

**27<sup>th</sup> Biennial National Conference of the  
Concrete Institute of Australia in conjunction with  
the 69<sup>th</sup> RILEM Week**

**concrete**  
30 August – 2 September  
Melbourne, Australia **2015**

**construction innovations:**  
RESEARCH INTO PRACTICE



## **Chair's Preface**

The proceedings contain 171 papers across 14 themes. All the papers included in the proceedings have been selected on the basis of least two peer reviews which were provided by independent reviewers (referees), who were experts in the subject field of the paper. We are grateful to the independent reviewers for their time and effort in reviewing the papers and providing reviews in a timely manner.

***Professor Jay Sanjayan***

Swinburne University of Technology

**Conference Chair**

Concrete 2015

Proceedings of the 27<sup>th</sup> Biennial National Conference of the Concrete Institute of Australia  
in conjunction with the 69th RILEM Week

*"Construction Innovations, Research into Practice"*

30 August – 2 September 2015, Melbourne, Australia

Published by the Concrete Institute of Australia

Suite 401, Level 4, 53 Walker Street, North Sydney NSW 2060, Australia

Tel: (02) 9955 1744

Fax: (02) 9966 1871

Email: [admin@concreteinstitute.com.au](mailto:admin@concreteinstitute.com.au)

Publication Date: 30 August 2015

ISBN: 978-1-943847-70-9



## **Organising Committee**

### **Chair**

Prof Jay Sanjayan, Swinburne University of Technology

### **Technical Program Committee Chair**

Dr Kwesi Sagoe-Crentsil, CSIRO

### **Committee Members**

David Millar, CEO, Concrete Institute of Australia

Prof Marita Berndt, Centre for Sustainable Infrastructure, Swinburne University of Technology

Simon Hughes, Westkon Precast

Fred Andrews-Phaedonos, Vic Roads

Vas Haitas, ITW Construction Systems

Shan Kumar, Hickory Group

Gary Wyatt, Calibre Consulting

Indubhushan Partnaikuni, RMIT University

Tuan Duc Hgo, The Melbourne University

Rebecca Gravina, RMIT University

### **Parallel Session Managers**

Chandani Tennakoon, Swinburne University of Technology

Max Un, Swinburne University of Technology

Behzad Nematollahi, Swinburne University of Technology

Rackel San Nicolas, University of Melbourne

### **Technical Committee and Reviewers**

Prof. Jay Sanjayan, Swinburne University of Technology (Conference Chair)

Dr Kwesi Sagoe-Crentsil, CSIRO (TC Chair)

Joanne Portella, EMS consultants

Prof Priyan Mendis, Melbourne University

Dr Rackel San Nicolas, Melbourne University

Behzad Nematollahi, Swinburne University of Technology

Dr Ahmad Shayan, ARRB Pty Ltd

Ahmad Mohd Ali, Swinburne University of Technology

Dr Pre de Silva, Australian Catholic University

Prof Riadh Al-Mahaidi, Swinburne University of Technology

Prof Emad Gad, Swinburne University of Technology

Prof Sujeeva Setunge, RMIT University

Prof Vijaya Rangan, Curtin University of Technology

A/Prof Faiz Shaikh, Curtin University of Technology

Dr Arnaud Castel, University of New South Wales

Prof Ian Gilbert, University of New South Wales

Dr Vinh Dao, University of Queensland

Dr Liza O'Moore, University of Queensland

Prof Hong Hao, Curtin University of Technology

Dr James Aldred, AECOM

Dr David Law, RMIT University

Dr Weena Lokuge, University of Southern Queensland

A/Prof Muhammad Hadi, University of Wollongong

Professor Hao Wang, University of Southern Queensland

Dr Sameh Salib, Ryerson University, Canada

Mr Prabir K Sarker, Curtin University

Chandani Tennakoon, Swinburne University

Fred Andrews-Phaedonos, Victoria Roads

Prof Marita Berndt, Swinburne University of Technology

Dr Michael Khrapko, RILEM

Chi Hou Un, Swinburne University of Technology

## **Table of Contents**

### **Keynote Presentations**

Ultra High Performance Ductile Concrete: The Delivery from Research into Practice Stephen Foster and Yen Lei Voo	1
Low Carbon Emission Geopolymer Concrete: from Research into Practice Jannie S.J. van Deventer and John L. Provis	12
Creep and Shrinkage of Concrete – from Theoretical Background and Experimental Characteristics to Practical Prediction Models Harald S. Müller Raphael Breiner and Vladislav Kvitsel	13

### **Construction Methods**

Concrete Hinges at Legacy Way Peter Boesch, Chin Cheah and Peter Miller	33
Challenges, Opportunities and Design Impacts for Different Construction Methods on Curtis Island LNG Jetties Jesper Jensen and Peter Kastrup	44
A Bond-Slip Modelling Approach for the Transfer Length of Pre-tensioned Concrete Rik Steensels, Lucie Vandewalle and Hervé Degée	55
Design for Construction Cockburn Gateway Stage 3 Case Study Bassam Matty	63
An Innovative Solution for Temporary Movement Joints in Concrete Floors Lance Rogers	73
Officer South Sewage Pumping Station – A Diaphragm Walling Case Study Marc Peril and Jaya Weerasinghe	83
Expansion and Mechanical Properties of Reactive Concrete incorporating Fused Thamer Kubat, Ahmad Shayan and Riadh Al-Mahaidi	94
Construction 3D Printing Laurie Edwards, Camille Holt, Louise Keyte, and Redmond Lloyd	101
The Application of Scattering-filling Stone Concrete on Highway Pavement Weiguo Shen, Xing Cheng, Liu Cao, Xinling Li, Chaochao Li and Guiming Wang	111
Preparation and Application of 3D Printing Materials in Construction Xiqiang Lin, Tao Zhang, Liang Huo, Guoyou Li, Nan Zhang, Baohua Wang	118

## **Repair and Retrofitting**

The restoration and repairs of the Sir William Goodman Bridge designed by Sir John Monash, Adelaide John Woodside and Leo Noicos	128
Condition Assessment and Structural Repair Solutions for the Renovation of the Sheraton Hotel at Doha, Qatar Satyajit Datar and Sajeev Kumar Krishnan	138
Adelaide Railway Station Façade Conservation Works Structural Engineering Aspects David Kennedy	147
A Variety of Remediation, Maintenance and Serviceability in its 15 Year Life Peter Kastrup and Andrew Turnbull	152
Design of FRP retrofitted concrete structures using AS5100 Part 8 Binh Pham	161
Investigation of Corrosion, Repair Assessment and Quality Assurance of a Basement subject to Saline Water Ingress Jonathon Dyson, Marton Marosszeky and Frank Papworth	167
Experimental Study on Anchorage Behaviour of the CFRP Grid in Mortar Bo Wang, Kimitaka Uji, Junlei Zhang, Atsushi Ueno, Kentaro Ohno and Tran Vu	177
Influence of Fiber Net Reinforced Mortar Repair Coating on the Crack Opening Resistance of Concrete Yoshinori Kitsutaka and Yukihiro Oyama	187
Performance of Fire-damaged Concrete Members Strengthened with NSM Laminates Embedded in Epoxy Adhesive Awad Jadooe, Riadh Al-Mahaidi and Kamiran Abdouka	193
Behavior of Squat Columns Strengthened with Fiber Reinforced Concrete Jacket Reza Hassanli and Minoru Kunieda	203

## **Failure Mode and Risk Analysis**

A Review of Limit State Design Principles and Practice Douglas Jenkins	218
Fasteners to Concrete: Failures and Solutions D. J. Heath, E. F. Gad and J. Lee	228
AEFAC Anchor Installer Certification Program Jessey Lee, David Heath and Emad Gad	238
Guide to Seismic Design & Detailing of Reinforced Concrete Buildings in Australia Scott Munter, John Woodside and Peter McBean	248

## Structures Research and Applications

Assessment of the Performance of a 24 Year Old Coating Applied to Concrete Bridge Piers Since Construction in a Saline Tidal Environment Fred Andrews-Phaedonos, Ahmad Shayan and Aimin Xu	259
Behaviour of Concrete Filled Steel Stub Columns During and After Fire Exposure Zhong Tao, Xing-Qiang Wang, Tian-Yi Song and Lin-Hai Han	268
Dynamic Performance Criteria for Suspended Courts at the National Tennis Centre Mark Sheldon and Benjamin Delaney	278
Flexural Response of GFRP-Reinforced Geopolymer Concrete Beams Ginghis B. Maranan, Allan C. Manalo, Warna Karunasena, Brahim Benmokrane and Priyan Mendis	287
An Experimental Study on the Long-Term Behaviour of Simply-Supported and Continuous Reinforced Concrete Slabs Md Mahfuzur Rahman, Gianluca Ranzi, Daniel Dias-da-Costa, Arnaud Castel and Raymond Ian Gilbert	297
Influence of environmental temperature and moisture conditions on the fatigue resistance of concrete Yasuhiro Koda, Shohei Minakawa and Ichiro Iwaki	307
An Approach for the Quantification of Ductility and Robustness of Reinforced Concrete Beams and Slabs R. Ian Gilbert, Stephen Foster and Ankit Agarwal	313
Experimental study of the mechanical behavior of shear-critical prestressed and reinforced concrete beams Kristof De Wilder, Guido De Roeck and Lucie Vandewalle	322
Development of a New Design Expression for the In-Plane Shear Capacity of the Partially Grouted Concrete Masonry Walls. Thangarajah Janaraj and Manicka Dhanasekar	332
Transient Heat Transfer Analysis of Reinforced Concrete Members Using a Discrete Crack Approach D. Dias-da-Costa, L. Godinho and G. Ranzi	343
In-Plane Behavior of Unbonded Post-Tensioned Concrete Walls Reza Hassanli	353
Concrete Slab and Footing Systems for Large Industrial Buildings. A Critical Overview of Current Design Methods for Reactive Clay Sites Anthony J Davis and Brian Ims	362

## **Fibres FRP Research and Applications**

Creep of Cracked Polymer Fiber Reinforced Concrete Rutger Vrijdaghs, Lucie Vandewalle and Marco di Prisco	373
Using FRP as Reinforcement in Precast Concrete Panels for Soil-Concrete Bridges Sameh Salib	382
Torsional Strengthening of Concrete Members Using Near-Surface Mounted CFRP Composites G. Al-Bayati, R. Al-Mahaidi and Robin Kalfat	390
Flexural Testing of Concrete Filled Fibre Reinforced Polymer Tubes (CFFT) with and without Internal Fibre Reinforced Polymer (FRP) Reinforcement Qasim S. Khan, Josiah S. Strong, M. Neaz Sheikh and M.N.S. Hadi	400
Durability Study of Textile Fibre Reinforcement Natalie Williams Portal, Nelson Silva, Katarina Malaga, Urs Mueller, Peter Billberg	408
Mechanical Properties and Post-crack Behaviours of Recycled PP Fibre Reinforced Concrete Shi Yin, Rabin Tuladhar, Tony Collister, Mark Combe and Nagaratnam Sivakugan	414
A Novel Ultra High Performance Fibre Reinforced Concrete Spandrel Cladding Panel Raafat El-Hacha, David Pesta, Gamal Ghoneim and Don Zakariasen	422
Upgrading the Dundas Point Boardwalk, Applecross with the use of GFRP Bar Reinforced Concrete Columns and Footings Joel Brown	433
A Design Methodology for Fibre Reinforced Concrete Slabs-on-grade Ravindra Gettu and Sunitha K Nayar	443
FRP Anchors for FRP-Strengthened Concrete Structures: Numerical Modelling Scott T. Smith, Jia-Qi Yang and Zhen-yu Wang	453
Joint Free Restrained Slabs – SFRC combined with mesh Alan Ross	459

## **Concrete Materials and Performance**

Neutron Pair Distribution Function Analysis of Synthetic Calcium-Silicate-Hydrate Claire E. White	471
Using Conventional Materials as Concrete Confinement Hua Zhao and Muhammad N.S. Hadi	476
Behaviour of Crumb Rubber Concrete Columns under Seismic Loading Osama Youssf, Mohamed A. ElGawady, Julie E. Mills, Xing Ma and Tom Benn	482
Sulfate Resistance Testing in Germany - Critical Review Johannes Haufe, Anya Vollpracht and Wolfgang Brameshuber	492

Linking New Australian Alkali Silica Reactivity Tests to World-Wide Performance Paul Rocker, James Mohammadi, Vute Sirivivatnanon and Warren South	502
Mechanical Properties of Mortar with Oil Contaminated Sand Rajab M. Abousnina, Allan Manalo and Weena Lokuge	514
Investigation into the Structural Properties of an Innovative Modified Concrete Negin Sharifi and Bijan Samali	523
Twisted Steel Micro-Reinforcement: Proactive Micro-Composite Concrete Reinforcement Luke Pinkerton, Kevin Fuller and Jeff Novak	533
Design of UHPFRC Mixtures to be used in Structures Subjected to Impact Loads Michael F. Petrou, Konstantinos G. Trezos and Anna L. Mina	543
Effect Rubberised Aggregates from Tyres on the Engineering Performance of M. Sonebi, R. Summerville and S. Taylor	552
The Effectiveness of Mineral Admixtures and Low Water to Cement Ratio in Concrete for Immobilizing Cesium, Sodium and Iodide from Radioactive Waste Irfan Prasetia and Kazuyuki Torii	559
Challenges contemporizing Australian Standards: Supplementary Cementitious Craig Heidrich	568
Effects of Chemical Admixtures and Aggregate Particles on Spatial Distribution of Cement Particles and Capillary Pores in Mortars Takuma Nakagawa and Shin-ichi Igarashi	578
The Effect of Type of Fly Ash on Mechanical Properties of Geopolymer Concrete M.P.C.M.Gunasekara, David W.Law and Sujeeva Setunge	586
Towards a More Sustainable Australian Cement and Concrete Industry James Mohammadi, Warren South and Des Chalmers	596
Steel, Concrete or Plastic? Support your Reinforcement! Scott Munter and Mark Turner	604
Performance of Architectural Concrete: New Approach Vyacheslav Falikman, Vyacheslav Deniskin and Alexander Vainer	611
Torsional Behaviour of Reinforced Concrete T-Beam Sections Douglas Anabalon	619
Effect of Ultraviolet Radiation on the Physical and Mechanical Properties of Polymer Matrix Wahid Ferdous, Allan Manalo, Thiru Aravinthan and Gerard Van Erp	630
Self-healing of Cementitious Composites via Coated Magnesium Oxide/Silica Fume Based Pellets Rami Alghamri and Abir Al-Tabbaa	637
Impact of Pore Structure of Lightweight Aggregates on Internal Curing Pietro Lura, Mateusz Wyrzykowski, Sadegh Ghourchian, Sakprayut Sinthupinyo and Clarence Tang	646

Reinforcing ordinary Portland Cement Mortar using Carbon Nanotubes Shu Jian Chen, Xiang Yu Li, Tong Bo Sui and Wen Hui Duan	652
The Significance of the Alkali Aggregate Reactivity Provisions in the VicRoads Structural Concrete Specification Section 610 Fred Andrews-Phaedonos, Ahmad Shayan and Aimin Xu	657
Long-term Experiments of Composite Slabs Using Recycled Coarse Aggregate Qinghe Wang, Gianluca Ranz, Yue Geng and Yuyin Wang	669
Implications of Alkali-Aggregate Reaction for three Concrete Bridges Ahmad Shayan, Aimin Xu and Fred Andrews-Phaedonos	679
Effectiveness of Traditional and Alternative Supplementary Cementitious Materials in Mitigating Alkali-Silica Reactivity Daniel Pospischil, Vute Sirivivatnanon, Uthayakumar Sivathasan and Kevin Cheney	694
The Use of Reaction Kinetics in Classifying Alkali Silica Reactivity Potential of Bob Bornstein, David Hocking, Johwelvic Bacolod and Vute Sirivivatnanon	704
Fresh and Early-Age Properties of Cement Pastes and Mortars Blended with Nickel Muhammad Ashiqur Rahman, Prabir Kumar Sarker and Faiz Ahmed Shaikh	712
Thermo-mechanical Behaviour of Epoxy Based Polymer Matrix Wahid Ferdous, Allan Manalo, Thiru Aravinthan and Gerard Van Erp	720
Development of an Acid Resistant Concrete Shamila Salek, Bijan Samali, Vute Sirivivatnanon and Georgius Adam	727
Effect of the Chemical Composition of Building Materials on Algal Biofouling Philippe Grosseau, Estelle Dalod, Alexandre Govin, Christine Lors, René Guyonnet and Denis Damidot	735
Expansive Behavior of Mortars - Containing Surf Clam Shell Powder at Early Age Akio Watanabe, Kazumi Hirokawa and Takashi Kondo	745
The use of Cementitious Coatings to Reinstat Low Nominal Cover on Reinforced Concrete Structures Neil Wilds	751
Behavior of Concrete after Exposure to Elevated Temperatures Yaman S. S. Al-Kamaki, Riadh Al-Mahaidi and Ian Bennetts	761
A Discussion on Service Life Prediction of Fly Ash Concrete Structures based on DuraCrete Methodology Zhuqing Yu and Guang Ye	770
Effect of Combined Fibres on Fire Resistance of Large Specimens Youngsun Heo and Byungyeol Min	779
Mechanical Properties of Fibre Reinforced High Volume Fly Ash Concretes Yashar Shafaei, Faiz Shaikh, Prabir Sarker and Salim Barbhuiya	788



## **Admixtures and Polymers**

Improving the Rheology of High Strength, very low W/C Ratio Concrete. 799  
Gary Boon and Tony Thomas

The Effects of Superabsorbent Polymers on the Water Vapour Sorption Properties of Cementitious Materials 805  
D.Snoeck, L.F.Velasco, A.Mignon, C.Vervaet, S.Van Vlierberghe, P.Dubruel, P.Lodewyckx and N.De Belie

Benefits of Water-Resisting Admixtures to Watertight Concrete 814  
Mohammadreza Hassani, Kirk Vessalas, Daksh Baweja and Zoe Schmidt

The Effect on Expansion of Wrapping Concrete Prisms with Cloth Saturated with Alkali Hydroxide 822  
Yasutaka Sagawa, Kazuo Yamada, Shoichi Ogawa, Yuichiro Kawabata and Masahiro Osako

Innovations in Admixtures for Piling Concrete 832  
Bruno D'Souza and Hairul Sarwono

Properties of Ultra-lightweight Concrete based on Protein and Surfactant foaming Agents 837  
Patrick Hartwich, Thomas Adams, Ali Shams, Anya Vollpracht and Wolfgang Brameshuber

Effect of Guar Gum Derivatives on Fresh State Properties of Portland Cement-Based Mortars 848  
Alexandre Govin, Marie-Claude Bartholin, Barbara Biasotti, Max Giudici, Valentina Langella and Philippe Grosseau

The Effect of Superplasticisers and Viscosity Modifiers on the Rheological Properties of Super Workable Concrete 858  
Greg Langton and Gary Boon

## **Durability and Serviceability**

Concrete Durability Performance Testing – The Approach Adopted in a Concrete Institute of Australia Recommended Practice 864  
W. Green and F. Papworth

A Discussion on the Autogenous Shrinkage Interpretation from the Experimental Shrinkage Measurement Based on the Australian Testing Procedure AS1012.13 875  
William A. Thomas, James Mohammadi and Warren South

Performance Test for Hydrophobic Impregnations for Protection against Chloride Ingress in Concrete 884  
Nelson Silva, Elisabeth Helsing, Katarina Malaga, Eva Rodum, Minna Torkkeli and Arvid Hejll

Durability of Concrete Caissons Made in Floating Docks 894  
Jose Vera-Agullo, Francisco Manuel Castro-Visos, Francisco Javier Larraz-Bordanaba, Claudio Troncone-Cusati, Juan Pedro Asencio-Varela, Nelson Silva, Urs Mueller and Katarina Malaga

Prescriptive versus Performance-based Design Approaches for Concrete Durability Hans Beushausen, Mark Alexander, Manuel Wieland and Stefan Linsel	904
Durability Performance of Crystalline-Modified Concrete Exposed to Severe Environment Farhad Nabavi	914
ISO 16204 and the Correct Solution to Fick Norwood Harrison	924
K-value for Carbonation of Concretes with Supplementary Cementitious Materials Christina Nobis and Anya Vollpracht	931
Feasibility of Digital Image Correlation Technique to Determine Mechanical Properties of Corroded Steel Rebars Ranjitha Rajagopal, Sameer Sharma, Radhakrishna G. Pillai and Sankara J.	939
Determination of Chloride Diffusion Coefficient of Concrete: Comparison of Bulk Diffusion and Electrical Field Method Aimin Xu and Ahmad Shayan	950
Frost Test and the Significant Influence of Small Amounts of Ions Dissolved in Surface Water Max J. Setzer	960
Durability Planning – a Formalised Approach in Concrete Institute of Australia Recommended Practice Rodney Paull and Frank Papworth	970
Time-dependent Stiffness of Concrete Members under Cyclic Loading Angus Murray, Raymond Ian Gilbert and Arnaud Castel	980
Role of Ettringite in Expansion and Cracking Potential in Steam Cured Precast Concrete Elements Johnson Mak, Paul Thomas, Kirk Vessalas and Daksh Baweja	990
Improved Sustainability by Design for Concrete Durability R. Doug Hooton	996
Exp-Ref: A Simple, Realistic and Robust Method to Assess Service Life of Reinforced Concrete Structures Roberto Torrent	1006
Durability Assessment of Concrete Immersed Tube Tunnel in Hong Kong-Zhuhai-Macau Sea Link Project Kefei Li, Quanwang Li, Pianpian Wang and Zhihong Fan	1016

## Geopolymers and Non-traditional Binder Concrete

Effect of MgO Incorporation on the Structure of Synthetic Alkali-activated Calcium Aluminosilicate Binders Brant Walkley, Rackel San Nicolas, Susan A. Bernal, John L. Provis and Jannie van Deventer	1026
Use of Geopolymer Concrete in Column Applications Weena Lokuge, Jay Sanjayan and Sujeeva Setunge	1033
Influence of Matrix Related Parameters on Strain Hardening Behavior of Engineered Geopolymer Composite (EGC) Behzad Nematollahi, Jay Sanjayan and Faiz Uddin Ahmed Shaikh	1041
EFC Geopolymer Concrete Aircraft Pavements at Brisbane West Wellcamp Airport Tom Glasby, John Day, Russell Genrich and James Aldred	1051
On Fly Ash Based Geopolymer Concrete and its Behaviour at Elevated Temperature Tian Sing Ng, Stephen J. Foster and Samantha Milojevic	1060
Development of Sugarcane Bagasse Ash Blended Geopolymer for use in Concrete Deepika S, Madhuri G, Bahurudeen A and Manu Santhanam	1070
Behaviour of Granulated Lead Smelter Slag-Based Geopolymer Concrete M. Albitar, M.S. Mohamed Ali, P. Visintin and M. Drechsler	1080
Influence of Binder on Alkali Reactivity of Aggregates in Geopolymer Concrete Chandani Tennakoon, Ahmad Shayan and Jay G. Sanjayan	1089
Rheological Properties of Sodium Carbonate Alkali-Activated Fly Ash/Slag pastes with Different Superplasticisers Ahmed Abdalqader and Abir Al-Tabbaa	1105
Direct Electric Curing of Alkali-Activated Concretes. Preliminary Study Maxim Kovtun, Julia Shekhovtsova and Elsabe Kearsley	1116
Investigation on Engineering Properties of Powder-activated Geopolymer Concrete Kamal Neupane, Daksh Baweja, Rijun Shrestha, Des Chalmers and Paul Kidd	1125
Alkali-Activated Foamed Concrete Elsabe Kearsley and Maxim Kovtun	1139
Alternative Concrete Materials from Industrial Waste Valle Chozas, Ignacio del Val, José Vera and Íñigo Larraza	1146
Progress Towards a Handbook for Geopolymer Concrete Marita Allan Berndt, Jay Sanjayan, Stephen Foster, Arnaud Castel, Pathmanatham Rajeev and Craig Heidrich	1156
Development of Low Shrinkage Water Repelling Foamed Concrete Kai Tai Wan, Honggang Zhu, Binmeng Chen and Chuanlin Hu	1166
A Resistivity-Based Approach to Indicate Chloride Permeability of Geopolymer Amin Noushini and Arnaud Castel	1172
Chloride induced Corrosion of reinforcing bars in Geopolymer concrete M. Babaee and A. Castel	1182
Specifying Fly Ash for Use in Geopolymer: A Conception of Reactivity Index Hao Wang, Zuhua Zhang, John L. Provis and Jin Zou	1188

## **Structural Monitoring and Assessment**

Evaluation of the Level of Damage of Concretes Affected by Expansive Reactions at Meso and Microstructural Scale. Relationship between Alkali-aggregate Reaction and Internal Sulfate Attack Esperanza Menéndez, Ricardo García Rovés and Nicanor Prendes	1197
The Impacts of Temperature and Salinity Variance on Service Life Modeling as a Result of Climate Change. Andrew Hunting, Sujeeva Setunge and David Law	1207
In situ and Laboratory Testing of Different Repair Materials. Lukovic, M., Gellweiler, W.A., Sierra Beltran, M.G., Blom, C.B.M., Savija, B., Zanten, van, D.C. Schlangen, E. , Ye, G. and Taffijn, E.	1217
Acid-soluble and Water-soluble Chloride – Testing Proficiency and Specification Warren South, Tony Thomas and Vute Sirivivatnanon	1225
Integrated Fracture-based Model for the Analysis of Cracked Reinforced Concrete Beams Tahreer M. Fayyad and Janet M. Lees	1233
Predicting Fire Induced Spalling in Concrete Structural Elements James M. de Burgh, Stephen J. Foster and Hamid R. Valipour	1243
In-situ Concrete Strength Assessment based on Ultrasonic (UPV), Rebound, Cores and the SONREB Method Frank Papworth, David Corbett, Reuben Barnes, Joseph Wyche and Jonathon Dyson	1253
Full Scale Concentric Punching Shear Testing of Two-way Floor with Bonded Post-tensioning and Studrails Fariborz Moeinaddini, Kamiran Abdouka and Andrew Barraclough	1263
Experimental Study on Carbon Fiber Reinforced Concrete for Strain Measurement of RC Portal Frame Fang-Yao Yeh, Kuo-Chun Chang and Wen-Cheng Liao	1273
<b>Early-age Concrete and Cracking</b>	
Temperature Monitoring of Concrete Elements for Insitu Strength Measurement and Prevention of Damage from Heat of Hydration Reuben Barnes, Frank Papworth, William Ward and Jim O'Daniel	1284
The Role of Dilation in Shrinkage Cracking of Concrete Suhaila Mattar and R.S. Al-Rawi	1295
High-absorptive Normal-weight Aggregates used as Internal Curing Agent Pericles A. Savva and Michael F. Petrou	1305
Tensile Properties of Early-Age Concrete Duy NGUYEN and Vinh T.N. DAO	1314
Experimental Study of Creep and Shrinkage in Early-age Concrete Inamullah Khan, Angus Murray, Arnaud Castel and Raymond Ian Gilbert	1325

## **Self-Compacting Concrete**

The Combined Influence of Paste Volume and Volumetric Water-to-Powder Ratio on Robustness of Fresh Self-Compacting Concrete 1335  
Farid Van Der Vurst, Steffen Grünewald, Dimitri Feys and Geert De Schutter

Instantaneous and Time-Dependent Behaviour of Reinforced Self-Compacting Concrete Slabs 1345  
Farhad Aslani, Shami Nejadi and Bijan Samali

Foam Concrete-aerogel Composite for Thermal Insulation in Lightweight Sandwich Facade Elements 1355  
Nelson Silva, Urs Mueller, Katarina Malaga, Per Hallingberg and Christer Cederqvist

## **Fib-C6**

Prefabricating in Unusual Environments 1364  
Marco Menegotto and Luciano Marcaccioli

Paddington Rail Station 1374  
George Jones

PCI Design Awards Program 1382  
Jason Krohn, Daniel Roman and Karla Vazquez

Sustainability of Structures with Precast Elements 1391  
D. Fernández-Ordóñez, B. González-Rodrigo, J. Ramírez and R. Valdivielso

## **Major Projects Case Studies**

Christchurch Art Gallery Foundation Strengthening and Building Re-Level 1400  
James O'Grady, William Lindsay and Russell Deller

Design of Berthing Dolphins on Curtis Island LNG Jetties 1408  
Jesper Jensen, Peter Kastrup and Matt Hodder

Lady Cilento Children's Hospital 1418  
Ken Gallie and Darryl Feodoroff

Documentation of Bridge Deck Construction Using Industrially Produced Internally Cured, High Performance Concrete 1430  
Timothy J. Barrett Albert E. Miller and W. Jason Weiss

## Posters

Comparative Performance of Recycled Plastic and Polypropylene Commercial Fibres with Plain Concrete Badr S. Al-Tulaian, Mohammad J. Al-Shannag and Abdulrahman M. Al-Hozaimy	1440
Finite Element Modeling of Shape Memory Alloy Confined Reinforced Concrete Khaled Abdelrahman and Raafat El-Hacha	1449
Modelling the Reactivity of Nano-silica in Cement Paste Madhuwanthi Rupasinghe, Rackel San Nicolas and Priyan Mendis	1457
A Study on the Estimation of ASR Expansion Based on CPT Kazuo Yamada, Shoichi Ogawa, Yuichiro Kawabata, Yasutaka Sagawa, Masahiro Osako and Takamasa Ochiai	1465
Enhancing Mechanical and Durability Properties of Recycled Aggregate Concrete George Dimitriou and Michael F. Petrou	1472
Effects of Silane Impregnation on Drying Shrinkage of Cement-based Compounds Pedram H. Mojarrad and Gary Boon	1482
Fresh Property and Matrix Distribution for Amorphous Steel Fiber Reinforced Byoungil Kim and Sea Hyun Lee	1488
Application of FRP Composite to Self-anchored Cable-stayed Bridge for Emergency Disaster Relief Fang-Yao Yeh, Kuo-Chun Chang, Yu-Chi Sung, Hsiao-Hui Hung	1495
Quick Uplift Rehabilitation for Differential Sunken Concrete Structure of Slab Ballastless Track Xinguo Zheng, Weichang Xu, Fei Cheng, Zhiyuan Zhang, Youneng Wang and Jing	1505
Investigation of Strain and Energy Ductility in SFRP-Wrapped Concrete Cylinders Nisreen Salameh, Raafat El-Hacha, and Khaled Abdelrahman	1510
The Possibility of using Inhibitors in New Repair Materials Vit Cerny, Rostislav Drochytka, Jiri Bydzovsky and Pavel Dohnalek	1518
Numerical Investigation of the Flexural Performance of RC Beam Strengthened with Iron-Based Shape Memory Alloys Bar Hothifa Rojob and Raafat El-Hacha	1528
Development of Double-Slotted Beam-Column Connection for the Seismic Design of Structures Fadi Oudah and Raafat El-Hacha	1547
Development of a Finite Element Analysis Design Tool for Future Study of a Novel Hybrid Steel-Free Multi-Girder Bridge Deck System Donna Chen and Raafat El-Hacha	1554
Investigation of Strength and Thermal Intake of Concrete Curing Through Means of Heated Water and Insulation Applied to the Exterior Surface Jamie Warr	1564
Comparative Performance of Recycled Plastic and Polypropylene Commercial Fibres with Plain Concrete Badr S. Al-Tulaian, Mohammad J. Al-Shannag, Abdulrahman M. Al-Hozaimy	1574

# Keynote Presentations

# ULTRA-HIGH PERFORMANCE DUCTILE CONCRETE: THE DELIVERY FROM RESEARCH INTO PRACTICE

Stephen Foster<sup>1</sup> and Yen Lei Voo<sup>2</sup>

<sup>1</sup>Professor and Head, School of Civil and Environmental Engineering, UNSW Australia

<sup>2</sup>CEO and Director, Dura Technology Sdn Bhd, Perak, Malaysia

**Abstract:** With the opening of Shepherd's Gully Bridge 150 km north of Sydney in 2005, Australia was amongst the leaders in the world in the utilisation of ultra-high performance concrete (UHPC) for road bridge construction. Ten years on, not one more bridge has been constructed and the uptake of UHPC technologies has been, at best, limited. In contrast, Malaysia's first bridge was opened in 2010 and in the time since a further 47 bridges have been completed, with many more under construction and on the drawing boards. Road bridges with spans as little as 12 metres and large as 58 metres are operational and of 100 metres are being built. Around the globe, UHPC is seeing slow, but steady, take up in many countries with more than 100 operational bridges worldwide. The question is asked "why has Australia gone from leading the world in the application of UHPC technology to watching from a distance" and "what is the future of UHPC for developing sustainable and resilient infrastructure"? This paper provides examples of two Malaysian UHPC bridges, the 51.0 metre span UHPC-composite deck Rantau Negeri Sembilan Bridge completed in December 2013 and the 100 metre span integral-deck precast segmental box girder bridge completed May 2015.

**Keywords:** Ultra-high performance, ductile, fibre, segmental, bridge, sustainable.

## 1. Introduction

One of the major breakthroughs in concrete technology of the 1990s was the development of ultra-high performance fibre reinforced concrete (UHPFRC), also known as the reactive powder concrete (RPC), by Richard and Cheyreyzy (1994, 1995). Compressive strengths and flexural strength of over 180 MPa and 40 MPa, respectively, have been reported. Since then, extensive research studies have been undertaken by academics and engineers alike with the view to industrialise this technology as an alternative for sustainable construction. While its take-up in practice has received gradual acceptance in many countries, this has not been the case in Australia. In the years 2004 and 2005, Australia was amongst the world leaders in development of UHPFRC for road bridge construction, through VSL Australia and their product Ductal. In the time since, and despite significant potential, the uptake of the technology has stalled, if not stopped in Australia.

The first major structures adopting UHPFRC technology were footbridges. In 1996, the 60-metre single span Sherbrooke Pedestrian Bridge was constructed, crossing the river of Magog, province of Quebec, Canada (Lachemi et al., 1998). The walkway deck, serving as the top chord to the truss, consists of 3.3 metre wide by 30 mm thin UHPFRC slabs. The web members are of a composite design involving UHPFRC placed in thin walled stainless steel tubing. April 2002 saw the construction of the Seonyu Footbridge (the Footbridge of Peace) in Seoul, South Korea (Behloul and Lee, 2003). Constructed by Bouygues Construction, the bridge is an arch with a 120 metre span supporting a 30 mm thick RPC deck. The structure required about one-half of the quantity of concrete that would have been used with traditional construction. At a similar time to the construction of the Seonyu bridge was the 50 metre footbridge constructed in Sakata (Sakata-Mirai footbridge), which is located in the north-western region of the island of Honshu, Japan (Tanaka et al., 2011). Other examples from Japan include the 36.4 metre span segmental construction Akakura Onsen Yukemuri Bridge (completed in 2004), the 64.5 metre span Hikita Footbridge (completed in 2007), the 81.2 metre span Mikaneike Footbridge (completed in 2007) (Tanaka et al., 2011, Musha et al., 2013). In the time since the construction of the Seonyu and Sakata-Mirai footbridges, UHPFRC bridges for pedestrian traffic have been constructed in France, New Zealand, Spain, Germany and elsewhere (Toutlemonde and Resplendino, 2011).

Internationally, private and governmental bodies are increasing their attention and initiative towards utilising performance advantages of UHPFRC, together with its being demonstrated as one solution towards more sustainable construction (Ng et al., 2012; Voo and Foster, 2010). UHPFRC is a highly workable material that may be used to form complex shapes, with reduced mass and reduced material. Figure 1 shows a 2.5 metre high UHPFRC retaining wall segment; Figure 2 shows the UHPFRC façade



elements of the Museum of European and Mediterranean Civilisations, Marseille, France and constructed in 2013.

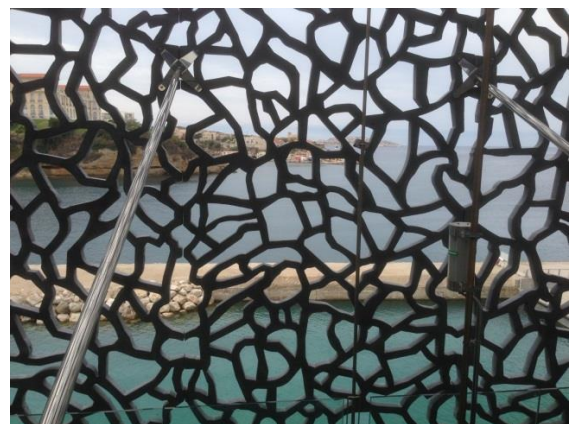
The first road bridges to be constructed using UHPFRC technology appeared in 2005, with four bridges constructed at around the same time (Voo et al. 2014). One of these was the 16 metre span, 21 metre wide, precast pre-tensioned I-girder bridge at Shepherd's Gully Bridge (Figure 3) located 150 km north of Sydney and constructed by VSL Australia (Foster, 2009, Rebentrost and Wight, 2011). The girders for these bridges were fabricated by VSL using the facilities of the Heavy Structures Laboratory at UNSW Australia. At this time, Australia was at the cutting edge of research into use of UHPFRC with doctoral theses by Voo (2004), Warnock (2005), Ngo (2005) Malik (2007) and Menefy (2007). The significance of such technology lies not only in the great enhancements in concrete strengths, leading to lighter weight construction and more efficiency of materials, but also in the contribution to sustainability through lower carbon footprints (Voo and Foster, 2010).



**Figure 1. Precast UHPFRC 2.5 metre high retaining wall segment.**



(a)



(b)

**Figure 2. (a) Museum of European and Mediterranean Civilisations - Marseille, France; (b) UHPFRC façade:**



**Figure 3. Shepherd's Gully Bridge, NSW, Australia constructed 2005: (a) 15 metre span 4 lane road traffic bridge (b) underside showing I-girders.**

In 2008, the world's first segmental UHPFRC composite deck road bridge was constructed; a single-span 46.0 metre ground support equipment (GSE) bridge was built over a road connecting the south and north apron in the extension of the Tokyo International Airport project. At the time, the road bridge was the largest UHPFRC road bridge in the world (Tanaka et al., 2011).

While construction of UHPFRC bridges in Australia has stalled, since 2006 Dura Technology Sdn Bhd (DTSB) has been pioneering research on the optimal uses of UHPFRC in bridge construction in Malaysia. During several years of research and development, DTSB has been collaborating with the Malaysia Works Ministry to design and build UHPFRC bridges, with a particular emphasis for bridges in rural areas where sourcing materials, site access and construction method are major constraints when using the conventional technology. From 2010 to now a total of 47 UHPFRC bridges have completed; a further 13 are in advanced stage of construction and another 15 are in the early stages of production. By the end of 2015, 75 bridges are due to be completed; 58 of these bridges are of segmental construction and 17 are pre-tensioned girders having spans of less than 22 metres.

In most cases UHPFRC precast bridge construction can be demonstrated to realise the following advantages (Voo and Foster, 2010, Voo et al., 2014):

- immediate and life-cycle cost saving;
- enhancement in design/service life of structures;
- low maintenance due to their high durability;
- reduced overall construction time and risk;
- reduced consumption of raw material;
- lighter superstructure dead weight permitting smaller and lighter substructure and foundations;
- reduced man-power and smaller plant;
- higher quality than in-situ wet work and precast high performance concrete structures; and
- lower impact on the construction site due to shorter-duration of temporary works.

In this paper, firstly, the mix design and mix performance properties of the Malaysian UHPFRC are outlined; next, two of the more than 40 bridges that have been completed are briefly discussed, the first the Rantau, Negeri Sembilan bridge, the largest single span composite deck UHPFRC bridge constructed to date, and the second the 100 metre span Batu 6 bridge, the world's longest UHPFRC single-span box-girder road bridge.

## **2. DURA Ultra-High Performance Fibre Reinforced Concrete**

There are many variations in mix design of UHPFRC with a number of commercial products in the marketplace (eg. Ductal, BSI, Taktl, myUHPC, Florida, etc). The mix design used in the beams in all bridges designed and constructed by DURA is given in Table 1; the material used to produce UHPFRC consists of Type I Ordinary Portland cement, densified silica fume containing more than 92% silica dioxide (SiO<sub>2</sub>) and with a surface fineness of 23,700 m<sup>2</sup>/kg and washed-sieved fine sand with a particle size

range between 100  $\mu\text{m}$  and 1000  $\mu\text{m}$ . A polycarboxylic ether (PCE) based superplasticizer is used. Two types of steel fibres are utilised in the mix; both manufactured from 2500 MPa high carbon steel wire. Type I steel fibre are straight in shape and are supplied with dimensions of 20 mm length by 0.2 mm diameter. Type II steel fibre is hooked-end and have dimensions of 25 mm long by 0.3 mm diameter. One percent of each fibre type is used; a total of 2%, by volume. Benchmark values for the specification of the UHPFRC are a 28 day characteristic cube compressive strength of 150 MPa and flexure strength of not less than 20 MPa; heat curing is applied for a period of 48 hours at a temperature of 90°C. The mechanical properties of the DURA UHPFRC are presented in Table 2.

**Table 1. Mix design of standard DURA UHPFRC.**

Ingredient	Mass (kg/m <sup>3</sup> )
DURA-UHPFRC Premix	2100
Superplasticizer	36-40
High strength steel fibres	158
Free water	168
3% moisture	32
Targeted W/B ratio	0.16
Total air voids	< 4%

**Table 2. Material characteristics of DURA UHPFRC.**

Characteristics	Standard	Value
Specific density, $\delta$	BS1881-Part 114 – 1983	2350 – 2450 kg/m <sup>3</sup>
Cube compressive strength, $f_{cu}$	BS EN 12390-3-2009	Min. 150 MPa (characteristic) Min. 160 MPa (mean)
Creep coefficient at 28 days, $\phi_{cc}$	AS1012.16 – 1996	0.2 – 0.5
Post-cured shrinkage	AS1012.16 – 1996	< 100 $\mu\epsilon$
Modulus of elasticity, $E_o$	BS1881-Part 121 – 1983	40 – 50 GPa
Poisson's ratio, $\nu$		0.18 – 0.2
Split cylinder. cracking strength, $f_t$	BS EN 12390-6 – 2000	5 – 10 MPa
Split cylinder ultimate strength, $f_{sp}$	ASTM C496 – 2004	10 – 18 MPa
Flexural strength or Modulus of rupture, $f_{cf,3P}$	BS EN 14651-2005 (Three-point test on notched specimens)	20 – 35 MPa
Rapid chloride permeability	ASTM C1202 – 2005	< 200 coulomb
Chloride diffusion coefficient, $D_c$	ASTM C1556 – 2004	0.05 – 0.1 $\times 10^{-6}$ mm <sup>2</sup> /s
Carbonation depth	BS EN 14630 – 2006	< 0.1 mm
Abrasion resistance	ASTM C944-99 – 2005	< 0.03 mm
Water absorption	BS1881-Part 122 – 2011	< 0.2 mm
Initial surface absorption	BS1881-Part 208 – 1996	< 0.02 ml/(m <sup>2</sup> s) (10 min) < 0.01 ml/(m <sup>2</sup> s) (120 min)

### 3. Rantau, Negeri Sembilan Bridge

The first example presented is the Rantau, Negeri Sembilan Bridge, which on 20 May 2013 became the world's longest single span UHPFRC-composite deck bridge, breaking the record of its predecessor, the 50 metre Kampung-Linsum bridge (see Voo et al., 2011). The project cost was MYR6.5 million (A\$2.1 million), which includes the construction of the new four lane road, river protection works, road furniture, earthwork, 400 metre by 16 metre wide approach pavement works, in addition to that of the bridge structure. The four lane wide bridge consists of five DURA UBG1750 beams with a conventional concrete cast in-situ deck (Figure 4). Being one of the busiest road accesses between the towns of Seremban and Port-Dickson, on the day of launching the existing road, and bridge, could not be closed to traffic for periods of more than 15 minutes at a time. The seven segments (2  $\times$  5.8 metres and 5  $\times$  8.0 metres) making up the 51.6 metre long beams were delivered from the factory to a site adjacent to the



construction, where they were assembled and stressed together. The girders were next transported the short distance to the new bridge site, utilising the existing bridge, and were lifted by two 500 tonne mega cranes in a single lift and placed on their abutments (Figures 5a and 5b). The whole launching process took just five hours to complete. There were no major disruptions to the heavy traffic and by 5 pm normal activity around the site was resumed and launching was complete. The composite deck slab was subsequently cast and the completed bridge is shown in Figures 5c and 5d.

The 18.3 metre wide Rantau, Negeri Sembilan Bridge remains the largest single span composite-deck bridge in plan area constructed to date; the longest span is held by the 58 metre span single lane Kampung Merdeka Bridge, completed in June 2015. The largest multi-span bridge is the 5 span, 200 metre long by 17 metre wide CFS Bridge, completed February 2015.

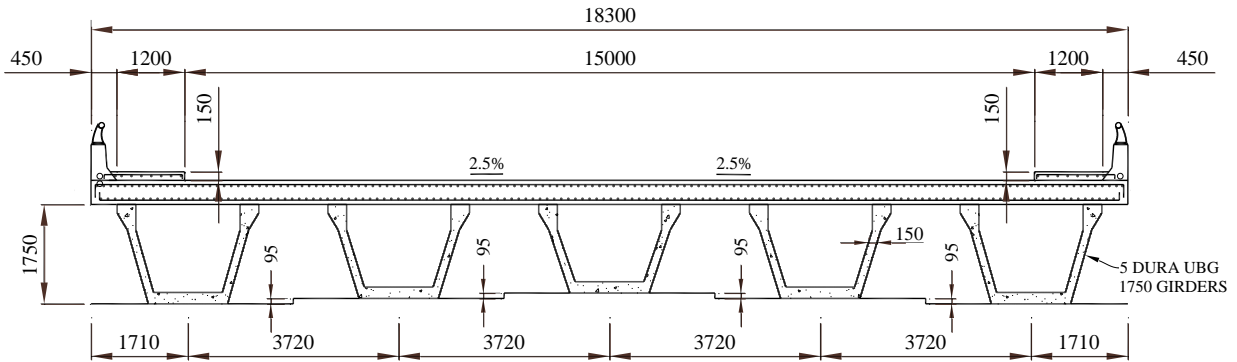


Figure 4. Rantau-Siliau Bridge cross section.



(a)



(b)



(c)



(d)

Figure 5. Rantau-Siliau Bridge. U-shaped UHPFRC girder with composite conventional strength concrete deck at different stages of construction: (a) and (b) during launching; (c) and (d) after completion.

#### 4. Batu 6 Bridge

The second example presented is the 100 metre span, integral-abutment box girder Batu 6 Bridge, located at Batu 6, Gerik, Perak, Malaysia. The construction cost was RM6.3 million (A\$2.2 million), which includes the foundation/piling, substructure (included wing-wall and approach slabs), superstructure, temporary works, road furniture, earthwork, 600 metre long by 6 metre wide approach road works and slope protection. The bridge was due for completion in February 2015; however, on December 22<sup>nd</sup> 2014, just one day before the planned pouring of the first of the integral abutments, the pour that would join the bridge to its foundations, saw the worst floods in Malaysia in decades with more than 100,000 people displaced.

The bridge is constructed of 40 – 4.0 metre high precast segments (Figures 6 and 7a), with each segment matched cast in the factory and delivered to site for placement and tensioning. The thickness of the webs between segment ends is 150 mm; the webs are locally thickened at the matched joints to accommodate the shear keys. The 36 middle segments each weight 16.5 tonnes, the segments second from the end 18 tonne and the end segments 20 tonne. With 26 tonnes of prestressing cable, 52 tonnes for the wearing surface and 20 tonnes for railings and ancillary fixtures, the total weight of the bridge is 770 tonne. For construction of the bridge falsework and positioning of the segments, crane access was available from one bank only and required the largest crane available; a 550 tonne crawler crane with a boom length of 108 metres. Even then, the last end segments at Abutment B could not be lifted into position and an innovative strategy was needed. To this end, a rail system was developed on the falsework to locate the precast segments to the accuracy needed for threading of the tendons. Figures 7b – 7d show the placement of the UHPFRC precast box segments. The 40 segments were placed over a period of 18 days (including two rest days). On day 11 of placement, five segments (12.5 metres of bridge) were positioned and aligned in a single day.

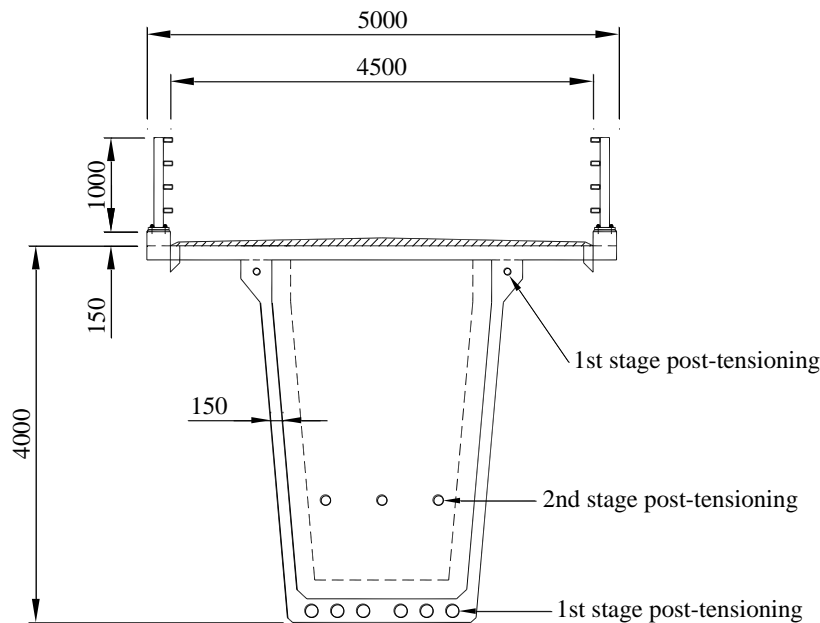


Figure 6. Batu 6 Bridge cross section.

The stage 1 prestressing work began on day 19 and the bridge was stressed on day 33 (29 November). On days 34 to 38 the strand ends were cut and grouting was completed (Figure 7e); the average prestress on the section ( $P/A$ ) is 17.1 MPa compression, the stress at the top and bottom of the section at mid-span is 19.3 MPa (compression) and 15.0 MPa, respectively. The calculated theoretical hog was 34.8 mm; the measured hog was 50 mm. After 7 days, the hog had reduced due to creep by 7 mm to 43 mm, consistent with predictions. Stage 2 stressing will be undertaken after completion of the integral abutment works.





(a)



(b)



(c)



(d)



(e)



(f)



(g)



(h)

**Figure 7. Batu 6 Bridge: (a) factory cast segments; (b)-(d) placing of segments; (e) after stage 1 stressing; (f) during flood; (g) shifting of girder on abutments downstream; (h) after completion of Abutment A.**



On 29 December 2014, from an unplanned release of water from Bersia Dam, the river Perak rose to a level of 3.0 metres above the soffit of the 4.0 metre tall girder (Figure 7f). This placed an extreme lateral pressure on the member, a load for which it had not been designed! The bridge, which had its first stage stressing a month before, carried the load without damage but had moved on its abutment 1.2 metres downstream, with the edge of the girder moving to within 50 mm of the edge of the abutment, and had tilted by 5 degrees (Figure 7g); it had come precariously close to topping into the river! On 20 January 2015 the flood waters had subsided to below the soffit of the girder and planning for restoration works began.

On 12 February the construction authority gave approval for the proposed remediation plan and work began shortly after. The girder was first lifted using hydraulic jacks and Teflon bearing plates were placed between the girder and the pile cap. The bridge was then repositioned by jacking laterally against a temporary structure that had been constructed around the pile caps for this purpose. The casting of integral Abutment A was undertaken over the days between 30 March and 3 April, 2015 (Figure 7h) and Abutment B is between 13 to 17 April. With the completion of construction in May mid-2015, the 100 metre span Batu 6 Bridge became the world's longest single span UHPCFRC integral-box road bridge (Figure 8).



**Figure 8. 100 metre span Batu 6 Bridge – completed May 2015.**

## **5. Concluding Remarks**

With the opening of Shepherd's Gully Bridge near Newcastle, Australia was at the lead of industrialisation of the latest in research in cementitious materials technology and in the utilisation of ultra-high performance concrete for road bridges – ten years ahead, not one more bridge has been constructed. The question that should be asked is: "where will we be in 2025"? In contrast, based on research begun in Australia and with Australian research training, Malaysian engineers built their first UHPC bridge in 2010; in the short time since, 47 more bridges, road and pedestrian, have been built. Similarly in other parts of Asia (particularly Japan) and in Europe (particularly France) some remarkable structures are being developed utilising UHPC technology.

In 2005 the German Government, through the German Research Foundation, invested €12 million (A\$16.7) in a programme that involved 34 research projects at more than 20 research institutes (Schmidt, 2012). Similarly, in 2007 the Korean Institute of Construction Technology (KICT) invested WON\$12 billion (\$A14 million) into research into UHPC for cable-stayed bridges in their Super 200 program (Kim et al., 2012). The US Federal Highway Administration (FHWA) began investigating the use of UHPC in 2001, with the first structure, the 33 metre Mars Hill road bridge in Iowa, constructed in 2006 (Graybeal, 2011). This compares to a general lack of investment in cementitious materials technology research throughout Australia by government, industry and, indeed, universities. Will we be looking for inspiration from overseas for the years ahead; will again Australia be at the lead or remain followers? It is time that that a new paradigm is found that unlocks the talent invested in Australian research institutions and brings the benefit more directly to Australian industry and the Australian economy.

## 6. References

1. Behloul, M., and Lee, K.C. (2003). "Ductal® Seonyu Footbridge", *Structural Concrete*, 4(4), 195-201.
2. Foster, S.J. (2009). "The Application of Steel-Fibres as Concrete Reinforcement in Australia: from Material to Structure", *Materials and Structures*, 42(9), 1209-1220.
3. Graybeal, B. (2011). "UHPC in US Highway Infrastructure", *Designing and Building with UHPFRC: State of the Art and Development*, Chapter 15, Eds. Toutlemonde, F., and Resplendino, J., John Wiley & Sons, Great Britain, 221-234.
4. Kim, B.-S., Kim, S., Kim, Y.-J., Park S.-Y., Koh, K.-T and Joh, C. (2012). "R&D Activities and Application of Ultra High Performance Concrete to Cable-Stayed Bridges", *Proceedings of Hipermat 2012 3rd International Symposium on UHPC and Nanotechnology for High Performance Construction Materials*, Ed., Schmidt, M., Fehling, E., Glotzbach, C., Fröhlich, S., and Piotrowski, S., Kassel University Press, Kassel, Germany, 865–872.
5. Lachemi, M., Bastien, J., Adeline, R., Ballivy, G., and Aïtchin, P.C. (1998). "Monitoring of the World's First Reactive Powder Concrete Bridge", *5th International Conference on Short and Medium Span Bridges*, Calgary, Alberta, Canada, July, 10 pp.
6. Malik, A.R. (2007). "An Investigation into the Behaviour of Reactive Powder Concrete Columns", PhD Thesis, School of Civil and Environmental Engineering, The University of New South Wales, Sydney, Australia.
7. Menefy, L. (2007). "Investigation of reactive powder concrete and its damping characteristics when utilised in beam elements", PhD Thesis, School of Engineering, Griffith University, Australia.
8. Musha, H., Ohkuma, H., and Kitamura, T. (2013). "Innovative UFC Structures in Japan", *Proceedings of the RILEM-fib-AFGC International Symposium on Ultra-High Performance Fibre-reinforced Concrete (UHPFRC)*, October 1-3, Marseille, France, Eds. Toutlemonde, F., and Resplendino, J., RILEM publications S.A.R.L, France, 17-26.
9. Ng, T.S., Voo, Y.L., and Foster, S.J. (2012). "Sustainability with Ultra-High Performance and Geopolymer Concrete Construction", *Innovative Materials and Techniques in Concrete Construction*, Chapter 5, M.N. Fardis (ed.), Springer, 379 pp.
10. Ngo, T.D. (2005). "Behaviour of high strength concrete subject to impulsive loading", PhD Thesis, Department of Civil and Environmental Engineering, University of Melbourne.
11. Rebstrost, M. and Wight, G. (2011). "Perspective on UHPCs from a Specialist Construction Company", *Designing and Building with UHPFRC: State of the Art and Development*, Chapter 13, Eds. Toutlemonde, F., and Resplendino, J., John Wiley & Sons, Great Britain, 149-187.
12. Richard, P., and Cheyrezy, M., 1995. "Composition of Reactive Powder Concretes", *Cement and Concrete Research*, Vol. 25, No. 7, pp: 1501-1511.
13. Richard, P., and Cheyrezy, M.H., 1994. "Reactive Powder Concretes with High Ductility and 200-800 MPa Compressive Strength", *ACI, SP-144(24)*, San Francisco, CA, pp: 507-518.
14. Schmidt, M. (2012). "Sustainable Building With Ultra-High-Performance Concrete (UHPC)—Coordinated Research Program in Germany", *Proceedings of Hipermat 2012 3rd International Symposium on UHPC and Nanotechnology for High Performance Construction Materials*, Ed.,



- Schmidt, M., Fehling, E., Glotzbach, C., Fröhlich, S., and Piotrowski, S., Kassel University Press, Kassel, Germany, 17–25.
15. Tanaka, Y., Maekawa, K., Kameyama, Y., Ohtake, A., Musha, H., and Watanabe, N., (2011). "The Innovation and Application of UHPC Bridges in Japan", *Designing and Building with UHPFRC: State of the Art and Development*, Chapter 12, Eds. Toutlemonde, F., and Resplendino, J., John Wiley & Sons, Great Britain, 149-187.
  16. Toutlemonde, F., and Resplendino, J. (2011). *Designing and building with UHPFRC: State of the art and development*, ISTE, London.
  17. Voo Y.L., and Foster, S.J. (2010). "Characteristics of Ultra-High Performance 'Ductile' Concrete (UHPdC) and its Impact on Sustainable Construction", *The IES Journal Part A: Civil & Structural Engineering*, 3(3), 168-187.
  18. Voo Y.L., Foster, S.J. and Voo, C.C. (2014). "Ultrahigh-Performance Concrete Segmental Bridge Technology: Toward Sustainable Bridge Construction", *ASCE, Journal of Bridge Engineering* [doi: 10.1061/(ASCE)BE.1943-5592.0000704 , B5014001].
  19. Voo, Y.L. (2004). "An Investigation into the Behaviour of Prestressed Reactive Powder Concrete Girders Subjects to Non-Flexural Actions", PhD Thesis, School of Civil and Environmental Engineering, The University of New South Wales, Sydney, Australia, 313 pp.
  20. Voo, Y.L., Augustin, P.C., and Thamboe, T.A.J. (2011). "Construction and Design of a 50M Single Span UHP Ductile Concrete Composite Road Bridge", *The Structural Engineer*, The Institution of Structural Engineers, UK, 89(15), 24 – 31.
  21. Warnock, R. (2005). "Short-term and time-dependent flexural behaviour of steel fibre-reinforced reactive powder concrete", PhD Thesis, School of Civil and Environmental Engineering, The University of New South Wales, Sydney, Australia.

# Low Carbon Emission Geopolymer Concrete: from Research into Practice

Jannie S.J. van Deventer<sup>1</sup> and John L. Provis<sup>2</sup>

<sup>1</sup>CEO, Zeobond Group, P.O. Box 23450, Docklands, Victoria 8012, Australia

<sup>2</sup>Professor, Department of Materials Science and Engineering, Sir Robert Hadfield Building, Mappin Street, Sheffield, S1 3JD, United Kingdom

**Abstract:** Geopolymers have received increasing attention in the literature and are rapidly gaining application in the construction industry. Nevertheless, there are obstacles to their wider adoption, including the lack of a long service track record, inflexible standards based implicitly or explicitly on the chemistry of Portland cement, questions about the applicability of durability testing, and the absence of many geopolymer precursors from the supply chain. Recent developments in nanostructural analysis and modelling of phase assemblages have provided insight into the nature and likely durability of the formed calcium aluminosilicate phases. This also provides indications that some accelerated durability testing methods will need to be modified to allow for the particular development of geopolymer gels at early age. The life-cycle analysis (LCA) of geopolymers needs to be conducted with caution regarding the origin of alkali activators, and for suitable mix designs an LCA will show significant reduction in CO<sub>2</sub> emissions compared with Portland cements. A case is made for the development of cement and concrete standards based on performance instead of prescription. It is shown here how a step by step approach involving all stakeholders, and by taking into account the drivers for adoption, has led to the commercialisation of geopolymers.

**Keywords:** geopolymer, nanostructure, durability, standards, commercialisation.

## 1. Introduction

Numerous papers have outlined the high CO<sub>2</sub> emissions of the Portland cement industry, mainly as a result of the calcination of the enormous quantities of limestone which must be processed to meet global demand for construction materials. Several alternative binder systems have been proposed as a means to reduce the CO<sub>2</sub> emissions of cement manufacturing; these include alkali-activated materials and geopolymers, calcium aluminates, sulphoaluminates, supersulphated slag cements, and magnesium-based binders. There has been much discussion of the term 'alkali-activated materials' versus 'geopolymers,' as coined by Joseph Davidovits (1), and while this is not the place to continue this debate, the term "geopolymers" will be used here to indicate all materials that are activated by alkalis.

The history of geopolymers, the binder chemistry, microstructure, different precursor materials, and engineering properties have been discussed extensively, especially in a recent RILEM report (2). The focus here will be to show how recent research on nanostructure has deepened our insight into phase assemblage and durability of geopolymers, that a critical analysis is required of durability testing methods, that the CO<sub>2</sub> footprint of geopolymers is a function of the origin of alkali activators, that there is a strong case for performance-based standards, and that despite obstacles, commercial adoption of geopolymer concrete has been achieved. In most commercial geopolymer concretes, Supplementary Cementitious Materials (SCMs) like fly ash from coal combustion and ground granulated blast furnace slag are used as precursors. Unless otherwise specified, the shortened terms 'fly ash' and 'slag' will be used here for these materials.

## 2. Understanding Phase Assemblage

### 2.1 Nanostructural Characterisation

The nanostructure of geopolymers is strongly dependent on the available Ca content of the precursors used in their formulation, with high-Ca systems based on materials such as blast furnace slag being dominated by a calcium aluminosilicate hydrate (C-A-S-H) gel with a tobermorite-like structure, while low-Ca systems such as those based on metakaolin or Class F fly ash tend to generate an alkali aluminosilicate (N-A-S-H) gel with a highly cross-linked, disordered pseudo-zeolitic structure (3). These gels can coexist in binders based on blends of high-Ca and low-Ca precursors, although the stability of the gel co-existence at high alkalinity is still the subject of some discussion (4).

Key analytical techniques which provide information about geopolymer gel structure include Fourier transform infrared (FTIR) and nuclear magnetic resonance (NMR) spectroscopy. Magic angle spinning (MAS) NMR studies of geopolymers often investigate  $^{27}\text{Al}$  and  $^{29}\text{Si}$  nuclei, and yield information about the coordination states of Al and Si. The information obtained through this method has been key to unlocking the details of the network structures of both C-A-S-H and N-A-S-H gels in geopolymers (3).

Particularly for low-Ca systems, FTIR spectroscopy provides information about the connectivity within Si-O-(Si,Al) frameworks, which can be observed via shifts in the infrared absorption peak corresponding to the Si-O-(Si,Al) asymmetric stretching vibration (3). Recent studies have also used in-situ time-resolved FTIR spectroscopy (5,6), and spatially-resolved infrared microscopy (6), the latter based on synchrotron radiation, to provide new insight into how the availability of silica (7) and alumina (8) controls gel structure.

Pair distribution function (PDF) analysis involves the calculation of interatomic distance correlations from 'total scattering' X-ray or neutron data, and can be applied to both ordered and disordered materials. This technique has shown differences in ordering between the C-A-S-H gels formed by hydration of tricalcium silicate and in alkali-activation of blast furnace slag (9). This is mainly because of the low Ca/Si ratio and the high Al content of the gel produced in slag-based geopolymers, which increases the likelihood of cross-linking between the silicate chains within the tobermorite-like gel (10).

A key question to be answered is whether the alkali metal cations in geopolymers are in fact structurally incorporated into C-A-S-H, or whether they are instead mainly sorbed onto its surface. This question is difficult to answer, particularly in view of the complexity in defining the 'surface' of such nano-scale particles (3), and so in some ways becomes a partly philosophical question. Nonetheless, Myers et al. (11) showed that the extent of alkali uptake by these gels is determined essentially by gel chemistry rather than being controlled by the available surface area. Thus, incorporation of the alkalis into the fundamental gel structure is important, and this may provide at least a partial explanation for the differences in PDF analysis results between slag-based geopolymers and tricalcium silicate hydration products, as mentioned above (9). Incorporation of alkali cations into the interlayer space of the C-A-S-H gel is inducing additional structural disorder in the gel (3).

## **2.2 Modelling**

The nanostructural and chemical complexity and disordered nature of geopolymers mean that it is difficult to study their phase assemblage by instrumental analysis alone, which is why there is increasing focus on thermodynamic and kinetic modeling in this field of research. The availability of appropriate structural models is essential in enabling the correct interpretation of spectroscopic data for C-A-S-H and N-A-S-H gels, as the models provide the necessary structural constraints which guide and validate the complex process of spectral deconvolution for quantification of individual sites. It is only in this way that structural parameters such as Ca/(Al+Si) ratios and mean chain lengths can be calculated from appropriately deconvoluted spectra. In recent examples of advances in this area, Myers et al. (10) implemented a structurally-based framework by which crosslinking degrees can be calculated in tobermorite-like C-A-S-H gels, and Richardson (12) also provided a crystal chemical model to describe layer spacings in these gels.

Krivenko (2,13) showed how the formation of sedimentary rock from weathered rock components could be used as a conceptual model for synthesising artificial materials such as geopolymers, which provides support for the durability of these concretes. Geochemical-type thermodynamic models have been successful in describing the phase assemblages formed in Portland cement and other Ca-rich systems, but until recently have not fully described the alkali metals and Al which are known to play important structural roles in the C-(N)-A-S-H gels in geopolymers. This gap has been filled by the thermodynamic model of Myers et al. (11) which describes this phase as an ideal 8-member solid solution, and can accurately describe solubilities in the full quaternary  $\text{CaO-Na}_2\text{O-Al}_2\text{O}_3\text{-SiO}_2$  aqueous system, as well as the pore solution chemistry of high-Ca geopolymers. This provides confidence in the long-term phase stability of the C-(N)-A-S-H gel and accompanying secondary phases, as the observed phase assemblages are consistent with predictions made from a thermodynamic basis. Unfortunately, such models are not yet available for N-A-S-H type gels, as the thermodynamics of this type of gel are much less well defined. It is envisaged that further developments in modelling of phase assemblage will aid in the prediction of phase changes over time, hence durability and in-service life, not just for geopolymers but also blended Portland cements.

The question is thus whether the currently available test methods for durability, which have been designed mainly for Portland cement systems, are applicable to geopolymers. Even for Portland cement systems

the prediction of service life based on accelerated testing remains problematic, so the prediction of service life for geopolymer concrete is a more challenging objective not yet achieved. The sections below review recent progress on the application of accelerated durability testing methods to geopolymers.

### **3. The Case for Durability of Geopolymers**

#### **3.1 Carbonation Testing**

The general assumption that a decrease in the alkalinity of concrete will always increase the susceptibility to corrosion of steel reinforcement requires further investigation and validation, especially when the chemical environment of the steel is different between various classes of concretes. The process of atmospheric carbonation is known to proceed differently in geopolymers compared with Portland cements (14). In Portland cement pastes, atmospheric  $\text{CO}_2$  dissolves in the pore solution and reacts rapidly with portlandite to form  $\text{CaCO}_3$ , and then once the portlandite is consumed, further  $\text{CO}_2$  decalcifies the C-S-H gel to form  $\text{CaCO}_3$  and silica gel (15). In contrast, the carbonation of geopolymer slag paste occurs first in the alkaline pore solution and then directly in the C-A-S-H gel because of the lack of portlandite, leaving an Al-containing siliceous gel in addition to  $\text{CaCO}_3$  (16).

While carbonation causes a loss of strength in geopolymer concrete (17), the hydrotalcite-type phases present in most slag-based geopolymers have been observed to bind carbonate ions and retard the progress of carbonation (18). The mechanism of strength loss in low-Ca gels induced by carbonation requires further research; the carbonation of low-Ca geopolymer gel mainly involves crystallisation of alkali carbonate or bicarbonate salts from the alkali-rich pore solution (19), with very little nanostructural alteration observable in the binder gel itself, as decalcification cannot happen in the absence of significant levels of calcium (16).

The most rapid carbonation of concretes occurs at relative humidities between approximately 50-70% (20), which is optimal for transport of  $\text{CO}_2$  into the pore solution, and so this is the condition specified in most testing standards. Unfortunately, exposure of immature concrete to relative humidities in this range can also result in significant drying shrinkage and microcracking (20), which contributes to the rapid carbonation of geopolymers in accelerated tests. The question arises whether such accelerated tests are representative of in-service natural carbonation conditions.

Xu et al. (21) evaluated the natural carbonation of in-service concretes older than 35 years as applied in the former Soviet Union, where the binders were based on alkali carbonate-activated metallurgical slags. In general, a carbonation depth of less than 8 mm was identified in these specimens, demonstrating the satisfactory durability of these materials against natural carbonation (2). Bernal et al. (22) showed that the depth of carbonation in a set of slag-geopolymers exposed to ambient conditions for 7 years was much lower than would be predicted through accelerated carbonation testing of specimens formulated to the same mix designs, demonstrating that the exposure conditions used in accelerated testing do not replicate the phenomena that take place under natural service conditions. In a recent study of in-service geopolymer concrete in the Netherlands it was shown that after 2 years the carbonation depths were comparable with those of blended Portland cement concrete containing slag or fly ash (23).

There appears to be a discrepancy between the results of accelerated carbonation testing of geopolymers, and the carbonation rates observed in-service under ambient conditions. This is attributed in large part to the thermodynamic differences between accelerated and natural carbonation conditions, which lead to different processes controlling the carbonation rates observed under different conditions. Accelerated carbonation testing over-predicts carbonation rates under actual service conditions, partly due to damage of the immature gel structure, and partly due to changes in alkali carbonate phase equilibria when the  $\text{CO}_2$  level is increased (17,24). Consistent with this observation regarding the importance of geopolymer binder maturity, accelerated carbonation testing of slag-geopolymer concretes showed that for carbonation depths less than ~8 mm, the carbonation process appeared to be predominantly chemical reaction controlled, and the rate-controlling step was close to first order with respect to  $\text{CO}_2$  (25). Beyond this point, where a more mature binder was being carbonated, diffusion control appeared to be more significant. This may indicate that as the geopolymer samples age the refinement of the pore structure of geopolymers means that diffusion of  $\text{CO}_2$  is limited by the carbonation reactions that can take place. This may partly explain the discrepancy outlined above.

It is also noteworthy that the chemistry of the precursors in geopolymer reactions may significantly affect carbonation behaviour. Bernal et al. (18) identified a strong interdependency between the formation of secondary phases, especially hydrotalcite-type phases, and the carbonation rate of the binder, as well as the chemistry and structure of the C-(N)-A-S-H type gels. A reduced content of MgO in the slag accelerates the early reaction process during alkali-activation, but reduces the overall extent of reaction which can be reached, and favours formation of C-A-S-H products with higher Al uptake, high chain length, and a lower degree of crosslinking. Conversely, the presence of more Mg reduces the Al/Si ratio in the C-(N)-A-S-H, as Al is instead bound through the formation of hydrotalcite. Under natural exposure conditions, hydrotalcite plays a clear role in determining the rate of carbonation by taking up CO<sub>2</sub> and preventing it from penetrating further into the material (18). The relationship between Ca/Si ratio and carbonation depth in geopolymers is not as evident as is the case for Portland cement.

### **3.2 Chloride Ingress**

The discussion about the corrosion of steel reinforcement in concrete has in general been focused mainly on the ratio of hydroxyl ions to chloride ions. However, the local oxidation-reduction potential is equally important in determining whether or not the steel will corrode. Much more needs to be done to understand these complex phenomena, not just in the case of geopolymer concrete but also in blended Portland cement concrete and other new binders which may have redox environments different from those of plain Portland cement. Nevertheless, the ingress of chloride is a major contributor to steel corrosion, especially in marine environments and in cold areas where de-icing salts are used.

Accelerated test methods aim to predict the time taken for the chloride to penetrate the concrete and initiate corrosion of the steel. The rate of ingress of chloride ion into concrete is a function of its diffusivity, hence the pore size and tortuosity, as well as its adsorption onto the pore walls. In general, geopolymers tend to show reduced chloride ingress compared with Portland concrete or even blended cements (2). However, as shown below, the interpretation of accelerated test data is complicated by the strong influence of the composition of the pore solution, which is a function of the nature of both the geopolymer precursor and the activator. This can yield unexpected results when comparing results obtained through tests such as the 'rapid chloride permeability test' (RCPT) with microstructural measurements for the same mixes (26). For example, mercury intrusion measurements have shown that sodium silicate-activated slag mortars exhibit much lower porosity and finer pore structure than when sodium carbonate or sodium hydroxide are used to activate the same slag in similar mix designs, but RCPT results revealed a much higher charge passed by the silicate-activated slag mortars. Thus, for slag-geopolymers the chemistry of the pore solution appears to contribute more to the electrical conductivity than does the pore structure, and the RCPT method may not always be accurate in predicting chloride resistance to ingress.

Bernal et al. (27) also found that the correlation between the RCPT and direct diffusion tests for determining chloride diffusion coefficients for geopolymer concretes was poor. It seems that the nature of the geopolymer gel hydration products strongly affects chloride ionic transport (28), but a full description of these processes has not yet been published. In high-Ca geopolymers, the C-A-S-H reduces porosity, while in low-Ca systems the N-A-S-H, which is more porous (29), appears to contribute significantly to higher chloride binding (28). The inherent deficiency of the RCPT method has led many workers to apply more advanced accelerated chloride migration tests such as the Nord Test method NT Build 492 (30), or long-duration chloride ponding tests such as ASTM C1543 (31). These tests use the colour change induced by spraying a silver nitrate solution onto a laterally split sample surface to provide a measurement of the chloride penetration depth, which is more appropriate than a pure electrical measurement as long as the pore solution chemistry is taken appropriately into account when defining the chloride concentration corresponding to the point of the colour change.

### **3.3 Sulphate Attack**

The mechanism of sulphate attack in geopolymer concrete is markedly different from that in Portland cement due to differences in phase chemistry of the hydration products, and specifically the absence or low concentrations of AFm phases, which are the Portland cement hydrate product most susceptible to sulphate-induced expansive processes, in geopolymers. From the summaries published by Shi et al. (32) and by RILEM TC 224-AAM (2) it can be concluded that geopolymers appear to resist expansion to a

higher degree than regular Portland cement under exposure to most sulphate solutions, and even show performance superior to that of sulphate-resistant Portland cement in the presence of sodium sulphate solutions. This is because sodium sulphate can be used as an activator in higher-Ca geopolymers (33), and thus can enhance the structural evolution and densification of the binding phases rather than inducing damage (32). However,  $MgSO_4$  exposure of calcium-containing geopolymers induces significant loss of compressive strength due to decalcification of the C-A-S-H, and gypsum and/or ettringite can also be formed as degradation products (34). To date, there has been little detailed investigation of the sulphate resistance of Ca-free geopolymer binders, but the expansive processes which take place in Ca-rich materials are unlikely to occur, and so the possible reduction in magnesium sulphate attack in geopolymer concrete which can be designed with very low permeability is worthy of further research.

### **3.4 Alkali-Aggregate Reaction**

Geopolymer concrete contains high levels of alkali as an intrinsic part of its binding phases, so there are valid – and widely asked – questions regarding whether alkali-aggregate reaction (AAR) is a concern for the durability of geopolymer concrete structures. In an interpretation of recent research, Provis et al. (3) concluded that, although AAR can occur in geopolymers, AAR in general does not contribute to deleterious expansive phases as is the case in Portland cement-based systems. In fact, AAR is close in nature to many geopolymer-forming reactions and when controlled correctly, could be expected to contribute substantially to longer term strength development through the formation of a strong and intimate paste-aggregate bond.

Based on the relationships between alkali-silica reaction expansion and slag content of Portland-slag cement, it has been observed that deleterious expansive processes would not be predicted to happen at slag contents higher than 80%, even at an alkali content over 4% (32). The reason for this behaviour is that the replacement of a high fraction of Portland cement with Al-rich supplementary cementitious materials will result in the formation of C-A-S-H with a low Ca/Si ratio, and this product can bind more alkali ions than C-S-H with a higher Ca/Si ratio, thus offering the potential to inhibit AAR. According to Provis et al. (3), many researchers have confirmed that AAR does indeed occur in slag-geopolymers, as significant amounts of AAR reaction product are able to be observed by electron microscopy around the interfaces between aggregate and paste, but the overall expansion of the specimens was in almost all cases less than that of conventional Portland materials tested in parallel, across a variety of testing protocols. In geopolymers containing low-Ca fly ash or metakaolin blended with slag, the expansion of the specimens was less than in solely slag-based specimens (3), and samples containing low levels of Ca demonstrated very small or negligible expansion, even with alkali-reactive aggregates.

The widely used accelerated mortar bar test (ASTM C1260) (35) for screening AAR-susceptible aggregates was designed for Portland-based reactions and may not be directly suitable for application to geopolymers (3), although in a practical sense it is unlikely that this test will be rapidly replaced due to its popularity and the lack of a validated alternative method specific to geopolymers. In the ASTM C1260 test, the mortar bars are cured for only 24 h (which is far from sufficient for almost all geopolymer formulations), then submerged in water for 24 h (inducing leaching of alkalis from the geopolymers and hindering further reaction (2)), and afterwards in 1 M NaOH solution at 80°C. Alternative curing regimes are therefore often applied to geopolymer mortars in variants of this testing methodology, but this does render the test non-compliant with the ASTM standard and causes problems in comparing the results between various published studies. Additionally, the alkali level of 1 M NaOH used in the immersion step of this test is actually lower than the intrinsic alkali content of most geopolymer binders (36), and thus the contribution of the external alkalis may be very limited (3). Clearly, the quantification of AAR for geopolymer concrete requires further investigation.

## **4. The Case for Performance-Based Standards**

In most jurisdictions, cement and concrete standards currently follow a cascade of dependency where the base standards assume and prescribe that Portland cement is the key binder, and is only aided by SCMs. Only a few standards do not prescribe the minimum level of Portland content of the cementitious materials, but most standards such as the European framework standard EN 206-1 prescribe a minimum Portland content for different applications or exposure classes. This prescription is highly inhibitive to

innovation and presents a formidable challenge to the commercial adoption of new cementitious binders, including geopolymers. When Portland cement is no longer the key binder and various non-Portland binder chemistries could be used instead, a prescriptive standards framework becomes inappropriate.

Prescriptive standards give users, including structural engineers, concrete specialists, contractors, asset owners and insurance companies, a sense of security. A key question in a dispute about concrete quality is whether the cement, the fresh concrete and the in-situ cast or precast concrete elements have all been manufactured according to the applicable standards. That often allows a shifting of the blame for a material or element failure to a specific party in the value chain. In contrast, if a performance standard is used instead, either for the cement binder, the wet concrete or the concrete elements, it places the onus for technical performance on the producer. Many producers find this situation a culture shock, which impedes attempts to change the standards framework from a prescriptive to a performance basis. Despite claims to the contrary, many vested interests are served by the current prescriptive and Portland-based framework. If the construction industry is serious in migrating to a performance framework of standards, it will allow the wider adoption of geopolymer concrete, and enable the industry to reduce its CO<sub>2</sub> footprint significantly. Moreover, such a shift will allow the utilisation of a wide range of precursors, provided that they are safe to use; this prohibition of intrinsically hazardous materials (which includes a significant fraction of unprocessed non-ferrous metallurgical slags as well as most unprocessed incineration ashes) must fundamentally be encoded in the standards documents, and should not dilute the 'non-prescriptive' philosophy of standardisation any more than is absolutely necessary.

A highly significant set of questions do arise regarding which performance testing and durability testing methods should be used in order to specify performance criteria. The discussion above shows the challenge of developing testing methods for durability that are independent of initial binder phase assemblage. In a critical review of performance-based approaches, Alexander and Thomas (37) explained that it is possible to relate service-life prediction models to durability testing, even when it is known that the diffusion parameters in concrete are complicated by several factors, including interaction between the diffusing species and the matrix and the reduction of diffusion coefficients with age. It is noteworthy that South Africa has developed a suite of durability index tests – oxygen permeability, sorptivity, and chloride conductivity – and these are linked to service-life models for the relevant deterioration mechanisms in reinforced concrete structures (37).

## **5. Geopolymers with Low CO<sub>2</sub> Emissions**

There have been a wide range of reported outcomes regarding the environmental performance of geopolymer concrete compared with Portland cement based concrete (38). Some authors report an 80% reduction in CO<sub>2</sub> emissions for geopolymer binders compared with blended Portland cement based on an independent lifecycle analysis (LCA) (39), while others like Habert et al. (40) have reported values which are more similar to that of Portland cement. The bulk of the CO<sub>2</sub> emissions attributed to geopolymeric binders are due to the production of the alkali activator(s), and it is here where caution is required in drawing conclusions.

There are various pathways to the production of sodium silicate, generally based on Na<sub>2</sub>CO<sub>3</sub> as a Na source. The different available processes for conversion of Na<sub>2</sub>CO<sub>3</sub> (or NaOH) and SiO<sub>2</sub> to sodium silicate, via either furnace or hydrothermal routes, differ by a factor of 2-3 in CO<sub>2</sub> emissions, and up to a factor of 800 in other emissions categories (41). It is therefore essential to state which of these processes is used as the basis of any LCA. Moreover, the best available data for emissions due to sodium silicate production were published in the mid 1990s (41), so improvements in emissions since that time have not been considered. Sodium carbonate itself can be produced via two main routes, which vary greatly in terms of CO<sub>2</sub> emissions. The Solvay process, which converts CaCO<sub>3</sub> and NaCl to Na<sub>2</sub>CO<sub>3</sub> and CaCl<sub>2</sub>, has emissions between 2–4 t CO<sub>2</sub> per tonne of Na<sub>2</sub>CO<sub>3</sub>, depending on the energy source used. Conversely, the mining and thermal treatment of trona for conversion to Na<sub>2</sub>CO<sub>3</sub> has emissions of around 0.14 t CO<sub>2</sub> per tonne of Na<sub>2</sub>CO<sub>3</sub> produced plus a similar level of emissions attributed to the electricity used. This indicates an overall factor of 5–10 difference in emissions between the two sources of Na<sub>2</sub>CO<sub>3</sub> (38). A similar situation is likely to exist in the production of NaOH, where various different processes are in use in different parts of the world; there will also be significant differences in the non-CO<sub>2</sub> emissions profile (particularly regarding mercury) between these processing routes.

Unfortunately, a high alkali activator addition is sometimes used in geopolymer concrete to compensate for the lack of reactivity of some precursors at low temperature, slow initial strength development, poor aggregate and particle grading design, and the deficiency of at least a portion of highly reactive precursors. When precursors could be custom ground, various precursor materials are available in the supply chain, alkali activators are better matched to the precursors, reagents are added to enhance dissolution and phase formation, and appropriate plasticisers are used to reduce water content, the achievement of high performance with a significantly lower alkali activator addition is possible, resulting in cost savings and greatly reduced CO<sub>2</sub> emissions.

## **6. Pathway to Commercial Adoption**

It is essential that the right drivers are in place to enable the commercial adoption of a new construction material. Usually, a substantial reduction in CO<sub>2</sub> emissions can be a driver for demonstration projects, or for inclusion as an innovation component as part of a larger project, but in general it is not a sufficient driver for widespread adoption. For the latter to happen, the strongest driver will be cost reduction, but enhanced technical performance such as enhanced resistance to aggressive media and fire, or utilisation of waste precursors to create a new value chain, may also be drivers.

Irrespective of the above drivers and the favourable CO<sub>2</sub> emissions of correctly designed geopolymer concrete, it is essential to gradually build industry confidence in geopolymers from a technical and commercial perspective. There are only a few examples of geopolymers in long term structural applications that can demonstrate the long service life of this emerging construction material (2), but confidence has been strengthened by recent large scale structural applications in Victoria, Queensland and South Africa. In Portland cement concretes, substantial technical advances since the 1970s have led to new engineering applications and cost reduction, most notably the chemical and mineral admixtures which are used to improve the properties of almost every concrete now produced in the developed world. For geopolymer concrete as an emerging technology, such advances are not yet available at the same level, which presents a challenge for wider commercial adoption beyond demonstration projects. The implementation of such advances is often dependent on scale and hence availability in the supply chain, so close collaboration is required between technology providers, materials suppliers, concrete manufacturers, contractors, asset owners, consulting engineers and regulatory authorities to build market confidence, achieve wider adoption and guide further research.

Regulatory progress has been made in Australia by VicRoads, that has recognised geopolymer concrete as being equivalent to Portland cement-based concrete for a range of applications. Nevertheless, geopolymer cement is not recognised as a binder in its own right in the Australian standards for structural concrete, and likewise in most other international standards frameworks. Beside the challenge associated with relating accelerated durability testing data to in-service life predictions as outlined above, there is also the question of whether existing structural engineering design methods calibrated for Portland-based concrete are applicable to geopolymer concretes. Laboratory research outcomes on these questions have given some comfort and certainly have supported commercial adoption, but it is indeed the success of in-service construction applications that has given the confidence to early adopters to continue with the technology. It is essential that research continues, not just on phase assemblage and durability, but that the industry should collaborate more with researchers in developing appropriate structural design methods and work towards the prediction of service life.

It has been necessary to build confidence in geopolymer concrete from scratch in each new market, as consumers wish to see success under local conditions. Small 'low risk' projects, where the cost of replacement is low if performance is not met, must first be completed to build confidence before more complex projects are tackled. The key challenge is often the availability of suitable precursors at the right price for demonstration projects in a new location, which is a more challenging situation technically and commercially than when there is a suitable supply chain at scale. This is the equivalent of building a car from components compared with delivery from an assembly line. These challenges are often underestimated by both researchers and experienced concrete professionals. Nevertheless, commercial adoption of geopolymer concrete has been achieved in selected applications (2). Recently, there has been an increase in interest in commercial application of geopolymers in new markets, with the driver being valorisation of fly ash in Australia, India and South Africa, a push to further reduce CO<sub>2</sub> emissions in



Europe, the Middle East and China, improved technical properties and if possible, cost reduction, in most markets.

## **7. Could Different Precursors be Used?**

Most of the published research on geopolymers has focused on SCM precursors like metakaolin, blast furnace slag and coal fly ash. According to Provis et al. (3), recent studies have greatly extended the sources and types of precursors, which may include non-ferrous slags, coal gangue, red mud, mine tailings, catalyst residue, coal bottom ash, rice husk ash, palm oil fuel ash, other biomass ash, municipal solid waste incinerator ash after removal of heavy metals, waste glass, waste ceramic, paper sludge ash, sludge resulting from water treatment, calcined clays, and natural minerals including natural pozzolans. Many of these precursors vary in reactivity over time, and could be more challenging than using fly ash and blast furnace slag. A bigger challenge is consistency of supply, associated with bringing these materials into the supply chain at a useful volume, which could pose a logistical challenge. In the same way as there is reluctance by Portland cement users to shift to geopolymers in fear of the unknown and the higher perceived risk, there is reluctance by geopolymer concrete producers familiar with using fly ash and slag to shift to other precursors. It takes a substantial amount of effort and time to prove again to the market that geopolymers made from new precursors perform well and are durable.

## **8. Conclusions and Final Remarks**

Geopolymers, or alkali-activated materials, have progressed from a laboratory research phase to industrial application in various structures and in different countries. Although further work is required to introduce a wider variety of precursors into the cementitious supply chain, and confidence building in the market will be ongoing, geopolymer concrete now offers a high-volume, affordable, and low-CO<sub>2</sub> alternative to Portland cement. Progress on the modification of existing accelerated durability testing methods and the development of methods to predict service-life will lead to the development of a performance standards framework, which is essential for the utilisation of various precursors in geopolymer cement. Such a framework will greatly enhance market adoption as it will simplify specification of geopolymers by structural engineers and reduce perceived risk, which will expand the scale of the supply chain, reduce costs and justify more expenditure on research, leading to further improvements in the technology.

Substantial progress has been made on the analytical characterisation and phase modelling of geopolymers at the nano-scale. Nevertheless, as is still the case with Portland cements, the link between nano-structure, microstructure and macroscopic/engineering behaviour of these materials remains a research challenge. This task is particularly challenging, because these materials are heterogeneous on every length scale from nanometers to centimeters, are crystallographically disordered, are multiphase, and are formed from precursors that are themselves often difficult to characterise. Further insight into the phase assemblage and nano-structure of geopolymers of industrially-relevant composition will aid the development of improved accelerated durability testing methods and service-life prediction, which will help to build further confidence in the market. There is a need to generate more data to describe the engineering behaviour of geopolymer concrete under different ambient conditions, so that existing structural design methods can be recalibrated. For this to happen in a productive manner, it is essential that structural engineers and materials scientists collaborate more closely.

## **9. References**

1. Davidovits, J., "Geopolymer Chemistry and Applications," Geopolymer Institute, Saint-Quentin, France, 2008, 592 pp.
2. Provis, J.L., Van Deventer, J.S.J., (Eds.), "Alkali-Activated Materials: State-of-the-Art Report," RILEM TC 224-AAM, Springer/RILEM, Dordrecht, 2014.
3. Provis, J.L., Palomo, A. et al., "Advances in understanding alkali-activated materials," Cement and Concrete Research, in press, DOI 10.1016/j.cemconres.2015.04.013

4. Provis, J.L., Bernal, S.A., "Geopolymers and related alkali-activated materials," Annual Review of Materials Research, 44, 2014, pp 299-327.
5. Rees, C.A., Provis, J.L. et al., "In situ ATR-FTIR study of the early stages of fly ash geopolymer gel formation," Langmuir, 23, 2007, pp 9076-9082.
6. Hajimohammadi, A., Provis, J.L. et al., "Time-resolved and spatially resolved infrared spectroscopic observation of seeded nucleation controlling geopolymer gel formation," Journal of Colloid and Interface Science, 357, 2011, pp 384-392.
7. Hajimohammadi, A., Provis, J.L. et al., "The effect of silica availability on the mechanism of geopolymerisation," Cement and Concrete Research, 41, 2011, pp 210-216.
8. Hajimohammadi, A., Provis, J.L. et al., "The effect of alumina release rate on the mechanism of geopolymer gel formation," Chemistry of Materials, 22, 2010, pp 5199-5208.
9. White, C.E., Daemen, L.L. et al., "Intrinsic differences in atomic ordering of calcium (alumino)silicate hydrates in conventional and alkali-activated cements," Cement and Concrete Research, 67, 2015, pp 66-73.
10. Myers, R.J., Bernal, S.A. et al., "Generalized structural description of calcium-sodium aluminosilicate hydrate gels: the crosslinked substituted tobermorite model," Langmuir, 29, 2013, pp 5294-5306.
11. Myers, R.J., Bernal, S.A. et al., "A thermodynamic model for C-(N)-A-S-H gel: CNASH<sub>ss</sub>. Derivation and validation," Cement and Concrete Research, 66, 2014, pp 27-47.
12. Richardson, I.G., "Model structures for C-(A)-S-H(I)," Acta Crystallographica, B70, 2014, pp 903-923.
13. Krivenko, P.V., "Alkaline cements," Proceedings of the First International Conference on Alkaline Cements and Concretes, Kiev, Ukraine 1994, pp 11-129.
14. Bernal, S.A., "The resistance of alkali-activated cement-based binders to carbonation," in: F. Pacheco-Torgal, J.A. Labrincha et al. (Eds.), Handbook of Alkali-Activated Cements, Mortars and Concretes, Woodhead, Cambridge, UK, 2015, 319-332.
15. Morandeau, A., Thiéry, M. et al., "Investigation of the carbonation mechanism of CH and C-S-H in terms of kinetics, microstructure changes and moisture properties," Cement and Concrete Research, 56, 2014, pp 153-170.
16. Bernal, S.A., Provis, J.L. et al., "Gel nanostructure in alkali-activated binders based on slag and fly ash, and effects of accelerated carbonation," Cement and Concrete Research, 53, 2013, pp 127-144.
17. Bernal, S.A., Mejía de Gutierrez, R. et al., "Effect of silicate modulus and metakaolin incorporation on the carbonation of alkali silicate-activated slags," Cement and Concrete Research, 40, 2010, pp 898-907.
18. Bernal, S.A., San Nicolas, R. et al., "MgO content of slag controls phase evolution and structural changes induced by accelerated carbonation in alkali-activated binders," Cement and Concrete Research, 57, 2014, pp. 33-43.
19. Criado, M., Palomo, A. et al., "Alkali activation of fly ashes. Part 1: effect of curing conditions on the carbonation of the reaction products," Fuel, 84, 2005, pp 2048-2054.
20. Bernal, S.A., Provis, J.L. et al., "Accelerated carbonation testing of alkali-activated slag/metakaolin blended concretes: effect of exposure conditions," Materials and Structures, 48, 2015, pp 653-669.
21. Xu, H., Provis, J.L. et al., "Characterization of aged slag concretes," ACI Materials Journal, 105(2), 2008, pp 131-139.
22. Bernal, S.A., San Nicolas, R. et al., "Natural carbonation of aged alkali-activated slag concretes," Materials and Structures, 47(4), 2014, pp 693-707.
23. Vermeulen, E., De Vries, P., "De uitdagingen van geopolymeerbeton" (English: The challenges of geopolymer concrete), Betoniek Vakblad (In Dutch), 2, 2015, pp 20-27.

24. Bernal, S.A., Provis, J.L. et al., "Accelerated carbonation testing of alkali-activated binders significantly underestimates service life: the role of pore solution chemistry," Cement and Concrete Research, 42, 2012, pp 1317-1326.
25. Bernal, S.A., Mejía de Gutiérrez, R. et al., "Effect of binder content on the performance of alkali-activated slag concretes," Cement and Concrete Research, 41(1), 2011, pp 1-8.
26. Douglas, E., Bilodeau, A. et al., "Properties and durability of alkali-activated slag concrete," ACI Materials Journal, 89, 1992, pp 509-516.
27. Bernal, S.A., Mejía de Gutiérrez, R. et al., "Engineering and durability properties of concretes based on alkali-activated granulated blast furnace slag/metakaolin blends," Construction and Building Materials, 33, 2012, pp 99-108.
28. Ismail, I., Bernal, S.A. et al., "Influence of fly ash on the water and chloride permeability of alkali-activated slag mortars and concretes," Construction and Building Materials, 48, 2013, pp 1187-1201.
29. Provis, J.L., Myers, R.J. et al., "X-ray microtomography shows pore structure and tortuosity in alkali-activated binders," Cement and Concrete Research, 42, 2012, pp 855-864.
30. Nordtest, "Concrete, Mortar and Cement-based Repair Materials: Chloride Migration Coefficient From Non-steady State Migration Experiments" (NT BUILD 492), Espoo, Finland, 1999.
31. ASTM International, "Standard Test Method for Determining the Penetration of Chloride Ion into Concrete by Ponding" (ASTM C1543-10a), West Conshohocken, PA, 2010.
32. Shi, C., Krivenko, P.V. et al., "Alkali-Activated Cements and Concretes," Taylor & Francis, Abingdon, UK, 2006.
33. Rashad, A.M., Bai, Y. et al. "Hydration and properties of sodium sulfate activated slag," Cement and Concrete Composites, 37, 2013, pp 20-29.
34. Ismail, I., Bernal, S.A. et al., "Microstructural changes in alkali activated fly ash/slag geopolymers with sulfate exposure," Materials and Structures, 46, 2013, pp 361-373.
35. ASTM International, "Standard Test Method for Potential Alkali Reactivity of Aggregates (Mortar-Bar Method)" (ASTM C1260-07), West Conshohocken, PA, 2007.
36. Lloyd, R.R., Provis, J.L. et al., "Pore solution composition and alkali diffusion in inorganic polymer cement," Cement and Concrete Research, 40, 2010, pp 1386-1392.
37. Alexander, M., Thomas, M., "Service life prediction and performance testing - Current developments and practical applications," Cement and Concrete Research, in press, DOI 10.1016/j.cemconres.2015.05.013
38. Provis, J.L., "Green concrete or red herring? - future of alkali-activated materials," Advances in Applied Ceramics, 113(8), 2014, pp 472-476.
39. Van Deventer, J.S.J., Provis, J.L. et al., "Technical and commercial progress in the adoption of geopolymer cement," Minerals Engineering, 29, 2012, pp 89-104.
40. Habert, G., d'Espinose de Lacaillerie, J.B. et al., "An environmental evaluation of geopolymer based concrete production: reviewing current research trends," Journal of Cleaner Production, 19, 2011, pp 1229-1238.
41. Fawer, M., Concannon, M. et al., "Life cycle inventories for the production of sodium silicates," The International Journal of Life Cycle Assessment, 4(4), 1999, pp 207-212.

# Creep and Shrinkage of Concrete – from Theoretical Background and Experimental Characteristics to Practical Prediction Models

Harald S. Müller<sup>1</sup>

Raphael Breiner<sup>2</sup>, Vladislav Kvitseľ<sup>3</sup> and Michael Haist<sup>3</sup>

<sup>1</sup>Prof. Dr.-Ing., Director, <sup>2</sup>Dipl.-Ing., Research Assistant and <sup>3</sup>Dr.-Ing., Research Associate, Materials Testing and Research Institute (MPA Karlsruhe), Karlsruhe Institute of Technology (KIT), Germany

**Abstract:** This contribution focuses on the newly developed creep and shrinkage models being included in the *fib* Model Code 2010. Emphasis will be paid to the background of these models and the underlying principles of constitutive behaviour and related modelling of modern structural concretes. Concerning shrinkage one of the main characteristics of the new model is the subdivision of total shrinkage into the components basic shrinkage and drying shrinkage. Furthermore, the creep deformation is introduced as the sum of the components basic creep and drying creep. The time-development functions of all deformation components were adjusted in order to predict properly the particular kinetics associated with the related mechanisms and the ambient conditions. The models will be briefly discussed in view of their prediction accuracy and application in the analysis and design of concrete structures. Finally, a brief outline on the microstructural mechanisms of concrete deformation behaviour will be given.

**Keywords:** Creep, shrinkage, prediction models, *fib* Model Code 2010.

## 1. Introduction

In the framework of the development of the new *fib* Model Code for Concrete Structures 2010 (MC 2010) creep and shrinkage prediction had to be revisited. The main reasons were that the models being included in the former CEB-FIP Model Code 1990 (MC 1990) reflect the knowledge of the 80s of the last century. Furthermore, some types of concrete being applied in practice today may differ considerably from those of that time. Finally, the fact that personal computers were not available to designers, when MC 1990 was developed, had some effect on the type of models being selected at that time.

While the mentioned weaknesses of the former MC 1990 models are overcome by the new models in MC 2010, one basic characteristic has been maintained. This concerns the consideration of the effect of the composition of concrete by means of the substitute parameter compressive strength of concrete. There are different reasons for that being indicated subsequently.

It is well known that the behaviour of structural concrete subjected to different types of loadings and actions depends primarily on its composition and its age. Modern concretes represent a five component system. They are composed of mineral aggregates like natural sand and gravel, cement, water, additions and admixtures. While the admixtures like plasticizer or air-entraining agents are added only in small quantities, additions like fly ash, stone dust, silica fume or finely ground blast furnace slag are often added in large amounts to the concrete mix. Depending on the reactivity of the additions and the water/cement or water/binder ratio, respectively, the properties of concrete can vary considerably, e.g. the compressive strength between approximately 5 and 200 N/mm<sup>2</sup>, see also *fib* Bulletin 51 [1].

It appears neither possible nor does it make any sense until today to develop code-type models, which take into account quantitatively all the parameters of the composition of concrete. The reasons are twofold. First, at the stage of structural analysis and design usually only the concrete strength, the dimensions of members, the exposure conditions and some other actions are known to the designer but not any details of the concrete composition. Second, too less systematic experimental data are available to cover all aspects of the effects of the composition of concrete and to derive reliable models. On the other hand, the strength of concrete may be used as a reasonable substitute parameter for the pronounced effect of the concrete composition. Hence this key parameter, in particular the compressive strength at the age of 28 days, partly complemented by information on the type of cement and the use of high amounts of additions in combination with the age of concrete, constitute the fundamental internal parameters to be used for code-type modelling of concrete. However, this simplification is also a source of the scatter which can be observed when the predictions of code-type models are compared with experimental data (see e.g. sections 4 and 5).

It has also to be kept in mind that the type of mineral aggregates used for concrete exerts a major effect on its deformation characteristics. Even if the aggregates may be characterised as quartzite material, their stiffness may vary considerably, depending on the place where the aggregates have been dug. This is another uncertainty in predicting creep and shrinkage, which is hardly to overcome unless tests are carried out.

Subsequently the newly developed creep and shrinkage models for MC 2010, including the approach to predict elastic strains, will be briefly presented and discussed. Their constitutive background will be explained and major features of the constitutive behaviour will be shown. In addition the prediction accuracy of the new models and possibilities for further improvement will be indicated. Temperature effects are not dealt with.

## 2. Definition of strain components of concrete

Concrete shows in addition to elastic deformations at loading both stress-dependent and stress-independent long-term deformations. The total strain  $\varepsilon_c(t)$  occurring at time  $t$  in a concrete member subjected to a sustained uniaxial stress at time  $t_0$  (age at loading) and at constant ambient humidity and temperature may be expressed by Eq. (1):

$$\varepsilon_c(t) = \varepsilon_{ci}(t_0) + \varepsilon_{cc}(t, t_0) + \varepsilon_{cs}(t) \quad (1)$$

where  $\varepsilon_{ci}(t_0)$  is the stress-dependent initial strain (elastic strain) at the time of stress application,  $\varepsilon_{cc}(t, t_0)$  is the creep strain at a concrete age  $t \geq t_0$  and  $\varepsilon_{cs}(t)$  is the shrinkage or swelling at a concrete age  $t$ .

This subdivision of the total strain into strain components, being a matter of convention, has been selected for MC 2010 [2]. One of the underlying key issues results from the fact that only overall deformations can be observed and measured on a single specimen, which means that the load- and time-dependent components cannot be separated. A second identical specimen is required in order to capture the shrinkage component that occurs after loading of the first specimen. In order to determine the load-dependent strains by subtraction of shrinkage strains the hypothesis has to be applied that the loaded and the unloaded specimen show the same shrinkage. This is very probably not the case, however, the hypothesis may neither be proven nor discarded by experiments. Further conventions are necessary to separate creep and elastic strains, or in general terms, time-dependent and instantaneous deformations considering both the age at loading and any later stage. Most usual is the procedure to measure the elastic strains (or the modulus of elasticity) on a separate specimen at the age at loading.

There are different approaches for creep prediction models where in particular the elastic strain is not distinctly separated from the creep strain, see e.g. [3]. However, it is of some advantage in the practice of design to use the descriptive parameters like elastic strain or creep strain, being connected with the modulus of elasticity of concrete and the creep coefficient. Basically, there is no restriction concerning the prediction accuracy of any models as long as the definitions for the strain components are consistent with the related derivation of the individual strain components from experimental data.

## 3. Elastic strains and modulus of elasticity

The initial elastic strain  $\varepsilon_{ci}(t_0)$  according to Eq. (1) may be directly related to the modulus of elasticity  $E_{ci}(t_0)$  applying Hooke's law, i.e.  $E_{ci}(t_0) = \sigma_c(t_0)/\varepsilon_{ci}(t_0)$ . Hence  $E_{ci}(t_0)$  is the tangent modulus of elasticity. At the age of  $t_0 = 28$  days,  $E_{ci}$  may be estimated from the subsequent Eq. (2), which is given in MC 2010 [2]:

$$E_{ci} = E_{c0} \cdot \alpha_E \cdot \left( \frac{f_{cm}}{10} \right)^{1/3} \quad (2)$$

In Eq. (2)  $E_{c0}$  is a constant in *MPa*,  $\alpha_E$  takes into account the effect of the aggregate type, and  $f_{cm}$  is the mean compressive strength of concrete in *MPa* at the age of 28 days. If  $f_{cm}$  is not available from tests, it can be estimated from the characteristic strength  $f_{ck}$  by means of the relation  $f_{cm} = f_{ck} + 8$  *MPa* [2].

By definition  $E_{ci}(t_0)$  and  $E_{ch}$ , respectively, do not contain any viscous or plastic deformations. However, at least at first loading of conventional structural concrete members, some plastic deformations due to micro-

cracking are observed, often termed as initial plastic set. Its magnitude decreases with the increase of the strength of concrete.

As a matter of convention, this initial plastic deformation is considered as part of the creep strain  $\varepsilon_{cc}(t, t_0)$  in MC 2010, i.e. it is included in the prediction of the creep function, see section 5. In cases where in practice at the design of a concrete structure creep effects are not considered and only an elastic analysis is carried out, a reduced modulus of elasticity  $E_c$  (secant modulus of elasticity) according to Eq. (3) should be used which takes into account the initial plastic strain:

$$E_c = \alpha_i \cdot E_{ci} \quad (3)$$

Herein  $\alpha_i = 0.8 + 0.2(f_{cm}/88) \leq 1.0$ , see MC 2010 [2]. For concrete grades higher than C80, the initial plastic strain may be neglected and  $\alpha_i = 1.0$  is calculated.

## 4. Shrinkage

### 4.1 Modelling

The shrinkage of concrete  $\varepsilon_{cs}(t, t_s)$  is usually defined as the load-independent strain or volume change (volume reduction) of concrete when concrete is subjected to drying, i.e. when hardened concrete evaporates at constant ambient environment. From a physical point of view various types and components of shrinkage may be subdivided [1]. However, as long as normal strength concrete is considered only the deformation caused by drying (drying shrinkage) is of practical significance. Hence for many decades this deformation of concrete, termed as shrinkage  $\varepsilon_{cs}(t, t_s)$  and achieving negative strain values of up to approximately 0.08 %, has been described by a simple product-type formula, see e.g. MC 1990 [4]:

$$\varepsilon_{cs}(t, t_s) = \varepsilon_s(f_{cm}) \cdot \beta_{RH} \cdot \beta_s(t - t_s) \quad (4)$$

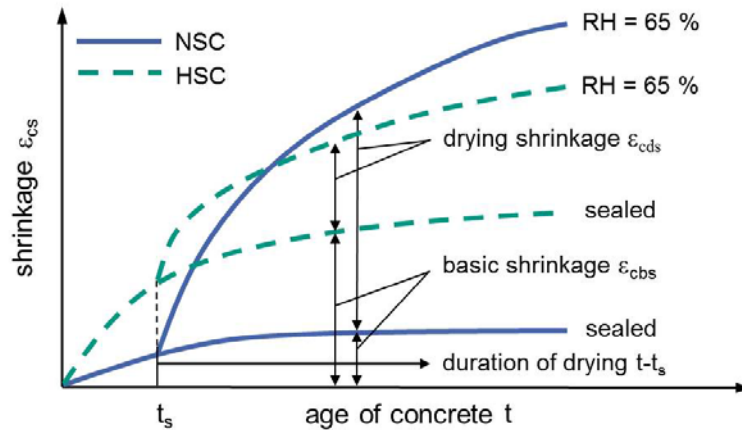
where  $\varepsilon_s(f_{cm})$  is a monotonic decreasing function with increasing strength,  $\beta_{RH}$  takes into account the average ambient humidity and the notional member size, and  $\beta_s(t - t_s)$  describes the development of shrinkage over time by means of a hyperbolic function. Here  $t - t_s$  is the duration of drying, i.e.  $t$  is the concrete age and  $t_s$  is the concrete age at the beginning of drying.

When high strength concrete is considered, which is the case in MC 2010, this type of formula can no longer be kept. The reason becomes clear from Fig. 1, where besides the drying shrinkage component also the basic shrinkage component is shown. Basic shrinkage is observed on sealed concrete specimens, i.e. when a concrete is prevented from drying. This particular shrinkage primarily results from self-desiccation and to a much lower extent from chemical shrinkage which both are associated with the hydration process.

While for normal strength concrete the basic shrinkage  $\varepsilon_{cbs}$  is very small ( $\varepsilon_{cbs} < 0.05 \cdot \varepsilon_{cs}$ ), compared to shrinkage or total shrinkage, respectively, for high strength concrete this component may become very large ( $\varepsilon_{cbs} \gg 0.05 \cdot \varepsilon_{cs}$ ), and even exceed the drying shrinkage component. Hence, a new approach for shrinkage must clearly distinguish between basic shrinkage  $\varepsilon_{cbs}$  and drying shrinkage  $\varepsilon_{cds}$ , and is formulated as a sum of both components in MC 2010:

$$\varepsilon_{cs}(t, t_s) = \varepsilon_{cbs0}(f_{cm}) \cdot \beta_{bs}(t) + \varepsilon_{cds0}(f_{cm}) \cdot \beta_{RH} \cdot \beta_{ds}(t - t_s) \quad (5)$$

Herein  $\varepsilon_{cbs0}(f_{cm})$  and  $\varepsilon_{cds0}(f_{cm})$  give the notional coefficient of basic and drying shrinkage, respectively. The functions  $\beta_{bs}(t)$  and  $\beta_{ds}(t - t_s)$  describe the time-development of the particular shrinkage component by means of an exponential function and a hyperbolic function, respectively, see MC 2010 [2].



**Figure 1. Total shrinkage subdivided into the components basic shrinkage  $\epsilon_{cbs}$  and drying shrinkage  $\epsilon_{c ds}$  for normal strength concrete (NSC) and high strength concrete (HSC). Note that the figure is not scaled.**

It should be noted that the term basic shrinkage is introduced in MC 2010 in analogy to the well-established term basic creep which describes the creep occurring when a loaded member is prevented from drying (see section 5). In the literature basic shrinkage is often termed as autogenous shrinkage or intrinsic shrinkage. Furthermore, the summation approach given by Eq. (5) represents a certain simplification as there is an interaction between basic shrinkage and drying shrinkage. However, for the sake of simplicity, and as the average prediction accuracy appears to be unaffected, this summation of individual strain components has been adopted.

While within MC 2010 detailed formulas are given to calculate the total shrinkage and its development with time, in many practical cases of design only the final value of shrinkage is of interest. Those final values of shrinkage (shrinkage after 50 years (service life) of drying) are given in Table 1. The final shrinkage values for other concrete grades and member sizes may be obtained roughly by linear interpolation.

**Table 1. Shrinkage values  $\epsilon_{cs,50y} \cdot 10^3$  after a duration of drying of 50 years for the concrete grades C20, C50 and C100**

Concrete grade	Dry atmospheric conditions (RH = 50%, indoors)			Humid atmospheric conditions (RH = 80%, outdoors)		
	Notional size $2A_c/u$ [mm]					
	50	150	600	50	150	600
C20	-0.68	-0.67	-0.53	-0.40	-0.39	-0,31
C50	-0.56	-0.56	-0.46	-0.37	-0.36	-0.31
C100	-0.48	-0.47	-0.42	-0.37	-0.37	-0.34
$A_c$ = cross-section [mm <sup>2</sup> ]; $u$ = perimeter of the member in contact with the atmosphere [mm]						

It should be noted that the difference in total shrinkage between normal strength concrete and high strength concrete is rather small from a practical point of view. However, the magnitudes of the individual components are different. Considering shrinkage after 50 years of drying for normal strength concrete C20, the basic shrinkage amounts to 7 % of the total shrinkage whereas this value increases up to 53 % for high strength concrete C100. While the drying shrinkage causes eigenstresses over the cross-section, the basic shrinkage does not, as it is uniformly distributed.

## 4.2 Prediction accuracy

The new prediction model for shrinkage of normal strength and high performance concrete in MC 2010 was developed and optimized on the basis of 168 different long-time shrinkage experiments. These data sets have been carefully selected and show a reasonable spread of the effecting parameters. Based on a procedure being defined in [5], a coefficient of variation of  $V = 32\%$  has been determined.

As the selected data sets cover a broad range of shrinkage under various conditions, the parameter  $V$ , indicating originally the quality of the regression analysis, may also be considered as a measure of the prediction accuracy of the shrinkage model given in MC 2010. For this reason comparisons with any other models, considering  $V$  and  $F$  in view of evaluating the prediction accuracy, would make only sense, if the other models would have been optimized applying the same data base.

For design purposes often only the final value of the shrinkage strain is of relevance which can be obtained by an extrapolation of the respective experimental data set. The mean prediction error  $F$ , indicating the average deviation between extrapolated and predicted final shrinkage values and being determined according to [5], amounts to  $F = 22\%$ .

## 4.3 Improvement of the shrinkage prediction

The prediction of the notional basic shrinkage coefficient  $\varepsilon_{cbso}(f_{cm})$  may be improved, if more detailed information on the type of cement, applied additives like silica fume, fly ash or blast furnace slag would be taken into account. Regarding the time-function of basic shrinkage no significant improvement of the overall prediction accuracy was obtained, when introducing the compressive strength as an affecting parameter.

The same aspects hold also true for modelling the notional coefficient and the time-development of the drying shrinkage component. Some further improvements might be obtained, if the parameter beginning of drying  $t_s$  would be introduced in the formulae. This holds true for both normal and high strength concrete. However, within typical durations of moist curing in practice, no significant effect of this parameter on the magnitude of shrinkage can be observed.

A general problem in finding an optimized prediction accuracy for shrinkage results from observed differences in the magnitude of shrinkage depending where the experimental investigation has been carried out. It is clearly evident from the shrinkage data included in the RILEM database [10] that the concretes investigated in the United States show always higher shrinkage deformations than comparable concretes in European investigations. This may partly be attributed to differences in the types and compositions of the cements and to some typical differences in the composition of the concretes (concretes according to EN 206 have a lower cement content than typical American concretes). In this context it should be noted, that the given prediction model for shrinkage is unbiased, i.e. the model has been optimized using all data sets included in the data base. Nevertheless, this may result in an underestimation of shrinkage of concretes outside of Europe up to approximately 20 %.

The prediction accuracy of the model could be improved without modifying the basic approach, if the parameter compressive strength of concrete is replaced by parameters describing the composition of concrete such as the water/cement-ratio, the cement content, the content and the type of additions and admixtures, etc. The reasons why such an approach has not been chosen for MC 2010 is explained in section 1.

If shrinkage is a decisive parameter in the design of concrete structures the most significant improvement of the prediction accuracy may be obtained by some short-term shrinkage tests on the particular concrete. The notional coefficients of autogenous and drying shrinkage, which are the most uncertain parameters of the model, may then be determined from the measured shrinkage data.



## 5. Creep

### 5.1 Modelling

The creep of concrete  $\varepsilon_{cc}$  is defined as the stress-dependent strain developing over time after the occurrence of the initial elastic strain when concrete is subjected to constant mechanical loads [1], [2]. For practical reasons creep is expressed by the so-called creep coefficient  $\varphi$ , which gives the ratio of creep strain and elastic strain at the concrete age of 28 days under the same stress  $\sigma_c(t_0)$ , i.e.  $\varphi(t, t_0) = \varepsilon_{cc}(t, t_0) / \varepsilon_{ci}(t_0 = 28d)$ , where  $t$  is the age of concrete and  $t_0$  is the age at loading in days. Hence  $\varphi(t, t_0)$  may be written as:

$$\varphi(t, t_0) = \frac{\varepsilon_{cc}(t, t_0)}{\sigma_c(t_0)} \cdot E_{ci} = \frac{\varepsilon_{cc}(t, t_0)}{\varepsilon_{ci}(t_0 = 28d)} \quad (6)$$

It has to be pointed out that in this definition of  $\varphi(t, t_0)$  the initial elastic strain at the concrete age of 28 days  $\varepsilon_{ci}(t_0 = 28d)$  is used, which can also be expressed by means of the modulus of elasticity at the age of 28 days, i.e.  $\varepsilon_{ci}(t_0 = 28d) = \sigma_c(t_0) / E_{ci}$ , where  $E_{ci}$  is the tangent modulus of elasticity at the concrete age of 28 days. Some confusion might be caused, as sometimes in the literature the creep coefficient is defined as  $\varphi^*(t, t_0) = \varepsilon_{cc}(t, t_0) / \varepsilon_{ci}(t_0)$ , where  $\varepsilon_{ci}(t_0)$  is the initial elastic strain at the time at loading  $t_0$ . Note, that  $\varphi^*(t, t_0)$  and  $\varphi(t, t_0)$  may differ considerably, in particular if  $t_0 \ll 28$  days. It is of veritable advantage to use  $\varphi(t, t_0)$  instead of  $\varphi^*(t, t_0)$  as it has been done also in former CEB Model Codes, see e.g. [6].

The total load-dependent deformation of structural concrete, i.e. the sum of elastic strain and creep strain per unit stress, is described by the creep function  $J(t, t_0)$ , see MC 2010:

$$J(t, t_0) = \frac{1}{E_{ci}(t_0)} + \frac{\varphi(t, t_0)}{E_{ci}} \quad (7)$$

Herein the creep function is connected with the descriptive values of  $E_{ci}(t_0)$ ,  $E_{ci}$  and  $\varphi(t, t_0)$  being defined above. The creep function has the dimension [1/MPa] and gives itself no descriptive value to the engineer in contrast to the creep coefficient which clearly indicates the relation between creep strain and elastic strain. Some other models for creep describe the creep function in a different way without using the descriptive parameters included in Eq. (7), see e.g. [3]. However, it has to be stated clearly that any type of expressing the creep function is correct as long as the total load- and time-dependent strains per unit stress are described as observed in experiments. This holds true for Eq. (7) as the definitions of the descriptive parameters  $E_{ci}(t_0)$ ,  $E_{ci}$  and  $\varphi(t, t_0)$  – being themselves derived from the experimental data – are absolutely consistent.

While in MC 1990 the creep coefficient  $\varphi(t, t_0)$  is modelled by a simple product-type approach applying a uniform deformation kinetics,

$$\varphi(t, t_0) = \varphi_0 \cdot \beta_c(t, t_0) \quad (8)$$

for MC 2010 a product type approach with a distinct separation into the deformation components basic creep and drying creep has been chosen. This approach is written as follows:

$$\varphi(t, t_0) = \varphi_{0,b} \cdot \beta_{bc}(t, t_0) + \varphi_{0,d} \cdot \beta_{dc}(t, t_0) \quad (9)$$

In Eq. (8)  $\varphi_0$  is the notional creep coefficient reflecting the effects of various parameters on the magnitude of creep such as the age at loading, concrete strength, type of cement as well as the member size and ambient conditions, see MC 1990 [4]. The coefficient  $\beta_c(t, t_0)$  describes the time-development function of creep, being of the same hyperbolic type as Eq. (11), however with a constant exponent of 0.3. In Eq. (9)  $\varphi_{0,b}$  and  $\varphi_{0,d}$  represent the notional basic creep coefficient and the notional drying creep coefficient, respectively, both reflecting parameters affecting the magnitude of creep, see MC 2010 [2]. The coefficients  $\beta_{bc}(t, t_0)$  and  $\beta_{dc}(t, t_0)$  describe the time-development functions of basic creep and drying creep, respectively, see the subsequent Eqs. (10) and (11):

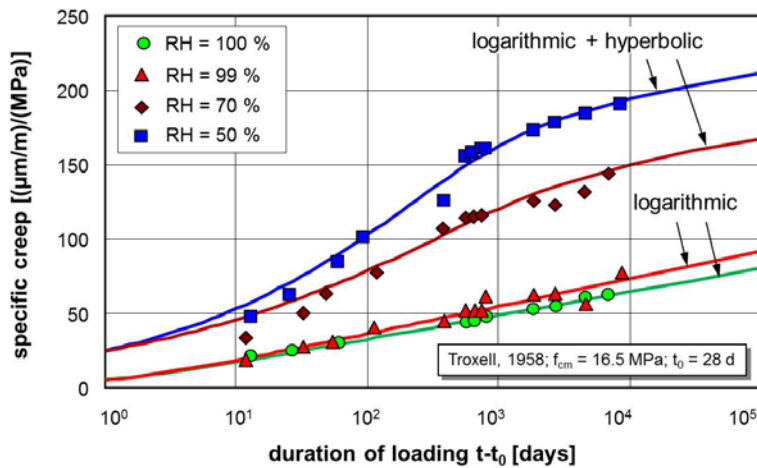
$$\beta_{bc}(t, t_0) = \ln \left( \left( \frac{30}{t_{0,adj}} + 0.035 \right)^2 \cdot (t - t_0) + 1 \right) \quad (10)$$

$$\beta_{dc}(t, t_0) = \left[ \frac{(t - t_0)}{\beta_H + (t - t_0)} \right]^{\frac{1}{2.3 + \frac{3.5}{\sqrt{t_{0,adj}}}}} \quad (11)$$

Herein  $t_{0,adj}$  is the adjusted age at loading,  $t - t_0$  is the duration of loading and  $\beta_H$  takes into account the member size and environmental conditions; for details see MC 2010 [2].

Note, that the basic creep is defined as the creep which occurs when concrete is prevented from drying (concrete loses no water), while drying creep is the additional creep which develops when concrete undergoes a drying process while being under load. This separation of the total creep into the components basic creep and drying creep, now realised in MC 2010 in contrast to MC 1990, became indispensable due to the fact that creep of normal strength concrete and high strength concrete should be covered best by one single model, and that the different deformation kinetics of these components should be considered properly. This is demonstrated in Fig. 2, which gives long-term experimental creep data for basic creep (RH = 100 % and RH = 99 %) and creep under drying conditions (RH = 70 % and RH = 50 %) together with a best-fit approximation.

The logarithmic function for basic creep (Eq. (10)) describes creep as an infinite on-going deformation process while the hyperbolic function for drying creep (Eq. (11)) approaches a finite value. Due to the addition of both components (see Eq. (9)), creep of concrete is now described as an infinite on-going process in MC 2010 in contrast to the approach given in MC 1990.



**Figure 2. Time-development of creep. Experimental data of Troxell et al. [7] and approximation by different types of time functions.**

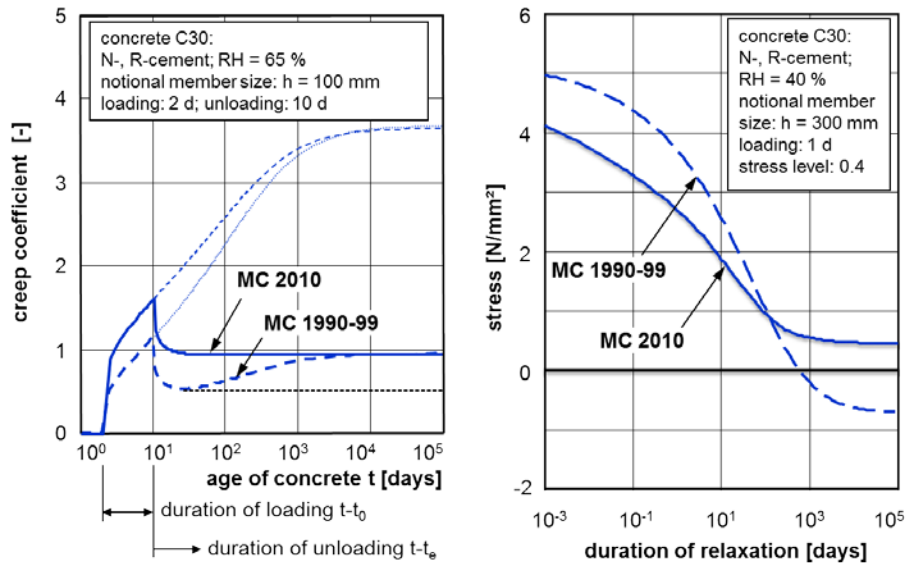
Comparing the different creep approaches of MC 2010 and MC 1990, respectively, it should be noted that the creep model in MC 1990 was valid up to the concrete grade C80. As high strength concrete up to the concrete grade C120 entered the practice only a few years after MC 1990 has been released, a modification of this creep (and shrinkage) model became necessary. This modification, where the main characteristics of the creep approach of MC 1990 have still been kept, is termed as MC 1990-99 and is given e.g. also in [1]. The actual creep model in MC 2010 now explicitly separates creep into the components basic creep and drying creep as described above while neither MC 1990 nor MC 1990-99 did.

When product-type creep approaches – their main feature is the product of the ageing function (age at loading) and the time-development function – are used in combination with the principle of linear superposition to describe creep deformations under variable stresses, some weaknesses could become evident under certain conditions, e.g. if a large member is loaded at a very young age. This is illustrated for the MC 1990-99 model in Fig. 3, left and right, considering the cases of creep recovery upon total unloading and relaxation. There a strain reversal and a change in sign, respectively, can be observed under the mentioned loading conditions. These weaknesses are nearly completely overcome by the new creep model in MC 2010 with the help of the exponent of the hyperbolic function in Eq. (11). In addition, this exponent also improves the prediction accuracy of creep development.

These weaknesses of the models MC 1990 and MC 1990-99, which were already known at the time when the models were developed (MC 1990 in the middle of the 80s of the last century), have been accepted in order to keep the approach as simple as possible and to facilitate hand calculations being typical at that time. On the other hand it was clearly stated that the creep prediction model of MC 1990 should only be applied for variable stresses and strains in combination with the effective age adjusted modulus method, see Eq. (12):

$$E_{c,eff}(t, t_0) = \frac{E_{ci}(t_0)}{1 + \rho(t, t_0) \cdot \varphi(t, t_0)} \quad (12)$$

Herein  $E_{c,eff}(t, t_0)$  is the effective age adjusted modulus and  $\rho(t, t_0)$  is the relaxation coefficient. If only final deformations or stresses are of interest,  $\varphi(t, t_0) = \varphi_{\infty}$ . Furthermore,  $\rho(t, t_0)$  may be assumed as  $\rho(t, t_0) = \text{const} \approx 0.8$  for the sake of simplicity. By means of Eq. (12) the creep analysis is reduced to an elastic analysis, and the fore-mentioned problems are overcome. For further details and background information see [8].



**Figure 3. Prediction of creep recovery (left) and stress relaxation (right) applying the principle of linear superposition in combination with the creep models given by MC 1990-99 and MC 2010.**

In many practical cases it is sufficient to know the final (corresponding to the service life) value of the creep coefficient. Those values are given in Table 2. The final creep coefficient for other concrete grades and member sizes may be obtained by linear interpolation.

## 5.2 Prediction accuracy

Corresponding to the shrinkage model, also the creep model has been optimized on the basis of a data bank, which includes in total 379 different long-time creep experiments of 39 different researchers. Compared to the large amount of publications on creep worldwide this number might appear rather small. However, one should keep in mind that strong selection criteria have been applied for data to be included

in the data base. In addition own experience in running creep tests since more than 40 years at the KIT helped to identify critical data suffering from certain experimental weaknesses.

Furthermore, when developing and optimizing a creep model it is not decisive to use as much data as can be found. It is more important to have a reasonable spread of the creep affecting parameters in the data sets. A higher number of selected data within the same range of criteria does not necessarily result in a better prediction model, but may well result in better looking statistical parameters for the accuracy like the coefficient of variation or the mean prediction error. Some more information on shrinkage and creep data bases may be found in [9].

As the result of the optimization of the MC 2010 creep prediction model a coefficient of variation of  $V = 27\%$  has been obtained for the creep function according to a procedure being described in [5]. This value may also indicate the prediction accuracy, as explained for shrinkage in section 4. In various practical cases, only the final value of the creep function or the creep coefficient is of relevance. The mean prediction error  $F$  for the creep function, determined according to [5], was found to be  $F = 27\%$ .

It is generally observed that after short durations of loading or drying (for shrinkage) the prediction error is higher than after long durations of loading and drying. Due to the inherent scatter of creep and shrinkage deformations, the weaknesses of a model simplifying the reality and the general uncertainty caused by randomness of material properties and environment, the prediction of deformations is inevitably associated with a high probability of a more or less considerable error, see also [9]. For concrete structures being very sensitive to creep it is recommended to run related tests.

**Table 2. Creep coefficients  $\varphi(50y + t_0, t_0)$  after 50 years of loading for the concrete grades C20, C50 and C100**

Concrete grade	Age at loading $t_0$ [days]	Dry atmospheric conditions (RH = 50%, indoors)			Humid atmospheric conditions (RH = 80%, outdoors)		
		Notional size $2A_c/u$ [mm]					
		50	150	600	50	150	600
C20	1	7.7	6.2	5.0	4.8	4.2	3.7
	7	5.5	4.5	3.7	3.6	3.1	2.8
	28	4.3	3.5	2.8	2.8	2.5	2.2
	90	3.4	2.8	2.2	2.2	1.9	1.7
	365	2.5	2.0	1.6	1.6	1.4	1.2
C50	1	3.5	2.9	2.5	2.4	2.2	2.0
	7	2.5	2.2	1.9	1.8	1.7	1.5
	28	2.0	1.7	1.4	1.4	1.3	1.2
	90	1.6	1.3	1.1	1.1	1.0	0.9
	365	1.1	1.0	0.8	0.8	0.7	0.7
C100	1	1.9	1.6	1.4	1.4	1.3	1.3
	7	1.4	1.2	1.1	1.1	1.0	1.0
	28	1.1	0.9	0.8	0.8	0.8	0.7
	90	0.8	0.7	0.7	0.7	0.6	0.6
	365	0.6	0.5	0.5	0.5	0.4	0.4

$A_c$  = cross-section [mm<sup>2</sup>];       $u$  = perimeter of the member in contact with the atmosphere [mm]

### **5.3 Improvement of the creep prediction**

It may come as a surprise to the informed layperson that research on concrete creep will continue to be facing significant challenges with regard to the further development of concrete constructions and the associated requirements for engineering models but also when considering the large number of remaining open questions in this area.

One of the many examples in this regard is the influence of varying ambient conditions on the magnitude of creep, which the KIT research activities are focussing on (see also [11]). This is of practical relevance, which is illustrated by the fact that almost all of the tests were carried out under constant ambient conditions, while by contrast, varying temperatures of structural components between -20 and +60 °C and varying ambient humidities between 30 and 100 % are not uncommon, even if only Central Europe is considered.

Furthermore, the creep models up to the date had predominantly been developed on creep experiments with higher ages at loading which holds also true for the new creep model given above. Nevertheless, in view of the large natural scatter of creep deformations the given model may be applied with sufficient accuracy also for younger concretes. However, regarding the limited number of experiments available on very young concretes, this previously insufficiently investigated behaviour and the prevailing nonlinear effects have recently been studied [12] to allow for improved predictions in the cases of very early loading (e.g. pre-stressing) of members.

The accuracy of the creep function depends on both the appropriate choice of the modulus of elasticity and the prediction accuracy of the creep coefficient itself. As long as no information is available on the concrete composition the modulus of elasticity at the age of 28 days may be estimated according to section 3 assuming the factor  $\alpha_E$  equal to 1.0. However, it is well-known that even for a given strength, the modulus of elasticity depends on the stiffness of the aggregates. The creep prediction may therefore be considerably improved by choosing factor  $\alpha_E$  according to the type of aggregates. Additionally, the modulus of elasticity at the age at loading does not only depend on the type of cement but also on the water/cement-ratio and the amount and type of additions.

Some attention has to be paid to the combination of ageing and time-development functions (product-type approach) when using the principle of superposition for the calculation of creep recovery or stress relaxation. Under certain conditions irrational results such as a strain reversal after complete unloading or a change in sign of stress relaxation may be obtained [5]. This weakness was tremendously reduced in *fib* Model Code 2010. However, some very special cases may be found, where these errors might occur to a rather small extent.

The logarithmic approach for the prediction of basic creep could be further optimised by introducing an additional exponent, which links the duration of loading  $t-t_0$  in Eq. (10) with the age at loading  $t_{0,adj}$ . It would enable a better adjustment to experimental data, i.e. it would result in slightly improved statistical parameters. However, a strain reversal after complete unloading will occur again, as the derivation of the function would be different for loading and unloading.

It may be generally stated that without modifying the given approaches, the prediction accuracy can probably be slightly improved if the parameter concrete compressive strength is replaced by parameters providing more detailed information on the concrete composition. However, a very significant improvement of the creep prediction may only be obtained if the notional creep coefficients, which are the most uncertain parameters of the model, are estimated on the basis of some short-term tests on the concrete to be used in the building or structure.

## **6. Understanding and controlling concrete creep and shrinkage deformation behaviour on the microstructural level**

The deformation behaviour of concrete as described by the models presented above can be traced back to partially reversible and irreversible changes in the microstructure of the material resulting from hygral changes and/or a mechanical loading. A detailed understanding of the mechanisms behind the long-term deformation behaviour would open up the chance to directly control and thus reduce the total deformation. However, the available knowledge on microstructural processes triggered e. g. by a drying or a mechanical loading of a building element is very limited. Today it is generally accepted that both shrinkage and creep of concrete are primarily a result of the deformation of the hardened cement paste, whereas the aggregates rather hinder this deformation process. Further it is known that the presence of water within the paste is a

prerequisite for deformations to occur. Therefore it is essential to understand the whereabouts and physical binding of water in the gel structure.

A large fraction of water is bound in hydrate phases such as calcium-silicate-hydrate (C-S-H) and calcium-hydroxide (CH), which form during the hydration process. According to Jennings, two different types of C-S-H, a low density (LD C-S-H) and a high density (HD-) C-S-H species have to be differed [13]. Despite their chemical binding, the water molecules bound in the C-S-H phases possess a certain mobility [14] and act as sliding plane allowing large irreversible shear deformations to occur. Feldman and Sereda identify this process as the dominating mechanism of concrete creep [15]. Newer computer simulations seem to confirm a significant contribution of this process to the total creep deformation [16]. In between the hydrate phases, water molecules are bound by van-der-Waals forces, resulting in a thermodynamic equilibrium, which however is disturbed by a mechanical loading of the sample [17]. So far it is unclear, to which extent these water layers act as sliding planes and contribute to the long term deformation behaviour. A great number of authors such as Powers, Wittmann or Bažant however identified processes on this level as the dominating mechanisms with regard to the creep deformation [17, 18, 14, 19]. Finally, depending on the w/c-ratio of the concrete, large fractions of water are stored in the capillary pores of the hardened cement paste. The role of this fraction of water with regard to concrete creep and shrinkage is still widely unknown.

All of the above model representations have in common that they essentially lack information on the mechanical behaviour of the microstructural constituents of the cement paste. Progress in this context can be expected from creep tests with in-situ small-angle X-ray scattering measurements [20]. Further, Vandamme and Ulm were able to conclude on the elastic properties and the creep modulus of the LD C-S-H and HD C-S-H phases using the statistical nano-indentation technique [21]. By implementing this data in a micromechanical model and combining it with data on the content of the individual phases in the concrete, they were able to show a good agreement with macroscopic creep results. Using this approach, a totally new class of creep models will become available in the future.

## 7. Summary and conclusions

In this paper it is shown which developments in structural concrete technology forced to modify the MC 1990 models for creep and shrinkage which have been applied with much success worldwide over two decades. One major point is the use of high strength concrete in practice nowadays. Concerning shrinkage, a model which should cover the characteristics of ordinary and high strength concrete must subdivide total shrinkage into the components basic and drying shrinkage, which is now realized in *fib* MC 2010. Similar to shrinkage also creep has to be subdivided into the components basic creep and drying creep. Hereby the time-development functions were adjusted in *fib* MC 2010 in order to predict more reliable the particular kinetics associated with the ambient conditions. On the other hand some basic features connected with diffusion-type processes and for reasons of practical application have been maintained also for the new models. The prediction accuracy of both models, being optimized applying an extended data bank, may be considered as rather good. Nevertheless creep and shrinkage tests are recommended when a structure is very sensitive to these deformations.

Considering future developments and improvements of the prediction models, respectively, some statistical evaluations indicate that there is only a very limited room left. Probably the consideration of the water/binder-ratio – if it is exactly known at the stage of design – might be associated with a minor improvement concerning the prediction accuracy. However, in view of the complexity of the composition of modern concretes and due to the pronounced effect and the variability of the characteristics of the type of aggregates, it makes hardly sense to go beyond using the substitute parameter compressive strength of concrete in prediction models. If the prediction accuracy achieved by the models is considered to be insufficient in view of the sensibility of the structure against deformations, tests have to be carried out. If these tests are run using the same concrete as applied for the structure, all effects concerning the concrete composition and the type of aggregates and cements are covered best, and the creep and shrinkage characteristics may be derived from the experiments with a coefficient of variation of approximately 10 %. Then these particular test results may be incorporated in the *fib* creep and shrinkage models by suitable algorithms to allow for the prediction of any deformation of this concrete under any given conditions. The development of these algorithms is underway.

Finally, significant progress in the next years is to be expected in understanding the microstructural mechanisms of creep and shrinkage. This knowledge will eventually allow the concrete engineer to develop concretes with significantly reduced long-term deformation tendency.

## 8. References

1. Fédération Internationale Du Béton (*fib*), *fib* Bulletin No. 51, Structural Concrete Textbook *fib*, 2009, Lausanne, Switzerland.
2. Fédération Internationale Du Béton (*fib*), *fib* Model Code for Concrete Structures 2010, Wiley c/o Wilhelm Ernst & Sohn, 2013, Berlin, pp. 402.
3. Bažant Z. P., Baweja S., "Creep and Shrinkage Prediction Model for Analysis and Design of Concrete Structures: Model B3", ACI Special Publication: Creep and Shrinkage of Concrete, Al-Manaseer A. (ed.), 1999.
4. Comité Euro-International Du Béton (CEB), "CEB Bulletin D'Information No. 213/214", CEB-FIP Model Code 1990, 1993, Lausanne, Switzerland.
5. Comité Euro-International Du Béton (CEB), "CEB Bulletin D'Information No. 199, Evaluation of the time dependent behaviour of concrete", 1999, Lausanne, Switzerland.
6. Fédération Internationale Du Béton (*fib*), "*fib* Bulletin No. 70, Code-type models for structural behaviour of concrete - Background of the constitutive relations and material models in MC 2010", 2014, Lausanne, Switzerland.
7. Troxell G. E., Raphael J. M. and Davis R. E., "Long time creep and shrinkage tests of plain and reinforced concrete", ASTM Proceedings, 1958, pp 1101-1120.
8. Comité Euro-International Du Béton (CEB), "CEB Bulletin D'Information No. 215, Structural Effects of Time-Dependant Behaviour of Concrete", 1993, Lausanne, Switzerland.
9. Müller H. S., "Considerations on the development of a data base on creep and shrinkage tests", Proceedings of the 5th International RILEM Symposium on Creep and Shrinkage of Concrete (ConCreep 5), Bažant Z. P., Carol I., (eds.), E & FN Spon, 1993, London, pp. 859-872.
10. RILEM TC 107, Subcommittee 5, "Data Base on Concrete Creep and Shrinkage", 1998, Institute of Concrete Structures and Building Materials, University of Karlsruhe, Germany.
11. Müller H. S. and Pristl, M., "Creep and shrinkage of concrete at variable ambient conditions", Proceedings of the 5th International RILEM Symposium on Creep and Shrinkage of Concrete (ConCreep 5), Bažant Z. P., Carol I., (eds.), E & FN Spon, 1993, London, pp. 15-26.
12. Anders I, "Stoffgesetz zur Beschreibung des Kriech- und Relaxationsverhaltens junger normal- und hochfester Betone", Dissertation, 2012, Karlsruhe Institute of Technology (KIT), Karlsruhe, Germany.
13. Jennings, H. M, "A model for the microstructure of calcium silicate hydrate in cement paste", In: Cement and Concrete Research, Vol. 30, No. 1, 2000, pp. 101-116.
14. Wittmann, F., „Einfluss des Feuchtigkeitsgehaltes auf das Kriechen des Zementsteines“, *Rheologica Acta*, Vol. 9, No. 2, 1970, pp. 282-287.
15. Feldman, R. F., Sereda, P. J., "A new model for hydrated Portland cement and its practical implications", In: *Engineering Journal*, Vol. 53, No. 8-9, 1970, pp. 53-59.
16. Manzano, H., Masoero, E., Lopez-Arbeloa, I., Jennings, H. M., "Shear deformations in calcium silicate hydrates". In: *Soft Matter*, Vol. 9, Royal Society of Chemistry, 2013, No. 30, pp. 7333-7341.
17. Powers, T.C, "The thermodynamics of volume change and creep", In: *Matériaux et Construction* Vol. 1, No. 6, 1968, pp. 487-507.
18. Bažant, Z. P., "Thermodynamics of interacting continua with surfaces and creep analysis of concrete structures". In: *Nuclear engineering and design*, Vol. 20, 1972, No. 2, pp. 477-505.
19. Setzer, M. J., „Oberflächenenergie und mechanische Eigenschaften des Zementsteins“, PhD Thesis, University of Munich, Germany, 1972.
20. Müller H. S., Eckhardt J.-D. and Haist M., "New experimental approach to study creep and shrinkage mechanisms of concrete on the nano-scale level", *Proc. 9<sup>th</sup> Intern. Conf. on Mechanics and Physics of Creep, Shrinkage and Durability of Concrete and Concrete Structures (ConCreep-9)*, Ulm, F.-J., Jennings, H. M. and Pellenq, R. (eds.), ASCE, 2013, pp. 150-157.
21. Vandamme, M., Ulm, F.-J., "Nanoindentation investigation of creep properties of calcium silicate hydrates". In: *Cement and Concrete Research*, Vol. 52, 2013, pp. 38–52.

# Construction Methods



# Concrete Hinges at Legacy Way

Peter Boesch<sup>1</sup>, Chin Cheah<sup>2</sup> and Peter Miller<sup>3</sup>

<sup>1</sup>Bridges Manager of Cardno (NSW/ACT) Pty Ltd, <sup>2</sup>Bridges Engineer of Cardno (NSW/ACT) Pty Ltd,  
<sup>3</sup>Design Manager, Transcity JV

**Abstract:** Legacy Way is Brisbane City Council's 4.6km road tunnel that will connect the Western Freeway at Toowong with the Inner City Bypass (ICB) at Kelvin Grove and is being constructed by Transcity Joint Venture.

The tunnels are driven from west to east requiring below ground box structures to facilitate TBM launch and TBM extraction respectively. The boxes are constructed using the Cut and Cover method. A significant innovation is the design and construction of the Eastern Cut and Cover box structure.

For the Eastern Cut and Cover roof, post-tensioned cast in-situ T-girders were used. The connection to the substructure, i.e. the secant pile walls, was achieved utilising a concrete hinge located between the T-girder support and a capping beam on top of the secant piles. Concrete hinges have been used in the past, as outlined in the NAASRA 76 standard, but design rules do not exist in the current standards. Often concrete hinges are used at the supports of arches to support significant axial compression forces while achieving a moment free connection. At Legacy Way, concrete hinges are used to reduce the fixity and therefore load transfer from the roof into the walls whilst achieving a maintenance free connection without bearings. Additional compression capacity was required in the throat of the hinge which was realised by post-tensioning the connection with high-tensile steel stress bars.

**Keywords:** Concrete Hinge, Cut and Cover Tunnel.

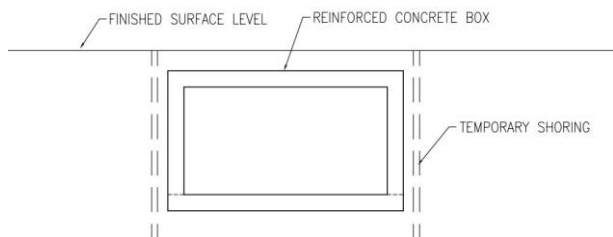
## 1. Introduction

The design and construction of Cut and Cover structures have the particular challenge of designing roof to wall connections without bearings and movement joints as those elements cannot be replaced once the structure is backfilled. The solutions adopted at the Legacy Way tunnel project are discussed, especially the solution for the Eastern Cut and Cover at Kelvin Grove, where post-tensioned girders and post-tensioned concrete hinges are used to provide a durable structure that minimises whole of life costs and improves sustainability.

## 2. Principal approach to design of cut and cover structures.

Cut and cover structures are often designed as cast in-situ reinforced concrete boxes. For the construction of these boxes from the bottom up, additional shoring is required as shown in Figure 1.

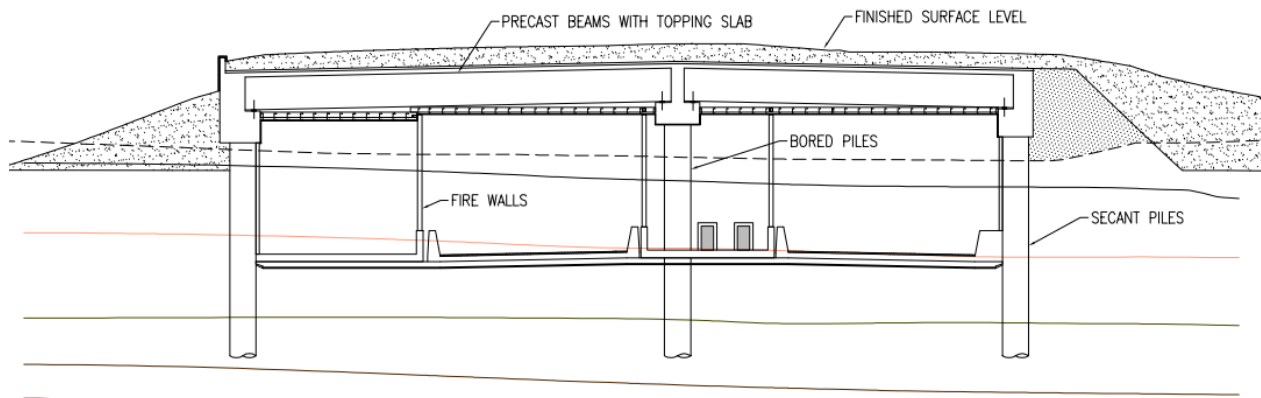
Another option is to use the required shoring, (diaphragm walls and secant pile walls) as walls of the permanent structure. To achieve a watertight structure the roof must be fixed to the walls. If the span between supports for these roofs is large, or if the backfill on top of the structure adds significant weight, the roof will need to be prestressed to gain



**Figure 1. Cut and Cover box.**

additional capacity and reduce deflection. Prestress, shrinkage and creep and backfill result in significant long term effects on the structure, resulting in high moments in the corners if the structure is designed as a fixed, continuous frame.

Achieving a high quality structure and speedy construction are important requirements. Consequently, precast, prestressed Super-T girders were initially used for the design of the Cut and Cover structures at Legacy Way. The girders were made integral with the secant pile walls, cast in-situ curtain walls, connecting pile caps and topping slab. An image of this solution is shown in Figure 2.



**Figure 2. Top down construction Legacy Way.**

The demand for precast, prestressed Super-T-girders was high and supply was identified as an issue. Consequently, another option was investigated which utilised cast in-situ, post-tensioned girders in a top-down construction. From previous experience, it was known that timing of the post-tensioning, backfill and excavation of the roadway was critical for the design of corners of the structure. A solution was sought which would allow rotation while transferring vertical and shear forces. With such a solution, bending moments in the corners of the structure would be negligible and would not govern the design of the piled walls. Bearings could not be used as their replacement would be impossible in service because the structure is covered.

Concrete hinges were considered a possible solution as they would transfer loads and still allow a degree of rotation. However, design rules for those hinges published in the 1970s have not been updated and most research into this construction type generally dates back to the 1930s to 1960s.

### 3. History of concrete hinges



**Figure 3. Salginatobelbridge.**

The background of construction utilising concrete hinges, their history, invention, applications and design rules, are described below.

#### 3.1 Invention and applications

Hinge connections for concrete bridges were initially used in 1880 in an arch bridge for a railway in Eastern Germany. These connections were first called rolling joint connections and their use for the support of concrete arches was well established. However, their construction proved to be very elaborate. Further developments in 1885 and 1933 introduced plumb plates between concrete blocks to

simplify construction. By the early 1900s, Mesnager introduced reinforced concrete hinges using crosswise reinforcement through the throat of the hinge and in 1910 Freyssinet proved that reinforcement can be omitted through the throat with the design based on compression and concrete confinement (Marx (1).

Documented testing of concrete hinges was undertaken by Parsons (2), Kluge (3) and Base (4). Tested specimens were generally based on the Mesnager-type-hinge and included reinforcement through the throat of the hinge. It was generally found that high compression forces and substantial corresponding

shear forces could safely be transferred. An example is the Salginatobelbridge built in 1929/1930 and is shown in Figure 3

Sims (5) emphasized the favourable use of concrete hinges in northern England for motorway bridges in mining subsidence areas. His research concluded that reinforcement through the throat should be avoided to reduce the risk of shrinkage cracks. Leonhardt (6) undertook considerable research resulting in design guidelines for concrete hinges. He found that unreinforced concrete hinges can be successfully utilised if the confinement reinforcement in both adjoining concrete blocks is thoroughly detailed. This research work suggests no throat reinforcement is necessary if the shear force is smaller than 0.12 x axial force. If the shear force is between 0.12 x axial force and 0.25 x axial force, straight reinforcement is suggested. If the ratio of shear force to axial force is larger than 0.25 a concrete hinge is not recommended unless additional measures are taken. These measures include prestressing of the throat to achieve additional compression.

### 3.2 Design rules

In Australia, there are no design rules for concrete hinges in current standards. The last code that covered concrete hinges was the 1976 NAASRA Bridge Design Specification. This approach described is largely based on a technical memorandum by the British Highways Agency (7) for the design and use of Freyssinet concrete hinges. It is very specific in regards to permissible axial forces and the shape of the notch either side of the throat. An image of the required notch shape is included in Figure 4.

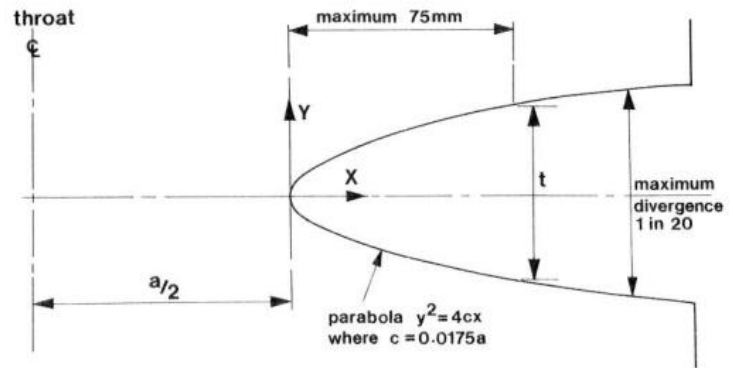


Figure 4. Typical shape of notch. British Highways Agency (7)

Basic rules as set out in NAASRA 1976 (8) are:

- No tensile forces in throat
- $f'_{c \text{ min}} = 40\text{MPa}$ ;
- Maximum aggregate size 10mm;
- Shear across throat 1/3 of co-existing axial load;
- Required short-term and long-term rotations can be accommodated without tensile stresses in the throat;
- Bending moments transmitted by the hinge is acceptable;
- Throat width "a" shall be not less than 50mm;
- Throat thickness at end of parabolic section between "a/2" and "a/3"; and
- Basic allowable stress  $P/a = \min (2 f'c \text{ or } 100\text{MPa})$ .

The high allowable stress is based on the confinement stresses of the concrete as included in current design standards for the design of bearing pressures, for example AS 5100.5, section 12.3 (9).

Further literature on the use of concrete hinges suggests that tensile forces in the throat may be allowed over a width of up to half the width of the throat. Forces and moments around the hinges are illustrated in Figure 5.

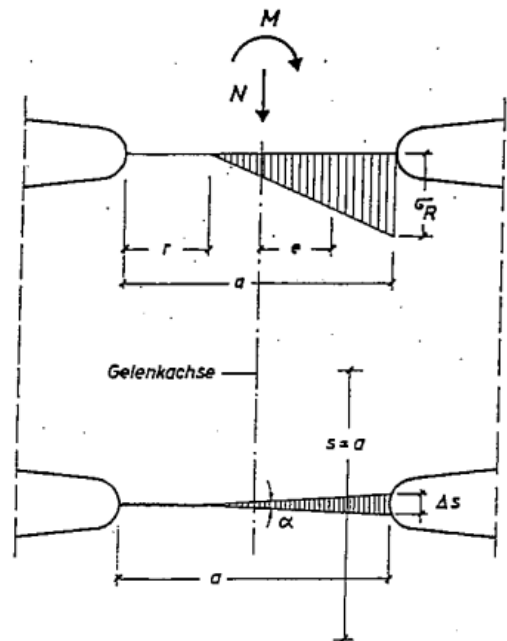


Figure 5. Forces on the throat. Leonhardt (6)

Leonhardt (6) derived a maximum allowable rotation for the hinge of:

$$\alpha \leq 12800000 \frac{N}{a \cdot b \cdot E} \quad (1)$$

With a = width of throat [mm], b = length of throat [mm] and E = Young's modulus [MPa].

### 3.3 General design detailing

From testing of concrete hinges as well as the design rules for concrete exposed to high bearing pressures it is known that the high compression forces through the throat cause bursting forces either side of the hinge. From testing it was found that the bursting force  $Z_1$  as shown in Figure 6 equals approximately  $0.3 \times$  the vertical force  $N$  (Marx (1)). This approximation is very close to the bursting force calculated in accordance with AS 5100.5, section 12.2.4 (9) which is given as:

$$T = 0.33 P (1 - k_r) \quad (2)$$

Where  $k_r$  is the ratio of the depth or breadth of an anchorage bearing plate to the corresponding depth or breadth of the symmetrical prism.

The provision of sufficient reinforcement to cater for the above bursting forces was found to be critical for the capacity of concrete hinges and is therefore an essential part of the design process.

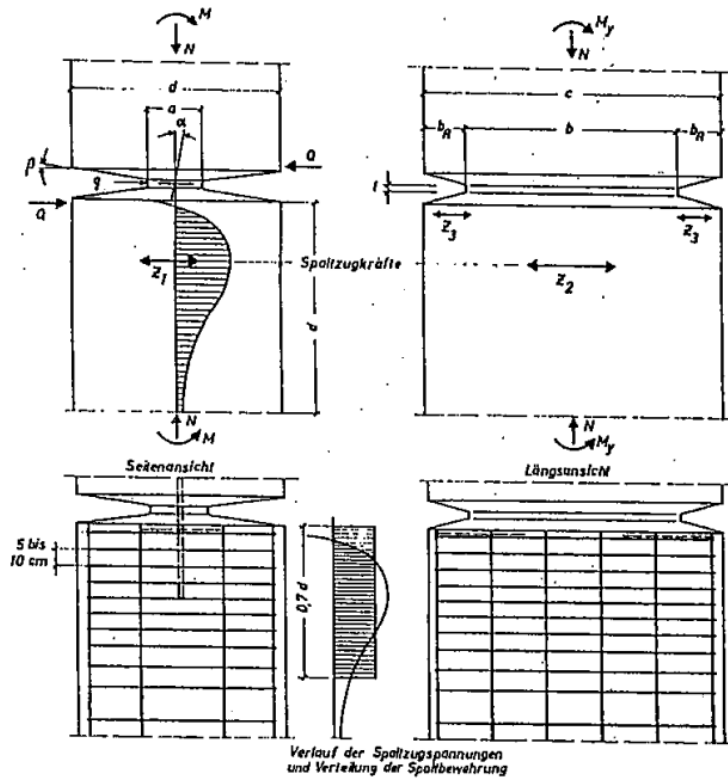


Figure 6. Bursting stress at concrete hinges. Leonhardt (6)

### 4. Design for Legacy Way

The design approach outlined above is particularly favourable for the case of concrete hinges with high axial forces such as would be found in the foundations of arch structures. For those arches, the hinge is oriented on an angle to achieve the highest possible direct axial force. At Legacy Way, secant piled walls are utilised for shoring and to support the roof structure. Locating the hinge at the lower foundation level was therefore not possible. The only practical solution was to locate the hinge at the top of the pile cap as shown in Figure 7 to allow cast in-situ construction of the throat and adjoining concrete blocks.

The roof was designed utilising cast in-situ post-tensioned T-girders. Post-tensioning of those girders was only possible once the rest of the structure was cast and hence, post-tensioning would create a significant shear force in the throat. Additionally, thermal effects during construction and in service had to be considered for the calculation of the shear forces. Consequently, the design shear force exceeded the design axial compression

in the throat. Since the advantages of allowing rotations in the support to reduce the bending moments at the top of the secant piles was considered significant, an option of introducing additional axial forces by post-tensioning the throat was agreed to be the best solution.

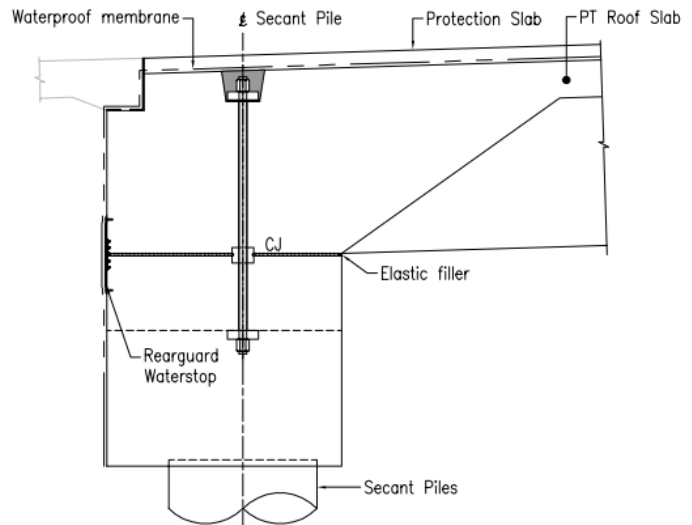
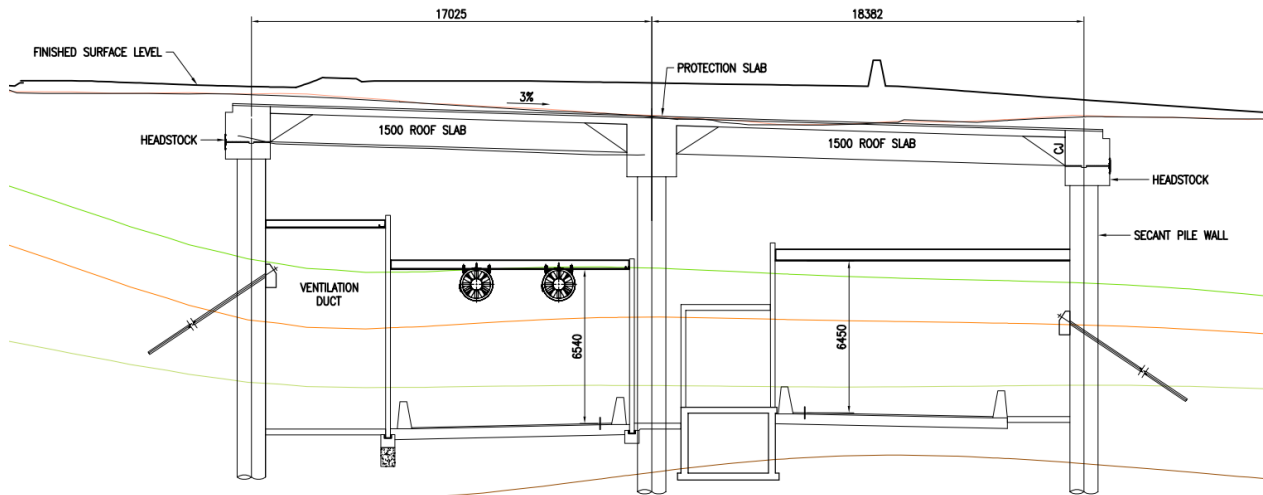


Figure 7. Typical arrangement of hinge.



**Figure 8. Typical geometry.**

Internal forces from post-tensioning, creep and shrinkage and thermal effects were calculated in a global model and a typical layout is shown in Figure 8. The design shear force was calculated to be 612kN/m and hence the resulting vertical force P was required to be 1836kN/m. The corresponding rotation angle was found to be  $\phi=0.0008$  rad.

In accordance with NAASRA section 8.12.4.2, the throat width required to eliminate tensile forces in the throat is calculated as follows:

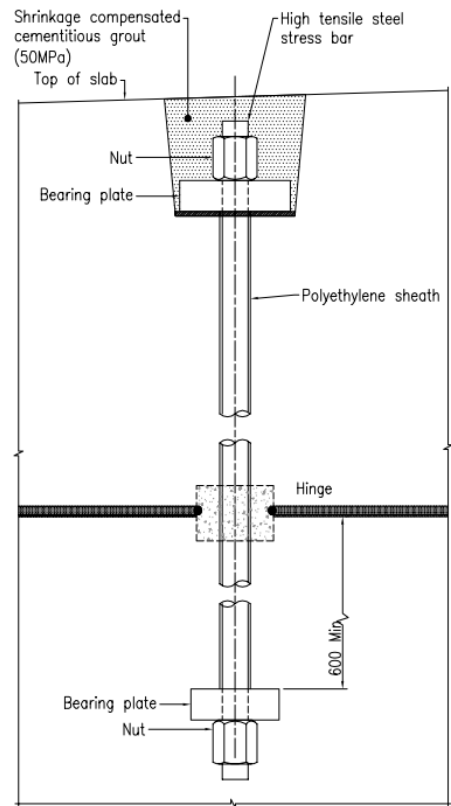
$$E'\phi \leq 2Kh_e \cdot \frac{P}{a^2} \Leftrightarrow a \leq \sqrt{2Kh_e \cdot \frac{P}{E'\phi}} \quad (3)$$

with:  $K=1.5$ ,  $h_e=125\text{mm}$ ,  $E=39162\text{MPa}$ , the throat width  $a$  is hence calculated to 148mm

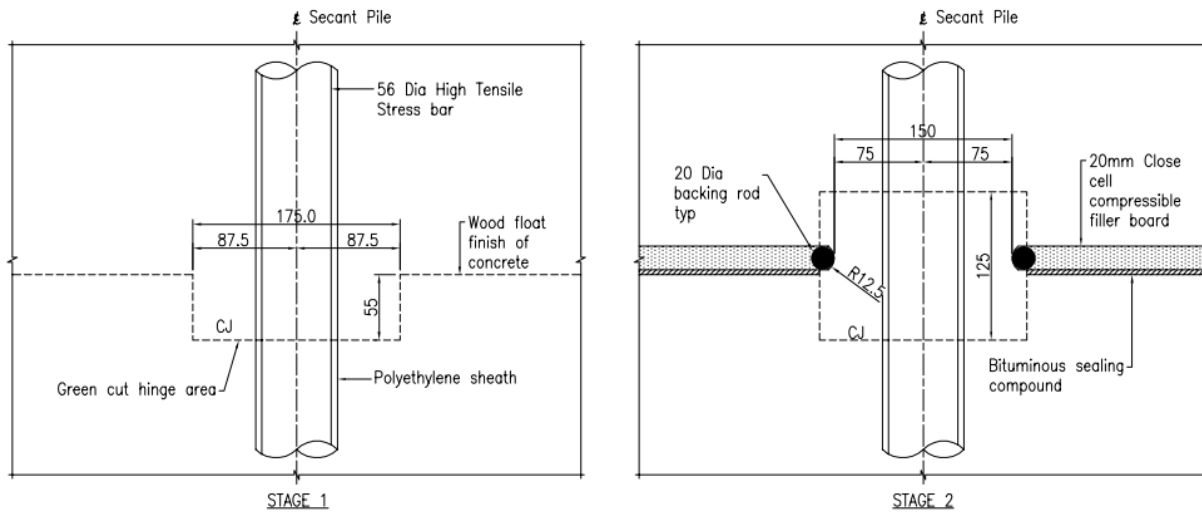
On that basis the throat width was chosen to be 150mm.

The shape of the notch shown in the NAASRA code was found to be impractical for construction and the rule was considered unnecessarily prescriptive. Instead, a simplified version was designed and detailed. It comprised a 12.5mm radius and a horizontal 25mm joint material comprising a closed cell compressible filler. Details of the solution are included in Figure 9.

Initially, it was planned to cast the pile cap and girders in one operation. However, access to the throat to ensure a high quality execution was considered an issue. Also, generally the concrete was planned to comprise 20mm aggregate but, for the throat, 10mm aggregate was planned to be used. Consequently, it was decided to construct the throat in several stages. Initially, the pile cap was constructed with a block out to form the hinge. In a second step the construction joint was prepared and the hinge area cast. Finally, the post-tensioned girders were cast, encapsulating the hinge area. The construction staging is described in more detail in the sections in Figure 9 and 10 and with photos and more detailed information in section 5.

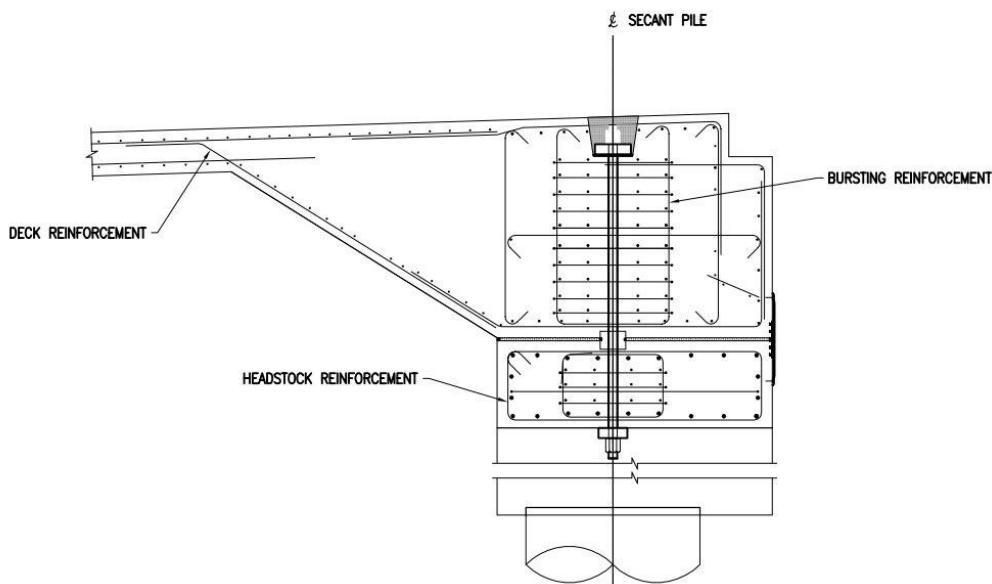


**Figure 9. Stressbar details.**



**Figure 10. Cross section details with construction staging.**

As detailed in section 3.2 bursting reinforcement is required in addition to the typical beam and headstock reinforcement. A detail of this reinforcement is included in Figure 11.



**Figure 11. Reinforcement details at the concrete hinge.**

## 5. Construction phase

The construction sequence is a critical aspect of the design of the concrete hinges to ensure the design intention is met. However, there were also a number of construction constraints and difficulties during the works including narrow width between the construction platforms, accessibility, limited lay down and storage areas and close proximity of the active Inner City Bypass. The Cut and Cover structures also had to be constructed early to ensure timely completion for TBM arrival, which put further constraint on the construction program.

The designers recognised this and, working with the construction team, focused on a way to combine innovative construction techniques with appropriate technical design solutions. The chosen construction sequence allowed the concrete hinge to be built off line to minimise traffic disruption to the Inner City Bypass.

The outline of the construction sequence has been divided into three stages as follows:



- Stage 1: Construction of the lower capping beam
- Stage 2: Construction of the concrete hinge and T Girder
- Stage 3: Stressing of the stress bars

### 5.1 Stage 1

The construction methodology for the lower capping beam was carried out in the following sequence:

- Construct blinding level to the lower capping beam and outside secant piles to give a flat and stable working space.
- Place and position capping beam reinforcement and bursting reinforcement.
- Erect formwork to the edges of the capping beam and install adequate falsework to support the forms off the ground.
- Install waterproofing membrane to manufacturer's specification.
- Erect scaffolding system to support the stress bars.
- Install high tensile steel stress bars including lower bearing plates and lock nuts.
- Form 55mm recess at the hinge centerline.
- Cast lower capping beam.
- Strip forms at hinge recess and provide wood float finish to the rest of the pile cap outside of the hinge recess.
- Green cut and apply concrete retarder to the hinge recess.



**Figure 12. Stress bars supported by scaffolding system.**



**Figure 13. Completion of stage 1 works.**

The stress bars were supported by a specifically designed scaffolding system as shown in Figure 12. The system was made using a closed frame slimshor system spaced at 2.5m centres. The frames were erected either side of the capping beam formwork. Each bay supports the weight of 4 stress bars. The longest steel stress bar was approximately 2.4m long and had to be lifted into position using machinery. Franna cranes were used to lift the stress bars into position and all slinging operations were carefully carried out by a competent dogman and rigger. The site surveyor provided the necessary support to ensure the set out of each stress bar was within the design tolerance and concentric with the throat centerline. Accurate placement of stress bars is required to eliminate any potential eccentric force on the hinge from the prestressing bars. The scaffolding system also provided the required support and bracing to the stress bars to ensure that the verticality and position of the stress bars were maintained at all times until the lower capping beam had been cast.

The capping beams were cast in 20m lengths to expedite the construction program, as requested by the construction team. To meet the project requirement of a maximum target concrete crack width of 0.2mm, additional reinforcement was placed. In addition, a low heat concrete mix was designed and imposed limit on the concrete placement temperature of 32 degree Celsius was in place to ensure the target concrete crack width can be achieved. A photo of the completed stage 1 works is included in Figure 13.

## 5.2 Stage 2

The Stage 2 works were more complex and the following procedures were adopted (Refer Figure 14 and 15 and diagrams in section 4):

- Form concrete nib above construction joint and cast 150mm wide x 125mm deep concrete nib.
- Place backing rod, compressible filler board and FC sheeting.
- Install stress bar bursting reinforcement and form grout pocket.
- Install T girder HDPE ducts and reinforcement.
- Install remaining waterproofing membrane.
- Erect formwork.
- Cast T girder roof slab.

Concrete with maximum aggregate size of 10mm was placed in the concrete nib forms from wheelbarrows as shown in Figure 14. The concrete was compacted through vibration transmitted from the formwork. The concrete nib surface was then screeded prior to commencement of the concrete curing.

To reduce the potential for early shrinkage and plastic cracks of the concrete nib, the concrete nib was covered in wet hessian and kept continuously damp for seven days after pour. The hinge is the critical item of the design and all construction risks were evaluated with the construction team to ensure the integrity of the design was not compromised. Wet hessian was therefore selected over the application of a curing compound because it was considered to be a more effective way of minimising evaporation in the hot Brisbane weather and thereby ensuring proper cement hydration and curing of the concrete.



**Figure 14. Forming and casting of concrete nib. Figure 15. Wet hessian applied on concrete nib.**

Due to the amount of the bursting reinforcement required for both the stress bars and the T girder tendons, the closed compressible fillers were under immense downward pressure from the weight of the steel reinforcement. Fibre cement (FC) sheeting was used to distribute the pressure adjacent to the hinge and prevent the closed cell compressible filler being crushed. This layer of the FC sheeting was placed above the compressible filler board adjacent to the hinge. The spacing of the fibre concrete bar chairs was also reduced to avoid excessive bearing stress on the compressible filler.

## 5.3 Stage 3

The Stage 3 works involved the setting up, stressing and grouting of the stress bars and these activities were undertaken after casting of the roof and edge beams. The following procedure was adopted:

- Install upper bearing plates, nuts and washers.
- Set up stressing equipment.
- Tension the stress bars up to design load after T girder concrete strength has achieved 35MPa.
- Tighten the permanent nut against the washer and bearing plate.
- Grout stress bars and infill pocket with shrinkage compensated cementitious grout.



- Stress T girder tendons.
- Grout T girders tendon and infill pockets.

A 200t capacity bar jack was used on site to stress the bars. The jack was connected to a hydraulic pump via hydraulic hoses and fitting which were powered by a site generator. A steel stool which was connected to the jack was placed on top of the infill pocket to allow access to the nut once the bar is stressed. A coupler and an additional pull bar were used to connect the stress bars to the jack. Once all equipment was fitted together, the bar was stressed to the required design load. The permanent nut was then fully tightened against the washer and bearing plate before the jack was released. Each bar was fully stressed before the jack was disassembled and moved to the next bar. See Figure 17 & 18 for details.

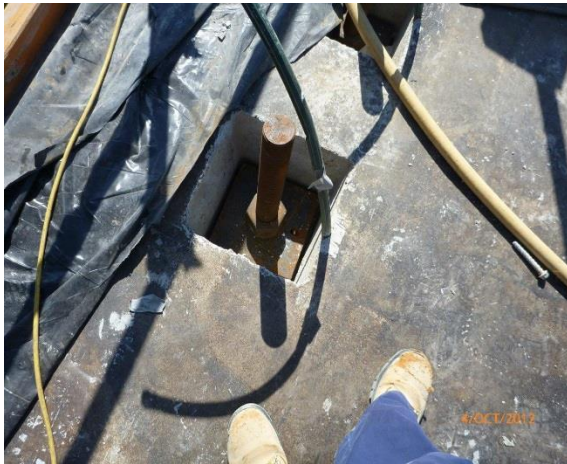


Figure 17. Stress bar infill pocket.



Figure 18. Stress bar stressing arrangement.

#### 5.4 Completed structure

Following construction of the roof, water proofing was provided to the top of the structure and the structure was backfilled. Excavation underneath the roof was carried out in parallel with roof construction. The excavation was carried out in stages to allow the progressive installation of water beams and prestressed anchors before full excavation depth was reached. The progressive excavation resulted in additional loads being applied onto the hinge joint. Due to the capacity for rotation, the additional loads applied are limited to shear forces and minor moments in the throat. The bending moments in the secant piles are largely due to earth pressure following excavation and prestressing forces when the ground anchors are stressed. A photo of the completed structure is shown in Figure 18.



Figure 18. Completed structure.

## 5. Conclusions

Design and construction of the cut and cover structures of the Legacy Way Project in Brisbane have required the provision of rigid or semi-rigid solutions and provision of structures without bearings and movement joints which would require later maintenance or replacement. Allowing rotations at the roof support while also providing a low maintenance structure resulted in a solution comprising secant pile walls, pile caps, a post-tensioned roof structure and a concrete hinge connection between sub and superstructure. It has been shown that a highly durable and sustainable structure was constructed.

However, there are no current design standards in Australia for this support type and the most recent codes date back nearly 40 years. In addition, the details provided in 1976 lack practicality on site and are over prescriptive. It is recommended that this support type be reassessed for current use in structures, in particular to address current whole of life and sustainability discussions. Since concrete hinges have been detailed for design and construction in previous versions of the Australian bridge design standard, consideration should be given to the re-introduction of this form of support. Finally, it appears prudent to carry out further testing of concrete hinges in particular since construction materials and the associated technology have changed significantly over past decades and these new materials could result in an improved design and construction approach.

## 6. Acknowledgement

We like to thank Transcity JV and Brisbane City Council for the opportunity to submit this paper.

## 7. References

1. Marx, S. and Schacht G. "Gelenke im Massivbau", Beton- und Stahlbetonbau 105 (2010) Heft 9, Ernst & Sohn Verlag.
2. Parsons, D. E., Stang, A. H., "Tests of Mesnager Hinges", National Bureau of Standards of the U.S.Department of Commerce, 1935.
3. Kluge, R. W., "An Investigation Of Rigid Frame Bridges Part III, Tests Of Structural Hinges Of Reinforced Concrete", The Engineering Experiment Station University Of Illinois, 1940.
4. Base, G. D., "Tests On Four Prototype Reinforced Concrete Hinges", Research Report No. 17: May 1965, Cement and Concrete Association.
5. Sims, F. A., Bridle, R. J., "The design Of Concrete Hinges", Construction & Engineering, August 1964
6. Leonhardt, F., Reimann, H., "Betongelenke", Deutscher Ausschuss für Stahlbeton Heft 175, 1965
7. The Highways Agency, UK, "Technical Memorandum (Bridges) Rules For The Design And Use Of Freyssinet Hinges In Highway Structures", BE 5/75, March 1975
8. National Association of Australian State Road Authorities, "Bridge Design Specification, Section 8, Bearings and Expansion Joints, Section 8.12 Concrete Hinges", 1976
9. Standards Australia, "AS 5100.5 – 2004 Bridge design Part 5: Concrete",

# Challenges, Opportunities and Design Impacts for Different Construction Methods on Curtis Island LNG Jetties

Jesper Jensen<sup>1</sup> and Peter Kastrup<sup>2</sup>

<sup>1</sup>Engineer, Arup

<sup>2</sup>Queensland Maritime Leader and Senior Engineer, Arup

**Abstract:** The demand for energy in South East Asia and the Pacific region has seen vast growth in gas exploration across the continent of Australia. With the approval of a number of liquefied natural gas (LNG) export facilities across the Australian seaboard, Arup Australasia has put its multi-disciplinary capabilities to full use in the delivery of a number of LNG Jetties in Gladstone, Queensland in a design and construct collaboration with contractor John Holland Group (JHG).

Marine construction methods often influence the permanent works design for which the importance of early constructability considerations is significant. The temporary works design and planning across the three projects required particular attention during the detailed design phase. Careful coordination between Arup's structural design team, John Holland's construction planning team and temporary works designers was vital in achieving a solution that achieved both the design intent and that could be constructed safely and efficiently.

As the projects were delivered in a high labour cost environment, pre-fabricated solutions were considered to be preferable. Where possible, a large number of precast and prefabricated elements were transported to site and installed on the driven steel piles. Adopting this type of modular construction meant that the temporary works were minimised where possible. The precast elements worked as permanent formwork for a large number of in-situ concrete pours above water.

The permanent walkways were utilised for temporary access allowing concreting dolphin pile caps by line pump instead of transporting agitators by barge at significantly increased transportation cost and with impacts on the concrete mix design.

**Keywords:** LNG Jetty Design, Concrete, Prefabrication, Precast, Constructability, Marine Construction

## 1. Introduction and Project Background

In 2010, the Queensland Government approved the Queensland Curtis LNG (QCLNG), Gladstone LNG (GLNG), and Australia Pacific LNG. The project partners across the three projects are (at the time of writing):

- QCLNG – QGC(BG), China National Offshore Oil Corporation (CNOOC)
- GLNG – Santos, PETRONAS, Total, KOGAS
- Australia Pacific LNG – Origin, ConocoPhillips, Sinopec

Bechtel was awarded as the engineering, procurement, and construction contractor of the three jetties. John Holland Group (JHG) was awarded the marine subcontracts, including procurement, fabrication, construction and commissioning of the structural, mechanical and electrical components of the product loading facility. JHG appointed Arup in a Design and Construct (D&C) collaboration for the permanent works design of the three liquefied natural gas (LNG) jetty facilities. Arup was also the engineer of record during construction, certifying that the works met the design intent.

With three different project stakeholders, the projects are considered as three separate projects. As such, each project required an individual assessment of the project-specific design requirements, geotechnical profile, and environmental conditions. Examples of impacts on constructability include different levels of the structures, which combined with different geotechnical supports leading to different requirements for member sizes and reinforcement. The three LNG plants are located on the south-western shoreline of Curtis Island and are only accessible by water. The three project sites are illustrated in Figure 1.



Figure 1. Top left: Overview of the Curtis Island LNG plants (from the bottom; Australia Pacific LNG, QCLNG and GLNG). Top right: GLNG. Bottom left: Australia Pacific LNG. Bottom right: QCLNG. @Bechtel

### 1.1 Concept Considerations

Constraints associated with constructing over water forms one of the defining considerations in the structural form selection. Early understanding of the contractor methodologies, plant preference and availability and programme needs are imperative to developing the optimum solution. The assessment of vertical piles vs. raked piles and reinforced concrete (RC) superstructure vs. steel frame were the major considerations during scheme development. Example considerations are summarised in Table 1 and Table 2 below.

Table 1. Examples of Pile Selection Comparison

Item	Advantages	Disadvantages
Vertical Piles	Simpler to install than raked piles.	Complex pile to superstructure connection to accommodate lateral loads.
	Flexibility to adjust rock sockets to manage geotechnical uncertainty.	
Raking Piles	Increased structural efficiency due to the ability of the pile to resist the lateral forces partially as an axial load.	Rely on increased certainty of ground conditions due to the difficulties to extend raked sockets.
	More robust structure than the vertical pile scheme.	Increased complexity of installation. Floating plant may not be practical. Pitch can be difficult to control when driven to seams of hard or firm material.



**Table 2. Examples of Superstructure Selection Comparison**

Item	Advantages	Disadvantages
RC Super-structure	Can be constructed in stages to satisfy the maximum crane lift capacity.	Availability of quality concrete and restrictions on concrete delivery to off shore location.
	Ability to accommodate pile installation out of tolerances.	Heat of hydration concerns with large concrete pours.
	Standard formwork allow quick installation of form base and reinforcement fixing.	Labour intensive. Practical issues when form is within tidal zone. Setting out cast-in items is a challenge.
	Permanent precast formwork save on temporary works, on site steel fixing, and removal of formwork.	Staged pours may be required. Preparing the horizontal construction joint can be challenging.
	Precast fabricated in a controlled environment, which give opportunity for improved appearance. Where marine grade precast concrete is used for the critical exposed sides and soffit, it may be possible to use in-situ concrete with lower durability and strength.	Consideration should be given to tidal variations in relation to the temporary support scheme.
	Increased control of material quality with steel truss typically fabricated off site in a controlled environment.	In-situ welding will likely be required for connection to piles – or a sleeved option may be preferred. Difficult to install with raked piles incl. sleeved option.
Steel Super-structure	Prefabrication can reduce in-situ labour and construction time significantly.	Reduced ability to accommodate piles installed out of tolerances.
	If no design corrosion allowance, full steel section can be utilised for structural capacity.	Potential vortex induced vibrations during transportation may be governing.

Early collaboration with the client to understand the ancillary functional requirements of the dolphins such as furniture, early Arup input during fender selection and involvement with the contractor to understand the constructability needs, was key to a successful scheme development.

## 2. Piling

The high variability of the ground conditions in Gladstone Harbour at Curtis Island and concerns over geotechnical risk governed the contractor's early decision to adopt a vertical pile solution. This was chosen over raking piles for the ease of installation and flexibility. Vertical piling also meant that more costly jack-up barge mobilisation would not necessarily be required. A traveler was utilized to install the trestle piles (and headstocks, pipe rack modules and deck units, refer Section 3). The use of a traveler allowed for the piling to be done independently from the water and intertidal area, which reduces risk of downtime due to wind, waves, tides and currents. Examples of the vertical piling is shown in Figure 2.

The vertical piling decision had a major influence on the structural jetty design, which is discussed in the following sections of this paper.



**Figure 2. Example of LNG Jetty Piling (from Australia Pacific LNG). Left: Piling using Traveler. Right: Piling using Floating Barge. @Arup**

### **2.1 Rock Socket/Anchor**

Due to the design criteria, loading and structural layout, some of the dolphin piles were subject to tension forces, which required rock sockets/anchors to fully transfer the design forces to the ground. Arup and JHG assessed options such as RC rock sockets and post-tensioned grouted rock anchors. The geotechnical conditions meant that the RC rock socket was deemed the most effective and flexible option. The bored in-situ concrete rock sockets could be practically extended where required to counteract the ground condition variability and manage geotechnical uncertainty.

This constructability decision impacted on incorporating this element into the pile design. When included in the dolphin pile analysis the RC rock socket attracted not only axial force, but also shear and bending moment and the connection detail to the steel liner had to be developed. To transfer the forces from rock socket to liner, Arup and JHG developed a solution using internal shear beads, which were designed to a size not protruding past the pile shoe to mitigate risk of damage during pile driving. In turn, this detail led to requirements for cleaning of the rock socket and bottom part of liner to ensure adequate concrete placement and bond.

### **3. Trestle**

As per Section 2, a traveler was utilized on all three projects to install the trestle piles, headstocks and deck units. This constructability decision impacted the pile and headstock permanent works design.

The crane on the traveler is used to lift piles, headstocks and deck units hence the reaction forces from these load cases were incorporated in the design of piles and headstocks. In addition, the deck units were transported from land to the traveler using a self-propelled modular transporter (SPMT), which the deck units were also designed for.

Arup and JHG assessed headstock options including a box section slotted into the pile and box section placed directly on top of the pile. Due to the preference for not cutting the slot in the pile, design loadings and criteria including a significant corrosion allowance, it was decided to adopt the steel box section welded to the top of the pile.

Although adopted for the abutment headstock, a typical concrete headstock was not preferred due to constructability considerations such as maximizing headstock installation time, traveler speed and practical design aspects requiring a steel section for load capacity at the critical locations.

Concrete deck units were designed for the temporary works load cases (in addition to permanent load cases) including the lifting case and to provide compression throughout the cross section. Arup and JHG developed the design of the deck units to fit within the lifting capacity of the crane proposed for the traveler.

### 3.1 QCLNG

The QCLNG trestle was designed for a typical span of 24 m. Images from QCLNG are shown in Figure 3.



Figure 3. QCLNG Trestle. Left: Headstock (Anchor Bent) During Welding to Pile. Right: One Deck Unit Installed. @Arup

### 3.2 GLNG

GLNG trestle is the longest of the three jetties. This jetty was designed for a typical span of 18 m. Figure 4 shows the GLNG trestle at two different construction stages.



Figure 4. GLNG Trestle. Left: Typical Bent View without Pipe Rack Modules. Right: View after Pipe Rack Module Installation. @Arup



### 3.3 Australia Pacific LNG

Australia Pacific LNG trestle is the shortest of the three jetties and a 24 m typical span was adopted, refer images in Figure 5.



**Figure 5. Australia Pacific LNG Trestle. Left: Traveler Trestle Construction. Right: Completed Trestle Roadway. @Arup**

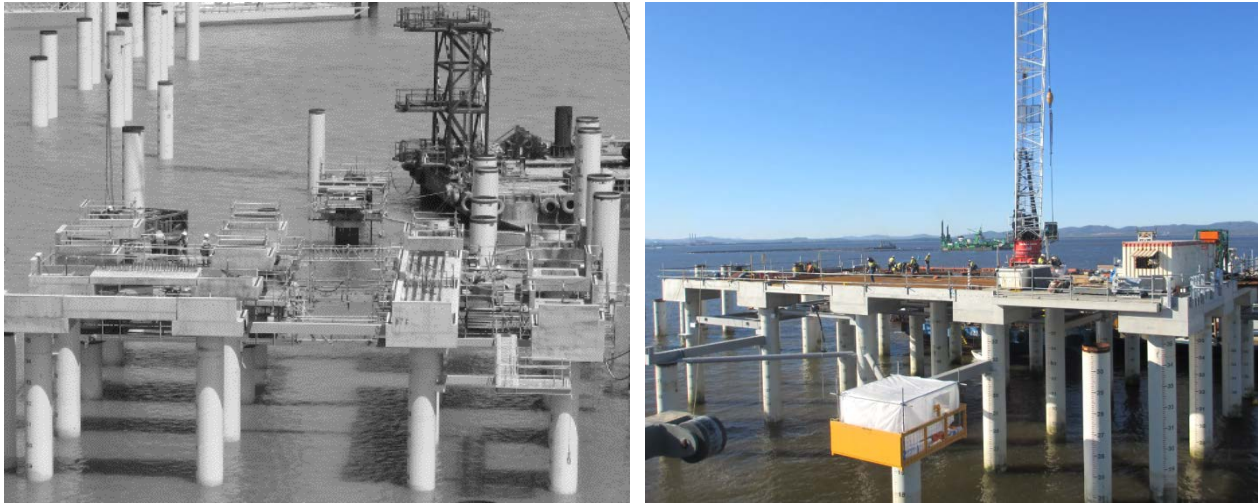
## 4. Loading Platform

The loading platform size and deck level varied between all three projects. JHG preferred a universal pile size to facilitate using the same piling equipment across all three projects. A concrete superstructure was adopted for all three projects and the designs were in all cases heavily governed by the constructability requirements. Wind forces on loading arms were also governing cases. The vertical pile arrangement meant that a relatively large quantity of reinforcement was required for the pile cap or headstock. Detailed space proofing was prepared considering piling and precast tolerances and cast-in temporary works members.

### 4.1 QCLNG

Precast pile caps were used on QCLNG. Primary precast deck planks were then placed on top of the pile caps followed by secondary precast deck planks placed to create the full soffit of the platform. However, one area of the deck had to be completed first such that JHG could install a crane here to facilitate the rest of the loading platform construction, refer Figure 6. A detailed staged analysis was performed to overcome the challenge of designing the precast including pile caps and in turn, assess and advise of allowable crane pad locations for an in-complete platform.



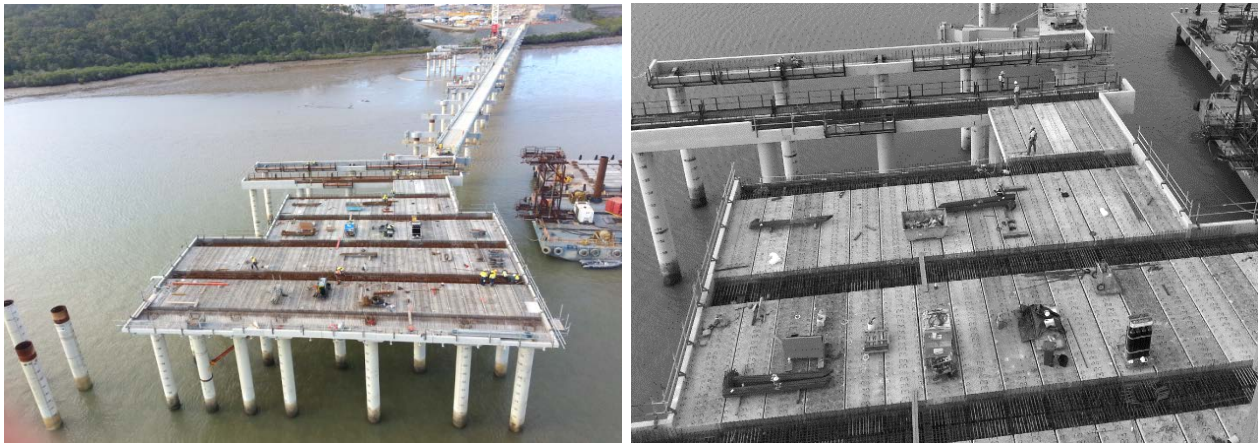


**Figure 6. QCLNG Loading Platform. Left: Pile Caps and Part Installation of Primary Precast. Right: All Precast Installed and Crane Working from a Section of the Platform. @Arup**

#### **4.2 GLNG**

The GLNG loading platform was designed and built with precast headstocks spanning in the direction of the quay line. Precast deck planks span the headstocks to complete the concrete soffit, refer Figure 7. This design avoided the need for pile caps, however requiring larger lifts than QCLNG.

The platform was built partly using a crane on a floating barge and partly using the traveler crane once it had reached the platform location.



**Figure 7. GLNG Jetty Loading Platform. Installation of Secondary Precast Deck Planks. @Arup**

#### **4.3 Australia Pacific LNG**

The Australia Pacific LNG loading platform was designed and constructed in a similar way to GLNG. Precast headstocks were placed directly on top of the piles without the use of concrete pile caps. Secondary precast planks span the headstocks to create the permanent soffit of the structure.



**Figure 8. Australia Pacific LNG Jetty Loading Platform during Construction. @Arup**

## **5. Dolphins**

The dolphin design was also heavily influenced by the construction method decisions. A main factor was whether or not to adopt a precast shell or use a conventional temporary formwork strategy for the reinforced pile cap. Another key component was the pile plug, which is a reinforced concrete plug within the top of the piles. The construction of these structures was challenging and was done in different ways on the three projects. Due to the vertical pile arrangement, a large quantity of reinforcement was required within the pile cap, which proved challenging when also having to account for piling tolerances and cast-in items such as fenders, mooring hooks and internal temporary works members.

### **5.1 QCLNG**

For the berthing dolphins, the pile extends into the cap. On QCLNG it was decided to prefabricate the pile plug reinforcement cage and attach this to the top part of the pile, which also had externally welded shear keys. This assembly was then welded with full penetration butt welds onto the pile at the surveyed level. Temporary works members was also incorporated into this assembly and facilitated less work over water when subsequently installing the temporary formwork. For QCLNG Arup and JHG further developed a modular concept for the pile cap reinforcement, which was another measure adopted to reduce work done over water, refer Figure 9.





**Figure 9. Left: Berthing Dolphin Pile Plug Prefabricated Assembly. Right: Modular Reinforcement Being Lifted into Pile Cap. @Arup**

## **5.2 GLNG**

The construction methodology Arup and JHG developed for GLNG was different to the other projects in a number of ways. A precast shell (soffit and sides) was utilized to avoid the need for temporary formwork over the water (temporary supports to the piles in the tidal zone were required to land the shell). Instead of traditional round reinforcement bars, a predominantly steel plate based reinforcement concept was adopted to provide less congestion within the cap. This steel plate arrangement was fully prefabricated off site and lifted into the cap in two pieces, refer Figure 10. The precast shell also facilitate the early installation of the walkways to utilize this access for staff and concrete pumping from trucks on the loading platform rather than by barge.



**Figure 10. Precast Berthing Dolphin Shell before and After Reinforcement Installation. @Arup**

## **5.3 Australia Pacific LNG**

The Australia Pacific LNG dolphins were designed and built using standard formwork. For the mooring dolphins the pile plug reinforcement cage extended fully into the pile cap and had to be designed to allow for the temporary works supports, refer Figure 11.

JHG also utilized early installation of walkways on the Australia Pacific LNG dolphins to improve access for staff and concrete pumping practicalities. This was also a critical factor in being able to reduce the time

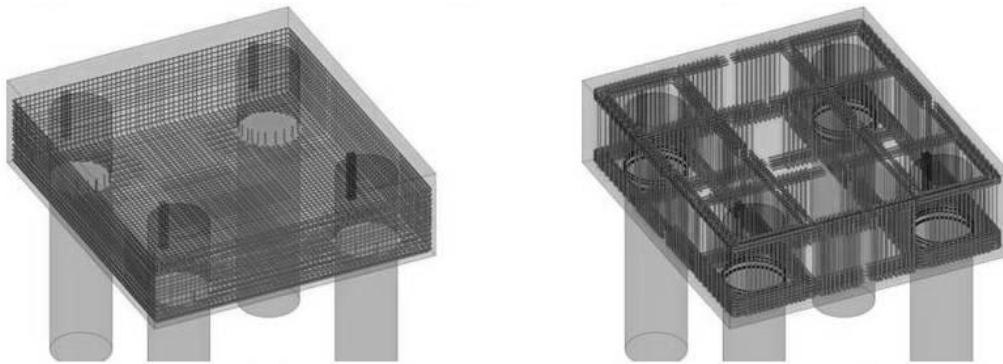
from concrete batching to the point of discharge. This was important to control the placement temperature during the summer months.



**Figure 11. Left: Berthing Dolphin Construction. Right: Mooring Dolphin Pile Plug Temporary Works Assembly. @Arup**

## **6. Modular Reinforcement and Clash Detection**

The opportunity to develop modular reinforcement and clash detection for the berthing dolphins was identified early in the projects. A 3D BIM model was developed to ensure that sufficient space was provided for all specified bars. As the projects were delivered in a high labour cost environment, pre-fabricated modules were developed for the reinforcement cage. The model was developed by Arup and transferred to JHG for construction. Adopting this type of modular construction had a positive impact on the critical path of the construction programme. In addition to the coordination of temporary works and the reinforcement, it was also a priority to develop a solution maintaining a safe working environment. An example of the 3D BIM model is shown in Figure 12.

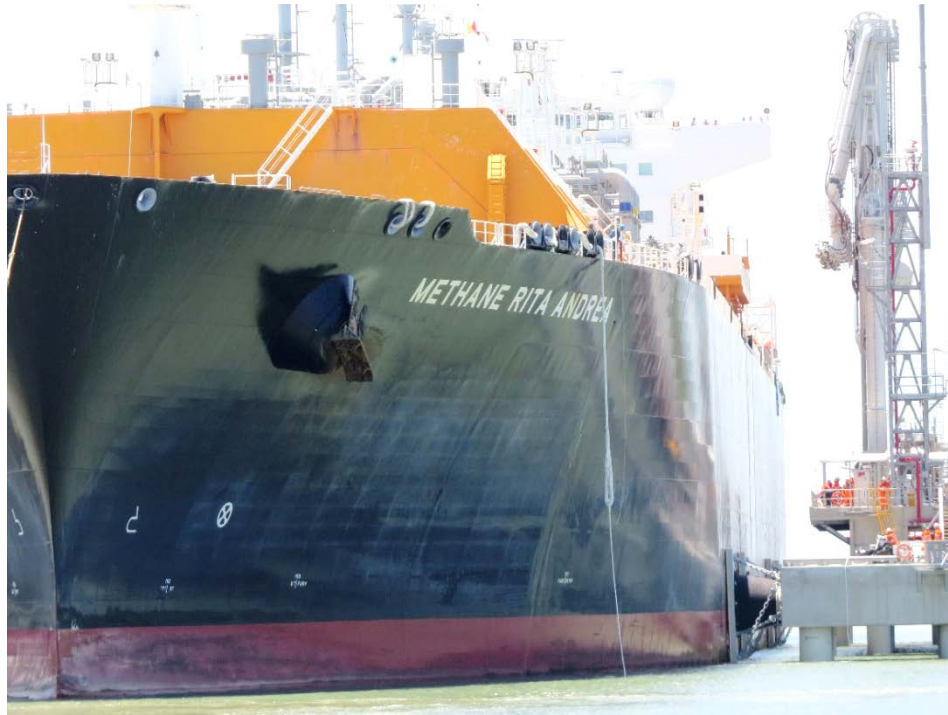


**Figure 12. Design BIM 3D Modular Reinforcement and Clash Detection Model. @Arup**

## **7. Conclusion**

Arup was expecting the design of these marine structures to be governed in a large part by the construction methodology decisions made by JHG. As per the examples in this paper, a number of critical design aspects had different impacts, challenges and opportunities across each of the three projects. The successful design and construct delivery of these projects is a demonstration of the positive collaborative relationship between the design team and contractor. Early engagement and an aligned understanding of the constraints helped in paving the way to designing efficient structures while incorporating innovative marine construction techniques. First gas was shipped from Curtis Island on 5 January 2015 from QCLNG. GLNG and Australia Pacific LNG are expected to commence shipping later in 2015.





**Figure 13 Methane Rita Andrea LNG Vessel at the QCLNG Berth (first vessel to ship gas from Curtis Island). @QGC**

## **8. Acknowledgements**

This paper is published with the permission of John Holland Group, Bechtel, QCLNG, GLNG, and Australia Pacific LNG. The authors acknowledge the encouragement of these parties in supporting this paper. Many people have contributed to these projects. The authors thank everyone involved and for the opportunity to deliver such challenging projects.

# A Bond-Slip Modelling Approach for the Transfer Length of Pre-tensioned Concrete

Rik Steensels<sup>1</sup>, Lucie Vandewalle<sup>2</sup> and Hervé Degée<sup>3</sup>

<sup>1</sup> PhD candidate, Hasselt University

<sup>2</sup> Professor at faculty of civil engineering, KU Leuven

<sup>3</sup> Professor at faculty industrial engineering, Hasselt University

**Abstract:** In this paper, a bond-slip relation at the prestress strand-concrete interface for pre-tensioned concrete is developed. The bond-slip behaviour is based on the confinement model developed by Den Uijl in order to properly address the influence of the nonlinear concrete material behaviour around the strand and the influence of the geometrical properties of the beam on the confinement of the prestress strand. Furthermore, this bond-slip behaviour is implemented in a finite element model to evaluate the transfer length of prestressed beams. The numerical model is compared to experimental results of two independent researchers and good agreement is achieved. This paper also presents the influence of several calibration constants of the bond-slip model on the resulting transfer length of the beam.

**Keywords:** Pre-tensioned concrete, bond-slip, confinement, transfer length, pre-stressed concrete.

## 1. Introduction

The transfer length of a prestressed element is an important parameter for the design of the anchorage zone reinforcement. In pre-tensioned elements, the driving phenomenon for the determination of the transfer length is the bond behaviour between the prestress tendons and the surrounding concrete. Overall, current evaluation of the transfer length is performed using empirically determined formulae based on experimental data (1). Furthermore, they often only take into account a couple of parameters like the prestressing force or the diameter of the prestressing strand. However, the bond behaviour governing the transfer length is influenced by an extensive amount of parameters ranging from geometric parameters, which determine the confinement of the concrete, to material parameters like the Young's modulus and the tensile strength of the concrete mixture. Furthermore, additional influences like the manner in which the prestress tendons are detensioned or the presence of additional confinement reinforcement around the prestressing strand impact the behaviour of the bond strength between steel and concrete and therefore also affect the transfer length. This study involves an implementation of a bond-slip relation based on the confinement model as described by Den Uijl (2). The bond-slip relation will be applied in a nonlinear finite element model to ascertain a numerical evaluation of the transfer length for concrete elements with different geometrical and prestressing conditions based on the experimental work of Mitchel et al.(3) and Oh et al.(4). The aim of this study is to achieve a numerical model which accurately describes the transfer of the prestressing force from the prestress tendon to the concrete, taking into account the geometrical and material properties of the element.

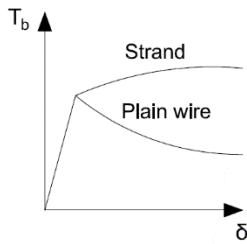
## 2. Modelling the bond behaviour

### 2.1 Bond mechanism of 7-wire strands

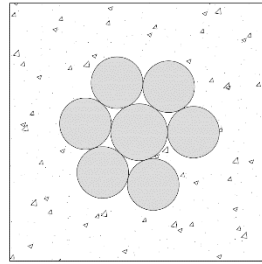
The bond mechanism describing the behaviour of 7-wire strands differs quite extensively from that of a plain wire as can be seen in figure 1. The bond strength can be attributed to three aspects; cohesion between steel and concrete, mechanical resistance and friction between steel and concrete. The effect of cohesion however is very small and thus of insignificant influence (5,6). Mechanical resistance is primarily of importance when deformed bars are examined due to the fact that concrete ribs will be formed and the associated bearing stresses will have a significant impact on the bond stresses. However when a 7-wire strand slips, it will follow the helical grooves in the surrounding material without substantial shearing off of the concrete (6).

The frictional aspect of bond carries the most weight when studying 7-wire strands. The friction can again be subdivided in three aspects, more specifically the poisson contraction, the 'lack of fit' and the pitch effect (7). Due to the stretching of the strand during the prestressing stage, the cross section of the strand

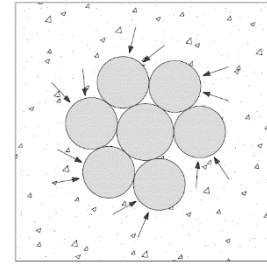
will narrow according to the Poisson ratio of steel. However when the strand is cut during detensioning,



**Figure 1. Bond-slip relation of strand vs plain wire**  
the



**Figure 2: 'Lack of fit'**



**Figure 3. Torsional moment attributed to pitch effect**

stress in the strand will decrease again at the end faces of the element and the cross section will want to expand radially to its original diameter. This expansion is partially restricted due to the surrounding concrete and causes a wedge-like shape of the 7-wire strand at the end faces of the element. Additionally, further bond strength can be attributed to the cross sectional properties of the strand. In a 7-wire strand, the middle wire has a larger diameter than the surrounding ones (figure 2). This causes the surrounding wires to leave a gap which is helically shaped along the length of the strand. Due to this 'lack of fit', cement particles form a small, helically shaped, concrete rib along the length of the strand. The additional compressive stresses which result when detensioning occurs further enhances the bond behaviour at the interface between concrete and steel. This increase in bond is known as the 'lack of fit' effect (7,8).

The final contribution to the bond behaviour is attributed to the pitch effect. When a 7-wire strand is released, it changes its pitch along its length. This pitch-change will be restricted by the concrete and consequently cause a torsional moment which further increases the bond strength of the strand (figure 3). However, the importance of the pitch effect is contested by several researchers, Stocker and Sozen (9) concluded that, due to low torsional stiffness of the strand, the frictional aspect of the pitch is small compared to other influences. This was contested by Russel and Burns (10) who stated that the boundary conditions of the test setup of Stocker and Sozen prevented them from effectively measuring the influence of the effect of the pitch change. Den Uijl lastly concluded from pull out and push in tests that frictional influence for prestress strands is greater than the effects which can be contributed to merely the Poisson effect and the 'lack of fit' of the strand. The third influence was denoted as the pitch effect without a clear mechanical explanation (2,7,11). The contribution of the wedging effect due to the Poisson ratio and the frictional forces to the bond are known as the Hoyer effect (12).

The bond phenomena described above cause a radial compressive pressure  $\sigma_{rr}$  at the strand-concrete interface. According to Tepfers (5), the bond stress  $\tau$  can now be calculated using a dry friction law.

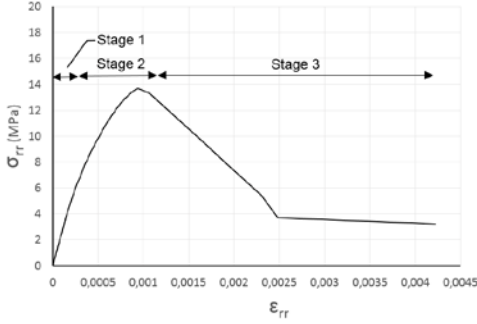
$$\tau = \tau_0 + \mu \sigma_{rr} \quad (1)$$

Where  $\tau_0$  is the initial bond strength caused by cohesion at the steel-concrete interface and  $\mu$  is the friction coefficient denoting the relation between the radial compressive pressure and the bond stress.

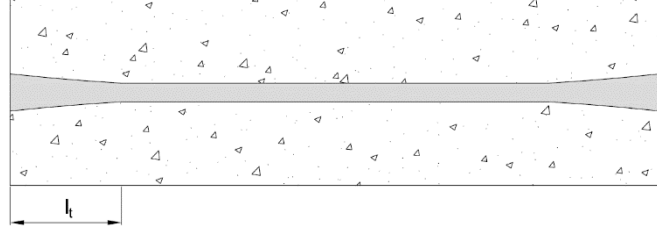
## 2.2 Confinement model

Based on the work of Timoshenko (13), Den Uijl gave a description of the radial compressive pressure  $\sigma_{rr}$  in function of the radial strain  $\epsilon_{rr}$  of a deformed bar using a thick-walled cylinder model (2). This approach was also used by Oh et al. (4), Abdelatif et al. (6), and Fellingner (11) to model the behaviour of prestressing tendons with good agreement to experimental results. Furthermore, the thick-walled cylinder model takes into account the confinement of the reinforcement due to the surrounding concrete. The radial compressive stress is described for three stages (figure 4). The first stage describes the relation between  $\sigma_{rr}$  and  $\epsilon_{rr}$  for uncracked concrete. The constitutive behaviour of concrete is linear elastic and isotropic. Due to the radial compressive stresses, tangential tensile stresses will occur at the steel-concrete interface and when the tensile strength of the concrete is reached, the second stage in the thick-walled cylinder model is introduced. In this second stage, the concrete of the thick-walled cylinder starts to crack and the crackfront moves from the cylinders inner radius to its outer radius. The constitutive

behaviour is changed to accommodate for the partially cracked region of the cylinder. The cracked concrete is modelled with the use of the fictitious crack model where concrete softening is taken into account following a bilinear softening law. When the crackfront has reached the outer radius of the thick-walled cylinder model, the third stage is initiated. The constitutive behaviour is now in accordance with a fully cracked cylinder and it further follows the softening function while the fictitious crack width increases.



**Figure 4. Confinement model Den Uijl**



**Figure 5. Wedge effect of prestress strand**

The loss of confinement at the steel-concrete interface due to the formation and the widening of splitting cracks around the reinforcement is hereby taken into account. For a full description of the constitutive behaviour of the thick-walled cylinder model and the  $\sigma_{rr}(\epsilon_{rr})$  relation, reference is made to Den Uijl (2).

### 2.3 Bond-slip relation

The confinement model of Den Uijl describes the radial compressive stress at the interface between the prestress strand and concrete taking into account possible concrete splitting cracks around the strand. Inserting this relation into equation (1) denotes the bond stress in function of the radial strain at the steel-concrete interface.  $\tau_0$  is assumed to be zero due to the small impact of cohesion to the bond stress.

$$\tau = \mu \sigma_{rr}(\epsilon_{rr}) \quad (2)$$

In order to obtain the bond-slip relation, the relation between the radial strain and the slip ( $\delta$ ) has to be setup. As mentioned above, the Poisson effect, 'lack of fit' of the strand and the pitch effect exert an influence on the radial stress and thus have to be taken into account. The total radial strain can therefore be described as follows;

$$\epsilon_{rr,tot} = \epsilon_{rr,v} + \epsilon_{rr,lof} + \epsilon_{rr,pitch} \quad (3)$$

Where  $\epsilon_{rr,v}$ ,  $\epsilon_{rr,lof}$ , and  $\epsilon_{rr,pitch}$  respectively denote the impact of the Poisson effect, lack of fit, and the pitch effect to the total radial strain at the interface. Denoting the Poisson effect in function of the slip is relatively straightforward. The slip causes a decrease of the longitudinal strain which, in turn, can be linked with a radial increase through the Poisson rate.

$$\epsilon_{rr,v}(\delta) = C_v \nu \frac{\delta}{l_t} \quad (4)$$

Where  $C_v$  is a calibration constant,  $\nu$  is the steel Poisson ratio and  $l_t$  denotes the transfer length. The transfer length is taken into account because the change in diameter occurs along the transfer length (figure 5). The longitudinal strain due to the slip is therefore denoted as the ratio between the slip and the transfer length. However, the presence of the transfer length in the description of the bond-slip relation compels an iterative approach to the model due to the fact that a re-evaluation of the transfer length has to be performed during the analysis in order to make a proper assumption of the transfer length. An overview of the steps performed during the analysis can be seen in the flow chart of the on figure 6. Obtaining the radial strain in function of the slip due to the 'lack of fit' and pitch effect however is more difficult. A formula was developed by Den Uijl (8) which describes the influence to the bond stress resulting from the 'lack of fit' as a function of the slip but this formula is based on experimental results without a clear physical explanation. Furthermore, as mentioned above, the mechanical background to the pitch effect is not fully clear. Therefore, it was opted to describe the influence of the 'lack of fit' and pitch effect in a similar way as the Poisson effect. The radial strain can be denoted as the ratio between a radial displacement at the interface ( $u_r$ ) and the radius of the strand ( $r_s$ ).



$$\varepsilon_{rr} = \frac{u_r}{r_s} \quad (5)$$

Using a second calibration constant, the influence of the slip to the radial displacement resulting from the lack of fit and pitch effect can now be denoted.

$$u_{r,lof+pit} = C_{lof+pit} \delta \quad (6)$$

The radial strain due to lack of fit and pitch can be found by inserting equation (6) into equation (5).

$$\varepsilon_{rr,lof+pit} = C_{lof+pit} \frac{\delta}{r_s} \quad (7)$$

Equation (7), (4) and (3) can now be combined and filled in equation (2) to obtain the bond-slip relation at the strand-concrete interface.

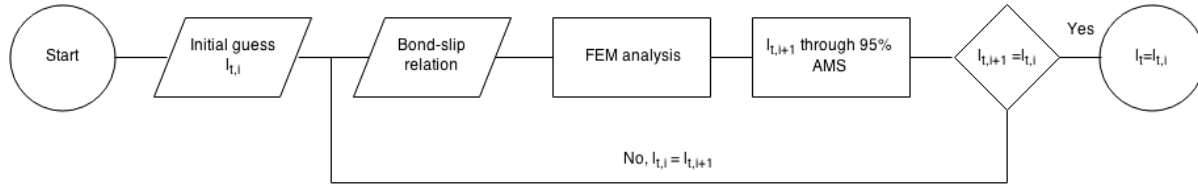
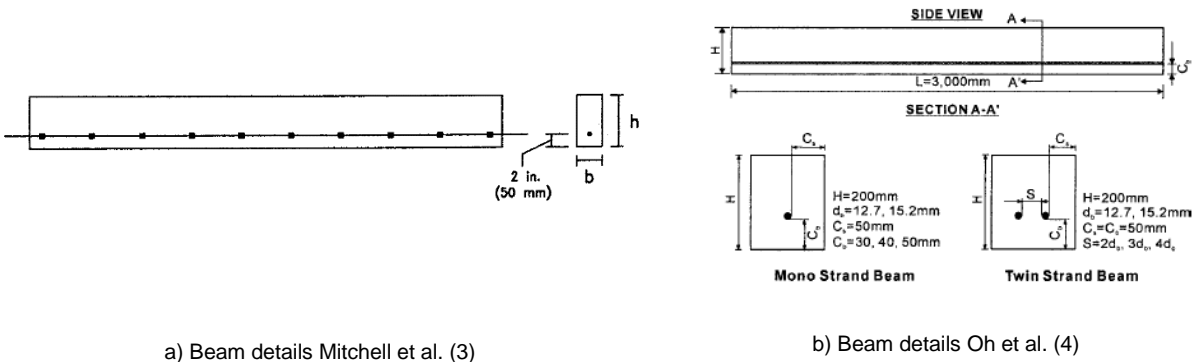


Figure 6. Flowchart of bond-slip model

### 3. Calibration and validation of the bond model

#### 3.1 Experimental tests

The constants and the friction coefficient of the bond model will be calibrated based on the experimental research of Mitchell et al. and Oh et al. Both authors conducted experiments where the transfer length was measured for small pre-tensioned concrete beams with different geometrical and material properties and for different values of the prestress force. The geometrical properties which are varied are the concrete cover of the strands, strand diameters, and in case of Oh et al. the number of strands in the beam (mono or twin strands). The material parameter which is altered is the concrete strength ranging from 31 to 89 MPa for the experiments of Mitchell et al. and from 47.4 to 61.2 MPa for the experiments of Oh et al. Prestress transfer was performed when the concrete was not yet at full strength but the transfer length development was monitored for the period necessary to reach full strength. The values of the initial stress in the prestress strand at transfer ranged from 922 to 1442 MPa for Mitchell et al. and from 1357.4 to 1418.0 MPa for Oh et al. Details of the beams of both authors can be found in figure 7.



a) Beam details Mitchell et al. (3)

b) Beam details Oh et al. (4)

Figure 7. Beam details of experimental tests

The transfer length is measured with two different techniques for the two authors. Mitchell et al. apply the slope intercept method in which the transfer length is determined as the distance from the end of the element to the intersection of a line which is fitted upon the strain values in the transfer region with the line representing the strain value beyond this region (3). Oh et al. use the Average Maximum Strain (AMS) method. This method implies that the readings of the strain gauges are first smoothed out to avoid the influence of locally diverging readings. Then, the transfer length is determined as the length from the end

of the beam to the point where 95% of the maximum average strain is reached. A drawback of the slope intercept method is that the method heavily relies on the number of data points available. Furthermore, it is a graphical method so it can occur that separate researchers will obtain different transfer lengths for the same data. The AMS method does not have this drawback but it is stated that this method relies heavily on the accuracy of the two readings between which the 95% line intersects the strain curve.

### 3.2 FEM model

The numerical implementation of the bond model was performed with the commercial software package DIANA. The concrete beam is meshed with 8-noded quadrilateral elements, the prestress strands are modelled as one-dimensional truss elements which are embedded in the concrete continuum elements. The concrete was modelled with a linear elastic material model and not with a nonlinear cracking model because this is currently outside of the scope of the study. Note however, that the influence of possible cracking and softening of the concrete around the tendon on the confinement and the bond behaviour is already taken into account using the bond-slip relation. DIANA offers a material model to implement bond-slip behaviour for embedded reinforcement, this material model was used to implement the correct behaviour of the prestress strands. The bond-slip behaviour determined in paragraph 2.3 was entered in the material model using a multi-linear bond-slip relation. Because the prestress force was transferred before the concrete hardened up to full strength, the values for the concrete cubic compressive strength ( $f_{cc}$ ) at the time of release were inserted into the model. Furthermore, an evaluation of the tensile strength and Young's modulus based on  $f_{cc}$  was made using formulas from the CEB FIB Model Code 2010 (14).

Due to the small runtime of the analysis it was opted that the beams could be modelled as a whole so no symmetry assumptions were made. The four corner nodes of the beams are restricted in X- and Z-direction and the lower nodes in the middle of the beam are restricted in the Y-direction (figure 8). The prestress load is applied as a force load which acts only on the outer nodes of the reinforcement. Due to the fact that embedded reinforcement is applied, no load is exerted on the continuum elements representing the concrete and the force transfer from the prestress strand to the concrete elements is done entirely through the bond-slip behaviour. Concerning the analysis, a full Newton-Raphson solution algorithm was employed to solve the nonlinear bond-slip model.

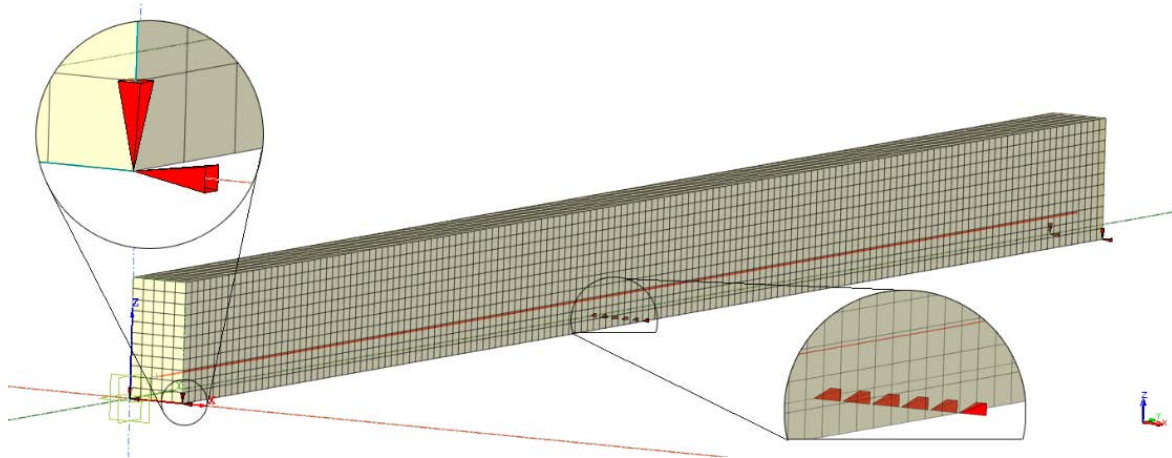


Figure 8: FEM model M15-N-C4

### 3.3 Comparison FEM model with experimental data

Based on the experimental results, the average values of the constants  $C_v$ ,  $C_{lof+pit}$  and  $\mu$  are set to 0.667, 0.3 and 0.75 respectively. With these values, good agreement is found for the experimental results of Mitchell et al. and Oh et al. as can be seen in figure 9 and 10. An average relative deviation of 9.66% was found between the numerical model and the experimental results of Mitchell et al. For the comparison with the experiments of Oh et al., the mean relative error was found to be only 5.61%. This can be attributed to the fact that the slope intercept method, which was used by Mitchell et al., to obtain the transfer length is more biased as was previously mentioned. The 95% AMS method applied by Oh et al. offers a more objective method for evaluating the transfer length. Figure 11a, displays the evolution of the longitudinal strain in the M15-N-C4 beam and figure 11b displays the stress build-up in the prestress strand for the

same experiment. For this particular experiment, the initial value of the prestress in the strand equals 1392.5 MPa. The typical parabolic curves associated with pre-tensioned prestressed concrete can be observed.

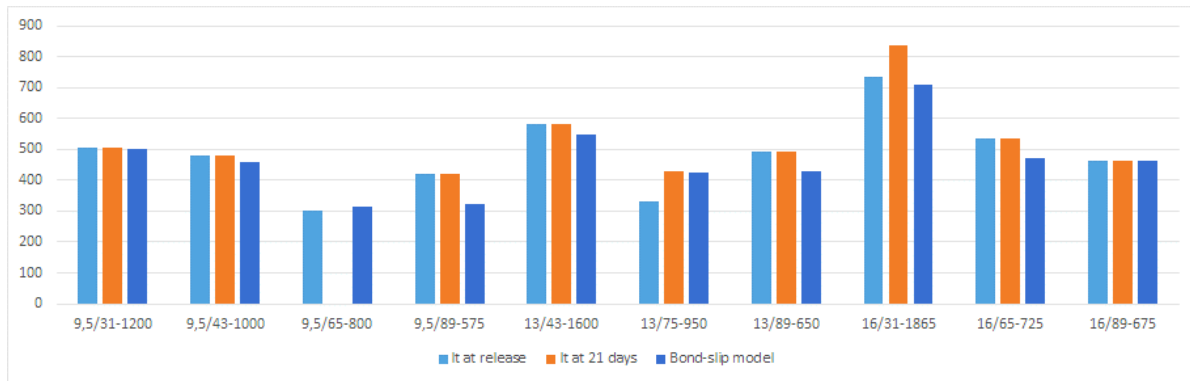


Figure 9. Comparison transfer length (mm) Mitchell et al. and bond-slip model

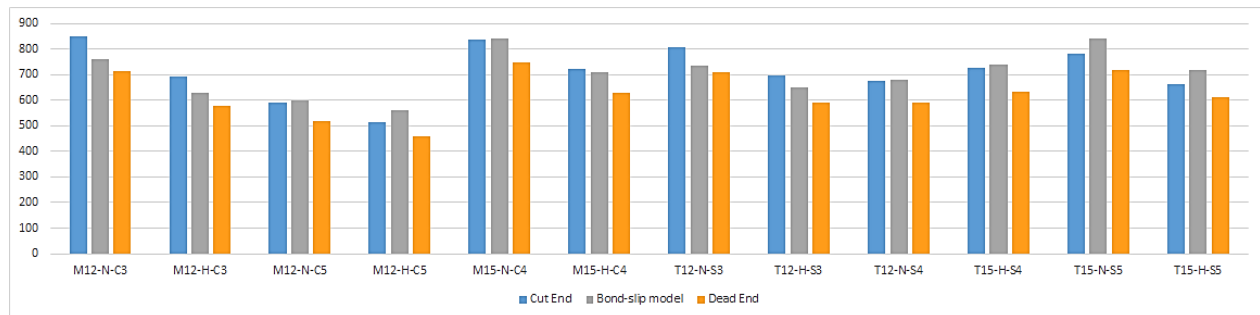
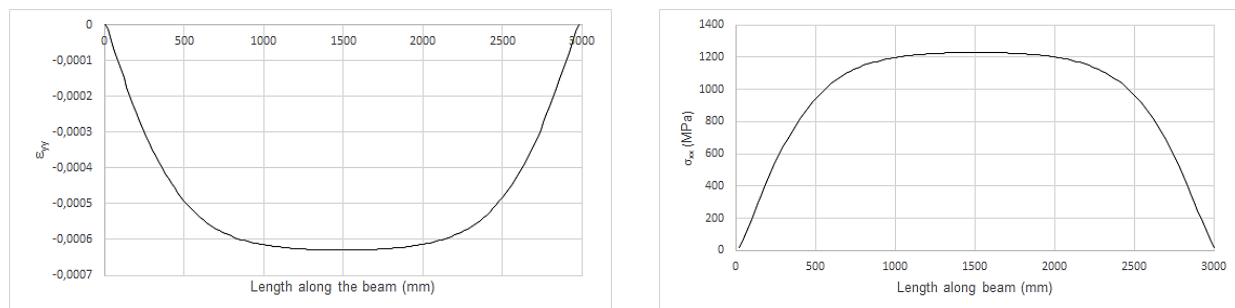


Figure 10. Comparison transfer length (mm) Oh et al. and bond-slip model



a)  $\epsilon_{yy}$  at the side end of the beam

b)  $\sigma_{xx}$  in the prestress strand

Figure 11. FEM output for M15-N-C4

#### 4. Discussion

The influence of the calibration constants on the transfer length can be found in figure 12. The change of the transfer length for  $C_v$  ranging from 0.4 to 0.93 is rather small and a linear relation can be denoted. When looking at equation 4, it can be seen that changing  $C_v$  has the same effect on the bond-slip relation as changing  $\nu$ . Therefore, the value of  $2/3$  for  $C_v$  can be physically attributed to adjusting the value of the Poisson ratio of steel to a value which is more representable for the strand-concrete interface. Altering  $C_{lof+pit}$  up to the value of about 0.5 appears to influence the transfer length according to a quadratic curve (figure 12b). However, when increased further this evolution changes to a more linear nature. It is noted that the convergence rate of the model for values of  $C_{lof+pit}$  higher than 0.5 decreases. This can be attributed to the fact that the confinement curve becomes more and more narrow as  $C_{lof+pit}$  increases and therefore, the area beneath the curve reduces and the total bond stress to be taken on by a certain amount of slip decreases. It is noted that the value of  $\mu$  is rather high. Common values of  $\mu$  range from 0.3

to 0.7, some authors (5,7) even adopt a value of 1 but often they also take into account some kind of measure for adapting  $\mu$  like for instance a plasticity model for  $\mu$  or a slip-dependent coefficient of friction (7). The influence on the transfer length of  $\mu$  ranging from 0.45 to 0.75 can be seen in figure 12c.

When observing the tensile stresses in the concrete, it is noted that in the top fibres of the beam the tensile strength of concrete is exceeded for some beams, though no report of whether or not cracks were formed at the top of the beams was made by Mitchell et al. or Oh et al. Nonetheless, the presence of these cracks would not have an influence on the bond behaviour.

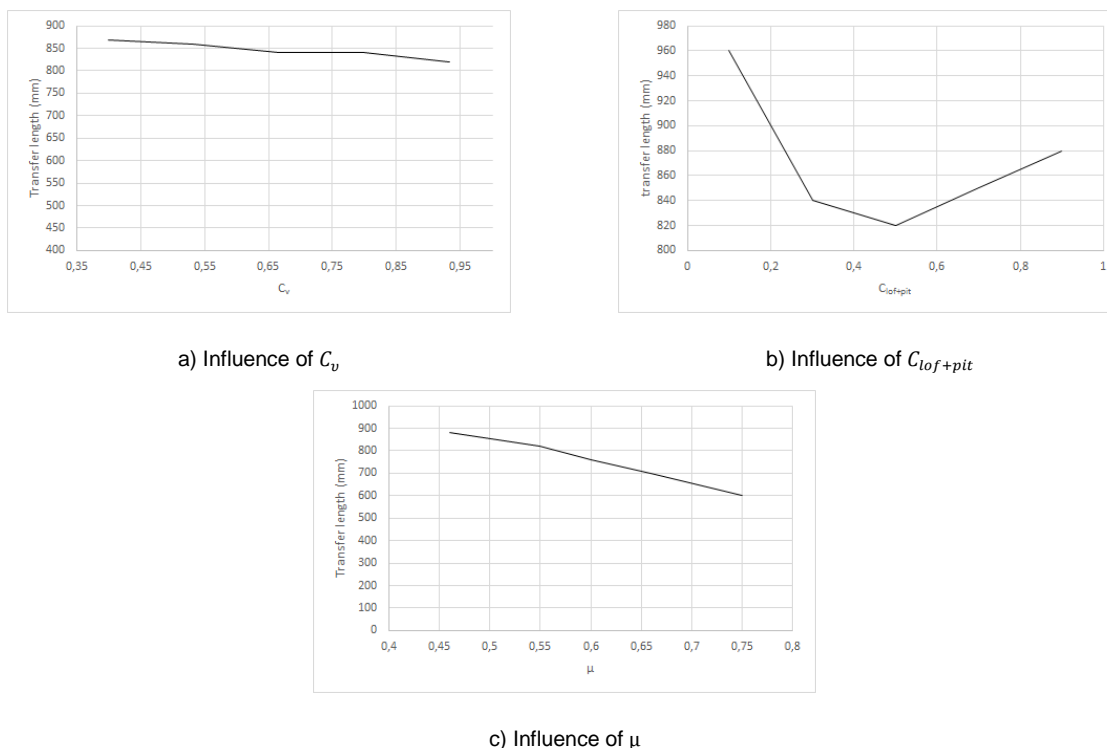


Figure 12. Influence of calibration constants

## 5. Conclusions

A bond-slip relation for the strand-concrete interface of pre-tensioned prestressed concrete was determined based on the confinement model of Den Uijl. The bond slip behaviour was implemented in a finite element model in order to evaluate the transfer length of pre-tensioned beams. Calibration constants were determined using experimental data from two independent researchers and good agreement with experimental results was achieved. Furthermore, the influence of the calibration constants of the bond-slip model on the transfer length was investigated and discussed.

## 6. Acknowledgement

The first author gratefully acknowledges Hasselt University for the financial support of the research.

## 7. References

1. Floyd, R. W., Howland M. B., et al., "Evaluation of strand bond equations for prestressed members cast with self-consolidating concrete", *Engineering structures* 33, 2011, pp 2879-2887.
2. Den Uijl, J. A., Agnieszka, J. B., "A bond model for ribbed bars based on concrete confinement", *HERON* 3, 1996, pp 201-226.
3. Mitchell, D., Cook, W. D., et al., "Influence of High Strength Concrete on Transfer and Development Length of Pretensioning strands", *PCI Journal*, pp 52-66
4. Oh, B. H., Kim, E. S. et al., "Theoretical Analysis of Transfer Lengths in Pretensioned Prestressed Concrete Members", *Journal of Engineering Mechanics*, 2006 pp 1057-1066

5. Lundgren, K., "Three-Dimensional Modelling of Bond in Reinforced Concrete Theoretical Model, Experiments and Applications", Chalmers Reproservice, 1999
6. Abdelatif, A. O., Owen, J. S. et al., "Modelling the prestress transfer in pre-tensioned concrete elements", Finite Elements in Analysis and Design 94, 2015, pp 47-63
7. FIB Bulletin No. 10, "Bond of Reinforcement in Concrete", FIB, 2000, pp 434
8. Den Uijl, J. A., "Bond modelling of Prestressing Strand", ACI special publication 180, ACI, 1998
9. Stocker, M. F., Sozen, M. A., "Investigation of Prestressed Concrete for Highway bridges; Part IV: Bond Characteristics of Prestressing Strand", Structural Research Series No. 344, 1969
10. Russel, B. W., burns, N.H., "Design Guidelines for transfer, Development and Debonding of Large Diameter Seven Wire Strands in Pretensioned concrete Girders", Research report 1210-5F, 1993
11. Fellingner, J., "Shear and Anchorage Behaviour of Fire Exposed Hollow Core Slabs", DUP Science, 2004
12. Briere, V., Harries, K. A. et al., "Dilation behavior of seven-wire prestressing strand – the Hoyer effect", Construction and Building Materials, 2013, pp 650-658
13. Timoshenko, S., "Strength of Materials Vol. 2", Lancaster Press, 1941
14. International Federation for Structural Concrete (FIB), Model Code for Concrete Structures 2010, 2013

# DESIGN FOR CONSTRUCTION COCKBURN GATEWAY STAGE 3

## CASE STUDY

Bassam Matty BSc MSc FIEAust, FAIM  
Director, Airey Taylor Consulting (ATC)

**Abstract:** This paper discusses the selection of a particular construction technique at the concept design stage to address site constraints and client operational requirements for designing a major extension to an operating Shopping Centre.

The selection of a non-common construction technique and the implication of that selection on the structural design parameters and construction tolerances are discussed. The advantages gained of adapting the structural design for the selected construction method and implementing it at the early structural design stage has delivered a 20% reduction in total investment cost.

The development comprises 19,200m<sup>2</sup> of underground parking, 21,200m<sup>2</sup> of ground floor retail and 19,700m<sup>2</sup> of part retail and part carpark upper floor. The significant cost reduction was achieved through the use of the top down construction technique. The design of special steel-encased pile shafts, for belled-end CFA piles to form the basement's columns and the use of short piles with micro fine cement grout to construct a unique reinforced retaining system are discussed. The top down construction technique combined with the use of hollow core planks resulted in a total reduction of formwork exceeding 80% when compared with conventional construction.

The use of post tensioning, significantly reduced the concrete used and a special fibre reinforced floating floor topping was used for facilitate the next stage of development. A lightweight floating floor for the retail area allows for the future replanning and service reticulation of the first floor without impacting the ground floor retail operation. The project was delivered on time and on budget.

**Keywords:** Construction, Sustainability, Innovation, Top down, Design, Economy.

### 1. Background

The Cockburn Gateway Shopping Centre is located in the City of Cockburn, Western Australia, approximately 21 kilometres south of the Perth city centre and 17 kilometres west of the City of Armadale. The development site is located on the south western side of the Kwinana Freeway and Beeliar Drive intersection. The existing Gateways Shopping Centre is located on a 7ha relatively flat site. With the completion of the stage three development of Gateways Precinct Shopping Centre, the shopping area were increased from 26,460m<sup>2</sup> Net Lettable Area (NLA) of shop/retail floor space to a total of 55,050m<sup>2</sup> (NLA) and the non-shop retail floor space was increased from 10,600m<sup>2</sup> (NLA) to 49,490m<sup>2</sup> (NLA)(1).

The ground sub surface profile consists of varying thicknesses of sandy fill overlying naturally occurring Bassendean sand with interbedded Coffee Rock bands. The historical groundwater level is approximately 10m below the existing ground level (2).

The stage-three development comprised 19,200m<sup>2</sup> of underground parking, 21,200m<sup>2</sup> of ground floor retail and 19,700m<sup>2</sup> of part retail part carpark upper floor. The top floor was designed to accommodate future utilisation of the entire upper floor deck as retail area.

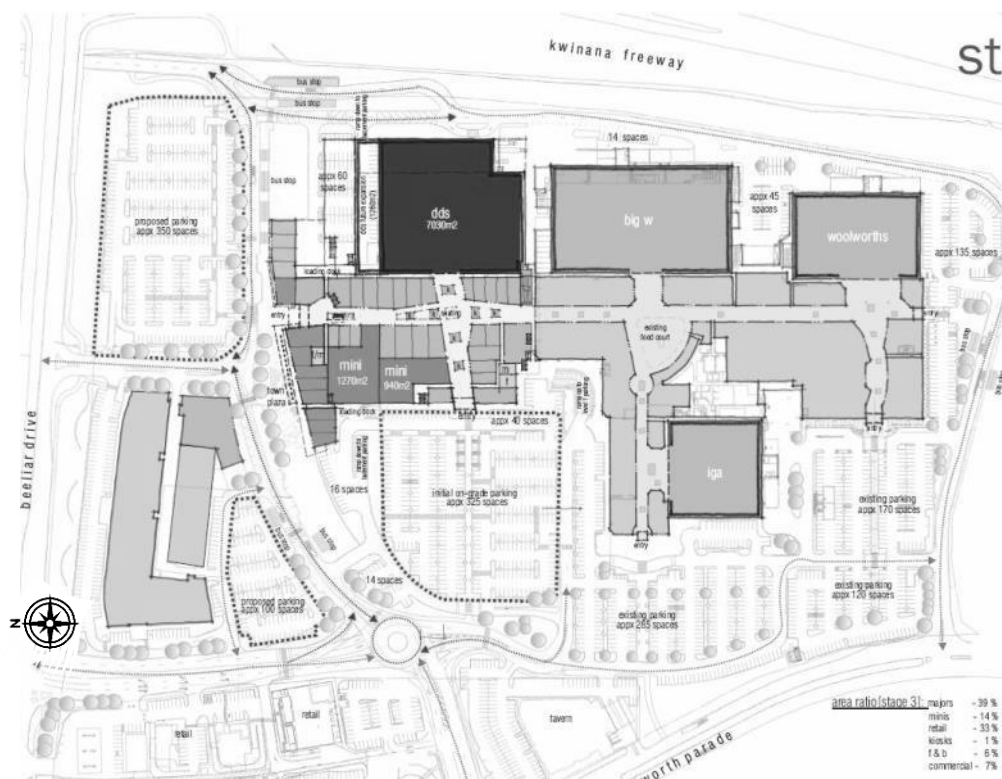
### 2. Construction Constraints

The close proximity of the existing building roads and services to the intended 19,200m<sup>2</sup> underground parking was assessed to add substantial capital cost of underpinning, re-routing of underground services and truck routes, and penalties to major tenants for service disruption and acquiring extra land for accommodate temporary car-parking to maintain normal trading. The cost of these extra requirements was assessed to be prohibitive and commercially unviable; however, without the basement carpark the expansion of the shopping centre was not possible.

To address the space and access constraints, ATC resolved that mining the dry Bassendean Sand in a confined space using small excavators was suitable. The amount of services and finishes are typically limited in a

basement and fall outside the critical path of the project planning, thus the extra time required to complete mining of the sand under the ground floor slab can be easily accommodated.

ATC proposed to the design team an alternative construction method to conventional open excavation; the alternative method employed a tailored top down construction technique that provided the prospect of addressing the operational restraints of the shopping centre whilst achieving substantial reduction in the construction cost and project delivery time without compromising the architectural intent. The alternative presented was based on ATC's past experience with a smaller sized building with comparable site geology, where we successfully developed and implemented similar techniques. The alternative construction method proposed allowed construction of the above ground structural elements to precede the basement excavation, thus facilitating overlapping construction activities and early site access to other trades to fit-out the retail areas while the mining of the basement progressed.



**Figure 1. The expansion to the existing Shopping Centre on Cockburn Gateways Site**

### 3. The Designed Solution

In top down construction, the walls are constructed first to support the excavation and these form the final external structural walls. Permanent piles or wall elements are installed internally between the soil retaining walls to reduce the span of the floor. Next the floor slab is constructed and tied into the walls. The building superstructure construction commences before or during the undercover excavation. The remainder of the excavation is completed under the protection of the top slab. Upon completion of the excavation, the base floor is completed and the services and finishes are installed within the completed structure.

The architect configured the basement using 8,550mm grid spacing in both directions with columns located at the grid intersection. This arrangement facilitates locating three spacious car-parking bays between the columns, with 2,700mm clear car bay width, leaving 450mm structural space for the columns. The same columns continue to support the first floor slab, with the exception of the elimination of 6 columns to form a column free 17,100mm span at the major retail.

A post tensioned floor plate was selected for the ground floor slab. The slab was designed to be cast directly onto the compacted sand. The post tensioning provided economy by reducing the slab thickness requirements

for punching shear and long term deflection as well as facilitating the driving of heavy construction equipment on the slab at an early age, prior to excavating the basement, as the pre-compression introduced increased the slab flexural capacity.

Assessment of the soil bearing capacity revealed the need for large diameter piles driven to a depth of 9.0~10.0m to achieve the geotechnical capacity required to support the column loads. The use of small shaft, enlarged base (belled-end) piles was investigated; 500mm diameter pile shaft with 900mm diameter belled-end base was selected. As the selected pile shaft was larger than the 450mm structural space considered by the Architect, a grouted pile was chosen to facilitate the installation of steel CHS caisson to form a smaller shaft for the exposed section of the pile shaft (407mm O/D).

Using Continuous Flight Auger piles (CFA) along the external perimeter of the basement and casting the Ground floor slab prior to excavating the soil offered the advantage of increased pile rigidity through the rotational restraint imposed on to the piles top end by the slab (Typical connection - Figure 2).

With the increased rigidity it was possible to reduce the diameter and depth of the reinforced piles and use micro fine cement injection to grout the soil block between well separated reinforced piles (Figure 3). The micro fine cemented block formed an infill between the reinforced pile while the reinforced piles provided the necessary wall strength and stiffness.

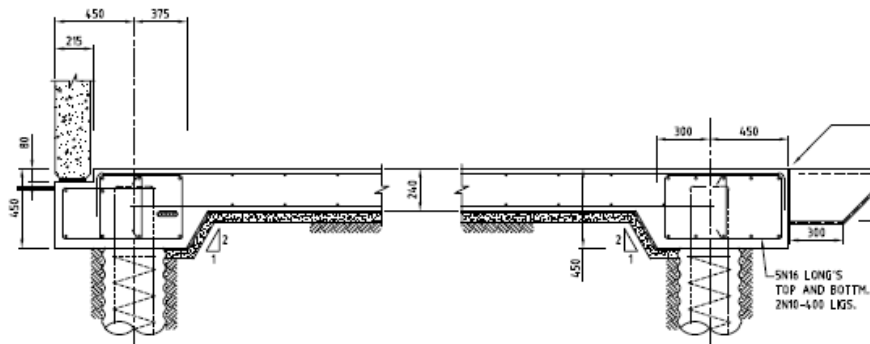


Figure 2, Slab / Retaining wall typical detail.

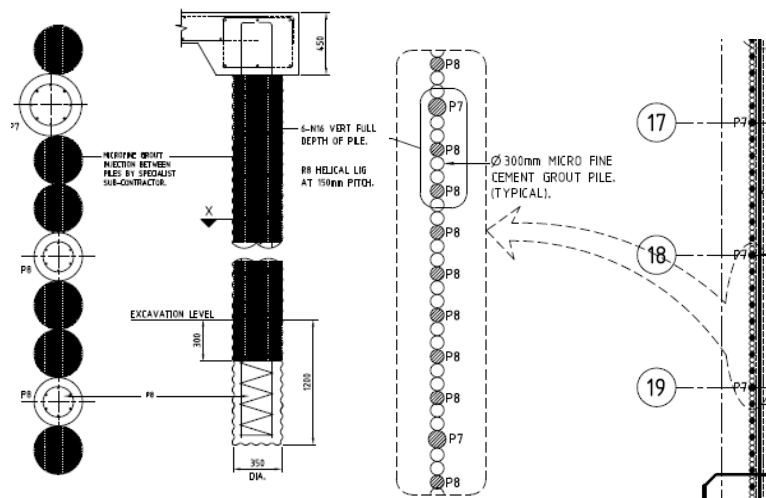


Figure 3, Reinforced cemented-block retaining wall.

#### 4. The Top down Challenge

Top down construction can impose a number of challenges and disadvantages including:



- Limited space and restricted access for excavation and construction of the floor below;
- A risk that the exterior walls (or centre columns) will exceed specified installation tolerances and impact the interior space;
- Potential water leakage through the soil retention system; and
- Inability to install external waterproofing outside the external walls.

Addressing these challenges is outlined below:

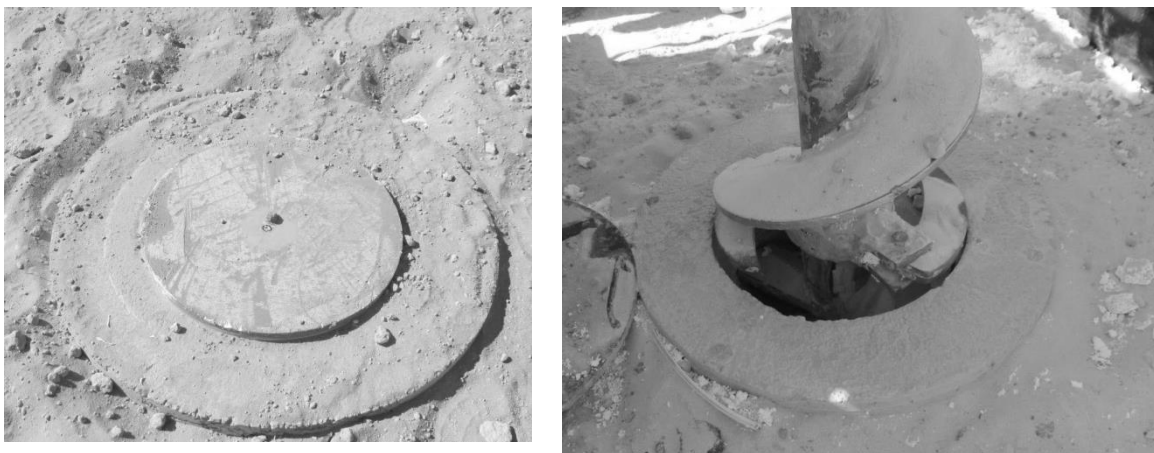
#### **4.1 Confined excavation**

Although the amount of services and finishes are limited in a basement and fall outside the critical path of the project planning, the use of small excavators to complete mining the sand under the ground floor slab was identified by the Builder as a risk factor that has the potential to impact the construction program. To reduce the risk, we looked at increasing the excavated depth between the internal piles to facilitate the use of large excavators. Agreement on the use of large excavators was made following evaluation and adjustment for the reduction in the shaft capacity of the piles due to the extra excavation depth. Mechanical ventilation and air quality monitoring were used at the start of the excavation to exhaust the fuel fumes. The need for the mechanical ventilation ceased once the excavation reached across to the first stair shaft, as natural ventilation provided adequate air flow.

#### **4.2 Installation tolerances**

Replacing the columns and footings with belled-end piles and achieving high positioning accuracy required careful design consideration. The Piling Code, AS 2159-2009 allows for 4% inclination to the vertical (3) in addition to out of position tolerance; if such tolerances were to be allowed, the out of plumb columns would be unsightly and would require architectural clad thus impacting the project cost and the car bay width.

To achieve high control in positioning the piles, the piling contractor elected to cast in-situ concrete guides cast around cylindrical polystyrene foams centred to surveyed pegs. Surveying the top level of the concrete guide prior to pile installation provided the necessary means to achieve high control on the cut-off level. The technique halved the out of position accuracy recommended in AS 2159-2009. Further adjustment was achieved by controlling the lowering of the caisson into the grout. Post construction survey of the projected UC sections of the piles confirmed the conformance of the installed piles/ columns with the tolerances for structures and members recommended in Clause 17.5, AS 3600-2009(4).

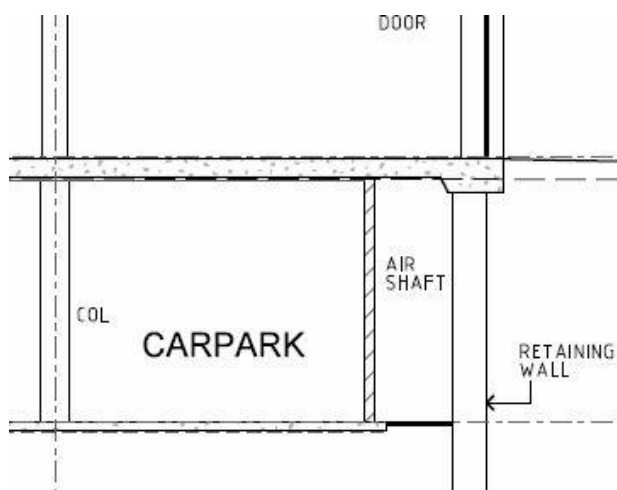


**Figure 4, Pile installation through the cast-in guide.**

#### **4.3 Waterproofing**

Although the water table is a few meters below the basement level, rain and surface water can enter the basement through the rather porous micro fine cement injected sand sections of the soil retention system. Waterproofing the external envelope was achieved through designing a free draining cavity wall around the external envelope. This was achieved by adding internal masonry leaf off the basement slab and maintaining the basement slab short of the piled wall to create a free-draining trench (Figure 5).

This formation was used to construct a plenum to circulate the air in the basement and exhaust the fumes. It was additionally beneficial in addressing the verticality issues and the micro fine cement injection protrusions.



**Figure 5. Detail of the free-draining cavity wall (left); Constructed air-shaft and soil retaining (right)**

## 5. The Structural System

### 5.1 Pile/Column Design

Conventional footings and columns were replaced with belled-end piles centrally located under the ground floor columns, at the grid intersections. Achieving high positioning accuracy was essential to control the load eccentricity imposed on the basement columns and that required careful design consideration.

To address the pile shaft size and verticality issues, the pile shafts were designed to have rigid composite columns rather than conventional steel cages. Steel CHS caissons with centrally located UC sections and interlaid reinforcing cage were used to form the pile within the basement's excavated zone. The composite columns were sized to provide the required ultimate load capacity. Careful detailing of the load transfer zones and the interface between the elements was essential. To address the load transfer between the ground floor reinforced concrete columns and the piles, the central UC sections were extended above the ground floor slab level to achieve the splice length, as shown in Figure 6. The extended UC section had the additional benefit of providing an above ground lever as a measure for checking and adjusting the caissons verticality during installation.

To achieve the fire rating of the basement columns without using fire proofing products, the interlaid reinforcing cages inside the CHS caissons were sized so that, for each pile, the central UC section and the reinforcing cage were capable of providing the fire design load capacity when acting compositely, while the CHS caisson was considered sacrificial in the fire load case. Upper and lower vent holes were provided in the caissons to relieve the hot gas pressure so that bursting of the CHS caissons in the event of fire is prevented(6)(7).

The pile reinforcement was detailed to have independently fabricated site lap spliced sections, a bottom reinforcing cage and an internally reinforced rigid caisson. This arrangement facilitated the lifting of the rigid caisson from a central hole located centrally to the UC section without damaging the rather flexible bottom reinforcing cage. The single point lifting allowed the caisson to act as a plumb bob enabling higher accuracy in achieving the column verticality. 75PFC sections were welded to the central UC section to control the pile cut-off level, guide the installation and enhance the punching shear resistance of the slab, as shown in Figure 7.

To accommodate for the thermal movement of the large floor area, the building was divided into five sections through full movement joints. Due to the use of belled-end piles, doubling the columns along the movement joints was not an option. Instead, all the ground floor movement joints in the post tensioned slab were located 1,650mm off their corresponding grid lines. The movement joints were articulated with high capacity stainless steel shear connectors; this arrangement eliminated the need for doubling the columns and achieved optimum structural design of the post tensioned floor slab through introducing negative bending movement to one end span and shortening the end span of the adjoining plate. (Figure 8 – detail; in Figure 9 – implementation)

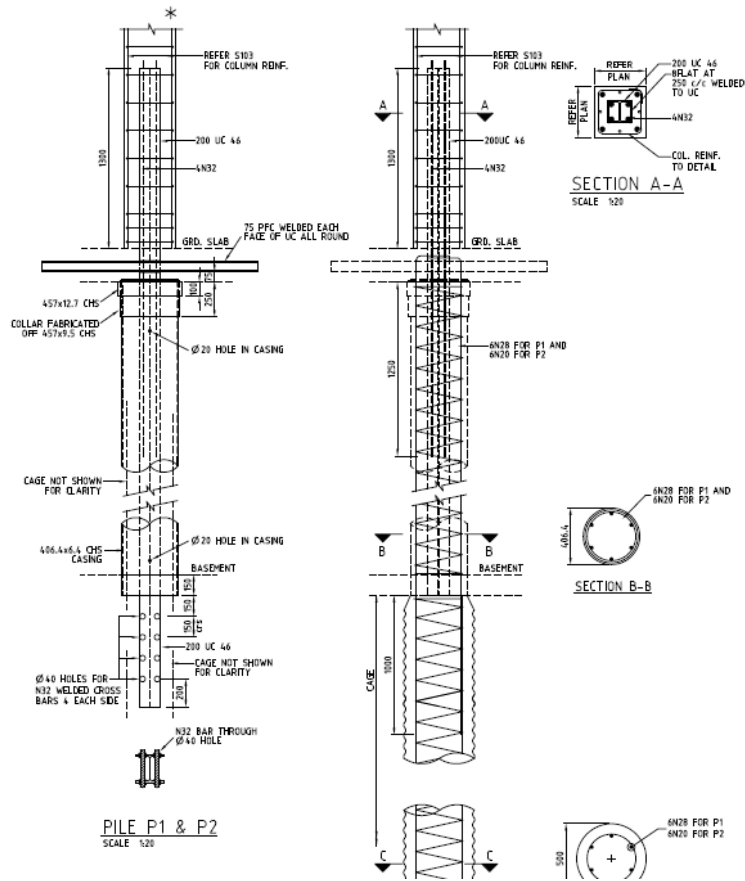
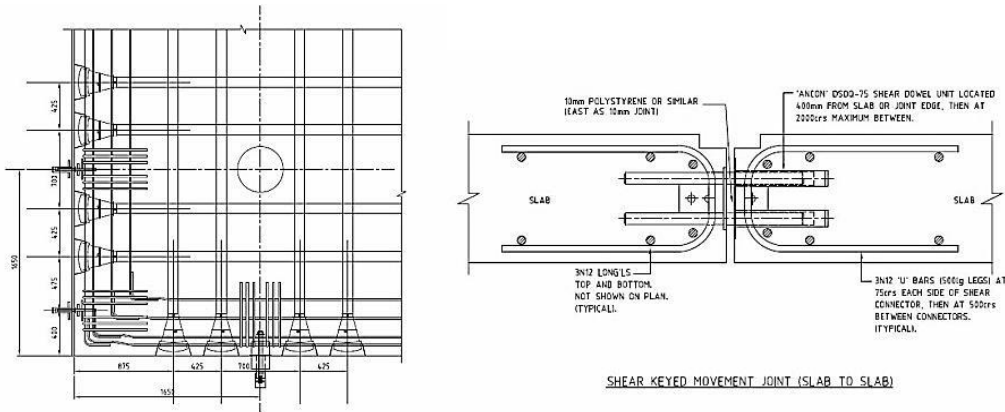


Figure 6. Details of the rigid shaft and the belled-end pile reinforcement



Figure 7. Caisson lifting and cage splicing



**Figure 8. Use of shear connectors at movement and construction joints**



**Figure 9. Offsetting the movement joint from the column line**

### **5.1 Upper Deck**

The ability to drive heavy construction machinery on the ground floor slab prior to mining the soil provided the opportunity to maximise the use of precast pre-stressed hollowcore planks for constructing the first floor deck, thus eliminating the need for long reach cranes. Cast in-situ post tensioned band beams were designed to be monolithically cast with the hollowcore plank topping. This arrangement facilitated the use of linear formwork towers to support the tray for casting the beam base while supporting the installed precast planks. The band beam and precast propping arrangement significantly reduced formwork needs for the upper deck (Figure 10).

Delayed mining of the basement meant large linear loads. As a result of supporting the planks, topping and beams were directly transferred to the soil supported ground floor slab, completely eliminating the need for back propping.



**Figure 10. Linear formwork arrangement for supporting the planks and casting the P/T beam**



**Figure 11. Linear formwork arrangement and use of P/T slab as high-capacity working platform**

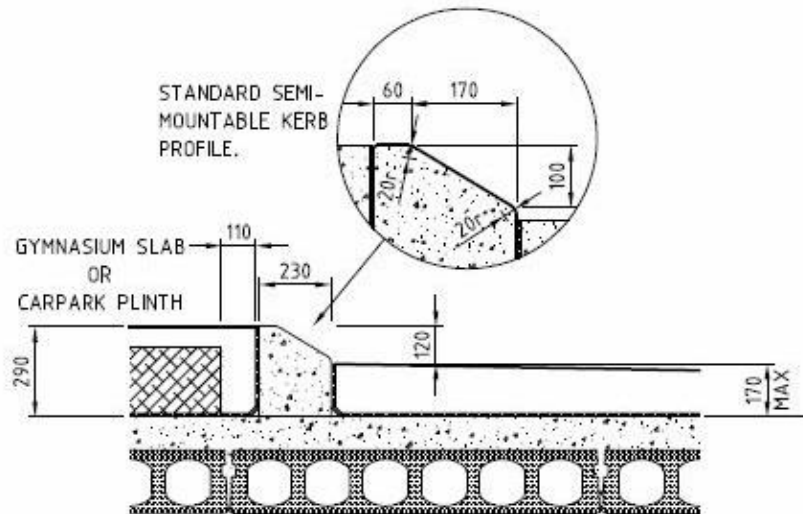
Casting the ground floor slab on compacted soil and the use of proprietary reinforced cemented soil block retaining achieved an 82% reduction in the formwork needs for the project when compared with conventional cast insitu construction.

## **6. Future proofing the deck**

To facilitate the planned future expansion of the retail area, which will incorporate the first floor car parking deck as future retail space, a floating floor was used. The space provided through the floating floor was selected to be sufficient to accommodate the future reticulation of the services above the structural floor. The future services shall be connected to pre-installed service risers. This configuration will facilitate the freedom of future service locations and will not affect the trading of the ground floor retail area.

The 290mm thick waffle floor was designed with 65mm topping (Figure 12 below) which allowed us to incorporate commercially available 1080mmx1080mmx225mm polystyrene void former pans, typically used for construction of raft floors for housing on clay soils. To construct the slab with reduced workmanship the use of steel fibre reinforced concrete at 15 kg/m<sup>3</sup> fibre dose rate, without supplementary reinforcing bars or mesh, was used. This configuration provided the required strength to resist the retail area design loads. The large void ratio of the waffle configuration assisted in reducing the design dead loads for the structure.

An independent plinth to falls was documented for the car parking area (Figure 12) for drainage. By removing the plinth and installing the implemented 290mm thick waffle, the full upper deck plan can be refurbished as retail area at the next phase of the development.



**Figure 12. Floating floor and car bay deck plinth**

## 7. Conclusion

The tendering process revealed the reality of the advantage offered by the tailored top down construction technique as opposed to conventional bottom-up construction for this particular project. Four contractors were invited to price the job. Three of the contractors provided their bid for constructing the building as documented with a variation of less than 5.5% between them, while the fourth bidder was fully against the use of the top down technique and offered an alternative bid to re-design and construct the development at a confirmed price of \$95.5 M. The project was awarded to the lowest bidder for a total construction cost of \$79.7 M, which is 16.5% lower than the alternative conventional construction bid. The construction was completed in 94 weeks, 16 weeks ahead of the alternative conventional construction bid.

The capital cost saving achieved was a direct result of the top down construction technique which delivered the following cost cutting advantages:

- Maintaining road access and securing uninterrupted trading operation to the existing shopping centre during construction of Stage Three;
- Elimination of the need to alter the main service supply route to the operating shopping centre;
- Significant reduction in the requirement to underpin the existing structure;
- Reduction in the excavation volume, backfilling requirements, total cement use and concrete volume and achieving 82% reduction in formwork usage;
- Significant saving in the cost of retaining the soil and eliminating the need for waterproofing the basement retaining walls;
- Maximisation of off-site production; and
- Shorter construction duration by effective overlapping of construction activities and providing an early start to critical path activities.



**Figure 13. Photo illustrating the achieved verticality and alignment of the pile installation**

Furthermore the approach developed achieved higher sustainability through the effective reduction in material usage, construction time and energy usage.

This design offered the owners the advantages of significant reduction in capital cost, lower holding cost and faster return to their investment.

## **8. Acknowledgement**

The writer would like to acknowledge the support provided by Mr Peter Airey and all Airey Taylor Consulting staff for their hard work and dedication in delivering this project. Mr Stuart Coutts and the Engineers of Bepile Australia Pty Ltd were critical in devising the installation technique for internal pile set- out and installation within very tight tolerances that made the construction technique viable.

## **9. References**

1. "Gateways Precinct Local Structure Plan", The Planning Group - WA, Report 708-034, February 2012.
2. Geological Survey of Western Australia. 1:50,000 Environmental Geology Series, Fremantle.
3. Piling – Design and Installation, AS 2159-2009, Standards Australia.
4. Standards Australia, "Concrete Structures", AS 3600-2009, Standards Australia Limited, Sydney, Australia
5. C. Jeremy Hung, PE, James Monsees, PhD, PE, NasriMunfah, PE, and John Wisniewski, PE, "FHWA Technical Manual for Design and Construction of Road Tunnels – Civil Elements", Report No. FHWA-NHI-10-034, March 2009.
6. Michael G. Goode, "Fire Protection of Structural Steel in High-Rise Buildings", Building and Fire research Laboratory, NIST GCR 04-872, National Institute of Standards and Technology, July 2004.
7. S J Hicks BEng, PhD, G M Newman BSc(Eng), CEng, MStructE, MIFireE, "Design Guide for SHS Concrete Filled Columns", The Steel Construction Institute, 2002.
8. B. Matty, BSc, MSc, FIEAust "Cockburn Gateway Stage 3 – Top down Construction" Proceedings of the 26th Biennial Concrete Institute of Australia's National Conference, October 2013.

# An Innovative Solution for Temporary Movement Joints in Concrete Floors

Lance Rogers<sup>1</sup>

<sup>1</sup>Product Development Manager, Refobar Australia

**Abstract:** Temporary movement joints are a complex and common joint used in post-tensioned concrete floors to relieve stresses from elastic pre-compression, shrinkage, creep and thermal effects. Common detail options available for temporary movement joints are pour strips, grouted dowel sleeves and stainless steel connectors. There are many issues associated with these options, including variation in material and site makeup as well as reliability of installation practice and standard site pressures of time and cost, leading to problems impacting joint quality and performance as a direct result. This paper presents the research and development of an innovative solution that has been engineered to eliminate the issues associated with the grouted dowel sleeve and stainless connector options. This latest product innovation is revolutionary as it fulfills all complex technical design criteria aspects as well as site installation reliability and efficiency requirements, whilst being economically advantageous through the use of low cost materials over all other options.

**Keywords:** Post-tensioned, Concrete, Grout, Dowels, Temporary Movement Joint,

## 1. Introduction

A paper written in 2011 titled “Temporary Movement Joints in Concrete Floors”, Sullivan et al (2011), presented the testing of the Grouted Dowel Sleeve System for various grout tube arrangements as well as the final locked tensile strength of various post-tensioned duct sleeve types. It is this prior paper along with its results and recommendations for further development of a proprietary product to resolve the issues, that motivated this paper and the research and development of an innovative solution. The final paragraph of the Sullivan et al (2011) paper quoted a recommendation as follows:

“There is also a possibility of developing proprietary sleeve that allows movement parallel and perpendicular to the joint with low resistance, then allows the sleeve to be grouted (for both load capacity and corrosion protection) including the bar length across the joint, without the necessity of filling the joint with grout.”

Temporary movement joints (TMJ) are a requirement within concrete floor structures to relieve initial restraint within floor plates due to fixed or stiff vertical elements, such as core walls. TMJs relieve this restraint effect to allow concrete to shorten ideally towards one fixed point of restraint, due to the actions of elastic shortening, shrinkage and creep. TMJs are more common in post tensioned floor structures due to the additional shortening actions associated with initial pre-compression elastic effects and long term creep effects.

TMJs are by far the most complex joint type as they are required to allow initial movement in two horizontal directions, the same as a permanent movement joint and then have a facility to lock the joining concrete elements together for permanent structural stability and integrity, similar to a common construction joint. The simpler and preferred design solution to achieve full initial movement and then final locking would be the pour strip. However, practical site installation aspects prove the pour strip system to be most undesirable due to typical site schedules and continuity pressures. As such the Grouted Dowel Sleeve option has proved to be the most popular and desirable option, mostly due to its initial low cost and lack of programme impact. It seems these initial up front time and cost attributes outweigh the immediate to long term issues associated with the Grouted Dowel Sleeve, despite being far less effective due to inherent system flaws and a heavy reliance on installation practices.

The problems associated with the Grouted Dowel Sleeve System, such as sealing and leaking grout, that lead to an ineffective joint, has been recognized for decades in the industry and is either largely ignored or remediated with band aid maintenance repairs such as re-sealing, re-grouting, crack injection and concrete patching. The reason the problem has remained unresolved for so long is down to the complex



nature of the joint itself. To be able to effectively seal and grout after movement has taken place calls upon structural engineers to think outside of standard structural engineering topics: To solve the problem, requires solutions from both mechanical and hydraulic engineering fields as well as material knowledge of plastics and rubbers. The added problem of the joint having an opening potential from a hairline crack up to 20mm or more poses the added problem of grout viscosity and pressure to fill the joint effectively.

Following the previous paper “Temporary Movement Joints in Concrete Floors” by Sullivan et al (2011) which tested and highlighted the issues of the Grouted Dowel Sleeve System, it is concluded that the key objective and desired outcome is to engineer and develop a product to provide a reliable, superior temporary movement joint system to raise the quality and safety of buildings while reducing cost of installation and maintenance. This paper outlines an innovative solution that answers these needs.

## 2. Previous Research

### 2.1 Paper by Sullivan et al (2011)

The Sullivan et al 2011 research paper had a primary purpose of understanding and developing an effective detail for grouted dowel sleeves, as there is limited information and an overall understanding in the post tensioned (PT) industry, both in Australia and the UK, that the current Grouted Dowel Sleeve System has many flaws and failings. The paper investigated four duct types and four grouting methods known within the industry to be common practice. The paper outlined a test procedure, presented observations and test results.

Despite test conditions being naturally more controlled and of higher quality than site conditions, the paper observations highlighted a number of issues relating to the ability to grout the sleeves and joint as follows:

1. **Blockages** – Grout flow from dowel sleeve into the joint is typically inconsistent due to concrete slurry or fines entering between the sleeve and pour 1 concrete face. The paper highlighted difficulty, even in a test environment, to ensure the sleeves were sealed against the first pour. This difficulty leads to concrete slurry entering the sleeve causing a blockage. Blockages were prevalent and random throughout the test sleeves.
2. **Grout Level in Joint and Sleeve** – General site practice demonstrates that grouting operations stop once grout flows out the top of the slab local to the sleeve. Naturally site personnel seek to avoid any cleaning up operations. As suggested by Sullivan et al (2011), the grout settles by flowing slowly along the joint and then settling below the level of the sleeve. This leads to the grout in the sleeve emptying into the joint and unless topped up multiple times as per the Sullivan et al (2011) test, the ducts will remain either empty or only partially filled.
3. **Gout leaking Underside** – The test demonstrated the underside seal to be insufficient causing grout to leak through the underside of the test slab.
4. **Initial movement restraint** – Jacking the test slabs apart to simulate initial free movement and attain a joint gap width of 10mm proved a considerable load of over 0.5T per sleeve in each direction, demonstrating the large amount of restraint in the Grouted Dowel Sleeve System.

The paper observations highlighted that the operation of grouting was a highly complex and sensitive task with many potential issues complicating the process resulting in an inconsistent performance outcome.

In addition there were some limitations to the test; the major limitation was the predetermined joint gap width of 10mm. The test method and setup ensured a 10mm joint opening was provided to enable the grout operator to visually determine if each sleeve had grout flow into the joint as part of the test observations. This process verified some sleeves were blocked from concrete fines, however, in reality the joint width can be as small as a hairline crack width due to the Grouted Dowel Sleeve System containing unreliable frictional restraint qualities. For this common situation a visual inspection would not suffice to witness flow of grout into the joint and places question on whether the joint is adequately filled to ensure fire and durability cover protection to the dowel bar across the joint itself.

## **2.2 Site Practices and Experience**

### **2.2.1 Grouted Dowel Sleeve**

Following the paper written by Sullivan et al (2011) and in conjunction with decades of knowledge and experience in the building industry, the many flaws associated with the Grouted Dowel Sleeve System have been identified below in relation to the two fundamental function requirements of a Grouted Dowel Sleeve TMJ system: Initial Movement and Permanent Lock.

Initial Movement is the first fundamental requirement of a TMJ. The criteria of free movement in both horizontal directions, x-direction for along the joint perpendicular to the dowel crossing the joint, and y-direction for moving away from the joint parallel to the dowel bar crossing.

Final Locking is the second fundamental requirement of a TMJ. The criteria for the joint to have the ability to lock two neighboring concrete elements together by grouting the dowel bar sleeves at a predetermined point in time, often 28 days after pour 2 concrete element has been cast.

The Grouted Dowel Sleeve System is simply a dowel bar (typically N grade 500 reinforcement) usually two meters long that has half its length installed and cast mid depth of the first concrete element pour. The second half of the dowel bar in the second concrete element pour is then sleeved with duct (either flat PT duct or round PT Duct). A grout tube arrangement is installed with the duct to facilitate the grouting and locking criteria at a later point in time.

Due to the many issues involved and interconnecting with the two function requirements, the issues will be explained per installation step.

### **2.2.2 Grouted Dowel Sleeve Issues**

**Stage 1 Pour 1 – Install Dowel Bar** –The first step is to drill an appropriate size hole in the edge form in order to pass half the length of the dowel bar through before chairing the end of the dowel bar to ensure the bar remains horizontal.

**Stage 2 Pour 2 – Install PT Duct** – The second step of the site installation process is to cut appropriate lengths of PT duct to sleeve the dowel bar protruding from pour 1.

Site manufacturing inconsistency is a major issue of this method as the dowel bars are all installed individually to slightly differing lengths protruding from the joint. In addition each sleeve is individually cut with a grinder or similar, which creates two problems, inconsistent lengths and inconsistent angle of the cut (i.e. not exactly 90 degrees). The combination of this site manual material preparation and installation leads to the following issues.

- **Sleeve Length not matching the Dowel Length** – When the sleeve is short a gap is left at the joint location. This gap allows concrete fines and often aggregates (with gaps of up to 30mm and more) surrounding the dowel bar at the joint face. This restricts the dowel bar and therefore the concrete elements moving in the x-direction along the joint generating a portion of restraint in the y-direction as well (depending on the gap width and amount of concrete slurry that has travelled up the duct).
- **Sleeve Cut Angle** – The cut is often roughly judged or measured, with each sleeve individually cut with a grinder or similar. This means each sleeve is slightly unique, close to 90 degrees though with a range of margin of error. As a result the duct often meets the joint face with a gap to one side allowing concrete fines and often small aggregates into the sleeve surrounding the dowel bar to block the duct sleeve. Again this restricts the dowel bar and therefore concrete element moving in the x-direction along the joint and generates a portion of restraint in the y-direction as well.
- **Sleeve Damage** – Often the typical flat PT duct is used which has an inside diameter of 19mm. In order to slide the duct over an N20 deformed reinforcement bar it is common for the duct to be manually manipulated out of shape. The result is a damaged piece of duct sleeve that is held to one or more sides of the dowel. In addition it is not uncommon for both flat and round duct to be trampled and so damaged in any case. All causing increased initial restraint.

- **Sleeve Horizontal** – Often the sleeve will not be installed horizontal. Transvers to the dowel bar (rotating about the dowel bar), it is not uncommon for the flat duct sleeve to be installed at a slight angle as there are limited means to ensure the light weight duct is not knocked or tied correctly from rotating. In addition, dowel bars, usually N20 (i.e. stiff bars) are not protruding horizontally from the face of the pour 1. These issue cause restraint and impact on the initial free movement requirement.
- **Sleeve Centralized Flat Duct** – It is extremely rare and uncommon for the dowel bar to be centralized within the flat duct as there is no real material system to achieve this. As such the dowel bar is often resting to one side and of course each dowel bar and adjacent sleeve will favour a random side. This deems any movement in the x-direction impossible and therefore causes restraint in the x-direction.
- **Sleeve Centralized Round Duct** – Evidence shows a similar issue as described above also occurs in the round duct, as the round duct is often damaged (squashed out of shape) making the requirement of initial free movement even clumsier. In addition, when the round duct is not damaged, the duct mostly hangs on the dowel bar so that the dowel bar is central at the top of the round sleeve. This means the concrete element the sleeve is encased in (pour 2) must move vertically upward in order to move in the x-direction. The forces due to self-weight are too great and so the system retains restraint in the x-direction.

**Stage 3 Pour 2 – Install Grout Tubes** – The third step of the site installation process is to cut and install appropriate lengths of PT grout tubing to the sleeves to facilitate the later grouting phase to lock the joint. Issues related to this phase are:

- **Grout Tube Arrangement** – There are a few different grout tube arrangements that Sullivan et al (2011) tested. Some arrangement can cause air void issues due to their arrangement design, however all arrangements have a potential of air voids due to blockages at the sleeve joint interface as described above.
- **Sealing Grout Tube & Duct** – Once the grout tube is installed, the end of the sleeve away from the joint must be sealed, again there are various ways and methods and likely left to what is available on site. A common method is duct tape, another is expanding foam. Both can be unreliable and completely open to the site operator installation practice per sleeve. I note the expanding foam is dangerous as it is quite difficult to judge the amount of expansion, which could potentially fill the sleeve.

**Stage 4 Pour 2 – Grouting** – The forth and final step of the site installation process is to grout the dowel bar sleeves and joint. This is by far the most crucial, however most complex stage.

- **Grout Joint and Sleeve Together** – The largest fundamental flaw of the Grouted Dowel Sleeve System is that it relies on the joint being grouted at the same time as the dowel sleeve. With the inconsistencies explained above coupled with the joint gap opening being inconsistent due to the systems inherent restraint issues explained above, then adding into the mix a reliance on the underside and edges being sealed sufficiently and effectively, make this process very unreliable and as shown in Sullivan et al (2011), often ineffective.
- **Sealing Underside** – There are no real set methods for sealing the joint on the underside and vertical edges to the joint and so each builder often try's their own solution. This makes the process unreliable and difficult to achieve. Typically a spotter has to be under the joint to spot any leaks and attempt to stop them as soon as possible. This can be quite messy, frustrating and sometimes impossible after grouting has begun.
- **Grout Pressure** – The pressure of the grout differs throughout the routable spaces. For example the size of the grout tube compared with size of the joint compared with the space in the sleeve and gaps through blockage zones. Ultimately this leads to the grout finding its way through the path of least resistance and so the path of most resistance is not filled of contains air voids. As per the testing results of Sullivan et al

(2011), which demonstrates all duct types and grout methods show the possibility of both air voids in the dowel bar sleeve and joint gap.

- **Blockages** – The above points regarding variance in dowel/sleeve length and sleeve cut angle and overall inability to seal the sleeve to the pour 1 concrete face, cause blockages that restrict the flow of grout into the joint and depending on the type of grout tube arrangement can result in the dowel sleeves being only partially full. This reduces the capacity of the tensile strength of the joint for the permanent locking.

### 2.2.3 Grouted Dowel Sleeve Consequences

Due to the above outlined issue there are a number of consequences to the Grouted Dowel Sleeve System:

- Corbels are required for all Grouted Dowel Sleeve System joints
- Labour inefficiency due to multiple sealing, grouting and cleanup activities
- Cracking (Initial) due to initial horizontal movement restriction (restraint)
- Cracking (Ongoing) due to insufficient grouting (locking) of the dowel sleeve
- Safety Risk Corrosion of dowel bar due to insufficient joint grout protection
- Safety Risk Fire to dowel bar due to insufficient joint grout protection
- Safety Risk structural stability of building reliant on joint transferring load

The above consequences outline that the Grouted Dowel Sleeve System has a number of manufacturing and installation inconsistencies that prove the system is an extremely low quality system and approach that is highly reliant on site manufacturing and installation practice, that even if perfectly installed such as the earlier test environment of Sullivan et al (2011), still contains all of the issues jeopardizing the quality and structural integrity of buildings long term. The system is definitely the most economical to initially install, however has the possibility of initial and long term maintenance issues associated that will often be ignored or missed years down the track.

### 2.2.4 Stainless Steel Option

There is a proprietary stainless steel product option available, however this option also relies on the joint being sealed and grouted effectively, which has similar sealing and joint gap width difficulties associated as the Grouted Dowel Sleeve System. In addition the product is extremely costly in comparison due to the stainless steel material used and therefore avoided and not preferred in the industry.

## 3. Product Development of an Innovative Solution for TMJs

### 3.1 Overview of the Innovative Solution for TMJs

The original innovative solution was initially conceived and designed for the “Slab to Slab” temporary movement joint connection type. Then as the product development stages unfolded the product range evolved to incorporate a “Slab to Wall” option, that allowed for both a compression situation, where the concrete slab element can move toward a wall structure (i.e. back of a core) and the standard tension situation pulling away from a wall. For ease of understanding, the full innovative solution range is best demonstrated in Figure 1 below.

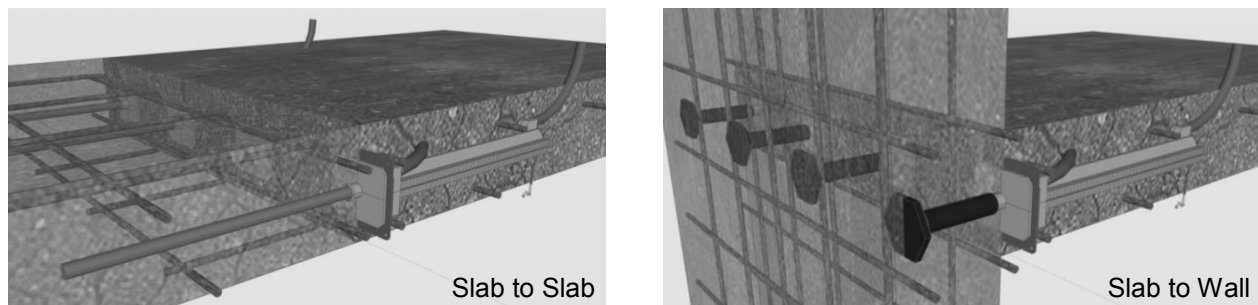


Figure 1. Product Innovation – Applications

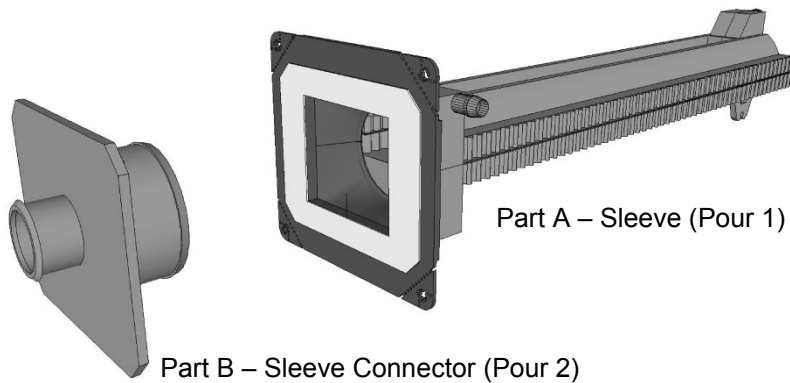
### 3.2 Prototype Design Development & In-House Testing

Prototype development occurred in conjunction with in-house testing over a period of 3 years from 2011 to 2014. There were a total of 8 prototypes manufactured each with their respective in-house testing regimes until the innovative solution had achieved all design criteria requirements set out in the beginning as follows:

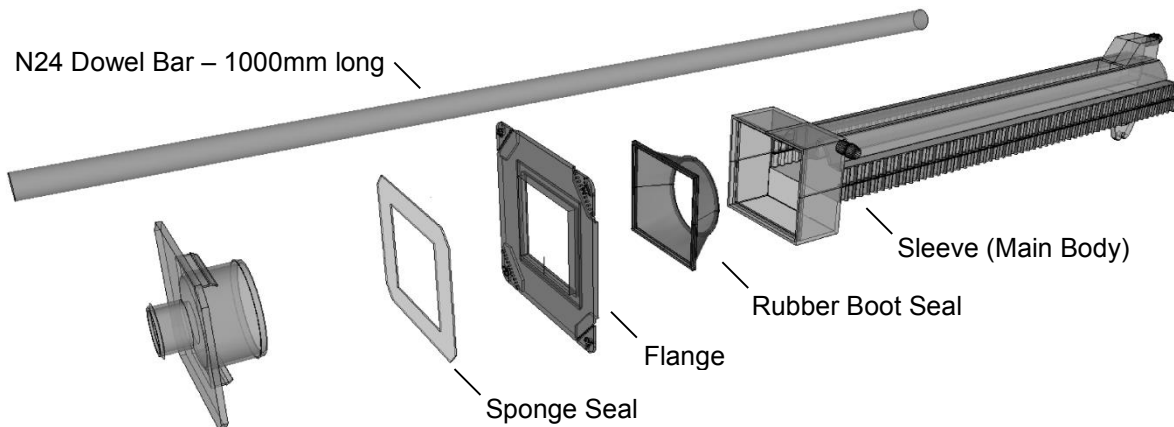
#### Innovative Solution Design Criteria

1. Initial Horizontal Movement – 10mm transverse (parallel to joint) movement prior to grouting
2. Initial Horizontal Movement – 20mm pull out (perpendicular to joint) movement prior to grouting
3. ZERO vertical movement in the grouted permanent state
4. Vertical shear capacity in the un-grouted temporary state and grouted permanent state
5. Watertight leak resistant seal during and after all temporary movement has taken place
6. No reliance on joint being sealed or grouted to provide minimum cover for durability (corrosion) and fire protection to reinforcement dowel through the joint
7. Economic materials – Use plastics rubbers mild steel (i.e. avoid stainless steel or galvanizing)

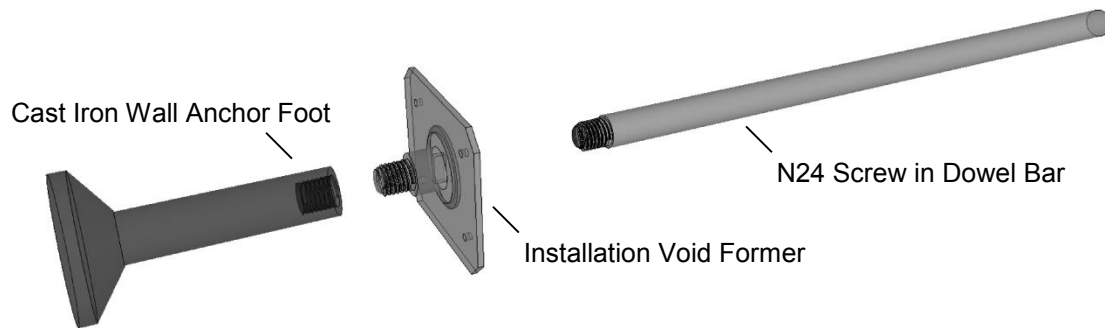
There were various developmental features that were engineered into the innovative solution over this period to achieve either a design or practical functional requirement. The following briefly describe some of the primary features in line with Figures 2, 3 and 4 below for clarity:



**Figure 2. Product Innovation – Assembled**



**Figure 3. Slab to Slab – Exploded View**



**Figure 4. Slab to Wall – Additional Parts**

**Rubber boot seal** – The rubber boot seal is arguably the most intelligent part of the product innovation as it primarily functions as a seal between the two sides of a temporary movement joint. The seal has two sealing ends; the first is the rectangular end that is mechanically locked into Part A of the product during the manufacturing process. The second is the opposite end of the rubber boot, which is a circular pressure seal that grips Part A (Pour 2) of the innovative solution. The secondary function of the rubber boot seal is to have the ability to stretch and compress in order to remain fully sealed while allowing movement in both horizontal planes. The thin rubber web between the two sealing ends is flexible enough to move in both horizontal directions while being robust enough for site installation purposes.

**Joint Zone Cover** – The second major feature is the cylinder section of Part B (Pour 2). This cylinder represents the potential joint opening zone, where the joint and product has the ability to open up to at least 30mm and even further with the rubber boot inverted, however the inverted position has not been seal tested and is unlikely to be a requirement as a horizontal slab element would have to be greater than 120m between fixed elements such as core walls and shear walls. The reinforcement dowel bar remains central to the cylinder at all times throughout any movement as the dowel bar and Part B move together with pour 2. The result of this design is that the dowel bar retains the initial 20mm cover around the dowel bar in the joint zone prior to and after grouting. This negates the need to grout the joint to provide protection to the dowel bar in the joint zone.

**Grout Integrity** – A major design focus and therefore feature of the innovative solution is the reliability of the sealed product to be fully grouted. As such, the products distinguishing twin grout rails are a major physical feature of Part A, refer Figure 3 top of the sleeve main body. There are three design aspects to the twin grout rails that ensure the product performs both technically and practically.

- 1) The top height of the grout rails in Part A represents the filled level of grout in the product, which is also the same height as the top level of the cylinder in Part B. This ensures the dowel bar has grout filled to the full cylinder height providing grout cover for durability and fire protection through the joint. Similarly, the box section of Part A has been design to contain a small void zone for any air bubble turbulence while grouting and facilitate the rubber boot initial movement function.
- 2) Secondly, the grout inlet and outlet ports have been designed at a higher level than the top of the twin rails and cylinder to ensure the product is completely filled before grout exits the product.
- 3) Finally the inlet and outlet ports have been design to be on one side of the joint (pour 1). This eliminates any confusion with a looping arrangement that would otherwise be required when installing Part B in pour 2. The inlet and outlet ports on one side also facilitate the slab to wall product option and retain the same product pieces for both “slab to slab” and “slab to wall” options.

**Shear Capacity** – The purpose for the two grout rails (twin rails) is to provide an upside down pyramid zone above the dowel bar to achieve an un-grouted shear capacity. The pyramid zone contains concrete directly above the dowel bar and also works in a reverse shear capacity situation as well.

**Tension Capacity** – In order to achieve maximum dowel bar tension resistance many concepts were tested, with the resulting design consisting of two waved edges to increase the friction, however maintaining flat top and bottom surfaces to ensure both un-grouted shear capacity and no air voids other than the purposely design air void space.

**Other minors** – There were many other minor design features that provide design protection from the practical installation rigors. For example the two clips on Part B provide a mechanism for the installer to plug Part B into Part A, with a guide and robust clipping feel to assert the parts are successfully engaged. The corners of the flange to Part A have a primary and secondary tear away feature in case the product is screwed to the formwork as opposed to installation advice to nail. The primary perforations mimic the natural failure path demonstrated by in-house testing. Also the grout inlet and outlet ports are integral and part of the main body injection molding. This provides a robust port to resist the rigors of site installation practices.

### 3.3 Laboratory Testing

In addition to the 3 years of in-house prototype development and testing, it was decided to engage a 3<sup>rd</sup> party university laboratory to carry out a series of tests to confirm the products actual capacity in shear and tension strength. The testing method and project also formed a thesis topic for a student capstone project. Full details of the project and testing results are documented by Boland (2014), however the main tests and results will be briefly outlined below.

- 1) Un-grouted Shear Test
- 2) Grouted Shear Test
- 3) Tension Test

**Un-Grouted Shear Test** – This test stage had been designed to replicate the possibility of a worst case scenario on site when activities of stripping formwork and progressive back propping occur. Typically this transpires in a post tensioned structure after final stress, extensions approved and cut/seal of pockets has occurred. The final stressing requirement is for the slab concrete element strength to reach 22Mpa or 25Mpa depending on the post tension system used. The un-grouted test was therefore performed at 22Mpa.

**Grouted Shear Test** – This test stage had again been design to replicate the design requirement for the grout in the product to be 40Mpa. Due to limitations in laboratory time, this stage had to occur slightly earlier than desired when the grout had only reached 28Mpa, rendering the results slightly conservative.

**Tension Test** – Again this stage had been designed to conduct the test at 40Mpa, however had to occur at 28Mpa.

A situational calculation was carried out to determine a desired capacity for the product within a residential loading scenario, 200mm thick slab, 8m x 8m span and the product spaced at 600mm centres. This calculation determined the desired shear capacities were **10.4KN** for the Un-grouted case and **12.8KN** for the grouted case per product (service loads).

The test setup configuration of the two shear tests involved loading adjacent to the joint via LC3, refer Figure 5 below. A frame analysis programme was used to determine the theoretical load through the joint dowel, and then compared to actual load cell readings for data validation. Refer Figures 7 and 8 below which demonstrate the theoretical load through the joint dowel is 80% and 55% lower than LC3 for the un-grouted and grouted case respectively. It is noted the un-grouted case utilizes 4 points of reaction support due to the hinge nature and only 3 points of support for the grouted case due to the joint being locked via grouting.

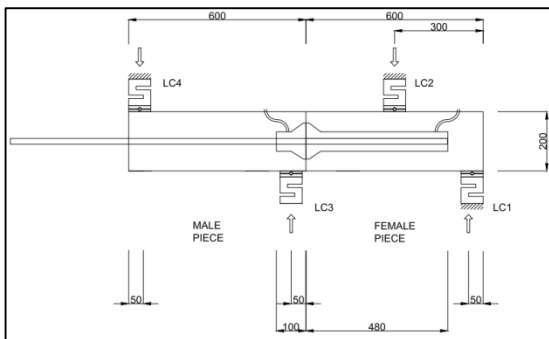


Figure 5. Shear Test Set Up

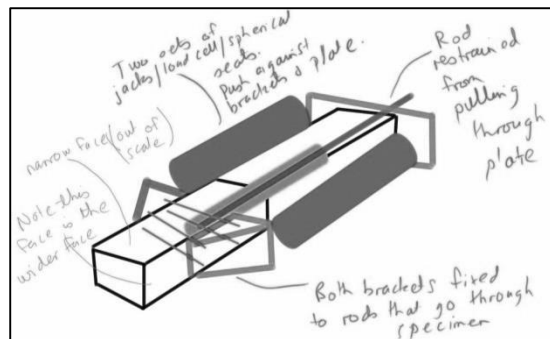
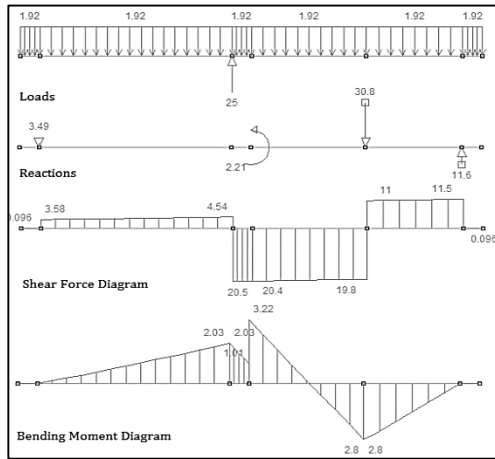
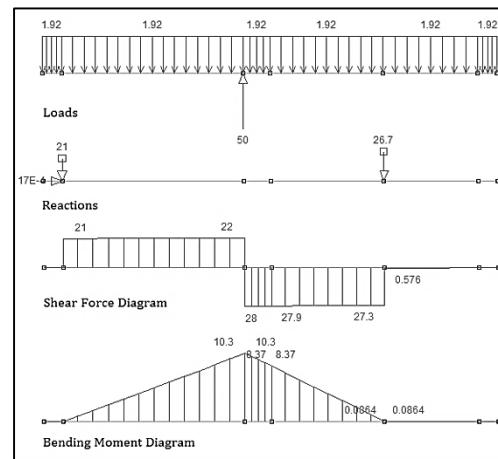


Figure 6. Pull out Test Schematic





**Figure 7. Theoretical Un-grouted Model**



**Figure 8. Theoretical Grouted Model**

Results in Tables 1 and 2 below show a comparison of the actual load through the dowel at the joint location compared to the theoretical models, for data validation.

The un-grouted test contained an anomaly in test 3 which could not be explained. By omitting test 3 results it is observed that test 1 and 2 are similar to the theoretical model calculation which validates the data and confirms an overall minimum factor of safety (**FOS**) of **1.96** has been achieved (20.4/10.4). It is noted the maximum FOS is unknown as the un-grouted case was not tested to destruction. It is noted that test 1 had errors for LC1 and LC2 as a result of the load cell rotating due to a lack of rollers under the pin, this was introduced for all following tests.

The grouted test results were very consistent and similar to the theoretical model calculations which validated all data. It is noted that the 3 tests reached different maximum shear results as the first test was to destruction, reaching **50.9kN** and the following 2 tests were restricted to preserve the specimens for the following tension tests. The following 2 grouted shear maximum loads were **39.2kN** and **27.9kN** respectively. Therefore, the **minimum FOS is 2.18** (27.9/12.8), with a **maximum FOS potential of 3.98** (50.9/12.8).

**Table 1: Comparison of Un-Grouted Results**

<b>Summary @ 20.4kN</b>	LC1 (kN)	LC2 (kN)	LC3 (kN)	LC4 (kN)	Self-Weight (kN)	Sum of Forces (kN)	Shear Force (kN)	Vert. Disp. (mm)	Horiz. Disp. (mm)
Theoretical	11.6	-30.8	25.0	-3.5	-2.3	0.0	20.4	-	-
Test 1	14.7	-34.1	25.0	-5.3	-2.3	-1.9	-	3.9	5.6
Test 2	13.8	-30.1	25.0	-5.9	-2.3	-0.5	-	5.2	5.6
Test 3	15.9	-31.0	25.0	-	-2.3	-	-	3.3	6.0
Average	14.8	-31.7	25.0	-5.6	-2.3	-1.2	-	4.1	5.7

**Table 2: Comparison of Grouted Test Results**

<b>Summary @ 27.9kN</b>	LC1 (kN)	LC2 (kN)	LC3 (kN)	LC4 (kN)	Self-Weight (kN)	Sum of Forces (kN)	Shear Force (kN)	Vert. Disp. (mm)	Horiz. Disp. (mm)
Theoretical	0.0	-26.7	50.0	-21.0	-2.3	0.0	27.9	-	-
Test 1	0.0	-26.7	50.0	-20.6	-2.3	0.4	-	0.2	0.6
Test 2	-0.3	-26.0	50.0	-21.2	-2.3	0.1	-	1.5	0.7
Test 3	0.0	-26.1	50.0	-21.0	-2.3	0.6	-	1.6	0.7
Average	-0.1	-26.3	50.0	-20.9	-2.3	0.5	-	1.1	0.7

There were 3 tension pull out tests, however 1 test had a bracket failure and was therefore omitted from the results. The remaining 2 tests achieved an average pull out tension capacity of 142.4kN with a grout strength of only 28Mpa.

### **3.4 Consumer Testing**

Following the success of laboratory testing the product was then trialed on one joint of a live project. The site testing plan was to investigate installation practicality and grouting practice. Observations from the installation lead to a minor modification to add a clip in chair to the product to speed up the installation process even further. Grouting was a success with no leaking.

## **4. Conclusions**

Overall, the 3 years of development and in house testing allowed multiple engineering modifications of the innovative product solution to occur to ensure the product evolved such that the full technical design criteria and practical site installation criteria were met. University laboratory testing has proved the product has a substantial shear and tension capacity, which can be utilized given a chosen factor of safety. The product application covers both a “Slab-to-Slab” connection and “Slab-to-Wall” connection, without the need for a corbel support. The product has been designed as a sealed unit that provides reliability of grouting and cover to the dowel bar across the joint, eliminating the need to seal and grout the joint. The innovative solution therefore meets the challenge posed by the previous paper Sullivan et al (2011), creating a high quality, professional TMJ product that will raise overall joint quality, performance and therefore building excellence.

## **5. Acknowledgement**

The author thanks all of the individuals involved from both SRG Limited and Refobar that contributed to the innovative product solution development as well as the cost involved.

The author thanks University of Technology Sydney for the use of their laboratory facilities, guidance with respect to the testing parameters and for their co-operation

The views expressed in this paper, and any errors, are those of the author.

## **6. References**

1. Sullivan et al (2011)., “Temporary Movement Joints in Concrete Floors”, Proceedings, 25th Biennial Conference of the Concrete Institute of Australia, Perth, Australia, Concrete 2011.
2. Boland (2014)., “Development of ‘SureLok’ a New Temporary Movement Joint Sleeve (Shear & Tensile Capacity Testing and Assessment)”, University of Technology, Sydney.

# Officer South Sewage Pumping Station – A Diaphragm Walling Case Study

Marc Peril<sup>1</sup> and Jaya Weerasinghe<sup>2</sup>

<sup>1</sup>Network Quality Manager, South East Water

<sup>2</sup>Chief Engineer (Structural) Asia Pacific, MWH

**Abstract:** Officer South Sewage Pumping station is a critical component of the \$40 M Pakenham Narre Warren Sewerage scheme to transfer sewage flows from Officer and Pakenham to Melbourne. Designed and constructed by the 'US' Alliance on a fast-tracked program, it is South East Water's largest sewage pumping station. It includes two large in ground water retaining structures in close proximity: A 12 m diameter 13 m deep circular shaft, and a 30 m by 11 m, 6 meter deep rectangular tank. Both constructed using diaphragm walling, enabling incorporation of temporary ground support into the permanent structures, and minimisation of formwork and falsework. Consequently, creating substantial time and cost savings and enhancing safety. Diaphragm walling enabled safe and rapid construction below the ground water table whilst achieving the required degree of water tightness to facilitate subsequent epoxy coating. Design of the diaphragm walls was based on the approach outlined by the ICE Specification for Piling and Embedded Retaining Walls. This proved particularly useful for delineating responsibilities of: the permanent works structural designer; diaphragm wall designer; diaphragm walling contractor; and site manager. It also mandated development and use of a walling manual, critical for safety control. The walling manual documented constraints on construction sequencing and lateral wall movement limits to monitor safety of the structures in the temporary condition. Inclinator tubes cast into the tank diaphragm walls were used to monitor wall movements against limits set in the walling manual. This supported validation of the design and proved safety of ground support during construction.

**Keywords:** Diaphragm wall, risk management, liquid retaining, sewage pump station, shaft, tank.

## 1. Project Background

The Officer South Sewage Pumping Station (SPS) is South East Water's largest SPS facility. It is a key link in the Pakenham-Narre Warren transfer scheme from the Pakenham Sewage Treatment Plant to the Eastern Treatment Plant (Bangholme, Melbourne). The \$17 M SPS project was a fast-tracked design and construct project delivered by the 'US' Utility Services Alliance made up of South East Water, Thiess Services, Siemens and design partner MWH. Other key members of the project delivery team included the diaphragm walling specialists Piling Contractors and their structural design subcontractor MJ Civil. This paper focuses on the application and integration of the diaphragm walling method to the construction of the main structures:

- a 13 m diameter, 12 m deep wet well shaft (Hereinafter referred to as the shaft); and
- a 30 m long x 11 m wide x 6 m deep 1.2 ML flow control tank with provision for expansion to 3.6 ML in the form of two additional tank cells (Hereinafter referred to as the tank).

### 1.1 Intent of this paper

This paper aims to present a project case study and share lessons learned from our experience of applying diaphragm walling technology to the construction of liquid retaining structures in the Australian context. It is written from the perspective of a generalist civil engineer and diaphragm wall procurement client. It is aimed at those new to diaphragm walling considering its application, however a basic understanding of the technique is assumed.

### 1.2 Diaphragm walling construction methodology

Diaphragm walls are reinforced concrete walls constructed in ground as a series of panels. A diaphragm wall panel is a reinforced concrete cast in-situ or precast wall panel installed within a pre excavated trench supported by bentonite slurry. Diaphragm walls are typically excavated using specialist grabs or hydrocutters. Trenches are set out at surface or working platform level using temporary cast in-situ guide walls. Once the desired excavation depth is reached, a prefabricated reinforcing cage including tremie pipes is lowered into the trench. Concrete is then placed in the trench from bottom to top via the tremie pipes within the reinforcing cage. The tremie pipes are gradually withdrawn as the concrete is placed. The trench walls act as formwork for the diaphragm wall and the heavy bentonite fluid serves as trench support both during excavation and during the concrete pour until it is totally replaced by concrete.

Diaphragm wall panel joints are sealed with water stops. Stop ends or metal forms are used at the edges of panels to hold water stops and maintain their position during concrete placement. Stop ends also protect the cast panel from damage whilst the adjacent panel is being excavated. Once an adjacent panel has been excavated, the stop end is removed laterally. This exposes the remainder of the water stop prior to concrete placement.

### 1.3 Author involvement

At the time of the project, Marc Peril was employed by MWH as a senior civil engineer and was the Design Manager for the Officer South SPS project. He is currently employed by South East Water. Jaya Weerasinghe was the permanent works structural lead and project structural reviewer.

## 2 Design Phase

### 2.1 Wet well shaft

The wet well shaft has an internal diameter of 12 m and a depth of 12 m (internal). Originally conceived as a rectangular shaft, it was changed to a circular shape to take advantage of its inherent structural efficiency and for ease of construction. The shaft comprised of three chambers: an inlet drop chamber and two wet wells each housing submersible sewage pumps. The chambers are separated by an internal tee wall from the base slab to cover level. Flow between the inlet chamber and either wet well is through base slab level penetrations controlled by penstocks to enable isolation for maintenance access. Closing of the penstocks applies hydrostatic loading to the internal tee wall. The tee wall also supports the 14 precast concrete panel/beam system which makes up the pump station shaft roof. The floor of the pump station shaft also includes substantial secondary concrete benching intended to optimise pump station operation. Figure 1 shows the wet well shaft layout.

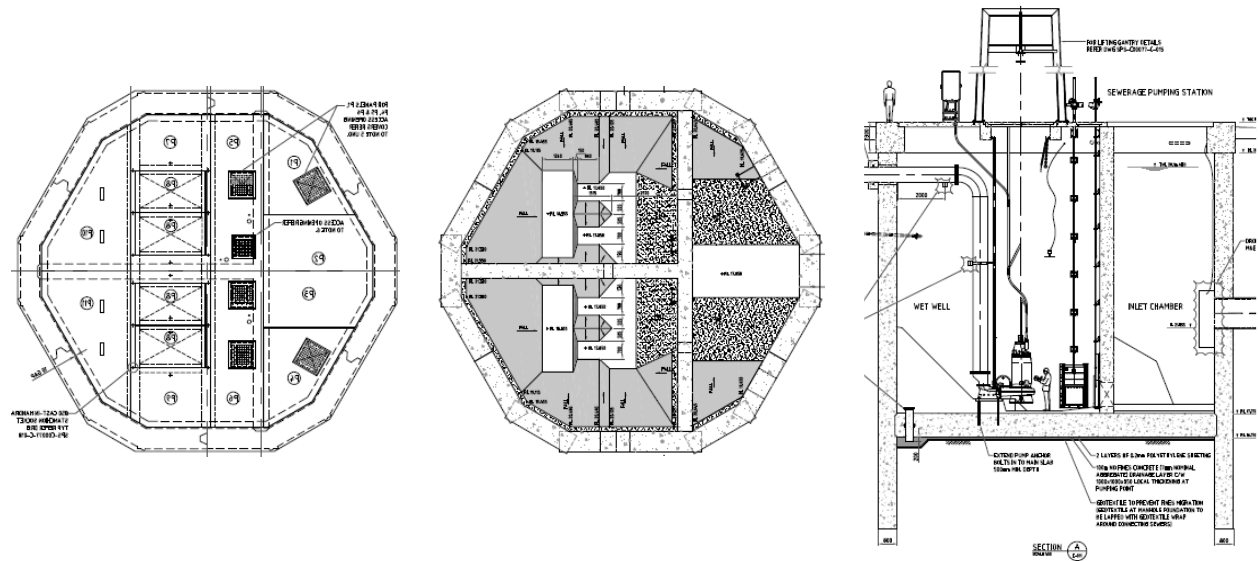


Figure 1. Officer South SPS wet well Shaft. From left: cover plan, benching plan, and section

### 2.2 Detention tank

The SPS facility also includes an in ground detention tank to attenuate peaks in flow and store flows in emergency scenarios. The detention tank is normally empty. The detention tank was planned to be developed progressively in stages. The first stage of development required an operational volume of 1.2 ML. At ultimate development, an operational volume of 3.6 ML is required. The first stage 1.2 ML detention tank is a single rectangular cell with internal dimensions of 30 m x 11 m and 6.25 m depth. The ultimate detention tank was originally conceived as comprising three rectangular cells with a common base slab and shared long walls.

Each detention tank cell includes four internal struts at roof level to prop long walls and support the roof system. The floor of each detention tank cell includes a secondary sloping concrete screed to facilitate cleaning and draining. Figure 2 shows the tank layout (Stage 1 only).

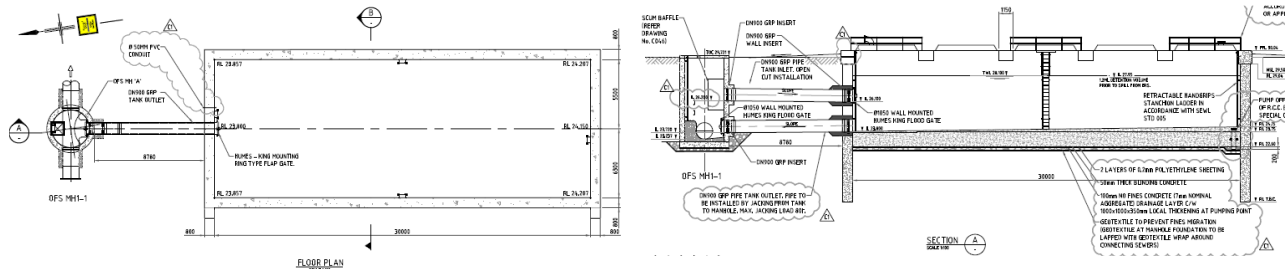


Figure 2. Officer South SPS detention plan and section

### 2.3 Ground conditions

The site geology encountered was predominantly clays with interbedded sands and silts. Of particular concern was a water bearing sand layer below the shaft at 14.5 m depth, 1.5 m below the shaft base. The water table was encountered at a depth of 3.5 m. Buttlings (1)

## 3 Diaphragm Wall Procurement and Design

### 3.1 Construction system selection

The 'US' Alliance design and delivery team faced the problem of building a 6 m deep tank structure and 13 m deep SPS shaft structure within mixed soft ground and below a high water table. It was evident that extensive temporary excavation would be required to enable construction. Design and construction planning commenced by investigating alternative temporary excavation support and construction solutions for the shaft. The tank was initially proposed to be constructed within an open battered excavation.

Options considered for shaft temporary excavation support included caisson construction (both cast in-situ and precast segmental ring types), sheet piling, cutter soil mixing and secant piling. Diaphragm walling was initially discounted due the relatively short length of wall in the shaft and the large mobilisation costs associated with this form of construction.

Tenders were called for the shaft temporary support. The tender documents included a performance based specification to encourage innovation and competition between the available technologies. The ability to incorporate the temporary works into the permanent works was explicitly encouraged.

The selected option was an alternative bid based on the use of diaphragm walling and inclusion of the detention tank in the scope of works. This alternative option was selected based on an estimated \$0.5 M construction cost saving.

By adding the detention tank into the scope of excavation support, the length of diaphragm wall increased sufficiently enabling it to become cost competitive with the other technology options. Diaphragm walls were able to perform the dual function of being temporary retaining structures during internal excavation and base slab construction. The 'temporary' excavation support walls were then incorporated into the permanent structures. The construction methodology eliminated the need for separate temporary structures and the requirement for extensive formwork and falsework.

## 4 Diaphragm Wall Specification and Design

Once diaphragm walling was selected as the preferred construction system, the temporary excavation support specification was re-written around the use of diaphragm walling. This specification [Peril and Weerasinghe (2)] was based on the example form provided by the ICE Specification for piling and embedded retaining walls 2<sup>nd</sup> edition (ICESPERW), ICE (3), which proved to be a valuable resource for this project. The revised specification paid particular attention to the following areas:

- detailed design criteria;
- the division of design and construction responsibilities;
- risk management in particular:
  - safety and stability of the diaphragm walls whilst in the temporary condition;
  - the use of a walling manual to construction sequencing and provide a reference for construction monitoring;
  - additional design criteria specific to diaphragm walling; and
- a high degree of water tightness (no damp patches etc. refer Section 4) to enable the subsequent application of internal coating to fulfil the requirements of the durability design.

### 4.1 Diaphragm wall design criteria

Both the wet well shaft and the detention tank were designed for the following criteria:

**Table 1. Design Criteria**

Design Life:	100 Years
Design Codes and References:	ICE Specification for piling and embedded retaining walls 2 <sup>nd</sup> ed
	BS EN 1538: Execution of Special Geotechnical works – Diaphragm Walls, BSI (4)
	AS3600 – Australian Standard for Concrete Structures, SA (5)
	AS3735 – Australian Standard for Concrete Structures for retaining liquids SA (6)
	AS4678 – Australian Standard for Earth Retaining Structures SA (7)
	AS2159 – Piling Design and Installation SA (8)
Internal Exposure Classification Ref AS3735 Table 4.1	D – Severe / Condensation/extremely corrosive environment due to sewage gases producing sulphuric acid due to bacterial activity.
Minimum Reinforcement Cover	75 mm + Epoxy coating (Note: Table 4.3 AS3735 requires only 55 mm cover for Grade 50 Concrete. Extra cover was specified to suit the construction method.)
Panel Maximum deviation from verticality	1 in 100
Concrete Mix (S50) Details	Minimum Characteristic Strength – 50 MPa Minimum cementitious content – 400 kg/m <sup>3</sup> Maximum cementitious content – 450 kg/m <sup>3</sup> Max w/c ratio - 0.40; Nominal 56 day shrinkage - 600 microns
Permissible lateral wall deflection	The maximum allowable lateral deflection of the diaphragm wall shall be compatible with the requirements of AS4678 and AS3735. The Subcontractor's design shall show the expected deflection of the wall giving due consideration to watertightness, crack widths and rebar stresses.
Ground water level	At surface for ultimate limit state 3.5 m below surface for serviceability limit state

## 4.2 Division of design and construction responsibilities

The 'US' Alliance design team was responsible for the design of the permanent works. The specialist diaphragm walling contractor carried responsibility for:

- interpretation of geotechnical data;
- diaphragm wall detailed design for the temporary and permanent cases;
- design of all temporary works required to ensure structural stability in the temporary condition;
- preparation of a walling manual; and
- conducting a seepage analysis providing estimated ground water inflow rates/quantities and identification of limits on ground water draw down including maximum head differential across the diaphragm walls.

The specialist diaphragm walling contractor was responsible for construction of the shaft and tank guide walls and diaphragm walls. The 'US' Alliance construction team carried responsibility for:

- wall trimming;
- carrying out excavation works in accordance with the walling manual;
- installation and removal of all temporary wallings and propping; and
- construction of all permanent structural elements other than the diaphragm walls.

## 4.3 Risk management

### 4.3.1 Safety and stability

The Singapore Mass Rapid Transit cut and cover diaphragm wall collapse, and subsequent Nicoll Highway incident, provides a vivid example of what can go wrong with the diaphragm walling technique. Both design and construction errors contributed to the diaphragm wall failure which resulted in four people losing their lives and three people being injured. Figure 4 shows the diaphragm wall collapse and associated impact on the Nicoll Highway.



**Figure 4. Singapore MRT Diaphragm wall collapse (Before and after), Singapore 2004 Photos reproduced from Chou (10)**

*“The key lessons from this event are:*

- *Trends of the temporary work during critical periods must be capable of being monitored.*
- *Those interpreting the analysis outputs must be competent to do so. The dangers of drawing conclusions from past behaviour, without careful consideration of the actual conditions, must be recognised.*
- *The management of uncertainty must be robust. There must be approved and tested contingency plans.*
- *The project must operate within a safety culture conducive to safe working. This means:*
  - *A ‘stop work’ procedure to be in place, clearly understood by all, and supported by management*
  - *Clarity in the chain of command and in responsibilities.”*

Reproduced from Chou (10)



#### **4.3.2 The walling manual**

The diaphragm walling specification included a requirement to prepare a walling manual [Buttling (11)] to encourage clear communication of key safety and technical information between all parties. In the case of this project, the walling manual was required to explicitly communicate:

- all design assumptions, in particular the intended construction sequence that the design was based on;
- the wall propping system;
- the maximum lateral deflections permitted and
- the monitoring requirements for the diaphragm walls whilst in the temporary condition.

#### **4.3.3 Monitoring lateral wall deflections using inclinometers**

As specified in the walling manual, both the shaft and tank structures were monitored using inclinometers. Inclinometer tubes were cast into the diaphragm walls at specified locations. During internal excavation of the shaft and tank, regular inclinometer readings were taken to monitor lateral deflections of the diaphragm walls whilst the structures were in the temporary condition. Actual lateral deflections were checked against predicted lateral deflections and specified deflection limits to ensure that the structures were stable and safe prior to construction of the base slabs.

#### **4.3.4 Geotechnical risk management**

Although it is not the focus of this paper, it is worth noting that substantial effort was made to manage geotechnical risk and uncertainty on this project. Following a traditional borehole and SPT (Standard Penetration Test) based investigation, a CPT (Cone Penetration Test) and dilatometer based investigation was undertaken at the request of the diaphragm walling contractor and geotechnical reviewer. Ground water sampling and testing was also undertaken to confirm the compatibility of the ground water with the proposed bentonite support fluid. The diaphragm walling contractor then prepared a geotechnical interpretive report [Buttling (1)] which was used by both the specialist diaphragm wall designer and the permanent works structural designer. The additional investment in geotechnical investigation increased the accuracy of the derived geotechnical design parameters and subsequent deflection predictions. This in turn enabled the diaphragm wall designer to be more aggressive when setting the depth of the tank diaphragm wall. The depth of the tank diaphragm wall was reduced from 15 m to 11 m based on improved geotechnical parameters. Essex (12) and ITIG (13) provide valuable guidance for the management of geotechnical risk and risks associated with construction of underground structures.

### **4.4 Water tightness specification**

To fulfil the requirement of a 100 year design life and to adequately protect the structures against the aggressive raw sewage internal environment (AS3735 Internal Exposure Classification D), the durability design called for coating all internal surfaces exposed to raw sewage gases within the shaft and tank. The ICESPERW water tightness specification adopted states:

- *“No weeping of water or greater rates of water ingress or flow is visible between the top of the wall and the WAL. Beading of water is permitted.*
- *Damp patches on the front face of the wall are permitted provided that the following criteria are met:*
  - *The total area of dampness does not exceed 10% of the visible area of the front face;*
  - *No individual patch of dampness has an area in excess of 4 m<sup>2</sup>.”*

Reproduced from ICE (3)

The ICE Specification for piling and embedded retaining walls defines damp patches, beading and weeping as:

- *“Damp patch; when touched, a damp patch may leave a slight film of moisture on the hand, but no droplets of water or greater degree of wetness are left on the hand. On a concrete surface a damp patch is discernible from a darkening of the colour of the concrete.*

- *Beading of water; beading of water is the state in which individual droplets of water (held by surface tension effects) form on the surface of the wall and adhere to the wall. The water beads do not coalesce with each other. The beads remain stationary on the surface and do not flow.*
- *Weeping of water; weeping of water is the state in which droplets of water form on the surface of the wall and coalesce with other droplets. The coalesced water does not remain stationary on the wall surface, but instead flows down the wall.”*

Reproduced from ICE (3)

## **4.5 Structural design**

The diaphragm wall/panel structural design and detailing and the temporary propping system was carried out by MJ Civil, the specialist diaphragm wall designer, and reviewed by MWH. MWH completed the remainder of the structural design and specified provisions for future extension of the detention tank including the capping beams, struts at roof level and base slab.

## **4.6 Diaphragm wall design outcomes**

### **4.6.1 Shaft**

The final shaft diaphragm wall layout is a dodecahedron in shape with six long sides and six short sides. The shaft perimeter wall is made up of six panels. Each panel has three sides. The panels are joined to each other along parallel edges with shear keyed joints. The shaft diaphragm wall panels were 17.5 m deep and 800 mm thick.

The shaft perimeter wall acts primarily in hoop compression, with each three sided panel acting horizontally as a pin jointed beam or arch to resist soil and ground water pressure. The major reinforcing of the shaft diaphragm walls included horizontal N32 bars and N24 vertical bars at 200 mm centres.

### **4.6.2 Tank**

The tank diaphragm wall is comprised of 14 panels. It includes two L-shaped corner panels and two T-shaped corner panels to enable construction of the second and third stages of the tank using diaphragm walling. The tank diaphragm wall panels were 11 m deep and 800 mm thick.

The tank structure also included four permanent struts, spanning between the capping beams, at roof level, to prop the long tank walls. The tank diaphragm walls act as vertical propped cantilevers resisting horizontal soil and water pressure. The major reinforcing in the tank diaphragm wall panels included: vertical N32 bars horizontal N20 and N24 bars at 200 mm centres.

Temporary steel struts (both transverse and diagonal) were installed at an intermediate level as the excavation progressed to control the wall panel deflection prior to the construction of the base slab.

## **4.7 Key details**

### **4.7.1 Vertical diaphragm wall panel joints**

All vertical diaphragm wall panel joints were formed using a temporary fabricated stop end. The use of the stopend also enabled a single rubber water bar to be installed in these joints.

### **4.7.2 Diaphragm wall - base slab joints and diaphragm wall internal wall joints**

Threaded female couplers were cast into the diaphragm walls to provide anchorage points for threaded starter bars for the base slabs and SPS internal wall reinforcing. The diaphragm wall base slab joints in both structures included hydrophilic water seals and a grout tube. The diaphragm wall internal wall joints in the SPS included a single hydrophilic water stop.

### **4.7.3 Diaphragm wall penetrations**

Penetrations through the diaphragm walls to enable installation of future piping were constructed using hexagonal timber box outs incorporated into the reinforcing cages at the relevant locations.

#### 4.7.4 Controlling ground water during base slab construction

The base slabs of both the tank and shaft were provided with temporary block outs/pipes and pumps to keep the excavation dry and relieve the build-up of ground water pressure whilst these slabs were in a plastic state. These penetrations were sealed once the base slab concrete had reached its' design strength.

## 5 Construction

### 5.1 Construction sequence

Table 2 outlines the construction sequence of the shaft and tank.

**Table 2. Shaft and tank construction sequence**

SHAFT	TANK
1. Preparation of working platform	1. Preparation of working platform
2. Construction of temporary guide walls	2. Construction of temporary guide walls
3. Construction of the diaphragm walls	3. Construction of the diaphragm walls
4. Removal of the temporary guide walls	4. Removal of the temporary guide walls
5. Wall trimming	5. Wall trimming
6. Construction of capping beam	6. Construction of capping beam and permanent struts
7. Excavation of SPS	7. Excavation (Stage 1 of 2)
8. Construction of SPS base slab	8. Installation of temporary bracing (wailers and raking struts)
9. Construction of pipe jacked SPS inlet sewer	9. Excavation (Stage 2 of 2)
10. Construction of internal tee wall from floor to roof	10. Construction of base slab
11. Construction of secondary benching concrete	11. Removal of DT temporary bracing
12. Construction of outlet pipe work	12. Construction of pipe jacked DT inlet sewer
13. Application of internal coating system	13. Construction of secondary floor screed
14. Installation of precast roof system	14. Installation of FRP roofing system
15. Mechanical and electrical fit out	15. Application of internal coating system

### 5.2 Quality control

#### 5.2.1 Diaphragm wall concrete mix testing

Extreme care was exercised in the concrete mix design with regard to the selection of good quality aggregates, proportioning of aggregates and selection and use of admixtures to arrive at a good quality flowing mix not prone to segregation with low drying shrinkage. This required good collaboration between the concrete supplier; Holcim and the design and construction teams. Extensive trials and testing of the as placed concrete was carried out to ensure good quality control.

#### 5.2.2 Verticality and deflection control

A steerable hydraulic grab was used to excavate the diaphragm wall trenches. This hydraulic grab was self-guided and self-levelling. A rig mounted inclinometer was used to validate the verticality of the diaphragm wall panels during excavation for each panel. Inclinometer tubes grouted into the Tank diaphragm wall panels at predetermined locations were used by the construction team to measure the actual lateral deflection of the diaphragm walls during excavation. The predicted lateral deflection of the diaphragm walls for each stage of construction was documented in the Walling Manual. The maximum lateral deflection predicted was 5 mm. Typical lateral deflections observed were in the order of 2-3 mm. Water tightness was achieved by adherence to verticality and deflection tolerances, and good workmanship which ensured the construction of sound homogeneous concrete wall panels with waterstops firmly embedded at all wall panel joints.

### **5.2.3 Diaphragm wall finish and internal coating application**

The diaphragm walls were cast against clayey soils. Upon exposure following excavation, they were found to be in reasonable condition however, relative to off-form concrete, substantial additional surface preparation was required to enable protective coating application: Additional cleaning was required due to the diaphragm wall surface being contaminated with bentonite. In some locations, the large concrete bar chairs dragged in clay as the reinforcement cages were lowered in to the excavations. Following excavation, these clay accumulations required removal and repair. The steel work and reinforcing left exposed at the temporary strut connection points required priming and covering. Polyurethane/water injection sealing was required in some areas of the panel – base slab joints, Wubben (14)

### **5.3 Beneficial outcomes**

The use of diaphragm walling technology for the shaft and tank structures enabled:

- Acceleration of the construction program and generation of an estimated \$0.5 M in savings due to:
  - Negating the need for temporary excavation support. The diaphragm walls provided temporary excavation support prior to being incorporated into the permanent structures;
  - Negating the need for 12 m of vertical internal and external formwork and falsework; and
  - Minimising the extent of works carried out at depth;
- Improved construction safety. Reinforcement cages for the wall panels were fabricated at ground level rather than in-situ, from scaffolding with difficult handling, using cranes etc.;
- Construction progressed in unfavourable wet weather - 2,000 mm of rain fell during the 18 month construction phase;
- Construction below the ground water table at 3.5 m depth and within close proximity to a water bearing strata – the sand layer at 14.5 – 16.0 m depth 1.5 m below the shaft base. The shaft diaphragm walls founded at 17.5 m in relatively impermeable clay provided ground water cut off for base slab construction.

### **5.4 Lessons learned**

With the benefit of hindsight performance aspects that could be improved include:

- Design management: Email based correspondence and paper based checking required very close collaboration and timely responses, sometimes requiring considerable extra work outside normal working hours as it was not time efficient. A project collaboration system such as a building information model, or file sharing platform, enabling a common CAD model able accessed by all parties involved would have made checking and change management far simpler;
- Water proofing: Additional measures could have been taken to enhance water tightness of the diaphragm wall panel joints at the level of the wall/base slab joint. Puller (15) provides useful insight to this problem. Some remedial polyurethane grouting was required at the wall base joint to enable coating work to proceed. Given its importance, greater treatment of water proofing in the walling manual would be warranted. Specifically work sequencing, timing of water proofing works, associated inspections and timing of secondary concrete placement;
- Walling manual: Along with additional treatment of water proofing suggested above, clarity of inclinometer reading interpretation responsibility, stop work procedures, chain of command, and contingency plans would be useful;
- Verticality: In the authors opinion, a tighter verticality tolerance is achievable in these ground conditions with the approach adopted. On this project typical panel verticality was in the order on 1 in 200+ for most panels. Depending on the ground conditions and construction methodology we understand a verticality tolerance of 1 in 400 is achievable;
- Wall trimming: Based on the project delays experienced, and the finish achieved using jack hammers, the use of high pressure water blasting for wall trimming in lieu of jack hammers for the majority of the panel surface may have been more efficient; and
- The use of diaphragm walling necessitates that greater allowance be made for substrate repair and preparation where protective coatings are to be applied.

## 6. Conclusions

On balance, the diaphragm walling based construction methodology had a substantially positive impact on the Officer South SPS project. However, the adoption of diaphragm walling as a construction system brings with it risk, complexity and differences to traditional cast in-situ construction. Particularly with respect to the division of design and construction responsibilities, risk management, water sealing, alignment of the design with the intended construction sequence and information hand over. Based on the good outcome and lessons learned on this project, for similar diaphragm walled based structures, we recommend utilising the specification framework provided by the ICE specification for piling and embedded retaining walls, following Pullers (15) water proofing recommendations. Developing an expansive walling manual and utilising a monitoring system to validate the safety and stability of the diaphragm walls during excavation is recommended.

For larger underground projects Essex (12) and ITIG (13) provide valuable guidance for the management of geotechnical risk and risks associated with construction of underground structures.

## 7. Acknowledgement

I would like to acknowledge the following people and organisations for their contributions to this project:

- Dr Julian Seidel of Foundation Specialists (Previously Foundation QA) The project geotechnical reviewer. Julian also introduced us to the ICE specification for piling and Embedded Retaining Walls;
- The MWH Sydney structural team involved in the design of the major shaft and tank structures including: Rafiqul Islam, Adam Chan-Sew, Maz Mahzari and Alan Gilbert;
- The Piling Contractors team including: Chris Simon (Project Manager), Dr Stephen Buttlng (Design Manager), and Branko Matkovic (Site manager);
- Mark Johns, MJ Civil, the specialist Diaphragm wall structural designer;
- The Thiess Services team: Craig Rogers (Project Manager), Ryan Bickerton (Project Engineer) and Alan Burns (Concrete Superintendent); and
- Rodney Wubben CorrCon the coating specifier and inspector.

## 8. References

1. Buttlng S, Geotechnical Interpretive report for the Officer South Pump Station and Detention Storage Tank, Piling Contractors, Brisbane, 2010,
2. Peril, M., Weerasinghe, J., "Officer South SPS & Detention Tanks Diaphragm Wall Specification" 13<sup>th</sup> May 2010. MWH Melbourne, Australia.
3. Institution of Civil Engineers (ICE), "ICE Specification for piling and embedded retaining walls, Second edition" Thomas Telford, 2007, London.
4. British Standards Institution (BSI), British Standard BS EN 1538: Execution of Special Geotechnical works – Diaphragm Walls, BSI, London 2000.
5. Standards Australia (SA), Australian Standard AS3600: Concrete Structures, Standards Australia Limited, 2001.
6. Standards Australia (SA), Australian Standard AS3735: Concrete Structures for Retaining Liquids, Standards Australia Limited, 2001.
7. Standards Australia (SA), Australian Standard AS4678: Earth-Retaining Structures, Standards Australia Limited, 2002.
8. Standards Australia (SA), Australian Standard AS2159: Piling Design and Installation, Standards Australia Limited, 2009.
9. Gaba A R, Simpson B, Powrie W, Beadman D R, Embedded retaining Walls – guidance for economic design (C580), Construction industry research and information association (CIRIA), July 2003

10. Chou, G., "Technical Note 002 Lessons Learnt: Collapse of Nicoll Highway in Singapore 2004" Version 2, Chun Wo Construction & Engineering Co Ltd, Jul 2013.
11. Buttlig S,. "Officer South Sewerage Pumping Station: Design Report Part 2 Wall Manual" Brisbane, 13<sup>th</sup> May 2010.
12. Essex, R. J. (Ed), "Geotechnical Reports for Construction Suggested Guidelines" American Society of Civil Engineers, Reston 2007.
13. International Tunnelling Insurers Group (ITIG), "A code of practice for risk management of tunnel works", 2006.
14. Wubben, R., "Coating auditing status report – Final (3)" (for internal coating of sewerage structures, Officer South SPS project), 16<sup>th</sup> December 2011, Corcon Pty Ltd, Melbourne, Australia.
15. Puller, M., "The Waterproofness of structural diaphragm walls", Proceedings of the ICE - Geotechnical Engineering, 107(1), 1994, pp 47-57.

# Expansion and Mechanical Properties of Reactive Concrete incorporating Fused Silica

Thamer Kubat<sup>1,2</sup>, Ahmad Shayan<sup>3,4</sup> and Riadh Al-Mahaidi<sup>5</sup>

<sup>1</sup>PhD candidate, Swinburne University of Technology, Melbourne, Australia

<sup>2</sup>Lecturer, Duhok Polytechnic University, Duhok, Iraq

<sup>3</sup>Chief Research Scientist, ARRB Group Ltd, Melbourne, Australia

<sup>4</sup>Adjunct Professor Dept. of Civil Eng., Swinburne University of Technology, Melbourne, Australia

<sup>5</sup>Professor of Structural Engineering, Swinburne University of Technology, Melbourne, Australia

**Abstract:** Fused silica was used to simulate reactive concrete in field structures. It was used as a replacement for fine aggregate at the dosage rate of 7.5% of total aggregate in the concrete. Expansion and mechanical properties of concrete mixes without and with fused silica were investigated. Incorporation of 7.5% fused silica in the concrete caused significant expansion and cracking of the specimens studied. Two high relative humidity (RH) values, 98% and 100%, were investigated to find the effect of this range of humidity on alkali aggregate reaction (AAR) and mass variation of concrete through two years of monitoring. Results showed that the RH conditions of 100% and 98% influenced the rate of expansion (being faster at 100% RH), but after two years, the magnitude of expansion was the same. The effect of reactivity of concrete on mechanical properties of concrete was also investigated after one year exposure at 98% RH. The mechanical properties of the concrete, especially compressive strength, flexural strength and modulus of elasticity, were adversely affected by AAR expansion. The decreases in the above properties at the age of one year were 74 %, 82 % and 93 %, respectively. These results indicate that the RH range of 98-100% is suitable for long term laboratory testing of concrete for AAR. More importantly, they highlight the significant damage that highly reactive aggregates can impart to the mechanical properties in concrete.

**Keyword:** AAR, fused silica, concrete expansion, mechanical properties

## 1. Introduction

Alkali aggregate reaction (AAR) is a chemical reaction between alkali hydroxides developed in the pore solution of concrete and certain silica-rich constituents within the aggregate in the presence of water to form an expansive gel. As the gel expands, an internal pressure develops, which may lead to cracking of the aggregate and the paste matrix. As a result of cracking, the rate of concrete deterioration will increase. The occurrence of AAR requires three main parameters to exist concurrently: reactive aggregate, sufficient alkali and humidity.

In the work reported in this paper, fused silica was used as the reactive aggregate, due to its uniformity compared to natural aggregates. Swamy and Al-Asali (1) also used fused silica as a reactive aggregate and found 15% of fused silica as a proportion of total aggregate caused large expansion in concrete. Abdullah (2) also used fused silica in an extensive laboratory investigation and found that 7.5% fused silica caused large expansion in concrete specimens. Alkali is usually derived from cement, but in laboratory expansion studies, alkali is added by dissolving sodium hydroxide to enhance the reaction and expansion.

Relative humidity (RH) is the expression of water content in concrete. The threshold of relative humidity to initiate and develop AAR has been investigated by several authors. Ludwig (3) concluded that 80-85% RH is sufficient to initiate AAR. Nilsson (4) stated that AAR degradation would not occur if the external RH is less than 80%. Most authors have found that higher external RH leads to more expansion and faster expansion rate.

The effects of AAR on concrete lead to loss in its mechanical properties, especially modulus of elasticity, tensile strength and, to a lesser extent, compressive strength (ISE (5)). Abdullah (2) investigated the effect of six percentages of fused silica (0, 3, 7.5, 10, 15 & 20%) as a replacement of fine aggregate to total aggregate used in concretes. The evolution of compressive strength of concrete with time up to 1 year was recorded and the results showed a decrease in the compressive strength of concrete which varied from 27 to 45%. The reduction in mechanical properties as the author explained is directly influenced by the amount of fused silica used and in general, the larger the percentage of fused silica, the lower the compressive strength of the concrete. Tensile strength is a sensitive parameter. The reduction in tensile strength due to AAR varied from 5% (Ahmed et al.(6)) to 85% (Siemes and Visser (7)). According to several authors, this variation depends upon the test method used.



For example, Han (8) explained that direct tensile strength testing showed the highest reduction in strength whereas the splitting tensile strength test (an indirect test) showed the least reduction in strength related to the AAR effect. Shayan et al. (9) stated that the flexural strength of concrete is significantly influenced by AAR expansion and is lower in specimens with greater AAR expansion. The flexural strength of concrete was reduced by as much as 40-50% when the expansion exceeded 0.12%. These authors also found that flexural strength is more sensitive to AAR than splitting tensile strength, especially at very low expansion. According to the expansion value, the authors classified the reduction in flexural strength into three groups:-

- Expansion value < 0.02% : no reduction
- $0.02 \leq$  Expansion value  $\leq 0.11$ : 30% reduction
- $0.12 <$  Expansion value : 40-50% reduction

The static modulus of elasticity is a sensitive parameter of concrete deterioration due to AAR (Ahmed et al. (6); Monette et al. (10); Mohammed et al. (11) and Giaccio et al.(12)). Marzouk and Langdon (13) found the modulus of elasticity of concrete containing rapidly reactive aggregate was decreased by 80%, whereas for concrete containing moderately reactive aggregate, the reduction was 20%. ISE (5) reported that the loss in elastic modulus varied between 20% and 50% at expansions ranging from 0.1 to 0.3% and could reach 80% at very high expansion levels.

As laboratory expansion tests are often conducted in the range of 98-100% RH, two RH values were investigated in this research to find the effect of humidity on AAR and the mass variation of concrete through two years of monitoring. The effect of the reactivity of concrete on the mechanical properties of concrete was also investigated for a period of one year after casting.

## 2. Concrete materials

Two types of concrete, reactive (RC) and normal (NC), were fabricated. The mix proportion was fixed according to the ASTM C1293 (14) requirements. One concrete mix of proportions 0.42: 1: 1.7: 2.54 (water cement ratio: cement: fine aggregate: coarse aggregate) was used throughout the research. General purpose cement was used for the mix. The percentage of alkalinity of this cement is 0.5% expressed as sodium oxide equivalent ( $\text{Na}_2\text{O}_{\text{equ}}$ ) according to the manufacturer's information. Crushed aggregate of 19 mm maximum size was used. Sodium hydroxide was added to water in the mix of RC and NC to increase the level of alkalinity in both concretes (RC & NC) to 1.25% expressed as  $\text{Na}_2\text{O}_{\text{equ}}$  according to the ASTM C1293 requirements. Fused silica of 0-1mm fraction grading from Sila Australia was used in the mix of RC. Table1 shows the chemical analysis of fused silica.

**Table 1. Percentages of chemical compounds of fused silica.**

Chemical Compounds	SiO <sub>2</sub>	Al <sub>2</sub> O <sub>3</sub>	Fe <sub>2</sub> O <sub>3</sub>	Na <sub>2</sub> O	K <sub>2</sub> O	TiO <sub>2</sub>
Percentage	99.8	0.05	0.015	0.007	0.003	0.01

The quantities of both types of concretes are shown in Table 2. Table 2 indicates that the unique difference between the two types of concretes is the use of fused silica in the mix of RC. Fused silica was used at a dosage rate of 7.5% by mass of total aggregate, replacing the fine aggregate component. According to Abdullah (2), this percentage leads to the highest expansion in concrete.

**Table 2. Reactive and normal concrete ingredients (kg/m<sup>3</sup>).**

Material		Reactive concrete (RC)	Normal concrete (NC)
Cement		420	420
Water		176	176
Fine aggregate	Sand	597	732
	Fused silica	135	-----
Coarse aggregate		1072	1072
Sodium hydroxide		4.07	4.07

### 3. Experimental work

Standard specimens were cast to determine the physical and mechanical properties of the concretes. Table 3 shows the distribution of specimens used throughout the research.

Samples for measuring the mechanical properties of concrete and those for assessing the expansion potential of concrete, using concrete prism test (CPT) method were stored in a chamber at 38 °C and 98% RH (Figure 1). To ensure that 100 % RH condition is achieved, a sealed stainless steel container, which could accommodate six prisms, was designed and used inside the larger chamber shown in Figure 1. This container was supplied with water at the bottom and wet cloth lining on the inside walls, without any contact with the prisms, which were placed vertically in the container.

**Table 3. Distribution of specimen sizes and numbers according to various tests.**

Test	Specimen size (mm)	Number of specimens
Accelerated mortar bar test (AMBT)	25*25*280	6
Concrete prism test (CPT)	75*75*280	12
Compressive strength, splitting tensile strength and modulus of elasticity	φ 100*200	60
Flexural strength	100*100*400	20



**Figure 1. Chamber where samples were stored at specified temperature and humidity.**

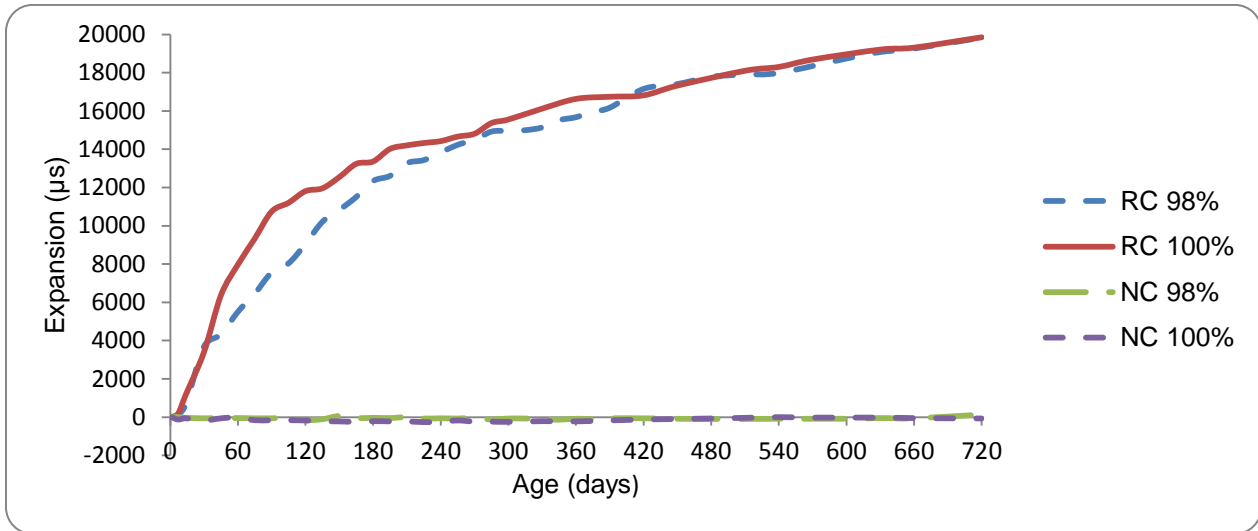
### 4. Results and discussion

#### 4.1 AMBT

Mortar bars measuring 25\*25\*280 mm were fabricated to test the reactivity of the fine and coarse aggregate phases. The coarse aggregate was crushed to appropriate size fractions in accordance with the ASTM C1260 (15) requirements, which are similar to those of the corresponding Australian Standard AS 1141-60-1(16). The average free expansion after 16 days of storage was 0.022% for fine aggregate and 0.045% for coarse aggregate, which are less than the 0.1% limit. In Australia for AS 1141.60.1, you need to compare the expansion at 21 days with the test limit of 0.10%. Therefore, you should also give the expansion values for the sand and coarse aggregates at 21 days. As a result, the fine and coarse aggregates are considered non-reactive according to both the ASTM C1260 and AS 1141.60.1 requirements.

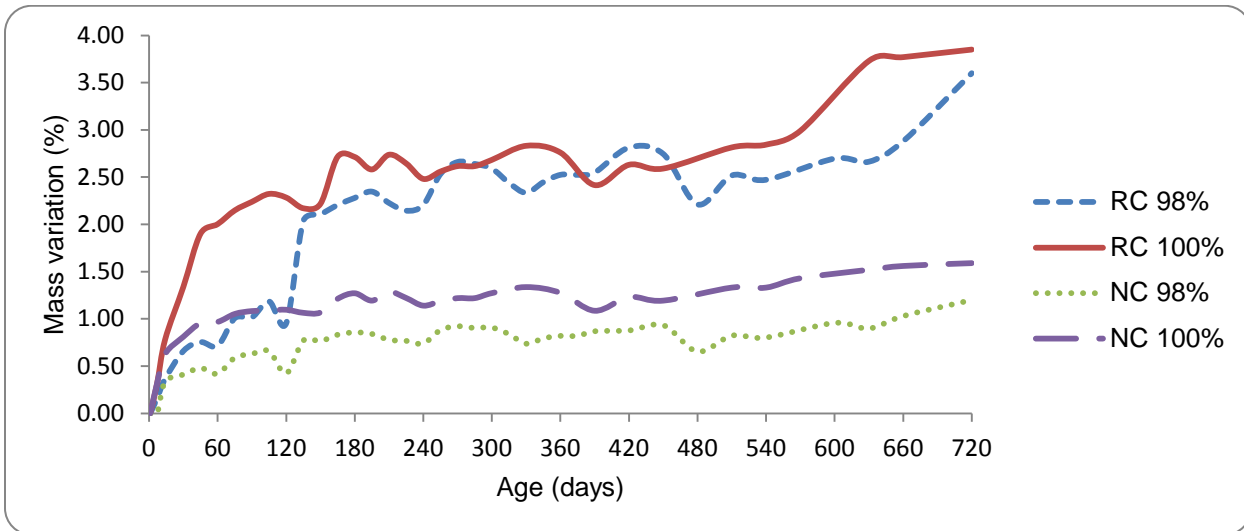
## 4.2 CPT and humidity effect

Two high RHs, 98% and 100%, were applied to find the effect of humidity on AAR expansion and the mass variation of concrete over two years of monitoring. The results of two years of measurement (Figure 2) showed that the difference in RH conditions of 100% and 98% influenced the rate of expansion, which was initially faster at 100% RH, but the value of expansion after two years was the same. The expansion is still increasing for both RH conditions, but a much slower rate.



**Figure 2. Free expansion for RC & NC concretes at 98% and 100% RH.**

The weight of concrete prisms was also recorded at the time of expansion measurement in order to monitor mass variation. Figure 3 shows the mass variation for the two types of concrete (RC & NC) over the two years of measurement. The difference in the mass variation is clear between the two concretes. Reactive concrete increases in mass due to water uptake by the AAR gel. Figure 3 also shows that the small change in RH conditions (98% & 100%) affected the mass variation rate of RC at early ages up to 120 days, after which the values appear to be approximately the same.



**Figure 3. Mass variation % for RC & NC concretes at 98% and 100% RH.**

### 4.3 Mechanical properties of concrete

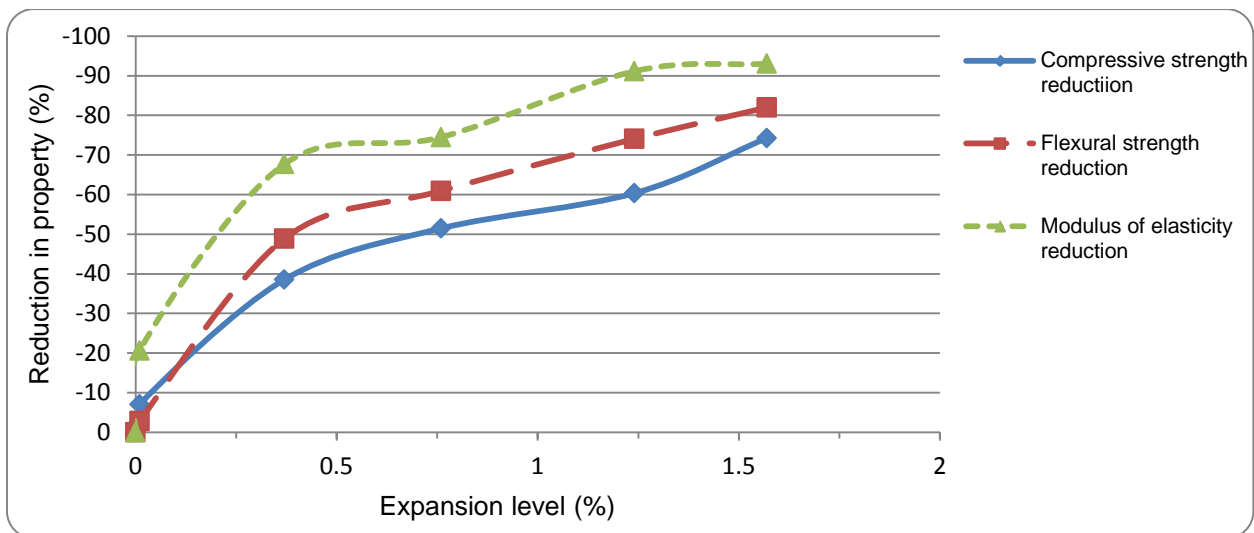
#### 4.3.1 Compressive strength, flexural strength and modulus of elasticity

Parallel strength testing is important to collect data about the relationship between expansion level and strength loss (Shayan et al. 2003 (9)). Table 4 represents the values of compressive strength, flexural strength and modulus of elasticity of RC and NC at the ages of 7, 28, 90, 180 and 360 days, which represent different expansion levels for RC (98% RH). More deterioration in the mechanical properties of RC was noticed as the expansion level increased. The reduction in compressive, flexural strength and modulus of elasticity at the age of one year reached 74 %, 81 % and 93 % respectively. Table 4 and Figure 4 show clearly that as the expansion level increased, the reduction in the property of RC also increased. The reduction in the modulus of elasticity of RC with respect to NC at the same age is higher than other properties, especially at early ages (i.e., at low levels of expansion), showing that the modulus of elasticity is more sensitive to expansion and microcrack development.

Figure 5 shows the stress-axial strain curves of compression tests on RC specimens at various levels of expansion: 0.01, 0.37, 0.76, 1.24 and 1.57%. As the expansion level increases, the stress-strain curve appears to be steeper and the slope of the curve (modulus) is less.

**Table 4. Summary of mechanical property results of RC and NC with different expansion levels at specified ages.**

Age (days)	Expansion level (%)	Compressive strength (MPa)		Flexural Strength (MPa)		Modulus of Elasticity (GPa)		Reduction in concrete property (%)		
		NC	RC	NC	RC	NC	RC	Compressive strength	Flexural strength	Modulus of elasticity
7	0.01	32.2	29.9	4.7	4.5	25.7	20.4	7	3	21
28	0.37	35.1	21.6	5.0	2.5	35.1	11.3	39	49	68
90	0.76	35.2	17.1	5.8	2.3	35.7	9.1	51	61	75
180	1.24	38.3	15.2	6.9	1.8	36	3.2	60	74	91
360	1.57	38.5	9.9	7	1.2	36	2.5	74	82	93



**Figure 4. Reduction in concrete properties with expansion level.**

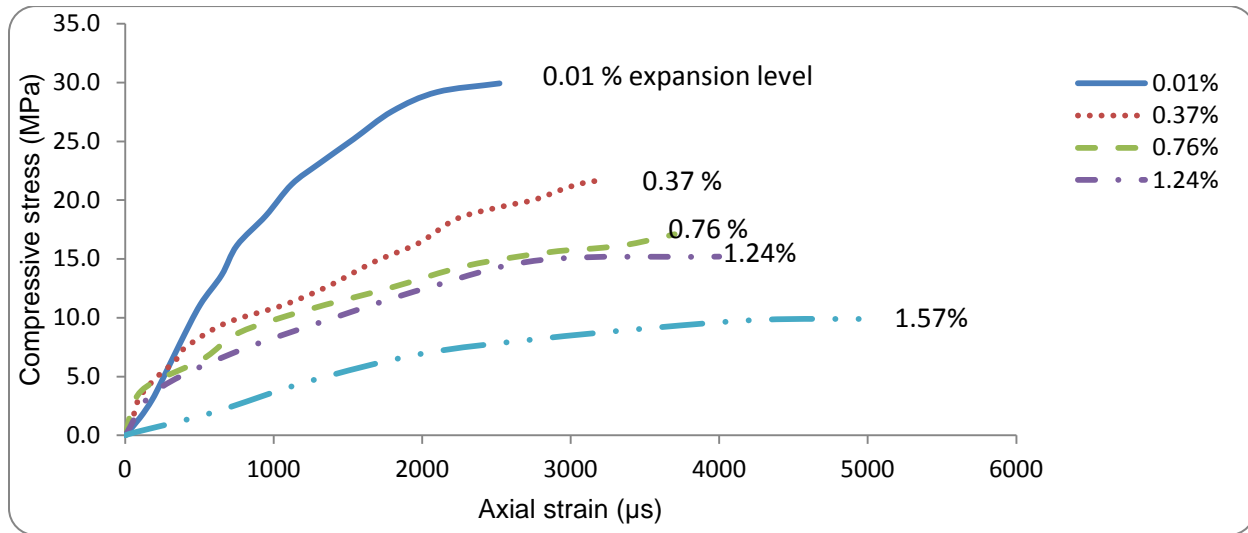


Figure 5. Effect of expansion levels on stress-strain diagram

#### 4.3.2 Splitting tensile strength

To find the effect of AAR on the splitting tensile strength of concrete, twenty four out of thirty cylinders were tested at the ages of 7, 28, 90 and 180 days and the remaining cylinders were tested at 360 days. As shown in Figure 6, the reduction in splitting tensile strength of RC compared to NC at the same age reached 62% at the age of 180 days. The loss in strength capacity does not occur at the same rate as the expansion.

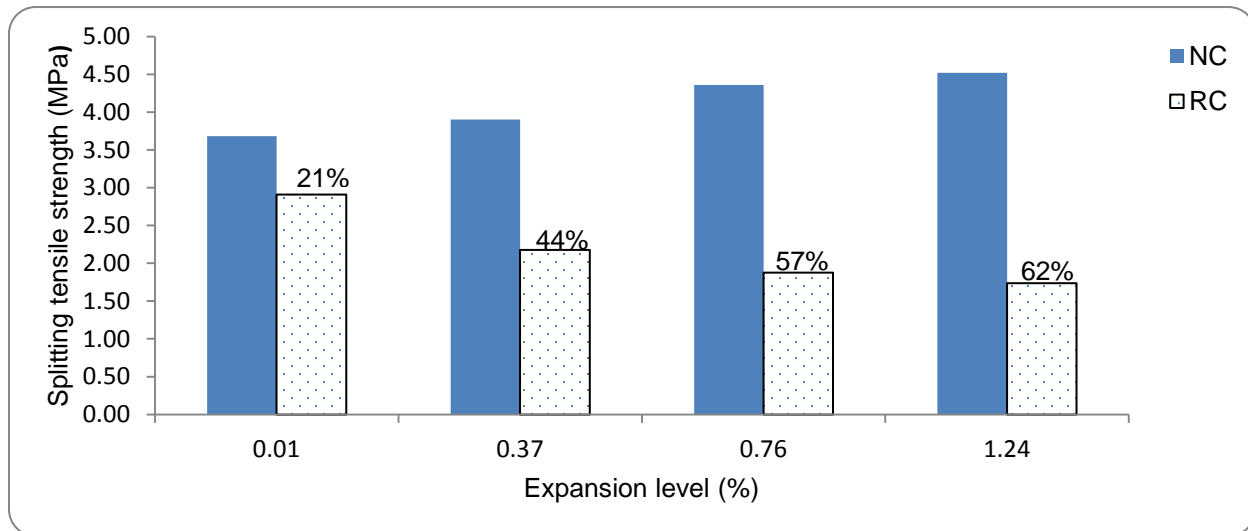


Figure 6. Results of splitting tensile strength against expansion levels.

## 5. Conclusions

The research focused on the effect of two high RH values, 98% and 100%, on the free expansion of reactive concrete, and the effect of various expansion levels (0.01%, 0.37%, 0.76%, 1.24% & 1.57%) on the mechanical properties of concrete. The results showed that the small difference in RH conditions of 100% and 98% influences the rate of expansion, but after two years of monitoring, the magnitude of expansion was the same. The mechanical properties of concrete, especially compressive strength, flexural strength and modulus of

elasticity, were adversely affected by AAR expansion. The reduction in the above properties at the age of one year was 74 %, 82 % and 93 % respectively, compared to normal concrete at the same age. In addition, the results showed the reduction in splitting tensile strength after six months age reached 62% compared to normal concrete at the same age.

## 6. Acknowledgement

The authors would like to thank all the staff of the Smart Laboratory at Swinburne University for their support.

## 7. References

1. Swamy, R.N. & Al-Asali, M.M., "Expansion of concrete due to ASR", *ACI Materials Journal*, 85(1), 1988, pp. 33-40.
2. Abdullah, S.R., "Fiber Reinforced Polymer Rehalibitation of AAR damaged Concrete Structures", PhD thesis, Monash University, 2013, Melbourne.
3. Ludwig, U., "Effects of environmental conditions on alkali-aggregate reaction and preventive measures". Proceedings, 8th International Conference on Alkali-Aggregate Reaction in Concrete, Society of Materials Science, Kyoto, Japan, 1989, pp 583-596.
4. Nilsson, L., "Moisture effects on the alkali-silica reaction", Proceedings,6th International Conference on Alkali-Aggregate Reaction, Copenhagen, 1983, pp 201-208.
5. Institution of Structural Engineers, "Structural effects of alkali- silica reaction , technical guidance on the appraisal of existing structures", ISE, London, 1992.
6. Ahmed, T., Burley, E. et al., "The effect of alkali-silica reaction on the fatigue behaviour of plain concrete tested in compression, indirect tension and flexure", *Magazine of Concrete Research*, 51(6), 1999, pp 375-390.
7. Siemes, T. & Visser, J., "Low tensile strength in older concrete structures with alkalis-silica reaction", Proceedings,11th International Conference on Alkali-Aggregate Reaction, Québec, Canada, 2000, pp 1029-1038.
8. Han,N., "Literature review of the effects of alkali-silica reaction on the tensile strength of concrete ", TNO report 2000-BT-0297, 2000, December.
9. Shayan, A., Xu, A. et al., "Development of a performance measure for durability of concrete bridges", Proceedings, 21st Biennial Conference of the Concrete Institute of Australia, Brisbane, Queensland, 2003, pp 739-757.
10. Monette, L., Gardner, J. et al., "Structural effects of the alkali-silica reaction on non-loaded and loaded reinforced concrete beams", Proceedings, 11th International Conference on Alkalies in Concrete, Quebec, Canada, 2000, pp 999-1008.
11. Mohammed, T.U., Hamada, H. et al., "Alkali-silica reaction-induced strains over concrete surface and steel bars in concrete", *ACI Materials Journal*, 100, 2003, pp133-142.
12. Giaccio, G., Zerbino, R. et al., "Mechanical behavior of concretes damaged by alkali-silica reaction". *Cement and Concrete Research*, 38(7), 2008, pp 993-1004.
13. Marzouk, H. & Langdon, S., "The effect of alkali-aggregate reactivity on the mechanical properties of high and normal strength concrete", *Cement and Concrete Composites*, 25, 2003, pp 549-556.
14. American Society for Testing Materials , "Determination test for length change of concrete due to alkali silica reaction, (ASTM C1293-08b)", American Society for Testing Materials, Annual Book of ASTM, 2011, pp 699-705.
15. American Society for Testing Materials, "Standard Test Method for Potential Alkali Reactivity of Aggregates,(ASTM C1260-07)", American Society for Testing Materials, Annual Book of ASTM, 2011, pp 694-698.
16. Australian Standard AS1141.60.1. "Method for sampling and testing aggregates-Potential alkali silica reactivity- Accelerated mortar bar method, Standards, Australia, Sydney, 2014, 14pp.

# Construction 3D Printing

Laurie Edwards,<sup>1</sup> Camille Holt,<sup>2</sup> Louise Keyte,<sup>3</sup> and Redmond Lloyd<sup>4</sup>

<sup>1</sup>Project Manager, Boral Innovation Factory

<sup>2</sup>Graduate Materials Scientist, Boral Innovation Factory

<sup>3</sup>R&D Manager, Boral Innovation Factory

<sup>4</sup>National R&D Manager, Boral Innovation Factory

**Abstract:** Additive manufacture or 3D printing is revolutionising manufacturing – from titanium aircraft parts to chocolate. 3D printing allows individually customised products to be produced without any of the tooling and set-up costs usually associated with manufacturing. The process of designing a 3D model and then fabricating it ‘layer-by-layer’ also allows complex shapes with optimised structural properties to be produced. There is no doubt that 3D printing will continue to grow as the technology matures, and will become one of the key manufacturing technologies of the 21st century.

Despite the clear benefits, the application of 3D printing in construction, and particularly concrete, has been relatively slow. This paper examines some of the key technologies in additive manufacture, their benefits and drawbacks, and explores how they will be applied in concrete construction.

**Keywords:** additive manufacture, 3d printing, concrete, construction.

## 1. Introduction

One of the most important trends in manufacturing over the past decade has been the rise of additive manufacture, or 3D printing. 3D printing allows direct manufacture of finished articles from computer models, unlike traditional mass production techniques, which require expensive tooling or moulds. 3D printing therefore allows ‘mass customisation’, where it is no more expensive to produce unique items than multiples.

3D printing techniques have been gaining traction in various industries as the technology has evolved. Some industries have embraced 3D printing much more rapidly than others. For example, direct manufacture of titanium parts through 3D printing has generated significant interest as it minimises waste of costly titanium metal, and allows highly complex shapes to be created. 3D printing has also generated interest in objects as diverse as bicycle frames, firearms and chocolates. [1] [2] [3]

This paper examines the drivers behind 3D printing, and explores how additive manufacture could revolutionise construction.

## 2. Background

3D Printing, or Additive Manufacture as it is also known, refers to a body of technologies that began to be developed in the 1980s. [4] Whilst these technologies are varied in both approach and material, they share the unique approach of constructing an object through layer by layer addition of material. This is fundamentally different from traditional approaches of manufacture such as casting in to a mould or die or removing material by machining.

All forms of additive manufacture follow the same basic process. First, a three-dimensional blueprint of an object is created and it is sliced into cross-sections using computer software. This is commonly referred to as Computer Aided Design (CAD) or Computer Aided Manufacturing (CAM). [5] Next, the design is converted to a set of manufacturing instructions which specify deposition of material at the required locations. Finally, material is deposited in successive laminations to build the object. Deposition of material can be achieved through a number of techniques that can mostly be divided into three key groups: Stereolithography (SLA), Fused Deposition Modelling (FDM) or Selective Laser Sintering (SLS).

In 1986, the first 3D printing related patent was issued to Charles (Chuck) Hull for the method Stereolithography (SLA). [6] He had invented a technique that could bypass the several week wait



normally expected when creating a plastic prototype and instead have it ready to be handled within a day. Hull's invention takes digital cross-sections which are then communicated to a Stereolithography machine consisting of a build platform suspended in a UV-sensitive liquid photopolymer resin filled basin and a guidable UV laser. This laser traces the path defined by the cross-section, applying energy to trigger solidification of the resin. Once a layer has been completed, the build platform drops slightly and the laser begins an adjacent cross-section, thus building the object one cross section at a time. For some applications stereolithography is the superior choice due to its ability to create highly detailed objects with thin walls and a clean surface finish. However there are also some challenges specific to this technique; as the object is being created in fluid, any objects with overhang require support structures. The necessity of support structures increases material wastage and labour time, as support materials are frequently difficult to remove. The phase-change of the material can sometimes cause shrinkage, warping or curling. Finally, due to the reliance on photosensitive liquids, materials are limited.

Concurrently, Carl Deckard was working on an entirely different method of Additive Manufacture at the University of Texas. By 1989 he was granted a US patent for the process of Selective Laser Sintering (SLS). [7] SLS enables three-dimensional models to be rendered in a similar fashion to SLA, however the basin is filled with a powdered material rather than a liquid. In this case a laser traces the cross section and applies thermal energy to sinter the material. The build platform within the basin is then lowered and a roller or scraper system deposits a fresh layer of powder so the process can be repeated; this time the laser simultaneously creates a new layer and fuses it to the layer below. Unlike stereolithography, the raw material provides support to the model as it is being created, meaning additional supports are rarely required. However selective laser sintering is also subject to limited suitable materials.

Perhaps the most similar technology to traditional two-dimensional printing is Fused Deposition Modelling or FDM. FDM was first patented in 1992 by Scott Crump [8] who partnered with his wife Lisa and founded a company called Stratasys. In early fused deposition modelling, a thermoplastic polymer or metal filament spool is fed to the print head in a similar way to thread on a sewing machine. The print head then melts the material and follows the path specified by the digital cross-section, depositing a layer of molten material. The successive layer is then deposited before the previous layer has fully solidified, enabling lamination. Depending on the machine being used, the build platform may be lowered as layers are printed or the print head may be raised. As FDM technology has advanced, the range of materials able to be "printed" in this way has broadened. Almost any substance that can start in a liquid state before solidifying can be used in this technique.

### **3. Applications in construction**

The construction industry is particularly well suited to take advantage of the benefits of 3D printing. 3D printing could bring improvements in safety, reductions in labour and time, and advances in customisation and form.

Perhaps the largest draw card for 3D printing in construction is the reduction in labour requirements, as this can translate to a saving in both cost and time. 3D printers would allow a house to be built by a skeleton crew, rather than a full team spanning multiple trades. [9] This reduction in labour would result in both decreased cost and an increased level of site safety, particularly in harsh or dangerous environments. Automated construction could also minimise costly errors and defects.

As well as the improved cost, timeline and safety, 3D printing also removes many design limitations. Rectilinear forms are known to be structurally weaker than curvilinear forms. [10] However, the creation of curvilinear forms in construction requires specialty formwork or engineering. This usually comes at a dramatic increase in expense and time. The use of 3D printing would enable curvilinear designs to be executed as easily as more traditional angular structures. This offers a structural advantage as well as an aesthetic one. Likewise, elements that are precast are limited to being solid whereas those which are printed are able to be created with cavities, saving on material and also creating channels for essential utilities. [11]

The construction industry is well positioned to capitalise on the benefits of 3D printing as the use of modelling is already commonplace. In fact, the majority of information needed to create a 3D blueprint is generated during the design of a building. In Building Information Modelling (BIM), which is rapidly

growing in popularity, it is standard procedure to create three dimensional CAD models of buildings. [12] It is a relatively small step to move from this type of model to instructions for a 3D printer.

#### 4. Current progress

At present, there are few examples of construction scale 3D printing. Early versions of concrete 3D printers operate by extruding very low slump concrete, designed to be self-supporting, from a deposition head mounted on a gantry. [13] This technique is analogous to Fused Deposition Modelling (FDM). Although FDM is not the only technique with potential application in the construction industry, it utilises the cheapest materials and is the favoured choice so far.

Since 2007, a team at Loughborough University in the United Kingdom, led by Dr Richard Buswell and Professor Simon Austin, have been focused on 3D printing applications within the construction industry. They are working to build and commercialize a 3D concrete printing robot, as well as helping to develop a supply chain for the required materials. [14] Construction company Skanska are collaborating with Loughborough University with the aim of facilitating the transition of 3D printing techniques to a commercially viable form of construction.

In 2014, Chinese company WinSun demonstrated how 3D printing could be used in practical terms by printing 10 basic dwellings in 24 hours. [15] The structures are claimed to have cost less than US\$5,000 each to manufacture and were created from mostly recycled materials. WinSun used a large FDM printer and high performance concrete to manufacture house components off-site. These completed parts were then transported and assembled in a similar fashion to traditional precast construction. Although the houses were produced rapidly and cheaply, the finish on the elements was poor compared to typical precast concrete. Furthermore, the true benefits of 3D printing were not realised, as the elements still required transport and assembly on site. This application may be better suited to providing affordable or emergency housing rather than typical residential construction.

WinSun are also pursuing production of taller structures, including a recently erected 5-storey apartment building, which currently holds the record as the tallest 3D printed structure. Next door, they also manufactured a 1,100 square metre concrete mansion, complete with interior fittings. This was printed at a cost of approximately US\$160,000 [6]. WinSun have since announced receiving an order for ten of these mansions from Taiwanese real estate company Tomson Group. [16]

US based Emerging Objects is employing entirely different technology to develop building components with a focus on the aesthetic advances that 3D printing has enabled. Using a proprietary cement-based material, the components produced are claimed to be lightweight and are toughened by the addition of fibre reinforcement. Emerging Objects offer a number of post-printing finishes, such as sand blasted, glossy or satin. Many of their products serve a dual purpose, which has been able to be incorporated due to the increased shape capabilities of 3D printing. These include interlocking seismically resistant blocks and acoustic dampening walls. [17]

Outside of engineering labs, Andrey Rudenko built and fine-tuned an FDM printer in his own backyard. By August 2014 Rudenko had successfully printed a castle in layers of concrete 10 millimetres high by 30 millimetres wide. [18] Due to limitations of the technique and material, the structure does not have a roof.

Another construction related application has been demonstrated by multinational engineering firm Arup, who have demonstrated steel components printed using selective laser sintering of powdered metal. The use of maraging steel has resulted in a low carbon, low weight, ultra-high-strength prototype. Arup are hoping further refining will result in a market ready product in the near future. Whilst these components are currently more expensive to create than their traditional counterparts, Arup believe this method of manufacturing will, in time, significantly reduce both cost and waste. [19]

A binder jetting method for 3D printing large structures with a stone-like finish called D-Shape uses sand mixed with a metal oxide catalyst as the powder bed onto which a low viscosity solution containing inorganic compounds, in particular chlorides, is printed. [20] Binder jetting is, in some ways, analogous to an inkjet printer wherein the printer head moves across the page depositing ink in predetermined locations. Once a layer has been printed a hopper deposits the next layer of sand which is then

compacted prior to printing. The binder for this system, a metal oxide combined with a solution of inorganic salts, is reminiscent of magnesium oxychloride (Sorel) cement which is made by mixing a solution of magnesium chloride with powdered magnesium oxide [21] and boasts strengths greater than those of traditional cement. A main advantage of this method in comparison with other examples of 3D printing in construction is that the whole structure is supported through the printing process by the excess sand surrounding the printed element. The D-Shape method also includes printing a wall around the structure as it is printed to hold the sand. Once the printing process is complete, this wall is broken and the excess sand removed to reveal the printed structure. Also, the printer itself is transportable and can be set up on site. Already, this method is currently being used in the construction of a four bedroom house in New York as well as military bunkers. [22] There is also talk of buildings in Perth being constructed from elements made using this technique. [23]

Contour Crafting (CC) [11] is a 3D printing system in which clay is extruded from a nozzle in a manner similar to that of the FDM technique. Attached to the nozzle is a pivoting trowel which smooths the sides of the structure as they are printed. The fact that the trowel can pivot means that curved structures such as cones or vases can also be produced with smooth surfaces. Individual printed layers are visible in the structures produced by both WinSun and Andrey Rudenko mentioned above and would need an extra finishing step to improve their aesthetic appeal. Given that the CC system is compatible with gantry systems which could be used on site, a combination of the CC technique with cementitious materials could result in a higher quality 3D printing system for construction.

## 5. Key challenges

Although some clear benefits of 3D printing are apparent in the construction industry, there are numerous challenges to be overcome before the technique is genuinely useful. Unfortunately concrete, as a material, is susceptible to the effects of weather, ambient temperature and deficiencies in mix design. These factors can make concrete unpredictable, even when utilising current technology. With the additional complications of extruding concrete through a finely tuned print head there is a lot of opportunity for errors to occur. [11] The setting time and rheology of concrete are also not ideal for layer-by-layer construction; however, these properties can be controlled to a certain extent through the use of admixtures. The problems associated with using hydraulic binders as 3D printing materials have, in part, begun to be addressed through the advances in large scale 3D printing discussed above. Whilst concrete itself is not amenable to extrusion due to the size of the aggregates it contains, a cement paste is and has been successfully utilised by WinSun in the construction of their buildings. Alternative binders, such as that used in the D-Shape system, are also another option to explore.

Another consideration is the finish produced when concrete is 3D printed. The clearly ridged texture is apparent; this may be irrelevant in applications where speed or large cost savings are the driving forces, such as emergency housing. However, structures like WinSun's mansion beg the question of how this finish will be received by consumers considering higher-end printed dwellings. [13] If the completed surface is deemed to require further finishing, the cost and effort may outweigh the initial savings. A simple answer to this problem has already been reported by Behrokh Khoshnevis, inventor of Contour Crafting. Through addition of a trowel to the system which smooths each layer as it is printed Khoshnevis is able to produce structures in a variety of geometries, including both curves and right angles, with a smooth outer wall. [11] Combination of such a system with a printer that extrudes cement paste may go some way in improving the appearance of objects printed in this manner.

A further challenge is in incorporation of reinforcement. Extrusion in layers makes conventional reinforcing difficult to achieve. Fibre reinforcement does not solve the issue, as fibres will be aligned with the direction of printing and therefore provide no inter-laminar bonding. Reinforcement is a key issue to overcome if structural concrete is to be 3D printed. Incorporation of reinforcement appears to be conversant with the CC methodology with printing able to take place over the top of an embedded metal coil due to the pressure with which the clay paste is extruded. It is not clear how the metal coil is incorporated into the system, however, nor have other materials such as cement pastes been tested. Another interesting enhancement to the CC system is the ability to produce hollow layers. It was suggested that a similar method could be used to extrude two materials simultaneously with the aim of having a reinforcing

material surrounded by clay. [11] The D-Shape system claims to be able to create structures so strong that traditional iron reinforcement is unnecessary. However, reinforcing fibres such as fibres or metal shavings are being investigated for incorporation into the house to be built in New York to ensure it can support a roof. [24]

Large scale printers face additional challenges created by transportation. Generally a printer remains in situ and can be expected to produce the same results with each task. 3D printers capable of constructing buildings must be sufficiently durable to withstand the rigours of transport and operation at construction sites. Ideally, a gantry system could be employed which would allow a building to be printed as a whole, saving time and money as the need for assembling individual parts would be eliminated.

Industry pushback could delay the rise of 3D printing applications in the industry. Mechanisation is almost always met with scepticism and any new technology that has the potential to automate industry jobs will encounter resistance. [25] Phillips & James Construction Consulting Firm estimates that construction of a typical family home can employ up to 63 construction workers over a four-month period. [26] 3D printing techniques could see this number drastically slashed; a prospect that may see sectors of the construction industry meet the new technology with some resistance. Retraining of current workers could provide a solution to this resistance whilst also addressing the lack of workers skilled in the use of this technology.

The types of materials that have already proven themselves useful for use with current 3D printing technology mostly consist of special preparations which are expensive to purchase, In addition, such materials are not fit for use in the construction of buildings. For 3D printing to prove itself as a viable construction method there needs to be a cheap, failsafe and readily available system that can be prepared easily on site. WinSun used recycled building materials along with glass fibres, steel and cement in their projects, while Rudenko used only cement made to a strict recipe. Whilst it is likely that cement is the main material from which 3D printed buildings would be constructed, there are still a lot of variables that need to be considered when designing a system to be used in a 3D printer such as the setting time of the cement. Once cement has started to set it will be harder to pump or extrude making printing impossible so a long setting time is, in this case, desired. However, once a layer of an object has been printed it would be advantageous to be able to complete the next layer in a short amount of time so the printed cement needs to set quickly so it can support the weight of subsequent layers. Alternatively, the D-Shape system utilises a quick setting 2 part cement which can be incorporated into the sand from which the structure is made. [20] Research and testing of potential cement mixtures for use in a 3D printing system would need to take place, along with long term stability testing to ensure the final structure is satisfactory.

Another unknown is if 3D printed structures will comply with building codes. This is a new method of construction which doesn't necessarily use standard materials and so no regulations exist to aid those designing and constructing buildings using 3D printing techniques. The first residential structures built using 3D printing have been built only in the past year so there is no information regarding long term performance. For 3D printing to become an acceptable method of construction it will need to be further investigated by regulatory bodies so that guidelines and standards can be written. Given the current difficulties in including traditional reinforcement in 3D printed structures and the fact that non-standard materials will likely be used, it is conceivable that elements produced using 3D printing may not be as durable or last as long as traditionally produced elements. Such elements may also have different requirements for maintenance.

Depending on the material or equipment used to make an object, some level of post-processing may also be required. For example, removal of rough edges or an additional treatment to improve the strength of the finished article may be required. Whilst the houses constructed by WinSun [9] did not require further treatment after printing to improve strength since they were made of cement, the overall finish was lacking. On the other hand, Contour Crafting [11] produces articles where the individual layers are considerably less pronounced but currently uses clay as the building material which requires firing to reach its final strength.

## 6. Limitations of 3D printing

3D printing has the potential to make a significant and positive contribution to the construction industry but in order to make the best use of this technology, not only should what it can do be investigated but the limits of 3D printing should also be recognised. Arguably, the most important limitation of current 3D printing technology is the range of compatible building materials. The structures made by WinSun and Rodenko, outlined above, use a cement paste which, in the case of WinSun, also contained building waste materials as reinforcement. It is unlikely that these methods could be altered in such a way so as to allow traditional concrete to be used in place of cement paste. D-Shape uses sand to form its structures which gives the system flexibility in that it can use sand from any source which can reduce the cost of materials.

There currently isn't a "one size fits all" 3D printer for fabrication of structural elements. Whilst there are similarities between the reported examples of 3D printing in construction, each is different and specific to an individual situation or set-up. It is envisioned that over time as the popularity of 3D printing increases and the price of the technology decreases further exploration into the use of 3D printing in construction will yield modifications to the current technology that will allow for increased flexibility and ease of set up.

Printing elements with overhanging areas is a challenge for 3D printing as support structures are needed to hold up overhanging areas until they have developed enough strength to support their own weight. Selective Layered Sintering (SLS) [7] and other powder bed methods, in which the unfinished object is supported by a bed of powder during fabrication, present a solution to this problem but require extra time and effort to remove the powder after production is complete. As far as examples such as the WinSun and Rudenko structures are concerned, this may mean that printing an entire building, including the roof, all at once is beyond the capabilities of current 3D printing technology. The D-Shape system, being a powder bed method, allows the object being printed to be entirely supported throughout printing but the current size of the printer means that the size of the object is limited to what can be printed in a 6 x 6 m space. This size is likely not going to accommodate an entire house.

## 7. Cost-benefit analysis of 3D printing in construction

At this particular moment in time, it is hard to evaluate exactly what impact 3D printing will have on construction. What is known, however, is that there is a potential for savings using 3D printing. In its current state, the largest immediate impact that 3D printing can have is in producing models from technical drawings and designs. Often, a three dimensional model can more easily communicate an idea or concern than technical drawings or computer models. In addition, a 3D printed model can cost less than a model made in a traditional manner. A recent study suggested that a sensible estimate of the cost of such a model is approximately 0.1% of the total project cost, not including costs relating to purchase of equipment, materials and software, or labour associated with building the model. Depending on the level of complexity of the model, it can be made in a short space of time ranging from hours to a number of days which compares favourably with current methods. [27]

A major cost associated with concreting is formwork. Cost estimates for construction in the Sydney CBD show that when the cost of building a concrete wall in a multistorey building is broken down, formwork contributed approximately 80% of the total costs (Table 1). By eliminating the need for traditional formwork during construction, there is the potential for considerable savings to be made (Table 2). The cost of the printer is currently unknown, and this is not included in Table 2. Given the magnitude of the gap, there is significant scope for printer costs to be absorbed and still provide a cost effective solution. Without the need for installation and removal of formwork, a saving of approximately 1 day per floor could also be achieved. The WinSun or Rudenko examples do not require the use of formwork to construct their elements but are unable to cope with overhanging sections without the incorporation of supports. Even so, buildings can be made piecewise without the need for formwork. As discussed above, powder bed methods (such as D-Shape) allow a great deal of flexibility in the types of shapes which can be produced

as the unreacted powder provides support to an object as it is being printed eliminating the need for formwork altogether.

**Table 1. Cost estimates for constructing a wall from 40 MPa concrete in a multistorey building in the Sydney CBD using formwork.**

	<b>Cost</b>	<b>Amount</b>	<b>Price</b>
<b>Supply of concrete</b>	\$200/m <sup>3</sup>	150 m <sup>3</sup>	\$30 000
<b>Pumping</b>	\$20/m <sup>3</sup>	150 m <sup>3</sup>	\$3 000
<b>Labour</b>	\$20/m <sup>3</sup>	150 m <sup>3</sup>	\$3 000
<b>Formwork</b>	\$100/m <sup>2</sup>	1500 m <sup>2</sup>	\$150 000
<b>Total</b>			\$186 000

**Table 2. Estimate of cost for constructing a wall from 40 MPa concrete using 3D printing.**

	<b>Cost</b>	<b>Amount</b>	<b>Price</b>
<b>Supply of concrete</b>	\$250/m <sup>3</sup>	150 m <sup>3</sup>	\$37 500
<b>Pumping</b>	\$20/m <sup>3</sup>	150 m <sup>3</sup>	\$3 000
<b>Labour</b>	\$20/m <sup>3</sup>	-	-
<b>Formwork</b>	\$100/m <sup>2</sup>	-	-
<b>Total</b>			\$40 500

Overall, the cost of labour would also be expected to fall as the number of workers required to construct a building would be decreased. Only those people required to oversee the printing activities, assembly and installation of utilities would be on site resulting in a reduction of labour costs. With less people working on site, the potential for injury is also decreased. With the reduction in traditional roles, an increase in new roles would also be seen. Staff with expertise in design and the ability to create commands for a printer, technicians conversant with the technology, as well as those skilled in the assembling and dismantling of the printer will all be required. There will also be costs associated with training and development of staff as new skills are acquired.

It is likely that the cost of building materials consumed during a project could be less for a 3D printing project. More exact placing of material means less waste is generated. There is also the possibility of incorporating construction waste materials into the printing media, such as was done by WinSun. [8] The inventors of D-Shape can use sand from any source, such as the building site itself, reducing the costs of raw materials and impact on the environment caused by production and transportation of these materials.

Another way in which an automated system can reduce waste is through lessening the impact of human error on the building process.

There are also cost savings to be realised through the speed with which building can take place with 3D printing versus traditional building methods. 3D printing boasts speed and efficiency and also greater transportability with systems that are able to be taken apart and rebuilt at the construction site. The completed elements can then immediately be placed without the need for transportation from a factory or warehouse to the site.

Another cost associated with the implementation of 3D printing is the cost of research and development. The current methods, whilst providing an exciting glimpse into the future, can be improved upon and scaled up to more effectively service the needs of the industry. There are also issues surrounding the incorporation of reinforcement; currently there are no systems which are compatible with traditional steel reinforcement and there is a reliance on fibres and metal shavings for additional strength. New binder systems may also improve the quality and strength of 3D printed systems. In addition, efforts into making more user friendly programs for creating digital models for use with 3D printers could increase the popularity of 3D printing techniques and make them a more cost effective option.

The nature of 3D printing is such that it costs no more in equipment to print a once off design than it does to mass produce that same design. Also, curved and irregularly shaped structures will likely cost no more to build with a 3D printer than a structure with a regular shape giving architects and designers a wider degree of freedom in choosing the shape of a building without inflating costs. However, this could result in buildings for which there exist no standards to use to evaluate structural integrity. Therefore a cost to governments and authorities will likely result as they introduce new standards specific for 3D printed structures. Intellectual properties issues must also be investigated to avoid plagiarism of technology and designs.

## 8. Conclusion

Recent activity indicates that there is growing interest in construction scale 3D printing. There are clear apparent benefits in safety, speed, design flexibility and cost, but also significant practical hurdles to overcome. The key benefits of 3D printing align well with the continual drivers of the construction industry: improve safety, reduce cost and increase design freedom. Although in its infancy, 3D printing may become an important part of construction in the relatively near future.

## 9. References

- [1] Empire Cycles Ltd., "Empire's 3D Printed MX6-R," 2014. [Online]. Available: <http://empire-cycles.com/article.php?xArt=31>. [Accessed 5 June 2015].
- [2] Defense Distributed, "Defense Distributed," 2015. [Online]. Available: <https://defdist.org/>. [Accessed 5 June 2015].
- [3] T. Edwards, "3D Systems Unveils CocoJet Chocolate 3D Printer At 2015 CES," 6 January 2015. [Online]. Available: <http://3dprint.com/35081/culinary-printing-3d-systems/>. [Accessed 5 June 2015].
- [4] RedOrbit, "The History of 3D Printing," 2014. [Online]. Available: [http://www.redorbit.com/education/reference\\_library/general-2/history-of/1112953506/the-history-of-3d-printing/](http://www.redorbit.com/education/reference_library/general-2/history-of/1112953506/the-history-of-3d-printing/). [Accessed 11 February 2015].
- [5] J. Kim and D. Robb, "3D printing: A revolution in the making," *University of Auckland Business Review*, vol. 17, no. 1, pp. 16-25, 2014.



- [6] C. Hull, "Method and apparatus for production of three-dimensional objects by stereolithography". European Patent Patent 0171069, 1986.
- [7] C. Deckard, "Method and apparatus for producing parts by selective sintering". United States Patent Patent 4863538, 1989.
- [8] S. Crump, "Apparatus and method for creating three-dimensional objects". US Patent 5121329A, 1992.
- [9] M. Fulcher, "Chinese firm 3D prints villa and apartment block," *The Architects' Journal*, 2015.
- [10] M. Abrams, "3D Printing Houses," 2014. [Online]. Available: <https://www.asme.org/engineering-topics/articles/construction-and-building/3d-printing-houses> . [Accessed 11 February 2015].
- [11] B. Khoshnevis, "Automated Construction by Contour Crafting – Related Robotics and Information Technologies," *Journal of Automation in Construction*, vol. 13, no. 1, pp. 5-19, 2004.
- [12] C. Eastman, P. Teicholz, R. Sacks and K. Liston, *IM Handbook: A Guide to Building Information Modeling for Owners, Managers, Designers, Engineers and Contractors*, 2nd Edition, Hoboken, NJ, USA: John Wiley & Sons, 2011.
- [13] G. Gibbons, R. Williams, P. Purnell and E. Farahi, "3D Printing of cement composites," *Advances in Applied Ceramics: Structural, Functional & Bioceramics*, vol. 109, no. 5, pp. 287-290, 2010.
- [14] L. University, "Partnership aims to develop 3D concrete printing in construction," 2014. [Online]. Available: <http://www.lboro.ac.uk/news-events/news/2014/november/204-skanska.html>. [Accessed 11 February 2015].
- [15] L. Hock, "3D Printing Builds Up Architecture," *Product Design & Development*, 2014.
- [16] M. Russon, "Chinese man creates world's tallest 3D-printed building and a villa in just 10 months," 2015. [Online]. Available: <http://www.ibtimes.co.uk/chinese-man-creates-worlds-tallest-3d-printed-building-villa-just-10-months-1485354> . [Accessed 11 February 2015].
- [17] E. Objects, "Emerging Objects," 2015. [Online]. Available: <http://www.emergingobjects.com/> . [Accessed 11 February 2015].
- [18] A. Rudenko, "3D Printed Concrete Castle is Complete," 2014. [Online]. Available: <http://www.totalkustom.com/3d-castle-completed.html> . [Accessed 11 February 2015].
- [19] S. Robarts, "Arup uses 3D printing to create structural steel component," 2014. [Online]. Available: <http://www.gizmag.com/arup-laser-sintering-construction/32457/>. [Accessed 11 February 2015].
- [20] E. Dini. United States of America Patent US 8,337,736 B2, 2012.
- [21] P. C. Hewlett, "Lea's Chemistry of Cement and Concrete Fourth Edition," Oxford, Elsevier, 2008, pp. 817-818.
- [22] E. Krassenstien, "D-Shape Looks to 3D Print Bridges, a Military Bunker, and Concrete/Metal Mixture," 18 December 2014. [Online]. Available: <http://3dprint.com/27229/d-shape-3d-printed-military/>.

[Accessed 29 May 2015].

- [23] E. Krassenstien, "D-Shape Intern Unveils Plans to 3D Print Unique Buildings in Australia & Beyond," 22 May 2015. [Online]. Available: <http://3dprint.com/64469/3d-printed-buildings-australia/>. [Accessed 29 May 2015].
- [24] M. Brassfield, "Home, Sweet 3-D Printed Home," 4 October 2014. [Online]. Available: <http://www.notimpossible.com/the-latest/3d-printed-estate>. [Accessed 29 May 2015].
- [25] F. Ishengoma and A. Mtaho, "3D Printing: Developing Countries Perspectives," *International Journal of Computer Applications*, vol. 104, no. 11, pp. 30-34, 2014.
- [26] D. Rivero, "Could 3D Printers Soon Kill Construction," 2014. [Online]. Available: <http://fusion.net/story/4565/could-3d-printers-soon-kill-construction/>. [Accessed 11 February 2015].
- [27] D. Foy and F. Shahbodaghlou, "3D Printing For General Contractors: An Analysis of Potential Benefits," in *51st ASC Annual International Conference Proceedings*, Texas, 2015.

## THE APPLICATION OF SCATTERING-FILLING STONE CONCRETE ON HIGHWAY PAVEMENT

Weiguo Shen<sup>1,2,3</sup>, Xing Cheng<sup>2</sup>, Liu Cao<sup>3</sup>, Xinling Li<sup>2</sup>, Chaochao Li<sup>3</sup>, Guiming Wang<sup>2</sup>,  
1.State Key Laboratory of Silicate Materials for Architecture, Wuhan University of Technology, Wuhan 430070, China;2.WUT-UC Berkeley Joint Laboratory on Concrete Science and Technology, Wuhan 430070China;3.Material Science and Engineering School, Wuhan University of Technology, Wuhan 430070, China;

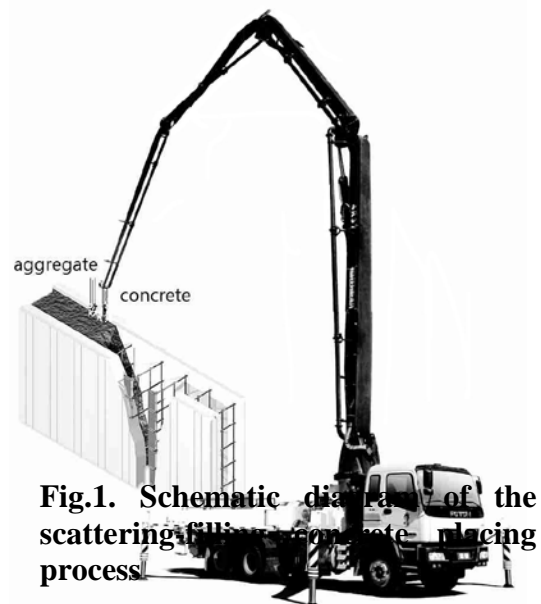
### Abstract

The coarse aggregate volume fraction in conventional plastic concrete is controlled relatively low to ensure a required workability, but its low aggregate content play negative roll on the service properties of the concrete. In this paper, we revealed the mechanism of a coarse aggregate interlocking concrete prepared by Scattering- Filling Stone Concrete (SFSC), it can keep the fresh concrete its workability but increase its service performance by scattering coarse aggregate during the concrete casting, the experimental and engineering application of SFSC indicated that: the strength of concrete prepared with this method increases obviously whereas the shrinkage decreases significantly when 20% cement dosage is saved, the adding aggregates absorbs water from cement paste so tighter and narrower ITZ is formed in the SFSC. The SFS process was utilized in a highway pavement, the core of the concrete is very dense and no obvious defect could be found when 8% pavement concrete was replaced by coarse aggregate. The SFSC is a type of low carbon concrete.

**Keywords:** Coarse aggregates; scattering-filling stone process; aggregate interlocking concrete; strength; shrinkage; interfacial transition zone

### Introduction

Concrete is arguably the most widely used manufactured materials in the world, the production processes of concrete result in tremendous environmental impact, cement is the most remarkable ingredient in the concrete which has the largest resource consumption, energy intensity, green house gases and acid rain gases emission [1,2,3], the manufacture of Portland cement (PC) is responsible for up to 10% of anthropogenic CO<sub>2</sub> emissions worldwide, to prepare qualified concrete with low cement content is a very effective approach to reduce the total environment impact of the concrete even the human activity CO<sub>2</sub> emission. The concrete is a three phased material: aggregate particles, interfacial transitional zone (ITZ) and cement paste matrix [4], the coarse aggregate is the strength framework of the plain concrete and it is the structure unit with highest strength, volume stability, durability and lowest cost in the most concrete [5,6]. As a composition material, the concrete's hydration heat, shrinkage, permeability and creep will decrease, whereas the strength, elasticity modulus and anti-cracking will increase with the increase of coarse aggregate content [7,8,9]. The conventional plastic or fluidal concrete is prepared by mixing the binders (cement and mineral admixture), fine aggregate, coarse aggregate and water together then placing and vibrating the mixture to fabricate a consolidated matrix. In order to keep the fresh mixture a reasonable flowability and avoid gravity segregation, the aggregate content in the conventional concrete (especially those high strength high performance concrete) keeps relatively low [10], the total aggregate volume



**Fig.1. Schematic diagram of the scattering-filling stone concrete placing process**

fraction in high performance concrete is around 65% [11], and the coarse aggregate volume ratio is around 40%, so the aggregates can't act fully as the matrix structure of the concrete, the high volume fraction of cement paste increases the permeability, creep and drying shrinkage of the concrete [11]. The first author invented a new concrete placing process named scattering-filling stone method: adding 10~30% (by the volume of the finished concrete) of coarse aggregate while the concrete is being poured, paved or placed, then vibrating the matrix to form a consolidated concrete [12,13,14] (illustrated in Figure 1). This concrete content 10~30% less cement than the conventional concrete so it is a typical low carbon concrete, in this paper, the mechanism of concrete is revealed, the experiment and engineering utilization of this technology is reported.

### The mechanism of the coarse aggregate interlocking concrete

As illustrated in figure 2, with the increase coarse aggregate in the concrete, the workability will become worse, to keep a reasonable workability, the w/c ratio need to increase therefor its strength of the concrete deduced. Whereas the increase of the coarse aggregate make the strength, modules of concrete increase but the permeability, shrinkage, creep, hydration heat reduce. Simplified it, the increase of coarse aggregate make worse the workability but make better the service performance.

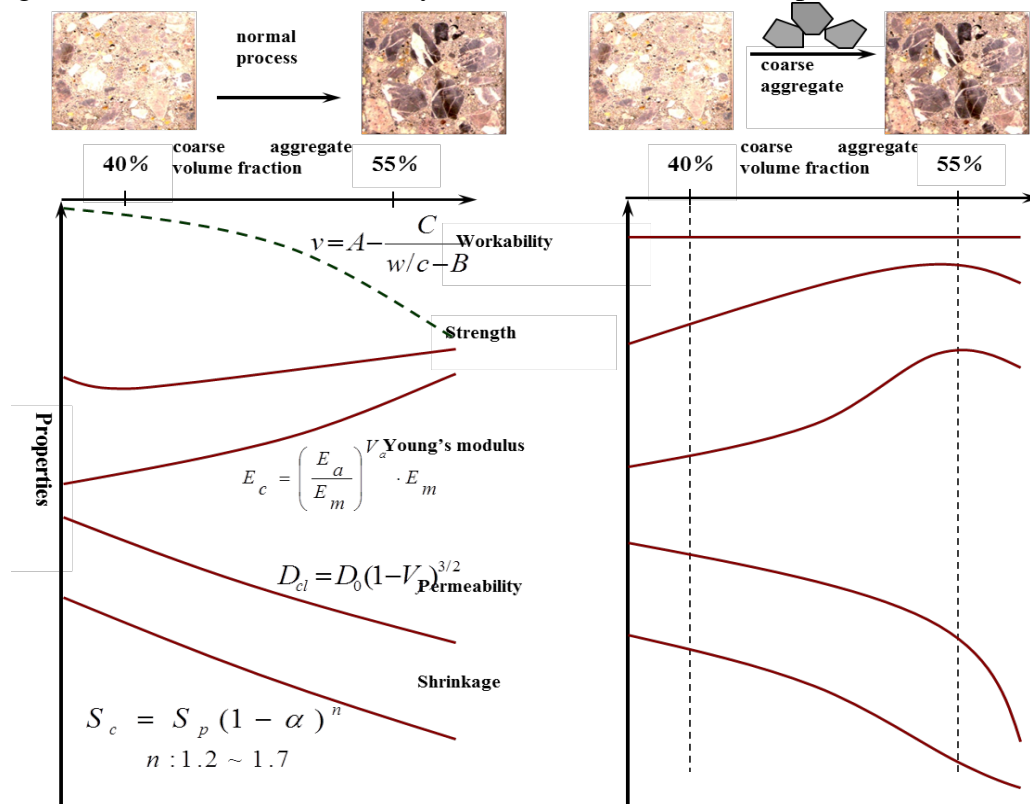


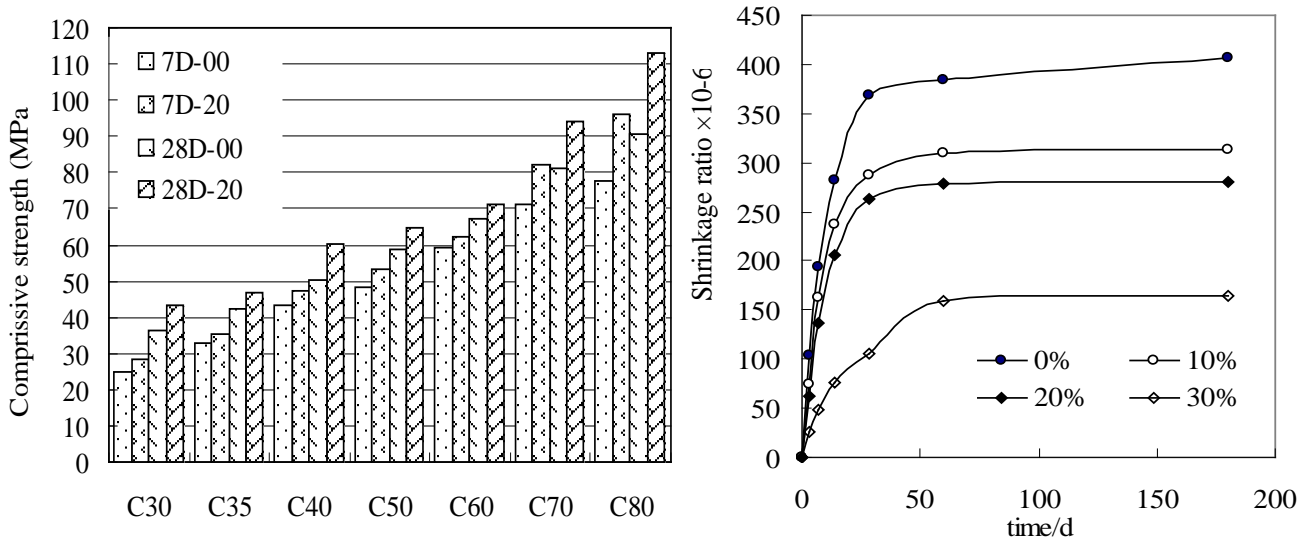
Figure 2 The mechanism of Scatering-Filling Stone Concrete

This new SFS process is a solution to this dilemma, the concrete is designed, mixed and ship with traditional method, so the fresh concrete keep the workability of itself, when the concrete is cast, the coarse aggregate (stone, it can be coarser than the original coarse aggregate in the concrete) is scattered in, the finished concrete has high coarse aggregate content, so the service performance increased. First of all, the coarse aggregate volume fraction increases dramatically in this type of concrete when more than 20% of coarse aggregate is scattered in the mixture, the coarse aggregates can interlock with each other, the friction forces among the aggregate contribute to the strength enhance in a certain extent. The second,

the coarse aggregate distributes more evenly in this kind of concrete than the concrete prepared with conventional process. With the vibration, the segregation of the coarse aggregate toward the bottom of the form and the of the cement paste toward the top may result in the conventional concrete [17], the surface of the concrete will be very weak, but when scattering-filling process is applied, the coarse aggregate will fill evenly at the top of the form. The third, the addition of extra amount of air dry coarse aggregates acts as somewhat water reducer, not only reduces the W/C of the paste close to the aggregate and make the paste stronger so the ITZ of the concrete is enhanced. With the volume fraction of the aggregate increasing, as a composite material, the concrete will become stronger and stiffer.

### Experimental study

The conventional concretes with strength grade varying from C30-C80 are prepared with various kinds of aggregates, cement, mineral admixture and mixing proportions, the aggregate interlocking concretes are prepared with scattering-filling stone process by adding 20% volume ratio of coarse aggregates to substitute the conventional concretes mixtures, the 7 day and 28 day strengths of those concretes with different content of adding coarse aggregate contents are illustrated in Figure 2 (a).



**Fig.3. The strength and shrinkage of original concrete or concrete prepared with SFS**

It can be found that the strengths of all those concretes with different mix proportions increase obviously with the 20% (the volume ratio of scattering concrete in the finished concrete) adding aggregate ratio only different in the extent. The increasing ratio can be as high as 25%. It is easy to find that concretes with 50-100 MPa have been prepared with only 362~440 Kg/m<sup>3</sup> of cement or binder when 20% coarse aggregate is scattered to substitute the original concrete mixtures through some simple calculation, this can be never achieved with the conventional concrete placing process. The scattering-filling stone can prepare concrete with very high coarse aggregate, although the “pre-placed aggregate” concrete process [16] can prepare concrete with as low cement dosage as this process, but it can only prepare low or middle strength concrete. The scattering-filling stone method can produce consolidated concrete with less cement but higher strength and performances at the same time, the decrease on cement dosage not only give the concrete good cost competitive but also good environmental harmonization.

The shrinkage crack of concrete sometime results in damage of concrete structures, increasing of the aggregate can reduce the crack of concrete [17], the shrinkage curves of the concretes with different

scattering-filling stone replacement volume fractions are illustrated in Figure 3 (b), which indicates that with the increase of the replacement volume fraction of the scattering-filling stone, the shrinkage of the concrete decreases significantly. With increasing of the volume fraction of the extra coarse aggregate is added to the concrete, the shrinkage of the concrete decreases markedly. The aggregate scattering-filling process is a very effective approach to reduce the shrinkage of the high strength concrete, which is highly desired by engineers [17].

#### 4.3 The micro-hardness distribution of the aggregate paste ITZ

Figure 4 illustrated the micro-hardness distribution of the ITZ in ordinary concrete and scattering-filling concrete, the rigid origin of X axis is the edge of the aggregate can be found in the microscopy. It is easy to see that the micro-hardness of the scattering-filling aggregate is much higher than that of the ordinary concrete. Generally, the ITZ has the lower hardness than aggregate and cement paste [18]. If the edge of ITZ is where the micro-hardness begin to increase, the width of the ITZ in the ordinary concrete is around 110  $\mu\text{m}$  but the ITZ in the scattering-filling aggregate concrete is 90 $\mu\text{m}$ . This test result also can be explained with the water absorption of the air dry coarse adding aggregate which enhance the microstructure of the ITZ.

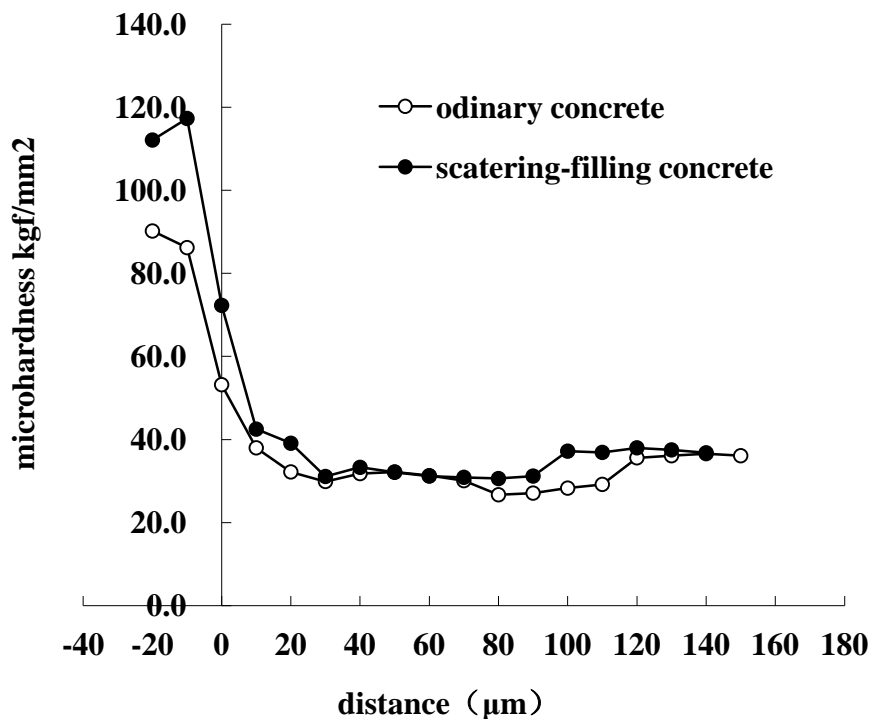


Fig.4. The micro-hardness of the ITZ

#### The utilization of Scattering-Filling Stone Concrete

The scattering-filling stone concrete was used in the pavement concrete in the Provencal highway project 305 in Xiangyang, Hubei (Figure 4), the mix proportion of the original concrete and Scattering-Filling Stone Aggregate Concrete is listed in Table 1.

**Table 1 The mixing proportion of original and Scattering-Filling Stone Concrete**

Concrete type	cement (kg/m <sup>3</sup> )	Crushed stone (kg/m <sup>3</sup> )	Water (kg/m <sup>3</sup> )	Sand (kg/m <sup>3</sup> )	Sand ratio	W/C
Ordinary	380	1211	167	652	0.35	0.44
SFSC	350	1323	154	600	0.31	0.44

The Scattering-Filling Stone Concrete is construction with a process nearly the same as the ordinary concrete, the only difference is this process need to scatter 8% of coarse aggregate by volume under at the surface of the base course of the pavement before the pavement concrete is cast. The pavement cores specimens were drilled 29 days after the ordinary and SFSC pavement were cast, the strength of those cores are listed at table 2, the cores of SFSC pavement have higher mean strength than that of the ordinary pavement.

**Table 2. The strength of core of the pavement at 29 day**

Core Site	Distance to middle (m)	Hight of core (mm)	Spilting strenght (MPa)	Flexual strenght (MPa)	Mean flexual (MPa)
K101+791	0.2	205	3.41	5.14	5.11 (Scattering-Filling Stone Pavement)
K101+780	1.5	214	3.39	5.12	
K101+752	0.2	207	3.34	5.06	
K101+740	0.2	220	3.33	5.05	4.97(Ordinary Concrete Pavement)
K101+732	0.2	224	3.25	4.97	
K101+721	0.9	217	3.18	4.90	

$$f_{sp} = \frac{2F}{\pi d_m \times l_m};$$

Note: the spilting strength is calculated by:

The flexual strength is writon:  $f_c = 1.607 + 1.035 f_{sp}$



**Figure 4. The building site of SFSC pavement**

8% to 10% of cement can be saved when SFSC is used in the pavement, the pavement has higher crack resistance than the ordinary concrete, the segregation of the mortar and aggregate is not so obvious, there are nearly no water bleeding above the surface of the pavement as usually. It is well known that the pavement concrete has very low slump, and not so high strength, there are nearly no the mortar more than needed in pavement concrete, whereas, this SFSC process can be used and get good technical and economic benefit. If we can invent an equipment to fulfil the scattering- filling stone process in the flowing especially the pump concrete, much more aggregate can be scattered and filled in the concrete, and much more cement can be saved, the performance of concrete can be improved more remarkably. Nearly all concrete except the roll compact and no fine concrete can use this process, if this concrete have the opportunity to be applied in all the possible concrete project, more than 15% of cement can be saved, around 1% of the anthropogenic CO<sub>2</sub> can be saved. It is promising to be a low carbon solution to the concrete industry.

## Conclusions

This article relates to a new type of SFSC process developed by the first author, the mechanism, experimental study and engineering application of this process is reported. The following conclusions can be drawn:

1. The increase coarse aggregate volume fraction increase the service performances but reduce the workability of fresh concrete, the SFSC keep the workability of fresh concrete but increase the service performance of the concrete at the same time.

2. C30~C80 concrete with higher strength is prepared but lower cement dosage is prepared with scattering-filling stone method, the dry shrinkage of the aggregate interlocking concrete decrease with the increase of volume ratio of the extra adding aggregate.

3. The application of SFSC in highway pavement indicate this process can be successfully used and increase the strength of the pavement 8-10% cement can be saved.



## Acknowledgments

The author acknowledges the funding support of Hubei Highway Bureau, Guangdong Transportation Ministry (2011-03-057, 2012-02-006) and the Key Laboratory of Road Structure & Material Ministry of Transport.

## References

- [1] Mehta P K. Concrete technology for sustainable development. *Concrete Intern* 1999; 21(11): 47-53.
- [2] Mizuguchi H. A review of environmentally friendly concrete. *Concrete Intern*. 1998; 36(1): 9-12.
- [3] Van Oss H G, Padovani A C. Cement Manufacture and the Environment, Part II: Environmental Challenges and Opportunities. *J Industr Ecol*. 2003; 7, (1): 93-126.
- [4] A.U. Nilsen, P.J.M Monteiro. Concrete: A Three Phase Material. *Cement and Concrete Res*.1993. 23(2): 147-151
- [5] Özturan T, Çeçen C. Effect of coarse aggregate type on mechanical properties of concretes with different strengths. *Cement Concrete Res*. 1997; 27(2): 165-170.
- [6] Beshr H, Almusallam A. A, Maslehuddin M. Effect of coarse aggregate quality on the mechanical properties of high strength concrete. *Constr Build Mater* 2003; 17(2): 97-103.
- [7] Stock A F, Hannant D J, Williams R I T. The effect of aggregate concentration upon the strength and modulus of elasticity of concrete. *Mag Concrete Res* 1979; 31(2): 225– 234.
- [8] Counto U.J. The effect of elastic modulus of the aggregate on the elastic modulus, creep and creep recovery of concrete, *Mag Concrete Res*. 1964; 16(2): 129.
- [9] Hirsch, T.J. Modulus of elasticity of concrete affected by elastic module of cement paste matrix and aggregate, *ACI Mater J* 1962; 59(3): 427–451.
- [10] Alexanderson J. The influence of the properties of Cement and aggregates on the consistency of concrete. *Proc. RILEM Seminar* 1971; 23(2): 12-22
- [11] Mehta P K, Monteiro P J M. *Concrete: Microstructure, Properties, and Materials*, New York, McGraw-Hill, 1993.
- [12] Shen W, Zhang T , Zhou M, et al. Investigation on the scattering-filling stone self-consolidating concrete. *Materials and structures*, 2010,43 (10):1343–1350
- [13] Shen W, Dong R, Li J et al. A study on the coarse aggregate interlocking concrete, *Construction and building material*, 2010,24(11) 2312–2316
- [14] Shen W, Cai Z, Zhou M. High Strength Coarse Aggregate Interlocking Concrete: Preparation And Properties, 8th International symposium on utilization of High-strength and High performance concrete (fib), 2008, Tokyo, 188-192
- [15] Beste U, Jacobson S, Micro scale hardness distribution of rock types related to rock drill wear, *Wear* 2003,254 (5):1147–1154
- [16] Neville F.M. *Properties of concrete*. London, Pitman publishing limited, 1981.
- [17] Mindess S, Young J F, David D. *Concrete (Second Edition)*, New Jersey. Pearson Education, Inc. 2003.

# Preparation and Application of 3D Printing Materials In Construction

Xiqiang LIN, Tao ZHANG, Liang HUO, Guoyou LI, Nan ZHANG, Baohua Wang  
China State Construction Co., Ltd. Technology Center, Beijing, China

**Abstract:** The main 3D printing material is cement and sand tailings, in addition to add coagulant admixtures, retarding admixtures, thixotropic agents and volume stabilizer. The material can be directly pumped to 3D building printers and applied in construction. The 3D printing materials have high early strength, its 2h compressive strength is 10 - 20MPa and 28days compressive strength is 50 - 60MPa. The setting time can be adjusted among 20-60min. It is low-cost, rapid coagulation, high early strength, good adhesion, stability and could meet the requirements of construction 3D printing.

**Keywords:** 3D printing material, R-SAC, coagulation, application

## 1. Development of 3D printing in construction

3D printing technology is widely used in the jewelry, footwear, industrial design, automotive, aerospace, dental and medical industry, civil engineering and firearms fields<sup>1-4</sup>. It is also popular in the field of construction. Compared with traditional architecture, its speed is faster. Without use of templates, it can save substantial costs. It doesn't need a huge number of construction workers which greatly improved the efficiency of production. It can easily print out otherwise difficult building construction curve with advances of low-carbon, green and environmentally friendly 3D printing technology. It could change the direction of building construction industry and obvious change the environmental, construction and ready-mixed concrete industry.<sup>5-7</sup>

In January 2012, the US space agency (NASA) fund collaboration with the University of Southern California and researched the 'outline the process' 3D printing technology.<sup>8</sup>

In January 2013, the Dutch designer Janjaap Ruijsenaars planned to use 3D printing to build houses. The imitation Mobius ring 3D printing houses. At the same time, the European Space Agency proceeded with the construction company of Forster to develop a space station on the moon used print projects which planned to use the lunar soil and other materials readily available to complete the construction of space station through 3D printing materials.<sup>9</sup>

In February 2013, the British designer Soft kill Design worked on the use of 3D printing to build large quantities of civilian houses with nylon fiber.

In March 2013, the Dutch company DAS' architects built the printer which was known as the construction of first 3D printing canal house. In January 2014, it achieved three-dimensional actual canal house component by 3D printing and expected to be completed in three years.<sup>10</sup>

In January 2014, Shanghai surplus company of china used high-grade cement and glass fiber to manufacture its first 3D printing building, causing much attention at home and abroad.

In February 2015, it showed 3D printed Villas with area of 1,100square meters and 6-storey residential buildings in the Suzhou Industrial Park<sup>11</sup>.

## 2. Research status of 3D printing materials

Currently, 3D printing materials mainly include four types which are plastics, metals, ceramics, waxes and like. The cost and the demand of 3D printing materials is difference. For example, plastic material is mainly used in printing and manufacturing industry, metal material used in aerospace and defense, automotive, medical and dental, and ceramics used in home decoration purposes<sup>12-15</sup>.

Among the four types of materials, the most likely used in 3D printing of construction is plastic material. However, the organic materials are prone to oxide, decompose and react under molten state at high temperature for 3D printing. It emits unpleasant toxic gases to the environment and is harm to humans. Besides, the requirement and cost of organic material is high and its mechanical properties are poor. So its use in 3D printing of construction is limit<sup>16-17</sup>.

For present, 3D printing materials used in the building are not yet ripe. Shanghai surplus company used waste of building materials in 3D printing. The material were crushed, ground and cement, fiber, organic binder was added to make toothpaste-like 'ink' to print. Experts from Netherlands made use of resin and plastic materials and US researchers studied resin, mortar, clay and concrete for 3D printing <sup>18</sup>.

3D printing material needs to settable quickly in construction. But the condense time of common concrete is too long, for example, the initial setting time is 6-10h and the final setting time is about 24 hours. Besides, common concrete generally showed to be mobility which could not meet requirements of 3D printing.

The paper researched kind of cement-based composite material suitable for 3D printing. It not only solved the problem of organic material, but also solved the setting time and mobility of cement-based materials.

## 3. Research of technical and mechanical properties of 3D printing material in construction

### 3.1 Cement-based building materials used in 3D printing

(1) Cement: Tangshan Polar Bear 42.5Rapid sulphoalumillte cement (R-SAC) made in China, the performance parameters are shown in Table 3.1 and Table 3.2.

**Table3.1 Chemical composition of cement**

Name	Al <sub>2</sub> O <sub>3</sub>	CaO	SO <sub>3</sub>	SiO <sub>2</sub>	Fe <sub>2</sub> O <sub>3</sub>	MgO	Loss
42.5R-SAC	35.17	42.54	10.79	6.13	1.53	1.24	2.10

**Table3.2 Physical-mechanics performance of cement**

cement	Setting time/min		compressivestrength/MPa		bending strength/MPa	
	Initial	Final	3d	28d	3d	28d
42.5R-SAC	45	73	47.6	55.7	7.70	8.60

(2) Superplasticizer: polycarboxylate superplasticizer (PC).

- (3) Fine aggregate: 20-40 mesh and mechanism tailings of 40-70 mesh.
- (4) Early strength agent: Lithium carbonate (J1), lithium hydroxide (J2), sulfates (J3).  
Retarder: boric acid (H1), sodium gluconate (H2), tartaric acid (H3), citric acid (H4), sodium tetraborate (H5), tripolyphosphate (H6)
- (6) Homemade composite volume stabilizer (VS):Complex admixture includes: thixotropic agents, cellulose ethers and fiber.

### 3.2 Key technology to control setting time of cement-based 3D printing material

#### 3.2.1 Selection of cement admixtures for rapid coagulation

R-SAC has faster condensation speed and higher early strength than ordinary Portland cement. But it also could not meet the requirement of 3D printing materials. In the hydration process of cement, coagulant could act as catalyst to promote hydration of  $C_3A$  and anhydrous sulfur calcium aluminate for formation large amount of ettringite which rapidly shorten the setting time of cement<sup>19</sup>. So the paper selected J1, J2 and J3 coagulant to research the effect on R-SAC and the results are shown in Figure 3.1.

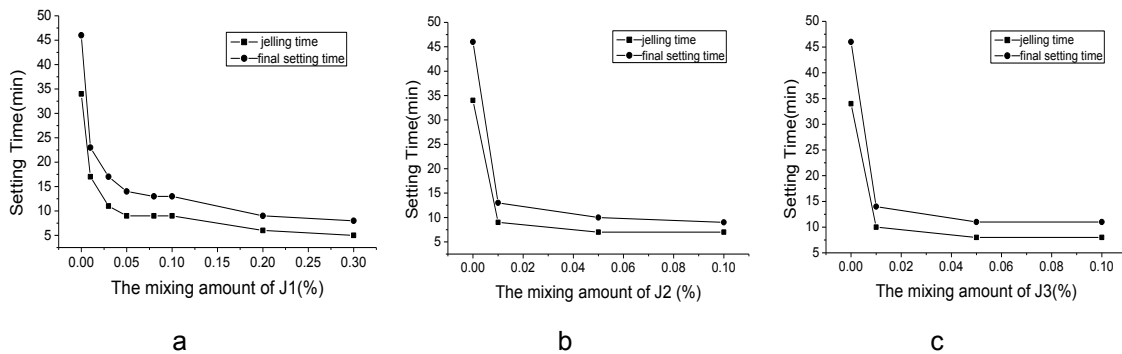
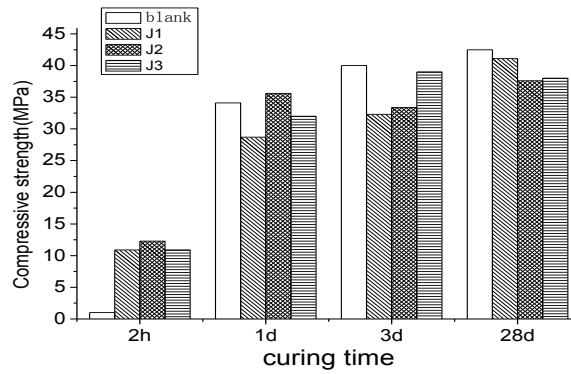


Figure 3.1 Effect of Coagulant J1, J2, J3 on setting time of R-SAC

Figure 3.1 shows that J1 has obvious effect on the setting time of R-SAC. With the ratio of 0.01%, the coagulation time is halved. With ratio of 0.05%, the initial setting time is shortened to nine minutes and when the ratio is 0.3%, the initial setting time is 5 minutes. J2 is a kind of strong base, the effect on the setting time of R-SAC is more than J1 and J3. When ratio of J2 is 0.01%, the setting time could be shortened to 9 minutes, which is the same with ratio of J1 is 0.05%. I. Jawed and J. Skalny et al said that with the presence of base, it promotes generation of ettringite (Aft)<sup>20</sup>. It could be explained that as J2 is a kind of strong base, it promoted the hydration of cement. J3 is ordinary Portland cement which is commonly used as coagulant is not good for the procoagulant effect of R-SAC. Therefore, the coagulant effect of J1 and J2 on R-SAC is more than J3.



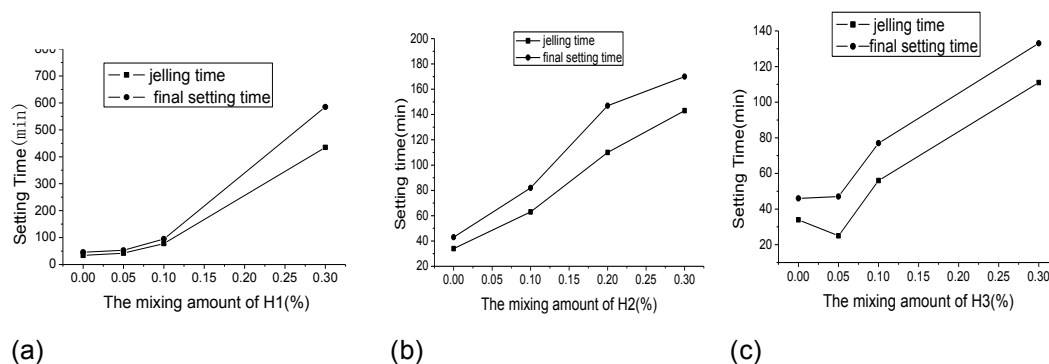
**Figure 3.2 Effect of coagulant on the strength of cement mixed with J1, J2 and J3**

Figure 3.2 shows results of strength of cement mixed with J1, J2 and J3. It could be seen that compared with the cement without coagulant, the 28-day strength of cement mixed with J1, J2 and J3 decreases. Among them, cement mixed with J1 declines the smallest which is 3.3%. But, the 2-hour strength of cement mixed with J1 and J2 is significantly improved which are 26.5% and 32.7% of 28-day strength respectively. It also shows that the 2-hour strength of cement mixed with J3 is low. It could suggest that J1 and J2 could be mixed with R-SAC. Due to the effect of J2 on late strength of cement, J1 is selected as coagulant of R-SAC. Its setting time is short and the early strength is improved at the same time.

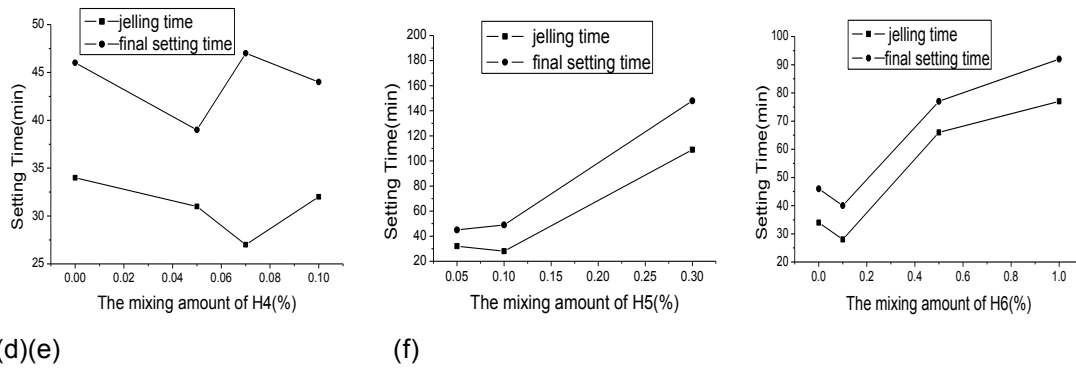
### 3.2.2 Selection of retarding admixtures of cement

Although the early strength of R-SAC is high and it is micro-expansion, the process of hydration is fast. In actual use, it often requires some working time. Especially in summer high temperature environment, it needs to be mixed with appropriate retarder to control the time of construction. Retarder could be adsorbed on the surface of cement particles and formed insoluble layer to delay the hydration of cement. It enables the setting time of 3D printing material to be more stable and easier controlled.

The research selected six common retarder H1, H2, H3, H4, H5 and H6 and tested the effect on the setting time and strength of R-SAC to find a suitable retarder to be mixed with R-SAC, the results are shown in Figure 3.3 and 3.4.



**Figure 3.3 Effect of coagulant on the setting time of R-SAC mixed with H1, H2 and H3**



**Figure 3.4 Effect of coagulant on the setting time of R-SAC mixed with H4, H5 and H6**

Figure 3.3 and 3.4 show the impact of different retarder on setting time of R-SAC, it has the trend of H1>H2> H3> H5> H6 and H4 could cause the setting time abnormal. With the increase of H1, the retarding effect and the setting time increases much. It is not conducive to control and resulted in a certain risk to actual use. H2 is commonly mixed with Portland cement as retarder and it also plays well effect to R-SAC. When ratio is 0.05%, H3 plays little procoagulant effect. With the ratio increase to 0.1- 0.3%, the retarding effect is similar to the trend of H2. It is also suitable to be mixed with R-SAC. H4 is also commonly mixed with Portland cement and to be mixed with R-SAC, the setting time is not stable. With the ratio of H5 increase, the procoagulant effect increases too. With ratio of H5 increase from 0.1% to 0.3%, the setting time increases from 28 to 109 minutes and final setting time increase from 49 to 148 minutes. Its procoagulant effect is more stable than H1 and available to R-SAC. As to H6, it would pay the opposite effect and is not suitable to be mixed as retarder.

**3.2.3 Complex retarder admixtures of 3D printing material**

In production and engineering applications, the setting time of R-SAC is commonly used accelerators and complex retarder to be adjusted. According to experiment, the complex of lithium carbonate as coagulant, anhydrous borax as retarder, lithium, sodium gluconate and tartaric acid could effectively regulate the setting time of R-SAC.

In the study, a lot of tests at different temperature were experiment, and the results were analyzed. Ratio of coagulant and retarder to R-SAC at different temperature is as shown in Table 3.3. Table 3.3 shows the ratio of coagulant and retarder to R-SAC which could effectively control the setting time of R-SAC from 10min to 1h at different temperature.

**Table 3.3 Ratio of coagulant and retarder to SAC at different temperature**

Temperature	Ratio of coagulant		Ratio of retarder	
	J1	H5	H2	H3
0°C~15°C	1.5‰~1.6‰	1.0‰~2.0‰	0~2.0‰	\
15°C~30°C	1.0‰	2.0‰~3.0‰	2.0‰	0~0.6‰
≥30°C	0.5‰~0.6‰	3.0‰~4.0‰	2.0‰~2.5‰	1.0‰

In the material both of coagulants and retarders are mixed in, because they have different role in hydration of cement and effect on different periods<sup>21</sup>. Retarder mainly play role in the induction period before hydration of cement, delaying the initial setting time. And the main role of coagulant is to shorten the induction period, which make both of the initial and final setting are setting time be shortened. So both of coagulants and retarders mixed in the 3D printing

materials could make the materials have particular setting time. It could meet the requirement of construction and the 2-h strength is high enough.

### 3.3 Preparation and study of mechanical properties of 3D printing materials

In the study, R-SAC and water quenched slag powder composite binder was used as the base of 3D printing materials. Industrial tailings sand, water reducer, complex of setting time modifiers and composite volume stabilizer was added to improve the performance of 3D printing material to meet its requirements. Table 3.4 shows the basic ratio of admixtures 3D printing material which were used to make 3D printing materials in the experiment.

The paper mainly studied the technology of controlling setting time and the effect on the mechanical properties of 3D printing materials. Therefore, it took 3 kind of coagulant complex to study the change of setting time and compressive strength of 3D printing materials with different ratio of three kinds of coagulant complex, the complex ratio is shown as in Table 3.5. The results of setting time and compressive strength change with different ratio are shown in Table 3.6.

**Table 3.4 Basic ratio of admixtures to 3D printing material**

W/B	Cement	Ore	Tailings 20-40m	Tailings 40-70m	PC	Coagulant	Other admixtures
0.35	400	100	300	200	1.0‰	JH	VS

**Table 3.5 Complex ratio of coagulant and retarder to 3D printing material**

	Coagulant		Retarder	
	J1	H5	H2	H3
HJ-1	1.5‰	2.0‰	/	/
HJ-2	1.0‰	3.0‰	2.0‰	/
HJ-3	0.6‰	3.0‰	2.0‰	1.0‰

**Table 3.6 Setting time and Strength of 3D printing material with different ratio at different temperature**

Temperature		Coagulant complex of JH	Setting time (min)		Strength (MPa)			
			Initial	Final	2h	1d	3d	28d
5-10°C	A-1	JH-1	33	50	16.1	37.2	48.6	60.5
	A-2	JH-2	58	122	7.6	36.5	40.4	58.3
	A-3	JH-3	140	175	/	35.9	45.8	61.6
15-20°C	B-1	JH-1	15	26	24.4	41.2	54.6	59.5
	B-2	JH-2	35	46	15.8	40.3	50.5	64.7
	B-3	JH-3	75	90	5.3	38.7	52.3	62.3
30°C	C-1	JH-1	8	15	28.9	47.1	56.1	64.1
	C-2	JH-2	26	38	23.1	43.2	54.5	60.8
	C-3	JH-3	47	59	19.2	46.8	55.7	67.5

Table 3.6 shows the setting time of 3D printing material could be flexibly controlled within 10-60min under three different temperatures by adjusting the ratio of coagulant and retarder in

the composition for the requirement of different seasons and environments.

The 3D printing material has high early strength and rapid coagulation. The 2h strength could be achieved to 10 - 20MPa, 3-day strength was 40 - 50MPa and 28-day strength was about 60MPa which could meet the requirements load-bearing walls and columns strength of 3D printing architectural. It could also make the printing members have good mechanical properties. The printing process used 3D printing materials is shown in Figure 3.5 and Figure 3.6 shows small 3D printing members.



**Figure 3.5 Printing process used 3D printing materials**



**Figure 3.6 3D printing construction members**

The raw materials of 3D printing materials are low-cost and friendly to the environment and humans. It also has the advantages that the adhesive of material is good, the stability is strong, the pump retention shape and bonding properties is good, and the 3D printing buildings has good printed form and volume stability. The 3D printing building and members could be mobile and assembled in short time, it has wide applications and could greatly promote the application and popularization of 3D printing technology.

#### **4. Conclusions**

(1) It used R-SAC in the 3D printing building materials to overcome the long setting time and low early strength of ordinary Portland cement-based materials. It have high early strength, its 2-h compressive strength could be 10 -20MPa and 28-day compressive strength is 50 -60MPa.



(2) At different application temperature, it could adjust the ratio of coagulant and retarder J1 H2, H3 and H5 to be suitable for the 3D printing material, and it could make the setting time of the material flexibility and easily controlled among 20-60min.

(3) It could change different kind of admixtures which have different functions to be mixed with R-SAC to adjust its performance. The shape is stability and the compressive strength is high enough for the continuity and security of 3D printing.

(4) The raw materials of 3D printing materials used in the study is low-cost and are friendly to the environment and humans which could promote the use of 3D printing technology in building construction.

## References

1. Arghavan Farzadi, Vicknes Waran, et al, "Effect of layer printing delay on mechanical properties and dimensional accuracy of 3D printed porous prototypes in bone tissue engineering", Ceramics International.41(2015)8320-8330
2. Benjamin Kading, Jeremy Straub," Utilizing in-situ resources and 3D printing structures for a manned Mars mission",Acta Astronautica.107(2015)317-326
3. A. Ovsianikov, V. Mironov, J. Stampfl, R. Liska, "Engineering 3D cell-culture matrices: multiphoton processing technologies for biological and tissue engineering applications". Expert Review of Medical Devices. Med. Dev. 9 (2012)613-633.
4. Fuping Li, Chunlin Deng, etc., "Outlook of 3D printing technology and commercial concrete construction industry", Concrete world. 3(2013) 28-29.
5. S.E. Hudson. "Printing teddy bears: a technique for 3D printing of soft interactive objects", Proceedings of the 32nd Annual ACM Conference on Human Factors in Computing Systems, 2014.
6. H. Seitz,W. Rieder, S. Irsen, B. Leukers, C. Tille, "Three - dimensional printing of porous ceramic scaffolds for bone tissue engineering", J. Biomed. Mater. Res. B 74 (2005)782-788.
7. Alexandros Selimis, Vladimir Mironov, Maria Farsari, "Direct laser writing: Principles and materials for scaffold 3D printing". Microelectronic Engineering 132 (2015) 83-89
8. Giovanni Cesaretti , Enrico Dini, et al., "Building components for an outpost on the Lunar soil by means of a novel 3D printing technology ", Acta Astronautica93(2014)430-450.
9. Yue Hong, "From theory to practical of 3D printing building", Frontiers of Science, 6 (2014) 58-62.
10. Yulei Du, Feifei Sun, etc., "Current Status of Materials for Three-dimensional Printing", Journal of Xuzhou Institute of Technology, 1 (2014) 20-24.
11. G. Cesaretti, E. Dini, X.DeKestelier , "Building components for an outpost on the lunar soil by means of a novel 3D printing technology",Acta Astronaut.93(2014)430-450.
12. Chelsea Schelly, Gerald Anzalone, "Open-source 3-D printing technologies for education: Bringing additive manufacturing to the classroom ". Journal of Visual Languages and Computing, 28(2015) 226–237.
13. Zhiguo Li, Ying Chen, et al., "3D printing materials related to the concept of discrimination", Tianjin Construction Science and Technology. 3 (2014)8-12.
14. M.Goldin, "Chinese Company Builds Houses Quickly With 3D Printing". April 28, 2014. Available: <<http://mashable.com/2014/04/28/3d-printing-houses-china/>>.
15. A. Butscher, M. Bohner, C. Roth, et al, "Printability of calcium phosphate powders for

- three-dimensional printing of tissue engineering scaffolds", Acta Biomater. 8 (2012) 373-385.
16. C.X.F. Lam, X. Mo, S. Teoh, D. Hutmacher, "Scaffold development using 3D printing with starch-based polymer", Mater. Sci. Eng. C Biomim. Supramol. Syst. 20 (2002)49-56.
17. R. Chumnanklang, et al., "3D printing of hydroxyapatite: effect of binder concentration in pre-coated particle on part strength", Mater. Sci. Eng.: C 27. 4(2007) 914-921.
18. M. Castilho, et al., "Structural evaluation of scaffolds prototypes produced by three-dimensional printing", Int.J.Adv.Manuf.Technol.56 (2011) 561–569.
19. Yanmou Wang, Muzhen Su, etc., "sulphoaluminate cement", Beijing Industrial University Press,1999, pp 3-4.
20. X. Feng, H. Wang, "The influence of gypsum on some properties of sulphoaluminate high early Strength cement", Journal of Chinese Ceram Soc. 12 (1984)166-178.
21. Jiankui Chen."Principles and Applications of concrete admixtures". China planning press,2004, pp 10-14.

# Repair and Retrofitting

# The restoration and repairs of the Sir William Goodman Bridge designed by Sir John Monash, Adelaide

John Woodside<sup>1</sup> and Leo Noicos<sup>2</sup>  
Principal, J Woodside Consulting Pty Ltd,  
<sup>2</sup> Principal, LN Engineering

**Abstract:** This paper examines the engineering design and project management of the restoration and repairs to a heritage listed tram bridge in Adelaide.

The bridge built in 1908 is the second oldest reinforced concrete girder bridge in South Australia. The bridge has performed remarkably well for over 100 years and is a tribute to the original designer, (Sir) John Monash, one of the early pioneers of reinforced concrete in Australia. The bridge was originally designed as a tramway bridge; it then became a one-way car bridge in the 1950s and now is a pedestrian/cyclist bridge. During an audit of the bridge in 2010, because of the extent of reinforcement corrosion and cracking of the concrete, the bridge was immediately closed causing concern to residents and the public who used the bridge.

From the repairs and reconstruction and other sources, it became evident that reinforcement corrosion was initiated by stray electrical currents from the trams, commencing early last century, although this was not initially understood.

The bridge was subject to many investigations and reports, and because two Councils owned the bridge, there was difficulty in agreeing on what should be done with the bridge. One Council wanted to restore the bridge, and one wanted to demolish it and build a new bridge. This political situation was overcome by one Council giving their half of the bridge to the other Council together with a monetary reimbursement. The restored and repaired bridge was reopened to the public in September 2014 as a cyclist/pedestrian bridge.

This paper reviews in particular the structural engineering and project management of the concrete repairs and restoration of a heritage concrete bridge, including the investigations, preliminary design, trial repairs, final design and documentation, construction and the lessons to be learnt from this project.

**Keywords:** Restoration, bridges, heritage, Sir John Monash, SARCC.

## 1. Introduction

To understand heritage restoration of concrete structures, it is important to understand the early history of reinforced concrete and the role of Joseph Monier (1). Miles Lewis in *"200 Years of Concrete in Australia"* (2) provides background to the early days of reinforced concrete in Australia. Many early reinforced concrete structures in Australia, including this bridge, used the proprietary Monier System of reinforcement (3).

The Sir William Goodman Bridge, as it is now known, is a SA heritage listed structure and is the second oldest reinforced concrete girder bridge in South Australia, built in 1908 originally as a tramway bridge spanning the River Torrens as shown in Figure 1. In recent times, the bridge has provided a direct route for pedestrians and cyclists across the Torrens River and connects with the River Torrens Linear Park and Path on the north side of the river which is a very important pedestrian and cyclist route in Adelaide.

Richard Venus has provided a marvelous historical record of the area, the bridge, Adelaide's tramways and the engineers involved originally in the bridge in the nomination of the bridge for engineering heritage recognition by Engineers Australia (4).

The design of the bridge was by (Sir) John Monash and the Reinforced Concrete & Monier Pipe Construction Co (RCMPC) with construction by the South Australian Reinforced Concrete Co (SARCC) (5,6,7).

In 1953 following the closure of the tram system, the Municipal Tramway Trust (MTT) offered the bridge to the SA Highways Department but they refused to take over as it unsuitable for vehicular use. In 1954, two councils had joint ownership of the bridge. In 1961, the Highways Department (now DPTI) became responsible for the bridge, and it was reopened in 1962 with a 5 ton limit and one-way traffic. Some upgrading work was carried out (but no concrete repairs) which included filling in the set down for the tram tracks with bitumen and the provision of guardrails on either side, inboard from the cast iron handrails.



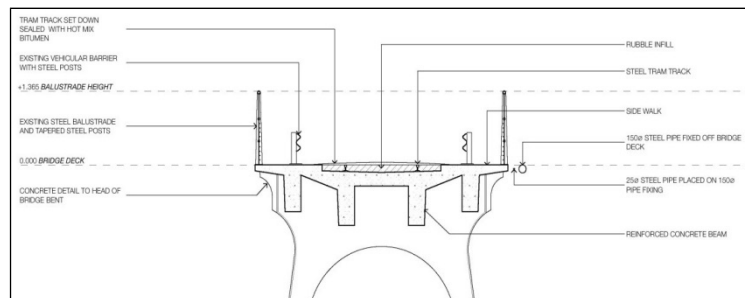
**Figure 1 The bridge under construction 1908**

(Photograph courtesy University of Melbourne Archives BWP/24366 Reinforced Concrete & Monier Pipe Construction Co.)

The bridge was SA heritage listed in 1986 due its historical significance and could not be demolished but could be retained as a managed ruin. With the merger of councils, the Holland Street Bridge, as it was then known, became jointly owned by the City of Charles Sturt and the City of West Torrens. The load limit of the bridge was lowered to 2 tons and closed to road traffic in 1990 and then became a pedestrian and cyclist shared use bridge. It was closed in 2010 because of safety concerns, following a bridge audit.



**Figure 2 The bridge prior to restoration**



**Figure 3 Typical Deck Section**

(Figure courtesy flightpath)

As shown in Figures 2 and 3, the bridge is a three-span continuous reinforced concrete deck slab and beams. Both ends of the bridge and the two middle A Frame-Bent-supports are integral with the bridge superstructure. The deck slab is supported by two interior and two exterior beams.

## 2. Sir John Monash

Much has been written about Sir John Monash, as he was brilliantly successful in three different careers during his life (8, 9, 10, and 11). Holgate and Taplin have provided an excellent background on the contribution of Sir John Monash to 20th-century engineering in Australia (12).

Monash established the *South Australian Reinforced Concrete Company (SARCC)*, which built this bridge, and he was one of the 4 directors of the SARCC. However, it was not as successful as its Victorian counterpart; the *Reinforced Concrete & Monier Pipe Construction Co* was. Holgate states (7) that after Monash established SARCC in 1906, its primary work seems to have been in the field of city buildings and elevated water tanks from 1909 in South Australia.

### 3. Investigations

The bridge was subject to a number of investigations over about two years with the final recommendation that the bridge be abandoned, and new pedestrian bridge be constructed. The City of Charles Sturt decided to explore the possible restoration of the bridge and engaged John Woodside of J Woodside Consulting (JWC) in 2011 to provide an independent second professional opinion on the structural deterioration and the possibility of restoring the bridge, suitable for a walking and cycling bridge.



**Figure 4 A view of the worst external beams 2011, which was the trial beam, repaired in 2013.**

The key question was could the bridge be successfully repaired, and its life extended and Figure 4 shows some of the damage observed in 2011. From a series of inspections, research and a long involvement with concrete and repairs, JWC believed that the bridge could be successfully repaired, with an estimated serviceable life of at least another 30 years. JWC also concurred with the Council's decision to close the bridge to all traffic. JWC findings were set out in their initial report to the Councils (13).

### 4. Preliminary and final design

The City of Charles Sturt then engaged the project team to carry out the preliminary design and design development of the restoration and repairs of the bridge to give a better understanding of the repairs and the likely costs. This stage also included trial repairs of one of the beams of the northern span of the bridge recommended by JWC, which was extremely successful. A further report in 2013 was prepared by JWC (14) confirmed that repairing the bridge was a significantly cheaper option than constructing a new bridge and maintaining the old one, by an order of 50%. The report concluded the bridge could be successfully repaired, based on the trial repairs and other design work, for a total budget cost of \$2.6m.

From the various investigations and reports, it was obvious that the structural deterioration of the bridge with reinforcement corrosion and cracking of the concrete had been occurring for many years. Together with other information and the trial repairs, it also became apparent that the corrosion of the reinforcement had been initiated by stray electrical currents from the trams rather than from carbonation as firstly supposed, as shown in Figure 5. When the trams ceased in 1953, the rate of corrosion slowed significantly.



The top reinforcement of the trial beam over the North “A” frame was also exposed, and it was found to be in good condition with no evidence of any corrosion.



***Figure 5 Corrosion of the original round reinforcement and the density of the uncracked concrete***

The trial repairs showed that where there was no corrosion and spalling, the existing concrete was in sound condition and of a satisfactory strength and those areas which were damaged could be successfully repaired to meet the requirements of the current Australian Standard AS 5100.

The architectural work included documenting the restoration of the existing cast iron balustrades on the outside of the bridge. As the existing balustrades did not comply with the requirements of the current Bridge Standard, new galvanised steel balustrades inboard complying with current requirements were provided. The new balustrades were designed using contemporary materials and included LED lighting in the posts and overhead lighting. Also to new lighting to the top bridge, there was up lighting under the bridge. The architectural design also included landscaping and urban design at either end of the bridge together with entrance statement and seating at the northern end of the bridge.

Discussions were held with Heritage SA on the colours for the coatings of the repaired concrete surfaces and other heritage matters during the design and construction stages. Heritage SA also required a simulated tram track to be cast into the new concrete surface, and the architect chose two lines of pavers in the concrete that were also lit, to represent the previous tram rails.

The electrical engineer was responsible for the lighting on top and lighting under the bridge to provide a visually exciting view of the bridge at night and to meet the P3 level required for safety reasons on top of the bridge as shown in Figure 9. The civil engineer designed the scour control around the two concrete A-frame bents in the river and one of the abutments, to protect the existing pile caps and piles and footing under flood in the River Torrens.

The structural engineer was responsible for the design and documentation of the concrete repairs including additional bar reinforcement to all the beams and carbon fibre reinforcement to all the beams to provide sufficient shear reinforcement. The existing reinforcement in the bottom of the external beams was only used in part, and additional bottom reinforcement added to take the design loads. Additional top reinforcement was included in the infill slab poured in the set down area on the top of the bridge, for the live load condition for the two inner beams. The structural design was based on carrying out a number of site inspections to confirm dimensions of the structure as taken from sketches and drawings included in previous reports and the identification of obvious major deterioration to the key structural elements of the existing bridge structure. The documentation of the structural work was also based on all visually accessible components of the bridge at the time of the inspections and the various reports. The data, which was collected was then used to carry out the structural analysis of the existing bridge structure. This data provided the basis for identifying the structural capacity of each element and the extent of the required upgrading and repair.

The structural analysis of the existing bridge was undertaken to check the existing capacities of the critical components for the most adverse combination of loadings that could act on the structure and to determine the strengthening procedure to restore the safe working condition of the bridge in accordance with the requirements of the current Australian Standards.

The assumed concrete compressive strength was 15 MPa for the structural analysis and design, consistent with the adopted strength in reports and analysis by others. The concrete strength was based on the average results of the laboratory testing carried out on the two sets of concrete cores taken from the existing bridge elements.

In the absence of original information on the properties of the existing reinforcement, 200 MPa yield strength of the existing reinforcement was adopted. This yield strength was in general agreement with the reported yield strength of 230 MPa (1914) of plain reinforcement bars which has compiled information on steel reinforcement as early as 1914 to the present time (15). Subsequent testing of a main reinforcing bar from the southern span confirmed yield strengths of 260 MPa, which was reassuring (16).

The design loads adopted for the structural analysis of the bridge structure were based on AS 5100 and included self-weight, imposed dead load, pedestrian live load, water flow drag force, debris load, wind load and earthquake load. In accordance with AS 5100 and AS 1170.0, these loads were combined to produce the most adverse case of loadings acting on the respective structural components of the bridge and to assess their structural capacities.

A 3-D computer model was created using the above information then to determine the local and global structural behavioural responses of the key elements of the bridge as shown in Figure 6. The converted three-dimensional frame model used section properties based on cracked concrete to account for the expected conditions of the concrete elements. The structural models assumed continuous beams over internal supports given the monolithic construction of the superstructures with the 'A Frame' and pinned supports at the abutments.

The sizes, dimensions, and arrangements of structural members were based on the reviewed sketches and drawings included in the previous reports and check dimensions obtained during site inspections.

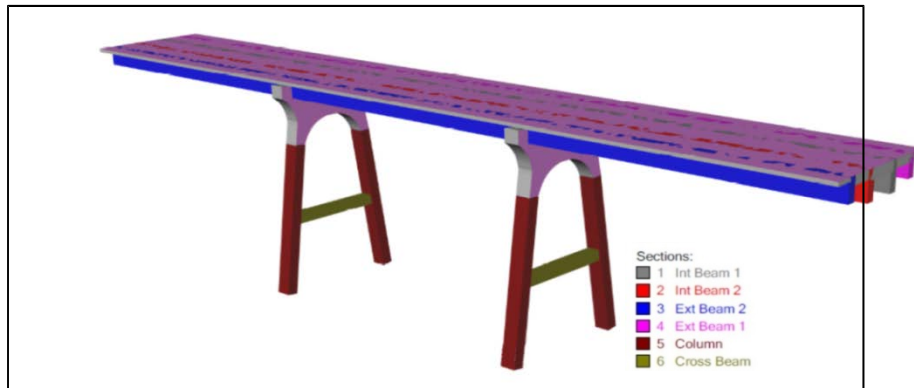
The design loads were combined in accordance with the provisions of AS 3600 and AS 5100 for concrete structures. The gravity loads applied to both the exterior and interior beams at the deck level were determined from the dead load, superimposed dead load, and pedestrian live load imposed between the new handrails. Furthermore, the bridge was analysed for transverse wind loads of 1.80 kPa and 3.0 kPa applied to the superstructure and 'A Frame' supports, respectively.

The earthquake load  $E_U$  was estimated to be  $0.04G_g$ , where  $G_g$  is the seismic weight in the order of 2580kN and was determined in accordance with the provisions of both AS 5100.2 and AS 1170.4. The bridge 'A Frame-Bent' was also analysed using 1.74 kN/m drag force and debris load of 50kN for each 'A Frame' from flood loads. These flood loads were determined in accordance with AS 5100.2 based on a river velocity of 2 m/s and water depth of 6.0 metres.

Based on the analysis, both the exterior and interior beams of the existing bridge were found to have insufficient capacities under vertical actions without strengthening to sustain the worst combination of the proposed loadings. The 'A Frame' internal supports were structurally sufficient to carry the proposed loadings; however the detailing of reinforcement particularly fitments did not meet the requirements of AS 3600 and AS 5100.

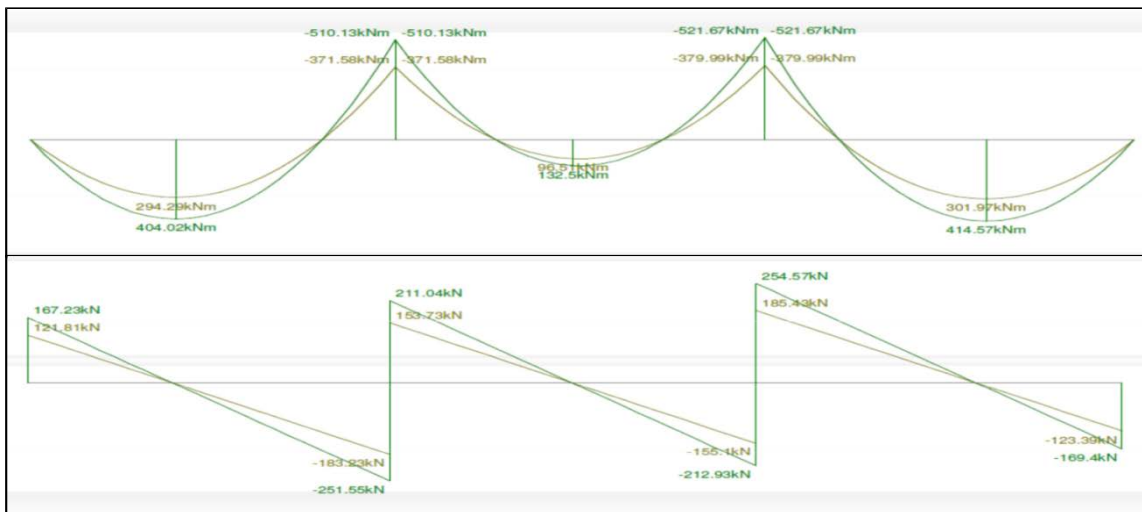
The sagging moment capacity of the outer beams were not adequate to provide resistance to the demand bending moment due to the reduced area of bottom reinforcement damaged by severe corrosion. The existing bottom reinforcement of the beams was 8 No  $1\frac{1}{4}$  inch diameter bars in two layers. However, the area of the reinforcement was estimated to be approximately 30% of the original area due to corrosion in certain places. Also, the beam had insufficient shear capacity near the supports due to the absence of required fitments required by the current relevant Australian Standards.





**Figure 6 Rendered 3-D Model of Bridge**  
(Figure courtesy URS)

The interior beams, which carry the majority of the applied pedestrian live load between the new handrails, were overstressed for both hogging moment and shear. Fortunately, the bottom reinforcement was largely undamaged, and additional top reinforcement could be added to the new slab on top of the bridge. The bending moment and shear force diagrams for the interior beams for both serviceability and ultimate limit states are shown below Figure 7.



**Figure 7 bending moments and shear force diagrams for inner beams**  
(Figure courtesy URS)

4 no. N24 additional bars were added to the bottom of the outer beams to increase the sagging moment capacity. All beams were also provided with U-wrap carbon fibre to increase their shear capacity and to comply with the minimum shear requirements of AS 3600.

The rectangular columns of the two 'A Frame-Bents' internal supports were found to be satisfactory to carry the proposed loadings but to ensure compliance with the minimum confinement requirements of AS 3600 and AS 5100, carbon fibre was wrapped around them also.

The footings were considered to be adequate with no sign of differential settlement observed based on the reviewed survey deck levels and a previous footings assessment report. Each column of the 'A Frame' internal supports was supported by 4 no 300mm x 300mm by 7610mm long concrete piles as shown on the existing original drawing and as recorded in a newspaper report at the time of the construction.

Following various political considerations and consultations, the City of West Torrens gave their half of the bridge to the City of Charles Sturt together with a contribution to the cost of future works and accepted no further responsibility. Together with a grant from the SA government and money from the City of Charles Sturt, this provided the funds to allow the final design work to be completed and the repairs and restoration to proceed under one owner.

The City of Charles Sturt then appointed the project team to finalise the design and documentation and to manage the restoration and repair work. The final design was undertaken in late 2013 and tendered by the Council by open tender, with tenders closing just before Christmas 2013. Five bids were received, and after careful evaluation, Synergy Remedial was awarded the contract. An updated cost plan by the QS also confirmed that the project could still be delivered for an overall budget cost of \$2.6 million.

## 5. Construction

Work on the repairs, restoration, and upgrading started in mid-January 2014 and was completed in mid-September 2014, a period of nine months.

The outermost beams were the most severely corroded together with local corrosion to the internal beams, the underside of the slab and the column A-frames. The beams and the underside of the slab were repaired using appropriate concrete repair techniques. Scaffolding and propping to repair the underside of the bridge was supported either on the banks of the river or hung from the centre span of the bridge.

The depth of the external beams was increased by approximately 75 mm to accommodate the additional bottom reinforcement as shown in Figure 8. This increase in depth is not obvious and had the approval of Heritage SA. The beams were repaired and strengthened, and all cracked concrete was removed, to provide space around the existing reinforcement to allow the new concrete to encase them. All existing reinforcement was grit blasted to bare metal, all existing and new reinforcement was coated with a zinc rich paint, and additional steel reinforcement was added to the bottom of the external beams as discussed previously.



**Figure 8 The existing & new reinforcement together with new concrete to half of an external beam**

The new concrete to the beams used 10 mm aggregate with a super plasticiser and was 20 MPa in strength to match the existing concrete strengths. Concrete was placed into formwork with bird mouths.

The new concrete enclosed the existing and additional reinforcement and restored the bottom of the beam previously cracked. It was also significantly cheaper than proprietary patch repair material. Carbon fibre reinforcement in discrete vertical strips was then applied to the sides and bottom of the beams as shear reinforcement. In a similar manner, the two A-frame bents were also repaired and strengthened. A thin render was then applied to the concrete surfaces under the bridge to provide a suitable surface for the application of the coating system with the colour to approval by Heritage SA.

The existing cast iron handrails were repaired and restored together with 12 new matching cast-iron posts but did not comply with current regulations. New handrails were installed inboard together with lighting.

The repair and restoration work were reasonably consistent with the expected extent of repairs and in accordance with the documentation and the trial repairs. However, there were a few hidden surprises with the concrete repairs; principally because there were no slabs at either end of the bridge; and there were also changes required to the new concrete slab on top of the bridge. This was in part due to the increased depth of set down which was not anticipated, resulting in an additional amount of bitumen to be removed.

Also, the extent of concrete repairs was more than was documented, which was not unexpected, and this additional work was allowed in the construction contingency.

The final construction cost including all fees, trial repairs and contingency was \$2.3 million, \$0.3 million under the \$2.6 million budget, which pleased everyone involved in the project, and in particular the client.

The reconstruction and restoration work included not only the repairs to the existing concrete with the coatings but also included a new concrete slab to fill the set down for the tram tracks to the top of the bridge, new lighting and scour protection at the base of the pier foundations as well as landscaping and signage and entrance statement at the northern end of the bridge. From the repair work carried out, it is obvious that the bridge will easily meet the brief requirements of 30 years additional life and should have at least another 50-100 years of life before possible further repairs and restoration are required.

Although load testing was not required since the design complied with the Australian Standards, testing was allowed for in the contract. The reason for the inclusion of load testing in the contract was to alleviate any concerns by other parties as to the structural adequacy of the bridge. Traditionally where a structure cannot be proved to be structurally adequate by structural mechanics, load testing of the structure is carried out. The proof load was 9kPa (900kg/m<sup>2</sup>), and the southernmost span was tested over the full width, with strains and deflections measured on two beams and corrected for temperature effects. The maximum deflection was of the order of 2 mm after correction, and the calculated internal stress was 9.2 MPa showing that the bridge was essentially uncracked, and the concrete had not reached its tensile strength. The test results were almost embarrassing, and the bridge may be suitable for future trams!

## **6. Existing tram tracks**

Initially, it was hoped that the existing tram tracks could be used in the project but they were badly corroded and after careful consideration, it was concluded that they could not be incorporated in any of the new works. As a result, they were given to the Tram Museum at St Kilda in Adelaide at no cost.

## **7. Lessons learnt**

With all concrete repair work, it is vital to determine the reasons for the deterioration of the concrete, consider the feasibility of repairs and reconstruction and then to proceed with the work if practicable.

It is important to select the right consultants and contractor to suit the project, with experience in heritage and concrete repair work. Use the same consultant team throughout, provided they are competent and work as a team, so design knowledge is not lost. Make the consultants responsible for preparing the as-built drawings of the final work. In a similar manner, it is important to have an architect experienced in heritage matters, and they may have a better overview than engineers of the final result. As lead consultant, they should manage the design team with input from the project manager.

Consult widely with those who are knowledgeable on all such projects to get their valuable input.

Do not use the currently fashionable method of documentation using partly finished and vague documents for tender or a design and construct tender and let the contractor sort out the details afterwards, it just does not work on these types of projects. Do not have liquidated damages and have a flexible construction period to allow for the unknown. Use an experienced project manager, as owners of such assets, do not have the experience for managing this type of project at a technical level. Heritage projects require a different mindset by all involved and the urgency for completion must be tempered with patience.

One of the major difficulties with concrete repairs is specifying the extent of repair work based on visual inspections as not all repair work can be identified. There are two approaches to this problem; one is to allow the contractor to take all the risk, but that can result in a loaded price but with no risk to the owner. The second approach based on previous experience by JWC on such projects is to use a cost plus approach for additional concrete repair work over above those repairs identified on the tender drawings. It is considered that this latter approach provides the best outcome for both the client and the contractor, and they share the risk between them. As a result, the contract price was not loaded at the time of tender,

a competent contractor will do all the necessary repairs required even if not documented without delaying the project and the final repair works can be readily measured, and variations agreed with rates established at the time of tender.

In heritage type projects such as this, unknown problems will always appear, and a construction contingency of 10% of the construction cost was included in the project budget. This allowance was found to be not be entirely sufficient, and should have been closer to 15%.

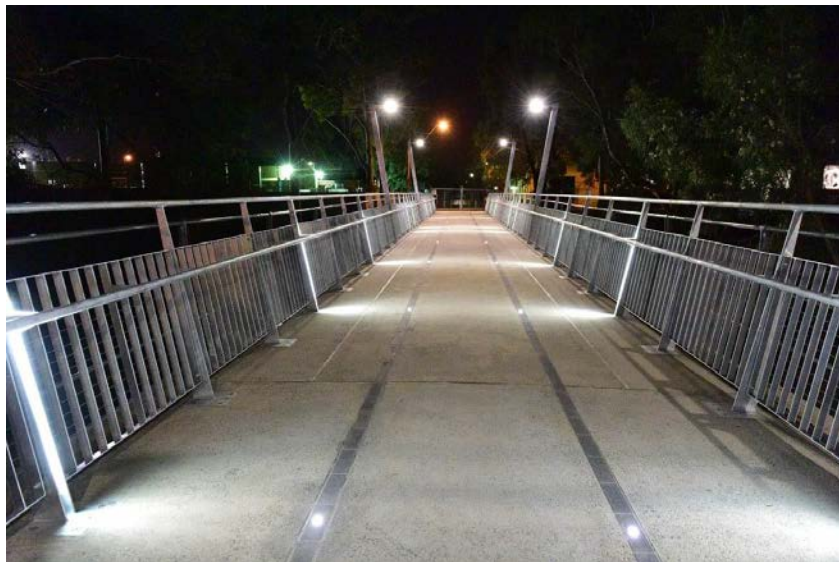
Cost management is also crucial in such works, and it is necessary for the QS to prepare cost plans at each stage of the design process to ensure that the works can be carried out within the approved budget and to maintain an accurate cost of the work and variations during the course of the construction.

A repair and maintenance regime must be established on completion of the project with a sufficient allocation of funds so that proper operational works can be undertaken on an annual basis with a major condition audit every 10 years. The bridge will require recoating of the top coat in 20 to 25 years' time.

## 8. Conclusions

The restored and reconstructed bridge was officially opened to the public and cyclists on the 13 September 2014 after more than 100 years of lack of care and uncertainty and 4 years of closure. The bridge has been recognised along with other bridges of that era in Victoria as having been designed by Sir John Monash and were celebrated as part of the 100<sup>th</sup> anniversary of the ANZAC landing at Gallipoli.

The whole team including the designers and the contractor worked together well on this project and with these projects, prompt information transfer is vital so that work on the site is not delayed over minor issues. Also, because the contractor was on a cost plus basis for the concrete repairs and other work, this meant that they were not delayed sorting out who is responsible for what and the contractor was able to proceed with the works without financial penalty and loss of time, knowing they would be fairly paid for the additional work.



***Figure 9 Photograph of the top of the bridge at night***

The restored and repaired bridge shown in Figure 9 was delivered at a significantly lesser cost than a new footbridge, justifying the decision taken to restore the bridge and in reusing the existing structure. The restored, and repaired bridge is a great sustainable result for a significant heritage bridge. It is also an outstanding example of perseverance by those involved to question the original advice, to take the time to understand the problems and to make the right decision to restore and repair the bridge. The restored and repaired bridge, beautifully lit at night, is a wonderful outcome for this heritage bridge, the environment and which the owner, the public, the users, the contractor and the design team are justly proud of.

## 9. Acknowledgement

Dr Alan Holgate and Dr Geoff Taplin for their wonderful recording of Sir John Monash's engineering work including this bridge.

The City of West Torrens and their consultants in carrying out the initial investigations and reviews of the bridge.

Councillors, Mayor Kirsten Alexander and Philip Hewitt, Manager Engineering Strategy & Assets, and the staff of the City of Charles Sturt for their support for the repairs and restoration of the Sir William Goodman Bridge. In particular, Phil Hewitt for allowing JWC to project manage this project on their behalf without undue intervention.

The design team and the contractor including J Woodside Consulting as project managers, flightpath as architects, URS as the engineers, Rider Levitt Bucknell as the cost planners and Synergy Remedial as the contractor for their work on this project but in particularly Leo Noicos for his contribution to the structural engineering for this project and Steve Freeman for his assistance during construction.

The University of Melbourne for permission to use the photograph of the construction of the bridge.

The South Australian Government for their funds for this project through their Open Space Grant system.

Richard Venus for his marvellous historical work in the submission of the bridge to Engineers Australia for engineering heritage, which has been approved.

Ian Maitland from Maitland Heritage Engineers in WA and Dr David Morris from David Morris Consulting in VIC for their invaluable advice and encouragement to the authors and the project.

Figures and photographs are by John Woodside unless otherwise credited

To others whom we have missed and who should be acknowledged.

## 10. References

1. G A Wayss, Das System Monier, Eisengerippe Mit Cementumhullung, in Seiner Anwendung Auf Das Gesamte Bauwesen (1887), Kessinger Publishing
2. Lewis, M (Ed), "200 Years of Concrete in Australia", Concrete Institute of Australia, 1988
3. Lewis, M. Monier and Anti-Monier: Early Reinforced Concrete in Australia, 2nd National Conference on Engineering Heritage Melbourne, Vic, 1985
4. Venus R, Nomination for Engineering Heritage Recognition, Holland Street Tramway Bridge, Engineering Heritage SA, April 2014
5. Holgate, A. Sir John Monash and the South Australian Reinforced Concrete Co. Trans. Inaugural South Australian Engineering Heritage Conference, Adelaide, 3 May 2012, 1-21
6. Taplin, G. and Holgate, A. Innovation in concrete technology - the contribution of Sir John Monash. Proc. Concrete Institute of Australia 2001 Conference, Perth, September 2001.
7. [http://www.aholgate.com/girdertexts/sa\\_bridges.html#thebarton](http://www.aholgate.com/girdertexts/sa_bridges.html#thebarton)
8. Serle G, John Monash, A Biography, Melbourne University Press, 1982
9. Perry R, Monash, The Outsider who won a War, Random House, 2007
10. Fischer T, Maestro John Monash, Monash University Publishing, 2014
11. Serle G, "Sir John Monash", Australian Dictionary of Biography, Australian National University, <http://adb.anu.edu.au/biography/monash-sir-john-7618>
12. Holgate, A and Taplin, G (2001), the Contribution of Sir John Monash to 20th-Century Engineering in Australia, The 11th National Conference on Engineering Heritage, Canberra, October 2001
13. Woodside J, Structural Report on the Sir William Goodman Bridge, (The Holland Street Bridge) Thebarton, Adelaide, South Australia, October 2011
14. Woodside J, Report on the Design Development and Preliminary Design Phase for the Sir William Goodman Bridge, (The Holland Street Bridge) Thebarton, Adelaide, South Australia, March 2013.
15. ARC-The Australian Reinforcing Company, Reinforcement Handbook, Your Guide to Steel Reinforcement, 2008
16. University of Adelaide, Report Number C131011-RP-01, Tension Testing of Reinforcing Bars and Compression Testing of Concrete for the Sir William Goodman Bridge, June 2014

# Condition Assessment and Structural Repair Solutions for the Renovation of the Sheraton Hotel at Doha, Qatar

Satyajit Datar<sup>1</sup> and Sajeev Kumar Krishnan<sup>2</sup>

<sup>1</sup> Principal Structural Engineer, GHD, B.E. (Hons), F.I.E. Aust., RPEQ

<sup>2</sup> Sr Structural Engineer, GHD, M.Tech (Structural), G Member IStructE (UK), PMP (USA), M.I.E. (India)

**Abstract:** Constructed in 1978, the iconic Doha Sheraton Hotel and resort complex of buildings having an area of 70,000m<sup>2</sup> with up to 20 storeys was completely renovated in 2014. This paper discusses the risk assessment and repair methodologies employed in the project for the various structural elements. The repair works were classified into repairs of damaged elements, strengthening of partly deteriorated elements and demolition and reconstruction of highly damaged elements. The repair strategy consisted of structural condition assessment by visual survey followed by non-destructive and destructive testing of concrete elements. A discussion of the results of testing and causes of identified defects was provided to the client. Based on a number of design life criteria contemplated by the client and building owner, various repair solutions were derived. Structural defects in concrete were primarily due to carbonation, chloride and sulphate attack, and corrosion of reinforcement. The types of structures affected included a sea water intake chamber, plant rooms, kitchen floors, underground water tanks, façade elements, roofs, walls, beams, columns and slabs at many locations. Solutions presented included protection against ingress, moisture control, salt extraction, concrete restoration, strengthening, cathodic protection and complete replacement of reinforced concrete. The paper discusses the challenges of addressing the time, cost, quality and risk constraints and outcomes inherent in a design and construct contract environment, and the practical problems faced in carrying out the repair works.

**Keywords:** structural defects, concrete, structural repair, strengthening.

## 1. Overview

The Sheraton Hotel at Doha was commissioned in 1982, designed by an American Architect Mr. William Pereira. Constructed over a plot area of 180,000 m<sup>2</sup>, the facility has a separate convention center, health and recreation center, swimming pool and many halls in addition to the main hotel building.

The ultimate client (the current Emir of Qatar) required a major renovation to restore the buildings back to their original condition. The project duration was only 9 months. The cost of the project was approximately 2 billion QAR (approx. AUD 700 Million). The scope of work included renovation of the rooms, public areas, lobbies, reception, ablutions, kitchens, back-of-house areas, MEP facilities, external landscaped areas, pools, sports facilities and external façades. The works constituted areas to be left unchanged, areas to be repaired, areas to be completely re-designed maintaining functionality and areas to be re-designed with a different functionality. GHD was the lead consultant for the architectural and structural works. This paper describes the structural assessment and subsequent repair solutions carried out on the buildings.

## 2. Structural systems

The structural system of the main hotel can be divided into two. The main building is a steel- concrete composite structure triangular in shape converging at the 16<sup>th</sup> floor. The shape appears as a truncated pyramid with a cantilever projection above the top floors. It consists of inclined steel frames supported at the top by concrete cores. Cantilevered floors project outwards from the steel frames. The remainder of the building consists of reinforced concrete (RC) columns, orthogonal slabs and beams of various spans and depths, with a podium roof, mezzanine, ground floor lobby and one basement floor. The steel structure is separated from the RC structure by means of expansion joints. Separate reinforced concrete structures served as liquid retaining underground water tanks and pump rooms. Chilled water for the air conditioning system, was drawn from the sea through an 8 meter deep intake chamber under the main pyramid building. All the main structures were supported on bored piles founded on bedrock up to 25 m below ground level.



### 3. Visual Assessment

A visual survey conducted by structural engineers in March and April 2014 consisted of inspections of representative and accessible areas of floors, soffits, walls, beams, columns, roofs, trusses, lintels, stairs and external pavements - identifying the general extent and location of visible deterioration. A photographic record was taken and visible defects logged.

Confined spaces such as tanks and concealed spaces such as behind ceilings, partitions and finishes, were partially inspected. The major defects noted were spalling of concrete at various locations, visible cracks in the beams and slabs, corrosion of exposed reinforcement and a number of non-structural defects such as damage to water proofing membranes and fire proofing coatings. The degree of corrosion of exposed steel reinforcement varied depending upon the location and proximity to moisture. The attempts of previous repair works were also visible at a number of areas. Generally the RC elements had the most deterioration but a few structural defects were noted on the major steel structure. Refer photos 1, 2, 3 & 4 for a representation of damage at various locations.



Photo 1- Sea water intake entrance beam: concrete spalling and reinforcement exposed.



Photo 2 – Sea water intake column: Extensive damage to the concrete and exposed reinforcement



Photo 3: Slab above the service corridor: reinforcement exposed after removing the damaged concrete.



Photo 4 : Pump room slab: spalling of concrete and exposed reinforcement

#### **4. Investigation and Testing**

Further investigation and testing was undertaken by an appointed local laboratory. Destructive and non-destructive tests were carried out that included:

- Initially 12 and eventually 18 no. 75 mm diameter cores, in the slabs across the site, for compressive strength, carbonation, sulphates and chloride ion tests
- Cover meter tests at 21 locations
- Rebound hammer tests at 21 locations
- Ultrasonic pulse velocity (UPV) tests at 21 locations
- Reinforcing bar tensile strength and chemical composition tests at 2 locations

The results indicated that carbonation at the surface level (less than 20mm depth) was extensive, where surfaces are exposed to water, moist air or both. Carbonation is deeper than the 20mm cover concrete for slabs, in a number of the cores taken; indicating that carbonation had been ongoing for several years and reinforcement corrosion had been accelerating. Two of the cores had a carbonation depth of 80mm.

Chloride levels in the tested cores were very high. The Qatar Construction Specification (QCS) limit for chloride % by mass of cementitious material is 0.10%. The actual values in all of the 18 measured samples were in excess of 0.10%, with a maximum of 1.26% and an average of approximately 0.45%. The chlorides were mostly at-or-above the corrosion activation threshold, considered to be between 0.4 to 0.5%.

Sulphates were very high with up to 20% by mass of cement in the cores tested. There is no prescribed QCS limit; however normal levels are usually expected to be less than 3 to 5 %. Though there was no sign of the concrete matrix having broken down in the cores tested, there was evidence of severe degradation of concrete in some areas, notably external suspended slabs on the sea side of the building.

It is likely that the chlorides and sulphates were a combination of external ingress and internal contamination present in the original sand and aggregate of 35 years ago.

#### **5. Causes of failure**

The causes of structural failure of the various structural elements can be broadly divided under the following topics:

##### ***5.1 Reinforcement corrosion and concrete spalling***

The two primary initiators of corrosion are carbonation (which reduces the inherent alkalinity of concrete) and chloride attack (which is the effect of chloride ions in contact with the reinforcement). The presence of moisture and oxygen in combination with carbonation and/or chloride ions, causes corrosion. When steel corrodes, it expands and exerts a force on the concrete. The cover concrete cannot resist this force and spalls.

##### ***5.2 Carbonation***

Carbonation is dependent on the carbon dioxide concentration in the atmosphere, the concrete porosity (including cracking) and moisture content, and the relative humidity and temperature. Each of these conditions was prevalent at the site.

The depth of carbonation is approximately proportional to the square root of time. The Sheraton concrete core samples showed carbonation depths of up to 80mm, indicating that carbonation was initiated many years ago.



### **5.3 Chloride attack**

Chloride attack arises most commonly, by external ingress from seawater and spray or internally cast-in the concrete constituents such as sea-dredged aggregates or calcium chloride admixtures.

Chloride ion concentrations increase, when in combination with carbonation, which appears to have occurred in the Sheraton structure.

### **5.4 Sulphate attack**

Sulphate attack also arises by external ingress or internally cast-in, and causes the concrete matrix to disintegrate into loose friable material, such as sand, gypsum and stones. Water/moisture presence is a must for expansive (deleterious) sulphate attack to occur.

The Sheraton structure was exhibiting extensive carbonation, chloride attack and some sulphate contamination of the concrete, and corrosion of the reinforcement, which had progressively worsened over the period since construction 35 years ago, principally in the reinforced concrete elements as described above. The main outcome was spalling of the concrete, in slabs, walls, columns and some beams. Where sulphate attack was advanced, the concrete matrix had deteriorated completely and required demolition.

Water ingress was a significant problem, from a variety of external sources (groundwater, irrigation, storm water) and internal sources (water supply and drainage pipes). Waterproof membranes and joint sealants to horizontal, vertical and sloping surfaces were in the majority of cases aged, degraded, ineffectual or absent.

## **6. Risk Assessment**

The full extent of concrete contamination, reinforcement corrosion and concrete degradation or spalling in the Sheraton structure was not known. The visual survey, investigation and testing was limited by constraints of time and access. There remained significant areas of structure not inspected nor tested due to concealment by services, ceilings, partitions and finishes. However, a majority of the reinforced concrete elements at the basement, ground, mezzanine, first floor and podium roof levels, exposed to humid atmosphere were able to be inspected.

An approach to risk mitigation, durability and protection of reinforced concrete structures was broadly taken from the BS EN 1504 Part 9, General Principles of:

1. Protection against ingress
2. Moisture control
3. Concrete restoration
4. Structural strengthening
5. Physical resistance
6. Resistance to chemicals
7. Preserving or restoring passivity
8. Increasing resistivity
9. Cathodic control
10. Cathodic protection
11. Control of anodic areas

Principles 1 to 6 are “must haves” for sound concrete, and are generally achievable by adhering to relevant British or other design standards, during the original design and construction, or retrospectively as applicable. Principles 7 to 11 are desirable or necessary for durable reinforcing steel, usually only under conditions where some or all of Principles 1 to 6 cannot be achieved.

Where carbonation and chloride depths in concrete cover are minimal, (such as, if carbonation depth is less than the reinforcement cover, or the chloride level is not high enough at the reinforcement level), it is

common to treat the symptoms only, by applying appropriate protective coatings to prevent or minimize future ingress of water, chlorides, carbon dioxide and sulphates. Removal and reinstatement of isolated damaged concrete may be required.

However, in the Sheraton hotel structure, the depth of carbonation and chloride contamination in many areas was likely to be well in excess of the depth of reinforcement. Under such conditions, treatment of the symptom alone was considered ineffective and may serve to move the corrosion cells to adjacent areas.

A specialist materials engineer was engaged to review the test results and recommend repair solutions. A number of meetings were convened with the contractor, project manager and owner's representative to convey the levels of risk to be accepted commensurate with the likely design life of each solution.

**Electrochemical repair solutions presented were:**

- Realkalisation
- Chloride extraction
- Cathodic protection (CP) – galvanic anodes or impressed current
- Penetrative/migratory corrosion inhibition
- Removal of contaminated concrete

**Realkalisation and chloride extraction** under the application of an electric current are temporary measures that would have taken several weeks to undertake and were not considered to be suitable at the Sheraton structure due to the high chloride levels present at the reinforcement level.

**Cathodic protection** of two types was considered: a permanent impressed current (ICCP) or with sacrificial galvanic anodes to accommodate future carbonation or chloride attack. Galvanic anodes were expected to provide a service life of up to 10 years, under the right conditions. ICCP would provide up to 25 years' service life if full electrical continuity (and monitoring) was able to be guaranteed.

**Penetrative corrosion inhibitors (PCIs)** were relatively new to the market having been introduced from 1996, and only one product in the Middle East, Sika Ferrogard 903, appeared to be proven in Europe in reducing corrosion and chlorides. Its success in the field had been mixed, with success rates for corrosion inhibition and penetration depths, ranging from 30% up to 80%. In our opinion, it would have a 50% chance of success in the Sheraton structure to extend the service life by up to 10 years. This was conveyed to the contractor and client and ultimately accepted, mainly due to time and cost constraints of the other solutions.

## **7. Proposed Solutions**

Solutions were developed based on the requirements of Principles 1 to 3 being implemented as far as practically possible:

1. Protection against ingress
2. Moisture control
3. Concrete restoration

This applied extensively for roofs, floors, walls and columns particularly throughout the back-of-house (BoH) areas of the complex and all areas (external and internal) exposed to humid air.

Conventional methods of concrete and reinforcement restoration were proposed wherever spalling or delamination was evident – by removal and cleaning of all deleterious material, replacement or addition of reinforcement as required, treatment of surfaces, followed by restoration with approved concrete mortars with protective coatings.

For the majority of the slabs and beams, cracking and spalling was not yet present, but the concrete was contaminated. A combination of protective coatings and galvanic anodes were recommended to achieve a design life greater than 10 years. Alternatively, impressed current cathodic protection (ICCP) was recommended in lieu of the coatings and anodes. Restoration alone was not recommended, as corrosion would likely accelerate in the un-restored areas. However, due to the lack of experience in ICCP or galvanic anodes of the contractor and the short duration of the project, only conventional methods of

repair works plus the application of PCIs were adopted, after careful examination of the various options and their design lives, by the owner's representative and contractor.

The general procedure adopted for repair work in slabs was as follows:

**1) Back Propping:**

Back prop the slabs and beams. The props were placed at the beams and at 1/3 span in each panel. During the repair operation, the max live load allowed on the slab was not to exceed 1.5 KN/m<sup>2</sup>.

**2) Repair first the top of the slabs.**

- a. Remove all material collected on top of the repair area
- b. Remove minimum 3 cm or the depth of concrete affected by carbonation.
- c. Clean the reinforced concrete. If reinforcement is corroded, remove the layer of corrosion using a mechanical brush.
- d. Apply a corrosion protecting, epoxy coating to the reinforcement.
- e. Fix anchoring steel to the top of slab. Use T12 @ 250 both ways. Anchor the rebar using a high performance anchoring adhesive. (This step was an option depending upon the location)
- f. To enhance further the long term durability of the concrete and embedded rebar, a corrosion inhibitor barrier to air and humidity was applied on the old concrete.
- g. Apply a PCI to the old concrete surfaces – both the residual surface after removal and the surfaces where concrete was not removed
- h. Apply a pre-packed concrete or mortar either by normal placement methods or by spraying.
- i. Apply an anti-carbonation coating to the finished surface.
- j. Apply a silane coating where exposed to external elements or a waterproof membrane.

**3) Repair the bottom of the slabs.**

- a. Remove the concrete cover around the corroded reinforcement; the area to be removed was defined by rebound hammer testing for delamination, but not less than 2m away from the visually corroded steel. The concrete was removed to a uniform depth not less than 40 mm or as determined from the carbonation tests.
- b. The surface of all exposed reinforcing rebar surfaces was be cleaned by means of wire brushing.
- c. Visible cracks, honeycombs or voids within the slab were injected with an epoxy mortar.
- d. All exposed rebar was coated with an epoxy resin for corrosion protection and as a bonding agent.
- e. Concrete surfaces were coated with a bonding agent.
- f. Remaining steps were as per the top of slabs including the PCI and anti-carbonation coating but excluding the silane or waterproof membrane.

A similar procedure was adopted for repair of beams and other elements with minor modifications based on element type, size of repair and location. For example, columns were repaired by following the above procedure with additional reinforcement and extra concrete at the base over a height of 1m.

Based on the initial repair methodology, a number of chemical products from various manufacturers were identified and the contractor was allowed to select the suitable material based on availability and support from the supplier.

In some cases where the corrosion and structural deterioration was prominent, a structural analysis was carried out to confirm the reinforcement and member sizes were satisfactory for the current structural code requirements and loadings. Where it was not satisfactory, CFRP (carbon fiber reinforced polymer) strips were adopted as a strengthening solution.

Where extensive damage wreaked the element beyond repair or strengthening, a full demolition and reconstruction of the element was undertaken.

## 8. Construction

Based on the nature and extent of the damage to the structural elements, repair and restoration, repair and strengthening of the elements or complete demolition and reconstruction of the elements were undertaken. The construction work for different areas based on the problem and repair methodology adopted are described below:

### 8.1 Seawater Intake Chamber & MER -1

The sea water intake and Mechanical & Electrical Room-1 (MER-1) were considered as one of the major areas where repair work and logistics caused critical impact on time and cost. The seawater intake chamber is 8m deep, 20m long and 10m wide, taking sea water to the mechanical room through two 2m diameter pipes connecting between them. The initial issue was to curtail the water inflow to the chamber. This was critical as the water was drawn directly from the sea without any control valves. The other issue was arrangement of alternate temporary cooling facilities once the plant closes. After many rounds of discussions and various proposals, a cost effective and efficient solution was established to contain the water inflow. The contractor used the excavated soil from the site to construct an earthen bund across the intake and continuously pumped out water that may leak in. The heavily damaged beams and slab were removed completely. The columns were found to be in good condition below the tidal water level and hence demolished only where damaged and re-constructed with additional rebar.

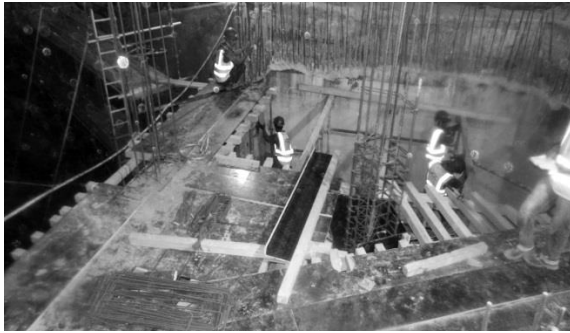


Photo 5 : The shuttering work for columns and slab of seawater intake structure



Photo 6: The beam and column of seawater intake structure after repair work

### 8.2 Underground Water tanks and Main Pump Rooms

The underground water tank and main pump rooms are separate structures situated around 100m away from the main building. The underground structure is rectangular in shape with a plan dimension of 22m x 84m. There are two expansion joints provided at 18m and 49m making 3 separate structures. The 250mm thick top slab is supported on 9m span secondary beams (400x750mm) provided longitudinally at every 2.75m. These are supported on main beams of size 750mmx1000mm spanning 11m laterally. The foundation is piles of various numbers under the walls with pile caps of various sizes. The top slab supports a dual carriageway and hence the slabs were analysed for bridge loads. Elements such as slabs and beams were checked to determine their structural compliance. The analysis and design was carried out employing current structural software applications, and the results were compared with the existing sizes and reinforcement. This approach helped to identify the mode of repair or strengthening required, or a combination of both to be carried out at damaged locations.

The design review showed that strengthening was required for some of the beams due to non-compliance with the structural design standards BS 5400, BD 21/01 and BD 37/01. In addition, repair work was required for a number of members, due to concrete contamination and reinforcement corrosion. In addition to standard procedures for repairing concrete work, approved hydrophobic impregnation (pure silane) to the entire surface was applied.

### **8.3 The Main Entrance Lobby**

The main entrance lobby was a reinforced concrete structure with a basement. It was found that the slab was extensively damaged due to ingress of water from the water fountain in the main entrance. A few bays were removed completely and reconstructed with fresh reinforcement and concrete. The rest of the area was repaired following the standard procedure.

### **8.4 Back of House areas**

All of the BoH areas (bulk store, service corridor, loading docks, five large plant rooms, several kitchens, engineer's offices, wet areas) were eventually repaired or reconstructed. This greatly increased the scope of works for the contractor, without increasing the project duration.

The bulk store was located near to the main entrance and was a reinforced concrete structure. It was found that the slab was deteriorated due to water ingress from kitchen floors above. A few areas of retaining wall also had cracks and corrosion of reinforcement. Standard procedure was adopted for repair work.

The service corridor also was a huge area away from the main building where damage to slabs and beams were noted extensively. A separate analysis was carried out for this area and as a result CFRP strips were provided to strengthen the beams in addition to the repair works for slabs and beams.

A lot of other areas such as large plant rooms and halls had extensive spalling and corrosion, and were repaired using the above repair methods and procedures and several areas were demolished and reconstructed.

A major non-structural item of the repair was replacing the existing water proofing membrane in almost all the podium roof slabs.

## **9. Key Lessons Learned and Conclusions**

The successful completion of the project within the prescribed time was hailed as a victory for the meticulous planning and nonstop implementation of the planned activities by the team behind the project. During its peak time an average of 16,000 labourers and more than 1,200 engineers and drafters worked on the site. Proper cooperation and coordination among various departments was paramount to the progress and success of the project.

One big lesson learned was that the anticipated repair work at the beginning of the project was multiplied many times as the project progressed as new areas were uncovered and the identified areas were extended during final inspections. Sufficient time and budget is needed for major repair works to be satisfactorily carried out for such large buildings in close proximity to the sea.

Another key lesson, working for a design and build (D&B) contractor; a consultant needs to always consider the multiple and often conflicting needs of many parties – the ultimate client and their representative, the contractor client, the local authorities, the subcontractor supply chain capabilities – in addition to the technical and ethical requirements inherent in professional engineering. Clear articulation of cause and effect, risks and consequences, design life, methodologies and cost estimates for each situation was required. Such articulation was difficult but achievable in a multi-lingual, multi-cultural project environment.

Managing expectations was another lesson - for example, the original aspirational design life of 50 years for all structural elements desired by the ultimate client, was not achievable given the time, cost and quality constraints for the location of the building and the climate. The typical design life warranted by subcontractors was 10 years. This required careful and persistent articulation by GHD of the design and repair options available – for acceptance by the contractor and the ultimate client's representative.

Professional lessons learned by the engineers and inspectors covered a wide range of technical aspects including:

- Concrete repair methodologies for numerous structural elements and conditions
- Climatic considerations in applications
- Variances in subcontractor/tradesmen skill levels
- Making informed judgements on the basis of incomplete investigations and small sample sizes of non-destructive and destructive testing

In summary, the project was exemplary in demonstrating the key challenges for engineers – to deliver practical design solutions that balance the competing drivers of time, cost, quality, risks and opportunities within a finite duration.



Photo 10: Renovated Hotel Sheraton Doha Front view.



Photo 11: Renovated Hotel Sheraton Doha right side view. ( Sea water inlet in the front side)

## 10. Acknowledgement

The authors hereby acknowledge the main contractor of the project, Urbacon Trading & Contracting and lead consultant GHD, for the help extended to them during the project.

## 11. References

1. BS EN 1504 Part 9: 2008 “Products and systems for the protection and repair of concrete structures. Definitions, requirements, quality control and evaluation of conformity. General principles for use of products and systems”.
2. BS 5400-4:1990 Steel, concrete and composite bridges. Code of practice for design of concrete bridges.
3. BD 21/01 : The assessment of highway bridges and structures, Design Manual For Roads And Bridges
4. BD 37/01 Volume 1, Section 3, Part 14 Loads For Highways Bridges, Design Manual For Roads And Bridges
5. QCS 2010 : Qatar Construction Specifications.

# Adelaide Railway Station Façade Conservation Works Structural Engineering Aspects

David Kennedy<sup>1</sup>

<sup>1</sup>Senior Structural Engineer, Aurecon Australasia Pty Ltd  
Adelaide, South Australia

**Abstract:** Aurecon was engaged by the South Australian State Government to review the condition of the façade of the Adelaide Railway Station, a 5 storey rectangular building constructed from a concrete encased steel frame with ribbed one way concrete suspended. The façade walls are predominantly clay brick masonry with decorative features made from precast concrete all rendered with a thin sand/cement finish to unify the external appearance.

Our diagnosis identified that deterioration of the concrete and reinforcing in precast elements was caused by carbonation and Aurecon recommended that concrete repair and the application of elastomeric coatings was required. Degradation was concentrated at horizontal surfaces where deteriorated screed coats allowed to pool for long periods and be absorbed into the concrete where it was able to initiate the damaging process of reinforcement corrosion.

The north façade was assessed to be the most heavily damaged and so conservation works were undertaken on the north façade throughout 2013.

The colour, texture and location of elastomeric coatings were negotiated in consultation with the heritage architect, and government authorities so that a balance could be struck between the need to satisfy the aesthetic and heritage requirements, and the need to provide lasting protection to the structure.

**Keywords:** Facade, Concrete, Repair, Heritage, Conservation.

## 1. Introduction

Aurecon was engaged by the Department of Planning Transport and Infrastructure (DPTI) to prepare an Asset Management Plan for the Adelaide Railway Station, which included consideration of the condition and maintenance of the façade of this historic building. The façade has been the subject of condition inspections by specialist façade contractors Synergy Remedial who issued reports in 2006 and 2009. Selective repairs of the more obvious defects, such as delaminating decorative features, have been carried out over the last 4 years. As part of the Asset Management Plan, Aurecon undertook a reassessment of the condition of the façades in conjunction with an appraisal of the 2009 Synergy report.



**Figure 1. North Façade.**

The following summarises the background information on the building, the investigation findings and subsequent conservation works undertaken:

## 2. General Façade Description

The railway station is a 5 storey rectangular building constructed from a concrete encased steel frame with ribbed one way concrete suspended slabs formed using cast-in sinter blocks laid in rows on formwork. The façade walls are predominantly clay brick masonry with decorative features made from precast concrete all rendered with a thin sand/cement finish to unify the external appearance.

The façades feature a range of decorative elements in addition to the solid walls:

- a) 2 storey fluted columns with Corinthian column capitals
- b) Cantilevering cornices around the full perimeter of the building incorporating two rows of major and minor dentil mouldings
- c) Fluted string course tiles at the mid-height position
- d) Scroll mouldings over archways

## 3. Inspection Findings

Inspections were carried out using zoom lens photography, close up inspections of accessible locations followed by inspections using abseil ropes and articulated boom towers.



**Figure 2. Precast columns undergoing carbonation North Façade.**

The following recommendations were made:

- e) Address the deterioration of the concrete and reinforcing, with particular reference to the external columns and the cornice mouldings (carbonation).
- f) Paint and treat corrosion to the steel windows (particular attention to the exterior) and steel tension rods for the external canopies.

Improve the stormwater disposal from the concrete slab roofs of the east, south, southeast and north external porticos





**Figure 3. Removal of loose items.**

It was determined that intervention was required to prevent the irretrievable loss of decorative components and a further acceleration in the rate of deterioration. Concrete cancer leads to structural failures with falling components threatening life safety, increases in water ingress and a reduction in heritage value. With the understanding that the costs of rectification of these types of façades increases exponentially with time, it was decided that repairs and installation of coatings would be undertaken in a progressive manner over several years.

Although general deterioration was observed in all locations, the north façade was assessed to be the most heavily damaged and so conservation works commenced on the north façade throughout 2013.



**Figure 4. First of 3 stages of scaffolding for the Northern Façade conservation works.**

## **2. Conservation Works**

A major contributing factor to the degradation of the façade was the lack of suitable vertical pathways for rainwater travelling down the face of the façade. Degradation was concentrated at horizontal surfaces where deteriorated screed coats were unable to provide adequate drainage. Water was then allowed to pool for longer periods and be absorbed into the concrete where it was able to initiate the damaging process of reinforcement corrosion.

The problem was compounded by the lack of “drip initiators” (vertical grooves on inverted surfaces used to break the surface tension which otherwise allows water to stick to the surface). Water flowed over the

edges of cornices and parapets and down the vertical faces of decorative features (such as dentils) in an uncontrolled manner leading to the growth of mould, which in turn trapped more moisture and exacerbated the effect.

Of equal concern was the integrity of the waterproofing membranes on the concrete portico decks and northern terrace.



**Figure 5 – Removal of defective concrete along the edge of the top ledge**

The works involved the following:

- a) Repair of leaking perimeter gutters and hip flashings of the roof turrets,
- b) Replacement of defective concrete, reinforcement and render
- c) Application of elastomeric membranes to all horizontal surfaces with modern membrane coatings to adequately shed rainwater and insulate the concrete from air and moisture,
- d) Localised repair of cracking external fluted columns.
- e) Use of elastomeric membrane coating of all external fluted columns to compensate for the low cover to reinforcing steel and disguise previous patch repairs,
- f) Localised repair to corbels, scrolls, dentils, beam soffits
- g) Repair and protection of corroded steel window frames and steel tension rods

The colour and texture of coatings and suitable locations for application were negotiated in consultation with the heritage architect, DPTI and the Heritage Division residing in the Department of Environment Water and Natural Resources. A negotiation was required so that a balance could be struck between the need to satisfy the aesthetic and heritage requirements, and the need to provide lasting protection to the structural elements.



**Figure 6 – Fluted column following removal of defective concrete with corroded reinforcement cage visible**

### **3. Conclusions**

All of the above measures were aimed at removing the hazard posed by loose material, managing rainwater flow paths and arresting the progress of corrosion by using modern coatings with the ultimate goal of reducing the requirement for expensive future maintenance to heritage fabric.

### **4. Acknowledgement**

Client: DPTI Project Services including Specialist Heritage Adviser: Lu Vitale, Facilities Manager: Jim Bray, Project Risk Managers: Augusta Soteriou and Nicky Will,

Aurecon team: Albert N van Grieken, David Kennedy, Niko Tsoukalas, Ryan Thyer.

Heritage Architect: Jason Schulz (DASH Architects)

Cost Consultant: Tom Bernard (Rider Levett Bucknall),

Contractor: Tom Pearce (Synergy Remedial),

Tenant Liaison: Wayne Coutts (Skycity)

Development Approval: Gabrielle MacMahon (Development Assessment Commission) & Peter Wells (DEWNR)

# A Variety of Remediation, Maintenance and Serviceability in its 15 Year Life

Peter Kastrup<sup>1</sup> and Andrew Turnbull<sup>2</sup>

<sup>1</sup>Queensland Maritime Leader and Senior Engineer, Arup

<sup>2</sup>Engineer, Arup

**Abstract:** The Redcliffe Jetty is a reinforced concrete structure and was constructed in its current form in 1999. Soon after construction was completed (1999-2000) significant immediate rectifications works were required to keep the structure in service. Following further assessment, further significant remediation works and subsequent load testing was carried out in 2003.

An engineering inspection was carried out in 2007 with minimal budget available for maintenance.

In 2013 a level 3 inspection including testing was carried out. Based on the findings of this inspection and the results of the testing, condition of each element of the structure was assessed and the remaining residual life estimated. A number of repair options for each element were used to investigate four different maintenance strategies: “Do Minimum”, “Reactive Maintenance”, “Preventative Maintenance” and “Replacement”. The specific repair applied to each element was varied depending on the overall strategy. The “Preventative Maintenance” strategy was selected for the main jetty and detailed repair design and tender documentation was prepared. This repair work was completed in mid 2014.

The lower level finger piers were deemed as in need of short term replacement. However, a further detailed tailored assessment was proposed to further investigate the life span. This assessment challenged the failure mechanism of the structure and revealed that the damage was not at a level warranting replacement, subject to a number of identified risks. In parallel, the replacement detailed design and tender documentation was prepared so the Council is ready to proceed when required.

**Keywords:** Concrete, Jetty, Steelwork, Maintenance, Durability, Repair, Structural

## 1. Introduction and Background

Redcliffe has had a number of jetties constructed since the late 1800s. In 1999, the current Redcliffe Jetty was constructed. Redcliffe is located within Moreton Bay Regional Council (MBRC) in Queensland, north of Brisbane. The coastal location is naturally sheltered from major offshore waves by Moreton Island, however local waves can occur and therefore a breakwater is located east of the jetty, refer **Figure 1**.

The jetty is approximately 250 m long in total and the water depth is up to 5 m at high tide at the seaward end. The different sections of the jetty are:

1. The Main Jetty is the longest part with the highest deck level comprising:
  - Jetty Stem landwards
  - Halfway House
  - Jetty Stem between halfway house and head
  - Jetty Head
2. The Jetty Fingers are the easternmost structures with low deck level and pontoon to facilitate vessel access:
  - Finger North (including pontoon and gangway)
  - Finger South (including pontoon and gangway)

Refer to **Figure 1** for plan showing the above description.



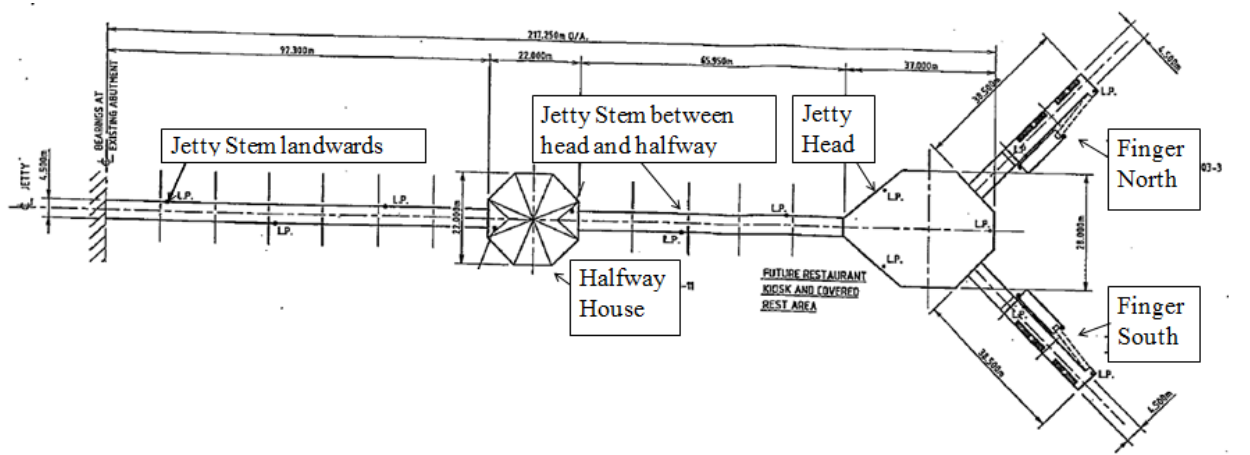
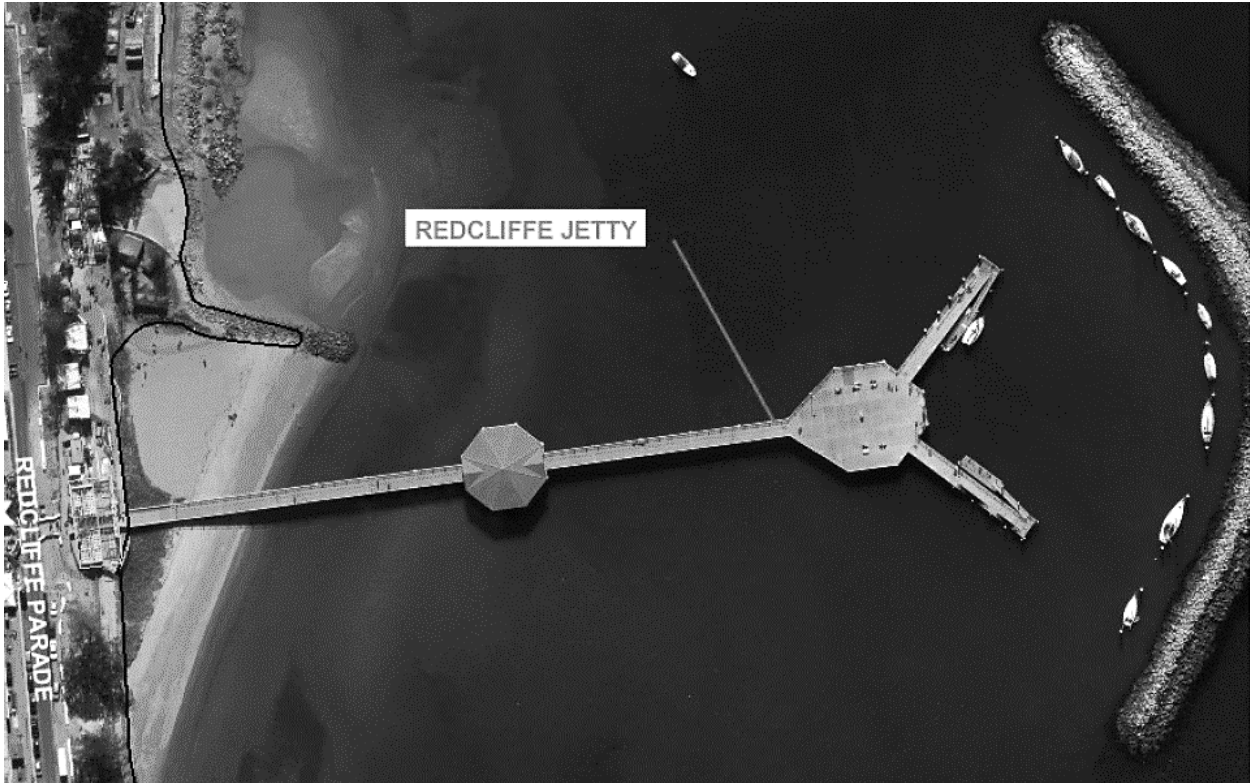
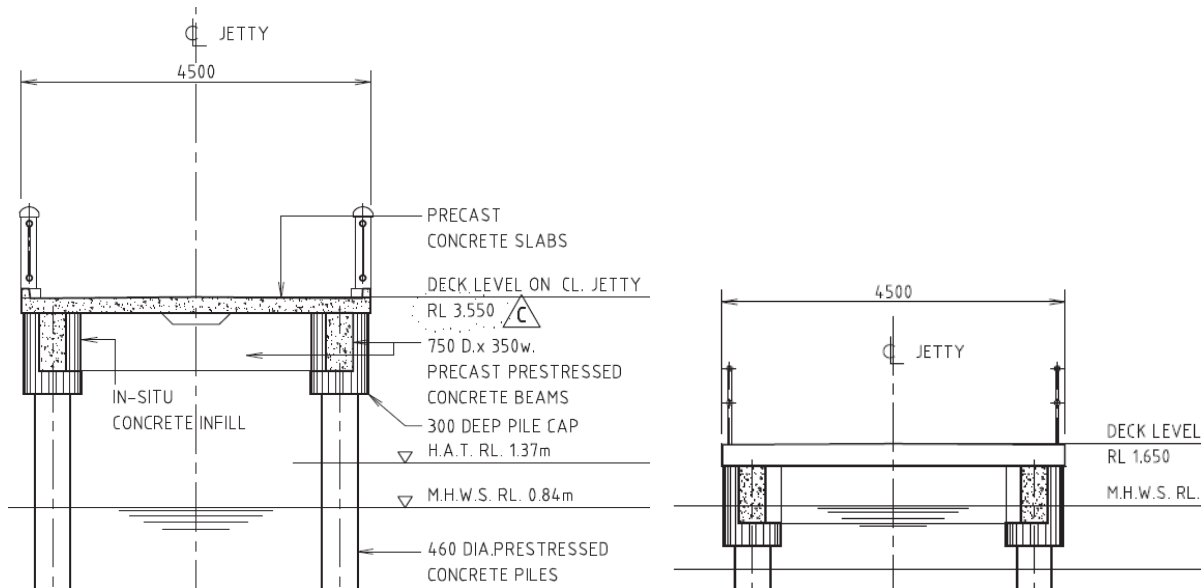


Figure 1. Top: Photo of Jetty from Land. Middle Aerial of Jetty and Breakwater. Bottom: Description of Jetty Structure. @MBRC/Arup

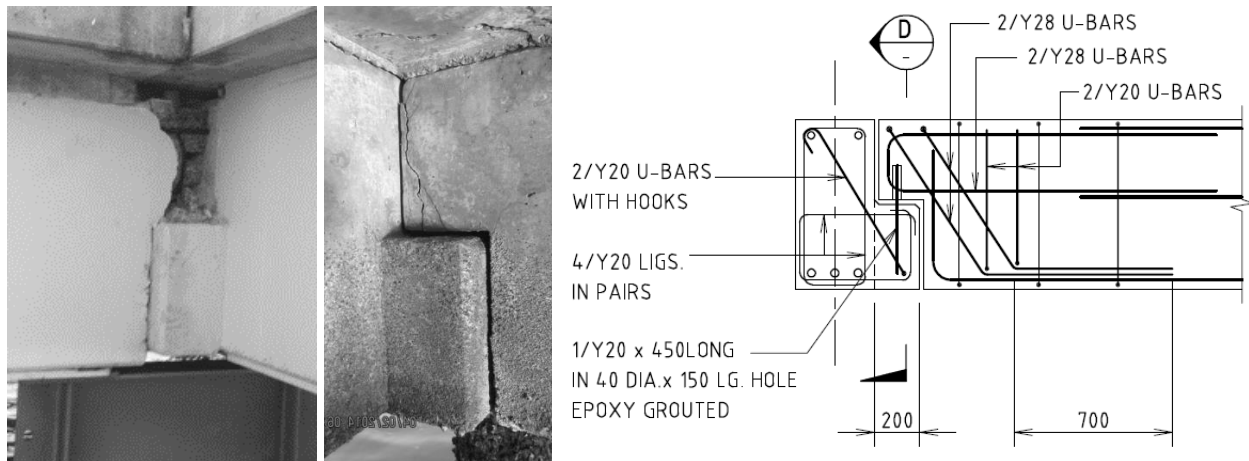
The jetty superstructure is predominantly a concrete structure consisting of precast hollow spun piles, in-situ pile caps, precast prestressed beams and precast deck panels. Refer **Figure 2** for typical sections and note the difference in deck levels.



**Figure 2. Left: Main Jetty Typical Section. Right: Jetty Fingers Typical Section. @MBRC**

## 2. 1999-2000 Immediate Remedial Works

Immediately after construction, issues were identified with the jetty superstructure, primarily relating to the beam supports. Arup was not the original designer, but was engaged to provide independent advice. Concerns were raised over the integrity of the half joints, refer **Figure 3**, as movement was observed and cracks were appearing. This led to the immediate localised installation of temporary steel supports, designed for the full joint loads. Shortly after installation, some of the concrete beams had deflected such that full support was provided by the steelwork.



**Figure 3. Half Joint Detail. Left: Main Jetty @Arup. Middle: Jetty Finger @Arup. Right: Reinforcement Detail. @MBRC**

The half joints (**Figure 3**) were found to have issues with limited capacity for the specific articulation and associated movements plus uneven bearing, which resulted in vertical capacity being compromised in the joints subject to the largest movements.

Another concern identified (not only for the half joints) was that design issues including inadequate allowance for tolerances had led to dowels for lateral capacity not being installed in a number of locations. Piling tolerance and precast installed directly on precast were key factors.

The purpose of the fingers is to facilitate vessel berthing and mooring, however due to the concern of insufficient lateral capacity of the timber fender piles, new independent berthing piles for the northern finger were designed and installed to accommodate a commercial tour operator vessel. The southern finger was not upgraded as there were no plans for accommodating more than one commercial vessel.

The observed issues and concerns for latent conditions and construction defects led to design of a number of permanent remedial works for the jetty.

### 3. 2003 Remedial Works

#### 8.1 Fingers

The decision was made to largely adopt a 'Do Nothing' strategy for the two fingers. It was assessed that it would not be financially viable to repair the fingers due to the nature of the relatively low level structures in combination with the fact that the remaining half joint defects were not severe enough to warrant strengthening at the time.

#### 8.1 Main Jetty

The previously identified half joint issues were further assessed and led to the detailed design of permanent remedial works. The most feasible and practical remediation option was determined to be structural steelwork supports. This was provided in all half joint locations, and where dowels were suspected missing brackets to address lateral restraint were installed. Some half joints were also located such that the loading provided a torsional load in the relevant beams. These beams were found to have insufficient torsion capacity and to counteract these loads, steel struts were designed to connect to the underside of the relevant beams opposite the half joints.

Due to the geometry of the jetty, a combination of vertical, torsional and lateral supports were specified where required, refer **Figure 4**.



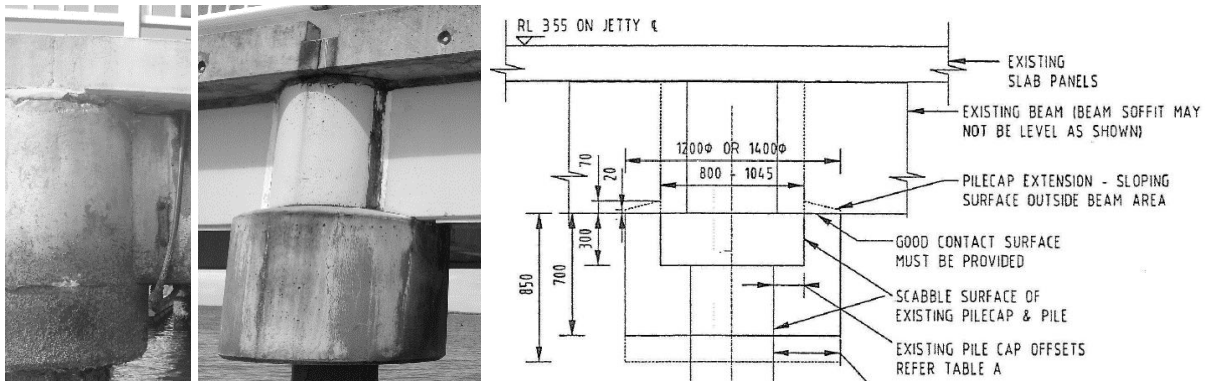
**Figure 4. Examples of Installed Steelwork Supports. Left: Vertical and Torsional Support. Middle: Torsional Support. Right: Lateral Support. @Arup**

Although well above the tidal zone, the steelwork is subject to salt water splash and spray and a maintenance manual was provided to advise Council of expected and recommended inspection and maintenance regime for the jetty including all remedial works.

The round in-situ pile caps was another element where remediation was required. The majority of the beams are supported on the pile caps and in a number of instances there was found to be insufficient bearing area and cover to reinforcement mainly due to inadequate allowance for piling and other tolerances.

The remedial solution adopted was the construction of a larger pile cap, which encapsulated the original element. The main objectives were to increase the bearing area for the beams, increase structural capacity and improve durability. To address these objectives, stainless steel reinforcement was used

throughout and the bars were dowelled into the existing pile cap and pile for load transfer, refer **Figure 5**. The dimensions of the remediation pile caps were tailored to suit the particular geometry at each location.



**Figure 5. Pile Cap. Left: Finger Pile Cap (original). Middle: Jetty Pile Cap (strengthened). Right: Remediation Design Detail. @MBRC/Arup**

Concerns over the quality and durability of the concrete lead to a decision to adopt a preventative intervention for the prestressed beams and deck panels. As prestressed strands has an inherent risk of sudden failure when subject to corrosion, it was decided to apply a protective coating to the highest loaded central span zone of the beams. Silane coating was applied to the remaining surfaces in the splash zone (soffits, beam edges).

To confirm the capacity of the structure a load test was carried out in increments up to a uniformly distributed load (UDL) of 6 kPa, which is 1 kPa higher than the characteristic design UDL.

#### 4. 2007 Inspection

The 2007 inspection focussed on assessing the current condition of the different components of the structure. The inspection included visible components of the structure as described in the maintenance manual. It was found that the structure appears to be in a fair to good condition (considering its pre-existing and latent conditions) and that no significant unexpected deterioration since 2003 was identified. The works carried out during remediation of the Jetty appear to be in a good condition and the repairs to beams and slabs are still in place. It appears that very few cracks had developed in the beams and the slabs since the remedial works. It was noted that most of the concrete beams had deflected such that the remedial steelwork provided full or partial support.

Redcliffe City Council previously decided not to carry out remedial works to the fingers of the Jetty and it was noted that these structures were showing further signs of deterioration. It was not expected that the fingers will fail in the short term under normal conditions but the condition of the fingers will need to be closely monitored in particular after significant weather events.

Overall, it was recommended that the Council continue to follow up the recommendations and carry out maintenance and inspections as outlined in the Redcliffe Jetty Maintenance Manual. With minimal maintenance budget available it was decided to postpone the minor maintenance actions identified.

#### 5. 2012 Inspection and Repair Strategy Option Study

Redcliffe City Council was amalgamated within Moreton Bay Regional Council in 2008 and staff changes meant that not all background knowledge and history of the previous work had been passed on. Others carried out an engineering inspection for Council in 2011 and provided advice, which highlighted concerns regarding the visible concrete damage. Recommendations included limiting public and vehicle access to the entire jetty.

Arup was engaged to peer review this advice and provided recommendations to Council on way forward. Council subsequently engaged Arup to undertake a level 3 inspection (including testing and structural



assessment) and to provide costed repair strategy options. The condition of each element of the structure was assessed and the residual life estimated. A number of repair options for each element were used to prepare four different maintenance strategies: “Do Minimum”, “Reactive Maintenance”, “Preventative Maintenance” and “Replacement”. The specific repair applied to each element was varied depending on the overall strategy. The costs and expected life extension of each repair or replacement option were estimated and this led to an overall quantitative analysis of the costs and benefits from each strategy.

Council decided to proceed with the preventative maintenance strategy (for the main jetty), which included an upfront capital maintenance cost with the aim of reducing the long term maintenance cost:

- Crack repair: Epoxy injection of most cracks suitable for crack injection to improve durability.
- Delamination repair: Patch repair of spalling or hollow sounding concrete areas. The spall repairs include breaking back the concrete and repairing the corroded reinforcement.
- Repair steelwork defects and coating.
- Re-apply protective and silane coating to the concrete beams.

This repair option is expected to increase the residual life of the jetty by up to 20 years. Minor maintenance is still to be expected in 5-10 year intervals, such as minor touch-up work.

Arup subsequently prepared the detailed design, cost estimate and tender documentation for the remediation works. Arup assisted Council in the tender assessment and provided technical advice during the construction phase, which was completed in 2014.

## 6. 2013 Breakwater Repair

As a separate but critical preventative measure to maintain the serviceability of the jetty, an assessment the breakwater revealed that this was damaged during a January 2013 storm event, refer **Figure 6**. The design of the jetty relies on the wave protection the breakwater provides. The assessment involved determining the likely immunity of the original breakwater overtopping and rock armour sizing. As a significant amount of rocks had been displaced from the breakwater crest the Council decided to re-instate the original breakwater profile with Arup assisting in completing this work.



**Figure 6. Redcliffe Jetty Breakwater During January 2013 Storm Event. @Arup**

## 7 2013-2014 Fingers Replacement Design

Based on the recommendations for the jetty fingers, Council decided to carry out a life span investigation for the existing structures as well as detailed design of the replacement works, refer **Figure 7** for images of the existing structures.



**Figure 7. Top: Southern Finger. Bottom: Northern Finger with Commercial Tour Operator Vessel (note the independent fender piles). @Arup**

### 7.1 Life Span Investigation

Based on visual inspection and structural calculations, the mode of failure that is of most concern to the fingers are the half joints which are showing signs of significant distress (large cracks). The investigation concluded that the major cracking in the half joints is probably due lack of adequate even bearing area in the half joints, refer **Figure 8**. The cracking observed in the half joints on the fingers seemed limited to the unreinforced edges/corners of the beams. It is believed that the cracking observed

has generally resulted in a relocation of the bearing area from the unreinforced edges/corners of the beam to the reinforced middle section of the beam.

If the fingers experience a significant vertical (crowd) loading, it is possible that further cracking of the half joints may occur. However it is also expected that this cracking will result in an increase in the bearing area. When this cracking occurs, the beams may “settle” which may result in cracking of the in-situ deck slab. In summary, it was not believed that the half joints are at risk of brittle failure and warning signs such as cracking in the slab is expected to be visible locally above the joints.



**Figure 8. Jetty Finger Half Joint Cracking Examples. @Arup**

A strut and tie analysis showed that the half joints have the structural capacity to transfer the 5 kPa vertical load if adequate bearing area is provided. The required bearing area was calculated in accordance with AS3600 with the required strut area which was output of the above strut and tie analysis. Based on observations and measurements from the visual inspection, it appeared that many of the half joints did not have adequate bearing area due to uneven bearing surfaces, precast supported directly on precast, temporary timber packers (not removed) and poor mortar pad grouting.

The movement joints of the main jetty are located at each end of the continuous stems (refer **Figure 1**), and these movement joints were constructed as half joints. This suggests that cracking in the half joints is partially due to shrinkage and temperature movement. For the fingers, the beams along the seaward side of the fingers are continuously restrained (with in-situ joints at the piles), this suggests that the unsupported half joints on the fingers are unlikely to crack to the extent of the main jetty half joints.

Furthermore, it is expected that the majority of the shrinkage in the concrete has already occurred reducing the risk of cracking due to shrinkage. However, there is still an inherent risk that damage can occur to the fingers should excessive lateral movement or loading occur (such as abnormal wave loading).

Arup did not identify a failure mechanism warranting replacement in ‘normal/calm conditions’, however a recommended 6 monthly inspection regime (to monitor the observed defects) has been implemented.

## **7.2 Detailed Design**

The detailed design of the replacement structures focused on re-using the existing piles. Minimal signs of deterioration was observed and demonstrated via testing including assessment of the chloride concentrations. To provide lateral capacity for wave loading, it was decided to adopt a superstructure design consisting of a new reinforced concrete headstock, which supports concrete deck units with a dowel detail designed for the expected movements and loads. This design allowed for a minor improvement of the durability as the soffit of the deck units were raised as much as possible (over 0.5 m higher than the soffit of the existing beams) to be clear of Mean High Water Spring tide level. As the replacement design was ‘like for like’ the basis of design did not include vessel berthing, which means retaining and refurbishing the existing independent fender piles.



The deck alignment was optimised to provide DDA compliance while re-instating the original deck level at the vessel access location. The detailed design was completed in 2014 and this construction work can be tendered by Council when required.

## 8. Conclusion

Over the years, Council and Arup's main objectives have been for the public to continue to safely enjoy this local community icon while adopting a long term value for money maintenance/upgrade strategy.

Having been involved with repairs, maintenance and serviceability for the Redcliffe Jetty over 15 years has provided the opportunity to learn a number of valuable lessons. Specific aspects include:

- To consider the complex movements and forces arising at half joints and other joints.
- To consider piling and other tolerances for pile caps, other bearing joints and dowel details.
- To consider avoiding details with precast supported directly on precast.
- To consider the durability of the key structural members. These concrete members are currently generally in a fair to good condition given the age and exposure to the marine environment.
- To consider and challenge failure mechanisms when observing visible defects and making decisions on load rating.
- The owner of the jetty structure is left with some inherent risks, which while partially mitigated still exist and have to be managed while the jetty is in service.
- In general, marine structures are likely to benefit from preventative maintenance work every 10-15 years with a view of extending the residual life.



Figure 9. Redcliffe Jetty 2014. @Concrete Diagnostics

## 9. Acknowledgements

This paper is published with the permission of Moreton Bay Regional Council. The author acknowledge the encouragement of Council in supporting this paper. Many people have contributed to projects relating to the Redcliffe Jetty over the years. The author thanks everyone involved and for the opportunity to deliver such challenging projects.

# Design of FRP retrofitted concrete structures using AS5100 Part 8

Binh Pham<sup>1</sup>

<sup>1</sup>Principal Structural Engineer, AECOM

**Abstract:** The increasing need to repair and strengthen existing bridges has led to the introduction of AS 5100 Part 8 “Rehabilitation and strengthening of existing bridges”. This standard will cover a range of topics relating to rehabilitation of concrete, steel, timber, and masonry. Appendix A of AS 5100 Part 8 will cover strengthening of reinforced and prestressed concrete structures using fibre reinforced polymer composites (FRP). The Appendix is still going through revisions but it will be a state-of-the-art guide which will address some critical issues with the international design guides that has been used in Australia. It might be possible there would be a surge in the use of this technique in Australia after the release of the code. This paper explains the principles of the new design standard to design FRP strengthening for bending, shear, torsion, and axial actions.

**Keywords:** FRP, strengthening, bridges.

## 1. Introduction

The Standards Australia working group BD-090-08 have been developing a new AS5100 Part 8 to cover rehabilitation and strengthening of existing bridges. Appendix A of AS 5100 Part 8 will cover strengthening of reinforced and prestressed concrete structures using fibre reinforced polymer composites (FRP). The Appendix is still going through revisions but it will be a state-of-the-art guide which will address some critical issues with the international design guides that has been used in Australia.

This paper presents the background and the principles behind Appendix A of AS5100 Part 8. The focus of this paper is on Sections A6 to A10 that cover the design aspects for FRP strengthening.

## 2. Design principles

The basic design principles for an FRP-strengthened element follow those of AS5100.1, AS5100.5 and AS5100.7.

Similar to ACI440 (2), a minimum strength requirement for un-strengthened members is included to ensure that the existing structure without FRP has a nominal strength for the scenarios of accidental loss of FRP.

## 3. Flexural strengthening

### 3.1 Basic principles for strengthening in bending

The principles of the analysis of a reinforced or prestressed concrete section strengthened with FRP under bending are similar to those of a ‘normal’ reinforced or prestressed section, i.e. basing on equilibrium and strain-compatibility conditions with an assumption that plane sections normal to the axis remain plane. In the ‘disturbed’ regions where the plane sections do not remain plane, other analysis and design methods might be used. The bond and anchorage of FRP shall be investigated in all cases.

One fundamental difference between a ‘normal’ reinforced/prestressed section and a section strengthened with FRP is that in most practical cases the ultimate load capacity is achieved not when the concrete top fibre strain reaches its limit but when the FRP strain reaches its bonding limit. As a result, the design of FRP strengthening for concrete members requires that concrete top fibre strains, steel reinforcement strains, and FRP strains are tracked through different load cases and different stages of section build-up. It is worth noting that FRP is often applied after permanent loads have been applied and calculation of strains shall take that sequence into account.

While formulas for a singly reinforced rectangular section are provided in the standard, in practice, formulas for bridge members are not possible due to the complexity of the section shape and construction

sequences. For example, the strengthening of a super-T bridge beam will involve analysing the beam sections at transfer, casting of deck slab, casting of barriers and installation of surfacing, service conditions and ultimate conditions. This can require a number of iterations.

Effects of creep and shrinkage on the behavior of FRP strengthened sections are often insignificant.

It is often necessary to define the concrete stress-strain curve in the analysis of a FRP strengthened section. The curve defined in Section 3 of AASHTO (1) can be adapted.

### 3.2 Strength limit states

It is fundamental the designer understands the failure modes that might occur in a FRP strengthened beam. Compared to a 'normal' reinforced beam, there are much more failure modes (5). All of these modes shall be accounted for in the design.

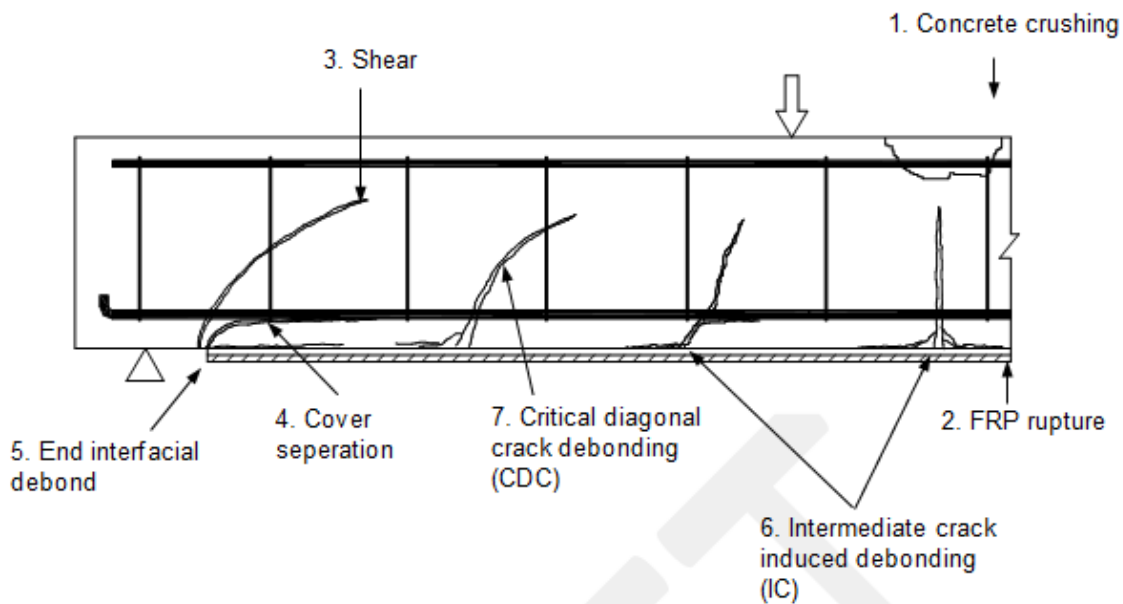


Figure 1. Summary of failure modes for members strengthened with FRP in flexure

Ductility and capacity reduction factors for FRP strengthened members are treated differently in international design guides. While FRP debonding or FRP rupture can occur in a brittle manner, experiments have shown that FRP strengthened beams resume their original strength and ductility after FRP debonding/rupture. Therefore, as long as the un-strengthened beam is ductile, i.e. it shows adequate warning prior to total collapse, a capacity reduction factor of 0.8 for bending can be adopted. Capacity reduction factors for shear are as defined in AS5100.5.

Guidance for FRP debonding is provided in Section A7.3.5.2 to A7.3.6.3 of the standard. The formula to calculate the FRP strain limit for IC debonding is based on the work by Teng et al. (7). This formula is adapted in ACI440 (2) and has been validated by Pham and Al-Mahaidi (5). For near surface mounted FRP strengthened beams, this limit is often higher due to larger bond area. The limit used in ACI440 (2) for near surface mounted FRP has been adapted in AS5100.8.

The formula to calculate the shear stress limit for end debonding (cover separation and end interfacial debonding) is based on Pham and Al-Mahaidi (6) and other research groups in the United State. This formula is adapted in AASHTO (1). To avoid FRP debonding caused by a high beam shear force, the factored shear force at the termination point of the FRP is also limited to two third of the shear strength of the section ( $V^* > 0.67V_u$ ).

The limits for serviceability are adapted from ACI440 (3) and AASHTO (1). The fatigue stress limit for carbon fibres is 55% of its strength. The fatigue stress limits for glass and aramid fibres are much lower.

FRP strengthening for bending is generally effective for non-composite reinforced or prestressed sections. The maximum percentage increase in bending capacity ranges from 20 to 60% for these sections. The controlling failure is often FRP debonding. The steel strain at ultimate varies but tends to be around 0.005 for reinforced sections and 0.010 for prestressed section.

FRP strengthening for bending is generally not very effective for pretensioned composite girders. The maximum percentage increase in bending capacity is typically less than 10% for these girders. For these girder sections, the fact that the neutral axis is typically close to the top fibre and the effect of construction sequencing lead to FRP reaches its debonding limit while the top concrete fibre strain is still low. For these sections, using thinner FRP and increasing bond areas would improve the strength enhancement. The enhancement is particularly small for highly reinforced and highly prestressed sections.

#### 4. Shear and torsional strengthening

The design of a reinforced or prestressed concrete beam strengthened with FRP in shear and torsion is covered in Section A8 of AS5100 Part 8. Compared to a 'normal' concrete beam, the shear capacity of a strengthened beam has an additional item,  $V_{uf}$ , which accounts for the contribution from FRP.

$$\phi V_u = \phi(V_u + V_{us} + P_v + C_E V_{uf}) \quad (1)$$

The expressions used to calculate the portion of the shear resistance contributed by FRP laminates,  $V_{uf}$ , are based on ACI440 (2).  $V_{uf}$  depends a great deal on the effective strain,  $\varepsilon_{f,e}$ , in the FRP, which is limited to 0.4% to account for stress concentrations or FRP debonding. For FRP not completely wrapped, the effective strain can be lower.  $C_E$  is the environmental reduction factor to take into account the environmental effects on FRP properties.



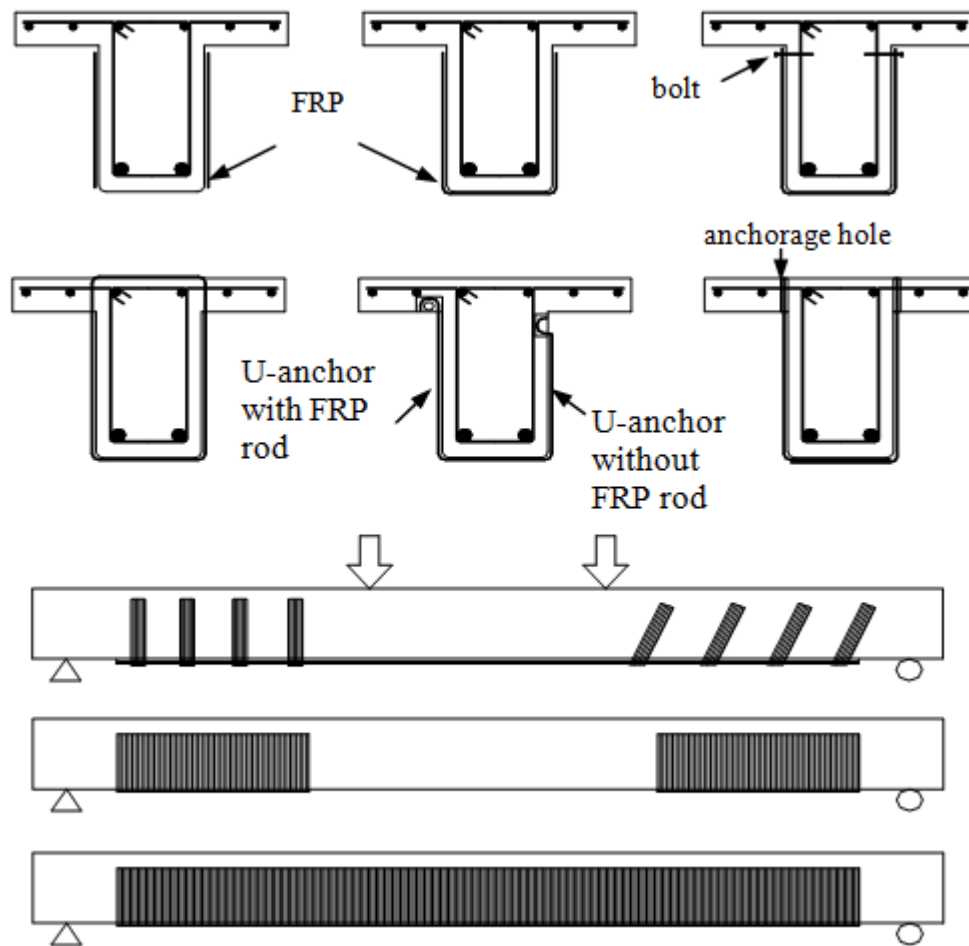


Figure 2. Examples of shear strengthening

Compared to a 'normal' concrete beam, the torsional capacity of a strengthened beam has an additional item,  $T_{uf}$ , which accounts for the contribution from FRP.

$$\phi T_u = \phi(T_{us} + C_E T_{uf}) \quad (2)$$

The expressions used to calculate the portion of the torsional resistance contributed by FRP laminates,  $T_{uf}$ , are based on Hii and Al-Mahaidi (3).  $T_{uf}$  depends a great deal on the effective strain,  $\varepsilon_{f,\theta}$ , in FRP which is dependent on the FRP modulus and FRP reinforcement ratio.

## 5. Axial strengthening with FRP confinement

By confining a concrete column with FRP, its ultimate strength in compression and in combined compression and bending can be improved. The improvement is resulted from higher confined concrete strength,  $f'_{cc}$ . Lam and Teng's stress-strain model (4) for FRP confined concrete was adapted in ACI440(2) and in AS5100 Part 8.  $f'_{cc}$  is dependent on the confinement pressure and the strain efficiency factor. FRP wrapping is most effective for circular sections.

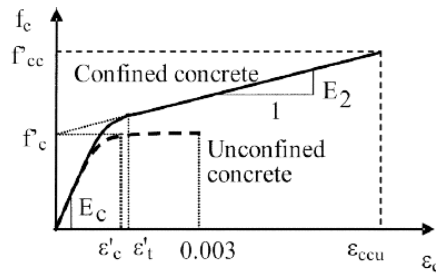


Figure 3. Typical stress strain curve for confined concrete (ACI-440 (2))

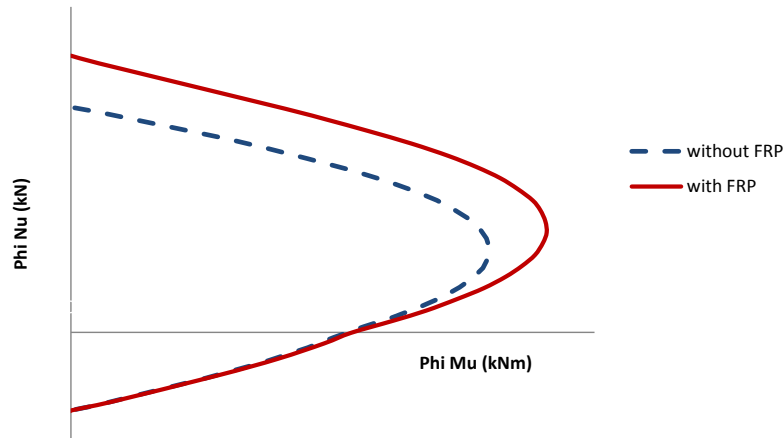


Figure 4. Example of interaction diagrams

## 7. Conclusions

Appendix A of AS 5100 Part 8 will cover strengthening of reinforced and prestressed concrete structures using FRP. The Appendix will be a state-of-the-art document which will provide practical and detailed guidance to design and construct FRP debonding. Designing FRP strengthening requires clear understanding of the system and how it behaves at both service and ultimate limit states.

## 8. Acknowledgement

The author would like to acknowledge Andrew Sarkady from BASF, John Hilton from Aurecon and other members of the Standards Australia Working Group BD-090-08 FRP Strengthening Sub-Group who, together with the author, developed Appendix A of AS5100.8.

## 9. References

1. American Association of State Highway and Transportation Officials, "Guide specifications for design of bonded FRP systems for repair and strengthening of concrete bridge elements", AASHTO, 2012, Washington.
2. American Concrete Institute, "Guide for the design and construction of externally bonded FRP systems for strengthening concrete structures (ACI 440.2R-08)", ACI Committee 440, 2008, Michigan.
3. Hii, A. K.Y., Al-Mahaidi, R., "Torsional capacity of CFRP strengthened reinforced concrete beam", Journal of Composites for Construction, January/February 2007, pp 71-80.
4. Lam, L., Teng, J.G., "Design-oriented stress-strain model of FRP-confined concrete", Construction and Building Materials, V.17, No. 6-7, pp 471-489.

5. Pham, H.B., Al-Mahaidi, R., "Assessment of available prediction models for the strength of FRP retrofitted RC beams", Composite Structures, 66, 2004, pp 601-610.
6. Pham, H.B., Al-Mahaidi, R., "Prediction models for debonding failure loads of carbon fibre reinforced polymer retrofitted reinforced concrete beams", Journal of Composites for Construction, January/February 2006, pp 48-59.
7. Teng, J.G., Smith, S. et al., "Intermediate crack induced debonding in RC beams and slabs", Construction and Building Materials, V.17, No. 6-7, pp 447-462.

# Investigation of Corrosion, Repair Assessment and Quality Assurance of a Basement subject to Saline Water Ingress

Jonathon Dyson, NSW Manager, BCRC; Marton Marosszeky, Director, BCRC; Frank Papworth, Director, BCRC

**Abstract:** Seawater penetration around the perimeter of a basement was leading to premature reinforcement corrosion in the boundary walls, adjacent internal beams, columns and slabs. An investigation was undertaken to determine the extent of repairs and develop a suitable repair approach. A key issue was that these repairs early in the life of the structure had to account for deterioration that might occur over the following 40 year life of the structure. Hence even though in some areas corrosion may not yet have commenced, issues of chloride penetration that might cause future corrosion had to be addressed. The exact extent of repairs and detail of the repair methods was determined during the repair management phase. Further extensive wet chemical analysis of chlorides based on cores was going to be both expensive and time consuming, hence the more detailed assessment of chloride penetration across the structure was completed on site using a calibrated silver nitrate colourimetric test. This paper discusses this method and provides reasons for the criteria adopted for the determination of remediation strategies including the extent of cathodic protection required.

**Keywords:** chlorides, profile, diffusion, concrete, corrosion, testing, silver nitrate, colourimetric, repair

## 1. Introduction

Seawater penetration around the perimeter of a reinforced concrete basement was leading to premature reinforcement corrosion in the boundary walls, adjacent internal beams, columns and slabs.

An investigation was undertaken to determine the extent of repairs and develop a suitable repair approach. A key issue was that these repairs early in the life of the structure had to account for deterioration that might occur over the following 40 year life of the structure. Hence even though in some areas corrosion may not yet have commenced, issues of chloride penetration that might cause future corrosion had to be addressed.

Initial methods employed included a combination of visual examination of concrete and reinforcement, laboratory analyses to determine total chloride ion (Cl<sup>-</sup>) profiles from core samples, half-cell potential measurements, cover meter surveys and carbonation testing. This identified that future corrosion issues were primarily associated with chloride ingress around the perimeter of the structure.

This paper discusses the investigation and testing methodologies employed and focusses primarily on the silver nitrate spray method used in field testing to assess chloride ion ingress into the concrete structure, the basis upon which test results were interpreted and how they informed the development of the cathodic protection (CP) scope of works.

## 2. Preliminary investigation

Initially a preliminary program of inspection and testing was completed to gain an understanding of the most likely causes of concrete deterioration and reinforcement corrosion.

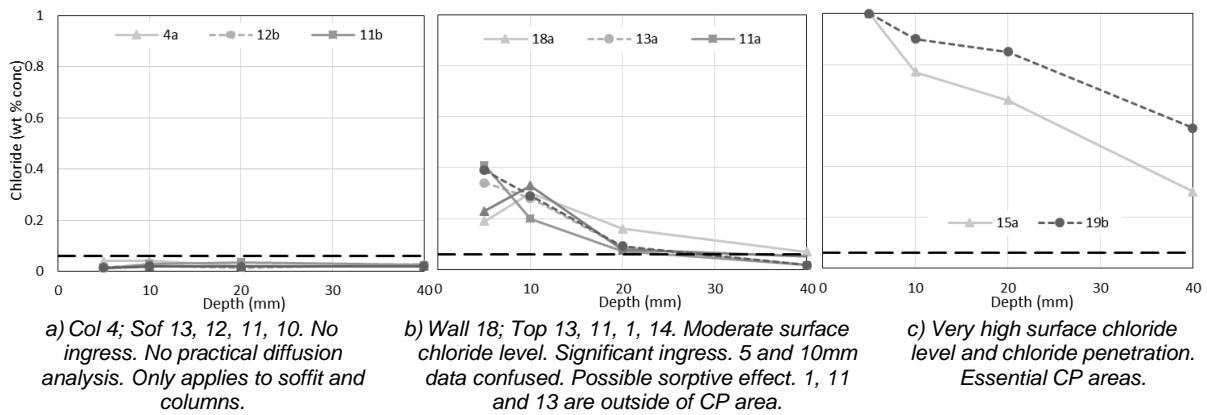
### 2.1. Chloride profile testing

Cores were extracted from various elements of the structure for laboratory analysis of chloride ions at several depth levels below the surface. The results were used to plot chloride profile curves.

The chloride profile plots were grouped into five categories (very low, low, medium, high, very high) to assess patterns of exposure. The “very low” category (*Figure 1(a)*) showed that there were areas of no contamination. It also gave a reasonable estimate of the base chloride level and showed that the original chloride level of the concrete was within code limits. Conversely, in some areas chlorides were very high. The surface chloride level of 1% by weight of concrete (approx. 6% by weight of cement), as shown in *Figure 1(c)*, is equivalent to a severe splash zone exposure.

### 2.2. Other testing (carbonation, half-cell potential, cover survey, visual survey)

Several other inspection and testing techniques were utilised during the preliminary investigation. Firstly, an overall visual forensic survey was completed to assess visual damage to the structure and begin to establish the possible causes of such damage.



**Figure 1** Three of the five different categories of surface chloride exposure found during results analysis.

Carbonation testing on extracted test cores was completed using a 1% phenolphthalein sprayed solution (pH indicator). This determined that for all elements only a small depth of concrete surface layer had been carbonated. Carbonation modelling was completed using a simple root time equation (Equation (1)) and from this it was predicted that the carbonated layer was unlikely to reach the level of steel reinforcement within the 50 year design life except in a few locations where concrete cover was very low.

$$D_c = k(t)^{1/2} \quad (1)$$

Also completed at selected locations were: half-cell potential surveys to assess corrosion risk, cover meter surveys to assess the reinforcement cover distribution, physical measurements of reinforcement cover at certain core locations (to verify cover readings) and visual condition assessments of exposed reinforcement (**Figure 2**).



**Figure 2** As part of the preliminary and subsequent investigations reinforcement was exposed for visual condition assessment. The bar in the left photo showed only slight superficial corrosion whereas the bar coincident with a crack in the right photo showed advanced corrosion.

### 2.3. Preliminary investigation findings

From the preliminary investigations it was determined the primary cause of distress was chloride-induced corrosion of the steel reinforcement in the concrete resulting from seawater inundation. The proliferation of both plastic and drying shrinkage cracks as well as low reinforcement cover in certain locations was found to have assisted in accelerating the structure's deterioration locally but was not the prime issue.

### 2.4. Preliminary CP extent

A preliminary extent of CP was estimated based on the limited initial investigations, in particular, visual confirmation of seawater inundation extent by recording wet areas & staining and chloride depth profile curves from a representative number of test locations around the structure. If a total chloride ion concentration of greater than 0.035% by weight of concrete at the reinforcement depth was observed, the general area was designated as requiring CP as a minimum. This 0.035% criterion was agreed as it was predicted via modelling this would equate to a 0.06% (by concrete weight) Cl<sup>-</sup> concentration at

the reinforcement after 50 years assuming the surface chloride level drops over time as further inundation is prevented and residual chlorides penetrate inward. 0.035% is also approximately equal to the chloride level permitted in AS 1379 [1] for new concrete.

The high chloride levels at reinforcement depth and significant cracking and spalling led to the conclusion that in order to achieve the design life with a normal reliability and minimal future additional disruptive repair CP would be required. Due to the limited extent of testing at this stage the minimum CP extent defined from preliminary tests was to be better detailed following a more extensive program of targeted chloride testing and additional cover surveys.

### 3. Detailed investigation

A second more extensive round of chloride testing was undertaken to confirm the extent of the CP scope of works, ensuring the carpark structure would achieve its 50 year design life while limiting the remedial works to only what was necessary on the basis of modelling. Because this further testing took place in parallel with the repair works, laboratory testing was not feasible (results would take too long). A quick, on-site, colourimetric test method was developed to assess the depth of chloride ion penetration into the concrete.

#### 3.1. Chloride field test method options review/feasibility study

From an initial review of field chloride testing options the authors quickly concluded a silver nitrate spray (colourimetric) test method warranted further investigation to determine its feasibility for this application. The colourimetric method involves spraying an aqueous silver nitrate ( $\text{AgNO}_3$ ) solution, typically 0.1mol/L, on a freshly fractured cross-section of concrete. The silver ions react with the free chloride ions in the concrete to form a white precipitate of silver chloride on the tested surface. When the free chloride ions in the concrete are below a certain concentration, the silver ions instead react with the hydroxyl ions, forming a brown precipitate of silver oxide from immediate decomposition of silver hydroxide. The obvious colour boundary represents a specific concentration of free chloride ions in the concrete.

**Table 1** Comparison of chloride concentration at colour change border for silver nitrate spray tests found by various researchers. This demonstrates the  $C_b$  value varies when using one set of materials let alone from project to project, showing project calibration as a minimum is required.

Researcher	Chloride % at colour border ( $C_b$ )				Comment
	Free (water soluble) chloride		Total chloride		
	Wt % Cem.	Wt % Conc.	Wt % Cem.	Wt % Conc.	
Yang, et al. [3]	Total chloride at the colour change roughly twice that the free chloride				
Otsuki, et al. [4]	0.15				Constant for pastes, mortars and concretes with varying w/c ratios
Kim, et al. [5]		0.045			Sprayed with a 0.1mol/L silver nitrate
Andrade, et al. [6]				0.18 ± 0.2%	
Sirivivatnanon & Khatri [7]	1.2%				Range 0.84% -1.69%
Meck & Sirivivatnanon [8]	0.9%	0.12%			Range 0.28% -1.41% for investigated concretes with different binders.

Chlorides in concrete can be either free chloride ions or combined chloride ions in Friedal salts (bound chlorides). The acid soluble chloride method used for assessing the chloride concentration in concrete in this project detects total (free + bound) chlorides present while in the colourimetric test the silver nitrate reacts only with free chlorides. The free to total chlorides ration is known to vary depending on circumstances. The Transportation Research Board [2] showed it could be as high as 0.8. Hence the two test methods will not always coincide. The total and free chloride ion concentration represented by the colour change boundary in the colourimetric method has been the subject of much research as shown in **Table 1**.

The considerable variation in the  $\text{Cl}^-$  concentration represented by the colour change boundary ( $C_b$ ) in literature may be the result of many factors. For example, the concentration of  $\text{AgNO}_3$  solution and the amount of solution sprayed on the exposed face have both been found to impact the value of  $C_b$  [9]. Others, though, found that different solution concentrations (0.05mol/L and 0.1mol/L) consistently produced almost the same diffusion coefficient when compared across concrete mixes with varying w/c ratios [5]. Because the colourimetric method involves a chemical reaction, varying chemistry of the concrete pour solution between different concrete mixes (e.g. with and without SCMs) likely contributes to variation in the value of  $C_b$ . In particular silica fume, by decreasing the hydroxyl ions in the concrete pore solution by an order of magnitude, may also decrease the  $C_b$  value similarly [10]. This was observed by Andrade, et al. [6]. From a review of the test results of Hamilton III, et al. [11] the authors deemed that inclusion of fly ash in a concrete mix (as in our case) appears not to significantly alter  $C_b$ .

The pH of the concrete has been found to affect the  $C_b$  value. Kim, et al. [5] suggest the colourimetric method is not appropriate when the concrete pH is lower than about 10 or 11 and when carbonation depth is lower than the colour change boundary depth (not an issue in our case). The water/cement ratio (w/c) has also been found to affect the  $C_b$  value, with a higher w/c coinciding with the colour change boundary occurring at a lower  $\text{Cl}^-$  concentration [9]. However, other researchers [5] found varying the w/c ratio had no effect on the value of  $C_b$ . It is also plausible that different test locations with the same concrete mix may have varying  $C_b$  values simply due to the inhomogeneous nature of concrete.

The above demonstrates the variability of the chloride concentration at the colour change boundary. Because of this uncertainty, BCRC conducted a program of trial field tests, calibrating the colourimetric test results against chloride diffusion curves (Figure 3) developed from laboratory analyses of existing and new cores to identify from the chloride depth profiles the average chloride concentration at the colour change boundary for this building.

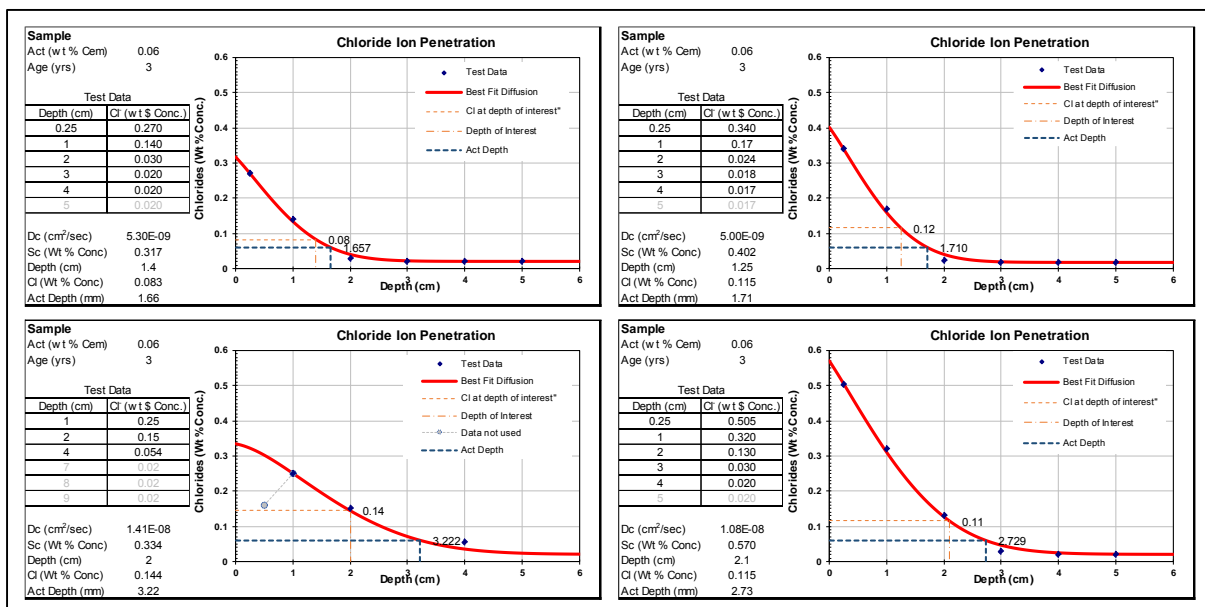


Figure 3 Example best fit diffusion curves developed from BCRC modelling.

### 3.2. Silver nitrate colourimetric test method calibration

Because the  $\text{AgNO}_3$  solution concentration might affect the value of  $C_b$ , it was decided to trial two different solution concentrations - 0.05mol/L and 0.1mol/L – during calibration testing. One solution type would be sprayed on each of the two freshly fractured faces for each calibration core.

The sprayed amount of  $\text{AgNO}_3$  solution may also affect the value of  $C_b$ . It has been suggested that an ideal amount of solution sprayed onto the exposed concrete test surface is a rate of about 0.015g  $\text{AgNO}_3/\text{cm}^2$  [9]. Given the discrepancy between studies as to the value of  $C_b$ , it was important to be consistent in the amount of solution sprayed in each test and to determine the approximate value of  $C_b$  this same amount represented through calibration testing.

The first step in tailoring the test method for this application was to determine the amount of solution imparted per spray in order to calculate the number of sprays required on each test surface. This was done as follows:

1. A decent quality plastic spray bottle suitable for chemical solutions was sourced.



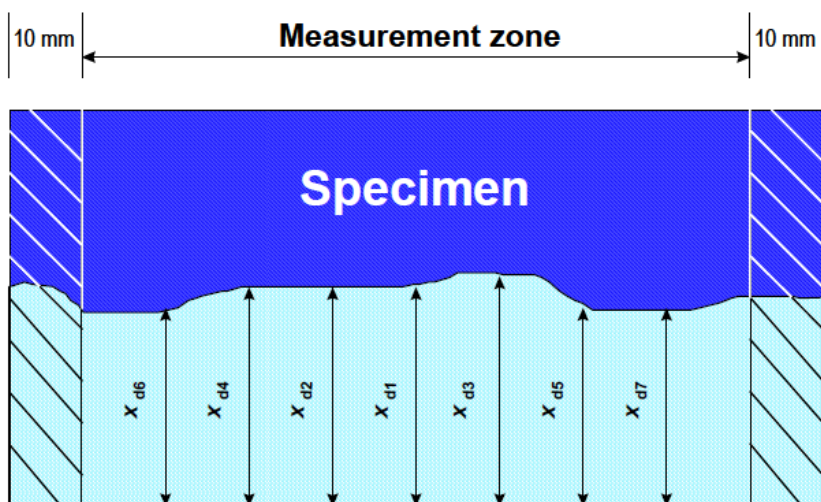
2. A spare dry concrete core was placed on reasonably high precision digital scales and the scales were zeroed.
3. The average weight of solution (water was used in testing) per spray onto the core from a distance of approximately 50-75mm away was calculated over several tests. The core surface was allowed to “dry out” and the scales re-zeroed prior to each further test.

The average weight of aqueous solution imparted onto the core per spray was calculated as 0.09 grams.

The test procedure (detailed in **Additional field chloride testing and cover survey**) included measuring the test surface area (A) and calculating the number of sprays (N) of solution required:

$$N = A \times 0.015g/cm^2 \div 0.09g \quad (2)$$

Nine calibration cores were sampled adjacent to previous lab tested cores. To assess the effect of time between chloride profile development and colourimetric trial testing, three more calibration cores for spray testing were sampled next to three newly lab tested cores. All cores were sampled from slab elements ensuring all calibration tests had the same concrete mix.



**Figure 4** Colour change boundary depth measurement procedure.

The calibration cores were rinsed of slurry, allowed to dry out (on the surface) then split and sprayed on their freshly fractured faces. For each core, one face was sprayed with 0.1 mol/L AgNO<sub>3</sub> solution and the other with 0.05 mol/L solution. The mean colour change boundary depth was measured at 15 mins and again at 24 hours to assess the effect of time on the C<sub>b</sub> value.

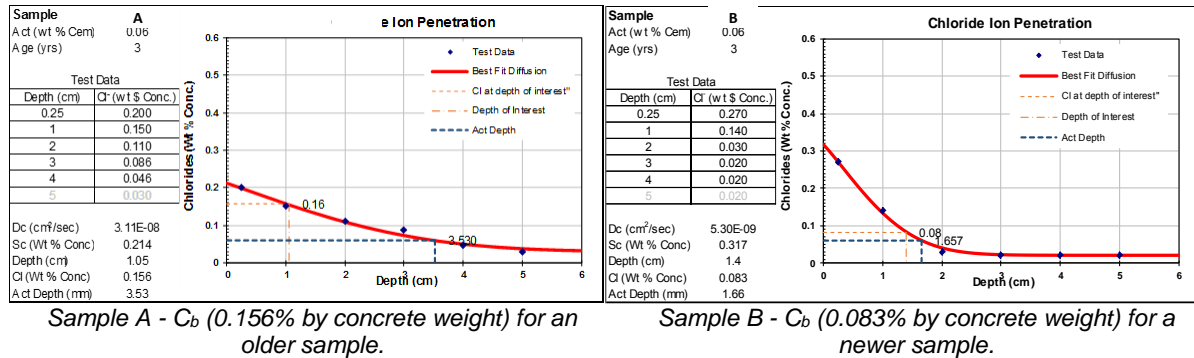
For each measurement, 7 depth readings were taken across the width of the test area and averaged (**Figure 4**), following the procedure detailed in NT Build 492 [12]. If the penetration front was obviously affected by a piece of aggregate, that particular measurement was either relocated or ignored. No measurements were taken within the 1cm or so wide zone at each edge to obviate the potential distortion of results near the external surface of the core from exposure to water during coring and rinsing.

Modelling was completed to plot best fit diffusion curves for the chloride profiles of the adjacent lab-tested cores. Diffusion was calculated based on Fick's 2nd Law of Diffusion with a constant diffusion coefficient and no allowance for sorption effects. This gave a reasonably accurate estimate of the current depth of the selected threshold value and a conservative value of the time to the activation front reaching the reinforcement. The modelling results showed:

- a) The high variation in chloride profiles from location to location, demonstrating the high variation in exposure severity.
- b) In some cases (for example the bottom left curve in **Figure 3**), the chloride concentration measured near the surface did not correlate with a diffusion analysis whereas the deeper measurements did. This may be due to sorption effects near the surface or an irregular surface chloride load (e.g. a short period of high surface chloride exposure followed by a period of low surface chlorides).
- c) The diffusion coefficients varied significantly (from 2 x 10<sup>-8</sup> to 67 x 10<sup>-8</sup> cm<sup>2</sup>/sec.). The variation is likely to be due a combination of variation in mix, placing, curing and exposure.

For each test, the average colour border depth was then overlayed with the appropriate calibration diffusion curve and the chloride ion concentration estimated from the curve (**Figure 3**).

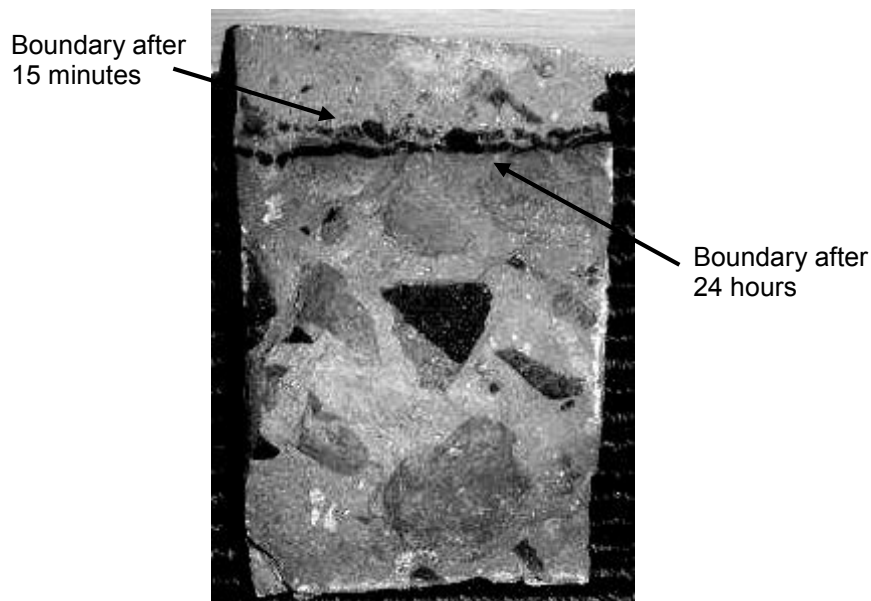
The average  $C_b$  value for all test results was then determined for both the 15 minute and 24 hour measurements. In estimating the “average”  $C_b$  value, the authors gave more weight to the calibration results from the newly lab-tested chloride profile curves on the assumption that calibrating against these was more accurate than calibrating against the older chloride profile curves. The newer calibration curves indicated a lower value for  $C_b$  than the older curves (**Figure 5**). The “average”  $C_b$  value will be referred to hereafter more accurately as the weighted average  $C_b$  value.



**Figure 5** Typical examples of  $C_b$  values derived from calibration against chloride profiles.

The colour change boundary depth was observed on average to be greater after 24 hours than after 15 minutes (**Figure 6**). This suggests that over time following spray application the value of  $C_b$  decreases (assuming a typical chloride diffusion profile for the concrete). This is consistent with Aoki, et al. [9] who also observed in their experiments the colour change boundary depth increasing with time albeit at a decreasing rate. Because of this it was important to consistently take colour border depth measurements at the same amount of time after spray application in the field testing. A 15 minute interval between spray application and colour change boundary depth measurement was included in the testing procedure.

It was concluded from analysis of the calibration test results against the lab test derived chloride diffusion curves that there was a small difference in the weighted average value of  $C_b$  between the two  $AgNO_3$  solution concentrations trialled. The weighted average  $C_b$  was calculated as about 0.08%  $Cl^-$  (by conc. weight) for the 0.05mol/L solution and 0.1%  $Cl^-$  (by conc. weight) for the 0.1mol/L solution. It was decided to use the 0.1mol/L solution in field testing because it was easier to source this concentration of solution and more research data exists relating to experiments at this concentration.



**Figure 6** The colour change boundary 24 hours after  $AgNO_3$  spray application is deeper than after 15 minutes.

To assure the service life for the structure, the level of free chloride ions at the reinforcement ( $C_R$ ) in the concrete at 50 years should be less than 0.06% by weight of concrete (0.4% by weight of cement), the widely accepted threshold at which reinforcement corrosion is predicted to initiate. From the modelling it was determined that to satisfy the  $C_R < 0.06\%$  (by weight conc.) at 50 years criterion,  $C_b$  at approx. 8 years (concrete age at time of field testing) should not occur deeper than 60% into the cover concrete layer above the steel reinforcement.

The authors believe there is inherent conservatism in the above detailed approach due to the use of a constant chloride diffusion coefficient ( $D$ ) and surface chloride concentration ( $C_o$ ) in the Fick's 2<sup>nd</sup> Law based modelling. In reality the observed diffusion coefficient typically reduces with time [13] and, due to repairs implemented to remove chlorides from the slab and slow the rate of seawater intrusion to the basement, the future surface chloride load will be significantly reduced from that assumed in the modelling.

### 3.3. Additional field chloride testing and cover survey

With calibration of the colourimetric field test method complete, testing was completed as per the following procedure. Example colourimetric test specimen images are included in **Figure 7**.

1. Core locations were planned to enable the final extent of CP to be adequately defined based on a sound understanding of the extent of chloride ion penetration into the structure.
2. Reinforcement was located at each core location using non-destructive techniques. Core locations were then finalised and marked on the slab. Most cores were located to miss reinforcement however some cores were located above reinforcement to allow further visual assessment of reinforcement condition. Some cores were located on cracks while others were located away from cracks. This was to assess the effect cracks had on chloride ion ingress into the structure and steel reinforcement corrosion.
3. A cover survey was completed in the vicinity of each core location to assess the minimum cover to top steel.



**Figure 7** Example colourimetric test specimens showing increasing depth of chloride ion penetration from left (no white precipitate, all brown i.e. no colour change border) to right.

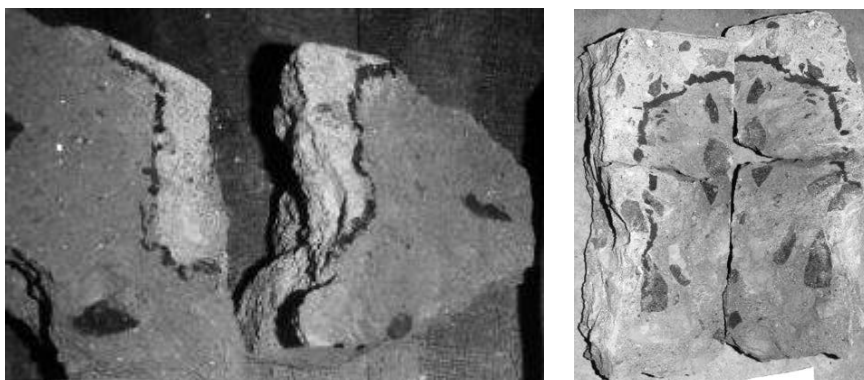
4. Cores were extracted. Cores were typically approx. 60mm diameter and varied in length from 20mm to about 100mm.
5. The external surfaces of the cores were rinsed of slurry to minimise contamination of the test surfaces when the cores were split.
6. Cores were numbered and the core number and location noted on a series of colourimetric testing drawings.
7. Cores were split using a bolster and the fresh split faces of the cores were immediately sprayed with 0.1mol/L silver nitrate solution. The amount of solution sprayed on each test area was determined by measuring the area of the exposed internal surface of the core and calculating the number of sprays of solution required using Equation (2). Cores taken on cracks were initially split along the crack, then split again perpendicular to the crack to end up with four segments. All internal fresh split faces were then sprayed (**Figure 8**).
8. Time of spray application was noted and the depth of colour change boundary measured, recorded and photographed approximately 15 minutes after spray application.
9. Relevant test data such as the average ( $d_{b,a}$ ) and maximum ( $d_{b,m}$ ) colour change boundary depth and the minimum cover to reinforcement ( $c$ ) was recorded in a test results spreadsheet.

10. A formula was included in the spreadsheet to calculate whether  $d_{b,a}$  and/or  $d_{b,m}$  were greater than  $0.6c$ , meaning the structure at the test location should be cathodically protected in accordance with the previously established criterion. This is discussed further in Section **CP extent**.

### 3.4. CP extent finalisation

A set of colour-coded chloride test result drawings was produced to assist in finalising the extent of cathodic protection. Colourimetric test results were marked on the drawing in their location in one of three colours: red ( $d_{b,a} > 0.6c$ ), amber ( $d_{b,m} > 0.6c \geq d_{b,a}$ ) or green ( $0.6c \geq d_{b,m}$ ).

Initial lab chloride test results were also included on the drawings using the same colour coding scheme. For the initial lab test results the colour coding criteria related to the level of total chloride concentration (% by concrete weight) at the reinforcement depth ( $C_r$ ) and were: red ( $C_r > 0.06\%$ ), amber ( $0.06\% > C_r \geq 0.035\%$ ) or green ( $0.035\% \geq C_r$ ).



**Figure 8** Example colourimetric test specimens at cracks showing deeper chloride penetration locally at the cracks.

Red test locations indicated CP was required and green locations indicated CP was not required. For amber test locations engineering judgement and consideration of various other factors was used to decide whether CP was required or not in each individual case. For example, for colourimetric tests completed at cracks,  $d_{b,m}$  at the crack would often be significantly larger than  $d_{b,a}$  when calculated from, say, 5mm away from the crack to the other edge of the test area (**Figure 9**). However although  $d_{b,m}$  at the crack was often high, studies have shown there is lower risk of reinforcement corrosion propagation resulting from chloride-transporting cracks that intersect rather than coinciding with a line of reinforcement [14]. Other factors considered included, for example, proximity to other “red” test results, proximity to the harbour side building edge, the extent to which  $d_{b,m}$  was greater than  $0.6c$ , how far the deeper chloride penetration extended away from the crack face and the comparative penetration depth of  $d_{b,a}$ .

Initial colourimetric test cores were located along the boundaries of the preliminary CP extent to confirm whether this CP extent was appropriate. Further rounds of field testing were completed where results from previous testing indicated CP was required but the boundary of CP extent could not yet be defined due to there being insufficient “green” test locations. Such further rounds of testing were conducted until the full extent of CP was able to be confirmed and finalised.

## 4. Benefits and drawbacks of the method

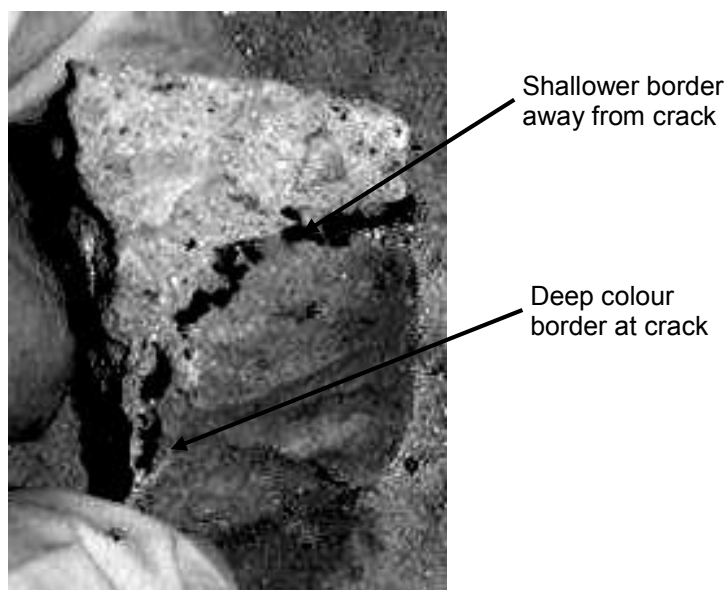
The key strengths of the silver nitrate spray test method are its simplicity, speed, comparatively small cost and practicality for use in the field. In this application, use of the method meant a fast (almost instantaneous) turnaround between testing and results, allowing the CP extent to be finalised much quicker than if laboratory testing was relied upon. This was a necessity considering the detailed investigation phase occurred at the same time as the completion of repairs.

The method does have some potential drawbacks that must be considered when assessing its suitability in any given situation. These include:

- The wide variation in the  $C_b$  concentration represented by the colour change boundary reported in the literature and the need to perform calibration testing to determine the likely  $C_b$  value in each unique situation.
- The method not being suitable for use in situations requiring high precision results, even when calibrated, due to the many previously discussed factors possibly affecting the value of  $C_b$  in each

unique test. Having said this, most field test methods are not suitable where high precision is required anyway, because less control during testing can be achieved than in a laboratory.

- Its unsuitability for use on carbonated concrete.



**Figure 9** Typical example of deeper chloride ion penetration at a crack face quickly reducing to shallower ingress away from a crack.

## 5. Conclusion

A two-stage investigation of a reinforced concrete basement was completed to determine the extent of damage and develop a suitable repair approach to achieve the 50 year service life. Initial methods employed included a combination of visual examination of concrete and reinforcement, laboratory analyses to determine total chloride profiles from core samples, half-cell potential measurements and carbonation testing.

Subsequently, a silver nitrate spray field test method to quickly and more extensively assess chloride penetration into the concrete elements and thus refine the preliminary cathodic protection scope of works was researched. It was concluded the method would be appropriate for use in the project context, provided it was calibrated to more accurately estimate the free chloride ion concentration represented by the colour change boundary given the high variation reported for this value in published literature.

Trial colourimetric tests were completed on the internal (freshly exposed) surfaces of a number of split test cores. The depth of the colour change boundary was calibrated against chloride profile diffusion curves developed from adjacent laboratory analysed test cores to determine the likely chloride ion concentration represented by the colour border. It was concluded that when the colour change border depth was measured 15 minutes after the test surface was sprayed with a 0.1 mol/L  $\text{AgNO}_3$  solution, the weighted average chloride concentration at the colour border was 0.1% by weight of concrete. From modelling on the basis of this value it was concluded that if the average colour change border depth for a test specimen was greater than 60% of the minimum concrete cover depth in the vicinity of the test location, the structure surrounding the test location required cathodic protection. This assumed reinforcement corrosion could commence once a chloride ion concentration of 0.06% (by concrete weight) occurred at the level of the reinforcement.

Following calibration of the method, a field colourimetric testing procedure was developed and iterations of testing were completed until the extent of CP works was finalised.

## 6. Acknowledgements

The authors would like to thank all project stakeholders for their cooperation and for allowing the publication of this paper.

## 7. References

1. Standards Australia, 2009. *AS 1379-2007: Specification and supply of concrete*. 3rd ed. Sydney: Standards Australia.

2. Transportation Research Board, 1979. *Durability of Concrete Decks, National Cooperative Highway Research Program Synthesis 57*, Washington D.C.: Transportation Research Board.
3. Yang, E., Kim, M., et al., 2004. Chloride diffusion in hardened concrete with concrete properties and testing method. *Journal of Korea Concrete Institute*, 16(2), pp. 261-268.
4. Otsuki, N., Nagataki, S., et al., 1992. Evaluation of AgNO<sub>3</sub> solution spray method for measurement of chloride penetration into hardened cementitious matrix materials. *ACI Materials Journal*, 89(6), pp. 587-592.
5. Kim, M.-Y., Yang, E.-I., et al., 2013. Application of the colorimetric method to chloride diffusion evaluation in concrete structures. *Construction and Building Materials*, Issue 41, pp. 239-245.
6. Andrade, C., Castellote, M., Alonso, C. & Gonzalez, C., 1999. Relation between colourimetric chloride penetration depth and charge passed in migration tests of the type of standard ASTM C1202 91. *Cement and Concrete Research*, 29(3), pp. 417-421.
7. Sirivivatnanon, V. & Khatri, R., 1998. *Chloride penetration resistance of concrete*. Brisbane, Concrete Institute of Australia.
8. Meck, E. & Sirivivatnanon, V., 2003. Field indicator of chloride penetration depth. *Cement and Concrete Research*, Issue 33, pp. 1113-1117.
9. Aoki, Y., Shimano, K. & Satoh, K., 2011. Effects of solution concentration and spray amount on the results of silver nitrate solution spray method. Singapore, CI-Premier.
10. Yuan, Q. et al., 2008. Effect of hydroxyl ions on chloride penetration depth measurement using the colorimetric method. *Cement and Concrete Research*, Issue 38, pp. 1177-1180.
11. Hamilton III, H., Boyd, A. J., Vivas, E. & Bergin, M., 2007. *Permeability of Concrete - Comparison of Conductivity and Diffusion Methods*, Tallahassee: Florida Department of Transportation.
12. Nordtest, 1999. *NT Build 492 - Concrete, mortar and cement-based repair materials: Chloride migration coefficient from non-steady-state migration experiments*, Espoo: Nordtest.
13. Tang, L. & Gulikers, J., 2007. On the mathematics of time-dependent apparent chloride diffusion coefficient in concrete. *Cement and Concrete Research*, Issue 37, pp. 589-595.
14. The Concrete Society, 1995. *Concrete Society Technical Report No 44 - The Relevance of Cracking in Concrete to Corrosion of Reinforcement*, Slough: The Concrete Society.

# Experimental study on anchorage behaviour of the CFRP grid in mortar

Bo Wang<sup>1</sup>, Kimitaka Uji<sup>2</sup>, Junlei Zhang<sup>1</sup>, Atsushi Ueno<sup>3</sup>, Kentaro Ohno<sup>4</sup> and Tran Vu Dung<sup>1</sup>

<sup>1</sup>Graduate Student of Dept. of Civil and Environmental Engineering, Tokyo Metropolitan University

<sup>2</sup>Professor of Dept. of Civil and Environmental Engineering, Tokyo Metropolitan University

<sup>3</sup>Associate Professor of Dept. of Civil and Environmental Engineering, Tokyo Metropolitan University

<sup>4</sup>Assistant Professor of Dept. of Civil and Environmental Engineering, Tokyo Metropolitan University

**Abstract:** Carbon Fiber Reinforced Plastic (CFRP) grid is usually used for strengthening of existing concrete structures. This is made by several layers of vertical and horizontal CFRP bars by means of pressing and adhesion. To investigate the behaviour between the CFRP grid and mortar comprehensively, three kinds of tensile tests of the vertical bar are conducted: (1) under bond condition with crossing section; (2) under no-bond condition with crossing section; (3) under bond condition without crossing section. Types of CFRP grids (CR5, CR8, CR13), grid interval (50mm, 100mm) and number of grid nodes (1, 2, 3) are selected as changing parameters. Based on experimental results of 135 pieces of pull-out specimens, influence rules of types of CFRP grids, grid interval and number of grid nodes on anchorage performance of CFRP grids in the mortar are analyzed. In addition, influence factors on the tensile strength utilization of CFRP grid, maximum tensile load growth gradient with increasing number of nodes, anchorage mechanism are discussed.

**Keywords:** CFRP grid, mortar, anchorage performance, tensile strength, pull-out test

## 1. Introduction

Concrete structure is one of most common structure in the world. As we know, many existing concrete structure have reached their planned service life. In order to enhance the safety of these structures, strengthening is necessary. Strengthening method by using sprayed polymer mortar and Carbon Fiber Reinforced Plastic (CFRP) grids has been applied in Japan.

For this strengthening technique, to ensure the oneness of CFRP grid, mortar and existing concrete is very critical. In the past, a lot of researchers studied the bond behaviour between base concrete and repairing material (Uji et al (2007), Ohno et al (2011), Zhang et al (2012, 2013)). Only several researches on bond behaviour between CFRP grid and mortar have been carried out (Sugiyama et al (2011)). The main purpose of this paper is to study the anchorage behaviour of the CFRP grid in the mortar comprehensively. Based on the initial analysis, it is clarified that anchorage actions between CFRP grid and the mortar could be divided into two parts: one is the resistance action of the horizontal bar in crossing section; the other is bond action between the vertical bar and the mortar. In order to investigate the behaviour between CFRP grid and mortar, three different anchorage conditions are conducted and a total of 135 pieces of specimens are fabricated to make pull-out tests.

## 2. Experimental Programs

### 2.1 Test specimens

Three kinds of pull-out tests (be equivalent to three kinds of anchorage conditions) of the vertical bar are conducted: (1) under no-bond condition with crossing section (abbr.: NBW); (2) under bond condition without crossing section (abbr.: BWO); (3) under bond condition with crossing section (abbr.: BW). Types of CFRP grids (CR5, CR8 and CR13), grid interval (50mm, 100mm) and number of grid nodes (1, 2, 3) are selected as changing parameters. Three identical specimens were manufactured for each specimen design. The total number of specimens is  $5$  (grid type and interval)  $\times 3$  (number of nodes)  $\times 3$  (anchorage condition)  $\times 3$  (sample), which is equal to 135.

No-bond condition is realized by wrapping tap around the vertical bar. Take CR8@50 for example, the fabricated grids corresponding to three different anchorage conditions are shown in Figure 1. Steel pipe (internal diameter is 93.2mm; thickness is 4.2mm) is applied to be the pouring mould as well avoiding the fracture of the mortar before the fracture of CFRP grid during the test. Figure 2 shows the pouring device of mortar and representative fabricated specimen.

Take the specimen with three nodes as example (abbr.: NBW-3, BWO-3, BW-3), dimensions are shown in Figure 3. To decrease the influence of inaccurate stress state of the mortar near the loading part when considering the bond action of vertical bar (BWO-type condition and BW-type condition), 30mm-length no-bond parts are conducted by using waterproof material as shown in Figure 3 (b) and (c). For dimensions corresponding to specimens with one node and two nodes, just need to replace  $3i$  with  $i$  and  $2i$  respectively in Figure 3.



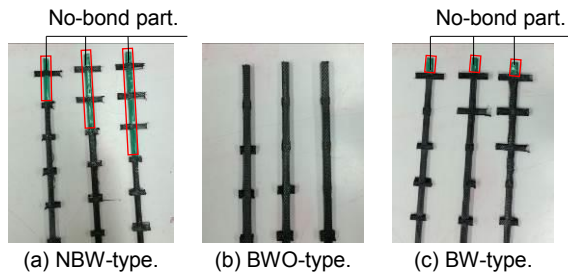


Figure 1. Three kinds of anchorage conditions.

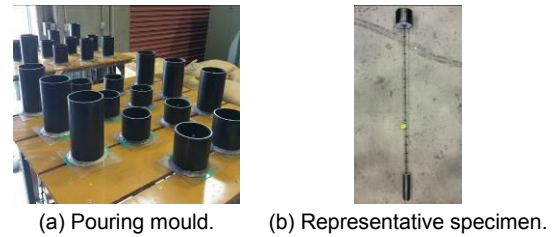


Figure 2. Fabricating of the specimen.

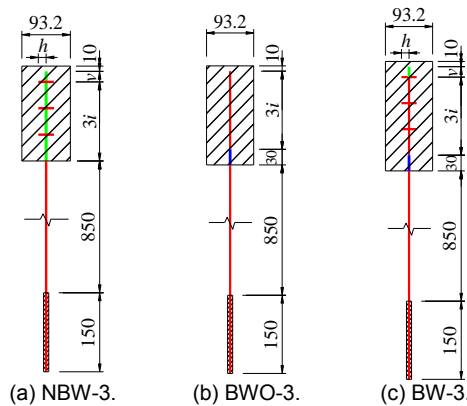


Figure 3. Dimensions of specimen with three nodes.

Notes:

$i$ —stands for the grid interval (50mm and 100mm);  
 $h$ —stands for the distance from the side of node to the end of horizontal bar (when grid interval is 50mm and 100mm, this value is taken for 15mm and 30mm respectively);  
 $v$ —stands for the distance from the side of node to the end of vertical bar (when grid interval is 50mm and 100mm, this value is taken for 20mm and 30mm respectively).

## 2.2 Material properties

In order to avoid the mortar occurring failure before the CFRP grid, high strength mortar which is usually used in practical retrofitting is applied. Table 1 provides the mix proportion of mortar. Test results show that the average compressive strength of the mortar is about 106.3 MPa. Table 2 provides the test maximum tensile load and the calculation maximum tensile load of CFRP grids. Calculation maximum tensile load is the product of theoretical tensile strength of CFRP grid (1400MPa) and the average cross sectional area (13.2mm<sup>2</sup>, 26.4mm<sup>2</sup>, 65mm<sup>2</sup> corresponding to CR5, CR8, CR13 respectively).

Table 1. Mix proportion of mortar and compressive strength.

Item	Cement (kg/m <sup>3</sup> )	Water (kg/m <sup>3</sup> )	Sand (kg/m <sup>3</sup> )	Expanding material (kg/m <sup>3</sup> )	Water reducer (kg/m <sup>3</sup> )
Value	1000	309	1000	50	2

Table 2. Tensile maximum load of CFRP grid.

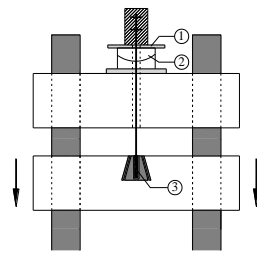
Type of CFRP grid	CR5	CR8	CR13
Test maximum tensile load ( $T_{tg}$ ) (kN)	24.5	45.7	108.8
Calculation maximum tensile load ( $T_{cg}$ ) (kN)	18.5	37.0	91.0
Calculation-test ratio ( $T_{cg}/T_{tg}$ )	75.5%	81.0%	84.3%

## 2.3 Measurement and testing procedures

According to the “Test method for bond strength between reinforcing steel and concrete by pull-out test (JSCE-G503)”, the pull-out test has been developed to investigate anchorage behaviour between CFRP grid and mortar. Figure 4 (a) shows the experimental equipment with 1000 kN load capacity. Figure 4(b) shows the experimental loading method. Displacement-control loading method is applied and the loading rate is set as 1.5 mm/min. Load and displacement data are acquired during the loading process.



(a) Experiment device.



(b) Loading method.

- ① steel plate;
- ② ball seat;
- ③ steel pipe and expansion material.

**Figure 4. Experiment device and loading method.**

### 3. Results and discussion

#### 3.1 Maximum load

Average maximum load of all specimens are shown in Table 3.

**Table 3. Maximum load of all specimens.**

Type	CR5@50	CR5@100	CR8@50	CR8@100	CR13@100	
NBW	NBW-1	11.2	12.0	17.0	18.5	48.5
	NBW-2	18.1	18.5	28.3	30.9	67.9
	NBW-3	19.1	21.4	31.3	35.9	79.9
BWO	BWO-1	10.8	22.3	14.0	25.3	34.0
	BWO-2	23.5	21.2	29.5	42.7	80.3
	BWO-3	22.5	24.4	38.6	43.0	96.0
BW	BW-1	19.2	23.2	24.9	35.9	73.3
	BW-2	23.6	23.3	40.9	45.3	110.3
	BW-3	22.8	23.3	42.6	43.5	109.4

Note: NBW-1, NBW-2, NBW-3 stand for the NBW-type specimen with one node, two nodes and three nodes respectively. Others analogize.

#### 3.2 Failure modes

For the external CFRP grid (the vertical bar outside the mortar), failure modes could be divided into three kinds:

- ① stands for the external CFRP grid still keep intact;
- ② stands for the break of the external CFRP grid;
- ③ stands for the smash of the external CFRP grid (It means the grid breaks into more than two parts).

For the internal CFRP grid (the grid inside the mortar), the failure modes also could be divided into three kinds:

- Ⓐ stands for the vertical CFRP bar be pulled out to a certain distance;
- Ⓑ stands for the vertical CFRP bar be pulled out completely;
- Ⓒ stands for the break of the vertical CFRP bar in the mortar.

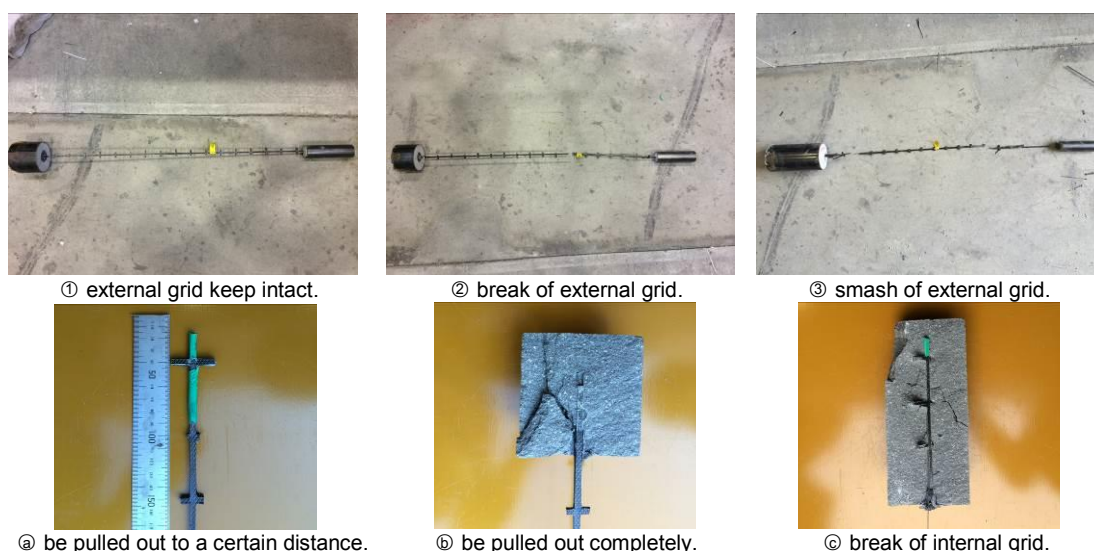
These failure modes above are shown in Table 4 and Table 5. Representative failure photos are shown in Figure 5.

**Table 4. Failure mode of the external CFRP grid.**

Type	CR5@50	CR5@100	CR8@50	CR8@100	CR13@100	
NBW	NBW-1	①	①	①	①	①
	NBW-2	②	③	②	①	②
	NBW-3	②	③	②	②	③
BWO	BWO-1	①	③	①	①	①
	BWO-2	②	③	②	③	②
	BWO-3	③	③	③	③	③
BW	BW-1	②	③	②	②	①
	BW-2	②	③	②	③	②
	BW-3	③	③	③	③	③

**Table 5. Failure mode of the internal CFRP grid.**

Type		CR5@50	CR5@100	CR8@50	CR8@100	CR13@100
NBW	NBW-1	a	a	a	a	a
	NBW-2	a	a	a	a	a
	NBW-3	a	c	c	c	c
BWO	BWO-1	b	a	b	b	b
	BWO-2	c	c	a	c	a
	BWO-3	c	c	c	c	c
BW	BW-1	a	c	a	a	a
	BW-2	c	c	a	c	c
	BW-3	c	c	c	c	c



**Figure 5. Representative failure photos.**

Combined with the maximum tensile load (as shown in Table 3), It shows that:

- (1) For each type of CFRP grid under the same anchorage condition, the external grid tends to break more and more seriously with the increasing number of nodes. When the maximum pull-out load is close to the maximum tensile load of CFRP grid (as shown in Table 2), the external grid occurs smash-type failure mode (③);
- (2) Maximum tensile load corresponding to break-type failure mode (②) is smaller than it corresponding to smash-type failure mode (③);
- (3) Under no-bond condition with crossing section (NBW), the internal grid tends to be pulled out to a certain distance under relatively lower pull-out load, while under higher pull-out load, the internal grid breaks, even smashes.
- (4) Under bond condition without crossing section (BWO) with one node except CR5@100, all the other internal grids are pulled out completely.

### 3.3 Analysis of tensile strength utilization of CFRP grid

#### 3.3.1 Definition and calculation of tensile strength utilization of CFRP grid

Define the tensile strength utilization  $\alpha$  by equation (1).

$$\alpha = \frac{P_u}{T_{ig}} \times 100\% \quad (1)$$

$P_u$ —average maximum pull-out load for each type of specimen, as shown in Table 3;

$T_{ig}$ —test maximum tensile load for CFRP grid, as shown in Table 2.

Calculation results of tensile strength utilization are shown in Table 6.

According to the calculation-test ratio of maximum tensile load of CFRP grid (as shown in Table 2) and considering the safety of practical engineering, it is regarded that when the tensile strength utilization is approximately equal to or greater than 70%, the tensile strength of CFRP

grid is fully used (underlined value as shown in Table 6).

**Table 6. Tensile strength utilization (%).**

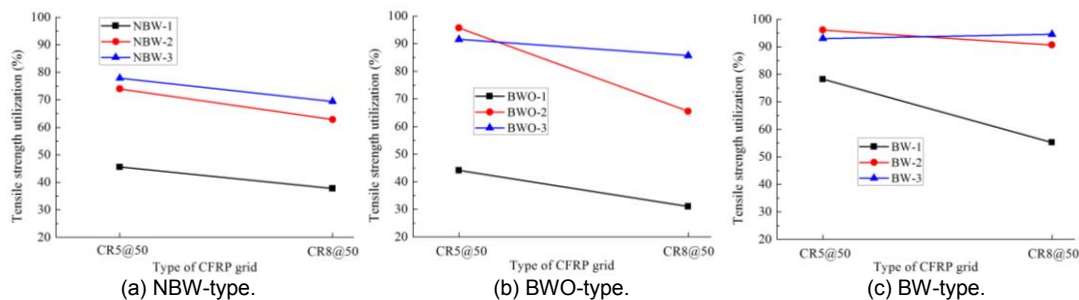
Type		CR5@50	CR5@100	CR8@50	CR8@100	CR13@100
NBW	NBW-1	45.6	49.0	37.8	41.1	44.5
	NBW-2	<u>74.0</u>	<u>75.6</u>	62.8	68.5	62.5
	NBW-3	<u>77.9</u>	<u>87.3</u>	<u>69.4</u>	<u>79.7</u>	<u>73.4</u>
BWO	BWO-1	44.1	<u>91.1</u>	31.1	56.2	31.2
	BWO-2	<u>95.7</u>	86.6	65.5	<u>94.7</u>	<u>73.8</u>
	BWO-3	91.6	99.3	<u>85.7</u>	95.3	88.2
BW	BW-1	<u>78.2</u>	<u>94.6</u>	55.2	<u>79.7</u>	67.4
	BW-2	96.1	95.1	<u>90.8</u>	100.0	<u>100.0</u>
	BW-3	93.2	95.1	94.5	96.5	100.0

Table 6 suggests that in order to make full use of tensile strength of CFRP grid:

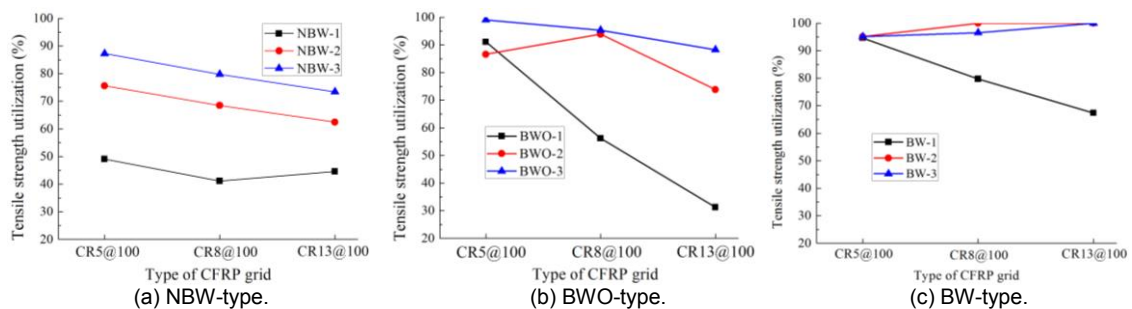
- (1) Under no-bond condition with crossing section (NBW), it needs two nodes at least for CR5@50 and CR5@100; it needs three nodes at least for CR8@50, CR8@100 and CR13@100.
- (2) Under bond condition without crossing section (BWO), it only needs one node for CR5@100; it needs two nodes at least for CR5@50, CR8@100 and CR13@100; it needs three nodes at least for CR8@50.
- (3) Under bond condition with crossing section (BW), it needs one node for CR5@50, CR5@100 and CR8@100; it needs two nodes at least for CR8@50 and CR13@100.

### 3.3.2 Influence rules of CFRP grid type on the tensile strength utilization

Figure 6 and Figure 7 compare the tensile strength utilization corresponding to different CFRP grid types under same grid interval (50mm and 100mm respectively).



**Figure 6. Influence rules of CFRP grid type (grid interval is 50mm) on the tensile strength utilization of CFRP grid.**



**Figure 7. Influence rules of CFRP grid type (grid interval is 100mm) on the tensile strength utilization of CFRP grid.**

Theoretically, under the same anchorage condition, the tensile strength utilization must increase with the increasing number of nodes. But from Table 6, Figure 6 and Figure 7, it shows that some values seem to be unreasonable. It shows that the tensile strength utilization decreases with the increasing number of nodes (for CR5@50: BWO-2 → BWO-3, BW-2 → BW-3; for CR5@100: BWO-1 → BWO-2; for CR8@100: BW-2 → BW-3.). Preliminary analysis shows that

with the increasing number of nodes under same anchorage condition, when two successive tensile strength utilization (as shown in Table 6, be equivalent to two successive maximum tensile load as shown in Table 3) is close, the comparative analysis in this part is meaningless. Because in this situation the tensile strength of CFRP grid has been fully used and this indicates that increasing the number of nodes couldn't continue to improve the tensile capacity of pull-out specimens. Therefore, when making comparative analysis of tensile strength utilization, discarding these meaningless data would be more reasonable.

Comparative analysis shows that the tensile strength utilization of CFRP grid decreases with the increasing of cross sectional area (CR5 (13.2mm<sup>2</sup>)→CR8 (26.4mm<sup>2</sup>)→CR13 (65.0mm<sup>2</sup>)).

### 3.3.3 Influence rules of CFRP grid interval on the tensile strength utilization

Figure 8 and Figure 9 compare the tensile strength utilization corresponding to different CFRP grid intervals under same grid type (CR5 and CR8 respectively).

Discarding the meaningless data as part 3.3.2 above, Figure 8 (b) (c) and Figure 9 (b) (c) show that the tensile strength utilization increases with the increasing of grid interval (50mm→100mm). Figure 8 (a) and Figure 9 (a) show that under no-bond condition with crossing section (NBW), the tensile strength utilization corresponding to 100mm grid interval is a little bigger than it corresponding to 50mm grid interval. However, under no-bond condition with crossing section (NBW), the tensile strength utilization should be much closer between two kinds of grid intervals theoretically. Because the elastic modulus of CFRP grid is rather large (about 10<sup>5</sup> MPa) which just could cause very small deformation of the vertical bar under tensile load. Preliminary analysis shows that it isn't the perfect no-bond condition by wrapping tap around the vertical bar, and there must be residual bond action which will increase with the increasing of grid interval. This will illustrate the phenomenon above.

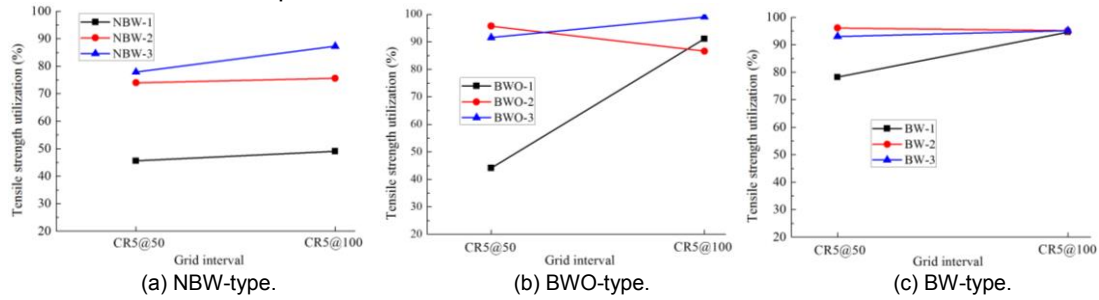


Figure 8. Influence rules of grid interval (CR5) on the tensile strength utilization of CFRP grid.

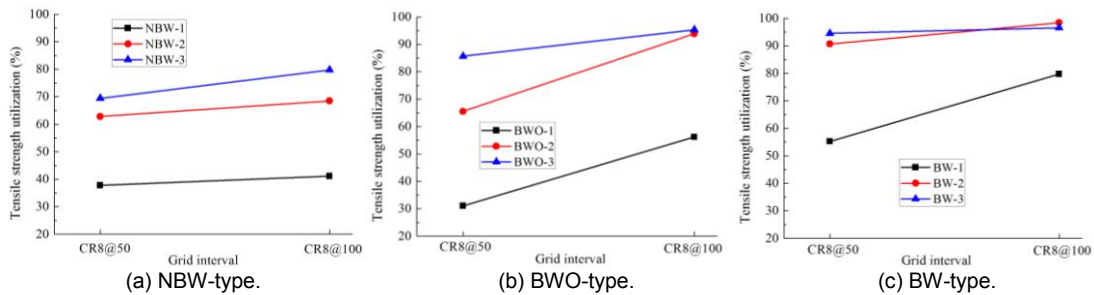


Figure 9. Influence rules of grid interval (CR8) on the tensile strength utilization of CFRP grid.

## 3.4 Analysis of maximum load growth gradient with increasing number of nodes

### 3.4.1 Definition and calculation of growth gradient of maximum load of CFRP grid

Define the growth gradient of maximum load  $\beta$  by equation (2).

$$\beta = \frac{P_{ij}}{P_{i1}} \quad (2)$$

$P_{i1}$ —average maximum tensile load for  $i$ -type of pull-out specimen with one crossing point (Be equivalent to the average maximum load of specimen NBW-1, BWO-1, BW-1 respectively), as shown in Table 3.;

$P_{ij}$ —average maximum tensile load for  $i$ -type of pull-out specimen with  $j$  crossing point, as shown in Table 3.



Calculation results are shown in Table 7. It is important to note that, as same situation and reasons shown in 3.3.2 part, when making comparative analysis, the meaningless values should be discarded.

**Table 7. Growth gradient of maximum load.**

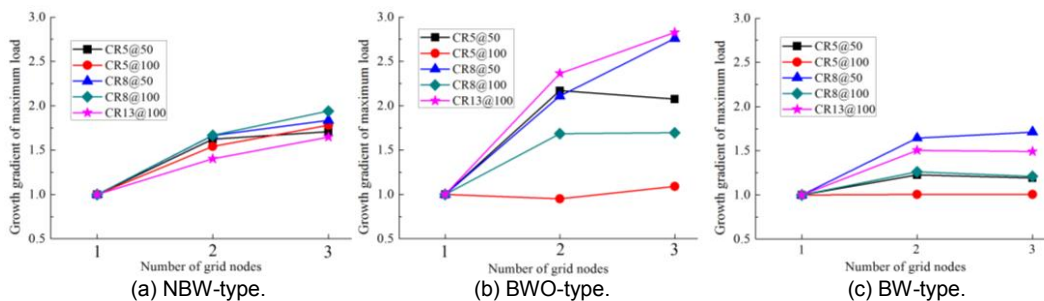
Type		CR5@50	CR5@100	CR8@50	CR8@100	CR13@100
NBW	NBW-1	1.0	1.0	1.0	1.0	1.0
	NBW-2	1.6	1.5	1.7	1.7	1.4
	NBW-3	1.7	1.8	1.8	1.9	1.6
BWO	BWO-1	1.0	1.0	1.0	1.0	1.0
	BWO-2	2.2	1.0	2.1	1.7	2.4
	BWO-3	2.1	1.1	2.8	1.7	2.8
BW	BW-1	1.0	1.0	1.0	1.0	1.0
	BW-2	1.2	1.0	1.6	1.3	1.5
	BW-3	1.2	1.0	1.7	1.2	1.5

### 3.4.2 Influence rules of grid type and interval on the maximum load growth gradient

Figure 10 compares the growth gradient corresponding to different grid types and intervals under the same anchorage condition. It shows that:

- (1) Under no-bond condition with crossing section (NBW), maximum tensile load corresponding to all types of CFRP grid increases with the increasing number of nodes from 1 to 3.
- (2) Under bond condition without crossing section (BWO), maximum tensile load corresponding to CR5@100 doesn't change much, while to other types of CFRP grids, maximum tensile load increases with the increasing number of nodes.
- (3) Under bond condition with crossing section (BW), maximum tensile load corresponding to CR5@100 nearly doesn't change with the increasing number nodes. Maximum tensile load corresponding to other types of CFRP grids increases obviously when the number of grid node increases from 1 to 2, while it doesn't change obviously when the number of grid node increases from 2 to 3.

Combined with analysis results of tensile strength utilization (3.3.2 part), it shows that when the number of nodes are enough to make full use of the tensile strength of CFRP grid, the maximum load growth gradient wouldn't increase any more with the increasing number of nodes.



**Figure 10. Influence rules of grid nodes on the growth gradient of maximum load.**

### 3.4.3 Influence rules of anchorage condition on the maximum load growth gradient

Figure 11 compares the growth gradient of maximum load corresponding to different anchorage conditions under each grid type and grid interval. It shows that:

- (1) For CR5@100 and CR8@100, maximum tensile load corresponding to NBW-anchorage condition is influenced highly by the number of grid node.
- (2) For CR5@50, CR8@50, CR13@100, maximum tensile load corresponding to BWO-anchorage condition is influenced highly by the number of grid node.

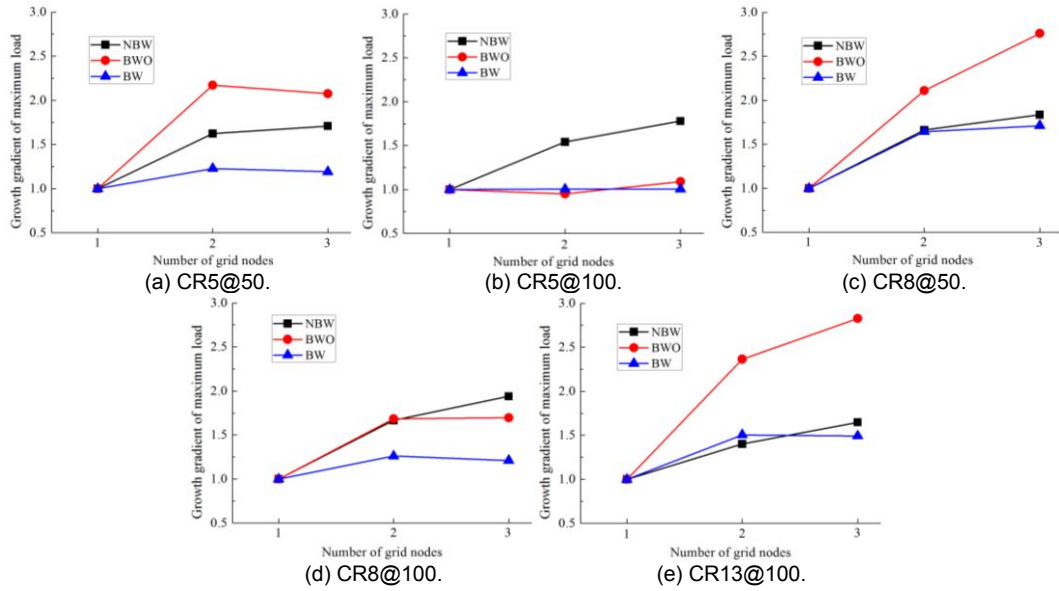


Figure 11. Influence rules of grid nodes on the growth gradient of maximum load.

### 3.5 Relationship of maximum load among three kinds of anchorage conditions

#### 3.5.1 Two kinds of anchorage actions

As above, three kinds of anchorage conditions were analyzed respectively. Based on the initial analysis, it is clarified that anchorage action of BW-type condition mainly be composed with the resistance action of horizontal bar (NBW-type condition) and bond action of vertical bar (BWO-type condition). In order to reveal the anchorage mechanism comprehensively, it is necessary to analyze the relationship of maximum load among three kinds of anchorage conditions.

Taking the maximum load corresponding to NBW-type specimen (under no-bond condition with crossing section) as the standard value, calculate the standardized value corresponding to BWO-type specimen and BW-type specimen. Specific calculation formula is shown as formula (3) below. Calculation results are shown in Table 8.

$$\begin{aligned} \gamma_1 &= \frac{P(NBW_i)}{P(NBW_i)} \equiv 1.0 & i = 1, 2, 3 \\ \gamma_2 &= \frac{P(BWO_i)}{P(NBW_i)} & i = 1, 2, 3 \\ \gamma_3 &= \frac{P(BW_i)}{P(NBW_i)} & i = 1, 2, 3 \end{aligned} \quad (3)$$

$P(NBW_i)$ —average maximum tensile load under NBW-type condition with  $i$  nodes, as shown in Table 3;

$P(BWO_i)$ —average maximum tensile load under BWO-type condition with  $i$  nodes, as shown in Table 3;

$P(BW_i)$ —average maximum tensile load under BW-type condition with  $i$  nodes, as shown in Table 3.

Table 8. Standardized maximum tensile load.

Type		CR5@50	CR5@100	CR8@50	CR8@100	CR13@100
One node	NBW-1	1.0	1.0	1.0	1.0	1.0
	BWO-1	1.0	1.9	0.8	1.4	0.7
	BW-1	1.7	1.9	1.5	1.9	1.5
Two nodes	NBW-2	1.0	1.0	1.0	1.0	1.0
	BWO-2	1.3	1.1	1.0	1.4	1.2
	BW-2	1.3	1.3	1.4	1.5	1.6
Three nodes	NBW-3	1.0	1.0	1.0	1.0	1.0
	BWO-3	1.2	1.1	1.2	1.2	1.2
	BW-3	1.2	1.1	1.4	1.2	1.4



Calculation results show that:

- (1) For all kinds of CFRP grids with three nodes and for CFRP grids with two nodes except CR8@50, the standardized maximum tensile load corresponding to BWO-type condition is greater than 1.0. This indicates that the bond action of vertical bar (be equivalent to BWO-type condition) is the predominant anchorage action;
- (2) For CR8@50 and CR13@100 with one node, the resistance action of horizontal bar is the predominant anchorage action; while for CR5@100 and CR8@100 with one node, the bond action of vertical bar is the predominant anchorage action;
- (3) For CR5@50 with one node and CR8@50 with two nodes, two kinds of anchorage actions divide equally.

### 3.5.2 Coupling effect between two kinds of anchorage actions

In order to make quantitative analysis, the proportionality coefficient  $\eta$  is calculated based on the formula (4) as below. Calculation results are shown in Table 9.

$$\eta = \frac{P(BW_i)}{P(NBW_i) + P(BWO_i)} \times 100\% \quad i = 1, 2, 3 \quad (4)$$

$P(BW_i)$ —average maximum tensile load under BW-type condition, as shown in Table 3;  
 $P(NBW_i)$ —average maximum tensile load under NBW-type condition, as shown in Table 3;  
 $P(BWO_i)$ —average maximum tensile load under BWO-type condition, as shown in Table 3.

**Table 9. Proportionality coefficient (%).**

Type	CR5@50	CR5@100	CR8@50	CR8@100	CR13@100
One node	87.2	67.5	80.2	82.0	88.9
Two node	56.6	58.6	70.7	61.6	74.4
Three nodes	55.0	51.0	61.0	55.2	62.2

Table 9 shows that the coefficient  $\eta$  isn't equal to 100% which indicates that there must be the coupling effect between two kinds of anchorage actions. Besides, the coefficient  $\eta$  decreases with the increasing number of nodes. And this indicates that with the increasing number of nodes, the coupling effect is more and more significant.

## 4. Calculation model of maximum tensile load

Based on the analysis of experimental results above, it is clarified that the anchorage action of CFRP grid ( $P_u$ ) is composed with resistance action of horizontal bar and bond action of vertical bar, which are marked by  $P_r$  and  $P_b$  respectively. As shown in equation (5) below,  $\Phi$  stands for one function relationship, which is related to the coupling effect between two kinds of anchorage actions as analysis above.

$$P_u = \Phi(P_r + P_b) \quad (5)$$

Suppose that the vertical bar has  $n$  nodes.

The calculation model of resistance action could be expressed by equation (6).

$$P_r = mP_0 + \sum_{i=m+1}^n P_i \quad (6)$$

Where  $P_0$  stands for the fracture load of single node;  $m$  stands for the number of fractured nodes under the tensile load.  $P_i$  stands for the tensile load beard by every no-fractured node.

In order to get the specific parameters in equation (6), the key is to reveal the resistance action transfer mode along the vertical bar under tensile load.

The calculation model of bond action could be expressed by equation (7).

$$P_b = f(\tau) \quad (7)$$

Where  $\tau$  stands for the bond stress between the vertical bar and mortar;  $f$  stands for one function relationship. And the bond stress is related to grid type, strength of mortar, anchorage length and other factors. Besides, in practical engineering, the bond condition of vertical bar is different with the condition illustrated in this paper. Three sides of vertical bar are bonded in the mortar, while the fourth side is attached on the surface of existing concrete. This will make the calculation of the bond stress

more complicated.

In order to reveal the anchorage mechanism comprehensively, more experiments and theoretical analysis should be made in late-stage research.

## 5. Conclusions

A total of 135 pull-out specimens were tested in this study. The main purpose was to investigate the anchorage behavior of CFRP grid in mortar under three kinds of anchorage conditions. The following conclusions can be made from the experimental results obtained in this study:

(1) In order to make full use of the tensile strength of CFRP grid: (a) Under no-bond condition with crossing section (NBW), it needs two nodes at least for CR5@50 and CR5@100; it needs three nodes at least for CR8@50, CR8@100 and CR13@100. (b) Under bond condition without crossing section (BWO), it only needs one node for CR5@100; it needs two nodes at least for CR5@50, CR8@100 and CR13@100; it needs three nodes at least for CR8@50. (c) Under bond condition with crossing section (BW), it needs one node for CR5@50, CR5@100 and CR8@100; it needs two nodes at least for CR8@50 and CR13@100.

(2) The tensile strength utilization of CFRP grid decreases with the increasing of cross sectional area, while it increases with the increasing of grid interval.

(3) The maximum tensile load growth gradient wouldn't increase anymore when the number of nodes is enough to make full use of the tensile strength of CFRP grid. Under no-bond condition with crossing section, maximum tensile load corresponding to all types of CFRP grids increases with the increasing number of nodes from 1 to 3.

(4) For CR5@100 and CR8@100, maximum tensile load corresponding to NBW-type anchorage condition is influenced highly by the number of grid nodes; For CR5@50, CR8@50, CR13@100, maximum tensile load corresponding to BWO-type anchorage condition is influenced highly by the number of grid nodes.

(5) For all kinds of CFRP grids with three nodes and for CFRP grids with two nodes except CR8@50, the bond action of vertical bar (be equivalent to BWO-condition) is the predominant anchorage action; for CR8@50 and CR13@100 with one node, the resistance action of horizontal bar is the predominant anchorage action; for CR5@100 and CR8@100 with one node, the bond action of vertical bar is the predominant anchorage action; for CR5@50 with one node, two kinds of anchorage actions divide equally.

(6) The coupling effect exists between the resistance action of horizontal bar and the bond action of vertical bar. And with the increasing number of nodes, the coupling effect is more and more significant.

(7) The anchorage behavior of CFRP grid in the mortar is rather complicated. Further study needs to be done with more experiments and numerical analysis to investigate the anchorage mechanism.

## 6. Acknowledgement

This research was supported by Asian Human Resources Fund from Tokyo Metropolitan government.

## 7. References

1. Uji, k., Satoh, K. et al. "Effects of retrofitting method using CFRP grid on the shear behavior of existing concrete members". Proceedings of FRPRCS-8(in CD-ROM), 2007, Greece.
2. Ohno, K., Kurohara, S., et al. "Failure process in shear bonding strength tests between existing concrete and repairing material by acoustic emission technique". Proceedings of International RILEM Conference on Advances in Construction Material through Science and Engineering (in CD-ROM), 2011, Hong Kong.
3. Zhang, J., Ohno, K., et al. "Investigation of shear bonding behaviour between base concrete and polymer-modified mortar with CFRP grid". Proceedings of the 3<sup>RD</sup> ICCRRR (in CD-ROM), 2012, Cape Town, South Africa.
4. Zhang, J., Ohno, K., et al. "Mechanisms of bond failure between existing concrete and sprayed polymer cement mortar with CFRP grid by Acoustic Emission", Concrete 2013 (in CD-ROM), 2013, Gold Coast, Australia.
5. Sugiyama, K., Yamaguchi, K., et al. "Stress transfer mechanism of the reinforced interface and seismic retrofit existing RC Pier by Polymer cement mortar for shotcrete with CFRP grid". JCI Proceedings of Structural Engineering, Vol.57A, 2011.3, pp 1042-1051 (in Japanese).

# Influence of Fiber Net Reinforced Mortar Repair Coating on the Crack Opening Resistance of Concrete

Yoshinori Kitsutaka<sup>1</sup> and Yukihiro Oyama<sup>2</sup>

<sup>1</sup>Professor, Tokyo Metropolitan University

<sup>2</sup>Ministry of Justice Associates

**Abstract:** For long-term and effective use of the concrete structure, the concrete wall repairing is getting more important. The use of the fiber reinforced cementitious composite for a repairing material on the cracked concrete surface or the damaged mortar finishing is effective to improve the durability of concrete structures. In this paper, the performance of the fiber net reinforced mortar from the viewpoint of concrete crack resistance was investigated. Three-point bending tests on pre-notched concrete beam specimens which coating the fiber net reinforced mortar on surface were performed. Load-load displacement curves were measured and the fracture toughness was evaluated. It was found that the toughness of cracked concrete was improved by coating the fiber net reinforced mortar. Material properties and the density of fiber net were important factors for improving the toughness of cracked concrete. Also the compiling direction of the fiber net was important factor for improving the toughness of cracked concrete. An analysis method to calculate the load-displacement relationship on the surface repaired concrete by the fiber net reinforced mortar was proposed and a good relationship was obtained between the test results and the analysis results.

**Keywords:** fiber net reinforced mortar, repair, coating, fracture toughness.

## 1. Introduction

Repairing of tiled and mortar external building walls has become increasingly important for the demand of long-term use of building structures and utilization of the existing building stock. The pin-net repairing system is a composite external wall repair system and is developed to prevent delamination of tiled and mortar external walls. The performance of individual pin-net repairing systems has been investigated in the literature, but comparison among various materials used for each method has not been well studied. Also, the resistance of netting to the propagation of tensile cracks in setting mortar and concrete is important from the aspect of a delamination-inhibiting effect.

The failure of fiber net containing mortar is characterized by being more ductile than that of conventional mortar finishing, bridging of fibers, which continues to transfer the tensile stress after cracking. The transferred stress may even increase after cracking, which is known as strain hardening (Kitsutaka and Oh-oka, 1998). In such a state, partial hardening in the failure process of a mortar causes new cracks in other parts of the mortar, dispersing the fracture area. This increases the energy-absorbing capacity of the mortar during failure, while avoiding brittleness due to localization of cracking, thereby leading to an ideal mode of failure.

The behavior of fiber net reinforcing mortar coatings during the tensile cracking process of the concrete substrate can be experimentally evaluated by the three-point bending tests on pre-notched concrete beam specimen which coating the fiber net reinforcing mortar on surface. The effect of fiber net reinforcing mortar coatings on tensile crack resistance can be evaluated by the load-load point displacement (L-LPD) curves obtained from the three-point bending tests. Also an area surrounded by L-LPD curve can evaluate the total energy consumed in the process of concrete cracking and this energy can be the evaluation index on the crack resistance of fiber net reinforcing mortar coating.

In this study, three-point bending tests were conducted on mortar specimens, to which multiaxial fiber netting was applied, with the aim of comparing the netting's effects of inhibiting tensile crack propagation in setting mortar and concrete.

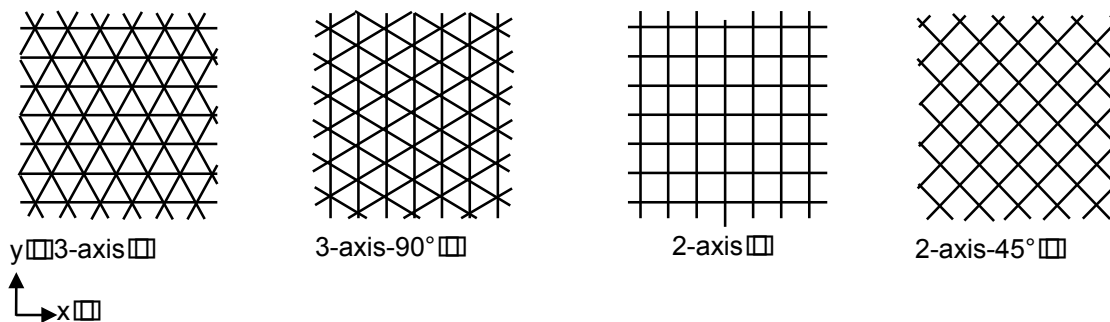
## 2. Experiments

### 2.1 Outline of specimens

Table 1 gives the outline of fiber nets. Nine types of specimens were fabricated: Six with six net types, one with no net (P), one with VF3-10 netting rotated 90° and one with VF2-10 netting rotated 45° to examine the effect of the direction of fiber nets, and types of fiber were vinylon, polypropylene and glass normally used for pin-net repairing system. Fig. 1 shows the directions of fiber net application.

**Table 1. Outline of fiber nets.**

Name of specimen	Sign	Net intervals (mm)	Properties of fiber					
			Weight (g/m <sup>2</sup> )	Diameter (μm)	Tensile strength (MPa)	Strain (%)	Young's modulus (GPa)	Dens. (g/cm <sup>3</sup> )
Plain	P	-	-	-	-	-	-	-
Vinylon fiber-3axis	VF3-10	10×10	88	13	1580	7.2	36.3	1.3
Vinylon fiber-3axis	VF3-15	15×15	57	13	1580	7.2	36.3	1.3
Vinylon fiber-2axis	VF2-10	10×10	100	13	1270	6.6	26.4	1.3
Vinylon fiber-2axis	VF2-15	15×15	70	13	1270	6.6	26.4	1.3
Polypropylene fiber-3axis	PP3-10	10×10	-	12	430	-	10.5	-
Glass fiber-2axis	GF2-5	5×5	150	10	2500	-	74.0	-
Vinylon fiber-3axis-90°rotate	VF3-10(90)	10×10	88	13	1580	7.2	36.3	1.3
Vinylon fiber 2axis-45°rotate	VF2-10(45)	10×10	100	13	1270	6.6	26.4	1.3

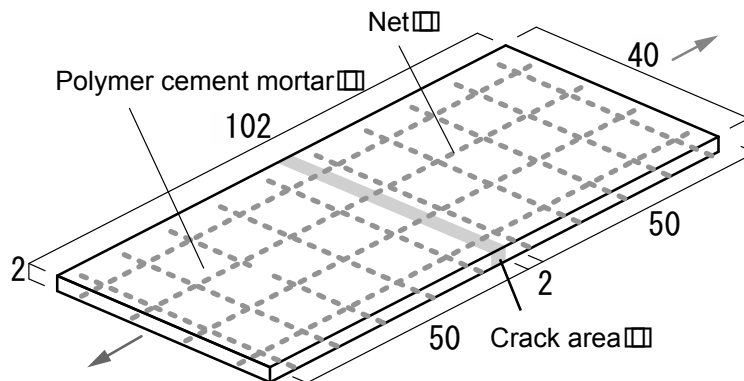


**Figure 1. Directions of fiber net application.**

Table 2 shows the mixture proportions and basic properties of polymer cement mortar. Fig. 2 shows the outline of a fiber net reinforcing mortar coating. In this study, in order to reduce the deviation of crack propagation caused by the coarse aggregate, mortar was selected for base specimens, which measured 200 by 100 by 100 mm. After curing base specimens as specified, a notch was cut to a depth of 25 mm in the longitudinal center of each of the four sides of each specimen. Nets were then applied to two opposite sides with polymer cement mortar following the instructions of the pin-net repairing system. Carbon fiber sheets were applied using epoxy.

**Table 2. Properties of polymer cement mortar**

Material	Contents	Properties
Polymer cement mortar	Cement	Cement : Admixture : Water 100:10:20(Weight ratio)
	Kation type SBR latex	Compressive strength 2 weeks : 28.3 (MPa)



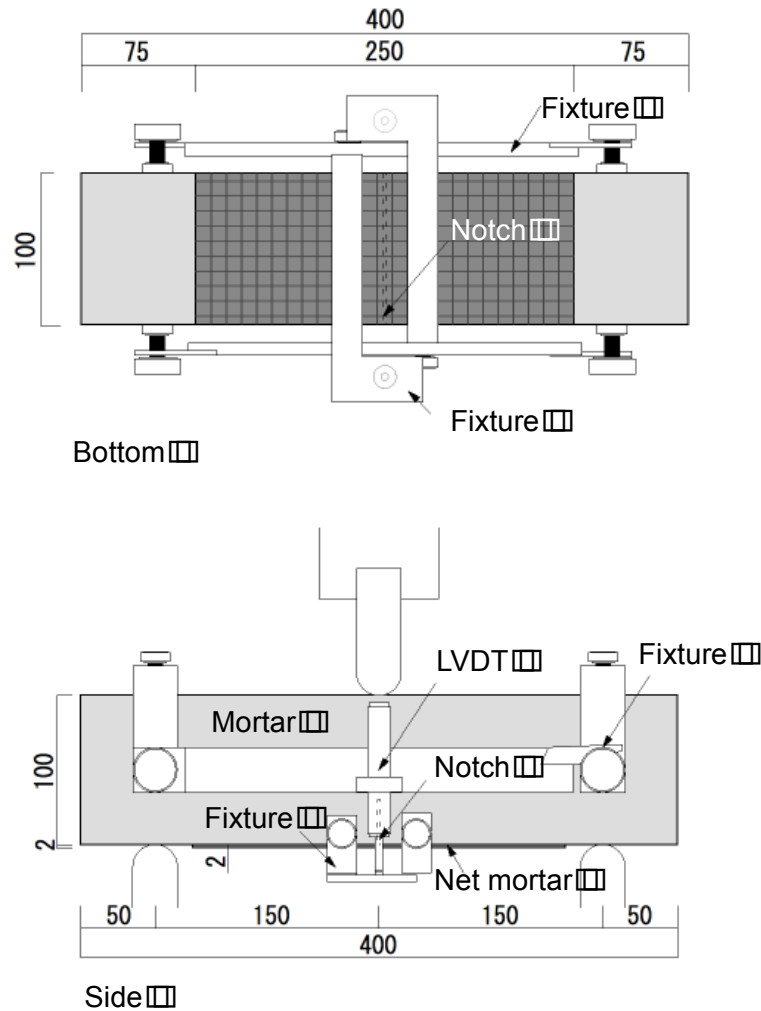
**Figure 2. Fiber net reinforcing mortar coatings**

## 2.2 Outline of tests

Three-point bend tests for the center notched beam specimen with net mortar on the notched surface were conducted to measure the load versus load point displacement (L-LPD) curves. Fig. 3 shows the outline of a specimen and the three points bending test. Photo 1 shows the actual appearance of three points bending test. A displacement-controlled load testing machine with a capacity of 250 kN was used for three-point loading. Specimen size, span length, notch length were 100 x 100 x 400mm, 300mm, 30mm according to the JCI standard (2003). LPD was measured by using two LVDTs with 0.001mm sensitivity. LVDT were attached on a support hanging on a specimen to avoid the displacement measurement error caused by load point caving (Fig. 3). The loading rate of the crosshead was 0.02 mm/min. The loading control was based on the displacement at the loading point.



**Photo 1 Three points bending test**



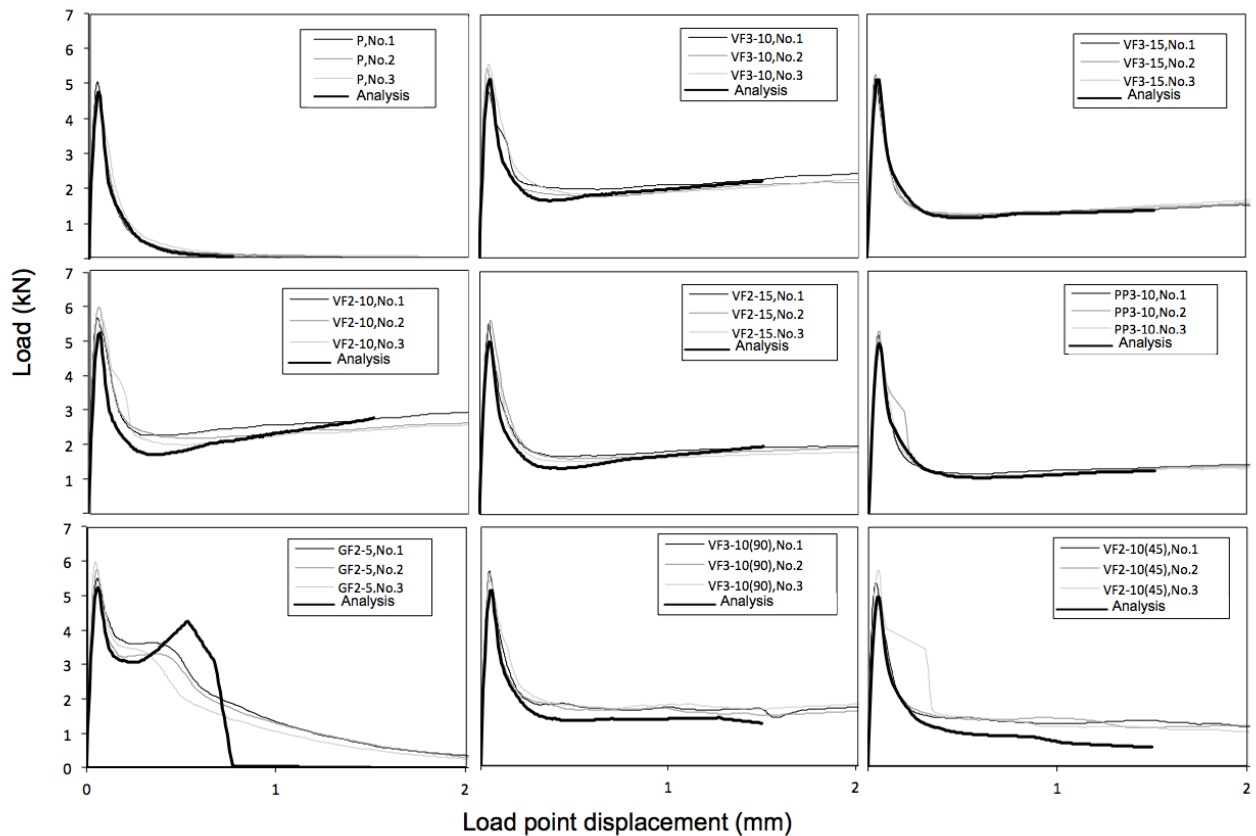
**Figure 3. Outline of specimen and three-point bending test**

### 3. Test results and discussion

Fig. 5 shows the L-LPD curves of the specimens of every test conditions. In Fig. 5, the specimen with fiber netting, no netting (p) were shown. No appreciable difference is observed between the maximum strengths of specimens with and without fiber netting. The differences between the maximum strengths of specimens with different fiber netting types are not significant either.

Plain specimens (p) underwent brittle failure after reaching the maximum load. In comparison, the LPD data of specimens with netting were measured to large displacement values, as a crack were restrained by the net layer to induce stable failure even after a crack propagation was formed. Also, the load of p specimens with no netting decreases after the maximum load, whereas no rapid reductions in the load after the maximum load are observed with specimens having netting. This can be attributed to the bridging effect of fibers composing the netting. This tendency is particularly evident with GF specimen with a high elastic modulus. Also GF specimen shows the hardening behavior, but those failure after the second maximum load is brittle. Because the fiber used for GF specimens is a high tensile strength fiber and shows a brittle failure.

From the comparison between VF3-10 and VF3-15V or F2-10 and VF2-15, the net intervals of fiber netting becomes lower the post peak crack resistance of specimens becomes higher. The post peak crack resistance of specimens with different fiber netting angle are not significant.



**Figure 5. Load and load point displacement curves**

Calculated L-LPD curves were shown in Fig. 5 by bold line. L-LPD curves have been calculated by the crack analysis (Kitsutaka, 1997) using the tension softening property of concrete substrate and tensile properties of fiber net reinforcing mortar coatings which were obtained by the direct tensile test. The original L-LPD curves and the calculated curves are agreed well, so this analysis method is considered to be an appropriate method to predicting L-LPD curves of pre-notched specimen adopting the fiber net reinforcing mortar coatings in three point bending test.

### 3. Conclusions

In the range of the specimen geometry and the materials used in this study, the following were found:

- (1) The maximum loads under three points bending testing of both specimens with and without fiber net reinforcing are similar.
- (2) Fiber net reinforcing improves the resistance to crack propagation of concrete substrate.
- (3) Fiber netting specimen made of a glass fiber with a high elastic modulus and high tensile strength shows the hardening behavior.
- (4) Interval of fiber netting becomes lower the post peak crack resistance of specimens becomes higher.
- (5) The observed L-LPD curves and the calculated L-LPD curves obtained from a crack analysis are agreed well.



#### 4. Acknowledgement

We thank JBR (Japan Building Repair Federation) for giving us materials and cooperation during our research.

#### 5. References

1. Kitsutaka, Y., Oh-oka, T., "Fracture Parameters of High-strength Fiber Reinforced Concrete Based on Poly-Linear Tension Softening Analysis", *Fracture Mechanics of Concrete Structures, FRAMCOS-3*, AEDIFICATIO Publishers, 1998, pp. 455-464
2. Japan Concrete Institute, "Method of test for fracture energy of concrete by use of notched beam (JCI-S-001-2003)", [http://www.jci-net.or.jp/j/jci/study/jci\\_standard/JCI-S-001-2003-e.pdf](http://www.jci-net.or.jp/j/jci/study/jci_standard/JCI-S-001-2003-e.pdf), JCI Standard, 2003
3. Kitsutaka, Y., "Fracture parameters by polylinear tension-softening analysis", *J. Engrg. Mech., ASCE*, 123(5), 1997, pp. 444-450

# Performance of Fire-damaged Concrete Members Strengthened with NSM Laminates Embedded in Epoxy Adhesive

Awad Jadooe <sup>1,2</sup>, Riadh Al-Mahaidi <sup>3</sup> and Kamiran Abdouka <sup>4</sup>

<sup>1</sup>PhD Candidate, Swinburne University of Technology, Melbourne, Australia

<sup>2</sup>Lecturer, Kerbala University, Kerbala, Iraq

<sup>3</sup>Professor of Structural Engineering, Swinburne University of Technology, Melbourne, Australia

<sup>4</sup>Senior Lecture, Swinburne University of Technology, Melbourne, Australia

**Abstract:** The repair and strengthening of existing concrete structures has become more common during the last decade. The most common application of FRP for the strengthening has been externally-bonded (EB) systems, where sheets or laminates of FRP are bonded to the external surface of the concrete with an epoxy adhesive. Despite the popularity of EB FRP strengthening techniques, they have a number of important limitations in practice and a limited ability to develop the full tensile strength of the FRP sheet. Near-surface mounted (NSM) systems have been proven to overcome the limitations of EB systems. The NSM technique was used in this research, where FRP laminates were bonded via an epoxy or cement-based adhesive in grooves cut into the concrete surface. Twenty fire-damaged concrete prisms were tested using a single-lap shear test. The results were compared with 20 reference specimens without fire damage. The results demonstrate that the residual tensile strength after the repair of fire-damaged concrete with rough CFRP is 94%, 79%, and 49% for temperature exposure of one hour at 200 °C, 400 °C, and 600 °C, respectively. The corresponding values for two hour exposure are 86%, 77% and 41% respectively.

**Keywords:** Fire, NSM, CFRP, Rehabilitation, Epoxy adhesive.

## 1. Introduction

Recent years have seen increased emphasis on the repair and refurbishment of all types of structures in preference to demolition and rebuilding. Concrete structures are no an exception. Since one of the problems facing buildings is exposure to high temperatures, they should be provided with sufficient structural fire resistance to withstand such circumstances, or at least to give the occupants enough time to escape before strength and or stability failure ensue (Tovey (1); Tovey and Crook (2); Haddad et al (3); Leonardi et al (4); Allen et al (5); ACI224 (6)).

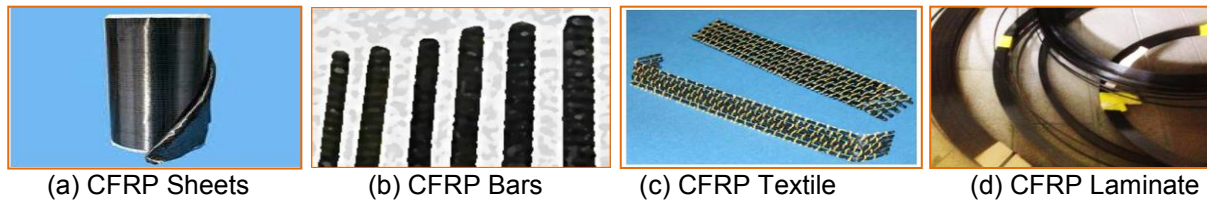
After a fire, an appraisal is normally required as soon as the building can be safely entered and generally before the removal of debris. To ensure safety, temporary false work may be required to secure individual members and stabilize the structure as a whole.

The primary on-site investigation technique is visual inspection, which is used to classify the degree of damage for each structural concrete member. Visually apparent damage induced by heating includes collapse, deflection, spalling, cracking, surface crazing, colour changes and smoke damage. A visual survey of reinforced concrete structures is performed using a classification scheme from Gosain et al. (7), as shown in Table 1. This scheme uses visual indications of damage to assign each structural member a class of damage from 0 to 4. Each damage classification number has a corresponding category of repair, ranging from decoration to major repair

**Table 1. Physical effect of temperature on concrete Gosain et al. (7).**

Temperature	Color Change	Changes in Physical Appearance and Benchmark Temperatures	Concrete Condition
0 to 550 °F (0 to 290 °C)	None	Unaffected	Unaffected
550 to 1100 °F (290 to 590 °C)	Pink to red	Surface crazing: 570 °F (300 °C); Deep cracking: 1020 °F (550 °C); Popouts over chert or quartz aggregate: 1070 °F (575 °C)	Sound but strength significantly reduced
1100 to 1740 °F (590 to 950 °C)	Whitish Grey	Spalling, exposing not more than 25% of reinforcing bar surface: 1470 °F (800 °C); Powdered, light colored, dehydrated paste: 1650 °F (575 °C)	Weak and friable
1740+ °F (950+ °C)	Buff	Extensive spalling	Weak and friable

Due to the main advantages of FRP, such as its durability, high strength, low weight, easy installation and the basically unlimited availability of different shapes, it has been extensively used in structural repair and strengthening (Kodur and Baingo (8); Hashemi and Al-Mahaidi (9); Al-Abdwais and Al-Mahaidi (10)). Moreover, the reduction of the cost of FRP has seen it being used more frequently in civil engineering, especially to repair damage and strengthen outdated buildings. Carbon fiber can be produced in different shapes such as bars, sheets, textiles and laminates, as shown in Figure 1. Therefore, it has been effectively used for different purposes, especially the strengthening of members.



**Figure 1. Types of CFRP materials**

The main purpose of the present research is to study the suitability and effectiveness of the CFRP NSM laminate strengthening system to repair reinforced concrete (RC) members after exposure to high temperature and/or fire. This research investigates the residual strength of RC members after exposure to fire with and without CFRP NSM laminates. Many variables were encountered in this investigation, which covered the following aspects:

- Investigation of the behavior of the bond properties and mode of failure of concrete prism specimens between CFRP NSM laminates embedded with epoxy and substrate concrete after exposure to temperatures of 200, 400, 600, 800, and 1000°C for exposure periods of one and two hours.
- Investigation of the effect of fire and/or high temperature on direct tensile strength values using a single-lap shear for testing after exposure to temperatures of 200, 400, 600, 800, and 1000°C for exposure periods of one and two hours.

## **2. Experimental Program**

In this section, the details of the experimental program are presented, including the materials used, the mix proportions, the preparation and curing of specimens and the testing program. Limited previous experimental work has been carried out on the effect of burning by fire on the mechanical properties of normal strength concrete such as compressive strength and splitting tensile strength to investigate the most effective repair techniques and the best bond properties. The following properties were investigated:

1. Compressive strength;
2. Splitting tensile strength;
3. Axial deformation;
4. Ultimate tensile load capacity.

The experimental variables investigated for the concrete prisms were:

1. Fire temperature (200, 400, 600, 800 and 1000 °C);
2. Period of exposure to fire (1.0 and 2.0 hours).
3. Strengthening with NSM laminates embedded in epoxy adhesives.

## **3. Materials and Mixes**

### **3.1 Introduction**

The properties of materials used in any structure are of considerable importance (Neville (11); ACI 211(12)). The properties of materials used in the current study are presented in this chapter. Standard tests according to the American Society for Testing and Materials (ASTM) and Australia Specifications (AU) were conducted to determine the properties of materials. The following sub-divisions describe types and properties of materials used in the research:-

### 3.1.1. Concrete

A target compressive strength of 35 MPa was specified. The concrete mix was designed according to the American mix design method ACI 211(12) specification with a 0.57 water cement ratio of 1(cement): 1.67(fine aggregate): 2.73 (coarse aggregate). The following sub-sections describe the ingredients of the concrete used.

### 3.1.2. Cement

General Purpose Ordinary Portland cement (OPC) (Type GP) manufactured in Australia was used for the concrete mix throughout the present work.

### 3.1.3. Aggregate

Crushed coarse aggregate of 14 mm maximum aggregate size and 1610 Kg/m<sup>3</sup> density was used.

### 3.1.4. Fine Aggregate

Well-graded natural sand from Australia was used for concrete mix.

### 3.1.5 Water

Tap water was used in the concrete mix.

### 3.1.6. FRP Laminate

The FRP laminate used had a rough texture. The rough FRP laminate was supplied by BASF Construction Chemicals Australia Pty Ltd). The dimensions of the CFRP laminate were 20\*1.4 mm<sup>2</sup> and the effective bond length equaled 175mm. The material properties of the rough CFRP laminates as provided by the manufacturer are presented in Table 2.

**Table 2. Properties of rough CFRP laminate**

Typical tensile strength MPa	3300
Typical tensile modulus GPa	210
Ultimate deformation %	1.4
Density g/cm <sup>3</sup>	1.6
Inter laminar sheer strength MPa	80
Thermal expansion	0.6*10 <sup>-6</sup>
Fiber content %	70

### 3.1.7. Adhesive

Epoxy resin adhesive for the FRP laminate system was used for exposed and unexposed concrete for this investigation. The typical properties provided by the manufacturer are presented in Table 3.

**Table 3. Properties of laminate adhesive**

Compressive strength	>60MPa
Flexural strength	>30MPa
Bonding ASTM D 4541 <ul style="list-style-type: none"><li>• Concrete</li><li>• steel</li></ul>	>30MPa (concrete failure) >5MPa
Mix ratio	3A : 2B by weight
Color	Red
Specific gravity@ 23 °C	1.5
Full cure@ 23 °C	7 days
Pot life <ul style="list-style-type: none"><li>• 23 °C</li><li>• 40 °C</li></ul>	40 min 20 min

#### 4. Program of the Work

During this research, the experimental work on the effect of fire on the behavior of concrete was based on 20 damaged concrete prisms cast in the laboratory and compared with 20 references not exposed to fire. The dimensions for all prisms were 250 mm in length and a square cross-section of 75×75 mm. The concrete prisms were designed to approximate the set-up for single-lap shear testing. A concrete mix with a target compressive strength of 35 MPa was designed, and the specimens were cast, cured for 14 days, and then air-dried in the laboratory. Forty concrete prisms were subjected to fire inside a large furnace as shown in Figure 2 for 45 days with temperature levels of 200, 400, 600, 800 and 1000 °C and for two exposure periods of one and two hours.

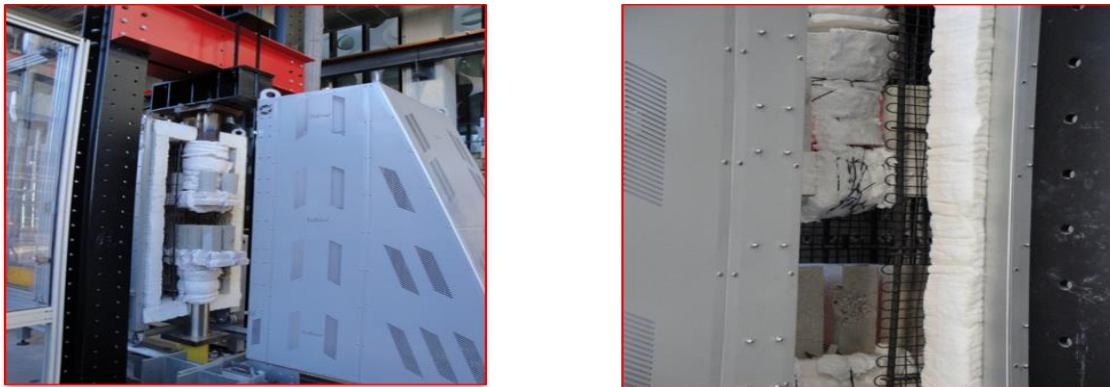


Figure 2. Exposure furnace

After exposure to fire, the specimens were repaired with NSM laminates that were embedded in epoxy adhesives. All damaged concrete prisms were repaired with working grooves inside the concrete prisms, such as slits on the surface of substrate concrete. The dimensions of the grooves were 250 mm in length 25 mm deep and 5 mm wide. All grooves were cleaned using air pressure to remove the dust from the surface of the concrete prisms. Epoxy resin primer with a mix ratio of 3:1 (A-B) was then placed inside the grooves to increase the adhesion between the epoxy resin and the surface of the concrete. MBrace laminate adhesive was applied inside the groove where the FRP should be in the center of the groove to ensure a straight FRP when the specimen was tested under the machine. Finally, the fibers were inserted in the center of the slits, and wire tie spacers were used to ensure a good bond between the adhesive and the FRP laminate.

#### 5. Effect of High Temperature on Compressive and Splitting Strength

In order to obtain a better understanding of the behavior of RC members in flexure after exposure to fire damage, it is important to first study the mechanical properties of concrete subjected to fire (Arioz (13); Chan et al (14); Li et al (15)). In the present study, three cylinders of concrete with dimensions of 100x200 mm of normal strength concrete were fired at each level of heating for each period to obtain the compressive and splitting strength of concrete after heating and to predict the effect of fire on the mechanical properties. Figures 3 and 4 show the relationship between compressive strength and fire temperature. It is clear from the results that the compressive strength decreases with exposure to fire temperature and splitting tensile strength is more sensitive to fire than compressive strength.

## 6. Test Set –up

Three days before testing, the concrete prism surfaces were cleaned and coated with white paint to clarify the propagation of cracks and make crack viewing easier. The prisms were then placed in a position using a single-lap shear for testing, as shown in Figure 5, to supply direct pull-off load with trend of FRP Laminate. The rate of the load used in the test was 0.2 mm/min. All the specimens were tested using an MTS 250 dynamic UTM model 819 high rate test machine.

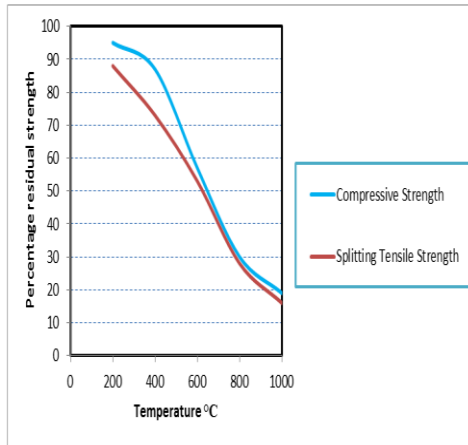


Figure 3. Relationship between compressive strength, tensile strength and fire temperature for (1) hour period.

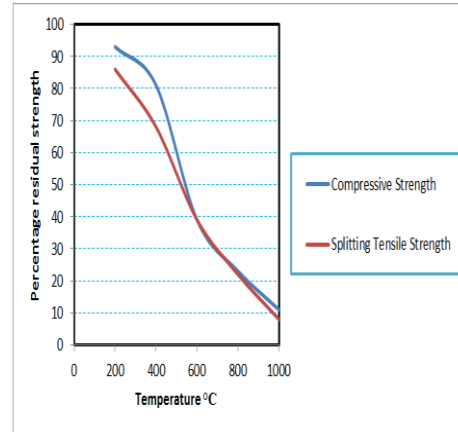


Figure 4. Relationship between compressive strength, tensile strength and fire temperature for (2) hour period.

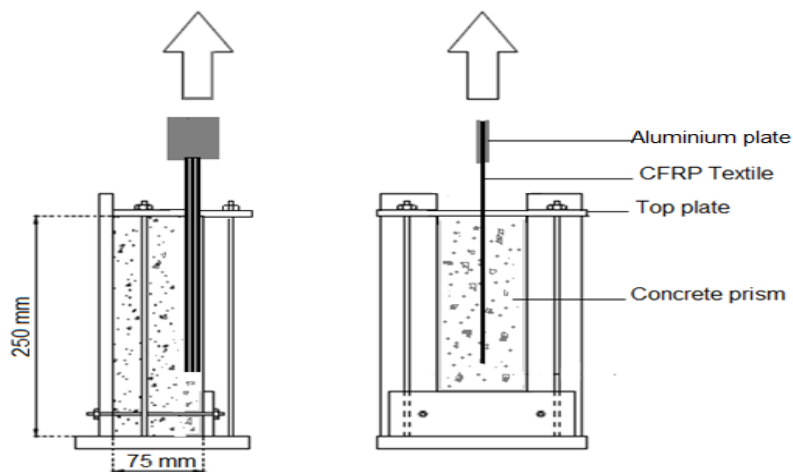


Figure 5. Single Lap test set-up

## 7. Test Result

The main objective of the current research is to investigate the effect of high temperature on direct tensile strength. Another objective is to repair damage after exposure to fire using NSM CFRP embedded with epoxy adhesive.

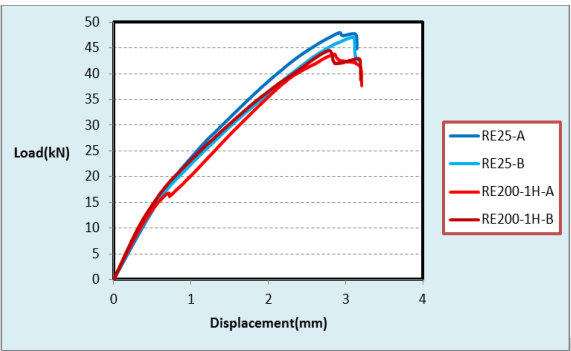
**8. Burning at 200 °C Fire Temperature:**

The residual direct tensile strength values were recorded for two series, for reference and damaged prisms strengthened with NSM CFRP using epoxy. The group is described in Table 4. The results show that residual strength decreased slightly when the prisms were exposed to 200 °C. The table also shows that the stiffness of concrete is little affected when the prisms are exposed to 200 °C. In the first period (one hour), the percentage of the residual direct tensile strength was 94%. In the second period (two hours fire exposure), the percentage of the residual direct tensile strength was 86%. Figures 6 and 7 illustrate the relationship between tensile force and displacement for damaged and undamaged concrete prisms. The failure mode for all the prisms subjected to fire was debonding at the interfacial zone between the concrete and the epoxy adhesive associated with cracking and peeling of adhesive at the surface.

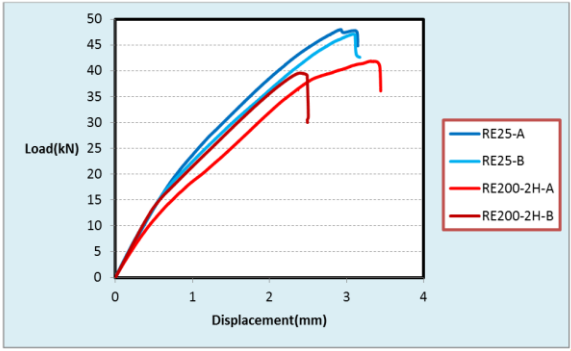
**Table 4. Details of prism specimens under temperature 200°C using epoxy adhesive and rough laminate.**

Specimen Type	Ultimate Pullout Load (kN)	Average Ultimate Load(kN)	Average Bond Strength(MPa)	Reduction in Bond Strength	Maximum Displacement (mm)
RE25-A	47	47.5	6.8	6%	3
RE25-B	48				2.9
RE200-1H-A	45	44.5	6.4		2.8
RE200-1H-B	44				2.9
<hr/>					
RE25-A	47	47.5	6.8	14%	3
RE25-B	48				2.9
RE200-2H-A	42	41	5.9		3.3
RE200-2H-B	40				2.4

R: rough FRP, E: Epoxy adhesive, 25: Reference, 200: Temperature in degrees C, 1and 2: duration times



**Figure 6. Relationship between tensile force and displacement before and after fire using epoxy adhesive for one hour and 200 °C.**



**Figure 7. Relationship between tensile force and displacement before and after fire using epoxy adhesive for two hours and 200 °C.**

**9. Burning at 400 °C Fire Temperature:**

When the temperature was raised to 400 °C, the residual direct tensile strength value for repairs with rough CFRP laminate was 79% for one hour. After two hours, the residual direct tensile strength value for repair with rough CFRP laminate was 77%. The group is described in Table 5. It is obvious from the results that after exposure to fire temperatures of 400 °C, the tensile strength decreases by 9-15 % for one and two hours, more than fire temperatures of 200 °C. It is generally agreed that the stiffness

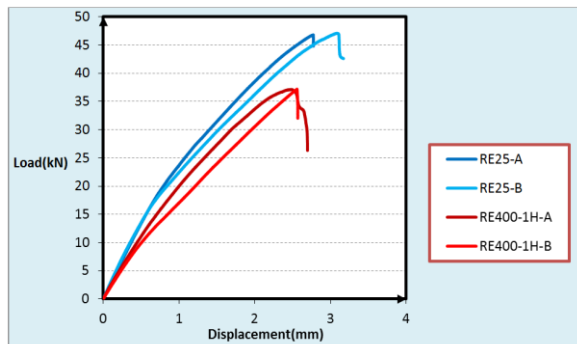


of concrete decreases with compressive and splitting strength, as shown in Figures 8 and 9. The failure mode was similar to that of specimens subjected to 200 °C.

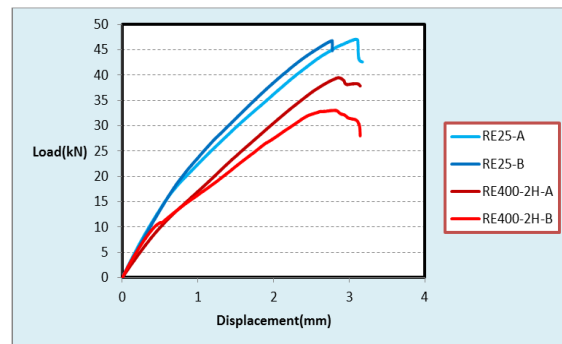
**Table 5. Details of prism specimens under temperature 400°C using epoxy adhesive and rough laminate**

Specimen Type	Ultimate Pullout Load (kN)	Average Ultimate Load(kN)	Average Bond Strength(MPa)	Reduction in Bond Strength	Maximum Displacement (mm)
RE25-A	47.1	47	6.7	21%	3.1
RE25-B	46.8				2.8
RE400-1H-A	37.1	37	5.3		2.5
RE400-1H-B	37.2				2.6
RE25-A	47.1	47	6.7	23%	3.1
RE25-B	46.8				2.8
RE400-2H-A	33.1	36	5.1		2.8
RE400-2H-B	39.5				2.9

R: rough FRP, E: Epoxy adhesive, 25: Reference, 400: Temperature in degrees C, 1 and 2: duration times



**Figure 8. Relationship between tensile force and displacement before and after fire using epoxy adhesive for one hour and 400 ° C.**



**Figure 9. Relationship between tensile force and displacement before and after fire using epoxy adhesive for two hours and 400 ° C.**

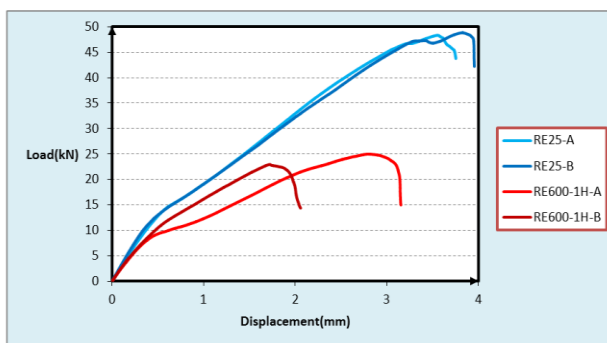
### 10. Burning at 600 °C Fire Temperature:

When the temperature was raised to 600 °C, the residual tensile strength of the prisms was 49% after repairing them with rough CFRP laminate using epoxy adhesive. However, the residual tensile strength was 41% for two hours. The group is described in Table 6. It can be seen that tensile strength for the 600 °C fire temperature decreases by 34-45 % after one and two hours, more than at a fire temperatures of 200 °C, whereas it decreases by 22-30 % after one and two hours, more than at a fire temperature of 400 °C, as shown in Figures 10 and 11. The failure mode for all the prisms subjected to fire at 600 °C was concrete crashing when epoxy adhesive was used.

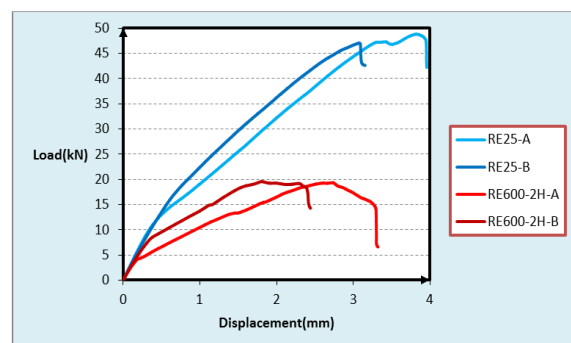
**Table 6. Details of prism specimens under temperature 600°C using epoxy adhesive and rough laminate.**

Specimen Type	Ultimate Pullout Load (kN)	Average Ultimate Load(kN)	Average Bond Strength(MPa)	Reduction in Bond Strength	Maximum Displacement (mm)
RE25-A	48.3	48.6	6.9	51%	3.8
RE25-B	48.9				3.6
RE600-1H-A	23	24	3.4		1.7
RE600-1H-B	25				2.8
RE25-A	48.8	48	6.9	59%	3.8
RE25-B	47.1				3.6
RE600-2H-A	19.4	19.5	2.8		2.7
RE600-2H-B	19.6				1.8

**R:** rough FRP, **E:** Epoxy adhesive, **25:** Reference, **600:** Temperature in degrees C, **1and 2:** duration times



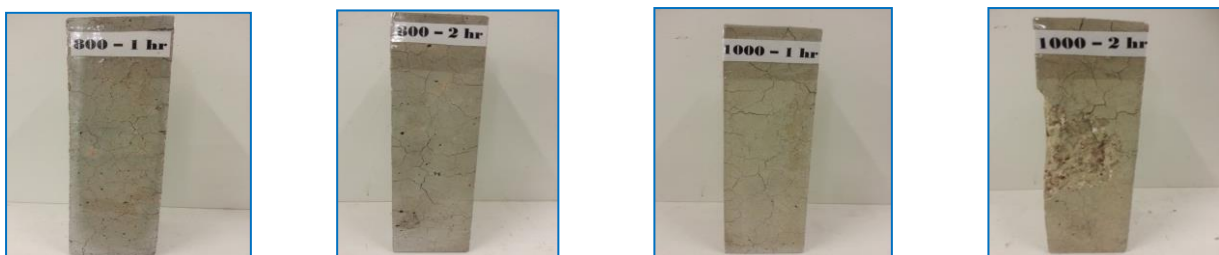
**Figure 10. Relationship between tensile force and displacement before and after fire using epoxy adhesive for one hour and 600**



**Figure 11. Relationship between tensile force and displacement before and after fire using epoxy adhesive for two hours**

### 11. Burning at 800 and 1000 °C Fire Temperatures:

When the temperature was raised to 800 and 1000 °C, the compressive strength and splitting tensile strength decreased sharply. Therefore, cracks were wide-spread along the concrete prism surfaces and inside the concrete cores, as shown in Figure 12. Due to the high magnitude of damage to concrete at temperatures of 800 and 1000 C, the efficacy of repairing using the NSM technique is limited. However, these prisms may not represent the full behavior of the concrete in actual full-scale members due to the propagation of cracks on the surface of the concrete prisms. Furthermore, plain concrete without reinforcement causes premature cracks before achieving the full ultimate load.



**Figure 12. Cracks after exposure to high temperature/ fire.**

## 12. Conclusions

The main objectives of the current research are to investigate the effect of high temperature on direct tensile strength, and to repair damage after exposure to fire using NSM CFRP embedded with epoxy. Based on the test results of the present study, the following conclusions can be drawn:-

- When the temperature is raised to 800 and 1000 °C, the efficacy of repairing with NSM is limited. However, these prisms may not represent the full behavior of the concrete in actual full-scale members due to the propagation of cracks on the surfaces of the concrete prisms.
- The residual tensile strength of the prisms was 49% for one hour after repairing them with rough CFRP laminate and epoxy adhesive. However, the residual tensile strength was 41% for two hours when the temperature was raised to 600 °C.
- The residual direct tensile strength value for repair with rough CFRP laminate was 79% for one hour. After two hours, the residual direct tensile strength value for repair with rough CFRP laminate was 77% when the temperature was raised to 400 °C,
- When the prisms were exposed to 200 °C, the percentage of the residual direct tensile strength in rough CFRP laminate with epoxy was 94%. In the second period (two hours), the percentage of the residual direct tensile strength in rough CFRP laminate was 86%.
- Although compressive strength and splitting tensile strength decrease sharply when the prisms temperatures increase, splitting tensile strength is more sensitive to fire exposure than compressive strength.

## 13. Acknowledgment

The authors thank the staff of the Smart Structures Laboratory at Swinburne University for their assistance.

## 14. References

1. Tovey, A., "Assessment and repair of fire-damaged concrete structures-an update", ACI Special Publication, Michigan, 92, 1986, pp 47-62.
2. Tovey, A. & Crook, R., "Experience of fires in concrete structures, evaluation and repair of the damage to concrete", American Concrete Institute, Michigan, 1986, pp 1-14.
3. Haddad, R., Al-Mekhlafy, N. et al., "Repair of heat-damaged reinforced concrete slabs using fibrous composite materials", Construction and Building Materials, 25, 2011, pp 1213-1221.
4. Leonardi, A., Meda, A. et al., "Fire-damaged R/C Members Repaired With High-Performance Fibre-Reinforced Jacket". Strain, 47, 2011, pp 28-35.
5. Allen, R., Edwards, S., et al., "The repair of concrete structures", 2<sup>th</sup> ed., 1993, Publication in the Taylor and Francis e- library, 2005. [www.eBookstore.tandf.co.uk](http://www.eBookstore.tandf.co.uk).
6. American Concrete Institute, "Causes, Evaluation, and Repair of Cracks in Concrete Structures (ACI224-1R-07)". Reported by ACI Committee 224, 2007, Michigan.
7. Gosain, N., Drexler, R. et al., "Evaluation and Repair of Fire-Damaged Buildings". Cement and Concrete Research 30, 2000, pp 247–251.
8. Kodur, V. & Baingo, D., "Fire resistance of FRP reinforced concrete slabs", Institute for Research in Construction Ottawa, Canada, 758,1998.

9. Hashemi, S. & Al-Mahaidi, R., "An investigation of CFRP application on reinforced concrete members using cement-based adhesives" Technical paper, department of civil engineering, Monash University, 11(2), 2011, pp129-139.
10. Al-Abdwais & Al-Mahaidi., "Modified cement-based adhesive for Near- Surface Mounted FRP strengthening system" Fourth Asia-Pacific Conference on FRP in Structures, International Institute for FRP in Construction, Melbourne, Australia, 2013.
11. Neville, A., "Properties of Concrete", Longman Group, Ltd., 4<sup>th</sup> and Final Edition, Pitman London, 2000, pp. (329-397), (674-687).
12. American Concrete Institute, "Standard Practice for Selecting Proportions for Normal, Heavyweight, and Mass Concrete (ACI 211-02)". Reported by ACI Committee 211 Committee Members Voting on 1991 Revision Contents.
13. Arioz, O., "Effects of elevated temperatures on properties of concrete". Fire Safety Journal, 42, 2007, pp 516-522.
14. Chan, Y., Luo, X. et al., "Compressive strength and pore structure of high-performance concrete after exposure to high temperature up to 800 C". Cement and Concrete Research, 30, 2000, pp 247-251.
15. Li, M., Qian, C. & et al., "Mechanical properties of high-strength concrete after fire. Cement and Concrete Research, 34, 2004, pp 1001-1005.

# Behavior of squat columns strengthened with fiber reinforced concrete jacket

Reza Hassanli<sup>1</sup> and Minoru Kunieda<sup>2</sup>

<sup>1</sup>PhD Student, School of Natural and Built Environments, University of South Australia

<sup>2</sup>Professor of Civil engineering, Department of Civil Engineering, Gifu University

**Abstract:** This paper reports on an experimental program that investigated the confinement effect of fiber reinforced concrete as a surface repair material. The effect of the repair material and the horizontal reinforcement (stirrup) ratio were studied. A total of 24 cylindrical concrete specimens were strengthened using jacketing technique by means of four different repair materials, including a type of ultra-high performance-strain hardening cementitious composite and three types of engineered cementations concrete. The effect of stirrup was studied by considering different reinforcement ratio, ranging between zero and 1.7%. All specimens were tested under uniaxial compression. According to the results, the specimens included both stirrups and fiber in the repair layer exhibited a better response and provided a higher strain capacity. This group of specimens presented a ductile failure represented by stable post peak behavior and gradual strength degradation. Moreover, the failure was characterized by small distributed cracks. This research concluded that a combination of surface repair using reinforced fiber reinforced concrete material and a level of reinforcement ratio can significantly improve the behavior of squat columns and effectively enhance the ductility and strength.

**Keywords:** engineered cementations concrete, UHP, squat columns

## 1. Introduction

As a result of advancement in the world of science and technology, new materials and techniques are developed which can be applied to structures for repair purposes. Fiber reinforced concrete (FRC) is one of the material which has been captured the attention of researchers. For concrete structures FRC is particularly favorable as it is compatible with the substrate concrete in terms of behavior and mechanical and physical properties [1, 2]. Repairing structures using a crack-free jacket of high-performance materials such as FRC will effectively protect the inner re-bar from corrosion and substrate concrete from carbonation. In this research two types of FRC jackets were considered. Ultra High Performance Strain Hardening Cementitious Composites (UHP-SHCC) and Engineered Cementitious Composite (ECC). Both materials are considered as composite materials with remarkable mechanical behavior and protective performance. Most research on surface repair using FRC has been focused on flexural members [3-5]. It has been found that a combination of strain hardening cementitious composites (SHCC) and a small amount of steel reinforcement helps develop higher strain in the strengthening layer at ultimate load and eliminates the formation of early cracks due to strain localization [3]. The technique of repair layer using high strength fiber reinforced concrete has been applied to other structural members such as columns [4, 6]. Kunieda et al. [6] developed a rapid jacketing technique to repair RC columns and investigated the behavior of the repaired column under cyclic load. The repair method involved spraying of high performance concrete to the column surface. The authors demonstrated that due to its inherent high tensile capacity, high performance repair layer, can significantly increase the strength and enhance the ductility of flexural members [6]. Moreover, due to high strain capacity, it is shown that FRC jacket can be considered as effective repair material to provide a free-crack surface in flexural members. However, no experimental research has focused on the behavior of axially loaded members retrofitted with high performance repair layer. For members basically subjected to axial stresses, surface repair jacket confines the substrate core and, hence, enhance the strength and ductility. This retrofit method can provide a free-crack compression member which is particularly favorable for bridge columns exposed to aggressive environment. Using FRC as a free-crack water-proof surface repair material of squat columns can not only preserve the substrate from steel corrosion and concrete carbonation and erosion but also potentially enhance the ductility and the strength of the member.

Wrapping with FRP is another method to enhance the behavior of columns. However, the brittle behavior of FRP wrapped columns, incomplete wet-out of the fabric and difficult release of trapped air bubbles and also uncertainty of the durability of the FRP material in aggressive environment are some of the main shortcomings of concrete columns wrapped in FRP [7]. In terms of physical properties and mechanical behavior, the cement based materials, such as UHP and ECC are well-matched with the substrate

concrete. Moreover, compared with FRP-wraps, FRC can effectively flow into the holes and fill the gaps and fix imperfections of the substrate surface. Moreover, using FRC material a designer can cope with different shapes and sections. Furthermore, the repair layer can protect the inner steel and prevent corrosion in aggressive environment.

This study intended to investigate the effect of surface repair material as well as the effect of horizontal reinforcement ratio (stirrup). The primary objectives of the research presented in this paper are:

- To observe the impact of different FRC material type on the stress-strain response of short concrete cylinders loaded in uniaxial compression
- To study and determine the effectiveness of thin layer of surface repair
- To investigate the impact of confinement provided by different surface repair materials and reinforcement ratio on crack formation, strain distribution, ductility and load-carrying capacity of squat columns

## 2. Experimental program

The experimental program consisted of uniaxial compressive tests on 24 concrete cylinders strengthened with four types of FRC jacket and three different ratios of horizontal reinforcement. The surface repair material included one type of UHP (UHP-SHCC) and three types of ECC with different fiber content (0.0%, 1.0% and 2.0% in volume). While the vertical reinforcement ratio was 0.87%, the horizontal reinforcement ratios of 0.00%, 0.56% and 1.70% were considered. The thickness of the strengthening jacket layer of all specimens was 25 mm. **Table 1** shows the notations used to specify the specimens. Each specimen identified by three parameters: Type of material, reinforcement ratio and the number of strain gauges. E0, E1, E2 and U account for the material type of ECC0, ECC1 ECC2 and UHP, respectively. R0, R1 and R2 represent the horizontal reinforcement ratio of 0.00%, 0.56% and 1.70% respectively. The last digit indicates the type of the specimen according to the number of strain gauges used. While specimens of Type 2 consisted of both internal gauges on the substrate surface and external gauges on the repair surface, the Type 1 specimens included only external strain gauges on the repair surface.

**Table 1. Specimens' identifiers and specifications**

Surface-Repair Material	Horizontal Reinforcement ratio (stirrup)			Type
	0.00%	1 $\phi$ 6 (0.56%)	3 $\phi$ 6 (1.70%)	
ECC0	E0-U-1	E0-R1-1	E0-R2-1	Type 1
	E0-U-2	E0-R1-2	E0-R2-2	Type 2
ECC1	E1-U-1	E1-R1-1	E1-R2-1	Type 1
	E1-U-2	E1-R1-2	E1-R2-2	Type 2
ECC2	E2-U-1	E2-R1-1	E2-R2-1	Type 1
	E2-U-2	E2-R1-2	E2-R2-2	Type 2
UHP	U-U-1	U-R1-1	U-R2-1	Type 1
	U-U-2	U-R1-2	U-R2-2	Type 2

The substrate concrete made from a mix of high-early-strength Portland cement, natural sand and gravel, as outlined in the mix proportion of

Table 2. All substrate concrete cylinders were cast from C40/50 ready-mix concrete with a maximum aggregate size of 24 mm. Steel cylinder molds 100 mm x 200 mm were used for casting concrete test substrate concrete. A total number of 27 concrete cylinders made from the same batch of concrete. The average compressive strength of the substrate concrete based on the tests results of three cylindrical specimens was 46.1 MPa, corresponding to an axial load of 362 kN. Using the average slope of the

stress-strain curve corresponding to stresses of less than 20% of the ultimate strength, the elastic modulus determined to be about 22700 MPa.

**Table 2. Mix properties of substrate material**

Material	Unit contents (kg/m <sup>3</sup> )					
	W/C	Water Content	Cement	Sand	Coarse Aggregate	AE Agent
Substrate Concrete	0.45	170	377	780	903	0.97

After water curing of concrete cores, the steel cages were fabricated and assembled as is presented in Figure 1. All strengthened specimens included three vertical  $\phi 6$  re-bars corresponding to a vertical reinforcement ratio of 0.87%. The specimens having horizontal ratio of 0.56% and 1.7% contained one and three  $\phi 6$  stirrups, respectively. The tensile yield strength and Young's modulus of the steel was 368 MPa and 186 GPa, respectively according to tensile test results of rebar specimens.



Specimen Type 2  
(without internal strain gauges)  
Stirrup: 3 $\phi 6$  (1.7%)



Specimen Type 1  
(consist of strain gauges on the core surface)  
Stirrup: 1 $\phi 6$  (0.56%)

**Figure 1. Details of the specimens, the substrate core and the external mold**

The mix proportions of materials used as the jacket surfaces are presented in **Table 3**. Material type of ECC0 representing a plain concrete without fiber which can be regarded as “mortar material”. Material type ECC1 and ECC2 included 1% and 2% of fiber content.



**Table 3. Mix Properties of the surface repair material**

Material	Unit contents (kg/m <sup>3</sup> )											
	W/C	Water Content	Cement	Sand	Coarse Aggregate	Fly Ash	Air Entrainment	Super-plasticizer	Air reducer	Viscosity Agent	Fiber	Silica Fume
<b>UHP</b>	0.22	340	1313	155	-	-	-	15.4	0.062	-	14.6	232
<b>ECC0</b>	0.45	384	599	630	-	255	5.99	-	-	1.9168	0	-
<b>ECC1</b>	0.45	384	599	604	-	255	5.99	-	-	1.9168	13	-
<b>ECC2</b>	0.45	384	599	577	-	255	5.99	-	-	1.9168	26	-

As some of the specimens included strain gauges which were sensitive to water, wet covering curing method used in the second stage of the curing (curing of the cover layer). To obtain the stress-strain curves, uniaxial compression test performed using a hydraulic testing machine. The specimens were tested using a 2000 kN compression machine and the data were monitored using an automatic data acquisition system (Figure 2). The bottom jaw of the testing machine was fixed. The top jaw was adjustable in the vertical direction and was attached to the loading actuator to record the applied load. The specimens were subjected to monotonically increasing axial concentric load. As shown in Figure , only the substrate core was subjected to the compression load.



**Figure 2 . Test setup**

### **3. Test results and discussions**

The strength of the cover materials was obtained using 50 mm x 100 mm cylindrical samples.

Table 4 presents the compressive strength of the jacket materials. According to the results, the maximum compressive stress carried by UHP material is considerably higher than that of the material type ECC0, ECC1 or ECC2.

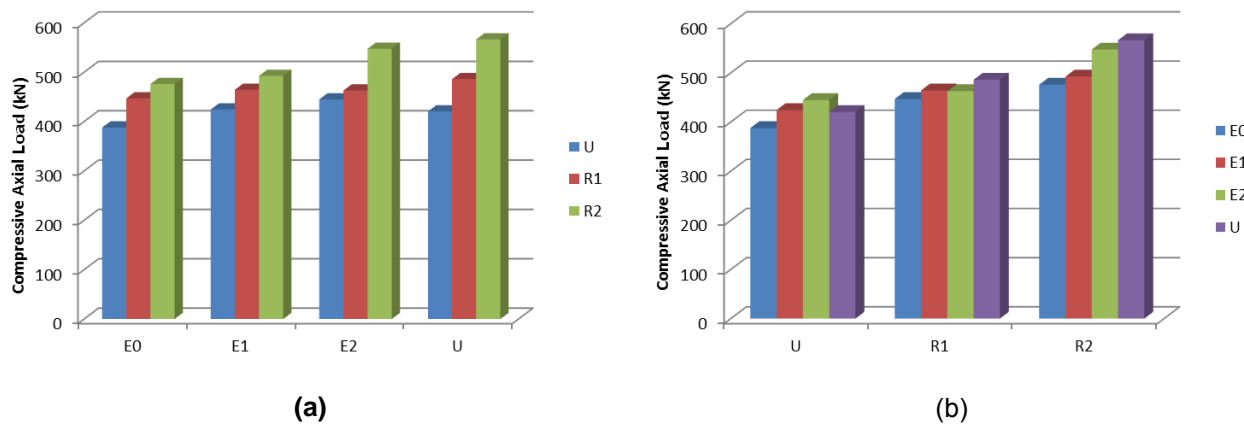
**Table 4. Compressive strength of the surface-repair materials**

Cover Material	Specimen	maximum compressive stress (MPa)	avg. of maximum compressive stress (MPa)
ECC0	Sample 1	42	39.7
	Sample 2	40	
	Sample 3	37	
ECC1	Sample 1	17	24.3
	Sample 2	30	
	Sample 3	26	
ECC2	Sample 1	26	28.3
	Sample 2	40	
	Sample 3	19	
UHP	Sample 1	112	99.0
	Sample 2	95	
	Sample 3	90	

The test results of the strengthened specimens are provided in Table 5 and Figure 3. Experimental results indicate an increase in the load carrying capacity of all strengthened specimens compared to the average of 362 kN in the control specimens.

Figure 3(a) compares the load carrying capacity of the specimens. As a general trend, as the stirrup ratio increases, the compressive load capacity increases. The average load carrying capacity of specimens with stirrup ratio of 0.56% (R1) and 1.7% (R2) was approximately 11% and 24% higher than the corresponding values of the unreinforced specimens (without stirrups), respectively. Moreover, the ratio of the average compressive strength of the retrofitted to the core specimen was 1.16%, 1.28% and 1.44% for specimens with zero, 0.56% and 1.7% stirrup ratio, respectively.

Figure 3(b) compares the load carrying capacity of the specimens retrofitted with different types of jacket layers. As shown, by increasing the fiber content from 0 in ECC0 to 1% in ECC1 and to 2% in ECC2, the load carrying capacity increased by about 5% and 11%, respectively.



**Figure 3. Load carrying capacity of the specimens in specimens**

**Table 5. Compressive strength and Elastic Modulus**

Cover Material	Specimen	Max force (kN)	Average maximum force (kN)	Max force/max force of unreinforced specimens	Elastic Modulus (MPa)	Average Elastic Modulus (MPa)	Force @ $\epsilon=2\%$ / maximum force	Mode of Failure
<b>ECC0</b>	E0-U-1	368	388	1.00	24586	22510	0.00	Brittle
	E0-U-2	408			20433			Brittle
	E0-R1-1	478	447	1.15	25019	24828	0.00	Brittle
	E0-R1-2	416			24637			Brittle
	E0-R2-1	485	476	1.23	26013	26752	0.00	Brittle
	E0-R2-2	467			27490			Brittle
<b>ECC1</b>	E1-U-1	419	424.5	1.00	30803	30688	0.00	Brittle
	E1-U-2	430			30573			Brittle
	E1-R1-1	461	464.5	1.09	29962	29796	0.15	Ductile
	E1-R1-2	468			29631			Ductile
	E1-R2-1	472	492.5	1.16	28917	29860	0.21	Ductile
	E1-R2-2	513			30803			Ductile
<b>ECC2</b>	E2-U-1	443	445	1.00	28280	29427	0.00	Brittle
	E2-U-2	447			30573			Brittle
	E2-R1-1	453	463	1.04	28051	22917	0.18	Ductile
	E2-R1-2	473			17783			Ductile
	E2-R2-1	562	547.5	1.23	32841	32484	0.39	Ductile
	E2-R2-2	533			32127			Ductile
<b>UHP</b>	U-U-1	378	420.5	1.00	14089	14089	0.00	Brittle
	U-U-2	463			—			Brittle
	U-R1-1	486	486	1.16	22268	25949	0.19	Ductile
	U-R1-2	486			29631			Ductile
	U-R2-1	549	566.5	1.35	29732	29108	0.44	Ductile
	U-R2-2	584			28484			Ductile

### 3.1 Failure mode and damage pattern

In this section the failure mode of the specimens are described. Figure 4 shows the final cracking pattern of the tested specimens. As it is indicated in Figure 4 (a), specimens with neither fiber nor stirrup in the jacket layer, exhibited a very explosive and sudden brittle failure. The specimens with zero fiber content but with stirrups in the cover layer, the failure was sudden and brittle, but less explosive than specimens without stirrups. All specimens without horizontal reinforcement showed a brittle failure, no matter if the cover layer contained fiber Figure 4 (b)) or not (Figure 4 (a)). In these specimens, as a result of Poisson's effect and the expansion of the substrate layer, strain localization occurred in the strengthening layer, which prevented the stress distribution, led to a brittle failure characterized by a wide vertical crack (Figure 4 (b)) or an explosive failure (Figure 4 (a)). The same immature type of failure was reported by Kamal [1] for strengthened beams. For these brittle categories of specimens, in which the specimen lacks fiber or stirrup or both, when the stress reached to ultimate, the compressive capacity drops to zero suddenly and the specimen fails without any sign of post-peak strength.

On the other hand, a more ductile type of failure was detected for the specimens in which the cover layer included both fiber and stirrup, characterized by a more stable post peak response and a gradual degradation of the strength after it reached the maximum strength. For the specimens with a ductile behavior, as is specified in

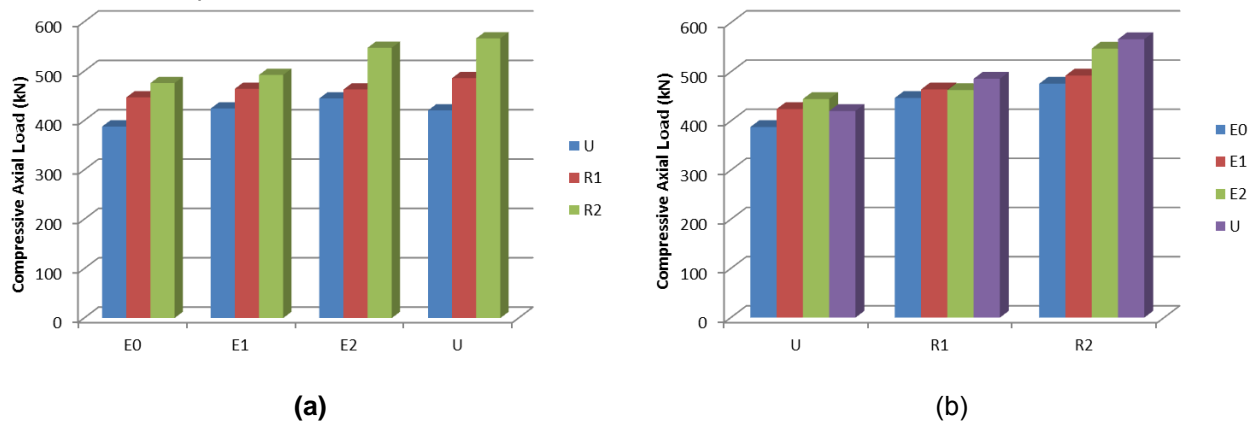


Figure 3. Load carrying capacity of the specimens in specimens

Table 5. Compressive strength and Elastic Modulus

Cover Material	Specimen	Max force (kN)	Average maximum force (kN)	Max force/max force of unreinforced specimens	Elastic Modulus (MPa)	Average Elastic Modulus (MPa)	Force @ $\epsilon=2\%$ / maximum force	Mode of Failure
ECC0	E0-U-1	368	388	1.00	24586	22510	0.00	Brittle
	E0-U-2	408			20433			Brittle
	E0-R1-1	478	447	1.15	25019	24828	0.00	Brittle
	E0-R1-2	416			24637			Brittle
	E0-R2-1	485	476	1.23	26013	26752	0.00	Brittle
	E0-R2-2	467			27490			Brittle
ECC1	E1-U-1	419	424.5	1.00	30803	30688	0.00	Brittle
	E1-U-2	430			30573			Brittle

	E1-R1-1	461	464.5	1.09	29962	29796	0.15	Ductile
	E1-R1-2	468			29631			Ductile
	E1-R2-1	472	492.5	1.16	28917	29860	0.21	Ductile
	E1-R2-2	513			30803			Ductile
<b>ECC2</b>	E2-U-1	443	445	1.00	28280	29427	0.00	Brittle
	E2-U-2	447			30573			Brittle
	E2-R1-1	453	463	1.04	28051	22917	0.18	Ductile
	E2-R1-2	473			17783			Ductile
	E20-R2-1	562	547.5	1.23	32841	32484	0.39	Ductile
	E2-R2-2	533			32127			Ductile
<b>UHP</b>	U-U-1	378	420.5	1.00	14089	14089	0.00	Brittle
	U-U-2	463			—			Brittle
	U-R1-1	486	486	1.16	22268	25949	0.19	Ductile
	U-R1-2	486			29631			Ductile
	U-R2-1	549	566.5	1.35	29732	29108	0.44	Ductile
	U-R2-2	584			28484			Ductile

, the test operation terminated deliberately beyond the strain value of 0.025. However, these ductile specimens maintained a fraction of compression capacity at the end of testing.

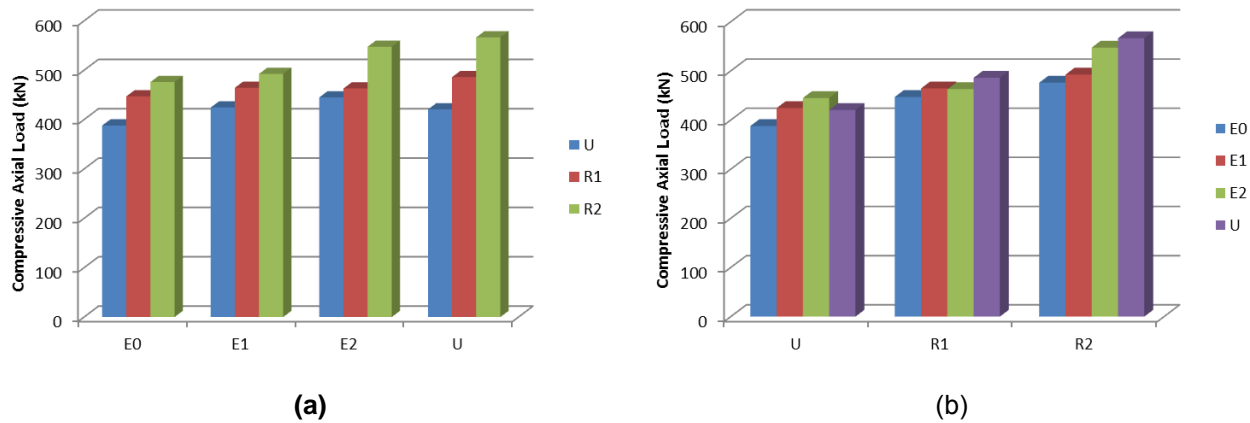


Figure 3. Load carrying capacity of the specimens in specimens

Table 5. Compressive strength and Elastic Modulus

Cover Material	Specimen	Max force (kN)	Average maximum force (kN)	Max force/max force of unreinforced specimens	Elastic Modulus (MPa)	Average Elastic Modulus (MPa)	Force @ $\epsilon=2\%$ / maximum force	Mode of Failure
<b>ECC0</b>	E0-U-1	368	388	1.00	24586	22510	0.00	Brittle
	E0-U-2	408			20433			Brittle
	E0-R1-1	478	447	1.15	25019	24828	0.00	Brittle
	E0-R1-2	416			24637			Brittle
	E0-R2-1	485	476	1.23	26013	26752	0.00	Brittle

	E0-R2-2	467			27490			Brittle
ECC1	E1-U-1	419	424.5	1.00	30803	30688	0.00	Brittle
	E1-U-2	430			30573			Brittle
	E1-R1-1	461	464.5	1.09	29962	29796	0.15	Ductile
	E1-R1-2	468			29631			Ductile
	E1-R2-1	472	492.5	1.16	28917	29860	0.21	Ductile
	E1-R2-2	513			30803			Ductile
ECC2	E2-U-1	443	445	1.00	28280	29427	0.00	Brittle
	E2-U-2	447			30573			Brittle
	E2-R1-1	453	463	1.04	28051	22917	0.18	Ductile
	E2-R1-2	473			17783			Ductile
	E20-R2-1	562	547.5	1.23	32841	32484	0.39	Ductile
	E2-R2-2	533			32127			Ductile
UHP	U-U-1	378	420.5	1.00	14089	14089	0.00	Brittle
	U-U-2	463			—			Brittle
	U-R1-1	486	486	1.16	22268	25949	0.19	Ductile
	U-R1-2	486			29631			Ductile
	U-R2-1	549	566.5	1.35	29732	29108	0.44	Ductile
	U-R2-2	584			28484			Ductile

also presents the strength ratio of the specimens at strain equal to 2% (which is four to five times of the peak strain) to the peak strength.

For specimens having fiber, the following modes of failure were observed:

- Having one stirrup  $1\phi 6$  (0.56%): Vertical cracks started from the bottom or top end, then deviated from the vertical direction to about 45 degree and extended to the mid-height of the specimen. The width of the crack was generally smaller than that in specimens without stirrup (Figure 4 (c)).
- Having three stirrups  $3\phi 6$  (1.7%): Inclined small cracks mostly extended up to the point in which horizontal steel was located. The horizontal steel extensively prevented the cracks to open-up. At the failure, larger number of cracks was observed compared with other specimens (Figure 4 (d)).

Stirrup and fiber caused the distribution of the cracks in macro and micro scale, respectively. As it is shown in Figure 4 (c) and Figure 4 (d), the stirrups resulted in formation of number of cracks with limited length and smaller width rather than a wide large crack. While the location and orientation of the large cracks are governed by the position of horizontal reinforcement, the distribution, direction and the location of small micro cracks are controlled by the fiber content ratio, properties, length, orientation and content.

### 3.2 Force-displacement response

The force displacement response of the tested specimens is presented in Figure 5-9. Comparing the ultimate strength of the substrate specimens (Figure 5) with that of retrofitted specimens (Figures 6-8), demonstrate that the strengthening method was successful in increasing the compressive strength. The repair layer confined the substrate concrete and hence caused an increase of 16% to 44% in compressive strength. Figure 6, Figure 7 and Figure 8 present the force displacement curve of specimens having stirrup ratio of zero, 0.56% and 1.7%, respectively. The slight slope of the tail of the force-displacement curves at the post-peak region of Figure 7 and Figure 8 indicates a more ductile response and stable post peak behavior of specimens having horizontal reinforcement compared with the response of specimens contained no horizontal steel (Figure 6). Figure 9 compare the force-displacement curve of the specimens

with surface repair material type of ECC0, ECC1, ECC2 and UHP. It can be seen that while the failure mode of the specimens retrofitted with material type ECC0 (zero fiber) is brittle (Figure 9), the specimens strengthened using fiber reinforced concrete exhibits a ductile response only if horizontal reinforcement is also provided.

Figure 10, presents the stress versus axial and hoop strain recorded for specimen E2-R2-1. The graph is presented as a sample as other specimens exhibited approximately the same trends. As shown in the figure, as can be predicted, throughout the test the tensile hoop strain increased as the axial stress increased. However, the behavior in the axial direction was completely different. The compressive axial strain increased as the axial stress increased. The rate of increase in the axial strain decreased prior to the peak strength. After the specimen reached the peak strength, the compressive axial strain started to decrease and became tensile toward the end of testing. The increasing compressive strain before the peak strength is due to the contribution of the jacket layer to carry axial stress, which attributed to the friction between the cover and the core layer by means of which the compressive stress can be transferred. At the peak strength, the compressive axial stress developed in the cover layer together with the radial stresses applied from the enclosed core, results in partially separation of the core and cover layers which reduce the friction and prevent a higher compressive stress develop in the cover layer. From this point onward, the compressive strain provided by friction reduces, and the tensile strain develops in the vertical direction as a result of core expansion.





a) specimens without fiber and stirrup



b) specimens with fiber, without stirrup



c) specimens having one stirrup 1φ6 (0.56%)



d) specimens having three stirrups 3φ6 (1.7%)

**Figure 4. Failure of specimens**

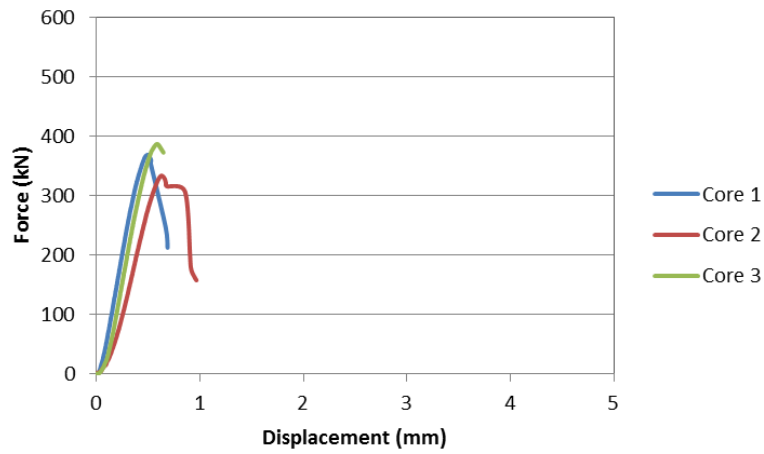


Figure 5. Force-displacement curve of the substrate core specimens

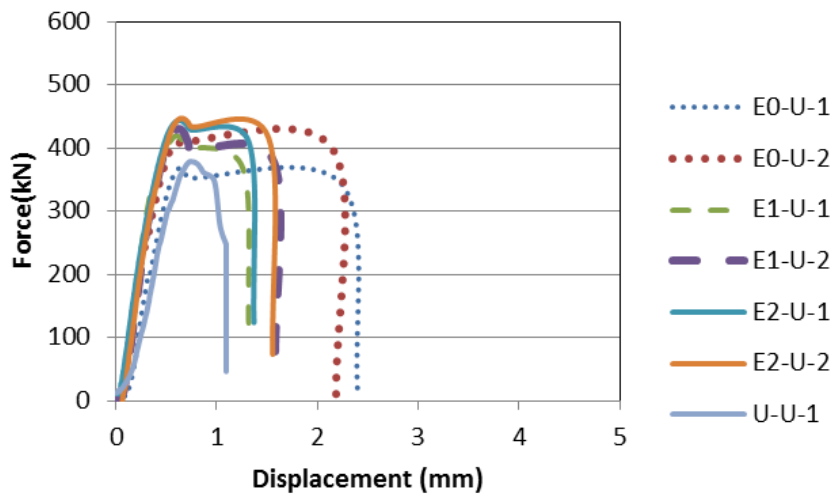


Figure 6. Force-Displacement curve of specimens without horizontal steel

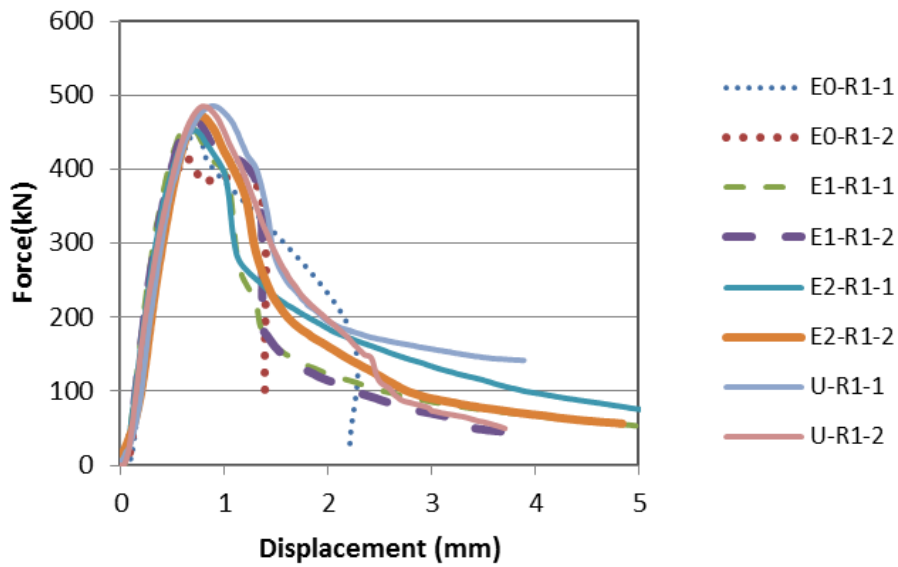


Figure 7 1. Force-Displacement curve of specimens Stirrup:  $3\phi 6$  (1.7%) in the jacket layer

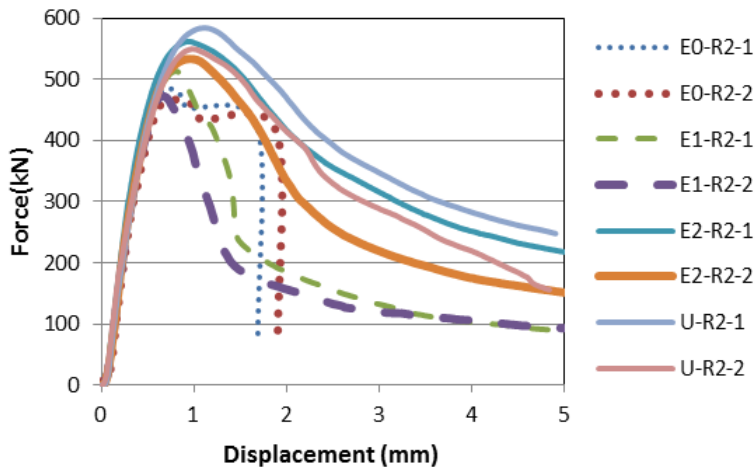


Figure 8. Force-displacement curve of the substrate core specimens

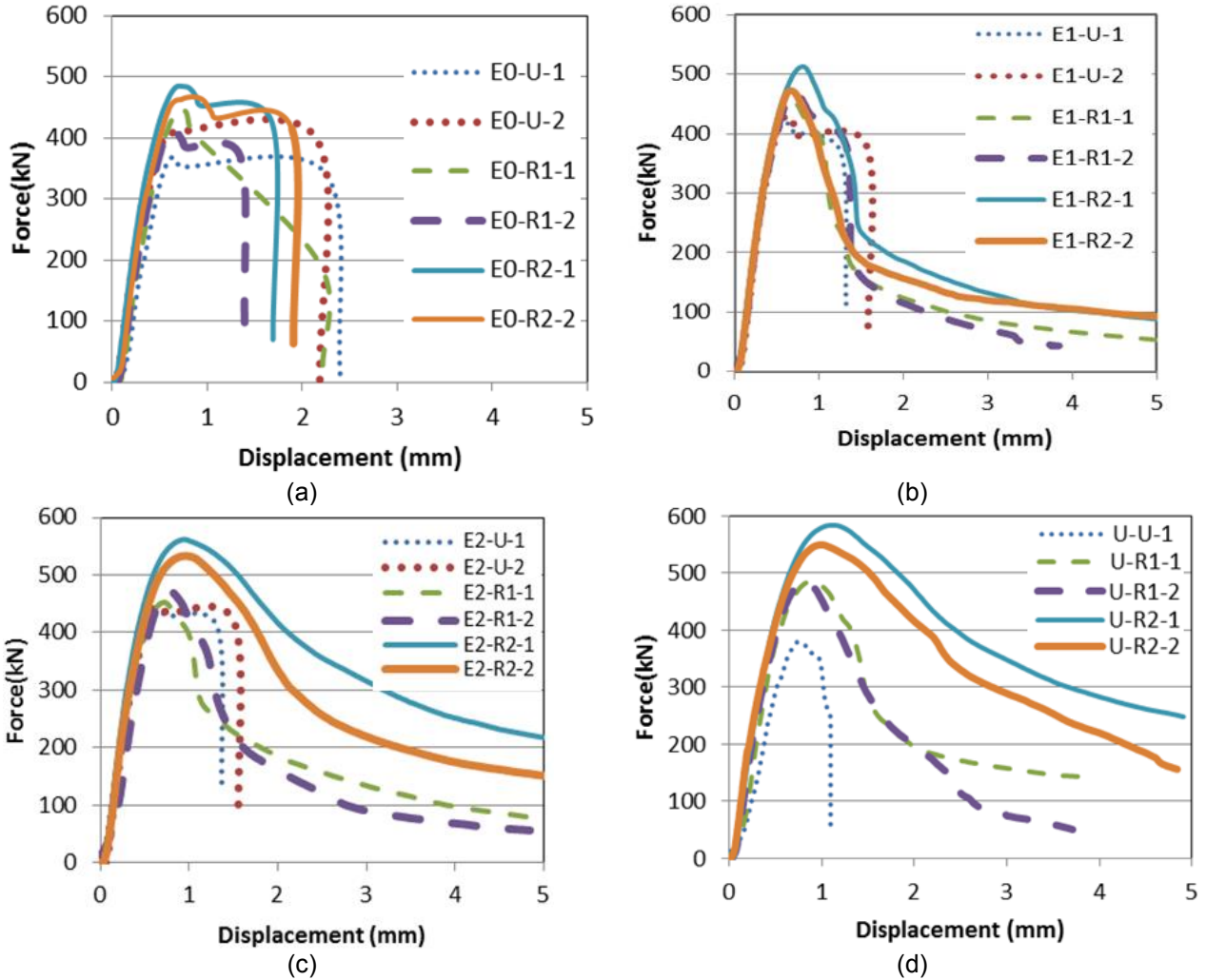
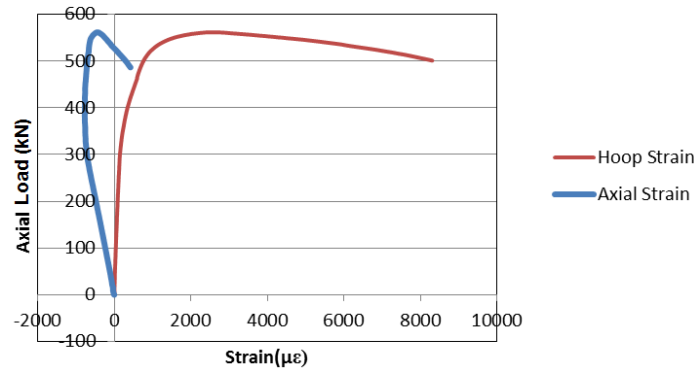


Figure 9. Force-displacement curve of specimens retrofitted with jacket of (a) ECC0, (b) ECC1, (c) ECC2, and (d) UHP



**Figure 10. Hoop and axial strain**

#### 4 Conclusion

- The main conclusion of this study is that the combination of fiber reinforced concrete and stirrup used in a repair jacket can significantly improve the behavior of concrete columns.
- The stirrup confines the core and hence increases the compressive strength. The average compressive strength of specimens having 0.56% and 1.7% stirrup ratio, determined to be 11% and 24% higher than the corresponding value for unreinforced specimens, respectively. Moreover, the ratio of the average compressive strength of the retrofitted specimens to the core specimens were 1.16%, 1.28% and 1.44% for specimens having zero, 0.56% and 1.7% stirrup ratio, respectively.
- Although the horizontal reinforcement enhanced the compressive capacity, it did not improve the ductility of the specimens having zero fiber content. For specimens having higher fiber content, increasing of horizontal reinforcement was more effective in terms of improving the post peak behavior, residual strength and ductility.
- Using FRC as a free-crack water-proof surface repair material in squat columns can not only preserve the substrate from steel corrosion and concrete carbonation and erosion, but can also enhance the behavior of the member under axial stresses.

#### Acknowledgement

The authors acknowledge the support provided by Concrete and Material Laboratory of Nagoya University and Mawson Lakes Fellowship Program for granting the scholarship to the first author.

#### References

1. Kamal, A., Kunieda, M., Ueda, N., and Nakamura, H., "Evaluation of crack opening performance of a repair material with strain hardening behavior." *Cement and Concrete Composites*, 2008. 30(10): p. 863-871.
2. Shin, S.K., J.J.H. Kim, and Y.M. Lim, "Investigation of the strengthening effect of DFRCC applied to plain concrete beams." *Cement and Concrete Composites*, 2007. 29(6): p. 465-473.
3. Hussein, M., M. Kunieda, and H. Nakamura, "Strength and ductility of RC beams strengthened with steel-reinforced strain hardening cementitious composites." *Cement and Concrete Composites*, 2012. 34(9): p. 1061-1066.
4. Kunieda, M., Ogurab, H., Ueda, N., and Nakamura, H., "Tensile fracture process of Strain Hardening Cementitious Composites by means of three-dimensional meso-scale analysis." *Cement and Concrete Composites*, 2011. 33(9): p. 956-965.
5. Zhang, Y.X., Ueda, N., Umeda, Y., Nakamura, H., and Kunieda, M "Evaluation of Shear Failure of Strain Hardening Cementitious Composite Beams." *Procedia Engineering*, 2011. 14(0): p. 2048-2057.
6. Kunieda, M., Umeda, Y., Ueda, N., and Nakamura, H., "Rapid Jacketing Technique by Using UHP-SHCC for Damaged RC Column under Seismic Loading, in *High Performance Fiber Reinforced Cement Composites*"
7. Li, G., "Experimental study of FRP confined concrete cylinders." *Engineering structures*, 2006. 28(7): p. 1001-1008.

# Failure Mode and Risk Analysis

# A Review of Limit State Design Principles and Practice

Doug Jenkins<sup>1</sup>

<sup>1</sup>Principal, Interactive Design Services

**Abstract:** The intent of the limit state design method is to provide adequate performance for the worst combinations of load and environmental conditions and material behaviour, having regard to the expected frequency of conditions and consequences of failure. The advantage of this approach is that design may be optimised to suit the worst combination of conditions, rather than providing a single arbitrary “factor of safety”. To achieve the greatest benefit of this approach design procedures should be appropriate to the type of loading, and load and reduction factors should take account of all sources of uncertainty.

In this paper the provisions of Australian and international concrete design codes are reviewed, in particular with regard to their provisions for dealing with unpredictable load conditions, and uncertainties in materials properties. It is concluded that whilst provisions are made for specific extreme load conditions, these are not handled in a consistent way within the principles of limit state design, and codes do not take adequate account of unknown sources of variability in structural resistance.

Recommendations are made to allow the full benefit of the limit state design approach to be achieved, including: 1) Design for expected maximum loads, and for extreme unpredictable loads should be recognised as two separate limit states, the former requiring adequate strength in all structural members, and the latter requiring adequate robustness to prevent collapse in the overall structure. 2) Load and reduction factors should take account of unknown sources of variation, as well as known statistical variations.

**Keywords:** limit state design, risk, uncertainty, consequences of failure, robustness

## 1. Introduction

The limit state design method identifies events or conditions that may have an adverse effect on the performance of a structure and seeks to reduce the risk of these outcomes as far as reasonably practicable, having regard to their expected frequency and the consequences of their occurrence. A number of “limit states” are specified, together with load magnification factors, material strength reduction factors, and any other design parameters appropriate to the particular limit state. The potential benefits of this approach, compared with methods relying on limiting material stresses with a single “factor of safety”, are:

- The design may be optimised to minimise the overall risk, allowing improved reliability at no additional cost, equal reliability at reduced cost, or some combination of the two.
- The focus on limit states and modes of failure encourages the use of design features appropriate to the particular mode of failure.
- In particular, where a structure requires additional ductility, energy absorption, or stability under extreme conditions, the limit state method is more likely to identify and provide these requirements than methods that focus on the strength of isolated sections under expected loads.

The limit state method also has a number of potential disadvantages:

- Analysis and design procedures are likely to be significantly more complex than those required by traditional “allowable stress” methods.
- Where limit state factors are closely calibrated against the results of earlier design methods there may be no significant improvement in the cost or safety of completed structures.
- Conversely, if design factors are optimised based on recognised risks there may be an overall reduction in safety due to risks not considered in the calibration process.

- Differing approaches to risk minimisation between technical documents and legal requirements for risk minimisation may increase the possibility of engineers being considered legally liable for structural failures, even if they have followed specified design procedures with due diligence.

## 2. Practical Significance

This paper examines the application of the limit state method as specified in Australian concrete codes, and in concrete and other structural codes in New Zealand, Europe, and the USA, with the intent to:

- Identify significant differences in the application of limit state design principles.
- Identify areas where changes to the application of limit state principles could be significantly improved.
- Make recommendations for changes to Australian structural codes to enhance the benefits of the limit state method, and reduce the likelihood of adverse outcomes.

It is found that although the basis of the limit state method is stated in similar terms in most of the codes, there are significant differences in the method of application. In particular, the Ultimate Limit State provisions in all codes largely consist of simplified procedures requiring the calculation of maximum design actions and design capacity at isolated sections, rather than a consideration of the collapse behaviour of the whole structure.

It will be argued that the Ultimate Limit State should be divided into two separate limit states, with different load factors and acceptance criteria:

- The Strength Limit State: considering maximum expected loads and minimum design strength of isolated sections.
- The Collapse Limit State: considering the behaviour of the whole structure under collapse conditions.

This recognition will provide a more logical framework for provisions that already exist; for instance for seismic and impact loads. It will also provide a better basis for ensuring that all structures are designed and detailed with an appropriate level of resistance to unexpected events, including gross overload, ductility demand, or deviations from specified construction or maintenance procedures.

## 3. Limit State Terminology and Definitions

The terms and definitions given in this section are based on Australian usage, in the structural concrete codes. Significant differences in other codes are discussed in later sections.

In AS/NZS 1170.0:2002 (1) the following definitions are given:

**Limit states:** States beyond which the structure no longer satisfies the design criteria.

**Limit states, serviceability:** States that correspond to conditions beyond which specified service criteria for a structure or structural element are no longer met.

**Limit states, ultimate:** States associated with collapse, or with other similar forms of structural failure. NOTE: This generally corresponds to the maximum load-carrying resistance of a structure or structural element but, in some cases, to the maximum applicable strain or deformation.

**Structural robustness:** Ability of a structure to withstand events like fire, explosion, impact or consequences of human errors, without being damaged to an extent disproportionate to the original cause.

Section 6 of AS/NZS 1170.0 provides general requirements for design and detailing of the “force-resisting system”:

- Structures shall be detailed such that all parts of the structure shall be tied together both in the horizontal and the vertical planes so that the structure can withstand an event without being damaged to an extent disproportionate to that event.
- The design of the structure shall provide load paths to the foundations for forces generated by all types of actions from all parts of the structure, including structural and non-structural components.

Other standards use the term “progressive collapse” and require (under some circumstances) provision of “alternative load paths”.



There is broad agreement between the international standards regarding the basic concept of limit states, and the specification of two limit states that must be satisfied; that is the serviceability and ultimate limit states. Detailed provisions for the Serviceability Limit State vary widely between different codes, but these detail differences are outside the scope of this paper. There are also significant differences in the wording of requirements for the Ultimate Limit State, which are examined in detail in the next section.

#### **4. Code Provisions for Limit State Design**

##### **4.1 AS-NZS 1170.0 and 1170.0 Supplement**

Section 7 of AS-NZS 1170.0 (1) provides requirements for two classes of Ultimate Limit States:

- 7.2.1 Stability: When considering a limit state of static equilibrium or of gross displacements or deformations of the structure, it shall be confirmed that ...
- 7.2.2 Strength: When considering a limit state of collapse, rupture or excessive deformation of a structure, section, member or connection it shall be confirmed that ...

Note that the overall stability of the structure, total collapse of the structure, and failure or excessive deformation of a single member or connection are all treated as examples of failure of the same limit state.

The Supplement to AS-NZS 1170.0 (2) provides further background information to the requirements of the standard. It states:

“The Standard incorporates the fundamentals of the limit states method and enables the designer to confirm the design of a structure. The intention is that confirmation establishes the ability of the proposed structure to resist known or foreseeable types of action appropriate to the intended use and design working life of the structure.”

It quotes ISO 2394 (3) as follows:

“In particular, they shall fulfil, with appropriate degrees of reliability, the following objectives:

- (a) They shall perform adequately under all expected actions.
- (b) They shall withstand both extreme actions and frequently repeated actions occurring during their construction and anticipated use.
- (c) They shall have structural robustness.’

These three objectives enunciate the serviceability, ultimate and fatigue, and progressive collapse (structural robustness) aspects of design.”

Section 6 of the Supplement provides more specific advice on design for structural robustness:

“... The potential damage may be avoided or limited by use of the following: ...

- (c) Selecting a structural form and design that can survive adequately the accidental removal of an individual element or a limited part of the structure or the occurrence of acceptable localized damage.
- (d) Avoiding as far as possible structural systems that may collapse without warning.

The design should provide alternate load paths so that the damage is absorbed and sufficient local strength to resist failure of critical members so that major collapse is averted. ...

Connections for example should be designed to be ductile and have a capacity for large deformation and energy absorption under the effect of abnormal conditions.”

Section 7 divides “Strength ultimate limit states” into 3 sub-classes:

- “(a) Attainment of the maximum resistance capacity of sections, members or connections by rupture (in some cases affected by fatigue, corrosion, and similar) or excessive deformations.
- (b) Transformation of the structure or part of it into a mechanism.
- (c) Sudden change of the assumed structural system to a new system (e.g., snap through).”

Appendix CA (Special Studies) states:

“Accidental actions include explosions, collisions, fire, unexpected subsidence of subgrade, extreme erosion, unexpected abnormal environmental loads (flood, hail, etc.), consequences of human error and wilful misuse. It is impractical to design for all accidental actions as they are very low probability events.

However, precautions should be taken to limit the effects of local collapses caused by such actions, that is, to prevent progressive collapse (see Section 6 and its commentary).”

## **4.2 AS 3600**

The Australian Standard Concrete Structures Code, AS 3600 (4) refers to the Loading Code, AS-NZS 1170.0 (1), for definitions and principles of the limit state method. Code clauses where the general provisions of the Loading Code are significantly amplified or varied are noted below:

Clause 2.2, Design for Strength, requires that:

“2.2.1 General: Strength checks for concrete structures and their component members shall be carried out ..., as appropriate to the strength check procedures being used.”

“2.2.5 The strength check procedure for use with non-linear analysis of framed structures at collapse shall be carried out as follows: ...”

The provisions of Clause 2.2.5 require consideration of the behaviour prior to collapse of the structure as a whole, including the margin between first yielding and peak load.

Clause 6.5, Non-Linear Frame Analysis, requires analysis of the structural behaviour at three separate levels: “This Clause applies to the non-linear analysis of framed structures at service load, at overload, and at collapse.”

The supplement to AS 3600 (5) contains the only specific requirement that the removal of one member from a framed structure should not result in a progressive collapse:

“C2.1.3 Design for robustness: A structure is to be designed such that ... , should one member be removed, the remainder of the structure would hang together and not precipitate a progressive collapse.”

## **4.3 AS 5100**

The Australian Standard Bridge Design Code, AS 5100 (6) includes detailed provisions for general design principles, loading, and the design of concrete structures, which whilst they generally follow the requirements of other Australian Standards (1,2,4,5), include significant variations where considered appropriate for the differing load conditions and longer design life of bridge structures. The extracts below relate to the major differences in wording and requirements for the ultimate limit state, and design for robustness:

### **4.3.1 Part 1: Scope and general principles**

Clause 6.3.2 Ultimate limit states:

“The ultimate limit states include the following:

- (a) Stability limit state, which is the loss of static equilibrium by sliding, overturning or uplift of a part, or the whole of the structure.
- (b) Strength limit state, which is an elastic, inelastic or buckling state in which the collapse condition is reached at one or more sections of the structure. Plastic or buckling redistribution of actions and resistance shall only be considered if data on the associated deformation characteristics of the structure from theory and tests is available.

Clause 11.3 Collision from railway traffic:

(b) ... supports adjacent to railway tracks may be permitted subject to ...

(i) Alternative load paths are available through the structure to ensure that the superstructure does not collapse in the event of removal of the supporting piers or columns as a result of collision...

### **4.3.2 Part 2 Design Loads**

Clause 14.7.5: Structural detailing requirements for earthquake effects; Ductile behaviour: “For bridge structures in BEDC-2, BEDC-3 and BEDC-4, a clearly defined collapse mechanism shall be established. The structural members shall be ductile at the potential plastic hinge locations defined in the mechanism.”

### **4.3.3 Part 5 Concrete**

Clause 2.11: Design Requirements and Procedures; Other Design Requirements:

“Requirements, such as progressive collapse and any special performance requirements, shall be

considered where relevant and, if significant, shall be taken into account in the design of the structure in accordance with the principles of this Standard and appropriate engineering principles.”

Clause 7.7: Seismic Analysis Methods:

“For a bridge structure in earthquake design category BEDC-4, the collapse mechanism shall be defined using a post-elastic analysis and it shall be ensured that there is a unique and enforceable strength hierarchy within the structural system.”

#### **4.4 NZS Codes**

The New Zealand loading codes are jointly published with Australian Standards (1, 2), but the New Zealand Concrete Structures Standard, NZS 3101 (7) is totally separate from the Australian Standard, other than referring to the same loading codes. NZS 3101 contains extensive requirements for design and detailing of structures under different levels of earthquake loading, but for the purposes of this paper only general requirements relating to the specification of limit states have been reviewed.

The code defines an “ultimate limit state”, rather than “limit states” as used in AS/NZS 1170.0 (1). The definition relates to the structure as a whole, rather than individual members or sections: “ULTIMATE LIMIT STATE. The state at which the design strength or ductility capacity of the structure is exceeded, when it cannot maintain equilibrium and becomes unstable.”

Clause 2.6 lists additional requirements for earthquake effects:

“2.6.1.1 Deformation capacity: In addition to the requirements of 2.3.2 for strength, the structure and its component parts shall be designed to have adequate ductility at the ultimate limit state for load combinations including earthquake actions.”

Clause 2.5 lists fatigue requirements as a serviceability limit state:

“2.5 Other design requirements: ...

2.5.2 Fatigue (serviceability limit state) “

#### **4.5 Eurocodes**

The Structural Eurocode series consists of ten documents covering the basis of structural design and application to different materials and load conditions. This paper examines the contents of EN 1990, Basis of Structural Design (8), and EN 1992, Design of Concrete Structures (9).

Code clause numbers followed by (P) in the quoted extracts below indicate clauses that are defined as “Principles” comprising:

- general statements and definitions for which there is no alternative, as well as ;
- requirements and analytical models for which no alternative is permitted unless specifically stated.

EN 1990 defines ultimate limit states as follows:

“1.5.2.13 ultimate limit states: states associated with collapse or with other similar forms of structural failure. NOTE They generally correspond to the maximum load-carrying resistance of a structure or structural member.”

Section 2 lists basic requirements, including:

2.1 Basic requirements ...

“(4)P A structure shall be designed and executed in such a way that it will not be damaged by events such as :

-explosion,  
- impact, and  
-the consequences of human errors,  
to an extent disproportionate to the original cause.

(5)P Potential damage shall be avoided or limited by appropriate choice of one or more of the following:  
avoiding, eliminating or reducing the hazards to which the structure can be subjected;  
selecting a structural form which has low sensitivity to the hazards considered;  
selecting a structural form and design that can survive adequately the accidental removal of an individual member or a limited part of the structure, or the occurrence of acceptable localised damage;

avoiding as far as possible structural systems that can collapse without warning; tying the structural members together.”

Section 3 lists ultimate limit states as follows:

### “3.3 Ultimate limit states

(1)P The limit states that concern:

- the safety of people, and/or
- the safety of the structure

shall be classified as ultimate limit states.

(2) In some circumstances, the limit states that concern the protection of the contents should be classified as ultimate limit states.

...

(3) States prior to structural collapse, which, for simplicity, are considered in place of the collapse itself, may be treated as ultimate limit states.

(4)P The following ultimate limit states shall be verified where they are relevant:

- loss of equilibrium of the structure or any part of it, considered as a rigid body;
- failure by excessive deformation, transformation of the structure or any part of it into a mechanism, rupture, loss of stability of the structure or any part of it, including supports and foundations;
- failure caused by fatigue or other time-dependent effects.”

EN 1992, Eurocode 2-1 (9) has the following requirement for prevention of progressive collapse:

#### “9.10.1 General

(1)P Structures which are not designed to withstand accidental actions shall have a suitable tying system, to prevent progressive collapse by providing alternative load paths after local damage. The following simple rules are deemed to satisfy this requirement ...”

## **4.6 ACI 318**

The ACI building code, ACI 318 (10) does not define design limit states; nonetheless its requirements for provision of adequate strength and resistance to collapse correspond to the ultimate limit state requirements in the other codes examined in this paper.

Requirements for strength design are stated in terms of the strength of individual members:

“8.1.1 — In design of structural concrete, members shall be proportioned for adequate strength in accordance with provisions of this Code, using load factors and strength reduction factors  $\phi$  specified in Chapter 9.”

Chapter 21 covers design of earthquake resistant structures, including provisions to prevent progressive collapse:

“21.1.1.1 — Chapter 21 contains requirements for design and construction of reinforced concrete members of a structure for which the design forces, related to earthquake motions, have been determined on the basis of energy dissipation in the nonlinear range of response.”

“R21.8.4 ... The design procedure should identify the load path or mechanism by which the frame resists gravity and earthquake effects.”

## **5. Limit State Provisions in Other Codes and Documents**

Whilst the great majority of structural design codes follow the practice of dividing limit states into the “serviceability” and “ultimate” categories, there are a number of documents that define a “collapse limit state”, either in addition to, or in place of the ultimate limit state. This usage is generally limited to those codes where design actions are much higher than can be accommodated by a strength design approach (such as earthquake loading in high seismic regions), or where the probability and/or consequences of failure are particularly high (such as off-shore drilling structures).

Documents related to seismic design of concrete structures, that include reference to a specific collapse limit state include:

- EN 1998-3, Eurocode 8: Design of structures for earthquake resistance – Part 3 (11) lists three limit states: “Near Collapse”, “Significant Damage”, and “Damage Limitation”. It states that “The definition of the Limit State of Collapse given in this Part 3 of Eurocode \* is closer to the actual collapse of the building than the one given in EN 1998-1: 2004 and corresponds to the fullest exploitation of the deformation capacity of the structural elements.”
- Procedures developed by The Engineering Advisory Group set up following the Christchurch earthquakes require consideration of building performance at the ultimate limit and collapse limit states (see Oliver et al. (12)).
- A paper presented to the Australian Earthquake Engineering Society 2011 Conference (Fardipour et al. (13)) deals with the “Collapse Limit State Assessment of Lightly Reinforced Concrete Columns”.
- The commentary to Part 5 of the AS-NZS Loading Code, NZS 1170-5 (S1), (13) states that “it is not currently considered practical to either analyse a building to determine the probability of collapse or base a code verification method around a collapse limit state ... it is possible to consider a limit state at a lower level of structural response, ... and then rely on margins inherent within the design procedures to provide confidence that acceptable collapse and fatality risks are achieved. In this Standard this limit state is referred to as the ultimate limit state (ULS).”
- Clause 2.1 of NZS 1170-5 (S1) states: “It is inherent within this Standard that, in order to ensure an acceptable risk of collapse, there should be a reasonable margin between the performance of material and structural form combinations at the ULS and at the collapse limit state. For most ductile materials and structure configurations it has been assumed that a margin of at least 1.5 to 1.8 will be available. This is intended to apply to both strength and displacement.”

The concept of separate “ultimate” and “collapse” limit states is further discussed in the Interim Report of The Canterbury Earthquakes Royal Commission (14).

Outside of earthquake design requirements, a number of codes and technical papers deal with requirements for an “accidental collapse limit state” and for prevention of “progressive” and/or “disproportionate” collapse, for example references 15 – 19.

## **6. Risk Management**

### **6.1 Approaches to Risk Management**

In “Safety of Structures, and a New Approach to Robustness” (20) Beeby writes: “It is proposed that the provision of adequate safety in structures depends on the satisfaction of three independent requirements: adequate safety factors, adequate control of the design and construction process, and adequate robustness.... The risks from failure may not be greatly changed by changes in safety factor”. This statement highlights the two main areas in which structural design codes may fail to minimise the risk of building collapse:

- Statistical analyses used to calibrate code load and resistance factors do not include significant sources of risk, such as failures in the design and construction process, or unforeseen events after completion.
- Increasing design loads, or reducing design strength capacity may have little effect on the risk of collapse where extreme conditions require ductility and energy absorption, or the ability to distribute loads to alternative load paths.

Analyses of risk in other areas arrive at similar conclusions. In “The Black Swan” (21) Taleb examines risk in global financial management, and finds (immediately before the start of the Global Financial Crisis) that focus on expected risks leaves institutions with increased susceptibility to collapse from the unexpected. He writes “the idea is not to correct mistakes and eliminate randomness ... *The idea is simply to let human mistakes and miscalculations remain confined*, and to prevent their spreading through the system, ...” (author’s emphasis).

## 6.2 Legal Requirements

Legal requirements to minimise risk have developed largely independently of structural design codes, and may have requirements that are inconsistent with the approach of the national codes. In some cases specific legal frameworks have developed over time as the result of a single incident. The most influential such incident is the Ronan Point Collapse of 1968, leading to widespread research into disproportionate and progressive collapse mechanisms, and specific requirements in the UK National Building Regulations, contained in “Approved Document A” (22).

In the Australian context requirements for prevention of collapse are much less well defined, however recent national safety in design legislation (23) requires that all risks be eliminated or minimised “so far as is reasonably practicable”, and this requirement applies to the design of structures, both for the construction stage and after completion.

The phrases “so far as reasonably practicable” (SFARP, or SFAIRP) and “as low as reasonably practicable” (ALARP) have a long history of use in the UK, which is documented in a publication by the Centre for the Protection of National Infrastructure (24). This document, and other reviews of the UK and Australian legislation (25, 26) suggest that the two phrases have effectively the same meaning. A recent paper by Robinson (27) however suggests that the two phrases reflect fundamentally different approaches to the design process, and that in the event of a structural failure the hazard focussed ALARP approach is unlikely to be found (in hindsight) to have satisfied the statutory requirements of the precaution focussed SFAIRP approach.

These issues remain to be resolved, but to minimise the risk of legal action against design engineers who have performed their duties with all due diligence (SFAIRP) it is highly desirable that design code provisions should be consistent in their requirements and terminology, and that where different levels of precaution are required for different classes of structure, these differences should be explicitly stated.

## 7. Summary and Conclusions

The design codes examined in this paper have a similar approach to the statement of the limit state method (other than ACI 318 (10), which does not use this terminology). They also have a similar approach in the application of design procedures to different classes of structure. They all shared an inconsistent approach towards design for the Ultimate Limit State in that:

- The Ultimate Limit State is characterised as a requirement to avoid structural collapse, but the great majority of the detailed code provisions relate to strength at a single cross-section, or in a single member (after limited allowance for load distribution).
- Code provisions for earthquakes and impact loads allow significant damage to the structure, provided that partial or total collapse is avoided, but these requirements are treated as being the same limit state as those that require the design strength of every section to be greater than the maximum design actions.

Of the codes examined in this paper only Eurocode 2 (9) contains specific general provisions (outside seismic or impact load requirements) intended to ensure resistance to disproportionate collapse after localised failure. In the UK further detailed provisions are given in the Building Regulations Approved Document A (22).

In Australia and New Zealand the joint loading codes (1,2) require structures to be robust, and to provide “alternate load paths”, but do not provide any specific guidance on how this should be achieved, or on the levels of robustness appropriate to different classes of building. In the Australian Concrete Structures Code and Commentary (4, 5) the code contains only general requirements for robustness, but the recently published commentary requires that “should one member be removed, the remainder of the structure would hang together and not precipitate a progressive collapse.”

Recent Australian legislation relating to “Safety in Design” (23) requires that all known risks should be removed or minimised “so far as is reasonably practicable”. Only very general guidance is given on how the limit of practicability should be determined and applied, and it has been argued that the design approach given in current standards and codes of practice is inherently incompatible with the legislated requirements (27).

In order to make design code procedures more internally consistent, to improve consistency with legal requirements, and to provide specific guidance on what measures should be considered practicable, the following changes to the Australian loading and structural design codes are recommended:

- Three separate levels of limit state should be specified:
  - Serviceability: the level at which unscheduled maintenance or repair is required, or specified performance requirements are no longer met.
  - Strength: the level at which any member fails or suffers excessive deformation.
  - Collapse: the level at which a structure is on the point of substantial or total collapse.
- Consideration of the Collapse Limit State should not be limited to seismic and impact loading, but should include all potential causes of collapse, including loss of support, deterioration of material properties, improper construction procedures, effects of fire, and extreme loads due to any cause.
- Where the degree of collapse resistance is considered to be related to the classification of the structure and the consequences of failure, specific guidance should be provided in the code regarding the type of analysis and the level of robustness required for different types of structure.

The advantages provided by these changes include:

- The limit state principles would be consistent with the actual requirements of the structures design codes.
- The code requirements would also be more consistent with the Safety in Design legislation.
- The risk of design engineers being held legally liable for failures due to unexpected causes would be reduced.
- A general increase in structural robustness would allow a review of load and reduction factors for the Strength Limit State, potentially allowing a significant improvement in design efficiency.

## 8. References

1. Standards Australia/Standards New Zealand, "Structural Design Actions Part 0: General Principles (AS/NZS 1170.0:2002)", SAI Global/ Standards New Zealand, 2002, Sydney and Wellington
2. Standards Australia/Standards New Zealand, "Structural design actions—General principles—Commentary (AS/NZS 1170.0 Supplement 1:2002)", SAI Global/ Standards New Zealand, 2002, Sydney and Wellington
3. International Standards Organisation, "ISO 2394 General principles on reliability for structures", ISO, 2015, Geneva.
4. Standards Australia, "Concrete Structures (AS 3600:2009)", SAI Global, 2009, Sydney
5. Standards Australia, "Concrete structures—Commentary (Supplement to AS 3600—2009) (AS 3600-2009 Supp 1:2014)", SAI Global, 2014, Sydney
6. Standards Australia, "Bridge Design (AS 5100:2004)", SAI Global, 2004, Sydney
7. Standards New Zealand, "Concrete Structures Standard Part 1: The Design of Concrete Structures (NZS 3101:Part 1:2006)", Standards New Zealand, 2006, Wellington
8. CEN/TC 250, "Eurocode – Basis of structural design (EN 1990:2002)", European Committee for Standardization, 2002, Brussels
9. CEN/TC 250, "Eurocode 2 – Design of concrete structures- Part 1-1: General rules and rules for buildings (EN 1992-1-1:2004)", European Committee for Standardization, 2004, Brussels
10. American Concrete Institute, "Building code requirements for structural concrete (ACI 318-08)", ACI Committee 318, 2008, Michigan.
11. CEN/TC 250, "Eurocode 8 – Design of structures for earthquake resistance – Part 3: Assessment and retrofitting of buildings (EN 1998-3:2005)", European Committee for Standardization, 2005, Brussels
12. Oliver, SJ., Boys AG. et al., "Nonlinear Analysis Acceptance Criteria for the Seismic Performance of Existing Reinforced Concrete Buildings", 2012 NZSEE Conference, Auckland



13. Standards New Zealand, "Structural design actions – Part 5: Earthquake actions – New Zealand Commentary (NZS 1170-5 (S1) 2004)", Standards New Zealand, 2004, Wellington
14. The Canterbury Earthquakes Royal Commission, "Interim Report", 2011, Wellington
15. Moan, T., "Development of Accidental Collapse Limit State Criteria for Offshore Structures", Special Workshop on Risk Acceptance and Risk Communication, 2007, Stanford University
16. Talaat, M., Mosalam, K., "Computational Modeling of Progressive Collapse in Reinforced Concrete Frame Structures", University of California, 2007, Berkeley, California
17. Hadi, M., Alrudaini, T., "New Building Scheme to Resist Progressive Collapse", ASCE Journal of Architectural Engineering, 18 (4), 2012, pp 324-331
18. Ellingwood B., "Load and Resistance Factor Criteria for Progressive Collapse Design", Georgia Institute of Technology, 2002, Atlanta, Georgia
19. Menchel K., "Progressive Collapse: Comparison of Main Standards, Formulation and Validation of New Computational Procedures", Universite Libre de Bruxelles, 2009, Brussels
20. Beeby, A., "Safety of Structures, and a New Approach to Robustness", Structural Engineer, 77(4), 1999, pp 16-21
21. Taleb, N., "The Black Swan", The Random House Publishing Group, 2007, New York
22. The Building Regulations, "Approved Document A", HM Government, 2013, London
23. Safe Work Australia, "Work Health and Safety Act 2010", Australian Federal Government, 2011, Canberra
24. Arup, "Review of international research on structural robustness and disproportionate collapse", Centre for the Protection of National Infrastructure, 2011, London
25. Institution of Civil Engineers, "A Review of and Commentary on, the Legal Requirement to Exercise a Duty 'So Far as is Reasonably Practicable'", Institution of Civil Engineers, 2010, London
26. Safe Work Australia, "Guide to the Model Work Health and Safety Act", Safe Work Australia, 2012, Canberra
27. Robinson R., "Near enough not safe enough", Engineers Australia, Civil Edition, 86(1), pp 30-32

# Fasteners to Concrete: Failures and Solutions

Heath, D. J.<sup>1</sup>, Gad, E. F.<sup>2</sup>, Lee, J.<sup>3</sup>

<sup>1</sup> National Technical Manager, Australian Engineered Fasteners and Anchors Council

<sup>2</sup> Chair of Department of Civil and Construction Engineering, Swinburne University of Technology

<sup>3</sup> Training and Development Manager, Australian Engineered Fasteners and Anchors Council

**Abstract:** Safety-critical fasteners to concrete are widely used in construction from small retro-fit applications to large infrastructure projects. To compromise their function endangers life and leads to considerable financial consequences, including disruption to the structure. The contributing factors to failures are largely avoidable through an awareness of the factors that influence fastener performance. This awareness is the cornerstone of risk mitigation strategies in the fastener industry and is achievable by reviewing education materials that are readily available. At present, there is a real risk that failures will continue to occur if lessons from past failures are not learned. The absence of guidance in Australian design standards and codes of practice and the lack of training and supervision during fastener installation dramatically increases the risk of failures occurring. Manufacturers, suppliers, design engineers, installers and field engineers may all be implicated in a failure investigation where ignorance is not a valid defence. The Australian Engineered Fasteners and Anchors Council was founded to address shortcomings in the industry and has developed technical guidance for specification and an installer certification program to lift quality and safety standards. This paper reviews a series of case studies of anchor failures from around the world, identifies the links with problems frequently encountered within the Australian construction industry and offers best practice solutions to prevent further failures from occurring.

**Keywords:** Post-installed, cast-in, anchor, fastener, failure

## 1. INTRODUCTION

Structural fasteners used in safety-critical applications involving metal inserts into a concrete or masonry substrate should be designed and detailed by a competent structural engineer. Applications are defined as 'safety-critical' when their failure may cause risk to human life and/or have considerable economic loss. Fasteners must be fit for purpose; durable, robust, and possess sufficient integrity for all design actions [1]. Structural fasteners in concrete or masonry are commonly referred to as anchors and form the focus of this paper.

In concrete, anchors may be grouped according to their installation method into cast-in-place and post-installed. Post-installed anchors may be further classified into two groups; direct installation (power actuated) fasteners and a much larger ensemble being drill installation fasteners which covers chemical bonded anchors and mechanical anchors (such as expansion and screw anchors).

The Australian Engineered Fasteners and Anchors Council (AEFAC, [www.aefac.org.au](http://www.aefac.org.au)) is an industry initiative that was formed in 2012 to introduce governance to the industry with support and guidance to be provided for design engineers, contractors, suppliers, installers and field engineers.

This paper outlines the details of a number of fastener failures that have been published, identifying common themes and lessons that should be learned from these failures to prevent them from occurring again. A summary is also provided of two new initiatives developed by AEFAC that are relevant to the case studies and will help lift safety standards in the Australian anchor industry. These include the development of the proposed AEFAC Standard for design engineers and the development of the AEFAC Installer Certification Program for installers of anchors.

## 2. ANCHOR FAILURES

The absence of suitable guidelines for anchors in safety-critical applications overseas has contributed to catastrophic failures ([2], [3], [4]). The following section outlines six different failure case studies that are relevant to fasteners and identifies common factors contributing to the failures.

### 2.1 Case study #1: prequalification

In 2012 a brace fixing bolt was being tightened to a ferrule when the ferrule fractured approximately 60 mm inside the panel at the location of minimum cross-sectional area corresponding to the hole for reinforcing bar (refer to Figure 1). A subsequent investigation was performed by WorkSafe Victoria

revealed that the product contained no marking as recommended by AS 3850:2003 [5], making identification and traceability difficult, particularly for reference to the specification and manufacturer's installation instructions, as well as reducing the possibility for product substitution [6]. Further, failure of the ferrule posed a crush hazard. A separate incident involving the erection of precast concrete panels highlighted this crush hazard when multiple panels collapsed into an adjacent car park (refer to Figure 2). Inspectors of the second incident were unable to confirm key details concerning the collapse including the choice of brace inserts (fasteners) supporting the temporary braces that pulled out of the concrete slab.



**Figure 1. Ferrule that fractured during installation (source: [7]).**



**Figure 2: Precast panel failure during erection crushes cars (source: [8]).**

The ferrule failure demonstrates not only the dangers of using fasteners without appropriate markings, it also highlights the need for a robust and transparent approvals scheme to demonstrate that the product is fit for its intended use. An example scheme employed in Europe for post-installed fasteners to concrete that provides this level of confidence is ETAG 001 [9]. This scheme includes quality assurance during manufacturer through factory production control, plus robust product assessment through standardised testing and evaluation procedures. The scope of this scheme covers tests addressing tolerances on installation practice and tests for admissible service condition to ensure that the fastener remains serviceable throughout its design life.

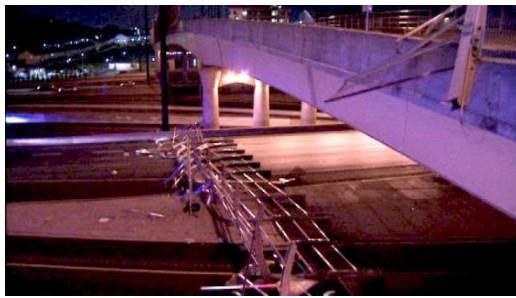
## **2.2 Case study #2: Canopy-fence failure on 17<sup>th</sup> Street Bridge**

At 11.20pm on August 13, 2011 approximately 190 feet (58 metres) of a canopy fence structure detached from the 17<sup>th</sup> Street Bridge in Atlanta, falling onto the roadway below [10]. There were no injuries and no damaged vehicles as a result of the collapse. The remaining canopy-fence on the 700 foot (213 metre) long overpass was removed a short time later. The bridge was opened in 2004 and spans over the Interstate Highway 75/85 which comprises 20 lanes of traffic. The southern side of the bridge includes the canopy-fence that was connected to the parapet wall. Each support frame for the canopy-fence was spaced 10 feet, six inches (3.2 metres) apart. A total of 19 support frames detached from the parapet during the collapse.

Wiss, Janney, Elstner Associates, Inc. were engaged to undertake a forensic examination of the collapse. The investigation into documentation revealed numerous shortcomings in the design and fabrication documents. One drawing referenced 7/8" (22 mm) anchor rods with sufficient embedment to develop 4 kips (17.8 kN) for the connection of the canopy-fence to the parapet, however the hole diameter and embedment depth as well as the anchor material and type of chemical system were not specified. A structural analysis revealed the eccentricity of the resultant load from the canopy structure relative to the fixture generated a net overturning moment that resulted in a sustained in-service tensile load equal to 1053 pounds (4.7 kN) on the bottom fasteners attaching each support frame of the canopy-fence. The Georgia Department of Transportation Office of materials and Research found that there were 15 different epoxy-resin products that met the standard specification and "Acceptance of Miscellaneous Construction Items".

Anchor rods from the fixtures were examined both in cases of failure as well as in fixtures that remained attached to the parapet. Failed anchor rods and those extracted from the fixtures remaining attached to the parapet were either 11" (279 mm) threaded rod or a combination of 6" (152 mm) threaded rod plus 5" (127 mm) smooth unthreaded rod. Of the 168 anchor rods remaining attached to the canopy after the failure, 112 had measureable withdrawal between 1/16" (1.6 mm) to 1.75" (44.5 mm). Holes that had experienced anchor pull-out were frequently observed to have voids between 1 –

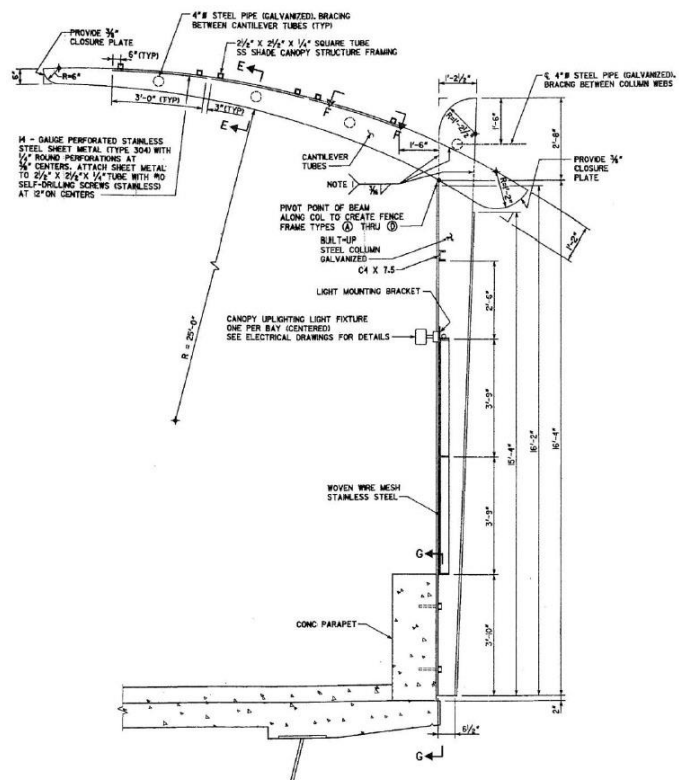
1.5" (25.4 – 38.1 mm) in length plus uncured epoxy was extracted from the rear of three holes in the failure area.



(a) Canopy fence collapsed onto roadway.



(b) Threaded and smooth anchor rods.



(c) Typical column-cantilever assembly detail.

**Figure 3. Canopy fence failure on Interstate Highway 75/85 in Atlanta (source: [10]).**

Laboratory tests confirmed the concrete was well consolidated and included well graded concrete with a compressive strength equal to 6787 psi (46.8 MPa). Analysis of the composition of the chemical anchors revealed differences in material composition from different sample locations, with results also suggesting hardener-rich areas and resin-rich areas. A creep test confirmed that the product used was susceptible to creep under sustained tensile loading.

The failure was attributed to: i) chemical anchors having poor resistance to long-term creep under sustained loading, ii) disproportionate and incomplete mixing of chemical anchor components, and iii) large voids in the chemical resulting in reduced embedment length and a greater effective shear stress needing to be resisted by the chemical anchor. The sustained in-service loads resulted in anchors withdrawing resulting in an increase in the eccentricity of loading, further increasing the magnitude of sustained load applied to the anchors.

The 17<sup>th</sup> Street Bridge canopy-fence failures case study is important because it highlights shortcomings in the specification, procurement and installation of the product. The specification for a chemical anchor should be accurate and contain a sufficient level of detail to ensure that there is no ambiguity for anchor procurement [11]. The type of product used was also found to be creep-sensitive and thus unsuitable for sustained in-service loads. The findings from the investigation also revealed shortcomings with the installation including poorly mixed products, excessive entrained air and product substitution without the written consent of the design engineer. Collectively, these factors resulted in safety being compromised for the project.

### 2.3 Case study #3: Awning collapse in Queensland

In 2012 an awning on a shop front swung down as the result of an anchor failure, resulting in one fatality and injuries to five other people. The awning was constructed in the 1970s and was fixed to adjacent reinforced concrete beams via torque-controlled expansion anchors. A safety alert published by Workplace Health and Safety Queensland revealed the structure had deteriorated with rust causing the fasteners to be prised out [12]. The design of the awning was such that fasteners were obscured from view making inspection difficult. The investigation that followed the failure revealed incorrect hole diameter and depth for the fasteners with the position of reinforcement in the concrete preventing



drilling from achieving the required depth. It was also established that additional sails had been added to the awning resulting in an increase in applied loads.



(a) Structure that swung down.



(b) End of awning with anchors showing.

**Figure 4: Awning collapse (source: [13]).**

This failure highlights the importance of a number of key requirements for fasteners:

1. Inspection and maintenance programs are necessary, especially for aging assets.
2. The selection of an anchor requires consideration of all likely loads encountered during the intended service life. Any variation to this constitutes change management, requiring a revision of the fastener design by the responsible engineer.
3. The installer needs to be aware that failing to achieve the correct drill depth may compromise the safety of the fixture and requires proper change management procedures to be followed, including notifying the responsible engineer. Further, there are strict tolerances on hole diameters for post-installed mechanical anchors – including torque-controlled expansion anchors – such that exceeding these tolerances may prevent the fastener from functioning as intended. If drilling meets refusal prior to achieving the required drilling depth, the responsible engineer should provide written approval for an alternative specification.

#### **2.4 Case study #4: Ceiling collapse in educational building**

A large educational building in the UK had been constructed when the suspended ceiling in a large teaching hall collapsed shortly before the opening of the building. There were no casualties since nobody was in the building at the time of collapse. The installation of the suspended ceiling was a variation on the original design intended to reduce noise levels from footfall impact in the facility. A report of the findings from the investigation that followed the failure was submitted to Confidential Reporting on Structural Safety (CROSS) in the UK [14]. The investigation found that the mechanism of failure was progressive collapse. Several key factors contributed to the collapse. Firstly, the specification was reportedly only partially complete. Secondly, although the correctly rated fixture had been procured, the fixture was appropriate for compression-only loads, not tensile loads.



**Figure 5: Ceiling collapse in educational building (source: [14]).**

Although the suspended ceiling was non-structural, it should be deemed to be safety-critical due to the potential consequences of failure. The lessons from this failure were the importance of a complete specification, as well as appropriate supervision on site to monitor installation.

### **2.5 Case study #5: Uster swimming pool concrete ceiling collapse**

The heavy concrete ceiling over a swimming pool in Uster, Switzerland had been in service for a period of 13 years when it suddenly collapsed, resulting in 12 fatalities and 19 people injured. The ceiling had been supported by a tension hanger system including stainless steel hanger rods. The failure investigation revealed that chloride stress corrosion cracking had severely weakened the austenitic stainless steel rods supporting the ceiling, leading to the collapse ([15], [16]). The condition is brought about by evaporation of chlorinated water with water vapour condensing in cooler regions of the interior space. With successive cycles, a concentration of chlorine deposits built up on the stainless steel components leading to localised corrosion and fine cracks developing. Stress corrosion cracking is a condition that may form in the presence of three conditions: i) inappropriate grade of stainless steel, ii) relatively high tensile stress developed in the element relative to yield strength, and iii) presence of a specific aggressive environment.



**Figure 6: Collapse of heavy concrete ceiling in swimming pool facility (source: [17]).**

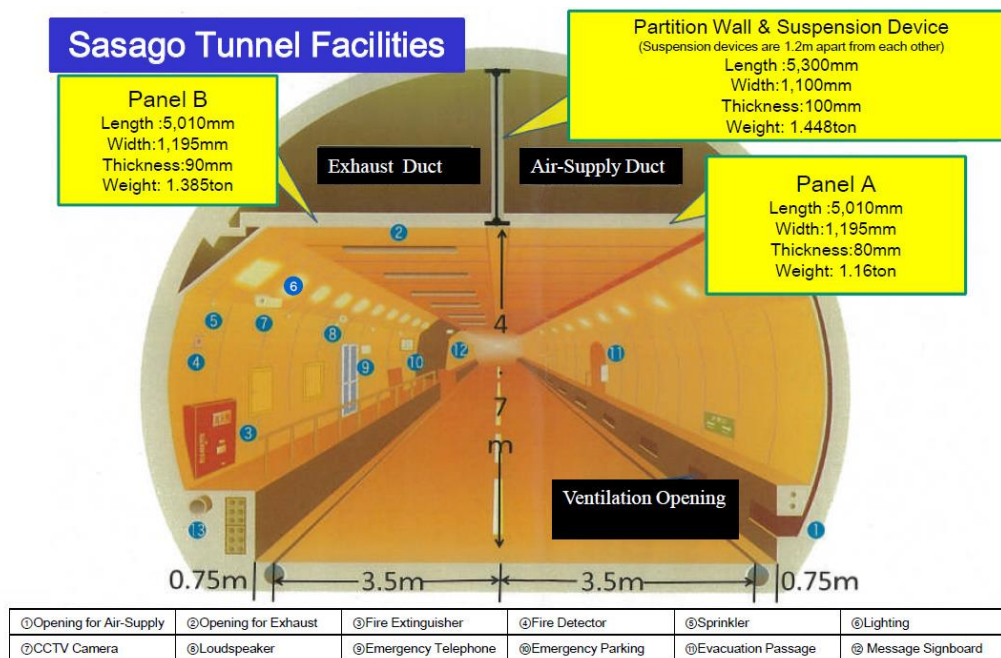
Although the failure occurred in the tension rods, the fasteners often form part of the tension system and are therefore an equally important consideration during design. General statements in project requirements result in the specification of austenitic stainless steel grades such as AISI 304 or AISI 316 that are inappropriate for corrosion conditions in an indoor swimming pool environment and render the fasteners susceptible to stress corrosion cracking. Since the collapse of the Uster swimming pool ceiling in 1985, other swimming pool ceilings have failed due to stress corrosion cracking such as the Steenwijk swimming pool in the Netherlands in 2001 [17]. These events reinforce the need for correct specification of material grades by consulting the fastener supplier's technical staff, as well as implementing an appropriate inspection and maintenance program.

### **2.6 Case study #6: Partial collapse of Sasago tunnel ceiling**

On December 2<sup>nd</sup>, 2012 a 130 metre section of concrete ceiling panels collapsed in the Tokyo-bound (inbound) Sasago Tunnel, 1.7km from the east portal of the 4.7km long tunnel (refer to Figure 7). Construction of the main body of the tunnel was originally completed in 1976 with the ceiling panel installation completed in 1977. The precast concrete panels were installed for the tunnel ventilation system and included ceiling panels and partition walls, weighing between 1.16 – 1.448 ton (refer to Figure 8). Chemical anchors were used to support the ceiling panels and partition walls [18]. In response to the collapse the "Research and examination committee for tunnel ceiling collapse incident" was formed to investigate the cause of collapse and to propose preventative measures to avoid recurrence. A preliminary report of the event published by the Ministry of Land, Infrastructure, Transport and Tourism of Japan noted that the incident caused three vehicles to be crushed, two of which caught fire, resulting in nine fatalities and two additional people injured [19]. Both inbound and outbound tunnels were immediately closed, with the outbound tunnel re-opened on 29<sup>th</sup> December, 2012 and the inbound tunnel re-opening on February 8<sup>th</sup>, 2013 more than two months after the failure.



**Figure 7: Partial collapse of concrete panels in Sasago Tunnel (source: [20]).**



**Figure 8: Structural system of Sasago Tunnel (source: [21]).**

As a safety precaution, ceiling panels in the outbound and inbound tunnels were removed and an investigation found 632 defects associated with the anchors securing the ceiling panels in the outbound tunnel and 1028 defects associated with anchors securing the ceiling panels in the inbound tunnel. Typical defects reported included loose anchors, missing anchors and cracked concrete.

Key findings from the investigating committee suggested the following factors contributed to the partial collapse:

1. Pressure differential between the two chambers separated by the partition wall had not been factored into the original design resulting in greater loading on the fasteners supporting the partition walls.
2. Inconsistencies were present among specifications, design reports and final drawings for the chemical anchors, with some anchor rods recovered onsite being shorter than the required length leading to insufficient tensile strength.
3. Insufficient level of detail in the specified performance requirements for the chemical anchor product.
4. Deterioration of the chemical compound in the chemical anchors attributed to repeated loading caused by operation of the ventilation system and pressure from passing vehicles as well as hydrolytic degradation of the chemical compound due to the aggressive environment.
5. No close visual testing or site testing of anchors for 12 years prior to the collapse.

The combination of the number of defects present in the structure and the lack of an inspection and maintenance program meant that a catastrophe was inevitable. The report of preliminary findings

revealed failure of the safety-critical fasteners resulted not only in injury and loss of human life, but also significant disruption to the facility and considerable economic impacts. Poor monitoring and programs have also contributed to other published failures such as the partial collapse of ceiling panels in the Interstate-90 connector tunnel ('Boston Big Dig') in Boston, Massachusetts, U.S. and the partial collapse of a steel structure in the Balcombe Rail Tunnel in the U.K. ([22], [23]).

Fasteners to concrete are manufactured to resist various conditions including highly aggressive environments and prolonged exposure to cyclic loads [9]. Additionally, guidance is available that provides the appropriate methodology to calculate the performance of these products under the application-specific requirements and to assist in the determination of appropriate maintenance programs ([24], [25]). These guidelines combined with technical support offered by reputable suppliers provide the engineer specifying a fastener with a high level of confidence that the fastener will remain fit for its intended use throughout its design life. Further, they provide important information to assist in developing an appropriate inspection and maintenance plan for the asset.

## 2.7 Summary

The case studies described above demonstrate the safety-critical nature of fasteners and the importance of learning from mistakes that have resulted in failures. A number of common themes are present:

- *Product prequalification:* A robust product approval process ensures the product is fit for purpose. The cast-in ferrule that failed (case study #1) not only lacked traceability, its failure during installation also demonstrated excessive variability in product performance that was not controlled to an acceptable level.
- *Product substitution and change management:* A proper change management procedure involving written consent by the responsible engineer must be followed for any deviation from the specification. The 17<sup>th</sup> Street Bridge in Atlanta (case study #2) had threaded rod substituted for only partially threaded rod, reducing mechanical interlock of the anchor rod with the chemical product that compromised performance and contributed to the collapse.
- *Quality of installation:* All fasteners to concrete exhibit some degree of sensitivity to installation such that their performance is limited to a certain degree by the quality of their installation. The installer needs to understand the dangers of deviating from the installation instructions. Poor installation technique for chemical anchor installation was identified in the 17<sup>th</sup> Street Bridge in Atlanta resulting in chemical compound that had not cured and the presence of large air voids. The collapse of the awning (case study #3) highlighted the danger of reducing drilling depth due to hitting reinforcement since the fastener cannot achieve its rated performance at the reduced depth.
- *Accurate and detailed specification:* A specification with insufficient information may lead to the same type of product being procured that exhibits very different performance. The limited information provided in the specification for chemical anchors for use in the 17<sup>th</sup> Street Bridge in Atlanta resulted in the potential to procure 15 different products. Further, the need to avoid creep-sensitive chemical product was not identified. Insufficient detail in the specification of fixtures to secure a suspended ceiling in an educational building (case study #4) was found to contribute to the ceiling's collapse. A proper understanding of project-specific requirements is imperative for fastener specification by the responsible engineer. The collapse of heavy concrete ceiling panels in a swimming pool (case study #5) was attributed to the selection of an inappropriate grade of stainless steel in the tension assembly supporting the concrete panels.
- *Inspection and maintenance program:* In the event that defects do occur, an inspection and monitoring program provides an early detection mechanism and the opportunity to undertake remedial work before defects escalate to a collapse situation. The corrosion of fasteners securing the awning that collapsed in Queensland had been in service for more than three decades but could not be easily inspected. Findings reported from the preliminary investigation into the Sasago tunnel collapse (case study #6) revealed an inspection and monitoring program had not been enacted during the 12 years preceding the collapse and that during the ensuing investigation 1028 defects were found in the fasteners securing the concrete panels remaining in the tunnel that experienced the collapse.

## 3. LIFTING QUALITY AND SAFETY STANDARDS

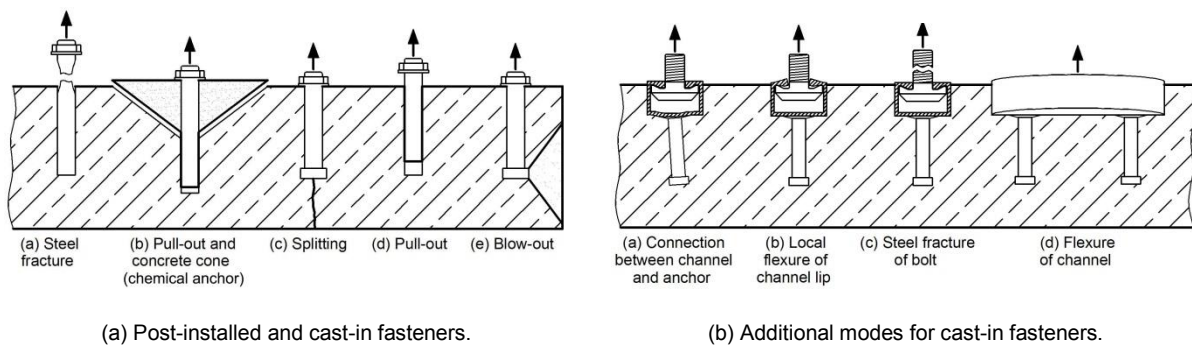
Internationally, failures of fasteners to concrete have been the catalyst for regulation such as collapse of a stair structure in Ireland in 2002 (one fatality) leading to the Code of Practice for the Design and installation of Anchors [26], and the Boston Big Dig leading to training for installers [27] and the inclusion of design provisions for adhesive anchors in ACI-318:2011 [28]. AEFAC has been formed to introduce the necessary measures to ensure that the risk of failure in the anchor industry is acceptably low. Two key initiatives that have been introduced to improve safety are discussed below.



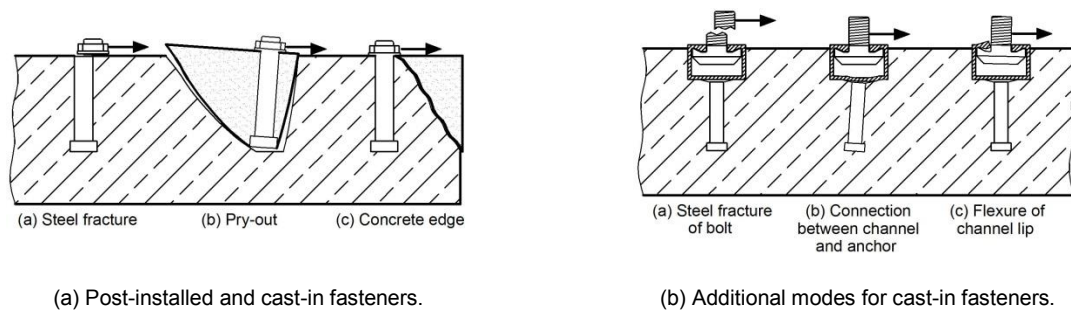
### 3.1 AEFAC Standard

Until now, guidelines for the design and evaluation of anchors in Australia have been minimal. The anchor industry has been self-regulated, relying on suppliers of products for information and performance data. However, this is often confusing for engineers due to there being a lack of consistency in testing and evaluation of products, as well as differences in terminology and design methodology. AS 3600 [29] states shallow anchorage failure should be investigated but provides no further guidance.

The proposed AEFAC Standard is closely based on prEN 1992-4:2013 [24] with a scope covering cast-in headed fasteners and anchor channel plus post-installed mechanical fasteners and chemical fasteners to concrete. Products eligible for use with the design methodology require strict quality assurance program at the factor as well as a robust testing and evaluation program to determine product performance ([9], [30]). The methodology underpinning the proposed AEFAC Standard is the Concrete Capacity (CC) Method that has been adopted in Europe and the United States for the design of cast-in and post-installed anchors ([24], [28], [31]). The document requires that the design engineer identifies the decisive mode of failure. The modes of failure for consideration under tensile loading are illustrated in Figure 9(a) for cast-in and post-installed fasteners with additional modes for consideration for anchor channel illustrated in Figure 9(b). Figure 10(a) illustrates the modes of failure requiring consideration for cast-in and post-installed fasteners under shear loading with additional modes of failure for anchor channel illustrated in Figure 10(b). A design check on combined loading must also be considered. A comprehensive overview of the design methodology has been presented elsewhere [32]. The proposed AEFAC Standard is due for publication in 2015.



**Figure 9: Modes of failure considered for fasteners to concrete under tensile loading.**



**Figure 10: Modes of failure considered for fasteners to concrete under shear loading.**

### 3.2 AEFAC Installer Certification Program

Anchor products that have been installed incorrectly will most likely perform in an unpredictable manner that differs from the specifier's intent. An awareness of this danger is critical. Most types of anchors that are presently used are reasonably sensitive to installation practice. The training of installers is frequently overlooked which may cause gross errors during installation that exceed tolerances acceptable by product suppliers and in turn could have catastrophic consequences [9].

The AEFAC Installer Certification Program has been developed specifically for installers of anchor products to ensure that the installation is consistent with the supplier's installation instructions. The training program is based closely on the ACI/CRSI Adhesive Installer program from the U.S. which is a requirement for installers of chemical anchors for use in sustained load applications, including orientations from horizontal to vertical ([27], [28]).

Installation by a certified installer provides the engineer with the peace of mind that the quality of installation allows the fastener to achieve its performance potential. The AEFAC Installer Certification Program ensures the installer possesses the following skills: i) ability to read, understand and execute anchor installation in accordance with a manufacturer's installation instructions, ii) understand risks of non-conformance with manufacturer's installation instructions, and iii) demonstrate practical competence for anchor installation including blind overhead installation of chemical anchors. A more comprehensive overview of the AEFAC Installer Certification Program and its background are included in [33]. The implementation of this training program together with appropriate prequalification and the design guidelines outlined in this paper, form a quality assurance system for the anchor industry.

#### 4. CONCLUSIONS

This paper seeks to raise awareness of problems that are commonly encountered in the anchor industry that have resulted in failures. The six case studies presented have highlighted the safety-critical nature of these fasteners whereby their failure has resulted in death, severe injury or substantial damage to property and disruption to the function of the structure. Factors contributing to failure of fasteners that are commonly encountered include a limited or no product prequalification, product substitution without following proper change management procedures, poor quality installation practice, insufficient and inadequate specification of products and a lack of inspection and maintenance programs to detect defects when they arise.

AEFAC is the peak body for the Australian anchor industry and has introduced two major initiatives to lift safety standards. The first is the proposed AEFAC Standard for the design of safety-critical cast-in and post-installed fasteners to concrete. The second initiative is the AEFAC Installer Certification Program to directly target installers of fasteners to ensure that the product performance is consistent with the specifier's expectations. Collectively, these initiatives will lift safety standards and reduce the risk of further failures from occurring in the Australian anchor industry.

#### 5. ACKNOWLEDGEMENTS

The authors wish to acknowledge the technical input from the following additional members of the AEFAC Technical Committee: Brett King (Allthread Industries), Gilbert Balbuena (Simpson Strong-Tie Australia), Hany Genidy (Ancon Building Products), Joe Rametta (Hilti – Aust.), Kamiran Abdouka (Würth), Neil Hollingshead (ITW Construction Systems), Ramil Crisolo (Hobson Engineering Co.), Tarun Joshi (Powers Fasteners Australasia). The authors would also like to acknowledge the ongoing financial support of the AEFAC Founding Members: Ancon Building Products, Hilti (Aust.), Hobson Engineering Co., ITW Construction Systems, Powers Fasteners Australasia and Würth, and Supporting Members: Allthread Industries and Simpson Strong-Tie Australia.

#### 6. REFERENCES

1. Eligehausen, R., Mallée, R. and Silva, J. F., Anchorage in Concrete Construction, Ernst & Sohn, 2006, Berlin, Germany
2. Salmon, M., Fixing Failures – Case Study 2: Collapse of a pre-cast concrete section – Ireland, Construction Fixings Association, [www.fixingscfa.co.uk](http://www.fixingscfa.co.uk), 2002
3. National Transportation Safety Board, "Ceiling Collapse in the Interstate 90 Connector Tunnel", Boston, Massachusetts, July 10, 2006, Accident Report NTSB/HAR-07/02, 2007
4. Salmon, M., Fixing Failures – Case Study 3: School ceiling collapse – West Midlands, Construction Fixings Association, [www.fixingscfa.co.uk](http://www.fixingscfa.co.uk), 2007
5. AS 3850, "Tilt-up concrete construction", Committee BD-066, Standards Australia, 2003
6. WorkSafe Victoria, Safety Alert, "Bracing insert fails on concrete panel", October 2012
7. WorkSafe Victoria, Safety Alert "Bracing insert fails on concrete panel", October 2012
8. Construction Industry Program Incident Report: Precast Panels Collapse & Crush Cars, WorkSafe Victoria, Ref. No. 05:004, 17 August, 2005
9. European Organisation for Technical Approvals, "ETAG 001, Guideline for European Technical Approval of Metal Anchors for Use in Concrete, Part one: Anchors in General", [www.eota.eu](http://www.eota.eu), 2013
10. WJE Associates Inc., "17<sup>th</sup> Street Bridge Canopy Failure Investigation", Report No. 2011.3732.0, 2011, Atlanta, Georgia, United States
11. Australian Engineered Fasteners and Anchors Council, "Sample specification: bonded anchors", [www.aefac.org.au](http://www.aefac.org.au)
12. WorkCover Queensland, "Awning collapse", Issued 13 November 2008, last updated 2 July, 2014, <https://www.worksafe.qld.gov.au/news/safety-alerts/whsg/2014/awning-collapse>
13. The Courier Mail, "One dead, five hurt in store awning collapse at Burleigh Heads on Gold Coast", December 24, 2012, <http://www.couriermail.com.au/news/queensland/one-dead-three-hurt-in-awning-collapse-at-burleigh-heads-on-gold-coast/story-e6freoof-1226542597203>

14. Confidential Reporting on Structural Safety (CROSS), Report ID 100, [www.structural-safety.org](http://www.structural-safety.org)
15. Page, Cl. L. and Anchor, R. D., "Stress corrosion cracking of stainless steels in swimming pools", *The Structural Engineer*, Vol. 66, No. 24, 20 December, 1988, p. 416
16. Baddoo, N. and Cutler, P., "Stainless steel in indoor swimming pool buildings", Technical note, *The Structural Engineer*, Vol 82, Issue 9, 4<sup>th</sup> May, 2004
17. Heselmans, J. and Vermeij, P., "Fatal accident in Dutch swimming pool caused by environmental cracked bolts", NACE International Corrosion 2013 Conference & Expo, Paper No. 2331, 2013
18. Ministry of Land, Infrastructure, Transport and Tourism, Japan, "Outline of the Report on the Tunnel Ceiling Panel Collapse by the Investigation and Examination Committee", Press Release, [http://www.mlit.go.jp/road/road\\_e/02topics/release/release\\_201307\\_1.html](http://www.mlit.go.jp/road/road_e/02topics/release/release_201307_1.html)
19. Ministry of Land, Infrastructure, Transport and Tourism (MLIT) of Japan, "Sasago Tunnel Ceiling Collapse on the Chuo Expressway (Sequence of Events and Countermeasures)", [www.mlit.go.jp](http://www.mlit.go.jp)
20. Japan Society of Civil Engineers, "Japanese Infrastructure Sustainability", <http://www.jsce-int.org/pub/iacnews/7>
21. World Road Association, "Accident at Sasago Tunnel on the Chuo Expressway", [www.poiarc.org](http://www.poiarc.org)
22. National Transportation Safety Board, "Ceiling Collapse in the Interstate 90 Connector Tunnel, Boston, Massachusetts, July 10, 2006", Accident Report NTSB/HAR-07/02, 2007
23. Rail Accident Investigation Branch, Department for Transport, "Partial failure of a structure inside Balcombe Tunnel, West Sussex, 23 September 2011", Report 13/2013, August, 2013
24. European Committee for Standardization, prEN 1992-4 "Eurocode 2: Design of concrete structures – Part 4: Design of fastenings for use in concrete", September, 2013
25. British Standards Institution, BS 3859-2012, "Code of practice for the selection and installation of post-installed anchors in concrete and masonry", 2012
26. Health and Safety Authority, "Code of Practice for the Design and Installation of Anchors", Ireland, 2010
27. American Concrete Institute, "ACI-CRSI Certification Program for Adhesive Anchor Installer", Publication CP-80 (12), [www.concrete.org](http://www.concrete.org)
28. American Concrete Institute, ACI 318-11 "Building Code Requirements for Structural Concrete and Commentary", Report by ACI Committee, 2011
29. Standards Australia, AS 3600-2009, "Concrete Structures"
30. Australian Engineered Fasteners and Anchors Council, "Prequalification of post-installed and cast-in anchors", Technical Note, [www.aefac.org.au](http://www.aefac.org.au)
31. Fuchs, W., R. Eligehausen, and J. E. Breen, Concrete Capacity Design (CCD) Approach for Fastening to Concrete, *ACI Structural Journal*, 92(1), 1995, pp. 73-93
32. Heath, D. J. and Gad, E. F., "Design guidelines for cast-in and post-installed anchors in Australia", Proceedings of the Australasian Structural Engineering Conference 2014, 9-11 July 2014, Auckland, New Zealand
33. Lee, J., Heath, D. and Gad, E., "AEFAC Installer Certification Program", Proceedings of Concrete 2015, 30 August – 2 September, 2015, Melbourne, Australia

# AEFAC Anchor Installer Certification Program

Jessey Lee<sup>1</sup>, David Heath<sup>2</sup> and Emad Gad<sup>3</sup>

<sup>1</sup>Training and Development Manager, AEFAC

<sup>2</sup>National Technical Manager, AEFAC

<sup>3</sup>Chair of Department of Civil and Construction Engineering, Swinburne University of Technology

**Abstract:** Performance of post-installed anchors in concrete and masonry is highly dependent on the way the anchors are installed. Failure of anchors often occurs due to incorrect installations. In recent years, there have been increasing awareness regarding poor installation practices leading to unreliable bonded anchors performance. As part of the industry's effort to enhance the standard of installation of post-installed anchors in Australia in line with international practice, the AEFAC Anchor Installer Certification Program is initiated to train and equip installers with necessary knowledge and skills to perform installation at the highest level. The AEFAC Anchor Installer Certification program is designed to verify that certified installers possess the necessary skills to properly install bonded and mechanical anchors as per manufacturer's recommendations. This paper outlines the steps for proper installation and commonly made mistakes by installers that will be highlighted in the training program. With the AEFAC Anchor Installer Certification Program in place to promote best practice for installation, the quality of installation of post-installed anchors will be lifted and this will help to safeguard human life against catastrophic anchor failures that had happened around the world in the past.

**Keywords:** post-installed anchors, safety-critical, installation, training, certification.

## 1. Introduction

Post-installed anchors are installed after concrete has been poured allowing greater flexibility for fixture alignment as compared to cast-in anchors. Two main types of post-installed anchors are mechanical anchors and bonded anchors as shown in Figure 1. Some common examples of safety-critical applications of post-installed anchors in the building industry are connection of structural steel floor members to a precast concrete core and connection of steel columns to concrete footings. Failure of safety-critical anchors may cause injury or death to human beings and lead to considerable economic loss. The structural performance of post-installed anchors are sensitive their installation. Installations of post-installed anchors are largely carried out on ad-hoc basis by tradesman without proper training resulting in many incorrect installations as observed by engineers and anchor suppliers and manufacturers in the industry. Anchor products that have been installed incorrectly will most likely perform in an unpredictable manner that differs from the design engineer's intent.

On the other hand, the skill set for welding industry is well established in Australia. Welding is the process of connecting steel members together and has been recognised as an area needing tradesmen to undergo specific training to become qualified welders. The AS1796 Certification of Welders (1) provides a curriculum and test regime for certification of personnel performing structural welding of connections and steel members and also for supervision of welders (2). Welding certification or qualification is an important part of the overall compliance to occupational health and safety obligations based on Statutory Law. It can be seen that although welds and post-installed anchors serve to connect structural members together, in the case of welding it is steel to steel connection whilst in the case of post-installed anchors, it is typically steel to concrete connection, the qualification or certification requirement for welders is not present for anchor installers; this resulted in varying competencies among installers which may cause gross errors during installation that in turn could have catastrophic consequences.

The best anchor product is only as good as its installation. Anchor failures have occurred both internationally and locally and sometimes with fatal consequences. In 2006, the Big Dig Tunnel ceiling collapsed in Boston (refer Figure 2) whereby 26 tonnes of concrete ceiling panel and debris fell, killing a motorist and causing a section of the tunnel to be closed for almost a year. A local failure documented by WorkSafe Victoria (4) in 2002 is shown in Figure 3 whereby a precast panel weighting 35 tonnes collapsed onto a crane during erection due to improper use of a coil anchor as a bracing insert. Following the collapse of the Big Dig Tunnel ceiling, the installation quality of bonded anchors was called into question. The American Concrete Institute (ACI) partnered with the Concrete Reinforcing Steel Institute (CRSI) developed the Adhesive Anchor Installers certification program (ACI,5). It is a regulatory



requirement in the USA for overhead anchors with sustained tension load to be installed by a certified installer and the inspection of anchor installation by specially approved inspectors.



a) Mechanical anchors

b) Bonded anchors

Figure 1. Types of post-installed anchors.



(a)

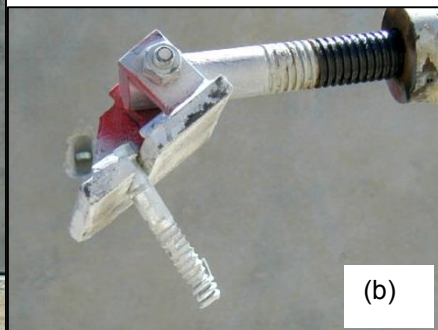


(b)

Figure 2. Concrete ceiling tiles collapse in the Big Dig Tunnel, 2006: (a) photo of aftermath; (b) photo of roof hangers pulled away from tunnel roof (Brady,3).



(a)



(b)

Figure 3. 35 tonnes panel that collapsed onto a crane during erection (WorkSafe Victoria, 4): (a) photo of collapsed panel; b) photo of a failed coil anchor used as a bracing insert.

The Australian Engineered Fasteners and Anchors Council (AEFAC, [www.aefac.org.au](http://www.aefac.org.au)) is an industry initiative that was formed in 2012 to introduce governance to the industry with support and guidance to be provided for engineers (specifiers), manufacturers, installers and field engineers. As part of the industry initiative to enhance the installation of structural anchors in the Australian construction industry, the AEFAC Anchor Installer Certification Program was initiated. This certification program is based on the

ACI-CRSI program but it has been extended to include mechanical anchors and adapted for Australian practice.

## 2. Installation Requirements

Bonded anchors are widely used in the construction industry due to their smaller edge and spacing requirements compared to mechanical anchors. However, they are prone to poor installation practices that have contributed to a number of failures in the past. An installer needs to properly understand the limitations and sensitivity of the product. The product should always be installed in accordance with the MII.

### 2.1 Performance considerations

In general, bonded anchors are sensitive to dust, roughness of drilled hole, water and temperature of substrate while mechanical anchors are sensitive to drilled hole tolerances. If water is present in the drilled hole, the installer needs to check whether the specified product is compatible with water. Most adhesive does not work well with the presence of water. Temperature of the substrate will affect the curing time of the adhesive, with a higher temperature leading to a shorter curing time. There is an allowable temperature range to install bonded anchors that installers need to adhere to. Figure 5 shows an example of capacity of bonded anchors decreasing with elevated temperature. Other factors that may affect the suitability of the product would be the type of substrate (refer Figure 4), whether it is concrete, masonry or lightweight concrete. Certain products may not be suitable for use in lightweight concrete. It is very important for installers to be aware of the different factors affecting performance of post-installed anchors during installation.

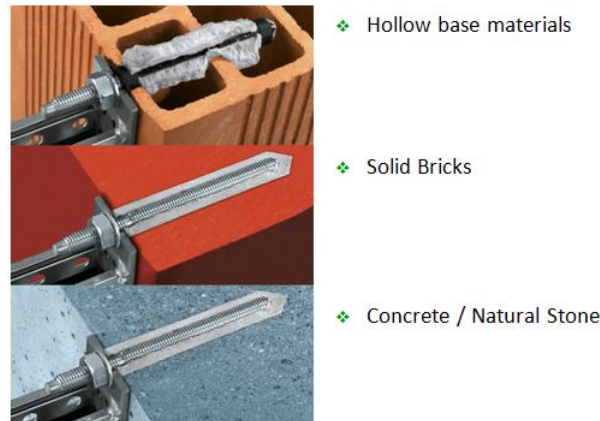


Figure 4: Different types of substrate for bonded anchor installations.

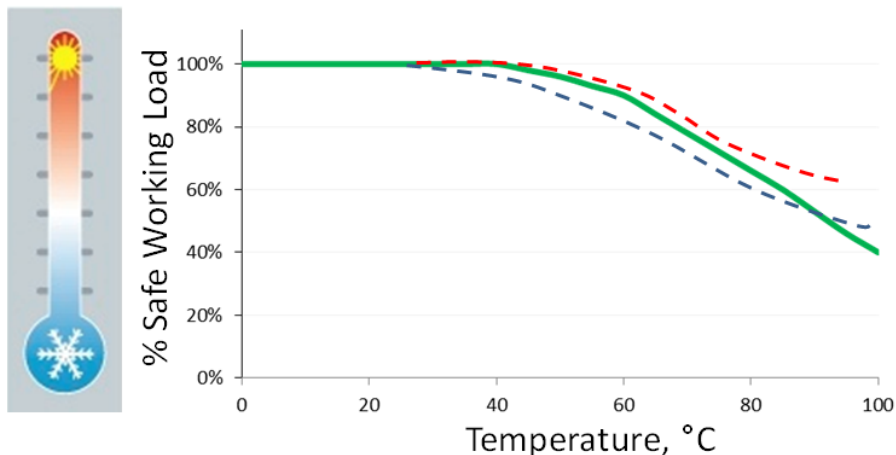


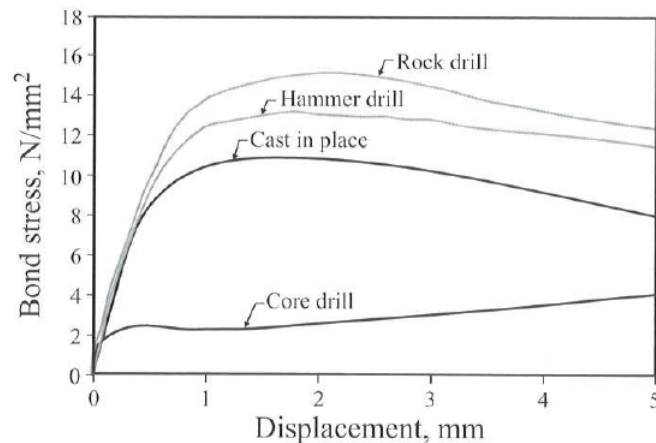
Figure 5: Graph showing example performance of anchors relative to temperature. At elevated temperature, performance decreases, necessitating a reduction in safe working load.

## 2.2 Drilling the hole

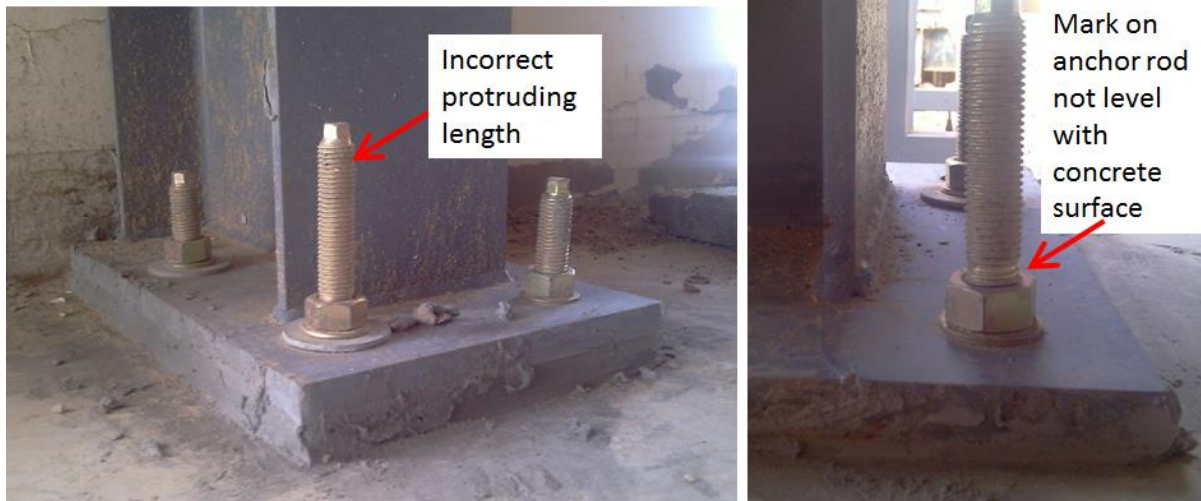
Good bonding between concrete surface and adhesive is correlated to roughness of drilled hole. The rotary hammer drill is the most common drilling method. Other drilling methods are rock drilling and core drilling. Using a rock drill will produce a rougher hole while a core diamond drill will produce a smoother hole which may reduce bond strength. This is not allowed unless explicitly permitted in the MII or if the design engineer has specified this method. Selecting the correct drill type and bit is important for drilling the correct sized hole and to achieve the appropriate hole roughness. Figure 6 illustrates the different bond strength that may be obtained from different drilling method.

Some anchor systems particularly mechanical anchors are sensitive to drilled hole tolerance. Using a worn drill bit may result in an elliptical shaped hole or an undersized hole whilst not steadying the drill while drilling may result in a hole that is not straight. For bonded anchors, the anchor rod may not be able to be inserted into the hole due to limited tolerances between the anchor and the hole size. The bit diameter can be measured with a caliper gauge to make sure that it is within tolerances. It is a good practice to insert an anchor rod into the hole to make sure the anchor can fit before injecting adhesive into the hole. Note that for bonded anchors the annular gap is typically several millimetres, meaning that if the anchor rod is a tight fit, it is highly likely that an incorrect drill diameter has been used or the hole has not been drilled straight. Bonded anchor holes are drilled oversize (relative to the steel insert) to ensure sufficient adhesive is between the steel insert and hole wall. Mechanical anchors on the other hand require strict adherence to specified drilled hole diameter to achieve their intended capacity; an oversized hole will result in the anchor not engaging the hole wall sufficiently thus significantly reducing the load carrying capacity of the anchor while in an undersized hole, the anchor may generate high expansion stress in the concrete such that concrete spalling may occur.

Performance of anchor system relies on specified embedment into the concrete as specified by the design engineer. Hitting reinforcement while drilling is a very common occurrence normally denoted by a change in the colour of dust, metal filings are observed or there is an increase in difficulty in drilling. The embedment depth of an anchor should never be reduced, i.e. anchor bars should never be cut short. Reducing embedment depth of the anchor dramatically reduces its strength; unfortunately leaving the anchor bar short of the designed embedment depth is a common practice in the industry. One such example is shown in Figure 7 whereby the anchor has an incorrect protruding length compared to other adjacent anchors and the mark on the anchor rod which should be level with the concrete surface to indicate that the anchor rod has achieved its designed embedment depth can be seen in the photo. The appropriate course of action when obstruction is met while drilling would be to cease drilling immediately and the design engineer should be consulted to determine the appropriate action. Options are drilling through the reinforcement if it is allowed by the design engineer or otherwise the hole needs to be relocated.



**Figure 6. Bond-stress displacement curves for 20mm diameter bonded anchors installed in holes with different drilling methods. All anchors are drilled in 20MPa concrete with 200mm embedment except for anchors in core drilled holes with 300mm embedment in 50MPa concrete (Wollmershauser,6).**



**Figure 7. Incorrect protruding length, anchor has not achieved required embedment depth.**

### **2.3 Hole cleaning**

Hole cleaning is a critical step in the installation procedure for bonded anchors and special care must be taken to ensure that cleaning instructions as per the MII have been followed. Cleaning accessories for post-installed anchors are shown in Figure 8. Improper hole cleaning is frequently a major source of poor bonded anchor performance. Figure 9 shows cut sections of installed bonded anchors. The photo on the right shows a layer of drill dust sticking to the face of the concrete indicating that the hole was not cleaned properly. This prevented good bonding between the adhesive and concrete to form, thus greatly reducing the performance of the anchor system. Figure 10 shows data from a sensitivity test carried out on a specific injection system product in dry concrete. The hole without cleaning resulted in a 60% reduction in bond strength.

The usual method of cleaning is blow-brush-blow i.e. blowing out the hole with sufficient clean compressed air followed by brushing the hole with a clean full brush then blowing the hole again. The MII will specify the sequence and number of brushing and blowing required for the product to best remove debris and dust particles from the drilled hole. Commonly encountered problems are installers using the wrong brush size, worn brushes, blowing into the hole through a straw or modified leaf blower and not following the number of times required for brushing and blowing when cleaning a hole which is detrimental to the performance of the bonded anchor system. Installers need to be mindful that water could adversely affect bonding of the adhesive. During the cleaning process if the hole is damp or filled with water, installers need to check the MII to determine if the product may be installed in wet conditions, if not water should be thoroughly removed and the hole should be dried out before installation can proceed.

From past experiences, cleaning deep holes and/or core drilled holes filled with slurry have posed great challenges to installers. Common problems are residual fines remaining on hole wall or a dust plug remaining in the bottom of the hole due to an incorrect cleaning method or unsuitable cleaning tools especially for deep holes.

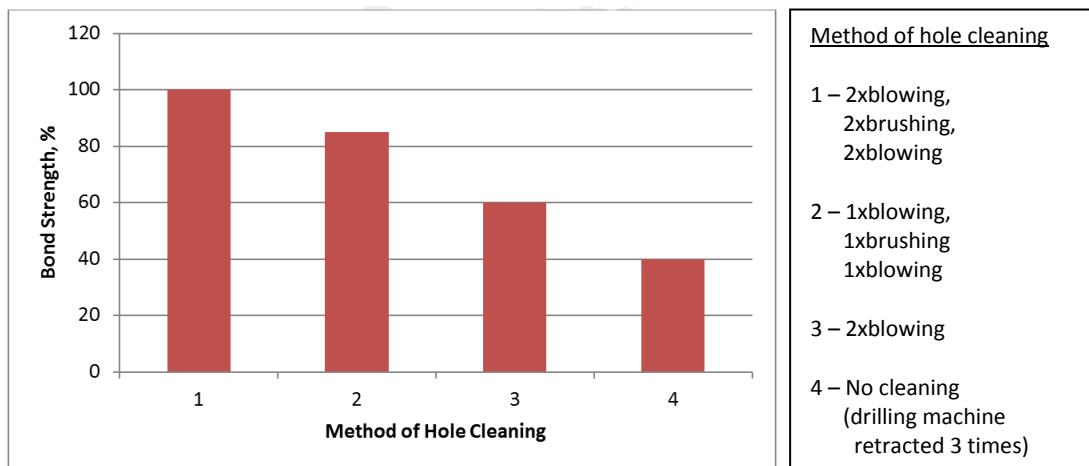


**Figure 8. Cleaning tools.**





**Figure 9. Cut sections of installed bonded anchors. The photo on the right shows a layer of drill dust between the adhesive and concrete (Courtesy of IWB, University of Stuttgart).**



**Figure 10. Graph showing sensitivity of a specific cartridge injection system product in dry concrete to cleaning method. (Data derived from (Eligehausen,7)).**

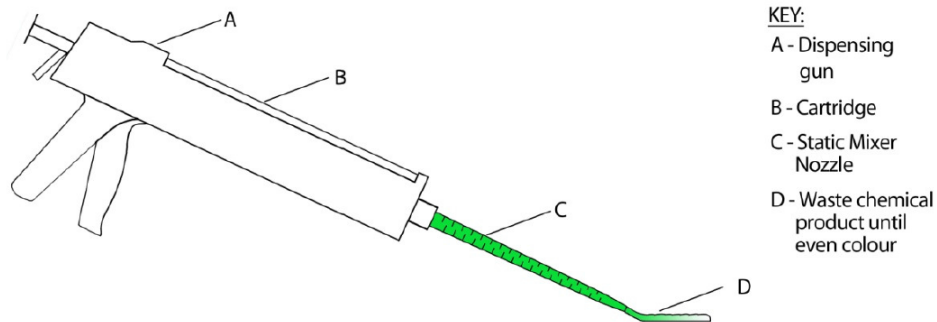
## **2.4 Injection of adhesive and inserting anchor**

For each bonded anchor product, the manufacturer's product specific complete installation system must be used. Components from one system may not be interchanged with those from another system, even though they may look and operate in a similar manner. Each system has been designed to deliver the correct proportion of components to ensure the correct mix ratio. Incorrect use of equipment or modification in any form may result in incorrect mix ratios that will reduce bonded anchor performance.

Installers need to first check the expiration date on the cartridge before placing it into an injection tool or dispenser. The cartridge needs to fit properly in the dispenser. After the cartridge has been inserted into the dispensing gun, the static mixer nozzle is attached. For injection into deep holes, an extension tube may be affixed to the mixing nozzle. Once the system has been correctly assembled, the first few trigger pulls of mixed adhesive from the dispenser should be discarded to ensure the correct mix ratio has been achieved as shown in Figure 11. If this initial material is not discarded, the quality of bonding achieved can be very poor. This is a very important step and is often overlooked by installers, especially when changing cartridge for installation of subsequent holes.

The mixing nozzle must reach the bottom of the hole, adhesive injected at a constant rate and the mixing nozzle is slowly withdrawn to prevent air voids from forming. Figure 12 shows air voids in injection which are detrimental to bonded anchor performance. The nozzle should be carefully removed when the hole is about two-thirds full followed by insertion of the anchor rod with a twisting motion. It is good practice to insert the anchor rod into the hole immediately after the hole is filled with adhesive to ensure that the

working time for the adhesive is observed. A clean, straight anchor rod must be used for installation. Contaminated anchors will hinder proper bonding with adhesive. Other common problems include anchors over tightened or overhead anchors not supported properly which may prevent proper bonding of adhesive to the anchor.



**Figure 11. Typical dispensing system.**



**Figure 12. Voids in injection**

## **2.5 Curing**

After the anchor rod is inserted, anchors must be protected from disturbance during curing and should not be loaded, tightened or tested until curing time has elapsed. Curing times are product specific. Higher temperature will lead to faster curing while lower temperature will slow down the curing process. When the temperature gets too cold, the reaction rate between the components of the adhesive may stop and this may result in the adhesive not adequately cured to achieve its designed strength and form proper bonding. This may cause premature failure to the anchor. The MII lists the minimum permissible ambient temperature for installation which must be adhered by the installers. Bonded anchors may appear to have cured at times shorter than the manufacturer's specification. However, it is not acceptable to load the anchor before the stated time.

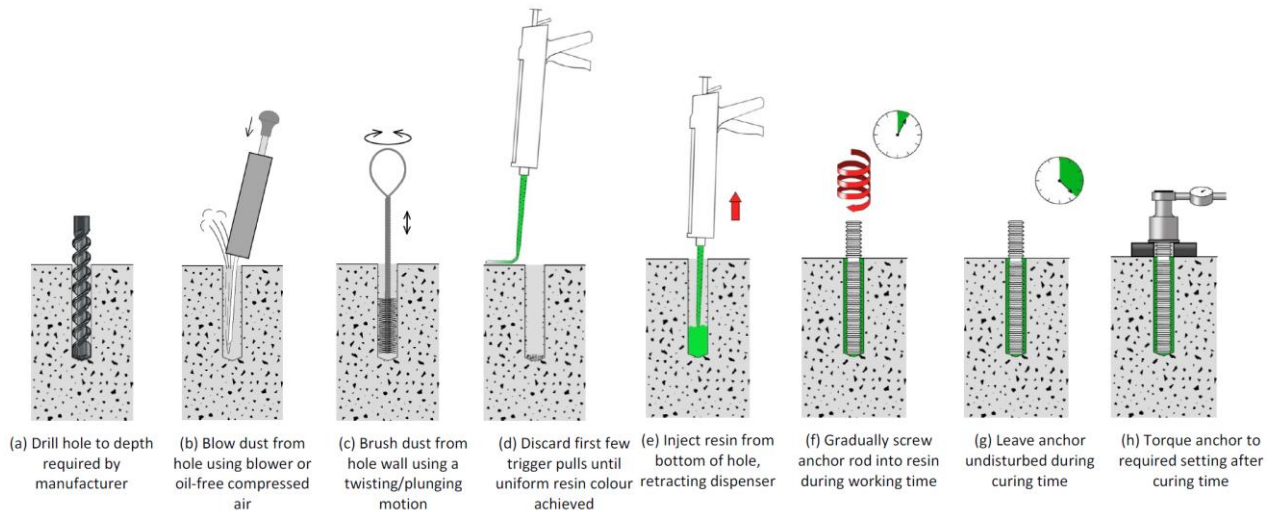
## **3. AEFAC Anchor Installer Certification Program**

The AEFAC Anchor Installer Certification Program has been developed to verify that certified installers possess the necessary skills to properly install bonded and mechanical anchors as per manufacturer's recommendations. The training and certification are intended for safety-critical applications. Illustrations of proper installation practices for a standard bonded anchor are shown in Figure 13.

An AEFAC Certified Installer will be able to demonstrate the following with the assistance of the Manufacturer's Installation Instructions (MII):

- Ability to understand and follow instructions
- Understand how to assess site conditions that impact installation (moisture in holes, drilling method, obstructions such as reinforcement, temperature of product and substrate, etc.)
- Demonstrate proper cleaning technique and hole preparation
- Demonstrate proper selection and assembly of equipment for the installation of injection-type and capsule-type chemical anchors

- Assess product storage conditions and shelf life, including when the product should be rejected.
- Demonstrate proper mixing technique
- Successful application of product in holes are various orientations (including vertical overhead) to the required depth using proper technique and equipment to minimise air voids
- Proper technique to install the anchor element in the chemical product to minimise air voids
- Recognise time limits for mixing, installation, positioning of anchor element and curing time
- Demonstrate the protection required of the anchor during curing
- Successfully tighten fixture to the anchor at the appropriate time and to apply the correct installation torque.



**Figure 13. Illustrations of proper hole preparation and installation practice for a standard bonded anchor.**

### 3.1 Assessment

AEFAC will grant certification only to those applicants who pass both the written and practical examination (refer Figure 14). The written examination is a closed book exam comprising of 65 multiple choice or true/false questions for completion within 60 minutes. All assessment material is covered by the Installer Training Manual (AEFAC,8).

The practical examination is a two part process testing the individual's competence with the installation of bonded anchor systems including assembly of tools and equipment, proper drilling and cleaning technique, proper injection technique and correct setting of the anchor component. Part one of the exam tests the ability of installers to install a bonded anchor in a vertical down orientation according to the MII and Material Safety Data Sheet (MSDS) (refer Figure 15) while part two of the exam test ability of installers to inject adhesive overhead using a piston plug (refer Figure 16). A maximum of two trials are permitted for each part of the practical examination. The examiner will advise the installer of a pass/fail outcome and advise on the error(s) made.

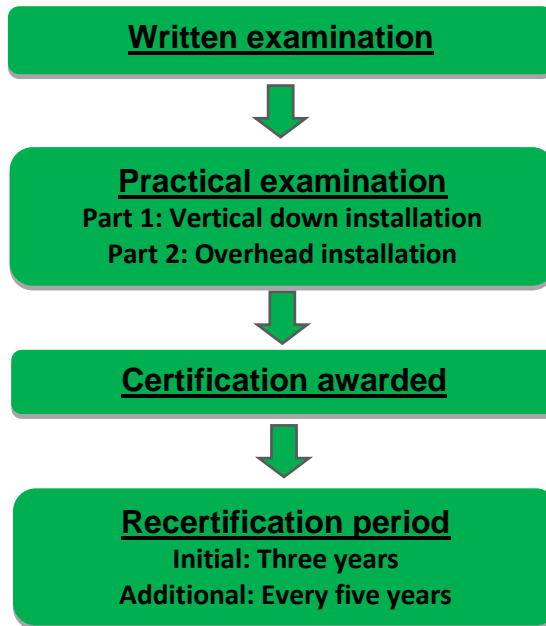


Figure 14. Process of Certification and Recertification



Figure 15. Vertical down bonded anchor installation



Figure 16. Overhead injection with a piston plug, tube is sliced after curing time is complete to check for voids.

### **3.2 Recertification**

Recertification requires the certified installer to re-sit the written and practical examinations periodically. The first recertification is required three years after initial certification, and every five years thereafter. Failure to comply with proper installation practices after being awarded certification would result in certification status being revoked and potential legal implications.

## **4. Recommendations**

As part of AEFAC initiative to lift quality and safety of anchors, it is recommended that safety-critical anchors shall be installed by AEFAC certified installer in strict accordance to the MII. Anchor products shall have the relevant prequalification such as an European Technical Assessment/Approval (ETA) or equivalent. An ETA is a certification that a product has been rigorously tested and independently confirmed to satisfy the requirements of European Technical Assessment Guideline 001 and demonstrated to be fit for its intended purpose (9). Current standard notes on engineering contract drawings allow the use of equivalent product in lieu of the specified anchor product by the design engineer. It is recommended that the substitution of equivalent products must be approved by the design engineer and have the appropriate prequalification. The implementation of this training program together with appropriate prequalification and the design of anchors, form a quality assurance system for the anchor industry.

## **5. Acknowledgement**

The authors would like to acknowledge the technical input and ongoing financial support from the AEFAC Founding Members: Ancon Building Products, Hilti (Aust.), Hobson Engineering Co., ITW Construction Systems, Powers Fasteners Australasia and Würth (Aust.), and Supporting Members: Allthread Industries and Simpson Strong-Tie Australia.

## **6. References**

1. Standards Australia, "AS 1796-2001 Certification of welder and welding supervisors", 2001, Sydney.
2. Standards Australia, "AS 2214-2004 Certification of welding supervisors - Structural steel welding", 2004, Sydney.
3. Brady, S., "Interstate 90 Connector Tunnel ceiling collapse", The Structural Engineer, 2013.
4. Construction Industry Program Incident Report: Precast Panels Collapses onto a Crane, WorkSafe Victoria, Ref. No. 02:015, 29 November 2002
5. American Concrete Institute (ACI), "Adhesive Anchor Installer Workbook CP-80(12)", ACI Committee 680, 2012, Michigan.
6. Wollmershauser, R., Mattis, L., "Adhesive Anchor Installation and Inspection", Concrete International, 2008, pp 36-40.
7. Eligehausen, R., Mallée, R. and Silva, J. F., 2006, "Anchorage in Concrete Construction", Ernst & Sohn, Berlin.
8. Australian Engineered Fasteners and Anchors Council (AEFAC), "Anchor Installer Training Manual", 2015.
9. ETAG 001, "Guideline for European Technical Approval of Metal Anchors for Use in Concrete, Part one: Anchors in General" European Organisation for Technical Approvals, [www.eota.eu](http://www.eota.eu)



# Guide to Seismic Design & Detailing of Reinforced Concrete Buildings in Australia

Scott Munter<sup>1</sup>, John Woodside<sup>2</sup> and Peter McBean<sup>3</sup>

<sup>1</sup> Executive Director, Steel Reinforcement Institute of Australia

<sup>2</sup> Principal, J Woodside Consulting Pty Ltd

<sup>3</sup> Joint Managing Director, Wallbridge and Gilbert, Adelaide

**Abstract:** The original Guide on the Seismic Detailing for Reinforced Concrete Buildings in Australia was published in 1995 by the SRIA following the publication of the second Australian earthquake standard AS 1170.4. There have been two revisions of AS 3600 Concrete Structures and a new earthquake standard AS 1170.4 since the original document. There have been significant advances in the analysis software for buildings, and the understanding of earthquake design has improved through advances in research, and actual seismic performance. AS 3600, provides Australian designers with the design rules for earthquake design to meet the typically lower seismicity of Australia. Most Australian commercial buildings are cast in situ reinforced concrete, designed and detailed to comply with AS 3600, for regions of lower seismicity, deeming the structure to have adequate ductility as a life safety measure.

The fundamental principle of concrete design is that the design and the detailing are inseparable. Appropriate detailing is required to ensure that the structure will respond under the seismic loading as assumed in the design. Technology and reduced design times can shift the focus away from the vital reinforcement detailing phase of the project.

The Guide's overall aim is to enable cost effective, simple design solutions by giving the designer the practical detailing information to efficiently determine requirements for the overall structural performance under seismic loadings. Reinforcement scheduler input in this specialised field provides current practice for graduate, practicing engineers with little seismic experience and senior engineers requiring refreshment. This paper describes the revisions to the Guide.

**Keywords:** Reinforcement, seismic, detailing, concrete.

## 1. Introduction

Unfortunately in Australia there is a generation of engineers, contractors and clients who do not believe that earthquakes occur in Australia, despite the long history of earthquakes in Australia and the 1989 Newcastle Earthquake (1,2). Because they have never experienced an earthquake, and with the pressures of modern design and construction, it does not allow them time to think about the issues as well as they should. It is anticipated and hoped that this Guide will provide the necessary design information to improve the design and detailing of reinforced concrete buildings for seismic loads.

Fortunately significant earthquakes in Australia are rare and probably will not occur during the average lifetime of a building. A major earthquake will generate the most severe structural demand ever experienced by a building. Given the rare and extreme nature of earthquakes, for economic reasons, designers are largely concerned about preserving life and preventing structural collapse. For most concrete structures, this will require the structural system to resist the imposed deformation in-elastically over a number of load cycles.

The first Guide on the Seismic Detailing for Reinforced Concrete Buildings in Australia was published in 1995 in response to the second Australian earthquake code AS 1170.4 (3). The updated and rewritten Guide is intended to assist graduate engineers, practicing engineers and other designers with limited seismic experience and senior engineers seeking to refresh themselves of the current developments and practical aspects of reinforcement design and detailing for seismic actions in Australia.

Since 1995, there have also been significant advances in analysis software; our understanding of earthquake design has improved through advances in research and combined with actual performance of buildings under seismic loads. AS 3600 (4) and AS 1170.4 (5), provides Australian designers with the minimum design rules for earthquake design for buildings to meet the typically lower seismicity of Australia. Most commercial buildings in Australia are in situ reinforced concrete, designed and detailed in accordance with AS 3600. Complying with the Standard for regions of lower seismicity deems the

structure to have adequate ductility [as a life safety measure](#). However, this concept of life safety is often poorly understood or not properly articulated by designers.

For lower values of the ductility factor  $\mu \leq 2$ , detailing of the concrete is only required in accordance with the body of the Standard and for higher values of ductility factor  $\mu$ , detailing is required in accordance with Appendix C of AS 3600. Levels of ductility  $\mu > 3$  are outside the scope of the Standard, and design and detailing to NZS 1170.5 (6), and NZS 3101 is suggested.

The fundamental principle of concrete design for the successful performance of a concrete structure under seismic actions is that [design and the detailing are inseparable](#). Appropriate detailing is crucial to ensure that the structure will respond under seismic loading in the manner for which it has been designed. Time and time again, earthquakes have shown that correct detailing of reinforced concrete structures can significantly improve the capacity of the building to resist seismic actions, even for a poorly designed structure.

This Guide is not a complete document covering all design situations or requirements, but an assortment of basic seismic principles, design advice, and fundamentals to assist and help designers. It also suggests further study of the principles and practice of seismic design and detailing. This information is presented by focusing on the key, functional and practical aspects of seismic design and detailing of reinforcement with references to specialist information. Technology and reduced design and construction times can shift the focus away from the vital reinforcement detailing phase of the project. The overall aim is to enable cost effective, simple design solutions by giving the designer the practical detailing information in order to efficiently determine the requirements for the overall structural performance under seismic loadings.

## **2. Risk mitigation and low damage design for buildings**

Unfortunately, clients and societies expectations compared with the reality of seismic performance may not match the minimum requirements of the Standards for life safety, as shown in Christchurch. For instance, does a building in the event of an earthquake require protection of irreplaceable contents such as a museum or is there a need for the continuing use of the building such as a hospital after the event or in the extreme condition that it contains dangerous materials such as a biological laboratory dealing with dangerous viruses. These are issues that the designer must consider in the early phase of the design.

The highest level of protection for a building available is base isolation, but it has not been used in Australia. The next level of protection is to minimise the damage by using a more robust and regular structure with a higher level of ductility. This will protect the primary structure even in the most severe earthquake with many alternative load paths and backup systems designed and detailed for greater forces than the minimum required by the Standard. The great advantage of this approach is that the structure should be operational and repairable; insurance may be less, and the mitigation of the risk of structural damage and business continuity is achieved but at an increased cost to the original construction of reinforced concrete building. It is thought that the increased order of the total cost would be as little as 1% to 3% of the total construction cost of a concrete building over the lowest level of protection required by the Standard. This assumption is based on a structural cost being 25% of the total cost of the building, and the additional design and detailing would result in an increased structural cost in the order of 5-10% including professional fees.

## **3. Analysis and design**

The aim of the analysis and design is to produce a safe, serviceable, aesthetic, economical and sustainable structure. Simple design does not mean elementary design but rather well conceived and quality design and adequate detailing including the earthquake design. Designers should always strive for simplicity, clarity and excellence in their design and detailing and maintain a strong focus on the detailing of reinforcement for seismic loads, as part of the design process.

Traditionally earthquake design has been based on a [quasi-static](#) forces approach where [hypothetical](#) static loads are applied to simulate the dynamic forces of an earthquake. Unfortunately, this may bear no resemblance to the actual earthquake forces when they occur, as earthquakes do not know about



Standards, methods of design or indeed the building being designed. For this reason, the earthquake actions will almost certainly not be those specified by the Standards.

There are a number of fundamental problems with the force-based method of analysis. These include choosing the right model, the selection of appropriate member stiffnesses and determining the static forces that are appropriate for the design being considered. Member stiffnesses cannot be resolved until the design is complete, and yet they will change during a seismic event. In addition, the static design forces applied to the structure may not bear any relationship to the actual dynamic forces applied. The distribution of local forces is based on elastic estimates of stiffness. This tends to concentrate the strength in elements of the greatest potential of brittle failure, such as walls.

There have been large advances in the past 20 years in our understanding of how concrete performs under seismic loads, in the technology and design of concrete, changes to reinforcement and enormous advances in computers and software and analysis tools. The computing power and software now available to designers has led to far more elaborate and sophisticated analysis and design of buildings and indeed more refined design.

This technology can lull the designer into a false sense of security, believing they fully understand how the structure will act under dynamic loads of an earthquake, when the actual effects of an earthquake may be far different from the computer model. This is because the structure is sized on non-seismic load considerations; member stiffnesses will change during the earthquake and other factors such as local failures will affect the model. This may result in the model and sophisticated analysis being entirely inappropriate in a major earthquake event.

Analysis is only part of the design process. Good designers know there is far more to design than just analysis and designers must understand the behaviour of each member and how they are expected to resist all of the applied actions and why these members need to be detailed for the seismic actions. In a real structure, the behaviour under load of individual elements can be complex depending on the materials used and many other factors, which will change under earthquake actions. Idealised computer models of the frame or structure are used for the analysis of a structure to simulate how the real structure may behave, but they can be very crude when assessing the structure under seismic loads.

#### **4. Reinforcement and concrete**

For a structural ductility factor  $\mu \leq 2$ , AS 3600 Appendix C, allows the structure to be designed and detailed in accordance with the main body of the Standard and both Class L and N reinforcement can be used. Although, not covered by AS 3600, any chord members, collector reinforcement or drag bars used in diaphragm action should be Class N reinforcement, because of the anchorage requirements and ductility demands for this reinforcement.

For a structural ductility factor,  $2 < \mu \leq 3$ , structures have to be designed and detailed in accordance with the main body of AS 3600 and Appendix C. Although Class L reinforcement is allowable under AS 3600 for walls and slabs, where Class L reinforcement is used for loadbearing walls and suspended floors and slabs when acting as diaphragms, designers need to ensure the reinforcement is capable of meeting the increased ductility and drift demands. For IL4 buildings, Class L reinforcement is not recommended in structural elements except as fitments for beams and columns, shrinkage reinforcement, for reinforcement to steel metal decking or non-structural elements, because of the increased ductility demands.

While structures will have concrete strengths typically in the range of 25 to 40 MPa, high strength concrete up to 100 MPa is allowed under AS 3600. High strength concrete is principally used in columns and walls where the size of such elements needs to be minimised. Designers should be careful using high strength concrete in columns and walls for buildings designed for a structural ductility factor  $\mu > 2$  or with a post disaster function, as high strength concrete is a brittle material requiring additional detailing of the reinforcement to prevent brittle failure.

## 5. Robustness

Structural robustness is discussed briefly in the commentary to AS 1170.0 (7) but is not well defined. There are no specific requirements for design for structural integrity (the prevention of progressive collapse) or robustness in the BCA (8) or AS 3600. The AS 3600 Commentary (9) has some limited information on this requirement. Nevertheless, because of overseas experience and failures, designers must consider the robustness of reinforced concrete building including reinforcement detailing.

In simple terms a structure should be safe and the Eurocode provides the following definition of robustness *“the structure shall be designed and executed in such a way that it will not be damaged by events like fire, explosion, impact, or the consequences of human error, without being damaged to an extent disproportionate to the original cause.”*

Progressive and disproportionate collapse must be avoided at all times. This means that the failure of one member should not set off a chain of events where the structure progressively collapsed as occurred in the failure of the columns of the Newcastle Workers Club in 1989, Melcher and Woodside (10,11) .

Robustness will require that all structures have a resistance to lateral loadings, and if none are specified, then a notional percentage of the vertical loads should be adopted. Redundancy is also an important issue as a failure of any load-bearing member must not lead to the collapse of the entire structure.

The building structural form will significantly affect its robustness and for this reason needs to be considered at the concept stage. An example of this might be a large transfer beam supporting a large part of the building so failure of this element would be catastrophic and should be avoided if possible or the design robust enough to provide a considerable reserve of strength.

Columns and walls should not be heavily loaded and designed so that the design values are below the balance point and well detailed (12). Compatibility of drift must also be considered.

Precast and tilt-up structures are more susceptible to the effect of abnormal actions than some traditional forms of construction because of the presence of joints between the structural elements. However, experience has shown that it is possible to manage these issues by effectively tying together the various elements of the structure and correct detailing. (13, 14)

Buildings should have sufficient robustness to survive without collapse if subjected to the ground motion in excess of that specified by Australian Standards. Well-proportioned and well detailed in-situ reinforced concrete structures are inherently robust. It is important to ensure that the structure is tied together; can resist some notional lateral load, and the failure of a particular element will not lead to progressive collapse. There are several overseas documents on structural robustness and progressive collapse (15, 16).

Reinforcement detailing for robustness also needs to address some basic requirements as follows:

- Minimum reinforcement should be provided in both faces of horizontal members such as beams and floor slabs even if the design does not require it or detailing is not required in the Standard.
- Detailing in accordance with Appendix C of AS 3600 will be required for buildings with a post-disaster function and for buildings where the ductility  $\mu > 2$ .
- Critical members should be reviewed for their role in the structure, detailed as required, and alternative load paths considered.
- Eliminate punching shear failures at columns at flat slabs and similar by providing additional bottom face reinforcement

## 6. Acceptable drift limits

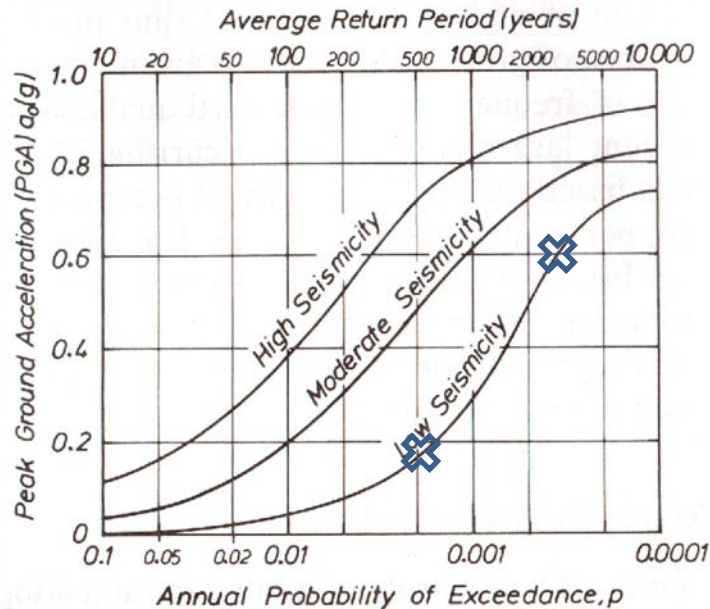
AS 1170 .4 sets out the maximum drift requirements for buildings. However, the maximum inter-story drift due to reduced stiffnesses must not exceed 1.5% of the storey height at each level at the ultimate limit state. These lateral displacements can be large (in the order of 30 to 50 mm). Many structures may not be

able to accommodate such drifts without premature failure of structural elements. Also, calculations associated with drift are often poorly understood, and stiffness assumptions are sometimes wrong.

Even if a part of a structure is not designed specifically to withstand seismic forces, it must be designed for the full drift (deflection) of the whole structure calculated in accordance with Clause 5.4.2, Clause 5.5.4 or Clause 6.7.1 of AS 1770.4. Moment frames systems are much more flexible than shear wall systems and need careful review for drift especially with associated shear walls.

## 7. Ductility demands

One of the issues when designing structures in an area of low seismicity such as Australia is that when a major earthquake occurs which exceeds the design return period (annual probability of exceedance of 1/500 or 1/1000 years), then the increase in peak ground acceleration over the design event can be significant and therefore the increase in the lateral forces can be large. For a rare event with say a return period of 1/2500 years, this can be of an order of 3 or more. This increase is shown in Figure 1 Pauly and Priestley (17). For structures however designed in areas of high seismicity, the increase in peak ground acceleration is not as significant, perhaps 30%.



**Figure 1. From Pauly & Priestley, 1992.**

## 8. Structural systems

Structural systems should be as simple as possible with readily understood gravity and lateral stability load paths. Some structural systems are more satisfactory than others in resisting earthquake-induced forces. One of the early tasks of the structural designer is to select a structural system that results in the best system for seismic performance of the building within the constraints dictated by the architect, the site and other conditions. Wherever practicable, alternative structural configuration should be considered at the concept stage to ensure that an undesirable geometry or structural form is not adopted before the detailed design of the building begins. In particular, structural irregularities both vertically and horizontally must be considered early in the design phase, and sound structural engineering principles applied to avoid or mitigate these effects.

AS 1170.4 specifies that all parts of a structure shall be interconnected, in both the horizontal and vertical directions. Connections between structural elements are typically the weakest chain in the link and should be detailed to fail in a ductile manner to avoid rapid degradation of strengths under earthquake actions.



**Figure 2. Failure of Transfer Beam, Copthorne Hotel, Christchurch**  
**(Photograph courtesy Peter McBean, Wallbridge and Gilbert).**

The connections must be capable of transmitting the calculated horizontal earthquake force in order to provide load paths from all parts of the structure, and the earthquake forces carried to the footings and foundation. In turn, the foundations must be robust enough to accommodate the overload due to large events without catastrophic loss of strength.

In Australia, stair and lift cores are typically constructed with concrete walls because of the fire rating and construction techniques, which have developed over many years. As a result, most buildings in Australia will be either a concrete shear wall system or a combination of concrete shear walls and moment frames or moment frame only. The designer has to choose whether the shear walls are ductile or limited ductile elements. Once the structural system is chosen, the structural ductility factor  $\mu$  and structural performance factor  $S_p$  can be determined in accordance with Table 6.5 (A) of AS 1170.4 or Table C3 of AS 3600. Ductile shear walls are often chosen where earthquake forces are higher than wind as the seismic reduction factor will lead to smaller members particularly foundations and the detailing is not too onerous. The decision as to which design route to take is left to the designer.

Because of the ratio of Structural Ductility Factor,  $\mu$ , to the Structural Performance Factor  $S_p$ , the earthquake design actions will be increased by about 73% if the designer chooses an OMRF over an IMRF. Ordinary Moment Resisting Frames (OMRF) are deemed to require no further detailing consideration from the detailing required in the body of AS 3600.

One problem with moment resisting frames (MRF) is their lack of lateral stiffness and the large displacements (or drift) under earthquake actions often together with incompatibility of the rest of the structure in resisting such drifts. This can result in significant damage to adjoining structural elements and non-structural parts and components. In addition, the importance of any plastic hinges forming in the beams and not the columns in an extreme event. Band beams usually are significantly stiffer than the columns, making the concept of strong columns and weak beams difficult to achieve.

Also where excess strength is provided above that theoretically required by the design through rationalising the design, less ductility is required for the element e.g. due to the provision of additional reinforcement for tying, or extra thickness or depth of section for fire requirements or deflections. Therefore, less detailing for seismic resistance may help buildability.

## 9. Responsibility for the design

It is recommended in the Guide that if a number of designers are working on the design and detailing of a concrete structure for seismic actions the overall responsibility for the structural aspects of the project should be taken by one structural engineer called the Principal Designer.,.

The principal designer and the design team should preferably carry out all the structural design of the building. Where part of the design is assigned or subcontracted to others, the principal designer needs to understand and fully coordinate those designs and take overall responsibility for them. Examples of design by others are the design of precast concrete elements and post-tensioned floors.

The failure of the CTV building in Christchurch where 115 people lost their lives in this extreme event is attributed to the designer of the building who was not experienced in earthquake design and did not fully understand what was required and the senior engineer did not supervise the inexperienced designer (18).

## 10. Detailing and drafting of concrete elements

Conceptualisation, structural analysis and design are the first part of the overall design process of a structure and detailing and drafting the second part. Detailing and drafting consists of satisfactory plans, elevations, sections and details and an understanding of how each part of the structure will perform under seismic loads.

Detailing of the reinforcement is a vital part of the seismic design process for reinforced concrete. There must be sufficient transverse steel to prevent shear or crushing failures, anchorage of reinforcement into areas of confined concrete and buckling of compression steel, once the cover to the concrete has been lost due to cyclic movements. The main steel bars must not lose their anchorage into the surrounding concrete during the repeated reversing loading cycles they would be subjected to in a major earthquake. The anchorage lengths combining various parts of the structure together must be sufficient and allow for local failures.

The art of reinforcement detailing is to provide the reinforcement in the right places required by the design and to meet the expected earthquake demands. If the reinforcement is correctly placed and fixed; the concrete correctly placed around the reinforcement which has not moved, then the structure will comply with the intent of the design and should perform satisfactorily during its design life including seismic actions, assuming it has been designed correctly.

Detailing involves practical and detailed considerations on how and where the reinforcement should be placed. Experienced designers who understand the overall design and the seismic requirements of the building should be responsible for the overall detailing. Detailing must not be carried out by graduate, inexperienced engineers or drafters without senior supervision.

*The basic assumption in any reinforced concrete design is that the designer is responsible to detail clearly and specify the reinforcement requirements on the drawings.*

The designer is responsible for ensuring that the information on the drawings and specifications is sufficiently clear so that each concrete element can be correctly constructed on the site, and the final structure will comply with the design requirements.

With the correctly detailed structural drawings, the reinforcement processor can then process the reinforcement using the reinforcement schedules produced by the scheduler from the structural drawings and deliver it to the site. This will allow the steel fixers to fix the reinforcement correctly and the builder/contractor to place the concrete around the reinforcement.

The detailing of reinforcement of concrete elements often occurs reasonably late in the documentation phase, after the design is substantially completed, and the final drafting of the structure has commenced.

Where possible, the structural design, including the drafting and detailing of the reinforcement should be completed prior to construction commencing.

Designers must allow enough time to complete the structural design and to detail the reinforcement adequately for all concrete elements, together with suitable checking and coordination. Checking should occur prior to issue of the drawings for construction and manufacture of reinforcement.

The detailing requirements of AS 3600 generally follow those of ACI 318 (19). With the trend to prefabrication of reinforcement off-site, attention needs to be given by designers as to how the components can be prefabricated and joined by drop in splice bars, known as loose bar detailing (20).

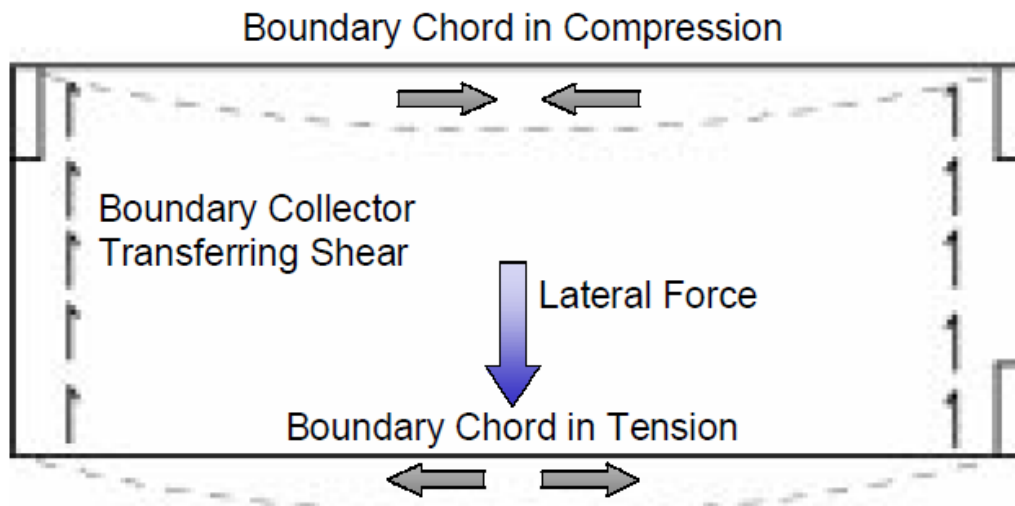
## 11. Diaphragms

Diaphragms in seismic design are the concrete floor and roof slabs. They are a critical element in the design of any building for seismic actions, as they tie the structure together and must be considered early in the design.

AS 1170 .4 makes passing reference to the deflection of diaphragms in Clause 5.2.5. AS 3600 in Clause 6.9.4, states that insitu concrete can be assumed to act as horizontal diaphragms. Unfortunately, there is no guidance in either Standard on the loads, the design of the diaphragm or the transfer of actions from diaphragms into the vertical elements.

Diaphragms have a number of roles in a building including carrying gravity loads and imposed vertical loads; to provide lateral support to vertical load bearing elements; to transfer the lateral earthquake actions applied at each floor level into the vertical elements. They also have a number of other functions such as redistribution of loads around openings, redistribution of forces due to torsion, and for resisting inclined or offset columns.

One method for the design of diaphragms has been to consider them as a horizontal deep beam where the flanges take the tension and compression as required as shown in Figure 3. Designers can also use a strut and tie approach. Diaphragms can also be rigid or elastic, regular or irregular, and have large penetrations, all of which can complicate their design.



***Figure 3. Floor as diaphragm after ATC/SEAOC briefing paper.***

Evaluating all the situations for the detailing of floor diaphragms requires experience and engineering judgement. For example, a building long and narrow in plan may be more flexible than thought, and the deformations may not be able to be accommodated by the walls at either end, resulting in separation of the walls from the diaphragm and possible failure.



Typically, edge beams form the edges of a diaphragm. They need to be continuously reinforced with the longitudinal bars fully lapped for tension and compression, restrained for compression and adequately anchored to the concrete walls and columns where they are attached.

Designers need to study how the forces from the diaphragm get into and out of the vertical elements, particularly shear walls and a good understanding of how these forces are transferred is necessary to ensure proper detailing.

Volume changes due to creep, shrinkage, thermal and post-tensioning also need to be considered with diaphragms. Where floors are temporally uncoupled from shear walls such as cores and lift shafts to allow for initial shrinkage, axial shortening, and post-tensioning effects, then correct detailing is required to ensure they will act as diaphragms in the final condition and are properly connected to the vertical elements.

Diaphragms will have a number of components depending on the design model adopted. Tension and compression members of the diaphragm are known as *collectors* or *collector bars* because they collect the shear forces and transmit them into the columns and walls. The earthquake forces must be transferred into the vertical element from the diaphragm, and these can be significant forces. The reinforcement used to transfer these forces is known as *drag bars*.

Failures of diaphragms in the recent high magnitude New Zealand Canterbury earthquakes were observed and a realisation that a more rigorous approach is required for the design of diaphragms. Designers need to consider these elements much more critically than they may have in the past (21, 22).

## 12. Conclusions

Australia is an area of moderate seismicity, of low probability but high consequence in comparison to areas such as California, Japan, and New Zealand. The provisions for both the design and detailing of reinforced concrete structures in Australia in accordance with the BCA and referenced Standards reflect this in the design and detailing required.

Many building structures in Australia will typically be designed and detailed in accordance with the main body of AS 3600 using the specific clauses for detailing in each section of the Standard. As a result, the detailing requirements are not that onerous and no more than would normally be required. Loose-bar detailing combined with efficient fabrication procedures and additional considerations, to provide the levels of ductility and continuity of reinforcement, will allow the structure to meet the anticipated earthquake loading satisfactorily in a life safety event.

With some additional design and detailing to Appendix C of AS 3600, the building can meet higher levels of earthquake resistance and minimise the damage requirements as required.

It is important to provide a minimum level of ductility in both beams and columns framing into a joint and to ensure adequate confinement of column reinforcement, regardless of the type of structural system employed.

With a limited additional quantity of appropriately detailed extra fitments and continuity reinforcement, plastic hinges can be induced to form at a given load. However, yielding will be ductile (gradual), even if the design earthquake load is exceeded (i.e. the hinge will act as a 'fuse' preventing transfer of the larger forces).

The choice for the designer is clear. A fully elastic response by the structure cannot be guaranteed, and a non-elastic response is allowed by the BCA and referenced Standards. Therefore, to prevent a catastrophic collapse and probable loss of life under a greater than design event, a ductile failure must be ensured. This minimum required level of ductility can be readily achieved by careful detailing and reducing the axial stresses in the columns and walls below the balance point on the interaction diagram

Precast and tilt-up concrete construction requires additional care in detailing to ensure connection detailing is satisfactory and that floors are adequately supported and will act as diaphragms in order to correctly transfer horizontal forces.



Comparable overseas experience has shown reinforced concrete, both in situ, precast and tilt-up concrete, is a simple, suitable and cost-effective solution for building structures in all seismic conditions. For low to medium seismic areas such as Australia reinforced concrete is eminently suitable. Designers and specifiers can remain confident of reinforced concrete's ability to function and to meet the needs of today's construction industry.

To further assist the client/building owner, designers and the builder/contractor specific seismic design checklists have been developed to provide a series of important questions for discussion and determination when conceptualising, designing and detailing reinforced concrete for structural performance under earthquake actions.

The new Guide will be a valuable resource for designers in Australia for the seismic design of reinforced concrete buildings.

### 13. References

1. The Institution of Engineers Australia, Newcastle Earthquake Study, 1990
2. The Institution of Engineers Australia et al, Conference on the Newcastle Earthquake, 1990
3. Standards Australia, AS 1170.4–1993, Minimum Design Loads on Structures, Part 4: Earthquake Loads.
4. Standards Australia, AS 3600–2009, Concrete Structures.
5. Standards Australia, AS 1170.4–2007, Structural design actions, Part 4: Earthquake actions in Australia.
6. Standards New Zealand, AS 1170.5–2004, Structural design actions, Part 5: Earthquake actions in New Zealand.
7. Standards Australia, AS 1170.0 Supplement 1:2002, Structural design actions- General Principles- Commentary
8. Building Code of Australia, the Australian Building Codes Board, July 2012
9. Standards Australia AS3600 Supplement 1, Concrete structures—Commentary (Supplement to AS 3600—2009), 2014
10. Melchers RE, Investigation of the Failure of the Newcastle Workers Club, Institution of Engineers Australia, Australian Journal of Structural Engineering, Vol 11 No 3
11. Woodside JW, Discussion Paper on the Investigation of the Failure of the Newcastle Workers Club, Institution of Engineers, Australian Journal of Structural Engineering, Vol 12 No 2
12. Wibowo A, Wilson JL, Lam NTKL, Gad EF, Drift performance of lightly reinforced concrete columns, Journal of Engineering Structures, Vol 59, pp 522-535, 2014
13. New Zealand Concrete Society & New Zealand National Society for Earthquake Engineering Guidelines for the Use of Structural Precast Concrete in Buildings 1991
14. Wilson JL, Robinson AJ, Balendra T, 2008, Performance of precast concrete load bearing panel structures in regions of low to moderate seismicity, Journal of Engineering Structures, Vol 30, July, pp 1831-1841
15. The Institution of Structural Engineers, Practical guide to structural robustness and disproportionate collapse in buildings, October 2010
16. Byfield M, Wjesundara M, Morrison C and Stoddart E, A Review of Progressive Collapse Research and Regulations, Proceeding of the Institution of Civil Engineers, Structures and Buildings 167 August 2014 Issue SB8
17. Paulay T and Priestley M J N, Seismic Design of Reinforced Concrete and Masonry Buildings, John Wiley & Sons Inc, 1992.
18. Canterbury Earthquakes Royal Commission, Volume 6, Canterbury Television Building (CTV) <http://canterbury.royalcommission.govt.nz>
19. ACI 318 – 11M, Building code requirements for structural concrete, American Concrete Institute, 2011
20. Concrete Institute of Australia, Recommended Practice, Reinforcing Detailing Handbook for Reinforced and Prestressed Concrete, updated and republished 2014
21. Gardner DR, Bull DK and Carr AJ, Internal forces in concrete floor diaphragms of multi-story structures during seismic shaking, 14th world conference on earthquake engineering, Beijing, 2008
22. NEHRP, Seismic Design Technical Brief Number 3, Seismic Design of Cast in Place Concrete Diaphragms, Chords and Collectors, a Guide for Practicing Engineers, 2010

# Structures Research and Applications

# Assessment of the performance of a 24 year old coating applied to concrete bridge piers since construction in a saline tidal environment

Fred Andrews-Phaedonos<sup>1</sup>, Dr Ahmad Shayan<sup>2</sup>, Dr Aimin Xu<sup>3</sup>

<sup>1</sup>Principal Engineer – Concrete Technology, VicRoads, Australia

<sup>2</sup>Chief Research Scientist, ARRB Group Pty Ltd, Australia

<sup>3</sup>Senior Engineer, ARRB Group Pty Ltd, Australia

**Abstract:** Lynch's Bridge (inbound) over the Maribyrnong River was constructed in 1991/92, supported on six piers each of which consists of five columns and a crosshead. Two of the piers function as abutments and stand on dry land, whereas the other four piers are in the saline tidal river with a tidal range of about 0.4 to 0.7 m. The pier columns and crossheads were treated with an acrylic decorative/anticarbonation coating soon after construction in order to improve their appearance and protect them against aggressive environmental agents, including seawater and atmospheric carbon dioxide. Although the expected service life of the coating was in the order of 10 to 15 years, this coating has been in place for the past 24 years without renewal.

Monitoring investigations commenced in 1999 on one pile cap and two pier columns (Pier 2 from Melbourne Abutment), and have continued since then on a regular basis in order to assess the effectiveness of the acrylic surface coating in protecting the concrete against the aggressive agents, particularly chloride ion penetration, and the consequent chloride-induced corrosion damage. The present work was carried out in line with scheduled monitoring to provide additional information on the performance of the surface coating. The corrosion activity of the reinforcement has not changed significantly in the past 15 years. The reinforcing bars in the tidal and splash zones have shown higher corrosion activity compared to the drier atmospheric zone. The chloride content at the depth of reinforcement in the column has not yet reached the corrosion initiation threshold. This may be why the corrosion rate of the steel bar in the tidal/splash zone of columns remains low. Since 1999, the chloride profile of the concrete at tidal zone has not advanced, which may be attributed to the barrier effect of the acrylic coating applied on the columns.

**Keywords:** Coating, protection, performance, durability, testing, service life, corrosion.

## 1. Introduction

Lynch's bridge (inbound) was constructed shortly before the introduction in 1993 of major durability provisions into the VicRoads structural concrete specification Section 610 (1). As such the piers were constructed using a 50 MPa strength grade concrete containing cement only with a tricalcium aluminate (C<sub>3</sub>A) content of 2-5% and without the inclusion of supplementary cementitious materials (SCMs)(i.e. fly ash, slag or silica fume). A protective decorative/anticarbonation acrylic coating was applied on the pier columns and crossheads immediately after construction.

The decorative/anticarbonation acrylic coating was applied onto the Lynch's Bridge substructure (2) prior to the standardisation of the VicRoads concrete coating specification Section 686 (3), and only based on the material manufacturer's technical data sheet. As such the original coating was applied in two coats with a variable dry film thickness (DFT) of 100 to 140 micron, compared to the minimum total DFT of 150 micron required by Section 686. However, it is likely that other performance criteria, including equivalent air layer thickness, equivalent thickness of concrete and CO<sub>2</sub> diffusion, coefficient would have satisfied the current minimum requirements for a decorative/anticarbonation coating as stated in Section 686. It should be noted that this same acrylic coating although not marketed for aggressive environments was found to have performed very satisfactorily when subjected to significant exposure in a severe tidal marine environment as part of a coatings research project undertaken by VicRoads in 1995 (4).

The monitoring investigation of Pier 2 from the Melbourne abutment (Fig. 1) has been conducted on a frequent basis over a number of years since 1999 (5) in order to obtain information on the reinforcement corrosion in the pier, and the effectiveness of the coating applied on the concrete surface in protecting it from chloride ingress. This current monitoring work was carried out as a follow up some 4 years after the 2010 investigation (6) in line with the future performance requirements as flagged in that investigation, to identify any further potential deterioration changes, which may affect the structure or the surface coating over the intervening 4 year period.

Electrochemical measurements were conducted on selected elements, and 75 mm diameter concrete cores were extracted from the pile cap and the atmospheric and splash zones of the column and tested for chloride penetration (7, 8). In addition, pull-off testing was conducted on the two cores extracted from the atmospheric and splash zones of the column to determine the bond strength of the coating.

The corrosion activity of the reinforcement has not changed significantly in the past 15 years. The reinforcing bars in the tidal and splash zones have shown higher corrosion activity compared to the drier atmospheric zone. The chloride content at the depth of reinforcement in the column has not yet reached the corrosion initiation threshold. This may be why the corrosion rate of the steel bar in the tidal zone of columns remains low. Since 1999, the chloride profile of the concrete at the tidal zone has not advanced, which may be attributed to the barrier effect of the acrylic coating applied on the columns (8).

On the other hand, the chloride profile in the pile cap was much more advanced. This strongly supports the suggestion that prevention of chloride penetration was due to the effectiveness of the acrylic coating as a barrier to chloride penetration. The bond strength of the coating applied to the concrete surface was stronger than the tensile strength of the underlying concrete, and surprisingly the strength shown was greater than the typical range for this type of coating (acrylic) even after 24 years in service.

## **2. Scope of Investigation (7, 8)**

The current investigation was carried out in line with scheduled monitoring to provide additional information on the performance of the surface coating. The following on-site sampling and testing were carried out:

- Examination for any evidence of peeling of the acrylic coating and any visible corrosion or other defects on Pier No. 2 from the Melbourne side.
- Extraction of one 75 mm core from each of the atmospheric and splash zones on one bridge column (upstream) and one 75 mm core from the pile cap, i.e., a total of three cores.
- Determination of chloride content in the cover concrete of the three cores at four depth increments, i.e., analysis of 12 samples for chloride content.
- Pull-off testing on the two cores extracted from the atmospheric and splash zones of the column to determine bond strength of the coating.
- Half-cell potential mapping on two adjacent faces of the column to a height of 1.5 m and one location on pile cap on a 250-300 mm grid.
- Measurement of concrete resistivity on the two adjacent faces of the column, in the atmospheric and splash zones and on the top surface of the pile cap.
- Measurement of corrosion rate in the same areas as for the resistivity tests.
- Analysis and assessment of results and review of both the durability performance of the column and the effect of the existing acrylic coating on the concrete performance.

The acrylic coating required removal by grinding at the locations of half-cell potential, resistivity and corrosion current tests. The removed coating was subsequently reinstated. The site work was undertaken at low tide when the pile cap surface was above the water level.

## **3. Results of the Investigation and Testing (8)**

### **3.1 *Visual Inspection of the Columns and extraction of concrete cores***

The acrylic surface coating on the columns showed no sign of peeling, although crazing and very fine cracks could be seen when closely examining the surface, and small spots of impact damage could be seen on the lower part of column (Fig. 1) (8).

Corrosion staining could be seen at the construction joint, but this did not appear to be from structural reinforcement (Fig. 1 and Fig. 2). Concrete core drilling at tidal zone revealed that vertical reinforcing steel was not corroded (Fig. 2). No obvious defects were observed on the pile cap.

With respect to extraction of concrete cores, concrete Core 1 was extracted from the atmospheric zone and Core 2 from the tidal zone of the middle column (P2C3). Core 3 was extracted from the top of the pile cap to its west side (between P2C3 and P2C4). The holes of the three 75 mm diameter cores were backfilled with a suitable fast setting repair mortar with similar strength to the existing concrete.



Figure 1. (L) Pier 2 Lynch's bridge (inbound), (C) Middle column of pier (P2C3) and location of cores. (R) Column P2C5- crazing, small spots of damage.



Figure 2. (L) Coating removed for measurement, some corrosion stain visible at construction joint. (R) Reinforcing steel at tidal/splash zone with no sign of corrosion.

### 3.2 Half-cell Potentials

Half-cell potential mapping of columns was conducted on the south east face of the two upstream columns of the pier identified as P2C4 and P2C5. The column surface was mapped on a grid of 300 mm (horizontal) by 250 mm (vertical), starting from the top line of the column chamfer which is 150 mm from pile cap top. The half-cell potential survey was made in accordance with ASTM C876, and the final output presented in the form of potential maps as shown in Figure 3. The probability of reinforcing steel corrosion based on the measured copper-copper sulfate half-cell potential values (CSE) as presented by these potential maps is shown in Table 1. Figure 4 shows the average values of the potentials measured at the same height in the past four investigations on Column 4. The data shows that the half-cell potentials have not significantly changed in the past 15 years since monitoring commenced in 1999. This is further supported by the fact that vertical steel reinforcement exposed through a core hole in the tidal/splash zone area showed no sign of corrosion (Fig. 2).

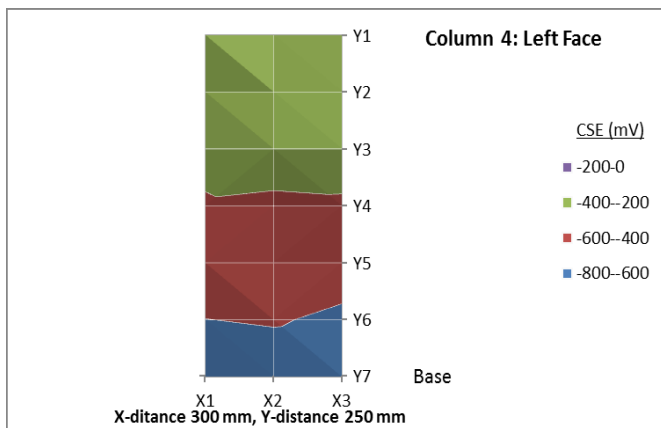


Figure 3. Half-cell potential mapping of P2C4 and P2C5 (8).

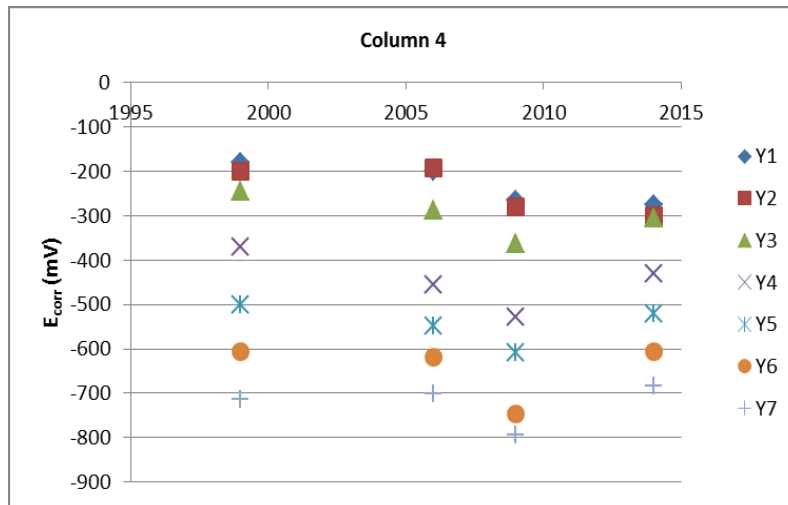


Figure 4. Average value of half-cell potential mapping of P2C4 since 1999 (8).

Table 1. Concrete Surface Potential Criteria.

Potential (vs. Copper Sulphate Electrode (CSE))	Indication for reinforcing steel
More positive than -200 mV CSE	A greater than 90% probability that no corrosion is occurring
Between -200 to -350 mV CSE	Corrosion activity is uncertain
More negative than -350 mV CSE	A greater than 90% probability that corrosion is occurring

### 3.3 Corrosion Rate and Concrete Resistivity

The corrosion rate was measured by using the Gecor6 Corrosion Rate Meter, which measures the corrosion current in the steel area confined beneath the sensorised guard ring of the measuring device, as well as the corrosion potential of the reinforcement and concrete resistance. The measured corrosion current is divided by the surface area of the steel bar in the confined area to obtain the corrosion current density. The resistance was converted to resistivity as described by the equipment procedure. Corrosion rate measurement was undertaken on the south east face of the two upstream columns of Pier 2, identified as P2C4 and P2C5.

The locations of measurement represented concrete exposed to air, tidal zone and splash zone. As shown in Table 2 and Figure 5, the corrosion rate of the steel in the columns was low in all three exposure zones, and the corrosion rate of steel bars in the wet areas of the columns (splash and tidal zones) was comparatively higher than in the atmospheric zone. The corrosion potentials became more negative and concrete resistivity became lower with decreasing height above the pile cap. Considering that the steel bar exposed by core drilling below the high water mark had no sign of corrosion, these results indicate that corrosion activity is low in the columns.

The values of corrosion rate measured over the past years appeared to be consistent except for that measured in 2010 for P2C4, which was higher than the values obtained in other years. Compared to the columns, the corrosion rate of steel in the pile cap was higher, the corrosion potential was more negative and resistivity was lower. The measured values of the corrosion current density presented in Table 2 can be interpreted in terms of corrosion activity of the steel and categorised as shown in Table 3. The concrete resistivity results can be empirically interpreted as shown in Table 4.

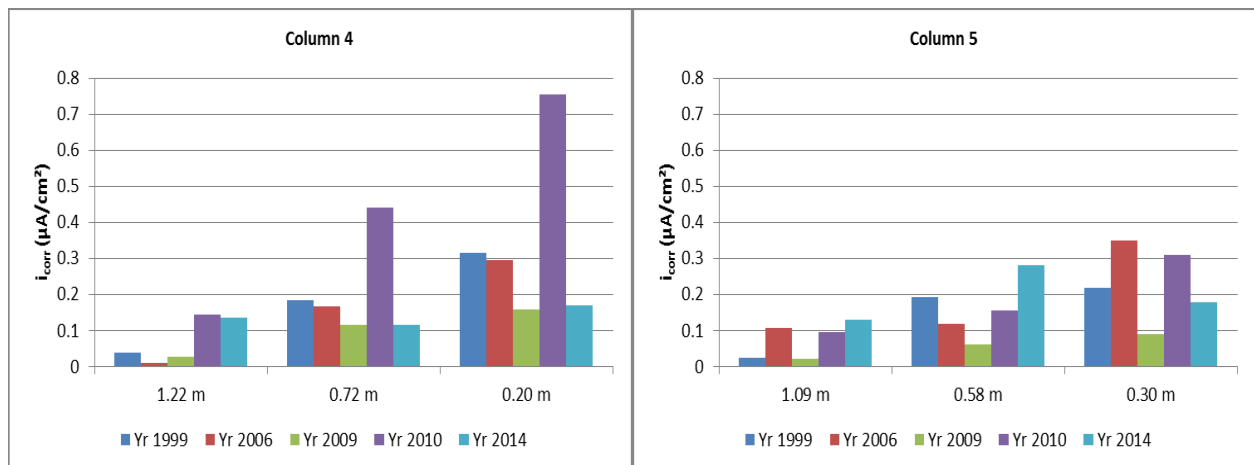
**Table 2. Results of rebar corrosion and concrete resistivity (8).**

Position	Current Density and Corrosion Rate	$E_{corr}$ , CSE (mV)	Resistivity (k $\Omega$ -cm)
P2C4, h=1.2 m, Atmospheric zone	$i_{corr}$ = 0.14 $\mu$ A/cm <sup>2</sup> , rate =1.6 $\mu$ m/year	-210	18.9
P2C4, h=0.7 m, Splash zone	$i_{corr}$ = 0.12 $\mu$ A/cm <sup>2</sup> , rate =1.3 $\mu$ m/year	-408	10.1
P2C4, h=0.2 m, Tidal zone	$i_{corr}$ = 0.17 $\mu$ A/cm <sup>2</sup> , rate =2.0 $\mu$ m/year	-600	3.6
P2C5, h=1.1 m, Atmospheric zone	$i_{corr}$ = 0.13 $\mu$ A/cm <sup>2</sup> , rate =1.5 $\mu$ m/year	-181	17.2
P2C5, h=0.6 m, Splash zone	$i_{corr}$ = 0.28 $\mu$ A/cm <sup>2</sup> , rate =3.3 $\mu$ m/year	-431	8.0
P2C5, h=0.3 m, Tidal zone	$i_{corr}$ = 0.18 $\mu$ A/cm <sup>2</sup> , rate =2.1 $\mu$ m/year	-581	3.4
Pile cap, near P2C4	$i_{corr}$ = 1.32 $\mu$ A/cm <sup>2</sup> , rate =15.3 $\mu$ m/year	-719	1.5
Pile cap, near P2C5	$i_{corr}$ = 0.86 $\mu$ A/cm <sup>2</sup> , rate =10 $\mu$ m/year	-722	1.3

**Table 3. Corrosion current density and estimated corrosion rate for steel in concrete.**

Corrosion current density, $i_{corr}$ ( $\mu$ A/cm <sup>2</sup> )	Corrosion rate category
< 0.1	No corrosion expected
0.1 to 0.5	Low to moderate rate
0.5 to 1.0	Moderate to high rate
> 1.0	High rate

Note 1: Theoretically, for steel, a corrosion current density of 1.0  $\mu$ A/cm<sup>2</sup> is equivalent to a corrosion rate of 11.6  $\mu$ m/year.



**Figure 5. Corrosion current density of the columns measured in the past years (8).**

**Table 4. Empirical Interpretation of concrete resistivity.**

Resistivity	Empirical interpretation
100 k $\Omega$ -cm	The resistivity will effectively stop corrosion
50 - 100 k $\Omega$ -cm	Low corrosion rate
10 - 50 k $\Omega$ -cm	Moderate to high corrosion rate when steel is active
< 10 k $\Omega$ -cm	Resistivity is not the controlling factor

### 3.4 Performance of concrete surface coating

Pull off tests were performed on the acrylic coating at the exterior surface of the two cores drilled from the middle column of the pier, i.e., P2C3. The pull-off test results obtained on the same column in 2010 showed that the bond strength was higher than 3.7 MPa, which is the limit of the instrument when using 50 mm dollies (the maximum force is 7.5 kN). Therefore, the pull-off test area on the coated surface of the cores was reduced to about 30mm X 30mm by cutting through the coating and about 1 mm into concrete, and performed the pull-off test within that area.

The bond between the coating and the column surface was unusually high for this type of coating, and all pull-off failures occurred in the concrete. Table 5 presents the test results, and visual features of the cores and dollies after pull-off testing are shown in Figure 6. The dolly glued on Core 2 could not be pulled off at the maximum force. Therefore, two 20 mm dollies were then glued on the core surface for additional pull-off



tests. However, the results were inconsistent and may not be reliable. The pull-off strength for the two 30mm X 30mm dollies were 6.6 MPa and > 8.5 MPa, for the cores drilled from dry and wet surfaces, respectively. It is possible that the effects of the epoxy adhesive which was left in place with the dollies for the minimum curing period prior to testing may be reflected in these results. The bond strength onto the concrete substrate would nevertheless be in the range of 1.5 MPa to 4 MPa as shown in Table 5 which would be in the typical range of this type of coating even after 24 years in service.

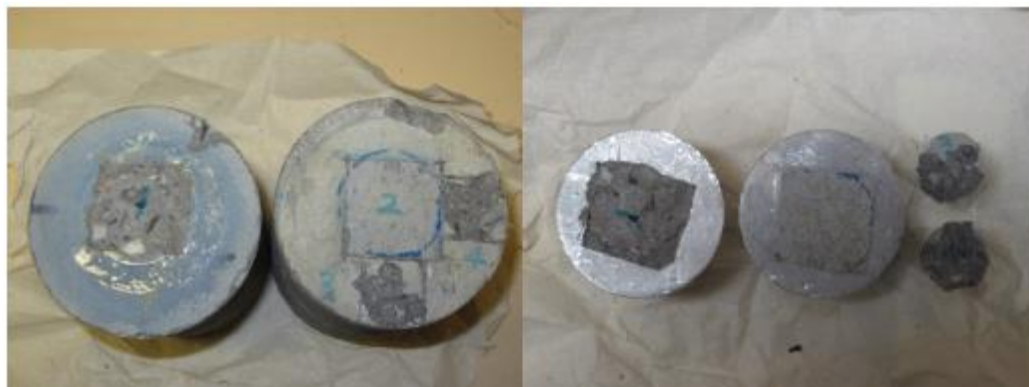
It should be noted that the 2010 monitoring investigation (6) showed that the in-situ coating thickness, based on measurements off the pull-off dolly ranged between 30 and 100µm (compared to original DFT in the order of 100–140µm). However, it is considered that the in-situ use of a paint inspection gauge consisting of a microscope, typically of 50× magnification in accordance with the relevant standard would have resulted in more accurate DFT determinations.

Nevertheless, it is evident that although the coating exposed to the river water may be deteriorating to some degree, it still exhibits effectiveness and provides some protection. This is also supported by the visual observations in that the coating is still adhering well onto the concrete substrate. The coating thickness is possibly reducing as expected due to the long term exposure and consequent degradation of the polymeric structure of the coating thereby gradually reducing the ongoing effectiveness of the acrylic coating applied some 24 years earlier. However, both the 2010 and 2014 monitoring investigations show that the acrylic coating still maintains some effectiveness and they also validate the appropriateness of the early application of protective coatings onto new concrete bridges and other structures.

**Table 5. Results of the Pull-off test (8).**

Sample	Force (kN)	Area (mm <sup>2</sup> )	Strength (MPa)	Note
Core 1, P2C3, dry surface	5.0	760	6.6	Failure in concrete 1.5-3 mm
Core 2, P2C3, wet surface	7.4	870	> 8.5	Could not be pulled off
	1.4	360	4.0	20 mm dolly, failure in concrete
	0.5	310	1.5	20 mm dolly, failure in concrete

The strength obtained by using small dollies was much lower than that obtained on larger dollies and may be unreliable.



**Figure 6. Views of cores and dollies after pull-off test. Core 1 is from atmospheric zone and Core 2 from tidal/splash zone. The 50 mm dolly on Core 2 was sheared off in the testing machine (8).**

### 3.5 Chloride Profiles

Chloride content in the concrete was determined as shown in Table 6 and the detailed chloride ingress profiles for the three zones are shown in Figure 7. The chloride ingress values represent the combined effect in resisting ingress of the in-situ concrete and the acrylic coating applied immediately after construction.

The 75 mm diameter Core 1 and Core 2 were drilled to depths of a lateral bar and a vertical bar, which revealed the cover thickness to be 82 mm and 92 mm, respectively. Core 3 was drilled on the pile cap and touched a bar at a depth of 120 mm. The holes of the three 75 mm diameter cores extracted from the atmospheric and splash zones of the middle column (P2C3) and the pile cap between P2C3 and P2C4, were backfilled with a suitable fast setting repair mortar with similar strength to the existing concrete.

Figure 7 demonstrates that the chloride content in the atmospheric zone at 80 mm depth is still below the threshold value for initiation of corrosion. According to the Drawings, the cover to reinforcement in pile caps should be 70 mm. The core probably touched the bar of the second layer, not the first layer, and the chloride content at the first layer of bars is likely to be significantly above the threshold value for the pile cap.

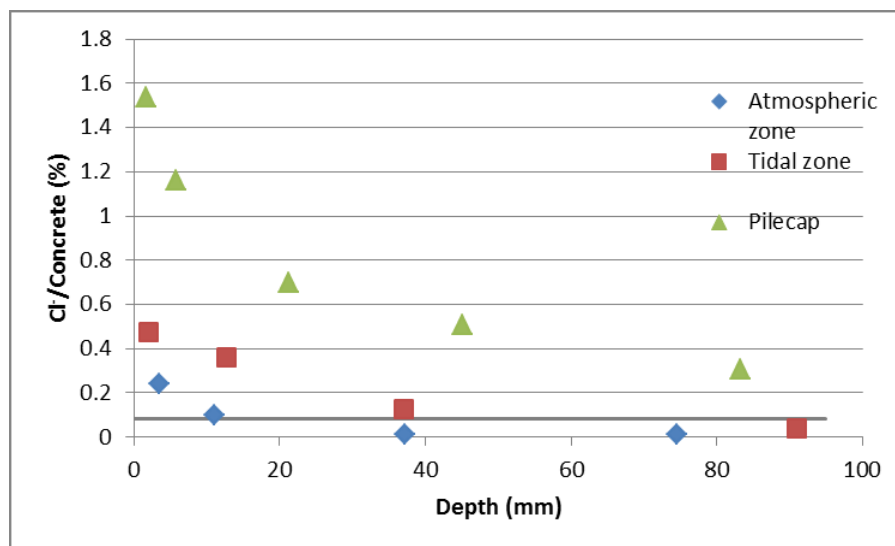


Figure 7. Chloride profiles of the samples obtained in this investigation (8)

Table 6. Chloride content in concrete (8).

Sample	From (mm)	To (mm)	Cl-/Sample (%)
<b>Core1, Column, Atmospheric zone</b>	2.4	4.7	0.239
	8.5	13.6	0.098
	32.9	41.4	0.012
	69.7	79.5	0.011
<b>Core2, Column, Tidal zone</b>	0	3.9	0.473
	7.9	17.5	0.363
	34.1	40.1	0.126
	87.9	94.0	0.040
<b>Pile cap (Chloride threshold is taken as 0.07% by wt of concrete)</b>	0	3.4	1.539
	3.4	8.1	1.159
	16.8	25.7	0.695
	38.6	51.6	0.506
	79.6	87.0	0.306
<b>Chloride ingress and diffusion parameters represent the combined effect of the in-situ concrete and the acrylic coating applied immediately after construction.</b>			

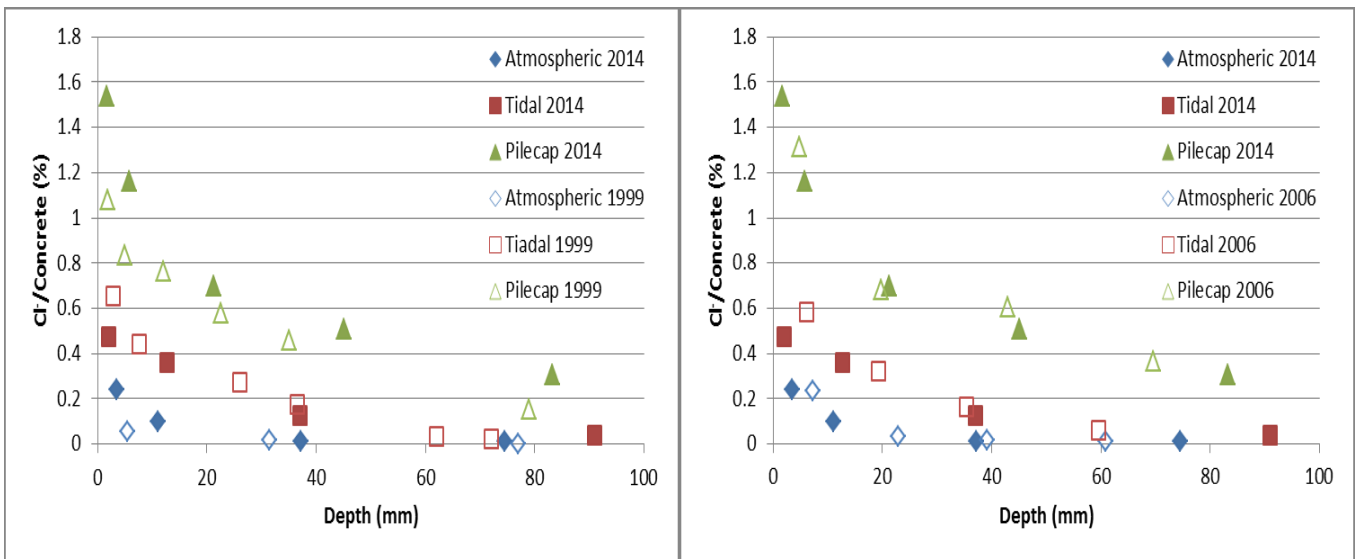
Compared with the chloride profiles obtained in 1999 and 2006 (9), in this 2014 investigation the chloride profile in the pile cap has gone slightly deeper. However, the chloride profiles obtained in 2014 are very similar, almost unchanged from the 2006 results in the tidal and atmospheric zones of the column (Figure 8). It appears that the acrylic coating has been effective in slowing down the chloride penetration in the tidal and atmospheric zones.

#### 4. Discussion

Two columns and the pile cap of Pier 2 of the 24 year old Lynch's bridge from the Melbourne side were investigated for reinforcing steel corrosion and chloride penetration. The acrylic surface coating on the pier columns was also tested for its bond strength.

It should be noted that the volume of permeable voids (VPV) of the pier concrete was determined at the initial investigation in 1999 at 15.5% which would represent the quality of the concrete after 8 years. The estimated corresponding 28 day estimate of VPV is in the order of 17.5% which represents the initial permeability condition and therefore microstructure performance of the original concrete. This would represent an in-situ

quality performance equivalent to a concrete grade of VR330/32 to VR400/40 as specified in Section 610 (1) instead of the required quality performance of a concrete grade VR450/50 which is essentially what was specified for use in the construction of the concrete piers for the bridge.



**Figure 8. Comparison of chloride profiles obtained in this investigation with those in 1999 & 2006 (8).**

The combined diffusion coefficient (D) determined in 2010 was  $2.9 \times 10^{-12} \text{ m}^2/\text{s}$  (atmospheric zone),  $1.3 \times 10^{-12} \text{ m}^2/\text{s}$  (tidal zone) and  $4.1 \times 10^{-12} \text{ m}^2/\text{s}$  (pile cap top face). Significantly, these diffusion coefficients (D) for the combination of acrylic coating and concrete is equivalent if not better than the specification requirements of RMS B80 - 50MPa of  $2 - 4 \times 10^{-12} \text{ m}^2/\text{sec}$  (durable concrete for Classification C, aggressive), and some 50% lower than RMS B80 - 40MPa of  $3.5 - 8 \times 10^{-12} \text{ m}^2/\text{sec}$  (for Classification B2) (10).

The relatively low chloride profiles obtained in the 2014 investigation which are similar to those determined in 1999 and 2006 as shown in Figure 8, and in conjunction with the low chloride diffusion coefficients determined in 2010, indicate that the combined effect of the average quality in-situ concrete (equivalent concrete grade of VR330/32 to VR400/40 instead of VR450/50) and the acrylic coating applied to the columns a short time after construction provide excellent protection to the steel reinforcement and enhanced performance in relation to the durability requirements. This outcome supports the fact that the acrylic surface coating applied to the columns during construction effectively slowed the chloride ingress in the tidal/splash and atmospheric zones of the columns.

The 2014 monitoring investigation showed that the corrosion activity of the reinforcement has not changed significantly in the past 15 years. Comparatively, the reinforcing bars in the tidal and splash zones have shown higher corrosion activity than in the drier atmospheric zone, in terms of steel corrosion rate and half-cell potentials and concrete resistivity.

The chloride profiles indicate that the chloride content at the depth of reinforcement in the column has not yet reached the corrosion initiation threshold. This may be one of the reasons why the corrosion rate of the steel bar in the tidal/splash and atmospheric zones of columns remains low. Since 1999, the chloride profile of the concrete at tidal/splash and atmospheric zones has not advanced, which may be attributed to the barrier effect of the acrylic coating applied on the columns after construction some 24 years ago.

On the other hand, the chloride profile in the pile cap was much more advanced, which strongly supports the suggestion that prevention of chloride penetration in the columns was due to the effectiveness of the acrylic coating as a barrier to chloride penetration.

## 5. Outcomes for Enhancing Structure Life

The ability of the acrylic surface coating applied to the columns of Lynch's bridge immediately after construction some 24 years ago to effectively slow down the chloride ingress in the tidal/splash and atmospheric zones of the columns, highlights the appropriateness of early application of protective coatings to bridges in all exposure conditions to enhance their ongoing performance.

It is considered that even if the protective coating which is initially applied to a new bridge is not re-applied as

part of ongoing maintenance, such initial application will protect the concrete for at least 15 to 20 years before the concrete structure is exposed to its in-service environment, thus providing the structure a valuable head start in its quest to achieve its required design life.

Furthermore, the monitoring investigations at Lynch's Bridge since 1999 revealed that even though the coating thickness may be reducing due to long term exposure and consequent degradation, coatings may still provide some protection to the concrete provided that they are still adhering well onto the concrete substrate.

The significance of the positive impact of early application of coatings is also demonstrated by the monitoring of the performance of an epoxy coating applied during construction on the columns of the Mordialloc Creek Bridge that are exposed to aggressive tidal marine conditions, some 8 years ago (11). The Mordialloc Creek Bridge epoxy coating investigation including the monitoring of other VicRoads bridges over the past 20 years demonstrated that early application of a protective coating provided enhanced performance, and contributed significantly to slowing down the ingress of chlorides into the columns concrete and lower the potential for earlier corrosion activity.

These evaluations further validate the case for the systematic application of protective coatings during construction of bridges and other structures in all types of exposure conditions, in combination with high quality concrete, to enhance their initial and long term durability performance even if such coatings are not re-applied during ongoing maintenance.

## **6. Acknowledgement**

The authors wish to thank VicRoads for permission to publish this paper. The views expressed in this paper are those of the authors and do not necessarily reflect the views of VicRoads. The testing as referenced in this paper was undertaken by Dr Ahmad Shayan and Dr Aimin Xu from the ARRB Group Pty Ltd to a specifically designed VicRoads brief.

## **7. References**

1. VicRoads Standard Specification, "Section 610 – Structural Concrete", 2013.
2. Andrews-Phaedonos, F., Shayan, A. and Xu, A, "Extending the Service Life of Concrete Bridges - Corrosion Monitoring of Lynch's Bridge over Maribyrnong River - Early Coating Provides Enhanced Performance" 25<sup>th</sup> Biennial Conference, Concrete Institute of Australia, October, Perth, 2013.
3. VicRoads Standard Specification, "Section 686 – Coating of Concrete", 2013.
4. Andrews-Phaedonos, F, Collins, F.G, Green, W.K, Peek, A. K, "Assessment of Protective Coatings for Concrete Bridges in Marine or Saline Environments", ACA Conference, Sydney (Awarded the 1997 ACA - "A. C. Kennett" award for best conference paper), 1997.
5. Shayan, A and Aimin Xu, ARRB Group Pty Ltd, "Management of Concrete Bridges to extend their service life. Investigation of three Victorian bridges, Extent of corrosion damage" Contract Report No. RC 91019, 1999.
6. Shayan, A and Xu, A, ARRB Group Pty Ltd, "Corrosion Monitoring of Lynch's Bridge over Maribyrnong River" Contract Report No. 001404, 2010.
7. Andrews-Phaedonos, F, "Consultant Brief, "Monitoring Investigation of a Pile Cap and Pier Column at Lynch's Bridge ", VicRoads, 2013.
8. Shayan, A and Xu, A, ARRB Group Pty Ltd, "Monitoring Investigation of a Pile Cap and Pier Column at Lynch's Bridge " Contract Report No. 007920, 2014.
9. Shayan, A and Xu, A, ARRB Group Pty Ltd, "Corrosion Monitoring of the Newer Section (Inbound) of Lynch's Bridge over Maribyrnong River" Contract Report No. VE71128, 2006.
10. RMS Specification B80, "Concrete Work for Bridges", 2013.
11. Andrews-Phaedonos, F., Shayan, A., Xu, A. and Walker, A, "Performance of epoxy coating on columns exposed to aggressive tidal marine conditions" 26<sup>th</sup> Biennial Conference, Concrete Institute of Australia, October, Gold Coast, Australia, 2013.

# Behaviour of Concrete Filled Steel Stub Columns During and After Fire Exposure

Zhong Tao<sup>1</sup>, Xing-Qiang Wang<sup>2</sup>, Tian-Yi Song<sup>3</sup> and Lin-Hai Han<sup>4</sup>

<sup>1</sup>Professor of Institute for Infrastructure Engineering, University of Western Sydney

<sup>2</sup>Associate Professor of Department of Civil Engineering, Shandong Polytechnic

<sup>3</sup>Career Development Fellow of Institute for Infrastructure Engineering, University of Western Sydney

<sup>4</sup>Professor of Department of Civil Engineering, Tsinghua University

**Abstract:** This paper investigates the behaviour of short concrete filled steel tubular (CFST) columns during and after fire exposure. A total of 10 circular CFST columns were loaded with different load ratios and heated to various temperatures for a specified fire exposure period. During the fire exposure phase, the temperature versus time curves of specimens were measured, and the strain developments of the steel and concrete in fire were measured by using photogrammetry method. The interaction between the steel tube and concrete was analysed accordingly. After the fire exposure, the specimens were cooled naturally in the furnace to room temperature and then the columns were compressed concentrically until failure. In the post-fire loading phase, the failure modes, load-bearing capacity and axial load–axial strain relationships were recorded and presented. The effects of temperature, initial load and hold time period of heating on the post-fire residual strength were discussed. A non-linear finite element (FE) model was developed to simulate the tests by using existing material models included the effect of fire exposure. The predictions indicate that the FE model can capture the post-fire residual strength of CFST columns reasonably, but improvement is required in predicting the post-peak response of the load–deformation curves.

**Keywords:** concrete filled steel tubes, fire exposure, failure mode, post-fire behaviour.

## 1. Introduction

Concrete filled steel tubular (CFST) columns have been widely used in building structures due to their excellent fire performance compared with bare steel columns. With the increasing use of CFST columns in structures, the post-fire performance of the composite columns has attracted increasing research interest. Since 2002, Han et al. (1-3) has started to investigate the post-fire performance of CFST columns after exposure to ISO-834 standard fire. A series of tests on circular, square and rectangular short and slender CFST columns were conducted. The test results indicate that CFST columns demonstrate improved ductility after fire exposure, and the major influencing parameters on the post-fire residual strength were identified as fire protection thickness, fire duration time, section size and slenderness ratio. David et al. (4) recently reported test results of CFST columns after exposure to ISO 834 fire and Eurocode smouldering (slow-growth) fire. The test results showed that the influence of selected fire curves was minor. The possible reason explained by David et al. (4) was that similar maximum temperatures were experienced for the two types of fire curves.

It should be noted that no initial load was applied to the test specimens reported in (1-4) during fire exposure. This is different from the real fire scenario, and the presence of initial loading may have remarkable influence on the post-fire performance of columns. To identify the influence of initial load, Yang et al. (5) and Song et al. (6) established finite element (FE) models of CFST slender and short columns, which aimed to simulate the behaviour of CFST columns subjected to different phases including initial loading at ambient temperature, heating and cooling with constant load and post-fire loading. However, in these FE models, the influence of loading and temperature histories on the post-fire material properties models was not considered. Currently, only Huo et al. (7) reported 8 post-fire test results of CFST stub columns with initial loads. The investigated parameters included section size, maximum temperature, fire duration time and initial load level. Opposite trends were observed for the specimens exposed to temperatures of 400 °C and 600 °C. At a temperature of 400 °C, the presence of initial load enhanced the ductility of CFST columns, but at a temperature of 600 °C, the trend was opposite.

Set against this background, it is necessary to conduct more tests to clarify the influence of initial load on the post-fire performance of CFST columns. Therefore, this paper reports test results of 10 specimens for investigating the performance of CFST stub columns during and after fire exposure. To investigate the interaction between the steel tube and concrete during fire exposure, photogrammetry method was

employed to measure the axial and lateral deformations of the steel tube and core concrete in fire. Strength tests were conducted on the post-fire specimens after cooled to ambient temperature. A FE model is developed to simulate the test results and possible improvement to the FE model is discussed.

## 2. Experimental investigation

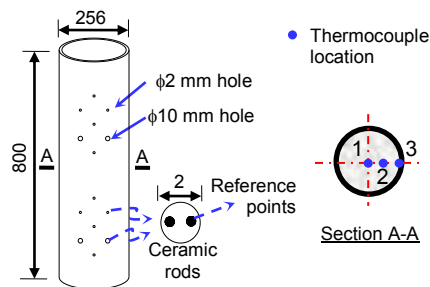
### 2.1 Specimen preparation

A total of 10 circular CFST columns were fabricated and tested. A summary of the specimens is shown in Table 1, in which  $D$  and  $t$  are the overall diameter and thickness of the steel tube, respectively. All the specimens have a same length of 800 mm. Specimen CFST-01 was reference specimen tested at room temperature, whilst the other 9 specimens were exposed to fire before strength testing.

**Table 1. Summary of test specimens.**

Specimen label	$D$ (mm)	$t$ (mm)	$T_t$ (°C)	$t_d$ (min)	$\Delta t$ (day)	$N_o$ (kN)	$n$	$f'_c$ (MPa)	$N_{uT}$ (KN)	$N_u$ (KN)	$RSI$
CFST-01	256	3	20	–	–	–	–	25.8	–	2103.2	–
CFST-02	256	3	400	45	42	650	0.25	32.1	2523.4	2601.4	0.970
CFST-03	256	3	600	45	8	650	0.22	37.6	2874.0	2901.5	0.991
CFST-04	256	3	700	45	132	650	0.22	38.8	2888.2	2918.7	0.990
CFST-05	256	3	800	45	60	650	0.20	43.7	2851.4	3220.6	0.885
CFST-06	256	3	800	0	60	650	0.20	43.7	2821.8	3220.6	0.877
CFST-07	256	3	800	90	56	650	0.20	43.4	2618.2	3219.8	0.813
CFST-08	256	3	800	135	92	650	0.20	42.8	1928.4	3193.8	0.604
CFST-09	256	3	800	90	61	0	0	29.2	2150.0	2488.1	0.864
CFST-10	256	3	800	0	55	1080	0.43	30.2	2555.7	2530.3	1.010

Photogrammetry method was used to measure strain developments of the CFST specimens in fire. Reference points were marked by using ceramic rods on the specimens during the fabrication stage. Ten holes with a diameter of 2 mm were drilled into the surface of the steel tube as shown in Figure 1. Then ceramic rods with two reference points were inserted into the  $\phi 2$  mm holes. The strain development of the steel tube in fire could be calculated based on the high pixel photos of these reference points. To measure the core concrete strains in fire, 4  $\phi 10$ mm holes were drilled through the steel tube to enable that the surface of the core concrete was exposed, and the ceramic rods with reference points were installed in the core concrete through the  $\phi 10$ mm holes.



**Figure 1. Location of ceramic rods and thermocouples (unit: mm).**

Three thermocouples were embedded into the CFST specimen to capture the temperature development in fire. Locations of the three thermocouples were shown in Figure 1, where point 1 is the centre of the

cross section, point 3 is located on the internal surface of the steel tube and point 2 is the midpoint between point 1 and point 3.

## 2.2 Material properties

The concrete used for specimens was made with ordinary Portland cement. The mix proportions of the concrete were: cement: 528 kg/m<sup>3</sup>; water: 210 kg/m<sup>3</sup>; sand: 664 kg/m<sup>3</sup>; coarse aggregate: 1027 kg/m<sup>3</sup>. Due to the availability of the furnace, the specimens were exposed to fire at a concrete age ranging from 53 days to 235 days. The compressive concrete strength ( $f_c'$ ) at the day of fire testing was measured from concrete cylinders. The obtained value of  $f_c'$  is presented in Table 1 for each specimen.

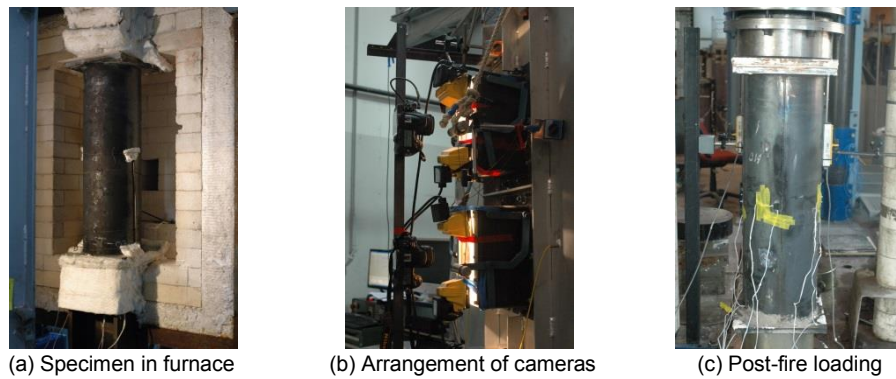
Steel coupons were cut from the same steel sheet which was used to fabricate the steel tubes of specimens. Tensile tests were conducted to obtain the steel material properties at room temperature. The yield strength ( $f_y$ ), tensile strength ( $f_u$ ), ultimate strain ( $\epsilon_u$ ) and modulus of elasticity ( $E_s$ ) of steel at room temperature are 330.4 MPa, 374.6 MPa, 0.154 and 206,500 MPa, respectively.

## 2.3 Test setup and procedure of the experiments

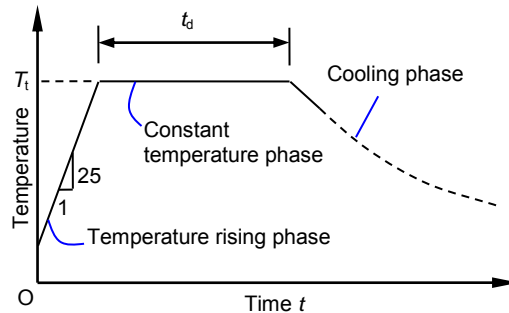
The following test procedure and setup were adopted:

- (1) Ambient temperature loading phase. Prior to the fire exposure, the column specimen was installed in the gas furnace located at the Structures Laboratory at the University of Western Sydney, Australia, as shown in Figure 2(a). Then the predetermined initial axial compression load ( $N_0$ ) was applied to the column specimen. The value of  $N_0$  corresponding to each specimen is shown in Table 1. The corresponding load ratio ( $n=N_0/N_u$ ) is given in Table 1, where  $N_u$  is the ultimate strength of the column at room temperature, which was determined based on FE prediction. The furnace chamber has a floor area of 640 mm in width and 630 mm in depth, and the height is 880 mm. The furnace is able to control the fire temperature following the specified temperature-time curve illustrated in Figure 3. Pin-pin end boundary condition was applied to the column specimen via two cylindrical hinges, and a loading jack with a capacity of 2,000 kN was used to apply load to the column.
- (2) Temperature rising phase. The applied load  $N_0$  was kept constant, and the furnace temperature was increased to the nominal target temperature ( $T_t$ ) with an average heating rate of 25 °C/min. The predetermined value of  $T_t$  for each specimen is shown in Table 1. During the test, there was some discrepancy between the actual maximum temperature and target temperature  $T_t$  due to the control accuracy. The difference was normally within 50°C. The temperature inside the furnace was controlled by four gas burners, and five thermocouples were used to monitor and record the furnace temperature. During the fire exposure, thermocouples in the specimen and a displacement transducer located at the top end of the specimen were used to measure the temperature and axial deformation of the column specimen. Two cameras, as shown in Figure 2(b), were installed outside the furnace to take photos of the reference points every 3 min until the end of cooling phase.
- (3) Constant temperature phase. After the furnace temperature reached the target temperature, the furnace temperature was kept constant until the predetermined hold time period of heating ( $t_h$ ) was reached. The value of  $t_h$  is shown in Table 1 for each specimen.
- (4) Cooling phase. After the hold time period of heating was reached, the heating was stopped and the specimen was cooled down to room temperature inside the furnace with the furnace door closed. In the cooling phase, the applied axial load was kept constant.
- (5) Post-fire loading phase. In the later stage of the cooling phase, the applied load to the specimen was removed. When the specimen cooled down to room temperature, the specimen was removed from the furnace and stored in the laboratory for a period ranging from 8 days to 132 days before conducting the residual strength testing. The stored period ( $\Delta t$ ) is presented in Table 1 for each specimen. The post-fire loading test was carried out using a testing machine with a loading capacity of 3,000 kN. All specimens were compressed under monotonic loading with a loading rate of 0.25 mm/min before the peak load and 0.75 mm/min after the peak load. The axial deformation of the column during the testing was measured by two displacement transducers as shown in Figure 2(c).





**Figure 2. Test setup.**



**Figure 3. Heating and cooling procedures.**

### 3. Temperature and strain developments in fire

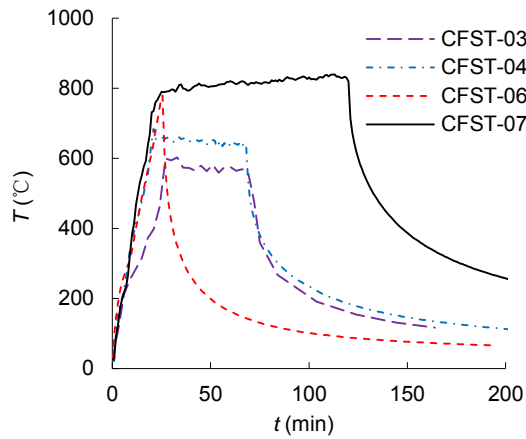
#### 3.1 Temperature versus time curves

The average furnace temperature ( $T$ ) versus time ( $t$ ) curves of typical specimens CFST-03, CFST-04, CFST-06 and CFST-07 are shown in Figure 4. For specimens CFST-03, CFST-04 and CFST-07, the temperature rising, constant temperature and cooling phases described in Figure 3 can be clearly identified. But for specimen CFST-06, there was no constant temperature phase since the predetermined hold time period of heating ( $t_d$ ) was set to be zero. It should be noted that the furnace took more than 24 h to drop to room temperature. But after 200 mins, the furnace temperature generally dropped below 300 °C. Therefore, only the first 200 min was shown for the furnace temperature to clearly illustrate the heating stage.

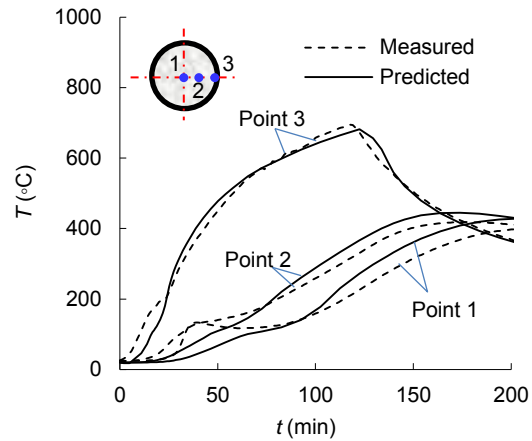
Figure 5 illustrates the measured temperature ( $T$ ) versus time ( $t$ ) curves corresponding to points 1, 2 and 3 for a typical specimen CFST-07. As expected, the further the thermocouple location from the surface of the steel tube, the lower the measured temperature. Meanwhile, the measured  $T-t$  curves at points 1 and 2 had a platform at around 100°C owing to the fact that the water in the core concrete started to evaporate at that temperature, which consumes heat and slows down the temperature rise. Compared with the furnace and the steel tube, the concrete core cooled down more slowly due to the heat sink effect of concrete.

#### 3.2 Strain development

Specimens CFST-07 and CFST-09 have same test parameters except that an initial load of 650 kN was applied to CFST-07. Therefore, the two specimens are chosen to illustrate the influence of initial load on the strain developments of CFST columns. Using photogrammetry method, the steel axial strain, steel lateral strain and concrete lateral strain during the fire exposure were measured, and strain versus time curves are shown in Figure 6, in which positive and negative strains represent expansion and contraction, respectively. Different phases of fire exposure are indicated in this figure.

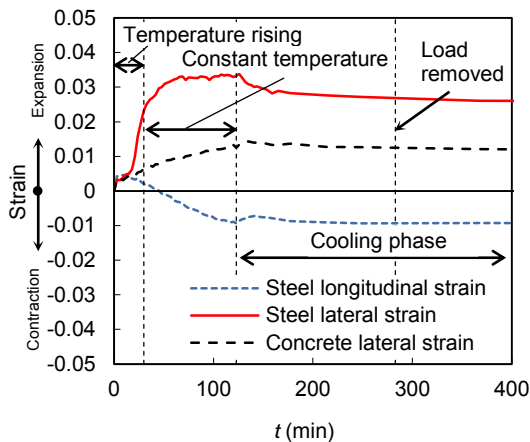


**Figure 4. Furnace temperature developments of typical specimens.**

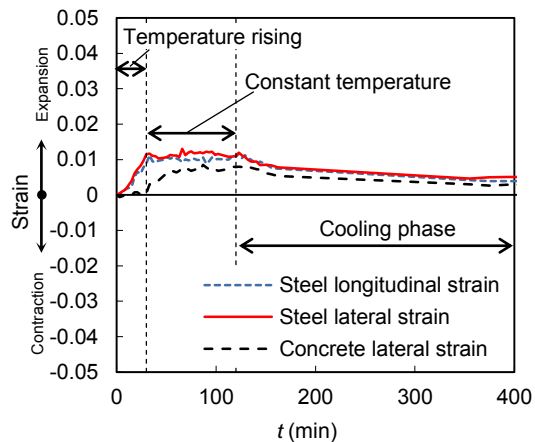


**Figure 5. Temperature development of CFST-07.**

For specimen CFST-07 with an initial load, the steel developed a maximum axial expansion of 0.005 at the beginning of temperature rising phase because of the thermal expansion of the steel tube. With the degradation of material properties at high temperature, the axial expansion decreased and changed to contraction soon after entering into the constant temperature phase. At the end of the constant temperature phase, the steel axial contraction reached -0.01. In the beginning of the cooling phase, the steel axial deformation reduced slightly due to the thermal contraction. But soon the steel axial contraction demonstrated gradual increase due to the thermal creep of steel. The removal moment of the load in the cooling phase is marked in Figure 6(a), which indicates that its influence on the strain development was minor since the strength of the specimen had recovered before the load was removed. During the temperature rising and constant temperature phases, the lateral expansion of the steel tube increased significantly due to the combined effects of thermal expansion and Poisson's effect. At the end of the constant temperature phase, the steel lateral deformation stabilised at a value of 0.033, which is about three times the steel axial deformation at that moment. In the cooling phase, the steel lateral expansion decreased slightly due to the thermal contraction. For the concrete core, the lateral deformation increased almost linearly until the end of the constant temperature phase. Then the concrete lateral deformation decreased slightly during the cooling phase.



(a) CFST-07 with an initial load



(b) Unloaded CFST-09

**Figure 6. Axial and lateral deformations for typical specimens in fire.**

For the unloaded specimen CFST-09, all the strains measured during fire exposure were free thermal strains. Therefore, only expansion was observed for the steel and concrete in both the axial and lateral directions. Due to the delay in temperature rise within concrete, the concrete developed smaller value of

expansion than the steel in the heating phase. During the cooling phase, the expansion of the steel and concrete decreased gradually until reaching a very close constant value of about 0.0015. This is owing to the fact that residual dilation occurred for the unloaded concrete after heating up to above 400 °C.

The difference between the lateral strain developments of the steel tube and concrete shown in Figure 6 clearly indicates the interaction between the steel tube and concrete. During the heating phase, a gap was formed between the steel tube and concrete for both specimens CFST-07 and CFST-09, which indicates the loss of lateral interaction of the two components. It can be seen that the presence of an initial load significantly increased the gap size between the steel tube and concrete. Based on the measured lateral expansions of the steel and concrete, it is found that the maximum gap sizes during the fire exposure are 2.97 and 1.37 mm for CFST-07 and CFST-09, respectively. After the fire exposure, a reduced gap with a size of 1.83 mm was observed for specimen CFST-07, whilst the gap closed for the unloaded specimen CFST-09. Therefore, it can be concluded that the presence of an initial load during fire exposure has a detrimental influence on the interaction between the steel tube and concrete.

#### 4. Test results of specimens after fire exposure

##### 4.1 Failure modes

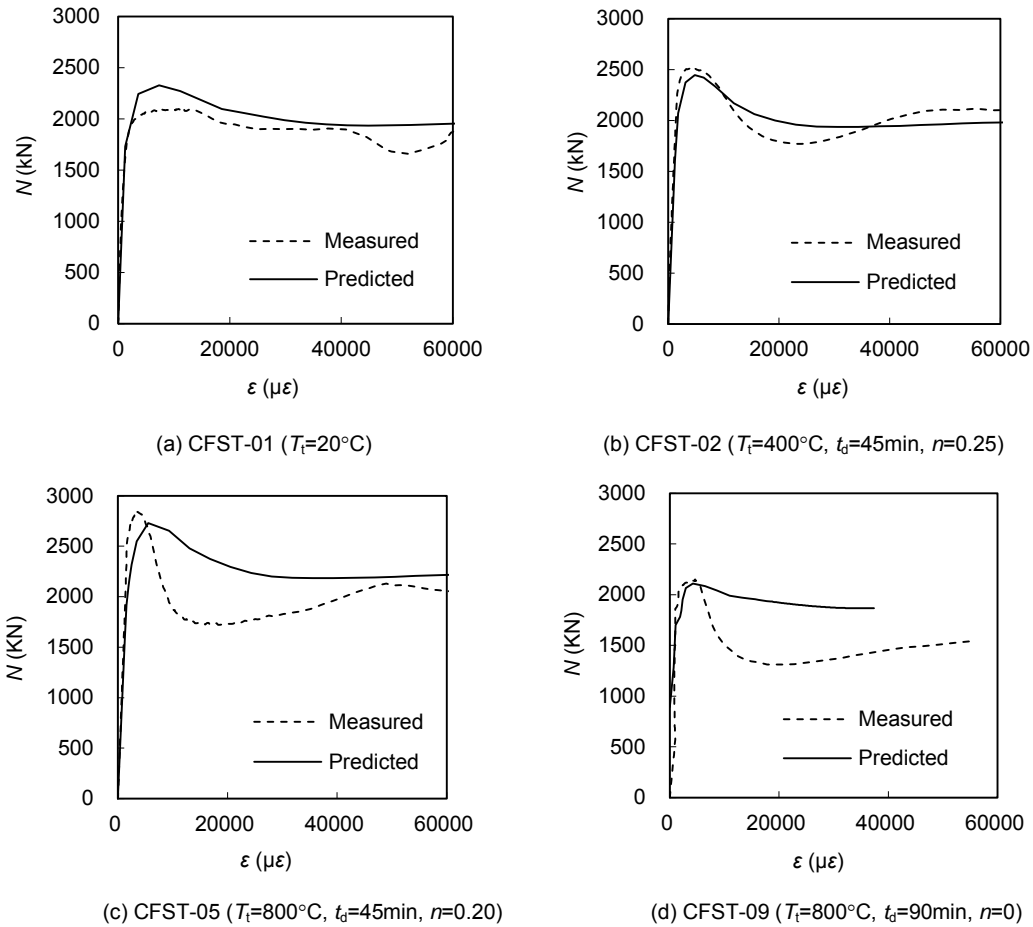
For specimens with an initial load, the steel tube buckled during the fire exposure. A typical specimen CFST-03 is chosen to demonstrate the local buckling of the steel tube, as shown in Figure 7(a). It is also found that oxide layer formed on the surface of the steel tube due to the fire exposure. In the post-fire loading phase, with the increase of the axial load, further deformation developed at the locations of initial local buckling until the column failed under axial compression, as shown in Figure 7(b).



**Figure 7. Failure mode of CFST-03.**

##### 4.2 Axial load versus axial strain curves

Figure 8 shows the measured axial load ( $N$ ) versus axial strain ( $\epsilon$ ) curves of typical specimens CFST-01, CFST-02, CFST-05 and CFST-09 tested in the post-fire loading phase. It can be seen that the  $N$ - $\epsilon$  curve of reference specimen CFST-01 without fire exposure exhibited good post-peak ductility as shown in Figure 8(a). But the  $N$ - $\epsilon$  curves of these fire-damaged specimens dropped sharply after the peak load compared with specimen CFST-01. At ambient temperature, the steel tube could provide effective confinement to the concrete core, thus improving the ductility of the concrete. Since there was a gap formed between the steel tube and concrete in fire-damaged CFST columns with initial loads, the interaction between the steel tube and concrete might be ignored. Due to the absence of proper confinement, the core concrete and steel tube worked independently, leading to the steep post-peak response of  $N$ - $\epsilon$  curves. Similar phenomenon was also observed for post-fire reinforced concrete columns reported by Huo et al. (8).



**Figure 8. Typical axial load ( $N$ ) versus average axial strain ( $\epsilon$ ) curves.**

### 4.3 Effect of different parameters on residual strength index

To quantify the influence of fire exposure on the ultimate strength  $N_{uT}$  of fire-damaged specimens, a residual strength index ( $RSI$ ) is defined, which is expressed as:

$$RSI = N_{uT} / N_u \quad (1)$$

in which  $N_u$  is the ultimate strength of corresponding column at room temperature determined based on FE prediction. The value of  $RSI$  corresponding to each specimen is given in Table 1. The effects of different parameters on  $RSI$  are described in the following.

#### 4.3.1 Effect of temperature

Figure 9(a) demonstrates the influences of temperature ( $T_i$ ) on  $RSI$  of CFST column specimens. The four specimens CFST-02 to CFST-05 were subjected to a same initial axial load (650 kN) during the fire exposure, and had a same hold time period of heating of 45 min. but they exposed to different target temperatures ( $T_i$ ) ranging from  $400^\circ\text{C}$  to  $800^\circ\text{C}$ . It can be found that when  $T_i$  is  $700^\circ\text{C}$  or less, the strength loss is generally less than 4%. But when  $T_i$  reaches  $800^\circ\text{C}$  for specimen CFST-5, a strength loss of 11.5% is obtained.

#### 4.3.2 Effect of hold time period of heating

The influences of hold time period of heating ( $t_d$ ) on  $RSI$  of CFST specimens is shown in Figure 9(b). The four specimens CFST-06, CFST-05, CFST-07 and CFST-08 were exposed to a same temperature of  $800^\circ\text{C}$ , but  $t_d$  of these specimens varied from 0 to 135 min. The influence of  $t_d$  on  $RSI$  is moderate when  $t_d$  is 45 min or less since  $RSI$  values of both specimens CFST-06 ( $t_d=0$ ) and CFST-05 ( $t_d=45$  min) are very close to 0.88. But when  $t_d$  is

greater than 45 min, a significant strength reduction is observed due to increased strength loss of the core concrete. When  $t_d$  increases from 45 to 135 min, the  $RSI$  value drops from 0.885 to 0.604.

#### 4.3.3 Effect of initial load

Figure 9(c) shows the influence of initial load on  $RSI$ . The two specimens CFST-09 and CFST-07 have the same test parameters except that an initial load of 650 kN was applied to CFST-07. But CFST-09 was unloaded during fire exposure.  $RSI$  for the unloaded specimen CFST-09 is 0.864, which is higher than the  $RSI$  value of 0.813 for loaded specimen CFST-07. This can be explained by the diminished confinement effect resulted from the presence of the initial load for specimen CFST-07. In contrast, Huo et al. (7) concluded that the influence of initial load on the post-fire strength of CFST stub columns is minor. Clearly, more tests need to be conducted in the future to reach a definite conclusion.

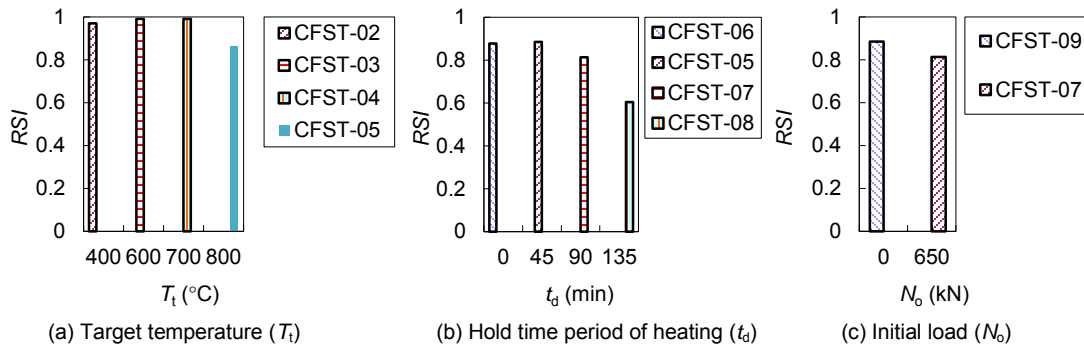


Figure 9. Influences of different test parameters on  $RSI$ .

## 5. Finite element (FE) analysis

### 5.1 FE model

Finite element analysis program ABAQUS (9) is used to simulate the behaviour of CFST stub columns during and after fire exposure. Heat transfer analysis model was established first to obtain the temperature distribution of CFST columns in fire, and then the predicted temperature field at the end of constant temperature phase was imported into the structural analysis model for conducting the post-fire analysis.

Extensive studies have been conducted by previous researchers to simulate the temperature distribution of CFST columns in fire. Tao and Ghannam (10) proposed refined thermal analysis models for CFST columns based on the analysis of extensive test data, and the proposed method can predict the temperature distributions of CFST columns with reasonable accuracy. Therefore, the FE model developed by Tao and Ghannam (10) was used in this paper to conduct the heat transfer analysis, in which the concrete was modelled using 8-node linear heat transfer brick elements (DC3D8), and 4-node heat transfer quadrilateral shell elements (DS4) were used for the steel tube.

For the structural analysis, the stress–strain models of steel at room temperature and after exposure to high temperature proposed by Tao et al. (11) were adopted. For concrete at ambient temperature, it expands laterally under axial compression, and the concrete will eventually be confined by the outer steel tube. This confinement is passive and should be considered in the concrete model (12). Concrete damaged plasticity model is a widely used concrete model, in which some key parameters, such as the dilation angle and strain hardening/softening rule, need to be determined very carefully to accurately simulate the behaviour of concrete in the steel tube. Tao et al. (12) recalibrated those important parameters in the concrete damaged plasticity model and proposed a FE model to simulate axially loaded CFST columns at room temperature. The FE model proposed by Tao et al. (12) was verified by a wide range of experimental data, and the accuracy of the proposed model is reasonable. Therefore, the FE model proposed by Tao et al. (12) is used in this paper to simulate CFST columns at room temperature. The concrete model after exposure to high temperature was determined according to Yang et al. (5). To simulate the interaction between the steel tube and concrete in the FE model, the Coulomb friction model

with a friction coefficient of 0.6 and 'hard contact' were employed in the tangential direction and normal direction, respectively. It should be noted that the initial gap between the steel tube and concrete was not considered in the FE modelling. The structural analysis model has the same mesh as heat transfer model, but different element types, i.e., 4-node shell elements (S4R) and 8-node linear brick elements (C3D8R) were used for the steel tube and concrete, respectively.

Based on the established FE models, the temperature versus time curves and axial load versus axial strain curves were predicted and the results will be discussed in the following subsection.

## 5.2 Discussion

Figure 5 shows the comparison between the predicted and measured temperature ( $T$ ) versus time ( $t$ ) curves. In general, the predictions agree well with the measured results. Although the predicted  $T-t$  curves cannot capture the platform stage at around 100 °C for points 1 and 2, it has very limited influence on the prediction accuracy at a later stage.

Figure 10 shows the comparison between the predicted and measured post-fire residual strengths. A mean ratio (predicted over measured strengths) of 0.965 is obtained with a coefficient of variation of 0.083. As can be seen, the predicted residual strengths are reasonable. The comparison of predicted and measured post-fire  $N-\epsilon$  curves is illustrated in Figure 8. Clearly, at a lower temperature ( $T_f \leq 400$  °C), the predicted  $N-\epsilon$  curves match well with the measured curves. But when  $T_f$  is higher than 400 °C, the predictions are reasonable for the initial stage of  $N-\epsilon$  curves and residual ultimate strengths. But the steep post-peak  $N-\epsilon$  curves are not captured very well in the FE predictions. The ductility of the fire-damaged CFST columns is overestimated. This can be explained by the fact that the initial gap was ignored in the current FE modelling, leading to the overestimation of the confinement effect. Further research is required for the FE modelling to accurately consider the influence of the initial load on the stress-strain model of concrete and interaction between the steel tube and concrete.

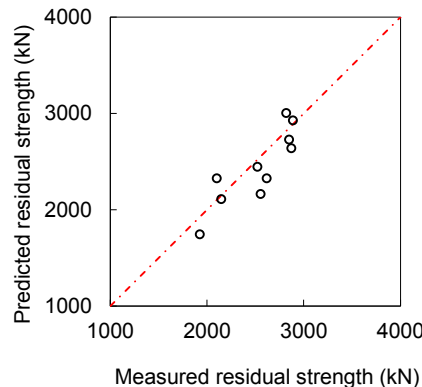


Figure 10. Comparison between predicted and measured post-fire residual strengths.

## 6. Conclusions

Based on the results of this study, the following conclusions can be drawn:

- (1) The measured steel and concrete lateral deformation versus time curves indicate that the presence of initial load can lead to the formation of a gap between the steel tube and concrete, which has a detrimental influence on the interaction of the two components.
- (2) The strength loss increases with the increase of temperature and hold time period of heating. A small load with a ratio of 0.2 has a detrimental effect on the residual strength in the current tests, but an increased load with a ratio of 0.43 increased the residual strength of the composite column.
- (3) Finite element models were established to simulate the test specimens. The accuracy of the predicted post-fire residual strengths is reasonable, but the predictions overestimate the post-peak ductility of fire-damaged CFST columns. For the FE modelling, further research is required to accurately consider the influence of the initial load on the stress-strain model of concrete and interaction between the steel tube and concrete.

## 7. Acknowledgments

This research was supported by the Australian Research Council (ARC) under its Discovery Projects scheme (Project No: DP120100971). The financial support is highly appreciated.

## 8. References

1. Han, L.H., Yang, Y.F. et al., "Residual strength of concrete-filled RHS columns after exposure to the ISO-834 standard fire", Thin-Walled Structures, 40(12), 2002, pp 991-1012.
2. Han, L.H., Huo, J.S., "Concrete-filled hollow structural steel columns after exposure to ISO-834 fire standard", Journal of Structural Engineering, ASCE, 129(1), 2003, pp 68-78.
3. Han, L.H., Huo, J.S. et al., "Compressive and flexural behaviour of concrete filled steel tubes after exposure to standard fire", Journal of Constructional Steel Research, 61(7), 2005, pp 882-901.
4. David, I.R., Luke, A.B. et al., "Post-fire residual capacity of protected and unprotected concrete filled steel hollow columns", Proceedings, 8<sup>th</sup> International Conference on Structures in Fire, Shanghai, China, 2014, pp 435-442.
5. Yang, H., Han, L.H. et al., "Effects of heating and loading histories on post-fire cooling behaviour of concrete-filled steel tubular columns", Journal of Constructional Steel Research, 64(5), 2008, pp 556-570.
6. Song, T.Y., Han, L.H. et al., "Concrete filled steel tube stub columns under combined temperature and loading", Journal of Constructional Steel Research, 66(3), 2010, pp 369-384.
7. Huo, J.S., Huang, G.W. et al., "Effects of sustained axial load and cooling phase on post-fire behaviour of concrete-filled steel tubular stub columns", Journal of Constructional Steel Research, 65(8-9), 2009, pp 1664-1676.
8. Huo, J.S., Zhang, J.G. et al., "Effects of sustained axial load and cooling phase on post-fire behaviour of reinforced concrete stub columns", Fire Safety Journal, 59, 2013, pp 76-87.
9. "ABAQUS analysis user's manual, SIMULIA", 2010 Providence, RI.
10. Tao, Z., Ghannam, M., "Heat transfer in concrete-filled carbon and stainless steel tubes exposed to fire", Fire Safety Journal, 61, 2013, pp 1-11.
11. Tao, Z., Wang, X. et al., "Stress-strain curves of structural and reinforcing steels after exposure to elevated temperatures", Journal of Materials in Civil Engineering, 25(9), 2013, pp 1306-1316.
12. Tao, Z., Wang, Z. et al., "Finite element modelling of concrete-filled steel stub columns under axial compression", Journal of Constructional Steel Research, 89, 2013, pp 121-131.



# Dynamic Performance Criteria for Suspended Courts at the National Tennis Centre

Mark Sheldon<sup>1</sup> and Benjamin Delaney<sup>2</sup>

<sup>1</sup>Technical Director, Aurecon

<sup>2</sup>Senior Project Manager, Major Projects Victoria

**Abstract:** The National Tennis Centre at Melbourne Park incorporates courts on the roof of a carpark building. As this has never been done at the home of a “Grand Slam” tournament, an appropriate structural design criterion for the suspended slabs was needed. A study was undertaken on how vibrations induced by the players and external sources would be perceived, and following testing on existing courts and undertaking real time studies on forces exerted by tennis players, a series of criteria for acceptable vibrations in the structure was developed. A bi-directionally banded post-tensioned concrete floor system was developed using FEA, and dynamically tested upon completion. The structure has now been successfully used during three Australian Open tournaments.

**Keywords:** Tennis court dynamic performance vibration

## 1. Introduction

The Eastern Plaza and National Tennis Centre are part of the Melbourne Park Redevelopment project which is being managed by Major Projects Victoria for Sport and Recreation Victoria, Melbourne & Olympic Parks, and Tennis Australia. The project, completed in late 2012, incorporates world-class tennis courts on the roof of the new carpark building. The new tennis courts are both indoor and outdoor, with the indoor courts covered by a metal and glass-clad architectural envelop as shown in the image below.



**The indoor tennis courts at the National Tennis Centre [1]**

Constructing international standard courts on top of a building is something not previously seen at the home of a “Grand Slam” tournament. This presented the design team with a new challenge – to determine an appropriate structural design criterion for the suspended slabs. The stiffness of the structure needed to be considered, in particular how vibrations induced by the players and external sources would be perceived. Following testing on existing courts and undertaking real time studies on forces exerted by tennis players, a design criterion for acceptable vibrations was developed for the suspended structure supporting the tennis courts.

Following completion of the design and construction, on-site testing was undertaken to compare the in-situ results to the theoretical predictions. The criteria was met, and the facility has now been successfully used by many of the world's top tennis players.

## **2. Background**

Most tennis courts suitable for international competition are located at ground level, on stable loadbearing layers supported by the ground. The structural design methodology for these courts is reasonably well understood within the structural engineering fraternity. However site constraints within the Melbourne Park complex dictated that for the new National Tennis Centre, opened just prior to the 2013 Australian Open, eight inside warm up courts and six outside courts needed to be located over the 1000 car carpark building. The National Tennis Centre also includes a player's gymnasium, a running track, and associated facilities which the design team identified could induce vibrations in the structure.

A study of major tennis venues around the world did not identify any design precedents for suspended "international standard" courts, so a design approach needed to be developed. The main concern was structure-borne vibrations, i.e. whether the movement of players or other external sources would cause unacceptable levels of vibration.

Structure-borne vibrations can be initiated from a number of sources. The simplest form of initiator is a single strike. Once struck, the structure will oscillate at its fundamental frequency or natural frequency. The length of time over which it will oscillate and the rate at which energy dissipates is a function of the inherent damping of the structure, which is influenced by the fixtures, services and furnishings attached to the structure, and the original form of the structure.

At the other end of the spectrum is the case where a cyclical load induces what could be considered a regular series of strikes on the structure. The effect of this type of loading is very dependent on the frequency of this cyclical load. If the load frequency does not match the natural frequency of the structure, then the resultant vibrations may not be significant. However when the load frequency matches the structure's natural frequency (or an integer multiple of the natural frequency), then significant vibrations can be induced.

In reality a tennis slab structure would be subjected to a wide range of forces, from single strikes generated by players jumping; a series of rhythmic strikes from players running; forces randomly generated from the movement of weights in the gymnasium; transient forces from cars moving around in the carpark or trains passing Melbourne Park on the nearby rail lines; and continuous forces from machinery in plantrooms. Each of these cases needed to be investigated.

Whilst the study of structure-borne vibrations can become quite technical, it was the desire of the client group (in particular Major Projects Victoria and Tennis Australia) that a quantifiable design approach be developed, so that this may be able to be used on similar future projects.

## **3. General Principles of Dynamics**

Under the influence of an applied load, or series of loads, a series of vibrations will be induced in the structure. As the structure will (typically) consist of slabs, beams, columns and foundations, these elements will all influence the frequency of the structure. Instead of having one natural frequency, a structure can have a number of resonant frequencies.

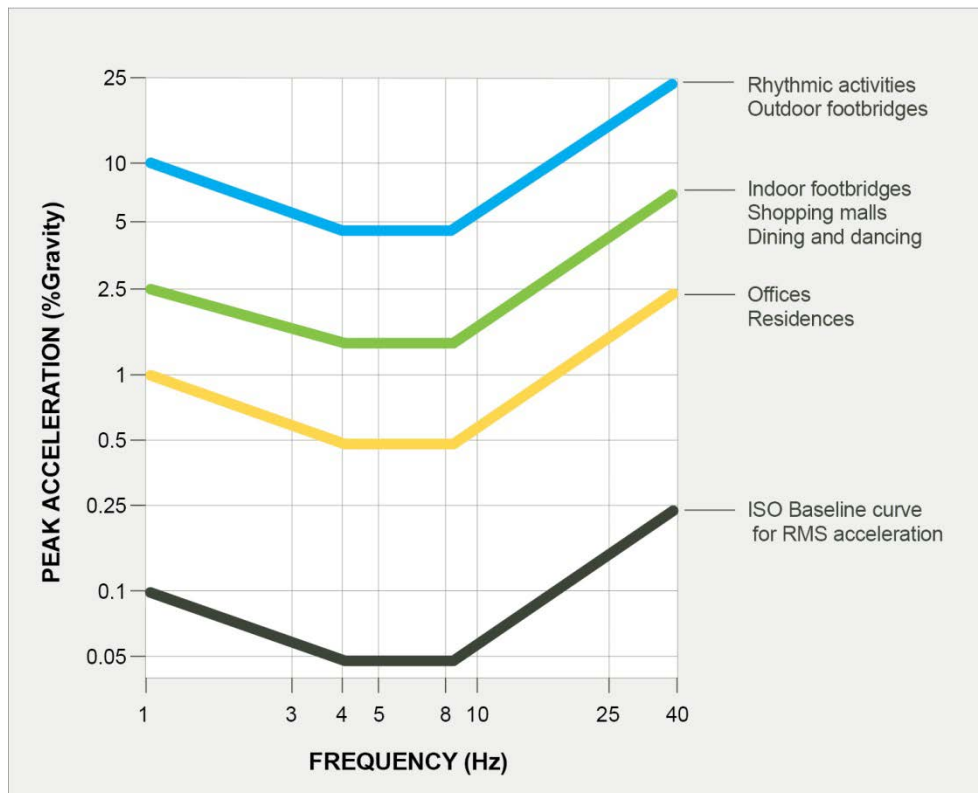
The main design parameter associated with an investigation into structure-borne vibration is usually the resultant acceleration. A person standing on the vibrating structure will feel this vibration. What they are actually sensing is the cycles of accelerations and decelerations. Interestingly, some people are more sensitive to the oscillating motion than others, and some people are more tolerant of this motion than others (and this may even change depending on the player's temperament).

Whilst the behaviour of the oscillation of a floor system can be quite complex, in simple terms under an applied striking force the following will occur:-

- The structure will vibrate at its “natural frequency” or one of its resonant frequencies
- The length of time over which it will oscillate is a function of the magnitude of the force and the damping in the building
- People will sense the acceleration of the slab caused by the vibration

There are various ways to measure and report accelerations, the relevance of which is dependent upon the type of floor and the predominant forcing loads. In this instance, it was determined that the as the frequency of forcing loads during play would be orders of magnitude above the frequency of the structure, then the most important structural response parameter is the peak acceleration. Immediately following the peak acceleration there will be a peak deceleration, both of which will contribute to the perceived vibration. It was therefore concluded that the average of these two peak figures would be used as the criterion.

A significant body of research has been undertaken over many years studying the perceptions of vibrations, particularly in North America based on work by Thomas Murray and David Allen. Much of this work has been published over a 30+ year period, and has formed the basis of the National Buildings Code of Canada’s design criteria [3] and the American Institute of Steel Construction’s Design Guide No 11 [4]. These studies have identified that humans are most susceptible to vibrations in the range of 4-8 Hz. It was also identified that people are more tolerant of vibrations in structures such as footbridges and shopping centres (where they only have limited exposure to the vibration) but are less tolerant of vibrations in an office environment and even less tolerant in their home. The following chart (Figure 1) is well known within the engineering fraternity as the basis for acceptable vibrations in different building types, based on the works of Murray and Allen.



**Figure 1: Acceleration Design Curves based on the works of Murray and Allen [2]**

A significant observation from these curves is that, above approximately 8 Hz the allowable accelerations can increase. This is due in part to the fact that people are less susceptible to higher frequency vibrations, but also recognizes that as the frequency increases, the displacement associated with the oscillation will be less (for a similar applied force).

In addition to the works by Murray and Allen, other structure-borne vibration studies have been undertaken in Australia and internationally over many years on buildings such as hospital wards, operating theatres and the like. These were referenced in the development of the criteria for the Eastern Plaza tennis courts.

Another critical factor in the development of the criteria for the tennis courts is the fact that a person using their own body weight to cause the load (by jumping, lunging, running etc) is generally not able to sense the resultant vibrations in a normal structure. This observation was central to the decision on where the accelerations should be measured in the structure, and is discussed in more detail below.

#### **4. Team Effort**

Developing a first-of-its-kind criterion that is practical and economical, yet still meets the “fitness for purpose” test requires buy-in from the whole team. Fortunately this occurred on this project. Similarly, it requires experienced people who are each able to contribute their inputs in their particular field of expertise, so that the important aspects of the whole issue can be identified and addressed. Again, this occurred on this project.

The client was concerned that if the courts were considered too bouncy by the world’s top players then the ensuing bad publicity would have significant impacts on the Australian Open. However they also had a budget to meet. The Eastern Plaza was tendered as a “Design and Construct” project by Major Projects Victoria. The three respondents to this tender each took different approaches to the issue of the dynamics of the tennis courts, proposing three different solutions. Each of the three proposals were based on a post-tensioned concrete structure, however the thicknesses and layout differed considerably as did their cost per square metre.

The contract was awarded to the team led by Watpac Construction, with Jackson Architecture, WSP as their structural engineer, and Marshall Day Acoustics providing vibration advice. After award, the final criterion was still to be resolved, and whilst different members of the team had different drivers, it was the professional approach by all parties that led to the successful conclusion.

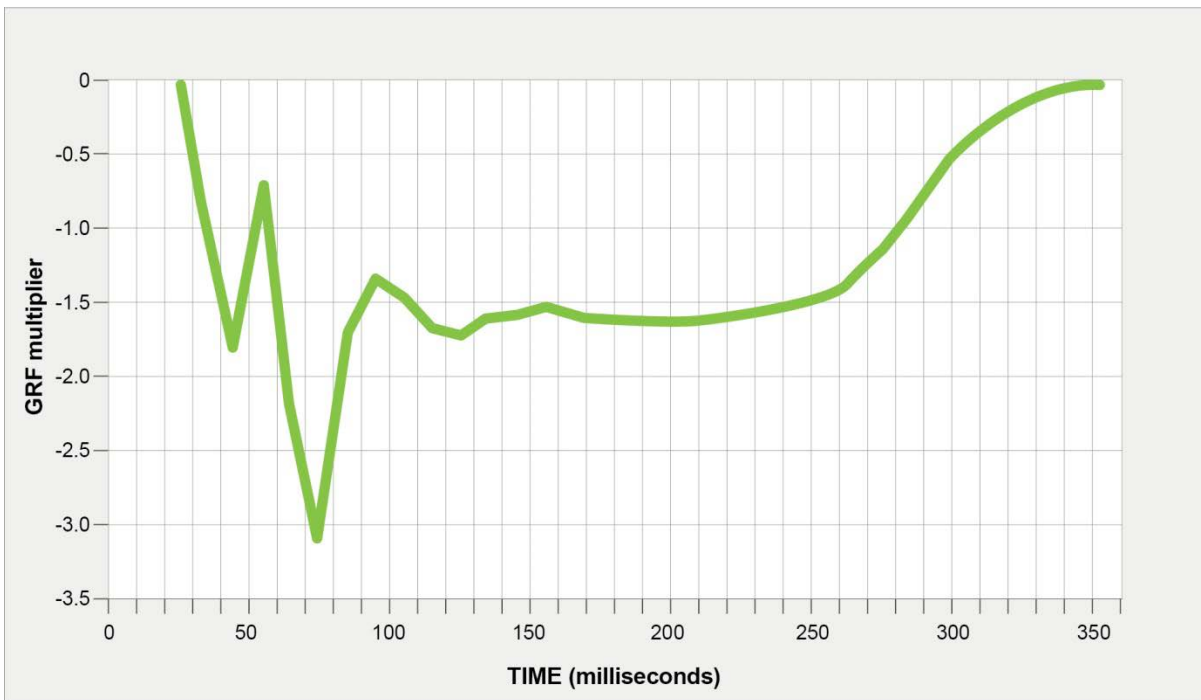
#### **5. Pre-tender investigation**

At the pre-tender stage of the Eastern Plaza project Major Projects Victoria and Tennis Australia recognised that this was an unusual project requiring additional inputs, so Tennis Australia commissioned testing to examine the dynamic performance of selected existing tennis courts. One court tested was the existing Margaret Court Arena, which has been used for many years during previous Australian Open Grand Slam tournaments, and consists of a post-tensioned slab-on-grade. The second test was on a tennis court located on a carpark building associated with a major hotel development. In addition, to accumulate more data for comparison a third series of tests were undertaken on a tennis court located on a suspended slab at a tennis facility in Auckland New Zealand during the final design stage. Measurements of accelerations and frequencies were taken at each of the facilities during a tennis match. As was expected, the dynamic response measured from these three tennis courts differed greatly. It was determined that for the Melbourne Park facility, the new suspended courts needed to be stiffer than the two suspended courts tested.

In addition, Major Projects Victoria and Tennis Australia also commissioned some actual impact load tests, undertaken at the Victoria Institute of Sport (VIS) Sports Science Department. A competition player was put through a series of typical tennis manoeuvres over a load cell. The actual forces exerted on to the floor from these manoeuvres were measured against time. Selected graphical outputs of these tests follow. The testing showed that under a “jump smash” action, the force exerted on the floor was equivalent to approximately 12.5 times the player’s weight, but for a very short period of time. Under actions such as running and changing directions, the Gross Reaction Force (GRF) is approximately 2 times body weight, but occurs over a longer time and is obviously likely to occur much more frequently during a match. Under a serve motion, the maximum GRF was approximately 2.5 times the body weight, increasing to approximately 3.2 times under a volley motion.



**Figure 2: Gross Reaction Force diagram for Change in Direction**



**Figure 3: Gross Reaction Force diagram for Volley**

The results of the Volley tests were of particular interest, as this represents an activity that would occur relatively frequently during a match. It was noticed that this action produces a GRF plot with a peak similar to a “Heel Drop”. A Heel Drop test is a universally accepted (albeit crude) test to study vibrations in structures. It was identified that a Heel Drop test could be used to simulate the Volley design case, and could be reproduced with reasonable consistency.

## 6. Development of a criteria

To design a structure with “imperceptible” accelerations under all load conditions was virtually impossible and, at best, extremely cost-prohibitive. It was accepted that a design criteria had to be developed. Rather than try to adopt a single criterion for the design of the structure, it was decided that a rational approach coupling the probability of a load occurrence with an appropriate allowable acceleration was more logical. The Jump Smash action was identified as the most severe of the design cases, however this activity is expected to occur less frequently than serving, volleying and significantly less than running / changing directions. In addition to these forces caused by the players, we also needed to consider structure-borne vibrations caused by vehicles in the carpark, trains and trams passing the facilities, activities in the gymnasium, and machinery in the plantrooms of the facility.

Given that the professional players normally play on “on grade” courts that experience minimal accelerations under impacts, it was deemed necessary that a tight criterion for the suspended slabs was necessary. The starting point was to consider a criterion for the most common forms of activity – running and changing directions during a match. Australian Standard AS2670.1 – 2001 [5], which is based on ISO 2631-1:1997, indicates that approximately 25% of alert fit persons cannot detect a vertical vibration with a peak magnitude of 0.2%g. Similarly, the Department of Environment and Conservation NSW’s “Assessing Vibration: A Technical Guideline” [6] provides a maximum recommended acceleration from a vertical continuous vibration source in a hospital operating theatre which equates to a peak acceleration of approximately 0.14%g. Anecdotal evidence from the design team on the National Tennis Centre was that a figure of 0.2%g had recently been used as the design criterion for a large Australian hospital. It was therefore decided that the criterion where the peak accelerations is limited to less than 0.2% g (for structures in the range of 4-8 Hz) would be appropriate, as it was deemed that even the most temperamental tennis player would agree that if a surface was stiff enough to for a doctor to operate, it would be acceptable for a tennis match. Following the precedent of the curves as shown above, the allowable acceleration could increase if a stiffer structure (with a higher natural frequency) was provided.

The “background” vibrations from external sources (vehicles, trains, trams, activities in the gym, mechanical plant etc.) was the second criterion to be determined. As this vibration could be expected to occur for extended periods of time, an acceleration limit less than the running/ changing direction criterion was deemed appropriate. Following an assessment of what could be realistically and economically achieved in design, an acceleration curve at 80% of the running / changing direction criteria was adopted. This is nearing the level at which many people would consider is imperceptible.

The next criterion to be considered was for the serve action and volley action. As this activity would occur less frequently than the running and changing direction, a higher acceleration was considered acceptable. A peak acceleration of 0.5%g was adopted, increasing in line with the curves shown above for frequencies greater than 8Hz. This is similar to what would be deemed acceptable in an office or residential environment, as shown in figure 1. A convenient aspect of this criterion is that the Gross Reaction Force generated from the players is similar in magnitude and duration to a heel drop test, which is relatively easy to replicate by technicians.

Under the jump smash action a more lenient criteria was necessary, as a cost-prohibitive structure would otherwise be necessary. Through consultation with Marshall Day Acoustics, it was agreed that as the duration of the significant force was extremely short, an allowable acceleration of 2%g (increasing for structures above 8Hz) would be acceptable. The resultant design curves are presented in Figure 4 below.

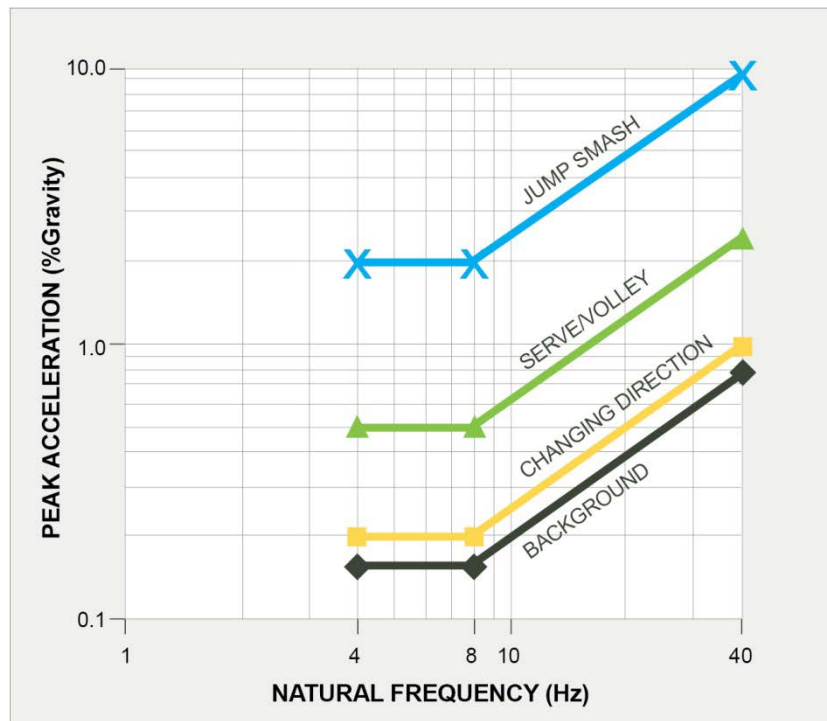


Figure 4: Adopted design criteria

## 7. Location of Acceleration Measurements

The location of the acceleration measurements on the structure is another important feature of the adopted design criteria. For the bottom-most curve, (the background vibrations), these accelerations should not be exceeded anywhere on the slab. For the remainder of the criteria, however, two different practical factors were considered. As noted previously, it is known that the person performing the forcing action does not feel the resulting accelerations. In a tennis match environment it is therefore typically the umpire or a doubles partner that is likely to be located within about 4 metres of that player.

It was decided that to have requisite stiffness to accommodate the design criteria, and to accommodate the carparking layout and other constraints below, the structure would have columns on a grid of 8.1metres x 7.8metres. By undertaking a preliminary 3D Finite Element Analysis (FEA) and studying the modeshapes of the resonant frequencies of the likely structural system, it was known that maximum and minimum accelerations are likely to occur at multiples of grids and half-grids of the structure. The design methodology was therefore to place the forcing load at the most severe location on the structure as determined by the FEA analyses and check accelerations at half-grid spacings (4.05m in the north-south and 3.9m in the east-west directions). Due to the length of a tennis court (and the fact that the players may be both located beyond the baseline) it was considered necessary to continue the measurements for a distance of approximately 25-30 metres.

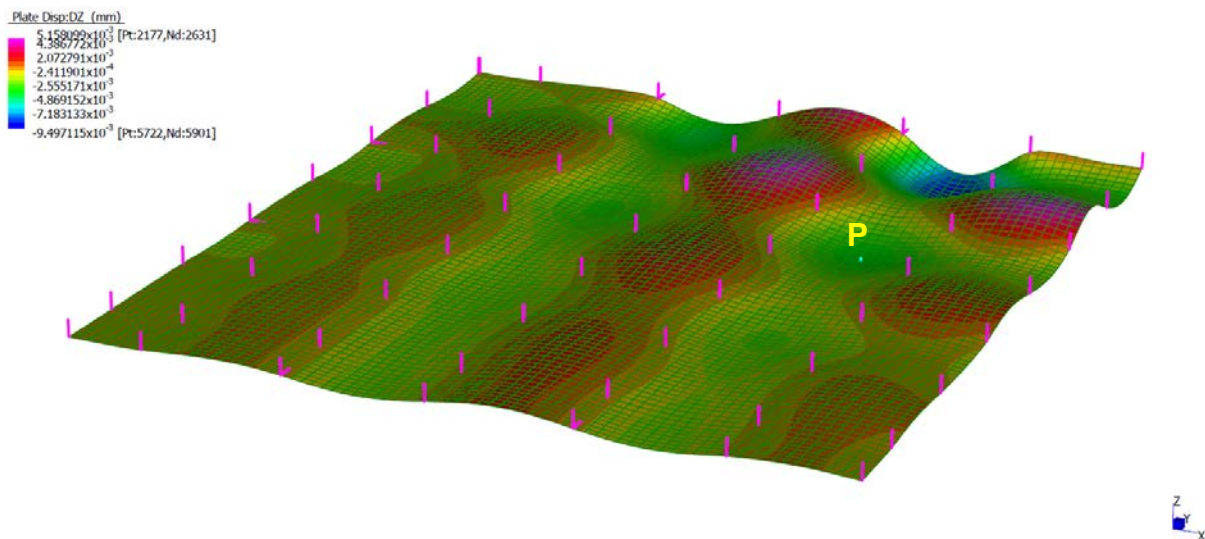
## 8. Pre-construction Dynamic Analysis

Significant analysis of the structure is required prior to construction, to determine the dimensions of structure to be constructed to meet the design criteria. A full 3D finite element analysis (FEA) with time history capability is necessary to model the characteristics of the load (from the GRF plots) and the response of the structure at multiple locations. To model the structure's response, an accurate assessment of the stiffness of the structural elements is essential. All flexural concrete members form fine cracks in the tensile zones which reduce its stiffness at these locations and increase deflections. These micro-cracks result in a varying effective Moment of Inertia across the structure. Similarly, under dynamic loads, publications such as the AISC Design Guide No 11 [4] recommend a dynamic modulus of elasticity



1.35 times higher for the concrete elements than what would normally be used for a static analysis. Whilst outside the scope of this paper, these parameters need to be carefully considered before a realistic dynamic FEA can be undertaken. It is wise to undertake a static analysis of the structure initially and compare moments, forces and deflections to results from a trusted flexural analysis program prior to embarking on the dynamic analysis. Modifications to the static design model may still be necessary, as the effect of the micro-cracking on the effective Moment of Inertia for very small amplitude deflections can be less prominent, especially in a post-tensioned structure.

The final design of the floor structure was undertaken by WSP using the ETABS software, and to test the accuracy of their model Aurecon produced our own Strand 7 FEA model. This reflected the edge conditions between the movement joints in the structure and the properties of the supporting columns below. The Aurecon model included the dynamic modulus of elasticity with a reduced effective Moment of Inertia in some elements. Based on the layout of the courts and the structural grids, it was identified that the maximum accelerations in the applicable portions of the building could be generated in the structure by locating the forcing load in the bay as shown in Figure 5. The structure was then designed and detailed based on this pre-construction dynamic analysis.



**Figure 5: Screen shot of the Aurecon Strand 7 model displacement under dynamic load (Load exerted at “P”)**

From the FEA analysis, a design evolved which essentially consisted of 450mm deep x 2400mm wide bandbeams in both the north-south and east-west directions, with 200mm infill slabs. Both the slabs and bandbeams are post-tensioned. This resultant structure is considerably stiffer than a “normal” slab that would otherwise be required for an office or retail development based on the same column grid.

## 9. Post-construction Dynamic Analysis

Once the structure had been completed, a series of tests were undertaken to measure the accelerations produced at the critical point located in figure 5. Tests were done whilst a player ran, changed direction, served, volleyed and hit jump smashes, with accelerometers at intervals up to 27metres away from the strike point. Tests were also performed using dropped loads, which were considered to more accurately reproduce the specified design GRF's in a repeatable manner. In addition, Heel Drop tests were undertaken to simulate the volley action. The results of the measured resonant frequencies of the structure were found to be around 20% lower than the theoretical figures. It is not unusual for there to be such a difference given the dependency of the results on numerous factors outside the control of the designer. This is accounted for in the performance criteria, as the allowable acceleration is a function of the actual frequency, as shown in figure 4. For the resonant frequency of the test bay the resulting accelerations were found to be within the criteria set for the project.

As the National Tennis Centre was opened prior to the end of 2012, it was used for the first time during the 2013 Australian Open, and again during both the 2014 and 2015 Australian Open. Feedback from the players and Tennis Australia was that the facility has performed well and met their expectations.

## 10. Summary

The National Tennis Centre at Melbourne Park incorporates courts on the roof of the new carpark building. Constructing international standard courts on top of a building is something not previously seen at the home of a “Grand Slam” tournament. This presented the design team with the challenge of how to determine an appropriate structural design criterion for the response of the structure to vibrations induced by the players and external sources.

Tests on existing courts were undertaken, as well as real time studies on forces exerted by tennis players. Based on a rational approach, relating how often an event may occur to an appropriate acceleration limit, a series of design curves was developed for acceptable vibrations in the suspended structure supporting the tennis courts. A criteria for the locations on the slab where the measurements should be taken was also determined. Using a Finite Element Analysis with a series of time history load inputs, a post-tensioned concrete structure was designed to satisfy the dynamic criteria.

This report provides guidance on the main parameters that should be considered, and the design approach that was applied for the dynamic performance of the suspended tennis courts at the Melbourne Park venue. The structure has now been constructed, and insitu testing has confirmed that it satisfies the design criteria. The structure was successfully used during the 2013, 2014 and 2015 Australian Open tournaments.

## 11. Acknowledgements

The authors wish to acknowledge the contributions made during the development of the design criteria by Tennis Australia, Melbourne Olympic Park Trust, Watson Moss Growcott, Watpac Construction, WSP, Marshall Day Acoustics, and the Major Projects Victoria and Aurecon teams.

[1] Photo courtesy of Peter Glenane

[2] Figure 1 adapted from American Institute of Steel Construction Design Guide No 11, AISC 1997

## 12. References

3. National Research Council Canada; User’s Guide – NBC 2005, Structural Commentaries (Part 4 of Division B).
4. Murray, Allen and Unger; Floor Vibrations Due to Human Activity, American Institute of Steel Construction Steel Design Guide 11, 1997.
5. Standards Australia; AS2670.1 – 2001, Evaluation of human exposure to whole- body vibration, Part 1: General Requirements.
6. Department of Environment and Conservation NSW (Aust); Assessing Vibration: a technical guideline, 2006.

# Flexural Response of GFRP-Reinforced Geopolymer Concrete Beams

Ginghis B. Maranan<sup>1</sup>, Allan C. Manalo<sup>2</sup>, Warna Karunasena<sup>3</sup>, Brahim Benmokrane<sup>4</sup>, and Priyan Mendis<sup>5</sup>

<sup>1</sup>PhD Candidate, University of Southern Queensland

<sup>2</sup>Senior Lecturer, University of Southern Queensland

<sup>3</sup>Professor, University of Southern Queensland

<sup>4</sup>Professor, University de Sherbrooke

<sup>5</sup>Professor, The University of Melbourne

**Abstract:** This study investigated the flexural response of glass fibre reinforced polymer-reinforced geopolymer concrete (GFRP-RGC) beams using a four-point static bending test. Three full-scale beams were cast and reinforced with nearly same amount of longitudinal GFRP reinforcements but of varying diameters at the bottom (4-12.7 mm, 3-15.9 mm, and 2-19.0 mm), two 12.7 mm GFRP bars at the top, and 9.5 mm GFRP stirrups spaced at 100 mm on-centre. The average compressive strength of the geopolymer concrete was 38.2 MPa. Based on the experimental results, all the tested beams showed nearly similar crack pattern, load-deflection response, bending-moment and deflection capacities, and strain readings, suggesting that the flexural response of a GFRP-RGC beam was not significantly influenced by the bar diameter; instead, by the properties of the geopolymer concrete. The  $0.3M_u$  criterion suggested by Bischoff must be adapted in the serviceability design of a GFRP-RGC beam. The flexural capacities of the tested beams were generally higher than the predicted values from ACI 440.1R-06 and CSA S806-12 standards. Furthermore, the GFRP-RGC beams have higher strength compared with their GFRP-reinforced concrete counterparts. Thus, it can be concluded that the GFRP-RGC beams have structural properties that are suitable for civil infrastructure applications.

**Keywords:** flexural response, geopolymer concrete, GFRP bars, four-point static bending test, civil infrastructure.

## 1. Introduction

Cement-based concrete is one of the oldest and most commonly used construction materials in the world. The demand for this material is expected to increase in the future owing to rise of infrastructure need by many developing countries and the growing number of old and deteriorated concrete structures needing urgent repair and rehabilitation. The production of cement, however, contributes billions of tons of waste materials and about 7% of the world's greenhouse gas yearly (1). In fact, several studies revealed that for every 1.0 tonne of cement produced, approximately 1.0 tonne of CO<sub>2</sub> are being released into the atmosphere (2). With the alarming increase of Earth's average surface temperature due to greenhouse gases, also known as global warming, the construction industry, specifically, are prompted to replace cement with a greener material like geopolymer. Geopolymer is a highly sustainable concrete binder as it can be manufactured using by-product materials, like fly ash and blast furnace slags. Davidovits (3) proposed the term "geopolymer" since the chemical reaction that takes place between the aluminum (Al) and silicon (Si) source material and the alkaline liquid activator is a polymerization process.

Many studies have shown that geopolymer concrete has physical and mechanical properties that are suitable for structural applications (4-6). In fact, the geopolymer concrete internally reinforced with steel bars has been successfully utilised in the construction of several civil infrastructures such as pavement, retaining walls, and bridges. However, in order to maximize its full potential for various structural applications especially in harsh environment, the corrosion of steel reinforcements must be avoided or must be eliminated, if possible, since this phenomenon results in geopolymer concrete cracking and spalling that can lead to early strength degradation and loss of serviceability of the structure before reaching its expected service life. Among the possible solutions that are being implemented to address this concern is to utilise fibre reinforced polymer (FRP) bars because, aside from being corrosion-resistant, these bars have high tensile strength, lightweight, high fatigue endurance, electromagnetic neutrality, and have low thermal and electrical conductivity (7).

With the advantageous properties of the geopolymer concrete and the FRP bars, their combination can be anticipated to yield a construction technology that is both more sustainable and more durable with adequate structural integrity. Limited studies, however, are available that deals with FRP-reinforced

geopolymer concrete and this has been the key motivation of this undertaking. This study presents an investigation of the flexural response of geopolymer concrete beams reinforced with sand-coated glass FRP (GFRP) bars subjected to four-point static bending test. Three full-scale beams with nearly same amount of bottom GFRP bars but with varying diameter were cast and tested. The crack patterns and failure modes, load versus deflection relationships, bending-moment and deflection capacities, and strains in the bars and geopolymer concrete are presented. Furthermore, the experimental flexural capacity of beams are compared with the predicted values using the current standards and with their GFRP-reinforced concrete (GFRP-RC) counterparts to verify the suitability of the proposed system for structural applications.

## 2. Experimental Program

### 2.1 Materials and test specimens

Three high modulus (HM) sand-coated GFRP bars with nominal diameters ( $d_b$ ) of 12.7 mm, 15.9 mm, and 19.0 mm were used to longitudinally reinforce the beams (Figure 1). The bars, as shown in Figure 1, were produced through the pultrusion process of E-Glass fibres impregnated in a thermosetting modified vinyl ester resin (Grade III, CSA S807-10 (8)). Table 1 summarises the physical and mechanical properties of the bars as provided by the manufacturer, including the guaranteed tensile strength ( $f_{tu}$ ) and elastic modulus ( $E_f$ ), computed based on the nominal area ( $A_f$ ), and the usable strain ( $\epsilon_{cu}$ ).

The geopolymer concrete used in the study was made up of fly ash and slag, fine and medium sands, 10 mm and 20 mm coarse aggregates, water, and alkaline liquid. Table 2 presents the mechanical properties of the geopolymer concrete. Based on the compression test of four 100 mm diameter by 200 mm high cylinders, the average 28-day compressive strength ( $f'_c$ ) and elastic modulus ( $E_c$ ) of the geopolymer concrete were 38 MPa and 38.5 GPa, respectively. Furthermore, the three-point static bending test of the three geopolymer concrete prisms (75 mm x 75 mm x 285 mm) yielded an average modulus of rupture ( $f_r$ ) of 3.86 MPa.

Three full-scale geopolymer concrete beams were cast and tested. The beams were longitudinally reinforced at the bottom with 4-12.7 mm, 3-15.9 mm, and 2-19.0 mm HM GFRP bars. Furthermore, each beam was provided with 2-12.7 top HM GFRP bars and 9.5 mm HM GFRP stirrups spaced at 100 mm on-center. The beams were 200 mm wide, 300 mm deep, and 3100 mm long and were designed as over-reinforced to achieve a concrete crushing failure mode. Figure 2 shows the beams' cross-sectional geometry and reinforcement details while Table 3 summarises the label and classification of each beam in accordance with their bottom longitudinal reinforcements. The actual and balanced reinforcement ratio ( $\rho_f$  and  $\rho_{fb}$ , respectively) were calculated using Equations 1 and 2. The terms  $\alpha_1$  and  $\beta_1$  were obtained from Equation 3 for ACI 440.1R-06 (9) and from Equation 4 for CSA S806-12 (10). These equations are summarised in Table 8. The maximum usable strain of the geopolymer concrete ( $\epsilon'_{cu}$ ) were assumed to be 0.003 and 0.0035 for ACI 440.1R-06 and CSA S806-12, respectively.

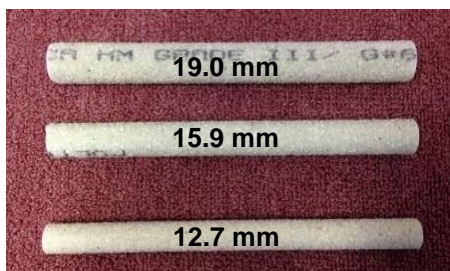
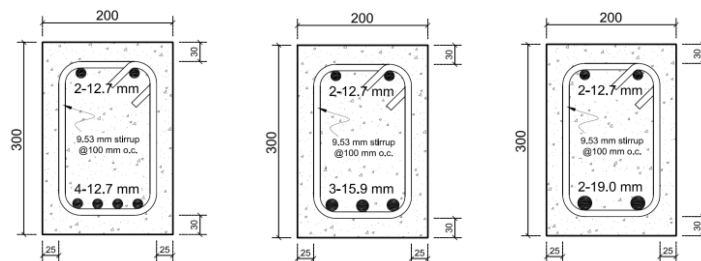


Figure 1. GFRP Bars.



(a) GFRP-RGC-4-12.7 (b) GFRP-RGC-3-15.9 (c) GFRP-RGC-2-19.0

Figure 2. Cross-sectional geometry and reinforcement details of the beams.

**Table 1. Properties of GFRP bars.**

$d_b$ (mm)	$A_f$ (mm <sup>2</sup> )	$f_{tu}^*$ (MPa)	$E_f$ (GPa)	$\epsilon_{cu}$ ( $\mu\epsilon$ )
9.5	71	1029	50	20580
12.7	129	1312	65.6 $\pm$ 2.5	20000
15.6	199	1184	65.6 $\pm$ 2.5	18914
19.0	284	1105	65.6 $\pm$ 2.5	17347

\*Guaranteed tensile strength: Average value – 3X standard deviation (ACI 440.1R-06)

**Table 2. Properties of geopolymer concrete.**

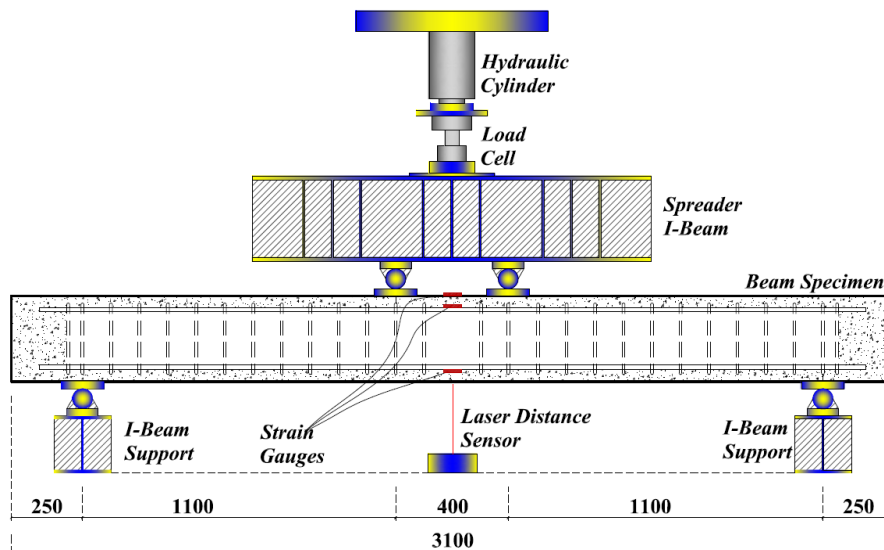
$f'_c$ (MPa)	$E_c$ (GPa)	$f_r$ (MPa)
38.2	38.5	3.86

**Table 3. Label and classification of the tested beams.**

Beam	Section		Tension Reinforcement			Remarks	
	$b$ (mm)	$h$ (mm)	#	$d_b$ (mm)	$\rho_f$ (%)		$\rho_{fb}^{\dagger}$ (%)
GFRP-RGC-4-12.7	200	300	4	12.7	1.13	0.38 (0.40)	Over-reinforced
GFRP-RGC-3-15.9	200	300	3	15.9	1.18	0.33 (0.35)	Over-reinforced
GFRP-RGC-2-19.0	200	300	2	19.0	1.00	0.29 (0.30)	Over-reinforced

## 2.2 Test method and instrumentations

Figure 3 shows the schematic diagram of the four-point static bending test employed in the study. The beams were loaded at midspan with two concentrated loads spaced at 400 mm, yielding a shear span of 1100 mm on both sides. The load was applied using a 2000 kN capacity hydraulic jack at a rate of approximately 3 mm/min. The midspan deflection was measured using a Laser Optical Displacement (LOD) device. Furthermore, electrical strain gauges were attached to the top surface of the geopolymer concrete beam and in the top and bottom reinforcements to measure the longitudinal strains during loading. The loads and strain readings were captured using the System 5000 data logger.



**Figure 3. The four-point static bending test.**

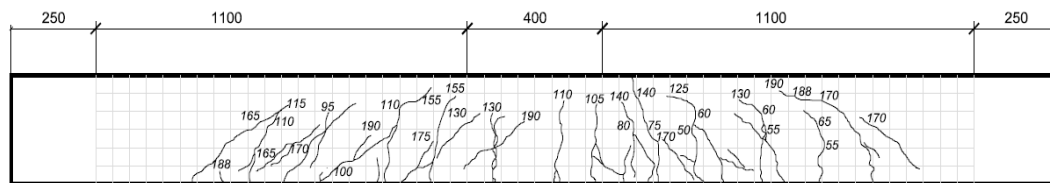
### 3. Results and Discussion

#### 3.1 Experimental results

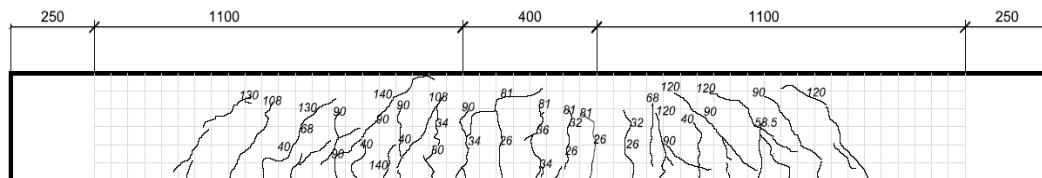
##### 3.1.1 Crack pattern and failure mode

All the tested beams were initially uncracked before loading. Then, several vertical cracks were formed along their constant bending-moment zone right after the applied load exceeded the geopolymer concrete tensile capacity. With further loading, these cracks became wider and propagated upward while new flexural cracks were developed on both shear spans of the beams. At higher loads, the vertical cracks within the pure bending zone further widen while the vertical cracks on both shear spans became more inclined due to the shear stresses. However, the rate of lengthening and widening of inclined cracks did not increase as the geopolymer concrete began to crush. At the final loading stage, few inclined cracks reached the crushed zone of the geopolymer concrete. Figure 4 shows the final crack patterns of the tested beams. Based on the figure, the cracks were almost uniformly distributed along the beam span with spacing of approximately 100 mm, similar to stirrups spacing. This observation demonstrated that a composite action existed between the GFRP bars and the geopolymer concrete, that is the stress is effectively transfer from geopolymer concrete to GFRP bars and vice versa, through the friction and mechanical interlock provided by sand-coats. No significant difference can be observed among the crack patterns of the beams.

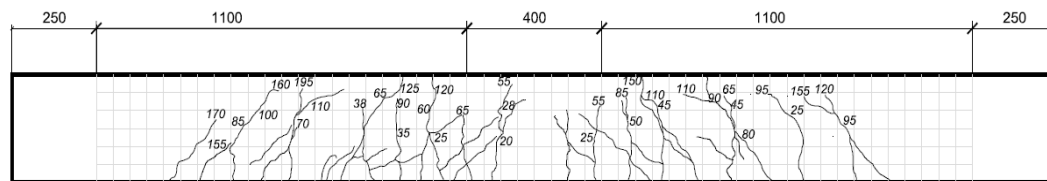
Figure 5 depicts the typical failure mode of the tested beams. As expected, the over-reinforced beams failed in flexure through crushing of the geopolymer concrete in the compression zone. Gangarao et al. (7) reported that, generally, the preferred failure mode for any FRP reinforced concrete beam is the concrete crushing since this failure is more gradual, less brittle, and less catastrophic with higher deformability compared with the FRP tensile rupture. Thus, it can be concluded that the tested beams were designed satisfactorily and accordingly.



(a) GFRP-RGC-4-12.7



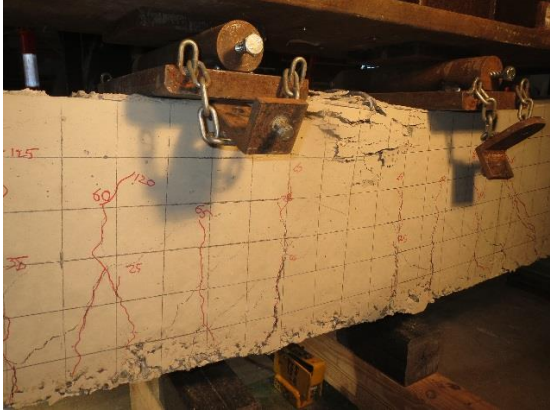
(a) GFRP-RGC-3-15.9



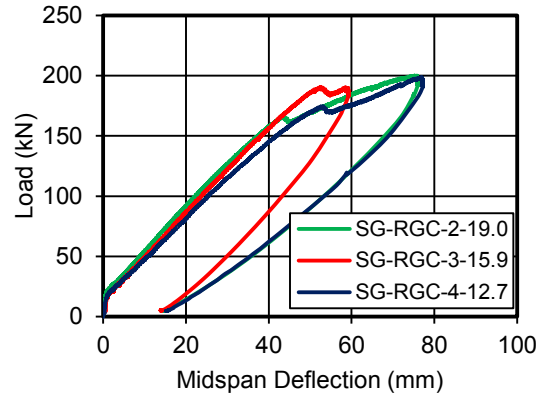
(a) GFRP-RGC-2-19.0

**Figure 4. Crack patterns of the tested beams.**





**Figure 5. Typical failure mode of the tested beams.**



**Figure 6. Load-deflection response of the tested beams.**

### 3.1.2 Load-deflection response

Figure 6 shows the relationship between the applied load and the midspan deflection of the tested beams. Generally, their load-deflection curves can be divided into three segments. The first segment embodies the typical steep linear response of an uncracked beam, wherein the load increases linearly with midspan deflection. This section is similar for all beams no matter the amount and type of reinforcements, because at this stage, only the geopolymer concrete is sustaining all the applied loads. The second segment represents the cracked response of the beam. It is composed of a linear response with reduced slope, similar for all the tested beams, followed by a non-linear response up until the crushing failure of the geopolymer concrete in the compression zone. This non-linearity can be attributed to extensive cracking and crushing of the geopolymer concrete. Lastly, the third segment represents the post-failure response of the beam wherein the beam continued to sustain additional loads after the crushing failure of the geopolymer concrete, owed to the stirrup confinement effect that enhanced the ductility and strength of the beams. The slope of this segment is lower than the previous segment due to the initiation of failure in the GFRP bars.

The beams were loaded just before its final failure to avoid any mishaps during testing. The behaviour during load removal was also recorded. The unloading segment showed the inherent elastic characteristic of the beams at higher loads, even after exhibiting a nonlinear behaviour or even after the concrete crushing failure.

### 3.1.3 Bending-moment capacity

Table 4 summarises the experimental flexural capacity of the tested beams at geopolymer concrete cracking ( $M_{cr-exp}$ ), at service condition ( $M_{s-exp}$ ), at geopolymer concrete crushing failure ( $M_{u-exp}$ ), and at peak ( $M_{peak-exp}$ ). The  $M_{cr-exp}$  was determined based on the recorded load when the first flexural crack appeared and was verified from load-deflection and moment-strain plots of beams. The GFRP-RGC-4-12.7, GFRP-RGC-3-15.9, and GFRP-RGC-2-19.0 beams yielded nearly similar  $M_{cr-exp}$  values of 10.4 kN-m, 11.5 kN-m, and 11.9 kN-m, respectively. This can be expected since the  $M_{cr-exp}$  is mainly dependent on the geopolymer concrete properties. The marginal difference can be attributed to the nonhomogeneous and anisotropic properties of the geopolymer concrete. The average cracking moment and the corresponding modulus of rupture ( $f_r$ ) were 11.3 kN-m and 3.76 MPa, respectively. This value of  $f_r$  was comparable to that obtained from the bending test of geopolymer concrete prisms.

In this study, the suggested criteria by ISIS-06 (11) and Bischoff et al. (12) were used to identify the  $M_{s-exp}$  of the beams. The first benchmark defines the  $M_{s-exp}$  as the bending-moment value that



corresponds to a tensile-strain reading of 2000  $\mu\epsilon$  in the reinforcement, the specific strain value that limits the crack width to 0.7 mm and 0.5 mm for interior and exterior exposures, respectively, in any FRP-RC components. The second benchmark, on the other hand, approximates  $M_{s-exp}$  as 30% of a beam's ultimate capacity ( $0.3M_{u-exp}$ ). Based on these criteria, all the tested beams yielded comparable  $M_{s-exp}$  values except that of GFRP-RGC-3-15.9 beams at 2000  $\mu\epsilon$ .

The  $M_{u-exp}$  of GFRP-RGC-4-12.7, GFRP-RGC-3-15.9, and GFRP-RGC-2-19.0 were 96.1 kN-m, 104.8 kN-m, and 91.4 kN-m, respectively. These values were relatively comparable to each other, suggesting that the nominal diameter does not influence the beams' bending-moment capacity, mainly because the failure of these beams was governed by geopolymer concrete crushing failure and not by tensile rupture of the GFRP bars. The slight variation can be attributed to, again, the intrinsic composite characteristic of the geopolymer concrete. All the tested beams, however, continued to sustain further loads even after the crushing failure and yielded another peak bending-moment, owed to the confinement effect provided by GFRP stirrups located in the constant bending-moment zone. The  $M_{peak-exp}$  were 109.3 kN-m, 104.7 kN-m, and 110.1 kN-m for GFRP-RGC-4-12.7, GFRP-RGC-3-15.9, and GFRP-RGC-2-19.0, respectively. The 25 mm gap, between the beam and the load applicator, prior to load application resulted in a relatively lower  $M_{peak-exp}$  of GFRP-RGC-3-15.9 compared with the other beams. Thus, it can be further concluded that the nominal bar diameter have no significant effect on beam strength even after crushing failure.

**Table 4. Flexural capacity and failure mode of the tested beams.**

Beam	$M_{cr-exp}$ (kN-m)	$M_{s-exp}$ (kN-m)		$M_{u-exp}$ (kN-m)	$M_{u-theo}$ (kN-m) <sup>†</sup>		$M_{peak-exp}$ (kN-m)	Failure Mode
		2000 $\mu\epsilon$	0.30 $M_{u-exp}$		ACI 440.1R-06	CSA S806-12		
GFRP-RGC-4-12.7	10.4	27.2	28.8	96.1	71.5 [74%]	77.2 [80%]	109.3	Concrete crushing
GFRP-RGC-3-15.9	11.5	21.3	31.4	104.8	73.9 [71%]	79.7 [76%]	104.7	concrete crushing
GFRP-RGC-2-19.0	11.9	27.0	27.4	91.4	72.3 [79%]	78.0 [85%]	110.1	concrete crushing

<sup>†</sup> The number inside [ ] represents the ratio between  $M_{u-theo}$  and  $M_{u-exp}$

### 3.1.4 Midspan deflection

Table 5 shows the midspan deflection at service load level ( $\Delta_{s-exp}$ ), at geopolymer concrete crushing failure ( $\Delta_{u-exp}$ ), and at unloaded phase or residual deflection ( $\Delta_{res-exp}$ ) of tested beams. As discussed earlier, the serviceability performance of the beams was described based on ISIS-07 and Bischoff et al.'s suggestions. The recorded  $\Delta_{s-exp}$  based on ISIS (Bischoff) criterion were 10.6 mm (11.5 mm), 7.1 mm (12.3 mm), and 8.7 mm (8.8 mm) for GFRP-RGC-4-12.7, GFRP-RGC-3-15.9, and GFRP-RGC-2-19.0, respectively. It was evident from these results that the nominal bar diameter have no significant correlation on the serviceability performance of the beams since the measured  $\Delta_{s-exp}$  for each criterion was comparable to each other. Generally, all the tested beams satisfy the deflection limit set by the ACI 440.1R-06, which is equivalent to L/240 or 10.8 mm. However, the results showed that the serviceability design of a GFRP-RGC beam should be based on 0.3 $M_{u-exp}$  criterion since the estimated deflections based on this criterion were higher than that of ISIS. El-Nemr et al. (13) also adapted the same criterion for the serviceability design of FRP-RC beams.

The  $\Delta_{u-exp}$  of GFRP-RGC-4-12.7, GFRP-RGC-3-15.9, and GFRP-RGC-2-19.0 were 53.2 mm, 52.5 mm, and 43.4 mm, respectively. From these results, it can be concluded that the deflection behaviour of GFRP-RGC beam is not dependent on the bar diameter. All the tested beams yielded similar  $\Delta_{res-exp}$  values, having an average of 14.3 mm. This magnitude of residual deflection shows the inherent elastic behaviour of the GFRP-RGC beams at higher loads, even after the crushing failure of the geopolymer concrete.

**Table 5. Midspan deflection of the tested beams.**

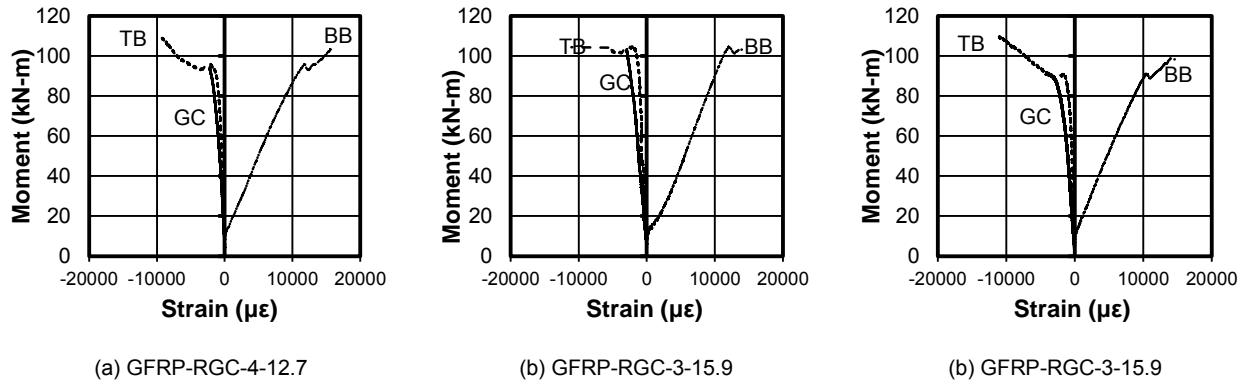
Beam	$\Delta_{s-exp}$ (mm)		$\Delta_{s-theo}$ (mm) <sup>†</sup>		$\Delta_{u-exp}$ (mm)	$\Delta_{u-exp}$ (mm) <sup>†</sup>		$\Delta_{res-exp}$ (mm)
	2000 $\mu\epsilon$	0.30 $M_{u-exp}$	2000 $\mu\epsilon$	0.30 $M_{u-exp}$		ACI 440.1R-06	CSA S806-12	
GFRP-RGC-4-12.7	10.6	11.5	7.4	8.2	53.2	36.3	35.3	15
GFRP-RGC-3-15.9	7.1	12.3	3.6	8.3	52.5	36.3	35.7	14
GFRP-RGC-2-19.0	8.7	8.8	6.6	6.8	43.4	32.9	32.9	14

<sup>†</sup>Based on ACI 440.1R-06

**3.1.5 Strain in the longitudinal reinforcement and geopolymer concrete**

Figure 7 shows the moment-strain relationships of the tested beams. Analogous moment-strain curvatures occurred among top bars (TB), bottom bars (BB), and geopolymer concrete (GC). Furthermore, the top and bottom reinforcements yielded trilinear curves, similar to the load-deflection curve, while the geopolymer concrete only yielded a bilinear curve because the strain gauge attached on geopolymer concrete’s top surface did not provide further readings after its crushing failure. These observations tend to show that no slippage occurred during the test, thereby demonstrating the effectiveness of anchoring the GFRP bars in geopolymer concrete using sand-coatings.

Table 6 shows the strain readings at service condition based on 0.3  $M_{u-exp}$ , at geopolymer concrete crushing failure, and at peak. The strains at bottom bars were all greater than 2000  $\mu\epsilon$ , showing the appropriateness of using Bischoff’s criterion for the GFRP-RGC beam serviceability design. On other hand, the maximum usable strain in the geopolymer concrete reached a magnitude of 4831  $\mu\epsilon$  that is higher than those normally assumed in ACI 440.1R06 and CSA S806-12 standards. The peak tensile strain at the bottom bars were just 79 %, 79 %, and 86 % of the bars’ tensile capacity for GFRP-RGC-4-12.7, GFRP-RGC-3-15.9, and GFRP-RGC-2-19.0, respectively. All the tested beams yielded nearly comparable strains at different load stages that further verified that bar diameter have no significant effect on the flexural performance of the GFRP-RGC beam.



**Figure 7. Moment-strain relationships of the tested beams.**

**Table 6. Strains in geopolymer concrete (GC), top bars (TB), and bottom bars (BB).**

Beam	At service condition ( $\mu\epsilon$ )			At failure ( $\mu\epsilon$ )			At peak ( $\mu\epsilon$ )	
	GC	TB	BB	GC	TB	BB	TB	BB
GFRP-RGC-4-12.7	348	247	2147	4831	2327	11547	9271	15746
GFRP-RGC-3-15.9	698	156	3508	2934	2115	12244	11083	14956
GFRP-RGC-2-19.0	502	203	2028	4226	2086	10855	11186	14963

<sup>†</sup>Based on ACI 440.1R-06

### 3.2 Theoretical Prediction

Table 7 shows the summary of the equations, suggested by ACI 440.1R-06 and CSA S806-12 standards, used in the study. The theoretical flexural capacities of the beams at geopolymer concrete crushing failure ( $M_{u-theo}$ ) were computed using Equation 5 and were summarized in Table 4. The stress in the bar ( $f_f$ ) was calculated from Equation 6 for ACI 440.1R-06 and from Equation 7 for CSA S806-12, where the neutral axis  $c$  was determined from Equation 8. The  $M_{u-theo}$  based on ACI 440.1R-06 were 71.5 kN-m, 73.9 kN-m, and 72.3 kN-m for GFRP-RGC-4-12.7, GFRP-RGC-3-15.9, and GFRP-RGC-2-19.0, respectively, while CSA S806-12 yielded 77.2 kN-m, 79.7 kN-m, and 78.0 kN-m, respectively. Generally, the prediction equations underestimated the flexural capacity of the tested beams due to several factors. First, the  $\varepsilon'_c$  used in the prediction, such as 3000  $\mu\varepsilon$  for ACI 440.1R-06 and 3500  $\mu\varepsilon$  for CSA S806-12, were lower compared with the actual strain that can reach a value of 4831  $\mu\varepsilon$ . Second, the flexural contribution of top GFRP bars was neglected in both equations. Finally, the confinement effect due to later ties provided in the pure bending-moment zone were not considered. By comparing the two standards, the CSA S806-12 yielded more accurate results than the ACI 440.1R-06.

The predicted midspan deflection at service condition ( $\Delta_{s-theo}$ ) and at geopolymer concrete crushing failure ( $\Delta_{u-theo}$ ) were shown in Table 5. These values were calculated from Equations 9, 10, and 11 for ACI 440.1R-06 and from Equations 12 and 13 for CSA S806-12. The computed  $\Delta_{s-theo}$  and  $\Delta_{u-theo}$  were lower than their actual deflection counterparts. The underestimation, however, was more evident at higher applied loads, owing to the overestimation of the tension stiffening parameter.

**Table 7. Summary of equations used for theoretical predictions.**

ACI 440.1R-06	CSA S806-12
$\rho_f = A_f/bd$	(1)
$\rho_f = \alpha_1 \beta_1 \frac{f'_c}{f_{fu}} \frac{E_f \varepsilon'_c}{E_f \varepsilon'_c + f_{fu}}$	(2)
$\alpha_1 = 0.85$ (3a)	$\alpha_1 = 0.85 - 0.0015 f'_c \geq 0.67$ (4a)
$\beta_1 = 0.85 - \frac{0.05(f'_c - 27.6)}{6.9}$ (3b)	$\beta_1 = 0.85 - 0.0025 f'_c \geq 0.67$ (4b)
$M_{u-theo} = \rho_f f_f b d^2 \left( 1 - \frac{\rho_f f_f}{2\alpha_1 f'_c} \right)$	(5)
$f_f = \sqrt{\frac{(E_f \varepsilon'_{cu})^2}{4} + \frac{0.85 \beta_1 f'_c}{\rho_f} E_f \varepsilon'_{cu}} - 0.5 E_f \varepsilon'_{cu} < f_{fu}$ (6)	$f_f = A_f E_f \frac{\varepsilon'_{cu} (d-c)}{c} < f_{fu}$ (7)
	$\alpha_1 \beta_1 f'_c b c - A_f E_f \frac{\varepsilon'_{cu} (d-c)}{c} = 0$ (8)
$\Delta = \frac{(Pa/2)}{24E_c I_e} [3L^2 - 4a^2]$ (9)	$\Delta = \frac{(P/2)L^3}{24E_c I_{cr}} \left[ 3\frac{a}{L} - 4\left(\frac{a}{L}\right)^3 - 8\eta \left(\frac{L_g}{L}\right)^3 \right]$ (12)
$I_e = \left(\frac{M_{cr}}{M_a}\right)^3 \beta_d I_g + \left[ 1 - \left(\frac{M_{cr}}{M_a}\right)^3 \right] I_{cr} \leq I_g$ (10)	$\eta = 1 - \frac{I_{cr}}{I_g}$ (13)
$\beta_d = 0.2 \left( \frac{\rho_f}{\rho_{fb}} \right) \leq 1.0$ (11)	

### 3.3 Comparison between GFRP-RGC and GFRP-RC beams

Table 8 shows the comparison between the normalized flexural capacity of GFRP-RGC and GFRP-RC beams. The GFRP-RC beams that were considered in the study have nearly similar dimensions, concrete strengths, and amount and type of reinforcements. In general, the bending-moment capacities of the tested beams (GFRP-RGC beams) were higher than the GFRP-RC beams owing to the enhanced mechanical properties of the geopolymer concrete compared with normal concrete, the provision of lateral ties within the constant bending-moment zone that provided confinement, and the higher tensile properties of GFRP bars used in this study compared with the previous ones.

**Table 8. Flexural capacity of GFRP-RGC and GFRP-RC beams.**

Reference	Beam	$\rho_f$ (%)	$M_u / f_c b d^2$
Current Study	GFRP-RGC-4-12.7	1.13	47.7
	GFRP-RGC-3-15.9	1.18	54.3
	GFRP-RGC-2-19.0	1.00	49.6
Toutanji and Saafi (14)	GB3-1	1.10	44.6
	GB3-2	1.10	47.3
Benmokrane et al. (15)	ISO1	1.10	35.1
	ISO2	1.10	36.7
Benmokrane et al. (16)	ISO30-2	1.01	35.9

## 4. Conclusions

The flexural response of geopolymer concrete beams reinforced with GFRP bars (GFRP-RGC beams) was investigated using a four-point static bending test. Based on the experimental results, the following conclusions were made:

- Nearly similar cracking pattern, load-deflection response, bending-moment and deflection capacities, and strain readings were obtained from all the tested beams. These results tend to show that the flexural performance of a GFRP-RGC beam is not dependent on the nominal diameter of the bottom longitudinal reinforcements.
- The uncracked and cracked response of the beams were relatively comparable since the strength of the beam mainly depends on the geopolymer concrete strength.
- The serviceability design criterion suggested by Bischoff et al. ( $0.3MU_{-exp}$ ) is more appropriate in designing a GFRP-RGC beam.
- The prediction equations recommended by ACI 440.1R-06 and CSA S806-12 underestimated the flexural and deflection capacities of the tested beams, suggesting that new prediction must be developed for a GFRP-RGC beam.
- The strength of GFRP-RGC beam is generally higher than that of GFRP-RC beam, indicating that the GFRP-RGC can be adapted for different structural applications; however, additional studies must be conducted to increase the approval of the proposed technology in the construction industry.

## 5. Acknowledgement

The authors would like to express their special thanks to V-ROD® Australia for providing the materials, the Natural Science and Engineering Research Council of Canada (NSERC), and the technical staff of the Centre of Excellence in Engineered Fibre Composites (CEEFC) at University of Southern Queensland.

## 6. References

1. Mehta, P. K., "Reducing the environmental impact of concrete", Concrete International, 2001.
2. McCaffrey, R., "Climate change and the cement industry". Global Cement and Lime Magazine (Environmental Special Issue, 2002, pp 15-19.

3. Davidovits, J., "Geopolymer chemistry and applications (3<sup>rd</sup> edition)" Institut Geopolymere, 2011, Saint-Quentin, France.
4. Rangan, B. V., Sumajouw, D. et al., "Reinforced low-calcium fly ash-based geopolymer concrete beams and columns", Proceedings, 31<sup>st</sup> Conference on Our World in Concrete and Structures, 2006, Singapore.
5. Sofi, M., van Deventer, J. S. J. et al. "Bond performance of reinforcing bars in inorganic polymer concrete (IPC)", Cement and Concrete Research, 37, 2007, pp. 251-257.
6. Duxson, P., Fernandez-Jimenez, A. et al. "Geopolymer technology: the current state of the art", Journal of Material Science, 42, pp 2917-2933.
7. Gangarao, H. V. S., Taly N. et al., "Reinforced concrete design with FRP composites", Taylor and Francis Group, 2007, NW, USA.
8. Canadian Standards Association, "Specification for fibre-reinforced polymers (CSA S807-10)", CSA Group, 2010, Ontario, Canada.
9. American Concrete Institute, "Guide for the design and construction of building materials with fibre-reinforced polymers (ACI 440.1R-06)", ACI Committee 440, 2006, Michigan, USA.
10. Canadian Standards Association, "Design and construction of building structures with fibre-reinforced polymers (CSA S806-12)", CSA Group, 2010, Ontario, Canada.
11. Intelligent Sensing for Innovative Structures, "Reinforcing concrete structures with fibre reinforced polymers: Design Manual No. 3, Version 2", ISIS Canada Corporation, 2006, Manitoba, Canada
12. Bischoff, P. H., Gross, S. et al., "The story behind the proposed changes to the ACI 440 deflection requirements for FRP-reinforced concrete", ACI Special Publication, 264, 2009, pp 53-76.
13. El-Nemr A., Ahmed E. A. et al., "Evaluation of flexural behavior and serviceability performance of concrete beams reinforced with FRP bars", ACI Structural Journal, 110, 2013, pp 1077-88.
14. Toutanji, H. A., Saafi, M., "Flexural behavior of concrete beams reinforced with glass fiber-reinforced polymer (GFRP) bars", ACI Structural Journal, 97(5), 2000, pp 712-719.
15. Benmokrane, B., Chaallal, O. et al., "Flexural response of concrete beams reinforced with FRP reinforcing bars", ACI Structural Journal, 1996, 91(2), pp 46-55.
16. Benmokrane, B., Chaallal, O. et al., "Glass fibre reinforced plastic (GFRP) rebars for concrete structures", Construction and Building Materials, 1995, 9(6), pp 353-364.

# An Experimental Study on the Long-Term Behaviour of Simply-Supported and Continuous Reinforced Concrete Slabs

Md Mahfuzur Rahman<sup>1</sup>, Gianluca Ranzi<sup>1</sup>, Daniel Dias-da-Costa<sup>1</sup>, Arnaud Castel<sup>2</sup>, Raymond Ian Gilbert<sup>2</sup>

<sup>1</sup>School of Civil Engineering, The University of Sydney, Australia

<sup>2</sup>School of Civil and Environmental Engineering, The University of New South Wales, Australia

**Abstract:** The behaviour at service conditions of a reinforced concrete member is highly dependent on the deformational properties of the materials, the extent of cracking, the creep and shrinkage deformations in the concrete and the magnitude and distribution of the applied loads. This paper presents initial measurements of an experimental study carried out on two simply-supported and three continuous reinforced concrete slabs aimed at evaluating the variation over time of the instantaneous flexural stiffness induced by time-dependent cracking. For this purpose, a particular loading device has been set-up based on the use of water tanks to provide different levels of sustained loads and to load/unload the sample in a short time (to simulate instantaneous loads). The long-term measurements have been recorded to provide insight into the influence of creep and shrinkage effects on the time-dependent response of the slab. Relative humidities have been measured through the thickness of the concrete samples to gain more insight into the development of drying shrinkage. It is envisaged that this experimental data represents valuable information for the calibration and validation of numerical and design models incorporating shrinkage effects for reinforced concrete slabs.

**Keywords:** Concrete, Creep, Instantaneous stiffness, Relative humidity, Shrinkage, Slabs.

## 1. Introduction

Reinforced concrete construction is widely used for building applications. Typical floor systems consist of statically indeterminate continuous reinforced concrete slabs. In the case of building floors, their design is usually governed by serviceability limit state requirements and their behaviour depends on the deformational properties of the materials, the extent of cracking, the creep and shrinkage deformations in the concrete, and the magnitude and distribution of the applied loads at service conditions. Typical slab systems used in Australia are lightly reinforced and their service loads induce maximum moments close to their cracking moments, therefore inducing cracking to develop over time (1, 2). Under these conditions, the flexural stiffness might reduce over time as highlighted from experimental measurements performed on reinforced concrete beams (3).

In this context, this paper presents initial measurements recorded as part of an experimental study aimed at investigating the time-dependent behaviour of lightly reinforced concrete slabs. In particular, two simply-supported and three continuous reinforced concrete slabs were prepared and tested subjected to different levels of instantaneous and sustained loads. A particular loading arrangement was devised to load the specimens by means of water pumped in and out from tanks placed on the samples, and its details are outlined in the following. All slab specimens were instrumented to monitor the instantaneous stiffness and time-dependent deformations. Separate concrete samples were prepared to measure the occurrence of shrinkage through the thickness of the slab considering different drying conditions for the slab surfaces. Relative humidity measurements were carried out on both reinforced and plain concrete samples to gain insight into the development and profile of drying shrinkage.

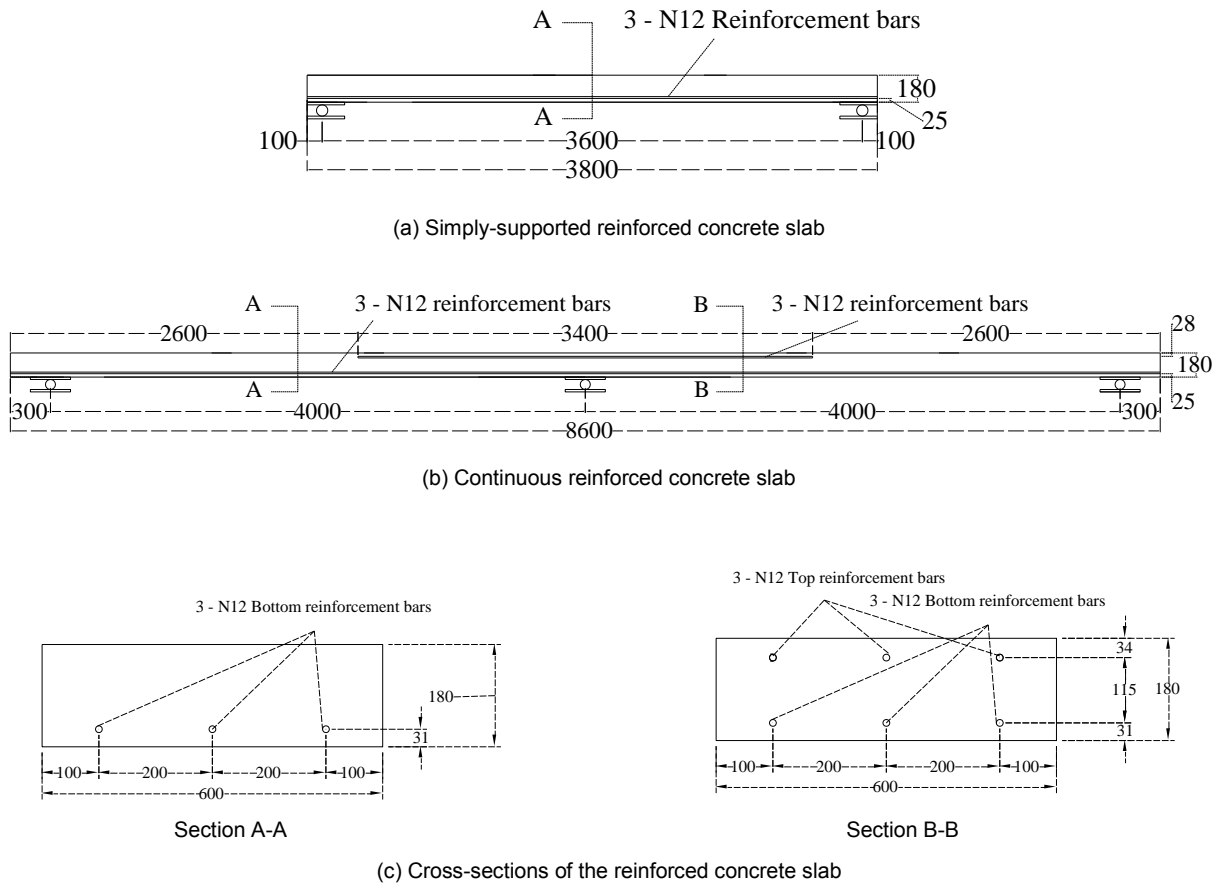
## 2. Experimental Program

### 2.1 Preparation of specimens

Two simply-supported and three continuous reinforced concrete slabs were prepared as part of this experimental program.

The simply-supported specimens had an overall length of 3800 mm and cross-sectional dimensions of 600 mm × 180 mm, as illustrated in Figure 1(a). Three N12 reinforcement bars were placed in a single layer at the bottom of the slab at a spacing of 200 mm. The continuous samples possessed identical geometric properties, with overall length of 8600 mm and rectangular cross-section of 600 mm × 180 mm. Samples were continuous over two equal spans of 4000 mm with an end outstand of 300 mm. Three N12 reinforcing bars were specified at the bottom of the slab and three N12 reinforcing bars were placed at the top of the slab over interior supports in the longitudinal direction with a transverse spacing of 200 mm, as shown in Figure 1(b). The tensile reinforcement ratio was about 0.4% for both simply-supported and continuous slabs.

The geometric characteristics and loading conditions adopted in the experiments are summarised in Table 1. All slab samples were wet cured for 7 days from the day of casting and then subjected to drying.



**Figure 1. Dimensions and reinforcement details for all specimens (all units in mm).**

**Table 1. Different geometric characteristics and loading conditions for reinforced concrete slabs.**

Type of Sample	Sample ID	Dimensions (mm) (Length × width × thickness)	Distance between supports (mm)	Instantaneous Load/Span (kN)	Sustained Load/Span (kN)
Simply-supported reinforced concrete slab	SS1	3800 × 600 × 180	3600	5	0
	SS2			5	5
Continuous reinforced concrete slab	CS1	8600 × 600 × 180	4000	5 followed by 10	10
	CS2			5 followed by 10	0
	CS3			5	0



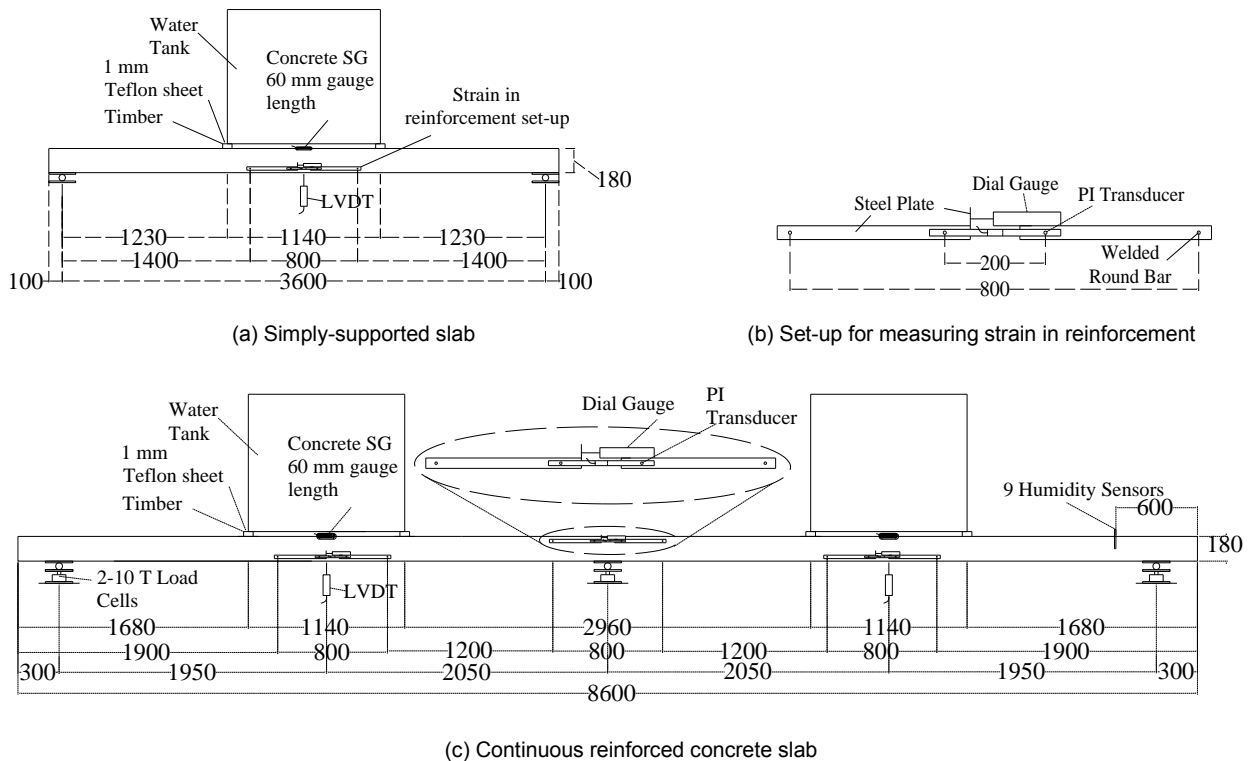
Material properties related to shrinkage were collected from four square plain concrete slabs cast with the same concrete mix of the reinforced concrete samples. These plain concrete slabs had dimensions of 600 mm × 600 mm × 180 mm to match the width and thickness of the reinforced concrete slab samples. Similar to the reinforced concrete slabs, shrinkage slabs were also wet cured for 7 days after the day of casting and then air dried. After curing, two shrinkage slabs, namely SH1 and SH2, were covered on their edges with moisture barrier paint to reproduce the continuity which the slab would have in a real floor system. Bottom surface and all four edges of other two shrinkage slabs, denoted as SH3 and SH4, were also covered with moisture barrier paint to obtain the non-uniform shrinkage distributions that would develop in a slab when its underside is sealed, as it would be the case in a composite floor. Exposure conditions specified for the shrinkage slabs are presented in Table 2.

**Table 2. Shrinkage slabs with different exposure conditions.**

Type of Sample	Sample ID	Dimensions (mm) (Length × width × thickness)	Exposure conditions: Top/Bottom Surface
Shrinkage slab	SH1	600 × 600 × 180	Exposed/Exposed
	SH2		
	SH3		Exposed/Covered with moisture barrier paint
	SH4		

## 2.2 Instrumentation

All samples were instrumented to measure deflections, strains in the concrete and reinforcement, and reactions during the experiment as shown in Figure 2. Mid-span deflections of the reinforced concrete slabs were measured by means of LVDTs. Concrete strain gauges were attached at mid-span to the top surfaces of the slabs while load cells were placed at support locations to monitor the reactions of the continuous reinforced concrete slabs over time. Average strains in the reinforcement bars were monitored with an 800 mm gauge length at mid-span for both continuous and simply-supported slabs, and over interior support locations for the continuous samples. These measurements were carried out using both dial gauges and PI transducers as shown in Figure 2.

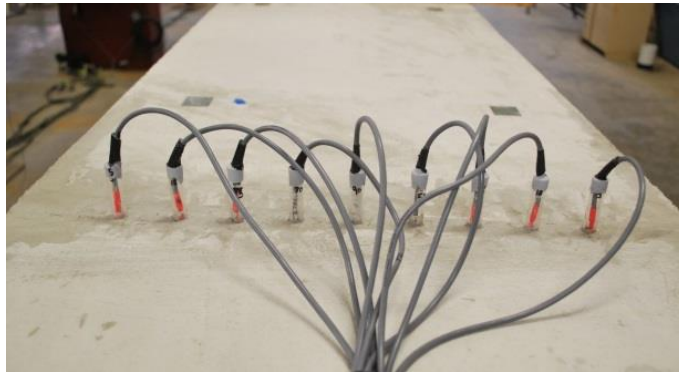


**Figure 2. Schematic diagram of instrumentation for all samples (all units in mm).**

Changes in relative humidity over the thickness of the slabs were measured over the time. Relative humidities were measured at 3, 5, 10, 15, 25, 35, 50, 70 and 90 mm depths from the top surface of each reinforced concrete slab and of two shrinkage slabs with top and bottom surfaces exposed to drying (SH1 and SH2). Relative humidities were measured at 3, 5, 10, 15, 25, 35, 50, 70, 90, 110, 130, 145, 155, 165, 170, 175 and 177 mm depths from the top of surface of other two shrinkage slabs (SH3 and SH4). Perspex tubes with cut at desired depths were held at position before casting to form holes inside the concrete as shown in Figure 3. Aluminum round bar with diameter slightly less than the inner diameter of Perspex tube was inserted to the Perspex tube to prevent the concrete flowing into the tube during casting. After few hours from casting, the aluminum bars were removed from the tube and the top of the tube was then sealed. All humidity sensors were inserted into the Perspex tubes after the end of curing and the tubes were then sealed with a silicon tape.



(a) Before casting



(b) After casting

**Figure 3. Set-up for the relative humidity measurements.**

### **2.3 Loading Arrangement**

The devise used for the loading and unloading of the slabs is outlined in this section. At the beginning of the tests, empty tanks were placed on top of the slabs. Double layers of 1 mm Teflon sheets were used between the water tank and timber supports to minimise the restraint during deformations, therefore avoiding the possible longitudinal restraint to the slab provided by the water tank frame. Details of the positions and dimensions of the water tanks are illustrated in Figure 2.

The loading and unloading was performed by pumping water into the loading tanks placed on top of the slab from the storage tank and vice-versa, respectively, as shown in Figure 4. With the adopted pump arrangement, the loading/unloading rate was about 4 kN/minute for each tank which was considered acceptable to represent typical instantaneous loads. The same arrangement was implemented to apply the sustained loads on the slab.

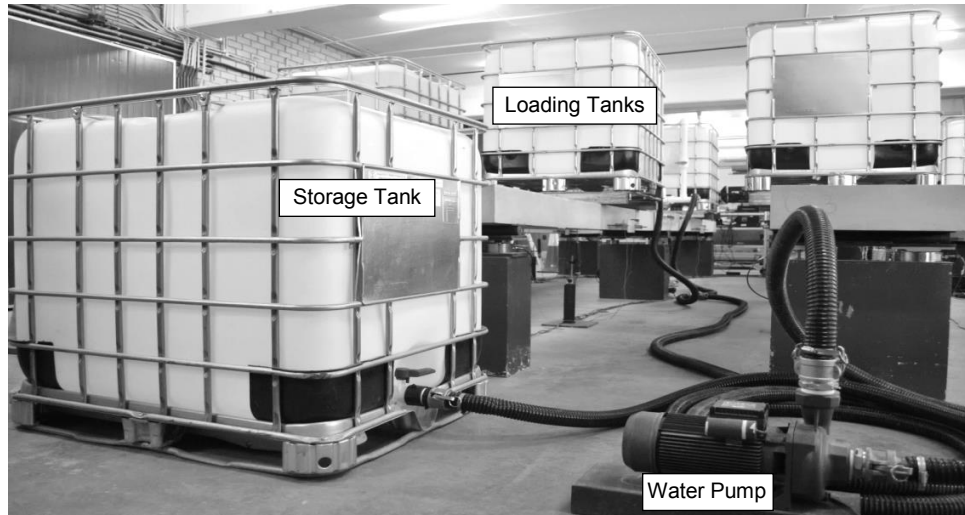


Figure 4. Loading/unloading arrangement using water tanks.

## 2.4 Testing Procedure

After curing, all continuous slab samples were unpropped and simply-supported slabs were placed in their simply-supported configuration and, therefore, were subjected to their self-weight and to shrinkage effects (Figure 5). After six weeks from casting, all samples were subjected to instantaneous loads to develop different level of cracking and to determine the stiffness of the slabs at that instant of time as shown in Figure 6. During the instantaneous tests, three loading/unloading cycles were applied for each sample. The levels of instantaneous loads applied during the tests are summarised in Table 1.

For the long-term tests, the slabs were monitored to evaluate the long-term deformations produced by different levels of sustained load and due to shrinkage. Different levels of sustained load for each sample are summarised in Table 1.

## 3 Material Properties and Environmental Conditions

### 3.1 Instantaneous Material Properties

All samples were cast from the same batch of ready-mixed concrete. Standard compressive strength tests and indirect tensile strength tests were carried out by testing standard cylinders of 150 mm diameter and 300 mm height. Average compressive and tensile strengths of concrete were 41.0 and 3.1 MPa, respectively, at 29 days from the day of casting. Average compressive and tensile strengths of concrete during the first application of external loading were 45.1 and 3.2 MPa, respectively, at the seventh week from casting. The measured yield and tensile ultimate strengths for the steel reinforcement were 590 MPa and 659 MPa, respectively.

### 3.2 Shrinkage and Relative Humidity Measurements

Free drying shrinkage was measured from the shrinkage slabs. Demec targets with 200 mm gauge length were attached on the top and bottom surfaces of the shrinkage slabs. To facilitate measuring the shrinkage strains at the top and bottom surfaces, all shrinkage slabs were placed in vertical position supported on three rollers (shown in Figure 7) after being cast horizontally.

The shrinkage strains of shrinkage slabs SH1 and SH2 (with top and bottom surfaces exposed to drying), and SH3 and SH4 (only top surfaces exposed to drying) are shown in Figure 8(a) and (b), respectively.



Figure 5. Reinforced concrete slabs subjected to only self-weight.



(a)



(b)

Figure 6. Reinforced concrete slabs with applied loading.

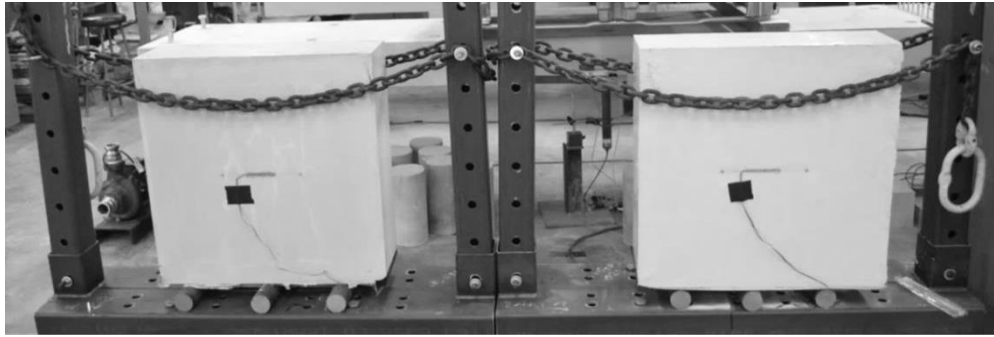


Figure 7. Shrinkage slabs in vertical position.

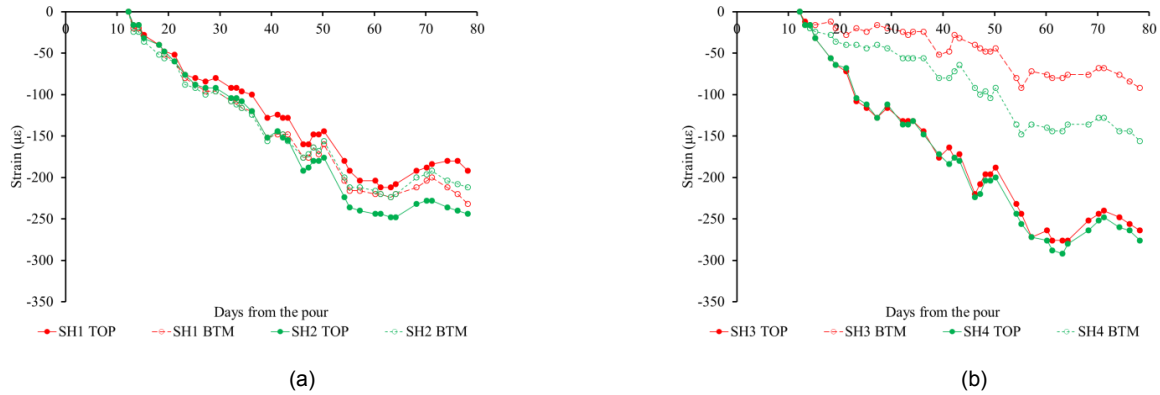


Figure 8. Shrinkage strains measured over time on shrinkage slab samples.

Over time, samples SH1 and SH2 experienced similar shrinkage values at the top and bottom surfaces, while samples SH3 and SH4 exhibited higher shrinkage strains at the top surface than that of the bottom surface because of the presence of moisture barrier paint at the bottom surface. This is consistent with previous work carried out on composite slabs by the authors (4, 5, 6, 7) and with the relative humidity profiles measured in the samples, highlighting the significance of the drying shrinkage component. Typical relative humidity profiles measured through the slab depths at different instants in time for the reinforced concrete slab and shrinkage slab samples are depicted in Figure 9.

### 3.3 Environmental Conditions

The samples were kept in a laboratory environment where the relative humidity and temperature were not controlled, and their variations are presented in Figure 10.

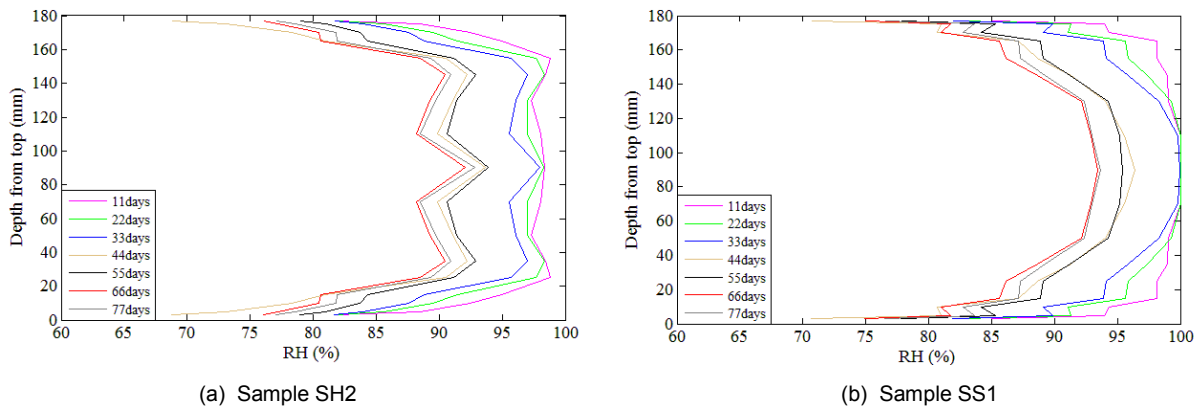


Figure 9. Representative measurements showing the variations in relative humidity over the cross-section taking place over time.

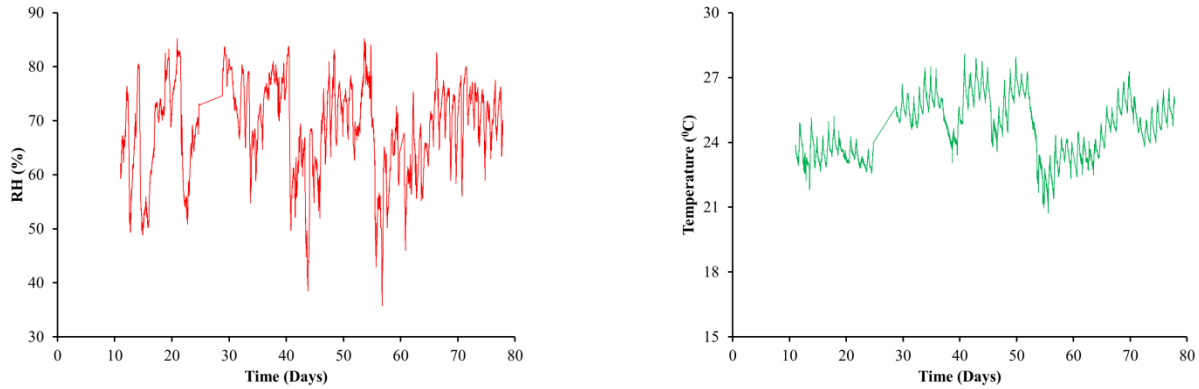


Figure 10. Ambient relative humidity and temperature over time.

#### 4. Test Results

The instantaneous and total deflections at mid-span for the two simply-supported slabs are shown in Figure 11(a) and (b), respectively.

Deflections measured at mid-span of all continuous slabs during instantaneous tests are plotted in Figure 12. During the tests, deformations at both adjacent spans were similar reflecting the symmetric behaviour of the geometry and loading conditions of the samples.

The loading/unloading cycles applied during the instantaneous tests for both simply-supported and continuous slabs exhibited an overall constant stiffness following an initial softening effect attributed to the formation of cracking. From Figure 11(a), comparing the slope of the load-deflection curves of the two simply-supported slabs, it can be observed that both specimens had similar stiffness at that time. Similarly, Figure 12(a) also confirms that all continuous slabs possessed similar stiffness at the time of the instantaneous tests.

In Figure 13, comparison between the total mid-span deflections of all continuous slabs is presented. Both instantaneous and long-term components of deflection are included in Figure 13. All samples exhibited similar deflections over time until the application of the instantaneous load. After that point of time, sample CS2 exhibited a similar incremental deflection as CS3 despite its higher instantaneous loading. After the application of the sustained load, sample CS1 showed higher deflection than that of other two samples due to creep produced by the application of the external sustained load.

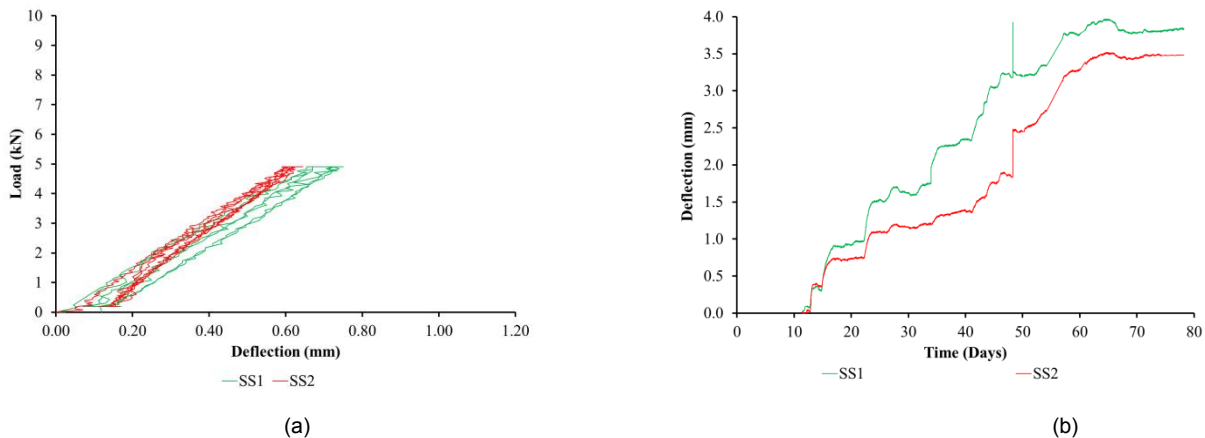


Figure 11. Mid-span (a) instantaneous and (b) total deflections for simply-supported slabs.

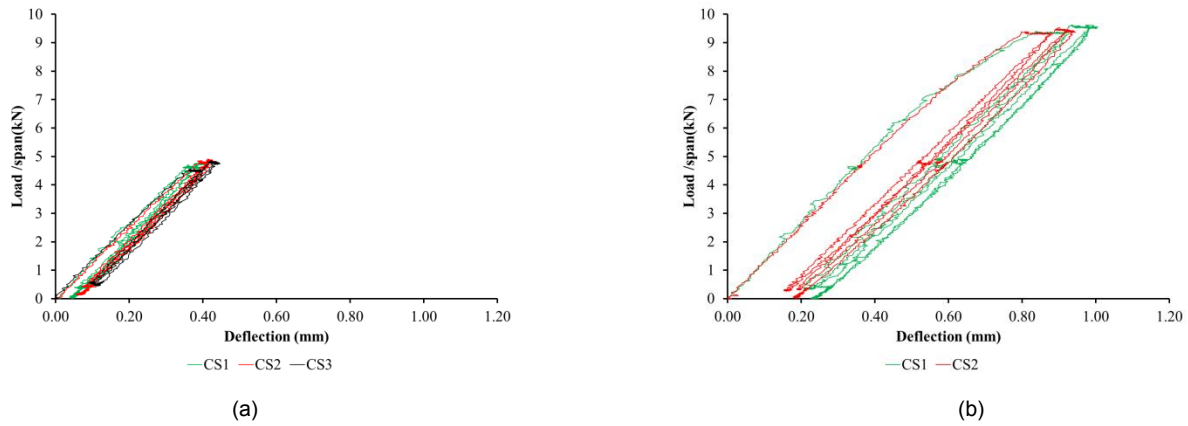


Figure 12. Mid-span load-deflection curves up to (a) 5 kN and (b) 10 kN for continuous slabs.

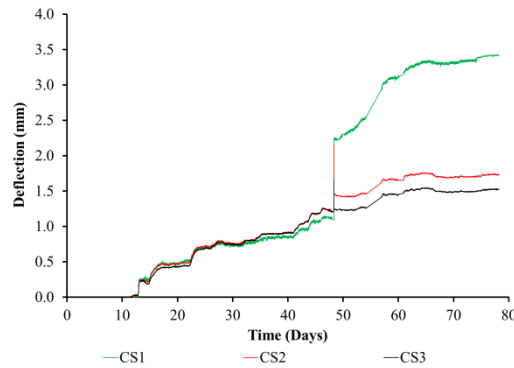


Figure 13. Mid-span deflections over time including both instantaneous and long-term components for continuous slabs.

## 5. Conclusions

This paper presented preliminary results of a series of tests carried out on two simply-supported and three continuous reinforced concrete slabs aimed at evaluating the change in flexural stiffness over time induced by cracking due to the effect of shrinkage and different levels of loads. A particular loading arrangement was set-up for applying different levels of sustained loads on the slabs and also to load/unload the specimens to investigate the stiffness of the slab at different instants of time.

Two different levels of instantaneous loadings were applied on the slabs before applying sustained loads by using the loading arrangement based on water tanks. From these tests, it was observed that all the slab samples showed an initial softening effect attributed to cracking followed by an overall constant stiffness during the instantaneous loading/unloading cycles. The load-deflection curves confirmed that both simply-supported and continuous slabs had similar instantaneous stiffness at that instant of time.

After the instantaneous tests, two continuous and one simply-supported slab samples were maintained unloaded and subjected to only their self-weight, while one simply-supported slab and one continuous sample were loaded with external sustained load (applied with water). These samples are currently being monitored to observe their long-term behaviour. First three months of readings were presented in the paper which showed that all three continuous slab samples exhibited similar deformations over time until the application of external loading and, after that, the sample with the sustained load exhibited higher deformations than the other two continuous samples because of the additional sustained load and its associated creep.



The development of shrinkage deformations taking place through the slab thickness was monitored considering different drying conditions applied to the slab surfaces. A qualitative overview of the variation of the drying shrinkage component over time was observed from the relative humidities measurements collected through the thickness of the slabs.

The long-term experiments presented in this paper are expected to continue in coming months and it is envisaged that these results will provide valuable benchmark data for the calibration and validation of numerical and design models.

## 6. Acknowledgement

The work in this article was supported under Australian Research Council's Discovery Projects funding scheme (project number DP110103028). The experimental work was carried in the J.W. Roderick Materials and Structures Testing Laboratory of the School of Civil Engineering at the University of Sydney. The assistance of the laboratory staff is also acknowledged.

## 7. References

1. Gilbert, R. I. (2007). Tension stiffening in lightly reinforced concrete slabs. *Journal of structural engineering*, 133(6), 899-903.
2. Gilbert, R.I., & Ranzi, G. (2011). Time-dependent behaviour of concrete structures, Spon Press, England.
3. Castel, A., Gilbert, R. I., & Ranzi, G. (2014). Instantaneous Stiffness of Cracked Reinforced Concrete Including Steel-Concrete Interface Damage and Long-Term Effects. *Journal of Structural Engineering*, 140(6).
4. Al-deen, S., Ranzi, G., & Vrcelj, Z. (2011). Full-scale long-term and ultimate experiments of simply-supported composite beams with steel deck. *Journal of Constructional Steel Research*, 67(10), 1658-1676.
5. Gilbert, R. I., Bradford, M. A., Gholamhoseini, A., & Chang, Z. T. (2012). Effects of shrinkage on the long-term stresses and deformations of composite concrete slabs. *Engineering Structures*, 40, 9-19.
6. Ranzi, G., Leoni, G., & Zandonini, R. (2013). State of the art on the time-dependent behaviour of composite steel-concrete structures, *Journal of Constructional Steel Research*, 80, 252-263.
7. Ranzi, G., Al-Deen, S., Ambrogi, L., & Uy, B. (2013). Long-term behaviour of simply-supported post-tensioned composite slabs, *Journal of Constructional Steel Research*, 88, 172-180.

# Influence of environmental temperature and moisture conditions on the fatigue resistance of concrete

Yasuhiro Koda<sup>1</sup>, Shohei Minakawa<sup>2</sup> and Ichiro Iwaki<sup>3</sup>

<sup>1</sup> Department of Civil Engineering, College of Engineering, Nihon University

<sup>2</sup> Civil Engineering Course, Graduate Schools of Engineering, Nihon University

<sup>3</sup> Department of Civil Engineering, College of Engineering, Nihon University

**Abstract:** The fatigue resistance of concrete declines in saturated conditions, such as in water, more quickly than it does under air-drying conditions. In addition, the compressive strength of concrete increases under low-temperature conditions. However, little research has been conducted on the influence of moisture conditions and environmental temperature on the fatigue resistance of concrete in low-temperature conditions. In this study, the fatigue resistance of concrete cylindrical samples under compression is investigated by means of a static loading test and a fatigue test. The experimental results show that the statically compressive strength decreases in normal temperature while the moisture content increases. On the other hand, the statically compressive strength increases in low temperatures. The test results show that the fatigue resistance of concrete decreases under wet conditions in normal temperatures and in low temperatures.

**Keywords:** fatigue resistance, environmental temperature, moisture content, compressive stress.

## 1. Introduction

The fatigue resistance of reinforced concrete members is influenced by both the fatigue strength of the steel reinforcing bars and the concrete. Concrete fatigue resistance is greatly dependent on the prevailing moisture conditions, for example, fatigue resistance decreases underwater more than in dry conditions especially (1). In addition, the compressive strength of concrete increases in low-temperature conditions, meaning that it is influenced by the environmental temperature (2). However, there have been few investigations into the influence of low temperatures and moisture conditions on the fatigue resistance of concrete. In this study, the fatigue resistance of concrete cylindrical samples is investigated by means of fatigue tests.

## 2. Experimental procedures

### 2.1 Mixture proportion

The water–cement (W/C) ratio of the test samples was 0.69. Thus, the water content of the mix ratio was 170 kg/m<sup>3</sup>. The target compressive strength of the concrete at the age of starting the load test was 24 MPa. Table 1 shows the mix proportions of concrete.

### 2.2 Test procedure

In this study, loading test types, environmental temperature, and moisture conditions were investigated as test variables. The following parameters were recorded: type of loading test carried out, static (S) and fatigue (F); environmental temperature, normal temperature (N) and low temperature (L, -20°C); and moisture conditions, dry and saturation. Table 2 lists the experimental conditions.

**Table 1. Mix proportions of concrete.**

G <sub>max</sub> (mm)	W/C	Air content	s/a (%)	Unit content (kg/m <sup>3</sup> )					
				W	C	S	G	Additives	
								Ad	AE
20	0.69	0.045	0.48	170	246	899	1000	3.696	0.004

Each specimen is 75 mm in diameter and 150 mm in length. Concrete samples were cured in water for 7 days.

In the loading tests, a static test and a fatigue test were conducted on specimens of the same age under identical environmental temperature and moisture conditions.

The cyclic range of fatigue load applied to the specimens determined 70% and 10% of the maximum compression stress from the static compressive strength test. The load, compressive strain, and number of load cycles were measured during the load test.

The saturated condition (S) defined the convergence of increase of mass by water absorption. The dry condition (d2) reduced the amount of water content to 0.75 from the saturated condition; and the dry condition (d1) was an air-drying condition with a water content of about 0.5. The moisture contained in the concrete was prevented from evaporating by sealing the surfaces of the samples with a layer of wax. Figure 1 shows the experimental setup used in this study.

**Table 2. Experimental conditions.**

Names	Types of loading test		Environment temperature		Moisture considerations		
	Static	Fatigue	Normal temperature	Low temperature (-20 degree C)	Dry 1 d1(0.5)	Dry 2 d2(0.75)	Sat s(1.0)
S-N-d1	○		○		○		
S-N-d2	○		○			○	
S-N-s	○		○				○
S-L-d1	○			○	○		
S-L-d2	○			○		○	
S-L-s	○			○			○
F-N-d1		○	○		○		
F-N-d2		○	○			○	
F-N-s		○	○				○
F-L-d1		○		○	○		
F-L-d2		○		○		○	
F-L-s		○		○			○



Figure 1. Experimental setup for low temperatures.

### 3. Results and discussion

#### 3.1 Compressive strength

Figure 2 shows the results of the compressive strength for different specimens. In normal temperature cases (N), the compressive strength for conditions d1, d2, and s are 28.6 MPa, 22.3 MPa, and 23.2 MPa, respectively. The compressive strength is seen to weaken as the water content increases. On the other hand, in low-temperature cases (L), the compressive strength for conditions d1, d2, and s are 27.3 MPa, 36.7 MPa, and 42.3 MPa, respectively. The compressive strength of s is 1.5 times higher than that of d1. This trend of increasing compressive strength under low-temperature conditions has been noted in past studies (2).

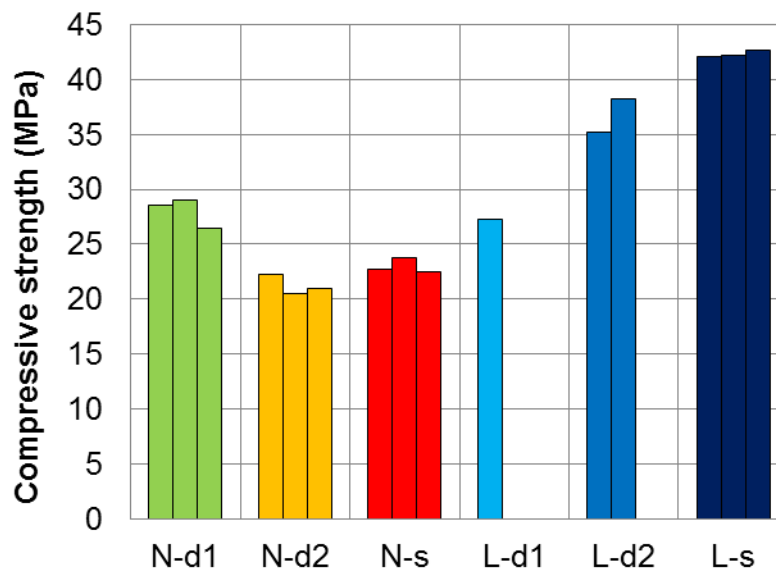


Figure 2. Results of compressive strength.

### 3.2 Fatigue resistance

Figure 3 shows the number of load cycles as the result of fatigue tests. The number of load cycles varied widely. In full consideration of this wide variation, the fatigue failure point is 16,150 for N-d1, 17,300 to 118,520 for N-d2, and 100 to 2,780 for N-s. In comparison with N-d1, it is not seen that the number of load cycles is less for N-d2 than for N-d1. For L-d1, the fatigue life was 17,000. Therefore, N-d1 and L-d1 were almost equivalent in terms of the number of cycles to fatigue failure. However, L-d2 endured 2,700 load cycles, and L-s underwent an average of 3,750 load cycles. This fatigue at low temperature indicates that concrete with a high water content has a reduced fatigue failure point compared with N-d1. In the experiments, the lowest fatigue durability was recorded for L-s, which had a remarkably higher static compressive strength than N-s. Thus, in terms of fatigue load under low temperature, it is possible that the fatigue failure process has a different mechanism than for normal temperature or underwater.

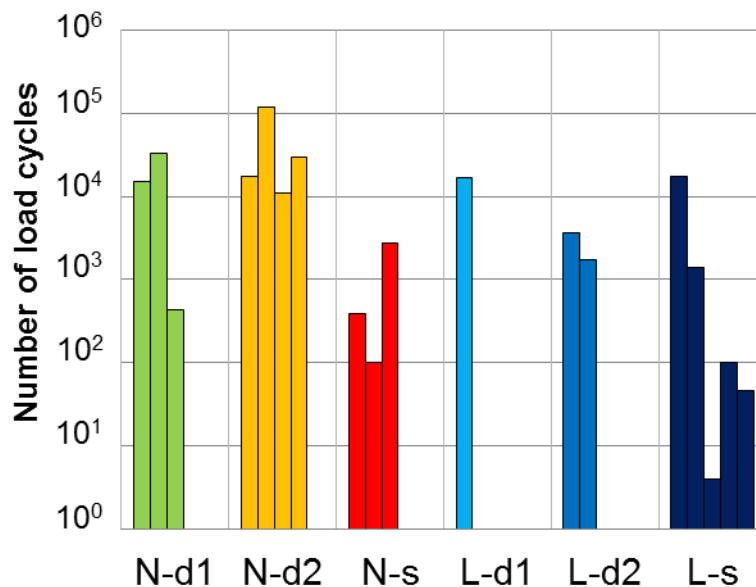
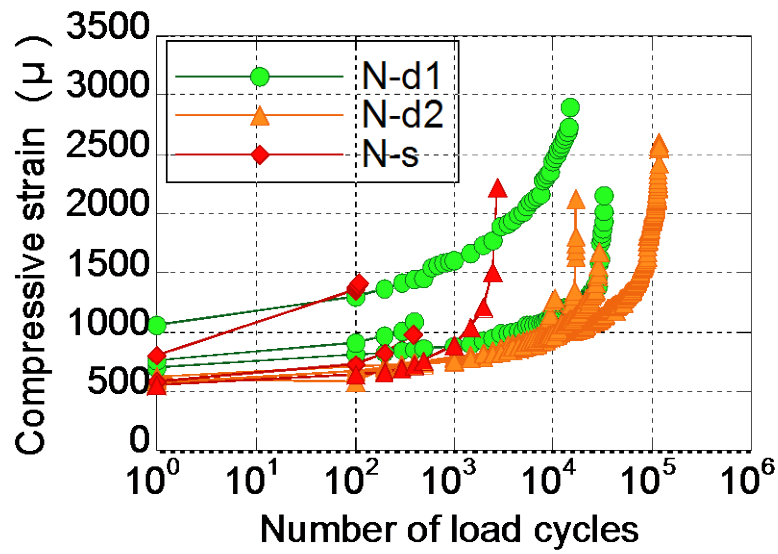
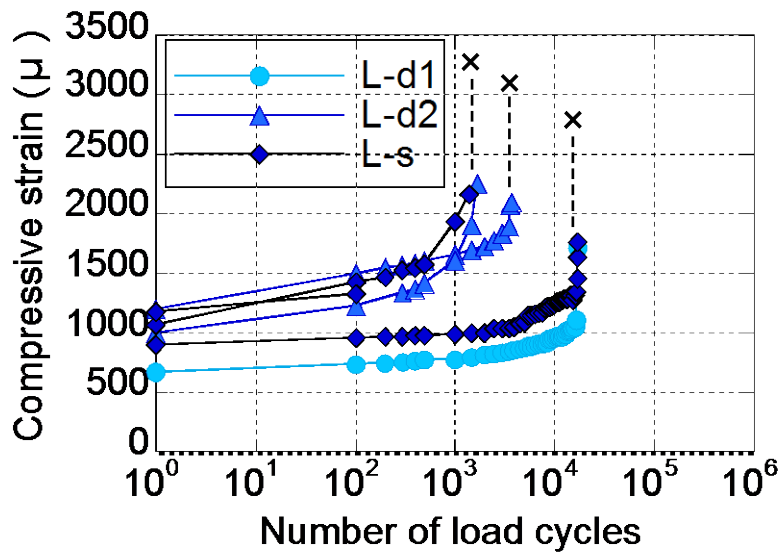


Figure 3. Number of load cycles to fatigue failure.

Figure 4 shows the relation between maximum compressive strain and the number of load cycles for (a) normal temperature and (b) low temperature. The compressive strain for the initial fatigue load was dispersion. The compressive strain showed a similar trend between L-d1 and N-d1. Thus, the results obtained show that the d1 case was not influenced very much by environmental temperature. In the d2 and s cases, the compressive strain was approximately 700  $\mu$  for normal-temperature conditions, and approximately 1000  $\mu$  for low-temperature conditions. The strains were basically classified by environmental temperature conditions such as the same maximum stress ratio. This tendency of compressive strain under normal-temperature conditions gradually increased toward fatigue failure with an increase in the number of load cycles. On the other hand, compressive strain under low-temperature conditions indicates that it increases rapidly just before fatigue failure. The results show that the stiffness of concrete was improved due to a freezing effect when moisture is present in concrete. However, this fatigue indicates that frozen concrete has a reduced fatigue durability compared with ordinary concrete without moisture.



(a) Results under normal temperature



(b) Results under low temperature

Figure 4. Relation between maximum compressive strain and number of load cycles.

#### **4. Conclusions**

The following conclusions were reached in this study.

- 1) The experimental results indicated that static compressive strength is reduced when the moisture content is increased under normal-temperature conditions. However, it increased under low-temperature conditions.
- 2) The fatigue durability of concrete by compressive stress was reduced when the moisture conditions are saturation at normal temperature and high moisture content at low temperature.

#### **Acknowledgement**

This work was supported by JSPS KAKENHI Grant Number 24760367. The author expresses appreciation to the members of the Concrete Engineering Laboratory at the College of Engineering, Nihon University.

#### **References**

1. Onoue, K. and Matsushita, H., "Energy consideration on decrease in compressive fatigue", Journal of JSCE, Vol. 66, No. 2, 2010, pp 166-178. (in Japanese)
2. JSCE Guidelines for Concrete, "STANDARD SPECIFICATIONS FOR CONCRETE STRUCTURES-2012 Design", 2013.



# An Approach for the Quantification of Ductility and Robustness of Reinforced Concrete Beams and Slabs

R. Ian Gilbert<sup>1</sup>, Stephen Foster<sup>2</sup> and Ankit Agarwal<sup>2</sup>  
<sup>1</sup>Emeritus Professor, <sup>2</sup>Professor and <sup>3</sup>Research Associate  
Centre for Infrastructure Engineering and Safety,  
School of Civil and Environmental Engineering, UNSW Australia

**Abstract:** Ductility is the ability of a structure or structural member to undergo large plastic deformations without significant loss of load carrying capacity. AS3600-2009 states that structures should be designed to be robust, but qualitative statements rather than quantitative recommendations are made. To design a concrete structure for robustness, a quantitative measure of ductility is required. In this paper, design guidance is given for the design and detailing of robust structures and a method is proposed whereby ductility and robustness of reinforced and prestressed concrete beams and slabs are quantified based on the ratio of internal energy absorbed by the structure before and after the formation of the first plastic hinge. Guidance is also provided on how to calculate the rotation at a plastic hinge and how much rotation is required to provide ductile and robust behaviour in a given situation.

**Keywords:** beams, ductility, elastic energy, plastic energy, plastic hinge, reinforced concrete, robustness, slabs.

## 1. Introduction

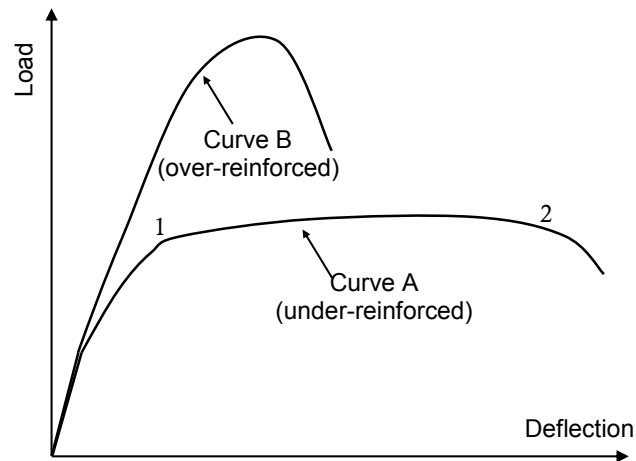
Ductility is the ability of a structure or structural member to undergo large plastic deformations without significant loss of load carrying capacity. Ductility is important for many reasons. It provides indeterminate structures with alternative load paths and the ability to redistribute internal actions as the collapse load is approached. Ductility is the reason why elastic analysis can be used to determine the internal actions in a statically indeterminate concrete structure. After the on-set of cracking, concrete structures are non-linear and inelastic. The stiffness varies from location to location depending on the extent of cracking and the reinforcement/tendon layout. In addition, the stiffness of a particular cross-section or region is time-dependent, with the distribution of internal actions changing under service loads due to creep and shrinkage, as well as other imposed deformations such as support settlements and temperature changes and gradients. All these factors cause the actual distribution of internal actions in an indeterminate structure to deviate from that assumed in an elastic analysis based on uniform stiffness.

Despite these difficulties, codes of practice, including AS3600-2009 (1), permit the use of elastic analysis based on uniform stiffness for the design of concrete structures at the strength limit state. This is quite reasonable provided the critical regions possess sufficient ductility (plastic rotational capacity) to enable the actions to redistribute towards the calculated elastic distribution as the collapse load is approached. If critical regions have little ductility (such as in over-reinforced elements) the member may not be able to undergo the necessary plastic deformation and the safety of the structure could be compromised.

Ductility is also important to resist impact and cyclic loading, and to provide robustness. With proper detailing, ductile structures can absorb the energy associated with sudden impact (as may occur in an accident or a blast) or cyclic loading (such as a seismic event) without collapse of the structure. With proper detailing, ductile structures can also be designed to resist progressive collapse.

Figure 1 shows the load-deflection curves for two reinforced concrete beams, one under-reinforced (Curve A) and one over-reinforced (Curve B). Curve A indicates ductile behaviour with large plastic deformations developing as the peak load is approached. The relatively flat post-yield plateau (1-2) in Curve A, where the structure deforms while maintaining its full load carrying capacity (or close to it) is characteristic of ductile behaviour. Curve B indicates non-ductile or brittle behaviour, with relatively little plastic deformation before the peak load. There is little or no evidence of a flat *plastic plateau* as the peak load is approached and the beam immediately begins to unload when the peak load is reached.

Structures with load-deflection relationships similar to Curve B in Figure 1 are simply too brittle to perform adequately under significant impact or seismic loading and they cannot resist progressive collapse. Reinforced and prestressed concrete beams can be designed to be robust and not to suddenly collapse when overloaded, but ductility is the key and a ductile load-displacement relationship such as that shown



**Figure 1. Ductile and non-ductile load-deflection curves.**

as Curve A in Figure 1 is an essential requirement. AS3600-2009 (1) states that structures should be designed to be robust, but qualitative statements rather than quantitative recommendations are made. To design a concrete structure for robustness, some quantitative measure of ductility/robustness is required.

## 2. Designing and Detailing for Robustness

The past twenty years, or so, has seen increasing emphasis on extreme event scenarios, such as blast loading, impact, fire and so forth. Earthquakes, tsunamis, and cyclonic events have placed increasing emphasis on the resistance of structures to withstand such hazards and of the reserve of strength available in Australia's infrastructure to withstand these events. In the case of building structures, the global response of the structure caused by the local event is of primary interest. For example, in the bombing of Murrah Federal Building in downtown Oklahoma in 1995, the effect of a local (blast) event was to cause the complete collapse of almost half the structure resulting in 168 deaths (2). It was not the blast loading that caused the majority of deaths but rather the progressive collapse of the structure. More recently, the Christchurch earthquake saw collapse and near collapse of many reinforced concrete framed structures, with perhaps the most notable being the 26 storey, 85 metre tall, Grand Chancellor Hotel built in 1985 and to the earthquake standards of the day. In 2012, an earthquake of magnitude 8.9 occurred off the coast of Japan, with devastating consequences. Such events highlight the need of a comprehensive understanding of structures and structural behaviour for extreme events.

For the above reasons, Standards bodies require engineers and designers to design robust structures. AS1170.0–2002 (3) defines structural robustness as:

*“Ability of a structure to withstand events like fire, explosion, impact or consequences of human errors, without being damaged to an extent disproportionate to the original cause.”*

and mandates that:

*“The design of the structure shall provide load paths to the foundations for forces generated by all types of actions from all parts of the structure, including structural and non-structural components.”*

Engineers generally tend to struggle with questions such as ‘What are the units of robustness?’, ‘How are these ‘load paths’ carried through a structure?’, ‘What are the design forces that must be guarded against?’. Little guidance is found in AS3600-2009, where the term ‘robustness’ is mentioned just twice, once in a two line Clause 2.1.3 mandating the designer to meet the requirements stipulated in AS1170, and the other noting that action effects can be determined using common methods of analysis.

For design purposes, AS/NZS1170.0 (3) requires that structures be designed and detailed such that adjacent parts of the structure are tied together in both the horizontal and vertical planes so that the structure can withstand an event without being damaged to an extent disproportionate to that event. In addition, structures should be able to resist lateral loads applied simultaneously at each floor level not less than  $0.01 (G + \frac{1}{6}Q)$  for each level of a structure taller than 15 m above the ground and  $0.015 (G + \frac{1}{6}Q)$  for each level

of all other structures, where  $G$  is the permanent gravity load and  $\frac{1}{6}Q$  is the factored imposed action on a particular floor level. In addition, AS/NZS1170.0 (3) requires that all parts of the structures be interconnected, with each connection able to transmit at least  $0.05 \times (G + \frac{1}{6}Q)$  for that connection.

Other general ways to increase robustness of the structure are to: (i) provide redundant load paths in the vertical load carrying systems; (ii) include additional ties as described below; (iii) increase the ductility of the structural frame; (iv) provide adequate shear strength of beams, such that it always exceeds the flexural capacity, in order to encourage a ductile response; (v) and provide capacity for resisting load reversals.

The inclusion of additional tie members in the structural frames provides improved protection against progressive collapse. Key elements of a structure must be tied together so that redistribution of the forces happens if a local failure occurs. Ties in a structural frame may consist of peripheral ties, internal ties, horizontal ties to columns and walls, and vertical ties, as shown in Figure 2.

Some general guidelines for providing ties in a RC structural frame are provided in (5) and include: (i) reinforcement provided to resist normal design loads may also be used to meet the requirement for structural integrity; (ii) if the bars extend (for an effective anchorage length) beyond all the bars of another tie, it may be anchored to that tie at right angles; (iii) where there is interruption in the continuity of the ties, the ties must be adequately anchored; (iv) internal ties must be continuous throughout their length, and should be anchored to the peripheral ties; (v) internal ties at each floor and roof level should be in two perpendicular directions (in walls, the ties should be relatively close to the top or bottom of the floor slabs); (vi) continuous peripheral ties should be provided at each floor and roof level; and (vii) all vertical load bearing elements should be tied continuously, including the corner columns, which should be tied into the structure in each of the two perpendicular directions.

To enhance the resistance of concrete building frames to progressive collapse and increase their robustness, the following factors need to be considered in design (5):

For the beams:

- (i) ensure flexural failure (ductile) rather than shear failure (brittle) and use ductile reinforcement (Class N or better);
- (ii) maintain continuous positive and negative moment reinforcement throughout. The non-seismic and seismic detailing of a beam according to AS 3600-2009 is shown in Figure 3;
- (iii) do not splice reinforcement near joint regions or near mid-spans;
- (iv) provide closely spaced confining steel to improve ductility and increase shear and torsional strength;
- (v) use 135 degree hooks at the anchorage of all stirrups; and
- (vi) consider the maximum plastic rotation after formation of plastic hinges. For plastic analysis, ensure that shear failure does not occur prior to developing the full plastic moment capacity.

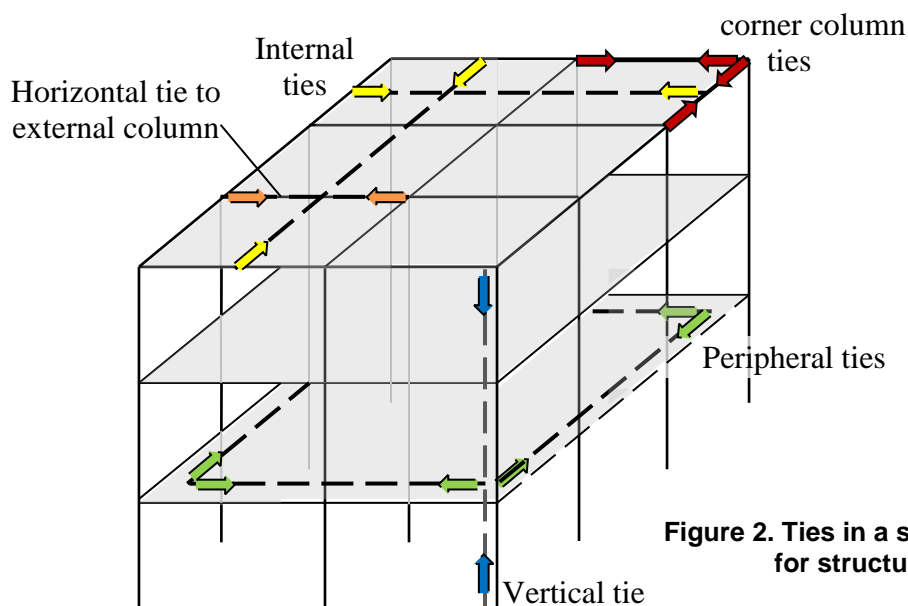
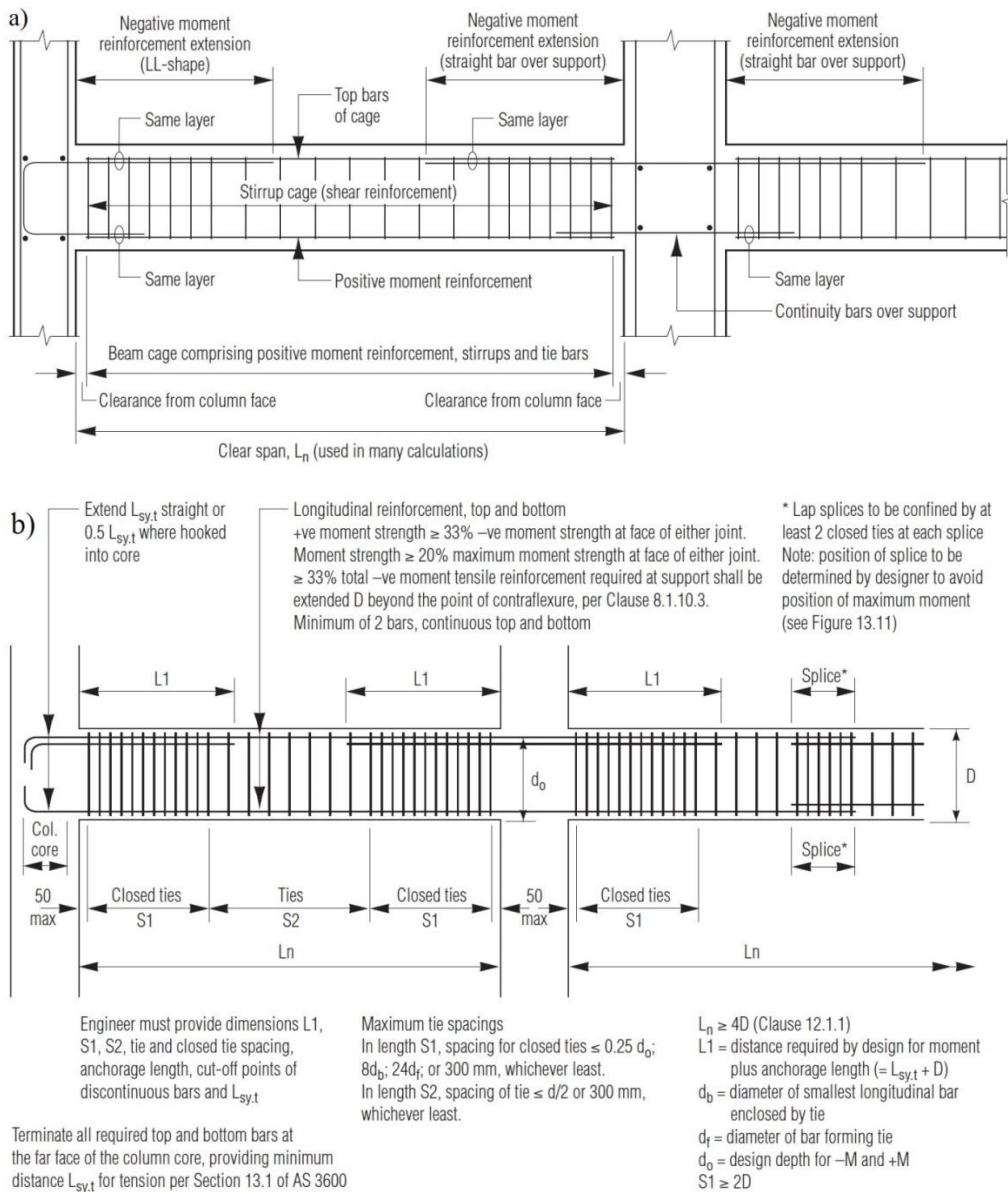


Figure 2. Ties in a structural frame for structural integrity (6).



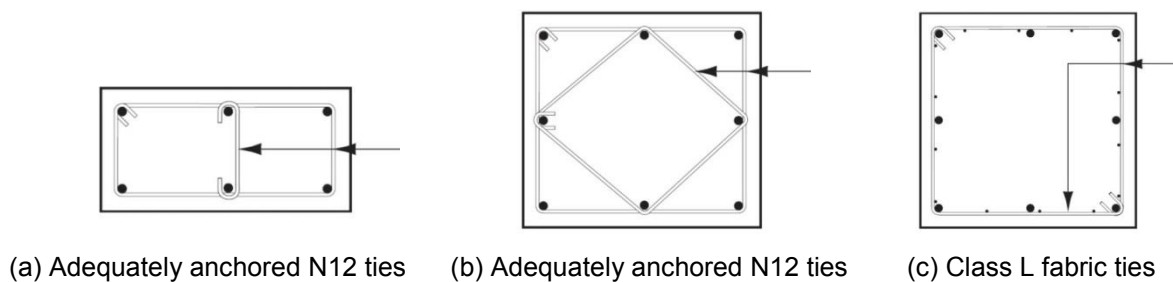
**Figure 3. (a) Non-seismic and (b) seismic detailing of the beam (7).**

For the columns:

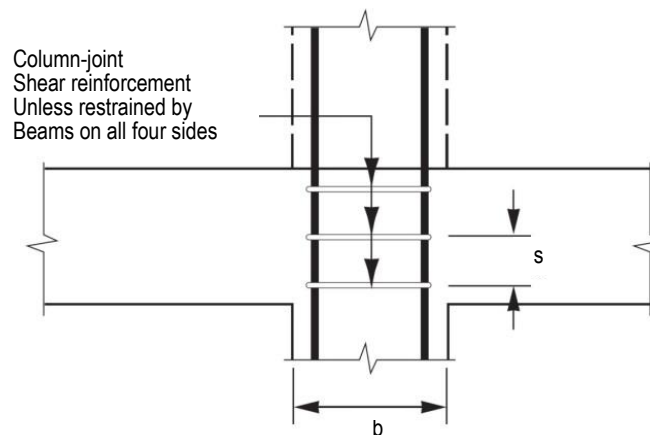
- (i) ensure flexural failure (ductile) rather than shear failure (brittle) and use ductile reinforcement;
- (ii) ensure plastic hinging in beams can occur by designing columns for larger moment than the beam can deliver (expected strength) (in AS 3600 this is included in the adoption of more conservative capacity reduction factors for less ductile members (eg. columns and walls compared to more ductile beams and slabs reinforced with N Class steel);
- (iii) Detail columns to have good confinement (Figure 4a and b show examples of good confinement, while Figure 4c shows potentially poor confinement because Class L ties may fracture at overloads and should be avoided in progressive collapse design scenarios);
- (iv) Splice column reinforcement at third-points along a column and not at the ends or at mid-span;
- (v) Continue confining ties through the joint region, as shown in Figure 5;
- (vi) For loss of a corner column, consider possible large moments and axial loads in adjacent columns.
- (vii) Identify critical elements where failure (or removal) could lead to large regions of damage and have high consequences on progressive collapse, and reinforce to resist such a possibility.

For the slabs:

- (i) use normal weight concrete floor slabs to enhance the blast resistance performance even though lightweight concrete will reduce the load;
- (ii) use of additional reinforcing steel to help tie-back adjacent beams to share load in event of column loss under a beam.
- (iii) provide continuous top and bottom reinforcement in both directions, and do not splice at mid-span or at the ends;
- (iv) cast slabs monolithically with beams and girders to provide better continuity and improve load redistribution;
- (v) the addition of a perimeter frame to a flat plate systems;
- (vi) consider reversals of load in design;
- (vii) provide sufficient tying of slabs into supporting walls;
- (viii) use N Class reinforcing steel for strength in flexure and, where needed, in column heads for punching shear.



**Figure 4. Tie configurations for confinement in columns (7).**



**Figure 5. Column-joint shear reinforcement (7).**

### 3. Beeby's approach for quantifying ductility and robustness

In his classic paper on the topic of robustness, Beeby (4) stated that

*“The problem with robustness is that, while we all have some intuitive idea what we mean by the term, it has never satisfactorily been put on a quantitative basis which would permit mathematical modelling or risk analysis to be carried out”.*

He further stated that a structure is robust if it is able to absorb damage resulting from unforeseen events without collapse. He also argued that this could form the basis of a design approach to quantify robustness. Explosions or impacts are clearly inputs of energy. Beeby (4) suggested that accidents or

even design mistakes could also be considered as inputs of energy and that robustness requirements could be quantified in terms of a structure's ability to absorb energy.

The area under the load deflection response of a member or structure is a measure of the energy absorbed by the structure in undergoing that deformation. Consider the load deflection response of a simply-supported under-reinforced beam shown in Figure 6. The area under the curve up to point 1 (before the tensile steel yields) is  $W_1$  and represents the elastic energy. The area under the curve between points 1 and 2 (when the plastic hinge develops and the peak load is reached) is  $W_2$ , which represents the plastic energy. A minimum value of the ratio  $W_2/W_1$  could be specified to ensure an acceptable level of ductility and, if all members and connections were similarly ductile and appropriately detailed, then an acceptable level of robustness (or resistance to collapse) could be achieved.

A ductile simply-supported member is one for which  $W_2/W_1$  exceeds about 0.5, but for statically indeterminate structures where significant redistribution of internal actions may be required as the peak load is approach, satisfaction of the following is recommended:

$$W_2 / W_1 \geq 1.0 \quad (1)$$

**Hinge rotation:** A typical moment curvature relationship for an under-reinforced concrete cross-section is shown as the dashed line in Figure 7 and an idealised elastic-plastic moment-curvature curve is also shown as the solid line. A plastic hinge is assumed to develop at a point along the span of a beam or slab when the peak (ultimate) moment is reached at a curvature of  $\kappa_y$  and rotation of the plastic hinge occurs as the curvature increases from  $\kappa_y$  to  $\kappa_u$ . The rotation at the plastic hinge  $\theta_h$  is the change in curvature

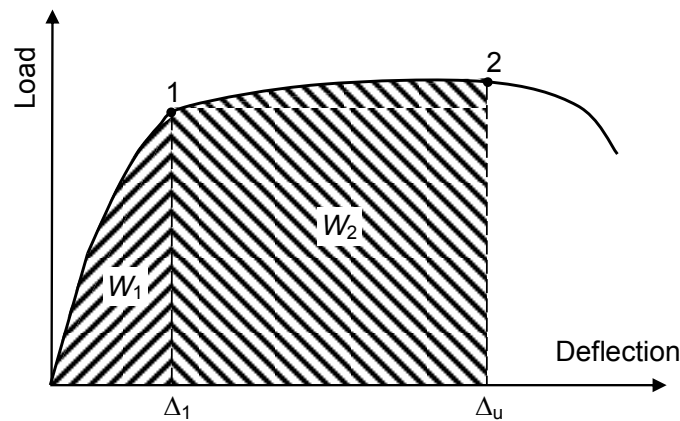


Figure 6. Typical load-deflection curve of an under-reinforced member.

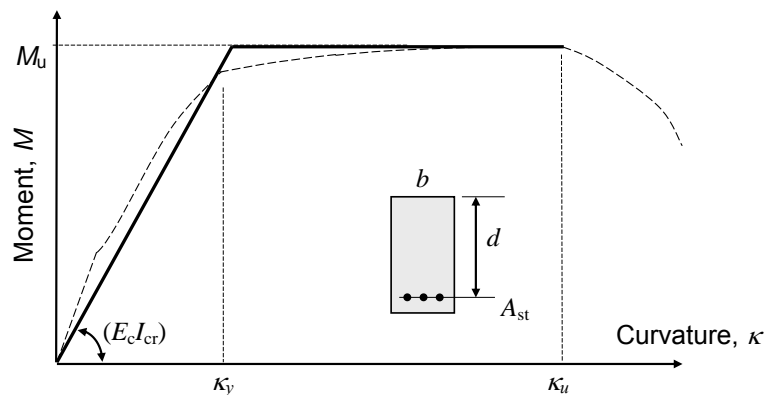


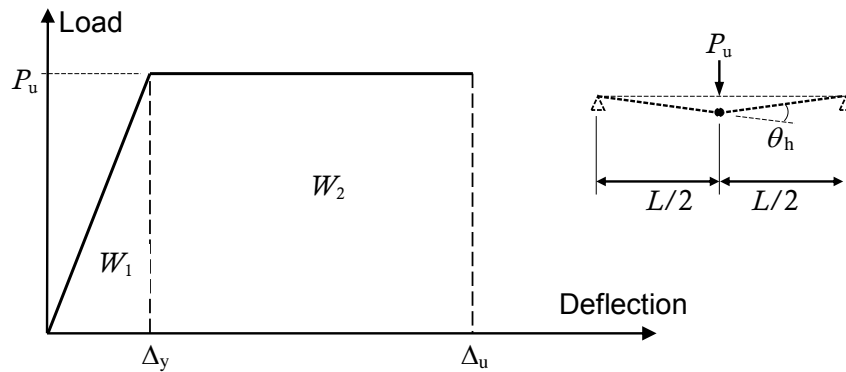
Figure 7. Idealised elastic-plastic moment-curvature relationship.

multiplied by the length of the plastic hinge  $\ell_h$  in the direction of the member axis. For under-reinforced cross-sections with ductile tensile reinforcement and tendons, the length of the plastic hinge  $\ell_h$  is usually taken to be equal to the effective depth of the beam or slab  $d$ . The maximum rotation available at a plastic hinge may therefore be approximated by:

$$\theta_h = \ell_h (\kappa_u - \kappa_y) \approx d (\kappa_u - \kappa_y) \quad (2)$$

**Ductility:** To investigate the ductility of reinforced concrete beam, it is convenient to idealise the load-deflection curve as elastic perfectly plastic. As an example, consider the idealised load-deflection response shown in Figure 8 of a simply-supported reinforced concrete beam of span  $L$  and subjected to a point load  $P$  applied at mid-span. A plastic hinge develops at mid-span when the applied load first reaches  $P_u$  and the mid-span deflection is  $\Delta_y$ . The moment at the plastic hinge is  $M_u = P_u L/4$ . After the formation of the plastic hinge, it is assumed that the deflection at mid-span increased from  $\Delta_y$  to  $\Delta_u$  by rotation of the plastic hinge through an angle  $\theta_h$  and this can be described as follows:

$$(\Delta_u - \Delta_y) = \frac{L\theta_h}{4} \quad (3)$$



**Figure 8. Idealised load-deflection curve.**

As an example, consider a singly-reinforced simply-supported beam of span  $L$  carrying a single point load  $P$  at mid-span. Let us assume that the reinforcement ratio is  $p = A_{st}/bd = 0.01$ , with  $f'_c = 32$  MPa,  $E_c = 28,600$  MPa and  $f_{sy} = 500$  MPa. Using the rectangular stress block specified in AS3600-2009 (1), the ultimate moment at the plastic hinge  $M_u$  and the corresponding ultimate curvature are given by:

$$M_u = f_{sy} A_{st} \left( d - \frac{\gamma d_n}{2} \right) \approx \beta b d^2 \quad \text{and} \quad \kappa_u = \frac{0.003}{d_n} \quad (4a, 4b)$$

where  $b$  is the section width and  $d$  is the effective depth to the tensile reinforcement and  $d_n$  is the depth to the neutral axis at the ultimate moment. The term  $\beta$  depends on the area, position and strength of the reinforcement and tendons. In our example,  $\beta$  is 4.54 and  $d_n = 0.223d$ .

For the centrally loaded simply-supported beam, the deflection  $\Delta_y$  may be approximated as:

$$\Delta_y = \frac{P_u L^3}{48 E_c I_{cr}} = \frac{M_u L^2}{12 E_c I_{cr}} \quad (5)$$

and, for the stated material properties and steel quantities, the cracked moment of inertia of the cross-section is approximated by:

$$I_{cr} = 0.0432 b d^3 \quad (6)$$



From Figure 7, the curvature  $\kappa_y$  is given by

$$\kappa_y = \frac{M_u}{E_c I_{cr}} = \frac{4.54bd^2}{28600 \times 0.0432bd^3} = \frac{3.67 \times 10^{-3}}{d} \quad (7)$$

Substituting Eqs. (4a) and (6) into Eq. (5) gives:

$$\Delta_y = \frac{L^2}{3266d} \quad (8)$$

If we assume that satisfaction of Eq. (1) is required for robustness, the minimum required plastic energy  $W_2$  must be 1.0 times the elastic energy  $W_1$  and, from the geometry of Figure 8,  $(\Delta_u)_{min} = 1.5\Delta_y$ . The elastic energy  $W_1$  (shown in Figure 8) may be approximated as:

$$W_1 = \frac{P_u \Delta_y}{2} = 0.5 \times \frac{4 \times 4.54bd^2}{L} \times \frac{L^2}{3266d} = 0.00278bdL \quad (9)$$

The minimum internal value for plastic energy  $W_2$  that must be absorbed during the hinge rotation is  $1.5W_1 = 0.00417bdL$  and this must equal the external work:

$$P_u (\Delta_u - \Delta_y) = W_2 = 0.00417bdL \quad (10)$$

Substituting Eqs. (3) and (4a) into Eq. (10), we get the minimum rotation required at the plastic hinge, as follows:

$$(4M_u / L)(L\theta_h / 4) = 4.54bd^2\theta_h = 0.00417bdL$$

$$\therefore \theta_h = 0.919 \times 10^{-3} \frac{L}{d} \quad (11)$$

It is evident that the plastic rotation required at the hinge at mid-span depends on the span to effective depth ratio. To achieve a ductility corresponding to  $W_2/W_1 = 1.5$ , the rotation required at the hinge at mid-span and the span to final deflection ratio ( $L/\Delta_u$ ) are determined from Eqs. (10), (3) and (5) and are given in the table below.

$L/d$	10	14	18	22	26	30
$\theta_h$ (radians)	0.0092	0.0129	0.0165	0.0202	0.0239	0.0275
$(L/\Delta_u)$	290	207	161	132	112	97

The maximum rotation available (given by Eq. 4 and using Eq. 4b and 7) depends on the reinforcement quantity and the effective depth. For this cross-section, Eq. (4b) gives  $\kappa_u = 0.0135/d$ , Eq. (7) gives  $\kappa_y = 0.00367/d$  and, from Eq. (2), the rotation available at the plastic hinge is  $\theta_h = 0.00983$ . For a singly-reinforced beam cross-section containing 1% reinforcement, the required ductility is only available for span-to-depth ratios less than about 11.

The rotation  $\theta_h$  required for ductility (according to the requirement of Eq. 1) and the rotation available at the plastic hinge for a singly reinforced simply-supported beam carrying a point load at mid-span are given in Table 1 for different reinforcement ratios and different span-to-depth ratios. The shaded cells in the Table represent those combinations of reinforcement ratio and span-to-depth for which the ductility requirement specified in Eq. 1 is satisfied. It is noted that cross-sections with any of the reinforcement ratios considered in Table 1 are classified as ductile in AS3600-2009, with  $d_n \leq 0.36d$  in all cases. When the reinforcement ratio is less than about 0.009,  $d_n < 0.2d$  and, according to AS3600-2009, up to 30% redistribution of moments is permissible irrespective of the span-to-depth ratio.

**Table 1. Rotation required for ductility and the rotation available at the plastic hinge in a singly reinforced simply-supported beam loads at mid-span.**

$A_{st}/bd$	Rotation required at plastic hinge at mid-span, $\theta_h$ (radians)						Rotation available at hinge (radians)
	Span to effective depth ratio ( $L/d$ )						
	10	14	18	22	26	30	
0.002	0.0076	0.0107	0.0138	0.0168	0.0199	0.0229	0.0643
0.004	0.0082	0.0115	0.0148	0.0180	0.0213	0.0246	0.0304
0.006	0.0086	0.0120	0.0155	0.0189	0.0224	0.0258	0.0190
0.008	0.0089	0.0125	0.0161	0.0196	0.0232	0.0268	0.0133
0.010	0.0092	0.0129	0.0165	0.0202	0.0239	0.0275	0.0098
0.012	0.0094	0.0132	0.0169	0.0207	0.0244	0.0282	0.0075
0.014	0.0096	0.0134	0.0172	0.0211	0.0249	0.0287	0.0058
0.016	0.0097	0.0136	0.0175	0.0214	0.0253	0.0292	0.0045

#### 4. Conclusions

Guidance is provided on the design and detailing requirements for robust structures. A method is proposed whereby ductility and robustness may be quantified based on the ratio of internal energy absorbed by the structure before and after the formation of the first plastic hinge. Guidance is provided on how to calculate the rotation at a plastic hinge and how much rotation is required to provide ductile and behaviour in a given situation.

#### 5. References

1. AS3600-2009, "Australian standard for concrete structures", Standards Australia, Sydney, 2009.
2. Corley, G., "Attacks on the Oklahoma City Federal Building, Pentagon and World Trade Centre: Using Reinforced Concrete to resist Progressive Collapse", CONCRETE 05, 22nd Biennial Conference of the Concrete Institute of Australia. 2005. Melbourne.
3. AS/NZS 1170.0:2002, "Structural design actions – General Principles". Amendments 1-5 (2003-2011). Standards Australia. Sydney. 2002.
4. Beeby, A.W., "Safety of structures, a new approach to robustness", *The Structural Engineer*, Vol. 77, No. 4, 1999, pp 16-21.
5. Ellingwood, B.R., Smilowitz, R., Dusenberry, D.O., Duthinh, D., Lew, H.S., and Carino, N.J., "Best Practices for Reducing the Potential for Progressive Collapse in Buildings", National Institute of Standards and Technology (NIST), US Dept. of Commerce, 2007, <http://fire.nist.gov/bfrlpubs/build07/PDF/b07008.pdf>
6. Department of Defense, "Design of Buildings to Resist Progressive Collapse," Unified Facilities Criteria (UFC) 4-023-03, 25 January, 2005.
7. Concrete Institute of Australia (CIA) (2010), "Recommended Practice: Reinforcement Detailing Handbook for Reinforced and Prestressed Concrete".

# Experimental study of the mechanical behavior of shear-critical prestressed and reinforced concrete beams

Kristof De Wilder<sup>1</sup>, Guido De Roeck<sup>2</sup> and Lucie Vandewalle<sup>3</sup>

<sup>1</sup> Dr. ir.-arch., Postdoctoral researcher, Department of Civil Engineering, KU Leuven, Belgium

<sup>2</sup> Prof. dr. ir., Full professor, Department of Civil Engineering, KU Leuven, Belgium

<sup>3</sup> Prof. dr. ir., Professor, Department of Civil Engineering, KU Leuven, Belgium

**Abstract:** This paper presents the results of 24 full-scale shear-critical (partially) prestressed and reinforced concrete members subjected to a four-point bending test with monotonically increasing load until failure. The main investigated parameters were the amount of prestressing, the amount of longitudinal and shear reinforcement and the shear span-to-effective depth ratio respectively. During the experiments, a vast amount of displacement and deformation data was gathered using two advanced optical measurement methods (i.e. 3D CCD-LED Coordinate Measurement Machine and Stereo-vision Digital Image Correlation). The experimentally observed failure load and failure mode are compared to analytical predictions using current shear design equations found in Eurocode 2.

A very poor correlation was found between the experimental results and analytical predictions (average experimental-to-predicted failure load ratio equal to 1.66, coefficient of variation equal to 36.8%). Based on the experimental data, it was found that direct strut action plays an important role in the overall structural behavior of the vast majority of the experimental test beams. This improved insight can be used to develop more suitable analytical modeling procedures.

**Keywords:** shear, structural concrete, optical measurement methods, FE modelling

## 1. Introduction

Despite more than a century of continuous research effort [1], shear remains one of a few areas into fundamentals of the behaviour of concrete structures where dispute remains amongst researchers about the mechanisms that enable the force flow through a concrete member and across cracks. The main reason for this contention can be attributed to the complexity of the shear phenomenon in structural concrete members. Firstly, various interrelated shear transfer mechanisms contribute to the overall shear capacity after the occurrence of cracking. Secondly, many parameters influence each shear transfer mechanism separately. Due to the complexity of the shear phenomenon, a generally accepted theoretical basis to model shear in structural concrete members is still absent within the research community.

Therefore, a multitude of analytical models dealing with shear in structural concrete members can be found in literature. Based on the cracking pattern typically observed during beam tests, Ritter [2] idealized the flow of forces by means of a parallel chord truss consisting of compressive diagonals inclined at 45°. This approach has ever since been referred to as the truss model approach. The necessary amount of shear reinforcement per unit length follows from the calculation of the axial force in the vertical tension ties.

The truss analogy is on one hand easy to understand and highly didactic but on the other hand a very simple representation of the actual structural behaviour. Moreover, in the case of structural concrete members without shear reinforcement, design engineers still mainly rely on empirical equations to estimate the shear strength. It is thus clear that more refined models are needed in order to optimize and economize the overall structural design of reinforced and prestressed concrete beams. An excellent overview of recent approaches to shear in structural concrete is given in references [3] and [4]. However, up until now, none of the existing theoretical approaches for shear in structural concrete elements has been able to fully explain the mechanics behind shear failure.

The ongoing debate in the literature on how to deal with shear in concrete members is also reflected by the code provisions. Current codes of practice [5-8] all recommend very different design approaches resulting in different design shear capacities and take parameters affecting the shear capacity into account in a different way. Due to our incomplete understanding and the brittle failure modes typically associated with shear, current codes of practice tend to propose highly conservative design equations, specifically in the case of prestressed concrete beams [9].

This paper therefore reports on the investigation of the mechanical behaviour of 24 full-scale shear-critical prestressed and reinforced concrete beams subjected to a combination of bending moment and shear force. In the first section, the experimental program is elaborated. Secondly, the experimental results are presented and compared to analytical predictions using current shear design equations found in Eurocode 2 [5, 6]. Finally, based on the experimentally observed deformation data, the mechanical behaviour is identified.

## **2. Experimental research**

### **2.1 Test specimens**

Each test specimen was labelled with the descriptive letter B followed by a number ranging from 1 to 12 or a number ranging from 101 to 112. The first set of beams, i.e. B1-B12, had a rectangular cross section, were 6000 mm long and 240 mm wide. The height of the aforementioned specimens varied between 400 mm, 500 mm and 600 mm. Specimens B101-B112 were characterized by an I-shaped cross section, were 7000 mm long, 630 mm high and had a flange width equal to 240 mm. The web width was equal to 70 mm. Specimens B2, B5, B7, B9, B12 and B101-B106 were provided with 8 low-relaxation seven-wire strands at the bottom (nominal diameter 12.5 mm) whereas beams B1, B4, B8, B10-B11 and B107-B109 were prestressed using 4 low-relaxation seven-wire strands at the bottom. All aforementioned beams were provided with two low-relaxation seven-wire strands (nominal diameter 9.3 mm) at the top. Specimens B8 and B10-B11 were additionally provided with two hot-rolled bars at the bottom (nominal diameter 25 mm). The same amount and diameter of reinforcement was used for the conventionally reinforced specimens (B3, B6 and B110-B112).

Shear reinforcement was provided in beams B7, B11-B12 consisting of closed double-legged stirrups (nominal diameter 6 mm, centre-to-centre distance equal to 300 mm). Shear reinforcement in beams B101-B102, B104-B105, B107-B108 and B110-B111 consisted of single-legged stirrups (nominal diameter 6 mm, centre-to-centre distance equal to 150 mm). Splitting reinforcement (nominal diameter 8 mm, centre-to-centre distance equal to 50 mm) was provided at both ends of all specimens. The geometry and reinforcement layout of all specimens are shown in Fig. 1-2.

### **2.2 Materials**

The self-compacting concrete mixture, used for both rectangular and I-shaped beams, was designed to have a characteristic cylindrical compressive strength  $f_{ck}$  equal to 50 MPa. Cement was specified as CEM I 52.5 R whereas the coarse aggregate consisted of 12 mm maximum size limestone gravel. Limestone filler and a high range water reducer were also used. The expected density of this mixture was 2378 kg/m<sup>3</sup>. The concrete mixture composition is listed in Table 1. The measured concrete material properties are reported in Tables 2-3. Tensile tests were performed on shear, splitting and passive reinforcement types to determine the modulus of elasticity  $E_s$ , the yield and ultimate stress,  $f_{ym}$  respectively  $f_{tm}$ , and the strain at failure  $\varepsilon_{su}$ . The characteristics of the prestressing strands were taken from the manufacturer. The results are summarized in Table 4.

### **2.3 Experimental setup**

All specimens were subjected to a four-point bending test as shown in Fig. 3. The tests were carried out in load control using a hydraulic press (Instron, maximum capacity 2.5 MN). The distance between the support points is equal to 4000 mm for the rectangular specimens and 5000 mm for I-shaped specimens. The distance outside the support points was equal to 1000 mm. The shear span  $a$  is equal to 1200 mm (specimens B1-B7 and B10), 1800 mm (specimens B8-B9 and B11-B12), 1600 mm (specimens B101, B104, B107 and B110) or 2000 mm (specimens B102-B103, B105-B106, B108-B109 and B111-B112). An overview of the investigated parameters is given in Table 5.

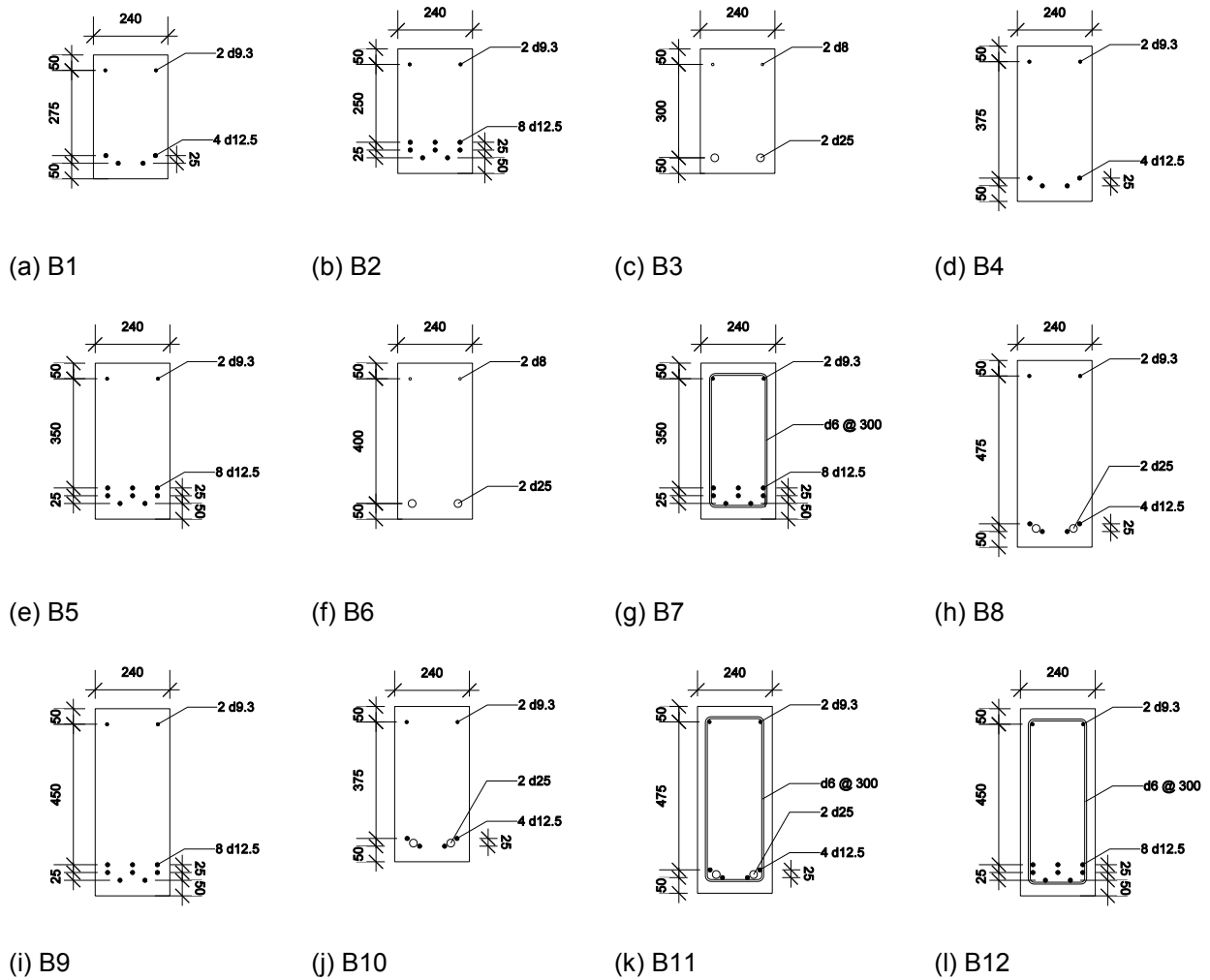


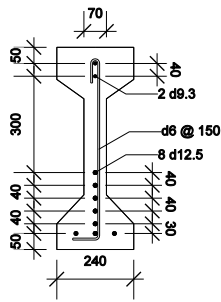
Figure 1. Cross sections and reinforcement details of rectangular specimens (note: units in millimetre)

Table 1: Concrete mixture composition

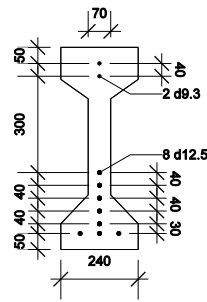
Material	Amount [kg/m <sup>3</sup> ]
CEM I 52.5 R	380
Limestone gravel 2/12	1042
Sand 0/2	631
Water	159
Limestone filler	160
High-range water reducer	6

Table 2: Concrete material properties for rectangular specimens

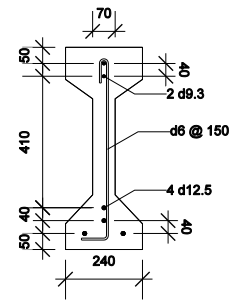
Specimens	$f_{cm,cube}$ [MPa]	$f_{ctm,fl}$ [MPa]	$\rho_m$ [kg/m <sup>3</sup> ]	Age [days]
B1,B4	84.1	7.1	2463	31-30
B2,B5	88.6	6.6	2381	55-51
B3,B6	85.5	9.8	2445	48-48
B7,B9	81.6	5.9	2459	35-48
B8,B10	89.3	9.1	2389	50-49
B11	79.4	5.8	2447	56
B12	72.7	n.a.	2453	49



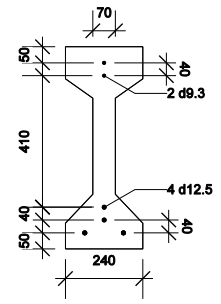
(a) B101-B105 except B103



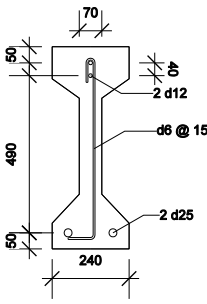
(b) B103, B106



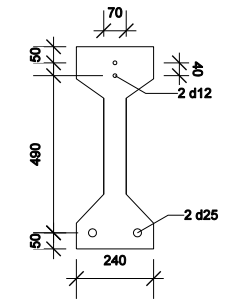
(c) B107-B108



(d) B109



(e) B110-B111



(f) B112

Figure 2. Cross sections and reinforcement details of I-shaped specimens

Table 3: Concrete material properties for I-shaped beams

Specimens	$f_{cm,cube}$ [MPa]	$f_{cm}$ [MPa]	$E_{cm}$ [GPa]	$f_{ctm,fl}$ [MPa]	$\rho_m$ [kg/m <sup>3</sup> ]	Age [days]
B101-B103	87.1	77.5	43.4	5.8	2399	28-233-393
B104-B106	82.8	88.9	43.5	6.5	2369	412-404-407
B107-B109	74.6	89.3	42.2	5.7	2376	428-424-412
B110-B112	85.2	96.5	34.3	5.7	2372	441-435-427

Table 4: Reinforcement properties

Reinf. type	Type	$d_p^*$	$E_p$	$f_{p0.1m}$	$f_{pm}$	$\epsilon_{pu}$
		$d_s$	$E_s$	$f_{ym}$	$f_{tm}$	
		[mm]	[GPa]	[MPa]	[MPa]	[%]
Top prestress. reinf.	7-wire	9.3	198.0	1737	1930	5.20
Bottom prestress. reinf.	7-wire	12.5	198.0	1737	1930	5.20
Shear reinf.	Cold worked	6.0	210.0	608	636	2.73
Splitting reinf.	Cold worked	8.0	203.0	542	603	5.97
Passive long. reinf.	Hot-rolled	25.0	212.0	530	635	12.91

Note: \* subscript  $p$  and  $s$  denote prestressing respectively conventional reinforcement types

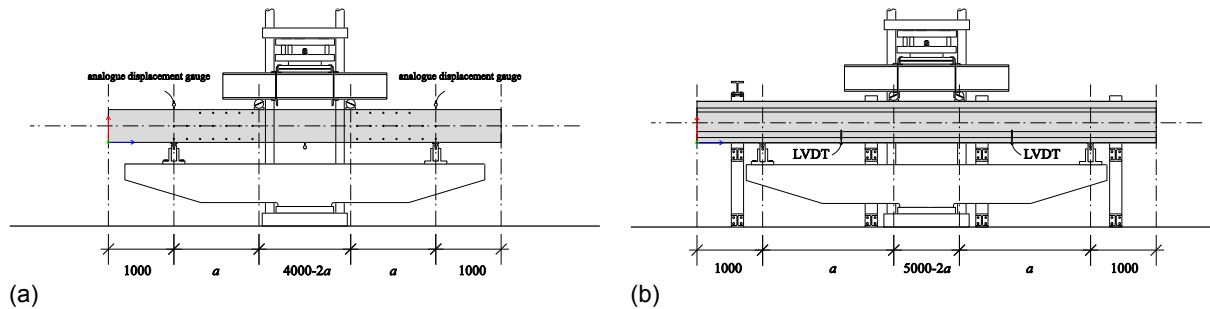


Figure 3: Schematic representation of experimental setup for (a) rectangular test specimens and (b) I-shaped specimens

Table 5: Overview of investigated parameters per specimen

Specimen	Type	$d$ [mm]	$\sigma_{p0}^*$ [MPa]	$a$ [mm]	$a/d$ [-]	$\rho_l^{**}$ [-]	$\rho_w^{***}$ [x 10 <sup>-3</sup> ]
B1	R	338	1488	1200	3.56	0.0046	0
B2	R	322	1488	1200	3.73	0.0096	0
B3	R	350	n.a.	1200	3.43	0.0117	0
B4	R	438	1488	1200	2.74	0.0035	0
B5	R	422	1488	1200	2.84	0.0073	0
B6	R	450	n.a.	1200	2.67	0.0091	0
B7	R	422	1488	1200	2.84	0.0073	0.785
B8	R	539	1488	1800	3.34	0.0105	0
B9	R	522	1488	1800	3.45	0.0059	0
B10	R	439	1488	1200	2.73	0.0129	0
B11	R	539	1488	1800	3.34	0.0090	0.785
B12	R	522	1488	1800	3.45	0.0060	0.785
B101	I	511	1488	1600	3.13	0.0208	2.693
B102	I	511	1488	2000	3.91	0.0208	2.693
B103	I	511	1488	2000	3.91	0.0208	0
B104	I	511	750	1600	3.13	0.0208	2.693
B105	I	511	750	2000	3.91	0.0208	2.693
B106	I	511	750	2000	3.91	0.0208	0
B107	I	550	1488	1600	2.91	0.0097	2.693
B108	I	550	1488	2000	3.64	0.0097	2.693
B109	I	550	1488	2000	3.64	0.0097	0
B110	I	580	n.a.	1600	2.76	0.0242	2.693
B111	I	580	n.a.	2000	3.45	0.0242	2.693
B112	I	580	n.a.	2000	3.45	0.0242	0

Note: \* initial stress in prestressing strands; \*\* longitudinal reinforcement ratio; \*\*\* shear reinforcement ratio

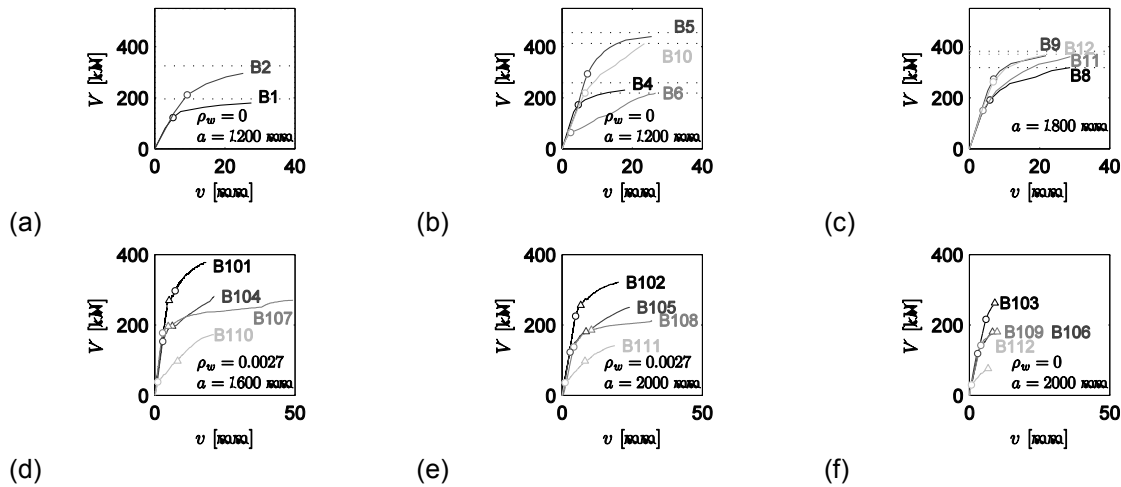
Discrete displacements and deformations of rectangular specimens were measured using analogue displacement gauges and demountable mechanical strain gauge points (DEMEC). Continuous displacements were measured during the tests on I-shaped beams using LVDTs. Additionally, advanced optical(-numerical) measurement techniques, i.e. *3D CCD-LED Coordinate Measurement Machines* and *Stereo-vision digital image correlation (DIC)*, were employed to investigate both zones where a shear force occurs in the case of I-shaped beams. The corresponding experimental setup and measurement precision are elsewhere described and reported in [10] and [11].

### 3. Experimental results

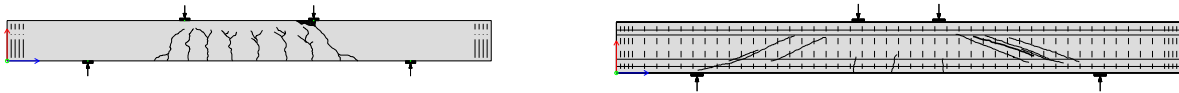
In this section, the experimentally observed structural behaviour is reported. Fig. 4 (a-f) show the experimentally observed load-displacement response curves for all investigated specimens apart from B3 and B7. During testing of B3, a sudden stage of unloading occurred. After increasing the load, the beam suddenly failed. The results of this specimen will therefore not be considered. Specimen B7 did not yield



any useful load-displacement data due to measurement errors. The onset of bending ( $\circ$ ) and diagonal ( $\triangle$ ) cracking is also indicated in the aforementioned Fig. 4 (a-f). Typical observed cracking patterns prior to failure are shown in Fig. 5(a-b) for both rectangular and I-shaped specimens.



**Figure 4: Load-displacement response curves for (a-c) rectangular beams (measured at mid-span) and (d-f) I-shaped beams (measured at 1200 mm from the support point)**



(a) B4 (b) B102  
**Figure 5. Typical cracking pattern prior to failure for (a) rectangular specimens and (b) I-shaped specimens**

Despite being designed to fail in shear, all rectangular specimens apart from beam B6 and B10, exhibited a bending failure mode due to severe yielding of the longitudinal reinforcement followed by brittle crushing of the compressive zone between the load points. Specimens B6 and B10 failed due to the loss of anchorage of the longitudinal reinforcement. All I-shaped beams but specimens B107 and B108 failed due to shear in a very brittle manner. The aforementioned specimens exhibited severe web cracking leading to excessive yielding and rupture of the shear reinforcement bars. Crushing of the diagonal struts was not observed. Table 6 summarizes the experimentally observed failure load and failure mode of each considered test beam. The experimental results can be compared to analytical strength calculations according to current Eurocode 2 (EC2) [5, 6] design guidelines. To better estimate the actual failure load, average material strength properties rather than characteristic values are to be used and all partial safety factors should be omitted. The results of the aforementioned calculation procedure are also incorporated in Table 6. Based on the results presented in Table 6, following observations and preliminary conclusions can be made.

1. For the vast majority of the reported test specimens, a poor correlation is found between the experimentally observed and analytically calculated failure load according to EC2 for both rectangular and I-shaped beams. A relatively good correlation was found between experimental and analytically predicted failure load in the case of reinforced I-shaped specimens with shear reinforcement (B110-B111) and prestressed I-shaped beams without shear reinforcement (B103, B106, B109 and B112), refer to Table 6. Even if all partial safety factors were omitted and average material strength properties were used rather than characteristic values, a mean experimental-to-predicted failure load ratio equal to 1.66 is found (coefficient of variation (COV) equal to 36.8%).
2. Although all considered rectangular specimens were characterized by a lower shear strength in comparison to their respective predicted bending capacity, no shear failure mode was observed. It can be noted that the experimentally observed failure load correlates well with the analytically calculated load necessary to obtain the bending capacity  $V_{u,bend}$ . All I-shaped beams were

characterized by a lower theoretical shear capacity compared to their respective bending strength. A shear failure mode was indeed encountered for all I-shaped beams except beams for B107 and B108 which failed due to bending. Table 6 clearly indicates that the experimental failure load is marginally higher than  $V_{u,bend}$  for the aforementioned beams.

**Table 6: Experimentally observed and analytically predicted failure load and failure mode**

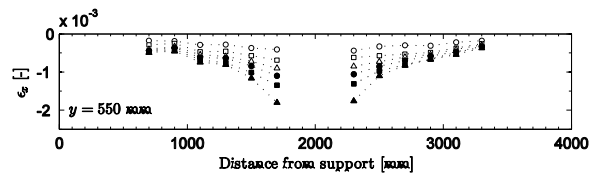
Specimen	Experiment		Eurocode 2 [5, 6]			
	$V_{u,exp}$ [kN]	Failure mode	$V_{u,pred}$ [kN]	$V_{u,bend}$ [kN]	Failure mode	$V_{u,exp}/V_{u,pred}$ [-]
B1	195.6	B*	154.4	172.0	S	1.27
B2	325.0	B	225.0	324.9	S	1.44
B4	259.2	B	167.3	226.3	S	1.55
B5	455.0	B	244.2	432.8	S	1.86
B6	222.0	A**	127.8	172.7	S	1.74
B7	445.5	B	130.6	430.8	S	3.41
B8	317.9	B	235.6	317.1	S	1.35
B9	380.7	B	256.8	346.2	S	1.48
B10	413.0	A	219.4	382.4	S	1.88
B11	370.1	B	166.8	314.5	S	2.22
B12	385.0	B	161.5	354.6	S	2.38
B101	377.7	S-DT***	158.1	412.2	S	2.39
B102	321.6	S-DT	158.1	329.6	S	2.03
B103	262.8	S-DT	243.3	329.6	S	1.08
B104	281.8	S-DT	135.2	406.6	S	2.08
B105	251.2	S-DT	135.2	325.3	S	1.86
B106	179.7	S-DT	206.9	325.3	S	0.87
B107	271.3	B	147.9	236.5	S	1.83
B108	213.8	B	147.9	189.2	S	1.45
B109	181.0	S-DT	197.0	189.2	S	0.92
B110	172.6	S-DT	149.6	195.7	S	1.15
B111	141.5	S-DT	149.6	156.6	S	0.95
B112	76.5	S-DT	87.1	156.6	S	0.88

Note: \* Bending failure; \*\* Anchorage failure; \*\*\* Shear (S) failure due to diagonal tension (DT)

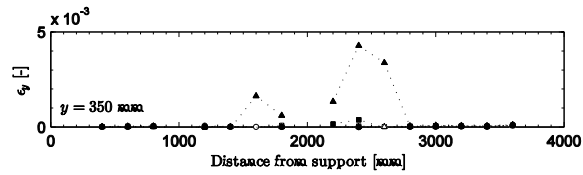
#### 4. Discussion

To further investigate the discrepancy between the experimentally observed and analytically predicted failure load, the measured (full-field) deformations are investigated. Fig. 6(a-c) show the typical horizontal and vertical strains for rectangular specimens as a function of the distance from the support point and applied load level. Fig. 7(a-c) show the same results observed for I-shaped specimens. From Fig. 6(a-c) and Fig. 7(a-c), it can be clearly seen that, near the support point, the horizontal strain  $\varepsilon_x$  at the top of both rectangular and I-shaped specimens rapidly decreases to low strains and thus also low stresses. Moreover, the vertical strains in the web of rectangular specimens remained relatively small in comparison to the vertical deformation in the web of I-shaped beams, refer to Fig. 6(b) and Fig. 7(b) respectively. For high load levels applied to I-shaped beams,  $\varepsilon_y$  rapidly increases and near failure, the strain in the web is nearly equal to the ultimate strain of the shear reinforcement bars as determined from uni-axial tensile tests, refer to Table 4.

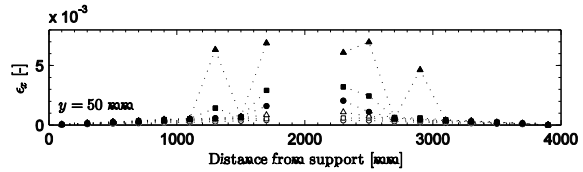
Fig. 8(a) depicts the experimentally measured full-field direction and magnitude of the principal compressive strain  $\varepsilon_3$  near failure of specimen B104 whereas Fig. 8(b) shows the measured angle  $|\theta_{\varepsilon_3}|$  between the principal compressive strains with respect to the horizontal as a function of the distance from the support point. Fig 8(a) indicates that, after the occurrence of inclined cracking in I-shaped beams, an inclined strut is formed which partly resists the applied shear force in the case of prestressed I-shaped beams. Apart from the direct compression strut, which develops through cracked concrete, refer to Fig. 5(b) two fan regions are developed which deviate the inclined web cracks and resist the remaining part of the applied shear force.



(a)

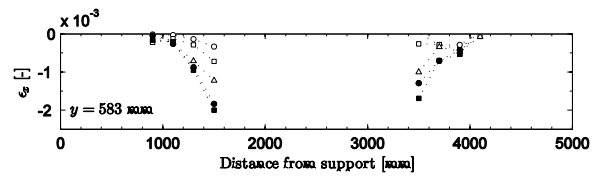


(b)

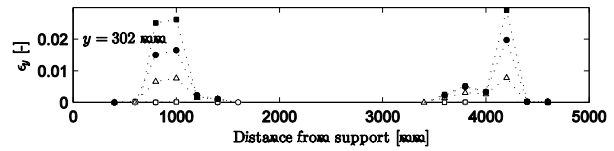


(c)

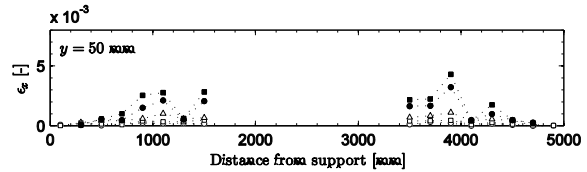
**Figure 6. Horizontal (a,c) and vertical (b) strain profiles of B9 at various load levels (○ 40%, □ 60%, △ 72%, ● 80%, ■ 88%, ▲ 96% of  $V_{u,exp}$ )**



(a)



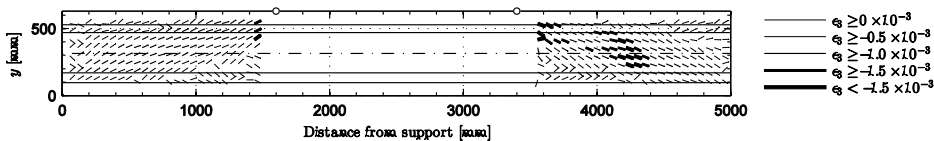
(b)



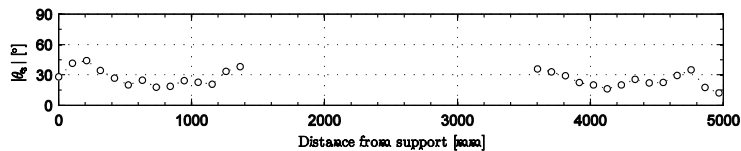
(c)

**Figure 7. Horizontal (a,c) and vertical (b) strain profiles of B101 at various load levels (○ 25%, □ 50%, △ 80%, ● 95%, ■ 99% of  $V_{u,exp}$ )**

The identified structural behavior of the above mentioned specimens corresponds to the observed parabolic course of the direction of the principal compressive strain  $|\theta_{z3}|$  along the axis of the member, as presented in Fig. 8(b). In view of the mechanical behavior described above, the experimentally observed failure mode can be understood as a splitting failure mode due to the spreading out of the compressive force in the web of the beam. Similarly, it can be assumed that direct strut action is the main bearing mechanism for the presented rectangular beams. However, different from I-shaped beams, the area where the direct compression strut can be developed remains uncracked, refer to Fig. 5(a). Hence, there is no reason for a fan region to be developed which deviates cracked zones.



(a)



(b)

**Figure 8. (a) Direction and magnitude of the principal compressive strain of specimen B104 at 95% of the experimental failure load; (b) Angle between the principal compressive strain and the horizontal for specimen B104 at 95% of the experimental failure load**

The identified structural behavior, as described above, provides a plausible explanation for the following experimentally observed phenomena:

1. The possibility of carrying the applied shear force by means of direct strut action significantly increases the shear carrying capacity in comparison to the shear capacity obtained using the variable angle truss model as proposed by Eurocode 2. This provides a possible explanation why the current sectional shear design provisions found in EC2 performed poorly in predicting the shear capacity of the reported (partially) prestressed concrete beams.

2. The direct strut action poses high demands on the anchorage of the longitudinal tensile reinforcement near the support point. This explains the anchorage failure of the partially prestressed specimen B10 which failed at the highest shear force in comparison to the other reported partially prestressed rectangular specimens.
3. In the case of rectangular (partially) prestressed concrete beams, no inclined cracks crossed the path between the support point and loading point. If the vast majority of the applied load is carried by means of direct strut action, then it is indeed expected that providing shear reinforcement does not contribute significantly to the overall structural behavior. This explains why a relatively small difference in failure load was observed for specimen sets (B5, B7), (B8, B11) and (B9, B12), refer to Table 6 and Fig. 4(c). The aforementioned specimen sets are identical apart from the provided amount of shear reinforcement.
4. In Fig. 6(a) and Fig. 7(a), the typically observed profile of the horizontal strain  $\varepsilon_x$  was presented at the top of rectangular respectively I-shaped beams. It was shown that the horizontal strain at the top of the presented beams rapidly decreases to relatively low strains, and thus relatively low stresses, away from the loading point. Due to the inclined strut action, it is indeed expected that low strain values occur at the top of the specimen near the support point.

## 5. Conclusions

This paper presented extensive experimental results obtained from 23 full-scale structural tests on prestressed and reinforced concrete members subjected to a four-point bending test until failure. The presented experimental results can be used in further research for model validation and model calibration. The main investigated parameters were the amount of prestressing, the amount of shear and prestressing reinforcement and the shear span-to-effective depth ratio respectively. Using either traditional mechanical measurement techniques or advanced optical(-numerical) measurement methods, a vast amount of displacement data was gathered from which deformations can be easily derived. All specimens were designed to fail in shear. However, 11 specimens exhibited a bending failure mode, 2 specimens failed due to the loss of anchorage and the remaining 10 specimens failed due to excessive yielding leading to sudden rupture of the shear reinforcement bars. The experimental results were compared to analytical calculations using the current design procedures as proposed by Eurocode 2 (EC 2). Based on the work presented in this paper, it can be firstly stated that, EC 2, using the variable angle truss model, in general significantly underestimates the load capacity of the presented test beams. Omitting all partial safety factors and using average material strength properties rather than characteristic values, an average experimental-to-predicted failure load ratio equal to 1.66 was found (coefficient of variation 36.8%). Moreover, the failure mode is wrongly predicted for 13 test specimens using current EC 2 design procedures. Secondly, direct strut action was found to be an important bearing mechanism for the presented rectangular beams and prestressed I-shaped beams with shear reinforcement. This mechanism, although generally believed to be only important for members with a shear span-to-effective depth ratio less than or equal to 2.5, significantly increases the failure load of the reported test specimens and form a plausible explanation for the experimental observations.

## 6. References

1. Balázs, G.L., *A historical review of shear*, in *Bulletin 57: Shear and punching shear in RC and FRC elements*, V. Sigrist, Minelli, F., Plizzari, G., Foster, S., Editor. 2010, Fédération Internationale du Béton (fib): Lausanne. p. 1-13.
2. Ritter, W., *Die Bauweise Hennebique*. Schweizerische Bauzeitung, 1899. **33**: p. 41-61.
3. Ramirez, J.A., et al., *Recent approaches to shear design of structural concrete*. Journal of Structural Engineering-Asce, 1998. **124**(12): p. 1375-1417.
4. fib, *Shear and punching shear in RC and FRC elements: Workshop 15-16 October 2010, Salò (Italy)*, in *fib Technical Report 57*, V. Sigrist, et al., Editors. 2010, fib: Lausanne. p. 262.
5. CEN, *Eurocode 2: Design of concrete structures - Part 1-1: General rules and rules for buildings*. 2004, NBN: Brussels. p. 255.
6. NBN, *NBN EN 1992-1-1 ANB in Eurocode 2: Ontwerp en berekening van betonconstructies - Deel 1-1: Algemene regels en regels voor gebouwen (in Dutch) - National Application Document*. 2010, NBN National Bureau for Normalisation: Brussels. p. 32 pp.
7. ACI, *ACI 318-11 Building Code Requirements for Structural Concrete and Commentary*. 2011, American Concrete Institute: Farmington Hills, Mich. (USA). p. 503.

8. CSA, *CSA A23.3 Design of Concrete Structures (CSA A23.3-04)*. 2004, Canadian Standards Association: Mississauga p. 230.
9. Nakamura, E., A.R. Avendano, and O. Bayrak, *Shear Database for Prestressed Concrete Members*. *Aci Structural Journal*, 2013. **110**(6): p. 909-918.
10. De Wilder, K., G. De Roeck, and L. Vandewalle, *Suitability of CCD-LED Measurements for the Characterization of the Mechanical Behaviour of Shear-Critical Prestressed Concrete Beams*, in *5th International Conference on Optical Measurement Techniques for Structures and Systems OPTIMESS*, J. Dirckx, et al., Editors. 2012, Shaker Publishing: Antwerp, Belgium.
11. De Wilder, K., et al., *Experimental investigation on the shear capacity of prestressed concrete beams using digital image correlation*. *Engineering Structures*, 2015. **82**(1): p. 82-92.

# Development of a new design expression for the in-plane shear capacity of the partially grouted concrete masonry walls.

Thangarajah Janaraj<sup>1</sup> and Manicka Dhanasekar<sup>2</sup>

<sup>1</sup>Research Associate of Civil Engineering, Queensland University of Technology; Email-  
thangarajah.janaraj@qut.edu.au

<sup>2</sup> Professor of Civil Engineering, Queensland University of Technology

**Abstract:** Partially grouted masonry walls subjected to in-plane shear exhibit a complex behaviour because of the influence of the aspect ratio, the pre-compression, the grouting pattern, the ratios of the horizontal and the vertical reinforcements, the boundary conditions and the characteristics of the constituent materials. The existing in-plane shear expressions for the partially grouted masonry are formulated as sum of strength of three parameters, namely, the masonry, the reinforcement and the axial force. The parameter 'masonry' includes the wall aspect ratio and the masonry compressive strength; the aspect ratio of the unreinforced panel inscribed into the grouted cores and bond beams are not considered, although failure is often dominated by these unreinforced masonry panels. This paper describes the dominance of these panels, particularly those that are squat, to the shear capacity of whole of shear walls. Further, the current design formulae are shown highly un-conservative by many researchers; this paper provides a potential reason for this un-conservativeness. It is shown that by including an additional term of the unreinforced panel aspect ratio a rational design formula could be established. This new expression is validated with independent test results reported in the literature – both Australian and overseas; the predictions are shown to be conservative.

**Keywords:** partially grout, in-plane shear, concrete masonry, design formulae.

## 1. Introduction

The existing in-plane shear design expressions in various national standards are based on additive approach. This method adds the capacity of masonry, the contributions of the pre-compression and the reinforcement. The masonry terms is accounted as a function of masonry strength and the wall aspect ratio. A fraction of the applied pre-compression and the steel reinforcement yield strength are also accounted. However, there are additional factors that influence the in-plane shear capacity of the partially grouted masonry shear walls, such as the boundary condition and the grout spacing / panel aspect ratio (Dhanasekar and Haider 2011; Haach et al. 2011; Janaraj et al. 2011). In the absence of these parameters, the current design formulae are often criticised as being highly un-conservative/ unsafe (Shrive et al. 2009; Nolph and ElGawady 2012; Janaraj 2014; Janaraj and Dhanasekar 2014).

The existing design expressions in the Australian, New Zealand and the USA standards ( AS 3700 (2011), NZS 4230 (2004) and MSJC (2008), respectively) are considered in this paper. These expressions attracted criticism of providing un-conservative predictions. This un-conservatism may be attributed to the complexity and to some extent, the lack of understanding of the in-plane shear behaviour of the walls. AS 3700 (2011) contains only masonry and reinforcement terms; although very simple, also is shown very highly non-conservative. The masonry term is expressed in wall aspect ratio while completely disregarding masonry strength. The exclusion of masonry strength might well be a problem. Further this formula completely neglects the effect of pre-compression and boundary conditions effects. AS 3700 (2011) in-plane shear expression is shown in Eq. (1).

$$V = (1.5 - 0.5\lambda_w)A_s + 0.8f_yA_s \quad (1)$$

Where  $\lambda_w$  is the aspect ratio of the whole wall  $\left(\frac{H}{L}\right)$ , in which  $H$  is height and  $L$  is length of the wall.

Walls of aspect ratio less than unity, low vertical and the horizontal reinforcement areas are particularly prone to provide highly non-conservative predictions; for example, a wall of 1.6 m high, 5.0 m long reinforced with N12 bars at 1.2 m c/c are shown to predict 234 % higher capacity compared to laboratory experiment, where care is taken on the quality of specimens. Therefore, using this expression for real world designs require urgent attention – this paper attempts to provide a rational base for making the predictions conservative.

The NZS 4230 (2004) expression is shown in Eq. (2).

$$V_n = \left[ (C_1 + C_2)v_{bm} + \frac{0.9P}{b_w d} \tan \alpha \right] b_w d + 0.8 \frac{f_{yh} A_{sh} d}{s_h} \quad (2)$$

Where  $C_1 = 33 \frac{A_{sv} f_{yv}}{300 b_w d}$

$$\frac{H_e}{L} < 0.25 \rightarrow C_2 = 1.5$$

$$0.25 \leq \frac{H_e}{L} \leq 1 \rightarrow C_2 = 0.42 \left[ 4 - 1.75 \frac{H_e}{L} \right]$$

$H_e$ ,  $A_{sh}$ ,  $A_{sv}$ ,  $b_w$ ,  $d$ ,  $f_{yh}$ ,  $f_{yv}$ ,  $L$ ,  $s_h$  and  $P$  stands for effective height of the wall, area of the horizontal steel, area of the vertical steel, effective wall width, design length of wall, yield strength of the horizontal steel, yield strength of the vertical steel, wall length, vertical spacing of the horizontal bars and pre-compression load, respectively.  $v_{bm}$  is the basic shear strength of masonry and  $\alpha$  is the angle of diagonal strut to vertical. The term  $(b_w d)$  accounts for the face shell area and does not include the area of grout. This assumption considers the shear flow continuity requirements and to avoid any potential for shear failures in the un-grouted shells. The design length ( $d$ ) of the wall is limited to 80% of the actual wall length.

The in-plane shear expression of the Masonry Standard Joint Committee (MSJC 2008) is shown in Eq. (3). This equation includes wall aspect ratio and the strength to masonry terms. The pre-compression load and the horizontal reinforcement terms are also included.

$$V = \left[ 0.166 \left( 2 - 0.875 \frac{M_f}{V_f d_v} \right) \sqrt{f'_m} \right] A_n + 0.25P + 0.5 f_{yh} \frac{A_{sh}}{s_h} d_v \quad (3)$$

In which the maximum in-plane load is limited to,

$$a) \frac{M_f}{V_f d_v} \leq 0.25 \rightarrow V_n \leq 0.083(6A_n \sqrt{f'_m})$$

$$b) \frac{M_f}{V_f d_v} \geq 1 \rightarrow V_n \leq 0.083(4A_n \sqrt{f'_m})$$

$\frac{M_f}{V_f d_v}$  is moment to shear arm length ratio of the wall and  $f'_m$  is compressive strength of the masonry.

The net area ( $A_n$ ) accounts the facially bedded area and the grouted area.

Partially grouted masonry walls were shown to exhibit panel failures while the grouted cores remain intact (Janaraj et al. 2011; Nolph and ElGawady 2012; Minaie et al. 2014). This panel failure is critical in determining the in-plane shear capacity of the wall. Therefore, this paper examines the significance of the panel aspect ratio and the factors influencing the wall failure and panel only failure. Further, an in-plane shear expression is developed based on the panel only failure walls which predict the in-plane shear



capacity conservatively. The panel aspect ratio ( $\lambda_p$ ) is defined in Eq. (4). Where  $h$  is panel height and  $l$  is panel length as shown in Figure 1.

$$\lambda_p = \frac{h}{l} \quad (4)$$

The in-plane shear capacity of the wall is non-dimensionalised as in Eq. (6).

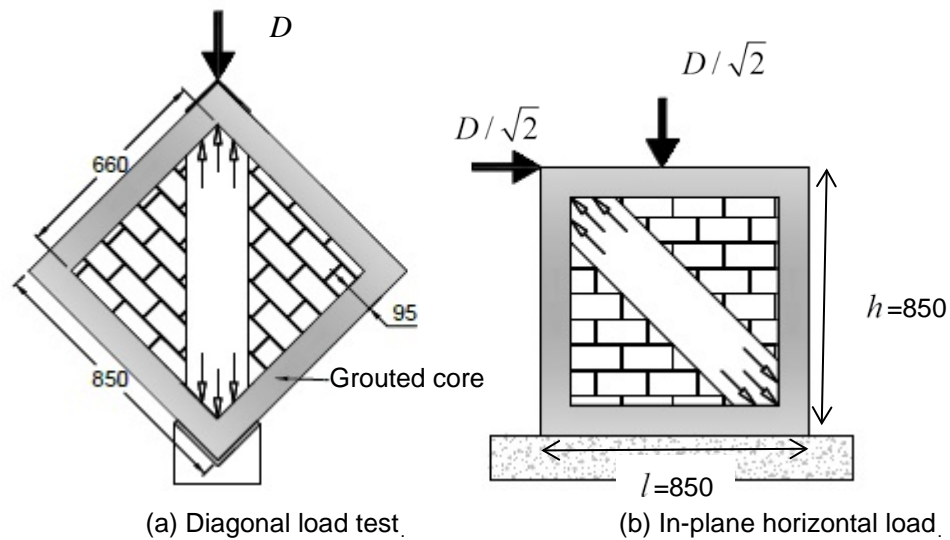
$$\ddot{X} = \frac{V}{A_n \times f'_m} \times 100 \quad (6)$$

Where  $\ddot{X}$  is non-dimensional shear strength and  $V$  is in-plane load capacity of the wall. The wall containing several panels is denoted as  $W_{x,y}$  where  $x$  indicated number of panels along the wall horizontal in-plane loaded direction and  $y$  indicates number of panel along the wall height direction. Number of panels along the height direction of the wall is also called as storey. Two storey wall defines a wall which has two panels along its height direction.

## 2. Experiment and Numerical validation.

Diagonal compression tests reflect the behaviour of laterally loaded shear walls, although the boundary condition and aspect ratio of walls could not be replicated in these tests; however, they are simpler and can provide reliable estimate of the shear strength of masonry (ASTM 2002; Petersen et al. 2012; Janaraj and Dhanasekar 2014). It is therefore prudent to develop finite element models to replicate the diagonal compression tests and then use the same FE model for various geometry of shear walls. The shear wall behaviour output from the FE models can be validated using other independent tests. This approach is followed in this paper.

The transmission of the diagonal compression test into the in-plane horizontal load is shown in Figure 1 where the diagonal strut formation of load resisting mechanism exists. This diagonal load test is widely used to examine the effectiveness of strengthening mechanism of the masonry with FE model development. This diagonal load test was conducted and tested in accordance with provisions of ASTM (2002). As large size wall cannot be tested under this method, half scale specimens were constructed to accommodate higher number of mortar joints within the panel.



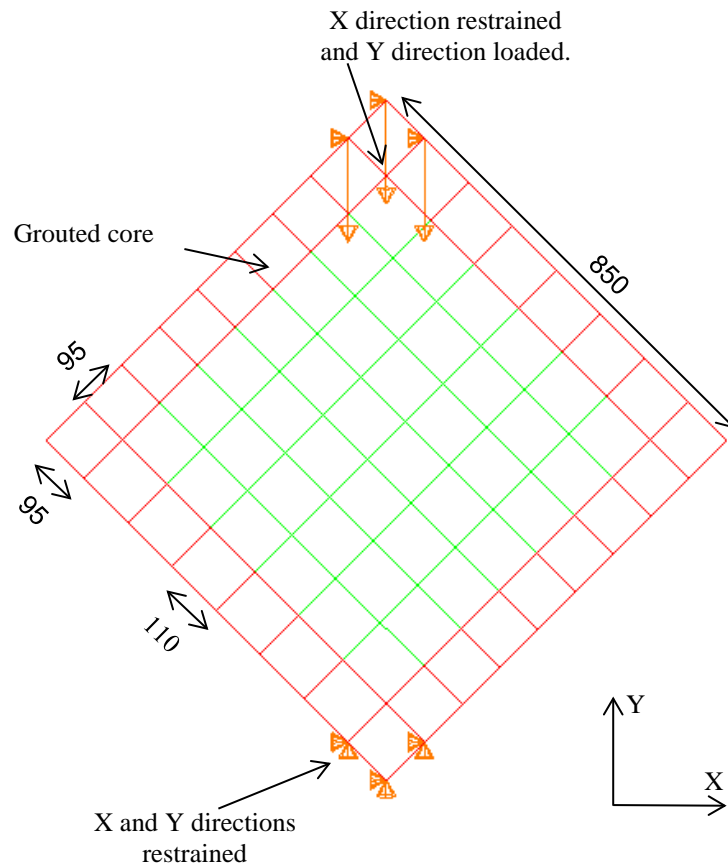
**Figure 1. Conversion of diagonal load test to partially grouted masonry walls.**

Four experimental walls were constructed and tested under diagonal load test; a) two un-grouted masonry walls and b) two grouted masonry walls. The wall dimension is 850 mm square as shown in the figure with the thickness of 90.5 mm. The face shell thickness is 15.75 mm. The grouted masonry wall has grout in its

edge recesses with a 12 mm diameter reinforcing bar placed at the centre. The diagonal load versus diagonal displacement was obtained and used for FE model validation. A non-linear FE modelling based on the homogenized macro element characteristics in explicit formulation was adopted as it predicting the masonry shear wall behaviours well (Dhanasekar and Haider 2008). A macro modelling strategy was deployed using ABAQUS Explicit formulation reported in Dhanasekar and Haider (2008) was adopted and reported in Janaraj and Dhanasekar (2014). The masonry mesh height was selected to represent one block height (90 mm) and one mortar thickness (5 mm). The length of the masonry mesh was selected by compromising the optimum mesh size from the mesh sensitive study which can sufficiently represent block and mortar. The FE model arrangement and the selected mesh sizes are shown in Figure 2.

Multi surface plasticity model was adopted to represent the masonry behaviours (Lourenço 1996). As the grouted cores are governed by similar masonry anisotropic behaviour, same masonry multisurface material model was selected to represent the grouted cores with different parameters. These masonry and the grouted cores parameters were determined from the conducted material testing of compression test, four point bending tests and triplet tests. The test results and the parameters can be found elsewhere Janaraj and Dhanasekar (2014).

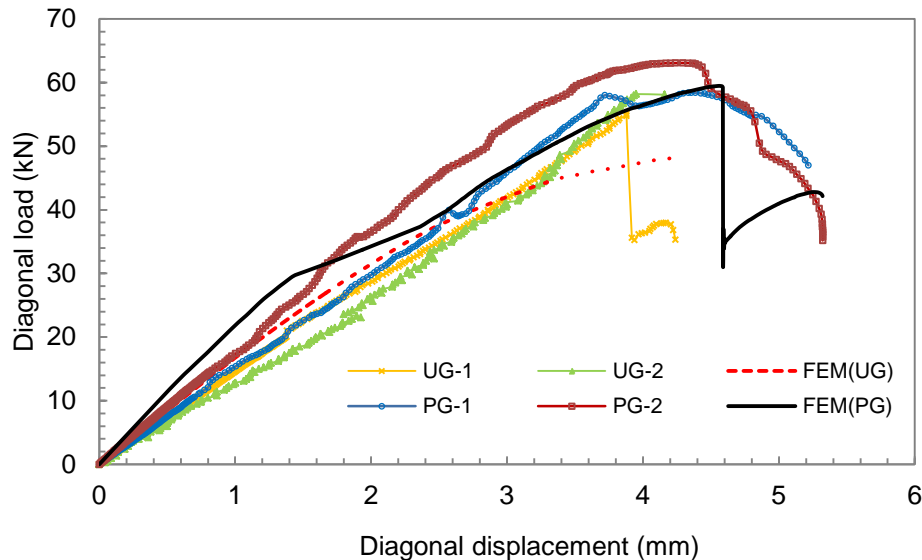
The reinforcement was represented by two node truss elements with the limited compression as the reinforcement was placed without any shear ties. From the conducted tensile coupon test, the yield strength and the elastic modulus was found as 500 MPa and 200 GPa, respectively. The stress strain curve was input as material parameters.



**Figure 2. Finite element model**

The predicted diagonal load versus diagonal displacement response of the diagonally loaded wall was compared with that of the tested panels and is shown in Figure 3. The un-grouted panel is denoted as (UG) and the partially grouted panel is denoted as (PG). Two walls of the each configuration are denoted by "1" and "2". It can be seen in the figure that the PG FE model FEM(PG) well predicts the average peak load of the tested panels (59 kN) and the failure displacement of 5.3 mm. Similarly the FEM(UG) predicts both experimental curves acceptable. Therefore, this model enables to study the behaviour of the partially

grouted masonry shear walls in-plane shear analysis. Further details of other validated parameters such as reinforcement strains, strains at centre of the panel, crack pattern can be found in Janaraj and Dhanasekar (2014), Janaraj and Dhanasekar (2015a) and Janaraj and Dhanasekar (2015b). This validated model is used for the further studies reported in the following sections.



**Figure 3. Diagonal load versus diagonal displacement**

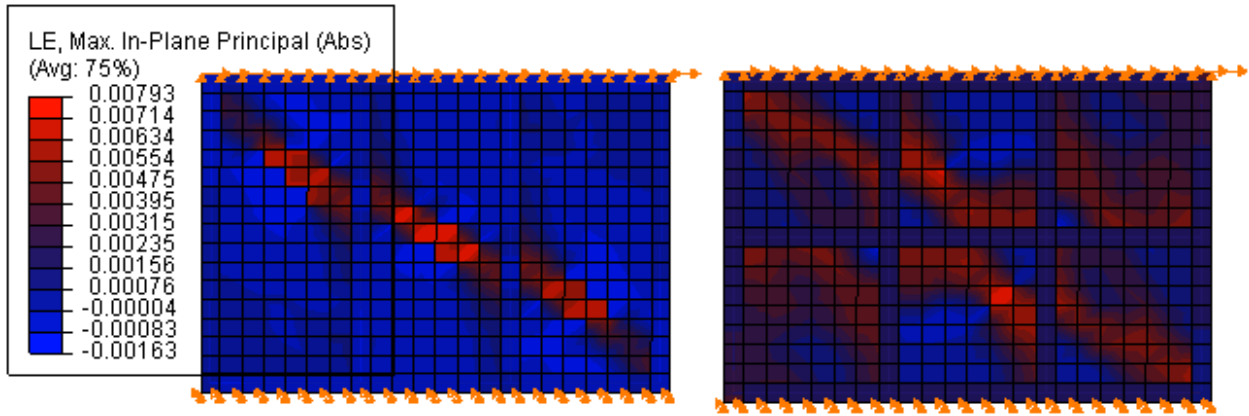
### 3. Influencing parameters

#### 3.1 Panel failure

It was found that the panel failure is determined by the aspect ratio of the panel. The study outlined such findings is reported in this section. For this purpose a wall with a wall aspect ratio of 0.68 walls containing  $\lambda_p = 1.9$  panels was selected as shown in Figure 4.a. The same wall was introduced with horizontal reinforced grout at the middle to form  $\lambda_p = 1.0$  panels as shown in Figure 4.b. The wall with three panels  $W_{3,1}$  is technically converted into six panels' wall  $W_{3,2}$  without changing its overall dimensions. The principal logarithmic strains are shown in Figure 4 where red shows tensile strains corresponding to failure of the wall. It can be clearly seen that the failure was obtained along the wall diagonal in Figure 4.a where  $\lambda_p = 1.9$ . The partition of wall using horizontal grout has arrested the diagonal failure within the panels. In this scenario, considering the wall aspect ratio to determine the in-plane shear capacity does not represent the actual resisting mechanism. Therefore, the sensitivity of the panel is analysed in the following sections.

#### 3.2 Effect of horizontal reinforcement

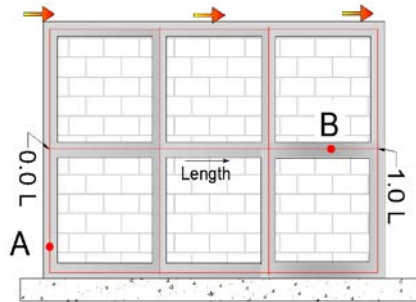
It is widely reported in the literature the horizontal reinforcements have limited contribution to the shear capacity of the masonry shear walls (for example Shing et al. (1990)). It has been found that the horizontal reinforcement activates in the post peak region of the wall hence no in-plane shear capacity will be attained. To examine this nature, the wall reported in Figure 4.b is considered.



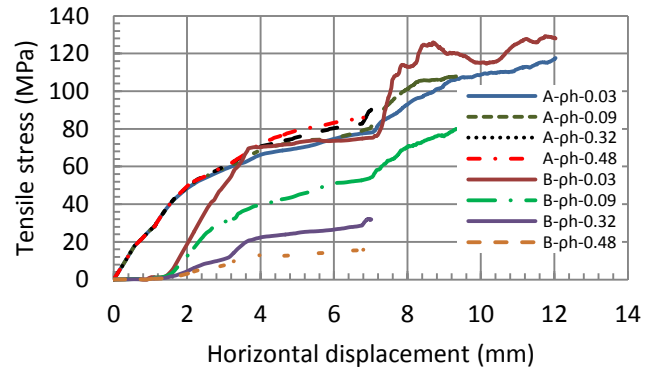
(a) Wall failure.

(b) Panel failure.

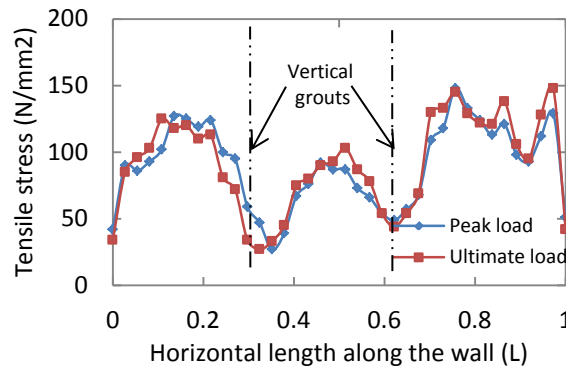
**Figure 4. Effect of horizontal reinforced grout**



(a) Tensile stress in the reinforcement.



(b) Tensile stresses at two loading



(c) Location definition

**Figure 5. Tensile stresses on the reinforcement**

Location A was selected at the heel side of the wall where higher tensile stress on the reinforcement exists and location B was selected in the horizontal reinforcement as shown in Figure 5.a. The graphs in Figure 5.b are denoted by the location followed by the net area of the reinforcements stated in percentage of net area of the wall. The amount of horizontal reinforcement was changed and its corresponding tensile stresses are shown in Figure 5.b. It can be seen from Figure 5.a that the reinforcement did not yield and reached only 25% of its yield capacity of 500 MPa. The increase on amount of horizontal reinforcement merely reduces the tensile stresses indicate it was in elastic region. As these A and B points were selected in two locations it was decided to study the tensile stress variation

along the length of the horizontal reinforcement. The tensile stress of the reinforcement at the peak load capacity of the wall and the ultimate capacity of the walls were selected as shown in Figure 5.c. The yield stress of the reinforcement had shown no significant difference for the ultimate and the peak load capacity of the wall. Therefore, it was decided the horizontal reinforcements do not contribute to enhance the in-plane shear capacity of the wall.

### 3.3 Panel efficiency

The panel efficiency measures the increase of the in-plane shear capacity of the wall than its individual arithmetic sum of individual panel in-plane shear capacity of the panels. This increase is achieved due to effective confinement induced in between panels. The panel efficiency is measured using Eq. (7).

$$\xi = \left( \frac{\ddot{X}_{x,y} - \ddot{X}_{1,1}}{\ddot{X}_{1,1}} \right) \times 100\% \quad (7)$$

Where  $\ddot{X}_{1,1}$  is shear strength parameter of single panel and  $\ddot{X}_{x,y}$  is the shear strength parameter of the wall containing  $x$  and  $y$  numbers of panels. Any value of shear strength parameter above zero indicates the increase of shear strength of the wall through effective confinement. The panel efficiency of the walls which has four different aspect ratios of the panels is shown in Figure 6.

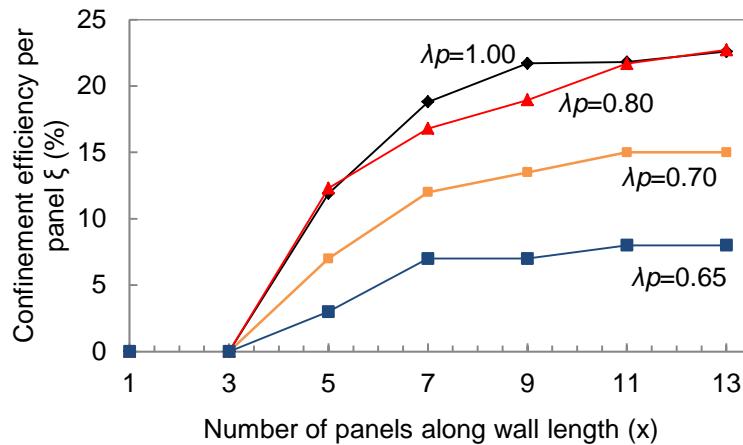


Figure 6. Panel efficiency of  $W_{x,1}$  walls.

For the walls containing  $\lambda_p=1.00$  panels along its wall loaded direction/ wall length, the increase of wall length from 1 to 3 did not increase any shear strength through confinement. However, the further increase of panels substantially increased the panels walls hear strength. For example, individual panel located in the nine panel wall produces 22% higher in-plane shear load than its individual capacity as confinement increased substantially. However, further increase of the panels within the wall does not increase the efficiency indicating saturation was occurred at 9 panel wall. It is also found that reduce in panel aspect ratio merely reduces the panel efficiency. This study was conducted on a single panel height wall or single storey height wall. When the panel height was increased, it was found that the efficiency reduces. This efficiency is implemented in the following sections of the equation development.

#### 4. In-plane shear expressions development

The in-plane shear expressions are formulated based on the capacity of the single panel. Then this single panel capacity is converted to wall in-plane shear capacity using panel efficiency factor. As these panel efficiencies were formed for single storey panel, the effect of multi storey was analysed and its correlation was found as below (Eq. (8)).

$$\ddot{X}_{1,y} = 0.9^{y-1} \ddot{X}_{1,1} \quad (8)$$

The in-plane shear capacity expressions of the partially grouted masonry wall are formulated by analysing masonry panel properties, Pre-compression load and boundary conditions. As horizontal reinforcement shows no effect on the in-plane shear capacity, it is completely disregarded in the equation formation.

##### 4.1 Masonry

A masonry panel was considered for the analyses. The panel was loaded in horizontal direction with fixed boundary conditions at the top while completely arresting bottom wall movements in both directions. The strength of masonry and the panel aspect ratio were considered as major variables. Initially, the panel aspect ratio was kept as constant and the in-plane shear capacity was correlated with  $\sqrt{f_m}$ . This correlation was performed separately for  $\lambda_p$  of 1.0, 0.80, 0.65 and 0.55 panels. An established linear correlation for the  $\lambda_p = 0.80$  panel can be seen in Figure 7. Similar linear correlation was observed in other aspect ratio panels.

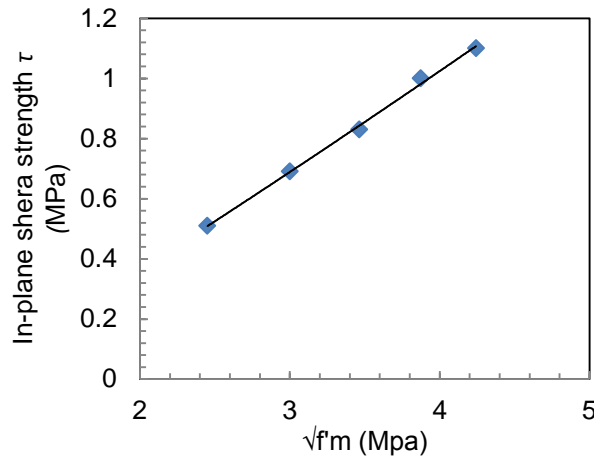


Figure 7. In-plane shear strength versus  $\sqrt{f_m}$ .

As the in-plane shear stress of the panel ( $\tau$ ) is linearly correlated with  $\sqrt{f_m}$ , further studies have been conducted by considering  $\tau / \sqrt{f_m}$  varies with panel aspect ratio ( $\lambda_p$ ) linearly as shown in Eq. (9).

$$\frac{\tau}{\sqrt{f_m}} = a(\lambda_p) + b \quad (9)$$

For this study, a compressive strength of masonry 6 MPa, 9 MPa, 12MPa, 15 MPa, and 18 MPa were considered. Curves were plotted in the  $\tau / \sqrt{f_m}$  versus  $\lambda_p$  space and 95% confidence line was obtained as shown in Eq. (10).

$$\frac{\tau}{\sqrt{f_m}} = 0.17(2 - 0.9 \times \lambda_p)$$

#### 4.2 Pre-Compression and boundary condition

A single panel was subjected to different levels of pre-compression changing from 0% of its compressive strength of the masonry to 50% of the compressive strength of the masonry. It was found that an inclusion of 25% pre compression load would conservatively measures the enhancement of the in-plane shear capacity of the panel through pre-compression. Further, any load exceeds 13% of the compressive strength of the masonry cause more brittle type failure of the wall. Similar limitation is enforced in 4230 (2004). It is also noticed that a transition of fixed boundary wall to cantilever type free boundary wall cause reduction in in-plane shear capacity of the wall. It was found that the release of boundary condition reduces the in-plane shear capacity by 50%. This effect is included through boundary condition factor  $\gamma$  in the equation which is 1.0 for fixed boundary wall and 0.5 for free boundary cantilever wall. Other factors are outlined in Table 1.

**Table 1. Design criteria for fixed boundary walls**

Wall height	Wall length	$\lambda_p$	$\xi$
Single panel	Less than 4 panels*	$\lambda_p=1-0.55$	1.00
	More than 10 panels	$1.0 \geq \lambda_p \geq 0.8$	1.22
		$0.8 > \lambda_p \geq 0.6$	1.00
		$0.6 > \lambda_p$	0.93
2-3 panels	All panels	$1.0 \geq \lambda_p$	1.00
4 panels	Less than 5 panels	$1.0 \geq \lambda_p$	1.00
	above 10 panels	$\lambda_p = 1.0$	1.00
		$1.0 > \lambda_p \geq 0.55$	0.94

\* Linear interpolation is permitted in between 4 to 10 panels.

For released boundary wall the factor need to be multiplied by 0.4.

After considering all the factors the final in-plane shear expressions is shown in Eq. (11).

$$V = \left\{ 0.17(2 - 0.9\lambda_p) \sqrt{f_m'} A_n + 0.25P \right\} \times (0.9)^{y-1} \times \xi \times x \times \gamma \quad (11)$$

Where  $V$ ,  $P$ ,  $x$  and  $\gamma$  are In-plane load capacity of the wall, pre-compression load, number of panel along wall length and boundary condition factor, respectively.

#### 4.3 Independent validation of the model

To examine the reliability of the model, nine independently tested walls published in Nolph and ElGawady (2011), Minaie et al. (2010), Shrive et al. (2009), Schultz (1996) and Ghanem et al. (1993) were considered as it contained  $\lambda_p \leq 1$  panels. Its prediction is shown in Figure 8, where  $V/V_{EXP}$  greater than 1.0 is un-conservative prediction. The prediction of AS 3700 is far away from the actual wall in-plane shear capacity whereas the propose expression average is 0.93 which is 7% conservative.



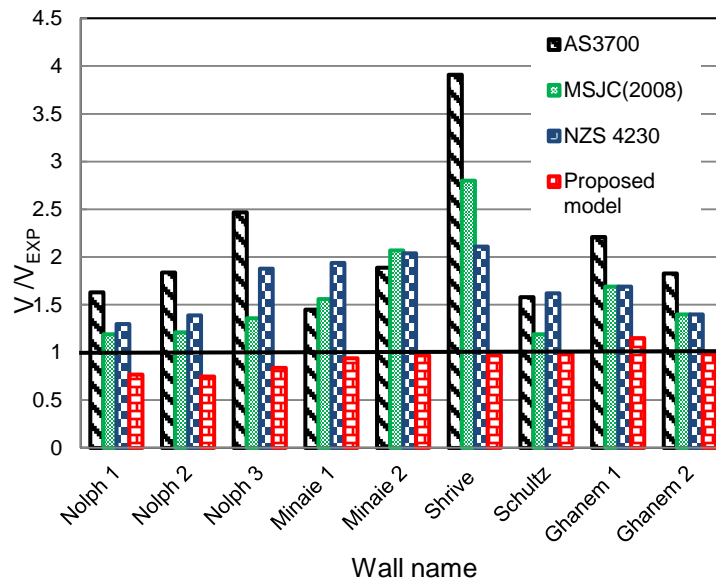


Figure 8. Prediction of the expressions.

## 5. Conclusions

The proposed model that accounts the effect of panel aspect ratio, pre-compression and boundary condition conservatively predicts the wall within acceptable safety margin. As 3700(2011) un-conservative prediction is quiet visible in the figure, hance it needs an urgent review.

## 6. References

- AS (Australian Standards). (2011). "Australian standard of masonry structures." *AS 3700*, Sydney, Australia, Standards Australia Limited.
- NZS (New Zealand Standards). (2004). "Design of reinforced concrete masonry structures." *NZS 4230*, Wellington, New Zealand, Standards New Zealand.
- ASTM (American Society for Testing and Materials). (2002). "Standard test method for diagonal tension (shear) in masonry assemblages." *ASTM E519-02*, West Conshohocken, PA, ASTM.
- Dhanasekar, M., and Haider, W. (2011). "Effect of spacing of reinforcement on the behaviour of partially grouted masonry shear walls." *Advances in Structural Engineering*. 14(2), 281-294.
- Dhanasekar, M., and Haider, W. (2008). "Explicit finite element analysis of lightly reinforced masonry shear walls." *Computers & Structures*. 86(1), 15-26.
- Ghanem, G. M., Salama, A. E., Elmagd, S. A., and Hamid, A. A. (1993). "Effect of axial compression on the behavior of partially reinforced masonry shear walls." *Proc., 6<sup>th</sup> North America Masonry Conf.* Philadelphia,
- Haach, V. G., Vasconcelos, G., and Lourenço, P. B. (2011). "Parametrical study of masonry walls subjected to in-plane loading through numerical modeling." *Engineering Structures*. 10.1016/j.engstruct.2011.01.015, 1377-1389.
- Janaraj, T. (2014). "Studies on the in-plane shear response of confined masonry shear walls." (*PhD thesis*), Queensland University of Technology, Australia.
- Janaraj, T., and Dhanasekar, M. (2015a). "Design expressions for the in-plane shear capacity of confined masonry shear walls containing squat panels." *Journal of Structural Engineering-ASCE (Accepted)*.

- Janaraj, T., and Dhanasekar, M. (2015b). "Effectiveness of two forms of grouted reinforced confinement methods to hollow concrete masonry panels." *Journal of Materials in Civil Engineering*. (in press). 10.1061/(ASCE)MT.1943-5533.0001295, 04015038.
- Janaraj, T., and Dhanasekar, M. (2014). "Finite element analysis of the in-plane shear behaviour of masonry panels confined with reinforced grouted cores." *Construction and Building Materials*. 65, 495-506. 10.1016/j.conbuildmat.2014.04.133, 495-506.
- Janaraj, T., Dhanasekar, M., and Haider, W. (2011). "Wider reinforced masonry shear walls subjected to cyclic lateral loading." *Architecture. Civil Engineering. Environment - ACEE Journal*. 4, 39-46.
- Lourenço, P. B. (1996). "*Computational strategies for masonry structures*." Delft university press, Netherlands.
- Minaie, E., Moon, F. L., and Hamid, A. A. (2014). "Nonlinear finite element modeling of reinforced masonry shear walls for bidirectional loading response." *Finite Elements in Analysis and Design*. 84, 44-53. 10.1016/j.finel.2014.02.001, 44-53.
- Minaie, E., Mota, M., Moon, F. L., and Hamid, A. A. (2010). "In-plane behavior of partially grouted reinforced concrete masonry shear walls." *Journal of Structural Engineering*. 136(9), 1089-1097. 10.1061/(ASCE)ST.1943-541X.0000206, 1089-1097.
- . (2008). "Building code requirement for masonry structures." *MSJC (Masonry Standards Joint Committee)*, ACI 530/ASCE 5, TMS 402, American Concrete Institute, Detroit.
- Nolph, S. M., and ElGawady, M. A. (2012). "Static cyclic response of partially grouted masonry shear walls." *Journal of Structural Engineering*. 138(7), 864-879. 10.1061/(ASCE)ST.1943-541X.0000529, 864-879.
- Nolph, S. M., and ElGawady, M. A. (2011). "Static cyclic response of partially grouted masonry shear walls." *Journal of Structural Engineering*. 138(7), 864-879.
- Petersen, R. B., Ismail, N., Masia, M. J., and Ingham, J. M. (2012). "Finite element modelling of unreinforced masonry shear wallettes strengthened using twisted steel bars." *Construction and Building Materials*. 33(0), 14-24. 10.1016/j.conbuildmat.2012.01.016.
- Schultz, A. E. (1996). "Seismic resistance of partially-grouted masonry shear walls." *Proc., 1996 CCMS of the ASCE symp. in conjunction with Structures Congress XIV*. ASCE, Reston, VA, Paper No. 1221.
- Shing, P. B., Schuller, M., and Hoskere, V. S. (1990). "In-plane resistance of reinforced masonry shear walls." *Journal of Structural Engineering*. 116(3), 619-640. 10.1061/(ASCE)0733-9445(1990)116:3(619), 619-640.
- Shrive, N. G., Page, A. W., Simundic, G., and Dhanasekar, M. (2009). "Shear tests on wide-spaced partially reinforced squat masonry walls." *Proc., Canadian Masonry Symposium*. Toronto, Canada., 223-232.

# Transient Heat Transfer Analysis of Reinforced Concrete Members Using a Discrete Crack Approach

D. Dias-da-Costa<sup>1,2</sup>, L. Godinho<sup>2</sup>, G. Ranzi<sup>1</sup>

<sup>1</sup>School of Civil Engineering, The University of Sydney, Sydney, NSW 2006, Australia

<sup>2</sup>ISISE, Department of Civil Engineering, University of Coimbra, Rua Luís Reis Santos, 3030-788 Coimbra, Portugal

**Abstract:** Transient heat transfer analyses of concrete structures can provide useful insight into their structural response when subjected to thermal effects, as for example in the case of exposure to elevated temperatures or when simulating the development of early-age thermal shrinkage. In these situations, the occurrence of concrete cracking can influence the temperature field and this effect needs to be included in the analysis. In early finite element formulations, the development of discrete cracks was based on progressive remeshing strategies to adapt the topology of the mesh and accommodate propagating cracks. It was a computationally demanding strategy, often leading to distorted meshes and inaccurate results. Recent nodal enrichment strategies (XFEM, GFEM) have overcome this drawback. However, in these simulations, the size of the problem increases dramatically with both number and size of cracks, i.e. with the increasing structural damage. In this context, this paper proposes an alternative element enrichment approach that can be efficiently used for transient heat transfer problems in cracked concrete members.

**Keywords:** Finite Elements, Element Enrichment Technique, Fracture Analysis, Transient Heat Transfer.

## 1. Introduction

The need for transient heat transfer analyses of concrete structures can arise in many different situations. For instance, in the case of concrete dams, predicting the heat distribution, and corresponding evolution, is critical for the optimisation of the construction procedure. Assessing the behaviour of a structure when exposed to elevated temperatures, or even predicting the impact of early-age thermal shrinkage on the serviceability behaviour of concrete members, are other examples in which transient heat transfer analyses can be very beneficial. In these situations, the development of accurate models has to take into account the coupling between mechanical behaviour, including possible fracture, and heat transfer analysis.

There are currently different numerical techniques for transient heat transfer problems, either formulated in the time domain (1-4), or in transformed domains (5-7). These procedures have been validated using different numerical discretisations, including finite differences, finite elements, boundary elements and meshless methods (8-11). Among all, the finite element method (FEM) is the most widely used since it easily caters for media with varying properties and different nonlinear features. In its standard form, the finite element model has to accommodate all discontinuities within the underlying mesh, hence thus it requires remeshing algorithms to progressively adapt the topology as cracks propagate or intersect (12). This, however, can lead to severely distorted meshes and inaccurate results without special approaches (13). Nodal enrichment techniques, such as XFEM or GFEM (14-16), entirely avoid this drawback by using additional nodal degrees of freedom directly placed on top of existing nodes and in the neighbourhood of all the cracks. The latter method was successfully applied to heat transfer analyses (17-19), even with heterogeneous domains (20-21). Nevertheless, these algorithms are computationally demanding, particularly when dealing with numerous discontinuities (i.e. when the additional degrees of freedom grow significantly).

This paper presents a preliminary study towards the development of an innovative and more efficient finite element enrichment strategy. The formulation is developed within the scope of the discrete crack approach (22-24) and uses the same variational framework for both mechanical and heat transfer analyses. Cracked finite elements are enriched with additional “rigid body” movements of the displacement field (in the case of the mechanical problem) and temperature field (in the case of the transient heat transfer problem) to account for the presence of strong discontinuities. The compatibility between mechanical and heat transfer formulations creates the possibility of evolving towards the proposal of a thermo-mechanical coupled model for concrete structures, based entirely on element embedded discontinuities.

## 2. Formulation

In this section, the element enrichment approach for simulating the mechanical behaviour of a fractured body is firstly presented. The framework is then extended for transient heat transfer problem.

### 2.1 Mechanical problem

The body  $\Omega$  shown in Fig. 1a is delimited by the external boundary,  $\Gamma$ , and contains an internal discontinuity,  $\Gamma_d$ , which defines two subregions,  $\Omega^+$  and  $\Omega^-$ . Loading is applied slowly, such that the response remains quasi-static, and is composed of body forces,  $\bar{\mathbf{b}}$ , and natural boundary conditions,  $\bar{\mathbf{t}}$ , the latter distributed on part of the external boundary,  $\Gamma_t$ . The essential boundary conditions,  $\bar{\mathbf{u}}$ , are applied on the remaining part,  $\Gamma_u$ , being  $\Gamma = \Gamma_t \cup \Gamma_u$  and  $\emptyset = \Gamma_t \cap \Gamma_u$ . Vector  $\mathbf{n}$  is orthogonal to the boundary surface, pointing outwards, whereas  $\mathbf{n}^+$  is orthogonal to the internal discontinuity and pointing inwards.

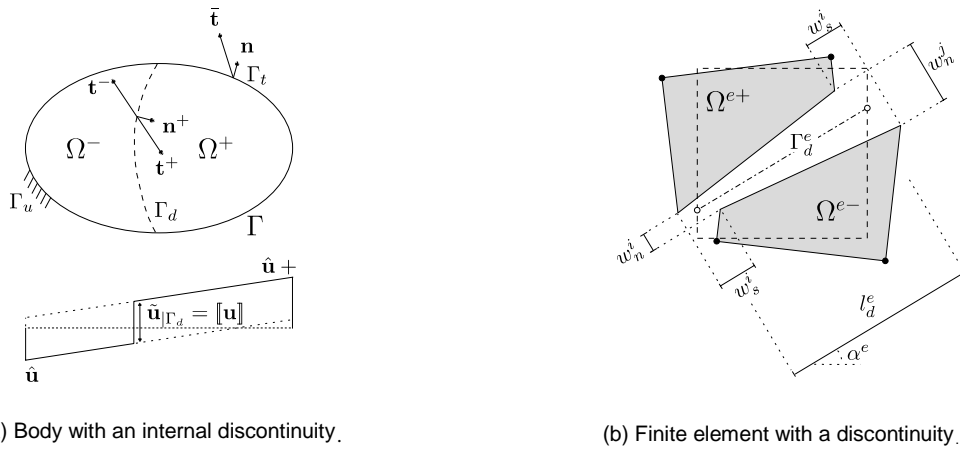


Figure 1. Adopted definitions.

The total displacement at any material point within the body is given by (22-24):

$$\mathbf{u} = \hat{\mathbf{u}} + \mathcal{H}_{\Gamma_d} \tilde{\mathbf{u}}(\mathbf{x}), \quad (1)$$

where  $\hat{\mathbf{u}}$  is the regular displacement field,  $\tilde{\mathbf{u}}$  is the enhanced displacement field solely due to the internal discontinuity, and  $\mathcal{H}_{\Gamma_d}$  is the Heaviside function taking the value 1 in  $\Omega^+$  and 0 otherwise.

The opening of discontinuity  $\mathbf{u}^{+/-}$ , or jump in the displacement field, across the discontinuity is calculated by applying Eq. (1) to both sides of the discontinuity and then equating the difference, which can be expressed as:

$$\mathbf{u}^{+/-} = \mathbf{u}^+ - \mathbf{u}^- = \tilde{\mathbf{u}}(\mathbf{x}_{\Gamma_d}). \quad (2)$$

The equations that govern this mechanical problem are as follows:

$$\nabla \cdot \boldsymbol{\sigma} + \bar{\mathbf{b}} = \mathbf{0} \quad \text{in } \Omega \setminus \Gamma_d, \quad (3)$$

$$\boldsymbol{\varepsilon} = \nabla^s \mathbf{u} \quad \text{in } \Omega \setminus \Gamma_d, \quad (4)$$

$$\boldsymbol{\sigma} = \boldsymbol{\sigma}(\boldsymbol{\varepsilon}) \quad \text{in } \Omega \setminus \Gamma_d, \quad (5)$$

$$\mathbf{u} = \bar{\mathbf{u}} \quad \text{at } \Gamma_u, \quad (6)$$

$$\boldsymbol{\sigma} \cdot \mathbf{n} = \bar{\mathbf{t}} \quad \text{at } \Gamma_t, \quad (7)$$

$$\boldsymbol{\sigma}^+ \cdot \mathbf{n}^+ = \mathbf{t}^- \quad \text{at } \Gamma_d, \quad (8)$$

$$-\boldsymbol{\sigma}^- \cdot \mathbf{n}^+ = \mathbf{t}^- \quad \text{at } \Gamma_d, \quad (9)$$

$$\mathbf{t}^+ = \mathbf{t}(\mathbf{u}^{+-}) \quad \text{at } \Gamma_d, \quad (10)$$

$$\mathbf{t}^+ = \mathbf{t}^- \quad \text{at } \Gamma_d, \quad (11)$$

being  $\mathbf{t}^+$  and  $\mathbf{t}^-$  the traction vectors at the discontinuity, respectively, on each side of the domain. The internal equilibrium is imposed by Eq. (3), whereas external and internal equilibrium are enforced by Eqs. (6), (7) and (11). The kinematic compatibility and constitutive laws are represented by Eqs. (4), and Eqs. (5) and (10).

The principle of virtual work for the cracked body can be seen as a particular case of the Hu and Washizu principle (25-27), where the independent unknown fields are  $\mathbf{u}$  and  $\mathbf{u}^{+-}$ . In this case the following variational equation applies:

$$-\int_{\Omega \setminus \Gamma_d} \delta \mathbf{u} \cdot (\nabla \cdot \boldsymbol{\sigma} + \bar{\mathbf{b}}) d\Omega + \int_{\Gamma_t} \delta \mathbf{u} \cdot (\boldsymbol{\sigma} \cdot \mathbf{n} - \bar{\mathbf{t}}) d\Gamma - \int_{\Gamma_d} \delta \mathbf{u}^{+-} \cdot (\boldsymbol{\sigma}^+ \cdot \mathbf{n}^+ - \mathbf{t}^+) d\Gamma = 0. \quad (12)$$

The first term of Eq. (12) can be expanded and integrated by parts, and after applying the Gauss theorem, the following equation is written:

$$-\int_{\Omega \setminus \Gamma_d} \nabla^s \delta \mathbf{u} : \boldsymbol{\sigma} d\Omega - \int_{\Gamma_d} \delta \mathbf{u}^{+-} \cdot \mathbf{t}^+ d\Gamma + \int_{\Omega \setminus \Gamma_d} \delta \mathbf{u} \cdot \bar{\mathbf{b}} d\Omega + \int_{\Gamma_t} \delta \mathbf{u} \cdot \bar{\mathbf{t}} d\Gamma = 0, \quad (13)$$

which is the classic virtual work principle for a medium with a discontinuity (28).

If the body is now discretised into a certain number of finite elements (as illustrated in Fig. 1b), the displacement field within each element is interpolated by (24):

$$\mathbf{u}^e = \mathbf{N}^e(\mathbf{x}) \left[ \mathbf{a}^e + \left( \mathcal{H}_{\Gamma_d} \mathbf{I} - \mathbf{H}_{\Gamma_d}^e \right) \tilde{\mathbf{a}}^e \right] \quad \text{in } \Omega^e \setminus \Gamma_d^e, \quad (14)$$

where  $\mathbf{a}^e$  are the total nodal displacements,  $\tilde{\mathbf{a}}^e$  are the nodal displacements due to the discontinuity,  $\mathbf{I}$  is the identity matrix,  $\mathbf{N}^e$  are the shape functions of the element, and  $\mathbf{H}_{\Gamma_d}^e$  is a diagonal matrix containing the Heaviside function evaluated at each regular degree of freedom of the element.

The enhanced nodal displacements result directly from assuming that the movement of  $\Omega^{e+}$  over  $\Omega^{e-}$  is a rigid body motion (22, 24). According to this:

$$\tilde{\mathbf{a}}^e = \mathbf{M}_w^{ek} \mathbf{w}^e, \quad (15)$$

where  $\mathbf{w}^e$  is a vector containing the jumps at additional nodes placed at both extremities of the discontinuity ('i' and 'j' in Fig. 1b), and  $\mathbf{M}_w^{ek}$  is the matrix transmitting the displacement due to the opening of the discontinuity, being calculated by evaluating  $\mathbf{M}_w^e$  at each node and then stacking it into rows:

$$\mathbf{M}_w^e(\mathbf{x}) = \begin{bmatrix} 1 - \frac{(x_2 - x_2^i) \sin \alpha^e}{l_d^e} & \frac{(x_2 - x_2^i) \cos \alpha^e}{l_d^e} & \frac{(x_2 - x_2^i) \sin \alpha^e}{l_d^e} & \frac{(x_2 - x_2^i) \cos \alpha^e}{l_d^e} \\ \frac{(x_1 - x_1^i) \sin \alpha^e}{l_d^e} & 1 - \frac{(x_1 - x_1^i) \cos \alpha^e}{l_d^e} & -\frac{(x_1 - x_1^i) \sin \alpha^e}{l_d^e} & \frac{(x_1 - x_1^i) \cos \alpha^e}{l_d^e} \end{bmatrix}. \quad (16)$$

The opening of the discontinuity is calculated by either using Eqs. (14) and (15), or by direct interpolation of the nodal jumps:

$$\mathbf{u}^{e+/-} = \mathbf{N}^e \mathbf{M}_w^{ek} \mathbf{w}^e = \mathbf{N}_w^e \mathbf{w}^e \quad \text{at } \Gamma_d^e, \quad (17)$$

where  $\mathbf{N}_w^e$  are the interpolation shape functions defined using the two additional nodes.

The stress within the element is incrementally given by:

$$d\boldsymbol{\sigma}^e = \mathbf{D}^e \mathbf{B}^e (d\mathbf{a}^e - \mathbf{H}_{\Gamma_d^e}^e \mathbf{M}_w^{ek} d\mathbf{w}^e) \quad \text{in } \Omega^e \setminus \Gamma_d^e, \quad (18)$$

$$d\mathbf{t}^{e+} = \mathbf{T}^e d\mathbf{u}^{e+/-} = \mathbf{T}^e \mathbf{N}_w^e d\mathbf{w}^e \quad \text{at } \Gamma_d^e, \quad (19)$$

where  $\mathbf{B}^e$  is the strain-nodal displacement matrix, and  $\mathbf{D}^e$  and  $\mathbf{T}^e$  are the linearised constitutive matrices for bulk and discontinuity, respectively.

Finally, Eqs. (14) and (17) to (19) are inserted into Eq. (13), leading to the following discretised set:

$$\mathbf{K}_{\hat{a}\hat{a}}^e d\mathbf{a}^e - \mathbf{K}_{aw}^e d\mathbf{w}^e = d\hat{\mathbf{f}}^e = \int_{\Omega^e \setminus \Gamma_d^e} \mathbf{N}^{eT} d\bar{\mathbf{b}}^e d\Omega^e + \int_{\Gamma_d^e} \mathbf{N}^{eT} d\bar{\mathbf{t}}^e d\Gamma^e, \quad (20)$$

$$-\mathbf{K}_{wa}^e d\mathbf{a}^e + (\mathbf{K}_{ww}^e + \mathbf{K}_d^e) d\mathbf{w}^e = d\mathbf{f}_w^e - (\mathbf{H}_{\Gamma_d^e}^e \mathbf{M}_w^{ek})^T d\hat{\mathbf{f}}^e, \quad (21)$$

where  $\mathbf{K}_{\hat{a}\hat{a}}^e = \int_{\Omega^e \setminus \Gamma_d^e} \mathbf{B}^{eT} \mathbf{D}^e \mathbf{B}^e d\Omega^e$ ,  $\mathbf{K}_{aw}^e = \int_{\Omega^e \setminus \Gamma_d^e} \mathbf{B}^{eT} \mathbf{D}^e \mathbf{B}_w^e d\Omega^e$ ,  $\mathbf{K}_{wa}^e = \mathbf{K}_{aw}^{eT}$ ,  $\mathbf{K}_{ww}^e = \int_{\Omega^e \setminus \Gamma_d^e} \mathbf{B}_w^{eT} \mathbf{D}^e \mathbf{B}_w^e d\Omega^e$ , and

$$\mathbf{B}_w^e = \mathbf{B} \mathbf{H}_{\Gamma_d^e}^e \mathbf{M}_w^{ek}.$$

It is worth pointing out that: i) when all forces are applied at the nodes, it can be shown that  $d\mathbf{f}_w^e - (\mathbf{H}_{\Gamma_d^e}^e \mathbf{M}_w^{ek})^T d\hat{\mathbf{f}}^e = \mathbf{0}$ ; and ii) only three degrees of freedom are required per element due to the rigid body movement assumption. Since the available degrees of freedom are indeed four (i.e. two nodes placed on the edges of the discontinuity) an additional constraint assures that the shear along the discontinuity remains constant. This is herein done by simply adding the following penalty matrix to  $\mathbf{K}_d^e$  (where  $w_p$  is the chosen penalty weight):

$$\mathbf{K}_p^e = \frac{w_p}{2} \begin{bmatrix} 1 + \cos(2\alpha^e) & \sin(2\alpha^e) & -1 - \cos(2\alpha^e) & -\sin(2\alpha^e) \\ \sin(2\alpha^e) & 1 - \cos(2\alpha^e) & -\sin(2\alpha^e) & -1 + \cos(2\alpha^e) \\ -1 - \cos(2\alpha^e) & -\sin(2\alpha^e) & 1 + \cos(2\alpha^e) & \sin(2\alpha^e) \\ -\sin(2\alpha^e) & -1 + \cos(2\alpha^e) & \sin(2\alpha^e) & 1 - \cos(2\alpha^e) \end{bmatrix}. \quad (22)$$

## 2.2 Transient heat transfer problem

This section describes the formulation for transient heat transfer. For this purpose, the body is now subjected to internal heat generated at a certain rate,  $\mathbf{g}$ , and to temperature,  $\bar{T}$ , and heat flux,  $\mathbf{q}_n$ ,

applied at the external boundaries  $\Gamma_T$  and  $\Gamma_q$ , respectively. With the adopted notation,  $\Gamma = \Gamma_T \cup \Gamma_q$  and  $\emptyset = \Gamma_T \cap \Gamma_q$ , while the internal discontinuity,  $\Gamma_d$ , divides the body into two subdomains,  $\Omega^+$  and  $\Omega^-$ .

The governing field equations in the strong form are:

$$\rho C_p \frac{\partial T}{\partial t} + \nabla \mathbf{q} = \mathbf{g} \quad \text{in } \Omega \setminus \Gamma_d, \quad (23)$$

$$\mathbf{q} = -k \nabla T \quad \text{in } \Omega \setminus \Gamma_d, \quad (24)$$

with corresponding boundary conditions:

$$T = \bar{T} \quad \text{at } \Gamma_t, \quad (25)$$

$$-\mathbf{q}^T \hat{\mathbf{n}} = q_n \quad \text{at } \Gamma_d, \quad (26)$$

$$0 = q_d \quad \text{at } \Gamma_d, \quad (27)$$

where  $\rho$  is the density of the material,  $C_p$  is the specific heat and  $k$  is the thermal conductivity.

The derivation of the mechanical formulation in the previous section can be easily reapplied to derive the discretised set of equations for the transient heat transfer problem, as is therefore omitted. It should be highlighted that the common framework used in the derivations assures compatibility between models.

### 3. Implementation

In the example discussed in the next section, mechanical and heat transfer problems are dealt with independently. The purpose is to gain a first insight on the performance of the embedded formulation for heat transfer analysis and to assess the feasibility of further extending it to a fully coupled thermo-mechanical model.

According to the adopted methodology, the mechanical analysis is first used to characterise the damaged state of the structure and corresponding crack pattern. In this stage, a discontinuity is assumed to always cross an entire finite element, being the additional degrees of freedom placed at the extremities (as represented by nodes 'i' and 'j' in Fig. 1b). An existing crack is propagated whenever the stress at the tip reaches the tensile strength of the material, with propagation angle orthogonal to the first principal stress.

After the mechanical analysis stage, heat transfer analysis is carried out independently for selected time steps with the underlying geometry defined in the mechanical analysis. A generic implicit solution scheme, known as Crank-Nicholson method, is used to then solve for the transient problem.

### 4. Single edge notched beam

This section uses the single edge notched beam benchmark test by Schlangen (29). The beam was  $400 \times 100 \times 100 \text{ mm}^3$  and had a notch located at the top with  $5 \times 20 \text{ mm}^2$ , as illustrated in Fig. 2a.

#### 4.1 Mechanical behaviour

The simulation of the behaviour of the single-edge notched beam until failure is herein presented and the complexity of the adopted constitutive models is kept to a minimum. The bulk is considered linear elastic with the following parameters: Young's modulus  $E = 35 \text{ GPa}$ ; Poisson ratio  $\nu = 0.15$ ; tensile strength  $f_t = 3.0 \text{ MPa}$ . The non-linear behaviour is solely due to the presence of discontinuities, which are modelled using a non-isotropic constitutive law from (30), with fracture energy  $G_F = 0.1 \text{ N/mm}$ , normal stiffness  $k_n = 10^5 \text{ N/mm}^3$  and shear stiffness  $k_s = 4 \times 10^2 \text{ N/mm}^3$ .

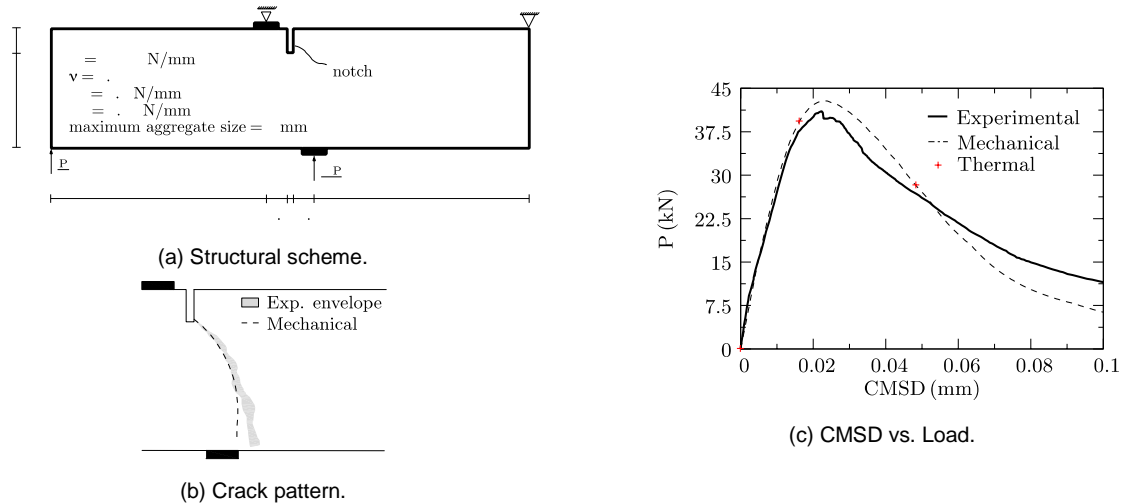
The loading procedure is controlled using the arc-length method, where the relative sliding displacement of the notch (CMSD) is monotonically increased. The discontinuity is propagated from the notch following the procedure detailed in Section 3.



The corresponding CMSD vs. load curve and crack path are shown in Figs. 2b-c, where it can be observed the good agreement between numerical and experimental results despite the simple constitutive representations specified in the modelling, highlighting that the structural response is predominantly governed by the development of the discontinuity. Near the support, the crack deflects towards the support due to the localised high gradients. These results could be further improved by adopting a more refined model.

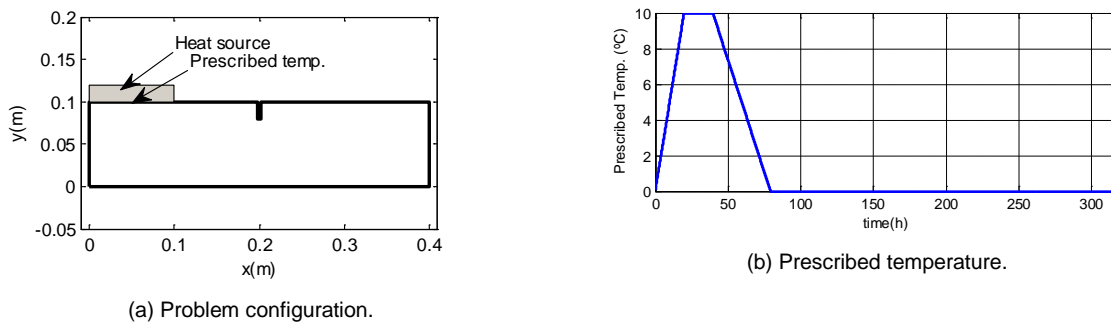
#### 4.2 Heat transfer analysis

The proposed algorithm is now applied to simulation of transient heat transfer within the beam at different stages. A prescribed heating curve is imposed at the top left surface, as identified in Fig. 3, whereas null normal flux is specified at all remaining edges. The domain is assumed to have a constant density of  $2500 \text{ kg/m}^3$ , a conductivity of  $1.4 \text{ W/m}^\circ\text{K}$  and a specific heat of  $840 \text{ J/kg}^\circ\text{K}$ . A constant time step of  $100 \text{ s}$  is adopted for all calculations.



**Figure 2. Single edge notched beam.**

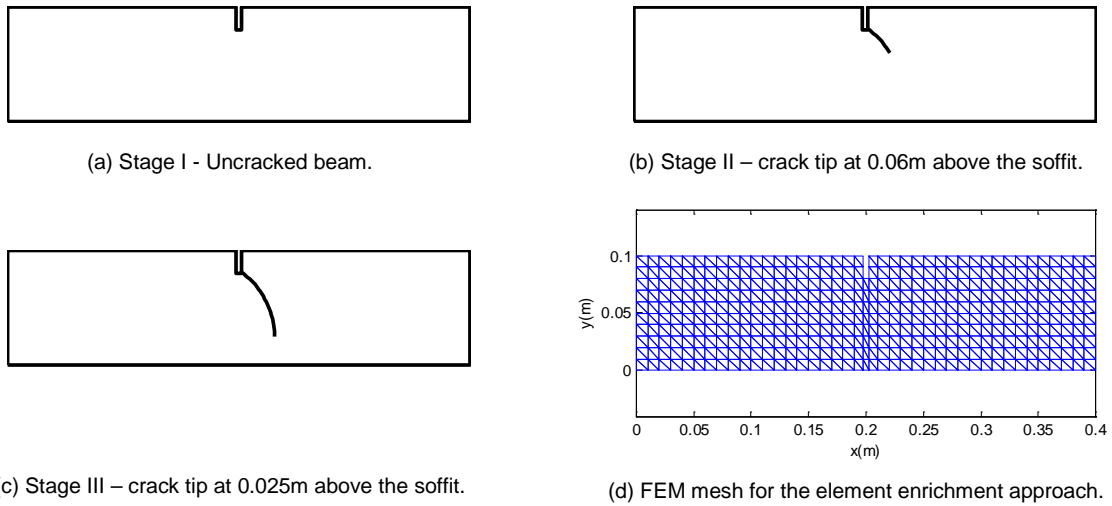
The three different stages of crack propagation previously identified on Fig. 2c, and characterised in Figs. 4a-d, are selected to illustrate the performance of the formulation and the impact of the crack length on both internal and surface temperature distributions of the beam. The same underlying FEM mesh is used throughout the analysis, being the discontinuities embedded using the technique described earlier in Section 2.



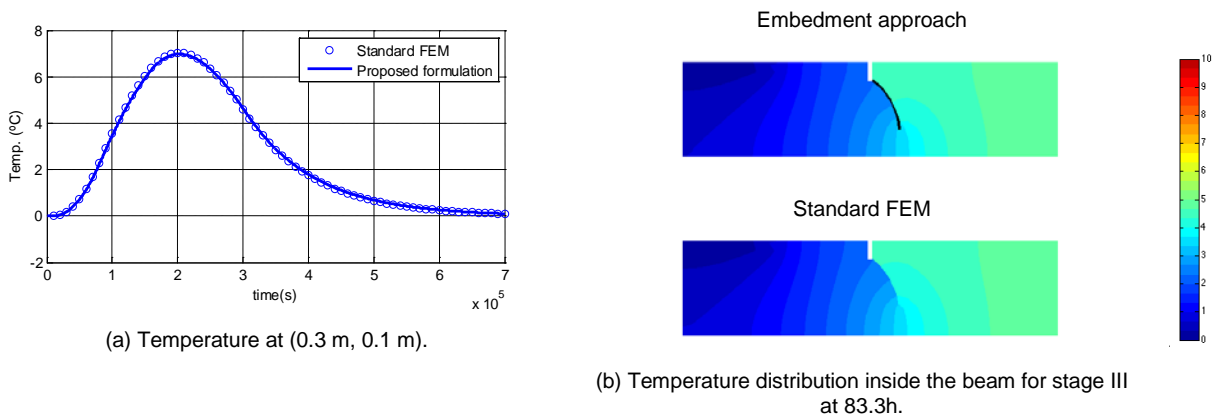
**Figure 3. Definition of the heat transfer problem.**

To first assess the accuracy of the proposed method in comparison with standard FEM, an additional FEM mesh with the crack fully discretised is considered in stage III. Fig. 5a shows the comparison between temperatures measured at a certain nodal location using both models, whereas Fig. 5b shows the internal temperature distribution at 83.3h. It is highlighted the good agreement between both approaches.

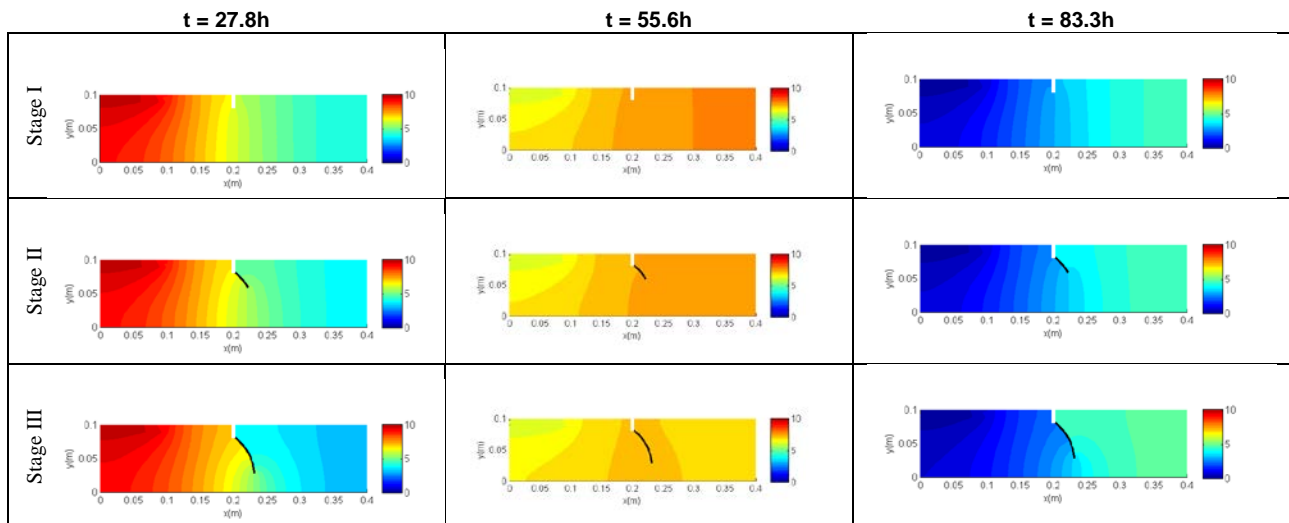
Following this preliminary validation, the internal temperature distribution is calculated for different time steps, i.e. 27.8h, 55.6h and 83.3h, and for all three stages. Fig. 6 shows the corresponding patterns.



**Figure 4. Stages of analysis.**



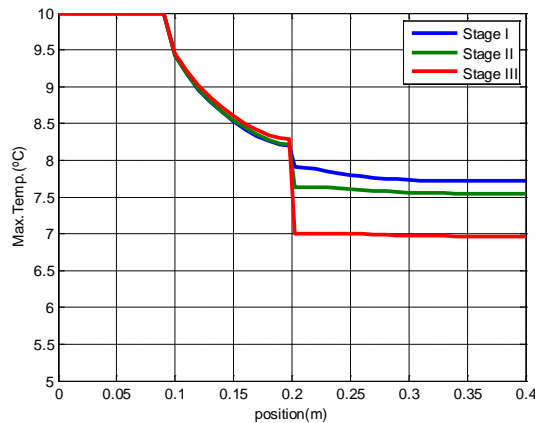
**Figure 5. Comparison between standard FEM and proposed embedment method.**



**Figure 6. Map of temperature distribution inside the beam for stages I, II and III.**

Fig. 6 clearly shows that the presence of the embedded discontinuity, across which there is no heat flux, modifies the temperature distribution by directing the heat flow towards the region between the soffit and the crack tip. As expected, this effect is more important as the crack extends, i.e. from Stages I to III.

Fig. 7 illustrates the variation of the peak temperature registered at the top edge of the beam. In particular, the maximum temperature decays exponentially in stage I between the heating source and the top-right corner. The notch can be identified by a sudden temperature drop which occurs at 0.2 m. As soon as the crack extends, the temperature drop becomes even higher. In fact, the presence of the crack severely restrains the heat flux along the beam. For this reason, when compared with Stage I, the maximum temperature on the top edge, between heat source and notch, tends to be higher. Opposite trend is observed moving away from the notch. In Stage III, the maximum temperature at the right side of the notch and on the top edge reaches a value which is about 70% of the prescribed maximum temperature and nearly constant throughout.



**Figure 7. Maximum temperature reached at the top edge of the beam.**

## 5. Conclusions

This paper presented a preliminary study on a new element enrichment approach for simulation of transient heat transfer problems in concrete structures. The formulation was derived in the scope of the discrete crack approach with the same variational framework for both mechanical and heat transfer analyses. According to the new formulation, the elements crossed by the discontinuity were directly enriched with the minimum kinematic degrees associated with the “rigid body” movement between the two sides of the discontinuity. This is a very effective way of embedding strong discontinuities on the displacement field, in the case of the mechanical problem, and on the temperature field, in the case of transient heat transfer problem.

In this study, both mechanical and heat transfer simulations were performed independently and their accuracy was evaluated against results obtained from known solutions. In particular, in the case of the heat transfer analysis, calculated values showed good agreement with those obtained using standard FEM, although avoiding the need for remeshing algorithms. The new embedded approach significantly decreased the number of additional degrees of freedom required in the analysis, particularly when compared to other existing nodal enrichment approaches, and adequately represented the thermal response on the entire domain of analysis. The proposed approach, in which discontinuities are described by means of embedded discontinuities, provides the basis for the development of a thermo-mechanical coupled model for the simulation of concrete structures.

## 6. Acknowledgement

This work was supported by Australian Research Council’s Discovery Projects funding scheme (project number DP140100529) and by the ECR Development scheme from the Faculty of Engineering and Information Technologies at The University of Sydney.

## 7. References

1. Chang, Y.P., Kang, C.S., et al., "The use of fundamental Green functions for solution of problems of heat conduction in anisotropic media", *Int. J. Heat and Mass Transfer*, 16, 1973, pp. 1905-1918, doi: 10.1016/0017-9310(73)90208-1.
2. Shaw, R.P., "An integral equation approach to diffusion". *Int. J. Heat and Mass Transfer*, vol. 17, 1974, pp. 693-699, doi: 10.1016/0017-9310(74)90202-6.
3. Wrobel, L.C., Brebbia, C.A., "A formulation of the boundary element method for axisymmetric transient heat conduction", *Int. J. Heat and Mass Transfer*, vol. 24, 1981, pp.843-850, doi: 10.1016/S0017-9310(81)80007-5.
4. Dargush, G.F., Banerjee, P.K., "Application of the boundary element method to transient heat conduction", *Int. J. Numerical Methods in Engineering*, vol. 31, 1991, pp. 1231-1247, doi: 10.1002/nme.1620310613.
5. Cheng, A.H.-D., Abousleiman, Y., et al., "A Laplace transform BEM for axysymmetric diffusion utilizing pre-tabulated Green's function", *Eng. Anal. Bound. Elmts.*, vol. 9, 1992, pp. 39-46, doi: 10.1016/0955-7997(92)90123-O.
6. Zhu, S.P., Satravaha, P., et al., "Solving the linear diffusion equations with the dual reciprocity methods in Laplace space", *Eng. Anal. Bound. Elmts.*, vol. 13, 1994, pp. 1-10, doi: 10.1016/0955-7997(94)90002-7.
7. Zhu, S.P.; Satravaha, P., "An efficient computational method for nonlinear transient heat conduction problems", *Appl. Mathematical Modeling*, vol. 20, 1996, pp. 513-522, doi: 10.1016/0307-904X(95)00170-O.
8. Ozisik, N., "Finite difference methods in heat transfer", CRC press, 1994.
9. R. Lewis, P. Nithiarasu, et al., "Fundamentals of the Finite Element Method for Heat and Fluid Flow", 2004, John Wiley & Sons Ltd, Chichester, England.
10. Minkowycz, W., "Advances in numerical heat transfer (Vol. 1)", 1996, CRC press.
11. Wrobel, L.C., "The Boundary Element Method, Applications in Thermo-Fluids and Acoustics. Vol. 1", 2002, John Wiley & Sons, Chichester, England.
12. Ingraffea, A. R., Gerstk, W. H., et al., "Fracture mechanics of bond in reinforced concrete", *Journal of Structural Engineering* 110 (4), 1984, pp. 871–890. doi: 10.1061/(ASCE)0733-9445(1984)110:4(871).
13. Areias, P. M. A., Dias-da-Costa, D., et al., "Arbitrary bi-dimensional finite strain cohesive crack propagation", *Computational Mechanics* 45 (1), 2009, pp. 61–75. doi: 10.1007/s00466-009-0418-z.
14. Melnek, J.M., Babuska, I., "The partition of unity finite element method: Basic theory and applications", *Computer Methods in Applied Mechanics and Engineering*, 139(1-4), 1996, pp. 289–314.
15. Belytschko, B., Black, T., "Elastic crack growth in finite elements with minimal remeshing", *International Journal for Numerical Methods in Engineering*, 45(5), 1999, pp. 601–620.
16. Duarte, C.A., Hamzeh, O.N., et al., "A generalized finite element method for the simulation of three-dimensional dynamic crack propagation", *Computer Methods in Applied Mechanics and Engineering*, 190(15-17), 2001, pp. 2227–2262.
17. Aragón, A.M., Duarte, C.A., et al., "Generalized finite element enrichment functions generalized finite element enrichment functions for discontinuous gradient fields", *International Journal for Numerical Methods in Engineering*, 82, 2010, pp. 242–268.
18. O'Hara, P., Duarte, C.A., et al., "Generalized finite element analysis of three-dimensional heat transfer problems exhibiting sharp thermal gradients", *Comp. Methods Appl. Mech. Engrg.*, 198(21-26), 2009, pp. 1857–71. DOI: 10.1016/j.cma.2008.12.024.
19. Soghrati, S., Aragón, A.M., et al., "An interface-enriched generalized FEM for problems with discontinuous gradient fields", *International Journal for Numerical Methods in Engineering*, 89(8), 2012, pp. 991–1008.

20. Yu, T.T., Wan, L.L., "Extended finite element method for heat transfer problems in heterogeneous material", *Chinese Journal of Computational Mechanics*, 28(6), 2011, pp. 884–890.
21. Yu, T.T., Gong, Z.W., "Numerical simulation of temperature field in heterogeneous material with the XFEM", *Archives of Civil and Mechanical Engineering*, 13(2), 2013, pp 199-208.
22. Dias-da-Costa, D., Alfaiate, J., et al., "A comparative study on the modelling of discontinuous fracture by means of enriched nodal and element techniques and interface elements", *International Journal of Fracture*, 161(1), 2010, pp. 97–119. doi: 10.1007/s10704-009-9432-6.
23. Dias-da-Costa, D., Alfaiate, J., et al., "A discrete strong discontinuity approach", *Engineering Fracture Mechanics*, 76 (9), 2009, pp. 1176–1201. doi: 10.1016/j.engfracmech.2009.01.011.
24. Dias-da-Costa, D., Alfaiate, J., et al., "Towards a generalization of a discrete strong discontinuity approach", *Computer Methods in Applied Mechanics and Engineering*, 198 (47-48), 2009, pp. 3670–3681. 10.1016/j.cma.2009.07.013.
25. Washizu, K., "On the variational principles of elasticity and plasticity", Tech. rep., Aeroelastic and Structures Research Laboratory, 1955, MIT, Cambridge.
26. Hu, H.-C., "On some variational methods on the theory of elasticity and the theory of plasticity", *Scientia Sinica*, 4, 1955, pp. 33–54.
27. Fraeijs de Veubeke, B. M., "Diffusion des inconnues hyperstatiques dans les voilures à longeron couples", *Bull. Serv. Technique de L'Aéronautique*, Imprimerie Marcel Hayez, Bruxelles 24, 56, 1951.
28. Malvern, L. E., "Introduction to the mechanics of a continuous medium", Prentice-Hall International, 1969, Englewood Cliffs, New Jersey.
29. Schlagen, E., "Experimental and numerical analysis of fracture processes in concrete", Ph.D. thesis, 1993, Delft University of Technology.
30. Wells, G. N., Sluys, L. J., "Three-dimensional embedded discontinuity model for brittle fracture", *International Journal of Solids and Structures* 38 (5), 2001, pp. 897–913. doi: 10.1016/S0020-7683(00)00029-9.

# In-plane behavior of unbonded post-tensioned concrete walls

Reza Hassanli<sup>1</sup>

PhD Student, School of Natural and Built Environments, University of South Australia

**Abstract:** In this study the behavior of unbonded post-tensioned concrete walls is investigated using experimental results. The displacement ductility of unbonded post-tensioned concrete walls is studied and the general behavior of PT-CWs is examined. The accuracy of an analytical approach to predict the force-displacement response of such walls is investigated using experimental results. The analytical method considers displacement compatibility and geometric compatibility conditions. According to the results, the approach can successfully predict the lateral strength, stiffness and neutral axis depth and the general behavior of the test walls, hence, is recommended to be considered for design purposes.

**Keywords:** post-tensioned, concrete walls, ductility, force-displacement, stiffness, unbonded

## 1. Introduction

Due to rocking mechanism, the rotation of the unbonded post-tensioned walls occurs mainly at the wall footing interface. Unbonded post-tensioning induces self-centering behavior to the structural systems and accordingly helps to eliminate or reduce the residual drifts and limits the structural damages [1-9]; hence, the system maintains its integrity following a ground excitation event. Moreover, the damage zone is limited to the walls' toe and the repair cost is minimal [5-6].

The seismic behavior of unbonded post-tensioned concrete walls (PT-CW) is not yet well understood and the ductility and force displacement response of these walls are needed to be more studied.

In this study, a total of 32 unbonded post-tensioned concrete walls (PT-CW) were collected as the experimental database. All the walls were tested by Henry [1-3] and the specifications are provided in Table 1. The walls were tested under monotonic lateral displacement applied to the top of the walls.

This study use the experimental test results to:

- i) Investigate the accuracy of an analytical approach to predict the force-displacement behavior of PT-CWs.
- ii) Study the ductility of PT-CWs

## 2. Analytical model

An analytical approach is employed to predict the force displacement response of wall specimens. The approach was developed based on mechanics of rocking walls and considers displacement and geometric compatibility conditions. The accuracy of the method has been validated against experimental results of unbonded post-tensioned masonry walls (PT-MWs) [10-11]. In this section the effectiveness of the approach to predict the force-displacement response of unbonded PT-CWs based on experimental results is investigated. The steps of the approach are not presented here due to space limitations and can be found in the referenced article [12]. Eight walls (series E and F) tested by Henry [1] (Table 1) were considered for validation. These walls were selected as they were the only specimens for which reliable strain measurements were reported [1].

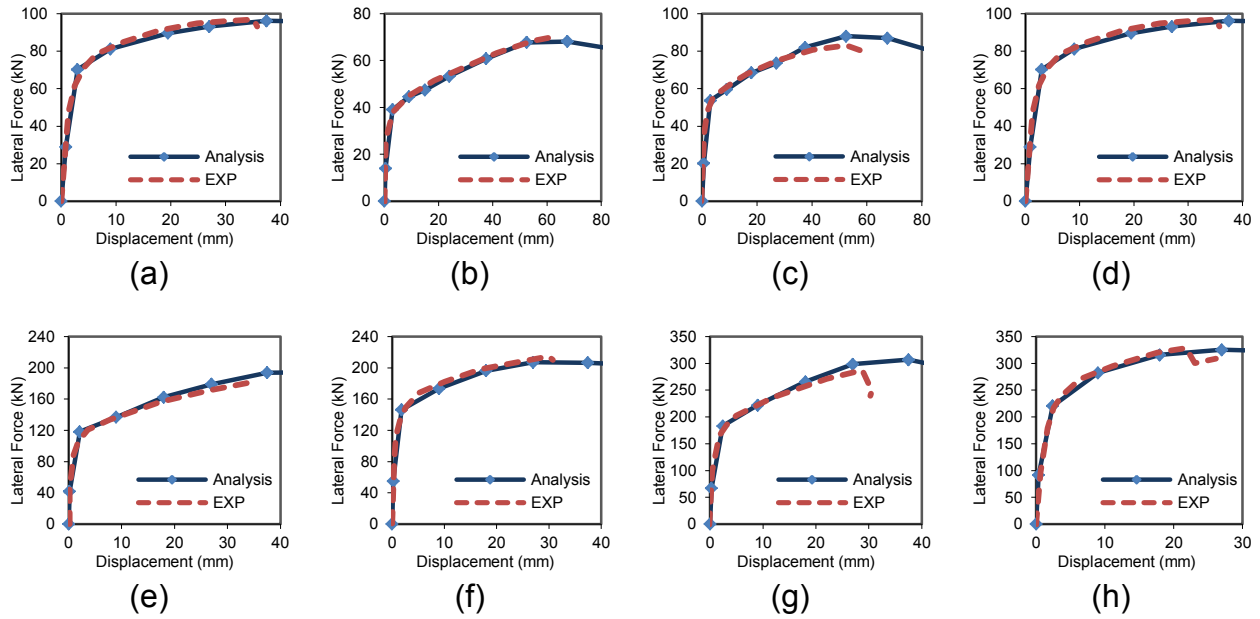
Figure 1 compares the lateral force-displacement curves determined using the analytical approach and the results obtained during the experimental work. As shown in the figures, the model can correctly predict the wall strength, initial stiffness and rotational capacity. The model can also capture the displacement recorded at the peak strength.

**Table 1. Wall database\***

Wall	$h_e$ (m)	$b_w$ (m)	$l_w$ (m)	$f'_c$ (MPa)	$f_c/f'_c$	$f_{py}$ (MPa)	No. of Tendons	$A_{ps}$ (mm <sup>2</sup> )	Tendon location, $d_i$ (mm)				
									$d_1$	$d_2$	$d_3$	$d_4$	$d_5$
Ai	3	0.14	2	32.9	0.043	1050	5	883.50	187	594	1000	1406	1813
Aii	3	0.14	2	32.9	0.063	1050	5	883.50	187	594	1000	1406	1813
Aiii	3	0.14	2	32.9	0.014	1050	2	353.40	187				1813
Aiv	3	0.14	2	32.9	0.026	1050	2	353.40	187				1813
Bi	3.3	0.14	1	31.7	0.019	1050	1	176.70			500		
Bii	3.3	0.14	1	31.7	0.036	1050	2	353.40	94		500		906
Biii	3.3	0.14	1	31.7	0.053	1050	3	530.10	94		500		906
Biv	3.3	0.14	1	31.7	0.078	1050	3	530.10	94		500		906
C1i	3	0.12	1	25.8	0.078	1580	2	293.10	94				906
C1ii	3	0.12	1	27.9	0.072	1580	2	293.10	94				906
C1iii	3	0.12	1	25.8	0.171	1580	3	439.65	94		500		906
C1iv	3	0.12	1	27.9	0.158	1580	3	439.65	94		500		906
C2i	2.2	0.12	1	28.1	0.071	1580	2	293.10	94				906
C2ii	2.2	0.12	1	28.1	0.071	1580	2	293.10	94				906
C2iii	2.2	0.12	1	28.1	0.156	1580	3	439.65	94		500		906
C2iv	2.2	0.12	1	28.1	0.156	1580	3	439.65	94		500		906
D1i	3	0.12	2	26.0	0.059	1580	3	439.65	187		1000		1813
D1ii	3	0.12	2	26.0	0.059	1580	3	439.65	187		1000		1813
D1iii	3	0.12	2	26.0	0.133	1580	5	732.75	187	594	1000	1406	1813
D1iv	3	0.12	2	26.0	0.133	1580	5	732.75	187	594	1000	1406	1813
D2i	2.2	0.12	2	28.1	0.033	1580	3	439.65	187		1000		1813
D2ii	2.2	0.12	2	28.1	0.053	1580	3	439.65	187		1000		1813
D2iii	2.2	0.12	2	28.1	0.088	1580	5	732.75	187	594	1000	1406	1813
D2iv	2.2	0.12	2	28.1	0.122	1580	5	732.75	187	594	1000	1406	1813
Ei	3	0.12	1	41.0	0.035	1580	1	146.56			500		
Eii	3	0.12	1	41.0	0.049	1580	2	293.10	94				906
Eiii	3	0.12	1	41.0	0.072	1580	3	439.65	94		500		906
Eiv	3	0.12	1	41.0	0.108	1580	3	439.65	94		500		906
Fi	3	0.12	2	39.5	0.039	1580	3	439.65	187		1000		1813
Fii	3	0.12	2	39.5	0.053	1580	3	439.65	187		1000		1813
Fiii	3	0.12	2	39.5	0.063	1580	5	732.75	187	594	1000	1406	1813
Fiv	3	0.12	2	39.5	0.087	1580	5	732.75	187	594	1000	1406	1813

\* $h_e$ : wall effective height,  $b_w$ : wall thickness,  $l_w$ : wall length,  $f'_c$ : concrete compressive strength  
 $f_c$ : axial stress on the wall,  $f_{py}$ : yield stress of pre-stressing steel





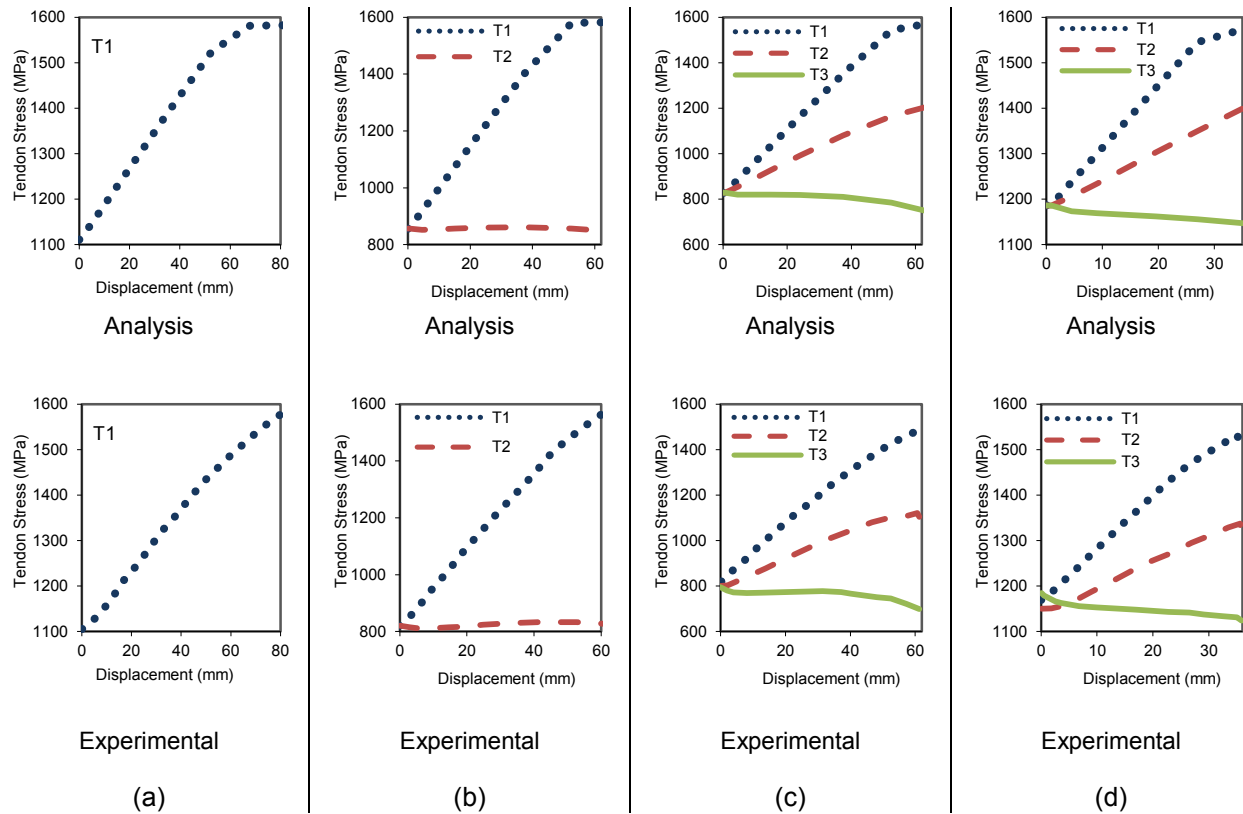
**Figure 1. Comparison of the experimental and analytical force displacement curves of walls (a)Ei, (b)Eii, (c) Eii, (d) Eiv (e) Fi, (f) Fii, (g) Fii, and (h) Fiv**

Table 2 compares the strength of the walls obtained from the experimental work,  $V_{EXP}$ , with the strength obtained from the analytical approach,  $V_{Analysis}$ . As presented in the table, the analytical approach could accurately predict the strength of the walls. According to the table, the predicted strength of the specimens using the analytical approach falls within  $\pm 6\%$  of the test results.

**Table 2. Prediction of the strength using analytical approach**

	Ei	Eii	Eiii	Eiv	Fi	Fii	Fiii	Fiv
$V_{Analysis}$	36.4	68.1	88.0	96.2	195.0	207.1	306.7	325.2
$V_{EXP}$	38.4	69.9	83.1	96.9	182.4	214.7	287.2	328.4
$V_{EXP}/V_{Analysis}$	1.05	1.03	0.94	1.01	0.94	1.04	0.94	1.01

Figures 2 and 3 compares the force developed in the Tendons obtained from the experimental work and analytical approach for series E and F of tested walls, respectively.  $T_i$  is the force in the tendon  $i$ . As shown, the analytical approach could effectively predict the force developed in tendons in different drift ratios. According to Figure 2 and Figure 3, in general the analytical model demonstrated a reasonable correlation with the experimental results, but slightly overestimated the force in some tendons. This can be attributed to the losses occurred in the tendons during testing.



**Figure 2. Force in tendons of series E of walls (a) Ei, (b) Eii, (c) Eiii , and (d) Eiv**

Figure 4 compares the neutral axis depth obtained from analytical approach and recorded during the experimental work. In general, the analytical model provides a reasonable correlation with the experimental data. However, for small displacement, the analytical approach tends to underestimate the neutral axis depth.

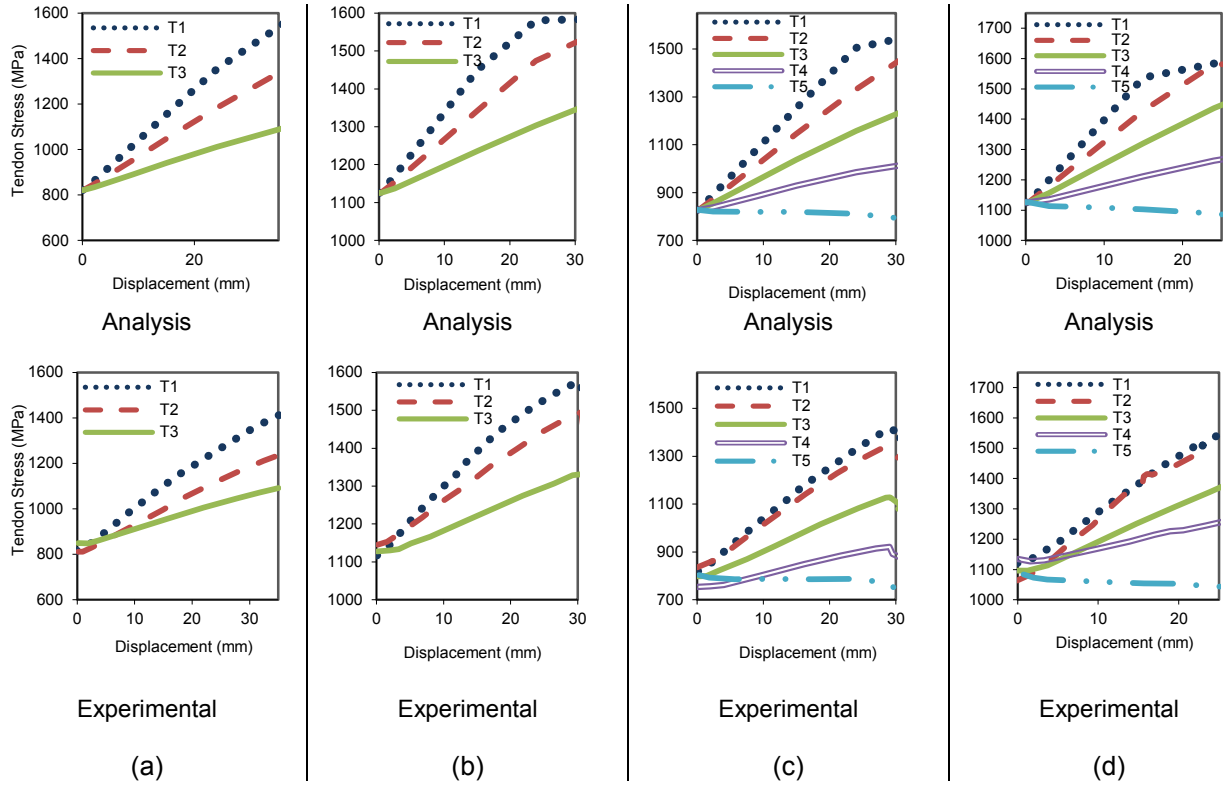


Figure 3. Force in tendons of series F of walls (a) Fi, (b) Fii, (c) Fiii, and (d) Fiv

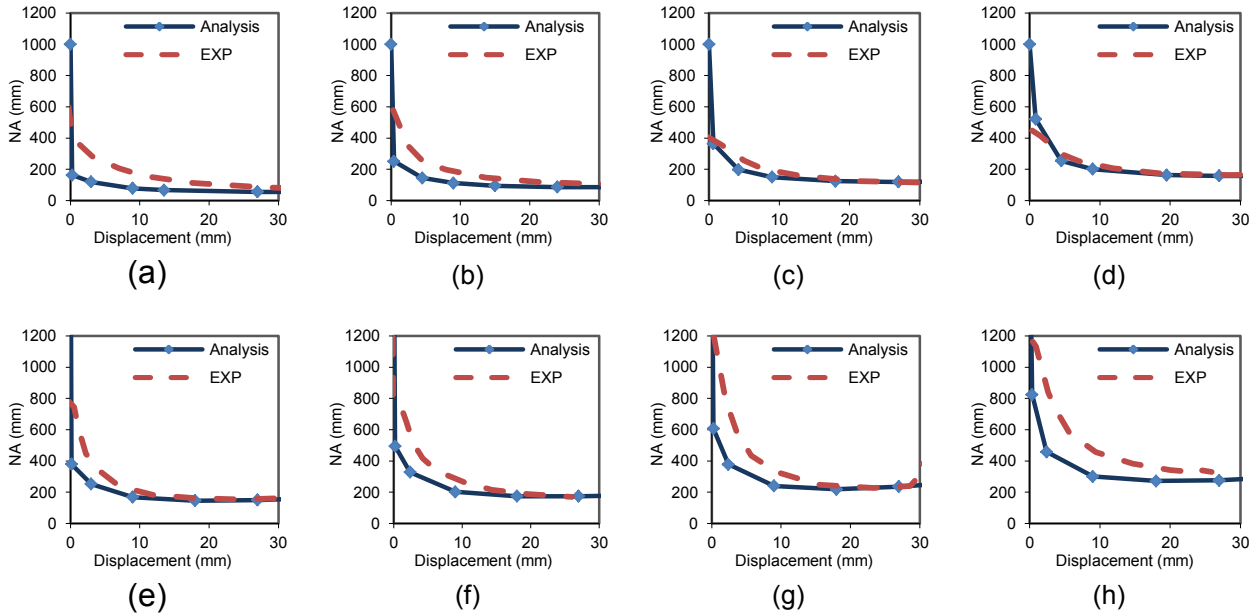
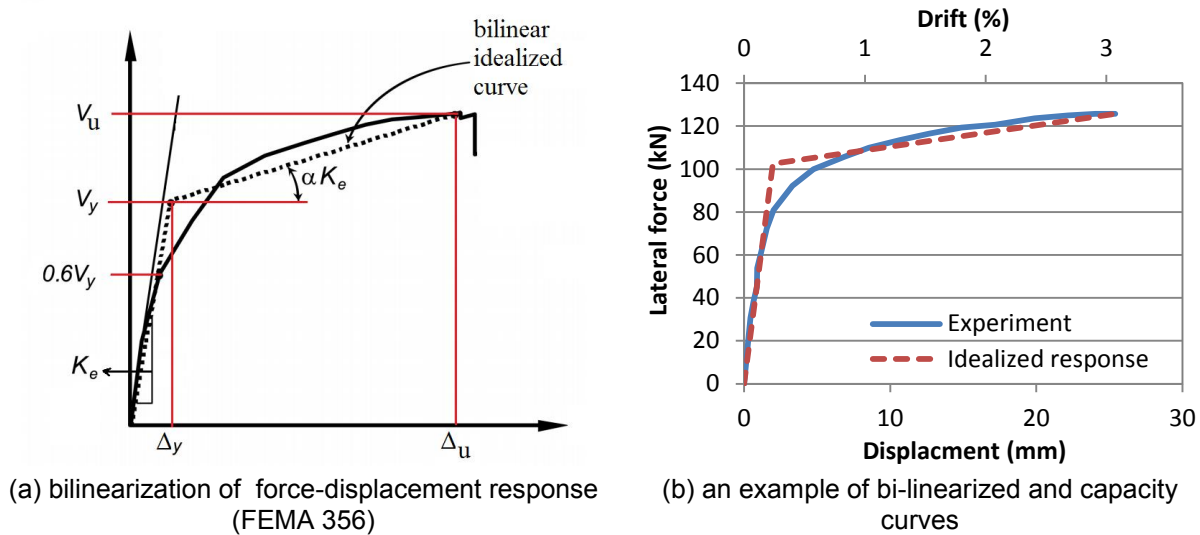


Figure 4. Neutral axis depth in, Analysis versus Experimental, of walls (a) Ei, (b) Eii, (c) Eii, (d) Eiv (e) Fi, (f) Fii, (g) Fiii, and (h) Fiv

### 3. Displacement ductility

The wall specimens presented in Table 1 are considered to investigate the seismic response of PT-CWs. Bilinear approximation of the force-displacement response is used to calculate the displacement ductility,  $\mu$ . The procedure provided by FEMA 356 [13] for force-displacement response with positive post-yield slope is used to obtain the idealized bilinear curves. As shown in Figure 5(a), the ultimate displacement,  $\Delta_u$ , is the displacement at the peak strength,  $V_u$ , and  $f_y$  and  $\Delta_y$  are the effective yield strength and yield displacement, and  $K_e$  and  $\alpha K_e$  are the effective yield and post-yield stiffness, respectively. Iterative procedure was used to determine the bilinear idealized curves. According to FEMA 356 [13], the idealized relationship can be determined by balancing the area above and under the capacity curve. The idealized and actual curve should also intersect at strength of  $0.6V_y$ . An example of bilinear approximation of the load displacement curve of the tested specimens is shown in Figure 5(b). As showed in Figure 5(b), the unbonded PT walls provide approximately a bilinear elastic response. Similar bi-linear elastic responses were also observed for the rest of the wall specimens of the database.



**Figure 5. Bi-linearization of the capacity curve**

Table 3 presents the parameters determined from bilinearization of the capacity curves of the test specimens. In this table  $\mu$  is the displacement ductility defined as  $\Delta_u/\Delta_y$ . As presented in the table, the considered walls presented a wide range of ductility, ranging between 7.1 and 74.8, with an average of 28.6.

In terms of ductility, of all parameters axial stress ratio seems to be the most critical one. Figure 6 presents the calculated ductility versus axial stress ratio,  $f_c/f'_c$ . The general trend of data in Figure 6 illustrates that ductility of unbonded PT-CWs is highly dependent on the axial stress ratio. Using regression analysis of ductility values of the wall specimens, the following expression is obtained to estimate the ductility of the unbonded PT-CWs.

$$\mu = 1.7 \frac{f'_c}{f_c} \quad (1)$$

Note that some of the specimens of wall test group A, presented in the Table 1, reported to have immature failure, hence, this group has been removed from analysis. The correlation between the data set and Equation 40 in Figure 10 indicates that in unbonded PT-CWs ductility is inversely proportional to the level of axial stress ratio.

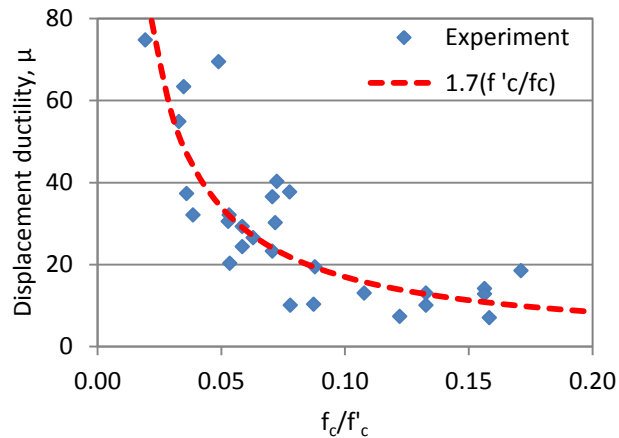


Figure 6. Ductility versus axial stress ratio,  $f_c/f'_c$

#### 4. Conclusions

- The analytical approach employed in the paper could accurately predict the lateral force behavior of unbonded PT-CWs. The wall strength calculated using the analytical approach was within 6% of the experimental results. Moreover, the analytical approach could effectively predict the force developed in post-tensioned bars in different drift ratios. It could also predict the wall initial stiffness and rotational capacity.
- The ductility of unbonded PT-CWs are highly dependent on the level of axial stress ratio.
- An increase in the axial stress ratio results in a decrease in ductility. The following equation is proposed to evaluate the displacement ductility of an unbonded PT-CW:  $\mu = 1.7 \frac{f'_c}{f_c}$

#### References

1. Henry, R. S. "Self-centering precast concrete walls for buildings in regions with low to high seismicity." PhD Thesis, Department of Civil and Environmental Engineering, The University of Auckland, 2011.
2. Henry, R. S., Brooke, N. J., Sritharan, S, and Ingham, J.M. "Defining concrete compressive strain in unbonded post-tensioned walls." ACI Structural Journal, 2012, 109(1).
3. Henry, R. S., Sritharan, S, and Ingham, J.M. "Unbonded tendon stresses in post-tensioned concrete walls at nominal flexural strength." ACI Structural Journal, 2012, 109(2).4.
4. Wight, G. D. and Ingham J. M. "Tendon stress in unbonded posttensioned masonry walls at nominal in-plane strength." Journal of Structural Engineering, 2008, 134(6): 938-946.
5. Rosenboom, O. A. and Kowalsky, M. J. "Reversed in-plane cyclic behavior of posttensioned clay brick masonry walls." Journal of Structural Engineering, 2004, 130(5): 787-798.
6. Wight, G. D., Kowalsky, M. J., and Ingham, J.M. "Direct displacement-based seismic design of unbonded post-tensioned masonry walls" ACI Structural Journal, 2007, 104(5).
7. Laursen, P. P. T. "Seismic analysis and design of post-tensioned concrete masonry walls", Ph.D dissertation, Department of Civil and Environmental Engineering, University of Auckland, New Zealand, 2002.
8. Rosenboom, O. A. "Post-tensioned clay brick masonry walls for modular housing in seismic regions." M.S. Thesis, North Carolina State University, Raleigh, NC, USA, 2002.
9. Ryu, D., A. Wijeyewickrema, ElGawady, M., and Madurapperuma, M. "Effects of tendon spacing on in-plane behavior of post-tensioned masonry walls." Journal of Structural Engineering, 2014, 140(4), [CID:04013096](#).

10. Hassanli, R., "Behavior of unbonded post-tensioned masonry walls." PhD Thesis, University of South Australia, Australia, 2015.
11. Hassanli, R., ElGawady, M. A. and Mills, J. E. "Experimental investigation of cyclic in-plane behavior of unbonded post-tensioned masonry walls." Journal of Structural Engineering (ASCE), 2015, Tentatively Accepted.
12. Hassanli, R. and Mills, J. E "Strength, force displacement behavior and seismic response of unbonded post-tensioned concrete walls.", Journal of Engineering Structures, under review.
13. FEMA-356, "Pre-standard and commentary for the seismic rehabilitation of buildings", American Society of Civil Engineers (ASCE),2000, Washington DC.

**Table 3. Seismic parameters\***

Wall	$\Delta_y$	$\Delta_u$	$V_y$	$V_u$	$K_e$	$\alpha K_e$	$\mu$
Ai	1.7	25.9	120.2	230.4	72.0	4.6	15.5
Aii	1.2	11.4	117.5	207.1	98.0	8.8	9.5
Aiii	0.6	36.1	47.8	109.7	75.0	1.7	56.5
Aiv	2.9	35.5	86.3	124.2	30.0	1.2	12.3
Bi	1.5	111.5	13.4	29.4	9.0	0.1	74.8
Bii	1.4	53.7	28.8	51.3	20.0	0.4	37.3
Biii	1.8	54.0	39.7	70.6	22.5	0.6	30.6
Biv	5.1	51.9	59.1	79.0	11.5	0.4	10.1
C1i	2.1	78.4	37.4	65.9	18.0	0.4	37.7
C1ii	2.1	64.3	36.8	60.9	17.3	0.4	30.2
C1iii	3.0	56.3	76.0	91.2	25.0	0.3	18.5
C1iv	4.7	33.2	70.2	88.8	15.0	0.7	7.1
C2i	1.3	30.4	45.6	81.9	35.0	1.2	23.3
C2ii	0.8	29.8	50.5	81.8	62.0	1.1	36.6
C2iii	1.8	25.7	101.7	125.4	56.0	1.0	14.2
C2iv	2.0	25.4	102.5	125.8	52.0	1.0	12.9
D1i	1.3	39.5	133.3	189.7	99.0	1.5	29.3
D1ii	1.7	42.6	130.8	201.1	75.0	1.7	24.4
D1iii	2.4	24.6	213.6	297.2	88.0	3.8	10.1
D1iv	2.7	35.1	80.6	96.9	30.0	0.5	13.1
D2i	0.5	29.7	105.3	231.9	195.0	4.3	55.0
D2ii	1.0	20.7	121.8	214.7	120.0	4.7	20.4
D2iii	1.2	22.9	276.2	407.6	235.0	6.1	19.5
D2iv	1.7	12.9	330.4	389.5	190.0	5.3	7.4
Ei	1.4	86.1	28.5	38.4	21.0	0.1	63.4
Eii	0.9	61.4	43.3	69.9	49.0	0.4	69.5
Eiii	1.3	52.5	61.3	83.1	47.0	0.4	40.3
Eiv	2.7	35.1	80.6	96.9	30.0	0.5	13.1
Fi	1.1	35.3	124.1	182.6	113.0	1.7	32.1
Fii	0.9	30.0	163.1	214.7	175.0	1.8	32.2
Fiii	1.1	28.8	194.4	287.2	180.0	3.4	26.6
Fiv	2.1	21.8	252.7	328.4	120.0	3.8	10.4
max	5.1	111.5	330.4	407.6	235.0	8.8	74.8
min	0.5	11.4	13.4	29.4	9.0	0.1	7.1
Avg.	1.8	40.7	105.4	154.8	74.5	2.0	27.9

\* Units:  $\Delta_y$ ,  $\Delta_u$ : mm,  $K_e$ ,  $\alpha K_e$ : kN/mm



# Concrete slab and footing systems for large industrial buildings. A critical overview of current design methods for reactive clay sites

Anthony J Davis<sup>1\*</sup> and Brian Ims<sup>2</sup>

<sup>1</sup> Davis Naismith & McGovern Pty Ltd Consulting Engineers. Email: tony@dnmconsulting.com

<sup>2</sup> Douglas Partners Pty Ltd Consulting Geotechnical Engineers. Email: ims@douglaspartners.com.au

## Abstract

The Australian Standard AS2870 Residential slabs and footings – Construction was first published in 1986 and is now in its 4<sup>th</sup> edition. The scope of this standard is generally limited to single dwelling houses or multiple townhouse developments and buildings classified as Class 1 and 10a under the BCA (3) but can be applied to commercial and industrial buildings if they are similar to houses in size, loading and superstructure flexibility. However, the unilateral application of AS2870 to large industrial buildings is problematic in terms of technical relevance and practicality given the significant differences in serviceability requirements, loadings and economics associated with larger plan area buildings as compared to housing or smaller scale Class 10a buildings.

This paper focuses on the engineering principles involved in the design of slabs and footing systems for larger commercial and industrial buildings such as situated in the highly reactive clay sites NW of Melbourne and western Sydney. Particular emphasis is placed on soil structure interaction, site characteristics, displacement sensitivity and the practicalities of footing system alternatives for large commercial and industrial buildings. Examples are presented to compare footing system solutions based on misapplication of AS2870 principles compared to systems based on fundamental geotechnical and building serviceability principles.

*Keywords:* Industrial footing systems reactive clay

## 1.0 Introduction

There is no independent Australian design guideline or standard that deals specifically with the design and construction of concrete slab and footing systems for large industrial and commercial buildings. The Australian Standard AS2870 - 2011 Residential slabs and footings (1) is often referred to in geotechnical reports and in legal expert reports as having relevance to these forms of slab and footing systems.

This paper details a number of technical issues and concepts that need to be addressed by the design and construction industry when considering the relevance of AS2870 to the design of concrete slab and footing systems for large industrial and commercial buildings and in particular those slab and footing systems constructed on reactive clay sites.

## 2.0 Practical issues – discussion

### 2.1 Serviceability

Most soils exhibit some form of reactivity (i.e. change in volume as the soil moisture changes), such as would occur throughout the year. These movements cannot be prevented but appropriate attention to design and construction details can go a long way to minimise their impact on a structure

The usual form of construction for industrial and commercial buildings differs from that for residential buildings. In the case of large industrial and commercial buildings the more common forms of construction generally involve the use of large open plan areas, highly articulated precast concrete facades, metal clad walls, glazing systems, and suspended ceiling and partition wall systems. In the case of residential buildings, the more common forms of construction still used in Australia involve the use of brick and brick veneer facades with limited articulation and plasterboard clad stud walls generally constructed with fixed plaster cornices at wall/ceiling junctions resulting in no internal wall articulation. In addition residential buildings typically have much smaller plan areas and as such

residential structures are far more visually susceptible to soil reactivity induced movements than large area industrial and commercial forms of construction.

## 2.2 Forms of construction

Large plan area industrial buildings constructed to accommodate modern warehousing and distribution materials handling requirements commonly require that floor slab construction be built to very tight levelness tolerance and high standards of finish. As such these floors are commonly constructed in relatively large areas using laser guided equipment and are generally articulated (i.e. jointed) in such a way as to minimize restraint to concrete shrinkage that might result in uncontrolled cracking. On the other hand, residential construction generally utilizes ribbed or stiffened raft slab construction to minimize slab distortion that could result in superstructure cracking. Such construction however often results in restraint to shrinkage (at the stiffening ribs) that generally results in slab cracking, albeit that such cracking is usually covered and hidden by non-brittle floor finishes.

Large industrial facilities often involve the construction of office space as part of the overall large area building footprint. Whilst these may be considered similar to a house and fall within the auspices of AS2870, these office areas may be relatively large in area and of multi-level construction resulting in higher wall or column loads in comparison to typical loadings for residential buildings. The office areas associated with industrial facilities are generally more open plan than residential buildings. The internal partitions that are provided are often of the demountable type and not fixed to the ceiling in the same manner as for residential buildings (i.e. no fixed cornices).

## 2.3 Construction methodology

The large spans of industrial and commercial buildings require the use of steel frame construction which is commonly incorporated with precast concrete and metal clad walls or glazed facades. Where site access allows, it is common practice to initially erect the steel framing, the roof cladding and then erect and fix the façade elements. This order of construction allows for the floor slab construction to be undertaken very late in the construction program and therefore in the protected environment which is required in order to achieve the higher level of finish required for warehouse floors. It does require however that footings for the columns and walls are constructed early and well in advance of floor construction whereas residential floor slabs are generally much smaller in area and constructed in the open air with the balance of the superstructure supported directly from the slab.

## 2.4 Economics and optimal performance

From an overall community point of view the cost of failures of footing systems should ideally be balanced against the costs of excessive construction and design costs (2) and as such the performance requirements and expectations should not be unrealistic. This issue is recognised in AS2870 which states at clause 1.3.1 that "*Buildings supported by footing systems designed and constructed in accordance with this Standard on a normal site that is (a) not subject to abnormal moisture conditions; and (b) maintained such that the original site classification remains valid and abnormal moisture conditions do not develop; are expected to experience usually no damage, a low incidence of damage category 1 and an occasional incidence of damage category 2*" and at clause 1.4.2 "*Foundation movement shall be assessed as the movement that has less than 5% chance of being exceeded in the life of the building, which is taken as 50 years*".

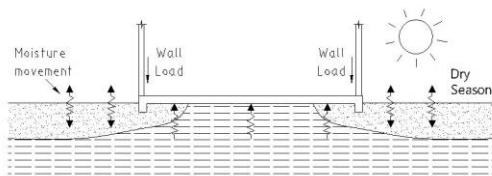
Further to the above, AS2870 Appendix B includes information on foundation performance and maintenance which expresses an expectation of some damage (cracking) occurring to residential buildings. At clause B1 AS2870 notes "*it is neither practicable nor economical to design for the extreme conditions that could occur in the foundation if a site is not properly maintained*" and "*some minor cracking and movement will occur in a significant proportion of buildings, particularly those on reactive clays*". AS2870 places a maintenance requirement on owners that involves attention to site drainage, limitations on gardens, restriction on the planting of trees and the need to repair leaking services, etc. all of which are applicable to industrial and commercial buildings.

In some regard it is not unreasonable to expect that a higher standard of maintenance on commercial and industrial properties would occur than would for a residential property. Also given the larger allotment sizes involved with industrial facilities as compared to residential subdivision should result in far less detrimental influences emanating from neighbouring properties (i.e. neighbours trees and poor neighbouring drainage control).

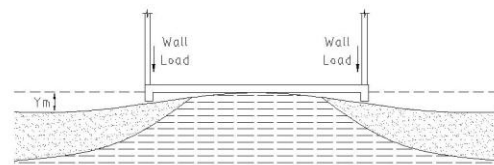
### 3.0 Technical issues – discussion

#### 3.1 Engineering design principles for reactive sites – residential buildings

AS2870 places emphasis on the use or modification of standard designs for residential buildings which are based on typical forms of residential construction and loading. However, the Standard also includes provisions for design by engineering principles which are primarily based around soil structure interaction through an idealized “soil mound” model. (i.e. it is assumed that more stable soil moisture conditions exist beneath the centre of the slab than at the edges). The idealized soil mound shapes in AS2870 represent the range of ground movement that could be expected over the life of the structure, on normal sites not subject to abnormal moisture conditions. In the case of central heave, the mounding is the result of an increase of soil moisture under the building cover (i.e. the slab) combined with a decrease in soil moisture around the perimeter. In the case of edge heave, the primary cause of the idealized mound shape is that the moisture increase occurs around the perimeter relative to the centre. Figures 1.1 to 1.4 below show the behaviour of covered areas in terms of moisture movements and expected ground heave for both centre heave and edge heave conditions.



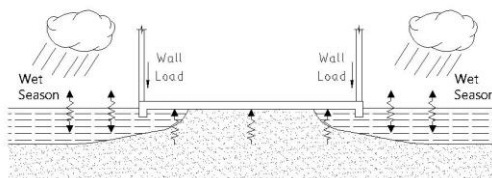
CENTER HEAVE (FIGURE 1.1)



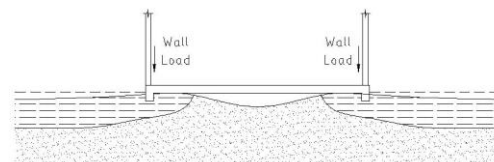
CENTER HEAVE (FIGURE 1.2)

$Y_m$  = Total differential due to combination of increase in moisture content under the slab and decrease in moisture content at edges.

Centre wetter than edge



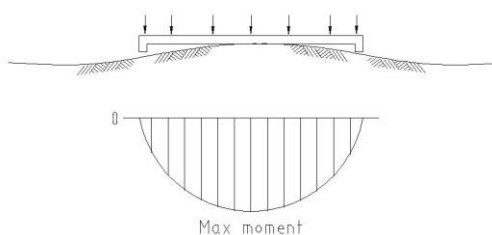
EDGE HEAVE (FIGURE 1.3)



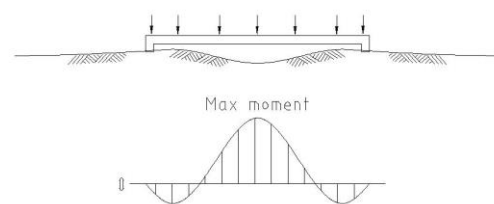
EDGE HEAVE (FIGURE 1.4)

Edge wetter than centre

The fundamental outcome of the soil mound model is the determination of bending moment and shear force effects on the footing system. For the central heave case the bending moments result from a “cantilevering” of the loaded edges of the building (i.e. loading primarily imposed by the external walls which also generally support roof and upper floor structure). The edge heave allows for determination of the impacts of internal loads on the slab span between edge mounds. Figures 2.1 and 2.2 show the resulting slab bending moments for the central and edge heave conditions.



CENTRE HEAVE (FIGURE 2.1)



EDGE HEAVE (FIGURE 2.2)

### 3.2 Engineering design principles for reactive sites – industrial and commercial buildings

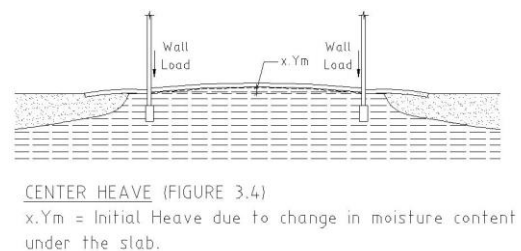
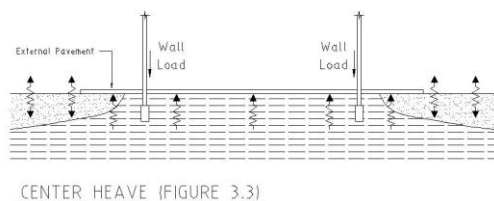
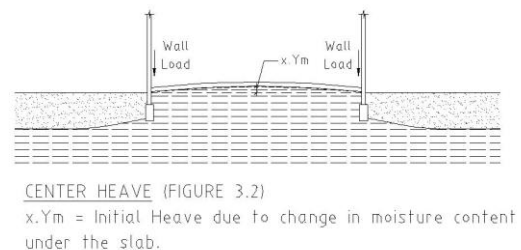
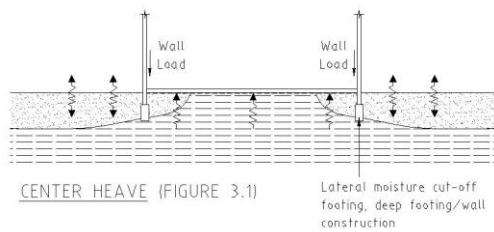
In the case of large industrial and commercial buildings the idealized soil mound concept can still be considered applicable but needs further consideration of the structural loading, slab shrinkage and structure articulation behaviour before application.

The edge loadings imposed by large industrial building construction (i.e. heavy column loads, heavy precast concrete wall loads, multi-level perimeter column loads and the like) would, likely result in excessive bending moments on an integrated raft or grillage beam style footing system. Hence, in practical and economic terms it is essential that these heavy concentrated type loads be supported directly on separate footings utilising the bearing capacity of the underlying soils. A similar argument can be made for high internal column loads. Hence the design task is to limit the formation of the centre heave mound or edge heave as much as possible so that footing systems do not need to be fully integrated.

In order to achieve desired practical and economic outcomes for industrial and commercial building construction it has been common practice over the past 30 years to incorporate either a deep wall/ footing “cut off” construction detail or impermeable paving to the building perimeter in combination with good site preparation, drainage design and limitations on the planting of trees or large bushes near the building perimeter.

The aims behind this approach have been to limit the initial soil heave that occurs when the floor slab is placed over the soil and at the same time limit edge effects at the perimeter caused by soil drying. Good drainage design limits the potential for edge heave effects and the limitation on tree planting is a fundamental requirement to prevent the development of excessive and abnormal moisture conditions that have been found to have the potential to cause excessive movement to almost any footing system. Site preparation should target obtaining as uniform as possible moisture regime over the area as close as possible to the expected long term conditions. When placing fill, care must be taken to ensure that the moisture content of the placed material is within the specified range and that there has not been excessive compaction of the materials (over compaction can be as detrimental to long term performance as would under compaction). In highly reactive ground this does require closer control of the operations than would a less reactive site.

Figures 3.1 to 3.4 show the behaviour of covered areas in circumstances where lateral moisture cut-off is provided by way of deep footing/wall construction or the adoption of perimeter paving external to the building perimeter.



## **4.0 Performance experience**

The performance experience with industrial footing and slab systems is difficult to quantify for a number of reasons not the least being the likely variability in performance expectations of industrial and commercial property owners or their tenants and a propensity for most legal disputes involving alleged footing system failures in the commercial arena to settle out of court and remain confidential. Accordingly, performance experience does have to rely largely on Engineering Practitioner experience.

While recent developments indicate that the commercial/industrial community performance expectations may be changing and may be becoming unrealistic, it is, however, the authors' collective experience that reported failures of footing systems for industrial and commercial buildings have been relatively minor over at least the past 30 years and that when taking into account the age of the overall industrial and commercial building stock in at least Melbourne and Sydney, the failure rate of slab and footing systems for industrial and commercial buildings is very low. The experience of the relatively recent severe drought conditions in Melbourne from around 1995 through to late 2009, which should have resulted in severe deep seated climate effects on building footing systems has not presented as being a particular cause of failures or damage during this period.

Similarly, the construction of industrial and commercial buildings during the extreme dry periods up until late 2009 should theoretically have resulted in at least transient edge wetting effects; however, to the authors' knowledge such incidences have not been widely reported.

In the case of buildings designed and constructed in the past 30 years and for which the authors have had experience or direct involvement, the total number would be many hundreds of which reported problems associated with the slab and footing systems would be less than 2% and actual failures requiring substantial structural rectification works minimal. It has also been the authors' collective experience that the reported failures of older style industrial building footing systems (i.e. brick wall, strip footing, bluestone footings etc) and more recent forms of concrete construction have been found to be primarily associated with the presence or development of abnormal moisture conditions caused by the planting and growth of trees too close to the footing systems or the general failure to maintain the drainage and plumbing systems in and around these buildings. The authors have also observed numerous failures of AS2870 compliant residential footing and slab systems where abnormal moisture conditions have been the primary cause of failure despite the inherent strength and stiffness built into these integrated forms of footing systems. In other words Practitioner observations are that it is the development of abnormal moisture conditions during the life of a building that are the major concern when it comes to footing and slab system performance irrespective of the structure and footing type.

## **5.0 Misapplication of AS2870 design principles to industrial and commercial buildings**

### **5.1 Soil classification issues**

A common observation in geotechnical reports carried out for industrial and commercial buildings is the reference to the Soil Classification based around AS2870. While most reports will qualify such classification as being a guide only, some designers in the industry tend to equate this classification to the general requirements and limitations of AS2870. These requirements and limitations include the exclusion of non-integrated footing and slab systems such as strip footing and infill slab construction on sites with classifications other than Class A and S.

Other observations are that designers feel compelled to adopt stiffened "infill" slabs (i.e. raft slabs built within a strip footing arrangement) in order to simply comply with particular AS2870 standard slab designs for site classifications other than Class A and S.

### **5.2 Soil Compaction Issues**

The large allotment sizes associated with industrial and commercial buildings often result in significant cut/fill requirements for developments and the resulting depth of fill means that these sites would technically be classified as "P" sites under AS2870 for which a common reaction is to resort to piles or piers despite the fact that the standard for earthworks on large industrial sites is expected to be at a higher level of supervision and testing in terms of moisture conditioning and compaction.

AS2870 places a limit of 400mm on controlled fill in the case of non – sand material before 'requiring an initial classification of 'P'. Because of the allotment sizes associated with commercial and industrial

sites the cut/fill depths will often exceed 400mm by a considerable margin. In such circumstances it has been the authors' experience that non – integrated footing systems and non-piled systems have performed satisfactorily on controlled fill depths greater than 400mm that have been compacted in accordance with Australian Standard "AS 3798 – 2007 Guidelines on earthworks for commercial and residential developments" to at least 98% standard compaction and within an appropriate range of moisture content.

### **5.3 Design by engineering principles to AS2870**

The rules for "design by engineering principles" as included in AS2870 require that the footing system be designed for the effects of the idealized mound model, which in the case of houses implies using two acceptable methods of analysis (i.e. Walsh or Mitchell) and an integrated footing system.

In the case of residential buildings the typical perimeter loading implied in the AS2870 standard designs is in the order of 25kN/m as an edge wall load which is equivalent to around 100kN concentrated load at the end of a cantilevering rib or grillage beam. The Standard does allow for loading from two level construction including suspended concrete floor slabs, however the latter is limited to Class A and S (i.e. non-reactive) sites.

For the case of two - level office buildings with suspended concrete slabs the concentrated load from roof and suspended floor construction on a perimeter column is likely to be in the order of 350kN – 400kN subject to the form of construction. Depending on the type of building façade the total concentrated load effect from floor loading and edge loading could be in the order of 450kN to 550kN excluding the self-weight of the footing system and the ground level superimposed loads. Accordingly, the proportioning in size and reinforcement of structural members for a fully integrated system designed for an idealized mound model will be influenced by the significant increase in load although the effects of this increase in load will impact on soil-structure interaction and in particular the calculation for the value of "Ym" and the edge distance "e". Essentially the idealized mound models used in AS2870 cannot be readily or reliably applied to commercial and industrial loading.

### **6.0 Cost implications**

The cost implications of adopting fully integrated footing and slab systems on large industrial and commercial buildings on all reactive clay sites would be significant in terms of increased design and construction costs resulting from the need for one off analysis of relevant soil-structure interaction effects and the likely increase in concrete and reinforcement requirements. While it is likely that the values for "Ym" and "e" will be reduced by the effects of the heavier loads the resulting design bending moments and shear forces for the centre mound condition are likely to be significantly increased in comparison to residential construction.

### **7.0 Non – integrated footing and slab systems**

The Commentary to AS2870 – 2011 states at clause C4.1, "*the design methods in Section 4 may be useful for strip footings although, more often, past satisfactory experience is appropriate*". As noted previously it has been the authors' 30 years+ experience that non-integrated footing and slab systems have been successfully adopted on industrial and commercial buildings in the reactive clay areas of Melbourne and Sydney for many years. The authors' also recognise their experience with the performance of older building stock which includes the common use of non – integrated footing and slab solutions.

#### **7.1 Design principles adopted**

It is the authors' experience that the primary design requirement with any footing and slab system is the avoidance of abnormal moisture conditions that may develop over the life of the building. In most cases abnormal conditions develop due to poor maintenance or non-adherence to design requirements and limitations, particularly related to the planting of trees too close to the footing system. It has been the authors' experience that these abnormal moisture conditions are equally problematic for both fully integrated and non – integrated slab and footing systems.

For the case of non – integrated systems the other key measures have been found to include:

- Good site preparation including moisture conditioning of the subgrade in order to limit initial heave effects caused by moisture increases resulting from the effect of the building cover.

- Provision of a deep perimeter moisture cut-off in the form of edge beams or wall and deep strip footings in order to minimise the drying effect of moisture migration from under the slab or the effects of moisture increase from external landscape areas to under the perimeter of the slab.
- Adequate external drainage away from the perimeter of the building so as to avoid the ponding of moisture and subsequent moisture migration under the perimeter of the slab.
- Adequate sealing of service trench penetrations under the slab at the point where they pass beneath the building edge. This includes the sloping of trenches away from the building perimeter and clay plugging at the point of penetration under the footing system.
- Adequate sealing of perimeter walls to the top of footings, particularly for precast concrete wall panels
- Avoiding the use of irrigation systems close to building edges.
- Provision of perimeter impervious pavement wherever possible.

By adopting and maintaining the above design features the development of the theoretical centre heave mound can be limited to that which occurs due to the effect of the building cover. The building cover cuts off evaporation and alters the moisture condition of the subgrade under the slab and depending on initial moisture content can result in very early heave of the slab. It is the combination of this initial heave and any subsequent edge drying that may occur due to poor detailing and maintenance that results in the formation of the full differential edge-centre movement.

## **7.2 Design circumstances and detail**

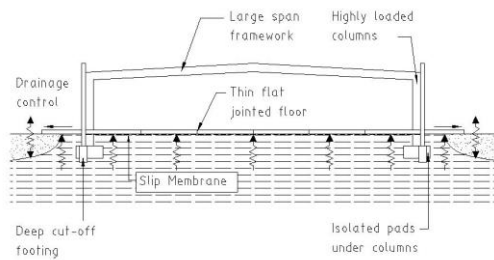
### **Warehouse Buildings**

For the case of large warehouse areas the adoption of integrated footing solutions is not practical or viable for many reasons including:

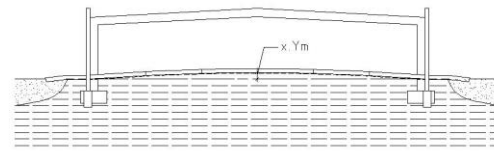
- Floor flatness and levelness requiring the use of laser guided screeds which need a relatively flat sub – base and which could not effectively operate over the top of slab rib trench excavations.
- The need to erect the superstructure prior to the construction of the floor slabs in order to avoid heavy construction traffic on the floor slabs and to provide protection from the elements during the construction of the floor slabs.
- The increasing adoption of steel fibre reinforced concrete floor slabs that require complete isolation from the structure and the sub-base in order to avoid major cracking due to shrinkage restraint conditions.
- High storage rack loads around the perimeter of buildings that would have a major impact on structural thickness requirements if the floor was to be designed as an integrated raft slab subject to edge drying effects.

For the above reasons warehouse floors are designed and constructed as relatively thin slabs of uniform thickness and generally fully isolated from the main building structure and placed on slip membranes in order to minimize shrinkage restraint conditions. The perimeter of the building is generally protected from edge drying effects by either impervious external pavements and surface drainage systems or the use of relatively deep cut off walls at the outside edge of the slab. In addition, these forms of floor construction are often articulated by control joints to minimize shrinkage restraint cracking.

Figures 4.1 and 4.2 shows the expected behaviour of a very large covered area such as a warehouse and which includes deep cut off footings, isolated pad footings and perimeter paving. These types of buildings are often large clear span structures involving relatively large external column loads and precast concrete wall loads and concrete floors that require articulation in the form of construction joints and shrinkage crack control joints. External drainage is usually provided by purpose designed and constructed in ground pipe systems and extensive use of impermeable pavement.



CENTER HEAVE (FIGURE 4.1)



CENTER HEAVE (FIGURE 4.2)

x.Ym = occurs over a large distance

Reports on slab edge failures in warehouse construction has been minimal in the authors' experience other than in extreme circumstances involving the growth of trees close to the building perimeter. Experience has shown that slab edges do tend to drop relative to the centre of the slab. Whilst it is usually difficult to determine if this is due to continuing centre heave or edge settlement, the degree of differential movement has generally been found to be minimal with no reports of slab failure caused by rack post loading of unsupported slab edges.

## Office Buildings

For the case of office buildings that are connected to or built into warehouse buildings, the slab and footing system requirements are often considered by engineers to be more stringent than for the warehouse part of the building. While there may be an argument that floor movement sensitivity in office areas is more problematic than warehouse areas, this is not necessarily the case depending on the use of the warehouse as there are some warehouse levelness limitations that can be more stringent than the general requirements of AS2870 for concrete floors. However, the issue with office areas appears to be seen as more problematic due to the presence of internal partitions, glazing and brittle finishes such as wall and floor tiling. In response, the engineering solution is often to incorporate a raft slab to the office areas even in circumstances involving multi-level construction where heavy column loads or wall loads are supported on independent pad and strip footings. Such solutions are thought likely to be in response to unwarranted pressure to be seen as responding to AS2870 solutions despite the fundamentals not supporting this approach. An isolated raft slab built within the confines of a multi – level structure serves no real purpose in the context of controlling the effects of soil movement.

As noted previously, the more flexible nature of construction detail in office buildings as compared to residential construction allows for more structural movement to occur without necessarily resulting in completely unacceptable incidences of damage or damage that cannot easily be repaired similar to Category 1 and 2 damage in residential buildings. The practical and economic solutions lay in the detail and in the adoption of more sophisticated and supervised earthworks and moisture migration protection/prevention measures that can be built into the office structures. Such measures may include the provision of a capping layer placed as early as possible over the slab area to induce as much initial site heave as possible in combination with a deep perimeter moisture cut off wall/footing arrangement that minimises subsequent edge drying effects and thus formation of the full extent of the idealized mound. Perimeter planting needs to be avoided in order to eliminate the risk of extreme abnormal moisture conditions and other solutions found for landscape and beautification treatment. If necessary such features can be placed within areas constrained by deep root barriers. In cases where internal partitions are built using plasterboard fixed to metal studs (as distinct from modular



demountable partitions) more attention needs to be paid to articulation of the walls and wall junctions, if only to reduce the need for minor maintenance and repair from time to time.

The authors' experience with regard to reports on office floor movement and damage have on occasion indicated likely incidences of initial heave caused by the building cover effect or in some cases lateral migration of moisture, however, the majority of cases have involved either the development of abnormal moisture conditions or defective construction detail, (for example the lack of recognition of potential movement when installing partitions and suspended ceilings can result in floor movements lifting partitions and hence ceiling panels, which while in themselves of no real consequence, appear unacceptable to an end user).

## **8.0 Conclusions**

On the basis of Practitioner experience over a period of 30 years, including a period of very severe and prolonged drought conditions from 1995 through to late 2009, it is the authors' view that current design methods incorporating the use of non – integrated slab and footing systems for industrial and commercial buildings on reactive clay sites have provided an economical and serviceable solution to the commercial and industrial user community. Where problems have been observed they have generally been associated with the development of abnormal moisture conditions caused by poor maintenance practices, non-conforming construction detail or the planting of trees too close to the footing system.

The approach taken by AS2870 to slab and footing design and construction is essentially based around single dwelling houses, town houses or similar structure with the intention of providing standard solutions wherever possible to take into account the inherent limitations in residential construction practices, particularly earthworks and to reduce overall costs to the general community whilst accepting that structures built in accordance with the code can never be considered damage free.

On the other hand large industrial and commercial building structures generally involve more sophisticated design input, construction techniques and supervision which allow the engineering designer more scope in achieving particular performance requirements.

The design and construction of non-integrated slab and footing systems which include pad, strip or pile footings are adequately covered by relevant Australian Standards such as AS3600 (4). It is just the application of such slab and footing systems on reactive clay sites that appears to invoke the use of AS2870 whereas in fact the application of logical engineering principles can be applied to these structures without the addition of unreasonable cost impost.

## References

1. AS2870 – 2011, Residential slabs and footings – Construction
2. SAA HB28 – 1997, the design of residential slabs and footings by Paul Walsh and Don Cameron.
3. National Construction Code Series 2014, Volume One, Class 2 to Class 9 Buildings
4. AS3600 – 2009, Concrete Structures

## Bibliography

1. Dr J.E. Holland, residential slab research – recent findings August 1978
2. Dr J.E. Holland, J Washusen & D Cameron, seminar residential raft slabs, September 1975
3. Technical Report 34 Concrete Industrial Ground Floors, a guide to design and construction, fourth edition, June 2014.
4. Building in accordance with AS2870 residential slabs and footings, P F Walsh

# Fibres FRP Research and Applications

# Creep of Cracked Polymer Fiber Reinforced Concrete

Rutger Vrijdaghs<sup>1</sup>, Lucie Vandewalle<sup>2</sup>, Marco di Prisco<sup>3</sup>

<sup>1</sup>Doctoral Researcher, Department of Civil Engineering, KU Leuven

<sup>2</sup>Professor, Department of Civil Engineering, KU Leuven

<sup>3</sup>Professor, Department of Structural Engineering, Politecnico di Milano

**Abstract:** Creep of cracked polymer fiber reinforced concrete is complex and not well understood. Fiber reinforced concrete creep can be attributed to fiber creep as well as interfacial fiber-matrix creep. The present work discusses the long-term behaviour of individual fibers and short-term bond strength between fiber and matrix. Polypropylene fibers, used as structural reinforcement, are being tested. A novel measuring method was adopted to measure the creep elongation of the fibers. Laser displacement sensors continuously measure the elongation of the fiber at a rate of 1 Hz. Different initial fiber lengths and sustained load levels are considered. The results show that at moderate load levels, the creep strain at failure can be an order of magnitude greater than the instantaneous strain. Additionally, experimental results of pull-out tests of the same fiber are reported. The results suggest that the age of the matrix is not influential in the pull-out behaviour. On the other hand, the matrix composition and imbedded length of the fiber have an important influence on the maximum pull-out force. The fiber embossment can increase post-peak performance. For the reported fiber, a continuous stress buildup and debonding mechanism is proposed to describe post-peak behaviour.

**Keywords:** Experimental, creep, pull-out, macro-synthetic fibers, FRC.

## 1. Introduction

Fiber reinforced concrete (FRC) is a composite material in which fibers are added to the fresh concrete mix [1, 2]. These fibers can improve the properties of the concrete in the fresh or hardened state. In structural applications, fibers can partially or totally replace the traditional reinforcement. For these purposes, the fibers provide an enhanced post-cracking tensile strength in the hardened state by bridging crack faces [3]. Commercially available fibers can be made from a number of different materials: steel, glass, synthetic and natural being the most common types [4]. Steel fibers are widely used in structural applications [5-8]. However, steel fiber reinforced concrete (SFRC) may not be suitable for all applications, and synthetic fiber reinforced concrete (SyFRC) [7] and glass FRC (GFRC) [9] have been successfully used as well.

Considerable research effort has been devoted in the last decades to study the properties of the fresh and hardened state of FRC [10-13]. It has been shown that the inclusion of fibers decreases plastic shrinkage cracking [14] and flowability [15] in the fresh state. In the hardened state, fibers provide a post-cracking strength as is shown in references [16-18]. However, only very limited research has been done on the long-term structural properties of FRC [19-21]. Time dependent effects may significantly alter the behaviour of structural elements, both in the serviceability limit state (SLS) and in the ultimate limit state (ULS). In the former, creep may cause unwanted and unacceptable deflections of FRC beams [22, 23], whilst in the latter, the residual load-bearing capacity of elements may be significantly lower than the design value based on the short-term strength assessment. Therefore, time-dependent effects should be taken into account during the design of FRC elements. The recently published Model Code 2010 [24] acknowledges this fact but does not provide design rules. It is clear that further research on the long-term structural properties of FRC is required.

One of these time-dependent phenomena is creep. Creep of FRC elements is different from creep of traditionally reinforced elements as the creep deformations of FRC are generally concentrated in the tensile zones. After matrix cracking, fibers allow forces to be transmitted across cracks. A crack can widen due to two main mechanisms: pull-out creep and fiber creep. Pull-out creep is the mechanism in which the fiber gradually slides out of the concrete matrix [25-27]. Fiber creep, on the other hand, is the time-dependent elongation of a stressed fiber itself. This fiber creep deformation is mainly a problem for synthetic and natural fibers [28, 29], but steel and glass fibers can exhibit creep behaviour at high temperatures as well.

In this paper, the first results of an multi-scale experimental program are presented. Firstly, results from creep tests on a polypropylene (PP) macrofiber are shown. A macrofiber is defined in EN14889-2 [30] as a polymer fiber of which the (equivalent) diameter  $d > 0.3$  mm. Secondly, pull-out tests of the same fiber from different matrices are reported as well.

## 2. Experimental setup

### 2.1 Fiber creep setup

A straight polypropylene fiber used for structural concrete reinforcement is tested. The fiber has an equivalent diameter of 0.95 mm, making it a class II fiber, according to EN14889-2 [30]. Two different initial lengths  $l_0$  are considered: 500 mm, and 200 mm. At its ends, the fiber is firmly held in place by a clamping system, which uses a combination of gluing and bolting to prevent fiber end slippage. An exploded view of the clamping system is shown in Figure 1. The fiber is pretreated with a chemical primer to increase the surface energy, which is quite low for polyolefins such as PP. This increase in surface energy allows the fiber to bond with a rapidly-drying cyanoacrylate adhesive. The fiber is glued to a roughened L-shaped aluminum plate over a length of 80 mm. The L-shaped plate has a thickness and width of 2 mm and 40 mm, respectively. As soon as the fiber is securely glued between the plates, 6 M6 bolts and nuts are fastened. The clamping action of the bolts actively holds the two plates together, and in combination with the rapidly drying adhesive prevents fiber slippage.

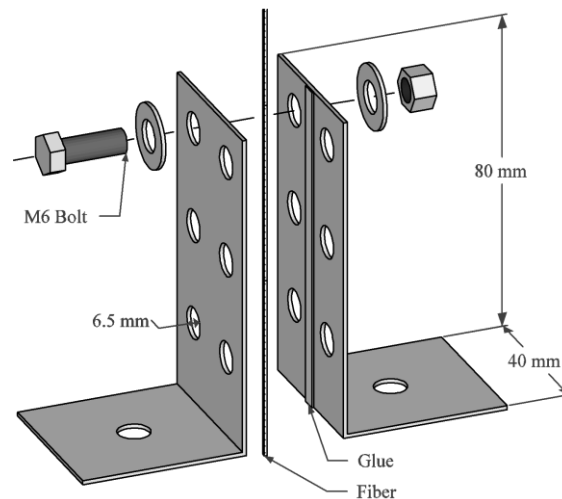


Figure 1: Exploded view of the clamping system

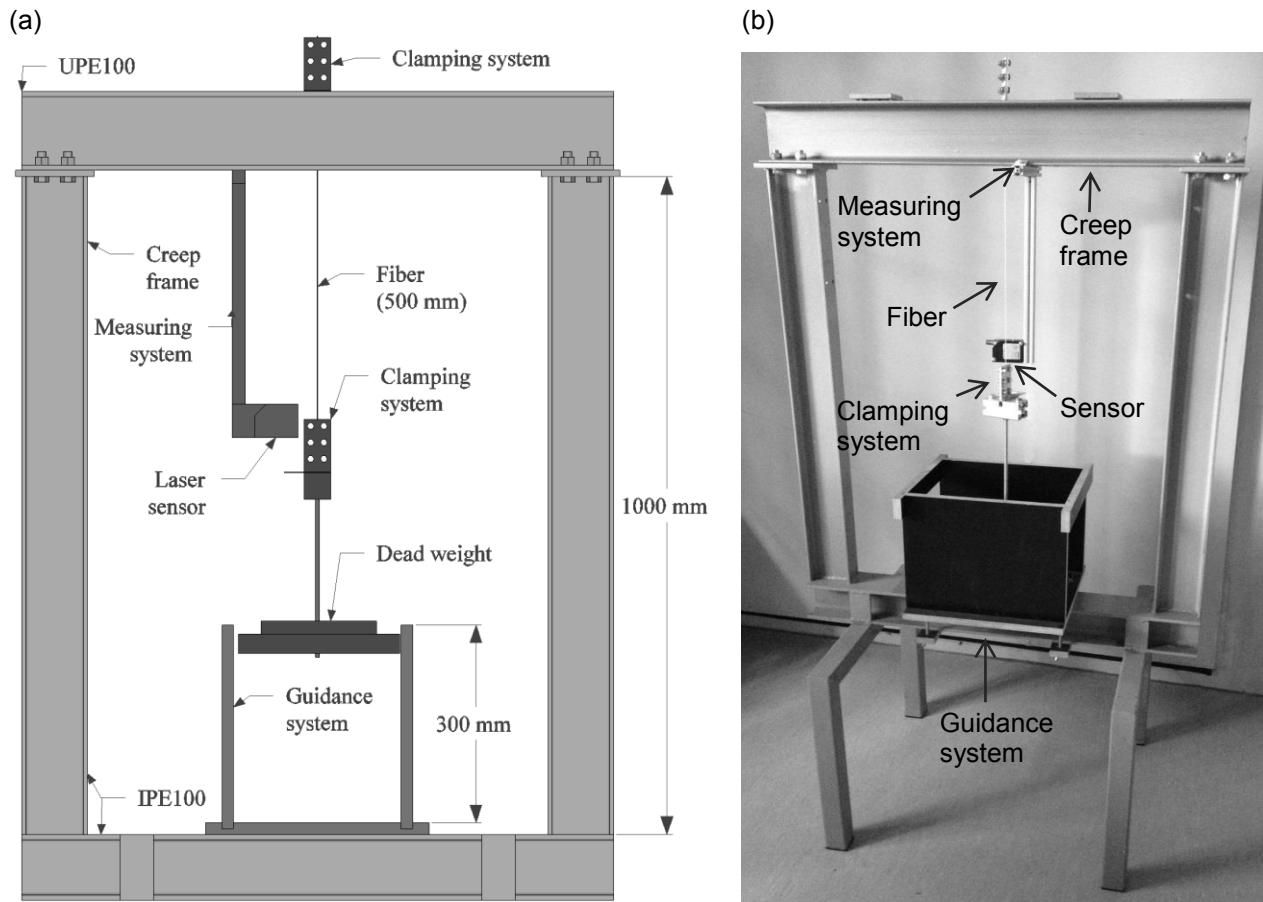
The creep specimen is placed in a creep frame in a climate controlled chamber at 20 °C and 60 % relative humidity. This frame is a steel structure consisting of 3 parts: a supporting frame, a measuring system, and a guidance system. An overview of the creep frame, and its 3 parts is shown in Figure 2 (a). A photo of the actual creep is shown in Figure 2 (b). There are 8 frames in total. It has been a deliberate choice to test only one specimen per frame. Failure of one of the specimens might induce unacceptable vibrations in the other samples if each frame supported more than one specimen.

The supporting frame serves as the main supporting structure for both the specimen and the guidance and measuring systems. The fiber with its two clamping systems attached is placed into the frame.

The measuring system is able to measure the fiber elongation. For this experiment, a contactless system was chosen. Optical laser sensors are fixed to a set of small (20 mm x 20 mm) aluminum profiles that allow the sensor to be moved in all directions. Measurements are taken at a rate of 1 Hz. The sensor has a maximum range of 250 mm and an accuracy of  $\pm 0.1$  mm. The maximum range corresponds to a maximum measurable strain of 50 % and 125 % for an initial length  $l_0$  of 500 mm and 200 mm, respectively.

In the reported setup, iron plates are used as dead weight to apply the tensile load to the specimens. Preliminary tests have shown the specimen may rotate at the application of the load. This may cause

problems for the optical measurement system. Therefore, all rotations of the specimens around its axis should be avoided and a guidance system is installed around the iron plates. The guidance system is made out of concrete plywood plates screwed together. The friction between the plywood plates of the guidance system and the iron plates is thought to be negligible during the creep test. This system simultaneously serves as an impact absorber at fiber failure.



**Figure 2: (a) Simplified creep frame with different components. The three parts of the creep frame are shown. Not shown is the supporting base (b) Picture of the actual creep frame**

In total, 16 creep specimens have been tested. The characteristics of the specimens are shown in Table 1. In this table, the load ratio is defined as the ratio between the applied load and the average fiber strength. The applied load is the sum of the weight of the clamping system and the dead weight, i.e. iron plates. The strength of the fiber is determined in a uniaxial tensile test on 6 test specimens which yielded an average value of 274 N and a standard deviation of 7 N.

**Table 1: Fiber Creep Specimens**

Category	Initial length	Dead weight / Load ratio	Number of specimens
1	500 mm	15 kg / 53 %	6
2	500 mm	12 kg / 43 %	2
3	500 mm	10 kg / 36 %	2
4	200 mm	15 kg / 53 %	6

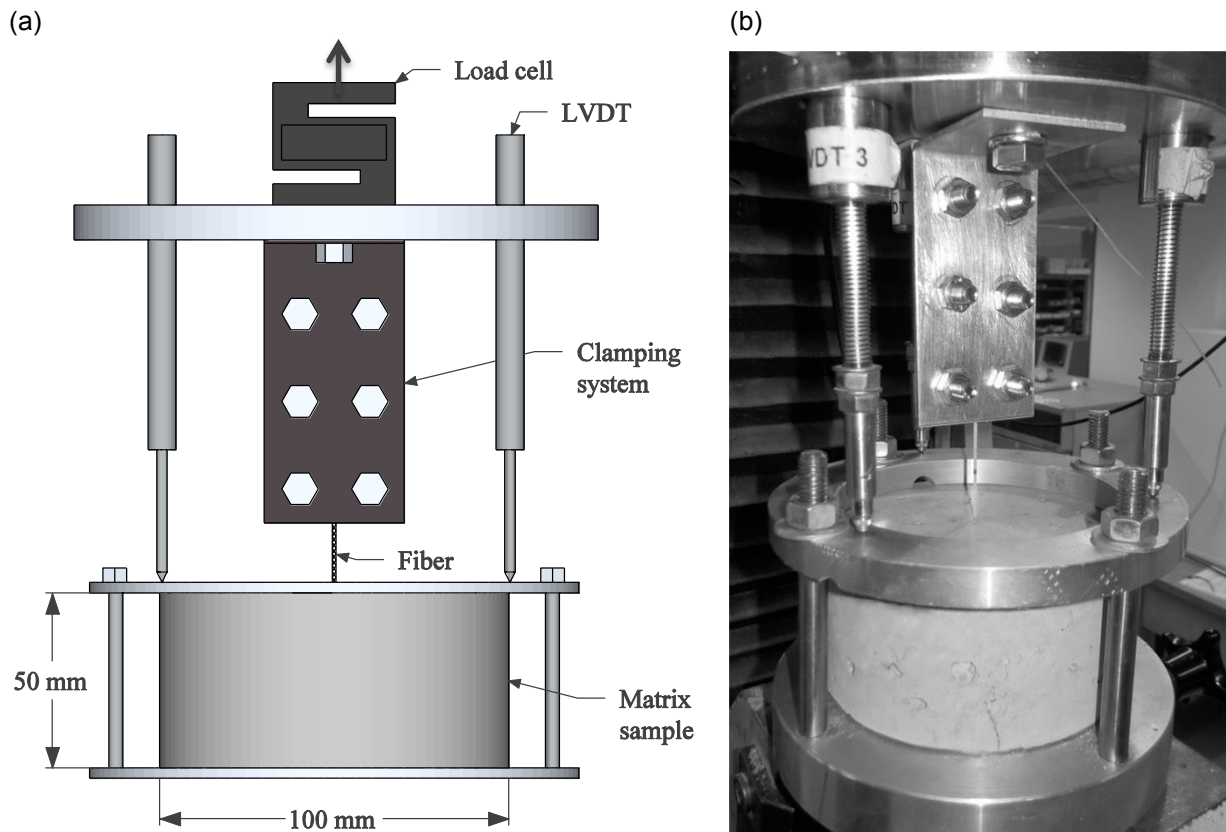
## 2.2 Pull-out setup

The same macro-synthetic fiber is subjected to pull-out tests as well. Three different matrices are considered: (1) a concrete matrix, (2) a mortar matrix obtained by omitting the coarse aggregates in the concrete matrix (3) a mortar matrix obtained by substituting the coarse aggregates of the concrete matrix with fine aggregates, i.e. sand. Table 2 summarizes the three matrices and presents the composition.

**Table 2: Matrix Composition**

	Concrete matrix	Mortar matrix 1	Mortar Matrix 2
CEM I 42.5R HES [kg/m <sup>3</sup> ]	350	350	350
Water [kg/m <sup>3</sup> ]	175	175	175
Sand 0-4 [kg/m <sup>3</sup> ]	835	1934	835
Gravel 4-14 [kg/m <sup>3</sup> ]	1099	0	0
Superplasticizer [kg/m <sup>3</sup> ]	1	1	1

The tests are performed on a universal test machine in a displacement controlled regime. The displacement rate is chosen to a relatively high value of 10 mm/min in order to minimize the effect of creep on the measured deformation. The initial length between the clamping system's end and the matrix sample is 20 mm. The displacement of the crosshead is accurately measured by 3 LVDTs placed around the fiber. The LVDTs can measure deformations up to 30 mm with an accuracy of  $\pm 0.01$  mm. The forces imposed on the system during the test are recorded by an external load cell with a capacity of 900 N. This load cell has a declared accuracy of  $\pm 0.05$  %. The load cell, LVDTs and matrix sample are held in place by steel profiles. In Figure 3, (a) a simplified drawing and (b) photo of the pull-out setup is shown.



**Figure 3: (a) Simplified pull-out setup (b) Picture of the actual pull-out sample**

In total, 18 specimens have been tested. The different specimens are reported in Table 3. During casting, the mold is filled in three layers, with manual compaction after every layer. The initial imbedded length of the fiber during casting is 30 mm in all cases. However, the first tests on the concrete matrix have shown that partial pull-out can occur during demolding. This problem has since been addressed and for the last concrete samples and for mortar samples, the actual imbedded length prior to testing is equal to the initial embedded length during casting. All samples are demolded 1 day prior to testing.

**Table 3: Pull-out Specimens**

Matrix	Age at testing [days]	Number of specimens [-]	Imbedded length [mm]
Concrete	11	3	30, 29, 24
Concrete	27	3	28, 28, 22
Mortar 1	7	3	All 30
Mortar 2	9	6	All 30

### 3. Results

#### 3.1 Fiber creep results

Table 4 presents the failure mode for the completed tests. Of the 16 specimens, 11 failed due to creep failure and 5 tests were aborted because the creep elongation had become or would become greater than 250 mm, the maximum range of the sensor. The experimental results are shown in Table 5. In this table,  $t_{failure}$  denotes the average time to failure in seconds. The average total strain at failure is denoted as  $\epsilon_{failure}$  in %. The results from the completed creep tests are shown in Figure 4 (a) and (b) on a linear and logarithmic time scale, respectively.

**Table 4: Failure Mode of the Completed Experiments**

Category	Number of specimens [-]	Failure mode (number of specimens)
1	6	Creep failure (5), Aborted: sensor out of range (1)
2	2	Aborted: sensor out of range (2)
3	2	Aborted: sensor out of range (2)
4	6	Creep failure (6)

**Table 5: Experimental Results**

Category	$t_{failure}$ [s] (#, s)	$\epsilon_{failure}$ [%] (#, s)
1	$2.00 \times 10^5$ (5, $25 \times 10^3$ )	35.8 (5, 1.8)
2†	$> 3.24 \times 10^6$ (2, N/A)	$> 50$ (2, N/A)
3†	$> 4.38 \times 10^6$ (2, N/A)	$> 33.7$ (2, 0.8)
4	$1.86 \times 10^5$ (6, $31 \times 10^3$ )	40.1 (6, 3.0)

† determined at the moment the creep test was aborted

# number of specimens

s standard deviation

N/A not applicable



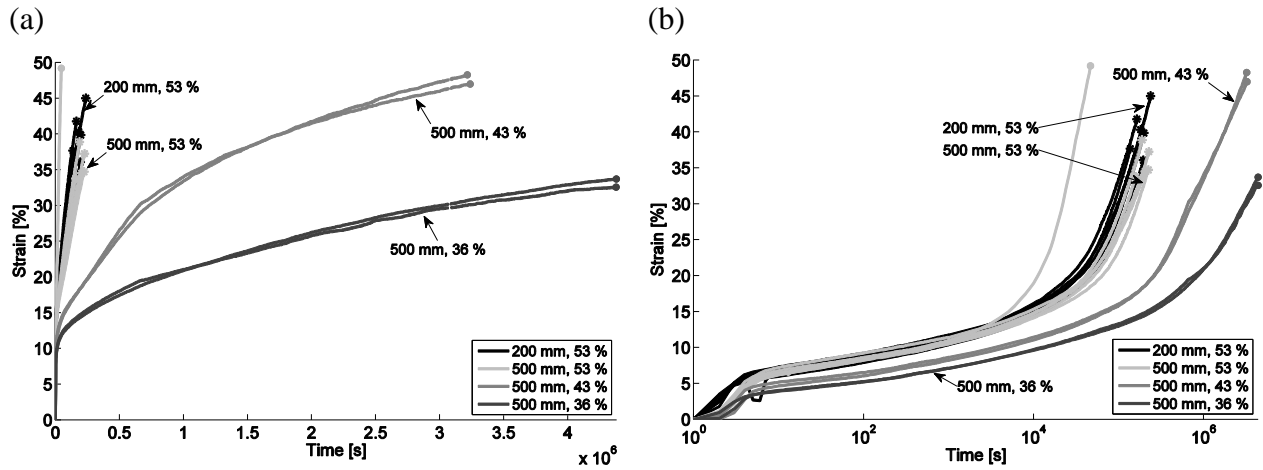


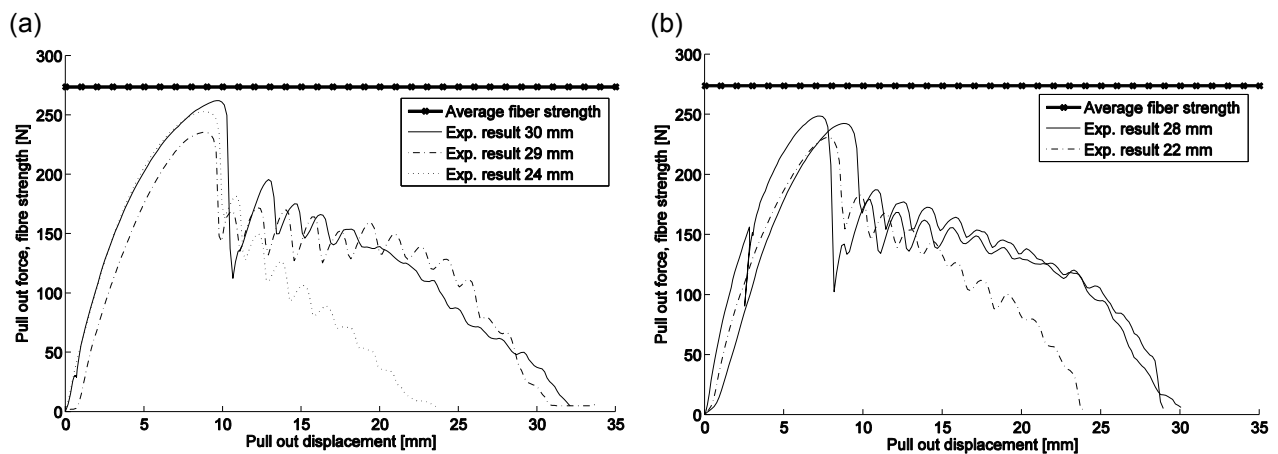
Figure 4: Total strain at (a) linear time and (b) logarithmic time. ○ denotes aborted tests, sensor out of range, × denotes fibre breakage due to creep failure.

### 3.2 Pull-out results

Table 6 presents the average maximum pull-out force  $F_{max}$ , as well as the standard deviation  $s$ , measured during testing. The number of specimens is shown as well. The pull-out results are presented in Figure 5 for all experiments. Shown as well is the average fiber strength in Newton. The fiber is pulled out from the matrix in all cases.

Table 6: Experimental Results of the Pull-out Specimens

Matrix	Age at testing [days]	$F_{max}$ [N]	$s$ [N]	Number of specimens [-]
Concrete	11	250	11	3
Concrete	27	240	7	3
Mortar 1	7	68	35	3
Mortar 2	9	217	27	6



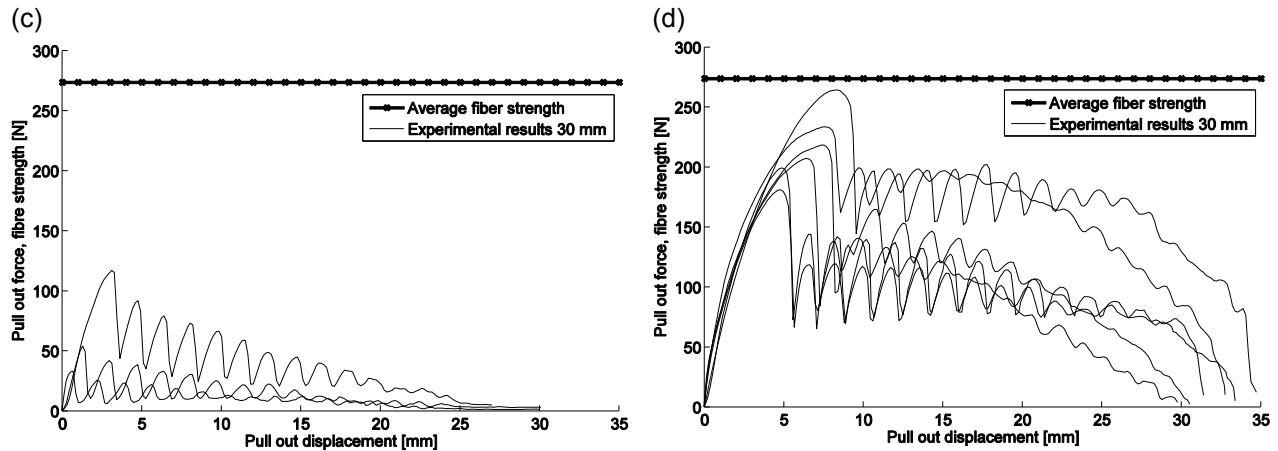


Figure 5: Results from pull-out samples from (a) a concrete matrix at 11 days (b) a concrete matrix at 27 days (c) a mortar matrix at 7 days (d) a mortar matrix at 9 days

## 4. Discussion

### 4.1 Fiber creep

From Figure 4, it can be observed that the total deformation greatly exceeds the instantaneous deformation. Let the creep coefficient  $\varphi(t)$  be defined as in Eq. (1)

$$\varphi(t) = \frac{\varepsilon_{creep}(t)}{\varepsilon_{inst}} \quad (1)$$

Where  $\varepsilon_{creep}(t)$  is the creep deformation at failure as a function of time, and  $\varepsilon_{inst}$  the instantaneous elastic deformation. Furthermore, let Eq. (2) and Eq. (3) hold

$$\varepsilon_{total}(t) = \varepsilon_{inst} + \varepsilon_{creep}(t) \quad (2)$$

$$\varepsilon_{inst} = \varepsilon_{total}(0) \quad (3)$$

Where  $\varepsilon_{total}(t)$  is the total strain that is measured experimentally. Using the results from Table 5, values for the creep coefficient  $\varphi(t)$  at  $t = t_{failure}$  are summarized in Table 7.

Table 7: Creep Coefficient Values of Completed Tests

Category	$\varepsilon_{inst}$ [%]	$\varepsilon_{creep}(t_{failure})$ [%]	$\varphi(t_{failure})$
1	5.0	30.8	6.2
2	3.8	> 46	> 12
3	3.0	> 30	> 10
4	5.0	35.1	7.0

It is very clear that for this type of fibers the creep strains can become many times greater than the instantaneous elastic strains. For samples loaded at 53 % of the ultimate load, the creep coefficient varies between 6 and 7. Furthermore, the creep coefficient increases as the load ratio decreases, exceeding 12 for samples loaded at 43 % of their ultimate load. Since these tests were aborted, the final creep coefficient is likely even greater.

### 4.2 Pull-out results

From Figure 5, it is clear that the pull-out behaviour from a concrete matrix is rather similar for 11 and 27 days. This has been confirmed in the literature as well [31]. The matrix composition, however, greatly

affects the pull-out behaviour. When replacing the coarse aggregates in a concrete matrix with sand, as has been done in mortar 1, the mix becomes very dry. This leads to a profound decrease of the maximum measured force  $F_{max}$ . On the other hand, a mortar with only a small amount of aggregates with respect to cement paste, such as mortar 2, can achieve almost the same maximum force  $F_{max}$  as a concrete matrix.

The maximum force measured during pull-out is related to the imbedded length of the fiber and to the interfacial bond strength between the fiber and the matrix. However, longer embedment lengths do not necessarily lead to higher maximum forces as can be seen in Figure 5 (a) and (b). This suggests that interfacial bond strength is not the only factor in play. Further research is needed to confirm this observation.

Shortly after  $F_{max}$  is achieved, a sudden drop in the load-displacement curve is observed. Experimentally, this drop corresponds to a snapping sound in the specimen, suggesting a sudden debonding of the fiber. After this maximum load, a recurring pattern of stress buildup and debonding is observed, giving rise to an oscillating curve. This process is repeated until the bonded length becomes too small to allow stress buildup in the matrix and the fiber is simply pulled out from the matrix. This can be observed for all matrices and at all ages. The surface embossment of the fiber can be the determining factor in this process.

## 5. Conclusions

The first results of an multi-scale experimental program are presented. Firstly, an experimental setup is shown used to determine the creep behaviour of a polypropylene fiber for structural concrete reinforcement. Three different load levels are considered: 53 %, 43 % and 36 % of the ultimate strength of the fiber, as determined in a uniaxial tension test. Two different initial fiber lengths are considered as well, 200 mm and 500 mm. The results show that the creep deformation can greatly exceed the instantaneous deformation, with creep coefficient values greater than 6 for all reported test results. Secondly, an experimental setup to determine the pull-out behaviour of the same fiber is presented. The results show that the age of testing does not greatly influences fiber performance. On the other hand, the matrix composition and imbedded length have a profound effect on the maximum pull-out load. The fiber embossment can increase post-peak performance of the fiber. For the reported fiber, a continuous stress buildup and debonding mechanism is proposed to explain post-peak behaviour.

## 6. Acknowledgement

The author would like to thank the financial support of the Agency for Innovation by Science and Technology in Flanders (IWT).

## 7. References

1. Balaguru, P. and S.P. Shah, *Fiber-Reinforced Cement Composites*. 1992, Texas, USA: McGraw-Hill.
2. Bentur, A. and S. Mindess, *Fibre Reinforced Cementitious Composites*. 1990, England: Elsevier Science Publishers LTD. 449.
3. di Prisco, M., G. Plizzari, and L. Vandewalle, *Fibre reinforced concrete: new design perspectives*. Materials and Structures, 2009. **42**(9): p. 1261-1281.
4. ACI Committee 544, *State-of-the-Art Report on Fiber Reinforced Concrete*, J.I. Daniel, Editor 2002, American Concrete Institute.
5. Serna, P., et al., *Structural cast-in-place SFRC: technology, control criteria and recent applications in Spain*. Materials and Structures, 2009. **42**(9): p. 1233-1246.
6. Caratelli, A., et al., *Structural behaviour of precast tunnel segments in fiber reinforced concrete*. Tunnelling and Underground Space Technology, 2011. **26**(2): p. 284-291.
7. Bernard, E.S. *Design of Fibre Reinforced Shotcrete Linings with Macro-synthetic Fibres*. in *Shotcrete for Underground Support XI*. 2009.
8. de la Fuente, A., et al., *Experiences in Barcelona with the use of fibres in segmental linings*. Tunnelling and Underground Space Technology, 2012. **27**(1): p. 60-71.
9. Ferreira, J.P.J.G. and F.A.B. Branco, *The use of glass fiber-reinforced concrete as a structural material*. Experimental Techniques, 2007. **31**(3): p. 64-73.
10. *Fibre Reinforced Concrete*. RILEM Proceedings of the 5th RILEM Symposium (BEFIB 2000), PRO15, BEFIB 2000, ed. P. Rossi and G. Chanvillard. Bagneux, France: RILEM Publications S.A.R.L.

11. *Fibre-Reinforced Concrete*. RILEM Proceedings of the 6th RILEM Symposium (BEFIB 2004), PRO39, BEFIB 2004, ed. M. di Prisco, R. Felicetti, and G.A. Plizzari. Bagnaux, France: RILEM Publications S.A.R.L.
12. *High Performance Fibre Reinforced Cement Composites (HPFRCC5)*, ed. H.W. Reinhardt and A.E. Naaman. Bagnaux, France: Rilem Publication S.A.R.L.
13. *Fibre Reinforced Concrete: design and applications*. BEFIB 2008, ed. R. Gettu. Bagnaux, France: Rilem Publication S.A.R.L.
14. Grzybowski, M. and S.P. Shah, *Shrinkage Cracking of Fiber Reinforced Concrete*. ACI Materials Journal, 1990. **87**(2): p. 138-148.
15. Pasini, F., et al., *Experimental study of the properties of flowable fiber reinforced concretes*, in *6th International RILEM Symposium on Fibre Reinforced Concretes*, M. di Prisco, R. Felicetti, and G.A. Plizzari, Editors. 2004, RILEM Publications SARL. p. 279 - 288.
16. Barros, J., et al., *Post-cracking behaviour of steel fibre reinforced concrete*. Materials and Structures, 2005. **38**(1): p. 47-56.
17. di Prisco, M., L. Ferrara, and M.G.L. Lamperti, *Double edge wedge splitting (DEWS): an indirect tension test to identify post-cracking behaviour of fibre reinforced cementitious composites*. Materials and Structures, 2013. **46**(11): p. 1893-1918.
18. Buratti, N., C. Mazzotti, and M. Savoia, *Post-cracking behaviour of steel and macro-synthetic fibre-reinforced concretes*. Construction and Building Materials, 2011. **25**(5): p. 2713-2722.
19. Babafemi, A.J. and W.P. Boshoff. *Preliminary creep behaviour of polypropylene fibre reinforced concrete (PPFRC) under a high tensile stress*. in *International Conference on Advances in Cement and Concrete Technology in Africa*. 2013. South Africa.
20. Babafemi, A.J. and W.P. Boshoff, *Time-dependent behaviour of pre-cracked polypropylene fibre reinforced concrete (PFRC) under sustained loading*. Research and Applications in Structural Engineering, Mechanics and Computation, 2013: p. 1593-1598.
21. Zhao, G., M. di Prisco, and L. Vandewalle, *Experimental Research and Numerical Simulation of Post-Crack Creep Behavior of SFRC Loaded in Tension*, in *Mechanics and Physics of Creep, Shrinkage, and Durability of Concrete*. 2013, American Society of Civil Engineers. p. 340-347.
22. Kurtz, S. and P. Balaguru, *Postcrack creep of polymeric fiber-reinforced concrete in flexure*. Cement and Concrete Research, 2000. **30**(2): p. 183-190.
23. MacKay, J. and J.F. Trottier, *Post-crack creep behavior of steel and synthetic FRC under flexural loading*, in *Shotcrete: More Engineering Developments*. 2004, Taylor & Francis. p. 183-192.
24. *fédération internationale du béton (fib), Model Code 2010 First complete draft*, 2010.
25. Zhao, G., et al., *Investigation on Single Fiber Pullout and Interfacial Debonding Mechanisms with Acoustic Emission Techniques*, in *8th RILEM International Symposium on Fibre Reinforced Concrete (BEFIB 2012)*, J. Barros, et al., Editors. 2012, RILEM Publications S.A.R.L.: Guimarães, Portugal. p. 111-112.
26. Li, V.C., Y. Wang, and S. Backer, *Effect of inclining angle, bundling and surface treatment on synthetic fibre pull-out from a cement matrix*. Composites, 1990. **21**(2): p. 132-140.
27. Wang, Y., V.C. Li, and S. Backer, *Analysis of Synthetic Fiber Pull-Out from a Cement Matrix*. MRS Online Proceedings Library, 1987. **114**: p. 159-165.
28. Sabuncuoglu, B., M. Acar, and V.V. Silberschmidt, *Analysis of Creep Behavior of Polypropylene Fibers*. Applied Mechanics and Materials, 2011. **70**(8): p. 410-415.
29. Drozdov, A.D. and J.d. Christiansen, *Creep failure of polypropylene: experiments and constitutive modeling*. International Journal of Fracture, 2009. **159**(1): p. 63-79.
30. *EN 14889-2: Fibres for concrete - Part 2: Polymer fibres - Definitions, specifications and conformity*, 2006, European Committee for Standardization.
31. Singh, S., A. Shukla, and R. Brown, *Pullout behavior of polypropylene fibers from cementitious matrix*. Cement and Concrete Research, 2004. **34**(10): p. 1919-1925.

# Using FRP as Reinforcement in Precast Concrete Panels for Soil-Concrete Bridges

Sameh Salib

Adjunct Professor, Civil Engineering Department, Ryerson University, Toronto, Canada

**Abstract:** Concrete is one of the most common construction materials world-wide. However, the corrosion of steel, conventionally used as concrete reinforcement, raises major durability and safety concerns for all types of concrete structures. This presents major risk for bridges as they are directly exposed to weather conditions, and further to the attack of de-icing salts in continents like North America and Europe. Therefore, soil plays a key role in improving the durability of buried concrete structures such as soil-concrete bridges. Besides, these bridges integrate the soil within their structural system which significantly reduces both the cost and time of construction. Yet, the need for steel reinforcement poses a challenging problem to durability. Recently, Fibre-Reinforced Polymers (FRP) are considered viable solution to such problems due to their non-corrosive nature. Herein, an innovative approach of using prefabricated/curved FRP deck units as formwork and reinforcement of precast concrete panels is proposed to form the structure of these bridges. A soil-structure interaction Finite Element Modelling (FEM) has been developed to conduct a parametric study that addresses the bridge structural capacity. This approach promises to introduce superior durability and, moreover, marks a substantial step towards a global sustainability of structures; above and below ground.

**Keywords:** FRP, precast concrete, reinforcement, buried structures, soil-structure interaction.

## 1. Introduction

Concrete is considered one of the first man-made materials to be used for massive construction projects. The utilization of concrete compressive strength in structural elements, subject mainly to compressive forces such as arches, ignited the idea of a three dimensional version of arches in the form of domes. Successfully, the Roman engineers were the first to introduce such approach in a colossal scale as in the 43 m diameter dome of the Pantheon about two millennia ago (1,2). Later, especially during the last few decades, concrete has been used to form structural elements subject to various straining actions like flexure, shear and torsion where significant tensile stresses are induced. Therefore, steel, with its significant tensile strength, is commonly used to reinforce concrete elements in order to provide the required tensile resistance. However, steel corrosion poses a significant threat to both durability and structural safety. Structural steel-reinforced concrete elements exposed to direct weather conditions like bridge decks and girders are severely damaged due to steel corrosion. Despite the billions of dollars spent every year world-wide over inspection, maintenance and repair of reinforced concrete bridges, several catastrophic failures are reported annually due to corrosion-related issues (3,4).

For special types of bridges, e.g. soil-steel and soil-concrete bridges, additional protection against weather conditions is achieved through their top soil cover. Therefore, these bridges are also classified as buried structures. Earlier, Abdel-Sayed and Salib (5) studied the behaviour and strength of soil-steel bridges with relatively long spans (up to 22m) and the recommendations of the study for an optimum depth of soil cover were considered through the Canadian Highway Bridge Design Code 'CHBDC' (6). Yet, steel corrosion still raises durability concerns of such buried structures especially under the attack of severe environmental conditions and de-icing salts in North America and Europe. During the last decade, FRP have been successfully introduced as a non-corrosive reinforcement alternative for bridge decks and girders in various forms such as bars and panels. Further, recently in USA, curved FRP tubes have been used as arch girders for soil-concrete bridges in few pilot bridges where the tubes were filled with concrete on-site and received a cast-in-place concrete layer over FRP corrugated sheets (7,8).

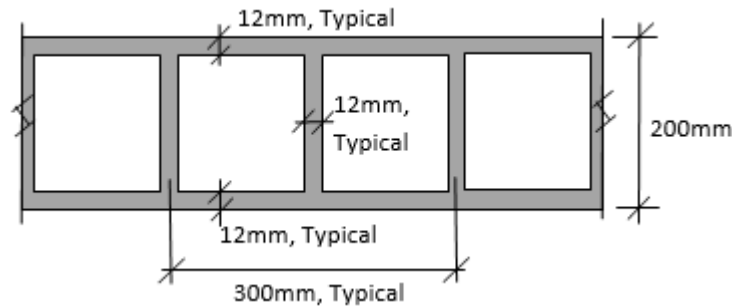
Herein, an innovative approach is proposed to utilize prefabricated/curved FRP deck units, fully or partially filled with concrete, as precast reinforced concrete panels to form the structure of soil-concrete bridges. This approach is encouraged by the recent achievements in producing FRP units with complex three dimensional geometry and curvatures; not only for aero-space industry and transportation vehicles but also for structural engineering applications (9). A FEM has been developed to present the soil-structure interaction of the investigated bridges. Through the developed FEM, a parametric study has been conducted to address the influence of bridge span, depth of soil cover and percentage of panel voids filled

with concrete on the bridge behaviour and strength. The conducted study provides an overall assessment of the performance of such bridges as well as guidelines for their optimum design.

It is believed the presented approach enables high quality control over of the produced structure, significant savings in both schedule and budget of construction and superior durability throughout the service life of the bridge. Moreover, this approach can be a major step towards achieving a substantial sustainability of transportation structures.

## 2. Material Properties

The material properties and cross section dimensions of the investigated Glass FRP (GFRP) deck have been proposed based on various GFRP decks available in the market, fabrication methods and related standards (10). The cross section of the deck is shown in Fig. 1. Also, the material properties of the deck, concrete and soil are listed in the Tables 1, 2 and 3 respectively.



**Fig. 1. GFRP deck cross section dimensions.**

**Table 1. The material properties of GFRP deck.**

Specific Weight (kN/m <sup>3</sup> )	Tensile Modulus of Elasticity (MPa)	Tensile Strength (MPa)	Compressive Strength (MPa)	Transverse Shear Strength (MPa)
18	32000	450	200	180

**Table 2. The material properties of concrete.**

Specific Weight (kN/m <sup>3</sup> )	Compressive Strength (MPa)	Modulus of Elasticity (MPa)
23.5	25	23000

**Table 3. The material properties of soil.**

Soil type	Specific Weight (kN/m <sup>3</sup> )	Angle of Internal Friction, $\phi$ (°)	Cohesion, C (kN/m <sup>2</sup> )
Native Soil	22	40	45
Compacted Granular Backfill	21	35	0

### 3. Live Load

The live load applied in the present study complies with that defined by the CHBDC (6) for the CL-625-ON standard truck as shown in Fig. 2.

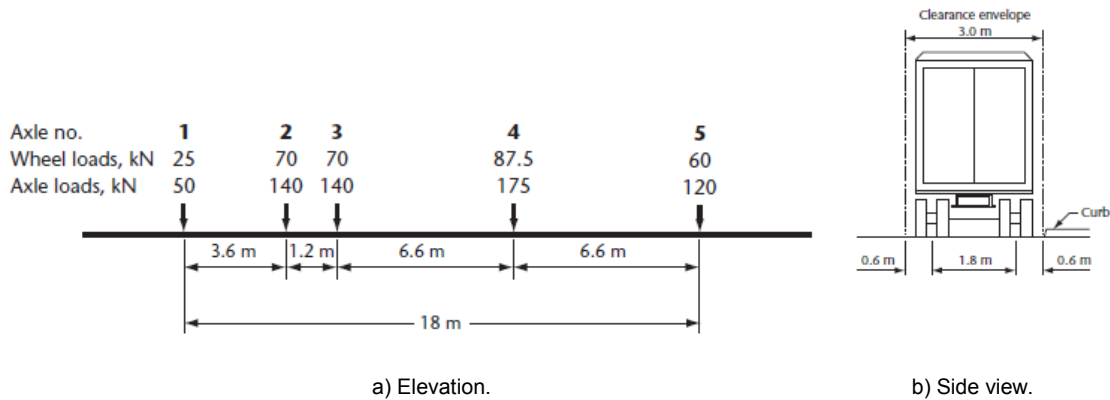


Fig. 2. The CHBDC standard truck 'CL-625-ON' (6).

### 4. Finite Element Analysis (FEA)

#### 4.1 Modelling

A non-linear 2D-FEM has been developed to investigate the subject soil-structure system as shown in Fig. 3. Plate elements and beam elements have been used to model the soil and the concrete-GFRP panels (buried structure) respectively. The structure has a half circle profile with a radius equals the span ( $S$ )/2.

#### 4.2 Investigated Parameters

Four different spans ( $S$ ) have been investigated; 10m, 15m, 20m and 25m. Also, different soil cover ( $h$ ) to span ( $S$ ) ratios are studied; 0.10, 0.15, 0.20, 0.25. These values of  $S$  and  $h/S$  are believed to cover the practical range of span and soil cover of such structures (5). Further, the influence of having half of the GFRP deck voids filled with concrete versus fully filled deck has been evaluated. This influence has been considered to reflect the interaction between the structure self-weight, stiffness and strength.

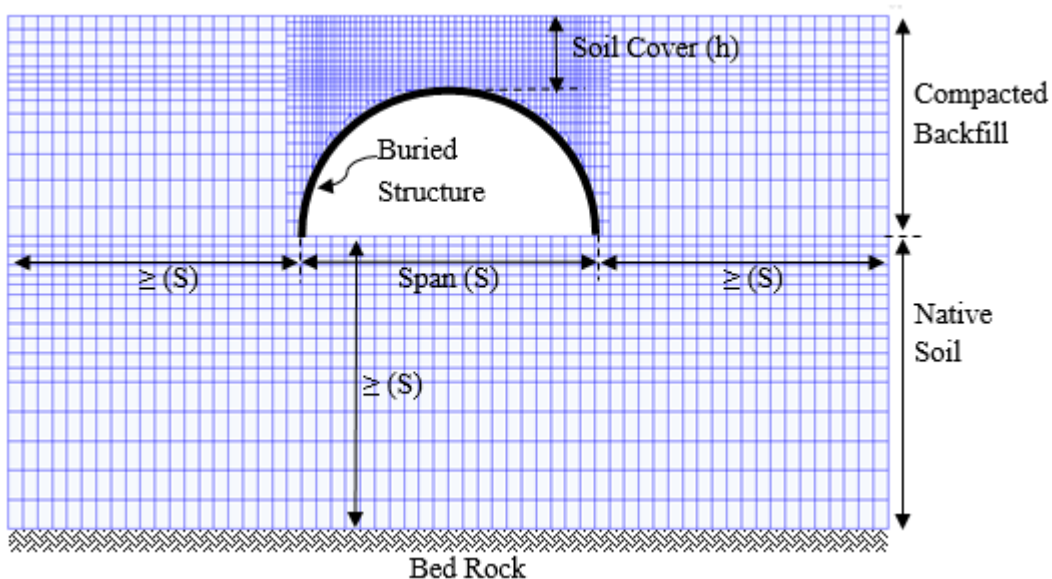


Fig. 3. Finite Element Model (FEM) geometry and materials

### 4.3 Assumptions

The analysis has been performed under the following assumptions:

- The model represents a typical 0.30m width of an infinite bridge width;
- The non-linearity of the soil behaviour is considered through the Drucker-Prager material modelling;
- There is full bond between concrete and GFRP deck;
- The FEM nodes along the model vertical sides are restrained in the horizontal direction while the nodes at the bottom edge are restrained in both horizontal and vertical directions;
- The live load is applied along the model top edge;
- The model represents a 0.30m width of a standard truck lane (i.e. carries 1/10 of the truck loads);
- The transverse distribution of the truck axle loads in the soil is considered with dispersion lines of slope equals 1 (horizontal) to 2 (vertical). Overlapped distributed loads at the level of the structure due to multiple adjacent lanes are considered as well; and
- The load and material strength factors are according to the CHBDC (6).

Also, the investigated soil-structure system is assumed to reach failure if one (or more; almost simultaneously) of the following conditions is satisfied:

- Shear (and/or tensile) failure of soil;
- Tensile failure of GFRP deck;
- Compressive failure of GFRP deck;
- Transverse shear failure of GFRP deck;
- Compressive failure of concrete; and
- Transverse shear failure of concrete.

## 5. Results and Discussion

The stresses induced in the soil-structure system due to the applied loads are obtained by the FEM. Fig. 4 shows an example of the obtained shear stresses in the soil under the own weight of the soil-structure system for a structure having a span ( $S$ ) of 25.0m and soil cover ( $h$ ) of 6.25m, i.e.  $h/S$  ratio of 0.25. For each component of the subject structural system (i.e. soil and concrete-GFRP panels) at each failure condition, the ratio between the factored strength of the component and the corresponding factored stress obtained due to the application of the entire dead and live loads has been calculated. The minimum value of these ratios obtained for each investigated bridge configuration is considered the Factor of Safety (F.S.).

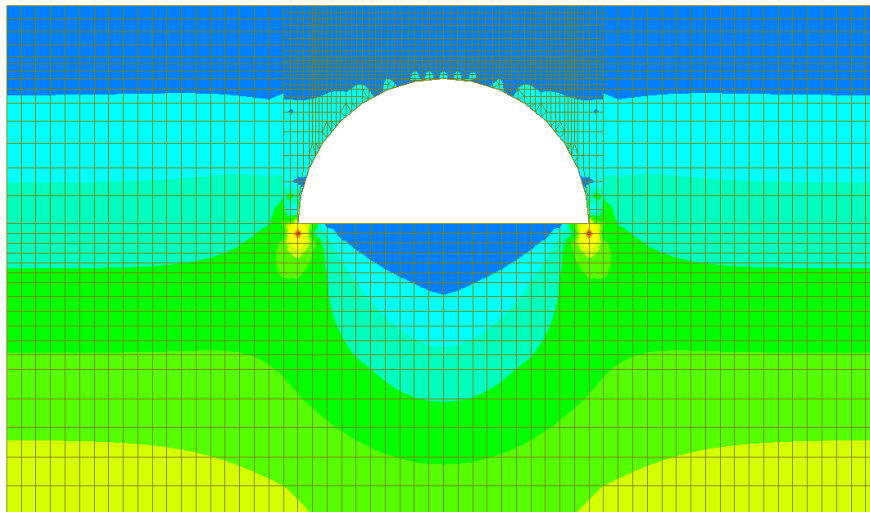


Fig. 4. Contours of maximum shear stress obtained by FEM under self-weight of soil and structure ( $S=25\text{m}$  and  $h=6.25\text{m}$ ).



Tables 4 and 5 list the configuration of each investigated bridge and the obtained failure conditions corresponding to full and half deck voids filled with concrete respectively. Also, the results are illustrated in Figs. 5 and 6.

**Table. 4. Analysis results-full deck voids filled with concrete.**

S (m)	h/S	h (m)	F.S.	Mode(s) of Failure	Location
10	0.1	1	1.02	Soil; Shear-Tension	Top soil cover
15	0.1	1.5	1.11	Soil; Shear-Tension	Top soil cover
20	0.1	2	0.67 < 1.0	Soil; Shear-Tension	Top soil cover
25	0.1	2.5	0.67 < 1.0	Soil; Shear-Tension	Top soil cover
10	0.15	1.5	1.82	Soil; Shear-Tension	Top soil cover
15	0.15	2.25	1.67	Soil; Shear-Tension	Top soil cover
20	0.15	3	1.18	Soil; Shear-Tension	Top soil cover
25	0.15	3.75	1.25	Soil; Shear-Tension	Top soil cover
10	0.2	2	3.33	Soil; Shear-Tension	Top soil cover
15	0.2	3	2.25	Concrete/FRP; Compression	At Foundations
20	0.2	4	1.41	Concrete/FRP; Compression	At Foundations
25	0.2	5	1.02	Concrete/FRP; Compression	At Foundations
10	0.25	2.5	3.21	Concrete/FRP; Compression	At Foundations
15	0.25	3.75	1.88	Concrete/FRP; Compression	At Foundations
20	0.25	5	1.25	Concrete/FRP; Compression	At Foundations
25	0.25	6.25	0.87 < 1.0	Soil; Shear-Tension	At Foundations

**Table. 5. Analysis results-half deck voids filled with concrete.**

S (m)	h/S	h (m)	F.S.	Mode of Failure	Location
10	0.1	1	0.91 < 1.0	Soil; Shear-Tension	Top soil cover
15	0.1	1.5	1.05	Soil; Shear-Tension	Top soil cover
20	0.1	2	0.77 < 1.0	Soil; Shear-Tension	Top soil cover
25	0.1	2.5	0.61 < 1.0	Soil; Shear-Tension	Top soil cover
10	0.15	1.5	1.67	Soil; Shear-Tension	Top soil cover
15	0.15	2.25	1.43	Soil; Shear-Tension	Top soil cover
20	0.15	3	1.03	Soil; Shear-Tension	Top soil cover
25	0.15	3.75	0.87 < 1.0	Concrete/FRP; Compression	At Foundations
10	0.2	2	2.81	Concrete/FRP; Compression	At Foundations
15	0.2	3	1.61	Concrete/FRP; Compression	At Foundations
20	0.2	4	1.02	Concrete/FRP; Compression	At Foundations
25	0.2	5	0.75 < 1.0	Concrete/FRP; Compression	At Foundations
10	0.25	2.5	2.25	Concrete/FRP; Compression	At Foundations
15	0.25	3.75	1.32	Concrete/FRP; Compression	At Foundations
20	0.25	5	0.87 < 1.0	Concrete/FRP; Compression	At Foundations
25	0.25	6.25	0.63 < 1.0	Concrete/FRP; Compression & Soil; Shear-Tension	At Foundations

It can be seen that filling the entire deck voids with concrete has, in general, a positive impact on improving the overall strength (i.e. higher values of F.S.) and eliminating the compressive failure of the concrete-GFRP panels. On the other hand, increasing the soil cover (h) to span (S) ratio results in soil and/or structure failure for relatively large spans. This observation can be interpreted as the associated significant increase of soil weight carried by the soil-structure system utilizes most of the system capacity with little or no reserve left to accommodate the applied live load. Similar behaviour was reported by Abdel-Sayed and Salib (5) and Abdel-Sayed et al. (11) for soil-steel bridges.

From the construction cost perspective, a value of F.S. just above 1.0 can be looked at as an indication to the optimum usage of material that achieves a safe design. In this case, for relatively large spans (20m to 25m), h/S ratio of 0.15 along with a GFRP deck fully filled with concrete achieves an optimum design with an F.S. value around 1.2 (Fig. 5). Further, the same h/S ratio (i.e. 0.15) provides an optimum design for relatively short spans (10m to 15m) with a value of F.S. equals approximately 1.5 when the GFRP deck is half filled with concrete (Fig. 6).

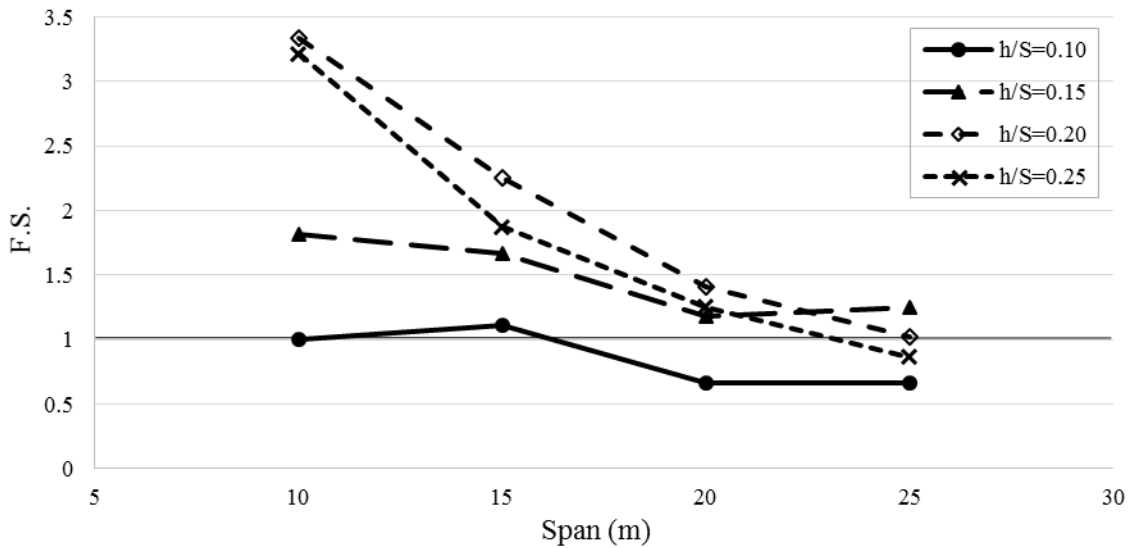


Fig. 5. Factor of safety-full panel voids filled with concrete.

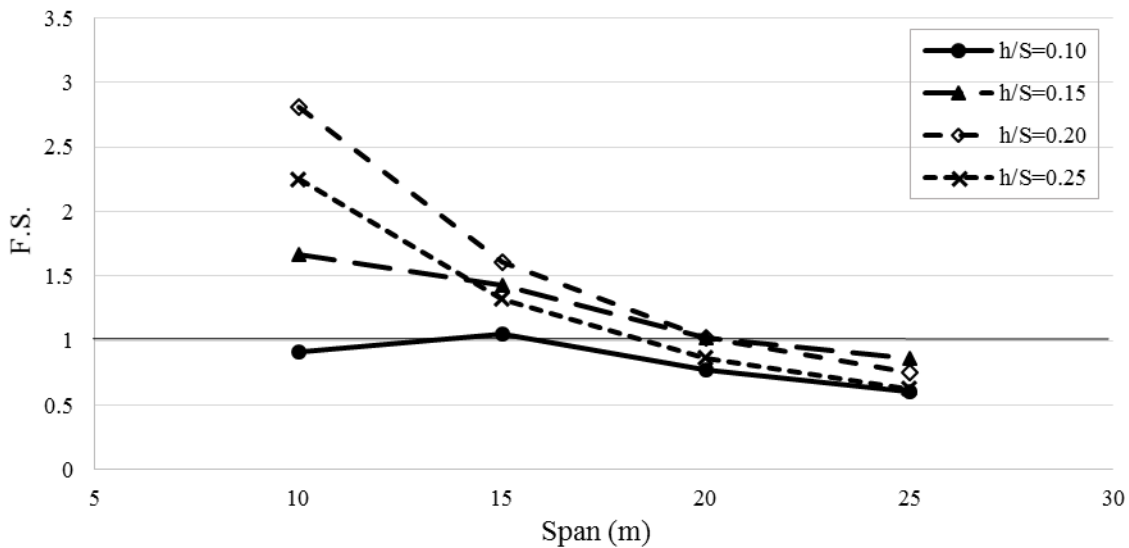


Fig. 6. Factor of safety-half panel voids filled with concrete.

## 6. Proposed Future Research

Few research programs have been dedicated to address the buckling of GFRP structural sections (12,13). Based on the available data, it is believed that the investigated concrete-GFRP panels should not experience global or local buckling prior to the considered modes of failure. However, it is recommended that future studies investigate this aspect in more details for verification purposes. Also, the influence of major structural behaviour and buckling parameters of the GFRP deck such as the modulus of elasticity, the depth and the thicknesses of both webs and flanges can be studied for further design refinement and cost optimization.

## 7. Conclusions

The paper presented an innovative approach to utilize prefabricated GFRP curved deck units, fully or partially filled with concrete, as precast reinforced concrete panels to form the structure of soil-concrete bridges. Based on the investigated configurations and the corresponding results of the conducted analysis, the following conclusions can be obtained:

- Filling the GFRP deck with concrete has significant improvement of the overall structure strength and eliminates the compressive failure of the concrete-GFRP panels;
- Increasing the top soil cover to span ratio does not necessarily increase the capacity of the soil-structure system. Further, ratios larger than 0.15 can cause soil and/or structure failure especially for relatively large spans;
- An optimum design can be achieved with top soil cover to span ratio around 0.15 along with panels fully filled with concrete for relatively large spans and partially filled panels for shorter ones;
- The presented approach enables high quality control over of the produced structure, significant savings in both schedule and budget of construction and superior durability through the service life of the bridge. Moreover, it is believed that this approach can be a major step towards achieving a substantial sustainability of such type of transportation structures; and
- Future research, especially in the area of GFRP deck buckling, can lead to further verification and optimization of the presented design.

## 8. References

1. Ward-Perkins, J. B., "Roman Imperial Architecture", Penguin Books, 1985, New York, USA.
2. Cowan, W., "The Master Builders", John Wiley and Son, 1977, New York, USA.
3. National Association of Corrosion Engineers, "Corrosion Control Plan for Bridges", NACE International, 2012, Houston, USA.
4. National Association of Corrosion Engineers, "Control of External Corrosion on Underground or Submerged Metallic Piping Systems", NACE International, 2007, Houston, USA.
5. Abdel-sayed, G. and Salib, S., "Minimum Depth of Soil Cover for Soil-Steel Bridges", ASCE Journal of Geotechnical and Geoenvironmental Engineering, 128(8), 2002, pp 672-681.
6. Canadian Standards Association, "Canadian Highway Bridge Design Code (CAN/CSA-S6)", CSA Committee S6, 2006, Mississauga, Canada.
7. Dagher, H. J., Bannon, D. J. et al., "Bending behavior of concrete-filled tubular FRP arches for bridge structures", Journal of Construction and Building Materials, 37, 2012, pp 432-439.
8. American Association of State Highway and Transportation Officials, "Guide Specifications for Design of Concrete-Filled FRP Tubular Arches for Flexural and Axial Members", AASHTO, 2012, Washington, USA.
9. Gelbrich, S., Ehrlich, A. et al., "Flexible Fibre Reinforced Plastic Formwork for the Production of Curved Textile Reinforced Concrete Structures", Proceedings, The 7<sup>th</sup> International Conference on FRP Composites in Civil Engineering (CICE 2014), Vancouver, Canada.

10. Harries, K. A., and Moses, J., "Replacing a Composite RC Bridge Deck with an FRP Deck- The Effect on Superstructure Stresses", Proceedings, Asia-Pacific Conference on FRP in Structures (APFIS 2007), Hong Kong, China.
11. Abdel-sayed, G., Bakht, K. et. al., "Soil-Steel Bridges-Design & Construction", McGraw-Hill Inc., 1994, New York, USA.
12. Laudiero, F., Minghini, F. et al., "Finite Element Buckling and Postbuckling Analysis of Pultruded FRP I-Section Columns", Proceedings, The 15<sup>th</sup> European Conference on Composite Materials (ECCM 2012), Venice, Italy.
13. Feng, P., Qian, P. et al., "Analysis of global buckling of FRP pipes under axial compression", Proceedings, The 4<sup>th</sup> International Conference on FRP Composites in Civil Engineering (CICE2008), Zurich, Switzerland

# Torsional Strengthening of Concrete Members Using Near-Surface Mounted CFRP Composites

G. Al-Bayati<sup>1</sup>, R. Al-Mahaidi<sup>2</sup> and Robin Kalfat<sup>3</sup>

<sup>1,2,3</sup>Faculty of Science, Engineering and Technology, Swinburne Institute of Technology  
PO Box 218, Hawthorn, Victoria, 3122, Australia.

<sup>1</sup>galbayati@swin.edu.au, College of Engineering, University of Baghdad, Al Jadriya, Baghdad, Iraq.

<sup>2</sup>ralmahaidi@swin.edu.au, <sup>3</sup>rkalfat@swin.edu.au

**Abstract:** To increase the strength of concrete members, numerous research studies on flexure and shear have been reported using carbon fibre-reinforced polymer (CFRP) with the near-surface mounted (NSM) strengthening technology, as it is considered a promising technology. However, to date research on torsional strengthening has been provided only for the externally-bonded reinforcement technique (EBR) and no studies have been conducted on NSM strengthening technology. In this paper, reinforced concrete (RC) beams with CFRP are considered and ATENA software is used to build a 3-D model of the beams and to analyse the beam structure. Finite element and experimental results of the control beam and beams strengthened for torsion with CFRP sheets using the EBR technique are compared. Further computer analysis of beams strengthened with CFRP laminate using the NSM strengthening technology is achieved by considering many parameters. The type of the adhesive, the method of strengthening, and the spacing between the grooves were examined. The performances of the beams and the ultimate strengths of the control and beams strengthened using the EBR technique were predicted with high accuracy by the models employed. According to the results for the beams strengthened using the NSM technique, the overall torsional behaviour of the beams with CFRP was improved by different percentages and the beams became stronger.

**Keywords:** Torsion, FRP laminate, strengthening, NSM, concrete beam, ATENA 3-D

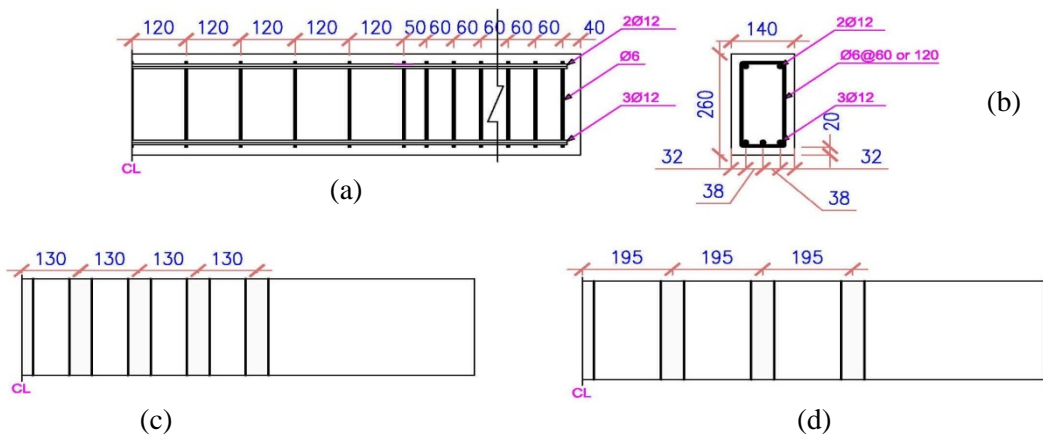
## 1. INTRODUCTION

Reinforcement concrete members may be presented with torsion in combination with bending and/or shear. Strengthening for torsion with carbon fibre reinforced polymer (CFRP) composite material has become an important matter and could be essential for members subjected to a torsional force (1). For torsional strengthening along with shear strengthening of concrete beams, CFRP materials can be applied by the following two major techniques: externally-bonded FRP sheets and strips applied to the external faces of the elements, and near-surface mounted (NSM) (2). Many configurations have been used to evaluate the contributions of external transverse FRP reinforcements applied to beams with rectangular cross-sections, such as full wrapping and U-jacketing (3). Hii and Al-Mahaidi (4) carried out an experimental study to examine the torsional behaviour of three solid reinforced concrete (RC) beams with vertical strips of FRP using the externally-bonded reinforcement (EBR) technique. The beams were 2700 mm long and 140 × 260 mm in cross-section. The results of this study showed that the use of EBR CFRP is applicable for the torsional strengthening of RC beams and it can increase the strength by a good percentage, depending on the spacing between the strips. Disregarding the increase in strength and ductility, the use of the U-jacket FRP strengthening technique is quite practical for most existing beams (Salom et al.(5)). Ameli et al. (6) tested four rectangular cross-section beams strengthened with U-jackets along the entire beam and U-jacket strips. The results were compared with full wrapping along the entire beam and strips. They found that the ultimate torque of the beams with the U-jacket strengthening technique can be increased by an acceptable percentage. However, the ultimate strengths for the full-wrap technique, were much higher than for the U-jacket technique. Early de-bonding has become a major issue in the EBR CFRP strengthening technique. To reduce this problem, the near-surface mounted (NSM) technique (Nanni et al. (7) provides greater resistance to de-bonding, and it has the ability to reduce the possibility of harm resulting from mechanical damage, fire, and vandalism. Many studies using epoxy adhesive as a bonding material have indicated that the NSM technique is feasible and beam strength capacity can be increased significantly compared with EBR application (Barros and Dias (8)). Because of the problems of epoxy with elevated temperature, cement-based adhesive has been used as an alternative bond material to epoxy. The first use of cement-based adhesive with the NSM technique was reported by Al-Abdwais and Al-Mahaidi (9).

The use of carbon fibre-reinforced polymer (CFRP) laminates with the NSM technique is one of the methods suggested for the strengthening and rehabilitation of concrete members. Both types of bonding agent, epoxy and cementitious adhesive, can be used to improve the torsional behaviour of RC members. In this paper, the experimental result of Hii and Al-Mahaidi (4) are compared with the FE analysis results using ATENA 3-D software in order to simulate and gain further understanding of the beams' behaviour and to validate the numerical modelling. Additional numerical analysis for beams strengthened with CFRP laminate using the NSM strengthening technology is reported for both epoxy and cement-based adhesive.

## 2. EXPERIMENTAL WORK

Three RC beams with 140 × 260 mm cross-section and a middle test zone of 1200 mm were constructed and tested by Hii and Al-Mahaidi (4). The concrete compressive strength of the concrete on the testing day was 51.3 MPa. The cover of the concrete was 20mm all round. All three beams were identical in the layout of the internal steel reinforcement. 12 mm diameter bars were used for the longitudinal steel, and two were at the top, while the bottom steel included three 12mm diameter bars. The diameter of all stirrups was 6 mm. The spacing between the stirrups in the test zone was 120 mm, while to avoid unwanted failure outside the test zone, the spacing was decreased to 60mm. The steel reinforcement properties are presented in Table 1. The beams were designed according to Australian code AS3600-2001 (10), and were intended to be deficient in torsion under new loading requirements. The first beam, C1, was the control beam, where no strengthening technique was applied. The second and the third beams were strengthened with CFRP sheet strips using the EBR strengthening technique. CFRP single layer hoop strips 50 mm wide were used to increase the torsional capacity for the second beam (F1) and the third beam (F2). The spacing between the strips was 130 mm centres, which is 0.5 of the full depth of beam (D) for the second beam. However, it was 195mm (0.75D) for the third beam. The beam dimensions, the steel reinforcement details, and the strengthening schemes are illustrated in Figure 1.



**Figure 1. (a) Side view of half of the beam, (b) beam cross-section, (c) strengthening for beam F1, (d) strengthening for beam F2.**

**Table 1. Steel properties**

Property	Area (mm <sup>2</sup> )	E (MPa)	Yield strength (MPa)	Ultimate strength (MPa)
Longitudinal Ø12	113.1	216000	600	733
Vertical Ø6	28.3	222000	450	515

The CFRP sheet and the resin were supplied by Master Builder's Technologies (MBT 2002), and the MBrace Application Guidelines (MBT 2003) were followed to apply it. The beams were tested using a special test rig and the results as shown in Figure 2.

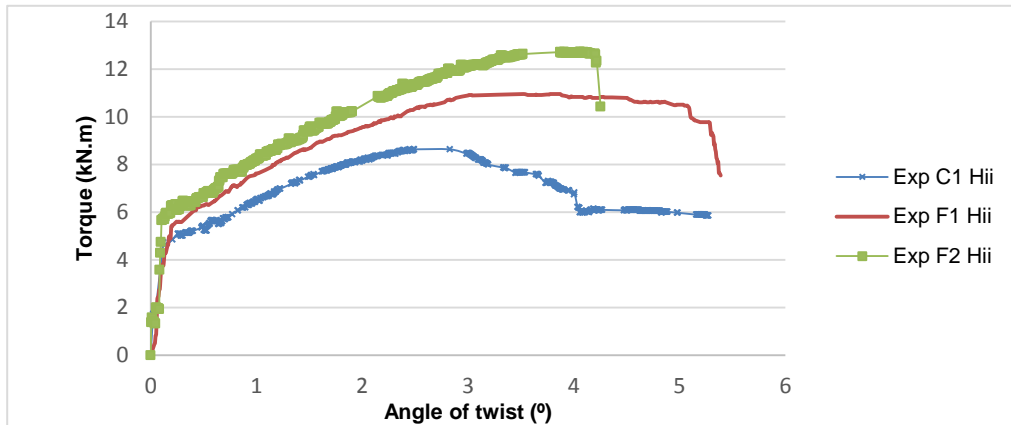


Figure 2. Torque-twist curves for control and strengthened beams (Hii and Al-Mahaidi)

### 3. FINITE ELEMENT ANALYSIS

In order to shed further light on the torsional behaviour of RC beams strengthened with EBR FRP, examine the modelling reliability, and provide a parametric study, non-linear finite element (FE) analysis was carried out using the ATENA 3-D software (Cervenka and Cervenka (11)). The data from parametric analysis can be used to identify future experimental work and provide advance understanding of the theories. The formulas recommended by CEB-FIP Model Code 90 have been adopted in this software to define the structural material and geometry. Figure 3 presents the complete uniaxial stress-strain results for concrete and mortar and the numbers 1-4 in this diagram are used in the results analysis for denoting the cases of damage. Figure 4 shows exponential crack opening law, whereas the area under the curve is a shear retention factor. To constitute the structural geometry for the beams using ATENA 3-D, basic steps taken during pre-processing should include: material properties, geometrical model, supports and actions, finite element mesh, and solution procedure.

3-D Nonlinear Cementitious is a fracture plastic model in ATENA 3-D used for brittle materials such as concrete and mortar. The 3-D elastic isotropic model is a suitable choice to model the test steel arm and the steel plates around the beams at each end to avoid any unrealistic stress concentration at the loading and support regions (Cervenka (12)). Reinforcement material can be used to define both steel and FRP material properties and the stress-strain laws for the steel and FRP are presented in Figure 5. 3-D interface material was used to define the contacts between the adhesive (mortar or epoxy) and the concrete. Three-dimensional solid regions called macro-elements with a higher order sophisticated 20-node brick element can be used in ATENA 3-D to model the geometry of the specimens. This element shows better numerical stability and convergence rates at higher load levels. Concrete and mortar and the steel arm and plates were modelled using this 20 node iso-parametric solid brick element with 120 degrees of freedom. The reinforcement pars elements were used in ATENA 3-D to model both the horizontal and vertical steel reinforcements.

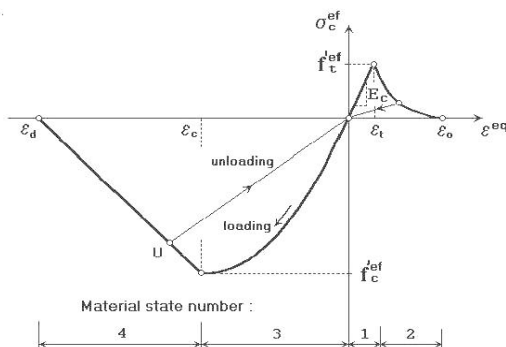


Figure 3. Uniaxial stress-strain for concrete and mortar (Cervenka et al. (13)).

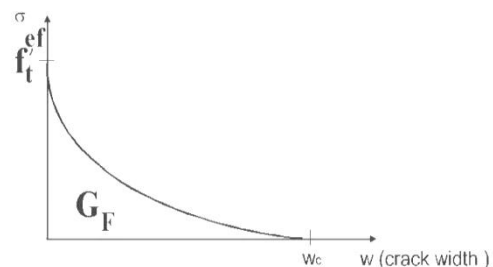
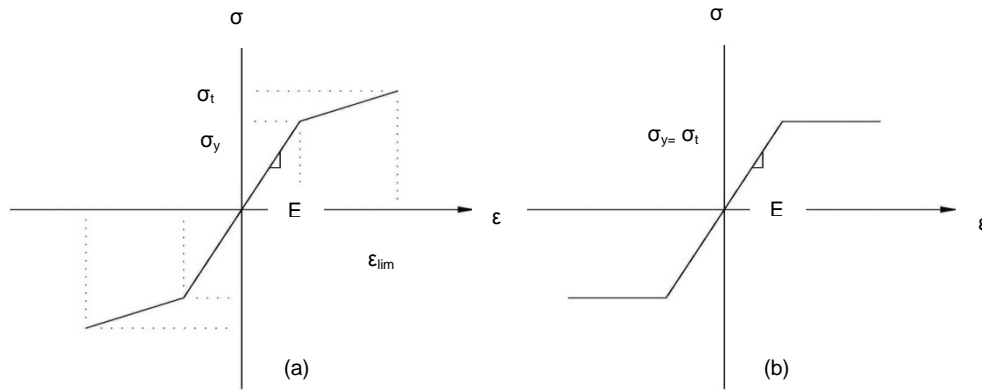


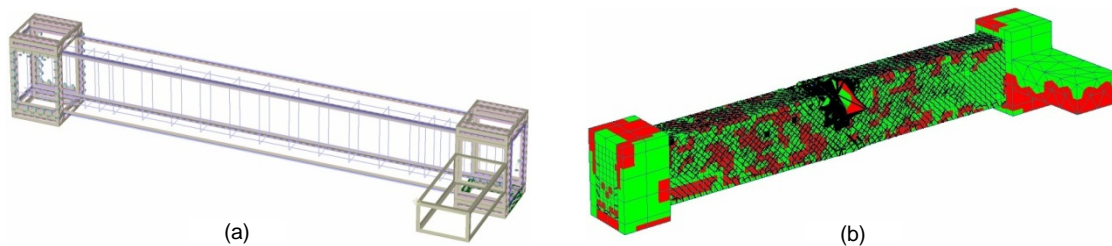
Figure 4, exponential crack opening law and shear retention factor (Cervenka et al. (13)).



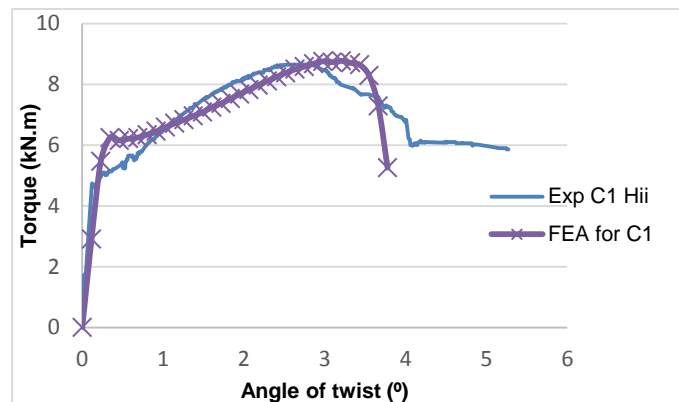
**Figure 5. Stress-strain law for: (a) steel reinforcement bars, (b) the CFRP laminate.**

Brick elements were created for the beam and an adequate mesh size was selected to make the analysis satisfactory. The Newton-Raphson method provided in ATENA 3-D was applied as the non-linear finite element solution method using displacement control to predict the numerical behaviour. The designated displacement per load step size was defined as 0.001m, which is equal to angle 0.11°. Displacement, residual and energy errors were found by assigning convergence criteria, and they were 0.01 for displacement error, 0.01 for residual error, and 0.0001 for energy error. A good compromise between the time and the accuracy was achieved by using these values. The load was applied on the end of the beam and the boundary conditions were used to simulate the experimental test.

The numerical model in Figure 6 (a) was adopted for control beam C1. Non-linear FE analysis was carried out using the ATENA 3-D computer program, as presented in Figure 6 (b). The results of the numerical analysis were compared with the experimental results. Figure 7 shows the torque-rotation curves for control beam C1. From the experimental and FE results, it is clear that the stiffness and ultimate failure load are captured with reasonable accuracy with excellent approximation to the experimental ultimate strength. The overall ultimate load was 1.1% lower than the experimental value. The failure mode and the crack pattern matched the experimental results. A good correlation between the experimental and numerical results is also achieved. Therefore, this model was used for the base in the F1 and F2 models.



**Figure 6. FE model of control beam , (a) microelements and the reinforcement bar model, (b) failure model.**



**Figure 7. Torque vs. rotation curves for beam C1 (numerical and experimental analysis).**



### 3.1 EBR MODELLING

Numerical models have been presented in this paper to compare the overall torsional performance in order to check the validity of the FRP modelling, the beams strengthened with the EBR FRP strips (beam F1 and F2) were numerically modelled and analysed prior to undertaking the parametric studies. The base model for beam C1 was strengthened with FRP strips with 135mm spacing for F1 and 195 mm for F2, as shown in Figure 8.

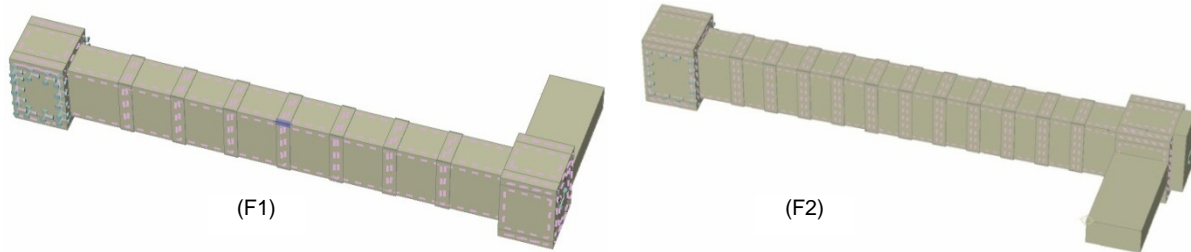


Figure 8. FE model for beams F1 and F2.

The FRP-epoxy layer was modelled using 3-D brick elements with 2 mm thickness around the beam cross-section. The 3-D linear elastic isotropic material was assigned to this layer using epoxy properties, and the FRP was defined as embedded FRP using the smeared reinforcement method. The FE predictions for torque-rotation responses for beams F1 and F2 are presented in Figure 9 and 10 respectively and compared with the experimental responses. These figures show that good correlations were accomplished with FE predictions. The predicted ultimate loads were higher than the experimental values by 6.6% for beam F1 and 1.5% for beam F2. Spiralled large cracks formed near the FRP strip before the failure of the beams, which provides a good correspondence to the experimental failure mode and crack patterns.

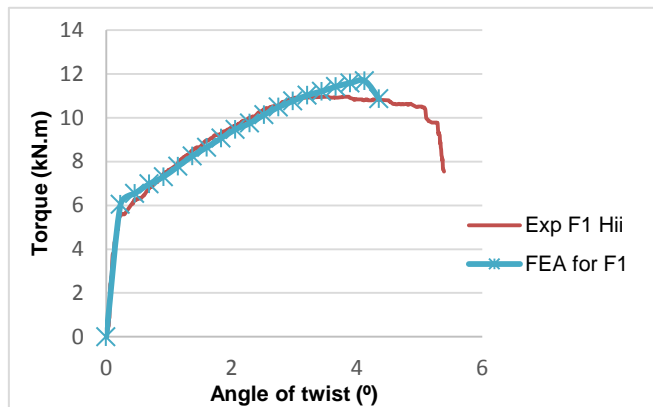


Figure 9. Torque vs rotation curves for beam F1 (numerical and experimental)

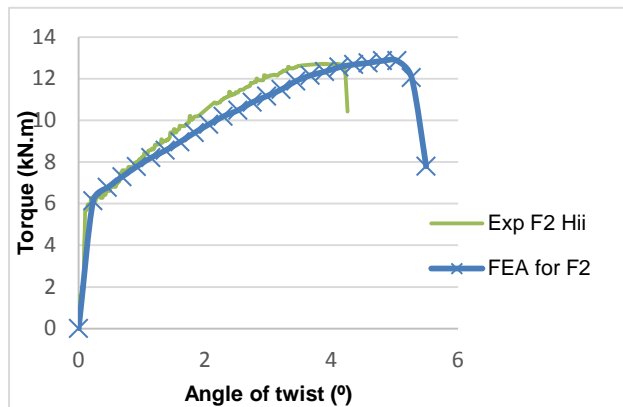


Figure 10. Torque vs rotation curves for beam F2 (numerical and experimental)

### 3.2 NSM MODELLING

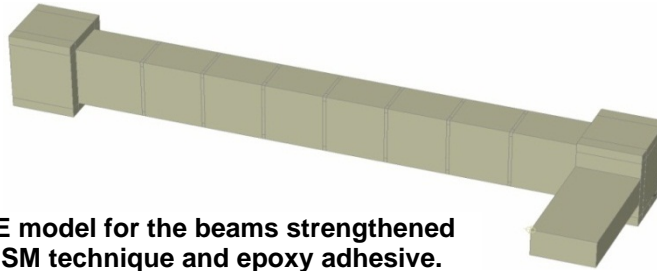
To the authors' knowledge, to date no theoretical or experimental studies have been carried out using the NSM technique to strengthen beams against torsion. The NSM technique can be used to strengthen beams against torsion by making grooves around the concrete cross-section in the concrete cover, and installing CFRP strips into the grooves using a bonding material.

From the previous numerical analysis, the validity of the FE models has been confirmed. In the following section, the same FE modelling steps are used to model the beams strengthened using the NSM technique, and the results of the parametric study are reported. The data from parametric analysis can be used to identify future experimental work by predicting the performance of the beams. It can also provide further understanding of torsional theories and provide data to develop theoretical models and design guidelines. Several parameters from many options of groove spacing and FRP configurations have been

selected and the results are presented and discussed. Both epoxy resin and cement-based adhesives were used as the bonding agent in this parametric study.

### 3.2.1 EPOXY

A new geometry was modelled for the beam by adding grooves around the beam cross-section with the same material properties and boundary conditions as the beam, as illustrated in Figure 11. The groove dimensions were 5 mm wide and 18 mm deep in the concrete cover (ACI 440.2R-2008(14)). It was known from the previous results that using the smeared model with FRP provides good results when the adhesive is epoxy. Therefore, 3-D brick elements filled the grooves as an epoxy adhesive material and the FRP was assigned as embedded FRP using the smeared reinforcement method. ATENA Interface elements were used to define the contact surface between the epoxy and the concrete.



**Figure 11. FE model for the beams strengthened using the NSM technique and epoxy adhesive.**

Many parameters were considered in this part of the study. First, it was assumed that the CFRP laminate strips were used and no connection between the laminate strips at the beam corners was achieved. The same FRP percentage as that in beam F1 was calculated and used with 195 mm spacing between the strips in the first FE model. The accomplished ultimate load was 6.5 % less than the value of the EBR model with a similar behaviour; a loss in the pre-cracking and cracking stiffness of the beam was also observed, where making the grooves around the beam may have been the reason. As it was not possible to apply the same FRP percentage in the groove and also to increase the FRP confinement efficiency, second and third beams were analysed with 97.5 mm strip spacing. To provide the same total FRP percentage per meter length, half FRP percentage was applied in each groove. The ultimate load in this case was almost similar to the EBR model value with more ductility. To provide the double FRP percentage per metre length, full FRP percentage was applied in each groove. The ultimate load in this case was 8.5% more than the EBR model value and a more ductile behaviour was revealed. The results of the three cases and the comparison with the EBR model result are presented in Figure 12.

For the EBR technique, it has been reported that complete wrapping around the cross-section is important to increase the torsional capacity of the beam (Ghobarah et al. (3); Mohammadzadeh et al. (15)). Two further FE analysis approaches were conducted to exhibit the difference in the results between the continuous FRP and non-continuous FRP at the beam corners. In the first analysis, small FRP sheet patches (50 × 50mm) were applied at each corner of the beam to increase the connection between the two embedded laminates in the adjacent beam faces, as shown in Figure 13. The second FE analysis was achieved by replacing the non-continuous laminate by equivalent continuous FRP rope. However, a bigger groove size needs to be used for the FRP rope in practice. The results for the two FE analysis cases compared with the previous FE case (non-continuous FRP) are presented in Figure 14. The comparison shows that small improvements in the ultimate loads of about 6.1 and 3.6 percentages were accomplished for the first and the second FE cases respectively.

Many existing beams in practice do not allow complete strengthening around the beams. To simulate this case, another FE model was implemented and analysed with U-jacketed NSM FRP laminate (three faces). The grooves were made on the bottom and both vertical sides of the beam cross-section. The comparison with the result of full groove wrapping is demonstrated in Figure 15. Although the ultimate load dropped by 3.11%, it was 20.6% more than the ultimate load of the control beam model.

### 3.2.2 CEMENT-BASED ADHISIVE

Because of the problems of epoxy with elevated temperature and the hazardous toxic fumes, the use of cement-based adhesive as an alternative bond material has become important in some cases.

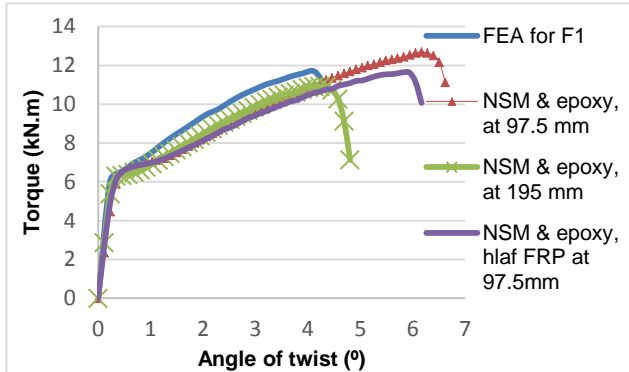


Figure 12. Torque vs. rotation curves for beam F1 (NSM and EBR models comparison).

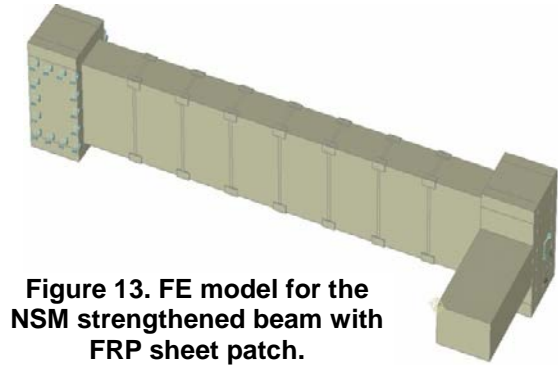


Figure 13. FE model for the NSM strengthened beam with FRP sheet patch.

The FRP modelling in the previous section using the smeared model provides a good correlation with the experimental work when the adhesive is epoxy, as there is no bond slip failure observed with the NSM strengthening technique (Dias and Barros (16)). However, a clear bond slip failure mode has been observed in experimental work using cement-based adhesive as the bonding agent (Al Bayati and Al-Mahaidi (17)). In order to model the cementitious mortar, the bond slip model for the CFRP laminate with modified cement-based adhesive proposed by Al Bayati and Al-Mahaidi (17) was adopted in this modelling. The CFRP laminate was modelled as discrete bars near the concrete surface with the area coinciding with the total CFRP cross-section (Pryl and Cervenka (18)), and the bond slip model was applied to these bars. Figure 16 shows the FE model for the beam strengthened using NSM and cement-based adhesive.

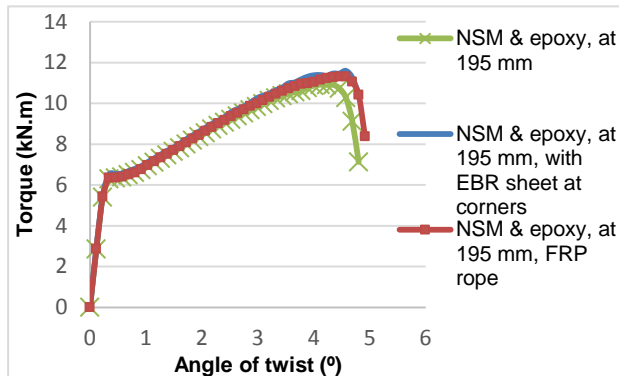


Figure 14. Torque vs. rotation curves for beam F1 (NSM continuous and non-continuous comparison).

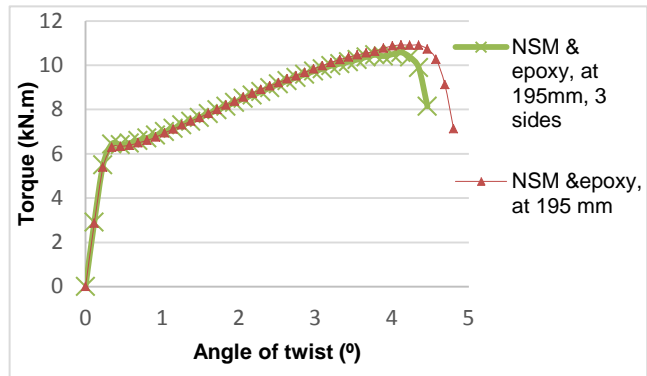


Figure 15. Torque vs. rotation curves for beam F1 (NSM full groove wrapping and U-jacket).

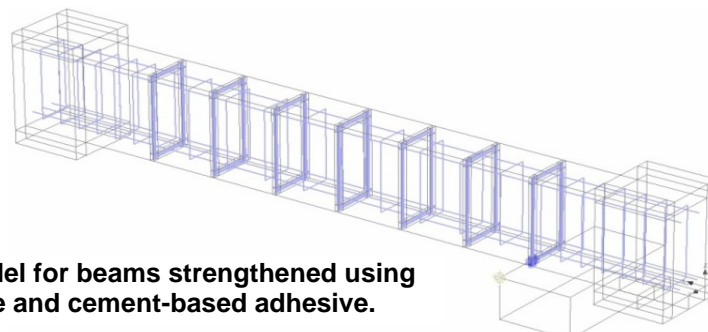
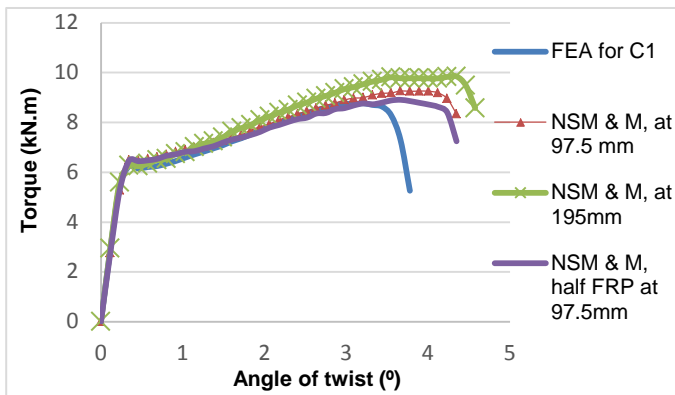


Figure 16. FE model for beams strengthened using NSM technique and cement-based adhesive.

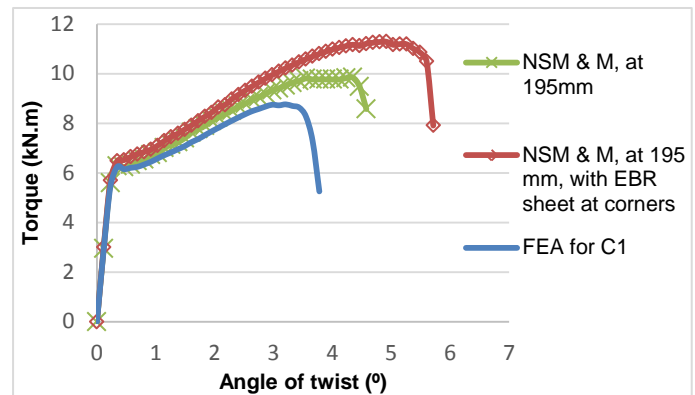
Many parameters were taken in consideration in this stage of the study. First, the same CFRP percentage used in EBR technique was used with mortar. The full percentage of CFRP was applied in the grooves of 195mm and 97.5 mm spacing. For the grooves of 97.5 mm spacing, double percentage per meter length was provided. Also, half FRP percentage in each groove (full percentage per meter length) was applied in the grooves with 97.5 mm spacing. The FE results of the three cases were drawn and contrasted with FE analysis of the control beam C1, and the results are displayed in Figure 17. As the figure shows, increases of 11.9% and 5.6% were obtained using full FRP percentages at 195 mm and 97.5 mm spacing respectively. However, only 1.6 % was obtained using the half FRP percentage in each groove at 97.5 mm spacing with an increase in the ductility of the beam. The mortar experienced less adhesive strength than epoxy, and increasing the groove numbers per meter length may reduce the whole stiffness of the beam, leading to reduced beam strength.

In order to investigate the effect of increasing the connection at the beam corners, a new FE analysis was accomplished for the beam strengthened using the NSM technique, cement mortar, and small FRP sheet patches (50x50 mm) applied at the each corner of the beam. These patches were intended to increase the connection between the laminate around the beam cross-section, but this does not simulate the real case of applying continuous FRP around the beam cross-section. The results were evaluated and compared with those for the control beam and non-continuous laminate strengthened beam, as shown in Figure 18. The figure shows improvement of about 15% for the strengthened beam and by 28.7% for the control beam.

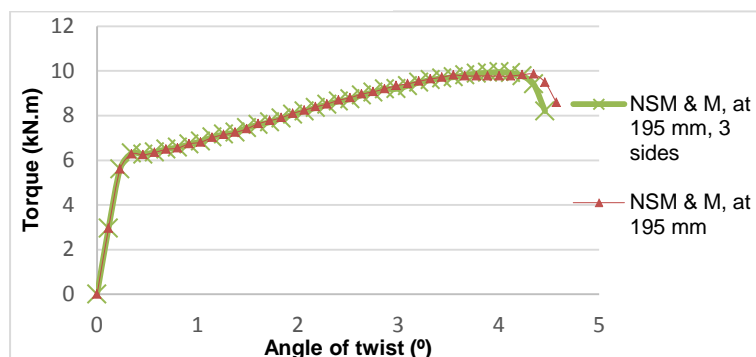
In order to simulate the practical case, U-jacketed NSM CFRP laminate (three faces) was applied on a new beam FE model. The results for the comparison with the result of full groove wrapping appear in Figure 19. The comparison shows a slight difference between the two cases (three and four face strengthening), which may indicate the type of beam failure. It is assumed that the four-face strengthened beam failed before the top laminate involved in the strengthening, which again indicates the less adhesive property of the mortar.



**Figure 17. Torque vs. rotation curves for beam C1 and strengthened beams with mortar (M), (half FRP% at 195 mm and full FRP% at 97.5, 195 mm).**



**Figure 18. Torque vs. rotation curves for beam C1 and strengthened beams with mortar (M), (half FRP% at 195 mm with and without corner sheet).**



**Figure 19. Torque vs. rotation curves for strengthened beams with mortar (M), (full groove wrapping and U-jacket).**

## 6. Conclusions

Numerical models have been presented in this paper to compare the overall torsional performance with the experimental results of RC beams strengthened with EBR CFRP sheet, and to predict the torsional behaviour of RC beams strengthened with NSM CFRP laminate using the ATENA 3-D computer program. According to the numerical results presented in this study, the main conclusions are as follows:

- 3-D finite element models are capable of simulating the performance of beams strengthened for resistance to torsion. The model results were successfully compared with the experimental data and provided good predictions for all tested beams.
- The influence of several parameters was predicted, the results were evaluated for both types of adhesives, and the following conclusions are indicated:-
  - It appears that using the same FRP percentage with less spacing between the grooves was effective for epoxy, and provides more improvement in the ductility and torsional strength, as more confinement is supplied to the beam. However, this is not the case if the bonding agent is not sufficiently strong.
  - The need to increase the connections at the beam corners between the two embedded laminates into adjacent faces was not effective enough with epoxy as the highly confined adhesive already provided, but it was more effective with the mortar. In practice, using FRP rope with mortar may be more efficient. However it may require different groove size. Further investigation is needed in this area.
  - Three-sided strengthening with NSM CFRP shows a significant reduction in the ultimate strength with epoxy.
- Further investigation is needed for developing and determining the mortar characteristics to increase the CRRP contribution in strengthening. It is recommended that future experimental torsion tests of beams strengthened using the NSM technique should consider the current results in choosing the CFRP configurations.

## 7. Acknowledgement

The scholarship support provided to the first author by Higher Committee for Education Development in Iraq (HCED) is gratefully acknowledged.

## 8. References

1. Irwin, R. and Rahman, A. (2002), "FRP strengthening of concrete structures—design constraints and practical effects on construction detailing", Available: Science Direct, [www.sciencedirect.com](http://www.sciencedirect.com). [Accessed September, 2009].
2. Hag-Elsafi, O., Lund, R. and Alampalli, S. (2002), "Strengthening of Church Street Bridge Pier Capbeam Using Bonded FRP Composite Plates: Strengthening and Load Testing", (Special report 138), Transportation Research and Development Bureau, New York.
3. Ghobarah, A., Ghorbel, M. and Chidiac, S. (2002), "Upgrading torsional resistance of reinforced concrete beams using fiber-reinforced polymer", *Journal of Composites for Construction* 6(4), 257-263.
4. Hii, A. K. Y. and Al-Mahaidi, R. (2004), "Torsional strengthening of reinforced concrete beams using CFRP composites", *FRP Composites in Civil Engineering-CICE 2004*, 551-559.
5. Salom, P. R., Gergely, J. and Young, D. T. (2004), "Torsional strengthening of spandrel beams with fiber-reinforced polymer laminates", *Journal of Composites for Construction* 8(2), 157-162.
6. Ameli, M. and Ronagh, H. R. (2007), "Analytical method for evaluating ultimate torque of FRP strengthened reinforced concrete beams", *Journal of Composites for Construction* 11(4), 384-390.
7. Nanni, A., Di Ludovico, M. and Parretti, R. (2004), "Shear strengthening of a PC bridge girder with NSM CFRP rectangular bars", *Advances in Structural Engineering* 7(4), 297-309.
8. Barros, J. A. O. and Dias, S. J. E. (2006), "Near-surface mounted CFRP laminates for shear strengthening of concrete beams", *Cement and Concrete Composites* 28(3), 276-292.
9. Al-Abdwais, A. and Al-Mahaidi, R. (2012), "Modified cement-based adhesive for Near-Surface Mounted FRP strengthening system" Swinburne University of Technology Report.

10. Standards Australia International (SAI) (2001), AS3600-2001 Concrete Structures, Standards Australia International Ltd.
11. Cervenka, V. and Cervenka, J. (2010), "ATENA Program Documentation, Part 2-2: User's Manual for ATENA 3D", Praha, Czech Republic.
12. Cervenka, V., Cervenka, J. (2007). "ATENA program documentation: Part 2-1, User's Manual for Atena 2D, Cervenka Consulting, Prague.
13. Cervenka, V., Jendele, L. and Cervenka, J. (2005), "ATENA Program Documentation, Part 1: Theory", Praha, Czech Republic.
14. ACI Committee 440 (2008), "Guide for the design and construction of externally bonded FRP systems for strengthening concrete structures", American Concrete Institute, United States.
15. Mohammadzadeh, M. R., Fadaee, M. J. and Ronagh, H. R. (2009), "Improving torsional behaviour of reinforced concrete beams strengthened with carbon fibre reinforced polymer composite", Iranian Polymer Journal (English Edition) 18(4), 315-327.
16. Dias, S. J. E. and Barros, J. A. O. (2010), "Performance of reinforced concrete T beams strengthened in shear with NSM CFRP laminates", Engineering Structures 32(2), 373-384.
17. Al-Bayati, G. and Al-Mahaidi, R. (2014), "Effective bond length of modified cement-based adhesive for frp-nsm strengthening system" 23rd Australasian Conference on the Mechanics of Structures and Materials (ACMSM23) Byron Bay, Australia, December-2014. PAGES?
18. Pyl, D. and Cervenka, J. (2013), "ATENA Program Documentation, Part 11: Troubleshooting Manual", Cervenka Consulting, Prague.

# Flexural Testing of Concrete Filled Fibre Reinforced Polymer Tubes (CFFT) with and without Internal Fibre Reinforced Polymer (FRP) Reinforcement

Qasim S. Khan<sup>1</sup>, Josiah S. Strong<sup>2</sup>, M. Neaz Sheikh<sup>3</sup>, M.N.S. Hadi<sup>4</sup>

<sup>1</sup> Ph.D Candidate, School of CME Engineering, University of Wollongong, NSW, Australia

<sup>2</sup> B.Sc. Civil Engineering, School of CME Engineering, University of Wollongong, NSW, Australia

<sup>3</sup> Senior Lecturer, School of CME Engineering, University of Wollongong, NSW, Australia

<sup>4</sup> Associate Professor, School of CME Engineering, University of Wollongong, NSW, Australia

**Abstract:** FRP reinforcement has emerged as an attractive alternate of steel reinforcement due to its higher ultimate tensile strength and weight ratio, and corrosion resistant properties. This study presents the behaviour of Concrete Filled Fibre Reinforced Polymer Tubes (CFFT) with and without longitudinal FRP reinforcing bars under flexural loading. Four circular normal strength CFFT (two carbon FRP tubes and two glass FRP tubes) specimens and a steel reinforced concrete specimen (Reference) of 204 mm and 200 mm diameters respectively were cast and tested. One of the CFFT of each type of CFRP and GFRP CFFT was unreinforced while the other was reinforced. The reinforced CFRP and GFRP CFFT were reinforced with longitudinal 6Ø15 CFRP reinforcing bars and 6Ø15.875 GFRP reinforcing bars, respectively. All the CFFT were tested under increasing flexural load until the fibres at the bottom of the CFFT were ruptured. Significant increases in the ultimate flexural load and ultimate midspan deflections were observed for reinforced CFFT than unreinforced CFFT. GFRP and CFRP reinforced CFFT demonstrated identical flexural behaviour while GFRP CFFT attained even higher ultimate flexural load than the Reference specimen, although both CFFT have similar ultimate midspan deflections.

**Keywords:** FRP Tube, FRP Reinforcement, CFFT

## 1. Introduction

Fibre Reinforced Polymers (FRP) has emerged as one of the most suited alternate option for steel reinforcement in Reinforced Concrete (RC) columns and beams. FRP reinforcement offers a number of advantages such as higher ultimate tensile strength, reduced corrosion and lower self-weight than steel reinforcement [1]. Pantelides et al. [2] concluded that larger proportion of the corrosion in steel RC specimens take place in steel helix. In the last two decades, to reduce the corrosion phenomenon in steel RC specimen, a new technique of Concrete Filled Fibre Reinforced Polymer Tube (CFFT) has been the focus of the research studies as an alternate of steel reinforcement particularly for steel helix. Ozbakkaloglu [3], Vincent and Ozbakkaloglu [4], Mirmiran et al. [5], Hong and Kim [6], Lillistone and Jolly [7], Mohamed and Masmoudi [8] investigated the effect of different geometrical aspects of FRP tubes such as tube thickness, orientation of fibres, height to diameter ratio and tube manufacturing method, unconfined concrete strength, bond between concrete and tube, and internal reinforcement ratio on the load and ductility capacity of CFFT. Nanni and Norris [9], Mirmiran et al. [10], Fam and Rizkalla [11] and Fam and Rizkalla [12] were amongst the early researchers who investigated the combined axial and flexural behaviour of CFFT. These studies showed that CFFT had significantly higher flexural strength and ductility capacity than steel (longitudinal bars and helix) reinforced specimens. Davol et al. [13] presented analytical models to characterise the flexural behaviour of circular CFFT and validated the models using a large scale 7.92 m long CFFT under flexural loading (four point loading).

Recently, FRP longitudinal reinforcing bars have also attracted significant research attention. Cole and Fam [14] investigated the flexural behaviour of longitudinal steel and FRP bars reinforced glass FRP (GFRP) CFFT. The study concluded that flexural strength and ductility attained in case of longitudinal steel bars reinforced CFFT were significantly greater than FRP reinforced CFFT; however, GFRP tubes exhibited a superior flexural behaviour than helical steel reinforcement as GFRP tubes confined the larger concrete area. Fam and Rizkalla [12] studied the flexural behaviour of circular concrete filled GFRP tubes, hollow GFRP tubes and steel tubes. They showed that the flexural behaviour of CFFT was dependent on modulus of elasticity of tube and diameter to thickness ratio of tube. Mohamed and Masmoudi [15] investigated the flexural behaviour of CFFT reinforced with longitudinal FRP and steel reinforcing bars. The study showed that confinement provided by FRP tube to the concrete core significantly increased both the flexural strength and ductility capacity. The study further showed that

CFFT exhibited smaller deflections, and higher strength and stiffness than commonly used steel reinforced beam specimens.

This experimental study investigates the flexural behaviour of unreinforced CFFT and longitudinal FRP bar reinforced CFFT under flexural loading (four point loading). In this study, the flexural behaviour of tested CFFT and steel RC (Reference) specimen is also compared.

## 2. Experimental Program

The experimental program reported in this study comprised four circular CFFT and a steel RC (Reference) specimen. The main objective of this study is to assess the behaviour of circular unreinforced and reinforced CFFT under four point loading. A comparison of flexural behaviour of circular unreinforced and longitudinal FRP bars reinforced CFFT, and the Reference specimen in terms of flexural load and midspan deflection has also been investigated. The key parameters studied in this experimental program were GFRP tubes, CFRP tubes, and GFRP and CFRP reinforcing bars. All the tests were conducted at the High Bay Laboratories of the School of Civil, Mining and Environmental Engineering, University of Wollongong, Australia.

### 2.1. CFFT Specimens and materials

Table 1 provides details of manufacturer provided values of modulus of elasticity ( $E$ ), ultimate tensile strength ( $f_{tu}$ ) and ultimate tensile strain ( $\epsilon_{tu}$ ) of fibres and FRP composites used in this experimental study. Moreover, steel reinforcing bars used in this experimental study has modulus of elasticity of 200 GPa and yield strength of 500 MPa.

**Table 1. FRP Tube and longitudinal FRP bars properties as reported by the manufacturer [16]**

Material	Modulus of Elasticity of fibres ( $E$ ), GPa	Ultimate tensile strength of fibres ( $f_{tu}$ ), MPa	Ultimate tensile strain of fibres ( $\epsilon_{tu}$ ), %	Modulus of Elasticity of FRP ( $E$ ), GPa	Ultimate tensile strength of FRP ( $f_{tu}$ ), MPa	Ultimate tensile strain of FRP ( $\epsilon_{tu}$ ), %
CFRP Tube	230	5080	2.2	146.1	3222.6	2.2
GFRP Tube	80	2000	2.5	49.3	1224.0	2.5
CFRP Bar	140	3100	2.2	78.4	1732.0	2.2
GFRP Bar	-	-	-	62.6	1184.0	1.9

Table 2 provides details of the type of FRP tubes, internal diameter, length and thickness of FRP tubes, types of longitudinal reinforcement, and number and diameter of longitudinal reinforcing bars. All the specimens tested in this study were designed to have a length to diameter ratio (H/D) of four. The internal diameter opted for CFFT and the Reference specimen was 204 mm and 200 mm, respectively.

**Table 2. Details of the specimens reported in this study**

Specimen Designation	Internal Diameter (D), mm	Length (L), mm	Type of FRP Tube	Nominal FRP Tube Thickness, (t) mm	Type of Longitudinal Reinforcement	Longitudinal Reinforcement
CT	204.07	812	CFRP	0.50	-	-
GT	204.00	812	GFRP	1.50	-	-
CT-CR	204.00	812	CFRP	0.50	CFRP	6Ø15
GT-GR	203.88	812	GFRP	1.50	GFRP	6Ø15.875
Reference	200	800	-	-	Steel	4N12

### 2.2. Specimen Designation

The CFFT specimens reported here were designated according to the type of FRP tube and type of longitudinal FRP reinforcing bars used in reinforced CFFT. In this experimental program the influence of two types of FRP tubes i.e., CFRP tube (CT) and GFRP tube (GT), and two types of longitudinal FRP reinforcing bars i.e., CFRP reinforcing bars (CR) and GFRP reinforcing bars (GR) have been investigated. For example a Specimen CT represents a concrete specimen confined with carbon tube with no longitudinal FRP reinforcement and tested under flexural loading. The control specimen was labelled as the Reference specimen i.e., a concrete specimen confined with helical steel reinforcement with longitudinal steel reinforcing bars and tested under flexural loading.



### **2.3. Fibre Reinforced Polymer (FRP) Tubes**

In this experimental program, CFRP tubes and GFRP tubes were used. CFRP tubes comprised 63% of carbon fibres and 37% of resin by volume, whereas GFRP tubes comprised 60% of glass fibres and 40% of resin by volume [16]. Both CFRP and GFRP tubes were designed to have an inner most layer of fibres oriented along the hoop direction (90° to the longitudinal direction) followed by skew layer of fibres (60° to the longitudinal direction). This stacking sequence of 90° and 60° was repeated until the required thickness of FRP tubes was achieved [16].

### **2.4. Fibre Reinforced Polymer (FRP) Reinforcement**

In this experimental program, two types of FRP reinforcing bars i.e., CFRP reinforcing bars and GFRP reinforcing bars were used. Both CFRP and GFRP reinforcing bars comprised 55-60% of fibres and 40-45% of resin by volume [16]. In both types of bars all of the fibres were oriented along the longitudinal direction.

### **2.5. Unconfined Concrete Strength**

A ready mix concrete was obtained from a local company in Wollongong. The target 28<sup>th</sup> day unconfined concrete strength of 32 MPa with maximum aggregate size of 10 mm and slump of 120 mm was requested. The unconfined concrete strength attained after 28 days was 37 MPa.

## **3. Test Methodology and Instrumentation**

All specimens were tested in flexure in the Denison 5000 kN Universal Testing Machine (UTM). The testing arrangement with CFFT loaded in flexure in the UTM is shown in Figure 1. All the specimens were initially loaded to 100 kN under a load control rate of 50 kN/minute and then they were unloaded to 20 kN. This was done so that specimen could align within the loading plates of the UTM and minor eccentricities due to unparallelled plate surfaces could be adjusted. After the initial loading and unloading, the specimens were loaded at a displacement control rate of 0.3-0.5 mm/minute until failure.



**Figure 1. Flexural testing arrangement used in this study**

The flexural testing arrangement consists of two platen rigs i.e. bottom platen rig and top platen rig having clear spans of 705 mm and 235 mm, respectively. The bottom platen rig was placed on bottom loading platen of the UTM. The specimen was placed on the two supports of bottom platen rig with equal portion (53.5 mm) of the specimen hanging from the supports. The specimen length between the supports of the bottom platen rig was equally divided into three segments of 235 mm length each. The top platen rig was then placed on the specimen centred over the middle segment. The top loading platen of the machine was lowered until it touched the top platen rig. The specimen was loaded in the UTM until the final failure due to rupture of the bottom FRP tube fibres was reached. The desired mode of failure under flexural testing (bending) was the rupture of the bottom fibres within the middle segment of the CFFT.

All specimens were instrumented with two Linear Variable Displacement Transducers (LVDT) fixed along the diagonal corners of the loading plates of the UTM, and laser triangulation fixed in the mid on the tension side of the specimen to measure midspan deflection. The UTM also recorded the midspan deflection along with the flexural load taken up by the specimens.

**4. Experimental Results and Discussions**

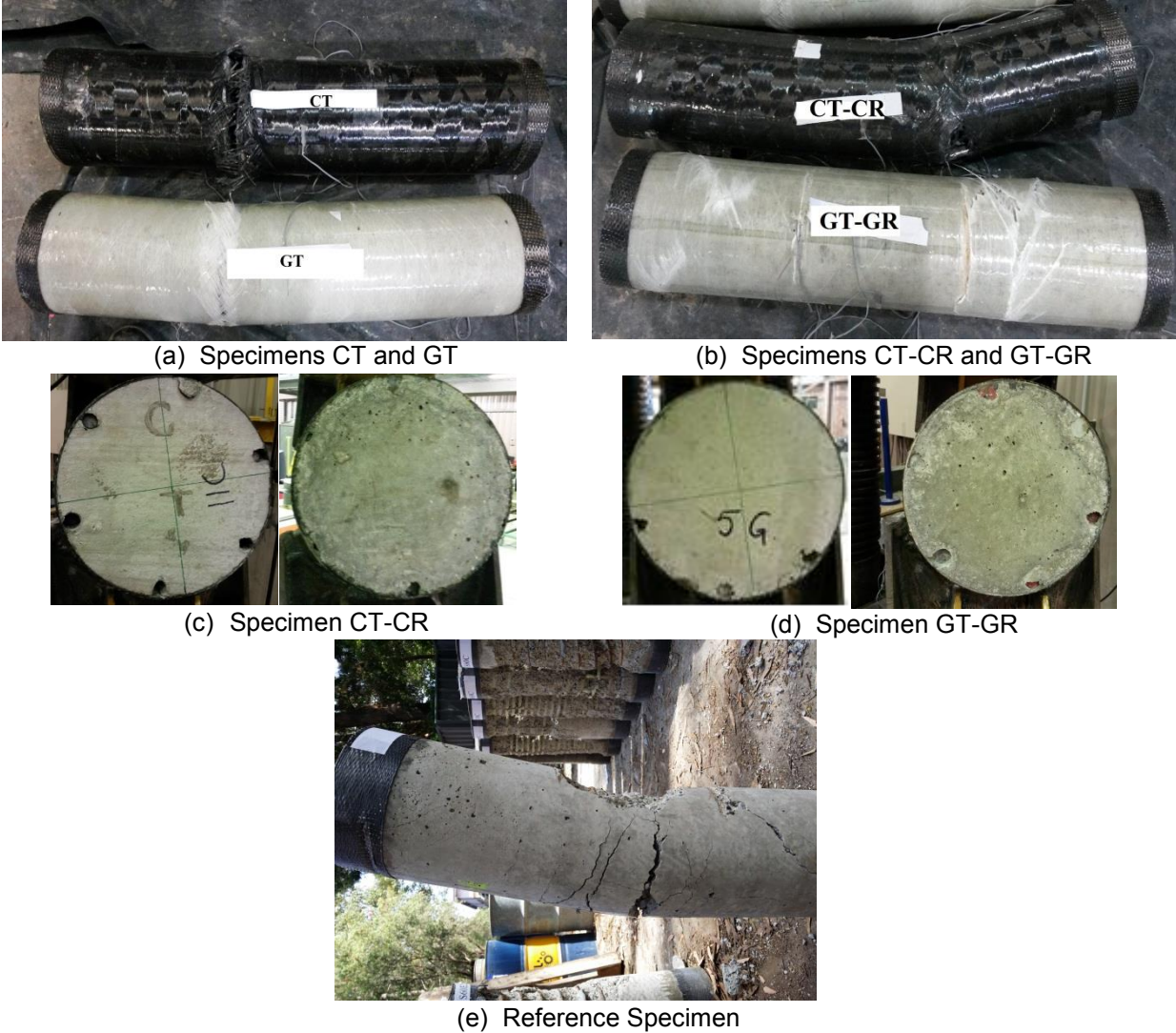
This section deals with the failure modes observed in circular CFFT and the Reference specimen, and the flexural load-midspan deflection behaviour of reinforced and unreinforced CFFT. It also investigates the influence of FRP tube and FRP reinforcement on the flexural load and midspan deflection. The ultimate flexural load and ultimate midspan deflection for all the specimens are presented in Table-3.

**Table 3. Summary of experimental results**

Specimen Designation	Ultimate Flexural Load (kN)	Ultimate Midspan Deflection (mm)
CT	93.2	26.61
GT	115.6	27.26
CT-CR	223.5	44.96
GT-GR	448.4	43.13
Reference	346.9	33.16

**4.1. Observed Failure Modes**

The observed failure mode in all of the CFFT was due to the rupture of the bottom fibres within the middle segment of the specimen as shown in Figure 2a and 2b. The failure in CFFT was initiated with snapping sound of the bottom fibres tearing apart followed by the tearing of the fibres along the hoop direction. Afterwards, crushing of concrete occurred and eventually fibres at the top compressive side were torn apart.



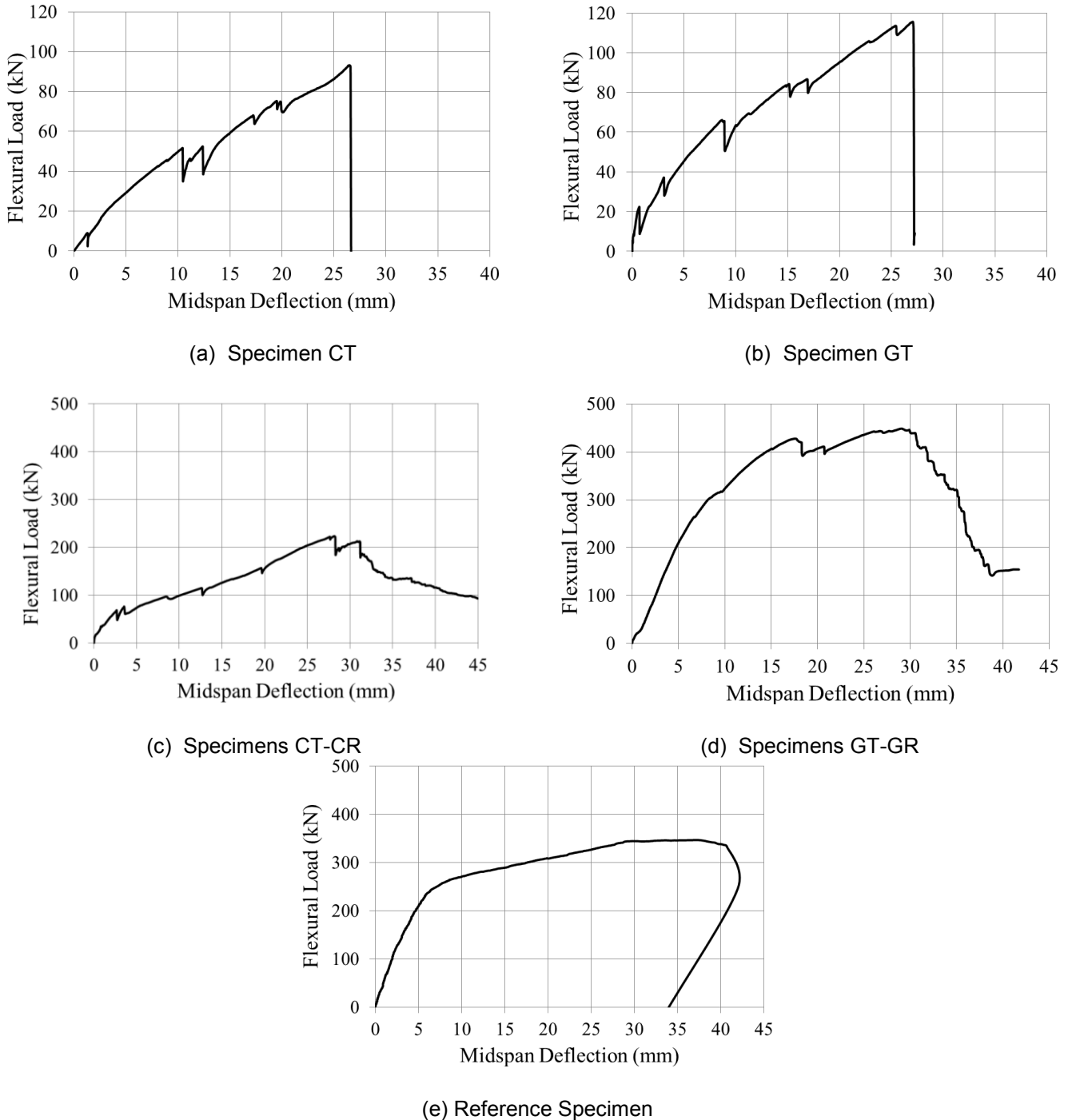
**Figure 2. Observed failure modes of the tested specimens**

The observed failure mode in case of the FRP bars reinforced CFFT was slightly different from that in the unreinforced CFFT. In FRP reinforced CFFT, FRP bars slipped with increasing flexural load as

shown in Figure 2c and 2d. The slippage observed in CFRP bar reinforced CFFT (CT-CR) was significantly more than that observed in GFRP bar reinforced CFFT (GT-GR). This was due to the fact that CFRP bars were smooth whereas GFRP bars were sand coated. Sand coating significantly increased the friction between the bars and the concrete and hence reduced the slippage of the bars and also increased the flexural strength of the CFFT.

#### 4.2. Flexural Load-midspan Deflection behaviour

Figure 3 shows the flexural load versus midspan deflection for all the specimens. It was observed that for CFFT, the flexural load-midspan deflection curve was not as smooth as of the Reference specimen.



**Figure 3. Flexural load versus midspan deflection behaviour of the tested specimens**

This difference was because in circular CFFT an increasing flexural load resulted in tearing apart of the inner layers of fibres which resulted in a sudden fall of load. However, the outer layers of fibres were still intact and resulted in again rise in load. It was noted that unreinforced CFFT failed in a highly brittle manner (Figure 3a and 3b) illustrating a sudden drop in the flexural load carrying capacity.

However, FRP bar reinforced CFFT (Figure 3c and 3d) experienced a reasonable ductile failure condition exhibiting a gradual decrease in flexural load similar to the Reference specimen (Figure 3e).

#### 4.3. Flexural load-midspan deflection behaviour of unreinforced CFFT

Flexural load-midspan deflection behaviour of unreinforced CFFT (Figure 3a and 3b) was characterised by a mild rising curve followed by a vertical falling curve. The rising curve has several drops in load which indicated rupture of inner fibres with increasing applied flexural load. However, the curve continued to rise until the inner and outer fibres were significantly ruptured and was followed by a vertical falling curve indicating a sudden release of applied load. The final failure mode was the rupture of the fibres initiated on the bottom tension side and completed with the rupture of the top compression fibres. Both unreinforced carbon and glass tubes (CT and GT) have exhibited an identical behaviour. However, Specimen GT has manifested higher flexural load and midspan deflection than Specimen CT.

#### 4.4. Flexural load-midspan deflection behaviour of reinforced CFFT

Flexural load-midspan deflection behaviour of FRP reinforced CFFT (Figure 3c and 3d) was characterised by a mild rising curve followed by a mild falling curve. Similar to unreinforced CFFT, mild rising curve in case of reinforced CFFT (CT-CR and GT-GR) also have several drops in load with an increasing applied load. However, drops in load were significantly smaller than those observed in unreinforced CFFT indicating the effectiveness of FRP reinforcement. Moreover, the mild rising curve continued to rise with longitudinal FRP reinforcing bars bending, and inner and outer layers of fibres rupturing with increasingly loud snapping sounds. After reaching the peak load, the load carried by the reinforced CFFT continued to decrease mildly with bending of FRP bars, and rupturing of inner and outer layers of fibres with increasingly louder snapping sounds. The test was stopped when the applied load stopped decreasing. During testing of FRP bar reinforced CFFT, a stage was noted when the flexural load almost stopped decreasing with increasing midspan deflection. Moreover, Specimen GT-GR has exhibited significantly higher flexural load than Specimen CT-CR, but identical midspan deflections in both types of tubes were observed.

#### 4.5. Comparison of flexural load-midspan deflection behaviour of CFFT and Reference specimens

Flexural load-midspan deflection behaviour of both unreinforced (CT and GT) and FRP longitudinal bars reinforced (CT-CR and GT-GR) CFFT, and a steel RC (Reference) specimen is presented in Figure 4. Unreinforced CFFT have exhibited about 4.5 and 2 times lower flexural load and midspan deflections, respectively, than the Reference specimen. However, reinforced CFFT have depicted a significant improved flexural behaviour than unreinforced CFFT. Specimen GT-GR has exhibited higher flexural load and midspan deflection than the Reference specimen, whereas, Specimen CT-CR has exhibited lower flexural load but higher midspan deflection than the Reference specimen. Lower flexural load capacity of Specimen CT-CR than the Reference specimen was attributed to the slippage of CFRP bars.

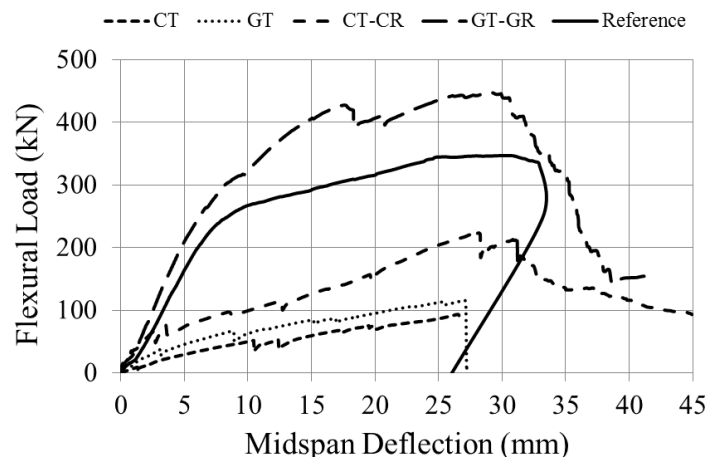


Figure 4. Comparison of flexural load-midspan deflection behaviour of the tested specimens

#### 4.6. Influence of Fibre Reinforced Polymer (FRP) Tubes

In this study two unreinforced CFFT specimens (CT and GT) were cast and tested to study the influence of FRP tubes on flexural load-midspan deflection. The experimental results presented in

Figure 3(a) and 3(b) showed that Specimens CT and GT have almost identical ultimate midspan deflections. However, Specimen GT has exhibited almost 24% higher flexural load capacity than Specimen CT.

#### **4.7. Influence of Fibre Reinforced Polymer (FRP) Reinforcement**

In this study two FRP reinforced CFFT (CT-CR and GT-GR) were cast and tested to study the influence of FRP reinforcement on flexural load-midspan deflection. The experimental results presented in Figure 3(c) and 3(d) showed that Specimen CT-CR exhibited slightly higher midspan deflection than Specimen GT-GR. The flexural load carrying capacity of Specimen GT-GR was almost 50% greater than that of Specimen CT-CR. The lower flexural load carrying capacity observed in Specimen CT-CR was due to the fact that CFRP reinforcing bars used in this experimental study were smooth bars without sand coating. This resulted in reduced friction between the CFRP reinforcing bars and concrete and consequently, CFRP reinforcing bars slipped towards the middle portion of the specimen.

### **5. Conclusions**

In this experimental study, four circular CFFT (two CFRP CFFTs and two GFRP CFFTs) were tested under flexural loading (four point loading). Two circular CFFT (one CFRP CFFT and one GFRP CFFT) were unreinforced and the other two CFFT (one CFRP CFFT and one GFRP CFFT) were reinforced with longitudinal FRP reinforcement. The experimental results of CFFT were compared to the steel RC specimen (Reference). The main outcomes of this study are as follows:

The observed failure mode in all CFFT was initiated by the rupture of the FRP tube fibres on the tension side followed by the crushing of concrete, and finally rupture of the fibres on the compression side. Longitudinal FRP bars reinforced CFFT failed in more progressive manner with significantly larger midspan deflections than unreinforced CFFT.

GFRP unreinforced CFFT exhibits moderately higher flexural load than unreinforced CFRP CFFT. However, GFRP longitudinal bar reinforced GFRP CFFT exhibited significantly higher flexural load carrying capacity than CFRP longitudinal bars reinforced CFRP CFFT. Moreover, midspan deflections in both types of CFFT were identical.

### **6. Acknowledgements**

The first author thanks the University of Engineering and Technology, Lahore and the University of Wollongong, Australia for funding his PhD studies. The authors thank the University of Wollongong, Australia for providing the funding and facilities to carry out the experimental work presented in this study. They also acknowledge the technical assistance provided by Senior Technical Officer Mr. Fernando Escribano.

### **7. References**

1. Afifi, M., H. Mohamed, and B. Benmokrane, *Strength and Axial Behavior of Circular Concrete Columns Reinforced with CFRP Bars and Spirals*. Journal of Composites for Construction, 2014. 0(0): p. 04013035.
2. Pantelides, C., M. Gibbons, and L. Reaveley, *Axial Load Behavior of Concrete Columns Confined with GFRP Spirals*. Journal of Composites for Construction, 2013. 17(3): p. 305-313.
3. Ozbakkaloglu, T., *Compressive behavior of concrete-filled FRP tube columns: Assessment of critical column parameters*. Engineering Structures, 2013. 51(0): p. 188-199.
4. Vincent, T. and T. Ozbakkaloglu, *Influence of fibre orientation and specimen end condition on axial compressive behaviour of FRP confined concrete*. Construction and Building Materials, 2013. 47: p. 814-826.
5. Mirmiran, A., et al., *Effect of column parameters on FRP confined concrete*. Journal of Composites for Construction, 1998. 2(4): p. 175-185.
6. Hong, W.K. and H.C. Kim, *Behaviour of concrete columns confined by carbon composites tubes*. Canadian Journal of Civil Engineering, 2004: p. 178-188.
7. Lillistone, D. and C.K. Jolly, *Concrete filled fibre reinforced plastic circular columns*, in *Composite construction-conventional and innovative conference, composite construction-Conventional and innovative*. 1997. p. 759-764.
8. Mohamed, H. and R. Masmoudi, *Axial Load Capacity of Concrete-Filled FRP Tube Columns: Experimental versus Theoretical Predictions*. Journal of Composites for Construction, 2010. 14(2): p. 231-243.

9. Nanni, A. and M.S. Norris, *FRP jacketed concrete under flexure and combined flexure compression*. Construction and Building Materials, 1995. 9(5): p. 273-281.
10. Mirmiran, A., M. Shahawy, and M. Samaan, *Strength and ductility of hybrid FRP-Concrete Beam-Columns*. Journal of Structural Engineering, 1998. 125(10): p. 1085-1093.
11. Fam, A. and S. Rizkalla, *Concrete filled FRP tubes for flexural and axial compression members*, in *ACMBS-MCAPC*. 2001.
12. Fam, A. and S. Rizkalla, *Flexural Behavior of Concrete-Filled Fiber-Reinforced Polymer Circular Tubes*. Journal of Composites for Construction, 2002. 6(2): p. 123-132.
13. Davol, A., R. Burgueño, and F. Seible, *Flexural Behavior of Circular Concrete Filled FRP Shells*. Journal of Structural Engineering, 2001. 127(7): p. 810-817.
14. Cole, B. and A. Fam, *Flexural Load Testing of Concrete-Filled FRP Tubes with Longitudinal Steel and FRP Rebar*. Journal of Composites for Construction, 2006. 10(2): p. 161-171.
15. Mohamed, H.M. and R. Masmoudi, *Flexural strength and behavior of steel and FRP-reinforced concrete-filled FRP tube beams*. Engineering Structures, 2010. 32(11): p. 3789-3800.
16. Dock, J. *CST COMPOSITES*. 2014 [cited 2014; Available from: <http://www.cstcomposites.com/products-and-services/tubes-rods-and-components/>].

# Durability Study of Textile Fibre Reinforcement

Natalie Williams Portal<sup>1</sup>, Nelson Silva<sup>2</sup>, Katarina Malaga<sup>3</sup>, Urs Mueller<sup>4</sup>, Peter Billberg<sup>5</sup>

<sup>1</sup>Researcher, CBI Swedish Cement and Concrete Research Institute

<sup>2</sup>Researcher, CBI Swedish Cement and Concrete Research Institute

<sup>3</sup>CEO, CBI Swedish Cement and Concrete Research Institute

<sup>4</sup>Senior Researcher, CBI Swedish Cement and Concrete Research Institute

<sup>5</sup>Project Manager, Consolis Strängbetong

**Abstract:** Conventional steel reinforced concrete is one of the most commonly used building materials, yet it has shortcomings in terms of weight, thick concrete covers, and durability namely corrosion of the reinforcement. Textile Reinforced Concrete (TRC), a combination of fine-grained concrete and non-corrosive fibre grids, has emerged as a promising alternative; corrosion is no longer an issue and much thinner and light-weight elements can be designed. Although TRC has been expansively researched, unknowns pertaining to the long-term durability arise when attempting to implement such innovative building materials. The aim of this article is to study the effect of accelerated aging on the tensile strength of various textile fibre grids according to ISO 10406-1 [1]. Carbon, basalt and alkali-resistant (AR) glass fibre grids were immersed into high alkali environment and elevated temperature for 30 days. Direct tensile tests were conducted before and after aging to observe the degree of stiffness and tensile strength loss. After aging, the carbon fibre grids were marked by an increase in both tensile strength and stiffness, while AR-glass and basalt were degraded to the extent that tensile tests could not be conducted. Specimens were therefore exposed to alternative conditions to identify the governing degradation factor.

**Keywords:** durability, aging, fibres, experimental tests, alternative reinforcement

## 1. Introduction

Textile reinforced concrete (TRC) is a combination of fine-grained concrete and non-corrosive fibre grids. Furthermore, it can be characterized as a three-phase material consisting of a cementitious matrix, fibre/yarn structure as well as a fibre/matrix interface. The individual fibres incorporated in the yarns which form the textile fibre grid are most often coated by a sizing material serving as a surface protection and improvement of bond between the fibres. This applied sizing could greatly influence the degradation process and long-term performance of the composite [2, 3]. During the service life, TRC could face harsh boundary conditions such as the highly alkaline environment of the concrete pore solution, varying temperature and humidity loads, carbonation as well as sustained and cyclic loading and fatigue which could all have an effect on its long-term mechanical behaviour and durability. Consequently, the critical zones of degradation are most likely the fibre sizing/coatings and the fibre/matrix interface.

Durability performance is most accurately measured in real-time [4]; however, as time is usually a constraint, accelerated aging tests or experimentally calibrated numerical models [5] have been used to predict the long-term performance of textile reinforcement or fibres in concrete. A common method to accelerate the ageing of the fibres, consists of immersing them, in the form of fibre-reinforced polymer (FRP) rods or textile reinforcement, in a simulated or actual concrete pore solution (i.e. alkaline environment) while simultaneously being exposed to high temperature [6].

In this study, accelerated tests paired with direct tensile tests were performed according to ISO 10406-1 [1] on fibre-reinforced polymer (FRP) bars and grids. Carbon, basalt and AR-glass fibre grids were immersed in a high alkali environment (pH=14) with elevated temperature (60 °C) for 30 days. It was of key interest to forecast the so-called long-term mechanical behaviour and material degradation of various commercially available textile reinforcement products for potential use in new façade solutions within the project H-HOUSE funded by the European Commission.



## 2. Experimental program

### 2.1 Materials

The durability related to the alkali-resistance of three commercially available textile fibre grids of carbon, basalt and alkali-resistant glass (AR-glass), listed in Table 1, were investigated in this study. TRC building applications have primarily focused on the use of AR-glass and carbon fibre materials, but natural and polymer fibres have also been researched for this application [4]. For the most part, the use and durability of AR-glass has been deeply investigated for use in TRC as it has been both cost effective and readily available [7]. Basalt fibres are mineral fibres extracted from volcanic rock and are often compared to glass fibres, such as E-glass and AR-glass, due to existing similarities in their chemical composition [2, 8].

**Table 1. Overview of tested textile fibre grids.**

Material	Sizing/coating	Grid spacing 0°/90° (mm)	Weight (g/m <sup>2</sup> )
Carbon	Styrene-butadiene resin (SBR), 15%	17/18	250
Basalt	Undisclosed resin, 17%	10/10	165
AR-glass	Styrene-butadiene resin (SBR), 20 %	7/8	210

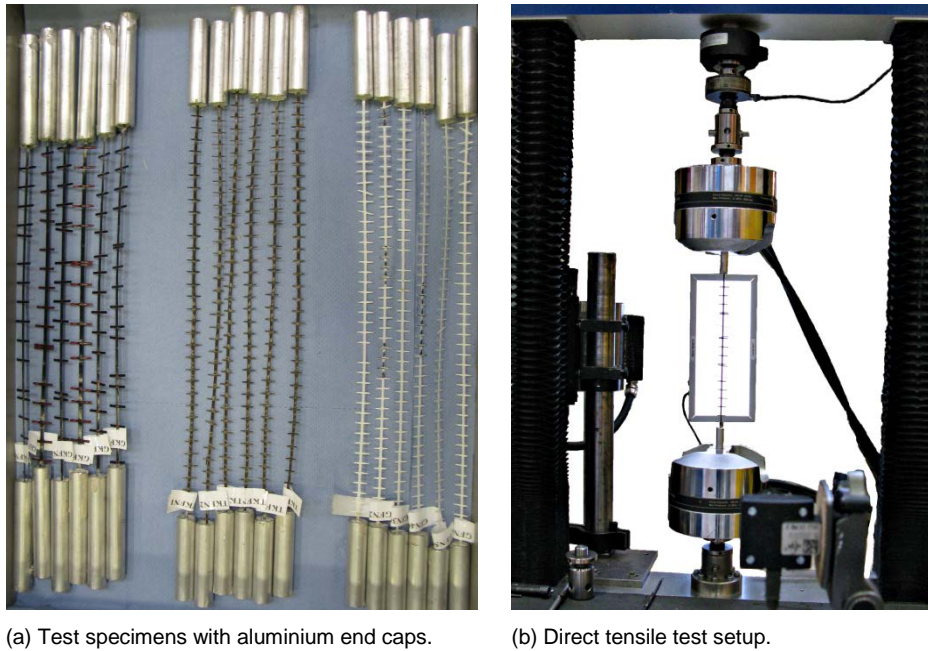
### 2.2 Direct tensile tests

Direct tensile tests were conducted on both reference samples and aged samples, denoted as pre-immersion (Case 1) and post-immersion (Cases 2 or 3), respectively. A total of five tests were conducted for each alternative before and after immersion. The tests were carried out using a universal testing machine (Sintech 20D) illustrated in Figure 1b and the force was recorded by a load cell with an accuracy of 1%. The deformation was measured by a Messphysik Videoextensometer ME46 with backlight technique in the background and digital camera in the foreground. A great advantage of using a video extensometer is that it is possible to measure the deformation up to failure of the specimen, i.e. the ultimate strain can be determined directly. A mechanical extensometer most often has to be removed before failure to avoid risk of damage, thereby causing the ultimate strain to be extrapolated by the assumption of linear elasticity.

The fibre reinforcement grid was cut into so-called individual yarns with a remaining 2 mm projection of the cross-points (crossbars) as well as a minimum of three cross-points along the length. An aluminium tube with epoxy resin as infill was found to be the most suitable solution for the end anchorage of the linear samples (Figure 1a). The main purpose of the end anchorage is to transmit only tensile force along the longitudinal axis of the sample. The tubes had a varying length of 75-100 mm, outer diameter of 15 mm and inner diameter of 12 mm. The inside of the tubes were roughened and cleaned with acetone to achieve superior bonding with epoxy.

The main outputs of the direct tensile tests were the tensile capacity, tensile rigidity and ultimate strain of the different alternatives. The tensile rigidity was calculated from the load-strain relation as the secant modulus between the load level at 20% and 50% of the ultimate tensile capacity. In addition, the tensile capacity retention rate was computed to measure the relative mechanical degradation of the post-immersed versus the pre-immersed specimens.

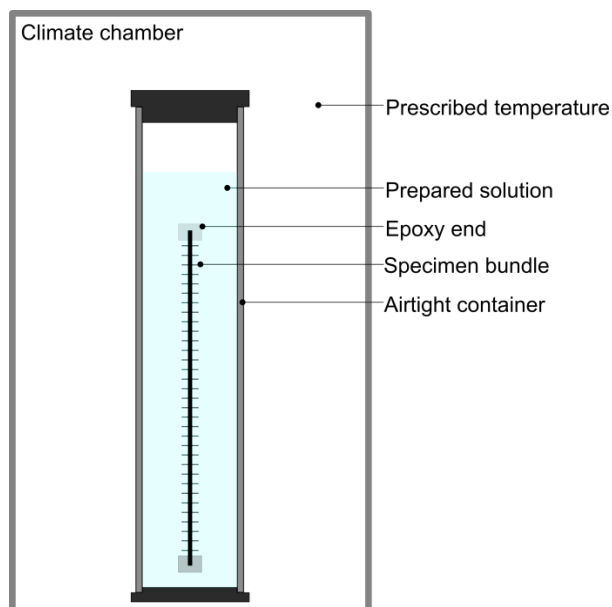




**Figure 1. Direct tensile testing.**

### 2.3 Accelerated testing

The accelerated tests involved the immersion of linear pieces of fibre reinforcement grid in an alkaline solution ( $\text{pH} > 13$ ) while being exposed to a temperature of  $60 \pm 3 \text{ }^\circ\text{C}$  for 30 days. The alkaline solution prepared according to ISO 10406-1 [1] consisted of 8.0 g of NaOH and 22.4 g of KOH in 1 l of deionized water. The pH of this solution was measured to be  $\text{pH}=14$ . The linear test pieces were bundled and sealed by epoxy resin end caps to prevent infiltration of the solution. These bundles were immersed in the alkaline solution in plastic cylindrical containers (see Figure 2) which were sealed and placed in a climate chamber. Once removed from the alkaline solution, the test specimens were rinsed in dionized water and visually examined prior to commencing with the aforementioned end anchorage preparation necessary for the direct tensile testing.



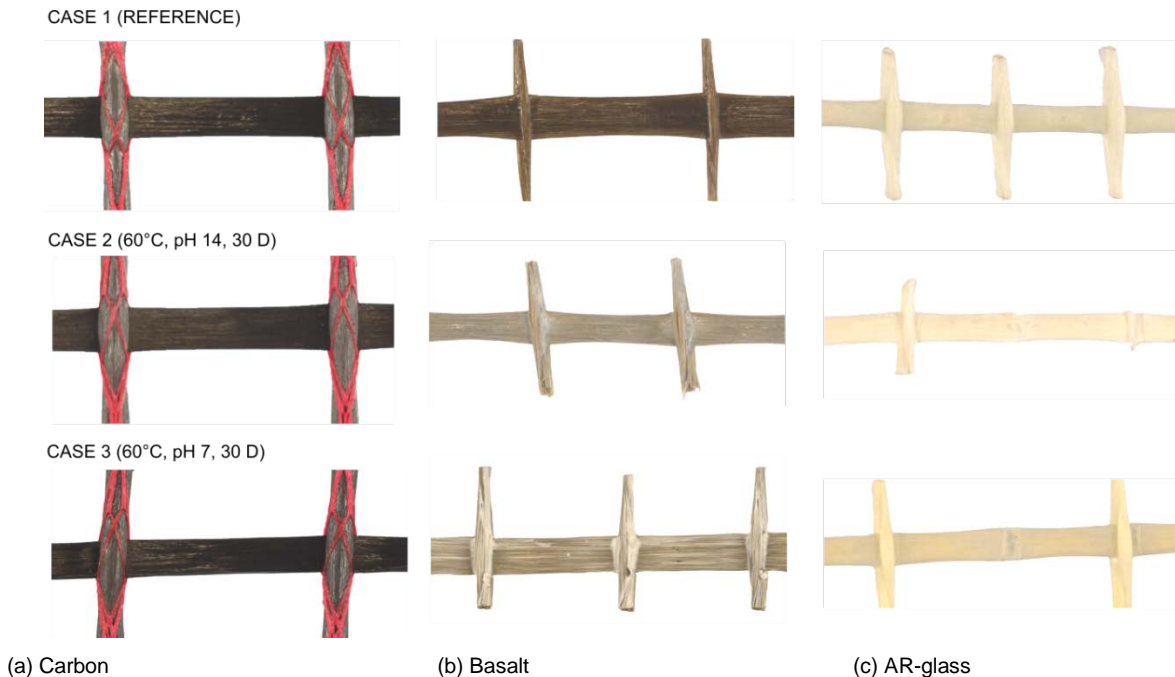
**Figure 2. Accelerated aging test setup.**

When tensile tests could not be conducted due to the extent of sample degradation based on the standard boundary conditions, which particularly applied to basalt and AR-glass, additional tensile tests related to alternative boundary conditions were executed. In the standard accelerated test (Case 2), the specimens face two upper bound variables simultaneously in terms of temperature (60 °C) and alkalinity (pH=14), which, in turn, makes it problematic to identify the actual cause of material degradation. Accordingly, in this study, test samples were also aged for 30 days at 60 °C and pH=7, denoted as Case 3.

### 3. Results and Discussion

#### 3.1 Visual observations

The external appearance of the fibre grid specimens was examined pre- and post-immersion, for comparison of colour, surface condition and change in shape. Photos depicting the visual macroscopic changes are shown in Figure 3.



**Figure 3. Visual observations pre- and post-immersion.**

For carbon fibre grids, no significant visible change of colour or surface texture were observed after 30 days of immersion in pH=7 and pH=14 at 60 °C (Cases 2 and 3). The basalt samples aged according to the standard conditions (Case 2) were marked by colour change and what appears to be the lifting of the coating to the surface. These samples lost a great deal of stiffness to the point that they broke prior to removal from the solution. For those exposed to Case 3, the observed degradation was similar to the Case 2 samples, yet these could be further tested in tension. The AR-glass specimens exposed to Cases 2 and 3 lost the majority of cross-threads which revealed an uncoated and transparent surface in these locations. These samples also lost a significant amount of physical stiffness and could be easily broken by hand at the cross-points.

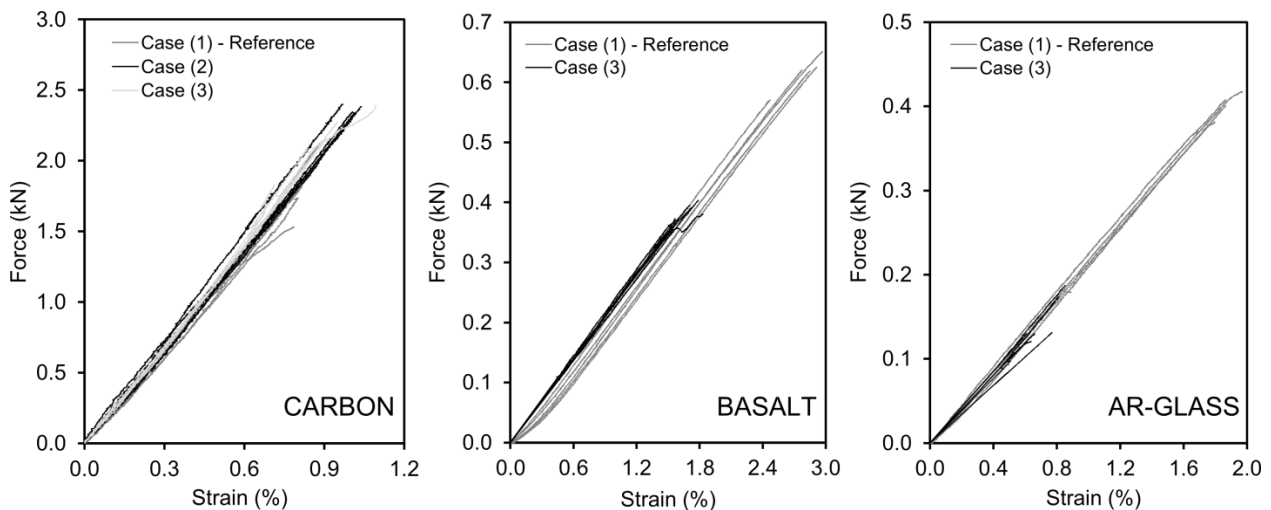
#### 3.2 Experimental results

A compilation of the mean tensile test results along with the associated standard deviations are reported in Table 2. It can be seen that both basalt and AR-glass samples aged according to the standard conditions (Case 2) were unable to undergo direct tensile testing due to the resulting extent of sample degradation. When exposed to alternative boundary conditions of 60 °C and pH=7 for 30 days (Case 3), however, basalt and AR-glass fibre grid samples could undergo direct tensile tests.

**Table 2. Mean tensile test results.**

Case	Reinforcement	Mean properties (st. dev.)			
		Tensile capacity (kN)	Ultimate strain (%)	Tensile rigidity (kN)	Tensile capacity retention rate (%)
(1) Reference	Carbon	1.88 (0.23)	0.87 (0.06)	221.38 (5.05)	-
	Basalt	0.62 (0.03)	2.85 (0.08)	23.73 (0.49)	-
	AR-glass	0.41 (0.02)	1.91 (0.10)	22.49 (0.49)	-
(2) 60 °C, pH 14, 30 d	Carbon	2.36 (0.03)	1.01 (0.03)	235.68 (18.60)	125 (2)
	Basalt	Not measurable			
	AR-glass	Not measurable			
(3) 60 °C, pH 7, 30 d	Carbon	2.14 (0.21)	0.91 (0.14)	234.33 (6.75)	114 (11)
	Basalt	0.39 (0.01)	1.70 (0.10)	23.13 (0.66)	62 (2)
	AR-glass	0.15 (0.03)	0.73 (0.10)	20.54 (2.62)	35 (7)

The tensile test results for the pre-immersed (Case 1) samples are compared to the post-immersed samples (Cases 2 and 3) in terms of applied load versus strain in Figure 4. The carbon fibre specimens appear to have increasing tensile capacity (14-25%) and rigidity (6%) after immersion which is thought to be due to a stiffening effect of the applied coating. In addition, the basalt and AR-glass samples were observed to have a significant degradation even after aging according to Case 3. The tensile capacity and rigidity of basalt were reduced by 38% and 3%, while those corresponding to the AR-glass decreased by 65% and 9%, respectively. It can be drawn from this outcome that AR-glass appears to have a greater sensitivity to the temperature effect. Furthermore, for all tested specimens, there was no significant difference in failure mode noted before and after immersion and failure primarily occurred at the cross-points.



**Figure 4. Applied load versus strain curves for all specimens.**

#### 4. Conclusions

The tensile capacity and alkali resistance of selected textile fibre grids were investigated using ISO 10406-1 [1]. According to the results, it can be concluded that the tested carbon fibre grid has a superior alkali and temperature resistance in comparison to the other alternatives. It was not possible to quantify the material degradation for basalt and AR-glass according to the standard boundary conditions. A downside of this method is that it simply describes the relative difference in durability between different samples, but does not predict the actual durability of the material neither does it specify requirements to be met.

It is believed that further parametric studies, in terms of varying boundary conditions, are needed to gain a deeper understanding of the degradation processes. Statistical analyses of these presented results could

also help highlight the significance of the observed trends. Moreover, the time-dependent degradation of fibre cross-sections could be additionally investigated using an electron-microscope to observe the effectiveness of sizings/coatings.

## 5. Acknowledgement

This research study was made possible with the support of the European Union's Seventh Framework Programme for research, technological development and demonstration under grant agreement no. 608893 (H-House, [www.h-house-project.eu/](http://www.h-house-project.eu/)).

## 6. References

1. ISO 10406-1, "Fibre-reinforced polymer (FRP) reinforcement of concrete - Test Methods, Part 1: FRP bars and grids", 2008.
2. Scheffler, C., Förster, T. et al., "Aging of alkali-resistant glass and basalt fibers in alkaline solutions: Evaluation of the failure stress by Weibull distribution function", Journal of Non-Crystalline Solids, 355(52), 2009, p. 2588-2595.
3. Butler, M., Mechtcherine, V. et al., "Experimental investigations on the durability of fibre-matrix interfaces in textile-reinforced concrete", Cement and Concrete Composites, 31(4), 2009, p. 221-231.
4. Mechtcherine, V., "Towards a durability framework for structural elements and structures made of or strengthened with high-performance fibre-reinforced composites", Construction and Building Materials, 31, 2012, p. 94-104.
5. Cuypers, H., Orlowsky, J. et al., "Durability aspects of AR-glass-reinforcement in textile reinforced concrete, Part 2: Modelling and exposure to outdoor weathering", Advances in Construction Materials 2007, 2007, p. 389-395.
6. Micelli, F. and Nanni, A., "Durability of FRP rods for concrete structures", Construction and Building Materials, 18(7), 2004, p. 491-503.
7. Büttner, T., Orlowsky, J. et al. "Enhancement of the Durability of Alkali-resistant Glass-Rovings in concrete", Proceedings, International RILEM Conference on Material Science, 2010, Germany, RILEM Publications SARL.
8. Wei, B., Cao, H. et al., "Tensile behavior contrast of basalt and glass fibers after chemical treatment", Materials & Design, 31(9), 2010, p. 4244-4250.

# Mechanical Properties and Post-crack Behaviours of Recycled PP Fibre Reinforced Concrete

Shi Yin<sup>1</sup>, Rabin Tuladhar<sup>1</sup>, Tony Collister<sup>2</sup>, Mark Combe<sup>2</sup>, Nagaratnam Sivakugan<sup>1</sup>  
<sup>1</sup>College of Science, Technology & Engineering, James Cook University, QLD 4811, Australia  
<sup>2</sup>Fibercon, QLD 4051, Australia

**Abstract:** Plastic macro fibres, inclusive of virgin and recycled plastic fibres, are becoming more popular in the construction of concrete footpaths, precast panels and shotcrete mine tunnels. In particular, the use of recycled plastic fibres has become increasingly attractive due to their low cost and sustainability. However, due to their production and service history, the recycled plastic fibres normally have lower mechanical properties than the virgin plastic fibres. Therefore, the feasibility of using recycled plastic fibres in concrete may be in doubt. This research assessed reinforcing effects of the recycled Polypropylene (PP) fibre and compared it with those of the virgin PP fibre. Crack mouth opening displacement (CMOD) and round determinate panel test (RDPT) were carried out to assess the post-cracking behaviours of the recycled PP fibre reinforced concrete. The results showed that the recycled PP fibre produced by the same process as the virgin PP fibre obtained lower tensile strength but higher Young's modulus than the virgin PP fibre. Although the recycled PP fibre had lower tensile strength, in the CMOD and RDPT the recycled PP fibre showed comparable reinforcement to the virgin PP fibre owing to its higher Young's modulus.

**Keywords:** Recycled PP fibre, fibre reinforced concrete, mechanical properties, CMOD, RDPT.

## 1. Introduction

Steel fibre and steel mesh have been widely and successfully used to reinforce concrete or shotcrete for industrial pavements (1, 2), non-structural precast elements (pipes, culverts and other small components) (3), and tunnels and underground structures (4, 5). However, the production of steel fibre and mesh is costly and leads to large amounts of carbon emission. For instance, around 180 kg carbon dioxide equivalents are emitted for the production of steel fibre and mesh, which are normally used to reinforce 1 m<sup>3</sup> concrete structures (6, 7). Therefore, more and more macro synthetic fibers, such as polypropylene (PP) (8, 9), high-density polyethylene (HDPE) (10) and polyethylene terephthalate (PET) fibres (11, 12), are used to replace steel fibre and steel mesh to improve post-crack behaviour, and to control dry and plastic shrinkages in concrete (13). These synthetic fibres can be eight to ten times cheaper than steel fibres and steel mesh, and emit significantly less carbon dioxide equivalents (around 16 kg for reinforcing 1 m<sup>3</sup> concrete structures) (14, 15).

These synthetic fibres are predominantly made of virgin plastics and have a tensile strength of 300-600 MPa and a Young's modulus of 4-10 GPa, depending on the materials and manufacturing techniques (16, 17). In recent years, recycled synthetic fibres have attracted great interest around the world. For example, Fraternali et al. (18) showed that the recycled PET fibre produced by extrusion, spinning and stretching could achieve 550 MPa of tensile strength and 27% of ultimate strain. Ochi et al (12) used analogous processing method to make the recycled PET fibre's tensile strength greater than 450 MPa. They also demonstrated that good workability could be achieved with up to 3% recycled fibres added to concrete mix. Another preparation method is to melt waste PET bottles first, and then press and roll them into a roll-type sheet (0.2-0.5 mm in thick), before slitting the sheets into thin strands. In this way the fibres could achieve 420 MPa of tensile strength and 10 GPa of Young's modulus (19, 20). Moreover, de Oliveira and Castro-Gomes (21) and Foti (11) produced lamellar fibres and 'O'-shaped fibres by simply cutting waste PET bottles, but the fibres have lower mechanical properties, in the order of 150 MPa in tensile strength and 3 GPa in Young's modulus.

Most of the past researches have focused on the use of recycled PET fibres in concrete; however, literature on recycled PP fibre is very limited. With this in view, this research focuses on application of recycled PP fibres to improve post-cracking behaviour of concrete. In this study, recycled PP fibres were produced by extruding, spinning and stretching recycled PP granules, which are made of industrial PP wastes (scrap off-cuts and off-specification items in the manufacturing industry that are not used by consumers). It is well known that fibre reinforcement is an effective means of enhancing the fracture

characteristics of concrete, where the fibres can effectively control the opening and slippage of concrete cracks (22). In this research, post-crack behaviour of the recycled PP fibre reinforced concrete was quantified through the crack mouth opening displacement (CMOD) test and round determinate panel test (RDPT).

In order to clarify the relationship between flexural load and post-cracking behaviour, which more accurately reflects how the fibres control cracks, crack-tip opening displacement (CTOD) and CMOD are normally measured in the flexural beam tests (18). According to ASTM E1290 (23), the CTOD is the displacement of the crack surfaces normal to the original (unloaded) crack plane at the tip of the fatigue precrack. However, due to inherent difficulties in the direct determination of CTOD, the CMOD test is considered a more appropriate test to assess post crack performance of the fibre reinforced concrete (24). The CMOD test just needs a displacement transducer mounted along the longitudinal axis at the mid-width of the test specimen, in accordance with the BS EN 14651:2005+A1:2007 (25). The test can clearly display the ability of fibres to redistribute stresses and bridge the cracks formed.

Panel tests are generally considered to better represent the relative behaviour of different fibre reinforced concrete in tunnel linings. The panel-based performance assessment is desirable because panels fail through a combination of stress actions that reflect the behaviour of an in-situ lining more closely than other mechanical tests (1). The round determinate panel test, based on ASTM C1550 (26), involves bi-axial bending in response to a central point load, and shows a mode of failure related to the in-situ behaviour of structures such as concrete slabs-on-grade and sprayed tunnel lining construction (27). This test has a significantly lower variation in post-crack performance than concrete beams, and hence energy absorption in the round determinate panel is considered the most reliable test method of post-crack performance assessment (28).

Recycled PP fibres used in this research were produced by using recycled PP granules. Its production processes and conditions are similar to those of commercial virgin PP fibre. The recycled PP fibre was also produced with the same size and indentation as the virgin PP fibre. Mechanical properties including tensile strength and Young's Modulus were tested for both virgin and recycled PP fibres. The performance of virgin and recycled PP fibre in reinforcing concrete was also tested through series of compressive strength, flexural strength with CMOD, and the round determinate panel tests to study the viability of using recycled PP fibre in concrete.

## 2. Material properties

### 2.1 PP fibres

The production processes of both recycled and virgin PP fibres were similar. The PP granules were extruded at 210-250 °C, and then spun and stretched at 140-170°C, before being stabilised at 110-130 °C. Smooth fibres with diameter of 0.8-0.9 mm were then produced. Further, indenting roller dies with line indents were used to mark indents on the smooth fibres to increase fiber-concrete adhesion. After indentation, the fibres were wound, polywrapped and finally cut into a length of 47 mm (Figure 1).

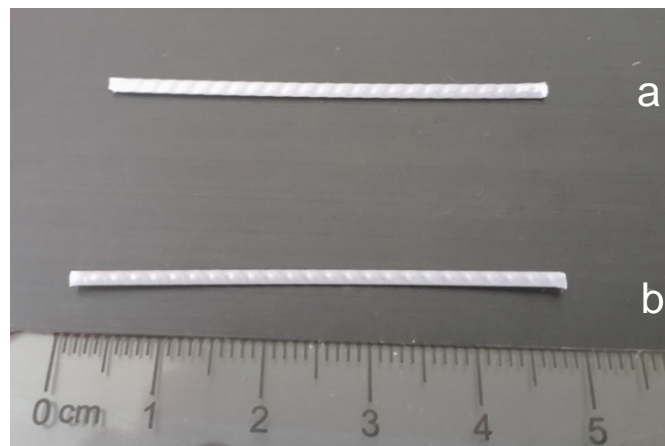
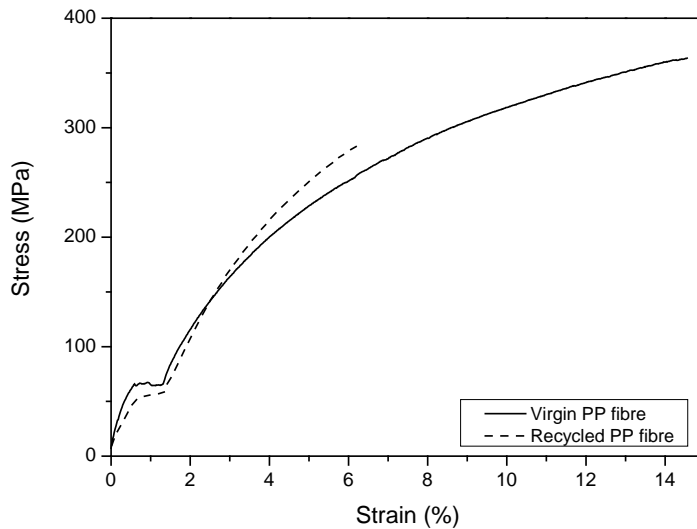


Figure 1. Virgin (a) and recycled (b) PP fibres

Tests for tensile strength and Young's modulus were performed on the virgin and recycled PP fibres according to ASTM D3822-07 (D3822, 2007). The tensile test instrument used for the tests was United STM 'Smart' Test System (STM-50KN) from United Calibration Corporation and was equipped with a 2 kN load cell and data acquisition software. Distance between the clamps was adjusted to obtain a gauge length of 25.4 mm, and extension speed was set as 60% of the gauge length/min (15.24 mm/min). 30 specimens were tested for each sample. Testing temperature was  $20 \pm 2$  °C.

Figure 2 shows stress-strain curve for recycled and virgin PP fibres. Table 1 presents average tensile strength, Young's modulus and elongation at break of these two PP fibres and their standard deviation. The virgin PP fibre showed higher tensile strength (359.2 MPa) and elongation at break (15 %), but lower Young's modulus (only 2801 MPa). The recycled PP fibre produced by the same processing method obtained much lower tensile strength (284.7 MPa), but much higher Young's modulus (5549 MPa) than those of virgin PP fibre.



**Figure 2. Typical stress-strain curves of PP fibres**

**Table 1. Mechanical properties of PP fibres**

PP fibres	Tensile strength (MPa)		Young's modulus (MPa)		Elongation at break (%)	
	Average	Standard deviation	Average	Standard deviation	Average	Standard deviation
Virgin PP Fibre	359.2	30.6	2801	564	15	2.8
Recycled PP Fibre	284.7	21.0	5549	1661	6	2.2

## 2.2 Concrete mix design

Based on industry practise, a 40 MPa standard concrete mix design for footpaths was used in this study. The concrete was delivered from the batch plant (Holcim Australia Pty. Ltd.) in a standard concrete truck without plastic fibres. The average slump of concrete was 125 mm. PP fibres were then added at a rate of 0.45% in volume ( $4 \text{ kg/m}^3$ ) and mixed using a concrete drum mixer. Good dispersion of fibres could be achieved using this method as fibres were sprinkled in to avoid fibre balling. After casting, based on AS 1012.8.1:2014 (29), all the concrete cylinders, beams and round panels were allowed to stand for 24 h in laboratory before demoulding. The demoulded specimens were cured in water at  $23 \pm 2$  °C for 28 days.

## 3. Experimental work

### **3.1 Compressive strength of concrete**

Compressive strength tests were performed on the PP fibre reinforced concrete specimens according to AS 1012.9:2014 (30). Fiber concrete cylinders of 100 mm diameter by 200 mm length were tested at an age of 28 days. The test involved axial loading of a cylindrical specimen until failure in the universal testing machine (UTM) with a maximum load capacity of 2000 kN. The results for each specimen type were based on an average value of four replicate specimens.

### **3.2 Residual flexural tensile strength with CMOD**

Post-cracking behaviour of the PP fibre reinforced concrete beams were studied using a residual flexural tensile strength test with crack mouth opening displacement (CMOD), according to BS EN 14651-2005+A1-2007 (25). All the beams had a size of 150 mm x 150 mm x 600 mm and a notch of 2 mm x 25 mm at mid-span. The notched beams were loaded using three-point loading with the distance between the supports at 500 mm, using a 500 kN hydraulic testing machine. The CMOD was measured using two clip gauges installed at the centre of the notch and averaged CMOD values were adopted. The clip gauges attached to knife edges glued to the bottom of the beam were connected to a data acquisition system Linear Variable Displacement Transformer (LVDT). The testing machine employed operated under displacement control with a constant rate of displacement (CMOD or deflection), and had sufficient stiffness to avoid unstable unloading phenomena in the softening branch of the load-CMOD curve. During the tests, the rate of increase of the CMOD was controlled at 0.05 mm/min. All the tests were carried out at K&H Geotechnical Services Pty Ltd in Australia. Three trials were performed for each test and one trial for the control.

### **3.3 Round determinate panel tests**

The round determinate panel specimens were tested in flexure according to ASTM C1550-12 (26). The diameter of the round panel was 800 mm and the thickness was 75 mm. A central point load was imposed on the round panel, which was supported on three symmetrically arranged hinged supports located on a 750 mm in diameter. The three pivoted supports ensured that load distribution was always determinate in the round panel specimens. A hydraulic universal testing machine with a capacity of 250 kN was used in this test. As specified in the standard, displacement was applied at a rate of 4.0 mm/min up to a central displacement of 45.0 mm. The deflection was recorded by a displacement transducer placed under the centre of the specimen. Three trials were performed for each test at K&H Geotechnical Services Pty Ltd in Australia.

## **4. Results and discussion**

### **4.1 Compressive strength**

Figure 3 shows compressive strength of the PP fibre reinforced concrete cylinders. As can be seen, the addition of fibres does not have significant effects on the compressive strength. Due to the relatively low fraction ( $4 \text{ kg/m}^3$ ) of fibres in the concrete matrix, the compressive strength mainly depends on the concrete mix design (8). Only at large fibre dosages (i.e.,  $13$  to  $18 \text{ kg/m}^3$ ) can improper distribution of fibres, causing balling and air voids, affect the compressive strength of concrete (12). This result correlates with the findings of many scientists (12, 31-33), who reported no notable change to compressive strength with the addition of PP fibres. Moreover, Figure 3 shows that all the recycled fibres had comparable compressive strength compared to virgin fibre. It should also be noted that, during the compression tests, the plain concrete failed suddenly with large single cracks at the peak load, while the PP fibre reinforced concrete cylinders failed with many minor cracks on the surface. The samples with fibres showed a more ductile mode of failure and a post failure structural performance.



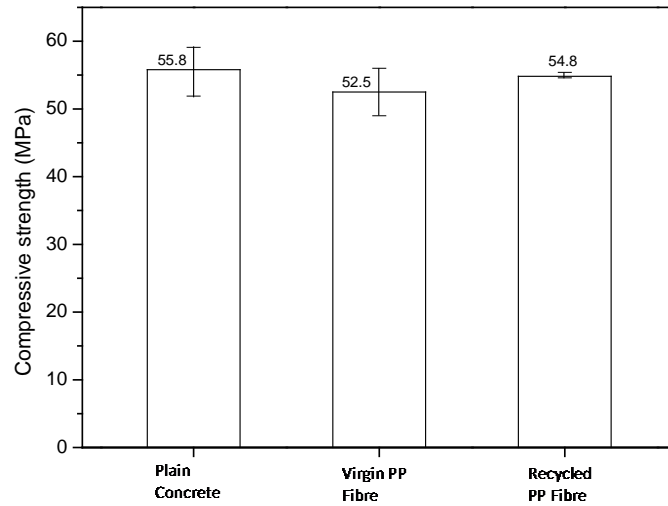


Figure 3. Compressive strength of the recycled and virgin PP fibre reinforced concrete cylinders

#### 4.2 Residual flexural tensile strength with CMOD

Figure 4 plots opening load-CMOD curves of PP fibre reinforced concrete beams. With increase of the CMOD, the flexural opening loads of both the recycled and virgin PP fibre reinforced concrete beams reached the highest points (around 20 kN) at the limit of proportionality (LOP), and then there was a significant drop in terms of the CMOD ranging from 0.05 mm to 0.46 mm. The flexural opening loads then increased with the increase of CMOD from 0.5 mm to 2 mm, and further kept flat within the range of 1 to 5 kN. As can be seen, the recycled PP fibre showed comparable post-crack control with the virgin PP fibre. Although the recycled PP fibre has lower tensile strength than the virgin PP fibre, its higher Young's modulus contributes to the reinforcement, thus showing the similar post-crack behaviour. However, for the control specimens, after the LOP, the opening load dramatically decreased to 0 kN. This indicated that both recycled and virgin PP fibre reinforced concrete beams showed outstanding post-cracking behaviour.

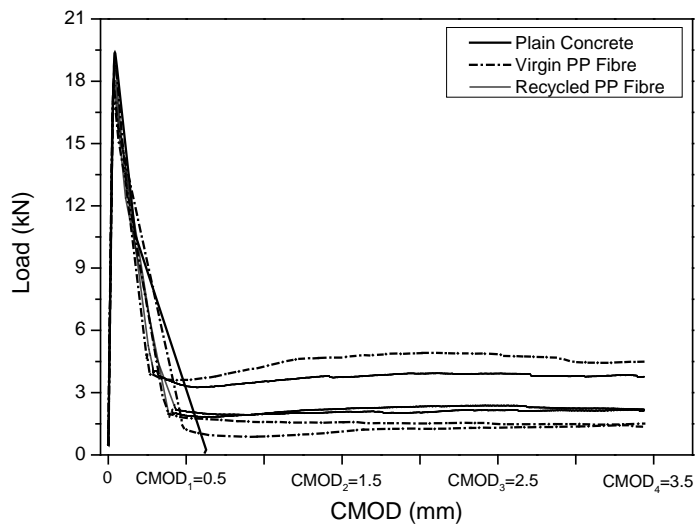


Figure 4. Load-CMOD curves of PP fibre reinforced concrete beams

### 4.3 Flexural strength and toughness of round determinate panels

Round determinate panel test (RDPT) is an essential tool for assessment of post-crack performance in fibre reinforced shotcrete within the underground construction and mining industries (27). The specimens can show a very low within-batch coefficient of variation in performance than any other test method for fibre reinforced concrete, mainly because of the large crack length experienced during testing (28). Figure 5 shows the comparison of the load capacity and the energy absorption of the RDPT on the recycled and virgin PP fibre reinforced concrete specimens. Table 2 shows the comparison of RDPT results in terms of the deflection of 5, 10, 20, 30 and 40 mm. The recycled PP fibre reinforced 40 MPa concrete round panels showed slightly lower load capacity and energy absorption than the virgin PP fibre reinforced panels, proving the feasibility of the recycled PP fibre in concrete.

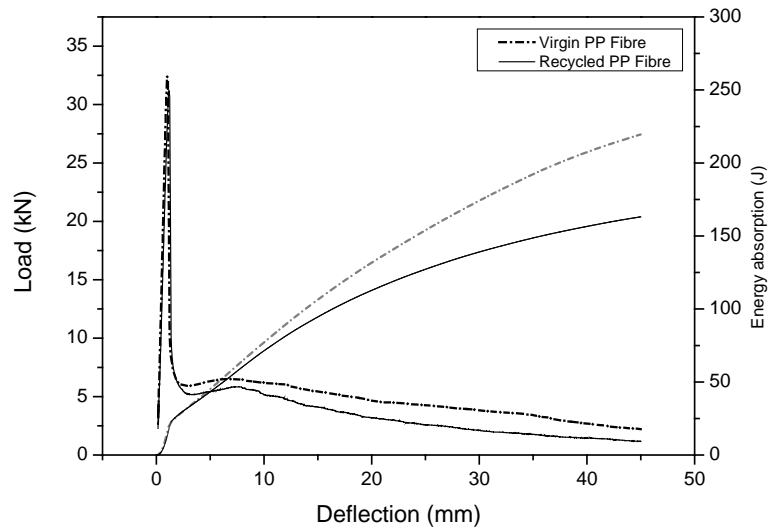


Figure 5. Energy absorption and load curves of round determinate panel tests

Table 2. Energy absorption and load of round determinate panel tests

	Deflection		At peak load	5 mm	10 mm	20 mm	30 mm	40 mm
	Specimens							
Energy absorption (Joules)	Virgin PP Fibre			44	74	126	166	198
	Recycled PP Fibre			42	69	108	133	149
Load (kN)	Virgin PP Fibre		32.4	6.3	6.2	4.7	3.8	2.7
	Recycled PP Fibre		31.2	5.4	5.2	3.2	2.1	1.5

## 5. Conclusion

The use of recycled plastic fibres has become increasingly attractive due to their low cost, lesser environmental impact, and sustainability. However, due to their production and service history, the recycled plastic fibres normally have lower mechanical properties than the virgin plastic fibres. Therefore, the feasibility of using recycled plastic fibres in concrete may be in doubt. This research assessed reinforcing effects of the recycled PP fibres and compared them with those of the virgin PP fibre. The recycled PP fibre produced by the same process with the virgin PP fibre obtained lower tensile strength but higher Young's modulus than the virgin PP fibre. The addition of recycled PP fibres did not have significant effects on the compressive strength, but offered the samples a more ductile mode of failure and a post failure structural performance. Although the recycled PP fibre has lower tensile strength, in the CMOD test the recycled PP fibre showed comparable reinforcement with the virgin PP fibre due to its

higher Young's modulus. In the RPDT the recycled PP fibre reinforced concrete panels showed slightly lower load capacity and energy absorption than the virgin PP fibre reinforced panels, proving the viability of the recycled PP fibre in concrete.

## 6. References

1. CENGIZ, O. TURANLI, L., "Comparative evaluation of steel mesh, steel fibre and high-performance polypropylene fibre reinforced shotcrete in panel test", Cement and Concrete Research, 34 (8), 2004, pp 1357-1364.
2. DING, Y. N. KUSTERLE, W., "Comparative study of steel fibre-reinforced concrete and steel mesh-reinforced concrete at early ages in panel tests", Cement and Concrete Research, 29 (11), 1999, pp 1827-1834.
3. BERNARD, E. S., "Behaviour of round steel fibre reinforced concrete panels under point loads", Materials and Structures, 33 (227), 2000, pp 181-188.
4. JOVICIC, V., SUSTERSIC, J. et al., "The application of fibre reinforced shotcrete as primary support for a tunnel in flysch", Tunnelling and Underground Space Technology, 24 (6), 2009, pp 723-730.
5. SORELLI, L. G., MEDA, A. et al., "Steel fiber concrete slabs on ground: A structural matter", Acı Structural Journal, 103 (4), 2006, pp 551-558.
6. STREZOV, L. HERBERTSON, J., "A Life Cycle Perspective on Steel Building Materials", Principals of the Crucible Group Pty Ltd 2006.
7. BPIC, "Building Products Life Cycle Inventory ", [www.bpic.asn.au/LCI](http://www.bpic.asn.au/LCI), assessed by Oct 2014.
8. HASAN, M., AFROZ, M. et al., "An experimental investigation on mechanical behavior of macro synthetic fibre reinforced concrete", International Journal of Civil & Environmental Engineering IJCEE-IJENS, 11 (03), 2011, pp 18-23.
9. KARAHAN, O. ATIS, C. D., "The durability properties of polypropylene fiber reinforced fly ash concrete", Materials & Design, 32 (2), 2011, pp 1044-1049.
10. ZHENG, Z. H. FELDMAN, D., "Synthetic Fiber-Reinforced Concrete", Progress in Polymer Science, 20 (2), 1995, pp 185-210.
11. FOTI, D., "Preliminary analysis of concrete reinforced with waste bottles PET fibers", Construction and Building Materials, 25 (4), 2011, pp 1906-1915.
12. OCHI, T., OKUBO, S. et al., "Development of recycled PET fiber and its application as concrete-reinforcing fiber", Cement & Concrete Composites, 29 (6), 2007, pp 448-455.
13. ALANI, A. M. BECKETT, D., "Mechanical properties of a large scale synthetic fibre reinforced concrete ground slab", Construction and Building Materials, 41, 2013, pp 335-344.
14. CHILTON, T., BURNLEY, S. et al., "A life cycle assessment of the closed-loop recycling and thermal recovery of post-consumer PET", Resources Conservation and Recycling, 54 (12), 2010, pp 1241-1249.
15. PERUGINI, F., MASTELLONE, M. L. et al., "Life cycle assessment of mechanical and feedstock recycling options for management of plastic packaging wastes", Environmental Progress, 24 (2), 2005, pp 137-154.
16. YIN, S., TULADHAR, R. et al., "Mechanical properties of recycled plastic fibres for reinforcing concrete", In: Proceedings of the 7th International Conference Fibre Concrete, pp. 1-10. From: 7th International Conference Fibre Concrete, September 12-13 2013, Prague, Czech Republic., 2013.
17. YIN, S., TULADHAR, R. et al., "Fiber preparation and mechanical properties of recycled polypropylene for reinforcing concrete", Journal of Applied Polymer Science, 132 (16), 2015.
18. FRATERNALI, F., CIANCIA, V. et al., "Experimental study of the thermo-mechanical properties of recycled PET fiber-reinforced concrete", Composite Structures, 93 (9), 2011, pp 2368-2374.

19. KIM, J. H. J., PARK, C. G. et al., "Effects of the geometry of recycled PET fiber reinforcement on shrinkage cracking of cement-based composites", Composites Part B-Engineering, 39 (3), 2008, pp 442-450.
20. KIM, S. B., YI, N. H. et al., "Material and structural performance evaluation of recycled PET fiber reinforced concrete", Cement & Concrete Composites, 32 (3), 2010, pp 232-240.
21. DE OLIVEIRA, L. A. P. CASTRO-GOMES, J. P., "Physical and mechanical behaviour of recycled PET fibre reinforced mortar", Construction and Building Materials, 25 (4), 2011, pp 1712-1717.
22. SOROUSHIAN, P., ELYAMANY, H. et al., "Mixed-mode fracture properties of concrete reinforced with low volume fractions of steel and polypropylene fibers", Cement & Concrete Composites, 20 (1), 1998, pp 67-78.
23. ASTM, "ASTM E1290-08e1 Standard Test Method for Crack-Tip Opening Displacement (CTOD) Fracture Toughness Measurement ", ASTM E1290. Book of ASTM Standards. ASTM Philadelphia, 2008.
24. ZHIJUN, Z. FARHAD, A., "Determination of crack tip opening displacement of concrete by embedded fiber optic sensor", ICF 11, JRESEARCH PAPERS, 2005.
25. EN, B., "BS EN 14651:2005+A1:2007 Test method for metallic fibre concrete. Measuring the flexural tensile strength (limit of proportionality (LOP), residual)", 2005.
26. ASTM, "ASTM C1550 - 12a Standard Test Method for Flexural Toughness of Fiber Reinforced Concrete (Using Centrally Loaded Round Panel)", ASTM C1550. Book of ASTM Standards. ASTM Philadelphia, 2012.
27. PARMENTIER, B., DE GROVE, E. et al., "Dispersion of the mechanical properties of FRC investigated by different bending tests", Tailor Made Concrete Structures: New Solutions for Our Society, 2008, pp 123-123.
28. BERNARD, E. S., "Correlations in the behaviour of fibre reinforced shotcrete beam and panel specimens", Materials and Structures, 35 (247), 2002, pp 156-164.
29. AS, "AS 1012.8.1:2014 Methods of testing concrete - Method for making and curing concrete - Compression and indirect tensile test specimens", 2014.
30. AS, "AS 1012.9:2014 Methods of testing concrete - Compressive strength tests - Concrete, mortar and grout specimens", 2014.
31. WANG, Y. J., ZUREICK, A. H. et al., "Properties of Fiber-Reinforced Concrete Using Recycled Fibers from Carpet Industrial-Waste", Journal of Materials Science, 29 (16), 1994, pp 4191-4199.
32. CHOI, Y. YUAN, R. L., "Experimental relationship between splitting tensile strength and compressive strength of GFRC and PFRC", Cement and Concrete Research, 35 (8), 2005, pp 1587-1591.
33. SOROUSHIAN, P., PLASENCIA, J. et al., "Assessment of reinforcing effects of recycled plastic and paper in concrete", Aci Materials Journal, 100 (3), 2003, pp 203-207.

# A Novel Ultra High Performance Fibre Reinforced Concrete Spandrel Cladding Panel

Raafat El-Hacha<sup>1</sup> David Pesta<sup>2</sup>, Gamal Ghoneim<sup>3</sup> and Don Zakariasen<sup>4</sup>

<sup>1</sup>Associate Professor of Civil Engineering, The University of Calgary, Canada

<sup>2</sup>Engineer, DIALOG, Calgary, Canada

<sup>3</sup>Associate, DIALOG, Calgary, Canada

<sup>4</sup>Director of Marketing, Lafarge North America, Calgary, Canada

**Abstract:** A novel spandrel cladding panel design using thin section Ultra High Performance Fibre Reinforced Concrete (UHPFRC) with Glass Fibre Reinforced Polymer (GFRP) reinforcing is load tested and compared to analytical calculations and the results of a linear-elastic finite element model constructed in S-FRAME Analysis for a new construction building in Victoria, Canada. Load testing was conducted on five test spandrel cladding panels due to the limited practical and theoretical information available regarding the behaviour of the panel materials and to approximations in the analytical and finite element calculations, including disregarding the contribution of the architectural surface texture. The deflection of the test panels under serviceability wind pressure load testing agreed well with the analytical values and the finite element model, in most cases deflecting less than the design limit. The comparison with the failure load in the finite element model is limited due the linear-elastic analysis. Failure strength of the panels reached as much as four times that predicted using design guidelines mainly because of UHPC's ductility and ability to carry load after cracking.

**Keywords:** spandrel cladding panel, Glass Fibre Reinforced Polymer, Ultra High Performance Concrete.

## 1. Introduction

A curtain wall system is a means of cladding a building with the benefit of the cladding support being predominantly separate from the primary structure of the building. This allows the primary construction to proceed independently of the cladding, easing construction scheduling. The curtain wall system typically supports its own self-weight plus any horizontal loads applied to the façade such as wind loading and the induced seismic loading from the motion of the primary structure during a seismic event. The system consists of mullions spanning vertically between floors, which may be divided by horizontal transoms if required. These mullions provide support for the infill panels, which can consist of stone veneer, metal sheets, glazing, or louvers, among others.

Curtain walls have been in use for nearly 100 years, but their use increased significantly in the 1930s with advances in the use of sheet metal, in the 1950s with the advent of float glass, and again in the 1970s with the use of aluminum mullions [1,2]. The mullions provide a continuous support along the edges for positive (into the building) wind pressure, while negative (suction) pressure is resisted by bolts through the mullions. Relevant to this research, the curtain wall system provides a backing frame to which the spandrel panels are attached.

The purpose of the study was to confirm the use of Ultra High Performance Fibre Reinforced Concrete (UHPFRC) as an alternative to stone or concrete to design and build spandrel panels for use in the curtain wall system of a mid-rise seven storey building located in Victoria, British Columbia, Canada.

Through collaboration with the designer, owner, and engineers, it was determined that an UHPFRC material, would be the ideal material for use as the spandrel panels in the cladding system. The primary factors dictating the use of UHPFRC was the potential for thin sections. The ability to achieve thin sections is important to reduce the seismic loading on the structure, since Victoria, British Columbia is a high seismicity zone. It is possible to achieve these sections due to the high tensile and compressive strengths and high stiffness of the UHPFRC material. This allowed some UHPFRC cladding panel sections to be as thin as 17 mm. A typical stone system can vary from 9.5 mm to 50 mm in thickness and the stone panel is limited to maximum panel dimensions of 300 mm to 400 mm [3], whereas the UHPFRC panels used in this project are 1300 mm in height and vary from 750 mm up to 2150 mm in length. Regular precast concrete cladding can be of similar overall dimensions; however they are typically 100 mm thick or greater. These dimensions are possible for the UHPFRC due to its high strength, in this case 100 MPa in compression and 4 MPa in tension [4]. The use of organic fibre reinforcing in the UHPFRC was preferred over steel fibres to reduce the potential for rust stains appearing on the surface of the cladding panels.

Initial design was done by analytical calculations and finite element modeling [5]. Due to the uncertainty of the performance of the UHPFRC in shear for the thin members, the lack of proven design codes or standards for UHPFRC and because there was limited data on the effects of size on tensile and flexural behaviour, full-scale prototypes testing of the selected design was performed for both static loading and fatigue loading to ensure satisfactory performance of the panels throughout the design life. Similarly, there is limited understanding on behaviour of Glass Fibre Reinforced Polymer (GFRP) reinforcing bars in thin sections. To validate the real-world feasibility of the cladding panels the full-scale testing was compared to analytical design calculations and an elastic finite element analysis of the panels in order to determine the acceptability for their use on the building.

## **2. Structural Validation of the UHPFRC Panels**

### **2.1 Materials**

#### **2.1.1 UHPFRC**

The UHPFRC mix used in these panels and its material properties were provided by the Lafarge Precast Group. A special mix of the UHPFRC utilizing a white aggregate was required in order to suite the architect and owner's design for a light coloured cladding panel. Relevant material properties provided by the concrete supplier for the purpose of design are compressive and tensile strength of 100MPa and 4 MPa, respectively, elastic modulus of 30GPa and fibre length 12mm [4].

#### **2.1.2 GFRP**

Glass Fibre Reinforced Polymer (GFRP) reinforcing bars were used in each of the ribs of the panels to provide greater ductility in the panels beyond the tension failure of the UHPFRC. The GFRP reinforcing bars are important to the strength and ductility of the panels beyond the cracking of the concrete in tension as demonstrated in the analytical calculations, and as such allow a greater utilization of the compression capacity of the UHPFRC. The GFRP is composed of glass fibres and vinyl ester resin, with a textured coating to enhance the bond with the concrete. This material performs in a pure linear-elastic manner to failure. According to the manufacturer, the relevant properties of the GFRP rods used are: nominal diameter of 6.35mm, cross-sectional area of 31.7mm<sup>2</sup>, tensile modulus of elasticity 46.1GPa, nominal ultimate tensile strength 874 MPa, guaranteed design tensile strength 784 MPa, ultimate tensile strain 1.9%, Poisson's ratio 0.25 [5].

## **2.2 Panels Geometry, Design and Test Matrix**

The scope of the testing included one full-scale short panel (1300 mm in height by 1287 mm in length) for static load testing, two full-scale long panels (1300 mm in height by 1757 mm in length) for static load testing, and an additional two full-scale short panels for fatigue load testing. All panels had thickenings around the perimeter of the panel as required to properly seal the joints between panels. In addition, the long panels had a thickening in the centre of the panel to assist with load carrying capabilities. All of the prototype panels were subjected to uniform pressures. The design of the panels (strength and deflections calculations) was achieved through analytical calculations [6]. The construction details and analysis of the short panel static load testing were previously discussed [6, 7], however, Figure 1 shows the construction details for the long cladding panels. Only the static testing results of one of the long panels, Long Panel #1, will be discussed in this paper while Long Panel #2 and the fatigue tests results can be found in [6].

## **2.3 Static Load Testing of Long Panel #1**

Curtain wall panels were subjected to transient wind loading resulting in both positive and negative pressures. The intent of the static load testing is to determine the panel's ability to withstand the design loads established through the National Building Code of Canada [8], and checked against the British Columbia Building Code [9]. Given the textured ribbed surface of the panels, there is the potential for increased localized wind pressures due to vortices forming adjacent to the panels. This effect could not be adequately determined without wind tunnel testing, however, because of the scale of the ribs compared to the size of the panels (5 mm ribs compared to a minimum of 750 mm smallest panel dimension) it was

assumed to average to a neutral pressure. The resulting net unfactored positive and negative wind pressure loads, including internal pressure effects and the effects at the corner or end zone of the building were 1.54 kPa and 1.91 kPa, respectively. The loading imparts both bending stresses and shear stresses on the panels as the forces are transferred back to the supporting curtain wall framing. Various load cycles were implemented on the panel. The selected load cycles are intended to simulate positive and negative pressure on the panel at Serviceability Limit States (SLS) and Ultimate Limit States (ULS) load levels, sustained loading (for 24 hours), and ultimately taking the panels through to failure. The testing included deformation and strain measurements of the panels at various points both on the top and bottom surfaces of the panels and strain measurement on the embedded GFRP reinforcing bars.

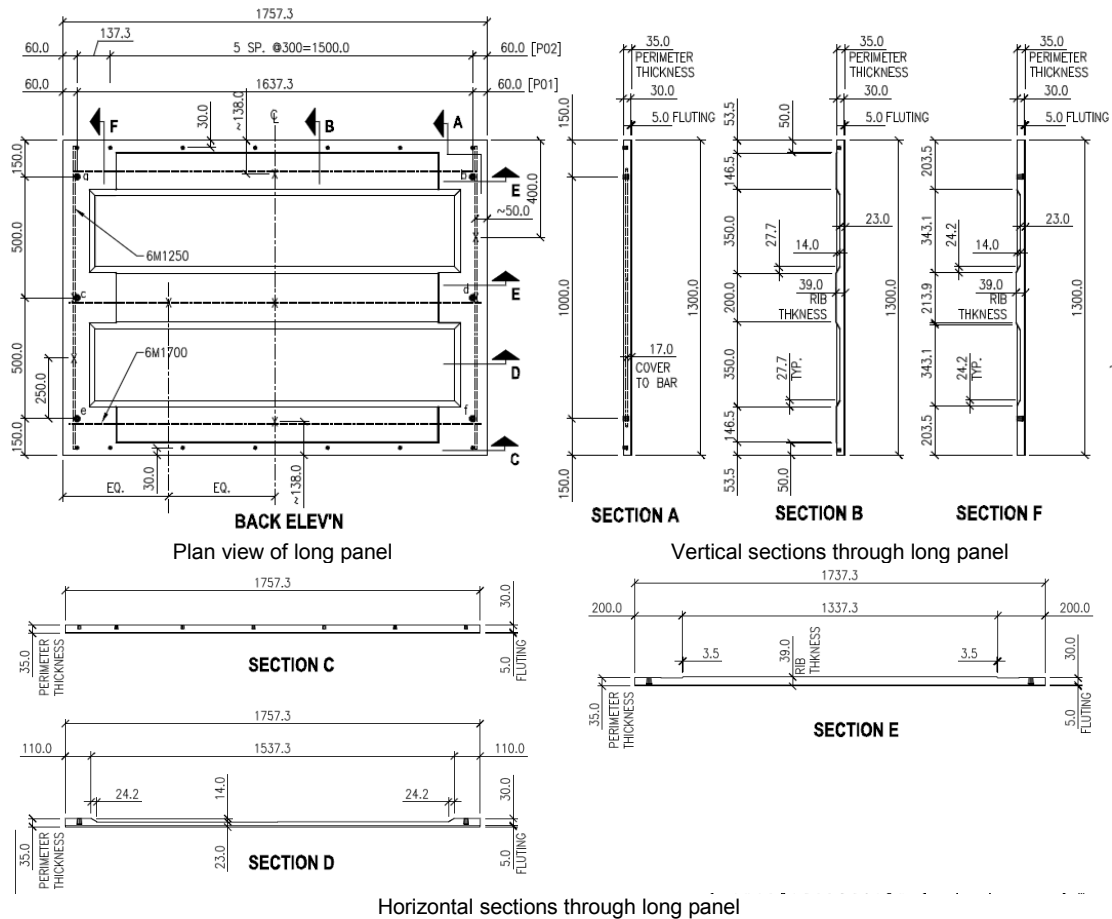


Figure 1. Construction details of prototype long cladding panel #1 (Lafarge Precast).

## 2.4 Finite Element Analysis of Long Panel #1

After the design of the spandrel panels through analytical calculations was complete [6], a finite element analysis (FEA) of the panels was undertaken in order to determine if any unanticipated effects occurred within the panels and to compare FEA deflections to those achieved through analytical calculations. Based on the results of the analytical calculations, it was assumed that the spandrel cladding panels would be in an uncracked state for SLS loading levels and as such the GFRP reinforcing bars would have little effect on the performance of the panel. Thus, for simplicity of modelling, the GFRP bars were not modelled and a purely linear-elastic analysis was used. This eliminates the ability of the model to calculate the anticipated failure load for the panels, and reduces the accuracy of the model beyond the cracking load. This was considered to be acceptable since the goal of the FEA was to verify the distribution of stresses and to show there are no unusual stress patterns. The structural analysis program S-FRAME was chosen to conduct the FEA of these panels. This software was chosen for the ability to quickly and accurately create models for design iterations during the initial design process. Details on the element types, material properties, model geometry, boundary conditions, mesh sensitivity analysis to provide the optimal mix of computation efficiency and result accuracy for the long panels can be found in [6].

The labels used throughout the analysis for each of the elements of the panel are shown in Figure 2. The long span edge member is the top, bottom, and middle thickened portion for the long spandrel panels, with dimensions of width of 200 mm, thickness of 34 mm, and span length of 1637.3 mm. The narrow edge member is the thickened portion on the left and right sides of the spandrel panel with dimensions of 110 mm wide and 30 mm thick with a 500 mm span for the long panel. The infill sections are 17 mm thick for the long spandrel panel, and are calculated for a per-metre width of panel for the purpose of comparison. For all of the members, any contribution from the interface of the infill panel with the thickened members to create a 'T' or 'L' section was ignored since loading is possible in both positive and negative directions, and these portions would be of little benefit during negative bending.

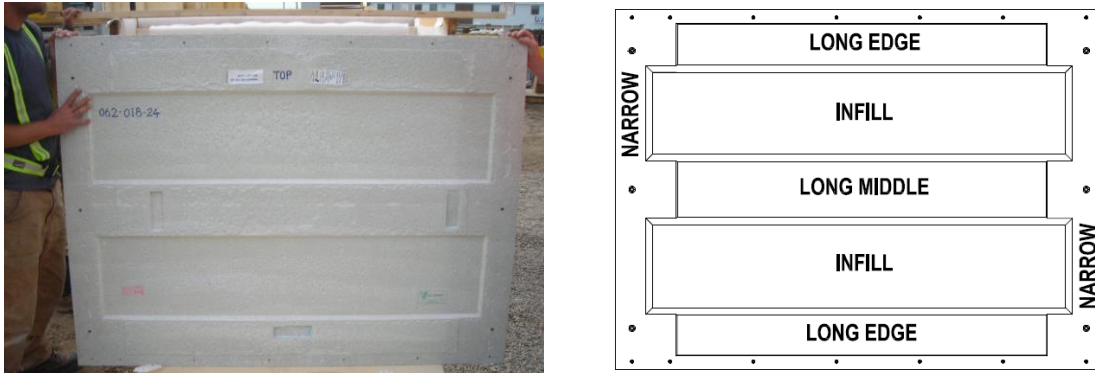


Figure 2. Labels used to identify long panel members.

#### 2.4.1 Results of Finite Element Analysis

Only select results are presented here, predominantly from the negative load case, as this is the case that applies the greatest pressure to the panels. Given the linear-elastic nature of the analysis performed, unfactored results are presented, since determining the response at the serviceability and ultimate limit states is simply a matter of proportion.

The stresses due to the self-weight of the panel in the upright position is shown in Figure 3. From this analysis, it is shown that the self-weight in this axis is a minor contribution to the total stress. Thus, the stresses from the self-weight are minimal in comparison to the stresses in the panel due to bending (0.041 MPa compared to 6.48 MPa expected from bending, or approximately 0.6% of the maximum stress) and can presumably be ignored during further analysis. The expected deflection of the panel under unfactored negative pressure is shown in Figure 4. Scaling this to the serviceability load level (multiplying the FEA results by the 0.75 SLS factor [8]), the expected deflection becomes 3.02 mm, and likewise for positive pressure, the expected serviceability deflection is 2.43 mm. For the purpose of comparison to the analytical calculations Figure 5 displays the moments in the long members of the panel for comparison to the analytical calculations. Finally, the maximum unfactored tension principal stresses for positive and negative pressure are shown in Figure 6 in order to determine if any portions of the panel are demonstrating unexpected behavior. A summary of the maximum and minimum stresses experienced in the long panel is given in Table 1.

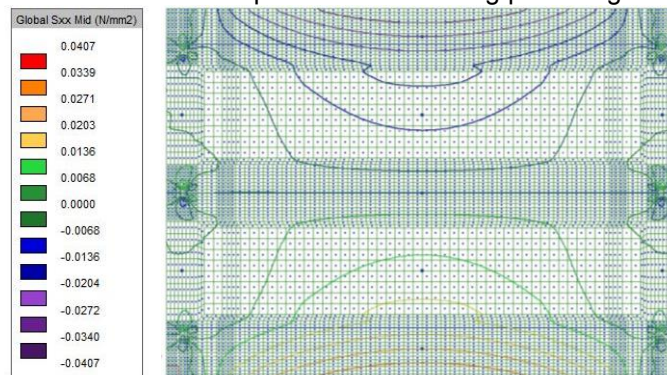


Figure 3. Stresses in the panel due to self-weight.



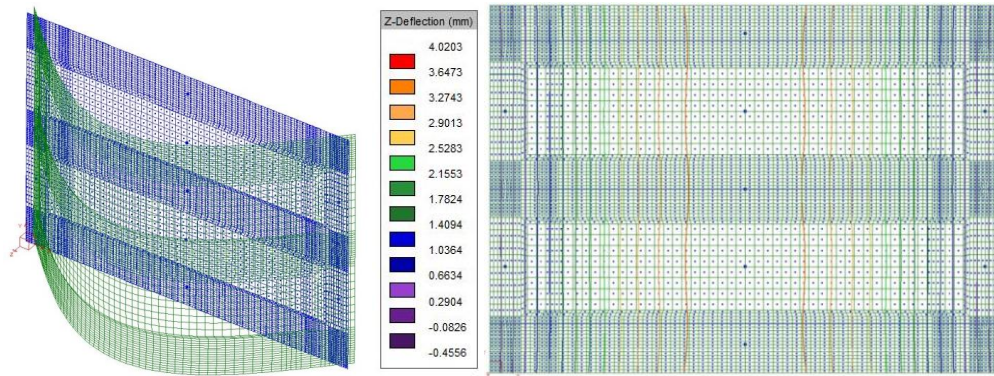


Figure 4. Undeformed and deformed geometry (left) and predicted lateral deflections (right) due to negative pressure.

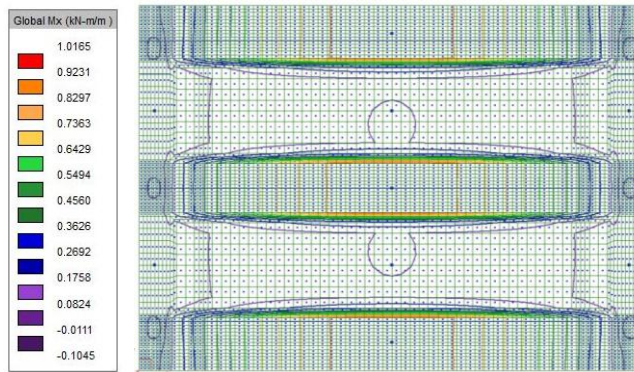


Figure 5. Moments in the long members for negative pressure.

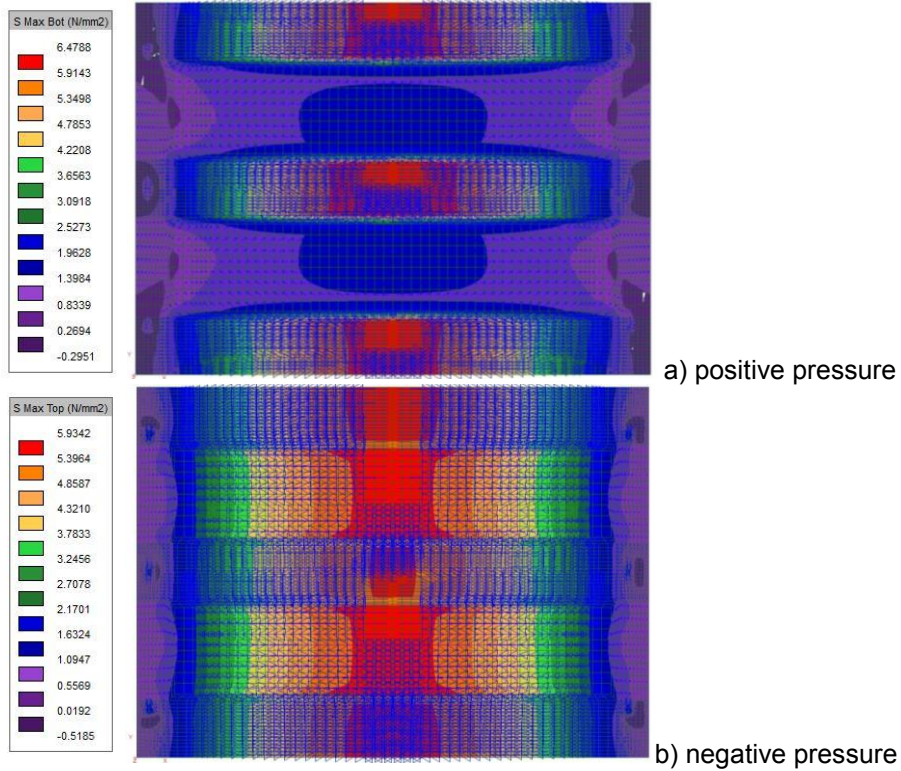


Figure 6. Maximum principal stress (tension).

**Table 1. Unfactored top and bottom stresses in long panel elements**

	<b>Positive Pressure (1.54 kPa)</b>		<b>Negative Pressure (1.91 kPa)</b>	
	Top Stress (MPa)	Bottom Stress (MPa)	Top Stress (MPa)	Bottom Stress (MPa)
Long	-4.582	6.227	5.683	-7.724
Middle	-4.461	6.450	5.533	-8.000
Infill y	-4.551	1.291	5.644	-1.601

The finite element model for the long panel shows that applying the ULS factor of 1.4 [8] to the above values, it is apparent that the stresses in many of the members of the panel exceed the cracking limit (4 MPa in tension) of the UHPFRC material. Thus, at this point it is expected that the loading has exceeded the linear-elastic nature of the finite element model and the exclusion of the GFRP reinforcing bars in the model becomes significant. In order to suitably verify the performance of the panels, it was deemed necessary to perform load testing on the panels.

## **2.5 Static Test Set-Up of Long Panel #1**

The full-scale static testing was performed with the panels in a horizontal position. Ideally, the panels would have been tested in a vertical position to include the in-plane self-weight effects in the test; however difficulties in accurately applying the required pressure made this impractical. As a result of using a horizontal test setup, the applied pressures were adjusted to account for the loading by the self-weight of the panel applied in this condition. It is important to note, however, that the deflection and strain measurements were zeroed with the panels supporting their self-weight, introducing a measurement offset bias in the testing.

The test frame was designed to replicate the supports that would be present in the real world condition, reproducing the mullions to act as primary supports. The positive and negative pressures were applied in independent tests in order to facilitate the testing setup. In order to ensure the pressure was uniformly applied to the panel, an inflatable mattress was placed between the load piston and the panel to distribute the loading. This also allowed the load to continue to be distributed as a uniform pressure even with the substantial deformations that were observed in the later stages of the testing. An example of this setup is shown in Figure 7. Once the capability of the air mattress to uniformly transfer load to the panels was exceeded in the loading to failure, the mattress was replaced with point loads at the quarter points of the panel to induce stresses similar to uniform pressure.

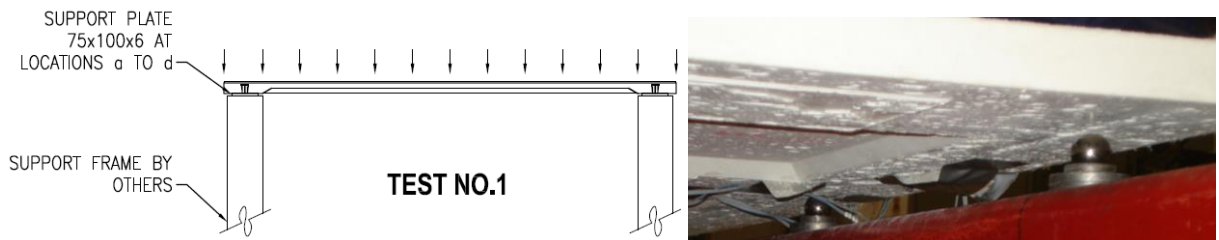
The load was applied in the downward direction for both tests; however the orientation of the panel was adjusted in order to test the appropriate pressure direction. For the positive load test, the panel was tested with the ribs directed upwards (external face upwards), whereas for the negative pressure case the panel was flipped, with the ribs directed downward (external face downwards).



**Figure 7. Use of an air mattress to provide uniform pressure**

### **2.5.1 Test No. 1 – Positive Pressure Supports**

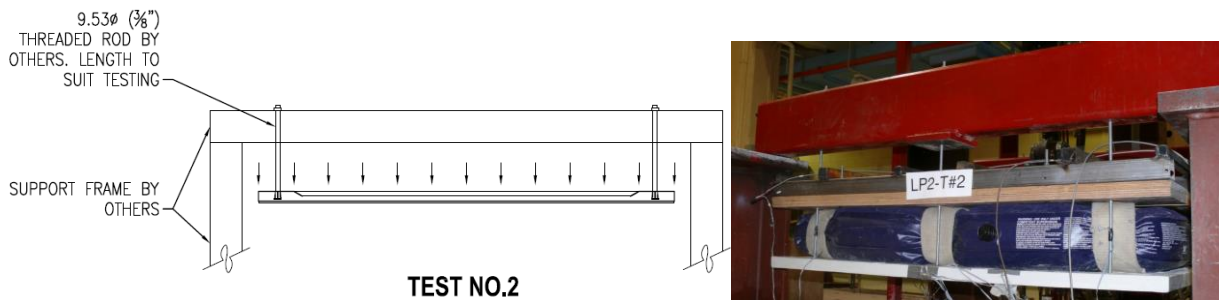
Test No. 1 applied positive pressure to the panels with the panels supported on ball bearings at each of the cast-in anchors. In this configuration, the panel was oriented with the textured surface (outside face) of the panel facing upwards. A schematic of the test setup is shown in Figure 8. The use of ball bearings at the support ensured that a true pin connected was provided. A close up of the supports provided is shown in Figure 8.



**Figure 8. Schematic of Test No. 1 test setup and positive pressure support condition**

### 2.5.2 Test No. 2 and Test No.3 – Negative Pressure Supports

Test No. 2 and Test No. 3 applied negative pressure to the panels with the panels supported from rods threaded into each of the cast-in anchors and suspended from the test frame. For this test, the panel was reversed, with the textured ribs oriented downwards, as shown in the schematic test setup in Figure 9. Suspending the panels was selected as the support method in order to prevent any membrane forces from developing within the panel. This support is shown Figure 9.



**Figure 9. Schematic of Test No. 2 and No.3 test setup and negative pressure support condition**

### 2.5.3 Instrumentations

The cladding panels were instrumented with strain gauges both on the exterior surfaces of the panels and on the GFRP reinforcing bars cast within. The strain gauges were placed to allow the determination of the cracking load and – once converted to stress – for the purpose of comparison to the analytical calculations and the finite element model. Additional instrumentation installed included Linear Displacement Sensors (LDS) and Laser Position Sensors (LPS) used to measure the displacement of the panels under load.

### 2.5.4 Applied Loading

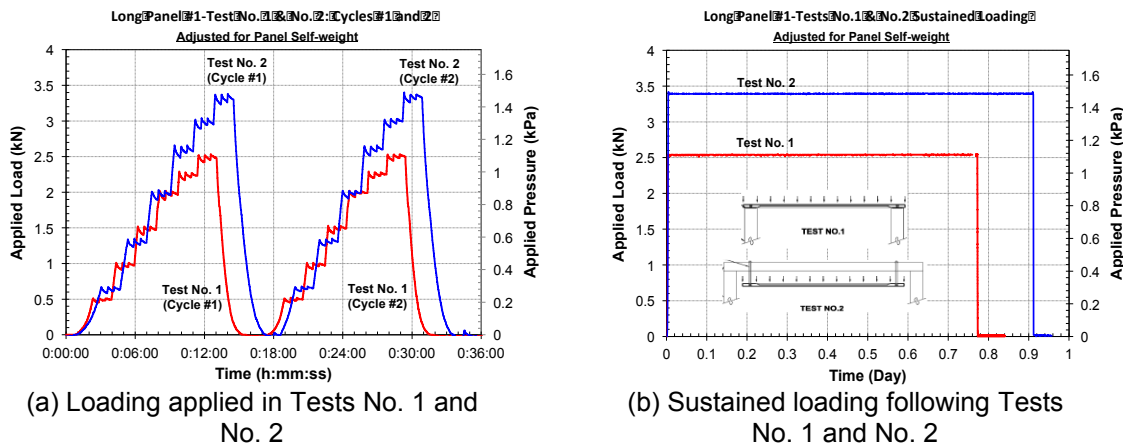
Loading of the panels in Test No. 1 and No. 2 was applied in steps and in cycles to simulate the variability of wind loading as shown in Table 2 for Test No. 1 (positive pressure) and for Test No. 2 (negative pressure). This pattern of loading is shown in Figure 10(a), with the 'Applied Load' as measured from the load cell in the testing apparatus, converted to the 'Applied Pressure' based on the area of the panel being tested. Since the panels were tested in the horizontal position, the self-weight of the panels was removed from applied loading (applied in the downward direction) in order to more accurately simulate the desired pressure. Note that in each load step the load is reinstated to the intended loading every 30 seconds to account for any load losses incurred in the system, either through dynamic effects or losses from the air mattress.

Following each of Test No. 1 and Test No. 2, a sustained load was applied to the panels for a period of 18 or 24 hours (depending on test facility availability). The intent of the sustained loading was to establish whether the panels displayed any time-dependent effects. These loading cases are shown in Figure 10(b), again as measured from the load cell during testing. The cause of the variability in applied loading in Test No. 1 is uncertain. Finally, after the previous testing was complete, the panel was loaded through to failure in Test No. 3.



**Table 2. Applied loading to long panel #1**

Load Step	% of non-Factored Load	Test No. 1		Test No. 2		Remarks
		Positive Pressure (kPa)	Positive Load (kN)	Negative Pressure (kPa)	Positive Load (kN)	
Cycle 1						
0	0	0	0	0	0	0
1	20	0.222	0.557	0.296	0.726	3 x 30 seconds
2	40	0.443	1.062	0.592	1.402	3 x 30 seconds
3	60	0.665	1.569	0.887	2.076	3 x 30 seconds
4	80	0.886	2.074	1.182	2.750	3 x 30 seconds
5	90	0.997	2.328	1.330	3.088	3 x 30 seconds
6	100	1.108	2.581	1.478	3.426	3 x 30 seconds
Cycle 2 – repeat loadings from Cycle 1						
7	100	1.108	2.581	1.478	3.426	Sustained 24 hrs



**Figure 10. Loading applied to long panel #1**

## 2.6 Static Test Results of Long Panel #1

The central deflection under Test No. 1 and Test No. 2, as shown in Figure 11 indicates that an amount of initial permanent deformation is observed in the panel prior to cycle 2. It is possible that this initial deformation is a result of 'setting-in' of the test apparatus, since in both tests, the second cycle of testing resulted in the panel rebounding to nearly the initial deformation. However, it is more likely that this permanent deformation is a characteristic of the panel, since under the sustained loading condition performed after Test No. 1 and No. 2, Figure 12(a) also indicates some creep as a result of the loading. This effect is also shown in Figure 12(b) which shows the deflection as a function of time under the sustained load. This figure clearly demonstrates that the panel central deflection progressively increases with no further increase in load, and having a resultant deformation of approximately 2.0 mm after Test No. 1 and 2.4 mm after Test No. 2. It is not apparent if this permanent deformation is a realistic expectation in real world use, since the variability and reversibility of the wind load means these deflections could cancel each other out.

The deflections measured at various points on the panel under loading were compared to ascertain the shape of the deflection and the similarity to the assumed one way loading in the analytical calculations. This comparison is made in Figure 13(a). The deflection curves for 'Def-L-Cen', 'Def-L-E', and 'Def-W' are the deflections for the long middle, and long edge at the top and bottom of the panel, respectively. The deflection curves for 'Def-S' and 'Def-N' are at the quarter points of the long middle member. Due to the close similarity of the deflections across the width of the panel (Def-W, Def-L-E, and Def-L-Cen), it is observed that the panel behaved as a single unit spanning between the supports.

Test No. 3, shown in Figure 13(b) shows the central deflection of the panel through to failure under negative pressure. In this test, elastic behaviour of the panel is shown under applied loading approaching 2.5 kPa, at which point cracking of the panel notably reduces the panel stiffness, indicated by the reduced slope of the graph. Ultimately, this panel failed at an applied load of approximately 8.4 kPa, which equals approximately 8.8 kPa including the self-weight of the panel, at a deflection of approximately 146 mm.

As expected for this panel, the ultimate failure occurred as a crack propagating across the short direction of the panel, located predominantly within the decorative ribs, as these act to reduce the effective section of the panel. The final failure crack is shown in Figure 13(b).

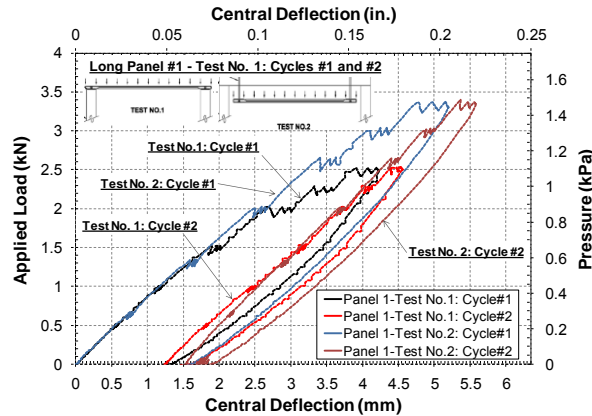
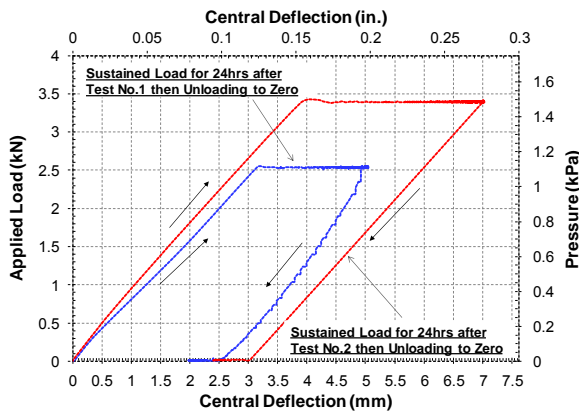
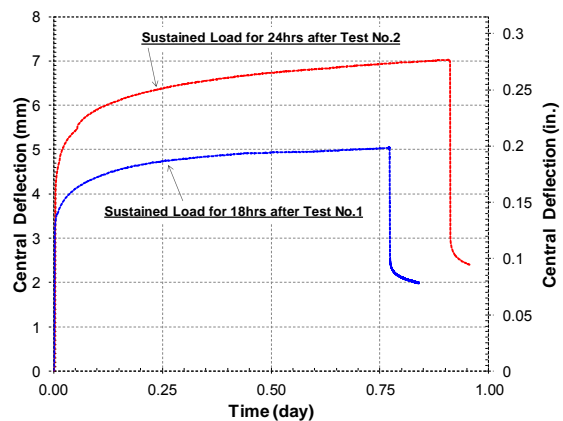


Figure 11. Central deflection under load through various loading cycles

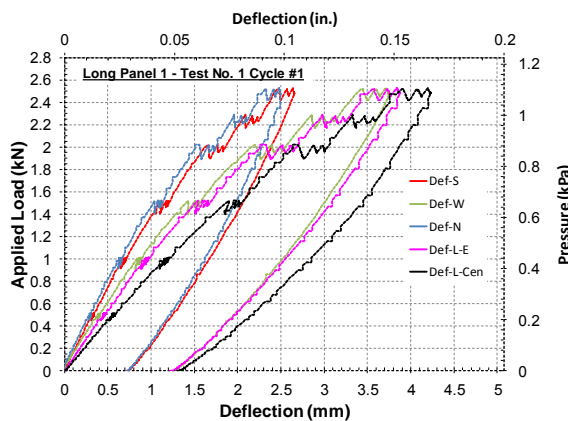


(a) Sustained loading

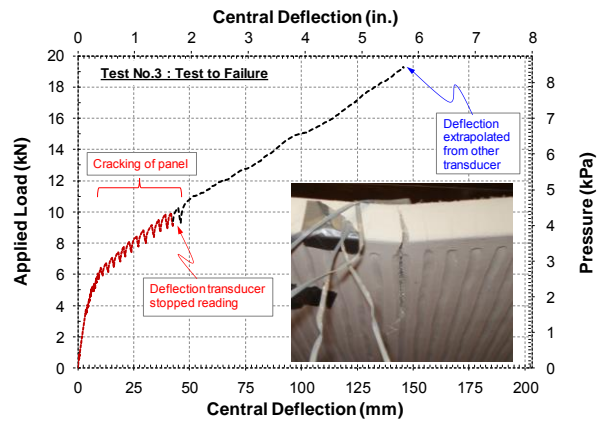


(b) Deflection vs. time under sustained loading

Figure 12. Central deflection under sustained loading for Tests No. 1 & 2



(a) Comparison of deflections at various points



(b) Test No. 3 and close-up view of failure crack

Figure 13. Load vs. Deflection for Tests No.1 and No.3

## 2.7 Static Tests Comparison and Validation

The primary criteria for acceptability of the wall panels is the deflection under serviceability load conditions. In this section, a comparison of all static test results is presented including the Short Panel [6], Long Panel #1, and Long Panel #2 [6]. A comparison of the deflection values obtained through the analytical calculations, the finite element model, and the static testing is shown in Table 3. It is noted that the analytical calculations predicted the highest deflections, most likely due to the number of simplifying assumptions made, including ignoring the contribution of the surface ribs to the panel strength, analyzing the panels as a one-way and two-way slab and beam system, and ignoring the contribution of the 'T' and 'L' sections to the member strength. For the short panel, the actual deflection at the SLS load level was significantly less, nearly half as much, as that calculated in the finite element model. This could be due to the additional stiffness offered by the textured rib surface, which was not accounted for in the modelling, but was shown to have a significant impact. The short panel static testing displayed deflections significantly below the established deflection limit for both the positive and negative pressures.

For the Long Panel #1, the average deflection of the panel agreed well with the analytical calculations, but was higher than the finite element analysis calculations. However, there was a substantial disparity in the performance of the two panels, for which there appears to be little explanation. Here, Long Panel #1 deflects less under load than both the analytical calculations and the finite element analysis predict and is within the acceptable deflection limit, while Long Panel #2 had measured deflections greater than expectations and limitations. Given that the performance of the Long Panel #2 continues the trend of deflecting less than the predicted deflection, similar to the Short Panel, it is theorized that Long Panel 1 is an anomaly and may not be representative of the typical panel behaviour. However, since only two Long Panels were tested, this could not be confirmed. When the average of the two long panels is considered, the maximum of 4.00 mm under negative SLS pressure results in a deflection of span/400, which is deemed to be acceptable given the established limit is based on masonry construction, and these Ductal® concrete panels exhibit much greater ductility than would be expected with masonry.

Based on the Short Panel and the Long Panel #2, the spandrel panels as designed satisfy the deflection design requirements.

**Table 3. Comparison of predicted and measured panel deflections**

Analysis Method	SLS Positive Pressure Deflection (mm)		SLS Negative Pressure Deflection (mm)	
	Short Panel [6]	Long Panel	Short Panel [6]	Long Panel
Established Limit: L/600	1.95	2.73	1.95	2.73
Analytical Calculations	2.03	3.02	2.53	3.96
Finite Element Analysis	1.41	2.43	1.75	3.02
Static Load Testing <sup>Note 1</sup>	0.84	<i>Panel 1</i>	1.24	<i>Panel 1</i>
		<i>Panel 2 [6]</i>		<i>Panel 2 [6]</i>
		4.38		1.71
		3.05 (average)		4.00 (average)

Note 1: The measured deflection from the static load testing does not account for the deflection caused in the panel under self-weight in the horizontal position.

In fact, the short panel cracked at a loading higher than the ultimate load condition, and as such would not be expected to crack at all through the life cycle of the panel. In general, the cracking loads predicted through analytical calculations were approximately three to four times less than the static test loads.

The measured failure load of the panel during the static testing was also notably higher than the load predicted through analytical calculations. This can likely be attributed to the simplifications made in the analytical calculations and the material reduction factors applied to the UHPFRC and GFRP reinforcing bars.

Given the fact that the panel was able to resist forces much higher than the ultimate limit states design loads and did not exhibit cracking under serviceability load conditions, it is determined that the panel is acceptable for the intended use as spandrel cladding panels. All of the panels demonstrated large deflection prior to the failure of the panels, thus a ductile failure mode was exhibited.

**Table 4. Comparison of calculated and measured cracking and failure pressure**

Panel	Analytical Calculations		Static Load Testing	
	Cracking Pressure (kPa)	Failure Pressure (kPa)	Cracking Pressure (kPa)	Failure Pressure (kPa)
Short Panel [6]	1.05	3.97	5.19	12.03
Long Panel #1	0.68	2.15	2.02	8.80
Long Panel #2 [6]			2.16	14.75

### 3. Conclusions

The UHPFRC spandrel cladding panels with GFRP reinforcing bars as designed and tested are sufficient to withstand the positive and negative wind pressures for the intended application in Victoria, British Columbia. The prototype panels proved to exceed expectations from both the analytical calculations and the FEA. Better realism in the FEA could have been achieved by developing a model that included the tension and compression properties of the UHPFRC by inputting the stress-strain relationship of the material, as opposed to the linear-elastic model that was used. Additionally, while the analytical calculation method undertaken proved to provide a reasonable approximation for the deflections, it was shown to estimate a failure load approximately three times lower than the failure load established through testing. It was also concluded that the textured rib surface did have a beneficial impact on the performance of the panel, contrary to the assumptions made in the initial analysis.

### 4. Acknowledgement

The authors would like to acknowledge the National Sciences and Research Council (NSERC) of Canada, University of Calgary and Lafarge Canada Inc. for their financial supports.

### 5. References

1. R. M. Sanders, R.M. "Curtain Walls: Not Just Another Pretty Façade," Hoffmann Architects' JOURNAL, vol. 23, no. 1, 2006, pp 1-8.
2. Yeomans, D., "The Pre-History of the Curtain Wall," Construction History, vol. 14, 1998, pp 59-82.
3. Michael J. Scheffler. (2010, Apr.) Building Envelope Design Guide - Thin Stone Wall Systems. [Online]. Available: [http://www.wbdg.org/design/env\\_wall\\_thin\\_stone.php](http://www.wbdg.org/design/env_wall_thin_stone.php).
4. Lafarge North America Inc., Ductal FO B3 Behaviour-10f2 Datasheet, 2011.
5. Pultrall Inc., V-ROD Std (50 GPa) Datasheet, May 2011.
6. Pesta, D., "Ultra High Performance Fibre Reinforced Concrete Spandrel Cladding Panels in Façade Applications", M.Eng. Thesis, University of Calgary, Department of Civil Engineering, November 2014.
7. Ghoneim, G., El-Hacha, R., Carson, G., and Zakariasen, D., "Precast Ultra High Performance Fibre Reinforced Concrete Replace Stone and Granite on Building Façade," in *Third fib Congress and Exhibition*, Washington, D.C., 2010.
8. National Research Council Canada, National Building Code of Canada, 2005.
9. British Columbia Building Code, 2006.

# Upgrading the Dundas Point Boardwalk, Applecross with the use of GFRP Bar Reinforced Concrete Columns and Footings

Joel Brown B.Eng GradIEAust  
Structural Engineer, Airey Taylor Consulting

**Abstract:** The use of Glass Fibre-Reinforced Polymer (GFRP) bars for internally reinforcing concrete structures has been growing to overcome common problems of steel reinforcement, such as corrosion. Areas for application are dominated by bridge decks where de-icing salts are used, although other applications include coastal structures or structures aiming for an extended design life.

The Dundas Point Boardwalk in Applecross, Western Australia is subject to a harsh marine environment and remedial works to the foundation system which included corroded steel piles were focused on achieving an extended design life and addressing the ongoing corrosion issues encountered in marine environments.

In stage one of the boardwalk repair, sixteen concrete columns and eight concrete footings were constructed, all internally reinforced with GFRP bars. The design of the footings and columns was performed using Canadian Code CAN CSA S806-12 (1) and ISIS Canada's guide 'ISIS Educational Module 3: An Introduction to FRP-Reinforced Concrete' (2).

As the boardwalk decking was constructed using steel supporting members, attention was paid to detailing the concrete to steel connections in order to avoid moisture ingress and bimetallic corrosion. This connection was designed using GFRP threaded bolts embedded into the concrete piles and connecting the supporting steel members.

Contractor feedback highlighted the ease of workability with the GFRP bars and all research suggests that there is no reason that a design life in excess of 75 years for the concrete elements cannot be achieved.

**Keywords:** GFRP, Reinforcement, Columns, Marine, Corrosion.

## 1. Introduction

### 1.1 Background of Dundas Point Boardwalk

Dundas Point Boardwalk is approximately 250 metres long, between 2.5 and 7 metres in width, and is located on the southern side of the Swan River Estuary near the north and western sides of Dundas Point in the City of Melville, Western Australia. The majority of the boardwalk is in the tidal zone of the Swan River and receives constant wetting and drying of its support structure. The boardwalk is used for foot and bike traffic only.

The boardwalk was designed and constructed in the 1990's utilising steel universal column (UC) piles encased in concrete a minimum of 200mm below ground level at the time of construction. This supported steel framing on which a timber deck was laid. All steel members including piles and steel framing were hot-dipped galvanised.



**Figure 1.**Left: Steel UC Connecting to Steel Framing. Right: Steel UC Below Concrete Encasing.



Steel thickness measurements were performed on a selection of the steel piles. They were assessed in accordance with AS 1627.0-1997: 'Metal finishing - Preparation and Pretreatment of Surfaces (3). All piles were classified as suffering from Grade H corrosion –'Large portion of surface is covered with rust, pits, rust nodules and non-adherent paint, pitting is visible.' The results of the thickness measurements were extrapolated through a detailed non-destructive visual inspection to give an assessment of all 76 of the boardwalk piles, Table 1 summarises these results.

**Table 1. Steel Pile Mass Loss Summary.**

<b>Steel Mass Loss Range</b>	<b>No.</b>	<b>%</b>
Not Inspected	1.0	1.3
No Assessed Loss	0.0	0.0
0 - 10% loss	0.0	0.0
10 - 20% loss	9.0	11.8
20 - 30% loss	36.5	48.0
30 - 40% loss	26.0	34.2
40 + % loss	3.5	4.6
<b>Total</b>	<b>76.0</b>	<b>100.0</b>

Due to funding limitations, it was decided to only remediate a 41 metre section of the boardwalk at the southwestern corner with the remainder of the required works programmed into the City of Melville's future works programme.

## **1.2 Background to GFRP**

Fibre Reinforced Polymers (FRP) are composite materials that can be used to strengthen concrete structures. They are made of fibres of a particular material selected, embedded in a polymeric resin. The most common fibres used in FRPs are glass, carbon or aramid. FRPs can come in woven sheets, which attach to the outside of reinforced concrete structures to offer strengthening, usually for remediation purposes. FRPs are less commonly produced as reinforcing bars.

Advantages of GFRP bars include; having high tensile strength, being corrosion resistant, nonmagnetic and lightweight with low thermal and electrical conductivity. This suite of characteristics is useful in many situations. GFRP bars are well suited for use in corrosive environments, in structures required to have a very long design life, in hospitals near MRI machines, for example, and provide easy workability because they are lightweight.

Disadvantages of GFRP bars include; no yielding before failure, low transverse strength compared to steel, low modulus of elasticity and possible durability issues of glass fibres in high alkaline environments. These characteristics need to be understood with guidelines to manage risk associated with these properties in concrete.

In 2001, the American Concrete Institute (ACI) released their first standard detailing recommendations of the use of FRP bars in reinforced concrete (RC). "Guide for the Design and Construction of Structural Concrete Reinforced with FRP Bars" (4) is the most current standard and was published in February 2006. ACI Committee 440 has chosen not to offer recommendations on the use of FRP bars in compression members due to the lack of experimental data at that time. The Canadian Code CAN CSA S806-12 (1) does include the use of GFRP in concrete compression members but ignores the contribution of GFRP when considering axial capacity.

## **1.3 Objectives**

Experimental research at University of Western Australia was undertaken by the writer in 2012 who compared the performance of axially loaded concrete columns reinforced with GFRP bars to traditional steel reinforcement "The Study of FRP Strengthening of Concrete Structures to Increase the Serviceable Design Life in Corrosive Environments" (5). The results concluded that the same axial capacity could be achieved using the same area of reinforcement providing the GFRP transverse reinforcement spacing

was lowered to approximately half that of the steel equivalent. That study led to the decision to construct concrete columns in an active project not only to achieve a corrosion resistant solution which would be economically beneficial, but to also monitor the performance of the columns, validating the findings of previous research.



**Figure 2. Existing Boardwalk in Tidal Zone.**

## **2. Initial Design Phase**

### **2.1 Constraints**

The project brief stipulated that remedial works undertaken must yield a similar appearance as the existing boardwalk. This therefore set column sizes at 300mm in diameter and required them to have a black exterior. The same size and arrangement of steel framing was to be used to support the decking. Whilst keeping to these aesthetic requirements, the Client required a design life of over 25 years. The portion of boardwalk being replaced was 23 years old.



**Figure 3. Typical Arrangement of Two Piles and Cross Beam.**

In the existing northeastern section of the boardwalk, there is pile support for the riverside of the boardwalk, with the steel cross beam which connects being supported in a recess into the limestone retaining wall on the land side. This connection was unstable as the retaining wall was rotating due to erosion issues below the boardwalk. This meant that new supports were needed to avoid reliance on the retaining wall for support.



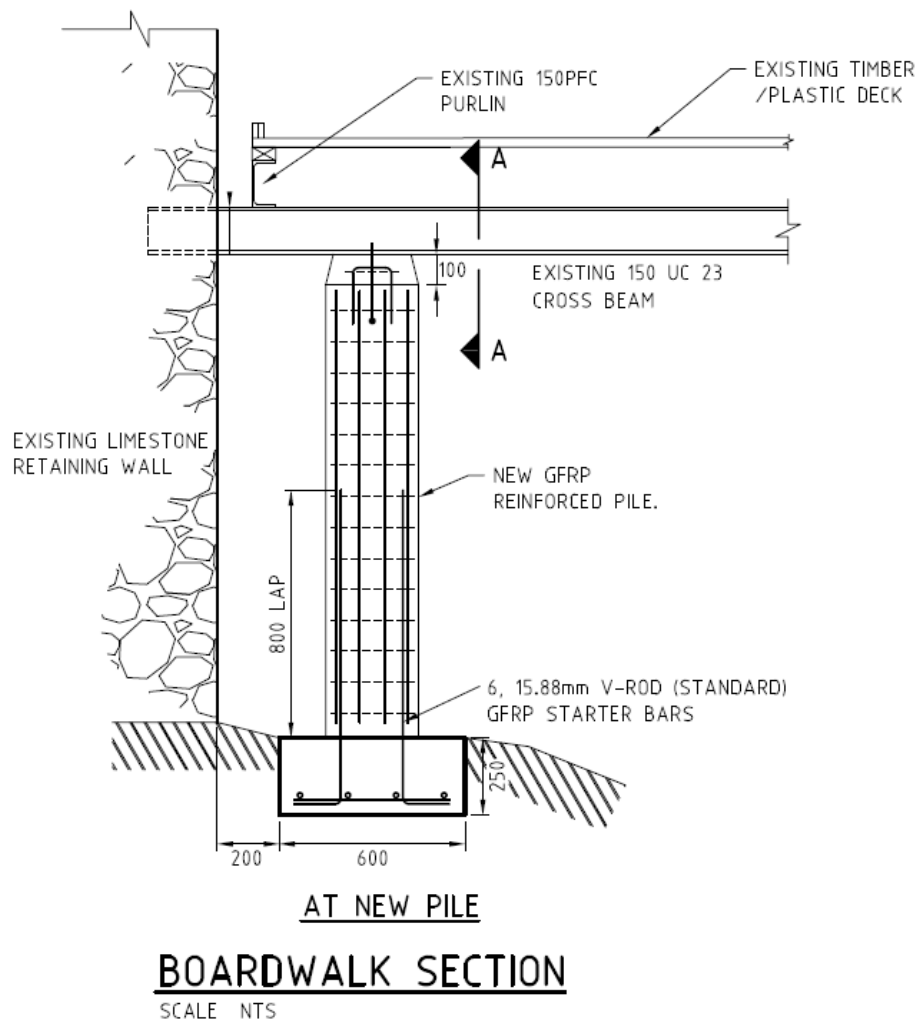
**Figure 4. Steel Cross Beam Embedded in Retaining Wall.**

## 2.2 Proposed Solution

The proposed solution included the replacement of pile supports whilst keeping a portion of the embedded steel UC pile to provide added anchorage of the element into the ground. The existing concrete encasement to piles was to be fully removed and replaced with a durable GFRP reinforced concrete solution. Whilst the existing steel UC pile was engaged, its requirement was designed out in the final design. This meant that a new footing would be required to support the concrete columns.

It was proposed that to eliminate the corrosion vulnerable column to superstructure connection, GFRP bolts would be cast into the new columns. This was deemed necessary as the steel framing for the decking was to be replaced and treated with an ultra-high build epoxy painting system so as to achieve a system that could be maintained over time and give a long design life of 20-25 years in a harsh marine environment.

Where the boardwalk cross beams were embedded in the limestone retaining wall adjacent, it was proposed to support them on new GFRP reinforced concrete columns identical to the replacement columns.



**Figure 5. Proposed Column and Footing Design.**

In the original construction there was a 300mm deep layer of sand extending up from the base of the concrete encasement of the steel piles. Over time this had been eroded away, in some cases exposing the limestone base below. This meant that two arrangements of footings were required to be designed, one founding on sand areas of the site and one founding on limestone.

### 3. Final Design

#### 3.1 Columns

The final design of the columns included six 15.88mm GFRP longitudinal bars with ligatures at 100mm centres made from 9.53mm GFRP bars. Although the bars are non-corrosive, it was decided that a pour blocker would be used in a 40MPa concrete mix to minimise concrete degradation. This was used with the intent of achieving a design life of the columns in excess of 75 years.

As there was the requirement for the new columns to look the same as the existing, permanent fibre cement formwork 300mm in diameter was specified and then painted black. This both allowed for easy forming and yielded a neat appearance.

The existing steel piles were nominated to be cut back to leave an 800mm lap to be embedded in the replacement column. Following this they were to be cleaned to a Class 2.5 finish according to AS 1627.4 using grinding to remove the bulk rusted layers followed by wet abrasive blast cleaning or a blasting / washing / blasting sequence to achieve effective removal of soluble salts. Surface chlorides were tested to ensure that they were less than 50 micrograms per square centimeter. Where otherwise, they were to be re-washed with inhibitor solution then re-blasted prior to coating with a corrosion inhibiting priming paint.

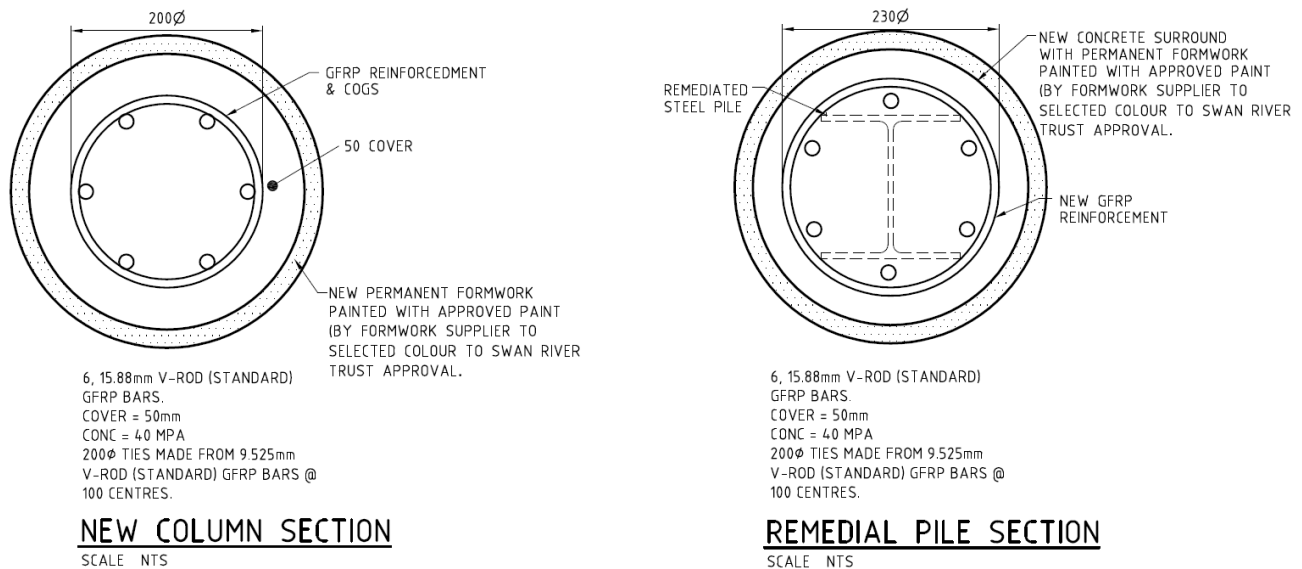


Figure 6. Final Column Design.

#### 3.2 Footings

The strip footings were designed to be able to support the loads through the new columns without the need for the engagement of the existing steel pile. One strip footing is used to support a pair of columns. The footing is 2.5 metres long, as required due to the placement of the columns, 600mm wide and minimum 250mm deep. The footing has bottom reinforcement, with six, 15.88mm GFRP bars equally spaced over the long span and four, 15.88mm GFRP bars over the short span. Six starter bars extend from the footings which would lap onto the main column reinforcement.

Due to the variable site conditions, the strip footing could be slightly altered for each case. Where sand is present, the footing and column are to be constructed with 500mm of sand above the top of the footing to allow for future erosion, or until bedrock is encountered. Where bedrock is exposed, the footing is to be recessed 250mm into the bedrock. These arrangements are shown in Figure 7.

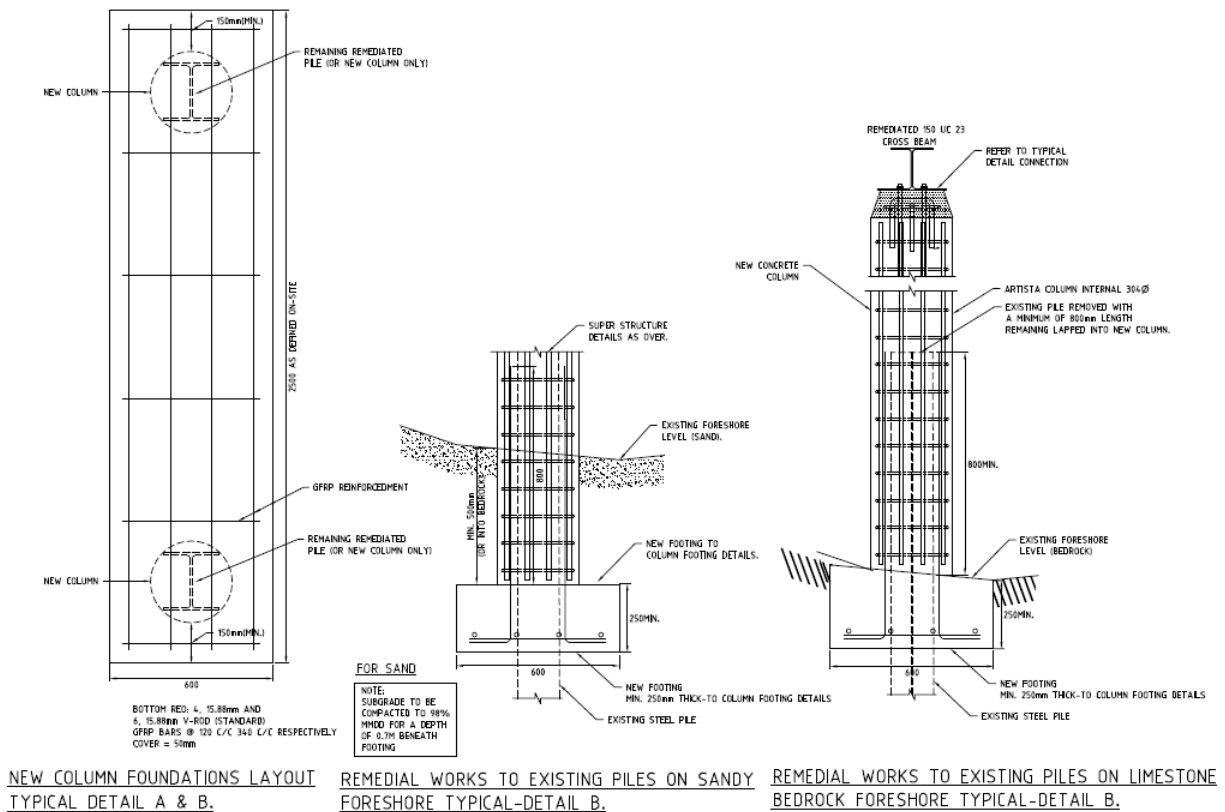


Figure 7. Final Footing Design.

### 3.3 Connection to Steel Framing

The connection detail between the new columns and the steel cross beams which support the decking is critical. As this zone was prone to the deposition of salts, GFRP bolts were assessed as the best material for fixing the columns to the steel. Four 24mm diameter GFRP threaded rods were anchored 1 metre into the new concrete column. The new steel UC cross beams which were fabricated had additional plates welded to the bottom flanges in order to allow for these bolts to be accommodated. Due to the high grade paint specification used, EPDM washers were used to protect the steel from the nut and washer fixings.

As there was a gap between the top of column and the underside of the steel cross beam, two 'U-bars' were fabricated from 15.88mm GFRP and cast into the top of the column. This allowed for a non-shrink structural epoxy grout to be used to infill the gap and be engaged by the remainder of the concrete column. The grout could then be tapered to the steel cross beam to minimise pooling of any moisture.

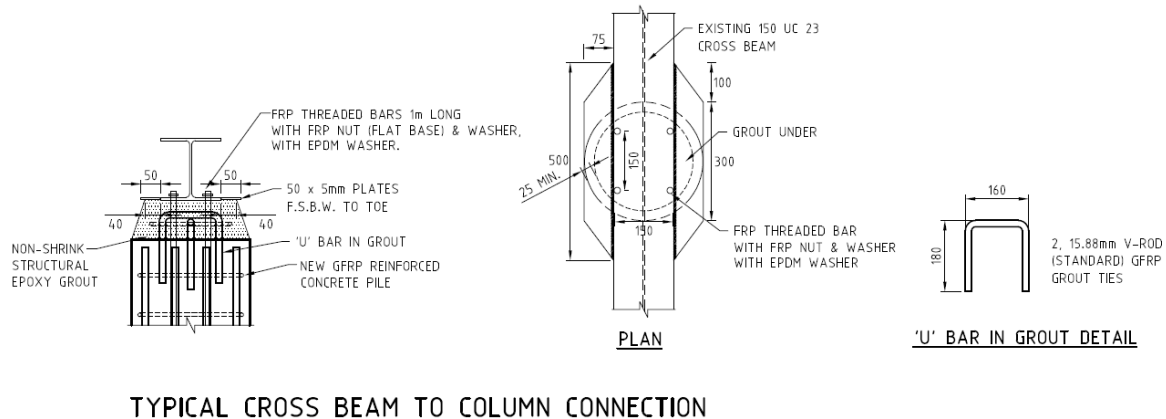


Figure 8. Final Column to Beam Connection.



## 4. Construction Phase

### 4.1 Footings

The existing steel UC piles were successfully cut back and cleaned via abrasive blasting and thorough wire brushing. Chloride tests were performed on five of the sixteen steel sections with all tests yielding results under the allowable 50 micrograms per square centimeter. The steel was then painted with the appropriate corrosion inhibitor within four hours of the chloride tests being undertaken. This ensured that no excess chloride deposition took place between the testing and painting phases.

The footings were formed and GFRP reinforcement and starter bars laid as per Airey Taylor Consulting drawings and specifications. All footings encountered bedrock and therefore all footings were recessed into the bedrock. Rock boulders would be placed at the base of the footings to assist in limiting erosion, protecting the retaining wall structure adjacent to the boardwalk. The Contractors noted the ease of laying the reinforcement due to its light weight. Plastic zip ties were used to tie bars together.



Figure 9. Forming and Pouring of Footings.

### 4.2 Columns

Once the footings were cast and cured, the column reinforcement cages, which were assembled on site, could be installed and the permanent formwork positioned and propped correctly. Timber plates were used to position the GFRP threaded rods at the correct height whilst the columns were poured.

The installation of GFRP reinforcement was completed in the same way that traditional steel reinforcement is. Contractor feedback focused on the lightweight material and the easy with which it was positioned.



Figure 10. Forming and Pouring of Columns.

### 4.3 Connection to Steel Framing

The steel cross beams were installed over the concrete columns and timber was used to hold the members at a slightly elevated level. The non-shrink structural epoxy grout was then placed and the steel lowered onto the grout to ensure there were no gaps between grout and steel. The grout was then tapered to give a rounded finish.

Once the cross beams were in place over the threaded rods, FRP washers and nuts, usually used for rock bolts, were installed over EPDM washers. This ensured that the paint on the steelwork was not damaged by the tightening of the nuts.



Figure 11. Column and Steel Connection.

### 4.4 Finished Boardwalk

Following installation of the steel framing, a composite decking was installed and the original hardwood handrails were reinstalled. After the remediation of the boardwalk reclaimed beach sand was placed over the top of the footings with a geotextile placed on top of that with additional rock armouring and beach re-nourishment. This was to aid in protecting the surrounding structures.

The construction phase was carried out in line with the final design and construction administration was performed by the writer throughout to ensure this was the case. The Client was very pleased with the outcome and the fact that the remediated portion of the boardwalk looked very similar to the existing, although now with a design life of 75 years for the columns and footings, minimizing their future maintenance costs in a very inaccessible area. The Contractor had no issues with the placement of GFRP and advised that it was similar to working with steel reinforcement but lighter.



Figure 12. New (left) vs Old Boardwalk (right).

## 5. Cost Analysis

Cost estimates were gathered from steel reinforcing suppliers in Perth for the fabrication and delivery of equal volumes of steel reinforcement compared to the GFRP bars specified. The steel estimates were approximately \$4,000 whereas the fabrication and delivery (via air freight) of GFRP came in at \$7,866. The price supplied for the same amount of GFRP but delivered via sea was \$6,810.



The difference of approximately \$4,000 is less than 1.5% of the total project cost which tendered for the amount of \$275,772.28 + GST. This was considered to be negligible, whilst the advantages in corrosion resistance and extended time prior to first maintenance are significantly increased.

## **6. Conclusion**

Previous experimental research performed by the writer in 2012 (5) concluded that concrete compression members reinforced with GFRP bars gave comparable capacities to concrete columns reinforced with traditional steel. This research was the basis of the design of the Dundas Point Boardwalk.

The use of GFRP reinforcement in compression members is not recommended by current guidelines and the Dundas Point Boardwalk is the first project in Australia known to have used the technique. This is considered a big step in the acceptance of GFRP as reinforcement not only in compression members but in all concrete structures in Australia. Whilst there are many projects overseas which utilize this material, Australia has been slow to adopt it, and as all things new, people want to see it used in projects before confidence can grow.

The additional 1.5% of the total project cost was assessed as a negligible outlay in order to achieve concrete members which are expected to give good in service duty for over 75 years. The lack of maintenance required will allow for this slight start-up price increase to be recouped multiple times over the life of the structure.

The Client was receptive to the use of GFRP reinforcement at the concept design phase of the project, and the Contractor had no negative feedback whilst using the material and commended the workability of the product. This project, the ease with which it was executed, and the attenuated durability expected will give confidence to others to adopt the material

## **7. Acknowledgements**

The writer would like to acknowledge the support provided by Mr John Clancy, Mr Peter Airey, Dr Anthea Airey and all Airey Taylor Consulting staff for their hard work and support in delivering this project. MMM WA Pty Ltd were crucial in ensuring the construction of the project went smoothly and were willing to learn and work with GFRP bars without any prior knowledge of the material. Thanks to the City of Melville team who were forward thinking and proactive in ensuring their public structure was designed and built to last, giving a very good return for the community they represent.

## **8. References**

1. CSA S806, 2012, "Design and Construction of Building Components with Fiber-Reinforced Polymers," Canadian Standards Association, Mississauga, ON, Canada
2. ISIS Canada Research Network, 2007, "Reinforcing Concrete Structures with Fibre Reinforced Polymers," ISIS Design Manual No. 3, ISIS Canada Research Network, Winnipeg, MB, Canada.
3. Standards Australia, 1997, AS1627.0 "Metal finishing - Preparation and Pretreatment of Surfaces - Part 0 -Method Selection Guide", Standards Australia International, Sydney.
4. ACI Committee 440, 2006, "Guide for the Design and Construction of Structural Concrete Reinforced with FRP Bars (ACI 440.1R-06)," American Concrete Institute, Farmington Hills, MI, 44 pp.
5. Brown, J., 2012, "The Study of FRP Strengthening of Concrete Structures to Increase the Serviceable Design Life in Corrosive Environments," University of Western Australia, Perth.

# A design methodology for fibre reinforced concrete slabs-on-grade

Ravindra Gettu<sup>1</sup> and Sunitha K Nayar<sup>2</sup>

<sup>1</sup>Professor of Civil Engineering, <sup>2</sup>Doctoral Research Scholar  
Indian Institute of Technology Madras, Chennai, India

**Abstract:** Slab-on-grade applications of fibre reinforced concrete have been widespread in the recent past. Design strategies based on inelastic analyses have been accepted for slabs-on-grade and utilized in many guidelines. Some of these have shortcomings due to the limitations of the material parameters adopted or due to the exclusion of critical failure modes, shrinkage and thermal stresses. This paper discusses a design methodology based on yield line analysis incorporating the equivalent flexural strength as the design material parameter, which can be used to choose a combination of fibre type and dosage, for a given concrete strength grade and slab thickness. All critical failure modes have been included in the analysis. The method also addresses the incorporation of thermal and shrinkage stresses systematically in the design. The outcomes of the method are compared with those of other guidelines in terms of slab thickness and fibre dosage.

**Keywords:** Fibre reinforced concrete, Slabs-on-grade, yield-line analysis, inelastic design, toughness.

## 1 Introduction

The effective exploitation of the crack resisting potential of fibre reinforced concrete (FRC) by the inclusion of appropriate material parameters in design methodologies is a necessity for applications such as slabs-on-grade, where FRC with relatively low dosages of fibres may be employed as "stand-alone" primary reinforcement. Many design guidelines are available in this area, in addition to those provided by manufacturers [1-7]. A detailed review of these methods brings out the following shortcomings:

- Most design methods use expressions from solutions of analysis done on large slabs, without considering the actual dimensions and behaviour of the slab [1-3], where the cracks interact with the boundaries. The consequent design solutions may underestimate the stresses generated since the failure mode is different in smaller slabs.
- Many methods use material parameters that may not appropriately represent the material in the slab systems. For example, the use of a constant multiplier (e.g., 0.7) for obtaining characteristic value from the mean value of toughness disregards the variations in the fibres due to differences in their production [1-3, 5]; and the use of an equivalent flexural strength ratio (instead of the absolute value) leads to the misinterpretation that the toughness is a multiple of the modulus of rupture (often calculated empirically from the compressive strength) [7-9].
- Thermal and shrinkage stresses are not dealt with, in detail, but could be significant when the slab is exposed to environmental changes and/or the joint spacing is large.

The present approach attempts to address the above mentioned limitations, as illustrated in the following sections.

## 2 Design philosophy

Incorporating fibres in concrete is expected to impart sufficient rotation capacity to the slab-on-grade during cracking so that the plastic moment capacity of the slab is fully mobilized. The ultimate load may then be estimated with the yield lines forming a mechanism and the regions bounded by the yield lines behaving as rigid-plastic sections. However, the yield line patterns and the corresponding ultimate loads are dependent upon the type of loading, slab dimensions and end conditions, as well as the soil pressure distribution [10-15].

### 2.1 Failure pattern

Based on the various possible cases, the following critical yield line patterns may be envisaged to occur in slabs-on-grade.

### Case 1: Circular fan type failure – for interior loading

Such failure has been typically considered in most design documents for FRC flooring, where radial cracks initially appear at the bottom of the slab and widen followed by circumferential cracking (Figure 1a). The moments along the radial yield lines equal the plastic moment capacity ( $M_p$ ) of the concrete and the negative moment ( $M_n$ ) at the top of the slab reaches the flexural capacity [1-3, 11-15]. The appearance of crack at the top is considered as the failure state. Such failure can occur only when the slab dimensions are large enough to allow the radial yield lines to develop followed by the circumferential yield lines. Meyerhof's solution [11], used by many design guidelines, for the ultimate collapse load is based on the large slab assumption; the condition is that the load should be at least at a distance of  $5l$  from where  $M_n/M_p = 1$ , with  $l$  being the radius of relative stiffness. This implies that such failure will occur only when the slab width is at least  $10l$ . Another possibility for this type of failure to occur is when the stress or load transfer mechanism between slabs is efficient enough for the adjacent slabs to behave monolithically as a large slab, which cannot normally be expected to happen, especially due to degradation of the concrete and shrinkage.

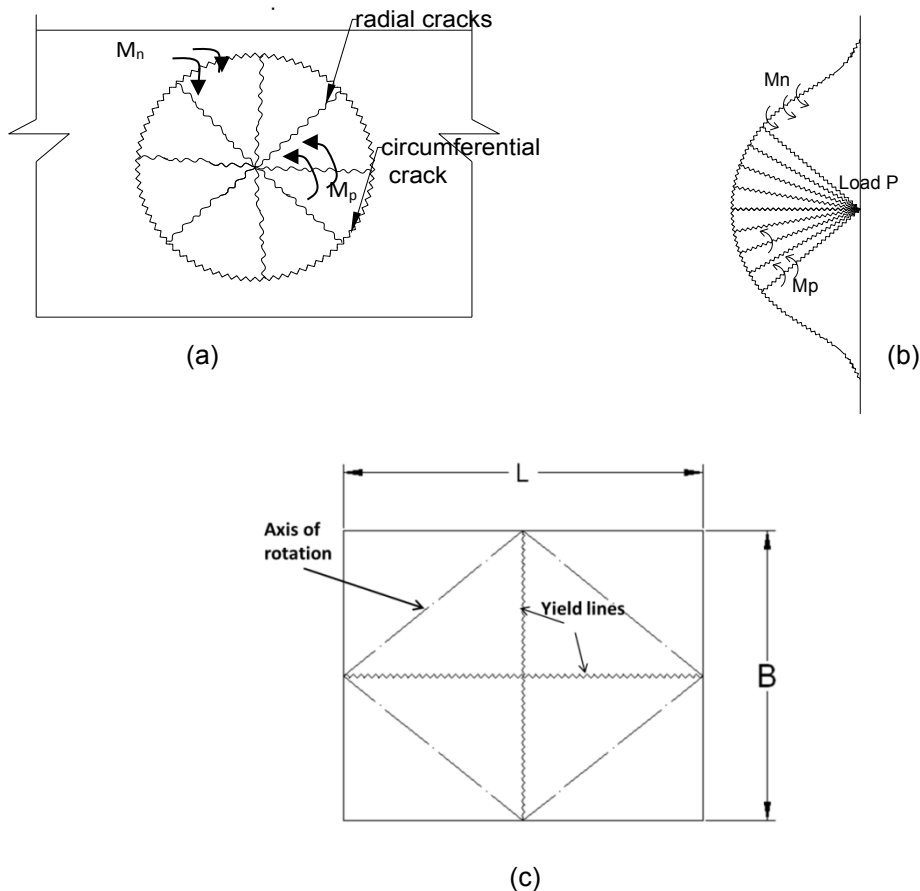


Figure 1. Yield lines: (a) Case 1, large slab; (b) Case 2, dominant edge load; (c) Case 3, free edges

### Case 2: D-cracking at the edges

In cases where the dimensions of the slabs are not large but more than 50% load transfer can be expected at the joints (i.e., enough to prevent free lifting of slab edges) or the loading is on or near the edge of the slab, the D-shaped failure pattern will govern [10, 11, 15]. Radial cracks start from under the load location followed by circumferential cracking, delimited by the edges of the slab (Figure 1b). As in the previous case, the radial yield lines are taken to have fully plastic moments and the circumferential yield lines are subjected to negative moments.

### Case 3: Centre line cracking – load in the interior of slab with free edges

Centre line cracking, as shown in **Figure 1c**, occurs when the slab is of finite dimensions and the edges are free to lift. The moment along all the yield lines may be assumed to be plastic as the slab rotates about the yield lines simultaneously; collapse is governed only by the plastic moment capacity [10].

#### 2.2 Limiting moment capacity estimate

The plastic moment capacity in the FRC slab is taken as the post-cracking moment carrying capacity, which is a function of the post-cracking flexural strength, such as the equivalent flexural strength specified in JSCE SF4 [16] or ICI/TC 01.1 [17]. Consequently, the plastic moment capacity per unit length of the slab is estimated as:

$$M_p = f_{e,nk} \frac{h^2}{6} \quad (1)$$

where  $f_{e,nk}$  is the characteristic equivalent flexural strength of concrete (obtained from the flexural test of an unnotched prism [16, 17]) corresponding to a specified deflection and  $h$  is the thickness of the slab. The equivalent flexural strength is used here instead of the residual strength since the former represents an average response over a range of crack widths rather than at a specific width, and exhibits lower variability than the latter [18-20].

The negative moment capacity is taken as a function of the flexural strength (or modulus of rupture) of the concrete (obtained from the same flexural test) as:

$$M_n = f_{ct,k} \frac{h^2}{6} \quad (2)$$

where  $f_{ct,k}$  is the characteristic value of the flexural strength of the concrete.

The corresponding moment estimates are used in the design equations suited to each yield pattern.

#### 2.3 Design equation and validation

The design equation is formulated to determine the required flexural strength and equivalent flexural strength for each critical loading condition as:

$$f_{e,nkrequired} = \left[ \frac{6M_{applied}}{h^2} - f_{ct,k} \right] \quad (3)$$

for cases where the limiting moments is given by the sum of the plastic positive and negative moment capacities (i.e., the circular and D-cracking cases), as  $M_{limit} = M_n + M_p$ .

For cases where the limiting moment is only the plastic positive moment capacity (i.e., for centre line cracking), the design equation is:

$$f_{e,nkrequired} = \left[ \frac{6M_{applied}}{h^2} \right] \quad (4)$$

$M_{applied}$  is obtained for each loading condition from yield line or other suitable inelastic analysis as:

$$M_{applied} = f\left(P, \frac{c}{l}\right) \quad (5)$$

where  $P$  is the factored applied load,  $c$  is the contact radius of the load application, and  $l$  is the radius of relative stiffness.

In accordance with the Winkler foundation approximation for subgrade, the value of  $l$  is taken as:

$$l = 4 \sqrt[4]{\left[ \frac{Eh^3}{12(1-\mu^2)k} \right]} \quad (6)$$

where  $E$  is the modulus of elasticity,  $\mu$  is the Poisson's ratio of concrete and  $k$  is the subgrade modulus.

In order to assess the validity of the methodology, the failure load obtained following the suggested method has been compared to the results of tests of FRC slabs by Falkner et al. [21]; the details of the test parameters are given in Table 1. The design was done assuming centre-line cracking to occur, since the slab dimensions do not meet requirements for circular cracking and the free edge conditions that permit the uplift of the slab rule out D-cracking. The limiting moment function is taken from the expressions given by Meda 2003 [10] as:

$$f_{e,3,krequired} = \frac{3P}{3h^2} \left[ 1 + \frac{1}{6} \frac{k}{K_s/B^2} \right] \quad (7)$$

where

$$K_s = \frac{86D}{\left( B\sqrt{2}/2 \right)^2} \text{ and } D = kl^4 \quad (8)$$

where  $B$  is the width of the slab = 3 m,  $h = 150$  mm,  $k = 0.025$  N/mm<sup>3</sup>. The terms needed for applying Eqn. (7) can be calculated as  $l = 540$  mm and  $K_s = 129$  kN/mm using the parameters in Table 1. The calculated load capacity is 185 kN, which falls between the reported fracture load of 165 kN and collapse load of 240 kN from the test results.

**Table 1. Parameters from the tests of Falkner et al. (21)**

Parameters	Values
Slab dimension	3.0 m × 3.0 m × 0.15 m
Loading plate dimensions	120 mm × 120 mm
Grade of concrete	C30/37
Fibre type used	Steel fibres, 60 mm long, diameter of 0.75 mm (Dramix RC 80/60 fibres)
Fibre dosage	20 kg/m <sup>3</sup>
Bedding type	Cork with $k = 0.025$ N/mm <sup>3</sup>
Elastic modulus of concrete	23400 N/mm <sup>2</sup>
Flexural strength of concrete $f_{ctk,fi}$	4.52 MPa*
Equivalent flexural strength $f_{e,150k}$	3.19 MPa*

\*Estimated from tests performed on similar FRC with same grade of concrete, fibre type and fibre dosage at IIT Madras

## 2.4 Thermal stresses

In cases where the temperature variations are significant, the design has to account for thermal stresses, especially in regions where the negative moment is critical. Axial tensile forces could occur if the temperature is uniform over the depth (usually occurs for thinner slabs) [22, 23]. A conservative estimate of the axial stresses has been suggested by Ghosh and Dinakaran [23], and Yoder and Witzack [22], as:

$$\sigma_{\Delta T_{axial}} = 24 \frac{wLf}{h} \quad (9)$$

where  $w$  = weight of slab, in N/m<sup>2</sup>,  $L$  = length of slab, in m,  $f$  = coefficient of subgrade restraint (<1.0), and  $h$  = thickness of slab, in m. However, these stresses are generally negligible and are, consequently, not taken into account in practice.

Flexural stresses could be generated when there are substantial temperature gradients [2, 4, 13], which can reduce the negative moment capacity to resist applied loads, affecting failure occurring with circular and D-cracking:

$$M_{limit} = M_p + (M_n - M_{\Delta T}) \quad (10)$$

Therefore, the required equivalent flexural strength value is to be modified to account for this, as:

$$f_{e, n_{krequired}} = \frac{6P}{h^2} f\left(\frac{c}{l}\right) - f_{ctk} + f_{\Delta T} \quad (11)$$

where  $f_{\Delta T}$  is the flexural stress due to the temperature differential ( $\Delta T$ ) in the slab. This could be estimated using the classical Bradbury's equation as:

$$f_{\Delta T} = \frac{E\alpha\Delta T}{2(1-\nu^2)} (C_1 + \nu C_2) \quad (12)$$

where  $\alpha$  is the coefficient of thermal expansion, and  $C_1$  and  $C_2$  are the Bradbury's correction factors for curling in finite slab, which are obtained from charts prepared for various values of  $L/l$ , where  $L$  is the joint spacing [22].

## 2.5 Shrinkage stresses

Proper concrete mix design and good construction practices are key to reducing shrinkage stresses in concrete, especially in the plastic stage. In hardened concrete, shrinkage stresses can be considerably reduced by providing friction relief layers, such as polyethylene sheets, so as to reduce the restraint against shrinkage, and by providing properly-prepared joints at adequate intervals [1-3]. Typically, sawn joints are recommended, with groove widths not less than 3 mm and depths of about 1/3<sup>rd</sup> to 1/4<sup>th</sup> the thickness of the slab [24]. The joint spacing depends on the amount of restraining stress and the tensile strength of concrete, both of which will depend on the composition and quality of concrete, and the length-to-width ratio of the slab. The following recommendations, compiled from existing standards, may be adopted:

- Joints may be located along the column lines with intermediate joints located at equal spacing between column lines (ACI 360R [3]).
- Maximum limit on length/width ratio = 1.5 (TR34 2003, TR34 2013 [1-2])
- Largest dimension between joints can be restricted to 4.5-6 m depending upon the thickness. (with smaller values for higher thicknesses) (TR34 2003, TR34 2013, IRC 15 [1-2,24])
- ACI 360R charts for joint spacing in unreinforced slabs or slabs with reinforcement for temperature or shrinkage stresses, obtained based on shrinkage measurements on concrete as per ASTM C157/ C157M, may be adopted in design [3].

Since the stress levels in concrete due to shrinkage could be considerable, an approach similar to that used for curling stresses is recommended in line with the method suggested in TR 34 2003 [1]. Thereby, the shrinkage stresses estimated from the ultimate (free) shrinkage strain values ( $\epsilon_{sh}$ ) may be reduced from the total negative moment capacity, as:

$$M_{limit} = M_p + (M_n - M_{\Delta T} - M_{sh}) \quad (13)$$

and the flexural stress associated with the moment due to shrinkage strain is calculated as:

$$f_{sh} = E \varepsilon_{sh} \quad (14)$$

where  $E$  is the modulus of elasticity of concrete and  $\varepsilon_{sh}$  is the ultimate shrinkage strain.

In the absence of data, a value between 300–500 microstrains may be assumed as the ultimate shrinkage strain of concrete. Further, a restraint factor of 0.2 may be assumed when a friction release layer is used, following TR34 (2003) [1], and the reduced shrinkage stresses may be computed as

$$f_{sh} = 0.2 E_{cm} \varepsilon_{sh} \quad (15)$$

## 2.6 Final design equations

Incorporating thermal and shrinkage stress in Eqn. (3), the final design equation for circular or D-cracking becomes:

$$f_{e, nkr} = \frac{6P}{h^2} f(c/l) - f_{ctk} + f_{\Delta T} + f_{sh} \quad (16)$$

Once the critical equivalent flexural strength value is determined by considering all possible loading and failure patterns, this can be specified as the performance requirement for choosing the fibre type, dosage and concrete mix, for the specified slab thickness. The choice can be made using any existing material database or test data.

From the actual parameters corresponding to the fibre type, dosage and concrete mix, preferably from test data, a design check has to be performed by calculating the allowable load, using the inelastic design equations (e.g., Eqn. 16), and ensuring that the following is satisfied:

$$P_{allowable} > P_{actual} \quad (17)$$

## 3 Comparison of design guidelines

The suggested method is compared in this section with design solutions obtained from various existing guidelines in terms of slab thickness and fibre dosage; comparisons were made with TR34 2003, TR34 2013, ACI 360 R-10 and the Losberg yield line method [1-3, 12]. The parameters that are significant for each method are shown in **Table 2**.

TR34:2003 uses the Meyerhof's equation wherein the equivalent flexural strength ratio is used to calculate the plastic moment capacity and the flexural strength for the negative moment capacity estimate to arrive at the allowable load. The TR34:2013 method uses the residual flexural strength (from a notched beam test) as the material parameter and neglects thermal and shrinkage stresses in the design equations, which results in an underestimation of stresses resulting in a less conservative design. ACI 360R uses the approximate equations suggested in Meyerhof's analysis for a slab on elastic foundation, with the assumption that the contact radius of the load ( $c$ ) is equal to or greater than the thickness of the slab, which leads to severe underestimation of the stresses. In Losberg's yield line analysis, the soil pressure distribution curves developed based on the elastic theories for the infinite elastic slab lead to more conservative estimates than the Meyerhof's analysis.

Allowable loads were obtained here, using the above-mentioned methods, for different slab thicknesses, for an M35 grade concrete having 20 kg/m<sup>3</sup> hooked ended steel fibres of length 60 mm and aspect ratio of 80. The material parameters for this combination were obtained from tests performed on notched and unnotched prism specimens, as listed in

**Table 3.** The stress due to thermal and shrinkage strains was taken as 1.5 MPa, based on TR34:2003 recommendations.

**Table 2 Details of parameters used in each method**

Design method	Input variables	Input material parameters	Dependent material parameters	Output variable
TR 34:2003 [2]	Load (P) Subgrade modulus (k) Thickness (h)	$R_{e,150}$ Grade of concrete	Type of fibre Dosage of fibre $f_{ctk}$	$P_{all}$
Losberg [12]	Load (P) Subgrade modulus (k) Thickness (h)	$f_{e,150mean}$ Grade of concrete	Type of fibre Dosage of fibre $f_{ctk}$	$P_{all}$
ACI 360 [3]	Load (P) Subgrade modulus (k) Thickness (h)	Grade of concrete	Type of fibre Dosage of fibre $f_{ctk}$	$R_{e,150}$ $P_{all}$
TR34:2013 [1]	Load (P) Subgrade modulus (k) Thickness (h)	$f_{r1}/f_{r4}$ Grade of concrete	Type of fibre Dosage of fibre $f_{ctk}$	$P_{all}$
Suggested method	Load (P) Subgrade modulus (k) Thickness (h)	Grade of concrete	$f_{ctk}$	$f_{ek,150}$ $f_{ctk actual}$ $P_{all}$

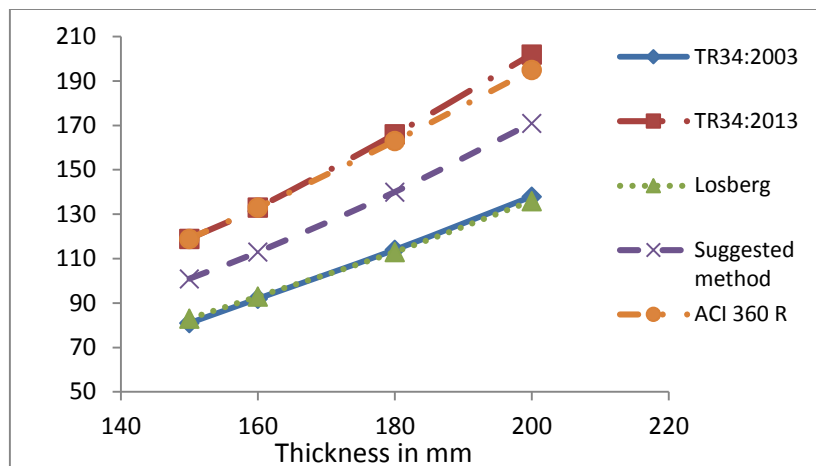
**Table 3 Material parameters used in the design comparison**

$f_{ct}$ , MPa		$f_{e,150n}$ MPa		$f_{r1}$ MPa		$f_{r4}$ MPa		$R_{e,150}$ %		Assumed stress due to thermal and shrinkage strains, MPa
Mean	Char	Mean	Char	Mean	Char	Mean	Char	Mean	Char	
5.80	4.87	3.72	2.8	3.96	2.86	4.17	3.26	64	64	1.50

Char: characteristics value

From **Figure 2**, it can be seen that the allowable load calculated as per the suggested method is higher than those obtained from the Losberg's yield line method and TR 34:2003 while it is lower than the allowable load as per TR34:2013 and ACI-360 R. For the case considered, the suggested method gives a higher capacity than TR34:2003 and Losberg yield line methods since it takes into account the characteristic value of the mechanical parameters from actual test results rather than taking the characteristic value as  $0.7 \times$  mean value; in this case, the actual characteristic strengths are higher than those obtained with the factor of 0.7. However, the suggested design method would give a lower estimate than TR34 2003 and Losberg's methods if the characteristic values were lower. It is, therefore, more realistic to take the actual characteristic values in the design rather than factored mean values.





**Figure 2 Comparison of allowable loads for different slab thickness**

Since the TR34:2013 and the ACI 360R methods are consistently less conservative than the other three methods, the next comparison only considers the suggested method, and the TR34:2003 and Losberg's yield line methods. The minimum required fibre dosage (for the same fibre type considered earlier) for a tyre load = 80kN, slab thickness = 120 mm and  $k = 0.02 \text{ N/mm}^3$  is calculated, assuming that the failure occurs by D-cracking, and reported in Table 4. The results suggest that for the same design parameters, the dosage of fibres required as per the suggested method is lowest thus providing the most economical design.

**Table 4. Minimum fibre dosage**

Design method	Minimum required $f_{e,150k}$ , MPa	Corresponding minimum dosage of the fibre considered, $\text{kg/m}^3$
TR34:2003	1.7	16
Losberg method	2.5	27
Suggested method	1.5	10

For the same combination of load and  $k$ , if the design by suggested method is done by assuming failure to be governed by centre line cracking (assuming a slab of  $3.0 \text{ m} \times 3.0 \text{ m}$  dimensions), then the design requires a minimum thickness of 150 mm (as opposed to 120 mm for D cracking) and a dosage of  $30 \text{ kg/m}^3$  of same fibres. Thus, it can be seen that the suggested method provides solutions that account for critical failure situations encountered in practice (normal size slabs without sufficient load transfer), and can be more conservative than other methods, such as the TR34:2003 method.

## 4 Conclusions

The prominent conclusions brought out in this study are

- A design methodology, for fibre reinforced concrete slabs-on-grade, based on yield line analysis is proposed wherein the material parameter adopted is equivalent flexural strength. The equivalent flexural strength has been taken as the basis since it gives a more realistic estimate of the post cracking capacity of the slabs-on-grade. The design equation estimates the required equivalent flexural strength for the given loading condition leading to a performance requirement for concrete.

- The governing design equations are dependent on the yield pattern that occurs based on the dimensions and end conditions of the slab. The design solutions of the suggested method are compared with existing design methods. It is seen that the current method can account for differences in the quality of concrete by the explicit use of the characteristic flexural strength and toughness parameter, instead of generic factors, and failure in small slabs by centre-line cracking.

## 5 References

1. The Concrete Society, "Concrete Industrial Ground floors: A Guide to Design and Construction (TR34)", England, U K, 2013.
2. The Concrete Society, "Concrete Industrial Ground floors: A Guide to Design and Construction (TR 34)", The Concrete Society, England, U K, 2003.
3. American Concrete Institute, "Guide to design of slab-on-ground (ACI 360R)", Detroit, USA, 2010.
4. Gettu, R., Schnütgen, B., Erdem, E., and Stang, H., "Design Methods for Steel Fiber Reinforced Concrete: A State-of-the-Art Report", Report of Sub-task 1.2. Test and Design Methods for Steel Fiber Reinforced Concrete Brite-EuRam Project, BRPR-CT98-0813 (DG12-BRPR), 2000, 55 pp.
5. Bekaert NV Dramix Manual, "Steel Fibre Reinforced Industrial floors – Design in Accordance with Concrete Society TR 34", Bekaert, 2001, 44 pp.
6. [http://www.maccaferri.com.au/webfiles/MaccaferriAu/files/Industrial\\_Flooring\\_Brochure\\_2011.pdf](http://www.maccaferri.com.au/webfiles/MaccaferriAu/files/Industrial_Flooring_Brochure_2011.pdf), last accessed 12.02.15
7. DiPrisco, M., and Mauri, M., "Fibre-Reinforced Concrete Industrial Flooring Slabs, FIBERFIX-BADESSI", A-fibres technology Pvt. Ltd., 2004, 26 pp.
8. Elsaigh, W. A., Kearsley, E. P. and Robberts, J. M., "Steel Fibre Reinforced Concrete for Road Pavement Applications", Proceedings of 24<sup>th</sup> Southern African Transport Conference (Pretoria), 2005, South Africa, pp 191-200.  
<http://repository.up.ac.za/bitstream/handle/2263/6329/021.pdf?sequence=1>; accessed 31st July 2013.
9. Altoubat, S. A., Roesler, J. R., Lange, D. A., and Reider, K. A., "Simplified method for concrete pavement design with discreet structural fibres", Construction and Building Materials, Vol. 22, 2008, pp 384-393.
10. Meda, A., "On the extension of the yield-line method to the design of SFRC slabs-on-grade", Studies and Researches, Vol. 24, Graduate School of Concrete Structures, Politecnico di Milano, 2003, Italy.
11. Meyerhof, G. G., "Load carrying capacity of concrete pavements", Journal of the Soil mechanics and Foundations Division, Vol. 88, No 3, 1962, pp 89-116.
12. Losberg, A., "Design methods for structurally reinforced concrete pavements", Transactions of Chalmers University of Technology, 1961, Sweden.
13. Losberg, A., "Pavements and Slabs on Grade with Structurally Active Reinforcement", ACI Journal, Vol. 75, No 12, December, 1978, pp 647-657.
14. Rao, K. S. S., and Singh, S., "Concentrated load carrying capacity of concrete slabs-on-ground", Journal of Structural Engineering, ASCE, Vol. 112, No 12, December, 1986, pp 2628-2642.
15. Baumann, R. A., and Weisberg, F. E., "Yield-line analysis of slabs-on-grade", Journal of Structural engineering, ASCE, Vol. 109, No 7, July, 1983, pp 1153-1568.
16. The Japan Society of Civil Engineers, "Method of Tests for Steel Fibre Reinforced Concrete (JSCE, Part III-2 (SF1 – SF4))", Concrete Library of JSCE, Tokyo, Japan, 1984.
17. Indian Concrete Institute, "Test Methods for the Flexural Strength and Toughness Parameters of Fiber Reinforced Concrete (ICI-TC/01.1)", Technical Committee Recommendation, ICI Journal, Vol. 15, No 2, 2014, pp 39-43.

18. Parmentier, B., Vandewalle, L., and Rickstal, F. V., "Evaluation of scatter of the post peak behaviour of fibre reinforced concrete in bending: A step towards reliability", Proceedings of Seventh International RILEM symposium of FRC: Design and applications, BEFIB, Ed. Gettu, R., Chennai, India, 2008, pp 133-144.
19. Vandewalle, L., Rickstal, F. V., Heirman, G., and Parmentier, B., "On the round panel and 3-point bending tests", Proceedings of Seventh International RILEM symposium of FRC: Design and applications, BEFIB, Ed. Gettu, R., Chennai, India, 2008, pp 173-182.
20. Merretz, W., Borgert, J., Smith, G., and Baweja, D., "Steel reinforced concrete in construction contracts and the 3 mm residual flexural strength beam test", Proceedings of Concrete 2011- Building a sustainable future, Perth, Australia, 2011.
21. Falkner, H., Huang, Z., and Teutsch, M., "Comparative Study of Plain and Steel Fibre Reinforced Concrete Ground Slabs", Concrete International, Vol. 17, No 1, 1995, pp 45-51.
22. Yoder, E. J., and Witczak, M. W., "Principles of pavement design", A Wiley Inter-Science publication, John Wiley and Sons, USA, 1975.
23. Ghosh, R. K., and Dinakaran, M., "Breaking load for rigid pavement", Transportation Engineering Journal, Proc. of ASCE, Vol. 96, No 1, February, 1970, pp 87-107
24. Indian Road Congress, "Standards, Specifications and Code of Practice for Construction of Concrete Roads (IRC: 15)", New Delhi, India, 1988.

# FRP Anchors for FRP-Strengthened Concrete Structures: Numerical Modelling

Scott T. Smith<sup>1</sup>, Jia-Qi Yang<sup>2</sup> and Zhen-yu Wang<sup>3</sup>

<sup>1</sup>Foundation Professor of Engineering, Southern Cross University, NSW, 2480, Australia

<sup>2</sup>Engineer, Country Garden Group, Foshan, Guangdong Province, China

<sup>3</sup>Professor, Harbin Institute of Technology + Key Lab. of Structures Dynamic Behavior and Control, China

**Abstract:** The application of anchorage devices to externally bonded fibre-reinforced polymer (FRP) strengthening systems for concrete structures is an intuitive solution to the debonding problem. While there have been experimental investigations of FRP anchors in FRP-concrete bonded interfaces to date, there has been decidedly less numerical modelling research. This paper presents the details of a finite element analysis of FRP-concrete joints anchored with FRP anchors. The finite element model as well as test results are also used to calibrate a constitutive model for the FRP anchor. The numerical simulations are shown to compare favourably with test results, and the simulations allow insights to be gained about the various components of FRP-concrete bonded interfaces anchored with FRP anchors.

**Keywords:** Finite elements, FRP, modelling, strengthening.

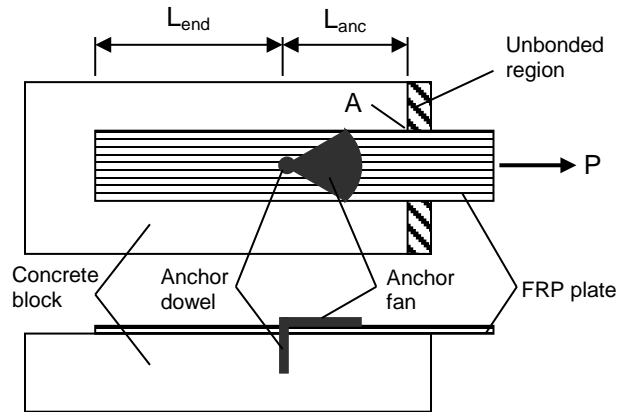
## 1. Introduction

Reinforced concrete (RC) structures can be strengthened with externally bonded fibre-reinforced polymer (FRP) composites. There have been numerous experimental studies conducted to date on FRP-strengthened RC members and a commonly observed failure mode has been premature debonding of the FRP [1, 2]. In order to delay or even prevent debonding failure, anchorage devices can be installed onto the FRP strengthening. The effectiveness of anchorage devices has been experimentally verified and quantified in a recent study by Kalfat et al. [3]. There have, however, been limited finite element investigations on anchorage devices and their use in FRP-strengthened structures thus far. Of central importance to such modelling are constitutive models for the anchorage devices. There has been limited development of such models to date.

Anchors made solely from FRP are referred to as FRP anchors. They are suitable for anchoring a wide variety of FRP strengthening applications ranging from beams to slabs. A convenient means to investigate the influence of FRP anchors is to incorporate them into FRP-concrete joints [e.g. 4, 5]. Figure 1 shows a typical joint as well as a FRP anchor hand-made from carbon fibre sheet and epoxy. A noticeable relationship between the position of the anchor relative to the loaded plate end has been observed from tests [6]. As the length  $L_{anc}$  is decreased, the load carrying capacity of the joint is increased. In addition, as the length  $L_{end}$  is increased past a threshold value, the load carrying capacity of the joint reaches a plateau. Other relationships between various geometrical parameters have been found to exist through experimentation, however, the trends concerned with anchor position and plate length are of most relevance to this paper.

A means to quantify the joint behaviour is to monitor the relationship between load applied to the free-end of the plate,  $P$ , versus the relative movement between the FRP and the adjacent concrete substrate at point A (i.e. slip,  $s$ ). Figure 2a is a generic load-slip relationship that has been compiled from numerous tests on FRP-concrete joints anchored with FRP anchors [6]. The anchor is activated once the load to initiate debonding  $P_{db}$  has been reached and the debonding crack has propagated to the anchor position. The peak load carrying capacity of the joint is reached at load  $P_{max,1}$ . At this stage the debonding crack has reached the unloaded plate end upon which the plate completely debonds at slip  $s_{max,1}$  and the load is reduced. A post-peak reserve of strength of load  $P_{max,2}$  is then maintained until anchor failure at slip  $s_{max,2}$ .

This paper presents the details of a constitutive model for FRP anchors that is derived from finite element analysis and calibrated with experimental results of FRP-concrete joints anchored with FRP anchors. ABAQUS [7] is utilised to perform the numerical simulations. An earlier paper has also developed a constitutive model for the FRP anchor using the same tests considered herein by Zhang and Smith [8]. This earlier model differed in that it utilised a partial interaction method of analysis with which to perform the numerical simulations.

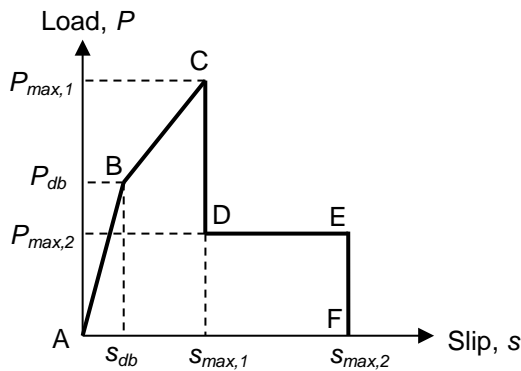


(a) FRP-concrete joint with FRP anchor: single shear arrangement

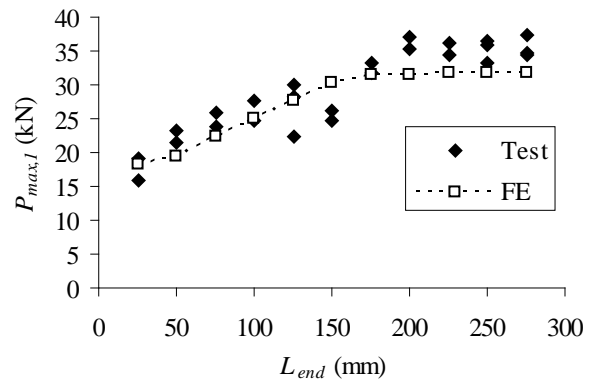


(b) Hand-made FRP anchor

**Figure 1. FRP-concrete joint and FRP anchor.**



(a) Generic Load-Slip model



(b) Test results

**Figure 2. Summary of results of FRP-concrete joints anchored with FRP anchors.**

## 2. Test results

Twenty five test results of FRP-concrete joints anchored with FRP anchors are utilised to calibrate the FRP anchor constitutive model. A detailed account of the test joints is provided in Zhang [6] although a brief overview is provided herein in relation to the features most relevant to this paper. For all joints, the anchor was located 75 mm from the loaded bonded plate end (i.e.  $L_{anc} = 75$  mm). The length of the plate between the anchor and the unloaded plate end ( $L_{end}$ ) was varied from 25 mm to 275 mm in 25 mm increments, and hence the total plate length was varied from 100 mm to 350 mm. The average concrete compressive cube strength was 55.1 MPa and the elastic modulus was 30.2 GPa. The FRP plate, which was made from three layers of carbon fibre sheet in a wet lay-up manner, had a tested tensile strength of 2978 MPa and elastic modulus of 227.5 GPa. Each FRP anchor was hand-made from a 200 mm wide carbon fibre sheet of the same type of fibre used to make the FRP plates. The cross-sectional dimensions of the concrete blocks were 200×200 mm<sup>2</sup> while the length of each block was 200 mm. In addition, a 20 mm unbonded zone was maintained at the loaded end of the joint. Figure 2a shows the test relationship between  $P_{max,1}$  and  $L_{end}$ . The load reaches a plateau at an  $L_{end}$  of about 175 mm.

### 3. Finite Element Model

#### 3.1 Element and mesh details

ABAQUS [7] was utilised to construct a two-dimensional finite element model of the generic joint shown in Figure 1a with the geometric and materials properties provided in Section 2. The model, along with the boundary conditions and element details, is shown in Figure 3.

A two-node truss element of ABAQUS designation T2D2 was utilised to model the FRP plate and concrete block components. In addition, a 4-node cohesive element designated as COH2D4 by ABAQUS was used to model the FRP-concrete interface as well as the FRP anchor. A single element was used to model the FRP anchor. The thickness of the cohesive elements was set to 1 mm in order to maintain a proportional relationship between the shear stress and the slip between the concrete and FRP nodes.

Mesh convergence studies yielded no significant variation on results and hence a 1 mm element size in the longitudinal direction was adopted. A linear-elastic analysis was utilised owing to the low stress level experienced in the concrete and the linear-elastic behaviour of the FRP and epoxy.

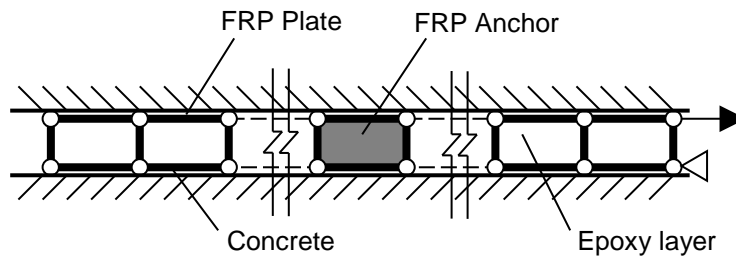


Figure 3. Finite element model and boundary conditions.

#### 3.2 Constitutive models

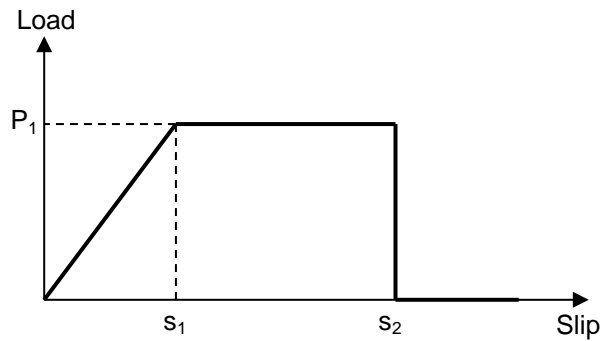
A linear-elastic relationship was used to define the response of the concrete block and FRP plate. Lu et al.'s [9] simplified bond-slip model was used for the cohesive FRP-concrete elements. The relationship for the cohesive element of the FRP anchor is derived from the P-s response of the anchor. In order to establish such a relationship, the FRP anchor can be idealised as a mechanical connector. Figure 4 shows a generic anchor response that is based on the response of mechanical shear connectors in steel-concrete composite structures [e.g. 10]. The response can be expressed algebraically as follows in Equation 1. Other relationships are provided in Reference [6] although the model shown in Figure 4 is satisfactory for its intended use.

$$P = (s/s_1) P_{anc} \quad 0 < s \leq s_1 \quad (1a)$$

$$P = P_{anc} \quad s_1 < s \leq s_2 \quad (1b)$$

$$P = 0 \quad s > s_2 \quad (1c)$$

The maximum shear force that the anchor can sustain is  $P_{anc}$  and this occurs at slip  $s_1$ . Afterwards, the load reaches a plateau. Anchor failure at slip  $s_2$  causes the load carrying capacity of the anchor to be lost. Note that tests have shown the slip  $s_2$  typically to be several times greater than the slip at debonding initiation and subsequent anchor activation.



**Figure 4. Constitutive model of FRP anchor.**

The force that is applied to the plate is assumed to be resisted by the intact (non-debonded) FRP-concrete bond, as well as the frictional resistance arising from the debonded plate. Measured responses of Figure 2a for selected test joints can therefore be used to extract these two components of resistance and hence such responses can be used to calibrate a constitutive model for the FRP anchor.

### **3.2.1 Calibration of $P_1$**

The anchor force capacity is denoted as  $P_1$  and it is equal to  $P_{\max,2}$  arising from the load-slip response of each test joint. The value of  $P_{\max,2}$  of each of the 25 test joints is reasonably consistent and the average value arising is 12.92 kN. This consistency means that the force capacity of the anchor depends more on the anchor properties than the geometric and material properties of the test joint.

### **3.2.2 Calibration of $s_2$**

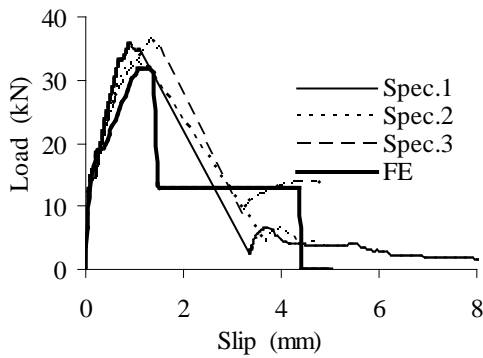
The slip capacity of the anchor,  $s_2$ , is equal to  $s_{\max,2}$  arising from the test load-slip responses. The average of the measured values is equal to 4.11 mm.

### **3.2.2 Calibration of $s_1$**

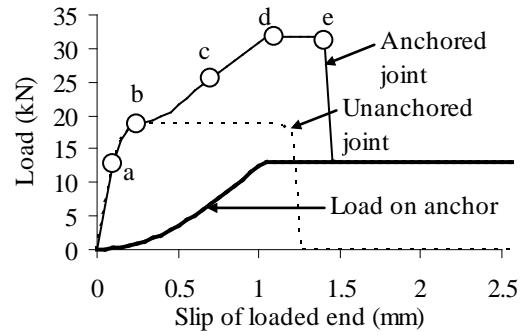
The anchor first reaches  $P_1$  at slip  $s_1$  (i.e. the anchor yields). As  $s_1$  cannot be directly extracted from the measured load-slip responses, recourse is therefore made to finite element analysis. According to the test results contained in Figure 2b,  $P_{\max,1}$  peaks when  $L_{\text{end}} = 175$  mm. This corresponds to a test joint of 250 mm bond length (i.e.  $L_{\text{anc}} = 75$  mm, plate length =  $L_{\text{anc}} + L_{\text{end}}$ ). Values of  $s_2$  are varied in the analysis of the test joint until  $P_{\max,1}$  coincides with yield of the anchor. Note that the value of  $P_{\max,1}$  is obtained from the simulated stress and the simulated value of  $s_1$  is determined to be equal to 0.1 mm.

## **4. Results**

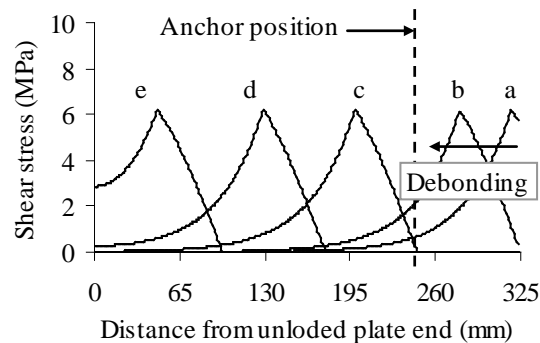
The simulated results of several joints of varying bond length are provided in Zhang [6]. The load-slip responses of one joint of long bond length (i.e. 325 mm) are presented herein in Figure 5. The long bond length ensures that the full load capacity (i.e.  $P_1$ ) of the anchor is able to be developed.



(a) Load-slip: prediction versus tests



(b) Load-slip: generic simulated behaviour



(c) Shear-stress distribution along plate length

**Figure 5. Simulation and test results.**

Figure 5a contains the simulated load-slip response as well as three test results for nominally identical specimens. The agreement between prediction and test is acceptable and hence gives confidence in the accuracy of the numerical technique.

Figure 5b contains an enlarged view of the simulated load-slip response up to a slip just in excess of  $s_{\max,1}$ . The load-slip responses for the anchored joint, as well as the anchor and an unanchored joint are provided. The anchor load is derived from the stress contained in the anchor cohesive element. It is evident that the plate completely debonds after the anchor has yielded (i.e. slip  $s_1$  has been reached) but before the anchor fails (i.e. slip  $s_2$  has not been reached). This results in a load plateau between points d and e. The existence of a load plateau is therefore of importance as it provides ductility to the FRP-concrete bond. Finally, the existence of a load plateau for the FRP anchor is evident and this occurs when  $P_1$  is reached.

Figure 5c contains the simulated distribution of shear stress at the FRP-concrete interface along the whole length of the bonded plate. Note that the shear stresses correspond to different levels of slip as indicated in Figure 5b by letters a to e. These five levels of stress correspond to:

- (i) Point a: The slip positioned midway between zero and point b.
- (ii) Point b: Initiation of debonding (i.e.  $P_{db}$ ) and it corresponds to zero shear stress at the loaded end of the plate.
- (iii) Point c: The slip corresponding to the peak shear stress occurring past the FRP anchor.
- (iv) Point d: Corresponds to  $P_{\max,1}$  and  $s_1$ .
- (v) Point e: Corresponds to complete plate debonding.



## 5. Conclusions

A constitutive model for FRP anchors has been provided in this paper. The model, which has been calibrated from tests on FRP-concrete joints anchored with FRP anchors, has then been incorporated into a finite element model. The model is shown to produce results consistent with experimental measurements. The finite element model results also reveal insights about the distribution of bond stress as well as the level of anchor activation in the test joints. Of particular importance, joints containing a long bond length have been shown to produce desirable ductile behavior.

Future studies can revolve around utilisation of the finite element model to conduct parametric studies. Such studies can then be used to develop design rules applicable to the design of FRP anchors in FRP strengthening applications.

## 6. Acknowledgement

This research was supported by the National Natural Science Foundation of China (Grant No. 51278150).

## 7. References

1. Teng, J.G., Smith, S.T., Yao, J. and Chen, J.F., "Intermediate crack-induced debonding in RC beams and slabs", Construction and Building Materials, 17(6), 2003, pp 447-462.
2. Hollaway, L.C. and Teng, J.G., "Strengthening and Rehabilitation of Civil Infrastructures Using Fibre-Reinforced Polymer (FRP) Composites", Woodhead Publishing Limited, 2008, Cambridge, UK.
3. Kalfat, R., Al-Mahaidi, R. and Smith, S.T., "Anchorage devices used to improve the performance of reinforced concrete beams retrofitted with FRP composites: a-state-of-the-art-review", Journal of Composites for Construction, ASCE, 17(1), 2013, pp 14-33.
4. Zhang, H.W. and Smith, S.T., "Influence of FRP anchor fan configuration and dowel angle on anchoring FRP plates", Composites Part B: Engineering, 43(8), 2012, pp 3516-3527.
5. Zhang, H.W., Smith, S.T. and Kim, S.J., "Optimisation of carbon and glass FRP anchor design", Construction and Building Materials, Special Issue on Strengthening and Retrofitting of Concrete Structures with Fiber Reinforced Polymer Material, 32, 2012, pp 1-12.
6. Zhang, H.W., "Influence of FRP Anchors on FRP-to-concrete Bonded Interfaces", Doctor of Philosophy Dissertation, University of Hong Kong, 2013, Hong Kong, China.
7. ABAQUS 6.10 Documentation, Dassault Systèmes Simulia Corp., 2010, Providence, RI, USA.
8. Zhang, H.W. and Smith, S.T., "Derivation and verification of a constitutive model for FRP anchors", Proceedings (CD-Rom), Fourth Asia-Pacific Conference on FRP in Structures, APFIS 2013, Melbourne, Australia, 11-13 December 2013.
9. Lu, X.Z., Teng, J.G., Ye, L.P. and Jiang, J.J., "Bond-slip models for FRP sheets/plates bonded to concrete", Engineering Structures, 27(6), 2005, pp 920-937.
10. Oehlers, D.J. and Bradford, M.A., "Composite Steel and Concrete Structural Members", Elsevier, 2004, UK.

# Joint Free Restrained Slabs – SFRC combined with mesh

Alan Ross CPEng IntPE(NZ)  
General Manager, BOSFA

**Abstract:** Controlling cracking to acceptable levels in concrete structures requires accurate detailing and good construction practices. This is more prevalent in ground supported slabs that are typically detailed to avoid cracks occurring under service stresses. Detailing the slab to avoid these cracks puts a number of limitations on the floor design and construction. There is an upper limit on panel size and shape, restraint should be limited as much as possible and of course joints are required, which can be expensive and may require on-going maintenance. And even with all this effort, cracks can still occur, and when they do they tend to be large and can have an adverse effect on the serviceability of the floor.

Recent Standards from Europe<sup>(5,6,7)</sup> enable the engineer to design using steel fibre reinforced concrete (SFRC) combined with conventional reinforcing. For floor slabs this means any panel size or shape can be considered, even when the floor is fully restrained, and importantly these solutions can be joint free. Using combined reinforcing also enables the design of economical liquid retaining structures, such as containment bunds, dangerous goods store floors, tank base slabs, watertight basement slabs.

This paper discusses the theory behind this design approach and provides a number of local and overseas project examples.

**Keywords:** CombiSlab, combined reinforcement, crack width calculation, SFRC, steel fibres, serviceability design

## Introduction

Concrete is a brittle material and cracking is normal. In fact, in order to take account of the reinforcing effect of bar or mesh, cracked section material properties and design capacities are used in the design of concrete structures. If these cracks are controlled within specified levels they are not detrimental to the integrity of the structure and do not affect its serviceability. This control is generally met by providing a minimum percentage of steel reinforcing and/or appropriate joint detailing.

With this in mind, a major design consideration for any concrete structure is the location and detailing of joints. This can become paramount for concrete pavements or slabs where joints have traditionally been the Achilles' heel of this form of construction. Being able to minimise or eliminate joints is an attractive proposition in terms of on-going maintenance costs.

This is one of the main reasons continuously reinforced concrete (CRCP) pavements, which are designed to eliminate the need for joints, are often preferred over jointed pavements with large numbers of closely centred crack control joints. CRCP are designed with enough steel reinforcing to keep the inevitable cracking within acceptable limits - by typically utilising 16mm or 20mm reinforcing bars at close (< 200mm) centres, the requirement for crack control jointing, such as saw cuts, is removed.

On the other hand, jointed pavements/slabs are detailed and designed in such a way as to limit the stresses in the slab due to restrained, temperature and shrinkage deformations to be less than the tensile capacity of the concrete, i.e. the design is based on the slab remaining uncracked in its serviceability limit state (SLS).

Innovation in this field of concrete design has led to the development of design rules that enable the use of steel fibre reinforced concrete (SFRC) in combination with conventional reinforcing. This makes it possible to design economic solutions for controlled cracking under service stresses. For floor slabs this means any panel size or shape can be considered, even when the floor is fully restrained, and importantly these solutions can be joint free.

## Say NO to Joints

Designing for controlled cracking in concrete elements is common practice, to suggest that this is a good idea for a ground supported slab requires quite a shift in thinking. A warehouse slab or external pavement is arguably the most important part of the tenanted space; it has to remain operational and serviceable with preferably as little maintenance as possible; and this maintenance typically involves joints.

There are flooring solutions that can reduce the number of joints, but as mentioned earlier, these put a number of limitations on design and construction. Particularly post tensioned slabs where wall block outs and pour strips may be required, joints over large distances open significantly and it's common for the slab to curl at joints and free edges. To avoid cracking a slab is normally tensioned incrementally as the concrete gains strength; this can put it on the critical path for construction. Importantly, limiting restraint is of paramount importance and the construction and design/detailing of these floors types is a specialist field.

Joints can work well, if detailed and constructed properly, but almost always require maintenance, as shown in figure 1. This dowelled movement joint will require a maintenance programme to reseal it possibly many times over the life of the floor. They can also perform poorly, as shown in figures 2 and 3. This costs the building owner and has a detrimental effect on the serviceability of the floor.



**Figure 1**  
**Figure 2**



**Figure 3**

The photographs in figures 4 and 5 show controlled fine cracking in a slab containing steel fibres and mesh. Figure 4, a close up and figure 5 showing two controlled cracks running parallel to each other, taken from head height, they are quite difficult to see.

**Figure 4**

**Figure 5**

So, instead of trying to detail and construct the slab with joints to avoid cracking under service stresses, another approach is to assume the slab will crack under services stresses but to design with enough tensile capacity at the cracked section to ensure any cracks are controlled and hence small enough not to affect the serviceability of the floor. To do this efficiently and economically you can use a 'CombiSlab' solution; steel fibres combined with mesh or bar.



This approach is particularly beneficial where there is unavoidable restraint in the floor. Rather than trying to detail round this restraint, by the judicious design and construction of a suitable arrangement of joints, the approach entails designing a suitable combination of mesh and steel fibre reinforcement to ensure an acceptable level of crack width whilst eliminating or minimising the need for either movement (dowel) or crack control (saw cut) joints.. Restraint may result from precast concrete panels being tied into the slab, pads or plinths that are poured integrally with the slab, or non-symmetrical shapes to the floor etc. etc.

It is worth noting, that in floors where restraint can be limited, joints are acceptable, the serviceability demands on the floor are small and there is no requirement for a crack width calculation, steel fibre only solutions can still be the most economically attractive option.

## Quantifying SFRC

Most current standards for design of SFRC provide guidance on how to quantify the reinforcing properties based on the measured post crack tensile strength of SFRC. The universally adopted approach is to measure the post crack performance in a flexural beam test, performed in the laboratory (Fig 5) and by means of suitable conversion factors, convert the laboratory measured flexural performance in terms of a load versus deflection or crack width curve into a tensile stress/crack width as shown in Figure 6 and hence into a stress/strain relationship that can then be used for design as shown in Figure 7.

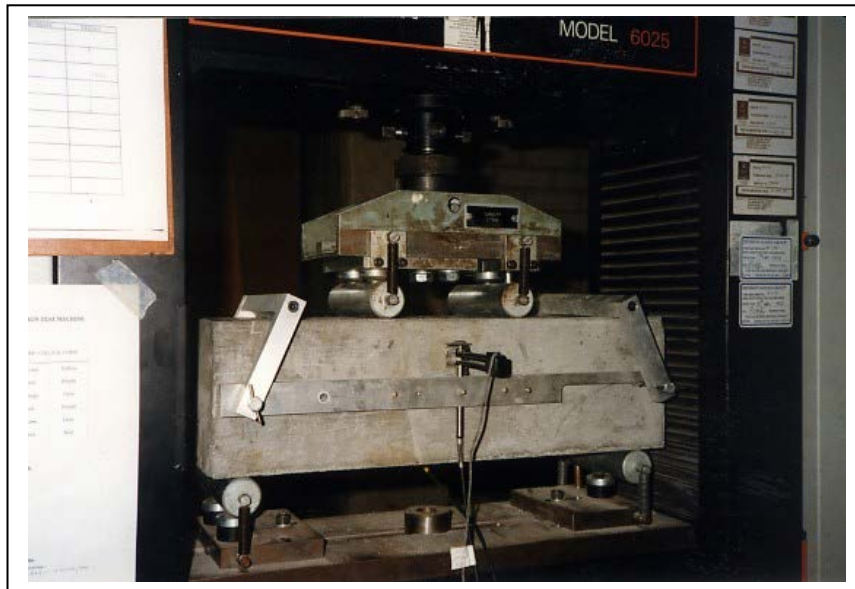


Figure 5 Typical Beam test setup in the laboratory

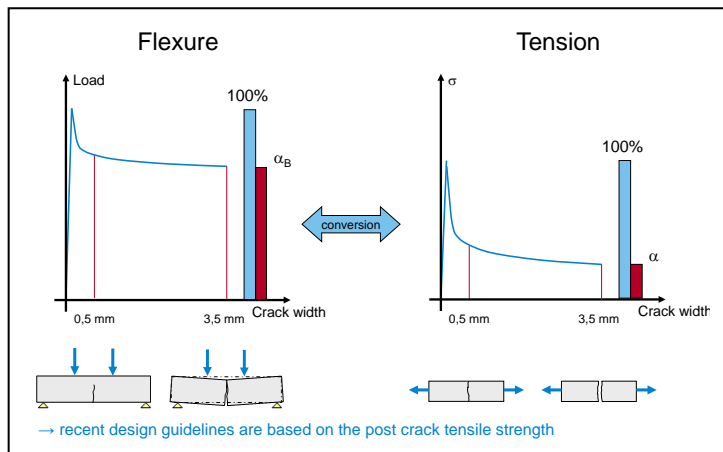


Figure 6 Converting Test results for SFRC

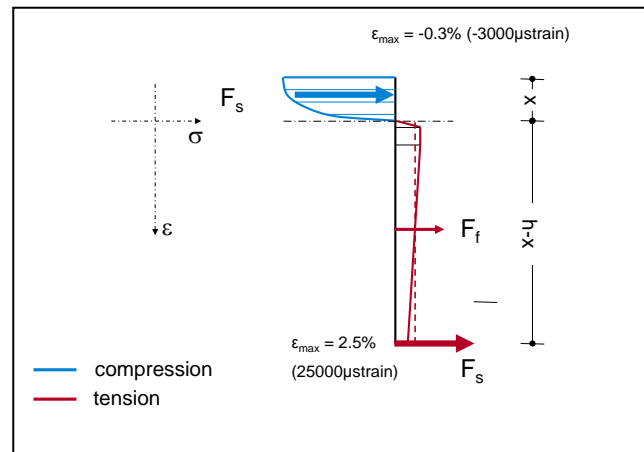


Figure 7 Stress/Strain for RC

There are a number of important points to be noticed about Figure 7 as follows:-

1. The stress strain diagram is exactly what is expected for conventionally reinforced concrete with the addition of a tensile stress block (dashed red line in figure 7) to model the effect of individual fibres crossing the crack that develops below a sections neutral axis. For more accurate modeling a refined stress-strain diagram should be applied (continuous red line in figure 7).
2. The strain nominated at the main reinforcing bar or wire can be chosen such that the steel will have yielded, as shown, or not. The nominated stress strain diagram is therefore suitable for determining either a sections Ultimate Moment Capacity or the tensile stresses that will exist in the section under working or service loads.

3. The compressive stress in the concrete and the tensile stress in the cracked fibre reinforced concrete (c.f. Figure 6) will in reality be curvilinear in shape. However, for simplicity it is acceptable to assume a stress block for both.
4. The value used for the magnitude of the steel fibre stress block varies with the section capacity that is to be determined. For the ultimate limit state moment capacity the tensile stress value used is the residual stress value shown in Figure 6 for a crack width of 3.5mm. For the serviceability limit state (e.g. for a crack width calculation) the tensile stress value used is the residual stress value shown in Figure 6 for a crack width of 0.5mm

Point 4 above brings into play an important concept for fibre reinforced concrete, namely the interplay between the stress in the reinforcement and the width of cracks. For conventionally reinforced concrete the lower the stress and hence strain in the steel the smaller will be the crack width. Conversely, for SFRC exhibiting strain softening behavior as shown in Figure 6, the lower the crack width the higher will be the residual stress value provided by the steel fibres. For this reason, to incorporate the effects of steel fibres in a combined reinforcement solution, it is critical that the stress values used in design for both the fibres and conventional reinforcement are those that will occur for the same, or at least consistent, values of strain.

As strain is a nebulous concept for SFRC, the fibres are actually pulled out rather than being strained over some imaginary fixed length that varies with a fibres orientation in 3-dimensions, it is more practical to fall back on crack widths. The difficulty of effectively and consistently relating crack widths to strain has been addressed in the DAfStb<sup>(4)</sup> guideline on SFRC, where crack width is defined as:

$w = \epsilon_{ct} \times 140\text{mm}$ , where  $\epsilon_{ct}$  is the concrete strain in the tensile zone.

The fixed value of 140mm is due to defining a crack opening of 3.5mm as being equivalent to a strain of 2.5% or 25000 $\mu$ strain.

This fixed relationship between strain and crack opening means that the defined stress/strain relationship applies to any depth of section, even when the material properties are derived from different sized beam tests; the same strain always gives the same crack width irrespective of the size of an actual element. This means the strain, crack width and design strength are the same irrespective of how deep your section is. RILEM (and NZS3101) on the other hand links design strength to section thickness, which means that they require a size factor to compensate. This latter approach is not being used in the recent design rules from Fib and DafStb; they have used the constant relationship between strain and crack width.

With the stress strain properties of SFRC, as well as concrete reinforced with combined reinforcement effectively defined, it is possible to determine, the tensile and ultimate moment capacity of a section reinforced with SFRC and/or SFRC combined with conventional reinforcing.

## The Importance of Crack Control

A crack width calculation is based on empirical guidelines and requires an understanding of the strains and stresses in the concrete section prior to cracking as well as a number of other assumptions in regards to the strength the concrete will be when cracking actually occurs. It is therefore not an easy calculation to perform and thus not often carried out in engineering design offices. The ability to avoid performing crack width calculations is typically addressed in Concrete Standards by the provision of guideline criteria that will indirectly provide a suitable level of serviceability/durability as well as strength in the finished structure, usually built around the service stress in reinforcing steel as well as the quality and amount of concrete cover in different environments.

As concrete standards are being revised and rewritten, both in Australasia and overseas, durability and serviceability of concrete structures is becoming more and more important. Typically this is done by means of additional requirements on material properties, detailing and minimum reinforcement. In fact what these concrete standards are typically achieving with their recommendations on durability and serviceability is to impose limits on crack widths i.e. higher durability and serviceability can very often be interpreted to mean the use of more reinforcement to effectively control crack widths.

Concrete Standards typically do a good job with these guidelines when it comes to cracking caused under load. However, when it comes to cracking caused by the restraint of shrinkage and thermal movements these recommendations become much less tangible. For instance in AS3600<sup>(1)</sup> there are

two recommendations for the minimum secondary reinforcement required in restrained slabs based on the degree of control over cracking that is required and a third level is added for slabs fully enclosed in a building. It is up to the engineer to decide what level of restraint is present.

The important parameters to judge if a crack is still acceptable or not will vary with the type of element, how the element is used and to what environment it is exposed. The owner of a concrete element or structure is really only interested in whether or not the element “works” and how long it lasts. It is therefore necessary that “works” is translated into an acceptable design crack width, which is the role of the designing engineer with guidance from suitable standards and technical recommendations.

An indicative example related to acceptable crack widths in reinforced concrete slabs on grade comes from DafStb<sup>(4,6)</sup> and DIN<sup>(5)</sup> as follows:

- Dry environment            0.5mm
- Soil or moisture            0.3mm
- Chlorides                    0.1 – 0.3mm (+possibly coated)
- Coated                        0.2mm
- Water tight                 0.1 – 0.2mm (+ possibly coated)
- Environmental              0.1 – 0.2mm (+ possibly coated)
- Chemical                    0.1 – 0.2mm (+ possibly coated)
- Heavily trafficked         0.2 – 0.3mm

A local example for designing concrete pavements can be taken from Austroads<sup>(2)</sup>, where continuously reinforced pavements are designed for a nominal crack width of 0.3mm.

It is obvious that the usefulness of such recommendations makes it essential that a crack width calculation be performed. Fortunately spread sheets can be developed that not only perform these calculations quickly and easily but can be used to investigate the sensitivity of the assumptions an engineer needs to make when using them. As an example, BOSFA can provide Dramix 4D CombiSlab designs to engineers, contractors and the like using a design tool based on relevant European Standards.

### **SFRC with No Conventional Reinforcement**

The strain softening behavior of SFRC is problematic in terms of calculating crack widths. Although it is theoretically possible to calculate a crack width in a section that has a permanent compression zone, the fact is that the tensile strength of the **uncracked** fibre reinforced concrete is higher than the tensile strength of the **cracked** fibre reinforced concrete. This means that for a concrete element where the full section is in tension, for example due to restraint of shrinkage and temperature stresses in a ground slab, the cracked section is the weakest section and it's not possible to determine accurately if and where the concrete section will crack again i.e. it is impossible to determine a theoretical spacing between cracks and without a crack spacing it is also impossible to determine a crack width using current crack width calculation theory. The determination of crack spacing and hence crack widths is discussed more in the next section.

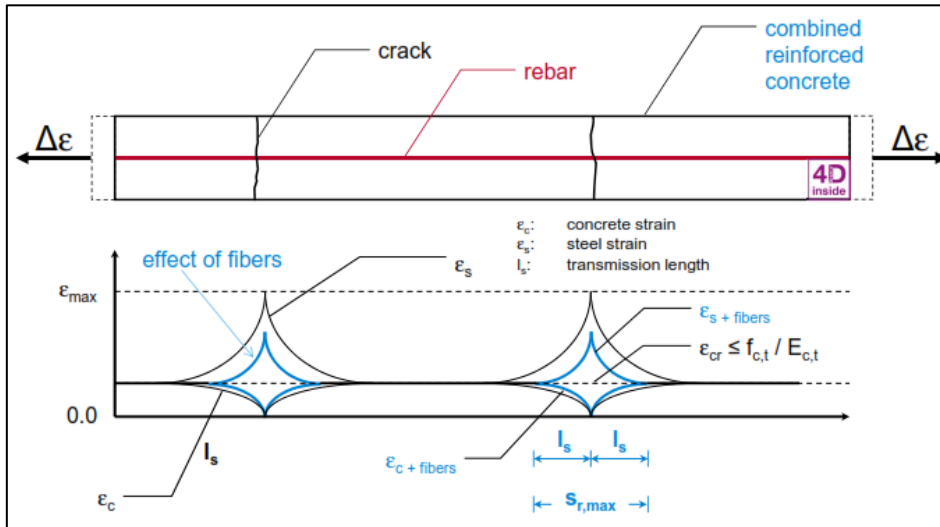
This situation can be likened to the determination of crack widths for conventional reinforcement where the tensile capacity of the reinforcement is less than that of the concrete. At a cracked section that is under reinforced it is possible for the steel to yield giving the possibility of uncontrolled and hence very large localized crack widths.

It should not be forgotten that steel fibres are effective in “locking off” or arresting the development of cracks at their earliest stage of development i.e. micro cracking. They effectively reduce the tendency of these cracks to propagate and as such fibre only saw cut free slabs on grade and rafts have been constructed successfully for many years. But it's not possible to effectively calculate a precise crack width, making it necessary to rely on experience when nominating joint centers, fibre type and dosage.

### **Combined Reinforcement, the synergies**

When conventional and steel fibre reinforcement are combined the strain softening behavior of SFRC does not change. However, the post cracking tensile capacity of the SFRC can be taken into account when calculating crack widths for the conventional reinforcement.

In conventionally reinforced concrete the width of a crack is a function of the distance between cracks and the distance between cracks is determined by the bond length of the reinforcing bars, this is shown graphically in figure 8 and explained below:



**Figure 8. Initial state of cracking**

At a crack the tensile force in the concrete is zero with all the tensile force being carried by the reinforcing steel. Away from the crack the reinforcing bars, being effectively bonded into the concrete matrix, transfer this tensile force into the concrete, with all the force being transferred into the concrete a distance from the crack equal to the reinforcing bars development length. This means that the minimum spacing between cracks is one development length and the maximum spacing is two development lengths. The maximum crack width will therefore result when the cracks are spaced at the maximum spacing of two development lengths. In practice, it may be somewhere in-between.

The effect of steel fibres is to increase the tensile force in the concrete at a crack from zero to the tensile capacity of the cracked SFRC. The result of this is that the tensile force in the conventional reinforcement at the crack is reduced and the development length of the steel is consequently reduced. The same holds for the strain in the steel. Reducing the development length and the strain of the reinforcement reduces the maximum distance between cracks and thus results in more but narrower cracks. This has a significant effect on the amount of bars or mesh required for a particular crack width design, using a SFRC with a residual tensile strength  $> 1.0 \text{ N/mm}^2$  can reduce the conventional reinforcing by about 50% for the same level of crack control.

As a simplification of this concept the crack width  $w_k$  may be seen as a function of the concrete tensile strength  $f_{ct}$  in the case of reinforced concrete and a function of the concrete tensile strength minus the cracked tensile strength of SFRC  $f_{ct,SFRC}$  in the case of combined reinforcement, this is shown in equation (1):

$$w_k = \text{function} [f_{ct} - f_{ct,SFRC}] \quad (1)$$

A number of related test programs <sup>(3,8,10,12)</sup> have been carried out and a number of design methods have been proposed. These approaches differ in some points but more or less follow the same principle, namely the reduction of the concrete tensile strength by the post crack tensile strength of SFRC.

Apart from serviceability and the determination of crack widths, the post crack strength of SFRC may also be taken into account for the ultimate limit state, where significant contributions to the load bearing capacity are possible. In joint free slabs there is also no requirement to model the floor loads on a joint, this leads to more efficient use of concrete – thinner slabs.

## Practical Experiences



Over 1m m<sup>2</sup> projects have been constructed utilising combined reinforcement in countries all over the world. A few examples are given to explain why combined reinforcement was used and what benefits were achieved.

### ***NZ, Container handling pavement***

Pavements designed for the handling and storage of containers need to accommodate high loads and constant wear and tear which invariably damages joints, resulting in expensive maintenance programs. Reducing or eliminating these joints is an attractive proposition to the asset owner. This project is about 13,000m<sup>2</sup>, the pavement winds its way round corners and up slopes, has been designed to accommodate stacked containers and is completely joint free. The SFRC was used in the ULS design, resulting in a thinner slab compared to PT and conventional reinforcing, AND it was used for SLS crack control in combination with one layer of mesh. Design crack width 0.25mm.



### ***Belgium, E17 motorway***

The E17, a major Belgian highway was constructed with a lane using SFRC in combination with 20mm reinforcing bars. Crack width is an important parameter for the long term performance of CRCP, particularly the development of punch outs (pavement failure). Using a CombiSlab enabled a reduction in calculated crack width, allowed a reduction in longitudinal reinforcing and improved the risk associated with punch out failure.



### ***NZ, Commercial building, restrained joint free floor***



The building is 95m x 45m and has full restraint along one 95m length from tied in precast panel walls. Using conventional methods of construction, this level of restraint would have required jointing in the floor. Taking this restraint into account in the design through combining SFRC with one layer of 441 mesh (7.5mm wires at 100c/c) enabled the construction of the floor without any joints. Eliminating construction, and importantly, maintenance costs associated with saw cuts and movement joints. The increase in load carrying capacity provided by the SFRC resulted in a slab thickness of 130mm. Design crack width of 0.25mm.



***NZ, Containment bund, joint free water tight***

Leakage of containment bunds can be an issue and costly to put right. Typical design and construction has sealed joints and expensive water stops. However, if the bund cracks outside these control points then there commonly isn't enough reinforcing to control them to acceptable levels. Combining SFRC with one layer of mesh enabled the design of a water tight layer and construction of the bund without any joints. 120mm thick, design crack width 0.2mm.



***NZ, Bulk Storage facility, restrained joint free floor***

This building is approximately 10,000m<sup>2</sup>, split into four rooms. The precast panel walls required large foundations due to the storage of bulk materials, and these were cast monolithically with the slab, fully restraining the floor. The whole building was constructed completely joint free using SFRC plus one layer of mesh. Design crack width 0.3mm.



***Australia, 15,000m<sup>2</sup> seamless floor***

The main challenge with this project was being able to accommodate 25t post loads, re-entrant corners, the slab being tied into the perimeter and tight time constraints. All this was taken into account in the design and a completely joint free floor was constructed using SFRC plus one layer of mesh. Design crack width 0.25mm.



***NZ, external saw cut free yard slabs***



Sealing of external saw cuts is time consuming, expensive and requires maintenance. Saw cut free panels approximately 30 x 30m, constructed using SFRC plus one layer of light mesh. Design crack width 0.25mm.



***Australia, dam spillway***

This joint free watertight spillway is approximately 700m long. The conventional design used 2 layers of bars plus mesh and very expensive jointing. The SFRC option was used in combination with one layer of heavy mesh. This resulted in a solution that was cost effective, joint free, more durable and quicker and easier to build, Design crack width 0.2mm.



## Conclusions

Combining SFRC with mesh or bar provides the engineer and contractor greater flexibility in slab construction; restraint, panel size and shape, as well as joint location are no longer a constraint on design. Importantly, designing for controlled cracking under service stresses and the elimination of joints will result in a floor that is more durable, serviceable and maintenance free, a very attractive proposition for the building owner. The CombiSlab solution also provides an economic option for liquid retaining structures such as containment bunds, dangerous goods store floors, tank base slabs and watertight basement rafts/slabs.

## References

1. Australian Standard AS3600-2009 Concrete Structures. Published by Standards Australia.
2. Austroads, A Guide to the Structural Design of Road Pavements
3. Brite-Euram, BRPR-CT98-0813: Test and design methods for steel fibre reinforced concrete
4. DAfStb, Deutscher Ausschuss für Stahlbeton: Richtlinie für Betonbau beim Umgang mit wassergefährdenden Stoffen (DAfStb, German Committee for Structural Concrete: technical rule on concrete structures for hazardous substances), Germany 1996 - 2011
5. DIN 1045-1:2008 Concrete, reinforced and prestressed concrete structures — Parts 1-3
6. DAfStb, Deutscher Ausschuss für Stahlbeton: Richtlinie Stahlfaserbeton (DAfStb, German Committee for Structural Concrete: technical rule on steel fibre concrete), Germany 2010
7. Fib: Bulletin 56, *Model Code 2010 – First complete draft, Volume 2* (chapters 7-10), April 2010, ISBN 978-2-88394-096-3.
8. H. Falkner, M. Teutsch: Stahlfaserbeton – Anwendungen und Richtlinie, Betonkalender 2006, Verlag Ernst und Sohn, Berlin, Germany (H. Falkner, M. Teutsch, Steel fibre concrete – applications and guideline, „Concrete Calendar 2006“, Verlag Ernst und Sohn, Berlin, Germany)
9. NZS 3101:2006 Concrete Structures Standard
10. P. Niemann: Gebrauchsverhalten von Bodenplatten aus Beton unter Einwirkung infolge Last und Zwang, Heft 165 der Schriftenreihe des iBMB, Eigenverlag TU Braunschweig (P. Niemann, Serviceability of ground supported concrete slabs subject to load and restraint deformation, publication No. 165 of iBMB at TU Braunschweig, Germany)
11. R. Ratcliffe, G. Vitt: Steel fibres combined with mesh, Amazing synergies using available design guidelines (2011)
12. RILEM TC 162 TDF: Design of Steelfibre Reinforced Concrete – Method, Recommendations, Material and Structures, March 2001

# Concrete Materials and Performance

# Neutron Pair Distribution Function Analysis of Synthetic Calcium-Silicate-Hydrate Gels

Claire E. White<sup>1</sup>

<sup>1</sup>Department of Civil & Environmental Engineering and Andlinger Center for Energy and the Environment, Princeton University, Princeton, USA

**Abstract:** The atomic structural arrangements in calcium-silicate-hydrate (C-S-H) gel in ordinary Portland cement-based pastes and blended pastes have been the subject of rigorous debate in recent years. Standard characterization techniques fail to fully capture the complex structure and morphology of C-S-H gel, primarily due to the nanocrystallinity of this important binder phase combined with the variability in calcium-to-silicon ratio and incorporation of aluminium in the structure for certain blended systems. Nevertheless, local structural tools such as X-ray and/or neutron pair distribution function (PDF) analysis are increasingly being employed to analyse the atomic structure of disordered materials. Here, for the first time, neutron PDF analysis is applied to a range of deuterated C-S-H gels with varying Ca/Si ratios (denoted C-S-D), including the in situ analysis of a C-S-D gel exposed to elevated temperature. The results highlight the water-containing bonding environments present in the gels, particularly through the use of deuterated samples. The in situ temperature study reveals that the local atomic bonding environments in C-S-D gel undergo large structural rearrangements due to exposure to elevated temperature, and sheds light on the non-crystalline structural transitions that cannot be accessed using standard crystallographic techniques.

**Keywords:** Calcium-silicate-hydrate, neutron diffraction, pair distribution function, temperature, dehydration.

## Introduction

Ordinary Portland cement (OPC)-based concrete has been used in the construction industry for more than 175 years, however, the main phase that controls strength and durability, calcium-silicate-hydrate (C-S-H) gel, remains a topic of significant debate since conventional characterization methods are ill-suited for elucidating the complex atomic structure of this important cementitious phase (1). C-S-H gel co-exists with multiple other phases in OPC concrete, including portlandite, ettringite and various sulphates phases, which makes isolation of the gel extremely difficult. The atomic structure of C-S-H gel has been debated rigorously in the literature, with new structural models derived from quantum chemistry failing to capture the known bonding environment existing in these gels (2,3). Experimentally-driven structural representations have been developed using techniques such as reverse Monte Carlo (4), with additional research required to fully-validate these models from a thermodynamics viewpoint to ensure that the models are chemically-reasonable (5).

Although the structure of C-S-H gel has been actively pursued in recent decades, little information is available regarding the atomic structural changes that occur when the gel is exposed to moderate (~ 100 °C) and high (> 100 °C) temperatures. These changes are extremely important for understanding how OPC concrete performs at high temperatures, especially in fire conditions (6,7). Some progress has been made in understanding the temperature-induced structural transitions in C-S-H gel analogues such as 11 Å tobermorite, which has been seen to decrease in interlayer spacing from 11.3 to 9.3 Å when heated to 300 °C (and remains intact with the interlayer spacing at 9.3 Å past 700 °C) (8). The thermal behaviour of C-S-H gel in OPC paste has been investigated using neutron diffraction (9), however, due to the existence of multiple phases in the sample the exact behaviour of the C-S-H gel remains unclear as studied using neutron diffraction.

Here, neutron total scattering measurements and subsequent pair distribution function (PDF) analysis is used to investigate the atomic structure of C-S-H gels together with the structural changes that occur due to dehydration and exposure to high temperatures (up to 650 °C). By using the high-flux available at the Spallation Neutron Source, Oak Ridge National Laboratory, it is possible to study the dehydration and high temperature reactions in situ (in real time) using neutrons, and therefore obtain information on the exact local structural changes that occur during exposure to these elevated temperature. Furthermore, the use of neutrons as opposed to X-rays enables the water-containing correlations to be measured and analysed.

## Materials and Methods

Calcium-silicate-deuterate (C-S-D) gels of varying Ca/Si ratios (0.83, 1.2, 1.5, 1.7 and 3.0) were synthesised using triclinc tricalcium silicate ( $C_3S$  in cement notation, CTLGroup) and amorphous fumed silica ( $SiO_2$ , Alfa Aesar, 325 mesh). The synthesis method used to produce these samples was previously outlined in detail in reference (10). The samples were measured on the Nanoscale-Ordered Materials Diffractometer (NOMAD) instrument at the Spallation Neutron Source, Oak Ridge National Laboratory (11). In order to produce each total scattering function and associated PDF, the measured intensities were normalised by scattering from a vanadium rod and then subjected to a background subtraction from the empty container. Prior to calculation of the PDF, the total scattering function was multiplied by a Lorch function in order to improve the signal/noise at the expense of real-space resolution. The PDF ( $G(r)$ ), was obtained via a sine Fourier transform of the total scattering function ( $S(Q)$ ) using a  $Q_{max}$  of  $20 \text{ \AA}^{-1}$ , as outlined in Eq. 1, where  $Q$  is the momentum transfer as defined in Eq. 2.

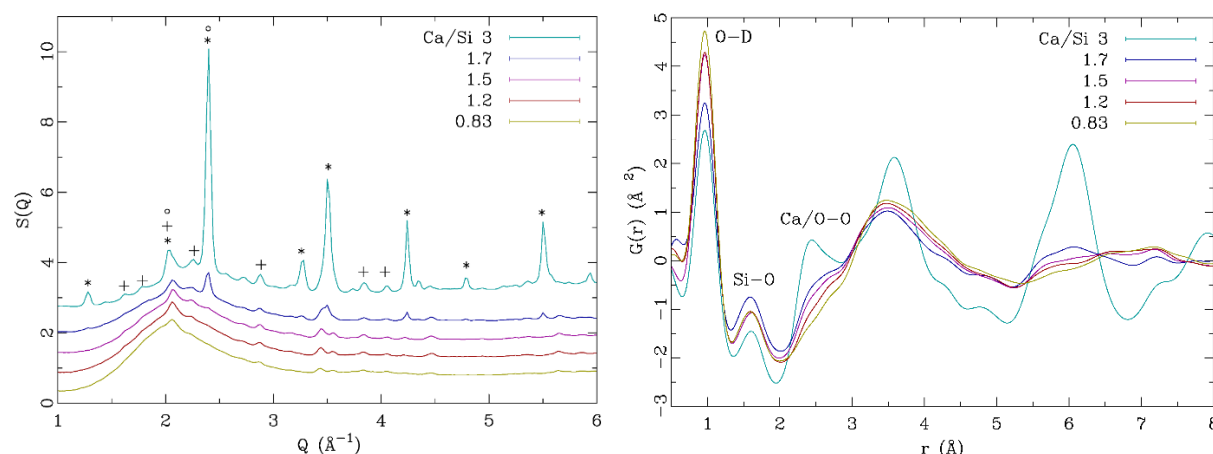
$$G(r) = \frac{2}{\pi} \int_{Q=Q_{min}}^{Q=Q_{max}} Q[S(Q) - 1] \sin(Qr) dQ \quad (1)$$

$$Q = \frac{4\pi \sin \theta}{\lambda} \quad (2)$$

## Results and Discussion

### Atomic Ordering at Ambient Temperature in Calcium-Silicate-Deuterate Gels

Figure 1 displays the neutron scattering data for the C-S-D gels, where Figure 1a provides the total scattering functions of the gels (in reciprocal space) and Figure 1b the neutron PDFs. It is clear that for increasing Ca/Si ratio the amount of crystalline portlandite dramatically increases (Figure 1a). However, the tricalcium silicate ( $C_3S$ ) peaks remain relatively small irrespective of the Ca/Si ratio, which is attributed to the smaller neutron coherent scattering length of silicon and calcium compared to oxygen and deuterium. Therefore, as more portlandite precipitates (as the Ca/Si ratio increases), and therefore additional deuteroyl units are associated with this crystal structure, the Bragg peaks associated with this crystalline phase are seen to increase significantly. A qualitative analysis of Figure 1a reveals that portlandite is present in the gels with Ca/Si ratios of 1.7 and 3. Figure 1a also contains information on the amount of water present in the sample in the form of  $D_2O$  or deuteroyl units (OD) via the broad amorphous peak situated between  $1$  and  $3.5 \text{ \AA}^{-1}$



(a) Total scattering functions. Bragg peaks assignments are as follows: C-S-H ( $^{\circ}$ ),  $C_3S$  ( $+$ ) and portlandite ( $*$ ). Offsets have been used to enhance clarity.

(b) Pair distribution functions. Nearest-neighbour atom-atom correlations are labelled.

**Figure 1. Neutron total scattering functions and pair distribution functions of C-S-D gels. The Ca/Si ratios are given based on the synthesis stoichiometry.**

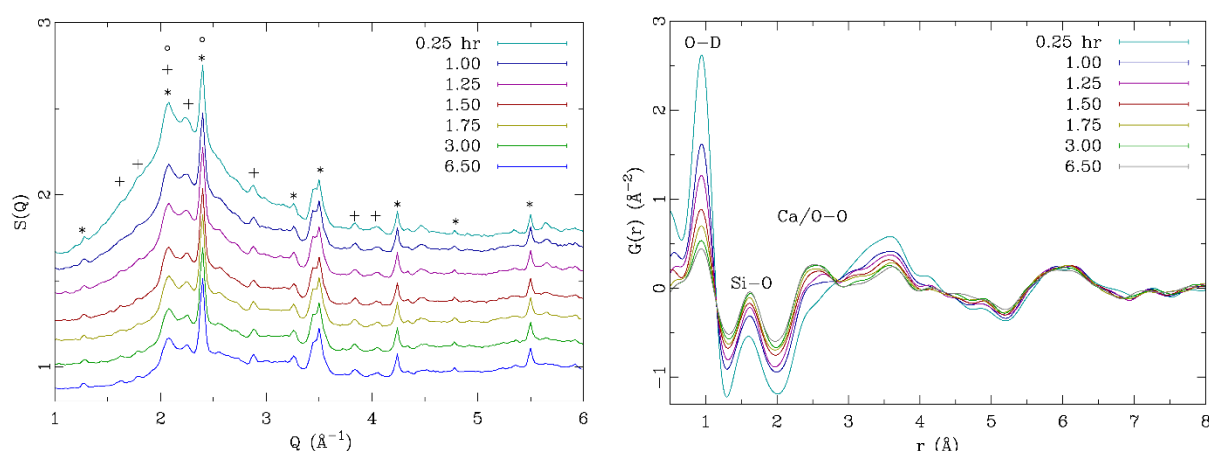
Figure 1b contains the neutron PDFs for the C-S-D gels, where it is apparent that the low Ca/Si ratio samples contain more water (intensity of the O-D correlation at  $0.96 \text{ \AA}$ ). This figure also shows that the Si-O correlation is similar for the gels in terms of overall intensity (taking into account the differences in



the atomic number density, as given by the sloping baseline at low  $r$  (12)). On the other hand, there are significant differences in the Ca-O correlation at  $\sim 2.44$  Å and O-O at  $\sim 2.7$  Å (where an inflection point is located in the data). At higher  $r$  values it becomes more difficult to assign specific atom-atom correlations without a detailed structural model.

### Drying-Induced Structural Changes at 110 °C

The main change seen in the total scattering patterns (Figure 2a) as a C-S-D gel (with Ca/Si ratio of 1.7) is exposed to 110 °C is the loss in intensity of the broad diffuse peak positioned between  $Q$  values of 1 and 3.5 Å<sup>-1</sup>, which is attributed to removal of water from the gel. The neutron PDFs (Figure 2b) directly show this loss of water via the reduction in intensity of the nearest-neighbour correlation (O-D) positioned at 0.95 Å. Although this correlation reduces significantly by 6.5 hrs, there is still a well-defined O-D correlation present. Hence, further drying would likely result in additional changes in the local atomic structure. The other major changes in the local structure due to drying at a temperature of 110 °C are the water-containing correlations (O-D and D-D) between 3 and 4.5 Å (2), which are seen to reduce in intensity, and the Ca-O and O-O correlations between 2 and 3 Å, where the intensity increases.



(a) Total scattering functions. Bragg peaks assignments are as follows: C-S-H (°), C<sub>3</sub>S (+) and portlandite (\*). Offsets have been used to enhance clarity.

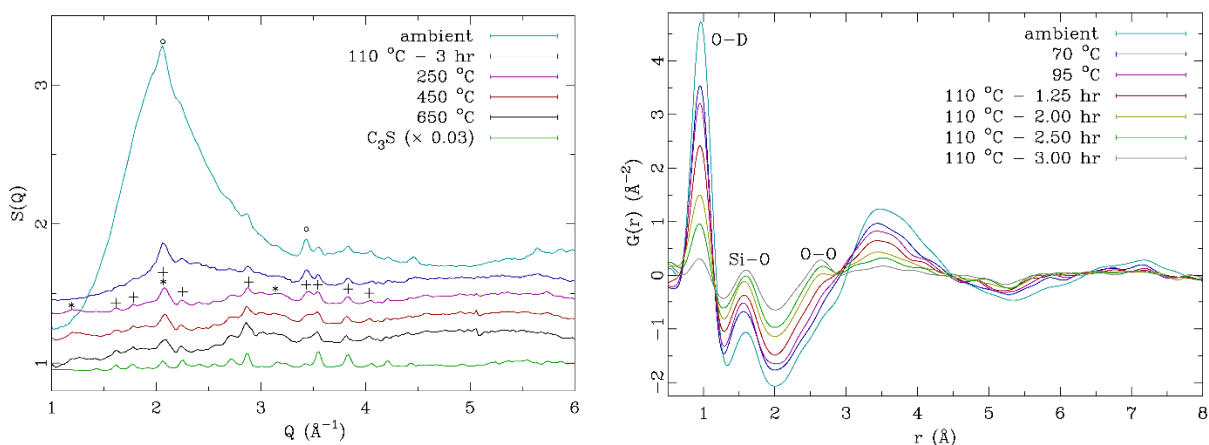
(b) Pair distribution functions. Nearest-neighbour atom-atom correlations are labelled.

**Figure 2. Neutron total scattering functions and pair distribution functions of the C-S-D gel with Ca/Si ratio of 1.7 exposed to drying conditions at 110 °C.**

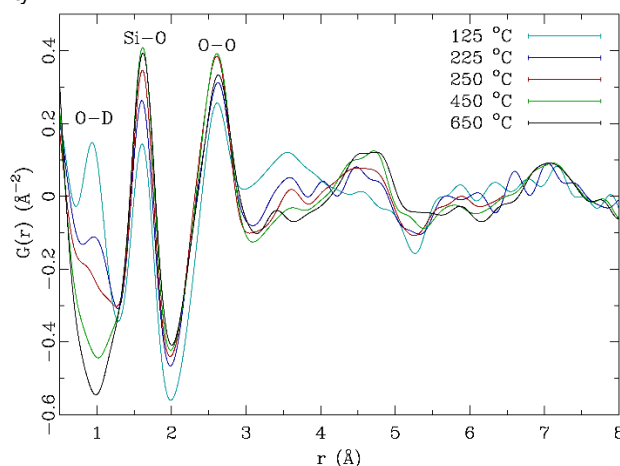
### High Temperature Behaviour of a Calcium-Silicate-Deuterate Gel

The local structural changes of C-S-D gels in response to exposure to high temperatures ( $> 200$  °C) are important from a macroscopic structural integrity viewpoint (concrete strength degradation), and therefore it is important to have a detailed understanding of the atomic structure of C-S-D gel and changes that occur upon heating. Figure 3 contains the neutron diffraction data for a C-S-D gel with Ca/Si ratio of 0.83 exposed to elevated temperatures (up to 650 °C), with Figure 3a containing the total scattering data (reciprocal space) and Figures 3b and 3c the real-space neutron PDF data. Figure 3a reveals that a significant amount of water is removed from the sample after 3 hrs at 110 °C, which is seen via the reduced intensity of the diffuse scattering attributed to the water correlations (between 1 and 3.5 Å<sup>-1</sup>). An additional reduction in the diffuse scattering is visible between 110 and 250 °C, with higher temperatures (up to 650 °C) revealing little change in the measured scattering patterns. Apart from the significant reduction in diffuse scattering during the in situ temperature measurement due to the removal of water from the sample, there are additional changes visible in Figure 3a, specifically the emergence of weak diffuse scattering located at  $Q$  values of 1.2 and 3.15 Å<sup>-1</sup>. Preliminary analysis of this diffuse scattering in conjunction with the existing Bragg peaks visible in the patterns reveals that this new diffuse scattering can be attributed to either larnite (C<sub>2</sub>S in cement notation) or 9 Å tobermorite. However, from analysis of the Bragg scattering it can be concluded that calcite, lime, wollastonite, and larger spacing tobermorite (11 and 14 Å) are not present in the sample.





(a) Total scattering functions. Bragg peaks assignments are as follows: C-S-H ( $\circ$ ),  $C_3S$  ( $+$ ) and 9.6 Å tobermorite ( $*$ ). Offsets have been used to enhance clarity. (b) Pair distribution functions ranging in temperatures up to 110 °C. Nearest-neighbour atom-atom correlations are labelled.



(c) Pair distribution functions above 110 °C. Nearest-neighbour atom-atom correlations are labelled.

**Figure 3. Neutron total scattering functions and pair distribution functions of the C-S-D gel with Ca/Si ratio of 0.83 exposed to dehydration conditions up to 650 °C.**

As seen in Figure 3b, at a temperature of 110 °C the atomic structure of C-S-D gel with a Ca/Si ratio of 0.83 is seen to go through similar structural transitions to that for a gel with Ca/Si of 1.7 (Figure 2b), where the atomic number density ( $\rho_o$ ) is seen to decrease as water is removed from the gel, and there is a significant reduction in intensity associated with the water-containing correlations (O-D at 0.96 Å, and O-D and D-D between 3 and 4.5 Å). There is also a slight shift in the nearest-neighbour O-D correlation from 0.96 Å at ambient temperature to 0.94 Å after 3 hrs at 110 °C, which may indicate that the remaining deuterium atoms at this stage of the reaction exist mostly as deuteroxyl units (OD) as opposed to  $D_2O$  molecules. Figure 3c shows that all the deuteroxyl units have been removed from the structure by 250 °C as there is no discernible O-D correlation at  $\sim 0.94$  Å in the neutron PDF. Also apparent in Figure 3b is the emergence of the O-O correlation at 2.65 Å, however, the positioning of this peak implies that there is limited contribution from a Ca-O correlation at  $\sim 2.4$  Å, which is attributed to the low calcium content of this C-S-D gel. Nevertheless, the emergence of the O-O correlation in Figure 3b is a strong indication of an increase in ordering of the Si-O-Si linkages, possibly via an increase in degree of polymerisation (conversion from  $Q^1$  to  $Q^2$  sites). Figure 3c contains the neutron PDFs for the C-S-D gel (Ca/Si of 0.83) exposed to higher temperatures (125 to 650 °C), where additional increases in the Si-O and O-O correlation are seen together with decreases in the nearest-neighbour O-D correlation and the water-containing correlations between 3 and 4.5 Å.

## Conclusions

Neutron PDF analysis has been utilised to investigate the local atomic bonding existing in synthetic C-S-D gels with different Ca/Si ratios, together with the changes in local structure of C-S-D gel that occur during (i) drying at 110 °C, and (ii) exposure up to a temperature of 650 °C. The results show that

neutron PDF analysis is extremely sensitive to the water-containing correlations in C-S-D gels, specifically the nearest-neighbour O-D correlation at  $\sim 0.96\text{\AA}$ , and the O-D and D-D correlations between 3 and 4.5  $\text{\AA}$ . Exposure to elevated drying conditions (110 °C) causes a significant loss of water together with an increase in ordering of the Ca-O and O-O correlation. Heating to higher temperatures (up to 650 °C) reveals that all water in the gel (structural and free water) is lost by 250 °C, and that the calcium silicate atomic structure undergoes additional ordering beyond 110 °C. Further analysis is required to assess the evolution of these phases with temperature, and to correlate the diffraction results with complementary spectroscopic analyses.

## Acknowledgement

This work was financially supported by the Princeton E-filiates Partnership award, Andlinger Center for Energy and the Environment (Princeton University). The author would like to acknowledge Dr. Monika Hartl and Dr. Luke Daemen with advice and assistance during sample synthesis, Dr. Jörg Neuefeind and Dr. Mikhail Feygenson for support and assistance on the NOMAD instrument at the Spallation Neutron Source, ORNL, and Mr. Michael Brusoski, Mr. Xie Xie and Prof. John Provis for assistance during the neutron experiments. This research at ORNL's Spallation Neutron Source was sponsored by the Scientific User Facilities Division, Office of Basic Energy Sciences, U.S. Department of Energy.

## References

1. Richardson, I. G.; Skibsted, J. et al., "Characterisation of cement hydrate phases by TEM, NMR and Raman spectroscopy", Advances in Cement Research 22(4), 2010, pp. 233-248.
2. Pellenq, R. J. M.; Kushima, A. et al., "A realistic molecular model of cement hydrates", Proceedings of the National Academy of Sciences of the United States of America 106(38), 2009, pp. 16102-16107.
3. Richardson, I. G., "The importance of proper crystal-chemical and geometrical reasoning demonstrated using layered single and double hydroxides", Acta Crystallographica Section B 69(2), 2013, pp. 150-162.
4. Skinner, L. B.; Chae, S. R. et al., "Nanostructure of calcium silicate hydrates in cements", Physical Review Letters 104(19), 2010, pp. 195502.
5. White, C. E., "Pair distribution function analysis of amorphous geopolymer precursors and binders: the importance of complementary molecular simulations", Zeitschrift für Kristallographie 227(5), 2012, pp. 304-312.
6. Alonso, C.; Fernandez, L., "Dehydration and rehydration processes of cement paste exposed to high temperature environments", Journal of Materials Science 39(9), 2004, pp. 3015-3024.
7. Bonnaud, P. A.; Ji, Q. et al., "Effects of elevated temperature on the structure and properties of calcium-silicate-hydrate gels: the role of confined water", Soft Matter 9(28), 2013, pp. 6418-6429.
8. Mitsuda, T.; Taylor, H. F. W., "Normal and anomalous tobermorites", Mineralogical Magazine 42(322), 1978, pp. 229-235.
9. Castellote, M.; Alonso, C. et al., "Composition and microstructural changes of cement pastes upon heating, as studied by neutron diffraction", Cement and Concrete Research 34(9), 2004, pp. 1633-1644.
10. White, C. E.; Daemen, L. L. et al., "Intrinsic differences in atomic ordering of calcium (alumino)silicate hydrates in conventional and alkali-activated cements", Cement and Concrete Research 67, 2015, pp. 66-73.
11. Neuefeind, J.; Feygenson, M. et al., "The Nanoscale Ordered Materials Diffractometer NOMAD at the Spallation Neutron Source SNS", Nuclear Instruments and Methods in Physics Research Section B: Beam Interactions with Materials and Atoms 287(0), 2012, pp. 68-75.
12. Egami, T.; Billinge, S. J. L. *Underneath the Bragg Peaks: Structural Analysis of Complex Materials*; Pergamon: Elmsford NY, 2003.

# USING CONVENTIONAL MATERIALS AS CONCRETE CONFINEMENT

Hua Zhao<sup>1</sup> and Muhammad N.S. Hadi <sup>2</sup>  
<sup>1</sup>PhD Candidate, the University of Wollongong  
<sup>2</sup>Associate Professor, the University of Wollongong

**Abstract:** Strengthening concrete members to improve the load carrying capacity and ductility at an economic cost has constantly been a challenge. This study aims to evaluate the effects of the conventional repair materials, mortar and galvanised wire mesh and mortar composite (MGWM) on the overall behaviours of confined concrete columns. The investigation was carried out on medium strength concrete (MSC) and normal strength concrete (NSC), respectively. Two methods were used to install the mesh reinforcement: cast integrally with concrete and wrapped to precast concrete core. The first method was applied to MSC specimens while the second was adopted for NSC cylinders.

The test results indicate that for MSC specimens, MGWM did not improve the load carrying capacity. However, ductility was substantially improved. The test results also show that for NSC specimens, mortar confined specimens outperformed MGWM confined specimens in terms of load carrying capacity, but the latter significantly improved ductility. Finally, the method for estimating the ultimate load of mortar-confined specimens is discussed.

**Keywords:** Mortar, galvanised wire mesh, load carrying capacity, ductility

## 1. Introduction

Due to the low material cost, wire mesh is considered for enhancing the performance of concrete members. The purpose of this series of experiments is to investigate the methods of using mesh to improve the behaviours of concrete columns. Two different methods were adopted: in the first experiment, wire mesh was formed into cage and placed into the steel moulds before medium strength concrete (MSC) cast, while in the second experiment wire mesh was wrapped onto the pre-cast normal strength concrete (NSC) core. In each case the layers of wire mesh (fracture volume) was the parameter.

In the first experiment, ten standard cylindrical specimens ( $\varnothing 150$  mm x 300 mm) cast, including two concrete controls and eight reinforced specimens, as shown in Table 1. In the second experiment, twelve ( $\varnothing 150$  mm x 380 mm) concrete specimens cast, among which were four controls and eight concrete cores, as shown in Table 2. All the specimens were tested under axial compression.

**Table 1 Specimen configuration \_Experiment 1**

Specimen Code	Cage <sup>1</sup> D <sub>m</sub> mm	Diametre D mm	Height H mm	Layer <sup>2</sup> n	Cover t mm
Control1	-	150	300	-	-
Control2	-	150	300	-	-
1L5C1	140	150	300	1	5
1L5C2	140	150	300	1	5
1L10C1	130	150	300	1	10
1L10C2	130	150	300	1	10
2L5C1	140	150	300	2	5
2L5C2	140	150	300	2	5
2L10C1	130	150	300	2	10
2L10C2	130	150	300	2	10

Note: 1 diametre of the outside wire mesh reinforcement cage  
2 the layer of wire mesh

**Table 2 Specimen configuration Experiment 2**

Specimen Code	Core $D_c$ mm	Cage $D_m$ mm	Diameter D mm	Height H mm	Layer n	Cover t mm
Control1	-	-	150	380	-	-
Control2	-	-	150	380	-	-
Control3	-	-	150	380	-	-
Control4	-	-	150	380	-	-
CM1	150	-	190	380	-	20
CM2	150	-	190	380	-	20
CM3	150	-	190	380	-	20
CM4	150	-	190	380	-	20
1M1	150	153	190	380	1	20
1M2	150	153	190	380	1	20
2M1	150	155	190	380	2	20
2M2	150	155	190	380	2	20

It is noted that in the first experiment the cover thickness was 5 mm and 10 mm, respectively, while in the second experiment the cover was identically 20 mm thick. The diameter of the confined specimens was 190 mm.

## 2. Experimental Program

### 2.1 Specimen Preparation

Due to the difference in applying wire mesh reinforcement, the specimens of the two experiments were prepared differently. In the first experiment timber plates were used to form a mesh cage. Wire mesh was overlapped at a length of 80 mm (6 x 13 mm), approximately, as shown in Figure 1. To ensure that the overlap would not loosen or slide from each other, it was tied with steel wire in two rows through the whole length at a space of every two grids. Additional ties were applied to the middle of the overlap area at every 6 grids. Wires were used to ensure space for 5 mm or 10 mm cover.



(a) Wire mesh cage (b) Wrapping mesh onto the precast core  
**Figure 1. Wire mesh reinforcement installation**

In the second experiment, concrete cores were cured for 28 days and each core was roughened evenly throughout the surface. Wire mesh was wrapped onto the surface in a continuous way. A working table was set up to facilitate installing wire mesh reinforcement. At the overlap area steel wires were used to tie up the mesh in a similar way as introduced in the first experiment.

All the confined specimens were strengthened with two layers of 40 mm wide CFRP strips at both ends and capped with high strength plaster before testing.

## 2.2 Properties of preliminary materials

Locally purchased galvanised wire mesh (12.7 mm x 12.7 mm) was used for this series of study. The tensile strength of single wire in both lateral and vertical directions was investigated, as shown in Table 3. The concrete used for the first experiment was mixed in the laboratory, while read mix concrete with target strength of 32 MPa was adopted for the second experiment. The slump test result and the average compressive strength at 28 days for the first and the second experiment were 150 mm, 55 MPa, 175 mm, 33 MPa, respectively. Due to the equipment constraint, four batches of mortar cast for the second experiment. The mortar compressive strength of each batch at 28 days was 62.4 MPa, 48.5 MPa, 59.5 MPa and 55.6 MPa, respectively.

**Table 3. Average single wire tensile strength**

Experiment	Orient.	Diametre $d_w$ mm	Ultimate Load N	Ultimate Stress MPa
I	Trans.	1.10	535	565
I	Long.	1.10	518	545
II	Trans.	1.12	614	620
II	Long.	1.13	584	587

Note: Orient. = Orientation, Trans.=transverse, Long.=longitudinal

## 2.3 Specimens testing

All specimens were tested under concentric loading, which was performed through displacement control. The specimens of the first experiment were tested using MTS 643, at a speed of 0.15 mm/min in the structural laboratory at Hong Kong Polytechnic University. The specimens of the second experiment were tested using the Denison testing machine, at a speed of 0.5 mm/min in the High Bay laboratory at the University of Wollongong.

## 3. Results and discussion

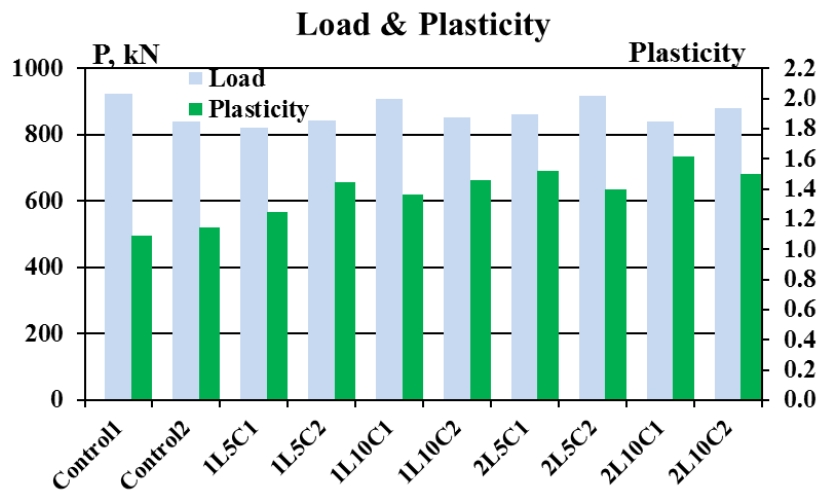
### 3.1 Experiment I: wire mesh cages cast integrally

The results of the first experiment are presented in Table 4 and Figure 2. The ultimate load of mesh confined specimens was less than the controls. The increment in the layer of wire mesh did not ensure the increment in the load capacity. The results also show that 5 mm difference in cover did not make significant difference in terms of load carrying capacity. Plasticity ratio was adopted to investigate ductility, which is defined as  $\beta = \Delta_{0.85} / \Delta_{ult}$ , where  $\Delta_{0.85}$  = the displacement corresponding to the load at 85 percent of the maximum axial load on the descending curve;  $\Delta_{ult}$  = the displacement corresponding to the maximum axial load. The specimens confined with wire mesh had significantly outweighed the controls in terms of ductility. However, the increment was not linear to the increase of wire mesh reinforcement.

**Table 4. Results of Experiment I**

Specimen Code	Ultimate Load kN	Ultimate Load, kN Average	Comp.	Plasticity Ratio $\Delta_{.85}/\Delta_{ult}$	Plasticity Ratio Average	Comp.
Control 1	924.			1.090	1.119	1.00
Control 2	841	883	1	1.148		
1L5C1	823			1.248	1.348	1.20
1L5C2	843	833	0.94	1.447		
1L10C1	909			1.365	1.411	1.26
1L10C2	852	881	1.00	1.457		
2L5C1	862			1.518	1.456	1.30
2L5C2	918	890	1.01	1.395		
2L10C1	840			1.615	1.556	1.39
2L10C2	881	861	0.98	1.497		

Comp. = comparison



**Figure 2. Load and plasticity of Experiment I**

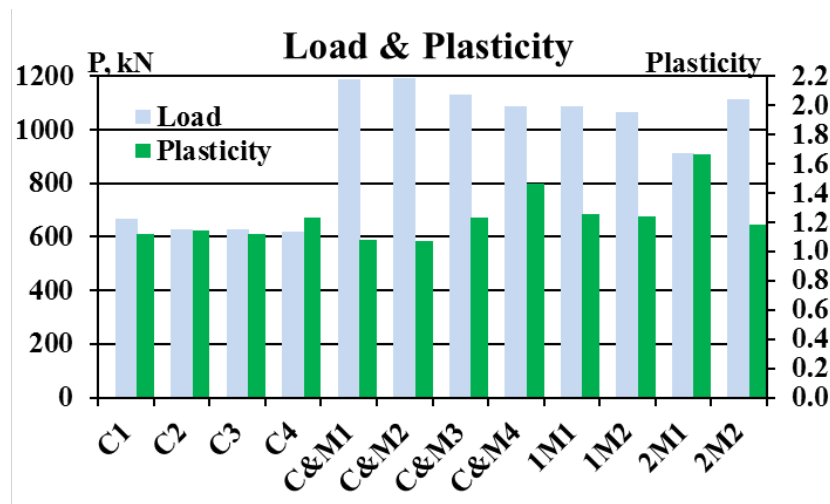
### 3.2 Experiment II: wrapping method

The results of the first experiment are presented in Table 5 and Figure 3. It is noted that the diameter of confined specimens were 190 mm, larger than that of control. In contrast to the first experiment, the load carrying capacity of mortar or MGWM composite confined specimens had been considerably improved. Moreover, the specimens confined with mortar had outperformed the specimens confined with MGWM composite in terms of load carrying capacity, which indicates that the increment in strength was related to the contribution of mortar. However, MGWM composite significantly improved plasticity. The second method, wrapping wire mesh onto precast concrete core combined with mortar, can improve both the load carrying capacity and ductility.

**Table 5. Results of Experiment II**

Code	Ultimate Load kN	Ultimate Load, kN Average	Mortar $f'_m$ MPa	Plasticity Ratio $\Delta_{.85}/\Delta_{ult}$	Plasticity Ratio AVE	Plasticity Comp.
C1	667	635	-	1.119	1.155	1
C2	627		-	1.147		
C3	630		-	1.119		
C4	618		-	1.235		
CM1	1186	1149	62	1.080	1.212	1.05
CM2	1194		49	1.070		
CM3	1130		60	1.231		
CM4	1088		56	1.468		
1M1	1086	1075	62	1.256	1.248	1.08
1M2	1064		49	1.239		
2M1	912	1013	60	1.665	1.423	1.23
2M2	1113		56	1.182		

Comp. = comparison



**Figure 3 Load and plasticity of Experiment II**

### 3.3 Estimated Load

Following AS 3600 (2009), the lateral confinement to the core was calculated for the MGWM composite confined specimens. Wire mesh was considered as steel reinforcement. The estimated values of the second experiment are shown in Table 6. The variation between the estimated values and the experimental results is large, which indicates that the strength contribution related to the wire mesh was marginal due to low reinforcement ratio. In other words, the contribution by concrete core and mortar are critical. A factor of 0.85 is considered for evaluating the mortar shell and the concrete core contribution to the load carrying capacity, as shown in the following equation:

$$P = 0.85(A_c f'_c + A_m f'_m) \quad (1)$$

where  $A_c$ ,  $f_c$  is the area and the compressive strength of concrete core, respectively;  $A_m$ ,  $f_m$  is the area and the compressive strength of mortar confinement, respectively.

**Table 6. Load estimation**

Specimen Code	$f'_m$ MPa	Layer L	VFR Vr	$f_{r,eff}$ MPa	$f_{c,c}$ MPa	$P_{est}^{**}$ kN	$P_{exp}$ kN	Comparison $(P_{est}-P_{exp})/P_{exp}$	$P^*$ kN	Comparison $(P-P_{exp})/P_{exp}$
MC1	62.1	-	-	-	-	1368	1186	15%	1163	-2%
1MOS1	62.1	1	0.0078	0.61	42.39	749	1086	-31%	-	-
MC2	48.5	-	-	-	-	1222	1194	2%	1039	-13%
1MOS2	48.5	1	0.0078	0.61	42.39	749	1064	-30%	-	-
MC3	59.5	-	-	-	-	1340	1130	19%	1139	1%
2MOS1	59.5	2	0.0155	1.21	44.88	793	912	-13%	-	-
M&C4	55.6	-	-	-	-	1299	1088	19%	1104	1%
2MOS2	55.6	2	0.0155	1.21	44.88	793	1113	-29%	-	-

VFR (Vr): volume fraction of reinforcement;

$f_{r,eff}$ : the effective confining pressure

$f_{c,c}$ : the compressive strengths of the confined concrete

$P_{exp}$ : the experimental results; \* Estimated using Equation 1; \*\* Factor 0.85 not considered

#### 4. Conclusions

Based on the series of experiments, the following conclusions are drawn:

At low reinforcement ratio, the contribution of wire mesh to the compressive strength is marginal. However, wire mesh can significantly improve the ductility of confined specimens in both cases. The method of wrapping wire mesh to precast core and compacted with mortar is sufficient to improve both the load carrying capacity and ductility. The contribution by concrete core and mortar is critical to predict the ultimate load. A factor of 0.85 might be adopted for a relatively close estimation for the ultimate load of mortar-confined specimens.

#### 5. Acknowledgement

Special acknowledgment is given to Prof. Teng Jin-Guang for hosting the PhD candidate's visit. The contributions of laboratory staff at the Hong Kong Polytechnic University and the University of Wollongong are gratefully acknowledged.

#### 6. References

1. Australian Standards, "Concrete structure (AS 3600)", 2009, Sydney
2. Australian Standards, "Determination of properties related to the consistency of concrete – Slump Test (AS 1012.3.1)", 1998, Sydney
3. Australian Standards, "Methods of Testing Concrete – Determination of the Compressive Strength of Concrete Specimens (AS 1012.9)", 1999, Sydney
4. Lam, L., and Teng, G. (2002). "Strength Models for Fiber-Reinforced Plastic-Confined Concrete." Journal of Structural Engineering, 128(5), 612-623.
5. Naaman, A. E. 2000, Ferrocement and Laminated Cementitious Composites, Techno Pr 3000, Mich., USA
6. Morales, S. M., "Spirally-Reinforced High-Strength Concrete Columns", Thesis for Doctor of Philosophy, 1983, Cornell University, USA
7. Waliuddin, A.M. and Rafeeqi, S.F.A., "Study of the behavior of plain concrete confined with ferrocement", Journal of Ferrocement, 24(2), 1994, pp139-150.



# Behaviour of Crumb Rubber Concrete Columns under Seismic Loading

Osama Youssf<sup>1</sup>, Mohamed A. ElGawady<sup>2</sup>, Julie E. Mills<sup>3</sup>, Xing Ma<sup>4</sup> and Tom Benn<sup>5</sup>

<sup>1</sup>PhD Student, University of South Australia

<sup>2</sup>Associate Professor, Missouri University of Science and Technology

<sup>3</sup>Professor of Engineering Education and Head of NBE School, University of South Australia

<sup>4</sup>Senior Lecturer in Civil Engineering, University of South Australia

<sup>5</sup>Lecturer in Civil Engineering, University of South Australia

**ABSTRACT:** This paper describes preliminary experimental work conducted to explore the possible use of crumb rubber concrete (CRC) for structural columns. Two reinforced concrete columns with a diameter of 240 mm and shear span of 1500 mm were tested under constant axial compression load and incrementally increasing reversed cyclic loading. One column was constructed out of CRC and the other one was constructed out of conventional concrete. A snap-back test was conducted to evaluate the damping properties of each column. The results indicated that the use of CRC in the column structure increased the hysteretic damping ratio and energy dissipation by 13% and 150% respectively, up to 4% drift. Beyond that the hysteretic damping ratio and energy dissipation slightly decreased by 0.33% and 1.8%, respectively compared to conventional concrete. However, using CRC decreased the viscous damping ratio compared to a conventional concrete. The CRC column was able to sustain a lateral load of about 98.6% of the load sustained by the conventional column. In addition, the CRC column showed an ultimate drift of about 91.5% of the drift shown by the conventional column. This investigation demonstrates that CRC has the potential to provide an environmentally-friendly alternative to conventional concrete in structural applications.

**Keywords:** Crumb rubber concrete, Cyclic loading, Seismic loading, Damping, Energy dissipation.

## 1. Introduction

Used tyres that are currently dumped to landfill are a significant problem throughout the world. Every year, one billion tyres reach the end of their useful lives and 0.5 billion more are expected to be discarded each year by 2030 [1]. Scrap tyres are among the largest and most problematic sources of waste of modern societies, due to their durability and the huge volumes of discarded tyres every year [2]. Recycling of used rubber conserves valuable natural resources and reduces the amount of rubber entering landfill [3]. One application where recycled tyres can be used is concrete. Crumb rubber concrete (CRC) is similar to conventional concrete but uses crumbed scrap tyre rubber as a partial substitution for mineral aggregates.

Well designed and detailed reinforced concrete structures under the prevailing capacity design codes will suffer from severe damage at predesigned locations (i. e. plastic hinges). Hence, more energy-dissipative materials and systems are highly desirable to reduce this damage. Experimental studies on rubberised concrete materials have shown that using rubber in concrete as a partial replacement of its mineral aggregates enhances its ductility, toughness, and damping ratio, but reduce its compressive strength, compared to conventional concrete [4-10]. However, limited studies have been carried out on larger scale structural elements and the results to date have been inconsistent [11, 12].

While tests at the material level showed that CRC generally has higher viscous damping compared to its counterpart conventional concrete, tests on structures constructed using CRC are rare and showed conflicting results. Xue and Shinozuka [11] have investigated the potential use of CRC as a structural material. They tested two very small-scale columns having dimensions of 40x40x500 mm on a shaking table with one column made out of conventional concrete and the other one made out of CRC. Their tests showed that the CRC increased the damping ratio by 62% and decreased the peak seismic response acceleration by 27% compared to conventional concrete. On the other hand, Bowland [12] has investigated the damping properties of two large-scale footbridges 9145x2135 mm using an electro-dynamic shaker. One bridge was constructed using conventional concrete, while the other one was constructed using CRC. This investigation showed that the crumb rubber did not significantly affect damping of the bridge and the crumb rubber sometimes reduced the viscous damping. The main differences between these two studies reported in [11] and [12] were the rubber particle size used and the scale of the tested structure as well as the test limit. In [11], the rubber particle size was 6 mm and it was applied on a relatively small scale column. By comparison, Bowland [12] used a smaller rubber particle size (0.25 mm) and applied it to a relatively large scale structure.

In addition, Xue and Shinozuka [11] have tested their columns up to failure. However, in Bowland [12] the footbridges were tested in the elastic range. This could have contributed to the differences in their findings.

Skripkiūnas et al. [8] observed a continuous decrease in damping ratio ( $\zeta$ ) with increasing rubber content up to 30% sand replacement. The rubber particle size in their study [8] was 1-3 mm. Resende et al. [13] used rubber particles of 2.4 mm size and found that there was no increase in  $\zeta$ . However, a significant increase in  $\zeta$  was observed when they used rubber and steel fibre together [13]. Therefore, it could be concluded that the rubber particle size also has a significant effect on structure  $\zeta$ .

The contradiction in the effect of crumb rubber on the dynamic properties of concrete structures indicates the need for future research and provided the motivation to investigate the performance of CRC as a construction material in reinforced columns under lateral cyclic loading simulating seismic loads. This paper provides the first investigation on seismic behaviour of relatively large scale CRC columns which can help explore the possible future use of CRC for structural columns.

## **2. Experimental program**

Two circular reinforced concrete columns with a diameter of 240 mm and shear span of 1500 mm were cast and tested under constant axial compression load and incrementally increasing reversed cyclic loading. One column was made out of CRC (CRC specimen) and the other one was made out of conventional concrete (CC specimen). Each specimen consisted of a 400x400x1200 mm footing, circular column of 240 mm diameter and 1325 mm clear height, and a 350x350x350 mm column head. The column head acted as a load stub through which the actuator for lateral loading was attached. Each column was reinforced by 6N12 (12 mm diameter) longitudinal bars. Shear and confinement reinforcement was provided by a RW10 (10.5 mm diameter) spiral at a pitch of 80 mm. These represent a longitudinal reinforcement ratio of 1.45% and a transverse volumetric reinforcement ratio of 1.42%. The column longitudinal reinforcement was extended into the footing and the column head to provide adequate shear capacity. Each column had a central un-bonded post-tensioned (PT) bar of 20 mm diameter with un-bonded length of 2253 mm that was used to apply an axial load of 110 kN, in conjunction with two disc springs that were used to keep the axial compression load constant during column loading.

### **2.1 Materials and concrete mixes**

General purpose Portland cement, according to AS 3972 [14], was used as the binder material in the concrete mixes. Two sizes of dolomite stone having nominal maximum sizes of 10 mm and 20 mm were used as coarse aggregate (10 mm : 20 mm = 1 : 2.34). River sand with a maximum aggregate size of 5 mm was used as fine aggregate. The crumb rubber used during the course of this study had only two particle sizes of 1.18 and 2.36 mm. The specific gravity, unit weight, and fineness modulus were 2.72, 1570 kg/m<sup>3</sup>, and 6.02 respectively for dolomite; 2.65, 1630 kg/m<sup>3</sup>, and 2.36 respectively for sand; and 0.85, 530 kg/m<sup>3</sup>, and 4.53 respectively for rubber. Polycarboxylic ether type superplasticizer (SP) with a specific gravity of 1.08 was added to the concrete mixtures to achieve the required concrete workability with a concrete slump of 130-150 mm.

The reinforcement in all column specimens consisted of N12 and RW10 for longitudinal and transverse steel bars, respectively. The yield strength, yield strain, ultimate strength, and ultimate strain provided by the supplier were 550 MPa, 0.00275, 698 MPa, and 0.11600, respectively for N12, and 612 MPa, 0.00306, 641 MPa, 0.02680, respectively for RW10. The yield strength and ultimate strength of the PT bar were 901 MPa and 1102 MPa, respectively.

In order to increase the rubber/cement interface adhesion, pre-treatment of the rubber particles with sodium hydroxide (NaOH) solution was used. The process commenced with the rubber particles being washed by tap water to remove any impurities and dust. They were then submerged into 10% NaOH solution for 30 minutes in a container. Finally, the rubber particles were washed again by stirring in water until its pH became 7, and then they were left to air dry. The final washing is essential to remove any existence of NaOH solution and to prevent any negative effect on the concrete durability [15-17].

The specimens were cast using two different concrete mixtures; conventional concrete of 60 MPa target compressive strength, and the corresponding CRC where 20% of the sand volume was

replaced by rubber particles. The concrete mixes were designed according to Australian Standard (AS) AS 1012.2 [18]. Table 1 summarises the different components and properties of the concrete mix used for each specimen.

**Table 1. Proportions of concrete mixes.**

Specimen code	Rs (%)	W/C	Mix proportions (kg/m <sup>3</sup> )							$f'_c$ (MPa)		E (GPa)
			Cement	Sand	Dolomite		Rubber	Water	SP	28 day	Test day	
					10 mm	20 mm						
CC	-	0.5	350	866	311	727	--	175	6.30	58.6	61.9	45.62
CRC	20	0.5	350	693	311	727	55.5	175	6.65	43.0	44.7	43.27

Rs Per cent of sand volume replaced by rubber.

The mixing procedure for the conventional concrete mix was as follows: mix dry sand and gravel for 1 min.; add half of the water and mix for 1 min.; rest for 2 mins; add cement, water, and admixtures, and then mix for 2 mins. The same procedure was followed for the CRC mix; except that the rubber aggregate was first mixed with dry cement for 1 min in an external container, aiming to increase the rubber/cement interface adhesion, which is one of the main factors affecting CRC strength. These are the same procedures previously followed by the authors in earlier work on CRC material properties [17].

## 2.2 Specimen preparation and cyclic test setup

The column reinforcement cage was placed in position during casting of the column footing to avoid using any steel splices in the column longitudinal bars. A PVC-225 stormwater pipe (240 mm inner diameter and 5.5 mm wall thickness) was used as the circular column formwork. A PVC-40 pressure pipe (45.1 mm inner diameter and 1.5 mm wall thickness) was centred along the whole specimen height to become a duct for the PT bar. Figure 1 shows a prepared test specimen. The concrete was cured until 28 days by showering the column specimens two times a day in conjunction with wrapping the specimens in plastic sheet. Ten 100x200 mm concrete cylinders were taken from each mix to record the 7 and 28 day compressive strengths, as well as, the column test day compressive strength according to AS 1012.9 [19].

After 28 days concrete age, the column footing was post tensioned to the lab strong floor. The MTS actuator ram was attached to the column head using two high-strength bolts passing through two horizontal ducts in the column head. The PT bar was loaded and anchored at the footing and head using two 160x160x40 mm steel plates and two 80 mm length hex nuts. The PT bar system was used to apply an initial axial force of 110 kN. This axial force was approximately 4.0-5.6% of the columns axial capacity ( $P_0$ ) calculated as  $P_0 = f'_c A_g$ , where;  $f'_c$  is the concrete compressive strength and  $A_g$  is gross cross-sectional area of the column.

The lateral load was applied using a horizontally aligned 100-kN hydraulic actuator under displacement control. The column specimens were subjected to reverse cyclic lateral loading at 1 mm/sec according to ASTM E2126-11 [20]. The displacement increment started with 0.25% drift ratio until reaching a total of 1% drift. Up to 1% drift, two complete cycles per drift were applied. Then, the displacement increment increased from 1% drift to 10% drift in increments of 1% drift. Each drift level in this stage consisted of three complete cycles. Figure 2 shows the loading pattern used in this study. The forces in the PT bars were measured using a load cell attached at the top of the column. All measurements were recorded using a data acquisition system and computer software (LABVIEW 8.6).

## 2.3 Snap-back test

Snap-back tests were carried out on each column specimen, before the cyclic loading tests, to estimate the structure damping ratio, natural frequency, and stiffness. Figure 3 shows the snap-back test setup. The column head was pulled with an initial displacement of 5 mm towards a reaction frame using steel wire of 16 mm diameter connected to the MTS hydraulic ram. Then, this initial displacement was suddenly released by using a double shear connection designed to fail at 5 mm displacement for each column, see Figure 3(b). The column displacement at the mid-height of the

column head was recorded using linear variable displacement transducers (LVDT). The column acceleration was measured using an accelerometer placed horizontally at the mid-height of the column head. The test was repeated three times for each column and the results were averaged.



Figure 1. Column specimen.

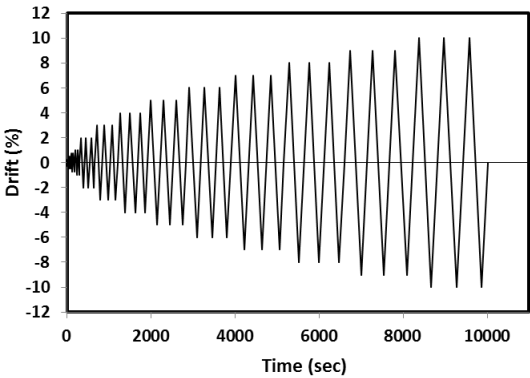
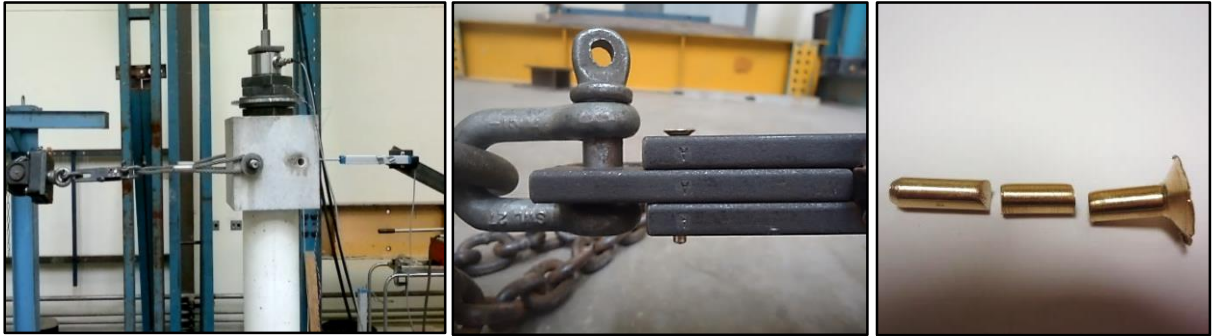


Figure 2. Loading pattern.



(a) Pulling system.

(b) Double shear connection.

(c) Pin double shear failure.

Figure 3. Snap-back test setup.

**3. Test results and discussions**

**3.1 Snap-back test**

Snap-back tests were carried out on the columns to determine their initial stiffness, natural frequencies, and damping ratios. The initial stiffness was determined as the slope of the linear load-displacement relationship recorded during the static pull of the column before the sudden snap failure. To determine the natural frequency for each column, Fast Fourier Transform (FFT) analyses were carried out to convert data from the time domain to the frequency domain. Damping ratios ( $\zeta$ ) were calculated from the recorded accelerations and displacements in time domains using the logarithm decrement method (Eq.1) after five cycles and in frequency domains using the half-power band width method (Eq.2). More details of each method can be found in Chopra 1995 [21].

$$\zeta = \frac{1}{2\pi n} \ln \frac{y_1}{y_n} \tag{Eq.1}$$

Where;  $y_1$  is the initial amplitude of displacement/acceleration in the response decay, and  $y_n$  is the amplitude of displacement/acceleration after n cycles in the time domain.

$$\zeta = \frac{f_b - f_a}{2f_n} \tag{Eq.2}$$

Where;  $f_b$  and  $f_a$  are the frequencies associated with the half power points ( $\frac{A_p}{\sqrt{2}}$ ) on either side of the peak amplitude ( $A_p$ ) in the frequency domain, and  $f_n$  is the natural frequency of the specimen.

Table 2 shows the detailed results of the snap-back tests. The natural frequency of the CRC specimen (18.3 Hz) was higher than that of the CC specimen (12.1 Hz). This was attributed to the higher initial stiffness of the CRC specimen which was 3.8 times the initial stiffness of CC specimen. However, the modulus of elasticity (E) for the CRC was less than that of the CC (see Table 1). The difference in the initial stiffness between the tested columns may be attributed to the casting of columns two days after the footing which can affect the bond at the footing/column interface. As shown in Table 2,  $\zeta$  for the CRC specimen was less than that of the CC specimen. By averaging the results of the two methods, it can be concluded that replacing 20% of the sand aggregate by rubber aggregates (specimen CRC) decreased  $\zeta$  by 56% compared to conventional concrete. This implies that using rubber aggregate in concrete in large scale structure applications is not as promising as what was found by researchers in most of the concrete material level studies [4-6, 22]. The rubber particle size used in this study ranged between 1.18 and 2.36 mm which is in the same range of 0.25-3.0 mm used by some previous researchers [8, 12, 13]. These researchers found that using this relatively small rubber size has no effect on concrete damping or sometimes decreased its damping properties. However, Xue and Shinozuka [11] used a rubber size of 6.0 mm and achieved 62% increase in concrete damping. Therefore, the rubber particle size plays an important role in affecting the concrete damping. More research is clearly required in this area.

**Table 2. Snap-back test results.**

Specimen code	Initial stiffness (kN/mm)	Natural frequency (Hz)			Damping ratio, $\zeta$ Log. dec.(%)			Damping ratio, $\zeta$ Half-power (%)		
		Disp.	Acc.	Average	Disp.	Acc.	Average	Disp.	Acc.	Average
CC	0.62	11.94	12.19	12.1	4.5	9.9	7.2	4.7	8.0	6.3
CRC	2.31	18.16	18.49	18.3	2.7	3.0	2.8	3.6	2.5	3.1

### 3.2 Cyclic test

Table 3 summarises the main results of the static cyclic test conducted in this study. The CC specimen reached an ultimate force of 28.9 kN at a drift of 5% before it reached an ultimate drift of 9.95%. The CRC specimen reached an ultimate force of 28.5 kN at a drift of 4% before it reached an ultimate drift of 9.10%. Thus, using rubber in concrete resulted in a decrease in the ultimate force and ultimate drift by 1.3% and 8.5%, respectively. The CC specimen had an average compressive strength,  $f_c$  of 61.9 MPa in comparison to  $f_c$  of 44.7 MPa for the CRC specimen, which would make it likely that the CRC column would have higher deformability. However, these specimens were tested under the same magnitude of axial load. Thus, the CRC specimen was subjected to a slightly higher percentage of its concentric capacity (5.6%) than the CC specimen (4.0%) which resulted in a reduction of the specimen deformability. The CRC specimen displayed residual drift 20% lower than that displayed by the CC specimen at their ultimate drift cycles, which were 9.10% and 9.95%, respectively. Residual drift is the drift that remains in the specimen at zero force of a given cycle drift.

**Table 3. Cyclic test results.**

Specimen code	Ult. disp. (mm)	Ult. drift (%)	Ult. force (kN)	Drift at ult. force (%)	Residual disp. at ult. drift (mm)	Residual drift (%)	Concrete cover spalling height (mm)
CC	149.3	9.95	28.9	5.0	105.0	7.0	250
CRC	136.5	9.10	28.5	4.0	84.0	5.6	230

#### 3.2.1 Test observations

Figure 4 shows the global damage, horizontal crack extensions, and concrete cover spalling regions of the tested specimens. In the CC specimen, at 3% drift, horizontal cracks began to occur at a height of 100 mm above footing. Spalling of concrete cover started at a drift of 4.5% in the bottom-most 100 mm

of the column above the footing, and then extended to 250 mm height above the footing at the end of the test (10% drift). In the third cycle of 9% drift the northern-most longitudinal bars ruptured. In the CRC specimen, up to 3% drift, only some horizontal cracks at a height of 150 mm above footing occurred without any concrete spalling. At 4% drift, concrete cover spalling started and extended up to 150 mm above the footing until 9.0% drift. Rupture of the most north and most south longitudinal bars occurred in the first cycle of 10% drift with extension of concrete cover spalling up to 230 mm above the footing. In the CRC, horizontal flexural cracks were observed to only 370 mm above the footing compared to observed horizontal flexural cracks to 860 mm above the footing in the CC specimen. These observations indicated that the rubberized concrete columns can behave almost like the conventional concrete columns. However, rubberized concrete can delay and reduce the amount of damage occurring under seismic loading. This is attributed to the higher deformability of rubberized concrete compared to conventional concrete.

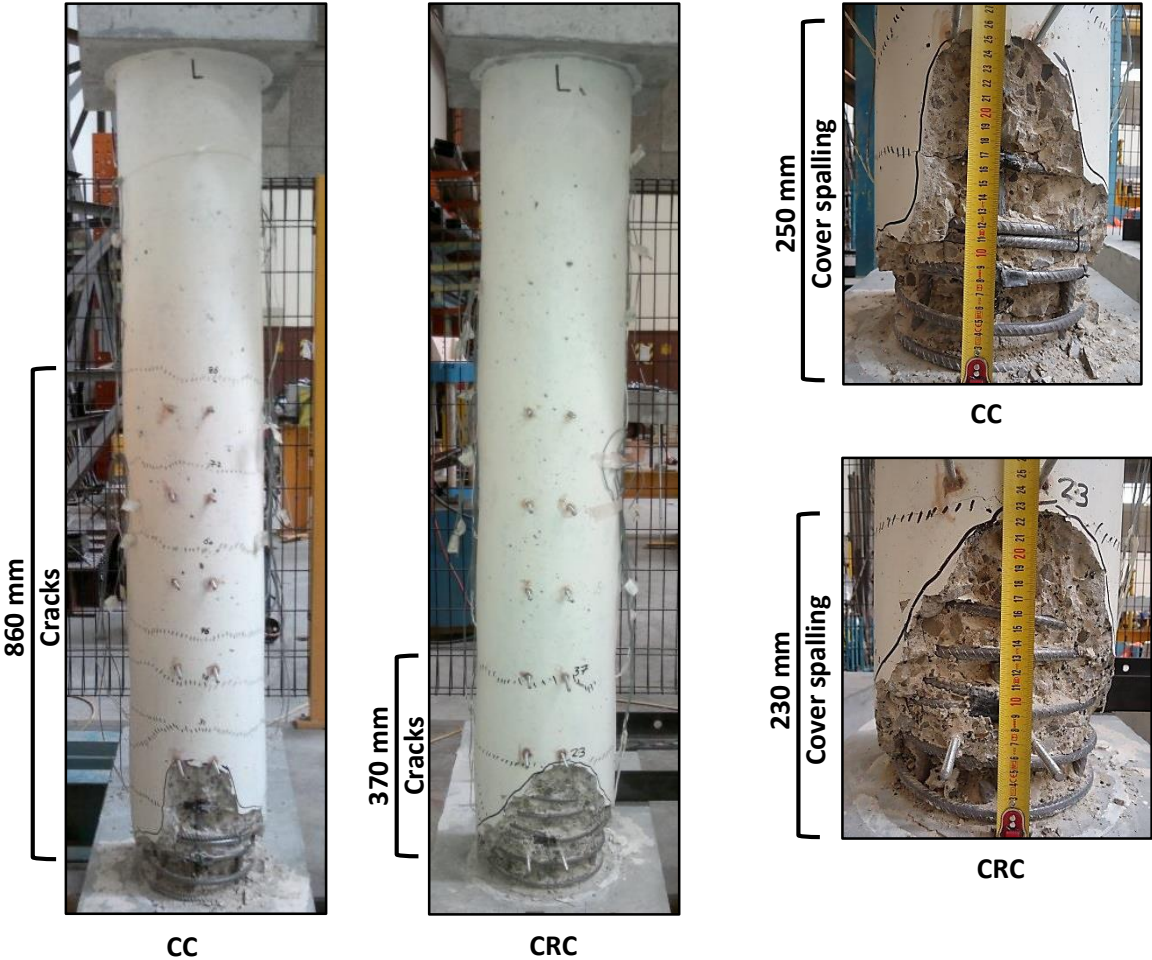


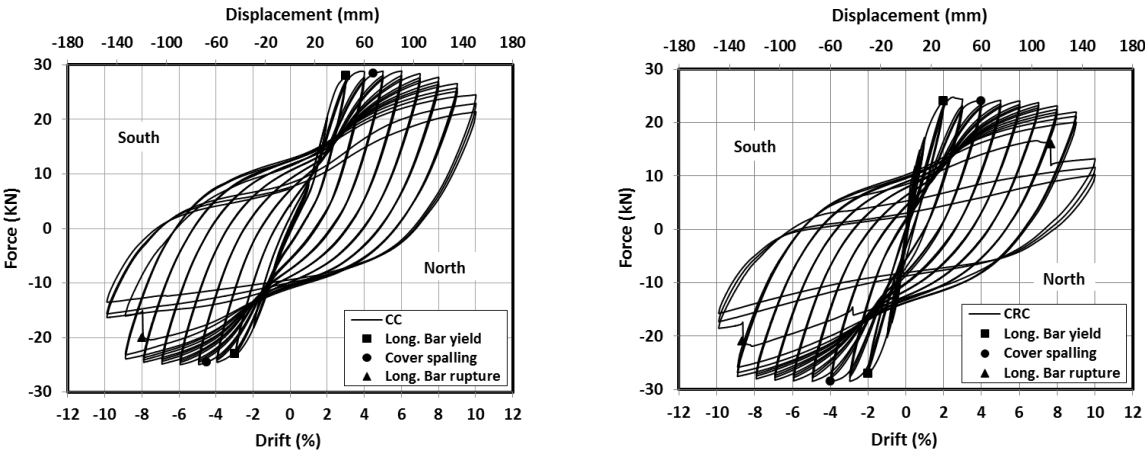
Figure 4. Global damage, horizontal crack extensions, and concrete cover spalling regions of tested columns.

3.2.2 Hysteretic behaviour and backbone curve

The recorded lateral force versus column displacement for each specimen is shown in Figure 5. The CC specimen showed linear behaviour until about 1% drift. However, the CRC specimen showed linear behaviour until only 0.5% drift. This was followed by stable nonlinear hysteretic loops until the end of the test for all specimens. The nonlinearity was attributed to the concrete cover spalling, horizontal flexural cracks, and longitudinal bar yielding. The hysteresis loops initially indicate typical well rounded curves until after a significant deterioration of the concrete has taken place. All specimens resisted the maximum lateral load for several cycles with minor strength degradation until the first rupture of the longitudinal bar that can be observed from the sudden drop in the specimen force at cycles of 9% and 10% drift for specimens CC and CRC, respectively. If a 20% drop in the

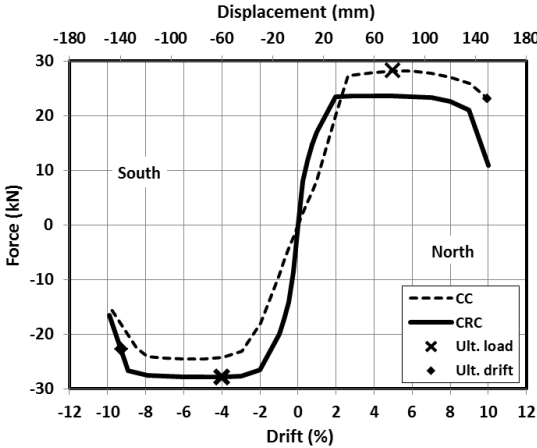
lateral force be considered as the point of specimen failure, then columns CC and CRC failed during the second cycle of 10% drift (north direction) and first cycle of 10% drift (south direction), respectively.

The backbone curves (envelopes of the hysteretic loops) of the tested specimens are shown in Figure 5(c). As shown in this figure, the CRC specimen had higher initial stiffness than that of the CC specimen (see Table 2). For all specimens, after the steel yielded the specimens possessed a constant post-yield stiffness until reaching their ultimate strengths of 28.9 kN and 28.5 kN for CC and CRC specimens, respectively. This was followed by strength degradation due to concrete cover spalling, longitudinal bar rupture and longitudinal bar buckling. In Figure 5(c), there is no significant difference in the stiffness degradation rate between the CRC and CC specimens. This indicated that the nonlinear behaviour of rubberized concrete is very similar to that of conventional concrete.



(a) Hysteretic behaviour of CC specimen.

(b) Hysteretic behaviour of CRC specimen



(c) Backbone curve for all specimens.

**Figure 5. Cyclic test results.**

**3.3 Energy dissipation and equivalent viscous damping**

High energy dissipation of structural elements subjected to earthquakes is a very desirable characteristic. The energy dissipation of the tested columns at each % drift can be calculated from the hysteretic behaviour as the area enclosed by the cycle of the lateral load versus displacement curve. Figure 6 shows the amount of energy dissipated at each % drift. The energy at each % drift has been taken as an average energy of all cycles at the same drift. As shown in Figure 6(a), up to 2% drift, there was insignificant energy dissipation due to the elasticity in the specimen’s behaviour (before bar yielding and concrete spalling). Beyond that, there was a significant linear increase in the energy dissipation with increasing applied drift until the specimens were not able to keep their post-yield



stiffness, see Figure 6(b). The CRC specimen dissipated mean energy about 2.5 times the energy that was dissipated by the CC specimen up to 4% drift. Beyond 4% drift, the CRC was not able to keep its post-yield stiffness due to the concrete cover spalling and then the peak force started to decrease. This resulted in a slight reduction in the CRC energy dissipation by 1.8% compared to the CC specimen.

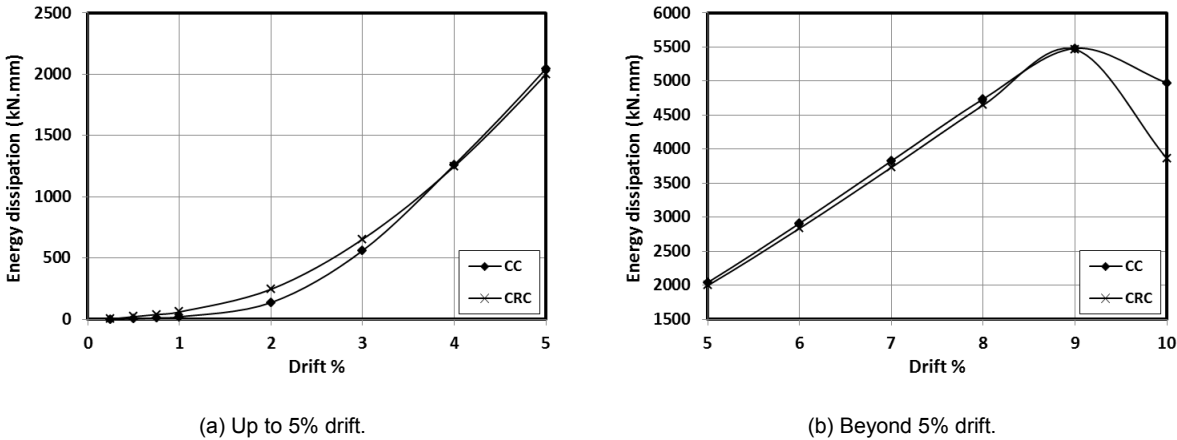


Figure 6. Energy dissipation.

Equivalent viscous damping ( $\zeta_{eq}$ ) is a central task in modern seismic analysis methods [23]. Hysteretic damping in structures can be represented by  $\zeta_{eq}$  as it is the simplest form of damping for numerical analysis [21]. In this study,  $\zeta_{eq}$  was calculated for each specimen using Eq.3 [24]:

$$\zeta_{eq} = \frac{1}{4\pi} \frac{E_d}{E_s} \tag{Eq. 3}$$

Where,  $E_d$  is the energy dissipated in a cycle and  $E_s$  is the stored energy measured at the peak force of the same cycle. The plot of  $\zeta_{eq}$  versus drift ratio for each specimen is shown in Figure 7.

The value of  $\zeta_{eq}$  increased with increasing drift ratio almost linearly up to approximately  $\zeta_{eq}$  of 25% for both specimens. This was due to the continuous increase in concrete spalling and horizontal flexural cracks opening until the specimens reached their failure mode. The  $\zeta_{eq}$  of CRC was about 1.13 times that of CC up to 5% drift, see Figure 7(a). Beyond 5%, drift due to the damage started in the CRC, the  $\zeta_{eq}$  slightly reduced by only 0.33% compared to CC, see Figure 7(b).

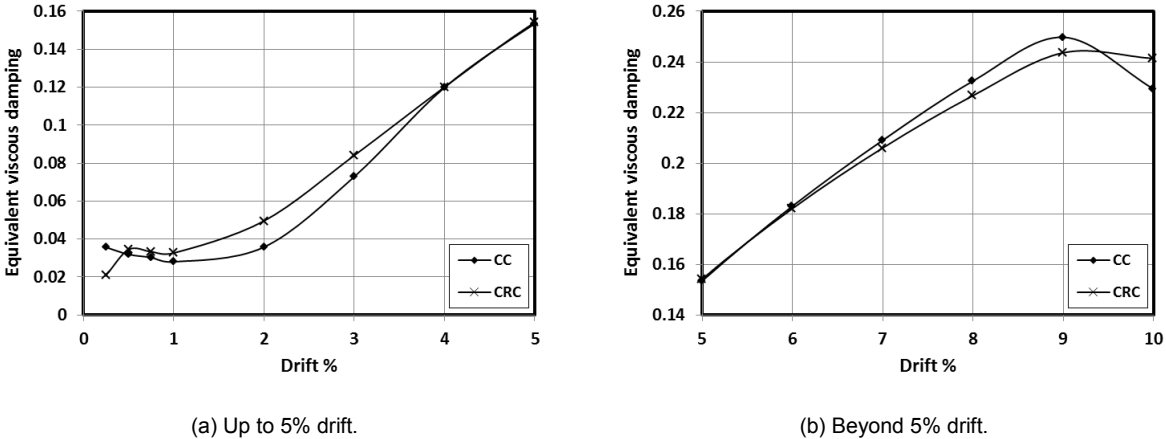


Figure 7. Equivalent viscous damping.

#### 4. Summary and conclusions

This paper presents an experimental investigation of the performance of crumb rubber concrete (CRC) in reinforced concrete columns. Two reinforced concrete columns having 240 mm diameter and 1500



mm shear span were tested under constant axial compression load and incrementally increasing reversed cyclic loading. One column was constructed out of CRC and the other one was constructed out of conventional concrete. A snap-back test was conducted to evaluate the damping properties of each column before the cyclic testing. The findings and conclusions of this investigation are summarised in the following points:

- 1) CRC in the column structure increased the hysteretic damping ratio and energy dissipation by 13% and 150%, respectively. However, it decreased the column viscous damping ratio by 56% compared to a conventional concrete column.
- 2) The CRC column was able to sustain a lateral load of 98.6% of the load sustained by the conventional column. In addition, the CRC column showed an ultimate drift of about 91.5% of the ultimate drift shown by the conventional column. This indicated that rubber can be used in concrete columns with no significant effect on its ultimate strength and deformability. However, CRC can delay and reduce the amount of damage occurring under the seismic loading.
- 3) CRC decreased the column residual drift by 20% compared to conventional concrete.
- 4) Using CRC in column structures delayed the concrete cover spalling and minimized the concrete cracks compared to conventional concrete.

Further research is recommended into the effect of rubber particle size and column size on both damping and seismic behaviour of column structures.

## 5. Acknowledgment

The authors gratefully acknowledge the donation of the following; steel reinforcement and fabricated cages by Bianco Reinforcing Australia Pty. Ltd.; sand by Premix Concrete SA Pty. Ltd.; aggregate by Hallett Concrete Australia Pty. Ltd.; cement by Adelaide Brighton Cement Pty. Ltd.; superplasticizer by BASF Construction Chemical Australia Pty. Ltd.

## 6. References

1. Silvestravičiūtė, I. and L. Šleinotaitė-Budrienė, *Possibility to use scrap tyres as an alternative fuel in cement industry*. Environmental research, engineering and management, 2002. **3**: p. 21.
2. Savas, B.Z., S. Ahmad, and D. Fedroff, *Freeze-thaw durability of concrete with ground waste tire rubber*. Transportation Research Record: Journal of the Transportation Research Board, 1997. **1574**(1): p. 80-88.
3. Li, G., Garrick G., Eggers, J., Abadie, C., Stubblefield, M.A., Pang, S.S., *Waste tire fiber modified concrete*. Composites Part B: Engineering, 2004. **35**(4): p. 305-312.
4. Fattuhi, N. and L. Clark, *Cement-based materials containing shredded scrap truck tyre rubber*. Construction and building materials, 1996. **10**(4): p. 229-236.
5. Zheng, L., X. Sharon Huo, and Y. Yuan, *Experimental investigation on dynamic properties of rubberized concrete*. Construction and building materials, 2008. **22**(5): p. 939-947.
6. Zheng, L., X.S. Huo, and Y. Yuan, *Strength, modulus of elasticity, and brittleness index of rubberized concrete*. Journal of Materials in Civil Engineering, 2008. **20**(0): p. 692.
7. Najim, K.B. and M.R. Hall, *Mechanical and dynamic properties of self-compacting crumb rubber modified concrete*. Construction and building materials, 2012. **27**(1): p. 521-530.
8. Skripkiūnas, G., A. Grinys, and K. Miškinis, *Damping properties of concrete with rubber waste additives*. Materials Science (Medžiagotyra), 2009. **15**(3): p. 266-272.
9. Eldin, N.N. and A.B. Senouci, *Rubber-tire particles as concrete aggregate*. Journal of materials in civil engineering, 1993. **5**(4): p. 478-496.
10. Son, K.S., I. Hajirasouliha, and K. Pilakoutas, *Strength and deformability of waste tyre rubber-filled reinforced concrete columns*. Construction and building materials, 2011. **25**(1): p. 218-226.
11. Xue, J. and M. Shinozuka, *Rubberized concrete: A green structural material with enhanced energy-dissipation capability*. Construction and Building Materials, 2013. **42**(0): p. 196-204.

12. Bowland, A.G., *Comparison and Analysis of the Strength, Stiffness, and Damping Characteristics of Concrete with Rubber, Latex, and Carbonate Additives*, 2011, Virginia Polytechnic Institute and State University.
13. Resende, F.M., et al., *Influence of Scrap Rubber Tires and Steel Fibers on the Damping Characteristics of Normal Concrete*. Civil Engineering Department, COPPE / Federal University of Rio de Janeiro, Rio de Janeiro, Brazil., 2003.
14. Standards Australia, *General purpose and blended cements, AS 3972.* , 2010.
15. Torgal, F.P., Y. Ding, and S. Jalali, *Properties and durability of concrete containing polymeric wastes (tyre rubber and polyethylene terephthalate bottles): an overview*. 2012.
16. Tian, S., T. Zhang, and Y. Li, *Research on Modifier and Modified Process for Rubber-Particle Used in Rubberized Concrete for Road*. Advanced Materials Research, 2011. **243 - 249**(0): p. 4125-4130.
17. Youssf, O., et al., *An experimental investigation of crumb rubber concrete confined by fibre reinforced polymer tubes*. Construction and Building Materials, 2014. **53**(0): p. 522-532.
18. Standards Australia, *Methods for testing concrete, Preparation of concrete mixes in the laboratory AS 1012.2*, 1994.
19. Standards Australia, *Methods for testing concrete, Determination of the compressive strength of concrete specimens, AS 1012.9*, 1999.
20. *Standard Test Methods for Cyclic (Reversed) Load Test for Shear Resistance of Vertical Elements of the Lateral Force Resisting Systems for Buildings*, 2011.
21. Chopra, A.K., *Dynamics of structures*. Vol. 3. 1995: Prentice Hall New Jersey.
22. Balaha, M., A. Badawy, and M. Hashish, *Effect of using ground waste tire rubber as fine aggregate on the behaviour of concrete mixes*. Indian Journal of Engineering and Materials Sciences, 2007. **14**(6): p. 427.
23. ElGawady, M., A.J. Booker, and H.M. Dawood, *Seismic behavior of posttensioned concrete-filled fiber tubes*. Journal of Composites for Construction, 2010. **14**(5): p. 616-628.
24. Jacobsen, L.S., *Steady forced vibrations as influenced by damping*. Trans. ASME, 1930. **52**(15): p. 169-181.

# *Sulfate Resistance Testing in Germany - Critical Review*

Johannes Haufe<sup>1</sup>, Anya Vollpracht<sup>2</sup> and Wolfgang Brameshuber<sup>2</sup>

<sup>1</sup>Research Assistant, Institute of Building Materials Research, RWTH Aachen University, Germany

<sup>2</sup>Professor, Institute of Building Materials Research, RWTH Aachen University, Germany

**Abstract:** The resistance of concrete to sulfate attack in aqueous solutions is often analysed using test methods on small mortar samples. The procedures are usually accelerated by using highly concentrated sulfate solutions. In this review, results on mortars made of sulfate resistant cement and mixtures of Ordinary Portland Cement (OPC) and fly ash are presented. The focus lies on the variation of the temperature and the sulfate concentration of the attacking artificial solution. The evaluation of the expansion caused by the aggressive solution is supported by the analysis of phase changes caused by the sulfate ingress. Artificial sodium sulfate solution is compared to a natural, sulfate bearing groundwater. These results and the assessment of a database containing previous results lead to the conclusion that an acceleration of the test by using high sulfate concentrations is not just unnecessary, but also leads to a change in the attack mechanism, which is not always suitable.

**Keywords:** Sulfate attack, Test methods, Fly ash

## **1. Introduction**

A major aspect concerning the durability of concrete is the resistance to sulfate attack. When exposed to water containing sulfate ions the formation of ettringite ( $\text{Ca}_6(\text{Al,Fe})_2(\text{SO}_4)_3(\text{OH})_{12}\cdot 26\text{H}_2\text{O}$ ), gypsum ( $\text{CaSO}_4\cdot 2\text{H}_2\text{O}$ ) and/or thaumasite ( $\text{Ca}_3\text{Si}(\text{OH})_6(\text{CO}_3)(\text{SO}_4)\cdot 12\text{H}_2\text{O}$ ) can lead to the deterioration of the cementitious matrix. The formation of ettringite and gypsum comes along with an increase in volume, causing expansive strains in the concrete, and thus leading to cracking. Thaumasite may precipitate when a source of carbonate, e.g. limestone powder or  $\text{CO}_2$  from the air is available. Since thaumasite is a mineral with a very low strength, its formation leads to a complete disintegration of the cement paste.

The intensity of the sulfate attack depends on the chemical composition of the cement, the permeability of the concrete, the temperature and concentration of the sulfate solution as well as the accompanying cation. Typically, sulfate resisting cements with a low content of  $\text{C}_3\text{A}$  are used, preventing the excessive formation of ettringite. The use of supplementary cementitious materials (SCMs) such as ground granulated blastfurnace slag, fly ash or silica fume usually results in a higher sulfate resistance.

Because of the differing environmental conditions and the great variety of binders the subject of sulfate attack on concrete is difficult to compress into one single testing procedure. Internationally a large variety of testing methods exists, trying to simulate and approximate the susceptibility of concrete to sulfate attack in the field using lab methods. A review on international methods can be found in [1].

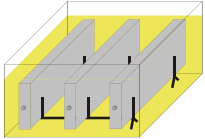
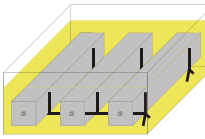
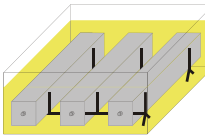
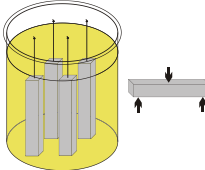
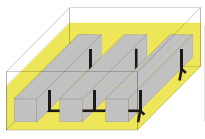
## **2. Test methods for sulfate resistance in Germany**

An overview on the test methods discussed in this paper can be seen in table 1.

The standard test method for sulfate resistance testing in Germany is the so called SVA method, which was developed from the method of Wittekindt [2]. Both methods concentrate on the evaluation of the expansion of flat prisms stored in a highly concentrated sodium sulfate solution. Originally designed to be conducted at ambient temperatures of 20 °C, the SVA method nowadays also includes testing at 5 °C to take the low temperatures usually found in German soils and groundwater into account. Recent findings concerning the attack mechanism and the influence of the concentration of the solution implicated new storage conditions: 3,000 mg  $\text{SO}_4^{2-}/\text{l}$  over a period of at least two years.

The expansions are compared to expansions of samples stored in a reference solution. For both methods (SVA and Wittekindt) a maximum difference between the expansion in sulfate and reference solution was defined: 0.5 mm/m. The assessment times are 91 days (SVA) and 56 days (Wittekindt). However, due to the recent changes in the SVA method, this criterion does no longer apply. Mixtures containing sulfate resistant OPC (CEM I 42.5 R-SR3) and blastfurnace slag cement (CEM III/B 42.5 N-LH/SR/NA) are taken as a reference to ensure the sulfate resistance of the tested binder.

**Table 1. Test methods for sulfate resistance used in Germany**

	SVA method	Wittekindt	CEN	Koch-Steinegger	MNS
Test setup					
Basic principle	Expansion measurement			Visual investigation, relative flexural strength	Relative tensile strength
Samples	Mortar flat prisms (10 x 40 x 160 mm <sup>3</sup> )		Mortar prisms (20 x 20 x 160 mm <sup>3</sup> )	Mortar prisms (10 x 10 x 60 mm <sup>3</sup> )	Concrete prisms (40 x 40 x 160 mm <sup>3</sup> ), cement content 360 kg/m <sup>3</sup>
w/c	0,5	0,6	0,5	0,6	
Storage temperature	20 °C, recently also 5 °C	20 °C	20 °C	20 °C	8 °C
Sulfate solution	Na <sub>2</sub> SO <sub>4</sub> , 30,000 mg SO <sub>4</sub> <sup>2-</sup> /l, recently also 3,000 mg SO <sub>4</sub> <sup>2-</sup> /l	Na <sub>2</sub> SO <sub>4</sub> , originally 14,400 mg SO <sub>4</sub> <sup>2-</sup> /l, later 29,800 mg SO <sub>4</sub> <sup>2-</sup> /l	Na <sub>2</sub> SO <sub>4</sub> , 16,000 mg SO <sub>4</sub> <sup>2-</sup> /l	Na <sub>2</sub> SO <sub>4</sub> , 25,000 mg SO <sub>4</sub> <sup>2-</sup> /l	Na <sub>2</sub> SO <sub>4</sub> , 33,900 mg SO <sub>4</sub> <sup>2-</sup> /l
Solution change	Every 2 weeks	Every month	Every month	-	Every month
Reference storage	Ca(OH) <sub>2</sub> solution	Water	Water	Water	Water
Storage before testing	Until age of 14 days in saturated Ca(OH) <sub>2</sub> solution	Until age of 14 days in water	Until age of 28 days in water	Until the age of 21 days in water	Water storage, Air storage, before immersion vacuum saturation at 150 mbar
Test duration	91 days 2 years for 3,000 mg SO <sub>4</sub> <sup>2-</sup> /l	56 days	Not determined	56 days	84 or 120 days
Criterion	30,000 mg SO <sub>4</sub> <sup>2-</sup> /l: Δε ≤ 0,5 mm/m	Δε ≤ 0,5 mm/m	Not determined	Relative flexural strength ≥ 0,7	Relative tensile strength ≥ 0,8 (84 days) or 0,7 (120 days)

The CEN method has been developed on a European level and is very similar to the SVA and the Wittekindt method, a major difference being the specimen geometry of 20 x 20 x 160 mm<sup>3</sup> and the concentration of the sodium sulfate solution being 16,000 mg SO<sub>4</sub><sup>2-</sup>/l. Extensive research has been carried out using this method in different research projects and round robin tests. However, the comparability between different laboratories has not been satisfying, and the evaluation of mixtures of cement and fly ash did not meet the expectations, since the results were not distinct [3].

Another method developed and applied in Germany is the method according to Koch and Steinegger [4]. Small mortar prisms are immersed into sodium sulfate solution of 25,000 mg SO<sub>4</sub><sup>2-</sup>/l and as a reference in water. In contrast to the three methods using expansion measurements for evaluation, this method

focuses on the relative flexural strength of the specimen after a storage time of 56 days at 20 °C. Publications presenting results achieved using this method are, however, scarce.

A relatively new procedure developed by Mulenga et al. is the MNS method (Mulenga-Nobst-Stark method) [5]. Focus of this method is the analysis of the relative tensile strength of concrete specimen vacuum saturated by and immersed in sodium sulfate solution of 33,900 mg SO<sub>4</sub><sup>2-</sup>/l at 8 °C in relation to water stored specimen. It is stated that the method allows to achieve repeatable results regarding the sulfate resistance of a concrete [5]. However, the application of tensile strength as the basic measurement principle results in a relatively high effort for testing compared to the other test methods. Additionally, the relatively high variance of the tensile strength compromises the validity.

## 2. Materials and Methods

### 2.1 Materials

In this study three different ordinary Portland cements with different composition and fines (CEM I 42.5 R, CEM I 42.5 R-SR, CEM I 52.5 N) are compared. A low calcium fly ash was used. The chemical composition of the materials is shown in table 2. Some of the results were previously presented at the International Conference on Durability of Concrete 2014 (ICDC), [6]. For the convenience of the reader, the material characterisation and the results are repeated in this paper.

**Table 2. Chemical composition of the cements and fly ash, [7]**

Content in wt.-%	CEM I 42.5 R-SR	CEM I 42.5 R	CEM I 52.5 N	fly ash
Loss on ignition	2.1	3.1	2.0	1.94
CaO	60.28	61.56	62.56	3.78
SiO <sub>2</sub>	18.98	19.58	21.10	57.85
Al <sub>2</sub> O <sub>3</sub>	4.12	5.27	5.03	20.07
Fe <sub>2</sub> O <sub>3</sub>	7.03	2.66	2.53	7.77
SO <sub>3</sub>	3.73	3.83	3.97	0.94
MgO	2.55	2.17	1.72	1.87
CO <sub>2</sub>	1.65	2.30	1.19	-
Na <sub>2</sub> O	0.16	0.23	0.22	2.05
K <sub>2</sub> O	0.95	1.03	0.73	1.88
Cl <sup>-</sup>	0.018	0.017	0.022	0.009

According to EN 196-1 five standard mortars with 450 g binder, 1350 g CEN reference sand and varying equivalent water cement ratio were produced. The high sulfate resistance cement was used for the reference mixture (SR). In mixtures M1 and M2 40 wt.-% of the cement were substituted by fly ash. In mixtures M3 and M4 30 wt.-% of fly ash were used as cement replacement. All five mixtures are summarized in table 3.

**Table 3. Mixture composition [7]**

Content in g	SR	M1	M2	M3	M4
CEM I 42.5 R-SR	450	-	-	-	-
CEM I 42.5 R	-	270	-	-	-
CEM I 52.5 N	-	-	270	317.6	317.6
fly ash	-	180	180	132.4	132.4
water	225	225	225	198.5	166.8
w/C <sub>eq</sub> <sup>1)</sup>	0.5	0.74	0.74	0.55	0.46
sand	1350	1350	1350	1350	1350

1) w/C<sub>eq</sub> according to DIN 1045-2

## 2.2 Methods

### 2.2.1 Sulfate resistance testing

For each mixture samples with dimensions of 10 x 40 x 400 mm<sup>3</sup> were produced. The flat prisms were stored for two days at 20 °C and > 95 % r. h.. Afterwards the framework was stripped. Subsequently the samples were pre-stored in a saturated solution of calcium hydroxide at 20°C until an age of 28 days.

Samples of each mixture then were stored in three different solutions: saturated calcium hydroxide solution, sulfate solution with 30,000 and sulfate solution with 3,000 mg/l. Four different temperatures were investigated: 5, 8, 12 and 20 °C. To remain a constant sulfate concentration, the sulfate solutions were exchanged every two weeks during the first three month and every four weeks afterwards.

Groundwater obtained in southern Germany was used for storage of specimen at 5 °C. The groundwater had an elevated sulfate concentration of approximately 1,500 mg/l and an ion composition according to table 4.

**Table 4. Ion concentrations (in mg/l) and pH of the groundwater**

Na <sup>+</sup>	K <sup>+</sup>	Ca <sup>2+</sup>	Mg <sup>2+</sup>	Cl <sup>-</sup>	NO <sub>3</sub> <sup>-</sup>	SO <sub>4</sub> <sup>2-</sup>	pH
22,0	5,7	597,0	74,5	123,98	55,53	1452	7,62

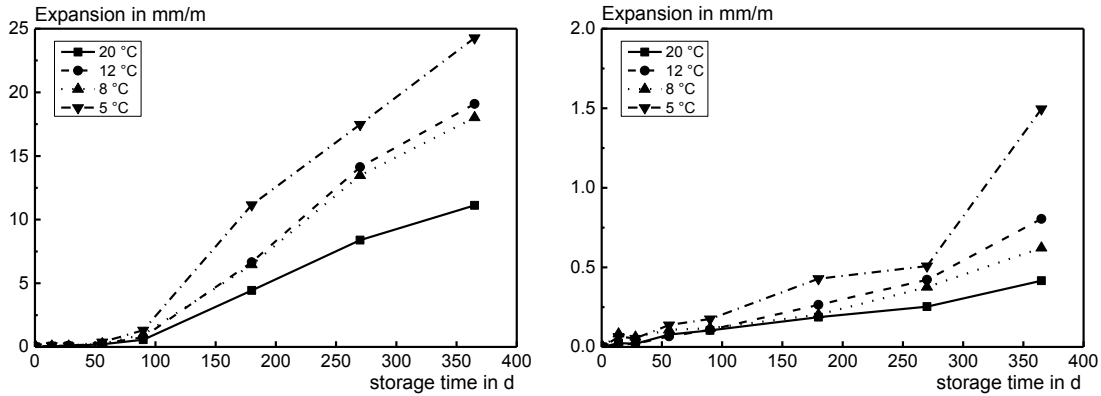
The samples were probed for their deformation and for their change of the modulus of elasticity. The measurements were performed after 0, 14, 56, 91, 180, 270 and 365 days of storage. The deformation was defined by their change of length measured with a digital indicator Mahr Millitast 1070. The dynamic modulus of elasticity was assessed by measuring the resonance frequency at the same dates.

### 2.2.2 X-ray diffraction

After 365 days of storage the sulfate intrusion was determined by means of X-ray diffraction. Therefore samples of 40 x 40 x 10 mm<sup>3</sup> were cut from the flat prisms. These samples were dried via solution exchange in isopropanol for 24 hours, followed by drying at 40 °C. The samples then were ground in steps of 0.5 mm until the middle of the sample. The powder of each step was collected and analysed with an X-ray powder diffractometer Panalytical X'Pert Pro with an X'Celerator detector in a 2θ range of 5 to 70 °2θ with a step size of 0.0167 °2θ. The samples were analysed qualitatively, followed by quantification using the Rietveld method [7].

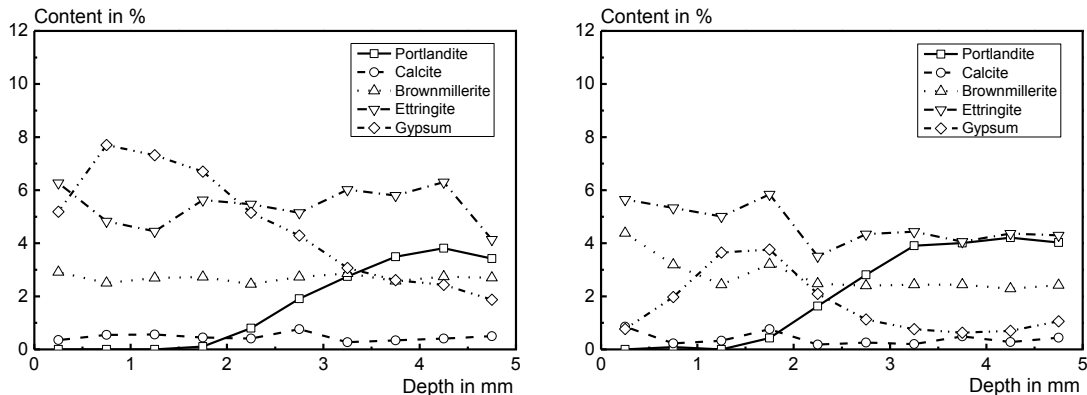
### 3 Experimental Results

The reference sample containing sulfate resisting cement shows a temperature dependence of the expansion rate (see Figure 1). A lower storage temperature leads to higher deformation. After one year of storage the highest deformation is 25 mm/m (30,000 mg/l at 5 °C). Despite the high deformation the samples are still intact. No spalling could be observed. The lower sulfate concentration (3,000 mg/l) results in a smaller expansion of only 1.5 mm/m at same temperature.



**Figure 1. Expansion of mixture SR stored in sulfate solution at 30,000 mg/l (left) and 3,000 mg/l (right), [6]**

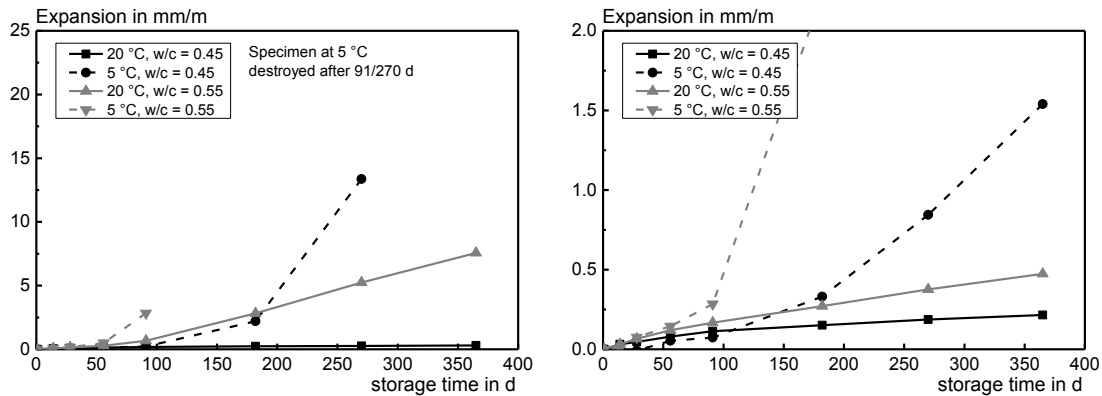
The results of XRD and Rietveld analyses are shown in figure 2. Inert phases like quartz and feldspars were disregarded in the graphs. Two variations of the reference mortar were investigated.



**Figure 2. Phase composition of mixture SR stored in sulfate solution at 30,000 mg/l and 20 °C (left) and at 3,000 mg/l and 5 °C (right), [6]**

The figure shows that there is a relatively high amount of brownmillerite ( $C_4AF$ ) remaining after one year whose content is constant over the depth of the sample. The amount of ettringite is essentially constant and is similar for both the 30,000 mg/l and 3,000 mg/l sulfate solutions. Probably it is primary ettringite formed during hydration. Due to the low alumina content of the cement this ettringite was not converted to monosulfate. In both solutions gypsum is formed. The use of the highly concentrated sulfate solution (30,000 mg/l) results in a doubled amount of gypsum throughout the sample in comparison to the lower concentrated solution. At sample depth of 1 to 2 mm the gypsum concentration reaches a maximum and decreases towards the middle. The lower gypsum content in the outer sample part might be caused by leaching of calcium caused by the deionised water that was used for the sulfate solution. That might be confirmed by the absence of portlandite up to depth of 2 mm.

Figure 3 shows expansions of the mixtures M3 and M4 with fly ash. The reduction of the equivalent water cement ratio of the fly ash containing mortars results in a higher sulfate resistance.

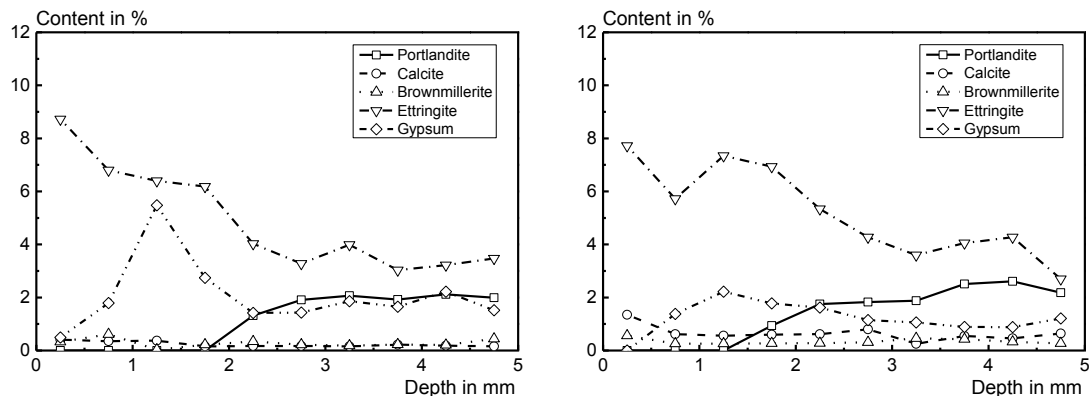


**Figure 3. Expansion of mixture M3 and M4 stored in sulfate solution at 30,000 mg/l (left) and 3,000 mg/l (right), [6]**

Compared to the sulfate resisting cement the fly ash containing mortars contain less  $C_4AF$ . Due to the pozzolanic reaction of the fly ash, the amount of portlandite is lower as well (cf. figure 4).

It is observed that the trend of the gypsum content over the depth of the sample is similar to the reference mortar. Yet, the amount of gypsum is far lower for the fly ash mixture for both sulfate solutions.

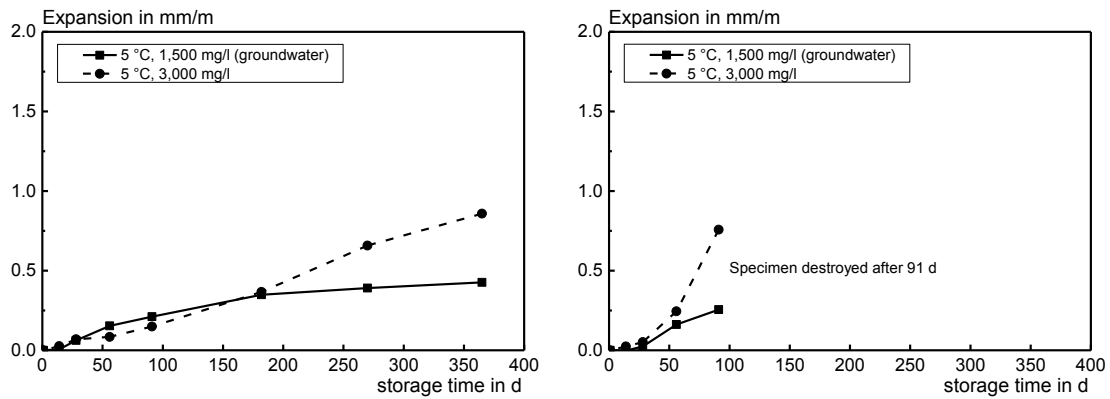
The lower cement content leads to a lower ettringite content in the center of the specimen compared to the reference sample. Close to the surface the amount of ettringite is much higher than in the middle and exceeds the one of the reference mortar. In these mixtures secondary ettringite has formed causing expansion and cracking.



**Figure 4. Phase composition of mixture M4 stored in sulfate solution at 30,000 mg/l and 20 °C (left) and 3,000 mg/l and 5 °C (right), [6]**

Storage of specimen in groundwater with a sulfate concentration of roundabout 1,500 mg/l (cf. table 4) has been conducted to investigate the influence of the artificial sulfate solution prepared with deionised water. Figure 5 compares the expansion of the samples stored in the artificial solution with 3,000 mg  $SO_4^{2-}$ /l with the groundwater storage. The tests were performed at 5 °C to increase the severity of the attack. The liquids have been renewed every 14 days to ensure constant conditions. In Figure 5 the results of the experiments on sulfate resistant cement and on a mixture of OPC and 40 % fly ash are illustrated.





**Figure 5. Expansion of a mixture containing CEM I 52.5 N-SR cement (left) and CEM I 52.5 N + 40 % fly ash (right) stored in sulfate solution at 3,000 mg/l and groundwater (w/b = 0.5)**

The expansion of the samples of both mixtures is lower when stored in the groundwater. This might on one hand be due to the lower sulfate concentration, on the other hand the availability of calcium in the groundwater reduces leaching of the specimens. Nevertheless severe damage was found for the samples with CEM I 52.5 and fly ash even in groundwater. In general, in natural groundwater the reactions are more complex because of a larger variety of ions available. Further analysis of the microstructure would be necessary to characterise the interaction between cement paste and groundwater.

The experimental data presented in this section has been added to a database of experimental results to achieve a more general view of the influence of different binders on the sulfate attack. The evaluation of this database is subject of the following paragraph.

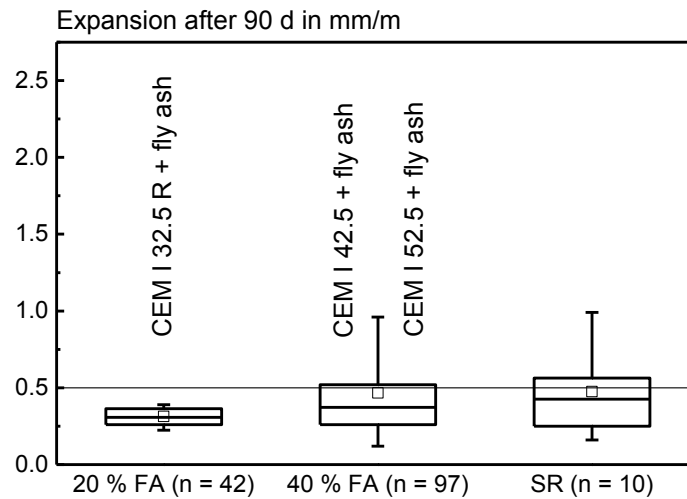
#### 4. Database analysis

Experimental data of sulfate resistance testing on flat prisms executed at the Institute for Building Materials Research has been collected in a database. The collected data includes the storage conditions, the composition of the particular mixture, the results of the determination of expansion and modulus of elasticity and the chemical composition of the constituents of the binder. Results from literature have been added to the database. The database consists of 580 data records, 519 records deal with the storage in pure sodium sulfate solution.

In a first step mixtures of OPC and fly ash (a total of 259 data records) and sulfate resistant OPC (overall 40 data records) were compared. The water-binder-ratio was 0.5, the concentration of the sodium sulfate solution was 30,000 mg  $\text{SO}_4^{2-}/\text{l}$ , and the storing temperature was 20 °C.

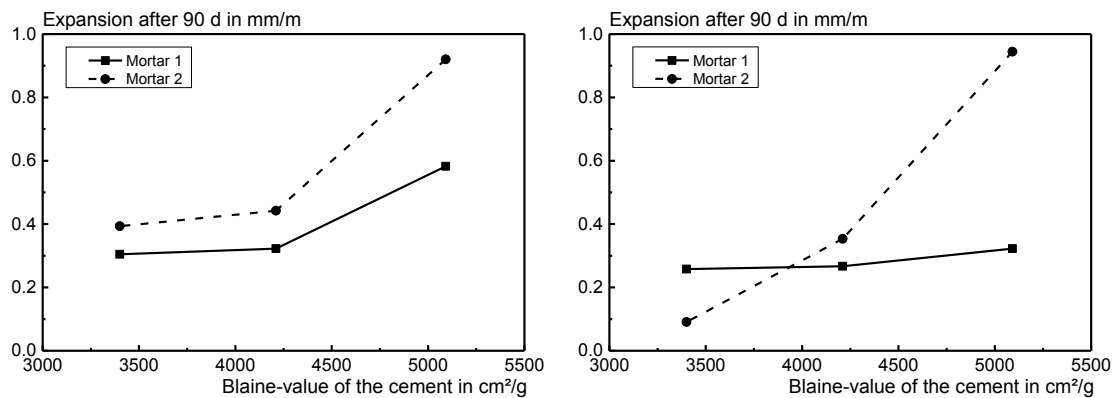
For the combinations of OPC and fly ash two groups of mixtures were distinguished: a group with a fly ash content of 20 % related to the binder (cement + fly ash) and one with 40 %.

In figure 6 the expansion after 90 days of storage in sulfate solution is shown. (4 data records for 20 % fly ash, one record for 40 % fly ash and one record for the SR cement mixtures were excluded by a statistical outlier test). It becomes apparent, that on average mixtures with 40 % fly ash and SR cement have the same expansion after 90 days. That speaks for the general applicability of such binder combinations to produce sulfate resistant concrete. In both cases the upper quartile of the data is above the criterion of 0.5 mm/m, which has been used in the SVA test until recently. That is the reason why the limit value was abolished.



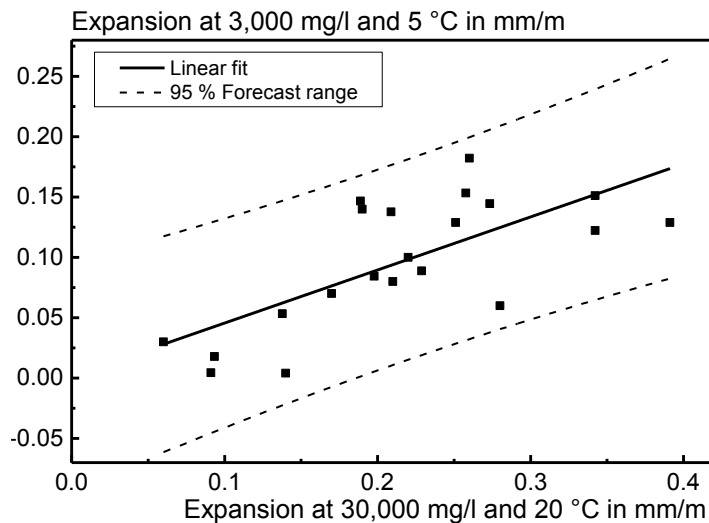
**Figure 6. Boxplot of the expansion at 30,000 mg/l and 20 °C for  $f/c = 0,25$ ,  $f/c = 0,67$  and sulfate resistant cement (SR)**

In contradiction to literature figure 6 shows increasing expansion with increasing fly ash content. Looking at the data in more detail it becomes apparent, that the mixtures with 20 % fly ash have always been produced with CEM I 32.5 R, the mixtures with 40 % fly ash were mostly prepared using cement of a strength class of 42.5 and 52.5. Results on the influence of the fineness of cement on the expansion of the mortar prove, that the expansion caused by sulfate attack increases with increasing fineness of the cement (cf. figure 7). Therefore, the apparent lower expansion of the mixtures with 20 % fly ash should not be overvalued.



**Figure 7. Expansion caused by sulfate attack after 90 days in correlation with the specific surface area of the cement of two mortars containing 40 % fly ash at 30,000 mg/l and 20 °C (left) and 3,000 mg/l and 5 °C (right)**

The results presented in section 3 indicate, that even at rather low sulfate concentration (3,000 mg  $SO_4^{2-}/l$ ) considerable expansion can be observed. In Figure 8 the expansion of mortar bars stored in 30,000 mg  $SO_4^{2-}/l$  at 20 °C is compared to that of specimen stored in 3,000 mg  $SO_4^{2-}/l$  at 5 °C. The results of 21 mixtures with different compositions with and without SCMs, and varying w/b ratios are included in the picture. An age of 56 days has been selected, because the results at 90 days had an increased variance due to partial damaging of the specimen.



**Figure 8. Correlation between the expansion after 56 days at 3,000 mg/l and 5 °C and 30,000 mg/l and 20 °C (Corrected  $R^2 = 0.47$ )**

The resulting  $R^2$  of 0.47 for the regression of the data points indicates a weak correlation. The expansion at 3,000 mg  $\text{SO}_4^{2-}/\text{l}$  and 5 °C is roundabout half of the expansion at 30,000 mg  $\text{SO}_4^{2-}/\text{l}$  and 20 °C.

#### 4. Conclusions and outlook

In this work the sulfate resistance of mortars containing OPC and fly ash were compared to mortars containing sulfate resistant cement by using the SVA method that is used to get a technical approval in Germany. The influence of storage temperature was tested, showing that a lower temperature leads to a more severe attack. The gypsum formation is boosted by higher sulfate concentrations in the attacking liquid. The correlation between more realistic concentrations (3,000 mg/l) at low temperatures and the accelerated test at 30,000 mg/l is poor. In conclusion the test method for determining the sulfate resistance of a binder should focus on lower and realistic sulfate concentrations at low temperatures. Depending on the exposure conditions (e. g. sea water or groundwater) other ions like magnesium or chloride have to be taken into account. Magnesium ions may lead to the formation of brucite or magnesium silicate hydrates (MSH). The latter have very low strength. This damage will not be recognised by expansion tests. Therefore other test methods will be needed [8].

By substituting OPC with fly ash a level of sulfate resistance comparable to that of sulfate resistant cement can be achieved, provided that adequate equivalent water cement ratios are used.

#### 5. References

1. van Tittelboom, K., De Belie, N. et al., "Test Methods for Resistance of Concrete to Sulfate Attack – A Critical Review", Performance of Cement-Based Materials in Aggressive Aqueous Environments, State-of-the-Art Report, RILEM TC 211 - PAE, Springer Netherlands, 2013, pp 251-288
2. Wittekindt, W., "Sulfatbeständige Zemente und ihre Prüfung", *Zement-Kalk-Gips*, 13(12), 1960, pp 565-572
3. Lipus, K., "Sulfatwiderstand", Proceedings, Beiträge zum 41. Forschungskolloquium am 11.und.12. Juli 2002 im Forschungsinstitut der Zementindustrie in Düsseldorf, Deutscher Ausschuss für Stahlbeton, 2002, Berlin, pp 147-159
4. Koch, A., Steinegger, H., "Ein Schnellprüfverfahren für Zemente auf ihr Verhalten bei Sulfatangriff", *Zement-Kalk-Gips*, 13(7), 1960, pp 317-324
5. Mulenga, D.M., "Zum Sulfatangriff auf Beton und Mörtel einschließlich der Thaumasitbildung", Thesis. Bauhaus-Universität Weimar, 2002, Weimar.
6. Haufe, J., Vollpracht, A., et al., "Sulfate Ingress on Fly Ash Containing Mortar Samples", Proceedings, 2nd International Congress on Durability of Concrete, ICDC 2014, New Delhi, India

7. Rietveld, H. M., "A profile refinement method for nuclear and magnetic structures", Journal of Applied Crystallography, 2, 1969, pp 65-71.
8. Menéndez, E., Matschei, T., et al., "Sulfate Attack of Concrete", Performance of Cement-Based Materials in Aggressive Aqueous Environments, State-of-the-Art Report, RILEM TC 211 - PAE, Springer Netherlands, 2013, pp 7-74

# Linking New Australian Alkali Silica Reactivity Tests to World-Wide Performance Data

Paul Rocker<sup>1</sup>, James Mohammadi<sup>2</sup>, Vute Sirivivatnanon<sup>3</sup> and Warren South<sup>4</sup>  
<sup>1</sup>Holcim Australia

<sup>2</sup>Research Analyst – Research & Technical Services, Cement Concrete & Aggregates Australia

<sup>3</sup>Professor of Concrete Engineering, University of Technology Sydney, Australia

<sup>4</sup>Director – Research & Technical Services, Cement Concrete & Aggregates Australia

**Abstract:** The long awaited Australian Standard test methods to detect alkali-silica reactivity (ASR) of aggregates - AS 1141.60.1 accelerated mortar bar test (AMBT) and AS 1141.60.2 concrete prism test (CPT) - were published in September 2014. Both test methods were adopted correspondently from the ASTM 1260 and ASTM C1294 test methods but with different performance limits leading to a new class of slowly reactive aggregates. This paper reviews international and Australian research which supported these new performance limits. It also reviews and examines the value of these testing methods in predicting the ASR of aggregates in field-exposed large concrete blocks and a limited number of concrete structures. The outcomes may lead to a consideration of the hierarchy of these two test methods.

**Keywords:** AMBT, ASR, CPT, ASR performance limits,

## 1. Introduction

There main types of tests for evaluating the alkali-silica reactivity (ASR) of aggregates are accelerated mortar bar test (AMBT), concrete prism test (CPT) and field testing. Recently, Standards Australia CE-012 Aggregate and Rock for Engineering Purposes Committee has published two new standard test methods to detect potential ASR:

AS 1141.60.1-2014 Potential alkali-silica reactivity - Accelerated mortar bar method (AMBT) [1] and AS 1141.60.2-2014 Potential alkali-silica reactivity - Concrete prism method (CPT) [2]

**Accelerated mortar bar test (AMBT)** is a rapid test method applied to determine the potential alkali-silica reactivity of aggregates by testing mortar specimens. In general, the procedure of mortar bar testing involves casting mortar bars (normally in the size of 25 x 25 x 285 mm) and curing for 24 hours in a relative humidity of at least 95%. Afterwards, mortar samples are kept in potable water and heated to 80°C and then mortar bars are put in the solution of 1N NaOH that is already at 80°C for 24 hours. After that, the initial length of mortar bars is measured as the zero reading. Until the next reading, samples remain in 1N NaOH for a period of time which can be 10, 14, 21 or 28 days according to the different standards and test methods.

During the development of the Standard AS 1141.60.1, three alternative AMBT methods namely the fixed flow (RMS T363 [3] or VicRoads CR376.03 [4]), fixed water-to-cement ratio (ASTM C1260 [5]) and fixed free water-to-cement ratio (RILEM AAR-2 [6]) were considered. The committee finally agreed to adopt the fixed water-to-cement ratio method because of the more conservative mortar mix composition in ASTM C1260 compared to the fixed flow method [7,8], reduced variability due to difficulty in determining the surface saturated dry condition (SSD) of crushed aggregates or flow measurement [9], and the possible benchmarking to international research data [10] and international proficiency program [11].

The procedure of Australian Standard AS 1141.60.1 is adopted from the ASTM C1260. In a recent study, Fournier et al [11] investigated the proficiency of different AMBT test procedures, including the American ASTM, Canadian CSA and the European RILEM test methods. It should be noted that the test procedure for ASTM and CSA tests are similar. As can be seen from **Table 1** coefficients of variation of AMBT methods showed a lower variation in the 14 days expansion for the ASTM and CSA methods compared to the RILEM test results. However, similar variations in the 28 days expansion were observed for all three test methods. By considering the 10 and 21 days limits for measuring the

expansion of mortar samples in AS 1141.60.1, the outcome of Fournier et al investigation provides support for the adoption of ASTM procedure.

**Table 1: Statistical analysis of different accelerated mortar bar test [11]**

Test age	Method of testing	Number of results	Mean [%]	Standard deviation	Coefficient of variation [%]	Min [%]	Max [%]
14 days	ASTM	26	0.375	0.043	11.6	0.307	0.486
	CSA	24	0.374	0.055	14.8	0.206	0.451
	ASTM + CSA	50	0.375	0.049	13.1	0.206	0.486
	RILEM	3	0.291	0.071	24.5	0.230	0.369
28 days	ASTM	26	0.591	0.067	11.3	0.450	0.725
	CSA	24	0.571	0.064	11.2	0.470	0.700
	ASTM + CSA	50	0.582	0.066	11.3	0.450	0.725
	RILEM	3	0.547	0.065	11.9	0.500	0.621

In addition, Thomas and Innis [12] stressed that the usefulness of various tests may be judged on the basis of the ease of testing, the repeatability or precision of the outcomes, the time taken to complete the test and, ultimately, the ability of the test to predict behaviour in the field.

**Concrete prism test (CPT)** is considered a more reliable test method than the accelerated mortar bar tests in the literature. The reason that the CPT test may provide a better measure for determining ASR compared to the AMBT test is that the CPT test samples are prepared using a concrete mix, and kept in less aggressive conditioning and lower temperature for a longer period of time. Moreover, CPT samples are larger in size (normally in the size of 75 x 75 x 285 mm). Another difference between CPT and AMBT test is related to the procedure of providing the available alkali for ASR reaction. While in the AMBT test mortar bars are kept in NaOH solution whereas in the CPT test the alkali content in the concrete was arbitrarily raised during mixing. For example the ASTM C1293 test measures the expansion of concrete prisms with a cement content of  $420 \pm 10 \text{ kg/m}^3$  and a dry mass of coarse aggregate per unit volume of concrete equal to  $0.70 \pm 0.02$  of its dry-rodded bulk density with a water to cementitious material ratio (w/cm) of 0.42 to 0.45 by mass. The cement has a total alkali content of 1.25% of  $\text{Na}_2\text{O}_{\text{eq}}$  equivalent by mass of cement. Specimens are placed in a container stored in a  $38.0 \pm 2^\circ\text{C}$ . Expansion measurements are performed up to 52 weeks for CPT samples. In addition, for samples prepared with supplementary cementitious materials (SCMs) to mitigate potential ASR, it is recommended in the CSA method to extend the test duration up to 104 weeks. Standard AS 1141.60.2 is adopted from ASTM C 1293 [13] procedure however there are differences in the interpretation of test results between both standards.

**Field testing (Outdoor exposure)** provides the most realistic condition for ASR testing. Outdoor exposure can simulate the temperature and moisture cycling. In addition, by conducting field tests, samples with larger dimensions can be casted that are closer to the scale of real structures. In addition, outdoor samples can be evaluated for longer periods of time (5 to 20 years).

It is implied by the literature [14] that the best method to determine whether an aggregate is potentially reactive or innocuous is to study the history of aggregates field performance. An aggregate can be used in concrete provided that satisfactory field performance was achieved and the cement content (the total alkali content of the cement) should be the same or higher in the field concrete than that proposed in the new structure. The outdoor field exposed concrete should be at least 10 years old. In addition, the exposure conditions of the field concrete should be at least as severe as those in the proposed structure [14].

## 2. Performance Limits

In both the AMBT and CPT methods, expansion limits after a particular period are used to indicate/classify the potential reactivity of aggregates tested. These expansion performance limits were derived from research and field experiences with the use of a wide range of aggregates.

## 2.1. Accelerated Mortar Bar Test (AMBT)

Shayan and Morris [7] compared the accelerated mortar bar expansion of 18 aggregates of known service record, based on the RMS T363 and ASTM C1260, and found lower expansion of the RMS mortars than the corresponding ASTM mortars for reactive aggregates. The lower expansion of the RMS mortars may be due to the lower water/cement ratio in the range of 0.40-0.42 in RMS T363 compared to 0.47 used in the ASTM method. The mortar bar expansions are similar for the less reactive aggregates possibly because they consume less alkali and are not affected by the differences in supply of alkali in the two methods. They found both test methods and their corresponding expansion limits to be capable of assessing the alkali reactivity of non-reactive or very reactive aggregates. However for slowly reactive aggregates, both methods can be used provided that the RMS expansion limits, reproduced in **Table 2**, are used to interpret the reactivity of the aggregates.

It was also found that the two methods would produce similar assessments for the effectiveness of fly ash in controlling ASR expansion for all except the very reactive aggregates. For such reactive aggregates, both methods could be used to obtain expansion curves but the RTA limits were recommended for the interpretation of the adequacy of the amount of fly ash used in controlling the expansion.

**Table 2: Aggregate reactivity classification in accordance with RTA T363 [7]**

Mortar Bar Expansion in 1M NaOH (80°C) [%]		Classification
10 days	21 days	
< 0.10*	< 0.10*	Non-reactive
< 0.10*	≥ 0.10*	Slowly reactive
≥ 0.10*	(much greater than) >> 0.10*	Reactive

\* For naturally occurring fine aggregates the limit is 0.15%

The non-mandatory appendix in ASTM C1260 provides guidance to the interpretation of test results with the following expansion limits: 14-day expansions of less than 0.10% to be indicative of “innocuous” behaviour whereas 14-day expansions of more than 0.20% are indicative of “potentially deleterious” expansion. Aggregates with 14-day expansion between 0.10% and 0.20% are known to be either innocuous or deleterious in field performance, and supplemental information in the form of petrographic examination or identification of alkali reaction products in specimens after tests, or field service record can be used in the assessment of the performance. It is noted in the same appendix that some granitic gneisses and metabasalts have been found to be deleteriously expansive in field performance, even though, their expansion in the test was less than 0.10%.

**Table 3 Comparison of ASTM and AS mortar bar expansion limits**

Interpretation	ASTM C1260		AS 1141.60.1	
	14 days	Classification	10 days	21 days
Innocuous	< 0.10%	Non-reactive	-	< 0.10%
Uncertain	0.10 to 0.20%	Slowly reactive	< 0.10%	< 0.30%
Potential deleterious	≥ 0.2*%	Reactive	≥ 0.10% or	≥ 0.30%

ASTM C1260 performance limits are compared with the Australian Standard AS 1141.1 limits in **Table 3**. The AS 1141.60.1 classifies aggregates with 21-day expansion below a lower limit of 0.10% to be non-reactive, and those with 10-day expansion equal or greater than the lower limit of 0.10% or 21-day expansion equal or greater than the upper limit of 0.30% to be reactive. For aggregates with 10-day expansion below the lower limit of 0.10% but 21-day expansion equal to or exceeding the lower limit of 0.10% but not exceeding the upper limit of 0.30% to be a “slowly reactive” aggregate. Note that the lower limit applicable to natural sand is 0.15%.

## 2.2 Concrete prism method (CPT)

The non-mandatory ASTM appendix states that an aggregate might reasonably be classified as potentially deleteriously reactive if the average expansion of three concrete specimens is equal to or

greater than 0.04% at one year. CSA indicated similar 0.04% expansion for determining ASR however, compared to the non-mandatory ASTM approach CSA has a more definitive approach (ASTM C1293 [13], CSA A23.2-27A-02 [15]). It is also suggested in CSA A23.2-28A-02 that the amount of pozzolan or slag used in combination with an aggregate is at least the minimum needed to prevent excessive expansion in field concrete if the average expansion is less than 0.04% at two years [16]. Similarly, the Standard ASTM C1293 confirmed the two years test duration.

In Australia, AS 1141.60.2 uses essentially the same concrete mix proportion and test method as the ASTM C1293 but classifies an aggregate with a prism expansion of less than 0.03% at 52 weeks as “non-reactive” and an aggregate with a prism expansion equal to or greater than 0.03% at 52 weeks as “potentially reactive”. The lower expansion limit is considered more conservative as it was adopted from the RMS T364 which tests concrete with a higher adjusted cement alkali of 1.38% of Na<sub>2</sub>Oeq equivalent. For mitigation, the standard does not state any particular limit but refer to classification contained in the supply agreement.

### 2.3 Hierarchy of test methods

There has been no agreed hierarchy of the two Australian Standard test methods. RMS T363 noted that some glassy basalt may cause excessive mortar bar expansion, due to the production of fine glassy particles in the fine aggregate grading required for mortar bars. The reactivity of coarse aggregate of the same source needs to be verified, because the glassy phase within compact coarse basalt aggregates may not be accessible to alkali and may not cause excessive concrete expansion. Concrete prism tests in accordance with RMS T364 or concrete block tests may be required for this purpose.

## 3. Australian and International Research

### 3.1 Consistency of AMBT & CPT reactivity classification

#### 3.1.1 Improved AMBT performance limits in AS 1141.60.1

**Table 4** presents alkali-silica reaction data from the investigation conducted by Stark [17]. ASTM C1260 limits were applied to check the potential alkali-silica reactivity of aggregates within two weeks. According to the ASTM C1260 limits, aggregates showing 14-day expansions exceeding 0.1% should be classified as being potentially deleterious aggregates and were labelled “reactive” in **Table 4**. Moreover, aggregates that showed 14-day expansions lower than 0.1% were classified as “innocuous”.

**Table 4 Comparison of ASTM and AS mortar bar expansion**

ID	Rock type	Field Performance	Expansion			ASTM 1260	AS 1141.60.1
			10 Days	14 Days	21 Days		
1	Granitic Volcanic	Reactive	0.713	0.867	1.035	Reactive	Reactive
2	Granitic Volcanic	Reactive	0.375	0.424	0.5	Reactive	Reactive
3	Argillite	Reactive	0.354	0.418	0.511	Reactive	Reactive
4	Chert, Quartzite	Reactive	0.328	0.409	0.515	Reactive	Reactive
5	Chert, Quartzite	Reactive	0.246	0.314	0.416	Reactive	Reactive
6	Granitic Gneiss	Reactive	0.239	0.309	0.385	Reactive	Reactive
7	Quartzite	Reactive	0.17	0.225	0.312	Reactive	Reactive
8	Chert, Quartzite	Reactive	0.116	0.177	0.27	Uncertain	Reactive
9	Chert, Quartzite	Reactive	0.073	0.106	0.142	Uncertain	Slow-Reactive
10	Granitic Gneiss	Reactive	0.065	0.096	0.132	Innocuous	Slow-Reactive
11	Granitic Gneiss	Reactive	0.064	0.086	0.124	Innocuous	Slow-Reactive
12	Metavolcanics	Reactive	0.052	0.082	0.115	Innocuous	Slow-Reactive
13	Limestone	Innocuous	0.029	0.026	0.035	Innocuous	Innocuous
14	Dolomite	Innocuous	0.066	0.066	0.077	Innocuous	Innocuous
15	Gabbro	Innocuous	0.029	0.044	0.066	Innocuous	Innocuous
16	Mixed Siliceous	Innocuous	0.181	0.278	0.329	Reactive	Reactive
17	Gabbro	Innocuous	0.061	0.075	0.157	Innocuous	Slow-Reactive

The last column demonstrates the interpretation of the results based on the Australian Standard criteria. As can be seen, the AS 1141.60.1 limits provided a significantly better understanding of the



aggregate performance. ASTM C1260 failed to provide the correct interpretation for the performance of aggregates No 8 to 12. However, the Australian Standard criteria showed the reactivity of those aggregates and classified them as “reactive” or “slow-reactive”. Overall, the ASTM C1260 limit failed to classify 6 aggregates correctly out of the total 17 tested aggregates (aggregate identification 8-12 and 16). On the contrary, the Australian limits failed to provide a correct performance only for two aggregates (identification 16 and 17). From the given data, it can be seen that the Australian limits provided a more accurate understanding of the aggregates ASR performance.

**Table 5** presents another set of data from the research conducted by Touma in The University of Texas at Austin [14]. Datasets presented in **Table 5** includes mortar and concrete expansion test in accordance with the ASTM C1260 and C1293, respectively. Tests were conducted to evaluate 15 types of aggregates while the field performances of aggregates were known. As can be seen from **Table 5** the ASTM C1260 (mortar test) failed to provide the correct interpretation for the performance of aggregates (8, 9, 10, 12 and 14). However, the Australian Standard criteria indicated a correct reactivity performance for some of those aggregates and classified them as “reactive” or “slowly-reactive”. Overall, the ASTM C1260 limit failed to classify 6 aggregates correctly out of the total 15 tested aggregates. In contrast, the Australian limits failed to provide a correct performance for only two aggregates (12 and 14). From the given data it is concluded that the Australian limits for mortar test provide a more reliable understanding of aggregates ASR performance.

**Table 5 Comparison of ASTM and AS mortar bar and concrete prism expansion**

ID	Aggregate	Expansion [%]				Field Performance	Classification			
		Mortar		Concrete			ASTM C1260	AS 1141.60.1	ASTM C1293	AS 1141.60.2
		11-day	14-day	21-day	52-week					
1	Rhyolite	0.21	0.24	0.31	0.073	Reactive	Reactive	Reactive	Reactive	Reactive
2	Rhyolite	0.27	0.29	0.34	0.107	Reactive	Reactive	Reactive	Reactive	Reactive
3	Quartzite, sandstone, limestone	0.75	0.79	0.89	0.379	Reactive	Reactive	Reactive	Reactive	Reactive
4	Rhyolite, andesite	0.83	0.91	1.04	0.411	Reactive	Reactive	Reactive	Reactive	Reactive
5	Argillite	0.28	0.31	0.39	0.085	Reactive	Reactive	Reactive	Reactive	Reactive
6	Pink granite, quartz, chert	0.23	0.28	0.39	0.051	Reactive	Reactive	Reactive	Reactive	Reactive
7	Quartz, chert	0.19	0.26	0.40	0.043	Reactive	Reactive	Reactive	Reactive	Reactive
8	Feldspar, quartz, chlorite	0.09	0.11	0.16	0.046	Reactive	Uncertain	Slowly-Reactive	Reactive	Reactive
9	Quartz, granitic rock	0.11	0.15	0.25	0.040	Reactive	Uncertain	Reactive	Reactive	Reactive
10	Quartzite, pyroxene, sericite	0.14	0.17	0.24	0.053	Reactive	Uncertain	Reactive	Reactive	Reactive
11	Dolomite	0.02	0.02	0.03	0.022	Innocuous	Innocuous	Innocuous	Innocuous	Innocuous
12	Glacial deposit, shale	0.38	0.25	0.44	0.025	Innocuous	Reactive	Reactive	Innocuous	Innocuous
13	Natural siliceous and glassy	0.18	0.25	0.34	0.060	Reactive	Reactive	Reactive	Reactive	Reactive
14	Natural siliceous	0.20	0.42	0.53	0.022	Innocuous	Reactive	Reactive	Innocuous	Innocuous
15	Rhyolite, andesite	0.33	0.36	0.46	0.064	Reactive	Reactive	Reactive	Reactive	Reactive

### 3.1.2 Consistency of both CPT classifications with field performance

The concrete prism test results for expansion of prisms in 52 weeks showed the ASTM C1293 criterion could accurately decide on the reactivity performance of aggregates. Using the ASTM C1293 0.04% expansion limit, all 15 aggregates were classified correctly regarding their performance. Similarly, the Australian Standard AS 1141.60.2 limit provided correct reactivity performance for all the aggregates. Results showed that there is no difference in the outcome of using the AS 1141.60.2 expansion limit (0.03 expansion over 52 weeks) and the ASTM C1293 expansion limit (0.04 expansion over 52 weeks). In addition, the assessment of data indicated a more reliable outcome for concrete prism test compared to the mortar bar test for both ASTM and the Australian test methods.

### 3.1.3 Relative value of AMBT and CPT methods

It is reported by Lane [18] that alkali-silica reaction has been a major cause of the deterioration for several concrete structures in Virginia. Lane examined the occurrence of the reaction in several Virginian structures. **Table 6** summarised the reactivity performance for the 13 aggregates. As can be

seen the aggregate evaluation based on the ASTM C1260 provided a correct decision on reactivity of some of the aggregates.

**Table 6 Comparison of ASTM mortar bar expansion and field performance**

ID	Rock Type	Field Performance	Expansion 14 Days	ASTM 1260
1	Dolomitic Limestone	Undetermined	0.23	Reactive
2	Argillaceous Dolomite	Innocuous	0.09	Innocuous
3	Diabase	Innocuous	0.13	Reactive
4	Quartzose Sand	Undetermined	0.09	Reactive
5	Quartzose Gravel	Undetermined	0.12	Reactive
6	Quartzose Sand	Reactive	0.19	Reactive
7	Quartzose Gravel	Reactive	0.32	Reactive
8	Metarhyolite	Reactive	0.39	Reactive
9	Qartzite	Undetermined	0.30	Reactive
10	Acrch Marble Calc Chist	Reactive	0.17	Reactive
11	Granite Gneiss	Suspected	0.17	Reactive
12	Granite Gneiss	Reactive	0.07	Reactive
13	Greenstone Metabasalt	Reactive	0.08	Reactive

Except for aggregate No 3 there is no disagreement between the field performance and ASTM C1260 mortar test results. For some aggregates with unknown field performance, ASTM C1260 classified them as “reactive”. However, the only notable drawback from the ASTM C1260 test is that it is significantly conservative and as can be seen from **Table 6** ASTM C1260 labelled performance of the most unknown aggregates as “reactive”.

The National Aggregate Association (NAA) performed the ASTM C1293 and ASTM C1260 tests on several aggregates. Results of this testing program was reported by Touma [14]. As can be seen from the listed results in **Table 7** there is no strong correlation between the outcome of ASTM C1260 and C1293. For 12 aggregates, results of ASTM C1260 test could not confirm the evaluation of ASTM C1293. In addition, for 8 aggregates there is a conflict between ASTM C1260 and C1293 interpretation. It is noted that the interpretation of test results at 14 days resulted in a conservative interpretation and led to labelling several aggregates as “reactive”. In addition, except for one aggregate (aggregate No 14), all other results showed that there is no difference in the outcome of using the AS 1141.60.2 expansion limit (0.03% expansion over 52 weeks) and the ASTM C1293 expansion limit (0.04% expansion over 52 weeks). It can be noted that the lower expansion limit based on the Australian CPT method did not make difference in the interpretation of the test results.

**Table 7 Comparison of ASTM and AS mortar bar and concrete prism expansion**

ID	Rock type	Expansion [%]		Classification		
		Mortar 14 days	Concrete 1year	ASTM C1260	ASTM C1293	AS 1141.60.2
1	Limestone	0.252	0.083	Reactive	Reactive	Reactive
2	Siliceous, Dolomite	0.227	0.009	Reactive	Innocuous	Innocuous
3	Dolomite, Siliceous	0.159	0.020	Uncertain	Innocuous	Innocuous
4	Limestone	0.285	0.015	Reactive	Innocuous	Innocuous
5	Limestone	0.335	0.070	Reactive	Reactive	Reactive
6	Siliceous	1.061	0.196	Reactive	Reactive	Reactive
7	Limestone	0.041	0.016	Innocuous	Innocuous	Innocuous
8	Siliceous	0.210	0.012	Reactive	Innocuous	Innocuous
9	Siliceous	0.139	0.018	Uncertain	Innocuous	Innocuous
10	Siliceous	0.250	0.012	Reactive	Innocuous	Innocuous
11	Siliceous	0.678	0.026	Reactive	Innocuous	Innocuous
12	Siliceous	1.072	0.016	Reactive	Innocuous	Innocuous
13	Siliceous	0.080	0.008	Innocuous	Innocuous	Innocuous
14	Dolomite, Limestone, Siliceous	0.154	0.038	Uncertain	Innocuous	Reactive
15	Siliceous	0.279	0.007	Reactive	Innocuous	Innocuous
16	Siliceous	0.316	0.005	Reactive	Innocuous	Innocuous

A research conducted by Berube [19] showed that even though the AMBT test was capable of detecting numerous of reactive aggregates, it was too severe for many aggregates that have performed well when tested using the concrete prism method and that have performed well in the field. Accordingly, it is stated that the ASTM C1260 should not be applied for rejecting aggregates.

### 3.1.4 Effect of different performance limits in AS 1141.60.2 and ASTM C1293

Test results from Berube [19] investigation are presented in **Table 8**. It can be seen that the ASTM C1293 CPT could accurately predict the field performance of reactive aggregates. In addition, except for one aggregate (aggregate identification 9) there is no conflict between the interpretation of AS 1141.60.2 and ASTM 1293. This outcome confirm the fact that the AS 1141.60.2 lower limit provides no difference in the interpretation of test results.

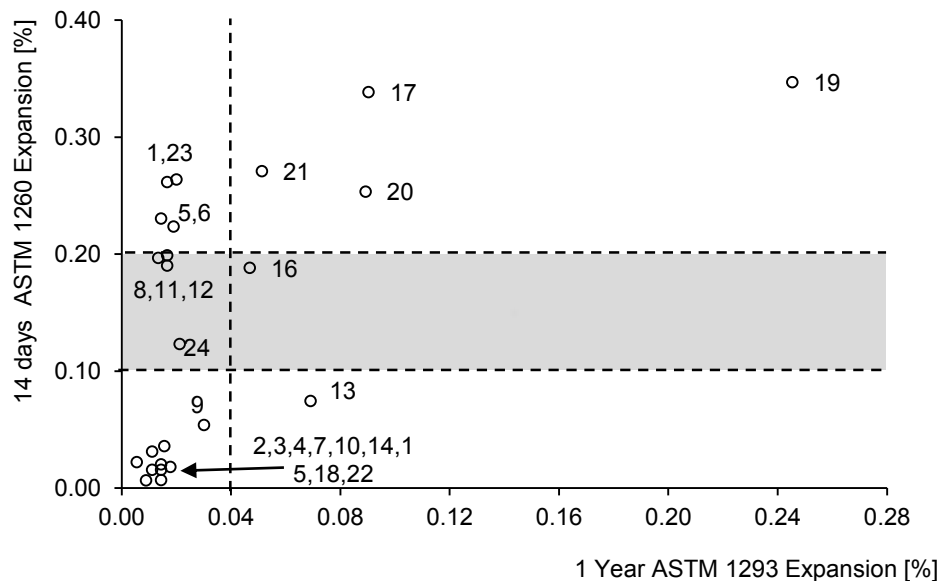
**Table 8 Comparison of ASTM (CSA) and AS mortar bar and concrete prism expansion**

ID	Aggregate type	Field performance	Expansion [%]		Classification		
			AMBT 14 days	CPT 52 weeks	ASTM 1260	ASTM 1293	AS 1141.60.2
1	Andesite	Innocuous	0.26	0.02	Reactive	Innocuous	Innocuous
2	Anorthosite	Innocuous	0.04	0.02	Innocuous	Innocuous	Innocuous
3	Basalt	Innocuous	0.03	0.01	Innocuous	Innocuous	Innocuous
4	Charnockite	Innocuous	0.02	0.01	Innocuous	Innocuous	Innocuous
5	Hornfel	Innocuous	0.22	0.02	Reactive	Innocuous	Innocuous
6	Hornfel	Innocuous	0.23	0.01	Reactive	Innocuous	Innocuous
7	Diorite	Innocuous	0.02	0.01	Innocuous	Innocuous	Innocuous
8	Gabbro	Innocuous	0.20	0.02	Uncertain	Innocuous	Innocuous
9	Granitic gneiss	Innocuous	0.05	0.03	Innocuous	Innocuous	Reactive
10	Granite	Innocuous	0.02	0.01	Innocuous	Innocuous	Innocuous
11	Greywacke	Innocuous	0.19	0.02	Uncertain	Innocuous	Innocuous
12	Greywacke	Innocuous	0.20	0.01	Uncertain	Innocuous	Innocuous
13	Potsdam sandst	Reactive	0.07	0.07	Innocuous	Reactive	Reactive
14	Phonolite	Innocuous	0.02	0.02	Innocuous	Innocuous	Innocuous
15	Quartzite	Innocuous	0.01	0.01	Innocuous	Innocuous	Innocuous
16	Chloritic schist	Reactive	0.19	0.05	Uncertain	Reactive	Reactive
17	Siliceous shale	Reactive	0.34	0.09	Reactive	Reactive	Reactive
18	Syenite	Innocuous	0.01	0.01	Innocuous	Innocuous	Innocuous
19	Rhyolitic tuff	Reactive	0.35	0.25	Reactive	Reactive	Reactive
20	Rhyolitic tuff	Reactive	0.25	0.09	Reactive	Reactive	Reactive
21	Rhyolitic tuff	Reactive	0.27	0.05	Reactive	Reactive	Reactive
22	Granitic sand	Innocuous	0.02	0.01	Innocuous	Innocuous	Innocuous
23	Lithic gravel/sand	Innocuous	0.26	0.02	Reactive	Innocuous	Innocuous
24	Carb sandstone	Innocuous	0.12	0.02	Uncertain	Innocuous	Innocuous

**Figure 1** is plotted based on the shown data in **Table 8**. It shows the effectiveness of the CPT results compared to AMBT results. CPT recognised most of the known reactive aggregates (aggregates 13, 16, 17, 19, 20 and 21 are reactive based on field performance), however, it did not misclassify other “innocuous” aggregates as “reactive”.

it can be seen that the AMBT has a conservative and incorrect interpretation for some aggregates such as No 1, 5, 6 and 23 which resulted in classifying these aggregates as “reactive”, while they are not reactive. On the other hand, the grey highlighted area of **Figure1** implies that most of the aggregates classified “uncertain” were “innocuous”, except for aggregate 16. Moreover, aggregate 13 labelled innocuous by AMBT test while it is a reactive aggregate based on field performance and CPT results. Although AMBT is not a time-consuming test compared to the CPT, it is a good measure only for highlighting the innocuous aggregates. AMBT is conservative and due to the aggressive nature that this test has, it labels some innocuous aggregates as “reactive” or “uncertain”, accordingly, no aggregate is suggested to be rejected by this test. It is suggested that the complementary CPT data

could provide a more reliable understanding of aggregates reactivity. Another shortcoming of the ASTM AMBT test is the 14-day limits. These limits could not provide any clear classification for several numbers of aggregates. In that case, other testing methods such as CPT or field data would be required for a reliable decision-making.



**Figure1: CPT vs AMBT test results [19]**

Ideker et al. [10] recently reported expansion data of ASTM C1260, ASTM C1293 and exposure concrete blocks made from 8 fine aggregates and 17 coarse aggregates as presented in **Table 9**. The mortar bar and concrete prism results were calibrated to those obtained from the large 710x380x380 mm concrete blocks exposed outdoor at the University of Texas in Austin.

**Table 9 Comparison of ASTM, AS, and exposure block results**

ID	Mineralogy	Expansion [%]			Classification			
		AMBT 14-day	CPT 1-year	Field block Exposure <sup>2</sup>	ASTM 1260	ASTM 1293	AS 1141.60.2	Field Exposure
F1'	Mixed quartz/chert/feldspar	0.64	0.586	1.239	Reactive	Reactive	Reactive	Reactive
F2	Mixed quartz/chert sand	0.31	0.119	0.991	Reactive	Reactive	Reactive	Reactive
F3	Quartz sand	0.29	0.057	0.487	Reactive	Reactive	Reactive	Reactive
F4	Quartz	0.28	0.059	0.575	Reactive	Reactive	Reactive	Reactive
F5	Quartz	0.17	0.038	0.333	Uncertain	Reactive	Innocuous	Reactive
F6	Tan dolomite carbonate	0.02	0.014	-	Innocuous	Innocuous	Innocuous	Reactive
F7	Mixed quartz/chert sand	0.29	0.207	1.363	Reactive	Reactive	Reactive	Reactive
F8	Mixed sand/gravel	0.29	0.111	0.582	Reactive	Reactive	Reactive	Reactive
C1	Chert & quartzite	0.02	0.129	0.212	Innocuous	Reactive	Reactive	Reactive
C2	Tan dolomite carbonate	0.33	0.112	0.315	Reactive	Reactive	Reactive	Reactive
C3	Limestone	0.11	0.055	0.141	Uncertain	Reactive	Reactive	Reactive
C4	Tan dolomite (marble)	0.14	0.020	0.119	Uncertain	Innocuous	Innocuous	Reactive
C5	Mixed quartz/chert	0.09	0.085	0.133	Innocuous	Reactive	Reactive	Reactive
C6	Tan dolomite (marble)	0.02	0.006	-	Innocuous	Innocuous	Innocuous	Reactive
C7	Limestone	0.37	0.204	0.379	Reactive	Reactive	Reactive	Reactive
C8	Mixed mineralogy gravel	0.31	0.144	0.368	Reactive	Reactive	Reactive	Reactive
C9	Chert	0.0	0.149	0.212	Innocuous	Reactive	Reactive	Reactive
C10	Rhyolite volcanic rocks	0.82	0.159	0.421	Reactive	Reactive	Reactive	Reactive
C11	Granodiorite & metadacite	0.08	0.086	0.220	Innocuous	Reactive	Reactive	Reactive
C12	Quartzite	0.14	0.163	0.183	Uncertain	Reactive	Reactive	Reactive
C13	Quartzite	0.12	0.098	0.271	Uncertain	Reactive	Reactive	Reactive
C14	Granite & quartzite gravel	0.23	0.097	0.294	Reactive	Reactive	Reactive	Reactive
C15	Rhyolite/mixed quartz	0.40	0.158	0.191	Reactive	Reactive	Reactive	Reactive
C16	Granite, meterhyolite	0.06	0.047	0.056	Innocuous	Reactive	Reactive	Reactive
C17	Greywacke	0.44	0.162	0.225	Reactive	Reactive	Reactive	Reactive

<sup>1</sup> F= Fine aggregates and C= Coarse aggregates, <sup>2</sup> Na<sub>2</sub>O<sub>eq</sub>=1.25%

It was found that the AMBT was a good indicator of reactivity of some aggregates. However, the concrete prism test could provide a more reliable evaluation of the most aggregates. In some cases, the results from the CPT disagreed with those from the AMBT. Ideker indicated that in no reported cases of deleterious expansion in the field, concretes containing aggregates that have passed the ASTM C1293 [10]. This evidence supports the better correlation between the reactivity diagnosed by CPT and reactivity in field exposure.

It is possible to re-evaluate the expansion data based on the performance criteria recommended in AS1141.60.2. It was found that except for aggregate F5, the proposed AS1141.60.2 would have classified all aggregate in a similar classification. However, the lowering of the CPT limit from 0.04% to 0.03% would have made no difference to the prediction. The results do not support the use of the lower 0.03% limit in the draft AS1141.60.2. They also show the exposure blocks to be a very useful calibration tool for the laboratory test methods.

### 3.2 Australian (AS) classification

In Australia, Shayan [20] tested five Australian aggregates with field evidence to be slowly-reactive using two accelerated mortar bar test methods. The ASTM C1260 classes them as non-reactive or uncertain while the RTA T363 correctly classified such aggregates as slowly-reactive aggregates. It was suggested that the Australian acceptance limit of <0.1% expansion at 21 days of storage in 1 M NaOH solution at 80°C be adopted by ASTM C1260 or that its 14-day expansion limit be lowered from 0.10% to 0.08%. The 300mm cube blocks showed large expansion or map-cracking usually after more than 1 year of exposure.

**Table 10** Summary of data from Shayan [20]

Structure	Prism Expansion after 1 year	Comments
Australian Railway sleepers. Gneissic granite rocks which produced about 0.10% expansion at 21 days in the AMBT	Prism in 50°C in water 0.06% with 1.4% alkali 0.09% with 1.9% alkali	300mm cube Block in 50°C in water 0.12% with 1.4% alkali 0.18% with 1.9% alkali
Canning dam, WA. Gneissic granite rocks	Just >0.05%	Blended cements: 44%HVFA, 42%FA/4.2%SF triple blend shown to reduce expansion below 0.04%.
Dam 1 gneissic quartz gravel. Tests conducted on 3 reactive quartz gravels No 1-3	No 1 just < 0.03% No 2 & 3 well < 0.03% RTA T363 classified aggregate No 1-3 as reactive.	Aggregate No 1 blocks in 38°C in water showed low expansion at 1 year but increased significantly at 2 years.
Dam 2 gneissic granite containing strained and microcrystalline quartz.	No CPT results.	Reactive aggregate as tested by RTA T363.
Dam 3 phyllite aggregate UY	Prism 0.019% at 1 year	410kg/m <sup>3</sup> cement with 1.76% alkali Block 0.117% at 1 year

Accordingly, the one-year concrete prisms test duration might not be enough for classifying the aggregates and may need to be extended. Results of the prism tests and field performance are summarised in **Table 10**. Using supplementary cementitious materials (SCMs) in mix designs is a common practice nowadays. It is important to take into account that the ASTM C1293 recommended the extension of the CPT duration to two years when SCMs are applied for mitigating the ASR. The two years test duration provides a more reliable time framework for evaluating the effect of the mitigation on slowly-reactive or reactive aggregates. This duration is supported by the observations of Shayan [20].

### 3.3 Slowly reactive aggregates

The term “slowly-reactive aggregate” has been introduced since 90s and is extensively used through literature [7,17,19–26]. However, lack of an existing appropriate test method or test limits for detecting ASR is observed throughout previous studies. It is significantly important to apply a reliable ASR test method, which can provide expansion limits for classification of aggregates as “non-reactive”, “slowly reactive” or “reactive” [20].

Some studies have shown the field evidence regarding the inability of ASTM 1260 14-day limit (expansion greater than 0.10%) for detecting slowly-reactive aggregates [27]. The failure in detecting slowly-reactive aggregate could cause serious damage to concrete structures in the long-term. In Australia, it is reported that meta-basalts or granitic gneisses cause serious damage to major structures [20]. In addition, studies in the United States showed that the slowly reactive aggregates could pass the existing AMBT tests but result in failure in field structures. These aggregate mostly included quartzites, gneisses, and schists [17]. For this reason, the AMBT test needs to be revised when slowly reactive aggregates are tested [28].

The proposed procedure should be rapid, requiring preferably not more than 28 days. Also the procedure should reliably discriminate between innocuous and slowly reactive as well as highly reactive aggregates [17]. In one study, it is recommended to extend the AMBT test duration up to 90 days and with the expansion limit of 0.20% to correctly classify the slowly-reactive aggregates [28]. Another suggested method is amongst the RILEM methods particularly the AAR-4 reactor method, which claimed to be as the proper method for identifying the reactivity of the slowly-reactive aggregate [23].

The Standard AS 1141.60.1 applies new limits to detect the “slowly-reactive” aggregates. The current CCAA research found a number of aggregates as “slowly-reactive”. The clear limits of AS 1041.60.1 classified these aggregate “slowly-reacted” instead of classifying them as “uncertain”. The slowly reacted aggregates can be utilised in concrete production while the proper ASR mitigation such as addition of SCMs to mix design is selected. In the case of slowly-reacted detection, it is suggested by this paper that the mitigation solution be tested by conduction the AS 1141.60.2 over the period of 2 years. This suggestion is supported by literature as it shown the CPT test could provide a more reliable indication of the performance of aggregates and the two years duration of testing will determine if the applied mitigation is effective to control the prism expansion to lower than 0.03%.

The test results proved that the proposed limits could distinguish between some innocuous and slowly-reactive aggregates. The Australian test method limits will enable the designer and concrete producer to distinguish slowly-reactive aggregates and safely use them in mix design by including the appropriate mitigation strategy. This approach is more efficient in term of asset management and provides a wider access to resources (local aggregates), which guarantees the more sustainable production of concrete. It is suggested by this research that the Australian test framework needs to provide an agreed hierarchy of the two Australian Standard test methods. This can help resolving issues when there is a conflict between the test results AS 1141.60.1 AMBT and AS 1141.60.2 CPT classifications.

#### **4. Conclusions**

Evaluation of the international and Australian test results by the Australian mortar bar (AS 1141.60.1) and concrete prism (AS 1141.60.2) tests support the reliability of both tests for determining the alkali-silica reactivity (ASR) of most aggregates and can be actively used by local industry.

Both the Australian and the ASTM mortar bar tests are quick and reliable means for determining non-reactive (innocuous) aggregates. However, the evaluation procedures of these test methods were found to be conservative and should not be applied for rejecting aggregates. In addition, international data for aggregates with known field reactivity showed that the Australian 1141.60.1 AMBT evaluation procedure is more reliable compared to the ASTM 1260 14-day limits.

Literature showed that the concrete prism test (CPT) has a better correlation with the performance of aggregates in field. The majority of international data showed that for cases which there are conflicts between AMBT and CPT classifications, the recommended approach was to accept the CPT test results. In addition, literature indicated that the 1-year expansion duration may not be sufficient, especially if supplementary cementitious materials (SCMs) are used for mitigating the ASR. In this case, it is suggested to extend the duration concrete prism testing up to two years in AS 1141.60.2

CPT test results indicated that there is no conflict between the Australian and ASTM CPT classifications. Although the Australian test procedure applies the lower 1-year expansion limit of 0.03%, however, there is no significant change observed in the outcomes of the both procedure. For this reason, it is suggested that the selected 1-year expansion limit of 0.03% may be increased to 0.04%.

There is a need for an extensive examination of available Australian and International data so that an agreement can be reached on the hierarchy of the two Australian Standard test methods. This can help resolving issues when there is a conflict between the AS 1141.60.1 AMBT and AS 1141.60.2 CPT classifications.

## 5. Acknowledgement

The authors acknowledged the contribution of Mr Peter Clarke, Chairman of Standards Australia CE-012 committee, who reviewed the accuracy of CE-012 committee consideration on performance limits leading to the final agreement and publication of the two Australian standards.

## 6. References

- [1] AS 1141.60.1. Methods for sampling and testing aggregates Part 60.1: Alkali aggregate reactivity—Accelerated mortar bar method. Sydney: 2014.
- [2] AS 1141.60.2. Methods for sampling and testing aggregates Part 60.2: Alkali aggregate reactivity—Concrete prism method. Sydney: 2014.
- [3] RMS T363. Accelerated Mortar Bar Test for AAR Assessment. 2001.
- [4] VicRoads CR376.03. Accelerated Mortar Bar Test - Alkali-silica reactivity of aggregate. 2013.
- [5] ASTM C 1260. Standard Test Method for Potential Alkali Reactivity of Aggregates (Mortar-Bar Method). West Conshohocken, United States: 2007.
- [6] RILEM Recommended Test Method AAR-2 (formerly A-TC 106-2). Selection of Potential Alkali Reactivity of Aggregates - The Ultra-Accelerated Mortar Bar Test. *Materials and Structures* 2000;33:283–9.
- [7] Shayan A, Morris H. A comparison of RTA T363 and ASTM C1260 accelerated mortar bar test methods for detecting reactive aggregates. *Cement and Concrete Research* 2001;31:655–63.
- [8] Thomas W. Private communication made available to CE-012 meeting. 2001.
- [9] Davies G, Oberholster R. An Interlaboratory Test Programme on the NBRI Accelerated Test to Determine the Alkali Reactivity of Aggregates (Special Report BOU 92-1987). Pretoria: 1987.
- [10] Ideker JH, Bentivegna AF, Folliard KJ, Juenger MCG. Do Current Laboratory Test Methods Accurately Predict Alkali-Silica Reactivity? *ACI MATERIALS JOURNAL* 2012:395–402.
- [11] Fournier B, Rogers C a, Macdonald C. Multilaboratory study of the concrete prism and accelerated mortar bar expansion tests with Spratt aggregate. 14th International Conference on Alkali Aggregate Reaction, 2012, p. 1–10.
- [12] Thomas M, Innis F. Use of the Accelerated Mortar Bar Test for Evaluating the Efficacy of Mineral Admixtures for Controlling Expansion due to Alkali-Silica Reaction. *Cement, Concrete and Aggregates* 1999;21:157–64.
- [13] ASTM C 1293. Standard Test Method for Determination of Length Change of Concrete Due to Alkali- Silica Reaction. West Conshohocken, United States: 2008.
- [14] Touma WE. Alkali-silica reaction in portland cement concrete: testing methods and mitigation alternatives. The University of Texas At Austin, 2000.
- [15] CSA A23.2-27A. Standard practice to identify degree of alkali-reactivity of aggregates and to identify measures to avoid deleterious expansion in concrete. Ontario, Canada: 2009.
- [16] CSA A23.2-28A. Standard practice for laboratory testing to demonstrate the effectiveness of supplementary cementing materials and lithium-based admixtures to prevent alkali-silica reaction in concrete. Ontario, Canada: 2009.
- [17] Stark D, Morgan B, Okamoto P. Eliminating or Minimizing Alkali-Silica Reactivity. Washington, DC: 1993.

- [18] Lane DS. Alkali-silica reactivity in Virginia. 1994.
- [19] Bérubé M, Fournier B. Canadian experience with testing for alkali-aggregate reactivity in concrete. *Cement and Concrete Composites* 1993;15:27–47.
- [20] Shayan A. Field evidence for inability of ASTM C 1260 limits to detect slowly reactive Australian aggregates. *Australian Journal of Civil Engineering* 2007;3:13–26.
- [21] Lindgård J. RILEM TC 219-ACS-P: Literature survey on performance testing. Norway: 2011.
- [22] Castro N, Sorensen BE, Broekmans M a. TM. Quantitative assessment of alkali-reactive aggregate mineral content through XRD using polished sections as a supplementary tool to RILEM AAR-1 (petrographic method). *Cement and Concrete Research* 2012;42:1428–37.
- [23] Nixon P, Lane S. Report 3.3 Experience from testing of the alkali reactivity of European aggregates according to several concrete prism test methods. Norway: 2006.
- [24] Islam MS. Performance of Nevada's aggregates in alkali- aggregate reactivity of Portland cement concrete. University of Nevada Las Vegas, 2010.
- [25] ACI221.1R-98. State-of-the-Art Report on Alkali-Aggregate Reactivity Reported by ACI Committee 221. 1998.
- [26] Shayan A. Aggregate selection for durability of concrete structures. *Proceedings of the ICE - Construction Materials* 2011;164:111–21.
- [27] Wigum B, French W. Sequential examination of slowly expanding alkali-reactive aggregates in accelerated mortar bar testing. *Magazine of Concrete Research* 1996;48:281–92.
- [28] Alaejos P, Lanza V, Bermúdez M a., Velasco A. Effectiveness of the accelerated mortar bar test to detect rapid reactive aggregates (including their pessimum content) and slowly reactive aggregates. *Cement and Concrete Research* 2014;58:13–9.



# Mechanical properties of mortar with oil contaminated sand

Rajab M. Abousnina\*, Allan Manalo, Weena Lokuge

Faculty of Health, Engineering and Sciences, University of Southern Queensland, Toowoomba, QLD  
4350, Australia

**Abstract:** The use of oil-contaminated sand in construction is now being considered as an alternative and cost effective remediation method to minimize its adverse effect in the environment. In this study, the effect of oil contamination on the mechanical properties of mortar under two different mixing methods and three different w/c ratios 0.4, 0.5 and 0.6 were investigated. Three different percentages of crude oil contamination (0, 2 and 10%) were considered. Similarly, the mortar was prepared using two mixing methods, i.e (i) cement is mixed with water first before sand is added (CWS) and (ii) cement and sand was mixed first before adding water (CSW) to examine its effect on the compressive strength. The results indicated that the oil contamination affects the compressive strength of mortar. While the compressive strength of 0 and 2% oil contamination is almost the same, a 25% of compressive strength reduction was obtained for 10% crude oil contamination. On the other hand, CWS provided higher compressive strength than the CSW mixing method under different crude oil content. These results show the importance of mixing method especially for mortar with sand with high percentage of crude oil contamination. While the optimum compressive strength was observed with w/c of 0.5 compared to 0.4 and 0.6. Furthermore, the results indicated that oil contaminated sand has the potential for use in construction application.

**Keywords:** Mixing, Compressive strength, Mortar, Contamination and Crude oil

## 1. Introduction

Oil contamination can adversely affect the ecosystem and contaminate ground water resources [1]. Moreover, the physical and chemical properties of the surrounding sand change as soon as they come into contact with crude oil [2]. To minimize its effect to the environment, a range of remediation methods for sand contaminated with oil have been implemented but the cost of these methods is prohibitive especially in developing countries [3]. Hence, a better and more cost-effective way of remediating oil contaminated sand is warranted. Several researchers [4-8] mixed the oil contaminated sand with cement and then use this mixture in construction as an alternative and cheap remediation method. While this approach is considered to be a clever and successful civil engineering solution in terms of cost and reducing the environmental impact; very limited studies have been conducted to investigate the properties of contaminated sand and its concrete in order to substantiate their beneficial use in construction.

The compressive strength of hardened concrete which is generally considered to be an index of its important mechanical properties, depends upon many factors, e.g. quality and quantity of cement, water cement (wc) ratio and aggregates; batching and mixing; placing, compaction and curing. Out of these factors mixing and wc ratios are considered as one of the most important factors that affects the compressive strength of concrete [9]. The workability of freshly mixed concrete is required for proper in practice and the hardened concrete needs to be durable in order to obtain a specific compressive strength [10]. The main purpose of a concrete mix design is to attain a workable concrete that meets a specific strength. Jézéquel and Collin [11] indicated that the compressive strength of concrete varies much based on the consistency achieved through mixing. Therefore, inability to achieve the design or required strength in concrete will have adverse effect on the structural behavior of the member that it will be used in.

Generally for any type of concrete, most literature recommends mixing the concrete until the mix is consistent and uniform in nature based on physical observation. For instance, ASTM C305 – 14 [12] and AS 2350 12-2006 [13] gives fine details on the procedure for preparation of mortar which includes “pouring water into bowl and, with the mixer in the operating position, add the cement to the middle of the

bowel then add the entire quantity of sand slowly". Based on ASTM C305 – 14 and AS 2350 12-2006 standards, cement needs to be mixed with water before sand is introduced, whereas, AS 1012.2:2014 [14] and ASTM C192/C192M-14 [15] give the details on the preparation of concrete mixes and curing concrete respectively. AS 1012.2:2014 and ASTM C192/C192M-14 standards recommend mixing the dry ingredients first (cement, fine aggregates, and coarse aggregates) when these materials are thoroughly blended water can then be introduced to the dry mix until the concrete is homogeneous in appearance and has the desired consistency. This recommendation of mixing priority, i.e, cement and water then sand (CWS) or cement and sand then water (CSW) may not significantly affect the compressive strength for a normal concrete mix. However, when oil contaminated sand is used; the mixing procedure may play an important role and affect the compressive strength of the prepared mortar or concrete due to the presence of crude oil which reduce or inhibit the hydration processes. Hence, two different mixing methods were considered to determine its effect on the compressive strength of the mortar mix. In practice, CWS mixing procedure was compared with that of CSW.

On the other hand, the ratio of water and cement is an important factor in concrete production because it affects the fresh and hardened properties of concrete. The wc ratio is directly related to the spacing between the particles of cement in the cement paste, such that the smaller the spacing the faster cement hydrates fill the gaps between the particles and the links between hydrated particles grow stronger and form a stronger concrete [16]. In this regard, the effect of the wc ratio on the compressive strength of mortar containing light crude oil is also investigated. Three different water cement ratios, 0.4, 0.5, and 0.6 under different contents of crude oil content (0, 2 and 10%) are prepared and tested. It is anticipated that the results of this study will give a better understanding on the effect of mixing methods and wc ratios for properties of mortar using oil contaminated sand, in order to evaluate its suitability as an alternative concrete materials for building and construction.

## **2. Experimental program**

### **2.1 Preparation of oil contaminated sand**

Air dried fine sand; with particle size less than 2.36 mm was used due to its similarity to sand in the Libyan Desert where the first author came from. On the other hand, mineral Fork w2.5 motor cycle oil was used because its density and viscosity are similar to light crude oil [17, 18]. The samples were prepared by mixing dry sand with two different percentages of light crude oil (2 and 10 %) by the weight of dry sand. In addition, uncontaminated (0%) sand was prepared as a control sample. These percentages were selected based on the previous results of this ongoing project on the mechanical properties of sand contaminated with oil [19]. The oil was mixed manually with the dry sand and then the samples were placed inside a plastic container for 72 hours to allow the mixture to attain a homogenous condition. A lid was placed on the plastic container to prevent the crude oil from evaporating during this period of incubation.

### **2.2 Preparing, casting and curing**

All laboratory work was conducted at a room temperature around 22°C. The specimens were de-molded after 24 hrs and were cured in in a fog room up to 28 days at a temperature of 25°C and 85% humidity. Figure 1 shows the protocol of sample preparation based on the AS 2350.12 [2006].

The composition of the mortar was based on AS 2350.12-2006 [13] with mix proportions of 1 part cement and three parts sand (by mass).

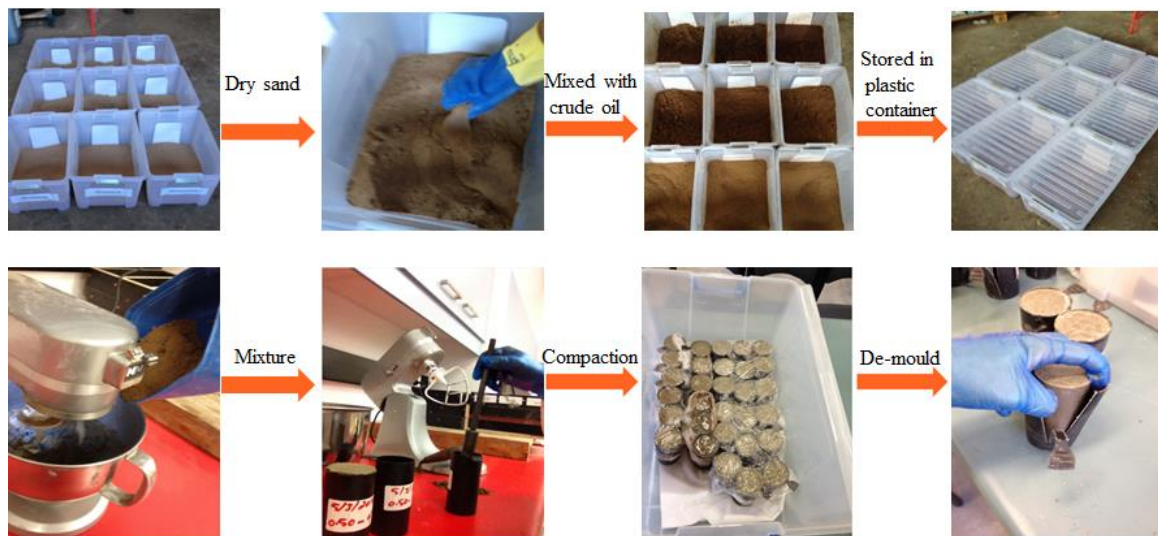


Figure 1: Sample preparation protocol.

### 2.3 Compressive Strength Test

Compressive strength tests were carried out for all the specimens after 28 days of curing. The specimens were tested to failure using a loading rate of 1.5 kN/min using 2 Channel Automatic Cube and Cylinder Compression Machine CT340-CT440 as shown in Figure 2(ab). The compressive strength of the samples was calculated by dividing the failure load by the actual cross sectional area. Both ends of the cylindrical specimens were ground before being placed in the testing machine mainly to smooth their cross sectional surface areas also the rubber capping was used to apply the load uniformly to the specimens as shown in Figure 2(c).

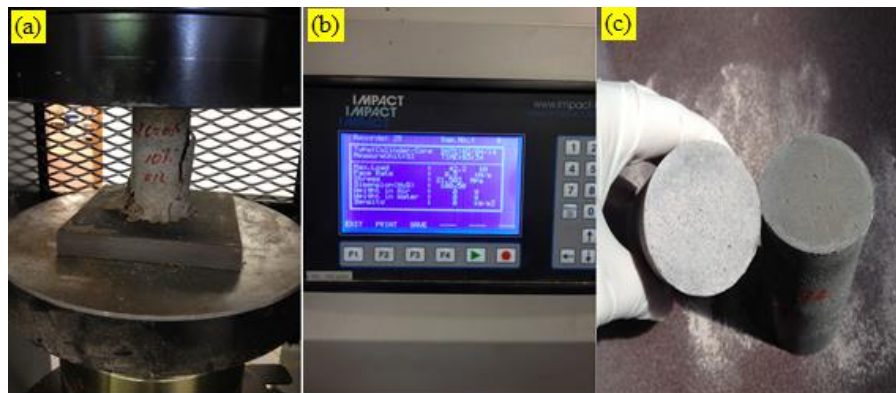


Figure 2: Compressive strength machine

## 3. Results and discussions

### 3.1 Effect of light crude oil on the flow

The flow table test was conducted based on the (ASTM C1437-07) as shown in Figure 3. The flow test results of the 0, 2 and 10% of crude oil contamination were 140mm, 147mm and 160mm respectively. Increasing the crude oil content increases the workability which indicates that the crude oil works as a plasticizer agent. This agreed with a previous study [20], which concluded that the oil acted like a chemical plasticizer and improved the fluidity and doubled the slump of the concrete mix, while maintaining its compressive strength. Furthermore, the increase in flow for mixes containing light crude oil is a similar outcome of the other studies by Hamad, Rteil and El-Fadel [7] and Nuruddin, Shafiq and Beddu [21]. In addition, Al-Mutairi [22] indicated a good effect with regard to slump of concrete made from oil contaminated sand.

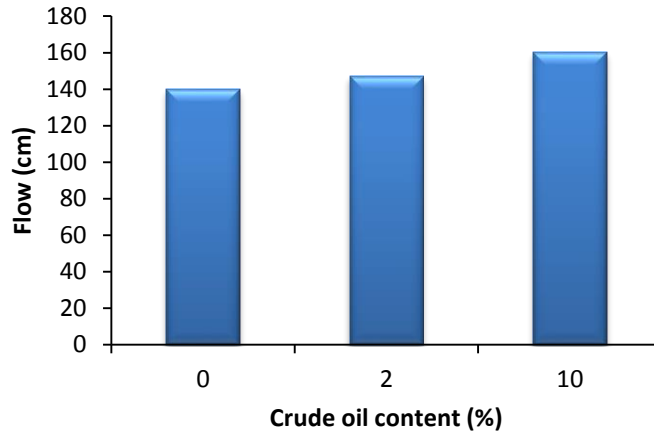


Figure 3: Flow values for mixes containing deferent percentage of light crude oil

### 3.2 Effect of mixing method on compressive strength

The compressive strength of mortar mixes after 28 days are shown in Figure 4, where two different mixing methods and three different percentages of oil contaminated sand were investigated. In general, results indicate that the compressive strength of cylinders is higher when CWS mixing method was used compared to CSW mixing method. Nevertheless, it can be seen that there was an insignificant variation between the two mixing methods with the uncontaminated sample. The compressive strength between the two mixing methods was only 0.1 MPa, but when the content of crude oil was increased to 2%. A higher compressive strength by 5.4 MPa was obtained using CWS mixing method. Similar results were obtained by increasing the content of crude oil to 10%, and the compressive strength increased by 5 MPa when cement was first mixed with water and then contaminated sand was introduced CWS; this indicated that the mixing method has a significant effect on the compressive strength of concrete when contaminated sand is used. Mixing cement with contaminated sand first may affect or inhibit hydration due to the presence of crude oil.

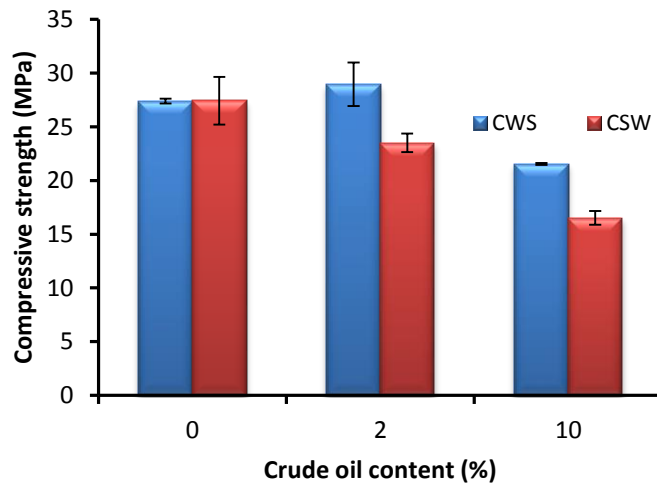


Figure 4: Compressive strength as a function of crude oil content.

Hydration is the process by which cement and water react together [23]. Mortar sets when solid particles in the mix, mainly ettringite and calcium silicate hydrates, become weakly connected by the hydration reactions. Contaminate sand with a high percentage of oil may have affected hydration. Figure 5 shows the contaminated sand with cement just before mixing it with water following the CSW. By increasing the content of crude oil it can be seen that the oil has merged into the cement, which may decrease the reaction between the cement and water and reduce the compressive strength, unlike the CWS mixing method which decrees that cement should be first mixed with water, and then sand.

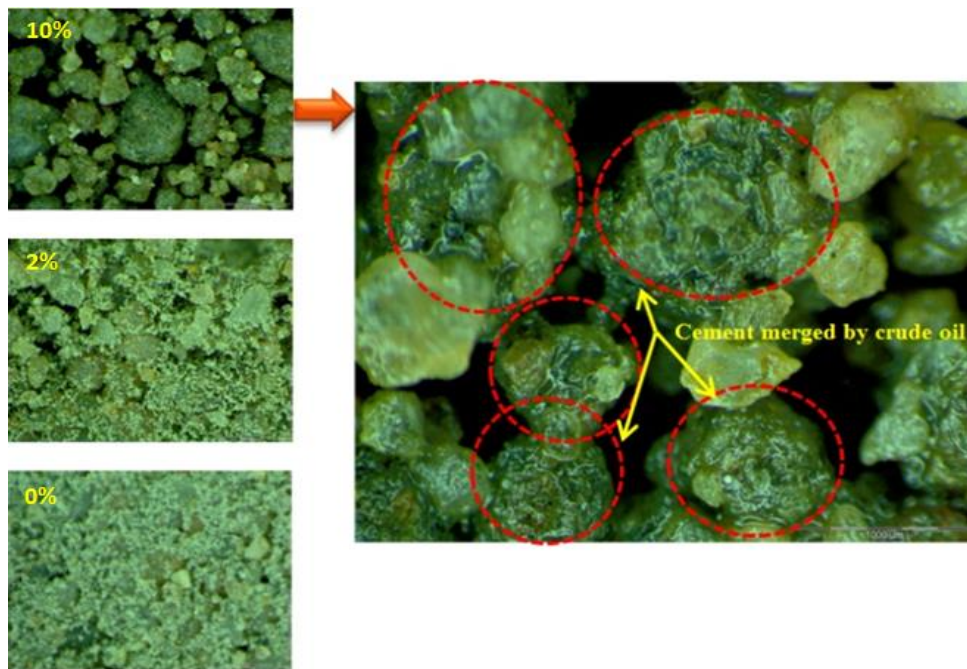


Figure 5: Oil contaminated sand mixed with cement

### 3.3 Effect of w/c ratio on the compressive strength

Figure 6 shows the effect of the water cement ratio on the compressive strength of mortar containing two different crude oil contaminations 2 and 10% and the uncontaminated sand (0%). Three different water cement ratios were investigated 0.4, 0.5, and 0.6. Disregarding the uncontaminated sample it can be seen that increasing the crude oil content from 2 to 10% decreases the compressive strength under the three different w/c ratios used. The reduction in the compressive strength of mortar when the crude oil content increased from 2 up to 10% agreed with the results of previous studies [24, 25]. Nevertheless the compressive strength of mortar under different w/c ratios with sand contaminated by 2% oil was higher than that for the mortar with uncontaminated sand. This result attributed to the degree of wettability caused by adding crude oil to dry sand because increasing its wettability by adding light crude oil decreased the amount of water the sand could absorb. Elsewhere it has been founded by Abousnina et al [19] that uncontaminated fine sand had the highest percentage of water absorption at 2.79%, but this percentage decreased as the amount of crude oil increased. However, water absorption was zero for sand with 2% of contamination and higher; this was due to the sand changing from dry to wet and met the saturated surface dry condition. Thus, all or most of the water added to the mix contacted the cement particles and helped complete the hydration process.



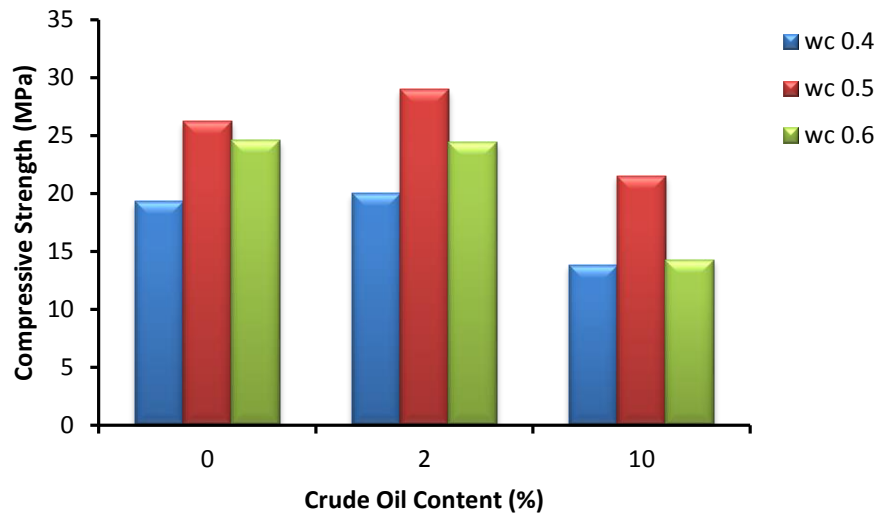


Figure 6: the effect of wc ratios on the compressive strength of mortar containing crude oil

Based on the literature, the effect of the wc ratio on the compressive strength has been studied widely and is very well known [26-28]. The compressive strength decreases with a higher water cement ratio. Of the three wc ratios used in this study, the compressive strength of the mortar mixes was highest with a 0.5 water cement ratio, whereas a water cement ratio of 0.6 caused a significant reduction in the compressive strength of mortar. These results agreed with previous studies [29-31] where it has concluded that increasing the w/c ratio decreased the compressive strength. The compressive strength of the uncontaminated sample of mortar decreased by 6% when a w/c 0.6 compared to the compressive strength obtained when w/c of 0.5 was used. The reduction of compressive strength by adding crude oil content with 2% and 10% was 15.7 and 33.6% respectively. The reduction in the compressive strength that occurred with wc ratio 0.6 compared to a w/c ratio of 0.5 may be due to an increase in porosity because by increasing the water cement ratio, the paste fraction of the mortar becomes increasingly porous and the mortar becomes weaker due to the increased porosity and more permeable because the pores are interconnected [32] which actually agreed with our visual observation showed in Figure 7. In addition to that, based on the visual observation as well as the microscope observation it can be seen that increasing the crude oil content from 2 to 10% increases the pore size and as a consequences the compressive strength decreased accordingly. Furthermore, X. H. Vu et al [33] claimed that the water/cement ratio, upon entering the concrete composition, is a major parameter affecting the porosity and strength of the cement matrix of hardened concrete.

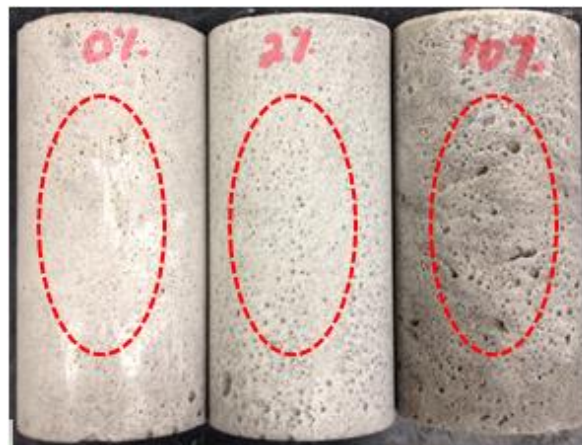


Figure 7: Air voids on the surface of specimens

One of the interesting findings in this study is that the lowest compressive strength was observed at a wc ratio of 0.4. The reduction of the compressive strength compared to w/c ratio of 0.5 under the three percentages of crude oil contamination used 0, 2 and 10% vary with 26.2, 31.0 and 35.7% respectively.

This may rely to the other factors that influence the compressive strength because the relationship between the w/c ratio and the strength of concrete is only approximate because it can be affected by other factors. Neville [34] stated that the influence of the wc ratio on the strength does not truly constitute a law because the wc ratio rule does not include the qualifications needed for its validity. Indeed the strength of concrete at any wc ratio depends on factors such as the degree of hydration of the cement and its chemical and physical properties, the temperature at which hydration takes place, the air content of the concrete, the change in the effective wc ratio, and the formation of cracks due to bleeding. Furthermore, Gilkey [35] stated that for a given cement and acceptable aggregates, the strength that may be developed by a workable, properly placed mixture of cement, aggregate, and water is influenced by wc ratio, and the ratio of cement to aggregate, grading, surface texture etc. This indicates that other parameters can also affect the strength of concrete with different wc ratios.

The wc ratio determines the porosity of the hardened cement paste at any stage of hydration, because it will directly affect the volume of voids in concrete. The wc ratio also influences the porosity of the cement matrix within the hardened concrete [36, 37], which itself heavily influences the durability of concrete. In fact there is a minimum w/c ratio for hydration products to form because there is insufficient space at low wc ratios. For complete hydration the wc ratio should not be below 0.42 by weigh [34]. When w/c 0.4 was used the actual water used was less than this amount due to the use of dry sand. This indicated that the hydration processes was not completed with a w/c ratio of 0.4, which may increase total porosity due to the lack of water in order to complete the hydration process. Furthermore, when a w/c ratio of 0.4 was used the workability was less than with w/c ratios of 0.5 and 0.6, which indicates that removing the air voids is much harder than with more workable mortar. Winter, N [23] stated that workability is an important factor in mortar/concrete because it indicates how easy concrete can be compacted; in other words, how easy all the air voids in the concrete can be removed to achieve maximum density. Obtaining the maximum possible density of a wet mix is important to maximize the strength of the hardened concrete and its resistance to deterioration. This the main reason for the reduction in compressive strength for a WC ratio of 0.4 compared with the w/c ratios of 0.5 and 0.6. As a consequence, reducing the water cement ratio decreases the workability, and hence, higher porosity is expected because all the air voids cannot be removed during compaction and hence, the total porosity will be higher.

#### **4. Evaluation of the suitability of mortar with oil contaminated sand for construction**

The results of the preliminary studies conducted by the authors point towards the sustainable use of fine sand contaminated with light crude oil for construction. Mixing method plays a great role in terms of the compressive strength obtained. The compressive strength of specimens mixed under CWS was higher compared to CSW especially for higher level of oil contamination. For this reason, it is suggested that CWS mixing method should be followed when preparing mortar or cement using sand with oil contamination, i.e. water and cement should be thoroughly mixed first before adding the oil contamination sand. Furthermore, the compressive strength of mortar mixed with contaminated sand 2% of oil contamination is found higher than the uncontaminated samples. However, when the amount of crude oil was increased from 2 to 10%, the compressive strength decreased significantly which may due to oil in the mix hindered the cement from being hydrated. These result indicated that the compressive strength of contaminated sand can be increased more than the uncontaminated sand by adding a certain amount of oil. This indicates that this material is suitable for building and construction. Similarly, the results indicated that even the mortar using fine sand with 10% oil contamination with wc ratio of 0.5 and mixed under CWS can be used because its compressive strength is around 21.5 MPa, which is only 20% lower of uncontaminated sample. In fact, the British standard for precast concrete masonry units (BSI, 1981) requires only a compressive strength of 2.8 and 7 MPa for blocks and bricks, respectively and a minimum compressive strength of 15 MPa is required by the Department of Transport in UK for sub-base and base materials. These results clearly showed the high potential of using oil contaminated sand for construction. Moreover, this remediation method will solve one of the major issues of sand contamination in oil producing but developing countries because the cost of this method is cheaper compared to the existing remediation methods.

#### **5. Conclusion**

This study investigated how mixing methods and water cement ratio affected the compressive strength of mortar containing light crude oil. Based on the results, the following conclusions were drawn:

- The mortar produced by mixing cement and water first before mixing contaminated sand (CWS) produced higher compressive strength compared to CSW mixing method. CWS mixing method gives a high probability that the hydration process would be completed, which is not the case when cement was first mixed with contaminated sand before the addition of water as in the CSW mixing method.
- By increasing crude oil from 2 to 10%, the compressive strength decreased in both the mixing methods as well as the three different w/c ratios used. This result was due to a decrease or reduction in hydration because the cement was coated with oil.
- The optimum water cement ratio occurred with a water cement ratio of 0.5, whereas a w/c ratio of 0.6 increased the porosity while a wc ratio of 0.4 resulted in the lack of water to promote the hydration process and hence, resulted in a lower compressive strength.
- The mechanical properties of mortar with oil contaminated were found suitable for use in building and construction. In fact, the compressive strength of mortar with 10% oil contaminated sand is only 20% lower than that of uncontaminated sample.

## 6. Acknowledgement

We acknowledge the scholarship provided by the Libyan Government to Rajab Abousnina

## 7. References

- [1] Z. A. Rahman, U. Hamzah, M. R. Taha, N. S. Ithnain, and N. Ahmad, "Influence of oil contamination on geotechnical properties of basaltic residual soil," *American journal of applied sciences*, vol. 7, p. 954, 2010.
- [2] A. Tuncan and S. Pamukcu, "Predicted mechanism of crude oil and marine clay interactions," *Proceedings of the Environmental Geotechnology*, May, pp. 25-27, 1992.
- [3] R. Riser, "Remediation of petroleum contaminated soils: biological, physical & chemical processes," ed: United States: Lewis Publisher, 1998.
- [4] V. M. Hebatpuria, H. A. Arafat, H. S. Rho, P. L. Bishop, N. G. Pinto, and R. C. Buchanan, "Immobilization of phenol in cement-based solidified/stabilized hazardous wastes using regenerated activated carbon: leaching studies," *Journal of hazardous materials*, vol. 70, pp. 117-138, 1999.
- [5] M. J. Cullinane'Jr and R. M. Bricka, "An assessment of materials that interfere with stabilization/solidification processes," 1987.
- [6] Abdul Ahad and Ramzi B, "Compressive And Tensile Strength Of Concrete Loaded And Soaked In Crude Oil," 2000.
- [7] B. S. Hamad, A. A. Rteil, and M. El-Fadel, "Effect of used engine oil on properties of fresh and hardened concrete," *Construction and Building materials*, vol. 17, pp. 311-318, 2003.
- [8] W. O. Ajagbe, O. S. Omokehinde, G. A. Alade, and O. A. Agbede, "Effect of Crude Oil Impacted Sand on compressive strength of concrete," *Construction and Building Materials*, vol. 26, pp. 9-12, 1// 2012.
- [9] B. Kocaman, R. Yanik, C. Kose, and A. Ozturk, "Effect of Different Cure Conditions on Compressive Strength of Concrete Having Different Properties," *Journal of Animal and Veterinary Advances*, vol. 10, pp. 1756-1759, 2011.
- [10] N. A.M., Ed., *Properties of Concrete*. 39 Parker Street, London: Pitman Publishing Ltd, , 2000, p.^pp. Pages.
- [11] P.-H. Jézéquel and V. Collin, "Mixing of concrete or mortars: dispersive aspects," *Cement and Concrete Research*, vol. 37, pp. 1321-1333, 2007.
- [12] ASTM-C305-14, "Standrad practice for mechanical mixing of hydraulic cement pastes and mortars of plastic consistency," ed. USA: American Society for Testing and Materials 2013.
- [13] A. 2350.12-2006, "Method 12: Preparation of a standard mortar and moulding of specimens," ed. Australia: Australian Standrad, 2006.



- [14] A. 1012.2:2014, "Method 2: Preparing concrete mixes in the laboratory," ed. Australia: Australian Standard, 2014.
- [15] ASTM-C192/C192M-14, "Standard practice for Making and curing concrete test specimens in the laboratory," ed. USA: American Society for Testing and Materials, 1944.
- [16] D. P. Bentz and P. Aitcin, "The hidden meaning of water-to-cement ratio," *Concrete international*, vol. 30, pp. 51-54, 2008.
- [17] C. Ltd. (2009 ). *C. Putoline HPX Fork & Suspension Oil* Available: <http://www.championmotouk.com/product-info-t.php?Putoline-HPX-Fork-Suspension-Oil-pid10650.html>
- [18] Simetric. ( 2011). *specific gravity of liquids*. Available: [http://www.simetric.co.uk/si\\_liquids.htm](http://www.simetric.co.uk/si_liquids.htm)
- [19] Rajab M. Abousnina, Jim Shiau, Allan Manalo, and W. Lokuge, "Effect of light hydrocarbons contamination on shear strength of fine sand," presented at the Fourth International Conference on Geotechnique, Construction Materials and Environment, Brisbane, Australia, 2014.
- [20] B. S. Hamad and A. A. Rteil, "Effect of used engine oil on structural behavior of reinforced concrete elements," *Construction and Building Materials*, vol. 17, pp. 203-211, 2003.
- [21] F. Nuruddin, N. Shafiq, and S. Beddu, "Effects of Used Engine Oil on MIRHA Concrete," 2010.
- [22] N. M. Al-Mutairi, "Kuwait oil-based pollution: effect on building material," *Journal of materials in civil engineering*, vol. 7, pp. 154-160, 1995.
- [23] N. Winter, "Understanding cement," *WHD Microanalysis Consultants Ltd, United Kingdom*, 2009.
- [24] R. B. Abdul Ahad, "Compressive And Tensile Strength Of Concrete Loaded And Soaked In Crude Oil," 2000.
- [25] S. Ejeh and O. Uche, "Effect of crude oil spill on compressive strength of concrete materials," *Journal of Applied Sciences Research*, vol. 5, pp. 1756-1761, 2009.
- [26] I. Soroka, "Portland Cement Paste and Concrete," Chemical Publishing Co," *New York*, 1980.
- [27] G. A. Rao, "Role of water–binder ratio on the strength development in mortars incorporated with silica fume," *Cement and Concrete Research*, vol. 31, pp. 443-447, 2001.
- [28] J. Schulze, "Influence of water-cement ratio and cement content on the properties of polymer-modified mortars," *Cement and concrete research*, vol. 29, pp. 909-915, 1999.
- [29] O. Alawode and O. Idowu, "Effects of Water-Cement Ratios on the Compressive Strength and Workability of Concrete and Lateritic Concrete Mixes," *The Pacific Journal of Science and Technology*, vol. 12, pp. 99-105, 2011.
- [30] V. Živica, "Effects of the very low water/cement ratio," *Construction and Building Materials*, vol. 23, pp. 3579-3582, 2009.
- [31] T. Nwofor, "Durability of block work: the effect of varying water/cement ratio of mortar joint," *Advances in Applied Science Research*, vol. 3, 2012.
- [32] N. B. Winter, *Understanding cement: an introduction to cement production, cement hydration and deleterious processes in concrete*: Microanalysis Consultants, 2012.
- [33] X. H. Vu, Y. Malecot, L. Daudeville, and E. Buzaud, "Effect of the water/cement ratio on concrete behavior under extreme loading," *International Journal for Numerical and Analytical Methods in Geomechanics*, vol. 33, pp. 1867-1888, 2009.
- [34] A. Neville, "Properties of concrete (4th and final ed.) Addison Wesley Logman," ed: England, 1996.
- [35] H. J. Gilkey, "Water-Cement ratio versus strength-another look," in *ACI Journal Proceedings*, 1961.
- [36] D. M. Roy and G. R. Gouda, "Porosity-Strength Relation in Cementitious Materials with Very High Strengths," *Journal of the American Ceramic Society*, vol. 56, pp. 549-550, 1973.
- [37] R. Sersale, R. Cioffi, G. Frigione, and F. Zenone, "Relationship between gypsum content, porosity and strength in cement. I. Effect of SO<sub>3</sub> on the physical microstructure of Portland cement mortars," *Cement and concrete Research*, vol. 21, pp. 120-126, 1991.

# Investigation into the Structural Properties of an Innovative Modified Concrete

Negin Sharifi<sup>1</sup> and Bijan Samali<sup>2</sup>

<sup>1</sup>Civil Engineer – Structures and Materials Technology Group, GHD Pty Ltd

<sup>2</sup>Institute Director, Prof and Program Director of Infrastructure Systems, University of Western Sydney

**Abstract:** Styrene Butadiene Rubber (SBR), sourced from truck and passenger car tyres retain much of their physical, structural and chemical properties at the end of their life. This has encouraged researchers to consider recycling them in civil engineering applications and to assist with decreasing the detrimental effects of their growing disposal.

This paper reports on the fundamental findings of utilizing SBR granules as a potential source for replacing fine and coarse aggregates in fabricating reinforced concrete components. Elastomeric modified concrete (EMC) beams incorporating 6% and 10% of SBR granules are assessed for their dynamic and mechanical properties compared to control beams devoid of SBR granule additions. The load-deflection and stress-strain relationships are evaluated during the four-point bending test and cyclic test, hysteresis loops are also analyzed for the beams. Dynamic (impact) test was carried out parallel to the four-point bending test. An increase in the energy absorption and damping properties of the EMC beams was observed; while the ductility factor of the control beams remains the highest showing that EMC beams are more resilient than ductile. Addition of SBR granules also prevented the sudden brittle failure of the EMC beams. Such results confirm the feasibility of incorporating SBR granules in concrete structures.

**Keywords:** Styrene Butadiene Rubber, cyclic test, hysteresis loops, ductility and damping.

## 1. Introduction

With an increased awareness of environmental pollution and a reduction in naturally existing resources, sustainable development practices could find a high stage among constructors and governmental decision makers. Civil structures, especially buildings, are among the largest consumers of natural resources such as aggregates, water, and metal. Moreover, the mentioned structures are responsible for a significant portion of greenhouse emissions, especially if they are constructed with the most commonly used construction material: concrete, Chen, Okudan et al. (1). Accumulation of solid waste without any secure market to absorb it, on the other hand, has raised the question of what is the best solution to reduce the significant amount of waste with the minimum usage of other energy resources.

One approach in solving the above issue is to identify wastes suitable for use in the construction industry. This approach is not only a solution to decrease the amount of waste in the natural environment, but it can also be an appropriate and economical option to utilise waste to build more sustainable civil infrastructure.

A number of detected recycling materials, such as waste tyre granules, have shown significant useful properties other than being environmental friendly, which distinguishes them from other construction materials. Therefore, styrene butadiene rubber (SBR) granules sourced from waste tyre has been introduced as a new approach to solve environmental challenges.

Several works have been devoted to the use of rubber particles recovered from waste tyres to replace natural aggregates in concrete mix. Khaloo, Dehestani et al. (2) have exclusively studied the mechanical and physical properties of concrete containing fine, coarse, and combined rubber as a substitute of aggregates. Toutanji (3) studied the effect of the replacement of coarse aggregates with different volume contents of rubber tyre chips (25, 50, 75 and 100%) on the mechanical properties of the EMCs. There are several studies that worked on the concept of the ductility and damping of the members incorporating fibres; for instance in a study by Son, Hajirasouliha et al. (4), the improvement of the deformability of rubber-filled reinforced concrete (RC) columns by making concrete mixes with different strengths and waste tyre particle size and content was examined. Toutanji and Eldin (5) also reported that traditional concrete incorporating rubber particles showed more deformability and ductility in members. Ilker, Bekir et al. (6) in a paper entitled “The properties of rubberised concrete” examined the ductility properties of concrete. In a study by Yan, Jenkins et al. (7), the damping properties of fiber-reinforced concrete were assessed.

Due to the fact that most of the studies were focused on the mechanical and physical properties of EMCs, there is a need for further investigation, such as examining the energy absorption of EMC under dynamic loading. In this study, EMC reinforced beams were made in order to fulfil this need, and also to study the effect of SBR granules on real members.

## 2. Research Program

### 2.1 Styrene Butadiene Rubber (SBR)

The SBR granules used in this study are a general purpose synthetic elastomer, manufactured from a copolymer of styrene and butadiene. These elastomeric granules were sourced from waste passenger and four-wheel drive tyres with the size varying from 1 to 4 mm and 12 to 15 mm. The relative wet density of the SBR granules was determined to be 920 kg/m<sup>3</sup>. Illustrations of the typical small and large SBR granules used in this study are shown in Figure 1 and Figure 2. The 1 to 4 mm SBR granules were used to partially replace blended fine and coarse manufactured sand at proportion of 10%, and the 12 to 15 mm SBR granules were employed to partially replace 10mm and 20mm manufactured coarse aggregates at proportion of 6%.

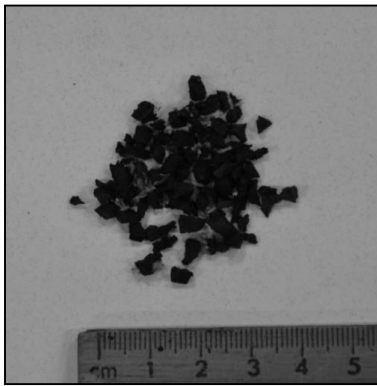


Figure 1 SBR granules 1-4 millimetres

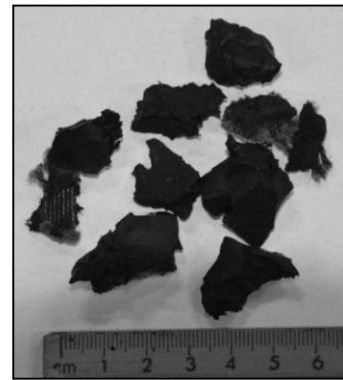


Figure 2 SBR granules 12-15 millimetres

### 2.2 Mix Materials

The raw materials used in batching of the concrete mixes included shrinkage limited Portland cement (PC), manufactured blended 50/50 fine and coarse sand (BS) as the fine aggregate component, and 10 mm and 20 mm gravel as the coarse aggregate (CA) fraction. In addition, fly ash (FA) sourced from Eraring power station was used as a supplementary cementitious material (SCM) addition to partially replace Portland cement (PC) at 30%. Drinkable grade water conditioned to 23 ± 2 °C was used for all mixes. The physical properties of all aggregates are summarised in Table 1. A high range water-reducing admixture (HWR) was also used to obtain the desired slump of 80 ± 20 mm. For all mixes, a fixed water-to-cementitious-material ratio (w/cm) of 0.35 was employed.

Table 1 Physical Properties of Aggregates

Aggregate Type	Particle Bulk Density (kg/m <sup>3</sup> )	Water Absorption (%)
10 mm CA	2700	1.8
20 mm CA	2710	1.6
Blended Sand	2650	1.2

### 2.3 Specimen Preparation and Testing

The proportioning of aggregates is shown in Tables 2 and 3, respectively. SBR granules were replaced by total mass of aggregates. SBR granules were premixed with other aggregates for 3 min prior to the adding of PC, FA and water. The raw materials were mixed based on the listed test method criteria of AS 1012.2-1994.

**Table 2 Experimental Program**

Mix	SBR Granules (%)		Fly Ash (%)	Blended 50/50 Sand (%)	10mm Coarse Aggregate (%)	20mm Coarse Aggregate (%)	SB Latex (%)
	(1-4 mm)	(12-15mm)					
C1	0	0	0	100	100	100	0
C2F	0	0	30	100	100	100	0
R4SBR6	0	6	30	100	97	97	0
R3SBR10	10	0	30	90	100	100	0

**Table 3 Concrete Mix Proportions**

Mix	Portland Cement (kg/m <sup>3</sup> )	Fly Ash (kg/m <sup>3</sup> )	Blended Sand (kg/m <sup>3</sup> )	10 mm Coarse Aggregate (kg/m <sup>3</sup> )	20 mm Coarse Aggregate (kg/m <sup>3</sup> )	Water (kg/m <sup>3</sup> )	Styrene Butadiene Rubber Granules (kg/m <sup>3</sup> )
C1	430.0	0.0	635.0	390.0	700.0	150.5	0.0
C2F	301.0	129.0	635.0	390.0	700.0	150.5	0.0
R4SBR6	301.0	129.0	633.0	378.0	674.0	151.0	33.0
R3SBR10	301.0	129.0	569.0	390.0	695.0	151.0	63.0

Beams were designed based on the specifications of Ultimate Strength Design Method and the final dimensions were as follows:

- Height 150 mm
- Width 200 mm
- Length 1,900 mm
- Length between supports 1,800 mm

#### 2.3.1 Four-point Bending Test Set up

In order to undertake the four-point bending test, ten channels were employed to capture the data via different tools as follows:

- Two channels for load cells
- Three channels for Linear Variable Differential Transformers (LVDTs)
- Three channels for strain gauges on the body of the beam
- Two channels for strain gauges on the reinforcing bar

Schematic of the four-point bending test set up is shown in the Figure 3 below.

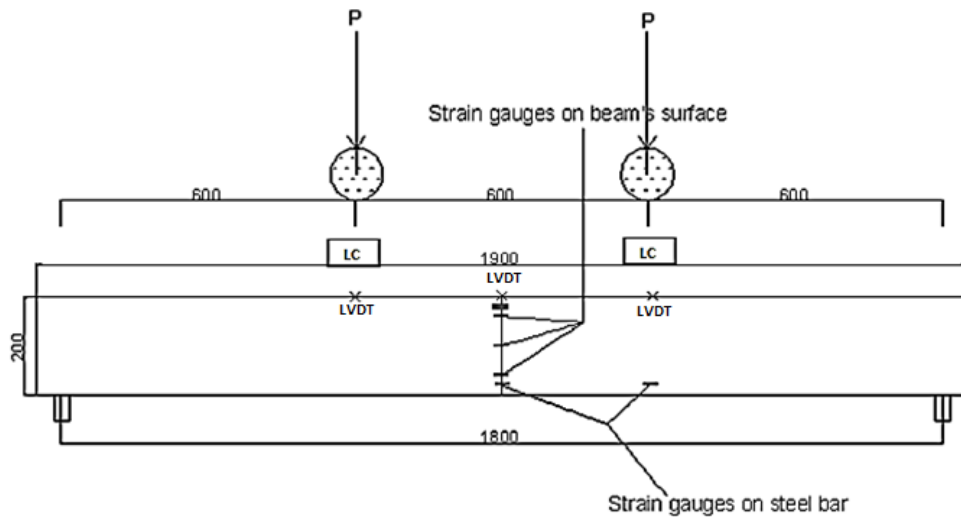


Figure 3 Schematic of the Four-point Bending Test Set up

### 2.3.2 Three-point Bending Test Set up

In order to carry out the three-point bending (cyclic) test, there were six channels as below:

- One channel for load cell under the applied load
- Three channels for LVDTs at half and one-thirds of the beam
- Two strain gauges at half span and one-third of the reinforcing bar

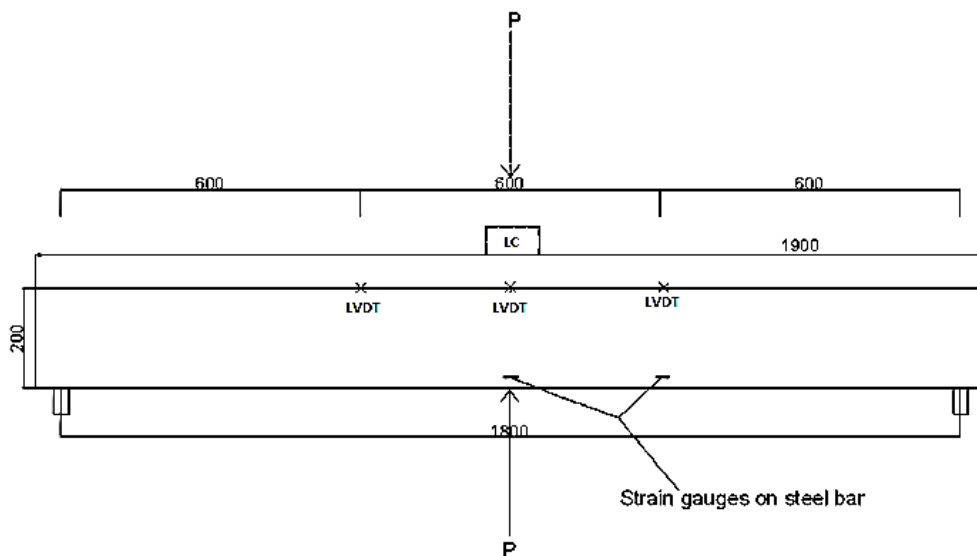


Figure 4 Schematic of the Three-point Bending Test Set up

### 2.3.3 Dynamic Test Set up

The hammer test is carried out parallel to the four-point bending test in order to study the transverse vibration (natural frequency and damping). The concrete beam is struck in two different places (close to two different accelerometers) three times prior to applying the load, and also after the failure. The schematic of dynamic tests on beams is shown in the Figure 5 below:

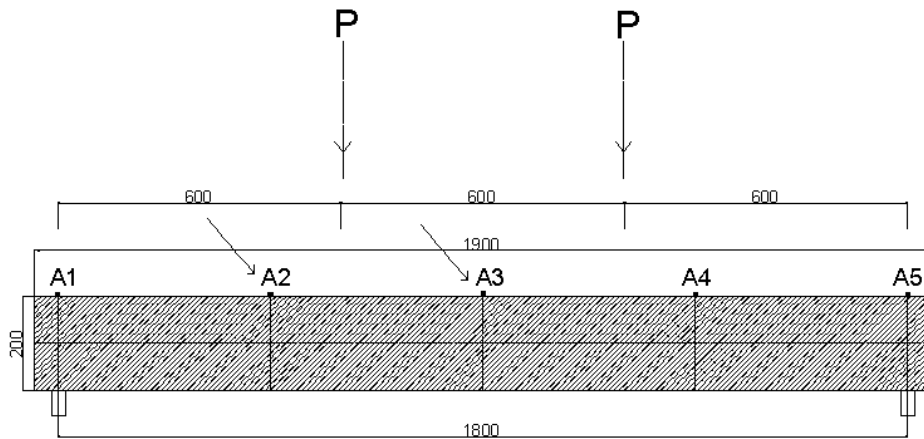


Figure 5 Schematic of Dynamic Tests on Beams

### 3. Results

#### 3.1 Four Point Bending Test

##### 3.1.1 Parameters Calculated in Four-point Bending Test

Using the data of the four-point bending test, the following parameters were calculated for each beam:

- The load and the corresponding deflection at the first crack; the location of first crack is assumed as the point where the curvature first increases sharply and the slope of the curve shows a definite change;
- The load and the corresponding deflection at proportional limit. Proportional limit is defined as a location on the curve where the elasticity region finishes and beyond which the slope changes. This limit is prior to the yield point;
- The maximum load and corresponding deflection: the deflection at the maximum load that the beam can take before failure; and
- Ductility Factor: defined as the ratio of maximum post-yield deformation to yield deformation which usually comes from steel yielding.

The Load – Deflection graph of the beams is shown in Figure 6 below:

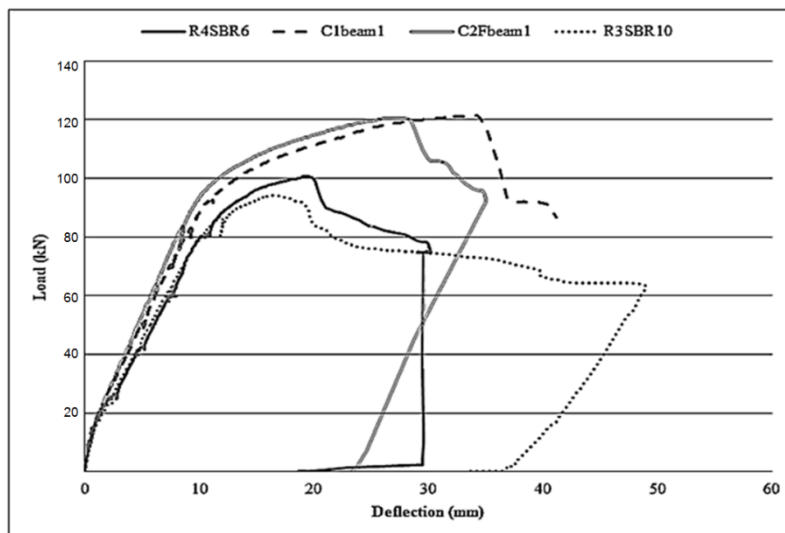
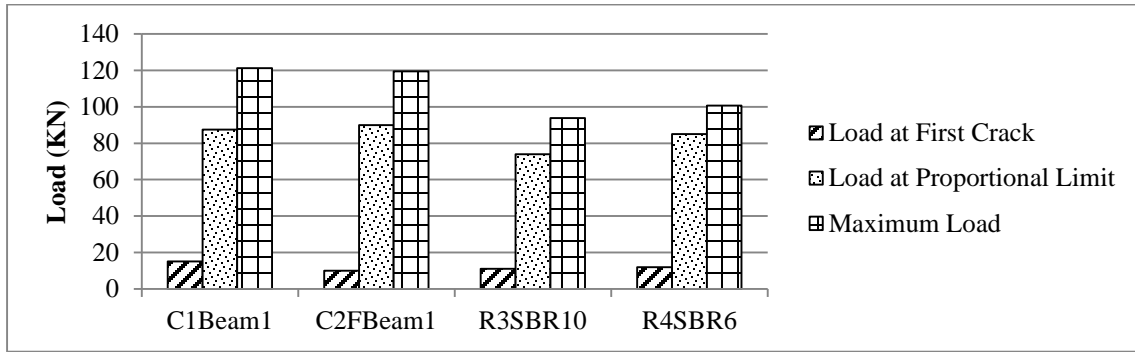
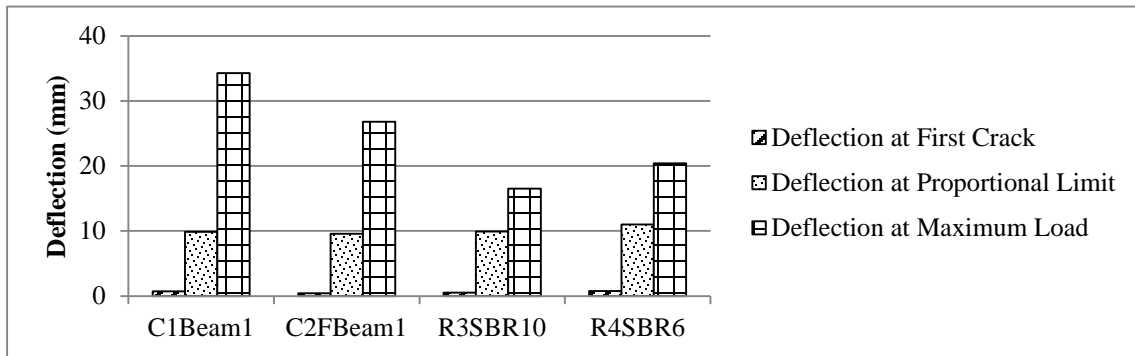


Figure 6 (Load – Deflection) Curve of the Beams

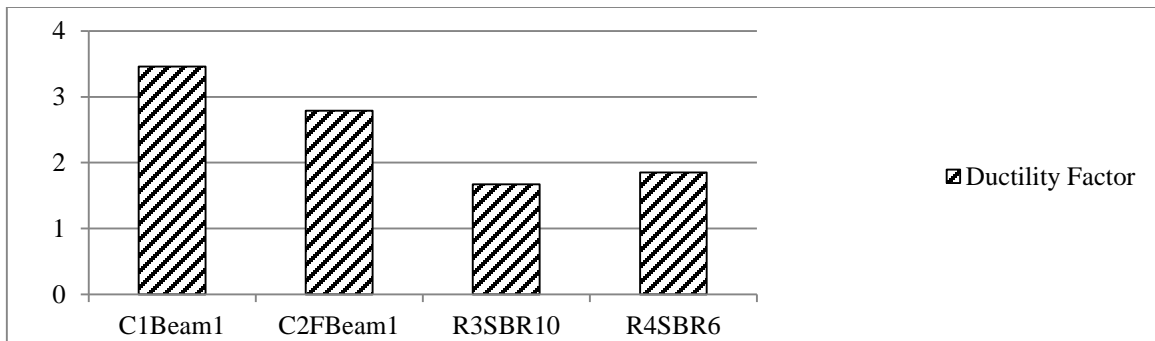
The following graphs (Figures 7 to 9) show the results of the four point bending test.



**Figure 7 Load at Different Points of Four-point Bending Test**



**Figure 8 Deflection at Different Points of Four-point Bending Test**



**Figure 9 Ductility Factor of Beams**

With the calculated values described in Section 3.1.1, the area under the graphs were calculated roughly and shown in the Table 4 below:

**Table 4 Area under Load - Deflection Curve**

Area under the Curve (kN.mm)			
	Up to First crack	Up to Proportional Limit	Up to Maximum Load
C1	5.6	469.0	2542.0
C2F	2.3	458.0	1801.0
R3SBR10	3.0	399.0	555.0
R4SBR6	4.6	497.0	873.0

The area under the graph up to the proportional limit can be assumed as the Modulus of Resilience with a small change in its definition. The modulus of resilience is defined in the literature as the area under the curve up to the yield point (where the material remains unaffected by the applied load and will return to its initial shape when unloaded), however, in this paper, due to the fact that finding the yield point was not possible, the area up to the proportional limit is calculated as the Modulus of Resilience. Based on the test results, the resilience of R4SBR6 was the highest; this could be because of the presence of the larger size SBR in the mix and the mechanical properties of the SBR granule itself.

### 3.2 Three Point Bending Test (cyclic test)

The goal of this test was to investigate the energy absorption for each concrete reinforced beam; this was done by numerically calculating the area enclosed by the load-deflection curves for each hysteresis loop.

#### 3.2.1 Results

Total area and area up to 30 kN of three-point bending load-deflection curves are provided in Table 5 below:

**Table 5 Total Area and Area up to 30kN of Three-point Bending Load-Deflection Curve**

Specimen Name	Total Area	Area Up to 30kN
C1	531	28.3
C2F	268	9.1
R3SBR10	284	34.0
R4SBR6	519	56.1

All beams suffered a tension failure, and all exhibited almost the same general flexural behaviour. The total area under hysteresis loops is the highest in the control concrete followed by the beam incorporating 6% (12 – 15 mm) SBR granules. Concrete beams incorporating SBR granules have a higher resilience and the area under the curve at lower amounts of load is more significant, whereas at higher loads, the areas under the curves in beams without SBR granules are higher.

### 3.3 Dynamic Properties

#### 3.3.1 Results

The values for first frequency retrieved from relevant plots are shown in Table 6 below:

**Table 6 First Frequency of the Beams (from graph)**

Beam Identification	Before the Load Application (Hz)
C1	82.40
C2F	76.80
R3SBR10	76.70
R4SBR6	78.81



As can be seen in the table above, the first frequency of the reference beam with 100% PC is the highest before applying the load followed by the Beam with 6% SBR (12-15mm). By using the results of the hammer test and plotting the Acceleration–Time history graphs, damping ratio in very low damping is approximated as the following equation, Samali (8):

$$\xi = \frac{u_n - u_{n+m'}}{2m'\pi u_{n+m'}} \quad (1)$$

where:

$u_n$  = displacement on the curve at  $n^{\text{th}}$  cycle

$u_{n+m'}$  = displacement on the curve at  $(n+m')^{\text{th}}$  cycle

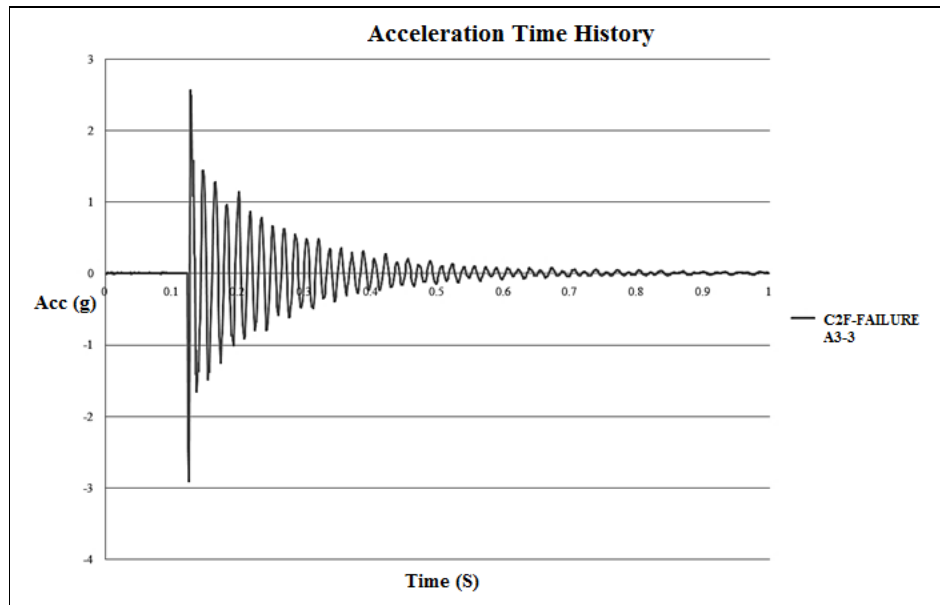
$m'$  = number of cycles

**Table 7 - Damping Ratio of Beams Before and After Failure**

Beam Identification	Damping Ratio (%)	
	Before failure	After failure
C1	3.71	3.89
C2F	3.27	2.67
R3SBR10	4.09	5.96
R4SBR6	4.96	6.12

In accordance to Table 7 above, the addition of rubber particles improves the damping properties of the concrete mix. This statement is supported by a study by Zheng, Huo et al. (9), which finds that with the increase of rubber content, the damping ratio will be improved, up to an optimum point of 30% rubber content.

An example of the Acceleration–Time history graph under free vibration is shown in Figure 10 below:



**Figure 10 Acceleration- Time History of C2F at Failure**

### **3.4 Modes of Failure**

In the current research, the failure of the control concrete is observed to be explosive, whereas by the addition of rubber the failure became more gradual and less explosive. Moreover, specimens containing SBR granules remained intact even after the failure. This could be due to the bridging of the rubber across the cracks which can decrease the crack propagation within the specimen. It is predicted that the gradual failure of the hardened concrete containing SBR granules could help with ductility and the ability to bear loads even after ultimate failure load. This property is also vital to prevent concrete shattering due to likely explosions and the safety it offers to potential victims. The statement above is supported in a study by Eldin and Senouci (10), which showed that the rubberised concrete did not show the typical brittle failure, but instead was observed to have a ductile, plastic mode of failure.

## **4. Conclusions**

This study highlights the feasibility of using SBR granules in concrete specimens. The main conclusions of this paper and the performed tests are as follows:

- The general observation indicates a lower stiffness and lower maximum load for beams incorporating SBR granules. This could be due to the weaker bond between rubber particles and cement matrix.
- The deflection of the beams did not vary much up to the proportional limit before the yield point, though, this value decreased between the yield point and the maximum load for EMC beams.
- The presence of SBR granules increased the resilience of the beams, however, the ductility factor decreased in EMC beams.
- The total area under hysteresis loops is the highest in the control concrete followed by the beam incorporating 6% (12 – 15 mm) SBR granules. Concrete beams incorporating SBR granules have a higher resilience and the area under the curve at lower amounts of load is more significant, whereas at higher loads, the areas under the curves in beams without SBR granules are higher.
- The value of frequency prior to Four-point bending test did not vary much among different beams.
- The addition of SBR granules improves the damping properties of the concrete beams.

## **5. Acknowledgement**

Support from Centre for Built Infrastructure Research (CBIR) at the University of Technology Sydney (UTS) is gratefully acknowledged. Also the authors would like to thank the technical support provided by the Faculty of Engineering and Information Technology (FEIT) and Concrete and Structures Laboratory at UTS.

## **6. References**

1. Chen, Y., Okudan, G.E. et al., "Sustainable performance criteria for construction method selection in concrete buildings", *Automation in Construction*, 2010, vol. 19, no. 2, pp 235-244.
2. Khaloo, A.R., Dehestani, et al., "Mechanical properties of concrete containing a high volume of tire-rubber particles", *Waste Management*, 2008, vol. 28, no. 12, pp 2472-2482.
3. Toutanji, H.A., "The use of rubber tire particles in concrete to replace mineral aggregates", *Cement and Concrete Composites*, 1996. 18(2): pp 135-139.
4. Son, K.S., Hajirasouliha, I. et al, "Strength and deformability of waste tyre rubber-filled reinforced concrete columns", *Construction and Building Materials*, 2011. 25(1): pp 218-226
5. Toutanji and Eldin, "The use of rubber tire particles in concrete to replace mineral aggregates", *Cement and Concrete Composites*, 1996. 18(2): pp 135-139.
6. Ilker, Bekir et al, "The properties of rubberized concretes", *Cement and Concrete Research*, 1995. 25(2): pp 304-310.
7. Yan, L., Jenkins, C.H. et al., "Polyolefin fiber-reinforced concrete composites: Part I. Damping and frequency characteristics", *Cement and Concrete Research*, 2000. 30(3): pp 391-401
8. Samali, B. 2011, "Structural Dynamics and Earthquake Engineering Lecture Notes", Sydney
9. Zheng, L., Sharon Huo, X. et al., "Experimental investigation on dynamic properties of rubberized concrete", *Construction and Building Materials*, 2008. 22(5): pp 939-947

10. Eldin, N.N. and Senouci, A.B., "Measurement and prediction of the strength of rubberized concrete", *Cement and Concrete Composites*, 1994. 16(4): pp 287-298.

# Twisted Steel Micro-Reinforcement: Proactive Micro-Composite Concrete Reinforcement

Luke Pinkerton<sup>1</sup>, Kevin Fuller<sup>2</sup>, Jeff Novak<sup>3</sup>

<sup>1</sup>Chief Technology Officer, Helix Steel

<sup>2</sup>Chief Executive, Helix Steel Australasia

<sup>3</sup>Vice President of Engineering, Helix Steel

**Abstract:** Reinforced concrete is a two-part system that at best can be described as a “macroscopic” composite made of reinforcement bar and a concrete matrix. The bar is designed to carry load only after the concrete fails – reactive reinforcement. Adding Twisted Steel Micro-Reinforcement (TSMR) at a specified dose to an ordinary concrete matrix creates a “microscopic” composite. The unique design of the TSMR allows for efficient load re-distribution prior to failure of the concrete. The result is a significant increase in the concrete’s strain capacity. TSMR provides proactive reinforcement as, unlike conventional reinforcement and other forms of reinforcement, it engages the material before it actually fails. Similar to conventional methods of reinforcement, TSMR also provides reactive reinforcement as it continues to provide stable tensile resistance after the concrete’s strain capacity is exceeded. With existing design methods, structural engineers are not able to calculate the required dosage of TSMR. The authors present a simple design method to determine the necessary TSMR dosage to resist the tensile forces in an area of concrete equal to or greater than the conventional reinforcement. The TSMR design models specifically for TSMR reinforcement have been developed and have been validated through third party testing at an IAS/NATA certified laboratory, full scale field-testing, calibration, and peer review by structural engineers in multiple countries.

**Keywords:** concrete, elastic, fibre, testing, design

## 1. Introduction

Reinforced concrete, by definition, gives the concrete its required tensile strength after the formation of a dominant crack in the concrete. While there are many interesting academic pursuits in Ultra High Performance Concrete that promise true composite behavior under high loads and deflections, the cost is prohibitive due to the quantity of fibre required and the need for expensive component materials. On the other hand, the fibre industry has promoted use of deflection controlled bending tests of deflection softening mixtures to derive tensile resistance of fibre concrete. In these tests, the machine is programmed to very carefully remove load from the specimen (so it does not fail suddenly) as deflection increases (1). Over the last several years the deflection limit at which the performance is measured using such tests has continued to increase. There are testing standards that actually compute strength based on crack widths near 20 mm, which are 50 times the code limit and twice the limit for a structure to be deemed stable for occupational health and safety (2). The industry has missed the fact that in practice a load would certainly not be so carefully applied and therefore security/safety that is being promoted with such standards is misleading. Also, there is no direct relationship between flexural strength and tensile strength once a crack has formed in the concrete and therefore several assumptions must be made to estimate the tensile strength (3). Finally, while testing has shown an alarming degree of creep in certain types of low modulus, non-metallic reinforcements, the industry has largely ignored the issue (4).

Twisted Steel Micro-Reinforcement (TSMR) offers a solution to these problems both in the product’s performance and in its design methodology. TSMR increases the flexural tensile strength of the concrete (Modulus of Rupture, MOR) and decreases the coefficient of variation of the MOR. TSMR increases the ductility of concrete in tension prior to the formation of a crack (more deflection at the point of crack). While it does exhibit strain-softening behavior at certain dosages after a crack forms, TSMR provides stable tensile resistance in the range of maximum allowable code crack widths. Its design method (Uniform Evaluation Service (UES), Evaluation Report (ER) # 279) fully recognizes its limits and gives the designer a safe, reliable, peer-reviewed design and field QA guidance. TSMR is made of high tensile, high modulus steel, which has been shown to perform well over time (5). Testing measures the real pre-crack properties (MOR, Splitting Tensile) of the TSMR concrete using methods that apply a constantly increasing load to failure just as would occur in real life (i.e. when an overloaded fork truck drives on a floor). Post crack design of TSMR is permitted when restrictions aimed at controlling maximum crack width to sizes consistent with codes are in place.

## 2. Testing and Design Approaches

### 2.1 Test Methods

Unlike traditional reinforcement, the performance characterization and design of steel fibre concrete is not uniform throughout the industry. There are many competing test standards (Table 1) and design procedures (Table 2). While direct tensile resistance is the performance measurement needed for design, most test standards involve flexural tests. Tensile resistance is derived by assuming a relationship between flexural stress (which only exists in linear elastic materials and is invalid after a crack forms) and direct tensile stress (6). A multiplier of 0.37 is typically used to relate the flexural stress in beams with large cracks (3.5 mm) to direct tensile strength (3). Beam testing is also plagued with so called “size effect,” the non-scalability of results to larger or smaller sections and/or cross correlation of crack size, fibre length and specimen size on results (7).

**Table 1. Common Test Methods.**

Test Standard	Type	Control	Measurement	Single Operator COV
ASTM C78 AS 1012.11-2000	Flexural Beam	Load	Peak only Post crack*	5.7%
ASTM C1609	Flexural Beam	Deflection	Peak Post crack	Peak: 8.2% Post: 17%
ASTM C1399	Flexural Beam	Load	Post Peak only	13%
ASTM C1550 RDP	Flexural Round Panel	Deflection	Peak Post crack	Peak 6.2% Post 10%
EFNARC	Flexural Square Panel	Deflection	Peak Post crack	Not Reported
EN 14651	Flexural Notched Beam	Crack Width	Post crack only	Not Reported
EN 12390-5	Flexural Beam	Load	Peak only Post crack*	Not Reported
RILEM TC 162-TDF	Flexural Notched Beam	Deflection	Post crack only	Not Reported
ASTM C496 EN 12390-6 AS 1012.10-2000	Splitting Tensile	Load	Peak Post crack*	5%
<b>UES EC 015</b>	<b>Direct Tension</b>	<b>Deflection</b>	<b>Peak crack Post crack</b>	<b>Peak 6.3% Post 11%</b>

### 2.2 Design Methods

While the fib Model Code 2010 (8) aims to become the general standard for fibre design in Europe, recently a new fibre design method was approved in Australia that is similar to the Model Code approach but contemplates an option to use direct tension design (9). There are still several competing design approaches and methods (Table 2). The design crack widths are different for different design methods. Some of the more robust approaches, like RILEM TC 162 TF (3), include some statistical considerations for variations in test results. UES EC 015 (10), is the only method evaluated that employs the Load and Resistance Factor Design (LRFD) method for deriving resistance factors employed by the world’s major design codes (11,12,13).

The Papworth 2002 method of design for shotcrete is the only empirical approach evaluated. It uses the relationship between energy (too large deflection) in the round or square panel testing to rock type presented in a prescriptive table instead of a physics-based tensile strength approach. This method favors fibres that behave well at large deflections in the round panel tests.

**Table 2. Fibre Design Methods.**

Design Approach	Application and Criteria	Design Assumption	Test	Test vs design Stress Model
ACI-360	Slabs only cracked stress	4 mm crack Yield Line	ASTM C1609	Linear, Re3
RILEM TC 162-TDF (3)	General, cracked stress & strain	1.5 mm 3.5 mm crack	EN 14651	Bi-Linear $f_{R,1} \times 0.45; f_{R,4} \times 0.37$
Concrete Society TR-34	Slabs only cracked stress	3.5 mm crack Yield Line	EN 14651	Bi-Linear $f_{R,4} \times 0.37$
Fib Model Code 2010 (8)	General, cracked stress	0.5 mm or 2.5 mm crack	EN 14651	Bi-Linear $f_{R,1} \times 0.45; f_{R,3} / 3$
Papworth 2002 (14)	Shotcrete Energy	Energy to 40 or 80 mm deflection	ASTM C1550, RDP	Empirical Table of Energy
DR AS 5100.5 -16 (15)	Bridges	1.5 mm crack	Direct Tension or EN 14651	Director or Bi- Linear $f_{R,4} \times 0.4 ; f_{R,2} \times 0.7$
<b>UES EC015/ ER 279 (5,10)</b>	<b>Stress &amp; Strain</b>	<b>Peak or 1 mm crack</b>	<b>EC 015</b>	<b>Not Required</b>

The properties of TSMR reinforced concrete with higher tensile strength could provide benefit to designs using provisions for elastic design (Table 3) and plain concrete design. Unlike with conventional non-linear reinforced concrete design, these approaches consider concrete tensile strength. Testing of MOR of TSMR reinforced concrete may be used along with the “deemed to comply” provisions of these codes to allow the use of the enhanced MOR.

**Table 3. Elastic Design Provisions**

Design Approach	Application and Criteria	Design Assumption	Test	Test vs design Stress Model
EN 1992	General Section 5.4	Elastic Design	EN 12390-6	Elastic
AS 3600	General Section 3.1.1.3	Elastic Design	AS 1012.11- 2000	Elastic
ACI 318	General Chapter 22	Elastic Design	ASTM C78 ASTM C496	Elastic
CSA 23.3	General Section 22.6.5	Elastic Design	ASTM C78 ASTM C496	Elastic

### 3. Twisted Steel Micro Reinforcement (TSMR)

TSMR is made from high carbon, cold-drawn, deformed steel wire complying with ASTM A 820, Type I. The steel wire has a tensile strength of 1850 MPa. TSMR comes in two sizes: TSMR 5-25 (0.5 mm x 25 mm length) and TSMR 8-50 (0.8 mm x 50 mm length). TSMR 5-25 has been proven to enhance MOR, splitting tensile and provides stable post crack performance. It has been employed successfully to replace conventional reinforcement and wire mesh for over a decade. TSMR 5-25 design and code approval is provided with an ISO Guide 65 Accredited Evaluation Report (10). TSMR 8-50 uses the same TSMR technology and advantages as 5-25, but its performance is optimized for standard post crack beam test performance (EN 14651) while still offering enhanced MOR and splitting tensile strength.

### 3.1 Functional Mechanism

Twisted Steel Micro-Reinforcement (TSMR) is produced with a unique twisted profile (Figure 1) that allows each piece to bond to the matrix over its full length. In addition, the reinforcement must untwist as it pulls out of the concrete. This makes the product significantly different from traditional steel fibres because pullout is governed by untwisting resistance rather than friction. TSMR is active in both the “Proactive Phase” (pre-crack), increasing peak tensile strength, and during the “Reactive Phase” (post-crack) providing ductility and stable tensile resistance to large crack widths.

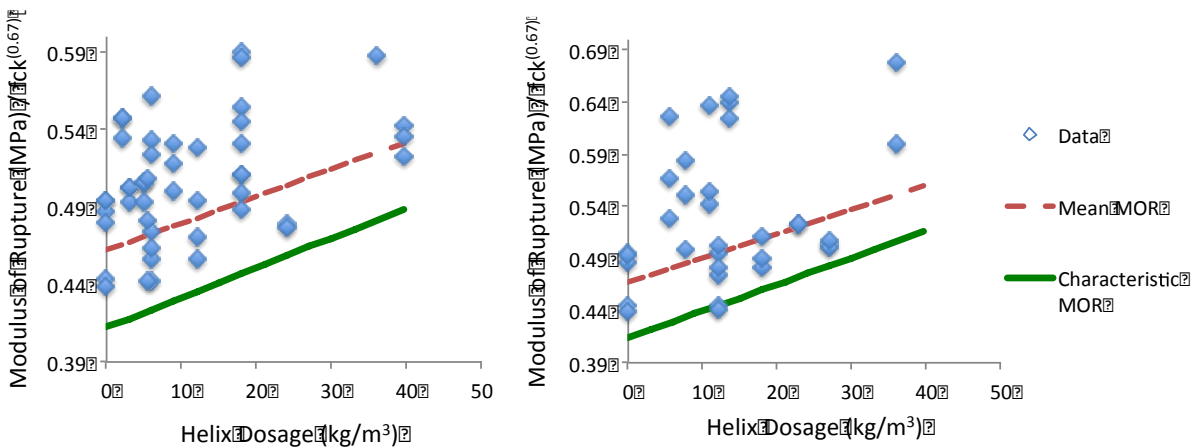


Figure 1: Twisted Steel Micro Reinforcement

## 4. TSMR Advantages

### 4.1 Flexural Tensile Strength (Modulus of Rupture)

Testing at independent laboratories has established a statically significant increase in the modulus of rupture (MOR) of concrete reinforced with TSMR. This is a unique feature of TSMR (as shown in Figure 2) as most codes and design guidance documents state that fibres do not increase the modulus of rupture (MOR) of concrete. The values are computed in accordance with RILEM TC 162 TDF Equations 5 and 6 (3). These equations take into account the mean and coefficient of variation of each of the source data sets. A mean and characteristic value is computed at each dosage tested. Linear regression is used to fit these points to establish the mean and characteristic curves.



(a) TSMR 5-25 (16)

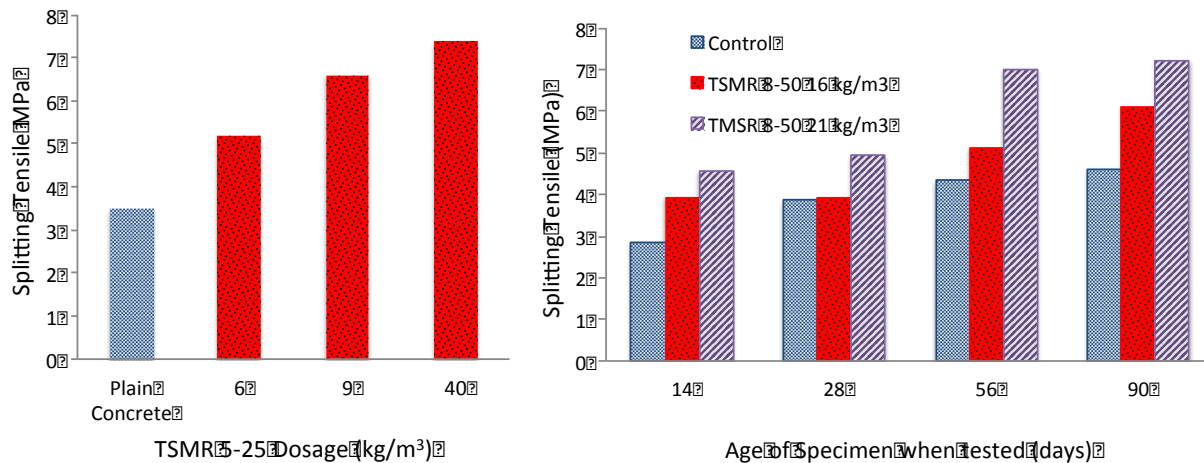
(b) TSMR 8-50 (17)

Figure 2. Flexural Tensile Strength

### 4.2 Splitting Tensile Strength

Testing at multiple independent laboratories has shown significant increase versus the control (plain concrete) in splitting tensile with TSMR reinforced concrete as the dosage increases and as the age increases. The tests show that TSMR does not suffer from the age embrittlement (shift of failure

mechanism from pullout to fibre fracture over time) that traditional steel fibres have exhibited in testing (18). Instead, the testing shows the strength of TSMR reinforced concrete increases as age increases. The increase in splitting tensile strength has particular advantages in tunnel construction where a tunnel boring machine's ram forces are high during segment installation. As a result, larger concrete segment designs may be viable with TSMR than previously thought possible.



(a) TSMR 5-25 Splitting Tensile Vs Dosage (19)

(b) TSMR 8-50 Splitting Tensile Vs Curing Time (20)

**Figure 3. Splitting Tensile Strength**

## 4.3 Modulus of Elasticity

### 4.3.1 Modulus of Elasticity of TSMR Vs Plain Concrete

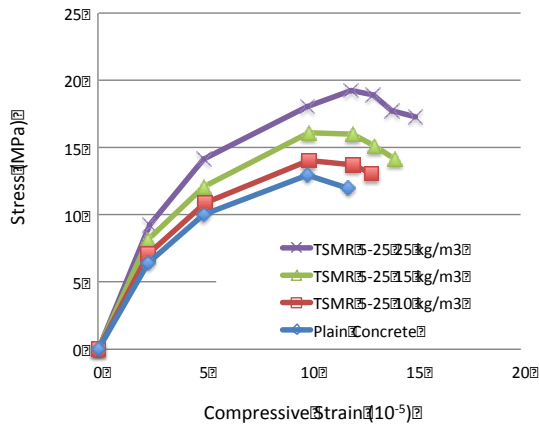
The stiffness of TSMR is equal to that of structural steel (200 GPa), 8 times stiffer than 25 MPa concrete (25 GPa) and 24 times stiffer than polymer fibres (8 GPa). Given polymer fibres have stiffness significantly less than concrete, it is physically impossible for them to carry any load until the concrete has cracked and become effectively softer than the polymer from which they are made. This helps explain why some testing and design methods that currently exist are based on large crack widths and do not conform with current concrete standards for allowable crack widths. While it is tempting to claim that a polymer fibres can provide the same structural integrity as steel, it's impossible to do so without allowing large cracks to form allowing the fibres to stretch enough to carry load (as Hooke's law requires).

### 4.3.2 Modulus of Elasticity of TSMR vs Reinforced Concrete

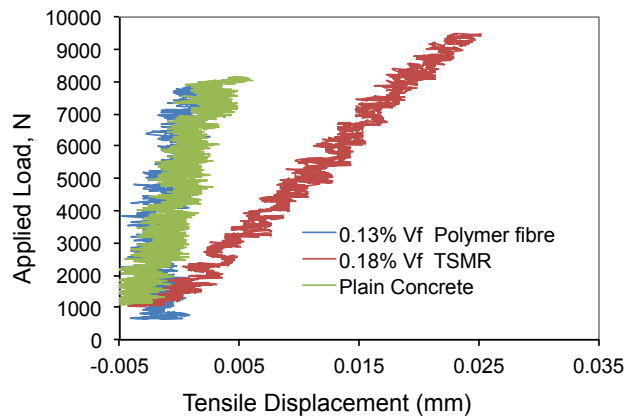
TSMR significantly increase the compressive modulus of elasticity (initial tangent modulus) of concrete. Tests have shown an increase of up to 38% (at 25kg/m<sup>3</sup> dosages). The strain at failure in compression, however, increases to 40% over the control as the dosage increases to 25 kg/m<sup>3</sup> (21). This is a clear indication of increased plasticity prior to failure and increased ductility (Figure 4a).

TSMR also increases the strain at failure in tension (Figure 4b). Testing of TSMR confirmed the increase in strain at first crack with TSMR versus the control with 99% and 98% confidence respectively. TSMR technology is the only fibre type studied – steel or polymer – that exhibits this behavior (22). The strain at which force is transferred through shear into TSMR is very low due to the efficient bond the twist provides. TSMR can carry load almost immediately after strain is applied due to the high stiffness of the material. This condition provides alternative load paths that allow micro-cracking to initiate and higher strains than plain concrete at the development of the first visible crack. While this affect can appear as an increase in deflection at peak measurement in flexural testing, this value is typically ignored in favour of looking at the residual load after the formation of a crack up to 20 mm wide, well after the concrete would have catastrophically failed.





(a) Compressive Stress Vs Strain (21)



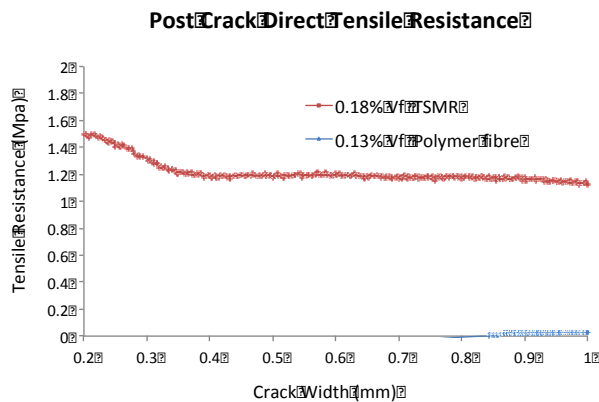
(b) Tensile Load Vs Displacement (22)

**Figure 4. Modulus of Elasticity**

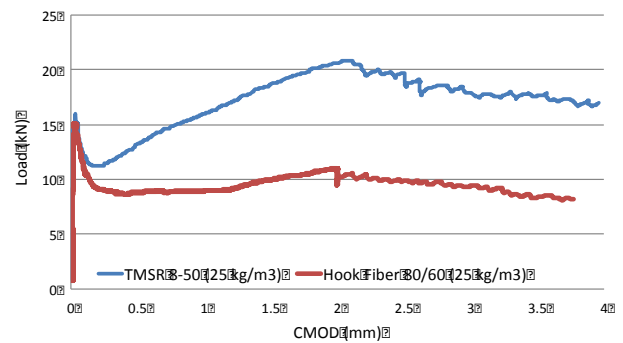
#### 4.4 Post Crack Behavior

Direct tension testing of TSMR (Figure 5a) shows stable load carrying capacity at code maximum crack widths (EN 1992 states that the maximum crack width in a low environmental exposure area is 0.4 mm).

Flexural testing of notched beams (for the EN 14651) indicates TSMR 8-50 performed 40% better than hook ended steel fibre at 3.5 mm crack width with more consistent results (Figure 5b). Post crack performance of 8-50, as measured in ASTM C1609, exceeds levels required in recent underground construction specifications at dosages lower than ever possible before with traditional steel fibres (23).



(a) TSMR 5-25 Direct Tension Vs Polymer (24)



(b) TSMR 8-50 Vs Steel Fibre EN 14651 (25)

**Figure 5. Post Crack Testing**

Round Determinate Panels (RDP) Testing of TSMR confirms the deflection at peak post-crack stability in the design crack width range exceeds hook ended steel fibres (Figure 6). TSMR holds a constant 15 kN load up to nearly 5 mm central panel deflection. While at very large cracks (40 mm central panel deflection) the product provides similar performance to hook fibres and polymer fibres, the behavior at these deflections is irrelevant due to the instability of the structure with cracks this large as determined by NIOSH, one of the worlds largest occupational health and safety organizations (2). In contrast, it should be noted that polymer fibres exhibit a sharp drop off in load carrying capacity to levels well below TSMR immediately after the crack. But, due the elasticity of the material, the polymer fibres provide a constant or increasing resistance as the crack is allowed to grow beyond the NIOSH limit of stability by the careful loading of the test machine (2).

## ASTM C1550

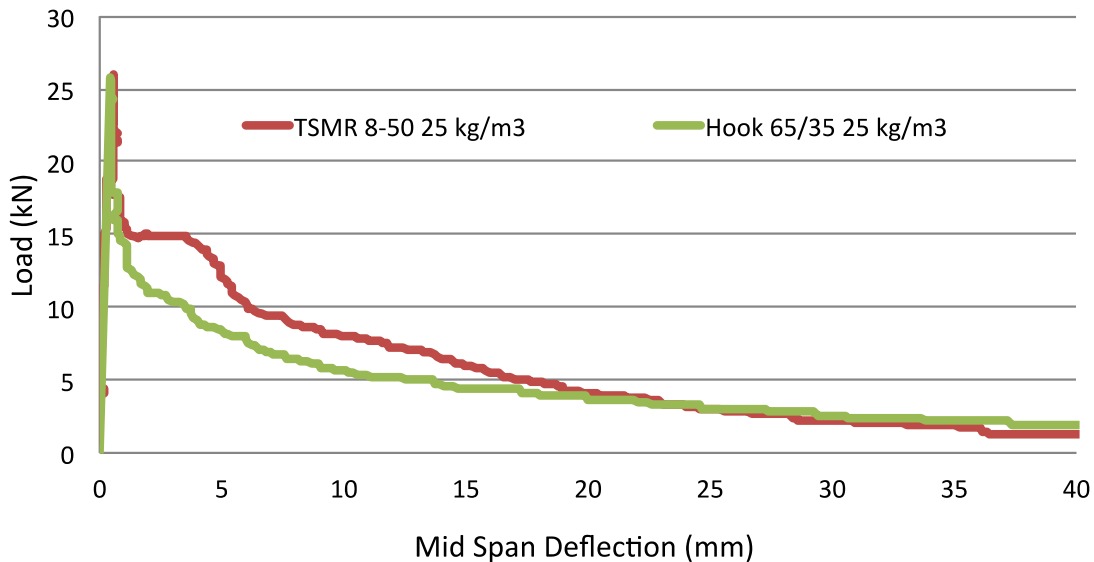


Figure 6. Post Crack Testing (26)

### 4.5 Fire and Blast Resistance

TSMR reinforcement does not adversely affect the fire resistance ratings when compared to conventionally reinforced concrete designs (5). Testing of steel fibres in general has shown enhancement of properties in precast tunnel segments (27). Blast resistance testing of TSMR shows efficacy of its use in conjunction with a reduced amount of conventional reinforcement to enhance the resistance of concrete to breach when exposed to explosives at close range, similar to a wearable improvised explosive device.

Figure 7 shows two 150 mm thick panels of equal cost after being exposed to 10 lb C4 at 380 mm standoff. Figure 7(a) is a concrete panel with two layers of 10 mm diameter bars at 100 mm spacing each way and Figure 7(b) is a concrete panel with 33% less conventional reinforcement than Panel 1 (two layers 10 mm bar at 150 mm) and 18 kg/m<sup>3</sup> TSMR.



(a) Control 2 Layers of 10 mm Bar at 100 mm

(b) TSMR 5-25 at 18 kg/m<sup>3</sup> with 10 mm Bar at 150 mm

Figure 7. TSMR Blast Testing (28)

## 5. Design of TSMR Reinforced Concrete

Extensive research and testing has been carried out to develop a suitable design methodology and provide practical and safe applications of TSMR. TSMR design methodology has been independently evaluated (ISO Guide 65 Evaluation Report 279). TSMR 5-25 reinforced concrete using this method of

design has been used successfully in Australia in hundreds of projects. Based on this approach to design, Elastic Design of TSMR 5-25 has also been used successfully in slabs-on-grade in hundreds of projects globally for 10 years. Furthermore, TSMR 8-50 provides the benefits of TSMR technology (increased MOR, Splitting Tensile, Pre-crack Ductility) along with improved post crack strengths at large crack widths. This improved large crack width performance allows TSMR 8-50 to conform to existing design methods listed in Table 2.

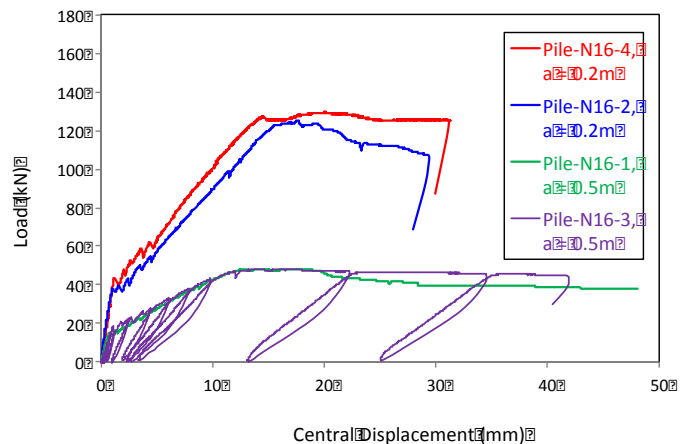
## 5.2 Evaluation Report 279 of TSMR 5-25

A unique method of design based on rigorous peer reviewed direct tension testing is available for TSMR 5-25. The ISO Guide 65 Evaluation Report (UES ER 297) described in other works (5, 10, 29), has been validated against hundreds of laboratory and field tests over a period of 10 years in nearly 30 countries. Furthermore, the ISO report is recognized in nearly 100 countries via mutual recognition treaties. The report includes a design guideline structured in a way that is familiar to engineers who are used to designing with conventional bar reinforcement. The report provides the required restrictions on its use and field QA procedures. This report is available for download at [www.iapmoes.org/Documents/ER\\_0279.pdf](http://www.iapmoes.org/Documents/ER_0279.pdf). This document provides a building official with a third party review of all the performance testing required to meet the performance based “deemed to comply” provisions in the BCA for alternative building materials.

Testing conducted at the University of New South Wales illustrates the accuracy of of ER 279 design when using a combination of TSMR and conventional reinforcement as well as the ductility TSMR provides in both static and cyclic loading. Four 200 mm diameter by 1.5 meter span circular beam with one N16 in the center and 25 kg/m<sup>3</sup> Helix were tested, three statically and one cyclically. Two different shear spans, (minimum distance between support and load point) were evaluated, 0.5 and 0.2 m). A maximum bending moment of 11.5 kN-m was computed. The tests results ranged from 12-13 kN-m (4 beams). All of them, even the specimen tested under cyclic loading, exceeded the ER 279 prediction. The beams exhibited ductility that exceeded what was expected with ordinary plain concrete producing a stable response even when 15 mm cracks were present (30). A similar test confirmed that shear was also accurately predicted by ER 279.



(a) Circular Pile Test Setup  $a = 0.5$



(b) Load - Deflection Results  $a=0.5, 0.2$

**Figure 8. UNSW TSMR Hybrid Beam Testing (30)**

## 5.2 Elastic Design

Until now, the usefulness of the elastic (plain concrete) provisions of the building codes (Table 3) was limited due to the requirement for very thick and/or high strength concrete needed to develop the same resistance of thinner reinforced concrete sections. Both TSMR 5-25 and 8-50 exhibit increased modulus of rupture with low coefficient of variation with increasing dosage as reported in section 4.1. The curves in Figure 2 may be used in place of the standard values used to compute flexural tensile strength in the code. Many codes require a resistance factor or factor of safety be applied to this value. When the dosage is low, below 15 kg/m<sup>3</sup>, the standard plain concrete resistance factor should be used. At higher

dosages, an increased resistance factor of 0.9 is recommended for both the mean and characteristic curves (16, 17) The factor is computed in accordance with the Load and Resistance Factor Design (LRFD) method assuming reliability levels ( $\beta=4$ ) appropriate for plain concrete design (31).

In the case of AS 3600 section 3.1.1.3, one would use the Characteristic MOR value in Figure 2 to compute the flexural tensile strength,  $f_{ctf}$  and use 0.9 in place of the standard value of  $\phi$  for plain concrete as stated in table 2.2.2. When designing structural concrete, the standard plain concrete resistance factor should be used when the TSMR dosage is below 15 kg/m<sup>3</sup> because testing indicated that while there is an increase in MOR, there is still high variation at low dosage (Table 4). The mean value rather than the characteristic value is allowed for slab design in many slab design approaches (ACI 360). All other restrictions of the code for structural plain concrete/elastic design or slab design must be followed when using the enhanced design with TSMR. Since this method relies on enhanced modulus of rupture versus code values, engineers need to obtain approval through the “deemed to comply” provision of the code BCA. The reference documents (16,17) provided the test data needed to satisfy these provisions.

## 6. Conclusions

After 10 years of successful implementation worldwide, the success of TSMR reinforced concrete is undeniable. This very fact, in addition to the significant increases in modulus of rupture and splitting tensile strength TSMR provides, calls into question common fibre testing and design guidelines that assume the concrete has failed prior to any contribution. A fundamental question must be addressed, is it really OK to design fibre concrete assuming large cracks have formed? And why do we give up on the concrete so easily?

- TSMR has successfully achieved what the fibre industry has been in search of for decades – a fibre reinforcement that engages the concrete before it fails, i.e. TSMR increases the modulus of rupture of concrete. This increase starts at very low dosage and increases further as dosage increases. The variability (COV) is also lower on average, than the control. All existing design procedures examined in this report completely ignore the pre-crack phase.
- The existing design procedures in table 2, examined in this report use post crack performance measurements for design, ignoring the pre-crack phase.
- Current test and design methods fail to provide adequate tools to the engineering community to design safe, reliable, structural concrete with fibres as they place too much emphasis on capacity at large crack width (after the structure would have far exceeded its ultimate limit state in real life).
- Steel and Polymer fibres are designed for optimum performance in these tests but most do not perform well until cracks larger than code limits (about 0.4 mm) have formed.
- TSMR increases splitting tensile strength of concrete. The increase becomes even larger as the concrete ages and as dosage increases. This addresses concern with age embrittlement of TSMR concrete and may allow design of larger tunnel segments than ever before possible with other fibres.
- The modulus of elasticity of TSMR is 24 times that of polymer fibres and 8 times that of plain concrete. The high modulus of elasticity, in addition to the efficient bond provided by the twist provides enhanced ductility in both tension and compression.
- Both TSMR 8-50 and 5-25 exhibit deflection softening but stable post crack behavior at typical dosages (below 30 kg/m<sup>3</sup>) beyond code allowable crack widths (0.4-1 mm) in standard beam and panel tests. TSMR 8-50 outperforms leading hook ended fibres even at large crack widths (R4 value at 3.5 mm crack width).
- The enhanced ductility of TSMR is dramatically demonstrated in blast testing where spalling was almost completely eliminated by partially substituting traditional reinforcement with TSMR.
- Design of TSMR 5-25 may be accomplished using an ISO Guide 65 Evaluation report that demonstrates compliance with the “deemed to comply” provisions of various building codes including the BCA.
- Design may alternatively be accomplished using the elastic design provisions of the code along with the enhanced MOR values provided by TSMR reinforcement at respective dosages.

## 8. References

1. Bernard, S, New Round-Panel Test Evaluates the Performance of Alternative Concrete Reinforcement Systems. ASTM Standardization News, November (2002).
2. L. Martin, B. Seymour, et al., "An analysis of flexural strength and crack width for fibre-reinforced shotcrete used in weak rock mines", The National Institute for Occupational Safety and Health (NIOSH), 2010.
3. TDF 162: Test and design methods for steel fibre reinforced concrete. Materials and Structures, RILEM, March (2004)
4. DeRiverez, Benoit – EFNARC Creep Test Procedure Description for Sprayed Concrete and Test Results with Steel and Synthetic Fibres, Ed Kusterle, W, Alpach Austria, February 2015
5. ER-279, Uniform Evaluation Service Evaluation Report #279, Uniform Evaluation Service, 5001 E. Philadelphia St. Ontario, CA 91761 – USA (2014).
6. Megson, T.H.G, "Structural and Stress Analysis. Second Edition, Elsevier Butterworth-Heinemann, Great Britain", 2005, 744 pp.
7. Wille, K., Parra-Montesinos, G.: Effect of Beam Size, Casting Method and Support Conditions on Flexural Behavior of Ultra High Performance Fibre Reinforced Concrete. ACI Materials Journal, May June (2012) 379-388.
8. CEB FIB Model Code 2010, Federation of Structural Concrete (2010).
9. Ali Amin\*, Stephen J. Foster\*, et al. "Evaluation Of The Tensile Strength Of SFRC As Derived From Inverse Analysis Of Notched Bending Tests", VIII International Conference on Fracture Mechanics of Concrete and Concrete Structures, 2013
10. EC-015, Uniform Evaluation Service Evaluation Criteria #015, Uniform Evaluation Service, 5001 E. Philadelphia St. Ontario, CA 91761 – USA (2014).
11. ACI 318-11: Building Code Requirements for Structural Concrete. American Concrete Institute, (2011).
12. EN 1992-2004, Eurocode 2, Design of Concrete Structures. European Committee for Standardization, (2004).
13. AS 3600, Australian Standard Concrete Structures, Standards Australia, 2009
14. Papworth, F.: Design guidelines for the use of fibre reinforced shotcrete in ground support. 27th Conference on OUR WORLD IN CONCRETE & STRUCTURES, (2002), 29-30.
15. DR AS 5100.5 -16, Section 16 Steel Fibre Reinforced Concrete
16. Helix 5-25 Elastic Design Coefficients and Data, Helix Steel, 2015, [www.helixsteel.com/elastic-design](http://www.helixsteel.com/elastic-design)
17. Helix 8-50 Elastic Design Coefficients and Data, Helix Steel, 2015, [www.helixsteel.com/elastic-design](http://www.helixsteel.com/elastic-design)
18. Bernard, "Embrittlement of FRS". Shotcrete, (2008)
19. A.S. El-Dieb, Mechanical, durability and microstructural characteristics of ultra-high-strength self-compacting concrete incorporating steel fibres, Materials and Design, 30 (2009) 4286–4292.
20. Report ESP016891P, Element Labs St Paul, MN USA (November 17, 2014)
21. Prashanth M.H., Indrani Gogoi, et al., Experimental Studies On Use Of Helix Fibres In Concrete, NITK Research Bulletin, Vol 21 No 2 Dec 2012.
22. Pinkerton, L, Hausfeld, H, et al., 2015 Twisted Steel Micro Reinforcement (TSMR) For Shotcrete, Ed Kusterle, W, Alpach Austria, February 2015
23. Euclid Creek OH, USA, Blue Plains MD, USA, Bay Tunnel, Central Subway, NY, USA, Construction Specifications for Fibre Concrete in Precast Tunnel Segments.
24. Report ESP017071P Direct Tension Testing of TSMR 5-25: Element St Paul (2014), Report ESP017071P, Direct Tension Testing of Polypropylene / Polyethylene Fibre), Element St Paul (2014)
25. Report SER-2013-0268L F1404-05A(18-19), SIKA Services AG (2014) 18 beam 2 and 19 beam 2.
26. Report SER-2013-0268M SIKA Services AG (2014), panel 3 (TSMR) and panel 1 (Hook)
27. Benoit de Rivaz, "Steel Fibre Reinforced Concrete (SFRC): The use of SFRC in Precast Segments for Tunnel Lining." World Tunnel Congress 2008 – Underground Facilities for Better Environment and Safety – India.
28. Walker, Martin, "Blast Testing of Helix Fibre Reinforced Concrete", Explora Foundation, UK (2013)
29. Pinkerton, L., Stecher, J., et al., Twisted Steel Micro Reinforcement. Concrete International, Vol 35, No. 10 (2013).
30. Chang, Zhen-Tia, "Report On Investigation Of Bending And Shear Behaviors Of Helix Circular Piles", University of New South Wales, 2014, [www.helixsteel.com/press](http://www.helixsteel.com/press)
31. MacGregor, J.: Safety and Limit States Design for Reinforced Concrete. Canadian Journal of Civil Engineering, V. 3, No. 4, Dec. (1976), pp. 484-513.

# Design of UHPFRC Mixtures to be used in Structures Subjected to Impact Loads

Michael F. Petrou<sup>1</sup>, Konstantinos G. Trezos<sup>2</sup> and Anna L. Mina<sup>3</sup>

<sup>1</sup>Professor of Civil and Environmental Engineering, University of Cyprus

<sup>2</sup>Associate Professor of Civil engineering, National Technical University of Athens

<sup>3</sup>Phd Candidate of Civil Engineering, National Technical University of Athens/ University of Cyprus

**Abstract:** This research presents the findings of an experimental study aiming to determine the mechanical properties of Ultra High Performance Fibre Reinforced Concrete (UHPFRC) specifically designed for sustaining impact loads. UHPFRC is a cement – based material that is composed of portland cement produced in Cyprus, sand from a local quarry grading 125 – 250micron and 250 – 500micron, microsilica, super plasticizer and a combination of steel fibers. The combination of steel fibers comprises of two different kinds of fibers: 6mm long with 0.16mm diameter and 13mm long with 0.16mm diameter. Three different mixtures were tested, each containing a different percentage by volume of steel fibers 6%, 2% and 0%. The specimens were submitted to hot curing at 90°C for 11 days. The effect of the steel fibers' volume on the compressive strength, direct tensile strength, the modulus of elasticity and the Poisson's ratio were measured at different ages. Finally, a complete stress – strain curve in compression was obtained for all UHPFRC mixtures. The mechanical properties were utilized in order to select the best UHPFRC design for concrete structures subjected to impact loading conditions.

**Keywords:** UHPFRC, Stress – Strain Curve in Compression, Modulus of Elasticity, Poisson Ratio, Impact Loads.

## 1. Introduction

During the last few decades, concrete industry was forced to develop and enhance concrete compositions following higher standards due to societies' higher demands (1). Thereby, today we are able to speak about Ultra High Performance Fibre Reinforced Concrete (UHPFRC) with great confidence. UHPFRC is a special type of concrete with advanced mechanical properties while many of its advantages result from the presence of steel fibres, silica fume, water reducing agent and lack of coarse aggregates. Much experimentation has been conducted on UHPFRC in order to improve its composition and utmost efficacy (2, 3, 4 and 5). In Cyprus, a series of experiments, recently completed, ended up into a mix design of an UHPFRC with the use of materials available in Cyprus (2). This design has been also tested for impact loads with very satisfying results (6 and 7). This mix design opened the field for further investigation regarding the full stress strain curve in compression, modulus of elasticity, Poisson ratio, and tensile strength. Thereby, the aim of this experimental study is to further investigate the original mix design and to measure the above mechanical properties for different mixtures. Three different mixtures were tested at the following steel fibers volumes, UHPFRC - 6%, UHPFRC - 2% and UHPC - 0% with the objective to show the effect of steel fibres on their mechanical properties and toughness which are equally important for reinforced concrete structures subjected to impact loadings.

## 2. Experimental Procedure

### 2.1. Mix Design – specimens

The details of the mix proportions used in the present study are illustrated in Table 1. This mix design was the first UHPFRC mixture in Cyprus and it was developed after an extensive experimental investigation by Nicolaidis et al. (2) based on a previous study by Benson and Karihaloo (2 and 3). Specifically, Nicolaidis et al. experimented with the different potential variations of the design composition in order to enhance its workability and mechanical properties. The variables considered were: water/cement ratio, the time of curing under different temperatures, the optimum percentage of silica fume, and the volume of steel fibres. In this study we used two types of steel fibres, one 6mm long with a diameter of 0.16mm and another one, 13mm long with a diameter of 0.16mm. In every mixture the quantity of the 6mm long fibres was five times the quantity of the 13mm long fibres.

**Table 1: Mix design (w/b=0.16)**

Constituents (Kg/m <sup>3</sup> )	UHPC - 0%	UHPFRC - 2%	UHPFRC - 6%
Cement	880	880	880
Microsilica (20%)	220	220	220
Silica sand 125-250µm	475	475	475
Silica sand 250-500µm	358	358	358
Water	176	176	176
Superplasticizer	67	67	67
Fibres 6mm	0	134	401
Fibres 13mm	0	27	80
Water / cement	0.20	0.20	0.20
Water / binder	0.16	0.16	0.16

We implemented the following mixing procedure, based on the studies by Benson and Karihaloo (3). First, the silica sand, the silica fume and the cement were mixed together for 6 minutes. Afterwards, steel fibres were added, while passing through a vibrating sieve, in 3 different dosages with 2 minutes of mixing in each one. Then, two – thirds of the superplasticizer were added in the water. The created liquid mixture was divided in three parts of one half, one quarter and one quarter. These proportions were continuously added in the dry mixture with 2 minutes stirring for each dosage. Finally, the remaining one – third of the superplasticizer was added in the mixture until the mix reached its required workability. All the specimens were cast into moulds and they were compacted on a vibrating table. All the specimens were created based on the CYS EN 12390 – 1:2009 standard (8). Specimens were composed of cubes 100x100x100mm, cylinders with a 100mm diameter and 200mm height and beams of 100mm height, 50mm width and 500mm length. The specimens were left for 24 hours in the moulds, covered with damp hessian sheets. Afterwards, they were removed from the moulds and placed in a hot curing tank of 90°C, where they remained for eleven days. Specimens from the three mixtures were tested as follows:

- Cubes at 14, 28, 56 days underwent uniaxial compression test in order to measure their ultimate compressive strength.
- Cylinders were evaluated at 14 and 28 days in order to determine their behavior in compression and capture the full stress – strain curve.
- Beams were tested under direct uniaxial tension in order to get the maximum tensile strength.
- Modulus of elasticity and Poisson ratio were measured in both compression and tension.

It is necessary to mention that all specimens for each mix design were cast from the same batch and the three different mixtures were made using the same equipment in order to eliminate any deviations in the results.

## **2.2. Tension Test**

Our aim was to use a technique for measuring the direct uniaxial tension strength without using dog – bone specimens which require preclusive moulds with casting difficulties. Subsequently, we followed a technique based on Stelios Koliass and R. I. T. Williams prototype (9). The technique – composed of a double scissor



friction grid system and plain geometrical specimens like beams – had the same efficacy as the dog – bone procedure. Since the distribution of the fibers depends on the shape and size of the specimens (10), the width of the beams for tensile tests was more than two times the length of the longer fiber. One longitudinal and one transverse strain gauge were placed on the beam’s surface to measure the modulus of elasticity and the Poisson ratio. Additionally, three linear variable displacement transducers (LVDTs) were placed on the specimen, at three different locations.

### 2.3. Compression Test

Cylinders were capped according to the ASTM C 617-98 (2003) standard (11). Loading was applied under displacement control for the compression tests. Two circular rings were mounted around the cylindrical specimen and were tightly fastened with four screws at 90° in order to maintain the rings’ stability. The rings should be horizontal with 70cm space between them symmetrically to the specimen’s center. On the top of the rings, three LVDTs were placed at 120° angle between them, in order to measure the occurring displacements. Two more LVDTs were placed on the machine’s plates in order to measure the plate’s displacement. This experimental setup was adopted from Hassan et al. study as a backup system (12). Additionally, for the investigation of the Poisson ratio and the modulus of elasticity one longitudinal and one transverse strain gauge were placed close to each other. The longitudinal strain gauge was placed at the mid-height of the specimen. The rate for the compression tests of the cylinders was 0.015mm/min. The cubes performance under compression was evaluated at a rate of 0.5MPa/s according to CYS EN 12390 – 3:2009 (13).

## 3. Results

### 3.1. Discussion

The results in Table 2 clearly show that the modulus of elasticity between the UHPC – 0% and UHPFRC – 2% remained constant while for UHPFRC – 6% was significantly increased. We also observe that Poisson ratio was slightly fluctuated. The above findings, however, need further investigation due to the fact that UHPFRC – 2% specimens provided slightly lower values for the tension tests than the rest of the specimens.

**Tables 2. Modulus of elasticity and Poisson ratio for three mixtures.**

		<b>UHPC - 0%</b>	<b>UHPFRC - 2%</b>	<b>UHPFRC - 6%</b>
<b>tension test</b>	<b>E (GPa)</b>	34,40	38,28	49,88
	<b>v</b>	0,25	0,17	0,24
<b>compression test</b>	<b>E (GPa)</b>	34,31	34,22	42,48
	<b>v</b>	0,22	0,24	0,20

Figures 1, 2 and 3 show the cubes’ compressive strength at three different ages, 14, 28, 56 days. It seems that after hot curing, and the passing of 14 days, compressive strength remains almost constant. The only mixture which presents a minor decrease with age is UHPC but this difference is due to fact that one of the tested cubes exhibited very low compressive strength. Additionally, these figures show that the compressive strength had an increase due to the increase of the fibers which is disproportionally less than the increase of the fibres. Subsequently, the UHPFRC – 6% is not recommended for cases requiring high compressive strength, due to its higher cost and low workability. The higher cost is due, not only to the increase in steel fibers, but also to the lower workability which necessitates extra amount of superplasticizer.



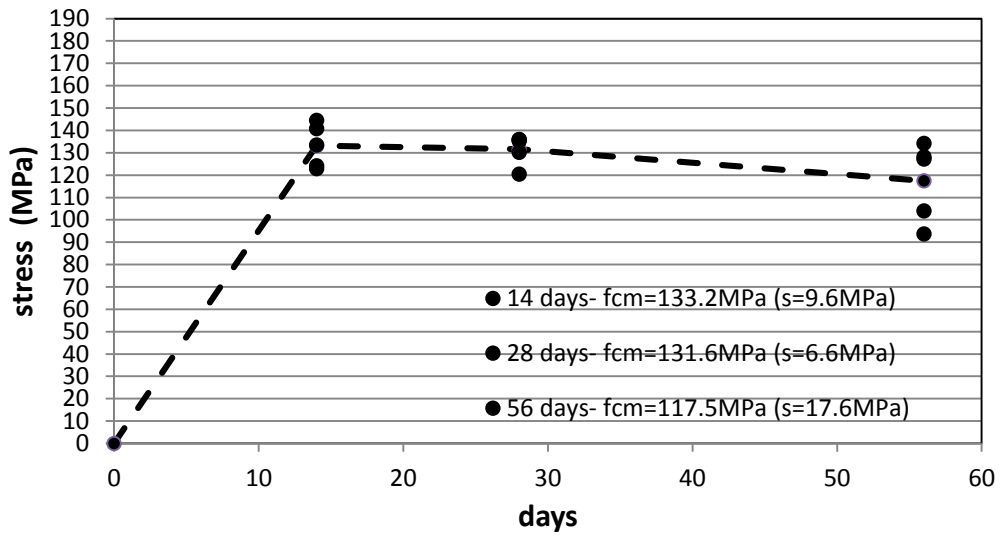


Figure 1. Compressive strength for UHPC – 0%.

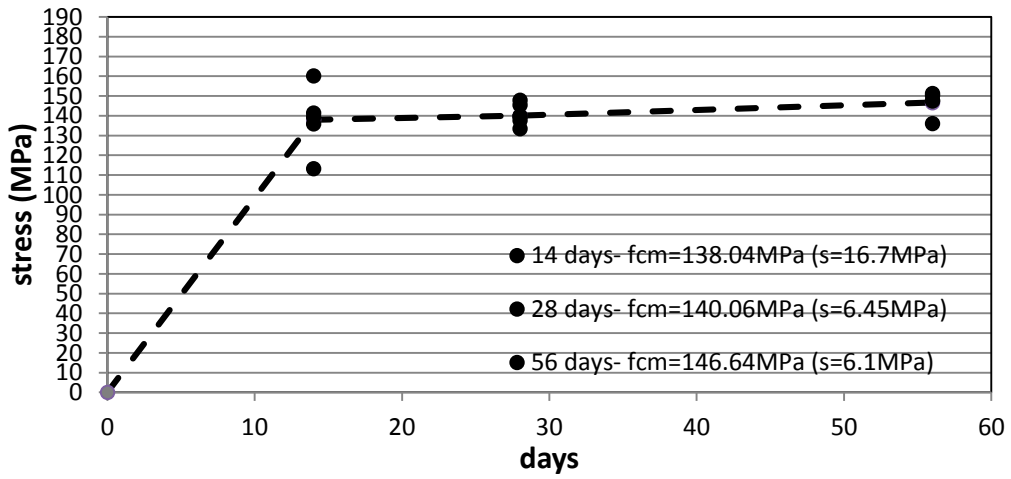


Figure 2. Compressive strength for UHPFRC – 2%.

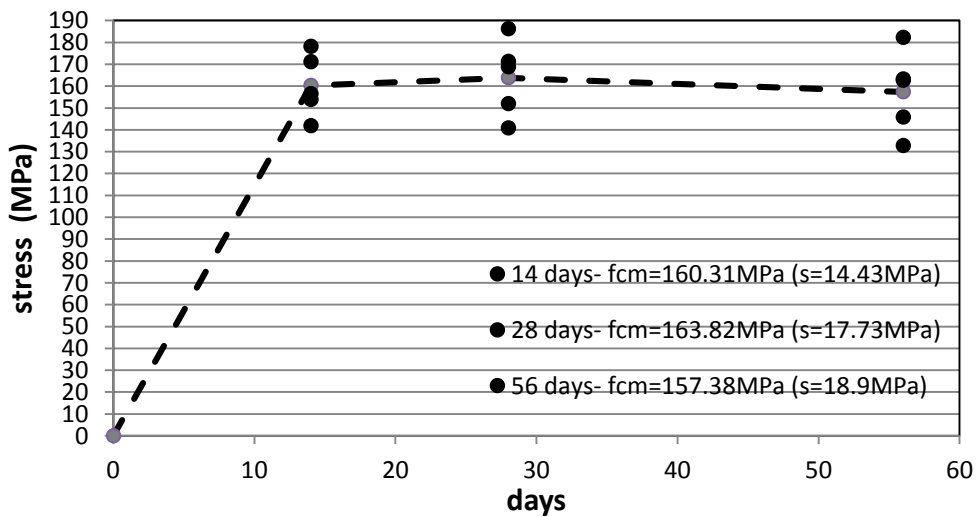
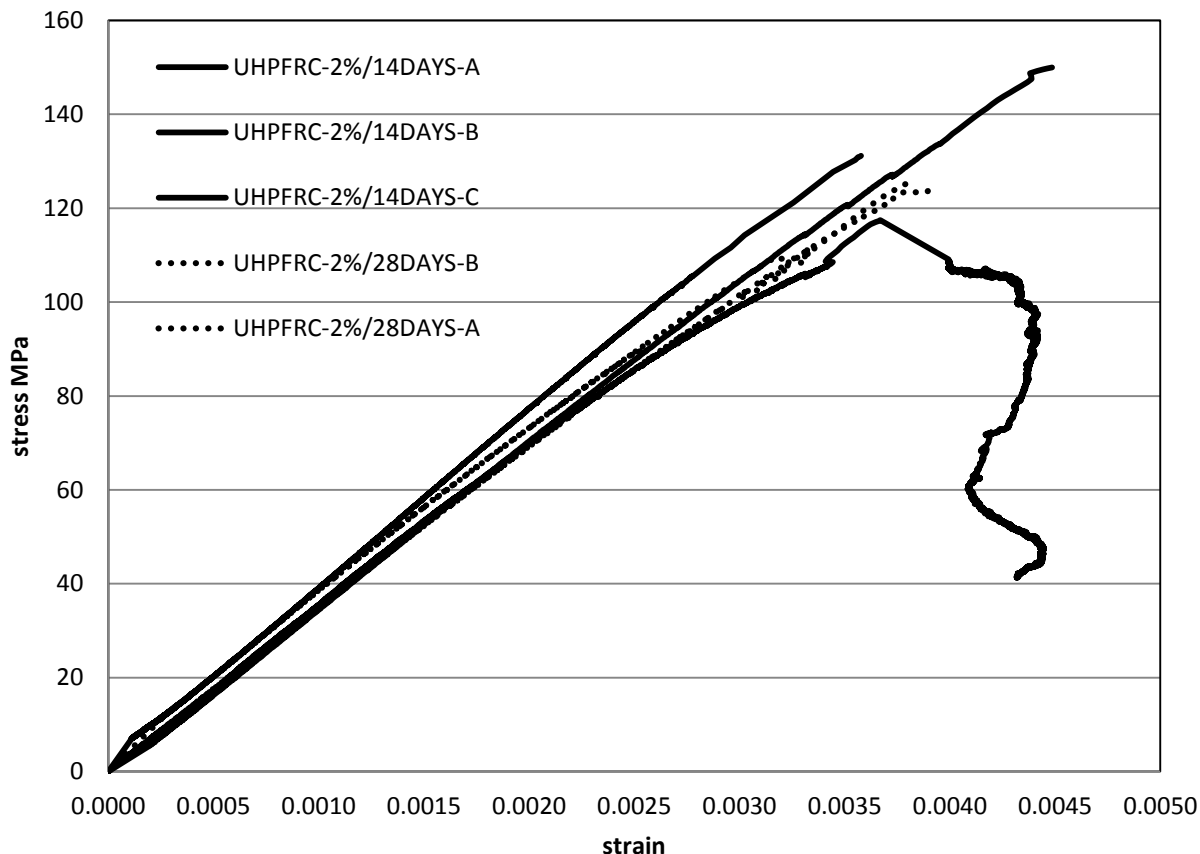


Figure 3. Compressive strength for UHPFRC – 6%.

UHPFRC – 2% during the compression test under maximum stresses was unable to sustain the imposed load and failed in a brittle way. This is confirmed by the results presented in Figure 4, where it is illustrated that out of the five cylinder specimens of UHPFRC – 2% that were examined under compression, only one was able to enter the strain softening phase.



**Figure 4. Full stress strain curve for UHPFRC – 2% cylinders.**

In comparison to the UHPFRC – 2% (Figure 4), all four cylinder specimens of UHPFRC – 6% exhibited strain softening behavior as shown in Figure 5. It is interesting to note that, Hassan et al. achieved strain softening behavior with UHPFC 2% steel fibres. Such a behavior may be observed depending on the properties of the fibers (length and diameter) and the mix design. The above findings, however, need further investigation.

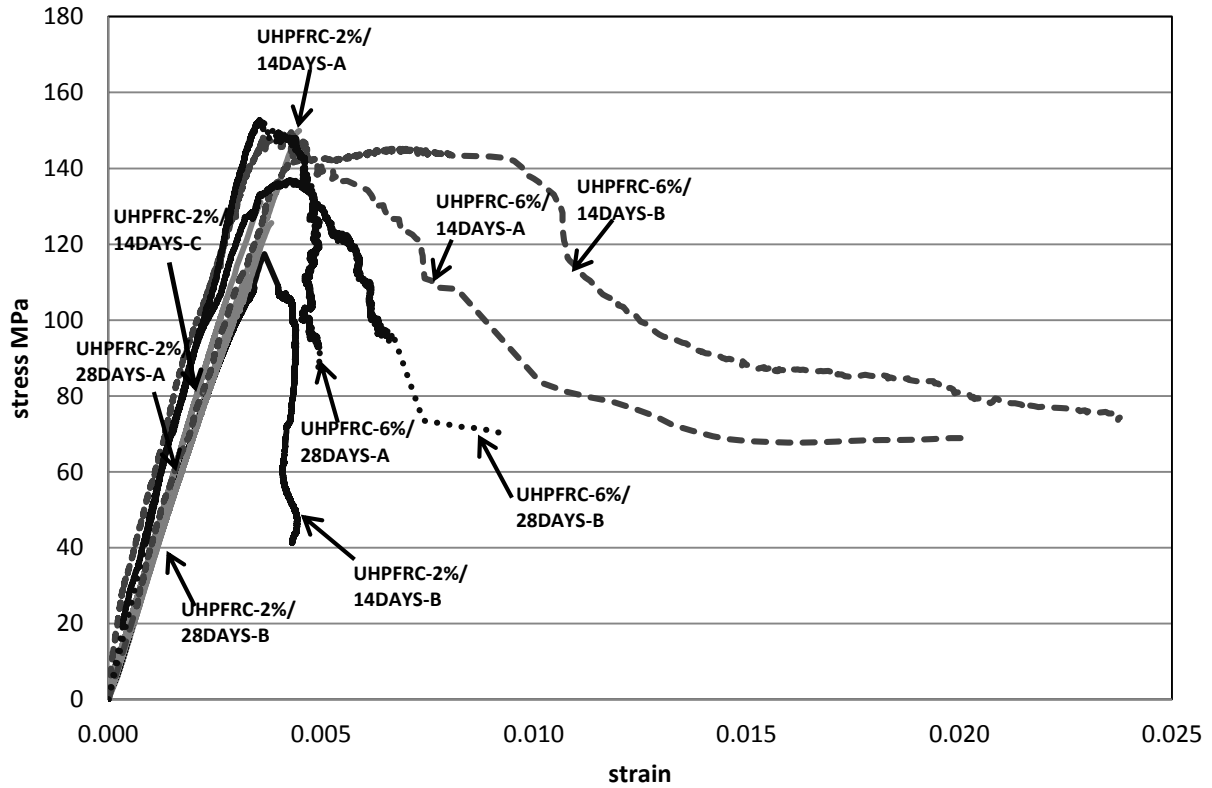


Figure 5. Full stress strain curve for UHPFRC – 6%.

What has been proven from the above stress strain curves is also confirmed by observation of the materials photos after failure. Figure 6 shows the specimen's typical failure of UHPFRC – 6% and UHPFRC – 2% respectively.

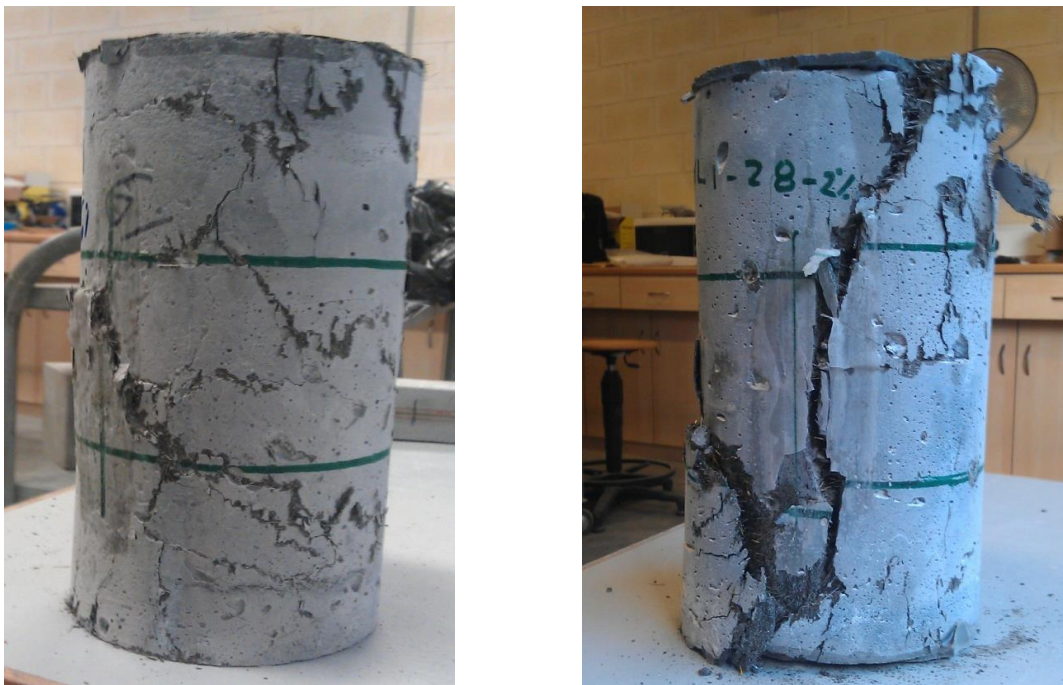


Figure 6. Typical failure of UHPFRC – 6% (left) and UHPFRC – 2% (right).

On the other hand, during the tension tests in all the three mixtures, beam specimens behaved elastically until peak strength was reached and then a sharp fall was observed. This proves that after, the first cracking, the resistance of the fibres in pull out is lower than the imposed load. The tensile strength of the three mixtures increases as the percent of the fibers increases (Table 3). Alike with the compression test results, Hassan et al. had also managed to obtain a full stress strain curve in tension with a softening phase. That could similarly be associated with the geometrical characteristics of steel fibres and the mix design.

**Table 3. Tensile strength for three mixtures**

UHPC - 0%		UHPFRC - 2%		UHPFRC - 6%	
beams specimens	tensile strength (MPa)	beams specimens	tensile strength (MPa)	beams specimens	tensile strength (MPa)
1	4,97	1	3,97	1	6,39
2	5,15	2	4,75	2	1,98
3	3,50	3	4,13	3	6,41
4	3,29	4	5,02	4	5,61
average	4,23	average	4,47	average	5,10

The illustrations below show cubes and beams of the UHPC – 0% taken after failure and reveal visible zones of matrix that are unhydrated. Those weak zones of the matrix and fibre distribution are probably the reasons for the high deviations of tensile strength observed among the specimens in Table 3.



**Figure 7. Weak Zones of Unhydrated Matrix**

For the impact resistance of structures, the concrete needs to have high compressive strength so that penetration is avoided. According to Zhang M. H. et al., a compressive strength beyond 150MPa does not affect significantly the penetration resistance on the concrete targets (14). Adequate compressive strength was achieved with both UHPFRC – 2% and UHPFRC – 6% mixes. The second substantial factor that has also been taken into consideration was to ensure the materials toughness against spalling. From the UHPFRC – 6% full stress strain curve it emerged that such a design is best suitable to achieve high levels of spalling resistance. As far as the UHPFRC – 2% is concerned further investigation is needed in order to increase its toughness by utilizing longer fibers and improving fiber distribution and hydration of the matrix.

### 3.2. Conclusions

The following conclusions can be drawn based on the results and the discussion presented above:

- The maximum compressive strength remains almost constant after 14 days of hot curing and exhibited a small increase with the addition of steel fibres.
- The modulus of elasticity improved by increasing the percentage of steel fibres and the Poisson ratio remained constant.
- Strain softening behavior – toughness of the UHPFRC in tension and compression, does not depend only on the percentage of steel fibres, but also on the geometrical characteristics of steel fibres and on the mix design. Further investigation is needed, in order to determine the parameters that control the toughness of these materials.
- For the impact resistance more suitable seems to be UHPFRC with high percentage of steel fibres because it achieved high compressive and tensile strength which are expected to increase its resistance to penetration. Furthermore, it has sufficient toughness to resist spalling.

### 4. References:

1. Pierre, R., Cheyrezy, M., "Composition of reactive powder concretes", *Cement and Concrete Research*, Vol. 25, No 7, pp. 1501-1511, 1995.
2. Nicolaidis, D., Kanellopoulos, A., Savva, P., Mina A., Petrou, M. F., "Mix Design and Mechanical Properties of Ultra High Performance Fibre Reinforced Cementitious Composites (UHPFRCCs)", *Proceedings of the 1<sup>st</sup> International RILEM Conference on Rheology and Processing of Construction Materials, Paris, 2013*.
3. Benson, B. S. D. P., Karihaloo, L., "CARDIFRC – Development and mechanical properties. Part I: Development and workability", *Magazine of Concrete Research*, 2005, 57, No. 6, August, 347–352.
4. Yang, S. L., Millard, S. G., Soutsos, M. N., Barnett, S. J., Le, T. T., "Influence of aggregate and curing regime on the mechanical properties of ultra-high performance fibre reinforced concrete (UHPFRC)", *Construction and Building Materials* 23 (2009) 2291–2298.
5. Song, P. S., Hwang, S., "Mechanical properties of high-strength steel fiber-reinforced concrete", *Construction and Building Materials* 18 (2004) 669–673.
6. Nicolaidis, D., Lampropoulos, A., Kanellopoulos, A., Savva, P., Mina, A., Petrou, M. F., "Static response and modeling of impact resistance of UHPFRCC slab specimens", *Fib Symposium 2013 Engineering a Concrete Future: Technology, Modelling and Construction, Tel Aviv, Israel, 22-24 April, 2013*.
7. Nicolaidis, D., Kanellopoulos, A., Petrou, M. F., Soutsos, M., "Mix design, Mechanical properties and impact resistance of UHPFRCCs", *Proceedings of the 3<sup>rd</sup> International Conference on Concrete Repair, Rehabilitation and Retrofitting, ICCRRR-3, Alexander, M.G.; Beushausen, H.D.; Dehn, F.; Moyo, P. (Eds.), Cape Town, South Africa, 2012, pp. 181-186*.
8. CY EN 12390-1. Testing hardened concrete – Part 1. Shape, dimensions and other requirements for specimens and moulds. Cyprus Standards.
9. S.Kolias., R.IT. Williams., "Uniaxial Tension Tests on Cement-Stabilized Granular Materials", *Geotechnical Testing Journal*, GTJODJ, Vol.1, No.4, Dec.1978, pp.190-198.
10. Benson, S. D. P., Nicolaidis, D., Karihaloo, L., "CARDIFRC – Development and mechanical properties. Part II: Fibre distribution", *Magazine of Concrete Research*, 2005, 57, No. 7, September, 421–432.
11. ASTM C617-98 (2003). Standard practice for capping cylindrical concrete specimens.

12. A.M.T. Hassan., S.W. Jones., G.H. Mahmud., “ Experimental test methods to determine the uniaxial tensile and compressive behaviour of ultra high performance fibre reinforced concrete (UHPRC) ”, *Construction and Building Materials* 37 (2012) 874–882.
13. CY EN 12390-3:2009. Testing hardened concrete – Part 3: Compressive strength of test specimens. Cyprus Standards.
14. Zhang, M. H., Shim, V. P. W., Lu, G., Chew, C. W., “Resistance of high-strength concrete to projectile impact ”, *International Journal of Impact Engineering* 31 (2005) 825–841.

# Effect rubberised aggregates from tyres on the engineering performance of concrete

M. Sonebi<sup>1</sup>, R. Summerville<sup>2</sup>, S. Taylor

<sup>1</sup>Senior Lecturer of Civil Engineering, School of Planning, Architecture and Civil Engineering, Queen's University Belfast, UK

<sup>2</sup>MSc Student, School of Planning, Architecture and Civil Engineering, Queen's University Belfast, UK

<sup>1</sup>Professor of Civil Engineering, School of Planning, Architecture and Civil Engineering, Queen's University Belfast, UK

**Abstract:** The disposal of waste tyres is becoming a major waste management problem in the UK. It is estimate that more than 40 million car and truck tyres are being discarded annually. Landfill has been one the most convenient ways of disposing of waste tyres. However, landfill is no longer a viable option and solution due to the implementation of European Union Legislation, which currently bans the disposal of whole tyres and shredded tyres in landfill sites. Therefore, there is an urgent need to identify alternative solutions in line with the UK Government's waste management hierarchy. One of the potential recycling routes is in construction, but currently only about 5% of tyres are recycled in civil engineering applications. The aim of this paper is to investigate the effect that replacing the virgin aggregate with recycled rubber tyre aggregates has on the mechanical properties of the concrete. The increase of the % of rubberized aggregate as replacement of virgin aggregates led to a reduction of density, compressive strength, modulus of elasticity, flexural strength, splitting tensile strength and improved impact resistance and energy absorption.

**Keywords:** Performance, impact resistance, splitting tensile, tyres, tensile strength, Young's Modulus, waste.

## 1. Introduction

In the past number of years, environmental issues have come into focus within the construction industry. These issues regard the materials currently used by the construction industry, many of which are a finite resource, with recycling of construction wastes becoming a major topic of concern. For example consider virgin aggregate, which makes up approximately 50% of construction material in the United Kingdom by weight. To encourage the recycling and the use of recycled aggregates, an aggregate levy of £1.60 per tonne on virgin aggregates was introduced in 2002. The introduction of this levy and similar environmental levies and taxes worldwide has shifted the focus on the use of recycled aggregates and other substitutes for virgin aggregates in the concrete mix. Some of these substitutes consist of glass, demolition concrete, recycled asphalt pavements and recycled tyres.

To coincide with the building boom experienced in the western world, is the growth in the automobile industry. This growth has prompted the significantly increased use of automobile tyres. In the UK alone, 450,000 tonnes of used tyres are discarded annually, with an estimated 100,000 tyres being removed from vehicles in the UK daily. The numbers of used tyres discarded in the US has reached 290 million, according to statistics from the Rubber Manufacturers Association (RMA). This large number of worn tyres has lead to accruals of large number of tyres in illegal and unsafe stockpiles throughout the country, with RMA suggesting that stockpiles around the country storing as many as 190 million tyres (1).

The disposal of these used tyres is a major environmental problem. It was generally believed that the easiest and cheapest method of disposal was to burn the tyres. This practise is prohibited by law in many countries due to the significant amount of harmful chemicals and gases emitted by this method of disposal, along with the chemicals being released from the melting tyres contaminating the soil and subsequently the groundwater below (2). In Europe, landfill disposal was the most widely used form of discarding worn tyres. However, as of July 2006, the introduction of the EU Landfill Directive meant that the disposal of whole or shredded scrap tyres to landfill was prohibited throughout Europe. In order to dispose of these used tyres in a safe and environmentally friendly manner, innovative techniques will have to be adopted. Several uses for waste rubber have been identified, such as being used as a fuel for power stations and cement kilns, as feedstock for the production of carbon black, and as artificial coral reefs in marine environments (3). Other options include the incineration of tyres for the production of steam and the reuse of ground tyre rubber in a number of plastic and rubber products, but, due to the high

capital investment involved, using tyres as fuel is technically feasible but economically not very attractive (4).

It is however, the use of recycled automobile tyre rubber as partial replacement for the virgin mineral aggregate in the concrete mix, which will be discussed in this dissertation. It is hoped that the use of rubber aggregate in concrete will offer a possibility to reduce the use of virgin aggregate resources, while disposing of used automobile tyre rubber in an environmentally friendly manner.

Although the use of rubber in concrete has notable positive environmental effects, along with positive effects on some characteristics of the resulting concrete, it must be realised that rubbers inclusion in the concrete mix does have drawbacks in that compressive, tensile and flexural strengths and stiffness of the concrete are reduced (1, 5; 6). In the early stages of investigations into the suitability of scrap rubber as a replacement for the virgin aggregates in concrete, many researchers were deterred by the resulting concretes reduction in compressive and tensile strengths (7). Due to this perceived flaw, many researchers' attention switched to the use of crumbed rubber in asphalt highways and extensive studies were carried out (8). In 1995, 5% of federally funded highway construction projects were required to use recycled rubber tyres in asphalt, this was increased in 1998 to 20%. However, due to the high cost of producing crumbed rubbers and the time consuming and expensive process of producing the modified asphalt using the "wet process", whereby the rubber is blended with asphalt cement before the binder is added to the aggregate (9), use of rubber in this manner was halted in the USA. Therefore, due to the problems associated with the production of modified asphalt and the greater understanding and appreciation of rubberised concretes positive properties, more attention was paid to its use. Unlike rubber modified asphalt, rubberised concrete utilizes the low cost "dry process", with a portion of the mineral aggregates replaced with recycled rubber tyre chips (9).

The objective of this paper is to investigate the effect of replacement of virgin aggregates by rubberised aggregates on fresh properties, density, mechanical performance and the impact resistance. The percentages of replacements of aggregates by rubberised tyres were 10, 15, 20, 30, and 40%.

## **2. Materials, test methods and mix proportions**

### **2.1 Materials**

The concrete mixes investigated in this study were prepared with Portland cement CEM 42.5 which conformed to Standard BS EN 197-1 CEM1. Continuously graded crushed gravel aggregate with a nominal particle size of 20 mm and 10 mm were used and well-graded quartzite sand with a fineness modulus of 2.60 was employed. The relative density values of the coarse aggregate and sand were 2.63, 2.63 and 2.65, and their water absorption rates were 1.2%, 1.2% and 1.6% respectively. 20-mm rubberised aggregates and having water absorption value obtained of 5.6% and density of 1.16 were used. SP based on chains of modified polycarboxylic ether was used and had 40% solid content and specific gravity of 1.08.

### **2.2 Test methods**

After measuring the slump and the fresh density, 15 cubes 100 mm, 2 prisms 100 x 400 mm, and 2 cylinders 100 x 200 were taken in order to determine the mechanical performance. The compressive strength test was performed at 3, 7 and 28 days. Tensile Splitting Strength test was carried out in accordance with BS EN 12390-6: 2009 at 28 days. The flexural strength of the beam is determined at 28 days by using the four-point test was conducted according to BS EN 12390-5: 2009. The static modulus was carried on cylinders 100 x 200 mm. The impact the BRE screed tester apparatus was used on the concrete cube specimens to simulate the impact experienced by concrete safety barriers.

The test consists of a 100mm cube specimen and BRE tester apparatus. The BRE screed testing apparatus consists of an anvil located at the bottom of the apparatus that is placed onto the concrete cube and 4 kg weight located at the top that is trigger released. The apparatus is held vertical using a small level, and the weight is dropped from a height of 1 m onto the anvil 4 times. After the 4th drop, the cube is inspected for damage and cracks etc., the measuring device is then place on top and an indentation reading taken in mm.



### 2.3 Mix proportions

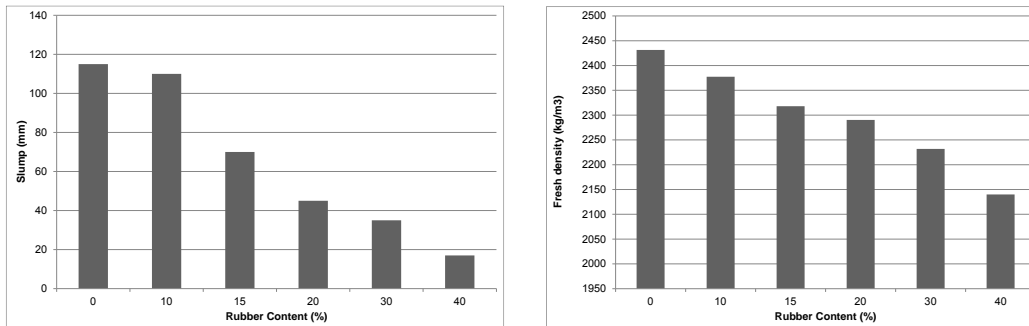
The mix compositions of 6 mixes is summarised in Table 1. The dosage of cement, water/cement ratio and dosage of superplasticiser were kept constant at 420 kg/m<sup>3</sup>, 0.45 and 0.7 L/m<sup>3</sup>. The dosage of replacement by mass of virgin aggregates was from 10 to 40% (48.5 to 197 kg/m<sup>3</sup>).

**Table 1. Mix proportions of all mixes.**

	Mix proportion (kg/m <sup>3</sup> )					
	0%	10%	15%	20%	30%	40%
CEM I	420	420	420	420	420	420
Water	190	190	190	190	190	190
Coarse Sand	630	630	630	630	630	630
10mm Coarse Aggregate	355	320	320	320	290	240
20mm Coarse Aggregate	745	670.5	625	570	490	430
Rubber Aggregate	0	48.5	73	98	147.5	197
Superplasticiser	0.7	0.7	0.7	0.7	0.7	0.7
Water / Cement Ratio	0.45	0.45	0.45	0.45	0.45	0.45

### 3. Results and discussion

The effects of a variation of percentage of rubberised aggregates on the slump and fresh density are shown in Figure 1. The results shown in Fig. 1 indicate that the slump and fresh density decrease with increasing percentage of rubberised aggregates. The most noteworthy is that when the percentage of rubberised aggregates in the mix exceeds 10%. It has been suggested that the rubberised concrete behaves in this manner as the rubber chips form an interlocking structure the rubber's rough surface texture that resists the normal flow of concrete under its own weight, and hence shows less fluidity than mixes containing lower quantities of rubber (7). This reduction can also be attributed to the reduction of the fresh density of concrete, which would affect the collapse of concrete under its own weight. The reduction of fresh density was also very important when more than 10% of rubberised aggregates were used.

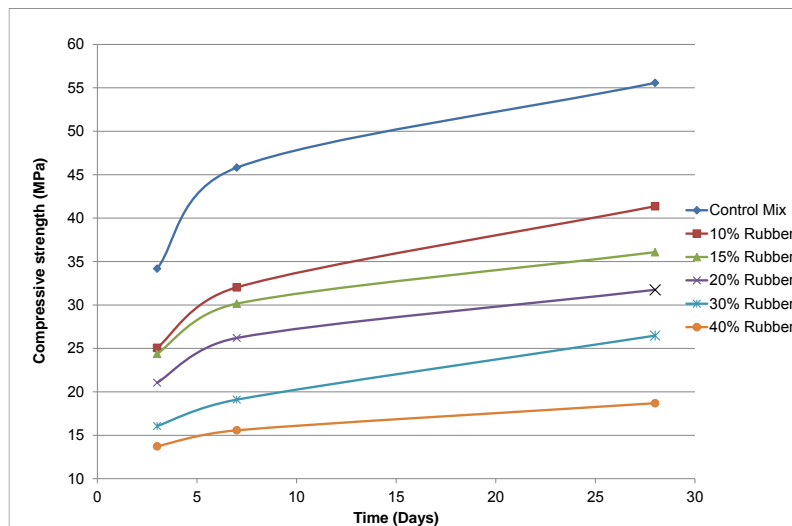


**Figure 1. Variation of slump and fresh density vs. % of rubberised aggregates.**

The effect of rubberised aggregates on the compressive strength at 3d, 7d and 28 days are shown in Fig. 2. From the results given in Fig. 2, it can be observed that the compressive strength at 3 ages rapidly decreases with the increase in the percentage of rubberised aggregates. Using rubberised aggregates to replace the virgin aggregates resulted in a reduction in the 3 days compressive strength by 27%, 29%, 38%, 53% and 60% for replacement levels of 10, 15, 20, 30, and 40%, respectively. Similarly at 7 days, the reduction in the compressive strength by 30%, 34%, 43%, 58% and 66%, for replacement levels of 10, 15, 20, 30, and 40%, respectively. In case of 28 days, the reduction was 26%, 35%, 43%, 52%, and 66%.

The reduction in strength had solely been due to a reduction in load carrying material in the concrete specimens. Therefore the loss of compressive strength can also be attributed to poor development of the interfacial transition zone (ITZ) and disparity between the rubber and hardened cement paste composite

(7). The significant disparity between the young's modulus of the rubber aggregate and hardened cement paste has been highlighted as a contributor to reduced compressive strength. When an external load is applied, the rubber acts as a stress concentrator within the concrete and deform elastically, debonding the rubber from the cement paste and causing micro-cracking around the ITZ, with the cracks spreading rapidly throughout the concrete matrix leading to the inevitable loss of compressive strength (1, 9; 10). Due to the hydrophobic properties of rubbers, the inclusion into the concrete mix may be disrupting the flow of water at ITZ of the rubber and cement paste, thus preventing the full hydration of the cement regionally within the concrete, contributing to failure of the concrete specimen (11). Finally, the reduction is due to the possible reduction of the concrete matrix density, which depends greatly on the density, size, and hardness of the aggregate. While the current investigation examined the use of virgin rubberised aggregates i.e., without any surface treatments, other researchers showed such surface treatments to enhance bond strength (12, 13, 14).



**Figure 2. Variation of compressive strengths vs. % of rubberised aggregates.**

The effects of the rubberised aggregates on splitting tensile and flexural strength are shown in Fig. 3. It can be seen that the introduction of rubber aggregate to the concrete mix led to a decrease in split tensile strength, with the decrease increasing as the rubber content is increased. Similar decrease in split tensile strength has been reported by Kew & Kenny (2008), Guneyisi et al (2004) and Eldin & Senouci (1994). It can be seen that the reduction in split tensile strength was up to 62% for 40% rubber content.

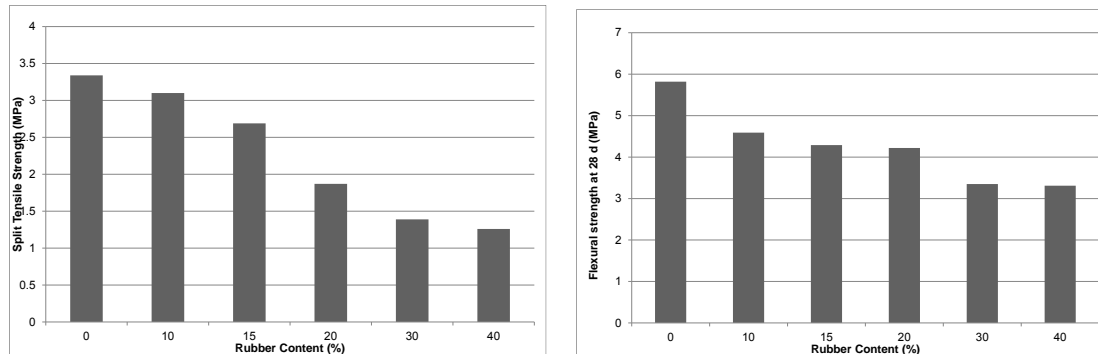
It was observed that the rubberised cylindrical specimens did not split into two halves like the plain concrete, except for one 10% rubberised specimen which was extremely difficult to open by hand. Similar observations were made by (15). This was due to the specimens exhibiting less virgin aggregate shear than the plain concrete, with the rubber aggregate holding the specimens together. From observing figure 56, it could be seen that when the two rubberised specimen halves were separated, there was evidence that the soft rubber aggregate debonded from the hardened cement paste, leaving a void, thus reinforcing the notion that poor development of the ITZ bonding has led to the accelerated and systematic reduction in split tensile strength.

The results of the flexural strength in Fig. 3, it can be seen that the introduction of rubber aggregate to the concrete mix also leads to a decrease in flexural strength, with the decrease increasing as the rubber content is increased. These results are similar to the findings by (1, 2, 16, 17).

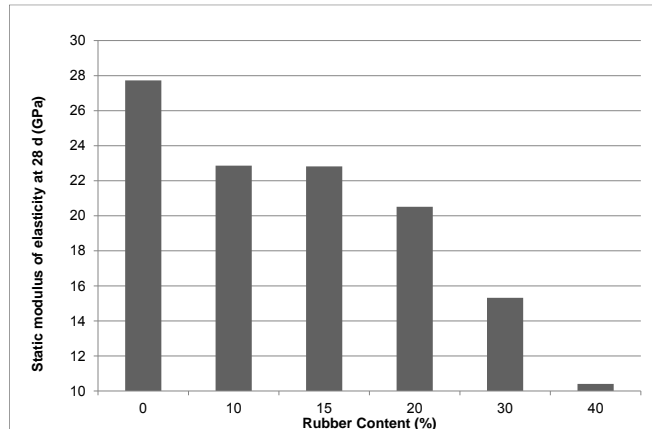
The control plain concrete flexural strength specimen demonstrated a characteristic brittle failure in that the control specimen broke into two separate pieces under flexural loading. The coarse aggregate was sheared as expected, however in case of the rubberised specimens demonstrated a notably less brittle mode of failure, with the modified concrete demonstrating a more ductile mode of failure under flexural loading. This behaviour of the modified concrete was expected as reported by (18), the brittleness index

decreased after 15% rubber content. It was also visible that the specimens after failure did not separate into two pieces due to the rubber chips holding the sample together, demonstrating increased toughness and flexibility.

It can be noted that when the rubberised concrete specimens were opened by hand, the rubber aggregate had debonded from the hardened cement paste. Further examination of the specimens show that as the rubber content was increased there was a noticeable decrease in aggregate shear, with a visible failure of hardened cement paste present. This poor interfacial bonding is a major factor in the reduction of flexural strength of the rubberised concrete specimens as compared to the plain control concrete, as good bonding is the key to high flexural strength (1).



**Figure 3. Variation of splitting tensile strength and flexural strength vs. % of rubberised aggregates.**

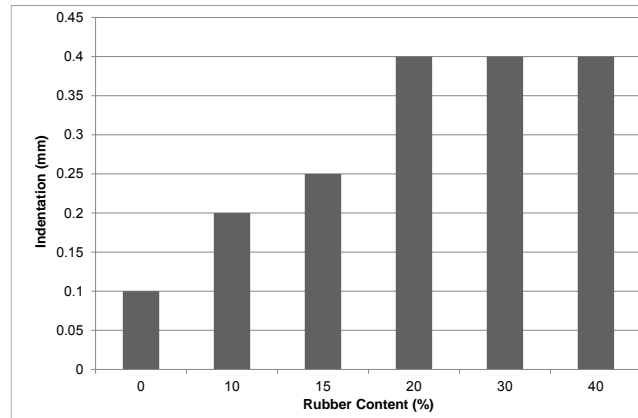


**Figure 4. Variation of static modulus vs. % of rubberised aggregates.**

Fig. 5 shows the effect of using different replacement levels of rubberised aggregates on the impact test. It can be observed that increasing the replacement level of rubberised aggregates significantly improved the impact strength of the concrete up to a replacement level of 20%. Further increase in the rubberised aggregates contents beyond this level resulted in a similar impact strength of the rubber concrete. This pattern of energy absorption in relation to the rubberised aggregates content might be explained by viewing the energy absorption of the concrete matrix as a trade-off between the composite matrix flexibility and strength. At low to medium replacement levels, the low stiffness of the rubberised aggregates allowed the rubber-cement composite to have a relatively high flexibility and thus absorb a considerable amount of energy higher than that absorbed by normal concrete. As the rubberised aggregates replacement level increases the rubber-cement composite gets weak as high strains are generated under loading which limits the material's ability to absorb energy. However, it is worth noting that even with this

relatively high replacement level, the impact resistance is still higher than that of concretes without rubberised aggregates. The ability of the rubberised aggregates to enhance the ductility and strain capacity as indicators of energy was reported by other researchers (18).

It is important to note that the low Young's modulus of the rubber aggregate compared with the cement paste will result in dissimilar deformation in the rubber aggregate phase compared to the cement paste phase (Fig. 4). This in its turn will result in cracking in the less deformable phase here the cement paste. While this mechanism represents an obvious limitation for developing high strengths in rubber concrete, it represents a favourable mechanism as it enables rubber concrete to have high deformability, toughness, and energy absorption characteristics. It is essential to realise that such micro-cracking would be relatively extensive and will occur at stress levels considerably lower than those observed in normal strength concrete.



**Figure 5. Variation of impact value vs. % of rubberised aggregates.**

#### **4. Conclusions**

The use of rubberised aggregates as aggregate in concrete showed promising results in producing a new type of concrete that has relatively enhanced energy absorption and fracture criteria compared with normal concrete. Incorporating rubberised aggregates in the concrete matrix as replacement of coarse resulted in a decrease in the fresh concrete slump and fresh density. While the compressive strength, the splitting tensile strength and flexural strength and static modulus of the rubberised concrete were significantly reduced as the rubberised aggregates replacement level increases, significant enhancements in the impact resistance of concrete were observed.

The major reduction of strength might be attributed to the behaviour of the rubberised aggregates as a soft aggregate rather than to the reduction of bond between the rubberised aggregates and the cement paste. It also becomes evident that the rubberised aggregates provide other energy consumption toughening mechanisms in the concrete such as particle pullout and rubber internal cracking that do not exist in normal concrete. It is obvious that the choice of the optimal replacement ratio of the rubberised aggregates should be governed by achieving a compromise between strength and the impact and fracture toughness based on field of application. Potential use of this material includes concretes with limited strength requirements and high fracture toughness/energy demand such as those used in bridge barriers and new-jersey barriers.

#### **5. References**

1. Ganjian, E., Khorami, M. & Maghsoudi, A. A. (2009). "Scrap tyre rubber replacement for aggregate and filler in concrete". *Journal of Construction and Building Materials*, Volume 23, pp. 1828-1836.
2. Sukontasukkul, P. & Chaikaew, C. (2006). "Properties of concrete pedestrian block mixed with crumb rubber". *Journal of Construction and Building Materials*, Volume 20, pp. 450-457.

3. Benazzouk, A., Douzane, O., Langlet, T., Mezreb, K., Roucoult, J. M. & Queneudec, M. (2007). "Physico-mechanical properties and water absorption of cement composite containing shredded rubber wastes". *Journal of Cement & Concrete Composites*, Volume 29, pp. 732-740.
4. Siddique, R. & Naik, T. R. (2004). "Properties of concrete containing scrap-tire rubber – an overview". *Journal of Waste Management*, Volume 24, pp. 563-569.
5. Guneyisi, E., Gesoglu, M. & Ozturan, T. (2004). "Properties of rubberized concretes containing silica fume". *Journal of Cement and Concrete Research*, Volume 34, pp. 2309-2317.
6. Sang Son, K., Hajirasouliha, I. & Pilakoutas, K. (2011). "Strength and deformability of waste tyre rubber filled reinforced concrete columns". *Journal of Construction and Building Materials*, Volume 25, pp. 218-226.
7. Eldin, N. N. & Senouci, A. B. (1994). "Measurement and Prediction of the Strength of Rubberized Concrete". *Journal of Cement & Concrete Composites*, Volume 16, pp. 287-298.
8. Epps, J. A. (1994). *Uses of Recycled Rubber Tires in Highways, Synthesis of Highway Practice*. Volume 198, Transportation Research Board, National Research Council; Washington DC.
9. Li, G., Stubblefield, M., Garrick, G., Eggers, J., Abadie, C. & Huang, B. (2004b). "Development of waste tire modified concrete". *Journal of Cement and Concrete Research*, Volume 34, pp. 2283-2289.
10. Meyer, C. (2009). "The greening of the concrete industry". *Journal of Cement & Concrete Composites*, Volume 31, pp. 601-605
11. Chou, L. H., Chang, J. R. & Lee, M. T. (2007). "Use of waste rubber as concrete additive". *Journal of Waste Management and Research*, Volume 25, pp. 68-76.
12. Raghavan, D., Huynh, H. & Ferraris, C. F. (1998). "Workability, mechanical properties, and chemical stability of a recycled tyre rubber-filled cementitious composite". *Journal of Material Science*, Volume 33, pp. 1745-1752
13. Uygunoglu, T. & Topcu, I. B. (2010). "The role of scrap rubber particles on the drying shrinkage and mechanical properties of self-consolidating mortars". *Journal of Construction and Building Materials*, Volume 24, pp. 1141-1150
14. Segres, N. & Joekes, I. (2000). "Use of tire rubber particles as addition to cement paste". *Journal of Cement and Concrete Research*, Volume 30, pp. 1421-1425..
15. Kew, H. Y. & Kenny, M. (2009) *Developing viable products using recycled rubber tyres in concrete*. In: *Excellence in concrete construction through innovation*. Taylor and Francis, CRC Press, London, pp. 523-531
16. Toutanji, H. A. (1996). "The Use of Rubber Tire Particles in Concrete to Replace Mineral Aggregates". *Journal of Cement & Concrete Composites*, Volume 18, pp. 135-139.
17. Topcu, I. B. (1997). "Assessment of the brittleness index of rubberized concrete". *Journal of Cement and Concrete Research*, Volume 27, No. 2, pp.177-183.
18. M. Nehdi and A. Khan [2001]. "Cementitious composites containing recycled tire rubber: overview of engineering properties and potential applications", *ASTM Journal of Cement, Concrete and Aggregates*, Vol. 23, No. 1, pp. 3-10.

# The Effectiveness of Mineral Admixtures and Low Water to Cement Ratio in Concrete for Immobilizing Cesium, Sodium and Iodide from Radioactive Waste Material

Irfan Prasetya<sup>1</sup> and Kazuyuki Torii<sup>2</sup>

<sup>1</sup>Dept. of Civil Engineering, Lambung Mangkurat University, Indonesia

<sup>2</sup>Prof. Dep. of Env. Design, College of Science & Eng., Kanazawa University, Japan

**Abstract:** Nuclear accident at Fukushima Daiichi Nuclear Power Plant has caused a huge leakage of radioactive materials such as cesium, iodine, and strontium. Therefore, in Japan, efforts and research works to overcome this problem are needed. This paper investigated the ion diffusivity of cesium and sodium iodide through cement pastes. The purpose is to find out the influence of mineral admixtures along with low water to cement ratio (W/C) on the immobilization of cesium (Cs<sup>+</sup>), sodium (Na<sup>+</sup>) and iodide (I<sup>-</sup>) ions. Blast furnace slag (BFS) and fly ash (FA) are used as the mineral admixtures with W/C set at 30%. The experiments are conducted through diffusion cell tests and followed by a range of post-analysis such as DSC, XRD and SEM. The results show that Cs<sup>+</sup>, Na<sup>+</sup> and I<sup>-</sup> ions are better absorbed in cement paste using 40% replacement ratio of BFS. These findings confirmed that the calcium aluminosilicate hydrate, which is formed from the hydration product in hardened BFS samples, absorb the ions from the solution. Experimental results also show that lower W/C significantly decreases the ion diffusivity. Finally, the experiment results and post-analysis indicate the effectiveness of mineral admixtures, especially BFS40%, and low W/C for immobilizing radioactive wastes materials.

**Keywords:** mineral admixture, diffusion, cesium, SEM.

## 1. Introduction

The 2011 Tohoku earthquake in Japan has caused extensive and severe structural damage in north-eastern Japan. This earthquake, followed by tsunami, has made three reactors in the Fukushima Daiichi complex suffered meltdowns. Due to this accident, huge leakage of radioactive materials such as cesium (Cs), iodine (I), and strontium (Sr) are occurred in Japan. Many efforts have been made to overcome this problem. One of which is an attempt to monitor the levels of radioactive material that leached to the environment. In addition, efforts to control, decontaminate and dispose the released radioactive waste material also have been started.

In terms of radioactive waste treatment facility, portland cement is commonly used to immobilize low level until intermediate-level radioactive waste (1). However, some researched found out that portland cement has low ability in immobilization of Cs ions (2; 3). As stated by McCulloch et al. (4) and Bagosi et al. (5), portland cement has low retention degree on Cs ions, which leads to relatively high leaching rates of cesium through portland cement. Moreover, hardened cement paste has intrinsically interconnected microspores, through which diffusion could readily occur, and will make the nuclides can easily leach out from the waste form (6).

One way to cover the shortage of portland cement for immobilizing Cs ions is by lowering the water to cement ratio (W/C). Reduction of W/C is at present one of the main possibilities to improve the properties of cement based materials (7). It is well known that a low W/C ratio leads to low porosity which, in turn, leads to greater strength and dimensional stability (8). In addition, lower W/C will also increase the biding capacity of the hydration products and increase the homogeneity of the pore structure (9).

In addition, another way to effectively confining radioactive waste materials is by using blended cement. Mineral admixtures, also called as Supplementary cementitious materials (SCMs), are known for its advantage in improving the final properties of the concrete. SCMs, such as blast furnace slag (BFS) and fly ash (FA), when used as replacement of portland cement, not only increase the final strength but also chemical resistance of concrete, and reduce the porosity of concrete. Thus, a durable concrete will be achieved. In terms of environment point of view, blended cement is also known as a green concrete which can reduce energy consumption and CO<sub>2</sub> emissions.

Recently, mineral admixtures also actively investigated to reveal its potential on absorbing the radioactive ions. Goni et al. (1) and Xuequan et al. (6) have confirmed the effectiveness of fly ash belite cement and alkali-activated slag cement for immobilizing radioactive waste material. Moreover, Hong et al. (10) and Glasser (11) have studied the potential of pozzolanic additives to improve the immobilization of highly soluble ion such as Cs.

Furthermore, as reported by Malhotra et al. (12), the Calcium Silicate Hydrates (C-S-H) gel produced from the pozzolanic reaction between amorphous silica from the SCMs and Calcium Hydroxide (CH), which is a product of cement hydration, showing a lower Ca/Si ratio compared with C-S-H gel from the hydration of cement. The lower Ca/Si ratio in the paste has advantage in showing higher binding capacity and bond strength of Cs ions to the cementitious pastes (10; 11).

In order to confirm the effectiveness of mineral admixtures and low water to cement ratio in concrete for immobilizing cesium (Cs<sup>+</sup>), sodium (Na<sup>+</sup>) and iodide (I<sup>-</sup>) ions from radioactive waste material, this study investigates the ion diffusivity of cesium and sodium iodide solutions through cement pastes according to self-diffusion cell tests. For this purpose, BFS and FA cement paste were prepared with W/C ratio set at 30%. As a control sample, ordinary portland cement (OPC) samples were also prepared. In addition, post-analysis such as DSC, XRD and SEM are also carried out to the cement paste samples after the completion of the diffusion cell tests.

## 2. Experiments

### 2.1 Materials and mix proportions

In this study, ordinary portland cement (OPC), from T Co, Ltd., (density: 3.16 g/cm<sup>3</sup>, blaine: 3300 cm<sup>2</sup>/g) was used. As for the mineral admixtures, fly ash (FA) from Nanao coal thermal power plant product (I-type fly ash classified by JIS A6201, density: 2.44g/cm<sup>3</sup>, blaine: 4780cm<sup>2</sup>/g, lg.loss: 2.0%), and blast furnace slag (BFS) manufactured by S Co. Ltd (density: 2.91g/cm<sup>3</sup>, blaine: 6030cm<sup>2</sup>/g, lg.loss 1.0%) were used. The chemical compositions of OPC, FA and BFS are shown in Table 1. Five types of cement pastes were prepared, which are OPC, 40% and 60% replacement ratio of BFS (BFS40% and BFS60%), and 15% and 30% replacement ratio of FA (FA15% and FA30%). In order to assess the effect of low water to cement ratio, the water to cement ratio (W/C) was set at 30% for all types of cement paste. Cesium iodide (CsI) and sodium iodide (NaI) solutions were selected as the electrolytes sources. The concentration was set at 1 mol/L.

### 2.2 Test method

After mixing, cement pastes were cast into PVC acrylic rings, with 5mm thickness and 30mm internal diameter, placed on glass plates, manually compacted and covered for one day to prevent early dryness and water loss. Then, the cement pastes were cured in Calcium Hydroxide (Ca(OH)<sub>2</sub>) saturated water solution for 28 and 91 days curing time under room temperature of 20°C and 60% R.H.

The diffusion cells were setup by adding 100ml of electrolyte sources of Cesium and Sodium Iodide solutions in the tracer cell (cell on the right side) and 100ml of de-ionized water in the measurement cell (cell on the left side) with the cement paste forming the partition between the two sides. After 24 hours, first sampling was performed by extracting 2ml of de-ionized water in the measurement cell and replaced again with the same volume of de-ionized water to keep a constant volume on the measurement cell. This procedure was repeated every 2 days afterwards. The ionic concentration was measured by a PIA-1000 ion analyzer. After the completion of the diffusion test, post analysis such as DSC, XRD and SEM were also conducted.

## 3. Results and Discussions

### 3.1 Diffusion starting time (DST)

The diffusion starting time (DST) of cesium (Cs<sup>+</sup>) and iodide (I<sup>-</sup>) ions from CsI solution, and sodium (Na<sup>+</sup>) and iodide (I<sup>-</sup>) ions from NaI solution at 28 days and 91 days curing time are shown in Figs. 1 and 2, respectively. The DST results were proportional to curing time. The figures show that there is

**Table 1. Chemical composition of OPC, FA and BFS (%).**

Mat.	SiO <sub>2</sub>	Al <sub>2</sub> O <sub>3</sub>	Fe <sub>2</sub> O <sub>3</sub>	CaO	MgO	TiO <sub>2</sub>	MnO	SO <sub>3</sub>	Na <sub>2</sub> O	K <sub>2</sub> O	Total
OPC	21.2	4.9	3.4	66.4	1.3	0.0	0.0	1.9	0.3	0.5	99.9
FA	53.6	28.9	6.7	3.2	0.8	1.4	0.1	0.2	0.3	0.7	96.2
BFS	33.0	13.6	0.1	42.6	5.8	0.6	0.2	3.1	0.2	0.2	99.3

a significant delay of DST from samples at 91 days curing time compared to samples at 28 days curing time. These results are more pronounced for BFS samples. Compared to portland cement, blended cement has a slower pozzolanic reaction, between 28 days until 6 months. However, within time, the blended cement will improve the engineering properties of the hardened concrete.

Overall, the occurrence of Cs<sup>+</sup> and I<sup>-</sup> ions were slower compared to Na<sup>+</sup> ions. Especially for the I<sup>-</sup> ion, there is a significant delay on the DST of I<sup>-</sup> ion from all samples including OPC sample. This might be the evidence that the low W/C ratio could decrease the porosity of cement paste, thus make the penetration of ions through cement paste becomes difficult. Table 2 shows the comparison of porosity of cement paste samples with W/C ratio set at 30% (W/C=0.3) and 50% (W/C=0.5) for OPC, FA15%, and BFS40% samples at 28 days curing time. It shows that by decreasing the W/C ratio, the porosity of the sample is significantly decreasing, especially for 0.3 OPC. In addition, the higher porosity that the blended cement paste samples have might be due to the fact that the pozzolanic reaction of blended cement is slower at 28 days. However, the difference in porosity for W/C ratio set at 30% is not significant.

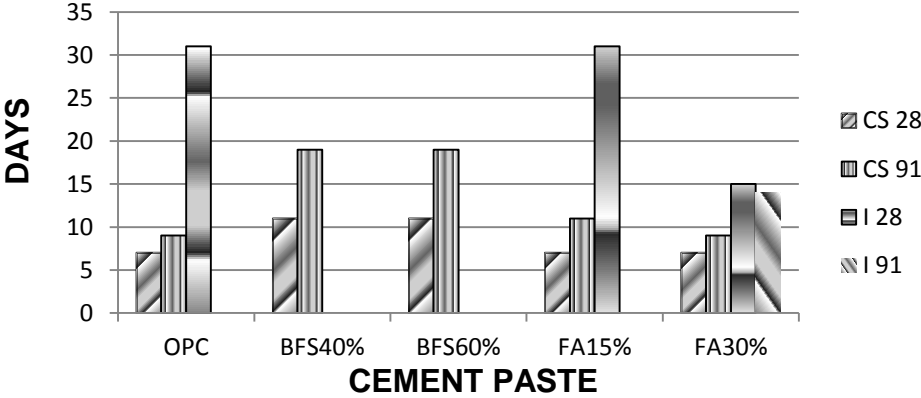


Figure 1. DST of Cs+ and I- ions from CsI solution.

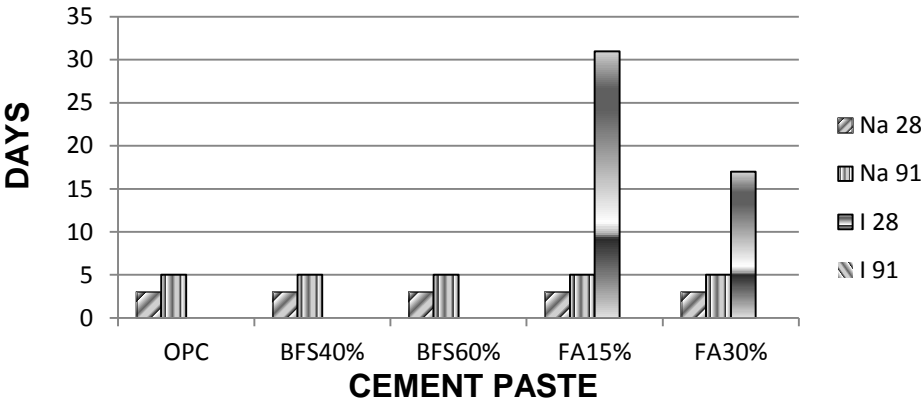


Figure 2. DST of Na+ and I- ions from NaI solution.

Table 2. Porosity of OPC, FA15%, and BFS40% samples at 28 days curing time.

Sample	Total Intrusion Volume (ml / g)	Total Pore Area (m <sup>2</sup> / g)	Median Pore Diameter (Volume) (µm)	Average Pore Diameter (4V/A) (µm)	Bulk Density at 0.50 psia (g / ml)	Apparent (skeletal) Density (g / ml)	Porosity (%)
28d OPC W/C=0.3	0.0523	26.025	0.011	0.008	2.0939	2.3513	10.9438
28d OPC W/C=0.5	0.1649	69.923	0.0165	0.0094	1.6399	2.2476	27.0402
28d FA15% W/C=0.3	0.0648	32.245	0.0103	0.008	1.9952	2.2912	12.9202
28d FA15% W/C=0.5	0.2054	79.267	0.0203	0.0104	1.5336	2.2387	31.4955
28d BFS40% W/C=0.3	0.0591	34.104	0.0093	0.0069	1.9781	2.24	11.6921
28d BFS40% W/C=0.5	0.1814	103.651	0.0075	0.007	1.5739	2.2031	28.5577



As for the BFS samples, the I<sup>-</sup> ion does not occur in both solutions and curing time. This finding suggests that I<sup>-</sup> ion was completely absorbed into the pozzolanic reaction of BFS cement. In addition, it is also important to note that the determination of DST for Na<sup>+</sup> ion from NaI solutions in the latter is fairly a difficult task. It is due to Na<sup>+</sup> ion is immediately released from the pore solution of cement pastes.

### 3.2 Diffusion coefficient (De)

The effective diffusion coefficient (De) of Cs<sup>+</sup> and I<sup>-</sup> ions from CsI solution, and Na<sup>+</sup> and I<sup>-</sup> ions from NaI solution, calculated by Fick's Law, are shown in Figs. 3 and 4, respectively. In addition, Table 3 shows the Effective Diffusion Coefficient (De) of all ions. The results show that the curing time also has a great influence in decreasing the De of all ions, especially for I<sup>-</sup> ions. The effect of lower W/C is also significant in decreasing the diffusivity of Cs<sup>+</sup>, Na<sup>+</sup> and I<sup>-</sup> ions. As could be seen on the OPC sample, the De for all ions are very low which the highest is only around 0.3e-12 for Na<sup>+</sup> ions. Moreover, the influence of lower W/C on OPC sample is significant for Cs<sup>+</sup> and I<sup>-</sup> ions, especially at latter curing time.

As for the blended cement pastes (BFS and FA samples), the combination between using mineral admixtures and low W/C ratio are showing more remarkable effect on confining Cs<sup>+</sup>, Na<sup>+</sup> and I<sup>-</sup> ions. Especially for 91 days curing time samples, the diffusion of Cs<sup>+</sup>, Na<sup>+</sup> and I<sup>-</sup> ions from the blended cement pastes are lower compared to OPC sample. However, higher replacement ratio of BFS and FA tends to have higher diffusivity of Cs<sup>+</sup> compared to OPC. Overall, BFS40% sample shows superiority in immobilizing Cs<sup>+</sup>, Na<sup>+</sup> and I<sup>-</sup> ions since the early curing time, while FA15% sample show almost the same effect as BFS40% at the latter time.

The ion immobilizing effect of the blended cement, especially BFS, can be explained due to the pozzolanic reaction of mineral admixtures with calcium hydroxide (CH) from cement hydration which produce calcium silicate hydrates (C-S-H) and calcium aluminosilicate hydrates (C-A-S-H) that have a 'pore-blocking' effect. This effect improves the binding and adsorptive capability of blended cement and gives higher strength and lower permeability (13). In addition, the CSH and CH formed in OPC paste may charge more negatively compared with FA or BFS samples, which will influence the immobilization of cation and anion ions. Moreover, in terms of Ca/Si ratios, previous experiment using the same OPC, FA and BFS show that the Ca/Si ratios for OPC paste, FA15% paste and BFS42% paste were around 1.7, 0.9 and 1.5, respectively, as been reported by Hasimoto, et al. (14). Lower Ca/Si ratios of FA and BFS will give higher ions binding capacity compared to OPC.

Moreover, blended cement increase the workability of concrete thus will reduce the water demand. Lower water demand will lead to smaller pore size in concrete due to the same mix water that hydrates the cement also occupies space between the cement particles, thereby the concrete strength continues to increase and permeability continues to decrease at lower values of W/C ratio (15). Thus, based on this facts, the combination of blended cement and low W/C ratio will give a significant influence for immobilizing radioactive waste material.

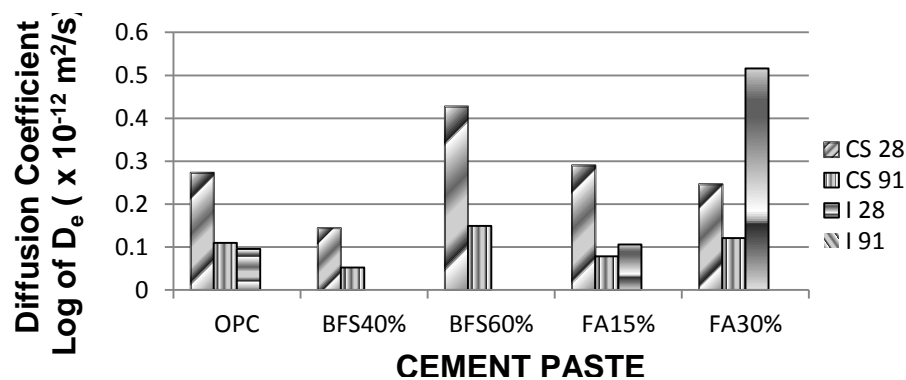


Figure 3. De of Cs<sup>+</sup> and I<sup>-</sup> ions from CsI solution.

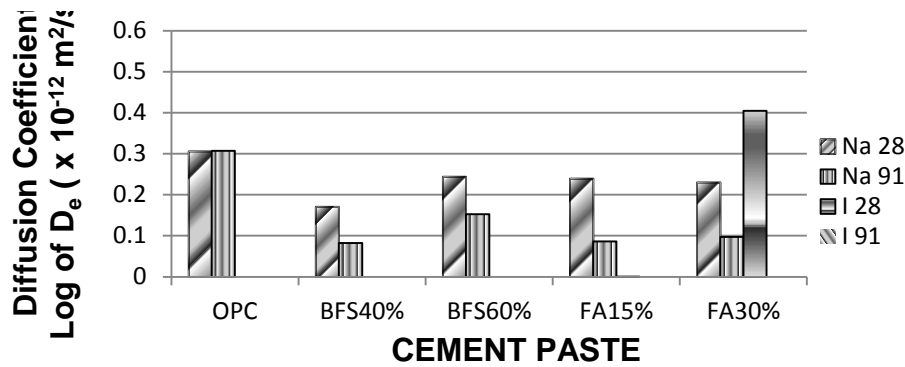


Figure 4.  $D_e$  of  $\text{Na}^+$  and  $\text{I}^-$  ions from NaI solution.

Table 3. Effective Diffusion Coefficient ( $D_e$ ) of all ions.

Curing Time	Samples	Effective Diffusion Coefficient ( $D_e$ ) ( $\text{m}^2/\text{sec}$ )			
		Csl [ $\text{Cs}^+$ ]	Csl [ $\text{I}^-$ ]	NaI [ $\text{Na}^+$ ]	NaI [ $\text{I}^-$ ]
28 days	OPC	0.273e-12	0.0957e-12	0.305e-12	0
	BFS 40%	0.144e-12	0	0.170e-12	0
	BFS 60%	0.427e-12	0	0.244e-12	0
	FA 15%	0.290e-12	0.106e-12	0.239e-12	1.31e-18
	FA 30%	0.246e-12	0.516e-12	0.230e-12	0.405e-12
91 days	OPC	0.110e-12	0	0.307e-12	0
	BFS 40%	0.052e-12	0	0.0822e-12	0
	BFS 60%	0.149e-12	0	0.153e-12	0
	FA 15%	0.0785e-12	0	0.0861e-12	0
	FA 30%	0.121e-12	0	0.097e-12	0

### 3.3 Differential scanning calorimetry analyses (DSC)

DSC analyses was carried out upon diffusion test completion. DSC curves of samples subjected to Csl and NaI diffusion tested at 28 days are shown in Figs. 5 and 6, respectively. The formation of ettringite (Ett) was confirmed by a peak between  $100^\circ\text{C}$  and  $130^\circ\text{C}$  in all samples. Calcium silicate hydrates (C-S-H) peaks were observed in all samples around  $160^\circ\text{C}$  to  $170^\circ\text{C}$ . Peaks similar to Friedel's salt ( $\text{FS}_t$ ) were observed in all samples around  $320^\circ\text{C}$  to  $350^\circ\text{C}$ . Residual calcium hydroxide was confirmed by sharp peaks in the vicinity of  $480^\circ\text{C}$ . Between  $680^\circ\text{C}$  and  $740^\circ\text{C}$ , flat exothermic peaks were observed in all samples. These peaks are a result of decarbonation of  $\text{CaCO}_3$  (CC), which is formed due to material exposure to air and probable contamination of CH with  $\text{CO}_2$  during the analysis.

In terms of residual CH, the formation of CH peaks on BFS samples are lower compare to the other samples. In addition, although FA samples have high residual CH at the early curing time, but within longer curing time the formation of CH peaks on FA samples are decreasing, especially samples tested with NaI solution. Smaller residual CH amount occurred on the DSC analysis is due to the pozzolanic reaction of BFS and FA consume CH to form C-S-H gel, thus it could reduce the amount of CH in the pore system. Moreover, the fact that the amount of residual CH of FA sample is higher compare to the BFS samples at 28 days curing time could be the evidence that the pozzolanic reaction of FA sample is slower and not yet stable compared to BFS sample at early curing time. Thus, lead to a larger diffusivity of  $\text{Cs}^+$ ,  $\text{Na}^+$  and  $\text{I}^-$  ions in FA samples at 28 days curing time.

Furthermore, in terms of BFS samples, although the BFS60% sample also shows a small amount of residual CH, the amount of C-S-H gel is smaller compared with other blended cement pastes, in both solutions and curing time. The small amount of C-S-H gel that produced might be the reason of larger diffusivity of  $\text{Cs}^+$  and  $\text{Na}^+$  ions in BFS60% sample. This result is in line with the experiment of Shariq, et al. (16) on the effect of fine aggregates on compressive strength development of cement mortar with GGBFS replacement. Shariq, et al. (16) found out that 40% replacement ratio of BFS is highly significant to increase the compressive strength of concrete compared to 60% replacement ratio. The reason is due to the presence of excessive fines on the 60% replacement ratio of BFS which will cause greater mobility of the unhydrated BFS particle. The failure takes place due to early crushing of paste and hence strength is found lower than 40% replacement of BFS.

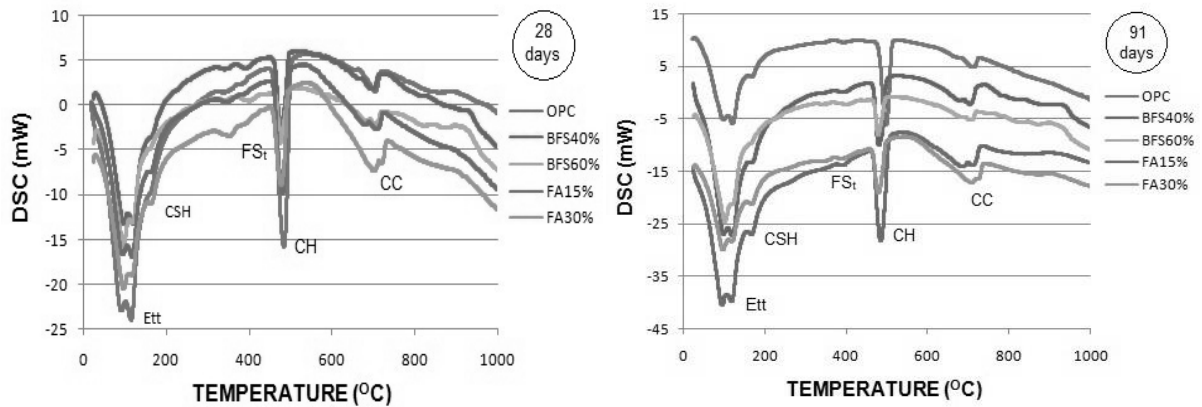


Figure 5. DSC of Cs<sup>+</sup> and I<sup>-</sup> ions from CsI solution.

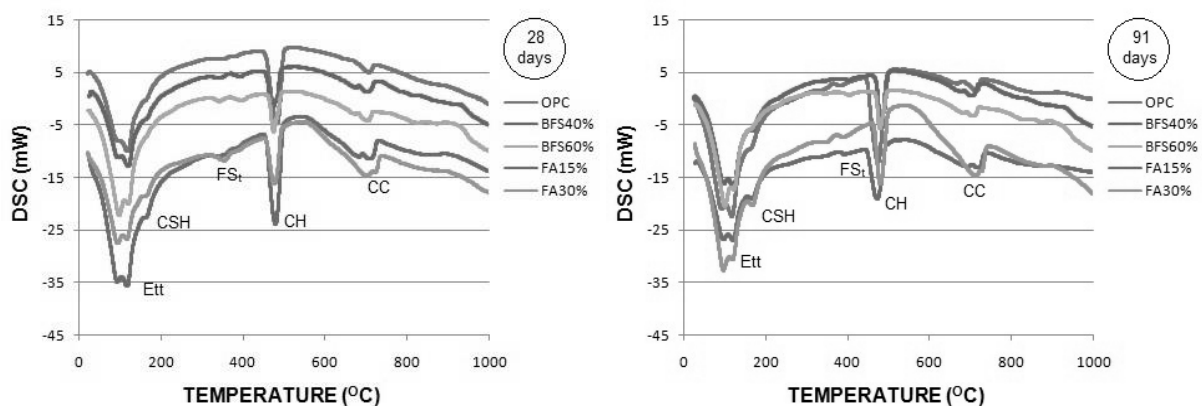


Figure 6. DSC of Na<sup>+</sup> and I<sup>-</sup> ions from NaI solution.

### 3.4 X-ray diffraction analyses (XRD)

XRD patterns subjected to CsI and NaI diffusion tested at 28 days are shown in Figs. 7 and 8, respectively. Ettringite peaks (Ett) were observed at 8.8°, 15.6° and 23° in all samples. At 11.2°, peak which resembles Friedel's salt (FS<sub>t</sub>) was observed in all samples. Residual calcium hydroxide (CH) peaks were confirmed by sharp peaks at 18° and 34°. Consistent calcium silicate hydrates (C-S-H) peak was observed in all samples at 29.4°. Small calcium carbonate (CC) peak was observed around 38°, as result of sample exposure to CO<sub>2</sub> during the analysis. Overall, the XRD analysis backed up the finding from DSC analysis.

As could be observed on the DSC results, peaks which resemble Friedel's salt (FS<sub>t</sub>) were also observed on XRD results in all samples. These peaks might be the evidence of iodine binding into the cementitious paste. As a result, as could be seen on the De results, the De of I<sup>-</sup> ions for all samples are very low. The Friedel's salt might be formed due to the chemical reaction between the anion (i.e. chloride or iodide) and tri-calcium aluminate (C3A) in the cement paste. Luo, et al. (17) and Cheewaket et al. (18) reported that the higher C3A content in the paste will lead to more anion will be bound.

Mineral admixtures such as BFS and FA are rich in aluminium oxide (Al<sub>2</sub>O<sub>3</sub>) compared to portland cement. Thus, it is expected that the iodide binding capacity of blended cement paste will be more pronounced compared to the OPC cement paste. However, slower pozzolanic reaction of fly ash will make the iodine binding effect of Friedel's salt in FA samples might be delayed compared to the BFS samples.

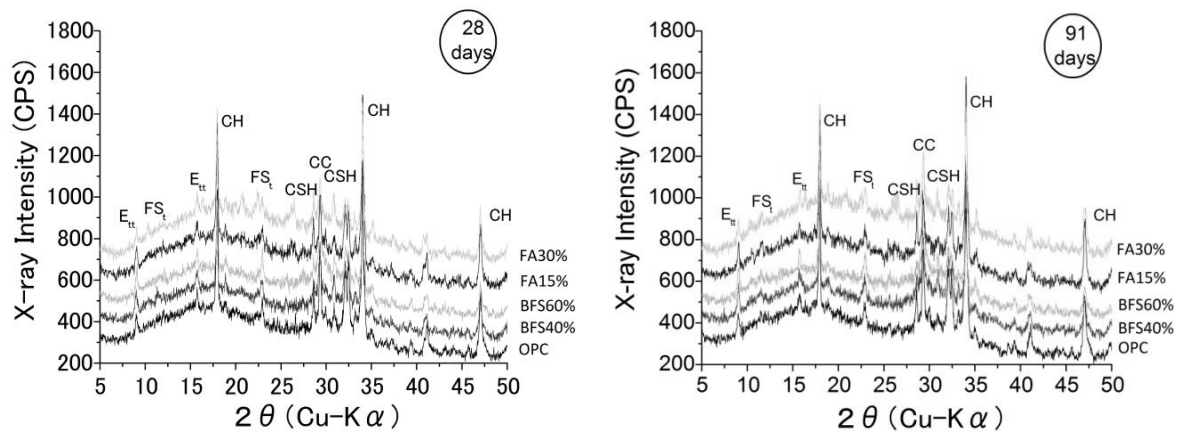


Figure 7. XRD of Cs<sup>+</sup> and I<sup>-</sup> ions from CsI solution.

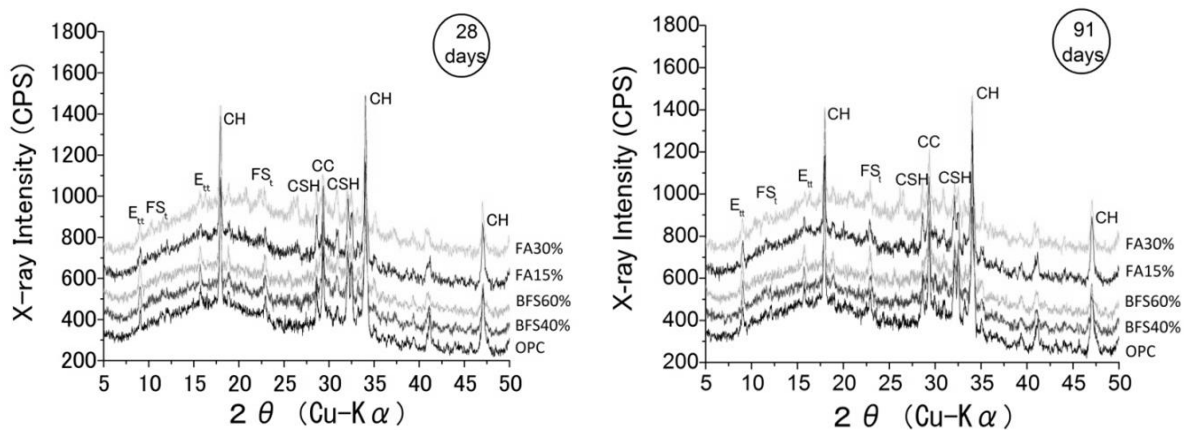


Figure 8. XRD of Na<sup>+</sup> and I<sup>-</sup> ions from NaI solution.

### 3.5 Scanning electron microscopy analyses (SEM)

Scanning Electron Microscopy analyses (SEM) were conducted to the samples at 28 days curing time tested with CsI solution. As shown in Fig. 9(a) the microstructure of BFS40% sample shows a denser structure. In this figure, it also could be observed that the larger slag is only partially reacted, but small slag is fully reacted. In addition, fibrous C-S-H gel could be easily detected in the microstructure of BFS40%. Moreover, as shown in Fig. 9(b), due to BFS is rich with Al<sub>2</sub>O<sub>3</sub>, the formation of Friedel's salt could easily be observed.

As for BFS60% sample, the microstructure for this sample is less dense compared to BFS40%. Ettringite (Fig. 10 (a)) and hydroxide crystal accompanied by hexagonal monosulfate plate (Fig. 10 (b)) are could be easily detected. The fibrous C-S-H gels of BFS60% are also much less compared to BFS40%. This finding is in the agreement with the DSC and XRD results. These results could be the reason of the high diffusivity of Cs<sup>+</sup> and Na<sup>+</sup> ions through the BFS60% sample. Furthermore, the formation of Friedel's salt (Fig. 10 (c)) could also be easily observed as well as BF40% sample.

As for the FA samples, both samples show a lot of unreacted fly ash as could be seen in Fig 11(a) and 11(b). However, it could be observed that the microstructures of both FA samples are dense. This is might be contributed due to the low water to cement ratio. Even though the pozzolanic reaction of fly ash is slow, but the hydration of cement is starting earlier. The low water to cement ratio reduces the porosity of the cement paste, thus make the microstructure become denser. In addition, in both FA samples C-S-H gel could also be observed. Moreover, it can be noted that slag or FA with bigger particle size tends to hardly reacted compared with the smaller particle size.

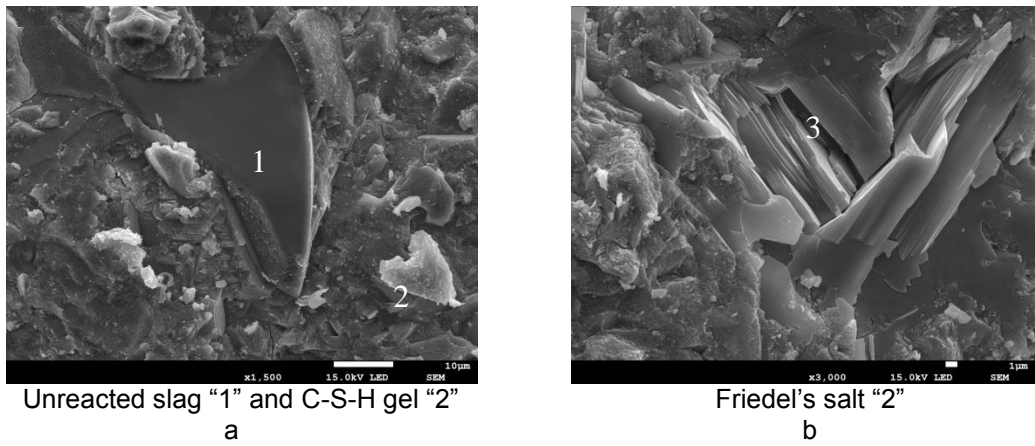


Figure 9. SEM images of BFS 40% at 28 days curing time tested with CsI solution.

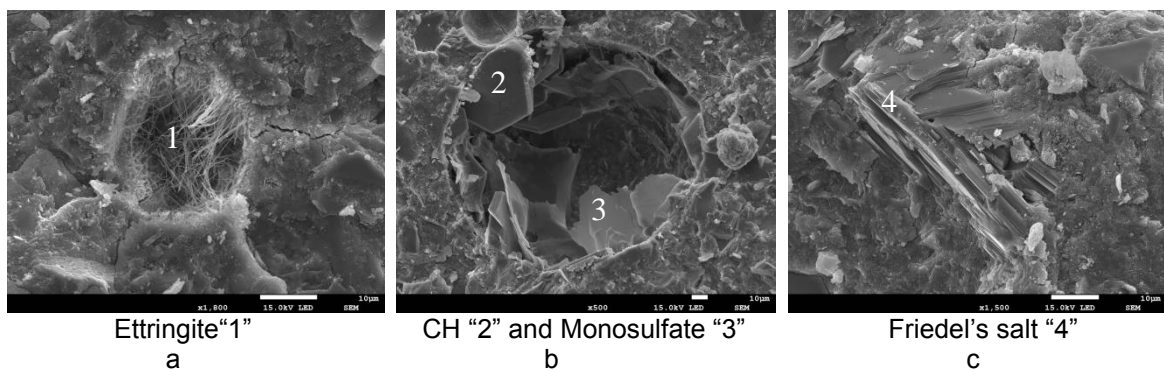


Figure 10. SEM images of BFS 60% at 28 days curing time tested with CsI solution.

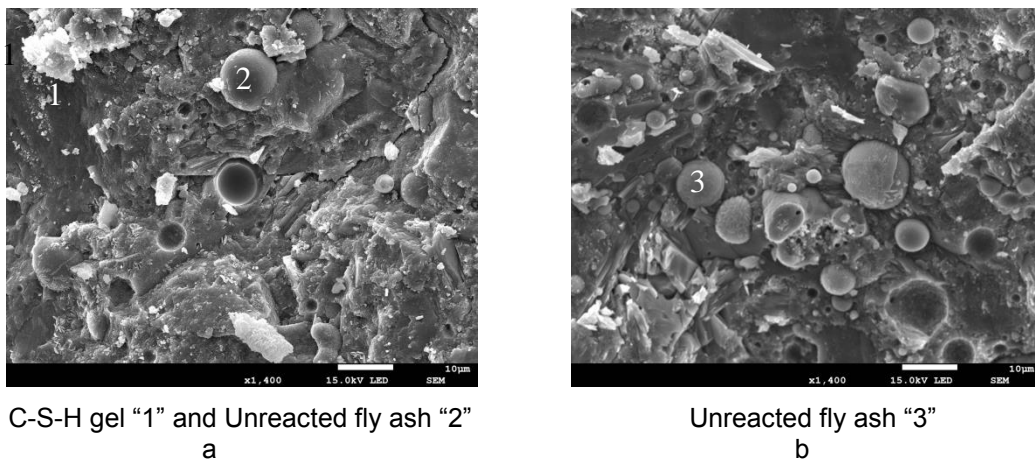


Figure 11. SEM images of (a) FA15%; (b) FA30% at 28 days curing time tested with CsI solution.

#### 4. Conclusions

The ionic diffusivity of cesium iodide (CsI) and sodium iodide (NaI) through cement pastes using mineral admixtures were measured according to self-diffusion test. These experiments, accompanied by post analysis such as DCS, XRD and SEM, are conducted to find out the influence of mineral admixtures along with low water to cement ratio (W/C) on the immobilization of cesium ( $\text{Cs}^+$ ), sodium ( $\text{Na}^+$ ) and iodide ( $\text{I}^-$ ) ions. The experiment results are confirming some concluding remarks.

From all the samples tested, BFS40% is showing smaller diffusivity compared to the other samples. Thus it is recommended to use BFS with this level of replacement ratio for immobilizing radioactive

wastes material. Although FA samples also show a good immobilizing effect of radioactive wastes material, the pozzolanic reaction of FA cement is slower and not yet stable at 28 days compared to BFS sample.

The ion immobilizing effect of the blended cement paste is due to the pozzolanic reaction of mineral admixtures with calcium hydroxide (CH) from cement hydration which produce calcium silicate hydrates (C-S-H) and calcium aluminosilicate hydrates (C-A-S-H). In addition, due to the pozzolanic reaction of blended cement pastes produce C-S-H gel with lower Ca/Si ratio, the binding and adsorptive capability of Cs<sup>+</sup>, Na<sup>+</sup> and I<sup>-</sup> ions were greatly improved compared to OPC sample. Moreover, it also could be noted that the formation of Friedel's salts also give influence in chemically bind the I<sup>-</sup> ions, especially for BFS samples, as could be confirmed by post analysis such as DSC, XRD and SEM analysis. Furthermore, ion diameter of Cs<sup>+</sup> is larger than that of Na<sup>+</sup> or K<sup>+</sup>. It is expected that the denser concrete with fine pores will give a significant immobilization effect of the Cs<sup>+</sup> ion.

In addition, decreasing W/C ratio is also significantly reducing the diffusivity of ions, especially for the I<sup>-</sup> ion, due to lower W/C ratio could reduce the porosity of cement paste. The lower W/C ratio not only significantly reduces the diffusivity of ions through OPC paste but also for the blended cement pastes. Especially for the FA samples, lower W/C ratio could replace the deficient of FA samples which have slower pozzolanic reaction.

## 5. Acknowledgements

The first author would like to acknowledge the Directorate General of Higher Education of Indonesia for providing his PhD scholarship.

## 6. References

1. Goñi, S., Guerrero A. et al., "Efficiency of fly ash belite cement and zeolite matrices for immobilizing cesium." *Journal of Hazardous Materials*, B137, 2006, pp 1608–1617.
2. Atkinson, A. and Nickerson, A.K., "Diffusion and sorption of cesium, strontium, and iodine in water-saturated cement." *Nuclear Technology*, 81, 1988, pp 100–113.
3. Holgersson, S., Albinsson, Y. et al., "Effects of gluco-isosaccharinate on Cs, Ni, Pm, and Th sorption onto, and diffusion into cement." *Radiochimica Acta*, 82, 1998, pp 393–398.
4. McCulloch, C.E., Rahman, A.A. et al., "Immobilization of cesium in cement containing reactive silica and pozzolans." in: G.G. Wicks, W.A. Ros (Eds.), *Advances in Ceramics*, vol. 8, Nuclear Waste Management, 1984, pp 413–428.
5. Bagosi, S. and Csetenyi, L.J., "Caesium immobilization in hydrated calcium–silicate–aluminat systems." *Cement and Concrete Research*, 28, 12, 1998, pp 1753–1759.
6. Xuequan, W., Sheng, Y. et al., "Alkali-activated slag cement based radioactive waste forms." *Cement and Concrete Research*, 21, 1991, pp 16-20.
7. Slamečka, T. and ŠKVÁRA, F., "The effect of water ratio on microstructure and composition of the hydration products of portland cement pastes." *Ceramics-Silikáty*, 46, 4, 2002, pp 152-158.
8. Skalny, J., Philips, J.C. et al., "Low water to cement ratio concretes." *Cement and Concrete Research*, Pergamon Press, Inc, 3, 1973, pp 29–40.
9. Živica, V., "Effects of the very low water/cement ratio." *Construction and Building Materials*, Volume 23, Issue 12, 2009, pp 3579–3582.
10. Hong, S.Y. and Glasser, F.P., "Alkali binding in cement pastes Part I. The C–S–H phase." *Cement and Concrete Research*, 29, 1999, pp1893–1903.
11. Glasser, F.P., "Characterisation of the barrier performance of cements." *Proceeding of Materials Research Society Symposium*, 2002, pp 721–732.
12. Malhotra, V.M., Ramachandran, V.S. et al., "Condensed silica fume in concrete." CRC Press Inc., 1987, Boca Raton, Florida.
13. Macphee, D.E., Atkins, M. et al., "Phase development and pore solution chemistry in ageing blast furnace slag-portland cement blends." *Materials Research Society Symposium*, 127, 1989, pp 475-480.

14. Hashimoto, T., Kubo, T., Sannoh, C., Torii, K. "A Development of Environmentally-Friendly and Highly-Durable Concrete Using Classified Fly Ash." Proceedings of Concrete Innovation Conference CIC2014, 11 – 13 June 2014, oslo, norwegia
15. Hover, K., "Curing and Hydration-Two half truths don't make a whole." L & M Concrete News, Vol.3, 2, 2002, [http://www.lmcc.com/concrete\\_news/0207/curing\\_and\\_hydration.asp](http://www.lmcc.com/concrete_news/0207/curing_and_hydration.asp).
16. Shariq, M., Prasad, J. et al., "Strength development of cement mortar and concrete incorporating GGBFS." Asian Journal of Civil Engineering (Building and Housing), 9, 1, 2008, pp 61–74.
17. Luo, R., Caib, Y. et al., "Study of chloride binding and diffusion in GGBS concrete." Cement and Concrete Research, 33, 2003, pp 1–7.
18. Cheewaket, T., Jaturapitakkul, C. and et al., "Long term performance of chloride binding capacity in fly ash concrete in a marine environment." Construction and Building Materials, 24, 2010, pp 1352–1357.

# Challenges contemporizing Australian Standards: Supplementary Cementitious Materials

**Craig Heidrich<sup>1</sup>**

<sup>1</sup>Ash Development Association of Australia, Suite 2 – Lvl 1 –336 Keira Street  
Wollongong, NSW Australia

**KEYWORDS:** Australian Standards, internationalization, fly ash, slag, amorphous silica

## ABSTRACT

The review of Australian Standards AS 3582, Part 1 – 1998 (Fly ash), Part 2 – 1991 (Slag – Ground granulated iron blast-furnace) and AS/NZS 3582, Part 3 – 2002 (Amorphous Silica) commenced in 2011 aimed at contemporising these material Standards of which selected standards have not been reviewed for more than 20 years.

In planning and undertaking this review process, a major function was to consult with, and seek the views of, major stakeholders prior to the commencement of the formal Standards review, through Standards committee BD-031. A collaborative pathway with Standards Australia was funded to achieve the review.

The review process included various producers, manufacturers and suppliers of these materials being consulted through the key industry association stakeholders. Considerable energy was spent on reviewing the existing national standards, elaborating proposed changes, collating supporting information for those changes and consulting across the appropriate membership groups to ensure alignment across the supply chain (generators, process and consumers). A review of international standards was undertaken to compare and contrast standards and test methods to ensure Australian standards are aligned, where appropriate.

The purpose of this paper is to inform of the work of Standards Committee BD031 which commenced in July 2014 on changes to Australian Standards AS 3582, Part 1 – 1998 (Fly ash), Part 2 – 1991 (Slag – Ground granulated iron blast-furnace) and AS/NZS 3582, Part 3 – 2002 (Amorphous Silica), rationale and supply uncertainty issues.

## INTRODUCTION

Large-scale use of coal in power generation gives rise to significant quantities of coal combustion products from which important ‘hard won’ end use markets have been established after many years, i.e. cement and concrete. The earliest recorded use of fly ash to enhance the properties of concrete occurred in the 1930s by the Cleveland Electric Illuminating Company based in the USA (Abdun-Nur 1961).



Existing and proposed end use markets for coal combustion products (CCPs) are not only of critical importance to the economics of power generation, but also to the established supply chain participants which have invested, researched, developed and promoted CCPs use into various applications, for example the construction sector use large quantities of CCPs. (Heidrich et al, 2013) reported globally, the continued growth in utilization of CCPs is dependent on many factors beyond the quality and characteristics, e.g. security of supply.

Appropriate legislation and regulation coupled with the development of international classification systems, standards and codes of practice are only a few of the important enablers for easing the way towards increasing utilization and securing the 'legal certainty' for continued investment. Maintaining contemporary standards are essential to functional supply chains (Heidrich et al, 2014).

## CONTEMPORIZING AUSTRALIAN STANDARDS

Focusing on Standards within Australia, a review of Australian Standards AS 3582, Part 1 – 1998 (Fly ash), Part 2 – 1991 (Slag – Ground granulated iron blast-furnace) and AS/NZS 3582, Part 3 – 2002 (Amorphous Silica) commenced in 2011 aimed at contemporising these material Standards of which selected standards have not been reviewed for more than 20 years. These supplementary cementitious materials (SCM's) account for more than 30 percent of all cementitious materials used in the Australia (ASA, 2013, ADAA, 2013, ASiAA, 2013).

In planning and undertaking this review process, Standards Australia strongly encouraged the stakeholder Association's to consult with, and seek the views of, major sectors prior to the commencement of the formal Standards review, through nominated representatives to Standards committee BD-031. The stakeholder Association's funded a collaborative pathway.

The review process, prior to submitting the 'Project Proposal' was conducted over two (2) years, during which time the various, generator, processor and suppliers of these materials were consulted through the respective industry associations of Ash Development Association of Australia (ADAA), Australasian (iron & steel) Slag Association (ASA), Amorphous Silica Association of Australia (ASiAA) and Cement Concrete Aggregates Australia (CCAA).

During this period considerable effort was committed to reviewing the existing documents, elaborating proposed changes, collating any supporting information for those changes and consulting across the appropriate membership groups to ensure alignment within the supply chain. In particular, changes in use and availability of materials meeting the requirements of AS 3582, was undertaken to understand the changing supply chain practices and emerging capacity constraints.

## EMERGING CAPACITY CONSTRAINTS

Over the last decade, a number of changes have occurred in the coal-fired power generation sector that has impacted on CCPs production volumes (supply), physical and chemical characteristics (quality), and environmental legislation. These changes include: modifications to coal-fired power generation plants to reduce emissions (in-

boiler and post combustion); the development of more fuel-efficient and more operationally flexible boiler plants; fundamental changes to the basic combustion process to prepare for carbon-capture technologies (for example oxyfuel combustion); changed legislative operating environment, e.g. impost of carbon tax, renewable energy targets, alone or together impacting of base load demand as reported by (Heidrich, 2013) and more recently the continued privatization of the public power generation.

Being by-products of coal fired power generation, CCPs in particular fly ash as defined in AS3582.1, has come under increased scrutiny for intermittent supply and quality issues in selected regions by major consumers. These regional shortages have raised concerns about changing economic impacts and practices of 'rationing' fly ash, from what is generally considered an abundant resource (ADAA, 2013). This supply uncertainty has resulted in major consumers conducting adhoc reviews of key specifications where, SCM's have secured hard won inclusions.

## SUPPLY UNCERTAINTY

Increasingly major consumers of CCPs report concerns regarding ongoing supply and availability issues across Australia. Examples of statements by major users such as *"...these supply shortages are unacceptable and costly....there clearly will be no [fly] ash available in 5 years as all power stations are shut down".... "we [major user] need to consider alternative materials for projects if these shortages continue"* and *".... we [major concrete pavement construction company] are aware of supply constraints on fine grade fly ash and are concerned about specifying fly ash in upcoming projects"*. These are just some examples of conversations with major consumers.

On investigation of these supply shortages claims during interviews with selected generator(s) advised they had undertaken various unplanned capital works (maintenance programs) with power stations units being placed into shut down, accordingly impacting on regional supply of graded fly ash. Given the planned nature and limited supply chain inventory associated with fly ash shortages had occurred. In isolation (one site) these activities would have limited impact, however in combination (multiple sites) these events seem to have resulted in what has been termed by major consumers that supply (cement and concrete) companies are 'rationing' fine grade fly ash, from what is an abundant resource.

Questions arising from this preprimary investigation identified the following questions

- Q. Is fly ash rationing occurring?
- Q. What are the facts about continued coal fired generation and accordingly coal combustion products supply?
- Q. Has coal fired generation capacity reduced i.e. Stations closed, resulting in shortages?
- Q. Are there capacity constraints and if so what capacity for other various grades exist and what is the role for the Standards review?

The first question.. *Is fly ash rationing occurring?..* is fraught with difficulties in determining, moreover uncovering the facts. The role of collection, processing and

distribution of fly ash is primarily controlled by companies owned or operated by cement companies, with a few exceptions. Requests for details are treated as commercial in confidence. Accordingly, no reliable analysis can be conducted on this question by the author. The remaining questions can be addressed using available primary and secondary data of the Associations to determine the facts about production and capacity to produced fine grade fly ash, moreover possible corrective measures and amendments to Standards.

## PRODUCTION AND CAPACITY ANALYSIS

Fortuitously a 'Production and Capacity Analysis', albeit limited in scope was undertaken, as part of the Cement Industry Action Agenda (DTIR, 2006), with the primary objective being to understand current coal fired generation capacity, fuel burned, coal combustion product generated and total stored which could be exploited by the cement industry. The analysis has been expanded and completed again in 2011 and 2013 providing some historical comparison and insights into changes for fly ash production; furnace bottom ash production; production capability for - Graded (fine), Ungraded (coarse & medium) and furnace bottom ash.

The production and processing capability stated in Table 1 is based on installed site design infrastructure capability at 100% utilisation. For example 'Generation Capacity' is the total MW installed for a given operating site at a given point in time, where as 'CCP Generated' is a function demand for energy i.e. 'Coal (fuel) Burned' x apparent ash content of coal. 'Fly Ash Graded Capability' means where processing capacity exists onsite to collect, capture and load vehicles with fine grade fly ash (AS3582.1). 'Fly Ash Ungraded Capability' means where processing capacity exists onsite to collect, capture and load vehicles with ungraded fly ash (1 to 300um). See Table 1 – Capacity Analysis 2006 to 2013.

State	Generation Capacity	Coal (Fuel) Burned	CCP Generated	Fly Ash	Furnace Bottom Ash	Fly Ash Graded Capability	Fly Ash Ungraded Capability	Furnace Bottom Ash Capability	CCP Diverted Storage	Total CCPs Stored
	MW	tonnes	tonnes	tonnes	tonnes	tonnes	tonnes	tonnes	tonnes	tonnes
NSW	11,991	24,623,900	6,292,781	5,126,302	991,479	1,150,000	2,000,000	600,000	2,542,781	196,325,000
QLD	8,046	20,437,483	5,611,975	4,770,179	841,796	1,200,000	1,370,000	560,000	2,481,975	126,932,430
VIC	5,800	55,572,204	1,111,444	944,727	166,717	0	0	0	1,111,444	35,295,241
SA	784	1,628,325	379,400	246,610	132,790	70,000	220,000	0	89,400	10,484,993
WA	2,097	5,175,000	459,000	398,400	60,600	140,000	120,000	40,000	159,000	6,732,000
NZ	1,000	794,940	55,646	38,952	16,694	10,000	5,000	7,000	33,646	100,000
2013	29,718	108,231,852	13,910,245	11,525,170	2,210,076	2,570,000	3,715,000	1,207,000	6,418,245	401,869,664
2011	29,704	126,461,941	14,553,568	11,972,761	2,349,947	2,560,000	3,710,000	1,200,000	7,083,568	391,645,908
2006	30,159	128,050,000	13,369,900							306,562,500
Change (+/-)	- 441	- 19,818,148	540,345							95,307,164
Change %	-1.5%	-15.5%	4.0%							31.1%
Utilisation			5,687,883	2,056,242	452,559	1,564,135	492,107	452,559		
Effective use			40.9%	17.8%	20.5%	60.9%	13.2%	37.5%		

Table 1 – Capacity Analysis 2006 to 2013

## OBSERVATIONS FROM THE ANALYSIS

Since 2006 total coal fired power generation capacity installed mega watts (MW) has decreased by 441MW or -1.5%. Plant maintenance upgrades to capacity at various

sites across Australia, less closure of older plant having been retired during the period. Retired sites were not identified as significant supply sites for fine grade ash. To summarise no significant change to installed power generation capacity has occurred.

The overall reduction in coal (fuel) used on the base line (2006) equates to 20 million tonnes or 15.5% reduction. Reduced fuel used means less total energy (MWh) being generated by coal fired power generation. In other words there is less demand for energy from coal with demand gaps being primarily filled by other renewable sources, driven mainly by government incentives and regulation, e.g. Renewable Energy Targets.

Interestingly, while there has been a reduction in total fuel used, coal combustion products generated have increased slightly by 0.540 million tonnes or 4%. This is consistent with trends identified in annual membership surveys that coal fired generators are using more marginal thermal coal sources with higher ashing contents - a trend that continues here and overseas. So in real terms, whilst energy from coal has reduced by some 15%, fly ash production has remained mostly unchanged over 10 years.

Focusing on graded<sup>1</sup> materials, capacity is reported at 2.5 million tonnes concentrated within NSW and QLD within two (2) power station sites. Whilst no data was captured in 2006, no significant change has been observed over the period. CCP used in cement and concrete applications for the 2013 was 1.6 million tonnes or 61% and in 2011 some 2.1 million tonnes or 81% of capacity utilised. Some possible factors attributed to a supply constraints;

- High concentration (> 60%) of fine grade (Graded) processing capacity centralized into limited coal fired power stations. Any unplanned interruptions in fly ash production will quickly translate to shortages
- No significant additional processing capacity for graded (fine) fly ash has been added in over 10 years
- Limited to no evidence of supply chain demand planning to compensate for low inventory capacity. Contributing factors to reduced volumes
- Renewables and lower emissions fuels being used in preference to coal
- Current Standards limit capability to use ungraded fly ash, where performance could be demonstrated

Installed coal fired power generation capacity and accordingly coal combustion products have not changed significantly in over ten (10) years, however capacity constraints for processing of fine grade ash have featured over the period through selective unit shut downs with sites where more 60% of processing capacity exists. Capacity for 3.7 million tonnes of ungraded materials has been installed over the past 10 years, but this material is poorly exploited by the current Standards. The question arises what is the role for the Standards review?

## ENABLING FUTURE CHANGE

<sup>1</sup> Fine Grade Fly ash -- Australian Standards AS 3582, Part 1 – 1998 (Fly ash)

The first change is in the title, and this change is proposed for all of the parts of AS 3582. The previous AS 3582 documents are entitled “Supplementary cementitious materials for use with Portland and blended cements”. The current proposal is to limit the title to “Supplementary cementitious materials”. There has been an attempt, for some time, to have the fly ash Standard in particular cover all aspects of fly ash use – not only for concrete, but for renders, mortars, grouts, stabilisation and various other potential uses such as geopolymers. The only real exception is when used as a mineral filler for asphalt residing in another Standard. By keeping the title to Supplementary Cementitious Materials (SCM) it is less specific about the options, but does at least confine them to cementitious uses.

The major areas of change in the draft are related to:

- alignment with AS3972 (2010) – Cement
- change in classification of the Grades of fly ash
- change in specified properties for Grades of fly ash
- adopt strength index (similar to ASTM)
- include measures of consistency for fineness and LOI values
- removal of available alkali test requirement given long term data
- review of testing frequency and reporting requirements
- alternate test method validation process
- alignment with AS3582.2 and AS3582.3

Standards are referenced in AS3600, AS1379 and AS3972. Where appropriate consequential amendments and alignment required to AS3600, AS1379 and AS3972 were considered along with consequential amendments and alignment with various Federal and State agencies infrastructure, building and construction related sector specifications. Alignment with international best practice adopted in similar standards globally will be considered as part of the review.

In summary the review consisted of updates of the standard requirements and inclusion of; scope of standard to include non-concrete related uses; new classes of materials; review appropriateness and confirm test methods and general updating of references to ensure the validity of the content. Test methods to be reviewed include

- 3583.1 Method 1: Determination of fineness by the 45 µm sieve
- 3583.2 Method 2: Determination of moisture content
- 3583.3 Method 3: Determination of loss on ignition
- 3583.5 Method 5: Determination of relative density
- 3583.6 Method 6: Determination of relative water requirement and relative strength
- 3583.8 Method 8: Determination of sulfuric anhydride content
- 3583.12 Method 12: Determination of available alkali
- 3583.13 Method 13: Determination of chloride ion content

Once finalized revisions to the Standard(s) will be reviewed by inviting public comment. The working committee currently expects to publish revised AS 3582 Series by the end of 2015.

## ABUNDANT AND POTENTIALLY EXPLOITABLE RESOURCE

The various utilisation pathways for CCPs reliant on the legislative, regulation and economics that drive the different participants (coal suppliers, generators, ash marketers and ash users) can have polarised interests in regards to the overarching utilisation goals. For example coal suppliers and generators prefer 'demand to be greater than supply' whereas ash marketers and ash users prefer 'supply to be greater than demand' with the corresponding value (Heidrich et al, 2014).

In microeconomics terms, supply and demand has important implications for price determination in any market. As an economic model used in competitive markets, the unit price for goods will vary until it settles at a point where the quantity demanded by consumers (at current price) will equal the quantity supplied by producers (at current price), resulting in an economic equilibrium for price and quantity.

The market for utilisation of CCPs however can be very broad, with an enormous range of potential applications. These applications range from cementitious uses through to bulk fills and emerging agricultural opportunities (Aiken et al, 2015). In addition a wide range of niche uses contribute small increases in total tonnages sold.

The beneficial use of coal combustion products (CCPs) consolidated during 2013 with 5.7 million tonnes or 52% effectively utilised resulting in the conservation of energy, finite natural resources, the reduction of greenhouse gas emissions and recovery of mineral by-product resources that would otherwise be placed into long term storage or emplacement.

The survey results for CCP production and categorised end uses for the period January to December 2013 can be found at ([www.adaa.asn.au](http://www.adaa.asn.au)) In summary from the 12.3 million tonnes of all CCPs produced some 52% of were effectively utilised within various civil and construction applications throughout Australasia (Australia and New Zealand). This compares well, given the uncertainty over with the introduction and subsequent withdrawal of Carbon Tax Legislation and wide ranging environmental reforms over the past 3 years. For previous periods of 2001, 2011, 2010, 2009 and 2008 resulted in effective utilisation of 42%, 48%, 41%, 34% and 31% respectively.

## SUMMARY

The review of the AS/NZS 3582 series was a planned process aimed at contemporizing these material Standards having not been reviewed for more than 13 years. In planning and undertaking this project a staged approach was considered in consultation with Standards Australia. That is, the project proponents consulted with, and sought the views of, major stakeholders prior to the commencement of the formal Standards review, through Joint Standards Australia/Standards New Zealand Committee BD-031.

The initial project review encompassed the various manufacturers, suppliers, users and academics with interest in these materials. Stakeholders were consulted through respective industry associations with a series of consultative meetings conducted to determined the review needed to address contemporary performance based

approach, widening the Standards application and methods of demonstrating compliance.

The major contributing supply chain factors were identified during the review were related to; closure/retirement of older coal fired power stations, the short-term closure of units to undertake earlier than planned maintenance; unplanned maintenance/repairs and ongoing privatization of coal fired power stations are contributing to uncertainty factors for supply. The net result during 2013 was a continuation of short-term interruptions within the supply chain for fly ash consumers, which highlight the limited and highly centralised processing and distribution capacity for fine grade fly ash across selected coal fired power station sites.

Accordingly, the Standards review introduces new classes of materials, definitions for proven and unproven sources and corresponding testing frequencies, incorporating product conformity requirements in the normative section which was previously in the 'informative' section.

The review considered and recommended, where appropriate, adopting international and national standards; existing referenced standards documents were reviewed, changes proposed and elaborated upon, and supporting information collated, with consultation across appropriate membership groups to ensure alignment across the supply chain.

In closing, the recovery and reuse of CCPs has been proven to provide positive and significant environmental impacts, including resource conservation and in this case, the reduction of greenhouse gas emissions from the processing of virgin resources, resulting in the reduction of carbon emissions. However, processors and major consumers singular focus on sourcing exclusively using fine grade fly ash, where other ungraded materials maybe suitable is unsustainable without significant investment into additional fine grade capacity.

Given uncertainty factors for with operation of coal fired power stations, more consideration should be given to exploitation or recovery of conditioned coal combustion products placed into ash dams.

## REFERENCES

Abdun-Nur, EA 1961, *Fly ash in concrete – an evaluation*, Highway Research Board Bulletin 284, Washington, USA.

ADAA (2013) <http://www.adaa.asn.au/resource-utilisation/ccp-utilisation>

Aiken, J. Heidrich, C. (2015) Australian Marketing Perspective Coal Ash for Agriculture. World of Coal Ash 2015. Nashville, TN, CEAR & ACAA

ASA (2013) <http://www.asa-inc.org.au/membership/annual-membership-reports>

ASiAA (2013) <http://www.asiaa.asn.au>

DITR (2006). *Punching Above its Weight - Australia's Cement Industry*. Canberra, Department of Industry, Tourism and Resources: pp. 87.

Heidrich, C., et al. (2013). Coal Combustion Products: A Global Perspective. World of Coal Ash 2013. Lexington, Kentucky USA, CEAR & ACAA. Vol 1: pgs 17.

Heidrich, C., et al., Eds. (2014). *Coal Combustion Products Handbook*. Wollongong, Australia, Ash Development Association of Australia.

Standards Australia (1991). *Supplementary cementitious materials for use with portland cement Part 2: Slag—Ground granulated iron blast-furnace*. AS 3582.2:1991. Sydney, NSW, Australia, Standards Australia.

Standards Australia (1999). *Supplementary cementitious materials for use with portland and blended cement Part 1: Fly ash*. AS 3582.1. Sydney, NSW, Australia, Standards Australia.

Standards Australia (2002). *Supplementary cementitious materials for use with portland and blended cement Part 3: Amorphous Silica*. AS/NZS 3582.3:2002. Sydney, NSW, Australia, Standards Australia.



# Effects of Chemical Admixtures and Aggregate Particles on Spatial Distribution of Cement Particles and Capillary Pores in Mortars

Takuma Nakagawa<sup>1</sup> and Shin-ichi Igarashi<sup>2</sup>

<sup>1</sup>Engineer, Aichi Prefecture Government Office, Japan

<sup>2</sup>Professor, Department of Civil and Environmental Engineering, Kanazawa University

**Abstract:** The point process statistics was applied to results of image analysis for backscattered electron images of cement pastes and mortars. Effects of chemical admixtures and sand particles on spatial distribution of unhydrated cement and capillary pores were investigated. Their distributions in actual mortars were compared to point patterns simulated by a thinning operation for the corresponding cement pastes. In cement paste specimens, cement particles dispersed randomly. However, spatial distribution of capillary pores exhibited clustered patterns if a superplasticizer or a viscosity enhancement admixture was not used. When the chemical admixtures were used, distributions of the pores nearly followed the complete random pattern. In mortars with a workable cement paste matrix, distributions of cement particles and the pores were the same as the ones obtained by thinning points from basic processes. Distributions of cement particles and capillary pores were not disturbed by sand in the workable mixtures. Sand particles had a simple role to delete points of cement and pores randomly. However, in mortars without the admixtures, clustering of cement particles and capillary pores was clearly reduced compared to the thinned processes. This mitigation of clustering depended on water/cement ratios. The more room for the particles, the greater mitigation was seen in mortars.

**Keywords:** point process, thinning, clustering, summary statistics, chemical admixtures

## 1. Introduction

It is needless to say that the most fundamental and important parameter to determine properties of concrete is a water/cement ratio, which is defined as a mass ratio. However, taking account of the fact that the density of Portland cement is not changed frequently, it is also possible to say in other words that properties of concrete are determined by the initial volume ratio of water against cement in a space available for a cement paste matrix. Furthermore, cement is a powder of which particle sizes are properly controlled in its production process. Therefore, as far as concrete is appropriately processed, the initial spatial distribution of cement particles can be regarded as a crucial parameter to determine the subsequent properties of concrete. Of course, pore structure affects strength and durability of concrete. However, its evolution with time is influenced by the initial arrangement of cement particles since the initial space for water, i.e. potential room for capillary pores is considered as a complementary set of cement particles dispersed in fresh cement paste.

In order to examine spatial structure of constituent phases in cement paste, image analysis techniques have been used. Geometrical features in images are evaluated based on the concept of stereology. The first-order stereology concept has been used for evaluating the quantity of constituent phases such as unhydrated cement and pores. However, these days, the summary statistics of second-order properties have been obtained for microstructure in cement paste since it enables to evaluate not only the quantity of the phases but also characteristics of spatial distribution such as clustering or regularly dispersing [1]. Furthermore, it also gives specific distances which characterize the distribution [2,3].

In this study, the point process statistics was applied to cement particles and capillary pores in backscattered electron images. They were converted to points. Effects of water/cement ratios and the addition of chemical admixtures on spatial distribution of the points are discussed. Furthermore, their distributions in actual mortars are compared with simulated patterns, which are obtained by a thinning operation for basic distributions in cement pastes. Effects of aggregate particles on the point patterns are discussed also from the viewpoints of interruption of free distribution and deflocculation of the points.

## 2. Experimental Procedure

### 2.1 *Materials and mix proportion of cement pastes and mortars*

The cement used was an ordinary Portland cement with a Blaine fineness value of 331m<sup>2</sup>/kg. River sand was used as a fine aggregate. Cement paste and mortar specimens of 100mm in height and 50mm in

Table 1 Mix proportion of cement pastes and mortars

Types	W/C	Cement	Water	Sand	SP(% wt/C)	VE(% wt/W)
Cement pastes	0.3	1	0.3	0	-	-
	0.3	1	0.3	0	1.0	-
	0.6	1	0.6	0	-	-
	0.6	1	0.6	0	-	0.6
Mortars	0.3	1	0.3	2	-	-
	0.3	1	0.3	2	1.0	-
	0.6	1	0.6	2	-	-
	0.6	1	0.6	2	-	0.6

SP: Superplasticizer, VE: Viscosity enhancement admixture

diameter were produced in accordance with JIS R5201. The water/cement ratios were 0.30 and 0.60. The mass ratio of sand to cement in mortars was 2.0. A superplasticizer (SP) and a viscosity enhancement admixture (VE) were also used to improve workability of mixtures. Mix proportions of cement pastes and mortars are given in Table 1. They were demolded at 24h after casting. The specimens with a water/cement ratio of 0.6 were then cured in water at 20°C for 3d.

## 2.2 Image acquisition and its conversion to a point process

At the age of 1d for w/c of 0.30, or 3d for w/c of 0.60, slices about 10 mm in thickness were cut from the middle of the height of cylinder specimens. They were dried by ethanol replacement and a freeze-drying procedure with t-butyl alcohol. Then they were impregnated with a low viscosity epoxy resin. After the resin hardened at room temperature, the slices were finely polished with abrasive papers. The polished surfaces were then finished with diamond slurry for a short time.

The polished samples were examined using an SEM equipped with a quadruple backscatter detector. In order to observe a wide field, the backscattered electron (BSE) images were acquired at a magnification factor of 60x (Fig.1(a)). The size of one pixel is about 1.85µm. Binary segmentation was made for pixels of unhydrated cement particles and pores (Fig.1(b)). Using a function of the image analysis software, coordinates of the centroid of each particle in the binary images were obtained. Then all the particles were converted to the points in the observation field. Those points in a 2-D image were regarded as a point process  $X = \{x_i; i = 1, \dots, n\}$  (Fig.1(c)).

## 2.3 Evaluation of cement paste matrix as a random field in mortar

A cement paste matrix in a mortar is considered as a complementary set of aggregate particles. If it is assumed that aggregate particles are distributed randomly throughout a mortar section, the cement paste matrix surrounding the aggregate particles is considered to occupy a region as a random field between the particles. In order to characterize geometrical features of the random field of the cement paste matrix, covariance function for the field was calculated. When a cement paste matrix is considered as a spatial set  $\mathcal{E}$ , its covariance function  $C(r)$  is given by Eq.(1).

$$C(r) = \Pr(x_1 \in \mathcal{E}, x_2 \in \mathcal{E}) \quad (1)$$

Where  $x_i$  ( $i=1, 2$ ) is a position vector of  $\|x_2 - x_1\| = r$ . To calculate the covariance function, a template with eight radial directions was placed on a binary image, in which a region of cement paste matrix was segmented. Whether both the center and the endpoints of the template fell in the cement paste matrix phase or not, was determined. This operation was repeated at different positions to obtain 10,000

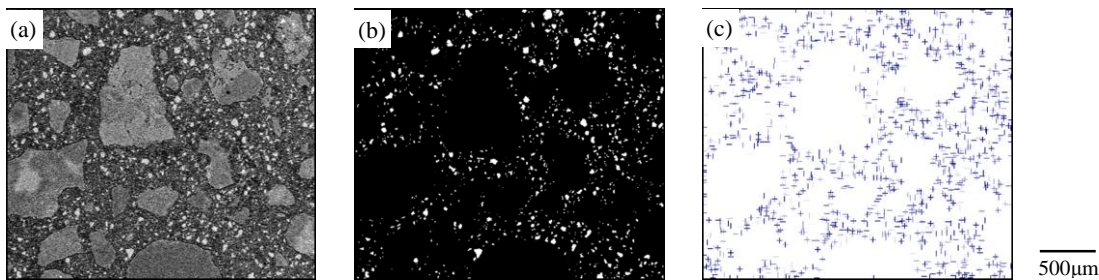


Fig.1 Example of conversion of unhydrated cement particles to a point process; (a) Backscattered electron image, (b) Binary segmentation of cement, (c) Point pattern

samples for a distance of  $r$ .

## 2.4 Point process statistics for cement particles and pores<sup>1)</sup>

### 2.4.1 K-function and the nearest neighbour distance function (G-function)

The point intensity  $\lambda$  of the point process  $X$  was determined from the images by the following equation.

$$\lambda = \frac{N(W)}{A(W)} \quad (2)$$

$N(W)$ : the total number of points in the observation window  $W=a \times b$

$A(W)$ : the area of  $W$

K-function ( $K(r)$ ) was calculated from the point pattern using Eq.(3).

$$K(r) = \frac{1}{\lambda^2} \sum_{i=1}^n \sum_{\substack{j=1 \\ (j \neq i)}}^n \frac{1_{[0,r]}(|x_j - x_i|)}{\bar{y}_W(|x_j - x_i|)} \quad (3)$$

Where  $1(\cdot)$  is the indicator function, i.e. equal to one if its argument is true and zero otherwise.  $r$  is distance, and  $\bar{y}_W(r)$  is the isotropized set covariance function of the window  $W$ . It is given as the mean area of the intersection of  $W$  with the  $W$  shifted by a random vector of length  $r$ .

The nearest neighbour distance function (G-function) was also calculated using Eq.(4).

$$\hat{G}(r) = \frac{\sum_{i=1}^{N(W)} \mathbf{1}(s_i \leq r) \cdot \mathbf{1}(s_i \leq b_i) \cdot w(s_i)}{\sum_{i=1}^{N(W)} \mathbf{1}(s_i \leq b_i) w(s_i)} \quad (4)$$

Where  $b_i$  is the shortest distance from each point  $x_i$  to edges of the window.  $s_i$  is the distance to the nearest other point in the point process.  $w(s_i)$  is a weighting factor, and given as the inverse of the window area eroded by a circle of radius  $s_i$  (Eq.(5)).

$$w(s_i) = \{(a - 2s_i)(b - 2s_i)\}^{-1} \quad (5)$$

From the K-function and the G-function, clustering tendency was simply judged for the point processes of unhydrated cement particles and capillary pores (Fig.2).

### 2.4.2 Thinning points from a basic process in a cement paste and K-function of the thinned process with a less point intensity

Spatial distribution of particles in cement paste specimens was used as a basic point process  $X_b = \{x_i | i = 1, 2, \dots, n\}$ . The K-function  $K_b$  for the basic pattern  $X_b$  was calculated following the same procedure as described in 2.4.1. Distribution of particles in actual mortar specimens was also considered as a point process  $X_p$ . If the point process  $X_p$  can be obtained by a thinning operation for  $X_b$ , then  $X_p = X_b \cap \Xi$ . Then the K- function of particles left in the thinned process,  $K_p$  can be calculated by Eq.(6) [1,4].

$$K_p(r) = \frac{1}{p^2} \int_0^r C(x) dK_b(x) \quad (6)$$

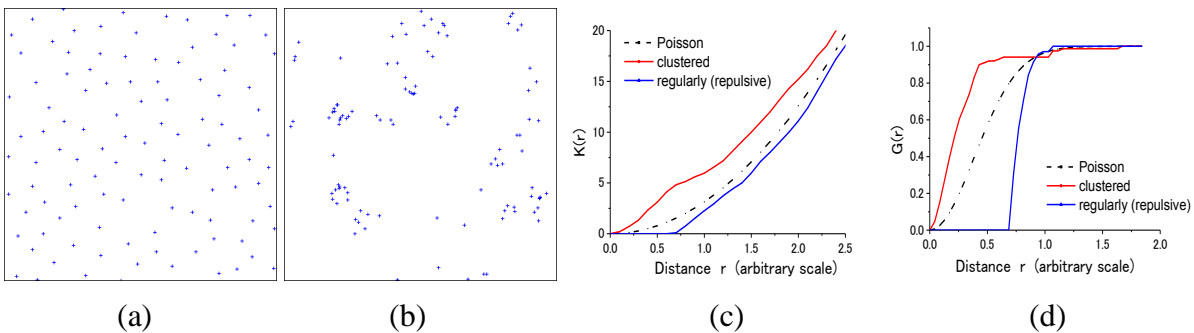


Fig.2 Examples of point patterns and their K- and G- functions (a) regular (repulsive) distribution (b) clustered distribution (c) K-function for the patterns (d) G-function for the patterns

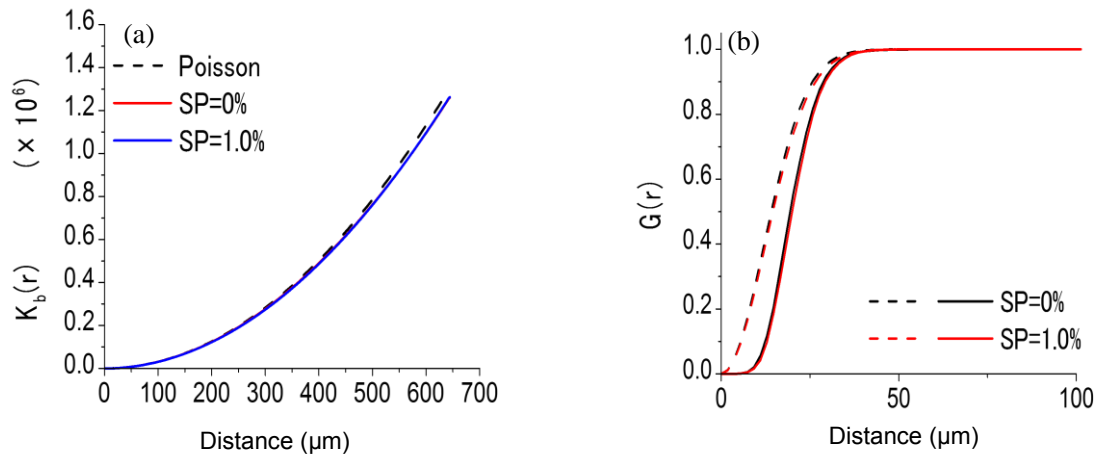


Fig.3 Distribution of unhydrated cement particles in cement pastes with a low w/c of 0.30; (a) K-function of unhydrated cement (b) G-function of unhydrated cement

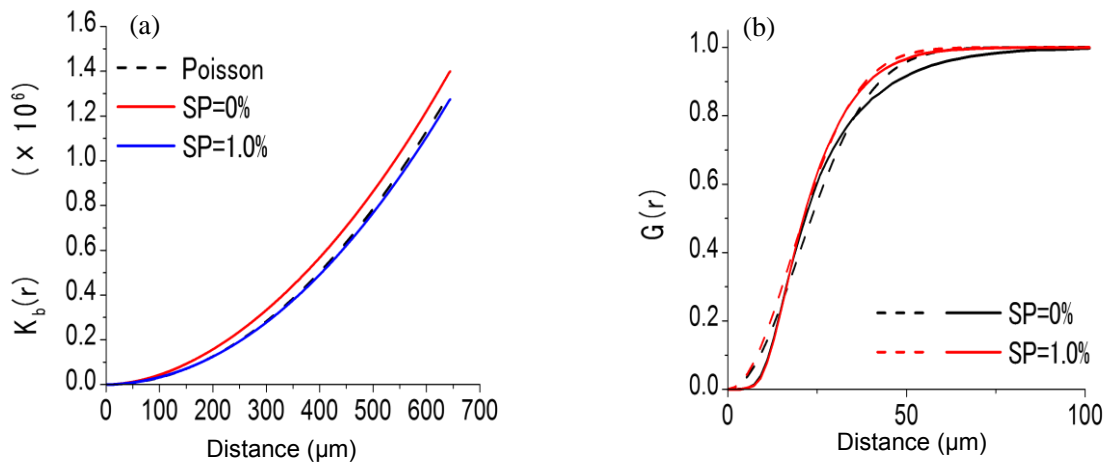


Fig.4 Distribution of capillary pores in cement pastes with a low w/c of 0.30; (a) K-function of pores (b) G-function of pores

Where  $p$  is the area fraction of a cement paste matrix in a mortar.

### 3. Results

#### 3.1 Spatial structure of cement particles and pores in cement pastes

Fig.3 shows K- and G- functions of unhydrated cement in cement pastes with a water/cement ratio of 0.30. Broken lines in the figures are the functions of completely random distribution, i.e. the Poisson point process. Regardless of the addition of a superplasticizer, the K-function of unhydrated cement particles follows the Poisson process. However, in the range shorter than  $50\mu\text{m}$ , the G-function of cement particles is smaller than the Poisson process. Hard core distances of about  $10\mu\text{m}$  are seen in the both cement pastes with and without the superplasticizer. This suggests that they dispersed regularly or repulsively in the short ranges. This distribution is due to the fact that the residual cement particles still have their own particle sizes. In particular, some of them are still large since it is at an early age of 1d. Therefore, points of the centroids cannot be closer each other.

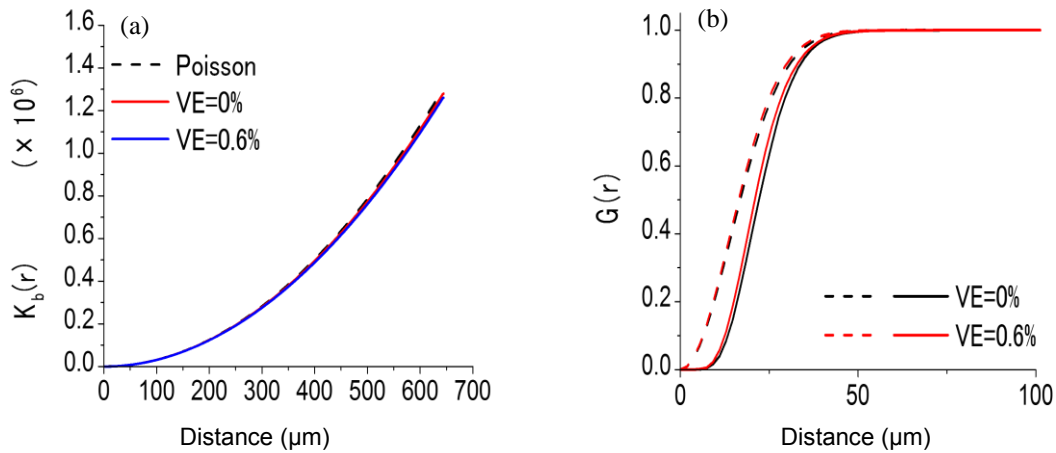


Fig.5 Distribution of unhydrated cement particles in cement pastes with a high w/c of 0.60; (a) K-function of unhydrated cement (b) G-function of unhydrated cement

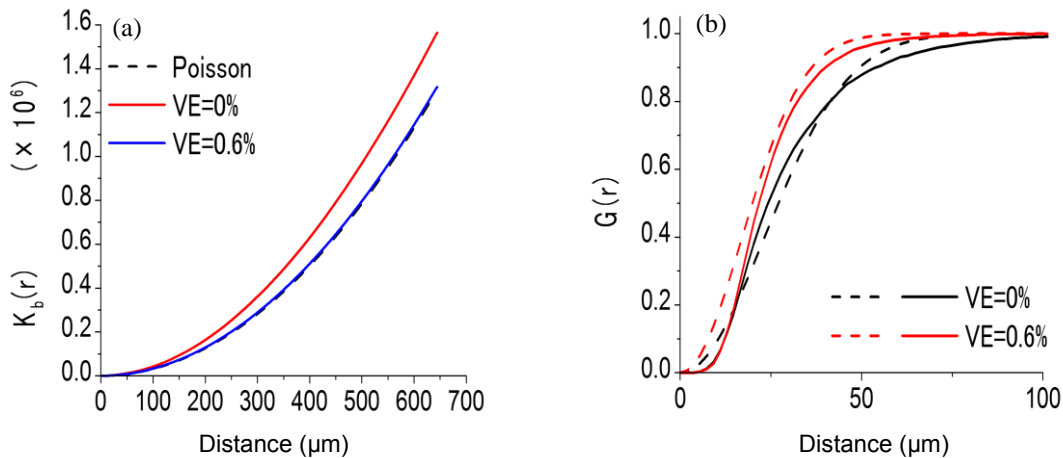


Fig.6 Distribution of capillary pores in cement pastes with a high w/c of 0.60; (a) K-function of pores (b) G-function of pores

On the other hand, situation of capillary pores (Fig.4) is different from that of the cement particles. When a superplasticizer is used, the K-function of the pores is almost the same as the Poisson process (Fig.4(a)). However, the K-function of the pores in cement paste without the superplasticizer exhibited a clustered pattern. The G-function of the pores in cement paste with the admixture exhibited a regular pattern within the distance of  $20\mu\text{m}$ , then followed the Poisson process beyond  $20\mu\text{m}$ . As for the pores in cement paste without the admixture, their distribution pattern varies with distances. In the range less than  $20\mu\text{m}$ , they are distributed regularly as well as in the cement paste with the admixture. In the range from about 20 to  $40\mu\text{m}$ , a clustered pattern is observed. However, beyond about  $40\mu\text{m}$ , the pattern follows a regular pattern again. It seems that the pores in the cement paste without the admixture are distributed more inhomogeneously. This heterogeneity is also found from convergence distances of the G-function. The convergence distance without the admixture is appreciably greater than that with the superplasticizer. This suggests that it is necessary to observe larger areas for unbiased evaluation of pore patterns since the pores disperse heterogeneously.

Fig.5 shows K- and G- functions of unhydrated cement in cement pastes with a water/cement ratio of 0.60. In this case, effects of bleeding on spatial distribution are of interest. Therefore, comparison is made between the distributions with and without the VE admixture. Cement particles in the cement pastes follow the Poisson process as well as at the water/cement ratio of 0.30. In other words, those particles dispersed randomly regardless of the addition of the VE admixture. Actually, bleeding was observed in the

specimens without the admixture. In this study, samples were taken from the middle of the height of specimens. In spite of some segregation, cement particles could disperse randomly in the middle of specimens. Capillary pores (Fig.6) also exhibit the similar patterns to those at the water/cement ratio of 0.30 (Fig.3). When the VE admixture was not used, the pores exhibited a clustered pattern (Fig. 6(a)). In the range of short distances, capillary pores were clustered between 20 and 40 $\mu\text{m}$  (Fig.6(b)). Their distribution is heterogeneous like the distribution with the w/c of 0.30.

It is found from Figs. 3 to Fig.6 that the admixtures did not greatly affect spatial distribution of cement particles in cement pastes. However, distribution of capillary pores was influenced by the admixtures to some extent. When the admixtures were used, their distribution became closer to the Poisson process as a whole. In other words, as long as cement pastes are workable due to the addition of the admixtures, cement particles and capillary pores disperse more randomly. However, if they are not used, inhomogeneous distribution appears for capillary pores. Capillary pores are considered as a complementary set of cement particles. However, they showed clustered patterns whereas cement particles showed almost random ones. This suggests that the evolution of pore structure depends on not only the initial arrangement of cement but also subsequent local geometrical conditions, which are changed by deposition of hydration products.

### 3.2 Spatial structure of cement particles and pores in mortar

Fig.7 shows covariance functions of cement paste matrices in mortars. It is difficult to specify a characteristic distance at which the function converges on the square of a volume fraction of the matrix. However, at least, it seems that two points are independent each other when the distance between them is beyond a few hundreds  $\mu\text{m}$ . Theoretically, the covariance at zero distance is equal to the area fraction (i.e. the volume fraction) of cement paste matrix in each mortar. They are 0.43 for the mortars with a w/c of 0.30, and 0.54 for them with a w/c of 0.60. When the chemical admixtures were used to obtain workable mixtures, the y-intercepts were almost the same as those theoretical values. However, in the mortars without the admixtures, there were certain differences between the theoretical values and experimental evaluations. This reflects inhomogeneous internal structure in the mortars with less workability.

Fig.8 shows K-functions of cement particles and capillary pores in mortars with a w/c of 0.30. In actual mortars, they are not allowed to disperse freely since there are aggregate particles. Therefore, the particles must exhibit clustered patterns. Actually, as expected, they exhibited clustered patterns in mortars. If these K functions for actual mortars agree with those for thinned point processes, then the actual distribution of the particles could be simulated by a simple thinning operation for the corresponding cement pastes. In view of the results of the thinning operation for cement particles in Fig.6(a), as expected, the particles in the thinned process exhibited clustered patterns regardless of the use of superplasticizer. In particular, a greater clustering tendency was seen when the superplasticizer was not used. Such a clustered distribution resulted from the fact that locations of cement particles were confined

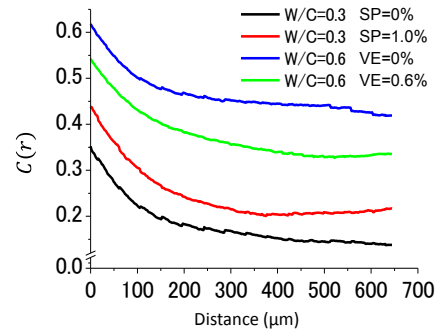


Fig.7 Covariance functions of cement paste matrices in mortars with and without admixtures

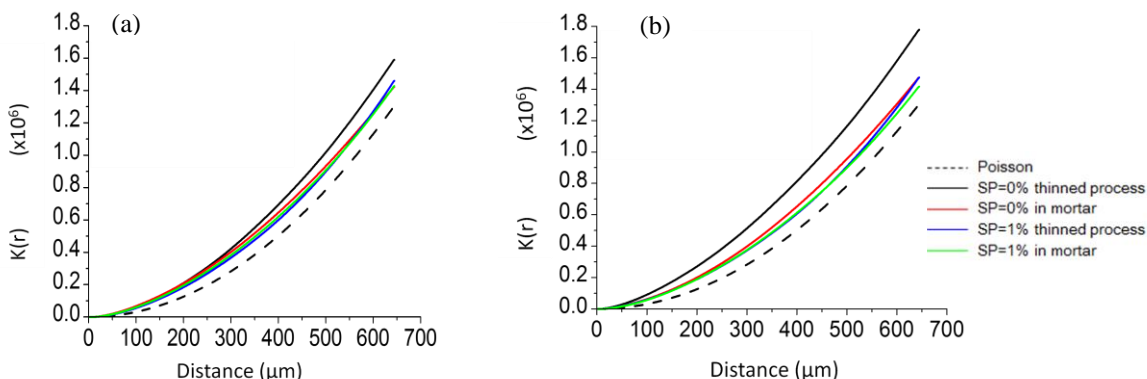


Fig.8 Comparison of K-functions of cement particles and pores between thinned processes and actual mortars with a w/c of 0.30; (a) cement particles (b) capillary pores



in the thinned point process also. The distribution of cement particles in actual mortars without the superplasticizer was similar to that in the thinned process in the range of a short distance up to 200 $\mu\text{m}$ . However, beyond this distance, the K function of cement in actual mortars showed less clustering than the simulation without the admixture. In other words, expected clustering of cement particles was mitigated. Contrary to this, there is little difference in the K-functions of cement particles and capillary pores between actual mortars and the thinned processes with the admixture. The agreement of the K-functions between the actual and the simulated point processes suggests that presence of aggregate particles simply reduces room for the particles. It does not affect spatial arrangement between the dispersed particles. This is quite different from the mortars without the admixture where clustering of the particles was appreciably mitigated by being mixed with aggregate.

Fig.9 also shows comparison of the K-functions at w/c of 0.60. As well as the distribution at w/c of 0.30 (Fig.8(a)), cement particles in the thinned processes were clustered (Fig.9(a)). When they were mixed with sand, their clustering was mitigated. Distributions of cement particles in the actual mortars were closer to the Poisson process. Mitigation of clustering was also clearly seen in distribution of capillary pores in mortars without the admixture. The K-functions for the actual mortars are appreciably smaller than those for the thinned processes. However, if the VE admixture was used, there were no differences in distribution of the pores between the thinned processes and the actual mortars. As long as the VE admixture was used as to obtain workable mixtures, in which no segregation occurred, spatial arrangement of capillary pores could be represented by the simulation. Deleting points in accordance with probability of being a matrix led to the actual distribution. Aggregate particles just played a role to reduce room for capillary pores.

#### 4. Discussion

It is found from Figs. 8 and 9 that aggregate mitigates clustering of the particles in mortars without chemical admixtures. As a result, distribution patterns become closer to the Poisson point process. On the other hand, when a superplasticizer or a viscosity enhancement admixture is used, effects of aggregate on spatial distributions of the particles are decreased so that characteristics of original distribution of cement and pores in workable cement pastes are substantially maintained in the mortars. Therefore, if the mixtures are workable, it is possible to simulate spatial distributions of constituent particles such as unhydrated cement and capillary pores by the thinning operation. The cement paste matrix in the workable mixture provides a random field in which the particles can survive. Each individual particle does not interfere with other particles.

In addition to workability, water/cement ratios also affect spatial distribution of the particles. When the superplasticizer was used, there was little difference in the K-functions of unhydrated cement particles between the thinned process and actual mortars at w/c of 0.30. On the other hand, when the viscosity enhancement admixture was used at w/c of 0.60, the K-function of unhydrated cement in actual mortars was smaller than in the thinned process. This means clustering of cement was mitigated at w/c of 0.60 whereas substantial mitigation was not seen at lower w/c of 0.30. This mitigation may result from a shear effect of aggregate particles, which breaks flocculation of cement particles during mixing of mortars. In order to break flocculation of cement, room for dispersion is necessary. At low w/c of 0.30, there is not enough margin for dispersing cement particles. As a result, similar distributions of cement are present in both of actual mortars and the thinned processes. However, at high w/c of 0.60, there is sufficient room for

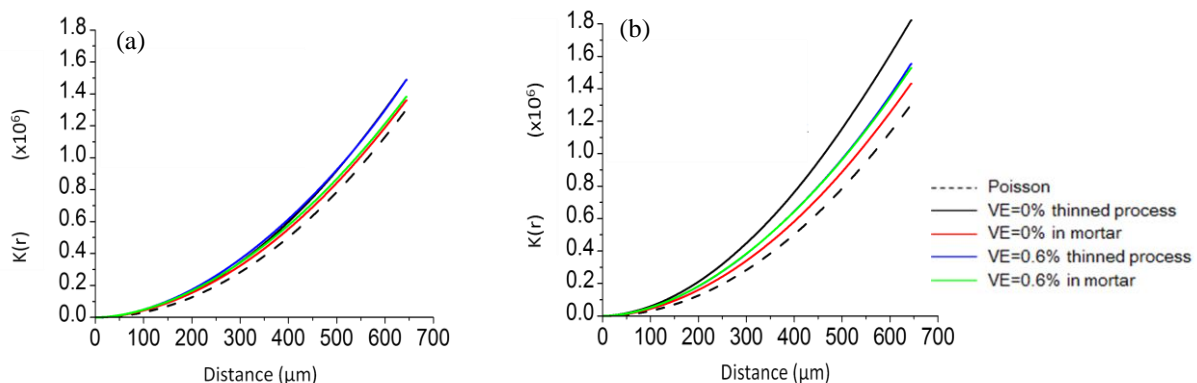


Fig.9 Comparison of K-function of cement particles and pores between thinned processes and actual mortars with a w/c of 0.60; (a) cement particles (b) capillary pores 584

dispersion of cement particles. Therefore, more random distribution of cement is possible so that the K-function of unhydrated cement in actual mortars is closer to the Poisson process.

## 5. Conclusions

In order to quantitatively evaluate spatial distribution of constituent particles of cement and capillary pores at early ages, the point process statistics was applied to 2-D distribution of unhydrated cement particles and capillary pores, which were segmented from backscattered electron images of cement pastes and mortars. Effects of the addition of a superplasticizer and a viscosity enhancement admixture on distribution of those particles were discussed in terms of summary statistics of the K-function and the nearest neighbor distance function (G-function). Effects of aggregate particles on distribution of those particles were also investigated based on the comparison between the simulated point patterns and the actual distributions in mortars. In the simulation, a cement paste matrix in each mortar was considered as a random field to keep the particles. The point process statistics were successful in evaluating differences in spatial distributions for cement and capillary pores. Major outcomes of this study are as follows;

- (1) In cement paste specimens, effects of the addition of a superplasticizer and a viscosity enhancement admixture on distribution of cement particles were relatively small. They distributed almost randomly irrespective of the chemical admixtures.
- (2) Capillary pores in cement paste specimens exhibited clustered distribution when the specimens didn't have proper workability. However, when the admixtures were used to obtain proper workability, clustering of capillary pores was mitigated. Their distributions followed a completely random process.
- (3) In the cement pastes without the admixtures, spatial distribution of capillary pores was inhomogeneous in the range of short distances.
- (4) Clustering of cement particles and capillary pores were mitigated in mortars with an unworkable cement paste matrix. Their distributions were closer to the random pattern.
- (5) In mortars with a workable matrix, characteristics of random distribution in the corresponding cement paste were largely maintained in the mortar.
- (6) If mortars are workable, distribution of cement particles and capillary pores in the mortars could be represented by the thinning operation, in which a cement paste matrix was regarded as a random field.
- (7) Effect of aggregate particles on spatial distribution of cement particles depended on water/cement ratios of the mixtures. Clustering of cement particles was effectively mitigated at a high w/c. The aggregate made a distribution of cement particles closer to the random point arrangement.

## 6. Acknowledgements

This study was supported by JSPS KAKENHI (Grant Number 24560564).

## 7. References

- [1] Stoyan, D., Kendall, W.S. and Mecke, J., "Stochastic geometry and its applications, second edition", John Wiley & Sons, 1995, Chichester, England.
- [2] Chermant, J.-L., Chelmant, L. et al., "Some fields of applications of automatic image analysis in civil engineering", Cement and Concrete Composites, 23(2-3), 2001, pp.157-169.
- [3] Dequiedt, A.-S., Coster, M. et al., "Study of phase dispersion in concrete by image analysis", Cement and Concrete Composites, 23(2-3), 2001, pp.215-226.
- [4] Stoyan, D., "Interrupted pointed process", Biom. J. 21(7), 1979, pp.439-449.



# The effect of type of fly ash on mechanical properties of geopolymer concrete

M.P.C.M.Gunasekara<sup>1</sup>, David W.Law<sup>2</sup>, Sujeeva Setunge<sup>3</sup>

<sup>1</sup>PhD Student, School of Civil, Environment and Chemical Engineering, RMIT University, Australia.

<sup>2</sup>Lecturer, School of Civil, Environmental and Chemical Engineering, RMIT University, Australia.

<sup>3</sup>Professor, School of Civil, Environmental and Chemical Engineering, RMIT University, Australia.

**Abstract:** The development of alkali activated binders with equivalent or better engineering properties has emerged as an alternative to Portland cement concrete. It is possible to use alkali activated fly ash to prepare environmentally friendly geopolymer concrete, which contribute to sustainable development. This paper presents a summary of an experimental program that has been conducted to determine mechanical properties of geopolymer concrete prepared with five different fly ashes obtained from different power plants in Australia. The variation in optimum 28-day compressive strength for the five fly ash based geopolymers was observed to be between 21.3 and 40.6MPa. The applicability of current relationships between compressive strength and tensile and elastic properties of concrete in AS 3600 for the range of fly ash geopolymers was then examined. The analysis showed that the flexural strengths of all geopolymer concretes are higher than the prediction of AS 3600, however, splitting tensile results appeared to depend on the fly ash source. When compressive strengths of fly ash based geopolymer concrete are below 40 MPa the model employed by AS 3600 for Portland cement concrete overestimates the modulus of elasticity. The Poisson's ratio's lie in the range reported for Portland cement concrete and show a general increase with increasing of compressive strength.

**Keywords:** Geopolymer, Fly ash, Concrete, Mechanical properties, AS 3600 standard.

## 1. Introduction

Concrete made with Portland cement (PC) is a major construction material used worldwide. However, the production of PC releases large amounts of CO<sub>2</sub> into the atmosphere, making a major contribution to the greenhouse effect and the global warming of the planet. The PC production involves very high temperatures (1400 to 1500 °C) and contributes between 5-7% of the anthropogenic CO<sub>2</sub> emissions worldwide [1, 2], with the production of 1 tonne of Portland cement producing from 0.6 up to 1 tonne of CO<sub>2</sub>, depending on the performance of cement kilns [3-7]. The 100% fly ash cements, widely known as geopolymer, is an emerging cementitious materials with greatest potential to provide a feasible alternative to PC in terms of CO<sub>2</sub> emissions. It is estimated that CO<sub>2</sub> emissions can be reduced by 26-45% with the replacement of PC concrete with geopolymer concrete [7, 8].

Fly ash (FA) production has increased up to 900 million tonnes per year by 2008 and it is anticipated to increase up to about 2000 million tonnes in 2020 [9]. While about 45% of this is being utilized for various purposes including cement and concrete production the balance is disposed of in landfills and storage lagoons at significant cost, posing a huge potential risk to local aquifers due to the possible leaching of heavy metals. Thus, producing geopolymer binders using FA is an added benefit is to convert a waste product into a useful by-product, conserving landfills and storage lagoons [10]. In the geopolymerization process, silica and alumina molecules contained in the FA react under highly alkaline conditions, typically provided by sodium based hydroxide and silicate solution. FA geopolymers need heat curing to increase the geopolymerization reaction while slag based geopolymers react at lower temperatures. However, couple with other environmental issues, FA based geopolymer production can contribute to precast concrete products such as structural elements, railway slippers and sewer pipes which can be highly resistant to the aggressive environments and fire expose.

In geopolymerization process, an amorphous three-dimensional network of silicon and aluminum atoms are linked by oxygen atoms in a four-fold coordination similar to the one exhibited by zeolites. While the formation mechanism of the geopolymer network is still debated, it was suggested that the reaction can be divided into three main stages, i.e. dissolution of silicate and aluminate species from the FA, transportation and coagulation/gelation, and condensation forming a three-dimensional network of alumino-silicates.

A number of studies have been conducted to investigate the material properties of FA geopolymer concretes and demonstrated the similarity of FA based geopolymer concrete to PC concrete in terms of the mechanical properties. However, most of the studies to date investigated the mechanical properties using a single type FA in each study using a mixing process unique to that study. The present study aims to investigate key mechanical properties of geopolymer concretes made with five Australian FAs with a range of chemical and physical properties, using the same mixing process. The mechanical properties investigated were compressive strength, tensile strength, modulus of elasticity and Poisson's ratio. The variation of test results in different FA geopolymers are explained in conjunction with the applicability of current relationships between compressive strength and the mechanical properties based on AS 3600 [11]. Finally, test results will be compared with previously reported research on mechanical properties of geopolymer concrete.

## 2. Experimental work

### 2.1. Materials

Class F fly ash conforming to Australian standard, AS 3582.1 were obtained from Gladstone(G), Port Augusta(PA), Collie(C), Mount Piper(MP) and Tarong(T) power stations in Australia. The chemical composition, particle size distribution and mineralogical composition of each FA, determined by X-ray fluorescence (XRF), Malvern particle size analyser instruments and X-ray diffraction (XRD), respectively are shown in Table 1, 2 and 3. Brunauer Emmett Teller (BET) method by N<sub>2</sub> absorption was used to determine the FA surface area. The alkaline liquid used in geopolymers consisted of a mixture of commercially available sodium silicate solution with a specific gravity of 1.53 and an alkaline modulus ratio (Ms) equal to 2 (where Ms= SiO<sub>2</sub>/Na<sub>2</sub>O, Na<sub>2</sub>O=14.7% and SiO<sub>2</sub>=29.4% by mass), and sodium hydroxide solution (15M). Both coarse and fine aggregate were prepared in accordance with AS 1141.5. The moisture condition of the aggregate was in a saturated surface dry condition. The fine aggregate was river sand in uncrushed form with a specific gravity of 2.5 and a fineness modulus of 3.0. The coarse aggregate was crushed basalt aggregate of two-grain sizes: 7 mm (2.58 specific gravity and 1.60% water absorption) and 10 mm (2.62% and 0.74%). Demineralized water was used throughout the experiment.

**Table 1. Chemical composition of FA**

FA type	by weight (%)										
	SiO <sub>2</sub>	Al <sub>2</sub> O <sub>3</sub>	Fe <sub>2</sub> O <sub>3</sub>	CaO	K <sub>2</sub> O	TiO <sub>2</sub>	P <sub>2</sub> O <sub>5</sub>	MgO	Na <sub>2</sub> O	SO <sub>3</sub>	MnO
GFA	47.88	25.10	15.54	4.66	0.86	1.76	2.20	0.96	0.0	0.38	0.19
PAFA	49.37	31.25	4.47	4.80	2.21	2.94	1.65	1.28	1.30	0.24	0.04
TFA	69.21	24.60	1.03	0.38	0.60	2.54	1.28	0.0	0.0	0.15	0.0
CFA	56.75	27.39	7.83	1.34	0.68	2.12	1.58	0.67	0.0	0.55	0.02
MPFA	65.24	25.20	1.12	0.83	4.21	1.74	1.16	0.0	0.0	0.25	0.0

**Table 2-Physical properties of FA**

Properties investigated	GFA	PFA	TFA	CFA	MPFA
BET Surface Area, (kg/m <sup>2</sup> )	2363	1228	1876	1095	1026
Fineness (%)	at 10 microns	43.1	46.7	43.0	36.0
	at 20 microns	61.9	62.1	63.0	57.1
	at 45 microns	82.7	80.2	81.8	70.0
Unburnt carbon content (%)	0.43	0.51	1.16	0.63	1.30

**Table 3- Mineralogical composition of FA**

Mineralogical composition (%)	GFA	PFA	TFA	CFA	MPFA
Amorphous	71.8	59.5	66.3	72.5	79.2
Quartz	6.8	29.2	14.8	18.2	7.2
Mullite	17.9	7.5	18.9	8.7	13.6
Others	3.5	3.8	0	0.6	0

## 2.2. Mix designs

A similar mix design procedure, based on FA geopolymer mortar, reported in reference [12] is used to optimize the mix design for each FA geopolymer concrete. The blended sodium silicate and sodium hydroxide solutions are characterized by the activator modulus (AM), i.e. SiO<sub>2</sub> to Na<sub>2</sub>O ratio in the activator solution, was varied from 0.75 to 1.75 by 0.125 intervals, until the optimum compressive strength for each FA geopolymer concrete at 28 days. Table 4 shows the ingredients of each optimum mix design. In this study, the Na<sub>2</sub>O dosage is fixed at 15% while the total aggregate in the concrete was kept to 64% of the entire mixture by volume for all mixes. The ratio of ingredients (FA, chemical activator, aggregate, and water) was calculated based on the absolute volume method [13], as a result, the total weight of binder and water was varied to keep the volume of material and water/solid ratio (0.37) constant. The mass of water in the mix was taken as the sum of mass of water contained in the sodium silicate, sodium hydroxide and added water. The mass of solid is taken as the sum of FA, the solids in the sodium silicate solution and the sodium oxide pellets.

**Table 4. Optimum mix design details (kg/m<sup>3</sup>)**

Geopolymer type	FA (kg)	Aggregates (kg)			Activator (kg)		Added water (kg)
		Sand	7mm	10mm	Na <sub>2</sub> SiO <sub>3</sub> (Liquid)	NaOH (15 M)	
GFA	416	699	309	618	292	65	8
PAFA	416	699	309	618	292	65	8
CFA	420	706	312	624	241	92	15
MPFA	425	714	315	631	163	132	30
TFA	412	693	306	612	342	39	0

## 2.3. Mixing, curing and testing

The mixing of geopolymer concrete was carried out using a 90 litre concrete mixer. The dry materials (FA, fine and coarse aggregates) were mixed first for 4 minutes. Then activator and water were added to the dry mix and mixed continuously for another 8 minutes until the mixture was glossy and well combined. The mixture was then poured into moulds and vibrated using a vibration table for 1 minute to remove air bubbles. After vibration the moulds were kept at room temperature for 1 day and then heat cured in an oven for 24 hours at 80°C temperature with 95% relative humidity. The inside surfaces of the moulds were coated with a high performance silicon grease to prevent the samples from sticking to the moulds surface during the heat curing process. Moulds were removed from the oven and left to cool to room temperature before demoulding, and then the samples were kept at room temperature.

Compressive strength test was performed by MTS machine with a loading rate of 20MPa/min according to AS 1012.9. The flexural tensile strength and splitting tensile strength tests were conducted to determine the tensile strength of fly ash based geopolymer concretes in accordance with AS 1012.11 and AS 1012.10, respectively. The flexural tensile strength test was carried out on a MTS machine with additional testing apparatus under a four point bending test with a loading rate of 1 MPa/min. The indirect tensile strength test was performed on MTS machine equipped with indirect tensile strength test equipment under a loading rate of 1.5 MPa/min. The static elastic modulus and poisson's ratio of geopolymer concretes was determined using TCM machine coupled with the compressometer/extensometer with a loading rate of 0.25 MPa/sec in accordance with AS 1012.17. The dry density of hardened geopolymer concrete was determined accordance with AS 1012.12.2. All tests were conducted at 28 days of casting. The reported test results in each specific test are an average of three samples.

## 3. Results and discussion

The 28-day strength properties related to different FA geopolymer concretes are presented in Table 5. Density of geopolymer concrete ranged from 2017 to 2167 kg/m<sup>3</sup> which agrees with the previously reported work [14, 15]. The density of FA geopolymer concrete is generally lower than PC concrete which is characteristically cited with a density of approximately 2400 kg/m<sup>3</sup> in accordance with Australian standard, AS 3600. This might be attributable to the specific gravity of the raw materials used to produce FA geopolymer concrete, i.e. experimentally measured specific gravity of the FA is 2.0–2.3 which is lower than that of PC with a specific gravity of 3.0–3.2. In contrast, all FA geopolymers except MPFA displayed a very high, collapsed slump, thus workability of this study is

represented by the average diameter of slump flow ranging from 365mm to 665mm. Demie et.al [16] also reported higher slump flow values attributed to low calcium FA which ranged between 625mm to 710mm. This is attributed to the spherical shape of fly ash particles combined with the lubricating effect of sodium silicate solution. However, MPFA leads to a very stiff mix and achieved a low workability with 40mm slump height.

**Table 5. Experimentally measured strength properties**

Geopolymer	Workability (Slump flow mm)	Dry density (kg/m <sup>3</sup> )	Strength property (MPa)		
			Compressive strength (fc)	Splitting tensile strength (fct.sp)	Flexural tensile strength (fct.f)
GFA	665	2142.1	40.6	3.67	5.07
PAFA	645	2017.9	33.5	2.87	4.40
TFA	560	2164.2	31.0	1.84	4.13
CFA	365	2115.8	22.8	2.78	4.56
*MPFA	-	2166.2	21.3	0.94	3.22

\*40mm of slump height is achieved.

### 3.1 Compressive Strength

In this study, the compressive strength ranged from 21.3 to 40.6 MPa while highest and lowest values were obtained by GFA and MPFA geopolymers, respectively. As specified in AS 3600, the 28 day compressive strength for standard site concrete under exposure classification B1 and B2 is  $40 \pm 10$  MPa. However, only GFA, PAFA and TFA geopolymers achieved this strength. The compressive strength achieved by other two geopolymer concretes only satisfied the exposure classification A1 compressive strength of 20 MPa. Hence, this significant variation of data clearly shows that properties of geopolymer concretes are strongly dependent on the characteristics of the source material, that is type of FA used in here. The GFA has highest surface area with higher level of finer particles passing at 10, 20 and 45 micron sieves. It further consists with higher percentage of reactive alumina-silica amorphous phase. Formation of aluminosilicate gel,  $[\text{Na}_z(\text{AlO}_2)_x(\text{SiO}_2)_y \cdot \text{NaOH} \cdot \text{H}_2\text{O}]$ , in the geopolymerization process primarily relies on the extent of dissolution of FA. The finer particles coupled with greater surface area increase the reactivity of FA, because a significant part of the reaction occurs at the particle-liquid interface [17]. On the other hand, the reactive amorphous alumina-silica species contained in FA precursor rapidly reacts with alkaline activator. Thus, aforementioned properties of GFA are attributed to the rapid gel formation, the dominant step in formation of an amorphous structure of FA geopolymers which determined the highest compressive strength for GFA.

The CFA and MPFA have lowest surface area coupled with higher percentage of coarser particles, Table 2, i.e. lower level of finer particles passing at 10, 20, 45 micron sieves. Hence, these FA characteristics lead both geopolymers to the lowest compressive strength while contained with high amount of reactive amorphous alumina-silica species than GFA. As well, both geopolymers show lower workability than GFA, which is also attributed to the higher content of coarser particles. Because, during the mixing of geopolymer, the activator solution demand rises as the fineness of the FA decreases due to the need to fill larger voids among coarser FA particles to achieve a workable material. And also high unburnt carbon in FA acts as an inert particulate and absorbs the activator solution [17], hence this further reduced the workability of MPFA, making a stiff, non-workable concrete mix.

While the PAFA and TFA contain higher percentage of finer particles (percentage passing at 10, 20, 45 micron sieves), both surface area and reactive amorphous content of these FAs are lower than GFA. This leads both geopolymers towards the moderate compressive strengths. Moreover, the PAFA has highest CaO percentage while TFA has the lowest. A high content of CaO in the FA allows the calcium silicate glass structure in the FA to react with the water and to form calcium silicate hydrate (C-S-H) compounds that improve the compressive strength of the resultant geopolymer. On the other hand, TFA contains higher unburnt carbon which attributes to its lower workability than PAFA. Hence, highest CaO coupled with lower unburnt carbon in PAFA leads to a slightly better compressive strength and workability though it has lower surface area than TFA.

### 3.2 Tensile Strength

Tensile strength of geopolymer concrete was measured using both splitting tensile and flexural tensile strength tests. The splitting tensile strength varied between 0.94 and 3.67MPa, whereas, the flexural tensile strength ranged from 3.22 to 5.07 MPa (Table 5). The flexural strength ranged between 12 and 20% of the compressive strength, compared to a range of 9 to 12% typically cited for PC concrete. Diaz-loya et al. [14] also reported a similar trend, that the flexural strength ranged between 7 and 26% of the compressive strength. The splitting tensile strength in this study ranged between 4 and 13% of the compressive strength which agreed with the Literature [18].

Similar to compressive strength, GFA gave the highest splitting and flexural tensile strength results while MPFA had the lowest. Fly ash is dissolved in sodium hydroxide while forming a gel layer on their surfaces. Then gel diffuses outward from the particle surface into larger interstitial spaces between the particles with precipitation of gel and concurrent dissolution of new fly ash grains. When the gel phase hardens, the separate fly ash particles are bound together by the gel which acts as a binder [19]. Tensile strength of FA geopolymer is highly dependent on the bond between this gel binder and aggregates. Due to high reactivity and concurrent gel formation of GFA geopolymer produce a strong bond between aggregates and gel binder which contributes to the highest tensile strength in concrete. In contrast, MPFA contains high unburnt carbon content which is hypothesised as weakening the bonding with aggregates, thus lower dissolution, reactivity and gel formation coupled with weak bonding characterise the lower tensile strength achieved in MPFA.

While TFA had a compressive strength in excess of 30 MPa, it had relatively low splitting tensile strength. Fernandez-Jimenez et.al [20] has reported that presence of  $\text{Si}^{+4}$  ions in the alkaline solution has a substantial negative effect on the very strong matrix/aggregate bond. TFA contains the higher amorphous  $\text{SiO}_2$  content, which may result in more  $\text{Si}^{+4}$  ions being leached into the alkaline solution and hypothesized as remaining as free ions, leads to lower tensile strengths. Though CFA geopolymer achieved very low compressive strength, it shows higher tensile strength which is almost similar to PAFA. This indicates that while CFA gel binder has less strength, it creates better bonding with aggregates. However, further study needs to verify this behaviour.

The uniaxial tensile strength of FA geopolymer concretes is calculated in accordance with AS 3600. The calculated uniaxial tensile strength based on measured flexural strength is higher than calculations based on splitting tensile strength in all geopolymers, except GFA which shows slightly higher value. However, both TFA and MPFA geopolymers showed significant variation in uniaxial tensile strength based on splitting and flexural strength data. Thus the choice of the test on which to base the uniaxial tensile strength is a critical factor. According to Neville [13], the splitting test is both simple to perform and gives more uniform results than flexural strength test. The splitting test gave the most conservative estimates for the uniaxial strength, which would provide more confidence in designing structures and as such would be recommended as the most appropriate test for geopolymer concretes.

**Table 6. Calculated uniaxial tensile strength,  $f_{ct}$  based on AS 3600**

Geopolymer	Based on Split tensile strength $f_{ct} = 0.9f_{ct.sp}$	Based on Flexural tensile strength $f_{ct} = 0.6f_{ct.f}$
GFA	3.28	3.14
PAFA	2.58	2.64
TFA	1.66	2.48
CFA	2.50	2.74
MPFA	0.85	1.93

### 3.3 Relationship between compressive and tensile strengths

For design calculations, it is usual to estimate the tensile strength from the compressive strength for PC concretes which is illustrated in AS 3600. In order to examine the applicability of this relationship for geopolymer concretes, splitting tensile and flexural strength data were plotted against measured compressive strengths of five concretes at Figure 1 and 2, respectively. Previously reported results and derivations based on FA geopolymers were reported in order to verify the spread of the present experimental data.

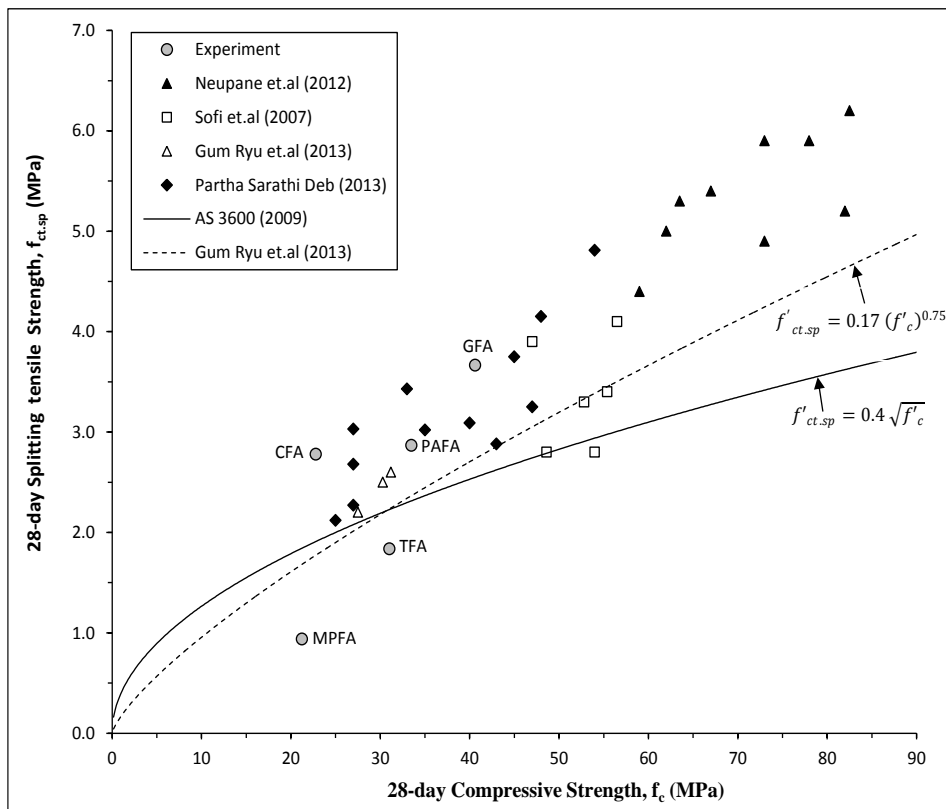


Figure 1. Splitting tensile strength vs. compressive strength

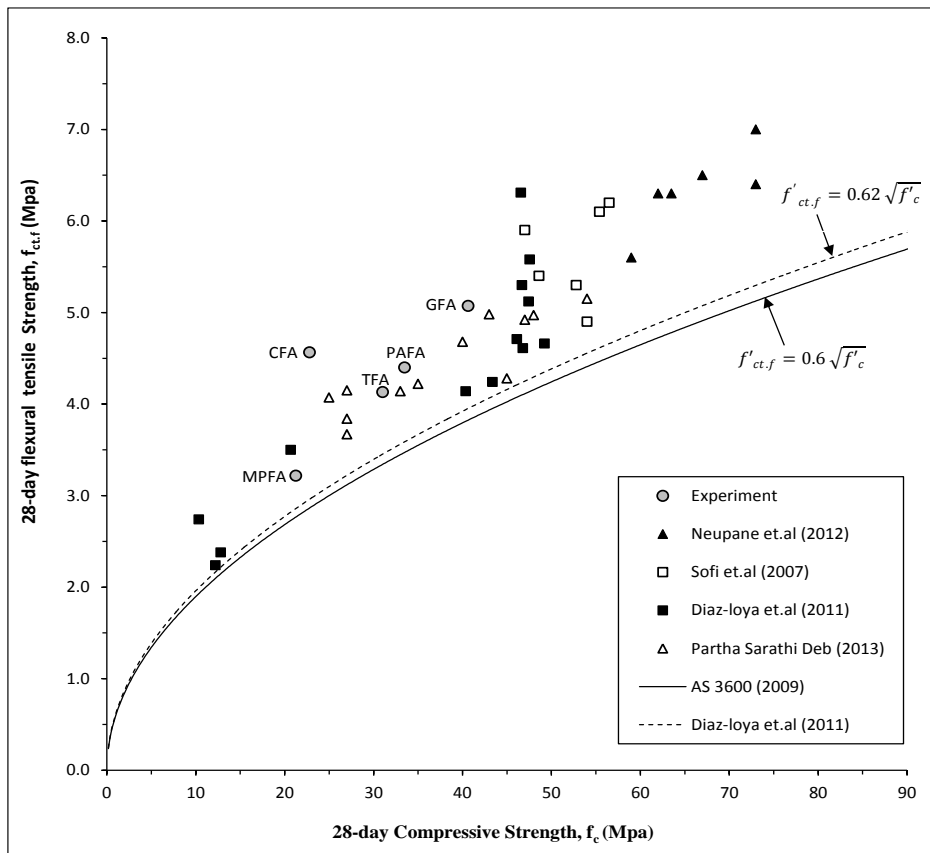


Figure 2. Flexural strength vs. compressive strength

Previously reported splitting strength data were based on the single type of FA and all of them exceeded the AS 3600 model whilst demonstrating spread of results (Figure 1). Three of five examined geopolymers, namely GFA, PAFA and CFA, achieved the splitting tensile

strengths above the AS 3600 prediction of PC concrete and Ryu et.al's [18] prediction of geopolymer concretes. However, TFA and MPFA geopolymer concretes had measured splitting tensile strength below those predicted by the AS 3600. This indicates that the correlation of splitting tensile strength with compressive strength depends on the type of FA used as source material and there is no direct relationship between the compressive and tensile strength of geopolymer concrete made with different FA materials. In contrast, both experimentally measured and previously reported flexural strengths of FA geopolymer concretes exceeded the prediction of AS 3600, Figure 2. That is unlike splitting tensile data, all five fly ash geopolymers showed the conservative approach at the design stage. In previously reported results, except Diaz-loya et.al. [14], all others worked with single type of FA. The present study results are slightly higher than the previously reported relationships by Diaz-Loya et al. [14] for geopolymer concrete. Hence, this analysis confirmed that while flexural strength is changed based on the type of FA, those variations may not affect the design standards.

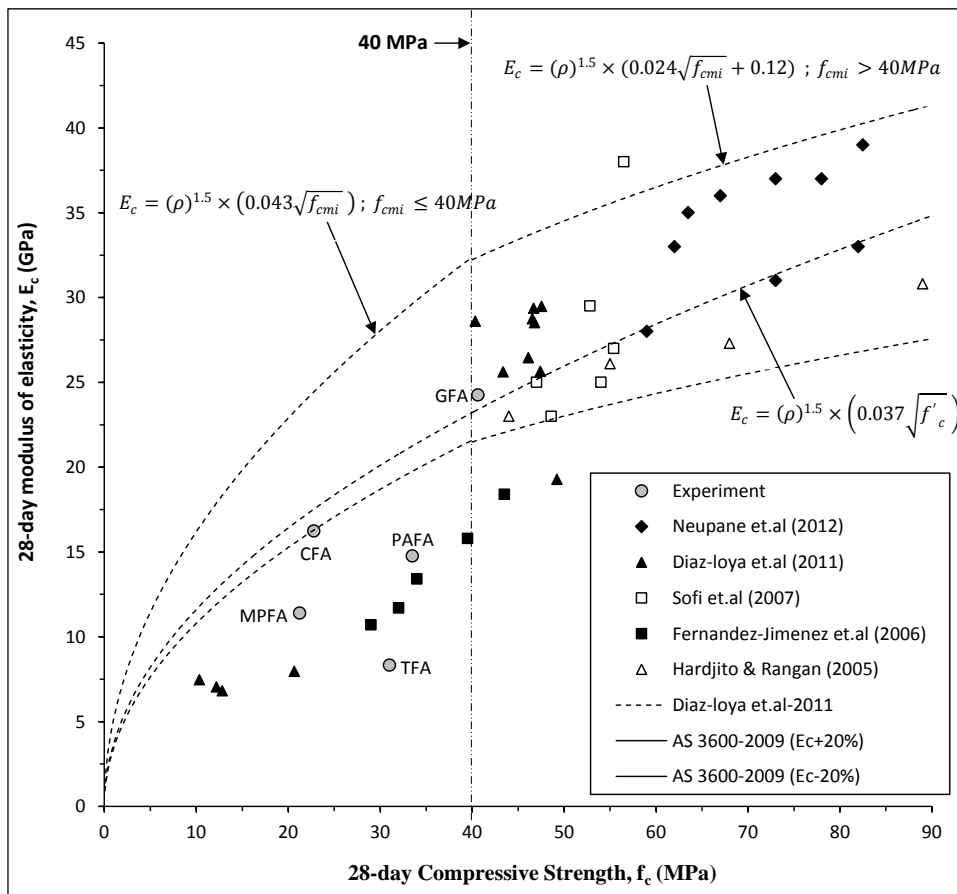
### 3.4 Modulus of Elasticity and poisson's ratio

**Table 7. Experimentally measured elastic properties**

GP	Elastic property	
	Modulus of Elasticity Ec, (GPa)	Poisson's ratio
GFA	24.3	0.16
PAFA	14.8	0.18
TFA	8.3	0.13
CFA	16.2	0.10
MPFA	11.4	0.09

The modulus of elasticity is a property of concrete defined as the stress retained to induce a unit strain within the elastic limit. A higher modulus of elasticity indicates a better quality of concrete. Measured modulus of elasticity and poisson's ratio of five FA geopolymer concretes are presented in Table 7. Modulus of elasticity of five FA geopolymers ranged from 8.3 to 24.3 GPa. The elastic modulus of geopolymer concrete is affected by the curing temperature, i.e. if water is lost due to evaporation at higher temperature curing before the full strength is gained, modulus of elasticity reduces [21]. MPFA geopolymer initially produced very stiff, non-workable mix that is opposed to the GFA mix which has highest workability, thus this workability difference which reflects the content of water in the initial geopolymer mix, may be attributed to the significant variation of concrete stiffness among the two geopolymers. On the other hand, formation of micro-cracks at the geopolymerization process with a higher curing temperature may reduce the stiffness of geopolymers than PC concrete. Liu et.al. [22] also reported that the pore volume and elastic modulus have a liner relationship, as the increase in the density of the geopolymer concrete enhances the stiffness. However, the present study showed FA geopolymer concretes have lower density compared to typical PC concrete that is again a factor of overall reduction of elastic modulus of FA geopolymers than PC concrete. The formation of micro-cracks at the geopolymerization of TFA is hence hypothesized as the reason for lowest elastic modulus observed despite having high compressive strength. However detailed microstructural analysis is required to confirm this phenomenon. PAFA and CFA geopolymers achieved moderate elastic modulus, however, the stiffness achieved by CFA is suspicious with respect to its lowest compressive strength and need further studies to understand the reason behind that.

The previously reported modulus of elasticity data coupled with present experimental data are plotted in Figure 3 against respective compressive strengths. Two regression models based on AS 3600 and Diaz-loya et.al. [14] are also presented in the same graph in order to compare the test results. In this study, only the elastic modulus of GFA was observed to fall within the limits provided by the AS 3600. The CFA concrete just achieves the lower limit of the standard though it has very low compressive strength, but all the other geopolymer concrete mixes fall below the lower limit. Analysis of these results and other data would suggest that if the concrete achieves a compressive strength greater than 40MPa, then the material will have a modulus of elasticity above the lower bound as predicted in AS 3600. Dias-loya et.al.[14] as well worked with range of fly ashes and his results confirmed this finding. Thus, when compressive strengths of fly ash geopolymer concrete are below 40MPa, the model in AS 3600 for PC concrete overestimates the modulus of elasticity when applied to FA geopolymer concretes.



**Figure 3. Modulus of elasticity vs. compressive strength**

The experimentally measured poisson's ratio of five FA geopolymers ranged between 0.09 and 0.18. Poisson's ratio values of PC concrete can range from 0.11 to 0.21 but usually fall in the range from 0.15 to 0.20 [23]. Values obtained for the geopolymer concretes, tend to populate the lower end of this range. The Poisson's ratio data in this study showed an increase with an increase of compressive strength while GFA showed a slight reduction than PAFA. A similar trend has reported by Setunge et.al. [24], which refers to the Poisson's ratio of high strength concrete.

#### 4. Conclusion

Based on the results of the experimental study, the following conclusions can be made:

- The density of FA geopolymer concrete is lower than PC concrete which is attributed to the lower specific gravity of the FA used to produce geopolymer concrete.
- The compressive strength of five different FA based geopolymers ranged from 21.3 to 40.6MPa. This strength variation is attributed to the characteristics of specific FA, mainly three parameters identified, i.e. surface area of FA coupled with amount of finer particles passing at 10, 20 and 45 micron sieves, the reactive amorphous alumina-silica percentage and CaO content of FA.
- Tensile strength of FA geopolymer concretes is also affected by the specific FA type. The splitting tensile strength varied between 0.94 and 3.67MPa whereas, the flexural tensile strength ranged from 3.22 to 5.07 MPa. Tensile strength of FA geopolymer concrete is dependent on the bond between aggregates and gel binder; that strong bond formation will leads to a higher reactivity and concurrent gel formation of FA which is again governed by the fineness and surface area.
- The unburnt carbon in FA precursor is hypothesised as weakening the bonding between geopolymeric binder and aggregates which is confirmed by the MPFA with lowest tensile strength. TFA contains the higher amorphous SiO<sub>2</sub> content, which may result in more Si<sup>4+</sup> ions being leached into the alkaline solution and hypothesized to stay as free cations that reduce the formation of very strong matrix/aggregate bond hence the lower tensile strengths achieved.



- The correlation between splitting tensile and compressive strength relies on a specific FA type, thus applicability of AS 3600 prediction is dependent on the FA source. However, flexural strength values of FA geopolymer concretes are higher than the AS 3600 predictions, while flexural strength is varied with FA source. In contrast, splitting test gave the most conservative estimates for the uniaxial tensile strength, hence would be recommended as the most appropriate test for design of FA geopolymer concrete structures.
- Modulus of elasticity of five FA geopolymers ranged from 8.3 to 24.3 GPa. The workability difference which reflects the content of water in the initial geopolymer mix affects the stiffness of the heat cured FA geopolymer concrete. This may be the reason for lower and highest elastic modulus for MPFA and GFA, respectively. The formation of extra micro-cracks at the geopolymerization of TFA is believed to be the reason for its lowest stiffness.
- When compressive strength of FA geopolymer concrete below is 40MPa, the model in AS 3600 for PC concrete overestimates the modulus of elasticity of geopolymer concretes.

## 5. Acknowledgement

The authors wish to express their thanks to Cement Australia Pty Ltd. and Flyash Australia Pty Ltd for the supply of fly ash. PhD scholarship provided by the school of Civil, Environmental and Chemical Engineering of RMIT is gratefully acknowledged.

## 6. References

1. Chen, C. ,Habert, G. et al., "Environmental impact of cement production: detail of the different processes and cement plant variability evaluation", Journal of Cleaner Production, 18(5), 2010, pp 478-485.
2. Meyer, C., "The greening of the concrete industry", Cement and Concrete Composites, 31(8), 2009, pp 601-605.
3. Peng, J. ,Huang, L. et al., "Modeling of carbon dioxide measurement on cement plants", Advanced Materials Research, 610-613, 2013, pp 2120-2128.
4. Li, C. ,Gong, X. et al., "CO2 emissions due to cement manufacture", Materials Science Forum, 685, 2011, pp 181-187.
5. Rehan, R. ,Nehdi, M., "Carbon dioxide emissions and climate change: policy implications for the cement industry", Environmental Science & Policy, 8(2), 2005, pp 105-114.
6. Davidovits, J., "Global warming impact on the cement and aggregates industries", World Resource Review, 6(2), 1994, pp 263-278.
7. Turner, L.K. ,Collins, F.G., "Carbon dioxide equivalent (CO2-e) emissions: A comparison between geopolymer and OPC cement concrete", Construction and Building Materials, 43, 2013, pp 125-130.
8. Habert, G. ,d'Espinose de Lacaillerie, J.B. et al., "An environmental evaluation of geopolymer based concrete production: reviewing current research trends", Journal of Cleaner Production, 19(11), 2011, pp 1229-1238.
9. Malhotra, V.M., "Role of fly ash in reducing greenhouse gas emissions during the manufacturing of portland cement clinker", Second International Conference on Advances in Concrete Technologies in the Middle East Conference Research Papers, Dubai., 2008, pp.
10. Khale, D. ,Chaudhary, R., "Mechanism of geopolymerization and factors influencing its development: A review", Journal of Materials Science, 42(3), 2007, pp 729-746.
11. AS, "Concrete structures", AS 3600, 2009, Standards Australia.

12. Gunasekara, M.P.C.M. ,Law, D.W. et al., "Effect of composition of fly ash on compressive strength of fly ash based geopolymer mortar", 23rd Australasian Conference on the Mechanics of Structures and Materials (ACMSM23), Byron Bay, Australia, 2014, pp. 113-118
13. Neville, A.M., "Properties of Concrete", Fourth and Final Edition. Standards updated to 2002, 1996, Pearson Education Limited, Harlow.
14. Diaz-Loya, E.I. ,Allouche, E.N. et al., "Mechanical properties of fly-ash-based geopolymer concrete", ACI Materials Journal, 108(3), 2011, pp 300-306.
15. Swanepoel, J.C. ,Strydom, C.A., "Utilisation of fly ash in a geopolymeric material", Applied Geochemistry, 17(8), 2002, pp 1143-1148.
16. Demie, S. ,Nuruddin, M.F. et al., "Effects of micro-structure characteristics of interfacial transition zone on the compressive strength of self-compacting geopolymer concrete", Construction and Building Materials, 41, 2013, pp 91-98.
17. Diaz, E.I. ,Allouche, E.N. et al., "Factors affecting the suitability of fly ash as source material for geopolymers", Fuel, 89(5), 2010, pp 992-996.
18. Ryu, G.S. ,Lee, Y.B. et al., "The mechanical properties of fly ash-based geopolymer concrete with alkaline activators", Construction and Building Materials, 47, 2013, pp 409-418.
19. Xu, H. ,Van Deventer, J., "The geopolymerisation of alumino-silicate minerals", International Journal of Mineral Processing, 59(3), 2000, pp 247-266.
20. Fernandez-Jimenez, A.M. ,Palomo, A. et al., "Engineering properties of alkali-activated fly ash concrete", ACI Materials Journal, 103(2), 2006, pp 106-112.
21. Bondar, D. ,Lynsdale, C.J. et al., "Engineering properties of alkali-activated natural pozzolan concrete", ACI Materials Journal, 108(1), 2011, pp 64-72.
22. Liu, M.Y.J. ,Alengaram, U.J. et al., "Evaluation of thermal conductivity, mechanical and transport properties of lightweight aggregate foamed geopolymer concrete", Energy and Buildings, 72, 2014, pp 238-245.
23. Warner, R.F. ,Rangan, B.V. et al., "Reinforced Concrete", 1998, Addison Wesley Longman,
24. Setunge, S. ,Attard, M.M. et al., "Static Modulus of Elasticity and Poisson's Ratio of Very High Strength Concrete", Civil Engineering Research Reports, 1990, pp

# Towards a More Sustainable Australian Cement and Concrete Industry

James Mohammadi<sup>1</sup>, Dr Warren South<sup>2</sup>, Mr Des Chalmers<sup>3</sup>

<sup>1, 2</sup> Research and Technical Services, Cement Concrete and Aggregates Australia (CCAA)

<sup>3</sup> Group Product Manager, Cement Australia

**Abstract:** This document provides a summary of results for the comprehensive test program to investigate the properties and performance of General Purpose (Type GP) cement prepared with up to 12% limestone content. An extensive literature review was carried out initially, and then an experimental research program designed. Cement, mortar, and concrete tests were conducted on a variety of mixes to evaluate the effect of introducing higher limestone mineral addition content to cement. The test results showed that there is no significant effect on most concrete properties due to increasing the limestone addition in cement. The result of this research supports the recommendation to increase the allowable limestone content of General Purpose (Type GP) cement to a maximum of 12%.

**Keywords:** General purpose (GP) cements; Limestone cement; Australian Standard AS 3972; Australian Standard AS 2350; Sulfate expansion; Rapid chloride penetration

## 1. Preface

The intent of the testing program was to study whether there is any detrimental effect on cement or concrete performance from the use of limestone mineral addition levels higher than the 7.5% allowed in AS 3972-2010 [1]. The upper limit chosen for this test program is 12%, based on the prevailing technical literature at the time the program was designed.

The program was designed and completed over 3 years (2011-2014) in two main stages under the supervision of Standard Australia BD-010 Working Group members. After the first stage of this research was completed, several members of the BD-010 Working Group sought to determine the effect of increasing limestone content in the cement used in a number of specific concrete systems. Therefore, an additional suite of tests was agreed among Committee members and carried out in 2014. The results of both research stages were documented and presented in two reports [2,3].

During the course of research program, combinations of different types of cementitious materials with plain Type GP cement were tested. Both plain cement and combinations of cement with supplementary cementitious materials (SCMs) were utilised to prepare cement paste, mortar, grout and different specific types of concrete samples. The research program included examining both laboratory and commercial mix designs. The suite of binder combinations included over two hundred different commercial concrete mixes, and involved standard laboratory mix designs, industrial grouts, normal and structural concrete grades, self-compacting, high-strength and durable concretes. The results of this research support the recommendation to increase the allowable limestone content of General Purpose (Type GP) cement to a maximum of 12%.

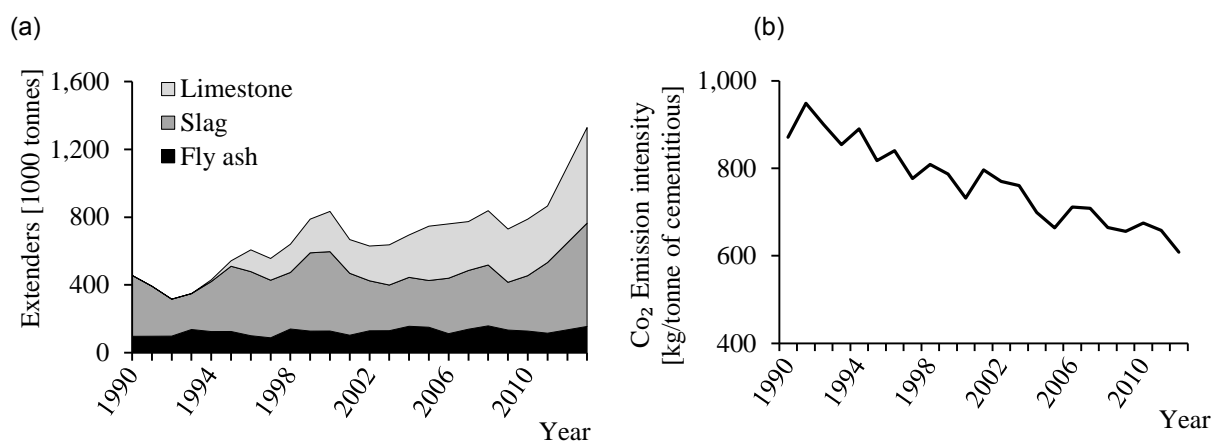
## 2. International Context for Cements with higher Limestone Contents

There is a strong international alignment for producing cement with higher limestone contents. For the past two decades European standards have permitted up to 20% and 35% limestone content for widely used CEM II types A/L and B/L, respectively. In a similar but later approach, Canada in 2008 and then in the USA in 2012 permitted higher limestone content in manufactured cement up to 15%.

The intent of this testing program is very clear. It is to determine whether there is any detrimental effect on cement or concrete performance from the use of limestone mineral addition levels higher than 7.5%, congruent with international practice.

### 3. Environmental Benefits of Cement manufactured with Higher Limestone Content

In the Australian context, the need to continue emissions reduction is clear. There is a long history of the use of supplementary cementitious materials in concrete in Australia. More recent data regarding the use of mineral additions in cement manufacturing are presented in Figure 1 (a). According to the Cement Industry Federation, gross emissions in 2010 were as shown in Figure 1 (b), at 660 kg per tonne of cementitious products, and further reductions have been seen in subsequent years [4]. A little over 25% reduction has been achieved since 1990. However, with community requirements influencing the use of alternative fuels, limited opportunity for thermal and electrical efficiency gains due to the relatively young age of cement manufacturing equipment, and little or no exploration of carbon capture & storage (CCS) strategies, clinker substitution remains the only viable alternative for emissions reduction. The most recent data, illustrated in Figure 1 (b), shows a continued downward trend in 2013/2014, co-incident with the increase in allowable mineral addition in cement. To continue this trend, an increase in mineral addition in the most commonly used cements is required.



**Figure 1: (a) Use of mineral components in Australian cement manufacture 1990-2012, (b) CO<sub>2</sub> emissions per tonne cementitious product produced, - Australia- 1990-2013 [4]**

Overall, from an environmental point of view, intergrinding of limestone and clinker reduces clinker content of cement, saves energy and produces cement with lower embodied CO<sub>2</sub> emissions. The use of mineral additions reduces the embodied emissions in cement roughly in proportion to the reduction in proportion of clinker in the cement. Increasing the mineral addition content of cement provides more sustainable Type GP cement, without compromising the existing structural and durability properties of concrete made with it.

### 4. Research Methodology

In practice, the achievable level of mineral addition and the material used as mineral addition will be determined by the cement manufacturer. Such decisions will be made with due reference to market requirements, cement manufacturing equipment capability and the availability of allowable materials. The cement Standard will prescribe the maximum level of allowable mineral addition in cements, but the actual level may vary from one cement manufacturer to another, as has always been the case.

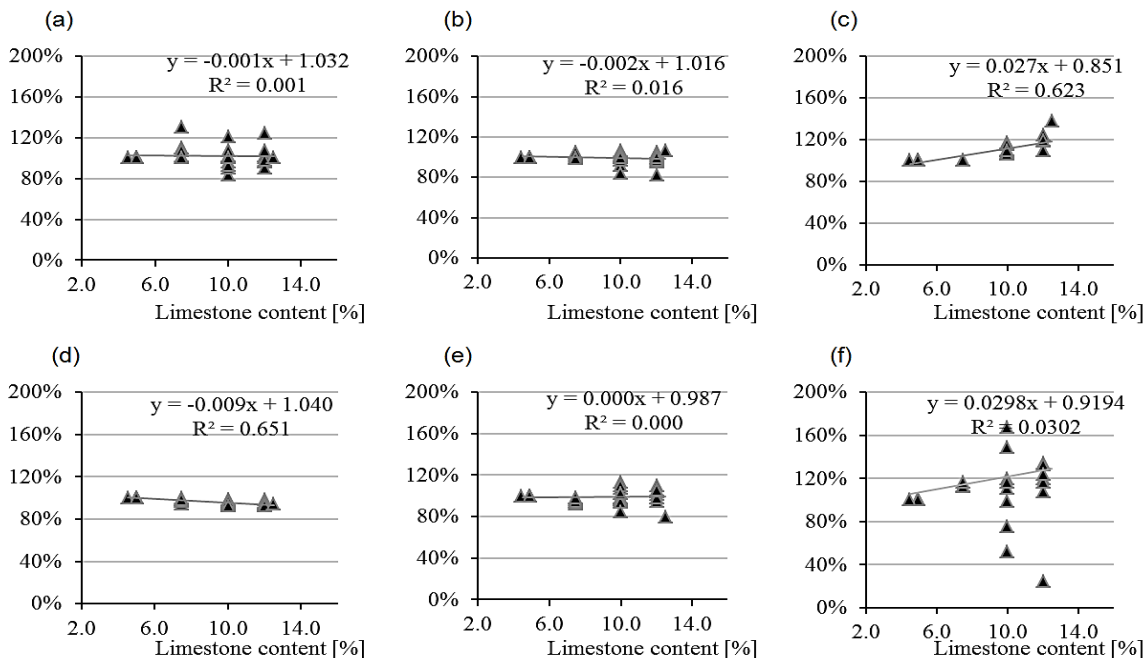
More than 200 high-quality international published research documents were reviewed. Accordingly a research methodology was selected which is congruent with the American research “Specifications and Protocols for Acceptance Tests on Processing Additions in Cement Manufacturing” conducted by NCHRP [5]. The statistical evaluation involved three stages. Firstly, investigating any correlation between laboratory test results and limestone content of cement; secondly, checking the compliance of the test results with Australian standards and industry specifications; and, finally, investigating if any significant change in properties of cement, mortar or concrete is due to the increase in limestone content of General Purpose (Type GP) cement by conducting experimental inferential analysis.

## 5. Results and Discussion

### 5.1. Cement, Cement Paste and Mortar Results

In total, 43 binder combinations from different Australian manufacturers were prepared, using Type GP cement and flyash or slag. Limestones used were sourced from the mines used by each of the cement suppliers providing product for the trials. Selected limestones contained not less than 75% by mass of  $\text{CaCO}_3$  as prescribed in the Australian Standard. Limestone with  $\text{CaCO}_3$  content equal to or greater than 75% and less than 80% was acceptable provided the clay content determined by the methylene blue test, as given in EN 933-9, did not exceed 1.20%, and the total organic carbon (TOC) content, as given in EN 13639, did not exceed 0.50% by mass. For limestone with  $\text{CaCO}_3$  content of 80% or greater, testing for clay content and TOC was not required. Cement samples with different limestone contents were prepared in plant trials carried out in the various cement plants providing product for the trials. This enabled an assessment of the performance of actual industrial product with increased limestone content.

Samples of cement were prepared with limestone mineral addition levels up to 12%. Thereafter, the effect of higher limestone on different properties of cement and cement paste, including chemical properties, setting time, hydration heat also compressive strength, drying shrinkage and sulfate expansion for mortar samples were examined.

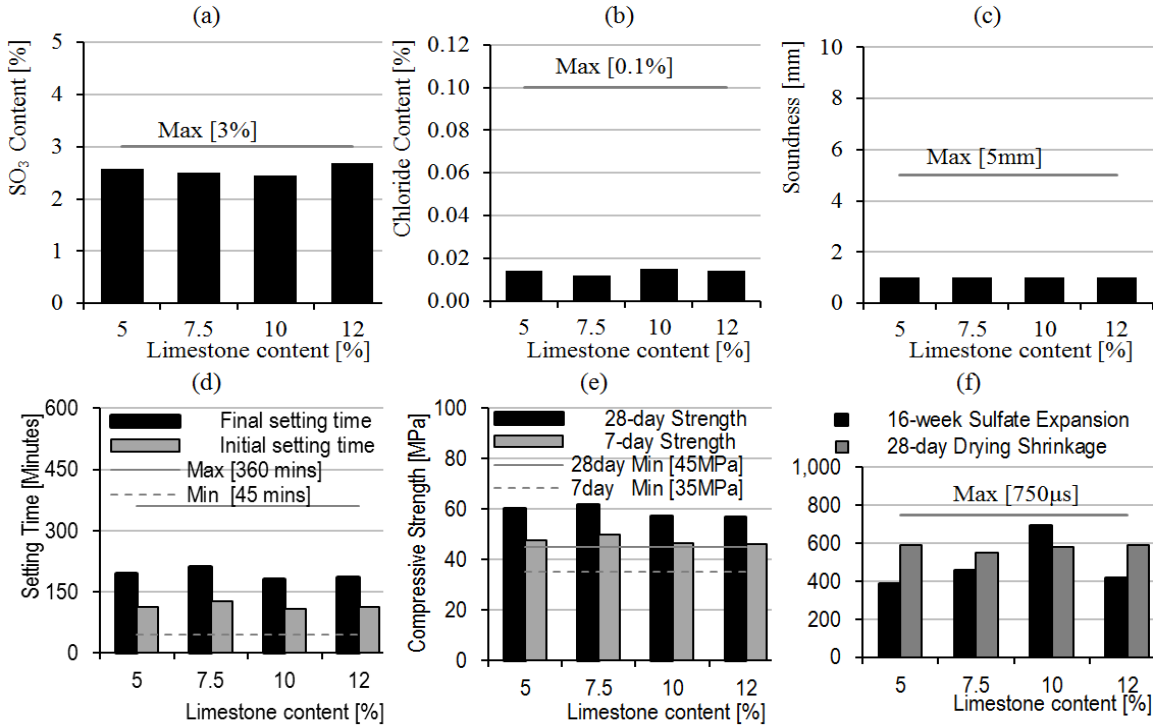


**Figure 2: Relative change of cement and mortar properties to control samples (a) Initial setting, (b) Final setting, (c) Fineness, (d) compressive strength, (e) Drying shrinkage, and (f) Sulfate expansion**

All tests were performed in accordance with the relevant Australian Standard testing procedure in different industrial laboratories. The correlational analysis of data showed there is no significant correlation between properties of cement or mortar with limestone content of cement up to 12%. An insignificant increase (<3%) in 16-week sulfate expansion of some samples was observed which was statistically scattered and had  $R^2$  of 3%. The only notable changes in characteristics were found for fineness. However, higher fineness and lower  $45\mu$  sieve residue were specifications set for the manufacturing process.

Results showed performance properties which were scattered within the usual statistical deviations arising from the number of test cements and binder combinations. Full cement and mortar correlational detail are available in the project reports. In addition to the conducted correlational study, test results for cement, mortar with higher limestone content were compared to the requirements of

Australian Standard AS 3972 as shown in Figure 3. All properties of 12% limestone content cement complied with the requirements of Australian Standards.



**Figure 3: Compliance with Australian Standards requirements (a) SO<sub>3</sub> content, (b) Chloride content, (c) Soundness, (d) Setting time, (e) Compressive strength, (f) Sulfate expansion and Drying shrinkage**

The third part of analysis included an inferential statistical analysis of cement and mortar test results. Considering the standard deviation, variation and distribution of test results, the statistical significance of test results was calculated. The majority of properties for cement and mortar samples prepared by higher limestone content did not show significant change from the samples prepared with control Type GP cement. The only statistically significant drawback found was a 5% reduction in mortar 28-day compressive strength, explained by the constraints of the test method, and congruent with reported international findings.

In summary, the results of cement, cement paste and mortar samples prepared with a higher limestone content demonstrated comparable properties with the control samples and there is no technical evidence that should limit the manufacture of Type GP cement with up to 12% limestone mineral content.

**5.2. Concrete Results**

The testing of the cements containing 7.5%, 10% and 12% limestone mineral addition was carried out in conjunction with relevant control cements as benchmarks. In addition to the 34 sets of standard laboratory concrete mixes using in-house mix designs, a wide range of concretes were prepared using current commercial mix designs for specific types of concrete. 52 sets of durable concrete; 24 sets of high-strength concrete; plus 35 and 32 sets of normal concrete grades N32 and N20 respectively were prepared. Moreover, an additional 33 sets of different specific types of concrete were provided from actual field concrete supplied for testing. Testing included those specified for fresh, hardened and durability properties namely (where applicable) concrete slump, concrete spread test, initial and final setting time, air content, bleed water, 1 day to 56 days compressive strengths, 56 day drying shrinkage, chloride ion penetration at 28 and 56 days, chloride ion migration, volume of permeable voids, creep test to 112 days, and modulus of elasticity at 28 and 56 days.

The evaluation of the data indicates there is little difference in performance between concrete using cement containing 12% limestone mineral addition and the control samples. This is supported by a statistical evaluation of the test results. Full correlational study, compliance with requirements, and inferential statistical evaluation details are available in the project reports. A summary of major findings is addressed as follows:

#### **Laboratory Standard Concrete**

The results of testing concrete based on standard laboratory mix design showed almost the same performance for 12% limestone mineral addition concrete samples and control samples. A statistically significant observed change was a reduction in bleed with increasing limestone content.

#### **Durable Concrete**

The test results for durable concretes indicated similar performance for 12% limestone mineral addition samples and control samples. The 12% limestone content durable concrete complied with all the benchmark requirements of this specific grade. Statistically significant changes were the reduction of bleeding and final setting time with increase in limestone content. Results for chloride ion penetration and chloride ion migration showed a significant improvement in concrete performance for the higher limestone content concretes.

#### **High-Strength Concrete**

Test results for high-strength concrete samples indicated similar performance for 12% limestone mineral addition samples and control samples. The 12% limestone content high-strength concrete complied with all the benchmark requirements of the high-strength specific grade. Similar workability and creep characteristics were observed for 12% limestone cement samples. Statistically significant observed changes were in the reduction of 1 day and 56 days strength by 7% and 1.6%, respectively. Test results for the modulus of elasticity at 56 days showed a 4% reduction compared to control samples.

#### **Normal Concrete Grades N20 and N32**

Test results for normal grade concrete samples showed almost the same properties for 12% limestone mineral addition samples and control samples. Both grades N20 and N32 prepared with 12% limestone content complied with all the benchmark requirements for these grades.

A statistically significant observed change for grade N20 was a reduction in bleed. No other significant change was detected.

A statistically significant observed change for grade N32 concrete was a reduction in bleed. In addition, relatively to the control samples, slump and air content results were 5% and 6% lower, respectively. However, higher strength values of about 3% to 6% for early ages (1, 3 and 7 days) test results were observed, which were statistically significant.

#### **Field Concrete**

Test results from field concrete samples exhibited similar performance for 12% limestone mineral addition concretes and control samples. The 12% limestone content concrete showed similar strength, drying shrinkage and fresh properties except for setting times, which were reduced by about 3-4%.

In general, it can be concluded that the test results for different specific types of field concrete did not show significant differences to control samples and supported the proposition of increasing the allowable mineral addition level in General Purpose (Type GP) cement, up to 12% limestone mineral addition.

### ***5.3. Supplementary Cement, Mortar, Grout and Concrete Results***

Several members of the BD-010 Working Group expressed concerned with the experimental program for the original test program (2011-2014). Specifically, they sought to determine the effect of increasing limestone content in the cement used in a number of specific concrete materials. Therefore,

an additional suite of tests and statistical analysis was agreed among Committee members and carried out in 2014 [3].

Cement, mortar and concrete tests were conducted on a variety of mixes to evaluate the effect of introducing higher limestone mineral addition to cement. These were to be tested according to normal test methods used in Australia. The total number of prepared mixes was 61 which were distributed between different types of concrete and grout. There are major differences in the performance requirements and properties of these specific types of concrete. Therefore, it was decided to report the result of the studies for the different groups of specific types of concrete separately from the original program. In addition to the cement, cement paste and mortar testing, six specific types of concrete included grout, self-compacting, general purpose, durable, high strength and structural concretes were examined.

### Cement, Cement Paste and Mortar

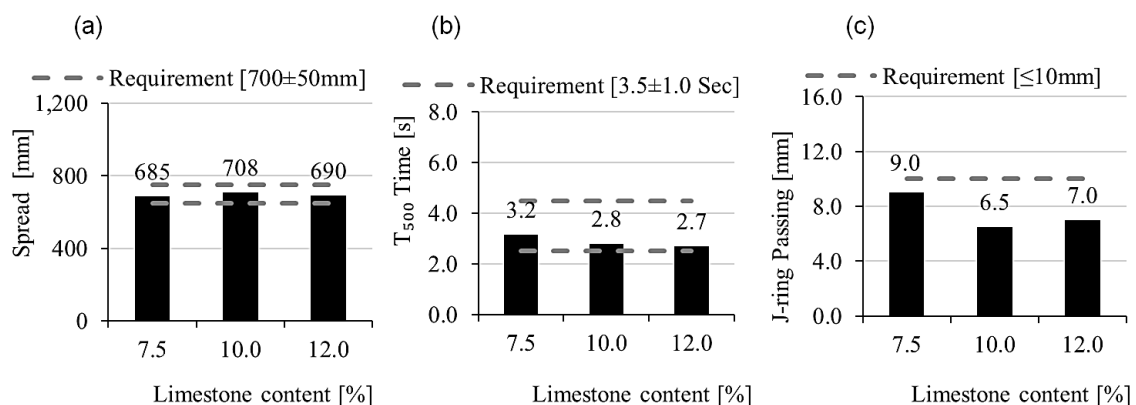
Some changes in chemical composition were noted due to a higher limestone content. In addition, there was a strong correlation between limestone content and surface area and the 45  $\mu\text{m}$  residue due to the influence of the manufacturing specifications. There was no correlation between cement limestone mineral addition content and the compressive strength or drying shrinkage of mortar.

### Grout

Grout test results include workability and strength results of three mixes prepared based on commercial mix designs. Results showed a significant improvement in the flow properties of grout made with cement containing the higher limestone contents in both the initial measurement and also after 45 minutes. The improvement may be due to the positive effect of higher limestone on the increase of water retention properties of grout. In addition, the better workability of mixes with higher limestone may be explained by softer and finer particles of limestone compared to the ground clinker particles. Literature supports the reported results for grout. Compressive strength tests were performed at different ages. Results revealed that there was no significant correlation between grout strength and limestone mineral addition content of cement.

### Self-Compacting Concrete (SCC)

The higher limestone content of cement did not result in a significant change in concrete flow. The results from additional tests such as  $T_{500}$  test and J-ring passing ability showed better workability of SCC with increased limestone content, however, the correlations were not strong.



**Figure 4: Self-compacting compliance with work-group requirements (a) Spread, (b)  $T_{500}$  time, (c) J-ring passing ability**

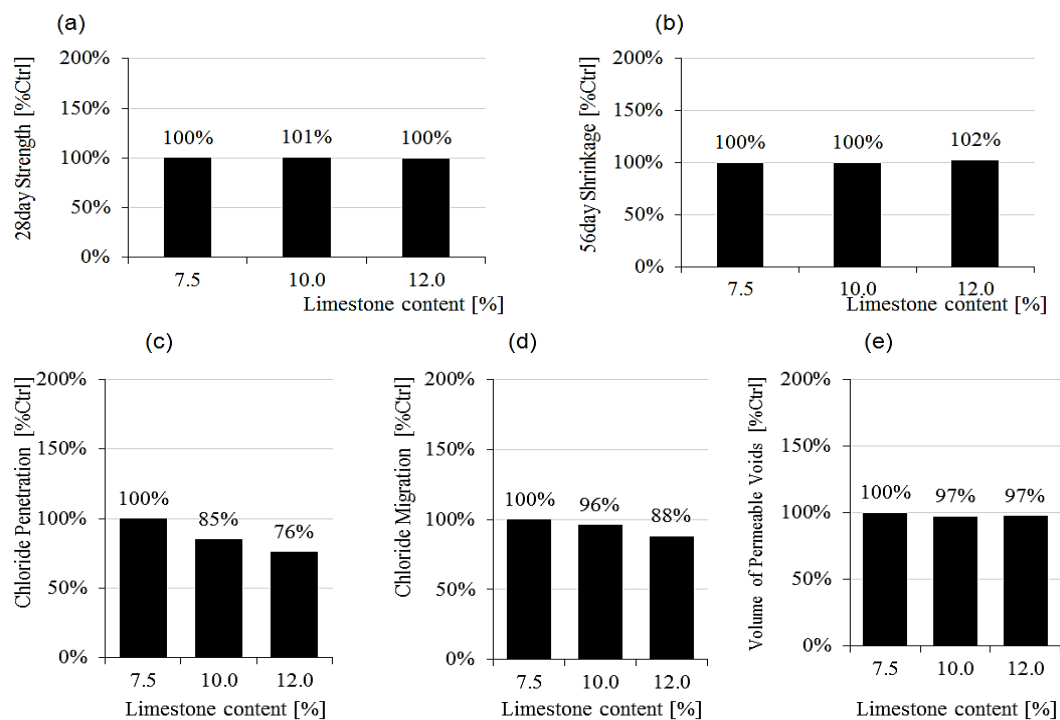
Considering results from all ages, slopes of trend lines and calculated values of  $R^2$ , it can be concluded that the increase in limestone content had no significant effect on the strength of SCC. SCC drying shrinkage results showed a slightly higher drying shrinkage for 12% limestone content, which may be due to the higher fineness of the cement, the increased limestone content or both factors. The correlations for chloride penetration and Volume of Permeable Voids (VPV) with limestone content of



cement were assessed for the SCC mix series. No significant correlation between limestone mineral addition content and chloride penetration or VPV was found.

### Normal, Structural, Durable and High-strength Concrete

In order to have a complete investigation regarding the effect of higher limestone on different types of concrete, 54 sets of concrete were prepared and tested by examining fresh, hardened and durability properties. It was found that the higher limestone content does not significantly affect the fresh properties of concrete. Results showed the air content decreased very slightly with the increase in limestone content. Moreover, the samples with increased limestone content did not have a significant effect on fresh concrete density or workability.



**Figure 5: Relative change of properties of concrete samples prepared with different limestone contents (a) Compressive strength (b) Drying shrinkage (c) Chloride penetration ASTM 1202 method, (d) Chloride penetration NT 492 method (e) Volume of permeable voids AS1012.21 method**

The test results showed that at very early ages, the compressive strength of concrete increased slightly with the increase of limestone content. For other ages, the compressive strength of concrete samples was not changed by the increase of limestone content.

An insignificant increase in the drying shrinkage was observed for the majority of concrete samples at different testing ages (Figure 5). Comprehensive analysis of drying shrinkage test results revealed that slightly higher drying shrinkage was observed only for concrete samples prepared with a combination of Type GP cement and fly ash. The higher drying shrinkage for 12% limestone content is possibly due to the higher fineness of the cements containing the higher limestone mineral addition levels.

Durability test results revealed that there were negative correlations between chloride penetration and the Volume of Permeable Voids with limestone content of cement. These lower Volume of Permeable Voids and chloride penetration results suggest improved durability of concrete using cement with higher limestone content. The observed improvements were more significant for concretes prepared with Type GP cement, while there were mild or insignificant correlations found for those prepared by Type GP cement and fly ash.

It was found that for most properties no significant change was found for up to 12% limestone mineral addition content (Table 1). The only drawback observed with 12% limestone mineral addition was a

higher drying shrinkage measured at 21 days compared to the control samples. However, the measured concrete drying shrinkage at 56 days did not show any significant increase. In addition, it is important to take into account that the reported repeatability of the drying shrinkage test is 8% at the 95% probability level. The measured shrinkage for 12% limestone samples was 7% higher than the shrinkage of control samples.

**Table 1: Overall evaluation of specific types of concrete test results for higher limestone cements**

Item	Correlation		Compliance		Inferential		Decision on addition		
	Trend	Condition	10% content	12% content	10% content	12% content	10% content	12% content	Consideration
Slump	neutral	insignificant	yes	yes	no effect	no effect	✓	✓	-
Air content	negative	insignificant	yes	yes	significant	significant	✓	✓	-
Mass per unit volume	neutral	insignificant	yes	yes	no effect	no effect	✓	✓	-
Strength 1day	positive	insignificant	-	-	significant	significant	✓	✓	improvement
Strength 3day	neutral	insignificant	-	-	no effect	significant	✓	✓	improvement
Strength 7day	neutral	insignificant	-	-	no effect	no effect	✓	✓	
Strength 28day	neutral	insignificant	yes	yes	no effect	no effect	✓	✓	-
Strength 56day	neutral	insignificant	-	-	no effect	no effect	✓	✓	-
Strength 91day	neutral	insignificant	-	-	no effect	no effect	✓	✓	
Shrinkage 21day	positive	insignificant	-	-	marginal	significant	✓	×	increased
Shrinkage 56dy	positive	insignificant	yes	yes	no effect	no effect	✓	✓	-
Chloride ASTM 1202	negative	mild	-	-	significant	significant	✓	✓	improvement
Chloride NT492	negative	mild	-	-	significant	significant	✓	✓	improvement
AVPV	negative	mild	-	-	marginal	significant	✓	✓	improvement

The test results showed an improvement in the chloride penetration (ASTM 1202 Method) and Volume of Permeable Voids (AVPV) for concrete prepared with 12% limestone mineral addition. The improvement was significant and confirmed at a 95% confidence level. The better durability performance of concrete prepared with 12% limestone GP cement suggests the potential to enhance concrete performance or service-life and reduce maintenance costs.

## 6. Conclusion and Recommendation

The results of this project supported the proposition of increasing the allowable mineral addition level in General Purpose (Type GP) cement. It was found that by increasing limestone content of cement to 12% most properties of cement, mortar and concrete were effectively unchanged. There were generally very limited performance reductions and these were statistically insignificant. It is concluded that variability in performance among the different tests was influenced more by concrete mix design and binder composition than by limestone content in the Type GP cement.

The result of this research supports the recommendation to increase the allowable limestone content of General Purpose (Type GP) cement up to a maximum of 12%.

## 7. References

- [1] AS3972-10, General purpose and blended cements, Sydney, 2010
- [2] BD-010 Working Group, Report on the use of Limestone in General Purpose Cement at levels up to 12 %, Sydney, 2013.
- [3] J. Mohammadi, W. South, Further Investigation into the Increase of Limestone Content of Australian General Purpose (GP) Cement, Sydney, 2014.
- [4] CIF, Statistics 2013, Cement-Industry-Federation (CIF). (2013) 1–16. <http://cement.org.au/Portals/0/Documents/Fast Facts/CIF Fast Facts 2013.pdf> (accessed October 16, 2014).
- [5] NCHRP Report607, NCHRP Report 607 Specifications and Protocols for Acceptance Tests on Processing Additions in Cement Manufacturing, Washington D.C, 2008. [http://onlinepubs.trb.org/onlinepubs/nchrp/nchrp\\_rpt\\_607.pdf](http://onlinepubs.trb.org/onlinepubs/nchrp/nchrp_rpt_607.pdf).

# Steel, Concrete or Plastic? Support your Reinforcement!

Scott Munter<sup>1</sup>, Mark Turner<sup>2</sup>

<sup>1</sup>Executive Director, Steel Reinforcement Institute of Australia

<sup>2</sup>Chairman Committee BD-084 Steel Reinforcing and Prestressing Materials

**Abstract:** The construction industry is witnessing increased levels of failure of critical cover control elements. Moreover, the global supply market, lack of quality control and traceability through the current procurement cost reduction approach is a critical factor in this lack of the minimum expected performance levels.

Until recently, there has been no standard for performance requirements for bar chairs and spacers in reinforced concrete. Unsatisfactory manufacture and application of bar chairs may compromise structural strength and reduce durability of reinforced concrete. AS/NZS 2425 – Bar chairs in Reinforced Concrete has been developed in response to this need. The strength grade, performance and classification of the three main product types: steel wire; plastic; and concrete bar chairs have been considered.

The specification, methods of test and traceability requirements will assist designers and builders to select appropriate reinforcement supports to ensure maintenance of specified cover within tolerance under self-load and anticipated construction loads. The ability to place, compact and cure the concrete around the reinforcement is also a critical consideration.

The benefits and shortfalls of the main types of bar chairs are reviewed and the practical application of appropriate products is presented for a range of construction tasks. All types of complying supports are shown to deliver cost-effective achievement of design intent.

**Keywords:** Bar chairs, steel reinforcement, standards, cover, durability.

## 1. Performance Critical – Reinforcement Placement

The construction industry is witnessing increased levels of failure of critical cover control elements. Moreover, the global supply market, lack of quality control and traceability through the current procurement cost reduction approach is a critical factor in this lack of the minimum expected performance levels.

The structural and durability performance of reinforced concrete depends significantly on securing and maintaining the position of reinforcement during fabrication, concrete placement and finishing. The end result seeks to provide the specified cover within tolerances to ensure that the concrete is compacted around the reinforcement. The use of bar chairs and spacers is critical to ensure design intent.

Until recently, there has been no standard for performance requirements for bar chairs and spacers in reinforced concrete. Unsatisfactory manufacture and application of bar chairs may compromise structural strength and reduce durability of reinforced concrete. Figure 1 shows that in extreme circumstances, no support is provided for reinforcement at all!



**Figure 1. Where's the support?**

There are few standards throughout the world that specify the performance of bar chairs and spacers. Unfortunately consideration of the type, quantity and spacing of reinforcement supports is often an afterthought of the design and detailing process. AS/NZS 2425 – Bar chairs in Reinforced Concrete (1) has been developed in response to this need.

## **2. Introducing AS/NZS 2425**

### **2.1 What is covered**

Design Standards such as AS 3600 (2) and NZS 3101 (3) specify the cover to reinforcement and the tolerances, which need to be met in placing and fixing reinforcement. These covers and tolerances form the underlying principles upon which AS/NZS 2425 is written.

The standard for bar chairs and spacers specifies their strength, permanent deflection, accuracy of manufacture, identification and traceability and fixing. It applies to chairs made from plastic-tipped wire, plastic and concrete. While primarily focusing on load-carrying capacity, the standard specifies durability requirements for concrete bar chairs, because the durability performance of these products is intrinsic to their suitability and selection.

While this new standard covers the majority of commercially available products there are some products which escape its application. These include:

- Custom made or “engineer specified” chairs such as may be required for heavily reinforced sections or extreme exposure classifications.
- Exotic materials. Some developments such as carbon fibre composites are being used for limited applications.
- Specialised supports for concrete products covered by their own standards including precast concrete access chambers and precast concrete pipes.
- Post-tensioning duct chairs. Heights of these chairs vary considerably. However the principles of AS/NZS 2425 may apply but are not designed to support construction loads.

AS/NZS 2425 notes that “engineer specified” chairs and the like should always be designed to comply with the fixing tolerances of AS 3600 and NZS 3101 as appropriate.

### **2.2 Load carrying Capacity**

The key classification for all bar chairs is their load carrying capacity. Four strength grades are nominated: 60 kg, 120 kg, 200 kg, and >300 kg. When tested in accordance with the standard, products need to carry not only the specified load but also maintain deflections and permanent set within certain limits. These are summarised in Table 1. The deflection and permanent set limits have been based on roughly half the fixing tolerance of AS 3600: allowing other site factors to be accommodated within the fixing tolerance.

Strength grade 60 would typically apply to non-vertical load bearing spacers such as those for columns and walls. For most building structures strength grade 120 would commonly be specified. The load carrying capacity allows for the mass of steel reinforcement, construction personnel, heaped concrete and equipment such as pumps and vibrators. Strength grades 200 and >300 would typically be used in heavily reinforced civil structures. Bridges and power stations are likely users of these products. The >300 grade chairs are often made from fine aggregate concrete. There are minimum compressive strength and durability requirements for concrete chairs but they should also be greater than or equal to the strength specification of the surrounding concrete.

Continuous bar chairs are often supported from bottom steel reinforcement rather than horizontal formwork. The table advises that the cumulative effects of supporting top steel from already supported bottom steel be considered. See Figure 2.

**Table 1. General Product Requirements**

Test		Strength grade			
		60	120	200	>300
Minimum test load capacity, kg		60	120	200	>300
Dimensional tolerance					
Height of bar chair, measured at pre-load	<75 mm	±1 mm generally For concrete chairs, -1 + 2 mm			
	≥75 mm	±2 mm			
Deflection under load		±3.0 mm max.			
Permanent set		After removal of load, the final recovered position of the test specimen shall be less than 2.0 mm For concrete chairs, no cracking shall be evident			

**NOTES:**

- 1 Strength grade >300 kg bar chairs are typically manufactured from a fine aggregate concrete. Specifiers should ensure that the concrete in the chair is greater than or equal to the strength specifications of the surrounding concrete.
- 2 Continuous bar chairs with heights >90 mm should be designed to ensure that reinforcement is supported within the placing tolerances of AS 3600 or NZS 3101, taking account of any cumulative effect of deflection from being supported on already supported reinforcement.



**Figure 2. Top steel supported from bottom steel using “engineer specified” supports.**

### 2.3 Durability

Consideration was given to inclusion of durability requirements. However, the Committee resolved that specification of durability resided with the design Standards such as AS 3600 and NZS 3101 except for concrete bar chairs where impermeability is intrinsic to their performance and is not covered in the design Standards.

Concrete bar chairs are required to have a minimum compressive strength of 60MPa. They also need to be classified on the basis of chloride permeability determined by the charge passed in a modified sample tested in accordance with ASTM C1202 (4). See Table 2

**Table 2**  
**Chloride Permeability Based On**  
**Charge Passed**

Maximum charge passed Coulombs	Chloride permeability class
>4 000	High
2 000–4 000	Moderate
1 000–2 000	Low
<1 000	Very low

This is one of the more controversial aspects of this new standard. Main Roads Queensland provided a modified test method. While the results from ASTM C1202 can be quite variable both in terms of repeatability and reproducibility, the drafting Committee acknowledges the need for an economically feasible test method.

### 2.4 Testing and Traceability

The new standard set out a regime for sampling and testing of bar chairs on a batch-by-batch basis. The general testing procedure requires samples from each batch to be statically load tested and measured against the criteria shown in Table 1. The batch is deemed to comply where the load and deflection requirements comply with Table 1 for the specified strength grade.

Where the sample does not meet the load and deflection requirements of Table 1, a further five samples must be tested. The batch is deemed to comply where all five samples comply with Table 1 for the specified strength grade.

All bar chair packaging is required to identify the strength grade. Packaging for concrete bar chairs is also required to display the permeability class. Each pack of bar chairs must be traceable to manufacturer and batch.

## 3. Protective-tipped Wire Bar chairs

### 3.1 Applications

Protective-tipped wire bar chairs are an economical choice for many applications. They will usually be grade 120 chairs. Figure 3 shows a range of wire bar chairs ranging in height from 20 mm to 360 mm. Protective tipped bar chairs can be used in suspended slabs, beams, vertical walls and slab on ground applications. When used in slab on ground applications, the chairs require a base to prevent penetration of the polythene film or soil base.

### 3.2 Limitations and Precautions

While an economical choice for many applications, protective tipped wire chairs should be used with caution in some situations and completely avoided in others. These include:

- **Durability Category B2 and above.** The Steel Reinforcement Institute of Australia (5) has advised designers and detailers not to use wire chairs in durability categories B2 and above. Typically these are exposed concrete structures within 1 km of the coast. The potential for corrosion and subsequent staining of the concrete surface cannot be ignored.

- **Architecturally sensitive slab soffits.** The potential for the wire to penetrate the protective coating and cause staining should be considered. Compliance with AS/NZS 2425 will mitigate this being a problem as testing requires the absence of any penetration of the wire through the protective coating. Recent innovations with protective-tipped wire chairs include a push-on Teflon cap system.



**Figure 3. Plastic tipped wire bar chairs.**

## **4. Plastic Bar Chairs and Spacers**

### **4.1 Applications**

Plastic chairs and spacers are finding an increasing and economic role. Figure 4 shows a selection of plastic products. They are available from a number of reputable manufacturers. Typical applications include:

- **Slab on ground and pavements.** Plastic chairs with an integral base are most suitable for these situations. They provide a stable platform for reinforcing bar and mesh and are available in a range of heights.
- **Suspended slabs.** Plastic chairs for these applications often have a clipping mechanism to keep reinforcement in place; reducing the need for tie wire. They can be substituted for wire chairs in durability categories B2 and above as they will not corrode or stain.
- **Vertical element spacers.** Wheel type plastic spacers are often used in maintaining cover to reinforcement in vertical elements such as walls, columns and piles. Because they are not required to be load bearing they will usually be grade 60 products. Recent innovations have seen this type of spacer produced as a carbon fibre polymer. While not specifically covered by AS/NZS 2425, the general principles of delivering covers within the fixing tolerances of the design standards should apply to carbon fibre spacers.

### **4.2 Limitations and Precautions**

AS/NZS 2425 has additional requirements for plastic chairs. The standard requires that plastic chairs be tested at a temperature of 30<sup>o</sup> C compared to 22<sup>o</sup> C for other products. The potential for a plastic chair to soften at elevated temperatures needs to be considered. One of the authors had experience as a younger engineer where 85 tonne of reinforcement for an insitu bridge span was supported on plastic chairs. High temperatures within the form caused the chairs to soften and collapse just prior to concrete placement: an expensive and time wasting event!

The standard also requires that the design of plastic chairs allows 20 mm aggregate concrete to readily penetrate the chair openings. Without this provision, the generally thicker walls of plastic chairs could lead to voids occurring in the finished concrete. Caution should be exercised if larger aggregate concrete is contemplated.

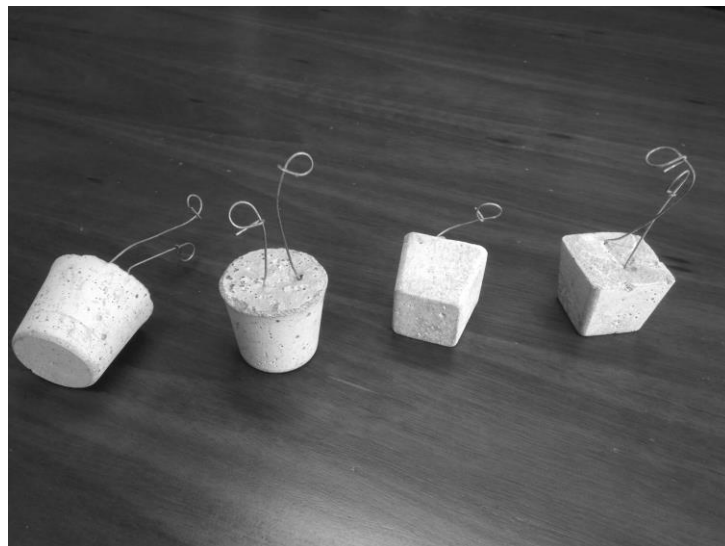


**Figure 4. Sample selection of plastic bar chairs and spacers.**

## **5. Concrete Bar chairs**

Concrete bar chairs find their best application where support of large amounts of reinforcement is needed or where durability is a major consideration. They usually have a strength grade of >300. The additional durability provisions, noted above, seek to ensure that the solid chairs are not a source of chloride penetration to reinforcing steel. A variety of manufacturing processes have been employed to create concrete chairs including moulding and extrusion. See Figure 5 below. The standard does not apply to site-manufactured bar chairs where product quality, dimensional tolerances and performance cannot be assured.

Concrete bar chairs and spacers may also be the preferred choice for water retaining structures or where water pressure against a concrete surface is a factor. Generally their bond to the concrete and low permeability offer the desired performance. A very low chloride permeability class as listed in Table 2 should be specified.



**Figure 5. Concrete bar chair with cast in tie wire.**



## 6. Continuous bar chairs

Continuous bar chairs are covered in AS/NZS 2425. They are chairs that are used to support reinforcing in a continuous line of support, which includes soffit-supported as well as middle deck chairs supported from a lower layer of reinforcement. Continuous chairs can be made from wire plastic and even concrete. See Figure 6. They rely on the mat of reinforcement to spread the imposed loads across the nodes. They are tested for compliance by applying pairs of the specified load at mid-node. Where middle deck chairs are used, detailers and designers should be aware of the cumulative effect of load deflection to ensure that the top layers of steel are placed within tolerance.

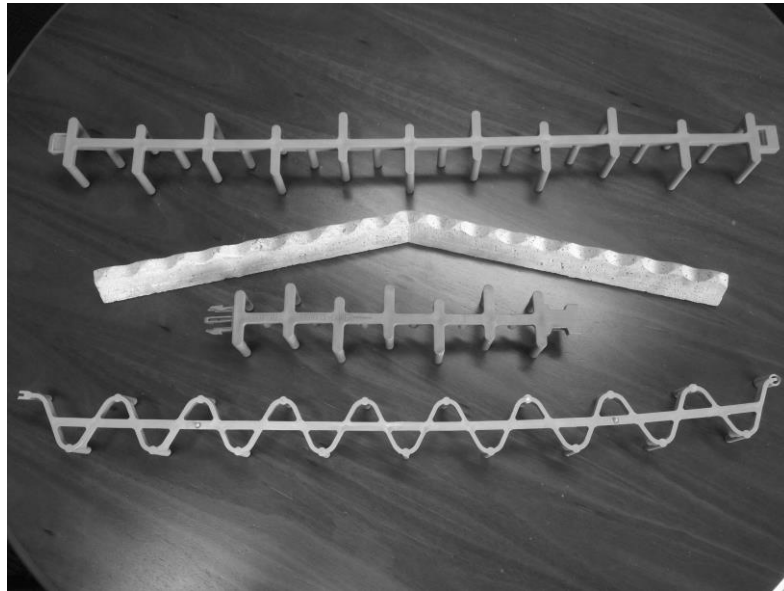


Figure 6. Sample selection of continuous chairs.

## 7. Conclusion

The publication of AS/NZS 2425 is a welcome addition to the suite of Standards intended to assist the delivery of structurally sound, durable and cost effective concrete structures. The specification of strength grade and product specific performance requirements gives designers and builders a tool to specify the quantity and spacing of reinforcement supports with confidence.

The selection of the most appropriate chair: plastic tipped wire chairs; plastic; or concrete, depends not only on the mass of reinforcement to be supported but the imposed construction loads during fabrication and concrete placement.

A specifier should also consider the environmental and durability conditions to which the finished structure will be exposed. While AS/NZS 2425 focuses primarily on the load-carrying capacity of bar chairs, durability aspects of concrete chairs are considered, as these are not adequately covered by the design standards.

The application and limitations of the various types of support have been briefly considered. Further useful information will be found in the product literature of compliant manufacturers and suppliers.

The new standard will need to be referenced in design standards such as AS 3600 (2) to realise its full potential.

## 8. References

1. Standards Australia, "AS/NZS 2425 Bar chairs in reinforced concrete - Product requirements and test methods" 2015.
2. Standards Australia "AS 3600 Concrete structure" 2009
3. Standards New Zealand "NZS 3101 Concrete Structures standard (series)
4. American Society for Testing Materials, "ASTM C1202 Standard Test Method for Electrical Indication of Concrete's Ability to Resist Chloride Ion Penetration"
5. Steel Reinforcement Institute of Australia, "Restrictions on the use of wire bar chairs" Technical Note 3, January 2007

# Performance of Architectural Concrete: New Approach

Vyacheslav Falikman<sup>1</sup>, Vyacheslav Deniskin<sup>2</sup>, and Alexander Vainer<sup>3</sup>

<sup>1</sup>Professor of Material Science, Moscow State University of Civil Engineering

<sup>2</sup>Researcher, Scientific Research Center "Construction"

<sup>3</sup>Consultant, Scientific Research Center "Construction"

**Abstract:** Architectural concrete technology is known to provoke often the growth of shrinkage strains, increase in permeability and reduction in frost-resistance. Methods of modifying of architectural concrete are proposed that provide an opportunity to control its structure and durability, concrete mix workability and hardening rate at all stages of manufacture. Performance of architectural concrete belonging to compressive strength classes B30 - B80 is assured by using mechanically activated composite binders and effective superplasticizers. The increased hydraulic activity of binders and rational design of new architectural concrete predetermine their high physical and mechanical properties and durability, particularly under favorable conditions of structure formation, e.g. when shrinkage reducing admixtures are used. Concrete mixes, including self-consolidating ones (slump-flow 60-70 cm, V-funnel time 7-15 sec), are characterized by 0 to 0.4% bleeding. Architectural concrete frost resistance reaches 300-600 freezing-thawing cycles and more and the open integrated voids rating does not exceed 2-4% vol. The values of the prism strength factor and the initial tangent modulus of elasticity of modified concretes meet or exceed regulatory requirements. Durability of architectural concrete may be additionally improved by impregnation with the special organic silicate compounds.

**Keywords:** architectural concrete, composite binders, self-consolidating concrete, shrinkage reducing admixtures, durability, impregnation.

## 1. Introduction

Development of the high-performance concrete (HPC) concept has revolutionized the concrete technology. By combining high strength with optimum structural characteristics, higher values of physical and mechanical properties and durability, the HPC extends the areas of application of artificial mineral composites [1].

One of the most promising areas of the HPC implementation is manufacturing of architectural concrete with improved decorative properties and performance. Application of concrete technology in decorative façade elements, sculptural plaster, and other elements of buildings requires, as a rule, the use of highly workable and fluid mixes. Additionally, plain and colored cements are used to improve decorative properties of material, while fine aggregates are required to create complex textured and highly detailed surfaces. A combination of these factors leads to increased water requirements for cement mixes, which in turn instigate the growth of shrinkage strains, increase in permeability and reduction in frost resistance of concrete. The features of cement chemical, mineralogical, and material composition (for example, increased content of C<sub>3</sub>A, increased content of belite, introduction of bleaching mineral agents during grinding, e.g. diatomite, etc.) contribute to the problem.

Within the framework of implementing the HPC concept, an integrated control system for the structural characteristics, hardening rate and strength of concrete has been developed having in mind to obtain a material with set-up physical and mechanical properties and durability in specific operating conditions. It envisages the use of mechanically activated composite binders, multifunctional chemical modifiers for various applications. Thereby a directional impact is possible upon the processes of structure formation and hydration, hardening and strength gain, as well as on parameters of concrete structure and durability at all stages of its preparation: from selecting initial materials, specifying material constitution and activation parameters of composite binders, introducing chemical modifiers into a concrete mix at the preparation stage to improve its workability, including efficient superplasticizing admixtures of the new generation, and up to concrete placing and hardening in special forms.

Elimination of the specified contaminating impurities from front face of ornamental elements, and upgrading of architectural concrete and architectural elements is attained by their treatment with the various compositions reducing permeability to water and water absorption. Among wide choices of treating and coating compositions and systems (acrylic, urethane, epoxide, silicone, siloxanic, silaned, etc.) the greatest technical and economic efficiency possess materials such as silicate and organosilicate

compositions combining comparative cheapness and accessibility of a raw-material base with a large-scale of decrease of water absorption, and permeability to water, and raise of working life.

## 2. Experimental Program

### 2.1 Materials

The Portland cement of CEM I 42.5 grade (**Table 1**) produced by Stary Oskol cement plant and White cement of CEM I 52.5 R grade produced by Aalborg cement plant were used for the tests.

**Table 1. Bogue cement composition.**

Cement	C <sub>3</sub> S	C <sub>2</sub> S	C <sub>3</sub> A	C <sub>4</sub> AF	R <sub>2</sub> O
CEM I 42.5	62.84	12.31	8.5	12.5	0.63
CEM I 52,5 R	77,26	15,52	4,5	1,0	0,25

Washed crushed granite of 5-20 mm fraction as coarse aggregate and standard siliceous sand were used for concrete preparation.

A superplasticizer based on polymethylene polynaphtalene sulphonates (PNS) and a retarder based on sodium triphosphosphate (TPPh) were used in some tests.

Titanium dioxide produced by DuPont was used as pigment. Samples of photo catalytic TiO<sub>2</sub> were synthesized according to [2].

Organic shrinkage reducing admixture (OSRA) was synthesized on the basis of aliphatic alcohols and their ethers [3]. The well-known commercial OSRA by Takemoto Oil & Fat Co. Hibidan® on the basis of polyalkyleneglycol was used for comparison.

### 2.2 Methods

Spread tests of mortars were performed according to [4]. Fresh concretes and mortars (fine-grained concretes) were tested according to [5], and hardened concretes (mortars) – according to [6-8]. Compressive strength of hardened samples was measured in accordance with [9].

Shrinkage for concrete samples was measured also starting from the 1-day age (zero reading); 100 mm × 100 mm × 400 mm prisms, prepared according to [10], were used for the measurement. Each curve is the average of results obtained in three specimens.

The performance criterion of OSRA was shrinkage strain reduction for three mortar samples (40 mm × 40 mm × 160 mm prisms) as measured using the method described in [11]. Shrinkage deformations of each specimen were measured using a length comparator, sensitivity of 1 μm, and gage studs on the end sections of the prisms.

The OSRA were incorporated in the mortar mixtures with gauged water (1:3 mixture proportions, 150 -170 mm cone flow) in dosage of 2%, 4% and 6% of cement weight. For the first 24 hours after casting the specimens were stored in a normal hardening chamber ( $t = 20 \pm 2^\circ\text{C}$ ,  $\phi = 95 \pm 5\%$ ), then after demolding and throughout the test – in air-dry conditions ( $t = 20-25^\circ\text{C}$ ,  $\phi = 60-70\%$ ). The shrinkage strains were measured starting from the 1-day age (zero reading). To assess the OSRA effect on the hardening rate and mortar strength the appropriate tests were conducted at the age of 1, 2, 3, 7 and 28 days.

The effect of admixtures on the concrete void structure characteristics was explored studying the kinetics of their water absorption in conformance with the methods described in [9].

To investigate the parameters of the specimen porous structure, the optical method based on the Gallery software was applied.

## 3. Results and Discussion

### 3.1 Low water demand binders.

In accordance with the developed process one of the main aspects of HPC producing is the use of mechanically activated composite binders. They are produced by controlled grinding of Portland cement clinker or finished Portland cement with chemical modifying agents, including water-reducing admixtures, and mineral admixtures; their types and quantities are specified from operating conditions and with

account of hydration and structure formation process optimization. As a result of the solid-phase reaction on the clinker mineral surface in the process of mechanochemical activation, finished binders are forming that combine increased dispersivity and, accordingly, high hydraulic activity, with very low water demand. Variations in a wide range in types and quantities of mineral admixtures confer to the binders such special properties as sulfate resistance, dimensional stability, reduced hydration heat, etc. The cumulative result of all above peculiarities is obtaining the mechanically activated binders with high performance properties and durability. It should be noted that the organic mineral compounds formed on the clinker grain surface in the activation process determine such technological properties of composite binder-based mixes as resistance to bleeding, a high degree of thixotropic shear thinning and increased reproductive performance, i.e. the ability to reproduce the finest details of the relief or texture without the formation of the large air pores and defects on the front surface, that is being especially important for decorative elements made from architectural concrete [12-14].

Below the test results are given (**Table 2**) based on composite binders from LWDB-90 – LWDB-100 test batches that were produced in ball mill with 0.5 t/h capacity from white cements (for composite binders LWDB designation is used, i.e. the binder having low water demand, the numeral in the designation denotes the content of clinker component in %).

**Table 2. The impact of binders and admixtures used in concrete mixtures preparation on technological properties and strength of concrete.**

№№	Quality index, measuring unit	Indicator values								
		White CEM I 52,5R		LWDB-100 (based on white CEM I 52,5R)				LWDB-90 (based on white CEM I 52,5 R, mineral additive – granulated blast furnace slag)		
Compound №		1	2	3	4	5	6	7	8	9
1.	Material consumption, kg/m <sup>3</sup>									
1.1.	Cement	490	496	480	485	490	472	469	471	487
1.2.	Sand	542	595	710	717	725	698	1641	1649	1705
1.3.	Aggregate	1068	1071	1100	1110	1124	1082	-	-	-
1.4.	Water	226	198	160	162	146	157	159	165	146
2.	Admixture dosage, % cement mass									
2.1.	PNS	-	0,6	-	-	0,5	0,5	-	-	0,6
2.2.	TiO <sub>2</sub>	-	-	-	1	1	1	3	3	3
2.3.	Retarder based on sodium tripolyphosphate	-	-	-	-	-	0,07	-	0,07	-
2.4.	OSRA	-	-	-	-	-	-	-	-	6
3.	W/C	0,46	0,4	0,33	0,33	0,3	0,33	0,34	0,35	0,3
4.	Slump, cm	18,5	20	15	5-9	14	20	14	16	18,5
5.	Fresh concrete density, kg/m <sup>3</sup>	2326	2360	2450	2475	2490	2410	2288	2295	2338
6.	Air content, %	2,5	3,0	2,7	2,3	2,3	2,5	4,5	5,6	4,7
7.	Compressive strength, MPa, in age									
	1 day	20,5	25,7	55,0	69,7	72,8	16,5	39,8	9,6	8,8
	2 days	36,4	47,4	64,8	70,5	78,4	72,0	55,2	48,4	23,1
	3 days	40,2	51,0	72,1	76,7	83,0	76,1	59,5	68,1	40,9
	7 days	47,6	58,4	83,3	90,0	90,6	84,2	73,4	77,9	73,0
	28 days	55,6	67,3	93,7	103,8	112,6	107,3	81,0	84,0	84,5

The use of mechanochemical activation allows considerably increasing the hardening rate and strength of white cement, while obtaining on its basis the composite binders with 60-100 MPa activity depends on the initial cement quality; this corresponds to the strength rise by 41-53% at 28 days, by 30-70% at 2-7 days and over 2 times at 1 day. Alongside with the above, the essential reduction (by 17-25%) of cement paste water demand is provided in spite of the rise in binder dispersivity as compared to initial cements. Introducing at the stage of binder production of mineral additives, such as natural alumina-containing pozzolana to reduce shrinkage or granulated blast furnace slag to control heat release and to increase sulfate resistance, does not result in considerable reduction of binder activity.

### **3.2 *Fresh concrete and structure formation of concrete.***

In accordance with the reduced water demand of binders the making of flow (or self-compacting) fresh concrete on their basis is achieved at significantly lower – by 20-30% - mixing water consumption (**Table 2**). At the same time the specific rheological properties of composite binders associated with mechanochemical activation provide the minimum bleeding, reduction of air entrainment in concrete mixes and increase their density, suggesting improvements of concrete structural characteristics.

Control of structure formation processes as well as performance and decorative properties of architectural concrete envisages at the stage of concrete mix preparation, first of all, a regulation of their slump loss and introduction of various chemical and mineral admixtures (mineral pigments, shrinkage reducing admixtures, etc.) when mixing. Slump loss of concrete mixes with composite binders, i.e. the rate and time of initial flow reduction, as a rule, corresponds to slump loss of mixes with ordinary cements. However, it may not be sufficient when concreting complex elements, for example, large-scale sculptural reliefs. Besides, the rapid loss of flow is in line with accelerated structure formation of concrete and intensive heat release during the first hours after placement. Introduction of retarding agents allows avoiding it. The data given in **Table 2** and related to the use of the admixture on the basis of sodium tripolyphosphate show that in this case slump loss of concrete mixes essentially decreases, while the beginning of the intensive strength gain occurs in 36-48 hours after molding. This process is accompanied also by the more uniform heat development.

### **3.3 *Role of titanium dioxide.***

Along with admixtures controlling the rate of structure formation, the coloring agents, in the first turn, titanium dioxide  $TiO_2$ , are introduced when mixing. Even when using binders based on white cement, the introduction of  $TiO_2$  allows neutralizing the color distortion due to contamination of the fillers and aggregates, and making the mix color more susceptible to the introduction of small doses of mineral pigments for accurate reproduction of colors. Adding small amounts of  $TiO_2$  (up to 3-5% of cement mass) does not affect actually water demand and rheology of concrete mixes, while affects positively the concrete strength. The data presented in **Table 2** show that for all periods of hardening the strength of concretes increases with the growth of  $TiO_2$  dosage. At the 1-day age the addition of  $TiO_2$  in the amount of 3% of cement mass is accompanied by the strength gain from 65 to 81 MPa, i.e. by 25%, at 7 days - from 82 to 101 MPa, i.e. by 23%, and at 28 days - from 92.5 to 109 MPa, i.e. by 18%. In combination with PNS the introduction of  $TiO_2$  is accompanied by even greater increase in strength. Using titanium dioxide sensibilized through a nanotechnology gives additional benefits connected with self-cleaning properties of architectural concrete and possibilities of the control over urban pollution [2].

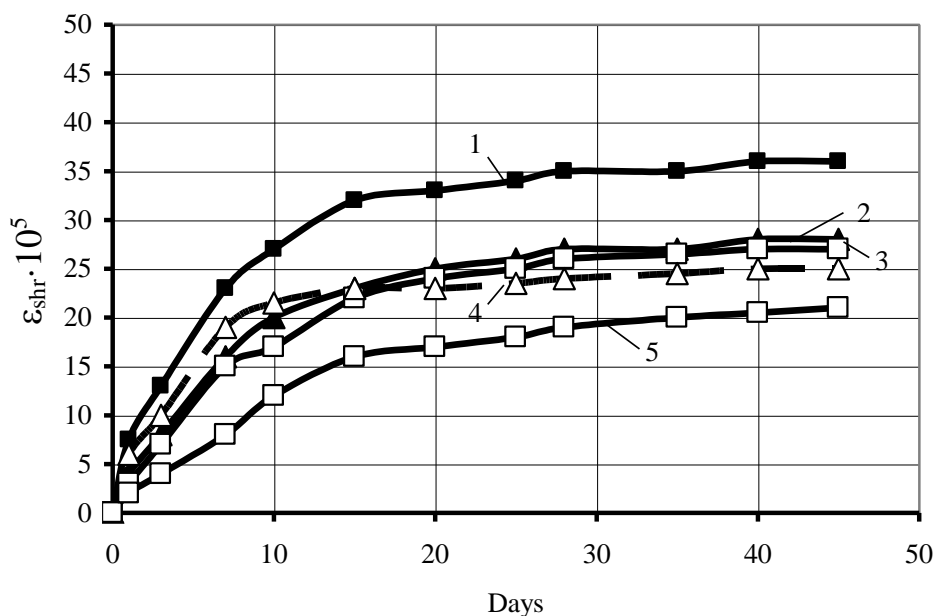
### **3.4 *Hardened concrete.***

The analysis of the data in Table 2 shows that the use of mechanically activated binders is accompanied in all cases by essential increase of the hardening rate as compared to concretes based on initial cements. Indeed, except for the cases, when a special aim was pursued to retard structure formation and hardening by using a retarder (**Table 2**, compounds 6, 8), the strength of modified concretes reaches 49-67% of the quality class strength as early as 1 day aging, while for concretes based on initial cements this value does not exceed 36-38%. These high hardening rates of concrete cured at ambient air confirm once more a possibility to produce architectural concrete articles without steam curing when used both sand and crushed stone (compounds 1-6) and graded sand mixtures as aggregates (compounds 7-9).

### 3.5 Control of shrinkage.

As already noted, at an early hardening stage the important factor of concrete defect-free structure formation is reduction of its shrinkage. The data given in **Figure 1** illustrate a possibility to control shrinkage of high performance architectural concrete owing to the use of OSRA. Being a product of chemical synthesis, the above admixture differs from mineral additives on the basis of sulfate and aluminat compounds by stability of its composition and properties. Besides, the OSRA admixture mechanism based on variation of water bond forms in concrete and regulation of mass-transfer processes presents a much lesser hazard for the concrete structure formed than appearance of calcium hydrosulfoaluminates, unbalanced conditions of hydration and composition of which alongside with reduction in shrinkage strains may also lead to structural failures. It follows from the data given in **Figure 1** that the reduction of their value is 22-45% by the moment of strain stabilization during hardening under air-dry curing when introducing OSRA in the amount of 2-6% of cement mass.

It should be noted that at equal dosages of admixtures OSRA and Hibidan based on polyalkylene glycol the equal degree of shrinkage reduction is reached thereby confirming efficiency of the admixture offered.



**Figure 1. Effect of admixtures on the shrinkage value of fine-grained concretes with the ratio of cement to sand 1:3,5 under air-dry curing.**

1 – no admixture; 2 – 2% OSRA; 3 – 4% OSRA; 4 – 6% OSRA; 5 – 4% Hibidan.

### 3.6 Mechanical properties and durability.

The increased hydraulic activity of mechanically activated binders and efficient mix design of architectural concretes predetermine their high physical and mechanical properties and durability, particularly under favorable conditions of structure formation, e.g. when introducing retarders or OSRA admixture. The data presented in **Table 2** show that show that the values of physical and mechanical properties of concrete correspond to high values of their strength.

The values of the prism strength factor and the initial tangent modulus of elasticity of modified concretes meet regulatory requirements or exceed them. Noteworthy increase of prism strength and modulus of elasticity of concrete with OSRA and sodium tripolyphosphate may be associated with reduction of the shrinkable nature microdefects in their structure, on one hand, and with the absence of structural changes connected with intensive heat development under fast strength gain at an early age, on the other hand.

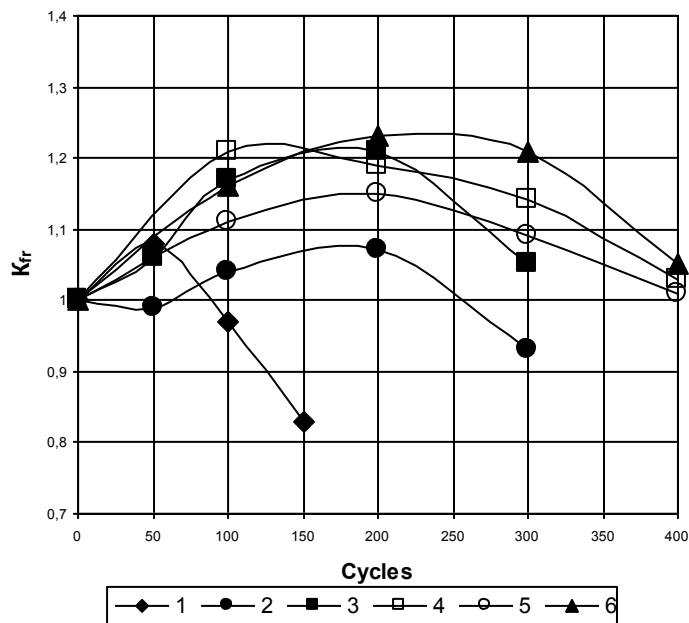
The value of volumetric water absorption of modified architectural concretes may also serve as an indicator of improving of their structural characteristics. The data in **Table 3** indicate that mentioned value does not exceed 10%, thus allowing attributing the obtained concretes to materials with compact structure.

Combination of high density and strength of modified concrete determines, in turn, their high frost-resistance. As follows from the data presented in **Figure 2**, frost-resistance factor  $K_f$  of concretes based

on LWDB (i.e. the ratio of strength of key samples after a given number of alternate freezing and thawing cycles to the strength of control samples) is over 1 even after 300-400 test cycles, that indicates to the available reserve of durability and to the predominance of constructive processes in the concrete structure over destructive ones. In contrast, the frost resistance of concrete based on initial white cements does not exceed 100-250 cycles depending on the type of cement.

**Table 3. Main characteristics of architectural concrete depending on binder and admixture types.**

№№	Quality index, measuring unit	Indicator values			
		White CEM I 52,5R	LWDB-100 (based on white CEM I 52,5R)	LWDB-90 (based on white CEM I 52,5 R, mineral additive – granulated blast furnace slag)	
1.	Admixture kind and dosage, % cement mass	PNS (0,6%)	TiO <sub>2</sub> (1%) PNS (0,5%)	TiO <sub>2</sub> (3%) TPPh (0,07%)	TiO <sub>2</sub> (3%), OSRA (6%), PNS (0,6%)
2.	Compressive strength, MPa, in age 28 days				
2.1.	Cubic R <sub>c</sub>	67,3	112,6	84,0	84,5
2.2.	Prism R <sub>pr</sub>	48,5	85,6	68,0	65,9
3.	Prism strength factor R <sub>pr</sub> / R <sub>c</sub>	0,71	0,76	0,81	0,78
4.	Initial tangent modulus of elasticity E x 10 <sup>-3</sup> , MPa				
4.1.	Experimental	38,1	57,7	44,2	46,9
4.2.	Normative	39,0	–	>40,0	>40,0
5.	Volumetric water absorption, %	12,8	7,1	7,8	7,0



**Figure 2. Frost resistance of concrete with various binders and admixtures.**

1. Portland cement (CEM I 42,5) with PNS (0.6 % of cement mass).
2. White cement (CEM I 52,5R) with PNS (0.6 % of cement mass).
3. LWBD-100 (based on CEM I 42,5).
4. LWBD-100 (based on CEM I 52,5R) + 1 % TiO<sub>2</sub> + 0.5 % PNS.
5. LWBD-90 (based on CEM I 52,5R + granulated blast furnace slag) + 3 % TiO<sub>2</sub> + 0.07 % retarder.
6. LWBD-90 (based on CEM I 52,5R + granulated blast furnace slag) + 3 % TiO<sub>2</sub> + 6 % OSRA + 0.6 % PNS.

### **3.7 Impregnation with the special organic silicate compounds.**

In real building practice ornamental concrete products are exposed to pollution to some extent even prior to the beginning of maintenance - during transportation, warehousing and especially at installation which is carried out frequently without appropriate protection of exterior surfaces. Surface treating of architectural concrete with special organic-silicate compounds, which partially or completely seal the pores with high density air-silica-gel, improves performance and durability of material, decreases water absorption up to 20-37% and increases freezing-thawing resistance up to 20-50% [15]. Penetrating sealant systems were developed on the basis of the soluble sodium silicate which silica module varied within 1.98-3.36. It has been found that technological parameters of organosilicate compositions for concrete impregnating can be essentially improved when surface active agents (SAA) of the various natures were introduced to soluble silicate, anionic and nonionic surfactants including. These additives make significant impact on state of soluble silicates in an aqueous solution at low concentration of SAA. The surfacing of concrete by specified sealing system improves essentially physical-mechanical parameters of the impregnated concrete that allows to raise considerably operate reliability and durability both new concrete made articles and reinforced concrete structures, and products and buildings which are under service conditions. With reference to architectural concrete it means also raise of durability of a surface of ornamental elements to foulings and makes easily the process of their cleaning, and also possibility of protective coating while in service that is confirmed by experience of practical application during restoration of some historical monuments and buildings in City of Moscow (**Figure 3**).



**Figure 3. The Center of Orthodox Heritage in Peredelkino near Moscow. More than 24,000 purpose-made details of outside architectural decoration.**

## **4. Conclusions**

Thus, the above mentioned methods of modifying of the architectural concrete provide an opportunity to control its structure and properties as well as concrete mix workability and hardening rate at all stages of its making – from selection of initial materials to surface treatment at the final stage of manufacture or even at the operational stage. Thereby an optimum combination of construction and technical characteristics of concretes and decorative properties of products is achieved that should considerably expand a field of architectural concrete application and on the whole facilitate the growth of its social significance and attractiveness.



## 5. Acknowledgement

The authors would like to thank Dr. N.F. Bashlykov and recently deceased Dr. Yu.V. Sorokin for their valuable contributions.

## 6. References

1. Boyle, M.J., «Concrete as a substitute for granite cladding attains high performance concrete consideration as the result of exceptional materials and production control», International Symposium on High Performance Concrete, Orlando, Florida, U.S.A., 2000, pp 279-293.
2. Falikman, V., Vajner, A., Zverev, I., “New photocatalytic cementitious composites containing modified titanium dioxide nanoparticles”, Proceedings, 3<sup>rd</sup> Int. Symposium on High Performance Concrete and Nanotechnology for High Performance Construction Materials (Hipermat), Kassel, Germany, 2012, pp 147-152.
3. Falikman, V.R., Vajner, A.Ya., “Hydroxyl Organic Compounds to Reduce Shrinkage Deformations of Concrete”, Proceedings, Application of Superabsorber Polymers and Other New Admixture in Concrete Construction, Dresden, Germany, RILEM S.A.R.L., 2014, pp 159 – 168.
4. GOST 310.4, “Cements. Methods of tests of bending and compression strengths”, 1981.
5. GOST 10181, “Concrete mixtures. Methods of testing”, 2014.
6. GOST 12730.0, “Concretes. General requirements for methods of determination of density, moisture content, water absorption, porosity and impermeability”, 1994.
7. GOST 12730.1, “Concretes. Methods for determination of density”, 1994.
8. GOST 12730.4, “Concretes. Methods of determination of porosity parameters”, 1994.
9. GOST 10180, “Concretes. Methods for strength determination using reference specimens”, 2011.
10. GOST 24544, “Concretes. Methods of shrinkage and creep flow determination”, 1981.
11. GOST 11052, “Gypsum-alumina expanding cement”, 1974.
12. Bashlykov, N.F., Falikman, V.R., Serdyuk, V.N., et al., “Hydraulic Cement”, Russian Patent № 2096364, 1996, publ. in Bul. No.32, 1997.
13. Bashlykov, N.F., Falikman, V.R., Serdyuk, V.N., et al., “Method of Manufacturing of Decorative Binder with Low Water Demand”, Russian Patent № 2085525, 1991, publ. in Bul. No.20, 1997.
14. Bashlykov, N.F., Sorokin, Yu.V., Falikman, V.R., et al., “Method of Manufacturing of Decorative Building Products and Decorative Coatings”, Russian Patent № 2084416, 1992, publ. in Bul. No.20, 1997.
15. Falikman, V.R., Sorokin, Yu.V., Deniskin, V.V., “Surface protection of high performance architectural concrete” Proceedings of Concrete Solutions, 4<sup>th</sup> International Conference on Concrete Repair, Dresden, Germany, 2011, Taylor & Fransis Group, London, UK, pp 813-821.

# TORSIONAL BEHAVIOUR OF REINFORCED CONCRETE T-BEAM SECTIONS

*Douglas Anabalon, Bridge Design*

---

## ABSTRACT

The development of torsion design models has been primarily based on the analysis and behaviour of rectangular beam sections. With the exception of linear theory, the formulation of torsion design rules have based on empirical results, which are subsequently applied to non-rectangular sections.

An assessment of the response of an isolated beam and slab section is undertaken to identify the torsional behaviour of T shaped beam elements when subjected to pure torsion. A study of the torsional theory associated with the Softened Truss Model is discussed to demonstrate a comparison between the applied theory, design code rules and experimental tests results undertaken on T-shaped beams.

To demonstrate differences in torsional behaviour between rectangular and T-shaped sections, two finite element models are assessed to study the impact of flanges and web aspect ratios on concrete stress distribution, reinforcement stresses, structural response and torsional stiffness.

---

## INTRODUCTION

Early principles of torsion design define the linear elastic state of materials however its left to non linear models to define the post cracked behaviour of cross sections under torsion. Many of the design theories developed for non linear behaviour have been determined from empirical solutions, formulated to match the behaviour of rectangular sections observed in load testing of sections to failure. Design theories are then applied to non rectangular sections through simplified methods that approximate the torsional response of structures. This design approach can underestimate the behaviour of idealised T beam sections and the stiffening effect of the flange.

This paper seeks to present a discussion regarding comparative studies relating to the structural behaviour of rectangular and T-shaped beam sections subjected to pure torsion. Design theories adopted and review of experimental testing in torsion is discussed and reviewed relative to the study of T shaped beam sections. Four non-linear finite element models are assessed and discussed to identify behavioral differences observed in the structural performance of T-beams and rectangular cross sections subjected to torsion.

## DESIGN THEORY

Classical torsional theory, developed in the early 19th Century, was considered an adequate model for behaviour of concrete members in the pre-cracked state. For members such as T and L shape sections, the torsional strength of a section could be estimated by expressing the stiffness through the torsional modulus,  $J_t$ .

$$J_t = 0.33 \sum x^2 y \quad (1)$$

This function, defined as the torsional modulus, embraces the rigidity of each individual segment in a member and is commonly used in the 2004 Australian bridge code to evaluate the cracking torque.

In the post cracked state of concrete, the shear flow around the perimeter of a cross section is disturbed and engagement of reinforcement is achieved over an increasing rate of rotation. As a result alternative design theories have been established to describe the behaviour on concrete members after the onset of cracking.

One such theory is that of the Softened Truss Model (STM) developed by T. Hsu. The theory adopts the three principles of mechanics

- equilibrium
- compatibility and
- stress strain relationship of material

in much the same way as the Modified Compression Field Theory. The STM transforms the normal plane stresses into a rotated co-ordinate system which conforms to the angle of the twist rotation observed in crack patterns. The rotated angle assumes a changing angle of compressive struts and differs from the fixed angle model which assumes the compressive struts remain parallel to the direction of the initial cracks

The softened component of the model relates to a reduced stress-strain relationship of the concrete principal compressive stresses and equivalent strains. To account for the reduced concrete performance of the stress-strain relationship a softening coefficient was adopted to reflect the two dimensional softening effect experienced in the concrete under stress. Furthermore the relationship of the average stress and average strain of the reinforcement was adjusted to account for the potential of local yielding at the crack location.

## **EXPERIMENTAL STUDIES**

### **Testing of Rectangular beams**

Much of the early research undertaken on rectangular beams consisted in an attempt to vary structural properties. Although development of early design theories was based on the idealised linear response of circular hollow sections, the development of post crack torsional theories has been based on empirical solutions created to match test cases observed in understanding the post-crack behaviour.

- An increase in the aspect ratio for specimens with the same amount of reinforcement, led to a decrease in the extent of cracking observed albeit with larger crack widths. Furthermore the increased aspect ratio also led to a decrease in the ultimate strength of a reinforced section
- concrete strength affected the crack width, torsional stiffness and torsional capacity of rectangular sections. Increase in concrete strength increase torsional stiffness and capacity.
- crack widths were reduced and well controlled by an increase in longitudinal reinforcement at near ultimate torsional capacities.
- The proportion of reinforcement affects the behaviour of crack angles and crack width across shear planes in the diagonal struts. Figure 1 depicts an interaction diagram based on STM model identifying four modes of failure for different reinforcement ratios.
- Concrete sections were found to suffer significant loss in stiffness in the post crack range and as such affected the capacity of a section to resist torsional moment.

In assessing the degree of redistribution, the presence of the two types of torsion:

- Equilibrium Torsion: where torsion is required to maintain equilibrium in the structure; and
- Compatibility Torsion: where twist is required to maintain compatibility of the structure.

It was found that the ratio of torsion to bending stiffness significantly dropped causing a redistribution of torsion and bending moment. In adopting compatibility torsion design, it was deemed that elements should consider twist rotation and not torque and as such minimum reinforcement would be required to ensure ductility and crack control. A reasonable assumption of "zero torsional stiffness" was suggested to simplify torsional design.

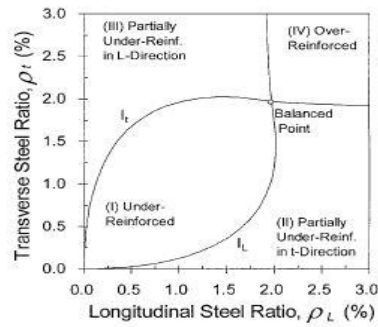


Figure 1: Failure interaction curve for rectangular beams

## Testing on T- shaped beams

Research in the area of T-beams that reflect slab on beam sections has been at best sporadic and random with varying results. Most of the effects noted previously were also found applicable to flanged sections. The effect of flanges on section capacity was assessed and deemed significant by a study assessing the Moment - Torsion interaction of flanged sections. Two failure mechanisms were identified in the study, these consisting of the following:

- Partial cracking of the beam faces at high bending to torsion ratios
- Full cracking of the beam at low moment to torsion ratios.

The first mechanism of failure consistently occurred for M/T ratios greater than 4 where as the second mechanism consistently occurred at ratios less than 4. The effect of reinforced flanges was considered a significant factor in the increase of torsional capacity in terms of both width and depth of flanges. The interaction diagram shown in Figure 2 highlights the significant effect of flanges compared to the rectangular section, with torque capacity up to 2.6 times greater than rectangular sections.

Failure of most sections was uniformly identified to occur after cracking along the top face of the web/flange. As a result, the influence of the flange width on the torsional capacity of the section was considered to be effective at overhang widths equal to six times the flange thickness. It was concluded that the behaviour of the slab and beam behave as box sections that cross each other with shear flows on each element generally unequal.

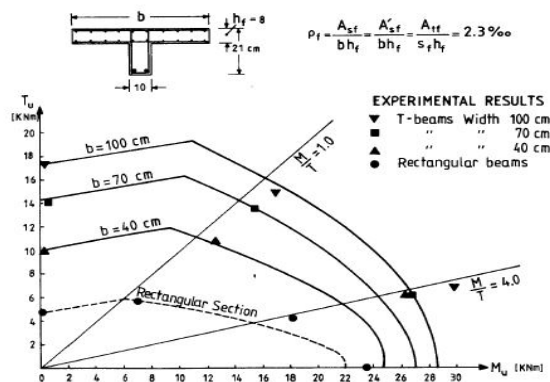


Figure 2: Moment/Torsion Interaction diagram for flanges sections (2)

A recent evaluation of torsional stiffness in beam and slab bridges decks was carried out by the University of Rijeka. The study looked at direct load testing of bridge structures with no transverse diaphragms. The intention of the analysis was to determine the design value coefficient of torsional stiffness reduction for the verification of serviceability limit state design. There study concluded that cross sections experienced a 70% reduction of torsional stiffness under serviceability limit state conditions.

## DESIGN MODEL

Two design models were selected to simulate a typical beam size section encountered in service with beam aspect ratios between 1.0 and 2.1. The beams only consider conventional reinforcement so to observe the overall pre and post crack behaviour and distribution of stress across the surface plane of the member. The Analysis of typical section models were carried out on a Strand 7 with models based on the stress-strain relationship of softened concrete truss theory.

## Model Analysis

An ideal flange width overhang of 4 times the flange depth was adopted for this particular study in accordance with the ACI code and previous studies on effective flange widths. A standard length of 2.0m was adopted, with axis - symmetric boundary conditions on one side to allow crack propagation over the peak stress regions and thus identify changing section stiffness. The design models were constructed using 2 node line element (Truss type) and 8 noded Quadrilateral Brick element (Hex 8)

The study considered four different design sections consisting of two rectangular and two T-beam sections as shown in Table 1. The dimension of the main web was carried throughout the length of the T-beam section so to assess the impact of flange stiffness.

**Table 1 - Analysis of beam torsional Stiffness**

Tag	Type	Beam section	Flange width	Flange Depth
R1_450	Rectangular	600 x 450	-	-
R2_600	Rectangular	600 x 600	-	-
T1_450A	T-Section	600 x 450	1 800	150
T2_600A	T-Section	600 x 600	1 800	150

Table 2 shows the degree of reinforcement adopted in the construction of the FE models. Two additional modifications were introduced into the T1\_450A beam to assess the impact in changing stirrup spacing and absence of reinforcement in the flange sections.

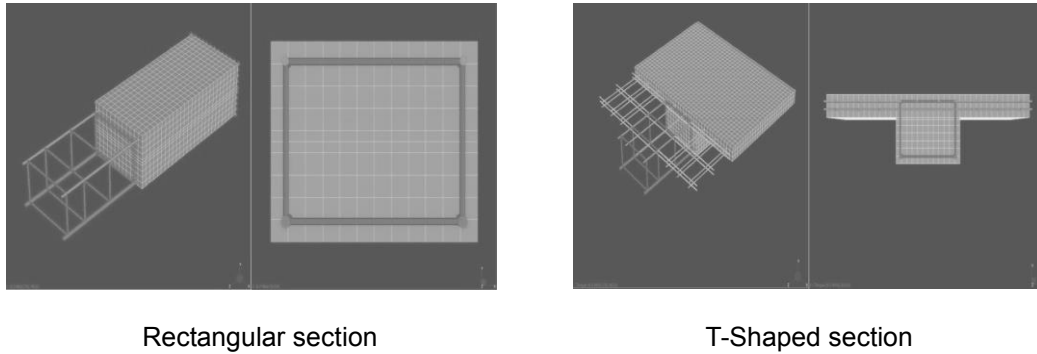
**Table 2 - Reinforcement details in finite element models**

Reinforcement Type	Location	Beam	Flange
Longitudinal	Top	2 - Ø20	Ø12 @ 200
	Bottom	2 - Ø28*	Ø12 @ 200
Transverse	Stirrups	Ø16 @ 300*	-
	Top	-	Ø12 @ 300
	Bottom	-	Ø12 @ 300

\*Reduced to 2-Ø20 bars longitudinally & Ø12 bars at 200 centers on 1 test beam.

The behaviour of reinforced concrete elements under shear stress was identified to differ from the normal constitutive laws of concrete in normal compression hence a softening of concrete strength in the truss model theory using redefined constitutive laws were adopted.

Defined boundary conditions reflecting rigid fixity at one end and axis symmetric conditions on the opposite end were adopted to reflect free end movement at midspan. Warping of the internal end face was restrained by the use of a loading beam on the end of the section and a coupling force was applied to a loading beam connected to the end of the beam segment.

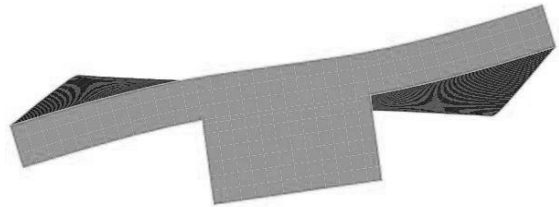


**Figure 3: Typical section of FE models**

## Results

General observations identified regarding the response behaviour included:

- no vertical or horizontal displacement about the center of the beam rotation
- Flanges tips displayed a hyperbolic deformation with internal curvature.
- Shear flow path within the web was consistent with rectangular sections however demonstrated a change in direction at the web - flange interface flowing through the flange. No shear flow between web-flange interfaces.
- Maximum shear stress zones around re-entrant corners and the middle of each surface element.



**Figure 4: Flange deformation**

Inspection of the diagonal strut angles found that the introduction of flange members resulted in keeping fairly uniform compressive strut angles between reinforcement nodes. No compressive strut was observed between web-flange interfaces. Increasing torque past the point of cracking caused strut angles to become steeper due to failure of beam elements and subsequent interruption of shear flow paths

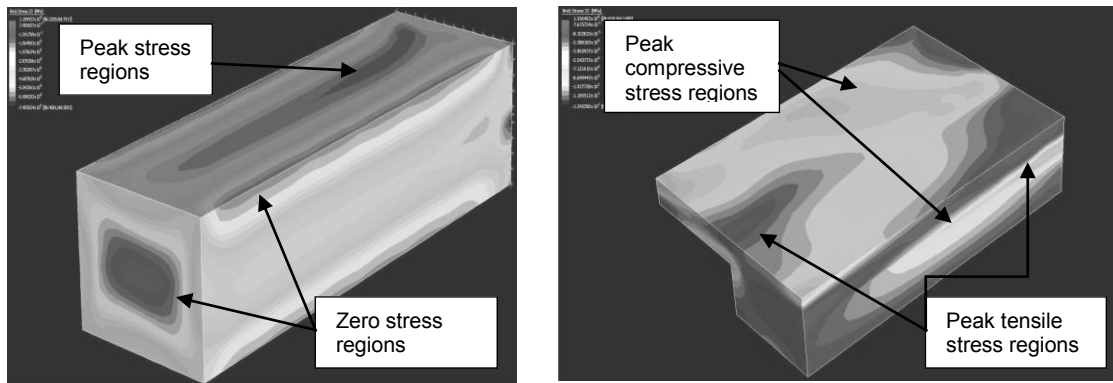
The impact of flange reinforcement was found to improve the behaviour and response of a T-beam subjected to torsion. Members with no flange reinforcement behaved similar to reinforced flange sections up until the onset of cracking at which point they behaved like rectangular sections. Strain distribution was observed in areas over the top and bottom of the flange. After cracking the extent of failure increases at the interface between the beams and flange until brittle failure results in the webs and flanges behaving as individual members. The use of flange reinforcement was found to:

- improve the ultimate torsional capacity;
- increase the level of ductility due to greater rotation tolerance;
- transfer shear stresses across the beam – flange interface thus enabling distribution of forces; and
- provide an effective bond between beam and flange sections after cracking has propagated through the interface.

Analyses of the concrete stresses present in a rectangular section were found to coincide with the location of maximum shear flow around the perimeter of the cross section. Concrete stresses of T-shaped members demonstrated similar behaviour with peak stress concentrations associated with the maximum shear flow path identified on the member surface. Differences identified between the two shapes are identified in Table 3.

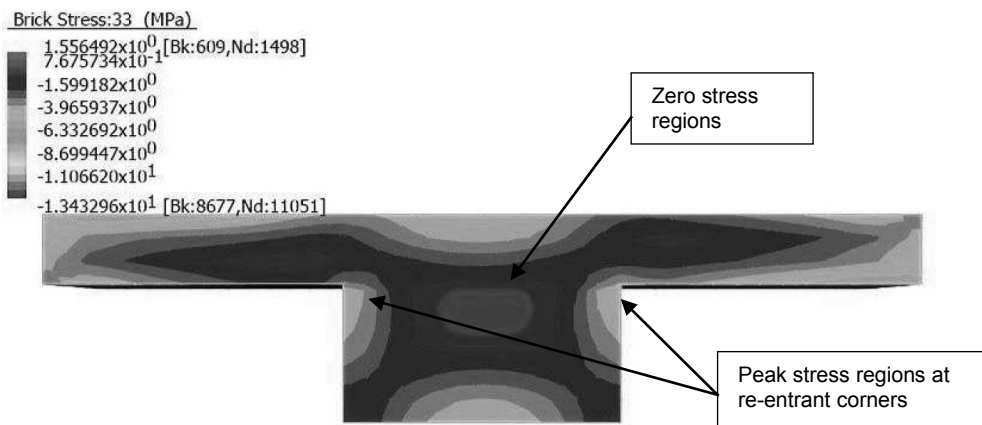
**Table 3 - Observations in Concrete Stress**

Rectangular Beams	T-Shape Beams
<ul style="list-style-type: none"> <li>• Uniform distribution over length</li> <li>• Minimum stress in the core</li> <li>• Minimum stress on the corners</li> <li>• Maximum stress on long length at shortest distance to centroid</li> <li>• Stress propagates uniformly over length with applied torque</li> </ul>	<ul style="list-style-type: none"> <li>• Diagonal distribution of stress</li> <li>• Uniform distribution of stress disturbed by flange</li> <li>• Stresses at mid length are lower but peak within the web sides</li> <li>• Stress concentrations near beam/flange interface</li> <li>• Peak tensile stresses at beam/flange interface located on beam ends and opposite faces</li> </ul>



**Figure 5: Concrete compressive stresses (post crack)**

Figure 5 demonstrates two main features associated with the compressive stresses which differ from that shown on rectangular sections. These include the non-uniform and uneven distribution of stress along the side face and change in distribution resulting from the flange.



**Figure 6: Concrete compressive stresses (post crack)**

Figure 6 highlights peak stress concentrations on the bottom re-entrant corners in addition to the stress distribution through the section near ultimate failure. Prior to failure, similar stress patterns are observed between each flange overhang and central beam. As the torque load increases to failure the stress disruption results in form of that shown in Figure 7. Each segment maintains connectivity to allow shear flow to remain present and thus distribute stress over the full cross section.

The shear center of the cross section was found to shift with increasing torque. In the pre-cracked state, the position of shear center was in accordance with theoretical assessment. . After cracking the shear center displaces vertically downwards ceasing midway between the original location and the shear center of the rectangular web section near ultimate failure. It is deemed that the transverse reinforcement across the flange assists in maintaining the distribution of shear flow across the T shaped cross section.

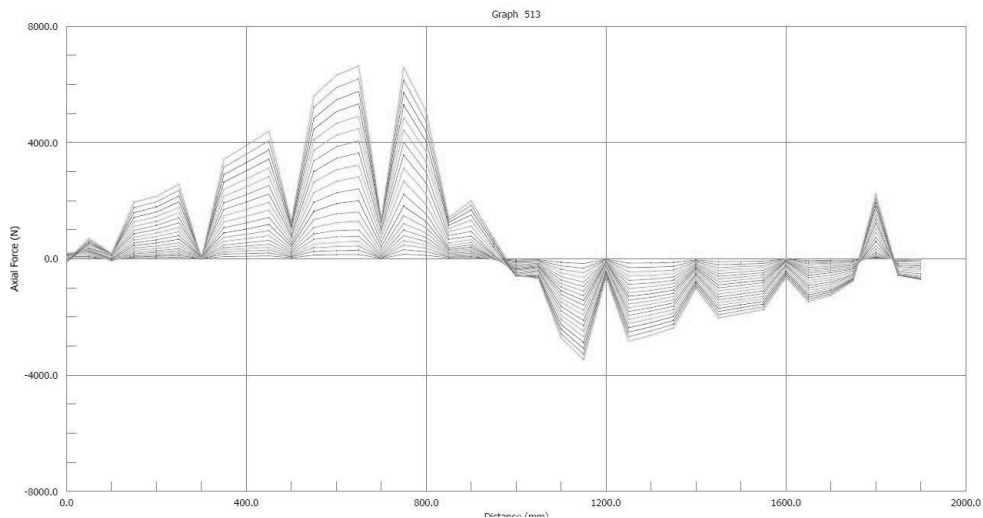
Stress levels in reinforcement were not found to significantly increase until after the onset of cracking. The depth of crack was also found to effect the stress increase. It was noted that the stress levels in the reinforcement depended on the location within the beam and the tensile forces acting on the truss elements.

The main areas where increased levels of steel stress were encountered included:

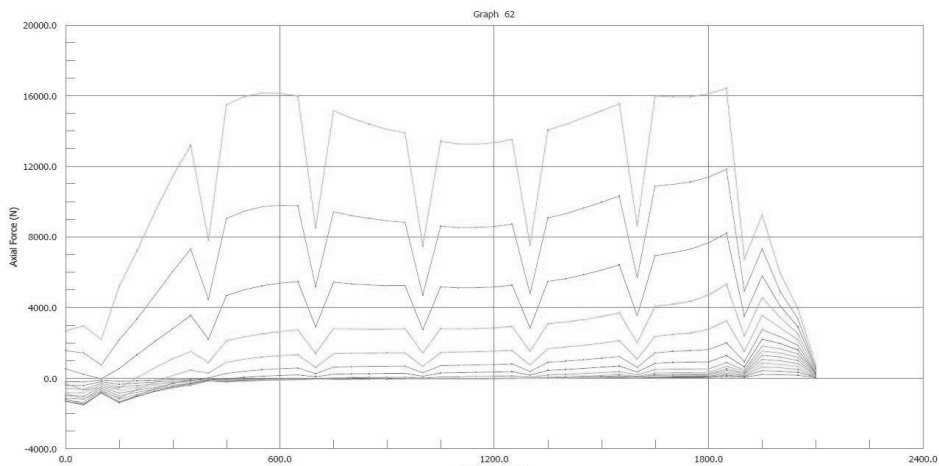
- Tensile face of the intersection between web and flange overhang
- main bottom longitudinal reinforcement and
- varying length of stirrup (subject to strut angle)

The degree of steel stress in the reinforcement was considered to be strongly associated with two factors:

- the deformation of the T-beam section and
- the stress distribution in the concrete

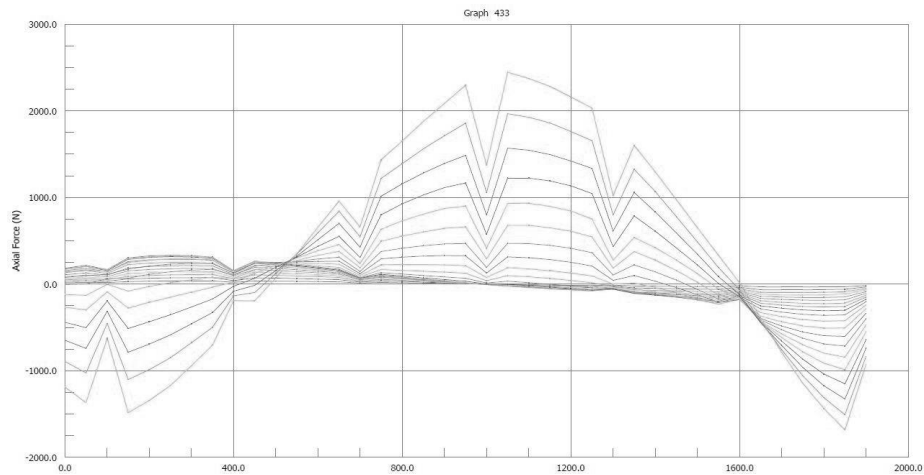


**Figure 7: Flange Reinforcement (loaded end)**



*i) Rectangular beam section*





ii) T-beam section

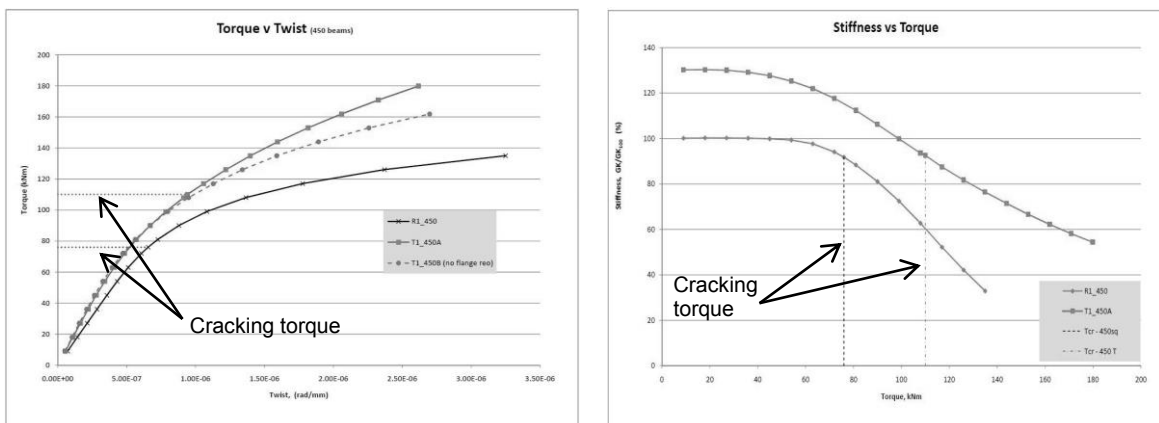
**Figure 8: Beam Longitudinal Reinforcement (Bottom face)**

Analysis of the torsional behaviour was carried out by generating two types of curves:

- Torque Vs Twist
- Stiffness Vs Torque

Based on the profiles observed on both graphs curves the following results can be obtained from the strength analysis of the beam section with an aspect ratio of 1.33.

- The rectangular beams experience increased rotation due to the lack of stiffness provided by the flanges
- The T-beams have greater torque capacity of than rectangular sections.
- The cracking torque of T-beams is relative to the cracking identified on the web. The stiffness of the flanges allows an increase in strength when compared to the rectangular section.
- Beams with unreinforced flanges have less ultimate torque capacity yet provide similar cracking torques.
- The torsional stiffness of T-beams has a flatter gradient after the onset of cracking resulting in increased degree of capacity.



**Figure 9: Load response graphs for 450 deep beams**

As shown in the graphs, the stiffness of the T-beam section at the point of cracking in the flange was closer to 90%. The results for cracking in the web of the T-beam sections clearly show a 30% loss in stiffness at first crack however suffer a significant loss of stiffness at ultimate torque limits. The torsional stiffness of beams in the ultimate limit state also appear to reduce with increasing aspect ratios of the web, although it is considered that this may have been the result of the FE models failing to converge before engaging full tensile capacity in the steel truss. In contrast with rectangular sections, the ultimate capacity of T-beam section can be seen to significantly increase with increasing aspect ratios of the web.

**Table 4 - Analysis of beam torsional Stiffness and strength**

Aspect ratio of Web	$GJ_{cr} / GJ$ (%)		$GJ_{ult} / GJ$ (%)		Torsional Capacity Ratio
	Rectangular	T-beam	Rectangular	T-beam	$Tu_{T-beam} / Tu_{rect}$
1.0	90	53	25	28	1.17
1.33	91.7	72	20	22	1.50
2.1	83	76	10	13	2.75*

## CONCLUSIONS

The study of the FE models found that the deformation of the structures was consistent with application of the applied torque. The key findings identified in the analysis and comparison of sections included the following:

- Shear stresses in T-beams reflected the behaviour of the shear flow around the typical cross section. Distribution was found to be diagonal along flange surfaces and not in a constant circulatory flow as identified in rectangular sections
- Maximum shear strains resulted in early cracking of the flange followed by the interface of the flange with the main web. The web surface was found to be the last of the elements to crack
- Flange reinforcement in T-beams was deemed important in maintaining compatibility between flange and web sections. It also increases torsional capacity of the beam at ultimate limit state conditions.
- Longitudinal stresses in the web reinforcement were found to behave differently between top and bottom bars, which were not consistent with rectangular beams
- Cracking torque of the main web was found to be 30% to 50% greater in T-beam sections when compared to equivalent rectangular sections.
- The relative torsional stiffness of T-beams with aspect ratios greater than 1 was greater by 12% to 16% in comparison with equivalent rectangular sections
- Ultimate torque levels were found to decrease with increasing aspect ratios of the main webs however torque capacities of T-beam sections are greater in T-beams relative to equivalent rectangular beam sections.
- Although initial flange cracking was observed at 90% of the torsional stiffness, the theoretical assessment to cracking torque coincided with cracking of the web. Torsional stiffness of sections at cracking torque was found to be equivalent to 70% of gross stiffness and 90% for rectangular sections.
- At ultimate torque, torsional stiffness was found to be between 10% to 25% of their gross torsional stiffness for both rectangular and T-beam sections.
- Principal failure mode consisted of surface yield lines located diagonally over the flange emanating from the point of load application and also located at the flange and web interface.

## REFERENCES

1. *Redistribution of Moments at Cracking - The key to simpler torsion design?* **Collins, Michael P. and Lampert, Paul.** 1973, Analysis of Structural systems for Torsion, American Concrete Institute, pp. 343-383.
2. *Diagonal Compression Field Theory - A Rational Model for Structural Concrete in Pure Torsion.* **Mitchell, Dennis and Collins, Michael P.** August 1974, American Concrete Institute Journal, pp. 396-408.
3. **ASCE, ACI Committee 445 I.** *Torsion in Structural Concrete.* s.l. : American Concrete Institute, 2013.
4. *Reinforced Concrete T-Beams in Torsion and Bending.* **Zararis, P. D. and Penelis, G. Gr.** Jan - Feb, 1986, ACI Journal, pp. 145-155.
5. **Stimac Grandic, Ivana, Grandic, Davor and Bjelanovic, Adriana.** *Evaluation of Torsional Stiffness in beam and slab bridge decks based on load testing.* Rijeka, Croatia : University of Rijeka, 2013.
6. **Tamberg, Karl G. and Mikluchin, P. T.** *Torsional Phenomena Analysis and Concrete Structure Design.* Farmington Hills, MI : American Concrete Institute, January 1973.

## AUTHOR BIOGRAPHIES

Douglas a Civil Structural Engineer with significant experience in the design of structures for both public and private sectors in Australia and the United Kingdom. Douglas has experience in design of structures particularly associated with road and rail application for the transportation of heavy loads; storm water drainage design; and overall structural design of infrastructure. He has also acquired design and project management skills associated with the delivery of various projects to road and rail clients. Over the last few years he has focused on specialising in the design of small to moderate size bridge structures and has recently completed his Masters of Engineering degree at UTS.

# Effect of Ultraviolet Radiation on the Physical and Mechanical Properties of Polymer Matrix

Wahid Ferdous<sup>1</sup>, Allan Manalo<sup>1</sup>, Thiru Aravinthan<sup>1</sup> and Gerard Van Erp<sup>2</sup>

<sup>1</sup>Centre of Excellence in Engineered Fibre Composites (CEEFC), School of Civil Engineering and Surveying, University of Southern Queensland, Toowoomba 4350, Australia

<sup>2</sup>Former Professor, Centre of Excellence in Engineered Fibre Composites (CEEFC), University of Southern Queensland, Toowoomba 4350, Australia

**Abstract:** In recent years, the use of polymer concrete have become a promising choice in outdoor applications such as repair concrete structures, beams and slabs of small cross section and coating of railway sleepers, is subjected to degradation caused by photochemical reactions from solar ultraviolet (UV) radiation. Any small damage in polymer matrix can be detrimental to the overall mechanical performance of the structure as it binds and transfers load to the reinforcement. This paper deals with the effect of UV radiation on the physical and mechanical properties of epoxy resin based polymer matrix. Seven different mixes containing filler materials from 0 to 60% with an increment of 10% were exposed to UV radiation using accelerated laboratory testing. Specimens were subjected to 2000 hours of UV radiation by Xenon 2200 watt air cooled lamp in the sunset XLS chamber and subsequently weighed, examined by microscope and mechanically tested. Surface degradation in the form of discoloration were observed by microscopic observation. It was found that, the loss of specimen's weight decreased with the increase of filler materials in the mix. Significant decrease of flexural strength were observed in the mixes containing filler volume up to 20%. However, no reduction of flexural strength were noticed for the higher filler ( $\geq 30\%$  filler) containing mixes indicating the filler can helps to preserve the structural performance by absorbing or blocking UV radiation before it reaching the chromophores in polymer matrix.

**Keywords:** epoxy resin, polymer matrix, ultraviolet radiation, physical and mechanical properties.

## 1. Introduction

The use of polymer concrete in outdoor structures such as bridge decking, pavement overlays, hazardous waste containers, waste water pipes and composite railway sleepers [1-3] are commonly exposed to ultraviolet (UV) radiation. UV radiation is found highly damaging to organic polymeric materials [4]. The solar UV radiations absorbed by the polymer are responsible for photolytic, photo-oxidative, and thermo-oxidative reactions that can degrade the polymer [5]. This photo-oxidative reaction reduces the molecular weight and makes the polymer brittle. Therefore, a special attention need to be provided for the application of polymer matrix in such kind of infrastructures. The wavelengths of UV radiation that reaches the earth's surface are ranged from 290 nm to 400 nm and most of the polymers have bond dissociation energies in that range of wavelength [6]. The UV ray caused by sunlight frequently combined with atmospheric oxygen, moisture, temperature, wind-borne abrasives, freeze-thaw and other environmental factors, and their photo-oxidative degradation can break the polymeric chains [6]. Due to photo-oxidation, the polymer matrix greatly affected by UV radiation and its effect on the physical and mechanical properties are essential to investigate for their widespread applications. Unfortunately, so far, a very limited research have been conducted on the performance of polymer matrix under UV radiation.

The effect of UV radiation are usually confined to the top few microns of the surface [6] that can reduce the mechanical properties which results in embrittlement, discoloration and an overall reduction in its physical and electrical properties [7]. This effect is severe for transparent polymer that allows UV ray to break the molecular bond of structure [8]. To reduce the transparency of epoxy resin, a non-transparent filler such as fly ash can be added. In contrast with the traditional concept of using fly ash as filler, this study incorporates two other filler materials, a fire retardant filler and hollow microsphere to improve the fire and shrinkage performance, respectively. However, the addition of filler can reduce the mechanical strength of polymer matrix as the flexural strength of polymer primarily depends on the amount of resin, the more resin in the mix- the more strength is.

The effect of different UV exposure time (500, 1000 and 1500 hrs) on fibre reinforced polymer composites have been studied by Yan et al. [9]. They found the deterioration of tensile and flexural properties after 1500 hrs of UV exposure. Chin et al. [10] investigated the UV radiation on thin polymer films that was exposed to a 1000 watt xenon arc source for 1200 hrs at 30 °C in an Oriel solar simulator. They observed surface oxidation results surface erosion and cracking for both vinyl ester and iso-polyester samples.

Peng et al. [11] studied the accelerated weathering on polypropylene composites reinforced with wood flour, lignin and cellulose at different loading levels from 0 to 960 hrs. They observed large cracks and delamination of polypropylene layer after 960 hrs of UV exposure. Cao et al. [12] investigated the degradation of polymer coating systems under 2000 hrs of UV exposure. The present study decided to expose the polymer matrix under UV radiation up to 2000 hours to achieve the more reliable results.

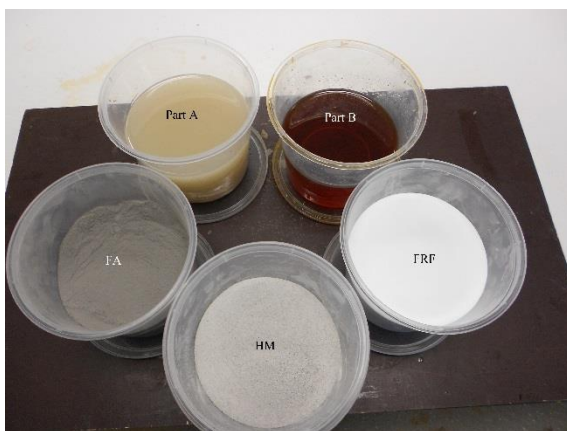
The lack of comprehensive knowledge on the effect of UV radiation on epoxy polymer matrix restricts their applications to the practicing civil engineers and designers. This paper explore some aspects related to physical and mechanical properties of polymer matrix under UV radiation and contributes to the scientific knowledge in the field.

## 2. Materials and Method

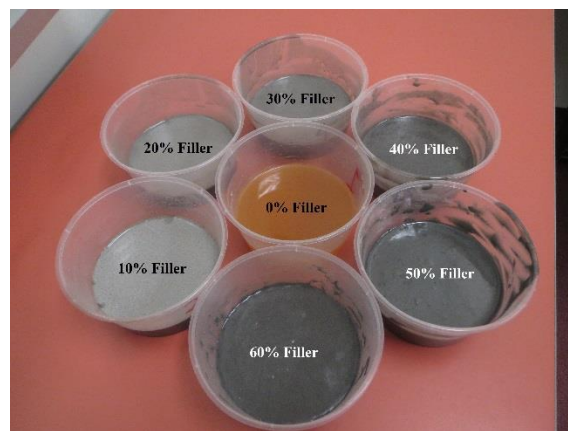
### 2.1 Materials

The materials employed in this investigation were epoxy resin and light-weight filler. Epoxy provides a high level of bonding properties compare to the traditional paste style glue. Generally two components of resin are required to get the gluing properties and need to be mixed together before use. In this study, two main components of the epoxy resin were DGEBA type (Part-A) and an amine based curing agent (Part-B). Epoxy resins are blended, filled, or modified with reactive and nonreactive components. It is then necessary to adjust the concentration of the curing agent to cure only the portion of the mix that is reactive. The resin producer furnishes the Epoxy Equivalent Weight (EEW) of 190 gm for Part-A and Amine Hydrogen Equivalent Weight (AHEW) of 60 gm for Part-B. To make the resin mix reactive, one equivalent weight quantity of amine curative will require for one equivalent weight quantity of an epoxy resin. Therefore, 32 gm of Part-B is required to react with 100 gm of Part-A, and otherwise it will not work properly.

Resin is the most expensive ingredients in polymer matrix and to minimise the cost and improving durability light weight filler materials were added in the mix. Three different filler materials such as Fire Retardant Filler (FRF), Hollow Microsphere (HM) and Fly Ash (FA) were mixed together by a certain percentage to get the effective filler mix. The mixing formulation of these three filler materials was established after several trial mixes. The fire retardant used is non-toxic and has low abrasiveness, acid resistance, chemically inertness, electric arc resistance and smoke suppression properties. On the other hand, hollow microspheres can contribute in reducing weight, controlling shrinkage, increasing thermal insulation of the polymer matrix. The by-product fly ash can improve the performance of matrix by resisting UV and reducing permeability of water and aggressive chemicals.



(a) ingredients before mixing



(b) solid polymer matrix after mixing

**Figure 1. Polymer matrix ingredients and specimens casting.**

## 2.2 Method

The addition of UV absorbers or UV stabilizers into the polymer is one of the best methods for protecting polymeric matrix against UV radiation [7]. In this study, filler materials were incorporated as UV absorbers for targeting the absorption of UV light and dissipating the absorbed energy harmlessly. The specimens were cast in plastic cups (Fig. 1b). Seven different mixes were prepared with an increment of 10% filler by volume starting from pure resin mix (0% filler) to the mix with 60% filler content. The detail mixing proportions are given in Table 1.

**Table 1. Details of mixing proportion.**

Identity of mix	Mix-1	Mix-2	Mix-3	Mix-4	Mix-5	Mix-6	Mix-7	
% Resin/Filler (by volume)	100/0	90/10	80/20	70/30	60/40	50/50	40/60	
Resin	Part A, (gm)	124	112	100	87	75	62	50
	Part B, (gm)	40	36	32	28	24	20	16
Filler (FRF+ HM+ Fly Ash), (gm)	0	30	59	89	119	148	178	

Specimens were demolded in the next day of casting and cut it to a nominal dimension of 80 × 10 × 10 mm using machine. The initial flexural properties of the specimens were determined and recorded before exposed to the UV radiation. The effect of UV can be determined either by accelerated laboratory testing or actual outdoor exposure. The latter is obviously time consuming method and therefore accelerated laboratory testing was conducted. UV-chambers basically consist of a UV-light source(s) and a specimen rack. A variety of artificial light sources including carbon arc lamps, xenon arc lamps, fluorescent sun lamps and mercury lamps can be used to simulate the natural sunlight. However, xenon arc and fluorescent lamps are the two most popular UV-sources for photo-degrading materials that can emit a similar type of harmful radiation [5]. In this study, specimens were subjected to 2000 hours of UV radiation by xenon 2200 watt air cooled lamp in the sunset XLS chamber. The exposure was carried out in an ambient atmosphere where the temperature was varied between 22 to 24 °C, with a relative humidity between 30 to 50%. After the specified time, the specimens were taken out from the UV chamber and subsequently weighed, examined by microscope and mechanically tested. Flexural test of the affected samples were conducted under three-point bending (Fig. 2b) set-up and compared the results with unaffected one.



(a) ultraviolet chamber



(b) bending test of polymer matrix

**Figure 2. Bending test of the UV affected samples.**

## 3. Results and Discussion

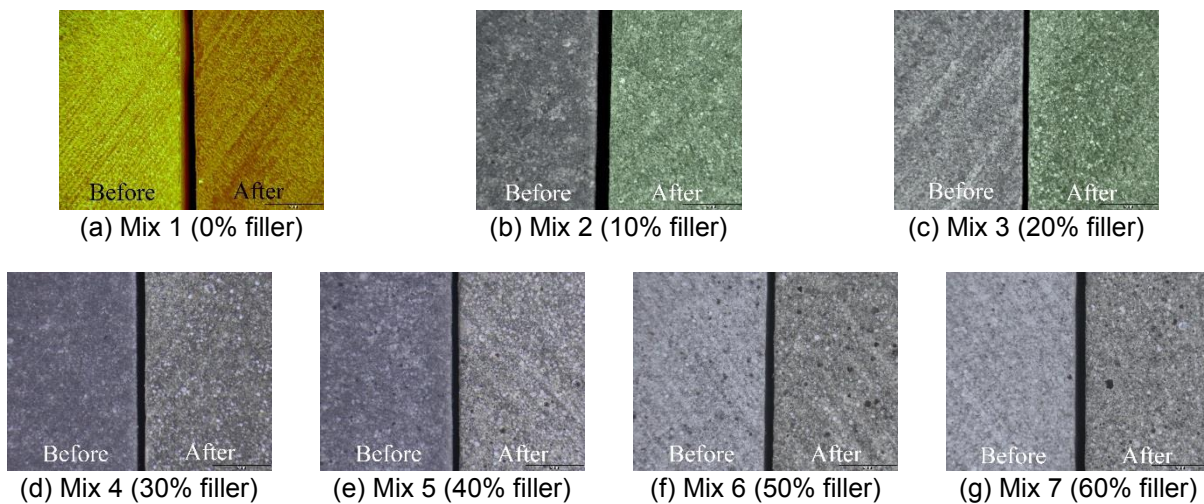
The polymer matrix usually generate heats while mixing two resins together and the maximum temperature was generated in the mix containing 0% filler. The addition of filler can absorb heat and maintain the temperature to the comfortable range for working. The physical properties in terms of



discolouration, depth affected by UV and loss of weight, and mechanical properties in terms of bending strength were examined once the samples were removed from the UV chamber.

### 3.1 Physical properties

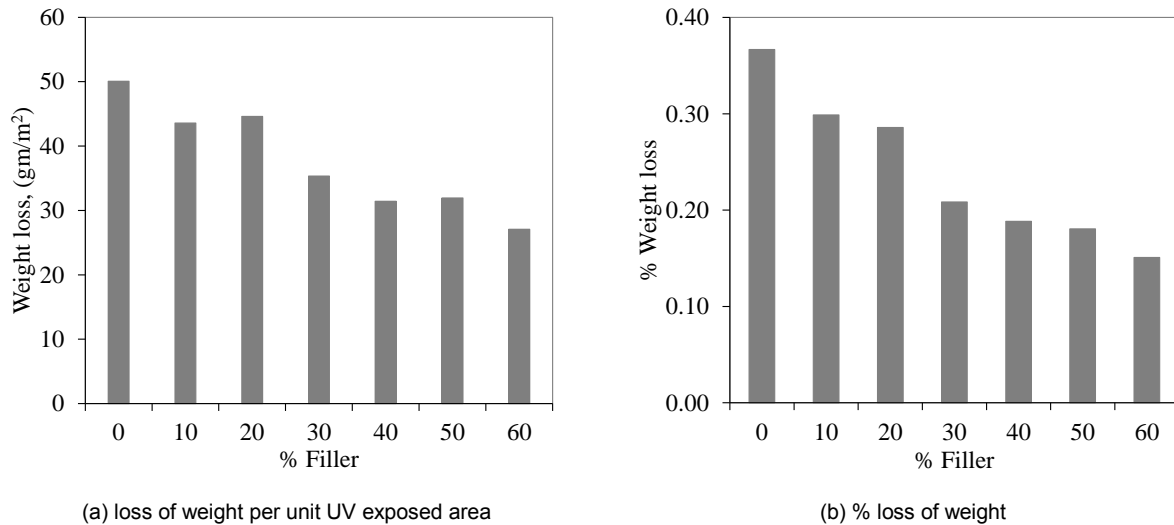
The mixes containing high resin or low filler (Mix 1 to mix 3) were severely affected by UV and surface degradation in the form of discoloration were observed by microscopic observation (Fig. 3 a-c). The discoloration is due to interaction between epoxy molecules on the exposed surface and the photons from UV radiations results in photo-oxidative reactions that alter the chemical structure [13]. No significant changes in colour were noticed for the mix having filler 30% or more (Fig. 3 d-g). It is noted that the Mix-1 which contains 100% resin or 0% filler is more transparent than the other mixes. This transparency is due to the physical properties of resin and the addition of filler can increase the darkness in the succeeding mix because the colour of fly ash which is grey or light dark in nature. Significant improvements were observed in 30% filler mix. Therefore, it can be concluded that the mix containing filler less than 30% is more prone to UV radiation. No significant variations were observed in the higher filler content mix (Mixes 4 to 7) because the darkness of filler can block the UV ray and protect the samples from physical and mechanical degradation. However, a minor changes in surface roughness were also visible by naked eye for all UV exposed specimens.



**Figure 3. Discoloration of UV affected samples after UV exposure.**

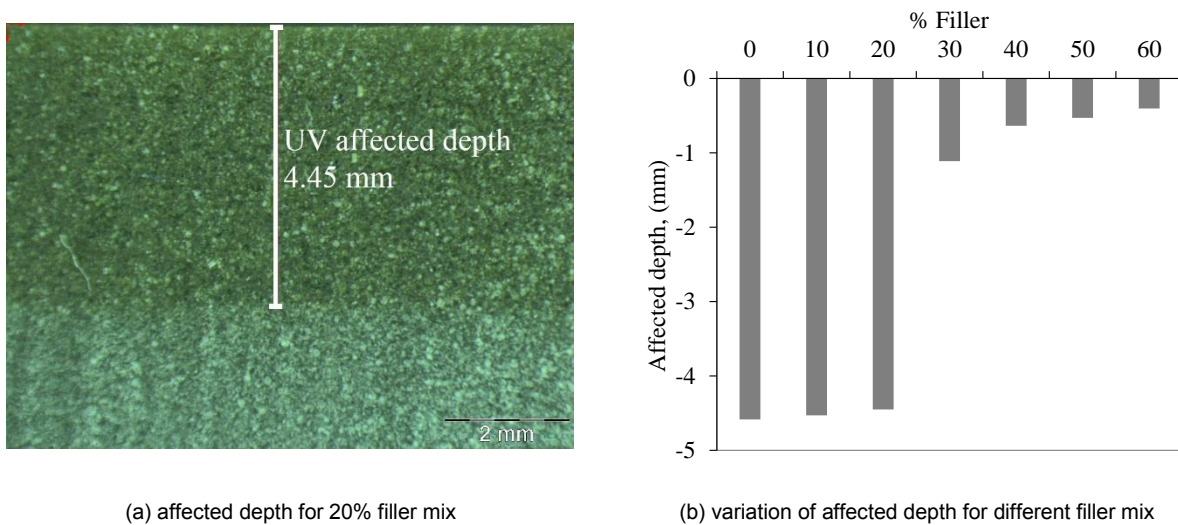
The weight of the specimens were measured immediately after taken out from UV chamber. As the UV lamp focused the specimens from the top, the top surface of the specimens were mostly affected by the UV light [14]. The loss of specimen's weight per unit UV exposed area was determined and it was found that the loss of weight follows a decreasing trend with the increase of filler in the mix (Fig. 4a). The highest loss of weight was found 50 gm/m<sup>2</sup> in 0% filler mix (Mix-1) and it decreased to 27 gm/m<sup>2</sup> for 60% filler mix (Mix-7). The loss was found more for the mix containing 0 to 20% filler and suddenly decreased from 45 gm/m<sup>2</sup> to 35 gm/m<sup>2</sup> when the filler increased from 20% to 30%. This sudden drop is expected because the depth of the specimen affected by UV for 20% filler mix was found significantly higher than 30% filler mix (Fig. 5b) and consequently the expulsion of moisture was higher. Moreover, the improvement rate is quite slow from 30 to 60% filler mix. The percentage loss of weight based on the initial weight of the specimens (before UV exposure) shown in Figure 4(b). It was also found that the loss of weight decreased from 0.37% to 0.15% with the increase of filler from 0 to 60%. This result is somewhat comparable with the loss of weight of carbon fibre reinforced epoxy composites after 500 hrs of UV exposure studied by Kumar et al. [13] where they found an average loss of 0.27%. The decrease of weight loss is due to the gradual improvement of UV resisting properties with the increase of filler which can protect the samples from deterioration.





**Figure 4. Loss of weight of polymer matrix after 2000 hours of UV exposure.**

The affected depth of the specimens due to UV light were measured using electronic microscope. There was a clear distinction of colours between the affected and unaffected layers (Fig. 5a). The affected depth was found higher for the mix containing filler up to 20%. The maximum depth was measured 4.58 mm for 0% filler mix and it was slightly decreased to 4.45 mm for 20% filler mix. However, a sudden decrease of the affected depth was found when the mix contained 30% filler (Fig. 5b). This indicates, the transitional polymer matrix that has superior resistance to UV radiation contains filler between 20 and 30%. The affected depth was gradually decreased from 1.11 to 0.40 mm for the mix having filler from 30 to 60%. Overall, the addition of filler in the epoxy polymer matrix can increase the resistance against UV radiation as the fillers block the penetration of UV thus only the resin near the surface is affected.

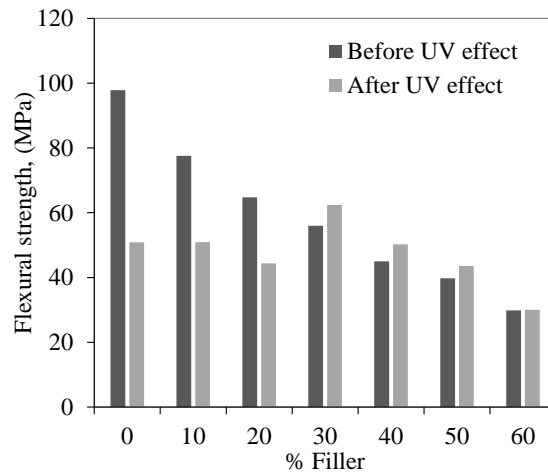


**Figure 5. Depth of the samples affected by UV light.**

### 3.2 Mechanical properties

The flexural strength of the UV unaffected group of specimens were measured before placing the identical second group in UV chamber. After 2000 hours of UV exposure, the flexural strength of the second group of samples were measured using three point bending test. To ensure the effect of UV on flexural strength, the specimens were placed in the testing machine in such a way that the UV affected side subjected to tension in bending. Results were compared with the unaffected samples and observed a significant

reduction of flexural strength up to 48% for zero filler mix (Mix-1). The reduction of strength was found 34 and 32% for the mixes containing filler volume of 10 and 20% respectively (Mix-2 and Mix-3). The reduction of strength due to the effect of UV should not be more than 10% in outdoor application [15], thus the mixes containing filler up to 20% is vulnerable to UV. However, no reduction of flexural strength were noticed for the higher filler containing mixes indicating the filler can help to preserve the structural performance by absorbing or blocking UV radiation before it reaching the chromophores in polymer matrix (Fig. 6).



**Figure 6. Effect of UV radiation on flexural strength of polymer matrix.**

Surprisingly, a slight increase of the flexural strength was found in the UV affected mix containing filler volume from 30 to 60%. It is previously mentioned that the effect of UV is only significant for the mix having filler less than 30% and no major change in colour was observed for the mix containing 30 to 60% filler (Fig. 3). Therefore, the slight increase of strength is probably due to the age of UV specimens which was at least 2000 hours (in-chamber period) longer than the unaffected samples.

#### 4. Conclusions

In this paper, the effect of UV radiation on some of the physical and mechanical properties of epoxy polymer matrix was studied by accelerated UV weathering. Microscopic observation was performed to analyse the change of colour and measuring the affected depth of the specimens under the effect of UV radiation. The loss of weight and the reduction of flexural strength was compared with unaffected samples. Some conclusions drawn from the investigation are listed as follows:

1. Significant surface degradation in terms of discoloration was observed in the mix containing filler up to 20%. However, no noticeable change in colour were found for the mixes containing 30 to 60% filler. The increase of filler reduces the transparency of the mix that can increase the UV resistance.
2. Specimens were affected up to a maximum depth of 4.58 mm when the mix contained pure resin without filler. A slight improvement was observed up to 20% filler mix (affected depth 4.45 mm). However, the addition of 30% filler can significantly improve the UV resisting properties as the affected depth drastically reduced to 1.11 mm indicating the transition polymer matrix containing filler between 20 and 30%. A minor variation was observed among 30 to 60% filler mix.
3. The loss of specimen's weight per unit UV exposed area decreased from 50 gm/m<sup>2</sup> to 27 gm/m<sup>2</sup> or 0.37 to 0.15% with the increase of filler from 0 to 60%. However, the loss of weight suddenly decreased from 45 gm/m<sup>2</sup> to 35 gm/m<sup>2</sup> or 0.29 to 0.21% when the filler increased from 20 to 30%. This is due to the significant improvement of UV resistance by the later when comparing with the former.

4. Reduction of flexural strength was observed for the UV exposed specimens containing filler from 0 to 20%. However, the addition of filler from 30 to 60% can protect the polymer matrix from mechanical degradation by improving the UV resisting performance.

## 5. Acknowledgement

The first author gratefully acknowledged the financial support by Australian Postgraduate Award (APA) scholarship from the University of Southern Queensland, and authors are also acknowledged the materials support by the Department of Industry Innovation, Science, Research and Tertiary Teaching Enterprise Connect Researcher-In-Business Funded by the Australian Government.

## 6. References

1. Jung, K.-C., I.-T. Roh, and S.-H. Chang, *Thermal behavior and performance evaluation of epoxy-based polymer concretes containing silicone rubber for use as runway repair materials*. Composite Structures, 2015. **119**: p. 195–205.
2. Lokuge, W. and T. Aravinthan, *Effect of fly ash on the behaviour of polymer concrete with different types of resin*. Materials & Design, 2013. **51**: p. 175-181.
3. Van Erp, G. and M. Mckay, *Recent Australian developments in fibre composite railway sleepers*. Electronic Journal of Structural Engineering, 2013. **13**(1): p. 62-66.
4. Signor, A.W., M.R. VanLandingham, and J.W. Chin, *Effects of ultraviolet radiation exposure on vinyl ester resins: characterization of chemical, physical and mechanical damage*. Polymer Degradation and Stability, 2003. **79**(2): p. 359–368.
5. Rabek, J.F., *Polymer photodegradation: mechanisms and experimental methods*. 1995, London, UK: Chapman & Hill.
6. Karbhari, V.M., et al., *Durability gap analysis for fiber-reinforced polymer composites in civil infrastructure*. Journal of Composites for Construction, 2003. **7**(3): p. 238–247.
7. Shah, V., *Handbook of plastics testing and failure analysis*. 2007, New Jersey: John Wiley & Sons, Inc.
8. Deanin, R.D., et al., *Mechanism of ultraviolet degradation and stabilization in plastics*. Polymer Engineering & Science, 1970. **10**(4): p. 228-234.
9. Yan, L., N. Chouw, and K. Jayaraman, *Effect of UV and water spraying on the mechanical properties of flax fabric reinforced polymer composites used for civil engineering applications*. Materials & Design, 2015.
10. Chin, J.W., K. Aouadi, and T. Nguyen, *Effects of environmental exposure on fibre-reinforced plastic (FRP) materials used in construction*. Journal of Composites Technology and Research, 1997. **19**(4): p. 205-213.
11. Peng, Y., et al., *Effects of UV weathering on surface properties of polypropylene composites reinforced with wood flour, lignin, and cellulose*. Applied Surface Science, 2014. **317**: p. 385–392.
12. Cao, H., et al., *Degradation of polymer coating systems studied by positron annihilation spectroscopy. 1. UV irradiation effect*. Macromolecules, 1998. **31**: p. 6627-6635.
13. Kumar, B.G., R.P. Singh, and T. Nakamura, *Degradation of carbon fiber-reinforced epoxy composites by ultraviolet radiation and condensation*. Journal of Composite Materials, 2002. **36**(24): p. 2713-2733.
14. Tcherbi-Narteh, A., et al., *Viscoelastic and thermal properties of full and partially cured DGEBA epoxy resin composites modified with montmorillonite nanoclay exposed to UV radiation*. Polymer Degradation and Stability, 2014. **101**: p. 81–91.
15. Lampo, R., et al., *Performance and safety issues regarding the use of plastic composite crossties*. 2001, AREMA 00039 AAR/TTCI Pueblo, Co.

# Self-healing of Cementitious Composites via Coated Magnesium Oxide/Silica Fume Based Pellets

Rami Alghamri<sup>1</sup> and Abir Al-Tabbaa<sup>2</sup>

<sup>1</sup> PhD Student, Department of Engineering, University of Cambridge, Cambridge, UK

<sup>2</sup>Professor of Civil & Environmental Engineering, University of Cambridge, Cambridge, UK

**Abstract:** Many studies have reported the use of mineral admixtures as an approach for the self-healing of cementitious composites. However, research has consistently shown that it is difficult to apply this approach because there could be a significant loss in workability of fresh concrete as well as the occurrence of early reactions with cementitious materials, which would lead to a decrease in the self-healing efficiency. Therefore, this work aims to improve the self-healing capabilities of concrete by developing pellets, which possess semi-capsulation effects, from powder materials. In this research, self-healing pellets were fabricated from a mix of magnesium oxide (MgO) and silica fume (SF) as potential self-healing agents and encapsulated within a cement paste coating. The produced self-healing pellets with a diameter range of 0.6-4.75 mm were added to mortar concrete samples in three dosages of 5%, 10%, and 15% by weight as partial sand replacement and all mortar specimens were then cured in water. The results indicated that the addition of up to 10% pellets increased the compressive strengths at 7, 14, 28, and 56 days. Same proportions presented promising results in both the flexural strength and its recovery. For instance, the addition of only 5% of pellets shows ~ 60 % and ~ 51% strength recovery in 28 days and 56 days respectively. The designed concrete samples containing the developed self-healing pellets possessed a promising crack self-healing performance.

**Keywords:** Self-healing, cementitious composites, pellets, Magnesium oxide, Silica fume.

## 1. Introduction

Concrete is the most used construction material worldwide and in comparison to many other materials it is cheap, can be moulded in any required shape easily, and has a high compressive strength [1]. Also, concrete has a greater durability than the majority of other building materials, for instance, it is very effective at fire resistance [2]. One drawback, however, is that concrete is a material sensitive to crack formation because of its limited tensile strength. Therefore, concrete is often combined with steel reinforcement to carry the tensile loads. These rebars restrict the crack width but cannot prevent crack formation completely and the propagated cracks may endanger the durability and functionality of concrete structures [3]. For instance, concrete cracks lead to an increase in the number of pathways open to the ingress of saline water, acid rain, and carbon dioxide. Depending on the type of concrete, the environmental conditions, and the chemical makeup of the infiltrating fluid, various degrading processes can occur which cause further cracking and substantially reduce the durability of the structure. These processes include freeze-thaw action, aggregate alkaline reaction, and reinforcement corrosion [1]. Additionally, cracking is aesthetically unsightly which is considered very important aspect in many structures [4]. Therefore, repairing of these cracks is very essential and indispensable.

The conventional repair methods increase the life-cycle cost of concrete, have a significant environmental impact, and need long time and intensive labour [5]-[6]. Therefore, it inspires the possibility that; if concrete were designed with a sufficient healing capability, cracks in concrete could be self-healed after cracking under specific conditions without human intervention. This may lead to a material with reduced lifetime costs and with improved durability and service life, both in terms of money and environmental impacts. In order to achieve this goal, many scientists and researchers have recently turned their attention to investigating this topic. Different approaches and materials have been proposed by research groups all over the world [7]. Among those some approaches are aimed at improving the natural mechanism of autogenous crack healing, which is generally attributed to the hydration of unhydrated cement grains and may be aided by carbonation of Portlandite (calcium hydroxide) [8]. Others are designed to modify concrete by embedding microcapsules or hollow fibers with a suitable healing agent, to heal the cracks autonomously [3].

A further approach used for healing concrete cracks is the incorporating of mineral admixtures [9–12]. For instance, Ahn (2008) [13] added some specific mineral and chemical admixtures in terms of swelling, expansion and precipitation to concrete mixture in the form of powder as partial cement replacement. Generally, concrete shows a promising healing capability with some mineral admixtures. However, it has been difficult to apply this approach to the construction industry as there has been a significant loss in workability of fresh concrete and self-healing efficiency, due to further reactions between the self-healing powder and mixing water during concrete casting. To control the reactivity of embedded materials, self-healing granules having a semi-capsulation effect, in which the inner material containing self-healing materials were closed by a coating layer of a cement compound, were proposed by Koide & Morita (2010) [14]. To date, few attempts in this area have been carried out and the application is still in its experimental steps.

On the other hand, pelletisation is a worldwide known technique in many industries including mineral processing, agricultural products, pharmaceuticals, and some chemicals [15]. However, it has not been widely used in the construction sector [16]. Few attempts have been made to produce lightweight aggregates (LWA) by using pelletisation technique and the developed pellets showed promising results to use them as artificial LWA in concrete structures [16,17].

Therefore, this paper focuses on introducing pellets from some self-healing powder minerals enclosed by a coating layer to produce self-healing pellets with semi-capsulation technique. These minerals may have the potential to heal concrete cracks, meanwhile, avoiding the problems in term of workability and early reactions with the existing cementitious materials.

## 2. Materials and Methods

### 2.1 Materials

The main materials used in this work were Portland cement, magnesia, and silica fume. Portland cement (PC) was the principal material for the concrete mixes while magnesium oxide (MgO) and silica fume (SF) were utilised as cargo for the developed self-healing pellets. CEM 1 (52.5N) which was supplied by Hanson, UK has been selected as PC cement. The MgO 92/200 was obtained from RBH Ltd., UK. The SF, which was adopted in this study, is undensified microsilica (MS) (from Elkem, UK), typically used in cement and concrete industries as an additive. The physical properties and chemical compositions of the raw materials, as provided by the suppliers, are listed in **Table 1**

**Table 1: Chemical and physical properties of PC, MgO, and SF as provided by the suppliers**

Chemical composition/properties		PC	MgO	SF
Chemical composition	CaO %	63.6	0.87	1.20
	SiO <sub>2</sub> %	19.50	2.25	93
	Al <sub>2</sub> O <sub>3</sub> %	4.90	0.22	1
	Fe <sub>2</sub> O <sub>3</sub> %	3.10	0.53	1
	MgO %	0.90	93.18	0.50
	SO <sub>3</sub> %	3.30	-	1
	Na <sub>2</sub> O %	-	-	0.50
	C %	-	-	2
	K <sub>2</sub> O %	-	-	-
Properties	Loss on ignition LOI %	2.10	2.59	≤ 3
	Mean Particle Size (µm)	5.00-30.00	75	≤ 45
	Particle density (g/cm <sup>3</sup> )	2.75-3.20	3.02	-
	Surface area (m <sup>2</sup> /g)	0.30-0.40	16.3	>15 & <30
	Bulk density (g/cm <sup>3</sup> )	0.90-1.50	-	200-350
	Reactivity* (sec)	-	136	-

(\*) As measured at the laboratory.

## 2.2 Pelletisation and coating

The cargo materials of the pellets were MgO and SF with 50% for each from the total solid. Water was used as a binder. The device used in this study is DP-14 “Agglo-Miser” which is a disc pelletiser supplied by Mars Mineral, USA, as shown in **Figure 1**. All the pelletisation trials were performed at room temperature. The two solid raw materials, i.e., MgO and SF, were dry-mixed together using Breville SHM2 Twin Motor Compact Mixer at the lowest speed for 3 minutes until a homogenous blend was achieved by visual inspection. Then the dry mix was loaded in the pelletiser drum wherein it was left to mix for 1 min  $\pm$  5 sec. Subsequently, the appropriate quantity of tap water was uniformly added by a venting bottle or spray gun within 1 min  $\pm$  5 sec. During the pelletisation process, the pelletiser was intermittently stopped to scrap the materials stuck to the pan and on the blades by spatula. Thereafter, the green pellets were dried in an oven at 60°C for one day. After that, the particle size distribution (PSD) analysis was performed. Then the pellets were stored in airtight plastic containers until the coating process.



**Figure 1: DP-14 “Agglo-Miser” pelletiser**

The produced pellets with diameters of 600  $\mu$ m to 4.75mm were selected for coating. Excluding the finer particles was due to the difficulty of coating them and their agglomerating while spraying the coating solution. While, the larger pellets with diameter  $\geq$  4.75mm were excluded because the pellets were used in concrete mixes instead of natural sand. The sand used in this study is a sharp natural sand with particles less than 4.75 mm. The coating solution was prepared by dissolving Portland cement in deionized water by a percent of 1 PC to 5 water. The spray gun used in the coating process is Gravity Feed Mini-HVLP gun with 1mm nozzle size. During rotation of the disc pelletiser, the pellets were sprayed with the coating solution. After that, the coated pellets were dried in the oven at 60°C for 3 days to raise the rate of cement hydration. Thereafter, the cured coated pellets were stored in an airtight plastic container until tested. Sample of these pellets from different sizes were examined under the microscope to ensure if they were coated or not. Typical images of the coating process are shown in **Figure 2**.



(a) (b) (c)

**Figure 2: (a) Preparation of cement solution for coating using a lab homogenizer, (b) Gravity Feed Mini-HVLP spray gun, and (c) Spraying the pellets while the disc pelletiser rotates.**

### 2.3 Mortar concrete mixes

Mortar concrete samples with water-to-cement ratio (w/c) of 0.5 were prepared for this study. The produced self-healing (S-H) pellets were incorporated as a partial sand replacement in four different ratios. The proportions of the four mixes are illustrated in **Table 2**. For each mix 12 cube samples (40 mm X 40 mm X 40 mm) were prepared for compressive strength analysis and 6 prism samples (40 mm X 40 mm X 160 mm) were prepared for crack forming through a three point flexural test, and crack healing analysis overtime. The samples were demoulded after 1 day of curing and then cured in a water tank at temperatures of 20°C ±2°C and a relative humidity 60°C ±2°C until the designed testing age.

**Table 2: Mix design of mortar samples by percentage weight**

Mix ID	PC (%)	Water (%)	Natural sand (%)	S-H pellets (%)
G1	22.2	11.1	66.7	0
G2			61.7	5
G3			56.7	10
G4			51.7	15

### 2.4 Tests to verify self-healing performance

Three-point flexural test was carried for prism samples from different mixing groups in order to examine the healing of the crack after certain periods and to evaluate the recovery of the flexural strength and study the effect of incorporating S-H pellets by comparing with the reference samples. Cracks were introduced in the prism samples instantly after de-moulding. Thereafter, the cracked samples were vertically setup into the water tank in order to keep the crack surface in contact. Digital microscope image analysis was used to analyse the crack healing of specimens at different ages (7 days, 14 days, 28days, and 56 days).

In order to study the effect of the addition of S-H pellets on the mechanical properties of concrete, the compressive strength testing was carried out using CONTROLS ADVANTEST9 with a maximum capacity of 250 KN and with a loading rate of 2400N/s. Three cubes (40 mm X 40 mm X 40 mm) were taken out for compressive strength test at ages of 7, 14, 28, and 56 days.

## 3. Results and Discussion

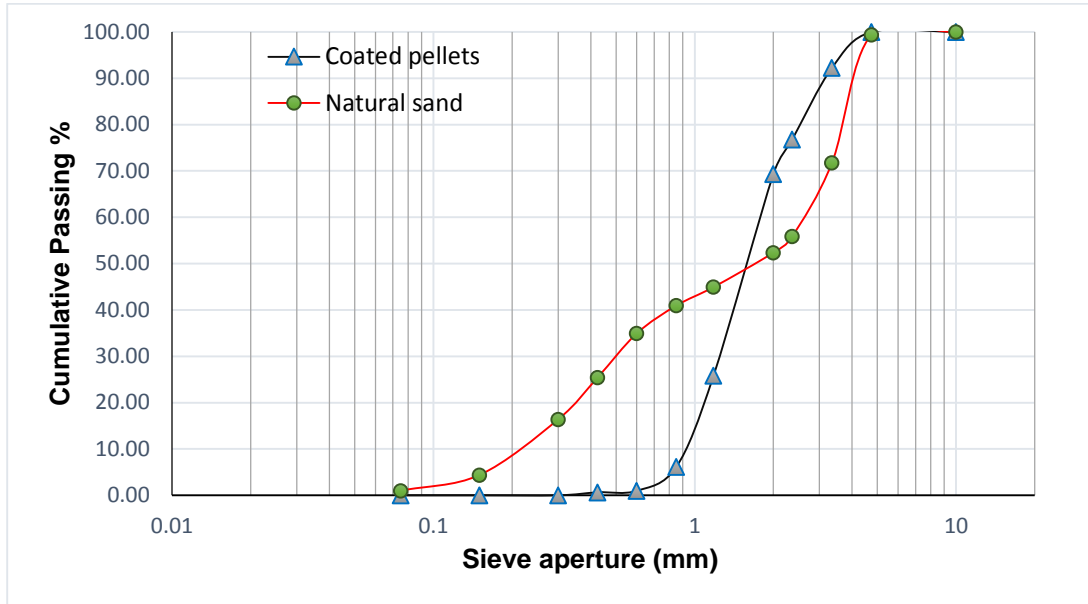
### 3.1 Pelletisation and coating

The PSD of the produced S-H pellets used in preparing mortar samples and the natural sand are shown in **Figure 3**. It is noticed that  $D_{50}$  and the gradation of particles of the both are very close. To examine the coating thickness, random samples from each size of coated pellets were selected for crushing and testing under microscope. **Figure 4** shows microscope images of some crushed pellets. It can be inferred that the thickness of the coating represents 20 to 35% from the total diameter of the pellets for most of the pellets that examined. Nevertheless, the un-coated pellets in all tested samples ranged between 30-40%.

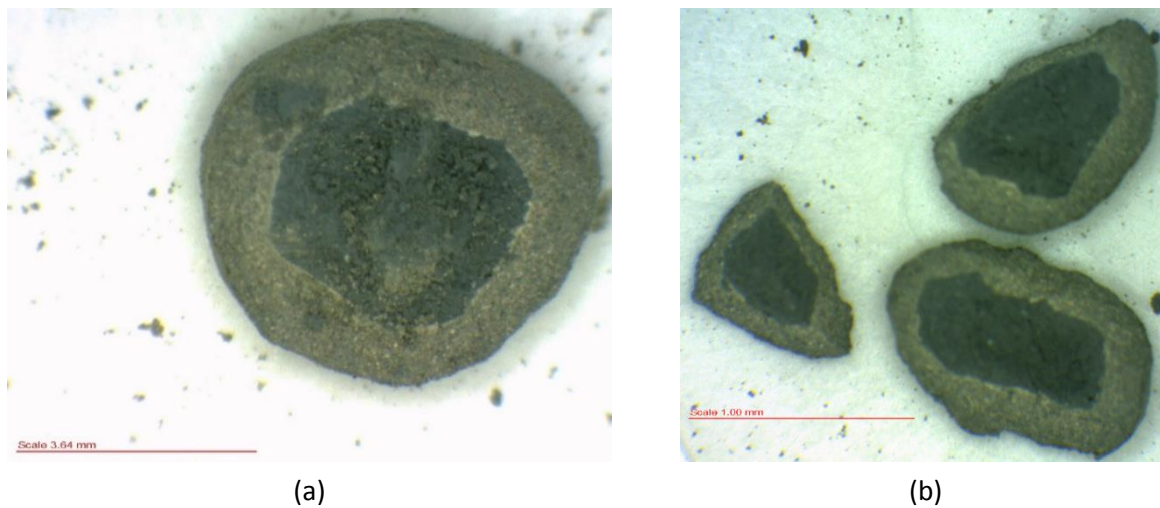
### 3.2 Three-point flexural strength

A three-point flexural test was carried out on six prism specimens from each of the four mortar groups just after de-molding with age of 1 day and before water curing. After 28 days of water curing for three specimens from each group, the crack was induced once again in each one by the same test to monitor their mechanical strength recovery. The other specimens were re-cracked after 56 days.





**Figure 3: PSD of the S-H pellets and natural sand used in preparation of mortar samples**



**Figure 4: Samples of crushed coated pellets**

**Figure 5** illustrates the average flexural strength of the samples on 0-day curing and the average regain strength after 28-days and 56-days for each group. The graph reveals that there is a sharp decrease in the regained flexural strength of the control samples (G1) where it is (794 N) 59% from the original strength at 28 days and it is (666 N) 40.3% after 56 days. Meanwhile, the addition of S-H pellets up to 10% achieved promising results. For example, the addition of only 5% of S-H pellets shows 60.3% and 50.5% strength recovery in 28 days and 56 days respectively. Similarly, G3 demonstrates 56.31% in 28 days and 47.4% in 56 days. However, G4 shows a dramatic decrease in the original flexural strength. Nevertheless, the samples of this group had a significant recovery compared with original strength i.e. 79.4% in 28 days and 81% in 56 days. The decrease in flexural strength with increasing the proportion of pellets is believed to be attributable to the increase of the uncoated pellets in the mix which adversely affects the workability and accordingly on the strength development.



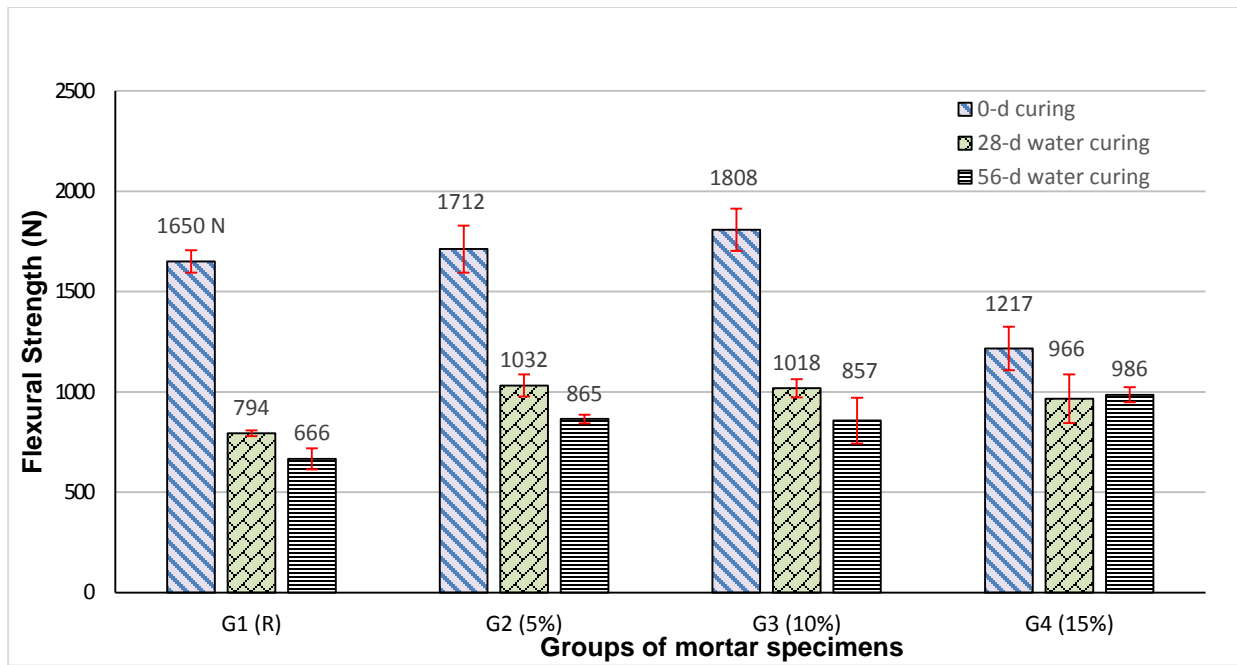


Figure 5: The flexural strength recovery for mortar specimens after 28 days and 56 days

### 3.3 Unconfined compressive strength (UCS)

Compressive strength was measured to find out the effect of partial replacement of sand by S-H pellets as presented in **Table 2**. The UCS values of mortar cube specimens at different ages (7, 14, 28, and 56 days) with their standard deviations are presented in **Figure 6** and **Table 3**. It is noticed that the addition of S-H pellets up to 10% increase the UCS values in all ages. In contrast, the addition of S-H pellets in 15% reduced the UCS for all ages in comparison with the control samples, although it had increased the self-healing capacity significantly. The main cause of the drop in the UCS values of G4 may be due to loss of workability. This is because some of uncoated pellets may be presented in the mix and this leads the free SF and MgO to consume large amounts mixing water. G2 and G3 samples show a significant increase in the UCS values at late ages particularly at 56 days. Therefore, it can be concluded that the replacement of natural sand by S-H pellets up to 10% has a positive influence on UCS.

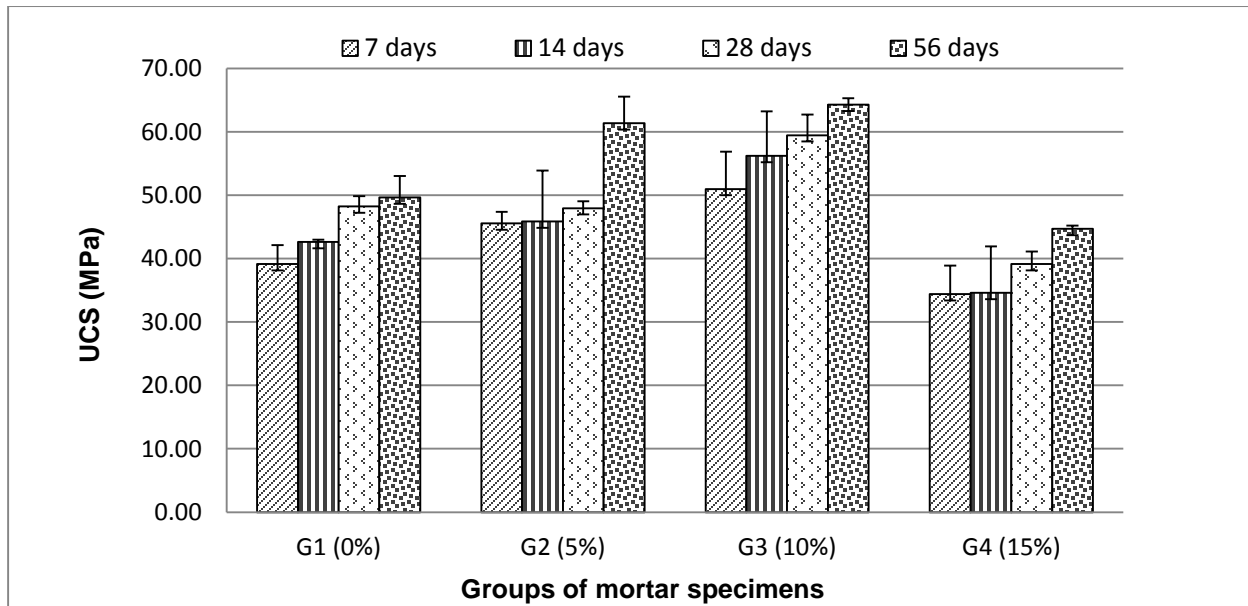


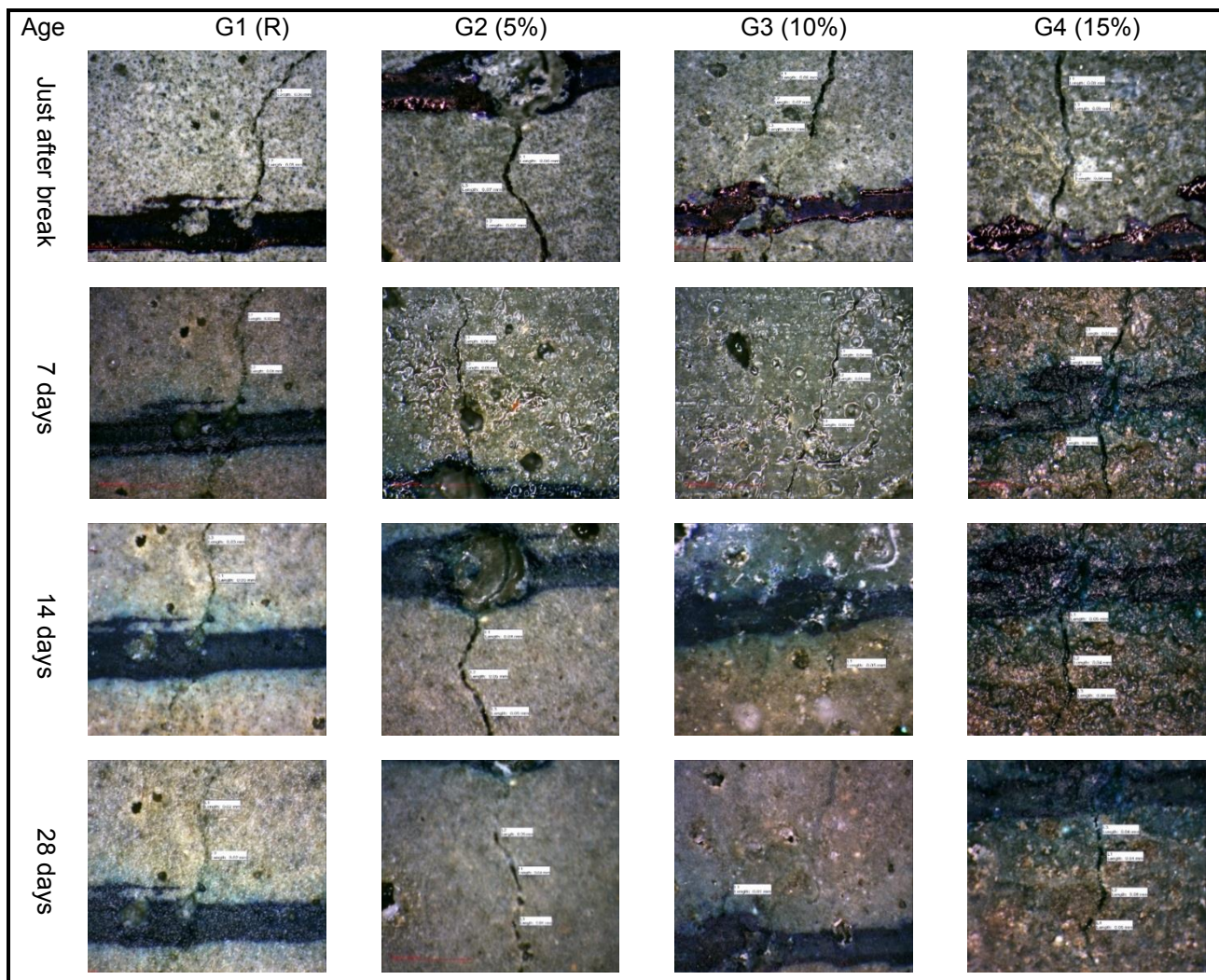
Figure 6: UCS of mortar samples with different proportions of pellets

**Table 3: Average UCS of mortar groups in different ages**

Age (days)	G1 (R)	G2 (5%)	G3 (10%)	G4 (15%)
7	39.2	45.6	51.0	34.4
14	42.6	45.9	56.2	34.6
28	48.3	48.0	59.5	39.1
56	49.6	61.4	64.3	44.7

### 3.4 Analysis of digital microscope images

The microscopic image analysis was conducted to monitor the change in the crack widths, which were induced in the prism mortar specimens. The crack-sealing process is used as an indication for efficiency of the self-healing cementitious composites [5]. The crack widths were measured in different ages (0, 7, 14, 28, and 56) days. **Figure 7** presents digital microscope images of cracks for the mentioned ages meanwhile **Figure 8** demonstrate the average crack widths for all groups in these ages. The results show that the average cracks for all groups ranged from 43 to 83.3  $\mu\text{m}$ . Variations in self-healing have been found in different mixes and generally, the crack width varied markedly overtime, as there were no reinforcing bars or fibers in the mixes. The average crack widths in G3 were approached to close earlier than other groups. However, all samples with S-H pellets showed promising results compared to the pristine samples.



**Figure 7: Digital microscope images of cracks at 0, 7, 14, 28 days**

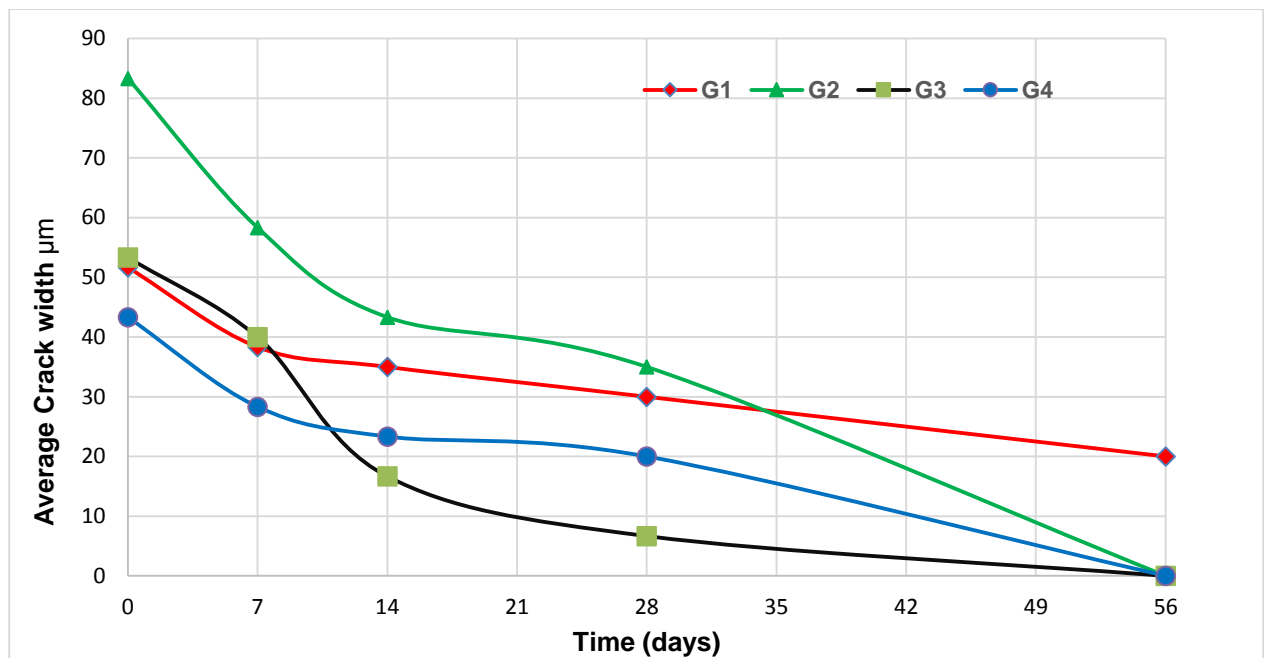


Figure 8: Average crack widths for all groups in different ages

#### 4. Conclusions

The following conclusions can be drawn from this study:

- The designed concrete samples containing S-H pellets of MgO and SF possessed a promising crack self-healing performance with the elapse of time in comparison to control samples. This includes both the sealing of the cracks and the recovery of flexural strength.
- Pelletisation of mineral admixtures is a cost-effective and a simple approach for self-healing of cementitious composites. This contributes to the possibility of applying broadly later.
- The major challenges of this investigation are increasing the efficiency of coating process and development the mechanism of realising the powder materials from the pellet to the surface of crack upon the crack occurrence.
- There are many other aspects need to be addressed in the future work to make this approach practically applicable.

#### 5. Acknowledgement

This research is supported by Yousef Jameel academic program through Cambridge Commonwealth, European & International Trust.

#### 6. References

- [1] Gilford, J., "Microencapsulation of self-healing concrete properties," Prairie View A&M University, 2012.
- [2] Neville, A. M., *Properties of concrete*, 4th ed. New York: Wiley, 1996, p. 844.
- [3] Van Tittelboom, K. and N. De Belie, *Self-healing in cementitious materials—a review*, vol. 6, no. 6. 2013, pp. 2182–2217.
- [4] Joseph, C., "Experimental and numerical study of the fracture and self-healing of cementitious materials," 2008.

- [5] De Rooij, M., Van Tittelboom, K., De Belie, N., & Schlangen, E., *Self-healing phenomena in cement-based materials. State-of-the-art report of RILEM Technical Committee*. 2011.
- [6] Oss, B. H. G. Van, G. A. Norton, and U. S. G. Survey, "Background facts and issues concerning cement and cement data," 2005.
- [7] Li, V. C. and E. Herbert, "Robust self-healing concrete for sustainable infrastructure," *J. Adv. Concr. Technol.*, vol. 10, no. 6, pp. 207–218, 2012.
- [8] Ahn, T.-H. and T. Kishi, "Crack Self-healing Behavior of Cementitious Composites Incorporating Various Mineral Admixtures," *J. Adv. Concr. Technol.*, vol. 8, no. 2, pp. 171–186, 2010.
- [9] Gruyaert, E., K. Van Tittelboom, H. Rahier, and N. De Belie, "Crack repair by activation of the pozzolanic or slag reaction," in *2nd International Conference on Microstructural-related Durability of Cementitious Composites*, 2012, pp. 1–8.
- [10] Termkhajornkit, P., T. Nawa, Y. Yamashiro, and T. Saito, "Self-healing ability of fly ash–cement systems," *Cem. Concr. Compos.*, vol. 31, no. 3, pp. 195–203, Mar. 2009.
- [11] Jaroenratanapirom, D. and R. Sahamitmongkol, "Effects of different mineral additives and cracking ages on self-healing performance of mortar," in *Proceedings of the 6th annual concrete conference, Petchaburi, Thailand*, 2010, pp. 551–556.
- [12] Hosoda, A., T. Kishi, H. Arita, and Y. Takakuwa, "Self healing of crack and water permeability of expansive concrete," in *1st international conference on self-healing materials. Noordwijk, Holland*, 2007.
- [13] Hung, V. V., T. Kishi, and T. H. Ahn, "Development of self-healing granules having semi-capsulation effect by using cement compound, chemical/mineral admixtures & its watertight performance through crack," 2008.
- [14] Morita, S., T. Koide, T. H. Ahn, and T. Kishi, "Evaluation of performance Upgrade for the Cracked Self-Healing Concrete Incorporating Capsuled Inorganic Materials," *Proc. Japan Concr. Inst.*, vol. 33, pp. 183–190, 2010.
- [15] Iveson, S. M., J. D. Litster, K. Hapgood, and B. J. Ennis, "Nucleation, growth and breakage phenomena in agitated wet granulation processes: a review," *Powder Technol.*, vol. 117, no. 1–2, pp. 3–39, Jun. 2001.
- [16] Gu, A., "Utilization of fly ash by pelletization process ; theory , application areas and research results," vol. 30, pp. 59–77, 2000.
- [17] Al-Ansary, M. S., "Stabilisation/solidification and pelletisation of petroleum drill cuttings," PhD thesis, University of Cambridge, UK, 2007.

# Impact of pore structure of lightweight aggregates on internal curing

Pietro Lura<sup>1,2</sup>, Mateusz Wyrzykowski<sup>1,3</sup>, Sadegh Ghourchian<sup>1,2</sup>, Sakprayut Sinthupinyo<sup>4</sup>, Clarence Tang<sup>4</sup>

<sup>1</sup>Empa, Swiss Federal Laboratories for Materials Science and Technology, Switzerland

<sup>2</sup>Institute for Building Materials (IfB), ETH Zürich, Switzerland

<sup>3</sup>Department of Building Physics and Building Materials, Lodz University of Technology, Poland

<sup>4</sup>Siam Research and Innovation, SCG Cement–Building Materials, Saraburi, Thailand

**Abstract:** Shrinkage of concrete may lead to cracking and ultimately to a reduction of the service life of concrete structures. Among the known methods for shrinkage mitigation, internal curing with porous aggregates was utilized in the last couple of decades for decreasing autogenous and drying shrinkage. In this paper, the internal curing performance of different types of lightweight aggregates (LWA) and porous mineral admixtures is evaluated in terms of impact on the internal relative humidity and on shrinkage. In particular, next to expanded shale/expanded clay aggregates, results on zeolite, bottom ash and LWA produced from biomass-derived waste are presented. For all these porous aggregates, it is shown that the internal curing performance is directly linked to their pore structure, which determines both their water absorption kinetics and their desorption isotherm. Most of the LWA and the bottom ash examined in this research had a substantial amount of pores larger than about 50-100 nm when measured with mercury intrusion porosimetry. They showed a rapid absorption under water, a steep desorption isotherm (they lost most of the water already at 98% RH) and were efficient internal curing agents. On the contrary, the zeolite aggregates absorbed most of the water in nm-sized pores, retained the water at low relative humidity levels and were unsuitable as internal curing agents.

**Keywords:** high-performance concrete; internal curing; porous aggregate; pore structure.

## 1. Introduction

In high performance concrete (HPC), even when water evaporation is prevented, self-desiccation of the cement paste results in high capillary stresses that cause autogenous shrinkage. Restrained shrinkage may result in cracking and loss of durability of concrete structures. For HPC with low water-to-cement ratio ( $w/c$ ), low porosity and permeability, external curing may not avoid self-desiccation because the curing water penetrates only the surface layer of the concrete (only several mm). On the contrary, internal curing consists in distributing small water reservoirs into the concrete mixture [1,2], which release the water locally and limit self-desiccation. The most common water reservoirs are porous lightweight aggregates (LWA) [3], followed by superabsorbent polymers (SAP) [4].

The efficiency of LWA as internal curing agents depends on their water absorption and desorption characteristics. Preferably, they should take up water rapidly before mixing when they are stored underwater and release it during concrete hardening, while the internal relative humidity is still high. Most porous aggregates absorb significant amounts of water (about 10–30% by mass) thanks to their high porosity [5]. However, not all of them are able to release rapidly a sufficient amount of absorbed water during self-desiccation of HPC. This issue of water availability has been discussed in [6], where the concept of thermodynamic and kinetic availability of water in the hydrating cement paste was introduced. Although it has been shown recently that the water has high mobility in hydrating cement paste in the first few days of hydration (see e.g. [7,8]), the water needs first to be rapidly released at high RH. The desorption behavior of porous aggregates depends critically on their pore size distribution. LWA with coarse pore structure perform better for internal curing [9].

In this paper, the internal curing performance of different types of LWA and porous mineral admixtures is evaluated in terms of impact on the internal relative humidity and on shrinkage. In particular, next to expanded shale/expanded clay LWA, results on zeolite, bottom ash and LWA produced from biomass-derived waste are presented. The results presented in this paper derive from published [9,10] and current [11] research of the authors. This comparison between different types of internal curing reservoirs allows drawing general conclusions about pore structures that are effective for internal curing.

## 2. Materials and Methods

### 2.1 Materials

#### *Internal curing agents*

LECA (Lightweight Expanded Clay Aggregate) is a porous expanded clay aggregate that is widely used in internally cured concretes [9]. The particle size was between 1 and 4.75 mm. Zeolite (clinoptilolite) is a natural porous aggregate with high absorption capacity [9]. The particle size was between 0.1 and 4.75 mm. LWA produced from pelletization of sugar cane bagasse fly ash (bio-LWA) had particle sizes between 0.5 and 1.4 mm [10]. Finally, bottom ash (BTA) derived from a stoker burning process had particle sizes between 63  $\mu\text{m}$  and 1.4 mm [10]. In this paper, only the water absorption, the pore size distribution and the sorption isotherms of LECA and zeolite are shown, while for their performance as internal curing agents reference is made to [9]. For the bio-LWA and the BTA, internal relative humidity and autogenous deformation data of internally-cured mortars are also shown [10,11].

#### *Mortars*

An ordinary Portland cement CEM I 42.5N was used. A polycarboxylate-based superplasticizer (SIKA Viscocrete 1S) replaced part of the mixing water (deionized water) in an amount allowing for obtaining similar spread (~170 mm after 15 shocks of the table) for all analyzed mixtures. The mixture composition is shown in Table 1. Different amounts of either bio-LWA or BTA were used based on their absorption (see Table 1) in order to introduce into the mixture the same amount of water. The bio-LWA or the BTA replaced part of the NWA and the total aggregate volume was fixed at 40%. The NWA was alluvial sand composed of (by weight): sandstone 37%, limestone 37%, dolomite 18% and metamorphic rocks 8% with grain sizes 0.25 – 1.0 mm.

**Table 1. Mix compositions of mortars.**

Material	Mass [kg/m <sup>3</sup> ]			
	REF w/c 0.30	REF w/c 0.35	bio-LWA	BTA
Cement	973.4	899.7	973.0	973.7
NWA (sand)	1063.8	1063.6	555.9	665.8
LWA	-	-	324.3	221.3
Mixing water	281.3	310.4	286.1	278.5
Water in LWA	-	-	48.6	48.7
Superplasticizer	10.7	4.5	5.8	13.6
w/c basic	0.30	0.35	0.30	0.30
w/c entrained	-	-	0.05	0.05
w/c total	0.30	0.35	0.35	0.35

### 2.2 Methods

#### *Density and water absorption*

Density and water absorption in saturated surface dry (SSD) conditions was determined according to the standard ASTM C1761/C1761M–12. In this method, LWA are immersed in water for 72 h before the SSD condition is determined using a cone. The water absorption is referenced to dry state obtained after 24 h oven drying at 110°C.

#### *Pore structure – MIP*

In order to relate the desorption properties with the microstructure of the aggregates, Mercury Intrusion Porosimetry (MIP) was performed, which allows determining the equivalent size distribution [12]. The dry aggregates were inserted into the sample holder, which was first filled with mercury at pressures up to 200 kPa in a low pressure porosimeter (Pascal 140). At this pressure range, mainly the intergranular spaces

were filled by the mercury. The sample was then moved to a high pressure porosimeter (Pascal 440) which reached intrusion pressures up to 200 MPa.

#### *Desorption isotherms*

The water desorption isotherms were determined with a VTI+ Dynamic Vapor Sorption (DVS) analyzer. Before performing the desorption tests, the samples were saturated with water for  $24 \pm 2$  h. 30-100 mg of saturated LWA were placed in a sample holder and changes of mass due to water desorption were monitored continuously at different RH steps. At the end of each test, the sample was dried to constant mass at  $105^\circ\text{C}$  and 0%RH in order to obtain the reference mass for water-content calculations. The equilibrium condition for proceeding to the next RH step was set as 0.001% of the initial mass per 5 min.

#### *Internal relative humidity*

Measurements of internal RH in reference mortars and mortars with BTA and bio-LWA were performed using water activity HC2-AW sensors by Rotronic. Each mortar obtained from a single mixing was measured at two stations in parallel. The nominal accuracy of the sensors was  $\pm 0.8\%$  RH. The sensors were calibrated at the beginning and at the end of each measurement with three saturated salt solutions with equilibrium RH in the range 98–85%. This procedure allowed reducing the difference between two sensors measuring the same mortar to below 0.5% RH. The temperature of the sample and the sensor was maintained at  $20 \pm 0.02^\circ\text{C}$  by means of tempered water circulating in the casings of the measuring chambers.

Right after mixing, the mortars were cast in sealed plastic containers. At the age of approximately 24 h the mortars were crushed into pieces of 2–5 mm. About 8 g of crushed mortar were inserted into sealed measuring chambers. The measurement continued until the age of 7 days.

#### *Linear autogenous shrinkage*

The linear autogenous shrinkage of mortars was measured using the corrugated tube method [13,14]. The length change was measured on a stainless steel bench, which can accommodate three specimens in parallel, with two linear variable differential transformers (LVDTs) for each specimen. The measuring bench was placed in a tempered silicone oil bath at  $20 \pm 0.1^\circ\text{C}$ . Duplicate samples from independent mixings were measured for each mixture; average results are presented in the graphs. Automatic measurements allowed recording the deformation starting approximately 1 h after mixing. Nevertheless, the results were zeroed at final set [13]. The setting times were estimated by Vicat needle on corresponding cement pastes (same composition as the mortars, but without aggregates).

## **2.2 Results and discussion**

#### *Density and water absorption*

The density and the water absorption of the LWA determined at SSD conditions are presented in Table 2. While LECA and BTA aggregates had similar density, the absorption of the BTA was double that of LECA. This might indicate the presence of closed pores in the LECA, or of pores into which water can be absorbed only slowly. The zeolite had the highest density, though the water absorption was comparable to the bio-LWA and substantially higher than for LECA.

**Table 2. Density and water absorption of LWA**

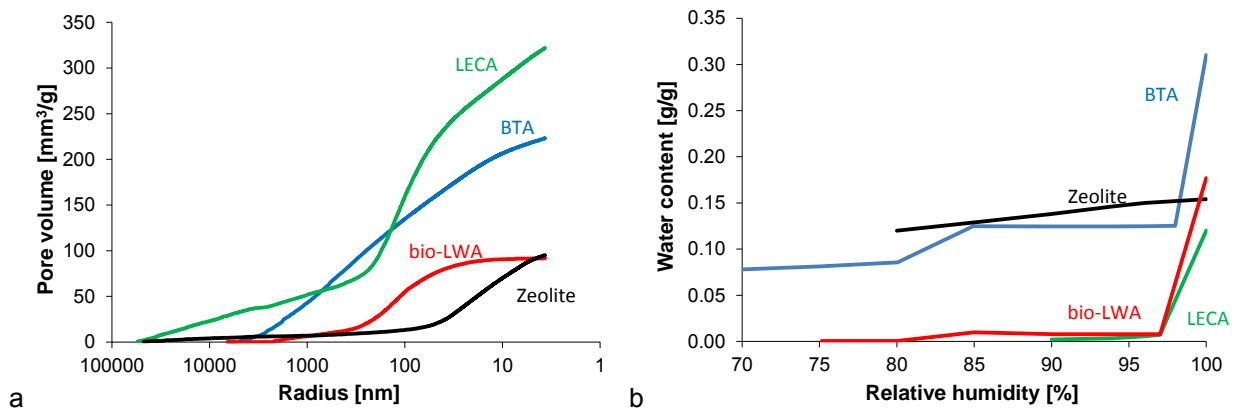
LWA type	Dry density [kg/m <sup>3</sup> ]	Absorption at 24 h [g/g]
LECA	1470	0.11
Zeolite	2250	0.16
bio-LWA	1700	0.18
BTA	1492	0.22



### Pore structure and desorption isotherms

The pore size distributions and the desorption isotherms of LWA are shown in Fig. 1. LECA had the highest porosity measured by MIP, followed by the BTA and by the bio-LWA and the zeolite with almost the same porosity (Fig. 1a). It should be noted that the 200 MPa used as maximum intrusion pressure allowed accessing pores of equivalent radii larger than approximately 4 nm. Depending on the LWA type, this may have not allowed to intrude the whole pore volume (consider also that for LECA, BTA and zeolite aggregates the pore size distribution did not reach a plateau at the highest intrusion pressures, Fig. 1 a). In LECA and BTA, a substantial amount of pores had equivalent entrance radii larger than 100 nm. The bio-LWA had slightly finer pores, with a majority between 100 and 30 nm. In the zeolite aggregates, instead, almost all the porosity were accessed through radii smaller than about 20 nm. A further analysis based on multi-cycle MIP [12] (results shown in [9-11] reveals that most of the pores in the LECA and the bio-LWA were ink-bottle pores, accessed only through pores with smaller radius. Also the BTA had a majority (about 70%, against the 90% of e.g. bio-LWA) of ink-bottle pores. It is expected that only the pore volume accessed through larger pores (larger than about 50-100 nm) might be useful for storing internal curing water. In fact, smaller pores would not be able to release the water at the high RH levels needed to avoid or limit autogenous shrinkage.

The results of the desorption isotherms presented in Fig. 1b appear to support this hypothesis. Whereas LECA, bio-LWA and BTA released a substantial amount of water already at 97-98% RH, this is not the case for the zeolite aggregate, which retains almost all the absorbed water down to 80% RH (when the experiments were stopped). Moreover, while LECA and bio-LWA were almost empty by 97% RH, the BTA retained a part of the absorbed water down to 70% RH and below. This could be explained by the presence of both large and small pores in the BTA, as suggested by MIP. The smaller pores of LECA were apparently not filled by water during the 24 h absorption period.



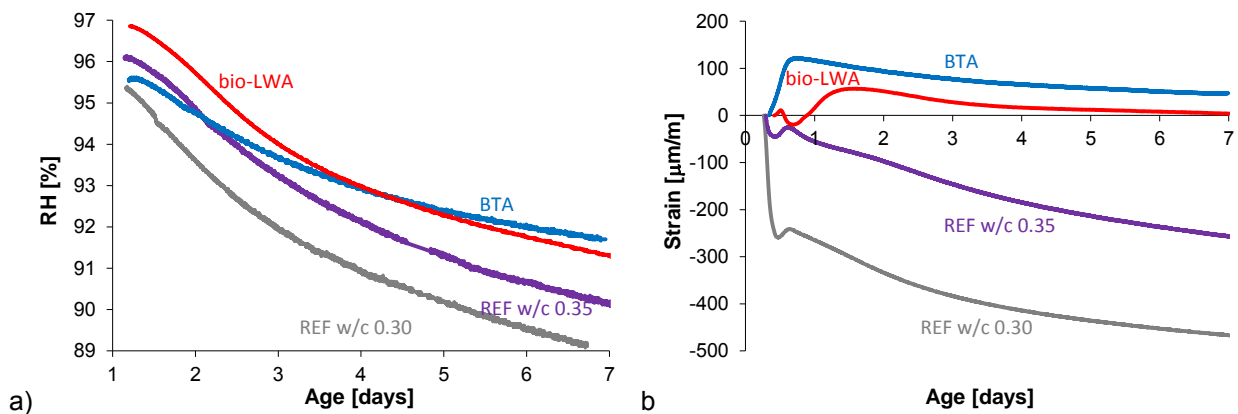
**Figure 1. a) MIP equivalent pore size distributions (cumulative curves); b) desorption isotherms.**

### Internal relative humidity and autogenous shrinkage

In Fig. 2a, the internal RH evolution in the mortars is presented, while the deformation in autogenous conditions, referred to the length at final set determined with the Vicat needle, is shown in Fig. 2b. The addition of both BTA and bio-LWA is keeping the internal RH considerably higher (especially in the first few days) compared to the reference mortar with w/c 0.30 (Fig. 2a). The RH is also higher than in the mortar with the same total amount of water, which is a confirmation of the principles of internal curing [1,2]. The autogenous shrinkage is strongly reduced in both mortars with BTA and with bio-LWA (Fig. 2b). It is noticeable that the two reference mortars differ only in the first day but have similar shrinkage rate afterwards, while the mortars with internal curing both show an initial expansion and a subsequent lower long-term shrinkage rate. Based on these results and others shown in [10,11], it is possible to conclude that both BTA and bio-LWA are efficient internal curing agents.

Results for LECA and zeolite presented in [9] show that LECA was able to delay and reduce drying shrinkage of mortars compared to the reference, while the mortars containing zeolite experience even higher shrinkage than the reference. This indicated that due to their small pores, the water absorbed in the zeolite aggregates was not available for internal curing.





**Figure 2. a) Evolution of internal RH in reference mortars and mortars with BTA and bio-LWA. b) autogenous deformation of mortars with BTA and bio-LWA.**

### 3. Conclusions

In this paper, the water absorption, the pore structures and the desorption isotherms of four different types of porous aggregates (LECA, BTA, bio-LWA and zeolite) were examined in view of their use as internal curing agents.

The principal conclusion is that the water absorption alone is not a good indicator of the internal curing efficiency. While e.g. BTA had high water absorption and was effective in keeping the internal RH high and reducing autogenous shrinkage in high-performance mortars, zeolite aggregates were not suitable as internal curing agents, despite their comparatively high absorption (16% by mass). The reason for this difference could be found in the pore structure of the different LWA. In particular, the zeolite aggregates had a majority of pores smaller than about 20 nm, which did not release the absorbed water even down to 80% RH. The other LWA types had larger pores (most of them in the range 50 nm – 1 µm) and were able to release a substantial amount of the absorbed water already at 97% RH.

A practical conclusion of this work is that MIP can be used instead of desorption isotherms measurements for a first evaluation of the suitability of a LWA for internal curing. In fact, for LWA, thanks to the prevalence of larger pores, it is possible to calculate a sorption isotherm from the MIP pore size distribution (see for example [10]). Depending on the availability of laboratory equipment and on measuring time, this approach can be more efficient than measuring a sorption isotherm.

### 5. References

1. D.P. Bentz, K.A. Snyder, Protected paste volume in concrete: extension to internal curing using saturated lightweight fine aggregate, *Cem. Concr. Res.* 29 (11) (1999) 1863–1867.
2. O.M. Jensen, P.F. Hansen, Water-entrained cement-based materials: I. Principles and theoretical background, *Cem. Concr. Res.* 31 (4) (2001) 647–654.
3. A. Bentur, S.I. Igarashi, K. Kovler, Prevention of autogenous shrinkage in high-strength concrete by internal curing using wet lightweight aggregates, *Cem. Concr. Res.* 31 (11) (2001) 1587–1591.
4. O.M. Jensen, P.F. Hansen, Water-entrained cement-based materials: II. Experimental observations, *Cem. Concr. Res.* 32 (6) (2002) 973–978.
5. J. Castro, L. Keiser, M. Goliás, J. Weiss, Absorption and desorption properties of fine lightweight aggregate for application to internally cured concrete mixtures, *Cem. Concr. Compos.* 33 (10) (2011) 1001–1008.
6. O.M. Jensen, P. Lura, Techniques and materials for internal water curing of concrete, *Mater. Struct.* 39 (9) (2006) 817–825.

7. P. Trtik, B. Münch, W.J. Weiss, A. Kaestner, I. Jerjen, L. Josic, E. Lehmann, P. Lura, Release of internal curing water from lightweight aggregates in cement paste investigated by neutron and X-ray tomography, Nucl. Instrum. Methods Phys. Res. A 651 (1) (2011) 244–249.
8. M. Wyrzykowski, P. Lura, F. Pesavento, D. Gawin, Modeling of water migration during internal curing with superabsorbent polymers, J. Mater. Civ. Eng. 24 (8) (2012) 1006–1016.
9. S. Ghourchian, M. Wyrzykowski, P. Lura, M. Shekarchi, B. Ahmadi, An investigation on the use of zeolite aggregates for internal curing of concrete, Constr. Build. Mater. 40 (2013) 135–144.
10. P. Lura, M. Wyrzykowski, C. Tang, E. Lehmann, Internal curing with LWA produced from biomass-derived waste, Cem. Concr. Res. 59 (2014) 24–33.
11. M. Wyrzykowski, S. Ghourchian, S. Sinthupinyo, N. Chitvoranund, T. Chintana, P. Lura, Internal curing of high-performance mortars with bottom ash, Waste Management 2015, submitted.
12. J. Kaufmann, R. Loser, A. Leemann, Analysis of cement-bonded materials by multi-cycle mercury intrusion and nitrogen sorption, J. Colloid Interface Sci. 336 (2009) 730–737.
13. ASTM, ASTM C1698-09 Standard test method for autogenous strain of cement paste and mortar, ASTM International, West Conshohocken, PA, 2009.
14. O.M. Jensen, P.F. Hansen, A dilatometer for measuring autogenous deformation in hardening portland cement paste, Mater. Struct. 28 (1995) 406–409.

# Reinforcing ordinary Portland cement mortar using carbon nanotubes

Shu Jian Chen<sup>1</sup>, Xiang Yu Li<sup>1</sup>, Tong Bo Sui<sup>2</sup> and Wen Hui Duan<sup>1</sup>

<sup>1</sup>Department of Civil Engineering, Monash University, Clayton, VIC, 3800, Australia

<sup>2</sup>Sinoma International, Beijing, China

**Abstract:** Carbon nanotubes (CNT), as the strongest fiber ever manufactured, are promising reinforcements in ordinary Portland cement (OPC) based materials. In this study, by dispersing CNTs with ultrasonication and polycarboxylate based surfactants, CNT-OPC mortar composites were made. The compressive strength of the material was increased by up to 20% for 28-day samples and the flexural strength of the sample was found to increase by 31%. The effect of CNT concentration was studied and it was found that 0.0375 wt% of CNTs in terms of the weight of cement gave the best results.

**Keywords:** cement, carbon nano tube, mortar, strength, ultrasonication.

## 1. Introduction

Ordinary Portland cement (OPC) based material is the second most consumed material in the world. However, its production consumes a huge amount of energy and releases greenhouse gases. The weak tensile property of OPC is one of its main limitations. Carbon nanotubes (CNTs), the strongest fibers ever manufactured, have the potential to improve the mechanical performance of cement based materials. Studies of CNT-reinforced OPC paste have shown improvements in compressive and flexural strength, fracture toughness, Young's modulus [1], porosity [2], electrical resistance [3], and piezoresistivity [4, 5] of the composite. However, little research into CNT-reinforced OPC mortar has been published. In this paper, CNT-OPC mortar composite is fabricated by dispersing CNTs with ultrasonication and surfactants. The compressive and flexural of the composite are tested.

## 2. Experimental Program

### 2.1 Materials

Type GP OPC, conforming to the requirements of Australian Standard AS 3972 [6], was used as the binder material. Multi-walled CNTs functionalized with COOH groups were purchased from Nanocyl s.a., Belgium. The physical properties of the nanotubes are shown in **Table 1**. The sand was provided by Sibelco Australia. The particle size distribution is shown in **Table 2**. A commercially available polycarboxylate-based concrete superplasticizer (PC) ADVA 210 (supplied by Grace Australia Pty. Ltd.) was used. The PC contains both active non-polar groups for adsorption on the surface of CNTs and polar groups to attach on cement particles/water in aqueous solution, thereby assisting the dispersion of both cement and CNTs [7-9].

**Table 1 Properties of functionalized CNTs**

Aspect ratio	Average diameter (nm)	Average length ( $\mu\text{m}$ )	Carbon purity (%)	-COOH functionalization (%)	Specific surface area ( $\text{m}^2/\text{g}$ )
150	9.5	1.5	>95	<4	250-300

**Table 2 Particle size distribution of silica sand**

Mesh size (mm)	% retained
0.710	0.1
0.600	1.5
0.500	20
0.425	32.5
0.355	24.5
0.300	12.3
0.250	5.6

## 2.2 Preparation of CNT suspensions

CNT suspensions were prepared by mixing CNT powder with PC in aqueous solutions under ultrasonication using a horn sonicator (VCX 500W) with a cylindrical tip (19 mm end-cap diameter). The input power of the sonicator was fixed at 150 watts. To prevent the temperature rising, the suspensions were placed in a water-ice bath during sonication. The ultrasonication energy was adopted from a previous study as 100J/mg of CNTs [10].

## 2.3 Preparation and testing of CNT-OPC mortar specimens

The mixing of the CNT aqueous dispersion, OPC and sand followed ISO 679 :1989, using a planetary mixing in compliance with ISO 681 :1989. A water-to-cement mass ratio of 0.5 was used for all the mixes. The sand-to-cement mass ratio of 3 was adopted. The mix design, as shown in Table 3, was based on the workability of CNT-OPC paste reported in a previous study [10] in order to produce very workable and consistent mortars. Based on a flow table test according to ASTM C1437 – 13, the three mixes had similar workability, yielding a flow diameter of 210±10 mm.

**Table 3 Mix proportion of CNT-OPC mortar specimens**

	Cement/g	Sand/g	CNTs*	Water/Cement ratio	SP*
Control	300	900	/	0.5	0.55%
CNT-0.0375%	300	900	0.0375%	0.5	0.85%
CNT-0.0758%	300	900	0.7058%	0.5	1.05%

Note:\* by weight of cement

The fresh mortars were poured into molds and vibrated to release residual air bubbles. The specimens were then covered under polyethylene sheets for 24 hours in the laboratory environment with temperature controlled at  $20 \pm 2^\circ\text{C}$  before demolding. After demolding, specimens were cured for 14 and 28 days in a tank of saturated limewater at  $23 \pm 2^\circ\text{C}$  as the moist-curing regime to satisfy ASTM C192 requirements [11]. Subsequently, the specimens were stored in a controlled environment maintained at relative humidity  $50 \pm 3\%$  and temperature  $23 \pm 2^\circ\text{C}$  for 1 hour before testing. This environment met the ISO requirements as a standard atmosphere for conditioning and testing of materials known to be sensitive to variations in temperature or relative humidity.

Following hardening, the mechanical properties of the hardened mortar were evaluated by compressive and bending tests to obtain the compressive and flexural strength. Cubes 20 mm in height were used in

compressive testing and 15 × 15 × 75 mm prisms were used in the three point bend tests. 50 and 2 kN load cells were installed on an Instron 4204 50 kN loading frame for compressive and bending tests, respectively. All the specimens were loaded to failure at a constant loading rate of 0.01 mm/min to maintain stable crack growth.

### 3. Test Results

Table 3 shows the strength of the CNT-OPC mortar in comparison with pure OPC mortar. Both batches of specimens containing CNTs show higher compressive and flexural strength than pure OPC specimens. It is found that 0.0375 wt% of CNT is the more effective, producing 18% improvement in compressive strength and 7% in flexural strength. The degree of improvement in the CNT-OPC mortar is lower than that obtained in CNT-OPC pastes [10], when 0.075wt % of CNTs was found to be more effective (with about 50% percent improvement in flexural strength). This might be due to the more complex nature of the mortar, where interfacial transition zones (ITZs) play important roles in the mechanical properties of the composite. The effect of CNTs on ITZs is still unclear and requires future investigation to optimize the enhancing effect of CNTs.

**Table 3. Compression (A) and bending (B) test results of CNT-OPC mortar (14 days) with different amounts of CNT incorporated (wt% is expressed in terms of the weight of dry OPC).**

(A)	Specimen No	Maximum load [N]	Compressive strength [MPa]	Average strength [MPa]	Standard deviation	Improvement
Control	1	7105.72	17.76	17.37	1.96	
	2	6099.07	15.24			
	3	7640.11	19.10			
CNT 0.0375 wt%	5	9239.02	23.09	20.42	3.00	18%
	6	6874.01	17.18			
	7	8389.52	20.97			
CNT 0.0758 wt%	9	8154.29	20.38	18.33	1.89	6%
	10	7176.14	17.94			
	12	6668.94	16.67			

(B)	Specimen No	Maximum load [N]	Flexural strength [MPa]	Average strength [MPa]	Standard deviation	Improvement
Control	1	232.09	4.64	5.00	0.36	
	2	268.36	5.36			
	3	250	5.00			
CNT 0.0375 wt%	5	311.29	6.22	6.10	0.17	22%
	6	308.44	6.16			
	7	295.08	5.90			
CNT 0.0758 wt%	9	267.54	5.35	5.35	0.02	7%
	10	266.51	5.33			
	12	268.76	5.37			

**Table 4. Compression (A) and bending (B) test results of CNT-OPC mortar (28 days) with different amounts of CNT incorporated (wt% is expressed in terms of the weight of dry OPC).**

(A)	Specimen No	Maximum load [N]	Compressive strength [MPa]	Average strength [MPa]	Standard deviation	Improvement
Control	1	6115.59	15.29	17.86	2.96	
	2	6878.54	17.20			
	3	8440.21	21.10			
CNT 0.0375 wt%	5	8695.90	21.74	21.35	1.28	20%
	6	8954.29	22.39			
	7	7969.97	19.92			
CNT 0.0758 wt%	9	8014.37	20.04	20.89	0.81	17%
	10	8661.02	21.65			
	12	8387.74	20.97			

(B)	Specimen No	Maximum load [N]	Flexural strength [MPa]	Average strength [MPa]	Standard deviation	Improvement
Control	1	299.87	5.9974	5.96	0.05	
	2	299.22	5.9844			
	3	294.98	5.8996			
CNT 0.0375 wt%	5	384.54	7.69	7.83	0.56	31%
	6	422.64	8.45			
	7	367.57	7.35			
CNT 0.0758 wt%	9	313.57	6.27	6.06	0.31	2%
	10	285.1	5.70			
	12	310.98	6.22			

### 3. Conclusions

CNT-OPC mortar composites were fabricated by dispersing CNTs with ultrasonication and a surfactant that was a polycarboxylate based superplasticizer. From the authors' previous research on CNT-OPC paste, the optimum ultrasonication energy and CNT-to-surfactant ratio for paste were used. The compressive strength of the material was increased by up to 18% and 20% for the 14-day and 28-day samples respectively. Greater improvement in flexural strength was obtained, 22% and 31% for 14-day and 28-day samples respectively. The improvement of strength in the mortar was found to be lower than that in paste, that was higher than 50%. This difference is due to the effect of ITZs in the mortar, indicating that more work is required for better understanding of CNT-ITZ interaction.

### 4. Acknowledgement

The authors are grateful for the financial support of the Australian Research Council in conducting this study.

### 5. References

1. Chen, S., et al., *Carbon nanotube–cement composites: A retrospect*. The IES Journal Part A: Civil & Structural Engineering, 2011. 4(4): p. 254-265.

2. Li, G.Y., P.M. Wang, and X. Zhao, *Mechanical behavior and microstructure of cement composites incorporating surface-treated multi-walled carbon nanotubes*. Carbon, 2005. **43**(6): p. 1239-1245.
3. Wansom, S., et al., *AC-impedance response of multi-walled carbon nanotube/cement composites*. Cement and Concrete Composites, 2006. **28**(6): p. 509-519.
4. Li, G.Y., P.M. Wang, and X. Zhao, *Pressure-sensitive properties and microstructure of carbon nanotube reinforced cement composites*. Cement and Concrete Composites, 2007. **29**(5): p. 377-382.
5. Xun, Y. and K. Eil, *A carbon nanotube/cement composite with piezoresistive properties*. Smart Materials and Structures, 2009. **18**(5): p. 055010.
6. AS 3972, *General purpose and blended cements*. 2010.
7. Uchikawa, H., D. Sawaki, and S. Hanehara, *Influence of kind and added timing of organic admixture on the composition, structure and property of fresh cement paste*. Cement and Concrete Research, 1995. **25**(2): p. 353-364.
8. Yamada, K., et al., *Effects of the chemical structure on the properties of polycarboxylate-type superplasticizer*. Cement and Concrete Research, 2000. **30**(2): p. 197-207.
9. Collins, F., J. Lambert, and W.H. Duan, *The influences of admixtures on the dispersion, workability, and strength of carbon nanotube-OPC paste mixtures*. Cement and Concrete Composites, 2012. **34**(2): p. 201-207.
10. Zou, B., et al., *Effect of ultrasonication energy on engineering properties of carbon nanotube reinforced cement pastes*. Carbon, 2015.
11. ASTM C192 / C192M - 13a, *Standard Practice for Making and Curing Concrete Test Specimens in the Laboratory*.

# The Significance of the Alkali Aggregate Reactivity Provisions in the VicRoads Structural Concrete Specification Section 610

Fred Andrews-Phaedonos<sup>1</sup>, Dr Ahmad Shayan<sup>2</sup>, Dr Aimin Xu<sup>3</sup>

<sup>1</sup>Principal Engineer – Concrete Technology, VicRoads, Australia

<sup>2</sup>Chief Research Scientist, ARRB Group Pty Ltd, Australia

<sup>3</sup>Senior Engineer, ARRB Group Pty Ltd, Australia

**Abstract:** Alkali aggregate reactivity (AAR) has been identified as a durability problem affecting a number of VicRoads concrete bridges since the late 1980s. At that time a number of bridges, built in the 1950s exhibited signs of distress in the form of cracking of various concrete elements, presenting costly rehabilitation requirements for these structures. Some of these bridges are situated inland and in moderate exposure conditions, whereas some others are exposed to salt water in coastal areas. VicRoads work into AAR continued throughout the 1990s and early 2000s with further investigation of additional structures for the presence of AAR. Extensive research work was also conducted on a relatively large number of aggregates, covering a wide range of aggregate types which established a strong correlation between the results of the accelerated mortar bar test (AMBT) (VicRoads RC376.03) with both the Concrete Prism Test (CPT) (VicRoads RC376.04) and field performance of the aggregates studied in a number of in-situ structures. As a consequence of the earlier investigation work, AAR testing of aggregates and mitigation measures were introduced into the 1996 version of the VicRoads structural concrete specification Section 610. This was followed by further improvements which culminated in the more recent AAR upgrade of Section 610 in 2013. The significance of the preventative AAR provisions in Section 610 is highlighted by the AAR investigation in 2014 of a relatively young bridge which was constructed some 5 years earlier in 1991, identified with AAR and premature cracking some 10 years later, and shown to have developed considerable amount of cracking and high residual expansion potentials as a result of AAR. In contrast, many VicRoads bridges monitored since the inclusion of the initial AAR provisions in Section 610 in the mid 1990s have not exhibited any signs of AAR related damage. The paper presents the updated AAR provisions in Section 610 and considered effectiveness in contrast to the investigation results of the young AAR affected bridge which will lead to further expansion and cracking and possible reduction in mechanical, structural and durability properties if costly protective measures are not undertaken.

**Keywords:** alkali aggregate reactivity (AAR), cracking, AAR damage, residual expansion, AAR provisions, cost protective measures

## 1. Introduction

Deterioration of concrete is of both internal and external origin. Deterioration of an internal origin is closely linked to the nature and chemical composition of the various constituents of concrete (cementitious materials, aggregates, water, admixtures etc), and to the internal chemical reactions in which they participate, particularly alkali aggregate reaction (AAR). The extent and rate of deterioration can also be controlled by the natural environment in which the concrete structure is situated (i.e. various exposure conditions of water etc), the technology and mechanical properties of the concrete and the construction practices adopted (1).

AAR occurs in a number of forms, the most common in Australia being that of alkali silica reaction. AAR can cause expansion and subsequent cracking of concrete, thus further compromising its durability by exposing the concrete to the easier ingress of aggressive agents such as moisture, carbon dioxide, oxygen, other gases, and salt solutions which lead to premature corrosion of the steel reinforcement(1,2,3,4). AAR also has important implications in the management of bridge assets and other concrete structures (2, 3).

AAR is a disruptive chemical reaction within the concrete matrix. The reaction, in susceptible aggregates and in the presence of moisture, is between the alkali hydroxides (sodium and potassium) and free or unstable, volatile silica minerals. It produces an expansive sodium or potassium rich (alkali) silica gel which has the ability to absorb further amounts of moisture and expand. When this expansive gel completely fills the pore system within the concrete it exerts excessive expansive stresses which can overcome its tensile capacity of the concrete. The result is severe cracking of the concrete (1, 4).

For deleterious AAR to occur in a structure, the concrete must contain aggregate with a high proportion of



reactive silica; the concrete pore solution must have a sufficiently high alkali hydroxide content; and there must be sufficient moisture, typically >85% internal relative humidity. The absence of any one of these inhibits the reaction.

The alkali aggregate reaction is normally a slow process which may take many years to manifest itself in a structure that contains the necessary ingredients for the reaction, with older bridges taking 20 to 30 years to exhibit visible signs of AAR damage. However, it has been observed over recent years that even much younger structures of less than 10 years can exhibit significant signs of AAR. This is mainly due to the higher amounts of cement content and more refined pore system, if appropriate preventative measures have not been taken, such as the incorporation into the concrete mix of adequate amounts of fly ash, slag or silica fume or combinations of these Supplementary Cementitious Materials (SCMs), as is the case with VicRoads structural concrete specification Section 610 (5).

## **2. Sources of Alkali and Moisture and Types of Potential Reactive Rocks**

The alkali hydroxides are mainly derived from the cement as they are present in its raw materials. Other possible sources include chemical admixtures, SCMs (i.e. fly ash, slag, silica fume), water and alkali released from some aggregates. Ground water, sea spray and sea water can also supply alkali. Mixing water in excess of that required to hydrate the cement can be retained as moisture within the pore system. More moisture can become available from rain and runoff, condensation, seasonal increases in humidity, leaking joints and inadequate drainage scuppers. Structures in moist environments, with surfaces immersed in water or exposed to regular cycles of wetting and drying, are particularly vulnerable.

Rocks must contain free or unstable fine-grained silica such as glass, quartz and quartz derivatives to be potentially reactive to alkalis. Potentially reactive aggregates include some originating from basalt, rhyolite, dacite and andesite, hornfels, granite and quartzite. Potentially reactive sedimentary aggregates include those originating from river gravel and sandstone (1, 4).

## **3. Visible Signs of Damage**

The visible signs of AAR damage are characterised by a network of cracks known as map cracking. Cracking can be directional, influenced by the direction of the largest applied stresses, such as in the case of prestressed concrete components. This may also be the case where significant amounts of steel reinforcement are present in a concrete component, as cracking tends to be more prominent in the direction parallel to the steel reinforcement. Other visible signs of damage include damp patches, usually at crack junctions, and discolouration due to the calcium rich alkali-silica gel which migrates to the surface of the concrete.

A greater awareness of AAR and its potential damage to concrete in recent years has made it easier to identify the problem. Previously, AAR induced cracking of 20 to 40 year old bridges may have been attributed to other factors such as drying and plastic shrinkage, surface crazing or structural movements or loadings. Shrinkage cracks and surface crazing normally develop early in the life of the structure (i.e. within hours, or days/weeks after casting the concrete and certainly within the first year), whereas AAR induced cracking may appear after about 5 to 8 years, with further deterioration taking place in subsequent years.

## **4. Durability Considerations**

The main deleterious consequences of AAR are essentially related to potentially significant reductions in compressive strength (up to 30%), tensile strength (up to 50%), flexural strength, elastic modulus (up to 60% to 80%), bond strength of the steel reinforcement and increased creep strain for concrete affected by AAR. Although not much evidence exists of significant reductions in structural capacity, reductions in the above physical properties does have the potential to adversely affect structural capacity with subsequent rehabilitation and strengthening requirements. The issue of greatest concern is the long term durability of concrete structures due to the network of cracks which substantially increase the permeability to aggressive agents. This can further accelerate deterioration mechanisms such as carbonation, chloride attack and corrosion of the steel reinforcement. Very porous and low strength concrete may be less susceptible to AAR induced damage as the gel products will tend to fill the porous microstructure first before they start cracking the concrete.

## 5. Management of Structures Affected by Cracking caused by AAR

Given the potential durability consequences it is important that AAR affected structures are inspected on a regular basis by experienced personnel. Monitoring of cracks should be undertaken using suitable measuring devices. Concrete cores are extracted from structures and subjected to petrographic analysis by viewing thin sections with a petrographic microscope. Alternatively, a more detailed examination of polished sections of concrete can be done by scanning electron microscopy (SEM). An assessment is made of the existing and predicted level (magnitude of residual expansion) of AAR expansion to enable determination of the timing and type of remedial options. Measurement of residual expansion of AAR affected concrete may show that for some elements of a structure the reaction has been exhausted and they would not develop any further AAR related cracking (1, 4).

Remedial measures to prevent moisture ingress may include:

- the injection of cracks with flexible epoxy or elastomeric chemical grouts;
- the application of flexible epoxy, elastomeric acrylic or cementitious coatings; and
- silane impregnations where appropriate.

In severe cases, concrete encasement or concrete repairs and strengthening in combination with the above may be required whereas in the more severe cases, even propping and strutting may be required.

At present there is some precedent for extensive AAR repairs including the rehabilitation of Mitchell River and Tallangatta bridges undertaken by VicRoads some 15 years ago. More repairs will probably be carried out as AAR affected bridges and other concrete structures age and given the greater awareness of the problem by asset owners, especially State Road Authorities. Bearing in mind however, that cracking and subsequent deterioration occurs in the presence of water, cracks greater than 0.2 mm in width should be chased out and filled (injected) with a suitable flexible epoxy resin to prevent further ingress of water.

In atmospheric or splash zones, the structure should subsequently be coated with a pore-lining penetrant such as pure silane to dry it out (or in combination with acrylic top coats), a flexible urethane or epoxy coating or a suitable cementitious coating. Where cracks are less than 0.2 mm, an application with a pure silane, crack bridging or crack filling epoxy, urethane or flexible acrylic coating may be sufficient. In tidal or submerged zones flexible epoxy or urethane coatings, or polymer modified cementitious coatings may be the most appropriate. Re-application of these coatings will be required at regular intervals (in the order of 10 to 20 years) depending on the type of coating and exposure conditions until the problem is effectively controlled.

Based on the extent of cracking and other AAR related durability deficiencies, the required treatments may represent a significant ongoing cost to asset managers, given the expectation to significantly increase the service life of concrete bridges and other structures (1, 2, 3, 4).

## 6. VicRoads Specification Section 610 AAR Provisions

The AAR provisions of the 2013 version of VicRoads Section 610 (5) are aimed to further enhance and augment the momentum and knowledge already generated on the subject in the previous two decades including the initial AAR measures.

VicRoads Section 610 requires that a petrographic examination of aggregates be undertaken in accordance with ASTM C295. This is to characterise the aggregate source and to determine the presence of potentially reactive silica minerals.

The specification also requires that the potential alkali silica reactivity of the coarse and fine aggregates is determined using either the accelerated mortar bar or the concrete prism test methods in accordance with VicRoads test methods RC 376.03 and RC 376.04 respectively (6,7), as a minimum on a 3 yearly basis. Regular testing of aggregates for AAR is a very important requirement as the reactivity level of aggregates does change over time as influenced by the location within the bedrock deposits from which the aggregates are quarried. This is also strongly supported by AAR research work which shows several batches of low reactivity gneiss, dacite, hornfels and granite aggregates becoming more reactive than the batches tested some 5 and 10 years ago. Monitoring over time of AAR test results from the same source during concrete mix design assessment work also supports this.

Establishing the alkali reactivity of aggregates is fundamental to the long term management of VicRoads

concrete bridges which must be based on up to date knowledge of the actual reactivity of aggregates that are used in a particular bridge, to assist with any future condition assessments and to avoid limiting the range of options and adverse influence on the cost effectiveness of remedial measures that may have to be undertaken to ensure the 100 year design life requirements.

For the accelerated mortar bar test (RC 376.03), the average expansion should not exceed 0.1% at 21 days in the case of coarse aggregates and 0.15% at 21 days in the case of fine aggregates, when tested with straight Type GP cement. Where potentially reactive aggregates are used, the total alkali content within the concrete mix must not exceed 2.8 kg/m<sup>3</sup> and SCMs must be used to ensure that expansion does not exceed either 0.1% at 21 days for coarse aggregates or 0.15% for fine aggregates.

As an alternative, for a longer term evaluation of aggregates using the less aggressive concrete prism test method (RC 376.04), the average expansion at 12 months is to be less than 0.03%, when tested with straight Type GP cement. Aggregates classed as reactive by the concrete prism test method in a concrete mix design, cannot be used in that particular concrete mix design. Alternative aggregates and/or alternative concrete mix designs must be used subject to compliance with the requirements of the specification.

The specification requires that where blended aggregates are used, the aggregates from different sources must be tested individually, and where fine and coarse aggregates are procured from the same source, only one alkali silica reactivity evaluation per source is required to be undertaken.

Further to the minimum testing requirements above, where it is proposed to use aggregates that have been classed as reactive, the specification requires the use of concrete mixes which contain as a minimum the proportions of supplementary cementitious material as stated in Table 1 (5).

**Table 1 - Minimum proportion of supplementary cementitious material (SCM) combination with Portland cement in the concrete mix to mitigate alkali aggregate reactivity (%) (5).**

Supplementary cementitious material (SCM)	Minimum proportion of SCM in single combination with portland cement in the concrete mix to mitigate alkali aggregate reactivity (%)	Minimum proportion of SCM in double combination with portland cement in the concrete mix to mitigate alkali aggregate reactivity (%)		
		Fly Ash	Slag	Amorphous Silica
Fly Ash	20	-	-	-
Slag	50	-	-	-
Amorphous Silica	8	-	-	-
Fly ash + Slag	-	15	15	-
Fly Ash + Amorphous Silica	-	15	-	5
Slag + Amorphous Silica	-	-	40	5

Where it is proposed to deviate from the minimum blended cement requirements stated in Table 1, the specification explicitly requires that further testing is undertaken to demonstrate compliance with both the maximum mortar bar and concrete prism expansion limits as determined by VicRoads test methods RC 376.03 and RC 376.04.

In addition to the above provisions, reference in Section 610 to the ATIC-SPEC SP43 (Cementitious Materials for Concrete published by ATIC (Australian Technical Infrastructure Committee)), limits the amount of alkali content within the concrete mix in order to prevent or minimise the risk of AAR. These include:

- (a) General purpose cement and Portland cement clinker to AS 3972, plus additional acceptance criteria within ATIC-SPEC SP43, including the total alkali content (Na<sub>2</sub>O equiv) not to exceed 0.6%.
- (b) Fine grade fly ash to AS 3582.1 and the following acceptance criteria. 'Significant oxides', defined as silicon oxide (SiO<sub>2</sub>), aluminium oxide (Al<sub>2</sub>O<sub>3</sub>) and iron oxide (Fe<sub>2</sub>O<sub>3</sub>), to be greater than 70%, plus the total and available alkali (Na<sub>2</sub>O equiv) to meet either of the following criteria:
  - Total alkali content to be less than 3.0%, or
  - For total alkali content greater than 3.0%, but less than 4.5%, the available alkali not to exceed 2.0% for any single determination.

- (c) Slag to AS 3582.2 plus additional acceptance criteria within ATIC-SPEC SP43, including the available alkali content (Na<sub>2</sub>O equiv) not to exceed 0.5%.
- (d) Amorphous silica (silica fume) to AS/NZS 3582.3 plus additional acceptance criteria within ATIC-SPEC SP43, including the available alkali content (Na<sub>2</sub>O equiv) not to exceed 0.5%. For slurried and densified (i.e.: condensed or microsilica) amorphous silica, sampling and testing to be done from the raw silica used to make these products.

Minimum sampling and testing as appropriate for both available alkali content and total alkali content within the cement, fly ash, slag and amorphous silica is prescribed within ATIC-SPEC SP43.

The use of SCMs as cement replacements has proven to be very effective in reducing the negative effects of AAR. SCMs reduce the availability of alkalis for expansive reactions and make the concrete more water tight. Depending on the type of aggregate and magnitude of potential reactivity the minimum effective cement replacement levels are as indicated in Table 1.

It must be emphasised that from ongoing monitoring of VicRoads bridges constructed since the introduction of the AAR provisions into VicRoads Section 610 in 1996, no bridges have been found to exhibit any signs of AAR.

## 7. Influence of Fly Ash in reducing the AAR Effect

Fig. 1 demonstrates the effectiveness of fly ash in reducing AAR induced expansions (4). However, what Fig. 1 also shows is that whereas, 25% fly ash would definitely suppress the AAR expansion, 15% fly ash is unlikely to suppress the AAR reaction into the longer term and especially in-situ, as it appears to be taking off when the test actually ceased at 21 days. As such insufficient amounts of SCMs may show up as being adequate to suppress AAR, whilst in reality could lead to expansion and cracking of concrete structures in-situ. The minimum proportions of supplementary cementitious material as stated in Table 1, aim to address this deficiency.

A research project currently undertaken by the ARRB on behalf of Austroads is studying the appropriateness of both the test methods and current test limits to be able to evaluate the effectiveness of SCMs to effectively suppress AAR. In addition, it is studying, the efficiency of the SCMs concerned and the optimum amount to be used in concrete to suppress AAR. These findings will be reported in a future technical paper. Based on these findings further improvements and refinements may also be undertaken in VicRoads Section 610 with respect to its AAR provisions including the requirements of Table 1.

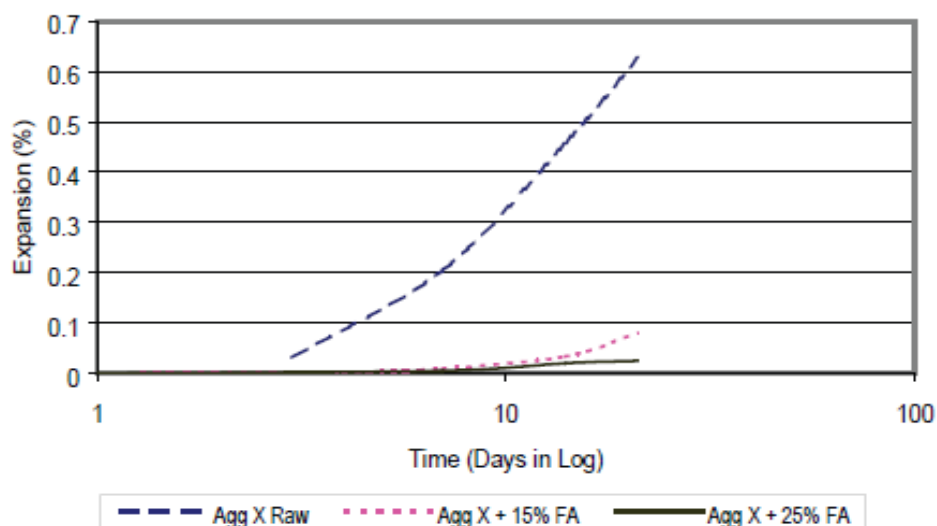


Figure 1. Comparative Mortar Bar Expansion - Results of Aggregate X with and without Fly Ash (4).

## 8. Testing for Potential Alkali Reactivity of Aggregates

The assessment of concrete aggregates for potential alkali reactivity can be undertaken using a number of laboratory test procedures.

- (a) **Petrographic examination:** an optical examination and analysis of the aggregate. This is undertaken to identify the types of minerals present and any suspect mineral phases. This is done using test method ASTM C295. Additional examination can be undertaken using scanning electron microscopy (SEM) and energy-dispersive X-ray (EDX) analysis.
- (b) **VicRoads accelerated mortar bar test method RC 376.03 (6):** Mortar bars are stored in caustic soda solution at 80°C and expansion is monitored for the required period. The test is rapid and provides results in about 3 to 4 weeks. The average expansion should not exceed 0.1% for coarse aggregate and 0.15% for fine aggregate at 21 days.
- (c) **VicRoads concrete prism test method RC 376.04 (7):** This test is considered to be less severe on the test samples and can be used to evaluate the aggregate performance over a 12 month period. The concrete prism test is appropriate when a longer period of time is available. Concrete prisms are produced using the actual concrete aggregates, with a minimum cement and alkali content, and are stored in sealed containers at 100% relative humidity and 38°C. The length of the prisms is measured at prescribed intervals for the 12 month period. Average expansion exceeding 0.03% at one year is considered deleterious.
- (d) **Determination of residual expansion (2):** Demec measuring studs are bonded onto the concrete cores with epoxy. Following the curing of the epoxy resin adhesive cores are soaked overnight in 0.5M NaOH solution at room temperature to allow them to absorb water without significant dilution of alkali in the pore solution of the concrete. The initial length is then measured, after which the cores are wrapped in moistened cloth and stored over water in sealed containers and transferred to a room kept at 38°C. The length change of the cores is measured periodically after equilibration at 23°C for a period of 12 months.

It should be noted that two new Australian standard test methods were published in 2014, namely, AS 1141.60.1 (Accelerated mortar bar test) and AS 1141.60.2 (Prism test). However, these test methods still require validation in practice with actual testing and a reliable performance correlation established with the respective VicRoads test methods, namely, RC 376.3 and RC 376.4, for local aggregates before acceptance by VicRoads.

## **9. 23 Year old Concrete Bridge affected by Alkali Aggregate Reaction (8, 9)**

### **9.1 General**

The investigation, assessment and associated results of this young bridge for AAR, highlight the significance of the AAR provisions in the VicRoads Section 610 introduced and further enhanced between 1996 and 2013. Importantly this bridge which was constructed in 1991 with a concrete comprising reactive aggregates and Type GP cement with a total alkali content exceeding 0.6%, and without the inclusion of any supplementary cementitious materials, was identified with AAR and premature cracking some 10 years later.

The two-span bridge which consists of a PSC box girder and a monolithic pier wall and the two abutments was identified with premature cracking some 10 years after construction. A brief examination undertaken in 2003, of cores taken only from the south east abutment, indicated that alkali aggregate reaction (AAR) was present in the concrete. However, no other concrete investigation was conducted at the time and it is unclear whether the pier wall had exhibited cracking in 2003, although at present cracking is clearly evident in the pier wall.

In 2014 an investigation (9) was commissioned into the concrete cracking at both the pier wall and the southern abutment crosshead. The aim of this investigation was to assess the concrete for AAR and its future expansion potential and to determine the relevant mechanical properties of concrete which may influence the bridge integrity.

### **9.2 Scope of investigation work (9)**

The investigation was limited to visual inspection and the extraction of five concrete cores taken from each of the pier wall and the southern abutment crosshead for the determination of the following properties:



- Visual features of cores
- AAR-related properties:
  - Petrographic examination
  - SEM examination
  - Available alkali content (soluble)
  - Residual expansion
- Compressive strength
- Modulus of elasticity
- Volume of permeable voids (VPV)

### 9.3 *Field Investigation*

#### 9.3.1 *Concrete Cores*

Five cores were drilled from each component; one 95 mm diameter core and four 74 mm diameter cores. Cores were drilled from the southern side of the pier wall adjacent to cracks and cores from the abutment were taken from near the west end of the element, where cracking was seen a few years ago. The abutment crosshead has been coated since that time and the cracks are no longer visible.

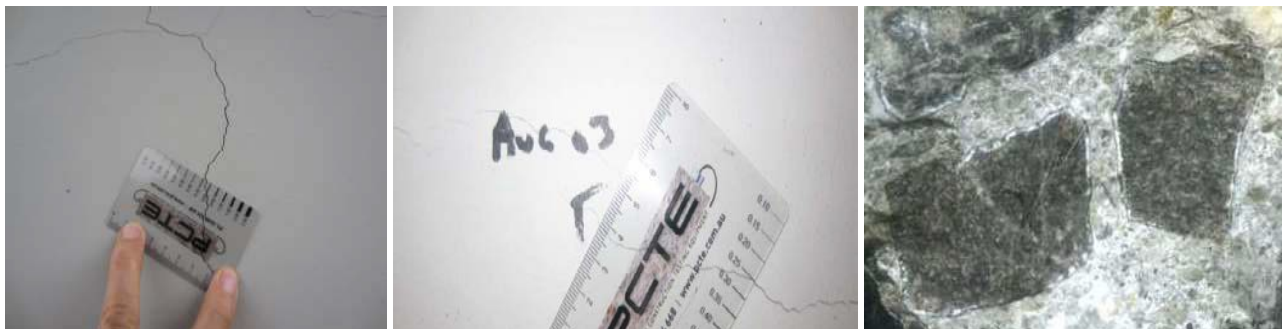
Examination of the cores showed that the coating was elastic and was about 140 µm thick. Additional cores which stopped as they intersected the steel reinforcement showed no corrosion on the exposed bars.

#### 9.3.2 *Cracking in Components*

Examination of the pier wall showed extensive cracking on all four faces. A few cracks were present on the side wall of the box girder and on the parapet near the abutments, where the components were accessible. Cracks in the abutment crossheads were covered over by the 140 µm grey elastic coating.

##### 9.3.2.1 *Cracking on Pier Wall*

Long vertical cracks have developed from top to bottom of the pier wall surfaces, which are visible on enlargement of photographs due to the masking effect of the concrete coating. The crack width was about 0.3 to 0.4 mm for finer cracks and 0.5 to 0.6 mm for the wider cracks (Fig. 2).



**Figure 2. (L) Crack (0.6 mm) pier wall; (C) Crack on box girder wall; (R) typical reaction rim (9)**

##### 9.3.2.2 *Cracking in Box Girder*

Horizontal cracking was observed on the side face of the box girder over the west end of the southern abutment, which was highlighted in previous investigation (Aug' 03). The widest part of the box girder crack was measured at 0.25 mm (Fig. 2).

##### 9.3.2.3 *Cracking in Parapet*

Cracking was noted in the lower part of the parapet, above the abutment crosshead, and in the kerb below the safety barrier. The vertical cracks are of regular space, which may be caused by shrinkage.

### **9.4.3 Visual Examination of cores**

#### *9.4.3.1 Cores from Pier wall*

Concrete Core 1 was noted as dense, with no cracking evident. One aggregate particle at the fracture surface showed signs of AAR gel formation. The coarse aggregate contains a dark variety of 7-20 mm size and white/cream variety of a small particle size. Some of the white aggregate pieces show faint signs of gel impregnation at the cement paste interface. Core 2 and Core 4 were noted to be very similar to Core 1.

Core 5 was found to be similar to Core 1 with dark aggregate particle exhibiting definite signs of AAR and a nearby void filled with AAR product. Some white aggregate particles also exhibit signs of gel impregnation at their boundaries with the cement paste. Weak to moderate AAR may be present in the concrete.

The coarse aggregate in Core 3 is also largely of the darker variety and the white aggregate is largely in the fine fraction. A few of the white particles of 7-10 mm show mild signs of gel formation at their interface with cement paste. Several dark aggregate pieces show stronger signs of gel impregnation at their boundaries with the paste. Some AAR seems to be present in the concrete.

#### *9.4.3.2 Cores from abutment crosshead (Surface coating on the outer face of cores)*

Both types of dark and white aggregate are present in Core 6. Two pieces of steel (16 mm dia.) are cut at depth of 60 mm and the edge of another bar is cut at 80 mm depth. A crack is present at the outer end of the core, which penetrates about 50 mm into concrete. A large pore and some small pores are filled with AAR products. Some aggregate pieces show AAR gel impregnating in the paste around them. Moderate AAR has occurred in the concrete. Internal aggregate cracking is present in some pieces.

The interior fracture surface of Core 7 shows several aggregate particles with AAR rims and a 5 mm diameter void was filled with AAR product. Many aggregate particles exposed at the drilled surface of core exhibited a sweating look indicating AAR gel impregnation in the surrounding mortar. Both the dark and cream/brown aggregates have reacted. Moderate AAR is present in the concrete.

The features of Core 8 are similar to Core 7, but there is also a crack at the outer end of the core (beneath the surface coating) which penetrates about 80 mm on one side and 60mm on the opposite side. Finer cracks also extend to 80 mm depth. Some aggregate pieces show internal cracking. Another Core 9 has features similar to Cores 7 and 8 but the AAR signs are milder. There is no cracking at the outer end of the core.

Core 10 has features are very similar to those in Core 9. Cores 9 and 10 are from the middle of the crosshead which appears to have weak AAR.

Overall, the visual examination of cores indicated that moderate AAR is present in the concrete. This is illustrated by the typical, white reaction rims around some aggregate particles (Fig.2).

### **9.4.4 Petrographic examination of cores**

#### *9.4.4.1 Pier wall*

The coarse aggregate in Core 3 is a mixture of metamorphic rock types of schist and gneissic rock types and all the particles exhibit strong signs of deformation and orientation, as indicated by elongated quartz grains and bands of micaceous minerals in parallel orientation. Some particles comprise a fine matrix of microcrystalline quartz and highly birefringent amphibole type minerals. Another variety includes a similar mineral assemblage, but with larger quartz crystals and the quartz also exhibits elongation. Some other particles resemble hornfels rock type. Particles of quartzite and quartz gravel with highly deformed quartz crystals are also present in which quartz shows patchy extinction and large undulatory extinction angles and sutured boundaries. All of these rock types are considered to be susceptible to AAR.

The fine aggregate fraction is a mixture of monomineralic quartz and feldspar crystals as well as finer fragments of the coarse aggregate particles. Some of the single quartz crystals also show moderate undulatory extinction angles. A portion of the fine fraction may be susceptible to AAR.

The cementitious matrix shows a considerable number of microcracks at the aggregate periphery, extending into the cement paste. AAR gel is definitely identified in some microcracks around the aggregate and in the microcracks within the paste. This concrete has clearly undergone AAR.

#### 9.4.4.2 Abutment crosshead

The coarse and fine aggregates in Core 6 are similar to those described for Core 3. In addition, one dark brown and one black particle with cryptocrystalline matrix were present, comprising very fine quartz and probably micaceous minerals. These particles could be of rhyolitic nature. Carbon may be present in the black particle. Similarly to the previous core, the coarse aggregate and part of the fine aggregate are considered to be prone to AAR. The cementitious matrix exhibits considerable microcracking and AAR gel is clearly identified in the concrete, even to a greater extent than in Core 3 from the pier wall.

The petrographic examination clearly shows that AAR is present in the pier wall and abutment crossheads concrete.

#### 9.4.5 Scanning electron microscopy (SEM) and energy-dispersive X-ray (EDX) analysis

The SEM/ EDX examination of both the pier wall and abutment crosshead cores provided strong evidence of the presence of AAR products in the concrete, both in and around aggregate particles, and in the microcracks in the cement paste. Some products were highly enriched with alkali and some contained aluminium, which indicated that in addition to the silica minerals, feldspar minerals may also have been involved in the reaction. Overall Core 7 from the abutment crosshead appeared to contain more extensive reaction products than the cores from the pier wall.

#### 9.4.6 Compressive Strength

The average value of compressive strength was 41 MPa, and there is no difference in the level of strength for the pier wall and abutment crosshead (Table 2). The strength indicates that the concrete may be of VR400/40 strength grade, although it is just on the borderline of the required 40 MPa for characteristic strength. These values of compressive strength may overestimate the actual strength of the element as cores are drilled in sound portions of concrete away from cracks, whereas the element itself would contain a considerable extent of cracking.

**Table 2 - Compressive Strength (9)**

ID	Component	Strength (MPa)	Mean ± 95% confidence range
Core 1	Pier wall	43.1	41.2 ± 4.0 MPa
Core 4	Pier wall	37.7	
Core 7	Abutment Crosshead	42.9	
Core 10	Abutment Crosshead	41.3	

#### 9.4.7 Volume of Permeable Voids (VPV)

VPV is a measure of porosity and permeability of concrete and influences several durability properties of concrete. VicRoads Section 610 states that cores drilled from a concrete of VR400/40 grade must not exceed a VPV value of 16%.

The VPV results for the cores taken from the pier and abutment crosshead were 15.4% and 15.6%, respectively. These values can be considered acceptable with respect to VicRoads requirements.



#### 9.4.8 Modulus of Elasticity

Cores 5 and 9 were subjected to modulus of elasticity testing, in accordance with AS 1012.17, *Methods of Testing Concrete. Method 17: Determination of the Static Chord Modulus of Elasticity and Poisson's Ratio of Concrete Specimens*.

Testing was conducted in accordance with AS 1012.17-1997 Appendix A, where compressive strain measurements were recorded by two bonded 120-Ohm strain gauges attached at 180° along the central 60mm of the cylinder. The cylinders were installed between the platens of a calibrated universal testing machine and load was applied until a stress of about 40% of the nominal compressive strength was achieved. At this point the load was released before repeating the loading cycle two more times. A fourth load cycle was then applied until a peak compressive stress was achieved. All testing was conducted in an enclosed environment at an ambient temperature of about 25°C and 50% humidity.

When tested, core 9 (abutment crosshead) achieved the lowest static chord modulus value (19 GPa). The static chord modulus value for Core 5 was of the order of 27 GPa (reduction of about 20% compared to design requirements for this type of concrete). The lowest modulus of 19 GPa (reduction of about 45%) for the abutment crosshead in young bridge is attributed to the more extensive occurrence of AAR in this concrete.

#### 9.4.9 Water soluble Alkali Content

The water soluble alkali content in the cores from the pier wall and the abutment crosshead was 3.78 kg/m<sup>3</sup> and 3.06 kg/m<sup>3</sup> (> than permitted maximum of 2.8 kg/m<sup>3</sup>), respectively, as shown in Table 3. Assuming that the concrete was of VR400/40 grade, the water soluble alkali as a percentage of cement mass would be 0.94% and 0.76% in the concrete of the pier wall and abutment crosshead, respectively. These values are higher than the 0.6% permitted, which may indicate that a local GP cement which is no longer available was used in the concrete, which had alkali contents in the range of 0.9 – 1.1 %. If the cement alkali content was actually lower than in the local cement, then the additional alkali may have been contributed from the Aggregate phase.

It is generally accepted that an alkali content of greater than 2.8 kg/m<sup>3</sup> is required to sustain AAR in concrete. Therefore, it can be expected that AAR will continue in the concrete, particularly if the aggregate phase releases alkali into the concrete. Petrographic features of the aggregate suggest that this may be possible.

**Table 3 - Water Extractable Alkali Content (9)**

ID and Component	Alkali per weight of concrete (%)				Alkali per volume of concrete (kg/m <sup>3</sup> )			
	CaO	Na <sub>2</sub> O	K <sub>2</sub> O	Na <sub>2</sub> O eq.	CaO	Na <sub>2</sub> O	K <sub>2</sub> O	Na <sub>2</sub> O eq.
Core 3, Pier	0.2494	0.1121	0.0859	0.1686	5.59	2.51	1.92	3.78
Core 8, Abutment Crosshead	0.2688	0.0899	0.0708	0.1365	6.02	2.01	1.59	3.06

#### 9.4.10 Residual Expansion

Cores 3 (pier wall) and 6 (abutment crosshead) which had a diameter of 95 mm were fitted with Demec studs and exposed to conditions of 100% RH, 38°C to enhance AAR expansion, which would reflect the residual expansion potential of the concrete. The expansion of the cores is being measured by using Demec gauge. The residual expansion potential is determined by the value of expansion measured at the age of one year, when the expansion usually flattens out.

The expansion results are presented in Figure 3 and at 365 days of exposure the expansion of both cores is relatively large and far exceeds the allowable limit of 0.03%. Core 6 from the abutment crosshead exhibits significantly higher expansion at the age of one year. The trend for both cores indicates that further reaction and cracking is likely in these elements.

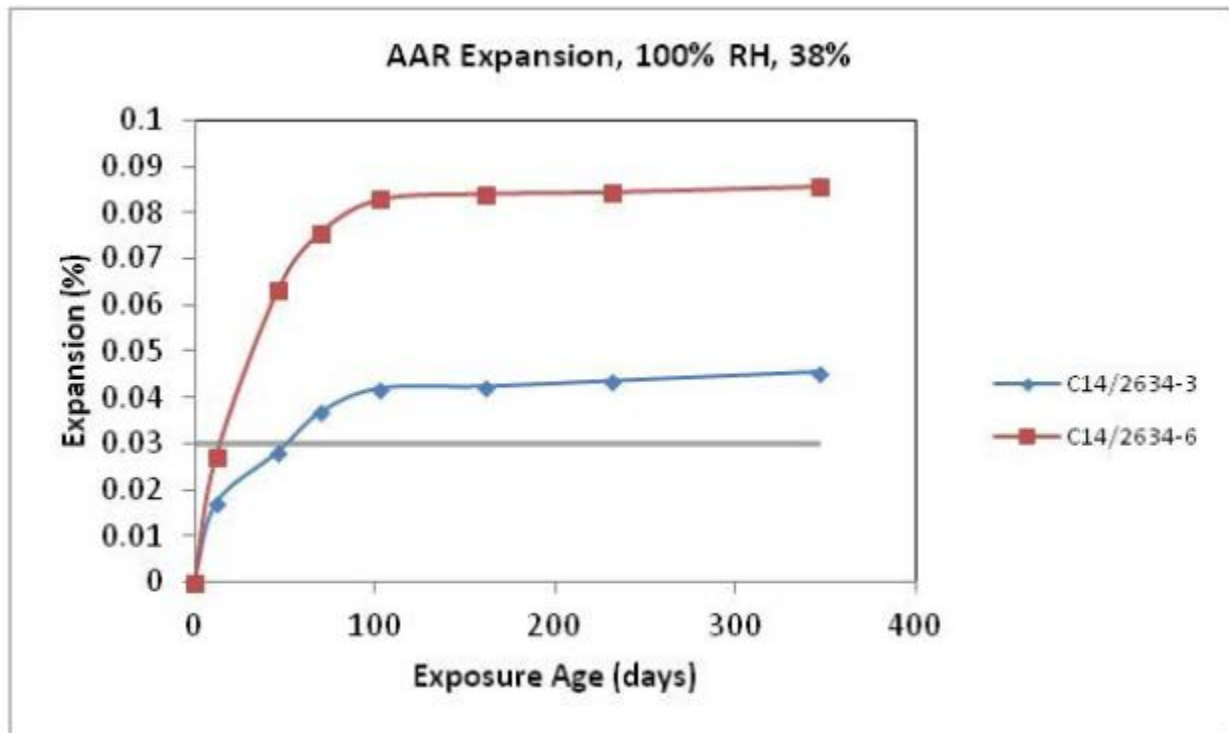


Figure 3. Residual expansion of concrete. Core 3 from pier wall. Core 6 from abutment crosshead(9)

## 10. Discussion

The 23 year old post-tensioned box girder bridge referenced in this paper (constructed in 1991) situated in a moderate environment (exposure classification B1), was constructed with a concrete comprising reactive aggregates, Type GP cement with a total alkali content exceeding 0.6%, and without the inclusion of any supplementary cementitious materials. Within 10 years in service it was identified as suffering from premature cracking. A brief examination undertaken in 2003, of cores taken only from the south east abutment, indicated that alkali-aggregate reaction (AAR) was present in the concrete. A more detailed AAR investigation undertaken in 2014 established that both the pier wall and the abutment crosshead of the bridge are suffering from AAR. Both elements have developed considerable amount of cracking as a result of AAR. Crack widths in the pier wall are in the range of about 0.4 mm to 0.6 mm. The cracks previously reported for the abutment crosshead have been masked by the newly applied, grey surface coating. In addition both elements have exhibited high residual expansion potentials as judged by measurements for up to 365 days of exposure. This trend is expected to continue and indicates that the concrete would develop further expansion and cracking. This is further supported with the water extractable alkali content in the concrete of 3.8 and 3.0 kg/m<sup>3</sup> (> than allowable of 2.8 kg/m<sup>3</sup>) in the pier wall and abutment concrete, respectively, which is adequate for AAR to continue.

The elastic modulus of the concrete in the pier wall at this stage was determined at around 27 GPa (about 20% lower than design requirements for this type of concrete) and that in the abutment crosshead 19GPa (about 45% lower than design requirements for this type of concrete), which suggest that the latter element was more seriously damaged by AAR. This is in agreement with other microstructural observations.

It is important to emphasise that given the high alkali content within the concrete to sustain further reaction and expansion and the confirmed high residual expansion potential into the future, further cracking and reductions in strength and modulus of elasticity and possibly flexural and bond strengths will occur.

Based on these results an effective coating should be maintained to reduce the rate of AAR induced expansion. It was also considered that suitable strengthening and/or durability measures may be required for the bridge in the longer term to reduce the rate of expansion. The box girder of the bridge was not tested. However, given its importance it is considered that the bridge box girder also required testing given the likelihood that it may be made from similar concrete. In addition, it was considered that other bridges in the area that used similar concrete would also need to be assessed for AAR induced deterioration.

The unsatisfactory results of this 23 year old freeway overpass bridge, the significant AAR investigation costs over the past 10 years and the expected high repair costs highlight the importance of the AAR provisions, the concrete mix design (aggregate and other ingredient properties change over time) requirements and the overall integrated durability provisions in Section 610 progressively introduced and further enhanced since 1996. The AAR provisions in Section 610 which would have prevented the AAR damage in the 23 year old bridge presented in this paper can be summarised as follows:

- Petrographic examination of aggregates.
- Alkali silica reactivity testing of both the coarse and fine aggregates on a 3 yearly basis.
  - AMBT testing has shown that low reactivity aggregates were found to be significantly more reactive than the same aggregates tested over a 10 year period.
- AAR expansion limits for both fine and coarse aggregate.
- Provision for both accelerated mortar bar test method (RC 376.03) and concrete prism test method (RC 376.04).
- Concrete mixes to contain minimum proportions of supplementary cementitious material to mitigate AAR.
- Limitations on alkali content within the cement and the various cementitious materials.
- Alkali content in the concrete mix not to exceed  $2.8 \text{ kg/m}^3$  ( $\text{Na}_2\text{O}$  equiv).

Finally, it should be noted that in contrast to the condition of the 23 year old freeway overpass bridge (which showed AAR affected cracking some 10 years after construction), ongoing monitoring of a number of VicRoads bridges constructed since the mid 1990s in various in-service exposure conditions have not exhibited any signs of AAR related damage, demonstrating so far the effectiveness of the AAR preventative measures included in VicRoads Section 610. It is considered that these preventative measures will ensure the long term durability performance of VicRoads bridges and minimise unnecessary and costly maintenance needs.

## 11. Acknowledgements

The authors wish to thank VicRoads for permission to publish this paper. The views expressed in this paper are those of the authors and do not necessarily reflect the views of VicRoads. The testing as referenced in this paper was undertaken by Dr Ahmad Shayan and Dr Aimin Xu from the ARRB Group Pty Ltd (9) to a specifically designed VicRoads brief (8).

## 12. References

1. Andrews-Phaedonos, F., "TB 51, Guide to the assessment, maintenance and rehabilitation of concrete bridges, TB51", VicRoads, 2010.
2. Shayan, A & Andrews-Phaedonos, F., "Investigation of the causes of cracking in some VicRoads bridges in East Gippsland, and estimation of their repair costs " 22<sup>nd</sup> Biennial Conference, Concrete Institute of Australia, October, Melbourne, Australia, 2005.
3. Shayan, A, Xu, A & Andrews-Phaedonos, F., "Development of a Performance Measure for Durability of Concrete Bridges" 21<sup>st</sup> Biennial Conference, Concrete Institute of Australia, October, Brisbane, Australia, 2003.
4. Andrews-Phaedonos, F., "TN 30, Alkali Silica Reaction in Concrete", VicRoads, 2008.
5. VicRoads Standard Specification, "Section 610 – Structural Concrete", 2013.
6. VicRoads Test method RC 376.0, Potential Alkali-Silica Reactivity (Accelerated Mortar Bar Method), September 2014.
7. VicRoads Method RC376.04, Alkali Aggregate Reactivity using the Concrete Prism Test, 2013.
8. Andrews-Phaedonos, F, Consultant Brief, "Investigation of concrete cracking at 23 year old Bridge over Freeway", VicRoads, 2013.
9. Shayan, A and Xu, A, ARRB Group, "Investigation of concrete cracking at 23 year old Bridge over Freeway", Contract Report No. 008490-1, 20 May 2015.

# Long-term Experiments of Composite Slabs Using Recycled Coarse Aggregate

Qinghe Wang<sup>1</sup>, Gianluca Ranzi<sup>2</sup>, Yue Geng<sup>3</sup>, Yuyin Wang<sup>4</sup>

<sup>1</sup> Ph.D student, School of Civil Engineering, The University of Sydney, Australia; Key Lab of Structures Dynamic Behaviour and Control of Ministry of Education, Heilongjiang, Harbin Institute of Technology, Harbin, China

<sup>2</sup> Associate Professor, School of Civil Engineering, The University of Sydney, Australia

<sup>3</sup> Lecturer, Key Lab of Structures Dynamic Behaviour and Control of Ministry of Education, Heilongjiang, Harbin Institute of Technology, Harbin, China

<sup>4</sup> Professor, Key Lab of Structures Dynamic Behaviour and Control of Ministry of Education, Heilongjiang, Harbin Institute of Technology, Harbin, China

**Abstract:** This paper presents an experimental study investigating the long-term behaviour of seven floor slab samples prepared with recycled coarse aggregate (RCA). In particular, three specimens consisted of slabs cast on steel-bars truss decks, while the remaining four samples were composite slabs poured on profiled steel sheeting. The slab specimens were tested in a simply-supported static configuration and monitored for a period of over five months. Separate concrete samples were prepared and tested to measure the occurrence of the non-uniform shrinkage profile through the slab thickness (developed due to the inability of the slabs to dry from their underside). Experimental results showed that the use of RCA produced increases in the measured long-term deflections when compared to the natural aggregate concrete (NAC) samples. It was also noted that time-dependent deflections were influenced by the shrinkage gradient and that the latter increased with RCA contents. The experimental measurements collected in this study are expected to contribute towards the development of adequate design guidelines for slabs prepared with RCA by providing benchmark data for the validation of numerical and design models.

**Keywords:** Recycled coarse aggregate, Recycled aggregate concrete, Floor slabs, Long-term deformation, Non-uniform shrinkage, Creep, Steel deck.

## 1. Introduction

Crushing waste concrete as aggregates for new concrete (recycled aggregate concrete) production represents an alternative to reduce the carbon footprint of natural aggregate concrete (NAC) [1-2]. Recycled aggregate concrete (RAC) has been commonly used to date for the casting of non-structural members, such as pavement, roadwork foundations, piles and mass concrete pours [3-6], because of its lower compressive strength and elastic modulus when compared to NAC [7-9]. Despite this, RAC has the potential to be applied over a broad range of structural applications and this has already been demonstrated from experimental work, for example, for RAC beams and columns, e.g. [10-17]. Full-scale tests were conducted by Sato et al. [10] on nine simply-supported beams to quantify the differences of flexural behaviour between RAC and NAC beams. They reported that the differences in the flexural capacities of beams made of NCA and RCA with the same reinforcement ratios were negligible. Etxeberria et al. [11] investigated the influence of RCA contents on the shear behaviour of twelve RAC beams with and without transverse reinforcement, and highlighted that beam specimens with transverse reinforcement and concrete with 50% and 100% RCA achieved approximately the ultimate shear load of NAC samples. Choi et al. [15] reported that the axial behaviour exhibited in RAC columns was comparable to that found in conventional reinforced concrete columns, and RAC could be effectively used as a structural material. A number of international design specifications regulate the use of RAC in reinforced concrete structures according to the quality of recycled coarse aggregate (RCA) [18-22]. In China, for example, the Type-I RCA with similar physical properties to NCA is permitted to be used in any reinforced concrete structure by JCJ/T 240-2011 [22], while the low-quality Type-III RCA is conservatively recommended for low-strength concrete applications (<25 MPa) which do not undergo freezing and thawing cycles. Due to the support of experimental research and international design specifications, increasing applications of RAC in reinforced concrete structures can be found worldwide, e.g. [23]. In the case of composite floor systems, recent research highlighted the ability for RAC composite slabs to obtain similar flexural capacity and longitudinal shear behaviour to NCA samples [24-26].

In this context, this paper intends to investigate how the use of RCA influences the long-term behaviour of composite steel-concrete slabs. Particular attention is devoted to the development of the non-uniform shrinkage profile which occurs due to the inability of the slabs to dry from their underside [27, 28]. As part of this study, seven full-scale slabs were prepared and tested. These included three specimens cast on steel-bars truss decks and four samples poured on profiled steel sheeting considering different levels of RCA replacement and slab thicknesses. Companion samples were subjected to shrinkage effects only and to the combined effects of external loads and shrinkage. Separate concrete samples were prepared and monitored to measure the development of non-uniform shrinkage through the slab depth. It is envisaged that the experimental measurements collected as part of this project will provide useful benchmark data for the validation of numerical and design models for RAC composite slabs.

## 2. Experimental program

### 2.1 Test overview

The experimental program involved the testing of seven full-scale slab samples with different RCA contents and slab depths for a period of five months. Two different decking profiles were considered and these consisted of steel-bars truss decks and profiled steel sheeting. Corresponding small-scale concrete samples were prepared to evaluate the development of non-uniform shrinkage through the thickness of the slab. Standard tests were carried out to determine the material properties of the components forming the cross-section. Details of the tests and measurements are reported in the following.

### 2.2 Aggregate properties

ASTM I Portland cement (with specific density of 3.17) was used as binder for the concrete prepared for this study. River sand (0-5 mm) with fineness modulus of 2.58 and limestone (5-25 mm) were used as natural aggregates. The RCA was sourced from a real demolition project of a 19-year-old building whose concrete properties consisted of a water-to-cement ratio of 0.45 and cubic compressive strength of about 30 MPa.

The demolished concrete underwent a two-stage crushing process. The first crushing treatment was carried out on the demolition site with clamp mechanical excavators and jackhammers, while the second crushing process was held in the laboratory with jackhammers and jaw crusher, during which the size of the waste concrete was reduced to less than 25 mm. The RCA was then sieved with square mesh to achieve a proper size fraction in accordance with the European Code UNE-EN 933-1 [29]. For comparison purposes, similar coarse aggregate gradations were used for the preparation of the RCA and NCA specimens and these are outlined in Table 1 (based on which the adopted RCA was graded as Type-I RCA and complied with the requirements of Chinese code JCJ/T 240-2011 [22]). Material properties measured during the experiments, e.g. density, water absorption, residual mortar content and index of crushing, are also reported in Table 1.

**Table 1. Basic properties of aggregates**

Properties	Size of test sieve (mm)	Cumulative passing by weight (%)		
		NCA	RCA	NFA <sup>a</sup>
Sieve analysis	26.5	100.0	100.0	—
	19.0	66.7	66.7	—
	16.0	50.0	50.0	—
	9.0	16.7	16.7	—
	4.75	0.3	0.4	—
Density (kg/m <sup>3</sup> )	Oven-dried	2777	2588	2623
	Saturated surface-dry	2792	2650	2714
Water absorption (%)		0.55	2.40	3.40
Residual mortar content (%)		—	40.2	—
Texture of rocky matrix		Limestone		River sand
Index of crushing (%)		4.3	15.2	—

<sup>a</sup> NFA—Natural Fine Aggregate.

### 2.3 Recycled aggregate concrete and steel properties

Three concrete mixtures were prepared in the laboratory and their details are provided in Table 2. A superplasticizer with specific density of 1.2 g/cm<sup>3</sup> was used to achieve a sufficient workability for the fresh concrete mix (Table 2). These were used for the preparation of three concrete mixes based on three RCA amounts, i.e. 0%, 50% and 100% of the coarse aggregate by weight, respectively. The effective water-to-cement ratio, the sand ratio and the cement content were kept constant at 0.45, 0.36 and 400 kg/m<sup>3</sup>, respectively. The effective water-to-cement ratio and workability of the RAC were controlled by pre-soaking the RCA in water for 24 hours and by draining it for about 1 hour before batching. Slump tests were carried out and slump values ranged between 140 and 190 mm. All samples, including full-scale slab samples, small-scale slab samples, and concrete samples for material tests, were wet cured for seven days from casting and then permitted to dry in air. Cubic compressive strength (150×150×150 mm<sup>3</sup>), splitting tensile strength (150×150×150 mm<sup>3</sup>) and elastic modulus (150×150×300 mm<sup>3</sup>) of all hardened concrete mixtures at 7, 28, and 90 days were measured, as summarised in Table 3.

**Table 2. Concrete mixture design and fresh concrete properties**

Mix designation	Replacement ratios (%)	Mix proportions (kg/m <sup>3</sup> )					Slump (mm)	
		Water	Cement	Sands	Coarse aggregates			SP <sup>a</sup>
					NCA	RCA		
NAC-0%	0	180	400	680	1208	0	4.0	170±20
RAC-50%	50	180	400	650	578	578	4.0	160±20
RAC-100%	100	180	400	620	0	1102	4.0	170±20

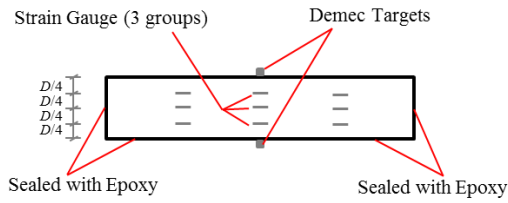
<sup>a</sup> SP—Superplasticizer.

**Table 3. Mechanical properties of hardened concrete**

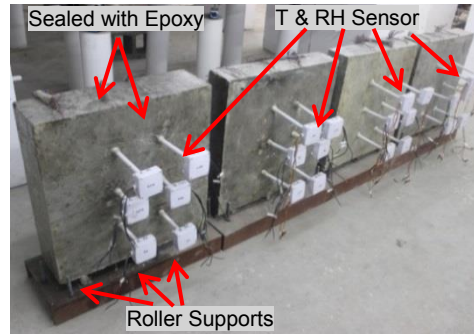
Mix designation	Compressive strength (MPa)			Splitting tensile strength (MPa)			Elastic modulus (GPa)		
	7 days	28 days	90 days	7 days	28 days	90 days	7 days	28 days	90 days
NAC-0%	33.2	40.9	45.9	4.3	4.9	4.6	31.8	35.5	33.8
RAC-50%	28.0	39.9	43.4	3.8	4.8	4.7	28.7	29.1	28.8
RAC-100%	27.3	36.3	42.1	3.1	3.4	3.6	25.1	26.3	26.3

As expected, when the RCA replacement levels increased from 0% to 100%, a decrease in compressive strength was observed. The corresponding reductions in the 28-day compressive strength were 2.4% and 11.2% for concrete made with 50% and 100% of RCA, respectively, when compared to the NAC measurements. Similar trends were noted for the splitting tensile strength, in which case concrete with 50% of RCA reduced by 2.1% the splitting tensile strength. This variation significantly decreased to 30.6% when using the 100% RCA replacement ratio. Only 74.1% of elastic modulus was achieved in RAC with 100% RCA replacement ratio compared to that of NAC, while 82.0% of elastic modulus was observed in RAC with 50% RCA replacement ratio.

The experimental arrangements used for the evaluation of the shrinkage properties of the concrete are illustrated in Figure 1. DEMEC gauges were used to measure the long-term shrinkage on both surfaces of the prisms (100×100×400 mm<sup>3</sup>) and of the small-scale shrinkage samples (600 mm×600 mm× 120 mm or 180 mm), while deformations taking place within the slab thickness of the small-scale shrinkage samples were monitored with embedded strain gauges, as shown in Figures 1 (a). The timber formwork was removed at 24 hours after casting, after which both four side edges and the bottom surface of the small-scale shrinkage samples were covered with epoxy to reflect the sealing condition provided by the steel deck without inducing its restricting action. Small-scale shrinkage samples were located on three roller supports vertically to eliminate any restraint due to friction between the specimen and the laboratory floor. Details of the small-scale shrinkage samples are listed in Table 4. The creep tests were conducted on concrete specimens (100×100×400 mm<sup>3</sup>) subjected to a sustained load ( $\approx 0.2 f_{cm}A$ ) applied at 28 days from casting. Figure 2 shows the temperature and relative humidity data that were recorded regularly for the duration of the experiments. The mean temperature and relative humidity measured during the tests were 19.0°C and 55.1%, respectively.



(a) Instrumentation for shrinkage

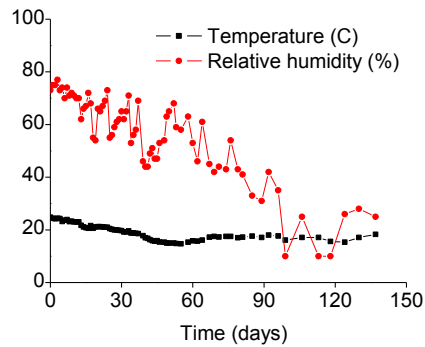


(b) Overview of the shrinkage test arrangement

**Figure 1. Instrumentation arrangement and long-term setup for small-scale shrinkage samples**

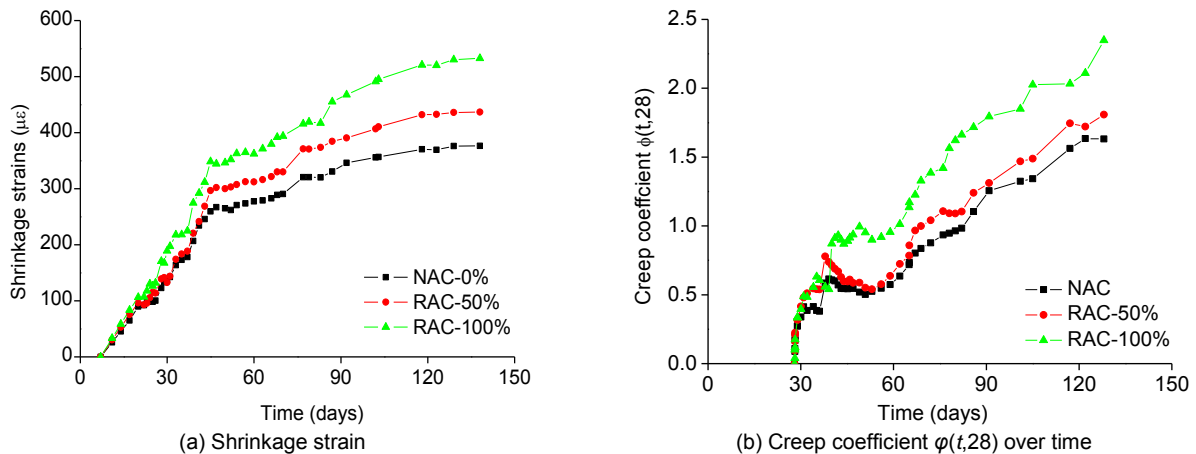
**Table 4. Detail of non-uniform shrinkage samples**

Shrinkage sample ID	Replacement ratio	Dimensions of samples (mm)	Exposed condition
SS-120-0%	0%	600×600×120	Only top surface exposed to the chamber condition, the other five sides sealed with epoxy
SS-120-50%	50%		
SS-120-100%	100%		
SS-180-100%	100%	600×600×180	



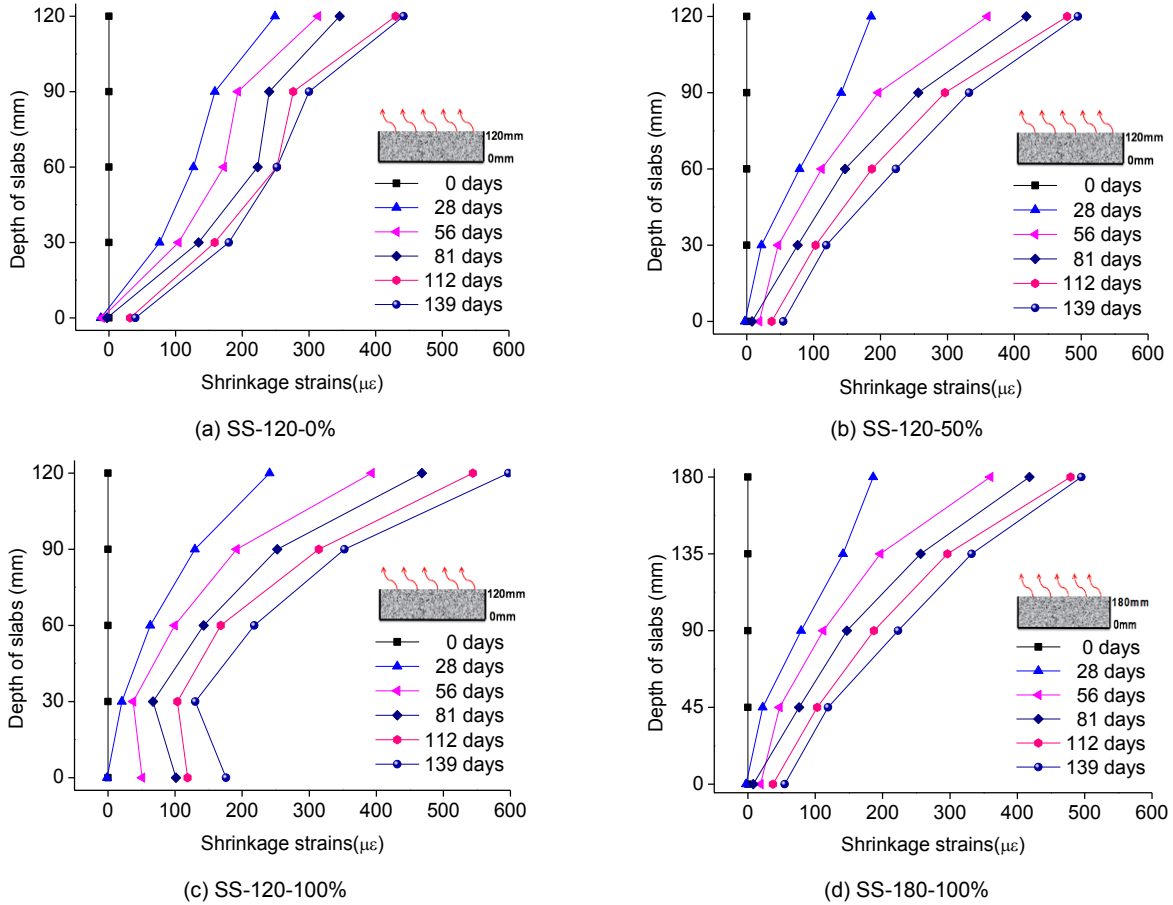
**Figure 2. Environmental conditions measured during the long-term tests**

Shrinkage deformation and creep coefficient measurements obtained from the 100×100×400 mm<sup>3</sup> samples are reported in Figures 3 (a) and (b). Significant increases of 41.5% and 52.9% for the shrinkage strains and the creep coefficients were observed for the concrete prepared with 100% RCA when compared to the measurements collected for NAC. Smaller increases (i.e. 16.0% and 12.2%) were recorded for concrete made with the 50% RCA replacement ratio.



**Figure 3. Long-term properties of hardened concrete**

The total deformations measured in the small-scale shrinkage samples are assumed in the following to reflect the shrinkage profile. As the purpose of this study is to develop adequate design guidelines, the simplifying assumption of using a linear distribution for the shrinkage profile is regarded as acceptable, even if more complex distributions develop in reality [30]. The shrinkage slab samples were sealed on one slab face (and on the four edges) to reflect the real condition in which the composite slab cannot dry from its underside due to the presence of the profiled sheeting. Typical strain profiles measured through the depth of the small-scale shrinkage samples at different instants in time are illustrated in Figure 4.



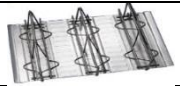

**Figure 4. Total deformations through the slab thickness of slab samples**

The strains measured on the top fibres increased with increasing percentages of RCA. In particular, maximum shrinkage strains on the top surfaces increased to  $495 \times 10^{-6}$  and  $597 \times 10^{-6}$ , respectively, when 50% and 100% of RCA were adopted, which were 12.0% and 35.1% larger than the NAC measurement (equal to  $442 \times 10^{-6}$ ). This was attributed to the residual mortar presented in RCA, which increased the porosity and reduced the volume of coarse aggregate in RAC. The non-uniform shrinkage gradient increased with RCA contents. At the age of 139 days, the shrinkage gradients were 2.91, 3.94, and  $5.19 \times 10^{-6} \text{mm}^{-1}$  for specimens SS-120-0%, SS-120-50% and SS-120-100%, respectively. A comparison of the shrinkage distributions in SS-120-100% and SS-180-100% showed that only 62.0% of the shrinkage gradient for SS-180-100% was observed compared to that of SS-120-100% after five months.

The section properties of steel-bars truss decks and profiled steel sheeting used in this study are provided in Table 5. The mechanical properties of the steel deck and reinforcement were obtained from standard tensile tests carried out in accordance with [31] and are reported in Table 6. Yield strength and elastic modulus of the profiled steel sheeting were 440.3 MPa and 199.7 GPa, respectively, while the corresponding measurements observed for the steel-bars truss decks were 414.3 MPa and 206.3 GPa, respectively. The yield strength of the 10 mm and 8 mm diameter reinforcing bars were 503.0 MPa and 510.0 MPa, respectively, with elastic modulus of 189.0 GPa and 166.3 GPa, respectively.



**Table 5. Geometric properties of steel-bars truss decks and profiled steel sheeting**

Deck profile ID	Depth $d$ (mm)	Width $b$ (mm)	Thickness $t$ (mm)	Dimension of reinforcement (mm)	$A$ ( $\times\text{mm}^2$ )	$I$ ( $\times 10^5\text{mm}^4$ )	Decking profile
Steel-bars truss decks	80	590	0.5	10/8/4.5 <sup>a</sup>	830	7.99	
Profiled sheeting	65	510	1.2	—	1200	7.75	

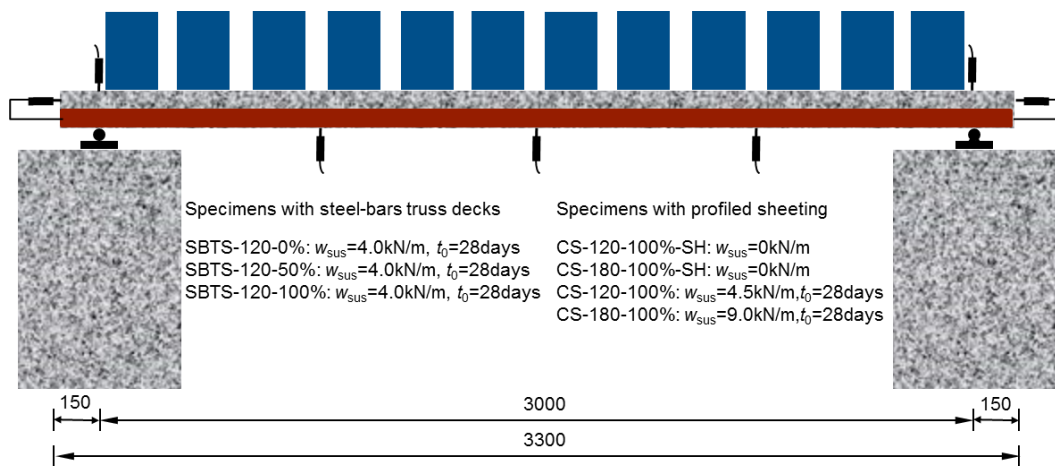
<sup>a</sup> 10/8/4.5—The diameters of reinforcing bars for compressive reinforcement, tensile reinforcement and stirrups.

**Table 6. Mechanical properties of reinforcement bars and steel deck**

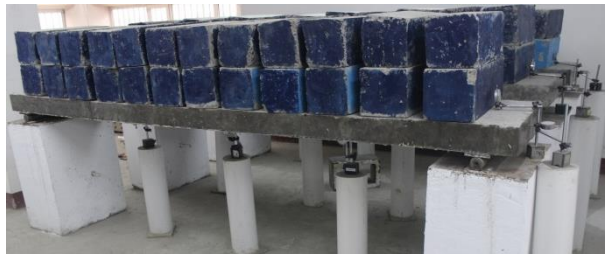
Diameter or Thickness (mm)	Elastic modulus (GPa)	Yield strength (MPa)	Ultimate strength (MPa)	Samples from
10	189.0	503.0	648.0	Steel-bars truss decks
8	166.3	510.0	661.3	
0.5	206.3	414.3	469.3	
1.2	199.7	440.3	517.0	Profiled steel sheeting

**2.4 Description of long-term experiments of the full-scale specimens**

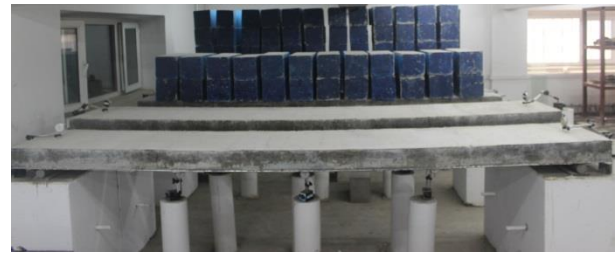
Three steel-bars truss slabs and four composite samples with profiled steel sheeting were prepared and tested as shown in Figure 5. All specimens were maintained propped during casting, after which the props were removed and the specimens were placed in a simply-supported static configuration. In this manner, the self-weight of the slabs was supported by the steel deck. Based on this, it was assumed that no creep developed in the concrete due to the slab self-weight. This condition was used to monitor the development of shrinkage only in two of the samples prepared which were kept unloaded for the entire duration of the long-term tests. The timber formwork was removed at 24 hours after casting, and then four side edges of the full-scale specimens were sealed with epoxy to prevent drying to take place from these locations as it would occur in a real slab due to its continuity.



(a) Instrumentation arrangement for long-term full-scale specimens



(b) Specimens with steel-bars truss decks


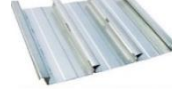


(c) Specimens with profiled steel sheeting

**Figure 5. Long-term test setup for full-scale specimens**

All slab samples were simply-supported with a total length of 3.3 m and a distance between roller supports of 3.0 m. The steel-bars truss samples had a thickness of 120 mm and were prepared with 0%, 50% and 100% RCA replacement ratios (Table 7). They were subjected to a sustained load of 4 kN/m applied at 28 days from casting. These samples have been referred to as SBTS-120-0%, SBTS-120-50% and SBTS-120-100%, respectively. The four composite slabs were poured with 100% RCA replacement ratio (Table 7). Two samples had a slab thickness of 120 mm and two specimens were 180 mm thick. One sample for each thickness was subjected to a sustained load at 28 days from casting. The two loaded samples were referred to as CS-120-100% and CS-180-100%, and were subjected to sustained loads of 4.5 kN/m and 9.0 kN/m, respectively. The remaining two specimens, referred to as CS-120-100%-SH and CS-180-100%-SH, were only exposed to shrinkage effects. Details of the full-scale specimens are provided in Table 7. The time-dependent deflections at mid-span, at quarter-span and at the supports of the slab samples were measured with dial gauges for the entire duration of the long-term tests.

**Table 7. Construction details of the full-scale slab samples**

Specimens	Replacement ratio $r$ (%)	Depth $d$ (mm)	Width $b$ (mm)	Length $L$ (mm)	$t_0$ (days)	Loading $w_{\text{SUS}}$ (kN/m)	Decking profile
SBTS-120-0%	0	120	590	3300	28	4.0	
SBTS-120-50%	50						
SBTS-120-100%	100						
CS-120-100%-SH	100	120	510	3300	—	—	
CS-120-100%		120			28	4.5	
CS-180-100%-SH		180			—	—	
CS-180-100%		180			28	9.0	

### 3. Experimental results

#### 3.1 Long-term experimental results for the steel-bars truss slab samples

The steel-bars truss samples exhibited greater mid-span deflections for increasing levels of RCA, as reported in Figure 6 (a). At the age of 139 days, the mid-span deflection was 8.78 mm ( $\approx L/340$ ) for SBTS-120-100%, which was about 14.5% and 35.5% larger than the measurements in the specimens prepared with 50% and 0% RCA replacement ratios, respectively. This was mainly caused by the shrinkage gradient and by the decrease of elastic modulus produced by the use of RCA, as the instantaneous mid-span deflections at 28 days were 1.72, 1.95 and 2.49 mm for SBTS-120-0%, SBTS-120-50% and SBTS-120-100%, respectively (Figure 6(b)).

It is worth mentioning that the slab samples presented initial upward deflections for the first few days when RCA was used. This was attributed to the expansion occurred in RAC at the beginning of the test caused by the additional water absorbed by RCA, as highlighted in [32]. This initial expansion was also observed in the RAC composite slabs, as shown in Figure 7.

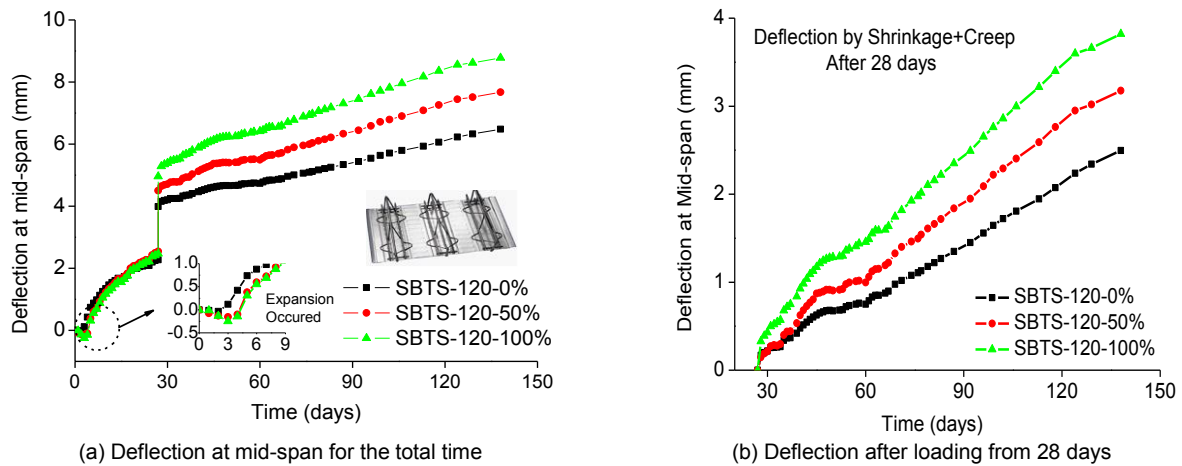


Figure 6. Mid-span deflection of slab samples with steel-bars truss decks

### 3.2 Long-term experimental results for the slab samples cast on profiled sheeting

Before the application of the external loads, the slab specimens with the same depth presented similar mid-span deflections, as reported in Figure 7. At the age of 139 days, the mid-span deflections of CS-120-100% and CS-180-100% under the combined effects of external loads and shrinkage were 8.33 mm ( $\approx L/340$ ) and 5.38 mm ( $\approx L/560$ ), respectively, while the mid-span deflections caused by shrinkage gradient were 5.33 mm and 3.22 mm for CS-120-100%-SH and CS-180-100%-SH, respectively. A comparison of the deflection composition of CS-120-100% showed that the deflection caused by shrinkage was about 64.0% of the total deflection. A similar influence was observed for the 180 mm thick samples (with the shrinkage deflection being equal to 59.9% of the total deflection).

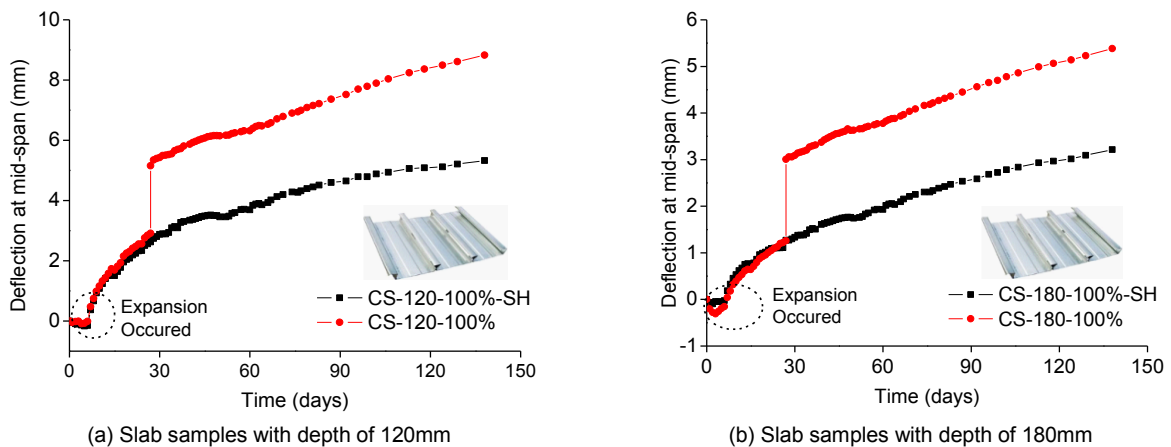


Figure 7. Mid-span deflection of composite slabs with profiled steel sheeting

## 4. Conclusion

This paper presented an experimental study on the time-dependent behaviour of seven floor slabs prepared with recycled coarse aggregate. These consisted of three steel-bars truss slabs and four composite slabs, and were tested in a simply-supported static configuration for a period of five months. Separate concrete samples were prepared and measured monitoring the shrinkage profile through the thickness of slabs. Experimental results showed that similar workability and compressive strength were achieved for RAC to corresponding NAC, due to the high quality of RCA used in this study, however, the decrease of elastic modulus and the increase of shrinkage and creep were still remarkable, when 100% RCA was selected. The non-uniform shrinkage gradient developed due to the inability of the slabs to dry from their underside and increased with RCA contents. The deflections of the RAC composite slabs were influenced by the non-uniform shrinkage gradient and increased with RCA contents. It is also expected

that more experiments should be carried out to quantify the non-uniform shrinkage profile though the thickness of the RAC composite slabs.

## 5. Acknowledgement

The research work reported in this paper has been supported by the National Natural Science Foundation of China (No.51178146), by 'Project 985'-Basic Scientific Research Capacity for Young Scholars of HIT, by the School of Civil Engineering of Harbin Institute of Technology and the School of Civil Engineering of Sydney. The contribution of the second author to the work reported in this paper was supported by the Australian Research Council through its Future Fellowship scheme (FT140100130).

## 6. References

1. Rahal K., "Mechanical properties of concrete with recycled coarse aggregate", *Building and Environment*, 42(1), 2007, pp 407-415.
2. Hansen T.C., "Recycled aggregate and recycled aggregate concrete. Second state of art report, development from 1945-1985", RILEM Technical Committee 37 DRC, *Material and Structures*, 19(3), 1986, pp 201-246.
3. Cheung H.K., "Use of recycled asphalt pavement—a practical approach to asphalt recycling", *Materials Science and Technology in Engineering Conference—Now, New and Next*, 2003, pp 15-17.
4. Hassan K.E., Brooks J.J., et al., "The use of reclaimed asphalt pavement aggregates in concrete, waste materials in construction: WASCON 2000", *Proceedings of the International Conference on the Science and Engineering of Recycling for Environmental Protection*, Harrogate, England, 2000, pp 121-128.
5. Poon C.S., Azhar S., et al., "Recycled aggregates for concrete applications", *Materials Science and Technology in Engineering Conference—Now, New and Next*, 2003, pp 15-17.
6. Yoda K., Yoshikane T., et al., "Recycled cement and recycled concrete in Japan, Demolition and Reuse of Concrete and Masonry: Reuse of Demolition Waste", Chapman and Hall, London, 1988, pp 527-536.
7. Katz A. "Properties of concrete made with recycled aggregate from partially hydrated old concrete", *Cement and Concrete Research*, 33(5), 2003, pp 703-711.
8. Corinaldesi V. "Mechanical and elastic behavior of concretes made of recycled-concrete coarse aggregates", *Construction and Building Materials*, 24(9), 2010, pp 1616-1620.
9. Belén G.F., Ferrnando M.A., et al., "Stress-strain relationship in axial compression for concrete using recycled saturated coarse aggregate", *Construction and Building Materials*, 25(5), 2010, pp 2335-2342.
10. Sato R., Maruyama I., et al., "Flexural behavior of reinforced recycled concrete beams", *Journal of Advanced Concrete Technology*. 5(1), 2007, pp 43-61.
11. Etxeberria M., Mari A.R., et al., "Recycled aggregate concrete as structural material", *Materials and Structures*, 40(5), 2007, pp 529-541.
12. Schubert S., Hoffmann C., et al., "Recycled aggregate concrete: Experimental shear resistance of slabs without shear reinforcement", *Engineering Structures*, 41, 2012, pp 490-497.
13. Ignjatović I.S., Manrinković S.B., et al., "Flexural behavior of reinforced recycled aggregate concrete beams under short-term loading", *Materials and Structures*, 46(6), 2013, pp 1045-1059.
14. Fathifazl G., Razaqpur A.G., et al., "Shear capacity evaluation of steel reinforced recycled concrete (RRC) beams", *Engineering Structures*, 33(3), 2011, pp 1025-33.
15. Choi W.C., Yun H.D., "Compressive behavior of reinforced concrete columns with recycled aggregate under uniaxial loading", *Engineering Structures*, 41, 2012, pp 285-293.
16. Xiao J., Sun Y., et al., "Seismic performance of frame structures with recycled aggregate concrete", *Engineering Structures*, 28(1), 2006, pp 1-8.

17. Choi W.C., Yun H.D., "Long-term deflection and flexural behavior of reinforced concrete beams with recycled aggregate", *Materials and Design*, 5, 2013, pp 742-750.
18. RILEM 121-DRG, "Specification for concrete with recycled aggregates", *Materials and Structures*, 27(173), 1994, pp 557-559.
19. British Standard Institution, "BS6543-Guide to the use of industrial by-products and waste materials in building and civil engineering", London, 1985.
20. German Committee for Reinforced Concrete (DAfStb)-Code: "Concrete with Recycled Aggregates", 1998.
21. ACI Committee 555, "ACI 555-01: removal and reuse of hardened concrete", Farmington Hills (MI, USA): American Concrete Institute, 2001.
22. JCJ/T 240-2011, Ministry of Construction of the People's Republic of China, "Technical specification for application of recycled aggregate", Beijing, China; 2011. (in Chinese)
23. De Brito, J., Saikia, N. *Recycled Aggregate in Concrete*. Lisbon, Portugal, 2013.
24. Xiao J, Li H, et al., "Longitudinal shear test on steel deck recycled aggregate concrete composite slabs", *Structural Engineers*, 26(4), 2010, pp 91-95. (In Chinese)
25. Zhang J, Zhu Y, et al., "Flexural behaviors of recycled aggregate concrete composite slabs with closed-section steel deck", *Journal of Beijing University of Technology*, 40(8), 2014, pp 1197-1203. (in Chinese)
26. Cao W, Zhang J, et al., "Experimental research on flexural performance of high strength recycled aggregate concrete slabs with steel bar truss", *Journal of Building Structures*, 35(10), 2014, pp 31-38. (in Chinese)
27. Ranzi G, Al-Deen S, et al., "Long-term behaviour of simply-supported post-tensioned composite slabs", *Journal of Constructional Steel Research*, 88, 2013, pp 172-180.
28. Gilbert R I, Bradford M A, et al., "Effects of shrinkage on the long-term stresses and deformations of composite concrete slabs", *Engineering Structures*. 40, 2012, pp 9-19.
29. UNE-EN 933-1. Test for geometrical properties of aggregates. Part 1: determination of particle size distribution. Sieving method.
30. Gilbert RI, Ranzi G. "Time-dependent behaviour of concrete structures". England: Spon Press, 2011.
31. GB/T 6397-86, Ministry of Construction of the People's Republic of China, "Metallic materials—Test pieces for tensile testing". Beijing, China, 1986. (in Chinese).
32. Gómez Soberón, J. M. V. "Relationship between gas adsorption and the shrinkage and creep of recycled aggregate concrete". *Cement, Concrete, and Aggregates*, 25, 2003, pp 1-7.

# Implications of Alkali-Aggregate Reaction for three Concrete Bridges

Ahmad Shayan<sup>1</sup>, Aimin Xu<sup>1</sup> and Fred Andrews-Phaedonos<sup>2</sup>

<sup>1</sup>ARRB Group Ltd., 500 Burwood HWY, Vermont South, VIC 3133

<sup>2</sup>VicRoads, 12 Lakeside drive Burwood East, VIC 3151, Australia

Corresponding Author: ahmad.shayan@arrb.com.au

**Abstract:** Alkali-aggregate reaction (AAR) can cause damage to concrete structures, which can vary from serious reductions in structural capacity to less serious maintenance problems, or minor durability effects. New cases of AAR continue to be discovered in different concrete structures in Australia, and exhibit different visual effects. The affected concrete needs to be characterised in order to determine the extent of damage caused by AAR, and to establish appropriate rehabilitation strategies.

Recently, three bridges were diagnosed with AAR and were characterised using petrography, scanning electron microscopy, measurement of residual alkali content and residual expansion potential, compressive strength and elastic modulus. The results show that AAR has impacted the three bridges differently, and the paper discusses the consequences of AAR and appropriate treatments for each case.

**Keywords:** AAR, Expansion, Cracking, Corrosion, Microstructure, Strength properties

## 1. Introduction

The most visible sign of alkali aggregate reaction (AAR) in concrete is cracking, which takes different forms and can occur to different extents, depending on the severity of reaction, and design details of the affected element. The severity of reaction, in turn, is a function of the type of aggregate, alkali content of concrete and exposure environment. The cracking adversely affects the durability of concrete by exposing the concrete interior to aggressive environmental agents.

In Australia, several major cases of deleterious AAR have been reported in dams and bridges (for example, 1-8), which have resulted in significant repair and rehabilitation expenditure, amounting to many millions of dollars in each case. Many more cases of AAR damage in concrete structures have been included in the updated version of HB70 (2015), "Guidelines on minimising the risk of damage to concrete structures in Australia", which may have suffered less severe damage.

The AAR-induced cracking of concrete is also often associated with reductions in the strength properties of concrete (8-11), the extent of which depends on the severity of the reaction. Some authors have reported that despite the reductions in strength properties of concrete, the load capacity of the affected element was not adversely affected (8, 9, 12-15). Deterioration of mechanical properties was found to be more severe in smaller elements than in larger elements, due to larger ratio of crack depth to dimension of element (16). The above indicates that several parameters influence the effect of AAR on the behaviour of affected elements, and that each case needs to be considered individually. This paper details the different impacts of AAR on three different structures, which require different treatments.

## 2. Structures investigated and methodology

The AAR-affected structures investigated are listed in Table 1. They represent structures incorporating different reactive aggregates, subjected to different exposure conditions.

Bridge A is 54 years old and carries freeway carriageways over a fresh water creek. Figure 1 shows the mild nature of cracking in the column and more extensive cracking in the crossheads of the bridge.

Bridge B is 24 years old and carries a State Road over a freeway. The concrete has been coated with heavy duty anti-carbonation coating, thereby masking the cracks. Figure 2 shows examples of cracks which have reopened.

Bridge C is 26 years old and is situated in a coastal area where the tidal river water is saline. This bridge has been inspected on a number of occasions and mild AAR-induced cracking identified in some columns and crossheads with wider cracks in pile caps, which are often submerged. The substructure elements have recently been painted, after patch repair and crack injection, which has masked the previously recorded cracks. However, in addition to AAR-induced cracks, corrosion-induced cracks were also noted at the corners of some columns. These cracks were not

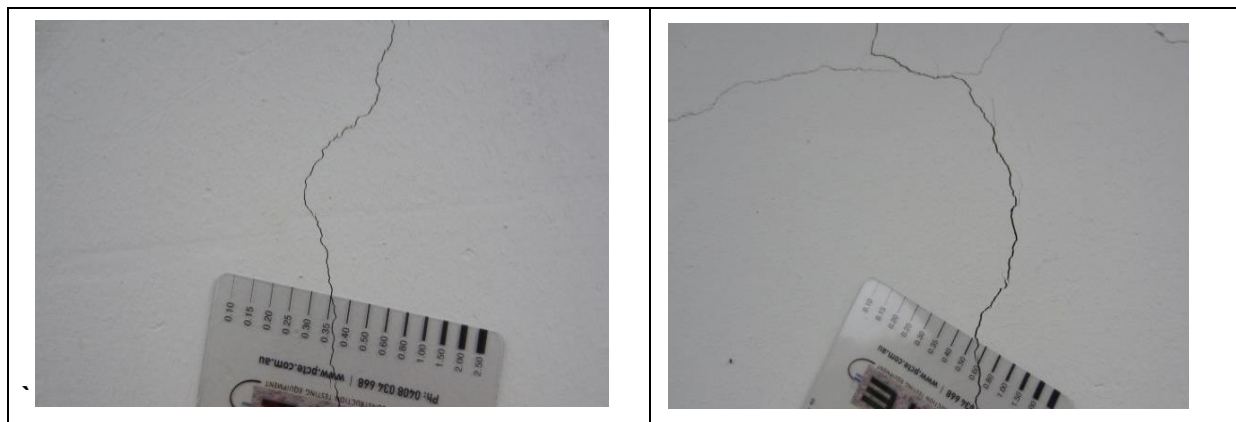
present in 2004. The bases of the columns to about 800 mm above the pile caps have been jacketed with a cement-based product in order to protect against scour (not against chloride ingress). Figure 3 shows some repaired elements in Bridge C.

**Table 1- Details of structures**

Bridge ID	Bridge type	Date Built	Environment	Cracking defects
A	3 spans- simply supported, consisting of pier columns & crossheads, supporting I-beams and deck slabs	1961	Over fresh water creek, carrying freeway lanes	Fine, mild vertical cracking at centre of some columns, and moderate cracking in crossheads varying in different locations from parallel horizontal to random and some vertical (bending) cracks
B	2 spans, continuous box girder T beam supported by central pier wall and abutment piers	1991	Over freeway, dry conditions	Random and oblique to vertical cracking in central pier wall and random cracking in the abutment crossheads.
C	6 spans- simply supported, consisting of pier columns & crossheads, supporting I-beams and deck slabs	1959	Over tidal river, exposed to salt water	Fine map-cracking throughout crossheads, central vertical crack in columns, cracking in pile caps, corrosion-induced cracks at column corners



**Figure 1- Mild cracking in column (left) and crosshead (right) of Bridge A**



**Figure 2- Vertical cracking in pier column of Bridge B, about 0.35- 0.40 mm wide**





**Figure 3- Views of repair in a crosshead and a column in Bridge C. Note jacket at the base of column applied later for scour protection**

### 3. Examination and testing of concrete cores

Each of the bridges was subjected to visual inspection and characterisation of concrete cores, drilled from various elements, by the methods listed below.

- Visual examination of core samples taken from different elements, and
- Petrographic examination
- SEM/EDX examination
- Available alkali content
- Residual expansion potential
- Compressive strength
- Modulus of elasticity
- Volume of permeable voids (VPV)
- Chloride content (Bridge C only)
- Onsite measurement of half-cell potential and corrosion rate of steel (Bridge C only)

These methods were used to assess the extent of AAR and its impact on the mechanical properties of the affected concrete. Table 2 shows the list of cores taken from each bridge. Most cores were of 75mm diameter, except those intended for residual expansion measurements, which were 95mm in diameter.

#### 3.1 Visual features of cores

Figure 4 shows representative photographs of cores from the three bridges. Cores from Bridge A contained uncrushed river gravel with some light and some dark particles. The dark particles exhibit stronger signs of reaction. The cores from the crossheads and columns appeared generally similar, to former has developed somewhat stronger reaction than the columns. Overall, the extent of AAR is considered to be mild in cores from Bridge A.

Bridge B cores exhibited stronger signs of AAR, as seen in Figure 4. A distinct layer of surface coating was present on the outer face of cores, particularly those from the abutment. Well-defined AAR rims and internal aggregate cracking were noted in some cores. Some air voids also appeared to contain AAR products. The extent of AAR in the cores is considered to be moderate to large and greater than those in cores from the other bridges.

Bridge C cores were similar in different elements and contained uncrushed river gravel. AAR signs were stronger in cores from the pile cap and included AAR rims at aggregate periphery and in some air voids. Cores from the jacketed areas of columns showed very weak bonding between the jacket and column, due to no cleaning of the column surface prior to application of jacket concrete. The latter comprised a different (proprietary) type of concrete with maximum aggregate size of 9mm.



**Table 2- List of cores taken from various elements**

Bridge	Location of Core <sup>†</sup>	Core ID
A	Two cores from P1C2	C14/2633-1 and C14/2633-2
	Three cores from P1C1	C14/2633-3, C14/2633-4 and C14/2633-5
	Five cores from south abutment crosshead	C14/2633-6, C14/2633-7, C14/2633-8, C14/2633-9 and C14/2633-10
B	Five cores from Pier wall	C14/ 2634-1 through C14/ 2634-5, inclusive
	Five cores from abutment	C14/ 2634-6 through C14/ 2634-10 inclusive
C	Three cores from Pier 1 Pile-cap	C13/2491-1, C13/2491-2 and C13/2491-3
	Two cores from P1C3	C13/2491-4A (jacket) and C13/2491-4B (behind jacket)
	Two cores from P1C2	C13/2491-5A (jacket) and C13/2491-5B (behind jacket)
	Three cores from east abutment crosshead	C13/2491-6, C13/2491-7 (included a 10 mm later of repair mortar) , and C13/2491-8
	Two cores from P3C3	C13/2491-9 (upper) and C13/2491-10 (lower)
	Two cores from P3C2	C13/2491-11 (upper) and C13/2491-12 (lower)
	Two cores from P3C1	C13/2491-13 (upper) and C13/2491-14 (lower)

<sup>†</sup>P= pier; C= Column, numbering of piers is from South to North.

## 4. Results and discussion

### 4.1 Petrographic examination of cores

**Bridge A:** The coarse aggregate in the cores from columns was predominately gneissic deformed quartz gravel, in which quartz crystals have been highly strained, producing strongly distorted crystal habit and patchy extinction. Some weathered andesite-like particles were also present in the thin section. The quartz gravel is susceptible to AAR, but the reactivity of the andesitic particles is uncertain.

The coarse aggregate from the abutment crosshead contained quartzite, in which the quartz grains appeared to be cemented together by fine micaceous materials. Foliated schist-like particles were also present. The fine aggregate fraction in both elements comprised a mixture of monomineralic quartz and feldspar as well as finer fragments of the same nature as the coarse aggregate, which are potentially reactive.

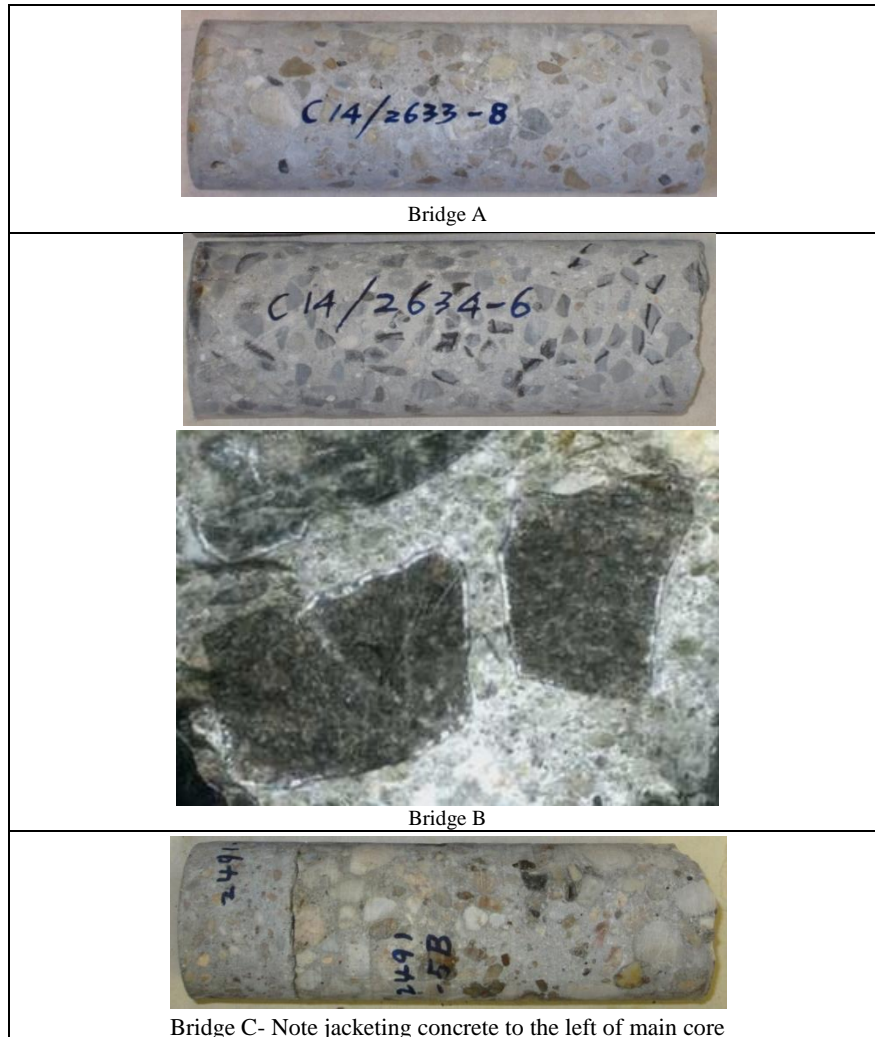
The cementitious matrix in the core from the column showed a few fine peripheral microcracks around a portion of some coarse aggregate particles, which extended a small distance into the cement paste. The core from crosshead exhibited more definite signs of AAR gel formation around aggregate particles and in parts of some microcracks in the cement paste.

**Bridge B:** The coarse and fine aggregate phases in the pier wall and abutment crosshead were the same. The coarse aggregates was a mixture of metamorphic rock types of schist and gneiss, and all the particles exhibited strong signs of deformation and orientation, as indicated by elongated quartz grains and bands of micaceous minerals in parallel orientation. Some particles comprised a fine matrix of microcrystalline quartz and highly birefringent amphibole type minerals. Particles of quartzite with highly deformed quartz crystals were also present, in which quartz crystals showed sutured boundaries and patchy extinction. These rock types are considered to be susceptible to AAR.

The fine aggregate fraction was a mixture of mono-mineralic quartz and feldspar crystals as well as finer fragments of the coarse aggregate particles. Some of the single quartz crystals also showed moderate undulatory extinction angles. A portion of the fine fraction may be susceptible to AAR.

The cementitious matrix in cores from both elements showed a considerable number of micro-cracks at the aggregate periphery, extending into the cement paste. AAR gel was definitely identified in some micro-cracks around the aggregate and in the paste. The petrographic examination clearly verified AAR is both elements.

**Bridge C:** The aggregate was a quartz gravel of gneissic origin, showing signs of strong deformation. The quartz crystals in the aggregate particles showed strongly patchy extinction. Stress lamellae are evident in the quartz crystals, which also show sutured boundaries. Some microcrystalline quartz was noted at quartz crystal boundaries. These petrographic features indicate that the aggregate is susceptible to AAR. In fact, AAR gel was clearly observed around the reacted aggregate particles in hand specimens of cores



**Figure 4- Views of representative cores from different bridges**

#### **4.2 SEM/EDX examination of cores**

The SEM/EDX examination was conducted on specimens coated with evaporated carbon. All the cores examined from the three bridges contained various forms of AAR products, but the amount of products varied amongst the cores even in each bridge.

Figure 5 shows examples of AAR products in Bridge A. Both elements contained AAR gel, which was found around reacted aggregate particles, as well as some crystalline AAR products that forms within the aggregate periphery. The number of reaction sites was larger in the cores from the crosshead than that from a pier column. This reflects the more extensive cracking noted in the crosshead. Some of the products appeared depleted in alkali and enriched in Ca, which is due to contact with cement paste over prolonged exposure to wet conditions.

Figure 6 shows representative SEM views of AAR products in pier column of Bridge B. Generally, AAR was stronger in Bridge B than Bridge A, as also indicated from the appearance of the cores, where

internal cracking of aggregate particles and AAR rimming of aggregate particles were evident in Bridge B cores. AAR gel was present in many sites. Some highly Na-rich fibrous products were present in the concrete, which also contained Al, indicating that in addition to the silica minerals, feldspar minerals may also have reacted with Alkali. The concrete from the abutment crosshead showed similar but even larger amounts of AAR products, indicating that AAR was probably stronger in the crosshead than in the pier wall. This probably resulted from higher cement content of concrete in the crosshead, as indicated by higher compressive strength (see later).

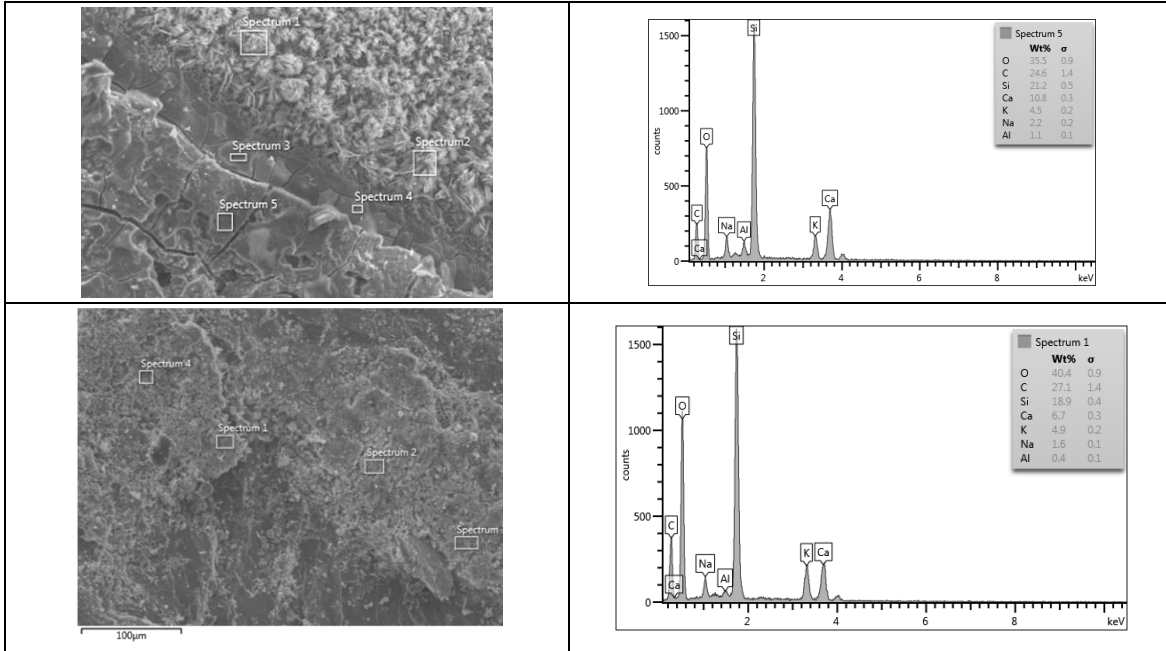


Figure 5- SEM views of AAR products in Bridge A. Top: AAR gel & Rosettes in pier column; Bottom: AAR Rim at aggregate periphery in crosshead

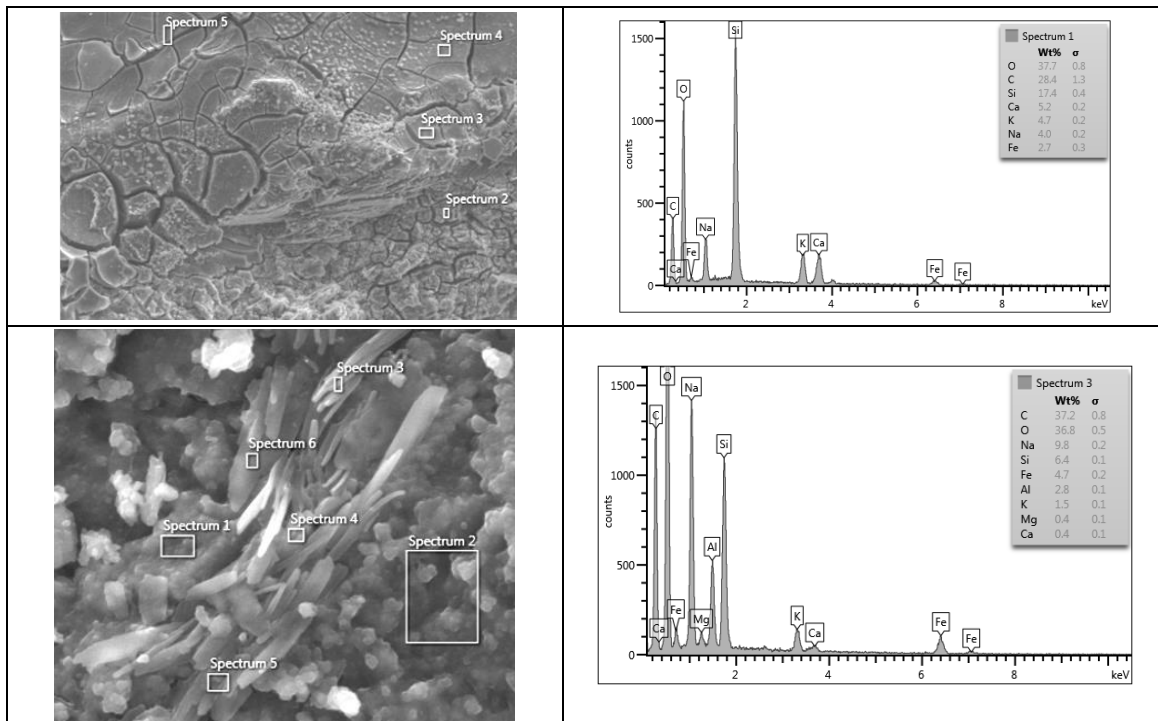
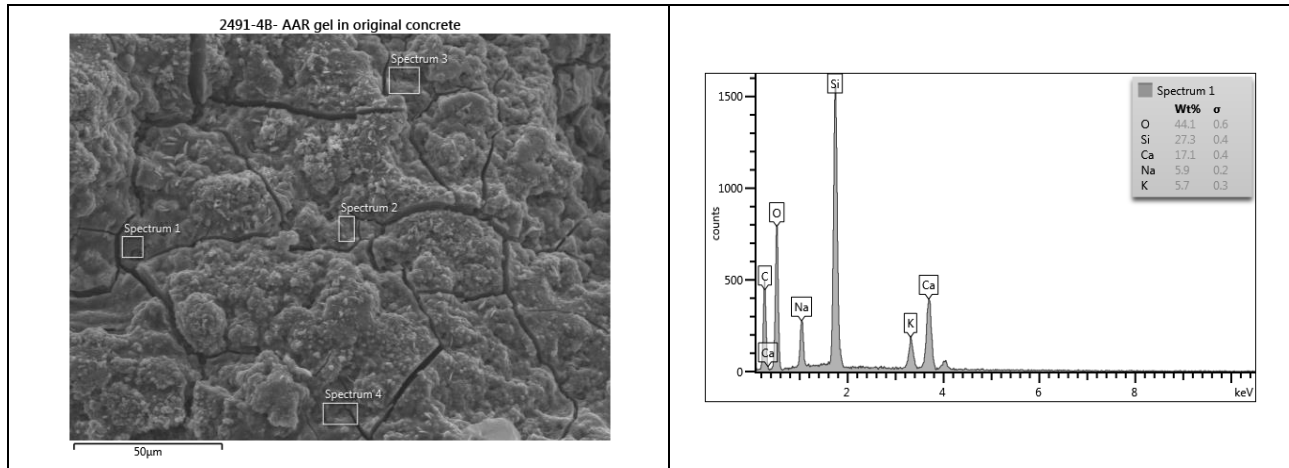


Figure 6- Representative SEM views of AAR gel around reacted aggregate and Na-rich fibrous crystals formed in reacted aggregate, both in pier wall of Bridge B

Figure 7 shows a representative SEM view of AAR gel in Bridge C. AAR products were present in all the concrete elements examined, except in one of the two jacket concrete from one of the columns (Core C13/2491-4A). The reasons for the difference in the concrete of the two jackets examined are not known, but may relate to the alkali content of the original mix. The concrete in the pile-cap exhibited more extensive signs of reaction than in other elements, and this is reflected in the larger extent of cracking reported for pile-caps. Both the concrete jackets, with and without AAR, have exhibited cracking. It was found that the relatively thin concrete jackets did not contain steel reinforcement, and the reason for the cracking of the jacket concrete that has not exhibited AAR may have been lack of reinforcement and low resistance to drying shrinkage.



**Figure 7- Representative SEM view of AAR gel in pier column of Bridge C. Note high Na content of the AAR gel, indicating high Na in original cement**

### 4.3 Compressive strength and Modulus of Elasticity

Table 4 presents the results of compressive strength tests conducted on the cores in accordance with AS 1012.14. The average values of compressive strength for the different elements in each bridge are also presented. Generally, the various elements exhibit adequate compressive strength. For Bridge A and Bridge B the crossheads showed higher strength than columns, whereas for Bridge C, columns showed the highest strength. These strength values may overestimate the actual strength of the elements concerned, as cores are usually drilled in sound portions of concrete, away from cracks, whereas the element itself would include a considerable number of cracks and microcracks. Nevertheless, the compressive strength of concrete could have been reduced by AAR. This is because, strength values of around 40 MPa indicate that the original concrete may have been VR400/40 grade (VicRoads Specification Section 610- Structural Concrete), and those of around 30 MPa of VR330/32 grade. Sound concrete of these grades should have had strength values of 50 MPa and 40 MPa, respectively, at the age of these bridges.

It is known that the compressive strength of concrete is less sensitive than other strength properties, such as tensile and flexural strength and modulus of elasticity, to the effects of AAR (17-19); therefore, the strength values given in Table 4 may not reflect the AAR-induced damage in the elements concerned. A number of cores were subjected to modulus of elasticity testing, in accordance with AS 1012.17-1997. In these tests, the compressive strain measurements were recorded by two bonded 120-Ohm strain gauges attached at 180° along the central 60mm of the cylinders, which were installed between the platens of a calibrated universal testing machine. Load was applied up to a stress of about 40% of the nominal compressive strength, and at this point the load was released and the loading –unloading cycle repeated twice more. A fourth load cycle was then applied to failure. The testing was conducted under controlled temperature and humidity conditions of 23°C and 50% RH.

The results are summarised in Figure 8 for Bridges A& B and in Figure 9 for Bridge C. The values of elastic modulus are also given in Table 4. The lowest modulus values were obtained for the pile-cap of Bridge C and Crosshead of bridge B, both of which had shown more extensive AAR products than other

elements. The AAR-induced internal microcracking significantly reduces the stiffness of the affected elements, which is reflected in the low values of elastic modulus. The stiffness of other elements is probably also somewhat reduced as the largest value of elastic modulus was 27 GPa, whereas concrete of VR400/40 would be expected to have an elastic modulus of around 35 GPa.

**Table 4- Strength properties of concrete in various elements of Bridges**

Bridge	Element	Core ID	Compressive Strength (MPa)	Elastic Modulus E (Gpa)
A	Pier column P2C2	C14/2633-2	35.18	-
	Pier column P1C1	C14/2633-3	33.5	29
	Pier wall P2C1	C14/2633-5	32.19	-
	Abutment Crosshead	C14/2633-6	36.19	-
	Abutment Crosshead	C14/2633-7	44.02	-
	Abutment Crosshead	C14/2633-10	43.2	29
B	Pier wall	C14/2634-1	43.08	-
	Pier wall	C14/2634-4	37.65	-
	Pier wall	C14/2634-5	36.8	27
	Abutment Crosshead	C14/2634-7	42.87	-
	Abutment Crosshead	C14/2634-9	50.3	19
	Abutment Crosshead	C14/2634-10	41.33	-
C	Pile cap	C13/2491-2	28.3	17.3
	Pile cap	C13/2491-3	36.5	-
	Cross- head	C13/2491-6	36.7	25.3
	Cross- head	C13/2491-8	36.5	-
	Column	C13/2491-9	40.0	-
	Column	C13/2491-11	42.3	29.1
	Column	C13/2491-12	41.1	-
Column	C13/2491-13	42.8	31.5	

It should be noted that the higher cement content in VR400/40 concretes could have favoured stronger AAR development than in VR330/32 grade, due to higher alkali content.

Overall, these results indicate that the strength properties of concrete in the various elements have deteriorated due to AAR.

#### 4.4 Residualalkali Content of concrete

The residual alkali content was determined on pulverised specimens of concrete for Bridges A & B only, as Bridge C is a coastal structure, being subjected to contamination by tidal salt water and salt spray. Instead, chloride ion penetration was investigated in Bridge C, as this is the major cause of chloride induced corrosion of steel-reinforced concrete.

Table 5 presents the results of determination of water-soluble, residual alkali content of concrete.

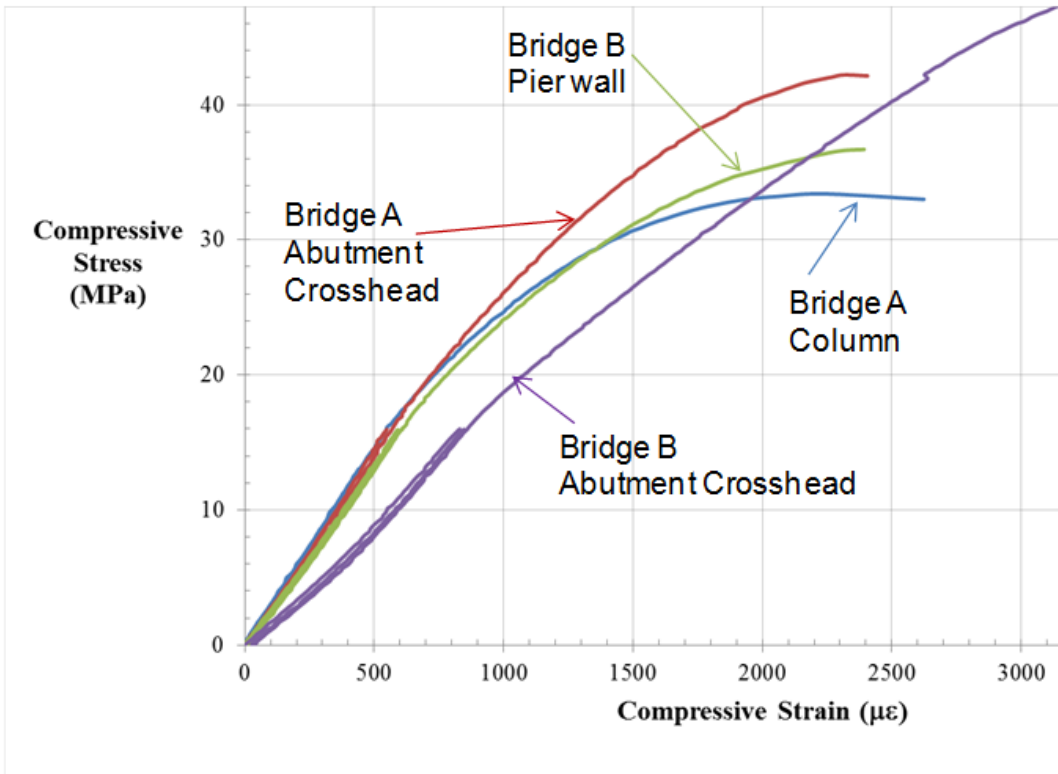


Figure 8- Stress strain curves for cores from different elements

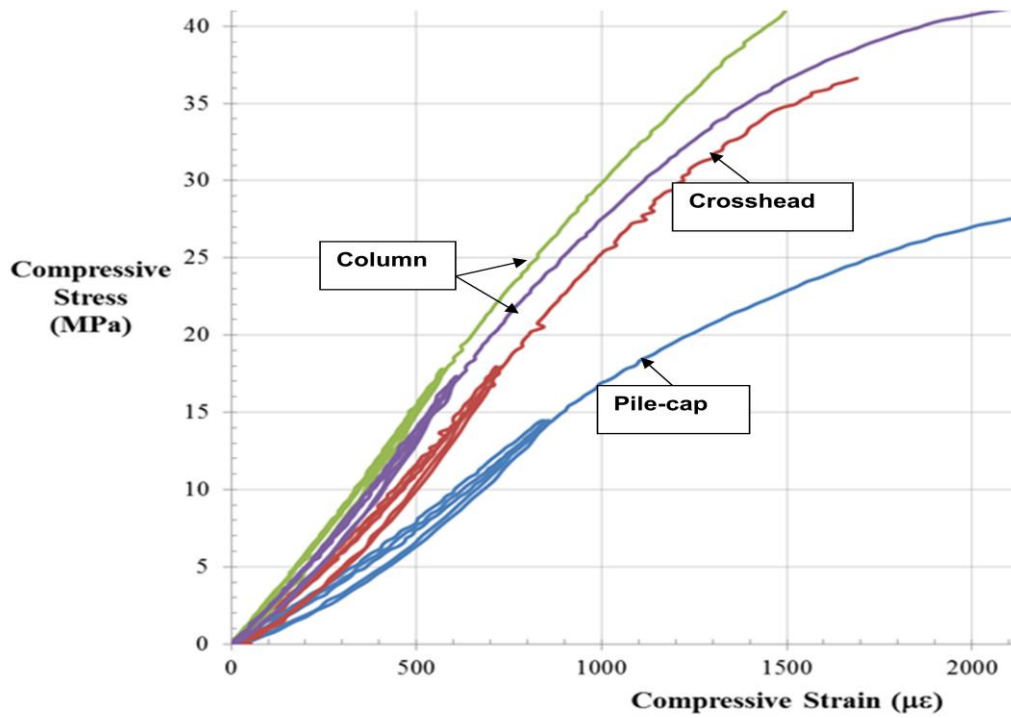


Figure 9- Stress strain curves for cores from different elements in Bridge C

**Table 5 --Residual Alkali Content of concrete**

Bridge	ID and Component	Alkali per volume of concrete (kg/m <sup>3</sup> )		
		Na <sub>2</sub> O	K <sub>2</sub> O	Na <sub>2</sub> O eq.
Bridge A	C14/2633, Pier Column	1.68	1.71	2.81
	C14/2633, Abutment Crosshead	1.91	1.60	2.97
Bridge B	C14/2634-3', Pier	2.51	1.92	3.78
	C14/2634-8, Abutment Crosshead	2.01	1.59	3.06

For Bridge A, the alkali contents in the cores from the pier column and the abutment crosshead were 2.81 kg/m<sup>3</sup> and 2.97 kg/m<sup>3</sup>, respectively. The corresponding values for the concretes from the pier wall and the abutment crosshead of Bridge B were 3.78 kg/m<sup>3</sup> and 3.06 kg/m<sup>3</sup>, respectively. Some of the measured alkali could have been released from the pulverised aggregate phase of the concretes; an artefact which would not occur in the structure, and needs to be corrected for. However, this would need fresh samples of the same aggregate, which were not available. In the case of Bridge A, which contained the quartz gavel the correction for alkali content would be small (around 0.1 kg/m<sup>3</sup>), whereas it could be considerably larger for Bridge B, which contained aggregate derived from igneous rock (perhaps around 0.5-0.7 kg/m<sup>3</sup>). However, in the latter case, there is also the possibility that the aggregate may release alkali into the concrete and increase the extent of AAR (21).

It is generally accepted that an alkali content of about 3 kg/m<sup>3</sup> is required to initiate AAR in concrete. Given that AAR has already occurred, the amount of available alkali could be sufficient to sustain further AAR in concrete elements concerned, particularly if the aggregate phase releases alkali into the concrete. The measurement of residual expansion would clarify the extent of remaining AAR potential.

#### 4.5 Chloride content of concrete in Bridge C

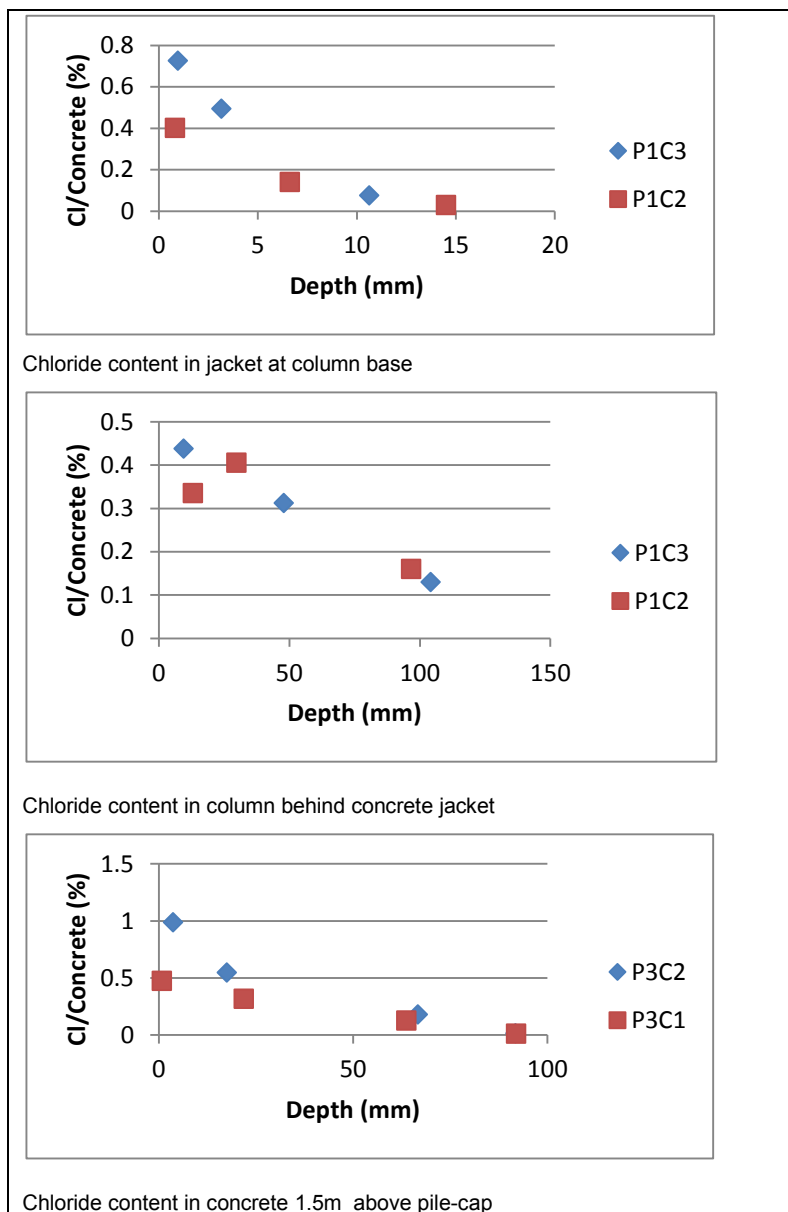
Chloride ion content in concrete was determined on pulverised concrete samples obtained at incremental depths from the concrete surface of selected elements in Bridge C, following AS 1012.20, which determines the total acid soluble chloride content. The chloride content required for corrosion initiation in reinforced concrete is related to the hydroxyl ion concentration in the pore solution of concrete, which varies depending on cement type and concrete quality. The Australian Standard AS 5100.5- Section 4 (Concrete durability) gives a limit of 0.6 kg/m<sup>3</sup> as the maximum acceptable chloride content in reinforced concrete structures. For medium strength concrete, this threshold value would correspond to about 0.1% chloride ion by mass of cement. It is considered that corrosion activity is very likely at chloride content of 0.4% by mass of cement, which would equate to 0.07% chloride by mass of concrete.

The results of chloride content determination in different columns, both at the water mark and at 1.5m height above pile-caps, showed that the chloride content at the depth of reinforcing bars (design cover thickness of about 89 mm) was high enough to cause steel corrosion, as illustrated in Figures 10.

The chloride profiles in the jacket concrete indicate that the surface coating had little resistance to chloride penetration, unless the coating was applied long after the installation of the jacket concrete, which was intended for scour protection rather than being as a chloride barrier.

The chloride content at the reinforcement depth at the base of columns, i.e. behind the jacket, is well in excess of the corrosion initiation threshold, which would have occurred before the installation of the jacket concrete. Therefore, the reinforcement is subjected to active corrosion in the columns and surface treatments (further jacking or coating) would be ineffective in preventing corrosion. In this situation, it is common to install a cathodic protection (CP) system, before corrosion damage becomes significant.

However, in the case of Bridge C, which includes reactive aggregate phases, care should be exercised in the application of CP because the CP current, particularly impressed current, could aggravate the AAR situation in the concrete (20) and cause further expansion and cracking.



**Figure 10- Chloride ingress profiles in concrete jackets and in columns**

#### 4.6 Residual Expansion of concrete

The results of residual expansion measurement, conducted on cores from various elements of the three bridges, under the storage conditions of 38°C and 100% RH, are presented in Figure 11 in the form of expansion curves. The initial, relatively rapid rise in expansion over the first couple of weeks is attributed to moisture absorption by the concrete and/or existing AARgel, and subsequent expansion due to continued formation of new reaction products.

**Bridge A:** Core C13/2633-1 from the column, which has exhibited the weakest manifestation of AAR, showed the lowest expansion and reached a plateau of 0.015%, including the initial expansion due to moisture absorption, which is considered insignificant. Core C13/2633-8 from the crosshead, which has exhibited a stronger case of AAR, showed larger expansion of 0.026%. The plateau indicates that the amount of alkali in the concrete is insufficient for further reaction. It is likely that leaching of alkali from the core, under the storage conditions of the test, could have contributed to the depletion of alkali.

**Bridge B:** Cores C13/2634-3 and C13/2634-6 from the pier wall and crosshead, respectively, showed larger residual expansion potential (0.045% and 0.086%, respectively) than cores from bridge A. These



levels of expansion indicate that further expansion and cracking may occur in these elements in the future, particularly in the crosshead. However, previous work (22) has shown that the expansion level that concrete elements can achieve under field exposure conditions in Australia would be around only 50% of the expansion experienced by cores which are cured at 38°C, 100% RH. Therefore, it would be expected that additional expansion of 0.043% could occur in the crosshead, which would probably lead to further cracking. These elements should be monitored to verify whether or not additional cracking occurs.

**Bridge C:** Large variations were measured in the residual expansion potential of cores from the pile-cap (C13/2491-1), lower part of column (C13/2491-10) and abutment crosshead (C13/2491-10), as illustrated in Figure 11.

The low expansion results for the pile-cap and lower part of column probably arise from alkali leaching effects, and the fact that these elements are often submerged in saltwater, would not induce further potential for AAR (23). It appears that only the crossheads could exhibit deleterious expansion in the future. However, if impressed current cathodic protection (CP) is applied to suppress reinforcement corrosion, then the other elements may also develop deleterious AAR-induced expansion (22).

#### 4.7 Possible treatments to protect various elements

The level of intervention required to reduce the rate of deterioration of AAR-affected elements depends on the impact that AAR had had on the condition of the elements concerned, their residual strength, as well as their current residual expansion potential. As noted above, the compressive strength of concrete appears to be adequate for all the elements examined. However, some elements exhibited reduced stiffness (low modulus of elasticity), which may also indicate deterioration of tensile and flexural strength of the respective elements. Such elements may need strengthening, e.g., post-tensioning or application of epoxy-bonded CFRP (carbon fibre reinforced polymer). Other elements would need lower levels of intervention, largely to suppress the rate of AAR expansion. Mitigation of chloride-induced corrosion of reinforcement in Bridge C, requires special attention due to the combined presence of AAR in the concrete.

On the basis of the above argument, the treatments recommended below could be applied to the various elements of the three bridges. This assumes that the elements tested are representative of other similar elements in each bridge.

**Bridge A:** Application of an appropriate penetrating silane product to the aerial parts of columns and crossheads, would reduce the water content of concrete and, consequently, further suppress that AAR potential. For elements which are prone to flooding, silane products may not be effective, and application of a heavy-duty surface coating (e.g., anti-carbonation acrylic coating) could prove more effective.

**Bridge B:** The exposure conditions for this bridge are benign and application of an appropriate silane would probably reduce the rate of expansion. In addition, application of appropriately designed epoxy-bonded CFRP system could, at least partially, restore the reduced strength and stiffness of the element.

**Bridge C:** Due to the fact that chloride-induced corrosion of reinforcement has already started in some elements, and the AAR-affected nature of the concrete, as well as low modulus of elasticity of pile-caps, three types of protection are required for the bridge elements, as follows:

- 1- Crack injection for the wide cracks noted in the pile-caps, and patch repair of corrosion-induced cracks in lower parts of columns, followed by an appropriate heavy duty surface coating to protect the repaired areas from chloride ingress.
- 2- Application of a cathodic protection system at low levels of impressed current or a sacrificial anode CP system, knowing that the aggregate is reactive and concrete expansion would need to be monitored. Application of an appropriate protective surface coating could be useful in limiting both the availability of oxygen and further chloride penetration.
- 3- Application of an appropriate silane to the crossheads and columns (above tidal zone) to allow the internal moisture of the elements to escape, without allowing moisture ingress, thereby reducing the rate and extent of expansion. The silane should be applied after a dry summer period to allow sufficient penetration. Once the concrete is drier, a heavy duty anti-carbonation coating could also be applied which would also reduce further chloride penetration.

- 4- With respect to strengthening to counter the effects of AAR, only parts of the pile caps may need attention.

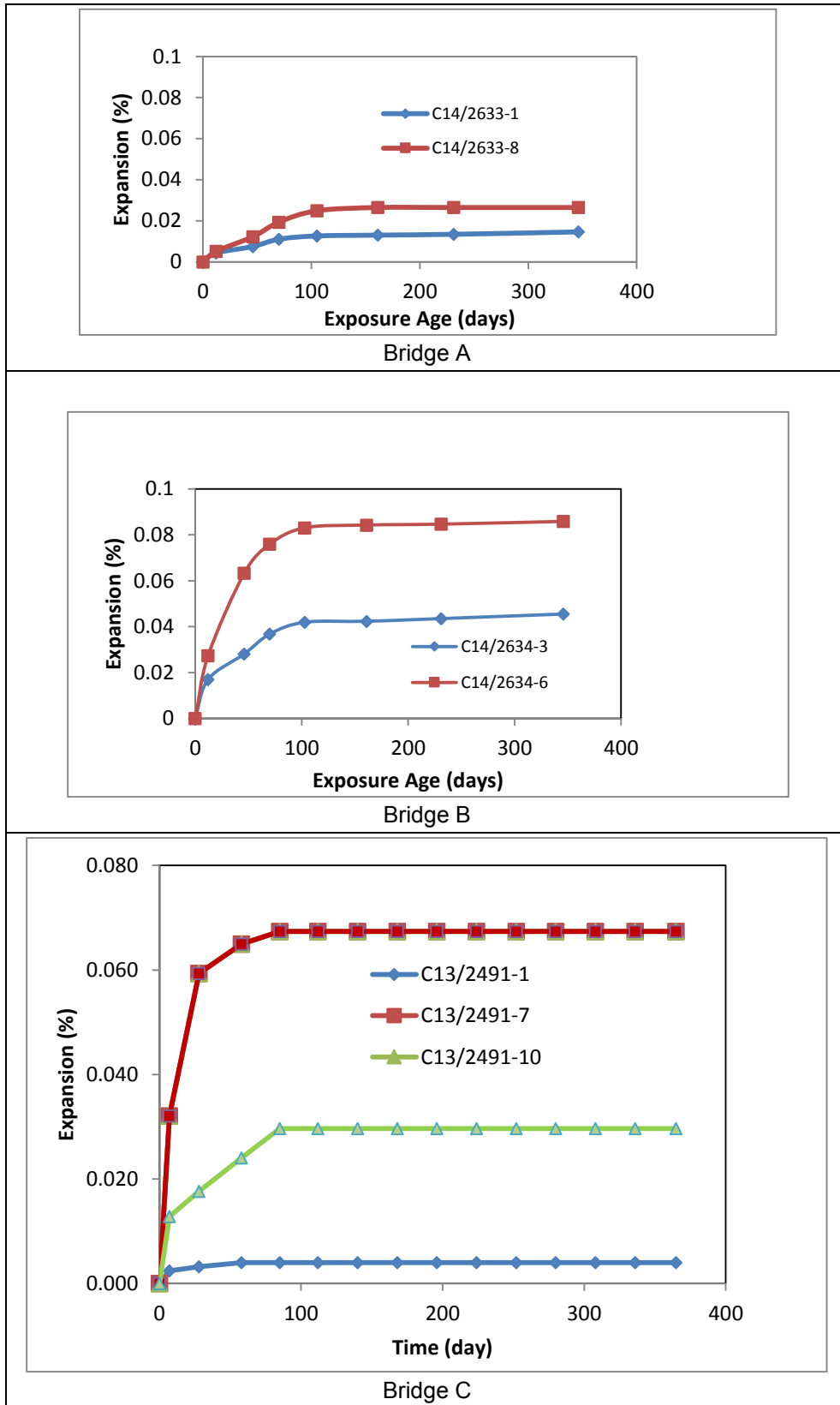


Figure 11- Residual expansion curves for cores from the three bridges, under storage conditions of 38°C and 100% RH

## 5. Conclusions

This work has confirmed the presence of AAR in all the concrete elements examined from the three bridges, arising from the reactive aggregate types used in these bridges. The severity of AAR varied in different bridges and amongst different elements of the same bridge. AAR was mild in Bridge A, and stronger in elements of Bridge B than those of other bridges. In bridge C, the pile-cap examined exhibited the greatest impact of AAR in the form of wider cracks. Cracking in the concrete jackets, which were unreinforced, was probably due to drying shrinkage effects than AAR.

The compressive strength of concrete in all elements appears to be adequate, although the stiffness of some elements has significantly deteriorated due to the effects of AAR. Such elements may ultimately need strengthening.

The measured residual expansion of concrete in most elements appears to be small, i.e., low potential for further reaction and cracking. The potential for further deleterious expansion is moderate for the crossheads of bridge B and Bridge C.

Recommendations for protection against corrosion and AAR have been made, taking into account the results of various tests.

## 5 References

1. Shayan, A. and Lancucki, C.J. (1987). Alkali-aggregate reaction in the Causeway bridge, Perth, Western Australia. In: Concrete Alkali Aggregate Reactions (P.E. Grattan-Bellew, editor), Noyes Publications, N.J., USA, pp. 392-397.
2. Shayan, A. (1988). Alkali aggregate reaction in a 60-year-old dam in Australia. *Int. J. Cement Composites and Lightweight Concrete*, Vol. 10, No. 4, pp. 259-266.
3. Shayan, A. and Quick, G.W. (1992). Microscopic features of cracked and uncracked prestressed concrete railway sleepers. *ACI Mat. J.*, July-August issue, pp. 348-361.
4. Ross, I. and Shayan, A. (1996). Alkali-aggregate reaction in Western Australia: Investigations on the Causeway bridge and some aggregate sources. *Proc. 10th Int. AAR Conf.*, Melbourne, Australia, 18-23 August 1996, pp. 257-264.
5. Shayan, A. (1999). Characterisation of AAR-affected concrete from a dam structure for rehabilitation purposes. *Proc. Int. Conf. On Infrastructure Regeneration and Rehabilitation*, June 1999, Sheffield Univ., U K, pp. 777-787.
6. Shayan, A., Wark, R.E., and Moulds, A. (2000). Diagnosis of AAR in Canning Dam, characterisation of the affected concrete and rehabilitation of the structure. *Proc. 11th Int. AAR Conf.*, June 2000, Quebec City, Canada, pp. 1383 - 1392.
7. Shayan, A. and Morris, H. (2002). Cracking in precast, prestressed deck planks in two bridges and rehabilitation options. *ACI Materials Journal*, Vol. 99, March-April 2002, pp 165- 172.
8. Shayan, A., Al-Mahaidi, R. and Xu, A. (2008). Durability and strength assessment of AAR-affected bridge deck planks. *Proc. 13th IAARC*, Trondheim, Norway, 16-20 June 2008, pp 422-432.
9. Inoue, S., Fujii, M., Kobayashi, K. and Nakano, K. (1989). Structural behaviours of reinforced concrete beams affected by alkali-silica reaction. *Proc. 8th IAARC*, Kyoto, Japan, pp 727.
10. Takemura, K., Ichitsubo, M., Tazawa, E. and Yonekura, A. (1996). Mechanical performance of ASR affected nearly full-scale reinforced concrete column. *Proc. 10th IAARC*, Melbourne, Australia, 18-23 August 1996, pp 410-417.
11. Mohammed, T.U., Hamada, H., Yamaji, T. and Yokota, H. (2004). ASR expansion of concrete beams with various restrained conditions – 612 days of accelerated marine exposure. *Proc. 12th IAARC*, Beijing, China, pp 1169-1190.
12. Thoresen, T. and Larsen, E.S.(1996). Alkali-silica reaction in damaged concrete-static and dynamic tests, material investigations. *Proc. 10th IAARC*, Melbourne, Australia, 18-23 August 1996, pp 402-409.

13. Blight, G.E., Alexander, M.G., Schutte, W.K. and Ralph, T.K. (1983). The effect of alkali-aggregate reaction on the strength and deformation of a reinforced concrete structure. Proc. 6th IAARC, Copenhagen, Denmark, pp 401-410.
14. Blight, G.E. (1996). Engineering properties of reinforced concrete damaged by AAR. Proc. 10th IAARC, Melbourne, Australia, pp 987-994.
15. Monette, L., Gardner, J. and Grattan-Bellew, P. (2000). Structural effects of the alkali-aggregate reaction on unloaded and loaded reinforced concrete beams. Proc. 11th ICAAR, Quebec City, Canada, pp. 999-1008.
16. Ahmed, T., Burley, E. and Rigden, S. (2000). The behavior of alkali-silica reactive concrete under high point load and under cyclic loading. Proc. 11th ICAAR, Quebec City, Canada, PP. 909-917.
17. Shayan, A. and Ivanusec, I. (1989). Influence of NaOH on mechanical properties of cement paste and mortar with and without reactive aggregate. Proc. 8th Int. Conf. on AAR, Kyoto, pp. 715-720.
18. Shayan, A., Xu, A. and Andrews-Phaedonos, F. (2003). Development of a performance Measure for Durability of Concrete Bridges. Proceedings of the 21st Biennial Conf , Concrete Institute of Australia, "Concrete in the third millennium", Vol. 2, Brisbane, Australia, pp739-757.
19. Shayan, A., Al-Mahaidi, R. and Xu, A. (2008). Durability and strength assessment of AAR-affected bridge deck planks. Proc. 13th IAARC, Trondheim, Norway, 16-20 June 2008, pp 422-432.
20. Shayan, A., Xu, A. and Pritchard, R. (2012). Influence of CP impressed currents on AAR expansion of concrete containing reactive aggregates. Proc. 14th ICAAR, Austin, Texas, USA, 20-25 may 2012.
21. Shayan, A. (2004). Alkali-aggregate reaction and basalt aggregates. Proc. 12th International Conference on Alkali-Aggregate Reaction in Concrete, 2004, Beijing, China, pp 1130-1135.
22. Shayan, A., Xu, A. (2012). Comparison between in-situ expansion measurements on AAR-affected beams, drilled cores and large sawn sections. Proc. 14<sup>th</sup> ICAAR, Austin, Texas, USA, 20-25 may 2012.
23. Shayan, A., Xu, A., Chirgwin, G. and Morris, H. (2009). Effects of seawater on AAR expansion of concrete. Cement and Concrete Research 40 (2010) 563–568.

# Effectiveness of Traditional and Alternative Supplementary Cementitious Materials in Mitigating Alkali-Silica Reactivity

Daniel Pospischil<sup>1</sup>, Vute Sirivivatnanon<sup>1</sup>, Uthayakumar Sivathasan<sup>2</sup> and Kevin Cheney<sup>2</sup>

<sup>1</sup>University of Technology, Sydney, Australia

<sup>2</sup>Hanson Construction Materials Pty. Ltd.

**Abstract:** With occasional disruptions in the supply of quality fly ash, and the global move towards sustainable means of power generation, it is timely for the Australian construction industry to examine the use of alternative Supplementary Cementitious Materials (SCM's) in various concrete applications. In this study, Metakaolin, Ground Granulated Blast Furnace Slag and Fly Ash were used to partially replace traditional Portland cement in mortar mixtures. The influence of these SCM's on the workability and early age strength development of mortars was examined, along with their effectiveness in mitigating the alkali-silica reactivity (ASR) of aggregates, which was evaluated using the new Australian Standard ((AS1141.60.1) (1)) for the Accelerated Mortar Bar Test (AMBT). Both the type and dosage of the two SCM's were studied.

**Keywords:** Accelerated mortar bar test (AMBT), alkali silica reactivity (ASR), supplementary cementitious materials (SCM).

## 1. Introduction

SCM's are not only widely used in concrete applications due to the range of benefits that such materials provide to the fresh and hardened properties of concrete, but also due to the range of environmental benefits associated with their use. With many SCM's being the by-product of existing and necessary industrial processes, the greenhouse gas emissions associated with the production of SCM's such as Fly Ash and GGBFS is considered to be negligible (Rubenstein (2)). The greenhouse gas emissions and energy requirements associated with the production of SCM's are attributed to the process from which the materials are wrought, and as such the use of certain SCM's is considered to be environmentally sustainable (Rubenstein (2)). In contrast, it is accepted that the production of 1 tonne of Portland cement results in emission of approximately 1 tonne of carbon dioxide alone, and as such, there is impetus within the construction industry to augment the use of blended cements and SCM's, which provide greater environmental sustainability (Rubenstein (2)).

Fly Ash and GGBFS are two of the most widely used and commercially available SCM's in Australia's construction industry, with Silica Fume also used in certain applications (Cement Australia 2014). With ongoing emphasis placed on the growth of sustainable energy production industries in Australia and on a global scale, it is estimated that the supply of Fly Ash to the Australian construction industry could halve by 2050 (Morrison, Graham et. al. (4)). In light of the popularity of the use of Fly Ash as a SCM, this paper seeks to present the effect that varying dosages of Fly Ash, GGBFS and an alternative SCM (Metakaolin) have on select fresh and hardened properties of mortars. This is crucial, as the findings of the report may deliver recommendations regarding types and dosages of SCM that can be used, should supply of traditional SCM's (namely Fly Ash) be constrained in the future.

The objectives of the reported work are as follows:

- To determine the impact of various dosages of Fly Ash, GGBFS and Metakaolin on early-age compressive strength of mortar, fresh properties (flow and air content) of mortar, and mitigation of mortar expansion due to alkali-silica reactions.
- If applicable, to propose types and dosages of SCM that can be used in concrete applications in place of Classified Fly Ash, (a commonly used SCM), should supply of Classified Fly Ash to the construction industry ever be constrained.
- To relate the mitigation of expansion of mortar bars due to alkali-silica reactions, to the physical and chemical characteristics of SCM's incorporated into mortars.
- To discuss variations in the compressive strength and workability of mortar specimens, in light of the physical and chemical properties of SCM's incorporated into mortars.

## 2 Scope and Experimental Procedures

With regards to the materials specifically used, two types of aggregate were tested:

- Dacite aggregate, denoted by 'DA'.
- Rhyolite aggregate, denoted by 'RH'.

These aggregates were used for the purposes of testing expansion of mortar due to ASR. For the determination of mortar air content and compressive strength, Sydney Sand was used as the fine aggregate; however, this is not denoted in the abbreviations used to identify such mortar mixtures.

Three types of SCM were tested: Fly Ash ('FA'), GGBFS ('SL') and Metakaolin ('MK').

Control mixtures, lacking any SCM, were also mixed and tested (denoted by the abbreviation, 'C').

### 2.1 Mix Design

**Table 1: Mix Design Compositions for ASR Tests.**

<i>Mixture</i>	<i>Cement (g)</i>	<i>SCM (g)</i>	<i>Aggregate (g)</i>	<i>Water (mL)</i>
DA-C	440	0	990	206.8
DA-FA10	396	44	990	206.8
DA-FA15	374	66	990	206.8
DA-FA25	330	110	990	206.8
DA-SL30	308	132	990	206.8
DA-SL40	264	176	990	206.8
DA-SL50	220	220	990	206.8
DA-MK7	409.2	30.8	990	206.8
DA-MK10	396	44	990	206.8
DA-MK15	374	66	990	206.8
RH-C	440	0	990	206.8
RH-FA10	396	44	990	206.8
RH-FA15	374	66	990	206.8
RH-FA25	330	110	990	206.8
RH-SL30	308	132	990	206.8
RH-SL40	264	176	990	206.8
RH-SL50	220	220	990	206.8
RH-MK7	409.2	30.8	990	206.8
RH-MK10	396	44	990	206.8
RH-MK15	374	66	990	206.8

**Table 2: Mix Design Compositions for compressive strength, mortar flow and mortar air content tests.**

<i>Mixture</i>	<i>Cement (g)</i>	<i>SCM (g)</i>	<i>Aggregate (g)</i>	<i>Water (mL)</i>
C	447.2	0	1229.7	268.3
FA10	402.5	44.7	1229.7	268.3
FA15	380.1	67.1	1229.7	268.3
FA25	335.4	111.8	1229.7	268.3
SL30	313	134.2	1229.7	268.3
SL40	268.3	178.9	1229.7	268.3
SL50	223.6	223.6	1229.7	268.3
MK7	415.9	31.3	1229.7	268.3
MK10	402.5	44.7	1229.7	268.3
MK15	380.1	67.1	1229.7	268.3

### 2.2 Experimental Methodology

Expansion of mortar bars due to ASR was tested and determined in line with AS1141.60.1-14 (1).

Flow of fresh mortar was measured in accordance with ASTM C1437-13 (5).

Air content of fresh mortar was measured in line with ASTM C185-08 (6).

Compressive strength of mortar cube specimens was determined in line with ASTM C109/C109M-13 (7).

Experimental conditions and methodologies which are referenced in the aforementioned standards, were followed where applicable.

### 3.0 Results and Discussion

#### 3.1 Alkali-Silica Reactivity

**Table 3: Mean expansion of mortar bars of different ages (Dacite aggregate).**

<i>Mixture</i>	<i>Expansion (%) at age</i>						
	<i>3-d</i>	<i>7-d</i>	<i>10-d</i>	<i>14-d</i>	<i>21-d</i>	<i>28-d</i>	<i>35-d</i>
<b>DA-C</b>	0.020	0.155	0.269	0.397	0.565	0.691	0.791
<b>DA-FA10</b>	0.011	0.059	0.113	0.180	0.286	0.367	0.432
<b>DA-FA15</b>	0.007	0.017	0.031	0.055	0.109	0.160	0.208
<b>DA-FA25</b>	-0.001	0.001	0.007	0.011	0.020	0.030	0.047
<b>DA-SL30</b>	0.017	0.079	0.132	0.200	0.290	0.359	0.414
<b>DA-SL40</b>	0.012	0.045	0.075	0.116	0.179	0.228	0.273
<b>DA-SL50</b>	0.002	0.013	0.020	0.031	0.060	0.090	0.118
<b>DA-MK7</b>	0.020	0.117	0.191	0.277	0.395	0.482	0.548
<b>DA-MK10</b>	0.015	0.081	0.135	0.200	0.293	0.367	0.422
<b>DA-MK15</b>	0.007	0.020	0.033	0.051	0.087	0.127	0.157

**Table 4: Mean expansion of mortar bars of different ages (Rhyolite aggregate).**

<i>Mixture</i>	<i>Expansion (%) at age</i>						
	<i>3-d</i>	<i>7-d</i>	<i>10-d</i>	<i>14-d</i>	<i>21-d</i>	<i>28-d</i>	<i>35-d</i>
<b>RH-C</b>	0.013	0.073	0.147	0.228	0.324	0.393	0.451
<b>RH-FA10</b>	0.010	0.026	0.041	0.070	0.117	0.159	0.191
<b>RH-FA15</b>	0.004	0.012	0.019	0.025	0.037	0.053	0.074
<b>RH-FA25</b>	0.001	0.005	0.011	0.012	0.017	0.021	0.028
<b>RH-SL30</b>	0.013	0.037	0.059	0.095	0.150	0.186	0.223
<b>RH-SL40</b>	0.013	0.027	0.035	0.051	0.083	0.107	0.136
<b>RH-SL50</b>	0.003	0.012	0.016	0.022	0.033	0.042	0.059
<b>RH-MK7</b>	0.013	0.055	0.108	0.167	0.239	0.297	0.338
<b>RH-MK10</b>	0.010	0.038	0.069	0.112	0.170	0.221	0.257
<b>RH-MK15</b>	0.007	0.017	0.023	0.032	0.047	0.070	0.085

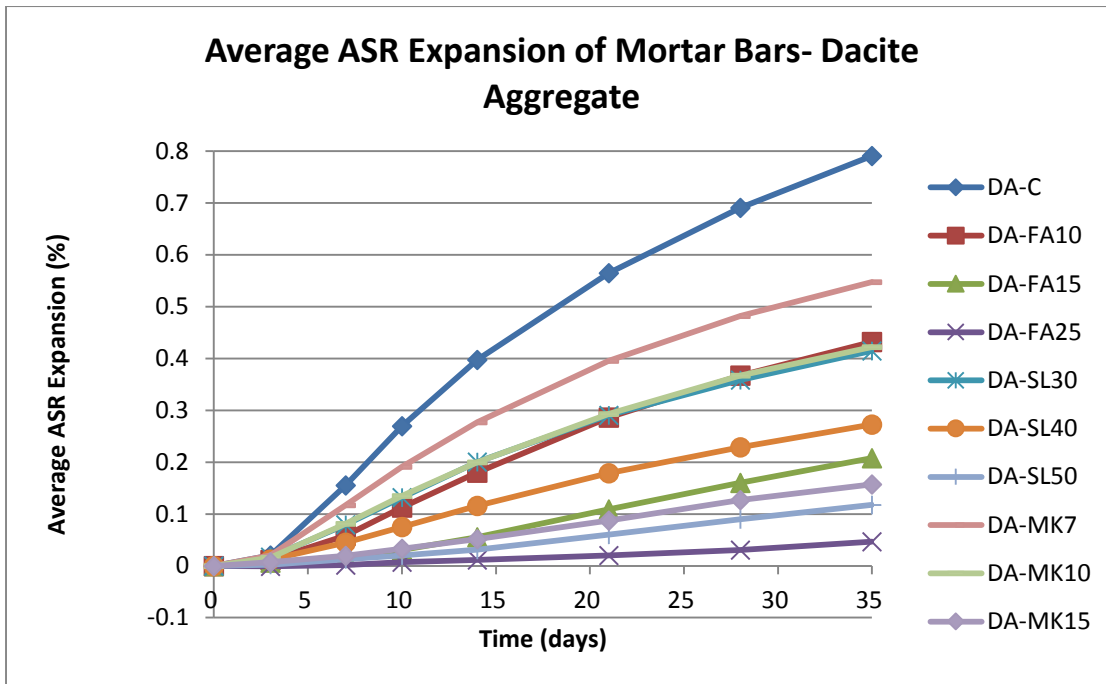


Figure 1: Average ASR expansion of mortar bars- Dacite aggregate.

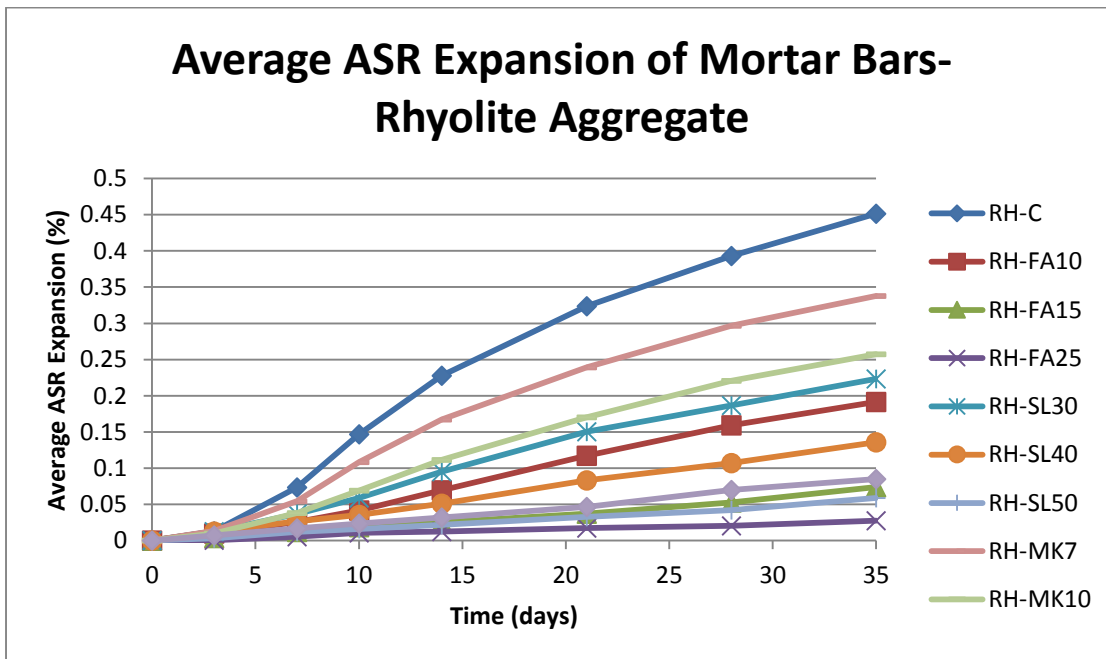


Figure 2: Average ASR expansion of mortar bars- Rhyolite aggregate.

Figures 1 and 2 above indicate that the expansion due to ASR of mortar bars containing Fly Ash increases at a decreasing rate with time, regardless of the type of aggregate used. It is expected that expansion of mortar bars containing Fly Ash as partial replacement of Portland cement would continue to increase with time in the accelerated mortar bar test. This is due to the saturation of mortar bars with sodium hydroxide solution, which provides an abundance of alkalis able to penetrate into the mortar mixture to facilitate alkali-silica reactions (Thomas (8)). However, the decreasing rate of expansion of mortar bars containing Fly Ash is attributed to the pozzolanic reaction associated with Fly Ash. An abundance of experimental work and literature exists, which outlines the efficacy of Fly Ash in consuming calcium hydroxide within mortars, thus reducing the alkali content of the mortar and mitigating the alkali-silica reaction (Kandasamy & Shehata (9); Shafaatian, Akhavan et al. (10)). Not only does the pozzolanic reaction allow Fly Ash to bind alkalis via this chemical reaction, but it also results in the formation of secondary C-S-H gel, which prevents the dissolution of soluble calcium



hydroxide with free water in the mortar mixture (Kandasamy & Shehata (9)). Dissolution of calcium hydroxide would otherwise increase the alkali concentration within the mortar mixture, facilitating the alkali-silica reaction (Kandasamy & Shehata (9)). Whilst effects of the pozzolanic reaction are noticeable after the age of 28-d, (and sometimes do not become prevalent prior to 90-d) (Sumer (11)), Figures 1 and 2 above indicate that at an age as low as 14-d, the rate of expansion of mortar bars containing Fly Ash begins to visibly decrease (evident as the gradient lines showing the mean expansion of each mortar bar begins to plateau).

The results indicate that the efficacy of GGBFS in mitigating expansions due to ASR became more prevalent with time, a likely indication of the pozzolanic reaction of GGBFS beginning. As Figures 1 and 2 demonstrate, at the early age of 3-d, the use of 40% GGBFS to replace Portland cement (using the Dacite aggregate) was not as efficacious in mitigating expansion of mortar bars due to ASR as mortars containing any dosage of Fly Ash, 50% GGBFS or 15% Metakaolin. Figures 1 and 2 also show that at the early age of 3-d, the use of 30% GGBFS to replace Portland cement was ineffective in curtailing expansion due to ASR, with all other mortar mixtures recording smaller expansion values, with the exception of the control mixture and the mixture containing 7% Metakaolin (when the Dacite aggregate was used). When the Rhyolite aggregate was used, mortar mixtures containing both 30% and 40% GGBFS were ineffective in curtailing expansion due to ASR at 3-d, with these mixtures recording the same expansion as the control. It is postulated that any initial benefits (or lack thereof), of GGBFS in mitigating expansion due to ASR can be attributed to the dilution of alkalis in the pore solution of mortars, associated with the use of GGBFS. At the early age of 3-d, the pozzolanic reaction associated with GGBFS has not had time to initiate, and thus, mitigation of expansion due to ASR associated with GGBFS mixtures, results from a reduction in the net quantity of available, soluble alkalis in the mortar pore solution (Kandasamy & Shehata (9); Kwon (12)). Regardless of the aggregate used, results indicate that incorporation of 50% GGBFS into a mortar mixture is able to sufficiently reduce the quantity of alkalis present in the mortar pore solution. However, the use of 30% and 40% GGBFS in mortar mixtures is less efficacious in achieving this end.

Being an artificial pozzolan, Metakaolin consumes portlandite and calcium hydroxide contained within the pore solution of cement paste, producing secondary C-S-H gel (Ramlochan, Thomas et. al. (13)). In doing so, the Metakaolin directly consumes alkalis, removing them from the pore solution of the cement paste, thus minimising the quantity of available alkali which is able to react with reactive silica introduced into the mortar mixture (Thomas (8), Ramlochan, Thomas et. al. (13)). When the Rhyolite aggregate was tested, the use of 15% Metakaolin was also highly effective, with only the expansion of mortar bars containing 15% Fly Ash, 25% Fly Ash or 50% GGBFS being less at 21-d. It is clear that as the dosage of Metakaolin used to partially replace Portland cement increases, the mitigation of expansion due ASR in mortar bars is enhanced. Not only is the retention of alkalis significant in the mitigation of ASR, but in the case of Metakaolin, so too is the retention of calcium, freely present in the pore solution of mortars. When alkali-silica gel forms, its expansion is widely attributed to the consumption of calcium (in the form of calcium hydroxide) (Thomas (8); Aquino, Lange et. al. (14)). Rather than forming an alkali-silica gel of low viscosity, which permeates into mortar pores with little expansive pressure, the consumption of calcium hydroxide creates a hygroscopic alkali-silica gel, which absorbs free water, expanding in the process (Thomas (8); Aquino, Lange et. al. (14)).

As shown in Figures 1 and 2 above, the use of 7% or 10% Metakaolin to partially replace Portland cement was relatively ineffective in mitigating ASR expansion, regardless of the type of aggregate used. Regardless of the aggregate used, the use of 10% Metakaolin in mortars recorded expansion lower than only the control mixture, and the mortar containing 7% Metakaolin. At the age of 28-d, the 10% Metakaolin mixture recorded expansion which was less than that of mortar containing 30% GGBFS, and equal to that of mortar containing 10% Fly Ash, an indication of the pozzolanic reaction of Metakaolin taking effect. The use of 7% Metakaolin was the most ineffective mortar mixture (with regards to the type and dosage of SCM used), as it recorded expansion values greater than those of all mortar mixtures, with the exception of the control mixture (regardless of the aggregate used). Ramlochan, Thomas et. al. (13) have shown experimentally, that the incorporation of less than 10% Metakaolin into a mortar mixture results in the formation of additional portlandite between the ages of 14-28-d (Ramlochan, Thomas et. al. (13)). This results because, once all the available Metakaolin has experienced the pozzolanic reaction, further calcium hydroxide ions are produced from subsequent hydration reactions in the mortar (Ramlochan, Thomas et. al. (13)). With time, this portlandite is able to leach alkalis into the mortar pore solution, facilitating the formation of expansive ASR gel (Ramlochan, Thomas et. al. (13)). Although this investigation did not seek to determine the alkali concentration of mortar bars containing dosages of various SCM's, let alone the portlandite content of such mortars, the ASR expansion results obtained for mortar bars containing 7% Metakaolin would seem to support the findings of Ramlochan, Thomas et. al. (13). The lack of efficacy of 7% Metakaolin

in mitigating ASR expansion can likely be attributed to its high reactivity (its high alumina content, relative to Fly Ash, GGBFS and Portland cement contributes to its pozzolanic properties). Consequently, Metakaolin is unable to effectively mitigate the formation of portlandite, and expansive alkali-silica gel with time, when used in small dosages.

### 3.2 Early-Age Compressive Strength

**Table 5: Effect of SCM type/dosage on mean 7-d and 28-d compressive strength of mortars.**

<b>Mortar Mixture</b>	<b>7-d Compressive Strength (MPa)</b>	<b>28-d Compressive Strength (MPa)</b>
<b>C</b>	24.00	35.76
<b>FA10</b>	18.12	37.24
<b>FA15</b>	19.56	38.00
<b>FA25</b>	17.52	36.56
<b>SL30</b>	18.04	35.80
<b>SL40</b>	17.80	29.96
<b>SL50</b>	16.44	26.28
<b>MK7</b>	20.40	34.40
<b>MK10</b>	20.60	36.88
<b>MK15</b>	23.80	37.04

As shown in Table 5, the fact that the mortar containing 15% Fly Ash records the greatest 7-d compressive strength of all mortars containing Fly Ash is attributed to the role of the dilution and filler effects at this early age. The filler and dilution effects have greater impact as the dosage of Fly Ash increases. As such, where 10% Fly Ash is used, the filler effect has a negligible impact on compressive strength, with the 24.5% decrease in 7-d compressive strength attributed to the dilution of the total quantity of Portland cement within the mortar, via partial replacement with Fly Ash. The compressive strength of mortars containing 25% Fly Ash is also decreased, due to the precedence that the dilution effect takes, over the filler effect in contributing to (inhibiting) compressive strength (which explains the 27% decrease in compressive strength at 7-d associated with this dosage). It would seem that the use of 15% Fly Ash represents an optimum dosage, whereby decreases in strength associated with the dilution effect are counteracted by compressive strength increases attributed to the filler effect. The fact that mortars containing 15% Fly Ash recorded the smallest decrease in 7-d compressive strength compared to other Fly Ash mixtures would seem to compliment this explanation.

The lack of early-age strength development exhibited by mortar mixtures containing GGBFS is attributed to both the slow onset of the pozzolanic reaction, and the dilution effect, a phenomenon especially prevalent due to the large dosages of GGBFS used to partially replace Portland cement. As GGBFS was used to partially replace Portland cement in dosages ranging from 30-50% in this investigation, the contributions that the filler effect and cementitious properties of GGBFS provided to the early-age strength development of mortar were outweighed by the dilution effect of the SCM. Due to the significant mass of GGBFS used to replace Portland cement in each mortar mixture, the total quantity of cementitious material able to contribute to the early-age strength development of the mortar decreases relative to the control mixture containing Portland cement alone (Barnett, Soutsos et al. (14)). The results shown in Table 5 above compliment this academic finding, whereby the compressive strength at both 7-d and 28-d of mortars containing GGBFS was reduced relative to that of the control mortar. Due to the dilution effect in particular, as the dosage of GGBFS used to partially replace Portland cement in mortar increases, inversely, the compressive strength of the mortar decreases (Miyazawa, Yokomuro et. al. (16)).

Metakaolin has a 'filling effect' when used in mortar, whereby, the small particle fineness and high specific surface area of the Metakaolin allows the SCM to fill voids between un-hydrated cement particles and aggregate particles in the mortar (Guneysi, Gesoglu et. al. (17)). This allows the formation of a mortar with a dense microstructure, which is relatively free of capillary pores, providing strength to the mortar. With a particle fineness approximately 40 times that of Portland cement, Metakaolin particles are able to pack the interfacial transition zone between cement paste and aggregate particles in mortar, filling voids and capillary pores. This increases the density of the microstructure of the mortar, whilst homogeneously dispersing cementitious by-products throughout the interfacial transition zone of the mortar (Wild, Khatib et. al. (18)). The filler effect that Metakaolin

provides is understood to outweigh the dilution effect associated with the SCM (Guneyisi, Gesoglu et. al. (17); Wild, Khatib et. al. (18)), allowing it to enhance the strength of mortar when used in dosages ranging from 5-15%. The results shown in Table 5 above compliment this academic finding, and in particular, explain the high 7-d compressive strength of mortar specimens containing Metakaolin, relative to mortars containing Fly Ash and GGBFS.

Being a predominately alumino-siliceous material, Metakaolin displays pozzolanic characteristics. Consequently, the material is able to hydrate and harden in the presence of moisture in mortar, consuming calcium hydroxide within the mortar pore solution to produce C-S-H gel, which contributes to the strength development of the mortar (Guneyisi, Gesoglu et. al. (17)). Despite having high contents of reactive silica and alumina relative to Portland cement (Megat Johari, Brooks et. al. (19)), the pozzolanic reactions associated with Metakaolin are most vigorous between the ages of 7-d to 14-d (Wild, Khatib et. al. (18)). This academic finding is supported by the experimental results presented in this investigation, whereby, the 28-d compressive strength of mortar specimens containing Metakaolin was found to be greater than that of the control mixture (with the exception of the mortar mixture containing 7% Metakaolin).

### 3.3 Mortar Flow

**Table 6: Effect of SCM type and dosage on fresh mortar flow.**

<b>Mortar Mixture</b>	<b>C</b>	<b>FA10</b>	<b>FA15</b>	<b>FA25</b>	<b>SL30</b>	<b>SL40</b>	<b>SL50</b>	<b>MK7</b>	<b>MK10</b>	<b>MK15</b>
<b>Flow (%)</b>	132	135	136	137	129	139	133	136	126	126

The results shown in Table 6 compliment a plethora of academic studies, which present experimental results that correlate increases in mortar flow with increasing dosages of Fly Ash. According to Sumer (11), “the morphologic effect states that there are many micro beads in Fly Ash, working as ‘lubricating balls’ when incorporated in fresh concrete” (Sumer 2012, p.531 (11)). The spherical shaped particles that constitute Fly Ash induce a ‘ball bearing effect’ regarding the fluidity and motion of mortar in the fresh state, which is manifested by way of enhanced workability (increasing mortar flow), when the Fly Ash is incorporated into a mortar mixture. This explanation is supported by Sahmaran, Christianto et. al.(20), who argue that the spherical shape of Fly Ash particles reduces friction between the particles themselves, Fly Ash and cement particles, and Fly Ash and aggregate particles in a mortar mixture, enhancing mortar flow. Consequently, when force is exerted on a mortar or concrete mixture during placement and consolidation, the decreased resistance to particle motion (aided by the lessened frictional forces acting between the cementitious paste and aggregate particles) improves the workability of the mixture. With regards to mortar, this phenomenon is manifested through a noticeable increase in the flow of mortars containing Fly Ash.

The increase in flow associated with mortars containing 40% and 50% GGBFS, as shown in Table 6, is indicative of other experimental and academic studies. As the dosage of GGBFS used to replace Portland cement was increased, so too did mortar flow. This is attributed to the smooth, glass-like texture of GGBFS, which allows the SCM to increase mortar flow, despite its angular and irregular particle shape (Sumer (11); Isikdag & Topcu (21)). A significant body of academic study indicates that GGBFS also disperses cementitious particles evenly in a mortar matrix, which enhances the flow of such mixtures (Megat Johari, Brooks et al. (19)). The improved workability that GGBFS provides to mortar (in the correct dosages) is also attributed to the particle size of GGBFS particles, which provides a micro bead effect within the mortar (Sumer (11)).

The results obtained compliment numerous academic studies, which show that as the dosage of Metakaolin used to partially replace Portland cement in mortar mixtures increases, the flow of the mortar mixtures decreases. This is primarily attributed to the water demand that Metakaolin particles exhibit, which is a combination of both the fineness and morphology of the material (Wild, Khatib et. al. (18); Siddique & Klaus (22)). With an average specific surface area of 15000 m<sup>2</sup>/kg (Megat Johari, Brooks et. al. (19)), Metakaolin has a specific surface area significantly higher than that of Portland cement (380 m<sup>2</sup>/kg). Consequently, Metakaolin exhibits a high water demand when introduced into mortar, absorbing mix water, and thus preventing the mix water from contributing to the fluidity and flow of the mortar (Wild, Khatib et. al. (18)).

### 3.4 Mortar Air Content

Table 7: Effect of SCM type and dosage on air content of mortar.

Mortar Mixture	C	FA10	FA15	FA25	SL30	SL40	SL50	MK7	MK10	MK15
Air Content (%)	3.5	4.2	4.3	4.3	4.7	4.5	4.2	4.6	4.4	3.9

As the results in Table 7 above indicate, the partial replacement of Portland cement with Fly Ash, GGBFS or Metakaolin increases the air content of mortar, relative to the control mixture. As the dosage of GGBFS and Metakaolin used to partially replace Portland cement in a mortar mixture increases, the air content of the mortar mixture decreases. This is attributed to the 'filler effect' associated with both these SCM's. The small particle size of GGBFS, and in particular, Metakaolin, relative to that of Portland cement, allows the SCM's to penetrate homogeneously throughout the microstructure of a mortar mixture, refining the size of microstructural pores within the mortar (Guneyisi, Gesoglu (17); Wild, Khatib et. al. (18); Siddique & Klaus (22)). Consequently, the volume of air retained within the pores of the mortar decreases, due to the enhanced microstructural density of the mortar which results (Guneyisi, Gesoglu (17); Wild, Khatib et. al. (18); Siddique & Klaus (22)). It is postulated that greater microstructural density and mortar pore refinement is associated with an increase in the dosage of GGBFS or Metakaolin incorporated into a mortar mixture. In turn, the air content of the mortar would be expected to decrease, a postulation complimented by the experimental data obtained.

The increase in the air content of mortar mixtures containing increasing dosages of Fly Ash (as a partial replacement for Portland cement) presents a counter-intuitive result. In line with academic findings, it was anticipated that, as the dosage of Fly Ash used to partially replace Portland cement was increased, the air content of the mortar mixtures would decrease. Such results would be attributed to the filler effect, whereby, the micro bead effect associated with Fly Ash allows the material to enhance the microstructural density of mortar, by penetrating homogeneously throughout a mortar mixture (Sumer (11)). The results obtained do not compliment current academic findings. As such, it is postulated that the particle-packing behaviour of the spherical Fly Ash particles influenced the air content of the mortar mixtures which resulted. When spherical Fly Ash particles pack within a mortar mixture, voids form between the particles, in which air can become entrapped.

### 4.0 Conclusions

Due to the need to address potential constraints regarding the supply of Fly Ash to the construction industry (for use in concreting applications), the results and discussion presented in this investigation indicate that dosages of GGBFS and Metakaolin can be used to partially replace Portland cement in concrete applications, rather than the more traditionally used Fly Ash. Furthermore, the experimental results presented in this report, outline that particular dosages of Fly Ash, GGBFS and Metakaolin can also be used to partially replace Portland cement in concreting applications, for the purposes of preventing expansion due to alkali-silica reactivity, without having deleterious effects on the early-age compressive strength, flow or air content of mortars. The following core results were found:

- 25% replacement of Portland cement with Fly Ash ought to ensure the mitigation of expansion due to alkali-silica reactivity. Whilst the use of 25% Fly Ash is not the dosage which optimises the 28-d compressive strength of mortar, this dosage will increase the 28-d compressive strength of concrete, relative to a control specimen. Furthermore, the use of 25% Fly Ash is also expected to enhance the workability of concrete in the fresh state, namely, flow and air content. Where such a dosage was used in this investigation, the air content of mortar was found to increase by 22.9%, and the flow of mortar was found to increase by 3.8%, indicating an increase in the ease with which concrete containing 25% Fly Ash can be placed and consolidated in the fresh state.
- 50% replacement of Portland cement with GGBFS ought to ensure the mitigation of expansion due to alkali-silica reactivity. It is not recommended that GGBFS be used in applications where

it is necessary to mitigate expansion due to alkali-silica reactivity, whilst also maintaining or enhancing the compressive strength of the concrete in question. This is because it is expected that using such a dosage (50%) of GGBFS, will decrease the 28-d compressive strength of concrete. Thus, concrete containing 50% GGBFS should not be used in high strength concreting applications. However, 50% GGBFS was found to enhance the workability (air content and flow) of mortars, which is desirable regarding fresh concrete. In particular, this dosage of GGBFS was found to enhance mortar air content by 20%, and flow by 0.8%, relative to the control, in this investigation.

- 15% replacement of Portland cement with Metakaolin ought to ensure the mitigation of expansion due to alkali-silica reactivity. This is ideal, as the use of 15% Metakaolin ought to maximise the 28-d compressive strength of mortar. In this investigation it was found that the use of 15% Metakaolin enhanced the 28-d compressive strength of mortar by 3.4%, relative to the control. However, the use of 15% Metakaolin has mixed effects on the workability of mortar in the fresh state. The use of 15% Metakaolin can be expected to enhance the air content of mortars (an increase of 11.4% relative to the control was noted in this investigation). However, the use of 15% Metakaolin significantly increases the water demand of mortar mixtures, and as such, decreases the flow of mortar in the fresh state.

As stated, the aforementioned dosages of Fly Ash, GGBFS and Metakaolin ought to be used in practice, so as to mitigate deleterious expansion of concrete elements due to alkali-silica reactivity. In summation, it is evident that, in the correct dosage, Fly Ash, GGBFS and Metakaolin can all be used to optimise the mitigation of ASR expansion, early-age compressive strength development, and the flow and air content of fresh mortars, and as such, these SCM's can find application in concrete practice within the Australian construction industry.

## 5.0 Acknowledgements

Dr. Vute Siriviatnanon, Mr. Rami Haddad, Mr. Antonio Reyno, Mr. David Hooper and Mr. Farzad Khamchin Moghaddam; University of Technology, Sydney.

Mr. Sivithasan Uthayakumar, Mr. Beda Aureus and Mr. Kevin Cheney; Hanson Construction Materials P/L.

## 6.0 References

1. Standards Australia 2014, *Methods for sampling and testing aggregates- Potential alkali-silica reactivity- Accelerated mortar bar method*, AS 1141.60.1-2014, Standards Australia, Sydney.
2. Rubenstein, M. 2012, *Emissions from the cement industry*, State of the Planet, accessed 20 October 2014, <http://blogs.ei.columbia.edu/2012/05/09/emissions-from-the-cement-industry/>.
3. Cement Australia 2014, *Why do we use Supplementary Cementitious Materials (SCM's)?*, Cement Australia, accessed 22 September 2014, <http://www.cementaustralia.com.au/wps/wcm/connect/website/bulk/bulk-home/faqs/#FAQ-bulk-q15.html>.
4. Morrison, A., Graham, P. & Nelson, P.F. 2005, 'Future ash availability- Potential consequences of transformation of Australia's energy generation portfolio to 2050', 2005 World of Coal Ash (WOCA), Lexington, viewed 20 October 2014, <http://www.flyash.info/2005/88mor.pdf>.
5. American Society for Testing and Materials 2013, *Standard Test Method for Flow of Hydraulic Cement Mortar*, ASTM C1437-13, American Society for Testing and Materials, Pennsylvania.
6. American Society for Testing and Materials 2008, *Standard Test Method for Air Content of Hydraulic Cement Mortar*, ASTM C185-08, American Society for Testing and Materials, Pennsylvania.

7. American Society for Testing and Materials 2013, *Standard Test Method for Compressive Strength of Hydraulic Cement Mortars (using 2-in. or [50-mm] Cube Specimens)*, ASTM C109/C109M-13, American Society for Testing and Materials, Pennsylvania.
8. Thomas, M. 2011, 'The effect of supplementary cementing materials on alkali-silica reaction: A review', *Cement and Concrete Research*, vol. 41, no. 12, pp. 1224-1231.
9. Kandasamy, S. & Shehata M.H. 2014, 'The capacity of ternary blends containing slag and high-calcium fly ash to mitigate alkali silica reaction', *Cement and Concrete Composites*, vol. 49, May 2014, pp. 92-99.
10. Shafaatian, S.M.H., Akhavan, A., Maraghechi, H. & Rajabipour, F. 2013, 'How does fly ash mitigate alkali-silica reaction (ASR) in accelerated mortar bar test (ASTM C1567)?' *Cement and Concrete Composites*, vol. 37, March 2013, pp. 143-153.
11. Sumer, M. 2012, 'Compressive strength and sulfate resistance properties of concretes containing class F and class C fly ashes', *Construction and Building Materials*, vol. 34, September 2012, pp. 531-536.
12. Kwon, Y-J. 2005, 'A study on the alkali-aggregate reaction in high strength concrete with particular respect to the ground granulated blast-furnace slag effect', *Cement and Concrete Research*, vol. 35, no. 7, pp. 1305-1313.
13. Ramlochan, T., Thomas, M. & Gruber, K.A. 2000, 'The effect of metakaolin on alkali-silica reaction in concrete', *Cement and Concrete Research*, vol. 30, no. 3, pp. 339-344.
14. Aquino, W., Lange, D.A. & Olek, J. 2001, 'The influence of metakaolin and silica fume on the chemistry of alkali-silica reaction products', *Cement and Concrete Composites*, vol. 23, no. 6, pp. 485-493.
15. Barnett, S.J., Soutsos, M.N., Millard, S.G. & Bungey, J.H. 2006, 'Strength development of mortars containing ground granulated blast-furnace slag: Effect of curing temperature and determination of apparent activation energies', *Cement and Concrete Research*, vol. 36, no. 3, pp. 434-440.
16. Miyazawa, S., Yokomuro, T., Sakai, E., Yatagai, A., Nito, N. & Koibuchi, K. 2014, 'Properties of concrete using high C<sub>3</sub>S cement with ground granulated blast-furnace slag', *Construction and Building Materials*, vol. 61, June 2014, pp. 90-96.
17. Güneş, E., Gesoğlu, M., Karaoğlu, S. & Mermerdaş, K. 2012, 'Strength, permeability and shrinkage cracking of silica fume and metakaolin concretes', *Construction and Building Materials*, vol. 34, September 2012, pp. 120-130.
18. Wild, S., Khatib, J.M. & Jones, A. 1996 'Relative strength, pozzolanic activity and cement hydration in superplasticized metakaolin concrete', *Cement and Concrete Research*, vol. 26, no. 10, pp. 1537-1544.
19. Megat Johari, M.A., Brooks, J.J., Kabir, S. & Rivard, P. 2011, 'Influence of supplementary cementitious materials on engineering properties of high strength concrete', *Construction and Building Materials*, vol. 25, no. 5, pp. 2639-2648.
20. Sahmaran, M., Christianto, H.A. & Yaman, I.O. 2006, 'The effect of chemical admixtures and mineral additives on the properties of self-compacting mortars', *Cement and Concrete Composites*, vol. 28, no. 5, pp. 432-440.
21. Isikdag, B. & Topcu, I.B. 2013, 'The effect of ground granulated blast-furnace slag on properties of Horasan mortar', *Construction and Building Materials*, vol. 40, March 2013, pp. 448-545.
22. Siddique, R. & Klaus, J. 2009, 'Influence of metakaolin on the properties of mortar and concrete: a review', *Applied Clay Science*, vol. 43, no. 3-4, pp. 392-400.

# The Use of Reaction Kinetics in Classifying Alkali Silica Reactivity Potential of Aggregates

Bob Bornstein<sup>1</sup>, David Hocking<sup>2</sup>, Johwelvic Bacolod<sup>3</sup> and Vute Sirivivatnanon<sup>4</sup>

<sup>1</sup>Manager Technical Services, Boral Construction Materials Australia

<sup>2</sup>Technical Manager Concrete, Boral Construction Materials Australia

<sup>3</sup>Civil Engineering Student, University of Technology Sydney

<sup>4</sup>Professor of Concrete Engineering, University of Technology Sydney

**Abstract:** The Australian Standard accelerated mortar bar test (AMBT) method, AS 1141.60.1, adopts the expansion limits at two exposure periods to classify the alkali silica reactivity (ASR) of aggregate. This was a first step toward the use of 'reaction kinetics' or 'rate of reaction' to detect and classify alkali silica reactivity. The AS 1141.60.2 concrete prism test (CPT), on the other hand, uses a single expansion limit at one year to classify ASR. This paper examines the validity of the use of reaction kinetics, evaluated from the AMBT expansion data, to gauge and classify the reactivity. This may enable a better quantification of the degrees of reactivity and a more fundamental approach to ASR mitigation.

**Keywords:** Accelerated mortar bar test (AMBT), concrete prism test (CPT), reaction kinetics.

## 1. Introduction

Alkali Silica Reactivity (ASR) is an internal reaction that can lead to deterioration of concrete. While only a small proportion of concrete suffers from deterioration due to ASR, its effects can lead to a significant reduction in service life of affected structures. Consequently, much effort has been expended in developing test methods to evaluate ASR reaction potential.

International accelerated mortar bar (NBRI method, ASTM C1260 and CSA A23.2-25A methods) and concrete prism test methods (ASTM C1293, CSA Test method A23.2-14A) have been used in Australia, together with derived test methods adopted by various statutory authorities such as RTA T363 Rapid Mortar Bar Test and Vic Roads RC376.04 Concrete Prism Test. These test methods were joined in 2014 by two new standard test methods published by Standards Australia CE-012 Aggregate and Rock for Engineering Purposes committee:

AS 1141.60.1:2014 Potential alkali-silica reactivity - Accelerated mortar bar method (AMBT) and

AS 1141.60.2:2014 Potential alkali-silica reactivity - Concrete prism method (CPT).

AS 1141.60.1 accelerated mortar bar method (AMBT) adopts the expansion limits at two exposure periods to classify the alkali silica reactivity (ASR) of aggregate, while AS 1141.60.2 concrete prism test (CPT), on the other hand, uses a single expansion limit at one year to classify ASR.

However, alkali silica reaction is a phenomenon occurring over time. These test methods do not address the issue of how much time is likely to pass before deleterious expansion occurs. Johnston, Stokes and Surdahl (2000)<sup>[2]</sup> attempted to develop a kinetic based model for better interpreting results from the ASTM C1260 mortar bar test. A literature search resulted in the selection of the Kolmogorov-Avrami-Mehl-Johnson (KAMJ) model, which describes nucleation and growth transformation reaction kinetics. A number of tests were done at various ages using extremely reactive sand and fitted into the KAMJ model. The conclusion from the research in this paper was that a kinetic based model can provide a means of interpreting the results of ASTM C1260 independent of the 14 day result.

A further study was undertaken by Johnston, Stokes, Fournier and Surdahl (2004)<sup>[3]</sup> to try to correlate the rates of reaction determined by the KAMJ model to the onset of cracking of concrete in service and large slabs and blocks stored externally. The study concluded that using the kinetic approach of the KAMJ model allows for a significant improvement in the reliability in predicting the reactivity of aggregates. Results from the study indicate that the same equation is applicable to laboratory test ASTM C1260 and slab and block concrete specimens exposed outdoors and in predicting the time to onset cracking of concrete pavements, all of which support its suitability as a model.

This paper examines the validity of the use of reaction kinetics, evaluated from both the AS 1141.60.1 (AMBT) and AS 1141.60.2 (CPT) expansion data, to gauge and classify the reactivity. This may enable a better quantification of the degrees of reactivity and a more fundamental approach to ASR mitigation.

## 2. Value of AMBT & CPT

Rocker, Mohammadi, Sirivivatnanon and South (2015)<sup>[1]</sup> reviewed international data on AMBT and CPT tests, as well as field performance of large concrete blocks.

It was found that the AMBT was a good indicator of reactivity of some aggregates. In many cases, however, the results from the AMBT disagreed with those from the CPT and the outdoor simulated field tests. In general, reactivity diagnosed by CPT was found to correlate well with reactivity in field exposure.

This mirrors the experience of Boral Construction Materials testing over many years and the requirements of some authorities that, where an aggregate is classified as reactive by AMBT, it be tested using the CPT. This often results in a non-reactive result.

While there is no agreed hierarchy of the two test methods, experience and current practice suggests the CPT has a closer correlation to reactivity in field exposure.

### 2.1 Aggregate classification based on AMBT

The non-mandatory appendix in ASTM C1260 provides guidance to the interpretation of test results with the following expansion limits: 14-day expansions of less than 0.10% to be indicative of “innocuous” behavior whereas 14-day expansions of more than 0.20% are indicative of “potentially deleterious” expansion. Aggregates with 14-day expansions between 0.10 and 0.20% are known to be innocuous and deleterious in filed performance, and supplemental information in the form of petrographic examination or identification of alkali reaction products in specimens after tests, or field service record can be used in the assessment of the performance

**Table 2.1 Comparison of ASTM and AS Mortar bar expansion limits**

ASTM C1260		AS 1141.60.1		
Interpretation	14 days	Classification	10 days	21 days
Innocuous	< 0.10*%	Non-reactive	-	< 0.10*%
“uncertain”	0.10*-0.20%	Slowly reactive	< 0.10*%	0.10*% to <0.30%
Potential deleterious	≥ 0.20*%	Reactive	≥ 0.10*% -	- ≥ 0.30%

\*The value of the lower limit for natural fine aggregate is 0.15%

The AS 1141.60.1 classified aggregates with 21-day expansion below a lower limit of 0.10% to be non-reactive, and those with 10-day expansion equal or greater than the lower limit of 0.10% or 21-day expansion equal or greater than the upper limit of 0.30% to be reactive. For aggregates with 10-day expansion below the lower limit of 0.10% but 21-day expansion equal to or exceeding the lower limit of 0.10% but not exceeding the upper limit of 0.3% to be a “slowly reactive” aggregate. Note that the lower limit applicable to natural sand is 0.15%.

### 2.2 Aggregate classification based on CPT

The ASTM C1293 tests the expansion of concrete with a cement content of  $420 \pm 10 \text{ kg/m}^3$  and a dry mass of coarse aggregate per unit volume of concrete equal to  $0.70 \pm 0.02$  of its dry-rodded bulk density with a water to cementitious material ratio (w/cm) of 0.42 to 0.45 by mass. The cement has a total alkali content of 1.25% of  $\text{Na}_2\text{O}$  equivalent by mass of cement. Specimens are placed in a container stored in a  $38.0 \pm 2 \text{ }^\circ\text{C}$ . The non-mandatory appendix states that an aggregate might reasonably be classified as potentially deleteriously reactive if the average expansion of three concrete specimens is equal to or greater than 0.04% at one year (CSA A23.2-27A-00 Table 1). It also suggests that it is reasonable to



conclude that the amount of pozzolan or slag used in combination with an aggregate is at least the minimum needed to prevent excessive expansion in field concrete if the average expansion is less than 0.04% at two years (CSA A23.2-28A-02).

The AS 1141.60.2 uses essentially the same concrete mix proportion and test method as the ASTM C1293 but classifies an aggregate with a prism expansion of less than 0.03% at 52 weeks as “non-reactive” and an aggregate with a prism expansion equal to or greater than 0.03% at 52 weeks as “potentially reactive”. The lower expansion limit is considered more conservative as it was adopted from the RMS T364 which tests concrete with a higher adjusted cement alkali of 1.38% Na<sub>2</sub>O equivalent.

### 2.3 Aggregate classification based on reaction kinetics

The current standard methods adopted by Australia in determining ASR involve the collection of information regarding whether or not deleterious expansion occurs and should be expected for the concrete in service. This process and the information gathered fails to address the time frame; that is the amount of time that passes until significant damage might occur in the concrete in question. For this reason it is desirable to develop a model and method that explores the correlation between rates of reaction, and the development of cracking in concretes in service. By implementing a kinetic-based method for interpreting AMBT or CPT test data not only can relative potential for ASR be evaluated and determined by the existing laboratory tests, but more information regarding the time frame in which damage occurs in field concrete may also be obtained and determined from these same tests.

#### 2.3.1 The Kolmogorov-Avrami-Mehl-Johnson (KAMJ) model

The study performed by Johnston et. al. (2000, p. 142)<sup>[2]</sup> was conducted to determine an appropriate model to represent ASR expansion in the C1260 test. The Kolmogorov-Avrami-Mehl-Johnson (KAMJ) model which describes nucleation and growth transformation reaction kinetics was selected as potentially applicable and has the following form:<sup>[2]</sup>

$$\alpha = 1 + \alpha_0 - e^{-k(t-t_0)^M} \quad (1)$$

$$\alpha = \alpha_0 + (1 - \alpha_0)(1 - e^{-k(t-t_0)^M}) \quad (2)$$

Johnston et. al. (2000, p. 142-144)<sup>[2]</sup> explains the equations:

$\alpha_0$  is the degree of reaction at time  $t_0$  when nucleation and growth become dominant, and  $k$  is a rate constant which combines the effects of nucleation, multidimensional growth, the geometry of reaction products, and diffusion. For expansion,  $\alpha$  is the degree of reaction and  $\alpha_\infty$  cannot exceed 1.

For the study, ASTM C1260 tests were conducted using extremely reactive sand from South Dakota, and length measurements taken at 3, 7, 11, 14, 17, 21, 25, and 28 days with data being fit into the above equations. A value of three days was selected for  $t_0$  with the corresponding expansion value used for  $\alpha_0$ . The fit was determined with linear regression using:<sup>[2]</sup>

$$\ln \ln \left( \frac{1}{1 + \alpha_0 - \alpha} \right) \text{ vs. } \ln (t - t_0) \quad (3)$$

The table 2.2 below taken from Johnston et. al. (2000, p. 145)<sup>[2]</sup> shows the expansion values and kinetic parameters for the different test conditions.

Table 2.2: ASTM results with different base concentrations<sup>[2]</sup>

*ASTM results with different base concentrations.*

Time (days)	ASTM C 1260 Percent Expansion (NaOH Normality)					
	0.5	0.6	0.7	0.8	0.9	1.0
3	0.017	0.026	0.036	0.045	0.055	0.065
7	0.025	0.041	0.087	0.122	0.156	0.196
11	0.043	0.102	0.182	0.240	0.248	0.290
14	0.071	0.162	0.248	0.303	0.303	0.336
17	0.100	0.207	0.297	0.347	0.368	0.373
21	0.129	0.256	0.343	0.391	0.384	0.430
25	0.160	0.301	0.390	0.432	0.420	0.467
28	0.174	0.324	0.407	0.454	0.464	0.488
$\ln k$	-7.1320	-6.2530	-4.4130	-3.7460	-3.3430	-2.9550
$M$	1.715	1.694	1.179	1.001	0.850	0.743
$R^2$	0.989	0.960	0.971	0.965	0.983	0.996

Where  $\ln k$  is the intercept and  $M$  is the slope of the regression line, the figure below is a plot of  $M$  versus  $\ln k$ . Figure 2.1 shows a uniform response with respect to the exponential and rate components of the kinetic parameters.

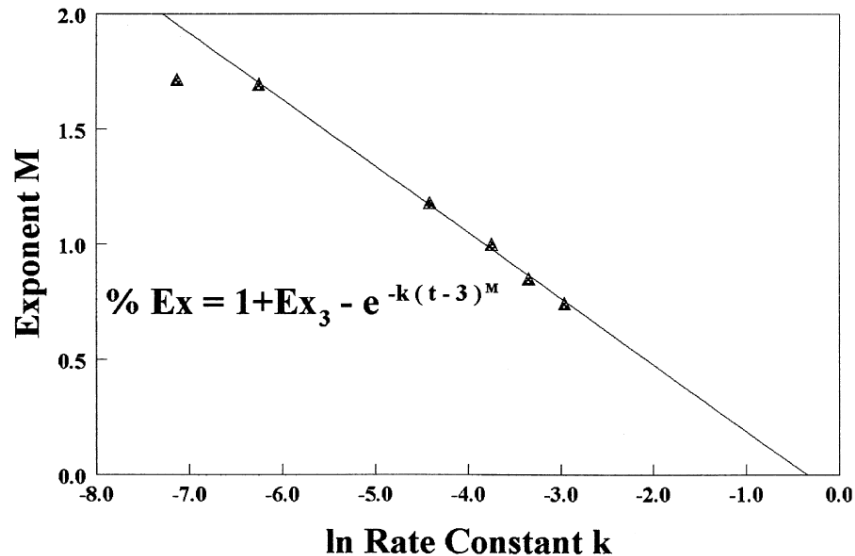


Figure 2.1: Exponent versus  $\ln$  rate constant: ASTM C1260 at different concentrations. <sup>[2]</sup>

The results of Johnston et. al. (2000)<sup>[2]</sup> conclude that an application of a kinetic model based on the KAMJ equation provides a means of interpreting the results of ASTM C1260 independent of expansion values obtained at 14 days. The use of a kinetic plot of slope  $M$ , and intercept,  $\ln k$ , obtained from a least-squares fit to the logarithmically transformed kinetic equation differentiates between reactive aggregates having  $\ln k > -6$ , and innocuous aggregates with  $\ln k < -6$ .

### 2.3.2 Analysis of Australian Data

Existing test data on 56 Australian aggregates tested for ASR in accordance with procedures detailed in AS1141.60.1 and AS1141.60.2 Table 2.3 below is an extract from that data.

Table 2.3: ASR classification results based on AMBT and CPT to Test Methods 1141.60.1 and 1140.60.2

Identifier	Aggregate type	Aggregate Reactivity Classification		AMBT Expansion	
		(AS1141.60.1)	(AS1141.60.2)	% Expansion (14 days)	% Expansion (28 days)
A1	Olivine Basalt	Non- Reactive	Non- Reactive	0.020	0.049
A2	Basalt	Non- Reactive	Not completed	0.013	0.035
A3	Basalt	Non- Reactive	Non- Reactive	0.030	0.056
A5	Pyroxene Andesite	Reactive	Non- Reactive	0.403	0.739
A6	Latite	Non- Reactive	Non- Reactive	0.012	0.055
A7	CRG	Reactive	Non- Reactive	0.230	0.462
A8	Rhyodacite Porphyry	Reactive	Reactive	0.318	0.533
A9	Hornfels	Slowly Reactive	Non- Reactive	0.081	0.217
A10	Limestone	Non- Reactive	Non- Reactive	0.008	0.011

The complete set of results for AMBT is plotted in Figure 2.2 showing expansion vs time for the AMBT test data. Also plotted are indicator lines at 0.1% and 0.3% as per the classification criteria of aggregates expansion based on AS11411.60.1.

Kinetic parameters were then calculated at 14 days and 28 days and analysed using the KAMJ model to establish any correlation between test results and a kinetic based method of interpretation. This is shown in table 2.4 below.

Table 2.4: Kinetic Parameters based on AMBT (1141.60.1)

Identifier	Aggregate type	Kinetic Parameters							
		$\ln k_{14}$	$k_{14}$	$M_{14}$	$R^2_{14}$	$\ln k_{28}$	$k_{28}$	$M_{28}$	$R^2_{28}$
A1	Olivine Basalt	-6.6494	0.001295	0.935	0.948	-7.0670	0.000853	1.165	0.969
A2	Basalt	-5.7956	0.003041	0.321	0.695	-7.1331	0.000798	1.084	0.852
A3	Basalt	-6.2066	0.002016	1.012	0.994	-6.1822	0.002066	1.001	0.995
A5	Pyroxene Andesite	-6.2644	0.001903	2.367	0.986	-5.2587	0.005202	1.805	0.959
A6	Latite	-7.7286	0.000440	1.370	0.996	-8.2360	0.000265	1.661	0.988
A7	CRG	-5.0423	0.006459	1.548	0.993	-4.6093	0.009958	1.304	0.987
A8	Rhyodacite Porphyry	-3.7765	0.022903	1.151	0.991	-3.5206	0.029582	1.008	0.990
A9	Hornfels	-6.5472	0.001434	1.702	1.000	-6.2498	0.001931	1.538	0.994
A10	Limestone	-9.2881	0.000093	1.534	1.000	-8.2226	0.000269	1.008	0.920

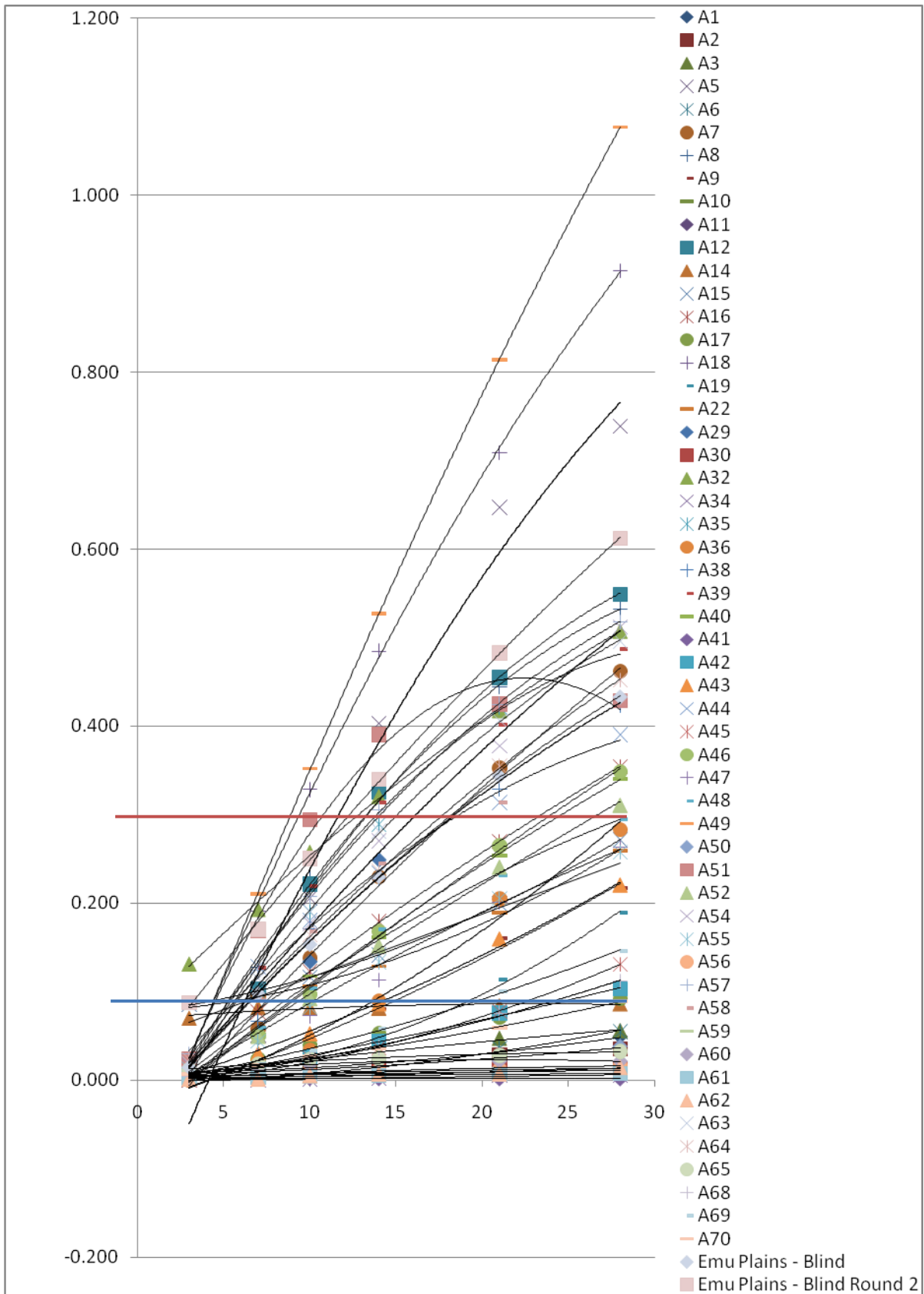


Figure 2.2: Plot of percent expansion vs time: AS1141.60.1 data

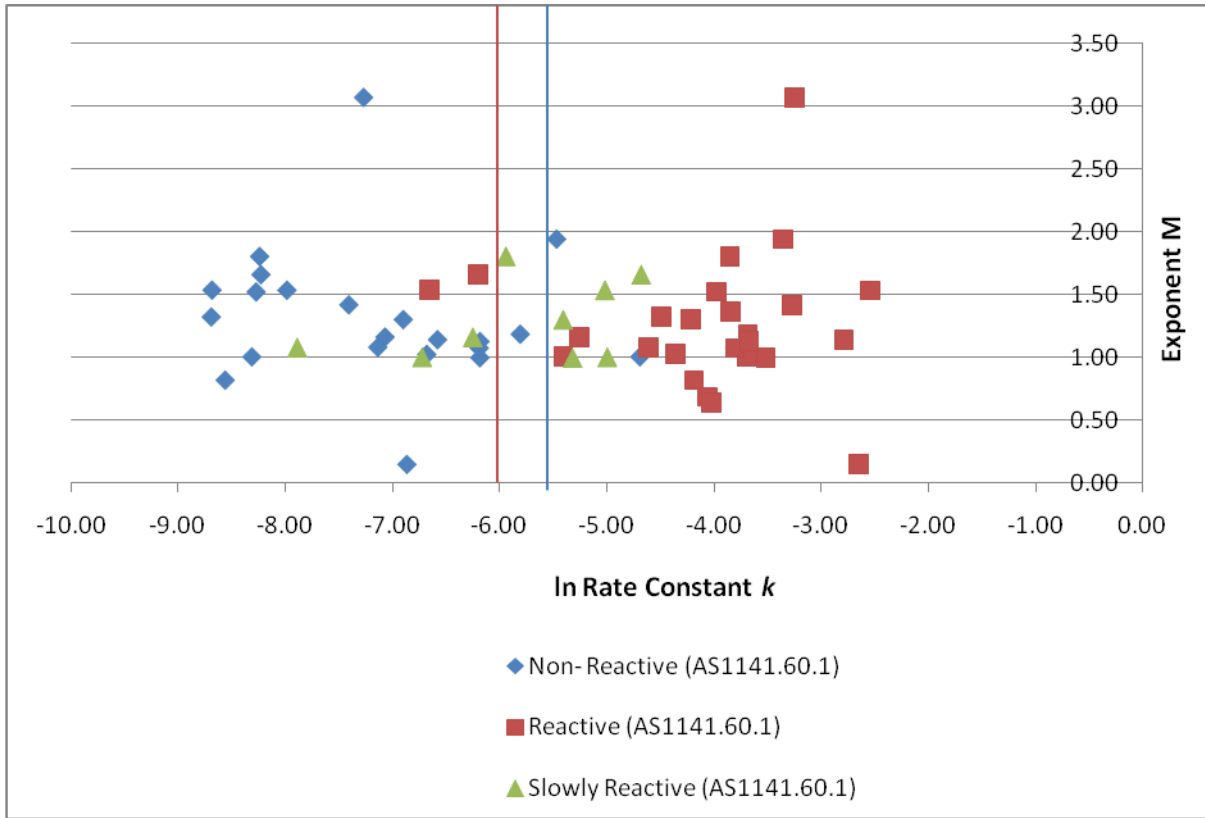


Figure 2.3: Reactivity plot based on AMBT (AS1141.60.1 test data) – 28 days

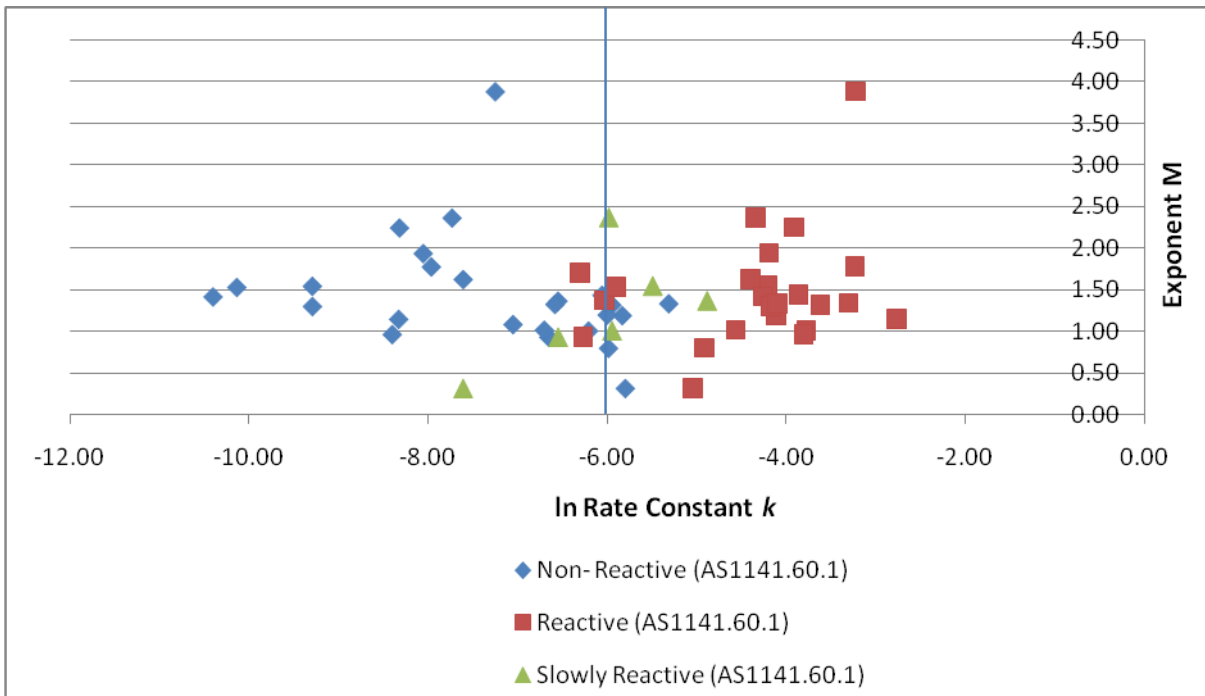


Figure 2.4: Reactivity plot based on AMBT (AS1141.60.1 test data) – 14 days

From figure 2.3 and 2.4 above, adopting the conservative value of  $\ln k$  below which all aggregates are innocuous as -6 specified in Johnston et. al. (2000) results in a split in which most aggregates tested as

non-reactive with AS1141.60.1 fall below, and those tested as reactive with AS1141.60.1 fall above. However, for both 14 and 28 days, there are some aggregates which tested as slowly reactive using AS1141.60.1 expansion criteria that are deemed to be innocuous based on the kinetic parameters, as well as some aggregate types which are reactive falling in the innocuous category of the graph and vice versa.

When examining data points for aggregates with borderline results around  $\ln k < -6$  for 14 days ( $-6.5 < \ln k < -5.5$ ) there are 10 aggregates that fall into this area of the plot. Five (5) of these aggregates all have kinetic parameters that suggest the aggregates are non-reactive with correlating CPT classifications. While another 4 have border line reactive  $\ln k$  values, -5.8976, -5.9465, -5.9832 and -5.8292 respectively, and are classed as non-reactive by the CPT expansion criteria. This suggests that the kinetic model using AMBT data, can give classification results consistent with the 12 month CPT test, but at 14 or 28 days. In our analysis the 14 and 28 day kinetic results gave comparable results with the 14 day results having slightly better agreement with the CPT classification.

### 3. Conclusions

Using a kinetic approach, such as the Kolmogorov-Avrami-Mehl-Johnson model, can provide the potential for decision making based not only on a single expansion value, but also the rate of expansion for various aggregates.

The results of this study show that the application of a kinetic model based on KAMJ provides a means of interpreting the results of AS1141.60.1 independent of expansion values obtained at both 14 and 28 days. Using this method aggregates examined with  $\ln k < -6$  are non-reactive or innocuous, whereas those with  $\ln k > -6$  are reactive.

The literature search by Rucker et al (2015)<sup>[1]</sup> and work by Ideker et al. (2012)<sup>[4]</sup> found that the reactivity diagnosed by CPT was found to correlate well with reactivity in field exposure. In our study, reactivity classifications from the kinetic method achieved close correlation to those from the CPT at both 14 and 28 days. This suggests that the kinetic approach offers potential to determine reactivity classifications consistent with those of CPT at 14 or 28 days, rather than the 12 months required by the CPT. It also has the potential to determine the rate of expansion of the alkali silica reaction, aiding in the evaluation of potential service life of a structure.

### 4. Acknowledgement

The authors acknowledged the contribution of Messrs. Peter Clarke, Tony Thomas and Dr Ahmad Shayan who highlighted the importance of reaction kinetics and reaction rate in the assessment of potential alkali silica reactivity.

### 5. References

1. Paul Rucker, James Mohammadi, Vute Sirivivatnanon and Warren South, 'Linking New Australian Alkali Silica Reactivity Tests to World-Wide Performance Data', *Proceedings, 24<sup>th</sup> Biennial Conference of the Concrete Institute of Australia, Melbourne, Australia*
2. D. Johnston, D. Stokes, R. Surdahl, 2000. A Kinetic-Based Method for Interpreting ASTM C 1260. *Cement, Concrete, and Aggregates*, Vol. 22, No. 2, 142–149.
3. D. Johnston, D. Stokes, B. Fournier, R. Surdahl, 2004. Kinetic Characteristics of ASTM C1260 Testing and ASR-Induced Concrete Damage. *Proceedings of the 12<sup>th</sup> International Conference on Alkali-Aggregate Reaction in Concrete*, 338–346.
4. J. Ideker, A. Bentivegna, K. Folliard, M. Juenger, 2012. Do Current Laboratory Test Methods Accurately Predict Alkali-Silica Reactivity? *ACI Materials Journal*, 109-M37, 395-402.

# Fresh and Early-Age Properties of Cement Pastes and Mortars Blended with Nickel Slag

Muhammad Ashiqur Rahman<sup>1</sup>, Prabir Kumar Sarker<sup>2</sup> and Faiz Ahmed Shaikh<sup>2</sup>

<sup>1</sup>PhD student, Curtin University of Technology, Perth, WA 6102

<sup>2</sup>Senior Lecturer, Curtin University of Technology, Perth, WA 6102

**Abstract:** Usage of industrial by-product materials in concrete is increasing because this is a sustainable way to manage the by-products and convert them into economic values. This paper presents the properties of fresh and hardened cement pastes and mortars blended with a proprietary nickel slag. Water demand slightly reduced with the increase of the slag content in determination of normal consistency. Incorporation of the slag with cement slightly prolonged initial and final setting time. The Le-Chatelier soundness test results did not show any increase in expansion for cement replacement of up to 65% by the slag though it has high magnesium content. The strength activity index of the slag was found to be 84% at 28 days when 20% of cement was replaced by the slag. Cement was replaced by the slag at rates of 20-50% in mortar mixtures having water to binder ratio of 0.5. Results show that 30% and 50% replacement of cement by the slag provided about 83% and 66% compressive strength respectively compared to that of 100% cement mortar specimens.

**Keywords:** Cement paste, compressive strength, mortar, nickel slag, soundness.

## 1. Introduction

Global warming has become a significant issue in the last decade in Australia and the researchers are embarking on programs to reduce Australia's carbon emissions [1]. Cement is the conventional binder for concrete and is known as an energy intensive material. Concrete is the most widely used material [2] for construction due to its versatile properties, availabilities of raw materials, strength and durability. It is important to reduce the environmental impact of concrete production in terms of greenhouse gas emission. Hence, construction practices are being revised by allowing increased use of industrial by-products [1]. It is necessary to increase the use of supplementary cementing materials (SCMs) within the existing performance based specifications. This will reduce the 'carbon footprint' of cement manufacture and help the reduction of greenhouse gas emissions.

Researchers are working to produce concrete with better engineering properties by using SCMs and chemical admixtures [3]. These can be used individually with Portland or blended cement or in different combinations of them. SCMs are generally added to concrete mixtures to make it more economical, durable and stronger. These materials reduce the amount of required cement and can enhance the strength, workability and durability through hydraulic and pozzolanic activities [4]. Typical examples of SCMs are fly ash, ground granulated blast furnace slag, silica fume, rice husk ash, metakaolin and natural pozzolans such as calcined clay and calcined shale which are incorporated in concrete as an addition or as a partial replacement of cement. Over the last 20 years, the use of SCMs in concrete has been steadily increased in Australia. At present, more than 90% of concrete contains at least one SCM. Detailed standards and procedures for using fly ash, slag and amorphous silica as SCMs are included in the AS 3582.1 [5], AS 3582.2 [6] and AS 3582.3 [7] Standards respectively.

In this research, suitability of using a proprietary nickel slag (NS) as a supplementary cementitious material has been investigated. The raw nickel slag was collected from the industry and then ground to a fine powder with blain specific surface area of 512 m<sup>2</sup>/Kg. Paste and mortar specimens were prepared and tested using different proportions of this slag with cement. The Magnesium Oxide (MgO) content of the slag is about 30% by mass. According to AS 3583.9 [8], the value of MgO in an SCM should be less than 15%. However, the actual effect of using the slag with cement on various properties of the product needs to be investigated. It was shown by experimental work that when 8% Magnesium expansive agent (MEA) was used, the cement paste cracked; causing unsoundness [9], but the concrete prisms showed very good surface and strength after the complete hydration of MEA. Moreover, their mechanical performance was better than that of the control prisms. In fact, the soundness of concrete needs to be determined by assessing the extent of expansion and its mechanical performance that resists the possible disruption due to expansion. Therefore, during the initial study of this research, the soundness,

consistency, setting time and compressive strength properties of cement paste and mortar mixtures containing the nickel slag as a partial replacement of cement are experimentally investigated and outlined in this paper.

## 2. Experimental work

According to ASTM C618 -12a [10], the sum of  $\text{SiO}_2$ ,  $\text{Fe}_2\text{O}_3$  and  $\text{Al}_2\text{O}_3$  should be more than 50% for class C natural pozzolans. The sum of  $\text{SiO}_2$ ,  $\text{Fe}_2\text{O}_3$  and  $\text{Al}_2\text{O}_3$  for the slag used in this research is about 65%. Hence, it can be considered as a class C pozzolan.

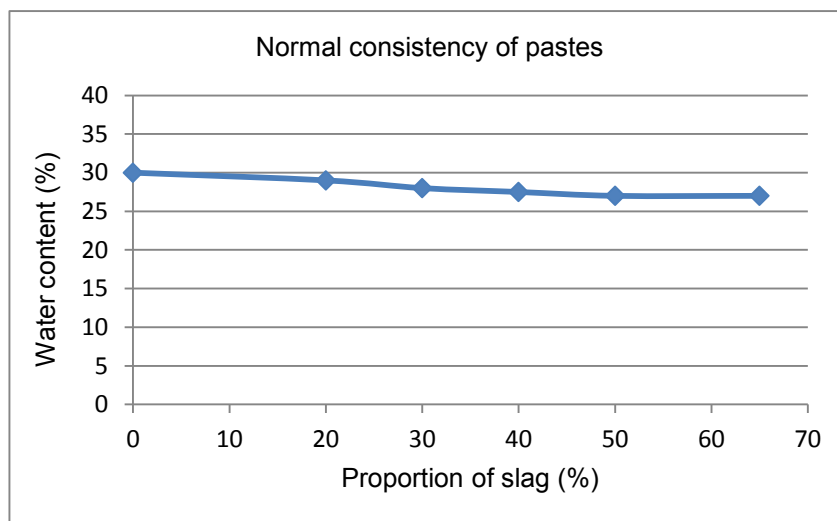
Several tests were conducted to assess the effects of blending of the nickel slag with cement. The test results of the nickel slag blended cement paste and mortars were compared with those of the control mixtures without the slag. Comparison was also made with the results of cement paste mixtures blended with fly ash (FA) and ground granulated blast furnace slag (GGBFS). The test results are discussed in the following sections.

### 2.1 Normal Consistency

The amount of water that brings the cement paste to a standard condition of wetness is called "normal consistency". It refers to the flow behaviour of a fresh mixture. Setting time and soundness properties need to be determined at a specified consistency rather than certain water cement ratio [11]. The nickel slag was used from 20 to 65% as partial replacement of cement. The normal consistencies of the mixtures were determined in accordance with AS 2350.3 [12] Standard. The results are given in Table 1 and plotted in Fig. 1. In the table, the paste mixtures were designated using the percentages of the slag and cement. For example, a mixture with the designation of 30NS70C had 30% nickel slag and 70% cement by mass. Thus, the mixture 0NS100C is the control mixture containing no slag.

**Table 1. Normal consistency and setting time of different mixes.**

Mixture	Consistency (% Water)	Initial setting time (mins)	Final setting time (mins)
0NS 100C	30	130	190
20NS 80C	29	130	200
30NS 60C	28	130	200
40NS 70C	27.5	140	200
50NS 50C	27	130	200
65NS 35C	27	150	230



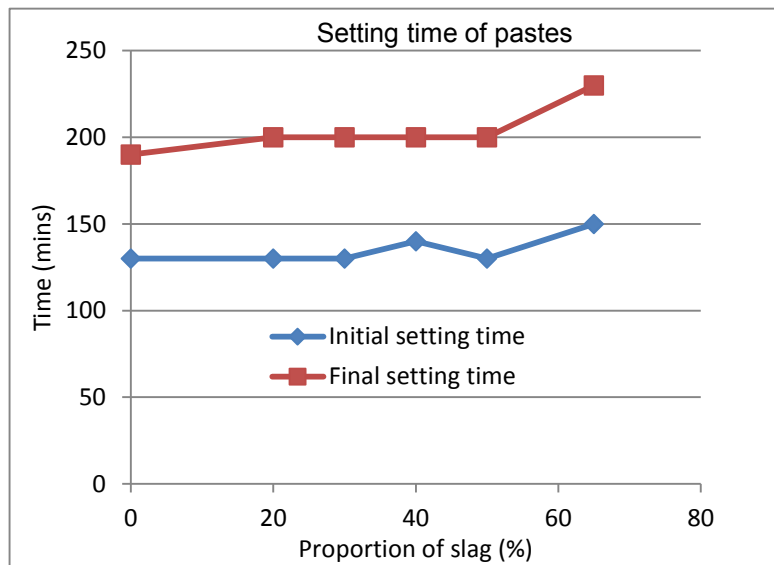
**Figure 1. Variation of water content for normal consistency with the addition of nickel slag.**



It can be seen from the results in Table 1 and Fig. 1 that the amount of water required for normal consistency slightly decreased with the addition of nickel slag. The required water content for normal consistency of the control mixture was 30% and that of the mixtures with nickel slag varied from 29 to 27%. Therefore, the required water content decreased from 30% to 27% with the inclusion of 65% nickel slag in the paste.

## 2.2 Setting time

The knowledge of the setting time of a cementitious mixture is required in order to determine the available time for mixing, transporting, placing and compacting the concrete effectively. Setting time tests are used to characterize how a particular cement paste sets. Setting time of cement paste is affected by a number of factors including fineness of cement, water-cement ratio, the chemical content and admixtures if used. According to ASTM C150 [13] specification, the initial setting time shall not be less than 45 minutes. However, an initial setting time of at least 90 minutes is usually preferred in practice. A smaller value of the final setting time is always preferred in order to avoid large expenditures on the formwork. Setting times of the pastes were determined in accordance with AS 2350.4 [14]. The setting time results of the control cement paste and the mixtures with up to 65% of nickel slag are given in Table 1. The values are also plotted against the percentage of nickel slag in Fig. 2.



**Figure 2. Variation of setting times with the addition of nickel slag.**

It can be seen from the results presented in Table 1 and Fig. 2 that initial setting times of the mixtures varied from 130 minutes to 150 minutes. The final setting time varied from 190 to 230 minutes. No significant difference in setting times was observed due to incorporation of nickel slag with cement at a rate up to 50%. At the replacement level of 65%, the nickel slag was found to retard the initial setting time by 20 minutes and final setting time by 40 minutes.

## 2.3 Strength activity Index

Strength activity index is the ratio of the strength of 20% nickel slag-blended cement mortar to the strength of the reference cement mortar at a specific age. The pozzolanicity of the nickel slag can be quantified by its strength activity index. The strength activity index of any material depends on the surface area, particle size distribution and silica content. The strength activity index can be increased by reducing the particle size thus increasing the fineness. The granulated nickel slag was ground by using a balling mill to the Blaine's fineness of 512 m<sup>2</sup>/kg, which is similar to the fineness of commercial ground granulated blast furnace slag. The control cement mortar mixture consisted of 500g of cement, 1375g of graded sand and 242g of water. The nickel slag blended cement mortar mixture contained 400g cement, 100g nickel slag,

1375g graded sand and 242g of water. Since the water demand for normal consistency of the 20% nickel slag blended paste was same as that of the control cement paste, the water contents of both the mortar mixtures were same. Cube specimens of 50mm sides were prepared and tested in accordance with the ASTM C311M Standard [15]. After casting, the specimens were placed in the moist room at 23±2°C for 24 hours. The specimens were then demoulded and cured in lime saturated water until tested for compressive strengths at the ages of 7 and 28 days. The average compressive strengths obtained from three specimens were used to determine the strength activity index. The results are given in Table 2.

**Table 2. Strength activity index of nickel slag.**

SI No	Composition	Mean 7 days strength (MPa)	Mean 28 days strength (MPa)	Strength activity index	
				7 Days	28 Days
1	Control	31	37	74%	84%
2	20% Slag	23	31		

Table 2 shows that the strength activity index for 7 days and 28 days were found to be 74% and 84% respectively. ASTM C618-08a [16] recommends the specific minimum strength activity index of 75% for SCM at 7 or 28 days. Since the value for the nickel slag at 28 days is above 75% and that at 7 days also very close to 75%, the slag meets the requirement of the ASTM standard as a supplementary cementitious material.

## 2.4 Soundness

Chemical analysis of the nickel slag showed that its MgO content is about 30%. According to AS 3582.2 [6], the value of MgO in SCM should be less than 15%. Therefore, the high magnesium content of the slag could raise concerns. However, MgO may not always be harmful for concrete depending on how it is chemically bound in the slag. Researchers found that the delayed expansion caused by slow hydration of MgO in cement had compensated the thermal shrinkage of concrete during the cooling stage [9, 17]. MgO powder is used as an expansive agent (MEA) [9, 18-19] at a rate of 5-10% weight of cement. Besides, minerals of Dolomite, Serpentine and Magnesite containing about 20-40% MgO have been used successfully for producing MEA [20-21].

The reactivity of MgO depends on its calcination temperature. MgO can be classified in three temperature categories of calcination: a) lightly burnt MgO (850-1200 °C), hydration takes place within 180 days b) heavily burnt MgO (1500-1800 °C), hydration can be up to 1000 days and c) dead burnt MgO, Periclase (>1800 °C), hydration can proceed up to 6-8 years. The higher the burning temperature, the smaller the magnitude of early-age expansion and the longer the MgO hydration process lasts. The quenching temperature of the slag used in this study was 1200-1300 °C.

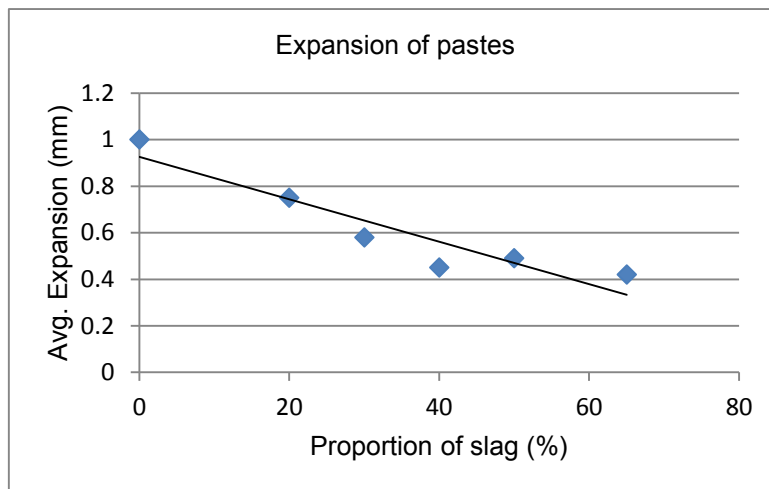
When MgO hydrates, it produces Mg(OH)<sub>2</sub> (Brucite), which has a volume of 17% higher [22]. The unsoundness caused by the excessive volume changes is usually accompanied by cracking and strength loss. The soundness of the nickel slag blended cement pastes has been evaluated using Le-Chatelier soundness test which is detailed below.

### 2.4.1 Le-Chatelier soundness test

Le-Chatelier soundness test was carried out in accordance with AS2350.5 [23]. The cement paste samples were prepared at normal consistency by replacing 0 to 65% of cement by the nickel slag. The Le-Chatelier mould was filled with the paste and submerged in water for 24 hours. After curing, it was boiled for 3.5 ± 0.5 hours and allowed to cool in the room temperature. The distance between the pointer of the mould before and after boiling is taken as the Le-Chatelier expansion. Three samples were prepared for each type of mixture and an average value of the measured expansions was calculated. The results are given in Tables 3. The values of expansion are plotted against percentage of the slag in Fig. 3. Expansions of two additional mixtures containing 40% fly ash (40FA 60C) and 40% GGBFS (40GGBFS 60C) were tested for comparison with the expansion of the mixture of 40% nickel slag (40NS 60C).

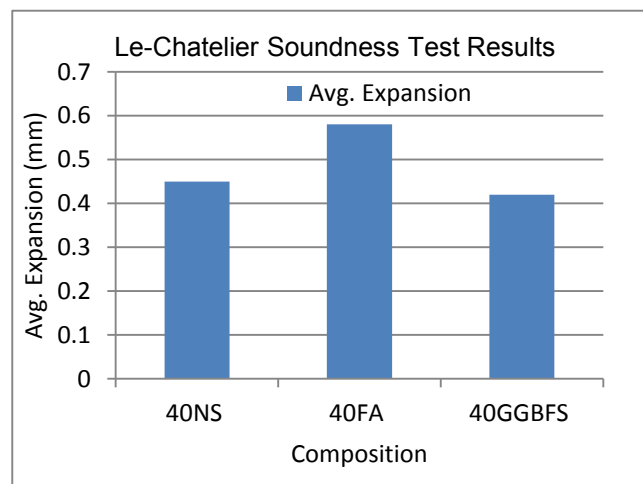
**Table 3. Le-Chatelier expansions of pastes containing nickel slag, fly ash and GGBFS.**

Proportion	Average Expansion (mm)
0 NS 100C	1.0
20NS 80 C	0.75
30NS 70 C	0.58
40NS 60C	0.45
40FA 60C	0.58
40GGBFS 60C	0.42
50NS 50C	0.49
65NS 35C	0.42



**Figure 3. Variation of expansion with the percentages of nickel slag.**

It can be seen from the results that the Le-Chatelier expansion of the mixtures varied from 0.42 to 1 mm. These values are well below 10 mm, which is considered as the limiting value of the expansion [24]. It can be seen from Fig. 3 that the values generally decreased with the increase of cement replacement by the slag. The value decreased from 1 mm to 0.42 mm when the cement replacement increased from 20% to 65%.



**Figure 4. Le-Chatelier expansions of pastes containing 40% nickel slag, fly ash and GGBFS.**

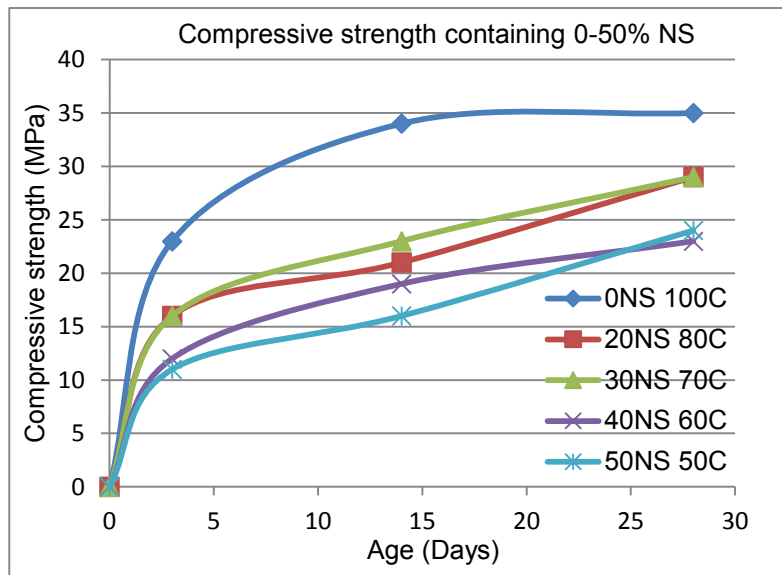
Fig. 4 shows the expansions of the mixtures containing three different SCMs at the rate of 40%. The values of the expansion varied between 0.42mm and 0.58mm for these three mixtures. It can be seen from the figure that the expansion of the mixture containing 40% nickel slag was similar to that of 40% GGBFS and less than that containing 40% fly ash. Thus, the Le-Chatelier expansion of the paste containing nickel slag up to 65% was found well below the usual limit of 10 mm and was not higher than those of the control mixture and mixtures with 40% fly ash and GGBFS.

## 2.5 Compressive strength of mortar specimens

The mortar mixtures consisted of one part of binder and three parts of standard sand by mass with a water-cement ratio of 0.50. A control mixture was prepared by mixing 450g of cement, 1350g of graded sand and 225g of water. Nickel slag was used to replace 20, 30, 40 and 50% of cement in the other mixtures. Specimens produced from fresh mortar were demoulded after 24 hours, and were then cured in water with at  $23 \pm 2^\circ\text{C}$  with  $70 \pm 10\%$  relative humidity until they were used for compressive strength tests. Tests were conducted following the ASTM C109 Standard [25] using a 2000 kN capacity machine. Three samples were tested for each mix at 3, 14 and 28 days of age. The mean compressive strength results are given in Table 4. The strength developments of the mixtures with age are plotted in Fig. 5.

**Table 4. Compressive strength of the mortar mixtures.**

Composition	Compressive strength (MPa)		
	3 Days	14 Days	28 Days
0NS 100C	23	33	35
20NS 80C	16	21	29
30NS 70C	16	23	29
40NS 60C	12	19	23
50NS 50C	11	16	24



**Figure 5. Compressive strength of cement mortars containing different percentages of nickel slag.**

It can be seen from the results that the 28-day compressive strength of the control cement mortar specimen was 35 MPa. The 28-day compressive strengths of the mixtures containing 20% to 50% nickel slag varied from 23 to 29 MPa. As seen from Fig.5, the rates of strength gain of the concretes containing nickel slag were higher during 14 to 28 days as compared to that of the control concrete. This is similar to the general behaviour of concretes containing pozzolanic materials. The results indicate that 20 to 30% cement replacement by the nickel slag resulted in about 83% of the 28-day compressive strength of the

control mortar mixture. Similarly 40 to 50% cement replacement by the nickel slag resulted in about 66% of the 28-day compressive strength of the control specimen. As shown in Fig.5, the strengths of the mixtures containing the slag show increasing trends beyond the age of 28 days. The ongoing study will determine the strength development at later ages.

### 3. Conclusion

This paper presented the properties of fresh and hardened paste and mortar mixtures containing a proprietary ground nickel slag as a partial replacement of cement. The water content required for normal consistency reduced from 30% to 27% due to 65% cement replacement by the slag. Thus, the slag did not have a significant effect of the water demand of the blended paste. There was no significant effect of the slag on the initial and final setting times of cement paste up to 50% cement replacement. The strength activity indexes of the slag at 7 and 28 days were 74% and 84% respectively. No negative effect on the expansion was shown by the slag in the Le-Chatelier soundness test. The values of expansion ranged between 0.42 mm to 1.0 mm for the mixtures containing 0 to 65% slag. These values are well below the 10 mm limit usually used for the test. Mortar specimens of 50 mm cube were cast with water to cementitious materials ratio of 0.5. The 28-day mortar compressive strength reduced from 35 MPa to 29 MPa due to 20% to 30% cement replacement by the slag. The corresponding compressive strength of the mortar containing 40% to 50% slag was about 24 MPa. Thus, the proprietary nickel slag did not show any negative effect on the properties of fresh mixtures and caused reduction in 28-day compressive strength with increasing trends at the later age. This is similar to the effect of other cement replacing materials such as Class F fly ash.

### 4. Acknowledgement

This research was funded and supported by SLN-ERAMET, New Caledonia. The authors gratefully acknowledge their contribution to this research. The authors are also grateful to BGC–Cement, Western Australia for their continuous support to the work.

### 5. References

1. AS 3972, "General Purpose and Blended Cements SAI Global Limited", 2010.
2. Siddique, R., and Khan, M.I., "Supplementary cementing materials", Springer-Verlag Berlin Heidelberg, 2011.
3. Muhl, A., "The use of supplementary cementing materials in residential concrete", Master's thesis, University of Toronto, 2003.
4. CSA A3001-03, "Cementitious materials for use in concrete", National standards of Canada, 2003.
5. AS3582.1., "Supplementary Cementitious Materials for use with Portland and Blended Cement - Fly Ash", Australian Standard, 1998.
6. AS3582.2., "Supplementary cementitious materials for use with portland and blended cement - Slag - Ground granulated iron blast-furnace ", Australian Standard, 2001.
7. AS3582.3., "Supplementary cementitious materials for use with portland and blended cement - Amorphous silica ", Australian Standard, 2002.
8. AS3583.9., "Methods of test for supplementary cementitious materials for use with portland cement - Determination of magnesia content ", Australian Standard, 1991.
9. Lingling, X., and Min, D., "Dolomite used as raw material to produce MgO-based expansive agent", *Cement and Concrete Research*, 35, 2005, pp 1480-1485.
10. ASTM C618-12a., "Standard Specification for Coal Fly Ash and Raw or Calcined Natural Pozzolan for Use in Concrete", ASTM International, 2012.
11. Lamond, J. F., and Pielert, J. H., "Expansive Mechanism of Magnesia as an Additive of Cement and Concrete-making Materials", *ASTM International*, 169(4), 2006.
12. AS2350.3., "Methods of testing portland, blended and masonry cements - Normal consistency ", Australian Standard, 2006.

13. ASTM C150., "Standard Specification for Standard Specification for Portland Cement", ASTM International, 2012.
14. AS2350.4., "Methods of testing portland, blended and masonry cements - Setting time ", Australian Standard, 2006.
15. ASTM C311., "Standard Test Methods for Sampling and Testing Fly Ash or Natural Pozzolans for Use in Portland-Cement Concrete", ASTM International, 2013.
16. ASTM C618-08a., "Standard Specification for Coal Fly Ash and Raw or Calcined Natural Pozzolan for Use in Concrete", ASTM International, 2006.
17. Yuan, M., and Tang, M., "Mechanism of the Autogeneous Expansion of the Concrete of Changbaishan Dam in Jilin Province," Journal of Nanjing Institute of Chemical Technology, 2, 1984, pp. 38-45.
18. Mo, L., Deng, M. et al., "Effects of calcination condition on expansion property of MgO-type expansive agent used in cement-based materials", Cement and Concrete Research, 40, 2010, pp 437-446.
19. Mo, L., Deng, M. et al., "Potential Approach to Evaluating Soundness of Concrete Containing MgO-Based Expansive Agent", ACI Materials Journal, 197(2), 2010, pp 99-105.
20. Peiwei, G., Xiaolin, L. et al., "Using a new composite expansive material to decrease deformation and fracture of concrete", Materials Letters, 62, 2008, pp 106-108.
21. Deng, M., Cui, X. et al., "Expansive Mechanism of Magnesia as an Additive of Cement", Journal of Nanjing Institute of Chemical Technology, 12(4), 1990, pp1-11.
22. Zheng, L., Xuehua, C. et al., "MgO-Type Delayed Expansive Cement", Cement and Concrete Research, 21, 1991, pp1049-1057.
23. AS2350.5., "Methods of testing portland, blended and masonry cements - Determination of soundness ", Australian Standard, 2006.
24. Bye, G. C., "Portland cement: Composition, Production and Properties", Thomas Telford, 1999.
25. ASTM C109., "Standard Test Method for Compressive Strength of Hydraulic Cement Mortars (Using 2-in. or [50-mm] Cube Specimens)", ASTM International, 2013.

# Thermo-mechanical Behaviour of Epoxy Based Polymer Matrix

Wahid Ferdous<sup>1</sup>, Allan Manalo<sup>1</sup>, Thiru Aravinthan<sup>1</sup> and Gerard Van Erp<sup>2</sup>

<sup>1</sup>Centre of Excellence in Engineered Fibre Composites (CEEFC), School of Civil Engineering and Surveying, University of Southern Queensland, Toowoomba 4350, Australia

<sup>2</sup>Former Professor, Centre of Excellence in Engineered Fibre Composites (CEEFC), University of Southern Queensland, Toowoomba 4350, Australia

**Abstract:** This study revealed the dynamic mechanical behavior of polymer matrix having different percentage of filler contents. Epoxy resin based polymer matrix were prepared and characterized their dynamic mechanical properties such as storage (elastic) modulus, loss (viscous) modulus and tan delta (damping coefficient) as a function of temperature. The temperature was applied from 30 to 120 °C with 5 °C increment and the specimens were clamped for dual cantilever bending. A total of seven different mixes with a filler volume increment of 10% started from zero filler mix (100% resin) were casted and the glass transition temperature were evaluated for each of the specimens. Knowing this temperature is important for the polymer matrix as the mechanical properties of material can change dramatically when the specimens are subjected to a temperature beyond this point. Results showed that the gradual increase of filler materials in the polymer matrix can shift the state of materials progressively from viscous to elastic. However, a slight increase of glass transition temperature were obtained among all seven mixes which ranged from 50 to 55 °C when using storage modulus or loss modulus curve and 60 to 65 °C when using peak of tan delta. To evaluate the effect of temperature and fatigue loading on specimens during the execution of Dynamic Mechanical Analysis (DMA), the flexural properties of the invaded samples were tested using three point bending once the specimens cool down to the normal temperature. It was found that the dual action of temperature and repeated loading can reduce flexural strength and modulus significantly.

**Keywords:** epoxy resin, polymer matrix, glass transition temperature, dynamic mechanical properties.

## 1. Introduction

The Glass transition temperature ( $T_g$ ) is one of the most important thermal property for designing polymeric composite materials [1]. Different from melting point,  $T_g$  is the temperature where a polymeric material changes from a hard, rigid or glassy state to a more soft, compliant or rubbery state. Glass transition temperature of polymer composites can be determined in several methods including: (a) differential scanning calorimetry (DSC) [2], (b) dynamic mechanical analysis (DMA) [3], (c) dynamic mechanical thermal analysis (DMTA) [4], (d) inverse gas chromatography (IGC) [5] and (e) differential thermal analysis (DTA) [6]. Of these methods, DMA is typically the most sensitive method to measure the glass transition temperature of polymers [7, 8].

DMA measures force and deflection while varying temperatures and/or frequency. The basic principles of DMA can be described as applying an oscillating force to a sample and analysing the material's response to that force. This cyclic nature of the test is equivalent to a creep test [8]. In reality, if a polymer heated above the glass transition temperature, the state of materials can change from glassy to rubbery and the stiffness drops dramatically. This sudden drop of stiffness can lead to serious problems in the structure.

The modulus measured from DMA is not exactly the same as the Young's modulus of elasticity. Young's modulus measures the material's stiffness at a fixed temperature, but DMA modulus measures the stiffness at variable temperature. It is well known that the Young's modulus of elasticity is determined from the slope of a stress-strain curve in the initial linear region. On the other hand, DMA measures the dynamic or complex modulus ( $E^*$ ) which is a function of storage modulus ( $E'$ ) and loss modulus ( $E''$ ), and can be expressed by Eq. (1).

$$E^* = E' + iE'' \quad (1)$$

$$\tan \delta = \frac{E''}{E'} \quad (2)$$

where,  $i$  is the imaginary unit. The storage modulus measures the stored energy per cycle while the loss modulus measures the dissipation of energy (as heat) per cycle. The ratio of loss modulus to storage modulus is called tan delta ( $\tan \delta$ ) or damping expressed in Eq. (2) which measures how well a material

can get rid of or absorbing energy under cyclic load. DMA can differentiate the glassy, viscoelastic, elastic and liquid polymers.

The glass transition temperature of epoxy grouts composed of resin with fine or coarse filler was investigated by Shamsuddoha et al. [3] using DMA. They found the  $T_g$  ranged from 60 to 90 °C depending on the mixing proportion of epoxy grouts. Goertzen and Kessler [8] measured the  $T_g$  of carbon/epoxy composites using DMA for structural pipeline repair. They found a wide range of  $T_g$  from 60 to 129 °C measured from tan delta peak for room temperature cured and post-cured specimens. The post curing system can enhance the structural and thermal properties.

The outdoor application of civil infrastructures such as bridge, railway sleepers are frequently heated by sun and when the vehicles passes over the structures they are subjected to fatigue loading at high temperature. The dual action can affect the serviceability of structures by reducing the structural performance. This study determined the glass transition temperature of polymer matrix and the residual flexural capacity of the invaded polymer matrices were evaluated.

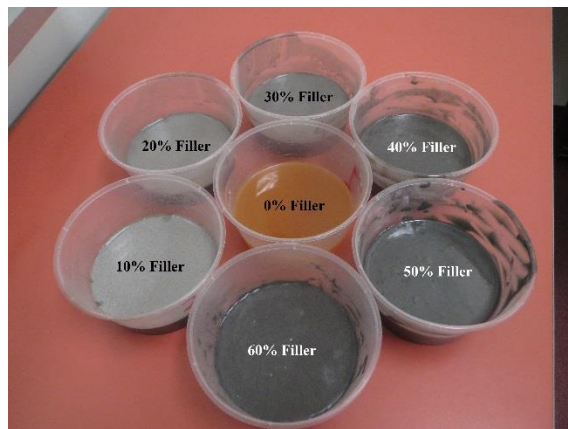
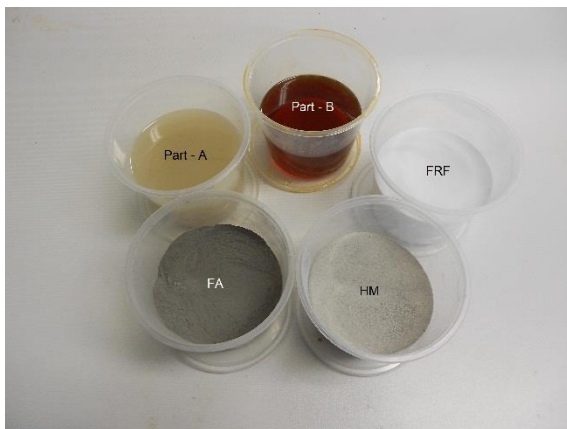
## 2. Materials and Method

In this study, the polymer matrix is composed with resin and filler. A DGEBA type epoxy resin (Part-A) and an amine based curing agent (Part-B) were mixed with a combination of three different fillers. The resin producer furnishes the Epoxy Equivalent Weight (EEW) of 190 gm for Part-A and Amine Hydrogen Equivalent Weight (AHEW) of 60 gm for Part-B. To make the resin mix reactive, one equivalent weight quantity of amine curative will require for one equivalent weight quantity of an epoxy resin. Therefore, 32 gm of Part-B is required to react with 100 gm of Part-A, and otherwise it will not work properly. To get the effective filler mix, three different fillers named Fire Retardant Filler (FRF), Hollow Microsphere (HM) and Fly Ash (FA) were mixed together by a certain ratio of mixing which was developed by LOC Composites Pty. Ltd. and could not be included in this paper due to the commercial in confidence. The functions of three fillers are different and their combined application can improve the structural performance and durability.

Mixes were prepared for different resin-to-filler ratio started from 0% to a maximum of 60% filler with an increment of 10% by volume (Figure 1). No further increase of filler were considered beyond 60% as because it was not workable. The mixing ratio are provided in Table 1.

**Table 1. Details of mixing proportion.**

Identity of mix	Mix-1	Mix-2	Mix-3	Mix-4	Mix-5	Mix-6	Mix-7
% Resin/Filler (by volume)	100/0	90/10	80/20	70/30	60/40	50/50	40/60
Resin Part A, (gm)	124	112	100	87	75	62	50
Resin Part B, (gm)	40	36	32	28	24	20	16
Filler (FRF+ HM+ Fly Ash), (gm)	0	30	59	89	119	148	178





(a) ingredients before mixing

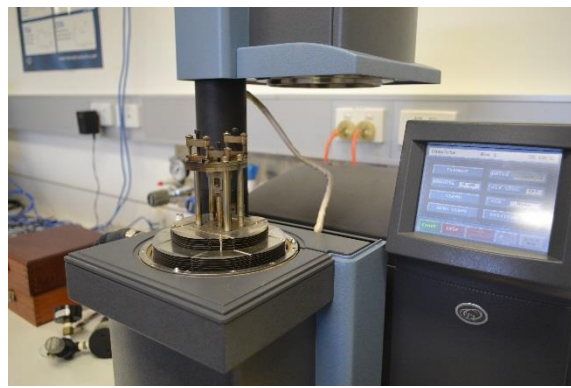
(b) solid polymer matrix after mixing

**Figure 1. Polymer matrix ingredients and specimens casting.**

Specimens were casted in the plastic cups which can be demolded quite easily as because the weak bond between resin and plastic. The solid polymer matrix were then cut to the specified dimensions using a cutting machine and tests were conducted in accordance with ASTM D7028 [9]. The machine was a Q800 type of TA instruments where the motor applies a force and displacement sensors measure strain, force and amplitude in the form of raw signals recorded by the machine. Test mode was DMA Multi-Frequency-Strain and the samples clamped with Dual Cantilever system. Temperature was set between 30 and 120°C, with an increment of 5°C, during temperature scans. Two specimens in each category were tested to determine the  $T_g$  of polymer matrix as shown in Figure 2. The surface of the specimens were prepared flat, clean, straight and dry to prevent slippage from the dual cantilever grips and any effects due to moisture.



(a) DMA specimens



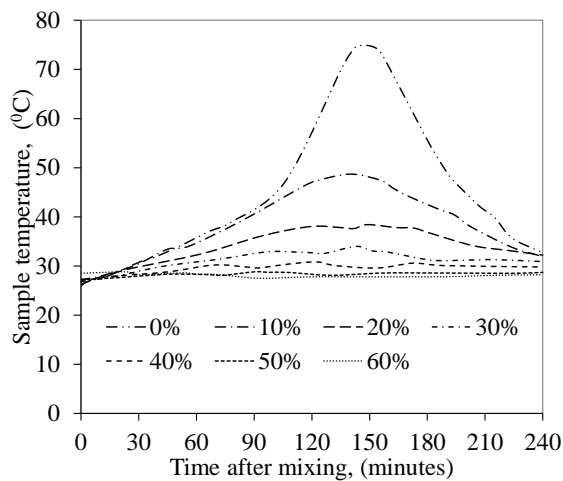
(b) DMA instrument

**Figure 2. Samples and the instrument for DMA.**

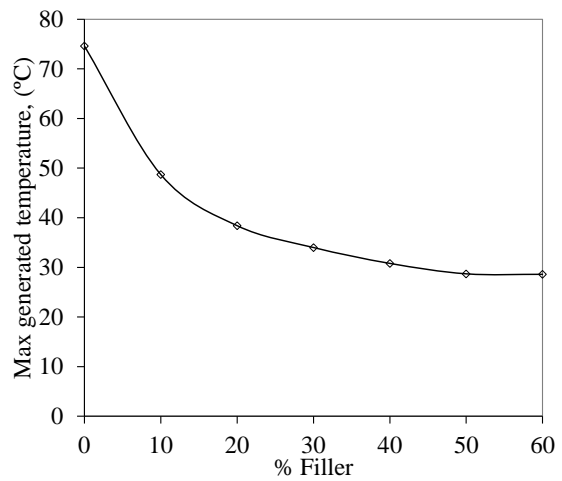
### 3. Results and Discussion

#### 3.1 Generation of heat during mixing

While mixing resin (Part-A) and hardener (Part-B) together, it generated heat and the temperature was measured by a temperature gun at 10 minutes interval. The recorded maximum temperature was 75°C for the mix containing 100% resin or 0% filler (Mix-1). However, the peak temperature was decreased in the succeeding mix with the gradual increase of filler up to 60% as shown in Figure 3.



(a) generation of temperature with time



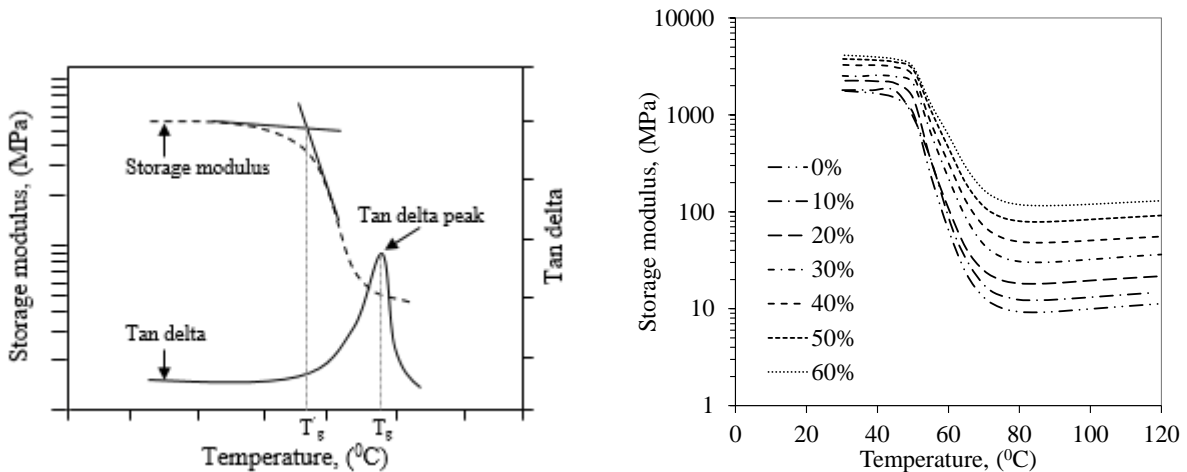
(b) variations of peak temperature with filler

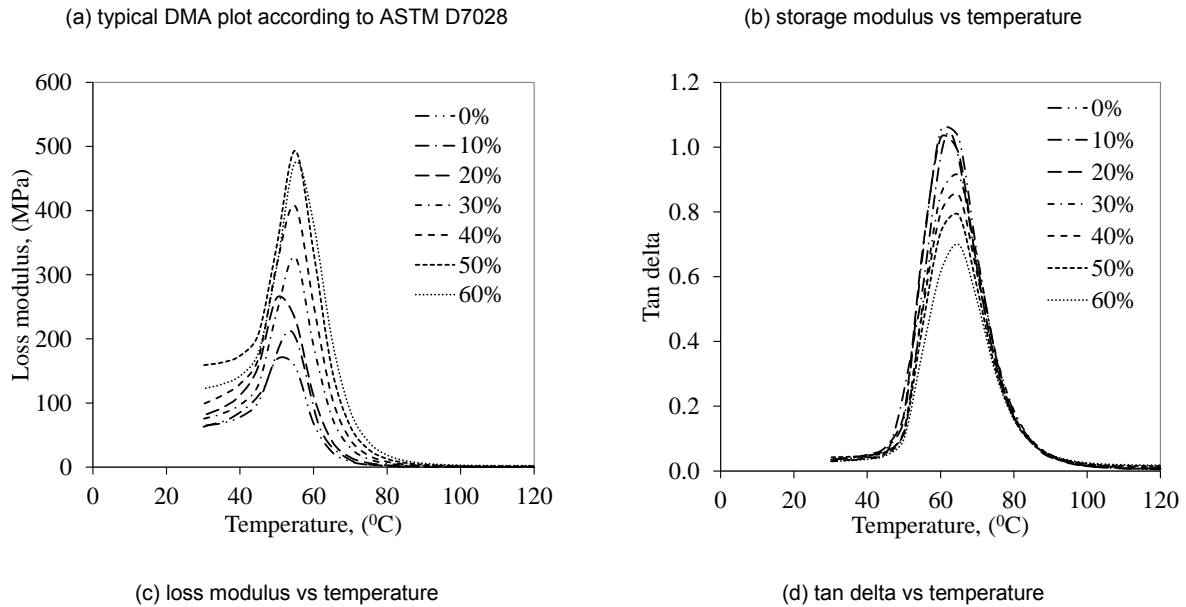
**Figure 3. Effect of filler on heat generation.**

Figure 3(a) shows that, for the mix with 0% filler, the peak temperature was obtained at 150 minutes after starting the mix and it was gradually decreased to 90 minutes for the mix having 60% filler. This indicates the exothermic reaction between resin and hardener was completed within this time period and the mixes started to lose their plasticity. A decreasing trend of heat with the increase of filler can be explained by the heat absorption capacity of filler. Filler can absorb heat and reduce the temperature to a comfortable range when 30% or more filler was added in the mix. The temperature of the mix varied between 34°C to 29°C for the addition of 30% to 60% filler which is a comfortable range of temperature to work with.

### 3.2 Glass transition temperature

The variation of storage modulus, loss modulus and tan delta with respect to temperature are presented in Figure 4(b-d). The corresponding temperature of the intersection of two tangent lines in storage modulus curve is the glass transition temperature, drawn the first tangent at a point where glass transition just started and the second tangent at the inflection point to approximately the midpoint of the storage modulus drop. The magnitude of  $T_g$  measured from storage modulus curve is slightly lower than the same measured from the peak of tan delta curve. The test standard ASTM D7028 [9] suggested to report both magnitude of  $T_g$  when using DMA. Li et al. [10], Goertzen and Kessler [8], and Shamsuddoha et al. [3] measured the  $T_g$  from the peak of tan delta curve. However, the standard practice for plastics ASTM D4065 [11] suggested to measure  $T_g$  from the peak of loss modulus curve.





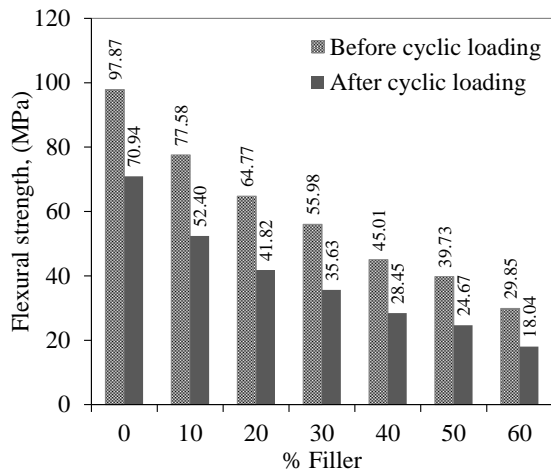
**Figure 4. Variation of dynamic mechanical properties with temperature.**

In all seven mixes, the magnitude of  $T_g$  ranged from 50 to 55 °C when using storage modulus or loss modulus curve and 60 to 65 °C measured from tan delta curve. This indicates the addition of filler from 0% to 60% in the polymer matrix can only increase the glass transition temperature by 5 °C. The  $T_g$  of the polymer mix primarily depends on the resin system where the type of resin was same for all mixes. Similar observation was noticed by Shamsuddoha et al. [3] where the increase of aggregates slightly enhance the glass transition temperature. However, in this study the samples were cured at room temperature, and the post curing system of polymer matrix could probably increase the  $T_g$  significantly. The height of tan delta indicates how viscous (large tan delta) or elastic (small tan delta) the material is. The magnitude of the peak of tan delta was decreased from 1.04 to 0.7 with the increase of filler from 0 to 60%. This indicates the response of zero filler mix (tan delta peak 1.04) is more viscous than any other mix under the application of load.

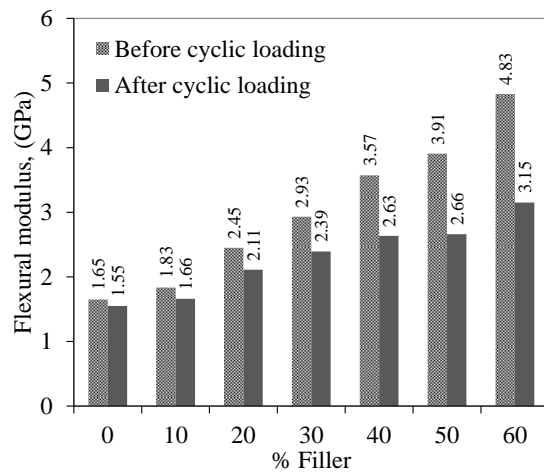
### 3.3 Residual flexural strength

The flexural strength and modulus of the unaffected specimens were determined before execution of DMA. The strength was gradually decreased from 97.87 to 29.85 MPa with the increase of filler from zero to 60%. However, the flexural modulus was increased from 1.65 to 4.83 GPa with the increase of filler from zero to 60%. The strength mainly depends on the amount of resin in the mix that explains their gradual reduction. The increase of flexural modulus is due to the modulus of filler material which is significantly higher than resin. The flexural modulus can be correlated to the peak of tan delta (Fig. 4d) curve where the peak was highest for zero filler mix and lowest for the mix containing 60% filler. The height of tan delta represents how viscous or elastic the material is, under the application of load. The lowest height for 60% filler mix indicates the mix is more elastic than others and that the Fig. 5(b) illustrated with increasing trend of elastic modulus.

As it is mentioned before, the specimens were subjected to cyclic loading with high temperature during the execution of DMA. To determine the effect of temperature and fatigue loading on the flexural properties of polymer matrix, the invaded specimens were tested under three point bending. Results are compared with the unaffected control samples and it is observed that the flexural strength and stiffness for all specimens are decreased from the unaffected one presented in Figure 5.



(a) reduction of flexural strength



(b) reduction of flexural modulus

**Figure 5. Effect of temperature and fatigue loading on flexural properties.**

It is also observed that the loss of flexural strength for zero filler mix (100% resin mix) is obtained 28% which gradually increases to 40% for the mix containing 60% filler. Similarly, the reduction of flexural modulus is only 6% for zero filler mix and is gradually increased to 35% for 60% filler mix. Results have indicated that the rate of losses is increasing with the increase of filler in the mix. This phenomenon is happened probably due to the bond between resin and filler which gradually weaken with the increase of filler under the application of high temperature and fatigue loading. The rate of loss was expected similar for all mixes as the percentage loss of storage modulus after glass transition were more likely similar for all mixes presented in Fig. 4(b). However it is important to mention that, when the polymer mix is subjected to a temperature higher than its glass transition temperature, the mobility of the polymer chains increase significantly and later it cured by high temperature. This is similar to post curing system where the high resin content mix can recover flexural properties more easily than those mixes which contains low resin as the resin is temperature sensitive but not the filler, and explains why the rate of loss increases with the increase of filler.

#### 4. Conclusions

This paper presented an experimental study on thermo-mechanical behavior of epoxy based polymer matrix using dynamic mechanical analysis. The generation of heat during the mixing of resin and hardener is measured and the reduction of flexural properties after the application of high temperature and fatigue loading during DMA is evaluated from which the following conclusions are drawn:

1. The mixing of resin and hardener can generate heat which increase the temperature of fresh polymer matrix. The addition of 30% filler can reduce the temperature to 34°C from 75°C which was obtained for pure resin mix with no filler. However, a further addition of filler can decrease the temperature quite slowly, for example, the temperature comes down to 29°C when 60% filler is added.
2. Only a minor increase of glass transition temperature was obtained for the addition of filler in the mix. The  $T_g$  was increased from 50 to 55 °C for the addition of filler from zero to 60% when measured from storage modulus or loss modulus curve. However, the  $T_g$  measured from tan delta curve provided 20% higher results and ranged from 60 to 65 °C. The response of low filler matrix was found more viscous than high filler polymer matrix under the application of loads.
3. The effect of fatigue loading at high temperature is increased with the increase of filler in the polymer matrix. The combined action makes the resin-filler bond weaker with the increase of filler.

## 5. Acknowledgement

The first author gratefully acknowledge the financial support by Australian Postgraduate Award (APA) scholarship from the University of Southern Queensland, and authors are also acknowledged the materials support by the Department of Industry Innovation, Science, Research and Tertiary Teaching Enterprise Connect Researcher-In-Business Funded by the Australian Government.

## 6. References

1. Ribeiro, M.C.S., et al., *Flexural performance of polyester and epoxy polymer mortars under severe thermal conditions*. Cement and Concrete Composites, 2004. **26**(7): p. 803–809.
2. Feng, L., et al., *Determination of ultra-low glass transition temperature via differential scanning calorimetry*. Polymer Testing, 2013. **32**(8): p. 1368–1372.
3. Shamsuddoha, M., et al., *Characterisation of mechanical and thermal properties of epoxy grouts for composite repair of steel pipelines*. Materials & Design, 2013. **52**: p. 315–327.
4. Bussu, G. and A. Lazzeri, *On the use of dynamic mechanical thermal analysis (DMTA) for measuring glass transition temperature of polymer matrix fibre reinforced composites*. Journal of Materials Science, 2006. **41**(18): p. 6072-6076.
5. Surana, R., et al., *Determination of glass transition temperature and in situ study of the plasticizing effect of water by inverse gas chromatography*. Pharmaceutical Research, 2003. **20**(10): p. 1647-1654.
6. Rieger, J., *The glass transition temperature T<sub>g</sub> of polymers—Comparison of the values from differential thermal analysis (DTA, DSC) and dynamic mechanical measurements (torsion pendulum)*. Polymer Testing, 2001. **20**(2): p. 199–204.
7. Wolfrum, J., G.W. Ehrenstein, and M.A. Avondet, *Dynamic mechanical thermoanalysis of high performance reinforced materials influences and problems*. Journal of Thermal Analysis and Calorimetry, 1999. **56**(3): p. 1147-1154.
8. Goertzen, W.K. and M.R. Kessler, *Dynamic mechanical analysis of carbon/epoxy composites for structural pipeline repair*. Composites Part B: Engineering, 2007. **38**(1): p. 1-9.
9. *ASTM Standard, ASTM D7028: Standard test method for glass transition temperature (DMA T<sub>g</sub>) of polymer matrix composites by dynamic mechanical analysis (DMA)*. 2008: United States.
10. Li, G., P. Lee-Sullivan, and R.W. Thring, *Determination of activation energy for glass transition of an epoxy adhesive using dynamic mechanical analysis*. Journal of Thermal Analysis and Calorimetry, 2000. **60**: p. 377–390.
11. *ASTM Standard, ASTM D4065: Standard Practice for Plastics: Dynamic Mechanical Properties: Determination and Report of Procedures*. 2012: United States.

# Development of an Acid Resistant Concrete

Shamila Salek<sup>1</sup>, Bijan Samali<sup>1</sup>, Vute Sirivivatnanon<sup>2</sup>, Georgius Adam<sup>3</sup>

<sup>1</sup>University of Western Sydney, <sup>2</sup>University of Technology Sydney, <sup>3</sup>Parchem Company

**Abstract:** Modern infrastructures are designed for long service life and are increasingly being built in more aggressive greenfield and brownfield areas. Sulfate, acid-sulfate and acid resistant concrete are engineering solutions to these challenges in infrastructures without the need for additional protective membrane associated with conventional concrete. This paper presents an experimental investigation on mechanical properties of concretes made from a new acid-resistant mortar and a conventional concrete, and corresponding reinforced concrete beams, subjected to accelerated acidic environments in UTS laboratory. Concrete properties including compressive strength, modulus of elasticity, modulus of rupture, indirect tensile and drying shrinkage were examined. The load carrying capacity of companion reinforced concrete beams were also determined. The specimens were tested before and after periods of exposure to sulphuric acid solution with the concentration of 7% and changes of their properties were evaluated. The results enable an understanding of the mechanism of acid attack and the benefit of the use of acid resistant concrete. On the other hand, the effect of acid attack on reinforced concrete beams is highly dependent on the design of the reinforced concrete beams and to a lesser extent on the acid resistant property of the concrete.

**Keywords:** Acid resistant mortar, Acid resistant concrete, Acid Attack on concrete.

## 1. Introduction

Given the existence of acidic soil and acidic groundwater in acid sulfate soils, particularly in coastal areas in Australia [1], introduction of new acid resistant materials and investigation of the effect of acidic environments on performance of reinforced concrete (RC) structures is of importance. These structures could be piers, footings or foundations of different structures such as buildings and bridges [2]. Acidic environments cause the degradation of concrete and hence, decrease of load bearing capacity in these structures as well as serious durability issues.

Penetration of aggressive agents into the concrete and their chemical reaction with the cement matrix including decalcification, gypsum formation and ettringite formation causes the deterioration of concrete [3]. These chemical reactions can lead to expansion and cracking of concrete and loss of strength and elastic properties of concrete [4, 5, 6, 7].

In Australian Standard AS 3600 there are some precautions for concrete structures in acidic environments such as, some recommendations about the use of Sulphate Resistant (SR) cement in harsh environments. However, for prolonged exposure periods, SRPC does not appear to provide a better resistance to sulphuric acid attack than that provided by conventional Portland cement (OPC) [8, 9]. Some polymer modified concretes have also shown a better performance against the sulphuric acid [10]. However, they have not been mentioned as a viable solution in these environments due to implied high cost [11].

In this study a new structural concrete is developed by use of a novel acid resistant mortar (ARM) which was initially used for lining and repair purposes in Australia. For this purpose, mechanical properties of the ARM, the new acid resistant concrete (ARC) made from the ARM and a conventional concrete as the control concrete were tested before and after exposure to sulphuric acid solution (7%). Then flexural strength of reinforced concrete members made from the ARC and conventional concrete was tested before and after exposure to acid that will be presented.

## 2. Experimental Work

Experimental tests of this research include two main parts, namely, mechanical properties tests and structural tests of reinforced concrete members. The details of experimental tests will be explained in this section.

## 2.1. Test materials

### 2.1.1. Conventional concrete (CC)

The first series of specimens were cast from a conventional concrete as control concrete. The characteristics of this concrete are shown in Table 1. The target slump was  $140 \pm 10$  mm.

**Table 1. Mix design of the conventional concrete (CC).**

Nominal compressive strength (MPa)	Coarse aggregate (kg/m <sup>3</sup> )	Fine aggregate (kg/m <sup>3</sup> )	Cement (Shrinkage limited) (kg/m <sup>3</sup> )	Water/Cement Ratio	Fly ash(kg/m <sup>3</sup> )	Pozzolith 80 (liter/m <sup>3</sup> )
40	960	661	350	0.4	150	2.3

### 2.1.2. Acid resistant mortar (ARM)

The second series of specimens were made from the acid resistant mortar (ARM). The ingredients of ARM are shown in Table 2. The mean 28-day compressive strength of ARM is 30 MPa.

**Table 2. ARM Compositions.**

Ingredients	Silica sand	Fly ash	Silicates and poly silicates	Silica fume	Portland cement	Other ingredients
* Proportion	30-60%	10-30%	1-10%	1-10%	1-10%	1-10%

\* The exact amount of the ingredients of ARC has not been mentioned here due to the confidentiality agreements with the manufacturer.

### 2.1.3. Acid resistant concrete (ARC)

The last series of specimens as the main purpose of this study was made from the acid resistant concrete (ARC) which contains ARM and coarse aggregates with the coarse to fine aggregate ratio of 0.5. Water to binder ratio for both ARM and ARC was 0.4 and ARC had a slump of  $140 \pm 10$  mm. Type and grading of coarse aggregates in the conventional concrete and acid resistant concrete (ARC) were the same and the maximum size of aggregates was 10mm.

## 2.2. Test procedure

### 2.2.1. Mechanical properties tests

The mechanical properties tests included the compressive strength, modulus of elasticity (MOE), modulus of rupture (MOR) and Indirect tensile test, according to the relevant standards in Australia, namely, AS1012 [12,13,14,15,16].

To investigate the mechanical properties, 120 standard cylinders with the dimensions of 100 in diameter by 200 mm in height; 50 cylinders with the size of 150 in diameter by 300 mm in height and 80 prisms with the size of 100mm by 100mm by 400 mm were tested. For each test, three concrete specimens were tested to ensure repeatability and the reported results are the average values of these three specimens.

Each series of the specimens were kept under standard curing conditions for 28 days. Afterwards, half of the specimens were washed with water, dried to a saturated surface dry condition and were then immersed in acid solution (five folds of their volumes) and then covered to eliminate evaporation of the solutions. The density of acid solution was monitored weekly to control the acid concentration (7%). Each time the same number of specimens, not exposed to acid, was also tested to compare the behaviour of ARC with CC in the presence and absence of acid.

As this concrete is developed for structural applications, the amounts of drying shrinkage are of importance. Hence, 9 prisms with the size of 75mm by 75mm by 400 mm were cast and their ultimate drying shrinkage was measured in accordance with AS 1012.13 (1992).

### 2.2.2. Flexural strength of reinforced concrete (RC) members

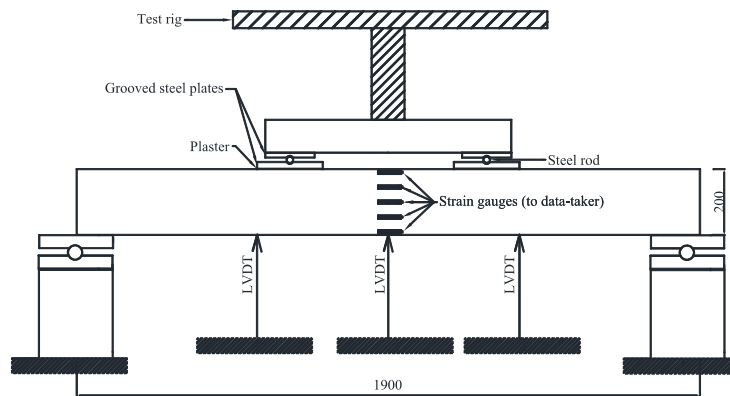
Flexural strength of 15 RC beams made from ARC and CC with the dimensions of 150mm by 200mm by 2000 mm were evaluated through four-point loading test before and after four, eight and twelve weeks of exposure to sulphuric acid solution. The RC beams were designed for tensile failure. Test set-up for these tests is shown in Figure 1 a, b and c and the beams' reinforcement details are shown in Figure 1 d. Three LVDTs were used at  $\frac{1}{4}$ ,  $\frac{1}{2}$  and  $\frac{3}{4}$  of the span of the beam to record the deflections. The beams were loaded with the rate of 0.5 mm/sec by deflection control method till failure.



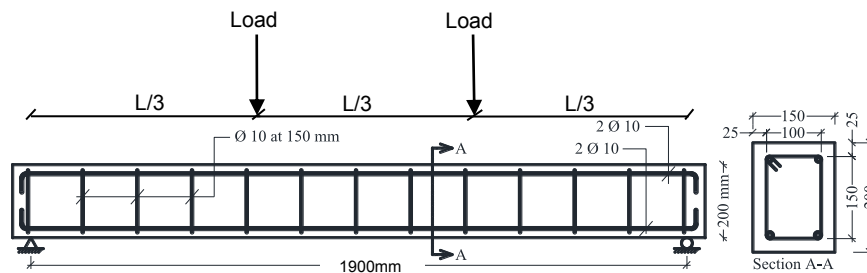
a)



b)



c) Test set up for flexural strength test



d) Details of RC beams

Figure 1. (a) & (b) Photos from the flexural strength tests, (c) & (d) Test set up and beam details for flexural strength tests.



### 3. Results and Discussion

The results of experimental tests including the mechanical properties tests and structural tests will be presented.

#### 3.1. Mechanical Properties Tests

The results of mechanical properties tests of the conventional concrete (CC), Acid resistant mortar (ARM) and acid resistant concrete (ARC) are summarized in Table 3. All reported times in this Table are the time of exposure to acid or water after 28 days of standard curing. Another important point in this table and Figure 2 is that the test results of control concrete have not been reported after eight weeks of exposure due to degradation of the concrete samples.

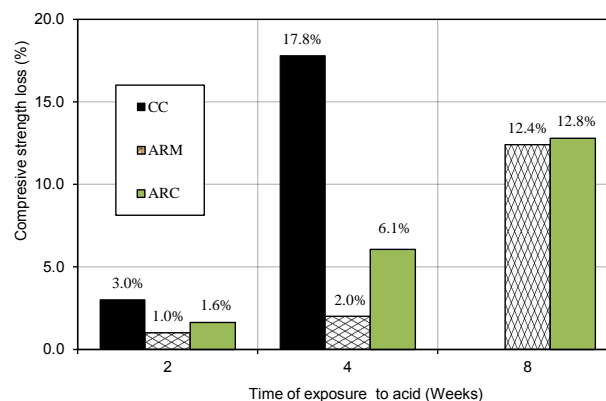
**Table 3. Mechanical Properties of CC, ARM and ARC after exposure to sulphuric acid.**

Type \ Time		2 weeks			4 Weeks			8 Weeks		
		exposure to water	exposure to acid	Change (%)	Curing	Acid	Change (%)	Curing	Acid	Change (%)
CC	Compressive Strength (MPa)	46.1	44.7	-3.0%	53.8	44.2	-17.8%	-	-	-
	MOR (MPa)	5.8	6.0	3.4%	5.9	6.2	5.1%	-	-	-
	MOE (GPa)	33.0	32.0	-3.0%	37.0	35.0	-5.4%	-	-	-
	Indirect Tensile (MPa)	6.6	7.1	7.6%	6.7	8.6	28.4%	-	-	-
ARM	Compressive Strength (MPa)	31.4	31.1	-1.0%	35.1	34.4	-2.0%	37.1	32.5	-12.4%
	MOR (MPa)	5.1	4.9	-3.9%	5.3	4.8	-9.4%	5.4	4.4	-18.5%
	MOE (GPa)	26.0	26.0	0.0%	28.0	28.0	0.0%	29.0	29.0	0.0%
	Indirect Tensile (MPa)	3.9	4.1	5.1%	4.1	4.5	9.8%	4.2	4.6	9.5%
ARC	Compressive Strength (MPa)	43.0	42.3	-1.6%	44.5	41.8	-6.1%	51.6	45.0	-12.8%
	MOR (MPa)	5.6	5.6	0.0%	5.7	5.7	0.0%	6.0	5.3	-11.7%
	MOE (GPa)	32.0	32.0	0.0%	33.0	32.0	-3.0%	33.0	28.0	-15.2%
	Indirect Tensile (MPa)	3.8	4.0	5.3%	3.9	4.5	15.4%	4.4	4.5	2.3%

#### Compressive strength

Regarding the compressive strength of concretes it should be mentioned that after introduction of coarse aggregates to ARM to produce ARC, compressive strength increased from 31.4 to 43 MPa at the age of six weeks (42 days) and from 35.1 to 44.5 MPa after eight weeks (56 days) of standard curing which suggests about 30% increase of compressive strength.

As shown in Figure 2, CC had 3% and 17.8% compressive strength loss after two and four weeks of exposure to acid solution respectively, whereas, these strength loss decreased by 1.6% and 6.1% for the ARC.



**Figure 2. Compressive Strength of CC, ARM and ARC after exposure to acid.**

This decrease was 1% and 2 % for the ARM, effectively unchanged. Comparison of the strength loss of CC and ARC after two weeks and four weeks of exposure to acid solution reveals that the strength loss of ARC was about 1/3 of CC.

- *Modulus of Rupture (MOR)*

Modulus of rupture (MOR) of CC had a slight increase in acid. ARM had 3.9% and 9.4% decreases after two and four weeks of exposure to acid, respectively. This shortcoming was resolved after addition of coarse aggregates to ARC and there was no change in MOR characteristics of ARC samples after two and four weeks (28 days) of exposure.

- *Modulus of Elasticity (MOE)*

Tests of modulus of elasticity (MOE) of CC showed a slight decrease after two and four weeks (14 and 28 days) of exposure to acid solution (3% and 5.4%), whereas, ARM did not show any change in MOE characteristics even after eight weeks of exposure to acid. ARC did not have any change of MOE after two weeks and 3% decrease after four weeks (28 days) of exposure that was less than CC. In addition, comparison of the MOE test results of ARM and ARC without acid confirms the increase of MOE by addition of coarse aggregates to the ARM. This was predicted due to the role of aggregate in stability of concrete.

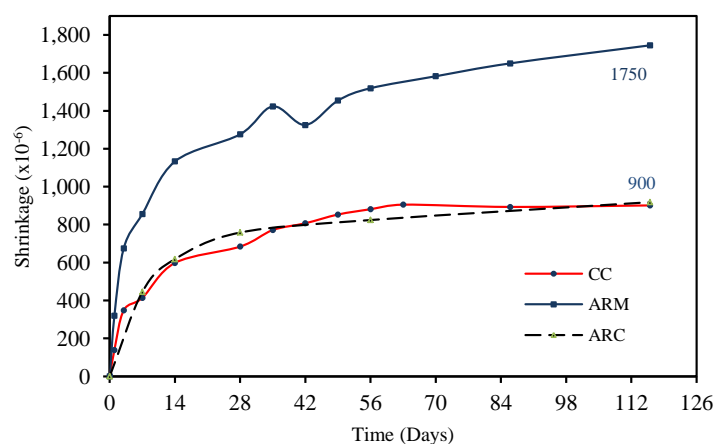
- *Indirect Tensile strength*

As shown, for all types of specimens, tensile strength measured by splitting test, increased after exposure to acid compared to the specimens under standard curing conditions. This unexpected increase was greater for the control concrete. For instance, after four weeks of exposure to acid CC had 28% increase compared to ARM (9.8%) and ARC (15.4%). The reason behind this increase is currently being explored through microstructural analysis in the UWS laboratory.

The same trend was initially expected for the changes of indirect tensile and flexural strength in acid. However, for MOR, the unaffected concrete at the extreme fibre of the conventional concrete is tested, whereas, for ARM and ARC the partially acid corroded extreme fibre of the ARM and ARC is tested. In indirect tensile test, the external layer that is to carry the compressive load is unaffected concrete in CC and the acid-affected layer in ARM and ARC.

- *Drying shrinkage*

Given the purpose of this project, which was developing the ARC for structural application, amounts of drying shrinkage of ARC was an important factor. ARM naturally had a high amount of drying shrinkage due to its fine nature. This issue was addressed by addition of coarse aggregate in ARC which led to the ultimate drying shrinkage of 900 micro strains which is within the acceptable range for structural concretes according to AS3600 (See Figure 3).



**Figure 3. Drying Shrinkage of CC, ARM and ARC**

### 3.2. Flexural strength of reinforced concrete (RC) beams

Two groups of RC beams were tested for flexural strength namely, CC and ARC. Figure 4 shows the load deflection of concretes before exposure to acid. As can be seen ARC had similar ultimate load but greater ultimate deflection comparing to CC, displaying more ductile behaviour.

Figure 5 shows the flexural behaviour of CC and ARC beams after exposure to acid. This reveals that after exposure to acid both types of concretes had some strength loss but there was no significant change. This loss was greater in CC beams comparing to ARC that can be attributed to reduction of the effective depth of the CC beam sections, causing the shortening of lever arm and, therefore, reducing the load capacity. This decrease of effective depth was found by measurement of the depth of the beams before and after exposure to acid. The initial depth of all beams was 200mm that decreased to 180mm and 162mm after four weeks and eight weeks (28 and 56 days) of exposure to acid, respectively. For CC the exposure to acid seems to increase the ductility of the beams, accompanied by loss of load carrying capacity from about 78 kN to about 62 kN after eight weeks (56 days) of exposure due to reasons mentioned above. The impact of acid exposure to ARC is less pronounced than CC with slightly better ductility and less loss of load carrying capacity with time of exposure.

In Figure 6 the normalized ultimate load of specimens is obtained by dividing the ultimate load of RC beams to the ultimate load of non-acid exposed beam. The normalized ultimate load of the beams predicts a dramatic decrease of flexural strength for CC in longer term dropping to 80% of the original strength after 12 weeks (84 days). This factor seems to remain almost constant (at about 90% of strength) for ARC and more resilient for long term exposure to acid. For the first 10 weeks of exposure, CC seems to display a better flexural strength, however, after 10 weeks the ARC behaves much better. Coincidentally the value at 10 weeks is about 90% for both CC and ARC. This confirms that ultimate load bearing of CC beams decrease much faster than ARC beams compared to not acid exposed beams from the same materials.

It is important to mention that despite degradation of surface layers of CC beams and loss of a considerable amount of concrete cover (20 mm loss of 25 mm concrete cover), the acid did not reach reinforcing bars after twelve weeks of exposure. However, a major loss of strength is predicted after long term exposure of CC beam to acid due to corrosion of reinforcing bars.

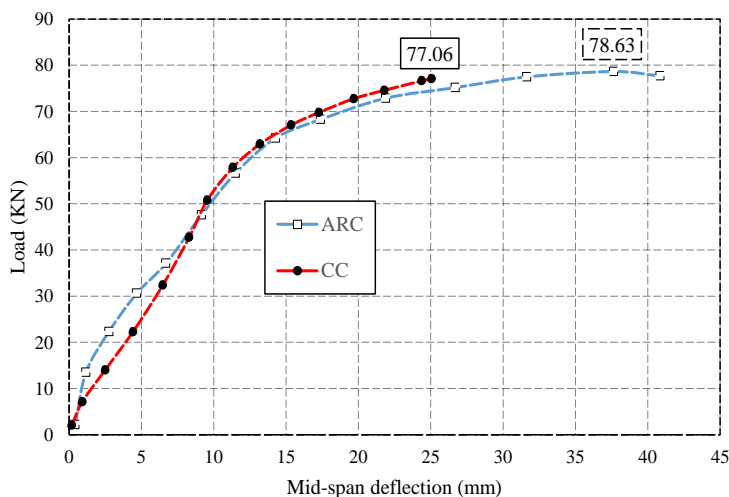
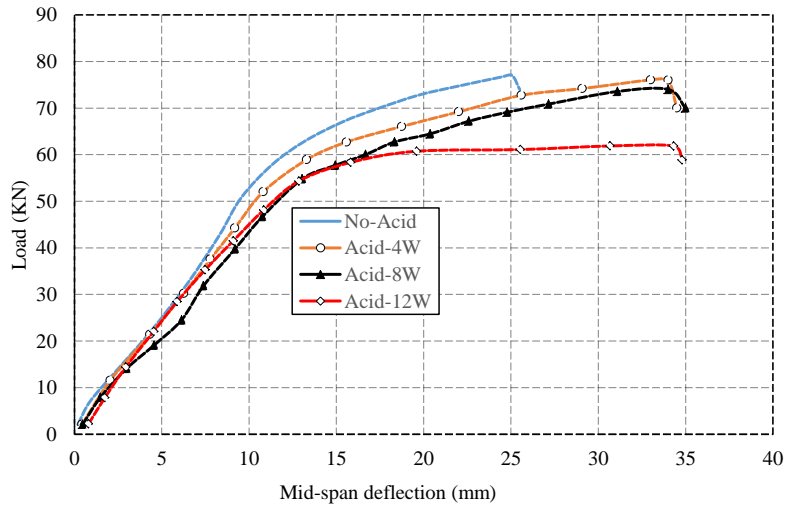
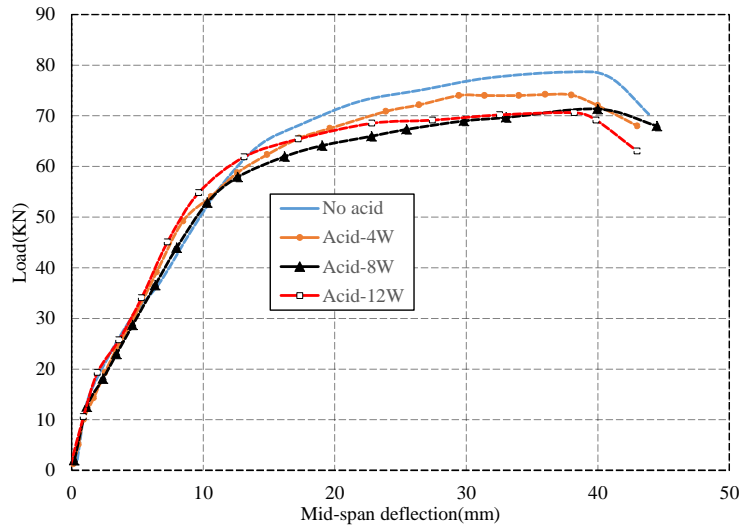


Figure 4. Load-deflection of ARC and CC beams in flexural test



a) Load-deflection of Conventional Concrete after exposure to sulphuric acid.



b) Load-deflection of ARC after exposure to sulphuric acid.

Figure 5. Load versus deflection in flexural test a) conventional concrete and b) ARC beams after exposure to acid.

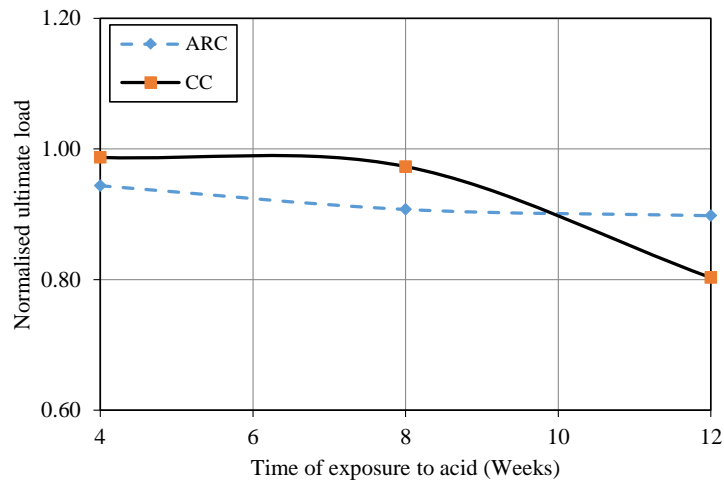


Figure 6. Normalized ultimate load of the RC beams versus time of exposure to acid.

#### 4. Conclusion

In this study, mechanical and structural properties of a new acid resistant concrete (ARC), were investigated and compared to a control concrete in the laboratory. The results of mechanical properties tests of ARC before and after exposure to accelerated acidic conditions were promising. Drying shrinkage of ARC was also in the acceptable range for the purpose of this study. Hence, flexural strength of reinforced concrete beams made from ARC was tested for structural applications and showed that as long as the acid has not reached the reinforcing bars the maximum load bearing capacity of RC flexural members, whether from CC or ARC, does not change significantly. However, there is some strength loss because of decreasing the effective depth of RC beam sections due to degradation of concrete surface layers. Study of the history of flexural strength of RC beams after exposure to acid suggests much better performance for ARC comparing to the conventional concrete.

#### 5. Acknowledgements

The authors gratefully acknowledge the support of Parchem Company in the provision of ARM materials for testing, the UTS for provision of laboratory facilities and financial supports and the Advanced Materials Characterisation Facilities (AMCF) in UWS particularly, the director of the AMCF, Dr. Richard Wuhrer, for his wonderful support and valuable suggestions.

#### 6. References

1. Australian Standards, "Analysis for Acid Sulfate Soil (AS 4969-0)", 2008, Australia.
2. The Environmental Protection and Heritage Council and Natural Resources Management Ministerial Council of Australia, "National guideline for the management of acid sulphate soils", 2011, Australia.
3. Neville, A, "The confused world of sulfate attack on concrete", Cement and Concrete Research, 34(8), 2004 ,pp 1275-1296.
4. Girardi, F. & Maggio, R. D. "Resistance of concrete mixtures to cyclic sulphuric acid exposure and mixed sulphates: Effect of the type of aggregate". Cement and Concrete Composites, 33, 2011, pp 276-285.
5. Gutierrez-Padilla, M. G. D., BIELEFELDT, et al., "Biogenic sulphuric acid attack on different types of commercially produced concrete sewer pipes". Cement and Concrete Research, 40, 2010, pp 293-301.
6. Zivica, V., T. Palou. et al., "Acid attack of cement based materials under the common action of high, ambient temperature and pressure". Construction and Building Materials, 36, 2012 ,pp 623-629.
7. Cement Concrete and Aggregates Australia, "Sulphate-resisting Concrete", 2011, Australia.
8. Attiogbe, E., Rizkalla, S, "Response of concrete to sulphuric acid attack". ACI Mater. J., 85, 1988, pp 481-488.
9. Fattuhi, N., Hhges, B, "SRPC and modified concretes subjected to severe sulphuric acid attack". Mag.Concr.Res, 40, 1988, pp159-166.
10. Mohamed, A.-M. O., Gamal, M. E., "Hydro-mechanical behavior of a newly developed sulphur polymer concrete", Cement and Concrete Composites, 31, 2009, pp 186-194.
11. Pacheko-Torgal, F., Jalali, S. "Sulphuric acid resistance of plain, polymer modified, and fly ash cement concretes", Construction and Building Materials, 23, 2009, pp 3485-3491.
12. Australian Standards, "Methods of testing concrete – Determination of the drying shrinkage of concrete for samples prepared in the field or in the laboratory (AS 1012.13)", 1992, Australia.
13. Australian Standards, "Methods of testing concrete - Determination of the static chord modulus of elasticity and Poisson's ratio of concrete specimens (AS 1012.17)", 1997, Australia.
14. Australian Standards, "Methods of testing concrete - Determination of the compressive strength of concrete specimens (AS 1012.9)", 1999, Australia.
15. Australian Standards, "Methods of testing concrete - Determination of the modulus of rupture (AS 1012.11)", 2000, Australia.
16. Australian Standards, "Methods of testing concrete - "Methods of testing concrete - Determination of indirect tensile strength of concrete cylinders (Brasil or splitting test) (AS 1012.10)", 2000, Australia.

# Effect of the Chemical Composition of Building Materials on Algal Biofouling

Philippe GROSSEAU<sup>1</sup>, Estelle DALOD<sup>2</sup>, Alexandre GOVIN<sup>3</sup>, Christine LORS<sup>4</sup>, René GUYONNET<sup>5</sup> and Denis DAMIDOT<sup>6</sup>

<sup>1</sup>Professor, SPIN-EMSE, CNRS:UMR5307, LGF, Ecole Nationale Supérieure des Mines de Saint Etienne, France

<sup>2</sup> PhD Student, SPIN-EMSE, CNRS:UMR5307, LGF, Ecole Nationale Supérieure des Mines de Saint Etienne, France and LGCgE- GCE, Ecole Nationale Supérieure des Mines de Douai, France

<sup>3</sup> Assistant Professor, SPIN-EMSE, CNRS:UMR5307, LGF, Ecole Nationale Supérieure des Mines de Saint Etienne, France

<sup>4</sup> Professor, LGCgE- GCE, Ecole Nationale Supérieure des Mines de Douai, France

<sup>5</sup> Professor, SPIN-EMSE, CNRS:UMR5307, LGF, Ecole Nationale Supérieure des Mines de Saint Etienne, France

<sup>6</sup> Professor, LGCgE- GCE, Ecole Nationale Supérieure des Mines de Douai, France

**Abstract:** The main cause of aesthetical deterioration of outdoor exposed building materials is the colonization by microorganisms. This phenomenon depends on factors such as geographical situation, environmental conditions and surface state of the substrate. Several researches have been devoted to the study of the effect of porosity, roughness and surface treatment on the biofouling of building materials. However, none of them has addressed the influence of cement composition. The main objective of this study is thus to highlight the influence of the composition of the material on its biocolonization by algae. The green alga *Klebsormidium flaccidum* was chosen because of its representativeness in France. It is indeed the species the most frequently identified and isolated from samples taken on sites. In order to characterize the influence of the composition of building materials on their biofouling, the behavior of mortars prepared with two types of Portland cement and two types of calcium aluminates cement is studied. The biofouling is followed by measuring the covering rate thanks to image analysis. This work is realized both on samples exposed outdoor and on samples tested in a laboratory bench. Obtained results prove that the composition of cementitious materials is a determining factor.

**Keywords:** biodeterioration, algae, mortars, Portland cement, Calcium Aluminate Cement.

## 1. Introduction

The colonization of building facades by microorganisms is the main cause of their aesthetical deterioration. The ageing of facades causes a change of the state of surface which favors the development of these species, in particular in the place where the rainwater flows and where run-outs appear. These latter are made of an association of organic particles and microorganisms called biofilm.

The main colonizing microorganisms are microalgae, fungi and bacteria (1,2,3). Barberousse (1) identified the micro-algae *Klebsormidium flaccidum* as the major microorganism developed on facades in France. *Klebsormidium flaccidum* is considered as a ground species. It is a green algae with a wide ecological amplitude (4). It can be found in the ground, on rocks, stone walls, and bark of trees. It is known for its wide presence in temperate regions (5,6,7).

The environment conditions the type of microorganism which colonizes a façade (3,8). The climate which includes temperature and moisture determines which microorganism will mainly grow. The rain and the wind favor the transport of microorganisms. The orientation of facades also impacts the biological development. An exposure toward North will be characterized by higher humidity and an absence of sun. These conditions favor the biofouling (1,9,10).

Organic materials such as paints and polymers and mineral materials such as mortar, concrete, natural stones or clay bricks are sensitive to biodeterioration. Barberousse (1) showed that the organic materials resist generally better to the colonization by algae and Cyanobacteria than mineral materials. The microorganisms observed are more diversified and more plentiful on mineral materials than on organic substrates.

Cementitious materials are heterogeneous, porous and their surface roughness can vary within a wide range. All these properties define the bioreceptivity of a material (2,11,12). Previous studies have

determined the influence of mortars' physical characteristics on their biofouling. Among them, the roughness of the surface (3,5,8,9,13) and the porosity (8,12,14) seem to be the most important ones.

Cementitious matrices partially weather because of the presence of carbon dioxide in the atmosphere. The natural carbonation of the mineral matrix leads to a decrease in surface pH and favors the microbiological colonization (8,10) and an alkaline surface pH can totally inhibit the colonization of a material by microorganisms. Indeed the pH affects the microorganisms because it regulates the ionization mechanism of metabolites (15).

The solutions developed to prevent the biocolonization of facades by microorganisms must take into account the preservation of the environment and the understanding of the interactions between microorganisms and materials is thus necessary for this purpose.

The main objective of this study is to highlight the influence of the chemical composition of the substrate on the biofouling, comparing the behavior of mortars prepared with cements of different mineralogy.

## 2. Materials and methods

### 2.1 Mortars formulation

In order to study the influence of the mineral chemistry on the biofouling of cement mortars, four types of cement were selected; two Portland cements and two calcium aluminate cements. The materials were a white Portland cement CEM I 52.5 N CE CP2 NF "SB" provided by Italcementi (coded CEMB), a grey Portland cement 52,5N-PM-ES-CP2 provided by Lafarge (coded CEMG) and two calcium aluminate cements provided by Kerneos, a white one (coded CACB) and a grey one (coded CACG). The chemical compositions obtained by X-Ray fluorescence are given in Table 1.

**Table 1 : Chemical Composition of the Cements CAC B, CAC G, CEM B and CEM G and the Siliceous Sand (%wt)**

Sample	SiO <sub>2</sub>	TiO <sub>2</sub>	Al <sub>2</sub> O <sub>3</sub>	Fe <sub>2</sub> O <sub>3</sub>	CaO	MnO	MgO	Na <sub>2</sub> O	K <sub>2</sub> O	P <sub>2</sub> O <sub>5</sub>	LOI
CAC B	4.98	1.89	49.99	1.70	38.61	0.06	0.58	0.39	0.26	0.15	0.47
CAC G	0.25	0.38	69.8	0.18	30.61	0.03	0.46	0.18	0.42	0.12	0.56
CEM B	21.70	0.16	4.25	0.41	69.53	0.01	0.79	0.32	0.07	0.05	2.79
CEM G	22.40	0.15	2.87	2.22	69.34	0.05	0.91	0.19	0.18	0.07	1.65
Sand	97.44	0.04	1.15	0.1	0	0.07	0.15	0.39	0.53	0.01	0.2

The mortars were prepared with either CAC B, CAC G, CEM B or CEM G and siliceous sand (Sifrac DURANCE DU 0.1-0.35 with  $d_{50}=254\mu\text{m}$ ). The formulation was 30% cement, 70% sand and the ratio w/c was 0.57 for the CAC B based mortars, 0.54 for CAC G based mortars and 0.5 for the CEM based mortars, in order to obtain similar consistencies.

The dry mix was added in water in a standard mixer. The mixing time was chosen accordingly to the procedure of the NF-EN-196-1 standard. The fresh mortar was then poured into polystyrene moulds of 50x50x1 cm (LxWxH). The air bubbles were eliminated by means of a vibrating table and of a ruler. For a higher roughness, the roughcast roller was applied during the setting. The arithmetical roughness was determined with an optical profilometer CHR-150-L. The mortars were stored 7 days in 100 % of relative humidity (RH) before being cut. The final dimensions of the samples were of 8x20x1 cm (LxWxH).

Accelerated weathering of mortar was carried out in a cell under pure CO<sub>2</sub> at 20°C and 65% RH. Carbonation reaction and decrease of surface pH were thus speeded up (16).

The pH-decrease was monitored with a surface electrode (WTW Sentix Sur). When the surface pH reached 9, carbonation was stopped and the mortars chemical composition was estimated by X-ray diffractometry and thermogravimetric analysis. The carbonation time was 30 days for CEM cement based mortar and 38 days for CAC cement based mortar.

The mortar porosity was measured via mercury intrusion porosimetry (Micrometrics Autopore IV 9400) after drying 24 hours at 60°C.

## 2.2 Algal culture

The algal culture of *Klebsormidium flaccidum* requires an appropriate culture medium: the Bold's Basal Medium, according to NF-EN-15458 standard. This medium contains macro-elements such as carbon, oxygen, phosphorus, nitrogen and hydrogen as well as some mineral salts (or trace elements).

Strains were supplied by the Museum National d'Histoire Naturelle (MNHN, Paris, France). The cultures were made in batches exposed to an artificial light for photoperiods of 12 hours. Two fluorescent lamps (Fluora Osram) provided a light intensity of 20  $\mu\text{mol}/\text{m}^2/\text{s}$  PPF (Photons Photosynthetic Flux) which corresponds to a power of 30 W. This type of lamp was chosen because the light emitting spectrum matches with the chlorophyll light absorbing spectrum. Temperature and hygrometry were regulated at 20°C and 60 % RH respectively. Algal growth was followed thanks to various microbiological techniques such as cellular counting, optical density via UV-visible spectrophotometer, and determination of dry mass via algal suspension filtration. The ionic concentration was measured by ionic chromatography. These techniques were also used to characterize the algal growth in the biofouling laboratory bench.

## 2.3 Biofouling laboratory test

The system consisted of a glass chamber of dimensions 100x50x50 cm in which were settled two stainless steel supports inclined at 45° (Figure 1). The mortar samples were exposed to the same conditions of light (20  $\mu\text{mol}/\text{m}^2/\text{s}$  PPF, photoperiods of 12 hours) and temperature (20°C) as for the algal growth. The temperature was maintained with a thermoregulator. The box was filled with 50L of microalgal suspension, (concentration of 4mg/L dry mass) which was pumped and sprinkled on the top of mortar samples. The watering was made by means of a full holes banister of 2 mm in diameter, every 1 cm. The flow was set to  $26 \pm 1$  L/h. The sprinkling was carried out for 90 minutes every 12 hours and enabled to reproduce the phenomenon of colonization of a facade: microalgae were transported by the solution and had the possibility of hanging on and of adhering to the surface according to the characteristics of the mortar.

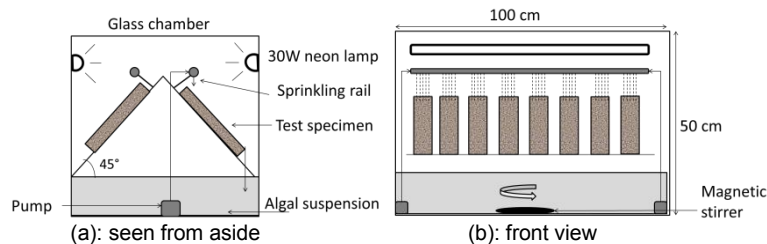


Figure 1. Laboratory bench for the colonization of mortars by streaming of algal suspension

## 2.4 Biofouling in-situ test

The in situ bench is set up at the “Ecole Nationale Supérieure des Mines de Douai” situated in Douai (North of France). The bench test on which are exposed 60 samples is constituted by a stainless steel structure (Figure 2). The angle of inclination is fixed to 45° which allows exposing samples to the weather conditions (period of sunshine, streaming, gusts of wind). Rows of samples are situated at least 1 meter above ground level, to avoid spatters phenomena. Samples are arranged so that the flow from one sample cannot contaminate the sample situated below and are spaced out by 5 cm to avoid contaminations. The site of exposure is a flat ground, distant from the traffic and close to some trees (situated at about 15 m from the bench)



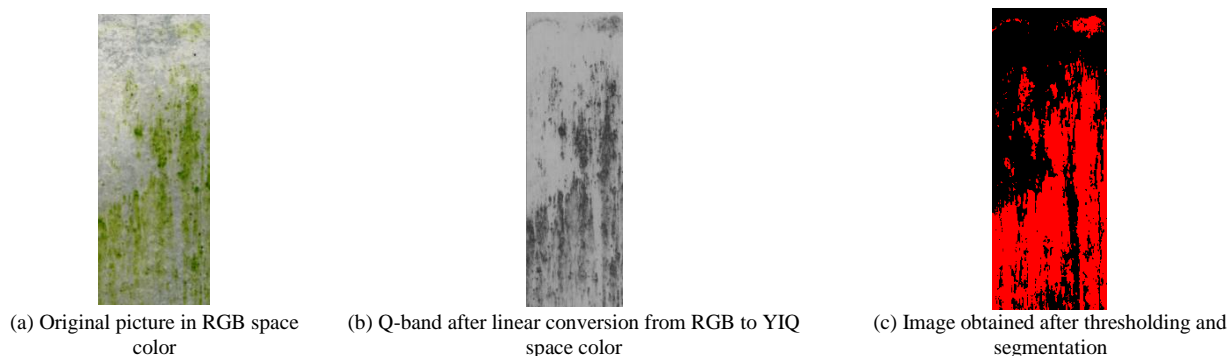


**Figure 2. In-Situ bench for the colonization of mortars**

## **2.5 Biofouling evaluation**

The biodeterioration intensity was measured by image analysis. Thanks to an office scanner, the surface of sample mortars was digitized at different times. These images were then treated with the software Aphélon® which calculates a covering rate (noted  $X(t)$ ) of samples by microalgae (13). The initial RGB color space was converted in YIQ color space in order to identify easily the green algae on mortars.

The Q channel was used to quantify the number of colonized pixels after thresholding and segmentation. The colonization rate was given by the ratio of colonized area to the total surface. The different steps of image analysis are detailed on Figure 3. After segmentation the binary image represents in red the fouled area and in black the unfouled one.

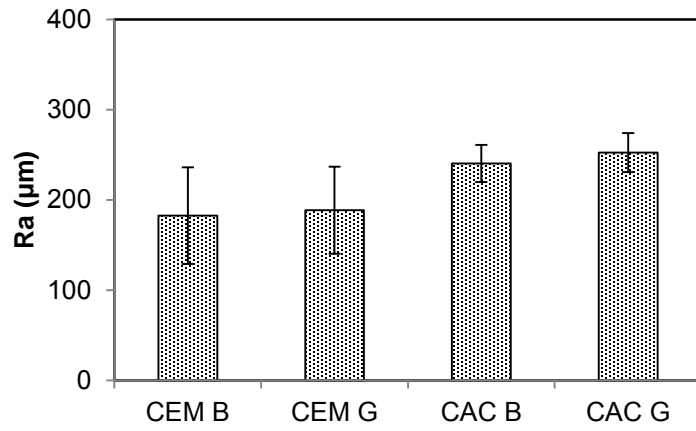


**Figure 3. Example of image analysis of a specimen after 9 days test**

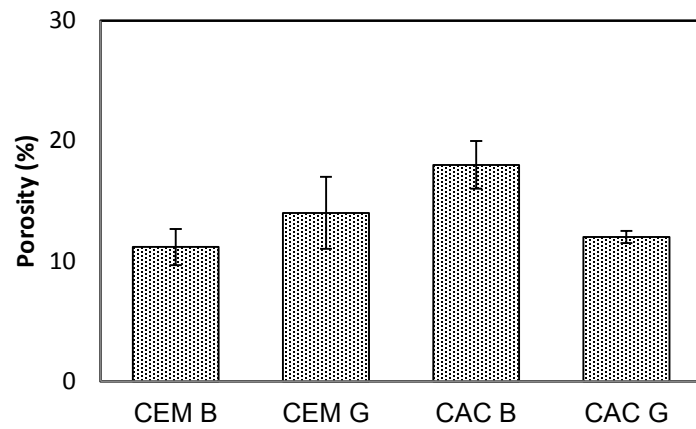
## **3. RESULTS AND DISCUSSION**

### **3.1 Characterization of the materials**

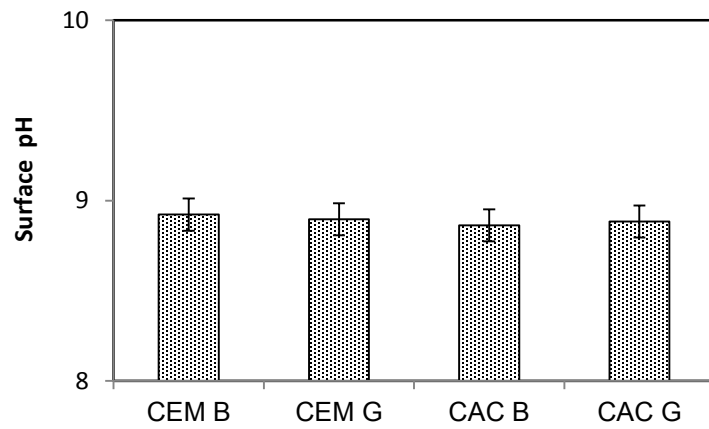
Results represented on Figures 4, 5 and 6 show that roughness, surface pH and porosity are not significantly different for all samples, around a value of about  $220 \mu\text{m}$  for roughness, 8.8 for surface pH and 14% for the porosity. This is an important result since it was already proven that these characteristics have a strong influence on the kinetics of biocolonization of mortars (4,5,9,12,13,14). As the physical characteristics of presently studied mortars are similar, we will thus be able to compare the effect of the chemical composition on the resistance to biofouling.



**Figure 4. Roughness of studied materials**



**Figure 5. Porosities of studied materials**



**Figure 6. Surface pH of studied materials**

### 3.2 Biofouling study in laboratory bench

The pictures of Figure 7 show the evolution of the surface of the specimens during the test period for Portland cement mortars and CAC mortars and we can thus notice that CAC based mortars were much less quickly colonized than Portland cement based mortars.

This phenomenon is fully confirmed by the evolution of the colonization rates of the specimens which is shown on Figure 8. The colonization of Portland cement based mortars both started earlier and was completed in a shorter time than the colonization of CAC based mortars.

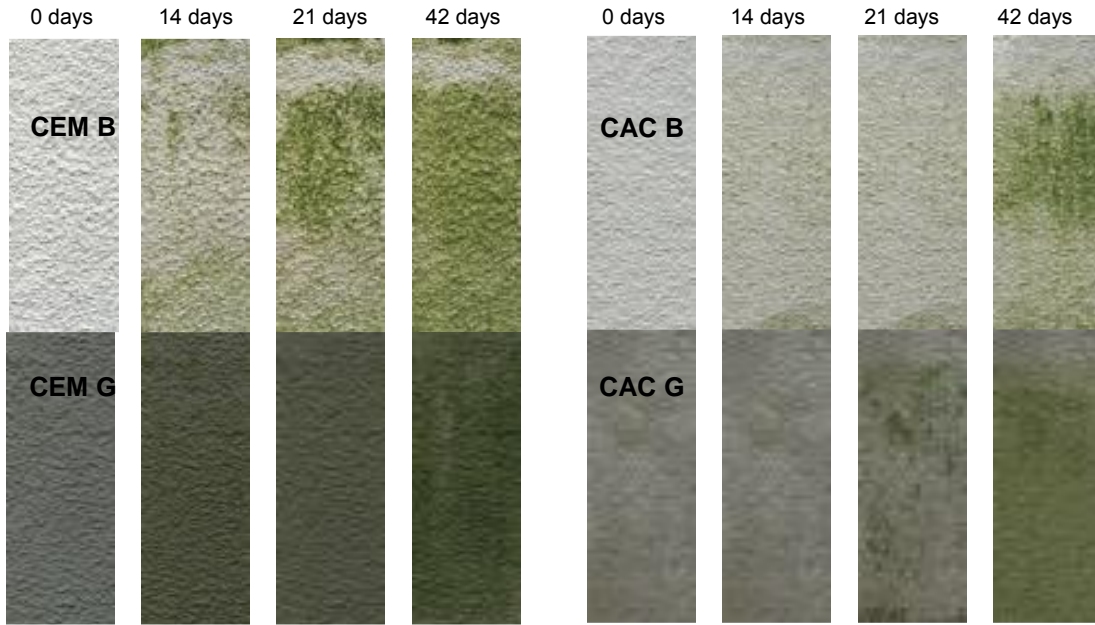


Figure 7. Evolution of the biocolonisation of the samples during accelerated laboratory test

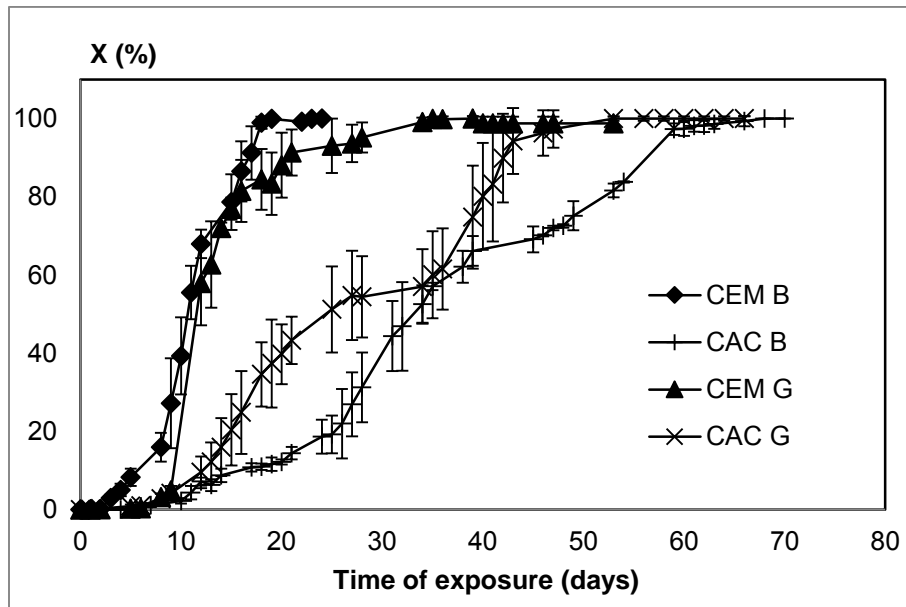


Figure 8. Evolution of the fraction of colonized area during accelerated laboratory test

### 3.3 *In-situ study of the biocolonization of mortars*

This part of the work was realised only with white mortars CEM B and CAC B. The samples were exposed from March 2012, at the beginning of spring. In a similar manner to what happened in laboratory tests, we can again notice that mortars containing CAC cement were more slowly colonized than the mortars which contain Portland cement (Figures 9 and 10).

On Figure 10, one can notice a decrease of the colonization rate after about 550 days and 900 days of exposure. This phenomenon was due to winter conditions which implied a detachment of algae from the material.

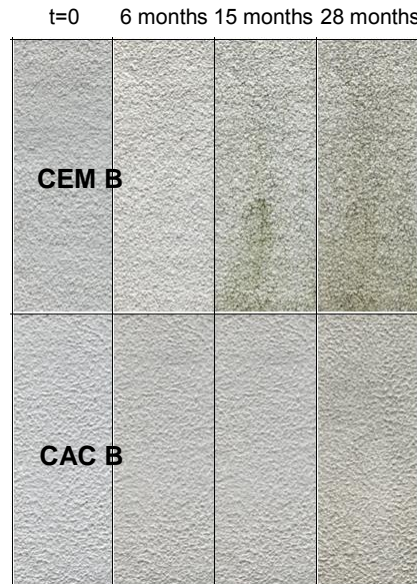


Figure 9. Evolution of the biocolonisation of the samples during outdoor exposition

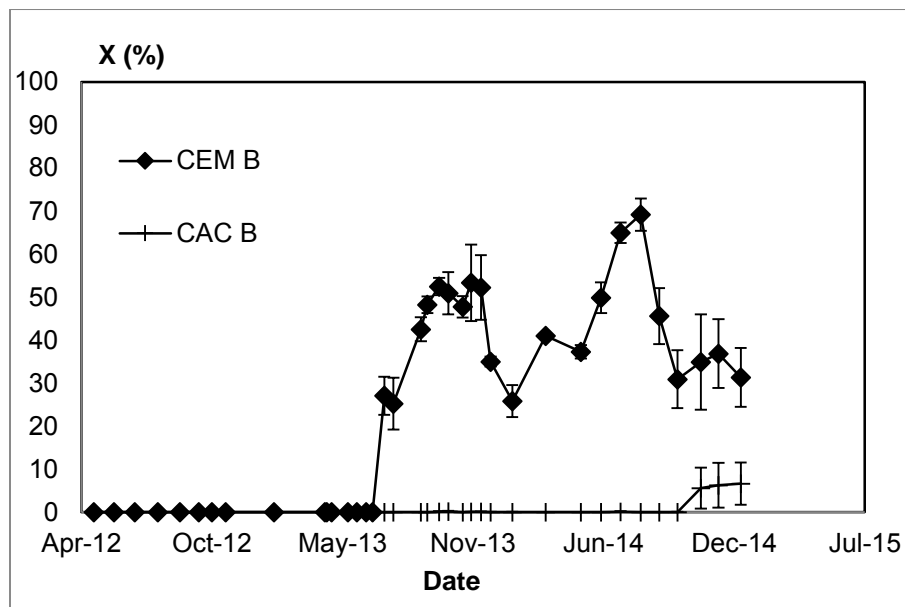


Figure 10. Evolution of the fraction of colonized area during outdoor exposition

### 3.4 Discussion

In order to verify that the observed phenomena were not due to a difference in the alkalinity of the studied mortars, we followed the evolution of surface pH of the samples and of the pH of the algal suspension all along the laboratory test. The results are shown in Figures 11 and 12. It is quite clear that there are no significant differences between the different materials tested, which is of course consistent with the fact that all samples are carbonated.

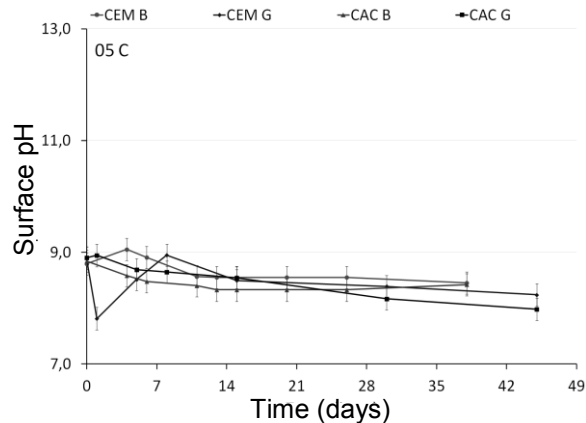


Figure 11. Evolution of the surface pH of samples during laboratory test

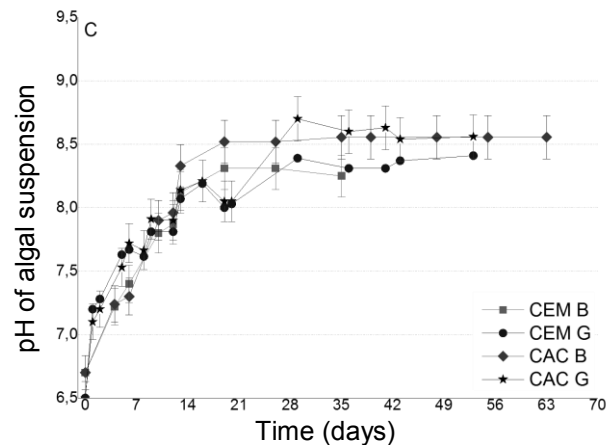


Figure 12. Evolution of the pH of algal suspension during laboratory test

Lindemann et al.(17) emphasize that aluminum toxicity is known in acidic pH and highlight a slowdown in the growth of algae at neutral pH ( $\sim 6.5$ ), pH range in which aluminum hydroxide  $\text{Al}(\text{OH})_3$  is predominant. A bacteriostatic effect of hydrated alumina gels formed by mild acid attack in sewage pipes is also proposed to explain the durability of aluminous cements for such applications (18).

It is thus likely that species containing aluminum such as the gel of  $\text{Al}(\text{OH})_3$ , present in significant amounts in carbonated aluminates cements (19,20), possess a bacteriostatic effect at the origin of the particularly high durability of CAC based mortars with respect to the algal biocolonization.

### 4. Conclusions

In this study, we have shown, both by accelerated laboratory tests and by outdoor exposition, that aluminate cement-based mortars present a resistance to algal biocolonization much higher than Portland

cement mortars. This study was performed using mortars with similar physical characteristics (roughness, porosity, surface pH) and which do not influence the pH of their environment in different ways. We can thus conclude that this effect is mainly due to mineralogical differences. Previous studies indicate that this phenomenon might be caused by a bacteriostatic effect of aluminum hydroxide. We plan to continue this study and verify this hypothesis by additional tests on the interaction between  $\text{Al}(\text{OH})_3$  and microorganisms.

## 5. References

1. Barberousse H. "Etude de la diversité des algues et cyanobactéries colonisant les revêtements de façade en France et recherche des facteurs favorisant leur implantation", 2006. PhD thesis, Museum National d'Histoire Naturelle, Paris, France.
2. Saiz-Jimenez C. "Biodeterioration vs biodegradation: the role of microorganisms in the removal of pollutants deposited on historic buildings", *International Biodeterioration & Biodegradation* 1997; 40:225-232.
3. Gaylarde C, Ribas Silva M, Warscheid T. "Microbial impact on building materials: an overview", *Materials and structure* 2003; 36:342-352.
4. Rindi F, Guiry MD, Lopez-Bautista JM. "Distribution, morphology and phylogeny of Klebsormidium (Klebsormidiales, Charophyceae) in urban environments in Europe", *Journal of Phycology* 2008; 44:1529-1540.
5. Ortega-Calvo JJ, Hernandez-Marine M, Saiz-Jimenez C. "Biodeterioration of building materials by cyanobacteria and algae", *International Biodeterioration* 1991; 28:165-185.
6. Rindi F, Guiry MD. "Composition and spatial variability of terrestrial algal assemblages occurring at the bases of urban walls in Europe", *Journal of Phycology*. 2004; 43:225-235.
7. Gaylarde CC, Morton LHG, Loh K, Shirakawa MA. "Biodeterioration of external architectural paint films – A review", *International Biodeterioration & Biodegradation* 2011; 65:1189-1198.
8. Warscheid T, Braams J. "Biodeterioration of stone: a review", *International Biodeterioration & Biodegradation* 2000; 46:343-68.
9. Morton LHG, Greenway DLA, Gaylarde CC, Surman SB. "Consideration of some implications of the resistance of biofilms to biocides", *International Biodeterioration & Biodegradation* 1998; 41:247-259.
10. Barberousse H, Ruot B, Yéprémian C, Boulon G. "An assessment of facade coatings against colonisation by aerial algae and cyanobacteria", *Building and Environment* 2007; 42:2555-2561.
11. Dubosc A, Escadeillas G, Blanc P. "Characterization of biological stains on external concrete walls and influence of concrete as underlying material", *Cement and Concrete Research* 2001; 31:1613-7.
12. Guillitte O. "Bioreceptivity: a new concept for building ecologies studies", *The Science of the total environment* 1995; 167:215-220.
13. Tran TH, Govin A, Guyonnet R, Grosseau P, Lors C, Garcia-Diaz E, et al. "Influence of the intrinsic characteristics of mortars on biofouling by *Klebsormidium flaccidum*", *International Biodeterioration & Biodegradation* 2012; 70:31-39.
14. Gaylarde CC, Gaylarde PM. "A comparative study of the major microbial biomass of biofilms on exteriors of buildings in Europe and Latin America", *International biodeterioration & biodegradation* 2005; 55:131-9.
15. Fogg GE. "Algal adaptation to stress - Some general remarks. In: *Algal adaptation to environmental stresses*", 2001. Page 1-19.
16. Chaussadent T. "Analyse des mécanismes de carbonatation du béton", *Comptes Rendu des Journées techniques AFPC-AFREM*. 1997. Page : 75-87.
17. Lindemann, J., Holtkamp, E., Herrmann, R., 1990. "The impact of aluminium on green algae isolated from two hydrochemically different headwater streams", *Bavaria, Germany. Environmental Pollution* 67, 61-77.

18. Herisson, J., 2012. "Biodétérioration des matériaux cimentaires dans les ouvrages d'assainissement : étude comparative du ciment d'aluminate de calcium et du ciment Portland", Université Paris-Est.
19. Scrivener, K.L., Capmas, A., 2003. 13 - "Calcium Aluminate Cements", in: *Lea's Chemistry of Cement and Concrete (Fourth Edition)*. Butterworth-Heinemann, Oxford, pp. 713–782.
20. Lamberet, S., 2005. "Durability of ternary binders based on Portland cement, calcium aluminate cement and calcium sulfate" (PhD Thesis). École Polytechnique Fédérale de Lausanne (EPFL), Lausanne.

# Expansive Behavior of Mortars Containing Surf Clam Shell Powder at Early Age

Akio Watanabe<sup>1</sup> Kazumi Hirokawa<sup>2</sup> and Takashi Kondo<sup>1</sup>

<sup>1</sup> Associate Professor of Civil Engineering, Tomakomai National College of Technology

<sup>2</sup> Professor of Civil Engineering, Tomakomai National College of Technology

**Abstract:** Reuse of surf clam shell has been of great interest in Japan, especially in fishing areas. The authors have investigated properties of concrete containing the clam shell powder, and they found that the clam shell powder could be used as an admixture of concrete. In this study, early age expansion between mortars with and without the surf clam shell powder was compared. Length changes of mortars at early ages were measured in accordance with ASTM C1698. As a result, regardless of the incorporation of the clam powder, the authors found them shrunken in the first few hours after mixing. However, subsequent behavior of mortars was quite different between them. It was observed that the mixed mortar, in which approximately 10 percent of the cement were replaced with surf clam shell powder, remarkably expanded by 10mm in length. This expansion may be related to formation of calcium hydroxide. The clam shell powder can be used as an effective expansive admixture for concrete.

**Keywords:** surf clam shell, ASTM C1698, Ca(OH)<sub>2</sub>, expansion.

## 1. Introduction

The enterprising use of industrial waste is required in the concrete structures. In Japan, approximately 480 kg of industrial waste, including blast furnace slag, fly ash, municipal solid waste incineration ash, and sewage sludge, is currently used per tonne of cement, and this proportion is increasing year by year. In Hokkaido, northern Japan, it is desired that waste generated as a result of processing seafood is also used as a construction material. This fishery-related waste includes approximately 200,000 tonnes of shells every year, but establishing methods of using these shells is a challenge. Research into the use of shell in concrete is being conducted in South Korea, where oyster shell is being studied as a concrete aggregate<sup>1</sup>. Furthermore, some scallop shells (of which there is also an abundance in Japan) are also being used as concrete aggregate.

However, surf clams, which are a specialty of Tomakomai City in Hokkaido, are caught in small quantities—6,000 tonnes in Hokkaido (of which 800 tonnes are caught in Tomakomai)—and so the amount of surf clam shells available is lower than that of scallop shells, and most are disposed of through methods that do not allow for recycling. Because large amounts of shells are required, using them in aggregate is thus an unsuitable method for utilizing waste surf clam shells. One idea is to use a mixture of scallop and surf clam shells, but it is best to avoid mixing the shells because their compositions are different. Whereas the surf clam shells are made of aragonite-type calcium carbonate, scallop and oyster shells are made of calcite-type calcium carbonate, and so the hardness and other properties of the shells differ. A mixture of shells of different quality could cause a decrease in the quality of the concrete. Therefore, a different method of use to that of scallop and oyster shells must be devised for surf clam shells.

Rather than using the surf clam shells as aggregate, the present research examines the use of the shell as an admixture that can be added in small amounts to improve the quality of concrete. The authors focused on the fact that surf clam shells are calcium carbonate and thought that by burning the shells to form calcium oxide they could be used as an expansive admixture for concrete. This paper examines the expansion characteristics of cement mortar that result from the addition of surf clam shells.

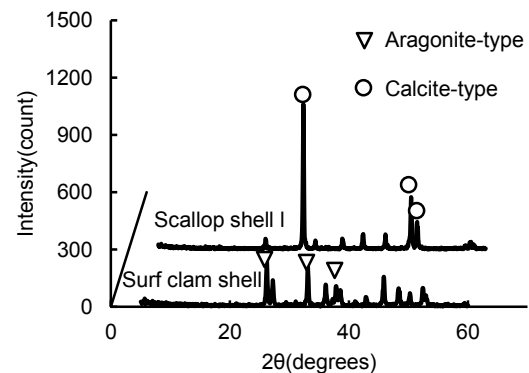


Figure 1. XRD of surf clam and scallop shell



## 2. Experiment

### 2.1 Material characteristics

#### 2.1.1 Surf clam shells

Surf clam shells are calcium carbonate-based, like scallop and oyster shells, but the crystalline structure is different. Figure 1 shows the results of powder X-ray diffraction measurements of the shells. The main peak values for aragonite-type calcium carbonate, 26.59°, 33.15°, and 38.10°, are identified in the surf clam shell, whereas the main peak values for calcite-type calcium carbonate, 29.65°, 47.57°, and 48.93°, are identified in the scallop shell. Lime made from limestone is ≥90% calcite-type calcium carbonate, and has a stable crystalline structure used in cement and steel. In contrast, aragonite-type calcium carbonate is described as being in a “metastable phase” and has a crystalline structure found only in some corals and shells. This structure is harder than the calcite-type, and its characteristics include changing into the calcite-type when burned at approximately 500°C.

The surf clam shells used in this research were ground to a grain size of 75 μm or lower, and burned for 1 hour at 1,000°C. Figure 2 shows the results of powder X-ray diffraction measurements of surf clam shell before and after burning. The aragonite-type calcium carbonate changes into calcium carbonate. Photo 1 is a scanning electron micrograph (SEM) of the shell powder. The surface of the shell powder becomes smooth as a result of burning.

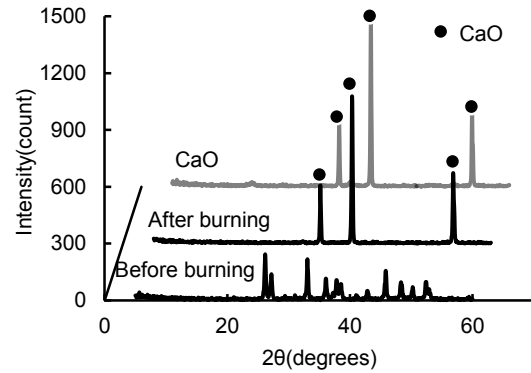
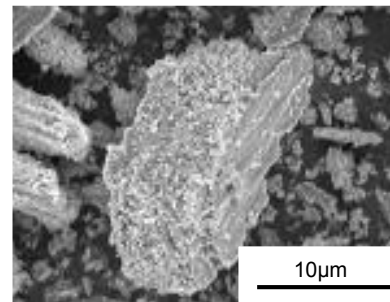
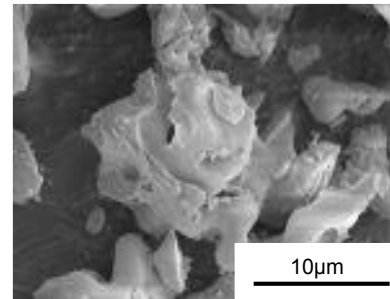


Figure 2. XRD of surf clam shell before and after burning



(a) Before burnig



(b) After burning

Photo 1. SEM of surf clam shell before and after burning

#### 2.1.2 Lime-based expansive admixture

An evaluation of the expansion characteristics of the surf clam shell was carried out by comparison with a commercial expansive admixture. Expansive admixtures can be divided into those containing calcium sulfoaluminate, which cause expansion by forming ettringite ( $3\text{CaO}\cdot\text{Al}_2\text{O}_3\cdot 3\text{CaSO}_4\cdot 32\text{H}_2\text{O}$ ), and those containing lime, which cause expansion by forming calcium hydroxide ( $\text{Ca}(\text{OH})_2$ ). Considering the composition of the surf clam shells, a lime-based expansive admixture was used in this research. Table 1 shows the chemical composition of the burned surf clam shell and the expansive admixture.

Table 1. Chemical composition of the burned surf clam shell and the expansive admixture

	Weight Percent						
	Ig.loss	SiO <sub>2</sub>	Al <sub>2</sub> O <sub>3</sub>	Fe <sub>2</sub> O <sub>3</sub>	CaO	MgO	SO <sub>3</sub>
Burned surf clam shell (HP)	1.4	0.05	0.03	0.19	98.0	0.08	0.24
Expansive admixture (B)	1.2	4.2	1.1	1.0	74.0	0.5	16.5

## 2.2 Mixture

A mortar (hereafter, N) comprising cement, water, and fine aggregate at a ratio of 1.0:0.5:2.0 was made using ordinary Portland cement (density 3.16 g/cm<sup>3</sup>) and river sand (density 2.77 g/cm<sup>3</sup>). Surf clam shell (HP) and expansive admixture (B) were substituted in proportions of 0.05 and 0.10 with respect to cement mass (hereafter, HP5, B5, HP10, and B10).

## 2.3 Compressive strength test

Square pillar specimens of size 40 × 40 × 160 mm were produced in accordance with Japanese Industrial Standards (JIS) R 5201. The specimens were removed from their molds 24 hours after pouring, and cured in water at 20°C. A compressive strength test was carried out at material ages of 7 days and 28 days.

## 2.4 Mortar specimen length change test

A length change test according to the American Society for Testing and Materials (ASTM) C1698 was employed as a method of measuring the expansion of the mortar, and it was decided to study the expansion characteristics of the mortar at an early age. This test was originally intended to evaluate autogenous shrinkage at low water-cement ratios, and is a method of examining length change in cement paste or mortar poured in a corrugated mold using a dial gauge based on the length when set<sup>2,3</sup>. This research enhanced the test apparatus by replacing the dial gauge with a laser displacement meter so that the length change could be measured directly straight after pouring.



Photo 2. Length change measuring device

A polyethylene corrugated mold approximately 30 mm in diameter and 425 mm in length was installed vertically on top of a shaking table, and the mortar was poured in from the top while the table was vibrated. Then, a Teflon stopper was put on to make a specimen for measuring length change. This was installed on a platform fixed at a 30° angle in a temperature-controlled room at 20°C, and length change was measured using the length change measuring device shown in Photo 2. The measurable range using this test apparatus was -10 to +10 mm.

## 2.5 Other tests

Samples were collected from the specimens after the compressive strength test, and these samples were immersed in acetone and, after the hydration reaction was halted, dried in a vacuum. Chemical analysis was carried out using thermogravimetry-differential thermal analysis (hereafter, TG-DTA) and powder X-ray diffraction. Pieces of samples were also collected from the specimens after the length change test and were examined using a scanning electron microscope (SEM).

# 3. Results and discussion

## 3.1 Compressive strength

Figure 3 shows the results of the compressive strength tests. If N is taken as the reference, the compressive strength of HP5 is slightly lower at material ages of both 7 days and 28 days. However, HP10 has a compressive strength of approximately 5 N/mm<sup>2</sup> at 28 days, which is a very low value. The reason for this is that, as shown in Photo 3, the HP10 mixture showed considerable expansion, such that a length change of approximately 10 mm in the direction of the longitudinal axis was identified, generating

many tiny cracks as a result. The cause of this expansion is considered to be calcium oxide reacting with water and forming calcium hydroxide, similar to a lime-based expansive admixture. Among the mortars in which the expansive admixture was used, the strength of B5 at a material age of 7 days was greater than N. The strength of B10 was slightly lower than N, and was at the same level as HP5.

### 3.2 Expansion characteristics

Figure 4 shows the measured results for length change. Displacement indicates length from the initial length of 425 mm. Each specimen demonstrated considerable shrinkage during the period from directly after pouring until 4 to 5 hours later. This is considered to be shrinkage due to a cement hydration reaction. Subsequently, almost no change in length was found for N, HP5, or B5. The reason why expansion was not found in specimens HP5 and B5 was considered to be that the added amount was small and the reactions that occurred were insufficient to cause expansion. However, HP10 demonstrated considerable expansion from after shrinkage until 1 day had passed, and subsequently showed almost no length change. The reason why there was almost no length change after the material age of 1 day is considered to be because the quantity of water for the reaction was limited inside the airtight space of the corrugated mold. B10 showed gradual, continuous expansion after the material age of 1 day. This is considered to be because the amount of CaO in B10 is lower than in HP and SO<sub>3</sub> is added instead, thus the reaction is controlled such that expansion occurs over a long period.

### 3.3 Formation of calcium hydroxide

Figure 5 shows the results of TG-DTA analysis at a material age of 7 days. The TG-DTA measurement conditions were an air flow of 25 ml/min. and a rate of temperature increase of 10°C/min., and the reference material was alumina. Figure 6 shows the results of quantitative evaluation of calcium hydroxide using the calibration curve method. N contains approximately 1.0% of Ca(OH)<sub>2</sub>, while HP5 contains approximately 1.5% and HP10 contains approximately 2.0% of Ca(OH)<sub>2</sub>. In other words, HP10 contains approximately twice the Ca(OH)<sub>2</sub> of the standard mortar. Therefore, the large expansion of HP10 is judged to be caused by the formation of Ca(OH)<sub>2</sub> due to the reaction of CaO in the burned HP with water. The reason why HP5

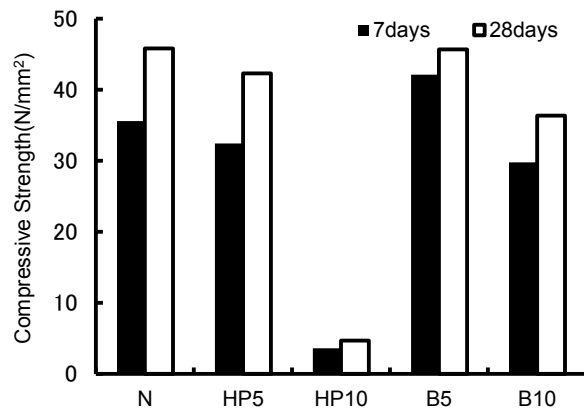


Figure 3. Compressive strength



Photo 3. Specimens (7days)

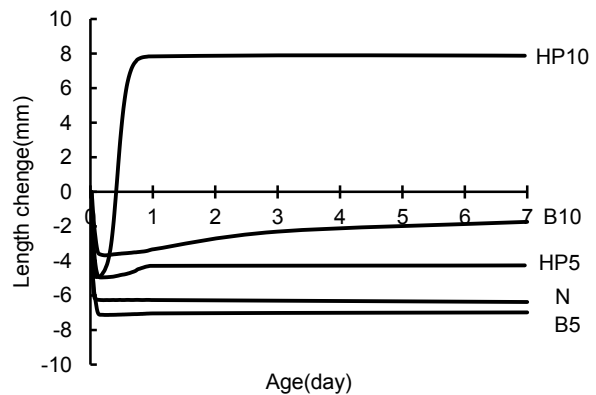


Figure 4. Length change at early ages

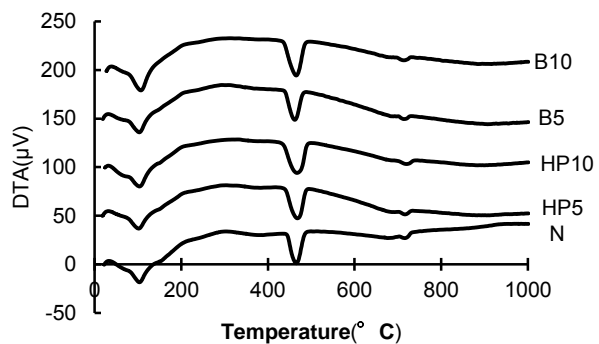


Figure 5. Results of TG-DTA (7days)

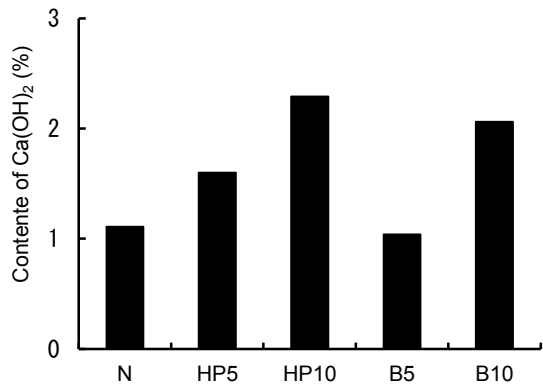


Figure 6. Ca(OH)<sub>2</sub> content of mortars (7days)

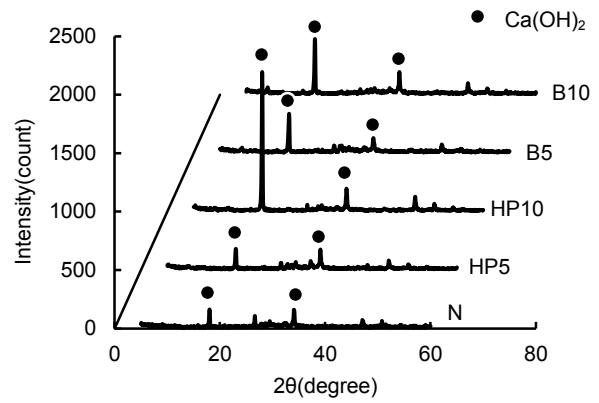
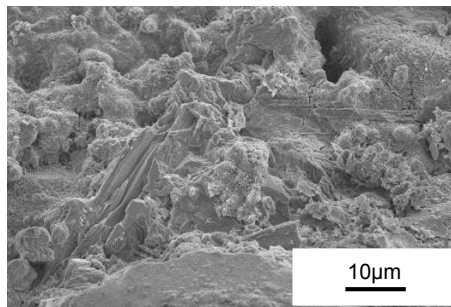
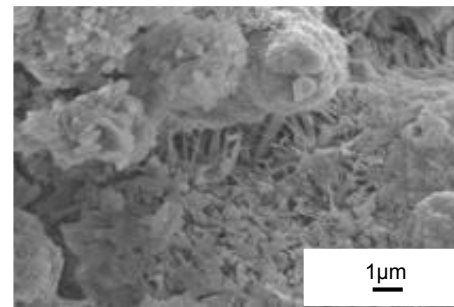


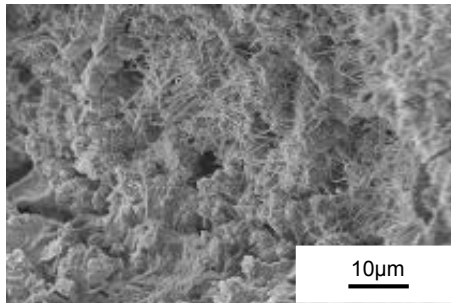
Figure 7. XRD of mortar (7days)



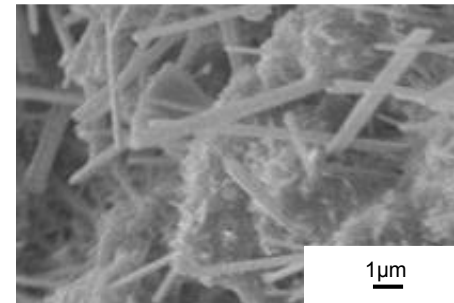
(a) N (×2,000)



(b) N (×10,000)



(c) HP10 (×2,000)



(d) HP10 (×10,000)

Photo 4. SEM images of N and HP10 after the length change test

did not expand is considered to be because the mixed amount of HP (CaO) was small and insufficient for Ca(OH)<sub>2</sub> to be formed.

### 3.4 Evaluation of calcium hydroxide using X-ray diffraction

Figure 7 shows the results of powder X-ray diffraction at a material age of 7 days. In HP5, the Ca(OH)<sub>2</sub> peak is roughly the same as in N. However, in HP10, the Ca(OH)<sub>2</sub> peak at 18° is very large compared to N, B5, and B10. The 18° peak increases in size according to the crystal orientation of Ca(OH)<sub>2</sub>. In other words, given that the content of Ca(OH)<sub>2</sub> in HP10 and B10 is roughly the same in the TG-DTA, it can be inferred that the cause of expansion is determined not just by the formation of Ca(OH)<sub>2</sub>, but also by the crystal orientation of the Ca(OH)<sub>2</sub>.

### 3.5 Electron microscopy of mortar fracture surface

Photo 4 shows SEM images of N and HP10 after the length change test. Some needle-like crystals of approximately 1 µm in length, considered to be ettringite, are visible in the SEM image of N. On the other

hand, in the SEM image of HP10, a large amount of rod-like crystals are found, and these crystals are of a size ranging from 5 to 10  $\mu\text{m}$ , making them visible even at a magnification of  $\times 2,000$ . These crystals are thought to differ from typical ettringite because of their large size.

Looking at the results of the powder X-ray diffraction measurements in Figure 7, ettringite peaks (e.g.,  $9^\circ$ ) are not visible in any of the specimens, and so it is unlikely that large amounts of ettringite were formed. However, the rod-like crystals are observed in large quantities, and so are considered to be relevant to mortar expansion. If these crystals originate in the  $\text{Ca}(\text{OH})_2$  detected using TG-DTA and powder X-ray diffraction, this could explain the size difference between the  $18^\circ$  peaks (Figure 7). In other words, although the cause is unclear, the results suggest that the powder X-ray diffraction peak may have increased in HP10 due to the thickness to which the crystals grew. The identity of this crystal requires investigation.

#### 4. Conclusion

This research investigated the expansion characteristics of a mortar in which the powder of burned surf clam shells was substituted for a portion of the cement, with the aim of using surf clam shells as an expansive admixture. The summarized results are as follows:

- (1) The surf clam shells change from  $\text{CaCO}_3$  to  $\text{CaO}$  as a result of burning at  $1,000^\circ\text{C}$ .
- (2) Mortar in which approximately 0.1 or more of the cement is replaced by burned surf clam shell demonstrates considerable expansion, and the formation of  $\text{Ca}(\text{OH})_2$  is increased.
- (3) In length change tests using a corrugated mold, all mortar specimens demonstrated shrinkage during the period from directly after pouring until setting. Subsequently, HP10 demonstrated considerable expansion until a material age of 1 day.
- (4) The cause of this expansion is considered to be the formation of  $\text{Ca}(\text{OH})_2$  due to  $\text{CaO}$  in the powder of burned surf clam shells reacting with water.
- (5) The intensity of the powder X-ray diffraction peak of  $\text{Ca}(\text{OH})_2$  at  $18^\circ$  was increased in HP10. Also, large amounts of rod-like crystals were observed in SEM images of pieces of the HP10 specimen.
- (6) These results show that mortar incorporating powder of burned surf clam shells causes expansion, and suggest that the powder of burned surf clam shells can potentially be used as a substitute for lime-based expansive admixtures. However, as there are points that are unclear in the expansion mechanism, research aimed at expansion control remains necessary.

#### 5. References

1. Yang, E.L., Yi, S.T. and Leem, M.L.: Effect of oyster shell substituted for fine aggregate on concrete characteristics: Part I. Fundamental properties, *Cement and Concrete Research*, 35(11), 2005, pp 2175-2182.
2. Millard, M. J. and Kurtis, K. E.: Effects of lithium nitrate admixture on early-day cement hydration, *Cement and Concrete Research*, 38(4), 2008, pp 500-510.
3. Sant, G. and Lothenbach, B. et al.: The origin of early age expansions induced in cementitious materials containing shrinkage reducing admixtures, *Cement and Concrete Research*, 41(3), 2011, pp 218-229.

# The use of cementitious coatings to reinstate low nominal cover on reinforced concrete structures

Neil Wilds<sup>1</sup>

<sup>1</sup>Technical Manager, Protective Coatings laboratory

<sup>2</sup>International Paint, Akzonobel, UK

**Abstract:** Reinforced concrete is used extensively in modern construction of numerous assets including bridges, jetties, public and industrial infrastructure. Structure design lives of 50 years and often significantly longer means durability should be a critical consideration. Durability of reinforced concrete depends on a variety of factors including the surrounding environment, mix design of the concrete and construction practices. A nominal design cover, thickness of concrete over steel reinforcement bars to provide corrosion protection, will typically be specified based upon the environment and the type of concrete used. In practice whether on site or in the pre-cast yard the specified concrete cover thickness is not always achieved. This will reduce the time to first maintenance and can lead to expensive repair costs particularly in severe coastal or industrial environments where high levels of chlorides and or acidic gases are present. When this occurs it can lead to project delays, scrapping of pre-cast units, potentially re-casting concrete on site or the use of protective coatings to reinstate the cover. Advanced cementitious coatings offer an innovative solution to this problem due to their ability to be applied to new, green, concrete and act as a barrier to moisture, Chlorides and acidic gases ensuring lasting protection.

This paper explores the problem and reviews the use of advanced cementitious coatings as a cost saving solution.

**Keywords:** concrete, concrete corrosion, durability, low cover, chloride protection, concrete repair and protection, cementitious coatings.

## 1. Causes of low cover

There are lots of causes of low cover and, although mistakes can happen on the project site, problems can sometimes be traced back to the design process. With the wish to make modern concrete structures more complex and aesthetically pleasing, the design becomes more complicated, and insufficient attention may be given to the practicality of turning the concept from the designer's drawings into reality. In some cases, designers do not picture the construction sequence or envisage the difficulties on project site, and so the requirements for steel reinforcement are based upon structural needs rather than the ease of assembly as subsequent encasement in concrete. This is seen as a common problem on highway and marine structures, where the sheer density of reinforcement provides big challenges for the contractor. In these instances, insufficient consideration is sometimes given to the mix design of the concrete to enable it to be poured into confined spaces.

Another cause of low cover can be poor workmanship, with the wrong or inadequate spacers being used or inadequate fixing of the formwork. Furthermore, great care must be taken when concrete is being poured and compacted to avoid displacement of the reinforcement. It must be remembered that, if the concrete fails to meet its specified characteristic strength, the cover quality will be inadequate to maintain the required durability requirements. Poor compaction and honeycombing will again reduce effectiveness of the concrete cover and will require remedial action. Therefore, it is vital to maintain tight quality control at all times to avoid such potentially costly mistakes.

## 2. Consequences of low cover

The concrete cover must have a minimum thickness for three main reasons:

- To protect the steel reinforcement bars (rebar's) from environmental effects to prevent their corrosion.
- To provide thermal insulation, this protects the reinforcement bars from fire.
- To give reinforcing bars sufficient embedding to enable them to be stressed without slipping.

The depth and quality of the concrete is vital as the relatively thin layer of concrete has to be able to maintain a passivating alkaline layer, formed by the release of calcium hydroxide as cement hydrates, whilst still forming a barrier to ingress of chloride ions or carbonation. Typical levels of cover are given in Table 1.

Country	Concrete Code	Range of Concrete Cover (mm)
UK	BS:8110	25-50
EU	EN 1992 (EC2)	diameter +10 - 55
USA	ACI:318	40-50
Australia	AS:3600	15-78

This is especially important where concrete structures are exposed to industrial or marine environments). The premature failure of corroded steel reinforcements and the expansion of the iron corrosion products around the rebar's are one of the main causes of the concrete degradation. The minimum concrete cover will depend on the environmental conditions encountered and must be thicker when the concrete is also exposed to moisture and chloride. A high quality concrete made with a low water-to-cement (w/c) ratio will have a lower porosity and will be less permeable to water and to the ingress of corrosive species (dissolved oxygen, chloride). A thicker cover or a more compact concrete will also reduce the diffusion of CO<sub>2</sub> in the concrete, protecting it better from carbonation and maintaining a higher pH for a longer time period, increasing so the rebar service life.

### 2.1 Remedial actions

#### 5.1.1 Demolition

Demolition is a drastic measure and the last resort, however once a client finds a major defect within a new structure the first suggestion is often to demolish those sections that do not meet the specification, or in the case of precast concrete elements reject the item. This is not always practicable, as it may be sometime before the problem is found or the costs in terms of delay to the project may be unacceptable.

### 5.1.2 Recasting

An alternative to demolition maybe partial recasting, which involves removing back to behind the level or the reinforcement using high pressure water jetting to avoid damage to the adjacent structure. The formwork is the repositioned to achieve the desired cover and the concrete is recast. However, depending when the problem is discovered, there may be problems with accessing the area to carry out the work.

### 5.1.3 Rendering

It may be practicable to increase the cover by building out the face of the concrete with a polymer-modified render, although it is important to ensure adequate key removing the surface laitance and achieving a rough surface using wet grit blasting. Depending upon the protective properties of the render, it may be possible to reduce the thickness of the cover while still providing the same degree of protection.

### 5.1.4 Protective Coatings

By far the easiest and most cost effective way of enhancing cover is to use cementitious protective coatings. These will not only reinstate the cover but also provides additional aesthetic and protective properties. But when selecting a coating system care must be taken to assess the film thickness required providing the necessary protection. In addition, the coating must be compatible with the substrate and its surroundings, and the products expected lifespan should be considered. The system must also be backed up by relevant independent test data and approvals.

## 3. Chloride Attack on Concrete

To use a well-known analogy, if a chloride ion were the same size as a tennis ball, then a capillary pore within even good-quality concrete would be the size of a railway tunnel (the radius of a chloride ion is  $0.18 \times 10^{-9}$ m. The size of the smaller capillary pores in concrete is  $1 \times 10^{-7}$ m. The diameter of a tennis ball is 670mm therefore multiply this by the difference in size (100) and you get 6.7m, which is certainly the size of a railway tunnel). Therefore, when concrete structures are exposed to salt spray or submerged in saltwater, chloride ions easily penetrate the concrete, eventually reaching the steel, breaking down the passivating layer and causing corrosion, even under highly alkaline conditions. Corrosion most rapidly occurs in the splash zone where the wet/dry conditions exacerbate chloride penetration and there is enough oxygen to facilitate the corrosion process.

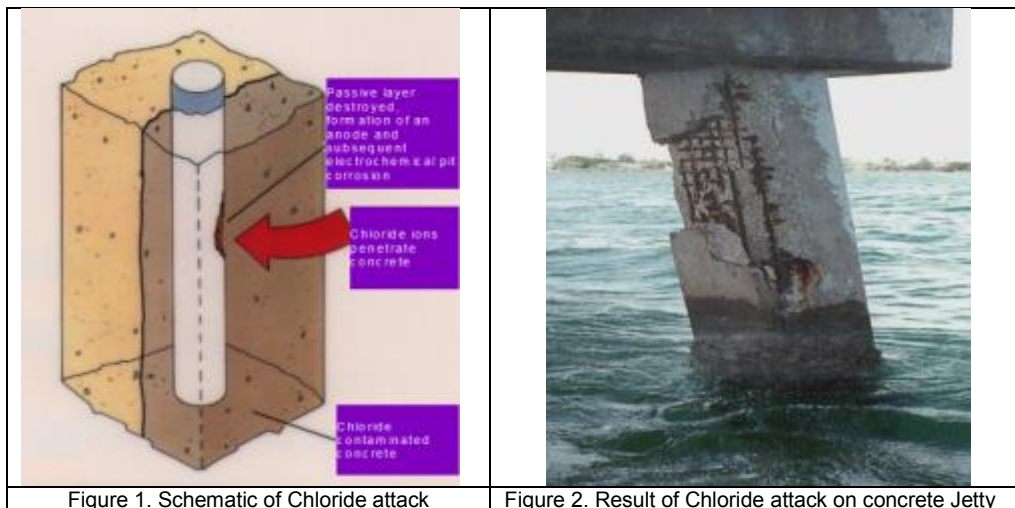
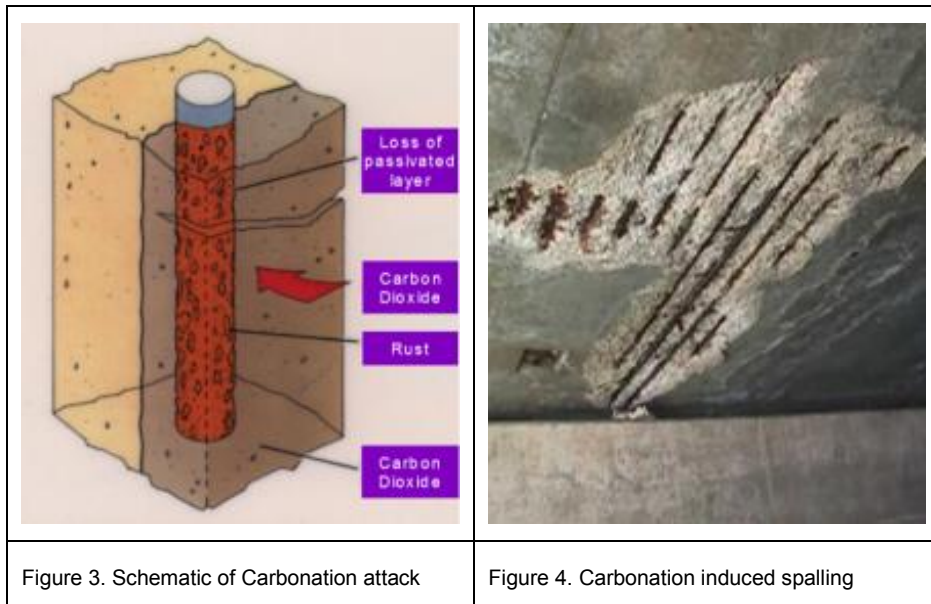


Figure 2. Result of Chloride attack on concrete Jetty



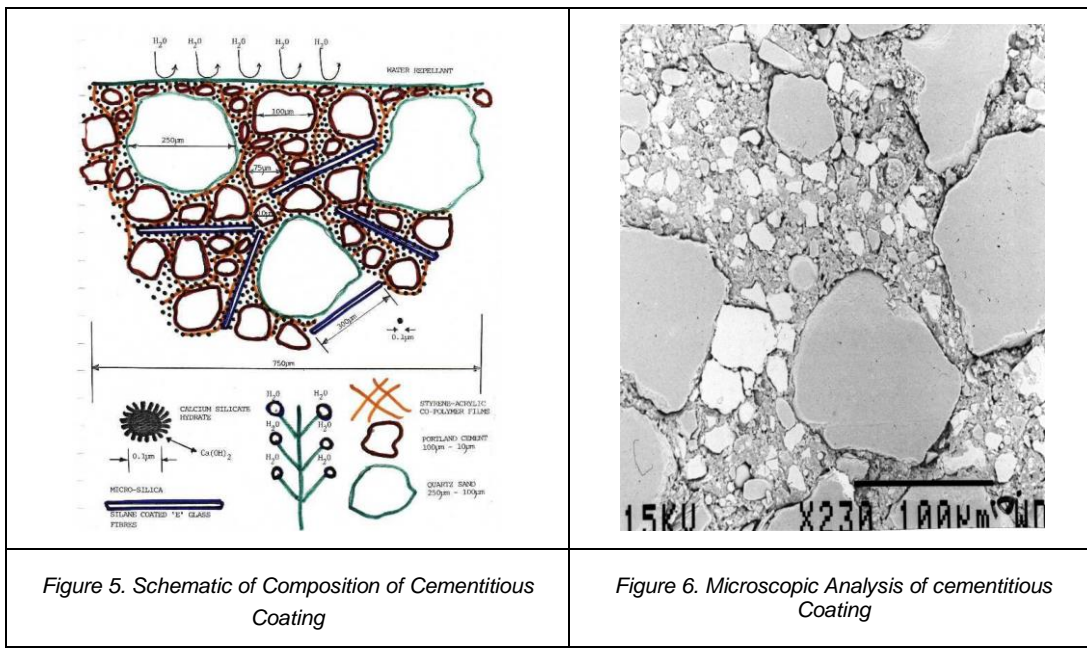
### 3. Carbonation of Concrete

The carbon steel of rebar is protected from oxidation by atmospheric oxygen by the high pH of concrete interstitial water. The rebar surface is passivated as long as the pH value is higher than 10.5. Fresh cement water has a pH of about 13.5 while evolved cement water pH ~ 12.5 is controlled by the dissolution of calcium hydroxide. Carbon dioxide present in the air slowly diffuses through the concrete and progressively reacts with the alkaline hydroxides (KOH, NaOH) and with calcium hydroxide leading to the carbonation of the hydrated cement paste. As a result, the pH of the cement drops and when its value is below 10.5 – 9.5, steel surface i.e. the rebar is no longer passivated and starts to corrode.



### 4. Cementitious Coatings a solutions for low cover

To achieve these barrier properties required to protect the rebar encased in concrete, the technology of cementitious coatings uses a number of different mechanisms to minimise both the porosity and permeability of what is essentially an ultra-thin but highly modified section of concrete. Low water:cement ratio and the use of pozzolanic materials such as fly ash, which react with the lime from the cement hydration to form further hydrates, reducing pore size, while micro-glass fibres dramatically reduce permeability. However the most influential raw material is silica fume, which is a byproduct of ferro-silicon steel production and is commonly referred to as a super-pozzolan due to its high reactivity with lime. It is 100 times finer than cement and contains material in the nano-particle range, which is capable of blocking the finest pores in the cement matrix. Many investigations have documented the dramatic reduction in the rate of chloride diffusion that can be achieved by incorporating silica fume into concrete<sup>1,2</sup>, which is largely attributed to the refinement of the pore structure. This modification in the pore structure also affects other properties resulting in 2mm film resisting water under 10 bar hydrostatic pressure (100m head of water). Gas diffusion resistance is also enhanced so that 2mm will provide the same resistance to carbon dioxide as 100mm of good quality concrete.



## 5. Performance of Cementitious coatings

As previously mentioned the two main modes of failure are carbonation and chloride attack of the rebar over prolonged exposure periods. This is obviously exacerbated with low cover issues resulting in the requirement that cementitious coatings must be shown to protect against these corrosive mechanisms. There are two relevant tests that can show this and can be used as a type of prequalification.

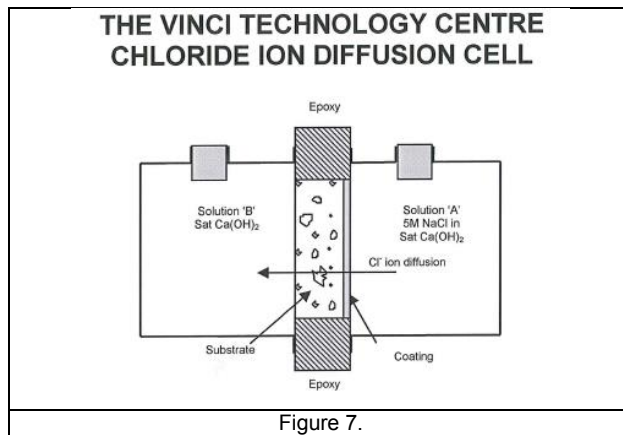
### 5.1 Chloride Diffusion Test

One such test for chloride diffusion began in 1988 initiated by Taywood Engineering (now Taylor Woodrow/Vinci construction Technology Centre).

#### 5.1.1 Test procedure

Two coats of the cementitious coating, each approximately 1mm thick were applied to one surface of a concrete slice using a palette knife. After this layer had cured for about 2 hours at 23°C and 60±5% relative humidity the second coat was applied at right angles. The coated specimen was then left to cure for 28 days under the same conditions prior to testing.

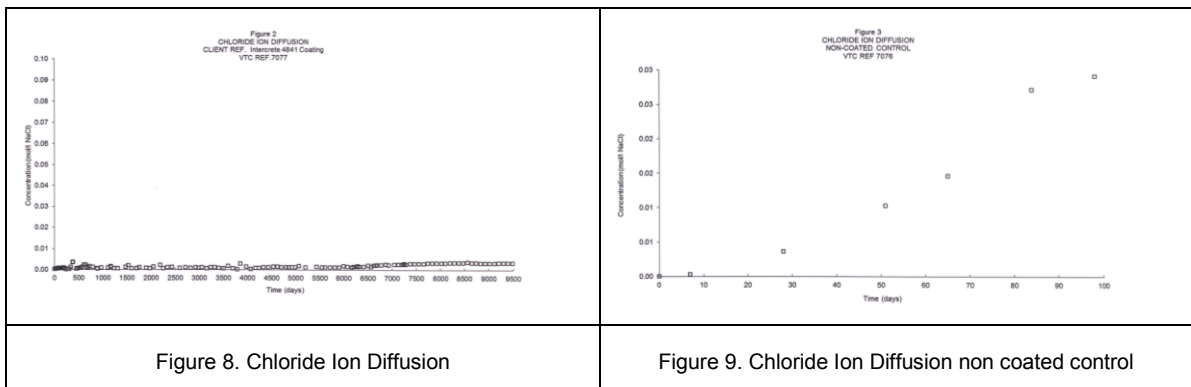
The coated specimen and an uncoated control had their top and bottom faces masked with plastic and tape respectively. They were then placed in individual moulds and the edges sealed with a cold curing epoxy resin. After allowing the resin to cure overnight, the specimens were immersed in saturated calcium hydroxide solution for 4 days. This was carried out to avoid anomalous effects due to chloride ingress by sorption rather than diffusion. Each specimen was the mounted in a diffusion cell as shown in Figure 7.



The cells were maintained at  $23\pm 2^{\circ}\text{C}$  and the chloride diffusing through the specimens was determined at suitable intervals. An aliquot of each sample was accurately pipetted into a clean oven dried glass container. Nitric acid (approximately  $50\text{--}70\text{cm}^3$ ) was added to the sample, which was then left to stand with occasional stirring. Automatic potentiometric titration with continuous stirring was used to analyse the samples. The titrator used was a Metrohm 798 MPT Tritrino and the course of the titration was monitored using a Metrohm electrode system. The accuracy of the method was checked using control samples of known chloride content ( $0.10\pm 0.01\%$ , by weight of sample).

### 5.1.2 Test Results

The following graphs Figure 8. & Figure 9. show the results from the titrations described above.



The cementitious coating has been on test for a period of 9484 days and counting (approximately 26 years). To allow the calculation of Chloride Ion Diffusion, CIDC, to be calculated, the chloride concentration must attain a steady state which is deemed when reaching  $>0.1$  mol/ltr. After 9484 days of the test, the chloride concentration was only  $0.0039\text{mol/ltr}$ , so no CIDC could be calculated. Results can be seen in Table 2 below.

Table 2. Chloride Ion diffusion Coefficient results ( After 26 years on test)		
Sample Ref	Cementitious Coating	Uncoated Control
Substrate thickness (cm)	1.414	1.465
Coating thickness (cm)	2100	n/a
Test area (cm <sup>2</sup> )	78.54	78.54
Chloride ion diffusion coefficient (cm <sup>2</sup> s <sup>-1</sup> )	n/a	1.03 x 10 <sup>-8</sup>

Although no CIDC could be calculated it can be stated that the cementitious coating on test proved a very good barrier to the ingress of chloride ions. The non – coated sample had reached a steady state after 98 days and CIDC has been calculated.

## 5.2 Carbon Dioxide Diffusion Coefficient

One such test for carbon dioxide diffusion was carried out in 2007 initiated by Taylor Woodrow Technology.

### 5.2.1 Test procedure

Taylor Woodrow Technology supplied four standard unglazed ceramic tiles 100x800mm for coating with the cementitious coating. Two coats of the cementitious coating, each approximately 1mm thick were applied to the test specimens using a palette knife. After this layer had cured for about 2 hours at 21±°C and 60±5% relative humidity the second coat was applied at right angles. The coated specimen was then left to cure for 21 days under the same conditions prior to testing. The coated samples were allowed to condition at 23±°C and ambient relative humidity at the test house prior to testing.

One coated tile was sealed in a circular steel rig such that the coated and uncoated faces were exposed. Due to the cementitious nature of the coating, oxygen at a known pressure and flow rate was passed over the coated face of the plate and helium gas was passed over the uncoated face at the same pressure and flow rate. The helium gas stream was continuously monitored by gas chromatography to analyse for oxygen. Equilibrium conditions were achieved after approximately 24 hours and the steady state flux was then calculated from the percentage of oxygen in the helium stream and the flow rate of gas.

The diffusion coefficient for oxygen (D<sub>O2</sub>) is calculated using Fick's law of Diffusion and Crank's equation.

Due to the cementitious nature of the coating, the testing was undertaken using oxygen and results converted for use with carbon dioxide using the following criteria;

$$*DC_{O_2} = 0.316 D_{O_2}$$

\*This equation has been derived from measurements of oxygen and carbon dioxide diffusion coefficients conducted with non-cementitious coating systems<sup>3</sup>

It is assumed that the relationship is valid for polymer modified cementitious materials such as that tested. This assumption is made as a direct relationship of D<sub>O2</sub> and D<sub>CO2</sub> is not available for polymer modified materials – direct measurement of DC<sub>O2</sub> cannot be carried out on such materials due to interference from the carbonation reaction.

## 5.2.2 Test Results

The results of the testing are tabulated below.

Table 3. Carbon Dioxide Diffusion Coefficient	
DC <sub>O2</sub> (cm <sup>2</sup> s <sup>-1</sup> )	8.02 x 10 <sup>-6</sup>
μ-value	1.86 x 10 <sup>-4</sup>
R (m)	39
Sc (cm)	10
Mean Dry Film Thickness (μm)	2121

Notes:

The equivalent air layer thickness (R-value) is calculated for the measured thickness of the specimen as follows;

$$\mu\text{-value} = 0.149 / DC_{O_2} \quad R\text{-value} = \mu \times \text{specimen thickness (m)}$$

DC<sub>O2</sub> and the diffusion resistance coefficient (μ-value) are calculated using the mean dft measured on a spare unused specimen.

DC<sub>O2</sub> for an uncoated plate is 1.0 x 10<sup>-3</sup> cm<sup>2</sup>s<sup>-1</sup>.

The equivalent thickness of concrete (Sc-value) is calculated for the measured thickness of the specimen as follows:

μ-mortar x specimen thickness (cm) = μ-concrete x Sc where the μ-value for an average grade of concrete is taken to be 400 (μ-concrete)

Klopfer criterion for effective anti-carbonation coating is R greater than 50 metres.

EN 1062-6 Classification C<sub>1</sub> for Carbon Dioxide Permeability requires S<sub>D</sub> value greater than 50 metres.

## 6. Example projects

### 6.1 Kwai Chung T8 Container terminal



Figure 10. Foundation coated with cementitious coating



Figure 11. Completed container terminal

Cementitious coatings were chosen to protect the supporting structure for the container terminal. The clients wanted to ensure an extended design life as any potential repairs due to chloride attack on the concrete supports would not be accessible.



## 6.2 Concrete Extension Doha Corniche



Figure 12. Application of cementitious coating system

Cementitious coatings have also been well proven in hot and humid climates, as demonstrated by the prestigious Doha Corniche project in Qatar's capital city of Doha. A waterfront promenade extending for 10km along Doha Bay, Doha Corniche was formed following extensive dredging work carried out during the late 1970s and early 1980s, which reshaped Doha's coastline; the Corniche is now popular among walkers, bikers and joggers. Protection from high seas is provided by a concrete breakwater, which suffers from erosion from wave action and chloride-induced corrosion of the steel reinforcement. When a new 500m precast concrete extension was constructed, the use of a chloride barrier was stipulated to extend the design life.

## 6.3 Link Bridge Belvedere London



Figure 13. Belvedere EfW

More recently, designer Royal Haskoning specified cementitious coatings to increase the durability on the new link bridge that forms part of the Belvedere Riverside Energy from Waste (EfW) facility in south-east London. The cementitious coating was applied to 91 precast, pre-stressed beams at Anchor Bay Wharf in Erith prior to transportation to site by barge and installation.

## **7. Conclusions**

Correctly formulated and tested Cementitious coatings present an ideal solution to non-conformance of concrete cover within specifications. Not only do they reinstate cover, they also provide structures with additional protection against carbonation, de-icing salts, water and chloride ion penetration. This ensures that the life span of the structure is both achieved and extended.

## **8. Acknowledgements**

Graham James and Christopher Lloyd Flexcrete Technologies, Leyland UK for all their support.

## **8. References**

<sup>1</sup> Richard J. Kessler, Rodney G. Powers (retired) and Mario A. Paredes, Florida dept of Transport – Corrosion Research Laboratory “Performance of Corrosion prevention Methods – 18 year study” Nace Corrosion Conference & Expo 2009 Paper No 09219

<sup>2</sup> Fabio Bolzoni, Marco Ormellese and Andrea Brenna, Politecnico di Milan, Dept.CMIC “Efficiency of Concrete Coatings on Chloride-induced Corrosion of Reinforced Concrete Structures” Nace Corrosion Conference & Expo 2011 Paper No 11001

<sup>3</sup> H.L. Robinson “Evaluation of Coatings as Carbonation Barriers”. Construction Repair, February 1987 pp 12-17

# Behavior of concrete after exposure to elevated temperatures

Yaman S. S. Al-Kamaki<sup>1</sup>, Riyadh Al-Mahaidi<sup>2</sup> & Ian Bennetts<sup>3</sup>

<sup>1</sup> PhD candidate, Faculty of Science, Engineering and Technology, Swinburne University of Technology, Hawthorn, Victoria, 3122, Australia & University of Duhok (UoD), Duhok, Kurdistan Region, Iraq.

<sup>2</sup> Professor of Structural Engineering, Faculty of Science, Engineering and Technology, Swinburne University of Technology, Hawthorn, Victoria, 3122, Australia.

<sup>3</sup> Adjunct Professor, Faculty of Science, Engineering and Technology, Swinburne University of Technology, Hawthorn, Victoria, 3122, Australia.

**Abstract:** The occurrence of a fire in a building raises a number of important questions regarding the post-fire or residual strength and stiffness of any exposed concrete members. Loss of residual strength and stiffness due to heating has been demonstrated by a number of previous studies, most of which have utilized experiments where unstressed specimens were heated and allowed to cool prior to testing them to failure at ambient temperature. This paper describes elevated temperature tests where the specimens were loaded during heating and cooling prior to testing them to failure at ambient temperature. This paper describes the results of such testing undertaken on eighteen identical plain concrete cylinders ( $\varnothing$  65mm  $\times$  150mm) which were exposed to temperatures of 100, 200, 300, 400, 500, and 600°C whilst they were subjected to 30% of maximum load during the heating and cooling phases, prior to testing at ambient temperature. The properties examined were residual compressive strength, residual secant modulus of elasticity and the effect on the stress-strain relationship of concrete. The exposure to high temperature decreased the residual concrete compressive strength, concrete modulus of elasticity and initial slope of stress-strain curves for the cylinders. It was found that the decrease in secant stiffness of concrete is more pronounced than the corresponding decrease in residual compressive strength. These results are compared with the findings from overseas studies which were conducted on specimens that were not loaded during heating. Finally, models for temperature-dependent residual compressive strength and modulus of elasticity are proposed.

**Keywords:** Concrete, Residual compressive strength, Residual elastic modulus, Stress-strain relationships, Elevated temperatures, Cooling, Constitutive model.

## 1. Introduction

Although concrete is considered to be resistant to heating, it is well known that the mechanical properties of concrete deteriorate after exposure to a fire and/or elevated temperatures (Lea 1922 [1]; Lea and Stradling, 1922 [2]; Malhotra, 1956 [3]; Mohamedbhai, 1982 [4]; Schneider, 1988 [5]; Phan and Carino, 1998 [6]; Khoury, 2000 [7]; Annerel and Taerwe, 2009 [8]). The degradation of mechanical properties of concrete due to short-term exposure to elevated temperature has been studied by Malhotra (1956) [3], Abrams (1971) [9], Mohamedbhai (1983) [10], Schneider and Kassel (1985) [11] and Schneider (1988) [5]. Studies have been conducted on the effect of elevated temperature on normal-strength concrete (NSC) (Castillo, 1987 [12]; Castillo and Durrani, 1990 [13]; Phan, 1996 [14]; Phan and Carino, 1998 [6]; Husem, 2006 [15]; Biolzi et al., 2008 [16]), with the specimens being tested using one or more of the following combinations of heating and loading: (a) stressed during heating and tested at high temperature, (b) unstressed during heating and tested at high temperature, and (c) unstressed during heating and tested after cooling. The unstressed residual properties of concrete after exposure to elevated temperature have been of great interest (Bazant and Kaplan (1996) [17]). In the present paper, a further combination of heating and loading, namely, stressed during heating and tested after cooling, is considered. This combination is of particular importance in the assessment and refurbishment of buildings after a fire, since it is necessary to have a sound understanding of the residual properties of concrete – i.e. the strength characteristics after cooling following heating due to a fire. In practice, all members are loaded during a fire event.

The adverse effect of extreme thermal exposure on the residual mechanical properties of concrete (i.e. combination (c)) has been demonstrated by many researchers. For temperatures less than 300°C, the reduction in residual strength is known to be small; however, the strength decreases significantly when heated above 300°C (Li and Li, 2010) [18]. NSC typically loses between 10 to 20% of its original compressive strength when heated to 300°C, and between 60 to 75% when heated to 600°C. According to the Concrete Society, (1990) [19], concrete loses 25% and 75% of its ambient compressive strength



when heated to 300°C and 600°C, respectively, following cooling. The residual modulus of elasticity decreases in a similar manner (Phan and Carino, 2000) [20].

The effect of elevated temperatures on the full stress-strain response of fire-affected concrete has been studied in the pioneering work of Furumura (1966) [21]. Later, Baldwin and North (1973) [22] attempted to establish a mathematical model for the full response using Furumura's (1966) [23] data.

There is a lack of studies where concrete members have been (i) heated under load (ii) cooled down to ambient temperature (iii) loaded to failure. This paper presents results which, in part, address the above gap in knowledge and form part of an on-going research project. The paper presents experimental results using the above sequence of loading and heating to examine the effects of heating temperature and cooling method on the residual strength of concrete. Models based on these experimental results have been developed.

## 2. Experimental Program

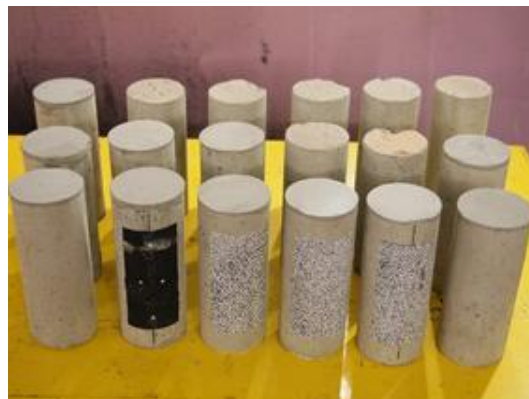
### 2.1 Concrete Mix and Details of Specimens

Small concrete cylinders were constructed using ready-mixed normal concrete prepared by a local supplier (Hanson Construction Materials Pty Ltd). The compressive strength ( $f'_c$ ) of the concrete was 32 MPa, the slump was 80 mm, and the maximum aggregate size was 14 mm, the properties of which are illustrated in Table 1. The test program involved 18 identical  $\varnothing$  65mm  $\times$  150mm small plain concrete cylinders, as shown in Figure 1. Of the 18 small cylinders, 2 were left as control samples and 16 were subjected to heating under stress.

The ready-mix concrete mixture was poured into small concrete cylinders followed by vibration using a vibration table for 6 minutes. The top surface of the concrete was then finished using a trowel and the specimens were left inside the molds for 24 hours to harden. After demolding, the specimens were placed in a water tank in the laboratory for curing for a further 28 days. At the end of the curing time of 28 days the specimens were removed from the water tank one day before the test and left in the laboratory to dry. Both ends of the concrete specimens were then capped using self-leveling grout (Ardex LQ 92) with a thickness of <5mm to ensure that the end surfaces of the concrete cylinders were flat in order to distribute the load uniformly. The capped specimens were air-cured until the day of heating exposure.

**Table 1. Properties of the concrete mix design per 1 cubic meter.**

Contents (kg/m <sup>3</sup> )	Quantity
Cement	158
Slag	158
Coarse sand	664
Coarse aggregate	1015
Hanson Kilmore manufactured sand	233
Water	170



**Figure 1. Identical  $\varnothing$ 65  $\times$  150mm small plain concrete cylinders**

## 2.2 Temperature Cycle and Cooling Regimes

All 16 specimens were subjected to a stress of  $0.3f_c$  at ambient temperature ( $25^\circ\text{C}$ ) during heating and cooling. Specimens were subjected to constant load by means of a 100kN capacity 8801 Instron testing machine. Specimens were heated at a rate of  $10^\circ\text{C}/\text{min}$  to a target chamber temperature for two hours after the target temperature was achieved. The specimens were then cooled to ambient by turning off the heating to the chamber and opening the door. For each of the chamber target temperatures ( $100^\circ\text{C}$ ,  $200^\circ\text{C}$ ,  $300^\circ\text{C}$ ,  $400^\circ\text{C}$ ,  $500^\circ\text{C}$  and  $600^\circ\text{C}$ ), two specimens were exposed in the environmental chamber, as shown in Figures 2 and 3. The heating inside the environmental chamber was controlled by putting one Type K thermocouple inside the environmental chamber in addition to the built-in thermocouple attached to the chamber.

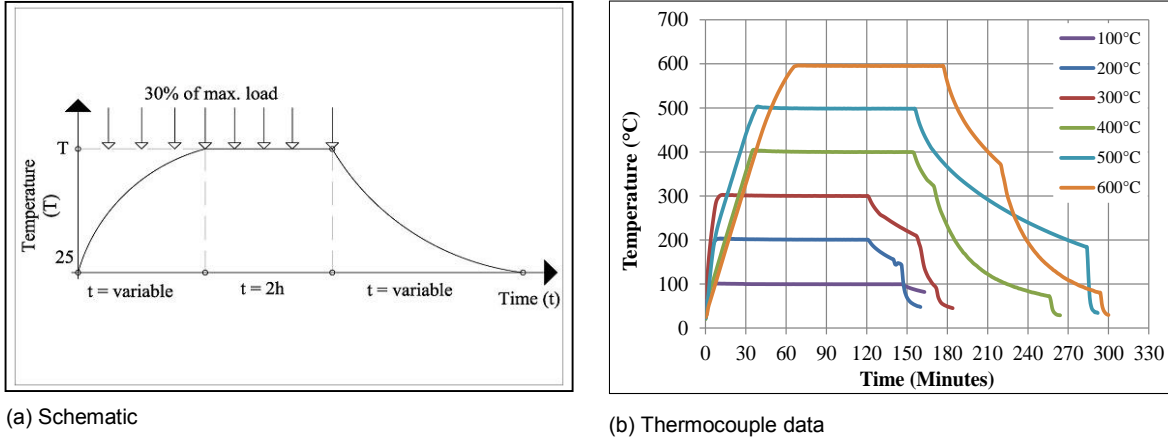


Figure 2. Heating cycles for  $\varnothing 65\text{mm} \times 150\text{mm}$  small concrete cylinders

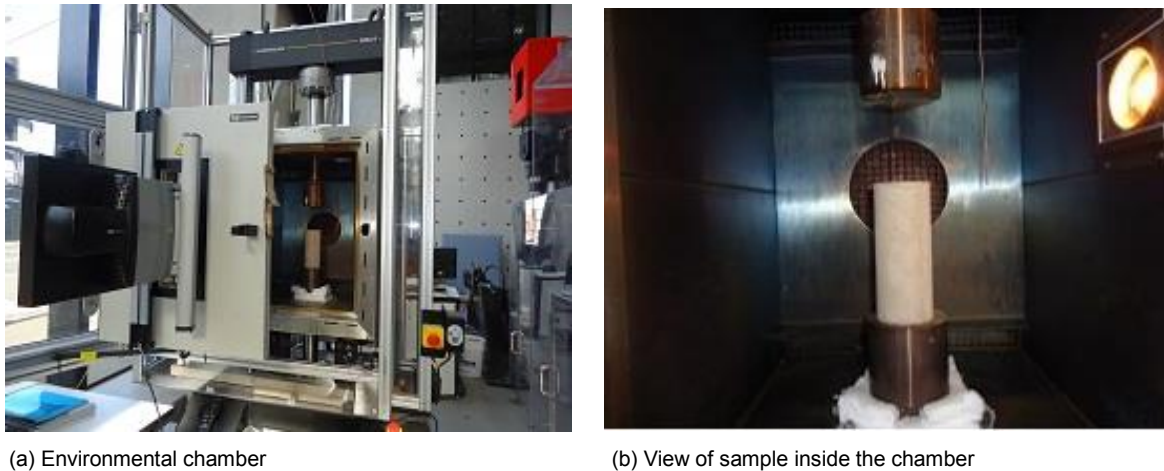


Figure 3. Environmental chamber

## 2.3 Surface Preparation for Strain Measurement

About half of each small concrete cylinder surface area was used for strain measurement purposes using a Vic-3D digital image correlation system camera [24] on 14 specimens including 2 control samples, or a video extensometer (on only 4 specimens). For the Vic-3D system, the area of interest on each specimen was painted with a random dot pattern (speckled) for displacement calculation purposes. A layer of white paint was applied to the specimen surface followed by black speckles using a black pen. Figure 4(a) shows the process of surface preparation with the speckled pattern.

The conversion of optical images to strains is achieved as follows. Two high-resolution cameras take a picture of the pattern before loading (during image calibration stage) using the Vic-Snap software and then new images at prescribed time or load steps when the specimen is under test and subjected to external loads (Sonnenberg and Al-Mahaidi, 2007 [25]; Lee and Al-Mahaidi, 2008 [26]). With computer software (Vic-3D) the images are analyzed considering the difference between pixels of the different images and correlated to create a contour map of strains.

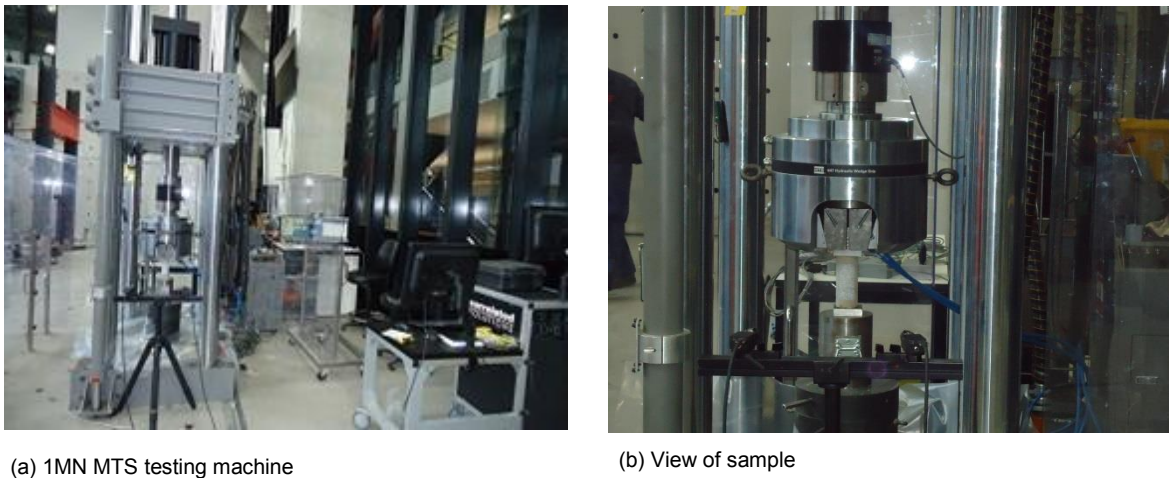
When using a video extensometer, the area of interest on each specimen must be painted with a layer of black paint followed by four white dots representing axial and lateral directions, as shown in Figure 4(b).



**Figure 4. Surface preparation for strain measurement**

## 2.4 Testing Technique

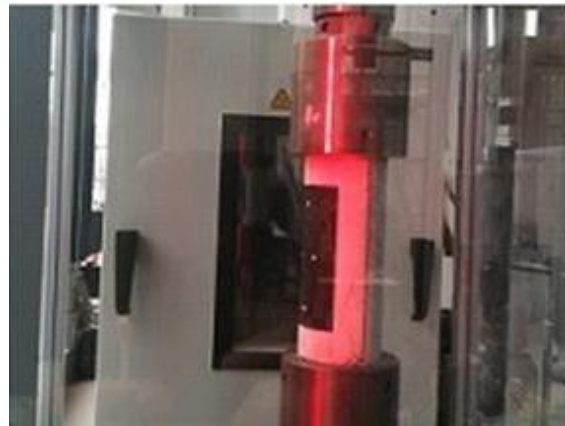
Residual concrete properties were determined as the mean value of the two tests per target temperature. The residual compressive strength for 14 specimens was obtained using a 1MN MTS testing machine (Figure 5) and a 100kN Instron testing machine for 4 specimens, as shown in Figure 6. A displacement rate of 0.25mm/min was used for both testing machines. The load and displacement records from the testing machines and the direct strains as determined by the Vic-3D camera or video extensometer were taken every second.



**Figure 5. 1 MN MTS machine and test set-up for Ø 65mm x 150mm small cylinders**



(a) 100kN Instron testing machine



(b) View of sample

**Figure 6. 100 kN Instron machine and test set-up for Ø 65mm × 150mm small cylinders**

### 3. Results and Discussion

The details of the test results for the small plain concrete cylinders are summarized in Table 2. These results include those for unheated specimens and for specimens tested after exposure to heating for two hours and subsequent cooling. These specimens were loaded during heating to 30% of the ambient crushing strength.

**Table 2. Test results of small plain concrete cylinders**

Sample	Temperature °C	* Average residual compressive strength (MPa)		Strain measurement method
1	25°C	38.8		Vic-3D digital image correlation camera
2	25°C			Vic-3D digital image correlation camera
3	100°C	32.6		Vic-3D digital image correlation camera
4	100°C			Vic-3D digital image correlation camera
5	200°C	36.7		Vic-3D digital image correlation camera
6	200°C			Vic-3D digital image correlation camera
7	300°C	32.3		Vic-3D digital image correlation camera
8	300°C			Vic-3D digital image correlation camera
9	400°C	26.2	25.6	Vic-3D digital image correlation camera
10	400°C			Vic-3D digital image correlation camera
11	400°C	25		video extensometer
12	400°C			video extensometer
13	500°C	20.3	20.2	Vic-3D digital image correlation camera
14	500°C			Vic-3D digital image correlation camera
15	500°C	20.1		video extensometer
16	500°C			video extensometer
17	600°C	16.4		Vic-3D digital image correlation camera
18	600°C			Vic-3D digital image correlation camera

\* The average of two 65 × 150mm small cylinders

#### 3.1 Effect of Temperature on Residual Compressive Strength

The residual strength of the small concrete cylinders is expressed as a ratio of the strength of the companion smaller concrete cylinders at ambient temperature (25°C). Figure 7(a), shows the variation of residual strength with temperature. It was observed that the cylinders exposed to temperatures ranging from 100°C - 600°C (in steps of 100°C) exhibited residual strengths of 84, 94.6, 83.3, 66, 52.1, and 42.3%



of the companion samples, respectively. It can be observed that the strength at 100°C is less than that for specimens heated to 200°C. This was also found by Li and Franssen, 2011 [27]. The reason for this is not apparent, but according to Naus, 2010 [28], it is due to cement gel layers moving closer to each other during heating. Cheng et al. 2004 [29] similarly attribute this phenomenon to general stiffening of the cement gel or the increase in surface forces between gel particles due to the removal of absorbed moisture.

Also shown in Figure 7(a), is a proposed model (Equation 1) for temperature-dependent residual compressive strength. The proposed model could be used for determining the effect of fire or other heating on the residual load capacity of concrete structures.

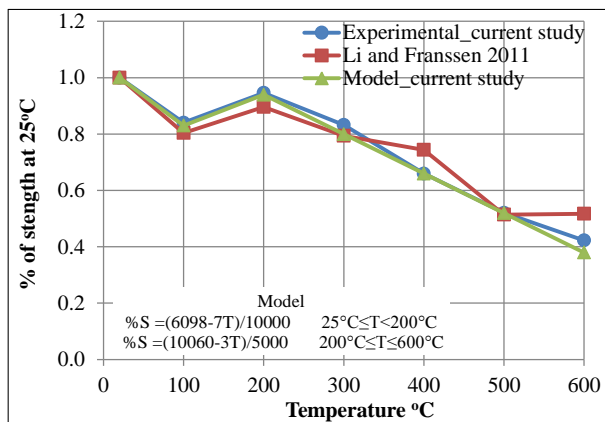
$$\% S = \frac{(6098 - 7T)}{10000}, \quad 25^\circ\text{C} \leq T \leq 200^\circ\text{C} \quad \& \quad \% S = \frac{(6098 - 7T)}{5000}, \quad 200^\circ\text{C} \leq T \leq 600^\circ\text{C} \quad (1)$$

### 3.2 Effect of Temperature on Residual Modulus of Elasticity

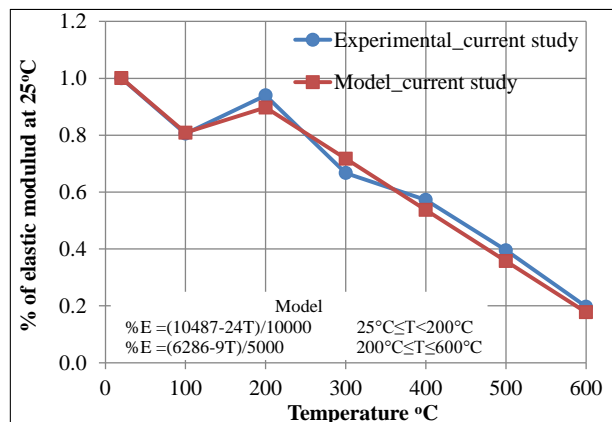
The static modulus of elasticity is defined as the slope of the concrete compressive stress-strain curve, either as a tangential slope at the origin or as the secant slope between the origin and a point on the stress-strain curve at approximately 30-40% of the peak stress. The decrease in the concrete modulus of elasticity due to elevated temperature exposure is more pronounced than the decrease in concrete compressive strength. The effect of high temperature exposure on the modulus of elasticity is shown in Figure 7(b). In general, the trend for the modulus of elasticity is that as the temperature increases, the stiffness tends to immediately decrease. However, it is clear that at lower temperatures between 100°C to 200°C, the modulus of elasticity experiences a slight increase compared to its original value at ambient temperature (25°C). From Figure 7(b), it is clear that the modulus of elasticity appears to degrade approximately linearly with temperature, particularly when  $T > 300^\circ\text{C}$ . The degradation in the elastic modulus of elasticity of concrete was 19.5%, 6%, 33.3%, 42.7, 60.5% % and 80.3% of its original value at ambient temperature (25°C) at 100°C, 200°C, 300°C, 400°C, 500°C and 600°C respectively. The reduction in the modulus of elasticity at 600°C is evidently due to micro-structural damage to the concrete with increasing temperature.

Furthermore, as Figure 7(b) indicates, a proposed model (Equation 2) for the temperature-dependent concrete residual modulus of elasticity is presented. Again, this model can be used for the evaluation of the residual modulus of elasticity of concrete structures after fire exposure or other heating.

$$\% E = \frac{(10487 - 24T)}{10000}, \quad 25^\circ\text{C} \leq T \leq 200^\circ\text{C} \quad \& \quad \% E = \frac{(6286 - 9T)}{5000}, \quad 200^\circ\text{C} \leq T \leq 600^\circ\text{C} \quad (2)$$



(a) Residual compressive strength



(b) Residual modulus of elasticity

Figure 7. Effect of heating on small cylinders

### 3.3 Stress-Strain Relationship

The residual stress-strain relationships for small plain concrete cylinders for temperatures between 25°C and 600°C are shown in Figure 8(a). It can be seen that the stress-strain relationships exhibit a linear portion, then as micro-cracking takes place, the shape of the curve becomes increasingly non-linear until it reaches the maximum stress. Beyond this point, as further cracking takes place, the curve descends until failure occurs. With the exception of the specimens exposed to 200°C, the strains corresponding to peak strengths are equal to or greater than those at ambient temperature (25°C). It is worth noting that the strains at peak strength do not necessarily increase with increasing exposure temperature. For example, the strain for the cylinders exposed to 300°C is greater than that for cylinders heated to 400°C.

Good correlation was also observed by comparing stress-strain relationships obtained using both new techniques (Vic-3D vs video extensometer), as shown in Figure 8(b).

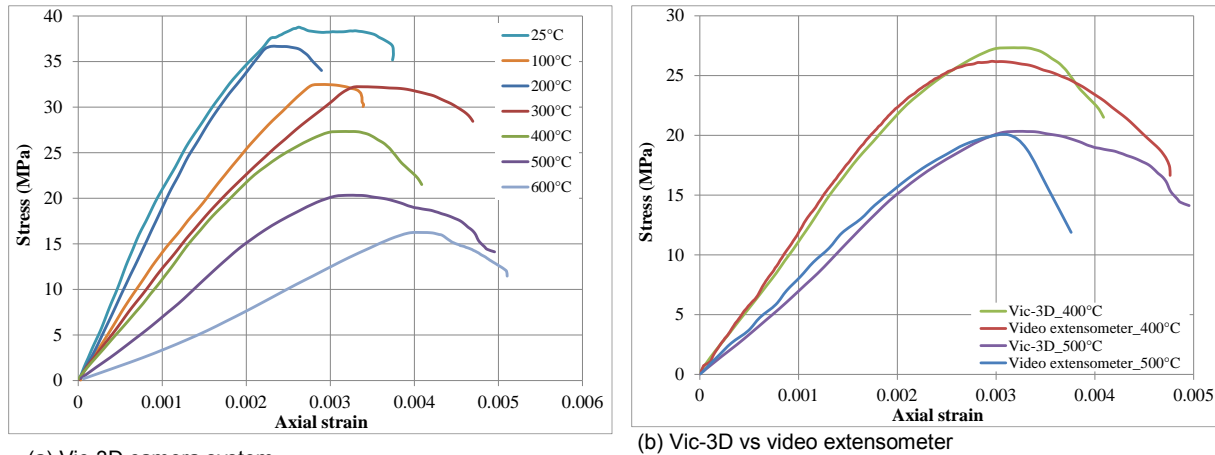


Figure 8. Stress-strain relationships of small cylinders

### 3.4 Cracking Pattern

The observed failure patterns for tested small cylinders indicated that, prior to failure, vertical cracking started from the top of the specimens and propagated downward along the length of the specimens in the direction of loading (see Figure 9). The specimens failed by splitting as the result of excessive shear stresses. The maximum compressive load of the specimens was achieved shortly after cracks developed and propagated. The load resistance of the specimens then reduced significantly.



Figure 9. Failure mode of small cylinders

#### 4. Conclusions

This experimental study reports the results of tests on specimens that were loaded (0.3 f'c) during heating subsequent to cooling. The following conclusions can be drawn based on the results of these experiments:

1. The testing described in this paper requires careful control of both the environmental (heating) chamber and the mechanical testing apparatus over a significant time duration. This was successfully achieved.
2. Surface strains were measured using an innovative visual technique which enabled the maximum strains to be reliably determined.
3. The effect of temperatures between 100-200°C on the residual strength of the concrete cylinders is unusual, in that a lower strength was obtained at 100°C compared with 200°C. This has been attributed to the effect of moisture changes on the cement gel structure.
4. The residual strength for the concrete cylinders decreases almost linearly for temperatures of 300°C and above.
5. The decrease in the concrete modulus of elasticity, whether measured as tangent or secant stiffness, is more pronounced than the corresponding decrease in concrete residual compressive strength.
6. In general, the initial slope of the stress-strain curves decreases as the temperature increases.
7. Equations have been proposed for both residual compressive strength and residual modulus of elasticity as a function of temperature.

#### 5. Acknowledgements

The authors would like to express their thanks to the staff of the Smart Structures laboratory at Swinburne University of Technology for their assistance.

#### 6. References

1. Lea, F., *The effect of temperature on some of the properties of materials*. Engineering, 1920. **110**(3): p. 293-298.
2. Lea, F. and R. Stradling, *The resistance to fire of concrete and reinforced concrete*. Engineering, 1922. **114**(2959): p. 341-344,38-382.
3. Malhotra, H.L., *The effect of temperature on the compressive strength of concrete*. Magazine of Concrete Research, 1956. **8**(23): p. 85.
4. Mohamedbhai, G.T.G., *Residual strength of reinforced concrete members subjected to elevated temperatures*. Proceedings of the Institution of Civil Engineers (London), 1982. **73**(pt 2): p. 407-420.
5. Schneider, U., *Concrete at high temperatures - A general review*. Fire Safety Journal, 1988. **13**(1): p. 55-68.
6. Phan, L.T. and N.J. Carino, *Review of mechanical properties of HSC at elevated temperature*. Journal of Materials in Civil Engineering, 1998. **10**(1): p. 58-64.
7. Khoury, G.A., *Effect of fire on concrete and concrete structures*. Progress in Structural Engineering and Materials, 2000. **2**(4): p. 429-447.
8. Annerel, E. and L. Taerwe. *Approaches for the assessment of the residual strength of concrete exposed to fire*. in *In Proc 2nd Int Conf Conc Repair, Rehabil Retrofit (ICRRR08)*. 2009. Taylor & Francis, UK, .
9. Abrams, M., *Compressive strength of concrete at temperatures to 1600 F*. Temperature and Concrete, 1971: p. 33-58.
10. Mohamedbhai, G., *The residual strength of concrete subjected to elevated temperatures*. Concrete, 1983. **17**(12): p. 22-27.
11. Schneider, U. and G. Kassel, *Properties of materials at high temperatures: Concrete*. 1985: Gesamthochschul-Bibliothek.
12. Castillo, C., *Effect of transient high temperature on high strength concrete*. 1987, Rice University, Houston, Texas: University Microfilms International.
13. Castillo, C. and A.J. Durrani, *Effect of transient high temperature on high-strength concrete*. ACI Materials Journal, 1990. **87**(1): p. 47-53.

14. Phan, L.T., *Fire performance of high-strength concrete: A report of the state-of-the art*. 1996, US Department of Commerce, Technology Administration, National Institute of Standards and Technology, Office of Applied Economics, Building and Fire Research Laboratory.
15. Husem, M., *The effects of high temperature on compressive and flexural strengths of ordinary and high-performance concrete*. *Fire Safety Journal*, 2006. **41**(2): p. 155-163.
16. Biolzi, L., S. Cattaneo, and G. Rosati, *Evaluating residual properties of thermally damaged concrete*. *Cement and Concrete Composites*, 2008. **30**(10): p. 907-916.
17. Bazant, Z.P. and M.F. Kaplan, *Concrete at high temperature: Material properties and mathematical models* 1996, Harlow, England: Longman Group Limited, Essex
18. Li, Z. and Q. Li. *Repair of fire-damaged concrete: Improvement of mechanical property*. in *Second International Conference on Sustainable Construction Materials and Technologies*. 2010. Marche Polytechnic University, Ancona, Italy.
19. Concrete Society, *Assessment and repair of fire-damaged concrete structures*. 1990, Technical Report 33, The Concrete Society, London.
20. Phan, L.T. and N.J. Carino. *Fire performance of high strength concrete: Research needs*. in *Proceedings ASCE/SEI Structures Congress*. 2000. Philadelphia, Pennsylvania.
21. Furumura, F., et al. *Mechanical properties of high strength concrete at high temperatures*. in *Proceedings of the Fourth Weimar Workshop on High Performance Concrete*. 1995.
22. Baldwin, R. and M.A. North, *Stress-strain relationship for concrete at high temperatures*. *Magazine of Concrete Research*, 1973. **25**(85): p. 208-212.
23. Furumura, F. *The stress-strain curve of concrete at high temperature*. in *Paper No. 7004: Annual Meeting of the Architectural Institute of Japan*. 1966. Tokyo Institute of Technology.
24. Vic-3D, *The Vic-3D™ measurement system*. 2010, Dutchman Blvd, Irmo, SC 29063, USA: Correlated Solutions.
25. Sonnenberg, A.M.C. and R. Al-Mahaidi, *Investigation of dowel shear in RC beams using photogrammetry*. *Magazine of Concrete Research*, 2007. **59**(9): p. 1-626.
26. Lee, T.K. and R. Al-Mahaidi, *An experimental investigation on shear behaviour of RC T-beams strengthened with CFRP using photogrammetry*. *Composite Structures*, 2008. **82**(2): p. 185-193.
27. Li, Y.-H. and J.-M. Franssen, *Test results and model for the residual compressive strength of concrete after a fire*. *Journal of Structural Fire Engineering*, 2011. **2**(1): p. 29-44.
28. Naus, D., *A Compilation of Elevated Temperature Concrete Material Property Data and Information for Use in Assessments of Nuclear Power Plant Reinforced Concrete Structures: Prepared by DJ Naus*. 2010: US Nuclear Regulatory Commission, Office of Nuclear Regulatory Research.
29. Cheng, F.P., V.K.R. Kodur, and T.C. Wang, *Stress-strain curves for high strength concrete at elevated temperatures*. *Journal of Materials in Civil Engineering*, 2004. **16**(1): p. 84-90.



# A Discussion on Service Life Prediction of Fly Ash Concrete Structures based on DuraCrete Methodology

Zhuqing Yu<sup>1,2</sup> and Guang Ye<sup>1,3</sup>

<sup>1</sup>PhD student, Microlab, Faculty of Civil Engineering and Geosciences, Delft University of Technology, Delft, the Netherlands

<sup>1</sup>Associated professor, Microlab, Faculty of Civil Engineering and Geosciences, Delft University of Technology, Delft, the Netherlands

<sup>2</sup>Assistant professor, State Key Laboratory of Materials-Oriented Chemical Engineering, College of Materials Science and Engineering, Nanjing Tech University, Nanjing, P. R. China

<sup>3</sup>Guest professor, Magnel Laboratory for Concrete Research, Department of Structural Engineering, Ghent University, Ghent, Belgium

**Abstract:** The DuraCrete project has provided one of the guidelines for durability design and assessment of concrete structures, and is used for many large projects in Europe and other countries. In DuraCrete probabilistic method, the rapid chloride migration (RCM) test is used as bases for predicting the service life of concrete structures. The chloride migration (diffusion) coefficient is determined by RCM test at the age of 28 days, which is used to evaluate the resistance to chloride penetration of concrete. It is believed that a substantial proportion of the hydration process has taken place for Portland cement concrete with a normal w/c ratio, and over 80% of final strength is reached at 28 days. The concrete would be considered as mature. However, when Portland cement is partially replaced by fly ash, the pozzolanic reaction of fly ash in concrete is slowed down during early curing age, even at 28 days. It appears that the current service life prediction model is not reliable for fly ash concrete structures. In this paper the reference time is redefined for fly ash concrete in view of service life predictions of fly ash concrete structures. The  $D_{RCM}$  value based on the redefined reference time in practice is discussed.

**Keywords:** DuraCrete methodology, fly ash concrete, chloride migration coefficient, RCM test

## 1. Introduction

Corrosion caused by chloride ingress is assumed to be the dominant mechanism determining the service life of concrete structures in the prevailing Dutch concrete standards (1-4). Previous study shown (5) that fly ash concrete has good resistance to chloride ingress. The chloride migration coefficient ( $D_{RCM}$ ) of fly ash concrete obtained from rapid chloride migration (RCM) test continuously decreases in the period up to 3 years at moisture curing condition. The  $D_{RCM}$  value is not only used to evaluate the resistance to chloride penetration of concrete, but also used in the DuraCrete model to predict the service life of concrete structures. In the DuraCrete model, the  $D_{RCM}$  value at the reference time  $t_0$  (28 days) is normally used (6). For Portland cement concrete, it is generally accepted that when concrete is properly cured for 28 days, a substantial percentage of the cement hydration has taken place (7) and the Portland cement concrete would be considered as mature. However, when Portland cement is partially replaced by fly ash, the pozzolanic reaction of fly ash in concrete is very slow during early curing age, even at 28 days (8-9). At 28 days, the Portland cement-fly ash binary systems shows high  $D_{RCM}$  value than pure Portland cement system (5). Therefore, it is believed that fly ash concrete needs longer curing time to reach the equal maturity like Portland cement concrete at the same temperature. The predicted service life of fly ash concrete would be underestimated if 28 days is used as reference time for fly ash concretes. It is noticed that Chinese standard (10) suggests that the chloride migration coefficient determined at 84 days is used for durability design and service life prediction of concrete structure. This method has been applied in the design of Hangzhou Bay Bridge (China) and Penang Second Bridge (Malaysia).

The aim of this paper is to define a proper reference time for fly ash concrete when DuraCrete methodology is used to predict the service life of fly concrete structures. The  $D_{RCM}$  value based on the redefined reference time in practice is determined.

## 2. DuraCrete model

## 2.1 General introduction

The DuraCrete methodology was developed in 1990s in a European research project, “Probabilistic Performance Based Durability Design of Concrete Structures” (11). The aim of this methodology was to develop a durability design concept, based on realistic and sufficiently accurate environmental and material models, being capable of predicting the behavior of concrete structures (11). Defining the desired performance of the structure is the first step in the process of designing durable concrete structures (11). Figure 1 schematically shows the performance of a concrete structure when suffering from reinforcement corrosion and related damages. In this figure two main phases are defined in the development of the performance of concrete structures with time, viz. the initiation phase and the propagation phase. The initiation period is the time for an aggressive substance to reach the reinforcement and cause corrosion of the steel. During the propagation phase, deterioration develops and loss of function is observed. The propagation phase includes several kinds of damages, such as cracking, spalling and collapse, as shown in Figure 1. In the DuraCrete methodology it is assumed that the deterioration mechanism of concrete structures is caused only by chloride ingress and subsequent corrosion of steel reinforcement.

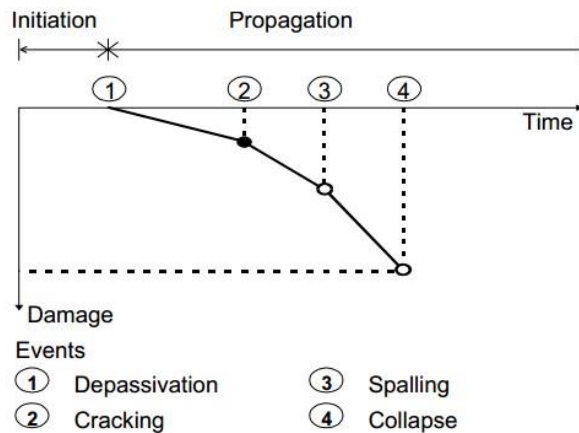


Figure 1: The performance of concrete structure with respect to reinforcement corrosion and related events (11)

## 2.2 Chloride transport model in concrete

Chloride ion transport in concrete can be driven by three mechanisms, i.e. capillary absorption, hydrostatic pressure and diffusion (12), among them diffusion is predominated. Fick's 2<sup>nd</sup> law can be used to describe diffusion-controlled chloride ion transport into concrete (13-17). When Fick's 2<sup>nd</sup> law is applied it is implicitly assumed that chloride ion penetration is primarily a diffusion process. Equation 1 was applied to calculate the chloride content at certain depth and time. In Equation 1,  $D(t)$  is the apparent diffusion coefficient, which is a time-dependent function as shown by Equation 2.

$$C(x,t) = C_s - (C_s - C_i) \operatorname{erf} \left[ \frac{x}{\sqrt{\{4k D(t)t\}}} \right] \quad (1)$$

$$D(t) = D_0 \left( \frac{t_0}{t} \right)^n \quad (2)$$

where:  $t_0$  is reference time of the concrete, normally is 28 days (18);  $D_0$  is achieved chloride migration coefficient at the reference time,  $t_0$  of the concrete (18);  $n$  is the ageing coefficient. It is theoretically range from 0 to 1 (18). It depends on the type of binder, the rate of cement hydration and environmental factors.

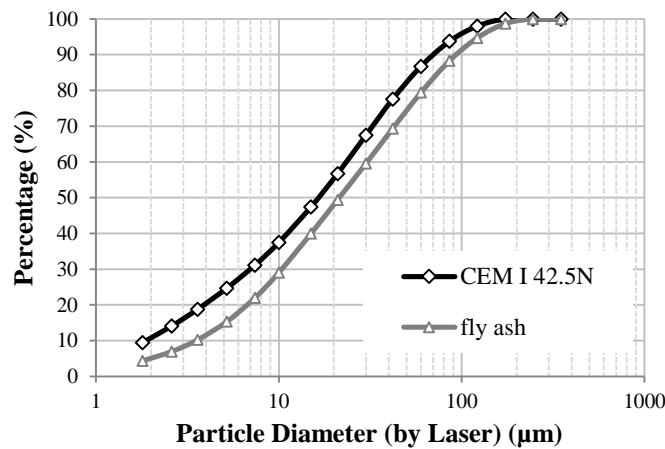
## 3. Materials and Methods

### 3.1 Materials

The concrete mixtures were prepared using Portland cement CEM I 42.5 N, fly ash (Low calcium), aggregate (the maximum size of 16 mm) and tap water. Table 1 shows the chemical compositions of Portland cement and fly ash. The crystalline phase of fly ash was about 41.29% determined by XRD method. The portion of mullite and quartz was 13.26% and 25.14%, respectively. The mean particle size of fly ash was about 21.46  $\mu\text{m}$  measured by Laser Method. Figure 2 presents the particle size distribution of Portland cement and fly ash. In the mixture, the replacements of cement by fly ash were 30% and 50%, respectively. Three water to binder ratios, 0.4, 0.5 and 0.6 are used. A series of samples with 50 percentages of fly ash and w/b of 0.6 were not cast because of significant bleeding.

**Table 1. Chemical compositions of fly ash and cement.**

Chemical compositions (% by mass)	SiO <sub>2</sub>	Al <sub>2</sub> O <sub>3</sub>	CaO	free-CaO	Fe <sub>2</sub> O <sub>3</sub>	P <sub>2</sub> O <sub>5</sub>	K <sub>2</sub> O	MgO	SO <sub>3</sub>	Na <sub>2</sub> O
CEMI42.5N	20.36	4.96	64.4	0.6	3.17	0.18	0.64	2.09	2.57	0.14
Fly ash	48.36	31.36	7.14	-	4.44	1.90	1.64	1.35	1.18	0.718

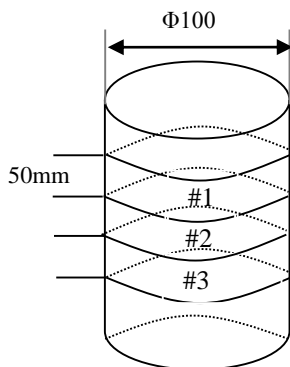


**Figure 2: The particle size distribution of Portland cement and fly ash (by laser method).**

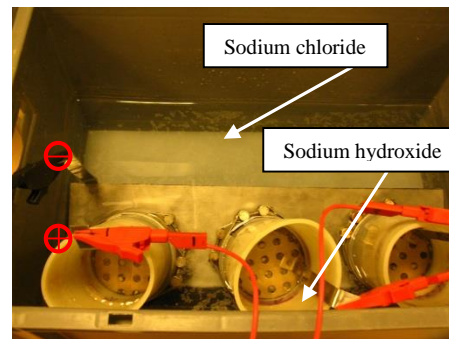
### 3.2 Methods

#### 3.2.1 Rapid chloride migration test

The concrete samples were cast in standard cylindrical mould with the dimension of  $\Phi 100 \times 300$  mm. After demoulding, the specimens were cured in a saturated limewater bath until preconditioning for testing in 28 days, 91 days, 180 days, 365 days, 730 days and 1095 days.



**Figure 3. The sawing plane of test specimens.**



**Figure 4. The migration set-up in laboratory.**

NT Build 492 method was used to determine the chloride migration coefficient of concrete from non-steady-state migration experiments (20). The preconditioning includes four steps, 1) cutting a  $50 \pm 2$  mm thick slice from the central portion of the cylinder as the test specimen, three specimens could be obtained from one concrete cylinder, with enough space (50mm) left at the sides to avoid any side effect; 2) placing specimen in the vacuum machine for three hours; 3) immersing saturated Ca (OH)<sub>2</sub> solution for one hour; 4) keeping the specimens in the solution for  $18 \pm 2$  hours. Figure 3 shows a sawing plane of test samples. After preconditioning, the test specimens were put in a rubber sleeve and fastened with two stainless steel clamps. The RCM set-up is shown in figure 4. The substrate surface was immersed in the anolyte solution of 0.3 M NaOH and the bottom surface was immersed in the catholyte solution of 10% NaCl. With the voltage preset at 30 V, the initial current through each specimen was recorded. The room temperature during the test was  $20 \pm 1^\circ\text{C}$  (20). Based on the initial current, a corrected voltage and appropriate test duration were chosen. After testing, each specimen were split into two pieces and 0.1M silver nitrate solution was sprayed over the freshly split section. After 15 minutes, the migration depth of chloride ion and the thickness of each specimen were recorded. The non-steady-state migration coefficient was calculated using equation 3.

$$D_{RCM} = \frac{0.0239 \cdot (273 + T) \cdot L}{(U - 2) \cdot t} \cdot \left( x_d - 0.0238 \sqrt{\frac{(273 + T) \cdot L \cdot x_d}{U - 2}} \right) \quad (3)$$

- $D_{RCM}$ : Non-steady-state migration coefficient,  $\times 10^{-12}$  m<sup>2</sup>/s;  
 U: absolute value of the applied voltage, V;  
 T: average value of the initial and final temperatures in the anolyte solution, °C;  
 L: thickness of the specimen, mm;  
 $x_d$ : average value of the penetration depths, mm;  
 t: test duration, hour.

### 3.2.2 Thermogravimetric analysis (TGA)

Thermogravimetric analysis (TGA) was performed on cement paste at atmospheric pressure in nitrogen, at heating rate 10 °C/min up to 1200 °C. The content of calcium hydration in cement paste can be calculated based on thermogravimetric curve at decomposition temperature around 460 °C.

## 4 Service Life Prediction of Fly Ash Concrete

### 4.1 Determination of reference time for fly ash concrete

In fly ash concrete, calcium hydroxide phase (CH) is consumed by the pozzolanic reaction of fly ash along with the formation of additional C-S-H gel. This has beneficial effects on the strength, permeability and the durability of concrete. Therefore, the CH content could be considered as an indicator to determine the reference time for fly ash concrete.

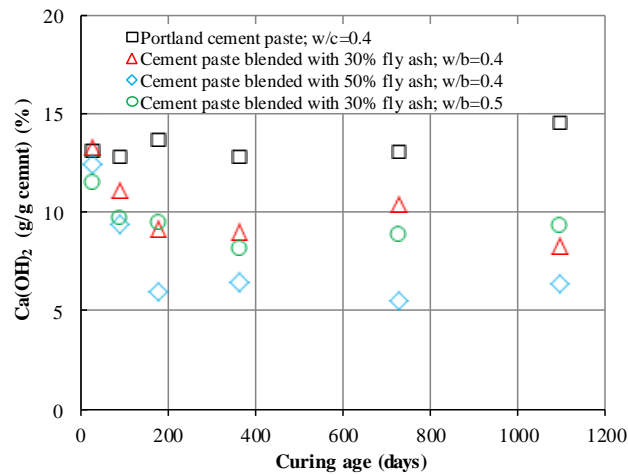


Figure 5. The CH content of cement paste.

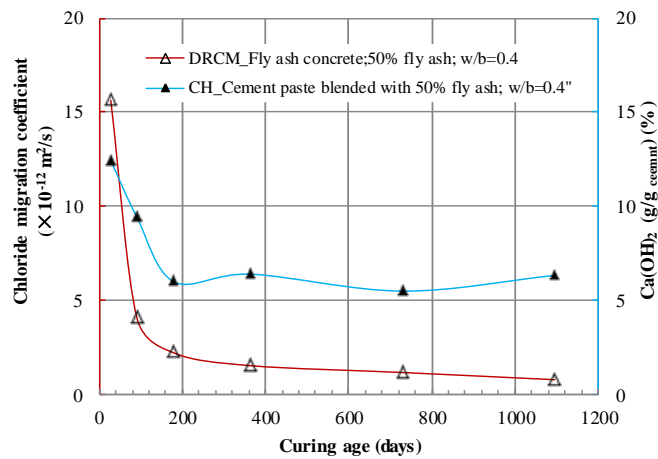


Figure 6. Comparison between the  $D_{RCM}$  and the CH content.

Figure 5 shows the CH content of Portland cement paste and blended cement paste at ages from 28 days to 3 years. It can be seen that after 28 days of curing, the CH content of pure Portland cement paste change little, from 12.44% to 14.50% (see Figure 5). The CH content of blended cement paste, however, decreases greatly at ages from 28 days to 180 days. After 180 days, the CH content of blended cement paste hardly changes. It is inferred that the pozzolanic reaction of fly ash takes place dramatically after 28 days, and a relative stable structure is reached in about 180 days. The CH content with curing age can be used as an indicator to reflect the degree of the pozzolanic reaction of fly ash.

Figure 6 plots a comparison between the chloride migration coefficient,  $D_{RCM}$  of fly ash concrete (50% fly ash; w/b=0.4) and the relevant CH content of blended cement paste. As can be seen from Figure 6, the CH content and  $D_{RCM}$  show a similar trend with increasing time, decreasing significantly from 28 days to 180 days and remaining almost constant after an age of 180 days. In this study, hence, 180 days is defined as the reference time to predict the service life of fly ash concrete structures based on the DuraCrete methodology.

#### 4.2 Service life prediction

By using the redefined reference time, 180 days, the service life of fly ash concrete structures is calculated. An example of concrete mixture (50% fly ash, w/b=0.4) served under the condition of marine atmospheric (XS1) is presented. For comparison, 28 days as reference time for fly ash concrete is also presented. Based on the DuraCrete report the input parameters used in the DuraCrete methodology are summarized in Table 2. Two reference times, 28 days and 180 days are specified.

With the redefined reference time of 180 days, the calculated service life is 116 years, which is much longer than 11 years when 28 days is used as the reference time. It means that the service life of fly ash concrete structures may be underestimated if 28 days is used as reference time as Portland cement concrete.

#### 4.3 Determination of the $D_{RCM}$ value at the reference time in practice

If 180 days is used as the reference time to predict the service life of fly ash concrete structures, 180 days is required to wait for the RCM test. In practice, the  $D_{RCM}$  of concrete is typically measured at the curing ages of 28 or 90 days. If there is a way which is able to deduce the  $D_{RCM}$  value at 180 days based on the results obtained at the age of 28 or 90 days, it would promote efficiency and cost savings.

In this research, two fly ash dosages, 30% and 50% and three w/b ratios, 0.4, 0.5, and 0.6 are adopted to investigate the influence of fly ash on the resistance of concrete to chloride penetration. Figure 7 shows the  $D_{RCM}$  of each type of fly ash concrete at ages from 28 days to 180 days.

On the double logarithmic coordinate, there is a good linear relationship between the  $D_{RCM}$  values and age of the concrete, as shown in Equation 4. In Figure 7, it is clear that the slope (b) of these curves is highly related to w/b ratio.

**Table 2. Input parameters for service life predictions with the DuraCrete methodology.**

Input Items	Symbol in DuraCrete model	Value	
Reference time, <i>year</i>	$t_0$	0.0767(28 days)	0.4932(180 days)
Chloride migration coefficient, $m^2/s$	$D_{RCM}$	$15.63 \times 10^{-12}$	$2.22 \times 10^{-12}$
Chloride resistance, $year/mm^2$	$R_{cl,0}^c$	0.0020	0.0143
Ageing factor	$n_{cl}$	0.8	0.8
Curing factor	$k_{c,cl}^c$	0.79	0.79
Critical chloride concentration, % relative to binder	$c_{cr}^c$	0.2	0.2
Water to binder ratio	$w/b$	0.4	0.4
Cover depth, <i>mm</i>	$x^c$	45	45
Margin for the cover depth, <i>mm</i>	$\Delta x$	8	8
regression parameter, % relative to binder	$A_{c,s,cl}$	4.42	4.42
Environment factor	$k_{e,0}^c$	0.68	0.68
	$k_{e,c}^c$	2.9	2.9
Partial factor	$\gamma_{cr}$	1.03	1.03
	$\gamma_{c,s,cl}$	1.2	1.2
	$\gamma_{R_d}$	1.50	1.50

$$D_{RCM,T} (\times 10^{-12} m^2 / s) = b \times t + c \quad (4)$$

where: b is slope related to different type of fly ash concrete; c is a constant; t is curing age, days;

According to Equation 4 the  $D_{RCM}$  value at an age of 180 days can be directly calculated based on the  $D_{RCM}$  values measured at the curing ages of 28 days (see Equation 4). The values of b for fly ash concrete mixtures with different w/b ratios are shown in Table 3. Figure 8 shows the  $D_{RCM}$  values at different curing ages from reference (21). The value at point "x" shows the calculated result according to Equation 5 (w/b=0.53; b=-0.951).

$$\lg[D_{RCM,180days} (\times 10^{-12} m^2 / s)] = \lg[D_{RCM,28days} (\times 10^{-12} m^2 / s)] + b \times (\lg 180 - \lg 28) days \quad (5)$$

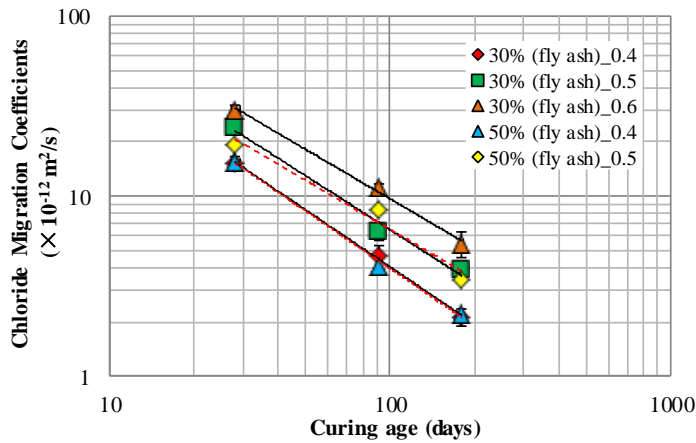


Figure 7. The  $D_{RCM}$  of fly ash concrete at ages from 28 days to 180 days.

Table 3. The value of  $b$ .

w/b ratio	$b$ (slope)
0.4	-1.055
0.5	-0.951
0.6	-0.913

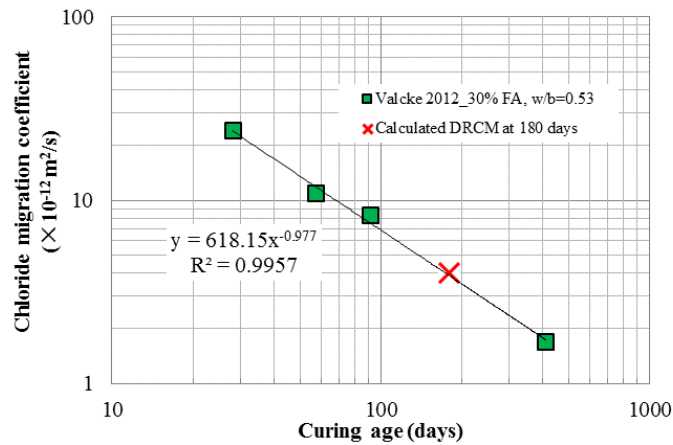


Figure 8. The  $D_{RCM}$  of fly ash concrete (20) and the calculated data at an age of 180 days.

## 5 Concluding Remarks

The prediction of service life is a particularly important step during the design phase of projects. In the DuraCrete methodology, the service life is defined and predicted by taking into account reinforcement corrosion. In this paper, the input parameters are discussed for fly ash concrete structures in order to predict the service life of fly ash concrete structures more reliably. The following conclusions can be drawn:

- 1) In Portland cement-fly ash binary systems, the calcium hydroxide (CH) content is one of the indicators reflecting the rate of pozzolanic reaction of fly ash. At ages from 28 days to 180 days, the CH content of blended cement paste decreases significantly. After 180 days, the CH content hardly changes. It is inferred that the pozzolanic reaction of fly ash takes place dramatically after 28 days, and a relative stable structure is reached after 180 days. 180 days is defined as the reference time for fly ash concrete structures in the DuraCrete methodology.

- 2) By using two reference time, 28 days and 180 days, the predicted service life of fly ash concrete (50% fly ash; w/b=0.4) is 11 years and 116 years, respectively. The service life of fly ash concrete structures, in this study, is underestimated when 28 days is used as the reference time.
- 3) In order to promote efficiency and save cost in practice, the  $D_{RCM}$  value at the reference time of 180 days can be deduced based on the experimental results of RCM test performed at age of 28 days.

## 6 Acknowledgement

The authors would like to thank National Basic Research Program of China (973 Program: 2011CB013800) and the China Scholarship Council (CSC) for the financial support.

## 7 References

1. NEN 6720:1995 nl TGB 1990 - Voorschriften Beton - Constructieve eisen en rekenmethoden (VBC 1995).
2. NEN-EN 206-1 Beton – Deel 1: Specificatie, eigenschappen, vervaardiging en conformiteit.
3. NEN 8005:2008 nl Nederlandse invulling van NEN-EN 206-1: Beton - Deel 1: Specificatie, eigenschappen, vervaardiging en conformiteit.
4. NEN 6722: 1989 Voorschriften Beton. Uitvoering (VBU 1988), met correctieblad van mei 1989.
5. Zhuqing Yu, Guang Ye, “New Perspective of Service Life Prediction of Fly Ash Concrete”, Construction and Building Materials, 48, 2013, pp. 764-771.
6. van der Wegen Gert, Polder Rob B., et al., “Guideline for service life design of structural concrete - A performance based approach with regard to chloride induced corrosion”, HERON, 57 (3), 2012, pp. 153-167.
7. Gonnerman, H. F., Lerch, W., “Changes in characteristics of Portland cement as exhibited by laboratory tests over the period 1904 to 1950”, ASTM Special Publication, 127, 1951.
8. Sybertz, F., Wiens U., “Effect of fly ash fineness on hydration characteristics and strength development”, Blended cements in construction. Papers presented at the international conference, university of Sheffield, UK, 9-12 September 1991.
9. Sakai Etsuo, Miyahara Shigeyoshi, et al., “Hydration of fly ash cement”, Cement and Concrete Research, 35, 2005, pp. 1135-1140.
10. “Standard for inspection and assessment of concrete durability”, JGJ/T 193-2009. China.
11. DuraCrete 2000, “Probabilistic Performance based Durability Design of Concrete Structures”, Contract BRPR-CT95-0132, Project BE95-1347. Document BE95-1347/R17, May 2000.
12. Neville, A. M., “Properties of concrete”, 1995, Wiley, New York.
13. Collepardi, M., Marcialis, A., et al., “La Cinetica Di Penetrazione Degli Ioni Cloruro Nel Calcestruzzo (The penetration kinetics of chloride ions into concrete)”, il Cemento, 67, 1970, pp. 157-164.
14. Oslakovic Irina Stipanovic, Bjegovic Dubravka, et al., “Evaluation of service life design models on concrete structures exposed to marine environment”, Materials and Structures, 43, 2010, 1397-1412.
15. Polder Rob B., de Rooij Mario R., et al., “Observed Chloride Penetration in Eastern Scheldt Storm Surge Barrier, The Netherlands, after 20 years in North Sea Environment”, Workshop "Risk based maintenance of Structures", 21 January 2003, TU Delft.
16. Polder R.B., de Rooij M.R., et al., “Validation of models for service life prediction –Experiments from the practice”, In Proceeding International RILEM-JCI seminar Concrete Life’06, Ein Bokek, 2006, pp. 292-301.
17. van Breugel, K., Polder, R., “Probability-based service life design of structural concrete”, in Proceeding 2<sup>nd</sup> International RILEM Workshop on Concrete Durability and Service Life Planning- ConcreteLife’09, Haifa, Israel, 2009; pp. 383-391.



18. Maage, M., Helland, S., et al., "Service life prediction of existing concrete structures exposed to marine environment", ACI Materials Journal, 93(6), 1996, pp. 602-608.
19. NT Build 492. "Concrete, mortar and cement-based repair materials: chloride migration coefficient from non-steady-state migration experiments". UDC 691.32/691.53/691.54. Approved 1999-11.
20. NT Build 492, "Concrete, mortar and cement-based repair materials: chloride migration coefficient from non-steady-state migration experiments". UDC 691.32/691.53/691.54. Approved 1999-11.
21. Valcke Siska L.A., Polder Rob B., et al., "High filler concrete using fly ash -Chloride penetration and microstructure", HERON, 57(3), 2012, pp. 169-184.

# EFFECT OF COMBINED FIBRES ON FIRE RESISTANCE OF LARGE SPECIMENS

Youngsun Heo<sup>1</sup> and Byungyeol Min<sup>1</sup>

<sup>1</sup>Fire Research Institute, Korea Institute of Civil Engineering and Building Technology (KICT), Republic of Korea

**Abstract:** In this study, effect of combined fibers on fire resistance of large specimens is investigated. The effect of the combined fiber technique on the level of spalling protection was experimentally confirmed by applying to large columns. Four different size of large columns were prepared for proving the effectiveness of the combined fiber technique. In addition, the authors presented the detailed procedure of the optimum fiber design for spalling protection of concrete in fire. In this design, critical parameters of fiber length, fiber diameter and the total number of fibers per unit volume were quantitatively established, so that the fiber addition can be reduced over 50% for the single type of fibers and can be further reduced for the combined type of fibers.

**Keywords:** Fire resistant concrete, Spalling, Fibers, Inter-aggregate spacing

## 1. Introduction

Normal strength concrete has been regarded as a fire-proof material because of its incombustibility and its high thermal insulating properties. However, since high strength concrete was introduced, concrete as a generic material has not existed when it comes to fire [1]. This is because the behavior of high strength concrete and normal strength concrete is at elevated temperature.

High strength concrete is at high risk of spalling when the concrete structures are exposed to fire [2-4]. The spalling is the detachment of pieces of concrete from the concrete surface, thus reducing the load-bearing cross-sectional area and capacity. It may be explosive in some cases. In extreme cases, it may result in the loss of entire cross section of a concrete member.

To mitigate the spalling problem of high strength concrete in fire, the addition of polypropylene fibers in the concrete is introduced in the open literature [5]. Since then, the effectiveness of the fibers has been proved by many researchers [6-8]. The fiber addition method has been the most widely used in concrete for the spalling protection than any other mitigating methods, due not only to the effectiveness but the simplicity and the cost effectiveness for their application to the concrete in practice.

In addition, it is expected that the use of fibers in concrete in a non-fire event has other beneficial effects on concrete such as reduction of plastic shrinkage and drying shrinkage.

In fire circumstance, the fiber addition technique can reduce the probability of spalling, or prevent it, by reducing the pore pressures that build-up during rapid heating of concrete structures in fire [9]. Polypropylene fibers initially in a form of solid phase undergo a melt phase at around 160°C. The spaces occupied by the melted fibers can provide pathways for water vapor within the concrete that can lead to pressure relief and the spalling protection of concrete.

## 2. Previous research work

In previous research, the authors have firstly proposed three critical fiber parameters providing effective pathway for water vapor in concrete in fire [10]. They are the total number of fibers per unit volume (N), the length of fibers (L) and the melting point of fibers (k). N determines the level of dispersion of fibers in concrete; L determines the level of connection of pores and k determine the commencing time of vapor evacuation. These three factors contribute an effective pore network in concrete at elevated temperature and relieve vapor pressure.

Based on the key findings from the investigations, the authors [11] have found that the addition of two types of fibers (nylon and polypropylene fibers) with selected dimensional characteristics could reduce the required fiber content up to three times less than the addition of the single type of polypropylene fibers commonly prescribed for the equal level of spalling protection of concrete in the literature. However, the findings from the previous work were drawn with small cylinders, in which a size effect may adversely affect the results.

Hence, in this current study, to further investigate the true effect of the combined fibers on the level of spalling protection, large column specimens with four different cross-sectional sizes were prepared. Finally, design of fire resistant concrete using the synthetic fibers were proposed.

### 3. Size effect of combined fiber technique

#### 3.1 Experimental outline

Table 1 shows the experimental outline. The combined fibers of 0.05% by volume and the conventional singled fibers of the same % were added in concrete. The combined fibers were nylon fibers of 0.025vol.% and polypropylene fibers of 0.025vol.%, and the singled fibers were polypropylene.

Four different sizes of columns were prepared, i.e. 300 × 300 × 1500, 500 × 500 × 1500, 700 × 700 × 1500 and 900 × 900 × 1500. The list of experimental tests conducted in fresh and hardened concretes are shown in Table 1.

**Table 1 Experimental outline**

Fiber type	Specimen size (mm)	Test conducted
Control (no fiber addition)	500 mm × 500 mm × 1500 mm	<ul style="list-style-type: none"> <li>· Compressive strength</li> <li>· Fire test (3h):               <ul style="list-style-type: none"> <li>- Spalling extent</li> <li>- Spalling area</li> <li>- Weight loss</li> </ul> </li> </ul>
Polypropylene fibers	300 mm × 300 mm × 1500 mm	
	500 mm × 500 mm × 1500 mm	
	700 mm × 700 mm × 1500 mm	
	900 mm × 900 mm × 1500 mm	
Combined fibers <sup>a</sup>	300 mm × 300 mm × 1500 mm	
	500 mm × 500 mm × 1500 mm	
	700 mm × 700 mm × 1500 mm	
	900 mm × 900 mm × 1500 mm	

<sup>a</sup> Polypropylene fibers of 0.025vol.% + Nylon fibers of 0.025vol.%

#### 3.2 Specimen preparation

The mixture proportion of the control concrete without fiber addition is shown in Table 2. Water to binder ratio of 0.25 was determined to cast high strength concrete. The binders included Fly ash of 20 % and silica fume of 10% by cement weight. A forced fan type mixer was used, and combined fibers were added for a dry mix of first 30 sec with cement, binders and aggregates, followed by mixing with water for 60 sec.

All specimens were demoulded after seven days and then placed in an atmospheric condition: temperature was 8°C - 20°C; humidity was 32% ~ 43% and wind speed was 1.4 m/s ~ 2.1 m/s. Fire tests were conducted at 91 days after casting the specimens.

**Table 2 Mixture proportion of control concrete**

W/B <sup>a</sup>	Unit water, kg/m <sup>3</sup>	S/a <sup>b</sup> , %	Weight mixture, kg/m <sup>3</sup>				
			C <sup>c</sup>	FA <sup>d</sup>	SF <sup>e</sup>	S <sup>f</sup>	G <sup>g</sup>
0.25	160	45	448	128	64	660	837

<sup>a</sup> Water to binder ratio

<sup>b</sup> Sand to coarse aggregate ratio

<sup>c</sup> Cement

<sup>d</sup> Fly ash

<sup>e</sup> Silica fume

<sup>f</sup> Sand

<sup>g</sup> Gravel

### 3.3 Materials

The Ordinary Portland cement (Density: 3150 kg/m<sup>3</sup> and fineness: 330 m<sup>2</sup>/kg) was used in this study. Fly ash (Density: 2210 kg/m<sup>3</sup>, fineness: 406 m<sup>2</sup>/kg and loss on ignition: 3.5%) and silica fume (Density: 2200 kg/m<sup>3</sup>, fineness: 20000 m<sup>2</sup>/kg and loss on ignition: 1.5%) were incorporated as mineral admixtures.

For aggregates (granite type), the combination of river sand and crushed rock (4:6) was mixed to obtain a 2.6 fineness modulus of fine aggregate. Density and absorption of the both fine aggregates were 2600 kg/m<sup>3</sup> and 0.46%. All coarse aggregates used in this study were a crushed aggregate type. Density and absorption of the coarse aggregates were 2610 kg/m<sup>3</sup> and 0.58%.

The physical properties of nylon and polypropylene fibers are shown in Table 3.

**Table 3 Physical properties of synthetic fibers**

Type of fiber	Diameter, mm	Length, mm	Density, kg/m <sup>3</sup>	Melting point, °C	Tensile strength, MPa
Polypropylene	0.040	19	910	160	560
Nylon	0.012	9	1150	220	918

### 3.4 Test methods

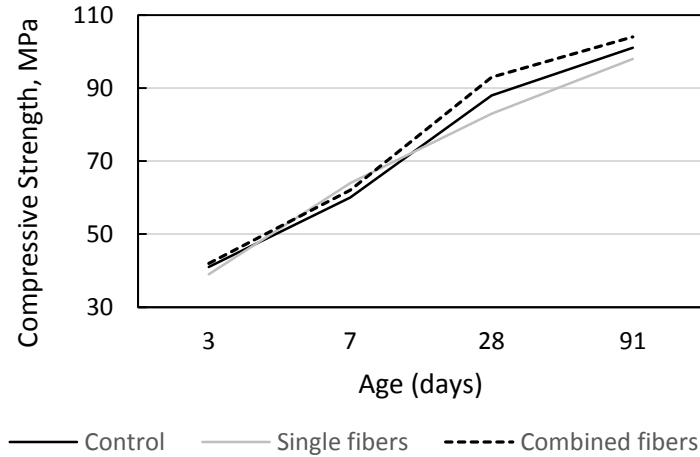
ASTM C 39 was conducted for compressive strength test of hardened concretes. Cylinders of size Ø100 × 200 mm were prepared and tested in triplicate for each type for this strength test. Fire tests were carried out for three hours according to the standard heating curve of ISO-834. After the test completed, the extent of spalling was visually observed, and weight loss due to spalling was examined by comparing the values before and after the test. The spalling area was calculated by using the automatic area measurement software after tracing and blacking out the contours of detached parts of heated concrete specimens on a transparent sheet.

### 3.5 Experimental test results

In this Section, experimental test results are presented. The compressive strength and spalling extent (i.e. spalling area, weight loss after fire exposure) of the concretes with single fibers and combined fibers are examined. Key findings obtained from the tests are discussed below.

### 3.5.1 Compressive strength of the concrete

Fig. 1 shows the compressive strength of the control concrete, single fiber-added concrete and combined fiber-added concrete to be placed in column specimens. Strengths of all concretes were properly developed and indicated around 100 MPa at the due date of fire tests, curing age of 91 days.

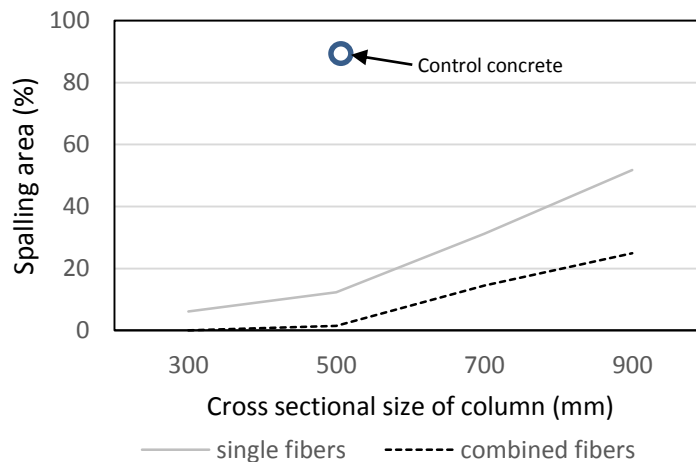


**Figure 1 Compressive strength of concrete**

### 3.5.2 Extent of spalling

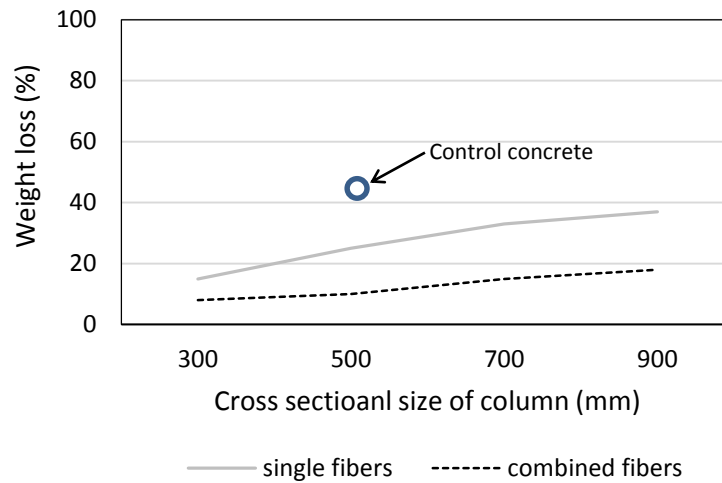
Fig. 2 shows the calculated % of spalling area of concrete column specimens. It was clear that the control column without fiber inclusion had severe damage due to spalling. The spalling area of the control column was 92.4%. Fiber addition in concrete improved the spalling resistance, but a fiber type significantly affected the results.

For the specimens with a cross sectional size of 500 mm that were exactly the same size with control, the spalling area of the column with singled polypropylene fibers was 12.0%, whereas that with combined fibers was only 1.5%. The good result of the column with the combined fibers was equally observed in other larger specimens tested in this study, which provides evidence that the combined fiber technique is effective in large specimens. It is noted that the larger the size of specimens, the higher was the results of spalling area.



**Figure 2 Spalling area of concrete after fire exposure**

Fig. 4 shows the weight loss of the column specimens after fire exposure. As expected, control concrete without fiber addition lost over 40% of its original weight before fire exposure. However, the combined fiber technique was much more effective on minimizing the weight loss of the concrete in fire, compared to the addition of single type of polypropylene fibers.



**Figure 3 Weight loss of concrete after fire exposure**

#### 4. Design of fire resistant concrete using combined fibers

In the literature, it was observed that the addition of polypropylene fiber of 1.8 kg/m<sup>3</sup> and 3.0 kg/m<sup>3</sup> had a similar effect on pressure relief in heated concrete exposed to fire [6]. In other words, this means that as soon as fibers constitute a connected network, the latter is large enough to evacuate gases and vapor, thus to reduce pore pressure, in which the level of reduced pore pressure is similar to former dosage.

Hence, it is very important that the amount of fiber inclusion should be just to resist the spalling of concrete to avoid any side effects that might occur when the fiber content unnecessarily increases. In fact, it should be noted that the capability of evacuating the vapor from the concrete in fire is dependent on the level of connected pores. Since the main role of fibers is to provide the connection between un-connected pores, the length of fibers and the total number of fibers are the essential parameters for spalling protection as characterized in previous work, by which the fiber content can be minimized.

By taking these essential parameters of fibers into the design of fire resistant concrete, the optimum level of fire resistant concrete can be achieved. The detailed procedure is presented as follows.

##### 4.1 Inter-aggregate spacing

It is important to note that for a given fiber content, the essential parameters, fiber length and total fiber number, are in inverse proportion to each other [12]. The relationship is given by

$$N = \frac{4V_f}{\pi d_f^2 L_f} \tag{1}$$

where  $N$  is the total number of fibers per unit volume,  $V_f$  is the volume of fiber content,  $d_f$  is the diameter of fibers, and  $L_f$  is the length of fibers. For a given fiber content, increasing  $N$  by decreasing  $d_f$  or  $L_f$  (Eq. 1) is beneficial to obtain a well distributed pore network in concrete at elevated temperature, but unlike limited effect of  $d_f$  on spalling protection,  $L_f$  has an effect to intersect un-connected pores in concrete, so that  $L_f$

should be long enough to provide effective pathways for water vapor, which in turn should decrease  $N$  accordingly for a given fiber content.

Percolation of concrete is one of the critical factors that can determine the level of spalling. According to a percolation theory, ITZ regions are normally percolated in normal strength concrete, but not definitely in high strength concrete. To achieve the high strength concrete to be percolated, it is believed that neighboring ITZs which is not connected due to the use of high strength concrete should be re-connected by the addition of fibers with a proper length. For a given fiber content, the addition of fibers shorter than the required length will result in the lack of interconnectivity between the ITZs and the fibers, and that of fibers longer than the required length will result in a decrease of  $N$ . In both cases, the concretes would not be percolated in the optimum level. Hence, to optimize the effectiveness of fiber addition, it is the first step to determine the least length of fibers required for percolating concrete.

Since ITZ thickness in high strength concrete is very small, the distance between neighboring ITZs is referred to as inter-aggregate spacing, which is a function of the size, grading and volume of aggregates as well as other mixture proportions of concrete. It should be noted that the inter-aggregate spacing of fine aggregate is not an important parameter for spalling protection. It is the inter-aggregate spacing of coarse aggregate,  $i$ , that is important, so that the least length of fibers should be longer than  $i$  for effective spalling protection.

Briefly, in previous study, a  $C_{shell}$  model [12] has been developed based on the assumption that all coarse aggregates are spherical, and they are uniformly distributed and covered by uniform thickness of mortar shells. Based on these assumptions, it can be said that  $i$  is twice the mortar shell thickness. The procedure for calculating  $i$  (equal to the least fiber length for percolated concrete) is summarized in Table 4.

**Table 4 Procedure for the calculation  $i$ , calculated for 1 m<sup>3</sup> concrete**

Parameter description	Equation
Void volume between the dry rodded aggregate occupied by the total amounts of the coarse aggregates used, $\eta$	$\eta = \gamma - \frac{\omega}{\rho_s}$ (2)
Specific surface area of spheres uniformly distributed in the size between the mesh size (mm), $d_x$ and $d_y$ of adjacent sieves, $S$	$S = \frac{6}{(1-\eta)\rho_s\sqrt{d_x d_y}}$ (3)
Specific surface area of actual used coarse aggregate having fractions of the total mass retained on different sieves, $S_{tm}$	$S_{tm} = \sum_{x=1}^n S_x x_x$ (4)
Excess volume of mortar after filling ' $\eta$ ', $\varepsilon$	$\varepsilon = V_{conc} - (\gamma + a)$ (5)
Mortar shell thickness covering each coarse aggregates by ' $\varepsilon$ ', $T_m$	$T_m = \frac{\varepsilon}{S_{tm}\omega}$ (6)
Inter-aggregate spacing of coarse aggregates, $i$	$i = 2T_m$ (7)

$\gamma$  is the total volume of dry rodded aggregate occupied by the amounts of the coarse aggregates used

$a$  is the volume of air content measured

$\omega$  is the weight of coarse aggregate

$\rho_s$  is the density of coarse aggregate

$S_1 S_2 \dots$  and  $S_n$  is the specific surfaces of uniform spheres distributed in the different sieves [Eq. 3], and  $x_1 x_2 \dots$  and

$x_n$  is the fractions of the total mass of the actual used aggregate retained on the corresponding sieves

$V_{conc}$  is the volume of concrete used, which is equal to 1 m<sup>3</sup>

#### 4.2 Total number of fibers per unit volume

For the next stage, it is important to estimate the least  $N$  required for spalling protection. With the pre-calculated  $i$ , the estimated  $N$  has an effect on the determination of the optimum fiber length. This is because, for a given fiber content, dramatically increased  $N$  can overtake the effect of fiber length, thus decreasing the optimum fiber length.

Prior to determine the least  $N$ , the effect of the influential factors into the design of the fire resistant concrete at the material level should be carefully considered. A way of measuring fiber content as  $N$  is due to the fact that essential parameters of fibers for spalling protection is  $N$  and  $L_f$ , and  $N$  is independent of  $d_f$ .

### 4.3 The optimum length of fibers

The optimum fiber length can be calculated based on the calculated  $i$  and pre-determined  $N$ . To finalize the optimum fiber length, another contributing factor, an aggregate size in concrete, should be introduced. Because the aggregate size in concrete affects an external tangent length of adjacent aggregates, which directly affect the required length of fibers for the interconnectivity of adjacent aggregates. An average aggregate size parameter,  $d$ , can be used to represent the aggregate sizes in the concrete. This is given by

$$d = \frac{6}{S_{tm}\rho_s} \quad (8)$$

It is important to note that there is a threshold of the critical number of fibers per unit volume,  $N_c$ , that can determine a dominant fiber parameter ( $L_f$  or  $N$ ) for spalling protection. This is because  $L_f$  and  $N$  have an effect to compensate each other in terms of the pressure relief of vapor in concrete in fire. By taking this into account, the equation for the optimum length of fibers for spalling protection is given by

$$\zeta = (i + d)\left(\frac{N_c}{N}\right)^{\frac{1}{3}} \quad (9)$$

where  $\zeta$  is the optimum length of fibers,  $N_c$  is a constant, empirically determined to be 250, which is believed to be the critical boundary of a dominant factor for fiber effectiveness parameters ( $L_f$  and  $N$ ), which can be said that if  $N$  is started to be higher than  $N_c$ , the dominant factor of the fiber parameters for spalling protection is likely to be  $N$ , so that the optimum fiber length decreases to achieve increased  $N$ ; and if  $N$  is lower than  $N_c$ , the dominant factor is likely to be  $L_f$ , so that the optimum fiber length increases.

### 4.4 New measurement for fiber content

At this stage, the quantity of calculated  $N$  and  $\zeta$  is finally examined to see whether these values are sufficient for spalling protection. In the literature, the addition of polypropylene fibers has been used for spalling protection of concrete for over a decade, and its excellent performance has been verified by many researchers. For the concretes having up to 100 MPa of compressive strength, it has generally been observed that the addition of polypropylene fibers with 0.1% to 0.3% is necessary for the spalling protection of the concretes. However, it has been demonstrated that these amounts of fibers being used in the past can be reduced to over 50% [8].

As discussed in Section 2, there is a method to quantify the required fiber content for spalling protection with dimensional characteristics of synthetic fibers. The new measure for fiber content to determine the critical threshold for fiber addition for spalling protection has been established. This is given by

$$N \zeta^3 k \geq 190 \quad (10)$$

where  $k$  is a factor introducing the effect of fiber melting point which is empirically determined as  $160/t_m$ , where  $t_m$  is the melting point of fibers in degrees Celsius. It can be said if  $N\zeta^3k$  is greater than 190 where the fiber addition is optimized, there is no or minor spalling occurred in concrete in fire.



#### **4.5 Combined fibers**

As discussed in Section 3, there is a synergistic effect of combined fibers showing outstanding performance of spalling protection. By combining nylon and polypropylene fibers, concrete spalling has started to be resisted (no or minor spalling) when  $N\zeta^3k$  is more than 52, which is over 3 times less than the critical threshold, 190, mentioned above.

This is because although polypropylene fibers have low melting point, this fiber can only provide limited number of fibers per unit volume due to their large diameter. Combining other types of fibers which are small in diameter such as nylon fibers can improve the deficiency of polypropylene fibers by providing larger number of fibers per unit volume [11]. In addition, since nylon fibers have higher melting point, the concrete containing both fibers can timely provide pathways for water vapor throughout fire exposure ( in early and latter stages), which also improve the effectiveness of combined fibers as compared with the addition of a single type of fiber.

### **5. Conclusions**

This study has investigated the effect of the combined fiber technique on the level of spalling protection by applying to large column specimens and proposed the design of fire resistant concrete using synthetic fibers. The conclusions are drawn as follows.

- 1) It is proved that the proposed combined fiber technique with significantly reduced fiber content is applicable to large concrete columns.
- 2) The size of a column has an effect on the level of spalling. The larger the size of specimen, the lower is the effectiveness of the combined fiber technique
- 3) To design the fire resistant concrete by using synthetic fibers, the melting point of fibers, the length of fibers and the total number of fibers per unit volume are the important parameters. In addition, it was found that the optimum length of fibers is mainly determined by the inter-aggregate spacing and the critical fiber number per unit volume parameters.

### **6. Acknowledgement**

This research was supported by a grant (391) from Infrastructure and transportation technology promotion research Program funded by Ministry of Land, Infrastructure and Transport of Korean government.

### **7. References**

1. Khoury G.A (2008) "Passive fire protection of concrete structures", Proceedings of the Institution of Civil Engineers-Structure & Buildings Vol. 161, pp.135~145
2. Han, C.G. (1998) "Concrete with spalling resistance", Magazine of Korea Concrete Institute Vol.10, pp.5~10
3. Phan, L.T. and Carino, N.J. (2002) "Effect of test conditions and mixture proportions on behavior of high-strength concrete exposed to high temperatures", ACI Materials J Vol. 99, pp.54~66
4. Jansson, R. (2013) "Fire spalling of concrete", PhD thesis, KTH, Sweden
5. Britenbucker, R. (1996) "High strength concrete C105 with increased fire resistance due to polypropylene fibers", Proceedings of 4th International Symposium on Utilization of High Strength/High performance Concrete, Paris, France, pp. 571~578
6. Kalifa, P., Chene, G. and Galle C (2001) "High-temperature behaviour of HPC with polypropylene fibres from spalling to microstructure", Cement and Concrete Research Vol.31, pp.1487~1499
7. Papworth, F. (2000) "Affect of synthetic fibres and silica fume on explosive spalling of high performance concrete exposed to fire:", South East Asia Construction, Trade Link Media Singapore, pp 1~6

8. Heo YS (2011) Identification of fibre parameters from spalling protection of concrete in fire. PhD thesis, Monash University, Australia
9. Consolazio, G.R., McVay, M.C. and Rish, III J.W. (1998) "Measurement and prediction of pore pressures in saturated cement mortar subjected to radiant heating", *ACI Materials J* Vol.95, pp.525~536
10. Heo, Y.S., Sanjayan, J.G., Han, C.G. and Han, MC (2011) "Critical parameters of nylon and other fibers for spalling protection of high strength concrete in fire", *Materials and Structures* Vol.44, pp.599~610
11. Heo, Y.S., Sanjayan, J.G., Han, C.G. and Han, MC (2010) "Synergistic effect of combined fibers for spalling protection of concrete in fire", *Cement and Concrete Research* Vol.40, pp.1547~1554
12. Heo, Y.S., Sanjayan, J.G., Han, C.G. and Han, MC (2012) "Relationship between inter-aggregate spacing and the optimum fiber length for spalling protection of concrete in fire", *Cement and Concrete Research* Vol.42, pp.549~557

# Mechanical properties of fibre reinforced high volume fly ash concretes

Yashar Shafaei<sup>1</sup>, Faiz Shaikh<sup>2</sup>, Prabir Sarker<sup>2</sup> and Salim Barbhuiya<sup>3</sup>  
<sup>1</sup>PhD student, <sup>2</sup>Senior Lecturer, <sup>3</sup>Lecturer,  
Department of Civil Engineering, Curtin University, Perth, Australia.

**Abstract:** This paper presents the mechanical properties of fibre reinforced high-volume fly ash (HVFA) concretes measured at 7 and 28 days. The effects of three class F fly ash contents of 40%, 50%, and 60% by wt. as a partial replacement of cement and two types of fibres (steel and polypropylene) with three different volume fractions of 0.15%, 0.25%, and 0.50%, on the compressive, tensile and flexural strengths of HVFA concretes are studied. Test results show that the addition of fibres (steel and polypropylene) reduces the workability of HVFA concretes and the workability decreases with increase in volume fractions of fibres and increases with increase in fly ash contents. The compressive, tensile and flexural strengths of all HVFA concretes increased due to addition of steel and polypropylene fibres and the above values also increased with increase in fibre volume fractions. Among all fibre reinforced HVFA concretes, the concrete containing 40% fly ash exhibited the highest mechanical properties at both ages. The steel fibre volume fraction of 0.5% exhibited the highest compressive, tensile and flexural strengths of HVFA concretes containing 40% fly ash and the improvement was by 73%, 40% and 36%, respectively. However, in the case of polypropylene fibre the above improvements were only 44%, 29% and 20%, respectively. This can be attributed to the lower elastic modulus and tensile strength of polypropylene fibres than steel fibre. Correlations among compressive, tensile and flexural strengths of the above concretes are also established.

**Keywords:** concrete, compressive, tensile, flexural strength, high volume fly ash, fibre.

## 1. Introduction

Concrete is the most widely used construction material in the world. In line with the concept of sustainable development, concrete technology now-a-days demands the production of high-performance materials by incorporating industrial waste as supplementary cementitious materials (SCM), both with regard to environmental pollution and curbing the rise in construction costs. The most available SCM world-wide is class F fly ash (FA), a by-product of coal fired thermal power stations [1]. Several studies involving concrete containing fly ash had reported excellent mechanical and durability properties [2-4]. The incorporation of fly ash as a partial replacement of cement in concrete is a common practice for many years. Replacement of 30% or more ordinary Portland cement (OPC) by FA is termed as high-volume fly ash (HVFA) concrete [5-6]. The HVFA concrete is one example of a construction material in harmony with the concept of sustainable development: having lower environmental impact (reduced CO<sub>2</sub> emissions), judicious use of resources (energy conservation, use of by-products), and being a high performance construction material [1].

Discrete short fibres are often added in concrete to compensate its low tensile strength and brittle failure behaviour. Addition of fibres also improves the mechanical properties of concrete such as flexural strength, compressive strength, creep behaviour, impact resistance, toughness, etc. [7-8]. Conventional fibre reinforced concrete (FRC) contains mostly OPC with little or no fly ash, which is not in line with sustainable development of concrete and its application in construction industries. Therefore, the replacement of OPC with high volume fly ash in conventional FRC will make it sustainable with reduced carbon footprint. However, limited research is reported on the properties of fibre reinforced concrete containing HVFA as partial replacement of cement. Different types of fibres with different fly ash contents are used in those studies. Topcu and Canbaz [9] studied the mechanical properties of FRC containing different contents of fly ash ranging from 10% to 20% reinforced by steel and polypropylene fibres. In another study, Atis and Karahan [10] studied the properties of steel FRC containing 15% and 30% fly ash as partial replacement of cement. In both studies the length of steel fibre was 35mm. In a number of studies on fibre reinforced HVFA concretes the fibres were polymeric e.g. polypropylene [11] and polyester [12] and natural fibre [5]. Sahamran and Yaman [13] reported steel fibre reinforced HVFA concrete containing coarse fly ash and lime stone powder. The length of steel fibre was limited to 30mm in that study. Kayali [14] reported a study on fibre reinforced HVFA concrete containing 50% fly ash as partial replacement of natural fines and cement in the concretes. Steel and polypropylene fibres of 18 and 19mm, respectively long were used to reinforce the concretes.

While the above studies on fibre reinforced HVFA concretes reported better mechanical properties due to reinforcement by different fibres, however, most of them are polymeric and natural fibres which are of low tensile strength. The length of those fibres is also limited to 20mm. Moreover, the studies considered steel fibres are also limited to the length of 35mm only. Recently, longer steel fibres of about 60mm are available in the market and are used to reinforce concrete for industrial floor application, rigid pavement, etc. Approximately similar length PP fibres are also available and widely used in concrete for shotcrete applications. However, those fibres are still used to reinforce the ordinary concrete, which is mostly based on cement based binders. The partial replacement of cement with high fly ash content in those concretes will make them sustainable competitive to counterpart ordinary fibre reinforced concrete. It is also anticipated that the replacement of OPC by HVFA affects the mechanical properties and behaviour of above concretes. However, the full potential of fibre reinforced HVFA concretes is still unexploited. This paper presents a thorough study to evaluate various mechanical properties namely compressive strength, tensile strength and flexural strength of steel and polypropylene (PP) fibres reinforced HVFA concretes containing three different fly ash contents of 40%, 50% and 60% as partial replacement of cement. Three different volume fractions of steel and PP fibres of 0.15%, 0.3% and 0.5% are also considered in this study. The effects of types and volume fractions of fibres and fly ash contents on the fresh properties e.g. workability of above concretes are also evaluated. Finally, correlations among above mechanical properties are also established.

## **2. Experimental program**

### **2.1 Materials**

The ordinary Portland cement (OPC) used in this study corresponds to ASTM type I. The commercially available class F fly ash (FA) of Australian origin was used in the mixes. The chemical composition and physical properties of FA and OPC are listed in Table 1. To reduce the difficulties of mixing and to prevent the segregation of aggregates in the production of HVFA fibre reinforced concrete, the maximum aggregate size was limited to 10 mm. Fine aggregate used in this study was natural sand and crushed coarse aggregates with two different size fractions of 10 mm and 7 mm with a ratio of 2:1 by mass. Both fine and coarse aggregates were prepared in SSD condition and used in all the mixes.

Two types of commercially available fibres such as, polypropylene (PP) and steel (ST) fibre were used in this study. The PP fibres used in this study were waved form for better bond with matrix, with an aspect ratio of 75 and length of 65 mm. This type of fibre is widely used in shotcrete applications. The steel fibres used in this study were hooked-end for enhanced pull-out resistance, having an aspect ratio of 65 and length of 60 mm. Detail properties of both fibres are shown in Table 2.

Fibres generally improved the tensile properties and brittle failure of concrete. However, excessive amount of fibres adversely affects the strength if not properly dispersed in concrete due to the introduction of additional defects during processing [14]. Excessive use of fibre volume fraction (0.5 %-1.0 %) increases the air content and voids in the fibre reinforced concrete [15]. High volume fractions of fibres adversely affect their uniform dispersion in concrete and form fibre balling. Hence, the maximum amount of fibres in this study is limited to 0.50 % by volume of concrete. For each of the two types of fibres, three different fibre volume fractions of 0.15%, 0.25% and 0.50% are considered. Total cementitious materials content e.g. cement and fly ash was kept to a certain minimum level of 400 kg/m<sup>3</sup> as recommended by Malhotra et al. [11] for proper dispersion of fibres in FRC. The concrete mix proportions in this study were based on the authors' previous study [16] while for all mixes the water/binder ratio was kept constant at 0.4.

### **2.2 Preparation, casting and testing of specimens**

In a typical mixing procedure, the materials were placed in a pan mixer in the following sequence: initially, sand and gravel were dry mixed for about 1-2 min. Then cement and fly ash were added to the mixture and mixed for 3-4 min. Water was then gradually added to the mix and mixed for 3-5 minutes. Finally, the fibres were gradually added to the wet concrete and mixed for additional 3-4 minutes. The prepared specimens were kept at 25 ±3°C for about 24 h and then they were demoulded and stored in water curing tanks until the day of testing.

**Table 1. Chemical composition and physical properties of cementitious materials**

Chemical Analysis	Cement (wt. %)	Class F Fly Ash (wt. %)	ASTM C618 limits for class F fly ash
SiO <sub>2</sub>	21.1	63.13	SiO <sub>2</sub> +Al <sub>2</sub> O <sub>3</sub> +Fe <sub>2</sub> O <sub>3</sub> ≥70%
Al <sub>2</sub> O <sub>3</sub>	5.24	24.88	
Fe <sub>2</sub> O <sub>3</sub>	3.1	3.07	
CaO	64.39	2.58	-
MgO	1.1	0.61	-
K <sub>2</sub> O	0.57	2.01	-
Na <sub>2</sub> O	0.23	0.71	-
SO <sub>3</sub>	2.52	0.18	<5%
LOI	1.22	1.45	<6%
Particle size	-	73% pass through 45 µm sieve	66% pass through 45 µm sieve
Specific gravity	3.17	2.68	-
BET Surface area (m <sup>2</sup> /g)	-	1.53	-

**Table 2 Properties of fibres**

Types of Fibre	Geometry	Length (mm)	Diameter (mm)	Aspect ratio	Modulus (GPa)	Tensile strength (MPa)
PP	waved	65	0.85	75	3	250
Steel	Hooked end	60	0.90	65	210	1345

**Table 3. Mix proportions of concretes**

Mix designation	Volume fractions of fibre		Cement (kg/m <sup>3</sup> )	Class F fly ash (kg/m <sup>3</sup> )	Water (kg/m <sup>3</sup> )	Water/binder	Sand (kg/m <sup>3</sup> )	Coarse agg. (kg/m <sup>3</sup> )
	Steel	PP						
FA40-control	-	-	240	160	163	0.4	684	1184
FA50-control	-	-	200	200	163	0.4	684	1184
FA60-control	-	-	160	240	163	0.4	684	1184
FA40-steel0.15	0.15%	-	240	160	163	0.4	684	1184
FA40-steel0.25	0.25%	-	240	160	163	0.4	684	1184
FA40-steel0.50	0.50%	-	240	160	163	0.4	684	1184
FA50-steel0.15	0.15%	-	200	200	163	0.4	684	1184
FA50-steel0.25	0.25%	-	200	200	163	0.4	684	1184
FA50-steel0.50	0.50%	-	200	200	163	0.4	684	1184
FA60-steel0.15	0.15%	-	160	240	163	0.4	684	1184
FA60-steel0.25	0.25%	-	160	240	163	0.4	684	1184
FA60-steel0.50	0.50%	-	160	240	163	0.4	684	1184
FA40-PP0.15	-	0.15%	240	160	163	0.4	684	1184
FA40-PP0.25	-	0.25%	240	160	163	0.4	684	1184
FA40-PP0.50	-	0.50%	240	160	163	0.4	684	1184
FA50-PP0.15	-	0.15%	200	200	163	0.4	684	1184
FA50-PP0.25	-	0.25%	200	200	163	0.4	684	1184
FA50-PP0.50	-	0.50%	200	200	163	0.4	684	1184
FA60-PP0.15	-	0.15%	160	240	163	0.4	684	1184
FA60-PP0.25	-	0.25%	160	240	163	0.4	684	1184
FA60-PP0.50	-	0.50%	160	240	163	0.4	684	1184

The experimental works were divided into two parts. The first part investigated the effect of different steel fibres contents on mechanical properties (compressive strength, tensile strength and flexural strength) of HVFA concretes containing 40%, 50%, and 60% class F fly ash by weight as partial

replacement of cement. The second part is same to the first part in every aspect except the type of fibre where PP fibre is used. Detail mix proportions of all concretes are shown in Table 3.

### 2.3 Test methods

Three cylinder specimens of 100Ø x 200 mm for each mix were cast and tested in accordance with ASTM C39/39M [17] standard for the compression test. Compression tests were conducted after 7 and 28 days of curing using a MCC8 compression testing machine with a loading rate of 0.333 MPa/sec. Three cylinder specimens of 150 Ø x 300 mm were prepared for each mix in accordance with ASTM C496/C496M [18] for splitting tensile strength test. Tensile tests were conducted after 7 and 28 days of curing using the same machine with a loading rate of 0.067 MPa/sec.

In order to evaluate the flexural behaviour of the concretes, the ASTM C1609/C1609M [19] standard was followed. The four-point bending test was conducted on 100 x 100 x 400 mm beams with a span length of 300 mm. Three specimens were considered for each mix. The specimens were tested in four-point bending using an Instron testing machine under displacement control with loading rate of 2 mm/min. The flexural strength of the fibre reinforced concretes was calculated from the ultimate load of the flexural load-deflection curve using the following formula [19].

$$f = \frac{PL}{bd^2}$$

Where:

$f$  = Flexural strength or modulus of rupture

$P$  = ultimate load

$L$  = span length

$b$  = width of the specimen

$d$  = depth of the specimen.

## 3. Experimental results and discussion

### 3.1 Workability

The effects of addition of steel and PP fibres of different volume fractions on workability of HVFA concretes are shown in Figs. 1(a) and (b), respectively. It can be seen that the workability of HVFA concretes increases with increase in fly ash contents. This can be attributed to the spherical shape of the fly ash particles and its lubricating effect in wet concrete. The same effect is also seen when either steel or PP fibres are added in those concretes. However, with increase in fibre volume fractions, this effect gradually diminished and resulted in reduction in workability. The results are in agreement with Siddique [20] who also reported reduction in workability of San fibres reinforced HVFA concretes.

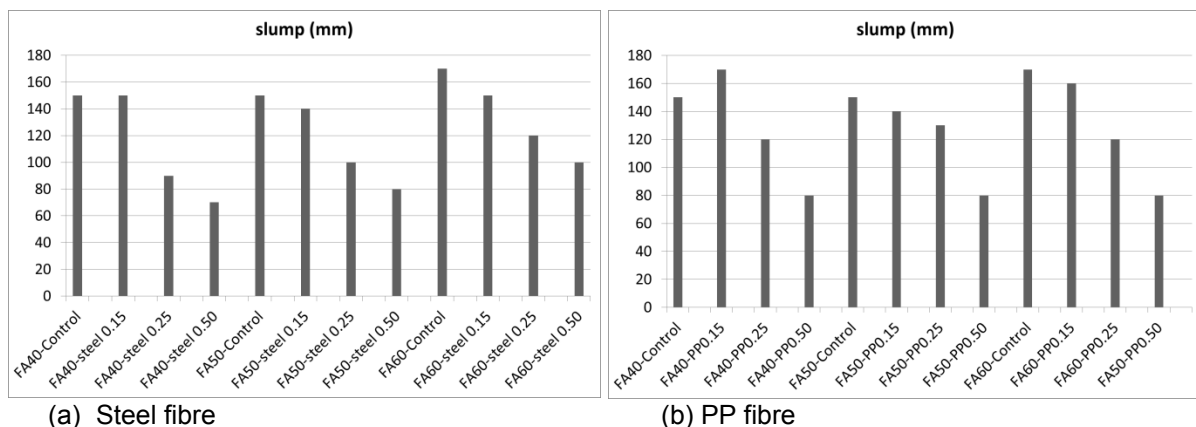
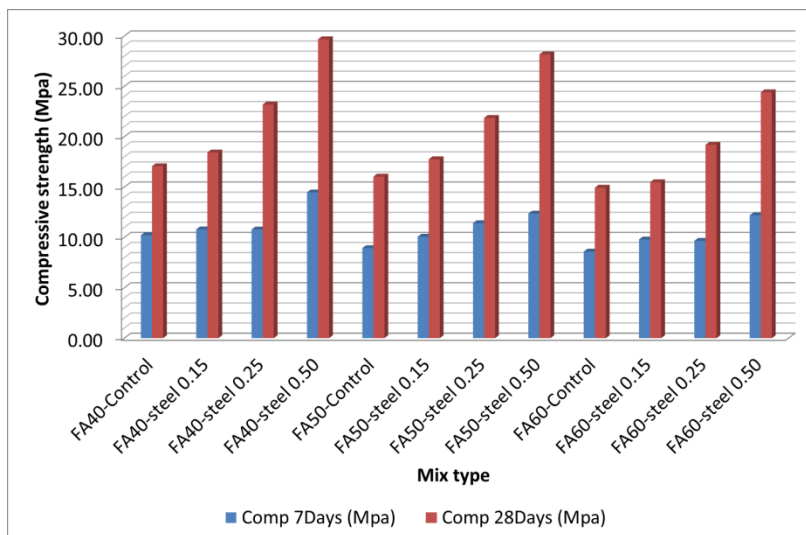


Figure 1. Workability of steel (a) and PP (b) fibre reinforced HVFA concretes.

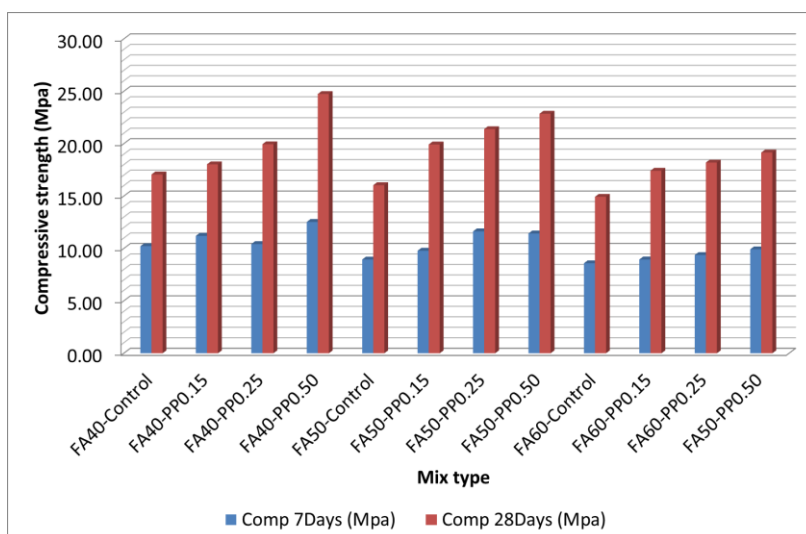
### 3.2 Compressive Strength

The effects of fibre types and their volume fractions on 7 and 28 days compressive strength of HVFA concretes can be seen in Figs.2a and 2b, respectively. The effects of replacement of cement by 40%, 50% and 60% fly ash on 7 and 28 days compressive strength of steel and PP fibre reinforced

concretes are also shown in the same figures, where the compressive strengths of above fibre reinforced concretes decreased with increase in fly ash contents. It can also be seen in Fig.2 that the inclusion of steel and PP fibres improved the 7 and 28 days compressive strength of HVFA concretes. At 7 days, the improvement of compressive strengths of both steel and PP fibre reinforced HVFA concrete is not very significant as compared to unreinforced HVFA concretes. This can be attributed to the slow pozzolanic reaction of fly ash in concrete at early age. However, at 28 days, the same concretes exhibited increase in compressive strength with increase in volume fraction of fibres and the improvement is better in steel fibre reinforced concrete than that of PP fibre reinforced HVFA concrete. The higher compressive strength of HVFA concretes provided by steel fibres than PP fibres is due to better anchorage provided by hooked ends of steel fibre and its higher modulus and tensile strength compared to PP fibre. Although the PP fibres are wave type deformed shape, which supposed to provide better bond with matrix, however the relatively lower modulus and tensile strength make them more susceptible to rupture at ultimate load, resulting in lower compressive strength. Failure behaviour at ultimate load of steel fibre reinforced HVFA concretes is also less brittle than that of counterpart PP fibre reinforced HVFA concretes due to the above reasons. The observed compressive strength results of the above concretes are in good agreement with other published results e.g. in Topcu and Canbaz [9] and Kayali [14], where researchers also observed increase in compressive strength with increase in fibre contents.



(a) Steel fibre



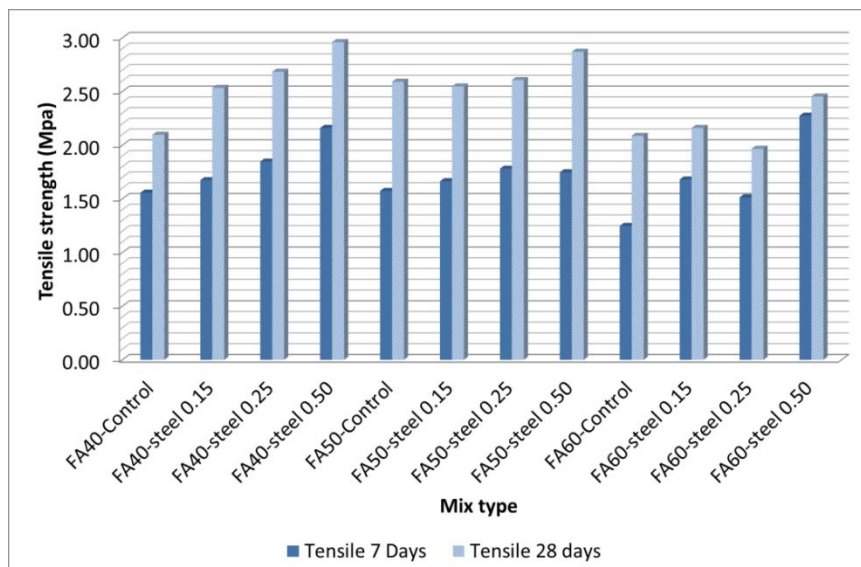
(b) PP fibre

Figure 2. Compressive strengths of steel (a) and PP (b) fibre reinforced HVFA concretes.

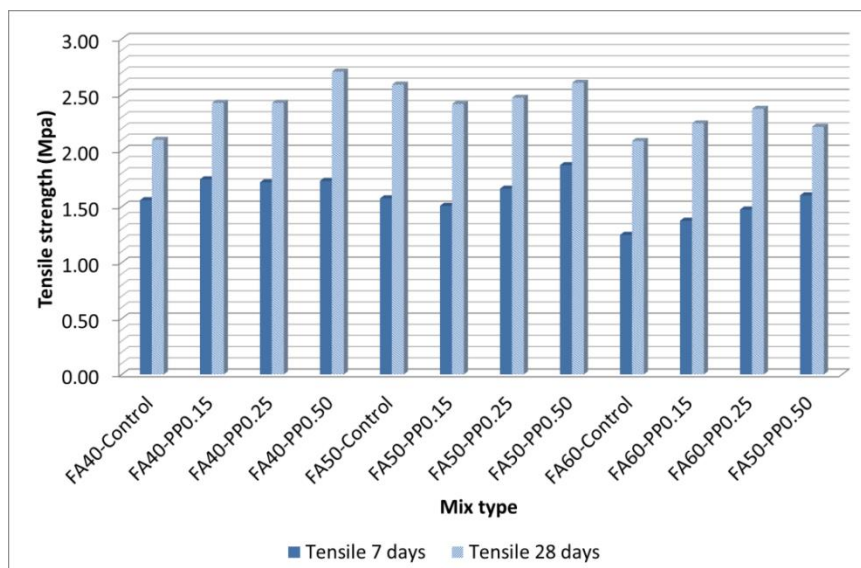
### 3.3 Tensile and flexural strengths

The indirect tensile strengths of HVFA concretes containing steel and PP fibres are shown in Figs. 3a and b, respectively. The test results show that the tensile strength of above fibre reinforced concretes decreases with increase in fly ash contents, which is consistent with that observed in compression tests. Results also show that the increase of fibre volume fractions of both fibres increases the tensile strength of the concretes and most significant improvement is observed in the case of steel fibre reinforced HVFA concretes. As expected the tensile strengths of PP fibre reinforced concretes are lower than those of steel fibre reinforced concretes due to lower modulus and tensile strength of the PP fibre than the steel fibre. The fibre end configuration of steel fibres might have also contributed to the better tensile strength of the concretes.

The flexural strengths of HVFA concretes containing steel and PP fibres are shown in Figs. 4a and b, respectively. Similar to tensile strength, the flexural strength of steel fibre reinforced concretes decreases with increase in fly ash contents irrespective of fibre volume fractions. However, in the case of PP fibre system, the concretes containing 50% fly ash deviated from this trend by showing slight increase in flexural strength. In general, the flexural strength of steel fibre reinforced HVFA concretes is higher than that of PP fibre system due to higher modulus and strength of steel fibres as well as hooks at both ends which facilitated the improved bond and better bridging of cracks during failure than that of PP fibre.



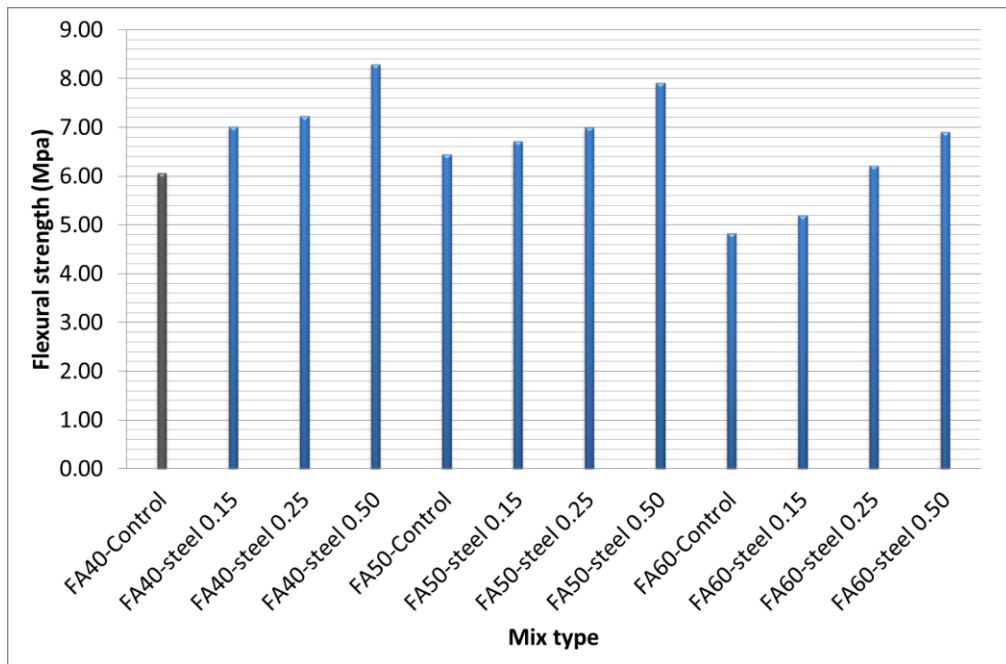
(a) Steel fibre



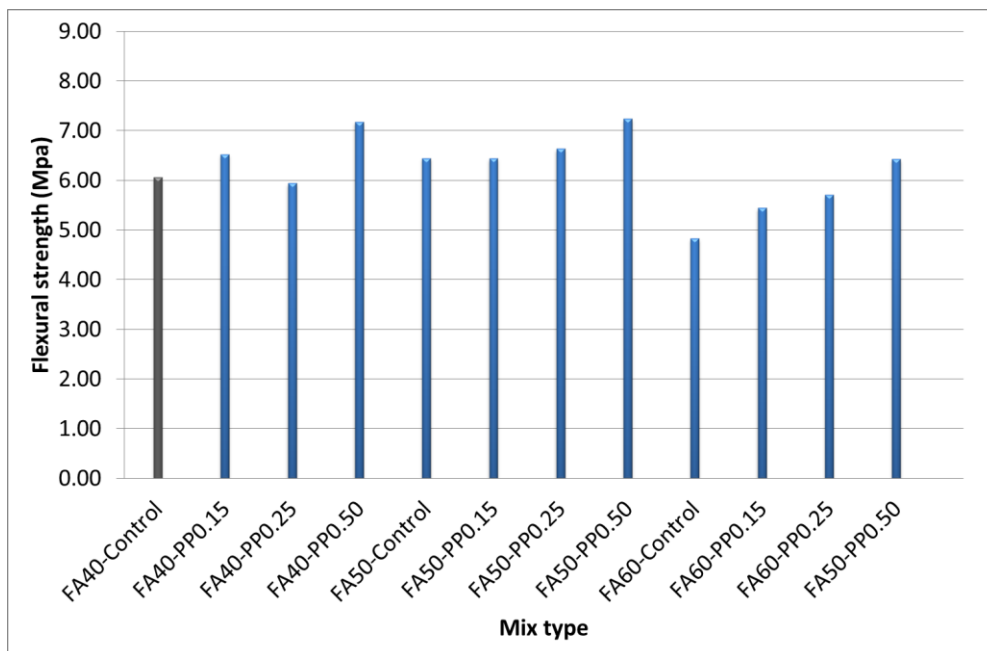
(b) PP fibre

Figure 3. Tensile strengths of steel (a) and PP (b) fibre reinforced HVFA concretes.





(a) Steel fibre



(b) PP fibre

**Figure 4. Flexural strengths of steel (a) and PP (b) fibre reinforced HVFA concretes measured at 28 days.**

### **3.4 Correlation of compressive strength with tensile and flexural strengths**

Based on the strength properties of steel and PP fibre reinforced HVFA concretes evaluated in this study, correlation between tensile and compressive strengths and between flexural and compressive strengths are also established and are shown in Figs. 5-6. Good correlation can be seen between tensile strength and square root of compressive strength at both curing ages in both steel and PP fibre reinforced HVFA concretes. The correlation coefficient of 0.54 can be reasonably used to predict the indirect tensile strength of both steel and PP fibre reinforced HVFA concretes. In the case of flexural strength, the correlation coefficient is 1.48. It should be noted that the above correlation coefficients are based on particular types of fibre e.g. steel and PP only. Moreover, they are valid for steel and PP fibres of certain properties shown in Table 2. In order to obtain a general correlation coefficient, extensive experimental program need to be conducted by having various aspect ratios,

volume fractions, elastic modulus, tensile strengths of fibres, different fly ash contents, etc. Nevertheless, the correlation coefficient of 0.54 for indirect tensile strength of steel and PP fibre reinforced HVFA concretes is reasonable if we compare it with unreinforced concrete e.g. 0.4 in AS 3600 [21] and between 0.42 and 0.56 in ACI 318 [22]. With regard to that for flexural strength, the correlation coefficient is higher than those used for ordinary concrete e.g. between 0.56 and 0.84 in ACI code and 0.6 in Australian code (AS3600). However, it should be noted that the ratio of flexural strength to tensile strength of fibre reinforced cementitious composites can be as high as 3 according to Maalej and Li [23]. The observed ratio of correlation coefficient for flexural and tensile strengths in this study agrees well with Maalej and Li's value.

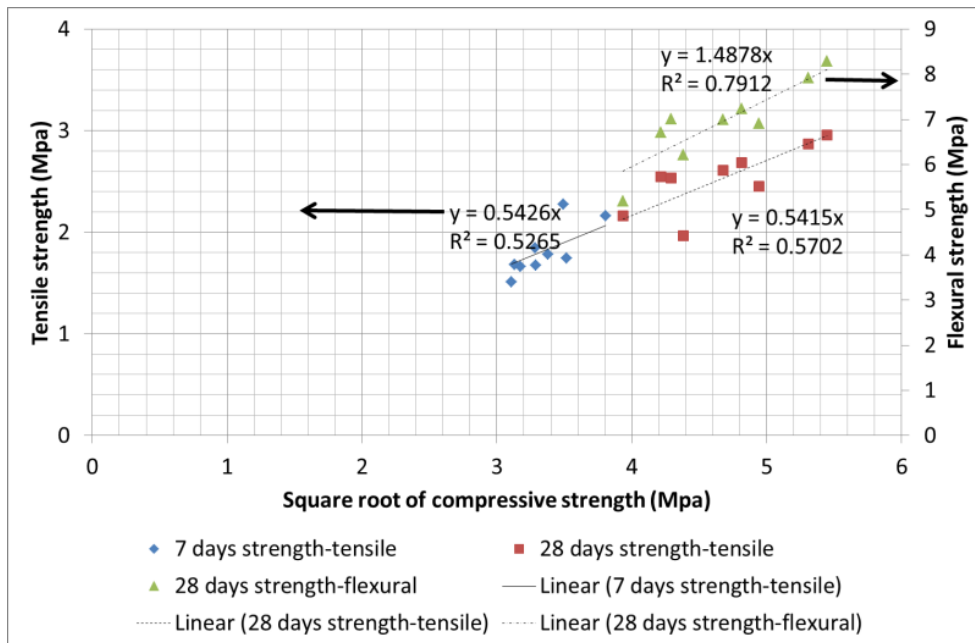


Figure 5. Correlation between tensile and flexural strengths and compressive strengths of steel fibre reinforced HVFA concretes.

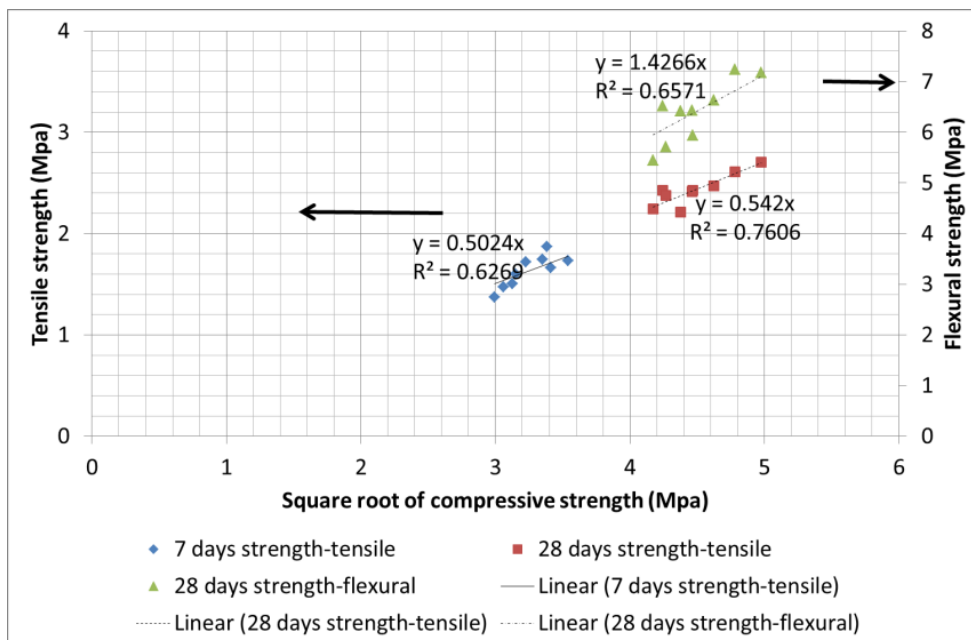


Figure 6. Correlation between tensile and flexural strengths and compressive strengths of PP fibre reinforced HVFA concretes.

## 4. Conclusion

This paper presented the compressive, tensile and flexural strengths of steel and PP fibre reinforced HVFA concretes containing three different fly ash contents of 40%, 50% and 60% by wt. and three different fibre volume fractions of 0.15%, 0.25%, and 0.50%. Based on these mechanical properties at 7 and 28 days the following conclusions can be made:

- The workability of fibre reinforced HVFA concretes decreases with increase in fibre volume fractions irrespective of fly ash contents. The workability of above concretes increases with increase in fly ash contents. It is also observed that the addition of fly ash helps to disperse the fibres in the mix due to its lubricating effect.
- The compressive, tensile and flexural strengths of above concretes increase with increase in volume fraction of fibres irrespective of their types at 28 days. However, at 7 days those increases are marginal presumably due to slow pozzolanic reaction of high contents of fly ash in those concretes. The above strength properties also adversely affected due to increase in fly ash contents.
- Correlations between tensile and compressive strength and between flexural and compressive strength are established in fibre reinforced HVFA concretes. The observed correlation coefficients for tensile and flexural strength of steel and PP fibres reinforced HVFA concretes are also found to be reasonable when compared to ordinary concretes.

## 5. Acknowledgement

Authors gratefully acknowledge BOSFA, Australia for providing the steel and PP fibres and Fly ash Australia for supplying the class F fly ash in this research.

## 6. References

1. Malhotra V.M. and Bilodeau A. (1999) High-volume fly ash system: the concrete solution for sustainable development. In: Mehta PK, editor. Concrete technology for sustainable development in the twenty-first century. New Delhi, India: Cement Manufacturers' Association; p. 43–64.
2. Malhotra VM. (1990) Durability of concrete incorporating high-volume of low calcium (ASTM class F) fly ash. *Cement and Concrete Composite*;12:487–93.
3. Bilodeau, A. and Malhotra, V.M. (1992) Concrete incorporating high-volumes of ASTM class F fly ashes: mechanical properties and resistance to de-icing salt scaling and to chloride ion penetration. In: Malhotra VM, editor. Proceedings of the fourth CANMET/ACI international conference on the use of fly ash, silica fume, slag and natural pozzolans in concrete, Istanbul, Turkey. ACI Special Publication, SP-132. American Concrete Institute; p. 319–49.
4. Langey, W.S., Crette, G.G. and Malhotra V.M. (1992) Strength development and temperature rise in large concrete blocks containing high-volumes of low-calcium (ASTM class F) fly ash. *ACI Materials Journal* ;89:362–8.
5. R. Siddique, (2004) Performance characteristics of high-volume class F fly ash concrete *Cement and Concrete Research*, 34 (3), pp. 487–493
6. Thomas, M. (2007) Optimizing the use of fly ash in concrete. Portland cement associations. [www.cement.org](http://www.cement.org).
7. Kurtz, S. and Balaguru, P. (2000) Post-crack creep of polymeric fiber reinforced concrete in flexure. *Cement and Concrete Research*; 30(2):183–90.
8. Luo, X., Sun, W. and Chan, Y.N. (2000) Characteristics of high performance steel fiber reinforced concrete subject to high velocity impact. *Cement and Concrete Research*;30(6):907–14.
9. Topcu, I.B. and Canbaz, M. (2007) Effect of different fibres on the mechanical properties of concrete containing fly ash, *Construction and building materials*, 21:1486-1491.
10. Atis, C.D. and Karahan, O. (2009) Properties of steel fibre reinforced fly ash concrete, *Construction and building materials*, 23:392-399.
11. V.M.Malhotra, G.G Cartte, and A.Bilodeau, (1994) Mechanical properties and Durability of Polypropylene Fibre Reinforced High-Volume Fly Ash Concrete for Shotcrete Applications, *ACI Materials Journal*, 91(5):478-486.
12. Rohit, M., Patel, I. and Modhera, C.D. (2012) Comparative study on flexural strength of plain and fibre reinforced HVFA concrete by destructive and non destructive techniques. *International journal of engineering and science*, 1(2):42-48.

13. Sahmaran, M. and Yaman, I.O. (2007) Hybrid fibre reinforced self-compacting concrete with a high-volume coarse fly ash. *Construction and building materials*, 21:150-156.
14. Kayali, O. (2004) Effect of high volume fly ash on mechanical properties of fibre reinforced concrete, *Materials and Structures*. 37:318-327.
15. V.C. Li, H. Mihashi, H.C. Wu., (1996) Micro-mechanical model of mechanical response of HPFRCC, in: A.E. Naamam, H.W. Reinhardt (Eds.), *High Performance Fibre Reinforced Cement Composites 2*, E & FN Spon, London, U.K., pp. 43–100.
16. F.U.A. Shaikh, S.W.M. Supit, P.K Sarker, A study on effect of nano silica on compressive strength of high volume fly ash mortars and concretes, *Materials and Design* 60 (2014) 433-442.
17. ASTM C39 (2013) Standard test method for compressive strength of cylindrical concrete specimens, Philadelphia, USA.
18. ASTM C496 (2011) Standard Test Method for Splitting Tensile Strength of Cylindrical Concrete Specimens, Philadelphia, USA.
19. ASTM C1609 (2009) Standard Test Method for Flexural Performance of Fiber-Reinforced Concrete (Using Beam With Third-Point Loading), Philadelphia, USA.
20. Siddique, R. (2003) Properties of concrete incorporating high volume of class F fly ash and san fibres, *Cement and Concrete Research*.
21. AS 3600 (2009) Australian standard for concrete structures.
22. ACI 318 (2011) Building code requirements for structural concrete, USA.
23. Maalej, M. and Li, V.C. (1994) Flexural/tensile strength ratio in engineered cementitious composites, *Journal of materials in civil engineering*, 6(4):513-528.

# Admixtures and Polymers

## Improving the rheology of high strength, very low W/C ratio concrete.

Gary Boon<sup>1</sup> and Tony Thomas<sup>2</sup>

<sup>1</sup>Technology Manager, Sika Australia Pty Ltd

<sup>2</sup>Chief Engineer-Concrete, Boral Concrete.

**Abstract:** The production of high strength concrete provides challenges with respect to the movement and placement of the concrete. High binder contents coupled with low water contents can give rise to concrete that is difficult to pump producing a concrete that can be classed as "sticky". The shear thickening tendency of "sticky" concrete can be measured and overcome by changing the concrete mix design. It is also important to measure and understand the thixotropy to avoid segregation.

The particle interaction and spacing has a large impact on the concrete rheology. This paper looks to evaluate the effect of the binder composition on the concrete rheology. We will show the effect of water content, binder content and composition, and the use of admixtures on the yield stress, viscosity and stress strain curve over a wide range of shear rates. The objective of this paper is to show how the binder and admixtures can be optimised to produce a more useable concrete that is easy to pump that still has the required hardened characteristics.

This paper provides experimental evidence of the role of binder composition and admixtures has on the rheology and therefore the useability of high strength concrete mixes.

**Keywords:** concrete, rheology, high strength, binder

### 1. Introduction

The rheology of concrete has been studied for many decades. There are many terms for describing the rheology of concrete, slump, workability, pumpability, flowability, compactability etc. Many of the test measurements for concrete rely on single point tests, such tests include L-box, V-funnel, slump cone, slump-flow. While fast and readily available, the single data points only provide the technician with limited information. Approximately 60 tests are available to measure various flow properties of concrete with most of these tests giving only a single parameter.<sup>1</sup> A rough way to calculate the workability of the concrete is the slump test and it can be used to prescribe the required workability for pumping, e.g. the concrete should have a slump of between 140-160mm for a pumping height of 30-60m.<sup>2</sup> A more comprehensive way to assess the concrete is to use a rheometer over a wide shear range.

When we change the mix design, the rheology of the concrete will change<sup>3</sup>. When we change the proportioning of the aggregate content, paste volume, we also change the concrete rheology<sup>4</sup>

Changing the powder content in the paste can dramatically affect the concrete rheology<sup>5</sup>.

The introduction of polycarboxylate-ether based admixtures has allowed for the increased use of high strength concrete with high fluidity. Based on the degree of fluidity achieved the concrete technology boundaries have been pushed further allowing for high strength concrete to be pumped vast distances over long working times. Therefore the study of concrete rheology has increased importance as it is how the concrete behaves under varying shear rates that will determine how it can be used in the field.

This paper explores changes in the mix design of high strength concrete using materials readily available in Australia.

How we measure the viscosity of concrete is important due to the torque required to shear the material. If the viscosity measurements are not taken at a steady state then the apparent viscosity at higher shear rates may be overestimated.<sup>6</sup>

### 2. Methodology

A concrete rheometer was utilised for the concrete rheology measurements. The rheometer was built in the Material Physics department of Sika Technology AG, Zurich. The rheometer setup is such that concrete is placed into a steel cylinder with an anti-slip cage and measurements done by rotating a double helical spindle<sup>7</sup>. The resultant shear stress was

measured vs. the applied shear rate. The shear rate was stepped downwards in a logarithmic spacing with the upper limit set to the torque limit of the device down to  $0.01\text{s}^{-1}$ , as in Figure 1.

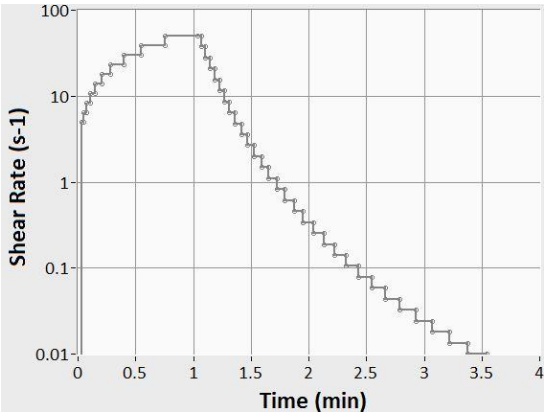


Figure 1. shear profile used in the test

Concrete mixes were prepared with differing mix designs and the same target flow. The flow and T500 (time to reach 500mm diameter) was measured using a standard Abram cone in the upright position, the concrete was then measured in the concrete rheometer using a standard measurement protocol. The concrete was mixed briefly in the rheometer (details of profile) and then the concrete sheared up to the maximum torque the RheoMix could withstand and then sheared back down to  $0.01\text{ s}^{-1}$  in logarithmic steps. The resulting rheogram was then analysed and compared.

The mix design programme is below in Table 1.

Effect of OPC/FA				
	FA-1	FA-2	FA-3	FA-4
	kg/m <sup>3</sup>	kg/m <sup>3</sup>	kg/m <sup>3</sup>	kg/m <sup>3</sup>
Boral 10mm	891	882	872	863
Boral C/Sand	438	434	429	425
Boral F/Sand	160	158	157	155
TOTAL WATER	190	190	190	190
Boral Berrima SL	470	440	415	390
Enviro GGBFS	250	240	225	210
Eraring Ash	0	40	80	120
total binder	720	720	720	720
w/b	0.264	0.264	0.264	0.264

Effect of silica fume			
	SF-1	SF-2	SF-3
	kg/m <sup>3</sup>	kg/m <sup>3</sup>	kg/m <sup>3</sup>
Boral 10mm	891	900	893
Boral C/Sand	438	443	439
Boral F/Sand	160	162	160
TOTAL WATER	190	190	190
Boral Berrima SL	470	460	420
Enviro GGBFS	250	250	230
Eraring Ash	0	0	0
Silica Fume	0	10	70
total binder	720	720	720
w/b	0.264	0.264	0.264

Effect of micro-ash				
MA-1	MA-2	MA-3	MA-4	MA-5

	kg/m <sup>3</sup>	kg/m <sup>3</sup>	kg/m <sup>3</sup>	kg/m <sup>3</sup>	kg/m <sup>3</sup>
Boral 10mm	891	905	894	884	873
Boral C/Sand	438	445	440	435	429
Boral F/Sand	160	162	161	159	157
TOTAL WATER	190	190	190	190	190
Boral Berrima SL	470	460	440	420	405
Enviro GGBFS	250	250	240	230	215
micro ash	0	10	40	70	100
total binder	720	720	720	720	720
w/b	0.264	0.264	0.264	0.264	0.264

Effect of water				
	WC-1	WC-2	WC-3	WC-4
Boral 10mm	891	891	964	1027
Boral C/Sand	438	438	474	505
Boral F/Sand	160	160	173	184
TOTAL WATER	190	200	190	190
Boral Berrima SL	470	470	388	306
Enviro GGBFS	250	250	206	162
total binder	720	720	594	468
w/b	0.264	0.278	0.320	0.406

Table 1: Mix design programme

The methodology was to change the proportions of the cement paste by changing the content of cement and supplementary cementitious materials (SCMs). The proposal was to change the psd of the fines to allow for better movement between fine particles and therefore improved rheology.

### 3. Results

Effect of silica fume

Mix Ref	SP dose (mL/100kg binder)	water (l/m <sup>3</sup> )	w/c	flow (mm)	T500 (s)	Viscosity infinity (Pa.s)	Yield stress (Pa)	shear stress at shear rate			7D UCS*
								0.1s <sup>-1</sup>	1s <sup>-1</sup>	10s <sup>-1</sup>	
FA-1	529	190	0.264	680	6	272.89	213	425	256	2770	87.0
FA-2	400	190	0.264	700	4	291.74	594	991	662	2551	79.5
FA-3	466	190	0.264	680	6	270.58	325	688	344	2508	79.5
FA-4	400	190	0.264	660		624.55	795	1449	875	9800	71.5

\*(200 x100 cylinder) AS1012.9

Effect of micro-ash

Mix Ref	SP dose (mL/100kg binder)	water (l/m <sup>3</sup> )	w/c	flow (mm)	T500 (s)	Viscosity infinity (Pa.s)	Yield stress (Pa)	shear stress at shear rate			7D UCS *
								0.1s <sup>-1</sup>	1s <sup>-1</sup>	10s <sup>-1</sup>	
MA-1	529	190	0.264	680	6	272.89	213	425	256	2770	87.0
MA-2	520	190	0.264	670	5	420.30	652	1507	674	4092	80.0
MA-3	451	190	0.264	670	4	332.27	792	1628	900	2850	75.5
MA-4	420	190	0.264	680	4	328.87	453	852	500	3031	72.5
MA-5	400	190	0.264	690	4	234.55	390	793	412	2045	73.0

Effect of silica fume

Mix Ref	SP dose (mL/100kg binder)	water (l/m <sup>3</sup> )	w/c	flow (mm)	T500 (s)	Viscosity infinity (Pa.s)	Yield stress (Pa)	shear stress at shear rate			7D UCS *
								0.1s <sup>-1</sup>	1s <sup>-1</sup>	10s <sup>-1</sup>	
SF-1	529	190	0.264	680	6	272.89	213	425	256	2770	87.0
SF-2	487	190	0.264	670	7	292.35	225	558	282	3295	79.0
SF-3	683	191	0.265	670	7	695.36	1183	2444	1235	8600	75.0



### Effect of water

Mix Ref	SP dose (mL/100kg binder)	water (l/m <sup>3</sup> )	w/c	flow (mm)	T500 (s)	Viscosity infinity (Pa.s)	Yield stress (Pa)	shear stress at shear rate			
								0.1s <sup>-1</sup>	1s <sup>-1</sup>	10s <sup>-1</sup>	7D UCS *
WC-1	468	190	0.264	690	4	466.96	715	2043	787	4193	80.5
WC-2	460	200	0.278	690	4	289.73	415	1023	346	2730	78.0
WC-3	451	190	0.320	670	3	206.03	903	1327	976	2330	69.0
WC-4	310	190	0.406	600	2	95.51	1230	1698	1266	2110	49.5

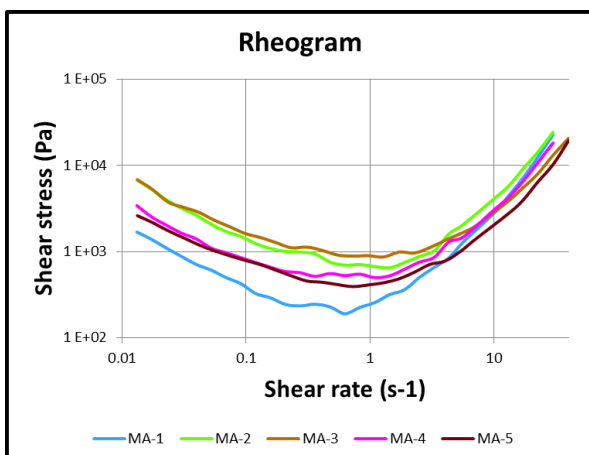
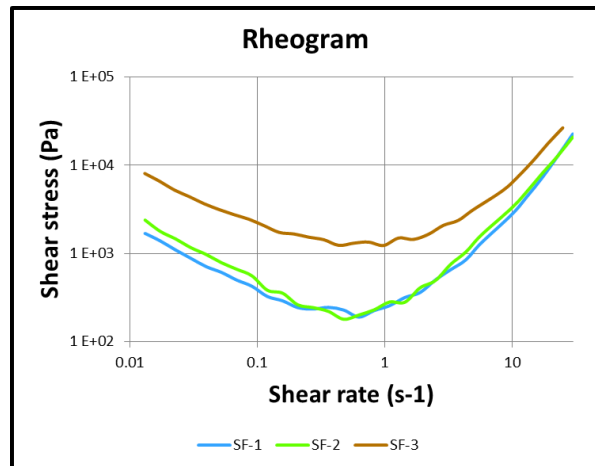
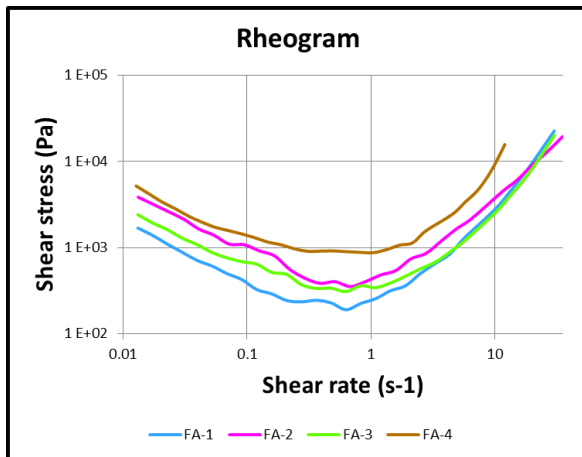
### Effect of Admixture

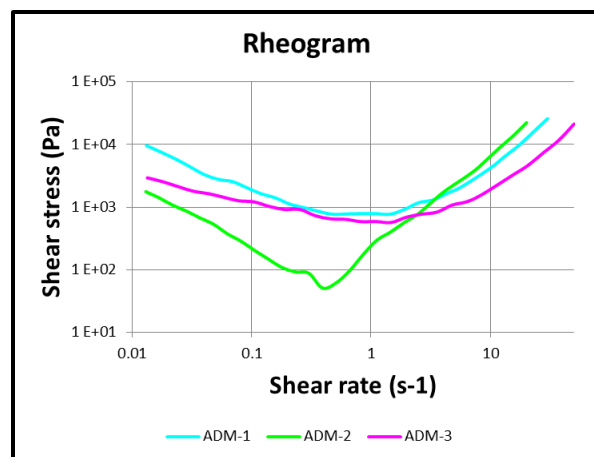
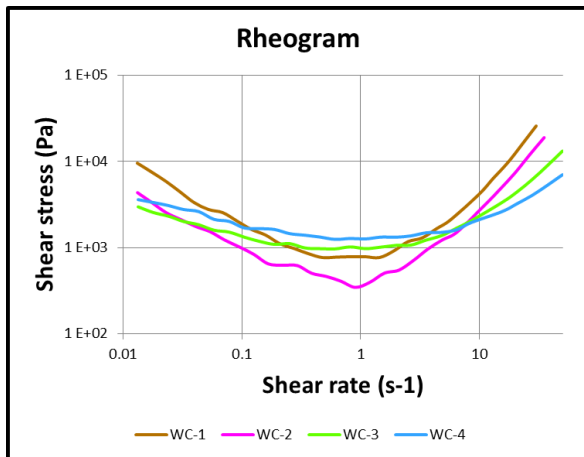
Mix Ref	Admixture dose (mL/100kg binder)	water (l/m <sup>3</sup> )	w/c	flow (mm)	T500 (s)	Viscosity infinity	Yield stress	shear stress at shear rate		
								1s <sup>-1</sup>	1 /s	10 /s
ADM-1	PCE-1 468 PCE-1 758 + VMA	190	0.264	690	4	466.96	715	2043	787	4193
ADM-2	500	190	0.264	690	5	-	74	220	240	6530
ADM-3	PCE-2 803	190	0.264	670	4	224.64	588	1230	590	1940

The rheograms give the continuous curve of shear stress vs. shear rate. We have taken 3 points as comparison being 0.1, 1, 10 s<sup>-1</sup>, which is an estimate of stability, flowability and pumpability. If the shear stress at 0.1 s<sup>-1</sup> is greater than the shear stress at 1 s<sup>-1</sup>, the concrete mix is likely to be stable, i.e. the aggregates will not settle to the bottom of the mix. The greater this difference the more stable the mix will be. If there is no difference or the difference is small, the aggregates will settle to the bottom of the mix and the mix is therefore unstable.

The shear stress at 10s<sup>-1</sup> is indicative if the pumpability with the higher the number, the greater pumping force required to move the material. The viscosity at high shear rates extrapolates to a linear relationship with shear rate, and is termed viscosity infinity.

### Rheograms





## 4. Discussion

The flyash series generally shows that an increased flyash replacement of the OPC gives a concrete with higher yield stress and higher shear stress at  $10\text{s}^{-1}$ . This indicates that the use of this flyash as an OPC replacement in this mix would lead to a less pumpable concrete.

Somewhat similarly, the silica fume series shows that at a low dose of silica fume, little effect is seen on the concrete viscosity, at a higher silica fume dose, a large increase in the shear stress across all shear rates is seen, the concrete is more viscous and requires more force to pump.

The use of micro-classified flyash appears to assist with reducing viscosity but variable results and seems to reduce strength significantly. The addition at  $40\text{kg/m}^3$  dose may be optimum.

Interesting that the use of Silica Fume seemed to increase the viscosity significantly as did higher levels of flyash, whereas micro-classified flyash at low doses significantly increased viscosity and this impact reduced at higher doses.

The water-cement variation series showed, not surprisingly, that increasing the water improves the pumpability of the concrete. There is a reasonable relationship between Viscosity and T500. From the data looks as if a "Viscosity Infinity" under 250 may produce a pumpable concrete. This correlates well with the previous studies showing  $200\text{Pa}\cdot\text{s}$  to give pumpable concrete.<sup>8</sup> From a practical perspective it has been found that a T500 needs to be  $<5$  seconds in order to produce commercially acceptable pumped concrete mixtures.

Overall, the 7 day strength to W/C ratio is fairly normal and so while added strength is achieved at the lower W/C ratio, the higher w/c ratio leads to better fine particle separation and so lower viscosity as expected. Unfortunately this means that very low W/C ratio is required for all of these mix binder combinations to achieve compressive strengths in excess of  $100\text{MPa}$  at 7 days. This along with the findings above underlines the importance of achieving a suitable viscosity of high strength concrete mixes to aid placement.

The admixture test series shows some useful data. The mix ADM-2 is the same as ADM-1, but additional PCE superplasticiser was added and an additional Viscosity Modifying Admixture (VMA) added to bring the initial flow back to the same as ADM-1. What we see is a rather large reduction in yield stress and a much improved concrete visually. The shape of the rheogram is changed significantly with a large dip around  $0.5\text{s}^{-1}$ . The curve increases at very low shear rates ( $0.01\text{s}^{-1}$ ) showing a stable concrete, while the shear stress at higher shear rates remain mostly unchanged indicating no improvement on pumpability of the mix. When the original PCE in ADM-1 is changed to a PCE with different chemistry (ADM-3) a large change is seen in the rheogram. Yield stress is reduced, and the concrete has lower shear stress at high and low shear rates, indicating a potential for improved ability to pump this mix at the target W/B as evidence also from the lower value of "Viscosity Infinity".

## 5. Conclusions

We can see that adjusting the proportioning of the powder in a concrete mix alters the rheological behaviour. Whilst the addition of water gives a flatter broader curve, the challenge is to reduce the water content to achieve the high target strength required. The

use of a VMA combined with a superplasticer allows the concrete technologist to modify the rheological behaviour of the concrete without changing the mix proportions.

<sup>1</sup> Chiara Ferraris, CONCRETE RHEOLOGY: WHAT IS IT AND WHY DO WE NEED IT?, SCC'2005-China: 1st International Symposium on Design, Performance and Use of Self-Consolidating Concrete, RILEM 2005.

<sup>2</sup> Yen Tsong, Tang Chao Wei, Chang Chao Shun, Chen Kuang Hong. Flow behaviour of high strength high-performance concrete. *Cem Concr Compos.* 1999;21:413–24.

<sup>3</sup> Kim Jae Hong, Noemi Nagy, Shah Surendra P. Effect of powder materials on the rheology and formwork pressure of self-consolidating concrete. *Cem Concr Compos* 2012;34:746–53.

<sup>4</sup> Domone PL. Self-compacting concrete: an analysis of 11 years of case studies. *Cem Concr Compos* 2006;28:197–208.

<sup>5</sup> Thixotropic behavior of self compacting concrete with different mineral admixtures M.K. Rahman a,†, M.H. Baluch b, M.A. Malik b

<sup>6</sup> The effect of measuring procedure on the apparent rheological properties of self-compacting concrete Mette R. Geikera\*, Mari Brandla, Lars N. Thranea, Dirch H. Bagerb, Olafur Wallevik

<sup>7</sup> F. Fabbris, W. De Carvalho, D. Lootens, „A Concrete Rheometer: Features and Industrial Applications“, Rheology and processing of Construction Materials – 7th RILEM International Conference on Self-Compacting Concrete and 1st RILEM International Conference on Rheology and Processing of Construction Materials, RILEM 2013.

<sup>8</sup> Ed. Å. Skarendahl and Ö Petersson, Self-Compacting Concrete - State-of-the-Art Report of RILEM TC 174-SCC, RILEM, 2000

# The Effects of Superabsorbent Polymers on the Water Vapour Sorption Properties of Cementitious Materials

D. Snoeck<sup>1,2</sup>, L.F. Velasco<sup>3</sup>, A. Mignon<sup>1,2</sup>, C. Vervaet<sup>4</sup>, S. Van Vlierberghe<sup>2</sup>,  
P. Dubruel<sup>2</sup>, P. Lodewyckx<sup>3</sup>, N. De Belie<sup>1</sup>

<sup>1</sup> Magnel Laboratory for Concrete Research, Ghent University, Belgium

<sup>2</sup> Polymer Chemistry and Biomaterials Group, Ghent University, Belgium

<sup>3</sup> Department of Chemistry, Royal Military Academy, Belgium

<sup>4</sup> Laboratory of Pharmaceutical Technology, Ghent University, Belgium

**Abstract:** Superabsorbent polymers (SAPs) are a new and promising additive used in the building industry. They are mostly used to mitigate autogenous shrinkage. SAPs, however, have various effects on concrete properties and the most important influence is the possible change in microstructure due to internal curing. The microstructure is closely linked to the strength of the material and the microstructure is thus a key property. Dynamic water vapour sorption (DVS) may be used to characterize the change in pore structure of cementitious materials, but the technique is difficult to interpret. In the present paper, DVS measurements were performed to characterize the changes induced by SAPs in the textural and sorption properties of the material. Different models were hereby applied to study pores in the micro- (Dubinin-Radushkevich) and mesopore (Barrett-Joyner-Halenda) range and to better interpret the sorption measurements. The results show that cement pastes with SAPs and without additional water show a slight decrease in the micro- and mesopore range. The results are closely linked to a cement paste with the same effective water-to-cement ratio. Cement pastes with SAPs and with additional water show no significant difference in the micropore range and a slight increase in larger mesopore range. These new findings give insight into the effects of SAPs on the microstructure and strength of cementitious materials.

**Keywords:** Hydrogel, microstructure, water sorption, densification.

## 1. Introduction

Superabsorbent polymers (SAPs) already found their way into the medical and health-care industry due to their high absorption capacity. They are new materials to be used in the concrete industry. The polymers are able to absorb up to 500 times their own weight in fluids and are therefore useful to improve some mortar properties as they take up mixing water and gradually release it towards the cementitious matrix. These improved properties include the mitigation of autogenous shrinkage, the increase in freeze-thaw resistance, the change in rheological properties, self-sealing and self-healing, amongst others [1-4]. However, the release of water results in the formation of macropores, impairing the strength as well. Furthermore, a change in the finer microstructural properties of the material can occur.

Previous research (mercury intrusion porosimetry and (scanning electron) microscopic analysis) already showed that the water release by the SAPs resulted in continued hydration, decreasing the microporosity at later ages, not taking into account the macropores [1]. The amount of smaller capillary pores is decreased due to the filling of existing pores with hydration products and the reduction of initial micro cracks induced by autogenous shrinkage. But overall, the capillary porosity should be the same for mixtures with the same effective water-to-cement ratio (ratio of the mixing water not held by the SAPs over the cement content) [5].

Another (not widely used) technique to study the pore structure is by means of water sorption and moisture transport processes, using the moisture fixation in the concrete pore system. The technique, however, is difficult to interpret but it can give a first impression of the pore microstructure [6-7]. Two models are applied, namely the BJH (Barrett-Joyner-Halenda) method for the mesopore range [8] and the DR (Dubinin-Radushkevich) method for the micropore range [9]. In this research, the pores are classified according to micro- (< 2 nm), meso- (2-50 nm) and macropores (> 50 nm) (originally proposed by Dubinin and subsequently officially adopted by the IUPAC [10]).

In the present study, the effects of superabsorbent polymers, additional water and supplementary materials on the microstructure were investigated using water vapour adsorption isotherms. In this way, knowledge is gained on the effects of the SAPs on the sorption properties, namely the formed microstructure of cementitious materials.

## 2. Materials and Methods

### 2.1 Materials

Cement pastes with a water-to-cement ratio of 0.50, 0.46, 0.41 and 0.35 were made and cast. The cement used was CEM I 52.5 N and the standard used for the mixing procedure was EN 196-1. A varying amount of SAP expressed as mass-% of cement weight (0.5 and 1 m%) and additional water were added on top. Two types of SAP were investigated (both obtained from the company BASF). These include SAP A being a copolymer of acrylamide and sodium acrylate (particle size  $100.0 \pm 21.5 \mu\text{m}$ ), and SAP B, a cross-linked potassium salt polyacrylate (particle size  $477 \pm 53 \mu\text{m}$ ). Both SAPs are bulk-polymerized and consist of irregular crushed particles. All SAPs were vacuum dried in a desiccator with silica gel prior to testing or mixing in the cement paste mixture. The polymers are able to take up  $305.0 \pm 3.7$  and  $283.2 \pm 2.4$  g de-ionized water/g SAP,  $61.0 \pm 1.0$  and  $58.4 \pm 1.7$  g cement filtrate/g SAP and 30.5 and 8.9 g mixing water/g SAP, respectively. The aforementioned swelling characteristics were determined by means of filtration tests [4-5]. Dry SAP particles were added to the cement and were first dry mixed to ensure a homogenous dispersion in the cement. Additionally, supplementary cementitious materials were studied. All raw material characteristics are shown in Table 1.

**Table 1. Chemical composition of CEM I 52.5 N, Class F fly ash and Blast Furnace Slag**

	<i>CEM I 52.5 N</i> <i>mass-%</i>	<i>Class F fly ash</i> <i>mass-%</i>	<i>Blast Furnace Slag</i> <i>mass-%</i>
CaO	63.12	2.47	40.38
SiO <sub>2</sub>	18.73	49.34	34.35
Al <sub>2</sub> O <sub>3</sub>	4.94	24.55	11.36
Fe <sub>2</sub> O <sub>3</sub>	3.99	6.23	0.48
SO <sub>3</sub>	3.07	0.30	1.65
MgO	1.02	1.73	7.57
K <sub>2</sub> O	0.77	3.84	0.37
Na <sub>2</sub> O	0.41	0.52	0.29
Cl <sup>-</sup>	-	-	0.013
S <sup>2-</sup>	-	-	0.77
Mn	-	-	0.165

The different mixtures are shown in Table 2. The letter R states Reference, and is followed by the water-to-cement ratio. The mixtures with SAPs are first described by the type of SAP (A or B), followed by the amount relative to the cement weight (0.5 or 1 m%). If that code ends with an a, additional water was used to compensate for the loss in workability and the uptake of mixing water by the SAPs. The amount was determined by comparing the flow values. The total, effective and additional water-to-binder ratio is given as well. The amount of additional water was added in such a way that an effective water-to-cement ratio of 0.50 was obtained for all SAP mixtures with additional water. Furthermore, mixes with supplementary cementitious materials are described by the type (FA = fly ash; BFS = blast furnace slag) together with their percent replacement of the cement.

### 2.2 Storage conditions and sample preparation

After one day of storage in a relative humidity of  $95 \pm 5\%$  and a temperature of  $20 \pm 2^\circ\text{C}$ , the samples were stored in water at  $20 \pm 2^\circ\text{C}$  for a minimum period of 6 months to ensure a stable formation of the cementitious matrix and to prevent carbonation. After being stored in water for 6 months, the samples were crushed and stored again in demineralized water for a minimum of 1 hour. This ensured the polymers to swell to their full extent. Subsequently, the crushed part was wet-sieved between 500 and 1000  $\mu\text{m}$ . The SAPs were separated from the cementitious material and the paste particles were collected. The best drying technique is the solvent exchange method in isopropanol followed by vacuum drying [7]. The final collected samples were thus stored in isopropanol for one week and vacuum dried for two additional weeks in the presence of soda lime to exclude the effect of contact with carbon dioxide and the effects of carbonation. The soda lime was replaced every day.

**Table 2. Used code for the different studied mixtures, supplementary materials replacement, amount of SAPs and corresponding water-to-binder ratios**

<i>Code</i>	<i>% SCM replacement</i>	<i>m% SAP</i>	<i>(w/b)<sub>add</sub> [-]</i>	<i>(w/b)<sub>tot</sub> [-]</i>	<i>(w/b)<sub>eff</sub> [-]</i>
R0.50	-	-	0	0.5	0.5
R0.46	-	-	0	0.46	0.46
R0.41	-	-	0	0.41	0.41
R0.35	-	-	0	0.35	0.35
A0.5	-	0.5	0	0.5	0.35
A0.5a	-	0.5	0.15	0.65	0.5
A1	-	1	0	0.5	0.2
A1a	-	1	0.30	0.8	0.5
B0.5	-	0.5	0	0.5	0.46
B0.5a	-	0.5	0.04	0.54	0.5
B1	-	1	0	0.5	0.41
B1a	-	1	0.09	0.59	0.5
FA15	15	-	0	0.5	0.5
FA50	50	-	0	0.5	0.5
BFS15	15	-	0	0.5	0.5
BFS50	50	-	0	0.5	0.5
BFS85	85	-	0	0.5	0.5

### 2.3 Water vapour sorption isotherms

The isotherms were determined by means of Dynamic Vapour Sorption (Surface Measurement Systems, London, UK). By measuring the mass change as a function of time with changing relative humidity (RH) of the sample versus an empty reference, sorption isotherms can be calculated while the humidity is regulated by mixing humid and dry nitrogen gases. The temperature was set to 20°C, and the mass criterion to proceed to the next RH step was  $dm/dt < 0.002$  wt%/min. Dried cement pastes were first conditioned at 0% RH inside the DVS equipment followed by an adsorption-desorption cycle. The RH levels at which samples (5–10 mg) were subsequently equilibrated included 0-1-2-5-10-20-30-40-50-60-70-80-90-98% RH [7].

The used models to study the pore structure are the BJH method for mesopores and the DR method for micropores. The BJH method makes use of the Kelvin equation which relates the equilibrium vapour pressure of a curved fluid surface in a pore to the equilibrium pressure of the same fluid on a plane surface [8]. The Kelvin radius is not the actual pore radius because some adsorption occurred on the pore wall prior to condensation. The DR method is based on the change in potential energy between the gas and adsorbed phases, and the characteristic energy of the solid with the Polanyi model [9].

### 2.4 Helium pycnometry

The porosity was determined by means of Helium pycnometry. A sample (4 - 7 g) of cement paste was placed in the measuring cell of the equipment (Accupyc 1330 Pycnometer, Micromeritics, Norcross, Georgia, US). After 10 purges with He-gas the chamber was pressurized to 19.5 psig. The equilibration rate to proceed to the next step was set at 0.005 psig/min. The volume of the sample was determined ten times, and based on the average volume its absolute density was calculated. The true density was determined on bigger samples by means of weighing.

### 2.5 Statistical analysis

A statistical analysis was performed using the program SPSS® in order to compare the obtained results. Multiple averages were compared using an analysis of variance (ANOVA) test with a significance level of 5%. The homogeneity of the variances was controlled with a Levene's test. The post hoc test for data with homogenous variances was a Student-Newman-Keuls test and if no homogenous variances were obtained, a Dunnett's T3 test was used.

### 3. Results

#### 3.1 Water vapour sorption isotherms

Taking into account that water is likely to impair the mechanical properties and durability of concrete structures, water vapour sorption measurements constitute an essential tool when characterizing the properties of cement-bound materials.

The water vapour sorption curves of all studied mixtures are shown in Figure 1. Figure 1a shows all mixtures with SAP A with their respective references. Figure 1b depicts the same for SAP B. Figure 1c gives the mixtures with cement partly replaced by supplementary cementitious materials (FA and BFS).

The shape of the found isotherms provides information about the pore structure of the cement pastes. With increasing relative humidity, first the micropores will adsorb water vapour, so the lower part of the adsorption curve corresponds with the finer pores. Further increasing the relative humidity will cause a filling of the larger pores (the mesopores). The steep increase in mass due to a relative humidity higher than 50% indicates that the cement pastes mainly consist of mesopores.

All isotherms show a pronounced hysteresis loop. This hysteresis can be explained by the occurrence of cavitation or by the presence of ink-bottle pores. These isolate and constrict the larger pores when desorption occurs. The water in the larger pores will only be released when the relative vapour pressure is the one from the smaller pore constricting the larger pore. This leads to the hysteresis found with the water vapour sorption isotherms. The desorption branch will not be used later on to calculate the pore size distribution due to this negative influence. The adsorption branch is more suitable for comparing the different pore size distributions as the mesopores are filled when the relative pressure corresponds to the Kelvin radius of that pore. A larger constricted pore will also be filled at its relative pressure as water can migrate towards these pores through the already filled smaller pores.

The sorption curve is shifted downwards with decreasing water-to-binder ratio. This points to the densification of the cementitious matrix as the cement grains are packed closer together. The hydration products which are then formed cannot grow expansively and will develop a tight cluster and thus a denser matrix [11].

When using SAPs, the curves are also shifted downwards as there is densification as well. The SAPs will hold mixing water during hardening and will only provide the entrained water for internal curing. The matrix is already formed and the water released will cause a densification of the cementitious matrix in between the eventual SAP macropores. This was already found in previous research on the capillary porosity [5]. If additional water was used, the capillary porosity was comparable to the one of the reference mixture with the same effective water-to-binder ratio. Additional water thus not only compensates for the loss in workability but also counteracts the densification and the change in capillary porosity.

The water vapour sorption isotherms of fly ash systems in Figure 1c show the same overall microporosity compared to a pure cementitious matrix. Only, with increasing replacement of cement by fly ash, the amount of larger mesopores seems to increase. This is seen as the steeper rise from a relative humidity of 80% onwards for the FA50 mixture. The FA85 mixture was impossible to make as there is not enough binder available for a stable microstructure during hardening.

The same conclusion can be made considering the blast furnace slag mixtures. The amount of smaller pores seems to be slightly higher compared to the reference mixture. Again, the amount of larger mesopores is higher. The microstructure is denser in the BFS85 mixture, where not all the slag is consumed and part is acting as a filler. The isotherm remains flat but at higher relative humidity, it becomes steeper and a high amount of mesopores can be expected.

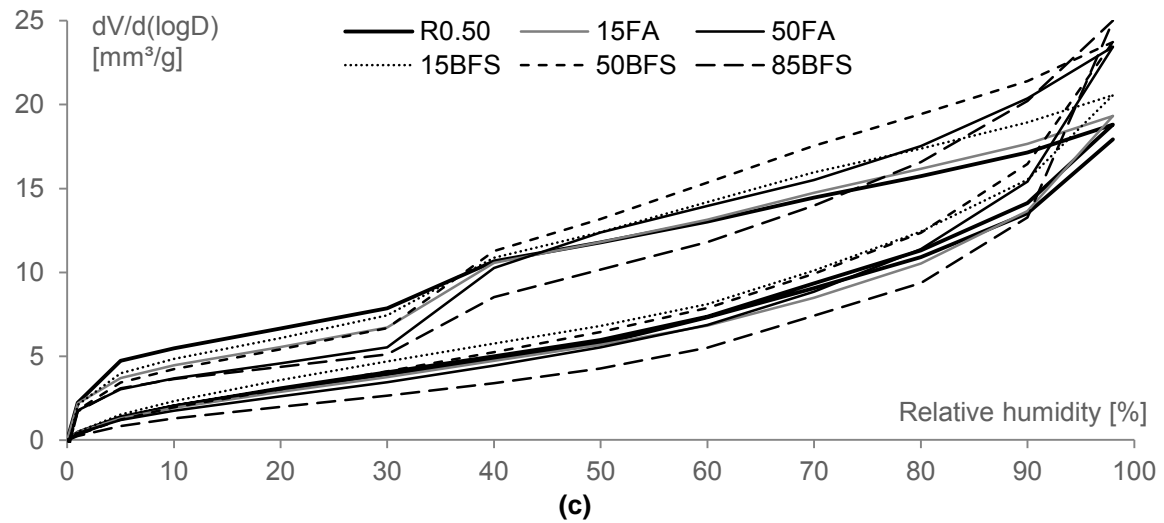
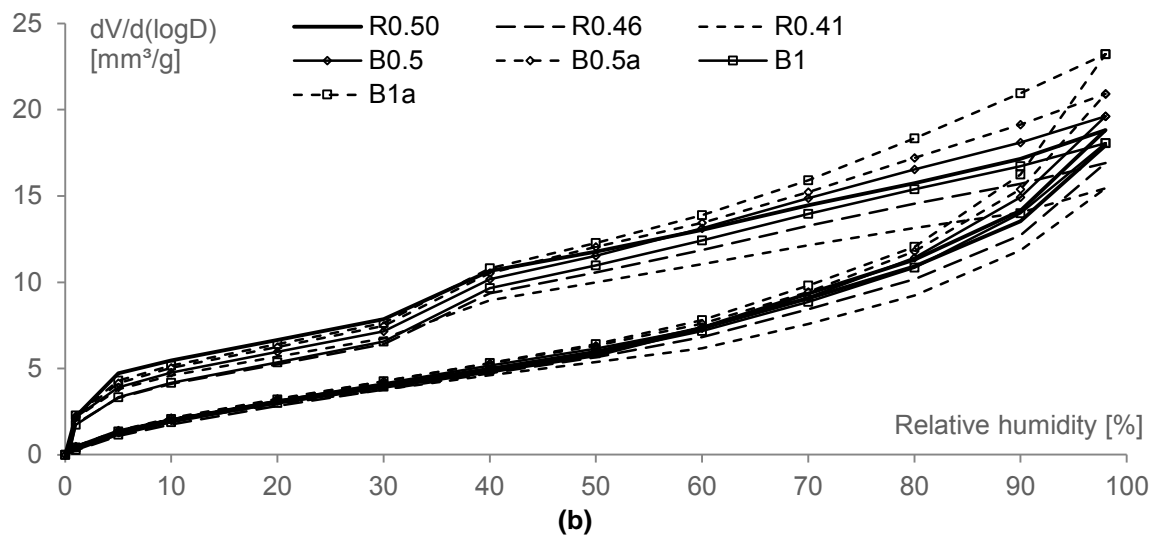
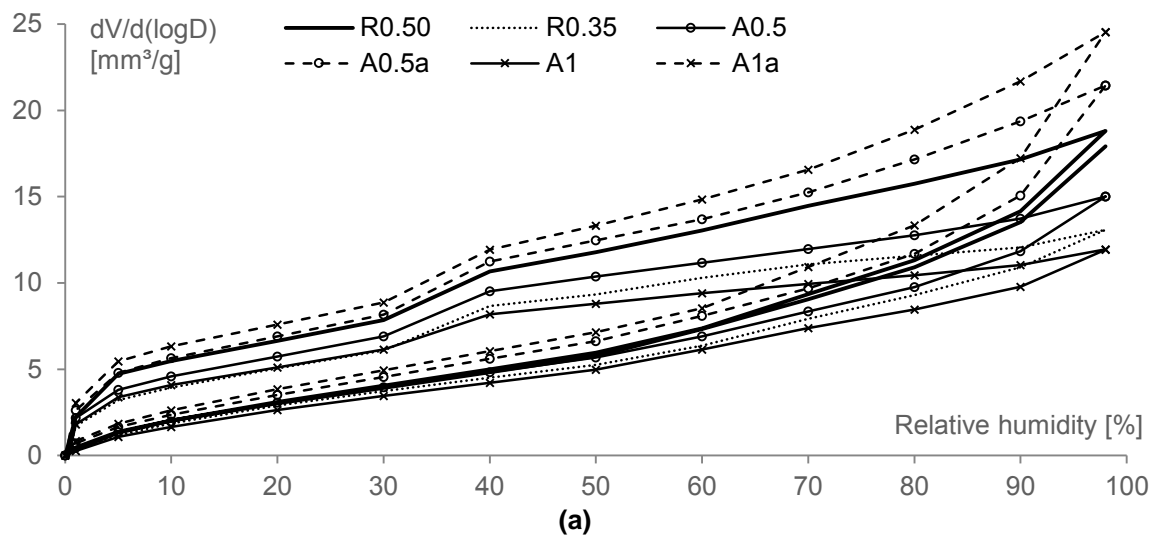


Figure 1. Water vapour sorption isotherms for specimens with or without superabsorbent polymers and additional water (a-b) and with supplementary cementitious materials (c).



### 3.2 Pore size distributions

The trends noticed in the water vapour sorption tests are reflected in the BJH mesopore size distribution calculations (Figure 2). Again, both SAP types are shown in Figure 2a and 2b, respectively, and the supplementary cementitious materials mixtures are shown in Figure 2c. All materials show an anticipated peak of narrow mesopores at 5-6 nm, which is typical for a cementitious material.

The BJH method showed an increased amount of pores with higher water-to-cement ratio. A lower water-to-cement ratio in mixtures leads to a less developed pore network with lower pore volumes, which could be expected.

Again, the densification due to the SAPs is clearly visible. The curves are shifted to the respective mixtures with the same effective water-to-cement ratio. This is for example the case for the A0.5 mixture which should be compared to the R0.35 matrix. The results show that cement pastes with SAPs and without additional water show a slight decrease in the mesopore range compared to the R0.50 reference. If mixtures with SAPs and without additional water are compared to the respective references, it is concluded that there is a slight increase in the larger mesopore range. On the other hand, the narrow mesopore range is similar. If additional water is used, the curves are shifted upwards towards the reference R0.50, which should give a matrix with the same effective water-to-cement ratio. Cement pastes with SAPs and with additional water show no significant difference in the narrow mesopore range and a slight increase in larger mesopore range.

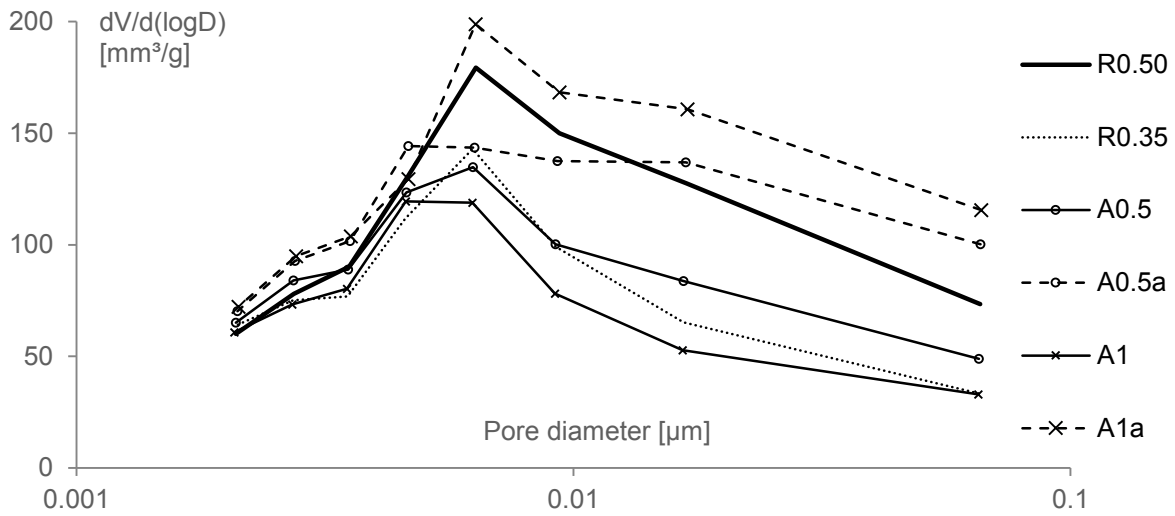
When supplementary cementitious materials like fly ash are present, the portlandite is consumed, producing calcium-silicate-hydrates (C-S-H). They contribute to the formation of the binding phases in the cementitious matrix and thus influence the resulting pore structure. Overall, mixtures with supplementary cementitious materials show more mesopores than a cement paste with the same effective water-to-binder ratio. This could indicate pore densification when the supplementary cementitious materials' reaction causes a change of capillary pores towards gel pores. In case of fly ash, there is a decrease of the narrow mesopores. This is a property which is inherent to a cementitious matrix which is partly replaced by fly ash. For example, at early age, the pozzolanic fly ash accelerates cement hydration in fly ash systems. Then it acts as a substrate for crystal nucleation on which C-S-H phases and calcium hydroxide crystals can form preferentially. The formation of these additional C-S-H phases on the surface of fly ash particles leads to an increase in the amount of bound water relative to the cement content. Hydrates formed by the pozzolanic reaction densify the microstructure.

In blast furnace slag mixture, only a small increase in amount of narrow mesopores is found. However, in the BFS85 mixture, the amount of small mesopores is less. In this mixture, there is not enough portlandite to activate all slag (also partly the case in the BFS50 mixture). The remaining part of the slag is considered to be filler.

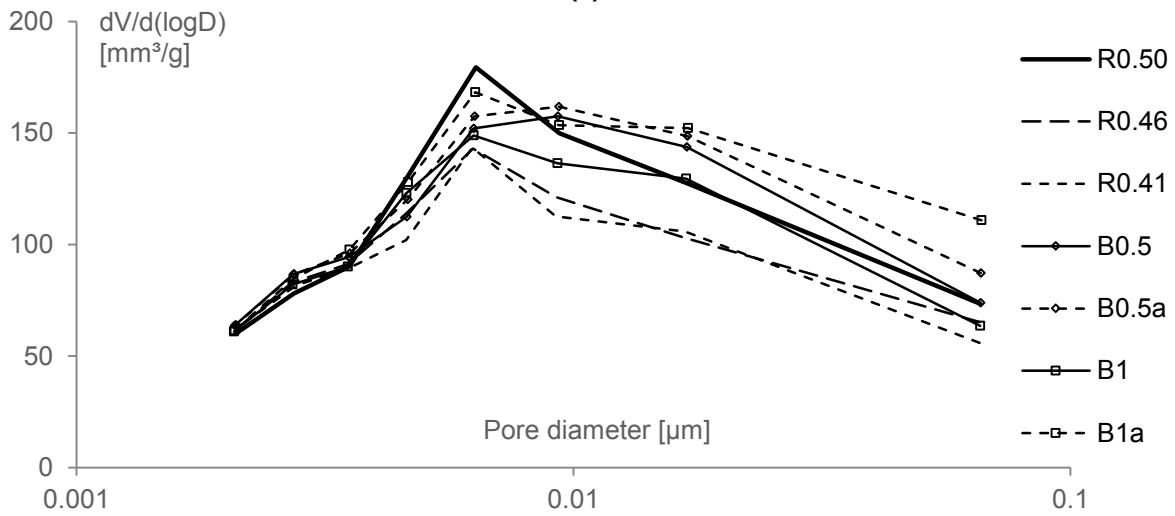
The micropore volumes, as determined by means of the DR method, are given in Table 3. The amount of micropores is lower than the amount of mesopores, which is typical for a cementitious material. In the table it can be seen that the use of SAPs decreases the amount of micropores and that additional water counteracts this phenomenon. However, these tendencies are less pronounced in this kind of pores.

**Table 3. Amount of micropores [ $\text{mm}^3/\text{g}$ ] calculated by means of the DR method**

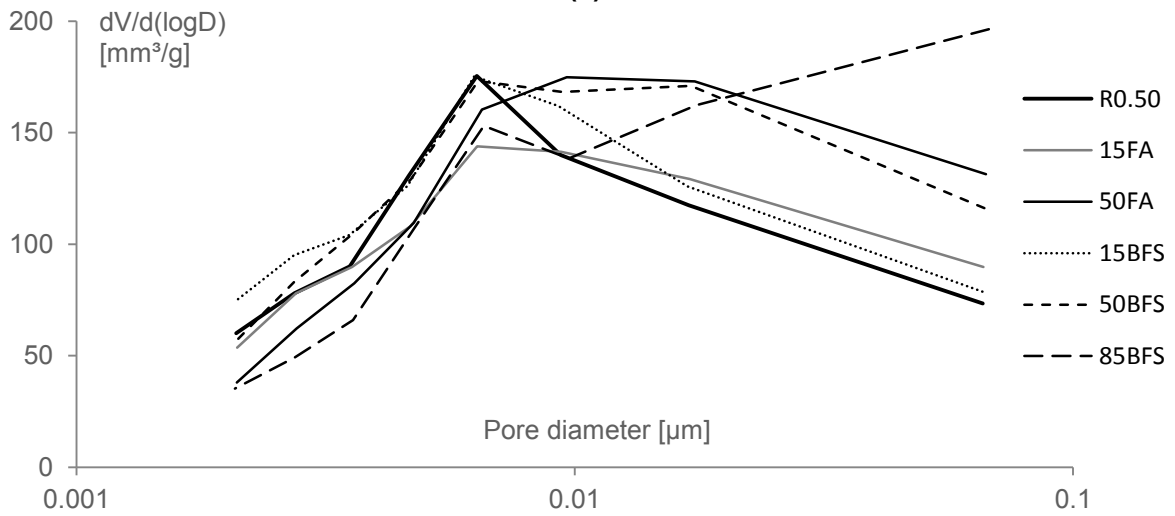
	<i>DR</i> [ $\text{mm}^3/\text{g}$ ]		<i>DR</i> [ $\text{mm}^3/\text{g}$ ]		<i>DR</i> [ $\text{mm}^3/\text{g}$ ]		<i>DR</i> [ $\text{mm}^3/\text{g}$ ]
R0.50	35	A0.5	32	B0.5	33	FA15	29
R0.46	32	A0.5a	34	B0.5a	33	FA50	27
R0.41	30	A1	31	B1	32	BFS15	38
R0.35	29	A1a	36	B1a	34	BFS50	35
						BFS85	22



(a)



(b)

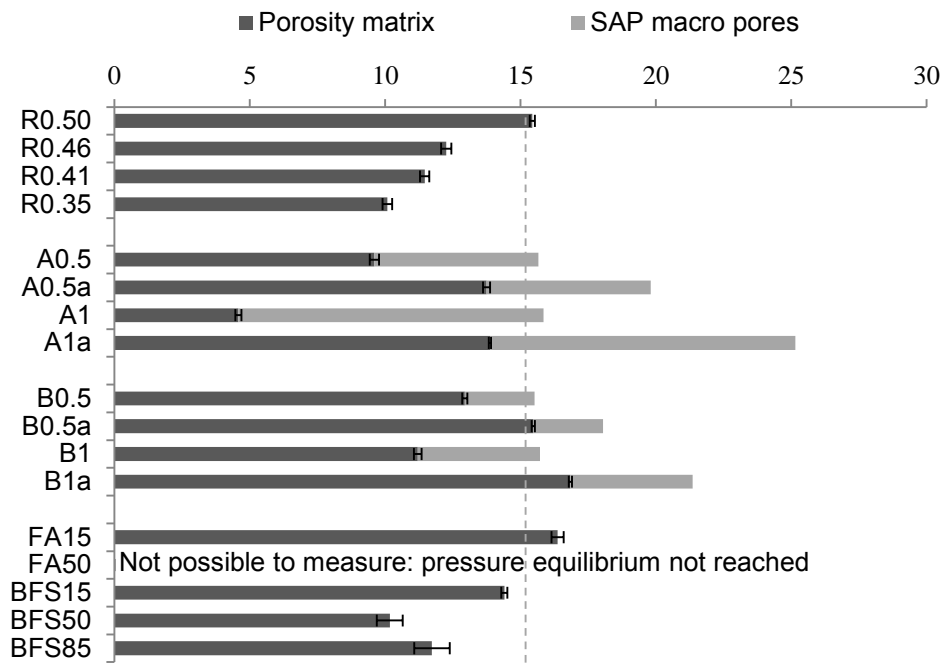


(c)

Figure 2. Calculated microstructure (BJH method) for specimens with or without superabsorbent polymers and additional water (a-b) and with supplementary cementitious materials (c).

### 3.3 Porosity by means of Helium pycnometry

The results found by means of Helium pycnometry are given in Figure 3. In this figure, the theoretical amount of SAPs has been subtracted from the obtained value. The amount of macropores has hereby been theoretically determined by calculating the volume of macropores through the total uptake of water during mixing. As the water is released towards the cementitious matrix, a macropore of approximately the size of the SAP particle and water uptake volume remained. The SAP particles do not adhere to the pore walls.



**Figure 3. Amount of pores and SAP macropores [%] found by means of Helium pycnometry.**

When adding SAPs without additional water, the total amount of pores was approximately the same. This is due to the macropore formation combined with densification. Additional water even increased the total porosity due to less densification. The results show that the mixtures with SAPs and without additional water show the same porosity of the cementitious matrix as a reference specimen with the same effective water-to-cement ratio (thus after subtracting the theoretical amount of SAP macropores). If additional water is added, the total porosity is shifted upwards, but the porosity of the matrix is approximately the same as the R0.50 reference mixture. These results were already found in previous research by means of mercury intrusion porosimetry and a study on the capillary porosity by means of backscattered scanning electron microscopy [5].

The capillary porosity ( $0.2 \mu\text{m} < d < 40 \mu\text{m}$ ) changes when using SAPs. As the cementitious matrix is affected by the internal curing by the SAPs, the microstructure will be different. As the effective water-to-cement ratio is lower in specimens containing SAPs without additional water, densification of the cementitious matrix occurs as the cementitious matrix in between the SAPs is denser. The water released from the SAPs hereby stimulated continued hydration. Additional water should be used to receive a similar capillary porosity of the cementitious matrix. Mixtures with the same effective water-to-cement ratio show nearly the same capillary porosity. The amount of pores is slightly lower in SAP A mixtures and this may be due to the local use of the entrained water by the SAPs filling the already formed pores. This effect is not as clear in SAP B mixtures due to the larger particle size of SAP B compared to SAP A, masking the overall effect.

## 4. Conclusions

Superabsorbent polymers (SAPs) are a new innovative material to use in cementitious materials due to their swelling capacity. This swelling causes the formation of macropores and the release of water by the SAPs causes a densification of the cementitious matrix. This results in a material which acts with a lower effective water-to-cement ratio, unless additional water is provided together with the SAPs.

Dynamic vapour sorption proved to be a useful technique to study the porous properties of cement pastes. The microporous range could be studied by means of the DR theory and the mesoporous range by means of the BJH method.

Use of SAPs thus leads to a denser matrix as if the water-to-cement ratio would be lowered. Additional water partly counteracts the densification and results in a material with the same global matrix and properties. The amount of mesopores of mixtures with the same effective water-to-cement ratio is slightly higher in mixtures with SAPs with or without additional water.

## 5. Acknowledgement

As a Research Assistant of the Research Foundation-Flanders (FWO-Vlaanderen), D. Snoeck wants to thank the foundation for the financial support (11D7413N). The authors also want to thank the Research Foundation-Flanders for funding the project entitled 'Effect of Tunable Hydrogels on Concrete Microstructure, Moisture Properties, Sealing and Self-Healing of Cracks' (3G019012). The authors want to thank Dr. G. Herth from BASF for providing SAP A and SAP B.

## 6. References

1. Technical Committee 225-SAP, "Application of Superabsorbent Polymers (SAP) in Concrete Construction", RILEM State-of-the-Art Report, 2012.
2. Jensen, O.M., Hansen, P.F., "Water-entrained cement-based materials I. Principles and theoretical background", Cement and Concrete Research, 31, 2001, pp 647-654.
3. Snoeck, D., Steuperaert, S. et al., "Visualization of water penetration in cementitious materials with superabsorbent polymers by means of neutron radiography", Cement and Concrete Research, 42, 2012, pp 1113-1121.
4. Snoeck, D., Van Tittelboom, K. et al., "Self-healing cementitious materials by the combination of microfibres and superabsorbent polymers", Journal of Intelligent Material Systems and Structures, 25, 2014, pp 13-24.
5. Snoeck, D., Schaubroeck, D. et al., "Effect of high amounts of superabsorbent polymers and additional water on the workability, microstructure and strength of mortars with a water-to-cement ratio of 0.50", Construction and Building Materials, 72, 2014, pp 148-157.
6. Baroghel-Bouny, V., "Water vapour sorption experiments on hardened cementitious materials - Part I: Essential tool for analysis of hygral behaviour and its relation to pore structure", Cement and Concrete Research, 37, 2007, pp 414-437.
7. Snoeck, D., Velasco, L.F. et al., "The influence of different drying techniques on the water sorption properties of cement-based materials", Cement and Concrete Research, 64, 2014, pp 54-62.
8. Barrett, E.P., Joyner, L.G. et al., "The determination of pore volume and area distributions in porous substances. I - computations from nitrogen isotherms", Journal of the American Chemical Society, 73, 1951, pp 373-380.
9. Dubinin, M.M., "Physical adsorption of gases and vapors in micropores", Progress in Surface and Membrane Science, 9, 1975, pp 1-70.
10. IUPAC, "Manual of Symbols and Terminology, Appendix 2, Pt.1, Colloid and Surface Chemistry", Pure Applied Chemistry, 31, 1972, pp 578-680.
11. Juenger, M.G.C, Jennings, H.M., "The use of nitrogen adsorption to assess the microstructure of cement paste", Cement and Concrete Research, 31, 2001, pp 883-892.

# Benefits of Water-Resisting Admixtures to Watertight Concrete

Mohammadreza Hassani<sup>1</sup>, Kirk Vessalas<sup>2</sup>, Daksh Baweja<sup>3</sup>, Zoe Schmidt<sup>4</sup>

<sup>1</sup>PhD Candidate in Civil Engineering, The University of Technology, Sydney

<sup>2</sup>Lecturer of Civil Engineering, The University of Technology, Sydney

<sup>3</sup>Associate Professor of Civil Engineering, The University of Technology, Sydney

<sup>4</sup>National Technical Manager, Sika Australia Pty. Ltd.

**Abstract:** An experimental investigation was carried out to study the effectiveness of using hydrophobic poreblockers and crystalline admixtures to reduce the absorption, permeability, and volume of permeable voids in concretes incorporating different water-to-binder ratios (W/Bs) and binder types covering GP cement, fly ash and slag. The main prerequisite for a low permeable concrete is a dense and durable concrete matrix. This is primarily achieved by lowering the W/B of the concrete, which also correlates with higher compressive strength. Employing water-resisting admixtures in concrete can be another effective means of lowering water penetration into concrete. The use of such admixtures provides a safety margin in design, particularly where relatively high W/B concretes are specified for use. In this study, a factorial analysis was carried out to rank the effect of influencing variables such as W/B, binder type and chemical admixtures on the performance of concrete. Results indicate that water-resisting admixtures are highly effective in reducing water penetration and their effect is more pronounced in low-quality concrete having high W/Bs. The results also demonstrate that such admixtures are beneficial when used in lower W/B concretes but to a lesser degree.

**Keywords:** Water-resisting admixtures, watertight concrete, crystalline admixtures, strength, durability.

## 1. Introduction

The watertightness of an in-service concrete structure should be assessed by evaluating the properties that can cause loss of water by leakage or absorption. The main sources of water loss are cracks, joints, construction defects, and permeation through concrete matrix (1). Cracks may be caused by factors such as applied tensile stresses, restrained shrinkage, and temperature-induced expansion and contraction. Unplanned joint movements in concrete elements due to shrinkage and restraint may also lead to water leakage. Honeycombing and segregation of concrete (construction defects) are the other sources of potential leakage. However, water may also permeate through uncracked concrete by different mass transport mechanisms including adsorption, diffusion, capillary absorption, and permeability (2). Concrete cannot be completely impermeable (1), but its permeation capacity varies according to the specific properties of constituents used in the concrete as well as employed mix design that are explored in this paper.

The penetration of water through uncracked concrete is influenced by different factors. Olivier et al. (3) classified these factors into three categories, namely aggregate porosity, matrix porosity, and transition zone porosity. Hearn and Figg (4) indicated that aggregates are, by comparison, effectively impervious. When the factors controlling the matrix and transition zone porosities are considered, two factors affecting both aspects are the water-to-cement ratio (W/C) and addition of supplementary cementitious materials (SCMs), showing their importance in achieving a watertight concrete (3). Studies by Powers et al. (5) showed that the permeability of cement paste is reduced as the W/C decreases. In terms of SCMs, it is difficult to gain a clear understanding of the effect of mineral additions on permeability due to the very varied results in the literature (3). However, lower permeability of three orders of magnitude can be achieved by adding natural pozzolans, fly ash or slag to the cement paste (3). In addition, curing (method and duration) plays an important role in achieving lower permeabilities. It is believed that the reaction of FA ceases in relative humidities below 80% (6). Thus, continuous moist curing is required when FA is used in concrete (particularly in early ages). Experimental investigations carried out by Thomas showed that the concretes with SCMs achieve parity with control concretes (100% GP) sometime between 28 and 91 days. This shows the significance of long term curing and testing of concretes with SCMs.

Currently, water-resisting admixtures are also widely used to improve the watertightness and durability of concrete. These admixtures are mainly utilised to reduce the porosity in the matrix and transition zone, in addition to blocking continuous capillary pores. AS 1478.1-2000 refers to these materials as permeability-reducing admixtures. ACI 212.3R.10 (7) subdivides them into admixtures for concrete exposed to hydrostatic (PRAH) and nonhydrostatic (PRAN) conditions. Since the permeability of concrete is defined as the flow rate under hydraulic pressure, the use of permeability-reducing admixture for nonhydrostatic condition seems to be technically invalid (8).

Water-resisting admixtures for hydrostatic conditions are crystalline admixtures, which are claimed to be beneficial in accelerating the autogenous healing of concrete and blocking capillary pores and cracks up to 0.4 mm (8). These admixtures are primarily developed for use in concrete members exposed to hydrostatic pressure, such as members in tunnels and water reservoirs. In such cases, the hydrophilic crystalline chemicals react with the cement and water to increase the density of the calcium silicate hydrate (C-S-H) and generate the pore-blocking deposits. Alternatively, water-resisting admixtures for non-hydrostatic conditions (PRANs) are recommended to be adopted in any application with a head pressure of up to 4 m (9) and even up to 14 m (10), including applications such as roof slabs and concrete pavements. These admixtures contain water repellent chemicals including various soaps, oils, and long chain fatty acid derivatives. When they are added to the concrete mix, the insoluble stearate created by the reaction between the admixture and lime forms a thin hydrophobic layer on the walls of the pores and voids in the concrete matrix, leading to higher contact angles to water (8).

Researchers have reported various results when water-resisting admixtures have been used in concrete mixes (8). Experimental investigations by Dao et al. (11), Justnes (12), Rixom and Mailvaganam (10), Trinder et al. (13) and Yodmalai et al. (14) revealed improvements in the reduction of permeation capacity. In contrast, Roberts and Adderson (15) reported significant variability in the performance of hydrophobic pore blockers, with only 4 out of 9 admixtures tested showing decreasing effects on water ingress. Moreover, in an experimental study by Dao et al. (11), a tested crystalline admixture had almost no noticeable effect on the permeation capacity of concrete.

Considering the debated performance of water-resisting admixtures and the rapidly increasing demand for such admixtures in the construction industry, this paper conducts a comprehensive experimental and numerical investigation into the factors influencing the watertightness of concrete. The effects of varying W/B, binder type, the addition of water-resisting admixtures and curing are examined and compared. For this purpose, concrete mixes with three different W/Bs (0.40, 0.50 and 0.60) and three different binder types, namely general purpose cement (GP), fly ash (FA), and ground granulated blast furnace slag (GGBFS) were selected to match commercially available mix designs in Australia. Furthermore, two different water-resisting admixtures were introduced to the mixes and their performance was assessed against the control mixes devoid of such additives. To obtain sufficient data regarding the porosity of the concrete matrix as well as its mass transport mechanisms, different test methods have been employed for measuring the volume of permeable voids, absorption and permeability of concrete. Results were analysed by factorial analysis (see Section 2) to rank the importance of influencing factors as well as the interactions between these factors. Section 3 provides research methodology of the experimental and numerical studies adopted in this study. The results and related discussions are presented in Section 4.

## **2. Factorial analysis**

A series of factorial analyses of variance (ANOVA) was conducted to evaluate the importance of influencing factors on the watertightness of concrete. Factorial analysis is a statistical technique that assesses the effects of several independent variables and their interaction effects on a single dependent response (16). The use of this technique in the present study had the advantage of separating the main effects of mix parameters (W/B, binder type and the addition of chemical admixture) and their interaction on any measured property (16). The basic approach for the factorial analysis of variance is to break down the observed variance in a particular response to components attributable to different sources of variation (main effects) and to test the significance of each variance. To test the significance of each factor the F-static test is used, in which the ratio of the mean square of the variable to the error mean square is generally determined and compared with the percentile from standard tables for a level of significance decided by the experimenter (17). Factorial analysis is also a useful technique for determining the significance of the interaction between factors. An interaction between factors occurs when the change in response from the low level to the high level of one factor is not the same as the change in response at the same two levels of a second factor (17). That is, the effect of one factor is dependent upon a second factor. For instance, factorial analysis can reveal whether the effect of water-resisting admixtures in reducing permeation capacity is dependent on the W/B of the mix.

## **3. Experimental procedure**

The aim of the experimental investigation in this study was to evaluate the water penetration characteristics of the concrete specimens with different W/B, binder types, and water-resisting chemical admixtures, and rank the significance of these three factors in achieving a watertight

concrete solution. For this purpose, 45 concrete mixes were prepared and sampled with W/Bs of 0.40, 0.50 and 0.60. These mixes contained three different binder types: 100% GP, GP:FA (75:25) and GP:GGBFS (60:40). Two types of water-resisting admixtures were added to the mixes in order to evaluate their performance against the control mixes (mixes devoid of water-resisting admixtures). For reproducibility in workability, the dosage of standard water reducer was varied in the mixes to achieve the target slump of  $100 \pm 20$  mm. The dosages and mixing sequences of the admixtures conformed to the respective manufacturers' technical information. Table 1 summarises the mix designs and the levels of the investigated variables. Moreover, the effect of curing was studied by changing the curing condition of samples (with W/B of 0.50 and no water-resisting admixture) from 28-days moist-curing to 7-days moist-curing followed by 21-days air-curing. Concrete samples were moist cured in lime-saturated water tanks, whilst air-curing was carried out in laboratory with ambient temperature of approximately  $20 \pm 3^\circ\text{C}$  and relative humidity of 70%

**Table 1. Summary of mix designs and levels of variables.**

Mix design variable	Case 1	Case 2	Case 3
Target slump	100±20 mm	100±20 mm	100±20 mm
W/B	0.40	0.50	0.60
Binder content	450	350	284
Binder Type (3 levels)	GP GP/FA (75:25) GP/GGBFS(60:40)	GP GP/FA (75:25) GP/GGBFS(60:40)	GP GP/FA (75:25) GP/GGBFS(60:40)
Water content	180	175	170
Water-resisting admixture (3 levels)	None (control) HP CP	None (control) HP CP	None (control) HP CP

The raw materials used in the concrete mixes were:

- General purpose Portland cement conforming to AS 3972-2010
- Fly ash (FA) conforming to AS 3582.1-1998
- Ground granulated blast furnace slag (GGBFS) conforming to AS 3582.2-2001
- Coarse aggregate with relative density of  $2700 \text{ kg/m}^3$
- Fine aggregate with relative density of  $2650 \text{ kg/m}^3$
- Chemical admixtures conforming to AS 1478.1-2000
- Potable water

The chemical admixtures investigated in this study were a hydrophobic pore blocker (HP) and a crystalline admixture (CP). HP is a liquid hydrophobic poreblocker, which consists of active components. These active components form non-soluble materials throughout the pore and capillary structure of the concrete, sealing the concrete against penetration of water and other liquids. HP is classified as 'water-repelling substance' as per Australian Standard AS 1478.1-2000. CP is a powdered crystalline admixture which is mostly used in hydrostatic conditions to improve water impermeability and self-healing properties of the concrete. CP is classified as a 'special purpose chemical admixture' as per Australian Standard AS 1478.1-2000.

### 3.1 Test methods

The watertightness of concrete was assessed by different test methods to establish its water penetration characteristics. The types of tests adopted in this study included evaluating the pore structure of concrete, permeability of concrete under hydrostatic conditions, and absorption rate of concrete under non-hydrostatic conditions. To assess pore structure, the apparent volume of permeable voids (AVPV) was measured in accordance with AS 1012.21:1999. In this test method, two standard cylinders (100 mm x 200 mm) were cured for 28 days in lime-saturated water and cut into 4 discs to perform the test in accordance with the standard test method requirements.

The permeability of the concrete subjected to water pressure (500 kPa) was tested in accordance with BS EN 12390-8:2009. Three cubes (150 mm x 150 mm x 150 mm) were cured for 28 days in lime-saturated water and subsequently pressurised for 72 hours. The water penetration depth was determined visually at the termination of the test by means of the application of methylene blue dye on the wet surface. Methylene blue was used to improve the accuracy of readings.

The absorption rate of the concrete in the absence of hydrostatic pressure was measured in accordance with ASTM C1585-11. Two standard cylinders (100 mm x 200 mm) were cured in lime-saturated water for 28 days and cut into 4 discs. In accordance with ASTM C1585-11, the test specimens were placed in an environmental chamber at a temperature of  $50 \pm 2^\circ\text{C}$  and relative humidity of  $80 \pm 3\%$  for 3 days. Then, each disc was placed in a sealable container and stored at  $23 \pm 2^\circ\text{C}$  for 15 days. The initial absorption rates were determined for each disc in accordance with ASTM C1585-11.

In addition to the aforementioned tests, compressive strength testing was carried out on cylinder samples at 28 days curing in lime-saturated water in accordance with AS 1012.9:1999.

### 3.2 Data analysis methodology

To analyse the data and rank the mix design factors influencing watertightness of the concrete, a series of full factorial analyses was performed. In these analyses, three factors, namely W/B, binder type and water-resisting admixture were considered as the variables. Table 2 shows the factorial experiment designs and the levels of variables. Main and interaction effects were considered to be significant when their corresponding confidence level was 95% or higher (17).

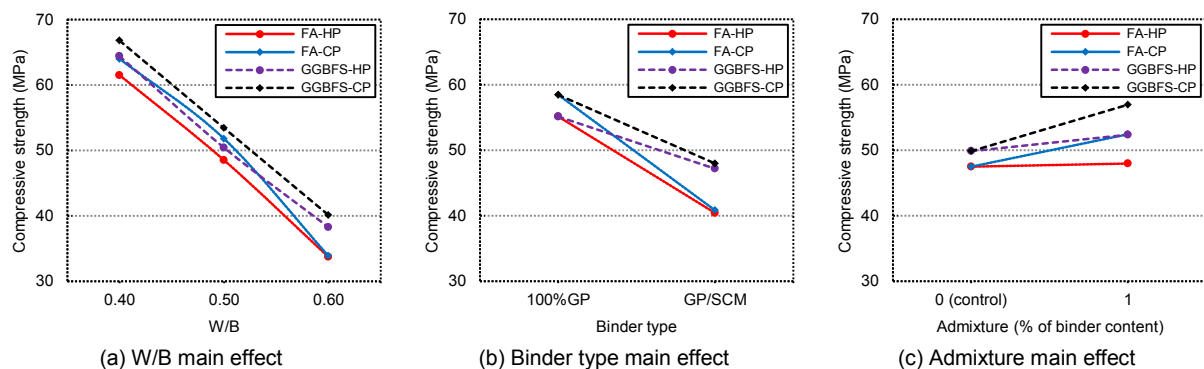
**Table 2. Factorial experiment design.**

Independent variable	Factorial experiment design for mixes with GP/FA		Factorial experiment design for mixes with GP/GGBFS	
	No. of levels	Nature of each level	No. of levels	Nature of each level
SCM	2	0% (control) 25%	2	0% (control) 40%
W/B	3	0.40 0.50 0.60	3	0.40 0.50 0.60
Water-resisting admixture	2	0% 1%	2	0% 1%

## 4. Results and discussion

### 4.1 Effect of factors on compressive strength

The plots shown in Figure 1 suggest that decreasing the W/B from 0.6 to 0.4 had the greatest effect on the outcome of compressive strength when compared to the effects of binder type and the addition of water-resisting admixtures (70% compared to 30% and 10%). Figure 1(b) shows that the addition of SCMs including FA and GGBFS decreased the compressive strength (30%). This decrease may be attributable to the slower hydration rate of SCMs given at 28 days curing (6). The addition of hydrophobic pore blockers had a minor effect on compressive strength whereas crystalline admixtures increased the strength (10%). This effect may be attributable to the formation of new C-S-H layers in the concrete matrix due to crystallisation of hydrophilic polymers (8).



**Figure 1. Effect (main) of factors on compressive strength.**



#### 4.2 Effect of factors on AVPV

Comparison of the slopes of the graphs in Figure 2 reveals that the addition of SCMs into concrete had the most significant effect on AVPV. The addition of FA and GGBFS increased the AVPV significantly (15%). As with the strength data, this may be attributable to the slower hydration rate of concretes incorporating SCMs and the presence of higher porosity in the concrete matrix at 28-days. This finding suggests that the performance of SCMs should be evaluated by long-term testing (up to 91 days). In addition, curing (quality and duration) is of more importance when SCMs are used compared to the concretes with 100% GP (7). Furthermore, the inclusion of admixtures together with GGBFS in the mixes resulted in lower AVPV (Figure 2(c)). This effect may be due to the differences in pore structure of the concretes with GGBFS compared to the concretes with FA and the capability of the admixtures in blocking particular pore sizes (12).

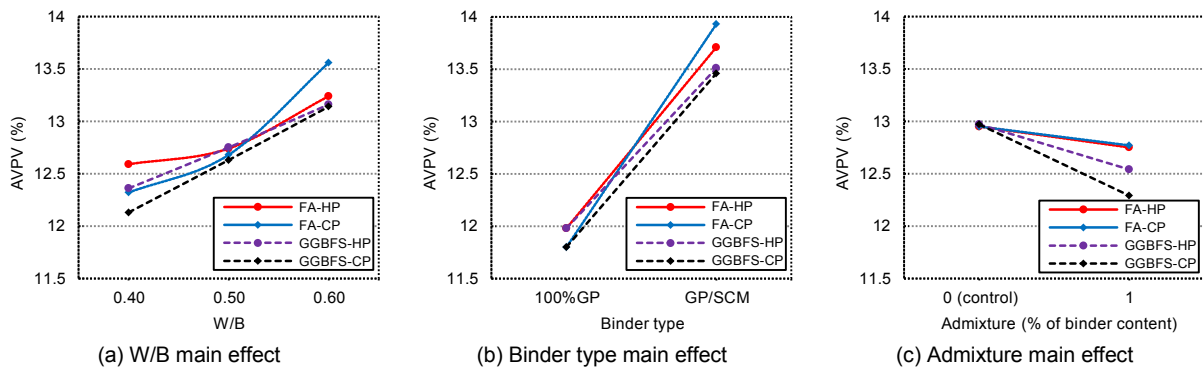


Figure 2. Effect (main) of factors on AVPV.

#### 4.3 Effect of factors on water penetration depth

Figure 3 shows the main effect of factors on permeability measured by the water penetration depth. Alteration of the W/B of the concrete had the most considerable effect on permeability. This effect was more pronounced for W/Bs ranging 0.50 to 0.60 than for W/Bs ranging from 0.40 to 0.50, which is similar to the results reported by Powers et al. (5); which indicated that the permeability increased at a much greater rate beyond a W/B of 0.50. Furthermore, the addition of FA increased the permeability (40%) whereas the addition of GGBFS decreased the same parameter significantly (65%). This finding may be attributable to the discontinuity of the capillary pores in concretes with GGBFS due to the finer particle size of GGBFS at 28 days as well as its higher CaO content, which gives cementitious properties to the binder (18). As with the AVPV data, water-resisting admixtures were more beneficial when used in concretes incorporating GGBFS. Similar performance was found for both hydrophobic pore blockers and crystalline admixture. This observation suggests that the hydrophobic pore blockers can also be used in hydrostatic conditions.

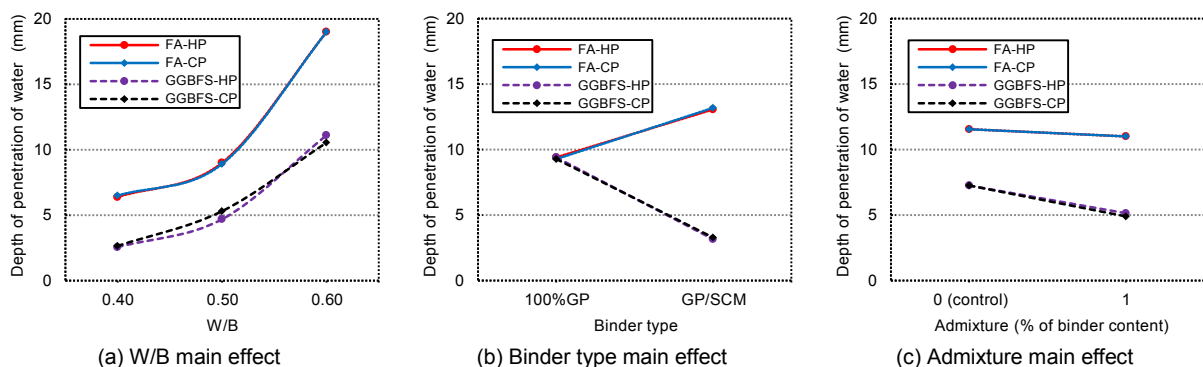


Figure 3. Effect (main) of factors on water penetration depth (permeability).

#### 4.4 Effect of factors on sorptivity

Sorptivity results shown in Figure 4 support the previous findings discussed in Sections 4.3. Comparison of the slopes shows that W/B and binder type had a more pronounced effect on reducing the absorption rate of the concrete (35% and 30% compared to 20% for water-resisting admixtures).

This finding demonstrates the significance of proper mix design in achieving a watertight system. The results also indicate that the behaviour of concrete in a non-hydrostatic condition is reasonably similar to its behaviour in a hydrostatic condition. However, the crystalline admixture was more effective than the hydrophobic pore blocker in reducing sorptivity (25% compared to 10%). This trend was apparent in mixes with FA as well as GGBFS.

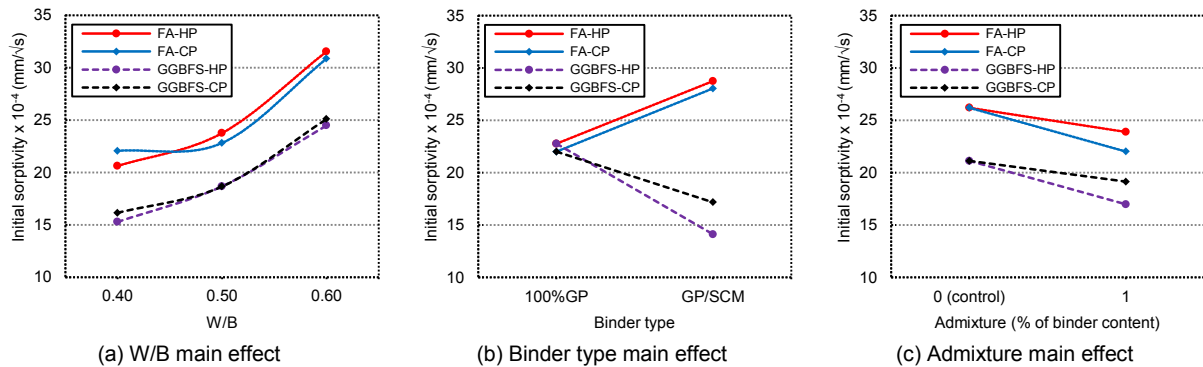


Figure 4. Effect (main) of factors on sorptivity (absorption rate).

To depict more precisely the performance of water-resisting admixtures, the interactions between the W/B and admixture factors are plotted in Figure 5 and Figure 6. In factorial analysis, interactions are considered to be significant when the interaction plots are not parallel (17). Accordingly, the relationships presented in Figure 5(a) show that there is no interaction between the W/B and admixture factors when the compressive strength of concrete is considered. This means that the effects of the inclusion of HP or CP are similar in mixes incorporating a W/B of 0.40, 0.50 and 0.60. In contrast, Figure 5(b) shows that the influence of HP in reducing AVPV is more pronounced in the mixes with higher W/Bs (2% compared to 6%). Similar performances were observed when the water penetration depth and sorptivity results were analysed (Figures 5(c) and 5(d)). These findings suggest that the watertightness of concretes with lower W/B (i.e. less than 0.50) might not be influenced by the addition of water-resisting admixtures. This may be attributable to the lower porosity (i. e., effective and absolute porosity) and discontinuous pore structure in the matrices of concretes incorporating lower W/Bs (2). Thus, water-resisting admixtures may be most beneficial in lower quality concretes such as the concretes used in suspended slabs.

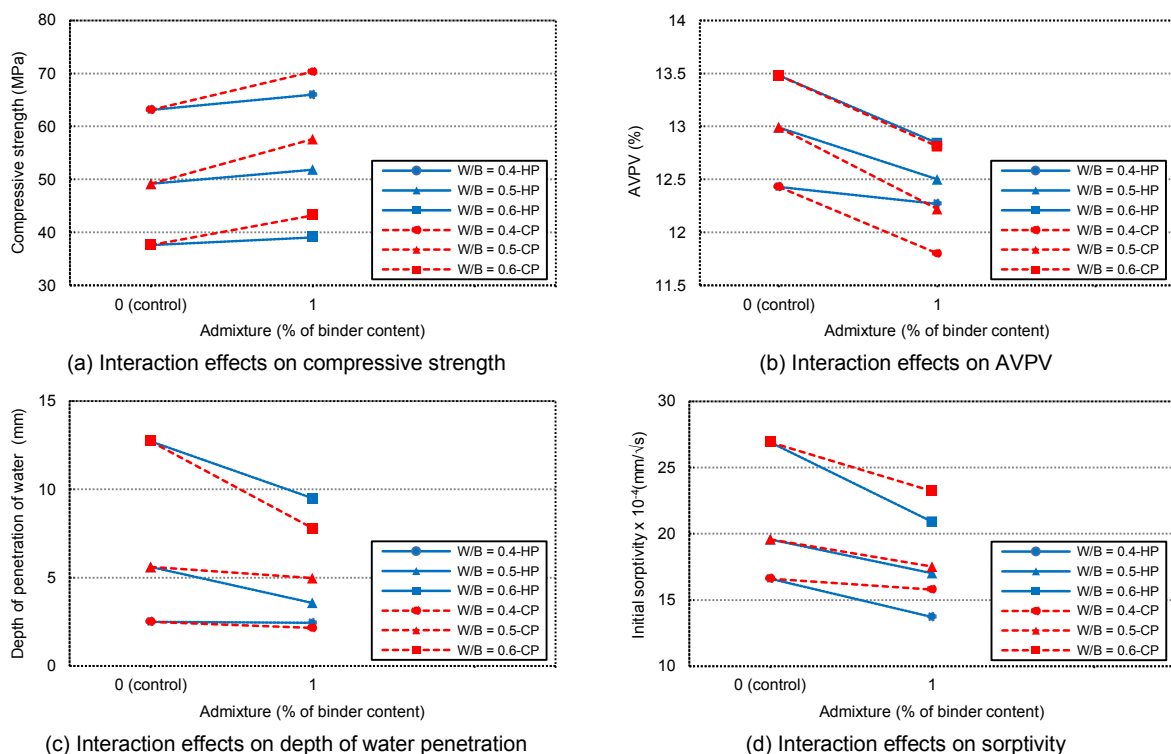


Figure 5. Effect (interaction) of W/B and admixtures.

#### 4.5 Effect of curing

Figure 6(a) shows that the AVPV of concretes with SCMs was highly influenced by the curing condition. The alteration of curing condition from a complete 28-days moist-curing to a combination of moist-curing (7 days) and air-curing (21-days) increased the AVPV of concretes incorporating FA and GGBFS by 13% and 10%, respectively. It may be attributable to the lower reactivity of SCMs in the relative humidities below 80% (6). However, this variation in curing had no considerable effect on the concretes with 100% GP cement.

Figure 6(b) illustrates the effect of curing condition on sorptivity. Generally, the change of curing condition from moist-curing to air-curing increased the absorption rate in all of the explored binder compositions. For instance, this variation in curing condition increased the sorptivity of concretes with 100% GP cement from  $8.5 \times 10^{-4}$  mm/ $\sqrt{s}$  to  $27.3 \times 10^{-4}$  mm/ $\sqrt{s}$  (300%). In addition, the sorptivity of concretes with FA increased from  $9.8 \times 10^{-4}$  mm/ $\sqrt{s}$  to  $39.1 \times 10^{-4}$  mm/ $\sqrt{s}$  (400%), whilst with concretes incorporating GGBFS, sorptivity increased from  $7.8 \times 10^{-4}$  mm/ $\sqrt{s}$  to  $23 \times 10^{-4}$  mm/ $\sqrt{s}$  (300%).

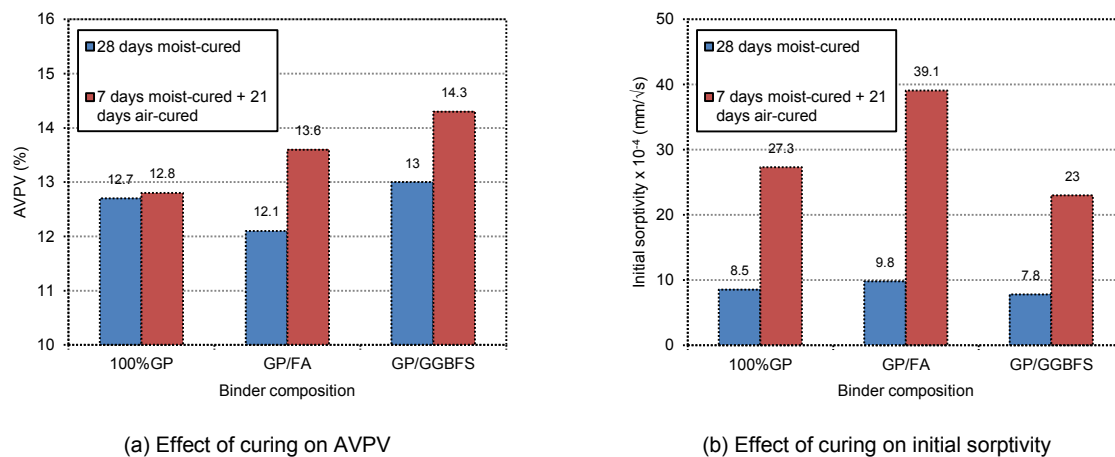


Figure 6. Effect of curing of concrete on water permeation properties.

#### 5. Conclusions

In this paper, the watertightness of concrete is evaluated, based on its pore structure and permeation properties, by means of different testing methods including AVPV, water penetration depth, and absorption rate (sorptivity). Accordingly, from the presented factorial analyses of the experimental data, the following conclusions are drawn:

- The watertightness of concrete is influenced by several factors such as W/B, binder type and water-resisting admixtures but at varying degrees. Therefore, advanced experimental mix designs are required to deal with these factors simultaneously.
- The W/B and SCM inclusions had a greater impact on watertightness when compared with water-resisting admixtures.
- At equivalent W/B, the inclusion of FA into the concrete mixes increased water permeation of concrete tested at 28 days and the addition of GGBFS improved its watertightness. Long-term testing and curing may be specified in practice when FA is to be added to concrete mixes. Caution must be exercised when the cement is replaced by FA in commercial mix designs.
- Hydrophobic and crystalline poreblockers are beneficial in both hydrostatic and non-hydrostatic conditions. However, their interaction with SCMs should be considered in any particular application.
- The addition of GGBFS to concrete mixes as a replacement for GP (40%) further aids water-resisting admixtures to achieve better performance in improving the watertightness of concrete.
- The effect of water-resisting admixtures on the watertightness of concrete is more pronounced in concretes with higher W/B (greater than 0.50). These admixtures are also effective in higher strength concretes (with lower W/B), but to a lesser extent.
- The sorptivities and AVPVs of air-cured concrete specimens were considerably higher than those for moist-cured concrete specimens. This observation was more pronounced in the

concretes incorporating FA and GGBFS when compared at equal W/B. Thus, proper curing of concrete is essential to achieve permeation reduction.

## 6. Acknowledgement

The authors gratefully acknowledge Sika Australia Pty Ltd for the materials and financial support provided through the research program. The authors also express their appreciation to Prof. V. Sirivivatnanon (University of Technology, Sydney) for his valuable advice and generous support.

## 7. References

1. ACI Committee 350 and American Water Works Association Committee 400, "Testing reinforced concrete structures for watertightness (ACI 350.1R/AWWA 400)", ACI Structural Journal, 90(3), 1993, pp 324-328.
2. Lamond, J.F. and Pielert, J.H., "Significance of tests and properties of concrete and concrete making materials", ASTM STP 169D-EB, 2006, [city of publication], PA.
3. Ollivier, J., Massat, O. et al., "Parameters influencing transport characteristics", in J. Kropp & H. Hilsdorf (eds), *Performance Criteria for Concrete Durability*, 1995, Chapman & Hall, UK, pp. 22-64.
4. Hearn, N., and Figg, J., "Transport Mechanisms and Damage: Current Issues in Permeation Characteristics in Concrete", Materials Science of Concrete VI, American Ceramic Society, 2001, Westerville, OH.
5. Powers, T.C., Copeland, L.E. et al., "Permeability of Portland cement paste", ACI Journal Proceedings, 51(3), 1954, pp. 285-298.
6. Thomas, M.D.A, "The effect of curing on the hydration and pore structure of hardened cement paste containing pulverized fuel ash", Advances in Cement Research, 81 (2), 1989, pp 181-188.
7. American Concrete Institute, "Report on chemical admixtures for concrete (ACI 212.3R-10)", ACI Committee 212, 2010, [city of publication], MI.
8. Day, K.W., Aldred, J. et al., "Concrete Mix Design, Quality Control and Specification, Fourth Edition", CRC Press, 2013.
9. Ramachandran, V.S., "Concrete admixtures handbook: properties, science, and technology, 2<sup>nd</sup> Edition", Noyes Publications, 1995, Park Ridge, NJ.
10. Rixom, M.R., Mailvaganam, N.P., "Chemical Admixtures for Concrete", E & F.N. Spon, 1986, London.
11. Dao, V.T.N., Dux, P.F., Morris, P.H. and Carse, A.H., "Performance of permeability-reducing admixtures in marine concrete structures", ACI Materials Journal, 107 (3), 2010, pp 291-296.
12. Justnes, H., "Low water permeability through hydrophobicity", COIN Project report 1, SINTEF Building and Infrastructure, 2008, Oslo, Norway.
13. Trinder, P.W., Chalmers, C. et al., "Resistance for concrete to harsh environment - Ammonium sulphate", Concrete in Australia, 1999.
14. Yodmalai, D., Sahamitmongkol, R. et al., "Chloride resistance of cement paste with crystalline materials", Annual Concrete Conference 6, Thailand.
15. Roberts M.H., Adderson, B. W., "Tests on water resisting admixtures for concrete", B.R.E Technical Note No. 159/85, 1985.
16. Basheer, P.A.M., Montgomery, F.R. et al., "Experimental Design for Concrete Durability Research", Proceedings of the ICE - Structures and Buildings, 104 (4), 1994, pp 449-462.
17. Box, G.E.P., Hunter, J.S. et al., "Statistics for Experimenters - Design, Innovation, and Discovery - Second Edition", John Wiley & Sons, 2005, NJ.
18. Nakamoto, J., Togawa, K. et al., "Water permeability of high slag content concrete", ACI Special Publication, 178, 1998, pp 779-795.

# The Effect on Expansion of Wrapping Concrete Prisms with Cloth Saturated with Alkali Hydroxide

Yasutaka SAGAWA<sup>1</sup>, Kazuo YAMADA<sup>2</sup>, Shoichi OGAWA<sup>3</sup>, Yuichiro KAWABATA<sup>4</sup> and Masahiro OSAKO<sup>5</sup>

<sup>1</sup>Associate professor of Faculty of Engineering, Kyushu University

<sup>2</sup>Senior researcher of Center for Material Cycles and Waste Management Research, National Institute for Environmental Studies

<sup>3</sup>Senior manager of Sales & Marketing Department, Taiheiyō Consultant Co. Ltd.

<sup>4</sup>Senior researcher of Structural Engineering Field, The Port and Airport Research Institute  
Visiting researcher of Materials and Structures Department, IFSTTAR-Université Paris-Est

<sup>5</sup>Director of Center for Material Cycles and Waste Management Research, National Institute for Environmental Studies

**Abstract:** In this paper, the effectiveness of wrapping by cloth impregnated with alkali hydroxide solution for concrete prism test (CPT) is discussed. First, RILEM AAR-4 and the CPT used in Japan are compared. Wrapping by cloth decreases leaching of alkali and drying during test period. Consequently, a new method in which concrete prisms are wrapped by cloth impregnated with sodium hydroxide solution and plastic film has been proposed. Except alkali wrapping with cloth and plastic film, the test procedure is the same as RILEM AAR-4. Following this method, the weight of prisms did not decrease, and stable expansion results were obtained. Furthermore, by this proposed method, ASR reactivity of two types of coarse aggregates was investigated in detail; one is andesite, another is chert. At 60°C, it results a clear relationship between expansion behavior and alkali content.

**Keywords:** ASR, CPT, wrapping, alkali hydroxide solution, expansion.

## 1. Introduction

Alkali silica reaction (ASR) is one of the possible deterioration mechanisms of concrete structures. ASR is due to a chemical reaction between reactive silica phases in aggregates and alkali hydroxides in the concrete pore solution, and it causes serious expansion and cracking in concrete. Although Stanton first recognized ASR in the late 1930's, it is still a significant problem regarding durability of concrete structures. Detecting methods of alkali-silica reactivity of aggregates and implementing ASR countermeasures have contributed to decreasing the risk of ASR. These methods, however, have imperfections and limitations.

It is necessary to improve the estimation procedure for highly reactive aggregate such as andesite containing opal or cristobalite/tridymite, or chert containing chalcedony (1). There are some difficulties for pessimum phenomena. First, the pessimum composition depends on the reactivity of aggregates (2). Second, at the pessimum composition, a higher content of pozzolanic materials is required than in the case that all aggregate is reactive (3).

Concrete prism test (CPT) is generally regarded as the best method to evaluate aggregate alkali-silica reactivity and to qualify preventive measures such as use of supplementary cementitious materials (SCMs). Some types of CPT have been already established. CSA A23.2 27A-09 and RILEM AAR-3 are famous methods. In order to accelerate ASR expansion, alkali content is increased to 5.25 or 5.5 kg/m<sup>3</sup> in concrete and temperature is set to 38°C, whereas RILEM AAR-4, which can accelerate reaction further of the temperature of 60°C, is now under preparation (4)(5). These methods use concrete specimens of 75\*75\*250 mm. Although they are easy to handle, alkali in concrete may leach out from concrete and alkali content may decrease significantly.

This paper investigates the effectiveness of alkali wrapping method in CPT to avoid alkali leaching. First, the result from two CPT methods are compared, and the necessity of water supply is discussed. The first one is based on the specification for the nuclear power related facilities in Japan, meanwhile, the other is RILEM AAR-4. In order to avoid alkali leaching and drying, wrapping by using an absorbent cloth including NaOH solution and a plastic film has been proposed. Then, the effectiveness of alkali wrapping in AAR-4 was examined. Moreover, this method was applied to the CPT varying the kind of aggregate type, alkali content in concrete and temperature.

## 2. Effectiveness of water supply in CPT

### 2.1 Experimental program

This section is based on the authors' previous paper (6). In order to provide the background to discussion in the following chapters, the results of previous experiments are necessary.

#### 2.1.1 Materials

Ordinary Portland Cement (OPC) ( $\text{Na}_2\text{O}_{\text{eq}} = 0.59\%$ ) specified in JIS A 5211, similar to CEM I 52.5 in EN197-1 was used. As SCMs, siliceous fly ash (FA) and ground granulated blast-furnace slag (BFS) were used. Physical characteristics are shown in Table 1.

**Table 1. Physical characteristics of cement and SCMs.**

Material	Density ( $\text{g}/\text{cm}^3$ )	Specific surface area ( $\text{cm}^2/\text{g}$ )
OPC	3.16	3110
FA	2.30	4190
BFS	2.89	4400

Coarse aggregate A1 and fine aggregate B1 are reactive aggregates, namely compose of andesite containing opal in vein. They have the same source, but the aggregate size is different. Moreover, andesite containing tridymite (aggregate C) and hornfels containing microcrystalline quartz (aggregate D) were used. As non-reactive aggregate, pure limestone (coarse aggregate G and fine aggregate H) was used. Aggregates G and H were from the same source. Physical properties of these aggregates are shown in Table 2.

**Table 2. Physical properties of aggregates.**

Aggregate	Dry density ( $\text{g}/\text{cm}^3$ )	Absorption (%)	Unit weight ( $\text{kg}/\text{L}$ )	Solid content (%)	Fineness modulus	Fines (%)
A1	2.46	2.33	1.41	57.2	6.60	4.2
B1	2.49	5.78	1.46	58.7	2.87	4.4
C	2.63	2.06	1.56	59.5	6.56	1.2
D	2.65	0.71	1.52	57.4	6.63	1.0
G	2.68	0.55	1.54	57.3	6.59	1.7
H	2.68	0.61	1.85	68.9	3.04	8.2

Table 3 shows the results of chemical method according to ASTM C 289. Aggregates A1 and B1 were judged as potentially deleterious. Aggregate C was judged as deleterious. Aggregate D seems to be innocuous because chemical method is not sensitive for late expansive aggregate containing micro/cryptocrystalline quartz. Andesite aggregate A1, B1 and C showed compositional pessimum effect at 30 mass% in the previous experiments.

**Table 3. ASR reactivity test results of aggregates checked by chemical method.**

Aggregate	Rc (mmol/L)	Sc (mmol/L)	Reactivity
A1, B1	207	672	Potentially deleterious
C	112	592	Deleterious
D	109	16	Innocuous
G, H	8	1	Innocuous

#### 2.1.2 Mixture proportions

Water content was kept constant as  $160 \text{ kg}/\text{m}^3$ . In some mixtures, OPC was replaced with 15, 25, or 35 mass % of FA, or 55 mass % of BFS. Slump was adjusted around 12 cm by

changing the dosage of air-entraining and water-reducing admixture. Air content was controlled to  $4.5 \pm 1.5$  % by changing the dosage of air-entraining admixture. Pellet type of sodium hydroxide (NaOH) was dissolved in mixing water to adjust alkali content of  $5.5 \text{ kg/m}^3$  in concrete.

### 2.1.3 CPT procedures

Table 4 shows the mixtures and test methods of CPT for each mixture. In this subsection, the results of two CPT methods are presented. The important differences between the two methods are the size of prism and whether prisms are wrapped by cloth or not.

**Table 4. Mixture proportions and CPT methods (O; Conducted).**

Mixture	Concrete materials			CPT	
	Aggregates		Binder	RILEM AAR-4	mJASS5N
	Coarse	Fine			
No.1	A1:G = 3:7	H	OPC100%	O	O
No.2	A1:G = 3:7	H	OPC75%+FA25%	O	O
No.7	G	B1:H = 3:7	OPC100%	O	O
No.8	G	B1:H = 3:7	OPC75%+FA25%	O	O
No.14	D	H	OPC100%	O	O

In the RILEM AAR-4 procedure, the specified size of the prisms is  $75 \times 75 \times 250$  mm. Specimens are stored in sealable stainless containers with water level of 35mm from the bottom, which are stored in a reactor generating  $60^\circ\text{C}$  and 100% relative humidity. After the test period, a sample of water at the bottom of container was taken, and the alkali concentration was measured so that alkali leaching was evaluated.

Another method exists in Japan, JASS 5N T-603. JASS 5N stands for Japanese Architectural Standard Specification "Reinforced Concrete Work at Nuclear Power Plants". In this method,  $100 \times 100 \times 400$  mm prisms are used, and they are wrapped with cloth impregnated by distilled water. The size of paper and weight of water are specified. In this study, two pieces of unwoven paper with  $355 \times 425$  mm were used, and 50 g of distilled water for each paper was added.

After having been wrapped with cloth, each specimen was covered by thin plastic film and was put into a thin plastic bag in order to prevent moisture movement between the specimen and surrounding environment. Then, three specimens for each mixture were placed vertically in a container, of which the temperature was controlled to be  $60^\circ\text{C}$  with a heater in water in the bottom of the thermally insulated container. JASS 5N T-603 specifies that the temperature shall be  $40^\circ\text{C}$ , however, in this experiment,  $60^\circ\text{C}$  was adopted (hereinafter, "mJASS5N" m; modified), as in RILEM AAR-4.

24 hours before length measurement, specimens were moved to a temperature controlled room at  $20^\circ\text{C}$ . Plastic bag, plastic film and cloth were removed. Then, the length and the weight of paper were measured. After measuring, distilled water was added to the same paper up to the weight of initial condition. After the whole test period, water content and alkali content in the paper were measured and alkali leaching were evaluated.

## 2.2 Results and discussion

The expansive behavior of specimens as measured according to mJASS5N and RILEM AAR-4 are shown in Figure 1. The relationships between the expansions between both methods are shown in Figure 2. In a wide range as shown in Figure 2(a), it seems to be a linear correlation for both methods. In the range of smaller expansion (Figure 2(b)), however, AAR-4 results in smaller expansion than mJASS5N.

It is possible that there was a difference in moisture supply. Figure 3 displays the relationship between mass change of specimens and expansions at 26 weeks. The mass gain in AAR-4 condition is always smaller than with mJASS5N procedure. However, the expansion according to AAR-4 was always slightly larger than with mJASS5N at the same mass gain and the moisture seems not to be the direct reason of discrepancy. Another possible reason is the difference in alkali leaching. Amounts of leached alkali were 2% or 3% of original 5.5 kg/m<sup>3</sup> for mJASS5N and 16% or 30% of that for AAR-4. The reason why limited amounts of alkali were leached in mJASS5N may be the use of the same paper, and the fact that just water was added in sealed condition. This means that all alkalis were kept in the paper and the plastic film, and no alkali go out from the system. More alkali leaching in AAR-4 may be caused by the water dropping when the container is cooled for the measurement even though the inclined inner roof is prepared, or moisture condensation in the container on the specimens when the container, especially the water in the bottom is heated after measurement during the specimens are cold. Therefore, because of the higher amount of alkali leaching, AAR-4 resulted in the less expansion. For rapid expansion, the effect of alkali leaching was limited because the most of expansion was happened before the first measurement. There is another possibility of the reason for limited alkali leaching of mJASS5N in its larger specimen size.

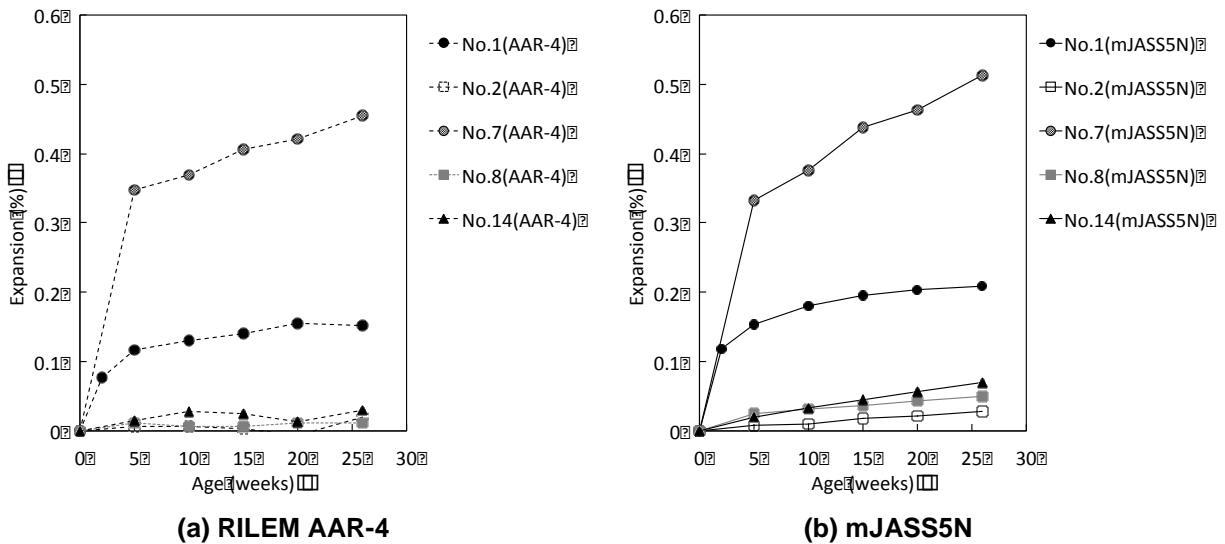


Figure 1. Expansion measured according to RILEM AAR-4 and mJASS5N.

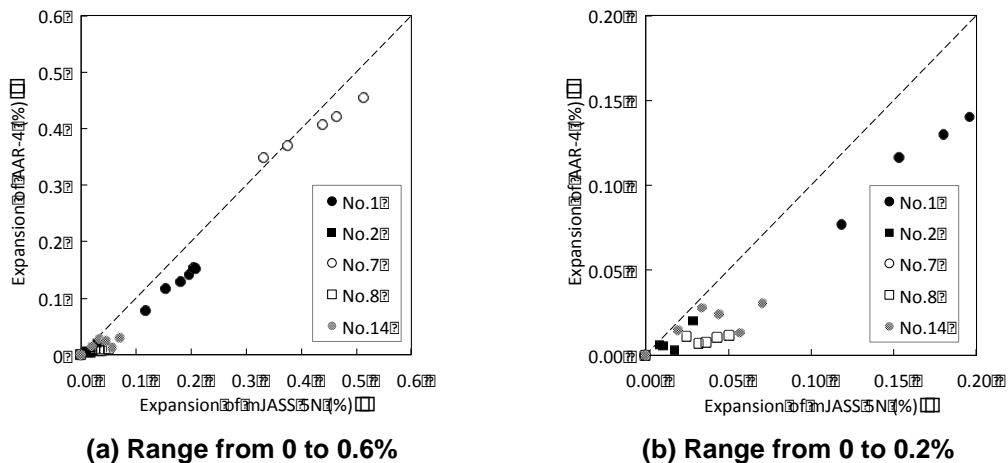


Figure 2. Relationship between expansion behaviors by AAR-4 and mJASS5N.



There is one more difficult point in AAR-4. Drying during cooling may happen because the stainless steel container gets cool faster than concrete prisms inside. Water in concrete prisms can move on the inside surface of container by condensation. When alkali amount is high, the equilibrium vapor pressure is low and vapor tends to be absorbed by concrete prisms. However, once the alkali content becomes less, the vapor absorbing tendency decreases and water may move from concrete prisms to the container. In real conditions of concrete structure, the most severe condition for ASR, except alkali supply from de-icing salt or sea salt, is continuous supply of water. Therefore, wrapping with cloth is considered as reasonably safe side.

The alkali leaching in the case of wrapping by cloth impregnated by distilled water is caused by the alkali movement from concrete specimens to cloth. Therefore, if appropriate amounts of alkalis are included in cloth in advance, the movement of alkalis is expected to be limited. CPT is an accelerated test in order to reproduce the worst case in field. Therefore, keeping alkalis and moisture is an essential point.

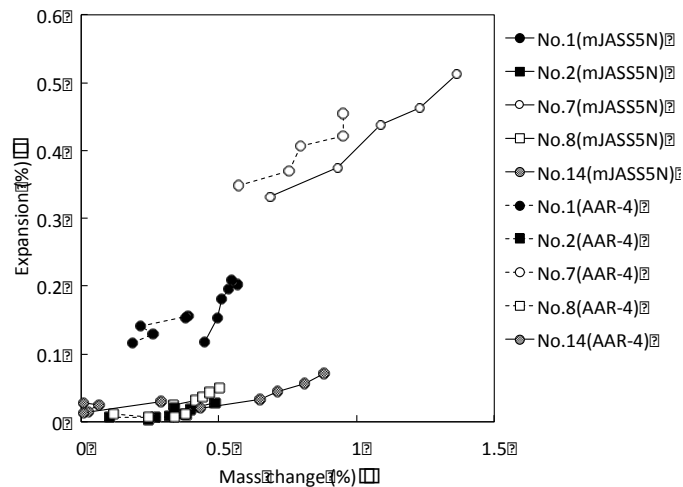


Figure 3. Relationship between expansion and mass change.

### 3. Proposal and examination of alkali wrapping method

#### 3.1 Experimental program

##### 3.1.1 Materials

Ordinary Portland Cement specified in JIS A 5211, similar to CEM I 52.5 in EN197-1 was used. In this subsection, reactive coarse aggregate A2 was used. Aggregate A2 was obtained from the same quarry as that of aggregate A1, but sampled season was different. Table 5 shows the result of reactivity analysis according to the chemical method. Limestone was chosen as the reference innocuous aggregate.

Table 5. ASR reactivity test results of aggregate A2 checked by chemical method.

Aggregate	Rc (mmol/L)	Sc (mmol/L)	Reactivity
A2	168	710	Potentially deleterious

##### 3.1.2 Mixture proportions

As shown in Table 6, there are 4 mixtures which have different alkali content. Alkali content was changed from 2.4 kg/m<sup>3</sup> to 5.5 kg/m<sup>3</sup>.

**Table 6. Alkali content, wrapping condition and mixture numbers (O; conducted).**

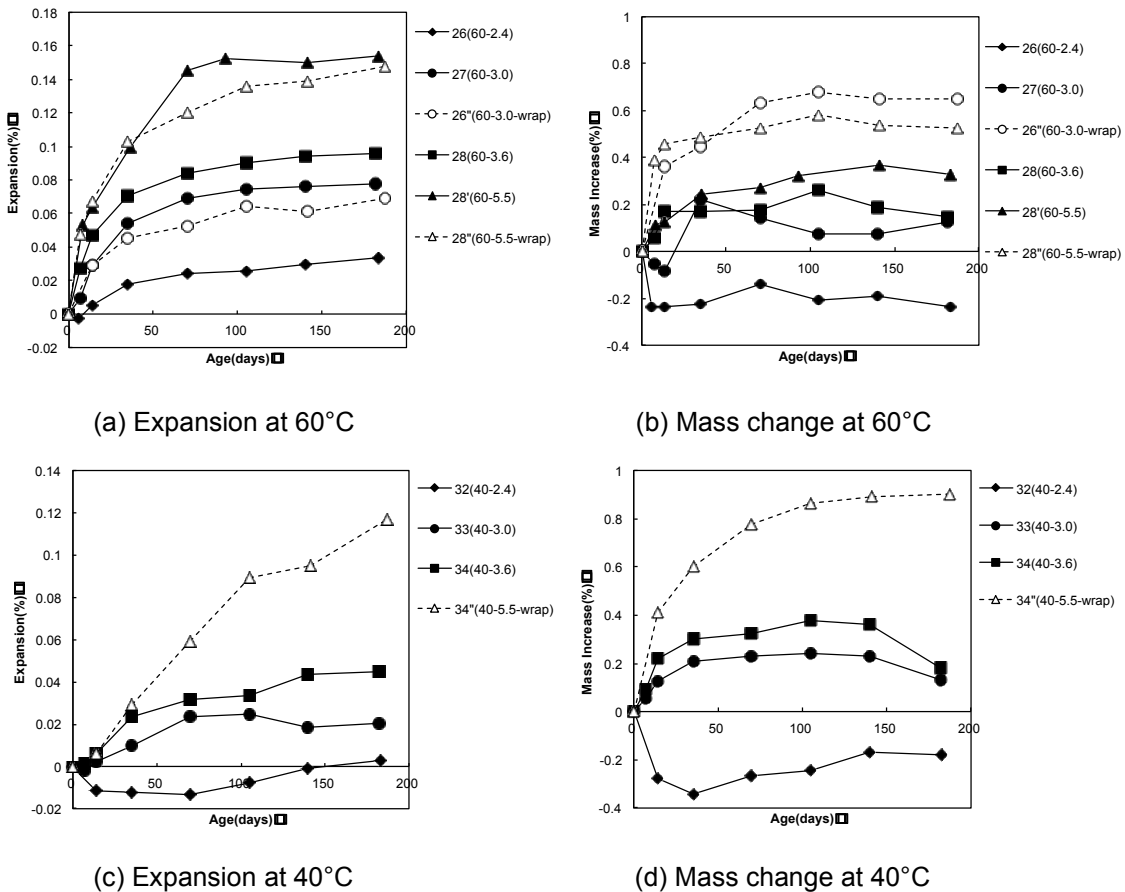
Alkali content (kg/m <sup>3</sup> )	60 °C		40 °C	
	AAR-4 (Without wrapping)	With alkali wrapping	AAR-4 (Without wrapping)	With alkali wrapping
2.4	O (No.26)		O (No.32)	
3.0	O (No.27)	O (No.26'')	O (No.33)	
3.6	O (No.28)		O (No.34)	
5.5	O (No.28')	O (No.28'')		O (No.34'')

**3.1.3 Test method**

Casting of concrete specimens and accelerated curing condition are almost same as according to AAR-4. The different point is whether the specimens were wrapped by the cloth including NaOH solution (alkali wrapping) or not. Concentration of NaOH solution was calculated by assuming chemical composition of C-S-H gel and alkali content in concrete (7).

**3.2 Results and discussion**

Figure 4 shows the expansion behavior and weight change at 60°C and 40°C. High temperature and high content of alkali correspond to the higher expansions. In the case of 2.4kg/m<sup>3</sup> of alkali, a weight reduction is observed. The test condition of AAR-4 is not enough to accelerate the ASR reaction. When the alkali content is low, specimens may dry. Meanwhile, when the alkali content is high, water absorption in pore solution will increase. In the concrete structure which has risk of ASR, actually, water will be supplied continuously. Therefore, the acceleration in AAR-4 method is not enough to examine the ASR reactivity.



**Figure 4. Relationship between expansion and mass change.**

From the results of this experiment, we propose new method detailed hereafter to evaluate ASR reactivity of concrete. This new method principally applies RILEM AAR-4 except for the wrapping procedure. Concrete prism shall be wrapped by cloth including NaOH solution and thin plastic film. The purpose of such wrapping is to avoid movement of water and alkali during test period. When the length and weight are measured, weight of paper also shall be measured. If the weight loss of paper is to be observed, water should be added to maintain the weight of paper. Concentrations of NaOH solution can be calculated by using alkali content of cement used and assuming chemical composition of C-S-H (7) .

#### 4. Verification of alkali wrapping method varying the temperature and alkali content

##### 4.1 Experimental program

In order to discuss the proposed CPT method, further experiments have been conducted. The effects of alkali content in concrete and temperature for acceleration of ASR reactivity were investigated. Picture 1 shows the wrapping procedure; (a) setting on a cloth (absorbable paper), (b) folding, (c) finish of folding, (d) fastening by rubber band, (e) wrapping by thin plastic film, (f) storage in stainless container.

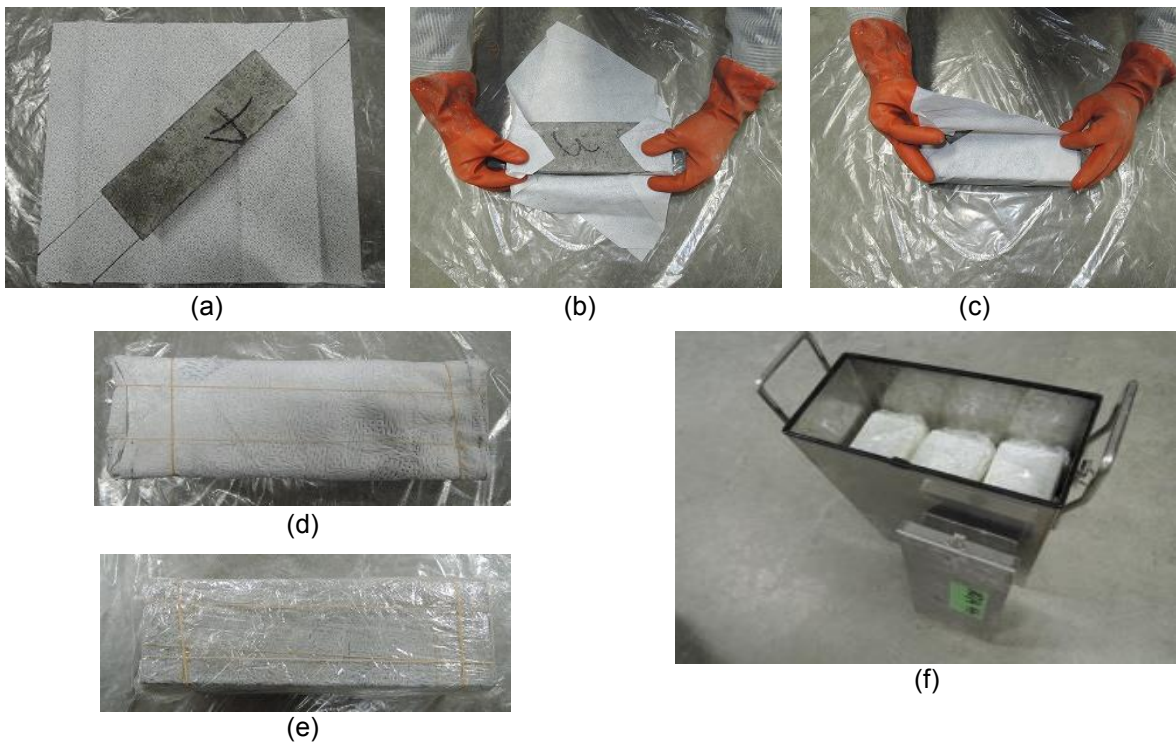


Photo 1. Proposed alkali wrapping method.

##### 4.1.1 Materials

Ordinary Portland Cement specified in JIS A 5211, similar to CEM I 52.5 in EN197-1 was used. In this subsection, the same reactive coarse aggregate A2 as in Section 3 and the reactive coarse aggregate T were used. The rock type of aggregate A2 was chert including cryptocrystalline quartz and chalcedony. Limestone was the reference innocuous aggregate. The result of chemical method for aggregate T is  $S_c = 158 \text{ mol/l}$  and  $S_c = 2 \text{ mol/l}$ . Meanwhile, the result of RILEM AAR-5 for aggregate T is that expansion at 14 days reaches 0.173%.

##### 4.1.2 Mixture proportions

As shown in Table 7, there are 22 mixes which have different alkali content. Alkali content was changed from  $2.00 \text{ kg/m}^3$  to  $5.50 \text{ kg/m}^3$ . While aggregate A2 was combined with

limestone by 30% : 70% in volume, aggregate T was used by itself. Furthermore, for the mixture using aggregate A2, fly ash was added, and mitigation effect by fly ash also examined. Temperature was controlled to 20, 40 and 60°C.

**Table 7. Alkali content, wrapping condition and mixture numbers (O; conducted).**

Alkali content (kg/m <sup>3</sup> )	Aggregate A2			Aggregate T		
	60 °C	40 °C	20 °C	60 °C	40 °C	20 °C
5.50	O (No.28+) O (No.59)* O (No.60+)**	O (No.52)	O (No.55)	O (No.41)	O (No.45)	O (No.48)
4.75				O (No.42)	O (No.46)	
4.25	O (No.27+)	O (No.53)	O (No.56)			
4.00				O (No.43)	O (No.47)	
3.00	O (No.49)	O (No.54)	O (No.57)	O (No.44)		
2.50	O (No.50)		O (No.58)			
2.00	O (No.51)					

\* : FA = 15%, \*\* : FA = 30%

## 4.2 Results and discussion

Figures 5 and 6 show the expansive behavior and the mass change of concretes using aggregate A2 and aggregate T, respectively. The color of the plots differs depending on the temperature condition.

### 4.2.1 Aggregate A2 (Andesite)

First, from Figure 5(a), in the case of 60°C, the higher the alkali content, the larger the expansion shows from early ages. After 10 weeks of test period, expansion speed decreased. Second, in the case of 40°C (Figure 5(b)), ranging the alkali content from 3.00 kg/m<sup>3</sup> to 5.50 kg/m<sup>3</sup>, expansion behaviors for 3 experiments seem to be almost the same. After 15 weeks, expansion of concrete with 3.00 kg/m<sup>3</sup> at 40°C exceeded the one with 3.00 kg/m<sup>3</sup> at 60°C. At 20°C, the beginning of expansion depends on the alkali content, and expansion with 3.00 kg/m<sup>3</sup> alkali reached to that of 4.25 and 5.50 kg/m<sup>3</sup>. Lastly, from the results of No.59 and No.60, 15% fly ash replacement was not enough for suppressing expansion, therefore, 30% replacement was required.

### 4.2.2 Aggregate T (Chert)

Both of 60°C and 40°C, the same trend of expansion behavior is observed. While expansion rate at 60°C until 5 weeks was very high, the expansion at 40°C also became remarkably large, and all mixtures of 40°C reached the same level as of 5.50 kg/m<sup>3</sup> at 60°C. There was no expansion for the specimen in 20°C.

### 4.2.3 Effect of temperature and alkali content

The relationship between alkali content and expansion at 26 weeks was clear as shown in Figure 7. In the case of 40°C and 20°C, however, the relationship was not clear. To clarify the mechanism of these behaviors, further analysis is required.

In addition, in the case of aggregate T which is chert including cryptocrystalline quartz and chalcedony, a test period of 15 weeks at 60 °C is able to detect ASR earlier than any other conditions. However, concretes with aggregate A2 including much crystalite continued expansion indefinitely. It would take much time to examine ASR reactivity.

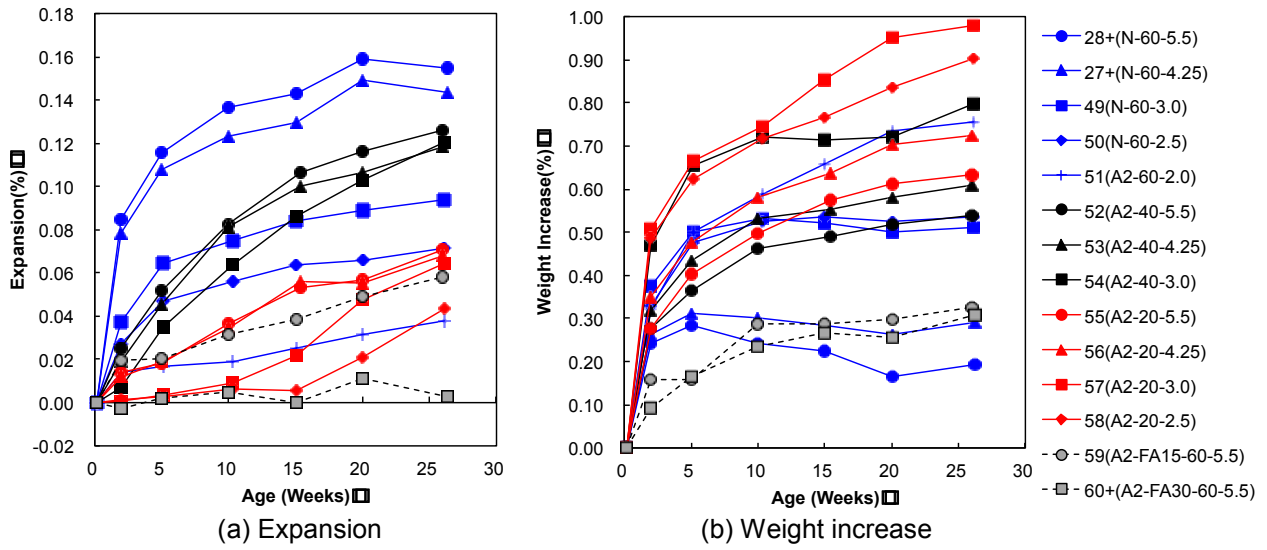


Figure 5. Relationship between expansion and mass change for aggregate A2.

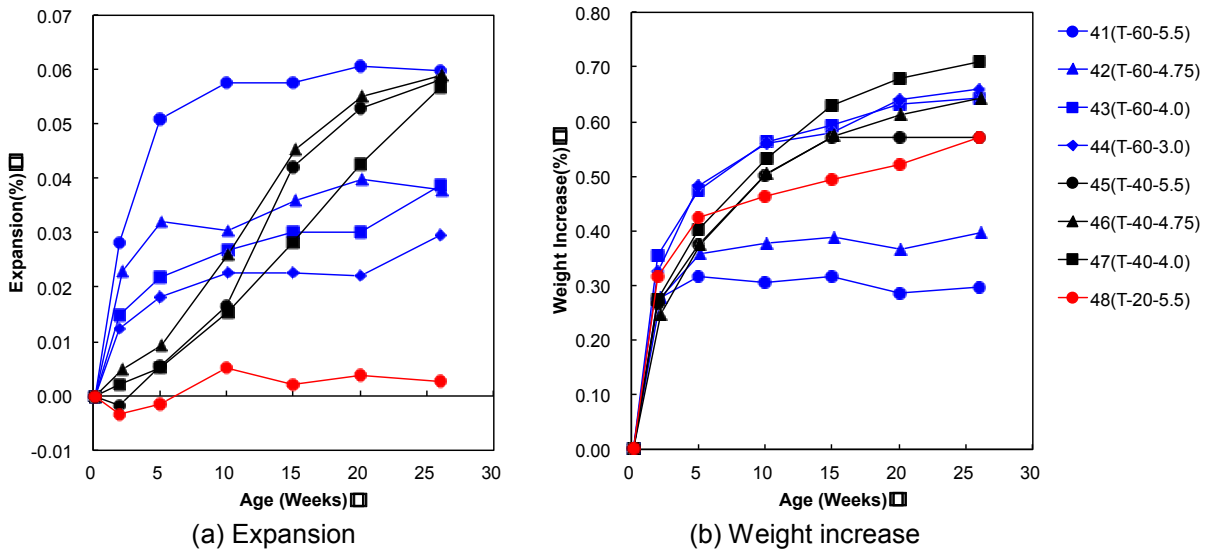


Figure 6. Relationship between expansion and mass change for aggregate T.

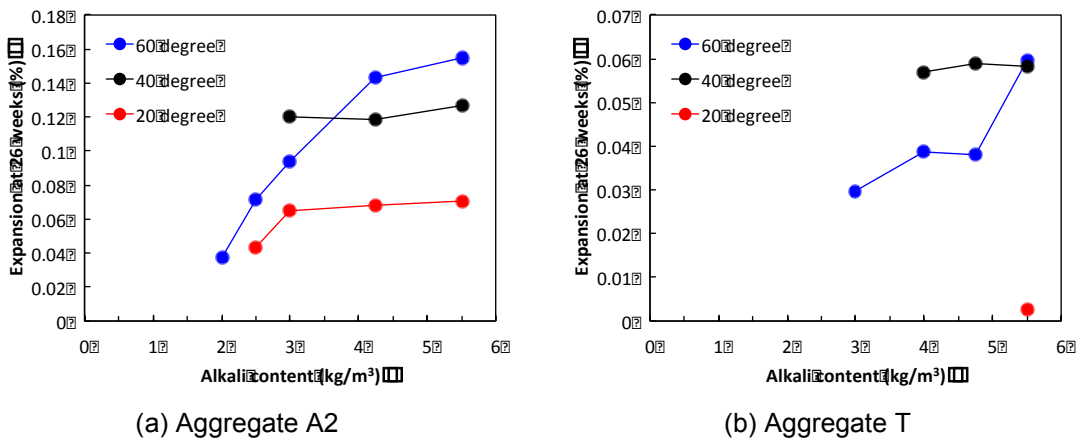


Figure 7. Relationship between Alkali content and expansion at 26 weeks.

Alkali wrapping method is able to decrease leaching of alkali and to avoid drying during test period. It is still yet difficult to evaluate the ultimate expansion from CPT test quantitatively.

## 5. Conclusions

In this paper, the significance of alkali wrapping for concrete prism test to evaluate ASR reactivity was presented. Several types of CPT were conducted. In Section 2, RILEM AAR-4 and CPT used in Japan were compared. In Japanese CPT, larger concrete prisms of 100\*100\*400 mm wrapped in cloth impregnated with distilled water and plastic film and plastic bag, were used. Wrapping by cloth decreased leaching of alkali and drying during test period. In Section 3, this new method where concrete prisms were wrapped by plastic film was qualified. This method did not decrease the weight of prisms, and it realized stable results of measurement. In Section 4, by this proposed method, ASR reactivity of two types of coarse aggregates were investigated; one is andesite, another is chert. As the results, in the case of 60°C, there was clear relationship between expansion behavior and alkali content, however, in the case of 40°C and 20°C, the trend was different from expected.

## 6. Acknowledgement

The authors are grateful to assistance from Mr. Karasuda, Mr. Morooka, Mr. Tanaka and Mr. Oda who were/are students of Concrete Engineering Laboratory in Kyushu University.

## 7. References

1. Katayama T., "The so-called alkali-carbonate reaction (ACR) - its mineralogical and geochemical details, with special reference to ASR", Cement and Concrete Research, 2010, Vol. 40, pp.643-675.
2. Katayama T., "A review of alkali-aggregate reactions in Asia – recent topics and future research", East Asia Alkali-Aggregate Reaction Seminar, Supplementary Papers, A33-43, 1997.
3. Kawabata Y., Yamada K., Matsushita H., "Suppression effect of fly ash on ASR expansion of mortar/concrete at the pessimum proportion", 13th International conference on alkali aggregate reaction, 031711-KAWA; 2012.
4. Lindgård J, Thomas MDA, Sellevold EJ, Pedersen B, Andic-Cakir O, Justnes H, et al., "Alkali-silica reaction (ASR) – performance testing: influence of specimen pre-treatment, exposure conditions and prism size on alkali leaching and prism expansion", Cement and Concrete Research, 2013, Vol.53, pp.68-90.
5. Lindgård J, Nixon PJ, Borchers I, Schouenborg B, Wigum BJ, Haugen M, et al., "The EU "PARTNER" project - European standard tests to prevent alkali reactions in aggregates: final results and recommendations. Cement and Concrete Research, 2010, Vol.50, pp.611-635.
6. Yamada K., Karasuda S., Ogawa S., Sagawa Y., Osako M., Hamada H., Isneini M., "CPT as an evaluation method of concrete mixture for ASR expansion", Construction and Building Materials, Volume 64, 14 August 2014, pp.184-191
7. Kawabata, Y., Yamada, K., Matsushita, H., "Relation of Phase Composition of Cement Hydrates with Supplementary Cementitious Materials to the Suppressing Effect on ASR Expansion", Journal of JSCE, Ser. E2, 69, 2013, pp.402-420 (in Japanese).

# Innovations in Admixtures for Piling Concrete

Bruno D'Souza<sup>1</sup> and Hairul Sarwono<sup>2</sup>

<sup>1</sup>Business Development Manager, Admixture Systems, BASF Australia Ltd

<sup>2</sup>Product Technologist, BASF Australia Ltd

**Abstract:** The use of Continuous Flight Auger (CFA) piles has gained considerable interest and popularity in recent years. With favourable geotechnical conditions CFA piling is the preferred method of deep foundation technology where installation speed and a large number of piles are required. In CFA pile construction it is considered good practice to commence drilling only after the concrete has arrived on the project site and delivery of the full volume needed for the completion of the pile without interruption is assured. The mix design, ambient conditions and characteristics of the soil at site play a significant role in the workability of concrete during reinforcement placing. In some soils, for example dry sandy soils may tend to dewater the concrete rapidly thereby reducing the workability of concrete. Loss of workability of concrete will in turn reduce the ability to successfully place the reinforcing cage. Conventional retarding admixtures can be used to achieve workability for an extended period of time but they also significantly retard the setting of concrete and hamper productivity. In long drilled shafts with higher than expected water contents it may be necessary to modify the concrete mix to prevent the washout of binder and fines for maintaining the integrity of the pile. Challenges like maintaining workability without excessive retardation and robustness during the installation of piles can be overcome through the use of innovative admixtures such as super slump retainers and colloidal materials capable of modifying the rheology of the mix.

**Keywords:** admixture, mineral additive, piling, slump retention.

## 1. Introduction

Deep foundation and ground engineering works include the construction of piles, diaphragm walls, displacement columns and retaining structures. A pile usually represents a slender structural member constructed in the ground. However, a pile is often used as a generic term to represent several types of deep foundations, such as CFA or driven pile, drilled shaft, caisson or an anchor.

Modern construction demands larger diameters and deeper shafts often with congested reinforced cages and steel elements. One of the challenges faced by engineers, contractors and concrete producers is to design an appropriate concrete mix for such specialized and often complex pours.

Large piles with diameters up to 2400mm and 45m in depth for high rise buildings in excess of 250m tall could use concrete with characteristic compressive strengths as high as 85 MPa. Moreover, cementitious binder contents in such high strength concrete mixes can exceed 600 kg/m<sup>3</sup> and therefore, present the concrete producer and contractor at the job site with issues related to workability & slump retention for the duration of the pour.

## 2. Properties of piling concrete

The integrity and high quality of the pile shaft is of paramount importance. With CFA piles, the pile is drilled to depth in one continuous operation using a continuous flight auger. The concrete then is pumped under pressure through a line from the top of the rig and delivered to the base of the auger via the hollow centre of the auger string. The concrete is continuously under pressure while the auger is smoothly lifted smoothly in one continuous operation. The reinforcement cage is then lowered into the fluid concrete to the required depth (1).

Some of the specific requirements for piling concrete used in continuous flight auger piles are high flowability or self-compacting yet non-segregating and cohesive properties without excessive bleeding over an extended period of time. The mix must also flow with ease between the reinforcing bars and into the interstices of the soil.

Therefore the other mix considerations are stability, filtration resistance with good workability life, passing ability and self-levelling properties that need to be maintained for the duration of the pour.

### **3. Admixtures for piling concrete**

Both low-range and high-range (superplasticizers) water reducing admixtures are routinely used in tremie, high flow and self-compacting concrete mixes for such applications. In addition, a retarder is commonly used in the same mix primarily to maintain slump for extended periods of time particularly for large pours, long hauls and in hot weather conditions. Conventional retarders maintain slump by retarding the set of concrete because they slow the rate of early hydration of cement. Retardation of concrete however, is accompanied by low early strength development. Extended set times and low early strengths are undesirable effects when speed and tight project construction schedules are of major consideration.

The authors would like to elaborate on the mechanism and potential applications of an innovative admixture and a mineral additive to meet some of the challenges posed by the construction industry described in the preceding section.

#### **3.1 Slump Retaining admixture**

Slump Retaining admixture (SR) is a relatively new class of admixture classified as Special Purpose, Normal Setting Admixtures or Type SN as per AS 1478.1-2000, Chemical Admixtures for Concrete, Mortar and Grout (2).

The chemical and physical behavior of polymers in concrete can be controlled through the efficient use of polymer chemistry and nanotechnology as depicted in the schematic modular diagram in Figure 1, Asmus, Kluegge et al (3).

SR is based on polycarboxylate ether polymers designed to a specific balance between electrical charges, side chains, length of the main backbone, new functional monomers and molecule geometry as shown in Table 1. For example a functional monomer (Block A) can be grafted to the polycarboxylate ether polymer to achieve control of workability without having the side effect of water reduction.

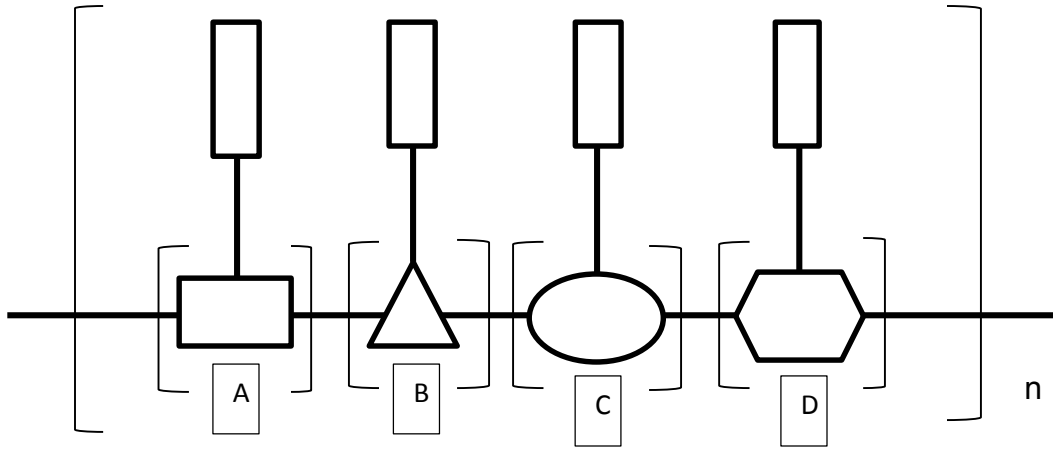
The functional monomer works by controlling the adsorption speed of the PCE to the surface of the cement particle thus providing workability retention after elapsed time without slowing the hydration process and retarding the set of concrete Asmus, Kluegge et al (3).

The attributes of such a functional monomer are beneficial for maintaining slump and workability for extended periods of time without impediment to the set times and early age strength developments of the mix. These benefits do not hinder the progress of work and aid in accelerating the project schedule.





These properties make it an admixture of choice in say CFA piling work where for example specifications call for a minimum of 15 MPa before pile construction can commence adjacent to a newly cast pile.



**Figure1. Schematic modular diagram of an engineered polycarboxylate ether polymer (3).**



**Table 1. PCE building blocks and their functionality in concrete (3).**

PCE Building block	Effect
Block A 	Slump retention
Block B 	Early strength
Block C 	Final strength
Block D 	Water reduction

A typical 50 MPa piling concrete mix used in the laboratory trials is shown in Table 2.

The performance of admixtures in these laboratory trials using identical mix designs is shown in Table 3.

Mix 1 containing a high range water reducer (superplasticizer) & retarder exhibits shorter slump & workability retention despite longer setting times compared with a SR incorporated in Mix 2 and 3.

**Table 2. 50 MPa piling concrete mix**

Ingredient	Quantity (kg/m <sup>3</sup> )
Cement	365
Fly ash	130
Water	198
20mm Coarse aggregate	720
10mm Coarse aggregate	180
Coarse sand	515
Fine sand	315

**Table 3. Performance summary of admixtures in 50 MPa piling concrete**

	<b>Mix 1</b>	<b>Mix 2</b>	<b>Mix 3</b>
Admixture (mls/100kg binder)			
High Range Water Reducer	500	450	450
Retarder	200	-	100
Slump Retaining admixture	-	200	200
Slump / Slump flow (mm)			
0 minutes	230 / 450	230 / 650	250 / 670
60 minutes	110	240 / 650	250 / 670
120 minutes	50	230 / 600	240 / 650
180 minutes		220 / 550	240 / 650
240 minutes		130	220 / 420
300 minutes			210 / 390
Setting time (hours:mins)			
Initial	7:30	5:50	6:20
Final	8:45	7:10	7:30
Compressive strength (MPa)			
1 day	9	17	16
7 days	41	41	42
28 days	59	58	61

### **3.2 Mineral additive**

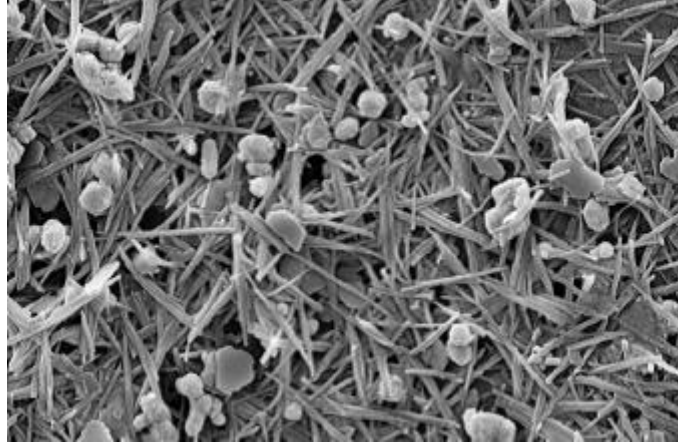
The mineral additive is a processed attapulgite, a hydrated magnesium aluminosilicate and principal member of the fuller's earth family of clay minerals. Attapulgite occurs as tightly packed bundles of submicron size particles whose lathe-like structure gives it unique colloidal and sorptive properties. The attapulgite needle-like particle shape is typically about 1 $\mu$  in length and approximately 0.10  $\mu$  across. Attapulgite can be characterized by its unique crystal structure. The 3-dimensional structure of attapulgite prohibits internal swelling action in the presence of water unlike some bentonites that swell owing the penetration of water between its layers Haden (4).

One of the reasons cast in situ piles fail is due to the discontinuity of concrete. Concrete stability is controlled by and related to the parameters of rheology and composition of the paste. Concrete placed at the base of a pile can be subjected to high hydraulic and hydrostatic head pressure and it needs to be designed to withstand this pressure. Working with less than ideal soils, soft, wet and in submerged conditions can also present difficulties with a propensity for washout of the binder from the concrete. Tremie concrete for example could be subject to free fall with a tendency to segregate and bleed especially with enlarged dimensions of the element.

The colloidal network created by the attapulgite particles forms a thixotropic gel as shown in Figure 2 that provides the concrete mix with anti-washout properties, improved cohesion, rheology, pumpability, stability and robustness required for concrete placed in environments and conditions described above. Due to the mode of action of attapulgite, the hypothesis is that the presence of such a mineral additive in concrete will not only enhance its ability to retain water under pressure but also improve the visibility stability index (VSI) making it suitable for the conditions and applications mentioned earlier. It is also envisaged that a concrete mix containing attapulgite will provide some support to the sidewalls of the drilled or bored shaft because of its thixotropic effect.

The additive complies with the requirements of a Special Purpose, Normal Setting Admixtures or Type SN as per AS 1478.1-2000, Chemical Admixtures for Concrete, Mortar and Grout (2). The testing and conformance of attapulgite to AS 1478 in a concrete mix confirms the compatibility for use in cement based applications including grouts and concrete for deep foundation works.

**Figure 2. Photomicrograph of particles in a colloidal network of attapulgite**



#### **4. Conclusions**

- Improved consistency and better control of slump, flowability, workability and stability can be achieved with the use of a Slump Retaining admixture
- A clay based mineral additive can impart stability, robustness and anti-washout properties to a mix by way of rheology modification
- New technology and traditional admixtures can be effectively used for piling concrete where quality, speed and economy are important

#### **5. References**

1. "Design and Construction of Continuous Flight", *Geotechnical Engineering Circular (GEC) No.8*, Auger Piles, US Department of Transportation Federal Highway Administration, April 2007, Chapters 2 - 4
2. AS 1478.1 Chemical Admixtures for Concrete, Mortar and Grout, Standards Australia 2000
3. Asmus, S, Kluegge, J, et al, "Influence of a New Family of Chemical Admixtures to Properties of Fresh and Hardened Concrete", Proceedings of the 31<sup>st</sup> Conference on Our World in Concrete & Structures, Singapore, 16-17 August 2006
4. Haden, W, "Attapulgite: Properties and Use", Proceedings of the Tenth National Conference on Clays and Clay Minerals, Texas, Austin, USA, 14 – 18 October 1961, pp 284 - 290

# Properties of ultra-lightweight Concrete based on Protein and Surfactant foaming Agents

Patrick Hartwich<sup>1</sup>, Thomas Adams<sup>2</sup>, Ali Shams<sup>3</sup>, Anya Vollpracht<sup>4</sup>, Wolfgang Brameshuber<sup>4</sup>  
and Josef Hegger<sup>5</sup>

<sup>1</sup>Scientific Staff, Institute of Building Materials Research, RWTH Aachen University

<sup>2</sup>Master Student, RWTH Aachen University

<sup>3</sup>Scientific Staff, Institute of Structural Concrete, RWTH Aachen University

<sup>4</sup>Professor, Institute of Building Materials Research, RWTH Aachen University

<sup>5</sup>Professor, Institute of Structural Concrete, RWTH Aachen University

**Abstract:** This study presents a newly developed physically foamed lightweight concrete with an oven-dry density of 400 kg/m<sup>3</sup> produced with foaming agents under standard conditions. The foaming agents are described in detail and the influence of their interactions with other admixtures on foam stability is evaluated. Subsequently different production processes for foam and foamed concrete as well as potential problems are discussed. The foamed concrete is characterized by its oven-dry density, compressive strength, Young's modulus and its thermal conductivity. By comparing the foamed concrete with other heat insulating materials, the advantages and disadvantages of the new material are pointed out. Finally an example of the use of the lightweight concrete is presented. The foamed concrete substitutes polyurethane foams in sandwich elements. The new composite material is characterized by its heat insulating properties.

**Keywords:** lightweight concrete, heat insulation, foaming agents, protein, surfactants, sandwich element.

## 1. Introduction

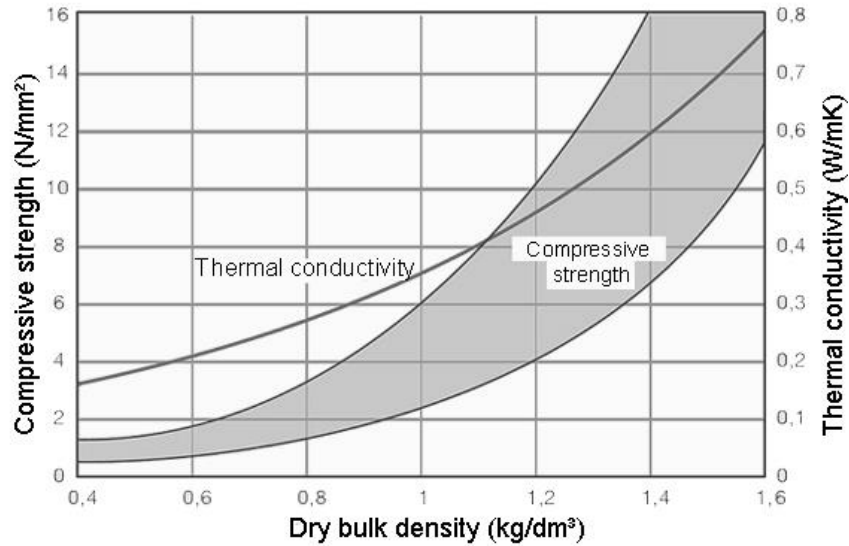
At the present time the conception of sustainable and efficient building materials is one of the most important objectives. Therefore it is requested to lower the ecological footprint of existing and new materials. One section deals with heat insulating materials. Those materials are widely used in civil engineering to fulfil new energy conservation guidelines [1, 2]. The concrete industry has developed lightweight concrete masonry units and prefabricated elements with densities between 500 kg/m<sup>3</sup> up to 1200 kg/m<sup>3</sup>. There are different types of lightweight concretes:

- a) Particulate porous concrete
- b) Concrete with lightweight aggregates
- c) Chemically aerated and autoclaved concrete (AAC)
- d) Physical foamed concrete.

The density of lightweight concrete types a) and b) is limited by the used (lightweight) aggregates to a value down to 500 kg/m<sup>3</sup>. Due to the artificial air entraining process concrete types c) and d) can achieve lower densities and as a result those are used as ultra-lightweight concretes with densities lower than 500 kg/m<sup>3</sup>.

AAC is produced by using fine aluminium powder as air-entraining agent. Due to the chemical reaction of aluminium and hydroxide ions elemental hydrogen is formed and evaporates. This causes an expansion of the fresh concrete. The expanded concrete is then autoclaved to accelerate the hydration process and thereby to stabilize the porous binder matrix, resulting in high energy consumption during the production process.

For the production of foamed concrete surfactants or proteins are used to generate foams. Subsequently the foam is merged with fresh concrete to incorporate air voids into the binder matrix. Since there is no curing under special conditions afterwards, it's crucial that the foam stays stable until the hydration sufficiently advanced. The use of lightweight concrete depends on its density. While concretes with densities from 800 – 2000 kg/m<sup>3</sup> are well known and standardized [3, 4], concretes with a density lower than 800 kg/m<sup>3</sup> are subject of ongoing research. They show improved heat insulating properties, while the compressive strength and modulus of elasticity are decreasing (see Figure 1). Therefore the application range of ultra-lightweight concrete is limited to non-load-bearing construction elements.

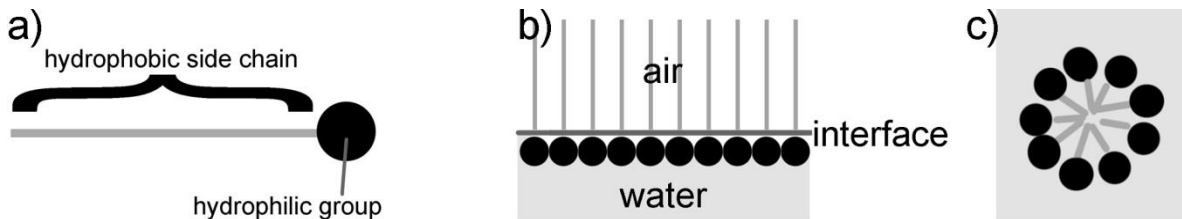


**Figure 1: Correlation between Compressive strength, thermal conductivity and oven-dry density [5]**

As mentioned before, the foam properties play a major role in lightweight concrete production. Therefore it is necessary to understand the mechanism of foam formation.

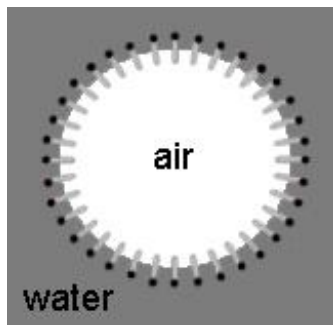
Speaking of foams, typically gas-liquid dispersions, in case of lightweight concrete air- water dispersions, are meant. To produce those dispersions, surface active substances are needed, which influence the surface tension of the continuous phase. One can differentiate between surfactants and proteins.

Surfactants are organic molecules, which consist of a hydrophobic and an ionic or rather non-ionic hydrophilic part, what makes them amphiphilic (see Figure 2a). By mixing them with water, surfactants start to assemble at the surface of the water, with their hydrophilic terminal groups orientated into the water. At low concentrations the interactions of the water molecules become weakened. Due to this effect, the surface tension is lowered. With increasing surfactant concentration, the whole surface is covered by the surfactant until a monomolecular surfactant layer has been formed as shown in Figure 2b. When this status is reached, the so called critical micelle concentration (cmc), the surface tension is minimized to a value defined by the used surfactant. If the concentration is further increasing, the surfactant will form micelles, due to their amphiphilic properties, as shown in Figure 2c.



**Figure 2: Pattern of: a) surfactant molecule; b) surfactant assembling at cmc; c) micelle formation above cmc [6]**

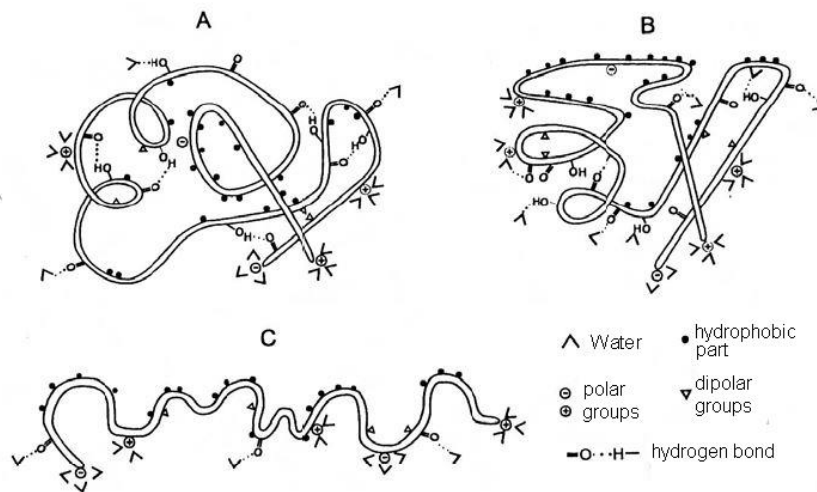
For foam production solutions with a surfactant concentration higher than the cmc are used. By introducing gas into the solution, e.g. via stirring, bubbles are formed and stabilized by the surfactant, due to their reorganization at the newly formed gas/liquid interfaces as seen in Figure 3 [7]. In this work four foaming agents based on surfactants were tested.



**Figure 3: Pattern of an air void stabilized by a surfactant**

Proteins are biological macromolecules, which are composed of amino acids. Due to the dominating functional groups – peptide bonds - within a protein, strong intermolecular interactions result and therefore proteins form complex tertiary structures as shown in Figure 4a.

If those complexes are unfolded, proteins become surface active as well. Due to different hydrophobic and hydrophilic side chains of the amino acids, the unfolded protein can assemble at an interface, where the hydrophobic side chains will emerge out of the aqueous phase (see Figure 4b).



**Figure 4: Unfolding Process of a protein: a) within the fluid; b) close to the interface; c) unfolded protein [8]**

By stirring a protein solution the unfolding process of the protein is accelerated and new air/liquid interfaces are formed (see Figure 4c). Thereby foam is generated. The intermolecular interactions of the protein chains should grant higher foam stability compared to surfactant based foam [9, 10].

## 2. Experimental details

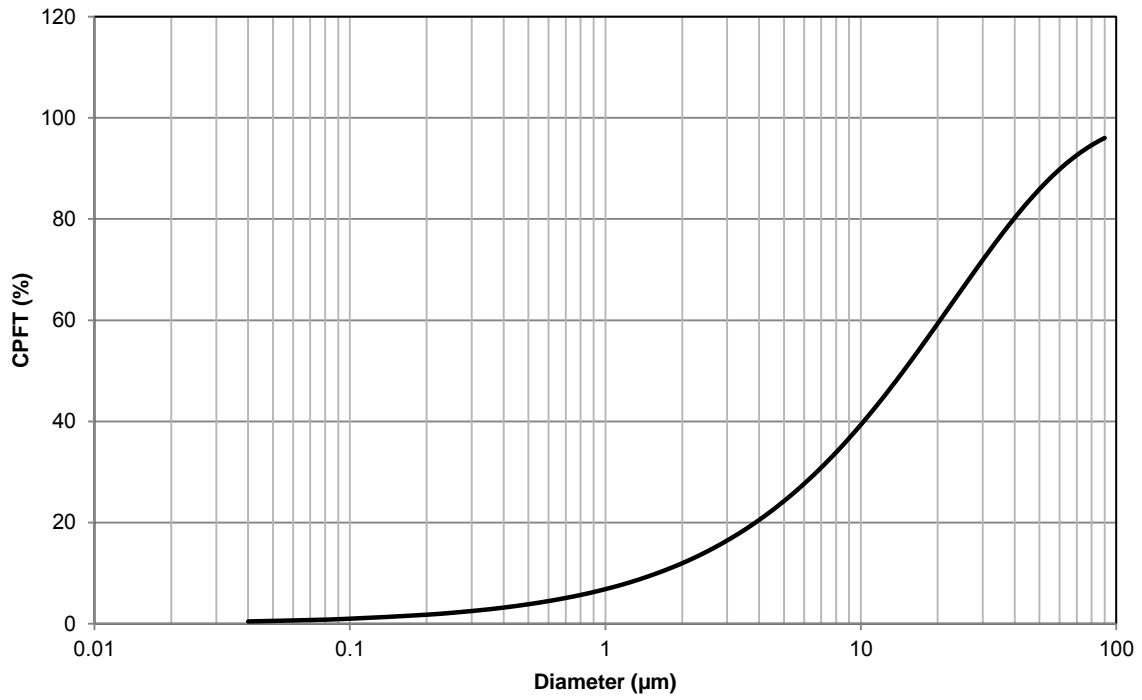
### 2.1 Raw materials

#### 2.1.1 Cement

The choice of cement is an important factor in foamed concrete development. Due to the fragile foam structure it is necessary, that the cement reacts fast enough to stabilize the thin foam lamellas before they collapse. Therefore an ordinary Portland cement CEM I 52.5 R with a fineness of 4500 cm<sup>2</sup>/g and a d<sub>50</sub>-value of 15 µm was used for the investigations. The composition of the cement is shown in Table 1, the particle size distribution in Figure 5.

**Table 1: Mineral composition and particle size distribution**

Mineral phase	Quantity (wt-%)
C <sub>3</sub> S	72.1
C <sub>2</sub> S	7.2
C <sub>3</sub> A	12.1
C <sub>4</sub> AF	1.1
Free lime	0.1
Arcanite	0.6
Bassanite	1.9
Anhydrite	4.2
Portlandite	0.1
Calcite	0.3
Quartz	0.3



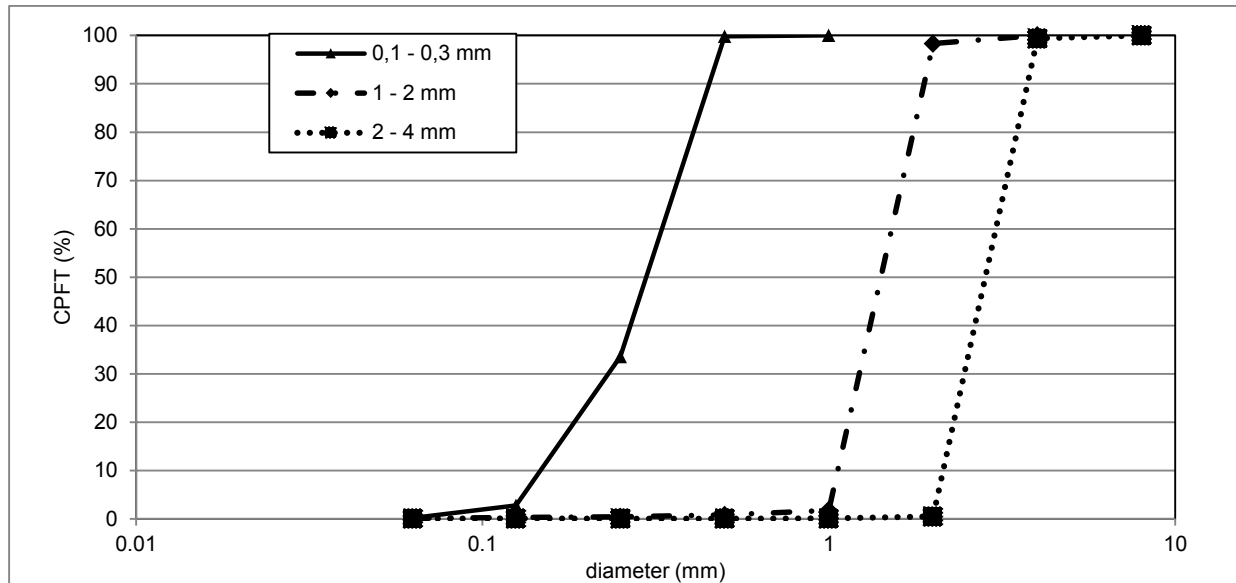
**Figure 5: particle size distribution CEM I 52.5 R**

### 2.1.2 Aggregate

Three different grain size fractions of a porous lightweight aggregate based on expanded glass were used. Material properties are listed in Table 2 and shown in Figure 6.

**Table 2: Manufacturer's data of the lightweight aggregate**

Grain size fraction (mm)	Bulk density (kg/m <sup>3</sup> )	Water adsorption (wt-%)	Mean grain strength (MPa)
0.1 - 0.3	950	35	2.8
1 - 2	400	19	1.6
2 - 4	320	14	1.4



**Figure 6: particle size distribution of the lightweight aggregates**

### 2.1.3 Admixtures

For the development of an ultra-lightweight concrete, an efficient foaming agent was needed. Therefore five commercially available substances were tested. Four of them based on surfactants (samples A-D), one was a protein based foaming agent (sample E, see Table 3).

Additionally a PCE based super-plasticizer was used to optimize the workability and flowability of the foamed concrete.

Referring to [9] a small amount of lithium carbonate was added for foam stabilization purposes.



**Table 3: Manufacturer's data of the foaming agents**

Sample	Ingredients
A	-Sulfohydroxypoly(oxy-1,2-ethandiyl- C10-C16-alkylether, sodiumsulfate (25-70%) -Sodiumolefin (C14/C16) sulfonate (10-20%) - Alkylaminoxid (3-5%)
B	-2-Butoxy-ethanol (25-50%) -Sulfonic acid, C14-16-alkanhydroxid- and C14-16-alkene, sodiumsulfate (2.5-3%) -Sodium laureth sulfate (1-2.5%) -Dodecan-1-ol (1-2.5%)
C	-Sulfonic acid, C14-16-alkanhydroxid- and C14-16-alkene, sodiumsulfate (5-10%) -Coconut oil, reaction product with diethanolamine
D	-Sulfonic acid, C13-18-alkanhydroxid- and C13- 18-alkene, sodiumsulfate (10-25%)
E	Unknown protein

## 2.2 Procedure

### 2.2.1 Foam optimization

In the first step the stability of the foam was optimized. Therefore 15 g of foaming agent solution were stirred with a hand mixer for 5 minutes. The produced foam then was poured in a measuring cylinder. The foam stability was quantified by the drained water over a defined period of time. The test was performed with different foaming agent concentrations (5 to 30 wt.-%).

### 2.2.2 Foamed concrete mixing process

Two mixing sequences were tested for their suitability. In the first methods, the fresh concrete and the foam are produced separately. Depending on the foam density and the targeted foamed concrete density, a defined amount of foam is subsequently added to the concrete slurry and homogenised. For the second method all raw materials are mixed simultaneously with high rotation speed (360 rpm). Due to the high shear forces the slurry foams up. The process is stopped, when the targeted volume is reached.

## 2.3 Characterization

The characterization of the foamed concrete was performed on an optimized mix (see paragraph 3). All samples were produced under standard conditions. Due to the low strength, they were retracted after two days with a following storage in a climate chamber (20 °C/ 65 % humidity).

### 2.3.1 Compressive strength and modulus of elasticity

The mechanical properties were tested after 7 and 28 days on cylinders with a height of  $h = 100$  mm and a diameter of  $d = 50$  mm and two installed displacement transducers. The load was increased by 500 N/min.

### 2.3.2 Thermal conductivity

Thermal conductivity was determined with the guarded hot plate method ( $\lambda$ -meter EP500, Lambda-Meßtechnik GmbH Dresden) referring to the EN 1946-2: 1999 [11] on coplanar samples with a base area of  $150 \times 150$  mm<sup>2</sup> and a height of 80 mm. The coefficient of thermal conductivity  $\lambda$  was measured at three different temperatures (10°C, 23°C and 40°C). For comparison a polyurethane foam sample with the same dimensions and a density of 36.1 kg/m<sup>3</sup> was tested.

### 2.3.3 Porosity and pore size distribution

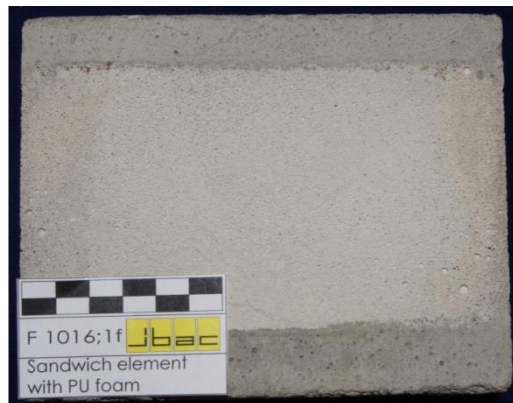
The porosity was measured with mercury intrusion porosimetry (AutoPore IV, Micromeritics) within a pressure range of 0.0138 to 420.5802 MPa. Additionally image analysis via transmitted-light microscopy on thin sections was used to determine porosity and the pore size distribution of the voids entrained by the foaming agent. For that purpose the pictures were edited with the image analysis software SIS to differentiate the pores introduced by the lightweight aggregates and those produced by the foam.

### 2.3.4 Sandwich elements for heat insulating purpose

Sandwich elements were produced from the samples used for the thermal conductivity measurements. Both sides of the sample were enclosed by a 20 mm layer of a mortar (see Table 4), resulting in a sample with a base area of 150 x 150 mm<sup>2</sup> and a height of 120 mm (see Figure 7). The heat conductivity was measured at a temperature of 23°C.

**Table 4: Composition of the sandwich element shell mortar**

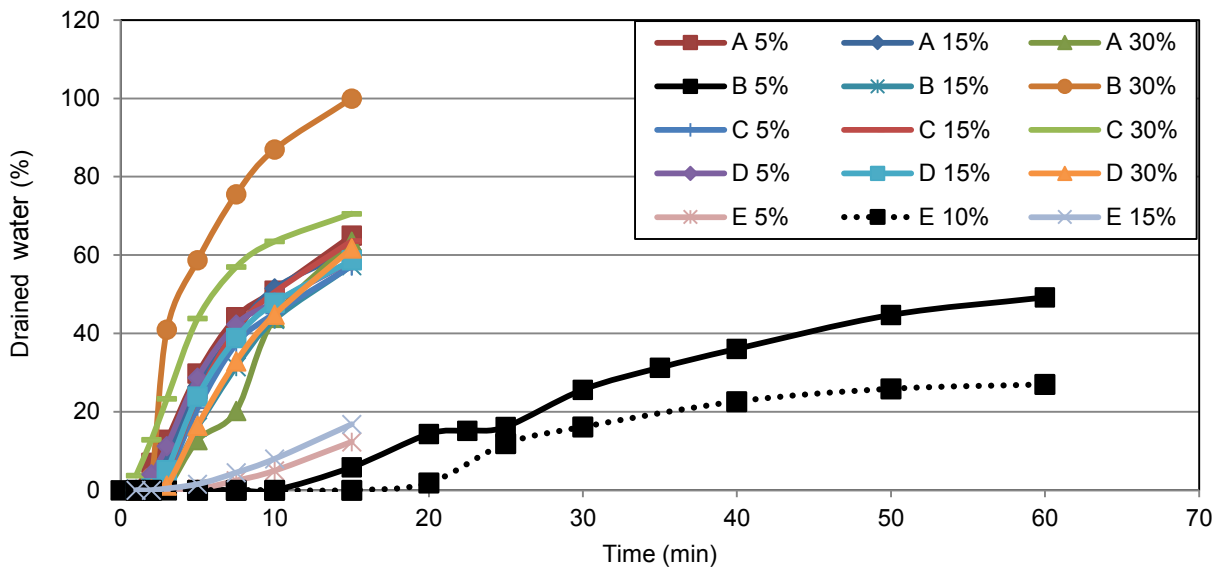
Component	Unit	Contents
CEM I 52,5 R	kg/m <sup>3</sup>	400
Aggregate		1600
Fly ash		100
Superplasticizer	% of cement	0,03
W/Z <sub>eq</sub>	-	0,463



**Figure 7: Produced sandwich element**

## 3. Results and discussion

Five foaming agents were tested for their stability in three different concentrations. The criterion for their stability was the drained water over 15 minutes. High foam stability results in a low amount of drained water. The results are shown in Figure 8.



**Figure 8: Results from the foam optimization experiments**

In general, foams made from foaming agents based on surfactants are less stable than protein foams, because of the intermolecular interactions between the unfolded and overlapping protein chains at the liquid-air interface. Accordingly the 10 % solution of protein foaming agent E produces the most stable foam. A 5 % solution of surfactant B shows competitive foam stability to the protein. For the following experiments surfactant B and E were used.

In a repetitive process the different raw materials and admixtures were tested in combination with the two described mixing methods until a stable foamed concrete with a density of 400 kg/m<sup>3</sup> was obtained. The final composition is shown in Table 5 and was produced with the simultaneous mixing method and foaming agent B.

**Table 5: Foamed concrete composition**

Component	Unit	Contents
CEM I 52,5 R	kg/m <sup>3</sup>	196
Lightweight aggregate		83,73
Superplasticizer	% of cement	0,25
Lithium carbonate		0,02
Foaming agent B 5%		0,25
Water/cement-ratio		-

The following remarks should be considered:

- The use of a superplasticizer is helpful to improve the dispersion of the concrete slurry in the foam.
- Because of the anti-foaming agent used in the superplasticizer, the dosage should not exceed 0.25 % of cement content.
- An optimized particle packing of the aggregates helps to stabilize the foamed concrete structure.

Despite of the protein foam stability it wasn't possible to produce a stable foamed concrete in our laboratory, which is contrary to the manufacturer who is capable to produce foamed concrete with densities down to 100 kg/m<sup>3</sup>.

The production volume of the in-situ mixed foamed concrete was limited to 4 liters due to the finite stirring possibility. For future investigations the pre-foaming method should be preferred.

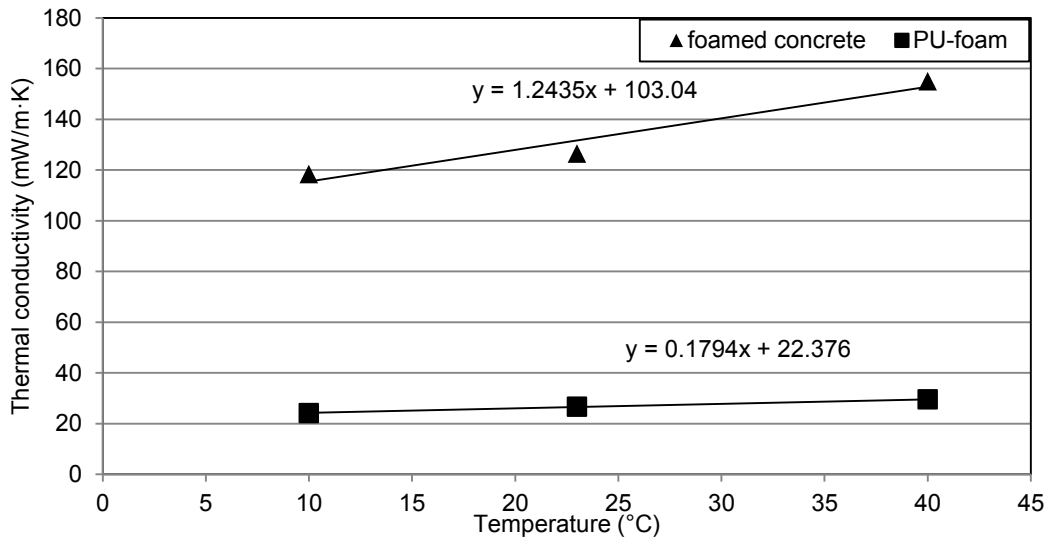
The achieved density of the foamed concrete varied between 400 and 430 kg/m<sup>3</sup>. Due to the void entraining process it isn't possible to maintain a higher accuracy.

Table 6 shows the results of the measured mechanical properties after seven and 28 days. The achieved compressive strength is  $0.61 \pm 0.16$  MPa and the modulus of elasticity is  $0.531 \pm 0.023$  GPa. Referring to the summary in [12] the compressive strength of foamed concrete systems with densities from 360-1400 kg/m<sup>3</sup> usually is between 1-10 MPa, but the high water to cement ratio ( $w/c = 1.0$ ) should be considered.

**Table 6: Results of the mechanical properties**

Sample	Compressive strength (MPa)		Modulus of elasticity (GPa)	
	7 days	28 days	7 days	28 days
1	0,23	0,54	0,327	0,579
2	0,288	0,541	0,422	0,507
3	0,296	0,639	0,337	0,52
4	0,297	0,703	0,397	0,52
5	0,327	0,92	0,397	0,52
6	0,266	0,468	0,397	0,541
7	0,296	0,357	0,389	0,554
8	0,233	0,569	0,406	0,527
9	0,248	0,517	0,401	0,512
Average value	<b>0,28</b>	<b>0,61</b>	<b>0,386</b>	<b>0,531</b>
Standard deviation	0,033	0,160	0,032	0,023

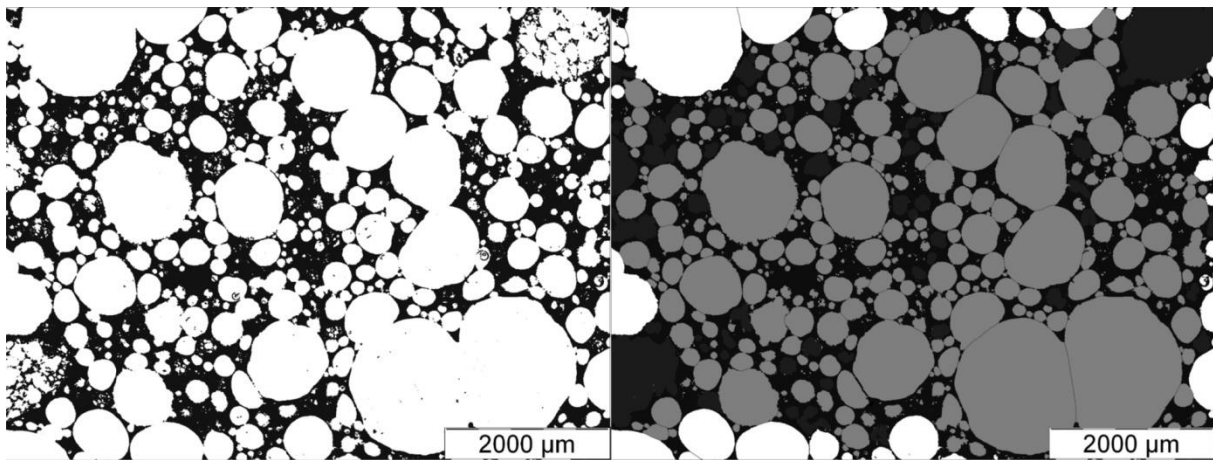
The averaged results of the heat conductivity measurements are shown in Figure 9. Due to the low density of polyurethane (PU) foam, the achieved foamed concrete thermal conductivity is about six times higher. To improve the heat insulating properties the density needs to be reduced.



**Figure 9: Correlation between thermal conductivity and temperature (average values)**

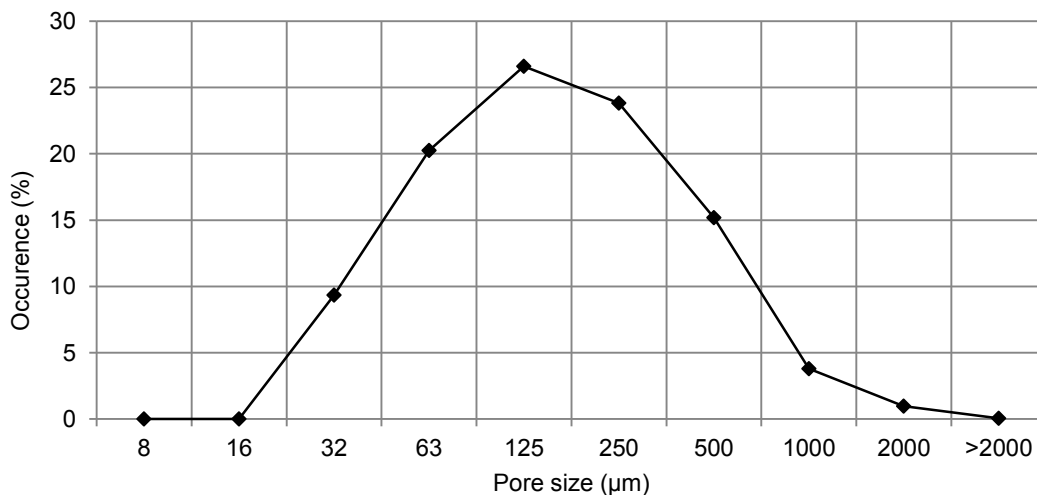
Measurements via mercury intrusion porosimetry gave a mean porosity of 65.3%. To determine the pore size distribution of the air voids, thin sections were analyzed via transmitted-light microscopy. The image analysis software allowed the detection of the void content via gray value differentiation between the bulk phase (dark) and the voids (bright). Figure 10 (left) shows an example of an analyzed picture. A Porosity of 63.4 % arises from the image analysis and is in very good agreement with the mercury intrusion porosimetry measurements.

Additionally the pore sizes were quantified. The edge voids and lightweight particles were excluded from the detection, because they would falsify the analysis. As shown in Figure 10 (right) only the colored voids are included for the quantification. The resulting pore size distribution is shown in Figure 11.



**Figure 10: Transmitted-light image (left), detected pore sizes (gray, right)**

It has to be considered that the detection via microscopy includes a systematic error because the three dimensional void shape is neglected. For spherical voids the diameter is usually smaller than the real pore size, because voids are usually not cut in the center. Therefore Figure 11 gives just a hint of the real pore size distribution of the air voids. Due to the low magnification, which was chosen to analyze a larger sample area, pores smaller than 8 μm couldn't be detected.



**Figure 11: Detected pore size distribution via image analysis**

The sandwich elements were tested for their thermal conductivity. The results of the single components and combined elements are shown in Table 7.

**Table 7: Results for thermal conductivity**

Sample	$\lambda_{23^{\circ}\text{C}}$ (mW/m·K)	$R_{23^{\circ}\text{C}}$ (m <sup>2</sup> ·K/W)
Foamed concrete	126.5	0.63
Sandwich shell mortar	495.5	0.06
Sandwich with foamed concrete	188.33	0.64

Due to the comparatively high thermal conductivity of the mortar the sandwich shell has no significant influence on the thermal properties of sandwich elements.

#### 4. Conclusion and outlook

The presented work gives a perspective for foamed concrete as sustainable alternative to polymers as heat insulating material. For that purpose the main target is to develop low density products ( $<150 \text{ kg/m}^3$ ) to reduce the thermal conductivity in order to compete with polymer foams. Otherwise the use of foamed concrete is uneconomical due to the necessity of large dimension construction elements to achieve comparable thermal properties to polymer materials. On the other hand, sustainability, e.g. recycling and long-term stability as well as fire resistance, should be taken into account when comparing cementitious with polymeric foams.

For that purpose our ongoing investigations deal with a foamed concrete based on calcium aluminate cement targeting a density between  $130 - 150 \text{ kg/m}^3$ .

Furthermore the characterization of the sandwich elements is an ongoing process to adjust the different components to obtain a high load-bearing capacity.

#### 5. Acknowledgement

Thanks to the RWTH Aachen University for funding the joint research project "Sustainable buildings of the future" in which scope this work took place.

#### 6. References

1. R. Mott, J. Steinhoff und W. Brameshuber, „Innovative wall construction made of foam SCC and textile reinforced concrete“ in *Third International fib Conference, Incorporating PCI Annual Convention Bridge Conference, May 29 - June 2, Washington, 2010*.
2. A. Shams, A. Stark, F. Hoogen, J. Hegger and H. Schneider, „Innovative sandwich structures made of high performance concrete and foamed polyurethane,“ *Composite Structures*, no. 121, p. 271–279, 03 2015
3. *DIN EN 206:2013; Concrete - Specification, performance, production and conformity; German version*, Berlin: Beuth Verlag, 2013.
4. *DIN EN 1992-1-1:2004; Design of concrete structures - Part 1-1: General rules and rules for buildings; German version*, Berlin: Beuth Verlag, 2004.
5. HeidelbergCement, *Betontechnische Daten*, Heidelberg: HeidelbergCement AG, Entwicklung & Anwendung, 2014.
6. B. Fabry, „Tenside. Eigenschaften, Rohstoffe, Produktion, Anwendungen,“ *Chemie in unserer Zeit*, Bd. 25, Nr. 4, pp. 214-222, 2001.
7. R. Prud'homme und S. Khan, *Foams: theory, measurements and applications*, New York: Marcel Dekker, Inc, 1996.
8. H. Besner, *Grenzflächenwechselwirkungen und Mechanismen der Schaumstabilisierung beim Ausschäumen von Sahne*, Dissertation Hrsg., Universität München: Fakultät für Brauwesen, 1997.
9. J. U. Pott, „Entwicklungsstrategien für zementgebundene Schäume,“ *Institut für Baustoffe*, Leibniz Universität Hannover, Hannover, 2006.
10. A. Saint-Jalmes, ..-L. Peugeot, F. H. und D. Langevin, „Differences between protein and surfactant foams,“ *Colloids and Surfaces*, pp. 219-225, 2005.
11. EN 1946-2 : 1999, „Thermal performance of building products and components – Specific criteria for the assessment of laboratories measuring heat transfer properties – Part 2: Measurements by the guarded hot plate method; German version,“ Beuth Verlag, Berlin, 1999.
12. Z. Zhang, J. Provis, A. Reid und H. Wang, „Geopolymer foam concrete: An emerging material for sustainable construction,“ *Construction and Building Materials*, Nr. 56, pp. 113-127, 2014.

# Effect of Guar Gum Derivatives on Fresh State Properties of Portland Cement-Based Mortars

Alexandre Govin<sup>1</sup>, Marie-Claude Bartholin<sup>2</sup>, Barbara Biasotti<sup>3</sup>, Max Giudici<sup>4</sup>, Valentina Langella<sup>5</sup> and Philippe Grosseau<sup>6</sup>

<sup>1</sup>Assistant Professor, Ecole des Mines de Saint Etienne

<sup>2</sup>Technician, Ecole des Mines de Saint Etienne

<sup>3</sup>Senior Scientist, Hydrocolloids Derivatives - Lamberti SpA

<sup>4</sup>Senior Scientist, BU Construction - Lamberti SpA

<sup>5</sup>Technology Manager, Hydrocolloids Derivatives - Lamberti SpA

<sup>6</sup>Professor, Ecole des Mines de Saint Etienne

**Abstract:** Mortars are traditionally made from a mixture of sand, a binder and water. However, modern factory-made mortars are currently, very complex materials. Indeed, to exhibit various properties from the fresh paste to the hardened material, mortar formulations are composed of many mineral and organic admixtures. Among organic admixtures, polysaccharides are widely used in mortar formulation to improve water retention capacity of the freshly-mixed materials. The water retention capacity is an essential property of mortars to enhance cement hydration and its adhesion to a substrate. Moreover, many polysaccharide admixtures, acting as viscosity-enhancing agents, prevent segregation and improve the homogeneity and workability of cement-based system. Indeed, the viscosity of the system strongly increases using polysaccharides. Nevertheless, polysaccharides, as sugars, act on cement hydration. The main drawback is the retarding effect in hydration mechanism and setting-time of the cement.

The aim of this study is to focus on the effect of guar gum derivatives on fresh state properties of Portland cement-based mortars, such as water retention, rheological behavior and the hydration delay. This work focuses on the guar gum derivatives since their manufacturing process is low pollutant and they provide very good properties to cement-based mortars. The results highlight that the chemical composition of guar gum derivatives (MS, DS, additional alkyl chain) are the key levers to improve water retention of mortars and to adapt the rheological behavior of the cementitious paste to a specific application.

**Keywords:** Cement; HydroxyPropyl Guar; Mortar; Rheology; Water retention.

## 1. Introduction

Modern factory-made mortars are complex materials, in which several kinds of admixtures are added in order to obtain specific properties, from the fresh state to the hardened material. Indeed, since many years, concretes, mortars or cement grouts with high fluidity have been developed, since their use implies many economical and technical advantages. However, the use of highly flowable mixtures may lead to segregation or excessive bleeding and subsequently, durability issues. In order to overcome this problem by enhancing the segregation resistance while maintaining high fluidity, viscosity-enhancing admixtures (VEA) are frequently introduced within the formulation (1,2,3,4). Among these admixtures, natural polysaccharides or their derivatives (such as welan gum, starch derivatives or cellulose ethers) are the most widely used. Moreover, the incorporation of these VEAs in shotcrete or render mortar is useful to ensure sagging resistance for thick application on vertical support, and to allow sufficient fluidity for normal pumpability by supplying shear thinning rheological behavior (5). Indeed, these admixtures provide, generally, high yield stress and apparent viscosity at low shear rate but low resistance to flow at high shear rate (6). However, their mode of action is not fully understood, since results are sometimes contradictory. Water retention (WR) is another essential property of monolayer render at fresh state. Indeed, high water retention improves the cement hydration and limits the absorption of the mixing water by a substrate and thus provides good mechanical and adhesive properties to the mortar (7). Among admixtures enhancing water retention capacity of the freshly-mixed mortars, cellulose ethers (CE) are the most widely used. Nevertheless, hydroxypropyl guar (HPG) are now also well-established in the construction industry as water retention agent for mortars (8,9,10,11). Since HPGs improve two main properties of mortar, they appear as suitable admixtures to be used in render formulation.

The aim of this study is to provide an understanding of the effect of chemical composition and structure of HPGs and its dosage on macroscopic properties of mortars. For this purpose, an original guar gum and five HPGs with specific chemical modifications, such as increase in MS<sub>HP</sub> or substitutions by hydrophobic

units, were selected. The impact of admixtures on the water retention capacity, on cement hydration and on the rheological behavior of mortars was investigated.

## 2. Materials and methods

### 2.1 Mineral products

Mineral products used in this study consist in blend Portland cement (Holcim), lime (Holcim), calcium carbonate (Calcitec V60, Mineraria Sacilese S.p.A.) and dolomite (Bombardieri and Leidi 0.1-0.4mm). The mineral compositions of the commercial Portland cement, CEM II/B-LL 32.5 R according to the European standard EN 197-1 (12), used are given in Table 1.

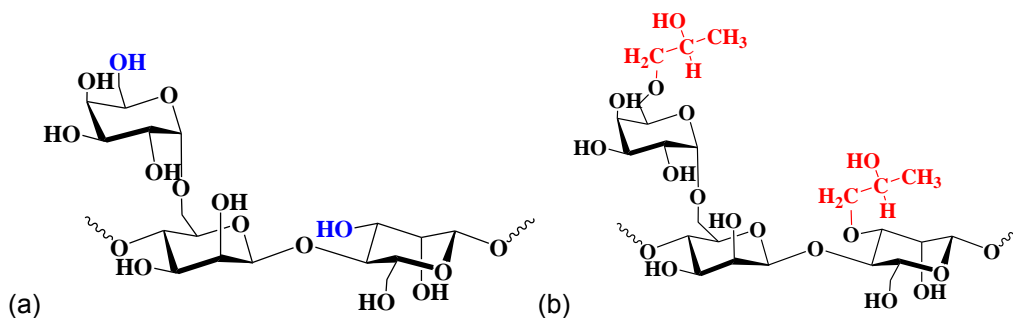
**Table 1. Mineral composition (% weight) of the investigated cement determined by XRF and XRD-Rietveld refinement.**

Chemical composition (% wt)				Phase composition (% wt)			
Oxides	XRF	Oxides	XRF	Phases	XRD (Rietveld)	Phases	XRD (Rietveld)
CaO	57.87	SO <sub>3</sub>	3.95	C <sub>3</sub> S	54.3	Calcite	28.9
SiO <sub>2</sub>	12.31	Na <sub>2</sub> O	0.99	C <sub>2</sub> S	3.5	Gypsum	3.0
Al <sub>2</sub> O <sub>3</sub>	5.25	K <sub>2</sub> O	1.66	C <sub>3</sub> A	4.7	Quartz	0.9
MgO	1.19	TiO <sub>2</sub>	0.16	C <sub>4</sub> AF	4.6	Free CaO	0.8
Fe <sub>2</sub> O <sub>3</sub>	4.05	LOI	13.7				

The phase composition was determined by Rietveld refinement method (Siroquant V2.5 software) after XRD analysis (D5000, Siemens) and the oxide composition was quantified by means of X-ray fluorescence spectroscopy. The median particle diameters by volume ( $d_{50\%}$ ) determined by means of laser diffractometry with dry powder disperser (Mastersizer 2000 and Scirocco dispersing unit, Malvern) was 5, 15, 20, 300 and 600 $\mu$ m for lime, cement, calcite and both dolomite fine aggregates, respectively.

### 2.2 Organic admixtures

Guar gum is a natural polysaccharide extracted from the seed endosperm of *Cyamopsis tetragonolobus*. This polymer consists in a  $\beta$ (1-4)-linked D-mannopyranose backbone with random branchpoints of galactose via an  $\alpha$ (1-6) linkage (Fig. 1(a)). Hydroxypropyl guar (HPGs) are obtained from the original guar gum via an irreversible nucleophilic substitution, using propylene oxide in the presence of an alkaline catalyst (Fig. 1(b)).



**Figure 1. Molecular structure of original guar gum (a) and HydroxyPropyl Guar (b)**

The manufacture of HPGs has the advantage of having a more reduced impact on the environment than cellulose derivatives. Indeed, guar gum is extracted by simple thermo-mechanical process, exhibits a higher chemical reactivity and is soluble in cold water thanks to its branched-chain structure with a lot of hydroxyl groups. Thus, the chemical modification of the original guar gum requires normal reaction conditions of temperature and pressure, does not generate large quantity of by-products, and requires minimal purification procedure (8). In this paper, five HPGs and an original guar gum provided by Lamberti S.p.A were studied. They exhibit roughly the same molecular weight, around  $2 \cdot 10^6$  g $\cdot$ mol<sup>-1</sup> since they are



all from the same original guar gum (noted HPG 6 in the paper) (13). Table 2 provides a qualitative description of the polymers used. The qualitative substitution degrees are provided by the manufacturers. The molar substitution ratio ( $MS_{HP}$ ) represents the number of hydroxypropyl units per anhydroglucose unit and is less than 3 for the investigated HPGs. The degree of substitution ( $DS_{AC}$ ) represents the amount of alkyl chain per anhydroglucose unit. The only difference between HPGs 1 and 3 is the molar substitution ratio, which increases, while HPG 4 exhibits an additional substitution (short alkyl chains).

**Table 2. Qualitative description of the HPG used.**

	$MS_{HP}$	$DS_{AC}$	Additional substitution
HPG 1	Low	-	
HPG 3	High	-	
HPG 4	High	Low	Short alkyl chain
HPG 6	-	-	-

### 2.3 Methodology

Mortars were prepared according to the following mixture proportions: 12% of cement, 3% of lime, 18% of calcium carbonate, 43% of dolomite Bombardieri and 24% of dolomite Leidi (by weight). The admixtures were in addition to the total dry mixture (i.e. cement, lime, calcium carbonate and dolomite) and are expressed in weight percent by weight of binder (% bwob). Dry mixture was blended in a shaker (Wab, Turbula, Germany) for 10 min. Deionised water was added in order to obtain a liquid-to-solid ratio  $L/S = 0.22$ . The mixing procedure was in accordance with EN 196-1 (14). All tests were carried out, at least, in triplicate and at a controlled temperature. A control test was also performed with a mortar without admixture.

### 2.4 Water retention measurements

The water retention capacity of freshly-mixed mortar was assessed using ASTM C1506-09 standard method (15). It had to be performed 15 min after mixing to measure the water loss of a mortar under partial vacuum. The standardized apparatus was submitted to a vacuum of 50 mm of mercury ( $6.6 \cdot 10^3$  Pa) for 15 min. Then, the water retention capacity, WR, was calculated using the following equation:

$$WR(\%) = \frac{W_0 - W_1}{W_0} \times 100 \quad (1)$$

where  $W_0$  represents the initial mass of mixing water;  $W_1$  is the loss of water mass after aspiration.

All the experiments were carried out at 23 °C. Three classes of water retention can be specified according to the DTU 26.1 (16). The first class (low WR category) contains mortars that exhibit WR lower than 86%. The second class (medium) corresponds to WR ranging from 86% to 94%. The last one (high) is defined by WR higher than 94%, corresponding to the required values in the field of rendering application.

### 2.5 Rheological behavior

The rheological measurements were performed with Rheometer MCR 302 (Anton-Paar), thermostated at 20 °C. The rheological properties of fresh mortars were investigated with vane-cylinder geometry (17,18). The mortar was introduced into the measurement system at the end of the mixing cycle. At 10 min, the mortar was pre-sheared for 30 s at  $100 \text{ s}^{-1}$  in order to re-homogenize the sample and to eliminate its shear history (19,20). After a period of rest of 5 min, the rheological measurements were started (total time = 15 min). The imposed shear rate was decreased by step from 300 to  $0.06 \text{ s}^{-1}$ . At each shear rate, the measuring time was adjusted in order to obtain a steady state whatever the formulation. The samples were systematically submitted to high shear rate ( $100 \text{ s}^{-1}$ ) for 30 s before each imposed shear rate in order to resuspend particles of mortar within the mortar mixtures. The results were expressed as shear stress  $\tau$  according to shear rate  $\dot{\gamma}$  and the Herschel-Bulkley (HB) model was applied to fit the experimental data and used to describe mortars rheological behavior (21):

$$\tau = \tau_0 + K\dot{\gamma}^n \quad (2)$$

where  $\tau_0$  correspond to the yield stress, K the consistency coefficient and n the fluidity index which characterizes shear-thinning behavior of mortar.

## 2.6 Adsorption curves of HPGs on binder

The adsorption isotherms were determined using the depletion method. The non-adsorbed polymer remaining within the pore solution was quantified by means of Total Organic Carbon (TOC) measurements. Prior to analysis, the pore solution was extracted from admixed or non-admixed mortar. The extraction was performed by means of two centrifuging steps. The first step consisted in the centrifugation of around 150 g of mortar at 5000 rpm for 5 min. The supernatant was, afterward, centrifuged again at 14500 rpm for 10 min in order to avoid the presence of mineral particles within the solution. The supernatant was diluted with hydrochloric acid solution at 0.1 mol.L<sup>-1</sup>. The total organic carbon was determined by combustion at 850 °C with a Vario-TOC Cube (Elementar). The adsorbed amount of polysaccharides was calculated from the difference of TOC content of the HPG reference solution and the TOC content of the supernatant.

## 2.7 Conductimetric measurement

Characterization of the delay induced by the studied admixtures on the cement hydration was performed by conductivity measurements. Conductivity measurements were carried out in lime suspension in order to obtain hydration kinetics close to that observed in cement pastes, in spite of a high liquid-to-solid weight ratio (L/S). Conductivity curves were interpreted according to explanations proposed by Comparet et al. (22). As soon as cement came in contact with liquid, the electrical conductivity increased as a consequence of the dissolution of the anhydrous phases. Then, nucleation of hydrates on the grain surface leads to a period where the conductivity evolves weakly. Conductivity then accelerated more quickly. The conductimetric slope is related to the growth rate of the hydration products. Meanwhile, cement dissolution still continued. The conductivity increases to the supersaturation with respect to portlandite and decreases rapidly due to its precipitation. Thus, an electrical conductivity drop is caused by the portlandite precipitation. The portlandite precipitation time was used as a benchmark to classify and to quantify the relative retardation ability of admixtures on cement hydration.

Experiments were performed in lime solution (20 mM), thermostated at 25 °C and continuously stirred. The liquid-to-solid weight ratio (L/S) used was equal to 10. Polymer-to-binder weight ratio (P/B) was fixed to 0.5%. Binder GUM 01 and admixture powders were blended in a shaker (Turbula, Wab) for 10 min before contact with the liquid phase. The control corresponds to the neat binder.

## 3. Experimental results

### 3.1 Impact of HPGs on the water retention property of fresh mortars

Fig. 2 represents the evolution of the water retention capacity of fresh admixed mortars, according to the polymer dosage. The non-admixed mortar exhibits a low water retention capacity of about 72% ± 0.3%. Then, as expected, the water retention increases with the use of HPGs and with increasing polymer dosage, until reaching a plateau with very high WR values (>97%). In the range of polymer dosage studied, the WR values reached for HPGs 3 and 4 are greater than 94% and therefore belong to the high WR class. The original guar gum and, to a lesser extent HPG 1, highlight a very limited impact, regardless of dosage until 0.2%. These results suggest that the substitution of hydroxyl units from original guar gum by hydroxypropyl units increases the WR of mortars. Furthermore, the increase in the MS<sub>HP</sub> (from HPG 1 to 3) improves the WR capacity of mortar, since HPG 3 provides the higher WR despite lower dosage.

The results highlight moreover the positive impact of additional alkyl chain on WR. Indeed, the highest WR are obtained with HPG 4 for the lowest polymer dosages. Moreover, concerning the shape of WR curves, an abrupt change in slope can be noticed for mortars admixed with HPGs 3 and 4, and with HPG1 but only above 0.15%. This occurs for a decreasing polymer dosage from HPG 3 to HPG 4.

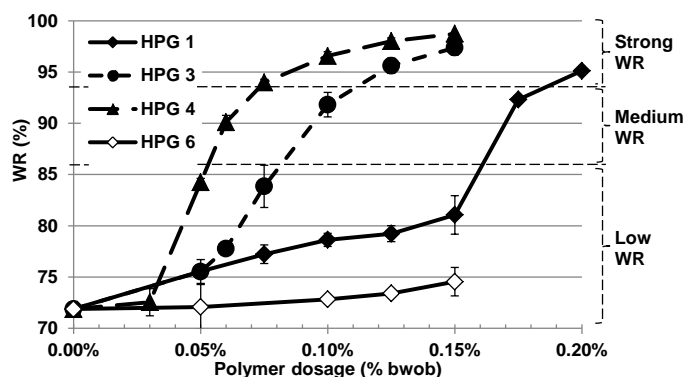


Figure 2. Impact of polymer dosage on water retention capacity of fresh admixed mortars

### 3.2 Modification of cement hydration by HPGs

The conductimetric data highlights the impact of HPGs on the kinetics of hydration (Fig. 3(a)). By focusing on the portlandite precipitation time, it appears a wide range of delays induced by the admixtures. Among HPGs, HPG 4 exhibits the weaker delay (4.5 h) (Fig. 3(b)). The most important delay is observed for HPG 1 (17.8 h). The native guar gum induces the lowest delay in the portlandite precipitation. The increase in  $MS_{HP}$  (from HPG 1 to 3) leads to a decrease in the portlandite precipitation time. The comparison between HPG 3 and HPG 4 suggests the low impact of the alkyl chain on the delay of the portlandite precipitation.

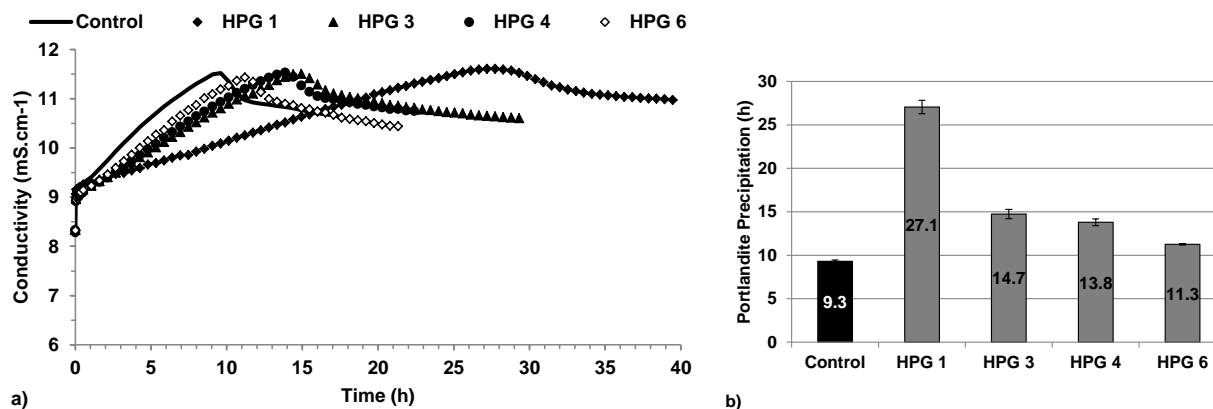


Figure 3. Influence of HPGs on conductimetric curves (a) and on portlandite precipitation time (b),  $[Ca(OH)_2]=20$  mM, L/S=10, P/B=0.5%

The conductimetric curves reveal a very low extension of the duration of the “period of low increase in conductivity” (Fig. 3(a)). This result highlights the weak influence of admixtures on the nucleation of the first cement hydrates. The same results were obtained by Poinot et al. (9). The delay of portlandite precipitation is mainly due to the slope decrease. The slope of the conductimetric curve, being linked to the growth rate of the hydrated cement phases, suggests that HPGs act preferentially on the growth of hydrates, rather than on their nucleation.

### 3.3 Adsorption curves of HPGs on binder

Fig. 4(a) shows the adsorption isotherms of the admixtures on Portland based-mortars. The results confirm the adsorption of original guar gum and HPGs on cementitious materials. It has been shown that the adsorption mechanism of galactomannose polysaccharides at solid–liquid interfaces involves strong hydrogen bonding (23). In the range of polymer dosage used in the study, no plateau was reached, and this, whatever the admixture. For the original guar gum (HPG 6), the adsorption is the highest of all the tested polymers and corresponds to a total adsorption higher than 98.5% of the introduced polymer. The presence of hydroxypropyl substitutions on the guar leads to a decrease in the affinity of the polymer with the binder since the adsorption of HPG 1 is lower by 35% than the original guar gum. Moreover, the

adsorption is further reduced by increasing values of  $MS_{HP}$  (64% for HPG 3 compared to HPG 6). This tendency is consistent with previous studies on HPGs and cellulose ethers (9, 24). Fig. 3(a) highlights also the effect of the additional alkyl chain on the adsorption. It appears that the hydrophobic side chains slightly intensify the adsorption of the hydrophobically modified HPG on surface of grains with respect to HPG 3.

From the TOC measurements, the real polymer concentration within the extracted pore solution was determined. Fig. 4(b) shows the evolution of this concentration versus the introduced polymer dosage. Excepted HPG 6, the amount of non-adsorbed polymer increases with increasing polymer dosage. According to the HPG, the concentration rises following this order: HPG 6 < HPG 1 < HPG 4 < HPG 3.

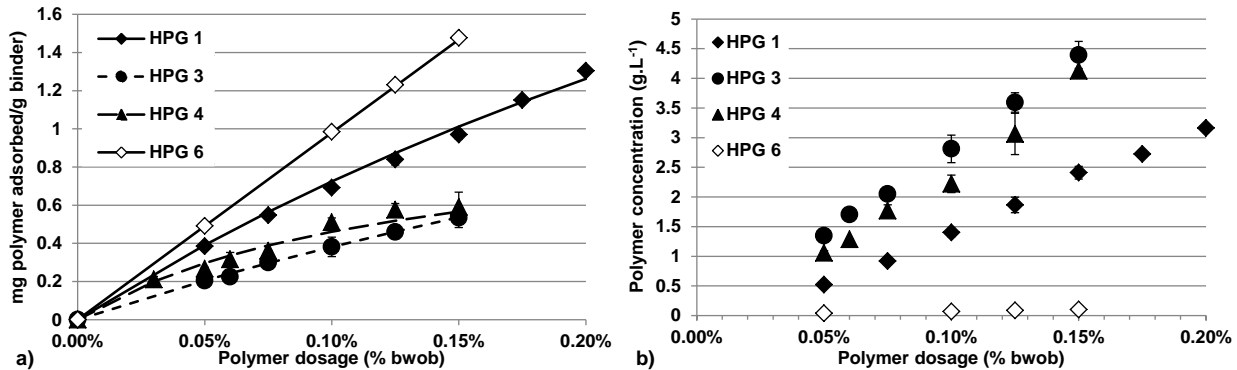


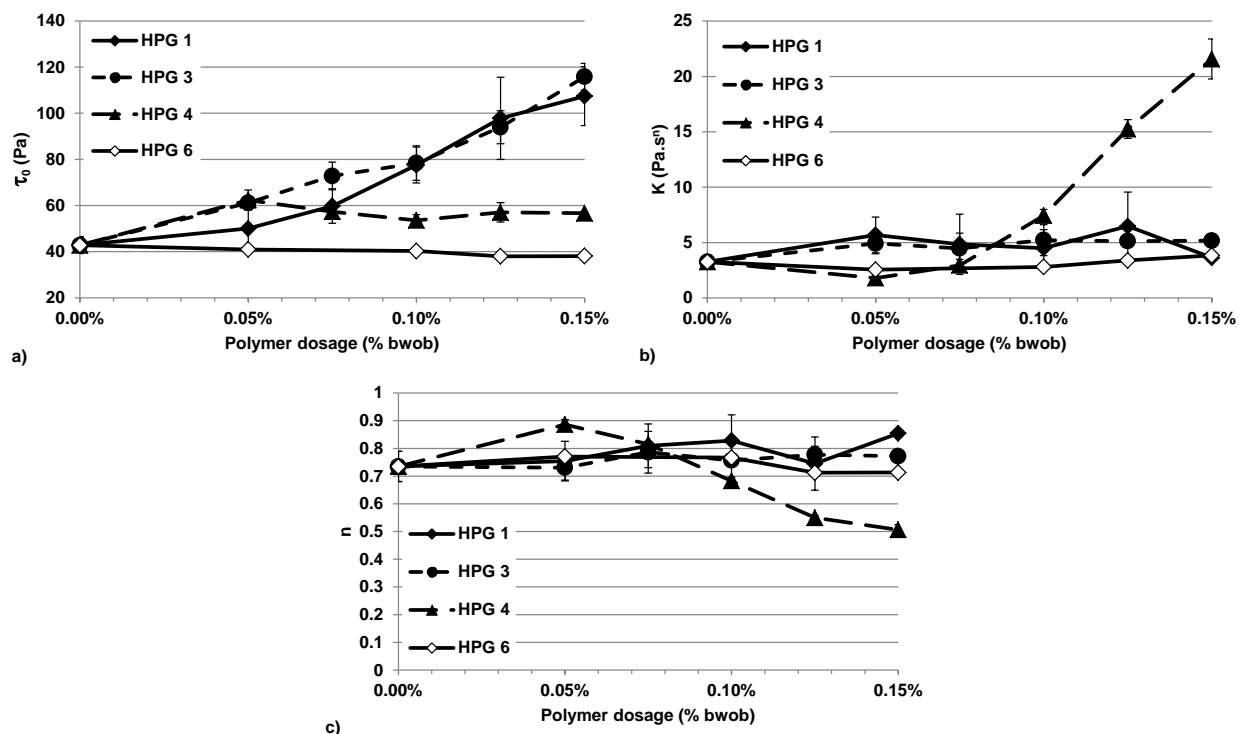
Figure 4. Adsorption isotherms of HPGs 1, 3, 4 and original guar gum (HPG 6) (a) and concentration of HPGs in extracted mortar pore solution (b)

### 3.4 Impact of HPGs on the rheological properties of fresh mortars

Fig. 5(a) shows the evolution of the yield stress, extracted from Herschel-Bulkley model, for all the studied mortars with and without admixture. The mortar without admixture exhibits a yield stress value of around 45 Pa. From the presented results, three different classes of HPG, inducing different evolution of the yield stress with the polymer dosage, can be highlighted for admixed mortars. The first category is only composed of the original guar gum (HPG 6), which induces a low and quasi linear decrease in the yield stress of mortar when HPG dosage increases. On the contrary, HPGs 1 and 3 lead to a continuous rise of the yield stress of mortars from 50-60 Pa to around 120 Pa with the increase in the HPG dosage from 0.05% to 0.15%. Finally, HPG 4 constitutes the third class of admixture. The use of this admixture leads an improvement of the yield stress compared to the non-admixed mortar, whatever the dosages tested in the study. However, the increase is not proportional to the admixture dosage. Indeed, our first dosage (0.05% bwob) leads to an increase in the yield stress. Beyond this dosage, increasing the dosage provides a slow and low decrease, before reaching a plateau. The value of the yield stress reached on the plateau is still higher than that of the mortar without admixture.

The evolution of the consistency coefficient ( $K$  from Herschel-Bulkley equation) during the increase of polymer dosage is presented Fig. 5(b). As in the case of the yield stress, the results can be divided into three classes of polymer. The first class is only composed of the original guar gum which provides a very low or negligible modification of the consistency coefficient with increasing polymer dosage compared to non-admixed mortar. HPGs 1 and 3, constituting the second group, induce first an increase followed by a plateau in the consistency coefficient. Finally, HPG 4 leads to a continuous increase in the consistency coefficient of admixed mortars.

Fig. 5(c) shows the evolution of the fluidity index ( $n$ ) versus the polymer dosage for all the studied mortars. It is worth to note that whatever the mortars, the values of the fluidity index are lower than 1, meaning that they are all shear thinning. Due to the high standard deviation, the value of the fluidity index of mortars admixed with HPGs 1 and 3 and 6 seem to be unchanged as the dosage of HPGs increase. However, HPG 4 leads to a low increase followed by a continuous decrease in the fluidity index until reaching values around 0.5. This means that the shear thinning behavior of mortars becomes more and more pronounced.



**Figure 5. Impact of polymer dosage on yield stress (a), consistency coefficient (b) and fluidity index (c) of fresh admixed mortars (HPGs 1, 3, 4 and original guar gum (HPG 6))**

## 4 Discussion

The effect of the original guar gum (HPG 6) is negligible from the WR point of view. Since the adsorption is higher than 98.5% of the initial amount of polymer, very few molecules are still in the pore solution. The composition of pore solution is thus close to that of the non-admixed mortar, leading to similar WR.

Concerning the hydroxypropyl guar, the results from WR experiments are consistent with those of previous studies performed with HPGs or CEs and with the proposed mechanism. Indeed, the WR of admixed mortars is mainly governed by the ability of polysaccharidic admixtures to form an associated polymer molecules network and to induce overlapping of polymer coils within the pore solution (10,25,26). When the polymer concentration in solution increases, the isolated polymer coils, existing at low concentration, begin to come into contact between them. This concentration is defined as the coil-overlap concentration (noted  $C^*$ ). Above this critical concentration, the polysaccharide aggregates stop the water flow by plugging the porous network of a thin polysaccharide-enriched filter cake at the interface mortar-substrate resulting in a sudden and sharp rise in WR curves (10). The abrupt change in slope is reached for a decreasing polymer dosage from HPG 1 to HPG 3. The only difference between these HPGs is the increasing substitution degree. According to literature, the increase in  $MS_{HP}$  does not lead to a change in  $C^*$  (27). However, the increasing substitution degree leads to a decrease in polymer adsorption on mortar components and hence an increase in polymer amount in pore solution (Fig. 4). Consequently, the coil overlapping occurs at lower dosage. The results highlight furthermore the positive impact of additional alkyl chain on WR. The presence of additional alkyl chains (HPG 4), despite slightly higher adsorption than HPG 3, leads to the formation of polymer associates at lower polymer dosage. Indeed, the interconnection between alkyl chains creates intramolecular and intermolecular interactions through specific hydrophobic interactions which cause a decrease in the coil-overlapping concentration (28,29). Consequently, the abrupt change in slope is reached for a lower polymer dosage of HPG 4 than HPG 3.

It is generally admitted that cement hydration delay induced by admixtures is due to adsorption of these molecules onto surfaces of the hydrating cement particles and/or surfaces of hydration products (30,31). Polysaccharides are molecules which contain a lot of polar functional groups (-OH). Therefore, strong interactions, through electrostatic forces and hydrogen-bonding, can occur between polysaccharides and the highly polar hydrated phases (31). This interpretation is consistent with our results, especially for

HPGs 1 and 3. Indeed, the increase in the  $MS_{HP}$  leads to a decrease in the amount of free hydroxyl groups on the backbone chain and in the polarity of the molecule. Therefore a drop in both adsorption onto the surfaces and delay of the portlandite precipitation, is observed. However, in the case of HPG 4, and more especially for HPG 6, the adsorption of the admixture is higher than that of HPG 3 but the delay in the portlandite precipitation is lower. Therefore, a competitive adsorption of admixture could occur between the constituents of the binder, promoting adsorption onto non-reactive phases (dolomites and/or calcite). To answer to this question, the conductimetric analysis should be carried out only with cement.

The rheological results (Fig. 5) highlight that HPGs 1 and 3, HPG 4 and HPG 6 behave quite differently. Indeed, HPGs 1 and 3 lead to a continuous increase in the yield stress, while HPG 4 modifies mainly the consistency coefficient and the fluidity index. HPGs 1 and 3 affect the rheological behavior of the admixed mortars in the same way, i.e. an increase in the yield stress, a low increase followed by a plateau in the consistency coefficient and a negligible modification of the fluidity index when the polymer dosage rises. Fig. 4(a) shows that HPGs adsorb onto particles constituting the mortar. Prima facie, this adsorption could be responsible for the increase in the yield stress because of bridging flocculation (24). However, despite a strong drop of the adsorption (50%) with the increase in the  $MS_{HP}$  (from HPG 1 to 3) the yield stress also increases. This suggests that the non-adsorbed polymer may be responsible for the yield stress increase. The potential loss of bridging can be compensated by an increase in the pore solution viscosity induced by the rise in the polymer concentration and/or by the depletion flocculation induced by the non-adsorbed coils (32). Moreover, the presence of HPG coils within the pore solution leads to an increase in the consistency coefficient ( $K$ ) compared to non-admixed mortars. However, the expected increase in  $K$  due to the rise of pore solution viscosity with the polymer dosage can be compensated by steric hindrance, leading to a plateau for  $K$ .

Since the adsorption of original guar gum is higher than 98.5%, one expects to detect a very strong increase in the yield stress compared to non-admixed mortar. However, the rheological behavior of the admixed mortar with HPG 6 is very close to that of the non-admixed mortar. This result suggests that the entire molecule of HPG 6 could be mainly adsorbed onto the surface of only one particle, limiting therefore the bridging flocculation. Moreover, the adsorption of the guar molecule onto a single particle leads to an increase in both steric hindrance and dispersion effects, leading to a low but continuous decrease in the yield stress. For dosages higher than 0.1% bwob, the concentration in polymer coils into the pore solution begins to slightly increase, leading to the beginning of the increase in  $K$  and of the decrease in  $n$ .

The additional alkyl chain also modifies the rheological properties of mortars. Contrary to HPG 3, HPG 4 leads to a strong and continuous increase in the consistency coefficient and a decrease in the fluidity index. These results highlight that mortars become more and more shear-thinning since the fluidity index decreases from 0.8 to 0.5. This rheological behavior gets more pronounced as the HPG dosage increases. These results are consistent with the fact that the hydrophobically modified HPG leads to the formation of coil overlapping at lower HPG dosage (0.05% in this study) since the presence of additional alkyl chains enhances the entanglement. Above this dosage, entanglement occurs between polymer coils, inducing a shear thinning behavior to the solution. At low shear rate, the entanglement of polymer coils leads to a higher pore solution viscosity and thus higher mortar viscosity. When the shear rate increases, the polysaccharide chains align in the direction of the flow resulting in less and less effect on mortar fluidity. The shear thinning behavior of the solution, and thus of the mortars, amplify with the increasing polymer dosage. The yield stress is also impacted by the additional alkyl chain. Indeed,  $\tau_0$ , of mortar admixed with HPG 4, increases for a dosage equal to 0.05% bwob then slowly decreases for dosages up to 0.075% bwob, before reaching a plateau for higher dosages. This result could be explained by a change in the HPG conformation due to the presence of additional alkyl chains. Indeed, as previously mentioned, alkyl chain creates intramolecular and intermolecular interactions through specific hydrophobic interactions. Intramolecular association of hydrophobic units tends to force the polymer chain into a more compact conformation (29,33). Moreover, the conformation of hydrophobically modified polymers in aqueous solution involves the presence of alkyl chains inside the coils in order to limit contacts between hydrophobic chains and water (29). Consequently, the hydrophilic groups, such as hydroxyl and hydroxypropyl, are preferentially on the outskirts of the coils, promoting the adsorption onto the surface of particles and therefore steric hindrance which implies a prevention of direct contacts between particles. Moreover, due to a more compact conformation and avoidance between water and hydrophobic units, the bridging ability of hydrophobically modified HPG should decrease. All these points should lead to a decrease in the yield stress.

## 5. Conclusions

In this paper, we studied the effect of several guar gum derivatives on water retention property and rheological behavior of mortars. Based upon the results, it was found that the original guar gum was totally adsorbed onto particle surface, leading to a negligible modification of WR and rheological behavior with respect to the non-admixed mortar. Depending of the chemical structure of HPGs, it is possible to promote the water retention according to two different ways. First, by increasing the MSHP of HPGs, the amount of adsorbed polymer drops, which leads to an increase in the HPG concentration within the pore solution and therefore to lower HPG dosage necessary to reach coil overlapping. Second, by enhancing overlapping, the hydrophobically modified HPGs improve the effectiveness of WR agent at low dosage. HPGs also modify the rheological behavior of the mortars. As in the case of WR, the hydrophobic characteristic of HPGs is the preponderant parameter. Indeed, it was shown that additional alkyl chain mainly leads to a more shear thinning behavior of the mortar and to a rise in the consistency coefficient, while classical HPGs strongly increases the yield stress.

## 7. References

1. Rols S., Ambroise J., Péra J., "Effects of different viscosity agents on the properties of self-leveling concrete", Cement and Concrete Research, 29 (2), 1999, pp 261-266.
2. Khayat K.H., Yahia A., "Effect of welan gum-high-range water reducer combinations on rheology of cement grout", ACI Materials Journal, 94(5), 1997, pp 365-372.
3. Lachemi M., Hossain K.M.A., Lambros V., Nkinamubanzi P.-C., Bouzoubaâ N., "Self-consolidating concrete incorporating new viscosity modifying admixtures", Cement and Concrete Research, 34(6), 2004, pp 917-926.
4. Sonebi M., "Rheological properties of grouts with viscosity modifying agents as diutan gum and welan gum incorporating pulverised fly ash", Cement and Concrete Research, 36(9), 2006, pp 1609-1618.
5. Paiva H., Silva L.M., Labrincha J.A., Ferreira V.M., "Effects of a water-retaining agent on the rheological behaviour of a single-coat render mortar", Cement and Concrete Research, 36(7), 2006, pp 1257-1262.
6. Khayat K.H., "Viscosity-enhancing admixtures for cement-based materials - an overview", Cement and Concrete Composites, 20(2-3), 1998, pp 171-188.
7. Jenni A., Holzer L., Zurbruggen R., Herwegh M., "Influence of polymers on microstructure and adhesive strength of cementitious tile adhesive mortars". Cement and Concrete Research. 35(1), 2005, pp 35-50.
8. Biasotti B., Giudici M., Langella V., Pfeiffer U., "Highly substituted hydroxypropylguar: a strong contribution to construction chemistry", International Dry mix Mortar Conference, Nürnberg, Germany, 2011.
9. Pointot T., Govin A., Grosseau P., "Impact of hydroxypropylguars on the early age hydration of Portland cement", Cement and Concrete Research, 44, 2013, pp 69-76.
10. Pointot T., Govin A., Grosseau P., "Importance of coil-overlapping for the effectiveness of hydroxypropylguars as water retention agent in cement-based mortars", Cement and Concrete Research, 56, 2014, pp 61-68.
11. Cappellari M., Daubresse A., Chaouche M., "Influence of organic thickening admixtures on the rheological properties of mortars: Relationship with water-retention", Construction and Building Materials, 38, 2013, pp 950-961.
12. Standard EN 197-1, "Cement-Part 1: Composition, specifications and conformity criteria for common cements", 2012.
13. Pointot T., Benyahia K., Govin A., Jeanmaire T., Grosseau P., "Use of ultrasonic degradation to study the molecular weight influence of polymeric admixtures for mortars", Construction and Building Materials, 47, 2013, pp 1046-1052.
14. Standard EN 196-1, "Methods of testing cement-Part 1: Determination of strength", 2006.

15. Standard C1506-09, "Standard test Method for Water Retention of Hydraulic Cement-Based Mortars and Plasters". American Society for Testing and Material, 2009.
16. NF DTU 26.1, "Travaux d'enduits de mortiers ", 2008.
17. Bouras R., Kaci A., Chaouche M., "Influence of viscosity modifying admixtures on the rheological behavior of cement and mortar pastes", Korea-Australia Rheology Journal, 24(1), 2012, pp 35-44.
18. Barnes H.A., Nguyen Q.D., "Rotating vane rheometry - a review", Journal of Non-Newtonian Fluid Mechanics, 98(1), 2001, pp 1-14.
19. Phan T.H., Chaouche M., Moranville M., "Influence of organic admixtures on the rheological behaviour of cement pastes", Cement and Concrete Research, 36(10), 2006, pp 1807-1813.
20. Roussel N., Ovarlez G., Garrault S., Brumaud C., "The origins of thixotropy of fresh cement pastes", Cement and Concrete Research, 42(1), 2012, pp 148-157.
21. Herschel W.M., Bulkley R., "Measurements of consistency as applied to rubber-benzene solutions", Proceedings of the American Society for the Testing of Materials, 26, 1926, pp 621-633.
22. Comparet C., Nonat A., Pourchet S., Guicquero J.P., Gartner E., Mosquet M., Chemical interaction of di-phosphonate terminated monofunctional polyoxethylene superplasticizer with hydrating tricalcium silicate, Proceedings, 6<sup>th</sup> International Conference on Superplasticizers and Other Chemical Admixtures in Concrete, Nice, France, 2000, pp 61-74.
23. Wang J., Somasundaran P., Nagaraj D.R., "Adsorption mechanism of guar gum at solid-liquid interfaces", Minerals Engineering, 18(1), 2005, pp 77-81.
24. Brumaud C, Baumann R, Schmitz M, Radler M, Roussel N., "Cellulose ethers and yield stress of cement pastes", Cement and Concrete Research, 55, 2014, pp 14-21.
25. Bülichen D., Kainz J., Plank J., "Working mechanism of methyl hydroxyethyl cellulose (MHEC) as water retention agent", Cement and Concrete Research, 42(7), 2012, pp 953-959.
26. Marliere C., Mabrouk E., Lamblet M., Coussot P., "How water retention in porous media with cellulose ethers works", Cement and Concrete Research, 42(11), 2012, pp 1501-1512.
27. Volpert E., Selb J., Candau F., "Influence of the Hydrophobe Structure on Composition, Microstructure, and Rheology in Associating Polyacrylamides Prepared by Micellar Copolymerization", Macromolecules, 29, 1996, pp 1452-1463
28. Cheng Y., Brown K.M., Prud'homme R.K., "Characterization and Intermolecular Interactions of Hydroxypropyl Guar Solutions", Biomacromolecules, 3(3), 2002, pp 456-461.
29. Simon S., Dugast J., Le Cerf D., Picton L., Muller G., "Amphiphilic polysaccharides. Evidence for a competition between intra and intermolecular associations in dilute system", Polymer, 44(26), 2003, pp 7917-7924.
30. Cheung J., Jeknavorian A., Roberts L., Silva D., Impact of admixtures on the hydration kinetics of Portland cement, Cement and Concrete Research, 41 (12), 2011, pp 1289-1309.
31. Jolicoeur C., Simard M.A., Chemical admixture-cement interactions: phenomenology and physico-chemical concepts, Cement and Concrete Composites, 20 (2-3), 1998, pp 87-101.
32. Palacios M., Flatt R.J., Puertas F., Sanchez-Herencia A., "Compatibility between Polycarboxylate and Viscosity-Modifying Admixtures in Cement Pastes", Proceedings, 10<sup>th</sup> International Conference on Superplasticizers and Other Chemical Admixtures in Concrete, Prague, Czech Republic, 2012, pp 29-42.
33. Aubry T., Moan M., "Rheological behavior of a hydrophobically associating water soluble polymer". Journal of Rheology, 38(6), 1994, pp1681-1692.



# THE EFFECT OF SUPERPLASTICISERS AND VISCOSITY MODIFIERS ON THE RHEOLOGICAL PROPERTIES OF SUPER WORKABLE CONCRETE

Greg Langton<sup>1</sup> , Gary Boon<sup>2</sup>

<sup>1</sup>Product Technologist, Sika Australia

<sup>2</sup>Technology Manager, Sika Australia

## Abstract

In order to achieve super workable concrete the use of a super plasticiser is required. The selection criteria for choosing a set of admixtures for super workable concrete usually relies on slump, flow and T500 tests to determine the combination to give a suitable concrete rheology for the application. While these tests can be valuable they provide limited rheological information due to the low variation in shear rate applied through gravity.

To better understand the effect of super plasticisers and viscosity modifiers on concrete rheology a range of commercially available PCE (polycarboxylate-ether) super plasticisers and VMAs (viscosity modifying admixtures) were tested using a concrete rheometer. The testing will show the concrete rheology obtained across a broad shear range encompassing the typical forces applied to concrete from static segregation to pumping. Through this testing the yield stress, and thixotropy can be quantified, as well as understanding the phenomenon of sticky and un-pumpable concrete.

**Keywords:** Rheology, super plasticiser, viscosity modifying admixture,

## 1. Introduction

Super workable or self-compacting (SCC) concrete has been increasingly used in the marketplace due to its flow characteristics. It can flow around obstacles such as reinforcement and intricate formwork, gives a better surface finish, and has the benefit of reduced workforce requirement, and improved health and safety conditions due to reduced exposure to noise, vibration and manual handling. The use of a super plasticiser is essential to reduce yield stress to achieve flowable concrete [1]. The introduction of PCE technology gives rise to the ability for customization to optimize the performance of admixtures. PCE admixtures are comprised of long chain polymer backbones to which side chains are attached. The length of the side chains and backbone, and the degree of side chain grafting leads to vast performance differences. This leads to a large number of available products to choose from. As segregation resistance is also an important factor in super workable concrete viscosity modifying admixtures are commonly used in conjunction with superplasticisers. The VMA improves the homogeneity of the mix by reducing the risk of dynamic and static segregation. They achieve this through hydrogen bonding interactions within the aqueous phase causing an increase in yield stress which gives reduction of slump flow [2,3]

Traditional selection criteria for determining an appropriate admixture combination involves testing to determine workability. The slump test is the most commonly performed test for fresh concrete properties due to its simplicity. For flowing concrete the addition of the T500 test is common with the time for the concrete to reach a flow spread of 500mm recorded. These tests give a single point indication of a rheological property commonly associated with yield stress. Other descriptive terms commonly used including "sticky" can give more rheological information that may not be distinguishable through common testing but no quantitative information can be obtained [4].

This paper aims to show the importance of rheological testing in admixture selection for super workable concrete to optimize plastic properties, and quantitatively assess the workability of concrete over a broad shear range applicable to concrete pumping, placement and stability.

## 2. Testing Program

Plastic properties of concrete mixes were investigated while using four PCE superplasticisers sourced from three manufacturers and a starch based VMA. The water cement ratio was fixed and a target slump

flow of 670-700mm was used. The properties measured were slump flow using a standard Abrams cone in the upright position, T500, and rheology using a concrete rheometer. UCS specimens were also cast

## 2.1 Materials

A fixed mix design was used comprising of a 10mm aggregate, and two sands. The binders comprised of a type GP cement – AS3972-2010, GGBFS – AS3582.2-2001, Fly Ash – AS23582.1 - 1998 and densified silica fume - AS3582.3-2002.

## 2.2 Mix Proportions & Mixing Procedure

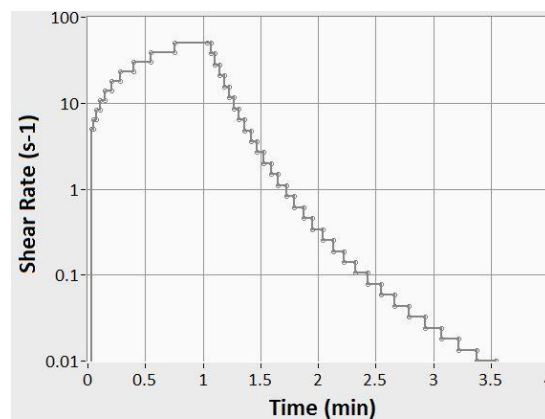
The binder proportioning and aggregate content is provided in Table 1. A fixed water content was used and adjusted for water contained in the admixtures. The materials were loaded in accordance with AS1012.2. All water and admixture was added within the first minute of mixing, and mixed for 10 minutes using a 70L Bennet pan mixer.

Material	kg/m <sup>3</sup>
Course Aggregate	900
Fine Aggregate	605
Type GP Cement	450
GGBFS	120
Fly Ash	90
Densified Silica Fume	40
Potable Water	180

Table 1: Mix proportions

## 2.3 Rheology Testing

Rheology tests were performed using Rheomix, a concrete rheometer built by the Material Physics department of Sika Technology AG, Zurich. The rheometer includes a steel cylinder with an anti-slippage cage, a rotating double helical spindle geometry [5], and is capable of testing over a broad shear and torque range. After a satisfactory workability is achieved as tested by slump flow, concrete is transferred to the rheometer cylinder and the geometry is attached. An initial manual test is conducted to determine the shear rate required to reach a torque of 20Nm. A test protocol is then assigned comprised of a pre shear increasing the shear rate in logarithmic steps to the predetermined maximum before a step wise reduction in shear rate to 0.01s<sup>-1</sup>. The typical protocol is shown below in graph 1.



Graph 1: rheology testing protocol

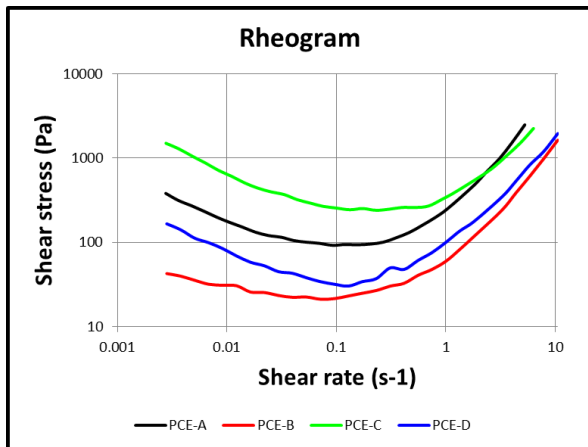
### 3. Results and Discussion

Admixture	Dose Rate ml/100kg binder	slump flow mm	T500 s	Viscosity Infinity Pa.s	Yield stress Pa	Amplitude Thixotropy Pa.s <sup>-n</sup>	1D UCS MPa
PCE-A	700	700	5	162	97	28	34.5
PCE-B	1060	690	4	45	23	9	25.5
PCE-C	700	670	5	147	248	98	34.5
PCE-D	820	690	3	66	36	9	33.0

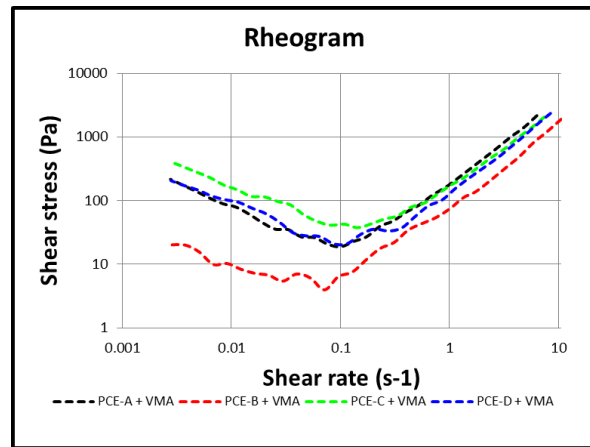
Table 2: PCE test results

Admixture	Dose Rate ml/100kg binder	VMA Dose Rate ml/100kg binder	slump flow Mm	T500 s	Viscosity Infinity Pa.s	Yield stress Pa	Amplitude Thixotropy Pa.s <sup>-n</sup>	1D UCS MPa
PCE-A	845	500	690	4	112	28	2	34.5
PCE-B	1261	500	690	4	49	6	0.3	21.5
PCE-C	810	500	680	5	105	51	8	33.0
PCE-D	930	500	690	5	87	31	4	31.5

Table 3: VMA test results



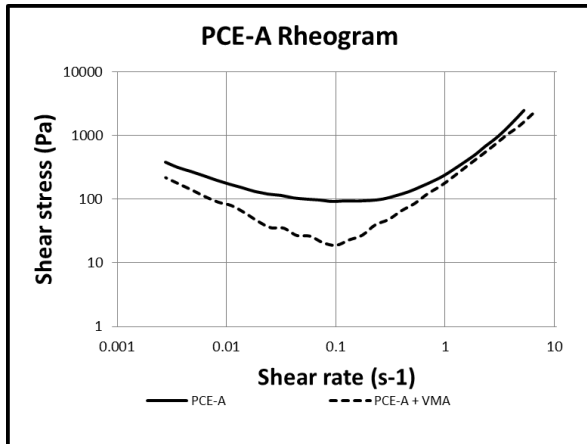
Graph 2: PCE rheograms



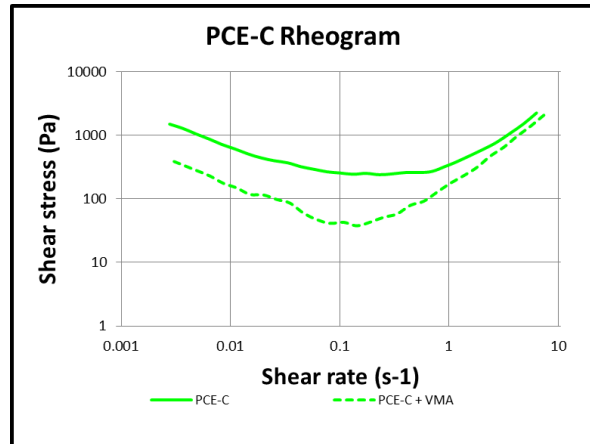
Graph 3: VMA rheograms

Table 2 shows the results obtained from four PCE samples. The admixture dose was fixed to achieve a target slump flow of 670-700mm. It can be seen that differing viscosity and yield stress are seen across the four tested PCE's. This suggests differing modes of dispersing action between admixtures. It can be seen from Graph 2 that PCE-C and PCE-D give lower yield stress than PCE-A and PCE-C. This would suggest improved flowability and an improve in placement. PCE-C and PCE-D also have a lower viscosity infinity. This gives an improvement in pumpability due to lower shear stresses being developed at higher shear rates. The lower viscosity achieved also gives the concrete a better feel (soft vs sticky). Difference is also seen in thixotropy, with PCE-C and PCE-D having a lower increase in shear stress that the added admixtures have improved dispersion effects at low shear rates. A lower 1 day compressive strength was seen with PCE-B. This is most likely due to retardation effects.

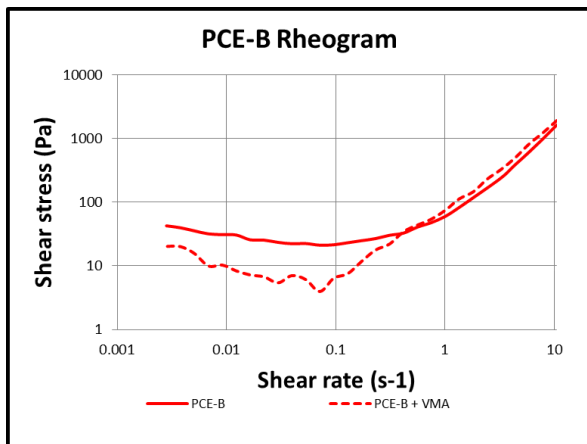
Table 3 and Graph 3 shows the results obtained when a dose of a starch based VMA is dosed with the four tested PCE's. As VMA's increase yield stress which leads to an increase in stability and loss of fluidity the dose of all PCE's had to be increased to maintain the target slump flow. From table 3 it can be seen that there is a reduction of the yield stress, and amplitude thixotropy when the tested PCE's are used with a VMA at a fixed slump flow. There is also a viscosity reduction for PCE-A and PCE-C, while an increase in viscosity is seen with PCE-B and PCE-D. A reduction in compressive strength at 1 day is seen with PCE-B to PCE-D when tested with the VMA. This is likely due to an increase in retardation due to increasing PCE dose to maintain the slump flow.



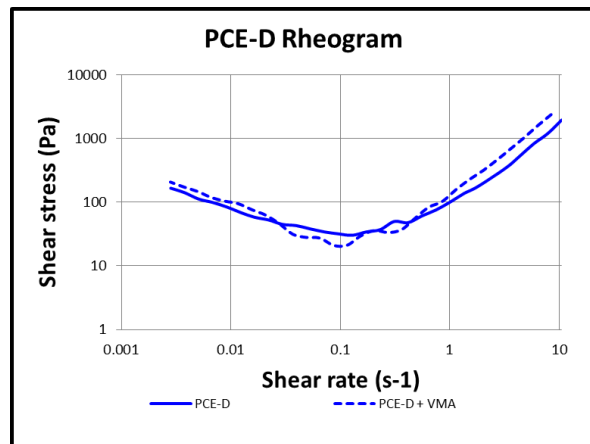
Graph 4: PCE-A vs PCE-A with VMA



Graph 5: PCE-C vs PCE-C with VMA



Graph 6: PCE-B vs PCE-B with VMA



Graph 7: PCE-D vs PCE-D with VMA

Graphs 4-7 compare the rheology between the tested PCE's and with the addition of a VMA. In graph 4 and 5 it can be seen that the addition of VMA with a fixed slump flow the yield stress is reduced leading to a more flowable concrete. The reduction in viscosity will also improve the pumpability of both mixes. Graph 6 shows a lowering of yield stress. Due to the low values achieved there is some noise in the results obtained under a shear stress of 10 due to the measurement resolution. In both graphs 6 and 7 an slight increase in viscosity is seen. From the above results it is clear that interactions between different PCE admixtures and the tested starch based VMA give differing rheological effects that cannot be measured by slump flow and T500 testing.

### 3. Conclusion

Through testing super workable concrete using a concrete rheometer over a broad range of sear stresses, detailed comparisons can be made between mixes to determine the most appropriate flow behavior for the application. The choice of superplasticiser has a large impact on the rheology of concrete with differences in yield stress, viscosity, and thixotropy being seen in the four tested admixtures. The inclusion of a VMA with an increased superplasticiser dose to maintain slump flow reduces yield stress and

thixotropy, and has variable impacts on viscosity. In determining a suitable admixture combination for super workable concrete the use of a concrete rheometer allows a fast and accurate characterization of concrete flow characteristics over a wide application range that cannot be determined by traditional single point testing such as slump flow and T500.

#### **4. References**

1. P.F.G Banfill, "The rheology of fresh cement and concrete-a review", *Rheology Reviews* 2006, pp61-130
2. J Kwasny, M Sonebi, et al, "The influence of different viscosity-modifying admixtures on the fresh properties of superplasticised cement-based grouts", 3<sup>rd</sup> International RILEM Symposium on Rheology of Cement Suspensions such as Fresh Concrete, 2009
3. W Wannaphahoun, "Effects of different viscosity modifying admixtures on rheology of cement past matrix of self-consolidating", 3<sup>rd</sup> International RILEM Symposium on Rheology of Cement Suspensions such as Fresh Concrete, 2009
4. M Khrapko, " Rheology of fresh concrete – practical significance", 3<sup>rd</sup> International RILEM Symposium on Rheology of Cement Suspensions such as Fresh Concrete, 2009
5. F. Fabbris, W. De Carvalho, D. Lootens, „A Concrete Rheometer: Features and Industrial Applications“, *Rheology and processing of Construction Materials – 7th RILEM International Conference on Self-Compacting Concrete and 1st RILEM International Conference on Rheology and Processing of Construction Materials*, RILEM 2013.

# Durability and Serviceability

# Concrete Durability Performance Testing – The Approach Adopted in a Concrete Institute of Australia Recommended Practice

W. Green<sup>1</sup> and F. Papworth<sup>2</sup>

<sup>1</sup> Corrosion Engineer, Vinsi Partners

<sup>2</sup> Managing Consultant, BCRC

**Abstract:** The Durability Series is a set of Concrete Institute of Australia recommended practices that provide deemed to satisfy requirements applicable to all concrete structure types based on standard input parameters for design life, reliability and exposure. The series includes details on project planning and implementation which if followed will increase the likelihood that the specification, design detailing and construction will be optimal to achieving the asset owner and community expectations regarding the long term performance of concrete structures. Also included are methods for modelling degradation over time and for crack control design. Thus the series provides what is described as a unified durability design process. This paper outlines the document in the series dealing with durability performance tests applied through design, construction and operational service life, i.e. Z7/07 Performance Tests to Assess Concrete Durability.

Z7/07 provides guidance on performance tests specific to the requirements of durability design, implementation and maintenance management. The document is intended to inform all parties involved in design, construction and maintenance about the benefits of durability performance testing and how as part of a durability planning and implementation process will lead to an increased likelihood of achievement of design life of concrete structures and buildings.

**Keywords:** durability, performance, testing, laboratory, field.

## 1 Introduction

In terms of durability performance testing, there has been a wide range of tests introduced to Australia over the years and this has caused considerable difficulty for:

- Asset Owners - appropriateness and the most cost effective testing regimes to achieve the outcomes and level of certainty sought.
- Designers –which tests are the most appropriate to specify and how much test data is required to ensure an appropriate level of statistical confidence from the test results underpinning the design is appropriate.
- Contractors – understanding and having confidence in the consistency, repeatability and validity of trial data and any quality control performance testing.
- Suppliers of Laboratory Testing Services – costs of registration for a wide range of tests despite some being rarely called for.
- General Users –gathering sufficient data to know the statistical confidence in the methods.

Durability performance testing can be required throughout the life of a project including the concept design stage (materials testing/trials, exposure assessment), design phase (concrete mix compliance), construction phase (concrete quality control testing) and the operation and maintenance phase (inspections, monitoring in situ service life performance). Z7/07 (1) provides an outline of durability performance testing under the following main headings:

- Mix Acceptance Tests

Testing during the design phase is conducted to support the design process, in particular to demonstrate that the combination of design details and practical concrete supply to the project will yield the desired performance.

The test methods are primarily required to provide measurements that are relevant to the potential durability of structural elements in specific exposures, and these values are used in predictive modelling processes to inform design decisions or to show a certain performance level has been achieved.

Prior to commencement of construction, trial mixes are generally required to produce samples for testing to demonstrate that the proposed mix design, using materials available to the project site, is suitable for the design life, exposure conditions and method of application.

- Tests For Quality Assurance

Quality assurance/control tests are primarily required to demonstrate consistency of supply in conformance with the works (project) specification and the properties established by acceptance trial mixes. Timeliness of results is therefore a highly important criterion, generally superseding the requirement to produce values for modelling purposes. Although strength tests of concrete are routine, durability tests are not and the type and frequency of tests must be specified in the project contract documents.

- Tests Where Placed Concrete is Suspect

The concrete performance in the field will differ to that in the trial mixes. To assess the extent of this, performance tests on the as-placed concrete might be required. This is often by non-destructive testing, or testing cores for strength or other properties. Such testing may be undertaken where there is doubt that the construction method or materials will have provided the required performance (e.g. routine testing has revealed an anomaly or trend of concern), or to verify the efficacy of the routine quality control testing program.

- Tests For Condition Monitoring

During the life of a structure it is necessary to check that the concrete is responding to the environment as expected. It is also often necessary to assess the residual life of the structure in order to determine what intervention is necessary (and when best performed) to reach the design life, or to assess the feasibility of extended operational service life. Some specifications now require that the maintenance manual for the structure be prepared at the time of design and that this include the type, frequency, extent and criteria for in-service testing.

For all test methods the limitations and advantages are given and where possible the variance of the test results stated. Variance is a major consideration in assessing the number of test results required and hence the practicality of applying the test.

## **2 Sampling and Sample Preparation**

Sampling and sample preparation requirements for fresh concrete and hardened concrete (including laboratory specimens and samples taken from in-situ concrete) and the frequency and extent of sampling are all necessary considerations prior to any durability testing whether it be concrete mix acceptance testing, quality assurance testing, testing where placed concrete is suspect or condition monitoring testing.

The accuracy of any test result is strongly influenced by the quality of the sample tested. Thus representative sampling, sample preparation, and the repeatability and reproducibility of the method are critical features. A sample may comprise one specimen or several replicate specimens. Several replicate specimens may be needed to comprise a representative sample of the concrete of interest.

The requirements for sampling fresh concrete are well developed in Australian Standards as it applies to compressive strength cylinders and these cylinders are generally used for other durability tests. However, Australian Standards only nominate requirements for compressive strength samples, the project concrete specification must nominate the number and type of samples required for durability related testing in addition to the frequency of sampling.

While the standard compaction procedures described in Australian Standards are satisfactorily consistent for measurement of macroscopic properties such as compressive strength, testing of durability related properties are inherently more sensitive to the microstructure and continuity of voids within the concrete. Published systematic repeatability studies of water permeability testing (2) have shown that consistency of concrete compaction of the sample is the primary factor that influences the often perceived poor repeatability/reproducibility of durability related tests. Compaction of test specimens using a vibrating table is preferred to other methods because it consolidates concrete with relatively little effort, therefore is the easiest way to consistently achieve good compaction in all samples. Where due care is taken in compacting the concrete, coefficients of variation for water permeability and absorption tests, for example, are comparable to those for compressive strength testing.

However, it is noted in Z7/07 that “durability” samples should not be given “special attention” to try and produce particularly high levels of compaction in order to secure favourable test results. For example, forensic investigation of past instances of failure to comply with specified water permeability criteria has found that over-zealous compaction can result in the formation of microstructural features such as segregation and bleed channels that adversely affect test results, even to the extent of compromising specification compliance (2).



The method of standard curing of concrete cylinders in temperate and tropical climates is well defined in Australian Standards. However, it is sometimes necessary to employ non-standard curing conditions in order to reflect the conditions under which the concrete will cure on-site. Examples of this include:

- Early age steam curing of precast elements.
- Temperature matched curing for maturity calculations.
- Unusually cold or hot conditions.
- Insulated conditions.
- Trial mixes that are performed in a different climatic zone to the project site.

Where non-standard curing conditions are required, these must be described in the project concrete specification.

Sampling from a concrete structure is often required to assess one or more properties. The sample type, size, locations and frequency of collection will depend on the properties to be determined, the reliability required for the results and the practicalities and cost of testing. Many test methods have specific requirements for the size and condition of samples. Unless sampling particular anomalies, a primary requirement is often to ensure that the extracted samples represent the bulk of the concrete in terms of properties such as aggregate distribution and voids.

The most common method for taking samples is by wet diamond coring. Where this is not convenient, drilled dust samples or dry grinding core cuts may be taken. A Section of the Z7/07 document (1) describes procedures for taking all three sample types.

Before taking the sample, the reinforcement position should be located and marked so that the sample can be taken over the reinforcement to inspect the physical condition of the reinforcement and measure the cover depth for verification of cover meter readings, or to avoid the reinforcement as required.

Furthermore, before taking the sample the concrete surface should be inspected and any defects recorded.

### **3 Concrete Mix Acceptance Tests**

If durability testing is required, the project specification should include:

- Test method according to some publicly available method.
- Sampling method (including curing), sample geometry and size (unless included in the method).
- Frequency of test and number of test specimens to be used to give one result (unless included in the method of test).
- Acceptance criteria (including tolerances) or details to be reported (if not clear in the method of test).

#### **3.1 Chloride Diffusion Tests**

While test methods have been developed that effectively measure chloride diffusion, there is still considerable debate about how these results should be applied. Tests that give the most precise estimate of chloride diffusion take a long time to complete. The original “steady state diffusion” (SSD) method of measuring chloride diffusion involved placing a sample in a cell with a chloride solution on one side and a solution with no chlorides on the other. The chloride concentration in the receiving cell was measured over time until a constant chloride ion concentration was achieved. The chloride diffusion coefficient was then calculated. However, the diffusion coefficient could take six months or more to measure, and require many chloride analyses. Because of the slow rate of increase in chlorides in the receiving side of the cell, it is easy to assume a steady state has been reached when it has not. This can lead to reporting of optimistic diffusion coefficients.

Rapid tests have been developed whereby the diffusion of chlorides is driven by a potential difference. The property measured under these conditions is often described as chloride migration rather than diffusion. The relationship between the results from rapid tests and the longer term tests is determined by the pore water chemistry of the individual concrete, which in turn is determined by the cement and supplementary cementitious materials (SCMs) chemistry, batch water supply, and admixtures. Therefore there is no universal relationship between results from each type of test, although calibration curves can be determined for individual concretes if required.

A range of test methods also exist for measuring or inferring the sample’s chloride ion diffusion coefficient. These include “non-steady state diffusion” (NSSD) and “non-steady state migration” (NSSM) methods. The resistance to chloride ingress is typically expressed as the chloride diffusion

coefficient. Because the test result is influenced by other ions present in the concrete, the result is often referred to as the apparent diffusion coefficient.

In Australia, the NordTest NT Build 443 (3) method is commonly used to test and pre-qualify concrete mixes for use in chloride-bearing environments. An alternative standard, ASTM C1556-11a (4), is based on NT Build 443. Although there are procedural differences between the methods, any effect on the test results has not been published at the time of writing such that the two methods are expected to produce similar results for practical purposes.

The diffusion coefficient will change with time as the concrete matures, therefore the age at which the test is carried out will determine the results. Thus apparent diffusion coefficients determined at early ages do not represent ultimate diffusion rates, particularly for concretes containing fly ash or slag.

Curing is followed by exposure to a chloride solution for at least 35 days. For a reliable result, the exposure period must be long enough for a measurable chloride ion concentration profile to develop. For high performance concretes, particularly those containing SCMs, exposure for 56 days or more is necessary to give time for sufficient chloride ions to penetrate.

NT Build 443 (3) or ASTM C1556-11a (4), modified in terms of a specific sample curing regime and to be consistent with standard Australian laboratory practice, are the recommended test methods for establishment of a concrete's chloride diffusion coefficient.

The 'modified NT Build 443 or ASTM C1556 method' is as follows:

- Production of concrete cylinders of dimensions used for standard compression test to AS 1012.8.1 (5).
- Curing of concrete cylinders to AS 1012.8.1 (5) to 28 days. This curing applies only to Portland and blended Portland cement concretes. The curing of other non-Portland cement binders is to be separately specified.
- At the age of 28 days, the specimens shall be exposed to water containing sodium chloride in accordance with NT Build 443 or ASTM C1556 at  $23 \pm 2^\circ\text{C}$ .
- The period of exposure to sodium chloride solution shall be 56 days typically.
- For core samples they shall be kept wet until delivery to the test laboratory. They must be representative of the concrete and/or structure in question and the concrete must be hardened to a minimum of 28 maturity-days.

There are no universal acceptance criteria for this test, as the required value is calculated based on modelling analysis. The following two-step process can be followed when specifying the chloride penetration resistance:

- 1) Establish a mean diffusion coefficient that gives the design life required by diffusion modelling and any allowances considered appropriate to provide a margin for error. It is essential that model values are reviewed by an experienced professional in terms of what can reasonably be expected to be achieved in practical concrete production prior to incorporation in a works (project) specification, otherwise there is a risk of specifying impractically low values that cannot be achieved in practice.
- 2) Specify the maximum diffusion coefficient to be achieved, or note the desired value and require that the actual value be reported. It is recommended that a specified value only be set where local suppliers have experience in meeting the proposed specified value. If local suppliers do not have the necessary previous experience in making this type of concrete then they will need to carry out trial batching to demonstrate they can produce this type of concrete with satisfactory consistency.

### **3.2 Carbonation Rate**

Under normal atmospheric conditions the deemed-to-comply concrete grade and cover requirements of Australian Standards will generally provide adequate protection. Because carbonation alone rarely causes significant corrosion, carbonation rate tests are not generally undertaken. However, carbonation rate testing is sometimes required, for example when:

- A mix does not perform well in general quality tests and the actual carbonation resistance of the mix is required.
- Non-standard materials are used and their performance has to be specifically assessed.
- The in-situ carbonation rates are high and/or the design life is 100 years or more, and a specific assessment of the concrete needs to be used to determine cover requirements.

Testing for carbonation rate is relatively simple. Concrete samples are cured for an appropriate time and are then placed in an airtight tank. The carbonation rate is accelerated by using a higher than

normal CO<sub>2</sub> content in the tank while temperature and humidity are held at a standard level. The CO<sub>2</sub> content must not be so high that it affects the chemical reactions that occur, or the morphology of the reaction products. When the results are used in modelling, allowance is made for the effects of actual exposure conditions compared to those in the tank.

The “Accelerated Carbonation Test” as detailed in FIB Bulletin 34 (6), modified to be consistent with standard Australian laboratory practice, is recommended in the Z7/07 recommended practice (‘modified FIB method’).

In the “FIB method”, the carbonation rate is accelerated by testing at a carbon dioxide concentration of 2% which is approximately 50 times the normal atmospheric CO<sub>2</sub> concentration but not so high as to change the reaction mechanisms or the morphology of the reaction products. After curing, concrete samples are exposed for 28 days. Thus, ignoring other factors the carbonation depth achieved during the test will be achieved in-situ in approximately four to five years (depending on wet/dry cycles in-situ).

### **3.3 Water Absorption and Sorptivity**

There has been a proliferation of this type of test in Australia. This may be due to the lack of clear standards being available before different methods were adopted by local authorities and variations of different tests were introduced into concrete product standards. A compounding factor is the different requirements of the test in different applications.

Absorption tests measure the total weight gained by concrete immersed in water. Absorption tests focus on filling the voids in concrete without reference to the rate at which this occurs, although in some tests water might only partially fill the voids. Results can be used as mix acceptance tests, but they cannot be used for modelling. Absorption test results are often referred to as the “volume of permeable voids (VPV)” or the “apparent volume of permeable voids (AVPV)”. Absorption values are expressed as percentage void space by volume of sample, or less commonly as the mass of absorbed water as a percentage of the dry mass of sample.

In contrast, Sorptivity tests measure the rate of water absorption. The results can be used in formulae for assessing the depth of penetration of water with time under capillary action. Sorptivity is measured by placing concrete in contact with water with no pressure head and measuring weight gain with time to obtain a sorptivity value. The corresponding visible height rise is often also measured, however this is a less accurate method for calculation of a sorptivity value. The result can be used for modelling of water ingress due to capillary rise, and can also be used as a quality assurance test. Sorptivity values are calculated as volume absorbed per unit surface area related to the square root of time, e.g. mm<sup>3</sup>/mm<sup>2</sup>/min<sup>½</sup> which is often reduced to mm/min<sup>½</sup>.

Both absorption tests and sorptivity tests are widely used in Australia for mix acceptance and quality assurance. Absorption tests are simple, therefore preferable where data for modelling is not required, while sorptivity tests are used where modelling of water ingress is required.

AS 1012.21 (7) is an Australian adaptation of the ASTM C642-06 (8) absorption test. In the AS1012.21 test method cylinders or cores are cut into four equal slices so that several results are obtained from one test specimen. The slices are dried to a constant weight then immersed and boiled in water in order to saturate the concrete’s permeable voids and thus give a measure of the total pore volume. Extensive work by VicRoads (9) has enabled them to assess the potential durability of concrete, as indicated by AVPV results, for concrete of different grades to ensure a high reliability that the mixes will be durable in the exposure for which they are intended.

The Taywood Sorptivity Test (10) was originally a brick test. Recognising the significance of the rate of water ingress due to capillary action, as opposed to tests which only measure the volume of pores, the original brick test was adapted for concrete in the late 1970’s. The test is mentioned in UK Concrete Society Technical Report TR31 (10) but was never standardised. The test has continued to be used by many people who had developed an understanding of concrete quality through the extensive use of this method and it is used in Australia for modelling purposes.

The ASTM C1585-11a (11) sorptivity test is relatively simple to undertake. Although it takes slightly longer than the Taywood Sorptivity Test and with shorter history of usage in Australia, it gives results that are more representative of in-situ concrete, and is an international standard. The fact that it is more representative of in-situ concrete is significant for modelling, which is a major advantage over alternative tests.

Recommendations in Z7/07 are:

- Where a general test of concrete quality is required for mix assessment or quality control it is recommended that the AS 1012.21 (7) AVPV test is used because it is already standardised and guidelines for interpretation of test results have been published, albeit for specific concrete mix designs.
- Where a sorptivity rate is required for use in modelling, the ASTM C1585 (11) test should be specified. This is because its method of specimen preconditioning means its results will more closely reflect the in-situ sorptivity.

The Z7/07 Recommended Practice also includes an analysis of assessment methods for water permeability, semi adiabatic tests to predict concrete adiabatic temperature rise, alkali aggregate reaction, delayed ettringite formation, sulphate resistance, abrasion resistance and concrete bleed.

## **4 Tests for Quality Assurance**

Testing for assurance that durability achieves expectations is undertaken throughout construction to verify durability is not compromised by unforeseen construction or material matters that may influence concrete performance.

### **4.1 Compressive Strength**

Z7/04 (12) notes that “One of the reasons that compressive strength is such a useful tool is that it is relatively simple to do, has a well-established methodology and hence low variance and established criteria for acceptance and sharing of risk. As such it is an essential part of the durability testing suite of tests”. However, it also notes that maintenance of the trial mix actual strength should be considered and provides a recommendation to that effect.

### **4.2 Cover**

After fixing the reinforcement and having largely completed formwork and screed rails in place the cover can be physically measured to ensure that it is within specification. This checking is particularly important as in some locations cover checking will not be practical after the concrete is placed. In these locations it also will not be possible to establish the cover distribution for residual life assessments later in the structure’s service life. Consequently Z7/07 provides a recommended procedure for pre-pour cover checks.

The placement of concrete can move the reinforcing within the formwork. It can either be weighed down or shift because of vibration, insufficient spacers etc. Confirming that the correct cover has been achieved is important to ensure that the construction process is properly managed. Where errors are made during construction of the first element, catching this early can prevent the problem persisting through every element. It is in the contractors’ interest to undertake post-pour checks on early pours to ensure the construction method will provide the cover specified, rather than checking cover at the end of a project and thus risk finding all pours have a cover deficiency due to a systematic error. Through the life of the structure the cover distribution will also be important for residual life assessments. Hence, Z7/07 includes a recommended procedure for post-pour cover checks.

### **4.3 Cracks**

If cracks form, investigation is required to determine whether they are acceptable or should be repaired. Whilst the design crack widths may be a guide, the actual cracks require specific evaluation of their likely significance over the design life. The cause and significance of cracks formed should be evaluated. Measuring crack width at the concrete surface to determine if the crack exceeds a given limit is not as straightforward as it seems because the width varies along the crack length. In addition, the crack width changes with concrete temperature (i.e. cracks close as the temperature increases) and moisture content (cracks close as concrete moisture content increases).

Z7/07 provides the following recommendations on crack measurement:

- a) The width values should be reported as maximum for each crack. A mean and distribution (with variance) can then be assessed for comparison with the design values.
- b) A measuring magnifier be used to give an accuracy of  $\pm 0.05$  mm. Crack width meters are suitable for first estimates of crack width (e.g. to assess which cracks need to be measured) but accuracy is only about  $\pm 0.1$ mm so they are not suited to more accurate assessments. With an appropriate crack width distribution the characteristic crack width can be assessed and used as the crack width.
- c) Crack widths should be measured during the coolest part of the day when they have a maximum width. This will make decision making conservative.

- d) Concrete core samples of 50 mm diameter can be taken through representative crack positions to the interior reinforcement depth to evaluate the crack depth and width beneath the concrete surface. When the core is removed from the structure, the loss of restraint from the surrounding concrete may result in widening of the crack, which requires evaluation for the specific crack and the measured crack width impact on durability, structural adequacy and contract requirements.

#### **4.4 Electrical Resistivity**

Electrical resistivity of saturated concrete is influenced by the nature of the cement (binder) system and in particular the use of SCMs, certain admixtures and water/cement (binder) ratio. Changes to binder composition and admixtures may not have a significant effect on strength, and hence resistivity is a useful quality assurance test on the concrete mix. There are two common types of resistivity test:

- Tests that are designed to measure resistivity, such as the 4 probe Wenner resistivity test.
- Tests that were designed to measure chloride ingress rate but in fact measure resistivity, e.g. Rapid Chloride Permeability Test, RCPT (i.e. AASHTO T277 (13) and ASTM C1202-12 (14)). RCPT tests are complex tests compared to resistivity and hence Z7/07 recommends that this test type not be included in specifications.

The four probe Wenner method of measuring concrete resistivity was developed for soils investigation and is used extensively to assess the resistivity of different soil layers. In this method four probes are spaced at equal distances apart. A current is passed between the outer probes and the voltage generated is measured between the inner two. In the adaptation of the test for concrete the probes are placed closer together than in soil tests. AASHTO TP95-11 (15) recommends a spacing of 1.5" or 38 mm. Different models of test equipment offer different probe spacings.

When used as a check on concrete variation, there are no established criteria for the test results. It is the variation in resistivity that is significant and the variation should only be used as an indication that there might be something untoward with the concrete that requires further investigation.

Temperature has a significant effect, therefore laboratory tests must be undertaken at a standard temperature (e.g.  $23\pm 2^{\circ}\text{C}$ ). Moisture content also has a significant effect, and hence samples should be tested for resistivity within 15 minutes of removal from the water bath. If core samples are to be tested, they should be preconditioned to a saturated state in accordance with AS 1012.14:1991 (16).

For structures in severe exposures it is recommended that:

- 1) 4 probe Wenner resistivity be measured in accordance with AASHTO TP95-11 (15) or equivalent to determine the mean resistivity for the concrete based on results from multiple batches with tests on three cylinders from each batch.
- 2) 4 probe Wenner resistivity be measured in accordance with AASHTO TP95-11 or equivalent on all 28 day age compressive strength tests undertaken. If resistivity trends up and results fall to 20% below the average result in the trial mix, then the designer and/or durability consultant should consider what actions should be undertaken to bring the mix back to the performance of the trial mix.

Z7/07 also includes an analysis of assessment methods for maturity, in-situ temperature and strain measurements and cross-hole sonic logging.

## **5 Tests Where Placed Concrete is Suspect**

The performance of a concrete in-situ will differ to its performance in trial mixes or laboratory tests on quality control samples taken during construction. Testing of as-placed concrete is not a common requirement, as in-situ concrete quality is generally accepted as being adequate if the mix supplied is in accordance with the specification and there is no reason to suspect that placing, finishing and curing were substandard. However, testing of the as-placed concrete during construction might be required for assurance of durability when the concrete mix, placing, or curing is suspect. This is analogous to non-destructive testing (NDT), or testing of cores for strength where the designer or contractor is not satisfied that the method of construction will provide the strength specified.

Z7/07 reviews tests for many aspects of concrete assessment and only the more common aspects are included here.

### **5.1 Cover**

Both the reinforcement location/spacing/position and the depth of cover over reinforcement are important, and may need to be determined when investigating the quality of a concrete placement.

The types of equipment available for non-destructively locating reinforcement and measuring its cover depth include magnetic reluctance and pulsed eddy current covermeters, ground penetrating radar (GPR) and ultrasonic pulse echo (UPE). The applications, limitations and recommended procedures for these are described in Z7/07. It is concluded that each instrument has its place. For example:

- Magnetic reluctance covermeters were first developed in 1955 and the method measures small changes in the electromagnetic field of the core, and it can be strongly affected by variations in the core e.g. temperature, external magnetic fields. Devices might have different heads with varying coil arrangements for specific purposes such as determining cover of congested reinforcement, measuring cover in different depth ranges, and for bar diameter estimation.
- In the pulsed eddy current method a pulse of current creates a magnetic field through the coils in the instrument, which induces an eddy current in the reinforcement. Devices have different heads with varying coil arrangements for specific purposes such as determining cover around core holes, measuring cover in different depth ranges, and for bar diameter estimation. Alternatively, various coil types might be housed in one measuring head and are tuned for sensitivity to bar spacing or cover depth. These coils can then be interpreted conjunctionally to give greater functionality.
- Widespread cover surveys are possible with small hand held GPR units and as it is not influenced by steel mass prior knowledge of the reinforcement layout is not required and complex and heavily reinforced sections can be measured. However calibration is vital.
- Higher performance GPR equipment is available that can detect reinforcement at greater depths, but its use is rarely warranted for development of cover distributions as the units are more cumbersome and more expensive. These units can be useful to measure reinforcement locations on both faces.
- Where cover is critical and reinforcement bars are masked by steel fibres, UPE is a consideration for post-pour quality assurance checks of standard rebar (e.g. edges of precast segments).

## **5.2 Compressive Strengths**

Tests for concrete strength fall into two main categories, destructive tests and non-destructive tests. Destructive tests give a definitive value directly measured from the structure, but as they damage the concrete they are generally restricted and only provide information about the small area tested. Non-destructive tests can be carried out over wide areas on the structure. However, they do not definitively measure strength, and accurate interpretation of results requires calibration against results from tests on laboratory specimens or destructive in-situ tests.

Measuring compressive strength of concrete in an existing structure will generally involve a combination of non-destructive tests (i.e. no concrete removal) and destructive tests (e.g. core samples extracted). The amount of concrete removed must not reduce the structural capacity or other performance parameters of the element.

CIA Z11 [17] gives general guidance on evaluating concrete strength from the results of testing cores taken from the structure. It describes the reasons for strength evaluation by the use of cores, and how to obtain cores from concrete structures so that they will be suitable for testing and the test results will be "significant" in the true statistical sense. Steps in the determination and evaluation of concrete strength from the results include providing for corrections to the indicated compressive strength of the core for length to diameter ratio of the core; presence of reinforcement in the core; position of the core axis in relation to the standard cylinder axis; age of the concrete; quality of compaction of the concrete; and, the curing regime experienced. A feature of the correction for quality of compaction of the cores is a series of photographs of concrete of known void contents. This visual means of correcting for excessive voids in the cores is presented with an alternative procedure using actual density measurements of the cores [18].

Z7/07 recommends that the practices in CIA Z11 be followed, with extra interpretation as in BS EN 13791 [19] and associated documents.

Z7/07 also reviews various non-destructive test methods for strength assessment of concrete. Although useful tools for an indication of strength they are more generally useful to indicate strength variations with core results used to gauge the strength of zones defined by NDT measurements.

## **5.3 Detecting Defects in Concrete**

Defects may be detected to a limited extent by visual inspection of the surface and/or core samples. A range of non-destructive test methods is available for determining whether defects are present over wider areas. Z7/07 indicates that many tests have a role to play in detecting defects and use of two or more tests in conjunction with each other generally provides a superior assessment. Tests

summarised in Z7/07 include ultrasonic pulse velocity (UPV), ultrasonic pulse echo (UPE), impact echo, impulse response and ground penetrating radar (GPR).

#### **5.4 Assessment of Concrete Surface Quality**

The quality of the concrete surface greatly influences the durability of the concrete. In turn, the surface quality is determined largely by curing method and duration. Inadequate curing may reduce compressive strength, but the effect on durability is likely to be greater. When the quality of curing is suspect, measurement of the surface's resistance to ingress of water or air by methods such as those described in Z7/07 (initial surface water absorption and torrent air permeability) is possible but is not frequently done.

The biggest issue with these types of tests is that the test result is affected by the concrete moisture content. Consequently, care is required when interpreting the results. They are also influenced by the surface finish/texture, which may affect the correct functioning of the test equipment. The most common methods of assessing the quality of as-cast concrete is to take samples and measure the performance using laboratory tests such as water sorptivity or volume of permeable voids (VPV) although a test related directly to the mechanism of deterioration may be considered.

### **6 Condition Monitoring**

Condition monitoring is an asset management function undertaken to assess whether a structure is still able to fulfil its levels of service and how it is performing with respect to its design life. This informs the asset owner on future maintenance expenditure and when either major renewals and/or replacement of the asset should be planned.

Monitoring is not solely collecting and storing data. It requires the data to be interpreted, and decisions made about when intervention is necessary to maintain serviceability or structural performance. Criteria for interpreting data and signalling a need to consider changing the monitoring methods or frequency intervention must be established at the same time as the methods for collecting and storing data.

Condition monitoring can be undertaken in various ways. The asset owner needs to be clear on the advantages and disadvantages of the approaches including:

- **Intermittent Visual Inspection:** Visual inspection will only detect visible damage. Unless conducted regularly, by the time damage occurs, deterioration might be advanced and options for preventative maintenance might be reduced or lost. Visual inspection can be undertaken relatively cheaply over the whole structure at frequent time intervals.
- **Intermittent Site Testing:** Site testing can be undertaken to monitor the rate of deterioration, and predict residual life based on the observed deterioration rate. Calculating residual life often requires various assumptions to be made as it is impractical to measure all parameters in the models. This can lead to large errors in predictions.
- **Permanent Surface Mounted and Embedded Monitoring:** These are installed preferably at the time of construction but can also be retrofitted. Some monitoring methods facilitate the assessment of residual life and because they establish a base line at construction for items like strain they give more extensive information not obtained from intermittent site testing that starts once the deterioration is imminent. This type of monitoring has a significant capital outlay and ongoing maintenance and operating costs, therefore it should only be installed where the asset's owner will commit to undertaking the monitoring throughout its service life. Where monitoring of this type is undertaken it must be considered throughout the design phase and into the construction phase.

Z7/07 provides useful background on visual inspection and various tests that are used within the monitoring frame work. These include intermittent site tests (e.g. electrode potentials, carbonation depth, chloride profiles, concrete resistivity, polarisation resistance, petrographic examination, microbial analysis) and permanent monitoring systems (e.g. corrosion initiation, corrosion rate, strain, vibration and deflection).

### **7 Conclusions**

Performance testing as part of a durability planning and implementation process will lead to an increased likelihood of achievement of design life of concrete structures and buildings.

Performance test methods used to inform durability design often do not accurately reflect processes that occur in the field. Whether the results are used to compare different materials or to predict their performance, it's important to account for the limitations of the method.

Therefore, it is strongly recommended that the selection of test methods, design of test programs, and interpretation of the results be performed by experienced professionals who have appropriate knowledge of both the testing processes and the deterioration processes that occur in structures exposed to various environments. This will ensure that test results, and the outcomes of predictive modelling based on the results, are interpreted appropriately.

## **8 Acknowledgements**

Thanks are afforded to the Z7/07 Task Group members, most particularly Andrew Peek, Susan Freitag, Miles Dacre and Reuben Barnes, Durability Committee members, most particularly Rodney Paull and the valuable contribution of CIA members from comments obtained through the peer review process.

## **9 References**

1. CIA Z7/07, "Concrete Durability Series – Performance Tests to Assess Concrete Durability", Recommended Practice Z7/07, Concrete Institute of Australia, Sydney, 2015.
2. Peek, A M, Nguyen, N and Wong T, "Durability Planning and Compliance Testing of Concrete in Construction Projects", Proc. Corrosion Control 007 Conf., Australasian Corrosion Association Inc., Sydney, 25-28 November, 2007.
3. Nordtest NT Build 443, "Concrete Hardened: Accelerated Chloride Penetration", Finland, 1995.
4. ASTM C 1556-11a, "Standard Test Method for Determining the Apparent Chloride Diffusion Coefficient of Cementitious Mixtures by Bulk Diffusion", American Society for Testing and Materials, West Conshohocken, PA, 2011.
5. AS 1012.8.1:2000, "Method of Making and Curing Concrete – Compression and Indirect Tensile Test Specimens", Standards Australia, Sydney, 2000.
6. fib Bulletin 34, "Model Code for Service Life Design", Lausanne, Switzerland, 2006.
7. AS 1012.21, "Methods of Testing Concrete Method 21: Determination of Water Absorption and Apparent Volume of Permeable Voids in Hardened Concrete". Standards Australia, Sydney, 1999.
8. ASTM C642:06, "Standard Test Method for Density, Absorption, and Voids in Hardened Concrete." ASTM International, West Conshohocken, PA, 2006.
9. Andrews-Phaedonos, F, "Assessment of Concrete Durability Using a Single Parameter with a High Level of Precision - The VPV Test", 25th ARRB Conference - Shaping the Future: Linking Policy, Research and Outcomes, Perth, Australia 2012.
10. UK Concrete Society, Technical Report TR31, "Permeability Testing of Site Concrete", Camberly, UK, 1988.
11. ASTM C1585-13, "Standard Test Method for Measurement of Rate of Absorption of Water by Hydraulic-Cement Concretes." ASTM International, West Conshohocken, PA, 2013.
12. CIA Z7/04, "Concrete Durability Series – Good Practice through Design, Concrete Supply and Construction", Recommended Practice Z7/04, Sydney, 2014.
13. AASHTO T 277-96, "Standard Test Method for the Electrical Indication of Concrete's Ability to Resist Chloride Ion Penetration", Standard Specifications for Transportation Materials and Methods of Sampling and Testing, Washington DC, 1996.
14. ASTM C 1202-12, "Standard Test Method for the Electrical Indication of Concrete's Ability to Resist Chloride Ion Penetration", American Society for Testing and Materials, West Conshohocken, PA, 2012.
15. AASHTO TP95-11, "Standard Method of Test for Surface Resistivity Indication of Concrete's Ability to Resist Chloride Ion Penetration", Standard Specifications for Transportation Materials and Methods of Sampling and Testing, Washington DC, 2011.
16. AS 1012.14:1991, "Method for Securing and Testing Cores from Hardened Concrete for Compressive Strength", Standards Australia, Sydney, 1991.
17. CIA Z11:2002, "The Evaluation of Concrete Strength by Testing Cores", Concrete Institute of Australia, Sydney, 2002.



18. CIA CPN22:2008, "Non- destructive Testing of Concrete", Concrete Institute of Australia, Sydney, 2008.
19. BS EN 13791:2007, "Assessment of In-situ Compressive Strength in Structures and Precast Concrete Components." European Committee for Standardization, Brussels, 2007.

# A Discussion on the Autogenous Shrinkage Interpretation from the Experimental Shrinkage Measurement Based on the Australian Testing Procedure AS1012.13

William A. Thomas<sup>1</sup>, James Mohammadi<sup>2</sup> and Dr Warren South<sup>3</sup>

<sup>1</sup>Chief Engineer, Concrete – Boral Construction Materials, Brisbane, Queensland, Australia

<sup>2,3</sup>Research and technical services – Cement Concrete and Aggregates Australia, Sydney, New South Wales, Australia

**Abstract:** This paper discusses a suggested experimental procedure for performing an accurate assessment of the concrete shrinkage. The suggested experimental procedure is based on the Australian shrinkage assessment terms and concept, addressed in the current version of Australian Standard AS3600. Following the introduction of the current version of Australian Standard AS3600, it has been noted that there are difficulties in relating test data from concrete drying shrinkage tests carried out in accordance with the Australian Standard AS1012.13 to the design shrinkage strain calculated in AS3600. This issue arises as a result of AS3600 approach for conducting shrinkage calculation by separating the forms of shrinkage into autogenous and drying shrinkage components. This paper discusses these types of shrinkage and their relationship to shrinkage measured according to AS1012.13. It goes on to propose possible procedure of using such test results to assist prediction of the design shrinkage strain by the methods proposed in AS3600. In addition, the proposed test method for measuring the autogenous shrinkage provides a consistent experimental method, which reveals the portion of autogenous shrinkage out of the total shrinkage. Besides, the proposed test method is used for assessing the effectiveness of mitigation methods applied specifically for the reduction of autogenous shrinkage.

**Keywords:** Drying Shrinkage of Concrete, Autogenous Shrinkage, Design Shrinkage Strain

## 1. Introduction

The current version of AS3600 [1] Clause 3.1.7.1 deals with the concrete shrinkage by introducing a parameter termed design shrinkage strain ( $\epsilon_{cs}$ ) of concrete. The design shrinkage strain ( $\epsilon_{cs}$ ) of concrete is determined from measurements on local concrete. In a situation which the design shrinkage is predicted, it can be estimated by calculations provided by AS3600 Clause 3.1.7.2. This calculation addresses in AS3600 Clause 3.1.7.2 separates the sources of concrete shrinkage between autogenous shrinkage ( $\epsilon_{cse}$ ) and drying shrinkage ( $\epsilon_{csd}$ ) as demonstrated in Equation (1).

$$\epsilon_{cs} = \epsilon_{cse} + \epsilon_{csd} \quad (1)$$

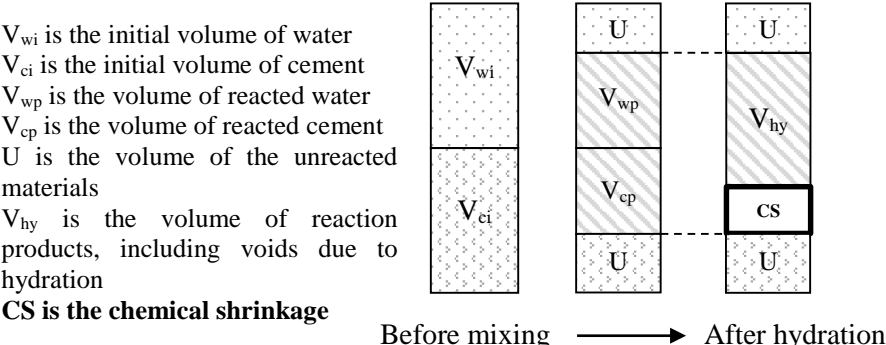
where,  $\epsilon_{cs}$  is the design shrinkage strain of concrete,  $\epsilon_{cse}$  is the autogenous shrinkage strain, and  $\epsilon_{csd}$  is the drying shrinkage strain

This change reflects the current European Codes EN1992-1-1 [2]. However, the two types of shrinkage noted in AS3600 Clause 3.1.7.2 now no longer have specific Australian Standard test methods from which the effect of intrinsic mix properties, such as concrete mix design values for these properties can be determined. The AS3600 code user is given the options of determining drying shrinkage “by tests after eight weeks of drying modified for long-term value, in accordance with the existing test method AS1012.13 [3], but the user is not advised as to how this data can be interpreted. In the previous version of AS 3600 [4] the value of basic shrinkage strain of concrete  $\epsilon_{cs,b}$  was either a default value of 850 micro-strains or directly assessed using the standard shrinkage test AS1012.13 value for drying shrinkage at 56 days as the value.

This problem arises from the fact that the Australian standard AS 1012.13 actually measures the entire shrinkage under the drying condition, which is different to just the drying shrinkage. The entire shrinkage under the drying condition includes both the drying shrinkage and autogenous shrinkage.

Autogenous shrinkage is considered to be a type of “drying” shrinkage that occurs when there is no loss of water from the concrete, but moisture is removed from the concrete pore structure through

internal hydration of the binder rather than drying from the exposed surfaces of a concrete structure. The hydration reaction starts after water is mixed with cement. This reaction is time-dependent and involves only a portion of the mixed cement and water. It is observed that the resultant products of this reaction have less volume compared to the summation of the volume of reacted water and cement. Figure1 illustrates the difference between the volume of concrete resources and products resulted from cement reaction, when the ambient temperature is kept constant (the thermal expansion negligible). This form of chemical shrinkage has two major stages. The first one is named the plastic deformation, which includes concrete deformation in the plastic state and before the concrete initial setting time. The second stage is after initial concrete setting, when the hydrating cement has formed some structure that is capable of resisting stress and further chemical reaction in concrete results in the autogenous shrinkage. Accordingly, when a sufficient structure is formed to restrain chemical shrinkage following initial setting, the volume of the movement becomes “self-desiccation” shrinkage or “autogenous shrinkage” [5].



**Figure1: Volume of Cement, Water and Hydration Products [6]**

The autogenous shrinkage magnitude is largely an intrinsic characteristic and is independent of member size, and concrete ambient condition. In contrast, the drying shrinkage where the size and shape of member as well as the surrounding environment are significant factors in the rate of drying from exposed surfaces and so the rate of “drying shrinkage”. In contrast to the autogenous shrinkage, which is caused by chemical reaction, the drying shrinkage is the shrinkage resulting from the effects of the loss of moisture from the concrete surface and is partly reversible when the concrete is re-saturated.

As mentioned above, factors affecting the autogenous shrinkage are different from the factors influencing the drying shrinkage. Although the current version of AS3600 proposes a model for estimating  $\epsilon_{cse}$  and  $\epsilon_{csd}$  separately, unfortunately the Australian Standards provide no means of separately measuring these values in sampled concrete. For a concrete test specimen, the given standard test method for drying shrinkage will contain both of these components of shrinkage. These components are varying in proportion, and it is difficult to now interpret and relate standard test data to AS3600 design values without further guidance being given. In the following sections the authors will review literature relating to interpretation of the two forms of shrinkage, review selected test data and recommend a method for interpretation of test data that can be applied by users of AS3600.

**2. Autogenous and Drying Shrinkage**

A review of the literature on this property of concrete yields a significant number of papers detailing the proposed mechanisms and magnitude of this form of shrinkage [7–9]. The complexity of trying to relate this data to that of the standard concrete shrinkage test AS1012.13, is that the test data incorporates a number of different forms of volume change as a result of the various elements of the curing process that a specimen is subjected to and how this may, or may not, be related to concrete formed into a structure. Some of the forms of volume change that need to be considered are:

- (a) Early Chemical Shrinkage

- (b) Thermal expansion or shrinkage
- (c) Autogenous Shrinkage
- (d) Swelling on saturation
- (e) Drying Shrinkage
- (f) Carbonation Shrinkage

In Table 1 below the authors suggest the likely volume changes (as above) that will influence the unrestrained shrinkage of a standard test specimen used for a drying shrinkage test carried out in accordance with AS1012.13.

**Table 1: Typical Characteristics of Free Volume Change of Shrinkage Samples**

Curing Period	Method of Curing	Likely Influences on Volume Change (from forms of volume change listed)
0 hours to 24 hours	Field or Laboratory specimen "sealed" in form.	(a), (b), (c) and possibly (e) to some extent
24 hours to 7 days	Specimen placed in lime saturated water at 23°C.	Possibly (c) to some extent and (d)
7 days to 63+ days	Specimen surface dried and maintained at 23°C and 50% Relative Humidity	(c), (e) and possibly (f)

Other test methods such as ASTM 1698 [10] provide a method for assessing autogenous shrinkage and is only suitable for cement pastes and possibly mortars. Neither of these methods are suitable for assessing the autogenous shrinkage component of a standard shrinkage test but do have value in gaining a better understanding of the nature of and time dependency of autogenous shrinkage at early ages. It can be seen that autogenous shrinkage is likely to have an influence on the final cumulative shrinkage on most parts of the test specimen's combined curing periods with the probable exception of the period of wet curing where, depending on the concrete permeability, there will be a ready supply of water to replace chemically reacted water with the net impact being expansion or swelling.

In the case of a concrete structural element cast in a dry environment (i.e. not in water or subject to wet curing) the main influences on volume change will be (a), (b), (c) and to a lesser extent (e) until initial in form or other form of curing is complete and then (b), (c), (e) and (f) after curing is complete. In this case it can be seen that autogenous shrinkage will have a continuing influence on the members volume change from the time of hardening after placement.

A literature review discovered a number of methods for assessing a concrete mix autogenous shrinkage. Holt (2005) proposes three methods ranging from assessing plastic concrete chemical shrinkage using water displacement to casting a test slab in forms and assessing dimensional change after casting [9]. Further, using a mechanical measuring gauge [6], or laser sensors [11] were also suggested in the literature. Although there are different methods available to be applied for measuring autogenous shrinkage, the selected method should be consistent with the current method AS 1012.13 used for measuring shrinkage under the drying condition. The proposed model in AS3600 for estimating the autogenous shrinkage is provided in equation (2) below.

$$\varepsilon_{cse} = \varepsilon_{cse}^* \times (1 - e^{-0.1xt}) = (0.06f'_c - 1) \times (1 - e^{-0.1xt}) \times 50 \times 10^{-6} \quad (2)$$

where,  $t$  is time in days after initial setting of the concrete,  $\varepsilon_{cse}^*$  is final autogenous shrinkage and  $f'_c$  is the 28-day characteristic compressive strength of concrete in MPa.

Literature revealed that the autogenous shrinkage is dependent on the chemical composition of cement and concrete materials, and also the mix proportioning [6]. In order to assess the effectiveness of any selected mix design, and selected mitigation methods applied for producing concrete with lower autogenous shrinkage, it is required to have a method specifically measure the autogenous shrinkage. There are different methods addressed by literature for mitigating the autogenous shrinkage such as using low heat (LH) cement, introducing expansive additives, using shrinkage reducing agents (SRA's), adjusting water reducer dose, adjusting gypsum level in cement, replacing a portion of cement with fly ash and increasing the water to cement (W/C) ratio. All these

methods can have effect in managing autogenous shrinkage and their level of effectiveness needs to be assessed by testing for any specific mix design.

In its defined form (from AS3600 [1] and EN 1992 [2]) drying shrinkage would be a combination of all shrinkage after taking account of autogenous shrinkage and any thermal shrinkage. To that extent it will contain some impact from carbonation shrinkage unless the measurement technique used seeks to avoid any availability of CO<sub>2</sub> or carbonation shrinkage is assessed separately removing the impact of carbonation removed from the over-all shrinkage measurement.

In its purest form “drying shrinkage” should be reversible. In other words, a concrete that has been dried for a period of time and the drying shrinkage component measured, with impacts of carbonation and autogenous shrinkage removed from the total shrinkage, may be re-saturated and the specimen should expand to the full amount of this drying shrinkage component. In reality the drying shrinkage is not fully reversible and literature suggests that the degree to which it is reversible will vary between 30% and 60% as a result of the introduction of additional links within the hydrating cement gel during the initial drying period [12].

Drying shrinkage occurs under drying conditions, which are not associated with chemical or autogenous self-desiccation of a concrete test specimen or a concrete structure, and takes place through the exposed surfaces of the concrete. The rate of drying is dependent on factors such as the concrete members’ size and shape as well as the exposed surface ambient conditions (temperature, air speed and relative humidity) and the permeability of the concrete. AS3600 and EN 1992 provide formulae for estimating the drying shrinkage component of a structure over time as impacted by environment (relative humidity) and member dimensions.

As shown in Equations (3), (4) and (5) from AS3600, at any time “*t*” after the commencement of drying, the drying shrinkage strain shall be taken as:

$$\varepsilon_{csd} = k_1 \times k_4 \times (1 - 0.008 \times f'_c) \times \varepsilon_{csd,b}^* \quad (3)$$

where, *k<sub>1</sub>* is the time after the commencement of drying in days, the value of the factors *k<sub>4</sub>* for the test prism is approximately 0.65 (drying room in AS1012.13 test environment is equivalent to an “interior environment” in AS3600), *f'<sub>c</sub>* is the 28-day characteristic compressive strength of concrete in MPa, and  $\varepsilon_{csd,b}^*$  is the final basic drying shrinkage strain, which is taken as  $800 \times 10^{-6}$  for Sydney and Brisbane,  $900 \times 10^{-6}$  for Melbourne and  $1000 \times 10^{-6}$  elsewhere.

$$k_1 = \frac{(0.8 + 1.2e^{-0.005t_h}) \times t^{0.8}}{t^{0.8} + 0.15t_h} \quad (4)$$

where, *t* is the time after the commencement of drying in days, *t<sub>h</sub>* is hypothetical thickness of a member in mm calculated using Equation (5)

$$t_h = \frac{2A_g}{u_e} \quad (5)$$

where, *A<sub>g</sub>* is gross cross-sectional area of a member in mm<sup>2</sup> and *U<sub>e</sub>* is exposed perimeter of a member cross-section plus half the perimeter of any closed voids contained therein in mm.

Finally, consideration should be given to the fact that the design shrinkage strains ( $\varepsilon_{cs}$ ) provided by Clause 3.1.7.2 of AS3600 has a range of  $\pm 30\%$  error. The test method for assessing concrete shrinkage, AS1012.13, uses a concrete prism of approximate dimensions 75mm×75mm×280mm. Accordingly, the calculation for the above AS3600 parameters based on the AS1012.13 sample size are tabulated in Table 2.

**Table 2: The calculated Drying Shrinkage parameters for Test Specimen based on AS 3600 Model**

$f'_c$ [MPa]	$t_h$	$k_d \cdot (1 - 0.008 \cdot f'_c)$					$k_d$	$\epsilon^*_{csd,b}$
		0-Day	7-Day	14-Day	56-Day	1000-Day		
20	37.5	0.000	0.690	0.897	1.231	1.475	0.65	800
50	37.5	0.000	0.493	0.641	0.879	1.053	0.65	800
100	37.5	0.000	0.164	0.214	0.293	0.351	0.65	800

<sup>1</sup> days after placing under drying condition (7 days from casting)

The above parameters (using  $\epsilon^*_{csd,b} = 800$  micro-strain) are further converted to estimated drying shrinkage values in Table 3 below.

**Table 3: The calculated Drying Shrinkage for Test Specimen based on AS 3600 Model**

$f'_c$ [MPa]	Drying Shrinkage (Microstrain)				
	0-Day	7-Day	14-Day	56-Day	1000-Day
20	0	359	466	640	767
50	0	256	333	457	548
100	0	85	111	152	183

<sup>1</sup> days after placing under drying condition (7 days from casting)

### 3. Estimate Concrete Shrinkage Using Numerical Models

The drying shrinkage test method used in Australia is AS1012.13. The test method assesses the total drying shrinkage of a concrete prism of approximate dimensions 75mm×75mm×280mm that has been cured for 7 days, 1 day at ambient temperature in moulds and 6 days in lime saturated water set at 23°C. Following this initial curing the specimen is placed in a drying environment kept at a temperature of 23°C and relative humidity of 50% for a further period (usually a further 56 days) with regular measurements of total shrinkage taken up to the end of the testing period.

As noted in Section 2 the “total shrinkage” measured by the test method AS 1012.13 is the total shrinkage under drying conditions, which contains components of “drying shrinkage”, autogenous shrinkage and possibly carbonation shrinkage. Based on information provided by Neville [12] the authors have estimated that it is probable that carbonation shrinkage of a concrete test specimen over 56 days drying is relatively low. The carbonation shrinkage is estimated by the authors as being in the likely range of 2 to 15 microstrains at most [12]. On this basis, the authors believe that it is reasonable to include any carbonation shrinkage as part of the overall drying shrinkage and not assessed separately [5].

Based on this, the shrinkage of concrete test specimens will be composed of a combination of residual autogenous shrinkage combined with drying shrinkage. On the assumption that the amount of remaining autogenous shrinkage between 7 days from casting to 63 days from casting (56 days of drying) can be estimated from a member with dimensions of the test specimen noted above and will have an estimated value taken from AS3600. Estimates from AS3600 in Table 4 below can provide an approximate comparison in the relative proportions of drying and autogenous shrinkage in three different concrete grades. Field test results to AS1012.13 on S50 grade concrete typically present values of shrinkage of approximately 650 microstrains at 56 days drying for sample S50, which is slightly higher than the total shrinkage of S50 grade concrete, calculate using AS3600 and EN 1992-1-1 models (refer to Table 4 & 5).

The autogenous shrinkage for different ages is calculated and presented in Tables 4 & 5. It should be taken into account that the presented autogenous shrinkage values are adjusted by subtracting the value of autogenous shrinkage at the start of drying condition (after 7 days of curing). This subtraction provides a similar reference point for measuring both autogenous and drying shrinkage.

Table 4 & 5 data ignore any potential differences in the impact of water saturation curing used from day 2 to day 7 in the test method on the value of the remaining autogenous shrinkage from 7 days to

63 days. This arises from the assumption that autogenous shrinkage is related to binder hydration and pore size. The autogenous shrinkage mechanism is more significant for higher strength, low W/C ratio concrete with a dense matrix with low porosity. Accordingly, concrete held at a constant temperature for the 6 days of saturation curing may have a relatively minor impact on these factors compared to a specimen which has no drying from the surface but no added water from curing and held at the same temperature for 6 days (stated for autogenous shrinkage only).

**Table 4: The Estimated Drying and Autogenous Shrinkage by AS 3600 Model**

Shrinkage Type	Applied Model	Concrete Grade [MPa]	Estimated Shrinkage by Type [Microstrain]				
			0-Day <sup>1</sup>	7-Day	14-Day	56-Day	1000-Day
Autogenous	AS3600	20	0	2	4	5	5
Drying			0	359	466	640	767
<b>Total</b>			<b>0</b>	<b>361</b>	<b>470</b>	<b>645</b>	<b>772</b>
Autogenous	AS3600	50	0	25	37	49	50
Drying			0	256	333	457	548
<b>Total</b>			<b>0</b>	<b>281</b>	<b>371</b>	<b>507</b>	<b>597</b>
Autogenous	AS3600	100	0	62	94	124	124
Drying			0	85	111	152	183
<b>Total</b>			<b>0</b>	<b>148</b>	<b>205</b>	<b>276</b>	<b>307</b>

<sup>1</sup> days after placing under drying condition (7 days from casting)

Table 4 above is can be repeated for the test specimen using the formulae provided in European Standard EN1992-1-1 as set out in Table 5 below.

**Table 5: The Estimated Drying and Autogenous Shrinkage by EN1992-1-1 Model**

Shrinkage Type	Applied Model	Concrete Grade [MPa]	Estimated Shrinkage by Type [Microstrain]				
			0-Day <sup>1</sup>	7-Day	14-Day	56-Day	1000-Day
Autogenous	EN1992-1-1	20	0	3	5	10	15
Drying			0	255	355	506	583
<b>Total</b>			<b>0</b>	<b>258</b>	<b>360</b>	<b>516</b>	<b>598</b>
Autogenous	EN1992-1-1	50	0	12	19	38	59
Drying			0	178	249	354	409
<b>Total</b>			<b>0</b>	<b>190</b>	<b>268</b>	<b>392</b>	<b>468</b>
Autogenous	EN1992-1-1	100	0	26	43	87	132
Drying			0	95	133	189	218
<b>Total</b>			<b>0</b>	<b>121</b>	<b>176</b>	<b>276</b>	<b>350</b>

<sup>1</sup> days after placing under drying condition (7 days from casting)

As can be seen from the data presented in Table 4 & 5 the two standards have slightly differing estimates on the amount of autogenous shrinkage that occurs between 7 days from casting and 63 days from casting and drying shrinkage over the period from start of drying to 56 days drying. For example grade S50 concrete will have an autogenous shrinkage portion from 7 days to 63 days (56 days drying) estimated as 49 micro-strains while it is estimated as 38 micro-strains using EN1992-1-1 model. The differences in total shrinkage estimated for shrinkage test specimens between the two standards are generally within the  $\pm 30\%$  suggested by both standards. It is evident that the estimate of total shrinkage for test specimens is significantly lower than is seen in these grades of concrete in practice (and as reflected in the 2001 and previous versions of AS3600 where typical 56-day drying shrinkage test data was used to estimate total shrinkage).

Considering reported data from literature, autogenous shrinkage can vary significantly for a concrete of the same characteristic strength based on constituents such as binder composition and admixtures (Holt [5]). In view of this the authors recommend that a test method for assessing the autogenous shrinkage component of the standard concrete shrinkage test is developed so that the “basic drying shrinkage” as defined in AS3600 may be better estimated from testing.

#### 4. Applying AS3600 Model for Concrete Shrinkage Estimation

The process of estimating the design shrinkage strain given in AS3600 is outlined by Gilbert (2002) [8] in his earlier proposal to Australian Standards. In essence the standard provides three ways to estimate this value. The first (default) method is to estimate the total shrinkage based on the Standard's formulae and a basic drying shrinkage strain value given for different regions. The second requires knowledge of typical drying shrinkage test values for given mixes available in a particular project location. The third method requires a test of the specific concrete mix in accordance with Australian Standard AS1012.13 to determine the shrinkage (typically after 63 days from casting or 56 days drying after the initial 7 days curing). In Standard AS3600 the total member shrinkage is given as being a combination of drying shrinkage ( $\epsilon_{csd}$ ) plus the autogenous shrinkage ( $\epsilon_{cse}$ ) at any given time ( $t$ ). Unfortunately the AS1012.13 test, as noted in previous sections, provides data that contains both drying shrinkage and autogenous shrinkage and these need to be separated out so that the test value can be useful in estimating the value of drying shrinkage component in either of the second or third methods noted above.

The problem here is one of timing and its impact on the test method used. Autogenous shrinkage effectively starts from when the concrete reached initial setting (normally within 4 to 12 hours of mixing the concrete) whereas drying shrinkage only starts after ceasing moist curing (in the case of the test method after 7 days). It would seem that in order to interpret the standard test results then the component of autogenous shrinkage in the test drying period needs to be estimated and removed from the result so as to report a final drying shrinkage value for the test prism of the standard dimensions. One way to achieve this is to use the AS3600 equation for the autogenous shrinkage from 7 days to 63 days (test specimen drying period) to determine the correction value to the 56 days drying test value so as to estimate the actual drying shrinkage component. This autogenous shrinkage component is dependent on characteristic compressive strength in the standard and the authors have calculated the relevant values in Table 4 above based on the AS3600 equations. The influence of time and curing on shrinkage based on AS1012.13 can be considered by the estimation of the autogenous shrinkage using equation (2) derived from AS3600 above. For example for the S50 concrete, the autogenous shrinkage is calculated from this formula to be 50 microstrain at the initial time of starting drying of the shrinkage test specimen (7 days). This value can then be subtracted from the estimated autogenous shrinkage from this equation at later ages and the net differential autogenous shrinkage deducted from AS1012.13 test results at these ages to estimate the drying shrinkage component.

The above method is an approximation and may be sufficient for estimation but the problem with the above analysis is that the actual value of the autogenous shrinkage test has been shown to vary significantly for the same concrete strength and needs to be assessed by testing of the same concrete rather than estimated in this way.

The authors propose a means of being able to carry out this testing is to cast duplicate specimens the same concrete used to cast test specimens for assessment of "drying shrinkage" to AS1012.13. These duplicate specimens need to be "sealed" after the initial 7-day curing cycle of the AS1012.13 method to prevent water ingress or surface drying and their shrinkage measured in the same curing temperature to that of AS1012.13 with the resultant shrinkage of these duplicate specimens measured being attributed to the autogenous shrinkage component of the same concrete over this curing period.

#### 5. Proposed Methods of Relating Shrinkage Test Data

As autogenous shrinkage is defined as the shrinkage that occurs through self-desiccation after setting of plastic concrete then the author's believe that it is feasible to assess the impact of this on a standard shrinkage test carried out in accordance with AS1012.13 by using duplicate samples of the same concrete as cast for the standard "drying shrinkage" testing that are subject to the same curing up to 7 days from casting as the standard "drying shrinkage" specimens as noted above.



The author's note that following the curing procedure for the proposed method is going to omit the significant proportion of autogenous shrinkage during the first 7 days after setting. Selection of the autogenous reference point for the samples cured 7 days results in neglecting almost 50% of the total autogenous shrinkage if using formula (2) above as a guide. This method is purely recommended for "correcting" the AS1012.13 method for the component of autogenous shrinkage over the period of the test and not as an estimate of the concrete total autogenous shrinkage including the period from setting to 7 days. The authors recommend that a separate test method for autogenous shrinkage from setting to 7 day's is developed along similar lines to those proposed by Holt [6].

Accordingly, after the standard curing regimes noted in AS1012.13 up to 7 days from casting the test specimens the "autogenous shrinkage" specimens are removed from moist curing and measured, in the same way as detailed in AS1012.13 for the specimens used for the current "drying shrinkage" test. The additional process of "towellling" the specimens is applied to dry to a saturated surface dry condition except that the authors recommend that each specimen mass is then measured to  $\pm 0.1$  gram accuracy (including the standard "drying shrinkage" specimens). After finishing each measurement, the autogenous shrinkage specimens are quickly returned to a storage that prevents loss of moisture through evaporation from the concrete surface. This storage will be maintained at  $23^{\circ}\text{C} \pm 2^{\circ}\text{C}$  and may be storage in a sealed container suspended over water on a rack or by sealing the surface of the concrete specimens to prevent moisture loss. These specimens are measured for shrinkage or expansion at the same storage ages (maturity) as the 'drying shrinkage' test specimens and each specimen mass recorded at the time of measurement as noted earlier. The "autogenous shrinkage" test specimen measurements will be accepted provided mass loss or gain does not exceed 0.2 gram over the measurement period. The results of autogenous shrinkage from 7 days to the time of measurement ( $\epsilon_{cset}$ ) can then be used to assess the drying shrinkage of the concrete by deducting  $\epsilon_{cset}$  from the standard total shrinkage value assessed by the method of AS1012.13.

It is the authors' opinion that this test method needs significant assessment to validate. The test method outlined here should be trialled to assess the drying shrinkage on a number of concrete mixtures ranging in grade strength from 20MPa to 100MPa as common grades used in construction. The method for storing the test specimens to prevent absorption or loss of water is varied to obtain "sealed specimen" behaviour with no loss or gain of moisture. The aim of the proposed test program will be to provide recommendations on suitable methods to prevent loss of moisture from the autogenous shrinkage specimens so that this may be adopted as a standard method in Australia and assist with aligning the resulting net drying shrinkage test data with the relevant provisions of AS3600.

## 6. Conclusions

This paper discusses the design and application of a test method, which may provide more accurate estimates of the actual drying shrinkage of concrete, specifically. A new method based on the Australian shrinkage test method AS1012.13 is proposed subject to a review of methods to be used in curing autogenous shrinkage test specimens. The suggested method follows mirrors the required procedure which is described in the current AS1012.13. The proposed method provides a means to interpret the characteristics of concrete based on experimental results and not just on the AS3600 model and assumed values, which only considers strength grade of concrete and has 30% error margin in prediction.

## 7. References

1. AS3600. Concrete Structures. vol. 2009. Sydney: 2009.
2. EN1992-1-1. Design of concrete structures Part 1: General Rules and Rules for Buildings. vol. 1. 2004.
3. AS1012.13. Methods of testing concrete Method13: Determination of the drying shrinkage of concrete for samples shrinkage of concrete for samples prepared in the field or in the laboratory. Sydney: 1992.
4. AS3600-2001. Concrete Structures. 2001.
5. Holt EE. Early age autogenous shrinkage of concrete. Technical Research Centre of Finland 2001;446.
6. Tazawa E. Autogenous Shrinkage of Concrete. CRC Press; 1999.
7. Yang Y, Sato R, Kawai K. Autogenous shrinkage of high-strength concrete containing silica fume under drying at early ages. Cement and Concrete Research 2005;35:449–56.
8. Gilbert I. Creep and Shrinkage Models for High Strength Concrete-Proposals for inclusion in AS3600. Australian Journal of Structural Engineering 2002;4:95.
9. Holt E. Contribution of mixture design to chemical and autogenous shrinkage of concrete at early ages. Cement and Concrete Research 2005;35:464–72.
10. ASTM-C1698. Standard Test Method for Autogenous Strain of Cement Paste and Mortar 1. 2009.
11. Morioka M, Hori A. Measurement of autogenous length changes by laser sensors equipped with digital computer systems. Proceedings of the International Workshop on Autogenous Shrinkage of Concrete, Hiroshima, Japan: E&FN Spon; 1998, p. 203–10.
12. Neville AM. Properties of concrete. London: 1963.

# Performance test for hydrophobic impregnations for protection against chloride ingress in concrete

Nelson Silva<sup>1</sup>, Elisabeth Helsing<sup>2</sup>, Katarina Malaga<sup>3</sup>, Eva Rodum<sup>4</sup>, Minna Torkkeli<sup>6</sup>, Arvid Hejll<sup>6</sup>

<sup>1</sup>Researcher, CBI Swedish Cement and Concrete Research Institute

<sup>2</sup>Senior Researcher, CBI Swedish Cement and Concrete Research Institute

<sup>3</sup>CEO, CBI Swedish Cement and Concrete Research Institute

<sup>4</sup>Senior Principal Engineer, Norwegian Public Roads Administration

<sup>5</sup>Head of Engineering Structures, Finnish Transport Agency

<sup>6</sup>Bridge Engineer, Swedish Transport Administration

**Abstract:** This paper describes the development of a common Nordic test method for the evaluation of hydrophobic impregnations for concrete, for protection against chloride ingress. The first stage of the experimental campaign served to evaluate the influence of the precondition environment before surface treatment, curing time and type of surface on the performance of the impregnation agent. In the second stage, a round robin test involving 3 Nordic laboratories was conducted; the results showed very little variation and were compared to results obtained according to previous standards in order to define performance requirements. Finally, data from field exposed specimens for more than 5 years was used to validate the suitability for use.

**Keywords:** Concrete, hydrophobic impregnation, chloride ingress, performance test, diffusion of chlorides.

## 1. Introduction

In the northern European countries de-icing salts are frequently used on road bridges during the winter season, causing a very harsh environment, especially for concrete edge beams. A large part of the maintenance costs of road bridges are due to repair or replacement of edge beams due to corroding reinforcement. With the aim to extend the service life of the edge beams, hydrophobic impregnation have been used in order to prevent or slow down the ingress of chloride ions into the concrete. Thus, the influence of the hydrophobic impregnations on the chloride penetration is a very important property for hydrophobic impregnation agents used for this purpose. However, according to the harmonized European standard EN 1504-2 [1], the property "diffusion of chloride ions" is for hydrophobic impregnations "subject to national standards and national regulations".

Therefore, the transport and road administrations of Sweden, Finland and Norway use separate national methods to evaluate this property of the hydrophobic impregnating agents for concrete. The existing methods differ in many ways and the results are not directly comparable. Therefore, the transport and road administrations of Sweden, Finland and Norway initiated a project with the aim to establish a common Nordic method to evaluate the protection against chloride ingress of this kind of products. The three administrations started the project by reviewing and comparing the three existing Nordic methods and other relevant methods, their advantages and draw-backs in order to create a basic setup for a new method.

It should be pointed out that the purpose of both the existing methods and the new method is to classify hydrophobic impregnating agents with regard to their capability to protect concrete from chloride ingress and not to monitor the performance of these agents under realistic conditions. However, the method should be able to distinguish between products which give a satisfying protection against chloride under field conditions and those who don't. Therefore, the method needs to be validated against data obtained from field experience. It is also an advantage if the results with the new method correlate to results obtained with the existing methods.

In all three methods the efficiency of the agents is obtained by comparing the amount of chlorides in impregnated concrete samples with the amount of chlorides in samples without impregnation after a certain period of exposure to chlorides. In the existing Norwegian method the chloride exposure consists of cycles of 4 hours spraying with 3% NaCl-solution and 4 hours drying in a chamber kept at 50% RH for a period of 42 days. In both the Swedish and the Finnish methods the exposure to chlorides is obtained by submerging the specimens in a solution with 15% NaCl-solution for 56 days.

The Norwegian method uses sawed surfaces (half cubes), the Swedish method uses sawed 20 mm thick concrete slices and whilst the Finnish method uses form surfaces of cubes. There are also many other diverging details of the testing procedure in the existing three methods, such as:

- type of concrete in the specimens used as substrates;
- the age of the concrete specimens;
- treatment and conditioning of the specimens before application of the impregnating agent;
- the way the impregnating agent is applied and the amount controlled;
- length of the period of curing after the impregnation is applied and before exposure to chlorides, as well as the climatic conditions during this period;
- the part of the specimens used for the chloride analysis (e.g. in the Swedish the outermost 2.5 mm are taken away before analysis);
- the way to express the efficiency of the impregnating product;
- the way to express the requirement: single limit value for acceptance or different levels.

The Norwegian exposure method is more close to the kind of environment a concrete surface may be exposed to in reality than the kind of exposure used in the other two methods. It has a more realistic chloride concentration of the exposure solution and more realistic climatic conditions. However, this method suffers from problems with reproducibility due to the difficulty to control the climate in the testing chambers. For this reason and also for the sake of simplicity submersion in a NaCl-solution was a preferred procedure.

In [2] four different exposure methods were compared; permanently submerged in 16.5% NaCl-solution; periodically submerged in 16.5% NaCl-solution (in principle 1 day submerged and 1 day in 50% RH); permanently submerged in 3% NaCl-solution and in a salt-spray chamber with 3% NaCl-solution (4 hours spraying and 4 hours drying). All exposures were continued for 56 days. Although the measured chloride levels varied substantially between the different exposure methods, there was not a big difference in the calculated efficiency of the impregnating agents obtained. This indicates that the impregnated samples and the reference samples are influenced in a similar and proportional way, regardless of the exposure method. A higher NaCl-concentration in the solution was preferred since it diminishes the effect of the detection limit of the chloride testing equipment on the result.

One inconvenience with the Swedish method is that the type of concrete to use reference is only made to EN 1766 [3] without specifying exactly which of several possible compositions (w/c ratio) should be used. There are cases where the product has first been tested on a concrete with w/c=0.45 and failed the test; the test was then repeated on a concrete with w/c=0.70 and the product passed.

One feature of the Norwegian method that was seen as something that should be kept in the new method was that the exposed sample was ground, in distinct levels, from the surface down to 15-25 mm to obtain a chloride profile. Another feature was the way to express the efficiency of the product, i.e. the filter effect defined as:

$$FE = 1 - \frac{Cl_I}{Cl_R} \quad (1)$$

where  $Cl_I$  is the amount of chloride ions in the impregnated sample and  $Cl_R$  is the amount of chloride ions in the reference samples: Both should be determined or estimated (if  $\sim 0$ ) down to the same depth.  $Cl_I$  and  $Cl_R$  can also be seen as the area under the chloride content profile of the impregnated and reference samples respectively.

Based on this review and the possibility to use supporting EN-standards a basic setup of the method was decided:

- Reference shall be made to MC (0.45) with  $D_{max}=10$  mm, according to EN 1766 [3] for substrates;
- The procedures shall have a well-defined starting point (specimens water cured for 28 days);
- Chloride exposure submersion of specimens in 15% NaCl-solution for 56 days shall be used;
- The chloride profile shall be determined;
- The efficiency of the product shall be expressed as a filter effect;
- It shall be possible to satisfactorily control the amount of impregnation agent applied;

It was also decided that before formulating the method and carry out a round robin test, a pre-study to clarify the influence of some unsettled parameters, primarily concerning the conditioning of the concrete samples before application of the impregnation and the treatment and curing of the specimens between the application of the impregnation and the submersion in the chloride solution.

Based on the basic setup and the results from the pre-study a method description should then be formulated and a round robin exercise with at least one laboratory from each country involved should be carried out, in order to ensure that the method gives reproducible results.

## 2. Pre-study: The influence of conditioning before and after application of the impregnation

### 2.1 Aim

The pre-study was set up to clarify the following questions:

Does the determined protective effect of the impregnations vary

- with type of application surface; sawed surface or form surface?
- if a sawed surface is let to dry directly or if it is treated with lime water?
- with the length of the drying period before application of the product?
- with the length of the period from application of the impregnation to the start of the exposure to the chloride solution?

### 2.2 Experimental

#### 2.2.1 Specimen preparation

The concrete used in this study was of the type MC (0.45) according to EN 1766 [2]; the mixture proportions are given in Table 1. Concrete cubes, with the dimensions of 100 mm x 100 mm x 100 mm, were cast in plastic moulds, demoulded after one day and stored in water for 27 days. At the age of 28 days, the cubes were cut in halves and all the surfaces, except the test surface (either cut or form) were coated with epoxy resin and allowed to dry for one day before preconditioning.

**Table 1. Concrete mixture proportions.**

CEM I 52.5 R (kg/m <sup>3</sup> )	Aggregates 0-10 (kg/m <sup>3</sup> )	Water (kg/m <sup>3</sup> )	Superplasticizer (wt.% CEM)	Air (%)	Slump (mm)
395	1800	178	0.5	1.5	180

#### 2.2.2 Specimen preconditioning

The influence of 3 different preconditioning environments, before application of the impregnation, on the protective effect of the impregnations was evaluated. Tests were conducted on cut surfaces.

- 7 days at (20±2) °C and (60±10) % RH, further on referred to as S;
- 3 days in saturated Ca(OH)<sub>2</sub> followed by 3 days at (20±2) °C and (60±10) % RH, further on referred to as H;
- 3 days in saturated Ca(OH)<sub>2</sub> followed by 7 days at (20±2) °C and (60±10) % RH, further on referred to as C;

Specimens aimed at studying the influence of the type of application surface were preconditioned during 7 days at (20±2) °C and (60±10) % RH (S).

### **2.2.3 Application and curing of the impregnation agent**

In this study two silane-based impregnation agents were used; a liquid, referred to as P1 and a gel, referred to as P2. Reference specimens are referred to as R. The hydrophobic agents, P1 and P2, were applied following the recommendations given by the producers, in the concentrations of 300 g/m<sup>2</sup> and 500 g/m<sup>2</sup>, respectively. After application of the impregnation the specimens were cured during 7, 14 and 28 days at (20±2) °C and (60±10) % RH and are further on simply referred to as 7, 14 and 28.

### **2.2.4 Exposure and chloride analysis**

After curing, both reference and treated specimens were immersed in 15% NaCl-solution, in separate containers, during 56 days. At the end of the exposure period, the samples were removed from the solution, surface dried with absorbent paper, sealed in plastic bags and stored at (20±2) °C before dry grinding on a lathe with a diamond tool. The following layers were ground: 0-2; 2-4; 4-6; 6-10; 10-15 and 15-20 mm (with an accuracy of 0.5 mm). After grinding, the powder samples were dried at 105 °C and stored in a desiccator prior to chloride analysis. The acid soluble chloride content in each layer was determined by potentiometric titration according to AASHTO-T260 [6] and expressed in wt.% of sample (oven dry concrete).

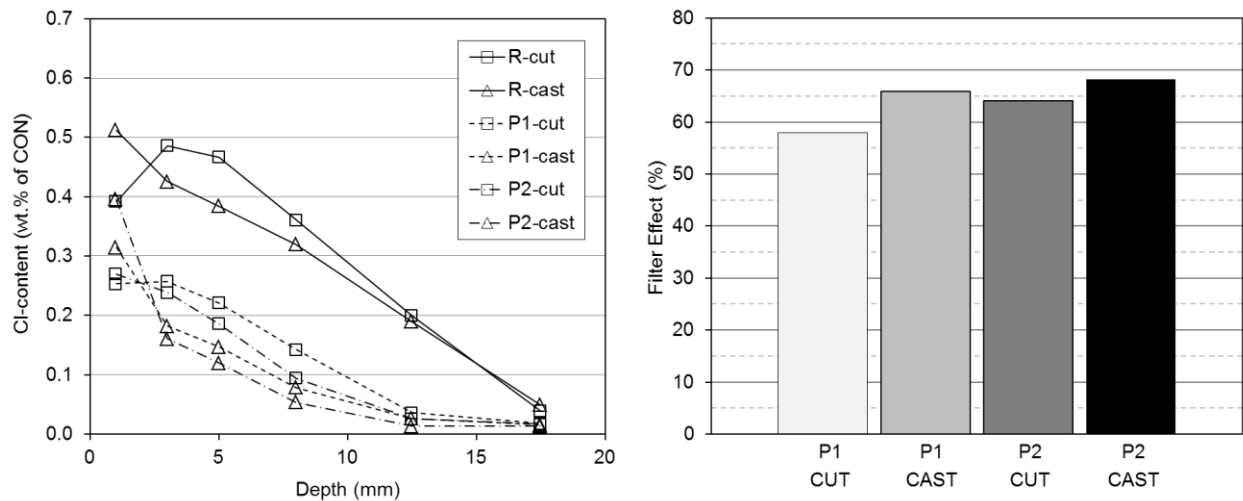
## **2.3 Results and discussion**

### **2.3.1 Influence of the type of application surface**

Figure 1 shows the chloride profiles obtained for the two types of treated surfaces (cut and form) as well as the respective filter effect for the 2 products tested. During casting, due to the presence of the formwork, concrete elements develop an outer layer richer in cement paste. When compared to the bulk concrete, such layer has a higher cement paste content, which gives a higher chloride binding capacity and a finer microstructure which can decrease the penetration depth of the impregnation agent.

The results in Figure 1 (left) show that except for the first layer, the chloride content is lower for the specimens in which the form surface was treated. Additionally, a higher filter effect for form surfaces was obtained (Figure 1 right), suggesting a somewhat beneficial effect when compared to cut surfaces. It is however unclear which effect is dominant: if the higher binding capacity of the first layer richer in paste (form surface) or the influence of the surface on the penetration depth of the treatment.

Therefore, if form surfaces are to be adopted for future reference, the chloride content should be expressed in weight % of binder. On the other hand, if cut surfaces are to be used, the results may be satisfactory expressed in weight % of concrete, as long as the curing period after application of the impregnation is short enough to avoid significant carbonation and the exposure period is short enough to avoid significant calcium leaching of the first few millimetres of the exposed surface.



**Figure 1. Results for cut and form surfaces cured during 28 days after application of the hydrophobic agent: (left) chloride profiles; (right) filter effect. Each data point is the average of 3 specimens.**

### 2.3.2 Influence of the preconditioning and curing time

Figures 2 and 3 show the chloride profiles taken as the average of three parallel specimens as well as the filter effect obtained with products P1 and P2. The results are shown for the different precondition environments and grouped as a function of the curing time.

The results show that the precondition environment before surface treatment does not significantly influence the resistance against chloride ingress.

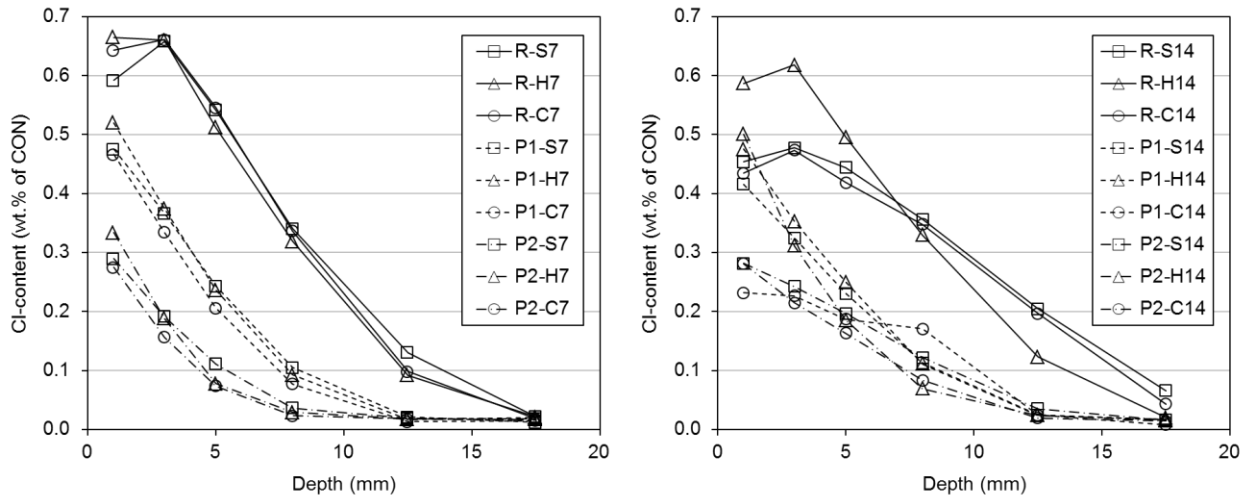
Essentially, for the specimens cured for 7 days after treatment, typical diffusion profiles were obtained; this is due to the relatively short drying period, implying that the degree of capillary saturation of the concrete pores is still very high. At this curing age, the main difference is observed at the surface layer of the reference specimens of the type S, which show a lower chloride level; such difference may be explained by the longer drying time when compared to type H and by the filling of the pores with calcium hydroxide when compared to type C.

Specimens cured for 14 days, do not present a clear behaviour in terms of the chloride transport mechanism and evaluation is not so straight forward, because the chloride profiles show characteristics typical of both diffusion and capillary suction. Apparently, for this curing length, the type of preconditioning environment has some influence, especially on the reference specimens; while specimens of the type S and C cured for a total of 21 days (7 days before treatment and 14 days after treatment) show profiles of the convection type, specimens of the type H cured for a total of 17 days (3 days before treatment and 14 days after treatment) show typical diffusion profiles.

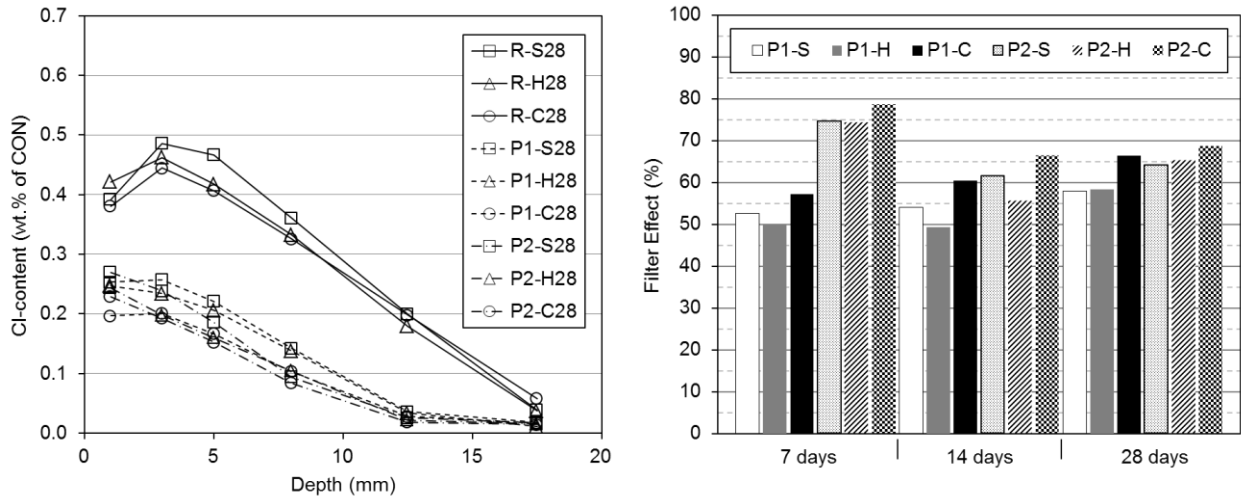
Finally, for the specimens cured during 28 days after treatment, typical convection profiles were obtained; due to the longer drying period, the degree of capillary saturation of the outermost layers is lower. Here chlorides are mainly transported by capillary suction and the chloride content up to a depth of 5 mm does not vary so much.

The results of the filter effect in Figure 3 indicate that, as long as the drying period before treatment is the same (7 days, specimens' type S and C), treatment with calcium hydroxide is beneficial; for all the curing ages (7, 14 and 28 days), higher filter effect was obtained. Whether chemical (binding) or physical (pore filling), the exact reason for this result is not clear.

Except for the specimens treated with P2 and cured for 7 days after treatment, the chloride protection slightly increases with the curing time. However, it is not clear which factor is most dominant: the polymerization of the impregnation agent or the cement hydration. Nevertheless, enough curing time is necessary for the treatment to be efficient, which may not be achieved at the end of 14 days.



**Figure 2. Chloride profiles measured for series cured during 7 (left) and 14 (right) days after application of the hydrophobic agent. Each data point is the average of 3 specimens.**



**Figure 3. Chloride profiles measured for series cured during 28 days after application of the hydrophobic agent (left) and filter effect (right). Each data point is the average of 3 specimens.**

### 2.3.3 Comments on the performance of the hydrophobic agent

The results in Figures 2 and 3 show that both products behave in a similar way with regard to the protection against chloride ingress; this is not surprising, since both are agents of the silane-type. However, while P2 is more effective for shorter curing periods, P1 requires longer curing time; the better short-term performance of P2 may be explained by the presence of bentonite clay which can efficiently block the capillary pores from the outermost concrete layers. With time, the difference between the effectiveness of the two products decreases. Regardless of the conditions tested, both products reduce the total chloride ingress to more than 50% when compared to non-treated samples.



### **2.3.4 Remarks on the development of the test method**

Concerning the development of a test method, none of the precondition environments clearly compromised to the robustness of the test results. Although not reported in this paper, the repeatability of the method was similar for all the tested conditions.

Although, precondition of the type C leads to better results expressed in terms of the filter effect, the results are consistent for all the curing periods after treatment of the samples; thus the absolute value becomes of no interest since it does not influence the filter effect and the fail/pass criteria for the test method. Moreover, under a practical point of view, precondition type C increases the number of experimental steps, without significantly better results, when compared to precondition type S; thus the latter is preferable. Finally, it should be pointed that such preconditioning (immersion in calcium hydroxide) is not representative for conditions in the field.

The preconditioning period after sample treatment should be 28 days: first, enough time should be given to the hydrophobic treatment to polymerize; secondly, the chloride profiles from the specimens cured for 14 days are difficult to evaluate and finally, the results of the filter effect are not consistent for the products tested.

## **3. Round robin exercise**

### **3.1 The tested method**

For the Round Robin test (RRT) three laboratories were involved; CBI in Sweden, SINTEF in Norway and VTT in Finland. A detailed experimental procedure (according to section 2.2) was distributed to the participating laboratories. Each laboratory was responsible for purchasing all the materials for their tests. The main features of the method were:

- MC (0.45) according to the mix design in Table 1;
- CEM I 52.5;
- Specimen precondition: 7 days at  $(20\pm 2)$  °C and  $(60\pm 10)$  % RH (type S);
- Curing of the hydrophobic agent: 28 days.
- Grinding steps for chloride analysis: 0-2; 2-4; 4-6; 6-10; 10-15; 15-20 and 20-25 mm.

For the test, three silane-based impregnation agents were used; a gel (P2), a liquid (P3) and a crème (P4). These were applied following the recommendations given by the producers, in the concentrations of 500 g/m<sup>2</sup>, 200 g/m<sup>2</sup> and 200 g/m<sup>2</sup>, respectively.

### **3.2 Comments on the execution of the round robin test**

Despite the attempt to make the method description as un-ambiguous as possible, some deviations between how the tests were performed at the three laboratories revealed that it was not precise enough.

According to the method description the specimens should be preconditioned and conditioned after application of the impregnating agent in a climate chamber at  $(20\pm 2)$  °C and  $(60\pm 10)$  % RH. At CBI and VTT climate rooms controlled at  $(20\pm 2)$  °C and  $(65\pm 5)$  % RH were used for both these periods. At SINTEF a room regulated  $(60\pm 5)$  % RH was used for preconditioning and one regulated at  $(50\pm 5)$  % RH was used after the application.

As regards the cement type, both CBI and VTT used a CEM I 52.5 R (from different manufacturers) with a high specific surface (500-600 m<sup>2</sup>/kg). SINTEF used a CEM I 52.5 N intended for use in infrastructures, with a much lower specific surface (360 m<sup>2</sup>/kg) and with a low alkali content (0.6%).

For the chloride analysis reference was made to AASHTO T 260, (or another method with the same or better precision), and the result should be given as percent of the dry sample mass. However, it was not stated if this meant oven dry or surface dry mass. According to AASHTO T 260 both options are possible. CBI and SINTEF have analyzed oven dry samples and VTT has analyzed surface dry samples.

### 3.3 Results and discussion

The results from the RRT are shown in Figures 4 and 5. Analysis of the chloride profiles (Figure 4) shows that highly reproducible results were obtained. Yet, some main differences are noticeable. The outermost layers (0-6 mm) of the reference specimens show the largest spread in the results. CBI shows a typical diffusion profile but in which chloride content in the first 4 mm is nearly maximum for this type of concrete, i.e. there is a saturation of free and bound chlorides. SINTEF shows a less steep chloride profile indicating a higher degree of capillary suction associated to more harsh drying conditions (50% RH). VTT shows a typical diffusion profile where the higher surface chloride content is associated to the higher paste content for the concrete tested (composition not given in this paper). When comparing the results from the treated samples, the main difference is the higher surface chloride content of the VTT specimens which is also due to the higher paste content. Finally, P4 shows higher spread in the results at a depth between 4 and 12 mm, the exact reason is unclear.

The fact that the major differences are associated to the chloride content at the surface layers indicates that handling of the specimens, especially after exposure, is crucial. Although the results, expressed in terms of the filter effect are very similar for all the laboratories (except for the specimens treated with P4), better instructions must be provided during the formulation of the test method.

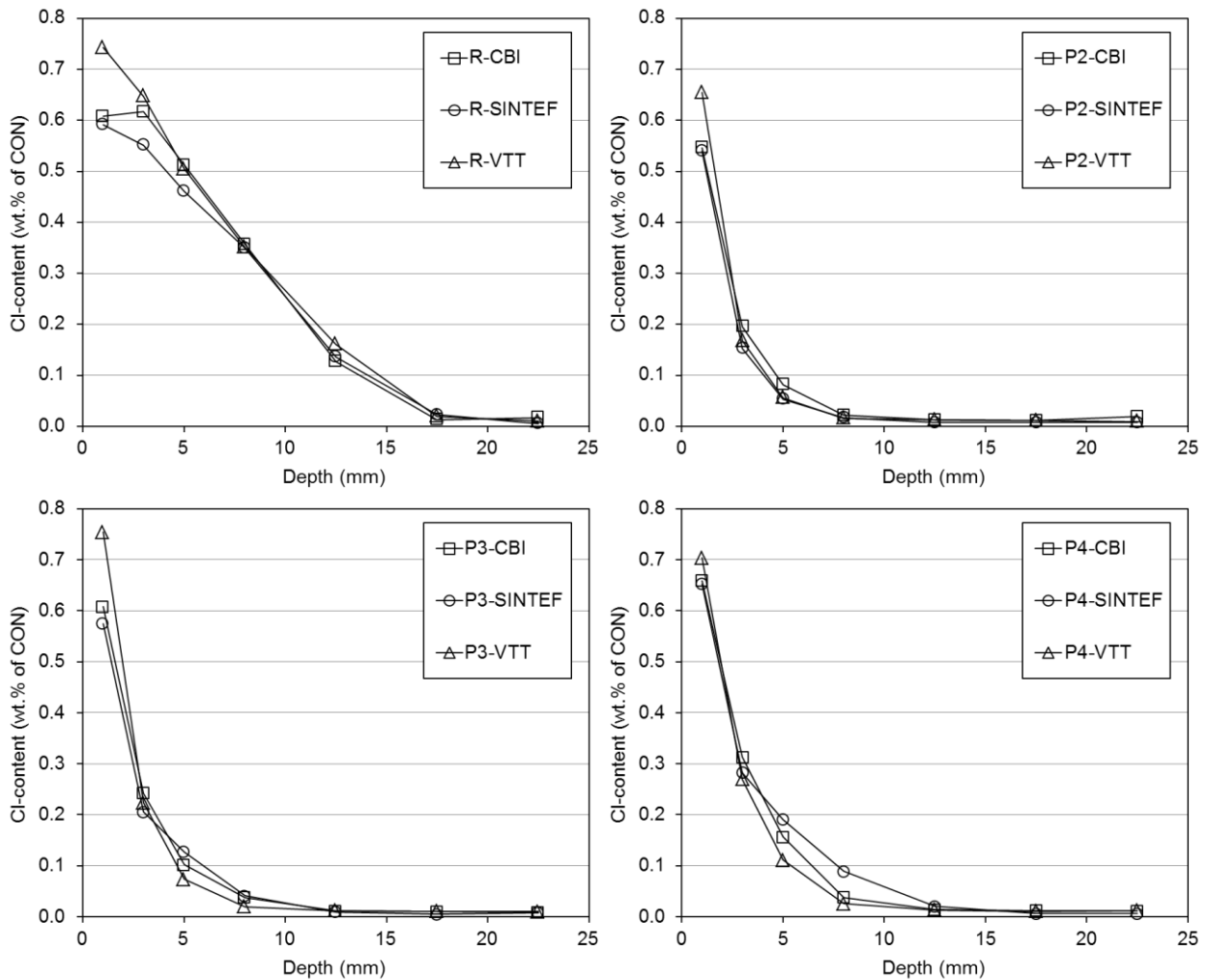


Figure 4. Chloride profiles measured at each laboratory. Each data point is the average of 5 specimens.

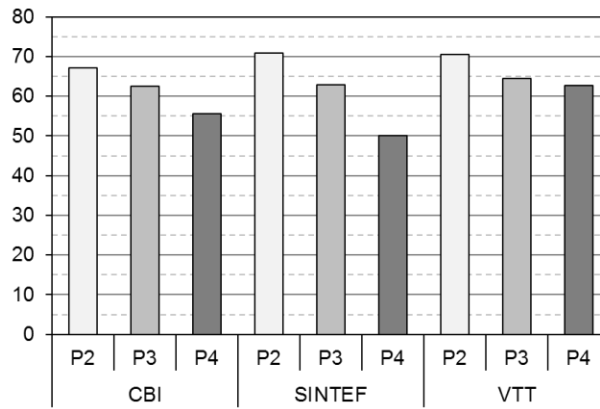


Figure 5. Filter effect obtained at each laboratory.

#### 4. Comparison with the existing methods and field results

It is not difficult to correlate the results with the new method ( $FE_{0-25}$ ) to results obtained with the existing Swedish method, when a concrete with W/C-ratio 0.45 has been used. Taking into account that 2.5 mm of the outermost surface is taken away and the 20 mm sample has been exposed to chlorides at both surfaces this will be equal to the relative chloride content of the sample between 2.5 and 17.5 mm depth. The difference between this content and the one obtained between 2 and 20 mm ( $FE_{2-20}$ ) will only be marginal, since beyond 17.5 mm the chloride content in both the impregnated specimens and the references is very close to 0. The requirement of the existing Swedish method corresponds to that  $FE_{2-20} \geq 0.85$ . Using all the results from the round robin exercise, it can be shown that a  $FE_{2-20}$  equal to 0.85 corresponds to a  $FE_{0-25}$  around 0.65. It is also rather easy to relate the results obtained with Finnish method to the filter effect of the new method. However, the Finnish method was recently modified and we have had difficulties to find any results acquired with it.

The requirements level when the Norwegian method is used is  $FE=0.75$ . It is not as easy to relate the results from the Norwegian method to the new method as for the Swedish or Finnish method, since the differences in the procedures are much greater. According to [3] somewhat higher filter effects are obtained when salt-spraying is used for the chloride exposure compared to permanent submersion. The Norwegian method uses much shorter periods for pre-conditioning and exposes the sawed surface to lime-water after sawing. Lengthening the preconditioning period and omitting the exposure to lime-water of the sawed surface both diminishes the value of the filter effect. Moreover, the Norwegian method uses shorter periods for the conditioning after application. As can be seen from the pre-study the influence of prolonging the conditioning periods also influences the filter effect, however not in the same way for all products. On the whole the  $FE_{0-25}$  obtained for a certain product will be lower than the filter effect obtained with the Norwegian method.

Based on the comparison and considerations above, a preliminary assumption of a requirement level for the protection against chloride ingress of hydrophobic impregnation agents can be around  $FE_{0-25}=0.65$  for the new method.

The influence of hydrophobic impregnations on the chloride ingress has also been the subject of several field studies, both in a road environment and a marine environment. However, finding results which can be compared is not without problems. There are many hydrophobic agents on the market, sometimes exactly the same product is sold under several different trade names. In many cases, products that were used in earlier studies do no longer exist or has been substantially modified. Thus, results for exactly the same product obtained with the different methods and from field studies are not easy to find. Another parameter that varies in the different studies is the amount of product applied and the conditions under which they were applied. Test results with the products P1, P2, P3 and P4 obtained with the different methods and the outcome of a couple of field evaluations are summarized in Table 2.

**Table 2. Classification and performance of different products.**

Product	Swedish Method	Norwegian Method	Pre-Study FE <sub>0-20</sub>	Round Robin FE <sub>0-25</sub>			Marine Environment after 10 years <sup>3)</sup>	Road Environment after 5 years <sup>4)</sup>
				CBI	SINTEF	VTT		
P1	Approved		55					Clear effect
P2	1)	Approved	63	66	69	68	Clear effect	Clear effect
P3	Approved			61	61	62		
P4	2)			54	49	60		
1) Did not pass at w/c=0.45; very good performance at w/c=0.70 2) Not tested with w/c=0.45; approved when tested with w/c=0.70 3) Data from [4] 4) Data from [5]								

## 5. Conclusions

The proposed method to classify hydrophobic impregnations with regard to protection against chloride ingress gives sufficiently reproducible results. Even though, the form of the obtained chloride profiles vary somewhat when determined at different laboratories, this does not influence the parameter chosen to describe the efficiency of the products, the filter effect, more than marginally. Since the filter effect is based on the amount of chloride in impregnated samples in relation to the amount of chlorides in un-impregnated samples, the variations in procedures causing differences in chloride profiles, influences the references and impregnated samples to the same degree. However, the reproducibility of the method may be enhanced if some parts of the procedures are made more precise.

Even though the method uses experimental conditions, such as submersion in a solution with unnaturally high concentration of NaCl and application of impregnations to sawed surfaces, the results seem to be relevant when compared to results with other test methods with more realistic conditions and field experiments.

## 6. Acknowledgement

The financial support of the Swedish Transport Administration, Norwegian Public Roads Administration and Finnish Transport Agency under grant agreement TRV 2012/75824 is acknowledged.

## 7. References

1. EN 1504-2, "Products and systems for the protection and repair of concrete structures - Definitions, requirements, quality control and evaluation of conformity - Part 2: Surface protection systems for concrete", CEN Standard, 2004.
2. EN 1766, "Products and systems for the protection and repair of concrete structures - Test methods - Reference concretes for testing", CEN Standard, 2000.
3. Rodum, E., "Accelerated testing of chloride ingress into surface treated concrete. Preliminary testing as basis for revision of procedures", NPRA Report No.189, Norwegian Public Roads Administration, February 2013 (in Norwegian).
4. Rodum, E. and Lindland, J., "R&D project Quay Sjursøya - Chloride retarding surface treatment of concrete - 10 years exposure", NPRA report No. 77, Norwegian Public Roads Administration, 2012 (in Norwegian).
5. Malaga, O., "Performance of impregnation of concrete structures - Results from a 5-year field study at Rv40 Borås", Master Thesis in Construction Management, Chalmers University of Technology, 2015.
6. AASHTO-T260, "Standard Method of Test for Sampling and Testing for Chloride Ion in Concrete and Concrete Raw Materials", American Association of State Highway and Transportation Officials, 1997.

# Durability of Concrete Caissons Made in Floating Docks

Jose Vera-Agullo<sup>1</sup>, Francisco Manuel Castro-Visos<sup>1</sup>, Francisco Javier Larraz-Bordanaba<sup>1</sup>, Claudio Troncone-Cusati<sup>1</sup>, Juan Pedro Asencio-Varela<sup>1</sup>, Nelson Silva<sup>2</sup>, Urs Mueller<sup>2</sup> and Katarina Malaga<sup>2</sup>

<sup>1</sup>ACCIONA Infraestructura

<sup>2</sup>CBI Swedish Cement and Concrete Research Institute

**Abstract:** ACCIONA Infraestructura, a Spanish contractor, uses the caisson method for the construction of breakwater structures. One of its floating docks, Kugira, is one of the largest of its kind in the world and it can produce concrete caissons measuring 70 m long by 36 m wide and 35 m high. Concrete caissons made in floating docks are gradually immersed in sea water as they are built; thus, the set concrete is exposed to sea water at a very early stage, within 18 to 48 hours after casting in sliding formwork. In order to study the durability of slag concrete using this construction method, the properties of concrete exposed to sea water at a very young age have been tested. Specimens were exposed to artificial sea water by the ponding method at different ages (16h, 1, 2, 3, 7 and 28 days) for a period of 6, 18 and 36 (analysis pending) months. The following properties were measured and compared with unexposed specimens: compressive strength, water and oxygen permeability, pore size distribution, migration coefficient DNT492 and chloride profiles. After 6 and 18 months ponding, lower chloride contents were measured for the specimens exposed to sea water after 28 days curing compared to those exposed at early ages. However, this difference significantly decreases within a small depth from the exposed surface. Also the migration coefficient DNT492 decreases significantly with the increase of the age of the concrete. With regards to water and oxygen permeability, no significant differences were found. In this paper, a summary of all these works is presented.

Apart from this laboratory analysis, real scale tests were performed at site with the aim to increase durability by the addition of nanosilica particles. The characterization of these real scale tests are also described and discussed in this paper.

**Keywords:** concrete, caissons, durability, chlorides, nanosilica.

## 1. The construction method

In the floating dock construction method, concrete is cured (mainly) under sea water; the caisson is progressively submerged as the caisson walls are casted and slide through the formwork. A typical caisson made with the Kugira floating dock (owned by ACCIONA Infraestructura) is 66.85 m in length, 34.60 m in width and up to 34 m in height. It is divided in 8 sections, in a total of 32 inner cells, weighing more than 12000 metric tons. More than 5000 m<sup>3</sup> of concrete and 500 tons of steel are used for the construction of each caisson. The construction method can be described in the following main steps:

- With the pontoon fully out of the water, the deck is cleaned and the caisson structure is stacked.
- The caisson base moulds are assembled, the reinforcement of the base slab and wall fixings are placed and the bottom slab is casted.
- The sliding mould and the steel truss are lowered.
- As the sliding of the caisson shaft starts, the base slab mould is removed and concreting of the caisson shaft starts. The concrete is poured in successive 30 cm thick layers at an average rate of 2 m every 12 hours.
- The floating dock is stage ballasted by flooding the ballast tanks to ensure that both the caisson and the dock are sunk in a balanced and proportionated way.
- When sliding has reached 8 m, several 300 mm tubes are put in place to communicate between the different shaft cells; this way the caisson is divided in 8 sectors so that when ballast is introduced the caisson will remain horizontal.
- At 12 m, 8 more tubes are placed in the exterior screens (1 per sector) to be able to locate the valves needed for anchoring the caisson.
- At 17 m, the towing hooks are placed to allow the caisson to be towed out to sea.
- Once the sliding is finished, the mould is removed and the caisson is ballasted with sea water.
- The floating dock is ballasted until the caisson rises of the deck and floats.
- Finally, the caisson is towed to the quay wall and the valves are open to fill the cells with sea water until the hole block is settle in the sea bed.



**Figure 1. Caissons construction method. Right) Kugira floating dock, and left) detail of the bottom part of the sliding formwork.**

## 2. Approach

### 2.1 Objectives

The objectives of this study were:

- To investigate the influence of early exposure to artificial sea water on the concrete's mechanical and transport properties.
- To determine the chloride transport properties in concrete by accelerated methods
- To analyze the influence of the use of nanosilica in the improvement of the strength and durability of concrete at real scale.

### 2.2 Test programme

All materials and the mix design are representative of those usually used in the construction process. Tables 1 and 2 show the composition and the sample matrix, respectively; the concrete follows the standard EN 206-1 (2000), fulfilling the minimum requirements for the exposure class XS3.

**Table 1: Concrete mix proportions.**

W/C	CEM III/A 42.5 N/SR (kg/m <sup>3</sup> )	Sand 0-4 (kg/m <sup>3</sup> )	Aggregate 4-16 (kg/m <sup>3</sup> )	Glenium C303 SCC (% of CEM)	Pozzoloth 488N (% of CEM)	Slump (mm)
0.45	350	918	1048	2.0	0.4	200

Specimens were tested at the ages of 16 h, 1, 2, 3, 7 and 28 d; these ages have been decided according to the details of the construction methods. The following curing conditions were employed:

- 16 h and 1 d: cured in the form;
- 2, 3 and 7 d: cured in the form for 1d and from then on under water;
- 28 d: cured in the form for 1 d, then 6 d under water and from then on stored at 20 °C and 65 % RH.

At the age of exposure (16 h, 1, 2, 3, 7 and 28 d), the specimens were immersed in artificial sea water, the composition of which is given in Table 3.

**Table 2: Sample matrix.**

Number/Type of samples	Cube 100 mm	Cube 150 mm	Cyl. Ø100 mm	Cyl. Ø150 mm							Total
					16 h	1 d	2 d	3 d	7 d	28 d	
Compressive strength (before exposure)	X				3	3	3	3	3	3	20 <sup>a</sup>
Compressive strength (after 6 months immersion)	X				3	3	3	3	3	3	18
Cl profile (after 6 month ponding - cast surface) (after 18 month ponding - cast surface) (after 36 month ponding - cast surface)		X				2 1 1	2 1 1	2 1 1	2 1 1	2 1 1	20
Cl profile (after 6 month ponding - cut surface) (after 18 month ponding - cut surface) (after 36 month ponding - cut surface)		X								2 1 1	4
Mercury Intrusion Porosimetry	X				1	1	1	1	1	1	6
Microscopy (SEM)	X				1	1	1	1	1	1	6
Rapid chloride migration			X		2	2	2	2	2	2	12 <sup>b</sup>

<sup>a</sup> 2 extra specimens were tested at the age of 180 days

<sup>b</sup> 2 extra cylinders (4 specimens) were tested at the age of 180 days

**Table 3: Composition of artificial sea water.**

Composition		Artificial seawater	
	(in ‰)		(in g/l) for 100 l (g)
Total salinity	35	NaCl	24.6 2460
Chloride	19.345	KCl	0.67 67
Sodium	10.752	CaCl <sub>2</sub> ·2H <sub>2</sub> O	1.36 136
Sulfate	2.701	MgSO <sub>4</sub> ·7H <sub>2</sub> O	6.29 629
Magnesium	1.295	MgCl <sub>2</sub> ·6H <sub>2</sub> O	4.66 466
Calcium	0.416	NaHCO <sub>3</sub>	0.18 18
Potassium	0.390	pH	8.2

### 2.2.1 Ponding tests and artificial sea water exposure

In these tests, the following properties were examined:

- Compressive strength before exposure to artificial sea water, at the ages of 16 h, 1, 2, 3, 7, 28 and 180d, according to EN 12390-3 (2009);
- Compressive strength after exposure for 6 months in artificial sea water, for specimens exposed at the ages of 16 h, 1, 2, 3, 7 and 28 d, according to EN 12390-3 (2009);
- Pore size distribution on paste samples, at the ages of 16 h, 1, 2, 3, 7 and 28 d by mercury intrusion porosimetry between 0.004 and 100 µm. This pore size range is important for all transport phenomena including capillary water transport and chloride diffusion. At the selected ages, the samples were immersed in 2-propanol (alcohol exchange) for 3 days in order to stop the hydration, vacuum dried and stored in a desiccator containing nitrogen to avoid carbonation.
- Microstructural analysis on polished cross sections of concrete, at the ages of 16 h, 1, 2, 3, 7 and 28 d by scanning electron microscopy (SEM). At the selected ages, hydration was stopped by means of alcohol exchange. After dried, the samples were impregnated with epoxy resin and finely polished using petroleum as grinding liquid.
- Chloride profiles on concrete samples, tested according to ASTM C1543-10a (2010) (ponding method). At the ages of 16 h, 1, 2, 3, 7 and 28 d the samples were exposed to chloride solution (3% NaCl) during 6, 18 and 36 (analysis pending) months. At the end of the exposure period, the samples were ground on a lathe in the following steps: 0-2, 2-4, 4-6, 6-9, 9-12 and 12-15 mm for the specimens exposed during 6 months; 0-2, 2-5, 5-8, 8-12, 12-16, 16-20 and 20-25 mm for the specimens exposed during 18 and 36 (analysis pending) months. The acid soluble chloride content (total chloride content) was determined according to AASHTO T-260 (1997). Additionally, for the age of 28 d, the influence of the exposed surface was studied by comparing the chloride profiles for both cast and cut surfaces.
- XRD on powder samples of concrete, after 18 months ponding: for the samples exposed at the ages of 1 and 28 d, grinding steps 0-2, 2-5, 5-8, 8-12, 12-16, 16-20 mm; for the samples exposed at the ages of 2, 3 and 7 d, grinding step 0-2 mm.

### 2.2.2 Rapid chloride penetration test

The chloride migration coefficient, based on non-steady-state experiments was measured according to NT Build 492 (1999). In this test, an external electrical field (10-60 V DC) is applied axially across a test specimen ( $\varnothing$  100 x 50 mm) to accelerate the process of chloride migration. At the end of the test period (typically 24 hours), the specimen is axially split into two half and the chloride penetration depth is measured using a colorimetric technique (silver nitrate spray). The chloride migration coefficient is then calculated from the chloride penetration depth.

## 3. Results

### 3.1 Ponding tests and artificial sea water exposure

#### 3.1.1 Compressive strength

Figure 2 shows the results from compressive strength measured before (left) and after (right) exposure to artificial sea water. Slow hydration continues throughout 6 months and the relative strength gain from 28 to 180 days is about 6 %. Figure 2 (right) shows that the age of the concrete at the time of exposure does not affect the strength development. The compressive strength after 6 months exposure is 5 to 10 % lower when compared to non-exposed specimens, which is within the variation of strength testing. From the results there seems to be no visible influence of the exposure to seawater on compressive strength.

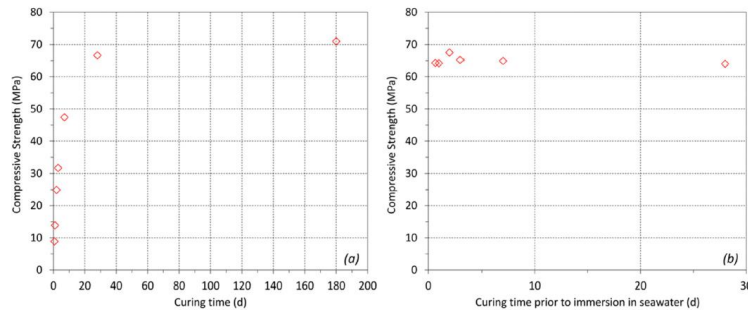


Figure 2. Compressive strength (left) before and (right) after 6 month exposure to sea water

#### 3.1.2 Pore size distribution

In practical terms, it is the capillary pores that are of major importance for the chloride ingress since the gel pores are too small to allow significant transport of species by diffusion or capillary forces. Although macro pores have no capillary action, these can also be of importance under submerged conditions.

The pore size distribution of cement paste samples at the ages of 16 h, 1, 2, 3, 7 and 28 d was characterized by mercury intrusion porosimetry (MIP).

The objective was to compare the pore size distribution of the cement paste at different ages of hydration. The results are shown in Figures 3. It can be seen that, as the hydration proceeds, there is a refinement of the pore structure together with a significant decrease (about 50 % from 16 h to 28 d) in the total pore volume. Most significant, is the increase in the gel pores (< 10 nm) and the decrease in both smaller (10-100 nm) and larger capillary pores (0.1-1  $\mu$ m).

Regardless of the exposure environment, concrete exposed at an early age will have a higher chloride diffusion coefficient since both the moisture content and the volume of capillary pores is higher; however capillary suction is relatively small. As the hydration proceeds, the volume of capillary pores decreases and with it also the diffusion coefficient.



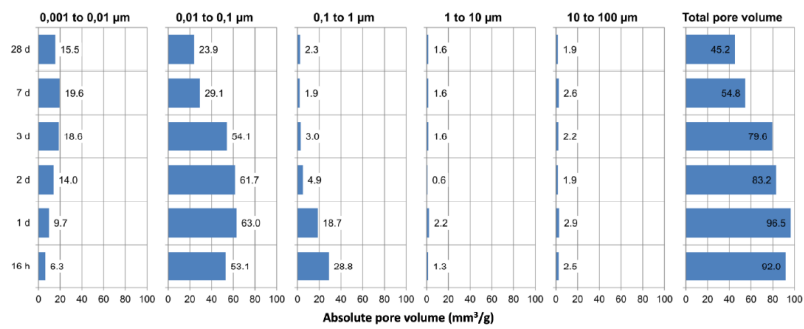


Figure 3. Absolute and total pore volume distributed according to the pore size at each age

### 3.1.3 Microstructural analysis

The microstructure of the concrete samples at the ages of 16 h, 1, 2, 3, 7 and 28 d was characterized by scanning electron microscopy. SEM images in Figure 4 show an overview of the cementitious matrix for samples 16 h, 1, 7 and 28 d. Detail pictures are shown in Figures 7 to 10.

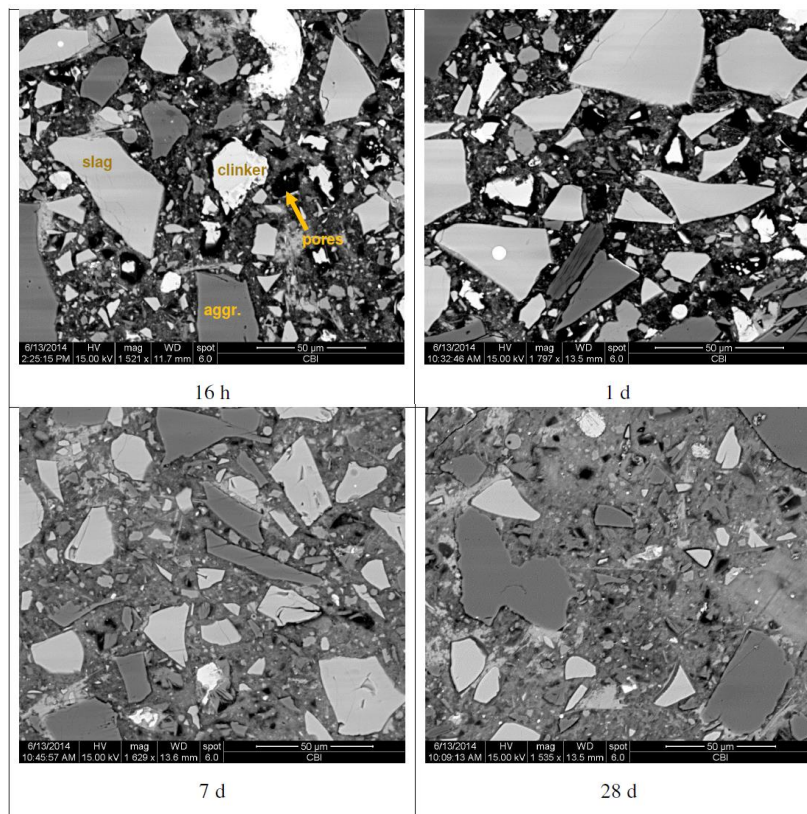


Figure 4. SEM photo micrographs of the cement paste at different ages (backscatter mode)

The micro structure of the slag cement containing concrete is, as expected, porous at young age  $\leq 1$  d, which is visible in the SEM backscatter images in form of black to dark grey areas (Fig. 4). Up to an age of 7 days the porosity is continuously decreasing (Fig. 4) and not so much different from the 28 day sample. This confirms the results from the development of the pore size distribution as shown in Fig. 3. The reaction of the slag is not visible at 16 h, where mostly the clinker phases are dominating the hydration. Some of the capillary porosity can be attributed to the clinker reaction: C3S and C2S are dissolving faster in the pore solution as hydration products are formed, which results in open space around the grains.

After 1 d, however, the slag started to react. In this stage only the partial dissolution of slag grains were visible. Hydration products in form of hydrotalcite like phases were not observable by SEM at this stage. After 7 d reaction of slag was clearly evident. In some of the grains the formation of a new Mg containing phase was observed. This phase is generally referred to as hydrotalcite  $Mg_6Al_2(CO_3)(OH)_{16} \cdot 4(H_2O)$ , which

is a main hydration product of slag with higher magnesium content and which composition and crystal structure may vary within certain limits.

After 28 d the micro structure of the concrete is denser and the hydration of slag and the formation of hydrotalcite around the slag grains are more pronounced. The hydration process of slag will not stop under water saturated conditions but will go on for several months or even years.

### 3.1.4 Chloride profiles

The chloride profiles after 6 and 18 months exposure (ponding method) are summarised in Figure 5. After 6 months exposure, no significant difference was found between the ages of 1 and 7 days except for the surface chloride content (CS). At early ages (1 day), the higher concrete permeability leads to distinctively higher chloride ingress, which is indicated by higher Cl concentrations in the first 5 millimetres. However, after a certain time with the refinement of the pore structure (Fig. 3) and because chloride diffusion is, in general, a slow transport process, the diffusion coefficients decrease with time and therefore almost the same chloride concentrations were analysed at depths larger than 5 mm.

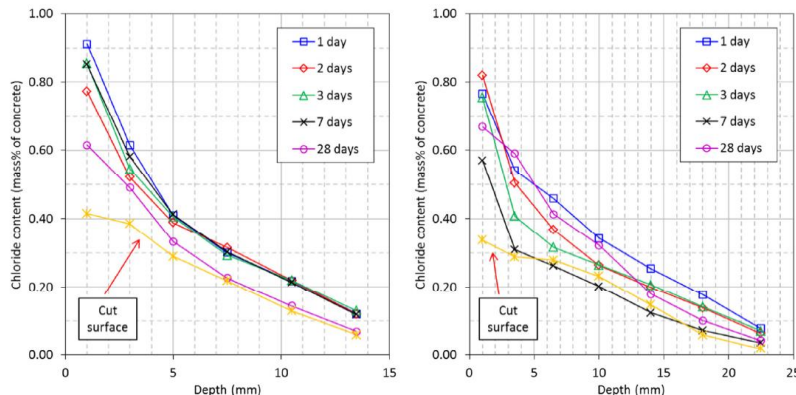
In general, the chloride ingress is more severe in specimens exposed at early age (1-7 days) when compared to those exposed at the age of 28 days. The main reason is associated with the strong decrease in porosity as shown in Figure 3, leading to lower permeability. While the curing age has, in general, a positive influence in reducing the total chloride content, it can be seen that this effect is more pronounced at the outermost layer. In fact, due to the combined transport mechanisms of capillary suction and diffusion, the relative difference in the chloride content between 28 days (circle) and 1-7 days (other curves) decreases with the penetration depth, since in the case of specimens exposed at 1-7 days the only relevant transport mechanism is diffusion.

The influence of the casting surface on the chloride ingress is also shown in Figure 5 for the case of specimens exposed at the age of 28 days. It can be seen that, up to a depth of 6 mm, the chloride content is higher for cast surfaces due to the higher cement content and therefore, chloride binding capacity; however, this does not seem to influence the chloride ingress.

Based on the mixture proportions the binder content can be calculated as 14 % by mass of concrete. In addition, based on the experience from Tang et al. (2013), a difference of 4 % binder per mass of concrete can be assumed between the outermost layer (paste rich) and the bulk concrete. Therefore, when expressed in terms of binder, the chloride contents shown in Figure 5 varied between 2.3-5 % at a depth of 0-2 mm and between 0.4-0.9 % at a depth of 10-15 mm.

After 18 months, however, there is a distinction between the chloride profiles of specimens exposed at different ages. Clearly, the influence of the exposure age becomes less pronounced. With exception of the surface chloride content, specimens exposed between 2 and 7 days show lower chloride contents when compared to those of specimens exposed at the age of 28 days.

Therefore, there is no reason to assume that the early age exposure has a negative influence on the chloride penetration. An interesting feature though is shown for the specimens exposed at the age of 7 days. The total chloride content is in general the lowest, showing also the lowest surface chloride content.



**Figure 5. Profiles of chloride ingress in concrete exposed at different ages: (left) after 6 months exposure; (right) after 18 months exposure (36 months analysis pending)**

### 3.2 Rapid chloride penetration test

Figure 6 shows the non-steady-state migration coefficients obtained at different ages. At the age of 1 day, the chloride migration coefficient is relatively high. However, only one day later (2 days old), this value drops drastically to about 50% and further on by about 90% at the age of 28 days. At the age of 28 days, the  $D_{NT492}$  obtained is within the range of those reported in ECO-Serve (2005), i.e. between 5 to 10  $\times 10^{-12}$   $m^2/s$ . A direct comparison between the two results,  $D_{NT492}$  and  $D_{F2}$ , is not possible since these are obtained under different experimental conditions (i.e. migration and diffusion). In the field, chloride penetration through concrete exposed in marine environments occurs mainly by combined capillary suction/diffusion in atmospheric and tidal zones and by diffusion only in submerged zone.

Since the concrete is exposed at very early ages, capillary suction is rather limited and the diffusion coefficients are much lower than the migration coefficients measured by accelerated methods. Nevertheless, accelerated methods give a good indication as to the resistance of concrete against chloride ingress.

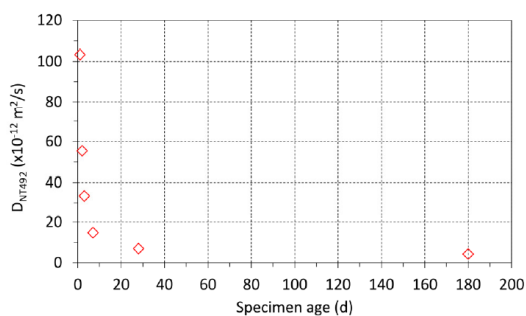


Figure 6. Evolution of the chloride migration coefficient  $D_{NT492}$  as a function of the specimen age

## 4. Real scale tests. Use of nanosilica to improve the concrete performance

Apart from the laboratory tests devoted to give durability guarantees for the floating dock construction method, real scale tests at work site are presented in this manuscript. A conventional concrete made following the standard EN 206-1 fulfilling the minimum requirements for the exposure class XS3 has proven to be durable; nevertheless, advanced concrete containing nanosilica has optimized to improve even more the performance of concrete and to give additional guaranties to the client.

The benefits of employing nanosilica in concrete have been widely studied in literature (Singh, 2013) and it is not the aim of this study to give additional light to this fundamental understanding. In this section the use of nanosilica in the construction of the Açu port complex located at São João da Barra, Rio de Janeiro (Brazil) is presented.

The Table 4 shows the mix design of the conventional concrete used at site and also the advanced concrete that was proposed and used in the second part of the works. The conventional concrete fulfilled all the requirements successfully, which was not easy at all taking into account the available raw materials and suppliers at site. Nevertheless, it was decided to improve even more the mix design, and then, an advanced mix design was proposed, developed, tested and used during the rest of the works. The requirements were a slump of  $22 \pm 2$  cm and a compressive strength class of C40/50.

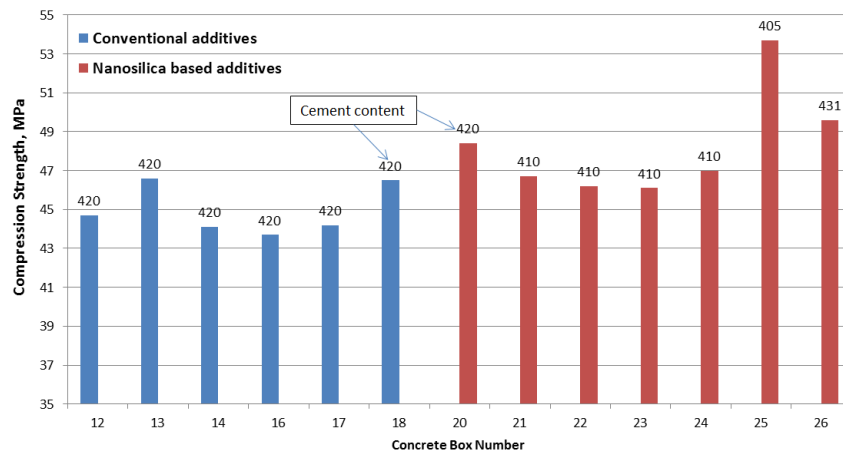
Table 4: Approximate concrete mix proportions.

Mix	W/C	CP III RS 40 (Brazilian standard)	Sand 0-2	Sand 0-4	Aggregate 4/12	Aggregate 12/19	Admixture		Slump
							1	2	
							Kg/m <sup>3</sup>		% of CEM
							WRA	Super plasticiser	mm
Conventional concrete	0.40	420	350	500	475	600	1	0.6	23
							0.4	0.6	
Advanced concrete	0.40	410	350	500	475	600	0.4	0.6	23
							0.4	0.6	



A total amount of 22 caissons of 6000 m<sup>3</sup> each was made using a nanosilica-based suplespastisicer at 0.55 % with respect to the cement content. Taking into account the solid residue of this admixture, more than 70 tons of nanosilica was used.

The observed improvement by adding nanosilica was quite significant in terms of workability and setting time robustness and compressive strength results. Also the bleeding was reduced. The main reason is that the concrete porosity decreases significantly with the addition of nanosilica. Then, the strength and durability (decreased water permeability up to a 30%) were highly improved. In fact, the production and quality control managers decided to decrease the cement content up to 10 kg/m<sup>3</sup> because the higher compressive strength obtained. Those results are statistically treated and shown in Figure 7.



**Figure 7. Statistical results of compressive strength of concrete made with conventional admixtures (boxes 12-18) and with nanosilica-based admixtures (boxes 20-26)**



**Figure 8. Work site pictures. Provisional Kugira protective dock, Kugira and 22 cm slump**

## 5. Conclusions

In this study, the influence of the early age exposure to sea water on the durability properties of slag concrete, generally used by ACCIONA Infrastructure for the construction of caissons by the floating dock method, was investigated.

For the tested concrete composition, the **compressive strength** was approximately 70 MPa at the age of 28 days. Early age exposure to chloride environment did not influence the compressive strength when compared to concrete cured for the same period under normal conditions (20 °C and 65 % RH).

**Mercury intrusion porosimetry** measurements have shown a significant decrease (about 50 %) of the total pore volume between 16 hours and 28 days mature samples. More importantly an increase in the gel pores and a decrease in the larger capillary pores was measured. Although the porosity (both total and capillary) is higher at early ages, its influence on the durability of the concrete, namely the resistance against chloride ingress, is limited. The main reason is that, at early ages, the degree of capillary saturation is expected to be higher than at the age of 28 days and thus diffusion is the only relevant mechanism for chloride transport.

**Microstructural studies** using scanning electron microscope (SEM) confirmed the results obtained by mercury intrusion porosimetry. SEM images showed that at very early ages ( $\leq 1$ d), the porosity of the cement paste is high and mainly the clinker phases react. The porosity then significantly decreases until the age of 7 days. The reaction of the slag is visible already from 1 day but more pronounced after the age of 7 days where the formation of hydrotalcite around the grains is clearly visible.

With regards to **chloride ingress**, after 6 months ponding no difference was found between specimens exposed at the ages of 1 to 7 days; lower chloride contents were measured for the specimens exposed after 28 days curing. However, the relative difference significantly decreases within a small depth, from 0.25% at the surface to 0.10% at a depth of 3 mm. The chloride diffusion coefficient appears to remain constant already after the age of 3 days. After 18 months exposure, only specimens exposed at the age 1 day show higher chloride contents. when compared to the remaining exposure ages. Again, no clear negative influence of the exposure age on chloride penetration was found: lower chloride values were measured for specimens exposed at the ages of 2 to 7 days when compared to those measured for specimens exposed at the age of 28 days. Except for the specimens exposed at the age of 1 day, after 18 months exposure, the chloride diffusion coefficients are much lower than those measured after 6 months exposure. It is recommended to compare the effect of the exposure age on the resistance against chloride ingress for concretes made with slag cement and ordinary Portland cement; although slag concrete is known to have a high resistance against chloride ingress due to its refined pore structure and binding capacity, sometime is required for the secondary pozzolanic reactions to take place, which may not be achieved in such short exposure times.

The **rapid chloride migration test** provides a good indication as to the resistance of the concrete against chloride ingress. The migration coefficient decreases significantly with the age of the concrete at the time of the test. However, at the age of 28 days,  $D_{NT492}$  was found to be in the range of values reported in the literature. In practice however, chloride transport through concrete exposed under submerged conditions occurs by means of diffusion mechanism meaning that the difference in chloride penetration between specimens exposed at the age of 1 day and 28 days is expected to be rather small (as indicated by the results from 6 months ponding experiments).

In **summary** the results indicate an only weak influence of early age exposure on the investigated concrete properties. Chloride ingress was higher in the surface zone of specimens exposed to artificial seawater at early stage but after ca. 5 mm depth the chloride levels tend towards the ones which were exposed after 28 d. Higher chloride content in surface zones in slag containing concretes with subsequent strong reduction in concentration is well known from other studies (e.g. Hong and Hooton, 1999) independent of the curing age and time of exposure. And these earlier studies showed also the lower chloride concentration and higher chloride binding capacities of slag containing concretes.

Regarding the **tests done at site in Brazil**, by means of the addition of nanosilica, the durability was improved and the concrete cost was reduced showing that it is possible to increase the lifetime of a civil structure without increasing the final cost.

## 5. References

1. AASHTO T260 (1997), Standard method of test for sampling and testing for chloride ion in concrete and concrete raw materials. American Association of State Highway and Transportation Officials.
2. ASTM C1543-10a (2010), Standard test method for determining the penetration of chloride ion into concrete by ponding. ASTM International.
3. Caballero, J., Polder, R.B., Leegwater, G.A. and Fraaij, A.L.A. (2012), Chloride penetration into cementitious mortar at early age. *Heron* 57(3):185-196.
4. EN 196-1 (2005), Methods of testing cement - Part 1: Determination of strength. European Committee for Standardization.
5. EN 206-1 (2000), Concrete – Part 1: Specification, performance, production and conformity. European Committee for Standardization.
6. EN 1015-11 (1999), Methods of test for mortar for masonry - Part 11: Determination of flexural and compressive strength of hardened mortar. European Committee for Standardization.
7. EN 12390-3 (2009), Testing hardened concrete - Part 3: Compressive strength of test specimens. European Committee for Standardization.
8. EN 12390-8 (2009), Testing hardened concrete - Part 8: Depth of penetration of water under pressure. European Committee for Standardization.
9. Hong, K., Hooton, R.D., (1999), Effects of cyclic chloride exposure on penetration of concrete cover. *Cement and Concrete Research* 29, 1379–1386.
10. Müller, C. (2005), European construction in service of society (ECO-Serve) - Production and application of blended cements. German Cement Works Association.
11. Neville A.M. (2002), *Properties of concrete*. Pearson Prentice Hall.
12. NT BUILD 492 (1999), Concrete, mortar and cement-based repair materials: Chloride migration coefficient from non-steady-state migration experiments. Nordtest.
13. Tang, L., Boubitsas, D. and Utgenannt, P. (2013), Chloride ingress in concrete exposed to marine environment – Field data up to 20 years exposure. CBI Report 2014.
14. Tang, L. and Nilsson, L-O. (1993), Chloride binding capacity and binding isotherms of OPC pastes and mortars. *Cement and Concrete Research*, 23:247-253.
15. Singh, LP, Karade, SR, Bhattacharyya, SK, Yousuf, MM and Ahalawat, S, Beneficial role of nanosilica in cement based materials – A review. *Construction and Building Materials*, 47:1069-1077.

# Prescriptive versus performance-based design approaches for concrete durability

Hans Beushausen<sup>1</sup>, Mark Alexander<sup>2</sup>, Manuel Wieland<sup>3</sup> and Stefan Linsel<sup>4</sup>

<sup>1</sup>Associate Professor of Civil Engineering, University of Cape Town, South Africa

<sup>2</sup>Professor of Civil Engineering, University of Cape Town, South Africa

<sup>3</sup>MSc Graduate, Civil Engineering, University of Applied Sciences Karlsruhe, Germany

<sup>4</sup>Professor of Civil Engineering, University of Applied Sciences Karlsruhe, Germany

**Abstract:** Durability specifications for reinforced concrete structures can be divided into the traditional prescriptive approach, in which limiting values are set for strength classes, cement contents and water/binder ratios, and performance-based approaches which should fundamentally be based on measurements of concrete properties that can be used as input parameters in service life prediction models. The research discussed in this paper compares the prescriptive approach presented in the Eurocode (EN 1992-1-1: 2004 [1]) to the performance-based approaches for concrete durability used in South Africa. A total of 12 different concrete mixes with 4 different binder combinations were designed according to the specifications given in the British National Annex (NA to BS EN 1992:1) [2] to the Eurocode, focusing on environmental classes related to chloride-induced reinforcement corrosion. The concretes were assessed with the South African Durability Index test methods. The results indicate that the prescriptive specifications of the Eurocode for concrete containing plain CEM I may not be adequate for the marine environment, resulting in lower durability than expected. In contrast, the prescriptive design specifications for the marine environment for concretes containing cement extenders such as fly ash, silica fume and slag, may be conservative, especially for environmental class XS1. As a consequence, it is proposed that engineers consider performance-based design approaches as a useful alternative for projects where traditional prescriptive approaches appear inadequate.

**Keywords:** Concrete durability, performance design, chloride ingress

## 1. Introduction

Durability design and specifications for reinforced concrete structures have become increasingly important in recent years, largely as a result of deteriorating concrete infrastructure and the financial burden associated therewith. The prescriptive design approach for durability, which is common to most national standards and specifications, sets limits on material selection and mix design parameters in relation to the prevailing environmental condition and assumes that the structure is inherently durable if these limits have been met. In contrast, performance-based design commonly includes the measurement of material properties that can be used to predict the performance of the structure and can therefore account for the important project-specific aspects of material selection and construction methods.

The prevailing mechanism causing premature deterioration of and damage to reinforced concrete structures is reinforcement corrosion resulting from carbonation, or the ingress of chlorides from the marine environment or the use of de-icing salts, often in connection with insufficient cover depth. The end of the service life of reinforced concrete structures is usually defined as the time when the corrosion initiation period ends and corrosion propagation starts. This is linked to the chloride concentration at the reinforcement exceeding a certain threshold value, or the carbonation front reaching the reinforcement. Performance-based design of reinforced concrete structures is therefore commonly based on the modeling of chloride ingress and carbonation. To this aim, the concrete's resistance against the ingress of harmful substances can be assessed with appropriate test methods. The South African performance method for durability design, which is already applied in practice on a large scale, makes use of transport properties such as oxygen permeability and chloride conductivity to model the service life of RC structures [3, 4].

The South African National Standards for the design of concrete structures are primarily based on (outdated) British Standards. Following the implementation of the new Eurocode in the UK [1, 2], it is anticipated that the Eurocode will in the near future also be adopted in South Africa. A South African National Annex will then need to be drafted as well. In this research, the potential durability of concrete mixes that meet the prescriptive design specifications of the Eurocode was evaluated using performance-based service life prediction models and test methods that are accepted in South Africa. Like this it could be evaluated if the durability specifications of the Eurocode offer a rational design concept for the South African industry.

## **2. Prescriptive design for durability according to Eurocode 2 and the British National Annex**

Eurocode 2, the European standard for the design of concrete structures consists of the common European document [1], which is the same for all member countries of the European Union, and the National Annexes (NA) which contain country-specific design parameters based on local conditions, experience and traditions. For durability design of concrete structures, Eurocode 2 prescribes indicative concrete strength classes in relation to different environmental exposure classes and presents requirements for minimum cover depths. For reinforcement corrosion a total of 10 environmental classes are presented, divided into corrosion due to carbonation (Exposure Class XC), general chloride exposure (XD) and chlorides from sea-water (XS). The design value for concrete cover depends on the so-called Structural Class, which relates to the required service life, concrete strength class, member geometry, and construction quality.

More detailed requirements for the composition of the concrete are presented in EN 206 (BS EN 206-1: 2000 [6]), which covers specification, performance, production and conformity of concrete and which needs to be considered in addition to the recommendations given in Eurocode 2. EN 206 allows the designer to use performance-related design methods for reinforced concrete structures, based on satisfactory experience with local practices in local environments or data from established performance test methods. EN 206 further includes prescriptive specifications for concrete durability and, in addition to the strength requirements of Eurocode 2, presents limiting values for maximum water/binder ratios and minimum cement contents in relation to the prevailing environmental exposure class. EN 206 therefore allows both performance-based and prescriptive design approaches but due to limited experience with the former, no further details are presented on appropriate test methods and conformity criteria for the performance-based approach.

The prescriptive durability requirements of Eurocode 2 and EN 206 are somewhat crude as they do not consider the influence of different binder types and, being restricted to limiting strength classes, water/binder ratios, and cement contents, leave only very limited design options and little room for innovation. However, the NA of the individual member countries generally offer a larger range of design possibilities based on locally available materials and local experience. For example, the British NA (NA to BS EN 1992:1 – 2004 [2]), which was considered for the design of concrete mixes used in this research, accounts for different cement combination types for exposure classes XS (marine exposure) and XD (de-icing salts) and therefore accounts for the potentially superior chloride resistance of concretes made with blended cements. In addition, the British NA relates requirements for strength class, cement content and water/binder ratio to different minimum cover depths, which results in the option to “trade off” concrete quality against cover depth. Compared to previous codes and standards, the current Eurocode and its National Annexes present a more detailed list of prescriptive requirements for concrete composition and cover depth, which can be considered a positive development. However, many researchers argue that the prescriptive approach to concrete durability fails to present a rational design tool as it cannot account for the use of innovative materials and the influences of the construction process [6-9].

As stated above, EN 206 also includes the option to apply performance-based design approaches for concrete durability, however without giving guidance on appropriate test methods or related service life models. Researchers and practitioners in many countries are currently developing and evaluating appropriate test methods and service life models (e.g. [10-12]) and it can be expected that in future performance-based design for durability will increasingly be applied to concrete structures.



### **3. Performance-based design for durability**

#### **3.1 Principles**

Performance concepts should be based on quantitative predictions for durability from exposure conditions and measured material characteristics. The resistance of the structure, measured through durability parameters of the actual concrete used, is compared against the environmental load, similar to the approach for designing and controlling compressive strength for certain loading conditions. On this basis, deterioration of a concrete structure during its lifetime is quantitatively predicted using appropriate deterioration models. The obvious advantage over traditional prescriptive approaches is that the influence of mix design parameters and mix constituents can be individually assessed for different types of concrete, which allows rational, economic and innovative design of concrete mixes that are tailor-made for the specific project requirements and environmental conditions.

Various approaches and philosophies for performance-based specifications for concrete durability exist around the world. Most of these approaches include experimental investigations on relevant concrete properties such as diffusion coefficients, which can be used in service life models to predict the rate of deterioration. For reinforced concrete, chloride ingress and carbonation are the most important deterioration processes and a range of test methods exist to characterize the concrete's resistance against these processes (see for example [13]).

Some performance-based approaches are solely based on pre-qualification of concrete mixes in the design stage. In this case, concrete mixes specifically designed or chosen for a project are tested for their resistance against the environment-specific deterioration processes. In this way, suitable constituent materials and concrete compositions can be selected and specified for the project. The structures built with concrete specified in this way are assumed to be inherently durable but no testing is carried out on the actual structure to confirm this. Examples of recent approaches that follow this methodology include the method discussed in [12] and the European "Equivalent Durability Concept" [14].

Another school of thought postulates that durability cannot be achieved unless relevant properties of the cover concrete of the *as-built* structure can be assessed. Approaches that follow this viewpoint include conformity-assessment of the as-built structure, commonly using test methods for transport properties such as permeability and conductivity (or the inverse, resistivity). With this approach, the important influences that construction procedures such as compaction and curing have on the potential durability of the structure can be assessed. An example of performance-based approaches that include conformity assessment is the South African Durability Index (DI) approach.

### **4. The South African Durability Index Approach**

#### **4.1 General**

The South African Durability Index (DI) approach for specification and conformity assessment of concrete durability is based on durability indicators (so-called durability indexes) such as oxygen permeability, chloride conductivity and water sorptivity.

Similar to most service life prediction models for reinforced concrete structures, the South African model assumes that the service life duration corresponds to the corrosion initiation period. As such, the service life is assumed to end when the concrete has carbonated to the level of the steel or when the chloride concentration at the level of the steel has reached a certain threshold value. Two corrosion initiation models have been developed, related to carbonation - and chloride - induced corrosion. The models derive from measurements and correlations of short-term durability index values, aggressiveness of the environment and actual deterioration rates monitored over periods of up to 10 years. The models allow for the expected life of a structure to be determined based on considerations of the environmental conditions, cover thickness and concrete quality [3, 15]. The environmental classes are related to the EN 206 classes as modified for South African conditions, while concrete quality is represented by the appropriate durability index parameter. The oxygen permeability index is used in the carbonation prediction model, while the

chloride model utilizes chloride conductivity. The service life models can also be used to determine the required value of the durability parameter based on predetermined values for cover thickness, environment, and expected design life.

## **4.2 Prediction of chloride ingress**

The South African Chloride Conductivity Index (CCI) test involves the measurement of a sample's conductivity [3, 15]. A 30 mm thick, 70 mm diameter specimen is dried in an oven and vacuum pre-saturated with a 5 M NaCl solution. A migration cell is used, in which the sample is placed between two cells containing 5 M NaCl solution. A 10 V potential difference is applied across the sample, causing a movement of chloride ions, and the corresponding current is used to calculate the concrete's conductivity. The apparatus allows for rapid testing under controlled laboratory conditions and gives instantaneous readings.

An international study [10, 13, 16] revealed that the chloride conductivity test is able to detect differences in w/b ratio, binder type, and curing condition on a statistically highly significant level and that test results obtained with the chloride conductivity method generally correlate well with results obtained from other accepted test methods for chloride resistance, such as the Rapid Chloride Permeability Test (ASTM C 1202 [17]) and the Bulk Diffusion Test (NordTest NTBuild [18]).

Chloride ingress into concrete is modelled with the South African service life model for concrete in the marine environment [3, 15]. This model is based on Fick's laws of diffusion and uses chloride conductivity values to evaluate chloride diffusion coefficients. Correlations between 28-day chloride conductivity results and diffusion coefficients after several years marine exposure have been shown to be good over a wide range of concretes [15]. The philosophy behind examining the correlation between diffusivity and conductivity is that conductivity of saturated materials is linearly related to steady state diffusivity, while apparent diffusivity is a function of steady state diffusivity and the chloride binding capacity. Having established a correlation between the apparent diffusion coefficient and the chloride conductivity makes it possible for the designer to use the Fickian service life models directly and input the appropriate conditions (cover depth, environmental classification, desired life, and material) to give material specifications in terms of the diffusion coefficient value that should be achieved using the chloride conductivity test. The correlation between the apparent diffusion coefficient and the chloride conductivity can also be used to establish chloride conductivity index limits used in durability design.

## **5. Experimental work**

### **5.1 Aims and methodology**

In this research, the prescriptive design approach for reinforced concrete durability in the marine environment according to the British National Annex to the Eurocode (2004 [2]) is compared with performance-based design approaches used in South Africa. The aim of the study was firstly to evaluate if the prescriptive specifications of the Eurocode are generally more or less conservative than the performance-based approaches in South Africa. Secondly, it was assessed if the prescriptive requirements make sufficient allowance for the influence of various binder types on the durability characteristics of concrete.

A total of 12 different concrete mixes were designed to meet the durability specifications of the British National Annex to EN 1992:1 (2004 [2]) and tested according to the South African Durability Index method. The test results were used to model chloride ingress using the South African service life prediction model for the marine environment. The assessment and analysis of durability parameters using accepted test methods and service life prediction models allowed evaluating if the prescriptive requirements given in Eurocode, in combination with materials locally available in South Africa result in a rational concrete mix design. In this context, rational concrete mix design can be considered to result in concrete mixes that are neither potentially non-durable, nor vastly over-designed and therefore not economical.

## **5.2 Concrete mix design and binder type selection**

In the British National Annex to the Eurocode (2004 [2]), specifications of maximum water/binder ratio, minimum cement content and strength class are made in relation to binder type and cover depth, as discussed earlier. For the experimental work, the selection of appropriate design cover depths and binder types was made based on South African construction practice. The considered design service life was 50 years.

In agreement with South African construction practice, the design cover depths chosen for this research was 50 mm for exposure classes XS (marine environment). The common South African binder type combinations (pure CEM I, or CEM I plus either 10% condensed silica fume (CSF), 30% fly ash (FA), or 50% granulated slag (GGBS)) correlate to the binder combinations stipulated in the British NA to the Eurocode (2004) for environmental classes XS, which include CEM I, CEM IIA, CEM IIB-V, and CEM IIIA. All of the above four binder type combinations were therefore used in this research.

Mix design parameters and strength classes were selected in relation to the above mentioned design cover depths and binder types to meet the specifications of the British NA to the Eurocode (2004 [2]), as summarized in Table 1. For comparability reasons, the amount of coarse aggregate in all mixes was kept constant at 1050 kg/m<sup>3</sup>. The water content of the mixes ranged between 170 and 190 l/m<sup>3</sup> and if necessary, adjustments to the workability were made with superplasticiser (SP) to achieve a desired slump of 70±10 mm. In the mix design process, the authors tried to be as close as possible to the specified minimum cement contents. However, for some mixes, workability requirements demanded slightly higher water contents and therefore higher cement contents.

With mix parameters and compressive strength values meeting the requirements of the specifications, all 12 mixes would be considered durable for their design environment according to the British NA to the Eurocode [2].

## **5.3 Chloride conductivity measurements (chloride ingress prediction)**

Mixes 1 – 12 were assessed for resistance against chloride ingress using the chloride conductivity index (CCI) values as input parameters in the South African service life prediction model for concrete in the marine environment. The test specimens consisted of 30 mm thick core slices (68 mm diameter) that were removed from concrete cubes (28 days water-cured at 23°C) and preconditioned and tested according to the test method's specifications [19]. A total of 4 test results were obtained per mix and, following exclusion of outliers, the mean conductivity values used in the analysis.

The CCI results of the laboratory-cured samples were converted to the “equivalent in-situ concrete”, as suggested in [6], using a conversion factor of 0.90 so that  $CCI_{Lab} = CCI_{Site} \times 0.90$ . This conversion takes into account that measurements taken on real structures under site conditions have a higher statistical variability, compared to measurements taken in the laboratory on fully cured samples. The test results (measured and converted) are presented in Table 1. Using the equivalent  $CCI_{Site}$  values, as well as binder type and environmental conditions as input parameters in the South African service life prediction model allows to forecast the chloride contents in the structure (by mass of binder) at a certain depth and time.

For interpretation of the predicted chloride contents in structures made with Mixes 1 – 12 it was assumed that the service life ends with the beginning of the corrosion initiation phase at a chloride content of 0.4% by mass of binder. Table 1 and Figures 1-3 present the results of the analysis in relation to the following:

- Chlorides by mass of binder at a cover depth of 50 mm (corresponding to the design cover depth) (Figure 1)
- Depth at which the chloride content exceeds 0.4% by mass of binder (after 50 years), corresponding to the cover depth actually necessary for a design service life of 50 years (Figure 2)
- Expected service life, assuming a chloride threshold of 0.4% by mass of binder and a cover depth of 50 mm (Figure 3)

**Table 1:** Prescriptive recommendations according to EC2 (reference) for exposure classes XS1, XS2 and XS3, assuming a cover depth of  $(40 + \Delta c_{dev}) = 50$  mm; concrete mix design and selected properties

Mix number	1	2	3	4	5	6	7	8	9	10	11	12
Exposure class	XS1				XS2				XS3			
Selected binder type (CEM)	I	II/A-D	II/B-V	III/A	I	II/A-D	II/B-V	III/A	I	II/A-D	II/B-V	III/A
Recommended mix parameters (EC2)												
Min. $f_c$ (cube)	45	45	40	40	35	35	30	30	55	55	45	45
Max. w/b	0.50	0.50	0.50	0.50	0.55	0.55	0.55	0.55	0.35	0.35	0.40	0.40
Min. cement (kg)	340	340	340	340	320	320	320	320	380	380	380	380
Mix composition (kg/m <sup>3</sup> )												
CEM I 42.5	360	324	280	180	345	310	242	172	498	448	298	213
GGBS	0	0	0	180	0	0	0	173	0	0	0	213
FA	0	0	120	0	0	0	104	0	0	0	128	0
CSF	0	36	0	0	0	35	0	0	0	50	0	0
Sand (0-2 mm)	820	820	780	820	860	860	860	860	700	700	740	740
Stone (19 mm)	1050	1050	1050	1050	1050	1050	1050	1050	1050	1050	1050	1050
Water	180	180	180	180	190	190	190	190	175	175	170	170
SP (l/m <sup>3</sup> )	2.25	2.25	0.75	1.25	3.00	1.38	0.50	1.25	2.25	3.75	0.75	1.25
w/b	0.50	0.50	0.45	0.50	0.55	0.55	0.55	0.55	0.35	0.35	0.40	0.40
$f_{c, 28 \text{ days}}$	47.7	55.9	43.7	42.9	44.1	55.2	31.1	34.8	65.7	83.2	50.9	56.1
Chloride Conductivity (CC) (unit)												
$CC_{\text{Lab (measured)}}$	1.06	0.2	0.53	0.37	1.22	0.29	0.81	0.37	0.63	0.12	0.35	0.17
$CC_{\text{Site}}$	1.18	0.22	0.59	0.41	1.36	0.32	0.90	0.41	0.70	0.13	0.39	0.19
Service life modelling												
Service life (years)	75	>100	>100	>100	22	>100	>100	>100	53	>100	>100	>100

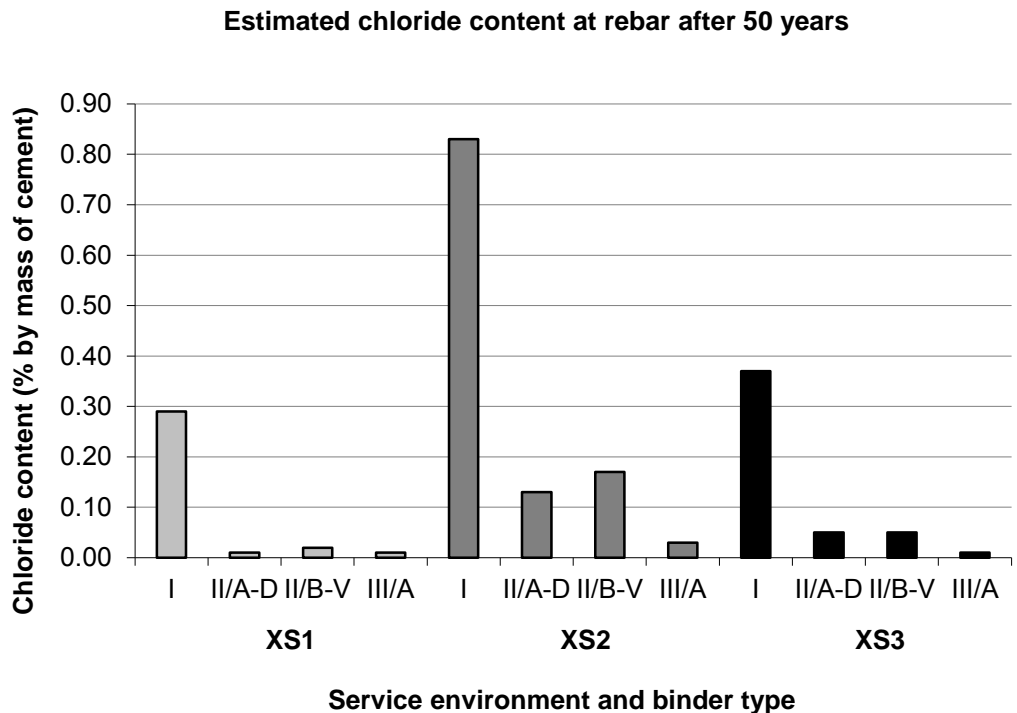
The South African service life prediction model for the marine environment uses Fick's law of diffusion to model chloride ingress into concrete and is therefore based on the model input parameters of chloride surface concentrations and time-dependent diffusion coefficients. The chloride surface concentrations are predicted based on binder type and environmental conditions, and the chloride diffusion coefficients are derived from chloride conductivity values, as discussed above.

Figures 1 – 3 show the results of the service life prediction model for mixes 1 – 12 and present an indication on how the prescriptive design approach of the British Annex to the Eurocode compares to the expected performance of the concretes in their respective design environments (based on the South African service life prediction model). It needs to be noted that the analysis presents a qualitative evaluation only, as the model is based on various assumptions and simplifications, such as a 0.4% threshold value for reinforcement corrosion and an estimated time-development of diffusion coefficients. A more accurate quantitative comparison of prescriptive and performance-based approaches in this way would need to be done based on long-term data of chloride ingress into concrete in real environments, which is currently not available. However, the service life prediction results shown in Figures 1 – 3 give a general indication on how conservative (or otherwise) the prescriptive durability requirements of the Eurocode are with respect to various binder types and environmental conditions in South Africa.

A limitation of the experimental research was that fully water-cured samples were used for the testing, which resulted in an upper-bound evaluation of chloride resistance. In real structures, where curing conditions influence the concrete quality, the chloride resistance can be expected to be lower. Nonetheless, the results allow identification of some interesting trends.

The results of the analysis indicate that the Eurocode specifications are on the conservative side with concretes made with blended cements. The predicted service life duration of all concretes made with silica fume, slag, or fly ash considerably exceeds the design service life of 50 years, even indicating a service life or more than 100 years, which was observed for all 3 exposure classes (Fig. 3). Correspondingly for these concretes, the predicted chloride contents at the level of the reinforcement after 50 years exposure are significantly below the threshold value of 0.4%, especially for environments XS1 and XS2 (Fig. 1).

The same trend, however less obvious, can be observed when the predicted required cover depths (the depths at which chloride concentration exceeds 0.4% by mass of binder) are considered (Fig. 2). The reason for the trend being less obvious in this case is that chloride ingress is fast in early years but slows down considerably with time. Considering, for example, Mix 7 (binder type II/B-V, exposure class XS2), the predicted chloride content at the level of the steel after 50 years is less than half that required for corrosion initiation but at 10 mm away from the steel, i.e. at 40 mm depth, the threshold has already been reached. This can be explained with the steep chloride profiles predicted in the model. A relatively small deviation from the specified cover (in the case of Mix 7, 10 mm, corresponding to 20% of the specified 50 mm) has therefore a significant influence on corrosion initiation and can reduce the service life duration by more than 50%.



**Figure 1:** Mixes 1 – 12: estimated chloride content at the reinforcement after 50 years

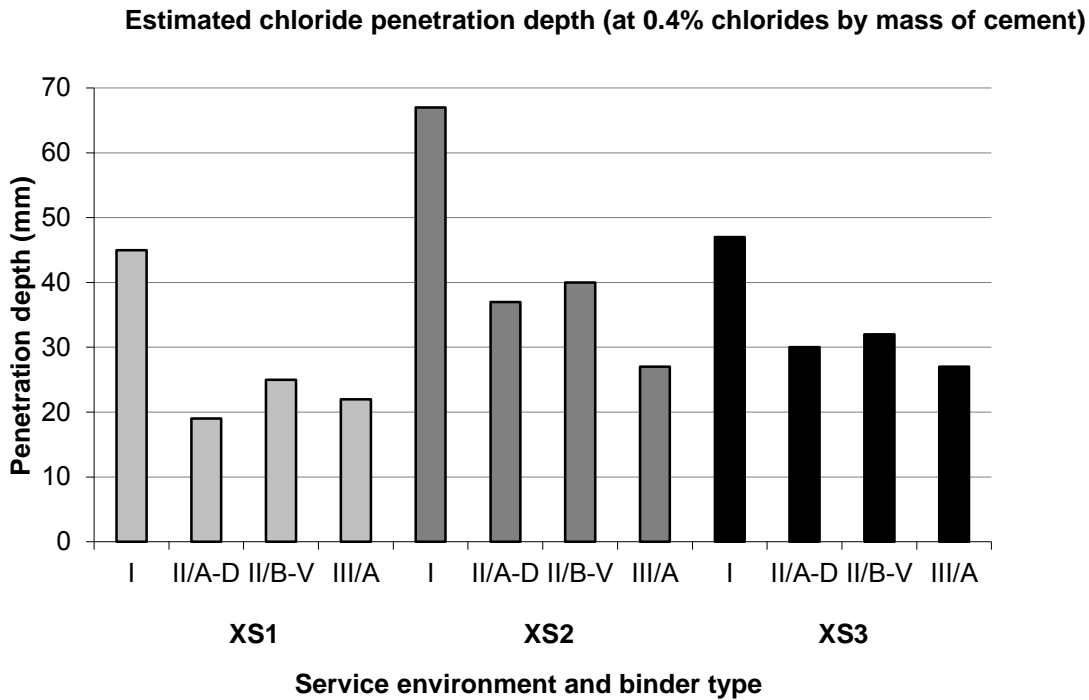


Figure 2: Mixes 1 - 12: estimated depth at which the chloride concentration reaches 0.4% (by mass of binder) after 50 years

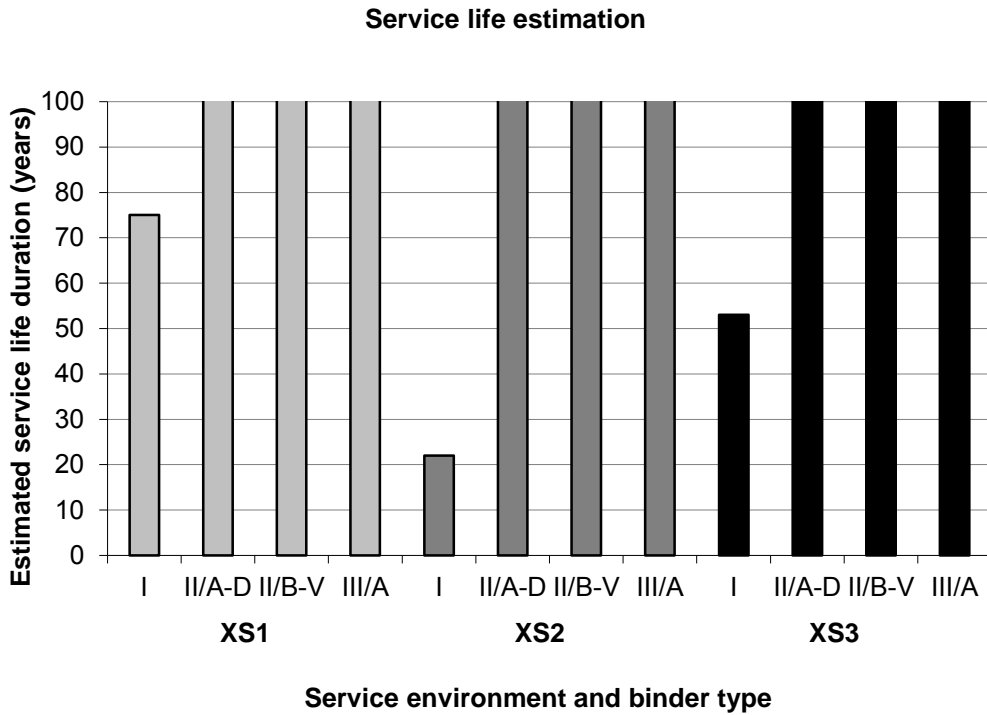


Figure 3: Mixes 1 – 12: estimate of service life duration (>100 years for all mixes with blended cements)

Interpreting the experimental data based on Figures 1 and 3 alone creates the impression that the prescriptive approach is extremely conservative with blended cements, considering the “potential” durability measured on fully cured concrete. However, Figure 3 shows that the safety factor may actually be relatively small with respect to concrete cover for environment XS2 in particular, XS3 less so, and XS1 considerably less so.

In comparison to the concretes made with blended cements, the prescriptive specifications for the mixes containing CEM I are far less conservative or even inadequate. In case of environmental classes XS2 and XS3, the predicted service life durations are just above 20 years and 50 years, respectively. Figure 2 shows that the required cover depth for environmental class XS2 is close to 70 mm and that very little safety in terms of cover depth is built into the specifications for environmental classes XS1 and XS3.

To identify a trend with respect to different exposure classes, the mean values of the required cover depths of all blended cement concretes are considered, which are 22, 37 and 30 mm for exposure classes XS1, XS2 and XS3, respectively. This suggests that, in comparison to the South African performance-based service life models, the prescriptive requirements of the Eurocode are particularly conservative for exposure class XS1. In contrast, for exposure class XS2, the safety margin with respect to cover depth is relatively small.

## 6. Summary and conclusions

The 12 different concrete mixes used in this research were designed according to the prescriptive specifications of the British NA to the Eurocode and would therefore be considered durable for the chosen cover depth and design environment. However, the predictions of chloride ingress into these mixes, based on chloride conductivity results and the South African service life prediction model, indicate that the design specifications may not be adequate for concrete made with plain CEM I cement. In contrast, concretes made with blended cements generally showed that the prescriptive provisions for the marine environments are somewhat conservative, especially for environmental class XS1. However, mixes used in this study were water cured for 28 days and do therefore only indicate the full durability potential of the concrete mixes. In real structures, the chloride resistance of the concrete will be influenced by construction procedures and curing conditions.

The prescriptive requirements seem to not fully take into account that blended cements incorporating silica fume, slag or fly ash have a much better resistance against chloride ingress, compared to CEM I cements, which is a result of pore structure refinement and superior chloride binding characteristics.

Compared to older versions of prescriptive specifications for concrete durability, the Eurocode accounts for a larger range of design environments and various binder types used, which is a positive development. However, this research indicates that even with concrete made with conventional aggregates and binder combinations, the design specifications of the Eurocode may fail to result in safe or economical concrete mixes. The limitations of the prescriptive approach can be expected to be even more pronounced when innovative and new materials or construction methods are used. For projects where durability is of major concern, the use of performance-based design and specification methods should therefore be considered.

## References

1. BS EN 1992:1 – 2004, Eurocode 2: Design of concrete structures – Part 1-1: General rules and rules for buildings
2. NA to BS EN 1992:1 – 2004, UK National Annex to Eurocode 2: Design of concrete structures
3. Mackechnie, J.R. and Alexander, M.G. (2002), ‘Durability predictions using early age durability index testing’, Proceedings, 9th Durability and Building Materials Conference, 2002. Australian Corrosion Association, Brisbane, 11p.

4. Alexander, M.G., Mackechnie, J.R. and Ballim, Y. Use of durability indexes to achieve durable cover concrete in reinforced concrete structures, *Materials Science of Concrete*, Vol. VI, Ed. J. P. Skalny and S. Mindess, American Ceramic Society, 2001, pp. 483 – 511
5. BS EN 206-1: 2000, Concrete – Part 1: Specification, performance, production and conformity
6. Alexander, M.G., Ballim, Y., and Stanish, K., 'A framework for use of durability indexes in performance-based design and specifications for reinforced concrete structures', *Materials & Structures*, Vol. 41, No. 5, June 2008, pp. 921-936.
7. Torrent R. & Jacobs F., 'Swiss Standard SIA 262:2003, a step towards performance-based specifications for durability', *Proceedings of the international RILEM TC 211-PAE Final Conference "Concrete in Aggressive Aqueous Environments; Performance and Testing"*, Volume 2, Toulouse, France, 2009, pp. 532-539.
8. Walraven, J. Design for service life: how should it be implemented in future codes, *International Conference on Concrete Repair, Rehabilitation and Retrofitting*, Proceedings ICCRRR 2008, Cape Town, 24-26 November 2008, pp. 3-10.
9. Simons, B. Concrete performance specifications: New Mexico Experience, *Concrete International*, 26(4), 2004, pp. 68-71.
10. Romer, M., Fernández Luco, L. (2005), 'RILEM TC 189-NEC: Non-destructive evaluation of the concrete cover: Comparative test - Part I: Comparative test of 'penetrability' methods - Part II: Comparative test of 'Covermeters'', *Materials and Structures*, 38(284), pp. 895 - 911
11. Andrade, C., Alonso, C., Arteaga, A. and Tanner, P, Methodology based on the electrical resistivity for the calculation of reinforcement service life, *Fifth CANMET/ACI International Conference on Durability of Concrete*, 2000, pp. 899-915.
12. Baroghel-Bouny V., Nguyen T.Q., Dangla P., Assessment and Prediction of RC Structure Service Life by Means of Durability Indicators and Physical/chemical Models, *Cement and concrete composites*, vol. 31, n° 8, 2009, pp 522-534.
13. Torrent, R. & Fernández Luco, L. (editors) State of The Art Report (STAR): RILEM TC 189-NEC: Non-Destructive Evaluation of the Covercrete, Zurich, Switzerland, 2007, 223 pp.
14. CEN/TC 104/SC1/TG17, 'Equivalent Durability Concept, a discussion document for CEN/TC 104/SC1 to decide upon what is achievable for the 2010 revision of EN 206-1, Draft 8 version 1, May 2008, 13 pp.
15. Mackechnie, J.R., 'Predictions of Reinforced Concrete Durability in the Marine Environment', *Research Monograph No. 1*, Department of Civil Engineering, University of Cape Town, 2001, 28 pp.
16. Beushausen, H., Alexander, M.G. (2008), 'The South African Durability Index tests in an international comparison' *Journal of the South African Institute of Civil Engineers*, Vol. 50, No. 1, South Africa, March 2008, pp. 25 – 31.
17. ASTM C 1202 – 1997. Standard Test Method for Electrical Indication of Concrete's Ability to Resist Chloride Ion Penetration. *ASTM*, USA.
18. NTBuild 492 1999. Chloride migration coefficient from non-steady state migration experiments. *Nordtest*, Espoo, Finland.
19. Alexander, M.G, Mackechnie, J.R and Ballim, Y. Guide to the use of durability indexes for achieving durability in concrete structures, *Universities of Cape Town and Witwatersrand*, 1999. (Research Monograph no.2).



# Durability Performance of Crystalline-Modified Concrete Exposed to Severe Environment

Farhad Nabavi, BEng, MTech, PhD<sup>1</sup>

<sup>1</sup>Technical Manager, Xypex Australia

**Abstract:** This paper presents the effect of crystals formation on mechanical properties and durability performance of concrete exposed to severe environmental conditions. Durability of the concrete is directly related to the mass transport property of the concrete. Penetration of aggressive substances such as chloride ions and carbon dioxide into concrete can significantly reduce the service life of reinforced concrete (RC) structures. Mass transport in concrete is a function of interconnected pores and cracks in concrete. Crystalline structure blocks the pores and heals the cracks permanently. Results from laboratory tests and field investigations as case studies indicated that formation of crystals in pores and cracks can reduce the diffusion rate of aggressive substances into concrete and enhance the durability of concrete significantly.

**Keywords:** crystalline technology, concrete durability, chloride diffusion, service life, concrete sustainability.

## 1. Introduction

Premature deterioration of RC structures exposed to severe environment such as marine environment has become a worldwide problem due to high cost effect, environmental impact, and safety issues [1,2]. Penetration of aggressive agents such as carbon dioxide, chloride ion, and sulphates into concrete, through interconnected pores and cracks result in the degradation of the concrete materials.

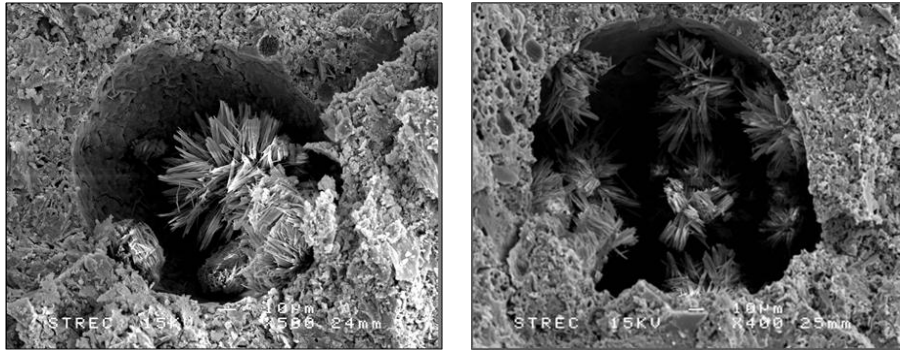
Degradation processes which cause reduction in the service life of RC structures may influence both concrete and steel reinforcement depending strongly on diffusion processes and type of diffusive substances into the concrete. Chloride-induced corrosion of steel reinforcement in concrete has received increasing attention in recent years because it has been the dominant factor in deterioration of RC structures [3,4].

Steel reinforcement in concrete is protected by a highly alkaline protective passive layer. Accumulation of the chloride ions at the surface of reinforcing steel results in a local fall in the pH of the pore solution. The protective film can be destroyed if the concentration of chloride ions at the depth of the steel reaches to a critical level which is called chloride threshold level (CTL). Depassivation of the protective film causes steel corrosion which consequently reduces the service life of the RC structures. Therefore, preventing chloride penetration into concrete, by blocking the pores and sealing the micro-cracks, increases durability of the concrete and consequently extends the service life of RC structures [5,6,7].

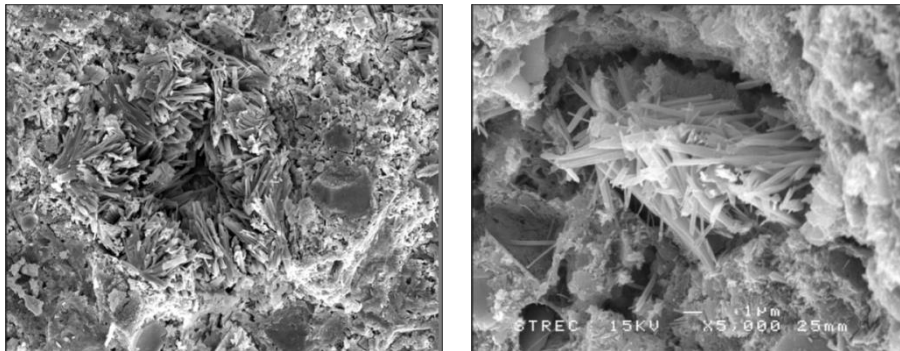
This paper investigates the effect of crystal formation on transport properties and durability of the concrete. Sorptivity, water permeability, and chloride diffusion as durability assessment tests are investigated. In addition, the effect of crystalline technology on compressive strength of concrete is examined.

## 2. Crystalline Technology

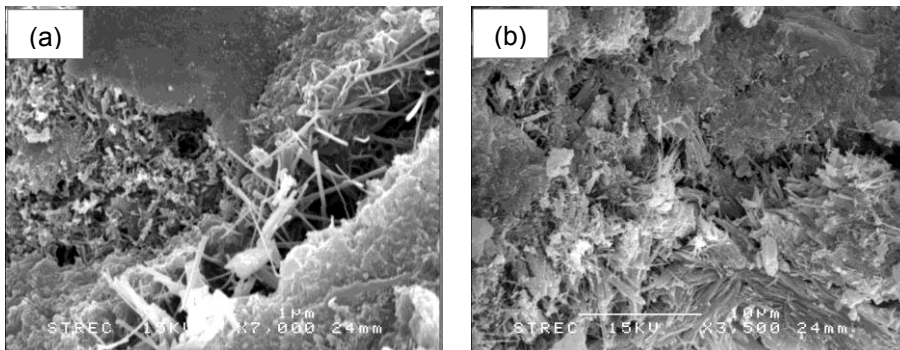
Crystalline materials are dry powder compounds composed of Portland cement, silica sand, and many active and proprietary chemicals. Active chemicals in crystalline materials react with the moisture and cement hydration products to cause a catalytic reaction. This chemical reaction generates a non-soluble crystalline formation which permanently blocks the pores and capillary tracts; and seals the micro-cracks of the concrete. Scanning electron microscope (SEM) images (Figure 1 to 3) confirm the pore blocking and crack sealing properties of the crystalline technology.



**Figure 1. Crystals growth in concrete pores**



**Figure 2. Pore blocking by crystals formation**



**Figure 3. Crack bridging (a) and crack healing (b) by crystals formation**

### **3. Experimental Program**

The experimental program includes laboratories and field investigations.

#### **3.1 Test Methods and Standards**

The conducted tests and utilised standards are summarised as follows:

- Slump: AS1012.3
- Compressive strength: AS1012.9
- Drying shrinkage: AS1012.13
- Apparent Volume of Permeable Voids (AVPV): AS1012.21

- Water permeability: ACCI Method
- Rapid chloride ion test: ASTM1202/CSIRO Modified
- Chloride ion diffusion coefficient: NordTest (NT Build 443)
- Chloride content measurement: ASTM C1152-04.
- Half-cell potential measurement: ASTM C876-91.

## **3.2 Laboratory investigations**

### **3.2.1 Materials**

Since the durability performance was the main objective of laboratory investigation, all concrete specimens were cast using supplementary cementitious materials (Fly Ash and GGBF Slag). Crystalline material was used as admixture with two proportions of 0.8% (CA1) and 1.2% (CA2) by weight of cementitious materials in concrete. Crushed limestone aggregate with specific gravity of 2700 kg/m<sup>3</sup> and maximum size of 20 mm as coarse aggregate, and river sand with specific gravity of 2600 kg/m<sup>3</sup> and maximum size of 4.75 mm as fine aggregate, were used. According to the AS 4997-2005 recommendations, the minimum of 400 kg/m<sup>3</sup> of cementitious material content and maximum water to binder (W/B) ratio of 0.4 were considered in all types of concrete.

### **3.2.2 Sample preparation**

Three types of samples were prepared as follows:

- Type-GB cement with 25% Fly Ash-class F (AS3582.1), (FA) with and without Crystalline Admixture (CA)
- Type-GB cement with approximately 38% Slag (AS3582.2) (S1) with and without Crystalline Admixture (CA)
- Type-GB cement with approximately 60% Slag (AS3582.2) (S2) with and without Crystalline Admixture (CA)

Based on these codes, for instance, S2-CA1 means a concrete sample with 60% slag and 0.8% crystalline admixture.

### **3.2.3 Conducted Tests**

Slump (workability) test as plastic concrete property, compressive strength and drying shrinkage as hardened concrete properties, and water sorptivity AVPA, water permeability, rapid chloride test, and chloride diffusion coefficient as durability characteristics of the concrete were examined.

## **3.3 Field Investigations**

Case studies presented in this paper are related to the durability performance of crystalline modified concrete (CMC) incorporating crystalline admixture materials in two marine structures exposed to severe environment for 19 years.

### **3.3.1 Cronulla Marina Jetty**

The prestressed crystalline modified concrete (CMC) panels (jetty slabs) were cast at the Cronulla Marina jetty, NSW in October 1994. Each panel has a thickness of 100 mm and has foam flotation attached to the soffit. The top surfaces of the concrete panels have a nominal distance of 350 mm from the sea level. The Cronulla Marina structure, which is located in Gunnamatta Bay, has been subjected to most severe environmental conditions within tidal/splash zone. The condition survey and assessment of the structure was conducted in 2013 after 19 years of service (exposure time). Crystalline admixture proportion in the concrete mix was 4.2 kg/m<sup>3</sup> which would be 0.8% by weight of cement content.

### **3.3.2 Lascelles Wharf**

The precast CMC slab was cast at Lascelles Wharf – Geelong Ports, VIC in 1995. This concrete slab has been in service as a bulk chemical and grain dock and also exposed to marine

environment which is classified as the most severe exposure condition. The condition survey and assessment of the structure was conducted in 2014 after 19 years of service (exposure time). Crystalline admixture proportion in the concrete mix was 4.0 kg/m<sup>3</sup> which would be 1% by weight of cement content.

### 3.3.3 Concrete mix design

Concrete mix designs for both case studies are presented in Table 1.

**Table 1. Concrete mix designs for both structures**

Project	Cement	CA (20mm)	CA (10mm)	Coarse Sand	Fine Sand	Water	W/C
	[kg]	[kg]	[kg]	[kg]	[kg]	[kg]	
Cronulla Marina	530	730	340	480	120	170	0.32
Lascelles Wharf	400	420	620	90	660	150	0.37

### 3.3.4 Conducted Tests

Visual inspection, half-cell potential, and chloride content measurement were conducted as criteria for durability assessment of the structures.

In both projects, Copper/Copper Sulphate (Cu/CuSO<sub>4</sub>) Electrode (CSE) was used to measure the half-cell potential. The standard that is typically employed to interpret the half-cell potentials measurements is ASTM C876-91. This standard provides a very general guide for probability of corrosion based on the half-cell potential values.

At Cronulla Marina, the half-cell potentials were measured on 150 mm × 150 mm square grid over an area of 3.6 square meters. At Lascelles Wharf, the half-cell potentials were measured on 200 mm × 200 mm square grid over an area of 3.0 square meters.

Chloride content measurements were carried out for both projects to specify the chloride resistance of CMC exposed to chloride environment after 19 years. Concrete cores were extracted from the slabs to measure the chloride content. The chloride content was measured in different depths up to the thickness of the concrete cover. The minimum concrete covers at the Cronulla Marina and Lascelles Wharf were 40 mm and 51 mm, respectively.

## 4. Results and Discussion

Results and discussion are presented for laboratory investigations and case studies separately.

### 4.1 Laboratory Test Results

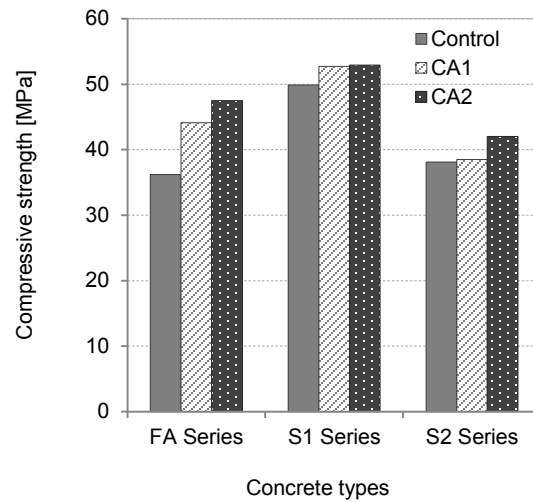
#### 4.1.1 Mechanical Properties

Test results of workability and hardened concrete properties are presented Table 2.

**Table 2. Concrete categories and properties**

Mix Code	W/B	Cementitious Content [kg]	CA [%]	Slump [mm]	Compressive Strength [MPa]			Drying Shrinkage [micron]
					3-day	28-day	91-day	
FA	0.4	435	Nil	95	21.9	36.2	46.7	719
FA-CA1	0.4	435	0.8	105	22.1	44.1	53.8	577
FA-CA2	0.4	435	1.2	100	28.0	47.5	58.0	562
S1	0.4	435	Nil	95	28.1	49.9	64.8	814
S1-CA1	0.4	435	0.8	100	28.6	52.7	65.7	689
S1-CA2	0.4	435	1.2	90	28.6	52.9	66.3	711
S2	0.4	435	Nil	100	14.2	38.1	49.3	803
S2-CA1	0.4	435	0.8	105	14.4	38.5	49.8	772
S2-CA2	0.4	435	1.2	95	15.7	42.0	53.4	772

All concrete mixes slump test results were within the normally acceptable range. 28-day compressive strengths for all types of concrete in this investigation are presented in Figure 4.



**Figure 4. 28-day Compressive strength of all types of concrete**

Concrete specimens with crystalline admixture showed higher compressive strength compared to the controls without CA. At age of 28 days, 31% improvement of compressive strength for FA series, 6% for S1 series and 10% for S2 series were observed.

In addition, drying shrinkage results indicated improved performance for all specimens with crystalline admixture. In particular, for FA series, results showed significant reduction in drying shrinkage up to 22%. This shrinkage reduction for S1 and S2 series was 15% and 4%, respectively

#### 4.1.2 AVPV Test

The AVPV test results are summarised in Table 3. Generally, crystalline modified concretes showed lower AVPV values than the control mixes under all curing conditions. Increasing the proportion of the crystalline materials decreases the AVPV value. Significant reduction in AVPV was found with concrete mix FA-CA2 with 11% lower AVPV than the control mix FA after 180 days limewater curing.

**Table 3. Summary of AVPV test results**

Mix Code	7d Lime + 49d Air AVPV [%]	Change [%]	7D Lime + 173d Air AVPV [%]	Change [%]	56d Lime AVPV [%]	Change [%]	180d Lime AVPV [%]	Change [%]
FA	13.06	Control	12.95	Control	12.71	Control	10.75	Control
FA-CA1	12.65	-3.1	12.05	-6.9	12.20	-4.0	9.87	-8.2
FA-CA2	12.80	-2.0	12.08	-6.7	11.54	-9.2	9.57	-11.0
S1	12.60	Control	12.44	Control	12.15	Control	10.22	Control
S1-CA1	12.05	-4.4	11.52	-7.4	11.24	-7.5	9.54	-6.7
S1-CA2	11.80	-6.3	11.25	-9.6	10.87	-10.5	9.32	-8.8
S2	12.05	Control	11.84	Control	11.37	Control	9.24	Control
S2-CA1	11.75	-2.5	11.20	-5.4	10.75	-5.45	8.64	-6.5
S2-CA2	11.55	-4.1	10.94	-7.6	10.47	-7.9	8.45	-8.5

The results confirmed that due to pore blocking by crystals formation, the overall volume of permeable voids decreased. This phenomenon is supported by water permeability test presented in next section.

#### 4.1.3 Water Permeability

All concrete types were tested for water permeability under 100 m water head. The concrete samples were cured in limewater for 90 days before testing. The test results have been summarised in Table 4 in terms of water permeability coefficient.

**Table 4. Water permeability coefficients of concrete types**

Mix Code	FA	FA-CA1	FA-CA2	S1	S1-CA1	S1-CA2	S2	S2-CA1	S2-CA2
Water Permeability Coefficient [ $\times 10^{-12}$ m/s]	1.76	0.98	NIL	1.14	0.31	0.12	0.82	NIL	NIL

Although, no visible water leakage was observed in FA-CA2, S1-CA2, S2-CA1, and S2-CA2 the water penetration depths of 22 mm, 16 mm, 14 mm, 11 mm, and 8 mm, respectively were measured. The results reveal, by increasing the dosage of crystalline material in the mix, water permeability of the concrete decreases. Considering the water permeability coefficient of crystalline modified concrete, this concrete can be categorised of high quality concrete in terms of mass transfer property which is suitable for structures exposed to severe environmental conditions.

#### 4.1.4 Rapid Chloride Test – ASTM C1202 / CSIRO Modified

The results of the rapid chloride ions test are presented in Table 5. As results show, crystalline formation can increase the chloride diffusion resistance of the concrete significantly.

**Table 5. ASTM C1202 / CSIRO Modified test results**

Mix Code	W/B	Cementitious Content [kg]	Crystalline Admixture [%]	ASTM C1202 [%]
FA	0.4	435	Nil	Control
FA-CA1	0.4	435	0.8	-76%
FA-CA2	0.4	435	1.2	-90%
S1	0.4	435	Nil	Control
S1-CA1	0.4	435	0.8	-71%
S1-CA2	0.4	435	1.2	-73%
S2	0.4	435	Nil	Control
S2-CA1	0.4	435	0.8	-47%
S2-CA2	0.4	435	1.2	-62%

#### 4.1.5 Chloride Diffusion Test – NT BUILD 443, Accelerated Chloride Penetration Test

The tests were conducted according to the Nordtest (NT Build 443) with exposure time of 35 days and 105 days. The test results are shown in Table 6.

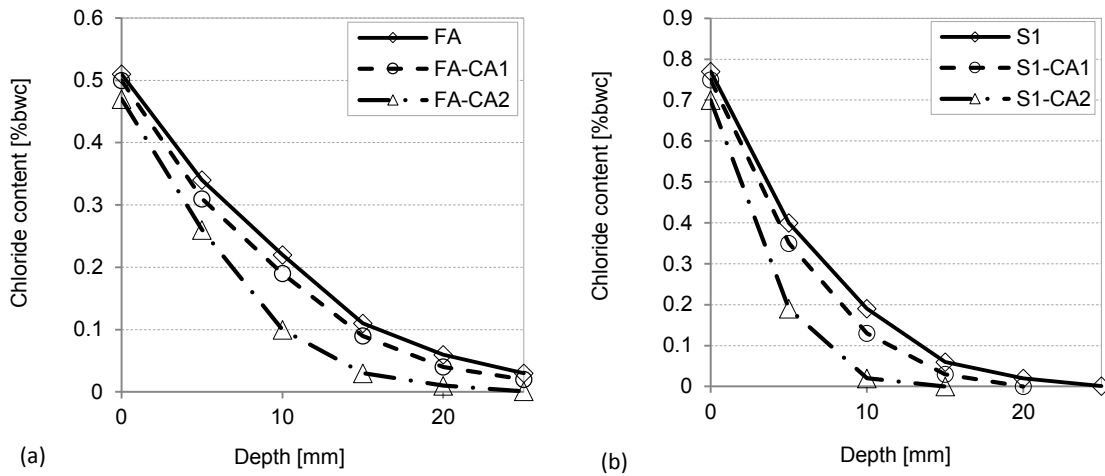
**Table 6. Chloride diffusion coefficient for all types of concrete**

Mix Code	CA [%]	Chloride Diffusion Coefficient [ $\times 10^{-12}$ m <sup>2</sup> /s]		Change (105 days) [%]
		35 days of Exposure	105 days of Exposure	
FA	Nil	15.0	8.0	Control
FA-CA1	0.8	8.5	6.8	-15%
FA-CA2	1.2	5.8	3.5	-56%
S1	Nil	4.0	3.5	Control
S1-CA1	0.8	2.2	2.5	-29%
S1-CA2	1.2	1.5	1.0	-71%
S2	Nil	3.0	1.7	Control
S2-CA1	0.8	3.5	1.2	-29%
S2-CA2	1.2	2.5	1.2	-29%

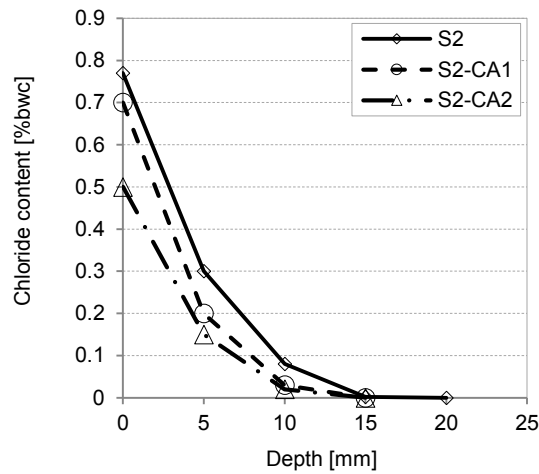
Crystalline modified concrete indicated significant chloride resistance property even compared to fly ash and slag concrete which are categorised as high quality concrete. Up to 56% and 71%

reduction in chloride diffusion rate in fly ash and slag concrete respectively proves that crystals formation can enhance the durability of the concrete significantly.

The chloride profiles of the different types of concretes are presented in Figure 5 and 6.



**Figure 5. Chloride profiles of FA (a) and S1 (b) series**



**Figure 6. Chloride profile of S2 series**

#### 4.1.6 Corrosion-Free Service Life

The prediction of corrosion-free service lives for S1 (38% slag) concrete samples have been estimated and are presented in Table 7. Concrete cover of 70 mm, chloride threshold level of 0.4% by weight of cement, and marine splash zone as environmental exposure were considered as assumptions in estimation of service life.

**Table 7. Prediction of corrosion-free service life**

Mix Code	S1	S1-CA1	S1-CA2
Crystalline Admixture [%]	0	0.8	1.2
Corrosion-Free Service Life [year]	42	59	147

## 4.2 Field Investigations, Case Study

### 4.2.1 Visual Survey

Site investigations conducted on both RC structures revealed that there was no sign of any concrete cracking, spalling or other defects and concrete slabs were in excellent conditions as shown in Figure 7.

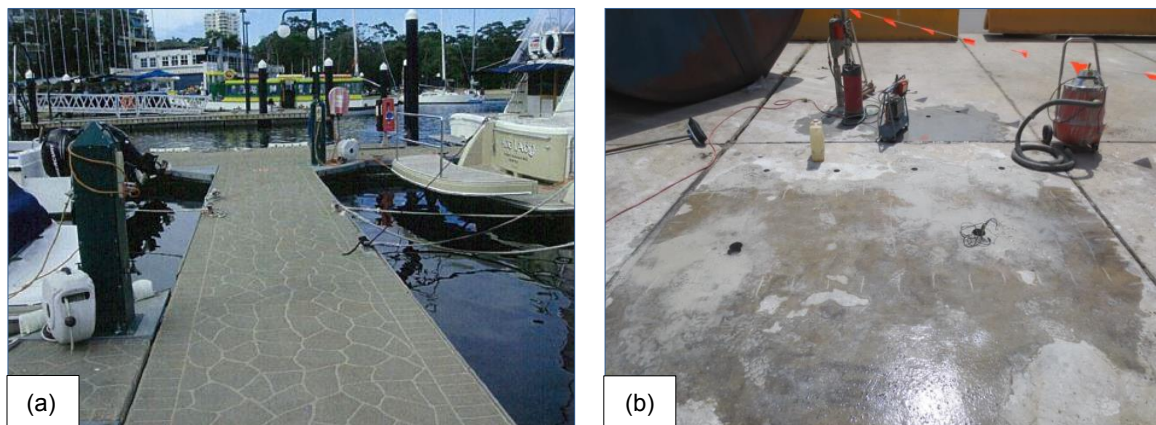


Figure 7. Cronulla Marina (a) and Lascelles Wharf (b) current conditions

### 4.2.2 Half-Cell Potential Results

The results of half-cell potential measurements of both concrete slabs are summarised in Table 8.

Table 8. Half-cell potential measurements for both concrete slabs

Project	Total Points	Max. Potential [mV]	Min. Potential [mV]	Average [mV]
Cronulla Marina	189	-140	-280	-154
Lascelles Wharf	96	52.9	-243	-51.3

Results indicated no corrosion activity in the concrete slabs. In Cronulla Marina the minimum potential was related to the area influenced by the exposed fittings fix on the slab at that point.

### 4.2.3 Chloride Content

The results of chloride content measurements are presented in Table 9.

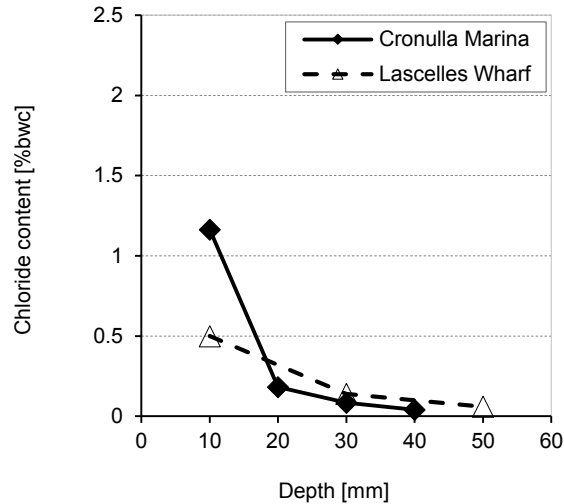
Table 9. Chloride content measurements

Average Depth [mm]	Cronulla Marina	Lascelles Wharf
	Chloride Content [% by weight of cement]	Chloride Content [% by weight of cement]
10	1.163	0.5
20	0.183	-
30	0.085	0.14
40	0.040	-
50	-	0.06

Considering the environmental exposure conditions, the chloride content measurements of both RC structures demonstrate a high quality of concrete after 19 years of exposure. For Cronulla Marina, to further quantitatively evaluate the resistance of crystalline modified concrete to chloride penetration, the chloride diffusion coefficient of the concrete was also calculated utilising Fick's second law and it



revealed an effective chloride diffusion coefficient of  $8.0 \times 10^{-14} \text{ m}^2/\text{s}$ . This chloride diffusion coefficient value is significantly lower than the high quality conventional concrete available in the literature. Chloride profile for the structures is shown in Figure 8.



**Figure 8. Chloride profiles for the structures**

## 5. Residual Service Life of the Structures

The free-corrosion service life for each structure has been calculated using chloride profiles and Fick's 2nd law. The design service life for both structures has been 50 years.

The free-corrosion service life of reinforced concrete structures is defined as the time required for the chloride concentration to reach to chloride threshold level (approximately 0.4% by weight of cement) at the steel reinforcement surface. The minimum concrete covers used in Fick's second law for Cronulla Marina and Lascelles Wharf were 40 mm and 51 mm, respectively.

The predicted residual corrosion-free service lives of structures are presented in Table 10.

**Table 10. Predicted residual corrosion-free service life for the structures**

Project	Residual Service Life [years]
Cronulla Marina	129
Lascelles Wharf	164

According to the calculations, crystalline technology increased the service life of the Cronulla Marina and Lascelles Wharf by approximately 100 years and 130 years compared to design service life, respectively.

## 6. Conclusions

This paper presented laboratory and field investigations on mechanical properties and durability performance of crystalline modified concrete. Compressive strength, AVPV, water permeability, and chloride diffusion characteristic of the concrete samples were examined as experimental investigation. Half-cell potential and chloride content were measured as the criteria for durability assessment of the reinforced concrete structures as case studies. Eventually, corrosion-free service lives for both experimental and case studies were calculated utilising Fick's second law. The conclusions of investigations can be summarised as follows:

- Non-soluble crystalline formation in concrete blocks the pores and heals the cracks permanently.
- Sorptivity and water permeability of concrete decreased by crystalline technology considerably.

- Crystalline modified concrete increased the compressive strength of concrete up to 31% for fly ash concrete and 10% for slag concrete.
- Crystalline modified concrete showed an excellent long-term performance in severe environmental exposure conditions.
- Chloride diffusion coefficient value in CMC confirmed that the interconnected pores in microstructure of the concrete have been blocked by crystals.
- By blocking the pores and healing the cracks by crystals formation in concrete, actual service life of the structure have been extended significantly.
- Increasing durability of the concrete can definitely reduce the maintenance and repair costs of the RC structures exposed to severe environment.
- Increasing service life of the structure will reduce the demand of raw materials such as aggregates, water, and cement in future which subsequently, will decrease the environmental impact. By enhancing the lifetime performance of the structure and environmental impact, concrete structure sustainability has been achieved.

## 7. References

1. Ann, K.Y., Ahn, J.H. & Ryou, J.S. 2009, 'The importance of chloride content at the concrete surface in assessing the time to corrosion of steel in concrete structures', *Construction and Building Materials*, vol. 23, no. 1, pp. 239-45.
2. Song, H.-W. & Kwon, S.-J. 2009, 'Evaluation of chloride penetration in high performance concrete using neural network algorithm and micro pore structure', *Cement and Concrete Research*, vol. 39, no. 9, pp. 814-24.
3. Costa, A. & Appleton, J. 1999, 'Chloride penetration into concrete in marine environment—Part I: Main parameters affecting chloride penetration', *Materials and Structures*, vol. 32, no. 4, pp. 252-9.
4. Zornoza, E., Garcés, P., Payá, J. & Climent, M.A. 2009, 'Improvement of the chloride ingress resistance of OPC mortars by using spent cracking catalyst', *Cement and Concrete Research*, vol. 39, no. 2, pp. 126-39.
5. Ann, K.Y. & Song, H.-W. 2007, 'Chloride threshold level for corrosion of steel in concrete', *Corrosion Science*, vol. 49, no. 11, pp. 4113-33.
6. Koleva, D.A., Hu, J., Fraaij, A.L.A., van Breugel, K. & de Wit, J.H.W. 2007, 'Microstructural analysis of plain and reinforced mortars under chloride-induced deterioration', *Cement and Concrete Research*, vol. 37, no. 4, pp. 604-17.
7. Maruya, T., Takeda, H., Horiguchi, K., Koyama, S. & Hsu, K.-L. 2007, 'Simulation of Steel Corrosion in Concrete Based on the Model of Macro-Cell Corrosion Circuit', *Journal of Advanced Concrete Technology*, vol. 5, no. 3, pp. 343-62.

# ISO 16204 and the Correct Solution to Fick

Norwood Harrison  
Humes Operations & Engineering

**Abstract:** In marine environments, chloride penetrates into concrete by diffusion, following a relationship known as Fick's second law. For a diffusion coefficient which varies with time, the Fick relationship differs from that applicable for a constant value, but there has nonetheless been widespread use of the constant-value form, with the diffusion coefficient (as would be measured by standard test) replaced by a related property having a different value. ISO 16204 presents guidelines for calculating chloride concentration at reinforcement depth, citing another publication as a source of input values. Both publications employ the alternative diffusion property, but values are easily converted to actual diffusion coefficients which can then be adopted in the correct Fick relationship. ISO 16204 does not endorse any model for estimating the remaining life after a threshold chloride level has been reached; in effect the threshold signifies the whole-of-life limit state and the resulting inherent conservatism is offset by relaxed target reliability. This development is taken here as an opportunity to re-asses values of the threshold to be used in design, referring to site investigations and the levels allowed by the provisions of Standards which reflect actual experience with marine exposure.

**Keywords:** concrete, chloride, marine, diffusion, fick.

## 1. Introduction

Modelling penetration of chloride into concrete has been through several phases, and is simplified in ISO 16204 "Durability – Service life design of concrete structures" (2012) to allow the concentration at chosen depth and time of exposure to be calculated from the initial chloride content, surface concentration during exposure and a time-dependent property of the concrete related to the diffusion coefficient. The International Standard does not itself provide representative or generic values for inputs, some of which are not obtainable from short-term measurements or observations but are nonetheless required in order to apply the model. For such data it nominates Concrete Society Technical Publication no. 61 (1), published prior to ISO 16204 and subsequently referred to here as TR61. Formulae in TR61 and ISO 16204 yield the same value for chloride concentration above the initial level, at any chosen depth or time of exposure.

## 2. ISO 16204 and the Correct Solution to Fick

TR61 introduces terminology "apparent diffusion coefficient" to denote a time-dependent property of the concrete related to diffusion, derived from measurements of chloride concentration in exposed concrete over an extended period of time. Quoting from TR61, "These values of apparent diffusion coefficient were then used in conjunction with the error function solution to Fick's second law of diffusion - - to predict rates of chloride ingress." At the time of publication of ISO 16204 it was known that the relationship given for calculating the concentration of chloride  $C(x,t)$  at any chosen depth and time of exposure is not in fact a solution to Fick's second law for a variable diffusion coefficient (2). To distinguish the "apparent diffusion coefficient" from actual values obtained by tests for this property. ISO 16204 provides explanation:

"The "apparent" diffusion coefficient after a period  $t$  of chloride exposure,  $D_{app}(t)$ , represents a constant equivalent diffusion coefficient giving a similar chloride profile to the measured one for a structure exposed to the chloride environment over a period  $t$ ."

This embodies the intention of obtaining values from exposed structures, but fails to clearly distinguish "apparent" from actual diffusion coefficients as obtained from tests such as Nordtest Build 443 (3), as this also assumes a constant value for the duration of the test. Such tests can be carried out on concrete at any age and as noted in TR61 (Figure 11.3 of that publication) yield widely different values from the apparent diffusion coefficient. TR61 shows the discrepancy but offers no explanation of its size. To some extent Nordtest Build 443 reflects early age exposure and so at early age the "apparent" coefficient is likely to be close to the value obtained from this test. Apparent diffusion coefficient applied using the ISO 16204 formula gives correct predictions only if values have been derived from long-term exposure, which in most instances will eliminate the use of this property for qualifying a new material.

The “apparent” diffusion coefficient is not in fact a diffusion coefficient at all in the context of Fick and is better referred to in a way which avoids any ambiguity, for which purpose it is suggested that the term “diffusivity” would be appropriate. Where the diffusion coefficient diminishes with time, diffusivity has a larger value than the diffusion coefficient.

The rate of change with time of either diffusion coefficient or diffusivity is denoted by an “age factor”  $n$ , which experimental data put in a range (approximately) from 0.25 to 0.7, higher values indicating a greater reduction in the property over time, as is obtained particularly with blended cements. The expression for  $C(x,t)$  using diffusivity has inputs of surface concentration of chloride, age factor and diffusivity at a chosen age. As well as replacing diffusivity with the diffusion coefficient, the solution to Fick has an additional input equal to the age of the concrete at the start of the exposure period, or an equivalent time depending on the curing treatment which the concrete has undergone. As it may be found elsewhere (2, 4), the algebraic expression of the solution to Fick is not reproduced here. However it is a property of the expression that when the time of exposure to the chloride environment greatly exceeds that prior to exposure, the effect of the pre-exposure time is diminished, allowing comparison with the relationship in ISO 16204 for which there is no input of this variable. If the ratio of diffusion coefficient to diffusivity is set at  $(1-n)$ , the two relationships converge. Conversely, data derived from exposure times long enough for the approximation to apply will yield the same value of  $n$ , whether fitted to the diffusivity relationship or the correct solution to Fick. Furthermore for the same inputs both relationships yield similar values of chloride concentration (identical if the pre-exposure time is set to zero), provided diffusion coefficient and diffusivity are set in a ratio  $(1-n)$ .

Table 1 shows values over time of the ratio of diffusion coefficient to diffusivity, this ratio being independent both of chloride levels and the depth at which concentrations are measured. It can be seen firstly that at high values of  $n$ , diffusivity has a much larger value than the diffusion coefficient; secondly that over time the ratio of the two measures converges to  $(1-n)$ , more rapidly with lower than higher values of  $n$ . At 20 years the ratio approximates to  $(1-n)$  even for the highest  $n$ -value encountered.

**Table 1. Convergence of the ratio diffusion coefficient / diffusivity**

n	(1-n)	Ratio diffusion coefficient / diffusivity for years exposure			
		0.3	1	5	20
0.3	0.70	0.80	0.74	0.72	0.70
0.5	0.50	0.64	0.57	0.53	0.51
0.7	0.30	0.52	0.43	0.37	0.34

Values for 7 days equivalent age prior to exposure.

TR61 provides typical or average values for diffusivity at 20 years, for a range of cement types and water/cement ratios. These are readily converted to 20-year values of diffusion coefficient simply by multiplying by  $(1-n)$ .

An explanation is provided immediately of the discrepancy between diffusivity and diffusion coefficient in the example from TR61 referred to above, which showed values of diffusivity more than double those of the diffusion coefficient. However it also shows up the possibility of gross error if diffusion coefficient should be used instead of diffusivity in the expressions set out in TR61 and ISO 16204. The spreadsheet provided with TR61 will accept either without distinction.

Replacing diffusivity with diffusion coefficient also removes an otherwise puzzling anomaly in the values for diffusivity provided in TR61 for portland cement (PC) and blended cement, in which contrary to the general understanding of properties blended cement exhibits higher diffusivity at an early stage of the exposure period. The effect is illustrated in Table 2, using fly ash blend as the example for blended cement.

At 1 year, PC concrete exhibits similar diffusivity to fly ash blend, while at 56 days the value is much lower; ie the diffusivity values would suggest that throughout most of the first year, chloride diffusion into PC concrete would be less than into concrete made with blended cement. With values of diffusion

coefficient derived from the same data the anomaly is removed, showing better chloride resistance for the blended cement throughout this period.

**Table 2. Representative values from TR61.**

Age of concrete	Diffusivity E-12 m <sup>2</sup> /s		Diffusion coefficient E-12 m <sup>2</sup> /s	
	PC	FA blend	PC	FA blend
56 days	2.7	5.0	2.0	1.7
1 year	1.6	1.5	1.2	0.5

Blend is fly ash 25%; w/c = 0.4 for both cement types  
 Values of diffusivity and age factor were obtained using the spreadsheet Ageddca in TR61.

Diffusion coefficients derived from TR61, obtained by multiplying the 20-year diffusivity by (1-n), can be applied directly for the purpose of design via the correct solution to Fick's second law, provided the cement (PC or blended) is known to be "typical or average" with regard to this property. A short-term diffusion test such as Nordtest Build 443 will indicate whether the cement proposed for a particular project does in fact have typical or average performance, provided other such short-term data are available for comparison. There are uncertainties associated with extrapolating 20-year diffusion coefficients back to a typical test age of 56 days, but the fly ash blend in Table 2 nonetheless provides a point of interest. In this example the extrapolated value for 56 days is 1.7E-12 m<sup>2</sup>/s. Results of this order are in fact obtained from fly ash blend using a good quality fly ash, reflected in a limit of 2.0E-12 m<sup>2</sup>/s (at 56 days standard cured) often specified for such a blend.

If it is impractical with locally available materials to achieve an initially specified 56-day diffusion coefficient there is the option of a revised design based on a higher w/c than would otherwise have been applied. Further to the fly ash example above, assuming that

- for cement materials of "typical or average" quality, w/c = 0.4 gives 2.0E-12 m<sup>2</sup>/s;
- the best achievable with local materials is 2.5E -12 m<sup>2</sup>/s;
- 2.5E -12 m<sup>2</sup>/s is obtained with the "typical or average" materials at w/c = 0.43;
- the design is revised to give the required performance with input w/c = 0.43,

local materials can be adopted, and the mix must then achieve a 56-day result of 2.5E -12 m<sup>2</sup>/s.

### 3. Threshold and progress of corrosion

#### 3.1 Threshold for corrosion

Immersed in air-saturated water containing chloride and having neutral pH, steel will rapidly corrode. If cement is dispersed into such a solution, the pH is raised to about 12.5, and immersed steel will remain uncorroded at surprisingly high concentrations of chloride – three times or possibly even higher than are found in sea water (5). Thus depassivation of reinforcing steel resulting from marine exposure depends on chloride from the seawater having at some stage become concentrated by evaporation. At average levels of surface chloride reported in TR61, moisture filling permeable voids (occupying a typical proportion of the concrete, as determined by the test for this property) has a concentration below what would be required in solution to depassivate the steel. One may conclude that, even if oxygen is present in the pore water, for corrosion to proceed there must be a further enhancement of the chloride concentration by some drying of the void space, and that whether or not the steel corrodes depends on the extent of such drying. A threshold level for initiation of corrosion then depends on other factors than just the concentration of chloride as a proportion of the concrete mass or of the cement. This is born out by observation, reported in TR61:

"Reported threshold levels vary from 0.25% to 2.5% (a tenfold difference), indicating that there is unlikely to be a fixed value for a given concrete."

and

“The commonly used value of 0.4% Cl (weight of cement) appears to be most applicable in conditions of wet/dry cycling of high (>0.6) w/c ratio mixes, whereas in mixes of low w/c ratios, under more stable moisture conditions, higher values may be tolerated.”

Some examples are included here for illustration.

Concrete ships (6):

The condition of reinforcement was examined in concrete ships moored or in service for 35 to 65 years. In two of the examples described, cover to reinforcement was in the range 10 to 25 mm, and chloride levels up to 1.2% of the cement were found at reinforcement depth. Reinforcement extracted from cores taken above and below the water line showed no evidence of corrosion.

Prefabricated harbour structures (7)

Harbour structures with pontoons made from reinforced concrete were deployed in northern France in June 1944 to offload cargo on beaches during the allied invasion of Normandy. The pontoons from one of these, Mulberry B, which came to be known as Port Winston, continued their exposure to the marine environment after the war and were inspected nearly 30 years later. It was reported that no corrosion of reinforcement was evident where cover exceeded 12 mm. Estimated chloride concentration at this depth is 0.9% of the cement.

Port Kembla swimming pool (8)

The Port Kembla seawater swimming pool, built in 1937, was exposed to a marine environment with some components permanently submerged, and others in the tidal or splash zone. The condition of concrete comprising the pool was assessed after 60 years of exposure. Of particular interest are reinforced concrete columns in the atmospheric zone, which exhibited concentrations of chloride essentially independent of depth from about 30 mm from the surface, and *lower* concentrations close to the exposed surface. The chloride threshold for steel corrosion was in the range 2.4 to 3.0% of the cement. Some of the stable interior chloride concentrations were as low as 0.6% of the cement, indicating that the levels leading to corrosion were derived from the exposure, not from chloride present in the concrete at the outset.

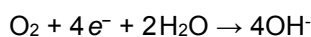
Concrete pipe (9)

Two cores were cut from a 900 mm diameter concrete pipe protruding through the sea wall into Hen and Chicken Bay, Sydney. Age of the installation was approximately 55 years. The concentration of chloride at the interior of the section including the reinforcement (cover in the range 8 to 18 mm) was about 4% of the cement. As with the Port Kembla swimming pool, there was a lower concentration, between 1.2 and 3.0%, at the surfaces of the concrete. As part of an overall petrographic investigation, reinforcement sections were examined, one showing no surface reactions and the other minor amounts of iron oxide and hydroxide.

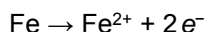
### **3.2 Progress of corrosion and damage to the concrete**

TR61 also presents a model for calculating a further time following initiation of corrosion, at which the concrete will crack. This time is derived from the rate at which corrosion occurs and the ability of the concrete to accommodate rust formed from the corroded steel. It may be questioned whether the rate of corrosion after initiation can be calculated with any useful degree of accuracy and further where the rust will actually form, if at all. In the corrosion process, cathode sites formed where there is oxygen present draw electrons from the steel to form negatively charged hydroxyl ions in the electrolyte, also rendering the steel positively charged. Metallic iron is released into the solution at anode sites as ferrous ions  $Fe^{2+}$ . In the absence of oxygen ferrous ions may subsequently combine with hydroxyl ions from the electrolyte to form ferrous hydroxide, which is insoluble and non-expansive. Elsewhere, ferrous ions combine with oxygen and water to form (expansive) rust. The relevant equations are:

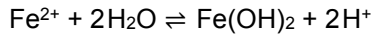
Cathode:



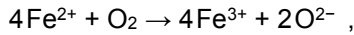
Anode:



In the electrolyte:



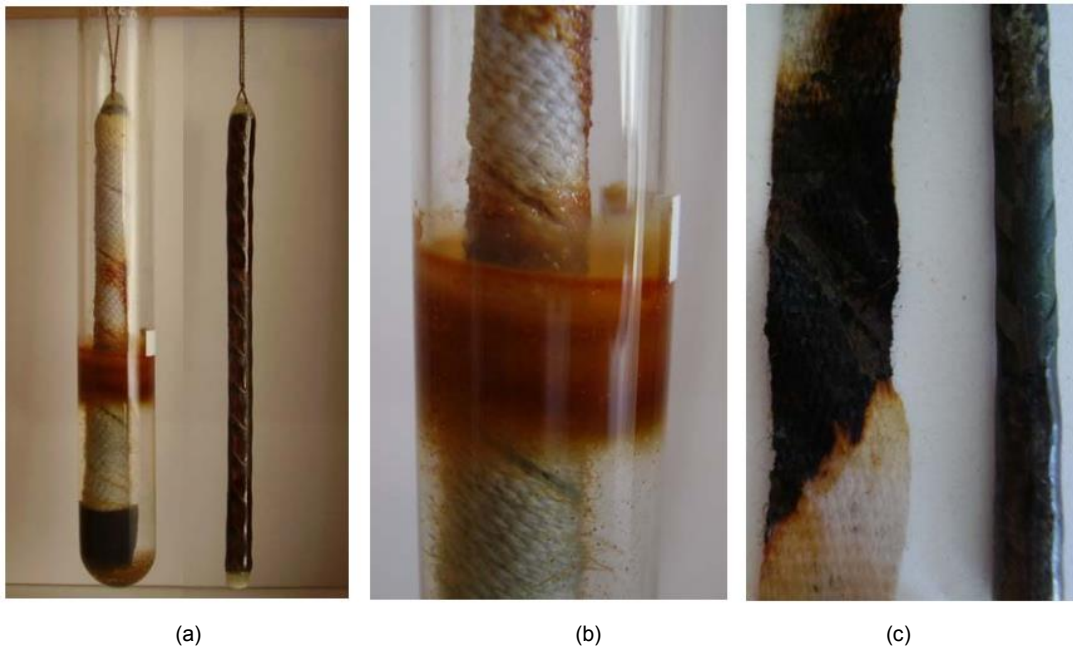
or if there is oxygen present,



the ferric ions together with oxygen and water being subsequently converted to rust.

Concrete in which steel is corroding will often exhibit highly visible rust staining on the surface, showing that ferrous ions or soluble compounds containing iron are able to diffuse in quantity away from the steel surface, and that some proportion of the metallic iron released at anode sites is only converted to the expansive, insoluble rust where oxygen is encountered at the surface.

The mechanism is illustrated in Figure 1, in which a piece of reinforcing wire, wrapped in cotton tape to simulate embedment in concrete, is immersed in a weak solution of sodium chloride. The first two photos (a) and (b) show the immersed sample, with rust formed outside the cotton wrap, near the water surface. In (c), the tape has been removed from the wire, revealing black hydroxide, but not rust, extending to the full depth to which the steel surface was in contact with the solution.



- (a) Immersed sample & twin piece of wire. Epoxy coating extends about four diameters (20 mm) from the lower end. Water level is at mid-height of the white paper strip.
- (b) Close-up of rust formation outside the cotton wrap.
- (c) Tape unwrapped from the steel wire.

**Figure 1. Reinforcing wire wrapped in cotton tape, immersed in dilute salt solution**

There are no doubt situations where rust forms on the surface of steel embedded in concrete, when passivity is lost either due to carbonation, chloride, or both, and cracking will be induced as a result, but the situation is by no means universal. Corroded steel in concrete commonly exhibits a black rather than red appearance and in these circumstances the expansive rust model described in TR61 simply will not apply.

The process has been described here as an explanation in part of the broad conclusion expressed in ISO 16204, Clause B.7:

“As with carbonation, there were no available models with broad international consensus available for predicting the length of the corrosion period till cracking, spalling or collapse of the structure occurs when this Standard was published. For this reason service life designs are normally based on the limit state of depassivation (reaching a critical a chloride concentration at the rebar

surface). As with carbonation, this rather conservative limit state is then normally linked with a relaxed target reliability level for failing, often in the order of  $10^{-1}$  to  $10^{-2}$ .”

In effect the design procedure treats the time for chloride to reach a threshold value as the whole-of-life for the structure. This by itself could be sufficient reason to adjust the threshold to a higher value than the level of 0.4% of the cement commonly applied. The above examples indicate that in some types of concrete the steel remains passive at much higher levels of chloride – in fact to equilibrium levels for at least the milder class of marine exposure, corresponding for example to C1 in AS 3600. For this situation the required depth of cover is not related to the ability of the concrete to slow ingress of chloride, but to maintain a stable moisture environment at reinforcement depth. For this purpose the crucial property is impermeability, low values depending on low w/c and being achievable with any cement type. Improved performance in marine exposure is obtained with concrete containing a high level of available alkalinity from calcium or magnesium (10), presumably because these are able to neutralise acidity generated by hydrogen ions released near anode sites at the steel surface. Calcium or magnesium carbonates may be present in aggregates while calcium is contributed by the cement. It can be assumed in the examples described in 3.1 above that the binder was portland cement, which for a given cement content will contribute a greater amount of alkalinity than blended cements (with fly ash or silica fume) in which no calcium is provided by the SCM.

#### 4. Chloride threshold for whole-of-life design

In its discussion of threshold values for chloride TR61 has reservations as expressed above about tangible evidence for a universal limiting value, but the point remains that where surveys of structures take no account of the composition or quality of the cover concrete, lower concentrations of chloride are associated with lower probability of corrosion. At 0.4% of the cement there is a low probability even of initiation; however achieving this level at the end of the design life may be expensive or even impractical and if the life can be achieved with a higher terminal level of chloride, the design method should allow this option.

Using the method set out in Section 2 above, with 20-year typical or average diffusivity from TR61 converted to diffusion coefficient and calculation using the correct solution to Fick, chloride concentrations at the end of the design life can be derived for examples encompassed by Standards or specifications. For any well-founded and widely accepted such specification, such calculations provide chloride threshold values which may then be applied elsewhere in design. Table 3 shows chloride concentrations at the end of design life, within the scope of the two generic Australian Standards, AS 3600 and AS 5100.5, and the corresponding British Standard BS 8500-1.

**Table 3. Chloride concentrations at design life**

Source	Exposure Class	Design life (y)	Chloride at minimum cover depth (% cem) for cement type	
			PC	FA blend
AS 3600	C1	50	0.92	0.27
	C2	50	1.09	0.20
AS 5100.5	C	100	2.07	0.33
BS 8500-1	XS3	50	1.30	0.33
	XS3	100	1.28	0.26

Blend is fly ash 25%; w/c = 0.4 & total cement 400 kg/m<sup>3</sup> for both cement types.

For AS 3600 & AS 5100.5, strength grade is 50 MPa and covers are those applicable to rigid formwork & intense compaction.

For BS 8500-1, selected cover is that allowed for maximum w/c 0.4.

For exposure class C1, surface chloride is the “typical” value from TR61; for other classes, those described as “characteristically high”.

Initial chloride 0.03% of the concrete, 0.19% of the cement.

The most striking pattern shown by this table is the contrast between levels allowed for PC and the example of blended cement. Even so, the highest for PC, 2.07% of the cement, is below levels in examples above (section 3.1) exhibiting no corrosion after exposure for up to 60 years. A reasonable



design limit for PC would be 1.5% of the cement. Given the margin between this and the nominally applied 0.4% for any cement type, there no longer appear to be any grounds for requiring such a low value for blended cement either and the limit for this type could be increased to 0.5 or even 1.0%. However both these proposals require qualification. The examples apply to situations where the specification limits the water/cement ratio to about 0.4 and also specifies a minimum cover. If either of these were relaxed the result could be a greater effect from the chloride at the allowed threshold values. Thus there is no immediate prospect of lower cover or grade of concrete. The effect of higher thresholds is to allow a wider choice of materials, where a limit is imposed on the diffusion coefficient as well as other requirements of the specification.

## 5. Conclusion

For long periods of exposure, as apply to the design life of a structure, inputs required for calculating chloride concentrations using the correct solution to Fick are provided by a simple adaptation of data from TR61. ISO 16204 does not acknowledge any model for life following a threshold level of chloride at reinforcement depth, in effect treating the time to reach the threshold as the design life of the structure. Observations of structures reveal concentrations of chloride required to initiate corrosion over too wide a range (more than an order of magnitude) for a single value to be used in design, and for this purpose the best indication of acceptable limits is obtained by estimating the end-of-life concentrations allowed by well-founded existing Standards. However the effect of chloride depends on other factors including alkali content of the cement and aggregate, and ability of the concrete to stabilise moisture at cover depth. Specified cover cannot be reduced just because a nominated threshold of chloride is not reached within the required service life.

## 6. References

1. Bamforth, P., "Enhancing reinforced concrete durability", Technical Report No. 61, The Concrete Society, 2004.
2. Tang, L., Gulikers, J., "On the mathematics of time-dependent apparent chloride diffusion coefficient in concrete", Cement and Concrete Research 90, 2007, pp 589-595
3. Method NT Build 443, "Concrete, hardened, accelerated chloride penetration", Nordtest, 1995.
4. Harrison, N., "The correct solution to Fick's law for variable diffusion coefficient", Concrete in Australia 40 (4), 2014, pp 38-41.
5. Harrison, N., "Concrete pipe in tidal flow or saline ground conditions", Concrete Pipe Association of Australasia, 2007.
6. Hofsoy, A., Hafskjold, P., "A survey of up to 60 Years old concrete ships in subarctic environment", FIP Notes, 1983/2.
7. "Concrete durability", letter to the editor of "Concrete", Dec. 1973.
8. Khatri, R., Guirguis, S. et al., "60 years service of Port Kembla concrete swimming pool", 2001.
9. Baker, C., "Durability of concrete Pipe in a Marine Environment", Concrete Pipe Association of Australasia, 2000.
10. Melchers, R., "Carbonates, carbonation and the durability of reinforced concrete marine structures", Australian Journal of Structural Engineering 10 (3), 2010, pp 215-225.

# *k*-value for carbonation of concretes with supplementary cementitious materials

Christina Nobis<sup>1</sup> and Anya Vollpracht<sup>2</sup>

<sup>1</sup>Research Assistant, Institute of Building Materials Research, RWTH Aachen University, Germany

<sup>2</sup>Junior Professor for Environmental Compatibility of Building Materials, Institute of Building Materials Research, RWTH Aachen University, Germany

**Abstract:** The performance of supplementary cementitious materials (SCM) such as fly ash (FA) or ground granulated blast furnace slag (GGBS) in concrete can be assessed by the *k*-value concept according to the Technical Report of the European Committee for Standardization CEN/TR 16639. This prescriptive method determines the performance of SCMs as concrete additives of type II in terms of concrete compressive strength. In recent years, the importance of durability aspects has become more apparent. Carbonation is generally one key issue for concrete with GGBS or FA. The integration of durability aspects into the *k*-value concept is a promising approach to the performance assessment of SCMs. This study presents results from a data evaluation of about 290 concrete mixtures with and without GGBS or FA. The analysis of the data is carried out based on the *k*-value concept and determines *k*-values for carbonation (*k<sub>c</sub>*) in relation to the SCM-content of the binder.

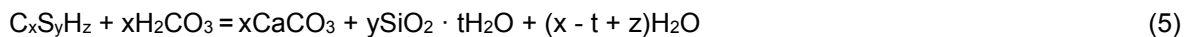
**Keywords:** carbonation, durability, granulated blast furnace-slag, fly ash, blended cement.

## 1. Introduction

Carbonation is one key aspect for the durability of reinforced concrete structures as it may induce steel corrosion. The pore solution of uncarbonated concrete with OPC usually exhibits a pH value in the range of 13.0 to 13.8 [1] due to the dissolution of alkali ions and OH<sup>-</sup>. Calcium hydroxide (Ca(OH)<sub>2</sub>) which was formed during cement hydration acts as a buffer for the alkalinity. Under these conditions, the steel forms a surface oxide layer, termed passive film. The atmospheric carbon dioxide (CO<sub>2</sub>) diffuses into the pore structure of the concrete, either dissolved in water or as gas. It dissolves in water and forms carbonate ions in the highly alkaline pore solution (equations (1) and (2)). The carbonate ions react with calcium ions in the pore solution to calcium carbonate (CaCO<sub>3</sub>) (equation (3)). This process reduces the calcium ion content in the pore solution and thus leads to the dissolution of crystalline Ca(OH)<sub>2</sub>, which has a lower solubility than CaCO<sub>3</sub> (equation (4)) [2].



This process continues until all Ca(OH)<sub>2</sub> in the affected area is consumed. The pH value of the pore solution will decline to a range of 8 to 9. In this condition the protective passive film of the steel reinforcement dissolves and, in the presence of water, corrosion may occur. The precipitation of the CaCO<sub>3</sub> will lead to a densification of the pore structure of the cement matrix due to the increase in volume when Ca(OH)<sub>2</sub> is transformed into CaCO<sub>3</sub>. The permeability of the carbonated area is reduced. Carbonation also effects the calcium-silicate-hydrate phases (C-S-H). When the Ca<sup>2+</sup> content in the pore solution is reduced, calcium ions will be released from the Ca-OH bonds of the C-S-H phases. Eventually this will convert part of the C-S-H phases to porous hydrated silica gel (ySiO<sub>2</sub> · tH<sub>2</sub>O) (equation (5)) [3, 4].



However, the carbonation of concrete is generally a slow process due to the low carbon dioxide content of about 0.03-0.04 vol.-% under natural environmental conditions. In general, concrete with OPC is more resistant to carbonation than concrete with GGBS or FA. The carbonation depth increases as cement replacement by SCM increases [5, 6, 7]. This is due to the reduced amount of Ca(OH)<sub>2</sub> in concrete with GGBS or FA. The Ca(OH)<sub>2</sub> content decreases in proportion to the replacement ratio and furthermore to the extent of the pozzolanic reaction (in case of FA). Therefore, the coarsening mechanism based on C-S-H modification outweighs the densification mechanism caused by CaCO<sub>3</sub> precipitation. This may

negatively affect other concrete properties such as freeze and freeze-thaw resistance [8] or chloride diffusion coefficient [9]. However, in concrete with OPC it is assumed that the formation of  $\text{CaCO}_3$  causes pore blocking which reduce further carbonation. On the other hand, concrete with GGBS or FA usually exhibits a refined pore structure and thus improved permeability [9, 10].

To assess the performance of SCMs in concrete such durability aspects have to be accounted for. In Germany, the efficiency of SCMs in concrete is determined via comparative analyses of concretes with and without SCM. The compressive strength is considered a proxy for durability. The principle method behind this is the prescriptive  $k$ -value concept. The concept was introduced by Iain A. Smith in 1967 for the design of fly ash concrete and has been further developed [11]. The  $k$ -value concept was established for FA (EN 450-1) and silica fume (EN 13263-1) in the European concrete standard EN 206-1 in 2000. The principle for the determination of the  $k$ -value is described in the Technical Report of the European Committee for Standardization CEN/TR 16639 [12]. It is used for the calculation of the equivalent water/cement ratio ( $w/c_{\text{eq}}$ ) according to the following formula (equation (6)):

$$w/c_{\text{eq}} = w/(c + k \cdot \text{SCM}) \quad (6)$$

$w$  = water content in  $\text{kg/m}^3$ ,  $c$  = cement content in  $\text{kg/m}^3$ , SCM = SCM content in  $\text{kg/m}^3$ .

The efficiency factor  $k$  indicates the contribution of a type II concrete additive to the compressive strength of concrete with OPC.  $k$  reaches values between 0 (no contribution) and 1 (OPC-equivalent contribution) or even higher. The durability of the concrete with SCM designed using the  $w/c_{\text{eq}}$  must be assessed in subsequent tests. Based on extensive studies the National Annex DIN 1045-2 gives a default  $k$ -value of 0.4 for FA in combination with specific cement types and other restrictions. Most recently, a  $k$ -value of 0.6 for GGBS was introduced to the European Standard that shall cover the minimum quality for GGBS according to EN 15167-1. The integration of durability aspects into the  $k$ -value concept is a promising approach to the performance assessment of SCMs. Based on this analysis it can be determined to what extent the carbonation resistance is a limiting factor for the applicability of GGBS or FA concrete.

## 2. Materials and Methods

### 2.1 Database

The Institute of Building Materials Research in Aachen has an extensive database concerning the carbonation of concretes with and without supplementary cementitious materials collected from internal reports of material testing and from literature. In particular, the database includes data on the carbonation of concrete with OPC, GGBS and FA under laboratory conditions. In the analysis no differentiation was made between SCM as additive or main cement constituent for the calculation of  $w/c_{\text{eq}}$ . The concretes differ considerably concerning their water/binder ratio ( $w/b$ ) and composition. To that end, the concretes presented in the database were divided into different categories according to their GGBS/clinker and FA/clinker ratio, respectively. The database is summarised in table 1. However, given the amount of the data only the key information will be shown in this paper.

**Table 1. Summary of the database on carbonation of concretes with OPC, GGBS and FA**

category	No. of concretes	SCM/clinker		range of w/b		binder content ( $\text{kg/m}^3$ )			
		min	max	min	max	clinker <sub>min</sub>	clinker <sub>max</sub>	SCM <sub>min</sub>	SCM <sub>max</sub>
0 no SCM	70	0/100		0.50	0.75	235	320	-	
1 low	23	20/80	39/61	0.50	0.75	162	248	68	96
2 medium	37	40/60	49/51	0.53	0.75	122	174	95	146
3 high	36	50/50	59/41	0.50	0.75	105	165	120	190
4 very high	16	> 60/40		0.50	0.67	46	127	178	276
1 low	18	10/90	24/76	0.44	0.67	240	300	30	70
2 medium	33	25/75	29/71	0.43	0.75	169	270	60	90
3 high	60	30/70	40/60	0.36	0.75	159	321	70	241

w/b: water/binder ratio ( $b$  = clinker content + GGBS or FA content as concrete additive and cement constituent)

### 2.2 Materials

The cement types used in the concretes and the combinations with GGBS or FA are listed in table 2. In order to ensure better comparability only cements with a strength class of 32.5 were selected for this

analysis as there are no sufficient data sets for the assessment of concretes with cement types of higher strength. The Blaine fineness of the used GGBS differed considerably and ranged from 2675 to 5050 cm<sup>2</sup>/g. Both, GGBS and FA, were obtained from several European countries. All concrete mixtures were prepared using quartzitic sand and coarse aggregates from the river Rhine. The maximum aggregate size was in the range of 8 to 16 mm. The specimens investigated were concrete beams with different dimensions (100 · 100 · 500 mm<sup>3</sup> and 70 · 70 · 300 mm<sup>3</sup>).

**Table 2. Summary of the cement types and additives used for the concretes of the database**

SCM	category 0	category 1	category 2	category 3	category 4
GGBS	CEM I 32.5 R	CEM I 32.5 R + GGBS CEM II/B-S 32.5 R CEM III/A 32.5 N	CEM II/B-S 32.5 R + GGBS CEM III/A 32.5 N	CEM I 32.5 R + GGBS CEM III/A 32,5 N	CEM I 32.5 R + GGBS CEM II/B-S 32.5 R + GGBS CEM III/B 32,5 N
FA		CEM I 32.5 R + FA	CEM I 32.5 R + FA CEM II/B-V 32.5 R	CEM I 32.5 R + FA CEM II/B-V 32.5 R	-

See table 1 for definitions of the categories.

## 2.3 Methods

### 2.3.1 Testing of the carbonation depths

All concretes with few exceptions were stored under water until an age of 7 d. Afterwards the concrete specimens were kept in laboratory conditions at 20 ± 3 °C and 65 ± 5 % RH during the experimental period. For the analysis only concrete specimens with a storage period longer than 1 year were chosen. The oldest specimens were tested up to eight and a half years. The specimens were tested at different times (e.g. 7, 14, 28, 56, 90, 180, 365, 730, 1825 d). The carbonation depths of the concretes were measured using a solution, which consists of 1 % phenolphthalein in 70 % ethanol. The indicator appears pink in pH values above 9 and colourless at lower levels. Hence, concrete pieces with a thickness of 30 mm were split off at testing time and the indicator was sprayed on the freshly exposed surface. After 24 h the carbonation depth was measured as the average thickness of the uncoloured carbonated layer.

### 2.3.2 Determination of the $k_c$ -value

In order to assess the performance of the SCMs in concrete, an efficiency factor  $k_c$  for carbonation similar to the  $k$ -value according to CEN/TR 16639 [CEN European Committee for Standardization, "Use of  $k$ -value concept, equivalent concrete performance concept and equivalent performance of combinations concept (CEN/TR 16639)", CEN/TC 104, 2014, Brussels, Belgium.] for compressive strength must be defined. The carbonation rate  $v_k$  was chosen as a substitute for compressive strength. To calculate the carbonation rate the carbonation depths of each concrete mixture was approximated as a function of the square root of the exposure time (equation (7)):

$$x = x_0 + v_k \cdot \sqrt{t} \quad (7)$$

- $x$ : depth of carbonation in mm,
- $x_0$ : initial carbonation (usually very small or zero),
- $v_k$ : carbonation rate in mm/ $\sqrt{t}$ ,
- $t$ : exposure time in d.

This function was determined by linear regression for each concrete mixture. To ensure comparability, only the carbonation depths up to an exposure time of 1 year were included in the analysis. The rate of carbonation was plotted against the w/b ratio of the concrete mixtures for each category. Next, the correlation between carbonation rate and w/b ratio was determined for each category via linear regression (equation (8) and (9)).

$$\text{reference concrete without SCM: } v_{k,0} = A_0 + B_0 \cdot (w/c)_0 \quad (8)$$

$$\text{tested concretes with SCM: } v_{k,SCM} = A_{SCM} + B_{SCM} \cdot (w/b) \quad (9)$$

- $v_{k,0}$ : carbonation rates of concretes without SCM in mm/ $\sqrt{t}$ ,
- $v_{k,SCM}$ : carbonation rates of concretes with SCM in mm/ $\sqrt{t}$ ,

$(w/c)_0$ : w/c ratios of concretes without SCM,

w/b= w/b ratio with b = clinker content + GGBS or FA content as concrete additive and cement constituent.

Figure 1 highlights, by way of example, the linear regression for the carbonation rates of the concrete mixtures without SCM and with GGBS of category 3. From the left picture it is obvious that the GGBS concretes have higher carbonation rates and carbonation rates increase with w/b ratio. In the right figure the w/b ratio is replaced by  $w/c_{eq} = w/(clinker + k_c \cdot SCM)$ . The  $k_c$ -value is varied until the performance of GGBS concretes is equal to the OPC concretes. This is the case if the two regression graphs are aligned. A  $k_c$ -value of 1 represents an OPC-equivalent performance of the SCM in regard to carbonation, whereas a value of 0 would imply that the SCM has no effect. In the example shown in figure 1 the best alignment was found for a  $k_c$ -value of 0.70.

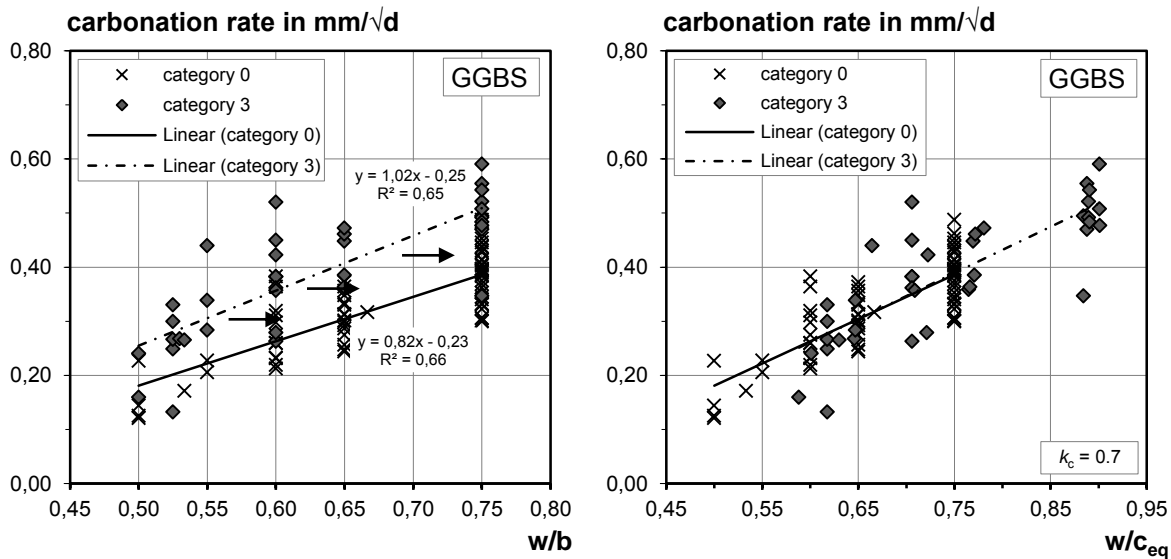


Figure 1. Exemplary illustration of the  $k_c$ -value determination

## 2.4 Results and Discussion

Figures 2 and 3 illustrate the spread of the measured carbonation depths of all concretes with and without GGBS and FA respectively up to an exposure time of 8.5 years. Since the process of carbonation is controlled by diffusion, the x-axis is shown in square root scale. The carbonation depths of all specimens increase almost linearly with square root of time. At the beginning of the testing period the carbonation rate is usually a bit higher than the carbonation rate at the end. In the database the majority of the concretes showed this behaviour. The reason for this is that the equation  $x = x_0 + v_k \cdot \sqrt{t}$  is based on a steady state performance with a constant carbonation rate over time. In reality, the carbonation process changes the microstructure of the affected concrete area and may cause a reduction of gas diffusivity. The carbonation depths of the concretes with SCM tend to be greater than those of the concretes with OPC. However, some concretes with GGBS or FA perform even better. Whether this might be ascribed to a refined pore structure or the concrete composition cannot be assessed.

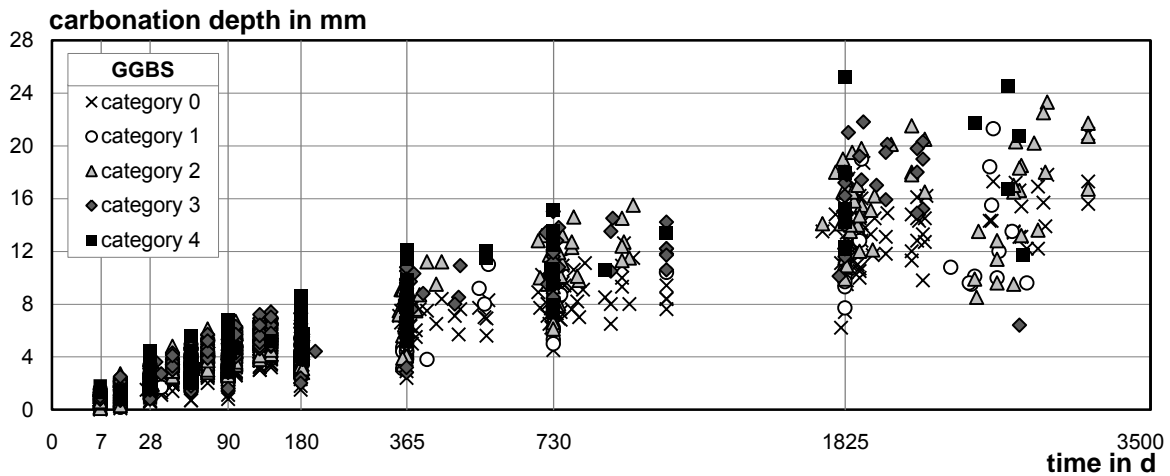


Figure 2. Carbonation depths for concretes with and without GGBS

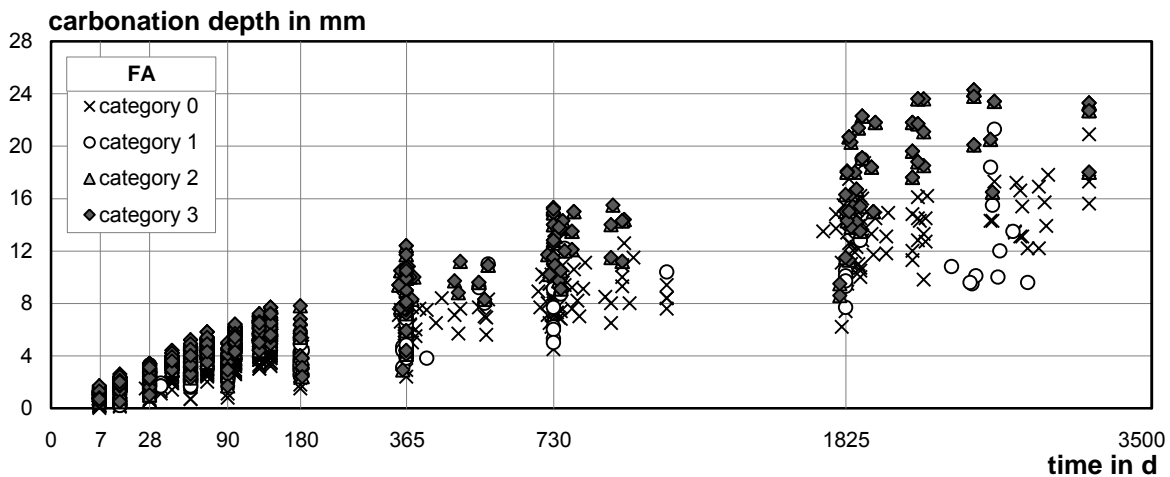


Figure 3. Carbonation depths for concretes with and without FA

The values show a rather big spread due to the wide range of concrete compositions and the different raw materials. To evaluate the influence of the SCM on the carbonation performance the carbonation rates are correlated with the  $w/C_{eq}$  ratio. A greater  $w/C_{eq}$  ratio produces a higher carbonation rate. This relation was plotted as a linear regression according to equations (8) and (9) for each category. The parameters of the linear regression and the determined  $k_c$ -value are shown in table 3 for each category. Figure 4 highlights the correlation of the carbonation rates and  $w/C_{eq}$ .

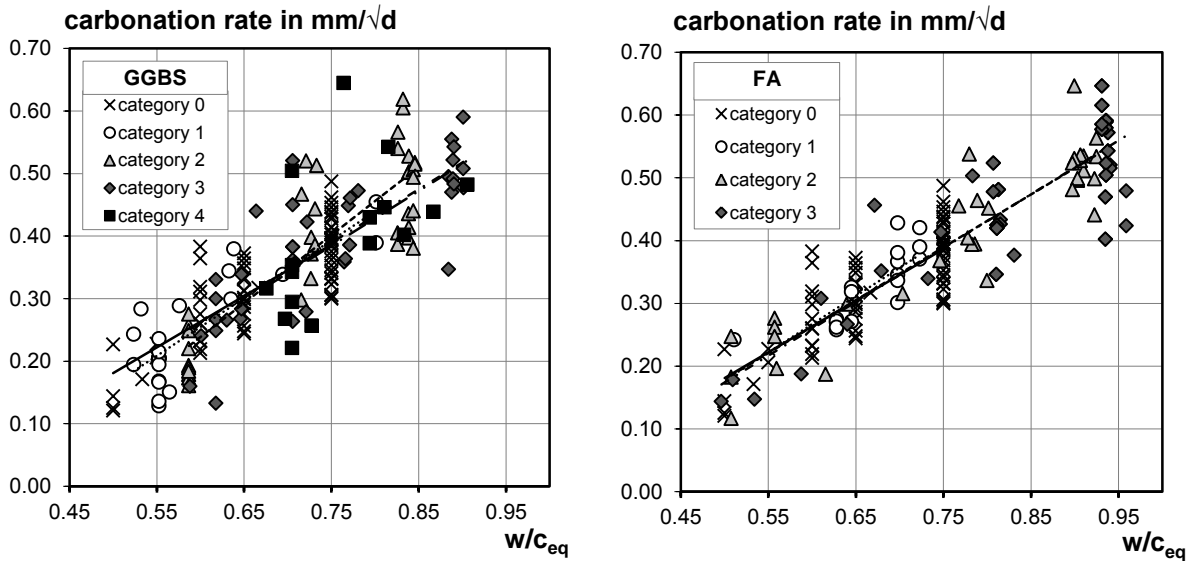


Figure 4. Correlation between carbonation rates and  $w/c_{eq}$  for concretes with and without GGBS (left) and FA (right)

Table 3. Summary of the database on carbonation of concretes with OPC, GGBS and FA

category	linear regression parameters			$k_c$ -value
	$A_0$ or $A_{SCM}$	$B_0$ or $B_{SCM}$	$R^2$	
0 none SCM	-0.23	0.82	0.66	-
1 low	-0.32	1.02	0.69	0.80
2 medium GGBS	-0.41	1.22	0.74	0.77
3 high content	-0.25	1.02	0.65	0.70
4 very high	-0.07	0.85	0.13	0.60
1 low	-0.17	0.84	0.63	0.30
2 medium FA	-0.26	1.05	0.86	0.35
3 high content	-0.19	0.98	0.74	0.34

See equation (8) and (9) for definitions of the linear regression parameters.

The coefficients of determination for all linear regressions graphs are not particularly high because of the large spread of data points. The comparison of the carbonation rates is only possible to a limited extent due to the differences in mixture composition and SCM quality. Since the focus of this analysis was to find a trend of the carbonation performance of blended concretes the poor coefficients of determination were considered sufficient, except for the GGBS blended concrete with more than 60 % GGBS in the binder. Nevertheless, the  $k_c$ -value for this category is included in the evaluation to indicate the trend.

In general, the efficiency factor for carbonation tends to decrease as the replacement percentage increases. This is particularly the case for GGBS blended concretes. The  $k_c$ -value ranges from 0.80 to 0.60 with increasing slag content. In comparison to the  $k$ -value of 0.6 that was introduced by EN 206 based on the 28 d compressive strength  $k_c$  is higher for categories 1 to 3.

Variation in FA content did not seem to have much effect on the  $k_c$ -value. This could be due to the small range of the investigated FA contents in present study. The  $k_c$ -value was found to be lower than the GGBS  $k_c$ -values. The  $k_c$ -value for concretes with a very low FA content (10 to 24 % of the binder) was 0.30 and for higher contents 0.35 and 0.34. Since the difference is very small it can be assumed that a constant  $k_c$ -value of approximate 0.3 complies for the investigated FA blended concretes. However, this efficiency factor seems to be low in comparison to the  $k$ -value of 0.4 which is used for the application of FA as concrete additive type II in Germany (DIN 1045-2). On the other hand, it is reasonable that the carbonation resistance of FA blended concretes is poorer than those blended with GGBS. The pozzolanic reaction of FA consumes  $Ca(OH)_2$  and thus may increase the carbonation rate.

### 3. Conclusions

In this paper, an efficiency factor  $k_c$  for carbonation was determined for concretes with GGBS and FA respectively based on the  $k$ -value concept described in CEN/TR 16639. To that purpose, a database of the carbonation performance of 290 concrete mixtures was evaluated.

- The  $k$ -value concept was initially linked only to the compressive strength. With the revision of the European concrete standard EN 206, durability aspects now have to be accounted for. However, no proposals were made for a concrete assessment method. The implication of the carbonation rate as a substitute for compressive strength in the well-known  $k$ -value concept is a promising tool to quantify SCM performance as concrete additive.
- The carbonation rate tends to slightly decrease over the testing period. Prognoses based on the carbonation rate of concrete measured very early, i.e. before one year, might lead to an overestimation of the carbonation depths.
- The performance of all concretes, even with equivalent binder concrete composition, exhibits a large spread. Some concretes with SCM perform even better than concretes without. This might be attributed to a refined pore structure due to the latent hydraulic or pozzolanic reaction.
- In general, the carbonation rate of concrete with GGBS or FA is higher compared to OPC concrete. This is expressed in the determined  $k_c$ -values  $< 1.0$  for all SCM concretes.
- The  $k_c$ -value ranges from 0.80 to 0.60 for GGBS concrete depending on the slag content. The carbonation rates for GGBS concrete are increased due to the lower amount of CH.
- The  $k_c$ -value of FA concrete does not differ appreciably with increasing FA content. However, the  $k_c$ -value of 0.3 is considerably low in comparison to the GGBS blended concretes. This might be attributed to the lower quality of the FA included in the database or to the consumption of CH in the pozzolanic reaction.
- The implementation of a durability based efficiency factor can be used for the assessment of blended concrete performance and proportioning of SCM. However, the efficiency factor might change with age, cement type, SCM content and curing conditions.

### 4. References

1. Vollpracht, A., Lothenbach, B., Snellings, R., Haufe, J.: "The pore solution of blended cements: a review", *Materials and Structures*. (*in preparation*)
2. Lagerblad, B., "Carbon dioxide uptake during concrete life cycle—state of the art", Swedish Cement and Concrete Research Institute (CBI), 2005, Stockholm, Sweden.
3. Pham, S. T., Prince, W., "Effects of Carbonation on the Microstructure of Cement Materials: Influence of Measuring Methods and of Types of Cement", *International Journal of Concrete Structures and Materials* 8(4), 2014, pp. 327-333. (DOI 10.1007/s40069-014-0079-y)
4. Borgesa, P. H. R., Costab, J. O., Milestonea, N. B., Cyril J. Lynsdaleb, Streatfield, R. E., "Carbonation of CH and C–S–H in composite cement pastes containing high amounts of BFS", *Cement and Concrete Research* 40(2), 2010, pp. 284-292. (DOI 10.1016/j.cemconres.2009.10.020)
5. Sisomphon, K., Franke, L., "Carbonation rates of concretes containing high volume of pozzolanic materials", *Cement and Concrete Research* 37(12), 2007, pp. 1647-1653. (DOI 10.1016/j.cemconres.2007.08.014)
6. Gruyaert, E., Van den Heede, P., De Belie, N., "Carbonation of slag concrete: Effect of the cement replacement level and curing on the carbonation coefficient - Effect of carbonation on the pore structure", *Cement and Concrete Composites* 35(1), 2013, pp. 39-48. (DOI 10.1016/j.cemconcomp.2012.08.024)



7. Papadakis, V. G., "Effect of supplementary cementing materials on concrete resistance against carbonation and chloride ingress", *Cement and Concrete Research* 30(2), 2000, pp. 291-299. (DOI 10.1016/S0008-8846(99)00249-5)
8. Ludwig, H.-M., "Zur Rolle von Phasenumwandlungen bei der Frost- und Tausalz-Belastung von Beton", Hochschule für Architektur und Bauwesen, Dissertation, 1996, Weimar, Germany.
9. Pedersen, B. M., Larsen, C., "Durability considerations on the use of blended cements with (high volumes of) fly ash and slag in concrete", *Proceedings of the International Congress on Durability of Concrete (ICDC)*, Norwegian Concrete Association, 2012, Trondheim, Norway.
10. Hårdtl, R., "Veränderung des Betongefüges durch die Wirkung von Steinkohlenflugasche und ihr Einfluss auf die Betoneigenschaften", Beuth Verlag, Deutscher Ausschuss für Stahlbeton Heft 448, 1995, Berlin, Germany.
11. Smith, I. A., "The Design of Fly Ash Concrete", *Proceedings of the Institution of Civil Engineers* 36(4), 1967, pp. 769-790.
12. CEN European Committee for Standardization, "Use of *k*-value concept, equivalent concrete performance concept and equivalent performance of combinations concept (CEN/TR 16639)", CEN/TC 104, 2014, Brussels, Belgium.

# Feasibility of Digital Image Correlation Technique to Determine Mechanical Properties of Corroded Steel Rebars

Ranjitha Rajagopal<sup>1</sup>, Sameer Sharma<sup>2</sup>, Radhakrishna G. Pillai<sup>3</sup> and Sankara J. Subramanian<sup>4</sup>

<sup>1</sup>Graduate Student, <sup>3</sup>Assistant Professor, Dept. of Civil Engineering, Indian Institute of Technology Madras, Chennai, India

<sup>2</sup>Graduate Student, <sup>4</sup>Associate Professor, Dept. of Engineering Design, Indian Institute of Technology Madras, Chennai, India

**Abstract:** To ensure safety and serviceability, it is essential to assess the residual capacity of corroding structures. For this assessment, it is essential to evaluate the residual mechanical properties of the embedded reinforcement bars (rebars) that are experiencing corrosion. Literature reports substantial difference of opinion on corrosion-induced changes in the residual mechanical properties. These differences could be due to the limitations of conventional techniques that are used to measure the strain (say, extensometers) and residual cross-sectional area (say, using Vernier calipers, average mass loss, etc.) and/or the methods to calculate mechanical properties of the corroded rebar specimens. The adoption of Digital Image Correlation (DIC), a non-contact, image-based deformation measurement technique, can overcome these limitations. In this study, mechanical properties measured using fixed gauge lengths (using virtual extensometer) and the Two-Dimensional Digital Image Correlation (2D-DIC) technique are compared. The data obtained using physical or virtual extensometers can be used only to obtain the 'average' strain along the gauge length and not the local strains at various locations within the gauge length. This study shows that 2D-DIC can capture the local strains and thereby the variations in strain along the entire gauge length of corroded rebars, which are very crucial in the assessment of residual mechanical properties. It is concluded that 2D-DIC is a feasible technique to estimate the residual mechanical properties of the corroded rebars extracted from concrete structures.

**Keywords:** steel, corrosion, concrete structures, residual mechanical properties, digital image correlation, extensometer, gauge length, strain, cross-sectional area

## 1 Introduction

The corrosion of embedded steel reinforcing bars (rebars) can adversely affect the safety and serviceability of concrete structures. It is essential to assess the residual mechanical properties of the rebars in order to assess the residual structural capacity and formulate timely structural repair/rehabilitation strategies, which in turn can help in assuring safety and serviceability. Researchers have attempted to characterize the residual mechanical properties of corroded rebars for several decades. The effect of the degree of corrosion on the elastic modulus, yield strength, ultimate strength, and ductility have been reported in literature (Almusallam 2001, Palsson and Mirza 2002, Du et al. 2004, Cairns et al. 2005, Apostopoulos and Papadakis 2007, and Francois et al. 2013). Because corrosion is a random phenomenon resulting in highly uneven surfaces, the evaluation of corroded specimens poses several challenges. Past studies vary from one another with respect to the type and diameter of steel rebars used, the measurement of residual cross-sectional area, the gauge length adopted, etc. These variations may be responsible for the difference of opinion among researchers on the effect of corrosion on the mechanical properties of rebar. The currently available information about the mechanical behavior of corroded rebars is not sufficient to model the behavior of structures with different levels of corrosion. Hence, there is a need for a precise estimation of the residual mechanical properties of corroded rebars, which can only be achieved by adoption of advanced methods of evaluation. In this study, Digital Image Correlation, an advanced non-contact, image-based deformation measurement methodology, is used to evaluate the residual mechanical properties of corroded rebars.

Following is a section on the significance of this study. Following this, a critical review on the contradictory findings in literature on the effect of corrosion on the yield strength, ultimate strength, and ductility of corroded bars is provided. Then, the probable reasons for these contradictions are discussed. Following this is a discussion on the experimental program to study the feasibility of 2D-DIC in evaluating the mechanical properties of corroded rebars, comparison of stress-strain graphs obtained from virtual extensometer and 2D-DIC, and the conclusions drawn from this study.

## 2 Research Significance

Characterizing the stress-strain behaviour and estimating the residual mechanical properties of corroded rebars are essential to reliably assess the residual capacity of the corroding structures. However, current techniques of evaluating corroded rebars using typical laboratory extensometer and currently adopted methods of measuring residual cross-sectional area are not sufficient to assess the mechanical behaviour of corroded rebars. This has led to difference of opinion among researchers who have studied the effect of corrosion on mechanical response of rebars. This work assesses the feasibility of a more advanced, non-contact 2D-DIC technique in (1) overcoming the limitations of conventional evaluation techniques (say, using contact extensometers) and (2) estimating the residual mechanical properties of corroded rebars in a more realistic and accurate manner.

## 3 Effect of corrosion on the mechanical properties of steel rebar

As mentioned earlier, the differences in the opinions on the effect of corrosion on the changes in the mechanical properties of rebars could be due to the differences in the type of test specimens and experimental techniques adopted. The specimens tested by various researchers varied with respect to the type of steel (ToS), pattern of corrosion (PoC) and degree of corrosion (DoC). The experimental techniques varied in the selected gauge length ( $L_0$ ), the method of inducing corrosion (MoIC), basis of estimating the degree of corrosion (DoC) and the method of measurement of residual cross-sectional area (RCSA). A summary these experimental features reported in literature is provided in Table 1. The following sub-sections discuss the key findings from the literature.

### 3.1 Yield strength of corroded rebars

Researchers have studied the effect of corrosion on the 'nominal' and 'actual' strength properties calculated using the original and residual cross-sectional areas, respectively. Herein, the term 'strength' indicates a parameter with units of stress (i.e., in MPa). Cairns et al. (2005) and Apostolopoulos and Papadakis (2007) concluded that corrosion does not significantly affect the 'actual' yield strength of the rebars; however, the 'nominal' yield strength of the rebars reduces significantly with increasing degree of corrosion as reduction in cross-sectional area of the specimens is not considered while calculating the strength. On the other hand, Palsson and Mirza (2005) and Francois et al. (2012) have observed a marginal increase in the 'actual' yield strength. The reason behind this difference in opinion is mainly due to the differences in the length over which the area is assumed to be uniform, which vary from 10 mm to 250 mm in the previous studies. (see Table 1 for details).

### 3.2 Ultimate strength of corroded rebars

Palsson and Mirza (2002) and Apostolopoulos and Papadakis (2007) reported that corrosion does not significantly reduce the 'actual' ultimate strength (in MPa) of the rebars, calculated using residual cross-sectional area. However, Du et al. (2004) concluded that the 'actual' ultimate strength reduces with increasing degree of corrosion. This difference in opinion could be due to the difference in the method of measurement of cross-sectional area (see Table 1 for details). On the other hand, Francois et al. (2012) reported a marginal increase in the 'actual' ultimate strength of corroded rebars with increasing degree of corrosion. Francois et al. (2012) reasons this behavior as "...Almost all the corroded bars failed at a pit location and the increase in the true ultimate strength at the pit can be explained by the fact that the failure path is imposed by the pit and does not correspond to the weakest point of the steel rebar as in the case for non-corroded bar...". Cairns et al. (2005) have provided a reason for this apparent increase in ultimate strength with section loss as "... if the position of the pit does not coincide with the location where steel is the weakest, an apparent increase in strength (which is based on the minimum cross-sectional area) will be measured...". This indicates the influence of the measured residual cross-sectional area on the calculated strength properties of the corroded rebar; the differences in opinion regarding the residual 'actual' ultimate strength of the rebars are likely due to the use of the average cross-sectional area over a specific length, which does not give an actual estimate of the cross-sectional area at the location of failure.

### 3.3 Ductility of corroded rebars

Almusallam (2001), Palsson and Mirza (2002), Cairns et al.(2005), Apostolopoulos and Papadakis (2007), and Francois et al. (2012) have unanimously concluded that corrosion has more impact on the ductility of the rebar than the strength properties. In this paper, 'ductility' is expressed quantitatively as 'ultimate strain' (i.e., the strain exhibited by the specimen at fracture point). Du et al. (2005) have concluded that

non-uniform distribution of cross-section along the length of a corroded rebar significantly reduces the measured ultimate strain, area under the stress-strain graph, and elongation. This is because the researchers have used the deformations over the entire gauge length for these calculations. Du et al. (2005) conducted a numerical analysis of the experimental results and showed that an average value of more than 10% corrosion can reduce ductility of the corroded rebars to a value less than the minimum requirement specified for Class S reinforcement. Class S reinforcement is defined as rebars with a strength ratio  $\geq 1.15$  and ultimate elongation  $\geq 6\%$ , as specified in CEB Model Code 90. Almusallam (2001) conducted a study on rebars conforming to ASTM A 615 Grade 60 steel and concluded that the rebars would exhibit brittle behavior if corrosion exceeds 12.6%. Francois et al. (2013) have concluded that the ductility is more influenced by the shape of the cross-section than both the cross-sectional area loss and pit depth. Cairns et al. (2005) and Apostolopoulos and Papadakis (2007) found that the strength properties decrease linearly with the mass loss; however, the ductility decreases exponentially with mass loss. Palsson and Mirza (2002) compared the ultimate strain measured using gauge lengths of 25 and 75 mm on the same specimens and concluded that the strain measured using 25 mm gauge length showed a higher value than that measured using 75 mm gauge length.

**Table 1. Summary of the experimental methods adopted in literature**

Type of specimen (ToS), Gauge length ( $L_0$ ), and Method of inducing corrosion (MoIC)	Basis for estimating the degree of corrosion (DoC) and residual cross-sectional area (RCSA) <sup>a</sup>	Pattern of corrosion (PoC) & Degree of corrosion (DoC) <sup>b, c</sup>	Reference
<ul style="list-style-type: none"> <li>ToS – Grade 60 ASTM A615</li> <li><math>L_0</math> – Not reported</li> <li>MoIC - Impressed current technique in cementitious system</li> </ul>	<ul style="list-style-type: none"> <li>DoC – Average mass loss over the length of the specimen</li> <li>RCSA – Effective diameter<sup>a</sup> calculated using average mass loss</li> </ul>	<ul style="list-style-type: none"> <li>PoC – uneven<sup>b</sup></li> <li>DoC – Up to 75-80%</li> </ul>	Almusallam (2001)
<ul style="list-style-type: none"> <li>Not specified</li> <li><math>L_0</math> – 25 mm within 75 mm</li> <li>Naturally corroded inside a concrete deck</li> </ul>	<ul style="list-style-type: none"> <li>DoC and RCSA – Average loss in cross-sectional area over 25 mm by measuring minimum and maximum diameter using Vernier Calipers</li> </ul>	<ul style="list-style-type: none"> <li>PoC – uneven</li> <li>DoC – &lt;10%, 10-20%, 20-30%, and &gt;30%</li> </ul>	Palsson and Mirza (2002)
<ul style="list-style-type: none"> <li>Not specified</li> <li><math>L_0</math> – 50 mm</li> <li>Impressed current technique in cementitious system</li> </ul>	<ul style="list-style-type: none"> <li>DoC – Weight loss over the length of the specimen</li> <li>RCSA – Average residual diameter over 10 mm calculated from volume of water displaced</li> </ul>	<ul style="list-style-type: none"> <li>PoC – uniform</li> <li>DoC – 20-25%</li> </ul>	Du et al. (2005)
<ul style="list-style-type: none"> <li>Not specified</li> <li><math>L_0</math> – Not reported</li> <li>Corrosion damage simulated by milling and accelerated corrosion by anodic polarization in cementitious system</li> </ul>	<ul style="list-style-type: none"> <li>DoC and RCSA – weight loss and pit depth measured using micrometer for lightly corroded specimens (up to 4%) and liquid displacement technique for heavily corroded specimens</li> </ul>	<ul style="list-style-type: none"> <li>PoC – Both uniform and localized<sup>c</sup></li> <li>DoC – Up to 50%</li> </ul>	Cairns et al. (2005)
<ul style="list-style-type: none"> <li>BSt 420 of DIN 488-1</li> <li><math>L_0</math> – 150 mm</li> <li>Accelerated aqueous corrosion using salt spray</li> </ul>	<ul style="list-style-type: none"> <li>DoC – Average mass loss over the entire length of rebar (250 mm)</li> <li>RCSA – Effective diameter over 250 mm calculated from mass loss</li> </ul>	<ul style="list-style-type: none"> <li>PoC – uniform and localized</li> <li>DoC – Up to 12 - 14.5%</li> </ul>	Apostolopoulos and Papadakis (2007)
<ul style="list-style-type: none"> <li>Fe500</li> <li><math>L_0</math> – 200 mm</li> <li>Long term exposure to chlorides in cementitious system</li> </ul>	<ul style="list-style-type: none"> <li>DoC – Average diameter loss calculated from mass loss</li> <li>RCSA – Mass loss over 1 to 2 cm long portion over the failure location</li> </ul>	<ul style="list-style-type: none"> <li>PoC – Localized</li> <li>DoC – Up to 25%</li> </ul>	Francois et al. (2013)
<ul style="list-style-type: none"> <li>Fe500</li> <li><math>L_0</math> – 200 mm</li> <li>Long term exposure to chlorides in cementitious system</li> </ul>	<ul style="list-style-type: none"> <li>DoC – Cross-sectional area loss</li> <li>RCSA – Mass loss of small pieces and diameter loss using Vernier calipers</li> </ul>	<ul style="list-style-type: none"> <li>ToC – uneven</li> <li>DoC – Up to 50%</li> </ul>	Zhu and Francois (2013)

a: 'Effective diameter'  $\neq$  the average diameter over a certain length of the corroded specimen.

b: 'Uneven'  $\rightarrow$  corroded sections randomly distributed along the length of the specimen.

c: 'Localized'  $\rightarrow$  corrosion concentrated at one location of the specimen

Though the researchers unanimously agree that ductility is reduced due to corrosion, they have used different the gauge lengths (a very crucial parameter influencing the measured ductility) to measure the ultimate elongation. Table 1 lists out the variations in the gauge length selected in the previous studies.

## 4 Influence of experimental techniques on the measured values of mechanical properties

Section 3 identified the limitations in evaluating the mechanical properties of corroded rebars using the conventional tension testing and data acquisition methods. The first challenge is to predict (prior to the testing) the failure location of corroded rebars, because the cross-sectional area generally varies randomly along the length. The second challenge is to select an appropriate gauge length. The third challenge is to appropriately define the length over which the residual cross-sectional area is assumed to be uniform. Ideally, the pattern of corrosion (PoC) must be considered to determine these experimental parameters, for which suitable standardized procedures do not exist. Therefore, researchers have been adopting various methods using engineering judgment, which are discussed in the following sections.

### 4.1 Gauge length

The strain,  $\epsilon$ , can be calculated as  $\Delta L / L_0$ , where,  $\Delta L$  is the change in length and  $L_0$  is the original length. In case of tension test specimens, the gauge length is considered as  $L_0$ . The ASTM E6-09 (2009) defines the gauge length as “the original length of that portion of the specimen over which strain, elongation or change of length are determined”. The total elongation of the rebar specimen is the sum of the elastic and plastic elongations. According to ASM, ‘...When a gage section that is very long (compared to its diameter), the necking elongation converted to percent is very small. In contrast, with a gage section that is short (relative to its diameter), necking elongation can account for most of the total elongation. For round bars, this problem has been remedied by standardizing the ratio of gage length to diameter as 4:1. Within a series of bars, all with the same gage-length-to-diameter ratio, the necking elongation will be the same fraction of total elongation...’. 5:1 as per ASTM E8M (2013) and IS 1608 (1995). This is to ensure that the necking elongation would be a constant fraction of the total elongation for all diameter specimens.

For corroded rebars, because the cross-sectional shape and size (and hence the effective diameter) varies along the length of the rebar, gauge length is not selected as per any code recommendations. The difficulty in predicting the failure location on the corroded specimens compels researchers to select a convenient gauge length that would also ensure that the failure will occur within the gauge length. Hence, the gauge length selected for testing the corroded rebars depends mostly on the test setup/fixtures and the number of probable failure locations and their distribution along the length. The measured ultimate strain (say,  $\epsilon_{max}$ ) is inversely proportional to the gauge length ( $L_0$ ) and hence the selection of the gauge length determines the measured ultimate strain (and therefore, the estimated ductility). Also, the typical laboratory extensometers assume that strain is uniformly distributed along the entire gauge length. However, the stress distribution is generally not uniform due to the variation in the cross-sectional area along the gauge length, and hence, the strain distribution is not uniform either. Hence, extensometers will not be able to capture the heterogeneity in the strain distribution and the actual elongation behaviour of the corroded rebars.

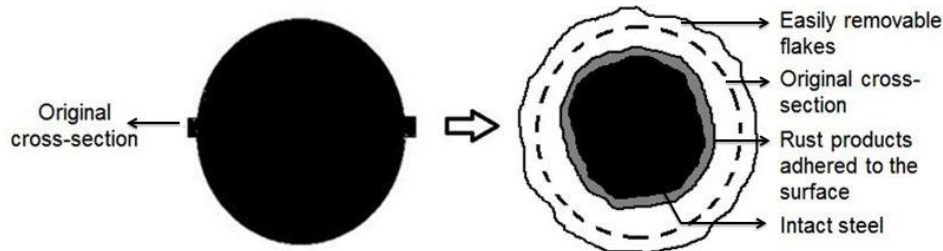
### 4.2 Residual cross-sectional area

Du et al. (2004) and Cairns et al. (2005) reported that the material properties of steel remain the same for the residual material obtained after the removal of corrosion products. Hence, the residual cross-sectional area is used for calculating the stress in the specimen. The cross-sectional area used to calculate the stress influences the ‘calculated’ residual strength of the rebar. The residual cross-sectional area of the corroded specimens are usually measured by two common techniques - (a) measuring the mass of the whole length or a specific part of the rebar specimen before and after corrosion, and (b) calculating the cross-sectional area from the volume of remaining steel measured using liquid displacement. These methods give an average cross-sectional area over the length considered for volume displacement or mass loss. For specimens with highly uneven cross-section, these methods may not capture the reduction in cross-sectional area at the weakest location and may underestimate the effect of corrosion.

Other than these methods, Vernier calipers are also used to measure the residual diameter of the corroded specimens. While calipers can measure the residual diameter at exact locations rather than over a length, this method is very tedious and does not give an actual estimate of the residual cross-sectional area, as the shape of the cross-section is not circular for a corroded bar. Figure 1 illustrates the schematic diagram of the conceptual cross-section of a corroded rebar. The white portion at the periphery of the cross-section indicates the loose corrosion products which can be easily removed by cleaning. The grey portion to the interior of this outer portion represents the corrosion products adhered to the residual steel which cannot be easily removed with acid. But this portion of the cross-section may not assist in carrying load. It is difficult to visually assess the area of the intact steel which is capable of carrying load.



Due to difficulty in predicting the exact failure location on the corroded specimen, the commonly adopted technique is to measure the ‘average’ cross-sectional area over the possible region of failure. The variability in the cross-sectional area along this considered length of the failure region influences the measured residual cross-sectional area. The strength properties – the ‘actual’ yield strength and ultimate strength of the corroded rebars – depend upon the residual cross-sectional area at the failure location. The closeness of the value of the ‘average’ residual cross-sectional area to the residual cross-sectional area at the failure location depends on the length over which the residual cross-sectional area is assumed to be uniform and the variability in the cross-sectional area in this considered length.



**Figure 1. Conceptual cross-section of a corroded rebar**

In short, there is a need for a more advanced method to evaluate the behaviour of corroded rebars. The 2D-DIC technique is an image analysis technique that can be used for studying the mechanical behaviour of materials. This paper aims at assessing the feasibility of 2D-DIC as a method of evaluating the mechanical behaviour of corroded reinforcing bars.

## **5 Two Dimensional Digital Image Correlation (2D-DIC) Technique**

Digital Image Correlation (DIC) is a versatile, non-contact image-based technique for estimating full-field displacements. When a single camera is used to capture in-plane deformations over a predefined planar area on the object, the technique is specifically called two-dimensional Digital Image Correlation (2D-DIC). DIC has been gaining acceptance in the field of civil engineering, especially to monitor live structures. This method has been employed to measure displacements in the longitudinal truss girder of a steel railway bridge in Nieporet, Poland (Malesa et al. 2010). Gencturk et al. (2013) have compared full-scale testing of prestressed concrete structures using DIC and conventional technique using LVDT. They found that DIC can produce more accurate strain measurements, can clearly identify the load path in the structures and provide a better understanding of the behavior of full-scale prestressed concrete structures. DIC is also being increasingly used to measure strain in the laboratory studies as well. McCormick and Lord (2010) have used DIC to measure crack opening in a loaded reinforced concrete bar. De Wilder et al. (2014) have used DIC to measure the shear capacity of the I-shaped prestressed concrete beams, as this technique can capture the brittle mode of failure due to shear.

The measurement of the deformation of an object using DIC involves tracking the change in position of the points on the surface of the object across the subsequent images of the specimen, captured using a suitable camera at different time intervals (i.e. *frame rate*). For a better understanding of the procedure of computation of the strains using 2D-DIC, an example of a simple tension test is chosen. The specimen is decorated with a stochastic pattern, composed of a distribution of light or dark blobs called speckles, to enable the identification of the pixel subsets across the images. The experimental setup consists of a UTM, a Charge Coupled Camera (CCD), illuminations such as fluorescent or LED lamps and the test specimen as shown in Figure 2. The camera is focused on the speckled specimen and during the test, a series of images is acquired at a suitable frame rate. The region of the specimen captured in the images is called the Area Of Interest (AOI). The image corresponding to the undeformed state of the specimen is labelled as the reference configuration and images of the intermediate deformed state are labelled as the current configurations at particular time instances. After the test is completed, these images are analysed with a 2D- DIC software, *VIC-2D<sup>TM</sup>* to obtain the full-field displacements and strain evolution with time. In the DIC algorithm, the displacement at a given pixel location in the reference image is computed by first choosing an image subset centred at this point and then finding its location in a subsequently acquired image (i.e. a deformed configuration) by minimizing a sum of squared intensity differences cost function. Typically, displacements can be accurately computed down to 1/100th of a pixel. Once the full-field displacement maps are computed, these are differentiated with respect to spatial coordinates and strain measures of interest are computed by the software.

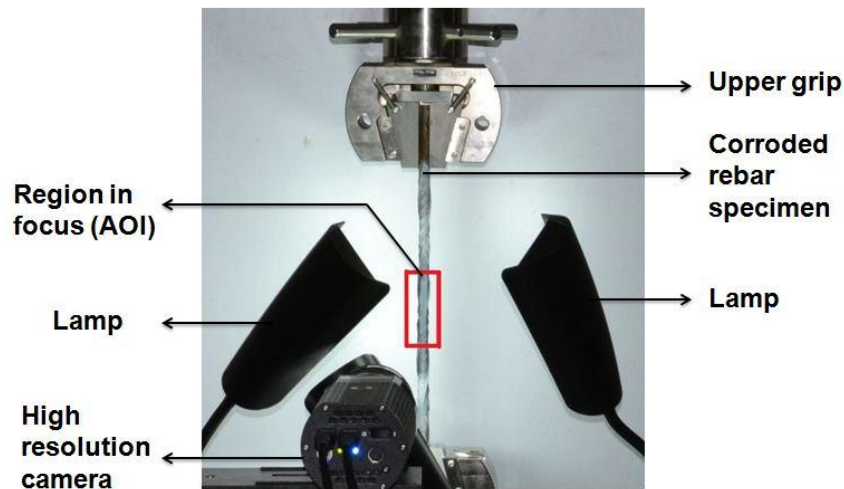


Figure 2. Experimental setup for the tension test of corroded rebar specimen

## 6 Experimental Design

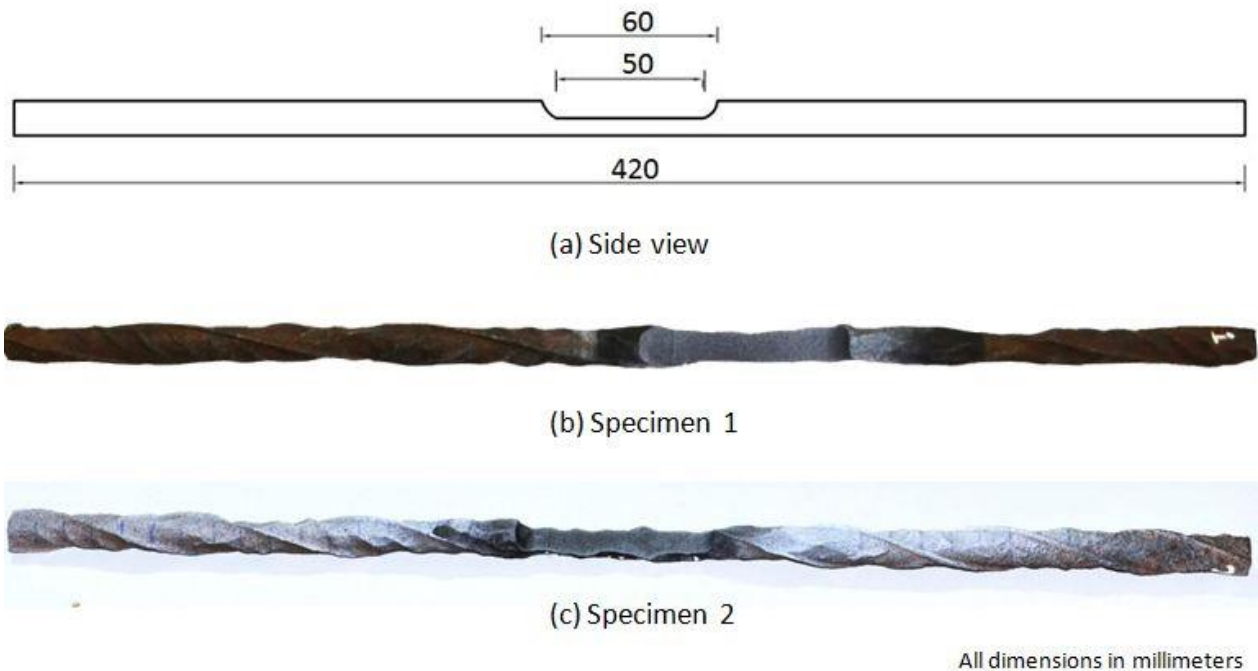
This section outlines the details of the experiment and the data analysis using 2D-DIC technique.

### 6.1 Specimen Preparation and Experimental Test Setup

Naturally corroded Cold-Twisted Deformed (CTD) steel rebars embedded in concrete were collected from a 10 year old building in Chennai, India. Chennai has a tropical wet and dry climate, with temperature varying from 15°C to 40°C and average annual rainfall of about 140 cm. The CTD steel rebars were introduced in the Indian construction industry in 1967 (Basu et al. 2004) and were discontinued from use in 1990s, due to their high vulnerability to corrosion. Rebars with different degrees of corrosion, ranging from mild to severe corrosion, were available in this lot of rebars collected. Sampling was done from this lot by cutting 420 mm long pieces such that the relatively weaker corroded section is at the middle of these pieces and the ends are relatively less corroded. This is done to ensure that failure occurs at the centre of the specimen and not inside the grips. These specimens were cleaned as per guidelines given in ASTM G1-90. Two rebars were selected for tension testing and were cut longitudinally into half for 60 mm at the centre, as shown in Figure 3 (a), using an Electric Discharge Machine (EDM) method, to get a smooth, planar surface for 50 mm long region, which can be speckled and images acquired. The two specimens selected were such that one is of fairly uniform reduction in cross-sectional area, while the other has an uneven reduction in cross-section along the length of the specimen, as shown in Figure 3 (b) and (c).

The cross-sectional area of the specimen was calculated by the liquid-displacement method. Primarily water was used for the measurement of the cross-sectional area. The cross-sectional area of the half-cut specimen to be measured was very small (less than 56 mm<sup>2</sup>). Liquid displacement technique using water did not give sufficiently accurate measure of the volume of the rebar because of the error due to the meniscus formed by water inside the container. Hence, water was replaced with kerosene to measure the cross-sectional area, which has a surface tension of 0.032 N/m compared to 0.072 N/m of water. This helped to minimize the error due to the meniscus formed by the liquid. To improve accuracy of the readings a micropipette was used to pour the liquid into the container containing the specimen. The area profile obtained is as shown in Figure 4. The average cross-sectional area was calculated for every 5 mm length of the 50 mm long longitudinally cut section of the specimen (named 'R1' to 'R10'). This half cut region of the specimens, which is the AOI, is speckled with white paint over a black background using spray paints, forming a pattern that is recognizable using a high resolution camera. It is kept undisturbed for 24 hours for the spray paint to dry.

The test setup is as shown in Figure 2. Tension test is conducted on the longitudinally half cut corroded specimen in a 100 kN capacity machine. The test was conducted at a displacement rate of 0.0125 mm/s, as per the lowest strain rate recommended in IS 1608:1995. Images were acquired using a high resolution camera at a rate of 1 image/sec till breakage of the specimen.



**Figure 3. Longitudinally half-cut specimens**

## 6.2 Data analysis using 2D-DIC

After completing the tension test (till fracture) on the two corroded specimens, each one of the images of the intermediate deformed states is correlated with the respective reference image (undeformed state), thus forming an image pair, to compute the full-field deformations in the AOI across all the images, acquired during the test for the specimen (1 or 2) under consideration. The commercial 2D-DIC package VIC-2DTM is employed for the DIC computations with the input parameters such as a) the AOI size (specimen 1 – 120 pixels x 700 pixels and specimen 2 - 125 pixels x 709 pixels), AOI is identified as the enclosing region of a polygon, defined by tracing the boundaries of the region of interest on the specimen, b) the subset size of 25 pixels x 25 pixels and the step or increment size of 3 pixels for both the specimens, c) Zero Normalized Sum of Square Differences (ZNSSD) optimization function. Using the mentioned parameters, VIC-2DTM estimated the displacements in unit pixels. To convert the displacements in the metric units (mm), a calibration is performed by first estimating the scaling factor (mm/pixels) and then multiplying it to the pixel displacements. Finally, full-field strains are computed using a filter size of 15 pixels x 15 pixels, the filter size defines the local region which is approximated by a smooth polynomial surface to compute the displacement gradients and hence the strains. VIC-2DTM can also compute linear one-dimensional (1D) strain (virtual extensometer), where the 1D element is defined by selecting the two (Top/Bottom) pixels spanning the undeformed length.

All the VIC-2D™ outputs are recorded and as the next step, each image is then correlated with the machine load applied at that instant corresponding to the time of image capture, to obtain the **load-displacement** or **stress-strain** plot of the specimens. To meet the objectives of this study, the data analysis involves:

- a) Comparison of the strain values measured by virtual extensometer and the strain computed using 2D-DIC.
- b) Comparison of the stress-strain curve plotted using residual cross-sectional area at the fracture location and the average residual cross-sectional area assumed to be uniform over the gauge length.

The conventional technique of strain measurement using typical laboratory extensometers was simulated using a virtual extensometer utility in VIC-2D™. Desirable gauge length can be selected on the images over which VIC-2D™ computes the strain, assuming strain distribution to be uniform over this length. 50 mm was selected as the gauge length for strain measurement using virtual extensometer. To



understand the heterogeneity in the strain distribution over the 50 mm long AOI, the AOI was sub-divided into 10 regions, each of 5 mm length as shown in Figure 4, and strains in each of these regions were computed using 2D-DIC. These regions are named 'R1', 'R2', and so on up to 'R10' with the region with the fracture location as 'RF'. It is assumed that the residual cross-sectional area in this 5 mm long sub-divided regions is uniform. This is a more accurate estimate than assuming the average cross-sectional area over the entire gauge length to be uniform over that length.

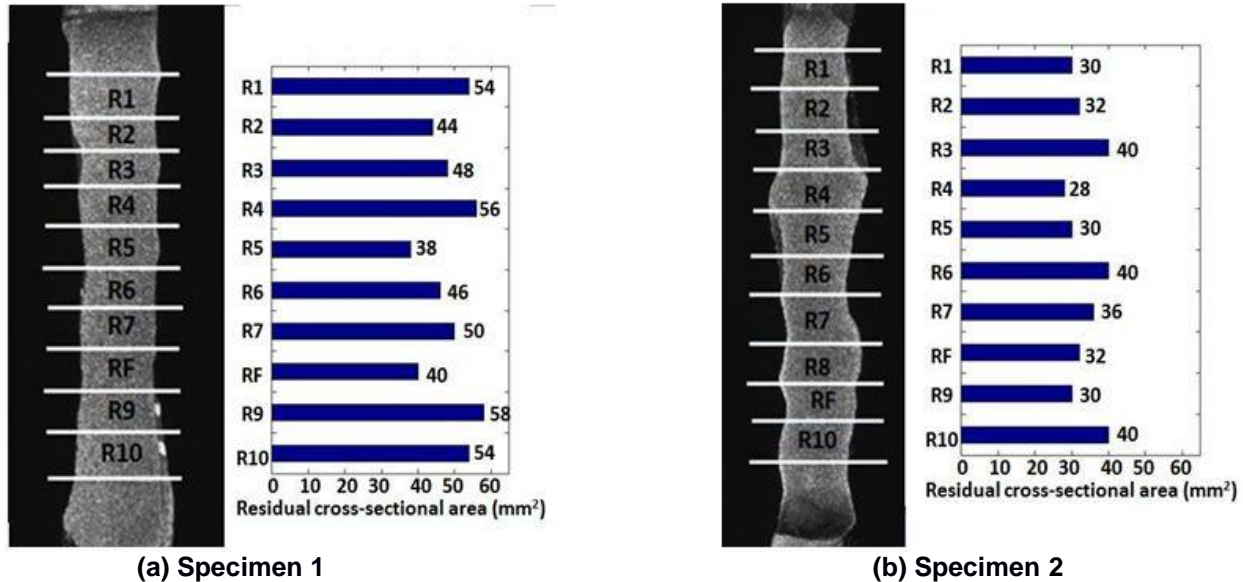


Figure 4. Variations in the cross-sectional area along the length of AOI

## 7 Results and Discussions

The following section details the results of the comparative analysis carried out on the two corroded rebar specimens tested.

### 7.1 Influence of the gauge length on measured mechanical properties

Figure 5 shows the stress-strain curves plotted with strain measured using virtual extensometer of 50 mm gauge length (the thicker curve labelled as 'G50') and strains computed for the regions 'R1' to 'R10' using 2D-DIC. The stress-strain plots for the regions 'R1' to 'R10' exhibits the non-uniform strain distribution over the AOI. Regions 'R1' to 'R10' exhibit dissimilar strain distribution due to the variation in the cross-sectional areas of these regions. The virtual extensometer measures the average strain over the AOI by means of the relative displacement of the two points 50 mm apart, assuming uniform strain distribution along the gauge length. The ultimate strain measured using the virtual extensometer is significantly lower than the ultimate strain exhibited by the 'RF' and adjacent regions. Table 2 shows the differences in ultimate strains measured using virtual extensometer and 2D-DIC.

Another observation is that, for specimen1, the region 'R1' exhibits a sudden decrease in the stress at a strain value of about 0.02 (the vertical line in the stress-strain curve in Figure 5. Similar behaviour is exhibited by regions R2, R3, R4, and R5, with a sudden reduction in the stress at about strains ranging between 0.02 and 0.05. Similarly, regions R1 to R6 of Specimen 2 exhibit a reduction in stress when strain is between 0.01 and 0.02. These reductions in stress exhibited by some regions that are away from the 'RF' and adjacent regions indicate that regions away from the RF are not influenced by the elongation due to necking. This shows that there can be significant variations in the strains experienced by the different regions within the gauge length. Thus, assuming uniform strain over a specific gauge length does not capture the actual mechanical response of the corroded rebars. Hence, an appropriate gauge length for corroded specimens would depend upon the variation in the cross-sectional area profile in the proximity of the probable failure location with least cross-sectional area. The 2D-DIC technique can help to determine appropriate gauge length for a corroded specimen by observing the strain distribution in the adjacent regions to the failure location. The computations involve a posterior analysis of the data (i.e., image analysis) collected during the tensile test.

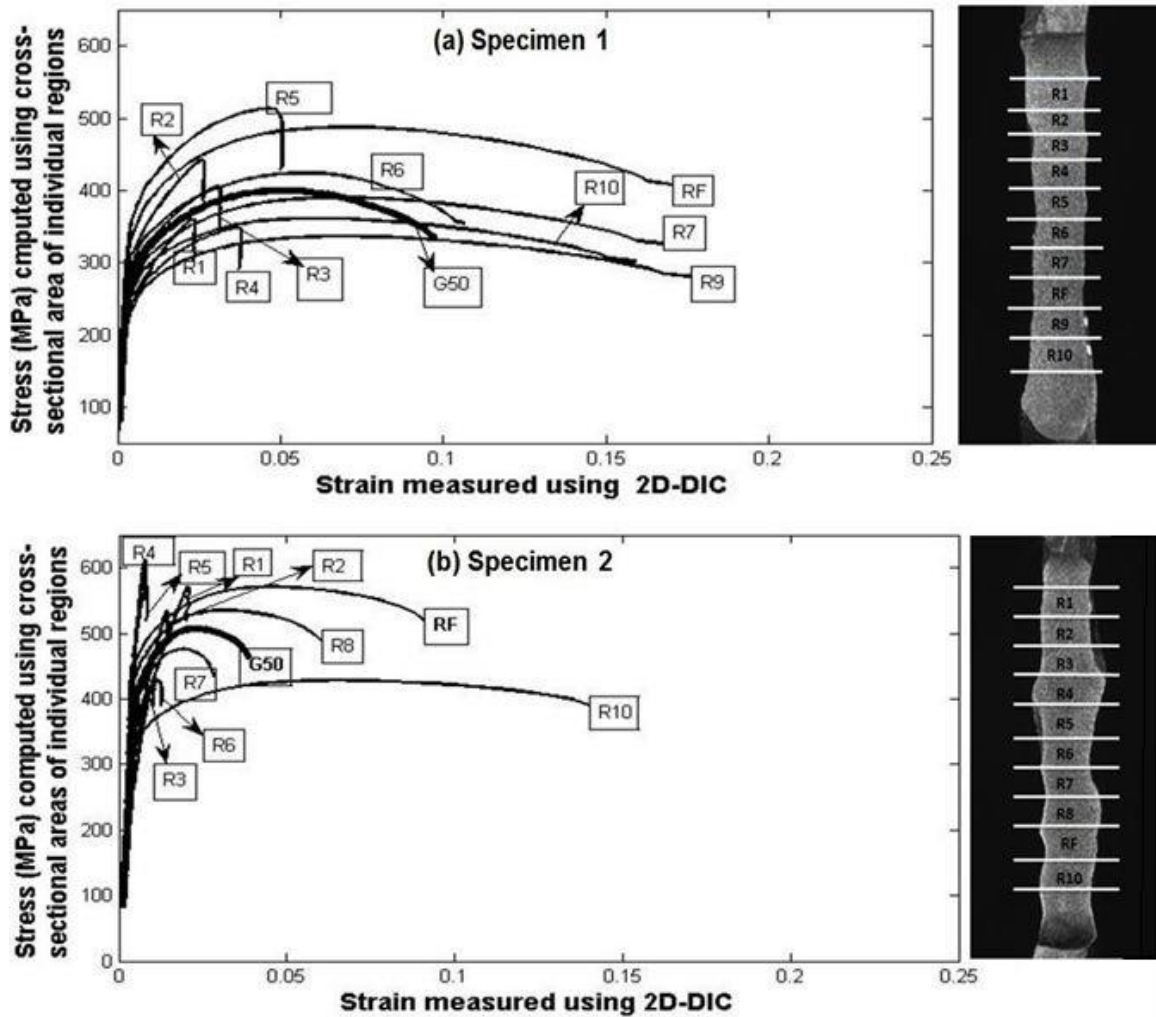


Figure 5. Comparison of stress-strain plots obtained using virtual extensometer and 2D-DIC

Table 2. Measured Mechanical Properties

Length over which residual cross-sectional area is assumed to be uniform (i.e., 'Gauge Length')	Specimen 1			Specimen 2		
	Yield strength (MPa)	Ultimate strength (MPa)	Ductility (%)	Yield strength (MPa)	Ultimate strength (MPa)	Ductility (%)
50 mm	300	400	10	400	500	4
5mm (RF)	340	490	17	450	580	8

## 7.2 Influence of the measured residual cross-sectional area on the measured mechanical properties

The length over which the average residual cross-sectional area is measured influences the calculated strength properties of the corroded rebars. The stress-strain curve plotted using 50 mm gauge length virtual extensometer and the average cross-sectional area measured over 50 mm is represented by the thicker line labelled 'G50' in Figure 5. The yield strength and ultimate strength values exhibited by this curve is significantly lower than the corresponding value calculated for the region 'RF' using the residual cross-sectional area measured over the region 'RF' (5 mm). Table 2 presents the strength properties measured using the average residual cross-sectional area measured over 50 mm and 5 mm for both the specimens. This indicates that the calculated strength properties assuming the residual cross-sectional area to be uniform over the gauge length are lower than those calculated using residual cross-sectional area at the region 'RF'. This is because the 'average' residual cross-sectional area over larger lengths cannot capture the actual local reduction in the cross-sectional area at the fracture location.

### **7.3 Influence of the pattern of corrosion on the measured mechanical properties**

Two specimens, one with uniform corrosion, (i.e., nearly uniform cross-sectional area along the length), and the other with highly uneven corrosion pattern, as shown in Figure 4 (a) and (b) respectively, were selected to study the influence of the pattern of corrosion on the mechanical behavior of corroded rebars. Figure 5 exhibits the variations in the stress-strain curves for different regions ('R1' to 'R10'). For Specimen 1 with uniform corrosion pattern over the AOI, the adjacent regions to the 'RF' (i.e., 'R7', 'R9' and 'R10'), exhibit similar ductility behavior, while strength properties are considerably different for these regions. However, for Specimen 2 with uneven corrosion pattern over the AOI, the adjacent regions to the 'RF', (i.e., 'R8' and 'R10') exhibit very different ductility as well as strength properties. This indicates that rebars with larger variation in the cross-sectional area along the gauge length exhibits higher heterogeneity in the strain distribution compared to the ones with uniform corrosion pattern. Hence, the measurement of strain using a typical laboratory extensometer for specimens with non-uniform cross-sectional area along its length cannot capture the actual stress-strain behaviour of the specimen. Also, assuming uniform residual cross-sectional area over the gauge length for the corroded rebars with uneven cross-sectional pattern (say, pitting corrosion) may fail to capture the actual residual cross-sectional area at the fracture location. Hence, the pattern of corrosion (i.e., the variability in cross-sectional area over the length) is an important parameter that would help in deciding an appropriate gauge length and the length of the specimen over which the residual cross-sectional area can be assumed to be uniform.

## **8 Conclusions**

Previous studies on the evaluation of the corrosion-induced changes in the mechanical properties of the rebars exhibit considerable differences in opinion among researchers. The reason for these differences is mainly the variations among the adopted test methods and the limitations of the conventional techniques of evaluation. This study has compared the mechanical properties measured using the virtual extensometer and the 2D-DIC technique and arrived at the following conclusions. The mechanical behavior of corroded rebars cannot be determined using an extensometer as there is considerable heterogeneity in the strain distribution along the gauge length. Also, the average cross-sectional area measured over a length may underestimate the actual reduction in cross-sectional at the failure location. The conventional techniques of evaluating corroded rebars have limitations in taking into account the effect of pattern of corrosion on their mechanical behavior. However, a posterior analysis of the images captured during the tensile test using DIC can capture the heterogeneity in the distribution of strain over the AOI for corroded rebars. DIC analysis can take into account the pattern of corrosion on the specimens and study its effect on the mechanical properties of rebars. Thus, evaluation of the corroded rebars using DIC can facilitate an accurate estimate of the mechanical properties and a better understanding of the mechanical behavior of corroded rebars.

## **9 Future Work**

An extensive experimental program is ongoing on a set of corroded CTD steel rebar specimens, with different levels of corrosion. This study aims to develop an improved methodology for the evaluation of the mechanical characteristics of corroded rebars using DIC. Mild and moderately corroded specimens are evaluated using 2D-DIC, which requires polishing a narrow region (planar) on the surface of the specimen. For severely corroded specimens, with highly reduced cross-sectional area, achieving a planar surface is not always feasible. In that case, a three-dimensional (3D) variant of the DIC, usually called as 3D-DIC is employed. It is a stereovision based technique, which employs two cameras to capture the same region of interest on the specimen. In recent years, 3D-DIC has emerged as an accurate technique for estimating both the in-plane and out-of-plane motion or displacement fields. This study also attempts to categorize specimens according to the corrosion pattern and define gauge lengths for each category. Instead of conventional methods of measurements, the 3D-laser scanning technique, is being adopted to obtain a better estimate of the residual cross-sectional area of the specimens, which would significantly help in identifying the potential failure locations.

## **10 Acknowledgements**

The authors are thankful to the financial support from the Department of Science and Technology (DST), and the Ministry of Human Resources Development (MHRD), Government of India through the Indian Institute of Technology Madras, Chennai, India.

## 11 References

- Almusallam, A. A. (2001) Effect of degree of corrosion on the properties of reinforcing steel bars. *Construction and Building Materials* 15, 361- 368.
- Palsson, R., Mirza, M. S. (2002) Mechanical response of corroded steel reinforcement of abandoned concrete bridge. *ACI Structural Journal* 99, 157-162.
- Du, Y. G., Clark, L. A., and Chan, A. H. C. (2004) Residual capacity of corroded bars. *Magazine of Concrete Research* 57 (3), 135-147.
- Cairns, J., Plizzari, G. A., Du, Y., Law, D. W., and Franzoni, C. (2005) Mechanical properties of corrosion-damaged reinforcement. *ACI Materials Journal* 102, 256-264.
- Apostolopoulos, C.A., Papadakis, V.G. (2007) Consequences of steel corrosion on the ductility properties of reinforcement bar. *Construction and Building Materials* 22, 2316–2324.
- Francois, R., Khan, I., Dang, V. H. (2013) Impact of corrosion on mechanical properties of steel embedded in 27-year-old corroded reinforced concrete beams. *Materials and Structures* 46, 899–910.
- Du, Y. G., Clark, L. A., & Chan, A. H. C. (2005) Effect of corrosion on ductility of reinforcing bars. *Magazine of Concrete Research* 57 (7), 407-419.
- Zhu, W., François, R. (2013) Effect of corrosion pattern on the ductility of tensile reinforcement extracted from a 26-year-old corroded beam. *Advances in Concrete Construction* 1 (2), 121-136.
- ASTM E6-09b (2009) Standard Terminology Related to Methods of Mechanical Testing. ASTM International, American Society of Testing and Materials, Conshohocken, PA.
- ASTM E8M-13a (2013) Standard test methods for tension testing of metallic materials. ASTM International, American Society of Testing and Materials, Conshohocken, PA.
- Basu P., C., Shylamoni P., Roshan A., D. (2004) Characterisation of steel reinforcement for RCstructures: An overview an related issues. *Indian Concrete Journal* 78 (1), 19-30
- IS 1608 (1995) Mechanical testing of metals - tensile testing. Bureau of Indian Standards, New Delhi-110002.
- Malesa, M., Szczepanek, D., Kujawska, M., Swiercz, A., and Kolakowski, P. (2010) Monitoring of civil engineering structures using Digital Image Correlation technique. *EPJ Web of Conferences* 6, 31014.
- Gencturk, B., Hossain, K., Kapadia, A., Labib, E., & Mo, Y. L. (2014). Use of digital image correlation technique in full-scale testing of prestressed concrete structures. *Measurement* 47, 505-515.
- McCormick, N., Lord, J. (2010) Digital image correlation. *Materials Today* 13 (12), 52-54.
- De Wilder, K., Lava, P., Debruyne, D., Wang, Y., De Roeck, G., & Vandewalle, L. (2015). Experimental investigation on the shear capacity of prestressed concrete beams using digital image correlation. *Engineering Structures* 82, 82-92.
- Sutton, M. A., Orteu, J. J., & Schreier, H. (2009) Image correlation for shape, motion and deformation measurements: basic concepts, theory and applications. Springer Science & Business Media.
- VIC-2D (2009), VIC-2D™ - Digital Image Correlation Measurement System, URL: <http://www.correlatedsolutions.com/vic-2d/>: Correlated Solutions Inc., Irmo, SC, USA

# Determination of Chloride Diffusion Coefficient of Concrete: Comparison of Bulk Diffusion and Electrical Field Method

Aimin Xu<sup>1</sup> & Ahmad Shayan<sup>2</sup>

<sup>1</sup> Senior Research Engineer, ARRB Group, Melbourne, Australia

<sup>2</sup> Chief Research Scientist, ARRB Group, Melbourne, Australia

**Abstract:** Chloride Diffusion coefficient of concrete is of prime importance in the service-life prediction for concrete structures, and it can also be used as a parameter for the concrete quality control. This paper presents the results of chloride diffusion tests in which the diffusion coefficient was determined by the two most commonly used acceleration methods; the bulk diffusion in solution of high chloride concentration, and the electric field accelerated migration test.

Two types of concrete mixes were used, one being of 40 MPa strength grade, containing plain Portland cement as binder, and the other of 50 MPa strength grade which contained blended cement as binder. This paper shows that the value of diffusion coefficients determined by the bulk diffusion test is considerably higher than that obtained on concrete structure exposed to seawater, and the value of diffusion coefficient determined by migration test under electrical field is even greater.

The paper discusses the possible reasons for the discrepancies including chloride binding, specimen age, and the appropriateness of using the diffusion coefficients so determined for concrete quality control.

**Keywords:** accelerated diffusion, chloride binding, chloride diffusion coefficient, concrete, electrical field.

## 1. Introduction

Chloride contamination of concrete can cause damage to concrete structures through alteration of chemical properties of concrete and chemical-electrical property of reinforcing steel which induces steel reinforcement corrosion. The latter occurs more rapidly in structures subjected to chloride containing sources, such as seawater, deicing salts and saline soil. The chloride ions enter concrete and gradually reach steel reinforcing bars which causes steel to corrode, when the concentration at steel is high enough. The duration since concrete is exposed to the chloride source till corrosion of reinforcing bar commence depends on the concentration of chloride in the source and the rate to transport through the concrete. This duration has been generally taken as the "service-life" of the component, which is a conservative approach.

There are several mechanisms for chloride transport in concrete and a few methods have been developed to evaluate the rate of chloride transport, as reviewed by Nilsson et al.<sup>1</sup> The most commonly encountered mechanism is the diffusion of ions, and the most tested property is the diffusion coefficient. The diffusion coefficient is a fundamental parameter for evaluating the service-life of the structural member, and can also be used for concrete quality control. However, the chloride ion diffusion in concrete in natural environment, such as normal seawater (about 3.5% NaCl by mass of water) is a very slow process, and the test will need a very long time to yield results, e.g. the ponding test by ASTM C1543 requires 6 months<sup>2</sup>. It is well known that concrete properties such as pore structure and strength improve with age, and that the improvement results in a reduction in the diffusion coefficient. For quality control, diffusion coefficient is determined at a designated exposure age which needs to be practical such as 28 days.

Therefore, accelerated test methods have been developed and used for testing the diffusion coefficient. The mechanisms and test methods are elaborated in Nilsson et al.'s comprehensive review<sup>1</sup>. The methods that have been adapted by standard organizations are NT Build 443 by Nordtest<sup>3</sup> which has also been designated as ASTM C1556 with minor change<sup>4</sup>, and NT Build 492 which uses basically the same test principle as ASTM C1202.<sup>5,6</sup>

NT Build 443 tests the natural diffusion of chloride ions into concrete at the age of 28 days (if it is for quality control) exposed to a strong chloride solution (NaCl 165 g/L) with exposure time of at least 35 days, and NT Build 492 tests migration of chloride under an electric field of 30 Volts across a 50mm thick slice of concrete for a period of 24 hours (the field strength and purging time can vary according to the anticipated migration speed). The experience of the present author is that neither test methods yields values of diffusion coefficient comparable to those obtained from concrete cores extracted from actual

structures<sup>7</sup>. In addition, the diffusion coefficient obtained by NT Build 443 will certainly be influenced by the exposure age.

Investigations have been conducted at ARRB to evaluate and compare the diffusion coefficients obtained by these methods. This paper discusses mechanisms of the transport process in the three methods and presents results of diffusion coefficients determined for two concretes; Grade 40 MPa made with GP cement and Grade 50 MPa made with blended cement. Particularly, the effect of specimen age on the magnitude of diffusion coefficient is investigated. The free chloride ion diffusion coefficient and chloride binding capacity, which can be evaluated from the results of these tests, are also discussed.

## 2. Transport Mechanisms Involved in the Test Methods

### 2.1 Bulk Diffusion

Diffusion of ions occurs where there is a concentration difference over a distance, i.e. the gradient is not zero. The distribution of a substance as a function time and space  $C(t,x)$  in a body exposed to a constant environment with a constant concentration can be described by the “Second Law of Diffusion” (or Fick’s Second Law). This law was originally derived for ion diffusion in solution. Nilsson<sup>8</sup> theorized that the diffusion law can be applied to the diffusion in concrete and that it can be expressed as:

$$C(t, x) - C_i = (C_s - C_i) \left[ 1 - \operatorname{erf} \left( \frac{x}{\sqrt{4D_a t}} \right) \right] \quad (1)$$

where  $C=C(t, x)$  is concentration of chloride ions which is a function of time ( $t$ ) and distance ( $x$ ),  $C_i$  is the original chloride content and  $C_s$  the content at surface of concrete, and  $D_a$  is the apparent diffusion coefficient. Values for  $C_s$  and  $D_a$  are obtained by curve fitting, i.e. by plotting the chloride content versus depth ( $x$ ) and fitting the data to Eq.(1), using trial values of  $C_s$  and  $D_a$  until the distribution in theory fits the data. The relationship between  $D_a$  and the diffusion coefficient of free moving ions ( $D_0$ ) can be expressed by the equation<sup>7</sup>:

$$D_a = D_0 / (1 + \partial C_b / \partial C_f) \quad (2)$$

where  $\partial C_b / \partial C_f$  is termed as “binding capacity” to describe the change of bound chloride ( $C_b$ ) with the change in equilibrium solution concentration ( $C_f$ ).<sup>8</sup>

In theory, there is no difference between the process of diffusion in seawater and that in NT Build 443 condition. However, the  $\partial C_b / \partial C_f$  is large at low concentration and becomes small at high concentration. This means that with increase in concentration, the change in chloride binding becomes relatively smaller and the  $D_a$  will be larger according to Eq.(2). Consequently,  $D_a$  obtained by NT Build 443 method will be larger than that of structure exposed to seawater. Comparative experimental tests have confirmed this.

Xu and Shayan<sup>7</sup> pointed out that all chloride ions must enter the specimen through the boundary ( $x=0$ ), therefore the total free chloride ions diffused into the specimen is the same as the bulk diffusion and that the diffusion coefficient of free chloride,  $D_0$  can be estimated in the bulk diffusion test by:

$$D_0 = [C(t)_{total} / A]^2 \pi / (4t), \text{ or } D_0 = \left[ (C_s - C_i) / (C_{ENV} - C_{i,free}) \right]^2 \quad (3)$$

where  $C(t)_{total}$  is the total amount of chloride ions entered the concrete at time  $t$ ,  $A$  is the area;  $C_{ENV}$  is the concentration of chloride in the solution (with the same unit as  $C_s$ ). The binding capacity,  $\partial C_b / \partial C_f$  can be estimated through the relationship shown in Eq.(2), i.e.  $\partial C_b / \partial C_f = D / D_a - 1$ .

### 2.2 Migration in Electrical Field

Under an electrical field ions at one surface are pushed into the specimen by the electrical potential difference. The distribution of free chloride ions (those that did not chemically react with cement paste during the process) in the specimen under such a condition before they break through the other side of the specimen can be described by<sup>9</sup>:



$$C(t, x) - C_0 = \frac{C_{ENV} - C_0}{2} \left[ e^{\frac{v}{D}x} \operatorname{erfc}\left(\frac{x+vt}{\sqrt{4D't}}\right) + \operatorname{erfc}\left(\frac{x-vt}{\sqrt{4D't}}\right) \right] \quad (4)$$

where  $C_{ENV}$  is the solution concentration at boundary ( $x=0$ ) and  $v$  is the velocity of the ions moving due to the electrical field. Under electrical potential of  $\Delta E$  across a specimen of thickness  $L$ , the velocity is:

$$v = \frac{zF}{RT} \frac{\Delta E}{L} D' \quad (5)$$

where  $F=96484.56$  C/mol,  $R=8.31441$  J/mol/K,  $T$  is the temperature (K), and  $z=1$  for chloride ions. It can be shown that Eq(4) is dominated by its second term (about 95% for a test of 6 hours). If the concentration at a depth  $x_d$  is known, the value of  $D'$  can be calculated by the relation derived by Tang,<sup>10</sup> which is:

$$D' = \frac{1}{vt} \left[ x_d + \frac{2\xi}{v} (1 - \sqrt{\xi^2 + vx_d}) \right] \quad (6)$$

where  $\xi$  is the invert of the error function complement, i.e.  $(C(x,t)-C_0)/(C_{ENV}-C_0)=\operatorname{erfc}(\xi)$ .  $D'$  is named as "non-steady state migration" coefficient by NT Build 492, and denoted as  $D_{nssm}$  which will be used in this paper.

The depth of chloride migration can be revealed by spraying a silver nitrite solution onto the cross section of the tested specimen, which results in a whitish zone (AgCl). The concentration of chloride that is revealed by 0.1 M AgNO<sub>3</sub> solution is believed to be 0.07 M.<sup>5,10</sup> If  $C_0 = 0$  and  $C(x_d, t) = 0.07$  M, then  $\xi$  equals 1.281214 and 0.842741, for the test using 2 M solution (NT Build 492) and 0.6 M (seawater), respectively.

It should be pointed out that 0.1 M AgNO<sub>3</sub> is a relatively strong solution with excess silver at the migration front, which turns black with exposure to sunlight and masks some of the AgCl formed. Therefore, the revealed depth is shorter than that if a diluted AgNO<sub>3</sub> solution is used.

## 2.3 Influences of Temperature and Time on Diffusion Coefficient

### 2.3.1 Temperature

Generally, diffusion coefficient increases with the increase in temperature and decrease in solution viscosity, as described by the Stokes-Einstein relation<sup>11</sup>:

$$D = k_B T / (6\pi\eta a) \quad (7)$$

where  $k_B$  is the Boltzman constant ( $1.38 \times 10^{-23}$  JK<sup>-1</sup>),  $T$  is the temperature (K),  $a$  is the effective dynamic radius of the diffusing particle (sphere) and  $\eta$  the viscosity of water. This leads to a simple relationship for evaluation of diffusion coefficients at different temperatures:

$$D(T_1) / D(T_2) = (T_1 \eta_1) / (T_2 \eta_2) \quad (8)$$

During the migration under an electrical field test the temperature of concrete specimen increases due to the electrical current induced heat. For comparison, the as-determined diffusion coefficient is to be expressed as that at a reference temperature by using Eq.(8) and the published values of water viscosity (CRC Handbook<sup>12</sup>).

### 2.3.2 Age of Concrete

Concrete properties improve with curing time because of the hydration of cement, e.g. strength increases and porosity decreases. Similarly the diffusion coefficient which is a function of porosity and cement hydration degree will decrease with time.

The diffusion coefficient has been found to decrease with concrete age, and a power function used by Poulsen<sup>13</sup> is typical:

$$D_a(t) = D_{ref} (t_{ref} / t)^m \quad (9)$$

where  $D_{ref}$  is the coefficient determined at “reference age”  $t_{ref}$ , and  $m > 0$  is a constant depending on cementing materials composition which is also termed as the “age factor” in the service life prediction softwares<sup>14,15</sup>. In the literature, the starting age of the test, e.g. 28 days has been denoted as  $t_{ref}$ .

This fact raises a question about the representatives of the diffusion coefficient obtained by the bulk diffusion test. Because the diffusion coefficient decreases with age, which is particularly true for a young concrete, and that the test is run from age of 28 days to 63 days (exposure duration 35 days) or later, the as-determined diffusion coefficient would be smaller than that at the starting age, e.g. 28-day. In another words, the common practice of using the diffusion coefficient determined by the bulk diffusion test as  $D_{ref}$  would be incorrect. Furthermore, the standard immersion duration is “at least 35 days”, which will result in further reduction in the diffusion coefficient.

Nilsson et al.<sup>1</sup> demonstrated that diffusion equation, Eq.(1) is valid even though the diffusion coefficient is time dependent, and during the period in which the diffusion coefficient is a continuous function of time, diffusion equation can be expressed as:

$$C(t, x) - C_i = (C_s - C_i) \left[ 1 - \operatorname{erf} \left( \frac{x}{\sqrt{4 \int_{t_1}^{t_2} D(t) dt}} \right) \right] \quad (10)$$

Clearly,  $D_a$  in Eq.(1) is an average value of the diffusion coefficient defined by

$$D_a(t_2 - t_1) = \int_{t_1}^{t_2} D(t) dt = \int_{t_1}^{t_2} D_{t_1} (t_1 / t)^m dt = D_{t_1} \frac{t_1^m}{1-m} \frac{t_2^{1-m} - t_1^{1-m}}{t_2 - t_1} (t_2 - t_1) \quad (11)$$

Eq.(11) can be rearranged to explicitly express  $D_a$  as function of age as shown by Tang and Gulikers.<sup>16</sup> For testing and quality control, the as-determined  $D_a$  by NT-build 443 (and ASTM C1556) must be recalculated to that at a certain reference age, e.g. 28-day. The values of diffusion coefficient at different ages during the test will be elaborated on in the following sections.

### 3. EXPERIMENTAL WORK

#### 3.1 Concrete Mix and Specimens

The investigation was conducted on two grades of concrete, 40 MPa concrete made with GP cement, and 50 MPa concrete made with blended cement (75% GP cement, 6.25% fly ash and 18.75% slag). Standard concrete cylinders (diam.100 mm, length 200 mm) were made and cured in a fog-room at 23°C until the age of 28 days, when three cylinders of each mix were tested for compressive strength and others for the diffusions. The mix proportions and the compressive strength at 28 days are shown in Table 1.

**Table 1. Concrete mixes and the strength and VPV at 28 days**

Code	Cementing material (kg/m <sup>3</sup> )	Mix proportion Cement : water : aggregate : sand	Strength at 28-day (MPa)	VPV (%)
VR40 (40 MPa)	400	1 : 0.450 : 2.775 : 1.725	59	11.8
VS50 (50 MPa)	480	1 : 0.375 : 2.188 : 1.437	70	12.2

Each cylinder for diffusion tests was sawn into three disks (cast/trowelled surface as top): top 90 mm for the bulk diffusion tests, middle and bottom 50 mm for the electrical field accelerated migration test. The side surface of the specimens was coated with epoxy glue.



### 3.2 The Bulk Diffusion Test

The test was carried out according to ASTM C1556. Two specimens were tested for each concrete. The cut face of the specimen was exposed to NaCl solution of concentration 165 g/L (2.82 M) and stored at 23°C. The tests were started at age of 33 days due to some practical problems encountered. The exposure time was 37 days and 49 days for the 40 MPa Grade and 50 MPa Grade concrete, respectively. The diffusion of chloride ions into concrete will inevitably reduce the solution concentration, therefore the concentration of the exposure solutions was determined at one week and three weeks since the start of exposure, and salt (NaCl) was added to the solutions to maintain the original concentration.

In the last day of the test, each specimen was ground from surface down by using a “profile grinder” (Germman Instruments, Denmark), which allows accurate incremental sampling (area of about 70 mm in diameter). For each specimen, the primary sampling depth was about 10 mm, and the sample from 10 mm depth used to determine its chloride content. The specimens after the primary sampling were stored at 5°C. Further sampling was done if the chloride content in this sample was much higher than the initial chloride content (tested on non-contaminated concrete). The total chloride content was determined by dissolving the concrete powder in nitric acid solution, heating the solution to boiling, filtering the acid-heat treated sample and then using potentiometric titration technique to determine the chloride ion content in the solution.

### 3.3 The Migration Test

The test was carried out following ASTM C1202 test method. That is, a specimen (50 mm disk) was placed between two cells, each cell with a metal mesh which is connected to an electric terminal. The potential across the specimen was maintained constant by the instrument. The cell connected to negative terminal contains NaCl solution (0.6 M) and the cell to positive terminal contains NaOH solution (0.3 M). The test was run at 60 Volts for 6 hours. The current and voltage across specimen were automatically recorded and the total charge passed through the specimen during 6 hours was calculated and reported by the instrument. After the completion of the ASTM C1202 test procedures, the tested specimens were split along the migration direction. The depth of chloride penetration was revealed by spraying a solution of 0.1M AgNO<sub>3</sub> on the exposed surface which forms a whitish AgCl zone, and the depth of AgCl ( $x_d$ ) was measured. The value of  $x_d$  is inserted into Eq.(6) to find a primary value of  $D'$  which is then inserted into Eq.(4).  $D_{nssm}$  is obtained by varying  $D'$  so that Eq.(4) gives  $C(t, x_d)/(C_{ENV}/2) = 0.6/0.035$  ( $C_0=0$ ).

To evaluate the age effect, the migration test was so planned that three sets of tests were conducted in relation to the time of bulk diffusion: (1) the starting day, (2) about the middle of the exposure duration, and (3) the finishing day. Two disks from the same cylinder were tested for each concrete at each age.

NT Build 492 standard indicates that the actual potential difference between the electric terminals is 2 volts less than the nominal potential, i.e.  $\Delta E = V - V_0$ , and  $V_0 = 2$ . In this investigation,  $V_0$  was measured for each specimen by using 10 volts and 30 volts (each for a minute) before setting the instrument to 60 volts. The current changes at the start and becomes stable after a few seconds.  $V_0$  (0-amp potential) is found by plotting the initial current (using the value recorded at 1 minute) against potential  $V$  (Figure 1). The extra time used for this determination was calculated as equivalent time under 60 volts and added to the purging time for the calculation of  $D_{nssm}$ .

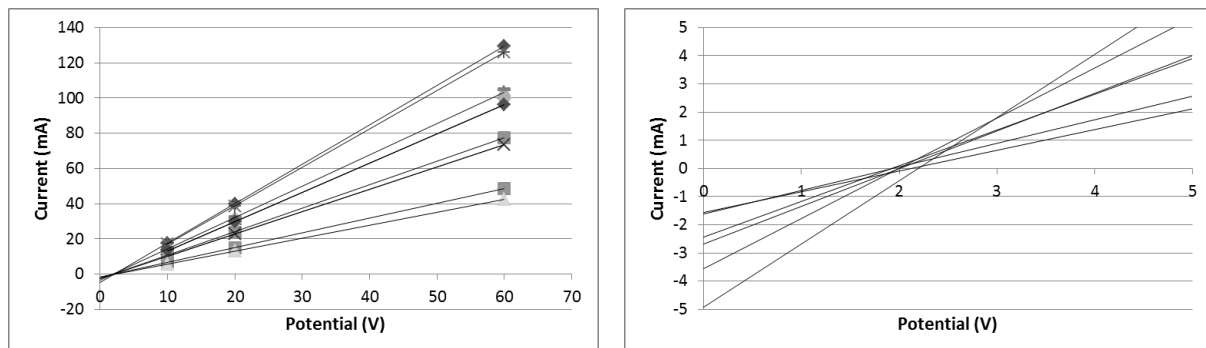


Figure 1. Initial current vs. potential to determine the 0-amp potential (all test results).

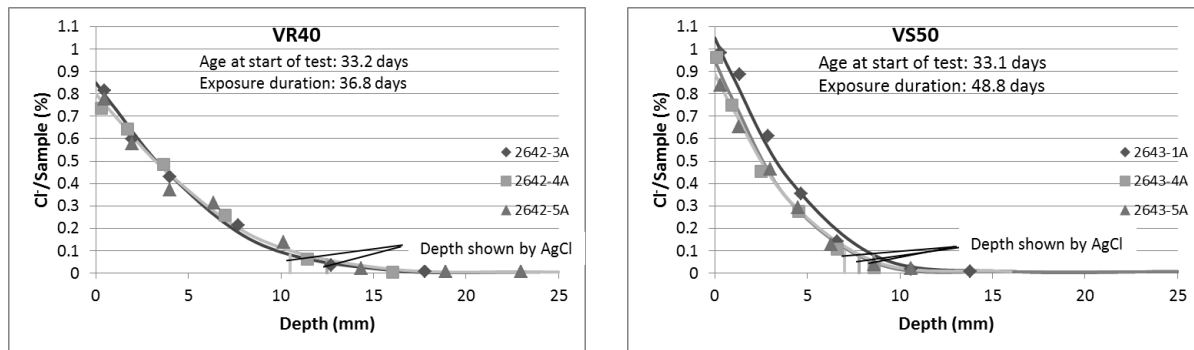
## 4. Results and Discussion

### 4.1 The Bulk Diffusion Test

The diffusion parameters,  $C_s$  and  $D_a$  of the two concretes are shown in Table 2, and the chloride profiles with fitted theoretical curves are shown in Figure 2.

**Table 2 – Results of bulk diffusion test**

Concrete type	Age during test	$C_s$ , Cl <sup>-</sup> per concrete (g/g)	$D_a$
VR40	33 – 70 days	0.81%, cv=0.05	$6.7 \times 10^{-12}(\text{m}^2/\text{s})$ , cv=0.07
VS50	33 – 82 days	0.96%, cv=0.08	$2.3 \times 10^{-12}(\text{m}^2/\text{s})$ , cv=0.12



**Figure 2. Chloride profiles.**

The as-tested apparent diffusion coefficient for Grade 40MPa concrete is about  $6.7 \times 10^{-12} \text{ m}^2/\text{s}$  and that for Grade 50MPa concrete is about  $2.3 \times 10^{-12} \text{ m}^2/\text{s}$ . These values are much higher than those tested on the actual concrete structures exposed to seawater. Besides, the as-tested diffusion coefficients do not represent those at the starting age due to the age effect. To present the results at 28 days and find out the actual age that these results represent, it is necessary to evaluate the age factor.

### 4.2 The Migration Test and Age Factor

The results obtained from the migration test include: the initial current (under 60 V), total charges passing through the specimen after 6 hours (calculated to that for the standard specimens: diameter 95 mm and length 50.8 mm), the class of resistance to chloride penetration specified by ASTM C1202; the 0-amp potential, depth of migration,  $D_{nssm}$  at 23°C. The results are shown in Table 3.

**Table 3 – Results of migration test (average of two specimens unless noted)**

Specimen code	Age at test (days)	Thickness $L$ (mm)	Initial current $I_i$ (mA)	Charge (Coulombs) & Class	0-amp volt $V_0$ (V)	Cl <sup>-</sup> depth $x_d$ (mm)	Coefficient $D_{nssm}$ , 23°C (m <sup>2</sup> /s)
VR40-1	33.4	52.0, 53.7	130, 103	2817 (M)	2.10	18.3, 14.3	$14.0 \times 10^{-12}$
VR40-2	49.9	51.0, 51.1	125, 100	2460 (M)	2.23	17.3, 12.8	$12.9 \times 10^{-12}$
VR40-3	69.9	51.7, 51.7	105, 96	2149 (M)	1.95	12.4, 11.8	$11.3 \times 10^{-12}$
VS50-1	33.4	53.8, 50.6	78, 74	1739 (L)	1.96	7.2, 6.7	$6.1 \times 10^{-12}$
VS50-2	55.9	50.5, 51.5	61, 54	1201 (L)	2.23	5.4, 5.8	$5.4 \times 10^{-12}$
VS50-3	82.1	51.0, 51.2	49, 42	1001 (L)	2.04	5.3, 4.2	$4.5 \times 10^{-12}$

Class of resistance to chloride penetration: M= moderate (2000– 4000 Coulombs); L= low (1000 – 2000 Coulombs)

The data obtained by the migration tests can be used for estimation of the “age factor”. To do this, the values to use must be comparable on the same base, i.e. not influenced by the change in temperature, actual size of specimens, and human errors (e.g. measurement of depth of chloride) and uncertainty in assumptions (e.g. assuming the free chloride concentration at the chloride front is 0.07 M). The best choice is the conductivity calculated from the initial current and specimen’s dimensions:

$$\kappa = \frac{I_i}{V - V_0} \frac{L}{\pi r^2} \quad (12)$$

where  $I_i$  is the initial current (mA),  $V - V_0$  is the effective potential (V),  $L$  and  $r$  are the thickness and radius of specimen (cm) respectively. The age factor estimated by the initial conductivity (Figure 3) is  $m=0.2$  for VR40 (Grade 40 MPa concrete) and  $m = 0.6$  for VS50 (Grade 50 MPa concrete). From the pattern of the conductivity decrease with age shown by Figure 3, one can predict that such decrease would be very little in the future, e.g. after 1 year. These results indicate that the chloride diffusion coefficient of concrete may not change significantly after a few years of construction.

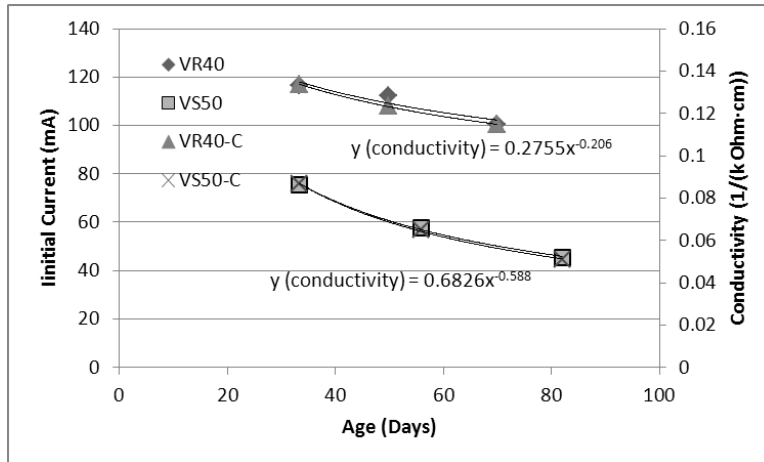


Figure 3. Estimation of the age factor.

#### 4.3 The Bulk Diffusion Coefficient at Different Ages

The diffusion coefficient at each age during the test can be calculated by using Eq.(9) when the age factor is known.

For the two concretes, the as-determined  $D_a$  represents that at an age between starting and end of the exposure, i.e. it was 42.4 days for VR40 (tested during age 33.2 to 70 days), and 54.6 days for VS50 (tested during age 33.1 to 82 days). The value of  $D_a$  at 28 days will be  $6.9 \times 10^{-12} \text{ m}^2/\text{s}$  and  $3.5 \times 10^{-12} \text{ m}^2/\text{s}$  for VR40 and VS50, respectively. The average values of the apparent diffusion coefficient for the two concretes are shown in Table 4 and Figure 4.

It can be calculated that if the test were started at age of 28 days and duration was 35 days,  $D_a$  would be  $6.9 \times 10^{-12} \text{ m}^2/\text{s}$  and  $2.7 \times 10^{-12} \text{ m}^2/\text{s}$  for VR40 and VS50, respectively. It is clear that the practice of using the starting age (e.g. 28 days) as the reference age for the determined  $D_a$  is imprecise for the newly made concrete. This is because the change in the diffusion coefficient during the test is significant.

Table 4 – Average apparent diffusion coefficient at various ages during testing

Concrete	Age (days)	$D_a$ ( $\text{m}^2/\text{s}$ )	Note
VR40	33.2	$7.3 \times 10^{-12}$	Start of test
	42.4	$6.7 \times 10^{-12}$	The test result (average)
	70.0	$6.3 \times 10^{-12}$	End of test
	28.0	$7.5 \times 10^{-12}$	Reference age
VS50	33.1	$3.1 \times 10^{-12}$	Start of test
	54.6	$2.3 \times 10^{-12}$	The test result (average)
	82.0	$1.8 \times 10^{-12}$	End of test
	28.0	$3.5 \times 10^{-12}$	Reference age

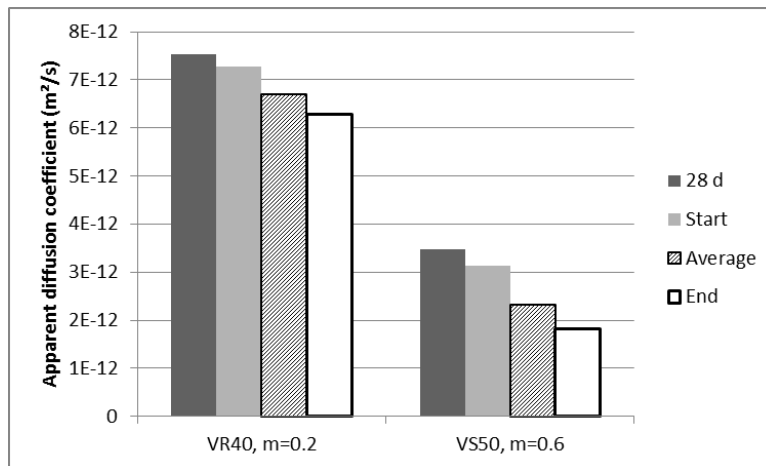


Figure 4. The diffusion coefficient at different ages during test, “Average” is the test result.

#### 4.4 Diffusion Coefficient of Free Chloride Ions

As described earlier, the diffusion coefficient of free chloride ions,  $D_0$  can be calculated using Eq.(3), and the mean chloride binding capacity,  $\partial C_b/\partial C_f$  can be evaluated. The environmental chloride is calculated by:

$$C_{ENV} = \frac{C_f}{m_{conc}} = \frac{C_f}{w} \frac{w}{m_{conc}} = \frac{C_f}{w} A_i \quad (13)$$

where  $m_{conc}$  is the mass of concrete,  $C_f/w$  the chloride content in the solution, and  $A_i$  is the concrete absorption. The solution used for the test (2.82M) gives  $C_f/w = 0.0905$ .  $A_i = 5.2\%$  and  $5.6\%$  for the VR40 and VS50 respectively. The average results for the two concretes are shown in Table 5.

Table 5 – Diffusion coefficient of free ions and chloride binding capacity

Concrete	$D_0$ (m <sup>2</sup> /s)	$D_a$ (m <sup>2</sup> /s)	$D_0/D_a$	$\partial C_b/\partial C_f$
VR40	$19.64 \times 10^{-12}$	$6.71 \times 10^{-12}$	2.93	1.94
VS50	$8.47 \times 10^{-12}$	$2.32 \times 10^{-12}$	3.64	2.60

The chloride binding capacity determined for in-situ concrete structures tested by the author was higher than 10. Published data on the chloride binding<sup>17, 18</sup> demonstrate that the slope of the curve of chloride content versus concentration of chloride in solution, i.e. the binding capacity, becomes smaller with increase in solution concentration, especially in the range where the environmental chloride ions concentration is above 0.6M. The reduction in the binding capacity may be the main reason for the high diffusion coefficient shown by concrete exposed to high chloride concentration.

On the other hand, this fact indicates that concrete exposed to environments with high chloride concentration would exhibit a higher chloride diffusion coefficient than that exposed to normal seawater.

#### 4.5 Comparison of $D_a$ and $D_{nssm}$

The second group of the migration tests had similar age as that of the average age of the bulk diffusion test, so that the results could be used for comparison. As shown in Table 6, the values of  $D_{nssm}$  are about twice that of  $D_a$  and 60% of  $D_0$ . This is likely because that the binding of chloride during the test was very limited.

Table 6 – Comparison of diffusion coefficients obtained from the two methods

Concrete	$D_a$ (m <sup>2</sup> /s)	$D_0$ (m <sup>2</sup> /s)	$D_{nssm}$ (m <sup>2</sup> /s)	$D_{nssm}/D_a$	$D_{nssm}/D_0$
VR40	$6.71 \times 10^{-12}$	$19.64 \times 10^{-12}$	$12.92 \times 10^{-12}$	1.9	0.66
VS50	$2.32 \times 10^{-12}$	$8.47 \times 10^{-12}$	$5.35 \times 10^{-12}$	2.3	0.63

Concrete powder samples were taken from the surface and near the AgCl boundary (migration front) of the specimens, one for each concrete, and the chloride content was analyzed. The distribution of chloride (Figure 5) demonstrates that the chloride content at the migration front was about 0.1%, and that at the it surface was much higher, which indicates that chloride binding occurred only in the near-surface zones. Note that the chloride content in the solution (0.6M), i.e.,  $C_f/w = 0.0208$ , which would result in 0.1% chloride in the concretes if chloride binding did not occur.

The maximum chloride content at concrete exposure surface is about 2/3 of that occurred during the bulk diffusion test (e.g. it is about 0.6% for the 40 MPa grade concrete) and becomes less toward the migration front. These indicate the binding of chloride by the concrete during the migration test could not complete due to the limited time (Figure 5). More comparative experiments are needed to establish the correlation between  $D_{nssm}$  and  $D_a$ .

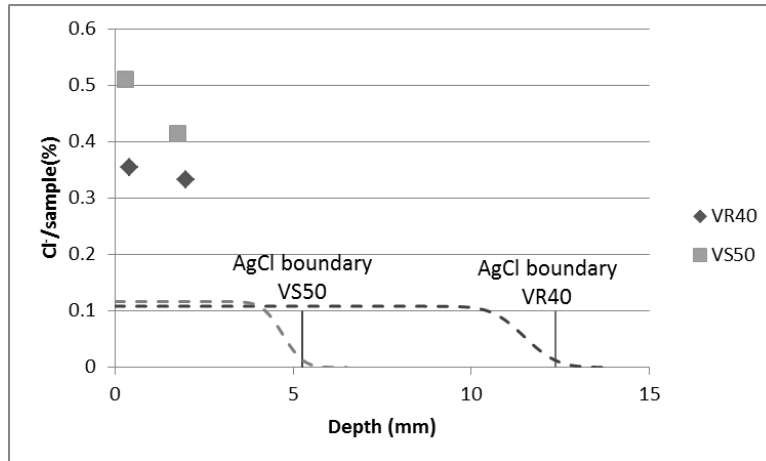


Figure 5. Chloride content in specimens tested for  $D_{nssm}$ . Dash lines represent free chloride ions distribution by theory.

## 5. Conclusions

This work has confirmed that the apparent diffusion coefficient,  $D_a$  determined by the bulk diffusion test method depends on the age of concrete and exposure duration. Its value decreases with age of concrete, especially for the newly made concrete.

The value of  $D_a$  at different ages can be estimated once the age factor is known. For quality control purpose, the reported  $D_a$  should be that for a specified age, but not a universal value.

The results of electrical field induced migration test can be used to estimate the age effect. The results presented in this paper indicate that the conductivity of the concrete at the start of the test, i.e. the initial conductivity is the best parameter to use to evaluate the age effect.

The estimated mean binding capacity of concrete,  $\partial C_b/\partial C_f$ , under the bulk diffusion test condition (exposed to 2.82M NaCl solution at 23°C) is 1.9 and 2.6 for the VR40 and VS50 concrete respectively, which are lower than that of concrete exposed to normal seawater.

For the two concrete mixes investigated in this work, the following results were obtained:

VR40: age factor  $m$  was 0.2,  $D_a$  at 28-day was  $6.9 \times 10^{-12} \text{ m}^2/\text{s}$

VS50: age factor  $m$  was 0.6,  $D_a$  at 28-day was  $3.9 \times 10^{-12} \text{ m}^2/\text{s}$

## 6. References

1. Nilsson, L.-O., Poulsen, E., Sandberg, P., Sørensen, H.E. and Klinghoffer, O., "Chloride penetration into concrete, State-of Art, Transport process, corrosion initiation, test methods and prediction models", Report No.53 (1996), Danish Road Directorate.

2. American Society for Testing and Materials, "Standard Test Method for Determining the Penetration of Chloride Ion into Concrete by Ponding (ASTM C1543-10a)", Annual Book of ASTM Standards, Vol.04.02
3. NORDTEST, "Accelerated chloride penetration (NT Build 443)", [www.nordicinnovation.org](http://www.nordicinnovation.org)
4. American Society for Testing and Materials, "Standard Test Method for Determining the Apparent Chloride Diffusion Coefficient of Cementitious Mixtures by Bulk Diffusion (ASTM C1556-11a)", Annual Book of ASTM Standards, Vol.04.02
5. NORDTEST, "Chloride migration coefficient from non-steady-state migration experiments (NT Build 492)", [www.nordicinnovation.org](http://www.nordicinnovation.org)
6. American Society for Testing and Materials, "Standard test method for electrical indication of concrete's ability to resist chloride ion penetration (ASTM C1202-97)", Annual Book of ASTM Standards, Vol.04.02
7. Xu, A. and Shayan, A., "Evaluation of Chloride Diffusion Coefficient in concrete by the Rapid Chloride Penetration Tests: Problems and observations," Proceedings of 23<sup>rd</sup> International ARRB Conference, Adelaide, Australia, July 2008, 15pp
8. Nilsson, L.-O., "The effect of non-linear chloride binding on chloride diffusivities and chloride penetration – A theoretical approach", Presented in the "Nordic Mini-seminar on Chloride Ingression in Concrete Structures," Göteborg, Sweden, 1993.
9. Jacob, B., Dynamics of fluids in porous media, Dover Publications, INC. New York, 1988. p.629.
10. Tang, L., "Chloride Transport in Concrete - Measurement and Prediction," Publication P-96:6, Department of Building Materials, Chalmers University of Technology, Sweden.
11. Atkins, P.W., (1987), Physical Chemistry, Third Edition, Oxford University Press, reprinted 1989.
12. CRC Handbook of Chemistry and Physics, 76<sup>th</sup> Edition, Davaid R. Lide, Editor-in-chief. Section 6-10.
13. Poulsen, E., "Four-parametric description of marine exposure and concrete's response to its chloride intensity", Proceedings of International Conference Repair of Concrete structures – from theory to practice in a marine environment, Svolvær, Norway (1997), pp.189-199.
14. Bentz, E. C. and Thomas, M. D. A., "Life-365 Service Life Prediction Model™ and Computer Program for Predicting the Service Life and Life-Cycle Costs of Reinforced Concrete Exposed to Chlorides", (2008.) [www.nrmca.org](http://www.nrmca.org)
15. Ferreira, M., Årskog, V., Jalali, S. and GjØrv, O.E., "Software for Probability-based Durability Analysis of Concrete Structures," Proceedings Fourth International Conference on Concrete Under Severe Conditions: Environment and Loading, ed. B.H. Oh, K. Sakai, O.E. GjØrv and N. Banthia, Seoul National Uni-versity and Korea Concrete Institute, Seoul (2004), pp.1015–1024.
16. Tang, L. and Gulikers, J., "On the mathematics of time-dependent apparent chloride diffusion coefficient in concrete," Cement and Concrete Research, Vol.37 (2007), pp.589-595.
17. Tang, L. and Nilsson, L.-O., "Chloride binding capacity and binding isotherms of OPC paste and mortars," Cement and Concrete Research, Vol.23 (1993), pp.247-253
18. Baroghel-Bouny, V., Wang, X., Thiery, M., Saillio, M. and Barberon, F., "Prediction of chloride binding isotherms of cementitious materials by analytical model or numerical inverse analysis," Cement and Concrete Research, Vol.42 (2012), pp.1207-1224.

# Frost test and the significant influence of small amounts of ions dissolved in surface water

Max J. Setzer<sup>1</sup>

<sup>1</sup>Professor em. of Civil Engineering, University Duisburg-Essen, presently WISSBAU, Essen

**Abstract:** The scaling of concrete during a freeze-thaw attack is dramatically increased by dissolved ions – not only as well known by de-icing agent (e.g. 3% NaCl = 513 mmol(eq)/l) but also even by small ion concentrations as found in tap or surface water (below 30 mmol(eq)/l). This is proved by outdoor exposure and in modified RILEM CIF-test. Effects of macroscopic physics or chemistry are too small to explain the phenomenon. The solution is found in the disjoining pressure relevant in the gel pores (typical pore diameter 2 nm to 30 nm). Additionally, it describes the following experimental results: (1) The gel-pore-water is prestructured by the surface interaction; (2) its density is increased to values between 1.15 g/cm<sup>3</sup> and 1.25 g/cm<sup>3</sup>; (3) its heat of fusion is reduced by app. 30% (1 to 3) depending on the type of cement; (4) the freezing point of gel-pore-water is lowered far below triple point – down to -45 °C. Since ice Ih is formed in the larger pores of concrete triple point condition – i.e. the coexistence of ice, gel-pore-water and vapor – is only fulfilled by additional high negative pressures in the gel-pore water; its value is increasing with falling temperature by app. 1 MPa/K. Experiments show that ice expansion is not relevant during the first freeze-thaw-cycles due to empty pores formed by self-desiccation. Freeze-thaw-cycles act as frost pump increasing the degree of saturation until ice damage sets in. Frost-test procedures – RILEM recommendations - should be modified on the basis of these results.

**Keywords:** Frost action, RILEM CDF/CIF recommendation, surface physics, dissolved ions, frost pump.

## 1 Introduction

Two principal questions concerning durability of concrete against freeze thaw attack are in the focus of this article. (1) Why concrete survives many freeze-thaw cycles even if it is saturated by isothermal capillary suction? (e.g. in ASTM C 666 it are 300 cycles, in Swedish test and CIF-test 56) In comparison a completely water filled steel container with much higher strength is destroyed during the first frost attack. (2) Why even small amounts of dissolved ions as found in surface water or tap water increase the scaling of concrete dramatically and this in a strength which cannot be explained by microscopic physics or chemistry (e.g. by depression of freezing point of chemical attack)?

The first question can be answered by a semi-macroscopic explanation. Starting point is that there exists a remarkable amount of unfrozen gel pore water even far below bulk freezing point. This aspect has already been pointed out by Powers [15]. He and Helmuth [23] used the hydraulic pressures and transport for the explanation. Fagerlund [6] claimed that if a critical degree of saturation is surpassed damage sets in. Already in 1977 calculated the author [28] the pressures and mass transport arising from surface tension of sub-microscopic ice crystals of different size in the gel structure which are trapped in submicroscopic pores and separated from the solid surface by an unfrozen molecular water-layer. Later the author [29, 30] used semi-macroscopic thermodynamics to calculate the temperature dependent negative frost-pressure in unfrozen gel-pore-water necessary to maintain the triple phase condition. Scherer [17] and Penttala [16] adopted similar pressures for the water ice interfaces. Scherer used it especially for his percolation model. The frost pressure generates frost shrinkage and a transport from unfrozen pore water to ice. As shown in [30] this effect generates macroscopically during a freeze-thaw cycle a frost-suction. It will be shown below that frost suction is by far more efficient than any other transport like isothermal capillary suction and of course than diffusion. For frost resistance it must be kept in mind that due to self-desiccation during the hydration of cement empty pore room is generated which is sufficiently large to balance the expansion of ice.

However, experiments proof that the macroscopic values for the properties of water deliver wrong values for the generated pressures. It is apparent from the experimental results that gel pore water deviates

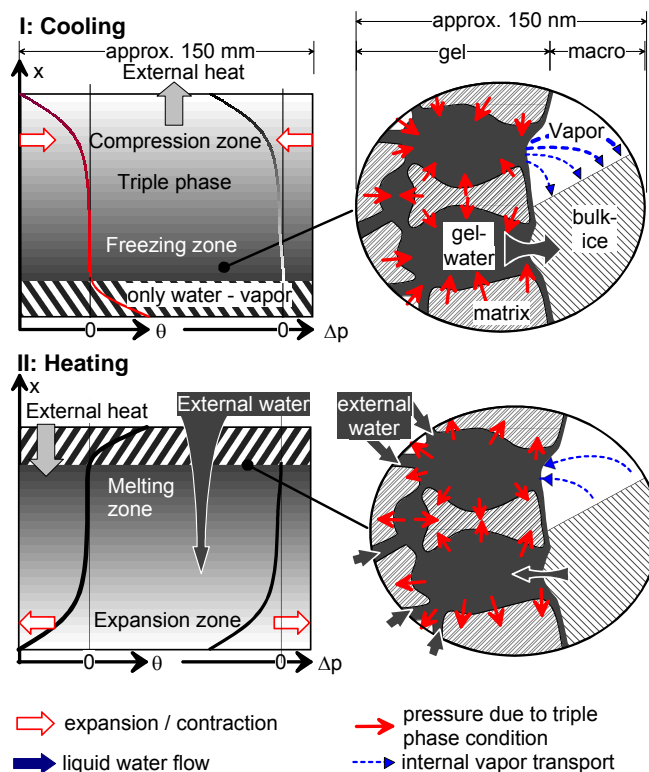
significantly from macroscopic bulk water. The heat of fusion and the density of gel-pore-water vary with the type of cement. Additionally, microscopic physical and chemical laws do not cover the influence of dissolved ions. To explain the impact of dissolved ions the disjoining pressure has to be introduced - a phenomenon which is only effective in the nanoscopic region i.e. far below  $1 \mu\text{m}$ . Especially the electrostatic part of the disjoining pressure is essentially changed by the concentration of dissolved ions and herewith important for the explanation of scaling.

At this point we should also keep in mind that we have to distinguish different sources of internal pressure. The micro-ice lens model and the negative pressure in the unfrozen gel pore water due to triple point conditions are strictly related to the pore water and its equilibrium with ice. A dry system will not show the effect. In contrast to this the disjoining pressure is primarily an interaction between the walls of the gel pore. It would be acting even in a dry system. However, it is significantly changed by the pore water and its dissolved ions.

Finally it must be taken into account that the frost phenomena act on different geometric scales. While disjoining pressure and all surface scientific aspects are most relevant around  $1 \text{ nm}$  and decay to become insignificant around  $100 \text{ nm} = 0.1 \mu\text{m}$ . The transport from gel pore water to the micro ice lenses takes place in the region around  $0.1 \mu\text{m}$  to  $100 \mu\text{m}$ . Here both thermal and thermodynamic equilibrium is reached much faster than any external change takes place. In the real structures above this we have as a rule transient thermal and hygral changes become more and more decisive i.e. no equilibrium is reached during normal cooling or heating process.

## 1. Micro-ice-lens model

### 1.1 Microscopic part and semi-macroscopic theory



**Figure 1:** The micro-ice-lens model. Comparison of microscopic / sub-microscopic scale (right) and transient macroscopic scale (left).

The micro-ice-lens model – figure 1 - describes the pumping effect leading to frost suction. It has three levels linked to scales – submicroscopic or nanoscopic, microscopic and macroscopic. In [29, 30] the author deduced the criteria for a thermodynamic equilibrium on the basis of the classical thermodynamics. Two criteria were derived: (1) a chemical stability criterion and (2) a mechanical stability criterion. Below bulk freezing point and after ice has formed in larger pores (above  $\approx 0.1 \mu\text{m}$ ) due to heterogeneous nucleation the macroscopic triple point condition is violated i.e. any unfrozen water has the tendency to



migrate to the ice. The triple point criterion can only be fulfilled in porous media if a high negative pressure can be generated in the unfrozen water. This is the chemical stability criterion. It bases on the equality of chemical potential of water. For unfrozen, liquid pore water (index L) and ice (index S) the equilibrium is established by equal chemical potential given by:

$$\int_{T_0}^T (s_S - s_L) d\tilde{T} = -v_L \Delta p_{LS} + (v_S - v_L)(p_S - p_0) \quad (1)$$

with the temperature T, the molar entropies s, the molar volumes v and the pressures p. In our context the second term is negligibly small giving

$$\Delta p_{LS} = -\frac{1}{v_L} \int_{T_0}^T (s_S - s_L) d\tilde{T} \quad (2)$$

As a rule the entropy changes with temperature and pressure (see [29]). However, the correction terms are small. The macroscopic properties and values of water are not applicable for gel pore water as found from detailed experimental results [19]. Its entropy and molar volume (density) is given in table 1.

The equation (2) can be simplified to a numerical relation between the pressure difference and the temperature  $\theta$  in Celsius scale with the coefficient  $\kappa$  dependent from the type of cement.

$$\Delta p_{LS} = \kappa \cdot \theta \quad (3)$$

Since  $\theta < 0$  and  $\kappa > 0$  the pressure in the liquid is negative. In table 1 data for bulk water and pore water are compiled. The value of pressure difference increases with falling temperature!

**Table 1: Data for prestructured gel pore water - from Setzer, Liebrecht [19]**

	Heat of fusion	Density	$\kappa$	$\bar{\gamma}/\kappa$
bulk	333 J/g	1000 kg/m <sup>3</sup>	1,22 MPa/K	27 nm*K
CEM I	186 J/g	1206 kg/m <sup>3</sup>	0,82 MPa/K	40 nm*K
CEM III A	238 J/g	1085 kg/m <sup>3</sup>	0,95 MPa/K	35 nm*K
CEM III B	226 J/g	1209 kg/m <sup>3</sup>	1,00 MPa/K	33 nm*K

The mechanical stability criterion defines until which temperature gel pore water remains unfrozen. For details see [29,30]. Here it is shown in a reduced way and combined with equation (3):

$$-\bar{\gamma} \frac{\partial \bar{A}}{\partial V} = -\frac{\bar{\gamma}}{R_H} = \Delta p_{LS}; \text{ and with (3): } R_H = -\frac{\bar{\gamma}}{\kappa \cdot \theta} \quad (4)$$

$\bar{\gamma}$  is the mean value of interfacial energy between ice and pore water. The value of the interfacial energy is quite uncertain in literature even under macroscopic aspects. Values are found between 20 and 44 mJ/m<sup>2</sup>. The value of Hobbs 33±3 mJ/m<sup>2</sup> is based on more direct experiments with interfaces and is used in table 1. In any case the given value gives only an approximation – however, a valuable guess for the magnitude and region.

$R_H$  is the hydraulic radius of the changing ice front. It is different during freezing and melting and depends from the pore geometry. During freezing it defines the progress or percolation of the ice into a pore; during melting the collapse of a pore-ice particle. In good approximation it is  $R_H(\text{percolation}) = R_H(\text{melting})/2 = d/4 = D/2$  where d is the diameter of a cylindrical pore and D the distance between the surfaces of a slit-pore.

At this point it is worth to note that the most relevant gel pore maximum in hardened cement paste is near to d=2 nm. Even if we consider the worst-case of bulk water in the table 1 and use as minimum temperature - 20° C as in most test procedures and especially in the RILEM recommendations than this gel pore water will not freeze.

## 1.2 Definition of size range – transition to macroscopic part and transient phenomena

The macroscopic range starts where the time of the externally generated temperature change faster than the necessary time to reach the thermal equilibrium this macroscopic volume of characteristic dimension length L. Following [12] the temperature within a slab of thickness L can be calculated by:

$$\theta(x,t) = \frac{4}{\pi} \theta_0 \sum_{n=0}^{\infty} \left\{ \frac{1}{(2n+1)} \exp\left(-\left[\frac{(2n+1)\pi}{L}\right]^2 a \cdot t\right) \sin\left(\frac{(2n+1)\pi}{L} x\right) \right\} \quad (5)$$

with:  $\theta(x,t) = T(x,t) - T_0$ ;  $\theta_0 = T_e - T_0$  and  $a = \frac{\lambda}{\rho c}$

where  $a$  is the thermal diffusivity of the material defined by the thermal conductivity  $\lambda$ , the density  $\rho$  and the heat capacity  $c$ . In equation (5) the exponential term is the dominant factor. It becomes less than 1% if the exponent falls below a value of  $-5$ . If we now consider a region of  $L_e$  then equilibrium is reached if it is:

$$\left[ \frac{(2n+1)\pi}{L_e} \right]^2 a \cdot t_e > 5; n=1 \Rightarrow t_e > \frac{5L_e^2}{3 \cdot a \cdot \pi^2}; \quad (6)$$

where  $t_e$  is called equilibrium time.

For wet concrete good approximations are  $\lambda = 2 \text{ W/(m}^*\text{K)}$ ,  $\rho = 2400 \text{ kg/m}^3$  and  $c = 1 \text{ kJ/(kg}^*\text{K)}$  and with that  $a = 0.83 \text{ mm}^2\text{/s}$ . Freezing is a phase transition; the situation is a moving boundary condition (Stefan problem) and equation (5) is not strictly correct. However, for our task to find an estimate for the region where quasi-equilibrium conditions change to a transient situation we can smear the heat of fusion over a temperature range where freezing takes place.  $0.1 \text{ K}$  is certainly a reasonable value. The heat of fusion in  $1 \text{ kg}$  of concrete we need the relative amount of freezable water in it which is until  $-10^\circ \text{ C}$  the bulk water. For a well hydrated concrete (degree of hydration app.  $0.9$ ) and a  $w/c$  of  $0.5$  we find approximately  $40$  liters of freezable water in one cubic-meter or  $0.017 \text{ kg(water)/kg(concrete)}$ . With an heat of fusion of  $333 \text{ kJ/kg}$  this gives  $5.5 \text{ kJ/kg(concrete)}$ . This smeared over  $0.1 \text{ K}$  the new  $c_{\text{frost}}$  is  $56.6 \text{ kJ/(kg}^*\text{K)}$  and  $a_{\text{frost}} = 0.0145 \text{ mm}^2\text{/s}$ . If we take as characteristic length  $L_e = 120 \mu\text{m}$  then the equilibrium time is  $t_e = 0.17 \text{ s}$  and at  $L_e = 300 \mu\text{m}$   $t_e = 1.05 \text{ s}$ . These equilibrium times are sufficiently below the values of a transient frost impact (typical  $10 \text{ K/h}$ ) and the length sufficiently above gel particle and pore size ( $\ll 1 \mu\text{m}$ ). At  $L_e = 4 \text{ mm}$  the equilibrium time is already a app.  $3 \text{ min}$ . This is critical even if external temperature changes are mostly slower than  $1 \text{ hour}$ . Therefore, we can now safely distinguish several regions:

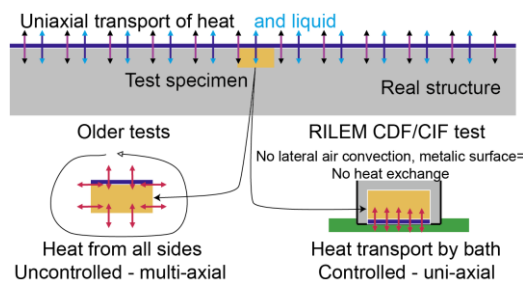
1. ( $>4 \text{ mm}$ ) In the **macroscopic scale** we have transient conditions where a frost-front is penetrating the object during freezing and a melting-front during heating.
2. ( $<4 \text{ mm}$  and  $>120 \mu\text{m}$ ) A **transition scale** where transient effects are still important. It is equivalent with the region of macro-capillaries. Here macroscopic transport of water etc. takes place.
3. ( $<120 \mu\text{m}$  and  $>4 \mu\text{m}$ ) In the **microscopic scale** local thermal equilibrium can be assumed. The mass transfer caused either by pressure or temperature gradients or by pressure differences between water and ice have time constants which are larger than the time constants of temperature waves without freezing. However, they are still significantly smaller than the macroscopic time constant. Therefore, in the submicroscopic scale we can assume a thermal equilibrium as well as a thermodynamic equilibrium.
4. ( $<4 \mu\text{m}$  and  $>0.120 \mu\text{m}=120 \text{ nm}$ ) **Submicroscopic scale**. Only local transport is significant. Region of micro-ice lenses, meso-capillaries and empty pores due to self-desiccation.
5. ( $<120 \text{ nm}$  and  $>4 \text{ nm}$ ) The **scale of gel** where the freezing point of pore-water is decreased by the surface interaction with the solid. It starts at meso-gel level (typical dimension  $d < 0.12 \mu\text{m}=120 \text{ nm}$ ) the upper diameter of meso-capillaries – hydraulic radius  $R_H = d/4 = 30 \text{ nm}$  - as given in [27])
6. ( $<4 \text{ nm}$ ) The **nanoscopic scale** where the natural law of surface physics and chemistry dominate over macroscopic bulk laws. The disjoining pressure as discussed below is dominant. Region of gel pores.

### 1.3 Macroscopic part of micro-ice-lens model

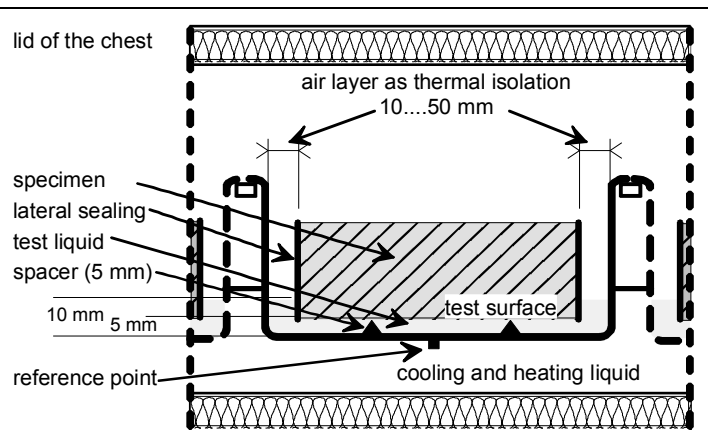
As pointed out above and can be seen in figure 1 gel pore water is transported during cooling to the micro ice particles until a sufficiently high negative pressure is generated in the unfrozen gel pore water following the equation (3); this transport is increasing with falling temperature. The phenomenon is called frost shrinkage. During heating the inverse effects takes place i.e. the value of the negative pressure in the unfrozen gel pore water is falling with temperature. However, ice remains unfrozen. A distinct hysteresis is observed between freezing and melting. Therefore, if external water is available it will be sucked in. The effect is called frost suction. This is by far the most efficient suction process. (See figure 1 for the description and in figure 5 for experimental results.) problem is proved by some thousand test results in CDF/CIF test [13, 14] and numerically modelled by Kruschwitz [9, 8].

## 2 Simulation of real conditions during a frost attack in laboratory by the RILEM CIF test – frost suction and internal damage

It is clear that this transient process of frost suction highly depends on the boundary conditions. Since any test procedure should simulate the real conditions as good as possible the boundary conditions of the real concrete structure shall be analyzed first – see figure 3. In real structures the heat and moisture transport takes place predominantly over one outer surface which can be called “surface of attack”. As long as they are laterally “infinitely” extended the heat and moisture flux are vertical to this surface. The horizontal heat transport is negligible as well as the water transport. A test specimen can be treated like a small cut out of such a structure. However, now additional surfaces lateral are generated. Any transport of both liquid and heat over these new surfaces would generate a deviation from the transient process in the real structures. Experimental data showed that in this case the effect of the micro-ice lens pump would be shortcut. Frost suction and herewith the result of the test and the durability prediction would deviate essentially from real situations. It is worth to keep in mind that 1 mm of liquid water on top of the surface of attack consumes as much heat during freezing as 10 mm of concrete. Therefore, a transport over any other surface of the specimen must be suppressed. This substantial requirement has been violated in nearly all test procedures (ASTM, ÖNORM, and even Swedish slab test) known to the author. CDF [13], CIF [14] test as proposed in the RILEM recommendations solve this problem - for a better understanding see figures 3 and 4. Since in the test procedures the relevant boundary conditions are adequately fixed the tests have a high precision as proved by several international round robin tests and evaluated following ISO 5725 (details see Auberg [1]). It is not reached by any other freeze-thaw tests taken into account.



**Figure 3. Comparison real structure and laboratory test.**

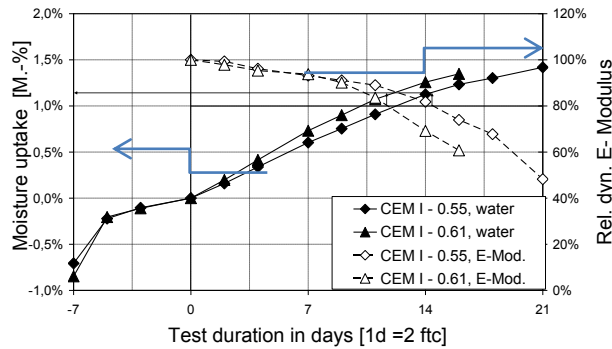


**Figure 4. Test set-up during RILEM CDF / CIF test procedure.**

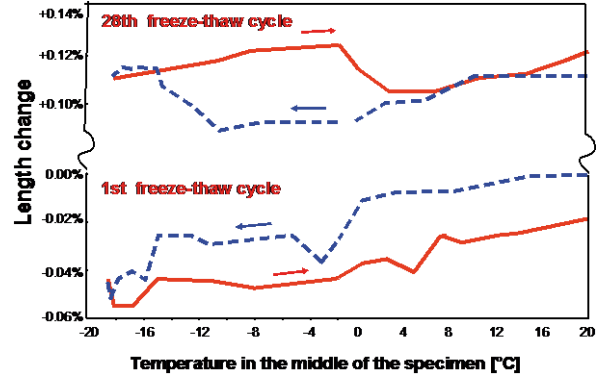
In the CIF/CDF test (figure 4) each specimen is in an individual container immersed in a liquid temperature controlled bath which allows both precise control of the freeze thaw cycle (<0.5 K) and an efficient heat transport. Lateral heat exchange by convection is suppressed due to the small distance between specimen and container wall and exchange by radiation by the use of metal surfaces.

In a frost test the degree of saturation is increased by frost suction until a critically and damaging degree is reached. Therefore, it is important to start the freeze thaw test is a well-defined degree of saturation. In CDF/CIF test the specimens are saturated by capillary isothermal suction during 7 days. Two freeze-thaw cycles are passed per day. Results are reached after 28 cycles or 14 days. For further detail it is referred to the RILEM recommendation.

## 2.1 Experimental results of CIF test



**Figure 5.** CIF Test results. Water uptake and rel. dyn. E-modulus as function of time / freeze thaw cycle ftc. Negative values relate to capillary suction.



**Figure 6.** Length change measured during CIF test. Abscissa has been cut to collect the data during contraction (1st cycle - negative!) and during expansion (28th cycle) in one graph. Data by Setzer, Kasperek

In figure 5 both internal damage characterized by the reduction of the relative dynamic elastic-modulus, and water uptake are plotted. It is seen: (1) The saturation by frost suction (positive values) is substantially larger than the saturation by the isothermal capillary suction. (2) The CIF test is able to distinguish even relatively small changes in concrete quality (here between w/c 0.55 and 0.61). The acceptance criterion RDM=80 % is transgressed with wc= 0.55 at the 29th freeze-thaw cycles (14.5 days) and for wc=0.61 at the 24<sup>th</sup> ftc (12 days). Since German regulations for waterways demand a minimum of 28 cycles before the RDM=80% is transgressed the wc=0.55 meets the test even if scarcely and 0.61 fails it. (3) Damage sets in after nearly the same amount of suction is reached in both cases as marked by arrows.

The thermal expansion during CIF test figure 6 reflects the length change measurement in figure 2: (1) At start of test – 1st cycle – frost shrinkage (negative values) dominates since apparently there is sufficient space due to autogenous shrinkage that ice expansion is not relevant here. The result also shows that even isothermal capillary suction cannot saturate the specimen sufficiently. However, due to frost suction ice expansion dominates at the end (28th cycle) where the critical degree of saturation is reached.

For durability of frost resistance the speed of frost suction is the decisive parameter. It should be noted that following our data entrained air is protective since it inhibits the suction process comparable to air in mechanical a hydraulic pump. This must be kept in mind when designing air content especially for high performance concrete with a dense matrix.

### 3 Scaling and the influence of dissolved ions

#### 3.1 Scaling experiments with changing concentration of solution including simulation of surface water

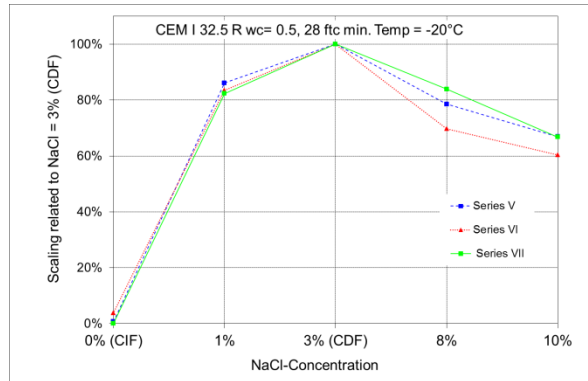


Figure 7. Change of scaling dependent from concentration of de-icing salt (NaCl) concentration – 28 ftc. 1% NaCl = 0.171 mol/l<sub>eq</sub>.

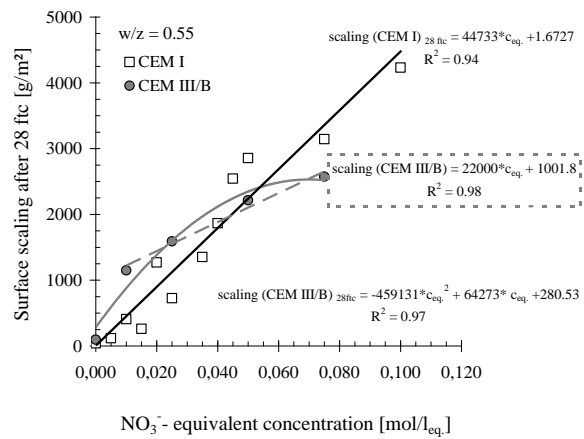


Figure 8. Influence of minor concentrations of dissolved ions (eq. surface water) on scaling after 28 freeze-thaw-cycles – ftc – with concrete.

It is well known that deicing chemicals increase the frost damage dramatically. In the RILEM technical committee TC 117 FDC recommendation the CDF test - has been proposed [13]; its precision has been assessed in several international round Robin tests and evaluated by ISO 5725. In a big additional research program [22] we found an acceptance level of 1500 g/m<sup>2</sup> after 28 freeze thaw cycles (ftc) for durability against frost and de-icing salt attack (In European Standard concrete class XF3). In this project more than 400 different types of concrete have been tested covering good and bad concretes. The selection of the mix design was advised by industrial representatives.

In another program we checked how a change of the concentration of deicing chemicals influences the scaling - figure 7. The 3% concentration as demanded in CDF test has been used as reference. It is clearly seen that at 3% - the CDF-value - the maximum damage is reached. From the macroscopic point of view this is astonishing since at this concentration neither the depression of freezing point nor a chemical attack are sufficiently strong to explain this maximum.

Even more astonishing was an experience during a round Robin test of RILEM TC 176 for the recommendation of CIF test [14] of frost resistance of concrete with **pure** water: It was found that already the different type of tap water in the different laboratories caused significantly different results. Auberg [1] reproduced the composition of the test-water in laboratory and could explain the differences in scaling by the influence of dissolved ions. However, since the precise causes were not understood sufficiently well to give clear recommendations RILEM TC 176 used demineralized water as test liquid in the RILEM recommendation for CIF test [14]. We were aware that for scaling these are minimum conditions.

Therefore, Bevanda studied the effect of dissolved ions systematically [2, 3]. She proved as well that the laboratory test results with well-defined ion concentrations can exactly be related to scaling under outdoor conditions with surface water. In figure 8 it is clearly seen that small concentrations dramatically change scaling. The “non-linear” progress of scaling can be attributed to the difference between carbonated and non-carbonated zone. The concentrations of test liquid are far below the well-known maximum condition for de-icing chemicals. Surface or tap water has a concentration of some milimol-equivalent/liter and is in the lower part of figure 8. This effect definitely cannot be explained by a microscopic physics or chemistry.

### 3.2 Explanation by the electrostatic part of disjoining pressure

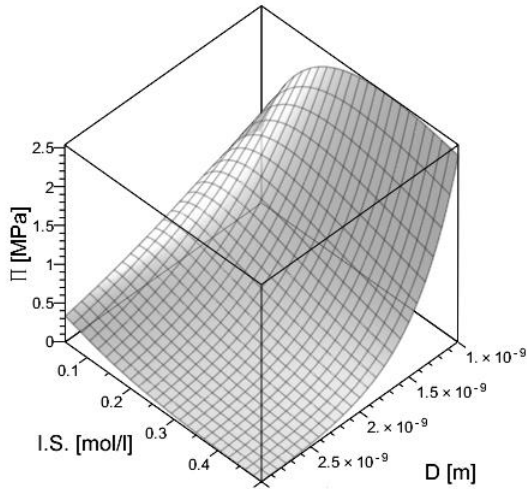


Figure 9. Disjoining pressure  $\Pi$  – electrostatic and molecular part - as function of the ionic strength (I.S.) and the pore diameter.

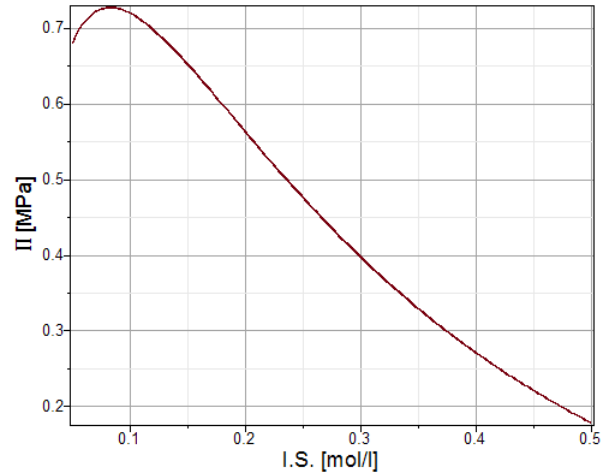


Figure 10. Disjoining pressure  $\Pi$  – electrostatic and molecular part - as function of the ionic strength (I.S.) – for a pore diameter of 2 nm.

A fair explanation of the rather high impact of even highly diluted dissolved ions on the surface scaling of concrete during a freeze thaw attack can be given by nanoscopic surface science. For this one must keep in mind (1) that hardened cement paste has a nanoscopic gel structure and (2) that in this structure special surface scientific laws become dominant. They are described best by the disjoining pressure  $\Pi$  which was published first by Derjaguin (1936) and which describes the interaction between two internal surfaces in the distance of a few nanometers. The disjoining pressure is characterized thermodynamically by the distance  $h$  of the two solid interphases.

$$\Pi(h) = - \left( \frac{\partial G}{A \cdot \partial h} \right)_{p, T, \mu_i} \quad (7)$$

It becomes relevant when the surface forces between the interfaces overlap. A precise description would go beyond the scope of this article. The background is found in the excellent text books by Israelachvili [7], by Derjaguin, Churaev and Muller [5] and by Churaev [4]. Three different types of disjoining pressure must be distinguished: the dispersive or molecular term (index  $m$ ) which is attractive in our case and compared to the other two relatively small, the electrostatic term (index  $e$ ) which is the most interesting here and the structural term (index  $s$ ) which is rather important and large in pre-structured and structured gel-pore water [25] but will not be treated here.

$$\Pi = \Pi_m + \Pi_e + \Pi_s$$

The molecular term decays with the distance by a power of six and ranges to the largest distance under the disjoining pressure terms i.e. until approximately 100 nm. The electrostatic term decays with distance  $d$  exponentially -  $\propto \exp(\kappa \cdot d)$  where  $1/\kappa$  is the Debye radius. It highly depends on the type of electrolyte and the electrolyte concentration.

$$\frac{1}{\kappa} = \begin{cases} 0.304 / \sqrt{[NaCl]} \text{ nm} & 1:1 \text{ elektrolyte} \\ 0.176 / \sqrt{[CaCl_2]} \text{ nm} & 2:1 \text{ elektrolyte} \\ 0.152 / \sqrt{[MgSO_4]} \text{ nm} & 2:2 \text{ elektrolyte} \end{cases} \quad (8)$$

The electrostatic and molecular part of the disjoining pressure following by DVLO theory and taking into account pore solution and distances as found in hardened cement paste has been calculated and is plotted in figure 9 and 10. In the plot the concentration is given by the ionic strength as defined by

$IS := \frac{1}{2} \sum_i z_i c_i$  where  $z$  is the valence and  $c$  the concentration of the ion type  $i$ . It must be emphasized

here that the electrostatic part of disjoining pressure is dominant and repellent. From squeezed out pore solution – Xu [32] - we can state that the ionic strength of the pore solution is near to 0.1 mol/l. The figure 9 and 10 show that this is near to a maximum of the electrostatic disjoining pressure. During freezing the concentration in the unfrozen pore water is increased since ice does not solve ions. The disjoining pressure is diminished.

This drop-down of disjoining pressure is added to the pressure discussed above in the micro-ice lens model. In contrast to the micro ice lens pressure which acts in the unfrozen water and is related to this water the change of disjoining pressure is related to the interaction of the solid gel particles even if this interaction is highly affected by the medium between the particles especially by the dissolved ions.

If by frost suction water with dissolved ions is sucked in the effect of electrostatic part of disjoining pressure is enhanced. For concentrations as found in deicing solutions this effect becomes detrimental as known from practical experience. However, the recent findings show as well that even small amounts of dissolved ions cannot be neglected.

## Conclusions

1. **Frost suction:** During the first freeze-thaw cycles a saturation process of concrete is observed which is caused by frost action and which significantly exceeds the usual saturation for instance by an isothermal capillary suction. The frost suction process is generated by the micro-ice-lens pump.
  - (1) Microscopically it bases on water in nanoscopic gel pores which is hindered from freezing by surface forces and which deviates from properties of bulk water (prestructured, density, heat of fusion). Below freezing point it is in equilibrium with ice due to negative pressure. This generates frost shrinkage during cooling and frost swelling during melting.
  - (2) Ice expansion is not observed during the first cycles since sufficient pore space has been generated due to autogenous shrinkage during hydration.
  - (3) Macroscopically there is a transient process. During cooling water is transported from gel to ice. During heating it remains trapped. The frost swelling sucks in external water if available.
  - (4) The degree of saturation increases with every freeze thaw cycle.
2. **Internal damage:** Only after a damaging degree of saturation is reached destruction by ice expansion and hydraulic pressures sets in as it is explained by the existing models of frost damage. The pure ice expansion effect is restricted to the inner part of concrete i.e. internal damage.
3. **Surface scaling** is highly dependent from dissolved ions in the pore solution. The electrostatic term of disjoining pressure is changed due to this especially during ice formation. Dissolved ions in the sucked in water increase the effect. Even small amounts are relevant as found in surface water. Concentrations like in de-icing solutions are detrimental.

## Acknowledgement

The author wants to thank his former co-workers and PhD students during his active work at IBPM at Univ. of Essen-Duisburg and before at Technical University of Munich.

## References

1. Auberg, R.: Zuverlässige Prüfung des Frost- und Frost-Tausalz-Widerstands von Beton mit dem CDF- und CIF-Test (Reliable testing of freeze-thaw and de-icing salt resistance). PhD thesis University of Essen. In Mitteilungen aus dem IBPM, Heft 6. Shaker, Aachen, 1998.
2. Bevanda, I.; Setzer, M.J.: Frost-scaling under minor concentration of dissolved ions – XF3 under laboratory and outdoor conditions. Proc. 17. Int. Baustofftagung IBAUSIL 2009 Finger-Inst. Bauhaus Univ. Weimar, p. 2-0445-2-0450
3. Bevanda, I.: Modifizierter CIF-Test – Auswirkung gelöster Ionen auf die Frostschädigung bei reinem Frostangriff. in Setzer (ed.): Mitteilungen aus dem Institut für Bauphysik und Materialwissenschaft der Univ. Duisburg-Essen. Heft 16, Cuvillier, Göttingen 2011
4. Churaev, N.V.: Liquid and Vapor Flows in Porous Bodies – Surface Phenomena. Topics in Chemical Engineering Vol. 13 (Gordon and Breach sci. Publishers, Amsterdam, 2000
5. Derjaguin, B.V., Churaev, N.V., Muller, V.M.: Surface forces. Cons. Bureau/Plenum, New York. 1987
6. Fagerlund, G.: The significance of critical degree of saturation at freezing of porous and brittle materials. ACI Spec. Publ. SP-47, Detroit (1977) p. 13

7. Israelachvili, J. N.: Intermolecular & surface forces. 2nd ed. Academic Press, Amsterdam 1991.
8. Kruschwitz, J., Setzer M.J.: From nano to macro: modelling freeze-thaw characteristics of cementitious materials. Proc. CONCREEP, 2008
9. Kruschwitz, J.: Instationärer Angriff auf nanostrukturierte Werkstoffe — eine Modellierung des Frostangriffs auf Beton., PhD thesis, Universität Duisburg-Essen, Cuvillier, Göttingen, 2008
10. Liebrecht, A.: Phasenübergänge, Frostschrumpfen und Schrumpfvorgänge im Zementstein. (Phase transition, frost shrinkage and autogenous shrinkage of hcp) PhD thesis. Mitt. IBPM, Univ. Duisburg-Essen, Heft 11. Cuvillier, Göttingen, 2005.
11. Liebrecht, A.; Setzer, M.J.: Sättigungsgrad und dessen Einfluss auf das Frostverhalten beim Zementstein. IBAUSIL 2003, FIB - Bauhaus-Universität Weimar, 2003, Vol.2 1043–1052
12. Özisik, M.N.: Heat conduction. Wiley, New York 1980
13. Setzer, M. J.; Fagerlund, G.; Janssen, D. J.(authors): RILEM Recommendation, RILEM TC 117 FDC: CDF Test- Test Method for the Freeze-Thaw Resistance of concrete with sodium chloride solution. Materials and Structures Vol. 29 (1996) 523-528
14. Setzer, M.J.; Heine, P.; Kasperek, S.; Palecki, S.; Auberg, R.; Feldrappe, V.; Siebel, E. (authors): RILEM. Recommendation - RILEM TC 176 IDC –CIF-Test–Capillary Suction, Internal damage and Freeze thaw Test – Reference method and alternative methods A and B, Materials and Structures, Vol. 37 (2004) 743-753
15. Powers, T.C.: A Working Hypothesis for Further Studies of Frost Resistance of Concrete. J. ACI Proc. (1945) 41, 245-272
16. Penttala, V.: Freezing-induced strains and pressures in wet porous materials and especially in concrete mortar. Adv. Cem. Based Mat (1998) p. 8
17. Scherer, G.W.: Freezing gels. J. Non-Crystalline Solids Vol. 155 (1993) 1
18. Setzer, M.J.: The Solid-Liquid Gel-System of Hardened Cement Paste. in [31] 237-243
19. Setzer, M.J., Liebrecht, A.: The properties of pore solution in hardened cement paste. in [24] p. 207-215
20. Setzer, M. J.: Modeling and testing the freeze-thaw attack by micro-ice-lens model and CDF/CIF-test. In: Proc. of the International Workshop on Microstructure and Durability to Predict Service Life of Concrete Structures, Sapporo, Japan 2004
21. Setzer, M.J.; Auberg, R. (eds.): Frost Resistance of Concrete RILEM Proc. 34. Spon, London 1997.
22. Hartmann, V.: Optimierung und Kalibrierung der Frost-Tausalz-Prüfung von Beton – CDF-Test. PhD thesis. Univ. Essen 1992
23. Helmuth, R.A.: Investigations of the Low Temperature Dynamic Mechanical Response of Hardened Cement Paste. Dept. of Civil Engineering, Stanford Univ., Technical Report 154, 1972
24. Setzer, M.J. (ed.): Transport in concrete – Nano to macrostructure. Proc. 5th Intern. Essen Workshop – TRANSCON07. AEDIFICATIO, 2007, Freiburg
25. Setzer, M.J.: Disjoining pressure in highly dispersed systems and shrinkage. In: Wittmann F. H.; M. Olivier (eds): Basic Research on Concrete and Applications, Proceedings of an ASMES International Workshop, Aedificatio Publishers Freiburg, Germany (2011) 195 – 216
26. Setzer, M.J.: Fundamentals of Frost Damage in Hardened Cement Paste. In: Wittmann F. H.; M. Olivier (eds): Basic Research on Concrete and Applications, Proceedings of an ASMES International Workshop, Aedificatio Publishers Freiburg, Germany (2011) 125 - 142
27. Setzer, M.J.: Mikroeislinienbildung und Frostschaaden. In.: Eilighausen R. (Hrsg.): Werkstoffe im Bauwesen – Theorie und Praxis (Construction Materials – Theory and application). Ibidem, Stuttgart. P. 397-413 (1999)
28. Setzer, M. J.: Einfluss des Wassergehaltes auf die Eigenschaften des erhärteten Betons. Schriftenreihe DAfStb. Heft 280 (1977) 43-117
29. Setzer, M.J.: Mechanical stability criterion, triple phase condition and pressure differences of matter condensed in a porous matrix. J. Coll. Interface Sci. 235 (2001) 170-182.
30. Setzer, M. J.: Micro-ice-lens formation in porous solid. J. Colloid Interface Sci. 243 (2001) 193-201
31. Tanabe, T.; Sakata, H.; Mihashi; H.; Sato, K.; Maekawa, H.; Nakamura;H. (eds.): Creep, shrinkage and durability mechanics of concrete and concrete structures; Proc. of 8<sup>th</sup> Intern. Conf. Ise-Shima, Japan. CRC Press, Leiden 2009
32. Xu, X.: Tieftemperaturverhalten der Porenlösung in hochporösen Werkstoffen. PhD thesis Univ. Essen 1995



# Durability Planning – a Formalised Approach in Concrete Institute of Australia Recommended Practice

Rodney Paul <sup>(1)</sup> and Frank Papworth <sup>(2)</sup>

<sup>1</sup>Materials Technology Service Line Leader GHD Pty Ltd, Perth, Australia,

<sup>2</sup> Managing Consultant BCRC, Perth, Australia

**Abstract:** This paper provides an overview of the Concrete Institute Australia (CIA) Recommended Practice Z7/01 Durability Planning (CIA Concrete Durability Series – Durability Planning. Concrete Institute of Australia Recommended Practice Z7/01. Sydney 2014.). Durability planning is cost-effective selection and usage of materials combined with design processes, construction methods and detailing to achieve the asset owner intended service life without premature unexpected operational maintenance.

CIA Z7/01 (1) provides information on durability planning during design, construction and operational service life phases for all concrete construction stakeholders. It is intended to inform and inspire designers about the benefits of durability design so they can inspire asset owners to elevate durability planning to a position alongside structural and architectural design. The planning process can be equally applied to all construction materials and this is commonly adopted by durability consultants in Australia.

Durability knowledge is available for engineering analysis but formal durability processes in design, construction and operational maintenance are missing. Durability planning as outlined in this technical paper and CIA Z7/01 (1) is the recommended change to formalise durability complementary with structural design.

A durability assessment report will explain the durability requirements and provide details to be included in the project design reports, specifications, design drawings, asset maintenance plans and/or operation and maintenance manuals. This report may be a page for simple structures or detailed for complex, critical or uncertain structures. Durability checklists in tabular form provide useful project guidelines complementary to the durability assessment report.

**Keywords:** Concrete, Durability Planning, Durability Assessment Report, Durability Consultant

## 1. Introduction

Information on processes involved in concrete deterioration are available for engineering analysis but a formal process for achieving durable structures in design, construction and operational maintenance is missing. Durability planning outlined in CIA Z7/01 (1) is a system to formalise the process of achieving durability through appropriate design, construction and maintenance.

The CIA durability series will provide the tools for managing durability through design, construction and maintenance. The series will comprise:

- Z7/01 Durability – Planning (published in 2014).
- Z7/02 Durability - Exposure Classes (in progress).
- Z7/03 Durability - Deemed to Comply Requirements (in progress).
- Z7/04 Durability – Good Practice through Design, Concrete Supply and Construction (published in 2014).
- Z7/05 Durability – Modelling (in progress).
- Z7/06 Durability - Cracks and Crack Control (in progress).
- Z7/07 Durability – Testing (to be published in 2015).

CIA Z7/01 (1) sets out the process of planning to achieve the required level of durability. The durability planning outcomes will be delivered in a durability assessment report or durability plan (alternative names for a durability deliverable report) specific for the project. This will describe how the desired level of durability will be achieved and ensured using appropriate tools and recommendations given in Codes and Recommended Practices (e.g. CIA Z7/02-07).

A durability assessment report provides a continuous link in durability objectives between design, construction and maintenance. Durability planning evaluates, explains and provides solutions for all stakeholders. Greater confidence is provided for the design and required service lives to be achieved.

Durability is provided with improved confidence when the concrete structure asset owner is actively involved starting from the project brief stating specific durability requirements. Designer and/or contractor provided durability without adequate asset owner defined formal requirements has uncertainty that an optimum whole of life cost will be achieved. In a worst case scenario of reduced structural adequacy and/or functionality, asset owner maintenance cost funding and resources may be excessive to keep the asset operational or the asset owner may face rapid premature depreciation.

Concrete structures recommended to use durability planning will have durability design requirements that are complex, critical or uncertain. Durability planning is not expected for simple structures in exposure conditions excluding moderate or severe (e.g. house slab and paths).

The durability assessment report issued will explain the durability requirements and provide details to be included in the project design reports, specifications, design drawings, asset maintenance plans and/or operation and maintenance manuals. This report may be a page for simple structures or detailed for complex, critical or uncertain structures. Durability checklists in tabular form provide useful project guidelines complementary to the durability assessment report.

## 2. Why Durability Planning

All capital works, whether government or privately owned assets, must achieve the design life intended, operational functionality, acceptable return on capital investment, safe operational environment (e.g. durability provides acceptable serviceability and ultimate risk to the community) and environmental sustainability. An appropriate durability philosophy throughout the project delivery will provide this.

In engineering terms, durability planning is cost-effective selection and usage of materials combined with design process, construction methods and detailing to achieve the asset owner intended service life without premature unexpected operational maintenance. A technical analysis determines the nature and rate of materials deterioration for given macro and micro environmental conditions, which is used to influence the design, construction and operational maintenance during the service life.

Design and construction to National or International Standards may not achieve the asset owner's required design life in aggressive exposure conditions. Significant premature maintenance and/or repair could be necessary. A durability review is required as Codes do not cover all environmental exposure conditions and specific location micro exposure conditions can be more severe than the general exposure conditions.

Asset owners may require a design life of 20, 50, 70, 100, 150 or 300 years whilst Standards may state 40 to 60, 50, 100 or not comment on design life. Owners may have specific desires for the performance of the structure at the end of the design life so that rehabilitation and extended life can be achieved. Future different owners may have upgrade requirements. They may also have views on reliability required through the design life. Durability planning allows owners to give specific design life requirements. Durability planning evaluates, explains and provides solutions to all parties and provides greater confidence that the design life will be achieved.

Durability design is expected by all construction parties but formal design by durability consultants is not a common specified requirement. The common informal expectation is someone completes the durability design within the design process and, in the absence of a named person, the structural engineer is deemed to have completed the task. This is not a reasonable obligation for the structural engineer who does not have durability training and /or experience. An alternative view is that Australian Standards take full account of durability such that structural design being acceptable equates to acceptable durability design.

However, Australian Standards state that compliance with the durability provisions of the standards is not sufficient given the complexity of the subject. For example, AS 3600: 2009 Section 4.1 Note 2 [4] "Durability is a complex topic and compliance with these requirements may not be sufficient to ensure a durable structure."

Furthermore, reliance on durability provided by a current Standard is not an acceptable legal defence for premature durability damage to a structure where a reasonable engineer is expected to have awareness of more recent related Standards or other technical society publications that require additional durability provisions.

Is premature deterioration or unacceptable maintenance a present day problem? Yes, in some aggressive environments where materials selection or construction techniques are inadequate, or design agreed maintenance is not implemented. Therefore acceptable durability is not always being achieved to the level expected.

It is recommended that asset owner project briefs include the requirement that design and non-compliance reports that effect durability are reviewed by a durability consultant. On projects where the contractor's construction method is different to the design or influences durability a durability consultant review is required. The durability planning process benefits all parties:

- The asset owner is likely to have a structure that more closely matches expectations in terms of reliability through the design life. The contribution to the proactive maintenance approach will lead to a lower maintenance cost.
- For the designer, inclusion of high level materials expertise reduces the risk of premature failure and over design.
- An unexpected outcome on some projects is contractors utilise the durability consultant expertise for advice on materials and methods even where not strictly required. Consequently they reduce the risk of not using optimal materials and this reduces the risk of failures and can lead to cost savings.
- For the operator of the structure it leads to reduced maintenance which means lower cost and less interference.

Examples of concrete structures recommended to use durability planning are listed below:

- Major civil and building structures, including:
  - Airport infrastructure.
  - Bridges and culverts, elevated viaducts, tunnels.

- Buildings for commercial, industrial, government and residential use, including weatherproof exterior façade and below water level basements.
- Mining and industrial structures, including material processing and handling.
- Power stations, including seawater structures.
- Structures of cultural, heritage, national or world significance.
- Transmission towers.
- Wharves, piers and jetties.
- Water retaining or excluding structures including dams, desalination plants, pipelines, pump stations, tanks and treatment plants.
- Wastewater treatment plants.
- Precast panels with complex metal arrangements and tight covers.
- Buildings with applications that lead to unusual exposures (e.g. where leakage with contaminants occurs like swimming pools in hotels or aquariums in restaurants).
- Industrial sites where elements or structures might be exposed to contaminated ground or air.
- Elements with critical leakage requirements.
- All concrete structures in corrosive exposure environments.

### 3. Formal Durability Planning

The need to incorporate durability into design, construction and maintenance to prevent premature deterioration of concrete structures has been identified in many international documents over a long period of time. Examples of technical concerns and improvement approaches for durability in the design, construction and maintenance of concrete structures are listed below from 2001 back to 1968. Technical society publications by the American Concrete Institute (ACI) in the 1960's and RILEM in the 1980's were state-of-the-art at that time, however, formal durability planning to coordinate technical improvements was missing.

- Australia: CIA: Z7 Durable Concrete Structures (2, first published in 1990 and second edition in 2001) states: "The aim of this Recommended Practice is to provide designers, specifiers and users of concrete with guidance on the provision of durable concrete structures by alerting them to potential problems that may occur at any phase from concept to completion." CIA Z7/01 (1) provides durability planning that is not given in CIA Z7 (2).
- Europe: CEB RILEM Durability of Concrete Structures (3, published in 1983), with the latter stating: "The international concrete profession is, therefore, challenged by acute demands to develop and implement rational measures of solving the present twofold problems of durability, namely: 1) Find measures to ensure a satisfactory remaining lifetime of existing structures threatened by premature deterioration; 2) Incorporate in new structures the knowledge, experience and new research findings, in order to monitor the structural durability, thus ensuring the required service performance of future concrete structures." And "Furthermore, an efficient voluntary coordination of activities in order to develop the proposed rationale 'Durability Technology' on a higher professional level than the present, would be welcomed by all parts of the concrete profession." This workshop brought together about 80 international leaders in concrete technology and durability who presented on the topics of state-of-the-art, deemed to satisfy rules and future work, which provided technical papers with references that was truly "state-of-the-art" for concrete durability at that time. Transfer of knowledge from theory to practice summary comments included, "...important task now is to use our already existing knowledge regarding materials technology, and transfer this knowledge in useable form to the structural engineer, i.e. to the designer and the contractor, as in practice a design engineer will ask for a certain type of concrete, not a certain type of cement or aggregate, etc." and "...one of the objectives of explicitly stated for this workshop, i.e. bridging the communications gap between materials science and engineering descriptions" and "...structural engineers should have a general understanding of what the materials scientists are doing – or could achieve – in order to ask the right questions to the materials science".
- United States of America: ACI Durability of Concrete Construction (4, published in 1968) states, "...is written for the intelligent engineer who wants to make or specify durable concrete, but who needs to be alerted to possible deterioration under various circumstances, and for students who wish to learn something about the subject" and "It will be assumed the reader is not a physicist, or chemist, or petrographer. This poses something of a problem because most of the properties and behavioural aspects of concrete of practical importance to engineers are very largely consequences of its microstructure and chemical nature, and detailed study of these matters lies mostly in the realm of the physical sciences. Furthermore, practical measures to achieve durable concrete usually comprise suitable control of microstructure or chemical properties, or both, although practitioners may not think about it in these terms. Yet they would be able to act more intelligently and with greater confidence if they had some general understanding of them."

CIA Z7/01 (1) has major sections on the formal durability planning process through the various stages of the structures life that include:

- Asset Owner brief.
- Project tender.

- Durability planning
- Concept design.
- Detailed design.

- Construction.
- Maintenance during operation

#### 4. Terminology

Definition of terms commonly used for durability is variable in Australian Standards with some important terms having different words or not being defined, which is a consequence of the many people involved in difference standards. In the absence of an Australian Durability Standard, CIA Z7/01 (1) provides in terminology that takes account of international durability use and can be referenced for common definition understanding in Australia. Definitions of durability and durability consultant CIA Z7/01 (1) are important for Australian future use and are given below.

- Durability: The capability of structures, products or materials of continuing to be useful after an extended period of time and usage. In the context of performance-based design of structures, durability refers to the fulfilment of the performance requirements within the framework of the planned use and the foreseeable actions, without unforeseen expenditure on maintenance and repair.
- Durability consultant: Person or group who completes the durability assessment and is the author of the durability assessment report and durability checklists. Intent is a person or group who can apply materials deterioration knowledge to construction materials and construction processes, additional to more common structural, civil, geotechnical and other engineering knowledge of design, construction and maintenance. Maybe an in-house employee of the design team, or an independent consultant engaged for the purpose. Intended to have a close working relationship with the asset owner, design team and construction team to ensure durability is provided to achieve the asset owner required service life. Practical experience is essential to ensure the durability assessment report and durability checklists do not become a research exercise. Contractor reviews are included to achieve a buildable final design for the asset owner service life. The durability consultant may be a person with relevant technical qualifications other than a qualified engineer (e.g. materials scientists), with the asset owner client (or authorised representative) responsible to approve the durability consultant for a project

Design life is one of the most important durability parameters yet this is not always clearly identified in codes and specification and definition are not always clear and consistent. CIA Z7/01 (1) provides some clear definitions which are also shown in Figure 1. The term “design life” is often used to convey the same intent as “design service life” and both terms are acceptable to convey the same intent. It is the period in which the required performance shall be achieved, used in the design of new structures construction. Service life (operational) however is the period in which the required performance of a structure or structural element is achieved, when it is used for its intended purpose and under the expected conditions of use. It comprises design service life and prolonged service lives.

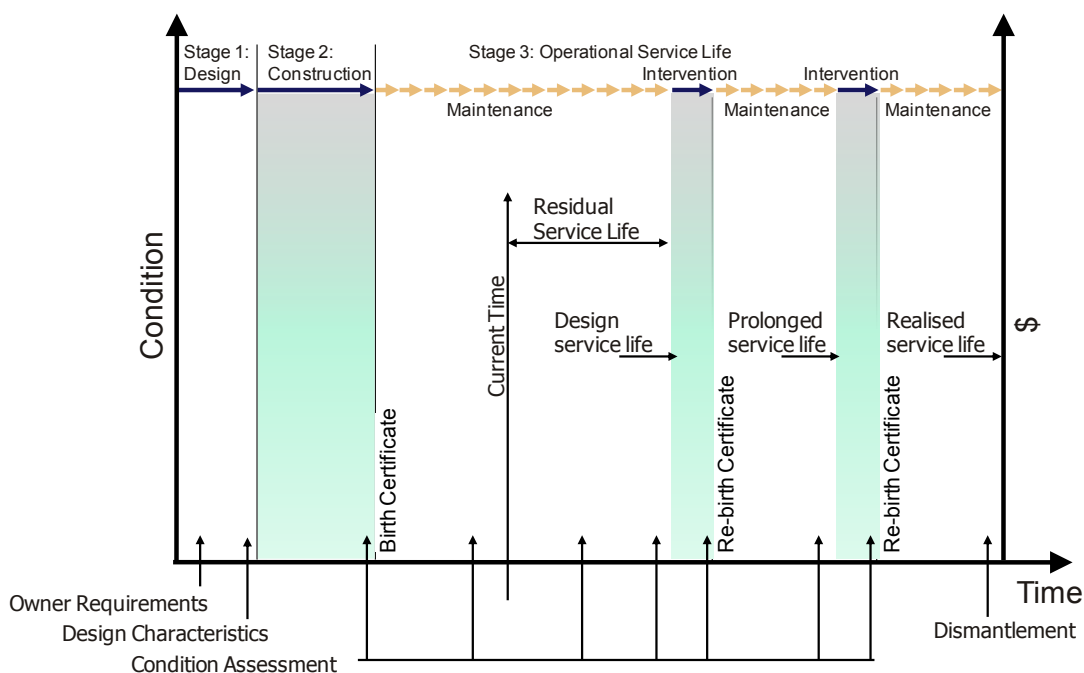


Figure 1 : Phase in the Life of a Structure (5)

## 5. Durability Tasks Through the Asset Life

An asset owner project brief is recommended to include service life, reliability, maintenance strategy, required condition at end of design life, durability requirements and who is to complete durability tasks and who is to review.

The contractor's tender should show that the contractor understands the project durability requirements, exposure conditions, mechanisms of deterioration, any issues with construction materials, workmanship requirements and maintenance after construction is completed. The scope of works should require that tender documents include an outline durability plan

It is recommended that the scope of works require that a durability assessment report be prepared at the detailed design stage. This should include the following:

- Modelling of deterioration mechanisms to determine future service life of materials where necessary.
- Assessment of durability requirements according to national codes, identification of where these requirements are deemed inadequate based on current state of the art and requirements that will be in accord with state of the art requirements.
- Durability audit of final design.
- Evaluation of proposed materials that will meet the required performance criteria.
- Review detailed material specifications for project elements with design and construction teams.
- Design details to minimise and/or avoid effects of aggressive environment (e.g. seals, flashings, waterproofing, cladding, etc.).
- Durability review of materials specifications.
- Proposed inspection, monitoring and testing programs that will ensure early identification of any premature deterioration, to be complemented by pro-active operational maintenance actions.
- QA/QC requirements for durability sensitive critical elements of materials and workmanship.
- Maintenance procedures to ensure the structure will remain in the required condition at the optimum whole-of-life cost.

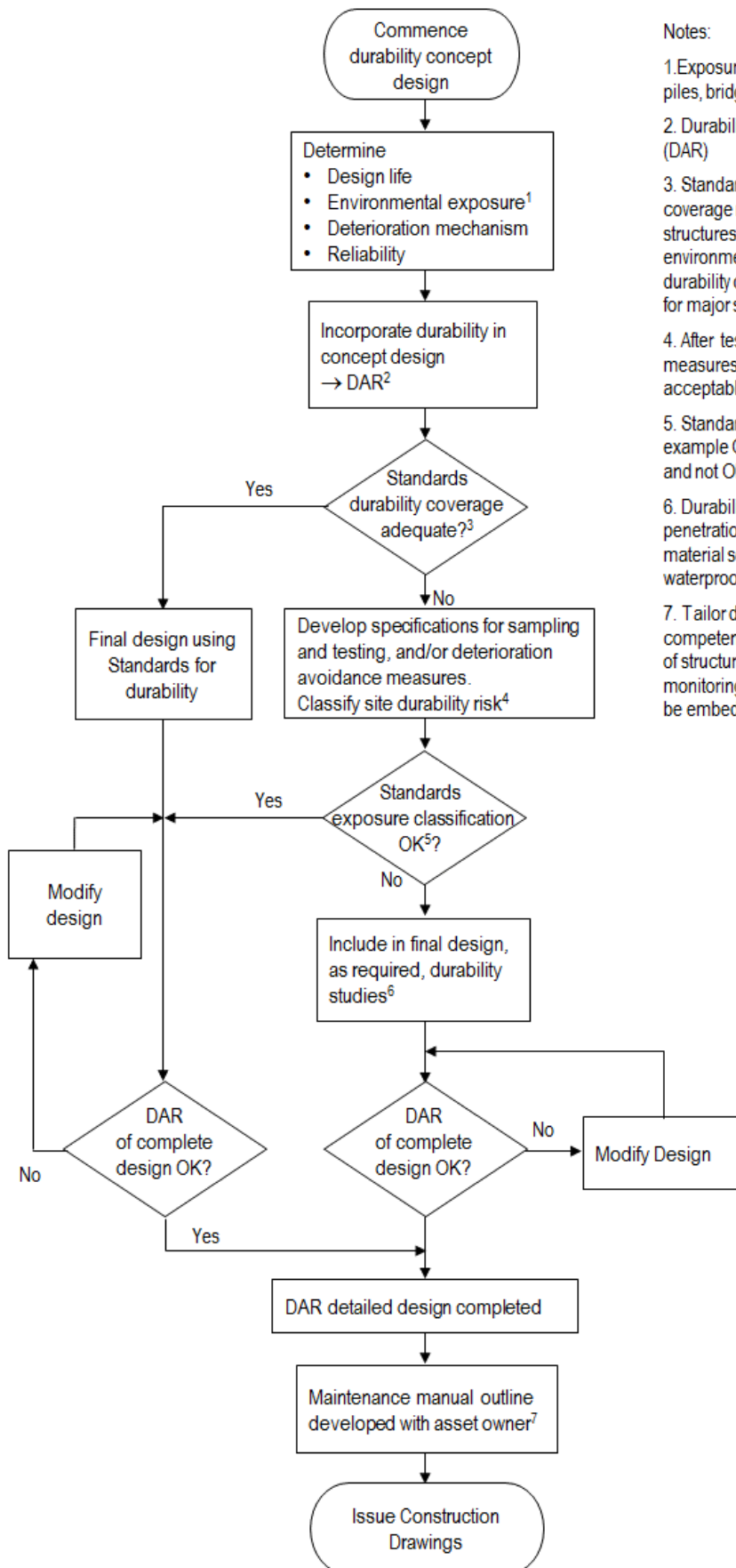
The process of durability planning through design, construction and maintenance phases is included in CIA Z7/01 (1) as flow charts. As an example the design flow chart is included here as Figure 2.

The main durability objective during construction is to ensure the durability design is properly implemented within the contractor's overall construction procedures for the project. To achieve this it is recommended that the contract require the contractor to demonstrate the following in the tender:

- A construction team with appropriate experience to implement durability requirements will be used including the naming of key personnel.
- Training proposed for the construction team, including workshops, tool box talks, etc. training to ensure all staff have appropriate expertise to give required construction quality.
- Procedures to be used to develop and assess materials of acceptable durability performance.
- Understanding of how to develop, implement and achieve a suitable QA/QC program.
- How site trials will be developed to prove materials and construction methods.
- How method statements will be developed.
- How the contractor will deal with non-conformances.

Maintenance is an integral part of ensuring durability through the life cycle. It is recommended that the scope of works require that the contractor detail a maintenance plan that includes the following:

- Details of asset management inspection audits including life cycle program of tests to be undertaken, assessment criteria and actions to be taken related to the inspection and test results.
- Maintenance materials and methods to be adopted
- Maintenance and asset management planning based on materials deterioration expectations and costs to achieve acceptable asset owner performance predicted at appropriate intervals but not exceeding 10 years.
- Identify repairs during maintenance audits to prevent further deterioration that may result in major problems.
- Minor repairs completed within required time schedule.
- System for keeping records of defects and repairs throughout structure life, including repair materials used.



Notes:

1. Exposure of various elements, e.g. piles, bridge deck.
2. Durability Assessment Report (DAR)
3. Standards (e.g. AS 3600) durability coverage may be acceptable for small structures in non-aggressive environments. Consider engaging a durability consultant (recommended) for major structures.
4. After testing and/or avoidance measures, Standards may still be acceptable for design DAR.
5. Standards exposure classification example OK is AS 3600 A1, B1, or B2 and not OK is U or C.
6. Durability studies to include: penetration modelling, chemical attack, material selection, detailing, waterproofing, etc.
7. Tailor detail to level of technical competence of asset owner, and size of structure. Determine inspection monitoring details and any probes to be embedded in the structure.

Figure 2 : Durability Process During Design

## 6. Key Durability Performance Criteria

When developing key performance criteria for a particular concrete structure, dialogues need to be opened between the durability consultant and the asset owner as to what role the structure participates regarding the key public, social, and economic needs as well as the technical aspects of structure type/function/exposure/construction methodology/operation and maintenance. This can entail detailed dialogue with the asset owner's financier, operator, designer, and builder that all have key roles that contribute to performance of the built concrete structure.

Within concrete structures the range of deterioration includes mechanical attrition (e.g. abrasion), physical thermal exposures (e.g. fire), chemical attrition (e.g. reaction between the cementitious paste and/or aggregates with sulphates, pure water, acids, alkali-aggregate reactions, salt crystallisation, etc.), biological (fouling, biogenic attack), structural (overloading, settlement, cyclic loading), and reinforcement corrosion. Although some of these risks may occur simultaneously on a particular structure, the magnitude and frequency/risk of each needs to be characterised before addressing durability performance as well as assessing whether two or more mechanisms have a cumulative impact on durability.

The characterisation of the actions that deteriorate a concrete structure entail the measurement and assessment of the types, magnitude and frequencies of exposures, or "durability loading". Significant existing data may already be available from the asset owner, namely existing condition survey reports on adjacent structures. This may include visual, non-destructive test data, and core sampling accompanied by chemical and physical test data. If the structure is to be an industrial facility, the process engineers working on the design of the new structure may supply the likely chemical compositions and treatment conditions that could impose on future durability. Environmental data may also be available, including air temperatures/chemical composition/prevaling winds/acid rain, soil and ground water permeability and chemical compositions. On most projects, only a subset of this data will be available and it may be prudent to undertake site environmental testing. Geotechnical investigations are commonly undertaken and additional chemical testing for assessment of durability risk is unlikely to impact significantly on the drilling and sampling cost that is already being conducted. Surface concentration of chloride within concrete is attained within a relatively short period (1-3 years) and can be measured on adjacent structures, although care is required when assessing the concrete composition, geometry of the structural member, and environmental exposure.

Following the "durability loading" assessment, the macro- and micro- environments for each structural component of the concrete structure can then be classified. Together with the asset owner's team, the key "durability loads" can be placed within the contexts whether impairment of the durability of the concrete component will impact functionality of the built structure. The risks and containment actions can then be assessed

## 7. Durability Planning Concept Design

Current industry practice is at best ad hoc in the involvement of durability planning at the project concept design stage. If it does happen it is usually driven by an individual in the asset owner's or the design consultant's team who has an understanding of the risk mitigation and whole-of-life cost benefit value that durability planning can bring to a project if effectively implemented.

The intent of this section is to inform and inspire asset owners so they understand the benefits and insist that durability planning be a key function on any major project and that it is consistently applied to achieve the short term and long term business goals that the project is intended to deliver to their organisation. By defining key durability requirements at the project concept design stage the asset owner can achieve the greatest impact in terms of influencing risk and cost outcomes and sculpt the project terms of reference/deed/technical specification that will deliver the optimal whole-of-life solutions no matter what contract delivery form is used.

Durability is generally seen as a straightforward assessment of the performance of the structural materials that make up the asset in the environment in which it is to be located. The structure form and function of the assets being created influences the materials performance, environment and creates micro environments. Therefore, the asset owner is justified to obtain advice at the concept stage to identify if certain options have significant risk and potential costs compared to others.

Similarly, and particularly in the case of concrete structures, the construction options adopted can impact on the build quality that in turn change the durability performance and likely future maintenance profiles and operational costs.

Another key variable is the range in quality and types of concrete and construction quality available in different geographic locations, which impacts on the identification, implementation and cost of the optimum technical solution both in terms of durability and sustainability.

It is vital that the asset owner participates in developing an effective durability risk review process to be applied at the options selection and concept design stage. The form and methodology of this review should suit the size and complexity of the project, but it would be advisable to use existing corporate risk processes so that risk assessments and mitigation measures are consistent project to project and can be verified/audited internally.

Durability predictive models are commonly used to determine chloride penetration into concrete and carbonation of concrete, which provides input to reinforcement corrosion analysis. Other durability models may

be considered, however, concrete resistance to chemical attack is more typically assured by relating performance criteria to exposure estimates (e.g. sulphates attack, acid attack, etc.). Many more aspects of concrete durability, including alkali aggregate reaction, delayed ettringite formation, etc. are controlled through the concrete materials testing and specification. CIA Z7/05 will provide guidance on durability predictive modelling (see durability series outline at section 1).

The use and selection of predictive models for materials performance evaluation as a design tool is at the discretion of the durability consultant. However, the benefits and limitations of the models considered must be explained and justified to the asset owner and designer.

The benefit of using models is they provide a measurable, verifiable basis for materials selection and performance criteria that can be measured during construction and in-service. It is recommended that modelling used in the durability assessment report includes:

- Relevant details of the durability model.
- Assumptions made in the modelling, how these relate to normal values adopted in codes, standards or technical literature and the implications of the values used.
- Comparison of modelling outcomes with requirements in codes/standards together with an explanation of why the model values were adopted.
- How modelling outcomes will be used in technical specifications.

Design life prediction by durability modelling is based on achieving a prescribed level of reliability at the end of the design life, typically a 90-95% probability of failure. CIA Z7/01 (1) provides a definition of reliability and gives guidance on reliability values that might be used in durability modelling. Reliability is not currently a stated parameter in current Australian codes for durability design but may be included subjectively by having higher performance requirements for more critical structures.

Cracks in concrete are often inevitable. The impact of cracks on durability can be a contentious matter for all stakeholders during asset design, construction and operation. Therefore, all stakeholders should have design stage awareness of potential crack formation, location and size. The concrete crack risk is proactively evaluated during design, and any unexpected cracks evaluated reactively. The importance of concrete cracks has justified a specific CIA Z7/06 Recommended Practice (see durability series outline at section 1).

It is appropriate to define maximum allowable crack widths for durability impact. This needs to be linked to exposure classifications, structural forms, crack types and loading conditions so that there is clarity with regards to the degree of risk associated with the concrete mix and structural design and the minimisation of crack formation.

As construction techniques and sequencing can impact significantly on the quality of the materials installed and thereby their in-service performance, it is highly recommended that during the concept stage a constructability review workshop is held to review potential risks and determine how they will be ameliorated.

If this cannot be achieved then the technical specification should contain a requirement for the contractor to evaluate their construction solutions against the requirements of the durability assessment report. The contractor will need to confirm that the build quality they can achieve will support the design assumptions and meet the durability design and material criteria in the durability assessment report.

It is recommended that durability testing requirements be clearly specified for four stages:

- Mix trials to confirm the mix is suitable.
- Quality assurance tests as construction proceeds. Variability of durability tests must be taken into account by the durability consultant, with specification test criteria allowing for alternative solutions to achieve the required durability if the test results do not achieve the specified values. This can be achieved by conservative durability design and/or provision for use of additional measures such as protective coatings or special additives or other measures.
- Tests at end of defects liability period to create a list of items for repair.
- Tests during the design and service lives including monitoring.

The key durability design requirements, the methodology of how it is to be delivered during the project and transition into the operation phase of the asset life should be set out in a project specific durability assessment report at concept design.

The durability assessment report does not need to define all of the material solutions but should identify critical issues and propose the steps needed to be taken to ensure that they are handled effectively and any key milestones and/or dates by which actions/issues need to be resolved.

Roles and responsibilities for the implementation and delivery of the durability assessment report need to be clearly defined along with the key outputs, their format and who they need to be delivered to; again with key milestones so that the durability program is aligned with and tied to the overall project program.

## **8. Durability Planning Detailed Design**

The design stage durability strategy needs to minimise the risks of long term deterioration of the project assets and asset components. The durability risks need to be identified, the durability design solutions determined, critical construction processes identified, operational inspection and monitoring requirements outlined and maintenance recommendations provided.



Durability inputs into the design process includes review of exposure and materials test data, review of owner requirements, identification of deterioration mechanisms and critical durability issues, review of proposed construction methods and identification of durability issues, undertake modelling, prepare options for construction, recommend materials and outline inspection and monitoring requirements.

Outputs to the process include durability requirements in design packages, input into specifications and construction drawings and a durability assessment report: detailed design.

Durability design objectives contained in the durability assessment report are then used in the construction process. The outcomes of the durability recommendations and addenda during construction (durability assessment report: verification report) can then be incorporated into the maintenance manual for the assets and asset components. A continuous link in durability objectives is therefore maintained between design, construction and maintenance.

The design durability strategy to minimise the risks of long term deterioration of the structural assets and asset components within a project needs to be consolidated into a durability assessment report: detailed design. The durability risks are identified, the durability design solutions are determined, critical construction processes identified, operational inspection and monitoring requirements outlined and maintenance recommendations provided. The durability checklists are consolidated and incorporated into the durability assessment report: detailed design.

The main objectives of a durability assessment report: detailed design is to provide guidelines on the following (6):

- Identify the critical construction elements at risk of long term deterioration.
- Identify critical construction processes.
- Develop a detailed work plan/program for future materials durability input.

CIA Z7/01 (1) provides examples of the key deliverables and the durability process for water or wastewater retaining structures and a bridge. These examples assume a design and construct (D&C) and traditional design/tender construction contractual arrangements. However, the general approach can be applied with minor modifications for Alliance or other forms of contractual arrangement.

Design stage durability awareness and planning outcomes need to be incorporated into operations and maintenance (O&M) documentation for use during the asset service life. The O&M documentation that is prepared for a project needs to incorporate the outcomes of the durability assessment reports, durability checklists and addenda as well as suitably address inspection, monitoring and maintenance requirements.

Inspection and monitoring may just entail visual inspection but can also include monitoring probe measurements (e.g. in the case of inaccessible concrete elements) and monitoring points on structures (e.g. for future coring and testing).

## **9. Durability Planning Construction**

The construction phase involves execution of the works and presents a risk of failure to achieve the project's durability targets, many of which may be difficult for the asset owner to appreciate for a considerable length of time. Monitoring for conformance with the durability assessment report during construction is therefore essential.

The usual conventions of quality management apply, and entail measuring against the durability criteria set out for materials, methods and workmanship, which are contained in the project specifications.

At design stage the durability consultant is proactively engaged with the design and construction teams. However, during construction the durability consultant is typically involved on a "by-request" basis with quality assurance by the contractor, design and construct (D&C) contractor or alliance as per the respective contractual arrangements. This process has a potential quality weakness by not involving the durability consultant in random audits to complement regular quality assurance by for example a D&C contractor. Such audits by the durability consultant can be considered by the asset owner to provide improved assurance on the construction activities.

## **10. Durability Planning MAINTENANCE STAGE**

Once the operation and maintenance phase of a structure has commenced, cognizance of the following factors will influence the operations and maintenance plan:

- Desired operational service life.
- Durability assessment report.
- Maintenance plan/asset management plan.
- Birth certificate
- Proactive or reactive approach to future maintenance
- Whole-of-life cost analysis

The birth certificate created at the completion of construction provides all relevant design and construction information.

A reactive approach to on-going maintenance will be limited to visual inspections only and these may be performed on a regular basis or ad-hoc. This may be adequate provided no major defects are found and may be

sufficient to prevent minor defects from becoming major ones, if appropriate follow up repairs are performed as required. This approach may be suitable for minor structures and/or structures with a short design life.

Proactive maintenance will involve early intervention to prevent or delay the onset of corrosion initiation. This will require regular inspections in conjunction with additional activities such as structural monitoring and non-destructive testing, as required. Corrosion monitoring systems provide an early warning of corrosion risk. Probes and instrumentation are commonly installed at the time of construction in reinforced concrete civil infrastructure projects, where justified by aggressive environmental conditions, to provide operational maintenance feedback on materials condition.

Corrosion monitoring systems are particularly beneficial for tunnels, bridges and wharf structures, to supplement maintenance inspection for defects carried out by visual observation.

If significant repairs/strengthening have been carried out, then a post-intervention inspection should be carried out along similar lines to a new structure first inspection mentioned above.

A common feature in new structures such as bridges, buildings below ground level, jetties, tunnels, wharves, etc. is to make provision for cathodic protection installation in the future should it be required. The durability design for future cathodic protection includes:

- Reinforcement electrical continuity ensured (e.g. welded connections and/or additional reinforcement installed).
- Provision for negative returns from reinforcement.
- Positions are available for cathodic protection hardware.
- A corrosion monitoring system is implemented to determine if cathodic protection is justified (see details below).
- Cathodic protection concept design completed to prove that a system can be economically and practically installed in the future.

## **11. CONCLUSIONS**

In engineering terms, durability planning is cost-effective selection and usage of materials combined with design processes, construction methods and detailing to achieve the asset owner intended service life without premature unexpected operational maintenance. Asset deterioration also impacts on the community and this must be accounted for in the design process. A technical analysis determines the nature and rate of materials deterioration for given macro and micro environmental conditions, which is used to influence the design, construction and operational maintenance during the service life.

Durability knowledge is available for engineering analysis but formal durability processes in design, construction and operational maintenance are missing. Durability planning as outlined in this technical paper and CIA Z7/01 Durability Planning Recommended Practice (1) is the recommended change to formalise durability complementary with structural design.

A durability assessment report will explain the durability requirements and provide details to be included in the project design reports, specifications, design drawings, asset maintenance plans and/or operation and maintenance manuals. This report may be a page for simple structures or detailed for complex, critical or uncertain structures. Durability checklists in tabular form provide useful project guidelines complementary to the durability assessment report.

## **12. ACKNOWLEDGEMENTS**

The authors acknowledge the CIA Z7/01 task group was primarily responsible for developing the CIA Z7/01 Durability Planning Recommended Practice, plus many others who have contributed to reviews.

The authors would like to thank GHD Pty Ltd and BCRC for the support and permission in publishing this paper.

## **13. REFERENCES**

1. CIA Concrete Durability Series – Durability Planning. Concrete Institute of Australia Recommended Practice Z7/01. Sydney 2014.
2. Concrete Institute of Australia, Z7 Durable Concrete Structures, first published February 1990 and second edition February 2001.
3. CEB-Rilem International Workshop, Durability of Concrete Structures, Copenhagen, May 1983 Structures.
4. American Concrete Institute, Durability of Concrete Construction, published jointly by American Concrete Institute and The Iowa State University Press, 1968.
5. fib Bulletin 65: Model Code 2010 – Final draft, Volume 1, March 2012.
6. Paull, R, “Concrete Durability Client Durability Requirements”, Concrete Institute of Australia, Concrete Durability Workshop, Adelaide, Brisbane, Melbourne, Perth & Sydney, June, 2009.

# Time-dependent stiffness of concrete members under cyclic loading

Angus Murray<sup>1</sup>, Raymond Ian Gilbert<sup>2</sup> and Arnaud Castel<sup>3</sup>  
<sup>1</sup>Ph.D. Candidate, <sup>2</sup>Emeritus Professor, <sup>3</sup>Associate Professor  
School of Civil and Environmental Engineering, UNSW

**Abstract:** In a cracked concrete flexural member, the difference between the stiffness observed at first loading to that observed after cycles of loading and unloading is measurable and significant. After cracking, concrete beams and slabs exhibit a permanent deflection in an unloaded state due to slip at the concrete-reinforcement interface. Existing models in the literature and in design codes for predicting the instantaneous stiffness provide reasonable estimates when the loads are increased monotonically, but these models underestimate stiffness even after a small number of load cycles. The instantaneous stiffness deteriorates still further when the beam is subjected to prolonged periods of sustained loading or after significant shrinkage has taken place, and this time-dependent loss of stiffness is accounted for with crude modifications to the existing models. The time-dependent decrease in stiffness after sustained loading and shrinkage is due to factors such as the formation of new cracks and the gradually diminishing effect of tension stiffening with time. In this paper, a tension chord model is described which accounts for the behaviour observed experimentally. Better estimates of the time-dependent stiffness of cracked RC members will enable designers to more reliably satisfy serviceability requirements of concrete structures.

**Keywords:** concrete, stiffness, cyclic loading, time-dependent, serviceability.

## 1. Introduction

Tension stiffening contributes significantly to the flexural stiffness of cracked RC members, particularly when they are subjected to typical service loads. In determining the short-term deflection of a cracked RC beam or slab, tension stiffening is usually accounted for by the application of one of a number of models commonly found in design codes. Both the Australian Standard for Concrete Structures (AS3600-2009) (1) and ACI 318-11 (2) make use of Branson's formula (3) to estimate the effective second moment of area of a cracked RC member. An alternative approach is that proposed by Bischoff (4) (based on the Eurocode 2 (5) approach for deflection calculations), which is known to be more reliable for lightly-reinforced members (6,7). Although both methods can predict short-term deflections with reasonable accuracy, they are not particularly accurate in assessing the stiffness of beams under cyclic loading.

When a RC flexural member is loaded beyond the point of cracking and is subsequently unloaded, it exhibits a permanent deflection. Fig. 1 illustrates the response of a RC beam subjected to two series of load cycles, separated by an extended period of sustained loading and drying (8). Immediately after the first cycle of load, the beam returns to a permanently-deflected state. The overall cyclic stiffness of the beam  $K_0$  (defined as the slope of the force-displacement curve) is greater than that which would be expected if this permanent deflection were ignored. The overall cyclic stiffness of the beam in the long term  $K(t)$  is again less than that in the short term (i.e.  $K(t) < K_0$ ).

The cause of the permanent deflection in cracked RC members is thought to be a combination of two main effects. Firstly, since the faces of a flexural crack are not perfectly imbricated, the crack is prevented from closing fully. This effect, cumulated over many cracks, results in a residual elongation of the tensile region of the member upon unloading (9,10). Secondly, a stiffer bond-slip response of reinforcement in a state of unloading compared to loading (11,12) means that upon removal of the load, a residual slip develops between the reinforcement and the concrete. It is beyond the scope of this paper to consider these two effects in any detail; rather, their combined effect on the cyclic response of RC members will be considered. The decay of the overall cyclic stiffness of RC members with time (as seen in Fig. 1) is also thought to be due to two main effects. Firstly, as the concrete shrinks and is restrained by the reinforcement, the tensile stresses that develop in it cause flexural cracks to form in regions where previously the applied bending moment was less than the cracking moment. As the extent of flexural cracking widens, the overall stiffness of the beam diminishes. Secondly, a time-dependent loss of tension stiffening occurs. The loss of tension stiffening is considered to be caused by the cumulative damage to the steel-concrete interface due to the propagation and formation of internal cracks in the region of the concrete surrounding the reinforcement (13,14). This process is also considered to be a result of shrinkage (4).

In this paper, a tension chord model is described that accounts for time-dependent effects in order to model the time-dependent stiffness of RC flexural members under cyclic loading.

## 2. Tension chord model

Consider the average stress-strain response of a symmetrically reinforced concrete tie subjected to axial loading, shown in Fig. 2. Prior to loading, the average strain of the tie at point A is zero, assuming that no significant shrinkage has taken place prior to loading. The straight line AB represents the linear-elastic behaviour of the tie before cracking and may be defined by an effective elastic modulus equal to:

$$E_{uncr} = E_s + E_c / \rho \quad (1)$$

where  $E_s$  and  $E_c$  are the elastic moduli of the reinforcement and the concrete, respectively; and  $\rho$  is the reinforcement ratio equal to  $A_s/A_c$ , where  $A_s$  and  $A_c$  are the cross-sectional areas of reinforcement and concrete, respectively. The curve BC represents the load-dependent loss of tension stiffening: as the applied load increases beyond the cracking load, the average response of the tie becomes increasingly similar to that of the bare reinforcement, whose stress-strain response is represented by the straight line AF, having an elastic modulus  $E_s$ . Suppose the tie were loaded beyond the cracking load to some point D and then subsequently unloaded. Due to the effects considered in Section 1, a permanent average tensile strain would remain (point E). The line DE would therefore represent the average axial stiffness of the tie under subsequent loading cycles. It is logical to assume that the effective elastic modulus of the tie subjected to loading cycles  $E_{cyc}$  is greater than that of the bare reinforcement, but less than that of the uncracked tie, thus:

$$E_{cyc} = E_s + k_{cyc}(E_c / \rho), \quad 0 \leq k_{cyc} \leq 1 \quad (2)$$

where  $k_{cyc}$  is a factor which represents the contribution of the concrete to axial stiffness during loading cycles. Over time, the value of  $k_{cyc}$  would be expected to decrease due to the time effects outlined in Section 1, resulting in an overall decay in axial stiffness of the tie. Despite the lack of experimental observations in the literature regarding the cyclic response of RC ties, a linear stress-strain response to loading cycles as depicted by the line DE in Fig. 2 may be assumed, based on the typical linear-elastic response of RC beams observed under loading cycles (8) (see Fig. 1).

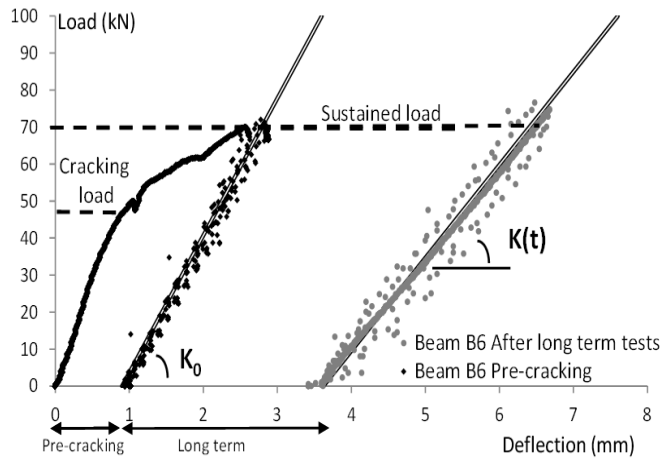


Figure 1. Response of a RC beam to load cycles before and after sustained loading (8).

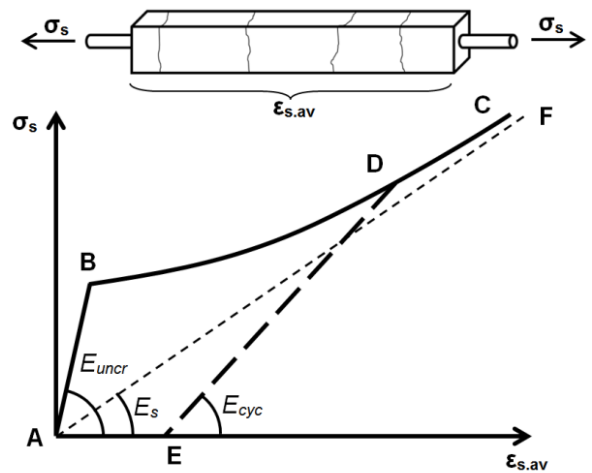


Figure 2. Typical average stress-strain response of RC tie to loading and unloading

### 2.1 General formulation

Consider a term  $\omega(x)$  (the *tension stiffening ratio*) defined as the ratio between the strain in a bare reinforcing bar  $\epsilon_{s,b}$  and the strain at some point in a concrete-embedded reinforcing bar  $\epsilon_{s,e}(x)$  subjected to the same tensile load. That is,  $\omega(x) = \epsilon_{s,b}/\epsilon_{s,e}(x)$ . Since the strain in a concrete-embedded bar is largely dependent on the distance from a crack face, it follows that the value of  $\omega(x)$  also depends on the position along the bar relative to a crack face. In this paper, a parabolic distribution of the concrete and steel strains between consecutive cracks is assumed. This assumption is made widely in the literature, including in (8), wherein the concrete strain distribution between cracks is assumed to take the form:

$$\epsilon_c(x) = g(x) \cdot \epsilon_{c,max}, \quad g(x) = 2(x/L_t) - (x/L_t)^2 \quad (3)$$

where  $g(x)$  is a parabolic distribution function;  $\varepsilon_{c,max}$  is the maximum concrete strain which occurs at a point  $x = L_t$ ; and  $L_t$  is the transmission length (i.e. the distance from the face of a crack over which slip occurs, and beyond which reinforcement and concrete strains are equal). At the point  $x = L_t$ , knowing that there is full interaction between the reinforcement and the concrete, it can be shown that the strain in the concrete  $\varepsilon_{c,max}$  is equal to:

$$\varepsilon_{c,max} = \frac{\sigma_s}{E_s + E_c/\rho} \quad (4)$$

where  $\sigma_s$  is the tensile stress in the reinforcement at a crack. Eq. (4) does not, however, take into account the diminished ability of concrete to develop tensile strain under increasing tensile load (i.e. the load-dependent loss of tension stiffening shown by the curve BC in Fig. 2). Therefore a term  $\lambda$  (the *bond damage parameter*) is introduced which accounts for the tendency of bond (and therefore tension stiffening) to decay under increasing load. Combining Eqs. (3) and (4) and the parameter  $\lambda$ , the concrete strain distribution between cracks may be expressed as:

$$\varepsilon_c(x) = g(x) \frac{\lambda \sigma_s}{E_s + E_c/\rho}, \quad 0 \leq \lambda \leq 1 \quad (5)$$

By equilibrium of forces, the strain in the reinforcement between cracks can be shown to be equal to:

$$\varepsilon_{s,c}(x) = \frac{\sigma_s}{E_s} \left( 1 - g(x) \frac{\lambda}{1+n\rho} \right), \quad 0 \leq \lambda \leq 1 \quad (6)$$

where  $n$  is the modular ratio  $E_s/E_c$ . Thus the tension stiffening ratio  $\omega(x)$  is found by dividing the strain in a bare reinforcement bar ( $\varepsilon_{s,b} = \sigma_s/E_s$ ) by the strain in a concrete-embedded bar given in Eq. (6), yielding:

$$\omega(x) = \frac{1+n\rho}{1+n\rho - g(x)\lambda} \quad \text{or} \quad \lambda = \left( 1 - \frac{1}{\omega(x)} \right) \left( \frac{1+n\rho}{g(x)} \right) \quad (7)$$

Consider now a RC tie that is subjected to both a sustained load (equivalent to a stress of  $\sigma_{s,sus}$  in the bare reinforcement) and a shrinkage strain  $\varepsilon_{sh}$ . Since the concrete is restrained by the reinforcement, a tensile stress will develop in the concrete with time. This time-dependent change in the concrete tensile stress, which may be found by applying the age-adjusted effective modulus method, can be thought of as the response to an equivalent tensile load (equal to a stress of  $\sigma_{s,eq}$  in the bare reinforcement), where  $\sigma_{s,eq}$  is:

$$\sigma_{s,eq} = \frac{1}{1+\bar{n}_e\rho} \left[ \sigma_{s,sus} - \frac{\lambda \sigma_{s,sus}}{1+n\rho} (1+n_e\rho) - \varepsilon_{sh} E_s \right], \quad \bar{n}_e = n(1+\chi\varphi), \quad n_e = n(1+\varphi) \quad (8)$$

where  $\varphi$  is the creep coefficient; and  $\chi$  is an ageing coefficient, which may be assumed to be a constant value (7). In Eq. (8), the value of  $\lambda$  is calculated for the maximum load experienced by the tie, which may be an initial loading of a greater magnitude than the sustained load. The application of an equivalent tensile load to account for time effects effectively induces further bond damage to the reinforcement-concrete interface. In this way, the influence of the time effects of sustained loading and shrinkage on the tension stiffening of the tie is accounted for.

## 2.2 Experimental analysis of RC ties

In order to calibrate the tension chord model, an analysis is undertaken of the average stress-strain behaviour of seventeen RC ties tested under monotonically increasing load in six different experimental programs (15-21). All ties were axially reinforced with deformed steel bars ranging in diameter from 11.3 to 32 mm. The dimensions of the concrete vary to give a range of covers between 1 and 3.67 times the bar diameter, and reinforcement ratios between 1.1 and 9.6 per cent. The compressive strength of the concrete ranged from 21.6 to 62 MPa. Specimens for which significant drying had occurred before loading were not considered in the analysis, since it was intended to study the tension stiffening effect in the absence of other effects. Considering the wide range of bar diameters, concrete covers, reinforcement ratios and concrete compressive strengths, the analysis should be useful in formulating a general model for RC structures.

In Section 2.1, the formula derived for the tension stiffening ratio  $\omega(x)$  given in Eq. (7) refers to a particular point relative to the face of a crack. However, in the analysis of RC ties, only the average stress-strain behaviour is known. Therefore, an *average* tension stiffening ratio  $\omega_{av}$  is introduced which is defined as the ratio between the strain in a bare reinforcing bar  $\varepsilon_{s,b}$  and the *average* strain in a concrete-embedded reinforcing bar  $\varepsilon_{s,e,av}$  subjected to the same tensile load. The average strain  $\varepsilon_{s,e,av}$  is found by integration of Eq. (6) between cracks. By symmetry, only one half of the crack spacing needs to be considered:

$$\varepsilon_{s,e,av} = \frac{2}{L_s} \int_0^{L_s/2} \frac{\sigma_s}{E_s} \left( 1 - g(x) \frac{\lambda}{1+n\rho} \right) dx = \frac{\sigma_s}{E_s} \frac{1+n\rho-0.744\lambda}{1+n\rho} \quad (9)$$

where  $L_s$  is the crack spacing and is taken to be equal to  $1.37L_t$ . In the literature, the ratio between the average crack spacing  $L_{s,av}$  and the transmission length  $L_t$  is taken to be either 1.33 (7,11,22) or 1.50 (8,23). The choice of 1.37 is for practical reasons only, since it yields a workable value of  $g(x) = 0.9$ . In any case, the value of  $g(x)$  is not particularly sensitive to the specific choice of this ratio. The average tension stiffening ratio  $\omega_{av}$  is then:

$$\omega_{av} = \frac{1+n\rho}{1+n\rho-0.528\lambda} \quad (10)$$

Alternatively, the bond damage parameter  $\lambda$  can be expressed in terms of  $\omega_{av}$ :

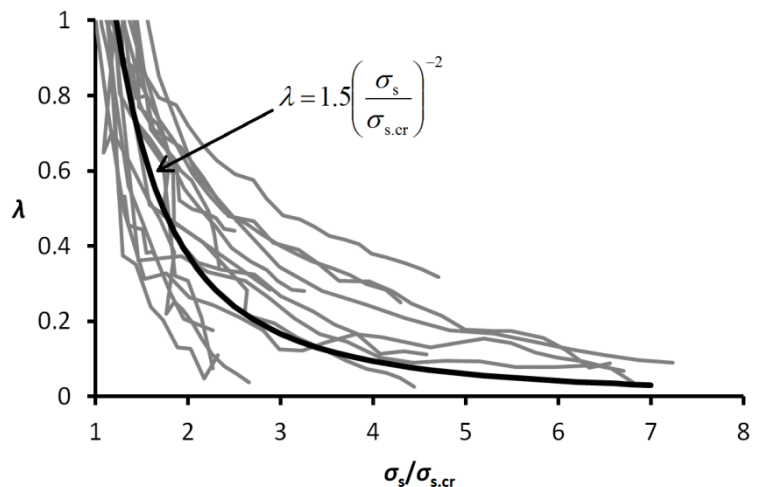
$$\lambda = (1.894 - 1.894/\omega_{av})(1+n\rho) \quad (11)$$

For each of the RC ties, the average tension stiffening ratio  $\omega_{av}$  was determined by considering the recorded average strain as a function of the normalised steel stress  $\sigma_s/\sigma_{s,cr}$ , where  $\sigma_{s,cr}$  is the stress in the reinforcement when cracking first occurs (i.e. at the cracking load). The bond damage parameter  $\lambda$  was then determined according to Eq. (11). The results of the analysis are presented in Fig. 3. The grey curves represent the relationship between  $\lambda$  and  $\sigma_s/\sigma_{s,cr}$  for each of the seventeen RC ties. It is immediately obvious that for levels of loading just in excess of the cracking load, the calculated values of the bond damage parameter  $\lambda$  are greater than 1.0, which is not permitted according to Eqs. (5) and (6). This is because the assumption that a stabilised crack pattern has been established is not justified at such low levels of loading and the relationship  $L_s = 1.37L_t$  is not accurate. For levels of loading greater than about  $\sigma_s/\sigma_{s,cr} = 1.3$ , the value of  $\lambda$  is generally less than 1.0 and at this level of loading a stabilised crack pattern has usually been established (24).

For each of these curves, a line of best fit in the form of a power function was determined, and the average of each of these lines of best fit is shown by the black curve, which is defined by the equation:

$$\lambda = 1.5 \left( \frac{\sigma_s}{\sigma_{s,cr}} \right)^{-2} \quad \text{when } \sigma_s/\sigma_{s,cr} > 1.3 \quad (12)$$

It is also important to note that in the analysis of the seventeen RC ties, none of the parameters considered (i.e. bar diameter, concrete cover, reinforcement ratio, and concrete compressive strength) appeared to have any apparent influence on the bond damage parameter  $\lambda$  as a function of the normalised steel stress  $\sigma_s/\sigma_{s,cr}$ . Although tension stiffening is known to be more pronounced in lightly-reinforced members (6), the formulation of  $\lambda$  in Eq. (11) tends to normalise this behaviour according to the reinforcement ratio. Therefore, the proposed model is expected to account for tension stiffening across a wide range of reinforcement ratios.



**Figure 3. Relationship between bond damage parameter  $\lambda$  and normalised load  $\sigma_s/\sigma_{s,cr}$ .**

### 3. Beam model (monotonic loading)

The tensile region of a RC beam or slab may be considered analogous to a RC tie, such as those analysed in Section 2.2. Fig. 4 depicts an uncracked cross-section of a typical RC beam as well as the cross-section of the same beam at some point between flexural cracks, where  $h$  is the overall depth of the member;  $b$  the width;  $d$  the effective section depth (measured from the extreme compressive concrete fibre to the centroid of the tensile reinforcement); and  $A_s$  the total cross-sectional area of tensile reinforcement. Between consecutive cracks, the cross-section may be considered to be composed of a compressive area of concrete located above an effective neutral axis depth  $d_{n,ef}(x)$  and a tensile zone comprising the tension chord model described in Section 2. The effective cross-sectional area of concrete within the tension chord is taken to be that given in the CEB-FIP Model Code 1990 (11):

$$A_{c,ef} = \min \{2.5(h-d)b, (h-d_{n,cr})b/3\} \quad (13)$$

where  $d_{n,cr}$  is the neutral axis depth of a fully-cracked section (i.e. at a point  $x = 0$ ) and may be evaluated using the modular ratio method. Previously, the tension stiffening ratio  $\omega(x)$  was introduced to represent the ratio between the strain in a bare reinforcement bar and the strain in a concrete-embedded bar subjected to the same tensile load. Therefore  $\omega(x)$  can be thought of as the ratio of the axial stiffness between the two cases. Consider, then, an *equivalent* cross-sectional area of tensile reinforcement  $A_{s,eq}(x) = \omega(x)A_s$  which represents the cross-sectional area of an equivalent bare reinforcement bar having the same axial stiffness of a concrete-embedded bar. In this way, the tension chord described in Section 2, comprising both reinforcement and concrete, can be replaced by this equivalent cross-sectional area of reinforcement alone. By applying the modular ratio method, it is possible to determine the effective neutral axis depth at any point between cracks:

$$d_{n,ef}(x) = \frac{-nA_{s,eq}(x) + \sqrt{(nA_{s,eq}(x))^2 + 2nA_{s,eq}(x)bd}}{b} \quad (14)$$

Considering the strain diagram in Fig. 4, the curvature between cracks is therefore equal to:

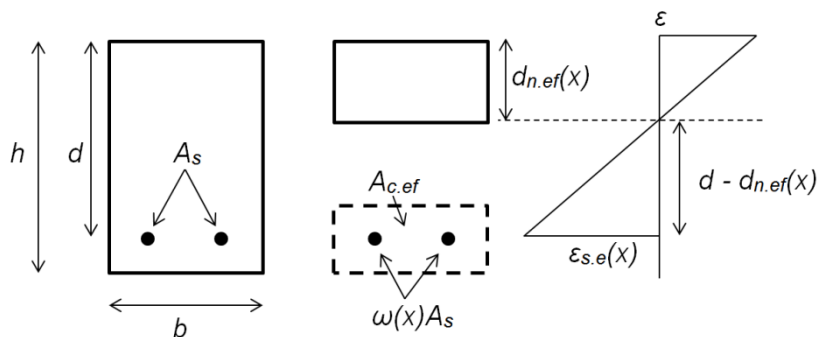
$$\kappa(x) = \frac{\varepsilon_{s,c}(x)}{d - d_{n,ef}(x)} = \frac{\varepsilon_{s,b}}{\omega(x)(d - d_{n,ef}(x))} \quad (15)$$

For a fully-cracked cross-section, the relationship between the applied bending moment  $M_s$  and the strain in the tensile reinforcement  $\varepsilon_{s,b}$  is given by:

$$M_s = \varepsilon_{s,b} E_s A_s (d - d_{n,cr}/3) \quad (16)$$

Finally, considering Eqs. (15) and (16), the second moment of area of the section at some point between cracks is derived as:

$$I(x) = \frac{M_s}{E_c \kappa(x)} = (d - d_{n,cr}/3) n A_{s,eq}(x) (d - d_{n,ef}(x)) \quad (17)$$



**Figure 4. Uncracked and cracked cross-sections of a typical RC beam**

Because the second moment of area formulation in Eq. (17) depends on the particular position under consideration between cracks, a simple alternative formulation is sought which, when applied uniformly between cracks, will yield the same overall flexural stiffness. Analysis of typical RC beams and slabs reveals that the second moment of area formulation in Eq. (17) is reasonably well approximated by a linear interpolation between the second moments of area calculated at a crack location and the mid-point between cracks. Thus:

$$I(x) \approx I_{cr} + \frac{2x}{L_s}(I_{mid} - I_{cr}), \quad 0 \leq x \leq \frac{L_s}{2} \quad (18)$$

where  $I_{cr}$  is the second moment of area at the location of a crack (i.e.  $x = 0$  in Eq. (17)); and  $I_{mid}$  is the second moment of area calculated at the mid-point between consecutive cracks (i.e. at  $x = 0.5L_s$  in Eq. (17)). For typical RC flexural members, considering the relatively small average crack spacing compared to the length of the member, it is reasonable to assume that the bending moment is more or less constant between consecutive cracks, regardless of the actual loading arrangement and bending moment distribution. Therefore, in order to determine an effective second moment of area to replace the linear approximation in Eq. (18), we enforce the criterion that the average curvature of a small beam segment between consecutive cracks having the linear second moment of area distribution in Eq. (18) and being subjected to a constant bending moment should be equal to the average curvature of a similar beam segment having a uniformly-applied *effective* second moment of area  $I_{ef}$ . By integration, this yields:

$$\frac{M}{E_c I_{ef}} = \frac{M(\ln(I_{mid}) - \ln(I_{cr}))}{E_c(I_{mid} - I_{cr})} \quad (19)$$

And therefore we derive the effective second moment of area to be:

$$I_{ef} = \frac{I_{mid} - I_{cr}}{\ln(I_{mid}/I_{cr})} \quad (20)$$

For a typical range of values for  $I_{mid}/I_{cr}$  in the order of 1-2, Eq. (20) becomes indistinguishable from a straight line and may be simplified to:

$$I_{ef} \approx 0.44I_{mid} + 0.56I_{cr} \quad (21)$$

Alternatively, substituting in a value of  $x = 0.22L_s$  into Eq. (18) achieves the same effective second moment of area. That is to say, the second moment of area determined at a point  $x = 0.22L_s$  may be considered to represent the effective second moment of area of the entire cracked region of the beam. At this point, there exists an *effective* tension stiffening ratio found by substituting  $x = 0.22L_s$  into Eq. (7):

$$\omega_{ef} = \frac{1 + n\rho}{1 + n\rho - 0.512\lambda} = \frac{1 + n\rho}{1 + n\rho - 0.768(M_s/M_{cr,t})^{-2}} \quad (22)$$

where  $\lambda = 1.5(M_s/M_{cr,t})^{-2} \leq 1.0$  (an equivalent expression to Eq. (12) for the case of flexure); and  $M_{cr,t}$  is the cracking load of the member at some point in time, taking into account the shrinkage that occurs.

### 3.1 Deflection calculations

The calculation of the mid-span deflection of a cracked RC flexural member is complicated by the fact that the flexural stiffness changes abruptly at the point where flexural cracking first occurs. In practice, the contribution to overall flexural stiffness of the uncracked parts of a RC member is often ignored. This approach would tend to overestimate deflections, particularly in cases where the RC member is loaded just in excess of its cracking load: for lightly-loaded members, the actual extent of flexural cracking might be restricted to a rather small region near the beam's mid-span. In this paper, the mid-span deflection is taken to be:

$$\Delta_{mid} = K_{ef} L^2 \kappa_{ef} \quad (23)$$

where  $K_{ef}$  is a parameter that accounts for the loading arrangement as well as the extent of flexural cracking;  $L$  is the length of the beam; and  $\kappa_{ef}$  is the effective curvature at the mid-span of the beam.



To illustrate the process of determining  $K_{ef}$ , a typically-encountered loading arrangement is considered. Fig. 5 depicts a cracked RC flexural member subjected to four point bending, with loads applied at the third span points. Point A is a simple support; point B represents the position along the beam at which the bending moment is equal to the cracking moment ( $x = M_{cr}/P$ ); point C is the third-point of the beam ( $x = L/3$ ) beyond which the bending moment remains constant; and point D is the mid-span. Within segment AB, the flexural stiffness is that of the uncracked section; within segments BC and CD, since cracking has occurred, the effective flexural stiffness in Eq. (17) is used, evaluated using the effective tension stiffening ratio  $\omega_{ef}$  in Eq. (22). By twice integrating the piecewise-defined curvature and applying the appropriate boundary conditions, an expression for the mid-span deflection is derived as:

$$\Delta_{mid} = \frac{1}{216} \frac{L^2 [8M_{cr,t}^3 (I_{ef} - I_{uncr}) + 23M_s^3 I_{uncr}]}{E_c M_s^2 I_{uncr} I_{ef}} \quad (24)$$

Equating the mid-span deflections in Eqs. (23) and (24) and noting that  $K_{ef} = M_s/(E_c I_{ef})$ , we get an expression for  $K_{ef}$ :

$$K_{ef} = \frac{1}{216} \frac{23a^3 b - 8b + 8}{a^3 b}, \quad a = \frac{M_s}{M_{cr,t}}, \quad b = \frac{I_{uncr}}{I_{ef}} \quad (25)$$

It is interesting to note that the formulation for  $K_{ef}$  in Eq. (25) is general and not restricted to the particular formulation of  $I_{ef}$  in this paper. A graphical representation of Eq. (25) is given in Fig. 6 for a typical range of values for  $\omega_{ef}$ , where  $\rho_{ef}$  is the effective reinforcement ratio for the tension chord equal to  $A_s/A_{c,ef}$ . For heavily-loaded members, for which the effective tension stiffening ratio  $\omega_{ef}$  is close to 1.0, the value of  $K_{ef}$  approaches the theoretical value of 0.107 for a uniformly-stiff beam. For lightly-loaded members, for which the value of  $\omega_{ef}$  is greater than 1.0, the value of  $K_{ef}$  decreases since the extent of flexural cracking is less. Similar results are observed in the derivation of  $K_{ef}$  for other load cases.

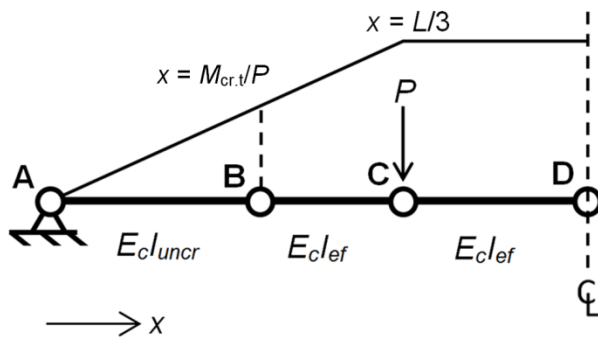


Figure 5. Beam model for the determination of  $K_{ef}$  (four point bending case)

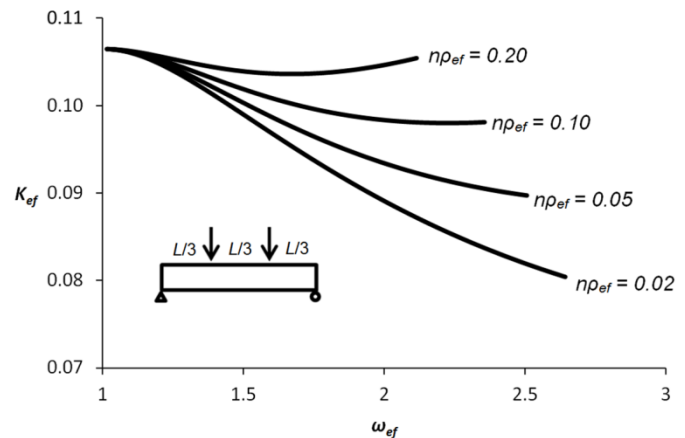


Figure 6. Plot of  $K_{ef}$  for a range of  $\omega_{ef}$  and  $n\rho_{ef}$  values (four point bending case)

### 3.2 Validation of model

In order to evaluate the validity of the proposed tension chord model and its application to RC flexural members, an analysis is undertaken of a large number of cracked RC beams and slabs that have been tested in 26 individual experimental programs, the results of which have been collated by Espion (25). In total, 181 rectangular RC beams and slabs subjected to monotonically increasing load have been selected for analysis. The specimens represent a very wide range of concrete compressive strengths, cross-sectional dimensions, reinforcement ratios and reinforcement types (round or deformed). Load levels are in the range of 1.02 to 8.32 times the cracking load. Given the limited knowledge of reported material properties such as the concrete elastic modulus and tensile strength, these values have been estimated based on the material models in AS3600-2009 (1). The proposed model is compared to deflection calculations made using the AS3600-2009 method based on Branson's formula (3) and that by

Bischoff (4) based on the Eurocode 2 (5) approach. The results of this analysis are presented in Table 1, where the values represent the ratios of predicted short-term deflections to reported values.

**Table 1. Results of short-term deflection analysis**

		Method of Analysis		
		This Paper	AS3600-2009 (1)	Bischoff (4)
All specimens ( <i>n</i> = 181)	Mean	1.09	0.94	1.05
	<i>Standard Deviation</i>	0.36	0.31	0.35
Beams ( <i>n</i> = 132)	Mean	1.13	1.00	1.08
	<i>Standard Deviation</i>	0.36	0.30	0.34
Slabs ( <i>n</i> = 49)	Mean	0.98	0.77	0.95
	<i>Standard Deviation</i>	0.33	0.28	0.36

Despite limited knowledge of the material properties of the specimens, the model was able to predict short-term deflections of RC beams and slabs very well on average. In the estimation of beam deflections, the proposed model yielded very similar results to those obtained using Bischoff's method. Both of these methods predicted slightly greater beam deflections than the AS3600-2009 approach. In the estimation of slab deflections, the proposed model performed very similarly to Bischoff's method. Again, both of these methods predicted greater short-term deflections in slabs than the AS3600-2009 approach. The results of this analysis confirm that the proposed model is able to reliably predict the flexural response of RC beams and slabs for a wide variety of load levels and is therefore effective in modelling the tension stiffening of RC flexural members.

#### 4. Beam model (cyclic loading)

Having validated the tension chord and beam models for the case of monotonic loading, a beam model for the case of cyclic loading is now considered, for which (in the absence of appropriate RC tie experiments in the literature) the parameter  $k_{cyc}$  must be determined according to the experimental results of beams subjected to cyclic loads. Considering the effective elastic modulus  $E_{cyc}$  given in Eq. (2), it can be shown that the elastic portion of the mid-span deflection of a RC member under loading cycles (i.e. excluding permanent initial deflections and creep and shrinkage deflection components) is equal to:

$$\Delta_{cyc} = K_{ef} L^2 \kappa_{ef,cyc} = \frac{K_{ef} L^2 M_s}{A_s (E_s + k_{cyc} E_c / \rho_{ef}) (d - d_{n,ef}) (d - d_{n,cr} / 3)} \quad (26)$$

where  $\kappa_{ef,cyc}$  is the effective curvature under loading cycles at the mid-span of the beam; and  $d_{n,ef}$  is evaluated at the critical point  $x = 0.22L_s$ . The value of  $k_{cyc}$  may therefore be estimated according to:

$$k_{cyc} = \frac{K_{ef} L^2 M_s}{\Delta_{cyc} A_{c,ef} E_c (d - d_{n,ef}) (d - d_{n,cr} / 3)} - n \rho_{ef} \quad (27)$$

For the evaluation of  $k_{cyc}$  in the long term, adjustments should be made to account for the shrinkage-induced reduction in the cracking moment, and the consequent change to the value of  $K_{ef}$ . Furthermore, the concrete elastic modulus may be modelled to increase over time. Finally, the effects of sustained load and shrinkage on the tension stiffening effect must be taken into account. That is to say, the value of  $d_{n,ef}$  in the long term, evaluated at the critical point  $x = 0.22L_s$ , will depend on the effective tension stiffening ratio  $\omega_{ef}$  which is determined by considering the equivalent tensile load in addition to the applied load.

##### 4.1 Experimental derivation of $k_{cyc}$

The results of an experimental program by Castel et al. (8) as well as more recent tests by the same authors are used to determine the average stress-strain response of the tension chord under cycles of loading. The two experimental programs involved the application of several initial cycles of load to RC beams ranging from about 1.1 to 2.0 times the short-term cracking load followed by an extended period of

sustained loading during which the beams were free to shrink. The period of sustained loading was six months and twelve months for the two experimental programs. Following this, each RC beam was again subjected to several cycles of load having the same magnitude as the short-term cyclic load. In total, thirteen RC beams were tested. Using Eq. (27), the values of  $k_{cyc}$  for both the short-term and long-term responses to cyclic loading were determined. The results of this analysis are presented in Fig. 7.

For levels of loading just greater than the cracking load, the value of  $k_{cyc}$  is relatively high, suggesting that, like the bond damage parameter  $\lambda$ ,  $k_{cyc}$  is highly dependent on the magnitude of loading.

Similarly, the value of  $k_{cyc}$  decreases as the applied load increases. Due to the effects of sustained loading and shrinkage, the value of  $k_{cyc}$  decreases in every case. In Fig. 7, the values of  $k_{cyc}$  are plotted against the normalised load  $M_s/M_{cr,t}$  where  $M_{cr,t}$  has been adjusted in the long term to reflect the shrinkage-induced decrease in the cracking moment. Both the short-term and long-term results appear to obey the same trend. In general, the value of  $k_{cyc}$  may be modelled according to:

$$k_{cyc} = A(M_s/M_{cr,t})^B \approx A(\sigma_s/\sigma_{s,cr,t})^B \quad (28)$$

For the thirteen beams analysed here,  $A = 0.6$  and  $B = -3.5$ . Fig. 1 shows the response to short-term and long-term cyclic loading of one of the beams in the experimental programs considered. Considering the expression for the elastic portion of the mid-span deflection under cyclic loading in Eq. (26), it can be shown that, in the case of a beam subjected to four point bending (as is the case for the thirteen beams analysed here), the overall stiffness of a RC flexural member subjected to cycles of load is equal to:

$$K = \frac{F_{cyc}}{\Delta_{cyc}} = \frac{6A_s(E_s + k_{cyc}E_c/\rho_{ef})(d - d_{n,ef})(d - d_{n,cr}/3)}{K_{ef}L^3} \quad (29)$$

where  $K$  refers to either the short-term overall stiffness  $K_0$  or the long-term overall stiffness  $K(t)$ ;  $k_{cyc}$  is the corresponding short-term or long-term value; and  $F_{cyc}$  is the total cyclic load applied to the beam.

## 5. Conclusions

- In the analysis of the average stress-strain response of seventeen RC ties to monotonically increasing load, no clear influence on the bond damage parameter  $\lambda$  by any of the parameters considered was found. These parameters include bar diameter, concrete cover, reinforcement ratio, and concrete compressive strength. The bond damage parameter was shown to be governed by the level of applied loading in excess of the cracking load.
- A tension chord model based on the observations made in that analysis has been shown to reliably predict the post-cracking behaviour of RC flexural members. The proposed model is demonstrated to yield very similar results to those obtained using the widely-accepted method by Bischoff (4).
- The introduction of the  $K_{ef}$  factor in Section 3.1 is thought to have improved deflection estimates significantly, particularly in lightly-reinforced members and members subjected to loads just greater than the cracking load.
- In the analysis of thirteen RC beams, it was found that the overall stiffness under cycles of load is closely related to both the magnitude of load cycles in excess of the cracking load as well as the degree of restrained shrinkage that occurs over time.
- A distinct lack of experimental observations reported in the literature regarding the average stress-strain response of RC ties subjected to cyclic loads warrants further experimental investigations.

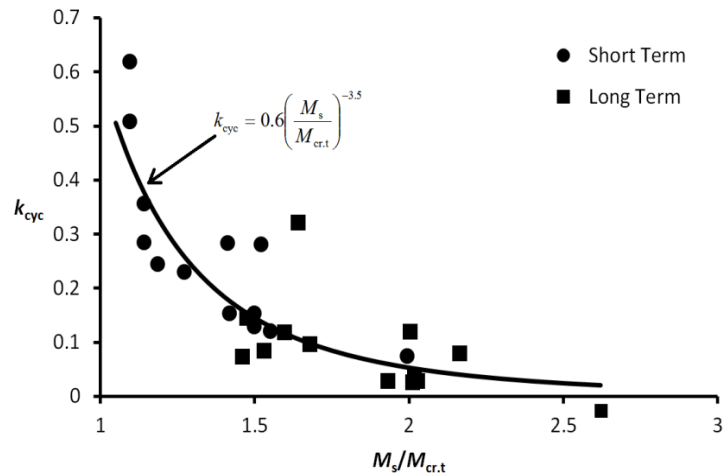


Figure 7. Plot of results of experimental analysis

## 6. References

1. Standards Australia, "Australian Standard for Concrete Structures, AS3600-2009", 2009, Sydney.
2. American Concrete Institute, "Building Code Requirements for Structural Concrete, ACI 318-11", 2011, Detroit.
3. Branson, D. E., "Instantaneous and time-dependent deflections of simple and continuous reinforced concrete beams. HPR Report No. 7. Part 1.", Alabama Highway Dept. Bureau of Public Roads, 1965, Alabama.
4. Bischoff, P. H., "Reevaluation of deflection prediction for concrete beams reinforced with steel and FRP bars", *Journal of Structural Engineering*, ASCE, 131(5), 2005, pp 752-767.
5. British Standards Institution, "Eurocode 2: Design of Concrete Structures – part 1-1: General rules and rules for buildings – BS EN 1992-1-1:2004", European Committee for Standardization, 2004, Brussels.
6. Gilbert, R. I., "Tension Stiffening in Lightly Reinforced Concrete Slabs", *Journal of Structural Engineering*, ASCE, 133(6), 2007, pp 899-903.
7. Gilbert, R. I. & Ranzi, G., "Time-dependent behaviour of concrete structures", Spon Press, 2011, London.
8. Castel, A., Gilbert, R. I. et al., "Instantaneous stiffness of cracked reinforced concrete including steel-concrete interface damage and long-term effects", *Journal of Structural Engineering*, ASCE, 140(6), 2014.
9. Muttoni, A. & Fernández Ruiz, M., "Concrete cracking in tension members and application to deck slabs of bridges", *Journal of Bridge Engineering*, ASCE, 12(5), 2007, pp 646-653.
10. Laurencet, P., "Précontrainte et armature pour contrôler l'ouverture résiduelle des fissures", Ph.D. Thesis, École Polytechnique Fédéral de Lausanne, 1999.
11. Comité Euro-International du Béton, "CEB-FIP Model Code 1990: Design Code", Thomas Telford, 1993, London.
12. Zanuy, C., "Investigating the negative tension stiffening effect of reinforced concrete", *Structural Engineering and Mechanics*, 34(2), 2010, pp 189-211.
13. Beeby, A. W. & Scott, R. H., "Mechanisms of long-term decay of tension stiffening", *Magazine of Concrete Research*, 58(5), 2006, pp 255-266.
14. Zanuy, C., "Analytical approach to factors affecting long-term tension stiffening", *Magazine of Concrete Research*, 62(12), 2010, pp 869-878.
15. Houde, J. & Mirza, M. S., "A study of bond stress-slip relationship in reinforced concrete", *Structural Concrete Series No. 72-8*, McGill University, 1972, Montreal, Canada.
16. Rizkalla, S. H., Hwang, L. S. et al., "Transverse reinforcement effect on cracking behaviour of R.C. members", *Canadian Journal of Civil Engineering*, 10(4), 1983, pp 566-581.
17. Wu, H. Q. & Gilbert, R. I., "An experimental study of tension stiffening in reinforced concrete tension members under short-term and long-term service loads", UNICIV Report No. R-449, The University of New South Wales, 2008.
18. Noghabai, K., Contribution No. 6 in Ref. (21) – "Tests and analyses with 16 and 32 mm bars".
19. Tork, B., Gálvez, J. et al., Contribution No. 7 in Ref. (21) – "Tests with 8 and 16 mm bars".
20. Bigaj-van Vlijet, A. & den Uijl, J., Contribution No. 3 in Ref. (21) – "Tests and analyses with 16 mm bars".
21. Elfgren, L. & Noghabai, K. (Editors), "Bond properties of reinforcement bars embedded in concrete", A RILEM Round Robin Investigation arranged by TC 147-FMB Fracture Mechanics to Anchorage and Bond, Research Report 2001:13, Div. of Structural Engineering, Luleå University of Technology, 2001.
22. Rizkalla, S. H. & Hwang, L. E., "Crack prediction for members in uniaxial tension at any given loading stage", *Journal of the American Concrete Institute*, 81(6), 1984, pp 572-579.
23. Aryanto, A. & Shinohara, Y., "Bond behavior between steel and concrete in low level corrosion of reinforcing steel", *Proceedings of the 15th World Conference on Earthquake Engineering*, 2012, Lisbon.
24. De Sousa, C. F. F., "Analysis of cyclic and long-term effects in continuous precast railway bridge decks", Ph.D. Thesis, Universidade do Porto, 2012.
25. Espion, B., "Long term sustained loading tests on reinforced concrete beams: a selected data base", *Bulletin du Service Génie Civil No. 88-1*, Université Libre de Bruxelles, 1988.

# Role of Ettringite in Expansion and Cracking Potential in Steam Cured Precast Concrete Elements

Johnson Mak, Paul Thomas, Kirk Vessalas, Daksh Baweja  
Centre for Built Infrastructure Research, University of Technology Sydney.

**Abstract:** The susceptibility of precast concrete elements to failure due to DEF is a significant issue to the construction industry in Australia although little work has been carried out on the potential susceptibility of precast concrete elements to DEF in an Australian context. In order to address this issue, a research program investigating the development of hydration phases in the presence of elevated sulfate and alkali contents over a range of curing temperatures has been carried out and related to expansion in the mortar specimens containing 25% fly ash as a partial Portland cement replacement. This paper reports on the relationship between the development of these phases and the expansion over a period of 400 days after the initial precuring and assesses the potential of these mortars to undergo expansion associated with DEF.

**Keywords:** Delayed ettringite formation (DEF), steam cure concrete elements, Portland cement, fly ash.

## 1. Introduction

In recent years cracking and potential failure of some concrete elements particularly in high sulfate environments or when manufactured by precast steam curing processes, has been linked to the expansive formation of ettringite at times long after the hardening process has been completed; a process commonly termed delayed ettringite formation (DEF). Crystalline ettringite has been observed in cracks (Lawrence et al, 1999) and laboratory experiments have demonstrated expansion in cured mortar prism specimens due to the hydrostatic pressure produced through the formation of the higher specific volume ettringite phase (Taylor et al, 2001; Tousin and Baradan, 2010). Laboratory experiments have identified a number of factors which increases the susceptibility of concretes to DEF formation such as elevated sulfate and alkali ion concentrations and at curing temperatures of greater than 70°C (Glasser, 1996; Odler and Chen, 1996), however, there has also been discussion associated with the presence of DEF and alkali-silica reaction (ASR) (Diamond, 2000) and that the formation of DEF occurs in conjunction with ASR as a secondary mineralisation process (Shanyan and Ivanusec, 1996).

The susceptibility of precast concrete elements to failure due to DEF is a significant issue to the construction industry although little work has been carried out on the potential susceptibility of precast concrete elements to DEF in an Australian context. In order to address this issue, a research program investigating the development of hydration phases in the presence of elevated sulfate and alkali contents over a range of curing temperatures has been carried out and related to expansion in the mortar specimens containing 25% fly ash as a partial Portland cement replacement. This paper reports on the relationship between the development of these phases and the expansion over a period of 400 days after the initial elevated temperature pre-curing and assesses the potential of these mortars to undergo expansion associated with DEF.

## 2. Materials and Methods

General purpose Portland cement (PC) manufactured in Gladstone, QLD, a Gladstone Class F fly ash (FA) (AS 3582.1-1998), Pink Lily course aggregate sand and Kinka Beach fine aggregate sand, whose compositions are listed in Table 1, were used in the preparation of 150 x 40 x 40 mm mortar shrinkage prisms which were prepared following the method outlined in AS2350.13 (2006). To control the flow properties of the mortars, ADVA Cast 620, a polycarboxylic high range water reducing type admixture was used in accordance with (AS 1478.1 – 2000). All materials required for preparation of mortar prisms were supplied through Humes Australia. Paste specimens, prepared for phase analysis, were also prepared based on AS2350.13 (2006) with the main alteration being that no aggregate sand was added. The mix design for both mortar and paste specimens are listed in Table 2.

Table 1. Composition of mortar components in oxide wt% determined using XRF.

Oxide	Portland Cement	Fly Ash	Pink Lily Course Sand	Kinka Beach Fine Sand
SiO <sub>2</sub>	19.13	52.15	95.6	95.72
TiO <sub>2</sub>	0.26	1.32	0.04	0.16
Al <sub>2</sub> O <sub>3</sub>	4.91	25.23	1.62	1.67
Fe <sub>2</sub> O <sub>3</sub>	3.33	3.33	0.88	0.77
Mn <sub>2</sub> O <sub>3</sub>	N/A	N/A	N/A	N/A
Mn <sub>3</sub> O <sub>4</sub>	0.1	0.17	0.04	0.19
MgO	0.87	1.56	0.16	0.05
CaO	64.7	3.54	0.19	0.07
Na <sub>2</sub> O	0.51	0.73	0.38	0.25
K <sub>2</sub> O	0.41	0.88	0.54	0.51
P <sub>2</sub> O <sub>5</sub>	0.09	1.02	0.05	0.01
Cr <sub>2</sub> O <sub>3</sub>	0.01	0.01	0.04	0.03
ZrO <sub>2</sub>	0.02	0.05	N/A	0.01
SO <sub>3</sub>	2.34	0.18	N/A	N/A
Loss on ignition (L.O.I)	4.3	0.88	0.4	0.5
Total Weight	100.98	100.04	99.91	99.94
Na <sub>2</sub> O Equivalent	0.78	1.31	0.74	0.59

Table 2. Mortar and paste mix designs.

Material	Mortar Specimen	Paste Specimen
Portland cement	337.5g	337.5g
Class F Fly ash	112.5g	112.5g
Total binder content	450.0g	450.0g
Water	135.0g	135.0g
Water:binder ratio	0.3	0.3
Superplasticiser	2.0mL	0.5mL
Coarse sand	1147.5g	N/A
Fine sand	202.5g	N/A
Total sand content	1350.0g	N/A

Control of the sulfate and sodium composition of the mortar and paste specimens was achieved by adding calcined (at 100°C for 24 hours) gypsum (CaSO<sub>4</sub>) and sodium hydroxide, both technical grade, obtained from Chemsupply, SA, Australia. Sulfate and sodium composition was altered to achieve addition based on equivalent oxide composition; SO<sub>3</sub> additions of 1, 2, 3 and 4% and Na<sub>2</sub>O additions of 0.5 and 1% in addition to the PC content to give a range of 2.3 to 6.3% SO<sub>3</sub> and 0.78 to 1.78% Na<sub>2</sub>O. The alkalis contained in the FA are considered to be bound by the presence of tetrahedral aluminium and, hence, not considered to be available to influence the reaction directly.

Mortar specimens were prepared in triplicate and transferred to a commercial sterilising autoclave set at 60, 70, 80, 90 or 100°C for 8 hours. At the termination of the eight hour curing period the autoclave was turned off and allowed to cool naturally to room temperature over a 16 hour period whereupon the mortar specimens were stripped from their moulds and transferred to enclosed vessels and submerged in distilled water. Room temperature (23°C) cured specimens were also prepared, however, these specimens were sealed in polypropylene bags and allowed to cure for 24 hours prior transfer to the enclosed vessels.

For each set of mortar specimens and equivalent set of paste specimens were prepared and cured in conjunction with the mortar specimens. The paste was transferred in 20g batches to small polystyrene cups and cured concurrently with the mortar specimens.

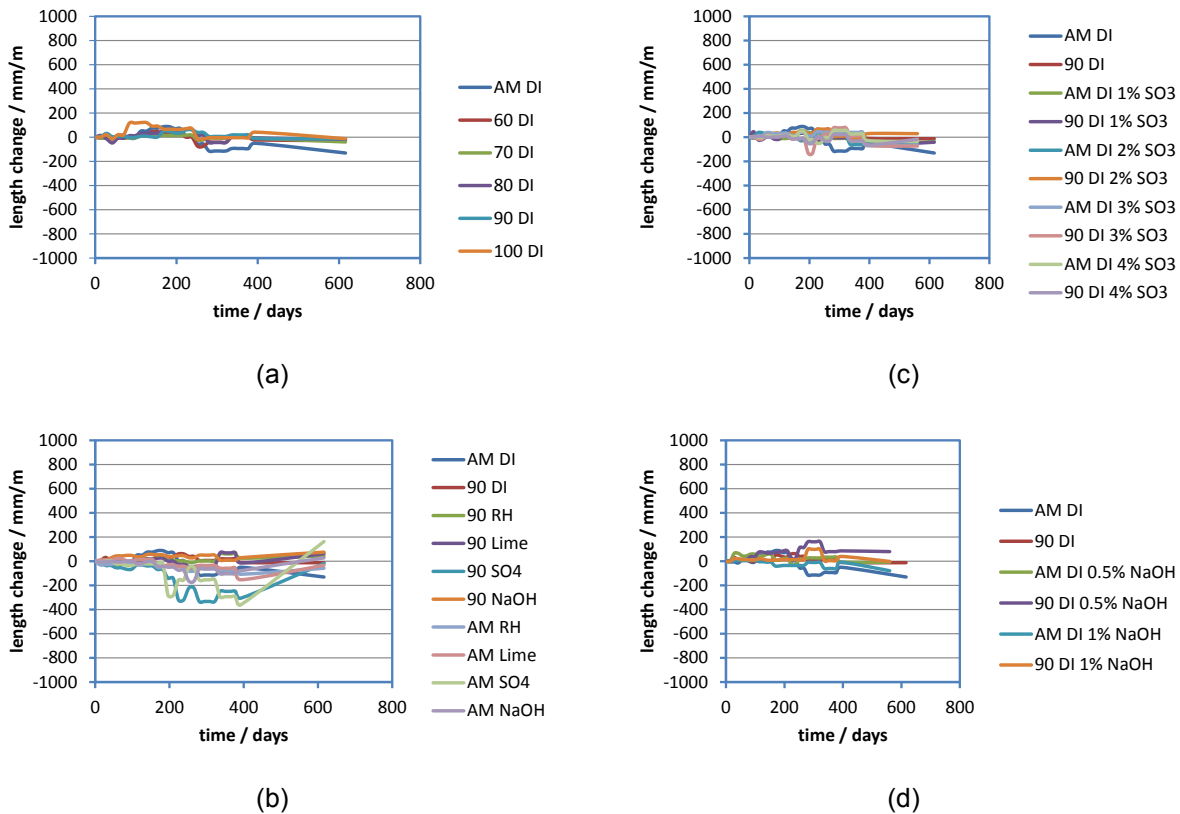


Figure 1. Expansion measurements carried out on mortars according to the procedures described in AS2350.13 (2006). Expansion has been plotted as length change in  $\mu\text{m/m}$  and has been plotted on a full scale of 2000  $\mu\text{m/m}$ , which represents a 0.2% expansion full scale. Data is plotted in series groups: (a) represents curing temperature, (b) environment in which the samples are submerged (DI – deionised water; RH – supported in saturated atmosphere above DI; NaOH – 1 M NaOH solution; Lime – saturated lime solution), (c) effect of increasing sulfate content showing  $\text{SO}_3$  equivalent % addition, (d) effect of increasing sodium concentration showing  $\text{Na}_2\text{O}$  equivalent % addition.

Dimension analysis was carried out on mortar specimens in accordance with the procedure laid out in AS2350.13 (2006). Dimension analysis was performed on specimens at 28 day intervals. The mortar specimens were removed from their submerged environments patted dry with paper towel and placed in a digital length comparator. Prior to returning specimens to their environment, the environmental liquid was replaced.

A paste specimen was also removed from the environment dried in a vacuum oven at RT and subsequently crushed and ground in a ring mill prior to characterisation by XRD using a Siemens D5000 diffractometer with an angular scan of  $3^\circ - 65^\circ 2\theta$  with a step size of 0.08 at 4 sec/step scanning time. Thermal analysis was carried out on a TA Instruments Simultaneous TG-DTA (SDT) Q600 instrument in  $\text{N}_2$  atmosphere with a flow rate of 120mL/min on  $30.0 \pm 0.1\text{mg}$  of binder paste powder using a  $10^\circ\text{C}/\text{min}$  heating rate over the temperature range of 30 to  $1200^\circ\text{C}$ .

## 2. Results

Mortar bars and cement paste specimens were prepared at a range of curing temperatures and stored in a range of environments. Mortar expansion (shrinkage) data were collected with a 4 week periodicity and are shown in Figure 1. Paste specimens were also collected at the same aging time and were dried ground and phase analysis was carried out using thermogravimetric analysis and x-ray diffraction (XRD). Only XRD data is presented in this paper and the data are shown in Figure 2.

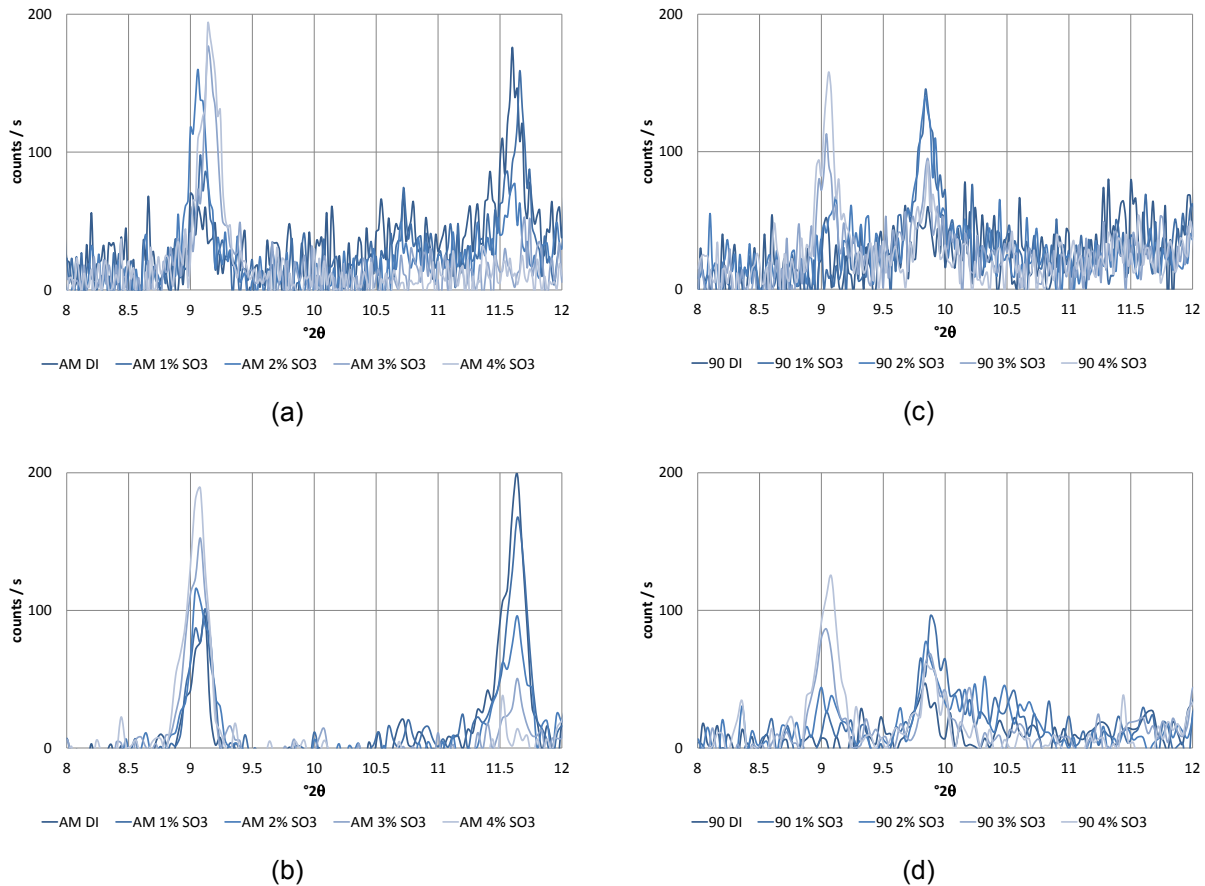


Figure 2. XRD data in the AFt, AFm region of the diffraction pattern: (a) ambient temperature (AM) cure, 28 days storage in deionised water (DI), (b) ambient temperature cure, 396 days storage in deionised water, (c) 90°C cure, 28 days storage in deionised water, (d) 90°C cure, 392 days storage in deionised water. Phases present:  $2\theta = 9.1^\circ$  - ettringite (AFt);  $2\theta = 9.8^\circ$  - monosulphate (AFm);  $2\theta = 11.6^\circ$  - monocarbonate.

## 2.1 Mortar Expansion Tests

The expansion (shrinkage) data is shown in Figure 1. The scales have been drawn so that full scale represents a 0.2% expansion. Expansion observed in laboratory experiments has been typically reported to be in the range 0.5 to 1% within a 400 days of curing (Yand, 1999, Ekolu 2007) which is significantly greater than the expansion observed in this study where no systematic expansion has been observed up to 600 days and length changes of less than 0.02% have been observed. Generally, laboratory experiments are carried out in the absence of mineral additions such as SCMs although reactive aggregates have been added to induce ASR (Ekolu 2007). In this study, all cement mortars contained 25% Class F fly ash.

## 2.2 XRD Phase Analysis

Figure 2 shows the XRD patterns for paste specimens collected at 28 and 392 days aging for ambient (AM) and 90°C curing for a series of cement pastes which have been modified with the addition of calcined (at 100°C for 24 hours) gypsum so that the  $\text{SO}_3$  equivalent is increased by 1, 2, 3 and 4%. Inspecting the ambient cured systems (Figure 2(a) and (b)), two peaks are observed in the range 8 to  $12^\circ 2\theta$  at 9.1 and  $11.6^\circ$ . The peak at  $9.1^\circ$  corresponds to ettringite. This peak increases in intensity with increasing proportion of sulfate addition suggesting that the proportion ettringite formed is linked to the sulfate present. A peak is also observed at  $11.6^\circ$  which indicates the presence of a (calcium aluminate)



monocarbonate phase (Matschei et al, 2007). The origins of this phase are uncertain, however, the Gladstone cement supplied by Humes Australia did contain an interground mineral addition of 7.5% limestone which could be a source of carbonate ions. Ettringite and monocarbonate are present in the ambient cured specimens at both 28 days and 392 days and, although these measurements are not truly quantitative, the relative peaks sizes appear consistent indicating that there is little change in the phase development with time.

Figure 2 (c) and (d) show the XRD patterns in this region for specimens cured at 90°C for 8 hours. In this case the monocarbonate peak at 11.6° is absent. Two peaks are still apparent at 9.1° and 9.8° indicating the presence of ettringite and (calcium aluminate) monosulfate. The monosulfate is more significant in the lower sulfate content cements while the ettringite peak is more significant in the higher sulfate content cements. This relationship of shift from monosulfate to ettringite with increasing sulfate content is consistent with increased sulfate concentration driving the equilibrium between these two phases toward ettringite. These data are also consistent with the reduced stability of ettringite at elevated temperature (Glasser, 1996). Again the relative size of the diffraction peaks suggests that there is little change in the phase composition from 28 days to 392 days.

### **3. Discussion**

Mortar and paste specimens were prepared and cured at ambient temperatures and at elevated temperature with varying sulfate composition in order to promote ettringite formation and in particular delayed ettringite formation resulting in expansion. A wide range of formulations have been prepared. The expansion measurements for many of these samples are shown in Figure 1. Within experimental error no expansion is observed in the timeframe of the study. This is surprising as a wide range of sulfate and alkali equivalent compositions have been incorporated and a range of curing temperatures has been applied. A compositional range from 2.4 to 6.4% sulfate in the presence of alkali ions should provide a pessimum composition. XRD phase analysis suggests that this compositional range is indeed enough as for an initial curing temperature of 90°C ettringite is absent in lower sulfate content pastes and present in the higher sulfate content pastes. This situation is mirrored in the ambient cured specimens although, qualitatively, it appears that there is a greater ettringite content for the higher sulfate content cements. Additionally, the observation of the presence of monosulfate in the 90°C cured specimens indicates that ettringite is depleted at elevated temperature in favour of monosulfate and as the sulfate content is increased, an equilibrium between ettringite and monosulfate is produced.

One significant difference between this study and other studies is that the cement used contained 25% fly ash in order to mimic field conditions in which this cement was used in the preparation of precast concrete element by Humes Australia. It is possible that the fly ash has a significant influence on the formation nucleation and precipitation of sulfo-aluminate phases. This study cannot draw any specific conclusions as only systems containing fly ash have been investigated.

### **4. Conclusions**

Mortar and paste specimens containing a range of sulfate and alkali contents and cured at a range of temperatures were investigated. Although ettringite has been produced, and elevated temperatures have aided the partial decomposition of ettringite in these systems, no expansion has been observed in mortar prisms containing elevated sulfate and alkali contents. A significant difference in the mortars and pastes studied was the presence of Gladstone fly ash which could influence the formation and stability of sulfo-aluminate phases that may be involved in DEF. In this study to date, although proportion of ettringite has been altered by changing the composition of the cements, no change in the ettringite content has been observed with time for a particular paste composition / curing temperature system. The role of the fly ash may be significant in mitigating DEF expansion, however, further work is required to demonstrate a relationship between fly ash and expansion mitigation in DEF susceptible systems.

## 5. Acknowledgement

The Authors would like to thank Humes Australia for financial support for this project and the supply of materials.

## 6. References

1. Lawrence B. L., Moody E.D. et al, "Evaluation and Mitigating Measures for Premature Concrete Distress in Texas Department of Transportation Concrete Elements" Cement and Concrete Aggregates, 21(1), 1999, 73-81.
2. Tosun K. and Baradan B., "Effect of ettringite morphology on DEF-related expansion", Cement & Concrete Composites, 32, 2010, 271-280.
3. Taylor, H.F.W., Famy, C. & Scrivener, K.L., "Delayed ettringite formation", Cement and Concrete Research, 31(5), 2001, 683-693.
4. Diamond, S., "The relevance of laboratory studies on delayed ettringite formation to DEF in field concretes", Cement and Concrete Research, 30(12), 2000, 1987-1991.
5. Glasser F. P., "The Role of Sulfate Mineralogy and Cure Temperature in Delayed Ettringite Formation", Cement and Concrete Composites, 18, 1996, 187-193.
6. Odler I. and Chen Y., "On the Delayed Expansion of Heat Cured Portland Cement Pastes and Concretes", Cement & Concrete Composites, 18, 1996, 181-185
7. Shayan A. and Ivanusec I., "An Experimental Clarification of the Association of Delayed Ettringite Formation with Alkali-Aggregate Reaction", Cement and Concrete Composites 18, 1996, 161-170.
8. Yang R., Lawrence C.D. et al, "Delayed ettringite formation in heat-cured Portland cement mortars" Cement and Concrete Research 29, 1999, 17-25.
9. Ekolu S.O., Thomas M.D.A. et al, "Implications of pre-formed microcracking in relation to the theories of DEF mechanism", Cement and Concrete Research 37, 2007, 161-165
10. Matschei T., Lothenbach B., et al, "The AFm phase in Portland Cement", Cement and Concrete Research, 37, 2007, 118-130.

# Improved Sustainability by Design for Concrete Durability

R. Doug Hooton<sup>1</sup>

<sup>1</sup>Professor of Civil Engineering, University of Toronto

**Abstract:** While many new types of concrete binder materials have been proposed and they can help in production of lower-carbon footprint concrete, far bigger contributions to sustainability over the whole life-cycle of concrete structures and infrastructure can be made through design and construction to ensure that sufficient durability is attained to extend their useful service life. To do this requires more than selection of limits on such things as maximum w/cm and minimum strength to meet durability requirements as required in national specifications. Influencing factors on attained durability include the materials, the concrete mix designs, volume stability, crack control (influenced by size, shape and restraint of structural elements, as well as structural detailing), as well as placing, protection and curing during construction. Prequalification testing of concrete placed in mock-up units, evaluation of the adequacy of the contractor's construction processes, as well as on-site inspection are required to ensure that in-place durability is obtained. Globally, the most severe environment that has resulted in premature deterioration of concrete structures is from corrosion of reinforcement in chloride exposures, from both marine and de-icing salts. Obtaining durability for a known service life in chloride exposures requires knowledge of the concrete properties, relevant transport processes, depths of cover as well as minimization of cracking and construction defects. For example, imperfect curing can result in depth-dependent effects on resistance to chloride ingress.

Several service life models with various levels of sophistication exist for prediction of time-to-corrosion of concrete structures exposed to chlorides. However, very few models deal with the influence of cracks or the fact that concrete in the cover zone will almost certainly have a higher diffusion coefficient than the bulk concrete as the result of imperfect curing or compaction. While many models account for variability in input properties, they will never be able to account for extremes in construction defects.

Therefore, to ensure the reliability of service life predictions and to attain a concrete structure that achieves its predicted potential, designers, contractors and suppliers need to work together to ensure proper detailing, minimize defects, and adopt adequate, yet achievable, curing procedures. As well, concrete structures are often also exposed to other destructive elements in addition to chlorides (eg. frost, ASR) and this adds another level of complexity since regardless of cause, cracks will accelerate the ingress of chlorides. These issues are discussed along with the need to use performance-based specifications together with predictive models.

**Keywords:** chloride ingress, diffusion, construction defects, cracks, performance specifications, durability.

## 1. Introduction

Concrete is a durable material and the most widely used construction material. Reinforced concrete structures can be designed to be resilient to severe storms, fire and earthquakes as well as to be durable in severe environmental exposures. Whether from marine or de-icing salts, chloride corrosion of steel reinforcement is the biggest challenge for both builders and owners of concrete structures. In addition to using materials and mix designs that will resist chloride ingress, construction detailing and practices have a large impact on durability. Achievement of concrete durability in-place is more likely with the use of appropriate performance specifications since temperature control, adequate compaction, protection of fresh concrete, and curing need to be detailed in specifications as well as requirements for sufficient inspection and testing to ensure that the specifications are being met.

In order to quantify the service life in severe environments, numerous predictive models have been developed over the last 25 years, especially related to the time-to-corrosion of reinforced concrete exposed to marine or de-icer salts. While early chloride ingress models, based on Fick's second law of diffusion were overly simplistic, newer models account for time-dependent changes in diffusion, the time to build up of surface chloride concentration, chloride binding and, in some cases, depth-dependent diffusion. However, diffusion is only one mechanism of ingress of fluids including aggressive ions such as chlorides. Other mechanisms including capillary absorption, permeability, and wick action can greatly accelerate ingress of chlorides, and some models have added terms to account for their effects. Taking a

different approach, more fundamental multi-species models have been developed such as Stadium (1, 2) that use effective diffusion values for different ions and account for their interactions and the nature of the pore structure and transport processes. In addition, deterministic models only provide average predictions which are not realistic given the level of uncertainty in concrete composition, rebar placement, and transport properties. However some models, such as DuraCrete (3) and LIFE-365 Version 2 (4) are at least semi-probabilistic and typically standard deviations as well as average values for each input value are used. The *fib* 2010 model code has incorporated some aspects of the Duracrete model (5). Unfortunately, space does not allow for more discussion.

## **2. Durability Design**

### **2.1 Design of Durable Concrete Mixtures**

Concrete mixtures that will be durable in aggressive exposures need to have low water/binder ratio, low unit water content, and contain appropriate levels of supplementary cementing materials. Typically, in order to minimize concrete permeability, a w/b of no higher than 0.40 is required. Using optimized total aggregate gradations and water-reducing admixtures, the unit water content can often be reduced to 135-140 L/m<sup>3</sup>, minimizing the paste volume fraction, thus reducing permeability while reducing thermal and drying shrinkage. Appropriate levels of supplementary cementing materials have many benefits in reducing paste permeability, reducing the porosity of the interfacial transition zones surrounding aggregates. Slag and fly ash will improve permeability at later ages, and silica fume improves properties at early ages, so ternary mixtures will work synergistically to improve initial properties and provide long-term benefits. In addition, SCMs improve the chloride binding capacity of the matrix, due to the lower Ca/Si ratio of the C-S-H and the incorporation of alumina into the hydrates, forming C-A-S-H (6, 7, 8).

Binder contents should be minimized, consistent with obtaining workable concrete, in order to minimize volume changes due to hydration temperatures and due to shrinkage. This will help minimize early-age cracking potential.

### **2.2 Types of performance testing**

Tests are or can be performed at various stages in construction.

- Pre-qualification Tests: Used by producers to demonstrate that a concrete mixture, when placed and cured under defined conditions, can meet the specification requirements and, if needed, provide input data for service life prediction. These tests often require significant lead time to complete and may include tests needed as inputs to service life models.
- Identity Tests: Performed when the concrete arrives on-site but before concrete is placed to demonstrate that the concrete being supplied is equivalent to the mixture that was pre-qualified (Similar to a DNA test). Unfortunately the range of identity tests that can be performed prior to acceptance of the truck load of concrete are quite limited. Typically, slump or slump flow is measured, and air content is determined. Useful information on concrete uniformity and air content can also be obtained from measuring the fresh density of the concrete, and some owners, such as the New York/New Jersey Port Authority have adopted the AASHTO microwave test to determine the water content of the delivered concrete (9) (as a partial check on w/cm (assuming that the cementitious materials are typically batched accurately) related to unintentional or deliberately added water).
- Quality Control: To document that the concrete supplied meets strength and other specification limits (a) at the change of ownership (the point of discharge from the truck) and (b) at the point of placement to demonstrate that pre-qualified placing practices are being followed.
- In-Place Testing: Using NDT and/or tests on cores extracted from the structure to ensure that the combination of the concrete supplied and the placement and curing methods used resulted in achieving the owner-defined performance levels. This is required in the End Result Specifications (ERS) used by several highway agencies.

Traditionally, concrete producers and contractors are often just interested in prequalification and quality control testing. However, owners are interested in performance of the hardened concrete in the structure, a number of highway agencies in North America have adopted or are currently considering the use of ERS where contractors are paid based on consistently meeting specified performance requirements using in-place testing of concrete in the structure. A number of these agencies have developed ERS with defined financial bonuses for consistently meeting performance, and penalties for failure to meet the in-place requirements. If performance is lower than a certain threshold, removal can be required. Regardless, of the type of performance specification adopted, the acceptance criteria and the responsibilities of the various parties in cases of failure need to be clearly defined.

While there are many types of aggressive exposures which could potentially require a multitude of durability tests, for resistance in all aggressive exposures the “permeability” or fluid penetration resistance of concrete needs to be minimized. Therefore, adoption of one or more tests for measuring fluid penetration resistance is fundamental to ensuring durable concrete.

Most deterioration processes involve two stages. Initially, aggressive fluids (water, ionic solutions with dissolved salts, gases) need to penetrate or be transported through the capillary pore structure of the concrete to reaction sites (e.g., chlorides penetrating to reinforcement, or sulfates penetrating to reactive aluminates) prior to the actual chemical or physical deterioration reactions. Therefore, a standard acceptance test or tests to measure rates of ingress of aggressive fluids, or a related rapid index test, is fundamental to the development of performance-based durability specifications. However, before tests are adopted in specifications, they must not only be shown to be useful and reliable, they must also be standardized and should include precision data based on interlaboratory evaluations (as is required for ASTM test methods), in order to set realistic specification limits that take account of test variability. Many tests have been proposed by researchers, but only a few have been found to be sufficiently robust to be adopted in recognised standards. Some interlaboratory data on non-destructive tests of concrete cover quality have been published (10, 11).

However, to be effective, the relevant mechanisms of fluid ingress for the environmental exposure of the structure or of specific structural elements need to be determined and appropriate test methods need to be adopted. Potential transport mechanisms include capillary absorption, diffusion, permeability and wick action, all of which are time-dependent. Many service life models only account for diffusion, but that is only one mechanism of chloride ingress. Capillary absorption into unsaturated near-surface zones can allow rapid ingress of dissolved ions in the so-called convection zone of the concrete cover. In some cases, pressure heads are also involved so permeability will also accelerate ingress. In the cases of tunnel liners, pipes, and slabs-on-grade, wick action from the air boundary can evaporate water from the near-surface capillary pores, leaving behind a buildup of precipitated chloride salts (12, 13, 14).

Test methods related to measurement of various durability properties exist in various North American standards (e.g. CSA, ASTM, AASHTO, US Corps of Engineers (CRD), and individual Departments of Transportation (DOT) in North America). Limits based on some of these test methods are specified in ACI, CSA and individual DOT specifications, amongst many others. Currently, standard test methods and/or limits do not exist for all of the relevant durability or performance concerns. As well, existing test methods are not always sufficiently rapid, accurate, or repeatable, nor do they necessarily adequately represent any or all of the in-situ exposure conditions. The lack of adequate performance-related test methods for concrete is one of the main factors that inhibit the move from prescriptive to performance specifications.

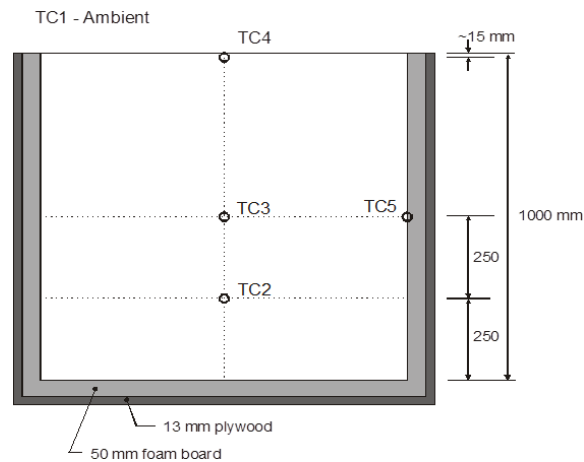
Limits on specific penetration resistance properties such as bulk chloride diffusion (ASTM C1556 (15), Nordtest NT Build 443 (16)), and water sorptivity (ASTM C1585 (17)) may be suitable for adoption in HPC specifications during pre-qualification and as inputs into predictive service life models, they are too time consuming to be used for acceptance purposes. For acceptance testing, a rapid permeability-index test should also be tested during prequalification and limits set that relate to the desired limits in the diffusion and sorptivity tests. Such rapid index tests include the ASTM C1202 (18) that was adopted in the CSA A23.1 concrete specification (19), the Rapid Chloride Migration Test (Nordtest NT492 (20) or AASHTO TP-64 (21)), a resistivity test (22, 23), or a chloride conductivity test (24). Because it is relatively simple, rapid and due to familiarity with its use, the ASTM C1202 test has become widely used for this purpose in North America. However, there is current activity at ASTM to adopt much simpler surface and bulk resistivity tests that may eventually replace the C1202 test. Many of these test methods are discussed by Lane et al (25).

In 2004, the Canadian CSA A23.1 concrete standard (19) introduced limits for the ASTM C1202 rapid chloride penetration test for prequalification of concrete mixtures to meet (a) C-1 exposure conditions (concrete exposed to freezing in a saturated condition with de-icer salts, 35 MPa, air-entrained, 0.40 w/cm max.) of 1500 coulombs at 56 days, and (b) C-XL exposure (similar exposure as the C-1 but where extended service life is required, 50MPa, air-entrained, 0.37 w/cm max.) of 1000 coulombs at 56 days. These limits effectively mandated the use of either blended cements or SCM's in all such concretes since 100% Portland cement concretes would be unable to meet these limits. The limits were originally set at 56 days of age to allow concretes containing slag or fly ash, that develop their properties more slowly, to be able to meet them, and have recently been revised to allow up to 91 days.

CSA A23.1 [19] includes statistical limits for acceptance purposes. The CSA coulomb limits were originally intended for prequalification, so notes were added that the 1500 coulomb requirement for Exposure Class C-1 an average value with no single result to be greater than 1750 coulombs. Similar wording was added for the high-performance C-XL Exposure Class concrete, except with different coulomb values (average of 1000, with no single value to exceed 1250). The 2014 revision of CSA A23.1 has moved these notes into the body of the specification. It is expected that the next revision will include a much simpler and less costly bulk resistivity test method and limits that will likely replace the C1202 test.

### **2.3. Identity tests and the monolith approach**

A challenging issue in implementation of performance specifications is the establishment of identity tests to confirm, at the start of a contract, that the concrete mixture being delivered is the correct one. Of necessity, these tests need to be done at the point of discharge from the truck and provide immediate confirmation that the mixture is essentially the same as the pre-qualified one. So how can it be determined that the measured slump, density, and air content, even if they are in the approved range, actually represent the concrete pre-qualified by the supplier to meet the specified strength and durability criteria? In connection with pre-qualification and constructability tests made by the authors for a proposed nuclear power station, casting of a pre-concreting monolith test procedure has been used (26). A similar performance approach was also developed for a series of underground transit stations). In these trials an insulated one cubic meter cube, suitably instrumented with thermocouples, was used as a pre-construction approval process. Specified performance criteria based on data and cores extracted from the monolith, were compressive strength, impermeability, freeze-thaw resistance, maximum temperatures, and temperature gradients. There are no instant tests for most of these properties so the monolith approach allows the Owner's design professional to check all the specified properties of the mixture that the contractor proposes to use. The sketch in Figure 1 shows a cross section of the monolith with locations of thermocouples. If needed to better determine thermal gradients, additional thermocouples can be added. The form is insulated so that curing is similar to the internal conditions in the mass concrete base slab. For this project compression tests up to 120 days were required, plus testing of in-place entrained air void systems, in-place rapid chloride permeability, and temperature gradients and maxima at all locations. The in-place tests were made on cores drilled from the monolith at different ages. On behalf of the owner the fabrication, concrete placing, compaction and curing can be witnessed. The owner can then make the tests on the concrete listed above and confirm that the concrete meets all strength and durability requirements. From then on the total responsibility for the quality of concrete delivered placed and cured rests with the contractor and the concrete supplier. This approach requires significant lead time, typically in excess of 3 months, but on most infrastructure contracts this is typically not a problem.



**Figure 1. Sketch of insulated one cubic metre monolith used for pre-qualification of concrete mixtures, showing locations of thermocouples (TC) (26)**

#### **2.4. Roles and Responsibilities in Performance Specifications**

Adoption of true performance-based specifications presupposes that we have a clear understanding of all the performance issues that can affect concrete. It also assumes that there are appropriate performance test methods in place to evaluate all of the performance issues for: concrete materials, fresh concrete, hardened concrete, and durability. It also assumes that performance can either be measured in time to affect the outcome, and/or can be used to pre-qualify concrete mixtures. Most parties to construction are familiar with testing for fresh properties and strength of concrete, but the biggest challenges in this regard relate to requirements for durability (27, 28, 29).

While there are many types of aggressive exposures which might require a multitude of durability tests, the common element is that most aggressive exposures require that the permeability or fluid penetration resistance of concrete be minimized. Therefore adoption of one or more tests for penetration resistance is fundamental to ensuring durable concrete.

The Canadian concrete standard CSA A23.1 (19) outlines the requirements and responsibilities for use in performance-based concrete specifications. The responsibilities of the various parties need to be clearly defined with a performance specification. This has been documented in CSA A23.1, as shown in Table 1. In addition, an Annex J to that standard explains each of the table items in more detail.

#### **2.5. Implementation of Performance Specifications**

The onus for meeting performance clearly rests with the producer up to point of placement. Since in-place performance is also affected by the contractor's placement methods, the producer must work with the contractor to ensure the owner's performance requirements are achieved: for example, the contractor (not the owner/specifier) should set the target slump to allow for proper placement and compaction for the situation, and the producer needs to design and provide this without reducing the intended performance of the hardened concrete.

Even if performance requirements are clearly stated in a specification, experience suggests that the successful implementation of a contract depends significantly on a dialogue between the contractors bidding for a contract and the Owner's design professional. Recent experience on a major HPC project suggests that where this requirement is established as an absolute and where there is constant and open communication across the construction team, all members will come to recognize the benefits of this approach.

A few important points are as follows:

- Require all contract bidders to attend a pre-bid meeting to hear about special requirements—so they cannot complain afterwards that they missed some of the performance requirements.

- Make contractors, including subcontractors, detail in their bid how they intend to meet the special requirements part of the bid submittal. eg. Concrete placement methods, protection, curing, hot/cold weather provisions.
- Do not accept low-price bids that are not responsive to the special requirements.
- Once work has commenced, require pre-pour meetings for important placements: The contractors, the suppliers, the subcontractors, including the finishers need to be aware of what needs to be done to ensure that the concrete can be delivered, placed, compacted, protected, finished, and cured to achieve the performance objectives. Even the person who will be fog misting, or applying other protective measures needs to be there to understand why it is important.
- During construction, the owner must be notified of any errors or problems without delay together with documentation and communication of the action being taken to rectify the problem.

Achieving the owner's performance requirements requires more cooperation between the concrete suppliers, the contractors, and concrete finishers than often exists in typical practice. As stated earlier, this type of information is detailed in Annex J of CSA A23.1(19).

## **2.6. Minimizing Construction Defects**

Construction detailing and practices as well as defects can significantly affect actual penetration rates of aggressive ions and fluids, but are rarely quantified or modeled. Almost no current service life prediction models can deal with the influence of cracks or the fact that concrete in the cover zone will almost certainly have a higher diffusion coefficient than the bulk concrete as the result of imperfect curing or compaction. An example of the variation in properties of similar bridge structures is given by Tikalsky et al (30).

It is the unpredictable areas of poorly compacted, poorly cured, or cracked concrete with less than the design depth of cover which will severely shorten the predicted the time to corrosion, regardless of what model is used. Therefore, one of the most effective ways to obtain the model-predicted service life of a structure is to address these site issues prior to and during construction. Pre-construction and pre-pour meetings mentioned previously are effective in ensuring that the contractor and sub-contractors understand the issues and have the required labor, materials and equipment on site to ensure best practices are followed.

As well, inspection of formwork placement and reinforcement cover depths prior to each placement of concrete can be used to correct areas of low cover deficiencies. In probability-based models, a common approach is to assume an average and range of properties such as concrete cover depth. But by correcting cover deficiencies prior to concrete placement, the variability in predicted service life can be significantly reduced. For example at the newest parking garage at Toronto's Pearson airport, this process of inspection prior to placement led to a standard deviation in cover depth of only 3 mm over a huge deck area (Figure 2) (the specified cover was 40 mm), significantly below the CSA A23.1 (19) allowable variation of 10 mm (31).

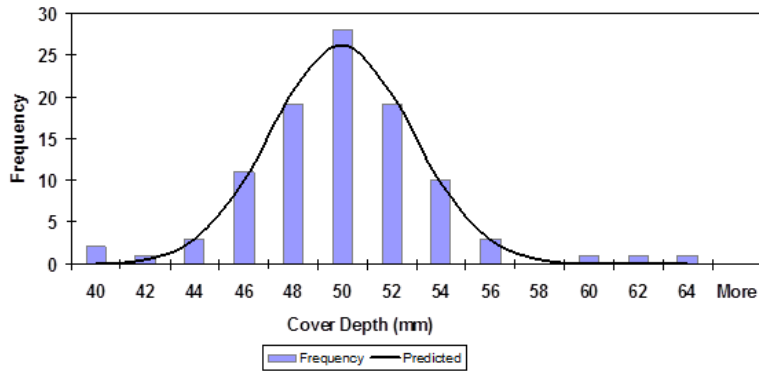
The ability to adequately place, vibrate and compact concrete in areas of congested reinforcement also needs to be established, preferably with test of mock ups but also by letting the contractor select the required workability required for the situation given the available equipment and labour. The concrete supplier can then design appropriate mixtures for the contractor's required workability. To address compaction and curing, cores extracted from the in-place concrete can be tested to assess the in-place performance of the final structural element (to avoid drilling cores from precast elements, extra elements for coring can be cast with the structural elements).

Early-age cracking can results from inadequate protection of plastic concrete, restrained drying shrinkage and from thermal gradients. Cracks wider than 0.05 to 0.10 mm have been shown to accelerate chloride ingress (36, 37). Therefore, in design detailing, mix proportions and construction practice, emphasis must be placed on minimizing cracking as well as the widths of cracks.



**Table 1. Prescriptive vs Performance Specification Responsibilities (adapted from CSA A23.1) (19).**

Alternative	The owner shall specify	The contractor shall	The supplier shall
<p><b>Performance:</b></p> <p>When the owner requires the concrete supplier to assume responsibility for performance of the concrete as delivered and the contractor to assume responsibility for the concrete in place.</p>	<p>(a) required structural criteria including strength at age;</p> <p>(b) required durability criteria including class of exposure;</p> <p>(c) additional criteria for durability, volume stability, architectural requirements, sustainability, and any additional owner performance, pre-qualification or verification criteria;</p> <p>(d) quality management requirements (Annex J)</p> <p>(e) whether the concrete supplier shall meet certification requirements of concrete industry certification programs; and</p> <p>(f) any other properties they may be required to meet the owner's performance requirements.</p>	<p>(a) work with the supplier to establish the concrete mix properties to meet performance criteria for plastic and hardened concrete, considering the contractor's criteria for construction and placement and the owner's performance criteria;</p> <p>(b) submit documentation demonstrating the owner's pre performance requirements have been met; and</p> <p>(c) prepare and implement a quality control plan to ensure that the owner's performance criteria will be met and submit documentation demonstrating the owner's performance requirements have been met.</p>	<p>(a) certify that the plant, equipment, and all materials to be used in the concrete comply with the requirements of this Standard;</p> <p>(b) certify that the mix design satisfies the requirements of this Standard;</p> <p>(c) certify that production and delivery of concrete will meet the requirements of this Standard;</p> <p>(d) certify that the concrete complies with the performance criteria specified;</p> <p>(e) prepare and implement a quality control plan to ensure that the owner's and contractor's performance requirements will be met if required;</p> <p>(f) provide documentation verifying that the concrete supplier meets industry certification requirements, if specified; and</p> <p>(g) at the request of the owner, submit documentation to the satisfaction of the owner demonstrating that the proposed mix design will achieve the required strength, durability, and performance requirements.</p>
<p><b>Prescription:</b></p> <p>When the owner assumes responsibility for the concrete.</p>	<p>(a) mix proportions, including the quantities of any or all materials (admixtures, aggregates, cementing materials, and water) by mass per cubic metre of concrete;</p> <p>(b) the range of air content;</p> <p>(c) the slump range;</p> <p>(d) use of a concrete quality plan, if required; and</p> <p>(e) other requirements.</p>	<p>(a) plan the construction methods based on the owner's mix proportions and parameters;</p> <p>(b) obtain approval from the owner for any deviation from the specified mix design or parameters; and</p> <p>(c) identify to the owner any anticipated problems or deficiencies with the mix parameters related to construction.</p>	<p>(a) provide verification that the plant, equipment, and all materials to be used in the concrete comply with the requirements of this Standard;</p> <p>(b) demonstrate that the concrete complies with the prescriptive criteria as supplied by the owner; and</p> <p>(c) identify to the contractor any anticipated problems or deficiencies with the mix parameters related to construction.</p>



**Figure 2. Range of measured in-place concrete cover on parking garage deck slab when inspected before placement (Specified cover = 40 mm) (31)**

#### 4. Conclusions

Achieving durability requires more than selecting an appropriate concrete mixture, construction practices and details also impact durability. In addition, performance specifications, making use of appropriate durability tests and limits, can help in the achievement of durable structures. While far from perfect, use of performance approaches in durability design is a step forward. Such approaches are being used successfully in large infrastructure projects and serve to focus attention on the whole construction process and not just on the concrete mixture being supplied. To achieve durability in the completed structure, designers, contractors and suppliers need to effectively communicate and work together to resolve problems quickly, to minimize defects, and to adopt adequate, yet achievable, curing procedures.

To quantify durability in chloride exposures, there have been impressive achievements in the development of predictive service-life models in the last 25 years. This is especially true in the area of time to onset of reinforcement corrosion where models have developed far beyond application of very simplistic Fick's 2<sup>nd</sup> Law methods to much more sophisticated multi-mechanistic, time-dependent, probabilistic transport models. Test methods have been developed to provide input values for these models, but often these tests are time-consuming, making them unsuitable beyond prequalification purposes. Some of these tests also suffer from high levels of variability. Faster, more reliable test methods will provide better predictions and will be better suited for quality assurance purposes during construction. In the meantime, rapid index tests for resistance to chloride ingress can be used for that purpose.

#### 4. Acknowledgements

The author would like to thank Dr. John A. Bickley, retired consultant, for ideas and useful discussions. As well, the support for the Author's Natural Sciences and Engineering Research Council of Canada / Cement Association of Canada, Industrial Research Chair in Concrete Durability and Sustainability, is greatly appreciated.

#### 5. References

1. Marchand, J., Samson, E. et al., "Predicting the performance of concrete structures exposed to chemically aggressive environment—Field validation", *Materials and Structures* 35 (10), 2002, pp 623-631.
2. Maltais, Y. Marchand, J. et al., "Predicting the durability of portland cement systems in aggressive environments – Laboratory validation", *Cement and Concrete Research* 34 (9), 2004, pp 1579-1589.
3. DuraCrete, Probabilistic Performance Based Durability Design of Concrete Structures, Final Technical Report, EU-Project-Euram III Document No. BE95-1347/R17, 2000.

4. Ehlen, M.A., Thomas, M.D.A. et al., "Life-365 Service Life Prediction Model Version 2.0", Concrete International 31(2), 2009, pp 41-46.
5. *fib* "Model Code for Concrete Structures", International Federation for Structural Concrete 2010, Geneva, Switzerland.
6. Zibara, H., Hooton, R.D., et al., "Influence of the C/S and C/A ratios of hydration products on the chloride ion binding capacity of lime-SF and lime-MK mixtures", Cement and Concrete Research, 38 ( 3), 2008, pp 422-426.
7. Hooton, R.D., Thomas, M.D.A. et al., "Use of Pore Solution Analysis in Design for Concrete Durability", Advances in Cement Research, 22 (4), 2010, pp 203-210.
8. Thomas, M.D.A., Hooton, R.D. et al., The Effect of Supplementary Cementing Materials and W/CM on the Chloride Binding Capacity of Cement Paste, Cement and Concrete Research 42 (1) 2012, pp 1-7.
9. Bognacki, C. J., Pirozzi, M. et al., "Increasing the services lives of concrete pavements", Concrete International 34(1), 2012, pp 27-33.
10. Rilem TC 189-NEC, "Non-destructive evaluation of the concrete cover, Part I-Comparative test of penetrability methods", Materials and Structures 38, 2005, pp 895-906.
11. Rilem TC 189-NEC, "Update of the recommendation of Rilem TC 189-NEC, Non-destructive evaluation of the concrete cover, Part I - Comparative test of penetrability methods", Materials and Structures 41, 2008, pp 443-447.
12. Buenfeld, N.R., Shurafa-Daoudi, M-T. et al., "Chloride Transport due to Wick Action in Concrete,' in Chloride Penetration into Concrete", Proceedings, RILEM International Workshop, St-Remy-les.Chevreuse, France, October 1995, pp 315-324.
13. Nokken, M.R. and Hooton, R.D., "Evaporative Transport of Chlorides in Concrete", Proceedings, Concrete Under Severe Environments, CONSEC'01, Vancouver, 1 ,2001, pp 357-364.
14. Aldred, J.M., Rangan, B.V. et al., "Effect of Initial Moisture Content on Wick Action through Concrete", Cement and Concrete Research, 34, 2004, pp 907-912.
15. ASTM C1556-11a, "Standard Test Method for Determining the Apparent Chloride Diffusion Coefficient of Cementitious Mixtures by Bulk Diffusion", ASTM Annual Book of Standards, V.04.02,ASTM International, 100 Barr Harbor Dr., P.O. Box C-700, West Conshohocken, PA USA 2013.
16. Nordtest NT Build 443, "Accelerated Chloride Penetration". P.O. Box 116, FIN-02151 Espoo Finland.
17. ASTM C1585-13, "Standard Test Method for Measurement of Rate of Absorption of Water by Hydraulic-Cement Concretes", ASTM Annual Book of Standards, V.04.02, ASTM International, 100 Barr Harbor Dr., P.O. Box C-700, West Conshohocken, PA USA, 2013.
18. ASTM C1202-12, "Standard test method for electrical indication of concrete's ability to resist chloride ion penetration", ASTM Annual Book of Standards, V.04.02, ASTM International, 100 Barr Harbor Dr., P.O. Box C-700, West Conshohocken, PA USA, 2013.
19. CSA A23.1/A23.2-14, "Concrete materials, methods of concrete construction, test methods and standard practices", Canadian Standards Association, Toronto, Ontario, Canada, 2014.
20. Nordtest NTBuild 492, "Chloride Migration Coefficient from Non-Steady-State Migration Experiments", P.O. Box 116, FIN-02151 Espoo Finland, 1999.
21. AASHTO TP64-03, "Standard Test Method for Predicting Chloride Penetration of Hydraulic Cement Concrete by the Rapid Migration Procedure", American Association of State Highway Transportation Officials, Washington, DC, 2003.
22. Hooton, R. D. and Karkar, E., "Evaluating durability of concretes using rapid measurements for fluid penetration resistance", Proceedings, Concrete Structures for Sustainable Community, *fib*, Stockholm, 2012, pp 315-318.
23. AASHTO TP95-11, "Standard Method of Test for Surface Resistivity Indication of Concrete's Ability to Resist Chloride Ion Penetration", American Association of State Highway Transportation Officials, Washington, DC, 2003.

24. Alexander, M. G., Ballim, Y. et al., "A framework for use of durability indexes in performance-based design and specifications for reinforced concrete structures", Materials and Structures 41(5), 2008, pp 921-936.
25. Lane, D. S., Detwiler, R. J. et al., "Testing transport properties in concrete", Concrete International 32(11), 2012, pp 33-38.
26. Hooton, R. D. and Bickley, J. A., "Prescriptive versus performance approaches for durability design - The end of innocence?", Materials and Corrosion 63(12), 2012, pp. 1097-1101.
27. Bickley, J.A., Hooton, R.D. et al., "Preparation of a Performance-Based Specification for Cast-In-Place Concrete", Report, RMC Research & Education Foundation, 2006, 168 pp. <http://www.nrmca.org/p2p>
28. Hooton, R.D., Hover, K.C., et al., "Performance Standards and Specifications for Concrete for Promotion of Sustainable Construction", Proceedings, CONSEC'07, Tours, France, 2007, 1, pp 815-830.
29. Hooton, R.D., Bickley, J.A. et al., "Specifying and Achieving High Performance in Concrete Structures", e-Proceedings, 9th International Conference on High Performance Concrete, Rotorua, New Zealand, 2011.
30. Tikalsky, P., Pustka, D. et al., "Statistical Variations in Chloride Diffusion in Concrete Bridges", ACI Structural Journal 102(3), 2005, pp 481-486.
31. Hooton, R.D. and Bickley, J.A., "Design for Durability: The Key to Improving Concrete Sustainability", e-Proceedings, First International conference on Concrete Sustainability (ICCS'13), Tokyo, 2013.
32. Crank, J., "The Mathematics of Diffusion", 2nd Edn, Clarendon, Oxford, 1975.
33. Mangat, P.S. and Malloy, B.T., "Prediction of Long Term Chloride Concentration in Concrete", Materials and Structures, 27, 1994, pp 338-346.
34. Bentz, D.P., Feng, X. et al., "Time-Dependent Diffusivities: Possible Misinterpretation due to Spatial Dependence", Proceedings, RILEM PRO19, Testing and Modelling the Chloride Ingress into Concrete, 2000, pp 225-233.
35. Hooton, R.D., Geiker, M.R. and Bentz, E.C., "Effects of Curing on Chloride Ingress and Implications of Service Life", ACI Materials Journal 99 (2), 2002, pp 201-206.
36. Garces Rodriguez, O. and Hooton, R.D., "Influence of Cracks on Chloride Resistance of Concrete", ACI Materials Journal, 100 (2), 2003, pp. 120-126.
37. Reinhardt, H-W. and Jooss, M., "Permeability and Self-Healing of Cracked Concrete as a Function of Temperature and Crack Width", Cement and Concrete Research 33, 2003, pp 981-985.

# Exp-Ref: A Simple, Realistic and Robust Method to Assess Service Life of Reinforced Concrete Structures

Roberto Torrent

Technical Director, Materials Advanced Services Ltd.

**Abstract:** The hereby proposed “Exp-Ref” method of Service Life Assessment presents two characteristic features. First, it is “Experimental”, because the prediction is based on the “in situ” ND determination of the cover depth  $d$  and of the coefficient of air-permeability  $kT$ . Second, the assessment is not based on a prediction starting from  $t=0$  as most other methods, but from a “Reference” condition corresponding to 50 years. This is the service life expected if the prescriptions of concrete quality (EN206-1 and EN 13670) and cover depth (Eurocode 2) are observed. By comparing the actual values of  $d$  and  $kT$  measured on site with those corresponding to the reference condition, it is possible to estimate the service life (SL) with the simple formula  $SL = \alpha \cdot d^2 / kT^{1/3}$ , with  $\alpha = f(\text{chloride exposure condition})$ . The proposed method is simple and realistic (is based on real data obtained on the end-product, referred to values for 50 years of SL) and is robust (neither ambiguities nor subjectivity by selective choice of model parameters as for other methods). It provides also a probabilistic representation of SL as a single value is assigned to each measurement point. A couple of application cases are presented.

**Keywords:** Service life, assessment, chlorides, cover, permeability.

## 1. Introduction: the Need for Service Life Assessment

Traditionally, Concrete Codes and Standards have applied the “Deemed-to-satisfy” approach [1] to specify durability requirements. Based on the accumulated experience in many countries, a set of primarily prescriptive rules has been established which, when rigorously observed, should result in a service life typically of 50 years (e.g. [2,3]). This applies also to codes that have adopted a more performance oriented approach, such as Australian and Swiss Standards [4-6].

Important structures, such as the Panama Canal and the Chacao Bridge (Chile) present a design Service Life of 100 years, reaching 120 years for the Hong Kong-Zhuhai-Macao Bridge (China), 150 years for the Port of Miami Tunnel (USA) and even 300 years for the 2<sup>nd</sup> Gateway Bridge in Brisbane (Australia).

All the above listed structures have something in common: the design should contemplate sufficient resistance against one of the most insidious deterioration problems of reinforced concrete structures, namely chloride-induced steel corrosion, for an extended service life well beyond 50 years.

These service lives clearly exceed the reach of existing experience with reinforced concrete and, therefore, some extrapolation via modeling is required for their design.

## 2. Modeling Chloride Ingress with Diffusion Fick’s 2<sup>nd</sup> Law

Most Service Life (SL) prediction models for chloride-induced steel corrosion assume that the penetration of chlorides into the exposed concrete follows a purely diffusive mechanism, governed by 2<sup>nd</sup> Fick’s Law which, for uniaxial flow is given by Eq. 1.

$$\frac{\partial C}{\partial t} = \frac{\partial}{\partial x} \left( D \frac{\partial C}{\partial x} \right) \quad (1)$$

Where  $C = C(x,t)$  is the concentration of chlorides in concrete at depth  $x$  and time  $t$  and  $D$  is the coefficient of diffusion to chlorides, expressed in  $[L^2]/[t]$  units, typically  $m^2/s$ .

Assuming that  $D$  is constant, i.e. independent of  $x$ ,  $C$  and  $t$ , and that the initial concentration of chlorides in the concrete mix is 0, an explicit solution, given by Eq. 2 can be derived.

$$C(x, t) = C_s \left[ 1 - \operatorname{erf}\left(\frac{x}{\sqrt{D \cdot t}}\right) \right] \quad (2)$$

$C_s$  = concentration of chlorides at the surface of concrete (assumed constant with time)

$\operatorname{erf}$  = error function

Eq. 2 is at the root of the most widespread models to predict service life.

From Eq. 2, the corrosion Initiation Time  $t = T_i$ , at which the concentration of chlorides  $C$  reaches a certain critical threshold value  $C_{cr}$  at the depth  $x$  equal to the rebar cover depth  $d$ , can be calculated. This Initiation Time  $T_i$  is commonly assumed as the limit state for the Service Life Design.

By making  $C(x, t) = C_{cr}$  at  $x = d$ , the initiation time  $T_i$  can be computed from Eq. 2, as:

$$T_i = \frac{d^2}{4 \cdot D} \cdot A^2, \quad \text{with} \quad (3)$$

$$A = \frac{1}{\operatorname{erf}^{-1}\left(1 - \frac{C_{cr}}{C_s}\right)} \quad (4)$$

where  $\operatorname{erf}^{-1}$  is the inverse error function.

Despite the fact that Eqs. 2 to 4 were derived assuming that  $D$  is constant, many models assume that the coefficient of diffusion of chlorides in concrete decreases with time (a fact that has been observed experimentally). The main justification for this phenomenon is the densification of concrete due to the hydration of cement at ages beyond that considered for the tests to measure  $D$  (typically 28 days). This is expressed as:

$$D = D_0 \left(\frac{t_0}{t}\right)^m \quad \text{for } t \leq t_h \quad (5)$$

where:

$D$  = coefficient of diffusion of chlorides at age  $t$

$D_0$  = coefficient of diffusion of chlorides measured at age  $t_0$

$m$  = exponent indicating the intensity of the "ageing" effect; if  $m = 0$ ,  $D$  is constant and not affected by age (only mathematically correct case)

$t_h$  = duration of the effect of hydration on the reduction of  $D$

The set of Eqs. 3 to 5 constitutes the core of the more widely used models to predict Service Life against chloride-induced corrosion: Life-365 [7], Duracrete [8], Duracon [9] and EHE-08 [10].

### 3. Limitations of Current Models

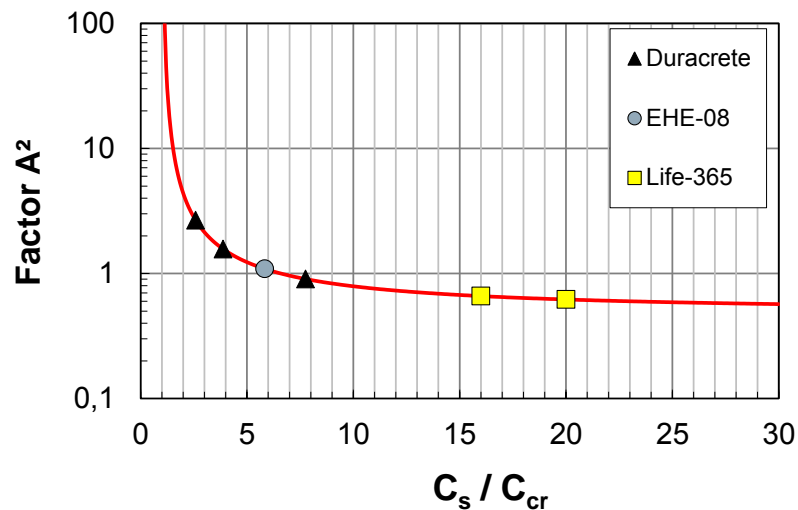
#### 3.1 Uncertainty of key parameters

Models based on the application of Eqs. 3 to 5 find application during the design stage, to make a preliminary SL assessment. As a result of their application, the durability design leads to the selection of the associated design variables  $d$  and  $D$  (or  $D_0$ ). The mix design should propose mixes that achieve the required  $D_0$  value used in the design and a binder compatible with the  $m$  and  $t_h$  values used in Eq. 5.

One of the limitations of the current models is the difficulties associated with the definition of key parameters  $C_s$ ,  $C_{cr}$ ,  $m$  and  $t_h$ , for the structure under design.

The validity of the power decay function (Eq. 5) and of the exponent  $m$  values proposed is a subject of much uncertainty and controversy [11,12]. In particular, the effect of  $m$  on  $T_i$  is "dramatic" [13]. The duration of the effect  $t_h$  is also controversial; Life-365 [7] proposes a maximum duration of 25 years, other models [8-10] extend the duration to the entire initiation time  $T_i$  of the structure. The experimental determination of  $m$  is difficult, due to the long-term nature of the exponent. Therefore it is not possible to count with representative values of  $m$  and  $t_h$  at the time of the SL design.

The factor  $A^2$  has also an important influence on  $T_i$  as shown in Fig. 1, where its relation to the ratio  $C_s/C_{cr}$  is presented. As shown in the figure, different models propose widely different values of  $C_s$  and  $C_{cr}$  (for Tidal and Spray exposure) and of their ratio, which have a strong effect on the SL designed.



**Figure 1. Effect of  $C_s/C_{cr}$  ratio on factor  $A^2$  (for Tidal and Splash Exposure)**

Hence, the rather arbitrary and sometimes subjective choice of key parameters  $C_s$ ,  $C_{cr}$ ,  $m$  and  $t_h$ , when applied to Eqs. 3 to 5, may lead to huge differences in the predicted service life, even to absurd results, such as  $1.5 \cdot 10^{29}$  years, which makes the Models non robust and extremely user-dependent.

### 3.2 Design and Real values of $d$ and $D_0$

As mentioned above, the SL design results in a selection of  $d$  and  $D_0$  values that satisfy the design Initiation Time  $T_i$  required by the project.

The cover depth  $d$  is usually specified in the project documents, as a minimum or nominal value and  $D_0$  is associated to the coefficient of diffusion measured by long-term tests (e.g. [14]), or by short-term migration tests (typically [15]), on laboratory-cast specimens, after 28 or 56 days of moist curing.

It is well known that the real values of  $d$  and  $D_0$  in the “as-built” structure are usually quite different to the ones assumed for the design or measured on laboratory specimens.

Neville [16], among others, has pointed out the differences (often on the unsafe side) between the specified and the real values of cover depth. From Eq. 2, we see that 10% less cover means 20% less service life.

The loss of quality, in terms of resistance to chloride penetration, of the real concrete (“Realcrete”) compared with that measured on laboratory specimens (“Labcrete”) has been well documented. Several laboratory and site investigations have shown that the transport parameters of the Realcrete may be significantly worse than those obtained on the Labcrete [17], due to segregation, lack of curing and the inevitable scale differences between treating a small specimen and a large structure.

Even when considered by coefficients (e.g. curing factor in Duracrete), the modeling will hardly consider the different and extremely variable quality of Realcrete.

## 4. The “Exp-Ref” Method

The proposed “Exp-Ref” Method for SL assessment aims at solving some of the limitations of the current methods, discussed in Section 3. As suggested by its name, it has two components:

Exp: It is based on the non-destructive “Experimental” assessment of  $d$  and  $D_0$  (indirectly through the measurement of the coefficient of air-permeability  $kT$ ), to get realistic values of the “Realcrete” quality

Ref: The method defines a “Reference” situation, established as a “deem to satisfy” condition, on which the SL prediction for different conditions is based.

A full description of the hypotheses and derivation of the formulae used to predict  $T_i$  from measured values of  $kT$  and  $d$ , can be found in [18]. In what follows, just the the fundamental concepts are presented.

#### 4.1 The Experimental Component of “Exp-Ref”

The principle consists in sampling the exposed surface of a concrete structure and, at the selected points, to measure non-destructively (using Standardized methods), both the cover depth  $d$  (e.g. [19]) and the coefficient of air-permeability  $kT$  [20], preferably at an age between 28 and 90 days. An experimental relationship (see Eq. 8) is used to transform the  $kT$  values into equivalent  $D_0$  values. Fig. 2 shows a possible arrangement of the readings, including the measurement of the moisture content of the concrete ( $m\%$ ) which, according to [20] shall not exceed 5.5% when measured by the electrical impedance method.

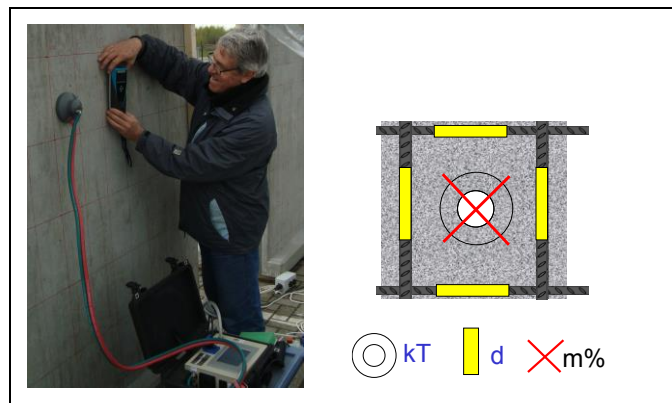


Figure 2. Arrangement of ND measurement of  $kT$  and  $d$ , after the Exp-Ref Method

#### 4.2 The Referential Component of “Exp-Ref”

In order to avoid the need to define the elusive key parameters  $C_s$ ,  $C_{cr}$ ,  $m$  and  $t_h$  for the prediction, a reference situation is assumed, for the exposure situation under consideration.

The concept is outlined in Fig. 3, based on the EN Codes and Standards.

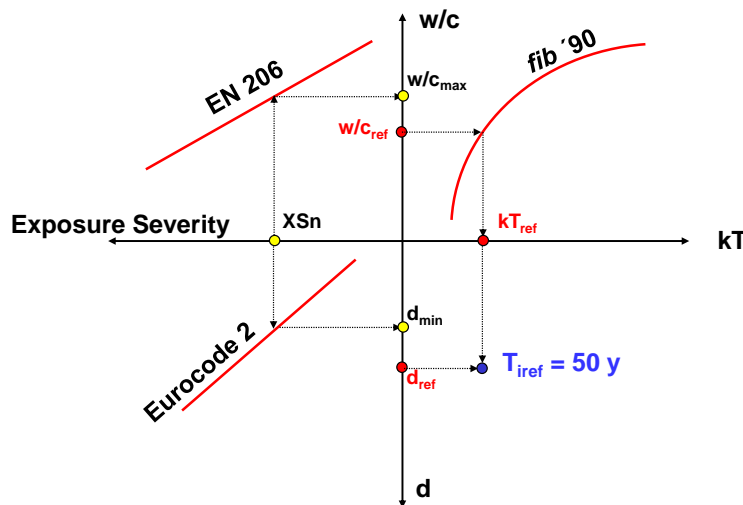


Figure 3. Concept of the Reference Condition in “Exp-Ref” Method



For the Exposure Severity of the Structure (e.g. XS3), the maximum  $w/c$  ratio and minimum cover depth  $d$  are obtained from EN 206-1 and Eurocode 2 (for 50 years SL), respectively. The reference values of  $w/c$  and  $d$  are the target values aimed at to satisfy these limiting values:  $w/c_{ref} = w/c_{max} - 0.02$  and  $d_{ref} = d_{min} + 10 \text{ mm}$ .

The relation between gas permeability and  $w/c$  ratio proposed in the CEB-FIP Model Code 1990 [21], applicable to air-permeability  $kT$ , is used to convert the  $w/c_{ref}$  value into a  $kT_{ref}$  value (Eq. 6):

$$\log kT_{ref} (\text{m}^2) = -19 + 5 \cdot w/c_{ref} \quad (\text{Eq. 2.1-107 of [21]}) \quad (6)$$

A point of the concrete structure, on which the values  $kT_{ref}$  and  $d_{ref}$  have been measured, is expected to have 50 years of service life. If the  $kT$  value measured is lower than  $kT_{ref}$  and/or the  $d$  value measured is higher than  $d_{ref}$ , the SL life estimated at the point will be longer than 50 years.

### 4.3 Relation between $kT$ and $D_0$

Any attempt to use values of air-permeability measured on site to predict service life of concrete exposed to chlorides requires a relation between  $kT$  and the coefficient of chloride diffusion  $D_0$ .

Results of  $kT$  and  $D_0$  (measured under  $\text{Cl}^-$  ponding/immersion long-term tests) are plotted with black symbols in Fig. 4. The empty circles in Fig. 4 correspond to  $kT$  and Coulomb ASTM C1202 [22] values available in the literature [23]. The Coulomb values were converted into  $D_0$  applying the following formula, established at Purdue University [24]:

$$D_0 (10^{-12} \text{ m}^2/\text{s}) = 0.4 + 0.002 \cdot \text{Coulomb} \quad (7)$$

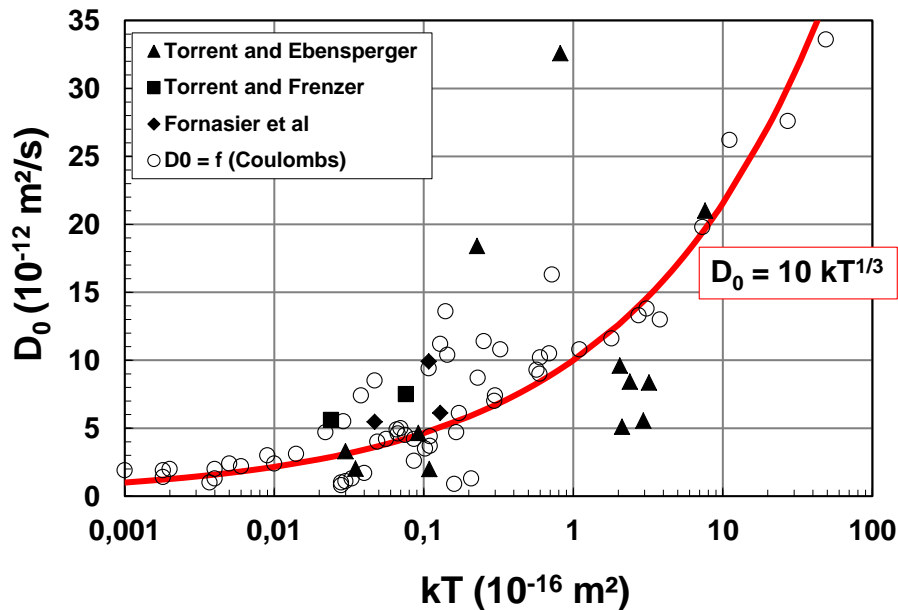


Figure 4. Relation between  $D_0$  and  $kT$

A relation between  $kT$  and  $D_0$  has been fitted to the values in Fig. 4, of the form:

$$D_0 = 10 \cdot kT^{1/3} \quad \text{with } D_0 \text{ in } (10^{-12} \text{ m}^2/\text{s}) \text{ and } kT \text{ in } (10^{-16} \text{ m}^2) \quad (8)$$

### 4.4 Calculation of Service Life with “Exp-Ref” Method

Combining Eqs. 3, 5 and 8 we have:

$$Ti = \frac{d^2}{4.10 kT^{1/3} (t/t_0)^m} A^2 \quad (9)$$

Applying Eq. 9 to the reference condition:

$$Ti_{ref} = \frac{d_{ref}^2}{4.10 kT_{ref}^{1/3} (t/t_0)^m} A^2 \quad (10)$$

Now, we can assume that  $C_s$ ,  $C_{cr}$  (and therefore  $A$ ),  $m$  and  $t_h$  are the same for the reference (50 y) and the Service Life condition (e.g. 100 y). So, dividing Eqs. 9 and 10 and rearranging:

$$Ti = Ti_{ref} \cdot \frac{d^2}{d_{ref}^2} \cdot \frac{kT_{ref}^{1/3}}{kT^{1/3}} \quad (11)$$

and making

$$\alpha = Ti_{ref} \cdot \frac{kT_{ref}^{1/3}}{d_{ref}^2} \quad (12)$$

The calculation of Service Life with the Exp-Ref Method is done through the simple formula:

$$Ti = \alpha \cdot \frac{d^2}{kT^{1/3}} \quad (13)$$

Where:

$Ti$  = Corrosion Initiation Time (years), usually assumed as the Service Life

$d$  = cover depth (mm)

$kT$  = coefficient of air-permeability ( $10^{-16} \text{ m}^2$ )

$\alpha$  = factor depending on the Exposure condition of the structure (see Table 1)

**Table 1. Values of factor  $\alpha$  for different Exposures and intermediate variables:  $Ti_{ref} = 50$  years**

Indicator	Environmental Aggressivity (Exposure Classes X)					
	Marine Chlorides			Other Chlorides		
	XS1	XS2	XS3	XD1	XD2	XD3
$w/c_{max}$	0.50	0.45	0.45	0.55	0.55	0.45
$d_{min}$ (mm)	35	40	45	35	40	45
$w/c_{ref}$	0.48	0.43	0.43	0.53	0.53	0.43
$kT_{ref}$ ( $10^{-16} \text{ m}^2$ )	0.25	0.14	0.14	0.45	0.45	0.14
$d_{ref}$ (mm)	45	50	55	45	50	55
<b><math>\alpha</math></b>	<b>0.0156</b>	<b>0.0104</b>	<b>0.0086</b>	<b>0.0189</b>	<b>0.0153</b>	<b>0.0086</b>

#### 4.5 “Exp-Ref” Method Application Examples

Two examples will be described, to show how the Exp-Ref Method can be applied.

##### Data from RILEM TC 230-PSC Application Test

Within the working program of Rilem TC 230-PSC [25], a series of reinforced concrete test panels were built with two different cements (OPC and Fly-Ash Cement) and two different w/c ratios, with one face of each panel having a nominal cover of 30 mm and the opposite face of 50 mm. All willing participants were asked to conduct ND measurements on the panels in order to predict their service life assuming them exposed to a XD3 environment (direct contact with chloride solution from deicing salts).

Two of the researchers worked on the panels at 3 months of age, measuring  $kT$  on at least 6 points randomly distributed across both panel surfaces. One of them also conducted measurements of  $d$  on the same locations, using an electromagnetic covermeter, as sketched in Fig. 1.

The values of  $d$  and  $kT$  obtained were used to compute the Initiation Time of corrosion for each location, applying Eq. 13, with  $\alpha = 0.0086$  (for XD3 exposure).

Fig. 5 presents the minimum, maximum and mean Initiation Time, estimated from the 6 pairs of data ( $d$  and  $kT$ ) obtained on each panel and nominal cover side. The cement type and w/c are indicated for each case.

The positive effect of a low w/c ratio and a higher cover depth are demonstrated by the corresponding longer Initiation Times.

Please, notice the large scatter of  $T_i$  obtained in some of the panels, which reflects the variability in permeability and cover depths within the panels.

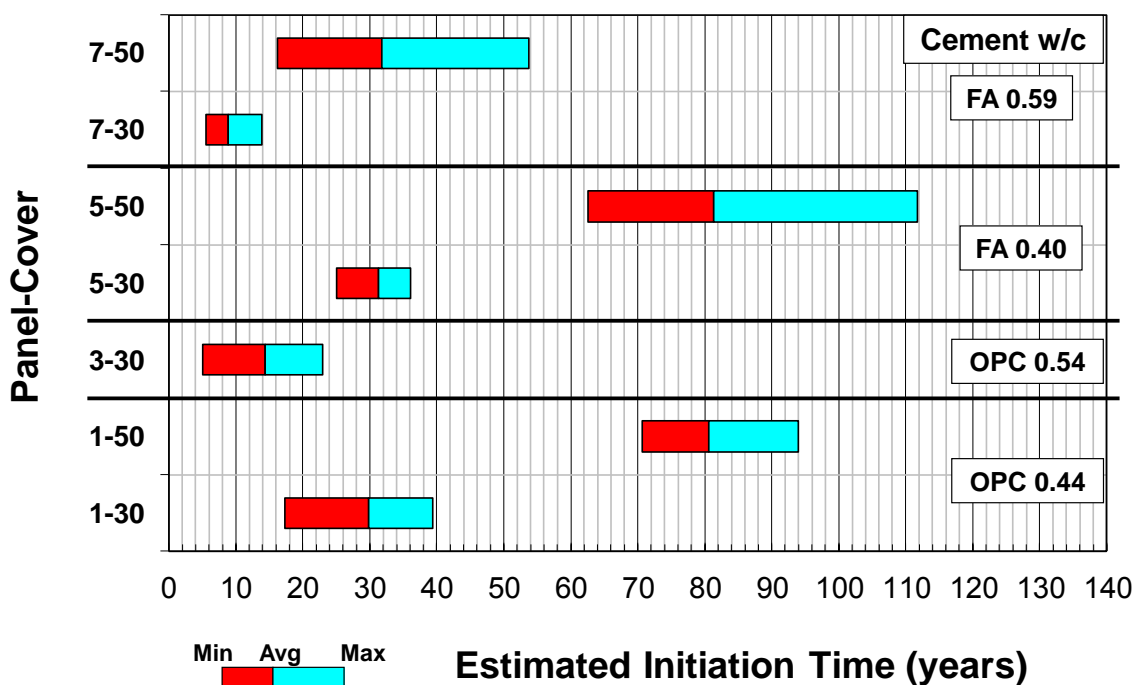


Figure 5. Estimated Initiation Time for panels made with different cements, w/c and covers

## Data from Hong Kong-Zhuhai-Macao Bridge

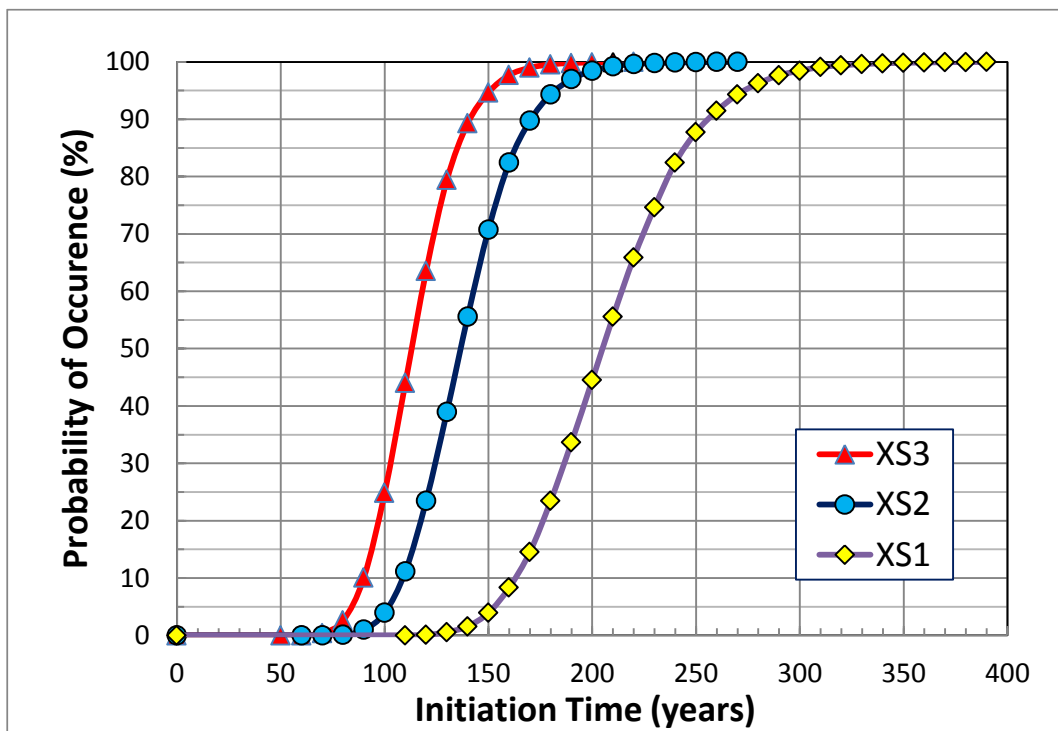
Statistical data for the HK-ZH-MA Bridge, measured on precast sections of submerged elements, have been reported [26], including values of  $kT$  of  $d$ , as shown in Table 2.

**Table 2. Statistical distributions and parameters assumed for  $d$  and  $kT$  [26]**

Variable	Extrados Cover Depth $d$ (mm)	Air-Permeability $kT$ @ 56 days ( $10^{-16}$ m <sup>2</sup> )
Distribution	Normal	Log-Normal
Mean	Arithmetic: 73.4	Geometric: 0.069
Standard Deviation	3.9 mm	of $\log_{10}$ of $kT$ = 0.179

A Monte Carlo simulation was made calculating the  $T_i$  values, applying Eq. 13, assuming  $d$  and  $kT$  as independent variables, with the results shown in Fig. 6 for Exposures XS1 (atmospheric), XS2 (submerged) and XS3 (tidal/splash zone), using the corresponding  $\alpha$  values given in Table 1.

Fig. 6 shows the predicted  $T_i$  probability distributions for a structure showing the values of  $kT$  and  $d$  reported in Table 2, under different exposure conditions. It can be seen that the results are compatible with the 120 years design service life expected for the structure (XS2 submerged condition).



**Figure 6. Calculated Probability Distributions of  $T_i$  for different Exposures**

## 5. Conclusions

A review of the more widely used SL prediction approaches has been made, pointing out two weaknesses:

- The difficulties in establishing the values of key and elusive parameters used in the calculations, namely: Surface chloride concentration  $C_s$ , Critical chloride concentration  $C_{cr}$ , ageing exponent  $m$  and duration of the Chloride diffusion decay effect  $t_h$

- The fact that the design values  $d$  and  $D_0$  are theoretical, or obtained from test on laboratory specimens that are not representative of the “as-built” quality of the real structure

The proposed “Exp-Ref” method, based on “Experimental” ND site measurements of cover depth  $d$  and air-permeability  $kT$  solves the second weakness. By taking a “Reference” situation, corresponding to a SL of 50 years, the method avoids the need of defining the above mentioned elusive parameters, thus solving the first weakness. It is simple (Eq. 13), realistic (based on hard data measured experimentally on the as-built product) and robust (no subjective influence of users).

Obviously, same as for other prediction methods, it is not possible to claim that the corrosion initiation times will be exactly the ones calculated by the proposed method. However, the Exp-Ref method will pinpoint areas of dubious quality, where to place especial attention during monitoring/maintenance of the structure. It is a useful tool for documenting the “Birth Certificate” of a structure.

## 6. References

1. Andrade, C., "Multilevel (four) methodology for durability design", RILEM Proceedings PRO 47, 2006, 101-108.
2. EN 1992-1-1: 2004, "Eurocode 2: Design of concrete structures - Part 1: General rules and rules for buildings", European Standards.
3. EN 206-1: 2000, "Concrete - Part 1: Specification, performance, production and conformity", European Standards.
4. AS 3600: 2001, "Concrete Structures". Australian Standards
5. SIA 262: 2003, "Concrete Structures", Swiss Standards.
6. SIA 262/1: 2013, "Concrete Structures – Complementary Specifications", Swiss Standards.
7. Life-365, "Service Life Prediction Model and Computer Program for Predicting the Service Life and Life-Cycle Cost of Reinforced Concrete Exposed to Chlorides", Life 365 Consortium II, January 2012, 80 p.
8. Duracrete, "Probabilistic Performance based Durability Design of Concrete Structures", The European Union–Brite EuRam III, BE95-1347/R17, CUR, Gouda, The Netherlands, 2000.
9. Ferreira, M., Jalali, S. and Gjørsv, O., “Software for Probability-Based Durability Analysis of Concrete Structures”, Concrete under Severe Conditions: Environment and Loading, CONSEC’04, Seoul, Korea, 2004, 1015-1024.
10. EHE-08, "Instrucción de Hormigón Estructural", Spanish Concrete Code, Annex 9, 2008
11. Gulikers, J., "Practical implications of performance specifications for durability design of reinforced concrete structures", Proc. 'Performance based Specifications for Concrete' (F. Dehn, H. Beushausen eds.), Leipzig, 2011.
12. Oslakovic, I., Bjegovic, D. and Mikulic, D., "Evaluation of service life design models on concrete structures exposed to marine environment", Materials and Structures, v. 43, 2010, 1397–1412.
13. Gulikers, J., "Considerations on the reliability of service life predictions using a probabilistic approach", J. Phys. IV France, v. 136, 2006, 233-241.
14. ASTM C1556, "Standard Test Method for Determining the Apparent Chloride Diffusion Coefficient of Cementitious Mixtures by Bulk Diffusion", ASTM Standards 2014, v4.01.
15. NTBuild 492, "Concrete, Mortar and Cement-based Repair Materials: Chloride Migration Coefficient from Non-steady-state Migration Experiments", Nord Test, 1995
16. Neville, A.M., "Concrete cover to reinforcement - Or cover-up?", Concrete International, v. 20, n. 11, 1998, 25-29.
17. Torrent, R., “The gas-permeability of high-performance concretes: site and laboratory tests”, ACI SP-186, 1999, Paper 17, 291-308.

18. Torrent, R., "Service Life Prediction: Theorecrete, Labcrete and Realcrete Approaches", Keynote Paper e577, SCTM3 Conference, Kyoto, Japan, 18-21 August, 2013
19. BS 1881-204:1988, Testing concrete. Recommendations on the use of electromagnetic covermeters, British Standards
20. SIA 262/1: 2013, " Concrete Structures – Complementary Specifications", Swiss Standards, Annex E: 'Air-Permeability on Site' (in German/French)
21. CEB/FIP (1991). "CEB-FIP Model Code 1990", CEB Bull. d'Information No. 203, p. 2-52
22. ASTM C1202, "Standard Test Method for Electrical Indication of Concrete's Ability to Resist Chloride Ion Penetration"
23. Torrent, R., Denarié, E., Jacobs, F., Leemann, A. and Teruzzi, T., "Specification and site control of the permeability of the cover concrete: the Swiss approach", Materials and Corrosion , V. 63, n 12, 2012, 1127–1133.
24. Olek, J., Lu, Aijiang, Feng, Xiuping and Magee, B., "Performance-Related Specifications for Concrete Bridge Superstructures, Volume 2: High-Performance Concrete", Purdue University – Joint Transportation Research Program, Technical Report Series 2002, 215 p.
25. RILEM TC 230-PSC, "Performance-based Specification and Control of Concrete Durability", H. Beushausen Chairman (2008-2014)
26. Li K. F., Li, Q., Wang, P. and Fan, Z., "Durability assessment of concrete immersed tube tunnel in Hong Kong-Zhuhai-Macau sea link project", Paper submitted to Concrete 2015, 30 Aug.-2 Sept. 2015, Melbourne, Australia.

# Durability assessment of concrete immersed tube tunnel in Hong Kong-Zhuhai-Macau sea link project

Kefei Li<sup>1</sup>, Quanwang Li<sup>2</sup>, Pianpian Wang<sup>3</sup> and Zhihong Fan<sup>4</sup>

<sup>1</sup>Professor of Civil Engineering, Tsinghua University, Beijing, China

<sup>2</sup>Associate professor of Civil Engineering, Tsinghua University, Beijing, China

<sup>3</sup>Master in Civil Engineering, Tsinghua University, Beijing, China

<sup>4</sup>Senior engineer, CCC 4<sup>th</sup> Harbor Research Institute, Guangzhou, China

**Abstract:** The concrete immersed tube tunnel in the Hong Kong-Zhuhai-Macau (HZM) sea link project was designed for a service life of 120 years. The concrete tunnel is exposed externally to the sea water and internally to traffic and marine air. This paper reviews the durability design of this concrete sea tunnel and the key durability parameters retained for the structural concrete. During the construction, the concrete properties were tested in the laboratory and nondestructive tests were performed on the prefabricated segments of concrete tube. The quality of structural concrete is evaluated on the basis of these in-situ data and their statistical properties. Further the achieved durability of the immersed tube tunnel is assessed through Fick's law for chloride ingress via a fully probabilistic approach. The safety margin for structural durability is represented in terms of failure probability and reliability index. Based on the durability assessment in construction phase, a preliminary maintenance planning is given taking into account the accidental working case of sea water infiltration.

**Keywords:** HZM project, immersed tube tunnel, durability design, chloride ingress.

## 1. Introduction

The Hong Kong-Zhuhai-Macau sea link project includes sea bridges of 28.8 km (three navigable spans), two artificial islands and an immersed tube tunnel of 5.6 km, with a total investment more than 12 billion US dollars. One of the main technical requirements is to achieve the service life of 120 years for the concrete structures in an aggressive marine environment. The hydrology data show the chloride (Cl<sup>-</sup>) concentration is within 10700-17020 mg/L, the sulfate (SO<sub>4</sub><sup>2-</sup>) concentration is within 1140-2260 mg/L, and the total salinity is between 25.4-32.9 (sea bottom).



**Figure 1. Segment of concrete tube tunnel in prefabrication of HZM project.**

The immersed tube tunnel is made of four cast-in-place segments of 112.5m long and 27 prefabricated segments of 180m long, and these segments are connected by water-proof connections. Each prefabricated segment itself is composed of 8 sub-segments of 22.5m long and these sub-segments are made in the prefabrication factory near the HZM project site, cf. Figure 1. Once these sub-segments are cast and cured to predetermined age, they are linked together to form one tunnel segment by prestress tendons. The cross section of tunnel amounts to 11.4m high and 38m wide, and the thickness of the external wall is 1.5m. No special protection measures are designed for the external wall of tunnel tube, and the structural concrete in external wall is the only barrier to ensure the durability of the tunnel exposed directly to the sea water environment. This paper is to review the durability design of the immersed tube

tunnel, analyze the construction quality from the in-situ test data and evaluate the achieved durability of these tunnel tube segments. On the basis of the durability assessment, a preliminary maintenance planning is proposed for the tube tunnel for the 120 years of service life.

## 2. Durability model and requirements

### 2.1 Model for chloride ingress

The durability related processes of this tunnel include the concrete carbonation from internal surface, sulfate attack from sea water as well as the reinforcement steel corrosion by sea water infiltration. In the preliminary study phase these deterioration processes were investigated for their criticality and the chloride-induced corrosion of steel reinforcement was identified as the control process for durability design. The relevant durability design was performed through a model-based approach (1,2). The model for chloride induced corrosion is adapted from the widely used analytical model of Fick's second law (3,4). The durability limit state (DLS) is specified as the corrosion initiation of the reinforcement steel, and the design equation is written as,

$$G = (C_{cr} - C_0) - (C_s - C_0) \left[ 1 - \operatorname{erf} \left( \frac{x_d}{2\sqrt{D_{Cl}t}} \right) \right] \geq 0 \quad (1)$$

where  $C_{cr,s,0}$  stand for the threshold chloride concentration for steel corrosion, the concrete surface chloride concentration and the initial chloride concentration in concrete (in mass percentage of binders) respectively;  $x_d$  is the concrete cover thickness (m);  $D_{Cl}$  is the chloride diffusion coefficient of concrete ( $m^2/s$ );  $t$  is the exposure age of structural elements; and  $\operatorname{erf}$  is the mathematical error function. The chloride diffusion coefficient,  $D_{Cl}$ , is assumed to decrease with the concrete exposure age  $t$ ,

$$D_{Cl}(t) = D_{Cl}^0 \left( \frac{t_0}{t} \right)^n = D_{Cl}^0 \eta(t_0, t) \quad (2)$$

with  $n$  as the exponential coefficient for  $D_{Cl}$  decrease law and  $D_{Cl}^0$  the diffusion coefficient at concrete age  $t_0$ . The term  $\eta(t_0, t)$  is the ageing coefficient of diffusion coefficient. Physically, the decrease of  $D_{Cl}$  with time is attributed to the microstructure evolution due to long-term hydration of binders after concrete hardening (5). Since the densification process of concrete cannot last infinitely with exposure age the decrease law of  $D_{Cl}$  is truncated at  $t=30$  years to obtain conservative results. Thus this models contains six parameters totally:  $C_{cr}$ ,  $C_s$ ,  $C_0$ ,  $x_d$ ,  $D_{Cl}^0$  and  $n$ (or  $\eta$ ). Note that the  $D_{Cl}^0$  in this model corresponds to the long-term exposure condition and the design values for this coefficient are converted to rapid migration test values  $D_{Cl}^{NSSM}$  through correlation analysis, see (1).

### 2.2 Durability requirements for tube tunnel

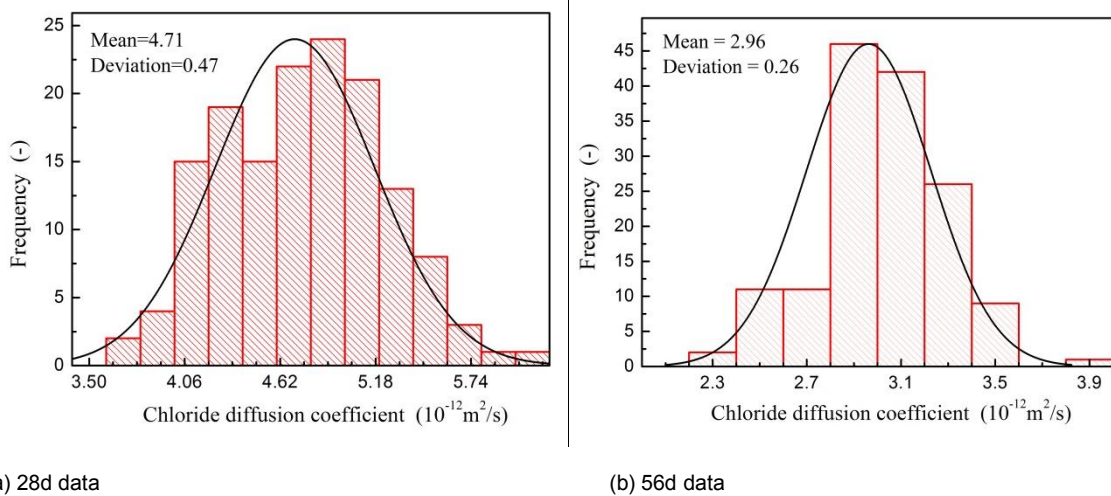
**Table 1. Durability requirements for structural concrete in tube tunnel segments.**

Condition and requirements	Tunnel intrados	Tunnel extrados
Exposure	Marine air (salty air)	Splashing
Design service life (year)	120	120
Durability limit state (DLS)	Steel corrosion initiation	Steel corrosion initiation
Concrete cover $x_d^{\min}$ (mm)	50	70
Concrete grade	C45	C45
Chloride diffusion coefficients ( $10^{-12} m^2/s$ )/28d	6.5	6.5
Chloride diffusion coefficients ( $10^{-12} m^2/s$ )/56d	4.5	4.5

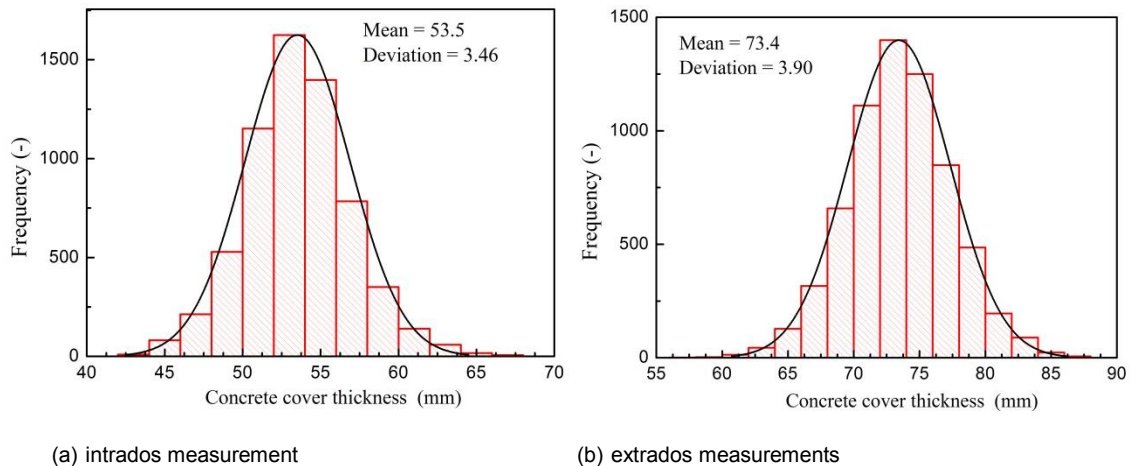
In the design phase, the model was used to specify the durability requirements for the tunnel tube segments through a fully probabilistic approach. The performance function was taken as Eq.(1) and the target reliability index was chosen as  $\beta=1.3$  for a service life of 120 years. Through Monte-Carlo simulations, the durability requirements were given in terms of the thickness of concrete cover and the chloride diffusion coefficient. The intrados of tunnel is exposed to traffic and a marine atmospheric



exposure condition is considered. For the extrados of tunnel, a splashing condition is considered since both the chloride in sea water and the oxygen in air can possibly be available to the reinforcement steel near the extrados, and the critical chloride concentration for corrosion initiation would be similar to the splashing condition. The detailed analysis can be found in the relevant publications (1,2). In Table 1 are summarized the retained durability requirements for the intrados and extrados of the tunnel segments. The tunnel concrete (C45) has a water to binder ratio  $w/b=0.36$ , and the binder materials contain ordinary Portland cement (50%), slag (30%) and fly ash (20%).



**Figure 2. Chloride diffusion coefficients for C45 concrete in tunnel segments through RCM method.**



**Figure 3. Statistical analysis on the thickness of concrete cover for tunnel tube segments.**

### 3. Quality control for durability in construction

#### 3.1 Chloride diffusion coefficients

The in-situ data of chloride diffusion coefficient of structural concretes were collected from the on-site laboratory for the prefabricated tunnel segments. The chloride diffusion coefficients were measured on concrete specimens under standard curing conditions ( $20^{\circ}\text{C}$  and  $\text{RH} > 95\%$ ) at given ages, 28d and 56d, by rapid migration method (RCM) (6). The data are presented in Figure 1(a) and 1(b) for 28d and 56d measurements. A total of 296 sets of data are collected for 28d and 56d with 148 sets of data for each age. The target mean values for  $D_{\text{Cl}}^{\text{NSSM}}$  are respectively  $6.5 \times 10^{-12} \text{m}^2/\text{s}$  and  $4.5 \times 10^{-12} \text{m}^2/\text{s}$  for 28d and 56d according to the durability requirements in Table 1. One can see that the mean values of measured  $D_{\text{Cl}}^{\text{NSSM}}$  are  $4.68 \times 10^{-12} \text{m}^2/\text{s}$  (28d) and  $2.95 \times 10^{-12} \text{m}^2/\text{s}$  (56d), much lower than the required values. The dispersion, variation coefficient in statistical terms, of this  $D_{\text{Cl}}^{\text{NSSM}}$  is 9.9% (28d) and 8.7% (56d), smaller

than the expected level of 20% in design phase, especially for 56d age. This decrease of dispersion will help to reduce the uncertainty associated with the chloride diffusion coefficients.

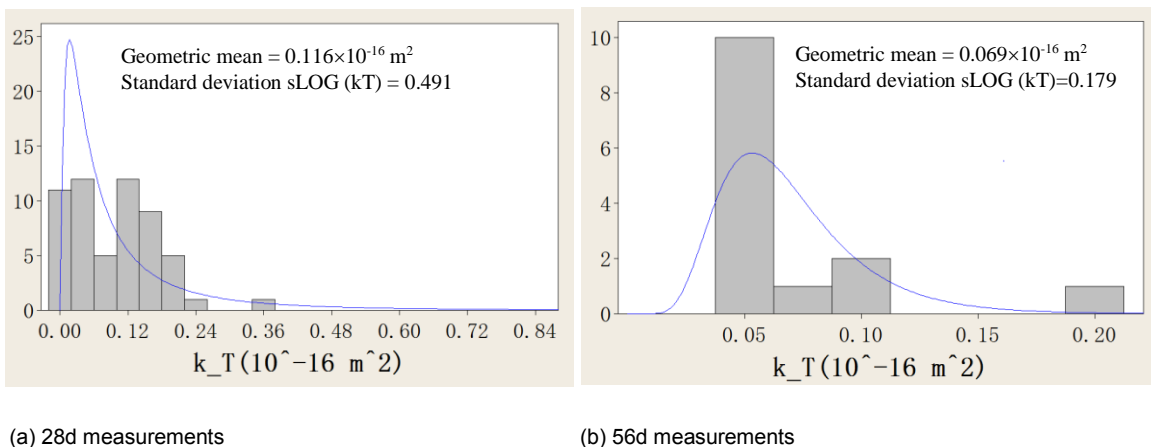
### 3.2 Concrete cover thickness

The measurements of concrete cover thickness are presented in Figure 3 for tunnel segments. The concrete cover was measured through the common midpoint (CMP) method and the principle of CMP method is to detect the depth of reinforcement bars through transmitting an electromagnetic wave pulse and receive the reflected waves from the steel bars by two adjacent antennas (7). The measurement error of the device used in HZM project is evaluated as around 3mm through the comparison with the measurement on extracted cores from test segments of tunnel in preliminary study.

Figure 3 illustrates the statistical analysis on the concrete cover thickness on the intrados and extrados of the tunnel segments. The data sets are 6,368 and 6,571 for intrados and extrados measurements respectively, thus sufficient to support a reliable statistical analysis. The required values for thickness are respectively 50mm (intrados) and 70mm (extrados). The analysis shows that the mean values are 53.5mm (intrados) and 73.4mm (extrados) and the construction error, corresponding to the distance between 5% percentile value and mean value, is 5.8mm (intrados) and 6.4mm (extrados), slightly larger than the expected construction tolerance, 5.0mm, for prefabricated elements.

### 3.3 Non-destructive tests: Air permeability

The NDT device of air permeability measurement used for prefabricated tunnel segments is the "Torrent Permeability Tester (TPT)", and its principle is to create a vacuum above the concrete surface and measure the steady flow of air coming through the concrete surface (8). The Torrent air permeability has been adopted by Swiss standard as the recommended method for in-situ concrete quality control (9). However, it should be noted that several factors can have important influence on  $k_T$  values, including the water content, hardening age and temperature of concrete surface. The results in literature show that extreme temperatures can also greatly affect  $k_T$  values (10) and the measurement temperature above 10°C was recommended (9). For these reasons, the air permeability measurements on the prefabricated segments were performed at 26d/56d ages with surface water content lower than 5.5% (measured by Tramex water content meter), as prescribed in (9).



**Figure 4. Lognormal statistics of air permeability measured at extrados of tunnel segments.**

From the in-situ measurement, a total of 56 data were obtained for 28d age and 14 data obtained for 56d age. The log-normal statistics of these two sets of air permeability data are given in Figure 4 with statistic parameters. The first observation on these data is that the  $k_T$  values are relatively low for the structural concrete, *i.e.* of the order of  $10^{-18} \text{ m}^2$ . Also, the 56d values are systematically lower than the 28d values. The dispersion of  $k_T$  values for 56d measurements is also quite low (sLOG below 0.2), according to Swiss experience [11]. It is interesting to note that both the geometric mean  $k_{Tgm}$  and sLOG compare well with results obtained on segments of the Port of Miami Tunnel ( $k_{Tgm}=0.57 \times 10^{-16} \text{ m}^2$  and sLOG=0.24 at 120d age), made with high-quality concrete [12], particularly when considering the two different brands of

instrument used in the investigations [13]. The correlation between the  $k_T$  values and the temperature, water content and hardening age of structural concrete is given in Figure 5. An analysis of the data shows that the changes in temperature (always above the critical 10°C) and water content (always below the critical limit of 5.5%), see Figure 5, do not influence significantly  $k_T$ . The dispersion is, therefore, the result of the inherent heterogeneity of structural concrete in different segments and sub-segments.

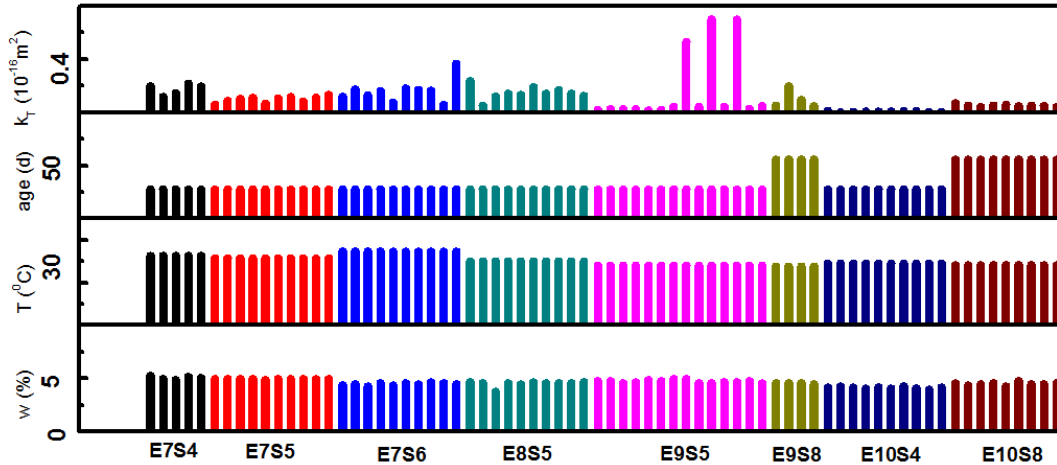


Figure 5. Correlation between  $k_T$  and temperature, water content and hardening age.

### 3.4 Non-destructive tests: Electrical resistivity

The principle of electrical resistivity measurement on concrete is to read the electrical current under a certain electrical potential. The resulted electrical resistivity reflects the pore space and its connectivity in concrete materials since the solid phases in concrete have very low electrical conductivity [14]. This measurement can be performed on both concrete specimens in the laboratory and concrete surfaces in project site. As air permeability, the electrical resistivity has also been regarded as a durability indicator for structural concrete. The device of electrical resistivity used is the Wenner probe that comes as accessory to the TPT instrument.

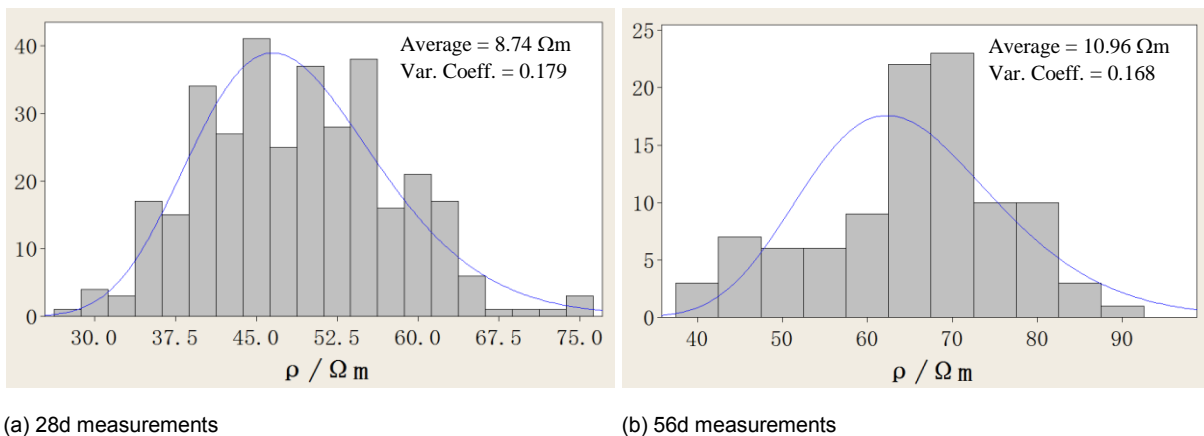


Figure 6. Statistics of electrical resistivity at 28d and 56d.

A total of 686 data were obtained for Wenner electrical resistivity on four tunnel segments for hardening ages from 3d to 56d. The log-normal distribution statistics of these data for hardening ages, 28d and 56d, are illustrated in Figure 6 with the corresponding statistical parameters. The first observation is that these values increase constantly with hardening age, which is related to both the densification of pore structure of concrete during hardening and the moisture drying on the concrete surface. Then, the values of

electrical resistivity values are relatively stable and show low variability with variation coefficient around 15% since age of 7d.

From the above figure, the resistivity values show a log-normal distribution. Certainly, the temperature, hardening age and water content all have impact on the resistivity measurement values, and their correlation is illustrated in Figure 7. It can be seen that the values are more correlated to hardening age, and less to other factors. The increase of electrical resistivity  $\rho$  with age is due to two mechanisms: the more compact microstructure of concrete achieved by further hydration with age, and the reduced water content resulting from evaporation.

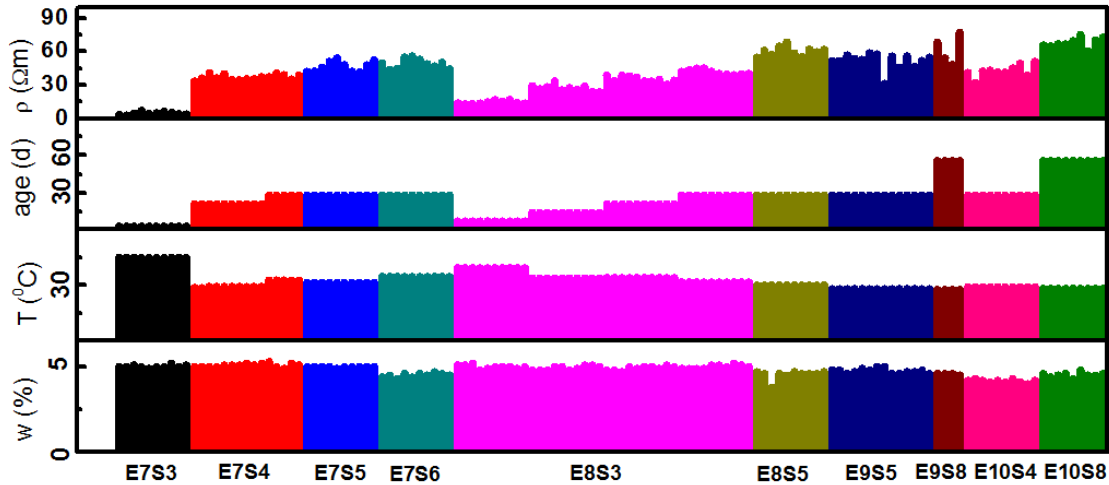


Figure 7. Correlation between  $\rho$  and temperature, water content and hardening age.

#### 4. Durability assessment of tube tunnel

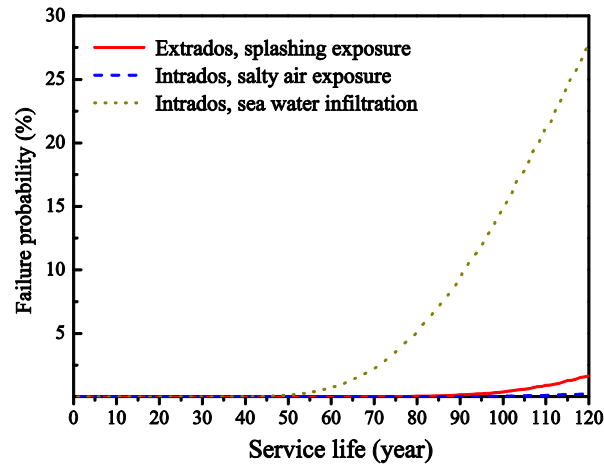
##### 4.1 Probabilistic assessment of durability

The model in Eqs.(1) and (2) is used to evaluate the durability performance with respect to the chloride ingress process through a fully probabilistic approach. To this purpose, the statistical properties of the model parameters, chloride diffusion coefficients  $D_{Cl}^0$  and concrete cover thickness  $x_d$ , obtained in the previous section are taken into account. Other model parameters, surface chloride concentration  $C_s$ , critical concentration  $C_{cr}$ , exponent coefficient  $n$ , adopt the same distributions as in the preliminary study phase, cf. Table 2.

Table 2. Statistical properties of durability parameters for probabilistic durability assessment.

Parameter (distribution)	Statistical properties	Extrados (splashing)	Intrados (Atmopsheric)
Initial chloride content $C_0$ (Rectangle)	Lower limit (%)	0.02	0.02
	Upper limit (%)	0.04	0.04
Surface concentration $C_s$ (Lognormal)	Average (%)	5.76	2.10
	Deviation (%)	0.86	0.32
Critical concentration $C_{cr}$ (beta)	Lower bound $L$ (%)	0.45	-
	Upper bound $U$ (%)	1.25	-
	Coefficient $\alpha$ (-)	0.22	-
	Coefficient $\beta$ (-)	0.36	-
Critical concentration $C_{cr}$ (Lognormal)	Average (%)	-	0.85
	Deviation (%)	-	0.13
Diffusion coefficient $D_{Cl}^0$ (Lognormal)	Average ( $10^{-12}$ m <sup>2</sup> /s)	4.71 (28d)	4.71 (28d)
	Coefficient of variance	9.8%	9.8%
Exponent coefficient $n$ (Normal)	Average (-)	0.47	0.53
	Deviation (-)	0.029	0.079
Concrete cover $x_d$ (Normal)	Average (mm)	73.4	53.5
	Deviation (mm)	3.90	3.46

The fully probabilistic analysis for the durability assessment is realized through Monte-Carlo simulations. A computer-based program is developed especially to perform the probabilistic assessment. In the simulation, six parameters are considered as joint occurrence random variables:  $C_{cr}$ ,  $C_s$ ,  $C_0$ ,  $x_d$ ,  $D_{Cl}^0$  and  $n$ . The statistical properties are presented in Table 2. For a given exposure age  $t$ , the Monte-Carlo simulations are performed to calculate the failure probability of Eq.(1), and 1,000,000 samplings are used to ensure the solution of “real” probability. Accordingly, the failure probability is solved with time from  $t=0$  to  $t=120$  years. The assessment results are presented in Figure 8 in terms of the failure probability with respect to corrosion initiation, for the intrados and extrados of tube segments. The assessment gives  $p_f=1.7\%$  and  $\beta=2.13$  for extrados and  $p_f=0.25\%$  and  $\beta=2.81$  for intrados at 120 years.



**Figure 8. Failure probability (corrosion initiation) of tube tunnel for extrados, intrados exposed to salt fog and intrados exposed to salt water infiltration (accidental scenario).**

In Figure 8 an accidental working case of sea water infiltration is also analyzed for the intrados. If sea water leakage occurs due to segment joint failure or local concrete permeability failure, the intrados will contact with liquid sea water and the splashing action should be considered. In Figure 8, the intrados is evaluated under splashing condition and the failure probability rises to 27% ( $\beta=0.59$ ) at 120 years. Accordingly, this accidental scenario should be monitored and the corresponding special maintenance actions should be planned.

#### 4.2 Preliminary maintenance planning

Following the analysis in Figure 8, this section investigates the maintenance planning for the accidental scenario of sea water infiltration. The only maintenance technique against the sea water infiltration is the installed cathodic protection in the tube segments. The following analysis is dedicated to the planning of the activation time of the cathodic protection in terms of the sea water infiltration intensity. The analysis is carried out in a rather engineering way and no physical model for the sea water leakage rate is included. Suppose the intensity of the sea water leakage can be represented by a ratio,  $\delta$  (-), between the area of intrados exposed to sea water infiltration and the whole intrados surface. In a straightforward way, the whole failure probability,  $p_t$ , of intrados is the addition of the two parts,

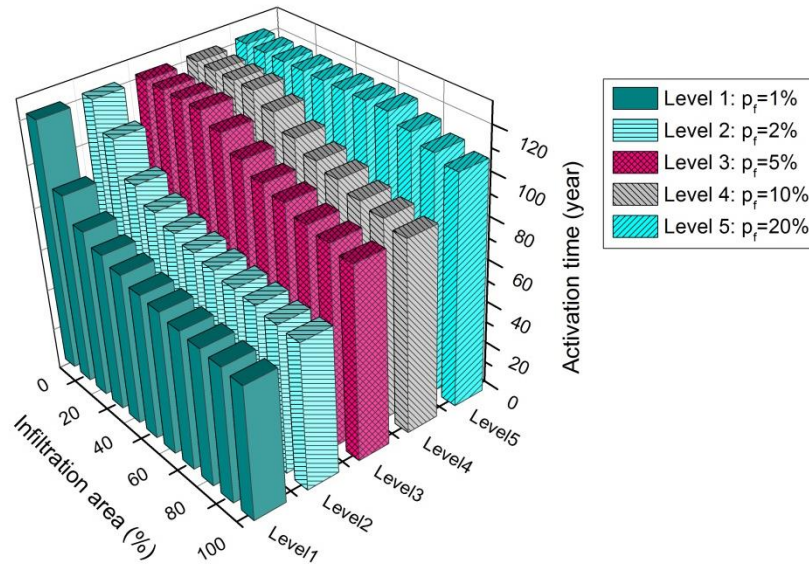
$$p_t(t) = \delta p_{sp}(t) + (1 - \delta) p_{air}(t) \quad (3)$$

where  $p_{sp,air}$  are respectively the time-dependent failure probabilities of intrados exposed to splashing action and to marine salty air. This global probability can be calculated from the results in Figure 7 for different infiltration area ratios. The analysis shows that a ratio of 10% intrados leakage will increase the failure probability to  $p_f= 3.0\%$  at 120 years and a ratio of 70% intrados leakage gives  $p_f=19.5\%$  at 120 years.

According to the state-of-the-art of the maintenance planning (15), different maintenance strategies can be adopted following different  $p_f$  values: The intervention at  $p_f=2\%$  corresponds to a preventive maintenance,  $p_f=5\%$  corresponds to a necessary strategy and  $p_f=20\%$  corresponds to a mandatory



maintenance. Early intervention of maintenance at low failure probability is considered cost-effective. The activation time of the cathodic protection corresponding to different  $p_f$  levels, from 1% to 20%, at intervention is illustrated in Figure 9. The activation times are around 65 years for preventive maintenance ( $p_f=2\%$ ) and 80 years for necessary maintenance ( $p_f=5\%$ ) for 100% infiltration area ratio.



**Figure 9. Maintenance planning for the activation time of cathodic protection in terms of intervention levels.**

## 5. Concluding remarks

(1) The concrete immersed tube tunnel in HZM project was designed for its durability of 120 years exposed to sea water and traffic/marine air. The durability requirements were specified from a model-based approach and involved mainly the cover thickness and the chloride diffusion coefficients of the structural concrete. The target reliability of the durability requirements was fixed to 1.3 at 120 years.

(2) The collected data included the measurements of chloride diffusion coefficients on concrete specimens, concrete cover thickness of prefabricated segments as well as the non-destructive test results of air permeability and electrical resistivity on the extrados of segments. The chloride diffusion coefficients showed less dispersed distribution than expected with the variation coefficient within 10%, and the statistics on concrete cover thickness gives a construction tolerance very near to the assumed value of 5mm. The air permeability results confirm that high compactness of the structural concrete in the segments. Both the air permeability and the electrical resistivity depend much on the hardening age and less related to the ambient temperature or the surface water content.

(3) The achieved durability of tube segments is evaluated on the basis of the collected data and their statistical properties in construction phase. A fully probabilistic approach is adopted and the Monte-Carlo simulations are used to calculate the failure probability with respect to the corrosion initiation DLS. The analysis gives  $p_f=1.7\%$  for extrados and  $p_f=0.25\%$  for intrados of segments, and the corresponding reliability index is much higher than the presumed reliability level ( $\beta=1.3$ ). The safety margin comes mainly from the lower and less dispersed chloride diffusion coefficients measured in the construction phase.

(4) An accidental scenario of sea water infiltration into the intrados of tube tunnel is considered in the analysis and the corresponding failure probability is as high as 27% at 120 years for the intrados. Thus this accidental working case should be monitored during service life. Following the analysis results, a preliminary maintenance planning is performed for this accidental case, and the cathodic protection activation times are calculated in terms of the infiltration intensity and the intervention  $p_f$  levels. In the most severe infiltration and most strict preventive planning, the activation time is estimated to around 60 years. By precaution, a minimum protection would be recommended once the tunnel is open to traffic.

## 6. Acknowledgement

The research is supported by the China National Science and Technology Support Planning Project No. 2011BAG07B04.

## 7. References

1. Li, Q.W., Li, K.F. et al., "Model-based durability design of concrete structures in Hong Kong–Zhuhai–Macau sea link project", Structural Safety, 53, 2015, pp 1-12.
2. Li, K.F., Li, Q.W. et al., "Durability Design of the Hong Kong–Zhuhai–Macau Sea-Link Project: Principle and Procedure", Journal of Bridge Engineering ASCE, DOI: 10.1061/(ASCE)BE.1943-5592.0000741, 2015.
3. DuraCrete, "Probabilistic performance based durability design: modeling of degradation." DuraCrete Project Document BE95-1347/R4-5, 1998, The Netherlands.
4. Fédération International du Béton, "Model code for service life design (Bulletin 34)", fib, 2006, Lausanne.
5. Andrade, C., Castellote, M. et al., "Measurement of ageing effect on chloride diffusion coefficients in cementitious materials." Journal of Nuclear Materials, 412(1), 2011, pp 209-216.
6. NORDTEST, "Concrete, Mortar and cement-based repair materials: Chloride migration coefficient from non-steady migration experiments (NT Build 492)." Nordtest Method, 1999, Espoo, Finland
7. Halabe, U., Sotoodehnia, A. et al., "Modeling the Electromagnetic Properties of Concrete", ACI Materials Journal, 90(6), 1993, pp. 552-563.
8. Torrent, R., "Torrent-a two chamber vacuum cell for measuring the coefficient of permeability to air of the concrete cover on site", Materials and Structures, 25, 1992, pp 358-365.
9. Swiss Standard, "Concrete Structures - Supplementary Specifications, Annex E: Air-Permeability on the Structure (SIA 262/1:2013)", SIA, 2013, Zürich.
10. Kucharczykova, B., Misak, P. et al., "Determination and evaluation of the air permeability coefficient using Torrent Permeability Tester", Russian Journal of Nondestructive Testing, 46(3), 2010, pp 226-233.
11. Jacobs, F., Denarié, E. et al., "Recommendations for quality control of concrete with air-permeability measurements", VSS Report 641, Office Fédéral des Routes, 2009, Bern.
12. Torrent, R., Armaghani, J. et al., "Evaluation of Port of Miami Tunnel Segments: Carbonation and service life assessment made using on-site air permeability tests", Concrete International, May 2013, pp 39-46.
13. Torrent, R., "Non-Destructive air-Permeability measurement: from gas-flow modelling to improved testing", 2nd International Conference on Microstructural-related Durability of Cementitious Composites, Amsterdam, 11-13 April 2012, pp 467-476.
14. Koleva, D.A., Copuroglu, O. et al., "Electrical resistivity and microstructural properties of concrete materials in conditions of current flow", Cement & Concrete Composites, 30(8), 2008, pp 731-744.
15. Yang, L.H., Li, K.F. et al., "Design and optimization of maintenance strategies for a long life-span port project", Materials and Structures, 46(1-2), 2013, pp 161-172.

# Geopolymers and Non-Traditional Binder Concrete



# Effect of MgO incorporation on the structure of synthetic alkali-activated calcium aluminosilicate binders

Brant Walkley<sup>1</sup>, Rackel San Nicolas<sup>2</sup>, Susan A. Bernal<sup>3</sup>, John L. Provis<sup>3</sup>, Jannie van Deventer<sup>1,4</sup>

1. Department of Chemical and Biomolecular Engineering, University of Melbourne, Victoria 3010, Australia

2. Department of Infrastructure Engineering, University of Melbourne, Victoria 3010, Australia

3. Department of Materials Science and Engineering, University of Sheffield, Sheffield S1 3JD, United Kingdom

4. Zeobond Pty Ltd, P.O. Box 23450, Docklands, Victoria 8010, Australia

**Abstract:** The precursors typically used for producing alkali-activated binders can be described within the CaO-Al<sub>2</sub>O<sub>3</sub>-SiO<sub>2</sub> system; however, depending on the source of the precursor, contents of different elements such as magnesium and iron can vary. In the case of alkali-activated slag binders, magnesium plays a significant role in formation and evolution of secondary reaction products, including layered double hydroxide (LDH) type phases, and consequently in the development of structural and physical properties of these materials. The formation of LDH can strongly affect the durability of alkali-activated slag binders, as it has the potential to chemically interact with aggressive agents such as CO<sub>2</sub> and chlorides. The inability to control key compositional parameters, due to the varying composition and mineralogy of commercial slags has made it difficult to isolate the effect of Mg on the structure and physical properties of alkali-activated materials.

In this study, stoichiometrically controlled alkali-activated binders containing both C-(A)-S-H and N-A-S-H gels with varying Mg content are produced by chemical reaction of a sodium silicate solution with magnesium-calcium-aluminosilicate nanopowders. These synthetic precursors were synthesised via a novel solution-polymerisation method utilising polyethylene glycol to sterically inhibit movement of precursor cations. The effect of the content of Mg, Ca, Si and Al on the chemistry, reaction kinetics and microstructure of the geopolymer is assessed using X-ray diffraction and scanning electron microscopy.

**Keywords:** Geopolymer, alkali-activated binder, layered double hydroxides, aluminosilicate powder synthesis.

## 1. Introduction

Alkali-activated binders offer a viable low-CO<sub>2</sub> alternative to Portland cement and exhibit desirable technical properties, as well as a potential reduction in CO<sub>2</sub> emissions by over 80% [1-3]. The main reaction product of an alkali-activated slag is an aluminium- and sodium-substituted calcium silicate hydrate gel (C-(N)-(A)-S-H), and the study of the microstructure and phase assemblage of this phase within alkali-activated slags has received significant attention in recent years [4-12]. Microstructural development of C-(N)-(A)-S-H is strongly dependent on the chemistry of the precursor slag, and most studies have focused on investigating reaction products within the quaternary CaO-Al<sub>2</sub>O<sub>3</sub>-SiO<sub>2</sub>-Na<sub>2</sub>O system. Magnesium plays a significant role in formation and evolution of layered double hydroxides, which have been identified as the main secondary reaction products in these binders, when a sufficient content of MgO is present in the slag, used. Its formation modifies the phase assemblage of alkali-activated slags and consequently its performance [13]. The content of magnesium varies significantly between commercial slags, and despite the vast number of studies investigating the chemistry of alkali-activated slags few have investigated the role of magnesium in microstructural development in these materials [4, 13, 14]. Further to this, the literature is often conflicting and the experimental analysis involves a large number of unrestrained parameters. It is then necessary to develop a method to study alkali-activated binders which enables strict control of the stoichiometry in these systems, to gain a more complete understanding of the relationships between thermodynamics, reaction kinetics and the initial compositions of the precursors used to produce these materials.

The sol-gel procedure [15] has been used to synthesise and investigate the effect of composition on C-(A)-S-H and N-A-S-H phase assemblages [16-20], as well as compatibility studies of C-S-H and N-A-S-H

gels [18, 20], however these studies mostly investigate the effect of addition of alkali cations, alkaline earth cations or aluminium on C-S-H or N-A-S-H gels after formation of the gel. In order to accurately represent the physical and chemical interactions occurring during alkali-activation, all of the ionic species of interest must be present in a precursor powder prior to alkali-activation. This study examines the effect of the content of Mg Ca, Si and Al on the chemistry, microstructure and phase assemblage of C-(N)-(A)-S-H by synthesising mixed oxide powders within the quaternary CaO-Al<sub>2</sub>O<sub>3</sub>-SiO<sub>2</sub>-MgO system via an organic polymeric steric entrapment solution-polymerisation route [21]. This method utilises polyethylene glycol (PEG) to sterically inhibit the movement of the metal cations during solution-polymerisation, forming a homogeneous mixed oxide powder upon drying. The stoichiometrically controlled reactive precursor powders are subsequently activated with an alkaline solution to form an alkali-activated binder.

## 2. Experimental

### 2.1 Precursor powder synthesis

A 5 wt.% polyethylene glycol (PEG) solution was produced by adding polyethylene glycol powder (Sigma Aldrich, MW=20,000 g/mol) to distilled water and stirring at 60°C. Aluminium nitrate nonahydrate, Al(NO<sub>3</sub>)<sub>3</sub>·9H<sub>2</sub>O (Sigma Aldrich, 98.5 wt.%), calcium nitrate tetrahydrate, Ca(NO<sub>3</sub>)<sub>2</sub>·4H<sub>2</sub>O (BDH Prolabo, VRW International, 99.0 wt.%), and magnesium nitrate hexahydrate, Mg(NO<sub>3</sub>)<sub>2</sub>·6H<sub>2</sub>O (Sigma Aldrich, 98.0 wt.%) were added to distilled water to produce 40 wt.% solutions of each, which were then added to the 5 wt. % solution of polyethylene glycol and stirred at 60°C. Colloidal silica, SiO<sub>2</sub> (Sigma Aldrich, 40 wt.% in water), was added to the 5 wt.% solution of polyethylene glycol containing aqueous aluminium nitrate, calcium nitrate and magnesium nitrate, and water was evaporated by stirring over heat at 80°C to form a viscous aerated gel. The stoichiometry of the metal cation-polyethylene glycol solution was designed so that the ratio of positive valences from the metal cations to negative valences from the polymer was 2. The viscous aerated gel was then placed in a drying oven at 100°C overnight. The dry polymer matrix was then calcined at 900°C to produce a fine white powder which was subsequently ground by hand using a mortar and pestle in preparation for characterisation and alkali-activated binder synthesis.

### 2.2 Alkali-activated binder synthesis

The activating solution was prepared by dissolution of sodium hydroxide powder (AnalaR, 99 wt.%) in sodium silicate solution (N grade, 37.5 wt.%, PQ Australia) and distilled water. The reaction mixtures had an activating solution modulus of SiO<sub>2</sub>/Na<sub>2</sub>O = 1 and a water/solids ratio and cation ratios as outlined in Table 1. The activating solution was mixed with the precursor powder to form a homogeneous paste, which was subsequently cast in sealed containers and cured at ambient temperature for 3 days. Previous work has shown the precursor powders to be sufficiently reactive such that any difference in w/b ratios is unlikely to affect the degree of saturation of each cation reached during alkali-activation.

**Table 1.** Molar ratios of the reaction mix for each sample.

Sample	Mg/(Al+Si)	Ca/(Al+Si)	Al/Si	Na/Al	Water/solids
A	0.05	0.67	0.15	0.5	0.75
B	0.25	0.67	0.15	0.5	0.75
C	0.05	1.00	0.15	0.5	0.83
D	0.25	1.00	0.15	0.5	1.13

### 2.3 Characterisation

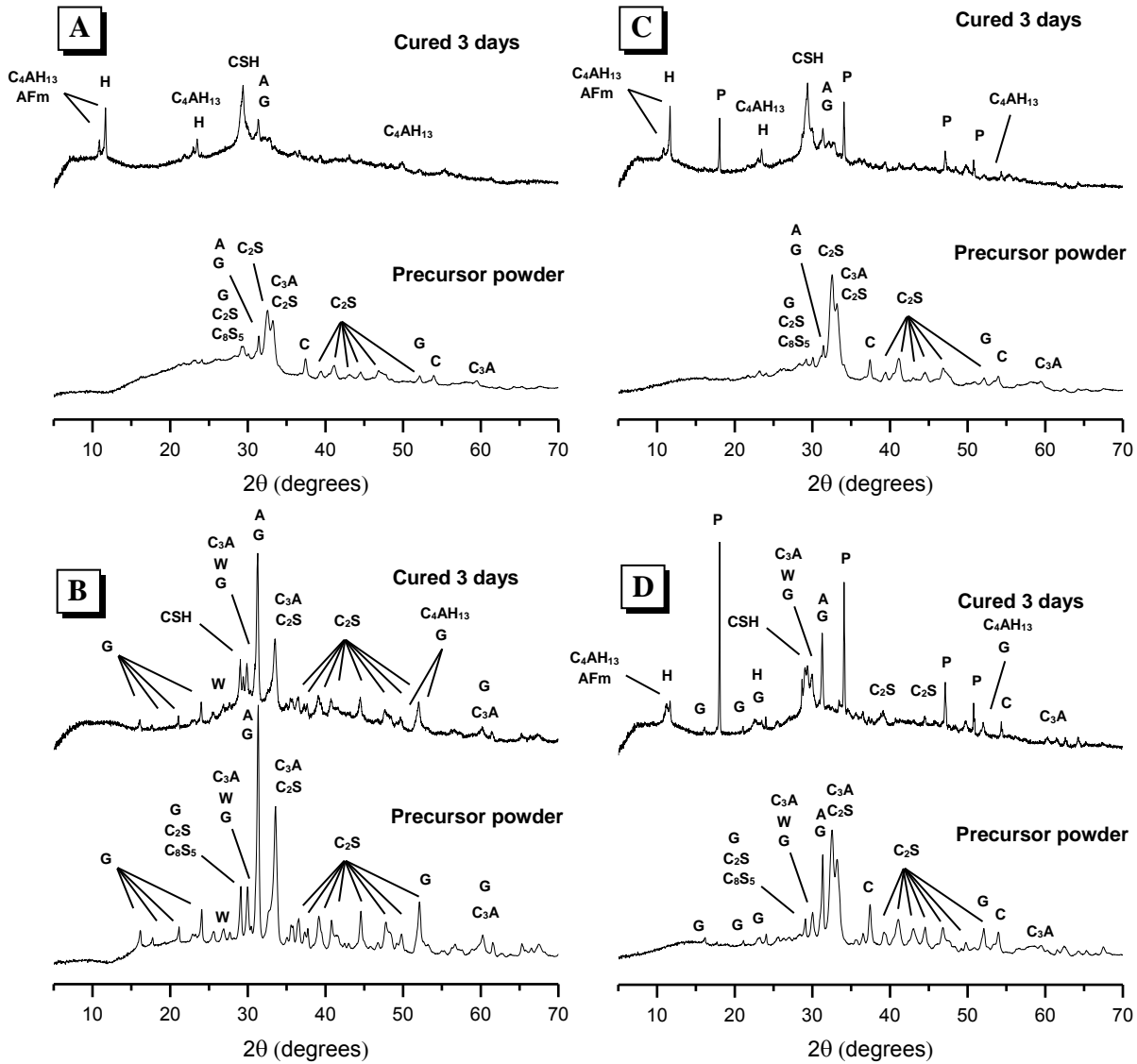
X-ray diffraction (XRD) data were collected using a Bruker D8 Advance instrument with Cu K $\alpha$  radiation, a nickel filter, a step size of 0.020°, and 3 s/step. Environmental scanning electron microscopy (ESEM) was conducted using an FEI Quanta instrument with a 15 kV accelerating voltage, a working distance of 10.0 mm and a Link-Isis (Oxford) X-ray energy dispersive (EDX) detector.

## 3. Results and Discussion

### 3.1 X-Ray diffraction

X-ray diffractograms of the calcined precursor powder and alkali-activated binders are presented in Fig. 1. The X-ray diffractograms of the precursor powders for each sample display a broad hump centred ~29°

CSH – calcium silicate hydrate C<sub>2</sub>S – dicalcium silicate C<sub>3</sub>A – tricalcium aluminate  
 C<sub>8</sub>S<sub>5</sub> – tricalcium silicate C – calcium oxide AFm – silica-substituted AFm H – hydroxalcite  
 A – åkermanite W – wollastonite G – gehlenite C<sub>4</sub>AH<sub>13</sub> – hydroxyl-AFm P – portlandite



**Figure 1.** X-ray diffractograms of the calcined precursor powder and alkali-activated binder cured for 3 days for samples A, B, C and D.

2θ, indicating a predominantly poorly crystalline nature of these powders, as is observed in granulated blast furnace slags (GBFS) [8, 9]. Small amounts of C<sub>3</sub>A (Ca<sub>3</sub>Al<sub>2</sub>O<sub>6</sub>) (PDF # 33-0251), calcium oxide (PDF# 48-1467), gehlenite (Ca<sub>2</sub>Al(AlSiO<sub>7</sub>)) (PDF # 35-0755), åkermanite (Ca<sub>2</sub>Mg(Si<sub>2</sub>O<sub>7</sub>)) (PDF # 98-000-0030), C<sub>8</sub>S<sub>5</sub> (Ca<sub>8</sub>Si<sub>5</sub>O<sub>18</sub>) (PDF # 29-0368) and two polymorphs of C<sub>2</sub>S (Ca<sub>2</sub>SiO<sub>4</sub>) (PDF # 33-0302 and 36-0642) are identified in all the precursor powders produced. Trace amounts of wollastonite (CaSiO<sub>3</sub>) (PDF # 27-0088) are also found in samples B and D. Calcination of the precursor powder to 900°C is necessary to remove any calcium carbonate present in the sample (converting it to free lime), however it is evident from the X-ray diffractograms in Fig. 1 that the calcination process has resulted in the formation of a small amount of crystalline phases. The lower calcium content of the precursor for samples A and B (Ca/(Al+Si) = 0.67) has resulted in greater formation of gehlenite and åkermanite when compared to samples C and D (Ca/(Al+Si) = 1.00). Alkali-activation of the synthetic precursors promoted the formation of a broad amorphous hump centred at approximately 29° 2θ, characteristic of alkali-activated slag cements [8, 9].

In sample A the crystalline phases present in the calcined precursor powder, with the exception of åkermanite and gehlenite, appear to be completely consumed upon alkali activation, leading to the formation of a poorly crystalline aluminium-substituted calcium silicate hydrate (C-(A)-S-H) phase with structural similarity to aluminium-containing tobermorite (PDF # 19-0052) as the main reaction product. Secondary reaction products crystalline  $C_4AH_{13}$  (PDF # 02-0077) and hydrotalcite ( $Mg_6Al_2CO_3(OH)_{16}\cdot 4(H_2O)$ ) (PDF # 41-1428) are also formed. Åkermanite and gehlenite do not appear to participate in the reaction, as the intensity of the reflection assigned to this phase remains unchanged upon activation. The diffractograms of the alkali-activated sample A also shows the formation of a partially silicate-substituted AFm phase type phase  $[(Ca_2(Al)(OH)_6] \cdot X \cdot xH_2O$  where X is a doubly charged carbonate or aluminosilicate anion), indicated by the peak at  $10.7^\circ 2\theta$  [22, 23]. In sample B the crystalline phases present in the calcined precursor powder, including gehlenite, appear to be only partially consumed upon alkali activation, and consequently small amounts of these phases are present in the alkali-activated sample B. The main reaction product in sample B appears to be a poorly crystalline C-(A)-S-H phase, as indicated by the broad amorphous hump centred at approximately  $29^\circ 2\theta$ .

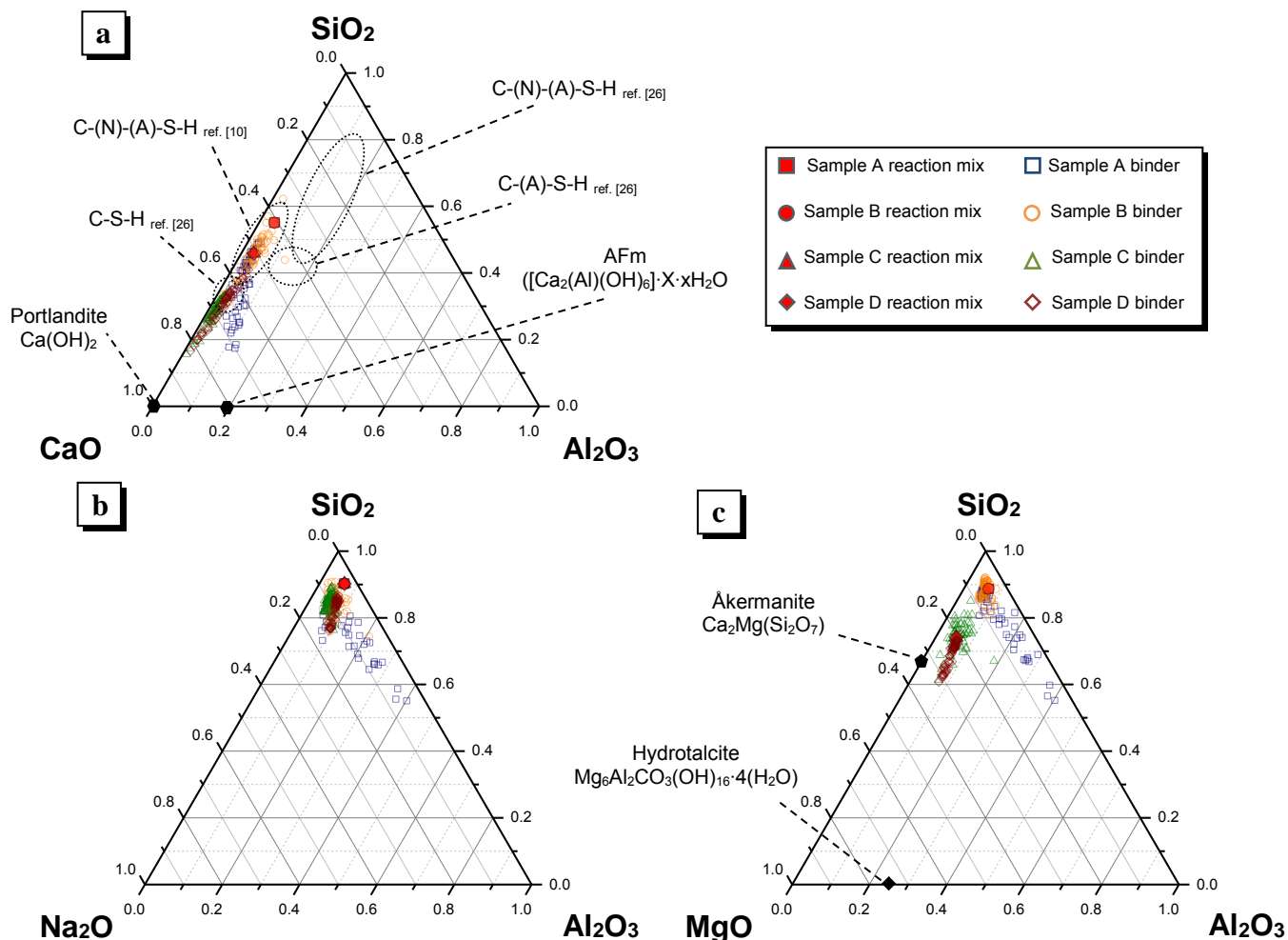
The crystalline phases in samples C and D, with the exception of åkermanite and gehlenite, appear to be completely consumed upon alkali-activation, leading to the formation of a poorly crystalline C-(A)-S-H phase as the main reaction product as well as secondary reaction products crystalline  $C_4AH_{13}$ , hydrotalcite, silicate-substituted AFm and portlandite ( $Ca(OH)_2$ ) (PDF # 44-1481). Again, åkermanite and gehlenite, and in sample D, wollastonite, do not appear to participate in the reaction.

The diffractograms for the alkali-activated samples A and B display each display a reflection attributed to poorly ordered C-(A)-S-H, but with significantly different intensities. The peak assigned to hydrotalcite (present at approximately  $11.5 2\theta$ ), identified in the diffractogram for the alkali-activated binder of sample A, is absent from the diffractogram of alkali-activated sample B, while the peak assigned to gehlenite and åkermanite (present at approximately  $30.7 2\theta$ ) in the alkali-activated binder for sample A has significantly less intensity than in sample B. Hydrotalcite is a common reaction product in alkali-activated slag where magnesium is present in the precursor, and as such is expected to be forming in the binders synthesised here [8, 9, 12, 24, 25]. These results suggest that, when the calcium and aluminium content in the precursor powder are held constant, a lower content of magnesium in the precursor powder ( $Mg/(Al+Si) = 0.05$ ) promotes greater formation of hydrotalcite during alkali-activation, while a higher content of magnesium in the precursor powder ( $Mg/(Al+Si) = 0.25$ ) results in no formation of hydrotalcite. This is contrary to what is observed during alkali-activation of ground granulated blast furnace slag (GGBFS), where increased magnesium content promotes formation of increased amounts of hydrotalcite [9]. In the samples here, increased magnesium content has resulted in increased formation of gehlenite and åkermanite during synthesis and calcination of the precursor powder. Consequently the amount of aluminium and magnesium available to participate in the reactions during alkali-activation at early age is significantly reduced, causing a reduction in the amount of hydrotalcite observed. Differences in the crystallinity of the hydrotalcite phases between samples may also be significant here.

This trend is also observed when comparing the diffractograms of samples C and D. As mentioned above, the formation of gehlenite and åkermanite during precursor synthesis is much less for these high-calcium containing samples. Consequently these samples will contain more freely available magnesium than samples A and B. Despite this, a higher content of magnesium in the precursor powder appears to have resulted in reduced formation of hydrotalcite and C-S-H and increased formation of portlandite, consistent with the trends observed for samples A and B. In samples with higher calcium content ( $Ca/(Al+Si)=1.00$ ), a higher magnesium content of the precursor powder also induces greater formation of portlandite, suggesting that magnesium also plays an important role in the formation of magnesium-free secondary reaction products.

### **3.2 Scanning electron microscopy**

The chemistry of each sample as determined by ESEM – EDX is reported in Fig. 2. Alkali-activated sample A binder exhibits a range of  $Ca/(Al+Si)$  ratios which lie along an imaginary line drawn between the  $Ca/(Al+Si)$  ratios of an aluminium- and sodium-substituted calcium silicate hydrate (C-(N)-(A)-S-H) phase and a partially silicate-substituted AFm phase (Fig. 2a). This is consistent with the XRD results of this sample (Fig. 1a). The main binding phase forming in the alkali-activated samples B exhibits a range of  $Ca/(Al+Si)$  ratios which lie within the region typically observed for C-(N)-(A)-S-H gels and C-S-H gels (Fig. 2a). This is consistent with that identified in the X-ray diffractograms where traces of a silicate-substituted



**Figure 2.** Projection of alkali-activated binder chemistry onto the a) ternary CaO – Al<sub>2</sub>O<sub>3</sub> – SiO<sub>2</sub> system, b) ternary Na<sub>2</sub>O – Al<sub>2</sub>O<sub>3</sub> – SiO<sub>2</sub> system and c) ternary MgO – Al<sub>2</sub>O<sub>3</sub> – SiO<sub>2</sub> system showing elemental is composition of alkali-activated binders cured for 3 days for samples A, B, C and D as determined by ESEM-EDX analysis. Approximate compositional regions in C-(N)-(A)-S-H, C-(A)-S-H and C-S-H have been determined from [26] and [10].

AFm phase were observed in sample A, while this phase is not identified in sample B. Given that the bulk calcium, silicon, aluminium and sodium content of the precursors were the same for each sample, it is clear that the magnesium content of the precursor plays a significant role in determining phase development. Increased magnesium content in the precursor powder appears to promote formation of C-(N)-(A)-S-H and less formation of C-S-H and silicate-substituted AFm phases. This is consistent with the relative intensities of the peaks assigned to C-S-H and silicate-substituted AFm in the X-ray diffractograms.

The chemistry of the alkali-activated binders for each of samples C and D ( $\text{Ca}/(\text{Al}+\text{Si}) = 1.00$ ) (Fig 2. b) exhibit a similar range of  $\text{Ca}/(\text{Al}+\text{Si})$  ratios which lie along an imaginary line drawn between the  $\text{Ca}/(\text{Al}+\text{Si})$  ratios of the reaction mix, C-S-H and portlandite, consistent with the phases observed by XRD. Alkali-activated binders for all samples exhibit  $\text{Na}/\text{Al}$  ratios clustered around that of the precursor powder ( $\text{Na}/\text{Al} = 0.5$ ) (Fig 2b). This suggests that despite formation of greater amounts of C-S-H and portlandite in binders where the precursor powder contained higher calcium content, sodium incorporation into the binder has occurred to approximately the same extent.

Each of the alkali-activated binders exhibits  $\text{Mg}/(\text{Al}+\text{Si})$  ratios similar to that of the precursor powders. Alkali-activated sample A exhibits an  $\text{Al}/\text{Si}$  ratio of approximately 0.35, while alkali-activated sample B

exhibits an Al/Si ratio which is similar to that of the precursor powder (approximately 0.16) (Fig. 2c). The higher Al/Si ratio in sample A is consistent with the observation by XRD of greater amounts of hydrotalcite compared to sample B. This is consistent with the mechanism discussed above (Section 3.1) where an increased content of magnesium in the precursor powder appears to have promoted the formation of greater amounts of åkermanite during the precursor synthesis and calcination, consequently decreasing the amount of freely available magnesium and hence inhibiting the formation of hydrotalcite upon alkali-activation. Consequently a greater amount of Al is freely available and greater substitution of Al into the calcium silicate hydrate (C-S-H) phase occurs, promoting the formation of a C-(N)-(A)-S-H gel. This is in contrast to observations for alkali-activated commercial slags [4, 9] and highlights the importance of consideration of freely available magnesium content rather than bulk magnesium content within the precursor.

The alkali-activated binders for each sample display a range of values for the ratios Ca/Si, Mg/Si and Al/Si which are very similar to those observed for alkali silicate-activated GGBFS slags where the precursor slag contained 1.17, 5.21 wt % and 7.44 wt % MgO, respectively [9]. This suggests that the chemistry of these binders produced from synthetic slags is representative of that of alkali silicate-activated commercial slags with varying magnesium content.

#### 4. Conclusions

Stoichiometrically controlled alkali-activated materials within the system CaO-MgO-Al<sub>2</sub>O<sub>3</sub>-SiO<sub>2</sub>, with varying Mg content, were synthesised via alkali-activation of precursor powders which were in turn synthesised from aqueous precursor solutions via an organic steric entrapment solution-polymerisation route. The main reaction product in all samples was a C-(N)-A-S-H gel, and the secondary reaction products hydrotalcite, crystalline C<sub>4</sub>AH<sub>13</sub> and a partially silicate-substituted AFm phase were also formed. Samples where the precursor powder contained higher amounts of calcium (Ca/(Al+Si)=1.00) also formed portlandite upon alkali-activation. Lower Mg content within the precursor appears to promote less formation of gehlenite and åkermanite during the precursor synthesis. More magnesium is then freely available during alkali-activation, and subsequently alkali activation promotes greater formation of C-(N)-(A)-S-H and less formation of hydrotalcite. Increased magnesium content promotes greater formation of gehlenite and åkermanite during the precursor synthesis. Less magnesium is then available to participate in the reaction, and subsequent alkali-activation promotes reduced formation of C-(N)-A-S-H and greater formation of hydrotalcite. This highlights the importance of considering freely available magnesium content rather than bulk chemistry when investigating the effect of network modifying cations on phase assemblage. Consequently, the availability of network modifying cations such as magnesium, among other factors, is expected to dictate microstructural changes occurring within alkali-activated materials induced by environmental factors (such as acidic attack, carbonation and other aggressive environments). The availability of magnesium during alkali-activation is then expected to be a significant factor controlling the physical properties and durability of alkali-activated materials.

#### 5. Acknowledgement

This work was funded in part by the Australian Research Council (ARC), including support through the Particulate Fluids Processing Centre, a Special Research Centre of the ARC. The University of Melbourne also provided support through an Overseas Research Experience Scholarship to support an extended visit by the first author to the University of Sheffield.

#### 6. References

1. Davidovits, J., *Geopolymers - Inorganic polymeric new materials*. Journal of Thermal Analysis, 1991. **37**(8): p. 1633-1656.
2. Duxson, P., et al., *The role of inorganic polymer technology in the development of 'green concrete'*. Cement and Concrete Research, 2007. **37**(12): p. 1590-1597.
3. Juenger, M.C.G., et al., *Advances in alternative cementitious binders*. Cement and Concrete Research, 2011. **41**(12): p. 1232-1243.
4. Ben Haha, M., et al., *Influence of slag chemistry on the hydration of alkali-activated blast-furnace slag — Part I: Effect of MgO*. Cement and Concrete Research, 2011. **41**(9): p. 955-963.

5. Ben Haha, M., et al., *Influence of slag chemistry on the hydration of alkali-activated blast-furnace slag — Part II: Effect of Al<sub>2</sub>O<sub>3</sub>*. Cement and Concrete Research, 2012. **42**(1): p. 74-83.
6. Le Saoût, G., et al., *Hydration degree of alkali-activated slags: A <sup>29</sup>Si NMR study*. Journal of the American Ceramic Society, 2011. **94**(12): p. 4541-4547.
7. Bernal, S.A., et al., *Effect of binder content on the performance of alkali-activated slag concretes*. Cement and Concrete Research, 2011. **41**(1): p. 1-8.
8. Bernal, S.A., et al., *Gel nanostructure in alkali-activated binders based on slag and fly ash, and effects of accelerated carbonation*. Cement and Concrete Research, 2013. **53**: p. 127-144.
9. Bernal, S.A., et al., *MgO content of slag controls phase evolution and structural changes induced by accelerated carbonation in alkali-activated binders*. Cement and Concrete Research, 2014. **57**: p. 33-43.
10. Myers, R.J., et al., *Generalized structural description of calcium-sodium aluminosilicate hydrate gels: the cross-linked substituted tobermorite model*. Langmuir, 2013. **29**(17): p. 5294-306.
11. Richardson, I.G., et al., *The characterization of hardened alkali-activated blast-furnace slag pastes and the nature of the calcium silicate hydrate (C-S-H) paste*. Cement and Concrete Research, 1994. **24** (5): p. 813-829.
12. Fernández-Jiménez, A. and F. Puertas, *Structure of calcium silicate hydrates formed in alkaline-activated slag: Influence of the type of alkaline activator*. Journal of the American Ceramic Society, 2003. **86**(8): p. 1389-94.
13. Bernal, S.A., *MgO content of the slag controls phase evolution and structural changes induced by accelerated carbonation in alkali-activated binders*. Cement and Concrete Research, 2013.
14. Bernal, S., et al., *Natural carbonation of aged alkali-activated slag concretes*. Materials and Structures, 2014. **47**(4): p. 693-707.
15. Iler, R.K., *The chemistry of silica : solubility, polymerization, colloid and surface properties, and biochemistry*. 1979, New York: Wiley.
16. Cui, X.-m., et al., *Characterization of chemosynthetic Al<sub>2</sub>O<sub>3</sub>-2SiO<sub>2</sub> geopolymers*. Journal of Non-Crystalline Solids, 2010. **356**(2): p. 72-76.
17. Zheng, G., et al., *Preparation of geopolymer precursors by sol-gel method and their characterization*. Journal of Materials Science, 2009. **44**(15): p. 3991-3996.
18. García-Lodeiro, I., et al., *FTIR study of the sol-gel synthesis of cementitious gels: C-S-H and N-A-S-H*. Journal of Sol-Gel Science and Technology, 2007. **45**(1): p. 63-72.
19. García-Lodeiro, I., et al., *Effect of calcium additions on N-A-S-H cementitious gels*. Journal of the American Ceramic Society, 2010. **93**(7): p. 1934-1940.
20. Garcia-Lodeiro, I., et al., *Compatibility studies between N-A-S-H and C-A-S-H gels. Study in the ternary diagram Na<sub>2</sub>O-CaO-Al<sub>2</sub>O<sub>3</sub>-SiO<sub>2</sub>-H<sub>2</sub>O*. Cement and Concrete Research, 2011. **41**(9): p. 923-931.
21. Gulgun, M.A., M.H. Nguyen, and W.M. Kriven, *Polymerized organic-inorganic synthesis of mixed oxides*. Journal of the American Ceramic Society, 1999. **82**(3): p. 556-560.
22. Lothenbach, B., et al., *Influence of limestone on the hydration of Portland cements*. Cement and Concrete Research, 2008. **38**(6): p. 848-860.
23. Matschei, T., B. Lothenbach, and F.P. Glasser, *The AFm phase in Portland cement*. Cement and Concrete Research, 2007. **37**(2): p. 118-130.
24. Ben Haha, M., et al., *Influence of activator type on hydration kinetics, hydrate assemblage and microstructural development of alkali activated blast-furnace slags*. Cement and Concrete Research, 2011. **41**(3): p. 301-310.
25. Escalante-García, J.I., et al., *Hydration products and reactivity of blast-furnace slag activated by various alkalis*. Journal of the American Ceramic Society, 2003. **86**(12): p. 2148-2153.
26. van Deventer, J.S.J., et al., *Microstructure and durability of alkali-activated materials as key parameters for standardization*. Journal of Sustainable Cement-Based Materials, 2015: p. <http://dx.doi.org/10.1080/21650373.2014.979265> (in press).

# Use of geopolymer concrete in column applications

Weena Lokuge<sup>1</sup>, Jay Sanjayan<sup>2</sup> and Sujeeva Setunge<sup>3</sup>

<sup>1</sup>Lecturer, Centre of Excellence in Engineered Fibre Composites (CEEFC),  
School of Civil Engineering and Surveying, University of Southern Queensland (USQ),  
Toowoomba, Queensland 4350, Australia

<sup>2</sup>Professor, Director, Centre for Sustainable Infrastructure,  
Faculty of Science Engineering & Technology, Swinburne University of Technology,  
Hawthorn, VIC 3122, Australia

<sup>3</sup>Professor, Deputy Head of School, School of Civil, Environmental and Chemical Engineering  
RMIT University, Melbourne, VIC 3001, Australia

**Abstract:** Geopolymer Concrete has been extensively studied in the past and recognised as a greener substitute for Ordinary Portland Cement (OPC) concrete. Geopolymer concrete is proven to have good engineering properties with a reduced carbon footprint. Geopolymers not only reduce the greenhouse gas emission but also use a large amount of industrial wastes such as fly ash and slag. This environmentally friendly material is being embraced by the construction industry after its use in the Global Change Institute at University of Queensland. However, research into the use of geopolymer concrete in structural applications is very limited.

This research paper aims at investigating the applicability of a constitutive relationship that authors developed for OPC concrete in predicting the constitutive relationship of geopolymer concrete. This model has the capacity to predict the lateral dilation of concrete which in turn will be used to establish the confinement provided by the lateral reinforcement in column applications. Load deformation behaviour of twelve geopolymer concrete slender columns reported in the literature is used to validate the proposed model. Since geopolymer concrete exhibits higher brittleness than OPC concrete, careful consideration should be given in the structural design of geopolymer concrete. Predicted behavior for slender geopolymer concrete columns using the proposed stress-strain relationship for confined geopolymer concrete is in good agreement with the experimental results. The outcomes of this paper will be useful in the structural analysis of geopolymer concrete columns.

**Keywords:** geopolymer concrete, stress-strain relationship, confinement, slender column.

## 1. Introduction

Emission of greenhouse gases such as carbon dioxide and nitrous oxide is a major contributing factor for global warming while the production of cement contributes about 5-7% of CO<sub>2</sub> emissions globally. Although the production of one ton of Ordinary Portland Cement (OPC) releases approximately one ton of CO<sub>2</sub> into the atmosphere [1, 2], it is widely used as a construction material around the world. As a result of few decades of research activities, geopolymer concrete (GPC) has become a potential candidate to replace the OPC concrete. It is reported that mechanical properties of GPC depend mainly on the source material, mix design and curing method [3]. However Reed et al. [4] proposed that fly ash based GPC is suitable for in-situ applications. The changes in the mortar with OPC and geopolymer are compatible with the changes in the OPC and GPC [5]. Some mechanical properties of GPC (tensile strength) are higher than those of OPC concrete [3, 5, 6], while some properties such as elastic modulus [5, 6] and flexural strength [6] are comparatively lower. Although design guidelines for geopolymer concrete are not very well documented, equations for some properties such as tensile strength, flexural strength and modulus of elasticity can be found in the literature [3, 7]. Commercial use of geopolymer concrete has taken place in the recent past for small scale applications. However the use of geopolymer concrete by Wagners, Australia in the Global Change Institute at University of Queensland and in the Wellcamp airport in Toowoomba are reported as its first structural application on large scale construction projects.

Geopolymer concrete has highly desirable structural engineering properties, which can lead to significant environmental and economical benefits. Its use is, however, limited by concerns regarding its increased brittleness compared with OPC concrete [5] and a lack of understanding of the behaviour under complex multi-axial loading conditions. The ductility of geopolymer concrete has not been investigated by many researchers in the past. The traditional method of improving ductility of columns is by using lateral confinement with steel reinforcement. However, effective methods of lateral confinement have not been reported for geopolymer concrete. The above concerns have led to very few research projects around the world [8], [9, 10]. In these studies the experimental/ analytical studies covered the behaviour of small-scale



square columns with a limited configuration of steel reinforcements, tested under laboratory conditions. In most studies, the confining pressure is assumed to be that corresponding to the yield stress of the confining steel. However the confining pressure exerted by the lateral steel is corresponding to the lateral dilation of concrete in that instance. Currently, with very limited research on the structural performance of geopolymer concrete, there is no agreement among researchers about the amount of lateral steel required in geopolymer concrete columns to provide a required level of ductility.

Based on experimental results, various stress-strain models for unconfined/confined normal or high strength concrete have been proposed in the literature [11-16]. These models can be divided into three broad categories. One group of researchers used a form of equation proposed by Sargin et al. [15]. The second group of researchers proposed a second order parabola for the ascending branch and a straight line for the descending branch and their studies were based on equations proposed by Kent and Park [14]. The third group developed stress strain relationships based on equations suggested by Popovics [16]. There are many developments to all the three preliminary equations. In these models, selected parameters were included in the stress-strain curves and then they were calibrated using the test results. There are very limited knowledge about the stress-strain relationship for unconfined/confined geopolymer concrete although it is the basis of any structural application of this new green construction material.

## 2. Existing stress-strain models for geopolymer concrete

There are two categories of constitutive models that have been discussed in the literature, one for geopolymer concrete [9, 17] and the other for geopolymer paste [18]. Haider et al. [18] developed a stress-strain model for geopolymer paste based on the experimental results with active confinement. The model proposed by the Concrete Institute of Australia is a modified version of Popovics [16] which gives a single curve for both the ascending and descending branches of the stress-strain curve for unconfined geopolymer concrete. Sarker [9] also proposed a modified version of Popovics [16] and applied this model for confined geopolymer concrete in column applications. Ganesan et al [17] used another version of Mander et al. [19] which was originally proposed by Popovics [16]. Ganesan et al [17] used the stress-strain relationship for geopolymer concrete to predict the behaviour of geopolymer concrete short columns confined by spiral reinforcement. These constitutive models are capable of predicting only the axial stress versus axial strain relationships. However, the confinement provided by lateral steel reinforcement depends on the lateral dilation of concrete. Therefore it is a timely concern to develop or investigate a complete deformational behaviour including both axial and lateral strains of laterally confined geopolymer concrete with axial compression. With the increased popularity in geopolymer concrete due to environmental and economic benefits, the greener material will be used in high-load-carrying structural members all over the world in the near future. Therefore a thorough knowledge of the material behaviour of the constituents (such as geopolymer concrete and steel) subjected to monotonically increasing loading is of great importance.

## 3. Methodology

Proposed stress-strain models for confined geopolymer concrete, steel and the procedure used in obtaining the load deformation curves are described in the following sub sections.

### 3.1 Proposed stress strain model for confined geopolymer concrete

The model proposed in this paper was originally developed by the authors for normal and high strength concrete. It is described in detail in Lokuige et al. [20]. Only one material parameter in the original model was changed to suit geopolymer concrete. Two different exponential curves form the complete stress-strain relationships for confined geopolymer concrete. The terms described in this model are illustrated in Figure 1.

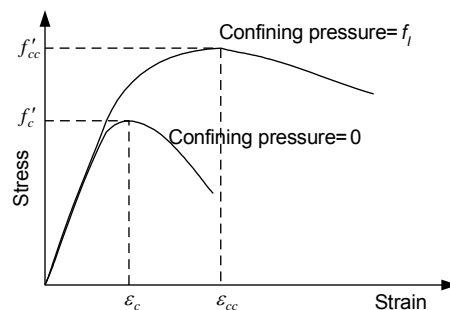


Figure 1. Typical stress-strain relationship for confined and un-confined concrete.

### 3.1.1 Relationship between axial strain and lateral strain

Relationship between axial strain  $\varepsilon_1$  and lateral strain  $\varepsilon_2$  is described below:

$$\frac{\varepsilon_2}{\varepsilon'_{cc}} = \begin{cases} \nu_i^a \left( \frac{\varepsilon_1}{\varepsilon_{cc}} \right) & \text{if } \varepsilon_1 \leq \varepsilon' \\ \left( \frac{\varepsilon_1}{\varepsilon_{cc}} \right)^a & \text{if } \varepsilon_1 > \varepsilon' \end{cases} \quad (1)$$

$\varepsilon_{cc}$  and  $\varepsilon'_{cc}$  are axial strain and lateral strain corresponding to peak axial stress.  $a$  is a material parameter which depends on the characteristic compressive strength of concrete ( $f_c$ ) and can be approximated by:

$$\mathbf{a} = 0.0177f_c + 1.2818 \quad (2)$$

$\varepsilon'$  can be obtained by equating the right hand side of Equation 1.  $\nu_i^a$ , the initial Poisson's ratio is defined as follows:

$$\nu_i^a = 8 \times 10^{-6}(f_c)^2 + 0.0002f_c + 0.138 \quad (3)$$

Equation 1 completely defines the relationship between axial strain and lateral strain if axial strain ( $\varepsilon_{cc}$ ) and lateral strain ( $\varepsilon'_{cc}$ ) corresponding to peak axial stress are known. Axial strain corresponding to peak axial stress  $\varepsilon_{cc}$  can be expressed as follows.

$$\frac{\varepsilon_{cc}}{\varepsilon_{co}} = 1 + (17 - 0.06f_c) \left( \frac{f_l}{f_c} \right) \quad (4)$$

$f_l$  is the confining pressure and  $\varepsilon_{co}$  is the axial strain corresponding to the peak uniaxial compressive strength. Peak axial stress for confined concrete  $f_{cc}$  is defined as:

$$\frac{f_{cc}}{f_c} = \left( \frac{f_l}{f_t} + 1 \right)^k \quad (5)$$

where  $k$  is a constant given by:

$$k = 1.25 \left( 1 + 0.062 \frac{f_l}{f_c} \right) (f_c)^{-0.21} \quad (6)$$

$f_t$  is the tensile strength. Tensile strength of geopolymer concrete is given by:

$$f_t = 0.9 \times 0.32(f_c)^{0.67} \quad (7)$$

Equations 1-7 can predict the lateral strain for a given axial strain if the unconfined concrete strength and lateral strain corresponding to peak axial stress are known.

### 3.1.2 Lateral strain at peak axial stress

Similar to the observations for normal and high strength concrete [20] and for geopolymer paste [18] it is assumed that geopolymer concrete samples will return to the original volume when the axial strain is corresponding to the peak axial stress. Therefore at peak stress:

$$\bar{\varepsilon}_v = \frac{\varepsilon_1 + 2\varepsilon_2}{\varepsilon_{v,\max}} = 0 \quad (8)$$

$$\varepsilon_{cc} = 2\varepsilon'_{cc} \quad (9)$$

By introducing Poisson's ratio, Equation 9 can be written as:

$$\nu_f^a = 0.5 \quad (10)$$

where  $\nu_f^a$  is the secant value of Poisson's ratio at peak stress.

### 3.1.3 Relationship between axial stress, axial strain and lateral strain

Based on shear stress factors and shear strain factors, axial stress ( $\sigma_1$ ), axial strain ( $\varepsilon_1$ ) and lateral strain ( $\varepsilon_2$ ) constitutive behaviour of geopolymers concrete can be expressed as:

$$\sigma_1 = \begin{cases} 2\tau_{mp} \left( 1 - e^{-c \left( \frac{\varepsilon_1 + \varepsilon_2}{2\gamma_{mp}} \right)} \right) + f_l & \text{before peak} \\ 2\tau_{mp} \left( 1 - e^{d \left( \frac{\varepsilon_1 + \varepsilon_2}{2\gamma_{mp}} \right)^2} - d \right) + f_l & \text{after peak} \end{cases} \quad (11)$$

$c$  and  $d$  are material parameters defined as follows:

$$\begin{aligned} c &= -0.0427f_c + 3.15 \quad \text{and} \\ d &= -0.0003f_c - 0.0057 \end{aligned} \quad (12)$$

$c$  is the only material parameter that was modified to suit geopolymers concrete better.

$\tau_{mp}$  is the maximum shear stress at peak and  $\gamma_{mp}$  is the maximum shear strain at peak. They are defined as:

$$\tau_{mp} = \frac{f_{cc} - f_l}{2} \quad \text{and} \quad \gamma_{mp} = \frac{\varepsilon_{cc} + \varepsilon'_{cc}}{2} \quad (13)$$

Therefore complete deformational behaviour of concrete can now be generated.

### 3.2 Stress-strain model for steel

A simple idealised elasto-plastic stress-strain model was used in this investigation.

$$f_s = \begin{cases} E_{st} \varepsilon_s & \text{if } 0 \leq \varepsilon_s \leq \varepsilon_y \\ f_{sy} & \text{if } \varepsilon_s > \varepsilon_y \end{cases} \quad (14)$$

Where  $f_s$  and  $\varepsilon_s$  are steel stress and strain,  $E_{st}$  is the modulus of elasticity and  $f_{sy}$  and  $\varepsilon_y$  are the yield strength and corresponding strain of steel.

### 3.3 Load-deformation relationships

The analysis was performed by assuming plane sections remain plane after bending, perfect bond between the longitudinal steel and the concrete and only tension steel resists the tensile forces. The stress-strain relationships for concrete and steel are assumed to be as described in the previous section.

A standard pin-ended column is used in analysing the slender columns used in the experimental results reported in the literature. The procedure used in obtaining the mid height deflection is the one suggested by Rangan [21]. The deflected shape,  $v(x)$  is assumed to be represented by a sine wave as follow:

$$v(x) = \delta \sin\left(\frac{x\pi}{L_e}\right) \quad (15)$$

$L_e$  is the effective length of the column. At mid height, when  $x = L_e/2$ , the relationship between the curvature and the deflection can be obtained by:

$$\varphi\left(\frac{L_e}{2}\right) = \frac{\pi^2}{L_e^2} \delta \quad (16)$$

The section is divided into a number of strips. For an assumed strain distribution (using curvature,  $\varphi$  and strain at extreme compression side,  $\varepsilon_t$ ), stresses in core, cover and reinforcement are calculated using the corresponding stress-strain relationships. Mid height deflection calculated using Equation 14 can be used to obtain the calculated eccentricity. For a given curvature,  $\varphi$  and eccentricity,  $e^*$ , strain at extreme compression side,  $\varepsilon_t$  is iterated until the calculated eccentricity is equal to the actual eccentricity within a given tolerance level. The procedure used in getting the load-deflection curve is shown in Figure 2.

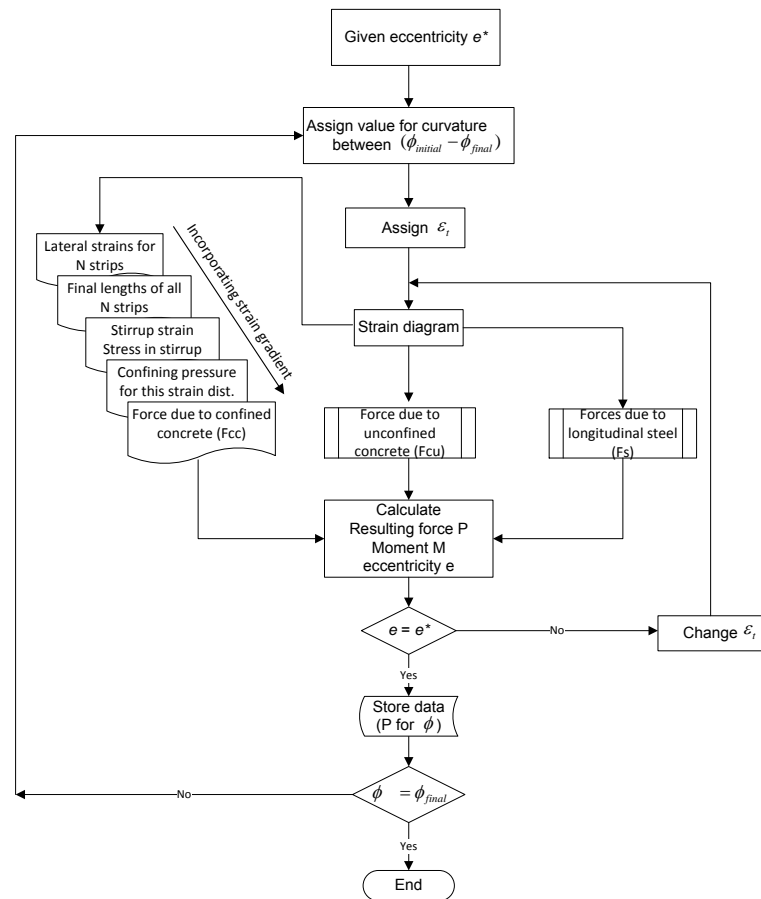


Figure 2. Flow chart used to draw load-deflection curves

#### 4. Experimental results used to compare model predictions

Twelve reinforced geopolymer concrete slender columns tested by Sumajouw et al.[8] are selected in this research to compare with model predictions. These columns were eccentrically loaded and two test series were utilized. Compressive strength of geopolymer concrete, reinforcement configuration and level of eccentricity were the test variables in their experimental program. Compressive strengths were in the range of 42-66 MPa and three level of eccentricities 15, 35 and 50 mm were used. Longitudinal reinforcement used in these columns are of type N12 deformed bars with cross sectional area of 110 mm<sup>2</sup> and yield strength of 519 MPa from tensile strength tests. Two different reinforcement configurations were used with 4N12 and 8N12. Lateral reinforcement used were 6 mm diameter hard drawn wires (W6) with 100 mm spacing for all the columns. Details of column specimens are shown in Figure 3 and Table 1. Length of all the columns was 1500 mm and the effective length was found to be 1684 mm.

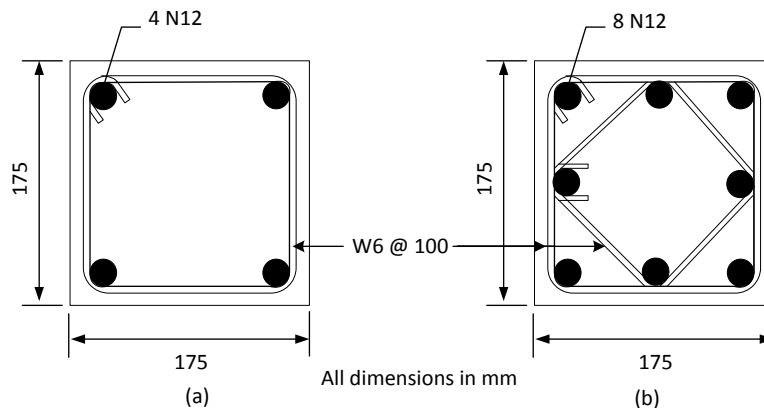


Figure 3. Details of columns [8]

**Table 1. Specimen details.**

Column	$f_c$ (MPa)	Tie reinforcement	Eccentricity (mm)
GCI-1	42	Figure 2(a)	15
GCI-2	42	Figure 2(a)	35
GCI-3	42	Figure 2(a)	50
GCI-4	43	Figure 2(b)	15
GCI-5	43	Figure 2(b)	35
GCI-6	43	Figure 2(b)	50
GCII-1	66	Figure 2(a)	15
GCII-2	66	Figure 2(a)	35
GCII-3	66	Figure 2(a)	50
GCII-4	59	Figure 2(b)	15
GCII-5	59	Figure 2(b)	35
GCII-6	59	Figure 2(b)	50

### 5. Results and discussion

Twelve slender column results reported in the literature [8] were used to validate the theoretical analysis described before. Figure 4(a) and Figure 4(b) show the experimental and theoretical load versus deflection curves for GCI and GCII series respectively.

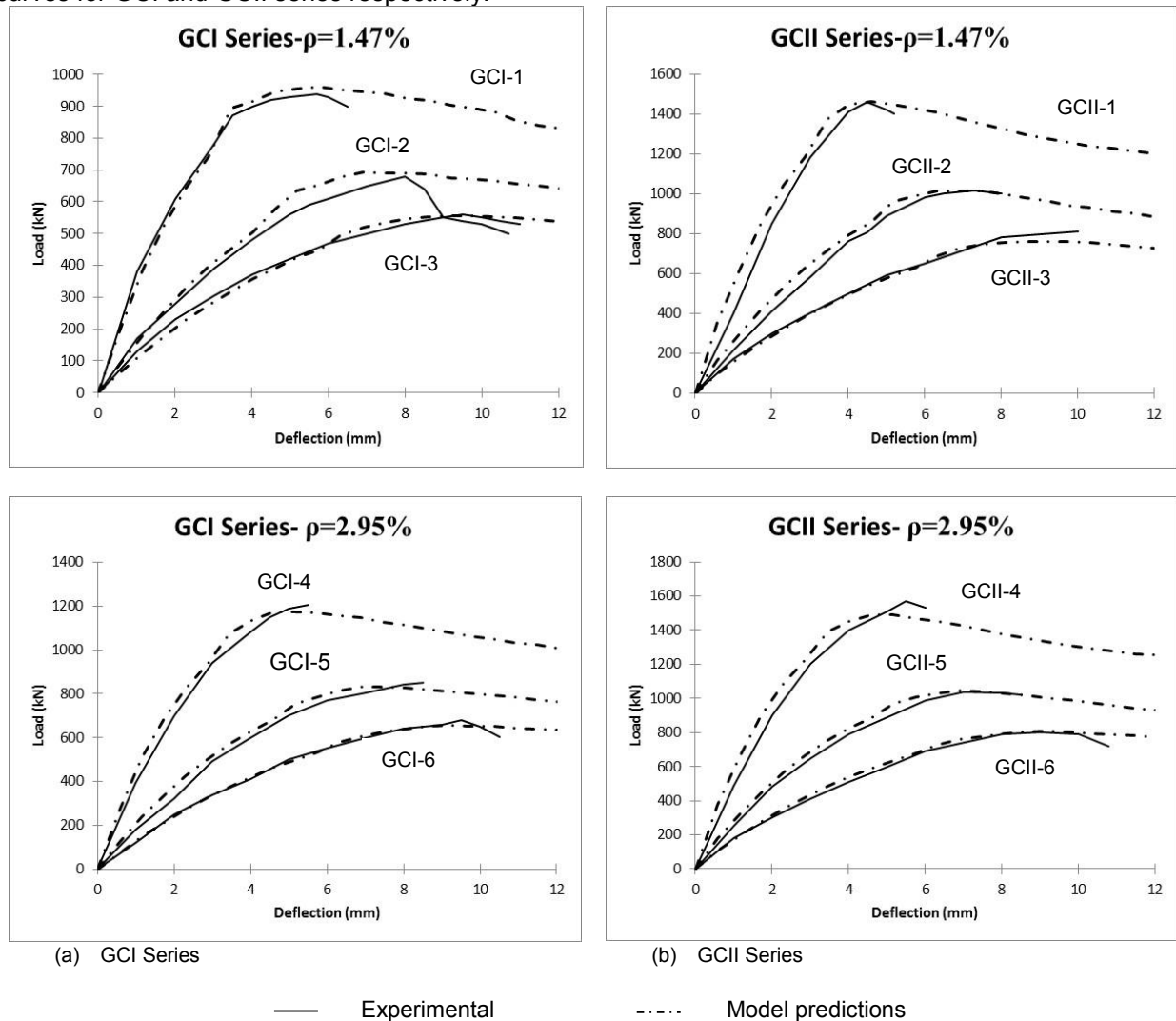


Figure 4. Load versus deflection curves for GPC slender columns

The analytical procedure was capable of predicting the ascending branch as well as the descending branch for all the twelve curves while a short post peak behavior is observed in majority of the experimental curves. Model predictions are in reasonable agreement especially for GCI series (low compressive strength) and for higher eccentricity values irrespective of the compressive strength. The load capacity of slender geopolymer concrete columns considerably decreases with increasing eccentricity for both experimental and model predictions. The predicted peak load and the corresponding deflection are always matching well with the experimental results. There are small variations in the ascending branches of GCII series (higher compressive strength). This needs to be investigated further with more experimental results in the future. The discrepancies between the experimental results and the model predictions may be due to the assumed sine wave function for the deflected shape.

## 6. Conclusions

The proposed constitutive relationship for confined/unconfined geopolymer concrete and the proposed analytical procedure to establish the load-deformation behaviour for eccentrically loaded slender geopolymer concrete columns compare well with the experimental results reported by Sumajouw et al. [8]. Conclusions resulted from this research are summarized below:

- The stress-strain relationship originally proposed by the authors for normal and high strength concrete [20] can be modified slightly and used for confined geopolymer concrete. It has been effectively used in the analysis of eccentrically loaded slender columns as it reflects both axial and lateral strain of confined geopolymer concrete.
- Proposed analytical procedure uses the confining pressure applied by the lateral steel which changes with lateral dilation of geopolymer concrete.
- With the increasing eccentricity, the strength of GPC columns decreases rapidly which is consistent with the experimental results as well as for NSC and HSC.
- Proposed analysis has good practical implications because the proposed model which was originally based on triaxial tests is more likely to work for a wide range of column configurations and sizes.
- The results discussed here for the slender columns not only depend on the moment-curvature of cross section, but also on curvature-deflection relationship of the column. The simplified sine-curve relationship is likely to have contributed to the slight discrepancies between the results which needs further investigation.

## 8. References

1. Rangan, B.V., *Fly ash-based geopolymer concrete*, in *Research Report GC4 2008*, Curtin University of Technology: Perth, Australia. p. 44.
2. Wallah, S.E., *Creep behaviour of fly ash-based geopolymer concrete*. Civil Engineering Dimension, 2010. **12**(2): p. 73-78.
3. Sofi, M., et al., *Engineering properties of inorganic polymer concretes (IPCs)*. Cement and Concrete Research, 2007 **37**: p. 251-257.
4. Reed, M., W. Lokuge, and W. Karunasena, *Fibre-reinforced geopolymer concrete with ambient curing for in situ applications*. Journal of Materials Science, 2014. **49**: p. 4297-4304.
5. Pan, Z., J.G. Sanjayan, and B.V. Rangan, *Fracture properties of geopolymer paste and concrete*. Magazine of Concrete research, 2011. **63**(10): p. 763-771.
6. Olivia, M., and Nikraz, H., *Properties of fly ash geopolymer concrete designed by Taguchi method*. Materials and Design, 2012 **36**: p. 191-198.
7. Diaz-Loya, E.I., E.N. Allouche, and S. Vaidya, *Mechanical properties of fly ash-based geopolymer concrete*. ACI Materials Journal, 2011. **108**(3): p. 300-306.
8. Sumajouw, D.M.J., Hardjito, D. and Wallah, S.E., *Fly ash-based geopolymer concrete: study of slender reinforced columns*. Journal of Materials Science, 2007. **42**: p. 3124-3130.
9. Sarker, P.K., *Analysis and geopolymer concrete columns*. Materials and Structures, 2009. **42**: p. 715-724.

10. Rahman, M., Sarker, P.K., *Geopolymer Concrete Columns under Combined Axial Load and Biaxial Bending*, in *CONCRETE 2011 Conference 2011*, The Concrete Institute of Australia: Perth Western Australia.
11. Sheikh, S.A. and S.M. Uzumeri, *Analytical model for concrete confinement in tied columns*. Journal of the Structural Division, Proceedings of the ASCE, 1982. **108**(12): p. 2703-2722.
12. Mander, J.B., M.J.N. Priestley, and R. Park, *Theoretical stress-strain model for confined concrete*. Journal of Structural Engineering, 1988. **114**(8): p. 1805-1826.
13. Cusson, D. and P. Paultre, *Stress-strain model for confined high strength concrete*. Journal of Structural Engineering, 1995. **121**(3): p. 468-477.
14. Kent, D.C. and R. Park, *Flexural members with confined concrete*. Journal of the Structural Division, Proceedings of the ASCE, 1971. **97**(7): p. 1969-1990.
15. Sargin, M., *Stress strain relationship for concrete and the analysis of structural concrete sections*. 1971(Study No.4).
16. Popovics, S., *A numerical approach to the complete stress-strain curve of concrete*. Cement and Concrete Research, 1973. **3**(5): p. 583-599.
17. Ganesan, N., et al., *Stress-strain behaviour of confined geopolymer concrete*. Construction and Building Materials, 2014. **73**: p. 326-331.
18. Haider, G.M., J.G. Sanjayan, and P.G. Ranjith, *Complete triaxial stress-strain curves for geopolymer*. Construction and Building Materials, 2014. **69**: p. 196-202.
19. Mander, J.B., M.J.N. Priestley, and R. Park, *Theoretical stress-strain model for confined concrete*. Journal of Structural Engineering, ASCE, 1988. **114**(8): p. 1804-1826.
20. Lokuge, W.P., Sanjayan, G.J. and Setunge, Sujeeva, *Stress strain model for laterally confined concrete*. Journal of Materials in Civil Engineering, ASCE, 2005. **17**(6): p. 607-616.
21. Rangan, B.V., *Strength of reinforced concrete slender columns*. ACI Structural Journal, 1990. **87**(1): p. 32-38.

# Influence of Matrix Related Parameters on Strain Hardening Behavior of Engineered Geopolymer Composite (EGC)

Behzad Nematollahi<sup>1</sup>, Jay Sanjayan<sup>1</sup>, Faiz Uddin Ahmed Shaikh<sup>2</sup>

<sup>1</sup>Center for Sustainable Infrastructure, School of Engineering, Faculty of Science, Engineering and Technology, Swinburne University of Technology, Melbourne, Victoria 3122, Australia

<sup>2</sup>Department of Civil Engineering, Curtin University, Perth, Australia

**Abstract:** This paper evaluates the influence of matrix properties on the behavior of a recently developed fiber reinforced engineered geopolymer composites (EGC) exhibiting strain hardening behavior under uni-axial tension. Randomly oriented short poly vinyl alcohol (PVA) fibers (2% v/v) were used to reinforce the relatively brittle low calcium (Class F) fly ash-based geopolymer matrix. The effect of matrix related parameters including activator to fly ash and sand to fly ash ratios on the matrix and composite properties of the developed fly ash-based EGCs including workability of the fresh matrix, density, compressive strength and uni-axial tensile behavior were evaluated. Experimental results revealed that the increase in the activator to fly ash ratio adversely affected the strain hardening behavior of EGC with reduction in ultimate tensile strength. The tensile strain capacity of EGC was significantly reduced when excessive amount of sand was added to the geopolymer matrix. However, the ultimate tensile strength of EGC was marginally increased.

**Keywords:** EGC, strain hardening, geopolymer, fly ash, PVA fiber.

## 1. Introduction

A special class of high performance fiber reinforced cementitious composites (HPFRCCs) with advanced ductility which is about 600 times the ductility of normal concrete in tension [1] has been referred to engineered cementitious composites (ECC) [2]. ECC is a micromechanics-based designed brittle matrix composite which utilizes a small amount of discontinues fibers (typically 2% or less by volume) and exhibits a tensile strain capacity of up to 6% [3]. High cement content is commonly found in the mixture design of several types of HPFRCCs, such as ultra-high performance fiber reinforced cementitious composites (UHPRCCs) [4-6] and ECC [7]. Typical ECC mix design contains considerably higher cement content than conventional OPC concrete [7]. Production of ordinary Portland cement (OPC) is responsible for almost 5% of total CO<sub>2</sub> emission which is the main cause of global warming in the world [8]. The high cement content in typical ECC mix design apparently compromises sustainability performance of this material [7]. Hence, it is essential to develop green ECC with lower cement content (i.e. lower global warming potential associated with CO<sub>2</sub> emission of OPC production) which sustain the tensile ductility properties but also include sustainability considerations. One of the solution to achieve this objective is partial replacement of OPC by supplementary cementing materials such as fly ash, palm oil fuel ash (POFA) and slag in the ECC mix design to reduce the use of OPC; thereby, reducing the global warming issues associated with the CO<sub>2</sub> emission of the cement industry [7,9]. However, a more sustainable approach to achieve this goal is to completely substitute the OPC binder in the ECC mix design by an alternative cement-less binder such as geopolymer.

Geopolymer is an emerging cement-less binder purported to provide a sustainable and environmentally friendly alternative to OPC. The term geopolymer was initially introduced by Davidovits [10]. Geopolymer is synthesized from materials of geological origin (e.g. metakaolin) or industrial by-products such as fly ash and slag that are rich in silica and alumina with high alkaline activators. In this study, a low calcium (Class F) fly ash which is an industrial by-product of coal-fired power stations [11] containing high amounts of silicon and aluminum was used as the source material. Production of fly ash based geopolymer requires approximately 60% less energy and has at least 80% less CO<sub>2</sub> emission compared to manufacture of OPC [12,13]. Recently, an initial study was conducted to demonstrate the feasibility of developing a geopolymer-based ECC, known as engineered geopolymer composite (EGC) where the OPC binder was completely replaced by fly ash-based geopolymer binder which exhibited strain hardening behavior in uni-axial tension, accompanied by multiple fine cracks [14]. However, the developed fly ash-based EGC possessed low to moderate compressive and uni-axial tensile strengths ranging from 17.4 MPa to 27.6 MPa and from 2.9 MPa to 3.4 MPa, respectively which may limit the widespread application of these composites in the construction industry. Following that study, Nematollahi et al. [15,16] evaluated the effect of different activator combinations on the matrix and composite properties of the recently developed fly ash-based EGC to improve its compressive and tensile strengths with relatively low concentration activator combinations. It should be noted that only fly ash (with no sand) was used in the matrix design of their



EGCs similar to the first generation of the conventional ECC that only utilized OPC and silica fume with no sand in the matrix [17,18]. Their experimental results revealed that although the concentration of the activator combinations was limited to 8.0 M to account for safety consideration; however, the developed fly ash-based EGC exhibited improved compressive strength, tensile strength and tensile ductility over 60 MPa, 4.7 MPa, and 4.3% on average, respectively with using the Na-based activator combination composed of 8.0 M NaOH solution (28.6% w/w) and Na<sub>2</sub>SiO<sub>3</sub> solution (71.4% w/w) with a SiO<sub>2</sub>/Na<sub>2</sub>O ratio of 2.0.

The behavior of randomly oriented short fiber reinforced composites such as fly ash-based EGCs are governed by three groups of parameters. The first group involves matrix related parameters such as compressive and tensile strengths, fracture toughness, elastic modulus, etc., while the second group consists of fiber related parameters such as fiber type, geometry and strength and so on, and the third group comprises matrix-fiber interface related parameters such as the frictional and chemical bond strengths [17]. Among these three groups, the focus of the current study is on the matrix related parameters. The geopolymer matrix properties such as compressive and tensile strengths, fracture toughness and elastic modulus are influenced by many parameters such as type of fly ash, type of alkaline activator, activator to fly ash ratio, sand to fly ash ratio, temperature and duration of curing and so on. For the purpose of the current investigation, activator to fly ash ratio (Act/FA) and sand to fly ash ratio (S/FA) were selected as the most significant parameters in governing the characteristics of the geopolymer matrix. Sand content can alter the matrix toughness, pre-existing flaw size distribution and fiber/matrix interface properties [19]. A systematic experimental program was conducted to understand the quantitative influence of these matrix related parameters on the matrix and composite properties of fly ash-based EGC with the aim of selecting an appropriate type of matrix for design of strain hardening EGC.

## 2. Micromechanics-based design criteria for strain hardening behavior

The pseudo strain hardening (PSH) behavior in fiber reinforced brittle matrix composite is a result of sequential development of matrix multiple cracking. A fundamental requirement for the multiple cracking behavior is that steady-state cracking prevails under tension. The condition for steady-state cracking was analyzed by Marshall and Cox [20] using J-integral method. When fiber bridging behavior is characterized by bridging stress-crack opening  $\sigma(\delta)$  relation, the condition for steady-state cracking, often referred as energy-based condition for PSH behavior, can be expressed in the following simple form:

$$J_{tip} \leq \sigma_0 \delta_0 - \int_0^{\delta_0} \sigma(\delta) d\delta \equiv J'_b \quad (1)$$

where  $J'_b$  is the complementary energy calculated from the  $\sigma(\delta)$  curve of the composite,  $\sigma_0$  is the maximum bridging stress corresponding to the crack opening  $\delta_0$  and  $J_{tip}$  is the crack tip toughness which for small fiber volume fraction can be determined from the following equation:

$$J_{tip} = \frac{K_m^2}{E_m} \quad (2)$$

where  $K_m$  and  $E_m$  are the fracture toughness and elastic modulus of the matrix, respectively [17]. Another condition for PSH behavior is that the tensile first cracking strength ( $\sigma_{fc}$ ) must not exceed the maximum fiber bridging strength ( $\sigma_0$ ). This condition, often referred as the strength-based condition, can be expressed in the following form:

$$\sigma_{fc} \leq \sigma_0 \quad (3)$$

where  $\sigma_{fc}$  is determined by matrix fracture toughness ( $K_m$ ) and the pre-existing flaw size [19]. When a brittle matrix shows PSH behavior, the ultimate strength of the composite ( $\sigma_{cu}$ ) coincides with the maximum bridging stress  $\sigma_0$ . Both criteria namely strength-based and energy-based conditions must be satisfied in order to achieve strain hardening composite; otherwise, conventional fiber reinforced concrete exhibiting tension softening behavior results [21]. Considering the random nature of fiber distribution and pre-existing flaw size in fiber reinforced composite, sufficient margin between  $\sigma_0$  and  $\sigma_{fc}$  as well as  $J'_b$  and  $J_{tip}$  should be obtained to ensure the possibility of PSH behavior [22]. In this regard, Kanda and Li [23] proposed two PSH performance indices namely stress-performance index ( $\sigma_0/\sigma_{fc}$ ) and energy-performance index ( $J'_b/J_{tip}$ ) to quantitatively evaluate the margin. Theoretically, both PSH performance indices must exceed unity to achieve PSH behavior in a fiber reinforced composite. The higher the performance indices values, the greater the possibility of saturated multiple cracking or saturated PSH behavior which results in higher tensile strain capacity of the composite. Unsaturated PSH behavior often results in small tensile strain capacity and large variation in tensile ductility of the composite [22]. Higher energy-performance index ( $J'_b/J_{tip}$ ) can be achieved by either

reducing  $J_{tip}$  which is correlated to  $K_m$  as shown in Equation (2), or increasing  $J'_b$ . Reducing  $J_{tip}$  is more desirable because low  $J_{tip}$  (i.e.  $K_m$ ) indicates low first crack strength [19].

### 3. Materials

The low calcium fly ash (class F) used in this study was supplied from Gladstone power station in Queensland, Australia. The sodium-based (Na-based) activator combination used in this study was composed of 8.0 M sodium hydroxide (NaOH) and D Grade sodium silicate ( $\text{Na}_2\text{SiO}_3$ ) solutions. NaOH solution was prepared with a concentration of 8.0 M using NaOH beads of 97% purity supplied by Sigma-Aldrich and tap water. The D Grade  $\text{Na}_2\text{SiO}_3$  solution was supplied by PQ Australia with a specific gravity of 1.51 and a modulus ratio ( $M_s$ ) equal to 2.0 (where  $M_s = \text{SiO}_2 / \text{Na}_2\text{O}$ ,  $\text{Na}_2\text{O} = 14.7\%$  and  $\text{SiO}_2 = 29.4\%$ ). NaOH and  $\text{Na}_2\text{SiO}_3$  solutions were mixed together with  $\text{Na}_2\text{SiO}_3/\text{NaOH}$  mass ratio of 2.5 to prepare the Na-based activator combination. Sieve graded high silica purity sands with maximum particle size of 212  $\mu\text{m}$  supplied by TGS Industrial Sand Ltd., Australia was used in this study. Properties of the PVA fiber used in this study supplied by Kuraray Co. Ltd., Japan are presented in Table 1.

### 4. Experimental procedures

#### 4.1. Mix proportions and mixing

In this study, four appropriate EGC mix proportions were designed through experiments using the principles of ECC development to establish strain hardening behavior in low calcium (Class F) fly ash-based EGC. Table 2 presents mix proportions of the fly ash-based EGCs used in this study. As shown in this table, two values of activator to fly ash ratios (0.35 and 0.45) with two values of sand to fly ash ratios (0.30 and 0.60) were selected. All EGCs were prepared in a Hobart mixer. To prepare the fly ash-based geopolymer matrix, fly ash and sand (if any) were dry mixed for about 3 min. Then alkaline solution as well as extra water in the mixture EGC35 were added and the mixing was continued for about 4 min. In each mix once a consistent matrix was reached, PVA fibers (2% v/v) were gradually added, taking care to ensure uniform fiber dispersion. The whole mixing procedure for each composite generally took 20-25 min.

**Table 1: Properties of PVA fiber**

Fiber type	Diameter ( $\mu\text{m}$ )	Length (mm)	Young's modulus (GPa)	Elongation (%)	Nominal Strength (MPa)	Density ( $\text{g}/\text{cm}^3$ )
RECS 15x8	40	8	41	6	1600	1.3

**Table 2: Mix proportions of the fly ash-based EGCs**

Mix designation	Fly ash	Activator	Water	Sand	PVA fiber
EGC35 <sup>1</sup>	1.0	0.35	0.014 <sup>2</sup>	---	0.02
EGC45 <sup>1</sup>	1.0	0.45	---	---	0.02
EGC45-S30	1.0	0.45	---	0.30	0.02
EGC45-S60	1.0	0.45	---	0.60	0.02

Note: All numbers are mass ratios of fly ash weight except W/GP solids ratios and fiber contents (volume fraction).

<sup>1</sup> Composed of only geopolymer paste with no sand.

<sup>2</sup> Extra water added to the activator.

#### 4.2. Casting, curing and testing of specimens

To determine flowability of fresh geopolymer matrix in each mix, mini slump tests also known as spread-flow tests were conducted. Each mix was tested twice. Details of the mini-slump test can be found in Nematollahi and Sanjayan [24]. The relative slump value was derived from the following equation:

$$\Gamma_p = (d/d_0)^2 - 1 \quad (4)$$

where  $\Gamma_p$  is relative slump,  $d$  is the average of two measured diameters of the matrix spread and  $d_0$  is bottom diameter of the conical cone, equals to 100 mm in this study [25].

For each mix design, compressive strength of the matrix specimens (before addition of the PVA fibers) and the composite specimens (after addition of the PVA fibers) were measured. In this regard, the fresh geopolymer matrices and composites were cast into standard 50 mm plastic cube molds and compacted using a vibrating table. For heat curing all molds were sealed to minimize moisture loss

and placed in an oven at 60° C for 24 hours. At the end of heat curing period, the specimens were removed from the oven and kept undisturbed until being cool and then removed from the molds and left in the laboratory at ambient temperature until the day of testing. All specimens were tested 3 days after casting. Previous studies have shown that age does not have considerable effect on strength of geopolymers after the completion of the heating curing period, thereby three-day compressive strength of geopolymer is equivalent to a typical OPC strength development after 28-days [26,27]. At the testing day the cube specimens were weighed to determine the density of the matrix and composite specimens. Compressive strength of all specimens were measured according to ASTM C109 [28]. For each mix, at least three matrix specimens and three composite specimens were tested in order to check the variability of performance under compression.

Uni-axial tension tests were conducted to evaluate the behavior of the developed EGC under tension. At least three coupon specimens with the dimensions of 400 mm×75 mm×10 mm were cast and cured similar to the cube specimens. All specimens were tested in uni-axial tension under displacement control using MTS testing machine with hydraulic wedge grips. Following Ahmed and Maalej [29], the displacement rate was 0.25 mm/min. Aluminum plates were epoxy glued onto the ends of the specimens to facilitate gripping. Care was taken to ensure proper alignment of the specimens with the machine hydraulic grips. Details of the uni-axial tension test can be found in Nematollahi et al. [15].

## 5. Results and Discussions

### 5.1. Workability, density and compressive strength

The average matrix workability of each mix in terms of relative slump value is presented in Table 3. According to this table, the EGC45 and EGC35 mixes exhibited the highest and the lowest matrix workability, respectively. In addition, as expected the matrix workability of the EGC45 mix was significantly (32%) higher than that of the EGC35 mix due to its higher Act/FA. Furthermore, as expected due to the addition of the sand, the workability of the mortar mixes was lower than that of the EGC45 mix (paste only mix with no sand) and the rate of decrease in workability depended on the sand content in the mortar mixes. Effect of the Act/FA on the matrix compressive strength of the EGCs is also presented in Table 3. According to this table, an increase in Act/FA from 0.35 to 0.45 resulted in a considerable decrease in compressive strength of the matrix. The matrix compressive strength of the EGC45 mix was 42% lower compared to that of the EGC35 mix. Similar trend was reported by other researchers for geopolymer paste and concrete [27,30]. This trend is somewhat similar to the well-known effect of water to cement ratio (W/C) on the compressive strength of the cement-based matrices [17,27]. The average matrix and composite densities of each mix are also presented in Table 3. As shown in this table, the EGC45-S60 and EGC35 composites exhibited the highest and the lowest matrix and composite densities, respectively. In addition, as expected matrix and composite densities of the mortar mixes were higher than those of the EGC45 mix (paste only mix with no sand). It should be noted that the composite density of each mix was relatively lower compared to its corresponding matrix density. This may be attributed to a fiber induced damage effect, which results in a composite with higher porosity compared with the matrix material alone [31].

**Table 3: Workability, density and compressive strength results**

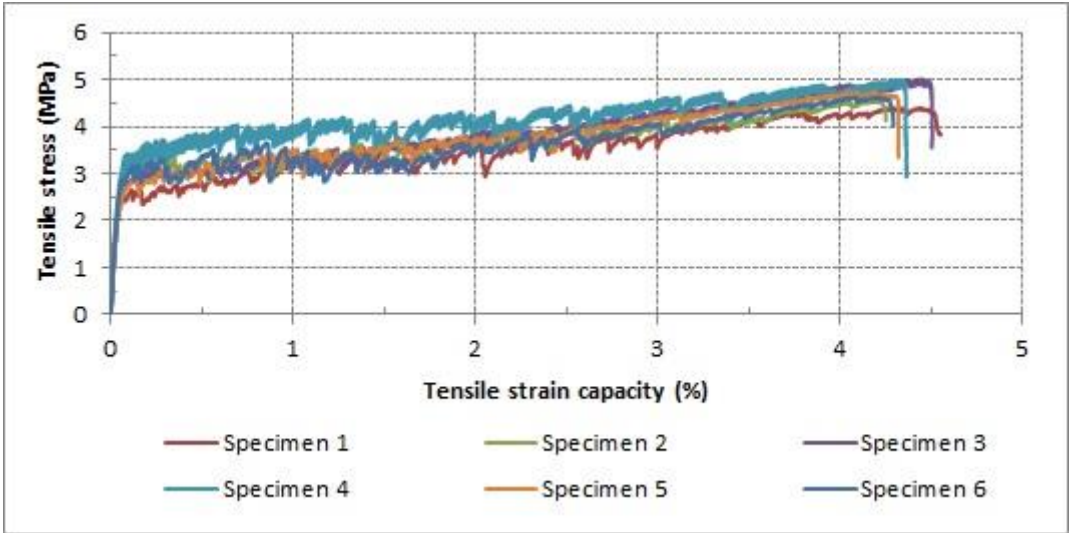
Mix designation	Relative slump value	Density; (kg/m <sup>3</sup> )		Compressive strength, (MPa)	
		Matrix	Composite	Matrix	Composite
EGC35	6.9	1859	1804	54.6	63.7
EGC45	9.1	1899	1824	31.6	52.6
EGC45-S30	8.8	1928	1828	36.4	56.8
EGC45-S60	7.3	2041	1912	35.3	60.7

Effect of the sand content (S/FA) on the matrix compressive strength of the EGCs is also demonstrated in Table 3. According to this table, an increase in S/FA from zero to 0.3 resulted in a marginal (15%) increase in the matrix compressive strength. However, increase in S/FA from 0.3 to 0.6 (doubling the sand content) did not cause any significant change in the compressive strength of the mortar matrices. In other words, the matrix compressive strengths of both mortar matrices, regardless of their sand content, were almost comparable. These results are in good agreement with those published by Temujin et al. [32] where the compressive strength of the fly ash-based geopolymer mortar mixes remained almost constant with varying the sand content. Effect of the Act/FA and S/FA on the composite compressive strength of the EGCs are also presented in Table 3. According to table, in all mixes the compressive strength of the composite was higher than that of the corresponding matrix due to the addition of the PVA fibers (2% v/v). Moreover, as expected it was

observed that in all composite specimens crack propagation was restrained due to the bridging mechanism of the PVA fibers; thereby the specimens kept their original shapes after peak load resulting in a ductile failure mode. It should be noted that although the concentration of the activator combination was limited to 8.0 M to account for safety consideration; however, the compressive strength of all EGCs developed in this study was significantly higher than that of the fly ash-based EGCs developed by Ohno and Li [14] which ranged from 17.4 MPa to 27.6 MPa. This could be mainly due to the longer heat curing period (i.e. 24 hours at 60° C) employed in this study. Among mortar mixes, the EGC45-S60 composite exhibited the highest compressive strength (60.7 MPa) as it contained the highest amount of sand. The fact that the EGC35 composite without sand exhibited higher compressive strength (63.7 MPa) compared to that of the EGC45-S60 composite with sand could be attributed to their different Act/FA (0.35 versus 0.45).

**5.2. Uni-axial tensile performance**

Tensile stress-strain behaviors of the fly ash-based EGCs are presented in Figures 1 to 4. As shown in these figures, all EGCs, regardless of their Act/FA and S/FA, exhibited clear PSH behavior with tensile strain capacities ranging from 1.3% to 4.3%. The experimentally measured ultimate tensile strength and tensile strain capacity as well as the estimated first-crack strength, the average crack opening at peak load (i.e. average loaded crack width) of each composite are presented in Table 4. The uni-axial tensile performance of the fly ash-based EGCs developed in this study are comparable to those of the fly ash-based EGCs developed by Ohno and Li [14]. However, as shown in Table 4, the ultimate tensile strength of all EGCs developed in this study was higher than that of the EGCs developed by Ohno and Li [14] which ranged from 2.9 MPa to 3.4 MPa. After unloading, clear trace of all visible cracks was obtained by using a permanent marker. The average crack opening at peak load was estimated based on the tensile strain capacity, gauge length and the number of visible cracks. It should be noted that the number of multiple cracks formed during loading was more than that of the unloading specimens as many micro cracks appeared during loading completely closed after unloading; thereby, making them very difficult to detect on the specimen surface after unloading. According to Li et al. [19], the actual crack opening at peak load should be smaller than the estimated values shown in Table 4 because as mentioned earlier the actual number of micro-cracks developed during loading was more than the number of visible cracks after unloading. In the EGC35, EGC45 and EGC45-S30 composites crack distribution was uniform with almost equal crack spacing and enormous micro-cracks with tightly controlled crack width (i.e. saturated cracking behavior) were observed which corresponds to their significantly high tensile strain capacities. However, in the EGC45-S60 composite the crack distribution was not uniform with un-even and wider crack spacing and fewer number of visible cracks (i.e. un-saturated cracking behavior) which corresponds to its significantly lower tensile strain capacity.



**Figure 1: Tensile stress-strain responses of EGC35**

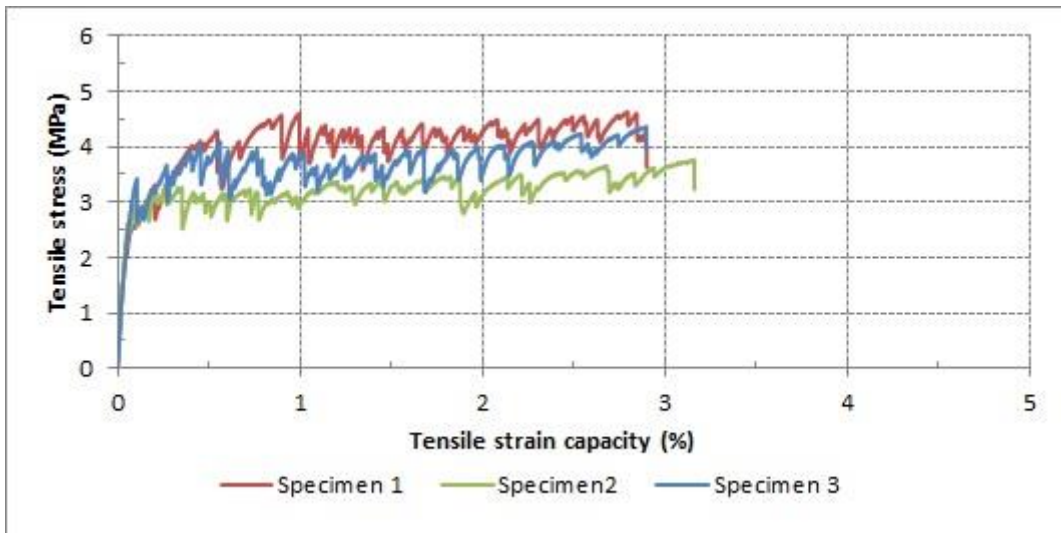


Figure 2: Tensile stress-strain responses of EGC45

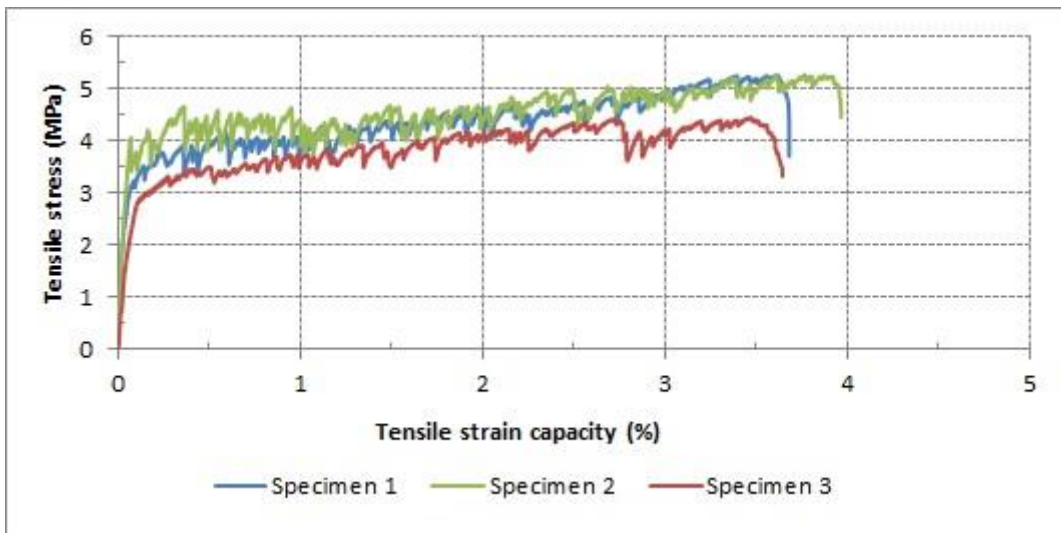


Figure 3: Tensile stress-strain responses of EGC45-S30

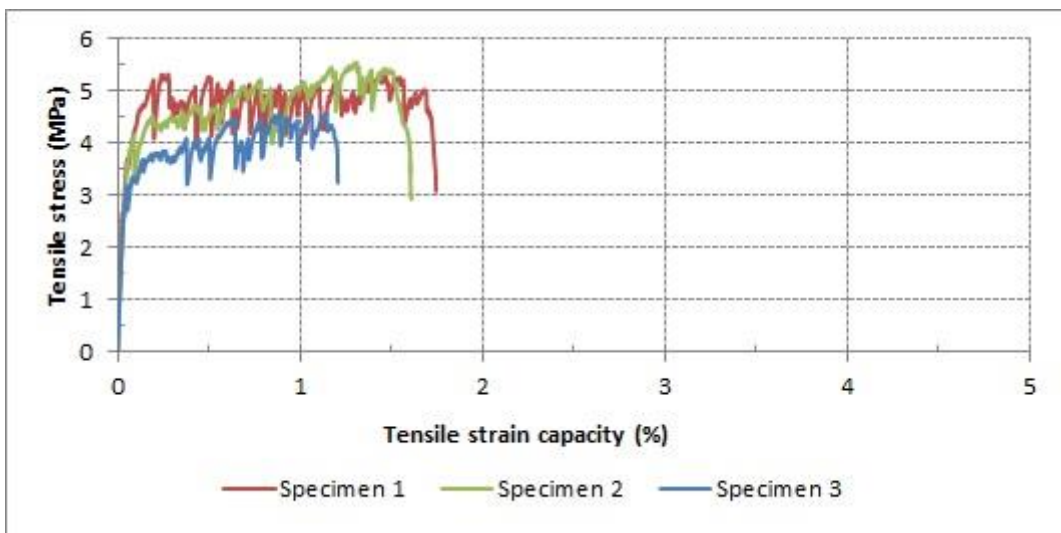


Figure 4: Tensile stress-strain responses of EGC45-S60

**Table 4: Uni-axial tensile test results**

Mix designation	First-crack strength, $\sigma_{fc}$ (MPa)	Ultimate tensile strength, $\sigma_{cu}$ (MPa)	Tensile strain capacity, $\varepsilon_{cu}$ (%)	Estimated loaded crack width; ( $\mu\text{m}$ )
EGC35	$0.66 \pm 0.053$	$4.7 \pm 0.25$	$4.3 \pm 0.14$	$119 \pm 9.53$
EGC45	$0.45 \pm 0.095$	$4.3 \pm 0.45$	$3.0 \pm 0.19$	$94 \pm 17$
EGC45-S30	$1.3 \pm 0.27$	$5.0 \pm 0.47$	$3.6 \pm 0.15$	$103 \pm 3.63$
EGC45-S60	$1.6 \pm 0.25$	$5.2 \pm 0.51$	$1.3 \pm 0.15$	$107 \pm 20.0$

According to Table 4, the increase in Act/FA from 0.35 to 0.45 resulted in a 32% decrease in first crack strength of the EGC45 composite compared to that of the EGC35 composite. The lower first crack strength of the EGC45 composite implies its lower  $J_{tip}$  compared to that of the EGC35 composite which is beneficial for PSH behavior of the composite [19]. In addition, the ultimate tensile strength of the EGC45 composite was slightly (9%) lower than that of the EGC35 composite which could be attributed to the interfacial properties. In other words, the chemical bonding energy and the frictional bond strength of the EGC45 composite was lower compared to that of the EGC35 composite; resulting in lower fiber bridging strength [33]. The reasons for different tensile strain capacities of the EGC35 and EGC45 composites could be explained in terms of the two PSH performance indices  $\sigma_0/\sigma_{fc}$  and  $J'_b/J_{tip}$ . With regards to the stress-performance index, the  $\sigma_0/\sigma_{fc}$  of the EGC45 composite was 35% higher than that of the EGC35 composite. With regards to the crack tip toughness, as mentioned earlier, the lower first crack strength of the EGC45 composite indicates that the  $J_{tip}$  of the EGC45 was lower than that of the EGC35 composite. The lower the  $J_{tip}$  value, the higher the energy-performance index. On the other hand, with regards to the  $J'_b$ , the higher ultimate tensile strength of the composite indicates the higher peak bridging stress in the  $\sigma-\delta$  curve of the composite. In addition, the higher loaded crack width indicates the higher crack opening corresponding to maximum bridging stress in the  $\sigma-\delta$  curve of the composite [33]. Considering the ultimate tensile strength and the loaded crack width of the EGC35 and EGC45 composites as presented in Table 4, it can be concluded that the  $J'_b$  of the EGC35 composite is higher than that of the EGC45 composite. The higher the  $J'_b$  value, the higher the energy-performance index. Consequently, with regards to the energy-performance index, it can be inferred that the  $J'_b/J_{tip}$  of the EGC45 composite is slightly higher than that of the EGC35 composite. As mentioned in Section 2, the higher values of the two PSH performance indices, the greater the possibility of saturated PSH behavior which results in higher tensile strain capacity of the composite. Considering the higher PSH performance indices of the EGC45 composite, it can be said that the EGC45 composite should theoretically exhibit higher (or at least comparable) tensile strain capacity compared to that of the EGC35 composite. However, as shown in Table 4, the tensile strain capacity of the EGC45 did not exceed that of the EGC35 composite. This may be attributed to the poor fiber dispersion (fiber bundles) of the EGC45 composite as fiber bundles were observed during mixing which adversely affected the composite behavior. According to Li et al. [34], fiber bundling is not desirable as it decreases the effectiveness of the fiber reinforcement and weak spots may be introduced by the fiber bundles.

As shown in Table 4, the addition of sand to the matrices of the EGC45-S30 and EGC45-S60 composites resulted in marginal (16% to 21%) increase in the ultimate tensile strength of these composites compared to that of the EGC45 composite with no sand. However, the addition of sand resulted in considerable decrease in the tensile strain capacity of these composites. It should be noted that, as mentioned earlier, the EGC45 composite should theoretically exhibit higher (or at least comparable) tensile strain capacity compared to that of the EGC35 composite. Similar results were reported by Ahmed and Maalej [29] regarding the adverse effect of the sand addition on the strain hardening behavior of conventional ECC composites. The undesirable effect of the addition of sand on the strain hardening behavior of the EGC composites could also be explained in terms of the two PSH performance indices  $\sigma_0/\sigma_{fc}$  and  $J'_b/J_{tip}$ . As shown in Table 4, the addition of sand to the matrices of the EGC45-S30 and EGC45-S60 composites resulted in significant increase in the first crack strength of these composites compared to that of the EGC45 composite with no sand. This significant increase in the first crack strength of these composites is not desirable as it results in significant reduction in the strength performance index ( $\sigma_0/\sigma_{fc}$ ) of the composite. For instance, the first-crack strength of the EGC45-S60 composite (with S/FA=0.6) was significantly (256%) higher than that of the EGC45 composite with no sand; thereby, the stress performance index of the EGC45-S60 was considerably (66%) lower than that of the EGC45 composite with no sand. In addition, the significant increase in the first crack strength of the EGC45-S30 and EGC45-S60 composites implies that the crack tip toughness of these composites would be considerably higher than that of the EGC45 composite with

no sand [19] which is not desirable as it results in significant reduction in the energy performance index ( $J'_b / J_{tip}$ ) of the composite. In conventional cement-based composites, it is well established that high sand content results in a matrix with high fracture toughness, which in turn increases the first crack strength of the composite compared to the maximum bridging stress of the fibers and violates the conditions for saturated strain hardening behavior ([35,36]Li and Maalej, 1996; Akkaya et al., 2000). In summary, it can be said that the excessive use of sand in the matrix of the EGC45-S60 composite resulted in considerable increase in the first crack strength and crack tip toughness of the composite; thereby, the two PSH performance indices ( $\sigma_0 / \sigma_{fc}$  and  $J'_b / J_{tip}$ ) of the composite decreased significantly which hindered the use of this matrix and still ensure saturated PSH behavior in the composite. These results are in good agreement with those published by other researchers regarding the conventional ECC composites which indicate that the sand content must be limited in the matrix to sustain tensile ductility of the composite [17,19].

## 6. Conclusions

Strain hardening behavior in randomly oriented short PVA fiber reinforced fly ash-based EGCs were developed in this study. The effect of matrix related parameters including the activator to fly ash and sand to fly ash ratios on the matrix and composite properties of the developed EGCs were experimentally evaluated. All EGCs, regardless of their alkaline solution to fly ash and sand to fly ash ratios, exhibited clear PSH behavior under uni-axial tension similar to the conventional PVA-ECC. Experimental results revealed that the increase in the activator to fly ash ratio decreased the first crack strength, ultimate tensile strength and tensile strain capacity of EGC. With regards to the effect of sand content, the tensile strain capacity of EGC was significantly reduced when excessive amount of sand was added to the geopolymer matrix. However, the ultimate tensile strength of EGC was marginally increased. The adverse effect of the addition of sand on the strain hardening behavior of EGC can be attributed to the increase of matrix fracture toughness due to the excessive use of sand in the geopolymer matrix, which in turn increases the first cracking strength of the composite and suppresses the desirable strain hardening behavior and accompanying composite ductility in tension. This result indicates that the sand content must be limited in the geopolymer matrix to sustain tensile ductility of EGC.

## 7. Acknowledgments

The authors gratefully acknowledge Kuraray Co. Ltd. of Japan for supplying the PVA fibers used in this study.

## 8. References

- [1] Li, V. C., and Kanda, T. (1998). "Engineered cementitious composites for structural applications". *ASCE Journal of Materials in Civil Engineering*, 10(2), 66-69.
- [2] Li, V. C., and Wu, H.-C. (1992). "Conditions for pseudo strain-hardening in fiber reinforced brittle matrix composites". *Applied Mechanics Reviews*, 45(8), 390-398.
- [3] Kong, H.-J., Bike, S. G., and Li, V. C. (2003). "Development of a self-consolidating engineered cementitious composite employing electrosteric dispersion/stabilization". *Cement and Concrete Composites*, 25(3), 301-309.
- [4] Nematollahi, B., Voo, Y.L., and Saifulnaz M.R., R. (2014). Structural behavior of precast Ultra-High Performance Fiber Reinforced Concrete (UHPFRC) cantilever retaining walls: Part I — Analysis and design procedures and Environmental Impact Calculations (EIC). *KSCE Journal of Civil Engineering*, 18(5), 1470-1480.
- [5] Nematollahi, B., Voo, Y.L., and Saifulnaz M.R., R. (2014). Structural behavior of precast Ultra-High Performance Fiber Reinforced Concrete (UHPFRC) cantilever retaining walls: Part II — Full scale experimental testing. *KSCE Journal of Civil Engineering*, 18(5), 1481-1495.
- [6] Nematollahi, B., Raizal Saifulnaz, M. R., and Voo, Y. L. (2014). Sustainability assessment of precast ultra-high performance fiber reinforced concrete (UHPFRC) cantilever retaining walls. *Research Journal of Applied Sciences, Engineering and Technology*, 7(19), 3971-3977.
- [7] Wang, S., and Li, V. C. (2007). "Engineered cementitious composites with high-volume fly ash". *ACI Materials Journal*, 104(3).
- [8] Huntzinger, D. N., and Eatmon, T. D. (2009). "A life-cycle assessment of Portland cement manufacturing: comparing the traditional process with alternative technologies". *Journal of Cleaner Production*, 17(7), 668-675.



- [9] Ahmed, S.F.U. Maalej, M. and Paramasivam, P. (2006). "Flexural responses of hybrid steel-polyethylene fibre reinforced cement composites containing high volume fly ash". *Journal of construction and building materials*, 21: 1088-1097.
- [10] Davidovits J. (1991). "Geopolymers: inorganic polymeric new materials". *Journal of Thermal Analysis*;37(8):1633–56.
- [11] Bakharev T. (2005). "Geopolymeric materials prepared using Class F fly ash and elevated temperature curing". *Cement and Concrete Research*, 35(6):1224–32.
- [12] Li, Z., Ding, Z., and Zhang, Y. (2004). "Development of sustainable cementitious materials". Paper presented at the Proceedings of the international workshop on sustainable development and concrete technology.
- [13] Duxson P, Provis JL, Lukey GC, Van Deventer JS. (2007). "The role of inorganic polymer technology in the development of 'green concrete'". *Cement and Concrete Research*. 37(12):1590–7.
- [14] Ohno, M., and Li, V. C. (2014). "A feasibility study of strain hardening fiber reinforced fly ash-based geopolymer composites". *Construction and Building Materials*, 57, 163-168.
- [15] Nematollahi, B., Sanjayan, J., and Ahmed Shaikh, F. (2015). "Tensile Strain Hardening Behavior of PVA Fiber-Reinforced Engineered Geopolymer Composite." *J. Mater. Civ. Eng.*, 10.1061/(ASCE)MT.1943-5533.0001242 , 04015001.
- [16] Nematollahi B, Sanjayan J. and Shaikh FAU. Strain Hardening Behavior of Engineered Geopolymer Composites: Effects of the Activator Combination. *Journal of The Australian Ceramic Society* Volume 51[1], 2015, 54 – 60
- [17] Li, V., Mishra, D. and Wu, H.-C. (1995). "Matrix design for pseudo-strain-hardening fiber reinforced cementitious composites". *Materials and Structures*, 28, 586-595.
- [18] Kanda, T., and Li, V. C. (1999). "New micromechanics design theory for pseudo-strain hardening cementitious composite". *Journal of engineering mechanics*, 125(4), 373-381.
- [19] Li, V. C., Wang, S., and Wu, C. (2001). "Tensile strain-hardening behavior of polyvinyl alcohol engineered cementitious composite (PVA-ECC)". *ACI Materials Journal*, 98(6).
- [20] Marshall DB, Cox BN. A J-integral method for calculating steady-state matrix cracking stresses in composites. *Mech Mater* 1988(8):127–33.
- [21] Yang E, Wang S, Yang Y, Li VC. (2008). "Fiber-bridging constitutive law of engineered cementitious composites". *J Adv Coner Technol*;6(1):181–93.
- [22] Yang, E. H., and Li, V. C. (2010). "Strain-hardening fiber cement optimization and component tailoring by means of a micromechanical model." *Constr. Build. Mater.*, 24(2), 130–139.
- [23] Kanda, T., and Li, V. C. (2006). "Practical design criteria for saturated pseudo strain hardening behavior in ECC". *Journal of Advanced Concrete Technology*, 4(1), 59.
- [24] Nematollahi, B. & Sanjayan, J. (2014). "Effect of different superplasticizers and activator combinations on workability and strength of fly ash based geopolymer". *Materials & Design*, 57, 667-672.
- [25] Okamura H, Ozawa K. (1995). "Mix design for self-compacting concrete". *Concrete Lib JSCE*;25(6):107–20.
- [26] Kong DL, Sanjayan JG. (2010). "Effect of elevated temperatures on geopolymer paste, mortar and concrete". *Cement and Concrete Research*;40(2):334–9.
- [27] Hardjito D, Wallah SE, Sumajouw DM, Rangan BV. (2004). "On the development of fly ash-based geopolymer concrete". *ACI Materials Journal*;101(6):467–72.
- [28] ASTM C109/C109M (2007). Standard test method for compressive strength of hydraulic cement mortars (using 50 mm [2 in.] cube specimens). United States: ASTM Standards.
- [29] Ahmed, S., and Maalej, M. (2009). "Tensile strain hardening behavior of hybrid steel-polyethylene fiber reinforced cementitious composites". *Construction and Building Materials*, 23(1), 96-106.
- [30] Barbosa, V. F. F.; MacKenzie, K. J. D. and Thaumaturgo, C. (2000). "Synthesis and Characterization of Materials Based on Inorganic Polymers of Alumina and Silica: Sodium Polysialate Polymers", *International Journal of Inorganic Materials*, 2(4), 309-317.



- [31] Li, V. C. and Mishra, D. K. (1992). "Micromechanics of fiber effect on the uniaxial compressive strength of cementitious composites", in *Fiber Reinforced Cement and Concrete*, Proceedings of the 4th RILEM International Symposium, Sheffield, U.K., edited by R. N. Swamy, pp. 400-414.
- [32] Temuujin, J., van Riessen, A., & MacKenzie, K. J. D. (2010). Preparation and characterization of fly ash based geopolymer mortars. *Construction and Building Materials*, 24(10), 1906-1910.
- [33] Lee B.Y., Cho C-G., Lim H-J., Song J-K., Yang K-H., Li V.C. (2012). "Strain hardening fiber reinforced alkali-activated mortar – a feasibility study". *Construction and Building Materials*, 37, 15–20.
- [34] Li, V. C., Wang, Y., & Backer, S. (1990). Effect of inclining angle, bundling and surface treatment on synthetic fiber pull-out from a cement matrix. *Composites*, 21(2), 132-140.
- [35] Li VC, Maalej M (1996). "Toughening in cement based composites, Part I: cement, mortar and Concrete". *Cement Concrete Compos*;18:223–37.
- [36] Akkaya Y, Peled A, Picka JD, Shah SP (2000). "Effect of sand addition on properties of fiber reinforced cement composites". *ACI Mater J*;97(3):393–400.

# EFC Geopolymer Concrete Aircraft Pavements at Brisbane West Wellcamp Airport

Tom Glasby<sup>1</sup>, John Day<sup>2</sup>, Russell Genrich<sup>3</sup>, and Dr James Aldred<sup>4,5</sup>

<sup>1</sup>EFC Manager, Wagners

<sup>2</sup>Group Technical Manager, Wagners

<sup>3</sup>EFC R&D Laboratory Manager, Wagners

<sup>4</sup>Technical Director, Aecom

<sup>5</sup>Adjunct Assoc. Prof., School of Civil & Environmental Engineering, UNSW

**Abstract:** Brisbane West Wellcamp Airport (BWWA) became fully operational with commercial flights operated by Qantas Link in November 2014. BWWA was built with approximately 40,000 m<sup>3</sup> of geopolymer concrete making it the largest application of this new class of concrete in the world. Heavy duty geopolymer concrete was used for the turning node, apron and taxiway pavements using a slip form paving machine. The proprietary geopolymer concrete, known as Earth Friendly Concrete (EFC), was found to be well suited for this construction method due to its high flexural tensile strength, low shrinkage and workability characteristics.

This paper describes the geopolymer concrete pavements delivery from both a materials and construction viewpoint and notes differences to conventional concrete where they occurred. The authors conclude by reviewing earlier projects with this particular geopolymer concrete and discussing how this body of work could help to increase the use of geopolymer concrete in Australia and globally.

**Keywords:** geopolymer concrete, BWWA, pavement, flexural tensile strength

## 1. Introduction

Brisbane West Wellcamp Airport (BWWA) is Australia's first greenfield public airport to be built in 48 years. BWWA became fully operational with commercial flights operated by Qantas Link in November 2014. This project marks a very significant milestone in engineering - the world's largest geopolymer concrete project.

EFC was supplied by Wagners for the construction of the 435 mm thick heavy duty pavements in the aircraft turning areas. There were three distinct areas of geopolymer pavement including the turning node at the Northern end of the runway, the taxiway on the Western side of the runway and the hangars on the Eastern side of the runway.

In preparation for the project both product testing and construction trials were undertaken to ensure that this geopolymer concrete could meet the performance criteria of the contract specification as well as be placed in the intended method using a slip form paving machine. The construction trials highlighted a number of challenges which were overcome by some innovative and novel solutions.

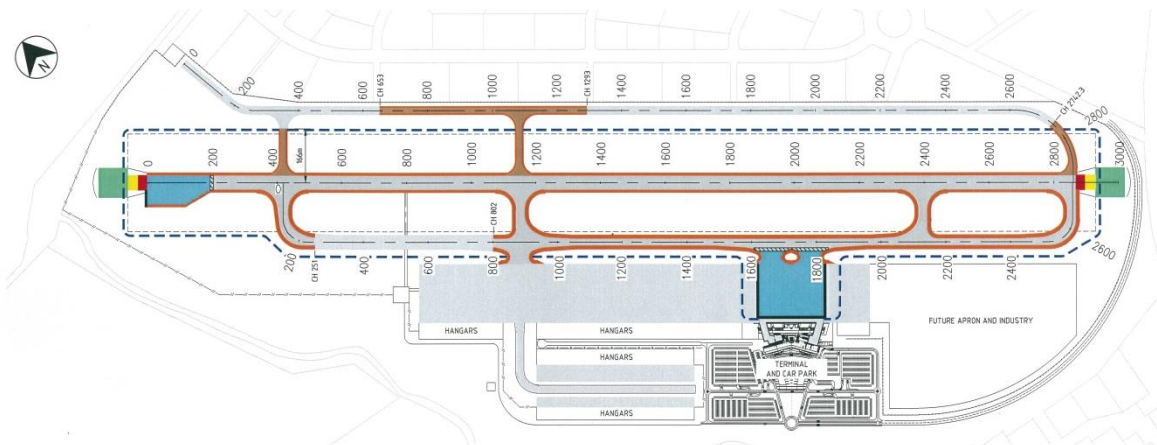
## 2. Project Outline

Figure 1 shows an overall plan and an aerial photograph of the completed pavement works at the BWWA site. The turning node is located at the Northern end of the runway and the apron is located on the Western side of the runway in front of the terminal and carpark. While not shown on the site plan, the private hangar pavement is located outside the boundary of the airport on the Eastern side of the runway which can be seen in the aerial photograph.

The private hangar pavement was constructed in the period May – July 2014 and served as a construction trial area to prove the intended geopolymer design mix and the pavement placement method. The pavement construction trials consisted of 10 individual pours of 5 m wide x 50 metres long that were placed by the paving contractor using a Gomaco slip form road paver.

In the 6 month period prior to pavement construction, Wagners had developed a geopolymer concrete design mix deemed suitable from laboratory trials and small scale pavement works around the BWWA site. The concrete materials specification written by independently commissioned ACG consulting engineers required:

- 4.8 MPa average flexural strength at 28 days of age, AS 1012.11 (1)
- 450 micro-strain maximum drying shrinkage at 28 days of age, AS 1012.13 (2)



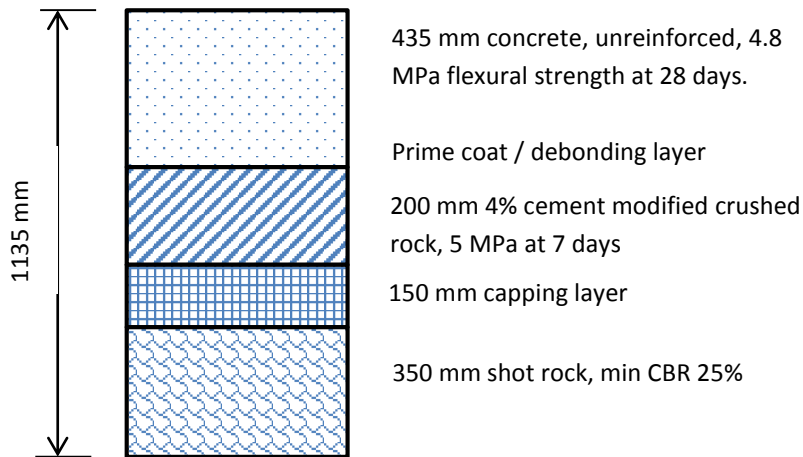
(pavement plan - excerpt from ACG Engineers drawings)



**Figure 1. Site plan and aerial photograph – BWWA.**

Following a successful trial phase, the geopolymer concrete mix and pavement construction method was approved by the engineers. Construction of the turning node pavements was undertaken during August and September 2014 and the apron pavements were constructed during October and early November 2014. BWWA was opened for its first commercial flight on 17 November 2014.

The pavement design was undertaken by ACG Engineers and is shown in Figure 2.



(pavement design by ACG Engineers)

**Figure 2. High Strength Concrete Pavement Design Cross Section.**

### 3. Geopolymer Concrete Mix

The proprietary geopolymer concrete mix used in this project follows approximately 10 years of work by Wagners developing a commercial product that is produced and handled in a similar manner to conventional concrete. The project mix was developed for the BWWA heavy duty pavements to suit placement with a slip form paving machine. Key criteria of the mix included:

- Workability, slump and slump retention suitable for transport in tippers and slip form pavement construction.
- Achieve specified flexural strength of 4.8 MPa

The summary mix parameters were:

- Total alumino-silicate binder comprising GGBS + Fly ash, 415 kg/m<sup>3</sup>
- Water:binder ratio 0.41
- Nominal 40 mm maximum aggregate size, conforming with 28 mm to AS 2758.1 (3)
- Chemical activator, 37 kg/m<sup>3</sup> solids content
- Proprietary water reducing admixture

Flexural strength testing was conducted by the project site NATA laboratory in accordance with Australian Standards AS 1012.11 at a frequency of 4 different loads taken evenly across the production of one work shift, as per the engineer's specification. The results achieved from making fresh concrete beam specimens across the turning node and apron pavements are shown in Table 1.

**Table 1. Flexural tensile strength results (28 days).**

No. of Samples	502
Average flexural strength (MPa)	5.8
Standard Deviation	0.6

#### 4. Geopolymer Concrete Production and Supply

The geopolymer concrete was produced in a twin mobile wet mix batch plant established on the BWWA project site as shown in Figure 3. The standard concrete production plants shown have been modified to accommodate the chemical activators which are added to the mix as a solution. An assembly of tanks and pumps are incorporated into the plant that mix, hold and accurately dispense the activators into wet mix bowl using an automated batch system.

A maximum supply capacity of 120 m<sup>3</sup>/hr was required to provide a continuous feed of concrete to the slip form paving machine which is shown in Figure 4. This requirement was successfully achieved using the plant configuration and several tipper trucks for delivery. An advantage of wet mix production is that concrete agitator trucks are not required for short transit times. The use of tippers allowed a significantly improved discharge rate at the paver face.



Figure 3. Geopolymer concrete twin batch plant.



Figure 4. Geopolymer concrete delivery to slip form paver.

#### 5. Geopolymer Concrete Pavement Construction

Aircraft pavement construction in Australia is normally undertaken by placing and compacting the concrete into and against steel side forms using a combination of internal mechanical vibration and vibrating beams. This method for the placement of deep lift heavy duty pavements has evolved from construction experience with Portland cement based concrete. The use of slip form paver machines as used in thinner concrete road bases have generally not been used in airport pavement construction due to concerns regarding incomplete compaction for thicker pavement bases.

Using geopolymer concrete in a series of successful trials at the hangar area demonstrated that a very high level of compaction could be achieved with a slip form paver machine. Steel side forms were chosen over the option of unformed extrusion to ensure the 435 mm thick pavements could be fully compacted at the sides without any loss in surface flatness. Slip form construction was adopted at



BWVA due to its efficiency and increased production rate compared to using a vibrating beam. It is estimated that a 30% reduction in the pavement construction program was achieved on this project compared with the traditional process.

The characteristic rheology and internal cohesion of the proprietary geopolymer mix at the specified slump allowed it to extrude considerably better than conventional concrete. This allowed for very efficient placement resulting in the noted speed gains. The level of admixtures and activators in the mix were able to be customised for the differing weather conditions and length of transit time across the project site. Winter to Summer (2°C minimum - 40°C Maximum, 5 minutes - 20 minutes transit time).

The proficiency of compaction using the slip form paving machine was validated by comparing in situ density test results with fresh concrete density results, (Table 2). In situ density was undertaken by using both the Nuclear density method (NDM) to AS 1289.5.8.1 (4) and in situ core density testing to AS 1012.14 (5) and AS 1012.12 (6). A density core specimen is shown in Figure 5.

**Table 2. Density measurements.**

	All areas	Turning node area – In situ testing				Apron area – In situ testing			
	Cast beams and cylinders	Core method middle	Core method top	Core method bottom	NDM method	Core method middle	Core method top	Core method bottom	NDM method
Max	2.540	2.500	2.540	2.510	2.511	2.490	2.490	2.590	2.520
Average	2.400	2.460	2.460	2.470	2.427	2.440	2.460	2.470	2.440
Min	2.280	2.420	2.410	2.410	2.312	2.400	2.430	2.380	2.370
No. Samples	1038	57	57	55	764	72	22	22	364
Standard Deviation	0.040	0.016	0.022	0.022	0.029	0.018	0.015	0.038	0.023



In situ density test specimen by coring method. Samples were cut into 3 sections – top, middle and bottom to detect compaction proficiency with depth of pavement, Table 2.

**Figure 5. Test core specimen.**

The geopolymer concrete required particular attention to curing and pre-curing evaporation control when placing exposed slab surfaces. It displayed very low bleed characteristics and the surface would rapidly dry out without intervening to maintain a moist sheen on the surface. From the supplier’s previous development work it was well understood that drying of this geopolymer concrete surface prior to initial set and the application of curing would render the extreme surface prone to wearing with time.

During trials on the hangar pavement area, a novel evaporation control and curing methodology was developed and adopted for the geopolymer concrete that well suited the slip form placement method. A new type of alkaline anti-evaporation spray was developed that reduced the evaporation rate while maintaining the alkalinity of the fresh geopolymer concrete surface that can be depleted through the application of traditional products. Curing consisted of applying a water based hydro carbon resin

curing compound, followed by covering with a geotextile to limit any thermal shock brought about by the difference of daytime and night time temperatures, Figure 6.



**Figure 6. Curing and side forms with dowels.**

Jointing design of the pavements followed conventional rules based on Portland cement concrete. In the direction of paving, joints were saw cut at 5 metres centres with isolation joints provided every 70 metres. Early age saw cutting was carried out as soon as possible, generally 1 to 5 hours after placement depending on the ambient temperatures as shown in Figure 7. Dowels were located between paving lanes as shown in Figure 6.

The geopolymer concrete’s lower shrinkage properties compared with conventional concrete would indicate that joint spacing could be increased compared with conventional concrete. However, this option was not pursued in order to maintain a low risk for this application of an innovative material. The supplier’s test data on this geopolymer concrete indicated an average 56 day drying shrinkage of 350 microstrain, tested to AS 1012.13 (2). A significant benefit and cost saving on future work would be to increase the joint spacing based on the higher flexural strength and lower shrinkage properties of this geopolymer concrete.



Fine crack in saw cut joint



saw suspended on bridge to allow earlier joint formation

**Figure 7. Early age saw cutting.**





**Figure 8. Operational BWWA.**

## 6. Commercialisation of Geopolymer Concrete

The pavements project at BWWA outlined in this paper is believed to be the largest commercial application of modern geopolymer concrete (defined by the authors as post-1970) in the world. Some 25,000 m<sup>3</sup> of aircraft pavement grade concrete was supplied and constructed over a 3.5 month period.

In addition to the pavements, a further 15,000 m<sup>3</sup> of geopolymer concrete was used throughout the BWWA project in a variety of applications including:

- Entry bridge to the airport, (Figure 9).
- Extruded kerb and road barriers, (Figure 9).
- Precast culverts.
- Site cast tilt panels for the terminal building.
- Footings, piles, pads and the tunnel slab for the terminal building.
- Footings, pads and site cast tilt panels for establishment of quarrying and concrete plants.
- Pavements for median strips and associated road works (some coloured).
- Sewer tanks.



**Figure 9. Other Geopolymer Concrete Works at BWWA.**



While alkali activated slag concrete has a history dating back to the 1930's in Eastern Europe (7), geopolymer concrete is still deemed a relatively new technology in modern concrete construction. The successful and rapid construction of the BWWA project serves as an excellent demonstration that geopolymer concrete is a viable alternative to Portland cement based concrete. Contractors, developers, specifiers and approval authorities can be confident that geopolymer concrete can be designed, produced and constructed within accepted quality control parameters at the commercial scale. However there exist a number of challenges to parties wishing to include geopolymer concrete in projects:

- No Australian or international standard for either manufacture or design
- Cost disadvantages due to lack of economies of scale
- Availability from suppliers
- Lack of older geopolymer structures in Australia to confirm long term durability.

The developers of the geopolymer concrete discussed here have made progress in overcoming these barriers as evidenced by the successful delivery of BWWA as well as a wide range of previous geopolymer concrete works, both commercial and internal projects with an R&D focus. This substantial body of work which includes results from independent durability studies by RMIT is reported by Glasby et al (8). A very significant previous project is the Global Change Institute (GCI) building in Brisbane on the University of Queensland campus that is reported by Bligh and Glasby (9). It is claimed to be a world first application of modern geopolymer concrete suspended floor beams in a multi-storey building.

It remains the case however that until significantly more progress is made on removing the barriers, new geopolymer concrete projects at the commercial scale will remain the domain of highly motivated parties that are willing to accept a price premium and 3<sup>rd</sup> party engineering certification of suppliers' data. One very positive step that the author is aware of is the writing of a Handbook on geopolymer concrete under a CRC grant that may lead to an Australian standard.

A key driver for the use of geopolymer concrete in Australia and elsewhere has been the environmental benefits of a concrete that utilises a large component of recycled material (slag and / or flyash) which completely replaces carbon intensive Portland cement (10). By using a figure of 80% reduced CO<sub>2</sub> emission compared to Portland cement, the binder content in this geopolymer concrete compared to a conventional 75% GP / 25% fly ash blended cement in an equivalent normal concrete, saved some 8,640 tonnes of CO<sub>2</sub> emissions in this project alone.

Another strong driver for geopolymer concrete is the performance and durability improvements that are possible due to the different chemistry of the binder. In this project the high flexural tensile strength coupled with low shrinkage of the particular proprietary geopolymer concrete used made it an ideal pavement concrete. In other projects, particular durability properties of acid, sulfate and chloride ingress resistance will offer high value to applications including sewer systems, marine structures and underground works through sulfate soils / ground waters. A cautionary note should be heeded that the term 'geopolymer' can apply to a wide range of alumino-silicate activated materials and their performance will vary depending on a range of factors, including:

- Source of alumino-silicate powder – type, reactivity, quality, etc.
- Alkaline activator chemicals
- Curing regime – ambient vs elevated temperature
- Total water and water:binder ratio for geopolymer concrete

Quality control during production and placement are extremely important in producing high quality geopolymer concrete, even more so than is the case for conventional concrete. Purpose made water reducing admixtures were a vital component in this proprietary geopolymer concrete having the necessary workability and slump retention at low water contents.

## **7. Conclusion**

The successful privately funded BWWA, Australia's first greenfield public airport in 48 years, is built on some 40,000 m<sup>3</sup> of geopolymer concrete making it the largest application of this new class of concrete in the world. This paper has reported on the heavy duty geopolymer concrete pavements that comprise the turning node, apron and taxiways. Production was undertaken using commercial scale concrete batch plants that delivered a continuous supply to a slip form paving machine and returned an excellent production rate. The proprietary geopolymer concrete proved an ideal material for the

construction method due to its high flexural tensile strength, low shrinkage and workability characteristics.

A comprehensive trial program leading up to the works ensured a suitable mix was developed that could be placed with a slip form paving machine. A new alkali anti-evaporation spray was developed that protected the geopolymer concrete surface from drying out prior to curing.

This successful application of geopolymer concrete at the full commercial scale should support future uptake of a truly novel and environmentally responsible technology.

## **8. References**

1. AS 1012.11-2000, "Methods of testing concrete, Method 11 – Determination of the modulus of rupture", Standards Australia, Sydney.
2. AS 1012.13-1992, "Methods of testing concrete, Method 13 – Determination of the drying shrinkage of concrete for samples prepared in the field or in the laboratory", Standards Australia, Sydney.
3. AS 2758.1-2009, "Part 1 Concrete aggregates", Standards Australia, Sydney.
4. AS 1289.5.8.1-2007, "Method 5.8.1: Soil compaction and density tests – Determination of field density and field moisture content of a soil using a nuclear surface moisture – Density gauge – Direct transmission mode", Standards Australia, Sydney.
5. AS 1012.14-1991, "Method 14: Method for securing and testing cores from hardened concrete for compressive strength", Standards Australia, Sydney.
6. AS 1012.12.1-1998, "Method 12.1: Determination of mass per unit volume of hardened concrete – Rapid measuring method", Standards Australia, Sydney.
7. Roy, D.M., 1999, "Alkali-activated cements -Opportunities and challenges", Cement and Concrete Research vol.29, pp.249–254.
8. Glasby, T., Day, J., Kemp, M. and Aldred, J., 2013, "Earth Friendly Concrete – A sustainable option for tunnels requiring high durability", Proceedings 1<sup>st</sup> Arabian Tunnelling Conference, Dubai, UAE.
9. Bligh, R. and Glasby, T., 2013, "Development of Geopolymer Precast Floor panels for the Global Change Institute at University of Queensland", Proceedings Concrete Institute of Australia Biennial Conference, Concrete 2013 – Understanding Concrete, Gold Coast, Australia.
10. Davidovits, J., 2014, "Geopolymer cement for mitigation of global warming", Geopolymer Institute website, <<http://www.geopolymer.org/applications/global-warming>>, accessed 12-02-2015.

# On Fly Ash Based Geopolymer Concrete and its Behaviour at Elevated Temperature

Tian Sing Ng, Stephen J. Foster and Samantha Milojevic

School of Civil and Environmental Engineering, University of New South Wales, Sydney, Australia

**Abstract:** This paper presents the results of an experimental investigation of the behaviour of two fly ash based geopolymer concretes following exposure to high temperatures up to 1000 °C. Two geopolymer concretes were manufactured using the same mixture proportion but the curing process was manipulated in order to achieve the target nominal compressive strengths of 20 MPa and 50 MPa. Residual compressive strength, static elastic modulus and density change were carried out for both mixes. Tests were also conducted for the 50 MPa high strength geopolymer concrete at hot state using a specially designed furnace–loading frame assembly. The hot-state deformation modulus, free thermal strains (FTS) and load induced thermal strains (LITS) were measured. In general, the compressive strength and elastic modulus decreased with increasing temperature. The FTS and LITS are found to be very different to that of Portland cement concrete where geopolymer concrete undergoes both expansion and contraction at different stages of heating. Further, stressed geopolymer concrete experienced an abrupt loss of stiffness and exhibited significant visco-plastic and deformation behaviours beyond 800 °C.

**Keywords:** Geopolymer; Elevated Temperatures; Fire; Stress-Strain; Hot strength; Residual strength; Modulus of Elasticity

## 1. Introduction

Over the last two decades, geopolymer concretes have emerged as novel engineering materials with the potential to form a substantial element of an environmentally sustainable construction and building products industry [1-2]. Geopolymer is a material resulting from the reaction of a material that is rich in silica and alumina with alkaline solution. Industrial waste materials, such as fly ash and blast furnace slag, are commonly used as the source of aluminosilicate to manufacture geopolymer concrete due to the low cost and vast availability of these materials.

Most of the research and investigation of fly ash based geopolymer concretes deal with their properties and behaviour at ambient temperature. Fire can cause substantial damage to concrete structures and the consequences could be enormous. At stake are not only lives but also can lead to significant financial losses. To evaluate the performance of fly ash based geopolymer concretes when exposed to a fire it is critical to know the effect of various temperature levels on the extent of deterioration of the concrete and the ability of the concrete to carry loads when exposed to a fire. Limited publications in this field of study are available in the literature. Most of the studies investigated the residual properties after cooling to normal room temperature [3-9] but the findings to-date is still not conclusive with some investigators observed strength losses and gains, respectively, on the concrete after exposed to elevated temperature. Little studies have also been carried out on the hot stressed and unstressed strength properties of fly ash based geopolymer concretes.

This study investigated the hot stressed and unstressed physical and mechanical properties of the fly ash based geopolymer concrete up to 1000 °C. The hot state deformation modulus, FTS and LITS of the concrete are reported herein. The residual strengths of the concrete after exposing to temperature up to 1000 °C were also investigated.

## 2. Experimental program

Fly ash based geopolymer concretes with target compressive strengths of 20 MPa and 50 MPa were studied initially. The authors have adopted two types of curing regime to achieve the two desired strengths of the geopolymer concrete, without changing the mixture proportions and initial chemical compositions. This manufacturing process is similar to that of undertaken by Pan et al. [3] and Sarker et al. [8]. Subsequently, however, it was found that the lower strength grade of geopolymer concrete obtained through this process is due to incomplete polymerisation of the concrete and, hence, the strength was not fully developed. This practice is not recommended in order to maximise the best performance of the concrete. Following this discovery, only the 50 MPa grade concrete was investigated.

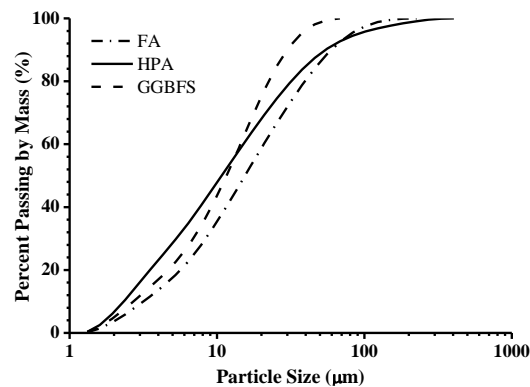
## 2.1 Source materials and mix design

Aluminosilicate source materials used in this study are ASTM Class F fly ash (FA) from Eraring power station in New South Wales, Australia and ASTM Class F Kaolite high performance ash (HPA) from Callide power station in Queensland, Australia. The two sources of fly ash were blended based on the findings of Ng and Foster [12] to achieve the optimal characteristic. Small amount of ground blast furnace slag (GGBFS) supplied by the then Blue Circle Southern Cement Australia was also used. The addition of slag is found to promote faster hardening process and give early structural strength based on the authors' preliminary work and the study by Li and Liu [13]. Without the addition of slag, Hardjito and Rangan [14] observed that their fly ash based geopolymer concrete did not harden for at least 24 hours when the room temperature was less than 30°C. Further, most commercial geopolymer concrete also includes the use of slag. The chemical compositions of the FA, HPA and GGBFS are presented in Table 1 while their grading curves are given in Figure 2.

**Table 1. Fly ashes and slag chemical composition (% by mass).**

Element	SiO <sub>2</sub>	Al <sub>2</sub> O <sub>3</sub>	Fe <sub>2</sub> O <sub>3</sub>	CaO	K <sub>2</sub> O	Na <sub>2</sub> O	MgO	MnO	P <sub>2</sub> O <sub>5</sub>	TiO <sub>2</sub>	SO <sub>3</sub>	LOI*
<b>FA</b>	66.56	22.47	3.54	1.64	1.75	0.58	0.65	0.06	0.11	0.88	0.1	1.66
<b>HPA</b>	45.14	33.32	11.99	4.13	0.13	0.07	1.37	0.23	0.56	2.19	0.48	0.41
<b>GGBFS</b>	31.52	12.22	1.14	44.53	0.33	0.21	4.62	0.36	0.02	1.03	3.24	0.79

\*LOI – Loss on ignition



**Figure 2. Particle size distributions for FA, HPA and GGBFS.**

The alkaline activator was comprised of a mixture of 12 molar sodium hydroxide (NaOH) solution and sodium silicate solution. The sodium silicate solution was obtained from PQ Australia, under the commercial name of D<sup>TM</sup> with Na<sub>2</sub>O = 14.7 %; SiO<sub>2</sub> = 29.4%; and H<sub>2</sub>O = 55.9%, by mass of chemical components. The ratio of NaOH solution to the sodium silicate solution was 1:2.5 by mass. The activator was blended and stored for at least 24 hours prior to the manufacturing of the geopolymer concrete in order to allow equilibration.

Kiln dried Sydney sand with maximum particle size of 600 µm and 10 mm nominal size air-dried basalt aggregate were used as the fine and coarse aggregates in the geopolymer concrete, respectively. Table 2 presents the details of the fly ash based geopolymer concrete mix used in this study.

**Table 2. Fly ash based geopolymer concrete mix data (% by mass).**

Material	FA	HPA	GGBFS	Alkaline Activator	Added water	Coarse Aggregate	Fine Aggregate
<b>Percentage</b>	8.2	2.2	1.8	6.7	2.7	48.3	30

## 2.2 Mixing and specimen preparation

The geopolymer concrete was produced using a horizontal pan type mixer. All the constituents were batched by an electronic balance. FA, HPA, fine aggregate and coarse aggregate were mixed for about 5 minutes. Following, the alkaline activator and water were added gradually and the product was mixed for

another fifteen minutes, making the total mixing time around twenty minutes. The reason for selecting a longer mixing time is that the rate of leaching and transportation of Al and Si atoms in the geopolymer mixture could be significantly increased, thus enhancing the strength of the geopolymer concrete [15]. Lastly, GGBFS was introduced gradually and mixing continued for a further 5 minutes. The GGBFS was added during the wet mixing rather than dry mixing in order to prevent rapid hardening of the mixture and to allow for a sufficient workable time for casting of the specimens.

The fresh geopolymer concrete was then cast as cylinder specimens of 100 mm diameter by 200 mm high. The geopolymer concrete was placed in the cylinder moulds in two layers and compacted on the vibration table. During the casting, two cylinders of 100 mm diameter and 200 mm height were cast with geopolymer mortar. The mortar was obtained by separating the coarse aggregate from the fresh geopolymer concrete using a 2.36 mm nominal size sieve.

After casting, all cylinder moulds were sealed with the cylinder lids to prevent excessive loss of moisture and were stored in a controlled environmental room at 50% relative humidity (RH) and 23°C for a period of 24 hours to allow the geopolymer concrete and mortar to be fully set, after which they were demoulded.

### **2.3 Curing regime**

Two types of curing regimes were initially adopted in order to achieve two desired strengths as discussed in Section 2 above. For the first curing method specimens labeled as 'GPC-AC' were continued to store in the controlled environmental room at 50% RH and 23 °C for a consecutive of seven days so as to achieve a nominal strength of 20 MPa. For the second method specimens labeled as 'GPC-HC' were cured under water in a hot water chamber at 80°C for seven days after they were demoulded in order to obtain a 50 MPa nominal strength.

### **2.4 Reference strength tests**

The stress-strain relationships for the two geopolymer concrete mixes were determined at ambient temperature after 28 days of casting and were used as the baseline data in this study.

### **2.5 Residual property tests after exposing to elevated temperatures**

An electric muffle furnace that is capable of heating up to 1200°C was used to heat the specimens to their desired temperatures. Five target temperature points were selected starting at 200 °C to 1000 °C, increments of 200 °C. Three cylinders were heated to the target temperature at a rate of 5 °C per minute from room temperature and allowed to soak at the target temperature for three hours to ensure uniform temperature distribution inside the cylinders. At the end of the soaking period, the furnace was turned off allowing the cylinders to naturally cool to room temperature. The cylinders were then tested to obtain the residual stress-strain relationship.

### **2.6 Hot state tests**

Two types of tests were undertaken: (i) hot state deformation modulus; and (ii) free and load induced axial thermal strains. The hot state tests were carried out in a purpose-built furnace-loading frame arrangement that allows simultaneous loading and heating of the specimens. The apparatus consisted of a vertical single zone split type furnace, and can be used to heat up to a maximum temperature of 1200 °C, and a stiff 1000 kN Instron servo-hydraulic controlled frame (Figure 3). A high temperature tolerant extensometer was used to measure the strains of the concrete.

#### **2.6.1 Hot state deformation modulus**

Five temperature points were selected for the measurements to be undertaken; 200 °C, 400 °C, 600 °C, 800 °C and 1000 °C. The cylinders were heated in the furnace-testing frame arrangement at a rate of 5 °C per minute to the target temperature and held at that temperature for 2 hours. Before the starting of heating, a small preload of 1 kN was applied during the heating to provide proper seating of the specimen and to engage the extensometer with the specimen. After the heat soaking period of 2 hours, which allowed uniform temperature distribution in the specimen, the cylinder was then tested for its deformation modulus while they were hot. The adopted measuring method was similar to that of prescribed by AS

1012.17 [16] with the specimens loaded to 40% of their residual compressive strengths that have been determined from Section 2.5 above.



(a) Arrangement of furnace with extensometer.



(b) Furnace and loading furnace during heating (furnace door was opened for photographic purpose only)

**Figure 3. Hot State Test Arrangement.**

### **2.6.2 Free thermal expansion (FTS) and load induced thermal strains (LITS)**

The cylinders were loaded at room temperature to one of the three initial loading levels: 0%, 5% and 10% of the room temperature uniaxial compressive strength. These loads were then maintained for the remainder of the test up to 800 °C.

## **3. Results and discussion**

### **3.1 Residual properties after exposing to elevated temperatures**

#### **3.1.1 Mass loss, volume change and density change**

Mass loss and volume change of the geopolymer concrete cylinders after exposure to the heating regime are calculated as a function of the concrete density. The density change predominantly takes place due to: loss of water reducing the mass of the specimen, swelling of high silicate phases at high temperatures resulting in expanding the volume of the specimen [11], increase in porosity caused by densification of the geopolymer gel during sintering [17] and bulk cracking caused by thermal incompatibility within geopolymer structures and fine and coarse aggregates [5, 6, 17]. Past thermogravimetric analyses [5, 6, 18] suggested that the vast majority of the mass loss taking place below 250 °C and is attributed to free or evaporable water loss. The mass loss between 200 °C and 300 °C may also likely due to the loss of water liberated from further geopolymerisation process [9]. The rate of mass loss is stabilised between 250 °C and 700 °C and after 700 °C, there is little change in the mass [5, 6].

Figure 4(a) shows the density curves for the mixes considered in this study as a function of exposure temperature. GPC-HC specimens show a steady and almost linear reduction in density over the temperature range. GPC-AC specimens, although having a lower strength value, are denser than GPC-HC specimens. When heated to 200 °C, a rapid reduction in the density is seen for GPC-AC specimens. As both GPC-AC and GPC-HC were made using the same mixture proportions, the difference is a direct result of the geopolymerisation or curing process. GPC-HC specimens were cured in 80 °C environment and it is therefore likely that (i) more free water was released during the curing process; (ii) more geopolymerisation occurred and the resulting water was expelled. The densities for both GPC-AC and GPC-HC specimens match at about 600 °C to 800 °C.

### 3.1.2 Physical colour change

The fly ash based geopolymer concrete experienced a range of colour changes through exposure to high temperature (Figure 4(b)). At 23 °C ambient temperature the GPC-AC specimen is dark grey in colour with traces of efflorescence (white salt deposits on or near the surface). The specimen colour progressively lightens through to 400 °C. The GPC-HC specimen is light grey at 23 °C, similar to that of GPC-AC specimen after exposed to 200 °C. After heating to 600 °C, there is a distinct change in colour in both mixes where the specimens become orange. Colour change can often signify a chemical reaction associated with a phase change, glass transition or melting point of a particular compound within the concrete. The colour develops further to a pinkish hue after heating to 1000 °C identifying continuation of the reaction. The colour changes of geopolymer concrete have been observed previously [8, 17] and are attributed to the iron oxidation in the fly ash [17]. In addition, during the experiment, when the cylinders were lightly tapped with a metal rod, the pitch of the note went up as the exposed temperature of the specimen increased; indicating the increase in the specimens porosity and brittleness.

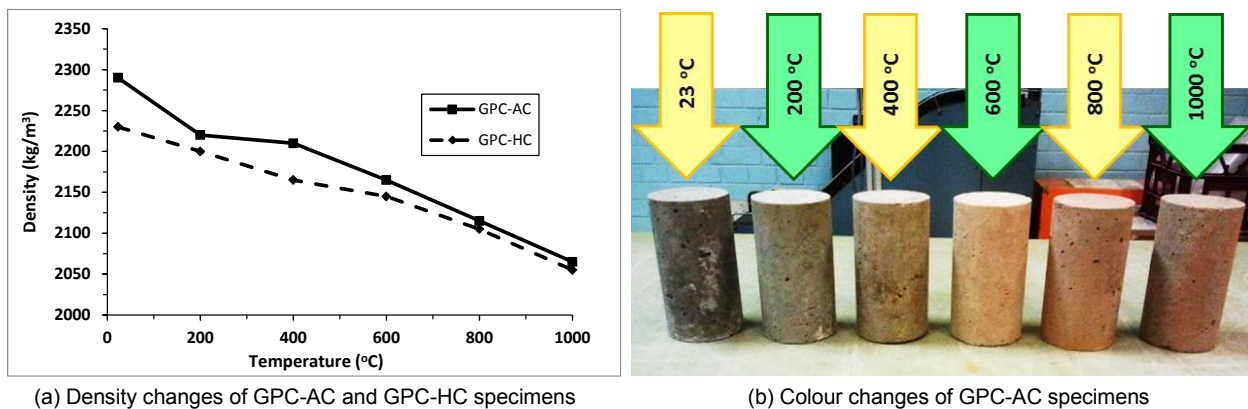


Figure 4. (a) Density; and (b) physical colour changes of specimens after heating.

### 3.1.3 Residual stress-strain relationship

Figure 5 shows the stress-strain relationships of GPC-AC and GPC-HC mixes after exposure to high temperatures while Figures 6(a) presents the residual compressive strengths for the mixes.

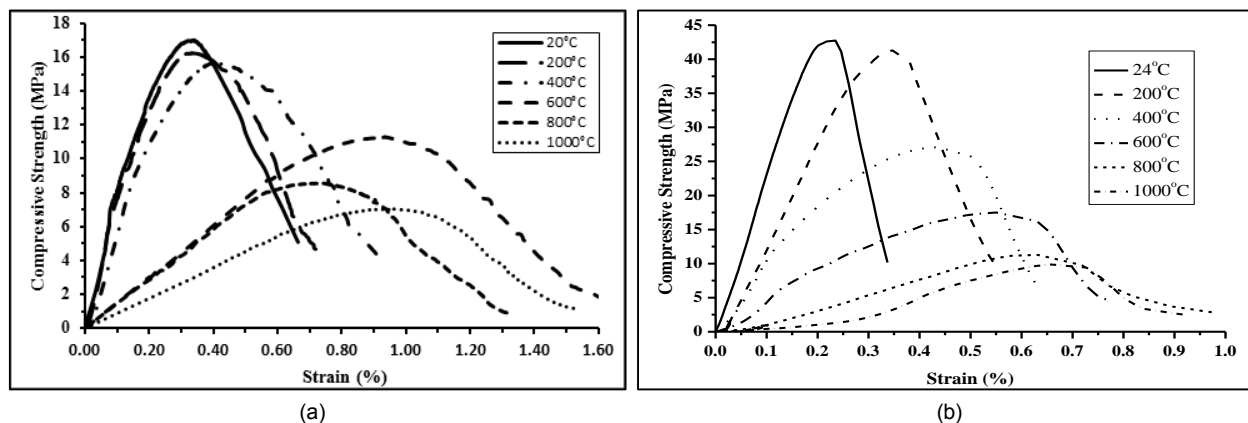
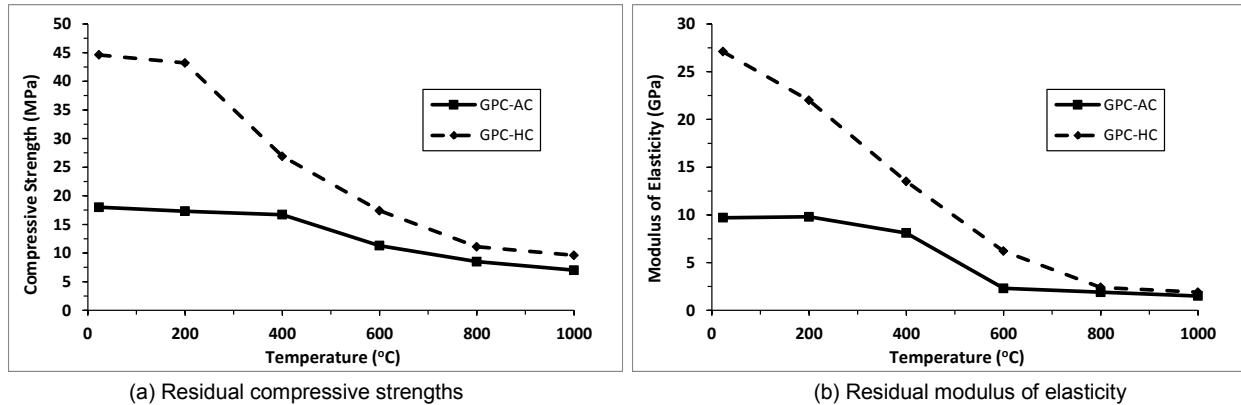


Figure 5. Residual compressive stress-strain curves for mixes (a) GPC-AC; and (b) GPC-AC.

Overall, the residual compressive strengths for both GPC-AC and GPC-HC mixes reduced with increasing temperature indicate the deterioration of geopolymer matrix during heating. GPC-AC specimens hold their initial strength steadily up to 400 °C while GPC-HC specimens only hold their initial strength up to 200 °C. The residual strengths for GPC-HC specimens decreased sharply with the increasing temperature beyond 200 °C, reaching 40% of the original value at about 600 °C. After exposure to 1000 °C, GPC-HC specimens have a compressive strength of approximately 20% of the initial strength. The strength

reduction for GPC-AC specimens with increasing temperature is relatively less than that of GPC-HC specimens. At 600 °C, GPC-AC specimens have a compressive strength of approximately 70% of the initial strength, further, GPC-AC specimens retained 50% of its original value at 1000 °C.

The compressive strengths for GPC-AC and GPC-HC specimens began to converge between 600 °C and 800 °C. Pan et al. [3] and Sarker et al. [8] also observed the strength convergence at about 650 °C to 800 °C for their lower and higher strength geopolymer concretes manufactured using the same mixture proportion but the curing process was manipulated in order to achieve different compressive strengths.

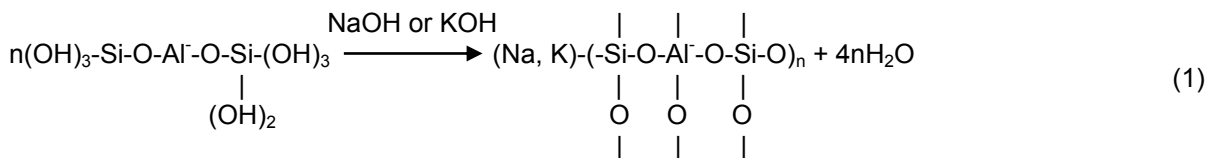


**Figure 6. Residual strength properties of the geopolymer concrete mixes.**

Pan et al. [3] suggested that two opposing processes occur in geopolymer concretes when heated: (i) further geopolymerisation and/or sintering at elevated temperatures leading to strength gain; (ii) the damage to the concrete due to thermal incompatibility between the geopolymer paste and the aggregates. Shrinkage of geopolymer paste was found to begin at 200 °C [5, 9] that would result in a steady deterioration from this point. Sintering of unreacted fly ash particles is unlikely to occur before the temperature reaches 800 °C as fly ash, which has been fired at high temperature up to 1600 °C in coal power station, only begin to sinter from 900 °C [20] but most research suggest the sintering temperature of fly ash is between 1100 °C to 1300 °C [21].

For GPC-AC specimens, it is likely that further geopolymerisation occurs with increasing temperature up to at least 600 °C. This is also supported by the observation from the density change studies, which indicated that the major amount of the density reduction for GPC-AC specimens, i.e. mass loss, occurred before 600 °C. As both the densities and residual strengths for GPC-AC and GPC-HC specimens have converged at about 600 °C, it is likely that the geopolymerisation process has completed for GPC-AC specimens or the remaining geopolymerisation rate for both GPC-AC and GPC-HC specimens is similar and the strength reduction is mainly due to the thermal incompatibility between the geopolymer paste and the aggregates, which causes internal damage and cracking within the concrete.

The schematic formulation of geopolymer can be shown in Equation (2) [1]. Geopolymerisation is a condensation polymerisation process and geopolymer is formed and hardened by loss of water. Higher temperature will provide for a more complete drying of the geopolymer. The more water is removed from the geopolymer bond, the higher will be its strength, due to more complete chemical reaction or polymerisation. The amount of water remaining in the geopolymer bond is governed by the temperature to which it has been exposed and its exposure duration.



From visual observation, GPC-AC specimens also showed trace of efflorescence but not on GPC-HC specimens as discussed in Section 3.1.2. The efflorescence product is found to be sodium carbonate heptahydrate (Na<sub>2</sub>CO<sub>3</sub>·7H<sub>2</sub>O) [22], which is likely due to the reaction of the unconsumed alkaline activator



with the carbon dioxide gases in the atmosphere. Zhang et al. [22] noted that fly ash based geopolymers synthesised at high temperature exhibit lower efflorescence than those synthesized at low temperature. This highlights that the lower strength grade of GPC-AC specimens is due to incomplete geopolymerisation and, hence, the strength was not fully developed. To maximize the full potential of the fly ash based geopolymer concrete and based on the above findings, heat curing is therefore recommended and a proper mix design is also required to increase the geopolymerisation process and reduce the unconsumed alkaline activator in the geopolymer.

The residual elastic moduli following exposure to high temperatures are plotted in Figure 6(b) versus exposure temperature. In the same manner as compressive strength, no appreciable change in modulus of elasticity for GPC-AC specimens was seen until 400 °C; thereafter, it dropped considerably to 20% of the original value at 600°C. For GPC-HC specimens, the modulus of elasticity reduced steadily up to 800 °C and thereafter it matched the modulus of elasticity of GPC-AC specimens.

### 3.2 Hot state deformation modulus

The hot state deformation moduli for GPC-HC specimens are presented in Figure 7 and are compared with the corresponding residual elastic moduli. The hot state elastic modulus shows a steady decline with increasing temperature. Both the hot deformation modulus and residual elastic modulus show no substantial difference up to 400 °C. However, the residual modulus was found to be lower than the hot state modulus for temperatures higher than 400 °C; this may be caused by micro cracking, which occurred during the cooling phase.

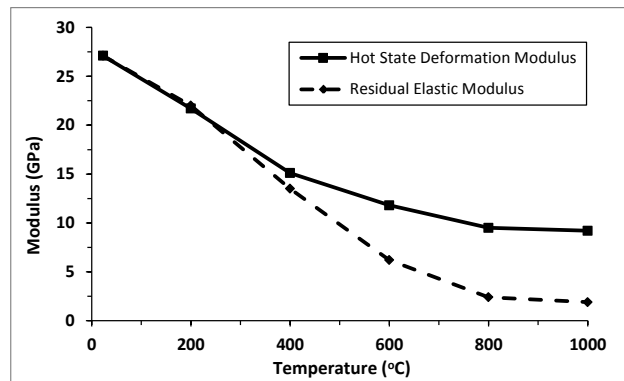


Figure 7. Hot state deformation modulus and residual elastic modulus for GPC-HC.

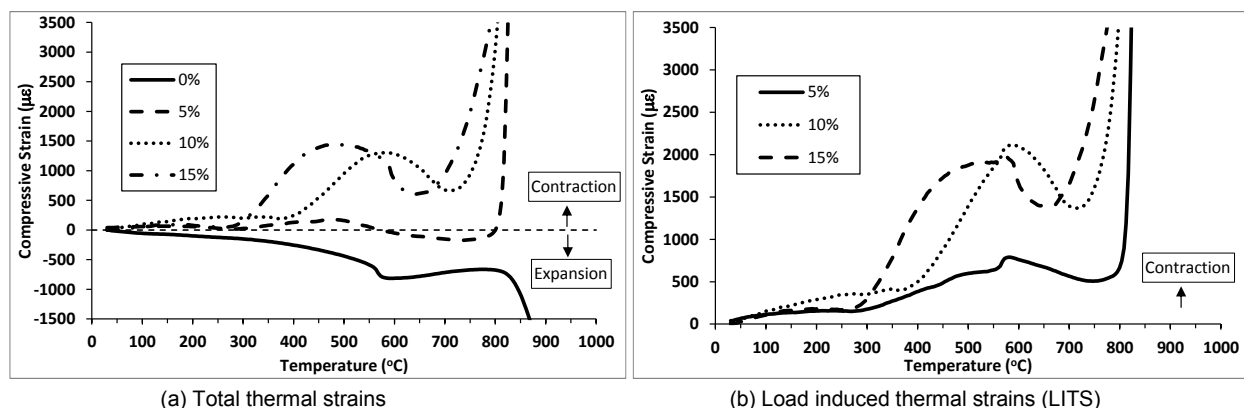
### 3.3 Free thermal expansion (FTS) and load induced thermal strains (LITS)

Figure 8(a) shows the evolution of axial thermal strains of GPC-HC cylinders when heated to 1000 °C under constant compressive load, plotted against the furnace temperature. The LITS is plotted in Figure 8(b). Positive strains indicate contraction; negative strains indicate expansion. Four loading levels were studied; 0%, 5%, 10% and 15% of the mean compressive strength obtained at ambient conditions. The results revealed very different behaviours for the different applied loads. Further, geopolymer concretes also exhibit non-linear and different thermal behaviour when compared to that of Portland cement concrete studied by Khoury [19] with both expansion and contraction occur when they are heated.

For no loading condition, the specimen expands freely by thermal expansion, which is the FTS component. A sharp expansion of the specimen occurred at about 560 °C to 570 °C and is likely due to the  $\alpha$ - $\beta$  phase change that occurs in the siliceous components in the mixes, mainly in the sand and the fly ash elements. At around 600 °C, the specimens appear to have contracted. Provis et al. [18] observed similar behaviour in the dilatometric study on geopolymer paste and suggested that densification attributed to a process resembling viscous sintering was commenced at this temperature. After heating to 800 °C, the specimens show a sharp and rapid expansion and this may be due to swelling of high silicate phases in the presence of alkalis above 800 °C or the specimens begin to melt.

When the specimens were heated while loaded, they initially shrunk progressively due to releasing of water from the specimen. Provis et al. [18] indicated that shrinkage occurs up to 250 °C as pore water is released

from the geopolymer gel and from 250 °C to 600 °C, shrinkage occurs gradually attributed to the loss of bound hydroxyls. Between 300 °C and 400 °C, the specimens were subjected to a rapid contraction. This contraction phase appears to be dependent on the applied load level. As the applied load increased, specimens contracted more rapidly and at a much lower temperatures. Pan and Sanjayan [9] observed the similar behaviour trend. While the actual reasoning may not be known, it is likely that the densification due to further geopolymerisation occurred and the geopolymer backbone or the polymer chain re-organised itself under the applied load. This remains as a hypothesis to be further researched. The specimens began to expand at about 570 °C, coincide with the  $\alpha$ - $\beta$  phase change that occurs in the siliceous components. Between 650 °C and 800 °C, the specimens experienced abrupt loss of stiffness and exhibited significant visco-plastic and deformation behaviours. Pan and Sanjayan [9] reported that the glass transition temperature for fly ash based geopolymer is 560 °C while Rickard et al. [11] and Provis et al. [18] argued that viscous flow of the aluminosilicate material causing sintering and subsequent densification and shrinking occur between 550 °C and 850 °C. Regardless, from structural engineering point of view, based on the observation from this study, the fly ash based geopolymer concrete, as a composite of geopolymer paste and aggregate, will deform excessively beyond 800 °C. Figures 9(a) and 9(b), respectively, show the deformed shapes of GPC-HC specimens subjected to 10% and 15% stress levels when heated to 800 °C. Physical tearing and rippling on the surface can be observed from Figure 9. The undulations and the exposed shapes of aggregates confirm that the aggregates were in solid state whilst the glass transitional geopolymer paste deformed and softened around them during the heating process.



**Figure 8. Thermal strains of GPC-HC under heating and constant compressive loading.**



(a) 10% stress level.



(b) 15% stress level

**Figure 9. GPC-HC specimens deformed during thermal strain test.**

#### 4. Conclusions

Experiments to evaluate the suitability for use in high temperature were conducted on two fly ash based geopolymer concrete mixes manufactured using the same mixture proportion but the curing process was

manipulated in order to achieve the target compressive strengths of 20 MPa and 50 MPa. The following conclusions were reached as a result of this study:

1. High strength geopolymer concrete demonstrates a steady loss in density when is heated up to 1000 °C. The reduction of density is likely due to loss of free or evaporable water, further geopolymerisation process occurred which caused additional water being expelled, densification of geopolymer gel that increased the overall concrete porosity, swelling of high silicate phases and internal damage and cracking caused by thermal incompatibility within the geopolymer structures and with the aggregates. The low strength geopolymer concrete, although is initially denser than that of high strength geopolymer concrete at ambient temperature, is subjected to drastically decrease in the density when is heated and its density converges with the density of the high strength geopolymer concrete at about 600 °C to 800 °C. This indicates that more geopolymerisation occurred and more water is released.
2. The fly ash based geopolymer concrete experiences a range of colour changes through exposure to high temperature, from grey to dark grey colour at ambient temperature to pinkish hue colour after heating to 1000 °C.
3. The compressive strength and modulus of elasticity of the high strength geopolymer concrete reduce after exposure to high temperatures but the low strength geopolymer concrete maintains its strength and modulus up to 400 °C before suffering strength and stiffness losses. Both strengths and moduli for the high and low strength geopolymer concretes converge at about 600 °C to 800 °C. The strength reduction and loss of stiffness indicate that the geopolymer concrete suffered considerable damage due to thermal incompatibility between the geopolymer paste and the aggregates. For the low strength geopolymer concrete, however, further geopolymerisation process occurs up to at least 400 °C, which supposedly leading to strength and stiffness gains, but the gains are compensated due to the thermal cracking.
4. The polymerisation process of the low strength geopolymer concrete that cured in the controlled environmental room at 50% RH and 23 °C for a consecutive of seven days is incomplete and, hence, resulting in the strength not fully developed. The unconsumed alkaline activator causes efflorescence on the concrete. To maximize the full potential of the fly ash based geopolymer concrete, a proper mix design and heat curing are required to increase the geopolymerisation process and reduce the unconsumed alkaline activator in the geopolymer.
5. The hot state deformation modulus of the high strength geopolymer concrete drops approximately linearly with increasing temperature.
6. The free and load induced thermal strains are found to be very different to that of Portland cement concrete, indicating that the geopolymer science is different to that of Portland cement concrete and the fundamental of Portland cement concrete cannot be used to explain the behaviour of geopolymer concrete.
7. Fly ash based geopolymer concrete, as a composite of geopolymer paste and aggregate, deforms excessively beyond 800 °C due to softening or melting of the geopolymer paste.

## 5. Acknowledgement

Financial support from the University of New South Wales Faculty of Engineering and Australian Defence Force Academy (ADFA) Research Collaboration Initiative Grant for carrying out this research project is gratefully acknowledged.

## 6. References

1. Duxson, P., Fernández-Jiménez, A., Provis, J.L., Lukey, G.C., Palomo, A., Van Deventer, J.S.J., "Geopolymer technology: The current state of the art". *Journal of Materials Science*, 42(9), pp 2917-2933.
2. Ng, T.S., Voo, Y.L., Foster, S.J., "Sustainability with Ultra-High Performance and Geopolymer Concrete Construction", in Fardis MN (ed.), *Innovative Materials and Techniques in Concrete Construction*, Springer, Dordrecht Heidelberg London New York, 2012, pp 81-100.

3. Pan, Z., Sanjayan, J. G., Rangan, B. V., "An investigation of the mechanisms for strength gain or loss of geopolymer mortar after exposure to elevated temperature", Journal of Material Sciences, 44, 2009, pp 1873-1880.
4. Kong, D. L. Y., Sanjayan, J. G., Sagoe-Crentsil, K., "Comparative performance of geopolymers made with metakaolin and fly ash after exposure to elevated temperatures", Cement and Concrete Research, 37, 2007, pp 1583–1589.
5. Kong, D. L. Y., Sanjayan, J. G., "Damage behavior of geopolymer composites exposed to elevated temperatures", Cement & Concrete Composites 30, 2008, pp 986–991.
6. Kong, D. L. Y., Sanjayan, J. G., "Effect of elevated temperatures on geopolymer paste, mortar and concrete", Cement and Concrete Research, 40, 2010, pp 334–339
7. Junaid, M. T., Khennane, A., Kayali, O., "Performance of fly ash based geopolymer concrete made using non-pelletized fly ash aggregates after exposure to high temperatures", Materials and Structures, 2014.
8. Sarker, P. K., Kelly, S., Yao, Z., "Effect of fire exposure on cracking, spalling and residual strength of fly ash geopolymer concrete", Materials and Design, 63, 2014, pp 584-592.
9. Pan, Z., Sanjayan, J. G., "Stress–strain behaviour and abrupt loss of stiffness of geopolymer at elevated temperatures", Cement & Concrete Composites, 32, 2010, pp 657–664
10. Junaid, M. T., Khennane, A., Kayali, O., Sadaoui, A., Picard, D., Fafard, M., "Aspects of the deformational behaviour of alkali activated fly ash concrete at elevated temperatures", Cement and Concrete Research, 60, 2014, pp 24-29.
11. Rickard, W.D.A., Temuujin, J., van Riessen, A., "Thermal analysis of geopolymer pastes synthesised from five fly ashes of variable composition", Journal of Non-Crystalline Solids, 358, 2012, pp 1830–1839.
12. Ng T.S., Foster S.J., "Development of a mix design methodology for high-performance geopolymer mortars", Structural Concrete, 14(2), 2013, pp 148 - 156.
13. Li, Z., Liu, S., "Influence of slag as additive on compressive strength of fly ash-based geopolymer", Journal of Materials in Civil Engineering, 19(6), pp 2-7.
14. Hardjito, D., Rangan, B.V., "Development and Properties of Low Calcium Fly Ash Based Geopolymer Concrete", Research Report GC 1, Curtin University of Technology, Perth, Australia, 2005.
15. Xu, H., "Geopolymerisation of Aluminosilicate Minerals", PhD Thesis, Department of Chemical Engineering, the University of Melbourne, Australia, 2002.
16. AS 1012.17, Methods of testing concrete - Determination of the static chord modulus of elasticity and Poisson's ratio of concrete specimens, Standards Association of Australia, 1997.
17. Rickard, W. D. A., Williams, R., Temuujin, J., van Riessen, A., "Assessing the suitability of three Australian fly ashes as an aluminosilicate source for geopolymers in high temperature applications", Materials Science and Engineering A, 528, 2011, pp 3390-3397.
18. Provis, J.L., Yong, C.Z., Duxson, P., van Deventer, J.S.J., 2009., "Correlating mechanical and thermal properties of sodium silicate-fly ash geopolymers", Colloids and Surfaces A: Engineering Aspects, 336, 2009, pp 57-63.
19. Khoury, G.A., "Effect of fire on concrete and structures", Progress in Structural Engineering and Materials, 2(4), 2008, pp 429-447.
20. Bijen, J., "Manufacturing process of artificial lightweight aggregates from fly ash," The International Journal of Cement Composites and Lightweight Concrete, 8(3), 1986, pp 191-199.
21. Kayali, O., "Flashag – New Lightweight Aggregate for High Strength and Durable Concrete", 2005 World Coal Ash, 11-15 April, 2005.
22. Zhang, Z., Provis, J. L., Reid, A., Wang, H., "Fly ash-based geopolymers: The relationship between composition, pore structure and efflorescence", Cement and Concrete Research, 64, 2014, pp 30-41.

# DEVELOPMENT OF SUGARCANE BAGASSE ASH BLENDED GEOPOLYMER FOR USE IN CONCRETE

Deepika S<sup>1</sup>, Madhuri G<sup>1</sup>, Bahurudeen A<sup>2</sup>, Manu Santhanam<sup>3</sup>  
<sup>1</sup>Graduate Student, Department of Civil Engineering, IIT Madras  
<sup>2</sup>Post Doctoral Fellow, Department of Civil Engineering, IIT Madras  
<sup>3</sup>Professor, Department of Civil Engineering, IIT Madras

**Abstract:** Development of alternative binders is imperative due to the severe impacts related to the production of ordinary Portland cement such as carbon dioxide emissions, rapid consumption rate of limited natural resources and high demand. Geopolymer concrete has emerged as a potential alternative material for a number of special applications. Sugarcane bagasse ash is obtained as a by-product from sugar industries in enormous quantities in major sugar producing countries and its disposal is problematic due to land constraints and environmental restrictions. Bagasse ash has reactive silica content (more than 70%) and can be blended with other industrial by-products such as fly ash and slag which are rich in alumina, silica and calcium sources to develop sustainable and high quality alkali activated slag concrete. The present study deals with the development of slag–bagasse ash as well as fly ash-slag based alkali activated binder. The influence of different parameters such as type and dosage of activators and curing methods on the compressive strength of the composite is discussed in the paper.

**Keywords:** Sugarcane Bagasse Ash, Alkali activation, Geopolymer, Curing

## 1. Introduction

In consideration of the serious impact of carbon dioxide emissions from the cement manufacturing process on the environment, there is a need to develop useful alternatives to Ordinary Portland Cement (OPC). Production of OPC is responsible for approximately 6 to 7% of the world's carbon dioxide emissions (1). In this context, geopolymers have emerged as potential binders for the concrete industry.

Geopolymers are inorganic polymers produced by chemical action of inorganic source materials that are rich in aluminates and silicates, and alkaline liquids (1). Silicates and aluminates present in the source material get dissolved in the alkaline activator solution and subsequently polymerize into molecular chains and become the binder. Calcined clay, fly ash or slag can be used as source materials. The three dimensional polymeric chain and ring structure consisting of Si- O- Al- O bonds is the backbone of the geopolymer matrix (2- 3). Heat resistance, non- toxicity, excellent durability are other important properties which are beneficial for use in construction sector (4).

In most cases such as when using fly ash or calcined clay, geopolymer binders need heat curing which significantly increases cost and hampers the use of geopolymer system in practical applications (5). Alkali activated slag, on the other hand, attains good strength in ambient curing conditions (4 - 8). However, rapid loss of workability is widely reported in the existing literature for slag based alkali activated binder (2, 4 - 6). It is important to develop good strength and workable slag based alkali activated concrete with the help of ambient curing. This can be accomplished by a partial replacement of the slag with other source materials that are not as fast to react. This study deals with the formulation of alkali activated slag-based binary blends with good workability and strength at ambient curing conditions. Bagasse ash and fly ash are used in combination with slag in this study, which also explores the influence on strength of the activator type as well as the curing method (heat curing and ambient curing).

## 2. Material and Methods

### 2.1 Materials

In this study, sugarcane bagasse ash, ground granulated blast furnace slag (GGBFS), and Type F fly ash were used as aluminosilicate mineral to prepare the alkali activated binder. Ground Granulated Blast-furnace slag (GGBFS) was procured from Jindal Steel plant, India. Class F fly ash was collected from a local thermal power plant (North Chennai Thermal Power Station, India), while Sugarcane Bagasse Ash (SCBA) was collected from a nearby sugar industry from a disposal site. The oxide compositions of fly ash, bagasse ash and GGBFS were determined by X-ray fluorescence spectroscopy and results are given in Table 1 (OPC is included for comparison purposes).

**Table 1. Oxide compositions by X-ray Fluorescence**

Oxide composition	OPC (53 grade)	SCBA	Fly ash (Type F)	GGBFS
SiO <sub>2</sub>	20.68	72.95	59.32	32.38
Al <sub>2</sub> O <sub>3</sub>	4.12	1.68	29.95	21.06
Fe <sub>2</sub> O <sub>3</sub>	5.44	1.89	4.32	1.87
CaO	60.36	7.77	1.29	31.46
MgO	0.83	1.98	0.61	8.57
K <sub>2</sub> O	0.27	9.28	1.44	0.49
Na <sub>2</sub> O	0.23	0.22	0.16	0.36
SO <sub>3</sub>	2.46	3.52	0.17	-

Sugarcane bagasse ash (SCBA) is a by-product from the sugar manufacturing industry. Sugarcane bagasse is burnt in the cogeneration boilers as a fuel at 500-550°C and the residual ash is collected using bag-house filter. Raw sugarcane bagasse ash has fine reactive particles and fibrous unburnt carbon particles, which lead to a high loss on ignition (~21%). The removal of these unburnt carbon particles increases reactivity of bagasse ash (9). For this study, the sugarcane bagasse ash was processed based on a methodology proposed by Bahurudeen and Santhanam (10), which entails sieving the material through 300µm sieve to remove the unburnt particles, and further grinding to cement fineness (300m<sup>2</sup>/kg) to obtain maximum reactivity of sugarcane bagasse ash.

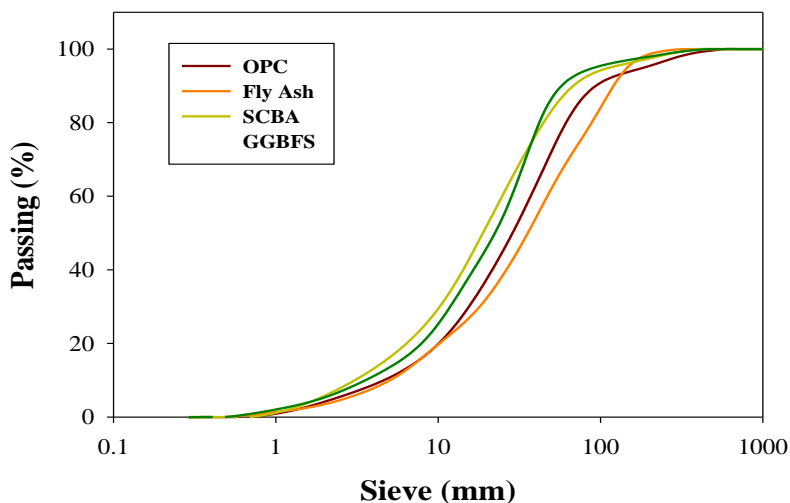
The physical properties of the source materials are presented in Table 2 (OPC is included for comparison purposes).

**Table 2. Physical properties**

Physical Characteristics	SCBA (as collected)	OPC	Fly ash (Type F)	GGBFS	Relevant standard
Specific Gravity	1.91	3.16	2.19	2.86	IS 4031-Part 11-2005 (15)
Specific surface area (Blaine)	145 m <sup>2</sup> /kg	310 m <sup>2</sup> /kg	330 m <sup>2</sup> /kg	360 m <sup>2</sup> /kg	ASTM C204-11 (11)
Loss on ignition	21 %	1.3 %	1.04 %	0.03%	IS 1727-2004 (12)
Consistency	50 %	30 %	29 %	30.5 %	IS 4031-Part 4-2005 (13)
Initial setting time	195 minutes	125 minutes	165 minutes	315 minutes	IS 4031-Part 5-2005 (14)
Final setting time	330 minutes	165 minutes	360 minutes	365 minutes	IS 4031-Part 5-2005 (14)
Soundness (expansion)	1.2 mm	1.61 mm	1 mm	0.67 mm	IS 1727-Part 3 (15)

After processing, the Loss on Ignition of SCBA comes down to 3-6%. Raw SCBA has a lower specific gravity compared to GGBFS and fly ash; however, this increases to 2.12 after processing(close to Type F fly ash). The soundness of processed SCBA when determined according to IS 4031(Part 3)-2005(15) was found to be 1.2 mm(well within the permissible limits).

The particle size distribution of the materials GGBFS, OPC, Type F Fly ash and sugarcane bagasse ash was determined by laser particle size analyzer and results are presented in Figure 1.



**Figure 1. Particle size distribution of source materials (OPC for comparison only)**

For preparation of the activator solution, Sodium Hydroxide (97% purity), Sodium Silicate, Potassium Hydroxide (97% purity) and Potassium Silicate laboratory grade reagents were used. The alkali solution of desired molarity was prepared by dissolving the appropriate mass of solid alkali in distilled water. This was allowed to attain thermal equilibrium over the duration of 24 hours. Then the alkali silicate was added to the hydroxide solution in the ratio of 1:1.5(alkali hydroxide: alkali silicate). This was allowed to attain constant temperature in a controlled environment of 25°C for at least 12 hours. The combination of alkali silicate and hydroxide to form alkali activator solution is known to give better strengths than alkali hydroxide used alone for alkali activated slag mortars (2, 16) due to the presence of additional silicate source for reaction.

Table 3 shows the activator modulus ( $\text{SiO}_2/\text{Na}_2\text{O}$  ratio) (also called water glass modulus) for the Sodium hydroxide based activator solutions used in this study. The silicate modulus of water glass (Sodium silicate) used in this study is 3.312 (8%  $\text{Na}_2\text{O}$  and 26.5%  $\text{SiO}_2$ ).

**Table 3. Activator Moduli**

Activator used		Activator Modulus
NaOH + Na <sub>2</sub> SiO <sub>3</sub>	6M NaOH + Na <sub>2</sub> SiO <sub>3</sub>	1.46
	8M NaOH + Na <sub>2</sub> SiO <sub>3</sub>	1.23
	6M NaOH + Na <sub>2</sub> SiO <sub>3</sub>	1.09

## 2.2 Methods

Mortar specimens for compressive strength testing were prepared in accordance with ASTM C109/C109M-13 (17). The mix details are presented in Table 4. The ratio of alkali activator solution to binder was fixed at 0.5:1 by weight and the ratio of binder to Indian standard graded sand (IS 383) (18) was kept at 1:2 by weight. 500g of binder was used to prepare 6 numbers of 50mm cubes. Four different types of mixes were cast and details of the mixes are presented in Table 4. Sand and binder were mixed for 1 minute in a Hobart mixer at low speed. Afterwards, the prepared activator solution was gradually added to the mix. 5 % of

additional water was added to the mix to achieve good workability and the mortar was further mixed for three minutes. The flow of the mortar was determined as per ASTM C1437-13 (19). Specimens were cast and kept in a controlled temperature (27 °C) environment for 24 hours.

The specimens were demoulded and then the first set was subject to ambient curing at room temperature (27°C) and the other set to heat curing at 65±5°C for 24 hours to compare the effect of curing on early age strength development. Compressive strength of specimens was determined after 3, 14 and 28 days of curing.

**Table 4. Mix details**

Molarity of Alkaline Hydroxide Solution	Activator Solution	GGBFS	BA	FA	Mix ID
6	NaOH + Na <sub>2</sub> SiO <sub>3</sub>	100	-	-	S 100-N 6
		90	10	-	SBA 90/10-N 6
		80	20	-	SBA 80/20- N 6
		50	-	50	SFA 50/50- N 6
	KOH + K <sub>2</sub> SiO <sub>3</sub>	100	-	-	S 100-K 6
		90	10	-	SBA 90/10-K 6
		80	20	-	SBA 80/20- K 6
		50	-	50	SFA 50/50- K 6
8	NaOH + Na <sub>2</sub> SiO <sub>3</sub>	100	-	-	S 100-N 8
		90	10	-	SBA 90/10-N 8
		80	20	-	SBA 80/20- N 8
		50	-	50	SFA 50/50- N 8
	KOH + K <sub>2</sub> SiO <sub>3</sub>	100	-	-	S 100-K 8
		90	10	-	SBA 90/10-K 8
		80	20	-	SBA 80/20- K 8
		50	-	50	SFA 50/50- K 8
10	NaOH + Na <sub>2</sub> SiO <sub>3</sub>	100	-	-	S 100-N 10
		90	10	-	SBA 90/10-N 10
		80	20	-	SBA 80/20- N 10
		50	-	50	SFA 50/50- N 10
	KOH + K <sub>2</sub> SiO <sub>3</sub>	100	-	-	S 100-K 10
		90	10	-	SBA 90/10-K 10
		80	20	-	SBA 80/20- K 10
		50	-	50	SFA 50/50- K 10

### 3. Results and discussion

#### 3.1 Effect of replacement of GGBFS

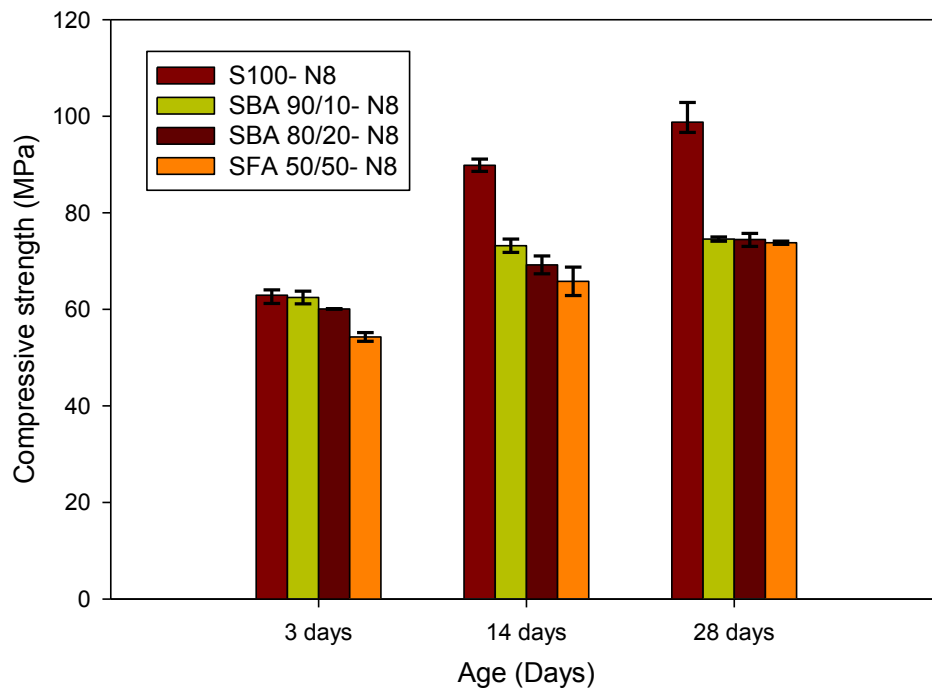
All the four mixes as mentioned in section 2.2 are compared to evaluate the effect of replacement. 8M sodium based activator solution was used as the alkaline activator. In addition, alkaline activator to binder ratio of 0.5 was maintained for all the four mixes. The flow value of the reference mortar (slag only) was measured just after mixing and it was found to be 101%. On the other hand, a sudden loss of workability was observed for the slag mortar mix within 10 minutes, at which time no flow was observed. Similarly, the flow value was determined for other mixes and 121% and 98% flow values were obtained for slag-fly ash mix and slag-bagasse ash mix respectively with similar workability retention (45 minutes). Compressive strength at the end of 3 days, 14 days and 28 days was determined. Figure 2 shows the comparison of compressive strength of all the mixes determined using displacement controlled universal testing machine.

The reference mix (GGBFS only) showed higher strength compared to other mixes. In ambient cured specimens, a reduction in strength was observed with increase in the replacement. This is due to the formation of Calcium Alumino-Silicate Hydrate phases (20 - 21) in addition to poly-sialates from the polymeric reaction in the case of the GGBFS only binder, which causes better strength development. The C-A-S-H is precipitated within 24 hours of reaction, resulting in early strength gain and pore refinement (8). Although the



strengths of blended mixes were lower, they increased with curing duration as shown in Figure 2. At 3 days, the strengths for GGBFS only mix and the binary component mixes were similar, and this can be attributed to the reactive silica and alumina present in SCBA and Fly Ash which contributes to early alkali activation (formation of aluminosilicate polymers). However, at later ages, the latent hydraulic nature of slag results in additional strength gain with increase in curing duration as seen in Figure 2. Similar observation was previously reported for fly ash-slag blended alkali activated concrete (22).

Although the fly ash – GGBFS blend was slower to being with, there was no difference in strength at 28 days compared to the SCBA – GGBFS system.



**Figure 2. Effect of replacement of slag on compressive strength**

### 3.2 Effect of curing methods

To investigate the influence of type of curing on strength of alkali activated binders, the specimens were subjected heat curing and ambient curing as described earlier and results are shown in Figure 3. It is interesting to note that ambient cured reference mortar specimens showed higher strength compared to heat cured specimens. Although heat cured specimens showed increase in strength with respect to curing duration, the reduction in strength was clearly observed compared to ambient cured specimens for the same curing duration. The observed reduction in strength for heat cured specimens is due to the loss of water from the system, which possibly causes a reduction in the level of slag hydration. In addition, drying shrinkage has been reported as a main disadvantage for slag based alkali activated binders in previous literature (4). Curing at higher temperature (and subsequent cooling prior to testing) may lead to formation of cracks in the specimens and cause reduction in strength compared to ambient cured specimens. In the case of ambient cured specimens, the increase in curing duration led to an increase in strength.

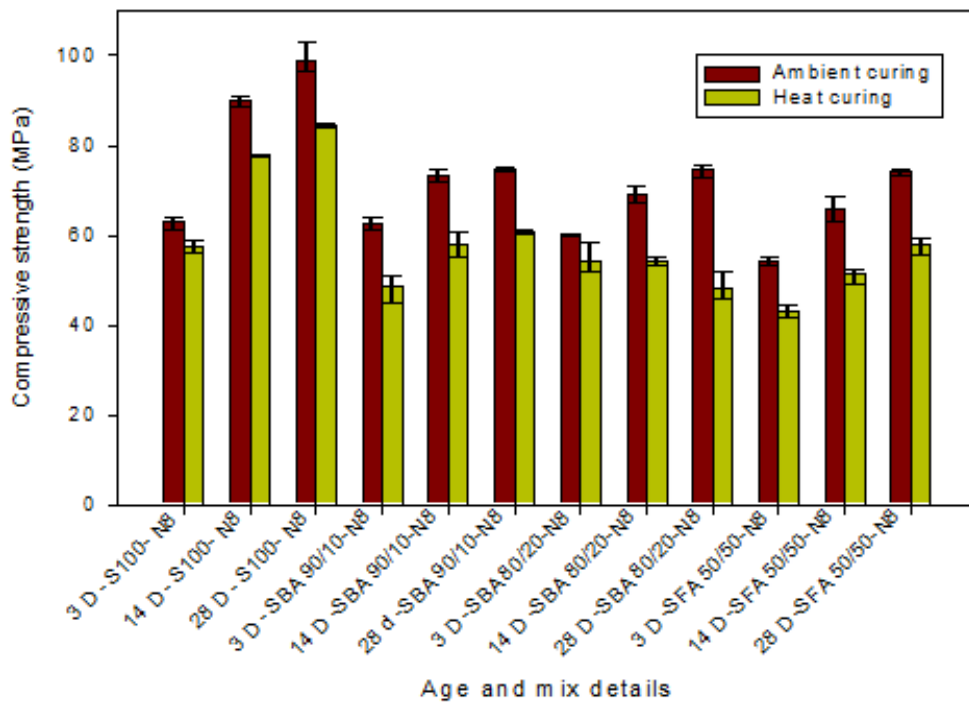


Figure 3. Effect of curing on compressive strength of blends

### 3.3 Effect of activator solution

Strengths of mortar specimens with Sodium Hydroxide with Sodium Silicate solution and Potassium Hydroxide with Potassium Silicate solution were determined to find the influence of activator on alkali activation and strength development. Figure 4 depicts compressive strength of all the specimens activated with both types of alkali activators. Constant molarity of alkali activator solution was maintained (8M) for all the mixtures and the specimens were cured in ambient condition. For the reference mix and slag-fly ash mix, sodium hydroxide/sodium silicate contributes higher strength. This has been validated in other studies which show that a more heterogeneous and porous micro-structure is created when slag is activated with potassium based alkali activators (23- 25). It is interesting to note that strength of slag blended with SCBA mixtures was found to be increased for KOH/K<sub>2</sub>SiO<sub>3</sub> activators compared to sodium based activators. Potassium Hydroxide with Potassium Silicate activator proves to be beneficial for SCBA blended specimens and this could be attributed to the higher K<sub>2</sub>O content in SCBA, which, along with the alkaline potassium oxide that is present in activator, helps as a cationic link between oligomers.

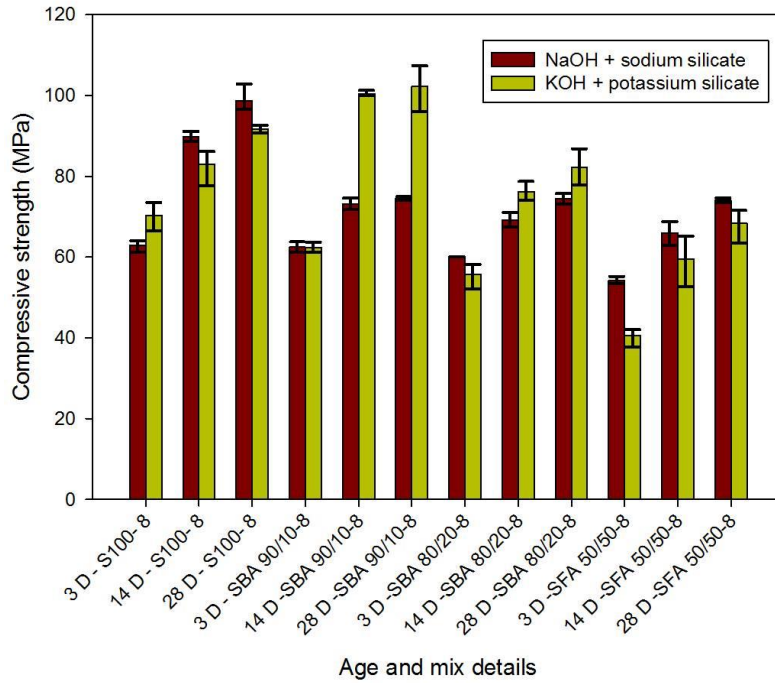


Figure 4. Effect of type of activator on strength of mixes

### 3.4 Effect of molarity and activator modulus

Three different molarities (6, 8, 10 M) were adopted for NaOH/Na<sub>2</sub>SiO<sub>3</sub> activator to find the influence of molarity as well as activator moduli on strength development under ambient curing, and results are presented in Figures 5 and 6.

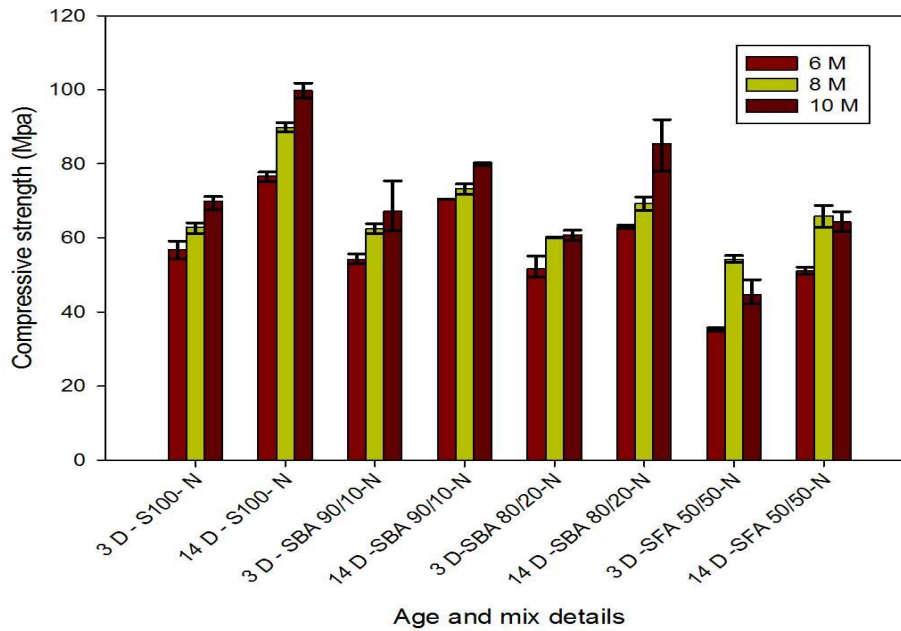


Figure 5. Effect of molarity on strength development in the alkali activated systems

The increase in molarity of the activator led to an increase in strength for the slag and slag-bagasse ash specimens. This is due to the increase in hydroxyl ion and alkali oxide concentration in the solution, which in turn accelerates the dissolution of  $\text{Si}^{4+}$  and  $\text{Al}^{3+}$  from the binder. Similar trend was reported in earlier literature for slag based activated binder (26). These in combination with calcium ion of slag form C-A-S-H gel phase. However, in fly ash slag blends there is decrease in strength with increase in molarity of alkaline activator beyond 8M (formation of Si-OH bonds rather than Si-O bonds). This may be due to the reduction in activator modulus, which inhibits the formation of fly ash reaction products (21).

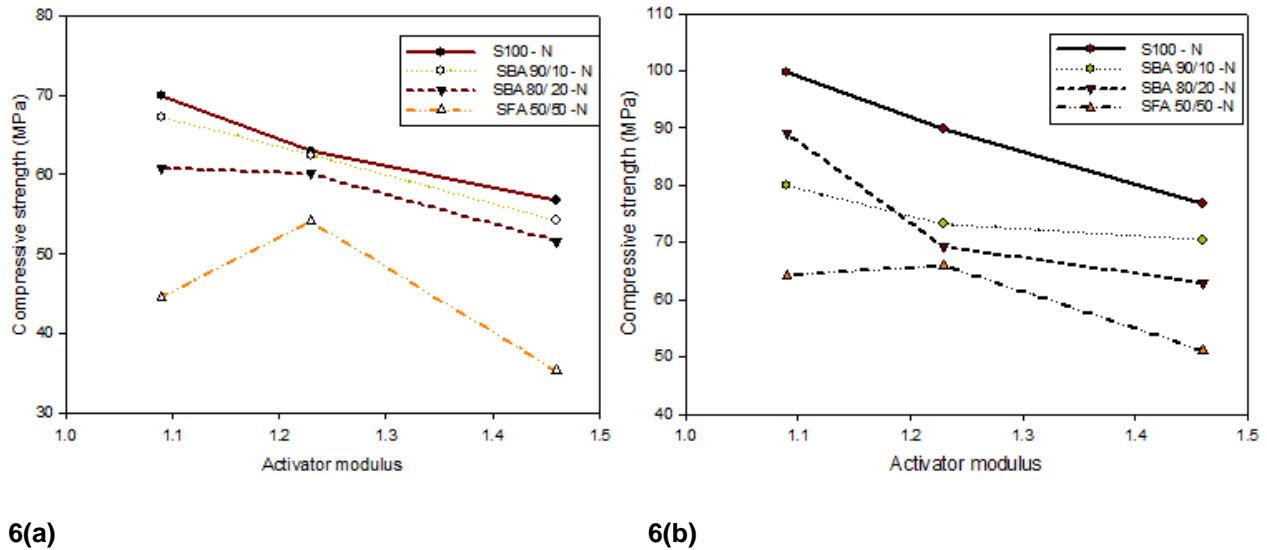


Figure 6(a) and (b). Effect of activator modulus on compressive strength at 3 and 14 days respectively

#### 4. Conclusions

- Ambient cured specimens had higher strength compared to heat cured specimens, possibly as a result of loss of water and micro crack formation in heat curing.
- Compressive strength increased with decrease in the activator modulus due to increase in alkali oxide concentration. Nevertheless for fly ash-slag blends optimal activator modulus was found to be 1.23 (i.e. 8M Alkali hydroxide solution). Further increase in molarity led to reduction in strength.
- Sodium based alkali activator proved beneficial for the slag and slag-fly ash blended binders. On the other hand, slag-SCBA mix exhibited better performance with potassium based activators compared to sodium based activators.
- Replacing GGBFS with other binders decreased the strength due to decrease in the calcium content of the binder. However, to achieve good workability retention of slag based alkali activators, blending with other bagasse ash/ fly ash sources is recommended.

#### 5. Acknowledgement

The authors wish to acknowledge the Ministry of Human Resources and Development (MHRD) for funding and Madras Sugar Limited and JSW Limited, India for providing the material for this study.

## 6. References

1. Jimenez, AF, Palomo, JG et al. "Alkali-activated slag mortars: Mechanical strength behaviour", *Cement and Concrete Research*, 29, 1999, pp 1313–1321.
2. Duxson, P, Mallicoate, SW et al. "The effect of alkali and Si/Al ratio on the development of mechanical properties of metakaolin-based geopolymers", *Colloids and Surfaces A: Physicochemical and Engineering Aspects*, 292(1), 2007, pp 8–20.
3. Xu, H, Deventer, JSJ. "The geopolymerization of alumina- silicate minerals", *International Journal of Mineral Processing*, 58, 2000, pp 247-266.
4. Rashad, AM. "A comprehensive overview about the influence of different additives on the properties of alkali-activated slag – A guide for Civil Engineer", *Construction and Building Materials*, 47, 2013, pp 29- 55.
5. Lee, NK, Lee, HK. "Setting and mechanical properties of alkali-activated fly ash/slag concrete manufactured at room temperature", *Construction and Building Materials*, 47, 2013, pp 1201–1209.
6. Chang, JJ. "A study on the setting characteristics of sodium silicate-activated slag pastes", *Cement and Concrete Research*, 33, 2003, pp 1005–1011.
7. Deb, PS, Nath, P, et al. "The effects of ground granulated blast-furnace slag blending with fly ash and activator content on the workability and strength properties of geopolymer concrete cured at ambient temperature", *Materials and Design*, 62, 2014, pp 32–39.
8. Gao, X, Yu, QL, et al. "Reaction kinetics, gel character and strength of ambient temperature cured alkali activated slag- fly ash blends", *Construction and Building Materials*, 80, 2015, pp 105–115.
9. Bahurudeen, A, Marckson, AV, et al. "Development of sugarcane bagasse ash based Portland pozzolana cement and evaluation of compatibility with superplasticizers", *Construction and Building materials*, 68, 2014, pp 465–475.
10. Bahurudeen, A, Santhanam M. "Influence of different processing methods on the pozzolanic performance of sugarcane bagasse ash", *Cement and Concrete Composites*, 56, 2015, pp 32–45.
11. ASTM C204 –11. Standard Test Methods for Fineness of Hydraulic Cement by Air-Permeability Apparatus, 2011, American Society for Testing and Materials, West Conshohocken, United States.
12. IS 1727:1967. Methods of test for pozzolanic materials, 2004, Bureau of Indian Standards, New Delhi, India.
13. IS 4031-4. Methods of physical tests for hydraulic cement: Determination of consistency of standard cement paste. 1983, Bureau of Indian Standards, New Delhi, India.
14. IS 4031-5. Methods of physical tests for hydraulic cement: Determination of initial and final setting times. 1988, Bureau of Indian Standards, New Delhi, India.
15. IS 4031- 11. Methods of physical tests for hydraulic cement: Determination of density, 1988, Bureau of Indian Standards, New Delhi, India.
16. Altan, E, Erdogan ST. "Alkali activation of a slag at ambient and elevated temperatures", *Cement and Concrete Composites*, 34, 2012, pp 131–139.
17. ASTM C109/ C109M-13. Standard test method for compressive strength of hydraulic cement mortars. American Society for Testing and Materials, West Conshohocken, United States.
18. IS 383. Specification for coarse and fine aggregates from natural sources for concrete. 1970, Bureau of Indian Standards, New Delhi, India
19. ASTM C1437 – 13. Standard test method for flow of hydraulic cement mortar. American Society for Testing and Materials, West Conshohocken, United States
20. Part, KW, Ramli, M, et al. "An overview on the influence of various factors on the properties of geopolymer concrete derived from industrial by- products", *Construction and Building Materials*, 77, 2015, pp 370–395.
21. Puertas, F, Jimenez, AF, et al. "Pore solution in alkali-activated slag cement pastes. Relation to the composition and structure of calcium silicate hydrate", *Cement and Concrete Research*, 34, 2004, pp 139–148.
22. Castaldelli, VN, Akasaki, JL, et al. "Use of slag/sugarcane bagasse ash (SCBA) blends in the production of alkali-activated materials", *Materials*, 6, 2013, pp 3108-3127.
23. Brough, AR, Atkinson, A. "Sodium silicate-based, alkali-activated slag mortars: Part I. Strength, hydration and microstructure", *Cement and Concrete Research*, 32, 2002, pp 865–879.

24. Bilima, C, Karahan, O, et al. "Influence of admixtures on the properties of alkali- activated slag mortars subjected to different curing conditions", *Materials and Design*, 44, 2013, pp 540–547.
25. Marjanovica, N, Komljenovica, M, et al. "Physical–mechanical and microstructural properties of alkali-activated fly ash–blast furnace slag blends", *Ceramics International*, 41, 2015, pp 1421–1435.
26. Izquierdo, M, Querona, X, et al. "Coal fly ash-slag-based geopolymers: Microstructure and metal leaching", *Journal of Hazardous Materials*, 166, 2009, pp 561–566.

# Behaviour of Granulated Lead Smelter Slag-Based Geopolymer Concrete

M. Albitar<sup>1</sup>, M.S. Mohamed Ali<sup>2</sup>, P. Visintin<sup>3</sup> and M. Drechsler<sup>4</sup>

<sup>1</sup>PhD Candidate, School of Civil, Environmental and Mining Engineering University of Adelaide, Australia

<sup>2</sup>Senior Lecturer, School of Civil, Environmental and Mining Engineering, University of Adelaide, Australia

<sup>3</sup>Lecturer, School of Civil, Environmental and Mining Engineering, University of Adelaide, Australia

<sup>4</sup>Adjunct Senior Lecturer, University of Adelaide, and Consultant Engineering Geologist, WorleyParsons, Australia

**Abstract:** Geopolymer concretes are manufactured from high-volume industrial waste materials and have emerged as an innovative engineering material with the potential to form Ordinary Portland Cement (OPC)-free concrete for both structural and non-structural applications. Utilising industrial waste materials to manufacture geopolymer concrete not only reduces carbon dioxide (CO<sub>2</sub>) footprint, but also resolves several issues associated with the dumping or disposal of high-volume waste materials. This paper studies the behaviour of a new industrial waste material known as granulated lead smelter slag (GLSS). The experimental program includes 32 mix designs to investigate the influence of incorporating GLSS with fly ash as fine aggregate, binder or both fine aggregate and binder. The paper also investigates the influence of particle size, activator dosage and mechanical properties of an optimised mix design. The results show little to no effect of GLSS as fine aggregate; however, it allows for a reduction of fly ash content, as it partially substitutes the polymerisation reaction that is reduced by the reduction of fly ash content. The results also show that the particle size of the slag plays an important role, as the compressive strength was significantly improved with super-fine particle size. Increase the activator-to-binder ratio (more than 0.4) has a detrimental effect on the compressive strength. Finally, the mechanical properties of geopolymer concrete (manufactured from 25% fly ash and 75% slag) were similar to that of 100% fly ash geopolymer concrete.

**Keywords:** lead smelter slag, geopolymer, fly ash, mechanical properties, particle size.

## 1. Introduction

Geopolymer concrete, also known as alkali-activated cement [1], inorganic polymer concrete [2], and geocement [3], has emerged as an innovative engineering material with the potential to form Ordinary Portland Cement (OPC)-free concrete for both structural and non-structural applications [4]. Geopolymer concretes are commonly formed by synthesising industrial aluminosilicate waste materials, such as metakaolin, fly ash and slags, with a highly alkaline activator solution. The polycondensation reaction of geopolymeric precursor and alkali polysilicates is known as geopolymerisation process. Geopolymer concrete relies on aluminosilicate molecules that join together to make very long molecules called polymers of which referred as geopolymeric aluminosilicate hydrate (A-S-H) gel. This process is called polymerisation and it differs from the process of conventional concrete, which relies on calcium silicate hydrate (C-S-H) gel to form a binder. Therefore, the chemical composition of a binder plays an important role in forming a certain gel. Yip et al. [5] and Yip and van Deventer [6] proved that it is possible to have geopolymeric aluminosilicate hydrate (A-S-H) gel and calcium silicate hydrate (C-S-H) gel forming simultaneously within a single binder. Thus, there is a compelling case to explore other types of slag-based geopolymer concretes as a sustainable alternative to traditional OPC concrete technologies.

Granulated lead smelter slag (GLSS) is an industrial waste material that is a by-product of heavy metal extraction during lead smelting process. The production of lead world-wide was estimated to be 3.9 million tonnes in 2009 from both primary and secondary resources [7], and the production of each ton of metallic lead generates around 100-350 kg of slag that is known as granulated lead smelter slag [9]. Given the potential suitability of GLSS for the use in structural and non-structural geopolymer concrete manufacture, it is of particular importance to understand the mechanical behaviour of GLSS-based geopolymer concrete. However, the studies on the behaviour of GLSS have so far focused on their characterisation and stability [8-12], and only one study to date has investigated the mechanical behaviour of geopolymer concretes with a 10% maximum substitution of fly ash with GLSS [7].

This paper presents the results of the first comprehensive experimental study on the behaviour of GLSS incorporated with fly ash as binder replacement and fine aggregate replacement to produce geopolymer concrete. Lead slags are typically available in the granulated form (sand sized fractions <2 mm) and are therefore less reactive than other types of geopolymer (i.e., fly ash <100 µm) due to the particle size [13-

14]. Therefore, this paper also investigates the effectiveness of super fine crushing to improve the GLSS reactivity as a geopolymer binder.

## 2. Experimental Program

A total of 32 mix designs were trialled to quantify the influence of granulated lead smelter slag (GLSS) on the compressive strength of fly ash geopolymer concrete. The mixture proportions of the mix designs are presented in Table 1. To investigate the influence of fly ash replacement with GLSS as a binder, five different GLSS ratios were investigated (0, 0.25, 0.5, 0.75, and 1). To investigate the influence of natural sand (NS) replacement with GLSS as fine aggregate, four different GLSS ratios were used (0, 0.5, 0.75, and 1). To investigate the influence of GLSS particle size, four different fractions of the GLSS grading were examined, including 550  $\mu\text{m}$ , 400  $\mu\text{m}$ , 250  $\mu\text{m}$ , and 150  $\mu\text{m}$ , and seven different grinding particle sizes D50 (D50 grain size of which 50% material passes) were examined, including 70  $\mu\text{m}$ , 63  $\mu\text{m}$ , 43  $\mu\text{m}$ , 20  $\mu\text{m}$ , 11  $\mu\text{m}$ , 8.2  $\mu\text{m}$ , and 5.8  $\mu\text{m}$ . In order to examine the degree of reactivity of the GLSS, three different alkaline-to-binder (a/b) ratios were investigated (0.37, 0.5, and 0.75). The mechanical properties of the optimised GLSS mix design were experimentally obtained and subsequently compared to those of fly ash geopolymer concrete.

**Table 1. Mixture proportions.**

Materials	Mixture proportions (kg/m <sup>3</sup> )
Binder	424.8
Coarse aggregate	1180.8
Fine aggregate	595.2
*NaOH with Na <sub>2</sub> SiO <sub>3</sub>	156.7
Superplasticiser	31.2
Water	9.84
*Except for mixes 17 and 19, which had 212.4 kg/m <sup>3</sup> of NaOH with Na <sub>2</sub> SiO <sub>3</sub> , and mixes 18 and 20, which had 318.4 kg/m <sup>3</sup> of NaOH with Na <sub>2</sub> SiO <sub>3</sub> .	

### 2.1 Material Specifications

The basis of the mixtures used in this investigation was low-calcium class-F according to ASTM C618-08 [15] fly ash produced at Port Augusta Power Station in South Australia and granulated lead smelter slag (GLSS) from the Nystar lead zinc smelter in Port Pirie (locally called 'black sand'). The chemical compositions of the fly ash and GLSS were determined by X-ray fluorescence (XRF) and are documented in Table 2. For all the mixes, the alkaline solution phase consisted of a combination of sodium silicate (Na<sub>2</sub>SiO<sub>3</sub>) and 14 molar sodium hydroxide (NaOH), pre-mixed with a ratio of Na<sub>2</sub>SiO<sub>3</sub>-to-NaOH of 1.5.

**Table 2. Chemical compositions by mass (%).**

Oxides	Fe <sub>2</sub> O <sub>3</sub>	SiO <sub>2</sub>	Al <sub>2</sub> O <sub>3</sub>	CaO	MgO	SO <sub>3</sub>
Granulated lead smelter slag	33.8	27.5	7.4	19.4	2.1	-
Fly ash	2.8	49.0	31.0	5.4	2.5	0.3

### 2.2 Testing Procedures

The experimental program consisted of the following two stages: (i) examining the behaviour of GLSS and developing a geopolymer concrete mix with high-volume of GLSS and a compressive strength of normal concrete, and (ii) examining the engineering properties of the optimised mix. The mixing procedures of all stages were accomplished by mixing the dry components for three minutes followed by the addition of liquid starting with water, alkaline solution and superplasticiser where applicable. The specimens in the first stage were heat-cured for 24 hours, and for allowing heat-curing period comparison, some specimens were heat-cured for 48 hours at a temperature of 70°C. The heat curing was applied to accelerate the curing time, so the specimens can be tested prior to 28-day. Thus, all specimens were placed in a fog room after heat curing and tested seven days after casting. Three replications were made for each mix. In the second stage, the optimised mix design was manufactured at a larger scale to examine the



engineering material properties, including compressive strength, stress-strain relationships, splitting tensile strength, flexural strength and modulus of elasticity. Both curing methods, 24-hour heat curing and ambient curing, were considered. All specimens in this stage were tested at 28-day of age.

### 3. Results and Discussion

Table 3 summarises the mix designs in terms of the parameter investigated in each mix design. The mixes were designed to investigate (1) the influence of granulated lead smelter slag, which includes (i) effect of GLSS as fine aggregate, (ii) effect of GLSS as a binder, and (iii) effect of GLSS particle size, (2) the influence of activator dosage, and (3) influence of curing period.

**Table 3. Description of mixtures.**

Mix No	Binder			Fine aggregates		GYP	a:b	Heat-curing period (Hour)	Slump (mm)	Density (kg/m <sup>3</sup> )	Strength at 7 days (MPa)
	FA Ratio	GLSS		NS	GLSS						
		Ratio	D <sub>50</sub> (µm)								
1	0.5	0.5	550	1	0	-	0.37	24	75	2355	37.2
2	0.5	0.5	400	1	0	-	0.37	24	27	2355	35.86
3	0.5	0.5	250	1	0	-	0.37	24	50	2355	36.06
4	0.5	0.5	150	1	0	-	0.37	24	50	2355	37.4
5	0.5	0.5	550	0	1	-	0.37	24	180	2360	51.94
6	0.5	0.5	400	0	1	-	0.37	24	130	2360	46.04
7	0.5	0.5	250	0	1	-	0.37	24	75	2360	50.06
8	0.5	0.5	150	0	1	-	0.37	24	100	2360	49.5
9	0.5	0.5	250	1	0	5%	0.37	24	0	2355	13.6
10	0.5	0.5	250	1	0	10%	0.37	24	0	2355	1.06
11	0.5	0.5	250	1	0	15%	0.37	24	0	2355	3.1
12	0.5	0.5	250	1	0	-	0.37	48	80	2355	36.4
13	1	0	-	1	0	-	0.37	24	155	2350	66.78
14	1	0	-	0.5	0.5	-	0.37	24	140	2355	63.8
15	1	0	-	0.25	0.75	-	0.37	24	200	2360	62.5
16	1	0	-	0	1	-	0.37	24	200	2350	63.22
17	0.5	0.5	250	1	0	-	0.50	24	235	2355	28.91
18	0.5	0.5	250	1	0	-	0.75	24	270	2355	16.85
19	0.5	0.5	250	0	1	-	0.50	24	240	2370	40.8
20	0.5	0.5	250	0	1	-	0.75	24	275	2370	23.19
21	1	0	-	0	1	-	0.37	48	155	2350	63.7
22	0.75	0.25	550	0	1	-	0.37	24	200	2360	62.41
23	0.5	0.5	550	0	1	-	0.37	24	200	2370	51.13
24	0.25	0.75	550	0	1	-	0.37	24	130	2400	31.52
25	0	1	550	0	1	-	0.37	24	0	2469	6.75
26	0	1	43	0	1	-	0.37	24	0	2548	11.9
27	0	1	63	0	1	-	0.37	24	0	2552	13.4
28	0	1	70	0	1	-	0.37	24	0	2548	16.4

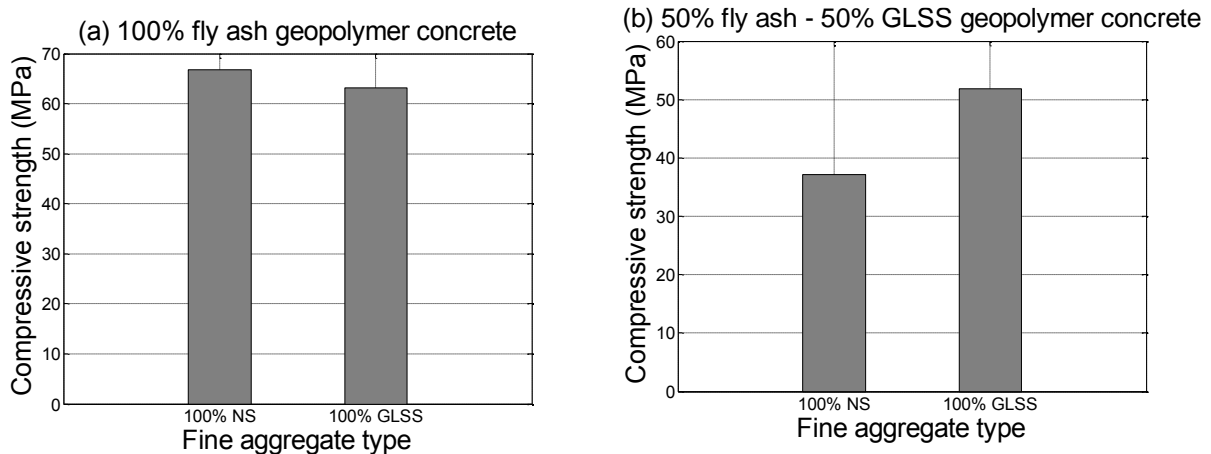
29	0	1	20	0	1	-	0.37	24	0	2646	48.1
30	0	1	8.2	0	1	-	0.37	24	0	2702	52.4
31	0	1	11	0	1	-	0.37	24	0	2701	60.1
32	0	1	5.8	0	1	-	0.37	24	0	2643	64.9
FA = fly ash, GLSS = granulated lead smelter slag, NS = natural sand, a/b = alkaline-to-binder ratio, GYP = gypsum, D <sub>50</sub> = grainsize of which 50% material passes.											

### 3.1 Influence of granulated lead smelter slag

In order to study the influence of granulated lead smelter slag (GLSS) on the behaviour of fly ash-based geopolymer concrete, the GLSS was substituted as fine aggregate, binder or both fine aggregate and binder.

#### 3.1.1 Effect of granulated lead smelter slag as fine aggregate

Granulated lead smelter slag (GLSS) was investigated as fine aggregate in two different mixture proportions. First, the natural sand (NS) was completely replaced with GLSS in a 100% fly ash-based geopolymer concrete (mixes 13 and 16). Second, 50% of the binder (i.e., fly ash) was replaced with GLSS alongside with the complete replacement of the NS with GLSS (mixes 3 and 7). The results show the utilisation of GLSS in a mixture proportions with 100% fly ash as a binder has little to no influence on the compressive strength of fly ash-based geopolymer concrete as shown in Figure 1(a). This is due mainly to the condensation polymerisation reaction that took place within fly ash-based geopolymer concrete in which the reaction was optimum. On the other hand, the utilisation of GLSS in a mixture proportions with 50% fly ash as a binder has a significant influence on the compressive strength of fly ash-based geopolymer concrete as can be seen in Figure 1(b). This indicates the GLSS contributed in the polymerisation reaction because when the fly ash content is reduced, the polymerisation reaction is also reduced, which in turn reduces the strength (as seen in mixes 1 to 4). However, once larger quantity of granulated lead smelter slag (GLSS) is added, the polymerisation reaction is substituted and hence the strength is enhanced (as seen in mixes 5 to 8).



(a) 100% fly ash geopolymer concrete.

(b) 50% fly ash geopolymer concrete.

**Figure 1. Effect of GLSS as fine aggregate on compressive strength.**

### 3.1.2 Effect of granulated lead smelter slag as a binder

The volume of fly ash was progressively replaced with granulated lead smelter slag (GLSS) to have fly ash ratios of 1, 0.75, 0.50, 0.25 and 0, as can be seen in mixes 21-25. It is evident from Figure 2 that the compressive strength decreased in proportion to the decrease of fly ash content. That is because the reduction of fly ash content affects the heterogeneous chemical reaction that is involved in the geopolymerisation between solid aluminosilicate oxides and alkali silicate solutions. It should be noted that the reaction contribution of GLSS is not optimum due to the particle size, which is relatively coarse compared to the particle size of fly ash. It is worth mentioning that the replacement of fly ash with GLSS up to 25% has little to no influence on the strength of geopolymers. This observation is in agreement with the findings previously reported by Ogundiran et al. [7].

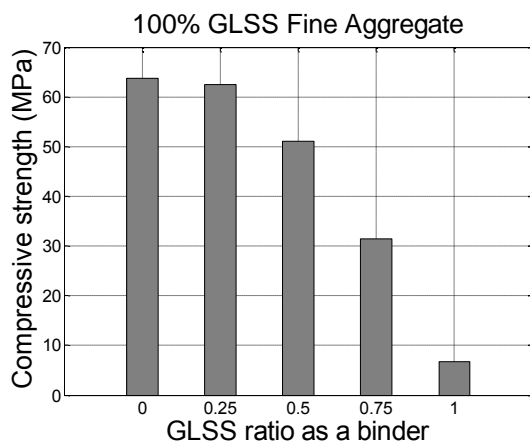


Figure 2. Influence of fly ash-to-GLSS ratio on compressive strength.

As the significance of the research is to utilise high volume of GLSS while maintaining the compressive strength in the range of the normal concrete strength (>20 MPa), mixture 24 (25% FA and 75% GLSS) was chosen to be the optimised mixture for further research.

### 3.1.3 Effect of granulated lead smelter slag particle size

The fineness of the binder has the most significant influence on the properties of the hardened concrete, even more so than the chemical and mineralogical composition of the binder [16-17]. The natural particles of GLSS are relatively large, angular and irregular, and for handling, health and environmental reasons, GLSS is produced as sand (i.e., <2 mm). To allow comparisons in reactivity of the GLSS to particle size, different fractions of GLSS were examined (i.e., fractions retained on the 550  $\mu\text{m}$ , 400  $\mu\text{m}$ , 250  $\mu\text{m}$  and 150  $\mu\text{m}$  sieves) as 50% substitution for fly ash (mixes 1-4 and mixes 5-8). The results showed that those size fractions did not have any significant influence on the final compressive strength. This can be attributed to the significant difference in the particle sizes of fly ash compared to GLSS, as slag of 150  $\mu\text{m}$  grading is still relatively coarse compared to that of fly ash ( $D_{50}$  of 12  $\mu\text{m}$ ).

To determine the influence of particle size of GLSS, different super fine crushed fractions of the slag were tested (mixes 25-32). It was found that the fineness of the binder has a significant effect on the reactivity of GLSS in geopolymer concrete, as can be seen in Figure 3. These results clearly demonstrate the effectiveness of super fine crushing the GLSS to grain sizes equal to or even finer than that of fly ash ( $D_{50}$  of 12  $\mu\text{m}$ ). That can be attributed to the significant increase in the surface area with reduced grain size, which consequently improves the reactivity of GLSS. It should be noted that the pozzolanic reaction takes place mainly on the surface of the particles [34]. Nevertheless, super fine crushing GLSS does require additional processing and energy, and the potential use of the oversize fraction was studied using a combination of fine GLSS and over size GLSS (mix 29). The combined

fraction ( $D_{50}$  of 20  $\mu\text{m}$ ) achieved a compressive strength of 48 MPa, suggesting that the fine fraction is providing most of the binder reactivity. The relationship between strength and various grain sizes ( $D_5$ ,  $D_{20}$ ,  $D_{50}$  and  $D_{80}$ ) is plotted in Figure 4. It can be seen that the compressive strength generally increases with reduced particle size of the slag.

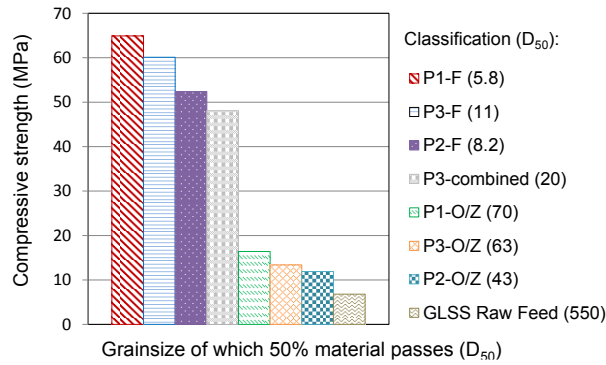


Figure 3. Influence of grainsize on strength of 100% GLSS geopolymer concrete.

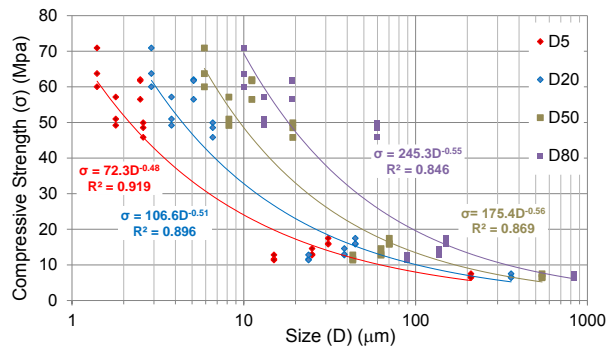


Figure 4. Strength versus grain size relationship of 100% GLSS geopolymer concrete.

### 3.2 Influence of activator dosage

Three different activator-to-binder ratios were used for the activation of slag geopolymer concrete, including 0.37, 0.5 and 0.75. These ratios were chosen to examine whether the reactivity of GLSS improves with an increase of the activator dosage using 50% fly ash and 50% GLSS geopolymer concrete mixes with two different fine aggregates, natural sand (mixes 3, 17, 18) and GLSS (mixes 7, 19, 20). It can be seen in Figure 5 that the compressive strength declined with the increase of the activator to binder dosage ratio. It can also be seen that the behaviour of the mixes that contain GLSS as fine aggregate attained higher compressive strength, which reflects the increase reactivity of the GLSS compared to the natural sand.

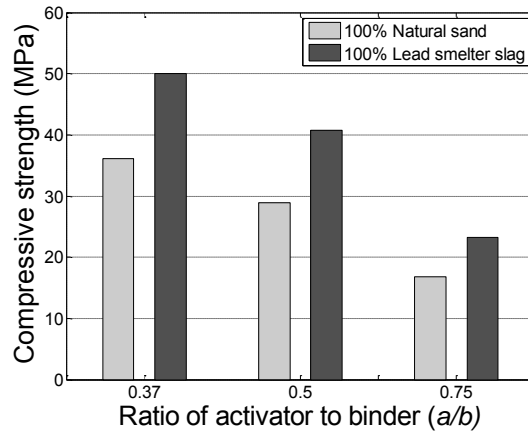


Figure 5. Influence of activator to binder (a/b) ratio in GLSS geopolymer concrete.

### 3.3 Mechanical properties of optimised mix design

Therefore, tests to determine the full-compression stress-strain relationships, the elastic modulus, the flexural strength and indirect tensile strength of slag geopolymer concrete have been undertaken on both ambient and heat-cured specimens tested after 28-day of casting. All the specimens were manufactured from mix 24, which utilises 75% of GLSS as the fly ash binder replacement. The results were then compared to that of 100% fly ash geopolymer concrete.

The full stress-strain relationships for both heat and ambient cured specimens are shown in Figure 6, together with Hognestad's [18] and Collins et al.'s [19] models. It is evident that the expressions of Hognestad [18] and Collins et al. [19] provide reasonable accuracy for slag geopolymer concrete stress-strain relationships.

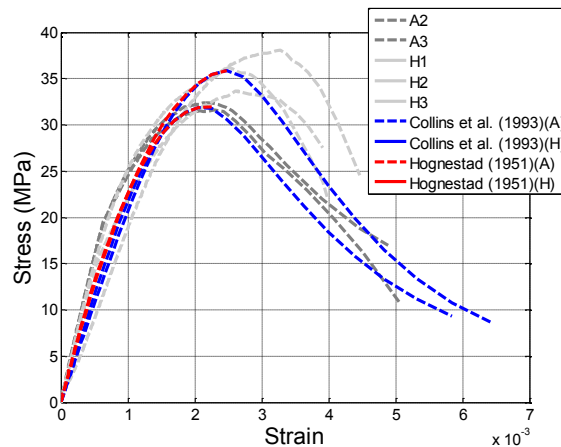


Figure 6. Stress-strain relationships.

The weight of three cylinders per mix was measured in order to calculate the density ( $\rho$ ) of a particular mix. The density, along with the respective compressive ( $f_c$ ), of each particular mix, is presented in Table 3. It can be noted that the density of fly ash geopolymer concrete is marginally lower than the equivalent OPC concretes, ranging between 2350-2355 kg/m<sup>3</sup>. It can also be noticed that the density slightly increased with the addition of raw feed GLSS and significantly increased to 2700 kg/m<sup>3</sup> when utilising super fine crushed GLSS. This is probably as a result of the high iron content of the GLSS, as well as a lower porosity of the geopolymer concrete when using super fine crushed GLSS.

Table 4 presents the results of splitting tensile, flexural strength and elastic modulus of slag geopolymer concrete, as well as fly ash geopolymer concrete results of ambient and heat cured specimens. The table also presents the results of prediction models of ACI [20]. It can be observed that the mechanical properties of slag geopolymer concrete are similar to those of fly ash geopolymer concrete.

**Table 4. Mechanical properties of slag and fly ash geopolymer concretes.**

Mix	Compressive strength (MPa)	Splitting tensile strength (MPa)	Flexural strength (MPa)	Elastic modulus (GPa)	American Concrete Institute (ACI [20])		
					Splitting tensile strength (MPa)	Flexural strength (MPa)	Elastic modulus (GPa)
Ambient-cured 25% FA & 75% GLSS	31.7	4.1	4.0	30.7	3.0	3.5	25.6
Heat-cured 25% FA & 75% GLSS	35.9	4.4	4.8	29.9	3.2	3.7	26.8
Ambient-cured 100% FA	32.3	3.1	4.2	27.0	3.0	3.5	25.8
Heat-cured 100% FA	49.8	5.1	5.3	30.1	3.7	4.4	30.3

#### 4. Conclusions

This paper has presented the results of an experimental study that was undertaken to investigate the influence of granulated lead smelter slag (GLSS) on the compressive strength of fly ash geopolymer concrete. The investigation involved the influence of (i) GLSS as fine aggregate, (ii) GLSS as a binder, (iii) particle size of GLSS, and (iv) activator-to-binder (a/b) ratio. The study also investigated the mechanical properties of the optimised mix design. The results showed that utilising GLSS as fine aggregate improved strengths when the volume of fly ash was reduced, and had little to no effect on 100% fly ash geopolymer concrete. The compressive strength of fly ash geopolymer concretes decreased in proportion to increasing fly ash binder replacement with GLSS. Nevertheless, strengths in excess of 20 MPa were still obtained by replacing fly ash with 75% GLSS. It was also shown that different fractions of GLSS between 550  $\mu$ m and 150  $\mu$ m did not have any significant influence on the compressive strength of geopolymer concrete. However, when the GLSS was super fine crushed to produce fractions with  $D_{50}$ 's less than 20  $\mu$ m, the size fractions had a significant positive impact on the compressive strength and density of geopolymer concretes. Increasing the activator-to-binder ratio above 0.4 had a negative impact on the compressive strength of geopolymer concretes. Moreover, the mechanical properties of the optimised geopolymer concrete mix design, which contained 25% fly ash and 75% GLSS as a binder and 100% GLSS as fine aggregate, were found to be similar to that of 100% fly ash geopolymer concrete.

#### 5. Acknowledgement

The University of Adelaide research team would also like to acknowledge the following contributors: WorleyParsons Services Pty Ltd, MSP Group, Nyrstar Port Pirie; IMP Technologies, Zero Waste SA and South Australian Department of Planning, Transport and Infrastructure (DPTI).

## 6. References

1. Duxson, P., Fernández-Jiménez, A., Provis, J. L., Lukey, G. C., Palomo, A., and van Deventer, J., "Geopolymer Technology: The Current State of The Art", Journal of Materials Science, 42, 2007, pp. 2917-2933.
2. Sofi, M., van Deventer, J. S. J., Mendis, P. A., and Lukey, G. C., "Engineering properties of inorganic polymer concretes (IPCs)", Cement and Concrete Research, 37, 2007, pp. 251-257.
3. Aldred, J., and Day, J., "Is geopolymer concrete a suitable alternative to traditional concrete", *37th Conference on Our World in Concrete & Structures, Australia*, 2012, pp. 1-14.
4. Komnitsas, K., and Zaharaki, D., "Geopolymerisation: A review and prospects for the minerals industry", Minerals Engineering, 20(14), 2007, pp. 1261-1277.
5. Yip, C. K., and van Deventer, J. S. J., "Microanalysis of calcium silicate hydrate gel formed within a geopolymeric binder", Journal of Materials Science, 38(18), 2003, pp. 3851-3860.
6. Yip, C. K., Lukey, G. C., and van Deventer, J. S. J., "The coexistence of geopolymeric gel and calcium silicate hydrate at the early stage of alkaline activation", Cement and Concrete Research, 35, 2005, pp. 1688-1697.
7. Ogundirana, M. B., Nugterena, H. W., and Witkamp, G. J., "Immobilisation of lead smelting slag within spent aluminate-fly ash based geopolymers", Journal of Hazardous Materials, 248-249, 2013, pp. 29-36.
8. de Andrade Lima, L. R. P., and Bernardes, L. A., "Characterization of the lead smelter slag in Santo Amaro, Bahia, Brazil", Journal of Hazardous Materials, 189, 2011, pp. 692-699.
9. Ettler, V., Legendre, O., Bodéan, F., and Touray, J. C., "Primary phases and natural weathering of old lead-zinc pyrometallurgical slag from Příbram", The Canadian Mineralogist, 39(3), 2001, pp. 873-888.
10. Ettler, V., Mihaljevič, M., Touray, J. C., and Piantone, P., "Leaching of polished sections: an integrated approach for studying the liberation of heavy metals from lead-zinc metallurgical slags", Bulletin de la Société Géologique de France, 173(2), 2002, pp. 161-169.
11. Ettler, V., Komárková, M., Jehlička, J., Coufal, P., Hradil, D., Machovič, V., and Delorme, F., "Leaching of lead metallurgical slag in citric solutions—implications for disposal and weathering in soil environments", Chemosphere, 57, 2004, pp. 567-577.
12. Lewis, A. E., and Hugo, A., "Characterization and batch testing of a secondary lead slag", Journal of the South African Institute of Mining and Metallurgy, 100, 2000, pp. 365-370.
13. Monzó, J., Payá, J., and Peris-Mora, E., "A preliminary study of fly ash granulometric influence on mortar strength", Cement and Concrete Research, 24(4), 1994, pp. 791-796.
14. Erdođdu, K., and Türker, P., "Effect of fly ash particle size on strength of Portland cement fly ash mortars", Cement and Concrete Research, 28(9), 1998, pp. 1217-1222.
15. ASTM C618-08, "Standard Specification for Coal Fly Ash and Raw or Calcined Natural Pozzolan for Use in Concrete", American Society for Testing and Materials, 2008.
16. Shi, C., Krivenko, P. V., and Roy, D., "Alkali-activated cements and concretes", 2006, USA.
17. Slanička, Š., "The influence of fly ash fineness on the strength of concrete", Cement and Concrete Research, 21, 1991, pp. 285-296.
18. Hognestad, E. N., "A study of combined bending and axial load in reinforced concrete members", University of Illinois at Urbana-Champaign, 49(22), 1951, USA.
19. Collins, M. P., Mitchell, D., and MacGregor, G. J., "Structural design considerations for high strength concrete", ACI Concrete International, 15(5), 1993, pp. 27-34.
20. American Concrete Institute, "Building code requirements for structural concrete (ACI 318-08)", ACI Committee 318, 2008, Michigan.

# Influence of binder on alkali reactivity of aggregates in Geopolymer concrete

Chandani Tennakoon<sup>1</sup>, Ahmad Shayan<sup>1,2</sup>, Jay G. Sanjayan<sup>1</sup>

<sup>1</sup>Centre of sustainable infrastructure, Faculty of Science, Engineering and Technology, Swinburne University of Technology, Hawthorn, Victoria, Australia.

<sup>2</sup>ARRB Group, Vermont South, Victoria, Australia

**Abstract:** Alkali aggregate reaction (AAR) is one of the main durability problems in Portland cement concrete, as it can cause significant expansion and cracking in concrete structures. Geopolymer is a new sustainable binder which is used as an alternative to Portland cement. Geopolymer binder is produced by activating alumino-silica sources using alkali activator. This work presents how AAR expansion varies with binder ingredients in geopolymers. Results show that geopolymer mortar specimens with at least 30% fly ash have negligible AAR expansion. In fly ash and slag blended geopolymer binder based mortars, microstructure changes are due to zeolite crystalline products in the pores instead of typical AAR products found in 100% alkali activated slag.

**Keywords:** Geopolymer, Alkali aggregate reaction, Fly ash, Slag, Microstructure, Durability

## 1. Introduction

Geopolymer is a novel binder which has given promising results, comparable or better than of Ordinary Portland Cement (OPC) binders in terms of sustainability, mechanical properties and durability. This binder is produced by the reaction of alumino-silicate rich source materials such as coal fly ash, slag etc. with highly alkaline activators. Geopolymer concrete has commonly been used for applications like footpaths, wall panels, pavements, footpath panels and sewer pipes [1]. However, use of geopolymer in large scale structural applications has been hindered due to lack of durability assessments and long term performance data.

OPC concrete can suffer from deterioration problems like alkali aggregate reaction (AAR). AAR is caused by the reaction between alkali hydroxide present in the hydrated cement and reactive phases that may be present in the aggregates. This reaction creates highly hydrated AAR gel in the concrete, which is an expansive product and can induce magnificent expansion and cracking of the affected elements. Major structures have suffered due to alkali-aggregate reaction reducing their service life or requiring large repair costs [2-4]. One approach to reduce AAR is the use of non-reactive aggregate in the concrete. However, this method is not always possible due to practical difficulties in acquiring non-reactive aggregates locally.

In previous studies, It has already been identified that AAR expansion can be reduced using supplementary cementitious materials like low calcium fly ashes [3]. This is due to factors such as reduction in alkalinity of pore solution and lower availability of calcium in the binder [5]. Geopolymer has a silica based polymer structure which has shown superior durability compared to OPC. It has less CaO and higher Na<sub>2</sub>O compared to OPC. Previous studies showed that the pH value of pore solution is above 11.5; which is adequate to attack reactive silica phases in aggregate [6]. However, AAR formation in geopolymer concrete is different from that of OPC concrete due to crossed link SiO<sub>4</sub> and AlO<sub>4</sub> in geopolymer compared to C-S-H in OPC. Therefore, it is worthwhile to identify the susceptibility geopolymer binder to AAR expansion. Geopolymer binder which is formed after a series of chemical reactions between silicon, aluminium and alkali hydroxides does not have hydrated phases or free calcium, which is an important factor in the expansion problems. Instead geopolymer contains three dimensional silicon polymer networks which can resist most of the above durability issues of OPC concrete.

Davidovits [7] stated that geopolymer based mortar bars which contained high alkali content (Na<sub>2</sub>O= 9.2%) have shown less expansion level compared to Portland cement binder based mortar bars. Kupwade-Patil and Allouche [8] reported that, mortar bars of alkali activated fly ash did not create any expansive gel due to absence of calcium. Although, they did not provide initial curing condition used in



their study, it is well known that 100% class F fly ash based geopolymer needs to be cured at elevated temperature (over 23 °C)[9]. García- Lodeiro et al.[5] also compared alkali aggregate reaction of alkali activated 100% class F fly ash binder with Portland cement binder using accelerated mortar bar method (1M NaOH, 80 °C). They reported that fly ash based geopolymer mortars showed less expansion compared to OPC mortars due to AAR. However, they cured samples initially at elevated temperature (85 °C). Expansion measurements after elevated curing are not ideal as expansion can occur before the zero measurement due to acceleration of AAR reaction at elevated temperature.

Although some aspects of AAR formation in class F fly ash based geopolymer has been studied so far, AAR in geopolymer mortars or concrete formulated with calcium rich material (i.e slag) and other aluminosilicate material has not been fully investigated. Bakrev et al. [10] and Puertas et al. [11], reported that concrete made with 100% alkali activated slag can show larger expansions than OPC concrete. However, addition of a calcium rich source into geopolymer systems is necessary as it enhances the setting behavior and mechanical properties of geopolymers [12]. Ground granulated blast furnace slag is mostly used as the calcium source in geopolymer systems due to its high reactivity in alkaline environment. The reaction product of slag contains calcium silicate hydrate (C-S-H) as well as geopolymer network. Despite the fact that slag improves the engineering properties of geopolymer binder excess Ca in geopolymer system can create phases like portlandite  $\text{Ca}(\text{OH})_2$  which may facilitate AAR. Fly ash and slag blended geopolymer binders contain less Ca, but their AAR susceptibility has not been thoroughly studied in the past.

This reports the results of accelerated AAR expansion tests conducted on geopolymer systems which were initially cured at room temperature (23 °C) prior to the accelerated testing in 1M NaOH at 80 °C. The analysis includes geopolymer with different fly ash to slag ratio and different with different aggregates that exhibit different levels of reactivity and different alkali contents. The microstructural features of representative specimen are also reported.

## 2. Experimental

### 2.1 Materials

#### 2.1.1 Geopolymer solids

A commercial Australian class F fly ash and ground granulated blast furnace slag from were used as main aluminosilicate source materials in geopolymer mixes. Anhydrous solid sodium silicate was used as alkali activator. General purpose (GP) cement was used for comparison. Table 1 shows the bulk chemical composition of source materials used in this study.

**Table 1: Bulk chemical composition of material**

Oxides	GP Cement	Slag‡	Fly ash
SiO <sub>2</sub>	19.3	32.0	51.5
TiO <sub>2</sub>	0.30	0.51	1.5
Al <sub>2</sub> O <sub>3</sub>	5.5	13.0	27.6
Fe <sub>2</sub> O <sub>3</sub>	2.9	0.40	11.8
Mn <sub>3</sub> O <sub>4</sub>	0.20	0.30	0.15
MgO	1.4	4.9	1.3
CaO	62	41.5	2.2
Na <sub>2</sub> O	0.06	0.20	0.4
K <sub>2</sub> O	0.4	0.33	0.6
P <sub>2</sub> O <sub>5</sub>	0.11	0.02	0.73
SO <sub>3</sub>	2.46	2.1	0.2

S <sup>2-</sup>	0	0.60	0
LOI	5.3 †	4.9	1.8
Total	99.93	100.7	99.78
‡ LOI in slag includes 3.7% sulfur in the form of SO <sub>3</sub>			
† indicate the presence of limestone in the cement			

### 2.1.2 Aggregates

Three types of aggregates including one non-reactive and two reactive were used in this study to identify the AAR behaviour.

- Non-reactive basalt (NR)
- Moderately reactive aggregate (R1) of gneiss origin
- Reactive aggregate (R2) of dacite origin

Aggregates were crushed and sieved according to (ASTM C-1260) to obtain required size range.

## 2.2 Test procedures

### 2.2.1 Geopolymer binder preparation for mortar bar expansion test

All geopolymer binders were formulated using material proportions shown in the Table 2. OPC binder was used to prepare specimens in the study. Total binder and crush aggregates masses were kept constant at 440 g and 990 g, respectively, in all tests. In geopolymer binders, the total solid content (combination of alumino-silicate source material and alkali activator) was considered as the binder. The mixing procedures followed that of RTA T363. The flow of each mortar mixture was measured using small flow table (ASTM C230). The mortar samples were cured in fog room at 23 °C for 24 hours. De-moulded samples were then cured further 3 days in the same curing condition before exposure to accelerated curing environment (1M NaOH, 80 °C). In this study, accelerated mortar bar test was used to measure expansion due to AAR. Shayan et al.[13] demonstrated that RTA-T363 test method, gives more reliable results compared to ASTM C-1260 procedures particularly for slowly reactive aggregates. Hence, all the mortar bar tests were conducted according to RTA-T363 procedures,

**Table 2: Binder formulations with different aggregates**

	Mix *	Aggregate type	Fly ash wt. (%)	Slag wt. (%)	OPC wt. (%)	Na <sub>2</sub> O wt. (%)
1	70F30S_4	NR	70	30	0	4%
2	50F50S_4	NR	50	50	0	4%
3	30F70S_4	NR	30	70	0	4%
4	100S_4	NR	0	100	0	4%
5	70F30S_6	NR	70	30	0	6%
6	50F50S_6	NR	50	50	0	6%
7	30F70S_6	NR	30	70	0	6%
8	100S_6	NR	0	100	0	6%
9	70F30S_4	R1	70	30	0	4%
10	50F50S_4	R1	50	50	0	4%
11	30F70S_4	R1	30	70	0	4%
12	100S_4	R1	0	100	0	4%
13	70F30S_6	R1	70	30	0	6%
14	50F50S_6	R1	50	50	0	6%
15	30F70S_6	R1	30	70	0	6%
16	100S_6	R1	0	100	0	6%
17	70F30S_4	R2	70	30	0	4%
18	50F50S_4	R2	50	50	0	4%
19	30F70S_4	R2	30	70	0	4%
20	100S_4	R2	0	100	0	4%
21	70F30S_6	R2	70	30	0	6%
22	50F50S_6	R2	50	50	0	6%
23	30F70S_6	R2	30	70	0	6%
24	100S_6	R2	0	100	0	6%
25	OPC	NR	0	0	100	0
26	OPC	R1	0	0	100	0
27	OPC	R2	0	0	100	0

\* F and S refer to fly ash and slag, respectively. The numerals refer to percentage of each component in the binder. Number 4 and 6 refer to percentages of Na<sub>2</sub>O content in the binder.

### **2.3 NMR technique for structure analysis of binders**

Geopolymer paste prepared using fly ash, slag and solid alkali activator was ground after 28 days to get NMR spectroscopy. <sup>29</sup>Si measurements were done at a bruker advance 3300 spectrometer operating at 59.6 MHz.

### **2.4 Scanning Electron microscopy (SEM) and Energy dispersive X-ray (EDX) analysis**

After mortar bar expansion measurements were conducted, sectioned mortar bars were subjected to SEM and EDX analysis. Samples were gold coated before analysis.

### 3. Results and Discussion

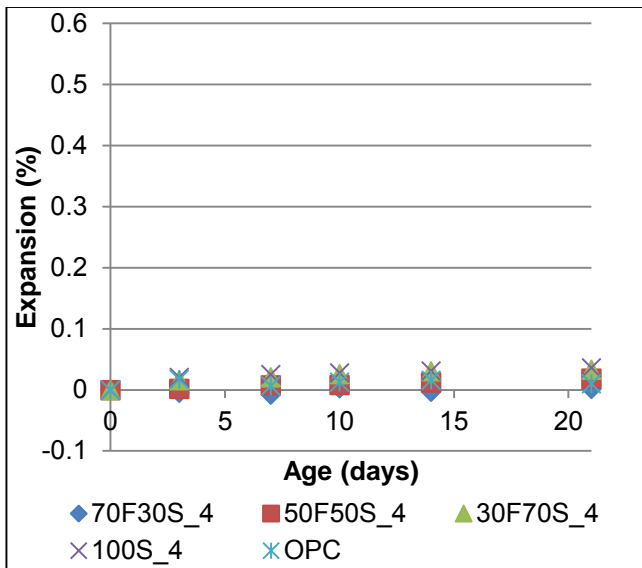
#### 3.1 AAR expansion of geopolymer based mortar bars

Length change of the mortar bars was measured using a digital comparator until the age of 21 days. The measurements were taken as described in Shayan et al. [14]. Three companion mortar bars were made for each test and the averages of the expansion values are shown in **Figure 1**, **Figure 2** and **Figure 3**.

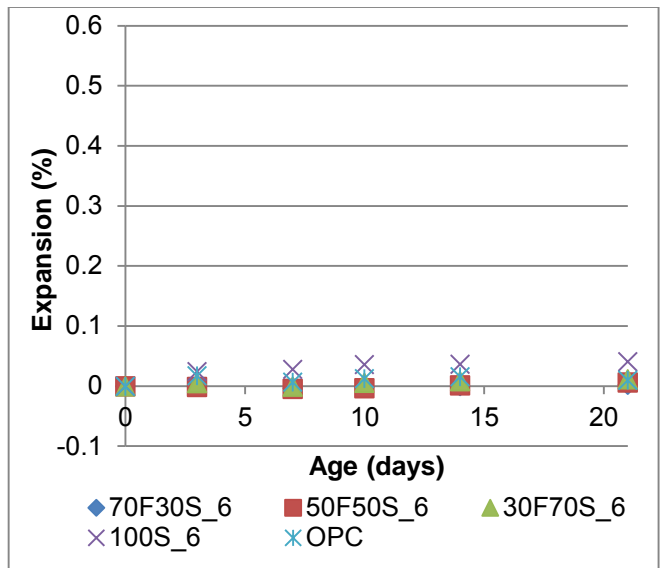
Figure 1a) and b) show the expansions of the mortar bars in geopolymer binders with NR aggregate. Fly ash slag blended geopolymer and OPCNR show almost no expansion in 21 days. The expansion level was very low even though the alkali content was increased in the binder to (6% Na<sub>2</sub>O). This showed that neither the NR aggregate nor the binder undergo expansion under the curing condition of the accelerated mortar bar test. The expansion limit of this test [14] note that values  $\geq 0.1\%$  expansion in 10 days indicate reactive aggregates and values  $\geq 0.1\%$  expansion in 21 days indicate slowly reactive aggregates. Expansion of NR basalt in geopolymer mortars was well below these limits. Reference OPC mortar bars also had high volume stability in presence of NR basalt aggregate. Basalt is minerally a silica-deficient, mafic rock, absent of free silica minerals, thereby it is not susceptible to AAR. The behavior of the binders in combination with reactive aggregates was also examined using two reactive aggregate types R1 and R2.

The two reactive aggregate types R1 and R2 are known to cause magnificent expansion when used in OPC concrete specimens containing elevated levels of alkali. Figure 2 (a/b) shows the expansion behavior of geopolymer based mortar bars with R1. The results show that 100S\_4, 100S\_6 and OPC binders caused large expansion in combination with R1 aggregate. Figure 2 also illustrates that OPC mortar bars exceed the acceptable expansion level in 10 days indicating the aggregates to be reactive. In 21 days, the expansion reached about 0.3%. Mortar bars with 100S\_4 showed a slower expansion rate compared to OPC but it also exceeded the 0.1% expansion limit in 21 days. Increase of the alkali content to 6% Na<sub>2</sub>O (100S\_6), increases the expansion up to 0.2% in 21 days. No significant expansion was observed in geopolymer systems with 30-70% fly ash. The expansion was slightly lower at the higher alkali content. This is probably because the geopolymer matrix becomes denser as a result of extensive reaction of fly ash and alkali in higher alkaline environment preventing AAR expansion in mortar bar.

Figure 3 illustrates the expansion behaviour of mortar bars containing R2 aggregate. Again mortar bars made with OPC binder showed significant expansion (0.2% and 0.4% in 10 days and 21 days respectively). The specimens made with alkali activated slag binder and R2 aggregate also showed significant expansion (0.1% and 0.2%, in 10 days and 21 days respectively). Moreover, the expansion of specimen made with alkali activated slag slightly exceeded that specimen containing OPC binder at high alkali content (6%) being 0.3% and 0.45% expansion in 10 and 21 days, respectively. Even though, specimens with 100S\_6 showed higher rate of expansion during the early period of measurements, the 21 days expansion values for specimens containing OPC and 100S\_6 were similar. These results show that slag-based geopolymers mortar containing high alkali content behave similar to OPC mortar, ie, the slag does not suppress AAR at high alkali content. However, fly ash and slag blended geopolymer binders show no expansion at either 4% Na<sub>2</sub>O or 6% Na<sub>2</sub>O contents. The results so far show that 70% slag usage in geopolymer synthesis is safe with respect to AAR.

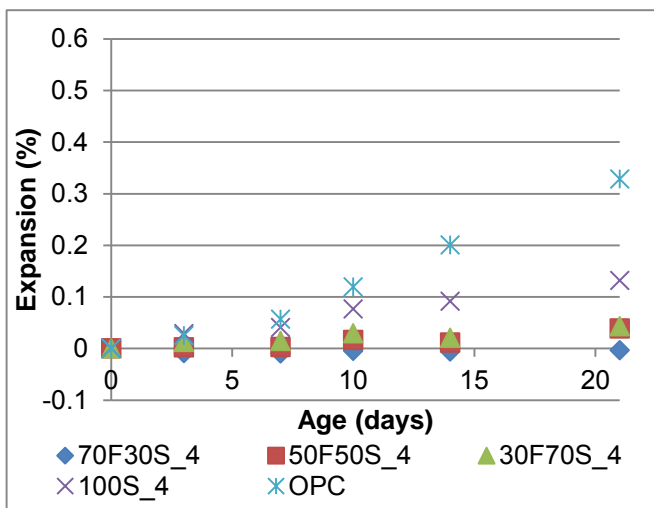


a

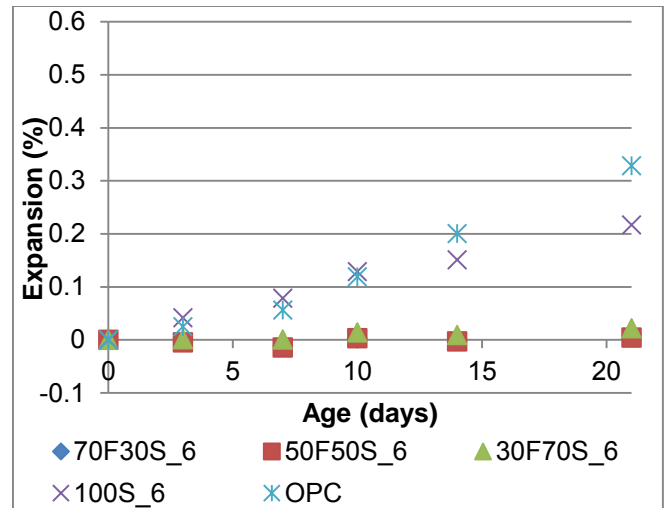


b

Figure 1: Average expansion of mortar bars containing NR aggregate at a) 4% Na<sub>2</sub>O b) 6% Na<sub>2</sub>O



a



b

Figure 2: Average expansion of mortar bars containing R1 aggregate at a) 4% Na<sub>2</sub>O b) 6% Na<sub>2</sub>O

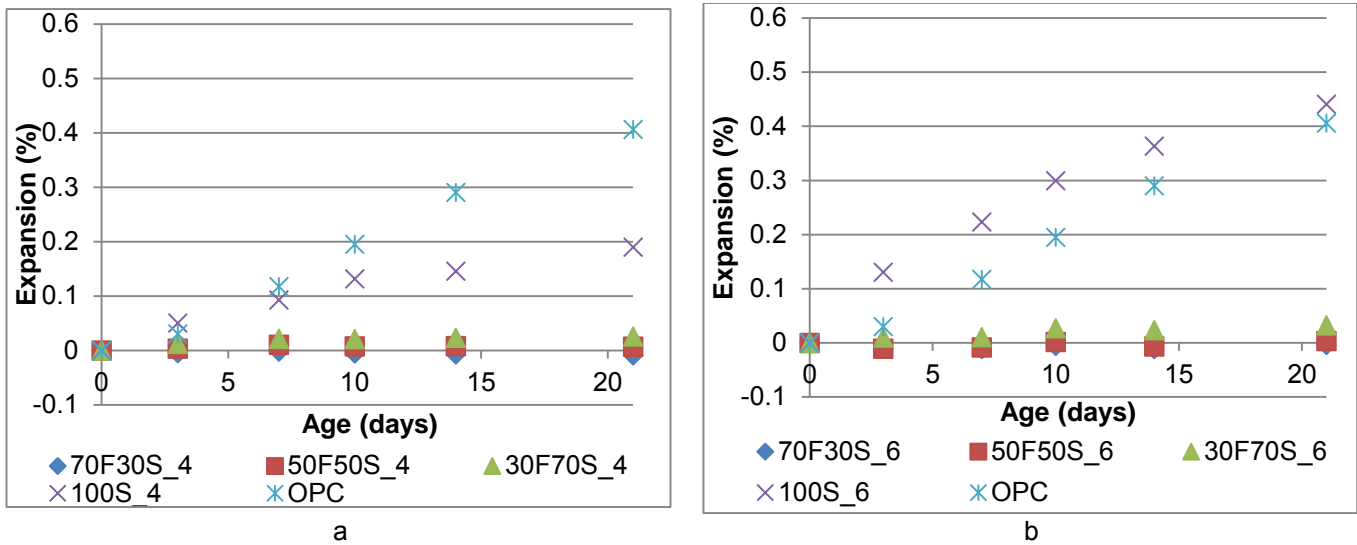


Figure 3: Average expansion of mortar bars containing R2 aggregate at a) 4% Na<sub>2</sub>O b) 6% Na<sub>2</sub>O

Slag addition to geopolymer synthesis increases the setting characteristics as well as the mechanical properties of the binders. Alkali activated slag creates calcium silicate hydrates (C-S-H) as the main reaction product while the introduction of class F fly ash into alkali activated slag mix generates Na<sub>2</sub>O-Al<sub>2</sub>O<sub>3</sub>-SiO<sub>2</sub>-H<sub>2</sub>O geopolymer matrix, C-S-H and (Ca/Na)-A-S-H phases as main products. When slag increases in the geopolymer synthesis, C-S-H percentage is also increased, resulting in durability issues like AAR. Hence, it is important to identify the optimum level of slag addition into geopolymer systems without causing AAR.

Figure 4 shows the AAR expansion of geopolymer mortar containing different levels of slag. Beyond 70% slag content, the mortar bars showed magnificent expansion. The rate of expansion also increases with higher slag content in the geopolymer. OPC mortars also have the same durability issue as the high slag based geopolymers due to high calcium contents. The results show that more than 80% slag content in the geopolymer can cause high AAR expansion in the later stages of testing.

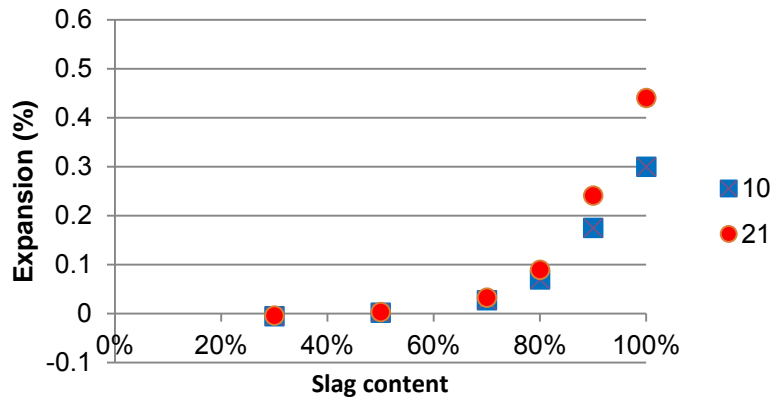
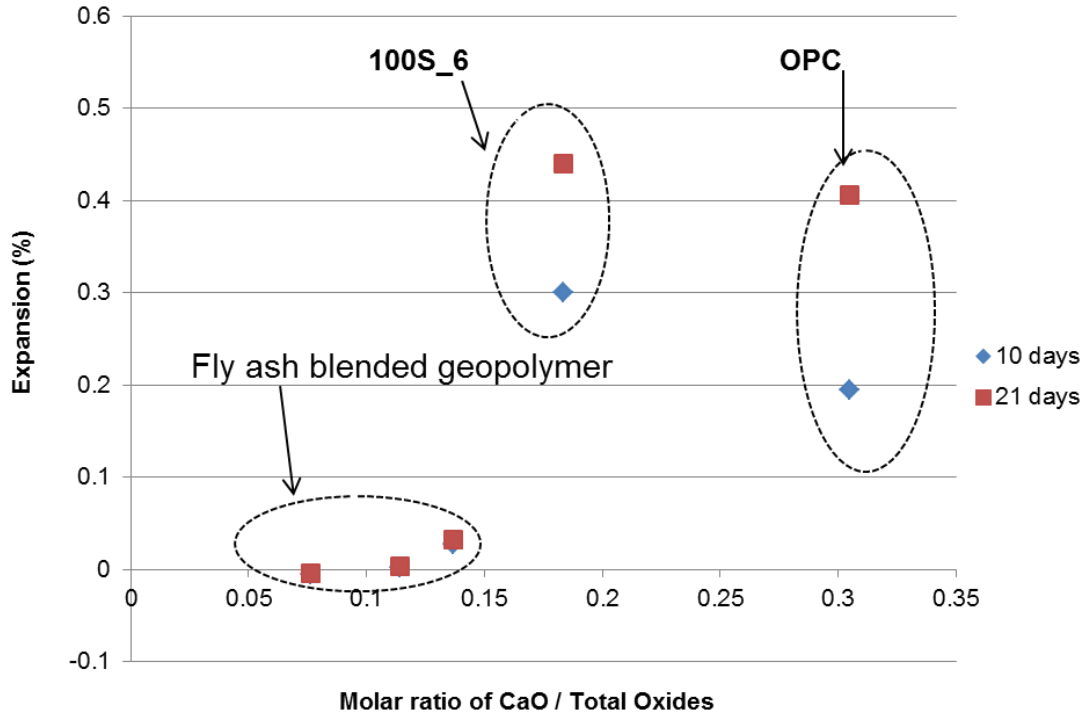


Figure 4: Expansion of geopolymer mortar bars containing different slag content and R2 aggregate at 6% Na<sub>2</sub>O

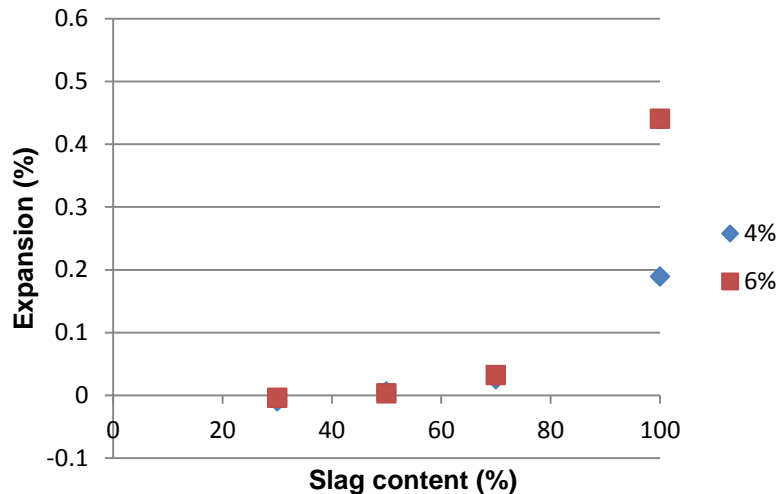
Figure 5 analyses the expansion behavior of geopolymer and OPC systems as a fraction of CaO content. It shows that a CaO fraction below 0.15 results in geopolymer systems without AAR expansions. Figure 5 also shows that CaO fraction significantly influences towards the AAR expansion of geopolymer mortars. 100% slag and Portland cement systems have calcium in form of Ca(OH)<sub>2</sub> which helps to maintain high alkaline levels in the concrete pore solution [15]. Thomas [16] reported that Ca<sup>2+</sup> can

replace alkali ions in the AAR gel, thereby more  $\text{Na}^+$  ions are released into the pore solution, allowing further reaction and expansion. He also showed that when class F fly ash is blended with OPC, it produced AAR gel with no harmful expansion (no expansion and cracking). This was attributed to low viscosity of AAR gel which can be dispersed into binder through pores. In presence of high calcium environment, the gel viscosity increases preventing it from being dissipated in the pores, eventually leading to expansion.



**Figure 5: Expansion variation with CaO fraction in the binder (total oxide molar =  $\text{Na}_2\text{O} + \text{CaO} + \text{K}_2\text{O} + \text{Al}_2\text{O}_3$ ) (note: R2 aggregate was used in this study)**

Alkalinity of geopolymer systems is one of the key parameters that control the reaction mechanism and structural characteristics of the binder. Influence of alkalinity in geopolymer systems for AAR can be discussed using Figure 6. Figure 6, which shows the expansion of geopolymer mortar bars in the presence of two different alkali levels. In this comparison, a reactive aggregate (R2) was used. Geopolymer mortar bars with 30-70% slag showed negligible length change at 4 and 6% alkali content. However, mortar bar made with 100% alkali activated slag expanded 0.45% in 6% alkali environment compared to 0.2% length change at 4% alkali level.



**Figure 6: Expansion variation of mortar bars with different alkali level and R2 aggregate (in 21 days)**

### **3.2 NMR spectra variation of different binders**

NMR is used to investigate the structure of silica species in crystalline as well as in amorphous form. Advantage of this analytical tool is that it can identify the nearest neighbour and next nearest neighbour in the atomic environment. Moreover, mobility of the associate protons can also be identified in NMR-MAS spectra. Hence, NMR-MAS spectroscopy was employed to examine atomic structures in various binders.

Figure 7 shows the  $^{29}\text{Si}$  spectra of 70F30S, 50F50S and 100S binders. In NMR spectroscopy, 'Q' is used to represent different silica species,  $\text{Q}^4$  denotes  $\text{SiO}_4$  tetrahedra which connects to four other atoms of the same type via shared oxygen atoms and  $\text{Q}^3$  denotes three oxygen bonded tetrahedral and so on.

70F30S and 50F50S geopolymers show signal at -110 to -120ppm indicating complete mixing of  $\text{SiO}_4$  and  $\text{AlO}_4$  units ( $\text{Q}^4$ ). Furthermore, 70F30S and 50F50S geopolymers also show shifts correspond to  $\text{Q}^3$  (-110 to -100 ppm),  $\text{Q}^2$  (-100 to -92 ppm) and  $\text{Q}^1$  (-94 to -84) and  $\text{Q}^0$  (-85 to -75 ppm) species apart from silica tetrahedral. On the other hand 100S shows signal around -85 to -79 ppm which corresponds to  $\text{Q}^1$  type species. It is observed in Figure 7, when fly ash was mixed with slag, this signal shifted towards negative direction. Provis et al.[17] stated that when  $^{29}\text{Si}$  NMR spectra signal is shifted towards negative direction the structure has higher connectivity.

The  $\text{Q}^4$  based structure found in geopolymer has rigid well organized framework preventing additional substitution of ions in alkali surroundings. Therefore, the structural changes are not easily allowed in geopolymer binders.  $\text{Q}^1$  species generates a chain type structure in 100S (mainly C-S-H) which is less polymerized compared to geopolymers. The chain type structure can be altered and rearranged in alkali environment. These results suggest that binders with  $\text{Q}^1$  chain type structure may favour AAR development in mortar in the presence of reactive aggregates.



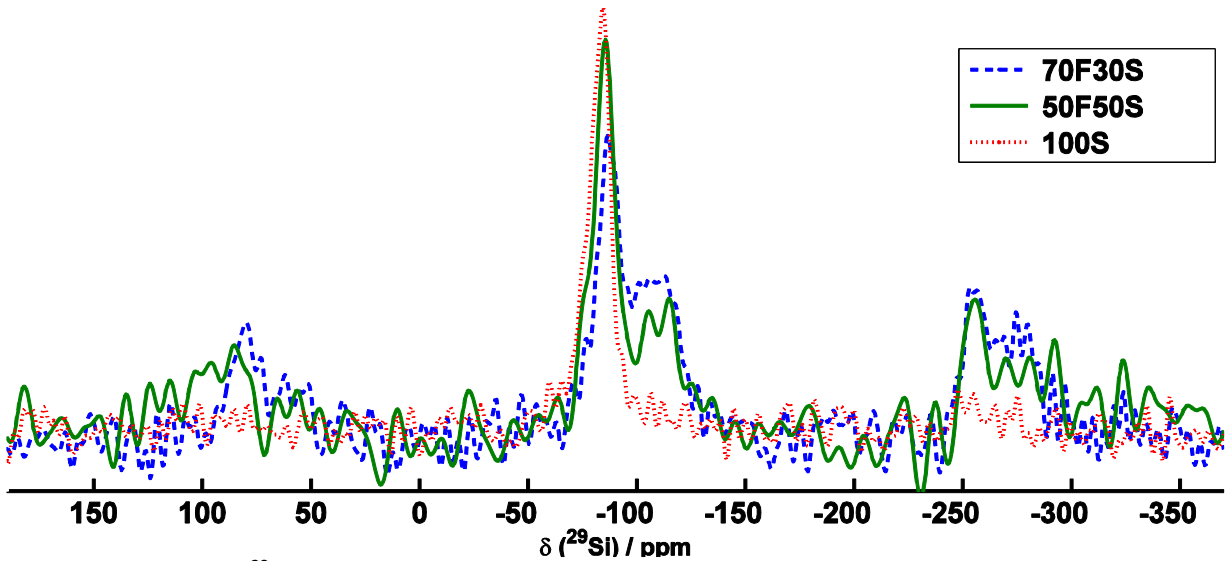


Figure 7:  $^{29}\text{Si}$  Spectra for geopolymer binders (activator content = 4%  $\text{Na}_2\text{O}$ )

### 3.3 Microstructural features of binders

Microstructural features of the binder were analysed using Scanning electron microscopy (SEM) and EDX Energy dispersive X-ray (EDX). Square sections (75×75×5 mm) were prepared for examination after the completion of expansion measurements. As discussed earlier, the ingredients of the binder significantly impact the AAR expansion. The combination of OPC or 100S with reactive aggregate caused excessive mortar bar expansion, whereas the use of at least 30% fly ash in binder prevented the expansion during the test period. SEM/EDX analysis was used to compare microstructural features of mortars incorporating the different aggregates in combination with 50F50S, 100S and OPC binders.

Figure 8, Figure 9 and Figure 10 show the different forms of products found in mortars with different binders in the presence of reactive (R1 and R2) and non-reactive aggregates (NR). Figure 8(a) shows a formed product in 50F50S geopolymer which contain NR aggregate. According to EDX composition, this product has zeolite-like composition. Figure 8(b) shows alkali activated 100S also shows a zeolite-like product but with less aluminium and high calcium compared to Figure 8(a). Figure 8(c) shows a reaction product found in OPC mortars in the presence of NR aggregate which has not been analyzed yet using EDX. Rosettes products in mortars in the presence of R1 aggregate with OPC and 100S binders are shown in

Figure 9(b) and Figure 9(c). These AAR products were found throughout the OPC and 100S specimens. Figure 9(a) shows that fly ash blended binder based mortars in the presence of R1 aggregate, formed zeolite-like product with less Al content compared to the product shown in Figure 8(a).

Figure 10 shows the composition of binder and AAR products of mortars in the presence of reactive aggregate R2. Area 'A' as marked on each image was analysed the binder composition. The EDX spectrum of OPC binder shows higher Ca and lower Si typical of calcium silicate hydrate, whereas the EDX spectrum corresponding to 100S also shows enhanced peak intensity for Si compared to Ca (unlike C-S-H). Even though, both spectra (OPC and 100s) show a composition of calcium silicate hydrate, Ca/Si ratio in OPC binder is higher than that of slag binder. It was observed that 50F50S binder generated a matrix rich in Al, Si, Na and Ca consistent with a hydrated calcium aluminium silicate type phase. Mg noted in the in the EDX spectrum of 50F50S binder originates from the slag.

Area 'B' marked on each image represents AAR products. As shown in Figure 10 all the mortars formed AAR products in the presence of R2 aggregate. The main reaction products formed in these binders were identified as typical AAR product like rosette-type crystals as seen in Figure 10. Most of the AAR related products found in the mortars in the presence of reactive aggregates are similar in nature. Observed AAR products were rich in Si, Na and Ca, but poor in Al which is typical of composite of AAR products.

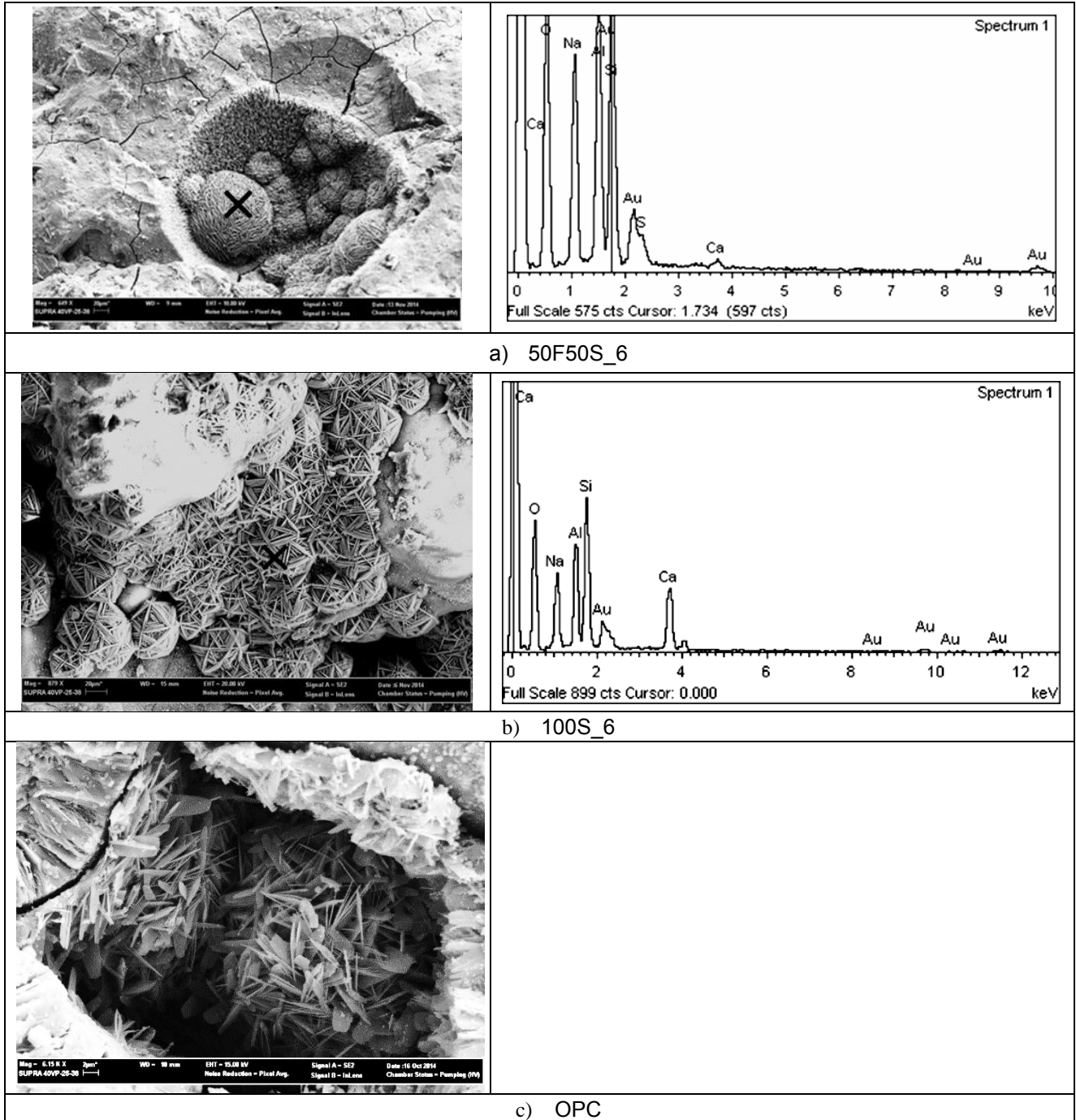
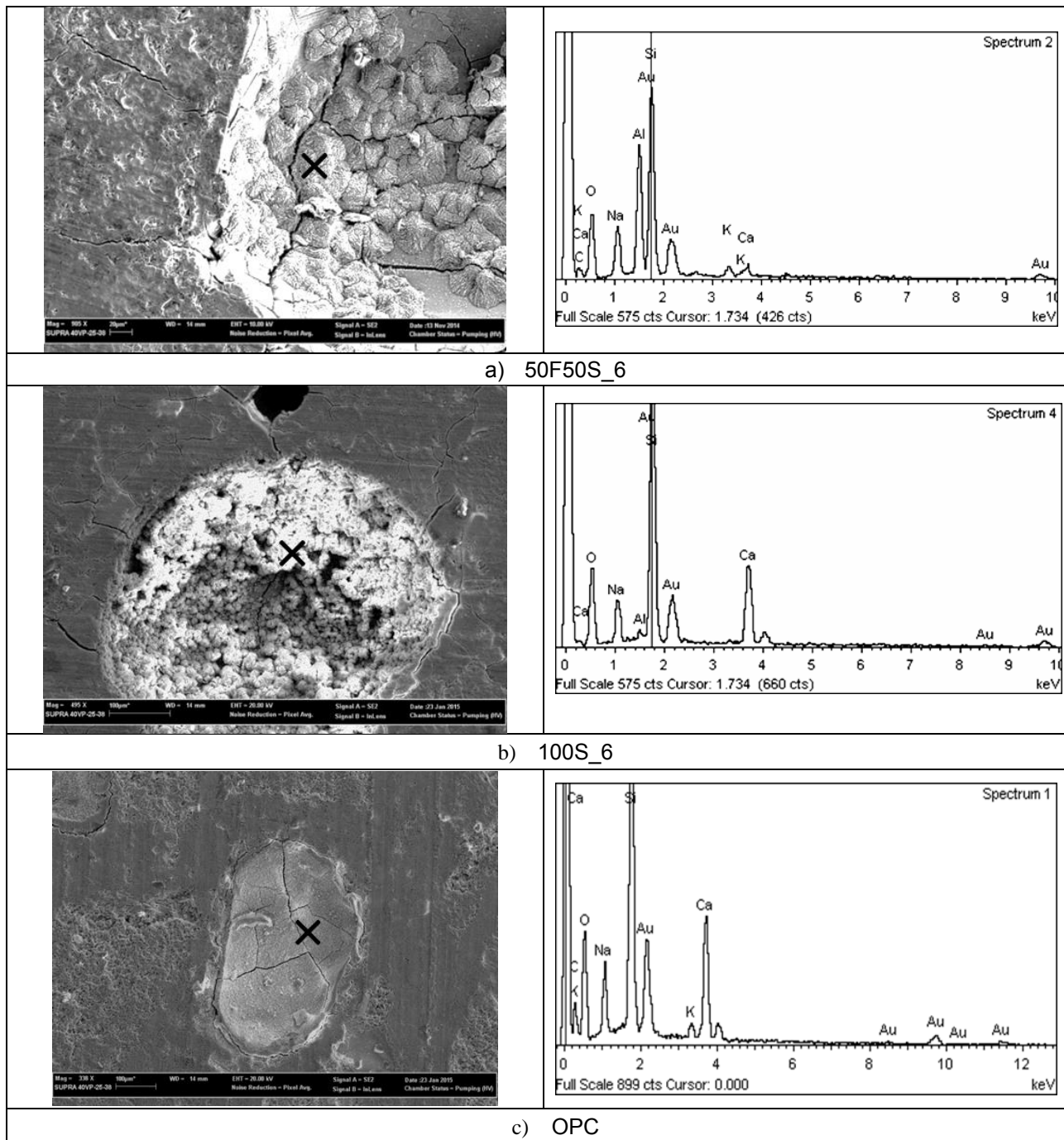
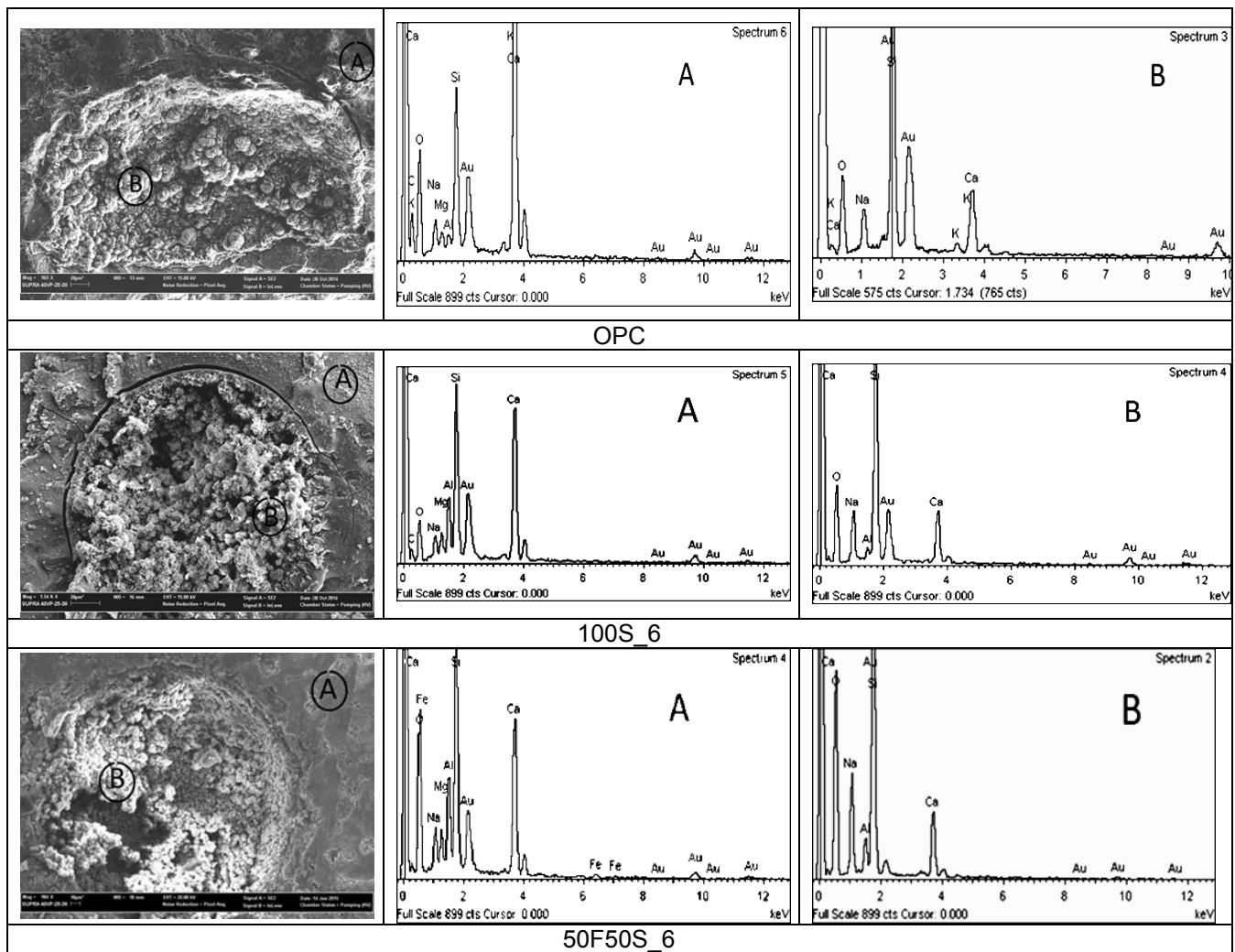


Figure 8: Reaction products found in mortars with different binders in the presence of NR basalts (EDX spectrum for OPC binder to be done). Each EDX spectrum represents the composition of the area marked on the corresponding image.



**Figure 9: Reaction products found in mortars with different binders in the presence of reactive aggregate R1. Each EDX spectrum represents the composition of the area marked on the corresponding**



**Figure 10: Reaction products found in mortars with different binders in the presence of reactive aggregate R2**

**Figure 11** shows that mortar specimens made with slag-fly ash blended geopolymer exhibit clear microstructural differences compared to those made with 100S. Whereas in the latter AAR products, such as the rosettes shown in Figure 11a, were present. In the fly ash blended geopolymer mortars, the composition of the observed products revealed large Al contents, indicating Na-aluminosilicate materials (**Figure 11(b)**). The Si/Al ratio in these products was found as approximately 1, whereas typical AAR products (As seen in **Figure 11(a)**) contain very small Al contents. The products formed in slag-fly ash blended geopolymers could belong to zeolite type phases generated in addition to geopolymer gel. García-Lodeiro et al.[5] also observed similar products in their fly ash based geopolymers.

EDX spectrum C in (Figure11) shows that AAR gel was present in this mortar (50F50S), and that the geopolymer phases were formed in association with the AAR gel.

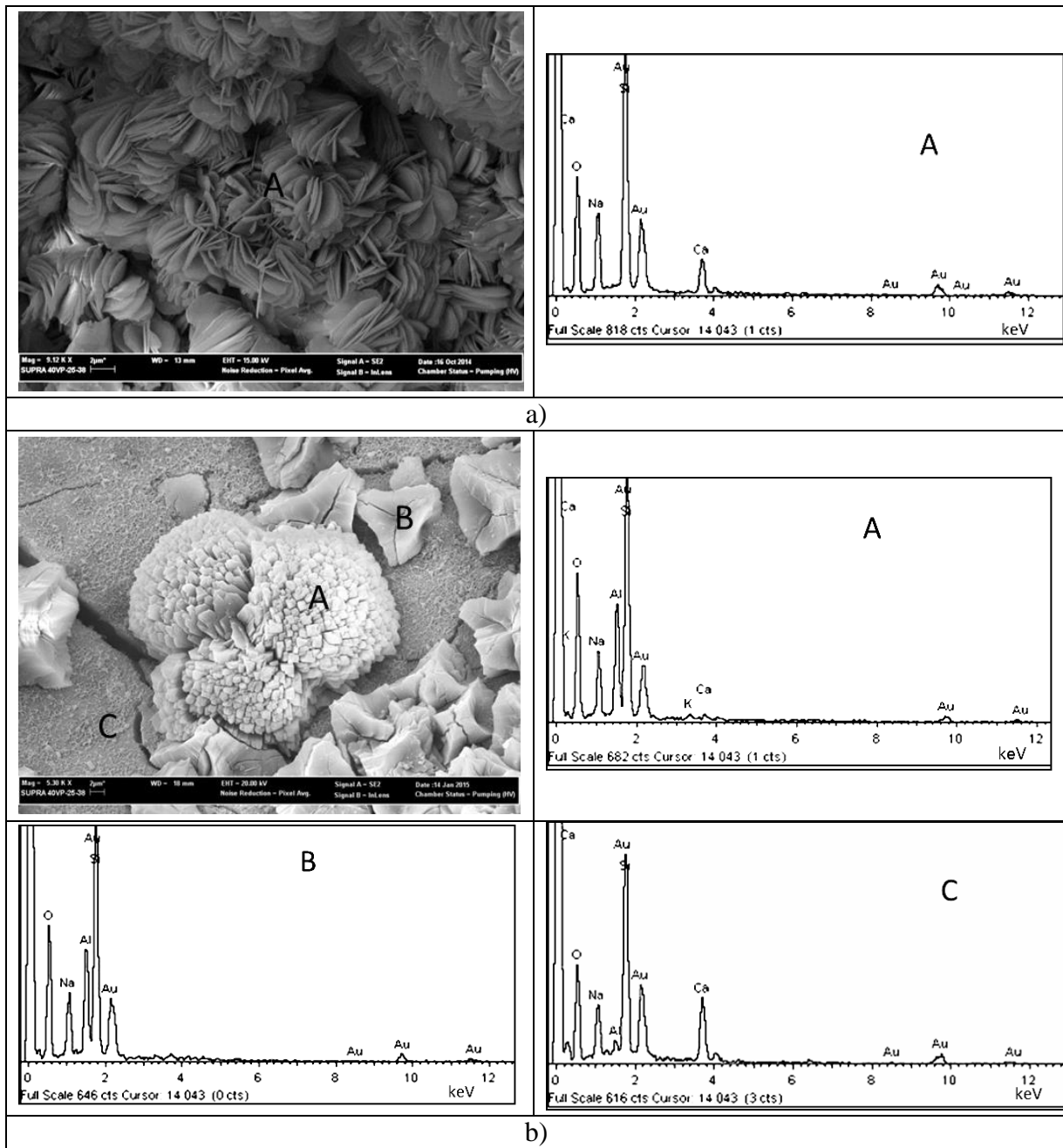


Figure 11: Products formed in mortars made with reactive aggregate R2 and binders a) 100\_6S b) 50F50S\_6

#### 4. Conclusions

The following conclusions can be drawn from this work:

1. The accelerated mortar bar test was used to analyze the performance of OPC, 100S and 50F50S binders in combination with two reactive aggregate and one non-reactive aggregate. At least 30% fly ash is needed in alkali activated slag to reduce the AAR expansion.
2. MAS-NMR  $^{29}\text{Si}$  spectroscopy results showed that alkali activated slag contains  $\text{Q}^1$  and  $\text{Q}^0$  species which are less polymerized (chain type structures). However, when fly ash was introduced into alkali activated slag (70F30S and 50F50S),  $\text{Q}^4$  and  $\text{Q}^3$  species were generated forming more stable 3 dimensional structures.
3. SEM and EDX analysis showed that OPC and alkali activated 100S mortars produced type typical AAR product such as rosettes, in the presence of reactive aggregates. On the other hand, fly ash and slag blended geopolymer generated zeolitic type products which contain significantly higher aluminum content compared to its binder composition.
4. AAR expansion could be related to the type of geopolymer reaction product that form in the binder and could be controlled by using at least 30% fly ash in the geopolymer composition.

#### Acknowledgement

The research was supported by Austroads project (TS1835) awarded to the ARRB group, Australia.

#### 5. References

1. Provis J., Deventer J.S.J.V., "Demonstration projects and applications in building and civil infrastructure", In: Alkali Activated Materials, 2013 pp 30-45.
2. Shayan A., Grimstad J., "Deterioration of concrete in a hydroelectric concrete gravity dam and its characterisation". Cement and Concrete Research, 36 (2), 2006, pp 371-383.
3. Shayan A., "Re-examination of AAR in an old concrete". Cement and Concrete Research, 19 (3), 1989, pp 434-442.
4. Shayan A., "Alkali aggregate reaction in a 60-year-old dam in Australia". International Journal of Cement Composites and Lightweight Concrete, 10 (4), 1988, pp 259-266.
5. García-Lodeiro I., Palomo A., Fernández-Jiménez A., "Alkali-aggregate reaction in activated fly ash systems". Cement and Concrete Research, 37 (2), 2007, pp 175-183.
6. Song S., Jennings H.M., "Pore solution chemistry of alkali activated ground granulated blast furnace slag". Cement and Concrete Research, 29, 1999, pp 159-170.
7. Davidovits J., "Properties of geopolymer cements", Paper presented at the First international conference on alkaline cements and concrete, 1994, Ukraine.
8. Kupwade-Patil K., Allouche E., "Impact of Alkali Silica Reaction on Fly Ash-Based Geopolymer Concrete", Journal of Materials in Civil Engineering, 25 (1), 2013, pp 131-139.
9. Bakharev T., "Geopolymeric materials prepared using Class F fly ash and elevated temperature curing". Cement and Concrete Research, 35 (6), 2005, 1224-1232.
10. Bakharev T., Sanjayan J.G., Cheng Y.B., "Resistance of alkali-activated slag concrete to alkali-aggregate reaction". Cement and Concrete Research, 31 (2), 2001, pp331-334.
11. Puertas F., Palacios M., Gil-Maroto A., Vázquez T., " Alkali-aggregate behaviour of alkali-activated slag mortars: Effect of aggregate type" , Cement and Concrete Composites, 31 (5), 2009, pp 277-284.

12. Provis J., Bernal S., " Binder chemistry – blended systems and intermediate Ca content. In: Alkali Activated Materials". 2013, pp 1-22.
13. Shayan A., Morris H., "A comparison of RTA T363 and ASTM C1260 accelerated mortar bar test methods for detecting reactive aggregates", Cement and Concrete Research, 31 (4), 2001, pp 655-663.
14. Shayan A., Diggins R.G., Ivanusec I., Westgate P.L., "Accelerated testing of some Australian and overseas aggregates for alkali-aggregate reactivity". Cement and Concrete Research, 18 (6), 1988, pp 843-851.
15. Hou X., Struble L.J., Kirkpatrick R.J., "Formation of ASR gel and the roles of C-S-H and portlandite", Cement and Concrete Research, 34 (9), 2004, pp1683-1696.
16. Thomas M.D.A., "The role of calcium in alkali-silica reaction", In: Materials Science of concrete, Sydney, Australia, 1998.
17. Provis J., Kamseu E. Leonelli C., Palomo A., "Binder chemistry – Low-calcium alkali-activated materials". In: Alkali activated material. 2013, pp 146-200.

# Rheological Properties of sodium carbonate Alkali-Activated Fly Ash/Slag pastes with Different Superplasticisers

Ahmed Abdalqader<sup>1</sup> and Abir Al-Tabbaa<sup>2</sup>

<sup>1</sup>PhD Candidate, Cambridge University Engineering Department

<sup>2</sup>Professor of Civil & Environmental Engineering, Cambridge University Engineering Department

**Abstract:** Alkali-activated fly ash/slag (AAFS) is a newly evolved type of alkali-activated material and a promising environmentally friendly alternative binder to Portland cement. The rheological properties of this type of binder were examined using a number of different commercial superplasticisers. Mini slump tests, flow table tests, and a rheometer were used to investigate the flowability and rheology of these binder pastes. It was found that increasing the sodium carbonate activator dosage increased the viscosity and the yield stress of the paste. The results also showed that the lignosulphonate-based admixture was the most efficient superplasticiser in improving the rheological properties of these mixtures.

**Keywords:** fly ash, slag, superplasticiser, rheology, lignosulphonates.

## 1. Introduction

The need for alternative and more sustainable binders to Portland Cement (PC) has fuelled significant research efforts in construction materials over the last few decades (1–4). The rapid growth in research and development related to alkali-activated materials (AAMs) has indeed indicated that the use of such systems as primary binders in the construction industry offers great potential in addressing not only the challenges of the damaging effect of PC on the environment, but also of the waste management problems related to the aluminosilicate solid waste materials from many industries (2,5–8). Ground granulated blast-furnace slag (GGBS) from the pig iron industry and pulverised fuel ash or fly ash (FA) from the burning of pulverised bituminous coals in power station furnaces (9) are the most used precursor materials in alkali activated systems.

Extensive research has been conducted on the activation of GGBS or FA. However, a growing literature has focused on the activation of a blend of both materials in part because of the limited availability of each and in part due to their potential synergetic effects (7,10–14), the purpose being to enhance the advantages and eliminate the disadvantages of the activation of each material alone (13,14). Because of their relatively low cost, low carbon footprint, and wider availability, the use of carbonate-based activators offers advantages over conventional activators, such as sodium hydroxide and sodium silicate, because of their low cost, availability, and low carbon footprint compared to the aforementioned activators (15).

More attention has, recently, been paid to understanding the role and mechanism of sodium carbonate ( $\text{Na}_2\text{CO}_3$ ) in the activation of GGBS and/or FA (13,14,16–18). Nevertheless, most research has concentrated on the mechanical properties of pastes, mortars, and concrete and the microstructural analysis of the reaction products. In contrast, very few studies have considered the rheological properties of AAMs (19–22); and to the authors' best knowledge, none have been conducted on  $\text{Na}_2\text{CO}_3$ -activated fly ash/slag. Like PC, AAMs display visco-plastic behavior (23). However, it is notable that there have been many conflicting reports with respect to the rheological properties of alkali-activated cement suspensions, with the majority of the studies indicating that admixtures have variable or inconsistent effects on these systems. Different behaviour and mechanisms with different superplasticisers have been reported in alkali-activated slag (AAS) and alkali activated fly ash (AAFA) (19,21,22,24–27). For example, some studies found that adding a superplasticising admixture based on selected sulphonated naphthalene polymers to AAFA improved the workability (27,28). On the other hand, other studies reported that neither polycarboxylate, vinyl copolymer-based admixtures, nor naphthalene-based superplasticisers had any influence on the workability (29,30). Palacios and Puertas (22) showed that naphthalene-based admixtures significantly increased the flow rate in NaOH-activated slag while polycarboxylate, melamine-based and vinyl copolymer admixtures led to a slight improvement in the flowability of the same system. However, the same admixtures exhibited no influence on the workability of waterglass-activated slag (22).

As alkali-activated fly ash/slag (AAFS) systems are still in their infancy and are an evolving field of research, there is a lack of studies on the rheological properties of these systems, and no research on systems activated by  $\text{Na}_2\text{CO}_3$ . Thus, the aim of this study was to investigate the effect of different commercial superplasticisers, activator dosage, and reactive magnesia incorporation on the rheological



properties of Na<sub>2</sub>CO<sub>3</sub>-activated fly ash/slag with reactive magnesia. The effects of these superplasticisers on the microstructure and mechanical properties of these mixes will be reported elsewhere.

## 2. Experimental materials and methodology

### 2.1 Materials used

The GGBS used had basicity ( $K_b = \frac{\text{CaO}+\text{MgO}}{\text{SiO}_2+\text{Al}_2\text{O}_3}$ ) and hydration modulus ( $\text{HM} = \frac{\text{CaO}+\text{MgO}+\text{Al}_2\text{O}_3}{\text{SiO}_2}$ ) values of ~1.0 and ~1.60, respectively. The GGBS was mainly amorphous, with merwinite (Ca<sub>3</sub>Mg(SiO<sub>4</sub>)<sub>2</sub>) identified as the only crystalline phase present. The FA is classified to meet the requirements of BS 3892: Part 1 for use with PC. The MgO 92/200 has a reactivity of 170s according to the acetic acid test, which indicates medium reactivity according to the classification of Jin and Al-Tabbaa (31). The chemical compositions of all materials are shown in Table 1. Sodium carbonate was supplied as a powder of 99% purity and was dissolved in the mix water.

**Table 1. Chemical composition and physical characteristics of the materials used (based on the suppliers' datasheets)**

Component	GGBS	FA	MgO92/200
CaO %	39.24	6.8±3.6	1.9
SiO <sub>2</sub> %	36.79	49.3±6.2	0.9
Al <sub>2</sub> O <sub>3</sub> %	11.51	24.1±0.4	0.1
Fe <sub>2</sub> O <sub>3</sub>	0.42	9.7±1.3	0.8
MgO %	8.10	1.1±0.2	93.5
SO <sub>3</sub> %	1.03	3.3±1.3	-
K <sub>2</sub> O %	0.63	3.5±0.3	-
Na <sub>2</sub> O %	0.37	1.2±0.1	-
SSA (m <sup>2</sup> /g)	0.545	2.600	15.9

Clinkerless systems were prepared from GGBS, FA, and MgO and activated by Na<sub>2</sub>CO<sub>3</sub>. Each material was given an appropriate notation for simplicity: G, F, M, and N refer to GGBS, FA, MgO, and Na<sub>2</sub>CO<sub>3</sub>, respectively. The ratio of the GGBS to FA was fixed at 3:1 by weight. MgO replaced between 0-10% of GGBS+FA and the content of Na<sub>2</sub>CO<sub>3</sub> varied from 0-10% by the weight of the total binder as an addition (Table 2). All mixes had water to binder (w/b) ratio of 0.31. Different commercial superplasticisers (SP) were used in this study in liquid forms:

(SP-A) a modified polycarboxylate-based high range water reducing/superplasticising concrete admixture;

(SP-B) a modified polycarboxylate-based mid-range water reducing/plasticising concrete admixture; and

(SP-C) a modified lignosulphonates-based water reducing/plasticising admixture were added to each mix at a dosage of 1%.

**Table 2. The cement paste mix proportions used in this study by % weight**

Mix ID	GGBS %	FA %	MgO %	Na <sub>2</sub> CO <sub>3</sub> % - forms part of the mix water
M0N5	75	25	0	5
M5N5	71.25	23.75	5	5
M10N5	67.5	22.5	10	5
M0N10	75	25	0	10
M5N10	71.25	23.75	5	10
M10N10	67.5	22.5	10	10

The mixing and sample preparation procedures are presented separately under each heading below and all mixing and tests were conducted in the laboratory at a room temperature of 20 °C ±1 °C.

## 2.2 Experimental procedure

### 2.2.1 Mini-slump test

The mini-slump test was developed to assess the early stiffening of cement paste in the first 60 minutes of hydration. To monitor the workability loss, the average diameter of the mini slump spread was plotted against time. Initially, all dry materials (GGBS, FA, MgO) were mixed for homogenisation. After dry mixing, 80% of the total water was added and mixed for 60s. Subsequently, the remaining water was added along with the superplasticiser and mixed for 60s. Then 2-minute-rest was applied and followed by a final mixing of 2 minutes. Between each stage the side walls were cleaned. After mixing the paste, the mini-slump test was performed using a small slump cone (Fig. 1). The paste was taken and poured into the cone. Excess paste was then removed by levelling the paste to the height of the cone and collected on the wide flange. Slight tapping was given on the flanges to release the entrapped air (if any). The mini-slump cone was lifted with a motion rapid enough without obstructing the flowing paste but slow enough to avoid disturbing the paste. After following a standard mixing schedule, samples of the paste were tested, at 2, 5, 10, 30, 45 and 60 minutes. For the last four readings, samples were remixed for 120s before performing the test. The diameter of the paste spread was recorded in two directions at right angles and the average was calculated (32). The test was replicated.



Figure 1. (left) Mini-slump cone dimensions, (middle and right) Test in action.

### 2.2.2 Flow table test

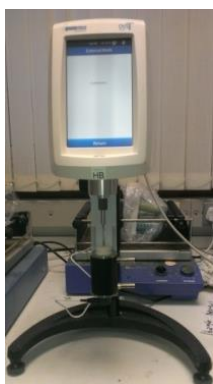
The standard flow table spread was determined in according to European standard EN 1015-3 (33) using an automatic table set (Figure 2). The test was conducted on cement paste rather than mortar. The truncated cone mould (larger base at the bottom) with its funnel in the centre was set on the disc of the flow table. The paste was introduced into the mould in two layers, each layer being compacted at least 10 times by a tamper to ensure uniform filling of the mould. Excess paste was then skimmed off with a palette knife and the disc was carefully cleaned of any paste or water. After 15s, the mold was lifted vertically and the disc was jolted 15 times at a constant frequency of one per second to spread out the paste. The diameter of the paste spread was measured in two directions at right angles and the average was stated to the nearest mm. The test was replicated.



**Figure 2. Flow table apparatus.**

### **2.2.3 Rheological studies**

Viscometric studies were conducted to explore the change in rheology due to the addition of the SP. The tests were performed on a coaxial cylinder type-smooth walled rheometer. The diameters of inner and outer cylinder were 11.76mm and 19.05mm respectively. The effective length of the inner cylinder was 39.3mm and the depth of the outer cylinder was 86.2mm (Figure 3). The volume of the sample taken was 10.4ml (34). In order to find the best test procedure, a preliminary study of the paste at a constant shear rate of  $50\text{s}^{-1}$  was conducted. The purpose of this test was to find out the time at which the test should start in order to eliminate the influence of the early changes in the paste due to the dissolution rate. To study the rheological parameters of yield stress and plastic viscosity, a shear profile was set up based on (32) who used similar apparatus. The procedure consisted of pre-shearing at  $30\text{s}^{-1}$  in 60s to erase any previous shear history due to mixing, and was followed by a 30s pause to stabilize the paste. Then it was followed by ramping up the shear rate from 0 to  $60\text{s}^{-1}$  in 105s, which data being recorded after every 15s, and finally the shear rate was ramped down from 60 to  $0\text{s}^{-1}$  in 90s, which data also being recorded after every 15 s. The yield stress and plastic viscosity values were calculated from the log-log scale of plotting shear rate (1/s) versus shear stress ( $\text{N/m}^2$ ) and were the average of at least three trials. The mixing time of all the mixes was fixed at 6 minutes. Immediately after mixing, the paste was transferred into the container of the used rheometer and left to rest for 5 minutes before running the test based on the results obtained from the preliminary study.



**Figure 3. (left) Rheometer, (right) inner and outer cylinder.**

### 3. Results and discussion

#### 3.1 Flow loss

Figure 4 shows the effect of both the activator dosage and MgO content on the paste spread with and without SP. For the sake of brevity, only the results of the mini-slump spread of mixes with SP-C are presented. In general, the flowability of the mixes without any SP (Figure 4-a) was low because of the low solution/binder ratio. The initial slump in this case varied in a small range between 39 mm and 44 mm. On the one hand, when the MgO content was 0%, the spread decreased with increasing the activator dosage from 5% (solid line) to 10% (dashed line). The flow loss in both cases increased gradually with time. This can be attributed to the viscosity of the alkali solution, which increased when increasing the activator dosage (35). This effect was clearer with the addition of SP-C in Figure 4-b. On the other hand, by adding MgO, the trend is unclear but, generally, the same behaviour can be observed. Mixes containing 5% (square shapes) and 10% MgO (triangle shapes) and activated by 10% Na<sub>2</sub>CO<sub>3</sub> (dashed lines) lost their flowability after 30 minutes and no longer would be cast in the cone. Adding SP-C This trend was also observed when adding SP-C as in Figure 2-b with higher fluidity and an extension of the fluidity of mix M5N10 to 45 minutes instead of 30 minutes. The negative effect of MgO on the flowability can be interpreted by the physical properties of MgO. Firstly, the irregular shape of its particles could lead to an increase viscosity and, secondly, its high specific area results in a higher water demand (36). This decrease in fluidity has been observed in PC-based cement with different MgO contents (37).

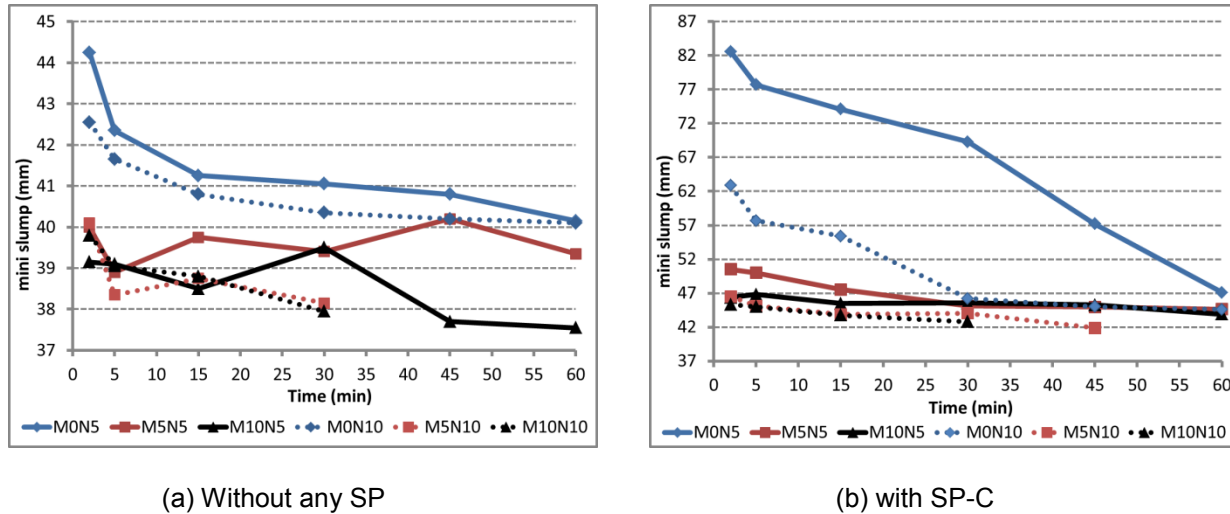


Figure 4. Effect of activator dosage and MgO inclusion on mini slump.

The effect of different superplasticisers on mix M0N5 is presented in Figure 5. It is clear that the addition of superplasticisers based on polycarboxylic ethers (SP-A and SP-B) had an insignificant influence on the fluidity of the mix with an initial increase of ~ 2% and 18%, respectively. It was also observed that a naphthalene-based admixture (not presented here) had no influence of the fluidity of this mix. However, lignusulphonate-based admixture exhibited salient influence on the fluidity of the observed mix.

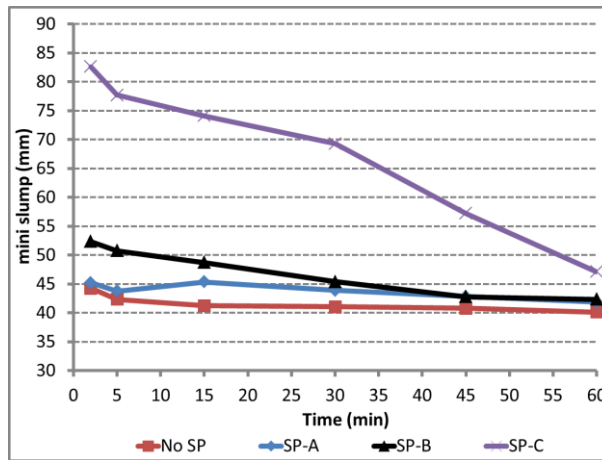


Figure 5. Effect of different SPs on mini-slump of mix M0N5.

The fluidity increased more than 80% from around 44 mm to more than 82 mm, then, decreased with time to reach 47 mm after 60 minutes. The same trends were noticed in all mixes with different degrees as shown in Figure 2-b. As SP-C is more effective in improving the workability of these mixes, results are hence presented for mixes without SP and with SP-C only.

### 3.2 Flow table

Figure 6 depicts the flow table results of all mixes without SP and with SP-C. Following the trend seen in the mini-slump tests, SP-C effectively improved the flowability of all mixes. For example, adding 1% of SP-C increased the spread of M0N5, M5N5, and M10N5 by 47%, 24%, and 17%, respectively. This indicates that this superplasticiser is more efficient with MgO-free mixes.

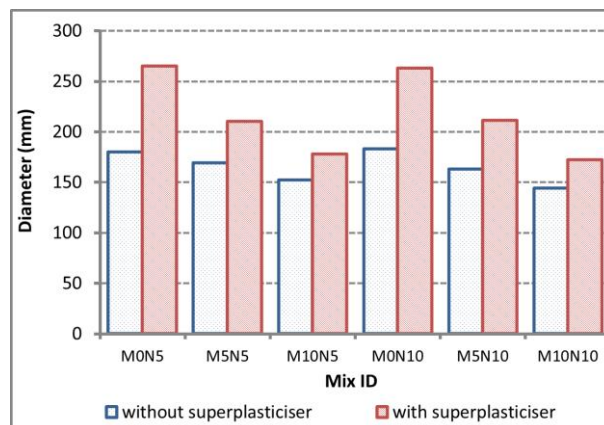


Figure 6. Effect of different SPs on mini-slump of mix M0N5.

### 3.3 Rheological parameters

The change in shear stress at constant shear rate was monitored for the first 30 minutes in order to define the best time to start the rheological test. This strategy was followed to alleviate the influence of the changes at early stages. It is clear from Figure 7 that there were many changes in the values of shear stress (viscosity follows the same behaviour) at the first 200 s in most of the mixes before the graph reached a plateau. Based on that, it was decided to run the test after 5 minutes. Another distinctive feature from the graph is that it confirms that increasing both the activator dosage and reactive magnesia

results in increasing the shear stress. This indicates that the attractive interparticle forces increase with increasing these factors.

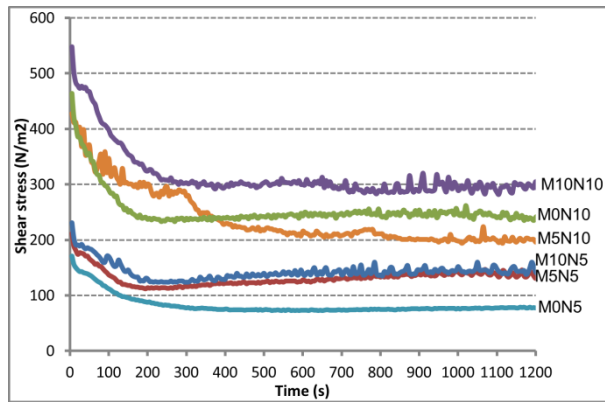


Figure 7. Shear stress change with time at constant shear rate.

### 3.3.1 Determination of plastic viscosity and yield stress

Figure 8 depicts the lower part of the flow curve in a log-log scale of different trials of Mix MON5. As noted, the lower part of the curve can be fitted to a straight line corresponding to the equation proposed by Bingham model (Eq. 1) to describe the rheological behaviour.

$$\tau = \tau_0 + \mu\dot{\gamma} \quad (1)$$

Where  $\tau$  is the shear stress applied to the paste,  $\dot{\gamma}$  is the shear rate,  $\mu$  represents the plastic viscosity of the system at any given time and  $\tau_0$  is the yield stress.

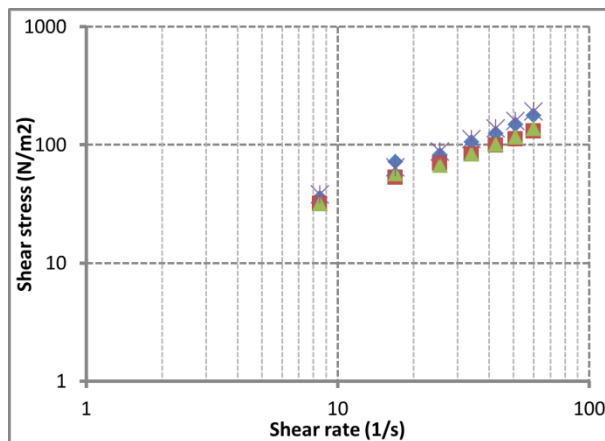


Figure 8. Flow curve of Mix MON5.

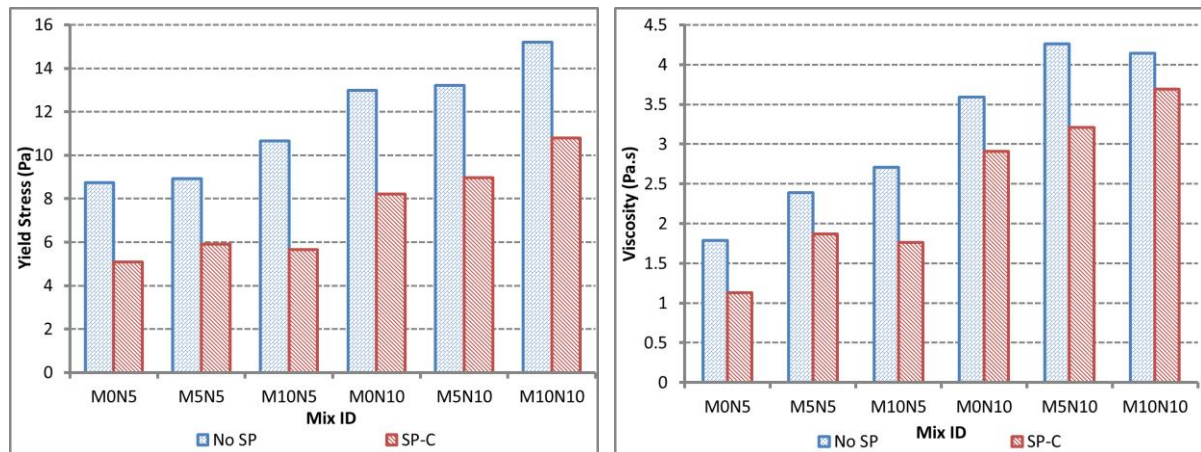
Figure 9 shows the yield stress (left) and the plastic viscosity (right) of all mixes without adding any superplasticisers and with the addition of SP-C (lignosulphonate-based admixture). It is clear that this superplasticiser decreased both the yield stress and the viscosity for all samples which made the pastes more fluid and hence less viscous. Again, it can be deduced that increasing the activator dosage and MgO content increased the yield stress and the plastic viscosity. The effect of increasing the activator dosage can be attributed mainly to the increase of the viscosity of the activation solution with concentration.



The yield stress varied between 8-15 Pa and 5-11 Pa in samples without and with SP-C, respectively. Different factors can influence the yield stress of a suspension such as the viscosity of the fluid, the interparticle forces (interaction potential and or steric forces and van der Waals forces), and particle jamming (38). The significant decrease of the yield stress when adding this SP may correspond to the increase in the net surface charge due to the absorption of the SP on the particles, thereby increasing the repulsive forces between particles.

Similarly, plastic viscosity decreased with adding SP-C from a range of ~ 1.8-4.3 Pa.s to a range of ~ 1.1-3.7 Pa.s without SP and with SP, respectively. The plastic viscosity relies on the volume friction of solid particles and the packed density (39). The results indicate that the viscosity is in the same range available in the literature review of AAMs (19,40,41). The viscosity ranges in both cases were higher the minimum viscosity required to prevent segregation as proposed by Nanthagopalan and Santhanam (32).

Organic admixtures based on sulphonic acids such as SP-C contain both a hydrophilic (sulphonic) and a hydrophobic (lignin) group. The electrical charge resulting from the adsorption of these compounds on the surface of binder particles generates the repulsive forces that increase paste fluidity (19). The effect of lignosulphonate-based admixture on workability of AAMs systems has been previously reported with some contradictions. Ren et al (41) concluded that the separation addition of lignosulphonate-based superplasticiser and the alkali solution led to better rheological properties than simultaneous addition. Criado et al (19) studied the influence of different admixtures, among them was a lignosulphonate-based one (Lig), on the workability of alkali activated fly ash and they found that Lig admixture had no effect on the workability.



**Figure 9. Rheological parameters of all mixes without and with superplasticisers (left) Yield stress, (right) Plastic viscosity**

#### 4. Conclusions

This study investigated the effect of different commercial superplasticisers, sodium carbonate activator concentration and the incorporation of MgO on the workability and rheological properties of AAFS. Based on mini-slump test results, the lignosulphonate-based admixture was the superplasticiser most effective in increasing the flowability of the mixes. It was found that the rheological properties largely depend on the activator dosage and the content of MgO. Increasing the contents of both parameters leads to a reduction in the fluidity of the mixes, thus increasing the yield stress and the plastic viscosity values. The addition of 1% lignosulphonate-based superplasticiser improves the rheological properties of all mixes. When introducing this admixture a maximum reduction in yield stress and plastic viscosity at 50% and 40% respectively. Additionally, this study demonstrates that the optimum timing for running a viscometric study for the mixtures used is 5 minutes, as at this point the shear stress stabilises at a constant shear rate.

## 5. Acknowledgement

The authors appreciate the financial support of the first author's PhD studentship from the Cambridge Overseas Trust (COT) and the Yousef Jameel Academic Program.

## 6. References

1. Benhelal, E., Zahedi, G., et al., "Global Strategies and Potentials to Curb CO<sub>2</sub> Emissions in Cement Industry," *J. Clean. Prod.*, vol. 51, pp. 142–161, Jul. 2012.
2. Provis, J. L. and van Deventer, J. S. J., Eds., *Alkali Activated Materials*, vol. 13. Dordrecht: Springer Netherlands, 2014.
3. Pacheco-Torgal, F., Jalali, S., et al., Eds., *Eco-Efficient Concrete*. Cambridge, UK: Woodhead Publishing Limited, 2013.
4. Pacheco-Torgal, F., Labrincha, J. A., et al., Eds., *Handbook of Alkali-activated Cements, Mortars and Concrete*. UK: Woodhead Publishing Limited, 2015.
5. Pacheco-Torgal, F., Abdollahnejad, Z., et al., "Durability of Alkali-Activated Binders: A Clear Advantage over Portland Cement or an Unproven Issue?," *Constr. Build. Mater.*, vol. 30, pp. 400–405, May 2012.
6. Provis, J. L., "Geopolymers and other alkali activated materials: why, how, and what?," *Mater. Struct.*, vol. 47, no. 1–2, pp. 11–25, Nov. 2013.
7. Puertas, F., Martinez-Ramirez, S., et al., "Alkali-Activated Fly Ash /Slag Cement Strength Behaviour and Hydration Products," *Cem. Concr. Res.*, vol. 30, pp. 1625–1632, 2000.
8. Shi, C., Roy, D., et al., *Alkali-Activated Cements and Concretes*. Oxon: Taylor & Francis, 2006.
9. Higgins, D., Sear, L., et al., "Cementitious Materials: The Effect of GGBS, Fly Ash, Silica Fume and Limestone Fines on the Properties of Concrete," Surrey, 2011.
10. Puertas, F. and Fernandez-Jimenez, A., "Mineralogical and microstructural characterisation of alkali-activated fly ash/slag pastes," *Cem. Concr. Compos.*, vol. 25, pp. 287–292, 2003.
11. Smith, A. M. and Osborne, J. G., "Slag/Fly Ash Cements," *World Cem. Technol.*, vol. 8, no. 6, pp. p. 223–224, Nov. 1977.
12. Wang, J., Wu, X., et al., "Hydrothermal synthesis and characterization of alkali-activated slag–fly ash–metakaolin cementitious materials," *Microporous Mesoporous Mater.*, vol. 155, pp. 186–191, Jun. 2012.
13. Abdalqader, A. and Al-Tabbaa, A., "Hydration and Mechanical Properties of Reactive Magnesia and Sodium Carbonate-Activated Fly Ash/Slag Paste Blends," in *the RILEM PRO092 proceeding of the Second International Conference on Advances in Chemically-activated Materials (CAM'2014-China), June 1-3, 2014, Changsha, China, 2014*, pp. 269–280.
14. Abdalqader, A. and Al-Tabbaa, A., "Factors Affecting the Properties of Na<sub>2</sub>CO<sub>3</sub>-activated Fly Ash/Slag Paste," in *the 34th Annual Cement and Concrete Science Conference, 2014*, no. 14–16 September 2014, pp. 329–332.



15. Deventer, J. S. J., Provis, J. L., et al., "Chemical Research and Climate Change as Drivers in the Commercial Adoption of Alkali Activated Materials," *Waste and Biomass Valorization*, vol. 1, no. 1, pp. 145–155, Feb. 2010.
16. Bernal, S., Provis, J. L., et al., "Role of carbonates in the chemical evolution of sodium carbonate-activated slag binders," *Mater. Struct.*, pp. 1–13, Sep. 2014.
17. Fernández-Jiménez, A. and Palomo, A., "Composition and microstructure of alkali activated fly ash binder: Effect of the activator," *Cem. Concr. Res.*, vol. 35, pp. 1984–1992, 2005.
18. Wang, S., Scrivener, K. L., et al., "Factors Affecting the Strength of Alkali-Activated Slag," *Cem. Concr. Res.*, vol. 24, no. 6, pp. 1033–1043, 1994.
19. Criado, M., Palomo, a., et al., "Alkali activated fly ash: effect of admixtures on paste rheology," *Rheol. Acta*, vol. 48, no. 4, pp. 447–455, Feb. 2009.
20. Vance, K., "Early Age Characterization and Microstructural Features of Sustainable Binder Systems for Concrete," PhD Thesis, Arizona State University, 2014.
21. Puertas, F., Varga, C., et al., "Rheology of alkali-activated slag pastes. Effect of the nature and concentration of the activating solution," *Cem. Concr. Compos.*, vol. 53, pp. 279–288, 2014.
22. Palacios, M. and Puertas, F., "Effect of superplasticizer and shrinkage reducing admixtures on alkali-activated slag pastes and mortars," *Cem. Concr. Res.*, vol. 35, pp. 1358–1367, 2005.
23. Palomo, A., Banfill, P. F. G., et al., "Properties of alkali-activated fly ashes determined from rheological measurements," *Adv. Cem. Res.*, vol. 17, no. 4, pp. 143–151, 2005.
24. Kashani, A., Provis, J. L., et al., "The interrelationship between surface chemistry and rheology in alkali activated slag paste," *Constr. Build. Mater.*, vol. 65, pp. 583–591, 2014.
25. Yang, K. and Song, J., "Workability Loss and Compressive Strength Development of Cementless Mortars Activated by Combination of Sodium Silicate and Sodium Hydroxide," *J. Mater. Civ. Eng.*, vol. 21, no. March, pp. 119–127, 2009.
26. Nuruddin, M. F., Demie, S., et al., "Effect of Superplasticizer and NaOH Molarity on Workability , Compressive Strength and Microstructure Properties of Self-Compacting Geopolymer Concrete," *World Acad. Sci. Eng. Technol.*, vol. 5, no. 3, pp. 1378–1385, 2011.
27. Reddy, B. S. K., Varaprasad, J., et al., "Strength and workability of low lime fly-ash based geopolymer concrete," *Indian J. Sci. Technol.*, vol. 3, no. 12, pp. 1188–1189, 2010.
28. Montes, C., Zang, D., et al., "Rheological behavior of fly ash-based geopolymers with the addition of superplasticizers," *J. Sustain. Cem. Mater.*, vol. 1, no. 4, pp. 179–185, Dec. 2012.
29. Puertas, F., Palomo, A., et al., "Effect of superplasticisers on the behaviour and properties of alkaline cements," no. 1, pp. 23–28, 2003.
30. Wallah, S. E. and Rangan, B. V., "Low calcium fly ash based geopolymer concrete: long term properties," Perth, Australia, 2006.
31. Jin, F. and Al-Tabbaa, A., "Characterisation of different commercial reactive magnesia," *Adv. Cem. Res.*, vol. 26, no. 2, pp. 101–113, Apr. 2014.

32. Nanthagopalan, P. and Santhanam, M., "A new empirical test method for the optimisation of viscosity modifying agent dosage in self-compacting concrete," *Mater. Struct.*, vol. 43, pp. 203–212, 2010.
33. BS-EN-1015-3, "Methods of test for mortar for masonry. Determination of consistence of fresh mortar (by flow table)." BSI, p. 5, 1999.
34. "More Solutions to Sticky Problems (2005) A guide to getting more from your Brookfield Viscometer. Brookfield Engineering Lab. Inc."
35. Favier, A., Hot, J., et al., "Flow properties of MK-based geopolymer pastes. A comparative study with standard Portland cement pastes," *Soft Matter*, vol. 10, p. 1134, 2014.
36. Shand, M. A., *The Chemistry and Technology of Magnesia*. JOHN WILEY & SONS, 2006.
37. Li, X., "Mechanical Properties and Durability Performance of Reactive Magnesia Cement Concrete," PhD thesis, University of Cambridge, 2012.
38. Barnes, H. a, "The yield stress — a review or 'παντα ροει'— everything flows?," *J. Non-Newtonian Fluid Mech*, vol. 81, pp. 133–178, 1999.
39. Struble, L. J. and Lei, W.-G., "Rheological changes associated with setting of cement paste," *Adv. Cem. Based Mater.*, vol. 2, no. 95, pp. 224–230, 1995.
40. Vance, K., Dakhane, A., et al., "Observations on the rheological response of alkali activated fly ash suspensions : the role of activator type and concentration," 2014.
41. Ren, J., Bai, Y., et al., "A Preliminary Study on the Effect of Separate Addition of Lignosulfonate Superplasticiser and Waterglass on the Rheological Behaviour of Alkali – activated Slags."

# Direct Electric Curing of Alkali-Activated Concretes. Preliminary Study

Maxim Kovtun<sup>1</sup>, Julia Shekhovtsova<sup>2</sup> and Elsabe Kearsley<sup>3</sup>

<sup>1</sup>Researcher, The University of Pretoria

<sup>2</sup>Researcher, The University of Pretoria

<sup>3</sup>Professor of Civil Engineering, The University of Pretoria

**Abstract:** Alkali-activated concretes containing fly ash as a prime aluminosilicate source have slow strength development at ambient temperatures. This is also relevant for acid and neutral granulated blast-furnace slags activated with a weak activator such as sodium carbonate. In order to accelerate hardening of the alkali-activated concretes on construction sites, direct electric curing can be used. Three alkali-activated cements were used to produce concrete mixes. Two cements contained fly ash and were activated with sodium hydroxide and sodium silicate ( $M_s=1.125$ ) respectively. The third cement was based on neutral granulated blast-furnace slag activated with sodium carbonate. The effect of duration of pre- and isothermal curing on compressive strength of the alkali-activated concretes was investigated. Electric properties of the alkali-activated cements were obtained.

**Keywords:** fly ash, GBFS, alkali activation, direct electric curing, strength.

## 1. Introduction

Alkali-activated cements have been used for over 70 years (1). Intensive research on these cements during recent decades is driven not only by the need of human society to reduce the CO<sub>2</sub> emissions associated with Portland cement production which is responsible for about 5 % of global anthropogenic CO<sub>2</sub> emissions (2), but also by several other advantages, such as resistance to chemical attack, fire resistance and low permeability, that alkali-activated cements can offer (3-7).

Various aluminosilicate precursors can be used to produce alkali-activated cements (8), but granulated blast-furnace slag (GBFS) and fly ash appear to be the most promising precursors for large-scale industrial production of alkali-activated cements. This is due to the more favourable rheological properties and lower water demand achievable when compared to mixes based on calcined clays (9).

One of the main barriers to the widespread use of alkali-activated cements and concretes is the slow strength development of fly ash alkali-activated cements at ambient temperatures. Curing temperatures from 60 to 80 °C are essential for alkali-activated fly ash cements to achieve good structural strength (10, 11). Alkali-activated slag cement has slow strength development when neutral or acid GBFS is activated with sodium carbonate (12). In the case of slag, the problem of slow strength development at ambient temperatures can be overcome by using different accelerating admixtures (12-14), while fly ash must be heat cured to overcome the thermal activation barrier which is a crucial aspect in the strength development of alkali-activated fly ash cements (10). Normally dry heat or steam curing is used to accelerate strength development of alkali-activated cements (10-12, 15). These types of curing are not easy to implement on construction sites, but almost all construction sites have electric power supply.

Electric power can be used for direct electric curing (DEC) of concrete when alternating electric current is passed through the bulk of fresh concrete to accelerate the curing process by means of direct ohmic heating (16-19). Direct electric curing needs much less initial capital investment in equipment and has substantially lower running cost in comparison to externally applied heat (steam, autoclave, etc.) (16-18). It is also a lot easier to provide DEC on a construction site than external heating.

Direct electric curing of Portland cement concretes has been used for decades (16-19) but there is no available information on alkali-activated concretes. This curing method has huge potential to increase in situ use of alkali-activated concretes. Power supply companies like Eskom in South Africa, will benefit, not only because the power demand will shift towards off-peak hours (16), but also the by-product of the electric power production process (which is fly ash in case of coal power plants) will be utilized in the production of a "green" construction material.

The aim of this research was to do a preliminary investigation on DEC of alkali-activated concretes and to determine the electric properties of alkali-activated cements.

## 2. Materials and methods

### 2.1 Materials

Unclassified low calcium fly ash and GBFS were used. The chemical composition of fly ash and GBFS determined by X-ray fluorescence is presented in Table 1. The specific gravity of the fly ash and GBFS were 2240 kg/m<sup>3</sup> and 2900 kg/m<sup>3</sup> respectively.

**Table 1. Chemical composition of fly ash and GBFS (LOI = loss on ignition at 1000 °C).**

Material	SiO <sub>2</sub>	Al <sub>2</sub> O <sub>3</sub>	CaO	Fe <sub>2</sub> O <sub>3</sub>	MgO	K <sub>2</sub> O	Na <sub>2</sub> O	TiO <sub>2</sub>	SO <sub>3</sub>	Other elements	LOI
Fly ash	56.2	30.7	4.5	4.4	0.5	0.8	0.3	1.6	0.4	0.3	0.3
GBFS	34.9	14.4	37.1	0.9	8.0	0.7	<0.01	0.7	2.0	1.1	0.2

Commercially available sodium hydroxide flakes (98.0 % purity), liquid sodium silicate (15.0 % Na<sub>2</sub>O, 29.5 % SiO<sub>2</sub>, remainder H<sub>2</sub>O), sodium carbonate (99.0 % purity) and tap water were used to prepare activator solutions. The specific gravity of the liquid sodium silicate was 1540 kg/m<sup>3</sup>.

Crushed dolomite stone (9.5 mm) and dolomite sand with a fineness modulus of 3.86 and 9.0 % passing the 75 µm sieve were used as the coarse and fine aggregates respectively. The specific gravity of the aggregates was 2860 kg/m<sup>3</sup>.

### 2.2 Mix design and preparation of concrete mixes

Alkali-activated concrete mix compositions are presented in Table 2.

**Table 2. Mix designs and workability of alkali-activated concretes.**

Mix	Binder, mass (kg/m <sup>3</sup> )	Activator	Na <sub>2</sub> O <sub>eq</sub> (wt.%)	Sand (kg/m <sup>3</sup> )	Stone (kg/m <sup>3</sup> )	Slump/Flow (mm)
S50	GBFS, 500	Na <sub>2</sub> CO <sub>3</sub>	4	650	1207	15/–
F40	Fly ash, 400	Na <sub>2</sub> SiO <sub>3</sub> +NaOH	9	668	1240	80/–
F50	Fly ash, 500	Na <sub>2</sub> SiO <sub>3</sub> +NaOH	9	584	1085	–/545
F35	Fly ash, 350	Na <sub>2</sub> SiO <sub>3</sub> +NaOH	9	709	1317	0/–
F35H	Fly ash, 350	NaOH	9	717	1331	0/–

Basic fly ash and slag mixes, used to investigate the influence of duration of precuring and isothermal curing on properties of alkali-activated concretes, contained 400 kg/m<sup>3</sup> (20) and 500 kg/m<sup>3</sup> (14) of binder respectively. All fly ash mixes had an activator concentration 9 % Na<sub>2</sub>O<sub>eq</sub> of fly ash mass (11). The slag mix was activated using sodium carbonate at 4 % Na<sub>2</sub>O<sub>eq</sub> (12, 21). Silicate modulus (Ms) of sodium silicate activator, produced from commercial sodium silicate (Ms=2) and sodium hydroxide, was 1.125 (22). Water/binder (GBFS or fly ash) ratio was designed as low as possible at 0.35 for all mixes (11). Fine to total aggregate ratio was kept constant at 0.35 by weight in all mixes. The activator solutions were prepared and cooled down to room temperature before mixing (11). All materials were pre-conditioned at 20±1 °C for at least 16 hours before mixing. The mixing was done in a pan mixer producing a homogeneous concrete mix. Workability of the alkali-activated concrete mixes was determined according BS EN 12350 (23). After workability testing, concrete was cast into modified moulds and vibrated.

### 2.3 Experimental set up

A rig for DEC of alkali-activated concretes used in this study (Figure 1) was designed taking into account previous research (16, 19). It consisted of modified moulds (Figure 2), a power supply with a capacity of 300 VA, maximum current 12 A and output voltage 0–250 V (ACDC Dynamics, South Africa), a temperature controller (TC600, Rhomberg, Australia), a digital ammeter (Rhomberg, Australia) and a digital voltmeter (Rhomberg, Australia). The modified moulds (100×100×100 mm) made from dielectric plastic and stainless steel plates (electrodes) (Figure 2), were placed in a 50 mm thick polystyrene shell to limit energy losses and were kept in a closed containment box for safety during the DEC process (Figure 1). The lid of the containment box consisted of a 50 mm thick polystyrene plate sealing the moulds to prevent extensive moisture loss during the DEC process which is critical for strength development of AAC (15) and the DEC process itself (18, 19, 24). Three rows of the modified moulds were connected in parallel with each row consisting of 4 moulds connected in series. The modified moulds are removable for ease of casting fresh concrete and were constructed in such a way that the electric current traverses the full area of the specimen (24), ensuring an equal electric field generated throughout the specimen. To eliminate the possibility of a short circuit while obtaining the true temperature of the concrete mix, a thermocouple with mineral insulation was placed in the centre of one mould used for temperature control measurements as shown in Figure 2,b.



Figure 1. DEC rig.



(a) Modified mould



(b) Modified mould for temperature measurements

Figure 2. Modified moulds.

## 2.4 Experimental procedures

All mixes were cured following a standard temperature cycle consisting of precuring, heating, and isothermal curing (25, 26). Precuring was done in closed containment box (Figure 1) to prevent extensive evaporation at  $25 \pm 1$  °C. After the isothermal phase, the DEC rig was switched off, and concrete specimens were demoulded immediately without any gradual cooling. Concrete mixes containing GBFS (S50, Table 2) and 400 kg/m<sup>3</sup> of fly ash (F40, Table 2) were precured for 2 and 4 hours. The alkali-activated slag concrete mix was isothermally cured for 8 hours and the fly ash mix for 8 and 16 hours. Alkali-activated concrete mixes containing 350 and 500 kg/m<sup>3</sup> of fly ash (F35, F35H, F50, Table 2) were only precured for 4 hours and isothermally cured for 8 hours. During the heating phase, the temperature increased at a rate of  $20 \pm 1$  °C/h (26). The temperature of the isothermal phase was set at 60 °C (11, 19), and this was maintained automatically by the temperature controller. Ammeter and voltmeter readings were recorded every 5 minutes during the heating phase. After demoulding, concrete specimens were stored in a fog room at  $90 \pm 5$  % relative humidity and  $20 \pm 1$  °C until testing. Three concrete specimens were tested at 1, 7 and 28 days according to BS EN 12390-3 (27).

The resistivity,  $\rho_c$ , of alkali-activated concrete mixes was calculated using the following formula:

$$\rho_c = \frac{RA}{L} \quad (1)$$

Where  $\rho_c$  – resistivity of concrete,  $\Omega \cdot m$ ;

$R$  – resistance of a concrete sample,  $\Omega$ ;

$L$  – length of a concrete sample, m;

$A$  – cross-sectional area of a concrete sample, m<sup>2</sup>.

Calculation of resistivity of alkali-activated cement pastes was done according to the formula found by Whittington et al (24) for Portland cement pastes. The formula was modified to take into account coarse porosity caused by the incomplete compaction of concrete mixes:

$$F = 1.04((1 - Por)\varphi)^{-1.20} \quad (2)$$

Where  $F$  – formation factor;

$Por$  – porosity of alkali-activated concrete samples at 1 day (measured by hydrostatic weighing);

$\varphi$  – theoretical fractional volume of alkali-activated cement paste in concrete mix.

$$Por = 1 - \frac{m}{(m - m_w)\gamma} \quad (3)$$

Where  $m$  – mass of concrete sample in air, kg;

$m_w$  – mass of concrete sample in water (hydrostatic weight), kg;

$\gamma$  – theoretical relative density of alkali-activated concrete.

$$F = \frac{\rho_c}{\rho_p} \quad (4)$$

Where  $\rho_p$  – resistivity of alkali-activated cement paste,  $\Omega \cdot m$ .

Temperature coefficient of resistivity was found from the following formula:

$$\rho_{p2} = \frac{\rho_{p1}}{1 + \alpha(T_2 - T_1)} \quad (5)$$

Where  $\rho_{p1}$ ,  $\rho_{p2}$  – resistivity of alkali-activated cement paste at temperature  $T_1$  and  $T_2$  respectively,  $\Omega \cdot m$ ;

$T_1$ ,  $T_2$  – temperature of concrete mix, °C;

$\alpha$  – temperature coefficient of resistivity, °C<sup>-1</sup>.

### 3. Results and discussion

#### 3.1 General observations

Workability of alkali-activated fly ash concrete mixes strongly depends on fly ash content at constant water/binder ratio (Table 2). Concrete mixes containing 350 kg/m<sup>3</sup> of fly ash had zero slump, but they could be properly compacted by vibration due to thixotropy of the mixes. Mix F50 had very high workability.

Thermal expansion of the plastic parts of the moulds resulted in an air gap between the electrodes and samples shortly after the heating phase. This was the case for concrete mixes containing GBFS, as well as fly ash mix activated with sodium hydroxide (S50, F35H, Table 2). Thus, these mixes were gradually cooling down for 8 hours. The thermal isolation of the containment box did not allow fast energy dissipation, therefore temperature only dropped to 48 °C before demoulding. Fly ash concrete mixes activated with sodium silicate did not lose contact with the electrodes due to the high adhesion to metal surfaces.

#### 3.2 Resistivity

Resistivity of all alkali-activated cement pastes and concrete mixes during the heating phase is presented in Table 3.

**Table 3. Physical and electric properties of alkali-activated cement pastes and concretes.**

Mix-Precurring (h)	Fractional volume, $\varphi$	Por	$\rho_{c1}$ ( $\Omega \cdot m$ ) <sup>1)</sup>	$\rho_{c2}$ ( $\Omega \cdot m$ ) <sup>2)</sup>	Formation factor, $F$	$\rho_{p1}$ ( $\Omega \cdot m$ ) <sup>1)</sup>	$\rho_{p2}$ ( $\Omega \cdot m$ ) <sup>2)</sup>	$\alpha$ , ( $^{\circ}C^{-1}$ )
S50-2	0.351	0.019	1.53	0.82	3.74	0.41	0.22	0.024
S50-4	0.351	0.018	1.62	1.03	3.73	0.43	0.28	0.020
F40-2	0.333	0.034	3.32	1.39	4.06	0.82	0.34	0.045
F40-4	0.333	0.029	3.39	1.37	4.03	0.84	0.34	0.045
F50-4	0.416	0.026	2.62	1.06	3.08	0.85	0.35	0.045
F35-4	0.291	0.035	4.35	1.63	4.77	0.91	0.34	0.045
F35H-4	0.284	0.034	0.89	0.64	4.91	0.18	0.13	0.020

<sup>1)</sup>  $\rho_{c1}$ ,  $\rho_{p1}$  – resistivity of alkali-activated concrete and cement paste at the beginning of the heating phase respectively;

<sup>2)</sup>  $\rho_{c2}$ ,  $\rho_{p2}$  – minimal resistivity of alkali-activated concrete and cement paste during the heating phase respectively (some mixes had a jump in resistivity due to the air gap that developed between the sample and the electrodes).

It can be seen that the resistivity of alkali-activated concretes containing cement paste of a certain composition (F35, F40, F50, Table 3) depends on the fractional volume of alkali-activated cement paste as the resistivity of the aggregates is several orders of magnitude higher than that of the paste, resulting in electric current being conducted through the paste, i.e. through the path of least resistance (24). Results show that formula (2) derived for Portland cement concretes by Whittington et al. (24) can be applied with success to alkali-activated concretes; the maximum and minimum resistivity of alkali-activated cement pastes in concretes with different paste content (F35, F40, F50, Table 3) are almost equal as it should be because the composition of the pastes is the same (Table 2). Only alkali-activated cement paste of mix F35 had slightly high resistivity at the beginning of the heating phase but it could be attributed to samples' compaction. Duration of precurring did not have any significant influence on the resistivity of alkali-activated concretes (S50-2 and F40-2 compare to S50-4 and F40-4 respectively, Table 3). The high value of minimum resistivity of mix S50-4 could be caused by the air gap that developed between the samples and the electrodes; this mix reached only 58 °C. The resistivity of the alkali-activated cement pastes strongly depends on type of activator used. Sodium hydroxide gives the lowest resistivity (F35H, Table 3) followed by sodium carbonate (SC50, Table 3; despite significantly lower concentration) and sodium

silicate (F35, Table 3). Lower resistivity leads to lower power demand during the heating phase (Joule–Lenz law):

$$Q = I^2 R t = \frac{U^2 t}{R} \quad (6)$$

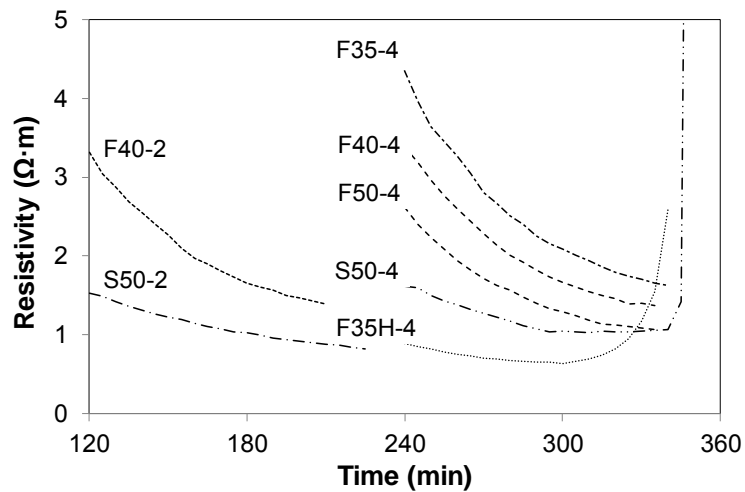
Where  $Q$  – generated heat, J;

$I$  – current strength, Amp;

$U$  – potential, V;

$t$  – time, sec.

Change in the resistivity of alkali-activated concretes during the heating phase can be seen in Figure 3.



**Figure 3. Electric resistivity development of alkali-activated concretes during the heating phase.**

The decrease in resistivity of alkali-activated concretes correlates to the behaviour of Portland cement concretes (16, 24). It is important to note that the resistivity of alkali-activated concretes (Figure 3) and cement pastes (Table 3) is significantly lower in comparison to Portland cement concretes and pastes (24).

The temperature coefficient ( $\alpha$ , Table 3) of all alkali-activated concrete mixes depends only on the composition of the alkali-activated cement paste, not the paste content in the concrete mix. The significance of the results is confirmed by the low standard deviation of the results of alkali-activated concrete mixes containing fly ash and sodium silicate (F35, F40, F50, Table 3);  $\alpha_{av}=0.0453 \text{ } ^\circ\text{C}^{-1}$ , st.dev.= $\pm 0.0027 \text{ } ^\circ\text{C}^{-1}$ . It is important to note that temperature coefficient of alkali-activated concrete mixes containing fly ash and sodium silicate is considerably higher than the value of  $0.022 \text{ } ^\circ\text{C}^{-1}$  found by Whittington et al. (24) for Portland cement paste. The higher value of the temperature coefficient indicates that fly ash activated with sodium silicate drops its resistivity faster than Portland cement paste. The degree of hydrolysis of electrolytes increases with temperature rise but it is more complex in case of sodium silicate solution due to its colloidal nature. Also, mobility of sodium ions in sodium silicate solution significantly increases with temperature rise. These two factors are responsible for the significant drop in the resistivity of alkali-activated cement paste containing sodium silicate. Thermal coefficients of alkali-activated concretes containing GBFS with sodium carbonate and fly ash with sodium hydroxide are similar to the thermal coefficient of Portland cement paste (24) and are comparable with a value of  $0.025 \text{ } ^\circ\text{C}^{-1}$  for most electrolytes.



### 3.3 Compressive strength

Compressive strength results are presented in Figure 4.

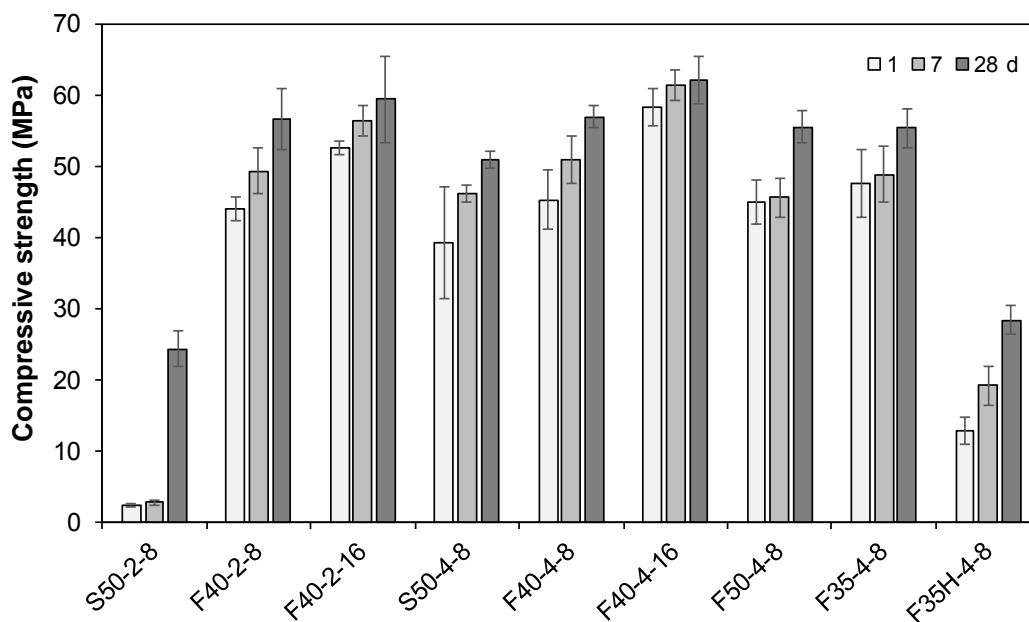


Figure 4. Compressive strength of alkali-activated concretes.

It is important to note that alkali-activated concrete containing GBFS had extremely low strength when precured for 2 hours and isothermally cured for 8 hours (S50-2-8, Figure 4). The reason for this phenomenon is not clear and can be studied in future. Alkali-activated slag concrete mix precured for 4 hours showed much higher strength which was equal to the strength of steam cured alkali-activated slag concretes with similar composition (14). High standard deviation of 1-day strength of S50 mix precured for 4 hours should be noted. Alkali-activated slag concretes were not cured for 16 hours due to the air gap described earlier; the concretes were cooling down gradually for 8 hours rather than being cured at 60 °C. It can be seen that, although the duration of precuring significantly affects strength development of alkali-activated slag concretes, it has much less effect on the strength of alkali-activated fly ash concretes, maximum difference is 10.8 % (F40 mixes, Figure 4), but compressive strength of alkali-activated fly ash concretes precured for 4 hours was always higher.

Variation of precuring and isothermal curing time showed that 4 hours of precuring and 8 hours of isothermal curing were the best in this study for alkali-activated fly ash concretes (F40 mixes, Figure 4). Precuring for 2 hours gave slightly lower strength and higher standard deviation of the strength at 28 days in comparison to 4 hours. Duration of isothermal curing affects compressive strength of alkali-activated fly ash concrete more when precuring is longer, and the effect on early strength is more significant than 28-d strength. Isothermal curing for 16 hours is therefore not economic due to higher power demand and marginally higher strength at 28 days.

Fly ash content did not significantly affect the compressive strength of alkali-activated fly ash concretes containing sodium silicate (compare F40-4-8, F50-4-8 and F35-4-8, Figure 4). Fly ash content can thus be chosen depending on specific application (required workability). Mix F35 is however the cheapest because it contains the least amount of fly ash and the activator amongst the mixes. To bring the cost of alkali-activated fly ash concrete down even more, sodium silicate was replaced by a sodium hydroxide activator. Unfortunately, it is not possible to compare actual performances of alkali-activated fly ash concretes containing sodium silicate (F35-4-8, Figure 4) and sodium hydroxide (F35H-4-8, Figure 4) due to the air gap that developed when the concrete mix activated with sodium hydroxide was cured. Previous studies conducted by our research group (28) showed that NaOH-activated fly ash concrete of similar

composition cured in dry heat could gain compressive strength up to 45 MPa at 28 days. Therefore F35H mix could gain higher strength if properly cured.

#### 4. Conclusions

The resistivity and the temperature coefficient of resistivity were found for three different alkali-activated cement pastes. The resistivity of alkali-activated concrete depends on the resistivity of cement paste.

Whittington's equation can be successfully used for predicting the resistivity of alkali-activated concretes, which is one of the main input parameters for the design of DEC equipment (transformer), based on content of a specific alkali-activated cement paste with known resistivity.

The resistivity of alkali-activated concretes is lower than that of Portland cement concretes. The decreased resistivity can potentially reduce the total power demand for DEC of alkali-activated concretes.

Pre-curing for 4 hours and isothermal curing of 8 hours can be suggested for practical application. The isothermal curing can be organized during the off-peak hours between 10 p.m. and 6 a.m. and will require less power in comparison with isothermal curing for 16 hours. The compressive strength will not be significantly compromised by the reduced isothermal curing time.

Alkali-activated fly ash concretes containing sodium silicate showed a very good response to DEC which opens new perspectives for much wider application of the material.

#### 5. Acknowledgement

Authors would like to thank postgraduate student Mateusz Ziolkowski for assembling and Krak Electrical, CC for sponsoring the electric curing rig. Editorial input of Alan Hall is gratefully acknowledged.

#### 6. References

1. Purdon, A.O., "The action of alkalis on blast furnace slag", Journal of the Society of Chemical Industry, 59, 1940, pp 191-202.
2. Hasanbeigi, A., Price, L. et al., "Emerging energy-efficiency and CO<sub>2</sub> emission-reduction technologies for cement and concrete production: A technical review", Renewable and Sustainable Energy Reviews, 16(8), 2012, pp 6220-6238. <http://dx.doi.org/10.1016/j.rser.2012.07.019>
3. Bakharev, T., "Resistance of geopolymer materials to acid attack", Cement and Concrete Research, 2005, 35(4), pp. 658-670. <http://dx.doi.org/10.1016/j.cemconres.2004.06.005>
4. Rashad, A.M., Zeedan, S.R., "The effect of activator concentration on the residual strength of alkali-activated fly ash pastes subjected to thermal load", Construction and Building Materials, 25(7), 2011, pp 3098-3107. <http://dx.doi.org/10.1016/j.conbuildmat.2010.12.044>
5. Shi, C., "Strength, pore structure and permeability of alkali-activated slag mortars", Cement and Concrete Research, 26(12), 1996, pp 1789-1799. [http://dx.doi.org/10.1016/S0008-8846\(96\)00174-3](http://dx.doi.org/10.1016/S0008-8846(96)00174-3)
6. Roy, D.M., Jiang, W. et al., "Chloride diffusion in ordinary, blended, and alkali-activated cement pastes and its relation to other properties", Cement and Concrete Research, 30(12), 2000, pp 1879-1884. [http://dx.doi.org/10.1016/S0008-8846\(00\)00406-3](http://dx.doi.org/10.1016/S0008-8846(00)00406-3)
7. Wang, S.D., Pu, X.C. et al., "Alkali-activated slag cement and concrete: a review of properties and problems", Advances in Cement Research, 7(27), 1995, pp 93-102. <http://dx.doi.org/10.1680/adcr.1995.7.27.93>
8. Pacheco-Torgal, F., Castro-Gomes, J. et al., "Alkali-activated binders: A review. Part 2. About materials and binders manufacture", Construction and Building Materials, 22(7), 2008, pp 1315-1322. <http://dx.doi.org/10.1016/j.conbuildmat.2007.03.019>

9. Van Deventer, J.S.J., Provis, J.L. et al., "Technical and commercial progress in the adoption of geopolymers cement", Minerals Engineering, 29, 2012, pp 89-104. <http://dx.doi.org/10.1016/j.mineng.2011.09.009>
10. Bakharev, T., "Geopolymeric material prepared using Class F fly ash and elevated temperature curing", Cement and Concrete Research, 35(6), 2005, pp 1224-1232. <http://dx.doi.org/10.1016/j.cemconres.2004.06.031>
11. Shekhovtsova, J., Kearsley, E.P. et al., "Effect of activator dosage, water to binder solids ratio, temperature and duration of elevated temperature curing on the compressive strength of alkali-activated fly ash cement paste", Journal of the South African Institution of Civil Engineering, 56(3), 2014, pp 44-52.
12. Wang, S.D., Scrivener, K.L. et al., "Factors affecting the strength of alkali-activated slag", Cement and Concrete Research, 24(6), 1994, pp 1033-1043. [http://dx.doi.org/10.1016/0008-8846\(94\)90026-4](http://dx.doi.org/10.1016/0008-8846(94)90026-4)
13. Glukhovskiy, V.D., Krivenko, P.V. et al., "Binder", US Patent 4410365, 1983.
14. Kovtun, M., Kearsley, E.P. et al., "Dry powder alkali-activated slag cements", Advances in Cement Research, <http://dx.doi.org/10.1680/adcr.14.00078>, (in press).
15. Kovalchuk, G., Fernandez-Jimenez, A. et al., "Alkali-activated fly ash: Effect of thermal curing conditions on mechanical and microstructural development - Part II", Fuel, 86(3), 2007, pp 315-322. <http://dx.doi.org/10.1016/j.fuel.2006.07.010>
16. Bredenkamp, S., Kruger, D. et al., "Direct electric curing of concrete", Magazine of Concrete Research, 45(162), 1993, pp 71-74. <http://dx.doi.org/10.1680/macrc.1993.45.162.71>
17. Kafry, I.D., "Direct electric curing of concrete: basic design", Whittles Publishing, 1993, Latheronwheel, Scotland.
18. Wadhwa, S.S., Srivastava, L.K. et al., "Direct electric curing of in situ concrete", Batiment international. Building research & practice, 20(2), 1987, pp 97-101. <http://dx.doi.org/10.1080/09613218708726799>
19. Heritage, I., Khalaf, F.M. et al., "Thermal acceleration of Portland cement concretes using direct electronic curing", ACI Structural Journal, 97(1), 2000, pp 37-40. <http://dx.doi.org/10.14359/803>
20. Ravikumar, D., Peethamparan, S. et al., "Structure and strength of NaOH activated concretes containing fly ash of GGBFS as the sole binder", Cement and Concrete Composites, 32(6), 2010, pp 399-410. <http://dx.doi.org/10.1016/j.cemconcomp.2010.03.007>
21. Kovtun, M.N., Kearsley, E.P. et al., "Producing alkali-activated slag concrete in South Africa", Proceedings, Innovations in Concrete Construction, UKIERI Concrete Congress, Jalandhar, Punjab, India, 2013, pp 919-928.
22. Hardjito, D., Rangan, B.V., "Development and properties of low-calcium fly ash-based geopolymers concrete", Research Report GC 1, Faculty of Engineering, Curtin University of Technology, 2005, Perth, Australia.
23. British Standards Institution, "Testing fresh concrete (BS EN 12350:2009)" BSI, 2009, London, UK.
24. Whittington, H.W., McCarter, J. et al., "The conduction of electricity through concrete", Magazine of Concrete Research, 33(114), 1981, pp 48-60. <http://dx.doi.org/10.1680/macrc.1981.33.114.48>
25. Neville, A.M., "Properties of concrete", 4th ed., Longman, 1995, Harlow, England.
26. Wilson, J.G., Gupta, N.K., "Equipment for the investigation of the accelerated curing of concrete using direct electrical conduction", Measurement: Journal of the International Measurement Confederation, 35(3), 2004, pp 243-250. <http://dx.doi.org/10.1016/j.measurement.2003.11.002>
27. British Standards Institution, "Testing hardened concrete – Part 3: Compressive strength of test specimens (BS EN 12390-3:2009)" BSI, 2009, London, UK.
28. Shekhovtsova, J., Kovtun, M. et al., "Evaluation of short- and long-term properties of heat cured alkali-activated fly ash concrete", Magazine of Concrete Research, <http://dx.doi.org/10.1680/macrc.14.00377>, (in press).

# Investigation on Engineering Properties of Powder-activated Geopolymer Concrete

Kamal Neupane<sup>1</sup>, Daksh Baweja<sup>1</sup>, Rijun Shrestha<sup>1</sup>, Des Chalmers<sup>2</sup>, Paul Kidd<sup>2</sup>

<sup>1</sup>University of Technology Sydney, NSW; <sup>2</sup>Cement Australia Pty. Limited, Darra, Qld

Geopolymer is an inorganic binder, generally synthesized by the activation of aluminosilicate materials by strong alkali solution. Several previous researches on geopolymer concrete around the world suggested that geopolymer concrete possess superior mechanical and durability properties over ordinary Portland cement (OPC) concrete, such as higher compressive, indirect tensile and flexural strength and better resistant to sulphate and acidic environment.

Two types of powder-activated geopolymer binders were used as binding materials. A detailed study in engineering properties (workability, compressive strength, indirect tensile strength and modulus of elasticity) of different grades (40, 50, 65 and 80 MPa) of geopolymer and OPC concretes with two workability levels (normal-workable and super-workable) was carried out. Geopolymer as well as OPC concrete cylinders were cured at ambient temperature. The compressive and indirect tensile strength development of geopolymer concrete at early age was relatively lower than OPC concrete; however, there was a continuous and higher growth in concrete strength at later age. Normal-workable geopolymer concrete exhibited higher 28 days indirect tensile strength than OPC concrete of same grade. Measured modulus of elasticity of geopolymer normal-workable concrete was similar to OPC concrete of same grade and complied with Australian Standard 3600 [1] relationship; despite, lower value of modulus of elasticity geopolymer concrete was reported in several previous investigations. Modulus of elasticity of geopolymer super-workable concrete was lower than normal-workable concrete of same strength level and below than estimated value using Australian Standard 3600 [1] relationship.

**Key word: powder-activated, normal-workable, super-workable, indirect tensile strength, modulus of elasticity**

## 1. Introduction

Geopolymer binder is generally synthesized by the chemical reaction between aluminosilicate compounds, such as fly ash and blast furnace slag with alkali activator solution. In this process, aluminium and oxygen atoms create a tetrahedral chain of  $\text{SiO}_4$  and  $\text{AlO}_4$  to shared oxygen atoms, known as geopolymerization process [2]. The silicon and aluminium compound in source material are activated by alkaline solution to form the geopolymer paste that binds the aggregates and other less reacting materials. As production of geopolymer binder produces significantly less amount of greenhouse gases compared to Portland cement (OPC), it has been regarded as sustainable construction material [3-5]. During the last two decades, several studies have been done to evaluate the chemical, microstructural and engineering characteristics of geopolymer binders and concrete in pursuit of an environmental friendly alternative binding material [6-10]. Industrial by-product such as fly ash and blast furnace slag are the most common source material for geopolymers because of their suitability in geopolymer and availability around the world [11, 12].

As fly ash based geopolymer concrete takes longer time to set and harden in ambient condition and develops significantly lower early age strength, therefore, most of the past researches were carried out by curing in elevated temperature [10,13,14]. The engineering properties of ambient temperature cured geopolymer concrete are still limited. Addition of blast furnace slag can play a significant role to reduce the setting time and increase early as well as later age strength of fly ash based geopolymer concrete in ambient temperature [15,16]. It was suggested that presence of calcium compound accelerate the geopolymerization process and there is the coexistence of geopolymeric gel and calcium-silicate-hydrate (C-S-H) in slag-fly ash based geopolymer paste, where C-S-H gel is responsible for developing early age strength [17-19].

Investigations on geopolymer binder around the world showed that concrete from geopolymer binder possessed superior engineering properties, such as higher compressive, tensile and flexural strengths than OPC concrete [13,20,21]. However, in several investigations, modulus of elasticity of geopolymer concrete (normal-workable) was found lower than OPC concrete of same grade, and also lower than estimated modulus of elasticity according to Australian Standard 3600 [1] and ACI 318 [22] equations [13, 21, 23].

Super-workable concrete is very similar to self-compacting concrete (SCC) in fresh and hardened concrete properties which generally contains higher amount of sand and binder in concrete mix than normal-workable concrete [24]. Super-workable concrete or self-compacting concrete generally contains higher amount of sand, binder and water compare to the normal-workable concrete with addition of mineral additives and high range water reducer [25]. These ingredients can bring significant differences in mechanical properties of super workable concrete despite same binding material. Previous investigations showed that some mechanical properties, such as indirect tensile strength and modulus of elasticity of SCC are relatively lower than normal-workable concrete of same grade because of significantly difference in mix compositions of concrete [26, 27]. The mechanical behaviour of SCC has not been addressed separately in structural concrete standards, such as Australian Standard 3600 [1] and ACI 318 [22].

This paper is an investigation of engineering properties (workability, compressive strength, indirect tensile strength and modulus of elasticity) of geopolymer concretes from two powder-activated geopolymer binders (Geopolymer 1 and Geopolymer 2) at ambient temperature curing at various ages (up to 90 days). Concrete of four strength grades (40, 50, 65 and 80 MPa) and two workability levels; normal-workable and super-workable were investigated. The engineering properties of geopolymer concrete were compared against the result of OPC concrete of same grade and relationship of mechanical properties suggested in concrete standards of current practice, such as Australian Standard 3600 [1], ACI 363R [28] and ACI 318 [22].

## **2. Experimental Program**

### **2.1 Materials**

Powder-activated geopolymers; Geopolymer 1 and Geopolymer 2 recently developed by Cement Australia, QLD were used as binding materials. The activators (combination of sodium silicate, sodium hydroxide and other alkalis), low calcium fly ash and ground granulated blast furnace slag are blended together to make these binders. Geopolymer 1 have 70% fly ash and 30% ground granulated blast furnace slag in source material and Geopolymer 2 contained 40% of fly ash and 60% of slag.

Ordinary Portland cement (type GP) was selected to produce control concrete for comparison. This GP cement complied with Australian Standard 3972 [29].

Crushed coarse gravels from river source of maximum sizes of 10 mm or 20 mm were used as coarse aggregates. A combination of medium and fine river sand was used as a fine aggregate.

Two types of chemical admixtures were used to produce the OPC concrete; normal water reducer (type WR) and high range water reducer (type HWR) which complied with Australian Standard 1478.1 [30].

### **2.2 Concrete mixing and testing of fresh concrete properties**

Normal-workable concretes from both OPC and geopolymer binders were mix design according to BRE method [31]. Based on preliminary studies, amount of binder and water content were adjusted for geopolymer concrete compared to Portland cement concrete for a comparable strength and workability. The mix design of super-workable concrete was based on recommended guidelines of practice [24, 32].

Concrete of four strength grades; 40, 50, 65 and 80 MPa were produced from OPC and geopolymers binders with two workability levels; normal-workable and super-workable concretes. Both OPC and geopolymer concretes were mixed in the same way in a rotating pan mixer of 65 litres capacity. Geopolymer concretes of both workability levels were mixed without addition of any chemical admixtures. OPC normal-workable concrete of Grade 40 and 50 MPa were prepared with addition of normal water reducing admixture and Grade 65 and 80 MPa concretes were prepared with addition of high range water reducing admixture. All super-workable OPC concretes were produced with addition of high range water reducing admixture.

The workability of normal-workable concrete was assessed by the slump test and slump flow (spread) and  $T_{500}$  (time to reach 500 mm circle) for super-workable concrete.

### 2.3 Casting, curing and testing of concrete specimens

Sufficient numbers of 100 mm by 200 mm concrete cylinders were cast from all three types of binders to determine compressive strength, indirect tensile strength and modulus of elasticity of concrete. A minimum five numbers of specimens were tested for 28 days and three numbers of cylinders were tested at any other age.

After casting, both OPC and geopolymer concrete cylinders were left in standard laboratory temperature (23°C) for 24 hours. Geopolymer concrete cylinders were wrapped with plastic sheet immediately after the demoulding as shown in Figure 1 to prevent the moisture loss. Small amount of water was sprayed prior to sealing the cylinders. The geopolymer cylinders were stored in the lab condition (23°C) until testing. OPC concrete cylinders were moist cured in lime saturated water at 23°C until testing.

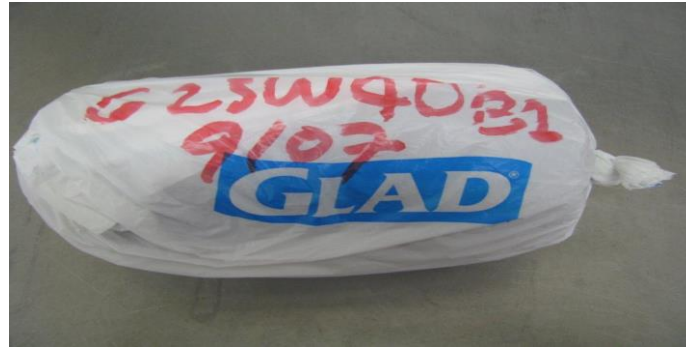


Figure 1: Curing of geopolymer concrete cylinder

The compressive strengths and indirect tensile strength of concretes of different grades and workability were tested according to Australian Standard 1012.9 [33] and Australian Standard 1012.10 [34] at the ages of 1, 3, 7, 28, 56 and 90 days. Modulus of elasticity of concretes was measured according to Australian Standard 1012.17 [35] at the age of 28 days.

## 3. Results and Analysis

Amount of water required on concrete mixes was based on comparable workability of concretes of different grades (average 120 mm slump for normal-workable concretes and 500–700 mm flow for super workable concretes). Concretes of different grades and workability levels were produced with the similar types (same source and grading) of aggregates. Therefore, the aggregate type is not considered as test variable.

### 3.1 Workability

The average water content in geopolymer concrete with Geopolymer 1 and Geopolymer 2 were 112 kg/m<sup>3</sup> and 121 kg/m<sup>3</sup> respectively. The average water content in OPC concrete for comparable workability was 166 kg/m<sup>3</sup>, although it was produced with addition of water reducing admixtures. In average, normal-workable concrete from geopolymer binders required around 30% less amount of water than from OPC for same workability.

The lower water demand in geopolymer concrete is due to high proportion (around 50%) of fly ash present in binder which is responsible to improve the workability of concrete because of its round shaped particles [36]. Fly ash itself is spherical and can be dispersed easily in the alkaline environment without addition of any admixtures [37]. The major difference between Geopolymer 1 and Geopolymer 2 binder is the proportion of fly ash which can be responsible for lower water demand in concrete from Geopolymer 1 than Geopolymer 2 for same level of workability.

In case of super-workable concretes, concrete from Geopolymer 2 binder required slightly less amount of water (around 7%) than OPC concrete for the comparable workability.

### 3.2 Compressive strength development

Figure 2 shows the compressive strength development of Grades 50 and 65 MPa concretes from different binders and workability levels. Similar trend of compressive strength development was observed in concretes of other grades. In both geopolymer and OPC concretes, compressive strength increased with time at a decreasing rate. For the same strength grade, geopolymer concrete exhibited relatively lower early age (1-3 days) compressive strength than OPC concrete. However, the later age (from 28-90 days) strength development was significantly higher in geopolymer concrete than in OPC concrete.

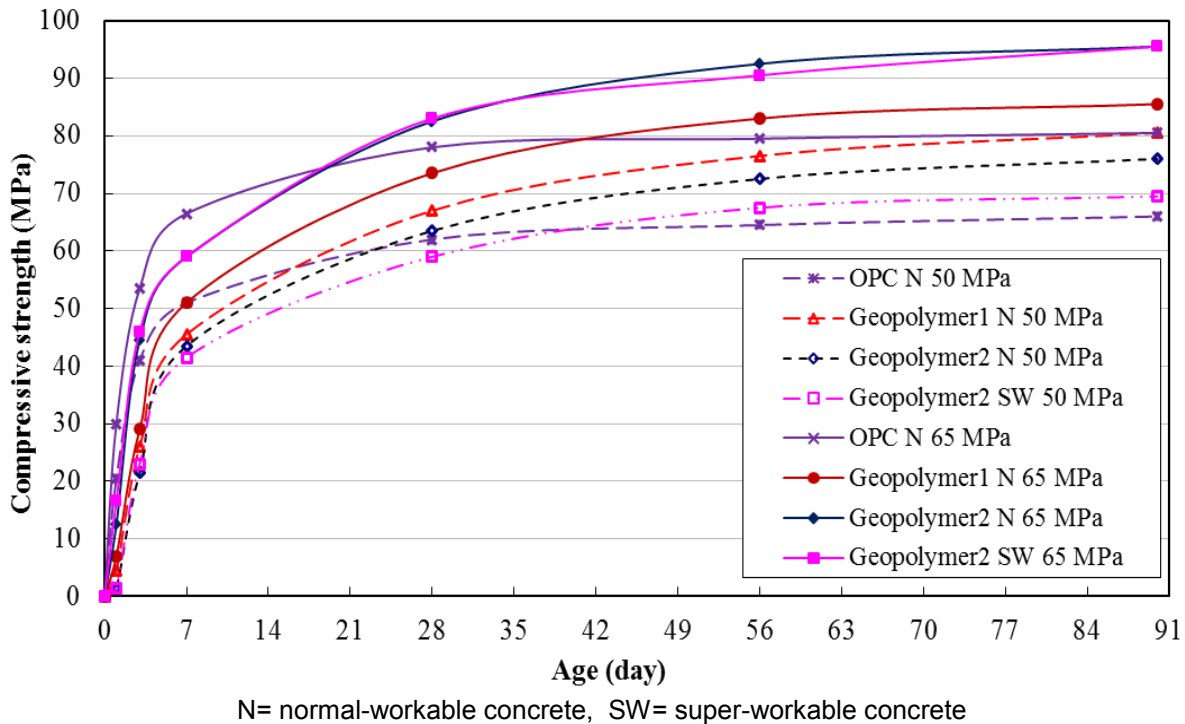


Figure 2: Compressive strength development 65 MPa grade concretes

The amount of binder required for the same 28-day compressive strength was significantly lower in geopolymer concrete compared to OPC concrete. In Grade 50 concrete, 295 kg/m<sup>3</sup> Geopolymer 2 binder and 395 kg/m<sup>3</sup> Portland cement developed 63.5 MPa and 62.0 MPa of 28-day compressive strength, respectively. Geopolymer 2 needs slightly less amount of binder than Geopolymer 1 for the same 28-day compressive strength which was due to the difference in slag content in those binders by 30%.

Compressive strength development of medium grade (40 and 50 MPa) geopolymer concrete at ambient curing condition was relatively lower at early age (1 to 3 days) compared to the OPC concrete. However, OPC concrete with Portland cement only (no supplementary cementitious materials added) are not common in field; generally Portland cement is replaced by 20 to 40% of fly ash or slag or combination of both. Partial replacement of Portland cement (20% to 40% by weight) by fly ash and slag or their combinations resulted significantly reduction in early age strength in previous studies. Johari, Brooks et al. [38] suggested around 60% reduction in 1 day compressive strength and 30% reduction in 3 day compressive strength due to replacement of Portland cement by 40% (by weight) of slag. Therefore, comparing with the early age strength results of OPC concrete having 20% to 40% of fly ash or slag, geopolymer concrete can attain same level of early age compressive strength to OPC concrete of same grade. High strength geopolymer concrete (65 and 80 MPa) exhibited significant early age strength equal to OPC concrete of this study. There was an average 18% growth in compressive strength in geopolymer concrete from 28 to 90 days period when compared to 7% increase in OPC concrete in for the same period.

### 3.3 Indirect tensile strength development

The Indirect tensile strength development of Grades 50 and 65 concretes is presented in Figures 3. The development of tensile strength was in similar pattern for all grades of concretes. Medium grade geopolymer concrete attained relatively lower indirect tensile strength than OPC concrete of same grade; however, the strength development at later age was significantly higher. The 28 days indirect tensile strengths of geopolymer normal-workable concretes were higher (15 to 20%) than OPC concretes for all strength grades. Both OPC and geopolymer super workable concretes exhibited lower indirect tensile strength (around 15%) than normal-workable concretes of same grades.

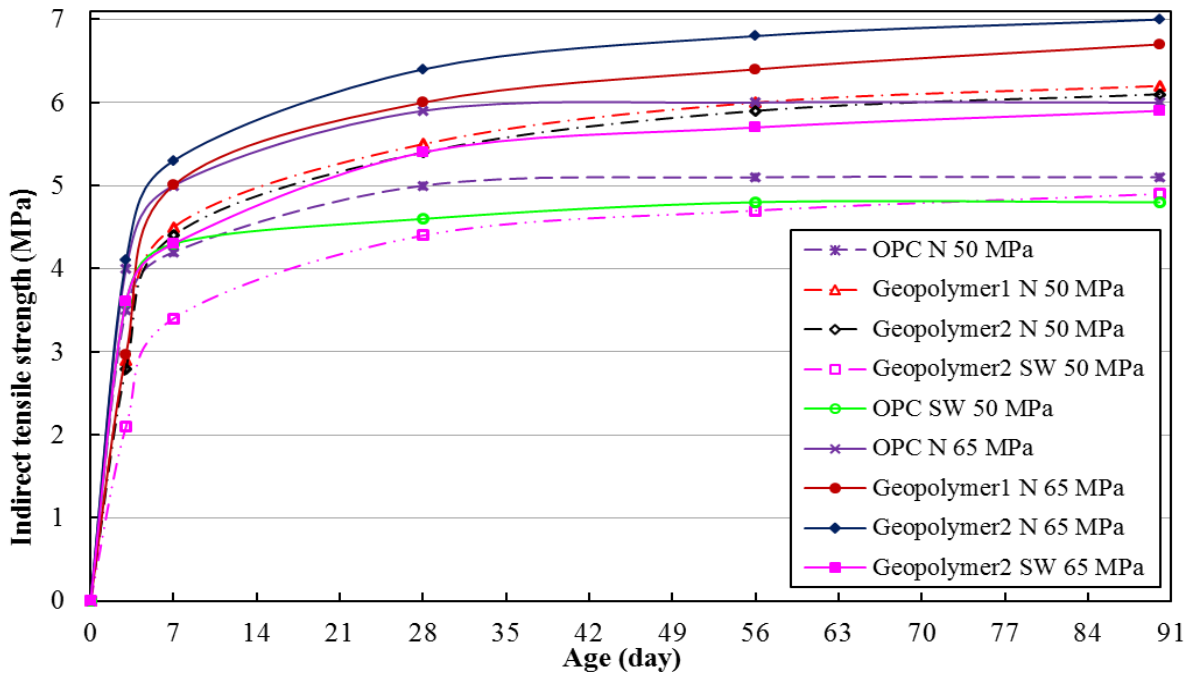


Figure 3: Indirect tensile strength development of Grades 50 and 65 MPa concretes

The early age development of indirect tensile strength of geopolymer concretes was significantly higher than compressive strength development at the same age. In Grade 50 MPa concretes, average indirect tensile strength development at 3 days was 53% of 28 days strength compared to average 35% of compressive strength at the same age. There was no significant development in indirect tensile strength of geopolymer concretes after 28 days compared to the post 28-day development in compressive strength. The average growth in indirect tensile strength from 28 to 90 days in geopolymer concretes was 12% when compared to 18% growth in compressive strength for that period.

#### 3.3.1 Formulation of relationship with compressive strength

The indirect tensile strength of normal-workable and super-workable concretes of same strength grade was different. So, these two types of concretes were analysed separately.

##### 3.3.1.1 Normal workable concrete

No equation has been suggested to define the relationship of mechanical properties of geopolymer concretes in any structural concrete standards so far. There are several concrete standards to define the relationship of mechanical properties of OPC concrete, some of them are as follows.

According to ACI 363R [28] indirect tensile strength concrete can be calculated as follows. (1)

$$f_{sp} = 0.59 \sqrt{f_c} \text{ MPa} \quad (\text{for } 21 \text{ MPa} < f_c < 83 \text{ MPa})$$

where,

$f_{sp}$  = characteristic indirect tensile strength of concrete

$f_c$  = characteristic compressive strength of concrete

Australian Standards 3600 [1] suggested following relationship between axial tensile and compressive strength of concrete applicable for 20 MPa to 100 MPa grade concretes.



$$f_{ct} = 0.36 \sqrt{f_c} \quad \text{MPa} \quad (2)$$

where,

$f_{ct}$  = characteristic axial tensile strength of concrete

Due to the differences in source material, alkali activators and their proportions, the results of indirect tensile strength were also diverse in previous investigations, hence, difference models were proposed. Some of them are as followings.

$$\text{Sofi, Van Deventer et al. [23]: } f_{sp} = 0.5 \sqrt{f_c} \quad \text{MPa} \quad (3)$$

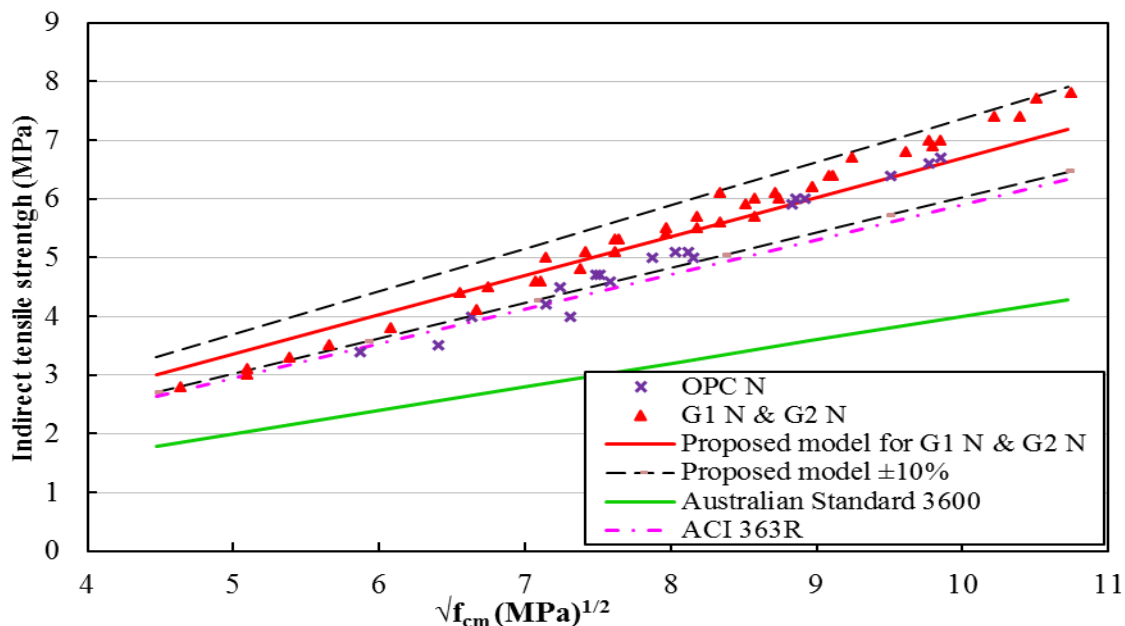
$$\text{Tempest [39]: } f_{sp} = 0.616 \sqrt{f_c} \quad \text{MPa} \quad (4)$$

Concrete Institute of Australia [40], recommended a very similar equation to AS 3600 [1] for geopolymer concrete which is as follows.

$$f_{ct} = 0.4 \sqrt{f_{cm}} \quad \text{MPa} \quad (5)$$

In above equations, the recommend equation by Concrete Institute of Australia [40] estimates lowest value of tensile strength for geopolymer concrete.

The relationship between indirect tensile strength and compressive strength of different grades of concretes is plotted in **Figure 4** including results at different ages (3 to 90 days).



**Figure 4: Relation between indirect tensile strength and compressive strength**

The line of ACI 363R is closely located to the data points of geopolymer concretes in lower range of compressive strength; however, there is a bigger gap in high strength range. Australian Standard 3600 [1] estimates lower value of indirect tensile strength, hence, it is located far below than data points of geopolymer concretes of this study.

A best fit line's equation for Geopolymer 1 and Geopolymer 2 normal- workable concretes, valid for the data range of 20 MPa to 110 MPa can be proposed as following.

$$f_{sp} = 0.67 \sqrt{f_{cm}} \quad \text{MPa} \quad (6)$$

In **Figure 4** all the data points of Geopolymer 1 and Geopolymer 2 normal workable concretes were located within the  $\pm 10\%$  range from this proposed line, hence this proposed equation can be used safely for design purpose. The line of ACI 363R is close with lower error range ( $-10\%$ ) of proposed model.

The difference in source materials and alkali activators can bring a lot of variations in engineering properties of geopolymer concrete as a final product of geopolymerization [9]. As such, significant variations in compressive strength, indirect tensile strength results of geopolymer concrete were observed among previous studies around the world.

### 3.3.1.2 Super workable concrete

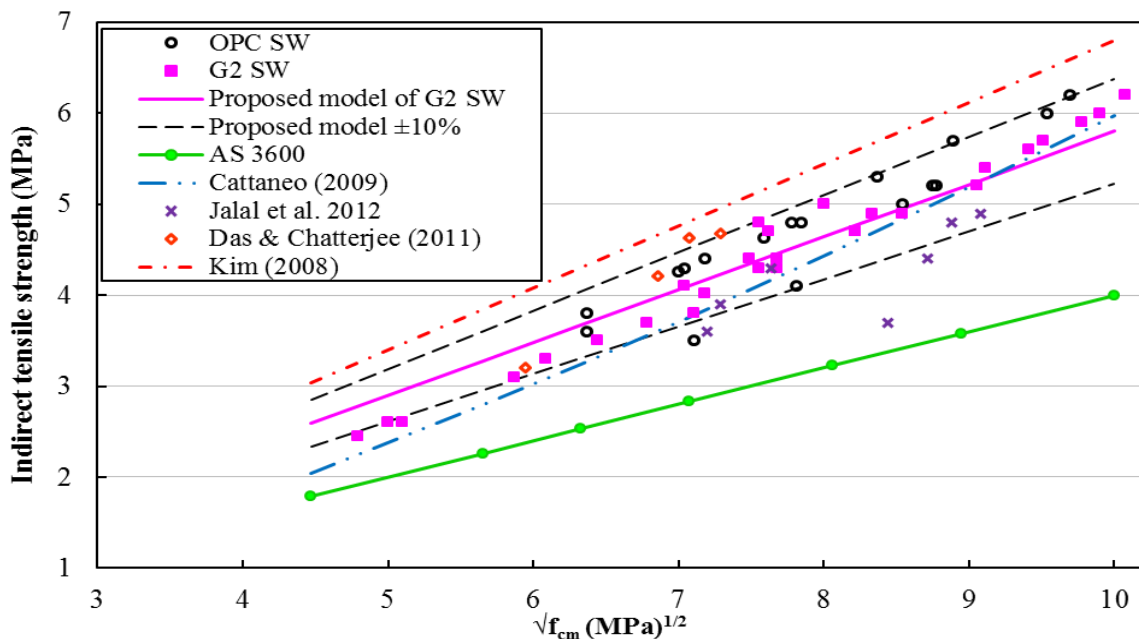
In the current study, the indirect tensile strength of super-workable concrete was found lower than normal workable concrete of same compressive strength by 15%. Some investigations were done in the past to compare the mechanical properties of OPC based self-compacting concrete. Jalal, Mansouri et al. [25] postulated lower splitting tensile strength of self-compacting concrete compared to normal workable concrete of same grade. On the contrary, Das and Chatterjee [41] found splitting tensile strength of self-compacting concrete slightly higher than normal workable concrete of same compressive strength and it was suggested due to improved microstructure and less porosity in super workable concrete. Kim [42] postulated a relationship model for splitting tensile strength of self-compacting concrete as following.

$$f_{sp} = 0.68 \sqrt{f_{cm}} \quad (7)$$

Cattaneo [43] also suggested that self-compacting concrete possessed similar or even higher indirect tensile strength than normal workable concrete and proposed an equation as following.

$$f_{sp} = 0.277 (f_{cm})^{2/3} \quad (8)$$

Indirect tensile strength results of super workable concretes of this study and previous results are plotted in **Figure 5**.



**Figure 5: Indirect tensile and compressive strength of super workable concretes**

In **Figure 5**, OPC super workable concrete exhibited slightly higher splitting tensile strength than geopolymer super workable for the same level of compressive strength. The line representing AS 3600 [1] was located below the data points of geopolymer super workable concrete.

As the data points and proposed model for self-compacting concrete were diverse in previous investigations, they may not be applicable to estimate the indirect tensile strength of geopolymer super-workable concrete. A relationship between indirect tensile strength and compressive strength of geopolymer super workable concretes can be proposed for the range of 20 MPa to 100 MPa.

$$f_{sp} = 0.58 \sqrt{f_{cm}} \text{ MPa} \quad (9)$$

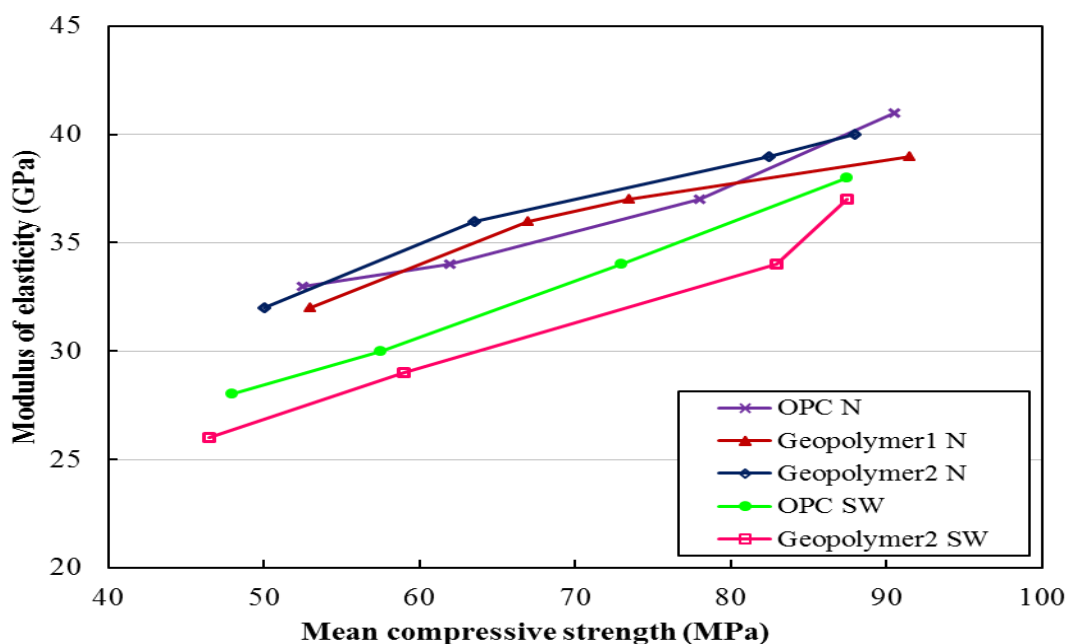
In **Figure 5**, all the data points of geopolymer super workable concretes of this study are located inside the  $\pm 10\%$  error range of the proposed equation. The line representing the equation suggested by Cattaneo [43] is located close to the data points of geopolymer super workable concretes despite her claim that SCC possess similar or higher tensile strength than normal workable concrete. The model proposed by Kim [42] estimates higher indirect tensile strength than this study. The binder types, use of mineral additives, proportions of sand and amount of binder in concrete mix are the major factors for the diversity of tensile strength results in previous investigations.

Super workable concrete were produced with smaller (maximum 10 mm) size of coarse aggregates, higher amount of binder and higher proportion. Walker & Bloem [44] found that tensile strength of concrete increase with the maximum coarse aggregate size. This was due to the reduction in area of aggregate-paste interface in concrete which is the weakest zone in concrete. Rao and Prasad [45] also found an increase in tensile strength of concrete with increase in maximum size of aggregate from 40 to 75 MPa. In current study, the average proportions of coarse aggregate in normal and super workable concretes were 61% and 49% of total aggregates respectively. Besides, the amount of binder in super workable concrete was significantly higher than in normal workable concrete. Those two ingredients contribute to make higher volume of mortar (binder and sand matrix) in the concrete mix which has lower tensile strength than aggregate rock, hence the lower tensile strength of concrete. Nikbin, Beygi et al. [46] found a decrease in tensile strength of concrete while the coarse aggregate proportion was decrease from 60% to 40%.

Mechanical properties of any material, such as compressive strength and indirect tensile strength are the function the constituent material. Geopolymer and Portland cement are based on different chemistry, therefore the material property of concretes from those materials should be different. Chemically, geopolymer binders are formed by the polymeric structure resulting from cross linking of polysilicate chains having a strong covalent bond [47]. This may be a reason for geopolymer concrete possessing higher indirect tensile strength than OPC concrete of same compressive strength level.

### 3.4 Modulus of elasticity

The experimental results of modulus of elasticity of concretes of different grades are presented in **Figure 6**. Figure shows that geopolymer concrete possessed similar elastic modulus to the OPC concrete of same strength grades. However, super- workable concretes possess relatively less elastic modulus than normal-workable concrete.



**Figure 6: Experimental data of modulus of elasticity**

Previous investigations suggested that modulus of elasticity of concretes also depends on the types and properties of coarse aggregates used; higher the modulus of elasticity of aggregate resulted higher modulus of elasticity of concrete [48, 49]. The majority of aggregate rock used in this experiment was greywacke having average modulus of elasticity 38.7 GPa [50] when compared to 49.0 GPa of limestone and 42.0 GPa of quartzite aggregates [51]. Therefore, the modulus of elasticity results could be different if other aggregates types were used.

#### 3.4.1 Relationship between modulus of elasticity and compressive strength

In some concrete standards of current practice modulus of elasticity of concrete is estimated from its density and compressive strength.

Modulus of Elasticity ( $E_c$ ) recommended by ACI 318 [22] is as following. (10)  
 $E_c = 0.043\rho^{1.5} \sqrt{f'_c}$  MPa

Modulus of elasticity recommended by Australian Standard 3600 [1] is as following (11)  
 $E_c = \rho^{1.5} (0.024 \sqrt{f_{cm}} + 0.12)$  MPa; when  $f_{mc} > 40$  MPa  
 Where,  $\rho$  = cylinder density ( $\text{kg/m}^3$ ) and  $f_{cm}$  = mean compressive strength (MPa) and  
 $f'_c$  = characteristic strength of concrete (MPa)

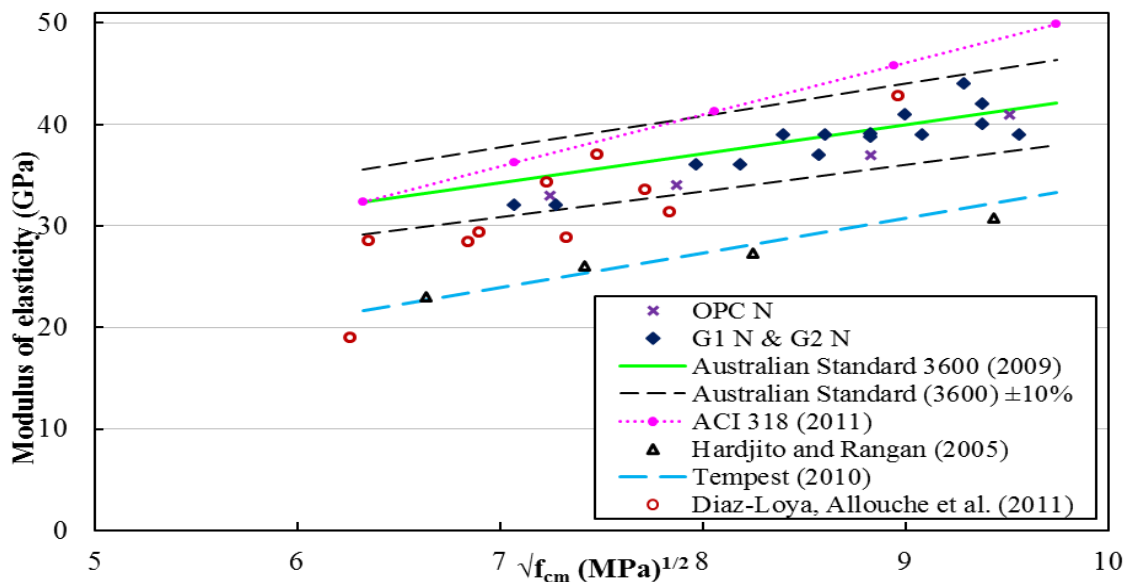
There are some publish investigations about the modulus of elasticity of geopolymer concrete synthesized from different types of source materials and activators. Most of the previous investigations were carried out in elevated temperature curing because of lower early age strength of fly ash based geopolymer concrete.

Tempest [39] postulated a model to estimate the modulus of elasticity from compressive strength as follows.

$$E_c = 3421 \sqrt{f'_c} \text{ MPa} \quad (12)$$

Modulus of elasticity of fly ash based geopolymer concrete reported by Diaz-Loya, Allouche, et al.[10] were similar with the results of this study but for the lower range of compressive strength.

Hardjito and Rangan [21] found that accelerated cured fly ash based geopolymer concrete possessed relatively lower modulus of elasticity then recommended by AS 3600 [1].



**Figure 7: Relationship of compressive strength and modulus of elasticity**

All above relationships and results are plotted in **Figure 7**. In this figure, the line representing Australian Standard 3600 [1] equation is close to data points of geopolymer as well as OPC concrete. This value has a range of  $\pm 20\%$ . However, in this plotting all normal-workable concrete data points are located well inside the  $\pm 10\%$  range of that line. Modulus of elasticity value is said to be overestimated by ACI 318 [22] because none of any data point are located above this line.

### 3.4.2 Compliance with AS 3600 and ACI 318

Measured modulus of elasticity of geopolymer concretes was compared with estimated values using Australian Standard 3600 [1] and ACI 318 [22] in this study. The calculated modulus of elasticity using Australian Standard 3600 [1] were very close to the measured results of geopolymer concretes for the same compressive strength. The ratios of measured to estimated value were in between 0.93 to 1.02 with an average of 0.98 for geopolymer concretes of different grades. Hence, modulus of elasticity for geopolymer binder concretes can be closely estimated using Australian Standard 3600 [1] equation. Equation suggested by ACI 318 [22] over estimates the modulus of elasticity of geopolymer concretes with an average 0.86 measured to estimated ratio.

### 3.4.3 Modulus of elasticity of super-workable concrete

In **Figure 6**, the modulus of elasticity of super workable concrete was relatively lower than normal-workable concrete for the same level of compressive strength. Similar to indirect tensile strength, modulus of elasticity of a lower self-compacting concrete was reported in some previous investigations. Holman, Myers et al. [26] found that SCC possessed relatively lower modulus of elasticity than normal-workable concrete despite higher compressive strength. Leemann and Hoffmann [52] study showed that self-compacting concrete possessed around 16% lower modulus of elasticity than normal-workable concrete of same compressive strength. Another study by Dinakar, Babu et al.[53] postulated a relationship to estimated modulus of SCC elasticity as following.

$$E_c = 4180 \sqrt{f_{cm}} \quad (\text{MPa}) \quad (13)$$

Similarly, Persson [54] postulated following relationship of modulus of elasticity of SCC.

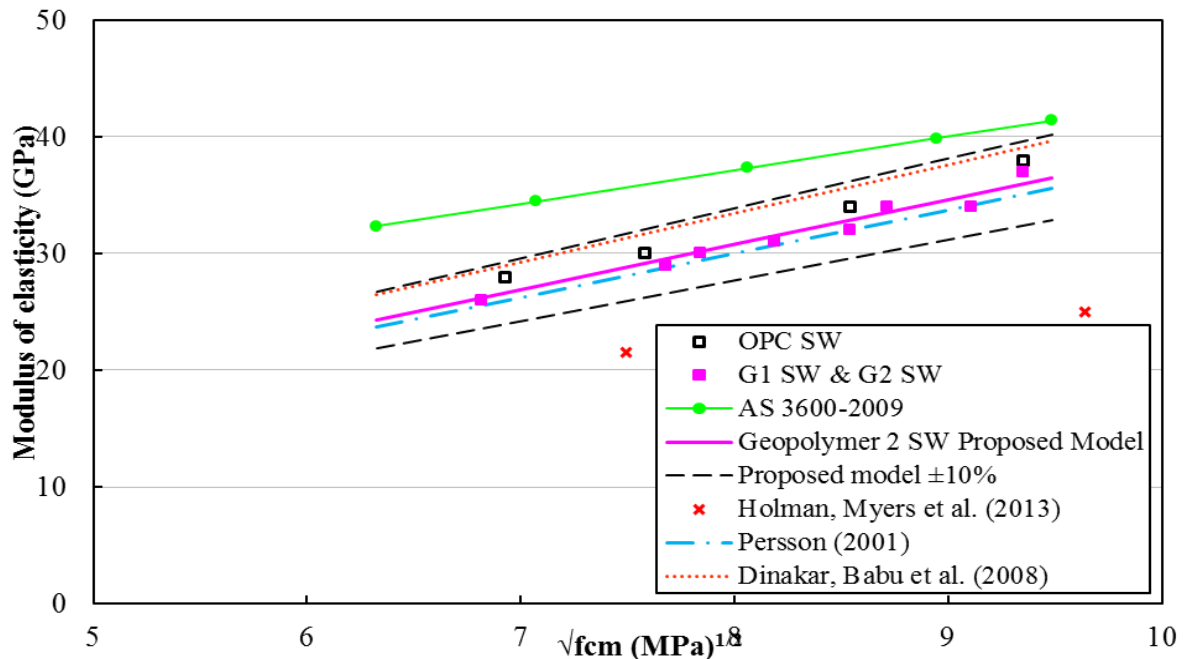
$$E_c = 3750 \sqrt{f_{cm}} \quad (\text{MPa}) \quad (14)$$

The moduli of elasticity of super-workable concretes are presented in **Figure 8**. In this figure, modulus of elasticity of super-workable concrete are located far from the line of AS 3600 [1]. Therefore, a model can be formulated representing the best fit line of the data points of Geopolymer 2 super-workable concrete.

$$\text{Modulus of elasticity } (E_c) = \rho^{1.5} 0.034 \sqrt{f_{cm}} \quad \text{MPa} \quad (15)$$

Where,  $\rho$  = cylinder density ( $\text{kg/m}^3$ ) and  $f_{cm}$  = mean compressive strength (MPa).

In **Figure 8**, all the data points of super workable concrete located within the  $\pm 10\%$  range from the proposed model, so this equation is safe for design practice. The relationship model proposed by Persson [54] is very close with the proposed model of this study, whereas equation proposed by Dinakar, Babu et al.[53] was slightly overestimate the modulus of elastic of super workable concrete but located within 10% range.



**Figure 8: Modulus of elasticity of super-workable concretes**

#### 3.4.3.1 Factor affecting the modulus of elasticity of super-workable concrete

Concrete as a composite material is affected from the properties of its ingredients; aggregates and binder. Kaplan [55] postulated following equation of effect of the modulus of elasticity aggregate and binder into modulus of elasticity of concrete.

$$E_c = V_a * E_a + (1 - V_a) * E_m \quad (16)$$

Where,  $E_c$ ,  $E_a$  and  $E_m$  are the moduli of elasticity of concrete, aggregate and binding paste respectively;  $V_a$  = volume concentration of aggregate.

The modulus of elasticity of concrete is the summation of modulus of elasticity of its ingredients; aggregates and binding paste with respect to their volume in concrete mix.

The average modulus of elasticity of greywacke aggregate rocks (used in this experiment) was 38.7 GPa [50], whereas modulus of elasticity of cement paste was measured around 24.0 GPa [56]. The binder content in super-workable concretes was around 35% higher (by weight) than in normal-workable concretes of same grade, thus higher volume of paste. This significant lower volume of coarse aggregates and higher volume of binder paste in super-workable concretes can contribute to lower the modulus of elasticity of super-workable concrete. Felekoğlu et al. [57] concluded that higher amount of binder was responsible to lower the modulus of elasticity of SCC.

The proportion of coarse and fine aggregates in the concrete mix is also a significant factor in modulus of elasticity of concrete. Nikbin, Beygi et al. [46] found a significant increase in modulus of elasticity with the increase in proportion of coarse aggregate in concrete mix. The average proportions of coarse aggregate in normal-workable and super-workable concretes of this study were 61% and 49% by weight of total aggregates respectively. The 12% difference in coarse aggregate may be responsible for the decrease in modulus of elasticity of super-workable concretes.

Lower density of super-workable concrete is also a major factor for the less modulus of elasticity according to Pauw [58]. In this study, average cylinder density of geopolymer super-workable concrete was around 2340 kg/m<sup>3</sup>, compared to the average density of 2430 kg/m<sup>3</sup> of geopolymer normal-workable concrete.

#### **4. Concluding remarks**

Normal-workable geopolymer Concrete required significantly less amount of water and binder for comparable 28 day compressive strength and workability level when compared to Portland cement concrete. Geopolymer concrete was produced without addition of any chemical admixture with sufficient workability.

Development of compressive strength in ambient cured medium grade geopolymer concrete was lower at early age (1 -3 days) when compared to OPC concrete. However, comparing with the early age strength results of OPC concrete having 20% to 40% of fly ash or slag, geopolymer concrete can attain same level of early age strength. Compressive strength development in high strength (65 and 80 MPa) geopolymer concrete was significantly higher at early age. The growth in compressive strength after 28 days was significantly higher in geopolymer concrete compared to OPC concrete of same grade which was ranged from 16 to 20% for 28 to 90 days period.

Normal-workable geopolymer concrete exhibited 15 to 20% higher indirect tensile strength than OPC concrete of same grade. Indirect tensile strength of normal-workable geopolymer concretes were higher than estimated value using Australian Standard 3600 [1] relationships. Therefore, a different relationship was proposed to estimate indirect tensile strength of geopolymer concrete. Indirect tensile strength of super-workable geopolymer concrete was relatively lower than normal workable concrete (around 15%) for the same strength grade. This was due to the small size of coarse aggregate, higher amount of binder and higher proportions of fine aggregates in the super workable concrete, therefore a separate equation has been proposed.

Normal-workable concretes from Geopolymer 1 and Geopolymer 2 binders exhibited similar values of modulus of elasticity to the OPC normal-workable concrete of same compressive strength. The measured moduli of elasticity of normal-workable concretes of this study can be close (within 10% error) estimated using Australian Standard 3600 [1] equations, hence, a different equation was not proposed.

Similar to tensile strength, geopolymer super workable concrete possessed relatively lower elastic modulus than normal-workable concrete of same grade. Previous investigations on OPC based self-compacting concretes also suggested lower elastic modulus. Higher proportion of sand, lower cylinder density and higher volume of binder paste in super-workable concrete are the major factors to decrease modulus of elasticity of super-workable concrete. Therefore, a different model has been proposed to estimate the modulus of elasticity of geopolymer super-workable concrete.

## References

1. Australian Standard-3600, "Concrete Structures", Standards Australia International Ltd, 2009, Sydney, NSW.
2. Davidovits, J., "Geopolymers and geopolymeric materials", Journal of Thermal Analysis and Calorimetry, **35**(2), 1989, pp 429-441.
3. Davidovits, J., "Geopolymers- Inorganic polymeric new materials" Journal of Thermal Analysis and Calorimetry, **37**(8), 1991, pp 1633-1656.
4. Raijiwala, D.B. and Patil, H.S., "Geopolymer concrete A green concrete", *Chemical, Biological and Environmental Engineering (ICBEE), 2nd International Conference on 2010*
5. Li, Z., Z. Ding, and Y. Zhang, "Development of sustainable cementitious materials", *Proceedings of the international workshop on sustainable development and concrete technology*, 2004.
6. Fernández-Jiménez, A., Palomo, A., et al. "Microstructure development of alkali-activated fly ash cement: a descriptive mode", *Cement and Concrete Research*, **35**(6), 2005, pp 1204-1209.
7. Wu, H.-C. and Sun, P., "Effect of Mixture Compositions on Workability and Strength of Fly Ash-Based Inorganic Polymer Mortar", *ACI Materials Journal*, **107**(6), 2010, pp 554-561.
8. Weng, L. and K. Sagoe-Crentsil, "Dissolution processes, hydrolysis and condensation reactions during geopolymer synthesis: Part I—Low Si/Al ratio system.", *Journal of materials science*, **42**(9), 2007, pp. 2997-3006.
9. Duxson, P., Fernández-Jiménez, A. et al., "Geopolymer technology: the current state of the art", *Journal of Materials Science*, **42**(9), 2006, pp 2917-2933.
10. Diaz-Loya, I.E., E.N. Allouche et al., "Mechanical Properties of Fly-Ash-Based Geopolymer Concrete" *ACI Materials Journal*,. **108**(3), 2011, pp 300-306.
11. Heath, A., et al., "The potential for using geopolymer concrete in the UK", *Proceedings of the ICE - Construction Materials*, **166**(4), 2013, pp. 195-203.
12. Swanepoel, J. and C. Strydom, "Utilisation of fly ash in a geopolymeric material", *Applied Geochemistry*,. **17**(8), 2002, pp 1143-1148.
13. Fernandez-Jimenez, A.M., A. Palomo, et al. , "Engineering properties of alkali-activated fly ash concrete" *ACI Materials Journal*, **103**(2), 2006, pp 106-112.
14. Hardjito, D., Wallah, S.E et al., "On the development of fly ash-based geopolymer concrete", *ACI Materials Journal-American Concrete Institute*,. **101**(6), 2004, pp 467-472.
15. Lee, N.K. and H.K. Lee "Setting and mechanical properties of alkali-activated fly ash/slag concrete manufactured at room temperature" *Construction and Building Materials*, **47**, 2013 pp 1201-1209.
16. Nath, P. and P.K. Sarker "Geopolymer concrete for ambient curing condition" *Proceeding of the Australasian Structural Engineering Conference, Perth, 2012*, Engineers Australia.
17. Yip, C.K., Lukey, G.C. et al. "The coexistence of geopolymeric gel and calcium silicate hydrate at the early stage of alkaline activation", *Cement and Concrete Research*, **35**(9), 2005, pp 1688-1697.
18. Oh, J.E., Jun, P.J.M., et al. "The evolution of strength and crystalline phases for alkali-activated ground blast furnace slag and fly ash-based geopolymers" *Cement and Concrete Research*, **40**(2) 2010, pp 189-196.
19. Catalfamo, P., Pasquale, S.D et al., "Influence of the calcium content on the coal fly ash features in some innovative applications", *Resources, Conservation and Recycling*, **20**(2) 1997, pp 119-125.
20. Raijiwala, D.B. and H.S. Patil, "Geopolymer Concrete: A Concrete of the Next Decade" *Journal of Engineering Research and Studies*, **2**(1), 2011, pp. 19-25.
21. Hardjito, D. and B.V. Rangan, "Development and properties of low-calcium fly ash-based geopolymer concrete", *Curtin University of Technology, Perth, Australia*, 2005.
22. American Concrete Institute, "Building Code Requirements for Structural Concrete; ACI-318 (Reported by ACI Committee 318)", 2011, Farmington Hills, , MI, USA.



23. Sofi, M., Van Deventer, J.S.J et al., "*Engineering properties of inorganic polymer concretes (IPCs)*", *Cement and Concrete Research*, **37**(2), 2007, pp 251-257.
24. Concrete Institute of Australia, "*Recommended Practice: Super-workable Concrete (Z 40)*". (CIA 2005)", National Office, St Leonard, NSW.
25. Jalal, M., Mansouri, E. et al., "*Mechanical, rheological, durability and microstructural properties of high performance self-compacting concrete containing SiO<sub>2</sub> micro and nanoparticles*", *Materials & Design*, **34**, 2012, pp 389-400.
26. Holman, K.R., Myers, J.J. et al., "*Mechanical and Durability Behaviour of Self-Consolidating Concrete (SCC)*", *Proceeding of the Fifth North American Conference on the Design and Use of Self-Consolidating Concrete*, 2013, Chicago, USA.
27. Domone, P., "*A review of the hardened mechanical properties of self-compacting concrete*. *Cement and Concrete Composites*", **29**(1), 2007, pp 1-12.
28. American Concrete Institute, "*State-of-the-Art Report on High-Strength Concrete; ACI-363R-(Reported by ACI Committee 363)*", 1992 (Reapproved 1997), Farmington Hills, MI, USA.
29. Australian Standard-3972, "*General purpose and blended cements*" 2010, Standards Australia International Ltd, Sydney, NSW.
30. Australian Standard-1478.1, "*Chemical admixtures for concrete, mortar and grout; Part 1- Admixtures for concrete*" 2000, Standards Australia International Ltd, Sydney, NSW.
31. Teychenné, D.C., Franklin, R.E. et al., "*Building Research Establishment-Design of Normal Concrete Mixes*" 2<sup>nd</sup> ed. 1997, Construction Research Communications Ltd. London, England
32. EFNARC, Association, "*Specification and Guidelines for self-compacting concrete*", 2002, EFNARC, Association House, Farnham, Surrey, UK.
33. Australian Standard -1012.9, "*Methods of testing concrete; Method 9: Determination of the compressive strength of concrete specimens*", 1999, Standards Australia International Ltd, Sydney, NSW.
34. Australian Standard-1012.10, "*Methods of testing concrete; Method 10: Determination of indirect tensile strength of concrete cylinders (Brazil or splitting test)*", 2000, Standards Australia International Ltd, Sydney, NSW.
35. Australian Standard-1012.17, "*Methods of testing concrete; Method 17: Determination of the static cord modulus of elasticity and Poisson's ratio of concrete specimens 1997*", Standards Australia International Ltd, Sydney, NSW.
36. Siddique, R., "*Waste Materials and By- Products in Concrete*" Springer, 2008, Berlin, Germany
37. Chindaprasirt, P., Chareerat., T. et al., "*Workability and strength of coarse high calcium fly ash geopolymer*", *Cement and Concrete Composites*, **29**(3), 2007, pp 224-229.
38. Johari, M.A.M., Brooks, J.J. et al., "*Influence of supplementary cementitious materials on engineering properties of high strength concrete*", *Construction and Building Materials*, **25**(5), 2011, pp 2639-2648.
39. Tempest, B., "*Engineering Characterization of Waste Derived Geopolymer Cement Concrete for Structural Applications*, in *Infrastructure & Environmental Systems*", 2010, The University of North Carolina at Charlotte, Ann Arbor, United States.
40. Concrete Institute of Australia, "*Recommended Practice: Geopolymer Concrete (Z16)*" 2011, National Office, North Sydney NSW.
41. Das, D. and A. Chatterjee, "*A comparison of hardened properties of fly-ash-based self-compacting concrete and normally compacted concrete under different curing conditions*" *Magazine of Concrete Research*, **64**(2), 2011, pp 129-141.
42. Kim, Y.H., "*Characterization of Self-consolidating Concrete for the Design of Precast, Pre-tensioned Bridge Superstructure Elements*", 2008, Texas A&M University, Texas, USA.
43. Cattaneo, S., "*Self-Consolidating Concrete*, in *Concrete Materials: Properties, Performance and Application*", J.T. Sentowski, Editor, 2009, Nova Science Publishers, Inc.: New York. pp 117-169.
44. Walker, S. and Bloem, D.L., "*Effects of aggregate size on properties of concrete*" *ACI Journal Proceedings*, 1960.



45. Rao, G.A. and B.K. Prasad, "*Fracture energy and softening behavior of high-strength concrete*", Cement and Concrete Research, **32**(2), 2002, pp 247-252.
46. Nikbin, I.M., Beygi, M.H.A et al., "*A comprehensive investigation into the effect of aging and coarse aggregate size and volume on mechanical properties of self-compacting concrete*" Materials & Design, **59**, 2014 pp 199-210.
47. Davidovits, J., "*Chemistry of geopolymeric systems, terminology*" Geopolymere '99 Proceedings, 1999 pp 9-39.
48. Beshr, H., Almusallam, A. et al., "*Effect of coarse aggregate quality on the mechanical properties of high strength concrete*", Construction and Building Materials, **17**(2), 2003 pp. 97-103.
49. Aïtcin, P.-C. and Mehta, P.K., "*Effect of coarse aggregate characteristics on mechanical properties of high-strength concrete*. ACI Materials Journal, **87**(2), 1990 pp 103-107.
50. Gokceoglu, C. and Zorlu, K., "*A fuzzy model to predict the uniaxial compressive strength and the modulus of elasticity of a problematic rock*", Engineering Applications of Artificial Intelligence, **17**(1), 2004, pp 61-72.
51. Baalbaki, W., et al., "*Influence of coarse aggregate on elastic properties of high-performance concret*", ACI Materials Journal, **88**(5), 1991, pp. 499-503.
52. Leemann, A. and Hoffmann, C., "*Properties of self-compacting and conventional concrete—differences and similarities*", Magazine of Concrete Research, **57**(6), 2005 pp. 315-319.
53. Dinakar, P., Babu, K. et al., "*Mechanical properties of high-volume fly ash self-compacting concrete mixtures. Structural concrete*", **9**(2), 2008, pp 109-116.
54. Persson, B., "*A comparison between mechanical properties of self-compacting concrete and the corresponding properties of normal concrete*. Cement and concrete Research,". **31**(2), 2001 pp 193-198.
55. Kaplan, M.F., "*Ultrasonic pulse velocity, dynamic modulus of elasticity, Poisson's ratio and the strength of concrete made with thirteen different coarse aggregates*", 1959, National Building Research Institute.
56. Alexander, M.G., "*Effects of aging on mechanical properties of the interfacial zone between cement paste and rock*. Cement and concrete research, **24**(7), 1994 pp 1277-1285.
57. Felekoğlu, Türkel, B., S. et al., "*Effect of water/cement ratio on the fresh and hardened properties of self-compacting concrete*", Building and Environment, , **42**(4), 2007 pp 1795-1802.
58. Pauw, A., "*Static Modulus of Elasticity of Concrete as Affected by Density*" ACI Journal Proceedings, 1960.

# Alkali-Activated Foamed Concrete

Elsabe Kearsley<sup>1</sup> and Maxim Kovtun<sup>2</sup>

<sup>1</sup>Professor of Civil Engineering, University of Pretoria, South Africa

<sup>2</sup>Researcher, University of Pretoria

**Abstract:** Foamed concrete has been used as isolating building material in many countries around the World. At the low densities required for high thermal resistance concrete strength is very low. Using alkali-activated cement as binder in foamed concrete instead of ordinary Portland cement does not only provide higher strength at low density but also results in reduction of associated CO<sub>2</sub> emissions. In this paper properties such as density, strength and abrasion resistance of Alkali-Activated Foamed Concrete (AAFC) is compared to that of traditional foamed concrete. The effect of manufacturing and curing techniques is compared. It is possible to manufacture alkali-activated foamed concrete using the same procedures and equipment than that developed to manufacture foamed concrete containing Portland cement. The density, strength and abrasion resistance of the AAFC is comparable to that of the normal foamed concrete and wet or dry heat curing does not seem to have a significant effect on the properties developed. At low density the heat curing does seem to result in crack formation indicating the heat developed during the chemical reaction stays in the concrete and cannot escape due to the high volume of voids acting as buffer.

**Keywords:** alkali-activated, fly ash, GGBFS, foamed concrete, heat curing.

## 1. Introduction

Foamed concrete has been manufactured for many years by replacing the aggregate in normal concrete with air voids. As larger volumes of aggregate are replaced with air voids both the density of the concrete and the strength of the concrete decreases. The compressive strength of foamed concrete is a function of density and foamed concrete is normally defined in terms of both density and strength requirements. The density of foamed concrete can vary between about 1800 kg/m<sup>3</sup> for foamed concrete that can be used for structural applications and 300 kg/m<sup>3</sup> for foamed concrete that is used for thermal insulation [1].

The air voids in foamed concrete can be generated through shear mixing, pre-foaming or pressure foaming. With both the shear mixing and pressure foaming the foaming agent can be added to the mixture in concentrated form, while pre-foaming requires that the foaming agent is diluted with water and foamed by forcing the diluted foaming agent and compressed air through baffles. Typically the pre-foamed foam has densities between 40 kg/m<sup>3</sup> and 100 kg/m<sup>3</sup> and the foam can then be blended into a cementitious paste to create foamed concrete. Both synthetic and protein based foaming agents are commercially available and the use of protein based foaming agents seem to produce smaller voids resulting in higher strength at any given density. High quality foam is stable for up to an hour and the viscosity of the paste should be such that the air voids created by the foam cannot escape once the foam starts breaking down.

The concrete mix composition of foamed concrete cannot be determined using the same procedures than that normally used for normal Portland cement concrete. The strength of normal Portland cement concrete is a function of the water/cement ratio and the water content is adjusted to ensure sufficient workability to make it possible to effectively place and compact the concrete. Foamed concrete on the other hand can only be manufactured with very limited variations in water contents. If too little water is added the foam breaks down too rapidly as the water in the foam is used in the hydration process. If too much water is used segregation takes place and the cement settles to the bottom and the foam start floating to the top thus resulting in significant variations in foamed concrete density.

The strength of foamed concrete is known to be a function of the porosity and the porosity is directly related to the volume of air entrained with the foaming agent [2]. It should be possible to manufacture foamed concrete with a given density containing a lower volume of air if the relative densities of the solids used in the foamed concrete can be reduced [3]. A reduction in porosity or air content should result in an increase in foamed concrete strength. As the relative density of both Ground Granulated Blast Furnace Slag (GGBFS) and Fly ash is significantly lower than that of pure Portland cement, Alkali-activated Foamed Concrete could yield higher strengths than traditional Foamed Concrete for constant densities.

Foamed concrete has been used as isolating building material in many countries around the World. At the low densities required for high thermal resistance concrete strength is very low. Using alkali-activated cement as binder in foamed concrete instead of ordinary Portland cement could not only provide higher strength at low density but also results in reduction of associated CO<sub>2</sub> emissions.

Alkali-activated Concrete has successfully been manufactured using both neutral and basic slag as well as low calcium fly ash [4, 5, 6]. The aim of current research is to determine whether it would be possible to manufacture alkali-activated foamed concrete by using existing foamed concrete technology and just replace the binder with alkali-activated fly ash and/or slag.

## 2. Background

### 2.1 Portland Cement based Foamed Concrete

Portland Cement based Foamed Concrete (PCFC) is normally classified in terms of density grade where the density is defined as the oven dry density of the foamed concrete [7]. The mix composition is determined based on the assumption that during cement hydration the cement will chemically bind some of the water resulting in the addition of 20% to the mass of the unhydrated cement. The design dry density can be established using equation 1:

$$D = 1.2 Cem + F \quad (1)$$

Where  $D$  is the design dry density of hardened foamed concrete (kg/m<sup>3</sup>),  $Cem$  is the cement content (kg/m<sup>3</sup>) and  $F$  is the sum of the weights of filler (kg/m<sup>3</sup>).

Besides the dry density formula, the sum of the volume of all the constituent materials should be one thousand litres for a cubic metre of materials as shown in equation 2 for mixtures containing cement, sand, fly ash and foam [3]:

$$1000 = \frac{x}{RD_c} + x (W/c) + \frac{x (a/c)}{RD_a} + \frac{x (s/c)}{RD_s} + V_f \quad (2)$$

Where  $x$  is the cement content (kg/m<sup>3</sup>),  $w/c$  is the water/cement mass ratio,  $a/c$  is the fly ash/cement mass ratio,  $s/c$  is the sand/cement mass ratio,  $V_f$  is the volume of foam,  $RD_c$  is the relative density of the cement,  $RD_a$  is the relative density of the fly ash and  $RD_s$  is the relative density of the sand.

The long-term strength of PCFC can be optimized by replacing significant percentages of the cement with fly ash. By reducing the relative density of the solids the volume of air than needs to be entrained into the matrix to obtain a given design density can be reduced, thus reducing the porosity of the foamed concrete and consequently increasing the strength of the PCFC [2].

The high heat-insulating capacity of low-density foamed concrete results in the conservation of the heat generated during the hydration of cement [7]. For constant cement content, there is an inverse relationship between the peak temperature recorded in foamed concrete samples and the foamed concrete density. The cement content of PCFC should be minimized to prevent temperatures developing in the matrix that could result in the collapse of the foam or the formation of cracks.

### 2.1 Alkali-Activated Cement

It has been established that South African fly ash can be efficiently activated using 9% Na<sub>2</sub>O and curing the samples in dry heat at 60°C for at least 12 hours [4]. Although basic ground granulated blast furnace slag (GGBFS) does not require heat curing to develop strength when more than 4% Na<sub>2</sub>O is used as activator, strength development of neutral slag can be accelerated through heat curing [8].

The strength of alkali-activated concrete is highly dependent on the water/binder ratio and this ratio should be minimized to optimize strength. The workability of mixtures can be significantly improved by adding Sodium Silicate as activator.

The combination of low water demand and resilience to thermal treatment indicates that it should be possible to manufacture A AFC.

### 3. Experimental setup

#### 3.1 Materials

The chemical composition and relative density of the fly ash, Portland cement, basic and neutral slag used in this investigation can be seen in Table 1. The Portland cement was only used to manufacture reference mixes for comparative purposes. Silica sand with a relative density of 2.65 was used as inert filler. Both sodium hydroxide and sodium silicate were used as activators. Sodium hydroxide flakes were dissolved in the mixing water and allowed to cool down before adding to the mixture. Liquid sodium silicate (water glass) consisted of 14.95% Na<sub>2</sub>O, 29.80% SiO<sub>2</sub>, and 55.25% H<sub>2</sub>O. A protein based foaming agent was used and for pre-foaming the foaming agent was diluted in water to a 2% concentration and then aerated to form foam with a density of 75 kg/m<sup>3</sup>.

**Table 1. Chemical composition of binder**

Material	Chemical composition, %										Physical characteristics
	SiO <sub>2</sub>	TiO <sub>2</sub>	Al <sub>2</sub> O <sub>3</sub>	Fe <sub>2</sub> O <sub>3</sub>	MgO	CaO	Na <sub>2</sub> O	K <sub>2</sub> O	SO <sub>3</sub>	LOI	Relative density
Neutral Slag	34.87	0.72	14.38	0.89	8.03	37.05	<0.01	0.72	1.96	0.16	2.90
Basic Slag	31.72	0.51	15.10	1.43	11.20	40.24	0.01	0.48	2.25	-	3.00
Cem I 52.5N	22.30	0.50	4.98	3.35	1.92	61.50	0.21	0.26	2.92	1.77	3.14
Fly ash	55.22	1.57	31.93	3.36	0.73	4.57	0.01	0.87	0.23	0.80	2.20

#### 3.2 Mixing and mix composition

Foamed concrete can be manufactured using three different mixing techniques (compressed air that is forced into the mixture under pressure, high speed shear mixing or pre-foaming) [9] and AAFC was cast using all three techniques. The lowest density foamed concrete can normally be manufactured by mixing the ingredients in a pressurized vessel thus forcing the entrained air into the mixture. For this method the foaming agent does not have to be diluted in water which means that the water content of mixes with extremely high foam volumes (in excess of 80% of total volume) can be limited. Although this method should be best suited for manufacturing AAFC for use as thermal isolation material, it has not yet been possible to manufacture stable mixtures using pressurization. Shear mixing can give the highest strength for foamed concrete mixes at relatively high densities (in excess of about 1100 kg/m<sup>3</sup>), while pre-foaming normally results in the most predictable and repeatable properties with the most uniform dispersion of air voids. This paper contains results of AAFC manufactured through either shear mixing or pre-foaming.

Fly ash was activated with approximately 9% Na<sub>2</sub>O, and slag with about 8% Na<sub>2</sub>O while different volumes of sand were replaced with foam to reduce the density of mixtures. The effect of combining fly ash and slag was investigated. Where combinations of ash and slag were used it was assumed that varying fractions of the ash would act as inert filler (varying between 100% binder to 100% filler).

The mix compositions for the AAFC results reported in this paper are listed in Table 2. For each mixture the "casting density" of the mixture was determined during the casting process. When the samples were demoulded 24 hours after casting a "demoulding density" was established as the average density of all the cubes cast from one mixture. From Table 2 it can clearly be seen that many of the densities increased significantly between casting and demoulding, indicating that the air entrained into the mixture escaped during the casting process.

#### 3.3 Curing and testing

Samples were cast in 100 mm steel cube moulds and all samples were left for 4 hours pre-curing, where after samples were placed in either a drying oven or a steam bath for 16 hours. Once the samples were placed in the oven or steam bath the elements were switched on and the temperature increased at a rate of approximately 20 °C per hour. After 16 hours all samples were removed from the heat curing environments and placed in a constant temperature room at 25 °C and 55% relative humidity. Sets of three cubes were tested 24 hours, 7 days and 28 days after casting.

**Table 2. Mix compositions**

Materials (kg/m <sup>3</sup> )	PCFC	AAFC 1	AAFC 2	AAFC 3	AAFC 4	AAFC 5	AAFC 6	AAFC 7	AAFC 8	AAFC 9
Cem I 52.5N	200									
Ash	400		330	321		285	233	252	285	381
Basic Slag								252	285	
Neutral Slag		261	330	321	250	285	233			
Sodium Hydroxide		15.3	19.4	18.9	14.7	16.8	13.7	14.8	16.7	44.3
Sodium Silicate		25.5	32.3	31.4	24.5	28.0	22.8	24.7	27.9	
Water	164	179	194	191	59	168	139	148	173	98
Silica Sand	200	573	396	385	20	342	279	303	342	22
Mixing method	Pre-foam	Pre-foam	Pre-foam	Shear	Pre-foam	Pre-foam	Shear	Pre-foam	Shear	Pre-foam
Casting density (kg/m <sup>3</sup> )	980	1100	1359	1295	400	1167	925	1025	1135	610
Demoulding density (kg/m <sup>3</sup> )	921	1437	1442	1372	831	1173	1095	1234	1382	542*

\*Density obtained by submerging wax sealed sample in water.

One of the main problems experienced with PCFC at low densities is the lack of abrasion resistance. The alumina-silicate reaction products that is formed in alkali-activated binder should result in an higher abrasion resistance than that of the calcium hydroxide products formed during Portland cement hydration. Abrasion resistance tests were therefore conducted on cube samples after 28 days. The abrasion testing was not conducted to any standard test method and the results only give an indication of the abrasion resistance of samples in comparison to other samples tested. A steel wire brush was attached to a small drill with a pre-set rotation speed as indicated in Figure 1. The time that it took for the brush to penetrate the foamed concrete to a depth of 5 mm was recorded. The result was taken as the average time obtained from conducting the test in four different positions on the face of a cube.



**Figure 1. Testing abrasion resistance of foamed concrete samples.**

## **4. Results**

### **4.1 Casting densities**

Visual observation indicate that sodium silicate affects the viscosity of mixtures to such an extent that the air entrained through the foaming agent can no longer remain entrapped by the paste and all the mixtures containing sodium silicates segregated with the solids migrating to the bottom of the cast samples while

the foam floated to the top. The mix compositions that segregated to the point that the cubes could not be demoulded are not provided in Table 2. The results in Table 2 do however indicate that the density of the majority of the mixtures containing sodium silicate increased significantly between the mixer and the mould. High quality foamed concrete should not experience this change in density.

Low density AAFC containing only fly ash activated with NaOH as binder was manufactured using pre-foaming (see AAFC 9 in Table 2). The casting density was  $610 \text{ kg/m}^3$  and after curing the top surface of the cubes showed no subsidence as indicated by the surface of the left-hand bottom cube in Figure 2. It was however impossible to demould these cubes as significant cracking took place below the surface. The cores of these cubes were also soft and powdery (as indicated in the two photos on the right of Figure 2) where the surfaces were hard with no obvious dust emission during handling.



**Figure 2. Damaged low density AAFC.**

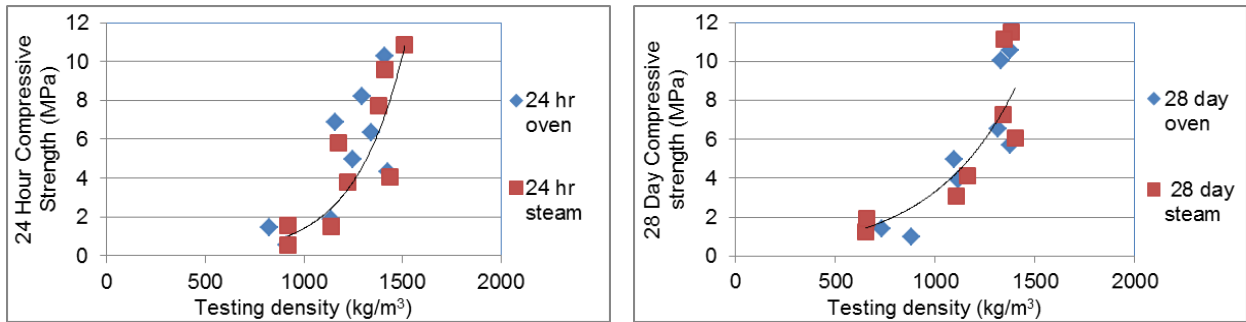
The cores of the samples seem to be damaged and it seems possible that the heat generated during heat curing is trapped in the cores of samples with high air contents, resulting in cracking caused by excessive heat. Although these results indicate that it would be possible to manufacture AAFC using only fly ash and NaOH as binder, further research is required to investigate suitable curing regimes.

#### **4.2 Compressive strength**

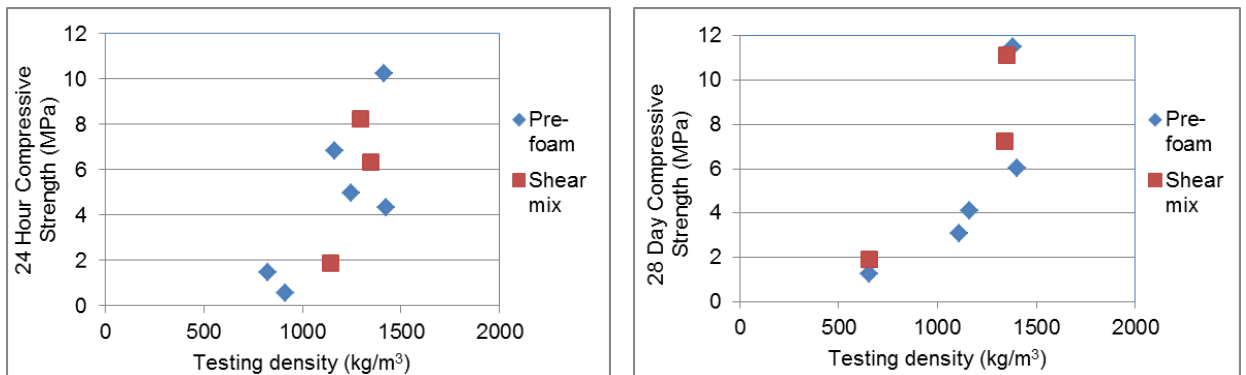
The effect of density on the compressive strength of the AAFC samples can be seen in Figure 3 and it is clear that the strength increases exponentially as the density increases. There is only a slight increase in strength between 24 hours and 28 days, indicating that the duration of curing is sufficient for factory manufactured samples to be dispatched directly after curing. The variation in strength does seem to be less for the 28 day strengths than for the 24 hour strengths indicating that older samples may have more predictable strengths. It is interesting to note that the humidity of the curing environment does not seem to have a significant effect on the strength development of AAFC. This differs from observations made for alkali-activated fly ash concrete where curing at low humidity resulted in significantly higher compressive strengths.

The effect of manufacturing technique on strength development can be seen in Figure 4. Although the shear mixes seem to have marginally lower early age strengths, the 28-day test results indicate that there is no real difference in the density-strength relationships obtained for shear mixing and pre-foaming. It was also interesting to note that the strengths obtained from the basic slag was marginally lower than from the neutral slag for both early age and 28 day strength tests. For a testing density of approximately  $1350 \text{ kg/m}^3$  the neutral slag yielded 8.2 MPa after 24 hours and 11.5 MPa after 28 days while the use of basic slag only resulted in 6.4 MPa and 7.3 MPa at similar ages. As basic slag is significantly more expensive

than neutral slag it cannot be justified to use basic slag in AAFC. The binder/solid ratio, binder content, binder combination or activator combination do not seem to have a significant effect on the strength.



**Figure 3. Effect of density on compressive strength.**

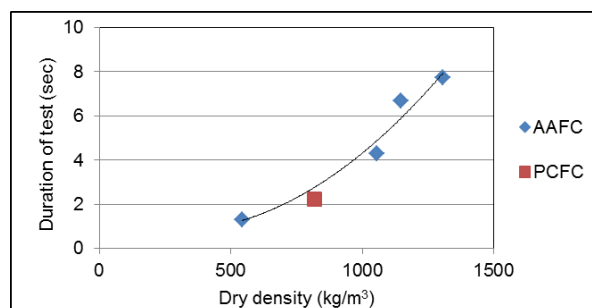


**Figure 4. Effect of manufacturing technique on compressive strength.**

From the results obtained to date it has not been possible to determine an optimum mix composition. Further research is required to establish the most suitable mix compositions for different applications.

### 4.3 Abrasion resistance

The results of the abrasion resistance test can be seen in Figure 5. These results clearly indicate that the abrasion resistance rapidly decreases as the dry density of the foam concrete decreases. The abrasion resistance of the AAFC is only marginally higher than that of the PCFC tested and at this stage it cannot be claimed that the use of alkali-activated cement in foamed concrete would yield higher abrasion resistance.



**Figure 5. Testing abrasion resistance of foamed concrete samples.**

## 5. Conclusions

It is possible to manufacture Alkali-Activated Foamed Concrete. The density, strength and abrasion resistance of the AAFC is comparable to that of the normal foamed concrete and wet or dry heat curing does not seem to have a significant effect on the properties developed. AAFC can be manufactured with fly ash, neutral slag or basic slag or combinations of fly ash and slag. There does not seem to be any benefit in using basic slag in foamed concrete.

When sodium silicate is used as accelerator care should be taken to ensure that the viscosity of the mixture is not affected to the extent that the air voids can escape from the AAFC matrix, resulting in non-homogenous and unpredictable densities.

At low density the heat curing does seem to result in crack formation indicating the heat developed during the chemical reaction stays in the concrete and cannot escape due to the high volume of voids acting as buffer. Further research is required to determine an optimum curing regime that would yield sufficient strength without resulting in overheating and structural damage to samples containing high air contents.

## 6. References

1. Kearsley, E.P., Mostert, H.F., 'Opportunities for Expanding the use of Foamed Concrete in the Construction Industry', Proceedings, The International Congress on Global construction: Concrete Opportunities, Use of Foamed Concrete, Dundee, Scotland, 2005, pp 143-154.
2. Kearsley, E.P., Wainwright, P.J., "The Effect of Porosity on the Strength of Foamed Concrete", Cement and Concrete Research, 32(2), 2002, pp 233-239.
3. Kearsley, E.P., Mostert, H.F., "Designing mix composition of foamed concrete with high fly ash contents", Proceedings, The International Congress on Global construction: Concrete Opportunities, Use of Foamed Concrete, Dundee, Scotland, 2005, pp 29-36.
4. Shekhovtsova, J., Kearsley, E.P. et al., "Effect of activator dosage, water to binder solids ratio, temperature and duration of elevated temperature curing on the compressive strength of alkali-activated fly ash cement paste", Journal of the South African Institution of Civil Engineering, 56(3), 2014, pp 44-52.
5. Shekhovtsova, J., Kovtun, M. et al., "Evaluation of short and long-term properties of heat cured alkali-activated fly ash concrete", Magazine of Concrete Research, (in press).
6. Kovtun, M., Kearsley, E.P. et al., "Dry powder alkali-activated slag cements", Advances in Cement Research, <http://dx.doi.org/10.1680/adcr.14.00078>, (in press).
7. Tarasov, A., Kearsley, E.P. et al., "Heat evolution due to cement hydration in foamed concrete", Magazine of Concrete Research, 62(12), 2010, pp 895-906.
8. Kovtun, M.N., Kearsley, E.P. et al., "Producing alkali-activated slag concrete in South Africa", Proceedings, Innovations in Concrete Construction, UKIERI Concrete Congress, Jalandhar, Punjab, India, 2013, pp 919-928.
9. Kearsley, E.P., Mostert, H.F., "The use of foamed concrete for housing", Proceedings, Innovations in Concrete Construction, UKIERI Concrete Congress, Jalandhar, Punjab, India, 2013, pp 390-400.



# Alternative concrete materials from industrial waste

Valle Chozas<sup>1</sup>, Ignacio del Val<sup>1</sup>, José Vera<sup>1</sup>, Íñigo Larraza<sup>1</sup>  
<sup>1</sup>Concrete Group, Technology Innovation Division, ACCIONA Infrastructure

**Abstract:** The large consumption of natural resources, the global warming caused by the anthropogenic emissions of greenhouse gases and the massive generation of industrial waste have generated the need to develop technologies that can offer integrated solutions and at the same time generate industrial benefits. Geopolymers have revealed as a very solid alternative to traditional constructive materials. This paper describes the synthesis and characterization of two sets of geopolymer materials that represent an alternative to traditional foamed and lightweight concrete, respectively, including recycled materials in their composition. In both cases the mechanical and insulation performance of these materials have been measured both at laboratory scale and in the case of the foamed material, also at pilot scale, demonstrating their viability as alternatives to their traditional homologous.

**Keywords:** geopolymer, industrial waste, alkaline activation.

## 1. Introduction

In the production of traditional clinker, carbonates undergo a heating process, generating 900 Kg of CO<sub>2</sub> for every ton of cement produced. The cement industry generates about 10% of anthropogenic CO<sub>2</sub>, favoring the climatic change. [1] Also, the extraction of aggregates for concrete production generates environmental concerns, such as dust release, noise, ground vibration and landscape alteration.

Parallel, every year millions of different industrial residues that can replace cement or aggregates in concrete are generated. For instance fly ash, blast furnace slags and the combination of both are able to harden in the presence of alkali solutions, yielding solid matrixes with similar properties to those of cementitious materials. Also, end life tyre rubber aggregates can be used as lightweight aggregates with good insulating properties. In both cases, millions of tons of these residues are generated and landfilled, which is an environmental concern.

In this paper the preparation, characterization and viability of two types of alternative concrete materials as environmentally friendly constructive elements is reported:

- A foamed concrete type material made of alkali activated fly ash as an alternative to traditional autoclaved aerated concrete (AAC). In the synthesis of this material, a foaming agent is added into the mixture, producing a cellular structure that confers excellent insulating properties. A prototype was built with this material and its properties were compared to an identical one built with traditional AAC, showing a very similar performance in terms of mechanical properties and thermal and acoustic insulation. This material has been produced within the GREEN CAST project.
- A lightweight concrete type material where the matrix is composed by alkali activated industrial waste cured at room temperature. In this case behaved very similar or even higher mechanical properties than traditional lightweight concrete. When traditional aggregates were substituted by tyre rubber aggregates, an alternative concrete with low thermal conductivity was obtained. This material has been produced in the framework of the SUS-CON project.

## 2. Materials and methods

### 2.1 Foamed concrete

The fly ash used in this project has been supplied by Cencatra, a waste management company located in Spain. Sodium hydroxide (50%) and hydrogen peroxide (33%) were supplied by Panreac. A commercial bubble stabilizer was used as received. All materials were used as received without any further purification.

The fly ash composition was analyzed by X-ray fluorescence (XRF). This technique allows detecting chemical species and their content in a given sample. The particle size and distribution were analyzed by granulometry. A Malvern Mastersizer 2000 equipment was used. Measurements have been made after ultrasonic dispersion of samples by using water as dispersant.

The materials were homogeneously mixed with a mechanical stirrer in plastic recipients in the following way: first the sodium hydroxide solution was diluted and allowed to cool down at room temperature. Then, the bubble stabilizer (BS) was added to the solution and stirred. The fly ash was weighted and placed in

the corresponding recipient, then homogenized mechanically. In each case the aqueous solution was added and mixed until complete homogenization. Finally the hydrogen peroxide solution was added to the mixture and mixed. The liquid mixtures were then immediately poured into the corresponding mold and covered with plastic film in order to prevent evaporation. The foaming process was allowed to take place prior to the curing stage.

The blocks were fabricated in PTFE coated wood molds (25x63x7 cm) with capacity for 5 independent blocks. All the samples were cured in laboratory furnaces at 80°C for 16 hours.

The density ( $\rho$ ) of the GREEN CAST samples was analyzed according to the UNE-EN 772-13 standard. Six specimens were extracted from different parts of three blocks.

The compressive strength (MC) was determined by following the standard UNE-EN 772-1. A constant load was applied at a constant rate of  $0.1 \pm 0.05$  MPa/s. The specimens were kept at a constant humidity of  $6 \pm 2\%$  prior to the tests. The dry density value is obtained from drying the specimens to constant mass.

The thermal resistance and conductivity was measured in a NETZSCH HFM 463 Lambda Heat Flow Meter, according to the UNE-EN 12664:2001 standard. The heat flow meter was used according to the norm ISO 8301:1991. In order to do that, 3 specimens were introduced horizontally in a heat flow meter, being the hot plate in the upper side. Said specimens were conditioned in a ventilation oven at 105°C until constant mass is achieved, then coated with a waterproof cover which prevents them from moisture. The state temperature and the average temperature difference through the specimen were set at 10 and 15°C, respectively.

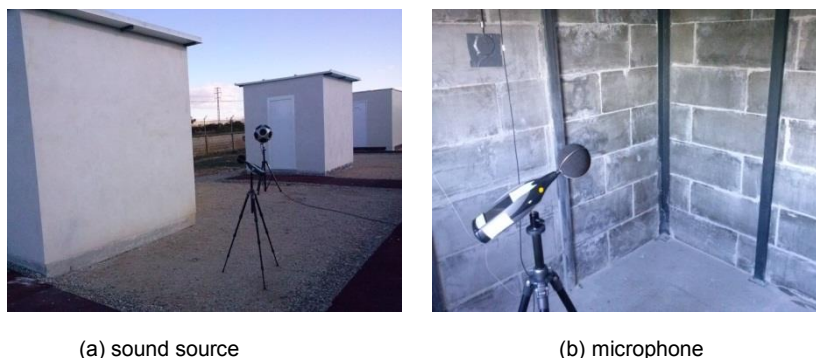
The free-thaw resistance was investigated by following the UNE-EN 15304:2010 standard. Six cubic specimens (7x7x7 cm) were extracted from different parts of two blocks, saturated and kept for 48 hours in a polyethylene bag for stabilization and preserve moisture. The samples were placed in a chamber and exposed to 15 cycles of freeze ( $-15 \pm 2^\circ\text{C}$ ) for 8 hours and thaw ( $20 \pm 5^\circ\text{C}$ ) and humidity 95% for 8 hours. Both the mass and compressive strength loss of the specimens after this test were determined and compared to that of references taken from adjacent parts of the blocks.

In order to demonstrate the viability of the developed technology as constructive element, two testing cells were built, one with the produced GREEN CAST blocks and an identical one built with commercial cement based AAC blocks. Both testing cells were built in ACCIONA's facilities in Alcobendas, Spain. The demo-scale buildings consisted of metallic structures anchored to onsite casted concrete ground slabs and the two types of blocks were used to build the walls of each of the testing cells. For the construction of the reference cells, Ytong blocks were used. The dimensions of the blocks were 25x63x7 cm and the density specified by the supplier 550 Kg/m<sup>3</sup>.

Both demo buildings possessed one window oriented to the east and one door oriented to the north. In both cases generic aluminum/polyurethane sandwich panels were used as ceilings. The blocks were glued together with insulating/waterproof mortar. Both testing cells were coated externally with such mortar, and finally, power supply was installed within them. The acoustic insulation of the developed material was studied by in situ measurements of the following parameters:

- Airborne sound insulation of façades, according to the standard ISO 140-5:1998. For this experiment, an omnipower sound source generating a sound field with a continuous spectrum was placed outside the prototype at 7 m from the analyzed façade. Then, the average sound pressure level is measured in a point at 2 m from the façade and 3 different points inside the prototype. The airborne sound insulation index was calculated as the difference between pressure levels, inside and outside, standardized by reverberation time. The airborne sound insulation index was calculated as the difference between pressure levels, inside and outside, standardized by reverberation time.

- Measurement of the sound reduction index. In this case, an omnipower sound source generating a sound field with a continuous spectrum was installed inside the prototype. The average sound pressure level was measured in a point at 1 m from the façade and 3 different points inside the prototype. Background noise reduction inside the prototype was recorded too. The sound measurements were carried out with the following equipment purchased to B&K: omnipower sound source 4292, audio power amplifier 2716, microphone 4189, hand held analyzer 2250 and sound level calibrator, **Figure 1**.



**Figure 1. Measurement of airborne sound insulation of façades.**

In order to study thermal behavior of the real scale demo-buildings, a data acquisition system was installed in both the reference and GREEN CAST testing cells. An Agilent 34972A Data Acquisition Unit with a built-in 20-bit resolution digital multimeter was selected as autonomous data logging system, combined with a pair of Type T thermocouples (Copper-Constantan) for internal temperature measurement (sensitivity  $40 \mu\text{V}/^\circ\text{C}$ , nominal accuracy  $\pm 0.5^\circ\text{C}$ ). A Davis Instruments Vantage Pro2 weather station was used for external temperature monitoring. Thermal sensors were previously calibrated using a FLUKE 724 Multi Function Calibrator, finding differences not higher than  $\pm 0.1^\circ\text{C}$ .

## **2.2 Lightweight GP concrete (GPC).**

Two recipes of lightweight geopolymer concrete (GPC) were designed with alkali activated wastes as binder. The first one was made from pulverized fly ash (PFA) and the second one was designed with a combination of PFA plus ground granulated blast slag (GGBS) as binder. This recipe was cured at room temperature. Expanded clay and natural sand were utilized as aggregates.

The GGBS utilized was supplied by Hanson, UK Company. The fineness is approximately  $500\text{m}^2/\text{Kg}$ . Commercially available chemicals were used as activators. Sodium hydroxide solution at 50% w/w was supplied by Panreac and a sodium silicate solution  $\text{SiO}_2:\text{Na}_2\text{O} = 2:1$  was supplied by Fisher Scientific. Expanded clay 3/8 mm was used as coarse aggregate and natural silica sand 0/4 mm as fine aggregate.

Mix parameters for activated waste binders developed by the geopolymer research group at the Queen's University Belfast, were used in order to design two lightweight GP concretes (GPC). The proportions set of recipe 1 and recipe two were the following:

-Recipe 1: 100% PFA in weight as binder. Alkali dosage were  $M+ = 7.5$  and  $AM = 1.25$ . For aggregates, 57% in volume was used, of which 50% in volume was expanded clay 3/8 mm and 50% in volume natural sand. The curing temperature was  $70^\circ\text{C}$  during 7 days. Then, they were kept in a wet room ( $20^\circ\text{C}$  and 90% humidity).

-Recipe 2: PFA/GGBS ratio = 30% / 70% in weight as binder. Alkali dosage were  $M+ = 7.5$  and  $AM = 1.25$ . For aggregates, 55% in volume was used, of which 50% in volume was expanded clay 3/8 mm and 50% natural sand. Regarding cured procedure, the specimens made were kept in a wet room ( $20^\circ\text{C}$  and 90% humidity).

A planetary concrete mixer was used and the sequence mix followed was the following: waste binders were placed in the mixer. Then, water plus sodium silicate solution plus sodium hydroxide solution premixed was added, stirred for 5 minutes. Expanded clay and natural sand were added and stirred for 5 minutes.

In order to characterize two different lightweight GPC formulations, mechanical and freeze/thaw tests were performed. The tests carried out in order to analyze mechanical properties were compressive strength according to Spanish standard UNE-EN-12390-3, tensile strength according to Spanish standard UNE-1239-6 and modulus of elasticity according to Spanish standard UNE-83-316-96. Regarding the freeze-thaw cycles analyses according to American standard ASTM C666 were carried out. For last, façade panels of  $62.5 \times 25 \times 7$  cm dimensions were made to analyze final surface finish and the occurrence of cracks.

### 3. Results and discussion

The ash was characterized by XRF and SEM. The ashes are mainly composed of  $\text{SiO}_2$ ,  $\text{Al}_2\text{O}_3$  and  $\text{Fe}_2\text{O}_3$ , with a low content in  $\text{CaO}$ , which corresponds to an F-class type of ash, **Figure 2**. The X-ray pattern, shown in **Figure 3** reveals the mineralogical phases of this material: Quartz, Mullite, Hematite, magnetite.

Muestra N°		$\text{Al}_2\text{O}_3$	$\text{SiO}_2$	$\text{Fe}_2\text{O}_3$	$\text{TiO}_2$	$\text{CaO}$	$\text{MgO}$	$\text{Na}_2\text{O}$	$\text{K}_2\text{O}$	$\text{P}_2\text{O}_5$	$\text{Cl}^-$	$\text{SO}_3$	C	Ppc
C.V.	Media	27.51*	44.02*	17.33*	0.89*	4.24*	0.89*	0.18*	1.35*	0.42*	<0.01*	0.42*	2.54*	2.76*
	desviación	0.06	0.18	0.02	0.01	0.01	0.01	0.01	0.01	0.01	---	0.07	0.05	0.04
	ITL	42	42	42	42	42	42	---	42	42	---	---	---	---

Figure 2. XRD analysis of the fly ash

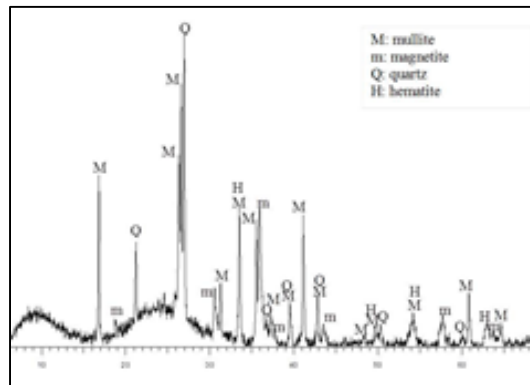


Figure 3. Mineralogical phases of the used fly ash. Composition:  $\text{Al}_2\text{O}_3/27.5\%$ ,  $\text{SiO}_2/44.0\%$ ,  $\text{Fe}_2\text{O}_3/17.3\%$ ,  $\text{TiO}_2/0.9\%$ ,  $\text{CaO}/4.2\%$ ,  $\text{MgO}/0.9\%$

**Figure 4** shows the particle size distribution of the analyzed fly ashes, as it can be seen that the majority of the particles ranged between 1 and 100  $\mu\text{m}$ .

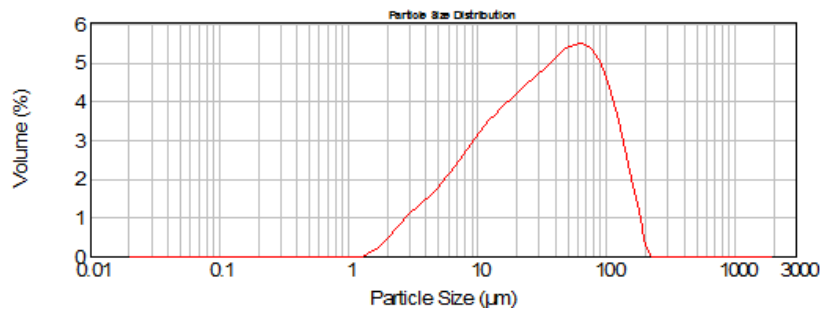
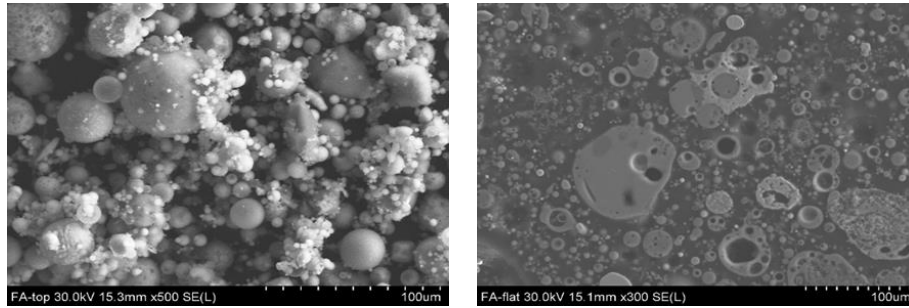


Figure 4. Fly ash particle size distribution

**Figure 5** shows the topology and internal microstructure of the fly ash. The particles are almost spherical and amorphous. Some spheres are hollow and others completely solid. The particles have a big range of sizes from 1.5 to 110  $\mu\text{m}$ . The media size is 33.5  $\mu\text{m}$ .



**Figure 5. SEM micrographs of fly ash.**

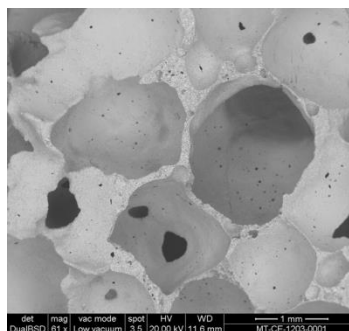
### 3.1 Foamed concrete

Previous research carried out showed that oxygen peroxide was the best performing foaming agent, and an optimization of the formulation proportions and the production process was carried out. Formulations with different proportions of the components were prepared and tested. Considering the heterogeneous properties of the fly ash due to its waste origin, the formulation was optimized in a range of proportions. **Table 1** shows a range of accepted formulations.

**Table 1. Range of weight percentages of each component in the mixture (wt.%)**

Fly ash	NaOH	Water	H <sub>2</sub> O <sub>2</sub>	BS
67-71	6-8	20-25	0.4-1	0-0.15

By following this procedure, 400 blocks were produced; some of them were kept for characterization. The material was prepared in form of blocks and their properties were measured. In **Figure 6** it is possible to appreciate a SEM micrograph of the porous structure of the material. The foaming agent added to the formulation generated a regular cellular structure that is the responsible for the low density of the material and its good insulating properties.



**Figure 6. SEM micrograph of the GREEN CAST material (scale bar is 1 mm).**

The main parameters of the samples were measured. The dry density was measured in 18 specimens extracted from 3 blocks. The average density was found to be  $790 \pm 21 \text{ Kg/m}^3$ .

Similarly, the compressive strength was measured by taking 6 specimens from 6 blocks. The average compressive strength for the tested samples was  $4.8 \pm 0.5 \text{ MPa}$ .

The thermal properties of the materials were studied through the measurement of the thermal resistance and the thermal conductivity. The average values for thermal resistance and conductivity, obtained after testing 3 specimens, were  $0.369 \pm 0.008 \text{ m}^2\text{K/W}$  and  $0.183 \pm 0.016 \text{ W/mK}$ , respectively.

In the case of a cellular material, such as AAC, the thermal conductivity is directly related to its density, since the air present in the structure, lightens the material and reduces the thermal conductivity, therefore improving the insulating behavior. Conventional AAC presents typical  $\lambda$  values of 0.1-0.2 W/mK). The reference AAC used in this work, with a density of  $550 \text{ Kg/m}^3$  presents a  $\lambda$  value of 0.16 W/mK according to the supplier. The slightly greater value of thermal conductivity obtained for the GREEN CAST material has been associated to its larger density.

Freeze/thaw cycles were carried out on the samples, measuring the mass and compressive resistance loss after said cycles. The temperature program consisted in cooling down to  $-15 \pm 2^\circ\text{C}$ , keeping at that temperature for 8 hours and heating up to  $20 \pm 5^\circ\text{C}$ , keeping at that temperature for 8 additional hours. After 15 cycles, for the tested samples, the average dry mass loss was  $0.6 \pm 0.4$  and the compressive strength loss was  $7.0 \pm 4.0$ .

In order to demonstrate the constructive viability of the developed material, as well as its insulating behavior, a testing cell was built with the GREEN CAST blocks and its performance was monitored. An identical testing cell built with reference AAC blocks was built and monitored in the same way. **Figure 7** shows pictures of the constructive process of both prototypes, as well as a picture of both finished ones.



**Figure 7. Testing cells being built with GREEN CAST blocks (left) and Ytong ones (center). Both testing cells finished (right).**

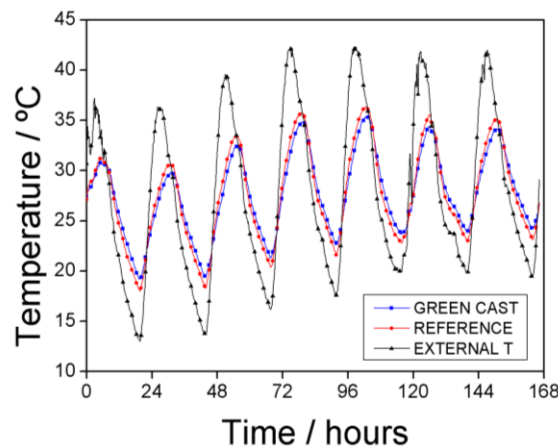
The acoustic insulation of the developed material was analyzed by in situ measurements. This method allows characterizing the developed technology as part of a constructive system. In order to enable the comparison with a reference, the same measurements were carried out for the reference testing cell. The sound insulation index ( $D_{2m,nT,Atr}$ ) is used to measure the level of sound insulation provided by a structure. This parameter can be expressed by a global value and by third octave bands. The results obtained for each of the façades of both testing cells are shown in **Table 2**.

In both prototypes the highest values for the sound insulation index were found in the West and South façades. This is because those walls do not contain elements with a low sound insulation such as windows. For this reason, these façades could be the most representative element of the prototype. The sound reduction index of a material characterizes the sound insulation properties of such material or the constructive system itself. It was obtained from a modeling of the acoustic field. The results obtained for each of the façades is collected in **Table 2**. Identically, West and South façades presented the best RW global values and in both cases both demonstrators showed very similar behavior.

**Table 2.** Airborne sound insulation for the measured façades. Sound reduction index ( $R_w$ ) obtained for the measured façades.

	$D_{2m,nT,Atr}$ (dB)		$R_w$ (dB)	
	GREEN CAST	Reference	GREEN CAST	Reference
North (door)	21.8	22.7	21	23
West	28.0	28.2	32	30
South	28.8	28.0	33	31
East (window)	25.1	26.4	25	25

**Figure 8** depicts testing cells internal temperature and external temperature from 7th August 2013 to 14th August 2013. Internal temperature for a given time is the result of averaging the output of two internal thermocouples placed at two different positions in the xy plane, keeping the height fixed at 1.5m



**Figure 8.** Testing cells internal and external temperatures measured in a period of one week.

For the analyzed period, the internal temperature inside the GREEN CAST testing cells showed a slightly attenuated thermal wave amplitude with respect to the reference case. This fact, in addition to the conservation of the observed frequency, confirms similar density and thermal conductivity values for both structures, corroborating GREEN CAST as an alternative to commercial solutions currently present in the market.

### 3.2 *Lightweight GP concrete (GPC).*

Two homogeneous lightweight concrete mixtures were obtained, and their fresh state presented good workability when concrete was placed compacted homogeneously without bleeding or segregation. In the case of recipe 2, it was decided to add a retarder additive after observing a fast setting of the fresh concrete in one test carried out without such additive. The consistency test was carried according to the Spanish standard UNE 83313:90 with the Abrams cone. In both cases a liquid consistency was obtained. **Figures 9** and **10** show Recipes 1 and 2, respectively.





Figure 9. GP fresh concrete Recipe 1 (cone 26 cm). Figure 10. GP fresh concrete Recipe 2 (cone 27 cm).

For the prepared samples, the mechanical performance was analyzed by measuring the compressive strength, the indirect tensile strength and the elasticity modulus. All specimens were tested at 28 days of age and the results have been collected in **Table 3**. The compressive strength was measured according to Spanish standard UNE-EN-12390-3, for cubic specimens (100x100x100 mm). The indirect tensile strength measurements were carried out according to Spanish standard UNE-1239-6 in cylindrical specimen (150 mm diameter and 300 mm length). The Young's modulus was measured on cylindrical specimens (150 mm diameter and 300 mm length) under standard UNE 83-316-96. **Figures 11** and **12** show pictures of the cubic specimens used for the mechanical characterization.

**Table 3. Mechanical performance of Recipes 1 and 2**

Sample	Density (Kg/m <sup>3</sup> )	Compressive strength		Indirect tensile		Elasticity modulus	
		Load (KN)	Stress (N/mm <sup>2</sup> )	Load (KN)	Stress (N/mm <sup>2</sup> )	Max stress (N/mm <sup>2</sup> )	Stress (N/mm <sup>2</sup> )
Recipe 1	1668	303.7	30.4	179.4	2.5	10.0	10959
Recipe 2	1741	549.4	54.0	220.7	3.1	18.1	13801

Compared to a conventional light-weight concrete with a density between 1600–1800 kg/m<sup>3</sup> and a compressive strength in the 20–35 N/mm<sup>2</sup> range, it can be pointed out that Recipe 1 is a light-weight GPC which properties are similar to its traditional homologous, however, it cures by action of the temperature. Recipe 2 reached better mechanical properties than conventional light-weight concrete and cures at room temperature. It can be highlighted that both materials represent an environmental alternative to cement based lightweight concrete.

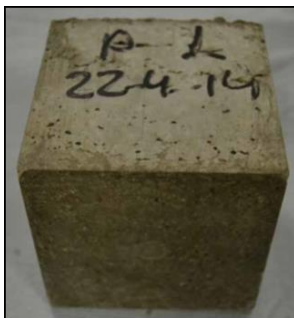


Figure 11. Cubic specimen (Recipe 1)

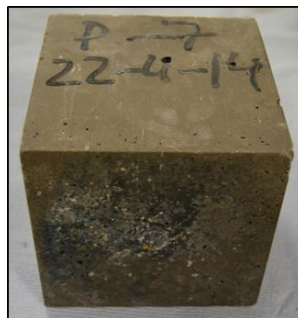


Figure 12. Cubic specimen (Recipe 2). Prior to the test (left), after the test (right)





The freeze/thaw tests were carried out according to the American standard ASTM C666/666M “Standard Test Method for Resistance of Concrete to Rapid Freezing and Thawing”. This analysis method establishes a freeze/thaw cycle with the following thermal program: from 4°C to -18°C at 2.2 °C/min, 20 minutes at -18 °C, from -18 °C to 4 °C at 2.2 °C/min and an isothermal step of 90 minutes at 4 °C. The whole cycle is completed within 2 hours. The duration of the test is limited to 300 cycles, until the elastic dynamic modulus is reduced to a 60% of its initial value or until the longitudinal percentage variation achieves a value of 0.10%.

These tests provided values of height length change (%), diameter length change (%), weight change (%), relative dynamic modulus of elasticity and the durability factor. The length change is related to the deformations and is considered a valuable indicator of the internal microstructural damage. The weight loss is not considered as a main damage indicator; however it can be useful as indicator of the spalling. The durability factor is given by the relative dynamic modulus of elasticity multiplied by the number of completed cycles and divided by the total number of cycles, generally 300. All results have been collected in **Table 4**.

As it can be observed both materials presented very similar dimensional variation, however the weight change is slightly higher in Recipe 1. Both lightweight GPC recipes resisted well 320 freeze-thaw cycles. However, after 420 cycles the recipe designed with 100% PFA (Recipe 1) was observed deterioration on top of the specimen, **Figure 13**.

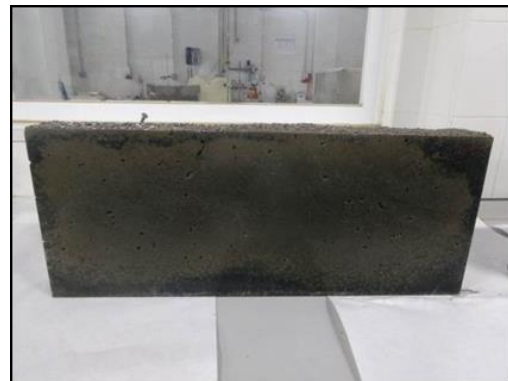
**Table 4.** Values of the different parameters of the durability tests

Sample	Height change (%)	Diameter length change (%)	Weight change (%)	Durability factor
Recipe 1	0.07	-0.02	5.5	110
Recipe 2	0.07	0.07	0.8	100

In order to compare lightweight GPC to commercial lightweight concrete, façade panels of 62.5x25x7 cm dimensions were manufactured. Regarding the surface finish, the pieces with the best surface finish were the façades made with Recipe 2, **Figure 14**. Neither segregation nor porosity was observed. The result was a very compact finish. Nevertheless, areas of different colors were observed.



**Figure 13.** Recipe 1 (100% PFA) after 420 freeze-thaw cycles.



**Figure 14.** Façade panel made of Recipe 2

### 3. Conclusions

The preparation of different geopolymer concrete formulations as well as their characterization has been reported in this paper. The first material consisted on a foamed geopolymer made of alkali activated coal fly ash which mechanical and insulation properties were analyzed at both laboratory and pilot scale, showing very similar density, compressive strength and thermal conductivity. This material was produced at large scale in form of blocks that were used in order to build a demo-building. An identical reference was built with commercially available AAC blocks. The thermal and acoustic performance of both demo-buildings was monitored, showing a very similar behavior in both cases. Two lightweight concrete

materials prepared with waste binder and aggregates were analyzed, revealing good workability, density, compressive strength and durability, compared to traditional lightweight concrete. In the second case, the material cured without a temperature program. Both sets of materials present feasible alternatives to non-structural traditional OP cement based materials.

#### 4. Acknowledgement

The SUS-CON project has received funding from the European Community's Seventh Framework Programme NMP.2011-1 under Grant agreement no: 285463. The authors acknowledge the European Commission for funding the GREEN CAST project within the CIP Eco-Innovation First Application and market replication projects framework.



#### 5. References

1. Damtoft JS et al. (2008) Cement and Concrete Research 38: 115-127; Olivier JGJ, Janssens-Maenhout G, Peters JAHW (2012), Report, The Hague: PBL Netherlands Environmental Assessment Agency; Ispra: Joint Research Centre.
2. "Building code requirements for structural concrete (ACI 318-05)", American Concrete Institute, ACI Committee 318, 2005, Michigan.
3. Rezansoff, T., Akanni, A. et al., "Tensile lap splices under static loading: A review of the proposed ACI 318 Code provisions", ACI Structural Journal, 1993, 90(4), pp 374-384.
4. Muttoni, A., Schwartz, J. et al., "Design of Concrete Structures with Stress Fields", Birkhäuser Verlag, 1997, Basel, Switzerland.
5. Smith, J., "The design of tensile lapped splices", Proceedings, 23<sup>rd</sup> Biennial Conference of the Concrete Institute of Australia, Gold Coast, Australia, pp 333-342.
6. Rafeet, A., Vinai, et al., "Alkali activated fuel ash and slag mixes: optimization study from paste to concrete building blocks", 34th Cement and Concrete Science Conference, Paper Number 179, 14-17 September 2014, University of Sheffield (UK).
7. Vinai, R., Rafeet, et al., "Slag valorisation in construction materials: mechanical properties and rheology of alkali activated concrete containing GGBS", 4th International conference Slag Valorisation Symposium, 15-17 April 2015, University of Leuven (BE).
8. Soutsos, M., Vinai, et al. "Effect of alkali dosage and modulus on strength development and microstructure of alkali-activated binders", accepted paper at 14th International Congress on the Chemistry of Cement (ICCC 2015) 13-16 October 2015, Beijing, China.
9. Olivia, M., Nikraz H. R., "Strength and water penetrability of fly ash geopolymer concrete", ARPN Journal of Engineering and Applied Sciences, VOL. 6, NO. 7, July 2011.
10. Enfedaque, A., Al-Assadi, G., et. al, "Durabilidad del hormigón frente a los ciclos hielo-deshielo evaluación de dos tipos de hormigón", Anales de Mecánica de la Fractura 28, Vol. 2, 2011.

# Progress Towards a Handbook for Geopolymer Concrete

Marita Allan Berndt<sup>1</sup>, Jay Sanjayan<sup>1</sup>, Stephen Foster<sup>2</sup>, Arnaud Castel<sup>2</sup>, Pathmanatham Rajeev<sup>1</sup>, Craig Heidrich<sup>3,4</sup>

<sup>1</sup>Swinburne University of Technology

<sup>2</sup>University of New South Wales

<sup>3</sup>Australasian Iron and Steel Slag Association

<sup>4</sup>Ash Development Association of Australia

**Abstract:** Our previous research conducted for the Cooperative Research Centre for Low Carbon Living identified several barriers to the widespread implementation of alternative, low CO<sub>2</sub> concrete such as geopolymers. It was found that the lack of standard specifications, lack of long-term performance data and non-compliance with AS 3600 were major obstacles to adoption. Therefore, current research is addressing these deficiencies through the preparation of a Handbook in association with Standards Australia. The primary purpose of the Handbook will be to assist engineers and end-users in specifying and constructing with geopolymer concrete. The Handbook will include background and properties of geopolymer concrete, a model performance-based specification, case histories and long-term durability studies, recommendations on testing and monitoring, and commentary on compliance with AS 3600. The objectives of this paper are to outline the proposed Handbook content, initiate discussion among stakeholders and seek input.

**Keywords:** Geopolymer, standards, specification, durability, test methods.

## 1. Introduction

Geopolymer concrete has been the subject of much research and offers a viable alternative to Portland cement concrete in a variety of applications. Potential benefits of geopolymer concrete include improved chemical resistance and reduced CO<sub>2</sub> impact. In 2013 a detailed study was performed to identify barriers to widespread adoption of geopolymer concrete (Berndt et al., 2013). Current practices with regard to concrete mix design and property requirements in Australian standards and state specifications were reviewed. Barriers to implementation of geopolymer concrete were analysed and case histories of how alternative can be successfully introduced into an established construction industry market were studied.

An industry survey was performed to better understand barriers particular to geopolymer concrete in Australia and to identify potential pathways to overcoming these barriers (Berndt et al., 2013). Based on review of prior studies and the industry survey, several actions and pathways were recognised. Highest priority activities identified were the development of a standard specification, development of new standards specific to geopolymer concrete that include performance requirements, provision for use of in state and local specifications and more independent research on engineering properties and long-term durability. Near-term research projects have subsequently been launched to address these needs. These were: (1) Development of a handbook (HB) through Standards Australia titled "Guide and Standard Specification for Construction with Geopolymer Concrete" and (2) Investigation of geopolymer concrete durability and field performance. It is intended that the handbook will be a platform for preparation of an Australian Standard on geopolymer concrete and will also build on the CIA Recommended Practice for Geopolymer Concrete (2011).

Geopolymer concrete is currently included in several VicRoads specifications and this is a major step forward in gaining acceptance and providing opportunities for use of geopolymers. National standardisation of geopolymer concrete, in conjunction with continued research, will give specifiers and end-users greater confidence with the material.

The proposed contents of the Handbook on geopolymer concrete are as follows:

1. Introduction
2. Constituent Materials

3. Properties and Applications of Geopolymer Concrete
4. Commentary on AS 1379 for Specification and Supply of Concrete
5. Commentary on AS 3600 for Design of Geopolymer Concrete Structures
6. Model Performance-Based Specification for Geopolymer Concrete
7. Recommended Performance Test Methods
8. Case Histories and Long-Term Durability
9. Summary

This paper describes current progress on Chapters 4, 5, 6, 7 and 8 listed above. Preparation of the Handbook contents commenced in mid-2014 and is a three year project.

## **2. Commentary on AS 1379**

AS 1379 (1997) covers specification and supply of concrete. The standard defines concrete as “a mixture of cement, aggregates, and water with or without the addition of chemical admixtures or other materials”. The cement type specified in AS 1379 is Portland cement complying with AS 3972. Geopolymer binders are not covered in the standard. Therefore, it is necessary to consider any deviations from AS 1379 that may be required for geopolymer concrete. The Handbook proposes to incorporate a commentary on AS 1379 to include such deviations and also provide explanation on assumptions with regard to aspects of materials, supply, testing and performance of geopolymer versus conventional concrete.

In general, specification and supply of geopolymer concrete can follow the majority of requirements given in AS 1379 for conventional concrete. The main deviation from AS 1379 is the description of binder materials. There are also aspects of supply and production of geopolymer concrete where further investigation is necessary to determine whether AS 1379 requirements and common practices for conventional concrete are applicable. Examples include the following:

- Alkali-aggregate reactivity and qualification testing of aggregates
- Temperature limits at point of delivery
- Hot and cold weather concreting precautions
- Curing practices

## **3. Commentary on AS 3600**

AS 3600 provides unified design and detailing rules (i.e., minimum requirements) for concrete structures and members with or without steel reinforcement and prestressing tendons. The standard also defines the performance criteria to assess the structural performance through its lifetime for concrete elements containing Ordinary Portland Cement (OPC) and blended cements. However, the material behavior and strength properties of geopolymer concrete show significant variability from the OPC concrete (OPCC) (e.g., Hardjito and Rangan, 2005; Ng and Foster, 2008; and Collins and Sanjayan, 1999) depending on the binder and method of curing etc. For example, geopolymer concrete has greater tensile and bond in comparison to OPCC.

Experimental studies have been undertaken to understand the shear and flexural behavior of geopolymer beam column members (e.g., Rahman and Sarker, 2011; Ambily et al, 2011; and Chang, 2009 etc). It was observed that AS 3600 estimates the flexural and shear capacities reasonably well. Due to high tensile and bond strength, the number of reinforcing bars and bond length of rebar may be reduced in geopolymer concrete. This eventually alters the detailing of design. Further, the serviceability limits set out in AS 3600 may not be adequate for geopolymer concrete members since the elastic modulus appears to be lower than OPCC. Therefore, it is necessary to make changes in AS 3600 in order to suit for geopolymer concrete. The proposed Handbook will provide a commentary on AS 3600 that includes modification to material strength, design equations and detailing. The focus will be devoted to following areas:

- Characterise the geopolymer concrete stress-strain behavior with and without confinements
- Determine the material properties including creep and shrinkage
- Assess the applicability of flexure and shear design rules in AS 3600 for geopolymer concrete member using experimental results and field performance data
- Assess the applicability of serviceability limit states provided in AS 3600
- Assess the applicability of fire design criteria provided in AS 3600
- Assess the applicability of strut and tie model provided in AS 3600

#### **4. Model Performance-Based Specification for Geopolymer Concrete**

A chapter of the proposed Handbook will present a model specification for geopolymer concrete. The specification has been designed to enable engineers to specify geopolymer concrete for projects in a manner similar to the current way in which conventional concrete is specified. The specification focuses on supply of geopolymer concrete and durability performance requirements. Existing Australian Standards and state transportation agency specifications relating to concrete have been used as a basis for this model specification on geopolymer concrete.

Given that geopolymer concrete does not have the same lengthy track record as Portland cement-based concrete, there are some uncertainties regarding long-term behaviour. Therefore, it has been necessary to make assumptions relating to properties and durability based on current knowledge. With ongoing research and practical experience with geopolymer concrete many uncertainties will be resolved. Hence, the specification will be subject to revision as more information becomes available.

The model specification sets out the requirements for the supply, testing and placement of geopolymer concrete. Currently, Australian standards such as AS 1379, AS 3600 or AS 4997 do not specifically cover geopolymer concrete. The only state specifications that include geopolymer concrete at the time of writing are VicRoads 701 (Underground Stormwater Drains), 703 (General Concrete Paving), 705 (Drainage Pits) and 711 (Wire Rope Safety Barrier). Further details are available in Andrews-Phaedonos (2014).

The specification is largely performance-based in that the required functional properties of the concrete are specified and limitations on concrete mix design or restrictions on binder type are not given. It has generally been assumed that the majority of requirements given in AS 1379 are applicable to geopolymer concrete. Therefore, areas where specification and supply of geopolymer concrete deviate from AS 1379 and the durability aspects of AS 3600 are covered.

Contents of the model specification are outlined below:

- Scope
- Definition of Geopolymer Concrete
- Existing Applicable Standard Clauses
- Material Requirements
- Geopolymer Concrete Classes, Mix Design and Property Requirements
- Sampling, Testing and Assessment of Compliance
- Placement, Finishing and Curing

A draft of the model specification has been prepared and comments from industry advisors and other interested parties are being invited so that the final document is practical, useable and achieves acceptance.

#### **5. Recommended Test Methods**

Existing testing protocols which are standardised worldwide have been developed specifically for Portland cement binder systems. However, chemical reactions characterising alkali-activated binder systems differ drastically from conventional hydration process of Portland cement. Thus, the mechanisms by which concrete achieves potential strength and durability are different between the two types of binders. As a result, existing testing methods are not necessarily suitable for geopolymer binders. This has been identified through the work of RILEM Technical Committee 224-AAM as being a key issue facing the widespread use of alkali-activated concretes in the industry (Provis and Van Deventer, 2014). Research

will be carried out combining laboratory work aiming to assess existing testing methods as well as field investigations required for the validation and the calibration of the new protocols. The project aims to determine:

- What are the best methods and protocols for testing a geopolymer concrete in laboratory?
- What are the performance requirements that should be specified?
- How do these correspond to in-service performance of real structure?

In addition to traditional standard tests related to the mechanical performance and the workability, the performance-based handbook will address the key issues surrounding the application of test methods to geopolymer concretes and mortars in the following areas:

- Creep and shrinkage
- Transport properties
- Atmospheric carbonation
- Concrete structures in marine environments
- Concrete structures in aggressive soils
- Sewer structures
- Alkali-aggregate reactivity

As an example, Table 1 shows the testing methods that will be assessed for chloride penetration in concrete structures. Laboratory experimentations will be carried out using different geopolymer concrete mix design. Results will be compared to the ones obtained in natural conditions for existing geopolymer concrete structures. The most suitable methods will be identified, protocols will be modified if necessary and performance based specifications will be calibrated for geopolymer concretes.

**Table 1. Test methods related to chloride penetration in concrete**

	Testing method	Standard protocol
1	Semi-natural chloride diffusion test	NT BUILD 443 / ASTM C1556
2	Rapid chloride permeability (RCP) test	ASTM C1202
3	Rapid chloride migration test	NT BUILD 492
4	Surface resistivity (SR) test	AASHTO TP95
5	Bulk electrical conductivity test	ASTM C1760

This work will be carried out in close collaboration with the RILEM Technical Committee 247-DTA: Durability testing of alkali-activated materials.

## **6. Case Histories and Long-Term Durability**

### **6.1 Laboratory Studies**

The majority of published durability research on geopolymer concrete has been laboratory-based. Table 2 compares broadly the laboratory tested durability properties of geopolymer and conventional Portland cement concrete. This is not a definitive list of research, but provides examples. Since properties of any concrete are highly dependent on mix proportions and constituent materials, only general comparisons have been made for concretes with similar compressive strengths.

**Table 2. Broad comparison between geopolymer and conventional concrete durability properties**

Property	Geopolymer versus Conventional Concrete	Examples of References
Carbonation Coefficient	Higher for accelerated tests	Bernal et al (2011, 2012a, b, 2014); Law et al (2012); Aperador et al (2009)
Chloride Diffusion Coefficient	Lower (migration test); lower (core test)	Bernal et al (2012a); Andrews-Phaedonos (2012); Kupwade-Patil and Allouche (2013a)
Rapid Chloride Permeability	Lower to similar depending on mix proportions	Bernal et al (2011, 2012a); Law et al (2012); Andrews-Phaedonos (2012); Kupwade-Patil and Allouche (2013a)
Corrosion Rate of Embedded Steel	Limited research, particularly field exposure, prevents conclusive comparison.	Aperador et al (2009); Aperador Chapparo et al (2012); Miranda et al (2005); Reddy et al (2013); Kupwade-Patil and Allouche (2013a)
Sorptivity	Higher	Law et al (2012); Bernal et al (2011)
Sulphate Resistance	Somewhat higher, depends on cation	Bakharev et al (2002)
Acid Resistance	More resistant to organic and inorganic acid attack	Literature reviewed by Pacheco-Torgal et al (2012); Bakharev et al (2003)
Alkali-Silica Reaction Susceptibility	Variable based on limited research, depends on composition	García-Lodeiro et al (2007); Fernández-Jiménez and Puertas (2002); Bakharev et al (2001); Literature reviewed by Pacheco-Torgal et al (2012); Kupwade-Patil and Allouche (2013b); Krivenko et al (2014)
Volume of Permeable Voids	Varies depending on mix proportions; higher	Bernal et al (2011); Andrews-Phaedonos (2012)
Water Absorption	Similar	Bernal et al (2011)
Gas permeability	Similar	Sagoe-Crentsil et al (2012)
Water Permeability	Higher	Sagoe-Crentsil et al (2012)

Table 2 indicates that the differences in properties and behaviour of geopolymer concrete compared with conventional Portland cement concrete are not always clear. This is frequently due to variation in materials, particularly activator concentrations and chemistry. Research between different organisations has not been coordinated, hence definitive comparisons are not always possible. The apparent variations and possible discrepancies highlight the need for greater understanding and verification of properties controlling service life in realistic exposure environments. It is also necessary to consider whether conventional test methods and procedures are applicable to geopolymer concrete and this is being investigated as part of the Handbook development.

## 6.2 Field Exposure Studies

Case histories and long-term durability data on geopolymer concrete in field exposure conditions are not as widely available as laboratory investigations. Recent reports on field performance of geopolymers and alkali-activated materials include work by Andrews-Phaedonos (2014), Shayan et al. (2013), Buchwald et al. (2015), Vanooteghem (2011) and Xu et al. (2008).

The research by Buchwald et al. (2015) and Vanooteghem (2011) is of particular interest as it refers to the long-term behaviour of alkali-activated slag cement concrete from buildings constructed in Belgium in the 1950s. The product used was known as "Purdocement". According to Buchwald et al. (2015) two types of Purdocement were produced. One was based on slag with a small proportion of Portland cement and the other was based on slag with a small proportion of calcium hydroxide. Both versions were activated by sodium sulphate.

Visual observations on the Purdocement buildings where the concrete was accessible showed variable performance (Buchwald et al., 2015; Vanooteghem, 2011). Some concrete was in sound condition and other concrete showed deterioration. Damage appeared to be due to water leakage or poor compaction and curing at the time of construction. Samples were extracted from damaged interior beams in a factory built in 1957 and analysed for composition, phases, microstructure, strength, carbonation and chloride ingress. Core samples from undamaged concrete in the factory were also taken for comparison. The compressive strength of cylindrical core samples from undamaged concrete was 52.2 to 54.8 MPa. The original strength was unknown. The cores were found to virtually be fully carbonated from both exposed

faces. Elevated acid-soluble chloride concentrations up to 0.49% by weight of binder were found in the damaged concrete whereas the concentrations in the undamaged cores were lower (up to 0.26% by weight of binder). The source of chloride ingress was attributed to fertiliser from leaking flower boxes. Sulphates from fertiliser may also have contributed to damage. Corrosion of reinforcement was observed in the damaged concrete and likely due to carbonation, chloride ingress or both. Corrosion was exacerbated by water leakage.

The carbonation data reported by Buchwald et al. (2015) and Vanooteghem (2011) showed that depths of carbonation for Purdocement located in an interior environment were 46 to 63 mm where measurable. In many cases carbonation of the concrete was complete and a depth of carbonation could therefore not be determined. Using the carbonation depths of 46 to 63 mm over a duration of 64 years gives carbonation rates of 5.7 to 7.9 mm/yr<sup>0.5</sup>. These values are relatively high even for an indoor environment, particularly considering that a coating had been applied to the concrete and that the calculated rates represent the lower range in the tested cores. Details on the coating and when it had been applied were unknown. However, it is possible that it may have provided some protection against carbonation. The carbonation rates can be compared with those reported for Portland cement-based concrete in indoor environments. Data is presented in Table 3 and shows the type of mixes with similar carbonation rates.

**Table 3. Indoor carbonation rates similar to “Purdocement” for conventional concrete mixes**

Mix	Curing (days)	Carbonation Rate (mm/yr <sup>0.5</sup> )	Reference
OPC, w/cm = 0.4	1	5.0	Burden (2006)
30% FA, w/cm = 0.4	1	8.0	Burden (2006)
20% FA, 46 MPa	1	8.5	Ho and Lewis (1987)
25% FA, w/cm = 0.5	28	5.9	Collepari et al (2004)
50% BFS, w/cm = 0.5	28	5.2	Collepari et al (2004)

Note: OPC = Ordinary Portland Cement, FA = Fly Ash, BFS = Blast Furnace Slag, w/cm = water/cementitious material ratio.

The data in Table 3 indicates that the measurable and, thus, lower range of indoor carbonation rates for Purdocement are similar to those for Portland cement and fly ash blends with water/cementitious material ratio of 0.4 and cured for only a short period of one day or for fly ash and slag blends with higher water/cementitious material ratio of 0.5 but cured for a longer period of 28 days. As noted above, the carbonation rates may actually have been higher, especially if the applied coating had given protection against CO<sub>2</sub> ingress.

The long-term performance of alkali-activated slag concrete in Ukraine has been reported by Xu et al. (2008). The slag was activated by carbonates or by carbonate/hydroxide mixtures and details of the original mix proportions were provided. The concrete was produced between 1964 and 1982 and had been exposed to freeze-thaw conditions typical of Kiev. The type of concrete elements included an underground drainage system, a high rise residential building, an outdoor precast slab and a silo. The age of the concrete elements at the time of testing ranged between 18 and 36 years. Chemical composition, phase analysis and microstructure of concrete samples were studied in addition to visual condition, compressive strength, depth of carbonation, surface pH and water absorption. The concrete appeared to be in good condition with no visible defects. Water absorption ranged between 4.76 and 8.04%. The compressive strengths of the samples ranged between 26 and 62 MPa. The pH of the surface was 9.08 to 11.57 and there appeared to be a correlation between surface pH and compressive strength. The depths of carbonation were 2 to 3 mm on the underground drainage system, 1 to 4 mm on the outdoor precast slab and 3 to 8 mm on the external surface of the silo. The depth of carbonation on the residential building was not reported but the concrete samples from this structure had the lowest surface pH of 9.08.

Based on the ages of the concrete and depths of carbonation for the Ukrainian alkali-activated slag concrete, the calculated carbonation rates were 0.3 to 0.5 mm/yr<sup>0.5</sup> for the drainage system, 0.2 to 0.8 mm/yr<sup>0.5</sup> for the precast slab and 0.7 to 1.9 mm/yr<sup>0.5</sup> for the silo. All of these carbonation rates are low. However, it is noted that the drainage system was likely to be wet and this would reduce carbonation. The



externally exposed concrete elements are also likely to have lower carbonation rates than might be experienced in Australia due to lower average temperatures.

The studies on Belgian and Ukrainian alkali-activated slag concrete that have been in service for decades offer insights to the long-term performance of such materials. Performance appears to depend on the type of activator and resultant chemistry of the concrete in addition to exposure conditions.

### **6.3 Proposed Field Testing**

As part of the development of a Handbook on geopolymer concrete, it is proposed to undertake detailed field testing of existing installations of geopolymers. Gourley (2014) summarised commercial use of geopolymers in Australia. Whilst the age of existing geopolymer concrete examples is relatively young, testing will provide an indication of performance to date and enable comparison with Portland cement concrete. One structure that will be tested as part of the research project is a slab constructed from geopolymer concrete at the former Zeobond batching plant in Campbellfield, Victoria. This slab was poured in 2006 and is exposed to an outdoor atmospheric environment.

The field testing programme will include non-destructive testing such as Schmidt hammer, resistivity, reinforcement corrosion activity and in-situ permeability. Extraction of core samples will also be performed and the cores will be tested for depth of carbonation, compressive strength, elastic modulus, density, sorptivity, volume of permeable voids and chloride diffusion coefficient. The microstructure of geopolymer concrete will also be examined to assist with understanding of microstructure-property relationships and identify any changes occurring with time. Comparisons will also be made with field studies on geopolymer concrete elements in Victoria reported by Shayan et al. (2013) and Andrews-Phaedonos (2014).

## **7. Conclusions**

Specific tasks are being undertaken towards preparation of a Handbook on geopolymer concrete to be published in cooperation with Standards Australia. The Handbook will assist development and adoption of geopolymer concrete in applications where an alternative to conventional concrete is sought. Widespread use of geopolymers requires engineering design and practical considerations to ensure successful construction, structural adequacy and durability. The current focus is on examination of existing standards such as AS 1379 and AS 3600, determination of how they can be applied to geopolymer concrete and identification of required deviations from the standards. A model specification suitable for use by engineers to specify geopolymer concrete for projects is being developed. Research is also investigating appropriate test methods and long-term durability investigations.

## **8. Acknowledgement**

The work reported in this paper was undertaken by Swinburne University of Technology (Centre for Sustainable Infrastructure), University of New South Wales (Centre for Infrastructure Engineering and Safety), Australasian Iron and Steel Slag Association and Ash Development Association of Australia on behalf of the CRC for Low Carbon Living whose activities are funded by the Australian Government's Cooperative Research Centre Programme.

## **9. References**

1. Berndt, M.L, Sanjayan, J. et al., "Overcoming barriers to implementation of geopolymer concrete", Proceedings, 23<sup>rd</sup> Biennial Conference of the Concrete Institute of Australia, Gold Coast, Australia, 2013.
2. Concrete Institute of Australia, Recommended Practice for Geopolymer Concrete, Z16, 2011.
3. Andrews-Phaedonos, F., Specification and use of geopolymer concrete, 9<sup>th</sup> Austroads Bridge Conference, Sydney, 2014.

4. Provis J.L. and Van Deventer J.S.J., Alkali Activated Materials: State-of-the-Art Report, RILEM TC 224-AAM, Springer, 2014.
5. Bernal, S.A., de Guitierrez, R.M et al., "Effect of binder content on the performance of alkali-activated slag concretes", Cement and Concrete Research, 41(1), 2011, pp. 1-8.
6. Bernal, S.A., de Guitierrez, R.M et al., "Engineering and durability properties of concretes based on alkali-activated granulated blast furnace slag/metakaolin blends", Construction and Building Materials, 33(1), 2012a, pp. 98-108.
7. Bernal, S.A., Provis, J.L. et al., "Accelerated carbonation testing of alkali-activated binders significantly underestimates service life: The role of pore solution chemistry", Cement and Concrete Research, 42(10), 2012b, pp. 1317-1326.
8. Bernal, S.A., San Nicolas, R. et al., "Natural carbonation of aged alkali-activated slag concretes", Materials and Structures, 47(4), 2014, pp. 693-707.
9. Law, D.W., Adam, A.A. et al., "Durability assessment of alkali activated slag (AAS) concrete", Materials and Structures, 45(9), 2012, pp. 1425-1437.
10. Aperador, W., de Gutierrez, D.M. et al., "Steel corrosion behaviour in carbonated alkali-activated slag", Corrosion Science, 51(9), 2009, pp. 2027-2033.
11. Kupwade-Patil, K. and Allouche, E.N., "Examination of chloride induced corrosion in reinforced geopolymer concretes", Journal of Materials in Civil Engineering, 25(10), 2013a, pp. 1465-1476.
12. Aperador Chapparo, W., Ruiz, J.H.B et al., "Corrosion of reinforcing bars embedded in alkali-activated slag concrete subjected to chloride attack", Materials Research, 51(1), 2012, pp. 57-62.
13. Miranda, J.M, Fernández-Jiménez, A. et al., "Corrosion resistance in activated fly ash mortars", Cement and Concrete Research, 35(6), 2005, pp. 1210-1217.
14. Reddy, D.V., Edouard, J.B. et al., "Durability of fly ash-based geopolymer structural concrete in the marine environment", Journal of Materials in Civil Engineering, 25(6), 2013, pp. 781-787.
15. Bakharev, T., Sanjayan, J.G. et al., "Sulfate attack on alkali-activated slag concrete", Cement and Concrete Research, 32(2), 2002, pp. 211-216.
16. Pacheco-Torgal, F., Abdollahnejad, Z. et al., "Durability of alkali-activated binders: A clear advantage over Portland cement or an unproven issue?", Construction and Building Materials, 30, 2012, pp. 400-405.
17. Bakharev, T., Sanjayan, J.G. et al., "Resistance of alkali-activated slag concrete to acid attack", Cement and Concrete Research, 33(10), 2003, pp. 1607-1611.
18. García-Lodeiro, I., Palomo, A. et al., "Alkali-aggregate reaction in activated fly ash systems", Cement and Concrete Research, 37(2), 2007, pp.175-183.
19. Fernández-Jiménez and Puertas, F., "The alkali-silica reaction in alkali-activated granulated slag mortars with reactive aggregate", Cement and Concrete Research, 32(7), 2002, pp. 1019-1024.
20. Bakharev, T., Sanjayan, J.G. et al., "Resistance of alkali-activated slag concrete to alkali-aggregate reaction", Cement and Concrete Research, 31(2), 2001, pp. 331-334.
21. Kupwade-Patil, K. and Allouche, E.N., "Impact of alkali silica reaction on fly ash-based geopolymer concrete", Journal of Materials in Civil Engineering, 25(1), 2013b, pp. 131-139.
22. Krivenko, P., Drochytka, R. et al., "Mechanism of preventing the alkali-aggregate reaction in alkali activated cement concretes", Cement and Concrete Composites, 45(1), 2014, pp. 157-165.
23. Sagoe-Crentsil, K., Yan, S. et al., "Effect of matrix permeability on durability of structural grade geopolymer and conventional concretes", in Concrete Repair, Rehabilitation and Retrofitting III, Alexander, M. et al (eds), Taylor and Francis, London, 2013, pp. 158-162.
24. Shayan, A., Xu, A. et al., "Field performance of geopolymer concrete used as a measure towards reduction of carbon dioxide emission", Proceedings, 23<sup>rd</sup> Biennial Conference of the Concrete Institute of Australia, Gold Coast, Australia, 2013.
25. Buchwald, A., Vanooteghem, M. et al., "Purdocement: Application of alkali-activated slag cement in Belgium in the 1950s", Materials and Structures, 48(1-2), 2015, pp. 501-511.

26. Vanooteghem, M., "Duurzaamheid van beton met alkali-geactiveerde slak uit de jaren 50 – het Purdocement", Master's thesis, Universiteit Gent, Belgium, 2011.
27. Xu, H., Provis, J.L. et al., "Characterization of aged slag concretes", ACI Materials Journal, 105(2), 2008, pp. 131-139.
28. Gourley, J.T., "Geopolymers in Australia", Journal of the Australian Ceramics Society, 50(1), 2014, pp. 102-110.
29. Hardjito, D. and Rangan, B.V., "Development and properties of low-calcium fly ash based geopolymer concrete", Research Report GC1, Faculty of Engineering, Curtin University, 2005, pp. 94.
30. Ng, T.S. and Foster, S.J., "Development of high performance geopolymer concrete", Proceedings of the 20th ACMSM, Futures in Mechanics of Structures and Materials, Toowoomba, 2-5 December 2008.
31. Collins, F.G. and Sanjayan, J.G., "Workability and mechanical properties of alkali activated slag concrete", Cement and Concrete Research, 29(3), 1999, pp. 455-458.
32. Ambily P.S, Madheswaran C.K., et al., "Experimental and analytical investigations on shear behavior of reinforced geopolymer concrete beams", International Journal of Civil and Structural Engineering, 2(2), 2011, pp. 673-688.
33. Rahman, M. and Sarker, P.K., "Geopolymer concrete columns under combined axial load and biaxial bending," 22<sup>nd</sup> Biennial Conference of the Concrete Institute of Australia, Perth Australia, 2011.
34. Chang, E. H., "Shear and bond behaviour of reinforced fly ash-based geopolymer concrete beams", Ph.D thesis, Department of Civil Engineering, Curtin University of Technology, 2009.

# Development of Low Shrinkage Water Repelling Foamed Concrete

Kai Tai Wan<sup>1</sup>, Honggang Zhu<sup>2</sup>, Binmeng Chen<sup>3</sup>, Chuanlin Hu<sup>3</sup>

<sup>1</sup>Lecturer in Civil Engineering, Brunel University London, UK

<sup>2</sup>Principal Research Engineer, Nano and Advanced Materials Institute Limited, Hong Kong

<sup>3</sup>Research Engineer, Nano and Advanced Materials Institute Limited, Hong Kong

**Abstract:** It is desirable to have better thermal insulation materials to reduce energy consumption for regulating indoor temperature. Common thermal insulation materials such as expanded polystyrene and foamed polyurethane are available in the market. However, because of high flammability and low abrasion resistance of polymer-based insulator, it is not suitable for building envelope without extra protection and precautionary measures.

The fire and wear resistance can be improved by changing the material from polymer-based to inorganic. There is lots of research on foamed concrete by incorporating large volume of controlled air void. However, the application is restricted to component with limited size due to excessive drying shrinkage. On the one hand, when more air void is trapped in the matrix, the density is lower and it results in higher thermal resistance. On the other hand, with lower density, the matrix is weaker and the water permeability is significantly increased. The high water permeability allows fast penetration of water and causes leaching that may lead to disintegration in relatively short time especially for ultra-lightweight concrete.

In this paper, drying shrinkage of non-foamed mortar made of different blends among ordinary Portland cement, ground granulated blast-furnace slag, calcium sulfoaluminate cement, calcine magnesium oxide condensed silica fume, limestone powder and surface-treated hydrophobic clag will be investigated. The drying shrinkage of non-foamed mortar and foamed concrete with the same mix proportion will be performed to verify the methodology. Finally, the modification of the hydrophilic matrix of conventional cement mortar to hydrophobic by using surface treated hydrophobic clag is demonstrated.

**Keywords:** water repelling, foamed concrete, drying shrinkage, CSA, calcined magnesium oxide.

## 1. Introduction

Most energy consumed in building is spent on heating/cooling. However, significant energy is wasted through the heat transfer of the building envelope. It is desirable to increase the thermal resistance of external walls of buildings. For floor heating system, it is more efficient to provide thermal insulator below the heating pipes to minimise heat transfer to the ceiling of the lower floor [1]. Polymer-based thermal insulators, such as expanded polystyrene and foamed polyurethane, provide excellent thermal insulation that the thermal conductivity is close to air as well as satisfactory mechanical strength. However, they are not suitable to be used in buildings, for which fire safety is one of the major design concerns. When fire safety is the prime concern, inorganic thermal insulator is preferable. Foamed concrete is one of the candidates. Foamed concrete consists of cementitious paste with macroscopic entrapped air void [2,3]. By reducing the density of the cementitious matrix, the thermal conductivity can be greatly reduced. One of the major problems of conventional foamed concrete is the excessive dry shrinkage because there is no coarse aggregates in the matrix. Also, by reducing the density, the matrix becomes more water permeable. In the presentation, different approaches of reducing the drying shrinkage as well as modifying the hydrophilic matrix to hydrophobic will be discussed.

## 2. Materials and methods

### 2.1 Materials

The studied lightweight foamed concrete consists of ordinary Portland cement (OPC), calcium sulfoaluminate (CSA) cement, ground granulated blast-furnace slag (GGBS), calcined magnesium oxide, limestone powder, uncondensed silica fume and surface-treated hydrophobic clag. The results of elemental analysis from X-ray fluorescence spectroscopy are shown in Table 1. To improve the

workability of the mix in fresh state, high performance polycarboxylate based superplasticizer (SP) is used. Boric acid is used to control the setting time of the mix with CSA cement. The particle size of OPC, GGBS, CSA, limestone powder and surface treated hydrophobic clag is in similar range (in 10-100  $\mu\text{m}$ ). Since the mix contains all fine powder, hydroxypropyl methylcellulose (HPMC) and uncondensed silica fume is added as a viscosity modifying agent to improve the cohesiveness of the mix. All CSA cement is blended with 15% wt of industrial grade gypsum dihydrate ( $\text{CaSO}_4 \cdot 2\text{H}_2\text{O}$ ) in powder form before mixing with other types of powder. [5] discusses the hydration process of CSA. Magnesium oxide is a common admixture for shrinkage compensation of cement based repair mortar. The magnesium oxide used in this study is the industrial grade lightly calcined from magnesium hydroxide. The as-received magnesium oxide is further calcined in an in-house furnace for 1 hour at 800°C, 900°C and 1000°C, respectively under normal atmospheric condition. The purpose of calcination of magnesium oxide is to increase the crystallinity and hence reduce the reactivity so that it can compensate the drying shrinkage in longer period. The foaming agent used for the foamed concrete is fatty alcohol-based liquid form (BASF Rheocell 30). To modify the surface of the matrix from hydrophilic to hydrophobic, a surface treated clag is used.

**Table 1. Elemental analysis of the raw materials of foamed concrete.**

	OPC	GGBS	CSA	Limestone	Silica fume	Clag
CaO	67.0%	46.5%	41.3%	96.9%	0.4%	4.5%
SiO <sub>2</sub>	19.4%	32.2%	8.2%	1.3%	92.1%	51.2%
Al <sub>2</sub> O <sub>3</sub>	3.4%	12.3%	32.9%	--	4.6%	12.9%
MgO	1.0%	4.1%	2.8%	1.8%	0.5%	5.1%
Fe <sub>2</sub> O <sub>3</sub>	3.5%	1.0%	1.6%	--	1.0%	2.7%
SO <sub>4</sub>	5.1%	3.1%	11.8%	--	0.4%	--
Na <sub>2</sub> O	--	--	--	--	--	22.9%

## 2.2 Specimens preparation and test

In this study, the drying shrinkage of the binder is investigated with different combination of binder and filler instead of making foamed concrete. The reason is to minimise the variation caused by adding air void. Also, the strength of foamed concrete is significantly reduced and it is damaged easily during continuous measurement of drying shrinkage. Foamed concrete specimens were made in three different sets of mix proportion to verify whether the trend and magnitude of drying shrinkage of foamed concrete is similar to the binder with the same mix proportion. To investigate the drying shrinkage of the non-foamed mortar, the specimens are divided into 3 groups as summarised in Table 2. All samples consist of the same content of uncondensed silica fume, SP and HPMC. Since the bubble stability of foamed concrete depends on the workability of the fresh state, the water content is kept the same. When boric acid is added, the workability of the fresh state of the mix may change significantly and hence the water content is adjusted to maintain similar workability. The first group consists of OPC, GGBS, uncondensed silica fume and limestone powder. The purpose of the first group is to investigate the conventional composition of foamed concrete. Conventional foamed concrete is made of OPC. To improve the greenness of foamed concrete, one traditional way is to replace OPC by GGBS. To reduce the cost of foamed concrete, part of OPC is replaced by limestone powder as well. The second group consists of fixed OPC-to-GGBS ratio and with addition of 4% mass of magnesium oxide with different calcination temperature. The reaction between the magnesium oxide and water to form magnesium hydroxide is expansive and it is conventionally used for shrinkage compensation in cement-based repair mortar. In this study, magnesium oxide with different crystallinity and reactivity is added to the mix for investigation of the effectiveness of using magnesium oxide to reduce the drying shrinkage in foamed concrete. The third group consists of more complicated blend among OPC, GGBS, CSA, uncondensed silica fume and limestone powder. Since the setting time of CSA cement with gypsum dihydrate can be as fast as 15 minutes, boric acid powder is added to retard the setting time to 60-75 minutes. While there is neutralisation reaction between boric acid and the alkaline in other powder and form water, the total water content is adjusted so that the mix in fresh state maintains similar workability.

**Table 2. Mix Proportion, compressive strength and dry shrinkage of non-foamed mortar.**

	OPC	GGBS	CSA	Silica fume	MgO	Lime-stone	Water	Boric acid	Compressive strength (MPa)	Dry shrinkage (Micro-strain)
GI-1	0.97	--	--	0.03	--	--	0.285	--	105.2	2,019
GI-2	--	0.97	--	0.03	--	--	0.285	--	40.8	2,273
GI-3	0.5	0.47	--	0.03	--	--	0.285	--	96.0	2,530
GI-4	0.23	0.74	--	0.03	--	--	0.285	--	90.5	3,090
GI-5	0.77	--	--	0.03	--	0.2	0.285	--	90.1	2,006
GII-1	0.221	0.71	--	0.029	0.04 (as-received)	--	0.285	--	93.1	2,662
GII-2	0.221	0.71	--	0.029	0.04 (800°C 1 hour)	--	0.285	--	99.1	3,139
GII-3	0.221	0.71	--	0.029	0.04 (900°C 1 hour)	--	0.285	--	101.4	3,055
GII-4	0.221	0.71	--	0.029	0.04 (1000°C 1 hour)	--	0.285	--	103.3	3,218
GIII-1	--	--	0.97	0.03	--	--	0.28	--	91.7	837
GIII-2	--	0.74	0.23	0.03	--	--	0.30	--	35.2	568
GIII-3	--	--	0.77	0.03	--	0.2	0.3	0.0021	72.5	1,014
GIII-4	0.115	0.54	0.115	0.03	--	0.2	0.27	0.0050	59.0	928
GIII-5	0.115	0.425	0.23	0.03	--	0.2	0.28	0.0075	76.8	493
GIII-6	0.115	0.225	0.23	0.03	--	0.4	0.28	0.0075	48.0	1,099

To compare the drying shrinkage between non-foamed mortar and foamed concrete, three sets of mix proportion is selected as shown in Table 3. Since it is too fragile to produce ultra-lightweight foamed concrete and it is broken easily during the measurement drying shrinkage manually, the wet density of foamed concrete is set at around 1600 kg/m<sup>3</sup>. For each mix proportion, three cubic samples for compression test and three prism samples for drying shrinkage measurement will be prepared for each binder and foamed concrete.

**Table 3. Mix proportion, wet density and compressive strength of non-foamed mortar and foamed concrete.**

	OPC	GGBS	Silica fume	Lime-stone	Water	Foaming agent (Liquid)	Wet density (kg/m <sup>3</sup> )	Compressive strength (MPa)
B1	0.667	0.333	--	--	0.285	--	2000	94.3
F1	0.667	0.97	--	--	0.285	0.0015	1626	43.0
B2	0.23	0.74	0.03	--	0.285	--	2061	90.5
F2	0.23	0.74	0.03	--	0.285	0.0015	1638	40.6
B3	0.184	0.592	0.03	0.2	0.285	--	2060	90.0
F3	0.184	0.592	0.024	0.2	0.285	0.0015	1611	38.0

To transform the hydrophilic surface of conventional mortar matrix to hydrophobic, the limestone powder is replaced by surface-treated hydrophobic clag. Since the particle shape of clag is clay-like, the water requirement is higher compared to limestone powder [4]. The hydrophobic property of clag affects the foam volume with the same amount of foaming agent. The detail mix proportion is still undergoing. Hence, only 70 mm x 70 mm x 140 mm cubes are fabricate to demonstrate the hydrophobicity of the matrix by using clag.

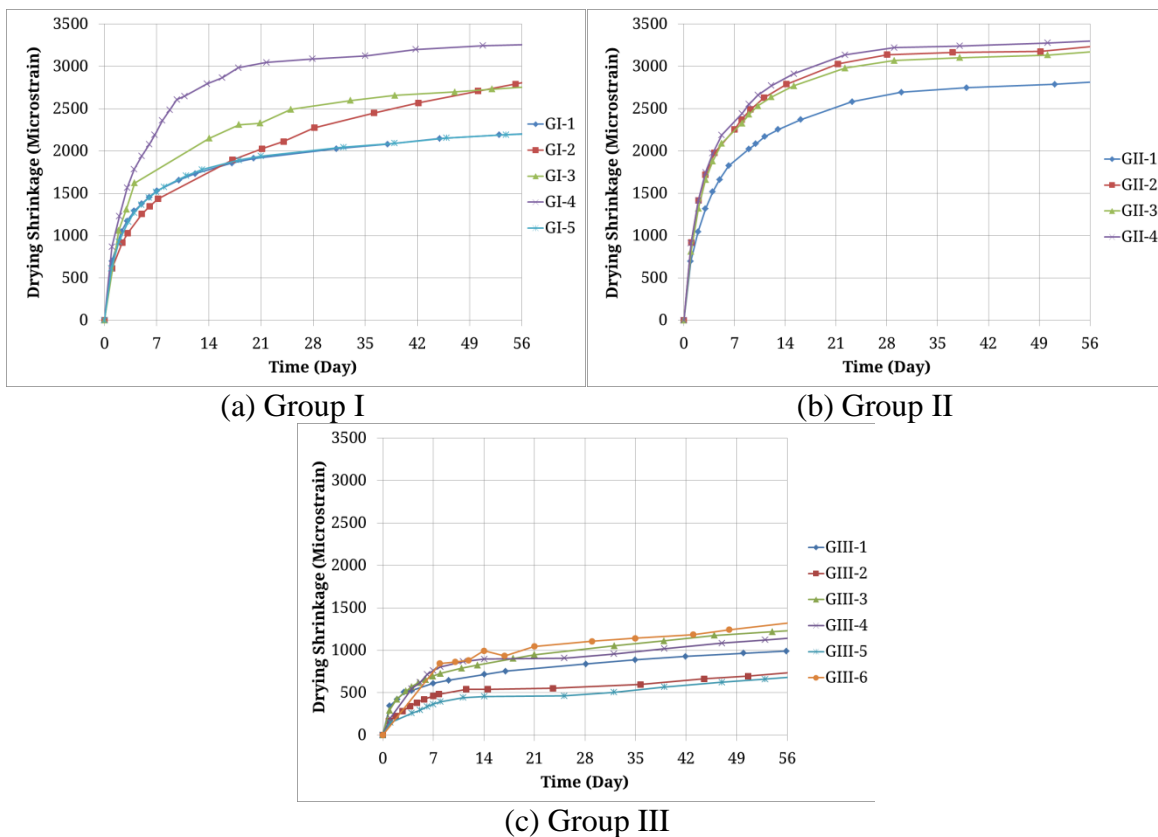
To fabricate non-foamed mortar, all dry powder including OPC, GGBS, CSA, uncondensed silica fume, limestone powder, calcined magnesium oxide, surface treated hydrophobic clag, boric acid and HPMC are mixed in the mixer. SP is mixed with water before adding to the mixed dry powder. The dosage of boric acid in Table 2 is the ratio to the total weight of OPC and CSA cement only. To fabricate foamed mortar, SP is mixed with 80% of the total water content while liquid form foaming agent is mixed with the remaining 20% water separately. The 80% water + 100% SP is thoroughly mixed with the dry powder mix. After the SP is effective, 20% water + 100% foaming agent is mixed to the wet mix to produce lightweight concrete. The amount of foaming agent added to achieve the desired wet density is based on trial-and-error process.

The wet density of the sample is measured in 100 mm x 100 mm x 100 mm cubes. The sample is cured at room temperature in the laboratory for 24 hours then the samples are demoulded. After demoulding, the cubic samples are put in a 60°C water bath for 7 days. Before the compression test, all samples are air dried for another 7 days. For each mix, three cubic samples are prepared. In the same batch of wet mixture, three 40 mm x 40 mm x 300 mm prisms are prepared for drying shrinkage measurement. A bolt is embedded at each end of the prism. A dial guage is used to measure the length of the sample. The wet sample is cured in normal laboratory for 24 hours then the samples are demoulded. After demoulding, the length of the sample is measured and then those samples are immersed in water bath in room temperature of the laboratory for 2 days. After 2 days of immersion in water, the length of the sample is measured and it is the initial length of the drying shrinkage measurement. The samples are put in a room with 23°C and 55% R.H. and the length change with time is measured by the dial gauge in the room manually. The frequency of measurement depends on the age of the sample since most drying shrinkage happens in the first week of test.

### 3. Results and discussions

The compressive strength of different mix is shown in Table 2. For group I, compressive strength of those mixes with OPC is similar. For GI-5, which contains 20% replacement of OPC by limestone powder, the

compressive strength is similar to those with high replacement proportion of OPC by GGBS. It is because there is no change in water content in the mix when binder is replaced by limestone powder and hence, the water-to-binder ratio increases. However, the strength development of GI-2, for which contains no OPC, is much lower comparing with other mixes in the group. It can be explained by the slow hydraulic reaction rate of GGBS. The drying shrinkage results of group I are shown in Figure 1a. The drying shrinkage at the 28<sup>th</sup> day is shown in the last column of Table 2. If there is no data at the 28<sup>th</sup> day, linear interpolation is used to deduce the drying shrinkage. In general, all drying shrinkage at the 28<sup>th</sup> day beyond 2,000 microstrain which is several times higher than normal concrete. The trends of drying shrinkage of GI-1 and GI-5 are identical. For GI-5, 20% of OPC is replaced by limestone powder. That means from the drying shrinkage reduction depends on water content instead of binder content. The drying shrinkage of those mixes with GGBS is generally with higher drying shrinkage (GI-2, GI-3 and GI-4). For GI-4, by replacing 75% of OPC by GGBS, the drying shrinkage at the 28<sup>th</sup> day is increased by 50% compared with GI-1 which contains no GGBS. For GI-2, for which contains no OPC, the drying shrinkage seems to be low compared to other mixed with blended OPC and GGBS. However, the low drying shrinkage is because of slow strength development. The trend of drying shrinkage of GI-2 keeps at much faster rate even after 28<sup>th</sup> day of measurement. Hence, the expected ultimate drying shrinkage of GI-2 is higher than the current value.



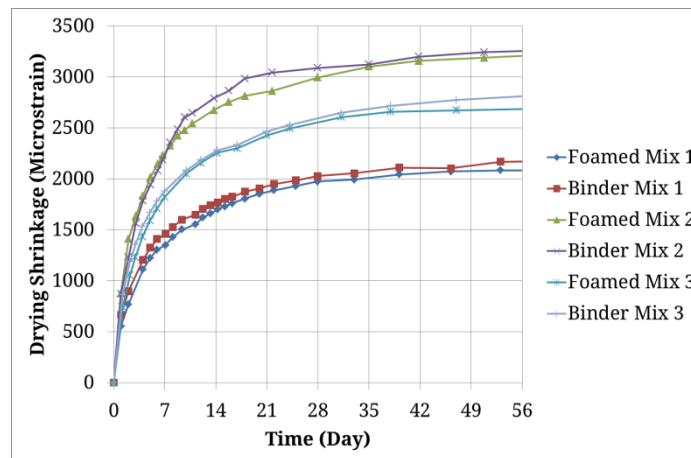
**Figure 1. Drying shrinkage of the specimens.**

In group II, in general, the calcined magnesium oxide does not reduce drying shrinkage of the mix GI-4 as shown in Figure 1b. For GII-1, which contains 4% as-received lightly calcined magnesium oxide, shows less drying shrinkage compared with other mixes in the same group. However, the compressive strength of the mixes with extra in-house calcination demonstrates higher strength. For higher the calcination temperature, that means higher degree of crystallisation, the higher the compressive strength. However, for lightly calcined magnesium oxide, the expansions reaction starts earlier compared with other cases in Group II. When the reactivity of magnesium is reduced by extra-calcination, the expansion reaction cannot compensate the drying shrinkage because the strength of the matrix has been developed.



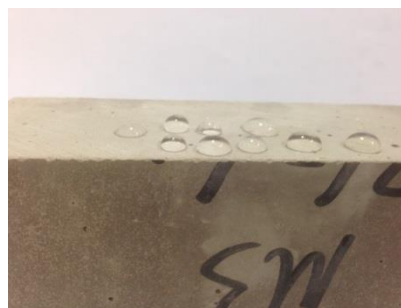
In group III, in general, the CSA cement can reduce drying shrinkage significantly as shown in Figure 1b. From the compression data from Table 2, the compressive strength of CSA mortar is significantly reduced when the ratio between CSA and OPC is less than 2. When CSA is blended with GGBS without OPC, the compressive strength is about one-third of pure CSA (Mix GIII-5). The minimum drying shrinkage is obtained when half of binder is GGBS and CSA-to-OPC ratio is 2 with 20% of limestone powder. The drying shrinkage is less than 500 microstrain at the 28<sup>th</sup> day which is comparable to conventional concrete with coarse aggregate. The compressive strength of GIII-5 is reduced by 16% compared with the GIII-1 with pure CSA.

The compressive strength of the three selected mix proportion of non-foamed mortar and foamed concrete is shown in Table 3. The compressive strength of the three non-foamed mortars is similar. With the same wet density of foamed concrete, the compressive strength is similar as well. Figure 2 shows the drying shrinkage of the non-foamed mortar and foamed concrete. Although the three selected non-foamed mortars achieve similar compressive strength, the magnitude of drying shrinkage is significantly different (varies from 2000 microstrain to more than 3000 microstrain). In Figure 2, the trend and magnitude of drying shrinkage of foamed concrete is very close to the non-foamed mortar. Hence, it is justifiable to investigate the drying shrinkage of foamed concrete by measuring the drying shrinkage of non-foamed mortar with the same mix proportion. When foaming agent is added, the viscosity of the wet mix becomes much higher. If the workability of the mix is too low, the shear stress in the wet mix may force merging of bubbles and the compressive strength of foamed concrete is significantly reduced. It is the major reason to keep the water content of the mix identical even through it increases the water-to-binder ratio when binder is replaced by inert filler (limestone powder or surface treated hydrophobic clag).

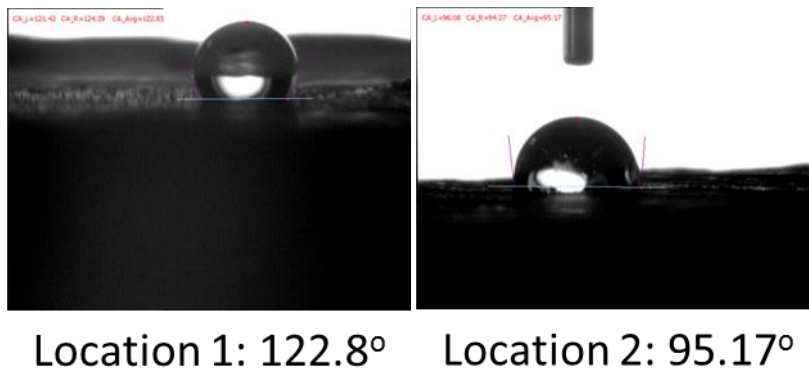


**Figure 2. Drying shrinkage of the specimens of non-foamed binder and foamed binder.**

Figure 3 shows water droplets on top of foamed concrete with replacement of limestone powder by surface treated hydrophobic clag. Figure 4 shows the contact angles of 2 randomly selected location. The contact angles of both locations are greater than 90° that means the matrix is modified from hydrophilic to hydrophobic. The drying shrinkage measurement and compressive strength test is still ongoing.



**Figure 3. Water droplets on hydrophobic foamed concrete.**



**Figure 4. Contact angle measurement of 2 randomly selected locations of foamed concrete with surface treated hydrophobic clag.**

#### 4. Conclusions

In this paper, the drying shrinkage of foamed mortar was investigated by measuring the drying shrinkage of non-foamed mortar blended with OPC, GGBS, CSA, calcined magnesium oxide, condensed silica fume and limestone powder. This methodology was verified by selecting 3 sets of mix to compare the drying shrinkage of foamed and non-foamed mortar with identical constituents with different densities. The optimal drying shrinkage of non-foamed mortar could be reduced to comparable to normal concrete. Finally, the modification of hydrophilic cement mortar to water-repelling matrix by using surface treated hydrophobic clag was demonstrated.

#### 5. Acknowledgement

The work of this paper is sponsored by CC003/12 from Nano and Advanced Materials Institute Limited.

#### 6. References

1. YANG, K.-., LEE, K.-., SONG, J.-. and GONG, M.-., 2014. Properties and sustainability of alkali-activated slag foamed concrete. *Journal of Cleaner Production*, **68**, pp. 226-233.
2. JUST, A. and MIDDENDORF, B., 2009. Microstructure of high-strength foam concrete. *Materials Characterization*, **60**(7), pp. 741-748.
3. ZHANG, Z., PROVVIS, J.L., REID, A. and WANG, H., 2014. Geopolymer foam concrete: An emerging material for sustainable construction. *Construction and Building Materials*, **56**, pp. 113-127.
4. KAWASHIMA, S., KIM, J.H., CORR, D.J. and SHAH, S.P., 2012. Study of the mechanisms underlying the fresh-state response of cementitious materials modified with nanoclays. *Construction and Building Materials*, **36**, pp. 749-757.
5. WINNEFELD, F. and LOTHENBACH, B., 2010. Hydration of calcium sulfoaluminate cements - Experimental findings and thermodynamic modelling. *Cement and Concrete Research*, **40**(8), pp. 1239-1247.

# A Resistivity-Based Approach to Indicate Chloride Permeability of Geopolymer Concrete

Amin Noushini<sup>1</sup> and Arnaud Castel<sup>2</sup>

<sup>1</sup>PhD Candidate, Centre for Infrastructure Engineering and Safety, School of Civil and Environmental Engineering, University of New South Wales, Australia

<sup>2</sup>Professor of Structural Engineering, Centre for Infrastructure Engineering and Safety, School of Civil and Environmental Engineering, University of New South Wales, Australia

**Abstract:** Chloride ion penetration in concrete is one of the major causes of deterioration of reinforced concrete structures by depassivation of reinforcing bars. Since testing of the natural chloride penetration is time consuming, utilising an accelerated test method is more desirable. Surface resistivity (SR) test is increasingly being used, due to its relative speed and ease of performing combined with the non-destructive nature, to assess the permeability of concrete and its resistance to chloride ion penetration. The test has been standardised as AASHTO TP 95 which consists of measuring the resistivity of water-saturated concrete cylinders using a four-pin Wenner probe array. This paper presents the results of an experimental investigation on the surface resistivity (SR) of a low-calcium fly ash-based geopolymer concrete (GPC). SR test results show that the resistivity of GPC samples are very low, this does not necessarily mean that they are having a high level of chloride penetrability since the AASHTO TP 95 limits are only applicable for conventional OPC concrete and not for the GPC. In case of geopolymer concrete, there are a large amount of mobile metallic ions such as Na<sup>+</sup> in the pore solution which could probably affect the resistivity test measurements. A further study is required to directly measure the chloride permeability of the GPC such as natural diffusion or ponding test to be able to properly correlate the surface resistivity measurements of GPC to its actual chloride permeability level.

**Keywords:** geopolymer concrete, surface resistivity (SR) test, chloride diffusion, permeability.

## 1. Introduction

Chloride ion penetration in concrete is one of the major causes of deterioration of reinforced concrete structures by depassivation of reinforcing bars [1]. The time taken by the chloride ions to reach the rebar and initiate corrosion depends on factors such as; mechanism of intrusion, external concentration of the chlorides, the transport rate of Cl<sup>-</sup> ions into concrete, the microstructure of the material and the matrix chloride binding capacity [1], [2].

Ion transport can take place by diffusion or by capillary suction [2]. In a completely water-saturated concrete, chlorides penetrate by pure diffusion mechanism due to the concentration gradients. However, in the case of partially saturated concrete, chloride ions penetrate by absorption, capillary forces or dissolving in the maritime fogs micro drops [1].

Since testing of the natural chloride penetration is time consuming, utilising an accelerated test method is more desirable. Rapid chloride permeability (RCP) test which has been first developed by Whiting (1981) and standardised as ASTM C1202, is an eminent test method using an electrical field. A potential difference of 60 V dc is applied to a 50 mm thick concrete disc over a 6 h period and the total charge passed, in coulombs, is used as an indication of chloride permeability of concrete. Although the RCP test is relatively simple and quick, the high voltage used causes heating and microcracking of the test specimen and the total current passed corresponds to the movement of all the ions (not only the Cl<sup>-</sup> ions) in the pore solution of the concrete. Considering the above mentioned uncertainties, the RCP test method may only be used as an approximate indication of concrete permeability.

Surface resistivity (SR) test is another accelerated test method which is increasingly being used, due to its relative speed and ease of performing combined with the non-destructive nature, to assess the permeability of concrete and its resistance to chloride ion penetration. The test has been standardised as AASHTO TP 95 which consists of measuring the resistivity of water-saturated concrete cylinders using a 4-pin Wenner probe array.

**Table 1. SR values to determine chloride ion penetrability in accordance with AASHTO TP 95-11 criteria**

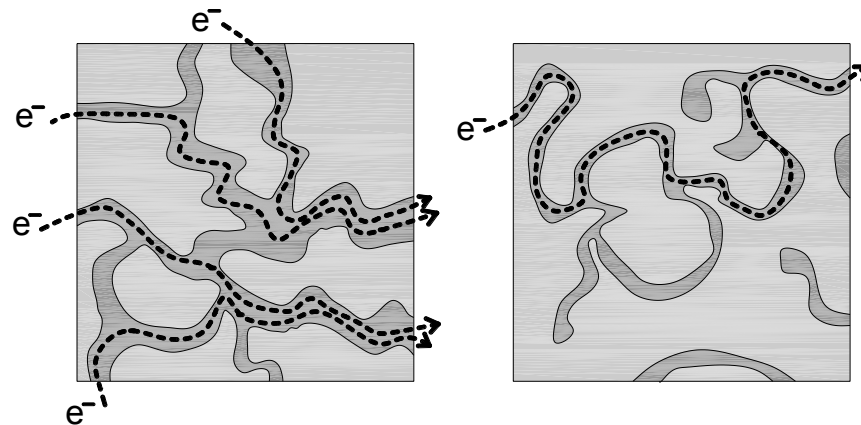
Chloride ion penetrability	Surface resistivity [ $k\Omega\text{-cm}$ ] SR test - AASHTO TP 95
High	< 12
Moderate	12 – 21
Low	21 – 37
Very low	37 – 254
Negligible	> 254

Previous research works [4]–[6] have demonstrated that SR test results can be related to chloride diffusivity and also to chloride ion penetrability (RCP test results) of conventional Portland cement and blended cement concrete. Furthermore, since SR test is non-destructive and can be applied to the same specimen at different ages, changes in resistivity over time can be used to evaluate the rate of microstructure development, pore refinement and strength development.

Resistivity is an intrinsic property of a material that indicates how resistant the material is to the flow of electric current. The factors that mainly influence the resistivity of concrete are similar to those that affect its permeability [7]. When a voltage is applied to concrete, it creates an electric potential gradient which drives the flow of electrons through the concrete (**Figure 1**). The electrons flow mainly through the saturated complex and multi-scale porosity in the concrete matrix structure. Although the flow of electrons through the aggregate and hardened binders is also possible, it plays a smaller role due to the higher resistivity of these materials [7].

As it is graphically illustrated in **Figure 1**, the concrete containing less interconnected pores with a more tortuous path will have a higher electrical resistivity as it would be more difficult for electrons to pass through these kinds of pore network. Accordingly, the measurements of concrete electrical resistivity can provide a good indicator of its permeability since both properties are mainly controlled by the tortuosity of the pore network. More compacted microstructures which tend to have more complex and refined pore networks result in a higher tortuosity and a lower permeability, whereas, less-dense microstructures (resulting for instance from a higher water to binder (w/b) ratio) would have greater porosity, lower tortuosity and higher permeability [7].

It worth mentioning that, to some extent, other factors including pore solution chemistry, curing conditions, temperature and moisture content could also affect the concrete's resistivity [8].



**Figure 1. Schematic representation of electron flow through saturated concrete mixtures: (left) highly porous microstructure; (right) dense microstructure [7].**

In this paper, the resistivity of a low-calcium fly ash-based geopolymer concrete (GPC) is investigated. Twelve different heat-cured GPC samples are studied for their surface resistivity after 28 days of age. The curing regimes include 3 temperatures of 60, 75 and 90 degree Celsius as well as 4 different curing durations of 8, 12, 18 and 24 hours. An ordinary Portland cement concrete (OPCC) having the same amount of binder and aggregate and being cured under the same conditions as the GPCs is also included

in the experiments as the reference point for comparisons. The surface resistivity results are compared to the ones obtained using the ultrasonic pulse velocity test which is another test method to assess the concrete microstructure and compactness.

## 2. Materials and mixing

Geopolymer concrete is produced by the alkali activation of aluminosilicate raw material, which is transformed into a reaction product by polymerization in a high pH environment under hydrothermal conditions at relatively low temperatures [9]. With regard to matrix formation, geopolymer paste differs substantially from ordinary Portland cement paste. While Portland cement relies on the presence of calcium, geopolymer does not utilize the formation of calcium silicate hydrates (C-S-H) for matrix formation and strength. Geopolymer contains aluminium and silicon species that are soluble in highly alkaline solutions. The dissolved species then undergo polycondensation to attain matrix structural integrity [10].

Three different sources of aluminosilicate materials have been used in this study in order to prepare the GPC mixes. A low-calcium type (ASTM C 618 Class F) fly ash (FA), sourced from Eraring Power Station in New South Wales, Australia, has been used. The fineness of FA by 45  $\mu\text{m}$  sieve was determined to be 87% passing (tested in accordance with AS 3583.1-1998). A special grade (ultra-fine) fly ash branded as Kaolite High Performance Ash (HPA) by Cement Australia has also been used as the second aluminosilicate source. The Kaolite HPA was obtained from Callide Power Station in Queensland, Australia. And finally, ground granulated blast furnace slag (GGBFS) supplied by Blue Circle Southern Cement Australia was used as the third aluminosilicate source of the geopolymer binding system.

The alkaline activator used is a mixture of sodium hydroxide (NaOH) solution and sodium silicate ( $\text{Na}_2\text{SiO}_3$ ) solution. The ratio of sodium silicate to sodium hydroxide solution used was 2.5:1 (by mass), according to the study conducted by Hardjito and Rangan [11] showing that more consistent test results could be achieved by using this ratio.

The sodium hydroxide solution used was prepared by dissolving the technical grade NaOH pellets in water. The sodium hydroxide white pellets with a purity of at least 98% were supplied by Ajax Finechem under the commercial brand of UNIVAR A-302. These pellets have a molecular weight of 40, a specific gravity of 2.1 and a pH of approximately 14. The concentration of sodium hydroxide solution used is 12 molar (M) consisted of 480 grams (g) of NaOH pellets per litre of NaOH solution or 361 g of NaOH pellets per kg of NaOH solution. The Sydney tap water was used in this study as the solvent to produce the NaOH solution.

The sodium silicate solution used, which was manufactured by PQ Australia under the commercial name of Vistrol D-A53 or grade D, has a chemical composition of  $\text{Na}_2\text{O}=14.7\%$ ,  $\text{SiO}_2=29.4\%$ , and  $\text{H}_2\text{O}=55.9\%$  (by mass). The  $\text{Na}_2\text{SiO}_3$  solution used, also known as waterglass, is a thick adhesive liquid with a viscosity of 400 cps at 20 °C, has a specific gravity of 1.53 and a pH of 12.9 (values provided by supplier, PQ Australia). Both alkaline solutions were prepared and mixed together 1 day prior to usage.

A maximum nominal size of 10 mm aggregate was used in this study. Sydney sand with specific gravity of 2.65 and water absorption of 3.5% was used as fine aggregate and 10 mm crushed basalt gravel, also known as blue metal, with specific gravity of 2.8 and water absorption of 1.6% was used as coarse aggregate. All aggregate was kiln dried at 105 °C for a period of 48 hours prior to batching. The drying procedure which removes all the moisture content of the aggregate and also the organic particles in sand could help to more accurately adjust the mix water and consequently enhance the consistency of the GPC.

Mix proportioning of the raw material ingredients, as shown in **Table 2**, was carried out by mass. For OPCC, mixing was performed in accordance with AS 1012.2 [12]. for GPC the below mixing sequence was followed. Using a vertical pan mixer, the solid constituents except for GGBFS were firstly dry mixed for 5 minutes to achieve a uniform dispersion. The alkaline activator solution and water were then gradually added and further mixed for 15 minutes. The longer mixing time could help to increase the rate of leaching and transportation of Al and Si atoms in the geopolymer mixture which leads to enhanced strength of the GPC [13]. Lastly, the GGBFS was introduced and mixing continued for another 5 minutes.

The reason for adding slag at the end of the mixing procedure is to prevent rapid hardening of the mixture due to high calcium content of GGBFS and to allow for sufficient workable time to complete casting.

Slump was measured to check the workability and, thereafter, freshly mixed concrete was placed into moulds and compacted using an external vibrating table to achieve proper consolidation and to minimise the amount of the entrapped air arising within the mix. Meanwhile, the mass per unit volume (density) and air content (AC) tests were also performed.

**Table 2: OPCC and GPC mix proportions (kg per cubic meter)**

Materials	GPC	OPCC
Coarse Aggregate	1221	1221
Fine Aggregate	621	621
FA	272	0
Kaolite HPA	77	0
GGBFS	39	0
Portland cement	0	388
Activator Solution (Na <sub>2</sub> SiO <sub>3</sub> :NaOH = 2.5:1)	194	0
Free Water	13	175
High-range water reducer (HWR)	0	1
Activator to geopolymer binder (SCMs) ratio	0.5	N.A.

Once casting and finishing the surface of all specimens completed, moulds were sealed with the lids and the plastic sheets to prevent excessive loss of moisture. One hour after finishing of the casting, sealed specimens were moved to the oven. 12 different curing conditions applied to the identical concrete samples consists of 3 different temperatures of 60, 75 and 90°C and four curing periods of 8, 12, 18 and 24 hours. After finishing of the heat curing period, samples were demoulded and stored in the controlled room at a temperature of 23 ± 2°C until the testing date.

### 3. Testing methods

#### 3.1 Static mechanical tests

Compressive strength and modulus of elasticity of hardened GPC and OPCCs are measured in accordance with ASTM C39-12 and ASTM C469-14, respectively. Cylindrical specimens of 100 mm diameter by 200 mm height were tested under a load rate control condition in a universal testing machine. The load rate was adjusted to apply a stress rate on the specimen of 0.25 ± 0.05 MPa per second. In order to measure the static chord modulus of elasticity of concrete samples, the axial and circumferential strain has been recorded by means of extensometers/strain gauges mounted on the specimen recording data up to the point equivalent to 40% of the measured maximum compressive strength.

#### 3.2 Surface resistivity (SR) test

The SR test has been performed in accordance with the standard procedure AASHTO TP 95-11. The test consists of measuring the resistivity of vacuum-saturated 100 × 200 mm cylinders by use of a 4-pin Wenner probe array (**Figure 3-right**). An alternative current potential difference is applied at the outer pins of the Wenner array resulting in current flow in the concrete (**Figure 2**). The resultant potential difference between the two inner pins is measured and used to calculate the resistivity of the concrete specimen. Resistivity ( $\rho$ ) can be obtained using Eq. 1.

$$\rho = R \frac{A}{L} = 2\pi a R = 2\pi a \frac{V}{I} \quad (1)$$

where  $\rho$  is resistivity,  $R$  is resistance,  $A$  is area of the element and  $L$  is the length of element and  $a$  is the spacing between the probs.

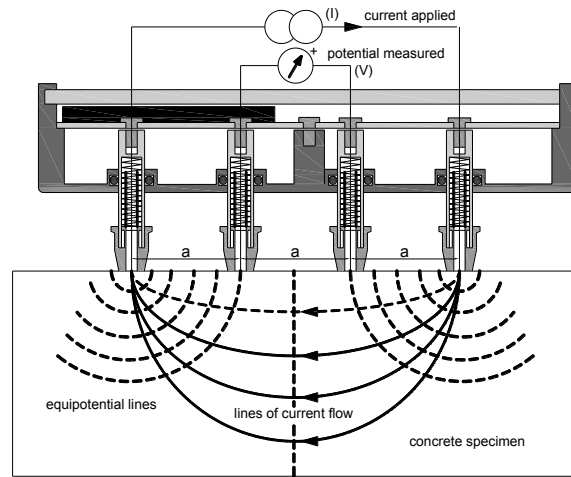


Figure 2. Four-point Wenner array probe setup (AASHTO TP 95-11)

### 3.3 Ultrasonic pulse velocity test

Ultrasonic pulse velocity (UPV) of concrete specimens is measured using PUNDIT (Portable Ultrasonic Non-destructive Digital Indicating Tester) equipment (Figure 3-left). UPV test is conducted on 100 mm diameter concrete cylinders based on the ASTM C597-09 test method. UPV method is based on measuring the velocity of compression stress waves (P-waves) to determine the material characteristics. PUNDIT generates low-frequency ultrasonic waves and measures the time taken for them to pass from one transducer to the other. The velocity of these waves traveling in a solid material depends on the density and elastic properties of material.



Figure 3. Pulse velocity (left) and surface resistivity (right) tests

## 4. Results and discussions

Compressive strength and modulus of elasticity test results of GPC and OPCC specimens are presented in **Table 3**. All the GPCs achieved 68% to 100% of their 28-day strength after 1 day, while this ratio ranges between 55% to 71% for the OPCCs. All the GPCs cured at 75°C and 90°C for 8 to 24 hours reached more than 90% of their 28-day compressive strength after 1 day which is a significant advantage for applications required high early-age strength such as precast industry.

The compressive strength of the geopolymer concretes cured for a short period of time (8 hours and 12 hours), increases with increase in the curing temperature from 60°C to 90°C. However, for a longer period of heat curing (18 hours and 24 hours) the optimum strength is achieved at 75°C. Heat curing at 90°C

leads to a strength reduction. Other researchers [14], [15] observed that curing geopolymer concrete for longer periods of time at elevated temperatures weakens its microstructure resulting in a lower compressive strength.

Among all the different curing durations and temperatures, the GPC cured at 75°C for a period of 24 hours shows the highest compressive strength at 28 days of 62.3 MPa. However, reducing the heat curing duration from 24 hours to 18 hours does not lead to a significant reduction in strength (around 4% reduction). As a result, 18 hours heat curing at 75°C could be considered as the optimum economical heat curing condition for low-calcium FA-based geopolymer concrete. Heat curing at 60°C for a period of less than 18 hours appears not to be a suitable option for the GPC in terms of strength.

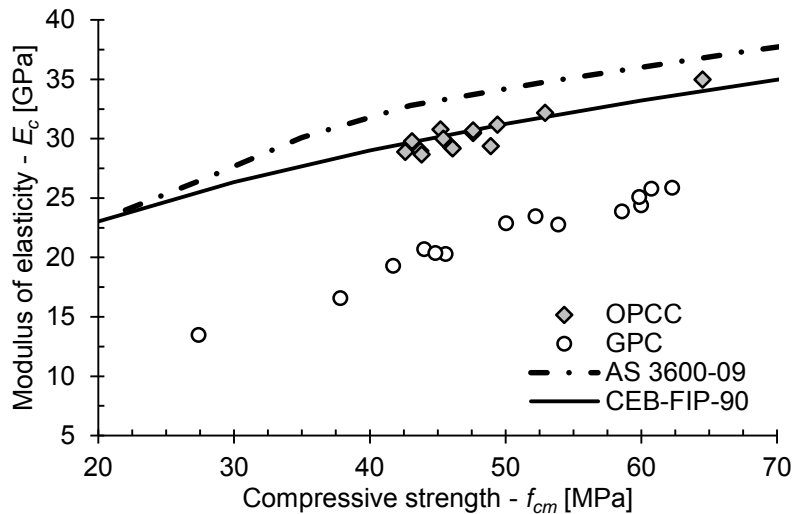
Furthermore, at any age, the compressive strength of GPC properly heat cured (i.e. temperature  $\geq 75^\circ\text{C}$  and duration  $\geq 12$  hours) is higher than that of their counterpart OPC concrete subjected to identical curing condition. The GPC cured at 75°C for 18 hours obtained a similar strength grade (only 7% lower) of the lime-water cured (WC) OPC concrete which is known as the ideal curing condition for the OPC concrete. As a result, for applications which require high early-age strength (e.g. precast industry), low calcium FA-based GPC appears to perform better than OPC concrete in term of both early and long term compressive strength.

**Table 3: Properties of GPC and OPCC at the age of 28 days**

Mix Designation	1-d Compressive Strength [MPa $\pm$ SD]	28-d Compressive Strength [MPa $\pm$ SD]	28-d Modulus of Elasticity [GPa]
GPC-60D-8h	18.6 $\pm$ 0.9	27.4 $\pm$ 0.9	13.5
GPC-60D-12h	29.7 $\pm$ 1.4	37.8 $\pm$ 0.3	16.6
GPC-60D-18h	40.8 $\pm$ 0.8	45.6 $\pm$ 0.4	20.3
GPC-60D-24h	43.6 $\pm$ 1.6	50.0 $\pm$ 0.8	22.9
GPC-75D-8h	45.2 $\pm$ 1.9	44.8 $\pm$ 0.2	20.4
GPC-75D-12h	50.5 $\pm$ 0.8	53.9 $\pm$ 0.5	22.8
GPC-75D-18h	55.9 $\pm$ 1.1	60.0 $\pm$ 0.1	24.4
GPC-75D-24h	60.2 $\pm$ 0.3	62.3 $\pm$ 0.2	25.9
GPC-90D-8h	51.1 $\pm$ 0.1	52.2 $\pm$ 0.7	23.5
GPC-90D-12h	54.1 $\pm$ 1.9	58.6 $\pm$ 0.9	23.9
GPC-90D-18h	56.0 $\pm$ 0.6	59.8 $\pm$ 0.2	25.1
GPC-90D-24h	60.5 $\pm$ 1.3	60.7 $\pm$ 1.2	25.8
OPPC-60D-8h	23.6 $\pm$ 0.1	42.6 $\pm$ 0.1	28.9
OPPC-60D-12h	27.1 $\pm$ 0.3	47.6 $\pm$ 0.7	30.5
OPPC-60D-18h	27.8 $\pm$ 0.2	47.6 $\pm$ 1.9	30.7
OPPC-60D-24h	28.7 $\pm$ 0.3	49.4 $\pm$ 0.9	31.2
OPPC-75D-8h	26.0 $\pm$ 1.1	45.2 $\pm$ 1.5	30.8
OPPC-75D-12h	29.0 $\pm$ 1.1	45.4 $\pm$ 0.4	30.0
OPPC-75D-18h	28.2 $\pm$ 0.4	46.0 $\pm$ 0.5	29.3
OPPC-75D-24h	31.4 $\pm$ 0.2	48.9 $\pm$ 0.1	29.4
OPPC-90D-8h	26.1 $\pm$ 0.6	46.1 $\pm$ 1.7	29.2
OPPC-90D-12h	28.5 $\pm$ 0.4	43.1 $\pm$ 0.4	29.8
OPPC-90D-18h	29.5 $\pm$ 0.6	43.7 $\pm$ 0.5	29.0
OPPC-90D-24h	31.3 $\pm$ 0.5	43.8 $\pm$ 0.9	28.7

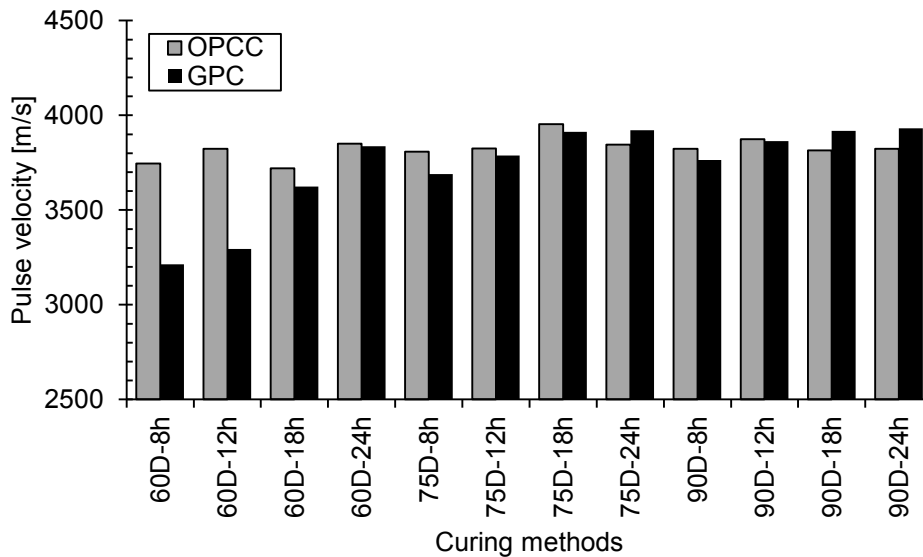
From the results listed in **Table 3**, it could be noticed that the modulus of elasticity of GPCs are significantly lower than that of OPCCs for all the curing condition. GPCs are having a modulus of elasticity ranging between 13.5 GPa to 25.9 GPa which is equal to 47% to 90% of the modulus of elasticity of their counterpart OPCC cured in the same condition. The low modulus of elasticity of the GPC is attributed to the lower modulus of elasticity of the geopolymer paste compared to the OPC paste [16]. In **Figure 4**, the modulus of elasticity of GPCs and OPCCs are plotted against the compressive strength together with the recommended models of the AS 3600 [18] and CEB-FIP-90 [19]. As expected, both the fib model code and the AS model significantly over-estimate the elastic modulus of the GPCs while providing an acceptable prediction for the OPC concrete.





**Figure 4. Relationship between modulus of elasticity of GPC and OPCC**

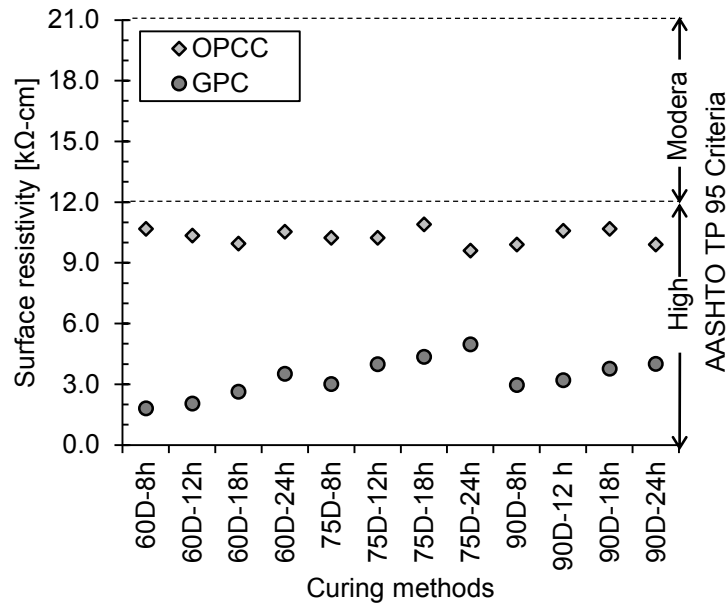
The pulse velocity test results of GPCs and OPCCs are shown in **Figure 5**. It could be observed that the pulse velocity of geopolymers increases with the increase in the curing temperature and duration. Since the speed of the wave varies as a function of the density of material, the increased pulse velocity for GPC shows that increasing the curing temperature up to 75°C and the curing duration to 18 and 24 hours lead to a more integrated matrix with higher density. The UPV results indicating that the appropriate heat-cured GPCs are having a similar or denser microstructure than their counterpart OPCCs.



**Figure 5. Pulse velocity of GPC and OPC concrete specimens after 28 days of age**

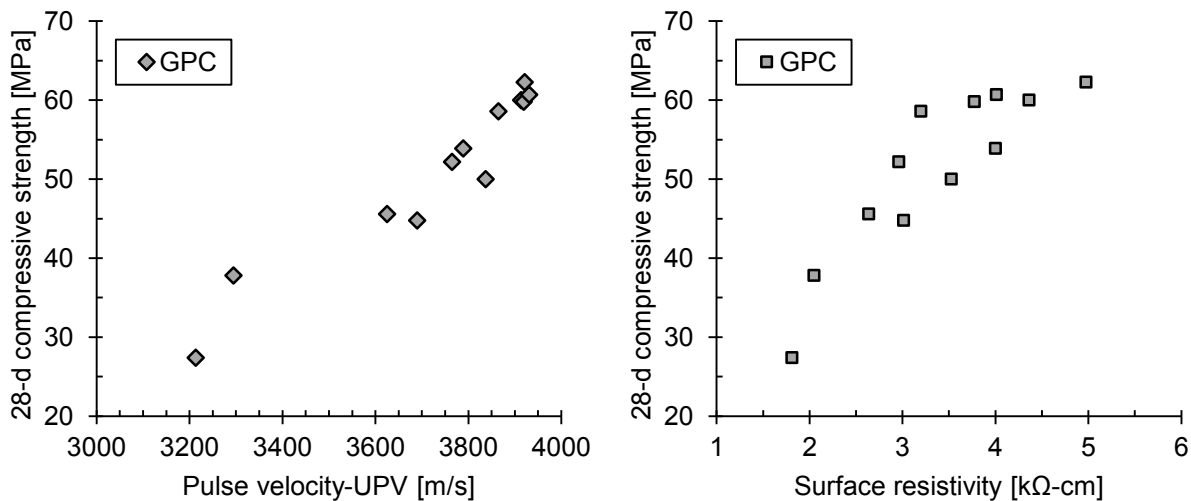
Both GPC and OPCC samples were tested for their surface resistivity after 28 days of age and results are presented in **Figure 6**. Four separate readings were taken around the circumference of the cylinder at 90-degree increments (0°, 90°, 180° and 270°). This process was repeated once again, in order to get a total of eight readings which were then averaged. An in-depth view of the test results show that the resistivity of the GPC samples increases by increasing the curing temperature and duration. This ongoing increase in resistivity is due to a continued geopolymerisation reaction following gelation. As the gel structure develops and becomes more cross-linked, the pore structure would be more disconnected leading to a reduction in the ions/electrons flow. This again confirms the fact that heat curing at 75°C for a

period of 18 to 24 hours could be considered as the optimum curing condition for geopolymer concrete since it leads to the highest achieved resistivity.



**Figure 6. SR test results of GPC and OPCC specimens at the age of 28 days**

As shown in **Figure 7**, there is strong correlation between the pulse velocity and compressive strength of GPC. Although both surface resistivity and pulse velocity of GPC are increasing with the increase in compressive strength, however, the correlation between the surface resistivity and compressive strength seems not to be as good as the UPV. Yet, it could be stated that heat curing improves the microstructure of the GPC and results in a higher strength, performance and density.



**Figure 7. Pulse velocity and surface resistivity of GPCs versus 28-d compressive strength**

However, SR test results show that resistivity of GPCs are much lower than that of their counterpart OPCC which is in contradiction with the UPV test results. From all the results obtained in this study, it could be stated that the surface resistivity test could properly reflect the mechanical and microstructural characteristics of GPC. Although the resistivity of GPC samples are observed to be very low according to the AASHTO TP 95 criteria, this does not necessarily mean that they are having a high level of chloride penetrability since the AASHTO TP 95 is only applicable to conventional OPC concrete and not to the GPC. Basically, the high level of chloride permeability is supposed to be the result of high porosity and high volume of permeable voids in the structure of a material, however, the UPV results indicating that GPCs are having a similar or denser microstructure than their counterpart OPCCs. Thus, there should be

other factors rather than the permeability and porosity (open pore network) which could affect the resistivity of a material and result in the significant reduction in surface resistivity of GPC samples compared to their counterpart OPCC. Conductivity of the pore solution is most probably an important contributor to the conductivity of the final material network structure. In case of geopolymer concrete, there are a large amount of mobile metallic ions such as  $\text{Na}^+$  in the pore solution which may affect the resistivity test measurements.

A further study is required to directly measure the chloride permeability of the GPC such as natural diffusion or ponding test. Identical GPC specimens should be tested for both surface resistivity and chloride permeability in order to set out new criteria against which the chloride penetrability of GPC could be judged.

## 5. Conclusions

Based on the AASHTO TP 95 limits, the low-calcium fly ash-based GPC investigated in this research work is prone to have high level of chloride penetrability since they were showing a very low resistivity. However, the UPV results showed that the GPCs are having a similar or even denser matrix than their counterpart OPCC which should basically results in higher resistivity. The reason for the observed contradiction might be the higher conductivity of the GPC's pore solution compared to OPCC which has nothing to do with chloride penetrability but could significantly affect the SR test measurements.

Hence, the true justification for the use of this accelerated test method (SR test) has to be based on how well the results correlate to long term diffusion test. Therefore, a further study is required to directly measure the chloride permeability of the GPC such as natural diffusion or ponding test. A more comprehensive research on the long term diffusion of the material is currently under process by the authors, following ASTM C1543 and NT BUILD 443 standard test methods, and results will be published in due course.

## 6. Acknowledgement

This research work is funded by the Cooperative Research Centre (CRC) for Low Carbon Living Ltd supported by the Cooperative Research Centres, an Australian Government initiative. The experimental work was carried out in the structures laboratory of the School of Civil and Environmental Engineering at the University of New South Wales. The assistance of the laboratory staff is acknowledged here.

## 5. References

- [1] C. Andrade, "Calculation of chloride diffusion coefficients in concrete from ionic migration measurements," *Cem. Concr. Res.*, vol. 23, no. 3, pp. 724–742, May 1993.
- [2] R. Mejía, S. Delvasto, C. Gutiérrez, and R. Talero, "Chloride diffusion measured by a modified permeability test in normal and blended cements," *Adv. Cem. Res.*, vol. 15, no. 3, pp. 113–118, Jan. 2003.
- [3] D. Whiting, "Rapid determination of the chloride permeability of concrete," Skokie, IL., 1981.
- [4] R. J. Kessler, R. G. Powers, E. Vivas, M. A. Paredes, and Y. P. Virmani., "Surface resistivity as an indicator of concrete chloride penetration resistance," in *Concrete Bridge Conference*, 2008.
- [5] X. Lu, "Application of the Nernst-Einstein equation to concrete," *Cem. Concr. Res.*, vol. 27, no. 2, pp. 293–302, Feb. 1997.
- [6] A. R. Chini, L. C. Muszynski, and J. K. Hicks, "Determination of acceptance permeability characteristics for performance-related specifications for Portland cement concrete," Tallahassee, FL, USA, Jul. 2003.

- [7] E. I. Nadelman and K. E. Kurtis, "A resistivity-based approach to optimizing concrete performance," *Concrete international*, pp. 50–54, 2014.
- [8] O. Sengul and O. E. Gjorv, "Electrical Resistivity Measurements for Quality Control During Concrete Construction," *ACI Mater. J.*, vol. 106, no. 6, 2008.
- [9] H. Rahier, B. Van Mele, M. Biesemans, J. Wastiels, and X. Wu, "Low-temperature synthesized aluminosilicate glasses," *J. Mater. Sci.*, vol. 31, no. 1, pp. 71–79, Jan. 1996.
- [10] Z. Pan, K. N. Feng, K. Gong, B. Zou, A. H. Korayem, J. Sanjayan, W. H. Duan, and F. Collins, "Damping and microstructure of fly ash-based geopolymers," *J. Mater. Sci.*, vol. 48, no. 8, pp. 3128–3137, Dec. 2012.
- [11] D. Hardjito and B. V. Rangan, "Development and Properties of Low Calcium Fly Ash Based Geopolymer Concrete," Perth, Australia, 2005.
- [12] AS, *AS 1012.2: Methods of testing concrete - Preparing concrete mixes in the laboratory*. Sydney, NSW, Australia: Standrads Australia, 2014.
- [13] H. Xu, "Geopolymerisation of Aluminosilicate Minerals," University of Melbourne, Australia, 2002.
- [14] J. G. . van Jaarsveld, J. S. . van Deventer, and G. . Lukey, "The effect of composition and temperature on the properties of fly ash- and kaolinite-based geopolymers," *Chem. Eng. J.*, vol. 89, no. 1–3, pp. 63–73, Oct. 2002.
- [15] K. Komnitsas and D. Zaharaki, "Geopolymerisation: A review and prospects for the minerals industry," *Miner. Eng.*, vol. 20, no. 14, pp. 1261–1277, Nov. 2007.
- [16] Z. Pan, J. G. Sanjayan, and B. V. Rangan, "Fracture properties of geopolymer paste and concrete," *Magazine of Concrete Research*, vol. 63, no. 10. Thomas Telford, pp. 763–771, 01-Oct-2011.
- [17] ACI, *ACI 318: Building code requirements for structural concrete*. United States, 1999.
- [18] AS, *AS 3600: Concrete Structures*. Sydney, NSW, Australia, 2009.
- [19] CEB-FIP, *CEB-FIP Model Code 1990: Concrete Structures*. Lausanne, Switzerland, 1990.
- [20] fib, *MC2010: fib Model Code 2010*. Lausanne, Switzerland, 2010.

# Chloride induced Corrosion of reinforcing bars in Geopolymer concrete

M. Babae<sup>1</sup> and A. Castel<sup>2</sup>

<sup>1</sup>PhD candidate, Centre for Infrastructure Engineering and Safety, School of Civil and Environmental Engineering, The University of New South Wales, Sydney, NSW, Australia

<sup>2</sup>Associate professor, Centre for Infrastructure Engineering and Safety, School of Civil and Environmental Engineering, The University of New South Wales, Sydney, NSW, Australia

**Abstract:** Geopolymer concrete (GPC) is considered as a very interesting alternative for ordinary Portland cement (OPC) concrete, because it needs less energy and emits a lot less carbon dioxide during the production process; which comes from employing industrial by-product precursors such as fly ash and Ground Granulated Blast Furnace Slag (GGBS). Reaction of these materials which are rich in aluminium and silicate with alkalis will form a highly cross-linked aluminosilicate binder which can develop high early-age mechanical strength and has a good performance in elevated temperatures, freezing-thawing cycles and against chemical attacks. However; there are some concerns over the durability aspects of these types of concretes and their long-term performance have yet to be assessed; particularly when it comes to the corrosion of reinforcing bars in GPC. In the current paper, the results of corrosion experiments on a number of chloride contaminated reinforced GPC samples which are manufacture using a blended low calcium (class F) fly ash and slag cement are reported. The initiation phase of corrosion is accelerated to study the propagation phase. Corrosion parameters such as free corrosion potential, polarization resistance and Tafel constants are investigated and compared to the reported values for OPC concrete. Direct mass loss measurement is carried out as well. Results show that the conventional test protocols which are used for OPC concrete can be applied to GPC. Besides, GPC can perform as well as a similar strength OPC concrete during the propagation phase of corrosion in marine environments.

**Keywords:** Geopolymer Concrete, Low-Calcium Fly Ash, Durability, Corrosion

## 1. Introduction

Over the last two decades, geopolymer concretes (GPC) have emerged as novel engineering materials with the potential to become a substantial element in an environmentally sustainable construction and building products industry [1–4]. GPC is the result of the reaction of materials containing aluminosilicate with an alkali solution to produce an inorganic polymer binder. Industrial waste materials such as fly ash and blast furnace slag are commonly used as the source of aluminosilicate for the manufacture of GPC due to the low cost and wide availability of these materials. Geopolymer binders can provide reduction of embodied CO<sub>2</sub> of up to 80% compared to OPC binders. Despite the very different chemical composition and reactions of geopolymer binders they exhibit many of the characteristics of traditional concretes [5,6]. The workability of freshly mixed geopolymer concretes and the mechanical characteristics of the hardened material appear to be similar to those for traditional OPC concretes. However, the quantity of available durability data such as chloride ingress properties or corrosion rate of embedded reinforcing steels, is limited and the long-term performance of GPC structures is yet to be determined [4]. Low calcium fly ash (Class F) GPC has been reported by some researchers to have lower chloride diffusion coefficients, chloride content and porosity compared to high calcium (Class C) fly ash GPC and OPC concrete [9], while others have found that the exact raw materials and mixture design can result in varying performance [10]. Previous studies reveal that due to the high alkalinity of the pore system, fly ash based geopolymeric binders can passivate the reinforcement steel as effectively as Portland cement binders [11–15]. Type and concentration of the alkaline activators have also been found to play a very important role in the stability of passive film [16,11,15]. While performance of fly ash GPC is observed to be similar to OPC concrete in passive state [12,15], There is not a consensus among researchers regarding the performance of low-calcium fly ash GPC compared to OPC concrete in severe marine environments during the propagation phase of corrosion [15,17,18].

In this paper, tests carried out using a blended class F fly ash and slag reinforced GPC are reported. Corrosion experiments were performed in order to assess the evolution of the steel corrosion potential and the linear polarization resistance with the chloride contamination. The Tafel constants are evaluated as well. The work aims to assess if existing testing methods and recommendations commonly used for OPC based concrete are suitable for GPC.

## 2. Experimental program

### 2.1 Geopolymer concrete mix and batching

The mix proportioning of the raw material as well as the stockpile/supplier details are provided in Table 1. The aggregate's mass shown in Table 1 is in the saturated surface dry (SSD) condition. The alkaline solution used was a mixture of 12 molar sodium hydroxide (NaOH) solution and sodium silicate ( $\text{Na}_2\text{SiO}_3$ ) solution with a ratio of 1:2.5 (by mass).

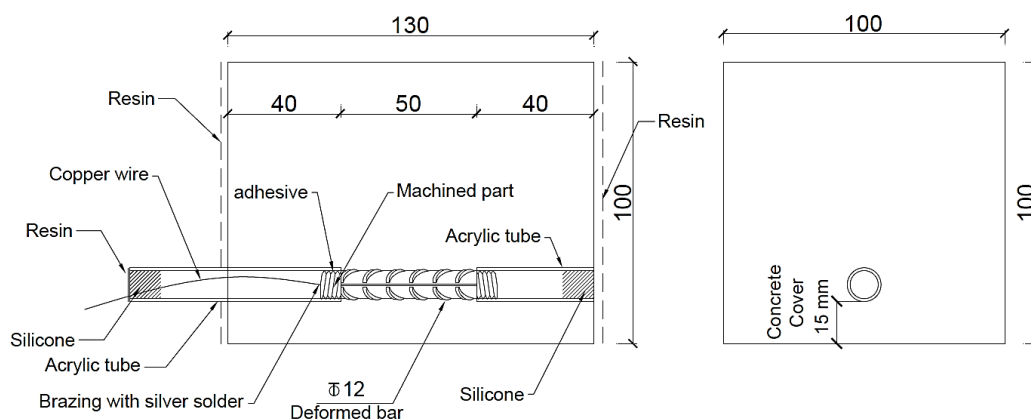
**Table 1: GPC mix proportions**

Material	Kg/m <sup>3</sup>
Coarse aggregate (10 mm nominal size crushed basalt)	1135
Fine aggregate (Sydney sand)	705
FA (Eraring Power Station, New South Wales, Australia)	200
Kaolite HPA (Callide Power Station, Queensland, Australia)	55
GGBFS (Blue Circle Southern Cement Australia)	45
Sodium hydroxide solution (NaOH)	45.7
Sodium silicate solution ( $\text{Na}_2\text{SiO}_3$ )	114.3
Free water	60

After casting, moulds were sealed and stored in a humidity chamber at 40°C for 24, followed by another 24 hours of curing at 80°C in hot water bath. Thereafter, samples were stored in a controlled room with a fixed temperature of  $23 \pm 2$  °C and relative humidity (RH) of 50% until the testing dates. The average compressive strength and elastic modulus of the concrete at 28 days were 54.5 MPa and 23.8 GPa respectively.

### 2.2 Corrosion experiments

To prohibit any external corrosion, normal ductility grade, 12 mm deformed bars with 500 MPa yield strength were embedded in the concrete. The deformed bars were cut and machined at both ends and then glued together with acrylic tubes. An electrical wire was welded on each steel bar to perform electrochemical measurements (**Figure 1**). The initiation period of the chloride-induced corrosion process (i.e. chloride diffusion through the concrete cover) was accelerated by drying samples in the oven, followed by alternative wetting/drying cycles in 35 gr/l NaCl solution and in controlled room respectively. This method has been already used for traditional OPC concrete [19] and allows obtaining a total chloride content of around 0.6% of binder mass after only 24 hours of immersion, which is beyond the suggested threshold chloride concentration values required to destroy the passive layer around the bars [20,21].



**Figure 1: GPC Specimen configuration**

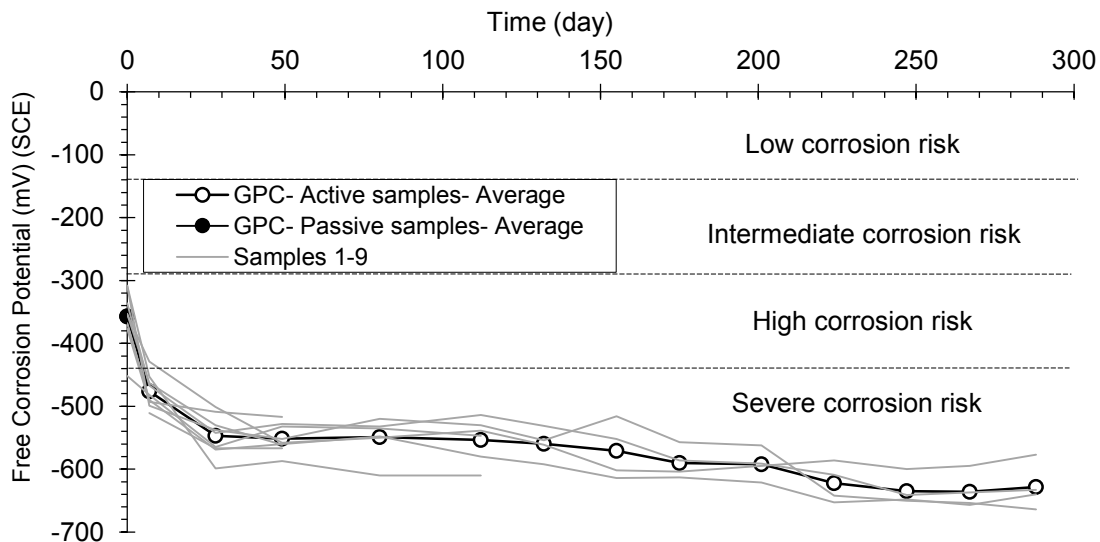
Alongside with the 9 active samples whose initiation phase of corrosion was accelerated, 6 samples were submerged in tap water for 6 weeks to be saturated and used for passive condition corrosion assessment. Electrochemical measurements are performed using a potentiostat. Free corrosion potential ( $E_{corr}$ ) was determined by open circuit measuring of the potential difference between the reinforcing bar and a saturated calomel reference electrode (SCE) while the stability of the half-cell potential was controlled beforehand. In order to monitor the time-dependent corrosion activity, the linear polarization resistance technique (LPR) was carried out in a limited range of over-potentials ( $E-E_{corr}= -20$  to  $+20$  mV) to avoid introducing any irreversible change into the system. To measure the corrosion current density and consequently the electrochemical mass loss by means of Faraday law, the destructive Tafel tests were conducted over a large range of overpotentials ( $E-E_{corr}= -200$  to  $+200$  mV) at 5 different time steps for active samples within the whole period of experimental program. The Tafel constants were measured to calculate the “B” parameter in the Stern-Geary equation [22,23]:

$$I_{corr} = \frac{\beta_a \beta_c}{2.3 R_p (\beta_a + \beta_c)} = \frac{B}{R_p} \quad \text{(Equation 1)}$$

Where  $I_{corr}$  is the corrosion current,  $R_p$  is the polarization resistance measured by conducting a LPR test and  $\beta_a$  and  $\beta_c$  are anodic and cathodic Tafel constants, respectively. A sweep rate of 10 mV/min is used for both LPR and Tafel tests [24]. To verify the results of LPR tests, Gravimetric mass loss measurements were conducted on samples which had been already used for Tafel tests based on the ASTM G1-03 protocols [25].

### 3. Experimental results

**Figure 2** shows variation of the corrosion potential ( $E_{corr}$ ) values and compares them to the reference values [26] which are commonly used to assess the corrosion state of OPC concrete structures. Since the active samples were also used to carry out the destructive Tafel test throughout the monitoring period, the average values are representative of only 4 data points at the end of the testing period.

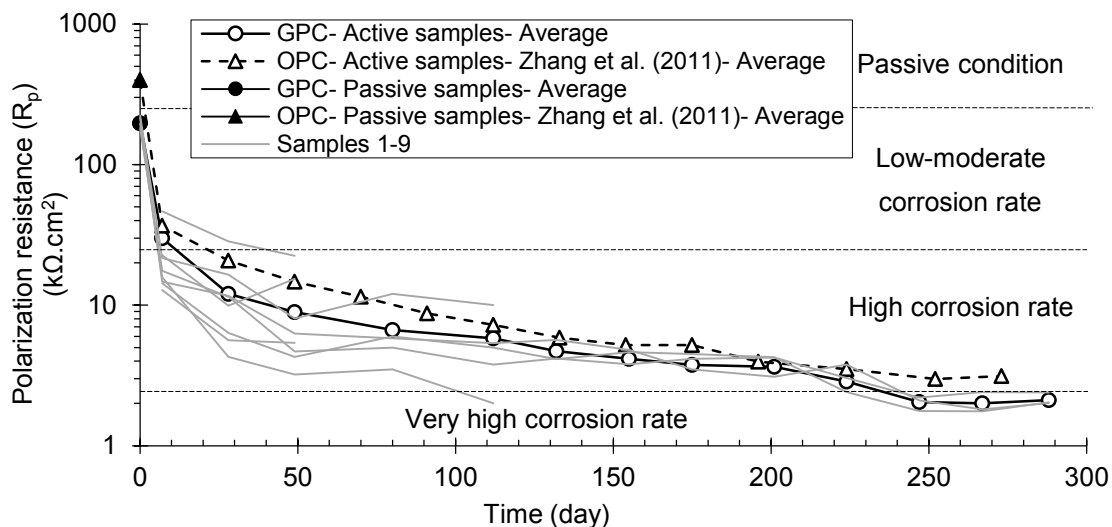


**Figure 2: Evolution of the average free corrosion potential ( $E_{corr}$ ) and the suggested reference values for OPC concrete (the initiation phase is accelerated)**

After only 7 days in the chloride solution, the measured corrosion potentials fall into the severe corrosion zone which can be attributed to the initial very low corrosion potential and the high chloride content of

samples due to the oven drying (accelerating the initiation phase). The corrosion potential reduction is about -200 mV in average which is comparable to the potential drop criterion which is used to distinguish between the passive and active steel reinforcements in OPC concrete [27,28]. Thus, the corrosion potential method seems to be suitable to assess qualitatively steel corrosion in GPC. However, the absolute value of the average corrosion potential of passive specimens (before chloride contamination) is more negative than the range in which reinforced Portland cement concretes are considered passive (i.e.  $E_{corr} > -140$  mV vs SCE). The more negative values are not necessarily indicative of a higher risk of corrosion; this can be attributed to a high concrete moisture content and lack of oxygen at the steel-concrete interface [29]. After 28 days, all the values have remained in the severe corrosion zone throughout the testing period; although, The absolute values of corrosion potentials are more negative than the reported figures for OPC concrete in active phase of corrosion, ranging between -550 and -650 mV vs SCE. These experimental results highlights the need for carefully interpretation of the measured corrosion potential values when assessing corrosion in reinforced GPC by using the reference values of corrosion potential commonly used for OPC concrete.

**Figure 3** shows the measured  $R_p$  values of GPC samples compared to Andrade and Alonso [23] recommendations for OPC concretes. Also, results of a set of similar tests on OPC concrete samples from Zhang et al. [19] with a similar fabrication method and almost the same exposure condition as the current study is presented in **Figure 3**. The presented OPC concrete results are the average of four data points. The  $R_p$  trend is consistent with the corrosion potential trend and the polarization resistance values fall into the high corrosion rate range after just two cycles of exposure to NaCl solution which means the initiation phase is successfully accelerated. The measured polarization resistance of passive specimens (the data point at day 0) are lower than expected according to Andrade and Alonso [23] recommendations (i.e.  $R_p > 250$  k $\Omega$ .cm $^2$  for passive samples). This suggests that the OPC concrete classifications might not be suitable for GPC samples in passive state. Moreover, the average polarization resistance trends for GPC and OPC concrete samples exhibit a remarkably good match and as a result, a similar performance of Portland cement binders and geopolymer binders in chloride contaminated environments during the propagation phase of corrosion (after depassivation of reinforcing bars) can be concluded.



**Figure 3: Polarization resistance for GPC and OPC concrete specimens before and after immersion in the chloride solution along with the suggested reference values for OPC concrete (the initiation phase is accelerated)**

By polarizing samples over a large range of over-potentials and using the Tafel plot method, parameters such as Tafel constants (and hence the B coefficient in Stern & Geary equation [22]) and corrosion current densities (and consequently electrochemical mass loss by means of Faraday law [23]) are calculated and presented in Table 2. It can be implied that using the conventional value of  $B=26$  [30] which is commonly used to calculate the corrosion current density of corroding OPC concrete systems instead of the actual values of B coefficient can lead to erroneous results when applied to GPC samples. Moreover, the recorded



values of predicted mass loss to actual mass loss ratios are similar to the reported values for corroding OPC concrete systems [30] which suggests that the employed electrochemical techniques have predicted the mass loss within a reasonable level of accuracy.

**Table 2: Stern-Geary “B” coefficient, predicted and actual mass losses**

Time after the first Immersion (day)	B (mV)	Electrochemical mass loss (mg/cm <sup>2</sup> )	Gravimetric mass loss (mg/cm <sup>2</sup> )
49	57	4.28	13.66
112	52	12.01	20.35
288	55	62	26.14
336	46	82.93	61.46

### 3. Conclusion

The work aimed to assess the performance of reinforced GPC in chloride contaminated environment during the propagation phase of corrosion and examine if existing testing methods and recommendations commonly used for OPC based concrete to assess steel corrosion are suitable for low calcium GPC. The half-cell potential measurements and the polarization resistance techniques as well as gravimetric mass loss measurements were used. Results show that both corrosion potential and polarization resistance reduce significantly with chloride contamination with a similar magnitude as the ones usually observed for reinforced OPC concrete. Indeed, both  $E_{corr}$  and  $R_p$  are lower than the reported values for reinforced OPC concrete, particularly in passive state and hence recalibration of the reference values traditionally used for OPC concrete might be required. The electrochemical mass losses compare rather well with the gravimetric mass losses; thus, the employed electrochemical techniques appear to be usable to assess steel corrosion in low calcium fly ash based GPC. However, special consideration should be given to analysing the results of electrochemical tests carried out on reinforced GPC in passive condition. The observed strong similarity between the measured trends of polarization resistance of reinforced GPC samples and their OPC counterparts along with the results of mass loss measurements can be interpreted as the equal performance of GPC and OPC concrete during the propagation phase of corrosion (after depassivation of reinforcing steel) in marine environments.

### 4. Acknowledgement

This research is funded by the CRC for Low Carbon Living Ltd supported by the Cooperative Research Centres program, an Australian Government initiative. The experimental work was carried in the concrete Laboratory of the School of Civil and Environmental Engineering at the University of New South Wales. The assistance of the laboratory staff is also acknowledged.

### 5. References

- [1] P. Duxson, J.L. Provis, G.C. Lukey, J.S.J. van Deventer, The role of inorganic polymer technology in the development of “green concrete,” *Cem. Concr. Res.* 37 (2007) 1590–1597.
- [2] T.S. Ng, S.J. Foster, Development of a mix design methodology for high-performance geopolymer mortars, *Struct. Concr.* 14 (2013) 148–156.
- [3] J.L. Provis, J.S.J. van Deventer, *Geopolymers: Structures, Processing, Properties and Industrial Applications*, 1st ed., Cambridge (UK), Woodhead, 2009.
- [4] J.L. Provis, Y. Muntingh, R.R. Lloyd, H. Xu, L.M. Keyte, L. Lorenzen, et al., Will Geopolymers Stand the Test of Time?, in: *Dev. Porous, Biol. Geopolymer Ceram. Ceram. Eng. Sci. Proceedings*, Vol. 28, Issue 9, John Wiley & Sons, Inc., 2007: pp. 235–248.
- [5] M. Sofi, J.S.J. van Deventer, P.A. Mendis, G.C. Lukey, Engineering properties of inorganic polymer concretes (IPCs), *Cem. Concr. Res.* 37 (2007) 251–257.
- [6] A.M. Fernández-Jiménez, A. Palomo, C. López-Hombrados, Engineering Properties of Alkali-Activated Fly Ash Concrete, *ACI Mater. J.* 103 (2006) 106–112.

- [7] S.A. Bernal, R. Mejía de Gutiérrez, A.L. Pedraza, J.L. Provis, E.D. Rodriguez, S. Delvasto, Effect of binder content on the performance of alkali-activated slag concretes, *Cem. Concr. Res.* 41 (2011) 1–8.
- [8] J.S.J. Van Deventer, J.L. Provis, P. Duxson, Technical and commercial progress in the adoption of geopolymer cement, *Miner. Eng.* 29 (2012) 89–104. doi:10.1016/j.mineng.2011.09.009.
- [9] K. Kupwade-Patil, E.N. Allouche, Examination of Chloride-Induced Corrosion in Reinforced Geopolymer Concretes, *J. Mater. Civ. Eng.* 25 (2013) 1465–1476. doi:10.1061/(ASCE)MT.1943-5533.0000672.
- [10] Y. Muntingh, Durability and diffusive behaviour evaluation of geopolymeric material, (2006).
- [11] R.R. Lloyd, J.L. Provis, J.S.J. van Deventer, Pore solution composition and alkali diffusion in inorganic polymer cement, *Cem. Concr. Res.* 40 (2010) 1386–1392.
- [12] J.M. Miranda, A. Fernández-Jiménez, J.A. González, A. Palomo, Corrosion resistance in activated fly ash mortars, *Cem. Concr. Res.* 35 (2005) 1210–1217.
- [13] M. Sufian Badar, K. Kupwade-Patil, S.A. Bernal, J.L. Provis, E.N. Allouche, Corrosion of steel bars induced by accelerated carbonation in low and high calcium fly ash geopolymer concretes, *Constr. Build. Mater.* 61 (2014) 79–89.
- [14] E. Bastidas-Arteaga, P. Bressolette, A. Chateaneuf, M. Sánchez-Silva, Probabilistic lifetime assessment of RC structures under coupled corrosion–fatigue deterioration processes, *Struct. Saf.* 31 (2009) 84–96.
- [15] A. Fernández-Jiménez, J.M. Miranda, J.A. González, A. Palomo, Estabilidad del estado pasivo del acero en morteros de ceniza volante activada, *Mater. Construcción.* 60 (2010) 51–65. doi:10.3989/mc.2010.53909.
- [16] D.M. Bastidas, A. Fernández-Jiménez, A. Palomo, J.A. González, A study on the passive state stability of steel embedded in activated fly ash mortars, *Corros. Sci.* 50 (2008) 1058–1065.
- [17] D. V. Reddy, J.-B. Edouard, K. Sobhan, Durability of Fly Ash–Based Geopolymer Structural Concrete in the Marine Environment, *J. Mater. Civ. Eng.* 25 (2013) 781–787.
- [18] M. Olivia, H. Nikraz, Properties of fly ash geopolymer concrete designed by Taguchi method, *Mater. Des.* 36 (2012) 191–198.
- [19] R. Zhang, A. Castel, R. François, Influence of steel-concrete interface defects owing to the top-bar effect on the chloride-induced corrosion of reinforcement, *Mag. Concr. Res.* 63 (2011) 773–773–781–781.
- [20] ACI, ACI committee 222: Corrosion of metal in concrete, *Concr. Int.* 7 (1985) 56–59.
- [21] RILEM, RILEM technical committee 124-SRC: Draft recommendation for repair strategies for concrete structures damaged by reinforcement corrosion, *Mater. Struct.* 27 (1994) 415–436. doi:10.1007/BF02473446.
- [22] M. Stern, A.L. Geary, Electrochemical Polarization: I. A Theoretical Analysis of the Shape of Polarization Curves, *J. Electrochem. Soc.* 104 (1957) 56.
- [23] C. Andrade, C. Alonso, Corrosion rate monitoring in the laboratory and on-site, *Constr. Build. Mater.* 10 (1996) 315–328.
- [24] I. Martínez, C. Andrade, Polarization resistance measurements of bars embedded in concrete with different chloride concentrations: EIS and DC comparison, *Mater. Corros.* 62 (2011) 932–942.
- [25] ASTM, ASTM G1 - 03(2011) Standard Practice for Preparing, Cleaning, and Evaluating Corrosion Test Specimens, *ASTM Int.* (2011).
- [26] ASTM, ASTM C876 - 09 Standard Test Method for Corrosion Potentials of Uncoated Reinforcing Steel in Concrete, *ASTM Int.* (2009).
- [27] P. Ghods, O.B. Isgor, G.A. McRae, G.P. Gu, Electrochemical investigation of chloride-induced depassivation of black steel rebar under simulated service conditions, *Corros. Sci.* 52 (2010) 1649–1659.
- [28] V. Garcia, R. François, M. Carcasses, P. Gegout, Potential measurement to determine the chloride threshold concentration that initiates corrosion of reinforcing steel bar in slag concretes, *Mater. Struct.* 47 (2013) 1483–1499.
- [29] H.R. Soleymani, M.E. Ismail, Comparing corrosion measurement methods to assess the corrosion activity of laboratory OPC and HPC concrete specimens, *Cem. Concr. Res.* 34 (2004) 2037–2044.
- [30] C. Andrade, J.A. Gonzalez, Quantitative measurements of corrosion rate of reinforcing steels embedded in concrete using polarization resistance measurements, *Mater. Corros. Und Korrosion.* 29 (1978) 515–519.

# Specifying fly ash for use in geopolymer: A conception of reactivity index

Hao Wang<sup>1</sup>, Zuhua Zhang<sup>1</sup>, John L. Provis<sup>2</sup> and Jin Zou<sup>3</sup>

<sup>1</sup>Centre of Excellence in Engineered Fibre Composites, University of Southern Queensland, West Street, Toowoomba, Queensland, 4350, Australia.

<sup>2</sup>Department of Materials Science and Engineering, The University of Sheffield, Sheffield S1 3JD, United Kingdom.

<sup>3</sup>School of Mechanical and Mining Engineering, and Centre for Microscopy and Microanalysis, The University of Queensland, St Lucia, Queensland 4072, Australia.

**Abstract:** Geopolymer is regarded as a green alternative to the current ordinary Portland cement. It uses industry wastes, such as fly ash, as source materials. Variations between fly ash lead to large differences in the performance of the geopolymer derived from them. This study aims to address the effects of physical, crystallographic and chemical characteristics of fly ash on geopolymerisation performances and the strength of deriving materials. Physical and glass chemistry are combined all these factors together to develop a single parameter, a fly ash reactivity index. This comprehensive index can be a powerful tool in evaluating the suitability of fly ash for the formation of high strength geopolymer, and can be further used to predict the performance of the resulting fly ash-based geopolymer materials. A reliable and predictable geopolymer will be a big step moving the new and greener cement towards the acceptance by industries.

**Keywords:** fly ash, geopolymer, reactivity index, glass, crystalline, particle size.

## 1. The problem of using fly ash as feedstock

Geopolymer is increasingly regarded as greener alternative cement-like binder [1-3]. It is a synthetic inorganic polymer produced by the alkali activation of aluminosilicates. This reaction takes place at room temperature or slightly elevated temperatures, totally bypassing the high temperature calcination process with significantly less energy consumption. By not using limestone, it also eliminates the chemical CO<sub>2</sub> emission during calcium carbonate decomposition, resulting in a binder with low CO<sub>2</sub> emissions [4,5]. Furthermore many industry waste materials, such as power station fly ash [6,7], blast furnace slag [8,9], alumina refinery red mud [10] and reservoir sludge [11], can be used as the aluminosilicate raw materials for geopolymer manufacture. While researchers still debate the reaction mechanism taking place during geopolymerisation, many agree the reaction can be divided into three main stages: (1) dissolution of the source material to form aluminate and silicate species; (2) aluminosilicate gel formation; and (3) condensation forming the 3D network [12], which gives geopolymer a set of properties that are equivalent, or even superior, to those of ordinary Portland cement (OPC).

Fly ash, a waste material from coal fired power stations, is commonly used for geopolymer manufacturing. However, inconsistent mineral compositions of source coal and variations in the combustion process can result in large variations of resulting fly ashes, in terms of the chemical and physical characteristics, varying from one source to another, and sometimes from one batch to another from a single power station. These variations could lead to varying properties of the deriving geopolymer [13-15], which will hinder its acceptance by civil and construction industries [16].

Chemical composition, particle size and morphology of fly ash are commonly used to characterise fly ash. In our previous research [17], five fly ashes with varied compositions were used to study the geopolymer synthesis. The results showed that there was no single correlation between the bulk composition, Si/Al molar ratio, reactive SiO<sub>2</sub> or fly ash particle size and the compressive strength of the derived geopolymers, as shown in Figure 1. Despite the use of many techniques to characterise and classify fly ash for geopolymer synthesis [18-20], the absence of a comprehensive method to effectively evaluate the raw fly ash and its variables has become one of the biggest barriers for geopolymer being fully adopted by the industries, especially in civil and construction industries, where predictable and consistent performance is critical.

In this paper we will present our new understanding on the behavior of fly ash during geopolymerisation, and the effects of physical, chemical and crystallographic factors of fly ash. We introduce the concept of a reactivity index to find a correlation between the fly ash characteristics and the properties of the resulting geopolymer. This proposed reactivity index can be used to assess the suitability of fly ash as the source material for geopolymer; it can also be used in the design of the activator system to match the fly ash

reactivity, which will achieve the maximum geopolymerisation with the minimal residual alkali solution. Knowing the extent of geopolymerisation will make the prediction of the properties of the resulting materials possible.

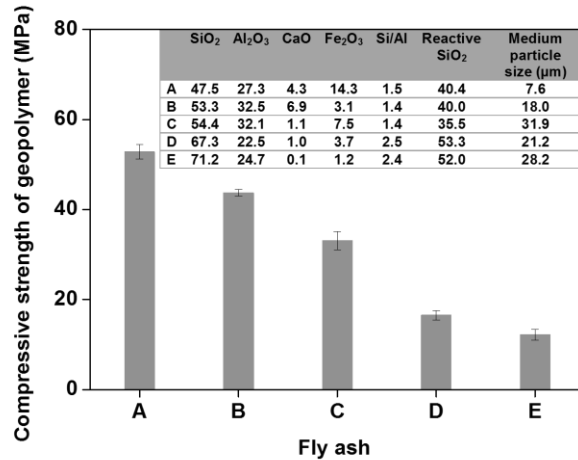


Figure 1. Compressive strength of geopolymers produced from different fly ashes. The inserted table shows the compositions and particle sizes of the ashes [17].

## 2. How the properties of fly ash affect the strength of geopolymer

### 2.1 Physical characteristics

Fly ash typically has a spherical morphology. Figure 2 shows the fly ash particles from fly ash A, B and E. Such a spherical shape is beneficial to the geopolymer formation as it results in good workability at low liquid/solid ratios [21]. The medium particle size for each of the fly ashes is given in Figure 1. Fly ash A has the smallest particle size, with medium size 7.6 µm. Fly ash B and D are in the middle with a particle size of about 20 µm, while fly ash C and E are the largest at about 30 µm. With the assumption that fly ash particles are perfectly spherical, the specific surface area (SSA) can be estimated from the particle size data from a particle size analyser (PSA). The results are listed in Table 1.

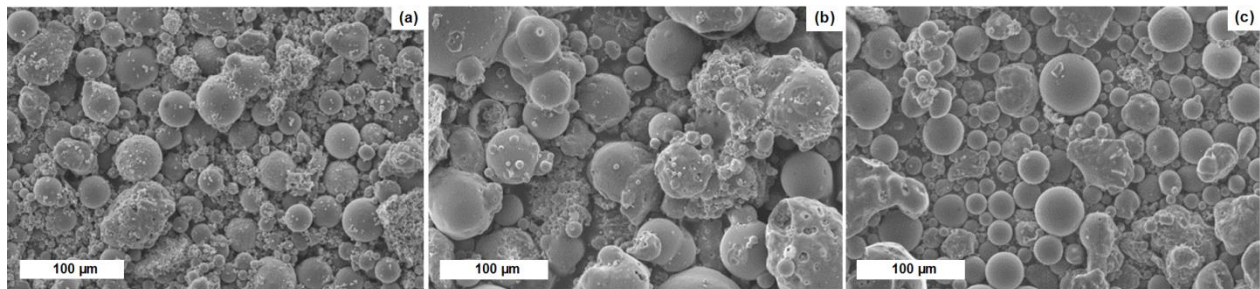


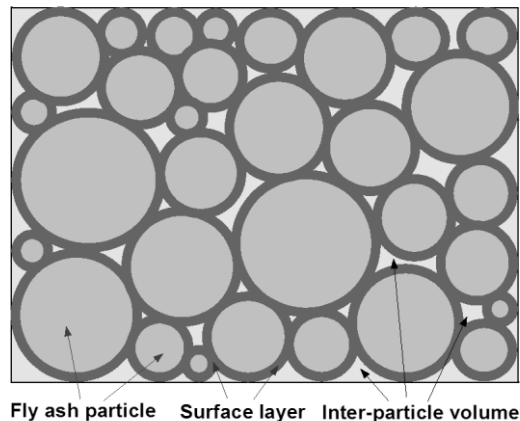
Figure 2. SEM images of fly ashes showing fly ash A (a) has much finer and fewer irregular particles than fly ash B (b) and E (c).

Table 1. Physical characteristics of fly ash particles. Residual carbon is determined by thermogravimetric analysis.

Sample	Geometric SSA by PSA, m <sup>2</sup> /g	Accessible SSA by BET, m <sup>2</sup> /g	Carbonaceous, mass%	Particle density, g/cm <sup>3</sup>	Packing density, g/cm <sup>3</sup>
A	2.1	1.9	0.6	2.3	1.4
B	2.4	2.5	0.5	2.0	1.2
C	0.9	1.2	0.9	2.1	1.4
D	1.0	1.1	0.9	2.0	1.3
E	0.6	0.8	0.7	1.8	0.9

Fly ash B has the highest SSA of 2.4 m<sup>2</sup>/g, followed by fly ash A 2.1 m<sup>2</sup>/g; while fly ash E has the lowest surface area 0.6 m<sup>2</sup>/g. We also used the Brunauer-Emmett-Teller (BET) method [22] to measure the SSA directly. The two sets of SSA have the similar order, however there are differences in the absolute value for a particular fly ash, which is caused by the particle shape and residual carbon. The shape of particles affects the surface wetting [21]. The fly ashes B and E contain many irregular particles (Figure 2), which may require a thicker liquid layer on the surface to overcome the friction for particle sliding. In addition to the particle shape, the residual carbon affects their SSAs and then liquid requirement as well. Table 1 lists the residual carbon as determined by thermogravimetric analysis. In combination with the BET surface areas, it is able to estimate the SSA of carbon particles in each fly ash, in a range of 25 - 60 m<sup>2</sup>/g, which is in agreement with the reported value [23]. The high SSA of the carbon particles leads to a high liquid requirement. In this study, as the residual carbon has not been removed from the samples, we assume that the SSA estimated by PSA is more accurate to describe the fly ash particle characteristic, therefore it is chosen for the evaluation of reactivity of fly ash.

Particle surface area is where the fly ash contacts with the alkaline activator solution and makes the dissolution occur. In the geopolymer formation process, the activator solution wets the fly ash particles, forming a layer of liquid around the surface. We describe this liquid requirement as 'surface layer volume (SLV)', as shown in Figure 3. It is one of the most important physical properties affecting the reactivity of fly ash in geopolymer formation. It has been reported that the SSA of fly ash has a direct correlation to the compressive strength of the derived geopolymers [24]. Our measurement shows that fly ash B has the highest SSA. It would be expected that this fly ash will have the fastest and largest dissolution and geopolymerisation, which will lead to the highest strength. But our strength results show that fly ash A has the highest strength. There must be other factors that contribute to the strength development in geopolymer system.

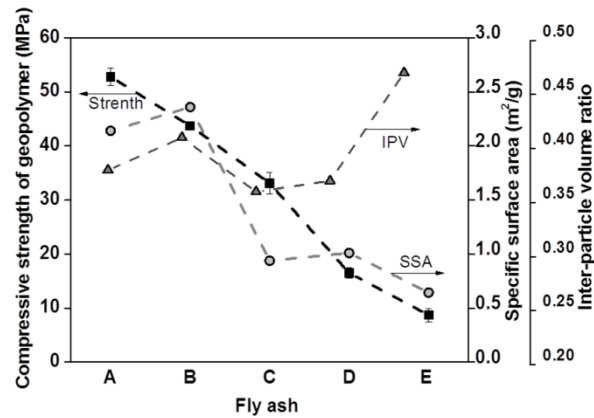


**Figure 3. A sketch of fly ash particles mixed with liquid activator.**

Here we introduce an additional geometric parameter, the inter-particle volume (denoted IPV), as a physical characteristic of fly ash to be incorporated into the ash activity index calculation. As indicated in Figure 3, when polydisperse particles are randomly packed up, small particles fill in the empty spaces between large particles to increase the packing density. However, there are still gaps between particles, forming the IPV. When a liquid activator is mixed with a dry fly ash powder, the SLV contributes to wetting the fly ash particles, while at the same time, additional liquid is required to fill the IPV to reduce the surface tension of activator (to air), lubricating the system to provide a necessary workability to the paste by enabling it to become a coherent fluid rather than a partially-cohesive granular system. For a given volume of fly ash, we are able to calculate the IPV by subtracting the particle volume from the total volume. When a liquid activator is mixed with dry fly ash powder, the SLV contributes to the wetting the fly ash particles. Additional liquid is required to fulfill the IPV to provide a necessary flowability (140-170 mm in this study) for paste. In general, the smaller the IPV, the less liquid required. The total liquid

requirement for a geopolymer system is the sum of the SLV and the IPV, which are determined by particle surface area and packing density, respectively.

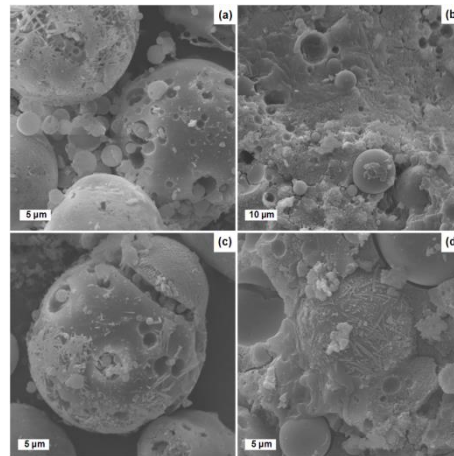
After geopolymerization, the excess liquid which is introduced into the system to provide the workability will eventually evaporate, leaving a certain volume of pores, if the space is not able to be filled by geopolymeric gels. It is well known in conventional cement and concrete systems that a smaller IPV will generate a more compact binder with lower porosity [25]. A lower porosity usually means a higher strength [26]. In Figure 4 we plot the SLV (using SSA) and IPV of the 5 fly ashes together with the compressive strength of the resulting geopolymers. Some kind of correlation is starting to show between the strength and these two physical characteristic parameters. In the 5 fly ashes, SLV is generally proportional to the strength while IPV is inversely proportional to the strength.



**Figure 4.** The relationship between specific surface area and inter-particle volume ratio of fly ash and the compressive strength of deriving geopolymer.

## 2.2 Crystallographic characteristics

Fly ash is the fine particle residue of coal after combustion. During coal combustion (temperatures may exceed 1600°C), most inorganic matters (except quartz) presented in coal particle melt. Molten aluminosilicate droplets cool rapidly and form amorphous, and some as crystalline, phases. The amorphous phase is described as aluminosilicate glass. Quartz and mullite, which are unmelted or crystallised during the melt droplet solidification, are generally presented as crystals in fly ash. Different phases in fly ash have substantially different dissolution rates and extents in alkaline solution [17].



**Figure 5.** SEM images of dissolved fly ashes by sodium silicate solution (4 M NaOH+1.3 M SiO<sub>2</sub>) at a liquid to solid ratio of 35 g/g, 80°C for 6 hours and the residual particles in geopolymer binders after 28 days: (a) dissolved fly ash A; (b) geopolymer A; (c) dissolved fly ash B; (d) geopolymer B.

Figure 5 shows the images of fly ash particles after dissolution in alkaline solution and after geopolymerisation. The crystals in fly ash particles remain unattacked or much less dissolved under the two conditions. The glassy phases are dissolved and participated in the geopolymerisation. This fact suggests that the molar ratio based on the bulk chemical compositions, which is used in most literatures for geopolymer design, is actually giving inaccurate information, if not misleading. We need to use the glassy phases and their compositions, rather than the overall composition, to calculate fly ash dissolution and geopolymerisation.

**Table 2. The mineralogical compositions (wt.%) of fly ashes as determined by Rietveld quantitative XRD method with 20 wt.% of internal reference material (corundum).**

Components (ICSD no.)	A	B	C	D	E
Mullite (66448)	18.7			15.7	24.1
Mullite (43289)		13.6	15.3		
Quartz (89280)	3.1	2.6	6.5	5.0	13.1
Magnetite (43001)	2.5	1.3	2.4	0.9	
Hematite (15840)	1.5	0.8			
Glassy phases	74.2	81.7	75.8	78.4	62.8
$W_{RP}$ , %	3.0	6.0	3.9	3.3	5.0

We used the RQXRD method [19] to determine the mineral components in the 5 fly ash samples, with the results listed in Table 2. RQXRD is better suited for quantitative analysis of fly ash as a complex material than other methods of analysis of XRD data, such as the reference intensity ratio method [27], because it uses the full profile of the diffraction patterns, which minimises the inaccuracies in the raw data raised from the systematic errors, such as peak overlap, preferred orientation, sample broadening and the lack of a pure standard [28]. This is particularly suitable when the fly particles in this study were sampled without any classification and grinding to avoid phase changing or separation. The results show that the fly ash E has the lowest amount of glassy phases. If it is assumed that glassy phases are the reactive components in geopolymerisation [29], fly ash E will certainly generate a weaker binder. However, the amounts of glassy phases in the other four fly ashes are not significantly different compared to their strength variations. This implies that the quantity of glassy phases is insignificant. The composition of glass phases is more likely another key factor that affects the 'apparent' reactivity of fly ash in geopolymerisation, through controlling its reaction rate and extent.

Table 3 shows the compositions of glassy phases in each fly ash. It is calculated by subtracting the mineral compositions (assuming all of the crystalline phases are 'pure') from the bulk composition determined by XRF analysis. This is an important correction to the use of bulk composition only (Figure 1).

**Table 3. Chemical compositions in the glassy parts of fly ashes as calculated from the bulk composition and mineral compositions. 'Others' includes  $P_2O_5$ ,  $SO_3$ , trace components and LOI, wt.%.**

Fly ash	SiO <sub>2</sub>	Al <sub>2</sub> O <sub>3</sub>	CaO	MgO	K <sub>2</sub> O	Na <sub>2</sub> O	Fe <sub>2</sub> O <sub>3</sub>	TiO <sub>2</sub>	Others
A	40.0	13.0	4.2	1.5	0.5	0.7	10.2	1.5	2.5
B	46.2	23.5	6.9	0.9	0.6	0.3	1.0	1.6	0.8
C	41.7	23.1	1.1	0.8	0.2	0.1	5.0	2.1	1.7
D	58.6	10.5	1.0	0.5	2.1	0.5	2.7	0.9	1.5
E	52.4	6.3	0.1	0.1	0.5	0.0	1.2	1.4	0.9

### 2.3 Chemical composition of glassy phases

During the geopolymerisation, the dissolved silicate and aluminate species in aqueous solutions are condensed to form geopolymeric gels. In this process [SiO<sub>4</sub>] and [AlO<sub>4</sub>] tetrahedral act as 3D network former sites while alkali cations (Na<sup>+</sup> and K<sup>+</sup>) act as charge balancer for the negative charge of anionic tetrahedral Al centre. The 3D network structure is the backbone, contributing to the strength of geopolymer. It is evident that the larger the quantity of dissolved glassy phase, the more sodium (or potassium) aluminosilicate hydrate gel (N-A-S-H) is formed, contributing to higher strength of the

hardened products. Therefore, as mentioned above, fly ash containing a higher quantity of the glassy aluminosilicate phase will generate a geopolymer with higher strength.

Si and Al are the network formers. It is reported that the availability of Al is critical to the properties of geopolymers [30,31]. Fly ash with large amounts of reactive Al usually generates high strength geopolymer [32]. In the 5 fly ashes we studied, fly A, B and C have high Al contents. So in the network formers of Si and Al, apart from their total quantity, the ratio of Si and Al in gel phases may also affect the mechanical properties of geopolymers [33]. The formed gels have varying Si/Al ratios, depending on the composition of the dissolved glassy phase and the alkaline activator. A more recent study [34] found that the strength of metakaolin-based geopolymer increased with the Si/Al ratio increase from 1.80 to 2.33 when  $Na/Al < 1$ . This is also probably due to the decreased porosity by mixing more dissolved silicate. Apparently, it is difficult to define an 'optimal' Si/Al ratio of geopolymeric gels for high strength.

The alkali cations, as the network modifiers, play important roles in affecting the intrinsic properties of geopolymeric gels. Alkali cation  $Na^+$  acts as a charge balancer, located around the negative site of  $[AlO_4]$ . It could present in the pore solution at a molecular level. This role helps the system to achieve stability. Alkali earth cations ( $Ca^{2+}$ ,  $Mg^{2+}$ ) may displace alkali cations through ion exchange and have similar roles as charge balancers. However, when the total charge of alkali and alkali earth cations (M) exceeds the concentration of  $[AlO_4]$ , alkali and alkali earth cations can also work as network modifiers, forming more non-bridge oxygen sites. This role prevents the formation of a polymer structure of a large molecular. From this point of view, alkali and alkali earth cations may have an optimal concentration, which is probably  $M/Al = \sim 1$ , i.e. fully compensating the negative charges of  $[AlO_4]$  in a geopolymer network. Indeed, it was reported that a maximum compressive strength was obtained at around  $Na/Al = 0.965$  in metakaolin-based geopolymers, with lower strengths observed at lower or higher  $Na/Al$  ratio [34]. It is probably reasonable to use the difference between  $(M+Me)/Al$  and 1 to indicate the integrity of the network.

If activator addition is designed to be sufficient, partial dissolution of glassy phases will increase the actual M/Al ratio in the resulting gels. Unfortunately, to date there are no effective methods developed for the prediction of the reaction extent of fly ash. It is therefore difficult to propose an optimal dosage for alkali addition in the design of the geopolymer mix. Again, if glassy phases are assumed to be fully dissolved, the M/Al values range from 0.7 in geopolymer C to 2.0 in geopolymer E. The closest value to 1 is obtained in geopolymer B, at 1.2, which is believed to partially contribute to its high strength. We want to emphasize the importance of this factor in the geopolymer formula, particularly for those systems with predictable dissolution extents of raw aluminosilicate.

#### **2.4 The reactivity index – a tentative format**

In the above results and analysis, we have shown three characteristics of fly ash having significant impacts on its reactivity: (1) physical properties, in particular, SLV affects the dissolution rate and extent of geopolymerisation reaction of fly ash particles, and IPV affects the liquid requirement and consequently the porosity in resulting geopolymer; (2) crystallographic characteristics decide it is only the glassy phase that participates the geopolymer formation; and (3) chemical characteristics of glassy phases determine the concentrations of network formers and network modifiers, which are combined to form the geopolymer 3D network.

We combine the three factors in a comprehensive function provided below:

$$RI = f(SLV, IPV, NF, NM) \quad (1)$$

where SLV and IPV are the effect of the physical characteristics; NF represents the contribution of network formers; NM presents the effects of network modifiers, which can be quantified by the difference between concentrations of M and Al.

At this stage, we have not obtained enough data to complete the format of this function; in particular, the magnitudes of each factor. For each of these identified factors, we have planned special experimental programs. For example, while keep other factors constant, we can study the influence of NF by using synthesized glass to mixing with synthesized crystals, such as mullite and quartz. In this way, we can figure out the basic relationship between NF and compressive strength or other mechanical properties. We can incorporate the relationships for each factor into a comprehensive equation, and finally have the reactivity index.



### 3. Conclusions

In summary, we proposed, for the first time, a reactivity index (RI) for fly ash, which combines the physical, crystallographic and chemical characteristics of fly ashes into one parameter. This comprehensive RI can be an effective tool in evaluating and grading the suitability of fly ash for geopolymer formulation. Then from the extent of the geopolymerization, we can predict the performance of the resulted fly ash-based geopolymer materials. A reliable and predictable geopolymer is a big step to make the new materials acceptable for industry as the green alternative to the current OPC. We acknowledge that in a real situation, a completely full dissolution of glassy phases will never reach, however, our proposed reactivity index provides a reaction potential of a given fly ash.

### 4. Acknowledgement

This work was supported by the Halok project and the Australian Research Council through a linkage project (LP130101016).

### 5. References

1. Davidovits, J., "Geopolymer chemistry and applications". Institut Géopolymère, 2008, Saint-Quentin, France.
2. Shi, C., Fernández-Jiménez, A., et al., "New cements for the 21<sup>st</sup> century: the pursuit of an alternative to Portland cement", Cem Concr Res, 41, 2011, pp 750–763.
3. Juenger, M.C.G., Winnefeld, F., et al., "Advances in alternative cementitious binders", Cem Concr Res, 41, 2011, pp 1232–1243.
4. McLellan, B.C., Williams, R.P., et al., "Costs and carbon emissions for geopolymer pastes in comparison to ordinary portland cement", J Cleaner Prod, 19, 2011, 1080–1090.
5. Yang, K.-H., Song, J.-K., et al., "Assessment of CO<sub>2</sub> reduction of alkali-activated concrete", J Cleaner Prod, 39, 2013, pp 265–272.
6. Palomo, A., Grutzeck, M.W. et al., "Alkali-activated fly ashes A cement for the future", Cem Concr Res, 29, 1999, pp 1323–1329.
7. Zhang, Z., Zhu, Y., et al., "Using fly ash to partially substitute metakaolin in geopolymer synthesis", Appl Clay Sci, 88–89, 2014, pp 194–201.
8. Mozgawa, W., Deja, J., "Spectroscopic studies of alkaline activated slag geopolymers", J Mol Struct, 924, 2009, pp 434–441.
9. Yang, T., Yao, X., et al., "Mechanical property and structure of alkali-activated fly ash and slag blends", J Sust Cem-Based Mater, 1, 2012, pp 167–178.
10. Dimas, D., Giannopoulou, I., et al., "Utilization of alumina red mud for synthesis of inorganic polymeric materials", Miner Proc Extr Metall Rev, 30, 2009, pp 211–239.
11. Chen, J.-H., Huang, J.-S., et al., "Use of reservoir sludge as a partial replacement of metakaolin in the production of geopolymers", Cem Concr Res, 33, 2011, pp 602–610.
12. Li, C., Sun, H.-F. et al., "A review: The comparison between alkali-activated slag (Si+Ca) and metakaolin (Si+Al) cements", Cem Concr Res, 40, 2010, pp 1341–1349.
13. Keyte, L., What's wrong with Tarong? The importance of coal fly ash glass chemistry in inorganic polymer synthesis (PhD Thesis). University of Melbourne; 2008.
14. Diaz, E.I., Allouche, E.N., et al., "Factors affecting the suitability of fly ash as source material for geopolymers", Fuel, 89, 2010, pp 992–996.
15. Kumar, S., Kumar, R., et al., "Influence of reactivity of fly ash on geopolymerisation", Adv Appl Ceramics, 106, 2007, pp 120–127.
16. van Deventer, J.S.J., Provis, J.L., et al., "Technical and commercial progress in the adoption of geopolymer cement", Miner Eng, 29, 2012, pp 89–104.
17. Zhang, Z.-H., Wang, H., et al., "Quantitative study of the reactivity of fly ash in geopolymerization by FTIR", J Sust Cem-Based Mater, 1, 2012, pp154–166.

18. Fernández-Jiménez, A., de La Torre, A.G., et al., "Quantitative determination of phases in the alkali activation of fly ash. Part I. Potential ash reactivity". Fuel, 85, 2006, pp 625–634.
19. Williams, R.P., van Riessen, A., "Determination of the reactive component of fly ashes for geopolymer production using XRF and XRD". Fuel, 89, 2010, pp 3683–3692.
20. van Riessen, A., Chen-Tan, N., "Beneficiation of Collie fly ash for synthesis of geopolymer: Part 1 – Beneficiation", Fuel, 106, 2013, pp 569–575.
21. Provis, J.L., Duxson, P., et al., "The role of particle technology in developing sustainable construction materials", Adv Powder Technol, 21, 2010, pp 2–7.
22. Brunauer, S., Emmett, P.H., "Adsorption of gases in multimolecular layers". J Am Chem Soc, 60, 1938, pp 309–319.
23. Hwang, J.Y., Sun, X., "Residual carbon in fly ash for mercury adsorption: I. Separation and characterization of unburned carbon", J Miner Mater Character Eng, 1, 2002, pp 39–60.
24. Kumar, S., Kumar, R., "Mechanical activation of fly ash: Effect on reaction, structure and properties of resulting geopolymer", Ceram Int, 37, 2011, pp 533–541.
25. Neville, A.M., "Properties of concrete (5th edition)", Pearson, 2011, London, UK.
26. Roy, D.M. New strong cement materials: Chemically bonded ceramics. Science, 253, 1987, pp 651–658.
27. Font, O., Moreno, N., et al., "X-ray powder diffraction-based method for the determination of the glass content and mineralogy of coal (co)-combustion fly ashes", Fuel 89, 2010, pp 2971–2976.
28. de La Torre, A.G., Bruque, S., "Rietveld quantitative amorphous content analysis", J Appl Crystal, 34, 2001, pp 196–202.
29. Duxson, P., Provis, J.L., "Designing precursors for geopolymer cements", J Am Ceram Soc, 91, 2008, pp 3864–3969.
30. Hajimohammadi, A., Provis, J.L., et al., "Effect of alumina release rate on the mechanism of geopolymer gel formation", Chem Mater, 22, 2010, pp 5199–5208.
31. Hajimohammadi, A., Provis, J.L., et al., "The effect of silica availability on the mechanism of geopolymerisation", Cem Concr Res, 41, 2011, pp 210–216.
32. Rickard, W.D.A., Williams, R., "Assessing the suitability of three Australian fly ashes as an aluminosilicate source for geopolymers in high temperature applications", Mater Sci Eng A, 528, 2011, pp 3390–3397.
33. Duxson, P., Provis, J.L., et al., "Understanding the relationship between geopolymer composition, microstructure and mechanical properties", Colloids Surf A 269, 2005, pp 47–58.
34. Saidi, N., Samet, B., et al., "Effect of composition on structure and mechanical properties of metakaolin based PSS-geopolymer", Int J Mater Sci 3, 2013, pp 145–150.

# Structural Monitoring and Assessment

# DAMAGE ASSESSMENT OF DAMS AFFECTED BY EXPANSIVE REACTIONS USING STEREO MICROSCOPY AND ELECTRON MICROSCOPY. RELATIONSHIP BETWEEN THE DAMAGE LEVELS DRI AND DL

Esperanza Menéndez<sup>1</sup>, Ricardo García Rovés<sup>2</sup>, Nicanor Prendes<sup>3</sup>

<sup>1</sup>PhD. Industrial Engineer, Institute "Eduardo Torroja" of Construction Science (CSIC)

<sup>2</sup>Mining Engineer, Institute "Eduardo Torroja" of Construction Science (CSIC)

<sup>3</sup>Geologist, Centre of Studies and Experimentation of public works (CEDEX)

**Abstract:** Currently, the analysis of the situation and potential future deterioration of concrete in dams affected by expansive reactions is considered a very complex problem. To evaluate and quantify the damage in the affected concretes, can be used complementary analysis such the assessment of macroscopic damage rating index (DRI), using optical stereomicroscopy, or determining the level of damage (DL) using electron microscopy techniques combined with X-ray microanalysis.

To determine the DRI polished concrete surfaces are prepared and evaluated using a stereoscopic microscope. During the observation the presence of microcracks and reaction products are observed and quantified with a relative weight to obtain the DRI. And, the damage of concretes is classified according to a certain ranges.

Also, the use of backscattering electron microscopy (BSE) combined with X-ray microanalysis (EDX) permits to evaluate the presence and degree of damage in concrete, due to internal expansive reactions, like ettringite formation or alkali-silica reaction. Then the deterioration degree of concretes is classified based on specific criteria of classification.

In this paper the results of assessment of concrete from dams are presented to evaluate the deterioration degree using both methodologies. Also, the classification of damage level obtained using macroscopic and microscopic techniques has been evaluated to analyze the relationship between these procedures to known the situation of the dam concretes.

**Keywords:** Damage Rating Index, Damage Level, expansive reactions.

## 1. INTRODUCTION

Throughout the useful life of concrete structures alterations can be produced as a result of environmental factors which could affect the loss of functionality in them, compromising the safety of the structures or the structural elements, according to the degree of deterioration [1], [2]. This deterioration might be associated with different types of factor: chemical, physical, mechanical, biological, etc. In some cases the origin of the damage is directly related to the characteristics of the components of the concrete (aggregates, cement, water, additives, etc.) and the interaction between them or with the environment. In the case of alterations arising from chemical reactions originating internally, in all cases water acts as a vehicle for the reaction and as a basic part of the expansive products formed. Within the expansive processes of an internal origin it is important to highlight, given its impact and the effects produced on the concrete, the alkali-silica reaction and the sulfate attack, although there are other phenomena of a physical origin that have an impact on the freezing and thawing cycles.

The alkali-silica reaction and the sulfate attack are phenomena brought about by the chemical reaction of different components of the concrete which give rise to the neo-formation of products whose main characteristic is that they are expansive.

The formation of these expansive products in the interior of the hardened concrete makes it overcome the resistance to traction of the material and gives rise to the formation of fissures. Another significant characteristic is that its appearance is affected by multiple factors, both proper to the material itself and its components as well as environmental conditions. The coincidence of influential factors and the manifestation of the damage, with similar characteristics, make it essential to carry out a suitable diagnosis in order to program actions on the structure and carry out repair work where deemed necessary. For a correct diagnosis of these phenomena a micro-structural analysis of the affected concrete is essential, specifically using electronic microscopy and microanalysis techniques, together with a correct interpretation [1].

The deterioration caused by the alkali-silica reaction and by sulfate attack can be differentiated using electronic microscopy and microanalysis techniques, considering the representativity of the samples of the structure [3]. On the other hand, could be possible also to observe the damage in concretes at optical microscopy level.

The damages caused by internal expansive reactions in the concrete can be diagnosed unequivocally by using micro-structural analysis techniques based on the study electronic microscopy combined with microanalysis by X-ray [1], by applying the damage level method (DL) [4]. Also, in several papers are described the consequence of ASR at microstructural level [5], [6], [7], [8]. However, it is essential to guarantee the representation of the samples in relation to the structure to be analyzed and the experience of the technicians to have a correct results.

The suitable diagnosis allows it to be established whether the deterioration observed is related with alkali-silica reaction, sulphate attack or the combination of the two processes. Likewise, it is possible to establish the origin of the damage, in spite of the alteration products having the same characteristics [4].

The damages caused by internal expansive reactions in the concrete also it can be diagnosed by using optical microscopy in polished samples, by applying the damage rating index (DRI).

The DRI consists in a semi-quantitative petrographic evaluation of damage in concrete either affected by ASR or other deleterious mechanisms [9]. However, the results can be significantly affected by the experience of the petrographer and since there is currently no standard test procedure available. The method can be fairly subjective and the results quite variable from one petrographer to another. The DRI method can provide very useful relative information when the examination of sets of cores from various parts of a structure (subjected to different exposure conditions or showing various external features of deterioration) is carried out by the same petrographer. The method also allows identifying the progress of ASR or other alterations than formed cracks when cores are extracted regularly from the same structural element and examined once again by the same petrographer. Although, until now the DRI method is currently not a standardized method and there are no accepted ratings for DRI results [10].

## **2. INSTRUMENTAL TECHNIQUES**

### *Backscattering electron microscopy and energy dispersive X-ray (BSE-EDX)*

The concrete samples were prepared and analyzed by BSE-EDX identifying the different structures and the distribution of its analyzing the elemental mapping associated with the images. The samples were imbibed in low viscosity resin, cutted and polished to generate a properly observation surfaces. Microscopic analysis has done with an electron microscopy JEOL JSM-5400 and with X-ray microanalysis OXFORD Link.

### *Optical microscopy*

The concrete samples were first cutted axially and then polished with a portable hand-polishing device. The polished concrete sections were prepared and examined using a strereomicroscope Nikon SMZ-2T.

## **3. CONCRETE SAMPLES**

For this study, concrete samples were extracted from different dams in operation. These dams are located in Spain, two buttress dams in the Northeast and an arch gravity dam in the Midwest. The current use of the dams is hydroelectric.

The concretes were manufactured with a cement type CEM I, without any addition. Aggregates used in the manufacture of the concretes of the two buttress dams, are classified according to standard ASTM C294 [11] as an arenaceous limestones. These limestones are compounds mainly of calcite, also containing quartz, feldspars and mica. Aggregate used in the manufacture of the concrete of arch gravity dam, is classified as a plutonic rock of granite type. This granite are compounds mainly of sodic and potasic feldspars, quartz and mica type biotite and muscovite.

Table 1 gives the location and details of the different concrete cores selected by this research.

**Table 1. Location of concrete samples.**

Structure	Sample	Location
Arch gravity dam Crest length: 418 m Height: 66 m	B5-AA-73	Block 5
	B11-AB-95	Block 11
	B16-AA-120	Block 16
	B16-C-91	Block 16
	B17-AA-118	Block 17
	B17-AB-118	Block 17
	B17-AA-91	Block 17
Buttress dam Crest length: 490 m Height: 31 m	B18-AA-120	Block 18
	UR-B-05(1)	Block 5
	UR-C-11A(4)	Block 11
	UR-C-11B(10)	Block 11
	UR-C-15A(1)	Block 15
	UR-C-16B(1)	Block 16
	UR-C-17A(4)	Block 17
Buttress dam Crest length: 535 m Height: 37 m	UR-C-17B(10)	Block 17
	UR-B-24(1)	Block 24
	UL-C-16A(7)	Block 16
	UL-C-16B(1)	Block 16
	UL-PC-14-02(3)	Block 14
	UL-PC-14-02(5)	Block 14

## 4. TESTING METHODOLOGY AND RESULTS

### 4.1 Testing methodology

#### Damage level (DL)

The DL is a method which permits to determine the grade of damage and assign a level of damage based on the microstructural studies, by using micro-structural analysis techniques based on the study electronic microscopy combined with microanalysis by X-ray. The gradation of the damage for concretes affected by the alkali-silica reaction and sulfate attack is set out in Table 2, describing the degree of damage for each level, the type of product formed and their location within the material. In both types of expansive reactions five levels of damage are established, which are increased in accordance with the deterioration from 1 to 5, each level corresponding to: low (1), moderate (2), average (3), elevated (4) and extended to the total (5). For its part, the levels of damage associated to an alkali-silica reaction are named DLASR (Level of Damage caused by Alkali-silica Reaction) and DLSA (Degree of Damage by Sulfate Attack) [4].

**Table 2. Definition of damage code as a function of the damage level in concretes affected by alkali-silica reaction and sulfate attack [4].**

Damage by Alkali-Silica Reaction					
Damage Code	DLASR-1	DLASR-2	DLASR-3	DLASR-4	DLASR-5
Damage degree	Low	Moderate	Average	Elevated	Extended to total
Reaction products	Vitreous gels	Vitreous gels and microcrystallines	Vitreous gels, microcrystallines and microcrystalline products	Vitreous gels, microcrystallines and microcrystalline products	Vitreous gels, microcrystallines and microcrystalline products
Location of products	Pores	Pores+aggregates	Pores aggregates+aggregate-paste interfaces	Pores+aggregates+aggregate-paste interfaces+paste	Pores+aggregates+aggregate-paste interfaces+paste (↑fissures)
Damage by Sulfate Attack					
Damage Code	DLSA-1	DLSA-2	DLSA-3	DLSA-4	DLSA-5
Damage degree	Low	Moderate	Average	Elevated	Extended to total

Reaction products	Needle-shaped crystallisations	Needle-shaped crystallisations	Needle-shaped and prismatic crystallisations	Needle-shaped and prismatic crystallisations	Needle-shaped and prismatic crystallisations
Location of products	Small pores	Pores+aggregate-paste interfaces	Pores+aggregate-paste interfaces+paste	Pores+aggregate-paste interfaces+paste+small filled fissures	Pores+aggregate-paste interfaces+paste+filled fissures

### *Damage rating index (DRI)*

The DRI method consists in a count of the number of petrographic features of deterioration commonly associated to ASR on polished concrete sections on which a grid is first drawn (minimum 200 grid squares to be examined, 1 by 1 cm in size). These studies are made using stereomicroscope technique ( $\approx 16\times$  magnification). The DRI thus represents the normalized value (to 100 cm<sup>2</sup>) of the frequency of these features after the count of their abundance, over the surface examined, has been multiplied by weighing factors representing their relative importance in the overall deterioration process [12]. This method is applied in different works for structures affected by expansive reactions [13], [14], [15], [16], [17], [18], [19].

According to Grattan-Bellew, 2012, it is difficult, if not impossible, to determine the minimum DRI that is indicative of significant deterioration of concrete due to ASR. The problem is further complicated frequently by large differences in the DRI's measured by different operators. [20]. From this point of view the DRI factor could be used as a comparison tool between different parts of one structure or the same areas with the time.

Table 3 gives a list of those features and the weighing factors [9], which were used in this research.

**Table 3. Petrographic features and weighing factors for the DRI [9].**

<b>Petrographic features</b>	<b>Factors</b>
Closed/tight cracks in coarse aggregate particle (CrCA)	0,25
Opened cracks or network cracks in coarse aggregate particle (OCrCA)	2
Cracks or network cracks with reaction product in coarse aggregate particle (Cr+RPCA)	2
Coarse aggregate debonded (CAD)	3
Disaggregated/corroded aggregate particle (DAP)	2
Cracks in cement paste (CrCP)	3
Cracks with reaction product in cement paste (Cr+RPCP)	3

## **4.2 Results and discussion**

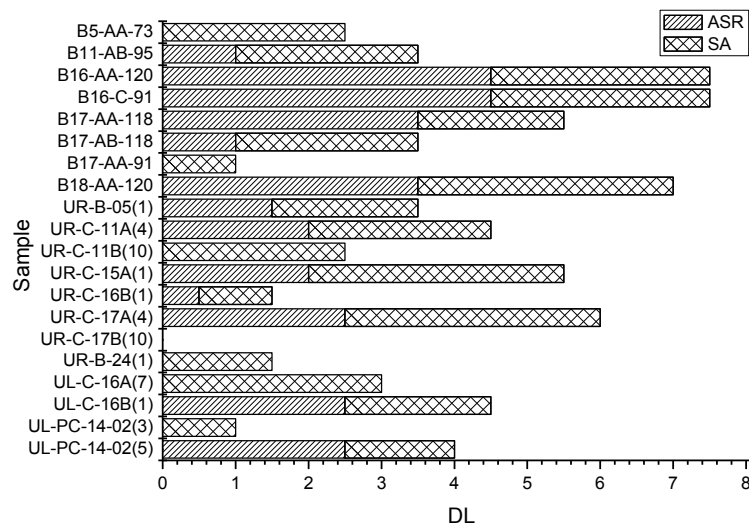
A calculation of DL, due to alkali-silica reaction and due to sulfate attack, and of DRI has been done to the different cores selected. Also, a comparison between both method of damage assessment is done to evaluate the relationship between them and value the most properly.

The results obtained by the application of DL method can be seen in the table 4. Table 4 shown the damage level of alkali-silica reaction (DL ASR), the damage level of sulfate attack (DL SA) and the combination of both damage (DL ASR-SA).

**Table 4. Results of the DL method for cores extracted from different dams**

Sample	DL ASR	DL SA	DL ASR-SA
B5-AA-73	0	2-3	2-3
B11-AB-95	1	2-3	3-4
B16-AA-120	4-5	3	7-8
B16-C-91	4-5	3	7-8
B17-AA-118	3-4	2	5-6
B17-AB-118	1	2-3	3-4
B17-AA-91	0	1	1
B18-AA-120	3-4	3-4	6-8
UR-B-05(1)	1-2	2	3-4
UR-C-11A(4)	2	2-3	4-5
UR-C-11B(10)	0	2-3	2-3
UR-C-15A(1)	2	3-4	5-6
UR-C-16B(1)	0-1	1	0-2
UR-C-17A(4)	2-3	3-4	5-7
UR-C-17B(10)	0	0	0
UR-B-24(1)	0	1-2	1-2
UL-C-16A(7)	0	3	3
UL-C-16B(1)	2-3	2	4-5
UL-PC-14-02(3)	0	1	1
UL-PC-14-02(5)	2-3	1-2	3-5

The graphic of figure 1 represent the results obtained by the application of DL method for ASR or SA damage and the addition of both.



**Figure 1. Graphic of results of the Damage Level (DL).**

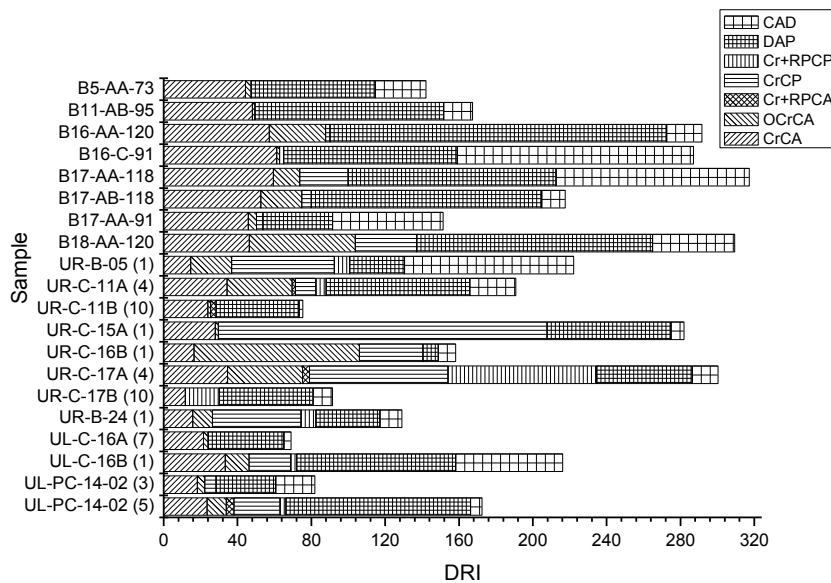
Also, the results obtained by the application of DRI method for each core samples can be seen in the table 5.



**Table 5. Results of the Damage Rating Index (DRI) for selected cores extracted from a dam**

Sample	DRI
B5-AA-73	142
B11-AB-95	167
B16-AA-120	292
B16-C-91	287
B17-AA-118	317
B17-AB-118	218
B17-AA-91	151
B18-AA-120	309
UR-B-05(1)	222
UR-C-11A(4)	191
UR-C-11B(10)	75
UR-C-15A(1)	282
UR-C-16B(1)	158
UR-C-17A(4)	300
UR-C-17B(10)	91
UR-B-24(1)	129
UL-C-16A(7)	69
UL-C-16B(1)	216
UL-PC-14-02(3)	82
UL-PC-14-02(5)	172

The graphic of figure 2 represent the results obtained by the application of DRI method. Cells with different fill patterns give the proportions of each petrographic feature to the DRI value. By this method a single valuation is performed regardless of the damage type.



**Figure 2. Graphic of results of the Damage Rating Index (DRI) (See Table 3 for the acronyms).**

The correlation between the results obtained by the DL and DRI assessment methods is analyzed. It is intended to verify the potential relationship of a general analysis method (DRI) with a specific analysis method for the type of damage (DL).

To compare the results between the method of assessment and taken into account the results obtained, some intervals have been defined. Three groups of damage have been defined, moderate, medium and

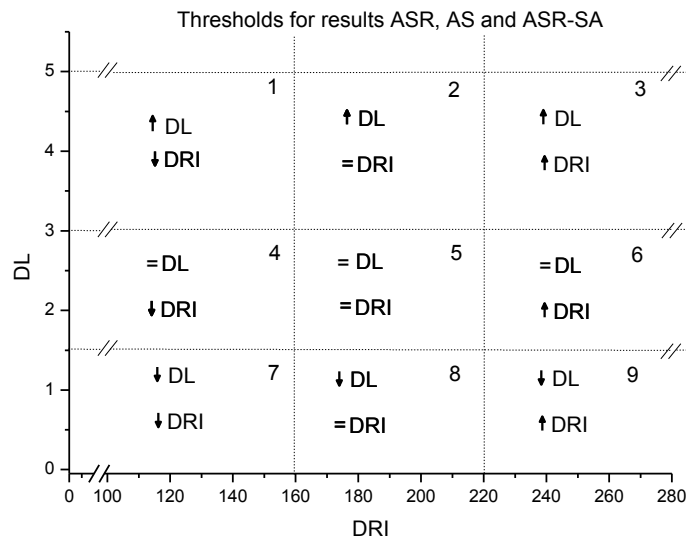
high. In table 6 the details of the damage are shown with the classification of DL and DRI damage to the structure analyzed. In the Figure 3 the different quadrants are represented with the limits between them.

**Table 6. Classification intervals**

Damage	DRI	DL ASR	DL AS	DL ASR-AS
Moderate	<160	<1,5	<1,5	<3
Medium	160-220	1,5-3	1,5-3	3-6
High	>220	3-5	3-5	6-10

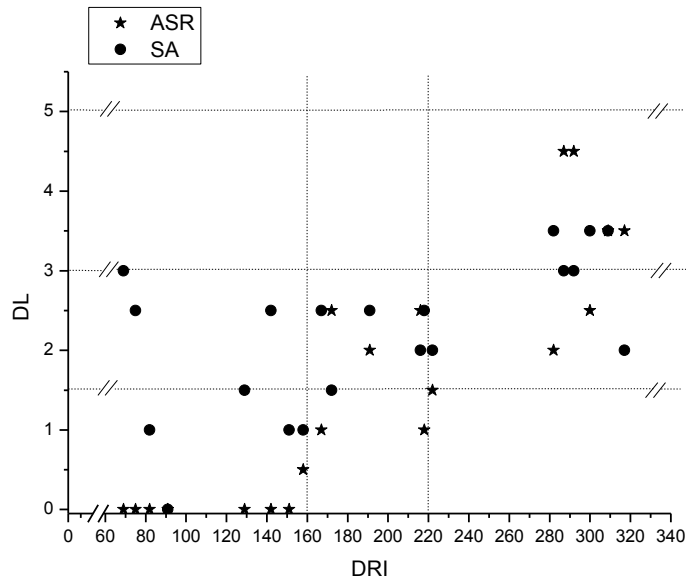
The evaluation of damage by DL method is considered as reference. Because it is possible to define clearly the origin of damage and qualify it. According with the reference of DL method the classification of intervals has the following characteristics:

- Good correlation with DRI method: Correlation values are localized in the quadrants 3, 5 and 7, according to the Figure 3
- The DRI underestimate the damage: Values sited in the quadrants 1, 2 and 4
- The DRI overestimate the damage: Values sited in quadrants 6, 8 and 9



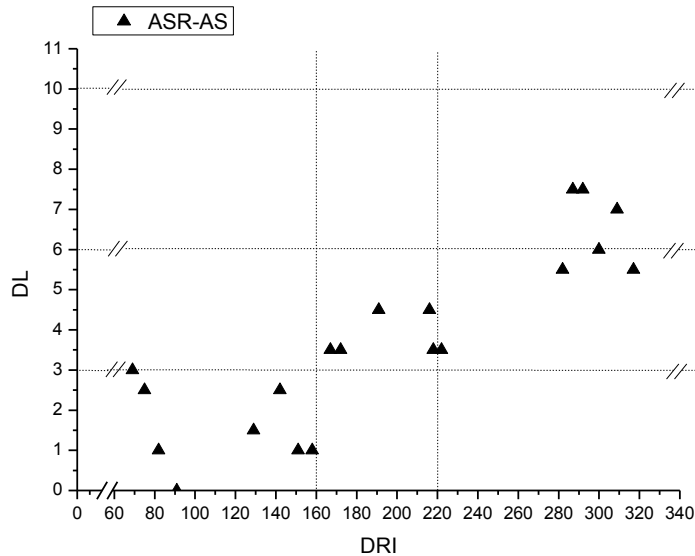
**Figure 3. Thresholds for DL results ASR, AS and ASR-AS versus DRI.**

Figure 4 represent the correlation obtained by the different evaluation methods of damage, with values DL ASR (Damage Level caused by alkali-silica reaction) and values DL SA (Damage Level caused by sulfate attack) in relation with DRI damage.



**Figure 4. Correlation graphic DL versus DRI with values ASR and SA.**

Figure 5 represents the correlation between the evaluation of damage DRI and the values of the combination of damage by alkali-silica reaction and sulfate attack, DL ASR-AS.



**Figure 5. Correlation between DL and DRI by ASR-SA.**

Analysis of Figures 3 and 5 shown a good fitting for ASR and AS, due to the correlation values are located in the quadrant 3, 5 and 7. Although, the evaluation of AS by DRI method occasionally underestimate the phenomenon (some values are located in the quadrant 4) and eventually overestimate it (values located in quadrant 6). Also when ASR+SA are evaluated jointly there is a good correlation.

The divergence between the mesostructural level of damage (DRI) and the microstructural level of damage (DL) is related with the type of damage caused by each type of deterioration (ASR or SA). In the case of ASR the formation of gels produce a partial densification of the cement paste. And, with the evolution of the reaction the formation of cracks in aggregates, interfaces and cement paste. These types

of cracks are well detected by the DL method. Although, the evolution of SA damage produces the increase of cracks with crystallization of ettringites inside. These cracks are not detected properly by stereomicroscopy. Due to this the SA phenomenon is occasionally underestimate and produces a bad correlation between DRI and DL methods.

### **3. Conclusions**

The use of the DRI and DL evaluation permits define a comparative level of damage between the concrete of different areas of one structure and between different concretes.

The application of these methods of assessment shall be done by well-formed technical, it is necessary to take into account the operator factor.

The DL method of assessment permits to diagnosis the origin of damage (alkali-silica reaction, sulfate attack, frost, etc.), while the method of assessment DRI evaluate the presence of cracks and alterations without the consideration of their origin.

The correlation between the method DL and DRI is good when the alteration is related mainly with ASR. Although, when the main damage phenomenon is SA there is a underestimation of the damage level of the concrete. This is because the cracks are filled by the reaction products and are not clearly detected by stereomicroscopy.

The DRI method is consider more adequate to evaluate the concrete affected by alterations with open cracks, like ASR or frost. While DL method is adequate to evaluate the concrete with cracks opened and filled.

### **4. Acknowledgement**

The authors are grateful to the financing provided by the CSIC of Spain through the project: PIE 201460E067.

### **5. References**

1. E. Menéndez, Analysis of concrete structures affected by alkali silica reaction, sulfate attack and frost-drawing cycles (in spanish) (IECA, 2010).
2. E. Menéndez, A. Gil, A. B. Martín, B. Aldea, C. Marquez, Analysis of concrete dams affected by internal expansive processes. Differences and similarities between internal sulfate attack and alkali-aggregate reaction (in spanish), Advance in Security and Durability, (Fundetel, 2011, pp.283-306).
3. Menéndez, E., 2013. Nueva metodología de evaluación del grado de daño por reacciones expansivas internas en el hormigón mediante análisis microestructural. Conpat 2013, Cartagena de Indias, Colombia.
4. Menéndez, E. Evaluation and Gradation of Simultaneous Damage in Concrete Affected by Alkali-Silica Reaction and Sulfate Attack, International Review of Civil Engineering (I.R.E.C.E.), vol.2, N. 2, march 2011.
5. British Cement Association, The diagnosis of alkali-silica reaction. (Report of a working party, 1988).
6. D.W. Hobbs, Alkali-silica reaction in concrete (Thomas Telford, 1988).
7. K. Scrivener, J. Skalny, Internal sulfate attack and delayed ettringite formation (RILEM Publications S.A.R.I, 2002).
8. E. Menéndez, Cracking and sulfate attack in field concrete in Spain, RILEM Workshop on Internal Sulfate Attack and Delayed Ettringite Formation, pp. 127-138, Villars (Switzerland),September 2002.

9. Villeneuve, V., Fournier, B., Duchesne, J., "Determination of the damage in concrete affected by ASR-The damage rating index (DRI), Proceedings of the 14th International conference on Alkali-Aggregate Reaction in concrete (ICAAR), Austin, Texas (USA), May 20 to 25, 2012.
10. Fournier, B., Bérubé, M., Folliard, K.J., Thomas, M., "Report on the Diagnosis, Prognosis, and Mitigation of Alkali-Silica Reaction (ASR) in Transportation Structures", U.S. Department of Transportation, FHWA, 2010.
11. ASTM C294-12, Standard Descriptive Nomenclature for Constituents of Concrete Aggregates, ASTM International, West Conshohocken, PA, 2012.
12. Grattan-Bellew, P.E., "Comparison of laboratory and field evaluation of alkali silica reaction in large dams". Proceedings of the First International Conference on Concrete Alkali Aggregate Reactions in Hydroelectric Plants and Dams, 1992, Fredericton, NB, Canada, 23p.
13. Dunbar, P.A. and Grattan-Bellew, P.E. 1995. "Results of Damage rating Evaluation of Condition of Concrete from a Number of Structures Affected by AAR". In Proceedings of CANMET/ACI International Workshop on AAR in Concrete, Dartmouth, Nova Scotia, CANMET, Department of Natural Resources Canada, pp. 257-265.
14. Fournier, B., Bérubé, M.A., Thomas, M.D.A., Smaoui, N., Folliard, K.J., "Evaluation and Management of Concrete Structures Affected by Alkali-Silica Reaction – A Review", CANMET Materials Technology Laboratory, Report Number MTL 2004-11, 2004.
15. Fournier, B., Thomas, M.D.A., Folliard, K.J., "Evaluation of Concrete Pavement on US Route 113, Delaware: Field Site and Petrographic Evaluation", U.S. Department of Transportation, FHWA, 2009.
16. Fichboeck, E.K., Harmutt, H., "An Austrian experience with identification and assessment of alkali-aggregate reaction in motorways", Concrete Repair, Rehabilitation and Retrofitting II – Alexander et al (eds), Taylor & Francis Group, London, 2009.
17. Rivard, P., Ballivy, G., "Assessment of the expansion related to alkali-silica reaction by the Damage Rating Index method", Construction and Building Materials, 19, 83–90, 2005.
18. Shrimmer, F., "Application and use of damage rating index in assessment of AAR affected concrete. Selected case studies, 11th International Conference on Alkali-Aggregate Reaction, Québec, 2000.
19. Smaoui, N., Bérubé, M., Benoit Fournier, B., Benoit Bissonnette, B., Durand, B. "Evaluation of the expansion attained to date by concrete affected by alkali-silica reaction. Part I: Experimental study", Can. J. Civ. Eng., vol. 31, 826-845, NRC Canada, 2004.
20. Grattan-Bellew, P.E., "Petrographic methods for distinguishing between alkali-silica, alkali-carbonate reactions and other mechanisms of concrete deterioration", Proceedings of the 14th International conference on Alkali-Aggregate Reaction in concrete (ICAAR), Austin, Texas (USA), May 20 to 25, 2012.

# The impacts of temperature and salinity variance on service life modeling as a result of climate change.

Andrew Hunting<sup>a</sup>, Sujeeva Setunge, and David Law

School of Civil, Environmental, and Chemical Engineering, RMIT University, Australia

[aandrew.hunting@rmit.edu.au](mailto:aandrew.hunting@rmit.edu.au)

**Abstract.** As the effects of climatic change become more evident and extreme, there is growing pressure on seaport infrastructure stakeholders to ensure that their assets are resilient to the effects of a more aggressive and corrosive climate. In almost all previous literature on condition modeling of concrete structures, a static or at least annually cyclic environment is assumed. However, given the anticipated changing futures in climatic parameters, this research will re-affirm the need for more accurate modeling to ensure that the effects of the changing environment on concrete are quantifiable and suitable for use in industry given today's context of climate change. In response to a gap in understanding of the influences of the environment, first part of this paper describes simulated exposures which were established with variations of salinity, temperature, humidity, and concrete mix design; with the ability of isolating each variable individually. Using these results and a broad review of literature, a more holistic service life modeling approach is presented in the second part which derives quantitative projections of how climate change is already invariably changing the rates of chloride ingress into concrete structures. Preliminary outcomes from the model indicate that the seaport structures will require earlier maintenance intervention compared to the maintenance regimes derived current models.

**Keywords:** Chloride ingress, salinity, climate change, concrete

## 1. Introduction

The ingress of chlorides is the ability for chloride ions to penetrate through the concrete protection cover to the reinforcement bar which initiates the corrosion process within the reinforcing steel.

This process is the principal mechanism responsible for corrosion-related damage to concrete infrastructure and it is directly related to its surrounding environment. This link to the surrounding climate variables implies an added vulnerability of the service life of structures to climate change.

This phenomenon is currently costing western countries around 2.5% of their national annual GDP, or costing the world economy over \$1.8 trillion a year (Schmidt, 2009). This corrosive process occurs more rapidly in structures that are exposed to saline-ridden environments with traces of chloride (i.e. sea water) than what it does in areas without exposure to such chlorides (Emmanuel, Oladipo, & Olabode, 2012). This ingress will often take place through pore spaces in the cement paste matrix and paste-aggregate interfaces or micro cracks (Lindvall, 2007) (Shi, Xie, Fortune, & Gong, 2011).

Work presented here aimed to develop and validate a tool which allows understanding of the effect of changes in climatic conditions on chloride ingress in reinforced concrete, which will lead to initiation of corrosion.

Typically, the time taken for an asset to exhibit structural failure from the corrosion initiation is a shorter than the time taken for corrosion initiation to occur. Therefore, the impacts that vary the time to corrosion initiation (that being the parameters explored in this paper) will heavily impact the service life of the structure.

## 2. Probabilistic Models.

Several studies (Emilio Bastidas-Arteaga, Bressolette, Chateauneuf, & Sánchez-Silva, 2009) (Rajasankar & Iyer, 2006) have attempted to use probabilistic methods to encompass the influence of variables in deteriorating mechanisms of RC structures and understanding the drivers that decrease

the corrosion initiation time. Kong et al. (Kong, Ababneh, Frangopol, & Xi, 2002) presented a concise reliability analysis which illustrated the inconsistencies around concrete mix design, however the research was restrictive as it assumed a static chloride threshold and static environmental salinity.

Further to this research, Trapper (Val & Trapper, 2008) presented a two-dimensional modeling of probabilistic evaluation of corrosion initiation time, however did not manage to encompass the environmental variables such as temperature and humidity. This research utilises this probabilistic evaluation of initiation time and extend this knowledge to encompass environmentally dependent parameters which will feed off the A1B and A2 climatic projections outlined in the Intergovernmental Panel on Climate Change's (IPCC) (IPCC, 2013) 5th assessment report.

### **2.1. Chloride Diffusion.**

The parameters affecting the interactions between moisture, the diffusion of heat, and chlorine concentration was presented by (A.V. Saetta, R.V. Scotta, & Vitaliani, 1993) however the ionic nature of the diffusion of chlorides was neglected. (Johannesson, 1993) examined a numerical model that examined the spatial, time, and interdependent variables influencing the movement of chlorides however excluded the dependency of the surface temperature. Despite the modeling of chloride movement simplistically being considered to occur in a 1-D fashion (i.e. perpendicular to the surface), (J.S. Kong, A. Ababneh, D. Frangopol, & Xi, 2002) developed a model by (Y. Xi & Bazant, 1999) which removed the consideration of convection and formulated the ingress into saturated concrete.

#### **2.1.1. Fick's 2nd Law**

Chloride ingress is typically modeled with the assistance of Fick's 2nd law of diffusion which can be simply described as the random motion of free chlorides from a region of high concentration to a region of low concentration. Fick's second law is used to predict the time variation of the concentration of chlorides for one-dimensional flow in a semi-infinite solid. There have been several models created to expand on Eq1 ((Tang & Nilsson, 1992), (Amey & Miltenberger, 1998; E. Bastidas-Arteaga, Chateauneuf, Sánchez-Silva, Bressolette, & Schoefs, 2010; Frederiksen & Geiker; Saetta, Scotta, & Vitaliani, 1993)), however the law in its most basic form is:

$$\frac{\partial C(x, t)}{\partial t} = \frac{\partial}{\partial x} \cdot \left[ D \frac{\partial C}{\partial x} \right] \quad (1)$$

#### **2.1.2. Crank's Solution**

To transfer this law and solve it with Crank's solution, the assumption can be made that the diffusion coefficient  $D$  and the surface chloride remain constant as boundary conditions. The initial condition as the concentration of chlorides ( $C = 0$ ) for depth from concrete surface  $x > 0$ , at time of exposure  $t = 0$ . Crank's solution of Fick's 2nd law is given below whereby erf is the error function.

$$C(x, t) = C_s \cdot \left[ 1 - \operatorname{erf} \left( \frac{x}{2\sqrt{Dt}} \right) \right] \quad (2)$$

## 2.2. LIFE-365 modeling.

This study and others document the effects of temperature on the results of migration tests, however, there is contention into how this can be accurately mapped and numerically incorporated into modeling. The modeling application known as LIFE-365 (Bentz & Thomas, 2000) uses the absolute temperature in kelvin (K), in which U, is the activation energy of the diffusion process (35000J/mol),  $T_{ref}$  is the reference temperature – typically 293K (20 degrees) and R is the gas constant (8.314J/mol.K) (Ababneh, Benboudjema, & Y. Xi, 2003) which presents the equation to be:

$$D(T) = D_{ref} \cdot \exp \left[ \frac{U}{R} \left( \frac{1}{T_{ref}} - \frac{1}{T} \right) \right] = D_{ref} \cdot f(T). \quad (3)$$

Furthermore, in determining the effective diffusion coefficient, at any time t, for any given temperature, T, Equation 4 may be used:

$$D(t, T) = D_{ref} \cdot f(t) \cdot f(T). \quad (4)$$

Despite the increasingly widespread use of this tool, there is reasonable concern that its inclusion of localised temperature is based upon a seasonal cyclic environment, with no allowance for increases over long periods of time such as those derived from global warming. It is for this reason that further research and definitive solutions on climate change influences are included into the modeling.

## 3. The Surrounding Environment

### 3.1. The Climate.

Following the release of the IPCC's 5th report (IPCC, 2013), there has been firm conclusions drawn that the climate is changing and the degrees of change, notably with respect to temperature; will vary depending on the emissions scenario that will society will follow.

Within this paper, the author will be principally focus on one climate emission scenarios: A1B – a world with very rapid economic growth, for comparison, scenario A2 which illustrates a heterogeneous world with a direction towards a self-reliance and preservation of local resources is also discussed. The specific temperature increases for these emission schemes are shown in table 1.

**Table 1 - Temperature °C increase for A1B and A2 Climate Scenarios**

2030		2055		2090	
A1B	A2	A1B	A2	A1B	A2
0.7 ± 0.5	0.7 ± 0.3	1.4 ± 0.5	1.4 ± 0.3	2.1 ± 0.8	2.6 ± 0.6

These temperatures give an indicative view on what is expected within the above emissions scenarios at three distinct intervals and will later be used in the modeling of probabilistic chloride ingress data.

### 3.2. Effects of the surrounding environment.

Condition modeling of in-situ concrete assets is often a very demanding and laborious task given the extent of variables which can affect any given asset throughout any particular season. One study conducted explored (through both controlled and uncontrolled environments) the effects that ocean salinity and temperature had on the rates of chloride ingress into reinforced concrete. The results illustrated that both salinity and temperature were significant positive influences to rate of chloride ingress (Lindvall, 2007). Despite graphically demonstrating this relationship, there was no numerical relationship drawn between these two events – both within Lindvall's research and more broadly within literature.



With respect to temperature, many studies consider the chloride ingress process to take place under isothermal conditions (Yuan, Shi, Schutter, & Audenaert, 2009), however to negate this cyclic environmental trend; or to a greater extent – climatic change, would inhibit drawing an accurate understanding of the service life implications given the changing climate. Again, there is wide acceptance through both case studies (Durack & Wijffels, 2010; Hussain, 1993) and simulated experiments (Lindvall, 2007) that warmer environments will increase the rate of chloride ingress, however localised temperature influences are often not incorporated into ingress modeling as a parameters, despite it being one of the most influential environmental variables that affect the ion mobility of chlorides (Andrade & Castillo, 2003; Yang, 1999).

Finally, a finite-element framework was created by (Shafei, Alipour, & Shinozuka, 2012) explored the impacts of the physical characteristics of the concrete (mix designs and diffusion characteristics) and the external environmental variables to develop a framework to illustrate that the impacts of these variables have time-dependant and non-linear characteristics. Once again, the ability for this framework to incorporate the effects of a changing climate were negated.

#### 4. Mix designs of concrete.

The typical transport mechanism of the ingress of chlorides is through the process of diffusion through the concrete matrix. The effectiveness of this diffusion is often governed by the contents and proportions of the concrete mix which determines its porosity. Since aggregates can represent up to 75% of the volume of concrete, aggregate will always play a significant influence on the porosity of the concrete.

Basheer et al (L. Basheer, 2005) examined the influences of these proportions, specifically the size distributions of aggregates and found that there was an inverse relationship between the larger aggregates and the increase in concrete strength. Within this aggregate variability, (M.M. Azari, 1995) found that the relationship between chloride diffusion in high w/c ratio concrete mixes is often more prevalent in low micro silica content aggregates which in turn, will significantly affect the diffusion coefficient. A practical investigation into the effects of the w/c ratio is presented in part 1 below.

#### 5. Part 1: Experimental Methodology

As explored above, there is a need to develop a firm link between the effects of a changing environment and future deterioration modeling. The numerical relationship between the environmental influences and the ingress of chlorides will be extrapolated and used within the development of a prediction tool that uses IPCC data to predict long term deterioration.

##### 5.1. Environmental Simulations

There is a increasingly large number of variables that impact the ingress of chlorides into concrete and are usually related to the surrounding environment. In order to segregate the effects of each of these parameters, controlled testing environments were constructed in established humidity/temperature chambers and samples were sprayed intermittantly to simulate different chloride laden environments.

**Table 2 – Proportions of elements within synthetic saline solution**

<b>NaCl</b>	<b>58.490%</b>
<b>MgCL2 – 6H2O</b>	<b>26.460%</b>
<b>Na2S04</b>	<b>9.750%</b>
<b>CaCl2</b>	<b>2.765%</b>
<b>KCL</b>	<b>1.645%</b>
<b>NaHCO3</b>	<b>0.477%</b>
<b>KBr</b>	<b>0.238%</b>

<b>H3BO3</b>	<b>0.071%</b>
<b>SrCL2 - 6H2O</b>	<b>0.095%</b>
<b>NaF</b>	<b>0.007%</b>

The saline concentrations were synthetically produced with a product containing balanced proportions to simulate the concentrations established by the American Standards for Testing Materials (Materials, 2013). Once the concentrate was added, continuous monitoring of the saline levels was recorded to illustrate the effects of the concrete leaching and any evaporation from the tanks with any variances greater than 5% ppt (parts per thousand) duly re-adjusted.

Within the experimental stage of this paper, differing mix designs were selected to illustrate the impacts that mix design will have pore matrix structure and thus chloride ingress. Both a high strength – taken from the specification of a recent port development; and a control mix were used to illustrate the influences of the surrounding environment. Further, it has been widely recognized that a reduction in the water to cement ratio will result in a reduction to the number of voids within the cement pore matrix thus reducing the mobility of chloride ions permeating through the concrete. This investigation will also demonstrate how the vulnerability in concrete to chlorides can be minimized with a change in the mix design of concrete. It is expected that the pozzolanic admixtures in the high strength mix may also provide some resistance to the ingress of chlorides, however this paper will focus primarily on the water/cement ratio being the dominating determinate for the chloride resistance of the concrete.

**Table 3 – Mix designs of concrete samples**

	<b>High Strength (mix 1)</b>	<b>Low Strength (mix 2)</b>
<b>Ingredient</b>	<b>kg/m3</b>	<b>kg/m3</b>
OPC	310	450
Silica Fume	20	-
Fly Ash	100	-
<b>w/b ratio mix</b>	<b>0.37</b>	<b>0.48</b>
20mm Aggregate	790	675
10mm Aggregate	310	675
Fine Sand	451	938
Manufactured Sand	250	-
GLENIUM 107 SURETEC	Slump of 140 +/- 30mm	N/A

Coarse and fine aggregate were tested for moisture content and absorption and the mixing water content was adjusted accordingly. A superplasticiser was added to the high strength mix to ensure workability into the sample moulds given the relatively low water content. 300 X150 \*X150mm samples were half filled, vibrated and finished before being placed into a lime solution curing tank at 20 degrees for 28 days.



**Figure 1 – Setup of testing in simulated environments**

Additional high and low strength cylinders and porosity samples were crushed and tested achieving an average of 37.06 and 59.10MPa respectively. Samples were then inserted into testing environments which included independent pumps and spray systems that showered twice daily to simulate the two high tides and drying time that is experienced within the splash zone. Samples were then exposed for 180 days continuously in climatic controlled conditions.

To facilitate the distinction between the effects of temperature and humidity, the atmospheric variables of the differing areas were as follows:

**Table 4 – Climate and salinity concentrations of chambers**

Chamber	Temperature	Humidity	Solution Concentrations
CH1	15 ° C	50% RH	10ppt, 20ppt, 30ppt, 40ppt
CH2	23 ° C	50% RH	10ppt, 20ppt, 30ppt, 40ppt
CH3	23 ° C	80% RH	10ppt, 20ppt, 30ppt, 40ppt

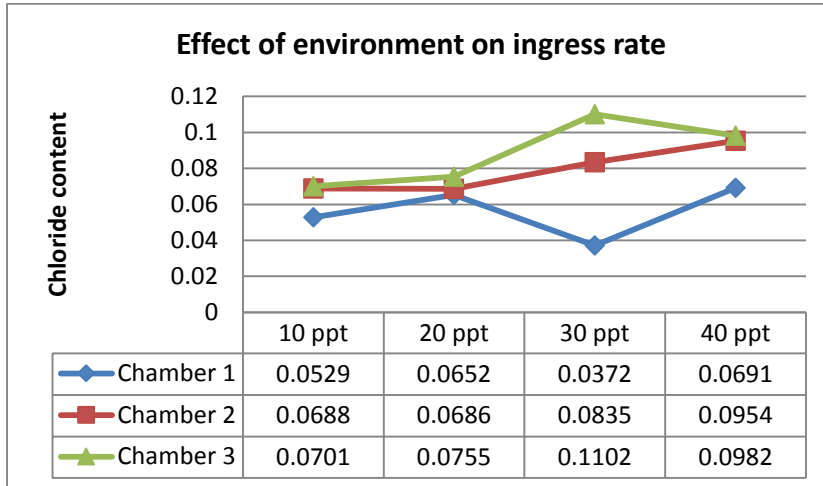
After 180 days of being exposed to the respective environments 50mm core samples were taken to a depth of 30mm and ground down in 10mm segments with a diamond tipped dry cut as not to wash away any chlorides. Once cut, the samples are ground down with a mortar and pestle and then individually packaged and sent for chloride content testing. Core holes are then filled with an impervious mortar and left to dry before being returned to the saline environments.

The results of the testing at the differing environments were translated into a chloride data analysis where the sum of squares reduction was performed to ascertain the surface chloride and chloride diffusion coefficient. This minimisation of squares was completed using the SOLVER application within Microsoft Excel.

## 5.2. Results

In the experimental planning, there was a variance of concrete mix design to prove the influence that the mix can have on the rate of chloride diffusion. The reduction of water to cement ratio (and thus inclusion of superplasticiser) in the high strength concrete was found to significantly improve the amount of void spaces within the pore matrix. In comparison to a controlled sample, the reduction of w/c ratio was responsible for a 25-30% decrease in the diffusion coefficient which is likely to cause a noticeable difference in the modelling of the chlorides.

The salinity of the solutions within the simulation tanks also acted as an accelerant in the absorption of chlorides through the concrete. Although some literature suggests that the external free chloride content has little influence on the rate of absorption (as there is a fixed diffusion coefficient); this was proved to be inaccurate as the tanks with higher salinity saw more chloride ions permeating through the material at lower depths.



**Figure 2 – Chloride content of concrete in varying environments**

The above illustrates a trend illustrating how an environment with higher saline concentration will inevitably increase the magnitude of free chlorides within the pore matrix. Further to this, the evidence suggests that the increase in both temperature, but more notably humidity – creates a more chloride aggressive environment whereby the chlorides diffuse through the concrete at a faster rate. This phenomenon results from a decrease in the bound chloride content, thus making the active corrosion easier to commence (Hussain, 1993). In addition, this increase in temperature also lowers the activation energy required to catalyse the passive film breakdown (Glass GK, 1997). In modeling the observed behaviour, active corrosion is considered when, in a small exposed area, the corrosion rate of the reinforcing bar is higher than 0.1  $\mu\text{A}/\text{cm}^2$ .

This information further allows the inputs of the model to be tailored to the specific environment and what the intended effects of climate change will be on the localised sea surface salinity.

## 6. Modelling the effects of future climate on concrete deterioration in a seaports context.

The data received from the experimental works outlays the quantifiable relationship between temperature, humidity, salinity, and w/c ratio. This data is then inserted as boundary conditions with a model that uses the most recent climate data for each year into the future and can formulate the change in corrosion initiation given the corrosion activation rate of 0.1  $\mu\text{A}/\text{cm}^2$ .

In bringing together the above temperature and salinity dependent formulae and incorporating them into one holistic equation, this paper is allowing a new version of Fick's 2nd law to be both time and environmentally dependent and responsive to changes in the environment into the future.

$$C(x,t) = C_0 * 1 - \operatorname{erf} \left( \frac{x}{2 * \sqrt{\left( K_t * K_e * K_c * \beta_t * D_c * 10^6 * \left( \frac{1}{t - (t_0 - 1)} \right)^{n * (t - t_0 - 1)} \right)}} \right) \quad (8)$$

Where  $C_0$  is the surface chloride which is extrapolated from the boundary conditions of each test sample in part 1 (dependant on the environment), erf is the error

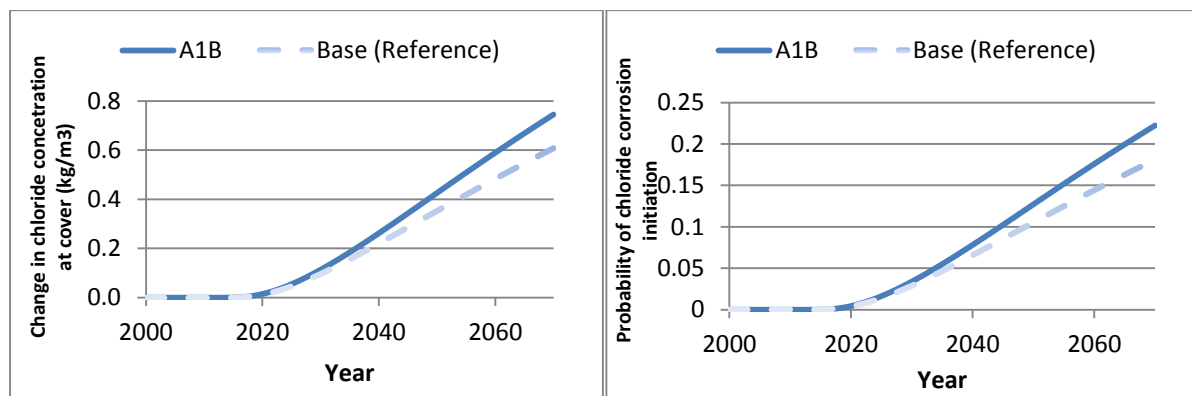
function,  $x$  is the depth of the test taken,  $K_t$  is the correction factor proposed by (Uji, Matsuoka, & Maruya, 1993),  $K_e$  is the environmental factor (Yoon, 2008),  $\beta_t$  is the temperature factor which has been modified from the works by (Yoon, 2008) to incorporate the results from Part 1,  $D_c$  is the diffusion coefficient which is taken from either of the two sample tests in part 1 (i.e. high or low w/c ratio),  $t$  is the year of observation,  $t_0$  is the time that the specimen was initially exposed to the saline environment, and  $C_{(x,t)}$  is the depth of chloride penetration.

### 6.1. Results of the modeling:

The below results illustrate how a changing climate is impacting on the chloride concentration at the cover depth and the timeframe until the initiation of corrosion. It is evident that the A1B scenario which details sea surface temperatures rising by 2.1 ° C and a slight increase in sea surface salinity brings forward the time for corrosion initiation of reinforcement. Unlike LIFE-365 modeling which assumes a repetitive annual climate, with no provision for long-term localised climatic change, the model proposed within this paper allows for the quantifiable forecasting of asset deterioration incorporating the effects of climate change.

Figure 3a below show the quantitative difference in projected corrosion induced by chloride intrusion for a high strength concrete asset following the IPCC A1B climate future. Figure 3b details a significant difference between the baseline and the climate impacted deterioration curve. Given that asset management remediation works will often commence at a certain corrosion initiation probability trigger, (e.g. 20%) the model indicates a reduction in serviceable lifespan of the asset by over a decade.

It is worthy acknowledging that within the future planning of seaport assets which are classed as long-term critical infrastructure, the accuracy of forecasting productivity downtime and economic spending is paramount.



(a) Change in chloride concentration at cover (50mm)

(b) Probability of corrosion initiation

**Figure 3 – Chloride concentration and corrosion initiation results**

## 7. Conclusion:

The existing numerical relationships between environmental change and concrete deterioration within literature varied significantly and within the context of seaports and high-strength concrete mixes; did not have a finite and quantifiable influencing factor on the ingress of chlorides.

In a changing climate, seaport authorities and governments are becoming increasingly dependent on research which depicts the effects that climate change may have on their structures. As competition on logistics and economic security through sea transport strengthens its hold on future planning, accurate condition deterioration modeling is pivotal for policy makers and seaport stakeholders alike.

Work presented here leads to following conclusions:

- Current climate models indicate a significant change in environmental factors which affect chloride ingress in reinforced concrete structures when exposed to marine environments
- Preliminary results of simulated lab experiments indicate that the temperature rise and increase in humidity as well as increase in salinity of the environment will increase chloride ingress in reinforced concrete structures exposed to marine environments
- Using the A1B climate model from IPCC [9], the results obtained from the experiments, and the approach presented by Trapper [8] a probabilistic model is developed to forecast probability of ingress in chlorides and corrosion initiation time of a selected port structure.

- Outcomes indicate that earlier intervention, as early as 10 years compared to current practice, will be needed to ensure protection of port structures from chloride ingress.

## 8. References

- A.V. Sietta, R.V. Scotta, & Vitaliani, R. V. (1993). Analysis of chloride diffusion into partially saturated concrete. *ACI Mater J*, 90(5), 441–451.
- Ababneh, A., Benboudjema, F., & Y. Xi. (2003). Chloride Penetration in non-saturated concrete,. *Civil Engineering*, 2(15), 183-191.
- Amey, S. L., Johnson, D. A., , & Miltenberger, M. A. (1998). Predicting the service life of concrete marine structures: An environmental methodology. *ACI Structural Journal*, 95(2), 205-214.
- Andrade, C., & Castillo, A. (2003). Evolution of reinforcement corrosion due to climatic variations. *Materials and Corrosion*, 54(6), 379-386. doi: 10.1002/maco.200390087
- Bastidas-Arteaga, E., Bressolette, P., Chateaufneuf, A., & Sánchez-Silva, M. (2009). Probabilistic lifetime assessment of RC structures under coupled corrosion–fatigue deterioration processes. *Structural Safety*, 31(1), 84-96. doi: <http://dx.doi.org/10.1016/j.strusafe.2008.04.001>
- Bastidas-Arteaga, E., Chateaufneuf, A., Sánchez-Silva, M., Bressolette, P., & Schoefs, F. (2010). Influence of weather and global warming in chloride ingress into concrete: A stochastic approach. *Structural Safety*, 32(4), 238-249. doi: <http://dx.doi.org/10.1016/j.strusafe.2010.03.002>
- Bentz, E., & Thomas, M. (2000). Manual of computer program for predicting the service life and life cycle costs of reinforced concrete exposed to chlorides. 1–55.
- Durack, P. J., & Wijffels, S. E. (2010). Fifty-Year Trends in Global Ocean Salinities and Their Relationship to Broad-Scale Warming. *Journal of Climate*, 23(16), 4342-4344,4347-4362.
- Emmanuel, A., Oladipo, F., & Olabode, O. (2012). Investigation of Salinity Effect on Compressive Strength of Reinforced Concrete. *Journal of Sustainable Development*, 5(6), 74-82
- Frederiksen, J. M., & Geiker, M. On an empirical model for estimation of chloride ingress into concrete. In Proceeding of the second international RILEM workshop on testing and modelling the chloride ingress into concrete, . *RILEM Publications SARL*, 355-371.
- Glass GK. (1997). Buenfeld NR. Chloride threshold levels for corrosion induced deterioration of steel in concrete. *RILEM International Workshop on Chloride Penetration into Concrete. St. Remy les Chevreuse*, 429-440.
- Hussain, S. E. (1993). Effect of temperature on pore solution composition in plain cements. *Cem Concr Res*, 23, 1357-1368.
- IPCC. (2013). Working Group I Contribution to the IPCC Fifth Assessment Report Climate Change 2013: The Physical Science Basis Summary for Policymakers". Switzerland.
- J.S. Kong, A. Ababneh, D. Frangopol, & Xi, Y. (2002). Reliability analysis of chloride penetration in saturated concrete. *Probab Eng Mech*, 17(3), 305-315.
- Johannesson, B. F. (1993). A theoretical model describing diffusion of a mixture of different types of ions on pore solution of concrete coupled to moisture transport. *Cement Concr Res*, 33(4), 481–488.
- Kong, J. S., Ababneh, A. N., Frangopol, D. M., & Xi, Y. (2002). Reliability analysis of chloride penetration in saturated concrete. *Probabilistic Engineering Mechanics*, 17(3), 305-315. doi: [http://dx.doi.org/10.1016/S0266-8920\(02\)00014-0](http://dx.doi.org/10.1016/S0266-8920(02)00014-0)
- L. Basheer, P. A. M. B., A.E. Long. (2005). Influence of coarse aggregate on the permeation, durability and the microstructure characteristics of ordinary Portland cement concrete. *Constr Build Mater*, 19, 682-690.
- Lindvall, A. (2007). Chloride ingress data from field and laboratory exposure – Influence of salinity and temperature. *Cement and Concrete Composites*, 29(2), 88-93. doi: <http://dx.doi.org/10.1016/j.cemconcomp.2006.08.004>
- M.M. Azari, P. S. M., S.C. Tu. (1995). Chloride ingress in microsilica concrete. *Cement Concrete Compos*(15), 215-221.
- Materials, T. A. S. f. T. (2013). Standard Practice for the Preparation of Substitute Ocean Water.
- Rajasankar, J., & Iyer, N. R. (2006). A probability-based model for growth of corrosion pits in aluminium alloys. *Engineering Fracture Mechanics*, 73(5), 553-570. doi: <http://dx.doi.org/10.1016/j.engfracmech.2005.10.001>

- Saetta, A. V., Scotta, R. V., & Vitaliani, R. V. (1993). Analysis of chloride diffusion into partially saturated concrete. *ACI Materials Journal*, 90(M47), 441-451.
- Schmidt, G. (2009). Global needs for knowledge, dissemination, research, and development in material deterioration and control. *World Corrosion Organisation, New York*.
- Shafei, B., Alipour, A., & Shinozuka, M. (2012). Prediction of corrosion initiation in reinforced concrete members subjected to environmental stressors: A finite-element framework. *Cement and Concrete Research*, 42(2), 365-376. doi: <http://dx.doi.org/10.1016/j.cemconres.2011.11.001>
- Shi, X., Xie, N., Fortune, K., & Gong, J. (2011). Durability of steel reinforced concrete in chloride environments: An overview. *Construction and Building Materials*, 30, 125-138.
- Tang, L. P., & Nilsson, L. O. (1992). Rapid determination of chloride diffusivity in concrete by applying an electrical field. *ACI Materials Journal*, 89(1), 49-53.
- Uji, K., Matsuoka, Y., & Maruya, T. (1993). Formation of an equation of surface chloride content of concrete due to permeation of chloride. *Corrosion of reinforcement in concrete, London, 1990*, 258-267.
- Val, D. V., & Trapper, P. A. (2008). Probabilistic evaluation of initiation time of chloride-induced corrosion. *Reliability Engineering & System Safety*, 93(3), 364-372. doi: <http://dx.doi.org/10.1016/j.ress.2006.12.010>
- Y. Xi, & Bazant, Z. P. (1999). Modeling chloride penetration in saturated concrete. *ASCE J Mater Civil Eng*, 11(1), 58-65.
- Yang, Q. (1999). Inner relative humidity and degree of saturation in high-performance concrete stored in water or salt solution for 2 years. *Cement and Concrete Research*, 29(1), 45-53. doi: [http://dx.doi.org/10.1016/S0008-8846\(98\)00174-4](http://dx.doi.org/10.1016/S0008-8846(98)00174-4)
- Yoon, I. S. (2008) Theoretical approach to calculate surface chloride content  $C_s$  of submerged concrete under sea water laden environment. *Vol. 385-387* (pp. 181-184).
- Yuan, Q., Shi, C., Schutter, G. D., & Audenaert, K. (2009). Effect of temperature on transport of chloride ions in concrete. *Concrete Repair, Rehabilitation and Retrofitting II*, 345-351.



# In situ and laboratory testing of different repair materials.

Lukovic, M.<sup>1</sup>, Gellweiler, W.A.<sup>2</sup>, Sierra Beltran, M.G.<sup>1</sup>, Blom, C.B.M.<sup>2</sup>, Savija, B.<sup>1</sup>, Zanten, van, D.C.<sup>2</sup>  
Schlangen, E.<sup>1</sup>, Ye, G.<sup>1</sup> and Taffijn, E.<sup>2</sup>

<sup>1</sup>Delft University of Technology, Faculty of Civil Engineering and Geosciences, Delft, Netherlands

<sup>2</sup>Engineering office municipality Rotterdam, Netherlands

**Abstract:** The Maastunnel in Rotterdam has to be renovated to ensure service life for a few more decades. The concrete of the tunnel is deteriorated. Chloride from deicing salts has penetrated into the concrete and has reached such levels in the material that the reinforcement is heavily corroded. Furthermore the concrete cover has spalled off and disappeared in large sections of the tunnel, especially in the floor of the tunnel. The cross section of the reinforcing bars at those places is also heavily decreased. The intention is now to perform a repair of the cover-zone concrete which will last for the remaining service life of the tunnel without any or limited maintenance.

In the Microlab at Delft University several novel repair materials are developed which are based on fibre reinforced cementitious composites. The new materials enable a good bond with the old concrete and have a crack distributing capability. Furthermore, if the reinforcement bars continue to corrode, the repair material will not fail because it can to a certain extent cope with the imposed strain by the expanding bars. With these materials several patches are repaired inside the tunnel and laboratory specimens for property testing and accelerated corrosion tests are prepared. The paper compares and discusses the performance of the different repair materials in situ and the results of the laboratory testing.

**Keywords:** Immersed tunnel, repair, SHCC, rebar corrosion.

## 1. Introduction

The Maastunnel in Rotterdam is Europe's first immersed tunnel with a rectangular cross section. It is completed in build in 1942 with a length of 1373 meter. Crossing the Maas river that flows through the heart of Rotterdam, the tunnel consists of four tubes combined within a single section: two tubes for cars, one for cyclists and one for pedestrians. It has to be renovated to ensure service life for a few more decades. The concrete of the tunnel is deteriorated. Chloride from deicing salts has penetrated into the concrete and has reached such levels in the material that the reinforcement is heavily corroded. Furthermore the concrete cover has spalled off and disappeared in large sections of the tunnel (Figure 1a), especially in the floor of the tunnel. The cross section of the reinforcing bars at those places is also heavily decreased. Analyses performed, commissioned by municipality of Rotterdam, showed however that the safety of the Tunnel is also guaranteed if the reinforcement at the inner surface of the floor is partly or completely removed from the cross section. Nevertheless, the intention is now to perform a repair of the cover-zone concrete which will last for the remaining service life of the tunnel, with no or limited maintenance.



**Figure 1: a) Inspected floor and ceiling of the ventilation tubes in the tunnel b) damage continuation in the previously repaired patches**

After studying internal reports provided by the municipality of Rotterdam and after having visited the tunnel it was concluded that the most logical and also feasible repair method is the following:



- Remove the concrete in the cover zone that is contaminated to a depth which is two times the original cover depth plus the rebar diameter. By doing so the new repair layer surrounds the rebars at all sides with a layer of uncontaminated material which has the size of the old cover depth.
- Clean the rebars by removing all the rust.
- Add a repair material which does not debond and crack. The risk for failure of the repair material is large because of different moisture conditions and related deformation in the repair material compared to the old concrete. Furthermore the corrosion of the rebars might continue after some time, which will lead to spalling of the repair material.

Even if the repair is performed with good quality materials and all the rust is removed from the rebars there is still a risk that the repair will fail in time (see for example Figure 1b). In the Microlab at Delft University currently several research project are ongoing on the development of new repair materials [1-4] and on the chloride ingress and corrosion of rebars in (cracked) concrete [5-7]. From this research several new repair materials are developed which are based on fibre-reinforcement and show strain hardening capacity (strain-hardening cementitious composites - SHCC [8]). The new materials create on the one side a good bond with the old concrete and have a crack distributing capability and therefore are an excellent candidate as repair material. Furthermore if the reinforcement bars might continue to corrode the repair material will not fail because it can to a certain extent cope with the imposed strain by the expanding bars.

The overall aim of the project is to develop a durable repair system for concrete in the Maastunnel that will prolong the service life of the tunnel for another 50 years without having to perform major maintenance.

This paper discusses part of the project, which is testing the performance of a number of repair mixes in the laboratory and in field tests. In the next section the tests that are performed are described. Subsequently this is followed by a presentation and discussion of the outcome of the tests. Finally some conclusions of the research are given.

## 2. Design of Testing

Two groups of tests have been done for investigating and comparing performance of different types of repair materials which are suitable for repair application in the tunnel. One set of tests has been performed in the laboratory and the second set has been done in the field, inside the tunnel. These tests are discussed in this section.

### 2.1 Laboratory tests

The tests performed on several repair mixtures in the laboratory research are summarized below:

- flexural performance test on the 5 different types of repair materials (Figure 2a). This test is done on 100x100x400mm prisms.
- compression test done on the samples after flexural testing (Figure 2b). 100x100x100mm<sup>3</sup> cubes are cut from the prism specimens and are tested in compression test.

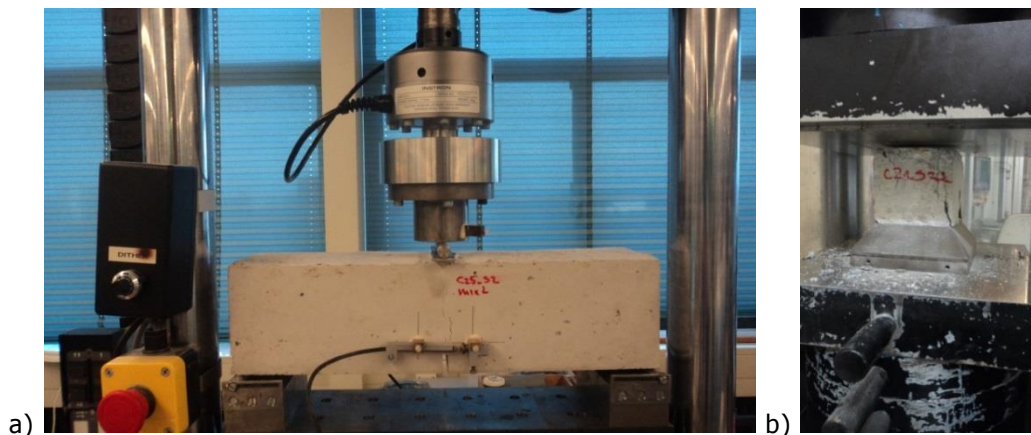
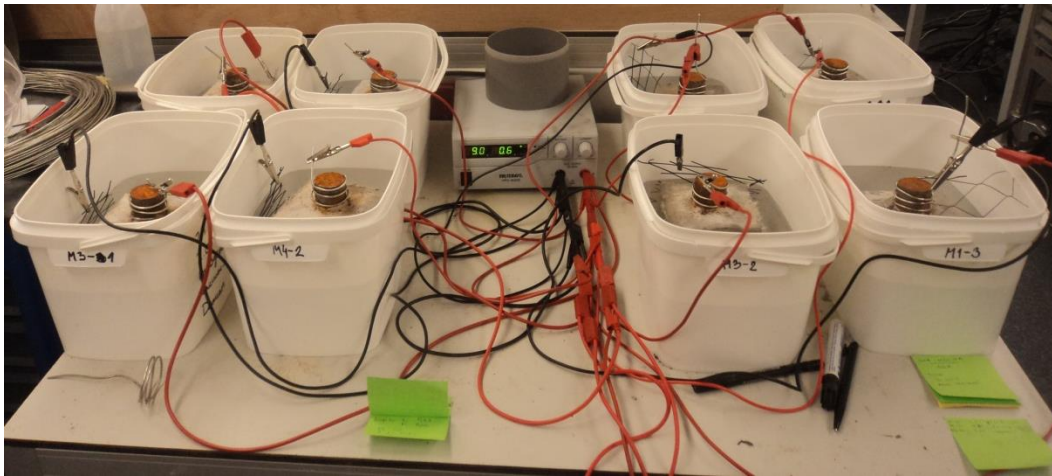


Figure 2: a) Flexural tests on 100x100x400mm<sup>3</sup> samples and b) compression tests on cubes 100x100x100mm<sup>3</sup> cut after flexural tests

Flexural and compression tests are done both on laboratory cured samples (two curing regimes: temperature,  $T=20^{\circ}\text{C} \pm 2^{\circ}\text{C}$  and relative humidity,  $\text{RH}=50\% \pm 2\%$  or  $T=20^{\circ}\text{C} \pm 2^{\circ}\text{C}$  and  $\text{RH}=95\%$ ) and also on the on situ samples. These samples are cast from the same material used in the patches, and were stored in the tunnel until testing (28days). This was done in order to compare laboratory made and cured mixtures with the mixtures that were mixed on-site and cured in the same conditions as patches.

- accelerated corrosion tests done on  $100 \times 100 \times 100 \text{mm}^3$  cubes with a single reinforcing bar of 35mm diameter placed in the middle of the specimen (Figure 3). 2 cubes were tested per each of the applied repair materials.

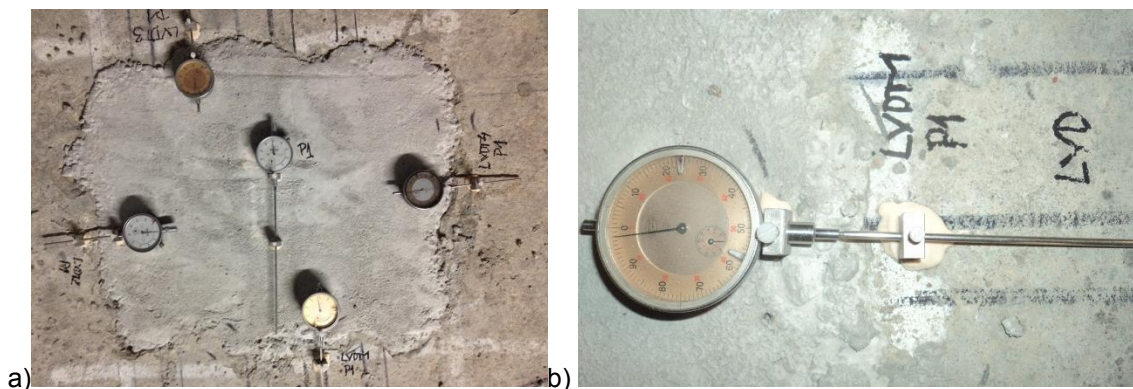


**Figure 3: Accelerated corrosion tests**

## 2.2 Field tests

The field tests in the tunnel can be described as follows:

- deformation measurements of the applied repair materials. To determine the magnitude of dimensional changes, length change is measured in each patch. This is done by attaching a dial gauge in the middle of the patch, with a measuring length of 10 cm and an accuracy of  $1 \mu\text{m}$  (Figure 4a). For each repair material dial gauge was attached.
- the interface delamination is measured also by dial gauges which were attached in the repair material on one side and in the concrete substrate on the other side (Figure 4b). Measuring length is 5 cm. For each patch, 4 dial gauges were attached around the edges of the repair material.

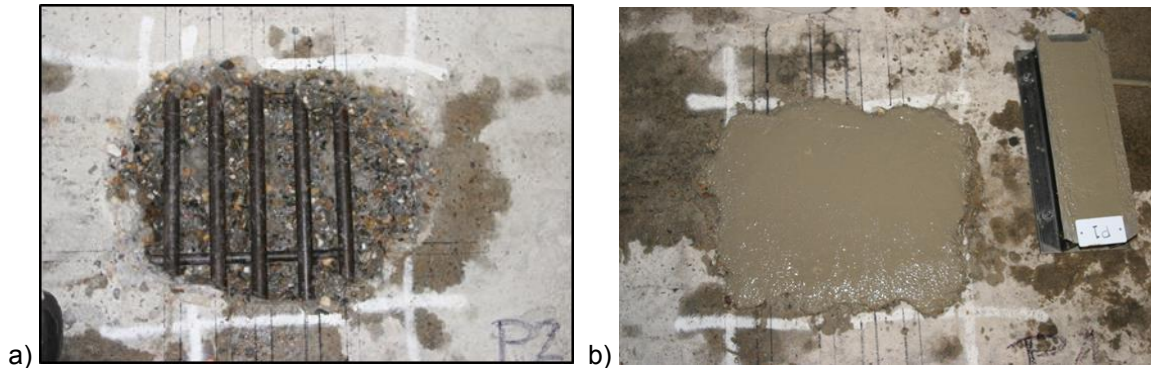


**Figure 4: a) Dial gauges for deformation measurement inside the material and b) delamination between two materials**

- the surface cracking in the repair materials was investigated with a portable microscope. The number of cracks and the crack width were measured manually.

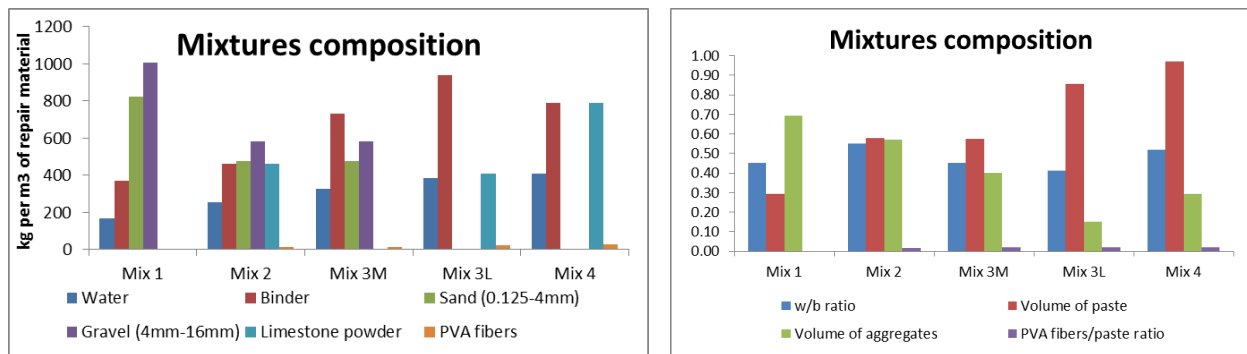
- pull-off test of the repair material to investigate bond strength between repair material and concrete substrate. These tests are done at the age of 41 days of applied repair materials.

For the field tests patches were prepared using hydro-jetting. Size of the patches were in the range of 500x500x110mm<sup>3</sup> (Figure 5). Patches were water saturated with a dry surface prior to application of the repair material. Patches were covered with a wet geotextile material for the first 7 days.



**Figure 5: Preparation of patch by hydro-jetting (a). Casting of repair patches and corresponding prisms (b)**

Five different mixtures were developed for the application in the tunnel. Overview of all mixture compositions (given without chemical admixtures) is given in Figure 6. In order to make a more clear comparison of the mixtures, also the volume of aggregates, paste and w/b ratio (per weight) is given. Mix 1 has the highest content of aggregates and the lowest content of paste. In order to enable good distribution of fibres and good workability of the mixtures, Mix 2 and mix 3M have the higher content of paste and lower content of aggregates. Mix 3L and Mix 4 are traditional SHCC mixtures without coarse aggregates [3, 4].

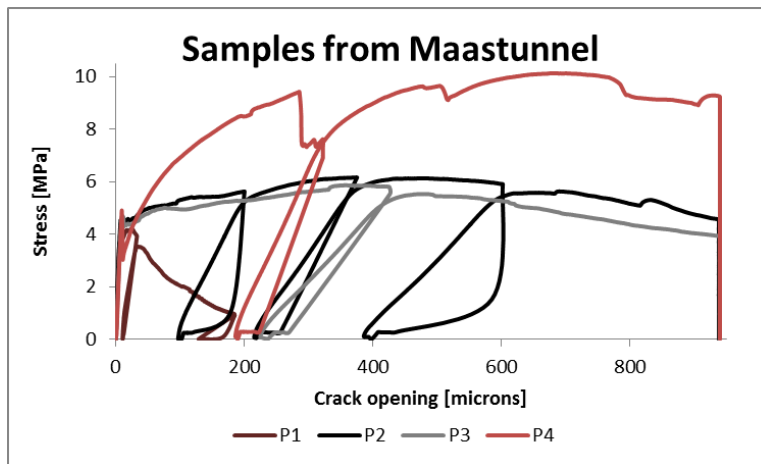


**Figure 6: Mixture compositions including amount of water, binder, aggregates and fibres**

### 3. Results

The beam specimens made in the laboratory and also the specimens made in the tunnel were tested at the age of 28 days in 3-point-bending. This is done for comparison with laboratory made and cured specimens, but also to check the properties of the material casted and cured in the same way as patches. First a notch of 25 mm was made in the middle of all of the samples. Then the samples are left to dry for 2 hours before three point bending test. Test was done by controlling the crack opening which enabled that the post-peak behaviour is measured. Samples made from mixtures Mix1, Mix2, Mix3M and Mix4 are labelled with P1, P2, P3 and P4, and correspond to Patch 1, 2, 3 and 4.

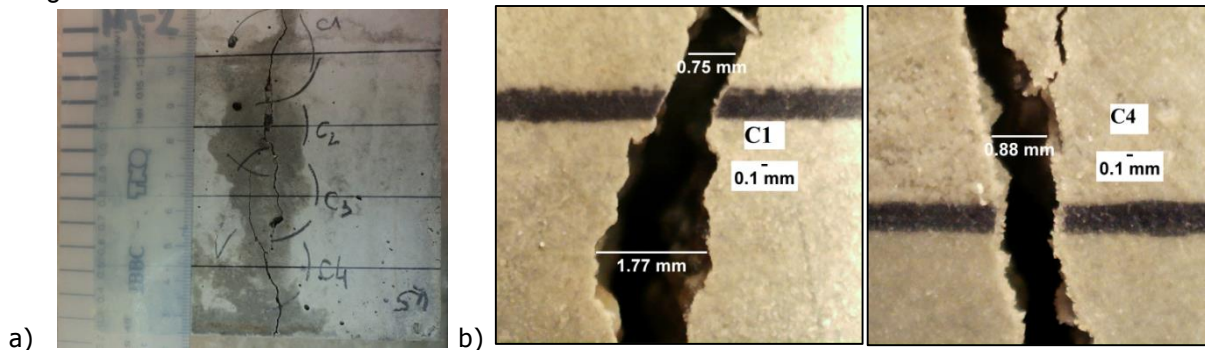




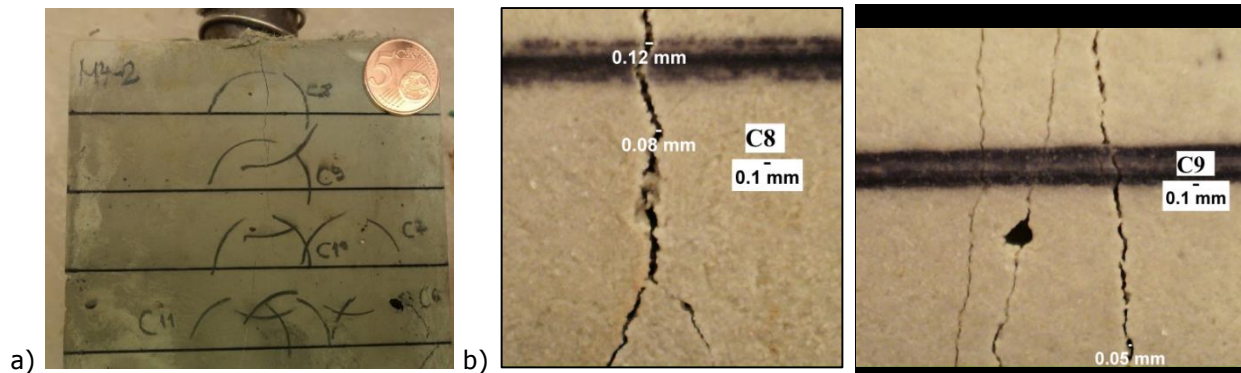
**Figure 7: Stress-crack opening diagram of beam specimens casted and cured in the tunnel.**

An example of the 3-point-bending results is given in figure 7, where the tests on the samples made inside the tunnel are shown. It can be seen from the stress-crack opening curves that all mixtures, except Mix 1 in P1 show strain-hardening capacity in bending. This means that after first cracking, stresses that the material can withstand do not reduce (as in Mix 1 where peak strength is equal to first cracking strength) but they increase with further crack opening. Differences are observed between cracking patterns of different samples. In specimen P1 only one crack forms. This specimen exhibits strain-softening behaviour, which is typical of concrete. As a consequence, after the peak load, the load-bearing capacity of the specimen drops. On the other hand, specimens P2, P3 and P4 show strain-hardening behaviour. This means that, after the first cracking, due to fibre activation, they can still withstand increasing stresses, resulting in ductile behaviour. This is important for repair materials, as repair systems are usually not crack free (due to restrained deformations, incompatibility between two materials [9, 10]), and it is important how they behave at higher strain levels. Mix 4 used in P4 shows the highest amount of strain hardening. This mixture has only sand and no larger aggregates. The fibres are more effective in this case. However Mix 2 and Mix 3M with larger aggregates might be more practical. The test results on the specimens made in the laboratory show similar behaviour.

For the accelerated corrosion tests, samples were cast in 100x100x100mm<sup>3</sup> moulds with a plain reinforcing bar with a diameter of 35mm, placed in the middle of the mould. This size and type of the rebar was chosen to be similar to the existing rebars in the tunnel. Note that accelerated corrosion results in uniform expansion around the reinforcement, which is somewhat different from chloride induced corrosion, which results in pitting (i.e. non-uniform expansion). After 1 day, the samples were demoulded and left for 4 days in the fog room ( $T=20^{\circ}\text{C} \pm 2^{\circ}\text{C}$  and  $\text{RH}=95\%$ ) for curing. At the age of 5 days, they were taken out and exposed to accelerated corrosion test. Samples were immersed in water and a titanium mesh was used as a cathode. Applied voltage was 18 V, which should enable that current density is about 200  $\mu\text{A}/\text{cm}^2$  of the steel rebar. The applied voltage was increased in time in order to increase and speed up damage development in the specimens. Images of damaged specimens are made during the exposure period. The results for Mix 1 and 4 are presented in figures 8 and 9. Mix1 exhibited only one crack with a large crack opening, while all fibre-reinforced mixtures had more cracks with by an order of magnitude smaller crack widths.



**Figure 8: Cracking pattern and representative cracks for Mix 1 captured with a) camera and b) microscope**



**Figure 9: Cracking pattern and representative cracks for Mix 4 captured with a) camera and b) microscope**

From the deformation and delamination measurements it is observed that all patches behave according to expectations. Deformation measurement increases only if cracking or delamination occurs. Generally, delamination was not observed in any of the repairs. Mix 1 did not exhibit cracking while the fibre-reinforced mixtures exhibited designed cracking. In pull-off tests, all failures with very low strength happened in the concrete substrate. Therefore, it seems that, in general, concrete substrate is more critical than repair material and bond strength. Still, due to the limited number of pull-off tests, small core diameter and difference in observed failure mode, no statistically reliable data is obtained from these tests.

#### 4. Discussion

High ductility is one of the most important requirements for a good repair material. In the repair system, due to drying and hydration, the repair material tends to shrink. Its deformation is, however, restrained by the concrete substrate, and either cracking or delamination results. However, delamination can only occur at a free end or around existing cracks in the repair material that propagated deep to the substrate. Otherwise, if there is no crack in the repair material or delamination at the free end, delamination beneath repair material, in the middle of the patch can never occur. This is not dependent on the size of the repair and therefore is also valid for bigger repairs. Further on, due to incompatibility in properties between the two materials (thermal properties, permeability properties, conductivity properties), any kind of thermal gradients will induce stresses that might cause cracking. Therefore, repair systems are very susceptible to cracking and are almost never crack free. That is why it is important not only to know how a material behaves under high loads, but it is more important how material behaves under large strain (after some cracking). Furthermore, maximum widths and distribution of these cracks are important for any further deterioration mechanism in the repair system (carbonation, freeze-thaw).

Mixture M1 has the smallest shrinkage. In the fibre-reinforced mixtures, as aggregate amount reduces from Mix1 to Mix4, the amount of material that is shrinking is increasing, meaning that more strain is developing. This strain is sufficient for inducing cracking. Due to the strain-hardening capacity, it might be considered that crack widths will not grow significantly, even in a larger patch, but will distribute at similar distances as already observed in the small patches in the tunnel. The cracks observed in the patches might however only be surface cracks at this stage. Therefore, both fibres and aggregates in repair material mixtures have their own benefits. Fibres are reducing crack widths, which is very important for solving the brittleness issue of a repair material. On the other hand, aggregates are beneficial as they enable reduction of total shrinkage, which is also an important aspect for concrete repair.

Due to big corrosion problems and observed damage in the existing repairs, a series of tests was also performed to assess the resistance of used repair materials to continued corrosion. For this purpose, an accelerated corrosion test was used. As expected, Mix1 exhibited only one crack with a large crack opening, while all fibre-reinforced mixtures had more cracks with much smaller crack widths. Therefore, it is clear that risk of continued corrosion will be less critical for the fibre-reinforced mixtures. In addition, as the material is more resistant to damage due to continued corrosion, it might be possible that less concrete need to be removed prior to repair. From these tests it might be concluded that if corrosion continues and Mix1 is applied, large cracks will develop and patches or repair will most likely spall. If a mix with fibres is applied the risk for large cracks is low and it will not likely result in loose patches.

An important aspect for concrete repair is the bond strength. Due to high restraint level of the repair material (restrained due to dense reinforcement) bond problems and debonding are not expected to be critical for the performance of the repair in these conditions. Furthermore, good bond is an important factor only if the material cracks and debonds. Bond strength will further determine how and where a crack or delamination will propagate. Compared to pull-off test, more influence of the bond can be observed through deformation measurement inside the repair system (delamination and deformation inside the repair material) and visual inspections of the repairs. This is because a pull-off test at certain location will, at best, give the bond strength (only if it breaks exactly at the interface and not in the concrete substrate or repair material), but not the probability of debonding. Due to the making the core, most of the eigenstresses that exist at the interface due to restrained deformations will be released and will not be measured during the pull-off test. Therefore, more crucial tests than pull-off tests for performance of the repair are: visual inspection, quantification of crack widths and crack spacing, and deformation measurements inside the repair system. This type of study will include all the most important parameters (repair material shrinkage, repair material relaxation, repair material E modulus, tensile strength, concrete substrate creep, amount of restraint at the interface, bond strength, environmental conditions, saturation level of the concrete substrate) and their interaction in the specific case study. All these factors are important, but their interaction is complicated and not well known. Therefore, based on a single parameter and test, e.g. bond strength or free shrinkage, performance of repair system cannot be reliably assessed.

## 5. Conclusions

From the laboratory tests and the field tests in the Maastunnel the following conclusions can be drawn:

- With all the proposed mixes a compression strength can be obtained that is in line with the concrete that is present in the tunnel.
- The strength of the concrete made on site in the tunnel is only a few percent lower than the concrete made in the laboratory.
- All mixes containing fibres show a strain hardening behaviour and multiple cracking. The fracture energy of the mixes containing fibres is much higher than the concrete without fibres. Mix 4 shows the highest amount of strain hardening.
- The accelerated corrosion tests performed in the laboratory show that Mix1 (concrete without fibres) results in a single crack with large crack opening (~1.0mm). In the tests with the other mixes the corrosion tests result in multiple cracking and the cracks width stay small (below 0.15mm)
- In the patches made in the tunnel no delamination occurred and only very small shrinkage cracks are observed in the mixes with fibres. Mix 1 (concrete without fibres) no cracks were observed, because of the high volume of aggregates and low amount of paste present, which results in lower shrinkage. In addition, shrinkage reducing admixture was used for this mixture.
- The pull-off tests show that, in general, good bond is achieved between the tested repair materials and the concrete substrate. In most of the tests it was observed that the concrete substrate was the weakest link in the system, probably due to the selected method of surface preparation. Therefore, the pressure that was applied during hydro-jetting in these patches did damage the surface of the concrete. This needs to be kept in mind during the final repair stage of the tunnel. One of the possible ways to reduce the amount of damage is to reduce the pressure that is applied during hydro-jetting. Then, however, it should be checked if the method is fast enough and practically feasible for removing large areas of concrete.

## 6. Acknowledgement

The expert help of the Microlab technicians Ger Nagtegaal and Maiko van Leeuwen in performing the field and lab-tests is highly appreciated.

## 7. References

1. Zhou, J. Performance of engineered cementitious composites for concrete repairs, PhD thesis, Delft University of Technology, 2011.

2. Lukovic, M., Savija, B., Dong, H., Schlangen, E., Ye, G.. Micromechanical study of the interface properties in concrete repair systems. Journal of Advanced Concrete Technology, 2014; 12: 320-339.
3. Lukovic, M. Influence of interface and SHCC material properties on the performance of the repair system, PhD thesis, Delft University of Technology, in preparation.
4. Sierra-Beltran, M.G., Jonkers, H.M., Schlangen, E. Characterization of sustainable bio-based mortar for concrete repair, Construction and Building Materials, Vol 67, Part C, pp. 344-352, 2014.
5. Savija, B. Experimental and numerical investigation of chloride ingress in cracked concrete, PhD thesis, Delft University of Technology, 2014.
6. Šavija, B., Luković, M., Pacheco, J., Schlangen, E. Cracking of the concrete cover due to reinforcement corrosion: a two-dimensional lattice model study. Construction and Building Materials 44, 626-638, 2013.
7. Pacheco, J. Corrosion of steel in cracked concrete, PhD thesis, Delft University of Technology, 2015.
8. Li VC, Horii H, Kabele P, Kanda T, Lim YM. Repair and retrofit with engineered cementitious composites. Engineering Fracture Mechanics. 2000;65(2-3):317-34.
9. Beushausen H, Alexander M. Bond strength development between concretes of different ages. Magazine of concrete research. 2008;60(1):65-74.
10. Tilly GP, Jacobs J. Concrete repairs: Observations on performance in service and current practice. CONREPNET Project Report, IHS BRE Press, Watford, UK; 2007.

## **ACID-SOLUBLE AND WATER-SOLUBLE CHLORIDE – TESTING PROFICIENCY AND SPECIFICATION**

(Theme: Concrete Materials & Performance)

Warren South<sup>1</sup>, Tony Thomas<sup>2</sup> and Vute Sirivivatnanon<sup>3</sup>

<sup>1</sup> Cement Concrete & Aggregates Australia.

<sup>2</sup> Boral Limited

<sup>3</sup> University of Technology Sydney, Australia.

### **Abstract**

The importance of limiting the chloride ion content in concrete has always been recognised and specified in structural concrete specifications. The Australian Standard test method for acid-soluble chloride has been revised and published as AS 1012.20.1. At the same time, a newly developed water-soluble chloride test method has been published as a parallel Australian Standard AS 1012.20.2. The paper reviews and report the proficiency of the two test methods and the relationship between acid- and water-soluble chloride based on research and proficiency testing program conducted by Cement Concrete and Aggregates Australia (CCAA). Performance limits specified in international concrete standards are reviewed and recommended to be specified in relevant Australian standards and specifications.

**Keyword:** Acid-soluble, water-soluble, chloride, performance limit

Corresponding author: Dr Warren South [warren.south@cca.com.au](mailto:warren.south@cca.com.au)



## 1. Importance of limiting chloride ion content

Chloride-induced corrosion of steel reinforcement has been found to be one of the most common causes of premature deterioration of reinforced and prestressed concrete structures. The more vulnerable structures are those exposed to external sources of chloride such as from marine environments or from the use of de-icing salts. Chlorides can also come from concreting materials and hence it is important that limits are placed on chlorides from these sources including cement, supplementary cementitious material (SCM), aggregates and chemical admixtures.

Chlorides can exist as surface contaminant as well as chloride-bearing minerals in the aggregates. In hardened concrete, chlorides exist as either '*bound*' or '*free*' chloride in concrete. Chlorides can be bound as reaction products between chlorides and cement hydrates such as calcium chloroaluminate (Friedels salt). It is well recognised (ACI 222R and Byfors *et al.*, 1986) that it is the free chloride that contributes to steel depassivation and subsequent corrosion. In determining the amount of chlorides in concrete, both '*water-soluble*' and '*acid-soluble (total) chloride*' test methods have been used to determine the '*free*' and '*free + bound*' chloride respectively. Bound chloride is therefore the difference between acid-soluble (total) and water-soluble chloride.

Glass and Buenfeld (2000) found that the time to corrosion initiation of embedded steel, due to chloride diffusion from the surface of concrete, is dependent on the corrosion risk presented by bound chloride. Bound chloride may participate in corrosion initiation when the establishment of pH gradients are required to sustain passive film breakdown. This is the result of the effect on the pore solution chemistry of the pH dependent solubilities of solid phases containing bound chloride that are very similar to that of calcium hydroxide. In some circumstances, the time to corrosion initiation may be reduced by an increase in binding because of the possible corrosion risk presented by bound chloride. Hence both free and bound chlorides are equally important and must be controlled.

## 2. Development of water-soluble chloride testing method

In 2007, Cement Concrete & Aggregates Australia (CCAA) began the development of a water-soluble chloride testing method for aggregates. Up to that time, there was very limited work carried out on the difference between water-soluble and acid-soluble chloride in aggregates. Hope *et al.* (1985) focused work on the influence of different testing techniques and sample subdivision on the resultant free water-soluble chloride. They found that subdivision of aggregate samples resulted in extraction of some chloride from the aggregate material that field experience with the aggregate used suggested that this chloride did not materially contribute to corrosion of the embedded steel. They also found that the Soxhlet (high temperature) extraction of ½ inch material was effective in recovering added chloride from the concrete samples and did not extract chloride from chloride-bearing minerals in the aggregate. They suggested that the Soxhlet extraction removed only the chloride which was mobile and able to take part in the corrosion process. In 1996, ACI Committee 222 has adopted a 'Provisional Standard Test Method

for Water-Soluble Chloride Available for Corrosion of Embedded Steel in Mortar and Concrete Using the Soxhlet Extractor’.

There have been reported instances (Gaynor,1985) where quarried stone, gravels and natural sand contained small amounts of chloride that have provided concrete with chloride levels that exceed the permissible levels of 0.2% chloride by mass of cement, the upper limit recommended in ACI 222R. Other reports (Rogers and Woda, 1977) of aggregates with an acid-soluble chloride content of more than 0.1 percent of which less than one-third is water soluble when the aggregate is pulverized for the test. Not all of that chloride will necessarily become available to the paste. Thus ACI 222R indicates that higher levels are tolerable if past performance has shown that the higher chloride content has not caused corrosion.

CCAA investigated the effectiveness of the extraction of water-soluble chloride methods, including the Soxhlet method, in terms of the type of extracting agent and degree of fractured surface of the aggregates. It was found that the use of boiling water on materials passing 850-micron sieve offered a well-balanced measure of the free chloride contents in aggregate. The findings were also confirmed valid in testing hardened concrete (Sirivivatnanon, Thomas & Waye, 2011). The methods and results of the investigation were the basis for the development of an Australian test method for water-soluble chloride.

### **3. Proficiency of Australian Standard testing methods**

Both the accuracy and proficiency of test methods are important to their successful applications. CCAA initiated and conducted proficiency programme for the existing acid-soluble chloride test method AS 1012.20 and the draft water-soluble chloride test method in 2010 and 2011 respectively. Details and findings are described below.

#### **3.1 AS 1012.20 Acid-soluble test method**

A proficiency programme on acid-soluble chloride was conducted based on AS 1012.20 test method. This programme focused exclusively on the analysis of chloride content and did not examine the possible variability due to sampling technique. Samples of three sands C1, C2 and C3, with a range of chloride contents were prepared by Boral Laboratory and sent to seven NATA registered laboratories around Australia.

Six laboratories submitted the results as listed below. One of these six laboratories tested replacement samples after reporting damages to the first samples. The results are summarised in Table 1.

There are inconsistencies in the reporting of test result in both the number of decimal points and significant figures. There appears also to be a limit to the accuracy of the method with some laboratories unable to test sand such as C2 and C3, with chloride content below 0.01%, to an accuracy of 0.001%. This is possibly due to the analytical method used by various laboratories ranging from Mohr’s and Volhard’s titration to potentiometry using various ion-selective electrodes.

Table 1 AS 1012.20 acid-soluble chloride test results (%)

Sand samples Lab	C1		C2		C3	
	No. 1	No. 2	No. 1	No. 2	No. 1	No. 2
1	0.0533	0.0517	0.0016	0.0013	0.0009	0.0008
2	0.044	0.044	<0.001	<0.001	<0.001	<0.001
3	0.038	0.043	0.004	0.009	0.003	<0.002
4	0.05	0.05	<0.01	<0.01	0.01	0.01
5	0.006	0.008	0.001	0.001	0.002	0.001
6	0.0210	0.0230	<0.005	<0.005	<0.005	<0.005
Mean	0.036		(0.0042)*		(0.0035)*	
Repeatability SD	0.0017		-		-	
Reproducibility SD	0.0179		-		-	

SD=standard deviation

( ) \*mean of test results using the upper limits eg. 0.001 as upper limit for <0.001.

For C1 with the mean chloride content is well in excess of 0.01%, the repeatability and reproducibility standard deviations are 0.0017 and 0.0179% respectively. The repeatability standard deviation is within the same range as 0.0015% reported in the ASTM C1152 - Standard Test Method for Acid-Soluble Chloride in Mortar and Concrete. However, the reproducibility standard deviation of 0.0179% is significantly higher than 0.0021% reported in the ASTM C1152. For sand C2 and C3 with lower chloride contents, it is not possible to determine the precision of the method. The cause of such differences in results from various laboratories is unknown, but highlights the need for re-examination of the test procedures.

It should be noted that the AS 1012.20 Acid-soluble chloride test method is re-issued as AS 1012.20.1 in 2014 with no significant changes to the method.

### 3.2 Draft AS 1012.20.2 Water-soluble chloride test method

CCAA sought collaboration from the same seven laboratories to conduct proficiency tests on water-soluble chloride content in accordance with the draft water-soluble chloride determination for aggregates and hardened concrete test method. Three aggregates (CL6, CL7 & CL10) and one chloride solution were prepared by Boral Materials Technical Services and sent to all laboratories. Six laboratories submitted the results as listed in Table 2.

Four out of six laboratories reported the concentration of the standard solution fairly accurately between 33 to 38 mg/L for the solution which was prepared at 35.45 mg/L. Laboratory 1 & 2 reported higher solution concentrations and generally higher results for the three aggregates.

All laboratories are able to report results to 0.001% which is an improvement on the accuracy when conducted to AS 1012.20. The repeatability and reproducibility standard deviations for all three aggregates are similar to those reported in ASTM C1218 – Standard Test Method for Water-Soluble Chloride in Mortar and Concrete.

Table 2 Analysis of all results (%)

Sand samples	CL6		CL7		CL10		Solution* <sup>1</sup>	Notes
Lab/Sample	1	2	1	2	1	2	mg/L	
1	0.010	0.010	0.009	0.009	0.017	0.019	45	or 0.0045% solution
2	0.008	0.008	0.008	0.008	0.025	0.025	43	or 0.0012N solution
3	<0.001	<0.001	0.001	0.001	0.015	0.015	36	Potentiometric titration on - 150µm
4	0.0015	-	0.0014	-	0.0147	-	38	or 0.0038% solution
5	0.0022	0.0012	0.0015	0.0029	0.0127	0.0130	38	
6	0.0085	0.0075	0.0073	0.0068	0.0177	0.0161	33	Dionex IC
Mean	(0.0050)* <sup>2</sup>		0.0048		0.0171			
Repeatability SD	(0.0004)		0.0004		0.0007		0.0013% in ASTM C1218	
Reproducibility SD	(0.0041)		0.0036		0.0043		0.0037% in ASTM C1218	

\*1. Solution was prepared as 35.45 mg/L.

\*2. Use 0.0009 for values reported <0.001 in the analysis.

For CL10 with higher mean chloride content of 0.017%, the coefficient of variation of repeatability and reproducibility are 4.4 and 25% respectively. These are within acceptable range and hence the water-soluble test method gives good precision for aggregates with the AS 2758.1 reportable chloride content.

This draft water-soluble chloride testing method was introduced to Standard Australia CE-012 committee in 2014, in consultation with Standard Australia BD-042 committee for designation as the new Australian Standard AS 1012.20.2. It went to a combined procedures process early in 2015 for possible publication around May 2015.

### 3.3 Conclusion on the proficiency of the two chloride test methods

Both proficiency test programmes focused exclusively on the analysis of chloride content and did not examine the possible variability due to sample preparation technique. The results show that the draft water-soluble test method provides results to 0.001% accuracy demanded by concrete specifications. The water-soluble test method also gives good precision in terms of both repeatability and reproducibility. However, the AS 1012.20.1 acid-soluble chloride test method has failed to provide the same precision except for the repeatability of aggregate with high chloride content well in excess of 0.01%.

## 4. Performance limits for concreting materials and concrete

Australian Standards AS 3972, AS 3582 and AS 2758.1 place limits on acid-soluble chloride in cement, SCM and reportable chloride in aggregates respectively. AS 1379 places a limit on total acid-soluble chlorides in the supplied concrete to ensure durability. There are challenges associated with AS 1012.20.1 acid-soluble chloride determination. The proficiency programme found large variations in the reported results leading to a low precision of the test method. The use of the test method in specifications creates problem in aggregate selection and in determining the risk of steel reinforcement corrosion in hardened concrete. On the other hand, the draft AS 1012.20.2 water-soluble chloride test method has proven to give much improved precision with better repeatability standard deviation than and comparable reproducibility standard deviation to the ASTM C1218 method.

Different international codes and standards have adopted different performance limits for concrete structures. American Concrete Institute (ACI) uses both water-soluble and acid-soluble limits whereas European and Australian Standards adopt acid-soluble chloride limits. These performance limits and corresponding type of chloride are summarised in Table 3.

Table 3 Performance limits and corresponding chloride determination methods

Maximum acid-soluble chloride-ion content, percent by mass of cement		Maximum water soluble chloride-ion (Cl <sup>-</sup> ), percent by mass of cement	
Standard	Reinforced	Standard	Reinforced
AS 1379	0.8 kg/m <sup>3</sup> or 0.20% <sup>a</sup> RC and concrete with tendons, ducts, cast-in inserts, embedded items or other items that require protection.	ACI 318-05 At 28-42 days	0.06, 0.30, [1.00], 0.15 % Prestressed concrete, RC exposed to wet chloride in service, [RC in dry condition in service], Parking structures and those near seawater
ACI 222R-01	0.08, 0.10, [0.20]% Prestressed, RC in wet condition, [RC in dry condition]	ACI 222R-01	0.06, 0.08, [0.15]% Prestressed concrete, RC in wet condition, [RC in dry condition]
European Standard EN 206-1	0.10-0.20 <sup>b</sup> % for prestressed 0.20-0.40 <sup>b</sup> % for RC 1.00% for plain concrete	Canadian CSA A23.1-94	0.06, 0.15, 1.00 % Prestressed concrete, RC in moist or chloride or both, RC exposed to neither moisture nor chloride
British Standard BS 5328-97	0.10 % for prestressed 0.40 % for RC No limit for plain concrete		
Norwegian Code NS 3420-L	0.6% for RC 0.002% for prestressed		

Note: (a). assumed cement content of 400 kg/m<sup>3</sup>.  
(b). the class to be applied depends upon the provision valid in the place of use of concrete.

It may be prudent for Australian standard AS 1379 and other specifications to consider adopting a water-soluble chloride limit for new concrete to alleviate the low proficiency problem in the acid-soluble chloride determination. A water-soluble chloride limit of 0.6 kg/m<sup>3</sup> for new concrete is recommended for AS 1379.

## 5. Discussions

In the Australian Standard for acid-soluble chloride content AS 1012.20, no precision statement is available nor is the stipulation of the accuracy of reporting. The problem affecting the precision of the acid-soluble chloride test (AS 1012.20) has been examined from the viewpoint of the size and sampling method by Forster & Bathgate (2009). The results reported in this paper show that AS 1012.20 test method does not provide a consistently accurate result to 0.001% demanded by concrete specifications. In the case of aggregate with reasonably high chloride content, the test method provides an acceptable repeatability but excessive reproducibility. With the reproducibility standard deviation of 0.0179%, results of two properly conducted tests from two different laboratories on samples of the same material could differ by 0.05% ( $2.83 \times 0.0179\%$ ) by mass. This renders the method and its test result to be unacceptable to all parties.

AS 1379 limits the level of acid-soluble chloride in reinforced concrete to be within  $0.8 \text{ kg/m}^3$ . A typical concrete mix may contain  $700 \text{ kg/m}^3$  of sand from  $1800 \text{ kg/m}^3$  of combined aggregates. The choice of testing laboratory can contribute a difference of  $0.35 \text{ kg/m}^3$  ( $0.05\% \times 700 \text{ kg}$ ) from the sand toward the limit of  $0.8 \text{ kg/m}^3$  for concrete which is clearly an unacceptable uncertainty derived from the testing method. If the method is used to determine acid-soluble chloride in hardened concrete, the results of two properly conducted tests from two different laboratories on the same hardened concrete sample could differ by 0.05% by mass of concrete. This amount is almost the chloride threshold associated with potential corrosion of steel reinforcement. Such discrepancy could easily lead to wrong decision regarding the risk of corrosion of steel reinforcement.

On the other hand, the newly developed water-soluble chloride test method has acceptable repeatability and the highest reproducibility standard deviation of 0.0043%, results of two properly conducted tests from two different laboratories on samples of the same material could differ by 0.01% ( $2.83 \times 0.0043\%$ ). The choice of testing laboratory can contribute a maximum difference of  $0.07 \text{ kg/m}^3$  ( $0.01\% \times 700 \text{ kg}$ ) from the sand toward the recommended water-soluble chloride limit of  $0.6 \text{ kg/m}^3$  for concrete which is a more acceptable level of uncertainty derived from the testing method.

## 6. Conclusions

The lack of precision of the Australian Standard test method for acid-soluble chloride content AS 1012.20.1 has been confirmed and shown to be potentially damaging to decision on the choice of concrete aggregates and the risk of corrosion of steel reinforcement in concrete. The draft AS 1012.20.2 water-soluble chloride test method gives significantly better precision with improved repeatability and reproducibility standard deviation comparable to the ASTM C1218 method. The permissible and reportable water-soluble chloride limits specified for new concrete and aggregate in AS 1379 and AS 2758.1 should also be revised accordingly.

## 7. Acknowledgement

Cement Concrete and Aggregates Australia (CCAA) acknowledges the collaboration by the following laboratories who participated in the proficiency programmes.

- Sharp and Howells. Bullen, Victoria 3105.
- Sydney Analytical Laboratories Pty Ltd. Seven Hills, NSW 2147.
- SGS Australia Pty Ltd. New Burn, WA 6105.
- SGS Australia Pty Ltd. Rocklea, Brisbane, QLD 4106.
- Boral Materials Technical Services. Baulkham Hills, NSW 2153.
- Queensland Department of Transport and Main Roads, Materials Services.
- RTA Chemical and Materials Laboratory, Auburn, NSW 2144.

## 8. References:

- American Concrete Institute, 'Protection of Metals in Concrete Against Corrosion, Part 1' ACI 222R-01.
- American Concrete Institute Committee 222, 'Provisional Standard Test Method for Water-Soluble Chloride Available for Corrosion of Embedded Steel in Mortar and Concrete Using the Soxhlet Extractor', ACI 222.1-96.
- ASTM C1218 Standard Test Method for Water-Soluble Chloride in Mortar and Concrete, American Society of Testing and Materials, West Conshohocken, PA, 2008.
- ASTM C1152 Standard Test Method for Acid-Soluble Chloride in Mortar and Concrete, American Society of Testing and Materials, West Conshohocken, PA, 2004.
- Byfors, K., Hansson, C.M. and Tritthart, J. (1986). Pore solution expression as a method to determine the influence of mineral additives on chloride binding. *Cement Concr. Res.* 16(5), 760-770.
- Forster, G. J., and Bathgate, S.N. The Significance of Chlorides in Concrete Trial Mixes. *Proc of Concrete Institute of Australia Concrete Solutions 2009*, Sydney, Australia.
- Gaynor, R.D. 'Understanding Chloride Percentages', *Concrete International*, V.7, No. 9, Sept 1985, pp 26-27.
- Glass, G.K. and Buenfeld, N.R., 'The influence of chloride binding on the chloride induced corrosion risk in reinforced concrete', *Corrosion Science*, V.42, Iss. 2, Feb 2000, pp 329-344.
- Hope, B.B., Page, J.J. and Poland, J.S. (1985). The determination of the chloride content of concrete. *Cement Concr. Res.* 15(5) 863-870.
- Lamond, J.F. and Pielert, J.H. (1998). Significance of tests and properties of concrete & concrete-making Material. ASTM International, West Conshohocken, PA, USA.
- Rogers and Woda (1997). The Chloride Ion Content of Concrete Aggregates from Southern Ontario. Report No. EM-17, Ontario Ministry of Transportation and Communications, Downsview.
- Sirivivatnanon, V., Thomas, W.A. & Waye, K. 2011, 'Determination of free chlorides in aggregates and concrete', *Australian Journal of Structural Engineering*, Vol. 12, No. 2, pp.151-158.
- Standards Australia. Determination of chloride and sulfate in hardened concrete and concrete aggregates, AS 1012.20, Sydney, 1992.



# Integrated fracture-based model for the analysis of cracked reinforced concrete beams

Tahreer M. Fayyad<sup>1</sup> and Janet M. Lees<sup>2</sup>

<sup>1</sup>PhD Candidate, Department of Engineering, Cambridge University

<sup>2</sup>Reader in Civil Engineering, Cambridge University

**Abstract:** Due to the rapid advances in the development of techniques for monitoring and retrofitting concrete, there is a need to revisit and generalize classical theories in order to better assess the strength of existing reinforced concrete structures and to encompass strengthening systems. An improved understanding of concrete cracking taking into consideration local phenomena such as tensile and compressive concrete softening as well as the bond between the reinforcement and the concrete is required. In this paper, a fracture-based model is developed to describe the cracking process in reinforced concrete by integrating different local phenomena to more precisely describe the flexural behaviour of reinforced concrete beams. The model results show a good correlation with experimental data obtained by testing small scale concrete beams subjected to three-point bending. The beams exhibited mode I fracture propagation and during testing crack measurements were undertaken using a non-destructive digital image correlation technique. The stability of the cracking process was found to depend on the concrete strength, reinforcement properties and reinforcement ratio.

**Keywords:** Reinforced concrete, fracture, cracking mechanism, crack propagation.

## 1. Introduction

The traditional analysis of a cracked reinforced concrete section is normally based on the assumption that under flexural loading plane sections remain plane. The effect of concrete in tension is typically ignored after cracking since concrete has a low tensile strength compared with its compressive strength. This approach does not consider the crack propagation process in detail and assumes that once the crack develops the concrete cannot sustain any tensile stresses. However, cracking in reinforced concrete is a sequential process and involves a gradual loss of tensile stresses with crack propagation. Furthermore, many studies have proved the existence of concrete softening in both tension and compression i.e. (1–4). This means that even in a cracked region, parts of the open crack still have some ability to transfer stress. Recognizing that traditional analyses are not sufficient to explain the cracking process in reinforced concrete, different approaches have been used to develop theoretical models for predicting the cracking behaviour of reinforced concrete members e.g. (5–9).

Numerous factors can influence the cracking process and crack bridging in reinforced concrete (RC). These include the concrete properties, the reinforcement properties, the ratio of the longitudinal reinforcement, the bond between the reinforcement and the concrete, and the geometrical properties and the size of the beam. These factors are interrelated and interdependent; for example, the concrete and steel properties can affect the bond which consequently affect the crack bridging and crack opening displacement. This means that developing a full understanding of the cracking mechanisms in reinforced concrete members is difficult and complex. Many variables and different phenomena have to be integrated into the study of fracture to produce more realistic material models that imitate the behaviour of a quasi-brittle material such as concrete.

## 2. Crack modeling using fracture mechanics

Fracture mechanics is a field of solid mechanics that deals with the mechanical behaviour of cracked bodies. It covers rules and principles of crack propagation and remains one of the most frequently used approaches to study and model cracks in concrete structures. Both Linear (LFM) and Non-linear (NLFM) fracture mechanics have been applied to concrete. LFM analysis assumes a singularity of the stress at the crack tip while NLFM approach considers a relaxation of the stresses in the fracture process zone (FPZ) such that there exists a finite value of stress at the crack tip. LFM was applied by Carpinteri (10) when developing a Bridged Crack Model used to study the flexural failure of reinforced concrete beams. It was assumed that when the crack starts to grow, the resultant stress intensity factor  $K_I$  equals the critical stress intensity factor  $K_{IC}$ . More recently, the model has been further extended to



analyze shear cracks where the diagonal tension failure load is determined from an analytical law for the crack trajectory based on experimental observations (11). As LFM is valid when the size of the fracture process zone is negligible, the Cohesive Crack Model (CCM) or Fictitious Crack Model (FCM) was developed as an alternative to model concrete cracks taking into account nonlinear behaviour in the fracture process zone (1). The difficulty of applying the CCM without a Finite Element framework led Gerstle et al (6) to simplify some assumptions related to the FCM to develop an analytical solution for flexural cracks in reinforced concrete beams; however, their model does not consider concrete compression softening or any bond-slip behaviour between concrete and steel. Yet strain softening of concrete in compression can affect the strength and ductility of reinforced concrete members. Fracture mechanics was used by Hillerborg (4) to study compression strain localization in concrete. However, the effect of concrete tensile softening was ignored in his model.

The aim of this paper is to present an analytical solution for the development of flexural cracks in RC beams from the onset of cracking until failure. The local phenomena associated with crack propagation will be considered as well as the interaction between the concrete and the reinforcement where further research is required to quantify appropriate material models.

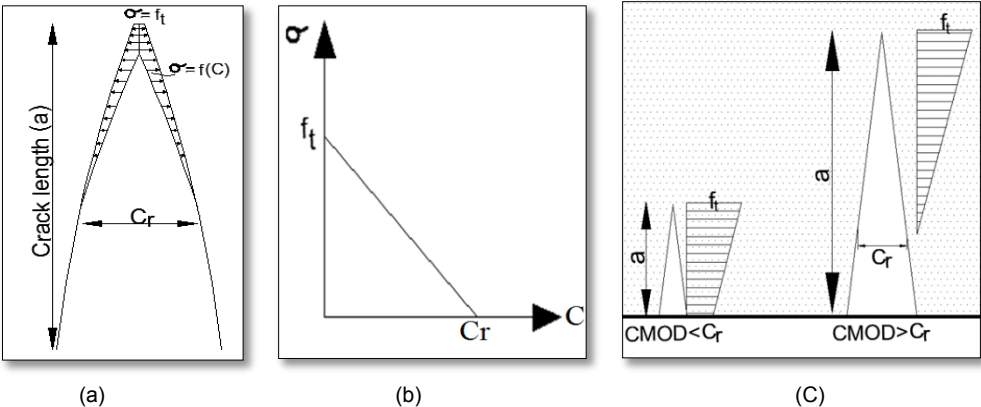
**3. Integrated fracture-based model formulation**

The proposed integrated fracture-based model incorporates post-cracking tensile stresses in the concrete, the bond-slip behaviour between the reinforcement and concrete, and compression softening in the concrete compressive zone. The modeling of each of these aspects is described in the following.

**3.1 Tension behaviour**

The Fictitious Crack Model (FCM) assumes that a crack will propagate when the stress at the visible crack tip reaches the concrete tensile strength ( $f_t$ ). As the crack opens, the stress decreases with increasing crack width ( $C$ ) until it reaches zero stress at a critical width ( $C_r$ ). The residual capacity to transfer stress in this region then needs to be overcome in order for the crack to propagate as shown in Figure (1a). The amount of energy absorbed per unit crack area to open the crack from a width of zero to  $C_r$  is the fracture toughness  $G_{IC}$ . The fracture toughness can be calculated as the area under the stress versus crack width curve ( $\sigma - C$ ) which is called a tension softening curve. For simplicity and suitability for use in a closed form solution, a linear tension softening curve is assumed in the current work (Figure (1b)). With a linear relationship between  $\sigma$  and  $C$ , when the crack mouth opening displacement  $CMOD < C_r$  the stress at the crack mouth opening equals  $(1 - \frac{CMOD}{C_r}) f_t$ . So, the total closing force ( $CF$ ) acting along the crack length ( $a$ ) per unit width is

$$CF = \frac{1}{2} a (f_t + (1 - \frac{CMOD}{C_r}) f_t) = \frac{1}{2} a f_t (2 - \frac{CMOD}{C_r}) \tag{1}$$



**Figure 1: (a) Fictitious Crack Model, (b) linear tension softening curve, (c) cracks with tension softening**

As the applied load increases, the crack opens and propagates but the crack still carries stresses which linearly decrease with the crack mouth opening displacement ( $CMOD$ ). When  $CMOD = C_r$ , the

total closing force =  $\frac{1}{2} a f_t$ . As the crack propagates further and the crack opening exceeds  $C_r$  at the crack mouth ( $CMOD > C_r$ ), the total closing force ( $CF$ ) then becomes

$$CF = \frac{1}{2} a f_t \left( \frac{C_r}{CMOD} \right) \quad (2)$$

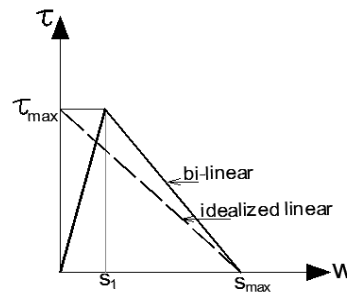
### 3.2 Bond between reinforcement and concrete

Bond between reinforcement and concrete is necessary for reinforced concrete to act as a composite material and to transfer load between the two materials. This interaction is represented in the literature as shear stresses ( $\tau$ ) on the interface between the reinforcement and concrete. These stresses are carried by different mechanisms such as mechanical interlock, chemical adhesion, and friction (12). The relative contributions of these mechanisms depend on the concrete and reinforcement properties. The development of bond stresses results in a relative displacement between the reinforcement and the concrete parallel to the reinforcement axis called slip ( $s$ ). The bond-slip behaviour of reinforced concrete affects the crack opening.

Based on test results on the local bond-slip relationship, Eligehausen et al (13) suggested a nonlinear relationship with increasing  $\tau$  and  $s$  when  $0 \leq s \leq s_1$  and until  $\tau = \tau_{max}$ . After the peak, the behaviour can be modeled using a linear relationship between  $\tau$  and  $s$  with a negative slope. Yuan et al (14) used a bi-linear approximation (Figure (2)) to study the performance of the interface between fibre reinforced polymers FRP and concrete. Mohamed Ali et al (15) further idealized a bi-linear relationship as a linear descending relationship and demonstrated its applicability to steel reinforced concrete (Figure (2)). In this case, the function that defines the bond-slip behaviour is

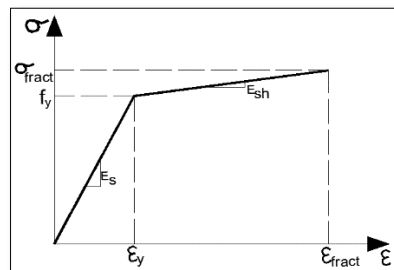
$$\tau(s) = \frac{\tau_{max}}{s_{max}} (s_{max} - s) \quad (3)$$

where  $\tau_{max}$  and  $s_{max}$  are determined experimentally and depend on the concrete and steel properties.



**Figure 2: Bi-linear bond-slip model and idealized linear bond-slip**

The stress-strain behaviour of steel reinforcement is characterized by the elastic modulus  $E_s$  until the steel yields at a stress  $f_y$ . The post-yield behaviour can be approximated as a linear relationship between the strain and stress but with a strain hardening modulus  $E_{sh}$  (Figure (3)).



**Figure 3: Idealized steel stress-strain relationship**

Haskett et al. (16) applied this steel stress-strain relationship and used an idealized linear bond-slip model like that shown in Figure (2) to study reinforced concrete. The stress-slip distribution was defined for two stages of behaviour. In the first stage the steel is elastic. During the second stage, the steel yields and the distribution of the stress-slip changes according to the strain hardening modulus  $E_{sh}$ . Considering the balance of forces and using a partial interaction numerical model, Haskett et al. (16) developed relationships between the applied axial load and the slip at the crack face by treating the elastic and the strain hardening behaviours separately and then summing them together. The elastic steel force  $SF_{el}$  was calculated considering  $E_s$ :

$$SF_{el} = \frac{\tau_{max} \pi d}{\lambda_{el}} \sin \left\{ \arccos \left\{ \frac{s_{max} - s}{s_{max}} \right\} \right\} \quad (4)$$

where  $\lambda_{el} = \sqrt{\frac{\pi d \tau_{max}}{s_{max} E_s A_s}}$ ,  $d$  is the diameter of the bar and  $A_s$  is the area of the bar cross section.

The force after yielding  $SF_{sh}$  takes into account  $E_{sh}$ :

$$SF_{sh} = \frac{\tau_{max} \pi d}{\lambda_{sh}} \sin \left\{ \arccos \left\{ 1 - \frac{s - s_{yield}}{s_{max}} \right\} \right\} + A_s f_y \quad (5)$$

where  $\lambda_{sh} = \sqrt{\frac{\pi d \tau_{max}}{s_{max} E_{sh} A_s}}$  and  $s_{yield}$  is the slip at yielding. For further details, please see (17).

### 3.3 Compression behaviour

Most of the investigations that have been carried out on strain localization in concrete under compression are based on the uniaxial compression behaviour e.g. (18–21). However, the mechanical behaviour of reinforced concrete beams with strain localization in the compression zone has not been studied extensively. Hillerborg (4) developed a fracture mechanics- based model to study compression strain localization. He treated the compression localization in a manner similar to the localization that occurs in tensile fracture. According to his model, the compression behaviour can be described by means of stress-strain diagram until the peak compressive strength is reached and thereafter using a stress-deformation diagram. It was assumed that this localization takes place within a length proportional to the depth of the compression zone which changes with loading. Jansen & Shah (20) showed that the post-peak stress-deformation relationship is a material property and depends on the specimen size. Based on this assumption, Carpinteri et al. (9) developed the overlapping crack model where he refers to the deformation that occurs after the peak load as interpenetration. In this model, instead of identifying a length where strain localization occurs, it was assumed that strain localization develops gradually in the compression zone in a manner similar to cohesive models used to describe the tension zone. The proposed stress-deformation relationship was similar to Hillerborg's. Based on the mathematical aspects of the overlapping model, a numerical algorithm was proposed (22) based on the finite element method to study the behaviour of RC beams. Borges et al. (23) adapted a linear softening curve (stress  $\sigma_c$  – strain  $\varepsilon$  response) (Figure(4)) which requires knowledge of the concrete compressive strength concrete ( $f_c$ ) and the critical damage strain ( $\varepsilon_{cr}$ ) as material properties of concrete. According to this softening curve

$$\varepsilon = \varepsilon_{cr} \left( 1 - \frac{\sigma_c}{f_c} \right) \quad (6)$$

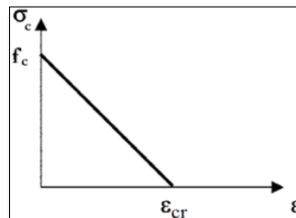


Figure 4: Compression softening in concrete

The assumption of a linear relationship between the concrete compressive stress and strain allows for an analytical solution for flexural cracking at the same time capturing the important features of the behaviour.

### 3.4 Model formulation

In this section, the local phenomena outlined above will be integrated to develop a fracture-based model to describe the cracking process in reinforced concrete and provide an analytical solution for the development of flexural cracks in RC beams from the onset of cracking until failure. To do this, an RC beam with a rectangular cross section and effective depth  $d$  and width  $b$  is subjected to an external bending moment  $M$  will be considered (Figure (5)). From the three cases indicated in the figure it follows that

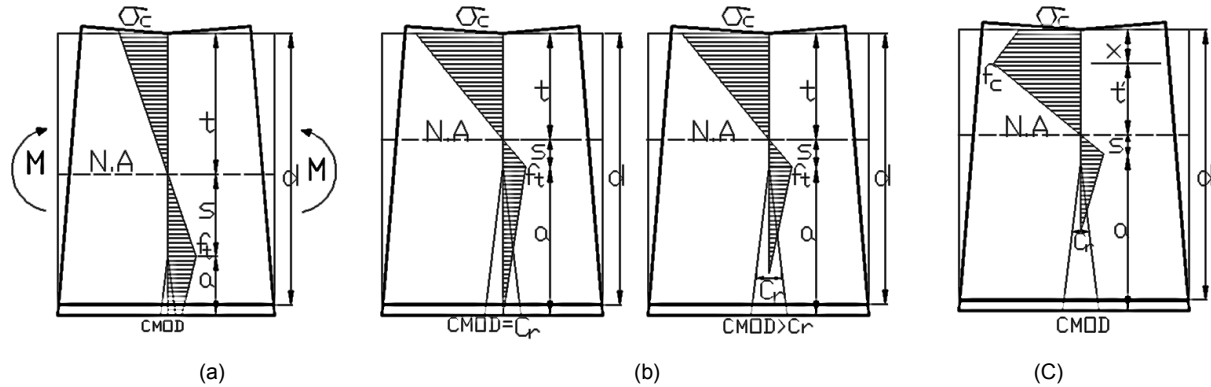


Figure 5: Crack development stages, (a) when  $CMOD < C_r$ , (b) when  $CMOD \geq C_r$  and (c) with compression softening

#### 3.4.1 Case (a) – $CMOD < C_r$ , Steel elastic

$$d = a + s + t \quad (7)$$

$$t = \frac{\sigma_c}{f_t} s \quad (8)$$

Longitudinal equilibrium gives

$$SF + 0.5 b a f_t \left( 2 - \frac{CMOD}{C_r} \right) + 0.5 b s f_t - 0.5 b \sigma_c t = 0 \quad (9)$$

While the reinforcement remains elastic, the steel force ( $SF$ ) can be determined from Equation (4) so  $SF = SF_{el}$ .

For a similar flexural crack, a relationship between  $CMOD$  and  $\sigma_c$  was developed (6) considering the deformation in concrete and the compatibility of stresses and strain in the top and bottom fibres of the beam section, where:

$$CMOD = \frac{2 \left( \frac{a}{d} \right)^2 \left( \frac{f_t d}{E_c C_r} \right) \left( 1 + \frac{\sigma_c}{f_t} \right)}{\left( 1 - \frac{a}{d} \right) \left( 1 - 2 \left( \frac{a}{d} \right) \left( \frac{f_t d}{E_c C_r} \right) \right)} C_r \quad (10)$$

#### 3.4.2 Case (b) – $CMOD \geq C_r$ , Steel may yield

$$d = a + s + t \quad (11)$$

$$t = \frac{\sigma_c}{f_t} s \quad (12)$$

Longitudinal equilibrium gives

$$SF + 0.5 b a f_t \left( \frac{C_r}{CMOD} \right) + 0.5 b s f_t - 0.5 b \sigma_c t = 0 \quad (13)$$

If the steel remains in the elastic region, the steel force  $SF = SF_{el}$  and can be calculated from Equation (4), and if the steel yields, the force after yielding can be calculated from Equation (5) since  $SF = SF_{sh}$ .

Considering the relationship between  $CMOD$  and  $\sigma_c$  (6)

$$CMOD = \frac{2 \left( \frac{a}{d} \right) \left( \frac{f_t d}{E_c C_r} \right) \left( 1 + \left( \frac{a}{d} \right) \left( \frac{\sigma_c}{f_t} \right) \right)}{\left( 1 - \frac{a}{d} \right)} C_r \quad (14)$$

### 3.4.3 Case (c) – $CMOD > C_r$ , Steel yields, Compression softening

$$d = a + s + t' + x \quad (15)$$

$$t' = \frac{f_c}{f_t} s \quad (16)$$

$$x = t \left( 1 - \frac{\varepsilon_0}{\varepsilon_0 + \varepsilon_{cr} \left( 1 - \frac{\sigma_c}{f_c} \right)} \right) \quad (17)$$

where  $\varepsilon_0$  is the strain corresponding to the compressive strength  $f_c$ .

Longitudinal equilibrium gives

$$SF + 0.5 b a f_t \left( \frac{C_r}{CMOD} \right) + 0.5 b s f_t - 0.5 b f_c t' - 0.5 b x (\sigma_c + f_c) = 0 \quad (18)$$

The steel force ( $SF$ ) can be calculated from Equation (5)

The relationship between  $CMOD$  and  $\sigma_c$  for case (b) can be modified as

$$CMOD = \frac{2 \left( \frac{a}{d-x} \right) \left( \frac{f_t (d-x)}{E_c C_r} \right) \left( 1 + \left( \frac{a}{d-x} \right) \left( \frac{f_c}{f_t} \right) \right)}{\left( 1 - \frac{a}{d-x} \right)} C_r \quad (19)$$

Considering the three cases indicated above, the crack propagation of lightly reinforced concrete beams can then be modelled by solving these equations for given steel and concrete properties.

## 4. Model results

A description of the cracking process is developed using the proposed model for different material properties and beams at different sizes. Figure (6) shows the predicted dimensionless moment  $\left( \frac{M}{f_{cb} d^2} \right)$  versus relative crack length  $\left( \frac{a}{d} \right)$  for an RC beam with the properties shown in the figure and for different reinforcement ratios (0.14% - 2%) where  $\tau_{max}$  and  $C_r$  are material properties to be determined experimentally. There are some kinks in the graphs which indicate a change between different stages of behaviour. With sufficient reinforcement the crack propagates with increasing applied moment. However, with low reinforcement ratios, in some regions, the applied moment shows a decrease in capacity with crack propagation.

The model assumes a gradual loss of tensile strength with crack propagation and that the concrete loses its tensile strength completely when the crack mouth opening equals the critical crack opening

( $C_r$ ). The point at which there is a decrease in the moment capacity is associated with the complete loss of the tensile stresses at the crack mouth as shown in Figure (6). Those stresses are then transferred to the reinforcement. If the reinforcement is not able to compensate for the loss of the concrete tensile stresses, the resistance decreases causing unstable crack propagation as noted for the beams with reinforcement ratios (0.14–0.77)% in Figure (6). Stable behaviour is associated with the development of the crack with increasing load whereas unstable behaviour is associated with the propagation of the crack under decreasing load. With higher reinforcement ratios, the crack propagation stage includes tensile softening until the tensile stresses diminish. If the stresses in the concrete exceed the compressive strength ( $f_c$ ), the concrete in compression exhibits a softening behaviour before failure and this depends on the geometrical and material properties.

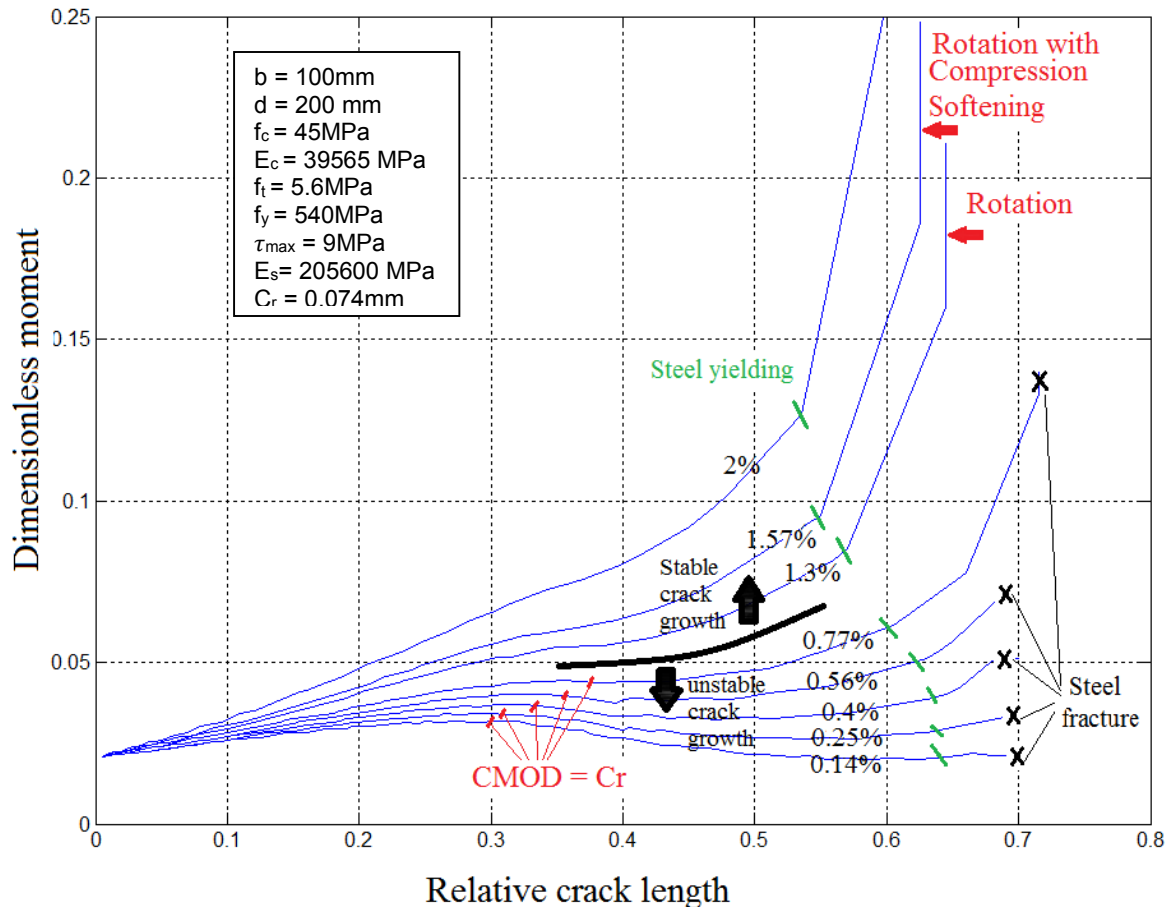
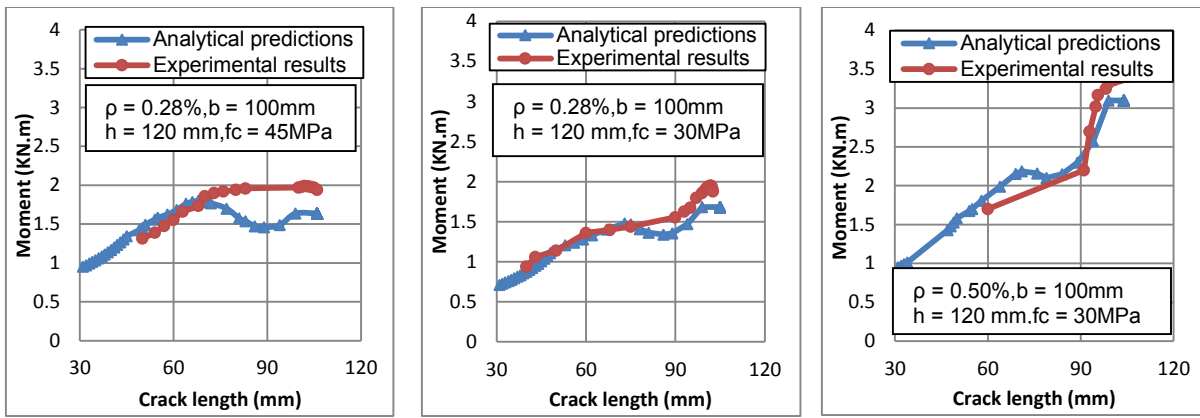


Figure 6. Moment-crack length prediction for RC beams with different reinforcement ratios.

## 5. Comparison with test results

To check the theoretical predictions, comparisons with experimental test results were undertaken. In Figure (7) the predictions are compared with experimental data obtained by testing small scale concrete beams subjected to three-point bending. The beams had a width of 100mm, a depth of 120mm and a total length of 840 mm with reinforcement ratios of 0.28% and 0.5% and a concrete compressive strength of 30MPa or 45 MPa. The beams exhibited mode I fracture (crack opening) and during testing crack measurements were taken by means of a non-destructive digital image correlation technique. For further details of the test specimens and analysis techniques, please refer to (24). The beams were tested under displacement control. It is of note that to get a better indication of a decreasing branch of the crack length-moment diagram, the beams should be tested under CMOD controlled tests. This may be a reason why the descending branches in Figure (7) are not always captured; otherwise the model results show a good correlation with the experimental data.



(a) (b) (c)  
**Figure 7. Theoretical predictions versus experimental results.**

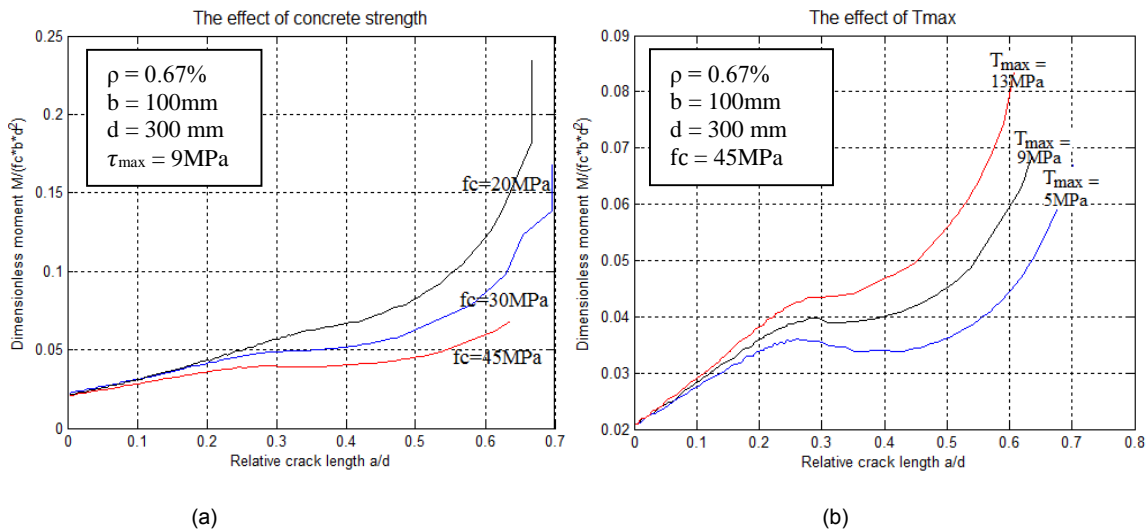
## 6. Ductility in reinforced concrete

Ductility can be defined as the ability of a material to provide sufficient deformation, and hence warning prior to failure. Ductility is very important to ensure adequate warning before collapse. Carpinteri (10) proposed a dimensionless brittleness number based on his developed LEFM Bridged Crack Model to study the stability of the cracking process in lightly reinforced concrete beams and suggested a brittleness number  $N_p$  (subsequently referred to as ductility number (25))

$$N_p = \frac{f_y d^{\frac{1}{2}} A_s}{K_{IC} A} \quad (20)$$

where  $K_{IC}$  is the critical stress intensity factor. Low values of  $N_p$  are a sign of brittle behaviour and high values give an indication of ductile behaviour.

The developed model includes further variables that are assumed to affect the cracking process. These variables include the beam depth  $d$ , beam width  $b$ , concrete compressive strength  $f_c$ , reinforcement ratio  $\rho$ , critical crack mouth opening  $C_r$ , maximum shear stress between the reinforcement and concrete  $\tau_{max}$ , elastic modulus of concrete  $E_c$  and elastic modulus of steel  $E_s$ . Figure (8) shows the effect of  $f_c$  and  $\tau_{max}$  on the behaviour of a reinforced concrete beam. It is noted that for the given parameters decreasing the concrete compressive strength increases the stability of the cracking process; on the other hand, decreasing  $\tau_{max}$  decreases the cracking stability.



(a) (b)  
**Figure 8: The effect of (a) concrete compressive strength (b) shear strength on the cracking process**

According to the developed model, it was found that in general increasing the values of  $d$ ,  $C_r$ ,  $\rho$ ,  $E_s$  and  $\tau_{max}$  increase the stability of the cracking process and helps to avoid a brittle failure due to the fracture of the reinforcement which can lead to a more ductile behaviour. In contrast, increasing the values of  $f_c$ ,  $E_c$  and  $b$  decrease the stability of the cracking process. Therefore, these properties should be reflected in a ductility measure to get a more representative indication of the ductility.

## 7. Conclusions

The proposed integrated fracture mechanics-based model is developed to describe the fracture process in reinforced concrete by integrating different local phenomena such as the tension softening of concrete to more precisely describe the behaviour of reinforced concrete beams. The model is capable of describing the initiation as well as the propagation of flexural cracks. Also, it is able to describe the post yielding behaviour as it considers the softening of concrete in compression and the strain hardening of the reinforcement after yielding. The bond between steel and concrete was modelled using a bond-slip model which gives a more accurate representation of the interaction between the concrete and the steel than the perfect bond assumption and helps to reveal the main parameters affecting the behaviour. Many assumptions related to the material behaviour were used to minimize the variables in the model to get a closed-form solution for the stresses associated with concrete cracking and the minimum reinforcement ratio, however, better accuracy can be achieved by implementing more sophisticated description of the material behaviour into the model i.e a non-linear softening behaviour can be assumed instead of linear behaviour.

## 8. Acknowledgements

The authors would like to thank the Yousef Jameel Foundation for their financial support of this research.

## 9. References

1. Hillerborg, A., Modéer, M., et al., "Analysis of crack formation and crack growth in concrete by means of fracture mechanics and finite elements," *Cem. Concr. Res.*, vol. 6, no. 6, pp. 773–781, Nov. 1976.
2. Crisfield, M. A., "Local instabilities in the non-linear analysis of reinforced concrete beams and slabs," *Proc. Instn Civ. Engrs, Part 2*, vol. 73, pp. 135–145, 1982.
3. Bažant, Z. P., Pan, J., et al., "Softening in Reinforced Concrete Beams and Frames," *J. Struct. Eng.*, vol. 113, no. 12, pp. 2333–2347, Dec. 1987.
4. Hillerborg, A., "Fracture mechanics concepts applied to moment capacity and rotational capacity of reinforced concrete beams," *Eng. Fract. Mech.*, vol. 35, no. 1, pp. 233–240, 1990.
5. Chan, B. H. C., Cheung, Y. K., et al., "Crack analysis of reinforced concrete tension members," vol. 118, pp. 2118–2132, 1993.
6. Gerstle, W. H., Dey, P. P., et al., "Crack growth in flexural members. A fracture mechanics approach," *ACI Struct. J.*, vol. 89, no. 89, pp. 617–625, 1992.
7. Ooi, E. T. and Yang, Z. J., "Modelling crack propagation in reinforced concrete using a hybrid finite element-scaled boundary finite element method," *Eng. Fract. Mech.*, vol. 78, no. 2, pp. 252–273, 2011.
8. Saleh, A. L. and Aliabadi, M. H., "Crack Growth Analysis in Reinforced Concrete Using BEM," *J. Eng. Mech.*, vol. 124, no. 9, pp. 949–958, Sep. 1998.
9. Carpinteri, A., Corrado, M., et al., "New Model for the Analysis of Size-Scale Effects on the Ductility of Reinforced Concrete Elements in Bending," *J. Eng. Mech.*, vol. 135, no. 3, pp. 221–229, Mar. 2009.
10. Carpinteri, A., "Stability of Fracturing Process in RC Beams," *J. Struct. Eng.*, vol. 110, no. 3, pp. 544–558, 1984.



11. Carpinteri, A., Ventura, G., et al., "Propagation of flexural and shear cracks through reinforced concrete beams by the bridged crack model," *Mag. Concr. Res.*, vol. 59, no. 10, pp. 743–756, Jan. 2007.
12. Lees, J. M. and Burgoyne, C. J., "Transfer bond stresses generated between FRP tendons and concrete," *Mag. Concr. Res.*, vol. 51, no. 4, pp. 229–239, Jan. 1999.
13. Eligehausen, R., Popov, E. P., et al., "Local bond stress-slip relationships of deformed bars under generalized excitations," 1982.
14. Yuan, H., Teng, J. G., et al., "Full-range behaviour of FRP-to-concrete bonded joints," *Eng. Struct.*, vol. 26, pp. 553–565, 2004.
15. Mohamed Ali, M. S., Oehlers, D. J., et al., "Interfacial stress transfer of near surface-mounted FRP-to-concrete joints," *Eng. Struct.*, vol. 30, pp. 1861–1868, 2008.
16. Haskett, M., Oehlers, D. J., et al., "Rigid body moment-rotation mechanism for reinforced concrete beam hinges," *Eng. Struct.*, vol. 31, no. 5, pp. 1032–1041, 2009.
17. Haskett, M., Oehlers, D. J., et al., "Yield Penetration Hinge Rotation in Reinforced Concrete Beams," *J. Struct. Eng.*, vol. 135, no. February, pp. 130–138, 2009.
18. Torrenti, J. M., Benaija, E. H., et al., "Influence of boundary conditions on strain softening in concrete compression test," *J. Eng. Mech.*, vol. 119, pp. 2369–2384, 1993.
19. Markeset, G. and Hillerborg, A., "Softening of concrete in compression — Localization and size effects," *Cem. Concr. Res.*, vol. 25, no. 4, pp. 702–708, May 1995.
20. Jansen, D. C. and Shah, S. P., "Effect of Length on Compressive Strain Softening of Concrete," *J. Eng. Mech.*, vol. 123, no. January, pp. 25–35, 1997.
21. Watanabe, K., Niwa, J., et al., "Localized failure of concrete in compression identified by AE method," *Constr. Build. Mater.*, vol. 18, pp. 189–196, 2004.
22. Carpinteri, A., Corrado, M., et al., "An integrated cohesive/overlapping crack model for the analysis of flexural cracking and crushing in RC beams," *Int. J. Fract.*, vol. 161, no. 2, pp. 161–173, Feb. 2010.
23. Borges, J. U. A., Subramaniam, K. V., et al., "Length effect on ductility of concrete in uniaxial and flexural compression," *ACI Struct. J.*, vol. 101, no. 101, pp. 765–772, 2004.
24. Fayyad, T. M. and Lees, J. M., "Application of Digital Image Correlation to Reinforced Concrete Fracture," *Procedia Mater. Sci.*, vol. 3, pp. 1585–1590, 2014.
25. Carpinteri, A., Cadamuro, E., et al., "Minimum flexural reinforcement in rectangular and T-section concrete beams," *Struct. Concr.*, vol. 15, no. 3, pp. 361–372, 2014.

# Predicting fire induced spalling in concrete structural elements

James M. de Burgh<sup>1</sup>, Stephen J. Foster<sup>2</sup> and Hamid R. Valipour<sup>3</sup>

<sup>1</sup>PhD Candidate, University of New South Wales

<sup>2</sup>Professor and Head of School of Civil and Environmental Engineering, University of New South Wales

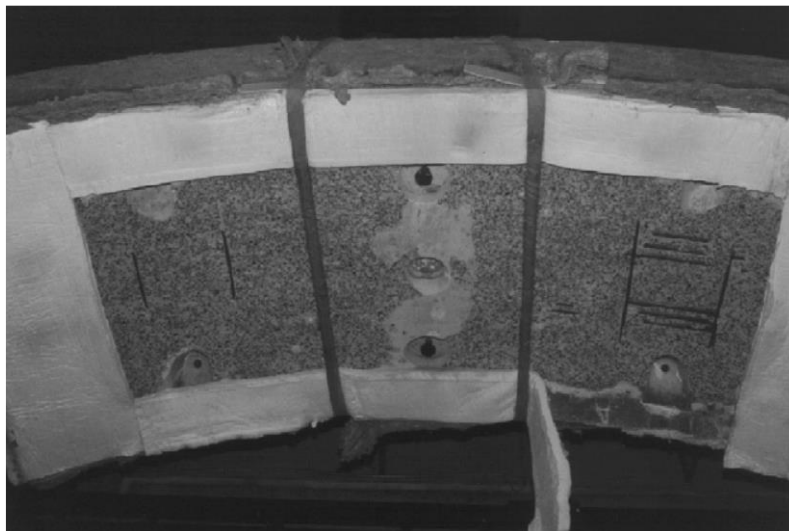
<sup>3</sup>Senior Lecturer, University of New South Wales

**Abstract:** When concrete structures are exposed to fire, they may exhibit fire induced spalling. This spalling severely reduces the ability of concrete to insulate steel reinforcement and may result in premature structural failure. As part of an ongoing research project into the numerical prediction of fire induced spalling, a new coupled hygro-thermo-mechanical model is developed – suitable for modelling the general heat and moisture transfer and mechanical response of concrete wall or slab type elements exposed to fire. This paper presents the developed hybrid fibre-type mechanical model together with mechanical constitutive behaviour, hygro-thermal model and associated coupling. The model is used to simulate an experimental test where spalling was observed and the results are used to propose and discuss a robust theory for the phenomena.

**Keywords:** fire, spalling, pore pressure, hygro-thermo-mechanical, high temperature

## 1. Introduction

Concrete thermal spalling has been defined as “the violent or non-violent breaking off of layers or pieces of concrete from the surface of a structural element when it is exposed to high and rapidly rising temperatures as experienced in fires” (1). It is typically characterised into various types, based on the appearance, sound and violence of the spalling damage. Surface spalling, and in particular explosive spalling (generally characterised by the significant violence of its action), is generally regarded as the most serious form of spalling – posing significant potential risk to structural survival.



**Figure 1. Spalled inner surface of a Great Belt Tunnel element (rebar visible), tested by Hertz (2).**

In traditional concretes (i.e. not densified by SCMs and not having a high strength (2)) spalling upon extensive heating is likely if the moisture content is high. For dense or high strength concretes, spalling is highly likely and may occur multiple times, resulting in a combined section loss of 25 – 100 mm or more from a fire exposed face (3). Any significant amount of spalling will dramatically change the geometry of a member – removing cover and its insulating ability from reinforcement. For these reasons and more, decades of research have been put into trying to understand and mitigate the phenomena behind surface and explosive spalling.

Despite this work, researchers have (as yet) been unable to fully understand the mechanisms behind fire induced spalling. For this reason, its prediction is currently reliant upon empirical data, expert opinion and large scale tests (3) – methods that are generally either inaccurate or expensive (and potentially both).

Since the 1960's, many researchers have speculated on mechanisms responsible for the surface/explosive spalling phenomena in fire exposed concrete. Generally speaking, earlier proposals relied upon quite simplified arguments – consistent with the prevailing basic understanding of the mechanical and hygral processes occurring. A good summary is provided by Connolly (4); the main theories established by the late 90's were:

- *Thermal stress induced spalling* – where sufficiently rapid heating rates lead to a non-linear temperature profile and result in compressive stresses coplanar and near to the exposed surface. When these mechanical stresses exceed the compressive strength of concrete; failure occurs.
- *Pore pressure induced spalling* – with an increasing temperature near a fire exposed face, evaporable moisture within the concrete (and non-evaporable water being liberated) vaporises. The build-up of vapour pressure trying to escape outwards, combining with moisture heading inwards creating an increasingly saturated zone – 'moisture clog' – leads to even greater vapour pressures. When gas pressures exceed the tensile strength of the concrete, spalling occurs.
- *Combined thermal stress and pore pressure induced spalling* – some combination of the previous two effects. For example, Sertmehemetoglu (5) proposed that the compression stresses create internal cracks parallel to the surface and that the internal gas pressures acted upon this weakened zone to cause spalling.

In the last 15 years, a number of sophisticated hygro-thermal and hygro-thermo-mechanical models have been developed by researchers attempting to better understand the phenomena responsible for fire induced spalling – with the eventual ambition of predicting its occurrence. With the development of these models, a number of complementary suggestions as to a 'criterion' for detecting the occurrence of fire induced spalling have been made. These modern criteria have typically taken one of three forms:

- *Simple mechanical model based criteria* – generally based on simplified hypotheses about the stability of a surface concrete laminate. Detailed information about the stresses etc. (from the HTM model) is taken as basic input for the simple model (6).
- *Damage level based criteria* – where spalling is considered to occur at an arbitrary magnitude of mechanical and/or thermo-chemical damage (7).
- *Failure envelope versus pore pressure* – in partly or fully uncoupled models (mechanical and hygro-thermal), spalling is considered to occur when a combination of a gas pressure related tension and mechanical stresses reaches a multi-axial concrete failure envelope (8) (9).

While these spalling criteria have been proposed with some success, none have yet been demonstrated to convincingly and reliably predict spalling within arbitrary concrete sections. Moreover, none adequately explain the mechanics behind the spalling phenomena in a quantitative way and in the context of the established 'ordinary' mechanical behaviour.

In this paper, a new contribution to the research on spalling prediction is presented. A coupled hygro-thermo-mechanical (HTM) model is developed and implemented for studying the detailed mechanisms behind spalling. The model is pseudo-one dimensional, making it appropriate for predicting the behaviour of planar type elements such as floor slabs, walls and tunnel linings. The experimental tests of Ozawa et al. (10) are simulated using the model, as a context for discussing the phenomena of fire induced spalling.

## **2. Coupled hygro-thermo-mechanical model**

### **2.1 Introduction**

With the spalling resistance of concrete floors, walls, road and rail tunnel linings and any other planar type elements being of critical interest, and given that the hygro-thermal processes within these elements is practically one-dimensional, it is logical to develop a pseudo-one dimensional approach to the analysis for spalling prediction.

A comprehensive hygro-thermal model, based largely on the work of Gawin et al. (11), has been described in (12). In this study, the hygro-thermal model is coupled to a suitable mechanical model (for modelling the behaviour of concrete at high temperatures). A partitioned solution approach is taken for the

hygro-thermo-mechanical problem, whereby the HT component is solved individually – followed by the mechanical model – then both are iterated until satisfactory convergence is achieved between exchanged variables. The mechanical model is briefly described below.

## 2.2 Kinematics of hybrid type fibre model

A pseudo-one dimensional mechanical model (referred to as the *fibre model*) is proposed, based on the classical assumption that “plane sections remain plane”. If we consider full 3-dimensional mechanical constitutive behaviour, a suitable infinitesimal (small) strain measure is  $E^T = \{\varepsilon_{xx} \varepsilon_{yy} \varepsilon_{zz} \gamma_{xy} \gamma_{yz} \gamma_{zx}\}$ , noting that shear strain terms are twice the strain terms found in the strain tensor form. The conjugate stress measure according to the usual vector form is  $S^T = \{\sigma_{xx} \sigma_{yy} \sigma_{zz} \tau_{xy} \tau_{yz} \tau_{zx}\}$ . Considering a planar type structural component of thickness  $t$ , a straight line may be defined in the direction of the thickness and the coordinate axis  $z$  defined along this line, with a complementary continuous displacement field being  $w$ . Accordingly, the strain at any location  $z$  along the fibre is described by:

$$\varepsilon_{zz}(z) = \frac{\partial w}{\partial z} \quad (1)$$

The coordinate  $x$  and  $y$  axes are defined perpendicular to the  $z$  axis and to each other. With the condition that plane sections remain plane, the in-plane elongation strains at depth  $z$  are described by:

$$\varepsilon_{xx}(z) = \varepsilon_{xm} + \kappa_x z \quad (2)$$

$$\varepsilon_{yy}(z) = \varepsilon_{ym} + \kappa_y z \quad (3)$$

The terms  $\varepsilon_{xm}$  and  $\varepsilon_{ym}$ , and  $\kappa_x$  and  $\kappa_y$  are the mean elongations and curvatures (respectively) in both  $x$ - and  $y$ -directions. Likewise, the in-plane shear strain at varying depth is described by:

$$\gamma_{xy}(z) = \gamma_{xym} + \kappa_{xy} z \quad (4)$$

Here  $\gamma_{xym}$  and  $\kappa_{xy}$  are the mean in-plane shear strain and twist, respectively. Assuming Mindlin plate theory, the out of plane shear strains  $\gamma_{yz}$  and  $\gamma_{zx}$  are considered constant throughout the thickness. From the described kinematics, the vector of strain parameters applicable to the whole fibre is:

$$\mathbf{p}_m = \{\varepsilon_{xm} \kappa_x \varepsilon_{ym} \kappa_y \gamma_{xym} \kappa_{xy} \gamma_{yz} \gamma_{zx}\} \quad (5)$$

When combined with the elongation strain, these completely define the strain field at any location along the fibre. The vector of net actions on the fibre (per unit width) is:

$$\mathbf{q}_m = \{N_x M_x N_y M_y N_{xy} M_{xy} Q_y Q_x\} \quad (6)$$

The axial forces on the fibre are  $N_x$  and  $N_y$ , for the  $x$  and  $y$  axis orientations respectively. The in-plane shear force acting on the fibre is  $N_{xy}$ , and out of plane shear forces acting on  $y$  and  $x$  oriented faces are  $Q_y$  and  $Q_x$ , respectively. Bending moments acting on the fibre are  $M_x$  and  $M_y$ , causing stress changes on the  $x$  and  $y$  axis faces, respectively, with twisting moment  $M_{xy}$ . These actions on the fibre are chosen (in this order) as they are complementary to the whole fibre strain parameters described in Equation 5.

Following these definitions, it is possible to discretise the fibre and utilise a traditional finite element type formulation along the  $z$ -axis (i.e. with a number of along-fibre displacement degrees of freedom). Combining with suitable numerical integration for the along-fibre stress fields, the equation assembly may be written in the same format as a typical non-linear finite element problem. Solution is achieved using a predictor-corrector type Newton-Raphson method. As the mechanical model makes use of a combination of curvature, strain and displacement degrees of freedom along the fibre, it is a hybrid approach.

Unlike existing approaches to the HTM analysis of wall-like elements, where unrealistic fully fixed boundary conditions and plane-stress assumptions are used (8) (13) (14), the approach described above is able to realistically model the un-constrained (or constrained) curvature and elongation that arises in

concrete walls/slabs. Additionally, it is possible to consider any pre-tension or applied load in the analysis, and the geometric effect of a 'large' element size may be considered by fixing curvature.

### 2.3 Mechanical constitutive model for fire exposed concrete

While the mechanical model (described in the previous section) is pseudo-one dimensional, the high temperature concrete material behaviour must be modelled in a fully three-dimensional sense. For this reason, a suitable comprehensive constitutive model is required. Following the established approach for modelling short term response of concrete in fire, a total strain rate decomposition is considered:

$$\dot{\mathbf{E}} = \dot{\mathbf{E}}_{\sigma} + \dot{\mathbf{E}}_{ft} + \dot{\mathbf{E}}_{tr} \quad (7)$$

The components of the total strain,  $\mathbf{E}$ , are the instantaneous stress-related strain,  $\mathbf{E}_{\sigma}$ , the free thermal strain (FTS),  $\mathbf{E}_{ft}$ , and transient creep strain,  $\mathbf{E}_{tr}$ . Any additional basic creep strain is neglected since for fire spalling analyses, where time duration is short, its contribution is typically minimal (15).

The free thermal strain of concrete heated to high temperatures is typically established by heating an unstressed specimen. It has been established that the expansion strain is dominantly determined by the quantity and type of aggregates in the concrete (3). For siliceous type aggregates the following phenomenological expression (developed from that proposed in (16)) provides a good correlation with experimental data for linear expansion, and is used in the model:

$$\varepsilon_{ft}(T) = \begin{cases} \frac{0.02 V_a}{\ln(5/63)} \ln\left(\frac{650 - \theta}{630}\right) & \text{for } 20^{\circ}\text{C} \leq \theta \leq 600^{\circ}\text{C} \\ 0.02 V_a & \text{for } \theta > 600^{\circ}\text{C} \end{cases} \quad (8)$$

The variable  $V_a$  corresponds to the volumetric ratio of aggregates within the concrete and  $\theta$  is the temperature in Celsius degrees. The three-dimensional strain rate is then given by:

$$\dot{\mathbf{E}}_{ft} = \dot{\varepsilon}_{ft} \mathbf{1} \quad (9)$$

where  $\mathbf{1}$  is the second order identity tensor expressed in matrix form,  $\mathbf{1}^T = \{1 \ 1 \ 1 \ 0 \ 0 \ 0\}$ . Since uncontrolled shrinkage strains occur during any heating process for the measurement of FTS (being almost impossible to separate from pure mechanical strains), they are considered to be implicitly included in this expression.

An approach similar to Nielsen et al. (17) has been taken to modelling the transient creep strains (TCS). Firstly, a dimensionless temperature is defined as  $\bar{T} = (T - 20^{\circ}\text{C})/980^{\circ}\text{C}$ , then a normalised TCS function is defined by:

$$\bar{\varepsilon}_{tr}(T) = \begin{cases} A\bar{T} & \text{for } 0 \leq \bar{T} \leq \bar{T}^* \\ A\bar{T} + B(\bar{T} - \bar{T}^*)^3 & \text{for } \bar{T} > \bar{T}^* \end{cases} \quad (10)$$

where the two constants are  $A = 0.025$  and  $B = 0.7$  and with the dimensionless transition temperature  $\bar{T}^* = 0.3$ . Following the work of de Borst and Peeters (18), the multi-axial transient creep rate is postulated as depending linearly upon the (effective) stress tensor,  $\mathbf{S}$ , according to:

$$\dot{\mathbf{E}}_{tr} = \frac{\beta}{f_c} \mathbf{H} \mathbf{S} \dot{T} \quad (11)$$

where  $\beta$  is the derivative of the normalised TCS function,  $\bar{\varepsilon}_{tr}$ , with respect to temperature  $T$ ,  $f_c$  is the ambient temperature compressive strength and  $\mathbf{H}$  is a compliance matrix (see for example (13)). In this study the Poisson's ratio like parameter used in the compliance matrix is taken as  $\nu_c = 0.35$ . The predictions of this approach have been confirmed to represent well the mechanical behaviour of loaded concrete under elevated temperatures.

Lastly a model for the instantaneous stress-related-strain type mechanical behaviour of the concrete itself is required. Considering that the hygro-thermal component of the overall model requires information on mechanical damage (as it strongly effects permeability), a model with a damage basis is suitable. As a first step, an isotropic damage model has been implemented in this study – while such models cannot

capture anisotropic stiffness effects and do not model unloading well, these limitations are unlikely to have any significant consequences for this analysis. Isotropic damage models have also been used successfully by the dominant HTM models presented in the literature (11) (13).

A modified non-local version (to better represent the multi-axial behaviour of concrete) of the Mazars (19) type isotropic damage model is used to represent mechanical behaviour in the concrete skeleton:

$$\mathbf{S} = (1 - D)\mathbf{C}_e\mathbf{E}_\sigma \quad (12)$$

The undamaged material stiffness matrix is  $\mathbf{C}_e$ , the total scalar damage variable,  $D$ , is determined from a combination of thermo-chemical,  $\chi$ , and mechanical damage,  $\omega$ , as proposed in (20). The damage parameters relate to secant stiffness according to:

$$(1 - D) = (1 - \chi)(1 - \omega) = \frac{E_0(T) E(T)}{E_0(T_a) E_0(T)} \quad (13)$$

where  $E_0(T_a)$  is a representative secant modulus for undamaged concrete at ambient temperature,  $E_0(T)$  is a representative secant modulus for mechanically undamaged concrete at elevated temperature, and  $E(T)$  is the total secant modulus of concrete at an arbitrary strain and at elevated temperature.

The growth of mechanical and thermo-chemical damage variables is controlled by a pair of damage loading functions. The mechanical damage loading function corresponds to  $\bar{\epsilon}$ , the non-local counterpart to the scalar valued function of the strain tensor (the Mazars type strain measure). Appropriate consideration of the effect of temperature on mechanical behaviour is considered through temperature dependence of the chosen damage evolution laws and damage threshold parameter.

Lastly, a total stress tensor is defined based on established poro-mechanics (i.e. akin to an effective stress principle):

$$\mathbf{S}^{tot} = \mathbf{S} - bP^s\mathbf{1} \quad (14)$$

where  $b$  is the Biot coefficient and  $P^s$  is a measure of the internal pressures acting on the solid skeleton (21). The pressure,  $P^s$ , is a combination of that from wetting (liquid water) and non-wetting (gas) phases. In this analysis, the effect of capillary pressure is assumed to be already implicitly considered in the stress-strain behaviour of the material – meaning that  $P^s$  is taken as just the gas pressure. A typical Biot coefficient of  $b = 0.5$  is considered, as suggested by Scherer et al. (22) for cementitious materials.

## 2.4 Effect of moisture on mechanical behaviour

It has long been established that the ambient temperature variation of moisture content (between dry and fully saturated conditions) has a non-negligible effect on the compressive and tensile strength of concrete specimens. While varying magnitudes of this effect have been reported, in general specimens pre-conditioned to a dry state will have a typical UCS increase of 10%, while conversely, samples saturated prior to testing will have a UCS reduction of 10-20% (23). While various hypotheses have been put forward to explain this effect, the most plausible relate to changes in surface energy and disjoining pressure associated with adsorption of water (24) or to a hydrolytic weakening phenomena (25).

Recently, Jansson and Boström suggested that a similar moisture weakening phenomena may also bear some responsibility for the observed spalling phenomena in fire exposed concrete (26). Citing several references, and from experiments of their own, they found that the observed ambient temperature moisture weakening effect only increased with temperature.

In this study, consideration of this moisture weakening effect is made in the HTM model. Based on the available experimental data, a weakening function (of both temperature and humidity) is proposed, whereby the ambient temperature saturated strength is considered 20% less than the dry state strength. At the critical temperature of water ( $T_{cr} = 374.14^\circ\text{C}$ ), the saturated strength is nominally considered to be fully 80% less than the strength when in a dry state. A linear variation of this reduction over varying temperature and humidity is assumed (the reduction is actually transitioned to 0% near the critical temperature, as humidity has no meaning past this point).

### 3. Numerical simulation

To demonstrate the efficacy of the hygro-thermo-mechanical model in simulating the behaviour of planar type concrete elements exposed to elevated temperatures, as well as providing a basis for examining the mechanism responsible for the fire spalling phenomena, a pair of experiments reported by Ozawa et al. (10) are simulated. The experiments were set up to facilitate essentially one-dimensional heat transfer through several unreinforced high strength concrete slabs, each having the plan dimensions of 0.4 m x 0.4 m and an overall thickness of 0.1 m. Each specimen was placed face-down onto an electric furnace that applied a linearly ramped temperature to the bottom face for approximately 50 minutes. At a nominal depth of 8 mm from the heated face each specimen contained 5 embedded steel pipes (filled with hydraulic oil) connected to pressure transducers – allowing internal gas pressures to be measured. A single thermocouple was also present centrally at the same 8 mm depth within each specimen. All samples experienced some spalling prior the termination of testing.

By applying two different curing conditions prior to testing, Ozawa et al. (10) examined the effect of a significant variation in the initial moisture content on the occurrence of spalling. One pair of tests was performed on fully saturated specimens (wet cured for 64 days before testing), and another pair of tests on air dried specimens (also water cured for 64 days, then held in a control room at 20°C and 40% RH for 118 days to partially dry before testing). The reported 28 day wet cured concrete compressive strength was 83.5 MPa and Young's modulus was 41 GPa. The water to cement ratio was 0.3.

Given the specimen geometry and roughly one-dimensional heating exposure, a pseudo-one dimensional HTM model (as proposed) is suitable. In this instance, the results of two of simulations are presented, one for each curing condition. The material properties used in the simulations are given in Table 1.

**Table 1. Material properties and initial conditions used in numerical simulations.**

Parameter	Analysis Value
Porosity (20°C)	10 %
Intrinsic Permeability, $k_{int0}$ (20°C)	$0.5 \times 10^{-19} \text{ m}^2$
Permeability coefficient, $A_{kt}$	0.006 1/°C
Apparent density (dry, 20°C)	2350 kg/m <sup>3</sup>
Dry Compressive Strength (20°C)	83.5 / 0.85 = 98.2 MPa
Dry Tensile Strength (20°C)	4.7 / 0.85 = 5.53 MPa
Initial internal temperature	35°C
Initial internal gas pressure	101325 Pa
Initial water saturation level	0.997 (Saturated) or 0.5 (Air Dried)

For the simulations, 100 quadratic type finite elements were used (refined at both exposed faces) for the hygro-thermal simulation and the discretisation of the mechanical simulation. Zero external loads (i.e. no in-plane moments or out-of-plane moments) are applied to the mechanical fibre model; however, the section is free to experience curvature and mean elongations as the analysis progresses. The analysis time-step is chosen automatically during the numerical simulation to maintain convergence.

In the coupled hygro-thermo-mechanical simulation, it is possible to consider the additional important effect of mechanical damage on intrinsic permeability. For this purpose, a multiplicative factor of the type suggested by Souley et al. (see (27)) is incorporated in the permeability formulation:

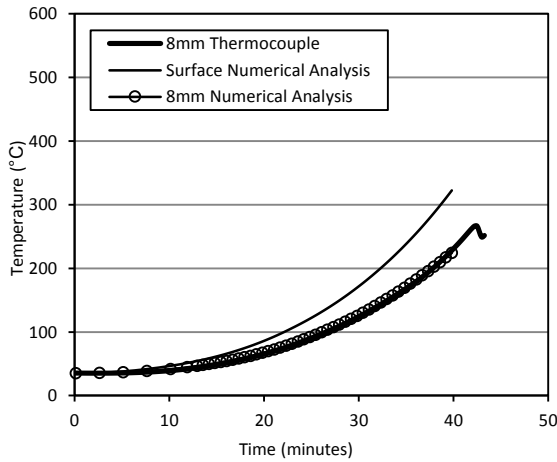
$$k_{int}^w = k_{int0} \cdot 10^{A_{kt}(T-T_{k0})} \cdot 10^{A_{\omega}(\omega-\omega_0)} \quad (15)$$

In the presented analysis, the multiplier for mechanical damage of  $A_{\omega} = 5.5$  and threshold for mechanical damage  $\omega_0 = 0.4$  were used, based on published experimental data.

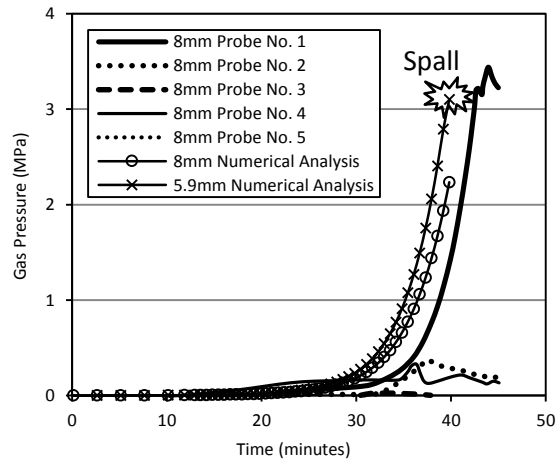
### 4. Numerical simulation results and spalling mechanism

In order to achieve close correspondence of the experimental tests and numerical simulations (giving the greatest chance that other simulation produced data is accurate), researchers will typically attempt to adjust unknown experiment parameters in HTM models so that simulation results match known measurements; e.g. see (8) (13). In the case of the experiments by Ozawa et al. (10), the quoted electric

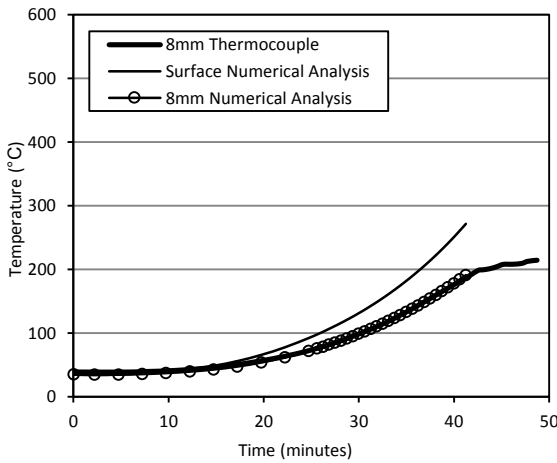
heater ramp rate was 20°C/min. For the presented simulations, the external thermal boundary conditions were adjusted within reasonable ranges for both air dry and saturated specimens to achieve a good match between simulated temperatures and the measured temperature profile (at 8 mm depth). The simulated temperatures at the surface and at 8 mm depth, compared with measured thermocouple data, are presented in Figures 2a and c. The simulation matches the non-linear development of temperature well.



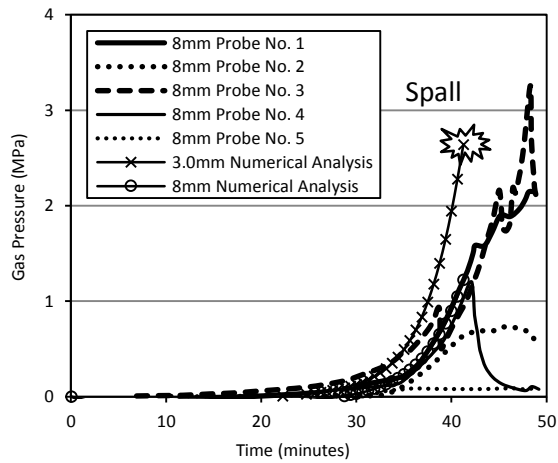
(a) Temperature vs. time (*Air Dried*)



(b) Gas pressure vs. time (*Air Dried*)



(c) Temperatures vs. time (*Saturated*)



(d) Gas pressure vs. time (*Saturated*)

**Figure 2. Experimental and numerical simulation results vs. time.**

The other main parameter able to significantly affect the results of HTM simulations is intrinsic permeability. No direct permeability measurements were made on the concrete used in the experiments of Ozawa et al., so an estimate must be made by comparison with other simulations. Gawin et al. used an intrinsic permeability of  $2 \times 10^{-19} \text{ m}^2$  for a similar concrete in their work (14). At least an order of magnitude lower permeability than that used for 35 MPa concrete modelled previously (12) is reasonable. In this study the ambient temperature (un-damaged) intrinsic permeability has been taken as  $0.5 \times 10^{-19} \text{ m}^2$ . The resulting simulated gas pressures, along with the measured gas pressures in each test specimen, are presented in Figures 2b and d. Noting that direct gas pressure measurements in heated concrete specimens are notoriously susceptible to leaks and cracking (resulting in low or no measured pressure development), the correspondence between predicted and measured gas pressure development is very good.

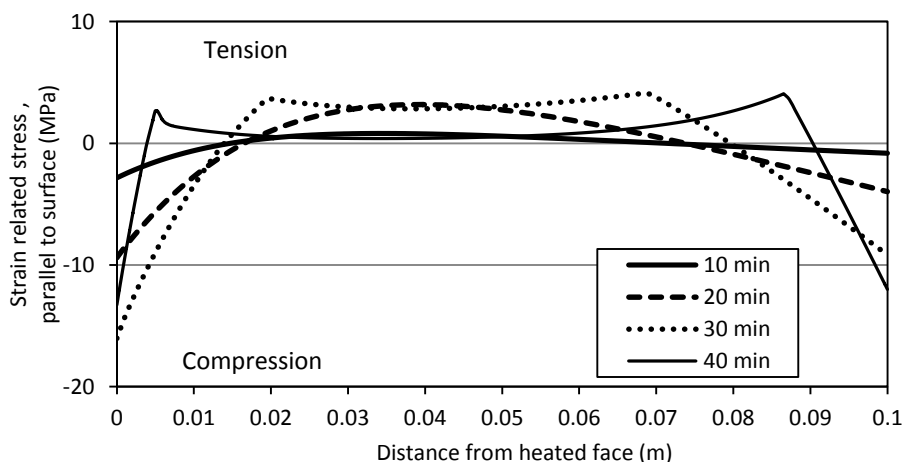
Having now fully described the conditions of the analyses, the results may be examined in more detail. Firstly, it is noted that the trend of development of gas pressures predicted in the model and those found experimentally are both very similar. An initial period of approximately 30 minutes having negligible gas



pressure development at approximately 8mm into the slab is followed by a relatively rapid pressure build up before spalling was experimentally observed. Peak gas pressures were measured as 3.5 MPa and 3.2 MPa (with several gauges reading moderately lower) for air dry and saturated specimens, respectively. Marginally lower gas pressures were recorded at the initiation of spalling, particularly for the wet specimen. Corresponding simulated peak gas pressures were 3.1 and 2.6 MPa at spalling – a good match.

In the air dry case, spalling was reported by Ozawa et al. to have occurred at approximately 43 to 44 minutes. In the saturated case, spalling was reported to have occurred between 44 and 49 minutes. In the numerical simulations, spalling is detected (as per the following Section) at approximately 40 minutes for the air dry specimen, and at 41 minutes for the saturated specimen, which is in close agreement. Observed spalling depths were up to 12 mm after testing, with an average depth of around 4-8 mm. The numerical simulations predict that spalling initiates at approximately 6 mm and 3 mm depth for air dry and saturated specimens, respectively.

Ozawa et al. also made some interesting acoustic emission (AE) measurements directly on the slabs during their tests (10). They found that from around 16 to 20 minutes into the tests, AE events gradually started to occur – these picked up from around 25 minutes into the test and continued constantly until spalling. While Ozawa et al. proposed that these events related somehow to water vapour movement, it is proposed here that they relate rather to the internal cracking processes associated with relief of (primarily) thermal expansion strains. Examining Figure 3, which shows the computed mechanical strain related stress along one axis (parallel to exposed surface), we see that from around 23 minutes into the analysis the core zone of concrete is predicted to reach its tensile strength. This matches well with the start of AE event detection. From this point onwards, further thermal expansion is associated with internal rupturing and softening of an expanding internal concrete zone in tension. Clearly fully restrained or plane strain analyses, as employed by many authors using advanced HTM models (i.e. (8) (14) (13)), must be unable to capture internal stress regimes and material behaviour to good accuracy.



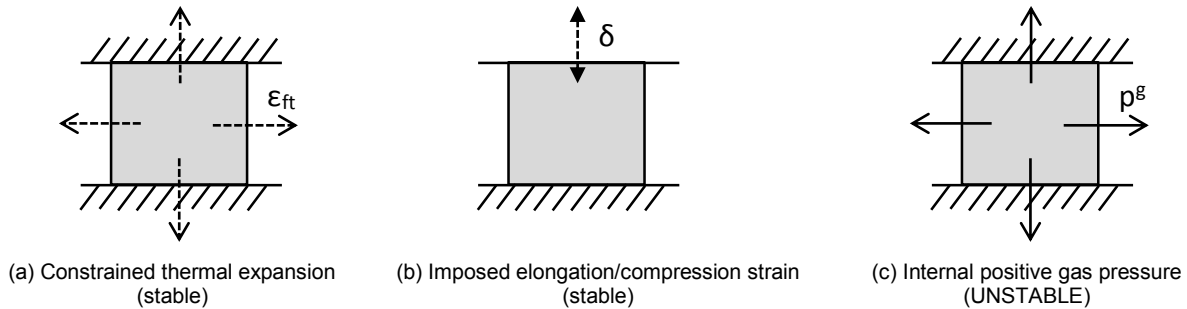
**Figure 3. Mechanical strain related stress, parallel to the exposed surface (Air Dried).**

## 5. Mechanics behind explosive spalling phenomena

A new criterion is proposed to explain and detect the occurrence of spalling. As a slab or wall like concrete structure (such as that being modelled) is rapidly heated, the mechanical processes primarily consist of a combination of those shown in Figures 4a and b. The large temperature differential between surface concrete and internal or un-heated concrete, combined with the plane-sections-remain-plane requirement, means that surface concrete fibres experience constrained thermal expansion (see Figure 4a). It is possible that the mechanical stresses, which build up, may exceed the compressive strength of the material – but regardless the displacement type nature of loading strongly encourages failure to be gradual (i.e. assuming no localisation effects).

Further to this, as indicated in Figure 3, it is normal that un-restrained concrete slab sections will experience internal tensile damage/cracking if exposed to rapid surface temperature rise. In this instance,

the imposed 'tension loads' are directly related to the mechanical surface strains and, as such, when the internal core softens, the loads dissipate – making this kind of mechanism also generally stable (see Figure 4b).



**Figure 4. Simplified consideration of imposed strains/actions within concrete near the face.**

Lastly, we consider the internal positive gas pressures, resulting from water vaporisation and dehydration and creating effective tensile stresses in the concrete skeleton (see Equation 14 and Figure 4c). In this case, when the internal gas pressure combined with the prevailing stress regime (which is complex and changes over time) leads to the material reaching the multi-axial strength envelope – the failure cannot be gradual. Once the strength envelope is reached, the mechanical resistance decreases and so the mechanical action must decrease for stability to be ensured. With vapour pressure being basically maintained, instantaneous rupture must eventuate, leaving an unstable cover zone with significant stored strain energy. Here it is proposed that explosive spalling is merely the consequence of pore pressure induced mechanical instability, as a consequence of a softening material. In the HTM simulation, this mechanical instability is generally detected as a negative pivot in the tangent stiffness matrix – where the problem becomes poorly-posed for the imposed gas pressure 'load'.

From the proposed spalling mechanism, it is possible to see why historic attempts at predicting and "simplifying" the spalling phenomena have been largely unsuccessful. The occurrence of spalling at a specific depth within a section appears intricately related to (at that depth) the moisture state, the mechanical stresses parallel to the exposed face (where the stresses at a local depth are strongly related to the rate of temperature increase, the degree of restraint and any external loads applied) and the pore pressures that develop (both in magnitude and the location of pressure peak relative to the current mechanical stress regime). Moreover, the moisture weakening phenomena may also be a significant factor in fire induced spalling – clearly it requires further research.

## 6. Summary and conclusions

Building upon a fully coupled hygro-thermal model for predicting the behaviour of concrete at high temperatures described previously by the authors (12) (28), an additional mechanical model component giving a coupled hygro-thermo-mechanical model has been described. This model has been formulated particularly for the efficient analysis of pseudo-one dimensional conditions, which are commonly encountered in both laboratory fire testing and in practice (e.g. walls, slabs, tunnel linings, etc.).

The instrumented fire spalling experiments of Ozawa et al. (10), on both fully saturated and air dry preconditioned samples, were simulated using the proposed model and a good correlation was observed for the model with the experimental temperature versus pore pressure measurements. The presented numerical model predicts that spalling type failures will occur at approximately 41 minutes from the start of tests, closely matching experimental observations. Additionally, the depths of spalling predicted correspond reasonably with experimental results. A new explanation of the spalling phenomena has been presented.

It is suggested that the described HTM approach shows significant promise for true model-based information on the spalling risk of fire exposed concrete structures. Further work is required to develop confidence in the model for predicting the spalling of arbitrary concrete mixes and fire/loading scenarios.

## 7. References

1. Khoury, G. A.; Anderberg, Y. *Concrete Spalling Review*; Report submitted to the Swedish National Road Administration, 2000.
2. Hertz, K. D. Limits of spalling of fire-exposed concrete. *Fire Safety Journal* **2003**, *38* (2), 103-116.
3. Khoury, G. A.; Fellingner, J.; Both, K.; Majorana, C. E.; Anderberg, Y.; Høj, N. P. *Fire Design of Concrete Structures - Materials, structures and modelling - State of the art report*; FIB, 2007.
4. Connolly, R. J. *The Spalling of Concrete in Fires (Thesis)*; The University of Aston: Birmingham, 1995.
5. Sertmehmetoglu, Y. *On a mechanism of spalling of concrete under fire conditions (Thesis)*; King's College: London, 1977.
6. Gawin, D.; Pesavento, F.; Schrefler, B. A. Towards prediction of the thermal spalling risk through a multi-phase porous media model of concrete. *Computer Methods in Applied Mechanics and Engineering* **2006**, *195* (41-43), 5707-5729.
7. Davie, C. T.; Zhang, H. L.; Gibson, A. Investigation of a continuum damage model as an indicator for the prediction of spalling in fire exposed concrete. *Computers and Structures* **2012**, *94-95*, 54-69.
8. Beneš, M.; Štefan, R. Hygro-thermo-mechanical analysis of spalling in concrete walls at high temperatures as a moving boundary problem. *International Journal of Heat and Mass Transfer* **2015**, *85*, 110-134.
9. Zhang, Y.; Zeiml, M.; Pichler, C.; Lackner, R. Model-based risk assessment of concrete spalling in tunnel linings under fire loading. *Engineering Structures* **2014**, *77*, 207-215.
10. Ozawa, M.; Uchida, O.; Kamada, T.; Morimoto, H. Study of mechanisms of explosive spalling in high-strength concrete at high temperatures using acoustic emission. *Construction and Building Materials* **2012**, *37*, 621-628.
11. Gawin, D.; Pesavento, F.; Schrefler, B. A. What physical phenomena can be neglected when modelling concrete at high temperature? A comparative study. Part 1: Physical phenomena and mathematical model. *International Journal of Solids and Structures* **2011**, *48* (13), 1927-1944.
12. de Burgh, J. M.; Valipour, H. R.; Foster, S. J. Fire induced Spalling of Reinforced or Prestressed Concrete; Overview and Initial Numerical Investigation. *Proceedings of Concrete 2013 - Understanding Concrete, October 16th-18th*, Gold Coast, Australia, 2013; p 10 pp.
13. Davie, C. T.; Pearce, C. J.; Bičanić, N. A fully generalised, coupled, multi-phase, hygro-thermo-mechanical model for concrete. *Materials and Structures* **2010**, *13* (0), 13-33.
14. Gawin, D.; Pesavento, F.; Schrefler, B. A. What physical phenomena can be neglected when modelling concrete at high temperature? A comparative study. Part 2: Comparison between models. *International Journal of Solids and Structures* **2011**, *48* (13), 1945-1961.
15. Gernay, T.; Franssen, J.-M. A formulation of the Eurocode 2 concrete model at elevated temperature that includes an explicit term for transient creep. *Fire Safety Journal* **2012**, *51*, 1-9.
16. Nielsen, C. V.; Pearce, C. J.; Bičanić, N. Theoretical model of high temperature effects on uniaxial concrete member under elastic restraint. *Magazine of Concrete Research* **2002**, *54* (4), 239-249.
17. Nielsen, C. V.; Pearce, C. J.; Bičanić, N. Improved phenomenological modelling of transient thermal strains for concrete at high temperatures. *Computers and Concrete* **2004**, *1* (2), 189-209.
18. de Borst, R.; Peeters, P. P. J. M. Analysis of Concrete Structures under Thermal Loading. *Computer Methods in Applied Mechanics and Engineering* **1989**, *77*, 293-310.
19. Mazars, J.; Pijaudier-Cabot, G. Continuum Damage Theory - Application to Concrete. *Journal of Engineering Mechanics* **1989**, *115* (2), 345-365.
20. Gawin, D.; Pesavento, F.; Schrefler, B. A. Modelling of hygro-thermal behaviour of concrete at high temperature with thermo-chemical and mechanical material degradation. *Computer Methods in Applied Mechanics and Engineering* **2003**, *192* (13-14), 1731-1771.
21. Gray, W. G.; Schrefler, B. A. Analysis of the solid phase stress tensor in multiphase porous media. *International Journal for Numerical and Analytical Methods in Geomechanics* **2007**, *31* (4), 541-581.
22. Scherer, G. W.; Valenza II, J. J.; Simmons, G. New methods to measure liquid permeability in porous materials. *Cement and Concrete Research* **2007**, *37* (3), 386-397.
23. Neville, A. M. *Properties of Concrete*; Prentice Hall, 2008.
24. Wittmann, F. H. Interaction of Hardened Cement Paste and Water. *Journal of the American Ceramic Society* **1973**, *56* (8), 409-415.
25. Hou, D.; Ma, H.; Li, Z.; Jin, Z. Molecular simulation of "hydrolytic weakening": A case study on silica. *Acta Materialia* **2014**, *80*, 264-277.
26. Jansson, R.; Boström, L. Fire spalling in concrete - The moisture effect, part II. *Concrete Spalling due to Fire Exposure: Proceedings of the 3rd International Workshop*, Paris, 2013; p 7 pp.
27. Jason, L.; Pijaudier-Cabot, G.; Ghavamian, S.; Huerta, A. Hydraulic behaviour of a representative structural volume for containment buildings. *Nuclear Engineering and Design* **2007**, *237* (12-13), 1259-1274.
28. de Burgh, J. M.; Valipour, H. R.; Foster, S. J. Hygro-thermal modelling of concrete exposed to high temperatures. *Proceedings of the 1st Australasian Conference on Computational Mechanics (ACCM2013), published in Applied Mechanics and Materials: Advances in Computational Mechanics* **2014**, *6*, 637-642.

# In-situ Concrete Strength Assessment based on Ultrasonic (UPV), Rebound, Cores and the SONREB Method

Frank Papworth<sup>1</sup>, David Corbett<sup>2</sup>, Reuben Barnes<sup>3</sup>, Joseph Wyche<sup>4</sup> and Jonathon Dyson<sup>5</sup>

<sup>1</sup> BCRC (WA); <sup>2</sup> Proceq; <sup>3</sup> PCTE; <sup>4</sup> Wyche Consulting; <sup>5</sup> BCRC (NSW).

## Synopsis:

The strength of concrete in a new structure is sometimes called into question. This may be due to cylinders not being taken, poor cylinder production, transport or testing, the actual concrete strength being low or the suspicion that in-situ cylinders are not representative of in-situ concrete. Whatever the reason testing of the in-situ concrete is generally called for. This paper gives a brief outline of the key aspects of strength assessment including a review of concrete supply and testing records, extent of testing required, assessment by cores to AS 1012.14 (1) and AS 3600 (2), ultrasonic (direct and indirect methods) and rebound hammer testing and analysis of in-situ strength using cores and NDT results (including published methods such as EN 12504 (3), EN 13791 (4), BS 6089 (5) and those under consideration by RILEM). If the concrete strength is found to be low, a structural analysis has to be undertaken. The paper includes information of six projects assessed. In two, strengths were low across the whole mine site but in each case only one structure required strengthening. In another, very low strength was identified at an early stage and a risk assessment identified the structure should be replaced. In the others, strengths were found to be adequate.

**Keywords:** Concrete, compressive strength, ultrasonics, UPV, rebound, cores, structural assessment, strengthening.

## 1. Introduction

For many years CSTR 11 (7) was the revered document on assessment of concrete compressive strength from cores. This was updated in 1987 (8). In 2002 CIA Z11 (9) was published and became the Australian reference for assessment of core strengths as a supporting document for AS 1012.14 (1). AS1012.14 provides performance requirements on sampling, conditioning, and reporting on cores and calls on AS 1012.9 (6) as the method of testing concrete samples for compressive strength. However, in 2004 a project report on core strengths by the Concrete Society (10) provided updated information on tests from a range of samples and findings were subsequently incorporated in an updated BS 6089 (5) which is complimentary to BS EN 13791 (4), the European standard on testing concrete strength in structures. Consequently CSTR 11 (7,8), and AS1012.14 (1) and CIA Z11 (9) which are at least partly based on them should be used with caution as some of the analysis methods have been superseded. The Concrete Society issued Advice Note 43 (11) in 2013 which summarises some of the approaches in the new European standards. In this paper some of the differences between European Standards and the methods used in Australia based on CSTR 11 are given.

BS EN 13791 now provides clear guidance on the use of ultrasonic pulse velocity and rebound hammer testing. These methods enable rapid scanning of the concrete to detect variations in strength and BS EN 13791 provides guidance on how their use can be incorporated into reducing the number of cores required. In this paper the methods are outlined with specific reference to direct and indirect UPV measurements and combined use of rebound, UPV and core strengths using the 'SonReb' method.

An outline of the strength assessment on seven projects is given in the paper to show the variety of approaches that may be appropriate. For each project a durability assessment was also undertaken for each structure but this is not included here as the paper's focus is strength and structural assessment. The methods employed for strength assessment range from reliance on 28 day strengths to the use of cores, UPV and rebound testing. The subsequent analysis of the structures included a full structural analysis to determine structural reliability and risk assessment if there is a reduced reliability.

## 2. Methods of Testing

### 2.1 Cores

To maximise the number of cores meeting AS 1012.14 requirements and to minimise damage to the core and structure, the engineer should ensure that the coring contractor has adequate experience in using his equipment to take cores for the specified purpose. On one project in remote Botswana the contractor arrived with a brand new coring machine, no hold down anchors and 5 people. His first core failed the requirements of AS 1012.14 because the machine was not properly secured and because of stop start coring. Being a remote location it took two days to get the team working.

Before coring the reinforcement locations are carefully mapped and marked with due allowance for bar diameter. The upper reinforcement layer can generally be identified using a covermeter but this may miss saddles which may be identified using ground penetrating radar.

Assessment of core strength can be based on BS EN 13791 and BS 6089. A comparison of these with current Australian standards is given in *Table 1*.

**Table 1 : Australian and European Standard Requirements for Assessing In-situ Concrete Strength**

	Not Yet Harmonised with European Practice (based on CSTR 11)		State of the art documents on in-situ strength assessment
	AS 1012.14	CIA Z11	BS EN 13791/BS6089
Core diameter	75mm	75min or 2.5 x agg size	100mm (increase number of cores if using diameters down to 50mm)
Core length:diameter ratio	Close to 2:1	1 to 2 (ideally 1.9 to 2)	1 to 2
<b>Actual Strength Corrections</b>			
Correction l:d	k <sub>1</sub> = 1 for l/d =2 reducing in steps to 0.87 for l/d=1		K <sub>cyl</sub> =2.0/(1.5+1/(l/d))
Correction rebar present	-	k <sub>2</sub> by formula	Avoid rebar
Correction core axis	-	k <sub>3</sub> = 1 perp. to casting direction and 1.08 if parallel	Influence noted but UK Annex NA says no allowance to be made
<b>Core locations limits</b>			
Vertical pours	-	Not from top 20% up to 300mm	Exclude top 300mm. Core top third
Face of concrete	-	Not within 50mm of face	Not within 50mm of face
Number of cores where suspect batch	-	3 from each suspect batch	15 with no NDT, 9 with NDT. Move to reduce the number with NDT
Conditioning	Wet 3d or air 7d	Dry (7d) as AS 3600	Air 3d but allowance can be made for wet cure
End preparation	AS 1012.9	Sulphur cap or ground ends	Ground ends recommended
Provision for outliers	-	No	Yes
NDT assessment	-	-	UPV, pullout and rebound accepted as means of reducing core numbers

### 2.2 Rebound

The original rebound hammer measured the hardness of a material by the degree of rebound. The instrument worked by firing a known mass using a standard spring loading to impact on a rod held in contact with the surface being tested. When the mass hits the rod it rebounds to an extent that depends on the hardness of the surface in contact with the rod. The original rebound hammer measured the rebound value R mechanically as a distance that the mass rebounded from the concrete surface. Extensive testing carried out in the late 1950's gave correlation curves between rebound value and concrete compressive strength.

In 2007 an electronic version of the original rebound hammer was introduced. This instrument measures rebound value (now Q) as the quotient between the velocity of the hammer mass just before and after impacting the rod. The validity of the new measurement principle has been recognized by the major standards bodies.

It should be noted that Q-values and R-values are not interchangeable. Correlation curves developed for the original rebound hammers cannot be used with Q-value and correlation curves developed for the new hammer cannot be used with the classical hammer. The manufacturer provide a strength relationship between Q values and compressive strength based on a lower 10<sup>th</sup> percentile curve. They do not provide direct relationships between Q values and R values, as testing on various types of concrete have shown that the relationship is not constant.

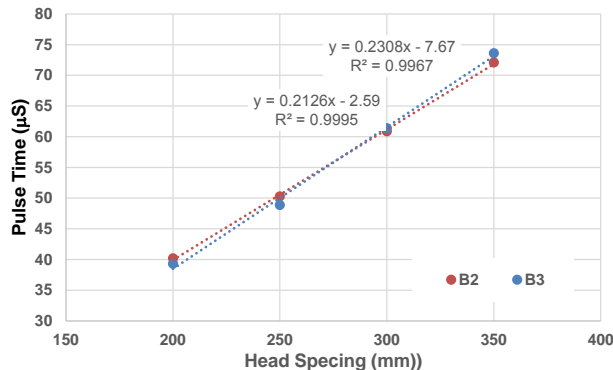
When assessing in-situ compressive strength using cores, EN 13791 requires at least 15 cores to be taken to establish the insitu concrete strength. The number of cores to be taken may be reduced to 9 when used in combination with NDT tests such as rebound hammer or ultrasonic pulse velocity.

In the German national annex to EN 13791 there is also the possibility to assign a compressive strength class based on rebound hammer testing alone, as in many cases, it is not allowed to take cores. EN 13791 is currently under review and there are proposals for reducing the number of cores further when used in combination with NDT testing and also to generally accept the method described in the German national annex.

Testing should be undertaken in accordance with EN 12504-2. A test location should be a minimum 100m thick, 300x300mm test area, minimum of nine readings, impact points >25mm apart, surface clean and smooth. Nine such test locations are required for a test region as described in EN 13791. A core should also be taken at each test location to establish the correlation. The method then uses the core correlation to shift a base correlation curve upwards. The same method may be used with ultrasonic pulse velocity.

### 2.3 Ultrasonic Pulse Velocity

UPV can be determined in number of ways direct, indirect and semi-direct. Only the first two are discussed here. Direct UPV is the most reliable as the velocity is measured across the entire element and gives an average velocity for a large thickness of concrete. Direct UPV can also be measured on cores to give a direct correlation between UPV and core strength.



**Figure 1** : Indirect Pulse Velocity Using Yaman's Five Point Method

However in cases where access to only one face is possible a direct velocity measurement is not possible. Yaman (16) developed a method of measuring the indirect velocity over 4 head spacings (200, 250, 300 and 350mm). This is very similar to the surface velocity method described in Annex A of EN 12504-4. The slope of a straight line plot of time vs head spacing (*Figure 1*) gives an indirect velocity that is very close to the direct velocity for homogeneous specimens. The principle difference between direct and indirect UPV's is that direct measurements are largely through the bulk concrete and indirect measurements are largely through the near surface but Yaman's five point method avoids direct surface effects such as carbonation and finishing. This is particularly useful for assessing slabs. It should be noted however, that typically concrete is an inhomogeneous material and the difference between indirect and direct pulse velocities can vary significantly if surface effects are deep.

In the indirect mode a particular issue is the low signal level compared with direct measurements. The first pulse may not trigger the timer unless the gain is suitably increased. For such measurements, it is advisable to use a waveform display to be certain of correct triggering. This may or may not be apparent from the best fit line through the four data points. Testing should otherwise be undertaken in accordance with EN 12504-4.

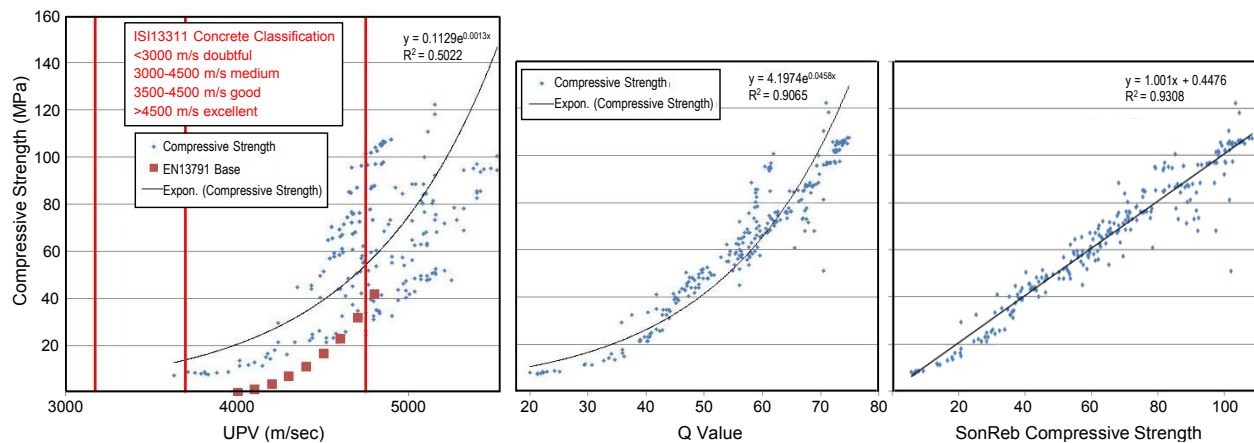
## 2.4 SonReb

One issue with combined use of NDT and cores for strength assessment is the number of core correlations required according to EN BS 13791. By reducing uncertainty by combining two NDT measurements the number of correlation points decreases. Breyse (15) describes the SonReb method of combined UPV and Rebound measurement as discussed by RILEM Technical Committee TC 207-INR as follows: *“This combination has received the name of SonReb, for Sonic and Rebound. Rebound and ultrasonic pulse velocity measurements can be carried out quickly and easily. The underlying concept is that if the two methods are influenced in different ways by the same factor, their combined use can cancel the effect of this factor and improve the accuracy of the estimated strength.”* Breyse describes two approaches to the combined assessment based on best fit of data but the multivariate approach A is preferred, i.e.: Approach A :  $f_c = aV^bR^c$  where a,b and c are constants ( $1.15 \times 10^{-10}$ ; 2.6 and 1.3 respectively); V is UPV; R rebound number.

Although standard values for a, b and c are given project specific values are determined.

Generally, the SonReb method provides an increase in correlation accuracy when compared with using either the rebound method or UPV method in isolation.

The data, presented in *Figure 2* was collected by the rebound hammer manufacturer to establish a SonReb curve using the Q-value. It illustrates the benefit of using the combined method. The SonReb method has been established as a national standard in several countries including Italy and China in particular and is currently being considered by the RILEM TC-249-ISC committee dealing with in-situ compressive strength estimation.



a) UPV correlation to compressive strength      b) Q-value correlation to compressive strength      c) SonReb correlation to compressive strength

**Figure 2** : Data from 240 Cubes to Establish SonReb Calibration Curves for Q Value

## 3. Structural Assessment of New Concrete Structures in a Ghana Mine

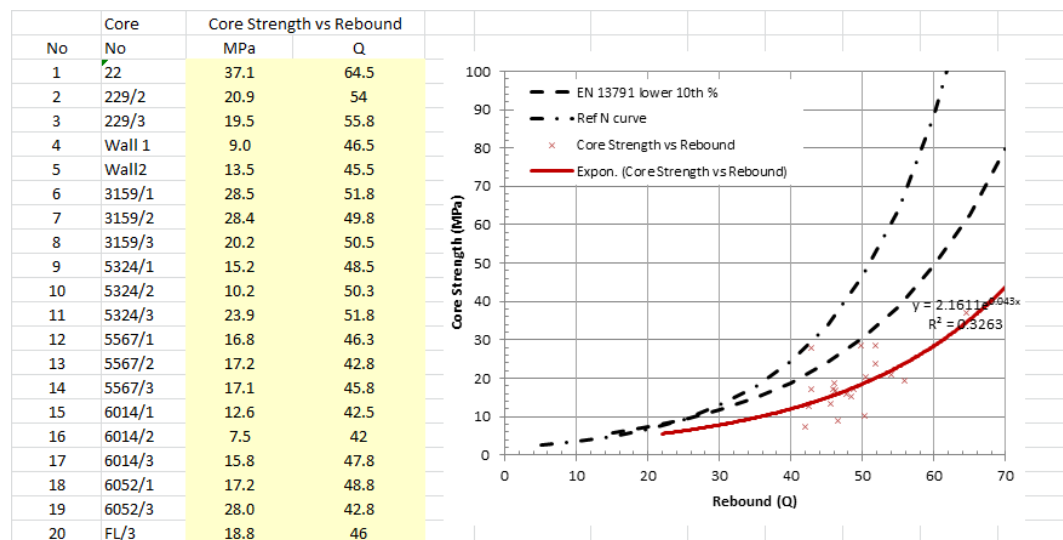
Shortly after construction deterioration of the primary crusher approach slab led to a preliminary investigation of the strength of concrete. This indicated that there was cause to suspect that the strength of concrete could be lower than design. Subsequently a detailed investigation of the concrete to identify if there are any significant deficiencies in construction was undertaken. For cores testing SANS standards were followed but as there were no SANS standards for non-destructive tests international standards were followed. The specified strengths varied and are shown together with core strength results in *Table 2*.

**Table 2 : Core Test Results From Ghana Mine**

Element Orientation	Vertical		Horizontal	
Specified Strength	40MPa	25MPa	40MPa	25MPa
No of Cores	3	4	-	19
No of Compressive Strength Tests	3	7	-	28
Average Strength (MPa)	34.0	16.1	-	17.8
Standard Deviation (MPa)	-	-	-	6.3
% Failing Individual Result	0%	57%	-	54%
% Failing Average Result	0%	100%	-	71%

The large fraction of cores that failed the individual and average strength requirements, and the margin by which some cores failed, was a serious concern.

Rebound hammer and core testing results from the same location are shown in *Figure 3*. The best fit relationship is achieved at compressive strength =  $2.161e^{0.043x}$  where x is the Q value. The rebound results are from the surface of slabs and the finishing may account for why a high Q value is achieved for a given compressive strength but more likely was that carbonation had occurred hardening the surface strength. This effect means rebound results on the top of the slab are not an effective method of assessing bulk strength. Consequently the assessment was based on core strengths.



**Figure 3 : Core Strength Vs Rebound Hammer**

Based on the core strength tests an equivalent characteristic cylinder strength of 15MPa was determined for the 25MPa concrete and 25MPa for 40MPa concrete. The structural assessment was undertaken in conjunction with the original designers with free and unfettered access to the design calculations. Jointly with the designer critical elements were identified and checked based on the strength of 15MPa and 10 year design life. The structural review identified all structures behaved acceptably at the actual in-situ strengths except for one tall conveyor support. Additional cores from this structure indicated there were still some concerns and hence strengthening was instigated.

#### 4. Structural Assessment of New Concrete Structures in a Botswana Mine Plant

25MPa and 32MPa concrete was specified for footings/slabs and walls/columns respectively but review of the cube test results showed a much lower strength was achieved in practice. Cores were taken from various locations and results were consistent with the cube results. Multiple cube results from the same batch tested at the same age were quite consistent and 7 day results were reasonably consistent at 67% of the 28 day results. This indicates that, failing an unexpected consistent error in testing, the results are a realistic and able to be used as a true indication of the strength of concrete supplied. The results are summarised in *Table 3*.



**Table 3 : Summary of 28day Compressive Strength Test Results**

Period	4 <sup>th</sup> -9 <sup>th</sup> May	Remainder
f <sub>c</sub> cube (MPa)	11	19
f <sub>c</sub> cylinder (MPa)	9	15

Compressive strengths from 2 cores taken from each of three different bases gave a characteristic in-situ cylinder strength of 17.5MPa. This was marginally higher than the 28day cube results and may have an improvement due to the aging.

28 rebound hammer results provided had an average cube strength of 28MPa and a standard deviation of 5.6MPa to give a characteristic cube strength of 18.8MPa.

A review of the mix indicated low coarse aggregate volume and a high proportion of crushed sand. The mix would have had a high water demand and it was concluded that to achieve a workable concrete extra water would have likely been added.

Hence for the project it was determined that:

- a) No further NDT testing was generally required as adequate data was available to give a reasonable estimate of the concrete strength. Originally the client had asked for more detailed NDT testing to show which elements had low strength concrete.
- b) A 28 day characteristic compressive cylinder strength of 15MPa was to be used for structural assessment of all bases except those produced between 4-9<sup>th</sup> May.
- c) For the concrete poured 4-9<sup>th</sup> May the location of the concrete placed was to be identified and design undertaken for strengthening to take the full design loads.

The structural assessment was undertaken of all structures by review of the original designs. This showed that in general the 15MPa cylinder strength was adequate. The exceptions were:

- a) Primary Crusher Base Slab – Development lengths up to 400mm to short due to low strength and low cover. Strengthen to reduce stresses or effectively increase development lengths
- b) Primary Crusher Rear Wall – Will crack as applied moments are 3 times the moment capacity

## **5. Structural Assessment of New Concrete in an Australian Mine Plant**

On this project the concrete strength was called into question when the supervisor recorded that after taking cylinders for strength assessment the concrete water was added to the mix for placement. Cores and NDT were used to establish the actual characteristic strength of 18MPa for most elements, well below the minimum specified strength of 32MPa.

Structural analysis was undertaken to show if these low strengths might be acceptable. A foundation slab was considered as 1m wide strips with actual load points imposed and resisted by soil spring nodes. Although the concrete strength was only 18MPa the authors believe that it is reasonable to extrapolate outside the range of characteristic compressive strengths of 20 MPa to 100 MPa, specified in Clause 1.1.2 of AS3600, provided that a reliable coherent set of core results can be obtained. Of note is the anchorage bond length where requirements will increase beyond those in AS3600 in highly stressed elements. The analysis undertaken indicated that although capacities were significantly reduced most parameters were predicted to be acceptable except for shear and hence a risk assessment was undertaken.

Risk is conventionally assessed by ISO 31000 (12) based on a combination of consequence and likelihood of failure. For some failure modes full probabilistic modelling can be undertaken to assess failure likelihood quite accurately. Where these methods are not possible a qualitative approach can be followed. The consequence of structural failure can vary significantly depending.

Discussions with the owner identified that the increased likelihood of failure was unacceptable because when combined with the consequence of failure the risks during operations became unacceptable. Consequently the concrete was replaced.

## 6. Strength Assessment of an Old Australian Shopping Centre Floor Slab

The strength of a concrete slabs on grade had been called into question. The strength of the surface layer is highly affected by finishing and curing and hence assessment using rebound hammer testing is not recommend as the results are very dependent on near surface properties. It was agreed to undertake widespread testing using indirect ultrasonic pulse velocity to show potential variations in strength. Cores were undertake for calibration of the UPV. Rebound hammer results were also taken over a wide area to determine if it gave any further insight into concrete performance.

UPV results were taken using the five point indirect method. Results were recorded on a spreadsheet which automated a linear regression analysis to check the four results gave adequate correlation (*Table 4*). The velocities, and the rebound results, were plotted in a spreadsheet using conditional formatting to highlight variations (*Table 5*).

**Table 4 :** Indirect UPV Data for Shopping Centre Floor Slab. D is the Transmitter/Receiver Separation and T the Corresponding Wave Transit Time

Separation	(mm)	Result No	B1	B2	B3	B4	B5	B6	B7	B8	B9	B10	B11
D1 (mm)	200	T1 (µs)		40.2	39.3	39.2	39.6	41.6	38.7	39.9	38.2	41.4	39.4
D2 (mm)	250	T2 (µs)		50.3	48.9	49.9	51.8	49.7	49.2	49.9	49.8	50.2	52.4
D3 (mm)	300	T3 (µs)		60.9	61.4	62.9	62.1	60.3	61.3	60.1	63.7	65.9	61.4
D4 (mm)	350	T4 (µs)		72.1	73.6	73.3	73.9	74.2	72.9	72.7	72.1	73.1	72.7
Sparkline				/									
Velocity (m/sec)				4701	4318	4329	4413	4547	4356	4589	4289	4423	4571
RSQ				0.999	0.997	0.998	0.999	0.986	0.999	0.997	0.992	0.980	0.995

**Table 5 :** Colour Coded Plot of Rebound and UPV Test Results

Rebound 10 Percentile Strengths (MPa)																Ultrasonic Sound Wave Velocities (m/sec)																
Grid No	1	2	3	4	5	6	7	8	9	10	11	12	13	Average	Std Dev	A	1	2	3	4	5	6	7	8	9	10	11	12	13			
A																4361	4310	4375	outlier	4424	4443	4709										
B						36.0		17.0								4701	4318	4329	4413	4547	4356	4589	4289	4423	4571							
C			35.0			33.5	22.5	22.0	29.0				29.5			4648	4390	4441	4399	4443	4694	4356	4728	4787	4494							
D	31.0	30.5	27.0	33.5	28.5	22.0	29.0	16.0	22.5	22.0	21.5	30.5								4379	4644	4690	4428	4681	4718							
E		21.0	37.0	22.5	20.5	22.0	23.5	18.5	22.5	23.0			18.5	19.5		4418	4528	4200	4554	4707	4627	4779	4541	4652	4572	4203						
F																4621	4539	4513	4559													
G																																
H																																
I																																
J	35.0	36.5	36.5	36.0	37.0																											
K	38.0	38.0	38.0	40.5	37.5	40.0	37.0	40.0																								
L																																
M																																
N																																

In the case of the rebound results there appears to be two distinct areas where the 10 percentile strengths are 24.9 and 38.2MPa. These variations are not seen in the UPV results. The Rebound variations may be due to variations in finishing and curing of the two pours and be limited to surface effects.

The UPV results were correlated with strength and gave the following relationship:

$$\text{Strength (MPa)} = 8.5344e^{0.3173v} \text{ where } v \text{ is ultrasonic pulse velocity in m/s.}$$

Converting the UPV to strength results gave a plot of strength as shown in *Table 6*. The colour coding is based on highlighting areas where the strength is less than the required 32 MPa.

**Table 6 :** Plot of Compressive Strength estimated using UPV measurements

	1	2	3	4	5	6	7	8	9	10	11	12	13
A					35	34	35		35	36	40		
B		39	34	34	35	37	34	37	34	35	37		
C		38	35	36	35	36	39	34	39	40	36		
D						35	38	39	35	39	39		
E	35	37	33	37	39	38	40	37	38	37	33		
F		38	37	36	37								
G											44		
H	35	40	40	35							35	40	
I				37	36	35	36	36	40	37	36	35	
J		36	36	36	40	38	34	40	34	36	38	40	41
K		35	36	42	37	37	37	36	35	35	35	36	34
L	38	38	38	37	33	33	36	34	36	35	40	35	
M					32	36	37	33	37	34			

## 7. Strength Assessment of New Columns and Walls of an Australian Office Tower

S65 concrete was poured in columns and stair well walls. Cylinder results were marginal and hence strength assessment was requested. An assessment of in-situ strength was undertaken using the SonReb method with UPV and rebound measurements calibrated against core strength tests. The process used for the SonReb method was:

- 1) Mark out reinforcement grid on the concrete surface using GPR so that UPV test results avoided the influence of reinforcement as far as possible.
- 2) Mark out sixteen measurement points for each element. These comprised eight pairs of measurement points precisely on opposite faces of the element. Typically four measurement points were at 0.5m, 1m, 1.5m and 2.0m above base level so that strength with height could be assessed. No significant variation was found (Figure 4)

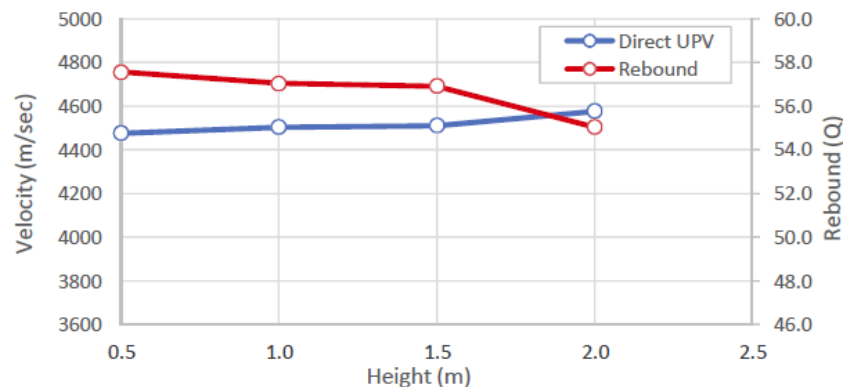


Figure 4 : Plot of UPV and Rebound With Height for a Shaft Wall

- 3) Assess the path length for the measurement points.
- 4) Take direct UPV measurements using digital UPV equipment with the transmitter on one face and receiver on the other for each of the eight pairs of measurement points. The transmitter and receiver were then swapped at each pair of points to give sixteen direct measurements. The UPV' equipment's built in measuring process takes multiple measurements to give an average of several reading for each result. Results were also verified by the strength of the received signal and only highly reliable results were recorded.
- 5) Prepare the concrete surface using a grinding stone at each of the sixteen points and take rebound measurements using the digital rebound hammer. Ten rebounds were used to give one Q value.
- 6) Enter the data in the results spreadsheet prepared for the project to verify results were sensible and consistent. The formula for strength generally used is  $f_{ck} = a \cdot V^b \cdot Q^c$  where a, b and c are constants V is the ultrasonic pulse velocity in m/s. Q is the rebound value as given in RILEM (14)

## 8. Strength Assessment of 50 Year Old Basement Columns in an Australian Building

On this city centre project the building height was to be increased adding several new floors of office space. This translated to additional load in the basement columns and diaphragm wall. The existing structure had reached its 50 year design life and hence a durability and strength assessment was undertaken to confirm that the load capacity was adequate and that the structure would provide an additional 50 year life commensurate with the requirements for the new structure.

The strength assessment was in two parts. Cores were taken from walls, columns and slabs. For the more critical columns a wider assessment of strength was required. This was achieved by correlating direct UPV results with core strengths and then using UPV results to give an indication of in-situ strengths. The correlation was based on compressive strength  $= 1.0828e^{0.8201v}$  where v is UPV.

**Table 7 : UPV Correlation with Core Strengths**

Col	Pulse Velocity (m/s)			Core Strength (MPa)			UPV Strength (MPa)		
	Bottom	Middle	Top				Bottom	Middle	Top
B10	4.781	4.817	4.849	48.51	63.52	56	43.5	45.1	46.7
G8	4.919	4.953	4.944	58.53	Broke	58.5	50.1	51.9	51.4

Piles were tested using a force vibration test as developed by Davis and Dunn (17). Testing was undertaken by measuring the response from a series of hammer blows on the concrete surface using a geophone held on the concrete surface adjacent to the hammer. Where there was no pile response the test location was moved along until a response was found. Having located the pile the test results were recorded. The received signal was put through a fast Fourier transform to give Mechanical Admittance and Frequency. Mechanical Admittance gives the load deflection curve based on wave theory. Frequency gives parameters of the pile model. Information obtained includes pile length, minimum pile diameter, presence of an end bulb, concrete modulus and safe pile load.

## 9. Strength Assessment of Old Shopping Centre Columns in Australia

Testing was undertaken on ground floor columns of a shopping centre in Queensland testing to assess the capacity for planned extensions. No coring was allowed in the structure and so the completely non-destructive NDT method was proposed. NDT results depend on the materials used and so cylinders made using local materials were used to create a calibration between NDT (UPV and rebound) and cylinder strengths.

Sixteen cylinders were tested. Direct UPV measurements were taken on the cylinders and then once the cylinder has been compressed to 3.5MPa the rebound values were taken using an original rebound hammer. The cylinders were then crushed. The calibration co-efficient were assessed using the equation proposed by Samirin (18), i.e.  $f'_c = aR + bV^4$ . Samin's approach was an early form of combined ultrasonic pulse velocity and rebound for strength assessment and the SonReb equation would be recommended today. Excel's 'Solver' function was used to give the values for a and b of 1.0695 and  $4.96 \times 10^{-15}$  respectively. The correlation achieved was 0.973.

Ten columns were tested. Two rebound hammer tests were carried out in accordance with BS 1881:202 on each face. Two UPV measurements (BS1881:203) were taken between each of the two sets of opposing faces. Care was taken to avoid any reinforcing steel by locating this first using a covermeter.

Column	1	2	3	4	5	6	7	8	9	10
Rebound Number	47.8	54.4	52.1	51.4	53.3	49.8	50	48.5	53.6	54.8
UPV (m/se)	4457.5	4300	4298.3	4173.3	4155	4295	3776.7	4175	4207.5	4100
Calculated Strength (MPa)	53.0	59.8	57.4	56.4	58.5	54.9	54.5	53.3	58.8	60.0

All of the columns were found to have strengths in excess of the 40MPa required for the extension.

## 10. Conclusions & Recommendations

The paper identifies recent changes in the state of the art for assessing the in-situ strength of structures and outlines some of the principles used on various structures. The principles include core testing, rebound hammer and ultrasonic pulse velocity use to support in-situ strength assessment, methods of structural assessment and use of risk assessment to determine acceptability of reduced reliability due to low strength concrete. AS 3600, AS 1012.14 and CIA Z11 represent the current recommendations for structural assessment in Australia. These are now inconsistent with overseas documents on which they were based due to recent developments with the overseas documents. They do not incorporate the use of NDT and do not give structural assessment guidelines. It is recommended that AS 1012.14 and CIA Z11 are updated to reflect the current state of the art and be expanded to give guidance from testing to structural assessment.

## Acknowledgements

The authors wish to thank their clients for involvement in their projects.

## References

1. Standards Australia "AS 1012.14 Method of testing concrete. Methods for securing and testing cores from hardened concrete for compressive strength" Standards Association of Australia, 1991, Homebush, Australia.
2. Standards Australia "AS3600-2009 Concrete Structures." Standards Association of Australia, 2009 Homebush, Australia.
3. BS EN 12504 "Testing concrete in structures. , Part 1 Cored specimens - taking, examining and testing in compression, (2009) Part 2 Non-destructive testing. Determination of rebound number (2012). Part 3 Determination of pull out force (2005). Part 4 Determination of ultrasonic pulse velocity (2004). BSI, London, UK.
4. BS EN 13791 "Assessment of compressive strength in structures and precast concrete component" British Standards Institute, 2007, London, UK.
5. British Standards "BS6089 Assessment of in-situ compressive strength in structures and precast concrete components – complementary guidance to BS EN 13791" British Standards Institute, 2010, London, UK.
6. Standards Australia "AS1012.9 - Method of testing concrete. Methods for the determination of the compressive strength of concrete specimens" Standards Association of Australia, 1999, Homebush, Australia.
7. Concrete Society "Concrete Testing for Strength" Technical Report 11, Concrete Society, 1976, Camberly, UK.
8. Concrete Society "Concrete Testing for Strength" Technical Report 11, Concrete Society, 1987, Camberly, UK.
9. CIA Z11 "The Evaluation of Concrete Strength by Testing Cores" Recomme, nded Practice Z11, Concrete Institute of Australia, 2002, Sydney, Australia.
10. Concrete Society "In situ concrete strength. An investigation into the relationship between core strength and standard cube strength." Concrete Society. Project Report 3, 2004, Camberly, UK.
11. Crook N. "Assessment of in-situ concrete strength using data obtained from core testing." Advice Note 47, Concrete Society, 2013, Camberly, UK.
12. ISO "ISO 31000:2009 Risk Management" International Organization for Standardization, 2009, Geneva, Switzerland.
13. *fib* "The *fib* Model Code for Concrete Structures 2010" Fédération internationale du béton, 2010 Lausanne, Switzerland.
14. RILEM "NDT4 Recommendation for in situ concrete strength determination by combined non-destructive methods", Réunion Internationale des Laboratoires et Experts des Matériaux, systèmes de construction et ouvrages. 1993, Bagneux, France,
15. Breyse D. "Main challenges of non-destructive evaluation of on-site concrete strength" Concrete Repair , Rehabilitation and Retrofitting III 2012 Taylor Franicis Group, 2012, London, UK
16. Yaman I.S., Inci G., Yesiler N. and Aktan H. " Ultrasonic Pulse Velocity in Concrete Using Direct and Indirect Transmission" ACI Materials Journal Nov/Dec 2001 pp450- 45
17. Davis A.G. and Dunn C.S. "From theory to field experience with non-destructive vibration testing of piles." Proc. Inst. Civ. Eng. Part 2, No 59, pp867-875, 1974
18. Samarin A., and Meynink, P. "Use of combined ultrasonic and rebound hammer method for determining strength of concrete structural members," Concrete International, vol. 3, no. 3, pp. 25–29, 1981

# Full Scale Concentric Punching Shear Testing of Two-way Floor with Bonded Post-tensioning and Studrails

Fariborz Moeinaddini<sup>1</sup>, Kamiran Abdouka<sup>2</sup> and Andrew Barraclough<sup>3</sup>

<sup>1</sup>PhD Candidate, Swinburne University of Technology

<sup>2</sup>Senior Lecturer, Swinburne University of Technology

<sup>3</sup>R&D Manager, ITW Construction Systems

**Abstract:** The Use of bonded post-tensioning strands in concrete flooring system is very popular in the Australian construction industry. Two-way post-tensioned floors are susceptible to punching shear failure, and quite often, they are strengthened with shear reinforcement at slab-column connection. Punching shear reinforcement in the form of studrail is favourable type in practice due to its ease of placement and the quick installation procedure compared to other types of shear reinforcement such as shearheads or closed-ties. However, the Australian Standard for Concrete Structures, AS 3600, does not give any guidelines for design and detailing of studrails. In this paper, results from an experiment on a full scale slab-column connection of a bonded post-tensioned flat plate with studrails are presented. In addition, the failure load of the specimen is compared to the failure load of similar post-tensioned and RC specimens with no studrails. The specimen, reinforced with studrails, showed a significant improvement in the punching shear strength and ductility in comparison to the specimens with no shear reinforcement. The significance of using shear reinforcement to avoid the punching shear failure is detailed. Further, different international codes of practice such as ACI 318-11, Model Code 2010 and Eurocode2 are used to calculate the punching shear strength of the experiments to compare the accuracy of prediction of failure load by these codes of practice.

**Keywords:** punching shear, flat plate, bonded post-tensioning, studrails

## 1. Introduction

The use of post-tensioning technique in concrete floors is very common in developed countries due to the better performance of post-tensioned floor in serviceability and ultimate stage as compare to reinforced concrete floors. Two-way flooring systems are susceptible to punching shear failure in the vicinity of slab-column connection. Since punching shear can occur without any warning and can lead to progressive collapse of the building, this phenomenon was researched extensively in the last decades. And as a result, different types of shear reinforcement such as shearheads, bent-bars, double-leg bars, shear bands and studrails were developed for strengthening of floors against punching shear. Studrail is a popular choice for designers nowadays due to its main advantage in placement and ease of use on the building site. As the use of post-tensioning technique in two-way flooring systems have become very common, Carvalho, Melo (1) investigated the performance of unbonded post-tensioning flat plates with studrails. The unbonded post-tensioning technique is the common practice in United States and most of the available literature on punching shear strength of post-tensioned flat plates are from experimental programmes on test specimens with unbonded post-tensioning technique (2). In Australia, however, the industry uses bonded post-tensioning technique predominantly and there is a lack of knowledge on performance of flat plates with bonded strands. In addition, Australian Standard for Concrete Structures, AS 3600-2009 (3), does not provide any guidelines for design of studrails which are the preferred type of shear reinforcement for punching shear in the industry. This has left Australian design engineers without a straightforward guideline on how to design and detail the shear reinforcement to avoid a punching shear failure mode. This paper reports an experimental programme which investigates the performance of bonded post-tensioned flat plates with and without studrails to a punching shear failure mode..

## 2. Background

If a flat plate is loaded by a uniformly distributed load and  $L$  is the spacing between columns, the point of contra-flexure occurs approximately at  $0.2L$  away from the internal columns. To investigate the punching shear strength of flat plates, most of researchers use the point of contra-flexure to test a subsection of the flooring system instead of the whole floor. The floor subsection includes a central column and a flat plate which extends  $0.2L$  from each sides of the column. During the test, the flat plate is supported around its perimeter, representing the point of contra-flexure, and loaded at the centre by an actuator which pushes the column till the failure occurs.

According to Broms (4), if little tensile reinforcement is provided in the flat section, the failure can take place by yielding of tensile bars in the flat plate which would result in a ductile and plastic failure. This type of failure is a flexural failure and the ultimate strength of the floor can be estimated by yield-line theory. The other failure mode can be sudden and without warning failure of the specimen which usually occurs before yielding of some of tensile bars in the flat plate. In this case, punching shear preceded the flexural failure and it can be characterised by the cone type mass of concrete detaching from the flat plate around the column.

## 2.1 Flexural strength of flat plates

Yield-line theory is an upper bound approach to calculate the flexural strength of a flat plate. For example, Guandalini, Burdet (5) carried out a test series with specimens supported on eight points representing the line of contra-flexure. Based on Yield-line theory, Guandalini, Burdet (5) suggested the following equation to calculate the flexural strength of their test specimen:

$$V_{flex} = \frac{m}{r(\cos\frac{\pi}{8} + \sin\frac{\pi}{8})} \frac{B^2 - Bc - (\frac{c}{2})^2}{B - c} \quad (1)$$

In Equation (1),  $V_{flex}$  is the flexural strength of test specimen,  $m$  is the moment strength of specimen per unit length,  $r$  is the radius of the support line,  $B$  is the side dimension of the test specimen and  $c$  is the side dimension of the column. The formula for  $V_{flex}$  can change depending on the position and boundary condition of supports.

## 2.2 Punching shear strength in Australian Standard AS 3600-2009

According to Clause 9.2.3 of AS 3600-2009 (3), the ultimate punching shear strength of concrete slabs  $V_{uo}$  can be calculated using Equation (2).

$$V_{uo} = u d_{om} (f_{cv} + 0.3\sigma_{cp}) \quad (2)$$

Where,  $d_{om}$  is the effective depth of slab,  $u$  is the perimeter around the column at a distance equal to the half of effective depth of slab from the face of column,  $\sigma_{cp}$  is the average effective prestress in the vicinity of column in MPa, and  $f_{cv}$  is calculated by Equation (3).

$$f_{cv} = 0.17(1 + 2/\beta_h) \sqrt{f'_c} \leq 0.34 \sqrt{f'_c} \quad (3)$$

Where  $\beta_h$  is the ratio of larger to shorter column sides, and  $f'_c$  is the compressive strength of concrete in MPa.

When the applied shear force on the critical perimeter is higher than the computed capacity, calculated by Equation (2), AS3600-2009 permits the use of shearheads by which the  $f_{cv}$  can be increased and Equation (4) can be used to calculate the strength of the floor.

$$V_{uo} = u d_{om} (0.5\sqrt{f'_c} + 0.3\sigma_{cp}) \leq 0.2 u d_{om} f'_c \quad (4)$$

Unlike other international standards such as ACI 318-11 (6) and Eurocode 2 (7) (EC2), AS3600-2009 does not provide any guidelines for the design and detailing of shearhead or other types of shear reinforcement.

To ensure adequate shear strength of the slab, Clause 9.1.2 of AS 3600-2009 requires that 25% of the negative bending moment in the column strip and half of the middle strip to be resisted by the reinforcement and prestressing tendons that cross over the column and of a width equal to the twice the thickness of the slab from the faces of the column.

### 3. Experimental programme

#### 3.1 Test setup

Three 3m x 3m concrete plates were built with a thickness of 200mm. Each concrete plate has a 300mm x 300mm x 300mm column cast at the centre of the concrete plate. The specimen was supported on 8 points around its perimeter at the distance of 1440mm from the centre during the test. The dimensions of test specimens and the position of supports are shown in Figure 1.

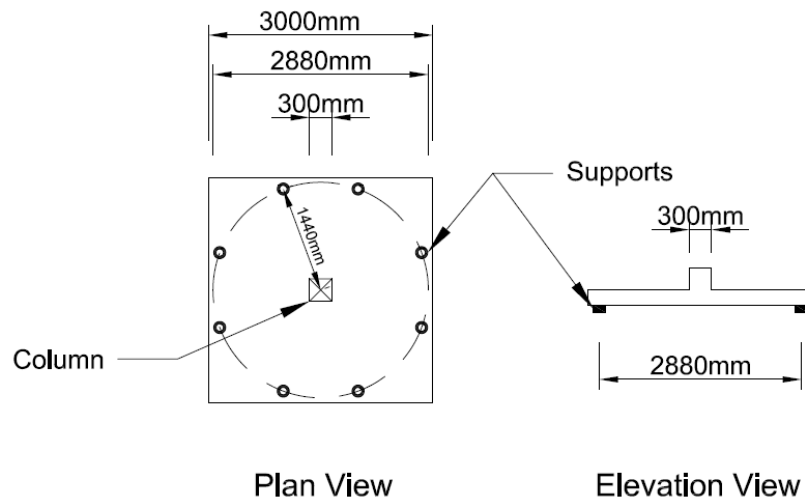


Figure 1 Dimensions of test specimens and position of supports

A cruciform reaction frame was designed for the purpose of this testing program. The cruciform consists of four 380 PFC beams in each direction. The reaction frame was supported on its four sides by four towers which supported the weight of testing rig and test specimen. The test specimen was suspended from the cruciform by four M36 high tensile bars. The hydraulic jack was placed between the reaction frame and the concrete panel to apply the load to the central column of the specimen. The test setup is shown in Figure 2.

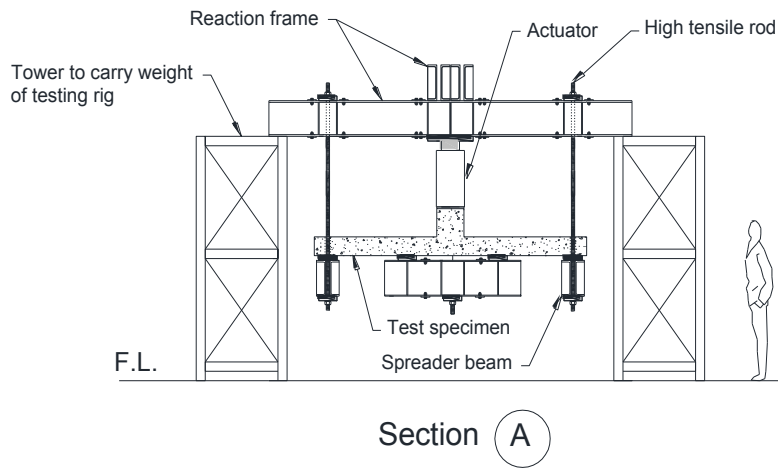
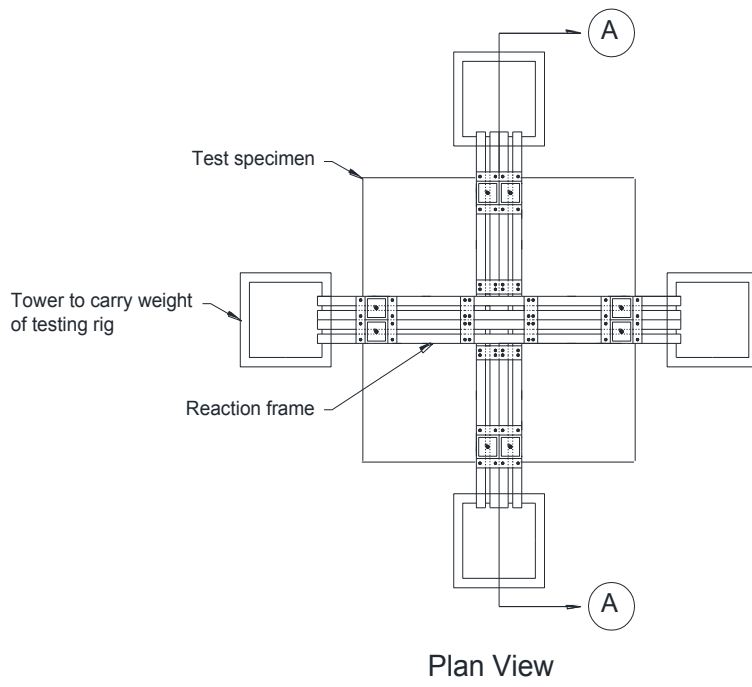
#### 3.2 Detail of reinforcement in specimens

Control specimen C1 was built without any post-tensioning strands and studrails. This specimen had N16 reinforcement bars with average effective depth of 164mm. The reinforcement detail for specimen C1 is shown in Figure 3.

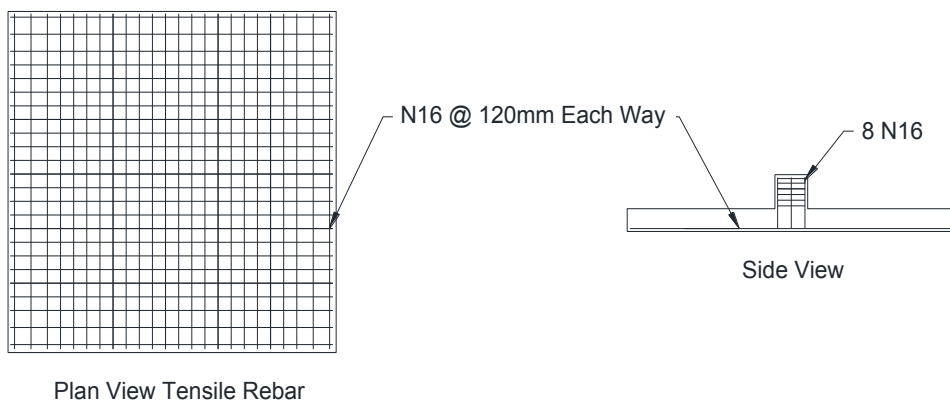
Reinforcement detail of Specimen PE1 was similar to specimen C1, and in addition it had bonded post-tensioning strands in both directions with a draped profile. It is a common practice to place the post-tensioning ducts with a profile to balance the applied bending moment in flat plates. Therefore, the post-tensioning ducts were placed with 100mm effective depth at the sides of the plate and on average 140mm effective depth at the centre of plate. The detail of post-tensioning strands in specimen PE1 is shown in Figure 4.

Specimen PES1 is similar to specimen PE1 except for additional eight studrails. The studrails consist of 10 shear studs that were welded on a rail to be placed around the column area. Figure 5 shows the detail of studrails which were used in specimen PES1. ACI-ASCE Committee 421 (8) recommended placing of the first row of studs at a distance between 0.35d and 0.4d from the face of column and the spacing between studs to be 0.5d. Therefore, the first row of studs was placed at 65mm from the face of column and the spacing between the studs was 82mm. One of the studrails had strain gauges on each of its studs. The strain gauges were installed to monitor the extent that each of the studs contributes in arresting the shear cracks from opening.

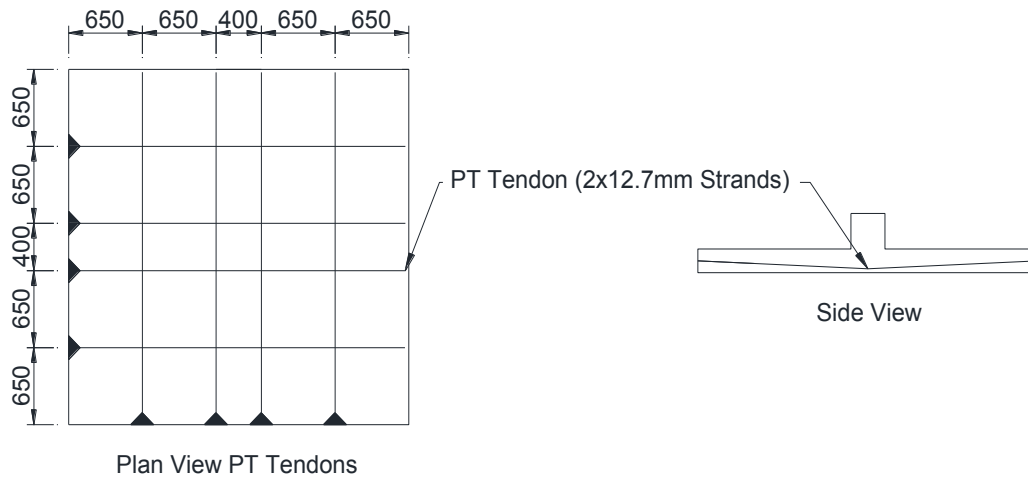




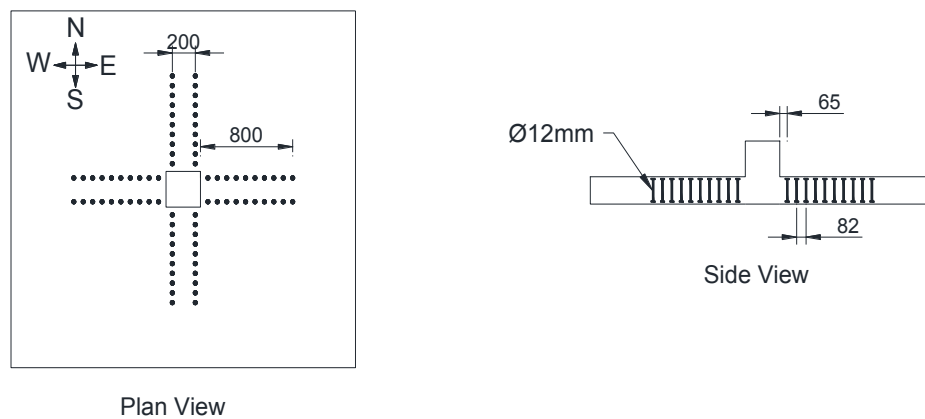
**Figure 2 Test setup for experiment on punching shear strength of flat plates**



**Figure 3 Position of tensile reinforcement in specimen C1, PE1 and PES1**



**Figure 4 Position of post-tensioning tendons in specimen PE1 and PES1**



**Figure 5 Position and detail of studrails in specimen PES1**

Specimens PE1 and PES1 were post-tensioned and grouted one week prior to the test at the age of 170 days. Strands were tensioned up to 156kN and anchored. There were immediate losses of post-tensioning strands due to the elastic compression of the concrete and the movement of the grips as the strands are anchored. The force in the strands was calculated with the use of readings from a strain gauge, which was attached to one of the wires of the strand. The forces were varied between 128kN and 131kN after losses. Specimen PE and PES1 had 8 strands in each direction and the average in-plane stress in the concrete was 1.7MPa. Post-tensioning ducts were grouted by a cement and water mix at the same day of stressing of strands.

### 3.3 Material properties

A 32MPa concrete with maximum aggregate size of 20mm was ordered from a local provider in Bayswater, Victoria to cast the specimens on 18<sup>th</sup> December 2013. The mix design was a typical concrete for post-tensioning slabs which would reach 25MPa in four days. The water-cement ratio was 0.57 and the requested slump was 100mm. Specimens were tested six months after they were cast, and within a period of one month. The tests on the properties of the concrete were carried out around the same time as the experiment. Table 1 gives the average properties of material which were determined by testing of samples of materials used in building of specimens. Six standard cylinder samples of 100mm diameter and 200mm height were tested to determine the compressive strength of the concrete ( $f_{cy}$ ). Three cube specimens with side dimension of 150mm were used to determine the cube compressive strength of the concrete ( $f_{cu}$ ). Three cylinder samples were taken from the grout to determine its compressive strength ( $f_{cgr}$ ). The reinforcement bars in the specimens were grade 500, N

type, with a modulus of elasticity of 200GPa. Samples of the rebar were used to determine the average yield strength ( $f_{sy}$ ). Studrails for specimen PES1 were made of normal ductility bars which their yield strength ( $f_{ssy}$ ) was determined by testing of six samples. A tensile test was carried out on a sample of the post-tensioning strands to determine its ultimate tensile strength ( $f_{psu}$ ).

**Table 1 Average value of material properties**

$f_{cy}$ (MPa)	$f_{cu}$ (MPa)	$f_{gr}$ (MPa)	$f_{sy}$ (MPa)	$f_{ssy}$ (MPa)	$f_{psu}$ (MPa)
34.5	44	30	540	510	1770

#### 4. Result and discussion

The first experiment was carried out on the control specimen C1. Specimen PE1 and PES1 were tested in sequence, two weeks after the first experiment. Since the concrete was cast 6 month prior to the testing, it is assumed the concrete properties were constant during the period of the experimental programme, ruling out the effect of varying concrete properties when comparing the test results. Specimen C1 and PE1 failed in a very brittle and sudden manner and a significant drop in the load resisted by the test specimen were observed. The punching action by column was apparent as the column was detached from the slab and the mass of column was held in place by catenary action of reinforcement bars. A different failure mode was observed in the experiment on PES1. The crushing of concrete occurred in the region where studrails were placed. The load resistance of the specimen decreased as the crushing of concrete progressed.

##### 4.1 Load-displacement

The applied load to the column was monitored by a load cell between the reaction frame and the actuator during test. Further, there were eight load cells between the test rig supports and the concrete panel. These load cells were used to have the load applied concentrically and there was no unbalanced moment transferring through slab-column connection during the test. The deformation of the flat plate was monitored by fourteen Linear Variable Differential Transformer (LVDTs) and a photogrammetry technique was used throughout the test load cycle. Specimen C1 resisted 798kN with central displacement of 19.4mm when punching shear occurred and the load dropped to 98kN. Specimen PE1 resisted 1074kN with the central displacement of 21.3mm before the punching of the flat plate. The load dropped to 300kN after the failure. Specimen PES1 resisted 1,264kN with the central deformation of 37.8mm which could attribute to the use of studrails. As the specimen reached the maximum load of 1,264kN, the crushing of concrete was apparent on the compression side of the plate and the load gradually dropped as the displacement increased. Test was stopped when specimen PES1 reached the central displacement of 50mm with corresponding load of 647kN. Figure 6 shows the applied load versus the displacement of the column for specimens C1, PE1 and PES1. It can be seen specimens PE1 and PES1, which have similar tensile reinforcement and post-tensioning strands, plot almost identical load-displacement up to 1,074kN where specimen PE1 fails by punching shear. Specimen PES1, however, could resist further load and displacement with the studrails arresting shear cracks from opening. One observation from Figure 6 is that specimen C1 and PE1, which have no shear reinforcement, fail at a similar displacement 19.4mm and 21.3mm respectively. However, specimen PE1 has a higher stiffness due to bonded post-tensioning strands and could reach a higher load for the same displacement before failure.

##### 4.2 Load-rotation

Rotation of the plate is one of main parameters in Model Code 2010 (9) (MC2010). This code uses Critical Shear Crack Theory (CSCT) (10) to calculate the punching shear strength of flat plates. CSCT suggests the rotation of the plate causes the opening of the critical shear crack, which leads to the punching shear failure. The rotation of the flat plate was monitored with the use of inclinometers on four sides of the square plate as shown in Figure 7 (b). The average rotation of plate is plotted against the applied load for specimen C1, PE1 and PES1 in Figure 8. The maximum observed rotation before failure was 0.0163rad, 0.0178rad and 0.0298rad for specimen C1, PE1 and PES1 respectively. At rotation of 0.001rad, specimen PE1 reached the decompression stage in the plate section at the face of the column. If the decompression rotation of specimen PE1 is deducted from its maximum rotation, the rotation of specimen C1 and PE1 are very similar prior to failure.

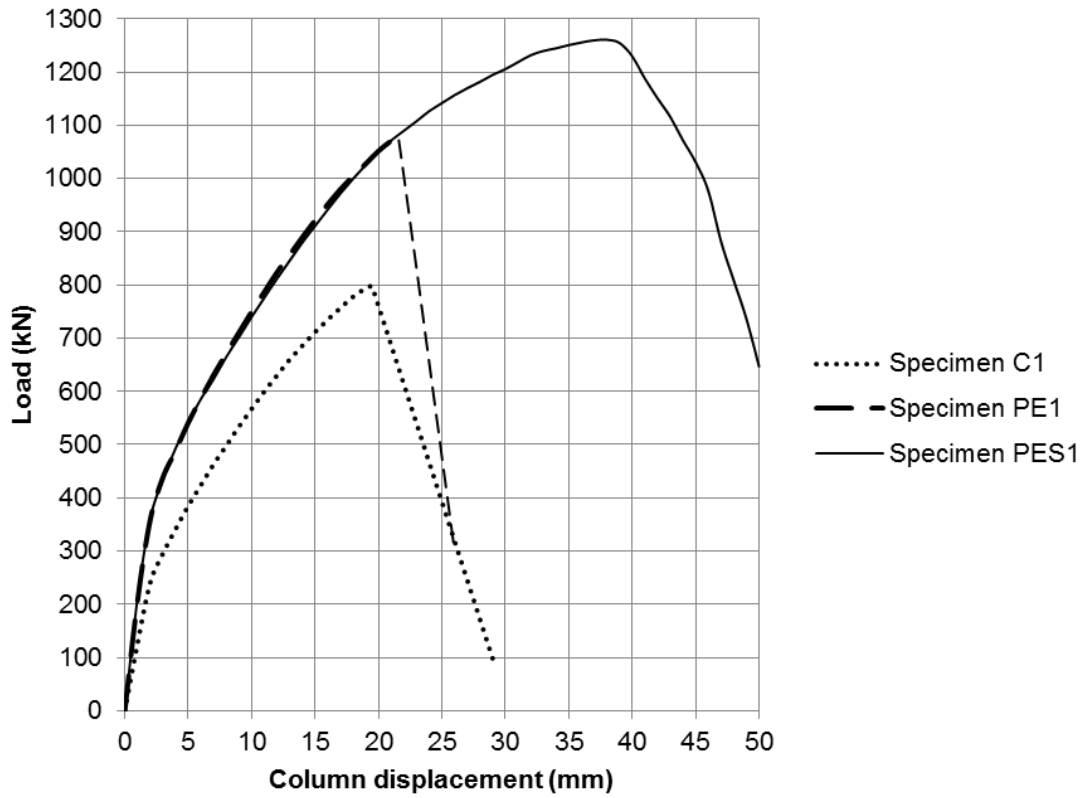


Figure 6 Load versus displacement of the column

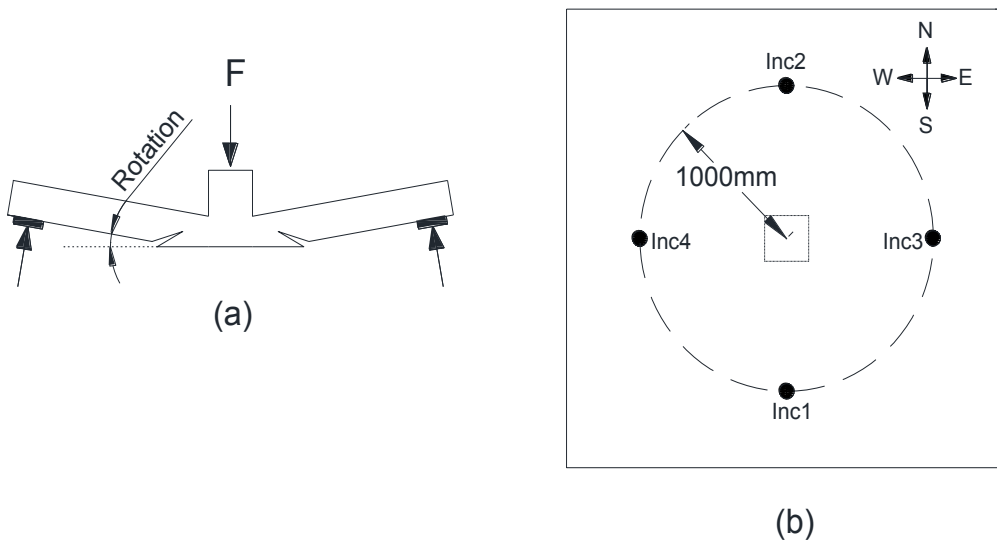


Figure 7 (a) Rotation of the plate (b) plan view of position of inclinometers

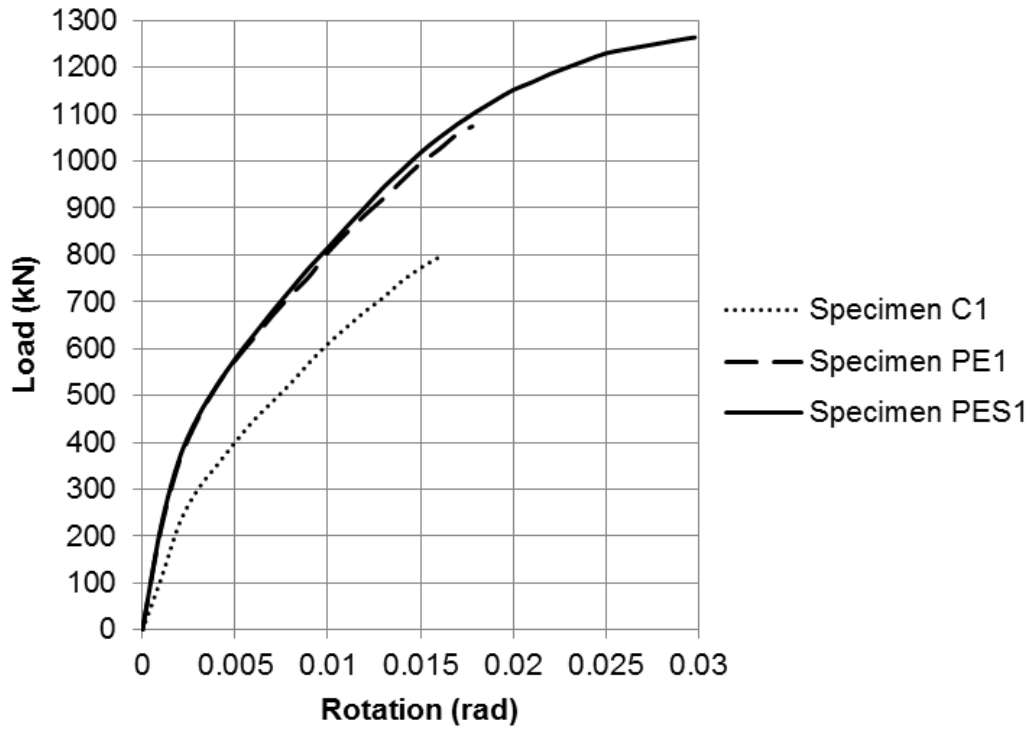


Figure 8 Load versus rotation of the plate in reference to the column

#### 4.3 Strain in studrails

Strain gauges were installed on studs of one studrail in specimen PES1 to monitor the strains during the test. Figure 9 shows the maximum monitored strains in studs during the testing of specimen PES1. Strains in the first six rows of studs are significantly higher than the rest of studs. The most critical studs are the second to fifth row of studs. The failure mode was crushing of concrete in the shear reinforced zone as shown in Figure 10. None of the studs reached the yield strength prior to failure. If it is assumed that strains of studs with strain gauges are similar for other studrails, the estimated load resisted by studrails at failure is 950kN. That means the concrete contribution in load carrying capacity of the plate is 314kN.

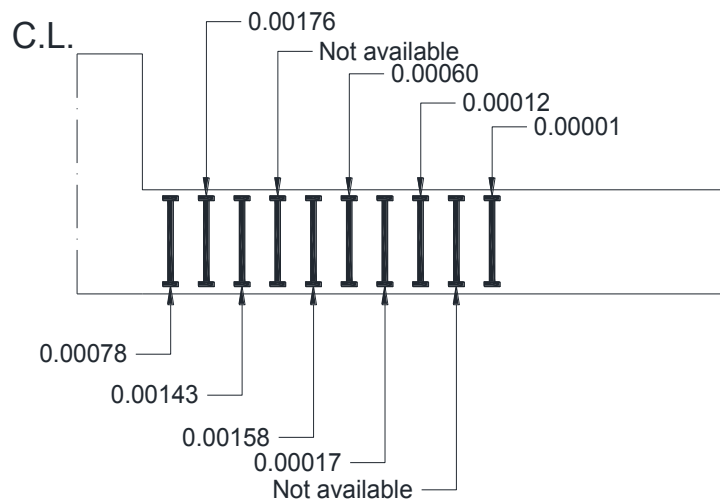
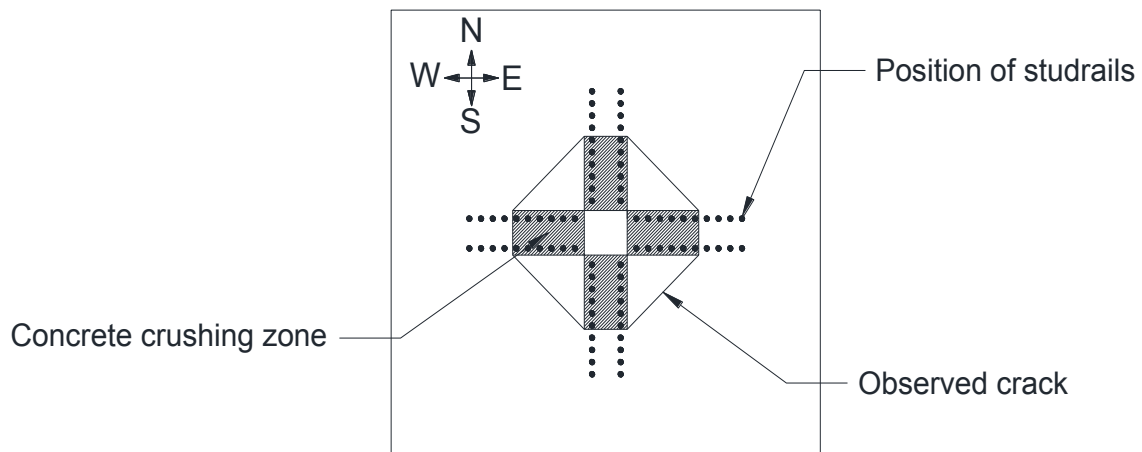


Figure 9 Maximum tensile strain in studs during experiment on PES1



Plan view of compression side of specimen PES1

Figure 10 Schematic view of concrete crushing zone in specimen PES1

#### 4.4 Comparison of predicted failure load

The results from the experiment are compared to the predicted punching shear strengths of some of the internationally recognised codes of practice such as AS 3600-2009 (3), Eurocode 2 (7) (EC2), ACI 318-11 (6) and Model Code 2010 (9). Table 2 provides the observed failure load of ( $V_{fail}$ ), the load which flexural capacity of the specimen would reach ( $V_{flex}$ ), the predicted strength by AS 3600-2009 ( $V_{AS3600}$ ), the predicted strength using EC2 ( $V_{EC2}$ ), the predicted strength by MC2010 ( $V_{MC2010}$ ) and the predicted strength by ACI 318-11 ( $V_{ACI318}$ ). The suggested formula for punching shear strength of flat plates with shearheads in AS3600-2009 was used to predict the failure load of PES1. EC2 was not applicable to calculate the punching strength of specimen PES1 since the detailing of placement of studrails did not meet the requirements by EC2. Level of Approximation Three was used to calculate the predicted strength by MC2010.

Table 2 Predicted failure load versus observed failure load

Specimen	$V_{fail}(kN)$	$V_{flex}(kN)$	$V_{AS3600}(kN)$	$V_{EC2}(kN)$	$V_{MC2010}(kN)$	$V_{ACI318}(kN)$
C1	798	1121	608	627	502	590
PE1	1074	1861	793	746	588	775
PES1	1264	1861	1079	Not applicable	1035	1180

All three specimens failed below their flexural capacity. Codes of practice in Table 2 predicted smaller failure loads as compared to the observed failure load. MC2010 has the most conservative prediction compared to the other codes of practice. AS 3600 formula for punching shear strength of flat plates with shearheads, Equation (4), predicts 1,079kN as the failure load of specimen PES1 which had studrails and reached the failure load of 1,264kN. This suggests the current formula of AS 3600, can be used to calculate the concrete crushing strength of flat plates with studrails.

## 5. Conclusion

The results from full scale tests on punching shear strength of three different flat plates presented. The increase in punching shear strength due to addition of bonded post-tensioning strands was apparent. It was observed that the punching shear failure in both specimens, which did not have studrails, occurred around the same central measured displacement. Further, the rotations of plates in the latter specimens were similar prior to failure. The use of studrails in flat plates with bonded post-tensioning improved the ultimate strength and increased the ductility significantly. The maximum strain in different rows of studs was reported and it was observed that the second to the fifth rows of studs underwent higher strains compared to the other rows of studs. Furthermore, studs, which were positioned beyond the sixth row, did not engage by carrying the applied load. The contribution of

studs and concrete in the load resisting capacity is estimated using strains in studrails at the maximum load. The mode of failure for the specimen with shear reinforcement was crushing of concrete in the vicinity of studrails and none of studs reached yield stress before failure. Various codes of practice such as AS 3600, EC2, MC2010 and ACI 318 were used to predict the punching shear strength of specimens. The results showed these codes of practice are predicting a lower failure load as compared to the observed failure load from the experiment.

## 6. Acknowledgment

The authors wish to express their gratitude to ITW Construction Systems Laboratory for providing the fund and space to carry out the testing programme, Smart Structures Laboratory of Swinburne University for providing instrumentation equipment, and Freyssinet for providing the post-tensioning services.

## 7. References

1. Carvalho, A., et al., *Punching shear in post-tensioned flat slabs with stud rail shear reinforcement*. ACI Structural Journal, 2011. **108**(5): p. 9.
2. Bondy, K., *Two-way post-tensioned slabs with bonded tendons*. PTI Journal, 2012. **8**(2): p. 7.
3. AS 3600-2009, *Australian Standard Concrete Structures*. AS 3600-2009. 2009, Homebush, NSW: Standards Australia. 205.
4. Broms, C.E., *Concrete Flat Slabs and Footings Design method for Punching and Detailing for Ductility*, in *Department of Civil and Architectural Engineering*. 2005, Royal Institute of Technology: Stockholm. p. 114.
5. Guandalini, S., O. Burdet, and A. Muttoni, *Punching tests of slabs with low reinforcement ratios*. ACI Structural Journal, 2009. **106**(1): p. 87-95.
6. ACI 318-11, *Building Code Requirements for Structural Concrete (ACI 318-11) and Commentary*, ed. A.C. 318. 2011, Framington Hills, Michigan: American Concrete Institute.
7. Eurocode 2, *Eurocode 2: Design of Concrete Structures-part 1-1: General Rules and Rules for Buildings*. 2004: British Standards.
8. ACI-ASCE Committee 421, *Shear Reinforcement for Slabs (ACI 421.1R-99)*, in *Technical report*. 1999, American Concrete Institute: Farmington Hills, Michigan. p. 15.
9. Model Code 2010, *Model Code 2010*, in *Final Draft*. 2012, International Federation for Structural Concrete (*fib*): Germany. p. 331.
10. Muttoni, A., *Punching shear strength of reinforced concrete slabs without transverse reinforcement* ACI Structural Journal, 2008. **105**(4): p. 440-450.

# Experimental Study on Carbon Fiber Reinforced Concrete for Strain Measurement of RC Portal Frame

Fang-Yao Yeh<sup>1</sup>, Kuo-Chun Chang<sup>2</sup>, Wen-Cheng Liao<sup>3</sup>

<sup>1</sup>Research Fellow, National Center for Research on Earthquake Engineering (NCEE)

<sup>2</sup>Professor of Civil Engineering, National Taiwan University (NTU)

<sup>3</sup>Assistant Professor of Civil Engineering, National Taiwan University (NTU)

**Abstract:** Structural monitoring systems are important in civil engineering. However, traditional structural monitoring systems have disadvantages such as the shorter life span of sensors relative to that of the structure being monitored. The present study uses carbon fiber reinforced concrete (CFRC) as a structural monitoring sensor to extend the life of a sensor to match that of the structure. There are some known advantages of carbon fiber reinforced concrete, such as high tensile strength and high ductility which increases the seismic capacity and security of structures. However, CFRC has functionality similar to piezoresistive materials which can be used as a self-sensing material for strain measurement and damage detection. This property is based on the reversible effect of the strain on the volume of electrical resistivity and the irreversible effect of material damage on its resistivity. The strain sensing behavior is such that the resistivity decreases reversibly upon compression due to the slight inward push of crack-bridging fibers and the consequent decrease in the contact electrical resistivity of the fiber-cement interface. Similarly, the resistivity increases reversibly upon tension due to the slight outward pull of crack-bridging fibers and the consequent decrease in the contact resistivity. To consider the economic benefits, the fiber content is only 0.2 vol. % which is less than half of the amount used in other references (0.48 vol. %). The experimental results show that the conductivity of current materials is significantly improved by CFRC and that it can be used for strain measurement and damage detection with fiber content of 0.2 vol. %. Moreover, the experimental results of CFRC coated beams and RC portal frame can be kept in a database for applications of structural health monitoring.

## 1. Introduction

This article shows that carbon fiber added into concrete becomes carbon fiber reinforced concrete (CFRC) and with the functionality similar to piezoresistivity material can be used as a self-sensing material for strain measurement and damage detection. It is based on the reversible effect of strain on the volume electrical resistivity and the irreversible effect of damage on the resistivity. The strain sensing behavior is such that the resistivity decreases reversibly upon compression due to the slight push-in of crack-bridging fibers and the consequent decrease of the contact electrical resistivity of the fiber-cement interface. Similarly, the resistivity increases reversibly upon tension due to the slight pull-out of crack-bridging fibers and the consequent decrease of the contact resistivity [1, 2]. The self-sensing ability of CFRC cement-based composite has been well demonstrated under compression and under flexure. With the use of CFRC's electrical resistance change and appearance of structural cracks, we are able to derive an integration of sensors which also possesses material smartness quotient of self-sensing, stability and repetitiveness.

## 2. Basic mechanical test plan

### 2.1 Preparation of materials

The design concrete strength was set at 49.05 MPa. The cement was blended Portland cement. Specimens were prepared from a mix with the following composition: water-to-cement ratio (w/c) = 0.4; sand-to-cement ratio (s/c) = 0.75; silica fume, 15% by weight of cement; methylcellulose, 0.4% by weight of cement; and carbon fiber, 0.2% of total volume. The fiber diameter was 7  $\mu\text{m}$ . The nominal fiber length was 15 mm. A standard mixing procedure was used. A rotary mixer with flat beater was used for mixing. After pouring the mix into oiled molds, an external electric vibrator was used to facilitate compaction and decrease the amount of air bubbles.

### 2.2 Preparation of specimens

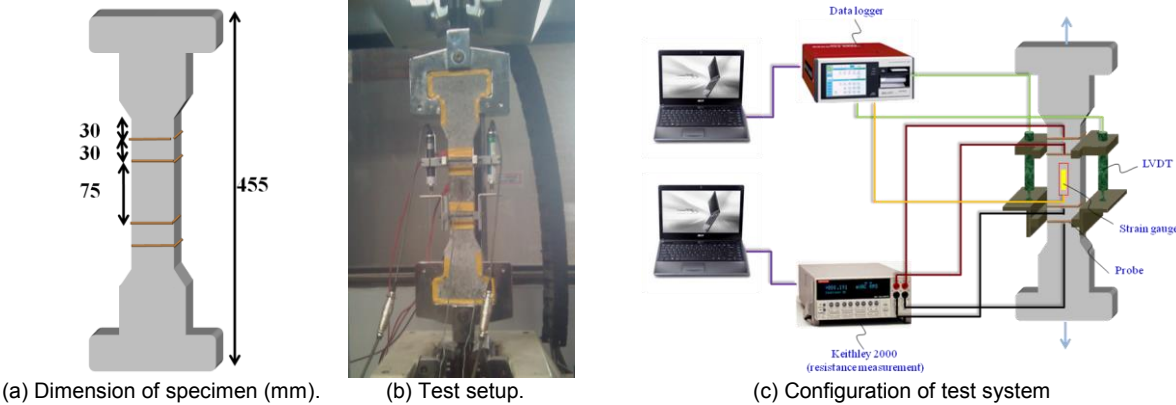
From the aforementioned concrete mixture, 5 CFRC dog-bone-shaped specimens, 4 CFRC cylinders, and 8 different styles of CFRC beams at 28 days age were fabricated for testing. Dog-bone-shaped specimens with dimension of 455  $\times$  50  $\times$  20 mm were prepared for uniaxial tension testing. Cylinders with dimension of  $\phi$ 100  $\times$  200 mm were prepared for uniaxial compression testing. Beam specimens



with dimension of 550 × 150 × 150 mm were prepared for three-point bending testing. The test setup is shown in Figs 1-3.

**2.2.1 Uniaxial tension test**

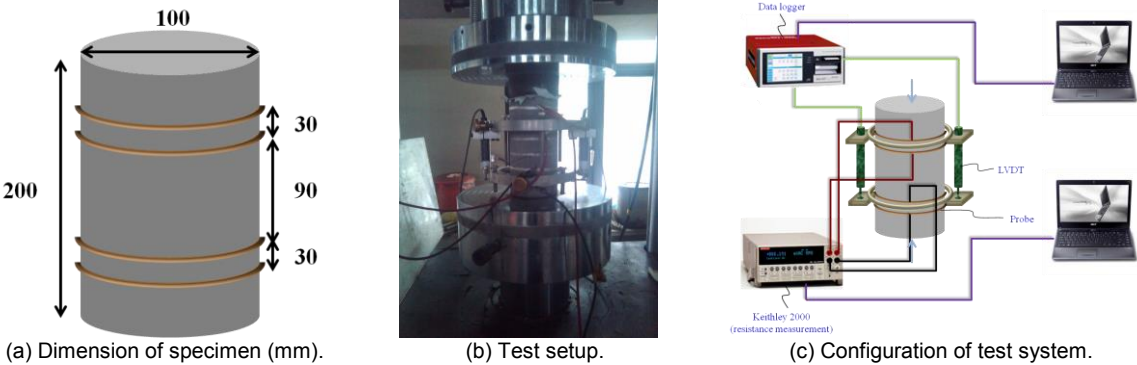
The monotonously tensile loading was applied on the specimen (Fig. 1). Tensile strain of CFRC specimen was measured by LVDT under gauge length equal to 105 mm. The electrical resistance measurements were conducted using the four-probe method, with silver paint in conjunction with copper wires for electrical contacts and the electrode distance was equal to 75 mm (Fig. 1a). The Keithley 2000 digital multimeter was used to measure the electrical resistance of the specimens (Fig. 1c).



**Figure 1. Uniaxial tension test.**

**2.2.2 Uniaxial compression test**

The monotonously compressive loading was applied on the specimen (Fig. 2). Compressive strain of CFRC specimen was measured by LVDT under gauge length equal to 100 mm. The electrical resistance measurements were conducted using the four-probe method, with silver paint in conjunction with copper wires for electrical contacts and the electrode distance was equal to 90 mm (Fig. 2a). The Keithley 2000 digital multimeter was used to measure the electrical resistance of the specimens (Fig. 2c)



**Figure 2. Uniaxial compression test.**

**2.2.3 Three-point bending test**

The cyclical loading was applied on the CFRC beam specimen (Fig. 3). Dynamic strain of CFRC beam was measured by strain gauge, the central deformation was measured by LVDT, and the electrical resistance was measured by Keithley 2000 digital multimeter under gauge length equal to 120 mm (Figs 3a, 3c).

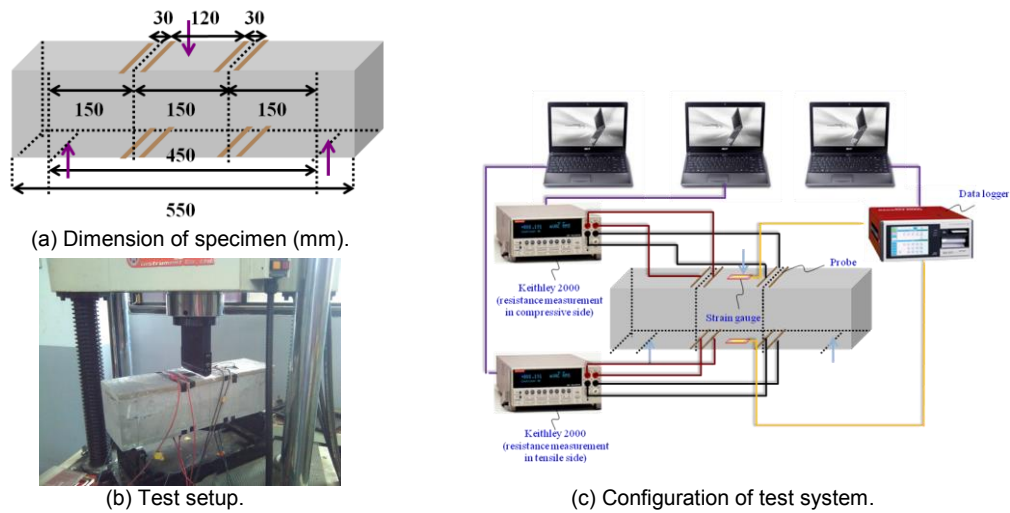


Figure 3. Three-point bending test.

### 3. Results and discussion of basic mechanical test

#### 3.1 Uniaxial tension test

The test results of specimens at 28 days age are shown in Figs 4-6. Fig. 4a shows the relationships between fractional change in electrical resistance (denoted as  $(R-R_0)/R_0$ ) of CFRC and strain measured by LVDT at the middle portion of the specimens. These data existed linear relationship between fractional change in electrical resistance of CFRC and strain measured by LVDT before proportional limit. If it exceeds the proportional limit, the fractional change in electrical resistance increases due to the increase of electrical resistance in CFRC specimen caused by the microstructure changes, micro crack density increases and damage occurrences.

In order to relate the fractional change in electrical resistance to tensile strain, the definition of gauge factor (GF) is fractional change in electrical resistance per unit strain. Before proportional limit, there exist strong linear relationship ( $R^2 \approx 1$ ) between fractional change in electrical resistance and tensile strain of T1 to T5 specimens (Fig. 4b). Similarity of fractional change in electrical resistance and tensile strain under uniaxial tension tests can be used as a self-sensing material for strain measurement within proportional limit.

Fig. 5 shows the stress-strain curves are very similar before proportional limits but have slopes change due to electrical resistances increasing if tensile strains exceed proportional limits. Based on the different phenomena of fractional change of electrical resistance, three regions are considered in this paper, (1) region-I: linear region, the strain sensing via fractional change in electrical resistance with linear relationship and reversibility; (2) region-II: plastic region, the strain sensing via fractional change in electrical resistance still with some proportional relationship and partial reversibility, owing to the crack occurrence and damage accumulation in specimen, but in tensile specimen these are not obvious; (3) region-III: damaged region, the strain sensing via fractional change in electrical resistance is meaningless, owing to the damage occurrence and material failure in specimen. The fractional change in electrical resistance should be changed very rapidly, which can be used for damage detection.

Fig. 6 shows the variation of tensile stress and fractional change in electrical resistance with tensile strain. The fractional change in electrical resistance has a linear relationship with tensile strain in region-I. The fractional change in electrical resistance rapidly decreases in region-III, because of the electrical resistance increase quickly, due to the damage accumulation. The slope of fractional change with tensile strain is a good indicator for damage detection under tensile loading.

The test results are summarized in Table 1. Before proportional limit (tensile strain =  $1 \times 10^{-4}$ ), there exist strong linear relationship between fractional change in electrical resistance and tensile strain, the range of  $R^2$  are 0.93 to 0.97, the similarity of fractional change in electrical resistance and tensile strain under uniaxial tension tests can be used for strain measurement. There gauge factors (GF) are 9.5 to 19.5 and the measurement ranges (MR) are 57.8% to 83.33% of ultimate tensile strain.

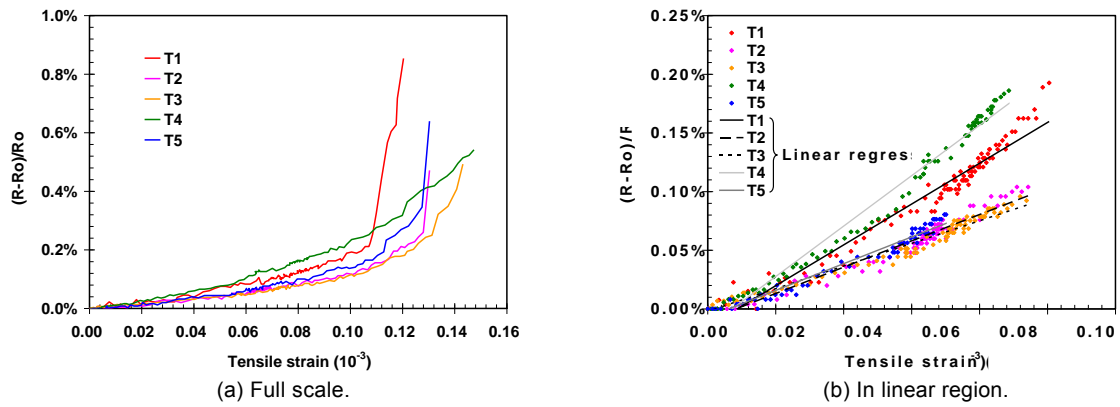


Figure 4. Comparison between fractional change in electrical resistance and strain measured by LVDT.

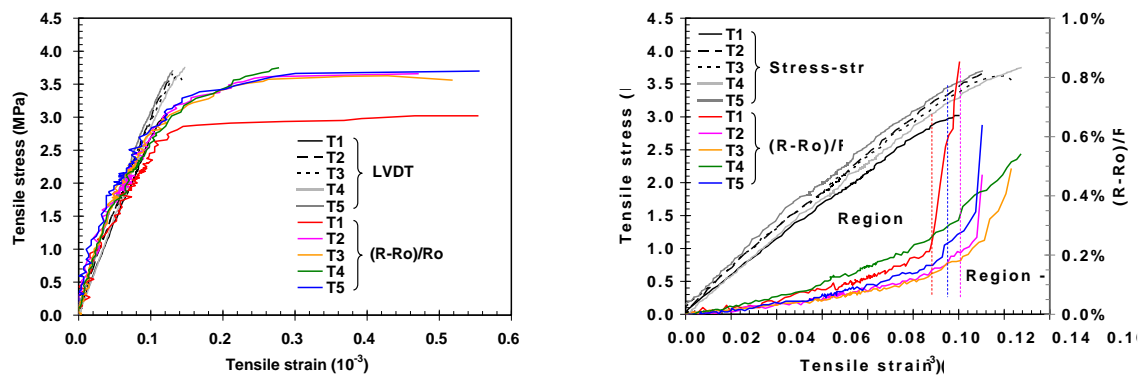


Figure 5. Variation of tensile stress with tensile strain measured by LVDT and CFRC.

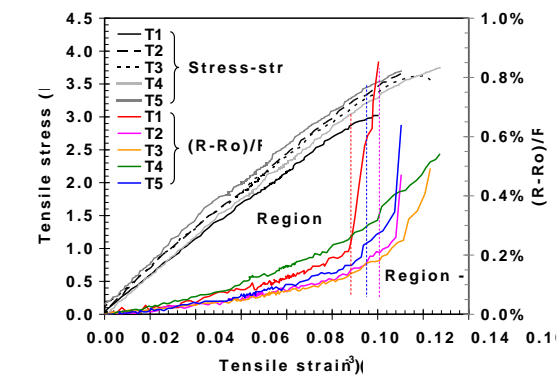


Figure 6. Variation of tensile stress and fractional change in electrical resistance with tensile strain.

Table 1. Results of uniaxial tension test.

Specimen	E	$f_t$	$\varepsilon_u$	$R_o$	GF	$R^2$	$(\Delta R/R_o)_L$	MR
	GPa	MPa	$10^{-3}$	$\Omega$			$10^{-3}$	%
T1	25.76	3.02	0.120	26.47	15.4	0.95	0.1	83.33
T2	29.36	3.66	0.173	25.03	10.0	0.94	0.1	57.80
T3	27.48	3.15	0.137	29.23	9.5	0.96	0.1	72.99
T4	27.74	3.75	0.147	36.54	19.5	0.97	0.1	68.03
T5	28.20	3.70	0.130	24.87	11.5	0.93	0.1	76.92

### 3.2 Uniaxial compression test

The test results of specimens at 28 days age are shown in Figs 7-10. Figs 7a, 7b show the relationships between fractional change in electrical resistance of CFRC and strain measured by LVDT at the middle portion of the specimens. These data existed bi-linear relationship between fractional change in electrical resistance of CFRC and strain measured by LVDT before proportional limit. If it exceeds the proportional limit, the fractional change in electrical resistance decreases due to the increase of electrical resistance in CFRC specimen caused by the microstructure changes, micro crack density increases and damage occurrences.

In order to relate the fractional change in electrical resistance to compressive strain, before proportional limit there exist bi-linear relationship between fractional change in electrical resistance and compressive strain. Fig. 8a shows the relation of the fractional change in electrical resistance to compressive strain smaller than  $2 \times 10^{-4}$  and the gauge factor of C1 to C4 specimens are approximately 200 to 250. Fig. 8b shows the relation of the fractional change in electrical resistance to compressive strain be-

tween  $5 \times 10^{-4}$  and proportional limit and the gauge factor of C1 to C4 specimens are approximately 20 to 30. The similarity of fractional change in electrical resistance and compressive strain under uniaxial compression tests can be used as a self-sensing material for strain measurement within proportional limit.

Fig. 9 shows the variation of compressive stress and fractional change in electrical resistance with compressive strain. The fractional change in electrical resistance has a linear relationship with compressive strain in region-I and region-II, the GF1 and GF2 are used for compressive strain measurement. Fig. 10 shows the fractional change in electrical resistance rapidly decreases in region-III, because of the electrical resistance increase quickly, due to the damage accumulation. The slope of fractional change with compressive strain is a good indicator for damage detection under compressive loading.

The test results are summarized in Table 2. Before proportional limit (compressive strain =  $2.57-3.25 \times 10^{-4}$ ), there exist strong bi-linear relationship between fractional change in electrical resistance and compressive strain, the range of  $R^2$  are greater than 0.94, the similarity of fractional change in electrical resistance and compressive strain under uniaxial compressive tests can be used for strain measurement. There gauge factors are 187.1 to 253.0 (for GF1) and 20.9 to 24.9 (for GF2) and the measurement range (MR) are 71.15% to 88.32% of ultimate compressive strain.

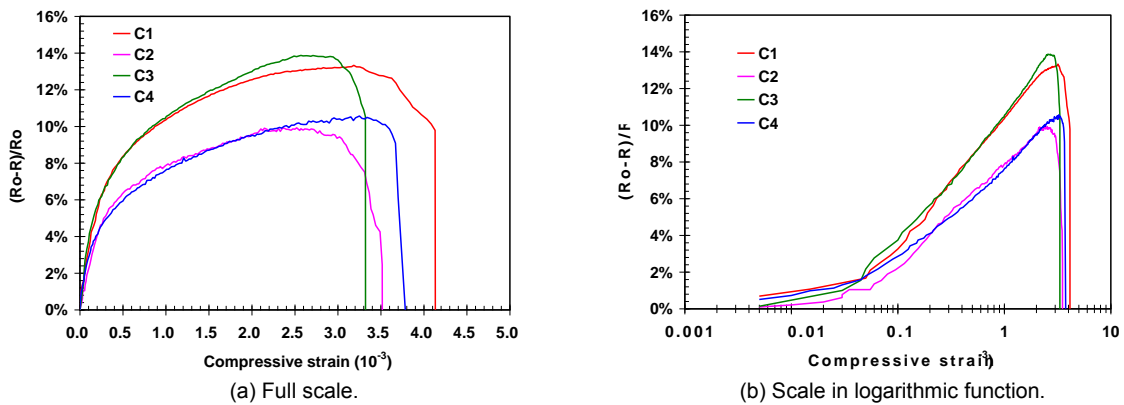


Figure 7. Comparison between fractional change in electrical resistance and strain measured by LVDT.

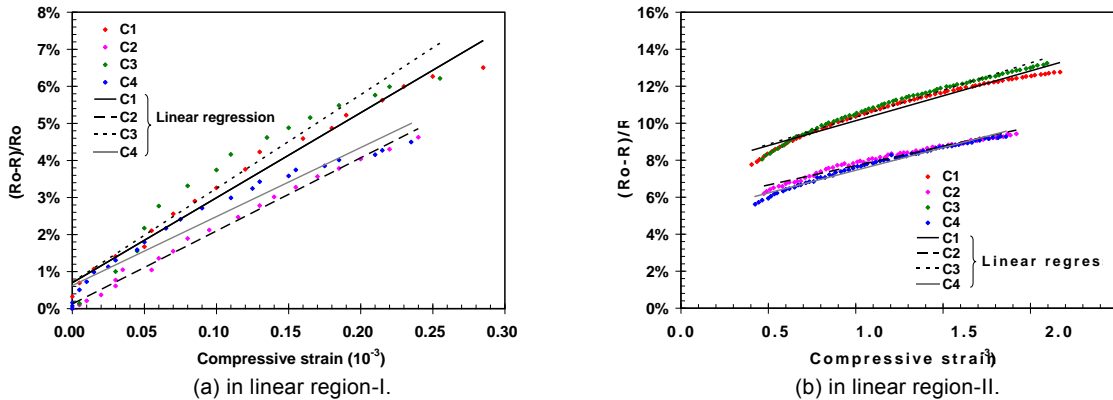


Figure 8. Comparison between fractional change in electrical resistance and strain measured by LVDT in Linear region.

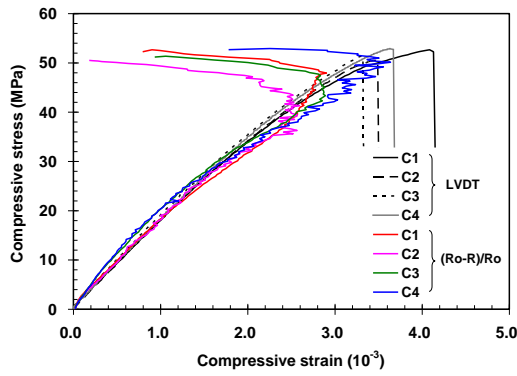


Figure 9. Variation of compressive stress with compressive strain measured by LVDT and CFRC.

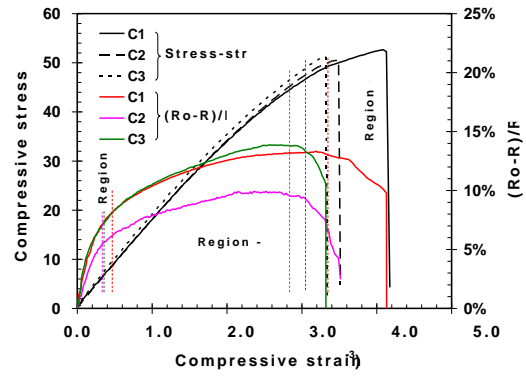


Figure 10. Variation of compressive stress and fractional change in electrical resistance with compressive strain.

Table 2. Results of uniaxial compression test.

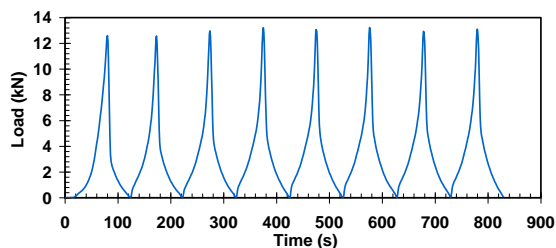
Specimen	E	$f'_c$	$\epsilon_u$	Ro	GF1	R <sup>2</sup>	GF2	R <sup>2</sup>	$(\Delta R/Ro)_L$	MR
	GPa	MPa	10 <sup>-3</sup>	$\Omega$					10 <sup>-3</sup>	%
C1	17.48	52.66	4.09	19.63	240.6	0.98	24.9	0.97	2.91	71.15
C2	17.77	50.51	3.49	31.38	197.2	0.99	20.9	0.97	2.57	73.64
C3	18.61	51.37	3.30	31.17	253.0	0.94	29.3	0.98	2.89	87.58
C4	17.62	50.98	3.68	19.93	187.1	0.95	24.7	0.98	3.25	88.32

### 3.3 Three-point bending test

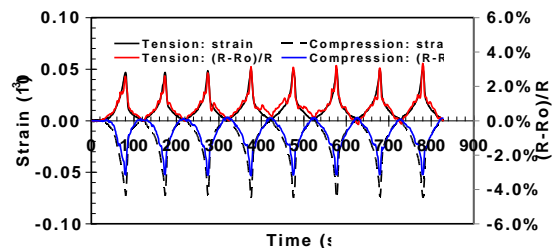
The test results of three-point bending specimens at 28 days age are shown in Table 3. There are several types of specimens in Table 3, including pure CFRC beam without steel reinforcement (P), pure CFRC beam with steel reinforcement (PS), concrete beam coating CFRC layer without steel reinforcement (Co) and concrete beam coating CFRC layer with steel reinforcement (CoS).

Figs 11a, 11b show the loading protocol, fractional change in electrical resistance, and strain measured by strain gauge at top and bottom of CoS3 specimen. Figs 12a, 12b show the relationships between fractional change in electrical resistance of CFRC and strain measured by strain gauge at top and bottom of CoS3 specimen. These data existed linear relationship between fractional change in electrical resistance of CFRC and strain measured by strain gauge before proportional limit. If it exceeds the proportional limit, the fractional change in electrical resistance increases (tension side) or decreases (compression side) due to the increase of electrical resistance in CFRC specimen caused by the microstructure changes, micro crack density increases and damage occurrences.

In Table 3, (1) comparison of pure CFRC beam, the strain in tension and compression side of P specimens are smaller than PS specimens, but the electrical resistance (Ro) and gauge factor (GF) are greater than PS specimens; (2) comparison of CFRC coating beam, the gauge factor of CoS specimens are greater than Co specimens; (3) comparison between pure CFRC beam and CFRC coating beam, the gauge factor of CFRC coating beam (Co and CoS) are greater than CFRC beam (P and PS). In general, the type of CoS specimen is with the greatest gauge factor.

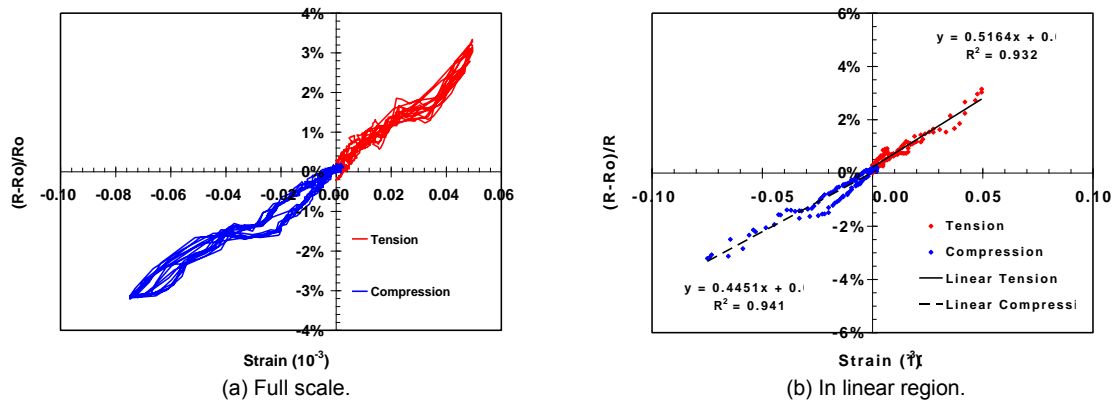


(a) Variation of load with time.



(b) Variation of fractional change in electrical resistance and strain measured by strain gauge with time.

Figure 11. Test results of CoS3 specimen.



**Figure 12. Test results of CoS3 specimen, comparison between fractional change in electrical resistance and strain measured by strain gauge.**

**Table 3. Results of three-point bending test.**

Bending	Specimen	Strain ( $10^{-3}$ )		Ro ( $\Omega$ )		GF		R <sup>2</sup>		Force kN
		c	t	c	t	c	t	c	t	
CFRC	P1	-0.08	0.040	36.8	53.3	175	220	0.97	0.81	7
	PS1	-0.17	0.075	14.7	18.9	52	87	0.96	0.90	10
	PS2	-0.15	0.075	15.3	15.9	78	89	0.92	0.89	10
Coating	Co1	-0.11	0.075	54.1	51.1	252	160	0.97	0.91	8.5
	Co2	-0.15	0.060	31.9	35.7	49	78	0.88	0.95	8.5
	CoS1	-0.15	0.060	81.9	49.7	1031	497	0.95	0.94	13
	CoS2	-0.06	0.045	40.6	84.3	603	844	0.98	0.93	13
	CoS3	-0.08	0.050	31.8	47.8	445	516	0.94	0.93	13

#### 4. RC portal frame push-over experiment

The practical application of pier strain measurement on RC portal frame push-over test is based on the test results of CFRC basic mechanical test. Columns to perform in accordance with the existing highway bridge seismic design specifications design, material strength of the requirements of generally reinforced concrete strength shall not exceed 41.20 MPa, reinforcement strength shall meet the relevant CNS-560 SD280W and SD420W regulations. The results could investigate the feasibility of CFRC for strain measurement of RC portal frame.

##### 4.1 Experiment plan

###### 4.1.1 Specimen design

The experimental plan includes a double-column framed pier, shown in Fig. 13, denoted as RCF (Reinforced Concrete Frame). According to the experimental field position, P1 column for the south side and P2 column for the north side of RCF, respectively. The clear span and clear height of RCF are 400 cm and the columns are using 60 cm square cross-section. Longitudinal reinforcement of RCF configuration are  $16 \times D25$  of steel, reinforcement ratio of about 2.3 %, and in each column, D14 @ 10 cm within the upper and lower plastic hinge zone of the rectangular cross-section of 1.5 times the depth range configuration closed stirrups and tie bars, transverse reinforcement and core concrete volume ratio of about 2.4 %, but non-plastic hinge zone transverse reinforcement spacing relaxed to 14 cm.

###### 4.1.2 Material properties

The material properties of RCF specimen are as follows: the concrete compressive strength = 42.2 MPa, the longitudinal reinforcement yield strength = 521 MPa, the trans-



verse reinforcement yield strength = 335 MPa, concrete compressive strength exceeds 41 MPa, so it is a high-strength concrete.

#### 4.1.3 Specimen configuration and loading protocol

Fig. 14 shows the configuration of the experimental test setup, including steel bracing system, vertical force loading system, lateral force loading system, and test specimen. Vertical force loading system consists of two sets of hydraulic pumps, two axial force beams and four  $\phi 69$  mm of high strength screw combination, which could provide a relatively stable axial force. Displacement control was applied to repeat push-over experiments. Firstly, the vertical load was applied to the top of the column, the design axial force for columns of RCF is  $0.1f'_cA_g$ , namely axial force required for 1500 kN. The first one hydraulic actuator is taken displacement control; but the second one is taken force control. In the course of experiments, the drift ratios (ratio of lateral displacement to column height) are representatives of plus or minus 0.25, 0.5, 0.75, 1.0, 1.5, 2, 3, 4, 5, 6, 7, and 8 %, sequentially. Finally, the fracture of experimental until occurs on longitudinal steel of columns. Each loop has several target displacements, the drift ratio for three laps before the 3 % and from 4 % for two laps until the end of the experiment. The target displacements and force steps are shown in Fig.15.

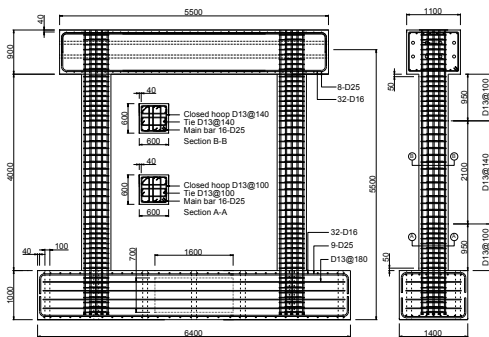


Figure 13. Design drawing of RCF specimen.



Figure 14. Push-over test setup.

#### 4.1.4 Strain measurement via CFRC

Select the bottom of south side P1 column as a strain measurement region, and CFRC conducted at this region is set to  $600 \times 600$  mm length and width, and thickness of 12 mm for CFRC coating layer. Fig.16 shows the four-wire method is used for electrical resistance measurement, the electrode length is set to 150 mm, and the electrode spacing is 120 mm. The detailed configuration is the same as the three-point bending test for CoS beams in section 2.2.3. Select three positions in which the electrodes are provided, and setting three strain gauges, such as CH-1, CH-2 and CH-3, respectively. After initial electrical resistance measurement of the three regions, select the middle portion for the final experiment. Simultaneous recording force, displacement, strain at three strain gauges, and electrical resistance change of the test, then relate the fractional change of electrical resistance to strain through gauge factor (GF).

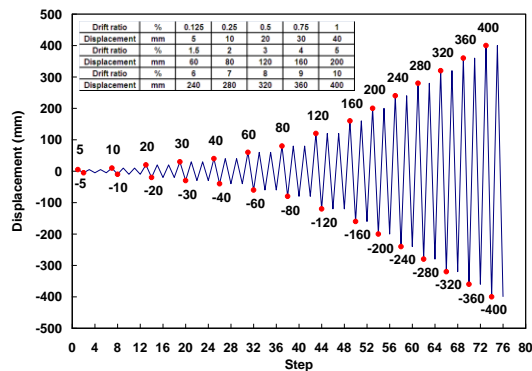


Figure 15. The target displacement and force steps.



Figure 16. Test setup of CFRC for strain measurement.

## 4.2 Results and discussion for strain measurement via CFRC

Fig. 17 shows the relationship between the strains measured by strain gauges, and the fractional change in electrical resistance with time. The measurement begin at lateral displacement reach 5 mm ( $t = 0$ ). Both the strain and the fractional change in electrical resistance versus time toward the same variation, and the start point of the electrical resistance change generated earlier than the strain, which displayed the sensitivity and ability of CFRC to predict the deformation of the structure. Referring to Table 3 that containing concrete beam coating CFRC layer with steel reinforcement (CoS) specimen, the mean value of gauge factor (GF) on compression side is 693, and on tension side is 619. Thus by using these two gauge factors, the measured fractional change in electrical resistance could relate to strain, and could be converted to strain. The relationship between strain measured by strain gauge and strain measured by CFRC at bottom of the column versus time are shown in Fig. 18.

Fig. 18 shows the strain measured by strain gauge (CH-3) and strain measured by CFRC versus time toward the same variation, within the lateral displacement of three loops of 20 mm. When the bottom of the column under compression: on the lateral displacement of the loop of 5, 10 and 20 mm, the strain gauges and CFRC could measure the strain on compression side, but the CFRC are more sensitive than strain gauge. The maximum amount of compressive strain is approximately  $5.9 \times 10^{-4}$ , under the lateral displacement of three loops of 20 mm. When the bottom of the column under tension: the strain gauges almost could not measure the strain on tension side, the reason is due to the strain gauge does not locate at the position of the maximum tensile strain occurrence, and therefore loss the sensitivity to measure tensile strain. Nevertheless, the CFRC have a higher sensitivity than strain gauge. The maximum amount of tensile strain is approximately  $1.7 \times 10^{-4}$ , under the lateral displacement of three loops of 20 mm. Obtained from the formula of ACI 318-05 [3] and ACI 363R-92 [4], the concrete at the bottom of the column should be cracking at this moment.

When the lateral displacement of column continues to increase to 30 mm, cracks occur between the CFRC coating layer and the column surface. At this moment, the fractional change of electrical resistance does not change, and the CFRC loss the function of strain measurement. When the lateral displacement of column continues to increase, the situation with the peeling and collapse occurs between the CFRC coating layer and the column surface. A subsequent of study on CFRC for strain measurement, the bond issue between CFRC coating layer and column surface will be the focus of research that must be overcome.

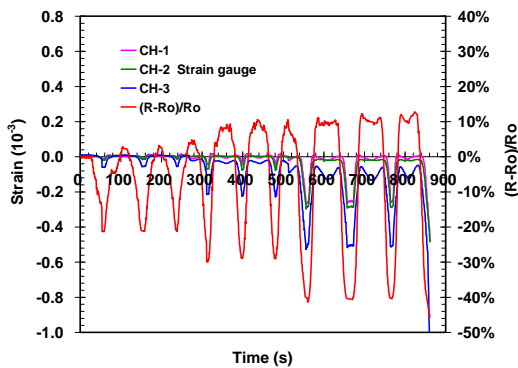


Figure 17. Variation of strain and fractional change in electrical resistance with time.

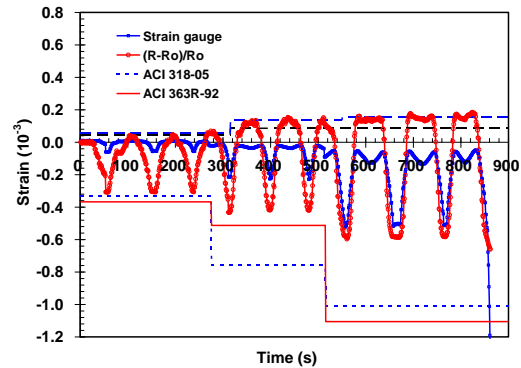


Figure 18. Comparison of strain measured by strain gauge and strain measured by CFRC.

## 5. Summary and discussion

To consider the economic, the fiber content is only 0.2 vol. % less than half of the amount of 0.48 vol. % used in references. The experimental results of uniaxial tension test, uniaxial compression test and three-point bending test show that the conductivity of materials is significantly improved and CFRC can be used as a strain measurement and damage detection in the fiber content of 0.2 vol. %.

For tension test, the similarity of fractional change in electrical resistance and tensile strain under uniaxial tension tests can be used as a self-sensing material for strain measurement within proportional limit. The slope of fractional change with tensile strain is a good indicator for damage detection under tensile loading.

For compression test, the similarity of fractional change in electrical resistance and compressive strain under uniaxial compression tests can be used as a self-sensing material for strain measurement within proportional limit. The slope of fractional change with compressive strain is a good indicator for damage detection under compressive loading.



For three-point bending test, the gauge factor of concrete beam coating CFRC layer with steel reinforcement is greater than concrete beam coating CFRC layer without steel reinforcement and pure CFRC beam with or without steel reinforcement. Moreover, the experimental results of coating beams can be the database for applications in the future.

For strain measurement of RC portal frame, the strain gauges and CFRC could measure the strain on compression side, but the CFRC are more sensitive than strain gauge. Nevertheless, the strain gauges almost could not measure the strain on tension side, but the CFRC have good accuracy and a higher sensitivity than strain gauge.

Self-sensing of tensile strain, compressive strain and damage detection is effective in CFRC under different loading. The self-sensing ability of CFRC, as shown for the sensing of strain and damage detection, is obviously presented in this paper.

## **6. Acknowledgement**

This work was supported by National Science Council of Taiwan R.O.C., under the project number NSC 99-2221-E-002-164-MY2.

## **7. References**

1. Wen, S., Chung, D.D.L., "Piezoresistivity-based strain sensing in carbon fiber-reinforced cement", *ACI Materials Journal*, 104(2), 2007, pp 171-179.
2. Han, B., Ou, J., "Embedded piezoresistive cement-based stress/strain sensor", *Sensors and Actuator*, A138, 2007, pp 294-298.
3. ACI Committee 318, "Building Code Requirements for Structural Concrete (ACI 318-05) and Commentary (318R-05)", American Concrete Institute, Farmington Hills, MI, 2005, 430pp.
4. ACI Committee 363, "State-of the-Art Report on High-Strength Concrete (ACI 363R-92)", American Concrete Institute, Detroit, MI, 1992, 56pp.

# Early-Age Concrete and Cracking

# Temperature Monitoring of Concrete Elements for Insitu Strength Measurement and Prevention of Damage from Heat of Hydration

Reuben Barnes<sup>1</sup> Frank Papworth<sup>2</sup>, William Ward<sup>3</sup> and Jim O'Daniel<sup>4</sup>

<sup>1</sup>Managing Director, PCTE

<sup>2</sup>Managing Consultant, BCRC (WA)

<sup>3</sup>Sales Manager (NSW), PCTE

<sup>4</sup>International Sale Manager, Engius LLC

**Abstract:** Cracking, strength loss and long term durability problems can arise if the concrete curing temperature is too high. Conversely high temperature can be beneficial as it gives high early age strengths but lower than expected temperatures can be catastrophic. In this paper the authors discuss various projects they have been involved with where temperature monitoring has been implemented so the project can avoid the problems noted or benefit from the early strengths.

The authors have experience with many methods and techniques for measuring the concrete's heat generating capacity and predicting and monitoring insitu temperature. The paper outlines key aspects of this experience including standardisation of the hot box tests, (CIA Z7/07), use of monitoring and logging devices and standardisation of insitu measurements (CIA Z7/07).

Temperature assessment criteria for prevention of Delayed Ettringite Formation and strength loss are often misunderstood and these are discussed. Thermal cracking criteria is a complex subject and is not included although monitoring temperatures and strain for quality assurance related to crack control is.

Early age strength is important in regards to curing required, time to prestress release, formwork removal and application of loads. Temperature measurement can be used to calculate concrete maturity for the estimation of insitu concrete strength. Examples of maturity implementation for cost and time saving on Australian and overseas projects are provided.

Keywords: Concrete, heat of hydration, maturity, temperature monitoring, insitu strength

## 1. Introduction

The chemical reactions that takes place when cement is mixed with water is exothermic. The heat generated depends on the nature of the cement and mix design but the temperature rise is also determined by how quickly the heat can escape. Controlling and monitoring the early temperature of concrete is extremely important in order that the following do not become problematic:

- a) Cracking due to restrained expansion or contraction as the concrete heats and cools
- b) Strength attained is significantly lower than the strength expected when cured at standard temperatures
- c) Durability is reduced due to the nature of the hydration products being changed by high temperatures. Delayed Ettringite formation is a known manifestation of this.

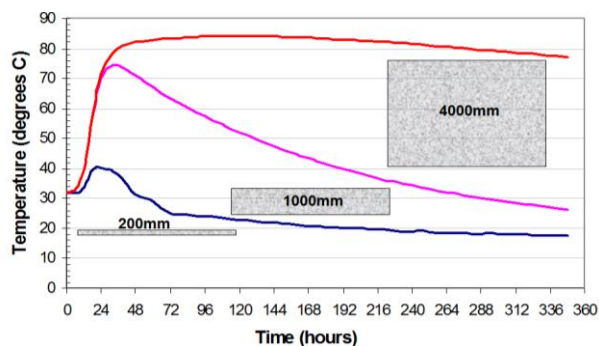
On the positive side high temperature speeds the cements reactions leading to higher early age strengths and durability. This gives the opportunity for early stripping, loading, stressing and cessation of curing. The insitu temperatures can be monitored to give an estimation of strength with time using a maturity method.

This paper provides information on predicting and monitoring concrete temperature development. A standardised "Hotbox" method for measuring the temperature generated by the cement in a particular mix is outlined and the method of calculating the adiabatic temperature rise of the concrete from this is discussed. Important aspects of modelling the temperature rise in a concrete pour is also provided. Based on the likely insitu temperatures the potential issues outlined above and early age performance can be assessed

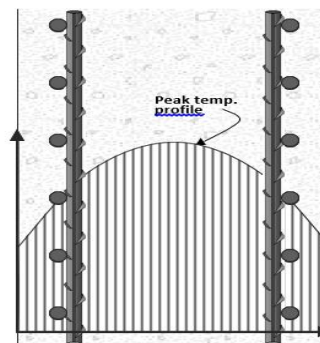
## 2. Heat Generation in Concrete

The reaction referred to as "hydration" commences when the cement is mixed with water, but it is not until some hours later that the reactions speed up and heat is released rapidly. This continues for around 15-30hrs after the concrete is placed in the forms. Heat at the centre of the pour can only escape slowly through

the surrounding concrete and hence the temperature at the centre of the pour builds up to a maximum in the first couple of days before heat loss exceeds the heat generated (**Error! Reference source not found.a**).



a) Maximum (slab centre) for different thicknesses



b) Temperature profile across the concrete section

**Figure 1. Temperature rise of concrete during hydration**

The internal temperature of the concrete at a discrete point is a function of how much heat is trapped. For example in a very thick element, a lot of heat will be trapped in the very centre, but closer to the surface there will be less self-insulation by the concrete and the effect of the ambient air temperature from the surrounding environment will become more predominant (**Error! Reference source not found.b**).

Independent of the cement chemistry, mix design and slab thickness there are other factors controlling the maximum concrete temperature and temperature differentials, for example:

- Formwork or insulation will keep the concrete surface warm this:
  - reduces temperature differentials
  - increase centre cool down and hence time to stripping based on allowable differentials
  - reduces the time it takes for concrete at the surface to attain a given strength and durability.
- Removal of formwork or insulation can lead to a dramatic reduction in concrete surface temperature and hence increase in temperature differential and internal restraint cracking risk.
- Use of cooling pipes to keep the centre of the pour cool and keeps temperature differentials low
- Curing by spraying with cold water can act as an extreme thermal shock and hence water should only be applied to the concrete surface immediately after placing and before the temperature rises. This water needs to be trapped in fabric under polythene until differentials have reduced sufficiently to enable stripping of thermal insulation.
- Wind (particularly with evaporative cooling) and rain (that impacts on the concrete surface) causes low surface temperatures and hence high temperature differentials and cracking risk.
- The temperature rise at the centre of the pour is added to the concrete delivered temperature to give the insitu temperature. Keeping the concrete delivered temperature down (by using chilled water, ice or liquid nitrogen in ascending order of cost), particularly combined with low cement contents, may be sufficient to dispense with the need for low heat cements and/or insulation of the concrete.

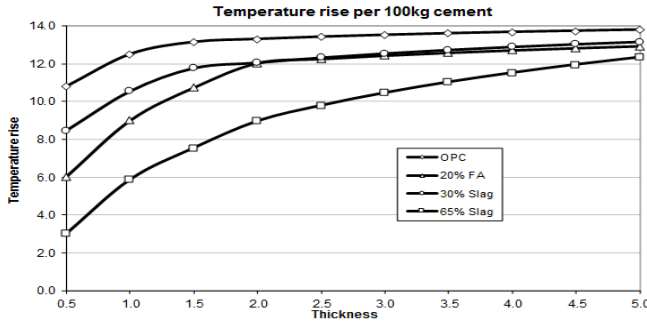
### 3. Predicting Insitu Concrete Temperatures

Mathematical models are used during design to predict concrete peak temperature, maximum temperature differentials, concrete strain and concrete crack risk.

On one project the concrete supplier's commercial manager undertook to supply the concrete and monitor temperature to ensure compliance with the maximum temperature and temperature differentials specified. It may seem natural for a supplier to take on management for the application of their product and the Contractor to pass the risk to the more knowledgeable supplier. An author was contacted by the supplier with a view to undertake the monitoring. During the phone call the concrete supplier conceded that they had not checked whether the slab would meet specified temperature limits and were simply monitoring to show it had complied. Using Bamforth's curves (Figure 2a) it was established during the call that based on the proposed cement content and type, proposed concrete delivered temperature and pour thickness the maximum allowable temperature and differentials were likely to be exceeded. Ironically if the only action were monitoring then the only result would be proof that the concrete was out of specification and liable for

replacement or significant remedial action. Before monitoring concrete pour temperatures (a relatively simple task indicated in Figure 2b) it is vital the more complex task of a proper thermal analysis is undertaken to ensure the concrete mix and pour are designed to:

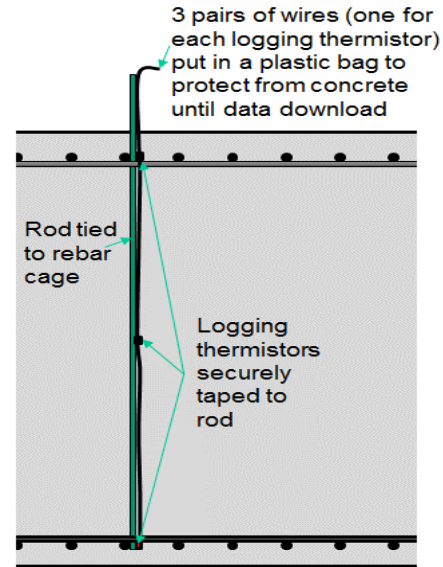
- meet specified temperature limits. On one pour in Singapore expensive strengthening was required when maximum temperature limits were exceeded.
- minimise contractors cost. Being overly safe on ensuring compliance can be expensive in time for the contractor but not impact on the concrete supplier.



Specific analysis	
Project	
Element	
Slab thickness	2.2 m
OPC content for strength	525 kg/m <sup>3</sup>
Concrete placing temperature	30 °C
Slag Efficiency	0.9
CSF efficiency	3.2
Fly ash efficiency	0.9

	Fly ash		Slag			CSF			OPC
	20%	30%	30%	50%	70%	4%	6%	8%	
Cementitious (same strength)	534	537	537	543	548	484	467	451	525
Temp/100kg	12.1	10.4	12.2	10.4	8.9	13.3	13.3	13.3	13.3
Maximum Temperature (°C)	95	86	95	87	79	95	92	90	100

a) Bamforth (8) curves for simple insitu temperature rise assessment



b) Insitu temperature measurement

**Figure 2. Simple Prediction of insitu Temperature Rise and Measurement of it.**

The Bamforth curves only give a first estimate of insitu temperatures but that will enable some refinement of the proposed concrete mix and placing method. Once these estimates show that temperatures may be acceptable, more detailed calculation are required before pouring to verify expected temperatures are safe. Traditionally the adiabatic temperature rise of the concrete was used to precisely predict the heat generating capacity of concrete and from that the insitu temperatures expected in the concrete after placement. However, adiabatic testing is complex, costly and generally laboratory based. More recently, semi-adiabatic testing has become more common because it is simple to undertake on site using concrete from the proposed batch plant as part of a trial mix.

There is no Australian Standard for measuring the semi adiabatic temperature rise but a method has been formalised within CIA Z7-07 (Concrete Institute of Australia “Concrete Durability Series, Performance Tests to Assess Concrete Durability” CIA Recommended Practice Z7/07, CIA 2015, Sydney) called the “Hot Box”. It uses a 1m x 1m x 1m cube of unreinforced concrete. The concrete temperature is measured by temperature sensors. The simplest configuration is to locate one at the centre of the pour and to also measure ambient temperature. An alternative arrangement requires the placement of plastic threaded rods within the box from which multiple temperature sensors are placed at specific points. Traditionally just a temperature sensor was located in the centre of the Hot Box, but a strain gauge can be used to give temperature and strain and this enables the coefficient of thermal expansion of the concrete to be calculated as well. The instrumented Hot Box assembly is held off the ground and sheltered from the elements to reduce external effects on the concrete temperature. It is then filled with concrete and the lid placed on.

From the concrete and ambient temperatures an allowance for heat loss is made to give the adiabatic temperature rise. The calculation assumes a heat loss coefficient which is then adjusted so that the calculated adiabatic temperature stays constant after reaching a maximum. Some contractors have assumed that the Hot Box temperature results are used directly to show whether the concrete meets specified temperature limits but that is not possible. Adiabatic and then insitu calculations have to be undertaken.

Calculating insitu temperatures from the adiabatic temperature rise of the mix, delivered concrete temperature, pour thickness, insulation proposed and ambient conditions is achieved using a spreadsheet

that calculates the temperature at discrete steps across the concrete section as heat is added by the cement hydration, is lost at the boundaries and is transferred from point to point. The effects of pouring in layers and shutter removal can all be built into the calculations.

For the Gorgon MOF wharf, a 0.8m thick slab with 2m edge beams, the construction schedule demanded removal of insulation as quickly as possible. The initial insulation proposed by the contractor was so effective that it would have taken weeks for the slab to cool down sufficiently for stripping to avoid thermal cracks. By minimising the insulation thickness to 10mm, so that allowable differentials were only just met, the stripping time was minimised.

On another project significant wide cracking to insitu decks cast on top of caissons occurred after an analysis to CIRIA C660 (Bamforth P. "Early Age Thermal Crack Control in Concrete": CIRIA Report C660, CIRIA, 2008 London, UK.) indicated crack width would not exceed 0.1mm. Investigation showed:

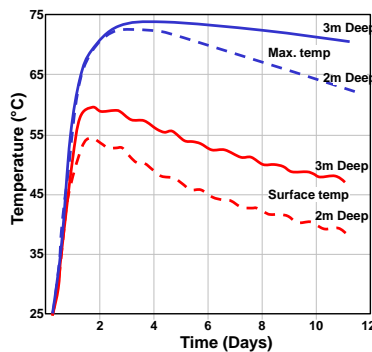
- a) The caissons were grouted together to form a continuous unit whereas the original analysis treated the caisson as separate units because no information on connection of caissons was provided. This led to very rigid caisson end walls and significant end restraint. A revised C660 analysis indicated the increased restraint increased predicted crack widths to 0.4-0.6mm.
- b) Cover was up to 150mm instead of the design cover of 50mm. The revised C660 analysis indicated the increased cover increased the predicted crack widths from 0.4-0.6mm to 0.8-1.3mm.

The importance of full disclosure and maintenance of maximum cover are apparent

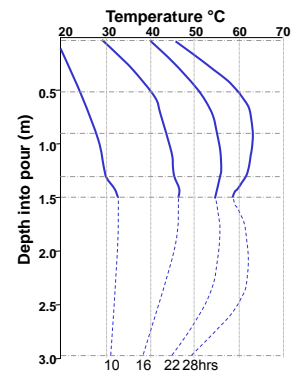
For the Jervoise Wharves temperature predictions for 1.5 and 2 m thick decks showed that the 17mm plywood insulation (Figure 3a) and shutters could be stripped in under 2 weeks. However for the 3m decks the stripping time of the 34mm ply insulations was going to be 3 weeks (Figure 3b). The Contractor was faced with requiring an additional set of shutters to keep up with the construction programme so accepted the use of cooling water pipes. This enabled stripping in 10 days. Water cooling pipes were highly effective (Figure 3c), fast to install and inexpensive in this case where a submersible pump was dropped in the ocean to pump water through the 75mm PVC pipes placed at the centre of the pour.



a) Insulation on a 2m Deep Jervoise Bay Deck



b) Predicted temperature with time for the 2m and 3m Jervoise Bay pour with 34mm of insulation. Note slow cooling of 3m centre.



c) Actual temperature through Jervoise Bay 3m pour using 34mm insulation and cooling water pipes.

**Figure 3. Thermal Analysis at Jervoise Bay**

#### 4. Monitoring Heat of Hydration

Monitoring of heat of hydration in concrete involves the installation of temperature sensors into the concrete before concrete placement. The temperature data is then logged at a certain interval for a specified amount of time. Aspects important for temperature monitoring are equipment choice as well as sensor placement and number. In terms of equipment choice; generally cost, reliability and ease of use are the key factors. Cheaper equipment generally comes with the inherent usability and reliability problems, whilst more expensive systems may alleviate these problems but budgetary concerns may make them prohibitive. The three prime systems used are:

- a) Thermocouple wire and a standard data-logger.
- b) Single channel wired or wireless data-loggers that collect the data for one sensor.
- c) A discrete robust sensor that measures temperature and logs it internally for subsequent download is installed into the concrete.

Potential issues are: Long cable runs and vulnerable on site loggers can make a) and b) expensive, unreliable and difficult to use. Many thousands of the discrete loggers are now used each year in Australia because of their ease of use and reliability.

Liquid nitrogen was used to reduce the concrete delivered temperature and hence insitu temperatures for mass concrete pours for a Dam in Queensland. A fully wired central data logging system was purchased to monitor all pour temperatures but frequent thermocouple failure meant results for many pours were not recorded. A discrete sensor system with internal logging as described in c) was purchased. Site engineers found the system easier to operate and totally reliable.

For temperature monitoring a set of temperature sensors is typically located at each measuring point. The set (Figure 2b) comprises:

- a sensor at the pour centre. This is generally close enough to be deemed the maximum temperature, which is of interest for assessment of DEF and low strength risk
- sensors tied to the reinforcement at each concrete face. This give the temperature differential to the centre and is used to assess internal restraint cracking

Sometimes a set of sensors are also tied to reinforcement at the edge and corner of a pour to enable analysis between the edge temperatures and temperature well away from the edge. Where differential temperatures between new pours and restraining old pours define the stripping time temperature adjacent to the old pour can also be monitored.

## **5. Temperature Induced Defects**

### **5.1 Delayed Ettringite Formation**

Ettringite formation is expansive, and if it occurs after the concrete has become rigid it causes cracking within the concrete. When it occurs after several months or years it is called Delayed Ettringite Formation (DEF). The exact cause of DEF is not entirely known, however it is generally thought to happen where gypsum decomposes during high curing temperatures only to lead to a later reaction causing expansive ettringite when exposed to water. The reaction does not however seem to be such an issue in concrete containing fly ash, slag, silica fume or cement with low alkalis.

The cracking caused by DEF is unsightly, reduces durability and may have structural implications. Micro-cracks allow carbon dioxide and chlorides to penetrate at much higher rates than normal leading to early onset of reinforcement corrosion. To eliminate DEF risk specifications limit maximum concrete temperature during hydration to 70°C for GP cement and 80°C for concrete with fly ash, slag or silica fume (Concrete Institute of Australia “Concrete Durability Series, Good Practice Through Design, Concrete Supply and Construction.” Recommended Practice Z7/04, CIA 2014, Sydney). Higher temperatures can be considered in specific circumstances.

DEF due to high curing temperature was first noted in Australia in steam cured railway sleepers but it can occur in any concrete cured at high temperatures. For example there are concerns that the temperature of diaphragms in steam cured T-Roff beams made from GP cement could exceed 70°C unless steaming is carefully controlled. Hence temperature monitoring of these blocks is often called for. Cases of DEF in mass concrete are uncommon but in the UK. 23 cases of DEF in abutments, wing walls, bridge beams and foundations have been identified by Quillin (Quillin K. “Delayed Ettringite Formation”. BRE Global. Information Paper 11/01, 2001, Watford, UK.).

It is generally practical to ensure critical temperatures for DEF are not exceeded, as it is simpler than detailed studies to enable higher curing temperatures and there is no accepted DEF test to check trial pours (this is the normal approach in specifications).

### **5.2 Damage from Restrained Thermal Cracking**

Where a concrete pour is restrained from contracting after it has reached its maximum temperature and starts to cool it can damage the concrete pour (cracking) or the restraint. The damage can be predicted by considering the restrained strains that occur in accordance with CIRIA C660 (8). Examples of such designs are given below.

Two similar unloaders were constructed at Port Hedland in 2008 and 2011. Both were subject to high ground water levels. It was recognised for the 2008 tunnel that AS 3735 (AS3735 “Concrete structures retaining liquids” Standards Australia, Sydney 2001) steel stress limits would not be an adequate means for

controlling crack widths and hence the crack width design was undertaken to the draft of CIRIA C660 which essentially followed provisions in EN1992-1-1 (9). At this point it had not been realised that the crack width predictions using EN1922-1-1 were significantly smaller than those predicted using the previous and validated UK code BS8007. Reasons for the difference in crack width predictions are given in Papworth (Papworth F. "Cracks in Concrete" Concrete in Australia. Journal of the Concrete Institute of Australia. Sydney, October 2009.). Significant cracking and leakage occurred in the 2008 built unloader walls although the reinforcement ratio was still higher than would have been required using AS 3735 requirements. By the time of the 2011 unloader, modifications had been made to the final version of C660 and a design based on crack widths of 0.15mm at the 95% confidence level and an alternative design of 0.3mm crack widths plus a waterproof membrane. The membrane alternative was pursued but when cost ballooned from an indicative price of \$1m to \$3m tender price the option for no membrane was pursued. Designing to 0.15mm at the 95% confidence level led to very few leaking cracks in the tunnels.

On the same 2011 unloader project the Ingo slab presented some unusual issues. The Ingo slab supports the rail line for the iron ore unloader. The slab incorporates bridge beams supported on pile caps. The interface of the bridge beams and piles was a steel surface to reduce friction and abrasion. The slab and beams would move due to train actions but shear pins at one of the beams were to be grouted after construction to fix it. Pins at the pile caps are intended to limit movement but not rigidly fix the beams. Thermal analysis showed that early thermal movement would exceed significantly the 5 mm tolerance originally allowed for the shear pins if the beams and slab were cast integrally. It was also identified that restraint due to friction with the high potential movement could lead to very high loads in the fixed shear pins. Another concern was for a potentially wide longitudinal crack in the slab due to restraint of the longitudinal beams.

Consequently the design intent was been changed to:

- allow for the high thermal and shrinkage movement in all pins initially (20mm)
- cast each beam in one length and the slab 14 days later in two lengths. The thermal contraction of the beams is then restrained by the slab reducing overall contraction
- delay fixing of shear pins by grouting at 60 days so that thermal contraction and some shrinkage has occurred.
- use a layer of polystyrene to compress and relieve lateral restraint
- cast the beams and slab to minimise frictional restraint.

## **6. Concrete Maturity for Strength Prediction**

### **6.1 Concrete Maturity Method**

Concrete maturity method is a means by which concrete temperature can be used to estimate in-situ strength during the early life. It uses the total exothermic heat produced by the hydration of the cement as a measure of the extent to which the cement has hydrated and as such the amount of strength that the concrete has been gained. In practical terms it makes use of the fact that insitu concrete elements will generally reach higher temperatures than standard cured strength cylinders and hence have hydrated to a larger amount at any given time. This means that concrete insitu will in a lot of cases have reached higher strengths earlier than the strength cylinders. In cold climates lower insitu strengths may results and this is also measurable by the maturity method.

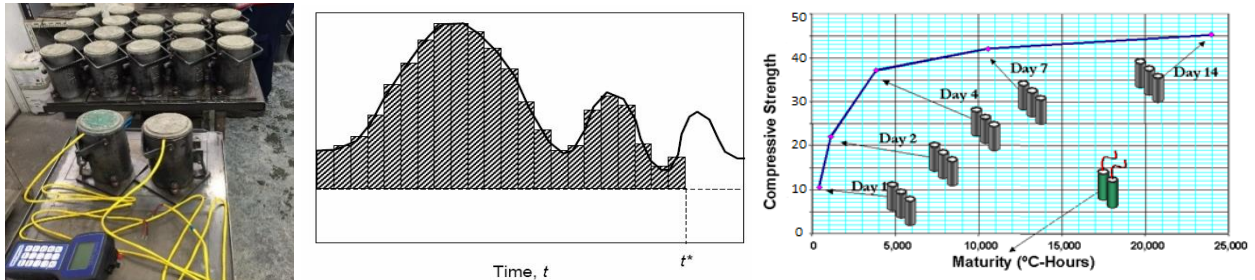
There are two methods by which maturity is calculated. The Nurse-Saul method and the Arrhenius method. The Arrhenius method accounts for nonlinearity in the rate of cement hydration. The Arrhenius method yields a maturity index in terms of an "equivalent age", which represents the equivalent duration of curing at the reference temperature that would result in the same value of maturity as the curing period for the given average temperature. The Nurse-Saul maturity function is the sum of the average temperature for the time interval minus the datum temperature multiplied by the time interval of interest (see figure 4 where the maturity is the sum of the area of the grey columns).

In practice a calibration which relates the maturity and strength for a particular concrete mix must be determined using lab trials. A method for this has been recommended by a manufacturer of temperature monitoring equipment. In the method 17 test cylinders are cast and held in standard curing conditions. Two of the cylinders are monitored purely for temperature and provide the maturity readings at a particular age. After 1 day three cylinders are crushed and the average strength is recorded against the average maturity of the concrete cylinders. This process continues for another 4 sets of strengths data at predetermined times



(e.g. 2, 3, 7, 14, 28 days). Once completed the 5 points on the Strength v Maturity graph are then joined using straight lines to interpolate the points. The use of a straight line between points means the interpolated points are conservative by nature.

In situ the temperature of predetermine points are monitored and the maturity is monitored over time. Using the strength-maturity calibration “goal” maturity levels are determined correlating to required strengths for construction processes such as stripping forms or stressing post tensioning. Once the sensors indicate the goal maturity has been reached then the process begins. Due to the fact that the cylinders for strength determination were kept in generally colder conditions the construction process is sped up as the concrete on site has undergone accelerated hydration at higher temperatures.



**Figure 4. (left) cylinders for a calibration (centre) Schematic of temperature time-factor and temperature history (right) Typical Maturity Curve**

The calibration only relates to the particular concrete mix that has been used in its formulation. Quality Assurance can be performed by which random batches of concrete are tested to see whether the curve is still valid. This entails one temperature monitored cylinder and the crushing of two others.

ASTM C1074-11 (5) details maturity measurement. The major limitations of the maturity method are:

- a) The concrete must be maintained in a condition that permits cement hydration. If the concrete is held in a dormant state at temperatures below a datum it will not increase in strength. The datum temperature is an important factor in the safe use of maturity
- b) The method does not take into account the effects of early-age concrete temperature on the long-term strength.
- c) The method needs to be supplemented by other indications of the potential strength of the concrete mixture.

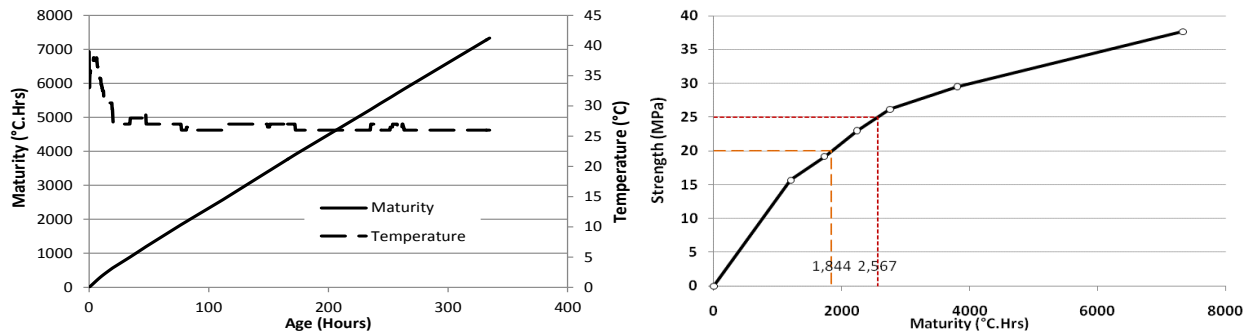
## 6.2 Port Hedland Unloader Rail Drive Floor

The Unloader TU603 at Port Headland has a rail drive floor. The construction schedule for these pours was tight. The specified minimum stripping time for tunnel roof soffit supports was 9 days for structural reasons. Time based stripping specifications are inherently conservative and the authors were asked to advise on use of maturity measurements for early stripping. The structural engineers indicated that concrete strengths of 20 and 25MPa were required for stripping and loading respectively. Roof slab thicknesses considered were 325mm, 535mm, 915mm and 1230mm.

Twenty cylinders were cast from the mix to be used in the pours. Two had maturity probes inserted and six sets of three cylinders were made for compressive strength tests. One set of cylinders was crushed at 2, 3, 4, 5, 7 and 14 days. The cylinders for strength testing and maturity probe cylinders were kept together at all times with cylinders for strength testing taken out of the curing bath just before testing. From the strength and maturity data of samples cured at identical temperatures (see Section 3) a graph of maturity vs strength was constructed (Figure 5). The maturity probes were set with a base temperature of 5°C.

a) Maturity and Cylinder Temperature

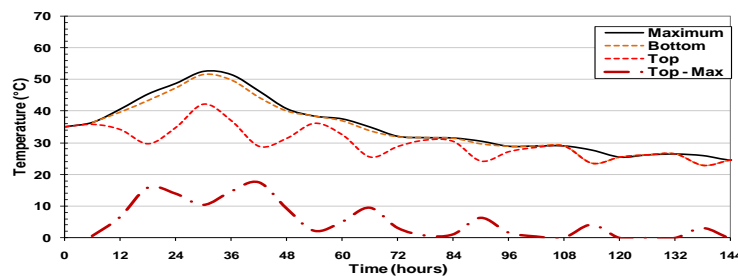
b) Maturity Curve for Project Concrete



**Figure 5. Development of Maturity Curve**

Maturity is calculated for specified strengths by assuming a linear plot between strength data points. From cylinder strength and maturity test results it was found that the strengths of 20 and 25MPa related to maturities of 1844°C.Hrs and 2567°C.Hrs respectively. Further analysis showed that these maturities were likely to be achieved at 2 to 4 days depending on slab thickness. Maturity was measured at the thinnest point of the pour at the level of the top reinforcing mat. Once the maturity criteria were met the formwork could be stripped provided the specified allowable temperature differentials were not exceeded due to thermal shock when the insulating formwork was removed. This was ensured by monitoring temperature differentials and only stripping once the allowable differential minus a thermal shock allowance was achieved.

**Error! Reference source not found.** shows an analysis for temperature with time for the 800mm thick slab cast on plywood but with no top surface insulation. This was calculated for the pour geometry, expected ambient conditions, probable concrete delivered temperatures and placing schedule based on an adiabatic temperature rise assessed from previous hot box test data. With a typical wind and no insulation the top surface is much cooler than the bottom and the top reinforcement is the location where the maturity probes were likely to record the lowest temperature.



**Figure 6. Predicted insitu Temperatures for an 800mm Thick Slab**

Based on the temperature with time profile for the top of the slab the likely time to achieve the required maturities was calculated as 60hours for the 1844°C Hrs (20MPa) and 84 hours for 2567°C Hrs (25MPa). Similar assessments were undertaken for other slab thicknesses.

After the pour was complete the maturity probes that had been installed prior to the pour were turned on and the base temperature set to 5°C. This is a conservative value for maturity assessment but doesn't make a significant difference to stripping times and simplifies the establishment of the system. For the first pour maturity was monitored at three locations on the top reinforcement and one on the bottom reinforcement. Results are shown in **Table 1**. For subsequent pours only the coolest mat (top) was monitored.

**Table 1 Maturity Data for First Tunnel Roof Pour**

Probe Location	Maturity (°C.Hrs)			
	24hr	48hr	72h	96hr
Bottom Rebar	1146	2469	3628	4635
Top Rebar loc. 1	835	1925	2905	3755
Top Rebar loc. 2	898	1992	2965	3820
Top Rebar loc. 3	896	1962	2911	3741

These results, and those on all other slabs, showed stripping at 2 days and loading at 3 days was acceptable subject to achieving other temperature limits related to thermal cracking. Construction of the tunnel roofs was completed in a month. All monitoring was undertaken by the site engineers who commented on the simplicity of managing it using the discrete maturity loggers after the maturity criteria were established.

### 6.3 NSW – Rail Infrastructure

This case study illustrates the use of maturity on precast bridge segments for a raised rail line in a major Australian infrastructure project. Pre-cast facilities producing large structural elements such as bridge segments operate on a tight schedule. They typically cast one segment per mould per day. This schedule is controlled by the strength at which moulds can be opened and segments moved out to cure while the mould is reset. The next hold point was a second strength requirement for segments to be lifted and taken to storage. Maturity was employed as a tool to measure insitu strengths.

A trial mix was tested to determine early age strength of the proposed concrete at critical moments in the casting schedule. 38 cylinders were cast. Two maturity loggers were embedded into two cylinders. Three cylinders were then crushed at 8, 10, 12, 14, 24, 32, 36, 48 hours and 7, 14, 21 and 28 days.

Maturity calibrations usually only entail 5 data points and so the effect of adding additional points to a maturity curve may make the prediction more precise but less conservative depending on the curve section being used. Figure 7 shows two maturity curves for the same concrete. One has five maturity points and one two points. At 280°C-Hours the left hand curve with five points gives a higher strength than the right hand curve with two points while at 560°C-Hours the maturity based strengths are the same.

Additional utility that can be gained from a trial mix with simultaneous maturity calibration includes trouble shooting during the test mix. For example if early strength gain is less than expected temperature graphs can be reviewed to capture heat of hydration information for the samples.

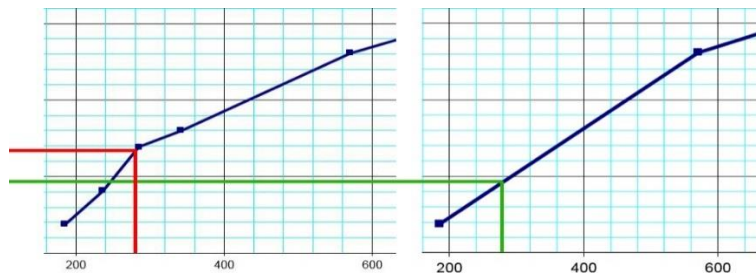


Figure 7. Strength v Maturity Calibrations



Figure 8 CEMEX Headquarters

### 6.4 CEMEX Headquarters, Houston

The 325,000 square foot CEMEX headquarters (Figure 8) is one of the largest green buildings in Houston. A major reason for the eco-rating, was the low amount of fly ash and cement used in the concrete mix. This led to a slow strength development and so maturity was used to maximise the use of early strength that was achieved. The construction company had previously used High Early Strength cement and high cement contents to achieve a 24 hour slab pouring and prestressing cycle based on standard cured cylinders. The use of maturity during Houston's high ambient temperature summer enabled the 24hour cycle to be achieved even with the eco-friendly concrete. Overall these factors also lead to cost saving on the project which was completed ahead of schedule. Switching mix designs was budgeted to save approximately \$130,000 in concrete costs alone for the 14-floor, 325,000 square feet building.

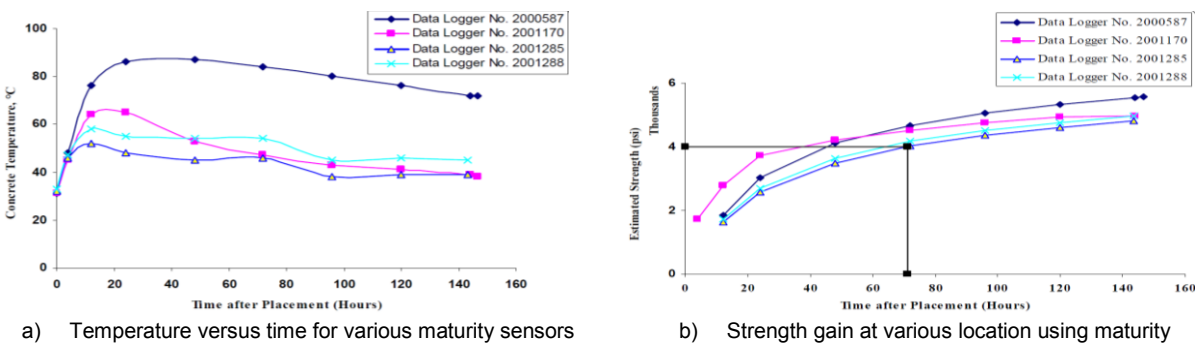
The temperature sensors strategically placed prior to each pour monitor the concrete's temperature and calculate the effects of elevated temperature on strength gain. Tracking the data transmitted by the sensors, the software converted the reported maturity data into actual strength values. Overall the project was finished on time, with the projected savings in time and money as well as the eco-friendly rating.

### 6.5 Amgen OPUS Project - Puerto Rico

This was a pilot project to check the implementation of maturity in Puerto Rico. The project entailed the expansion of a bio-pharmaceutical process facility with over 300,000 square feet to be added during construction. In total 6 placements were monitored for maturity with strength vs maturity calibrations for the design mix also carried out. During calibration 20 cylinders were used. Two for maturity data and eighteen

(i.e. six sets of three) for the strength testing. A line of best fit was used to match the strength-maturity data the equation being  $y=1305.1\ln(x) - 6630.9$ . Data between 800-4900° C.hrs gave an  $r^2$  correlation of 0.9981 (Note that interpolation should be done using straight lines between points, not line of best fit).

For one beam where early strength assessment was critical four locations were monitored for maturity. Loggers 2001170 and 2000587 were placed 1m deep inside a beam with 2001288 and 2001285 placed in the cover region (100mm deep) where the slowest strength gain was predicted. Figure 9a shows the concrete temperatures measured over 160 hours. All of the sensors measured an increase in temperature after placement with 2000587 getting extremely hot due to self-insulation. The two cover sensors do not get as hot. Using best fit equation the strength insitu was calculated from the temperature history. The strength at each sensor location are shown in figure 7b. The goal strength of 4000 PSI was required in the specification for stripping of forms. It was found that this strength was reached last on sensor 2001285 at around 70 hours. Forms were able to be removed 2 days earlier than would have been the case if maturity had not been used and therefore construction was accelerated. Also important to the pilot project were validation checks to make sure there were no significant variations in the concrete mix. None of the 6 validations performed during the project varied by more than 5% from the calibration curves used during the project.



**Figure 9: Maturity Assessment for the Amgen OPUS Project**

## 7. Conclusions

This paper discussed how the heat of hydration of cement leads to a rise in concrete temperatures. It detailed how these temperatures can be predicted and how they should be monitored.

Based on predicted insitu concrete temperatures the risk of damage due to high temperatures and temperature differentials can be assessed. Examples of how this was undertaken on various projects were given. The examples explored:

- Design to maintain crack widths to a level whereby durability is not compromised
- Mix design and placing methods to ensure maximum temperatures do not lead to delayed ettringite formation or low insitu strength
- Design of thermal curing methods to minimize stripping times thereby enhancing the construction program and minimizing construction time

High insitu temperatures can bring advantages. It leads to high early age strengths and this can be measured using maturity methods. Examples are given where maturity measurements were used to enable cost savings, use of eco-friendly concrete, early stripping and accelerated construction.

Temperature prediction and monitoring is an extremely important exercise that should be encouraged by the industry to allow for efficient and durable construction.

## 8. Acknowledgement

The authors would like to thank the companies who were able to provide data for the case studies illustrated within this paper.

## 9. References

1. American Concrete Institute, "Building code requirements for structural concrete (ACI 318-05)", ACI Committee 318, 2005, Michigan.

2. Concrete Institute of Australia "Concrete Durability Series, Performance Tests to Assess Concrete Durability" CIA Recommended Practice Z7/07, CIA 2015, Sydney
3. M. Collepari "A State-of-the-Art Review on Delayed Ettringite Attack on Concrete" Civil Engineering Faculty, Leonardo Da Vinci, Politechnic Milan, Italy
4. Winter N. [www.understanding-cement.com](http://www.understanding-cement.com) [2nd Feb 2015]
5. ASTM C1074-11, Standard Practice for Estimating Concrete Strength by the Maturity Method, ASTM International, West Conshohocken, PA, 2011, [www.astm.org](http://www.astm.org)
6. Goodrum, J.Dai, Cr.Wood, M.King "The use of the Concrete Maturity Methods in the Construction of Industrial Facilities: A Case Study" FIATECH P.M 2004 Stillwater OK USA
7. Quillin K. "Delayed Ettringite Formation". BRE Global. Information Paper 11/01, 2001, Watford, UK.
8. Bamforth P. "Early Age Thermal Crack Control in Concrete": CIRIA Report C660, CIRIA, 2008 London, UK.
9. Eurocode 2: Design of concrete structures - Part 1-1: General rules and rules for buildings, EN 1992-1-1:2004
10. Papworth F. "Cracks in Concrete" Concrete in Australia. Journal of the Concrete Institute of Australia. Sydney, October 2009.
11. Concrete Institute of Australia "Concrete Durability Series, Good Practice Through Design, Concrete Supply and Construction." Recommended Practice Z7/04, CIA 2014, Sydney
12. AS3735 "Concrete structures retaining liquids" Standards Australia, Sydney 2001

# The Role of Dilation in Shrinkage Cracking of Concrete

Suhaila Mattar<sup>1</sup> and R.S. Al-Rawi <sup>2</sup>

<sup>1</sup> Daphne Jackson Fellow, School of Civil Engineering, University of Leeds, UK

<sup>2</sup> Professor of Civil Engineering, College of Engineering, University of Baghdad, Iraq

**Abstract:** The aim of this investigation was to study the role of dilation in delaying shrinkage cracking of concrete and the possibility of producing shrinkage crack-free concrete. The experimental programme consisted of two parts. In the first part, end-restrained concrete beams were water-cured for one and three days before drying under controlled temperature (35 °C) and relative humidity (25%) conditions. In the second part, concrete beams were water-cured for one and three days before drying in outdoor summer conditions in Baghdad, Iraq. For all specimens, various parameters were measured, including free-shrinkage strain, tensile strain capacity, elastic tensile strain capacity, creep in tension and cracking time.

The experimental results show that none of the concrete specimens dried under natural outdoor conditions cracked in spite of high temperatures (up to 60 °C) and low relative humidity (less than 15%). This is due to dilation in the form of increased creep in tension with variations in temperature and relative humidity. Increasing water-curing duration usually delays shrinkage and always delays or prevents cracking; it increases tensile strain capacity, which reduces the probability of cracking for all specimens dried in natural or controlled conditions.

**Keywords:** concrete, shrinkage, creep in tension, tensile strain capacity, dilation, end restrained shrinkage.

## Introduction

Dilation can be defined as a strain opposite to shrinkage and thermal contraction. It can be expected to prevent or delay cracking and to reduce crack widths. In 1986, Al-Rawi and Al-Qassab (1) found that the observed crack width is less than the calculated maximum crack width for reinforced concrete beams cast in I-shaped moulds and subjected to drying shrinkage conditions. Many other researchers (2,3,4) and practical cases (2) have shown that crack widths observed by microscope are less than those measured by demec points and calculated by equations. Salman (5) reported that concrete beams treated with gypsum and cured for 3 days did not exhibit any cracking under outdoor exposure conditions. He attributed this to the addition of gypsum, which led to expansion and development of compressive stress along the concrete beam due to restraint at the end of the beam supported by the flanges. As a result, lower tensile stress will develop in the concrete beam which is less than the tensile strength of concrete. Another reason is that water-curing results in an increase in the tensile strain capacity of the concrete. These two effects combine to minimize restrained shrinkage stress within the concrete beam, thus delaying or preventing cracking.

Adday (2) found the same results. He indicated that covering concrete with polyethylene sheets for one day after casting, then water-curing for one week in the laboratory prevented cracking, even though the concrete beam was highly restrained and subjected to high temperature and low relative humidity for long periods. This showed that under outdoor exposure conditions, the cracking tendency of large beams seemed to be very low and the probability of cracking much less than under laboratory conditions.

Al-Rawi and Salih (6) showed that in a study of a concrete mass (850 m<sup>3</sup>), no shrinkage and thermal cracking takes place despite the fact that the temperature difference between the core and the surface of the concrete mass reached 41 °C and temperature cycles (daily rise and fall) on the surface of the concrete mass cause expansion at the surface due to repeated creep cycles (dilation), which reduces the possibility of cracking.

The above-cited studies (2,5,6) conflict with the prevailing conclusion in the literature, which is that subjecting concrete to high temperatures and low relative humidity increases the probability of cracking due to increased drying shrinkage, as the beams subjected to drying in outdoor exposure

conditions in the summer in Iraq did not show any cracking. This may be because the large variation in temperature and relative humidity between day and night increased creep in tension, which could be more than the increase in shrinkage. Therefore, the probability of shrinkage or thermal cracking decreases. The fact that creep increases with fluctuations in temperature and relative humidity has been studied by Al-Rawi and Kammouna (7).

Given the findings in the studies cited above (1,2,3,4,5,6,7), the term "dilation" of concrete is defined in this project to include factors that delay or prevent shrinkage or thermal cracking of concrete. These factors are:

- i. Water (moisture) movement caused by water-curing concrete before drying.
- ii. Increased creep of concrete in tension due to temperature fluctuations.

## Experimental Work

### Concrete Mixes

Four concrete mixes were designed according to ACI 211.1–91. The slump was chosen to be 100 mm for all mixes. Trial mixes were made, and slump testing was carried out according to ASTM.C143/C143M-05a to ensure the desired workability. Adjustments then were made to the calculated properties. Table 1 shows details of concrete mixes employed in this study. Mixes then were cast in special moulds and vibrated and trowelled to obtain an even surface.

**Table 1. Details of concrete mixes.**

Mix	Mix proportion (by wt.)	Water/cement (by wt.)	Cement (kg/m <sup>3</sup> )	Sand (kg/m <sup>3</sup> )	Coarse aggregate (kg/m <sup>3</sup> )	Water content (kg/m <sup>3</sup> )
A	1:2.8:3.64	0.75	288	791	1020	216
B	1:2.06:2.93	0.62	350	720	1020	216
C	1:1.74:2.66	0.55	400	667	1020	216
D	1:1.32:2.18	0.48	520	637	1020	216

### Moulds

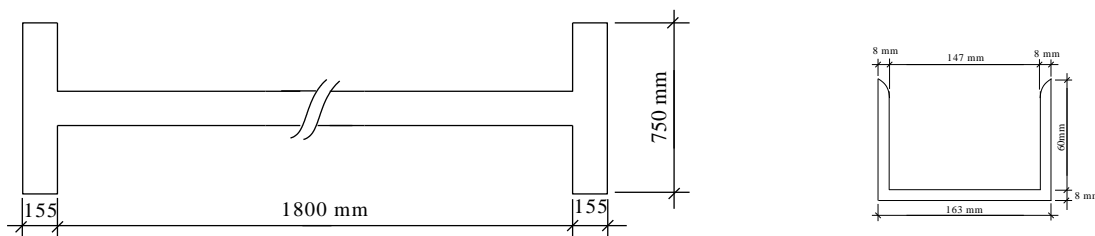
Moulds used were made of a steel channel section fabricated into I-shapes, as shown in Figure 1. Concrete was cast into them and subjected to drying shrinkage restrained by the flanges (8). Naturally, the restraint is not complete, and some contraction of concrete will take place. The mould is designed such that this contraction is relatively small, and the restrained shrinkage induces cracking across the web of the beam. Shallow mould depth enables fast drying, without significant differential shrinkage. To minimize friction between the steel mould and the concrete, the web part of the mould is greased and lined with a sheet of polyethylene.

For each mix, three moulds were cast and then dried, either in a room with controlled temperature and relative humidity, or exposed to the weather outdoors. For each mix, one of the three moulds was cast with an artificial opening in the middle of the web to allow determination of free shrinkage, and the two others were used for the restrained shrinkage test.

**Note:** Each specimen was given a set of letters and numbers to describe it.

A, B, C, D: Concrete mixes shown in Table 1; i: indoor exposure conditions; o: outdoor exposure conditions; 1 and 3: water-curing durations.





**Figure 1. I-Shaped mould (not to scale).**

### ***Curing and Exposure***

Generally, the surface was covered with polyethylene sheets for 24 hours to prevent plastic shrinkage cracking. Curing was effected by covering the concrete beam with canvas sheets wetted with water for the specified curing period. After curing, the concrete beams are left in the moulds to achieve restraint and dried either in a room with controlled temperature and relative humidity or outdoors, subjected to natural drying conditions. For those beams dried indoors, the temperature was constant at  $35\text{ }^{\circ}\text{C} \pm 5\text{ }^{\circ}\text{C}$ , and the relative humidity was  $25\% \pm 2\%$ .

### ***Free Shrinkage Strain Measurement***

Free shrinkage was defined as the average strain over the length of the web of concrete beams. A diaphragm was introduced in the middle of the web prior to casting, dividing the beam into two halves. The diaphragm was removed the next day, leaving an artificial opening. This arrangement allowed free shrinkage to take place, as there was no restraint. Demec points were fixed on either side of the artificial opening, 100 mm apart. The increase in gauge-length between these points was measured by demec extensometer when the beams were exposed to shrinkage conditions, with 100 mm in length in an accuracy of 0.002 mm/division, and it was taken as free shrinkage along the whole web length less the 100 mm distance between the demec points. This was based on the assumption that the coefficient of the thermal expansion of steel is approximately equal to that of concrete. The difference, if any, is usually not great, and in any case, it also exists in restrained shrinkage. The fact that free shrinkage strain was averaged over a fairly long length (1700 mm) minimized experimental errors.

### ***Restrained Shrinkage Strain Measurement***

The restrained concrete beams were water-cured in the laboratory for the specified curing periods. During that period, demec points were fixed at 100 mm intervals on the surface along the centre of the web and on the steel moulds. Then the beams, still in their moulds, were transferred either to a room with controlled temperature and relative humidity or outdoors to dry. The concrete was allowed to shrink until either cracking occurred or until it reached a fairly stable state, and demec readings were taken continuously by a demec extensometer until the end of the test. Then, parameters were calculated, as described below.

#### ***Loss of Restraint (LOR)***

In most practical cases, full restraint does not exist, i.e., not all the shrinkage of concrete is restrained. This means that some movement of moulds takes place and leads to some loss of restraint. In the moulds used in the present study, loss of restraint was measured as the mean contraction of the steel mould or, alternatively, contraction in the web length of the beams at the time of cracking.

#### ***Tensile Strain Capacity (TSC)***

Tensile strain capacity was defined as the difference between the free shrinkage strain during cracking time and the strain due to loss of restraint.

$$\text{TSC} = \text{Fsh} - \text{LOR} \quad (1)$$

where:

TSC = Tensile strain capacity (mlths).

Fsh = Free shrinkage strain (mlths).



LOR = Loss of restraint (mlths).

### ***Elastic Tensile Strain Capacity (ETSC)***

This was defined as the observed free contraction of concrete at the onset of cracking. In the present study, this was found by measuring the change in the strain at either side of the crack at the onset of cracking. This means that the elastic tensile strain capacity is equal to the difference between the strain just before cracking and the strain just after cracking.

$$\text{ETSC} = \text{Strain just before cracking} - \text{strain just after cracking} \quad (2)$$

### ***Creep in Tension (Creep Prior to Cracking)***

Concrete was subjected to very high tensile stress prior to shrinkage cracking, and the stress/strength ratio might have been close to unity for a considerable period of time. Under these conditions, significant creep can take place. This is because creep is time-dependent and it increases sharply with the increase in stress/strength ratios. It also increases under the environmental conditions that promote drying. This phenomenon can be termed relaxation, because it takes place at a practically constant length and is effective in reducing tensile stress in the concrete. Relaxation can be viewed as increasing the tensile strain capacity of concrete and consequently reducing the possibility of cracking. In addition, it can decrease crack width. Creep in tension is defined as tensile strain capacity less elastic tensile strain capacity.

$$\text{Creep in tension} = \text{TSC} - \text{ETSC} \quad (3)$$

### ***Cracking Time***

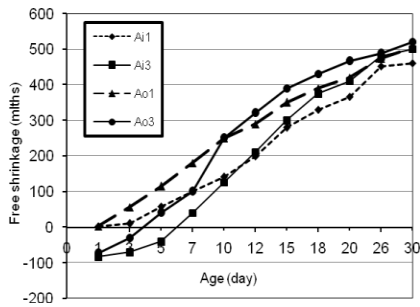
Cracking time is defined as the number of days required for cracking to occur. Cracking time has received little attention in other research. It seems, however, that cracking time can be used as an index to compare the possibility of cracking of various mixes exposed to differing conditions.

## **Results and Discussion**

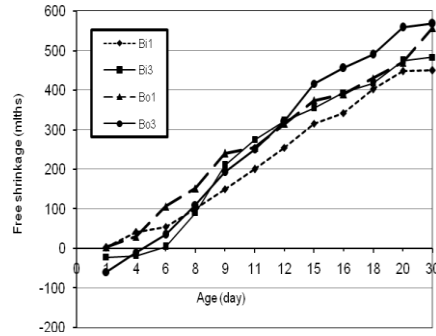
### ***Free Shrinkage Results***

Figures 2–5 illustrate the effects of prolonged water-curing on free shrinkage of concrete specimens. In general, long-term shrinkage of concrete specimens that have been water-cured for three days and then subjected to drying is higher than shrinkage of those water-cured for one day. However, in the first few days, the shrinkage of specimens cured for one day is higher than those cured for three days. The reason for this is that specimens cured for three days absorb more water than those cured for one day. During the three days, there is expansion of specimens rather than shrinkage. After water-curing, when the concrete begins shrinking, it reaches its original length (zero expansion) within three to six days. After a few more days, the shrinkage of specimens cured for three days usually exceeds that of those cured for one day.

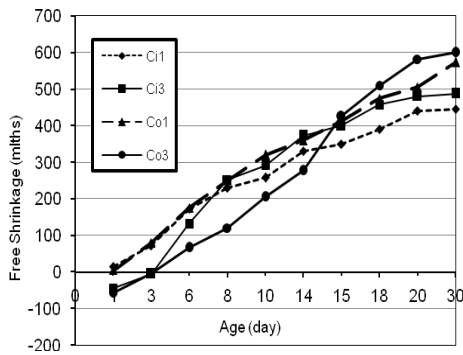
Figures 2–5 also show that drying conditions affect shrinkage. All specimens subjected to natural outdoor conditions have higher shrinkage than specimens dried in controlled temperatures and relative humidity indoors. The final (one-month) shrinkage values show the same trend, because the specimens subjected to natural outdoor conditions were exposed to maximum temperatures exceeding 60 °C and relative humidity of less than 15%, in contrast to the moderate conditions of 35 °C temperature and 25% relative humidity for specimens dried indoors.



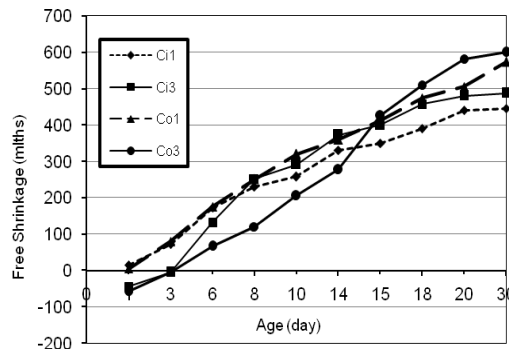
**Figure 2. Effect of water-curing duration and exposure conditions on free shrinkage development with age for concrete beams (mix A).**



**Figure 3. Effect of water-curing duration and exposure conditions on free shrinkage development with age for concrete beams (mix B).**



**Figure 4. Effect of water-curing duration and exposure conditions on free shrinkage development with age for concrete beams (mix C).**



**Figure 5. Effect of water-curing duration and exposure conditions on free shrinkage development with age for concrete beams (mix D).**

## **Restrained Shrinkage Results**

### **Indoor Concrete Specimen Results**

Table 2 shows the restrained shrinkage results of indoor concrete specimens. Results show that prolonged water-curing increases the tensile strain capacity of the various mixes of concrete up to 47%. This is because the necessity for curing arises from the fact that the hydration of cement is greatly reduced when the relative humidity within the capillary pores drops below 80% (9). Furthermore, water lost internally by self-desiccation must be replaced by water from outside. Therefore, the quality of the concrete depends on the gel/space ratio of the paste. Greater hydration will lead to a higher-strength concrete. In addition, prolonged water-curing delays the advent of shrinkage and produce stronger concrete that is able to withstand a larger shrinkage without cracking.

Table 2 shows that the trend of elastic tensile strain capacity is similar to that of tensile strain capacity, because the same factors affect them both. The elastic tensile strain capacity of concrete specimens cured for three days was not measured, because no cracks occurred in these specimens. Creep strain of concrete subjected to restrained shrinkage is the difference between tensile strain capacity and elastic tensile strain capacity. This has been ignored by some researchers, while others have attributed to it as much as 75% of free shrinkage. The results of Al-Rawi (8) show that the creep strain is quite significant and therefore must not be ignored.

Table 2 shows the creep values of concrete specimens water-cured for one day before drying. In general, creep increases with increased cracking time, and factors that increase cracking time also increase creep strain. Its value, however, depends to a large extent on test conditions. The creep of specimens water-cured for three days was not measured because the increase in curing time delays shrinkage and prevents cracking. This gives enough time to develop creep, which means higher creep than the specimens water-cured for one day.

Cracking time is defined as the number of days required for cracking to occur; it can be used as an index to compare the possibility of cracking of various mixes. Table 6 shows the cracking time of concrete exposed to indoor drying conditions after being water-cured for one day.

The reduction in water/cement ratio results in earlier shrinkage cracking, in spite of increased tensile strain capacity. This is consistent with increased drying shrinkage (rapid drying shrinkage does not allow relief of stress by creep and leads to cracking). This trend confirmed results reported by Al-Ali (4), who showed that the cracking tendency of concrete (cracking age) was affected by the mix richness; concrete with a higher cement content suffered a higher cracking tendency (earlier cracking age). Shah and Weiss (10) found that the reduction in water/cement ratio decreased cracking time. They explained this as a result of increased total shrinkage, decreased stress relaxation and increased brittleness and stiffness.

Table 2 shows that prolonged water-curing prevents cracking of concrete. Drying the specimens for 30 days resulted in no cracks in specimens water-cured for three days. Figures 2–5 show that shrinkage in specimens water-cured for three days exceeds that of those cured for one day. At the same time, water-curing increases concrete strength and tensile strain capacity.

This shows as incorrect the supposition that the higher the shrinkage of concrete, the higher the probability of cracking, because it ignores the possible increase in tensile strain capacity, as in the present case. In addition, the literature calls for low shrinkage of concrete to avoid shrinkage cracking, but this is not always correct, as the present results show that higher shrinkage leads to less probability of cracking.

**Table 2. Results of indoor concrete specimens.**

Specimen notation	Cracking time (day)	Free shrinkage (mlths)	Loss of restraint (mlths)	Tensile strain capacity (mlths)	Elastic tensile strain capacity (mlths)	Creep (mlths)
Ai1	18	330	30	300	178	122
Ai3	No cracking	500	70	>430	---	---
Bi1	17	344	34	310	189	121
Bi3	No cracking	483	45	>438	----	---
Ci1	13	331	20	311	200	105
Ci3	No cracking	487	30	>457	---	----
Di1	11	350	20	330	266	64
Di3	No cracking	510	40	>470	----	----

### **Outdoor Concrete Specimen Results**

Restrained shrinkage movements were measured for outdoor specimens cast for one month in the summer (July and August) in Iraq without any cracking. After 30 days, the specimens (water-cured for one day) were artificially cracked to measure the properties, as shown in Table 3.

Table 3 show the tensile strain capacity of outdoor specimens, which exhibit the same trends as indoor specimens. The tensile strain capacity of concrete increases with increased cement content. Longer water curing increases the tensile strain capacity of concrete specimens more than 6.0%, as illustrated in Table 3. This, as discussed previously, is because prolonged curing delays the advent of shrinkage and produces stronger concrete, which is able to withstand greater shrinkage without cracking.

The tensile strain capacity measured in outdoor specimens was greater than that of indoor specimens, and the increase in tensile strain capacity reached more than 75%. This is expected, because outdoor temperatures reached more than 60 °C, which means faster development of strength (accelerated curing), which means faster development of tensile strain capacity.

Generally, the tensile strength capacity of concrete achieved much higher values than those reported in the literatures, which generally are 100–200 mlths. Tensile strength capacity values found in the present work were more than 597 mlths. None of the specimens exposed to outdoor conditions cracked. The researcher cracked those specimens water-cured for one day at 30 days of age and then measured the elastic tensile strain at the time of cracking. Table 3 shows the elastic tensile strain capacity for cracked mortar and for the uncracked specimens that were cracked by the researcher. This means that the values obtained for elastic tensile strength capacity are greater than the values reported here. The creep of outdoor specimens was measured as the difference between tensile strain capacity and elastic tensile strain. Creep was measured when the specimens were artificially cracked at 30 days of age. Table 3 shows that creep values are relatively high. They also are greater than the creep values of indoor specimens because of the longer cracking time (30 days). The creep developed during the 30 days period is higher than the creep of indoor specimens.

**Table 3. Results of outdoor concrete specimens**

Specimen notation	Cracking time (day)	Free shrinkage (mlths)	Loss of restraint (mlths)	Tensile strain capacity (mlths)	Elastic tensile strain capacity (mlths)	Creep (mlths)	Average Temperature and R.H**
Ao1*	No cracking	503	26	477	221	256	Temp=65 °C R.H=12%
Ao3	No cracking	520	30	490	----	----	
Bo1*	No cracking	557	33	524	277	247	Temp=65 °C R.H=12%
Bo3	No cracking	568	28	540	----	----	
Co1*	No cracking	588	43	545	292	253	Temp=56 °C R.H=17%
Co3	No cracking	600	42	558	----	----	
Do1*	No cracking	603	40	563	305	258	Temp=56 °C R.H=17%
Do3	No cracking	633	36	597	----	----	

\* The specimens were artificially cracked at 30 days of age.

\*\* These data were recorded by the researcher.

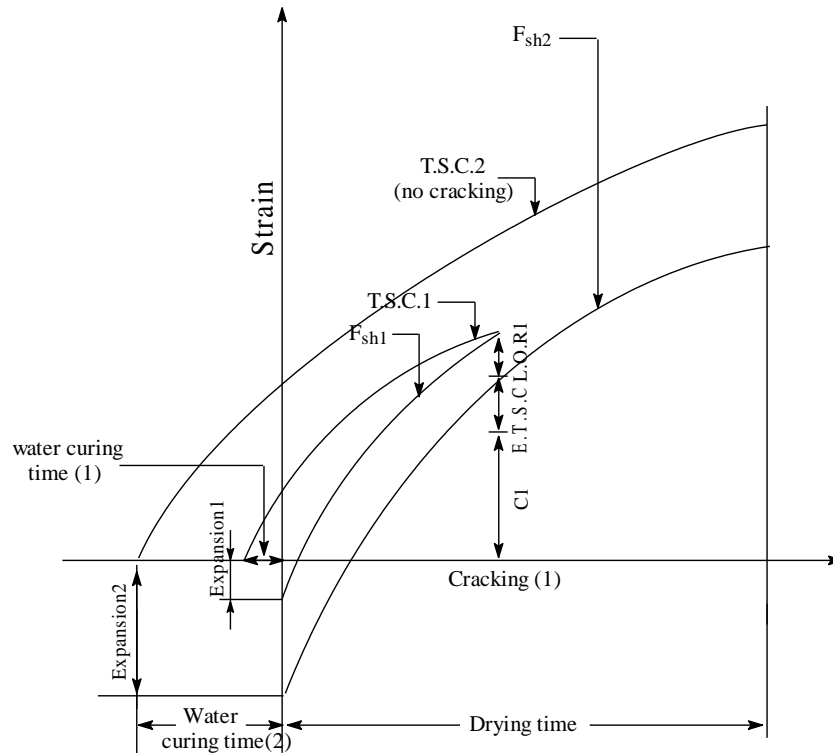
### **Results of Dilation**

The previous results show that dilation is associated with restrained drying shrinkage and is found in many forms. The effects of various factors on dilation are described below.

#### **Effect of Water Curing**

It can be seen from the results of both indoor and outdoor specimens that prolonging water-curing to three days prevents cracking. This is because increased water-curing duration causes expansion, which also can be called dilation. Dilation due to water-curing reduces the probability of cracking. It can prevent cracking or at least decrease crack width. In this case, dilation delayed early shrinkage of specimens, and consequently, the cracking resistance of the concrete was increased because water-curing increases the strength of concrete. The tensile strain capacity increased so that shrinkage strains remained less than the tensile strain

capacity, as shown in Figure 6. No crack occurred in any concrete specimen water-cured for three days.



**Figure 6. A sketch of tensile strain capacity and related concrete parameters for various water-curing periods under outdoor exposure conditions.**

TSC<sub>1</sub>: Tensile strain capacity for specimens water-cured one day.

F<sub>sh1</sub>: Free shrinkage for specimens water-cured one day.

LOR<sub>1</sub>: Loss of restraint for specimens water-cured one day.

ETSC<sub>1</sub>: Elastic tensile strain capacity for specimens water-cured one day.

C<sub>1</sub>: Creep for specimens water-cured one day.

TS<sub>2</sub>: Tensile strain for specimens water-cured three days.

F<sub>sh2</sub>: Free shrinkage for specimens water-cured three days.

Note: In outdoor exposure conditions, no cracking took place whether water-curing was for one day or three, i.e., in both cases curves (2) are applicable.

### ***Effects of Fluctuations in Temperature and Relative Humidity***

Specimens subjected to outdoor exposure did not crack whether cured for one day or three. This means that other factors affect the cracking tendency of outdoor specimens. Results reported in Table 3 show the maximum and minimum temperature, average relative humidity and wind speed of exposure durations in summer in Baghdad. It can be seen that the change in temperature between day and night is more than 40 °C. The relative humidity ranged from 12% during the day to 23% at night in July and from 17% during the day to 28% at night in August. These fluctuations in temperature and relative humidity led to higher rates and magnitude of creep, as shown in Figure 5, partially relieving the restrained shrinkage stress.

In this case, dilation occurs because of increased creep due to relatively large fluctuations in temperature and relative humidity. This agrees with the argument proposed by Al-Rawi and

Kammouna (7), who claimed that the temperature rise increases the rate of creep, resulting in higher creep values. They found that changes in temperature and relative humidity from 21 °C and 50% to 42 °C and 23% caused a sudden increase in creep of approximately 280 mlths. The increased creep of concrete in tension with increased variation in temperature is attributed to the fact that the coefficient of thermal expansion of water is much higher than the coefficient of thermal expansion of concrete. Therefore, with increases in temperature, the water in concrete pores expands much more than the concrete. This causes pressure, leading to expansion of the concrete. With decreases in temperature, the water in concrete pores contracts but obviously does not lead to contraction of the concrete. Repeated heating and cooling of the concrete means repeated expansion, but no contraction, which means higher creep (transitional thermal creep) of the concrete in tension.

## Conclusions

The following conclusions can be drawn.

- 1- Concrete water-cured for three days after casting shows significant expansion. When such concrete is dried indoors for one month, it shows shrinkage higher than concrete water-cured for one day followed by one month of drying indoors. Concrete dried outdoors shows similar trends as concrete dried indoors, but it shows higher shrinkage due to higher temperatures (more than 60 °C) and lower relative humidity (less than 15%).
- 2- All specimens subjected to natural drying conditions outdoors have tensile strain capacity higher than the specimens dried in rooms with controlled temperature and relative humidity. This is because outdoor temperatures reached more than 60 °C, which causes faster development of strength (9), resulting in increased tensile strain capacity.
- 3- Prolonged water-curing increases the tensile strain capacity of various mixes of concrete, whether they are exposed to indoor or outdoor drying conditions. Specimens water-cured for three days gain greater strength during these three days, and higher tensile strain capacity is gained compared with specimens water-cured one day.
- 4- Prolonging water-curing to three days prevents cracking of concrete. Concrete specimens subjected to outdoor conditions did not crack whether water-cured for one day or three. This is due to the higher rate and magnitude of creep (dilation) and to partial relief of restrained shrinkage stress. This dilation occurs due to relatively large fluctuations in temperature, which cause higher creep, resulting in relief of tensile stress on the concrete and prevention of cracking.
- 5- Fluctuations in weather conditions between day and night in the summer in Iraq could be an advantage regarding shrinkage and thermal cracking of concrete. This is because such weather increases tensile creep significantly (up to more than four times the tensile creep achieved in steady moderate weather), thus increasing tensile strain capacity of the concrete by more than 46% and reducing the possibility of cracking.
- 6- Considerable savings in steel reinforcement of concrete can be made in fluctuating, hot, dry weather.
- 7- Magnitude of shrinkage is not the only factor affecting cracking of concrete. Tensile strain capacity, including dilation, is another factor.

## REFERENCES

1. Al-Rawi, R. S. and Al-Qassab, F., "Laboratory test on small beam to study shrinkage cracking in continuously reinforced concrete pavement", ACI International Conference on Concrete Transportation, 8-10 September 1986, Canada.
2. Adday, S., "Development of mathematical relations for tensile strain capacity of concrete", Ph.D. Thesis, University of Baghdad, 2005.
3. Al-Badry, J., "Control of shrinkage cracking of steel fibre reinforced concrete end restrained members", MSc Thesis, University of Baghdad, 2000.
4. Al-Ali, B., "Control of shrinkage cracking in reinforced concrete", MSc. Thesis, University of Baghdad, 1985.
5. Salman, M., "The effect of addition of some local materials on dimensional changes and cracking of concrete", MSc. Thesis, University of Baghdad, 1987.

6. Al-Rawi, R. S. and Salih, S., "Control of thermal and shrinkage cracking of mass concrete in hot climate", Journal of Engineering, College of Engineering, University of Baghdad, 9(2), June 2003, pp 195-205.
7. Al-Rawi, R. S. and Kammouna, Z. M., "Development of a mathematical model for creep of concrete with reference to Baghdad climate", Journal of Engineering, College of Engineering, University of Baghdad, 9(1), March 2003, pp 49-61.
8. Al-Rawi, R. S., "A new method for determination of tensile strain capacity and related concrete properties", ACI Symposium, Singapore Chapter, August 1985, "Our world in concrete and structures".
9. Neville, A. M., "Properties of Concrete", Fifth Edition, Pearson Education Limited, 2011, England.
10. Shah, S. P. and Weiss, W. J., "High strength concrete strength, permeability, and cracking", Proceedings, PCI/FHWA International Symposium on High Performance Concrete, Orlando, Florida, 2000, pp 331-340.

# High-Absorptive Normal-Weight Aggregates used as Internal Curing Agent

Pericles A. Savva<sup>1</sup> and Michael F. Petrou<sup>2</sup>

<sup>1</sup>Phd candidate in Civil and Environmental Engineering, University of Cyprus

<sup>2</sup>Professor of Civil and Environmental Engineering, University of Cyprus

**Abstract:** High performance concrete (HPC) in the early age suffers high shrinkage. Two well established methods for compensating early-age shrinkage have been the incorporation of pre-saturated lightweight aggregates (LWA) and the addition of dry super absorbent polymers (SAP). LWAs and SAPs are purely water reservoirs which have little or no contribution to concrete final performance. Consequently, the space occupied by these reservoirs yield to additional porosity which is known to deteriorate concrete mechanical properties. An effort to reduce early-age shrinkage using high-absorptive normal-weight aggregates (HANWA) has been conducted on concrete mixtures with water to binder ratio of 0.25. The HANWA concrete mixtures were compared with a mixture including low-absorptive normal-weight aggregates (NWA) and two different mixtures including low-absorptive aggregates and two different types of SAP. Tests on resistance to chloride penetration, vacuum porosity, and compressive strength have been conducted, in order to assess the mechanical and durability properties. Furthermore, autogenous shrinkage and maturing temperature of these mixtures have been monitored during the first week of hardening. The results show that autogenous shrinkage can be reduced using HANWA for internal curing (IC) maintaining mechanical and durability properties intact.

**Keywords:** Internal curing, Shrinkage, High-absorptive normal-weight aggregates, Super Absorbent Polymers

## 1. Introduction

Concrete has a relatively low tensile strength compared to its compressive strength. The first week of the material's life-cycle is very crucial and along with the constituent material's it defines its final performance. Fresh concrete maturing is strongly depended on environmental conditions since the water evaporation and the cement hydration rates are greatly affected by temperature, humidity and wind speed. Consequently, drying rate and hydration products dispersion are two dominating parameters that define the material's quality. However, the volume variations that occur in early-age concrete are not exclusively attributed to the evaporation rate. It has been reported that shrinkage will occur due to chemical and physical intrinsic properties of cement even in a completely isolated environment (1). Swelling will occur during the initial maturing period due to the formation of ettringite and osmotic pressure (2). Neville (1) has clarified that in most cases shrinkage will overcome swelling. The mechanisms that cause shrinkage have been studied thoroughly and there are evidence that along with drying shrinkage, concrete contracts due to autogenous and chemical shrinkage.

Autogenous shrinkage was first recognized and introduced in concrete technology by Lynam in 1934 (3). It is a general term that describes the material's bulk volume variation. Autogenous shrinkage is the sum of chemical shrinkage and self-desiccation. Chemical shrinkage occurs because the reactants occupy 8-10 ml for every 100 g cement reacted less volume than the initial products (2), whereas in the case of supplementary material's such as silica fume, the reduction in volume may occur up to 20 ml for every 100 g silica fume reacted (4). Chemical and autogenous shrinkage begin to diverge when concrete develops adequate strength to support the formation of voids within its structure (2,5). Self-desiccation is the result of two governing physical processes that appear due to insufficient water. Specifically, disjoining pressure between the material's particles occurs where high RH levels exist and the water adsorption is obstructed due to insufficient space. Reduction in RH levels will result in disjoining pressure decrease causing the material contraction (4). Furthermore, a partially fluid filled pore will result in fluid-air menisci formation that exhibits tensile stress (4). The pore surrounding walls will develop compressive stresses in order to restore equilibrium resulting in further contraction (6).

It is therefore understandable that the practice of increasing cement quantity and decreasing water quantity has a severe influence on the material's shrinkage (7). During the last two decades, high performance concrete (HPC) has been introduced and increasingly used in the construction sector due to



its high strength and high durability properties. In order to achieve such properties, among other modifications in the mixtures constituent materials, cement quantity is increased whereas water quantity is decreased.

An effort to reduce HPC shrinkage has been focused on utilizing water from the inner structure of the material, by dispersing micro-reservoirs of water, providing IC. IC have attracted great attention after Ole Jensen's comprehensive work (8,9) at the early 2000s. Two well established methods of IC are the use of SAPs and LWAs. Both methods, however, evidently cause deteriorating side effects on the material's performance. The effort of this research was to provide IC to concrete and maintain its properties intact.

## **2. Research significance**

The main objective of IC is to provide additional water in dense concrete to reduce the early-age shrinkage. The quantity of IC water required to compensate autogenous shrinkage can be calculated based on Benz equation (10). The difficulty in IC is to provide the full quantity of IC water without compromising the material's performance. For example, increasing LWA in order to satisfy the IC requirements may endanger the mechanical properties of the mixture. Employing SAPs to compensate autogenous shrinkage has proven to be a very effective method but the material's mechanical properties are evidently deteriorated (11). Furthermore, using shrinkage reducing agents (SRA) in the mixture, although durability indicators may remain unaffected, the compressive strength is reduced (12). In this research, the water reservoirs employed were part of an existing constituent of the mixture (aggregates) and consequently the material's properties were expected to be improved.

## **3. Experimental methods**

### **3.1. Mixtures**

Five mixtures have been prepared in order to evaluate the IC effectiveness. Two mixtures included HANWA which are designated as HANWA-SSD and HANWA-DRY and their difference lies on the state of the aggregates prior entering the mixture. In the first case the aggregates were saturated surface dry (SSD) and in the second case the aggregates were dry and the appropriate amount of water needed to reach SSD was added to the mixing water. This practice lies on the assumption that the aggregates will absorb the additional water and therefore the w/b ratio would not be increased. If his assumption is true, then the mixtures' properties should remain the same. Furthermore, three mixtures with NWA have been also prepared. The two mixtures included two different types of SAP (T1, T2) and the third mixture was the control (CTRL) mixture with no IC agent.

The mixtures have been made in a horizontal rotary mixing machine. The slump of each fresh concrete mixture was measured in order to maintain consistent workability. Furthermore, the mixtures' temperature prior to cast was recorded as well as the ambient humidity and temperature. Finally, the mixing water was kept in a chamber for 24 hours before mixing to ensure constant temperature. After the specimens were cast, the molds were covered with wet burlaps in order to prevent moisture loss to the environment. 24 hours after casting the specimens were demolded and wrapped with polyvinyl chloride membrane in order to provide sealed conditions for curing. The efficiency of the membrane was verified with consecutively mass measurements. The specimens were kept in a room with controlled temperature and humidity. The concrete temperature evolution and autogenous shrinkage were monitored. Also, the compressive strength and vacuum porosity were measured at 3, 7, 28 and 90 days and rapid chloride permeability (RCP) at 7, 28 and 90 days.

### **3.2. Materials**

The cement utilized for this research was CEM I 52.5N. The fraction of the aggregates utilized as IC agents was 4-10mm since their  $WA_{24}$  was 5.2% (Table 1), which is considered adequate. A similar fraction (4-8mm LWA) has been also used by Weber who established their effectiveness (13). The aggregates water absorption ( $WA_{24}$ ) was calculated based on EN-1097-6 (14) (Table 1). The sand has a fraction of 0-4mm and its  $WA_{24}$  and fineness modules are presented on Table 2. Polycarboxylate polymer superplasticizer (SP) was used in order to maintain the mixtures workability within a slump range of 70-100mm (within a range of  $\pm 15$ mm). The utilized SAPs were Poly (acrylic acid) partial sodium salt for T1 and Poly (acrylic acid), partial potassium salt, slightly cross-linked for T2. The SAPs were prepared with bulk polymerization technique. It has to be mentioned that concrete using SAPs yielded from bulk polymerization technique demonstrate a superior performance as opposed to suspension technique in terms of strength evolution (15). The conclusions of a round-robin test (RRT) (11) support that small and

spherical SAP particles are more effective in terms of (11) compressive strength than irregular larger particles. The polymers were tested in suspended pore solution using the teabag method and it was concluded that their absorbing capacity was 29g/g for SAP-T1 and 26g/g for SAP-T2. Therefore, the amount of SAP required to carry the necessary quantity of IC water was 0.18% and 0.2% with respect to cement mass for T1 and T2 respectively.

The aggregates used as IC medium in this study (HANWA) are crushed limestone quarried in Cyprus. It has been shown that the specific aggregates contain mainly micritic calcite which in restricted areas yields to microspar. More specifically fossils, whose composition is mainly recrystallized sparry calcite, were observed, whereas micritic endoclasts and non-carbonate grains such as quartz, chert and spinel were sparsely observed. Traces of anhydrite were also observed. The HANWA high absorptivity is attributed to the significant intraparticle porosity obtained within fossils, whereas elongated pores have been formed due to recrystallization of spar crystals. More mineralogical information about the aggregates can be found in reference (16).

### 3.3. Mix proportions

The predominant reason for implementing IC in concrete is to reduce autogenous shrinkage which is more intense at low water to binder ratio (w/b) and increased cement content. The mixture was intentionally designed with low w/b ratio and high cement content (Table 2), in order to evaluate the effectiveness of the IC method. The amount of coarse aggregates was calculated based on IC water requirements (Bentz equation (10)) and the aggregates desorption properties (Figure 2). It has to be mentioned that the mixtures SAP-T1, T2 have a reduced amount of fine aggregates since the IC water occupies a specific volume.

Table 1: Aggregate properties EN 1097-6(14) (g/cm<sup>3</sup>)

	$\rho_b$	WA <sub>24</sub>	FM	Fraction
NWA	2,74	1,1%	-	4/10
HANWA	2,30	5,2%	-	4/10
SAND	2,63	1,2%	2,12	0/4

Table 2: Mix constituents ACI 211.1-91 (17) (kg/m<sup>3</sup>)

	CTRL	HANWA-SSD	HANWA-DRY	SAP-T1	SAP-T2
Cement	864	864	864	864	864
Water	216	216	216	216	216
Coarse	854	854	854	854	854
Sand	499	344	344	383	383
SP	0,09%	0,05%	0,05%	0,04%	0,23%
SAP	-	-	-	1,5	1,7
IC water	44,0	44,0	44,0	44,0	44,0
Slump	70	100	85	85	80

## 4. Results and Discussion

### 4.1. Aggregates desorption

In order to ensure that HANWA would be able to function as IC medium, the aggregates should be able to release the majority of the IC water at high RH levels. Javier Castro (18) suggested that an efficient aggregate would release its majority of moisture at high RH and more specifically at 93%. The HANWA used in this research were washed in a 63 $\mu$ m sieve and then oven dried until constant mass was reached. Afterwards the aggregates were placed in a wire basket and immersed in 20°C water for 24h. Then they were placed in an environmental chamber where the temperature was maintained at 23 $\pm$ 1°C and the RH was decreased gradually from 95% to 80% with 1% interval. The RH was decreased each time when the aggregates reached a constant mass. It has to be mentioned that based on Bentz equation the required amount of IC water was 0.51kg per kg of cement. Based on Figure 2, the HANWA aggregates release 65% of their moisture at 93% RH, whereas another 15% of their moisture is released to a RH level of

85%. It is expected therefore that HANWA will be able to provide the majority of IC water at early-ages. It was expected that due to their smaller pores as opposed to LWAs which is reflected on desorption curve, HANWA beneficial effect would occur more gradually and last for a longer period of time.

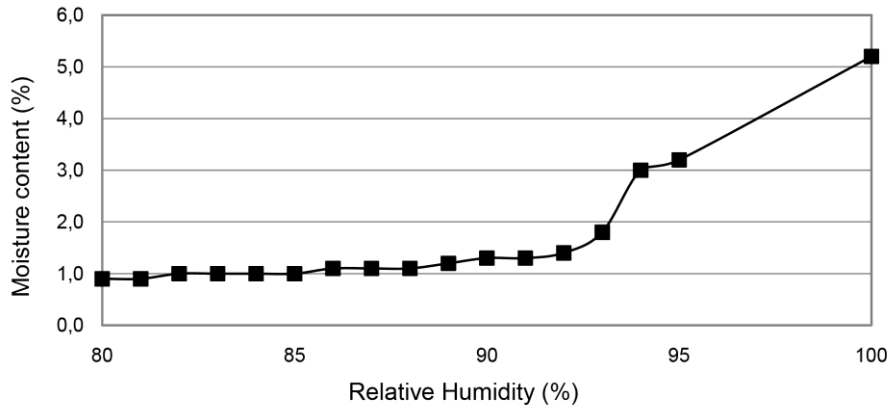


Figure 1: HANWA desorption properties

#### 4.2. Autogenous shrinkage

The effectiveness of an IC medium is also reflected on the mixtures shrinkage since the reason for implementing IC is to reduce the early-age volume variations that cause excessive internal stress and lead the material to cracking. Therefore autogenous shrinkage experiments have been conducted in order to evaluate the effectiveness of the selected IC medium. Sealed concrete prisms with strain gauges attached on their longitudinal opposite faces have been tested for 7 days after final setting. The mixtures have been cured for 7 hours after casting and directly sealed after demolded with polyvinyl chloride membrane. The membrane at the strain gauges location was removed using surgical blade and epoxy resin covered the surface. After the resin was solidified the strain gauges were attached and the specimen was wrapped again with membrane to ensure no moisture exchange with the environment. The experiments were conducted in an environmental chamber with constant temperature ( $25\pm 1^\circ\text{C}$ ) and RH ( $60\pm 1\%$ ). Each strain gauge was connected to a strain indicator and the results were logged using a pc unit with a time interval of 15 minutes.

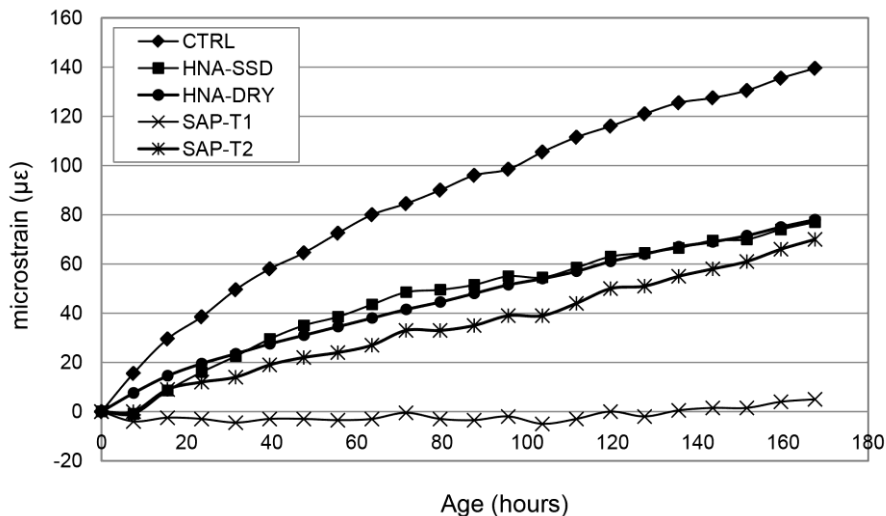


Figure 2: Autogenous shrinkage

The IC mixtures observe a clear reduction in autogenous shrinkage (Figure 3). The reference mixture as expected exhibited the higher shrinkage whereas SAP-T1 the lowest. SAP-T1 observes no volumetric variations in contradiction to others reports that have employed up to 0.6% SAP (with respect to cement mass) in order to fully diminish autogenous shrinkage (8). It has to be mentioned that concrete

performance is deteriorating when SAP quantity is increased. HANWA-SSD, HANWA-DRY and SAP-T2 exhibit similar behavior. HANWA mixtures appear to be effective in internal curing, since the lower of autogenous shrinkage can be attributed to water replenishment or increased w/b ratio. SAP-T2 seems to perform differently than SAP-T1. The performance of a mixture containing SAP in terms of autogenous shrinkage is not depended on the absorbing capacity of the polymer but it depends on their absorption and desorption rate. The fact that SAP-T1 and T2 have similar pore fluid absorption capacity does not imply that the absorption and desorption rate will be similar. Reinhardt (19) has concluded that the desorption or drying rate of SAPs would vary from the outer surface to the core of the polymer due to the large surface area and weak bond between the polymer particle and water molecule. It can be concluded that the surface area of the SAPs would significantly influence the desorption properties of each polymer. Furthermore, the absorption rate and carrying capacity of each polymer varies with its degree of anionicity whereas and cross-linking density. Based on Figure 3, SAP-T1 appears to be the most effective IC medium used in this research regarding autogenous shrinkage, whereas the rest of the IC agents. The rest of the IC agents reduce also significantly the autogenous shrinkage as opposed to the CTRL mixture.

### 4.3. Maturing temperature

Three thermocouples were embedded in a concrete prism at three mid-height points along the specimen right after the mixtures were cast. The specimen was sealed to ensure no moisture exchange and the temperature was kept constant ( $23\pm 1^\circ\text{C}$ ). The mixture's maturing temperature has been monitored until constant temperature has been reached.

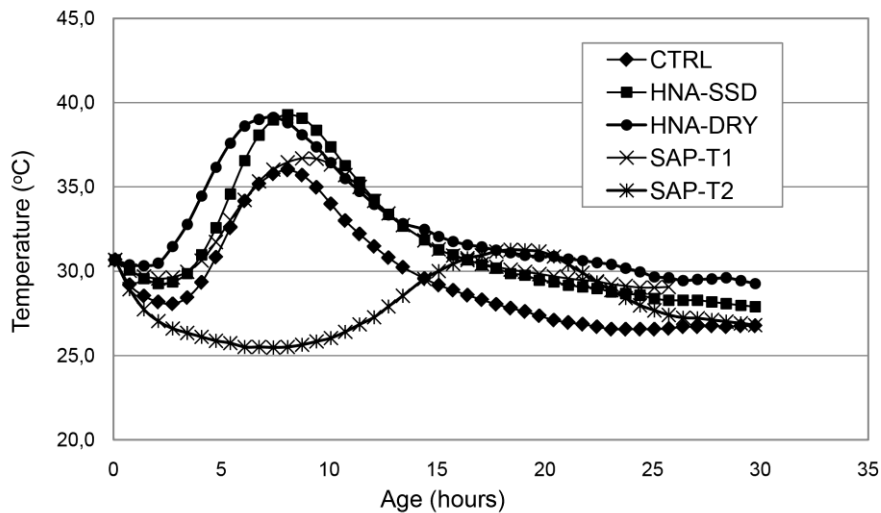


Figure 3: Maturing temperature

Based on Neville (1), the rate of heat evolution is comprised of three temperature peaks. The first which is the higher occurs at the point the cement comes in contact with water; its duration is very short and corresponds to the surface hydration of the cement particles and especially  $\text{C}_3\text{A}$ . The second peak happens at approximately 10 hours after the initial contact but occasionally can be observed as early as 4 hours. The third stage is observed in most types of cement and happens due to an extended hydration of  $\text{C}_3\text{A}$  because of gypsum exhaustion. It is widely known that gypsum is added in cement production in order to restrict the violent hydration that occurs after  $\text{C}_3\text{A}$  comes in contact with water. On Figure 4, the second stage of heat evolution is clearly observed as well as a very smooth increase at late hours which is likely to correspond to gypsum depletion. Furthermore, it has to be mentioned that the HANWA-IC mixtures exhibit a higher temperature at the second stage and this is attributed to the availability of IC water which is supplied to the mixture from the aggregates walls. It can be observed though that the slope of HANWA-SSD is steeper. It has to be mentioned that water is withdrawn from HANWA when the RH drops and negative pressure is developed within the material's pores. It is therefore concluded that the HANWA-DRY aggregates do not absorb the whole additional quantity of water which finally participates in the w/b ratio delaying the RH drop. The increased temperature peak is attributed to higher w/b ratio. Furthermore, SAP-T1 and CTRL mixtures have observed similar heat evolution; however the SAPs peak value is slightly shifted. The results of a RILEMs RRT (11) have shown that mixtures including IC water would observe an increased setting time. SAP-T2 exhibits a very different maturing behavior from the

other mixtures. In order to assess the behavior of the specific mixture the material's microstructure have to be examined. It has to be mentioned though that the specific type of polymers observed a high reduction in mass at the first hours during the tea-bag test.

#### 4.4. Compressive strength

The results of compressive strength as well as the standard deviation are presented on Table 3. The specimens have been cured in sealed conditions at temperature  $23\pm 1^\circ\text{C}$ . Each value represents the average of minimum three cubic specimens (100x100x100mm). It is concluded that the compressive strength of IC mixtures was reduced compared to the CTRL mixture. This was expected at early-ages since the IC mediums are not directly contributing to the material's mechanical performance. Their contribution though is reflected on the evolution of their mechanical properties and durability indicators (Table 2-4). Especially in the case of HANWA-SSD the material demonstrates a constant increase in its compressive strength and at the age of 90 days its compressive strength is equal to the CTRL mixture. Additionally, the water adjustment in HANWA-DRY mixture is not justified. The compressive strength of the specific mixture is consistently lower than HANWA-SSD and this is attributed to the additional water which participates to the w/b ratio and leads to additional porosity (Table 4) and reduced compressive strength (Table 3).

Based on the results (Table 3) it seems that unlike the rest of the mixtures, HANWA-SSD is the only mixture that is continuously gaining strength. The reduction in compressive strength for concrete including SAP is observed in both SAP-T1 and T2 mixtures. It seems, however, that both mixtures partially recover the initial loss at 28 days, due to extended hydration. It seems though that between 28 and 90 days, no significant gain in compressive strength has occurred in the specific mixtures and this is attributed to the SAPs water exhaustion. It can be concluded that despite the beneficial effect on durability indicators, a permanent reduction in compressive strength was observed when SAPs were included.

Table 3: Compressive strength

	3DAYS		7DAYS		28DAYS		90DAYS	
	$f_{cm}$ (MPa)	SD (MPa)	$f_{cm}$ (MPa)	SD (MPa)	$f_{cm}$ (MPa)	SD (MPa)	$f_{cm}$ (MPa)	SD (MPa)
CTRL	84,64	3,89	82,09	7,40	93,18	4,48	88,53	14,76
HANWA-SSD	76,24	3,85	76,68	0,74	80,27	3,25	86,13	3,37
HANWA-DRY	71,84	1,13	67,57	5,29	75,56	3,78	75,89	3,92
SAP-T1	62,58	4,07	72,92	2,25	80,43	5,14	81,66	1,55
SAP-T2	66,03	4,69	67,34	5,41	81,63	8,14	78,81	7,44

#### 4.5. Vacuum porosity

The specimens have been kept in a sealed chamber where the pressure was removed. The specimens were subjected to vacuum for 24 hours before being immersed in water. The specimens were then stored for another 24 hours immersed in water. Immersed and saturated mass was then recorded and after the specimens were placed in an oven with constant temperature of  $105^\circ\text{C}$  until constant mass was reached. The dry mass of the specimens was recorded and the porosity of each specimen was extracted. It has to be noted that the results correspond to a single test conducted on a different specimen at each time interval.

Table 4: Vacuum porosity

	3 DAYS	7 DAYS	28 DAYS	90 DAYS
CTRL	12,48%	11,42%	9,40%	8,22%
HANWA-SSD	14,81%	14,02%	13,69%	12,66%
HANWA-DRY	15,49%	14,70%	16,58%	17,10%
SAP-T1	17,49%	15,24%	15,27%	14,53%
SAP-T2	17,35%	16,32%	13,69%	17,77%

The difference of HANWA-SSD and HANWA-DRY mixture is also reflected on the results of their porosity (Table 4). The HANWA-DRY mixture exhibits higher porosity than the HANWA-SSD mixture. The results

support the argument that the water calculated for the aggregates to reach SSD state was partially participated to the w/b ratio increase. Furthermore, the HANWA-SSD mixture exhibits the lowest porosity after the CTRL mixture verifying its IC effectiveness. SAP-T2 porosity was unexpectedly high at the age of 90 days. SAP mixtures observe a high reduction in porosity at early-ages. It is believed that the majority of SAP water was exhausted and therefore a further reduction at late ages was not possible. The CTRL mixture is consistently improving. The continuous reduction in porosity is an indicator of pores sealing due to hydration products. The same observation was not possible in the case of SAP mixtures due to additional pores introduced by SAP particles.

#### 4.6. Rapid chloride permeability

The rapid chloride permeability (RCP) test was conducted based on ASTM C1202 (20). The experiment assesses the concrete's ability to resist chloride intrusion. The specific test is widely used because it is fast and needs about 24 hours to prepare the sample and 6 hours to complete an experiment (21). The experiment measures the electrical conductivity or resistance of a 50 mm thick disk concrete specimen for a period of 6 hours. It is assumed that the resistivity is directly related to the pore network or concrete permeability, although some claim that the relation is not strictly correct (22). The samples cannot be reused because of concerns over leaching in a moist environment and the exposure to chlorides during the test, which may change the pore solution conductivity. Rapid chloride permeability test can be used for quality control and concrete durability research (23). The specimens are positioned in a measuring cell which contains a fluid reservoir at each face. One reservoir is filled with sodium chloride solution and the other with a sodium hydroxide solution. The reservoir containing NaCl is connected to the negative terminal and the NaOH reservoir to the positive terminal of the microprocessor power supply unit.

The high charge indicates a highly permeable mixture. It can be observed that the lowest permeability at early ages was exhibited by the CTRL sample and its behavior is consistent with the previous measurements. Additional porosity in IC mixtures seems to enhance the pore network and increase the permeability. In the case of SAPs additionally voids interconnect the material's pore network whereas in the case of HANWA extended pore network occur due to the interconnection provided by the aggregates body. However, refinement of the pore network regarding the IC mixtures was expected at later ages due to solidification of the products extracted from the extended hydration.

Although porosity reduction is more effective in the case of HANWA-SSD, it seems that SAP-T1 mixture is more effective in terms of permeability reduction. Since permeability is highly depended on the pores interconnection and not the porosity, the small size of the SAP particles benefits the pore network sealing. Considering the smaller size of SAP particles which yields to better dispersion, the pore network is more likely to be sealed. After the SAP water exhaustion, however, the space occupied by the polymers remains empty, increasing porosity, without necessarily affecting permeability. The larger particles of HANWA are able to reduce the porosity since no additional porosity is introduced to the mixture. Regarding the pore network, however, their efficiency is limited.

Table 5: RCP results (Coulombs)

	7 DAYS	28 DAYS	90 DAYS
CTRL	3695	2352	1378
HANWA-SSD	5850	3022	2137
HANWA-DRY	5433	4410	2202
SAP-T1	6554	3831	2198
SAP-T2	4972	4258	2333

## 5. Conclusions

In this research, the effectiveness of using HANWA as IC agents without compromising any other properties of the mixture has been evaluated. The specific IC medium has been compared with well established IC mediums and the results indicate that it can perform very well. HANWA has been investigated in order to evaluate whether a reduction in autogenous shrinkage could be achieved, without compromising any other properties. Based on the results, the specific IC medium in SSD state reduces the autogenous shrinkage effectively. The specific mixture seems to recover the loss in compressive strength and continuously gain strength due to the presence of water from the inner core that benefits the degree of hydration. Additionally, in comparison with the rest IC mixtures, HANWA-SSD is the only mixture that consistently exhibits a reduction in porosity with time. It is believed that the specific IC

medium is able to utilize IC water even at later ages. This is attributed to the fact that the HANWA do not release their total moisture content at high RH which means that the aggregates' hold moisture in their small pores. The pressure required to extract water from smaller pores is higher, thus the water will be extracted when the RH drops at lower levels. Finally, the specific mixture along with SAP-T1 mixture has observed the greater reduction in RCP values. Even though the size of the IC particles utilized in the case of HANWA-SSD does not contribute to the pore network sealing as explained above, the specific mixture has exhibited a superior performance improving its durability properties. An extended investigation regarding the in depth material's performance is in progress.

## 6. References

1. Neville, a. M. *Properties of Concrete*. (Pearson Education Limited, 2002).
2. Henkensiefken, R., Bentz, D., Nantung, T. & Weiss, J. Volume change and cracking in internally cured mixtures made with saturated lightweight aggregate under sealed and unsealed conditions. *Cem. Concr. Compos.* 31, 427–437 (2009).
3. Jensen, O. M. & Hansen, P. F. Autogenous deformation and RH-change in perspective. *Cem. Concr. Res.* 31, 1859–1865 (2001).
4. Lura, P., Jensen, O. M. & Van Breugel, K. Autogenous shrinkage in high-performance cement paste: An evaluation of basic mechanisms. *Cem. Concr. Res.* 33, 223–232 (2003).
5. Schröfl, C., Mechtcherine, V. & Gorges, M. Relation between the molecular structure and the efficiency of superabsorbent polymers (SAP) as concrete admixture to mitigate autogenous shrinkage. *Cem. Concr. Res.* 42, 865–873 (2012).
6. Barcelo, L., Moranville, M. & Clavaud, B. Autogenous shrinkage of concrete: A balance between autogenous swelling and self-desiccation. *Cem. Concr. Res.* 35, 177–183 (2005).
7. Craeye, B., Geirnaert, M. & Schutter, G. D. Super absorbing polymers as an internal curing agent for mitigation of early-age cracking of high-performance concrete bridge decks. *Constr. Build. Mater.* 25, 1–13 (2011).
8. Jensen, O. M. & Hansen, P. F. Water-entrained cement-based materials I . Principle and theoretical background. 31, 1–13 (2000).
9. Jensen, O. M. & Hansen, P. F. Water-entrained cement-based materials II. Experimental observations. 32, 973–978 (2002).
10. Bentz, P. D. & Snyder, K. A. Protected paste volume in concrete Extension to internal curing using saturated lightweight fine aggregates. *Cem. Concr. Res.* 29, 1863–1867 (1999).
11. Mechtcherine, V. *et al.* Effect of internal curing by using superabsorbent polymers (SAP) on autogenous shrinkage and other properties of a high-performance fine-grained concrete: results of a RILEM round-robin test. *Mater. Struct.* 47, 541–562 (2013).
12. Lopes, A. N. M., Silva, E. F., Dal Molin, D. C. C. & Toledo Filho, R. D. Shrinkage-Reducing Admixture: Effects on Durability of High-Strength Concrete. *ACI Mater. J.* 110, 365–374 (2013).
13. Weber, S. & Reinhardt, H. W. A new generation of high performance concrete: concrete with autogenous curing. *Adv. Cem. based Mater.* 6, 59–68 (1997).
14. EN-1097. Tests for mechanical and physical properties of aggregates Part 6: Determination of particle density and water absorption. (2013).

15. J. Siramanont, W. Vichit-Vadakan, W. S. The impact of SAP structure on the effectiveness of internal curing. *Int. RILEM Conf. Use Superabsorbent Polym. Other New Addit. Concr.* 243 – 252 (2010).
16. Ioannou, I. *et al.* Crushed limestone as an aggregate in concrete production: the Cyprus case. *Geol. Soc. London, Spec. Publ.* 331, 127–135 (2010).
17. American Concrete Institute. Standard Practice for Selecting Proportions for Normal Heavyweight, and Mass Concrete, ACI 211.1-91. *Man. Concr. Pract.* 1–38 (2002).
18. Castro, J., Keiser, L., Goliias, M. & Weiss, J. Absorption and desorption properties of fine lightweight aggregate for application to internally cured concrete mixtures. *Cem. Concr. Compos.* 33, 1001–1008 (2011).
19. Reinhardt, H. W. & Mönning, S. Results of a macroscopic simulation of saturated lightweight aggregates (LWAs) and superabsorbent polymers (SAP) as internal water sources. 585–593 (2008).
20. Drilled, T., Concrete, C. & Statements, B. Standard Test Method for Electrical Indication of Concrete 's Ability to Resist Chloride. *Annu. B. ASTM Stand.* 1–6 (2008). doi:10.1520/C1202-10.2
21. Riding, K. a., Poole, J. L., Schindler, A. K., Juenger, M. C. G. & Folliard, K. J. Simplified concrete resistivity and rapid chloride permeability test method. *ACI Mater. J.* 105, 390–394 (2008).
22. Mindess, S., Young, J. F. & Darwin, D. *Concrete.* (Pearson Education Inc., 2003).
23. Bentz, D. P. A virtual rapid chloride permeability test. *Cem. Concr. Compos.* 29, 723–731 (2007).



# Tensile Properties of Early-Age Concrete

Duy NGUYEN<sup>1</sup>, Vinh T.N. DAO<sup>2</sup>

<sup>1</sup>Ph.D Student, School of Civil Engineering, The University of Queensland

<sup>2</sup>Lecturer, School of Civil Engineering, The University of Queensland

**Abstract:** Despite significant research, early-age cracking remains an ongoing major concern to the concrete construction industry, seriously compromising the performance and aesthetics of concrete structures. More effective crack control requires an improved knowledge of tensile properties of early-age concrete.

In this paper, the tensile properties of concrete at very early ages and their measurement are first reviewed, and the need for further study is clearly highlighted. On that basis, key features of an improved testing system that effectively addresses major drawbacks in current test setups are outlined. Notable features of this system include (i) an air-bearing box to float test specimen, thus effectively eliminating friction and (ii) the novel use of Digital Image Correlation (DIC) for reliable, non-contact capturing of the required displacement fields. The displacements as directly measured by DIC in this study appear much smaller than those estimated from LVDTs readings in previous research, leading to significantly smaller Young's modulus and fracture energy. The substantial variation highlights the need for an accurate and reliable displacement measuring system. Further improvement is being underway at The University of Queensland to develop such system.

**Keywords:** Early-age Cracking, Tensile Properties, Fracture Properties, Direct Tensile Test, Digital Image Correlation (DIC).

## 1. Introduction

Early-age cracking may occur in concrete structures from as early as several hours after casting. These cracks and their further development at later ages can seriously compromise the integrity, durability, aesthetics, and long-term service life of wide-ranging types of concrete structures. Despite significant research over the past decades (1-4), cracking in early-age concrete remains widespread, making it among the most common causes of structures' deterioration and litigation in the construction industry (5, 6).

In principle, cracking occurs when the tensile stresses arising in the concrete reach their tensile strength or, equivalently, when the restrained shrinkage strain reaches tensile strain capacity of concrete at that age. Once occurred, existing cracks would develop further if sufficient energy is provided. Indeed, very often, cracks developed at early-ages would propagate and become unserviceable at later stages due to subsequent shrinkage/loading.

Proper assessment of early-age cracking risk in concrete therefore requires an adequate knowledge of tensile and fracture properties of the materials being considered. Such knowledge can generally be derived from reliable data on complete tensile stress-strain curves of concrete at relevant ages. Unfortunately, such useful data are currently very limited, especially for concrete during the first hours after casting. (In subsequent discussion, the term "very early-age concrete" refers to concrete with ages of less than 12 hours after casting.)

As a corollary, there is a lack of appropriate technical guidelines for prediction of these properties in current codes of practice. Eurocode 2 BS EN1992-1-1:2004 (7) and Japanese standard JSCE-SSCS – 2007 (8) appear the only two available standards providing formulae for the estimation of concrete properties from an age of several days following casting, though their predictions differ greatly from each other – No formulae for concrete during the first day is available yet.

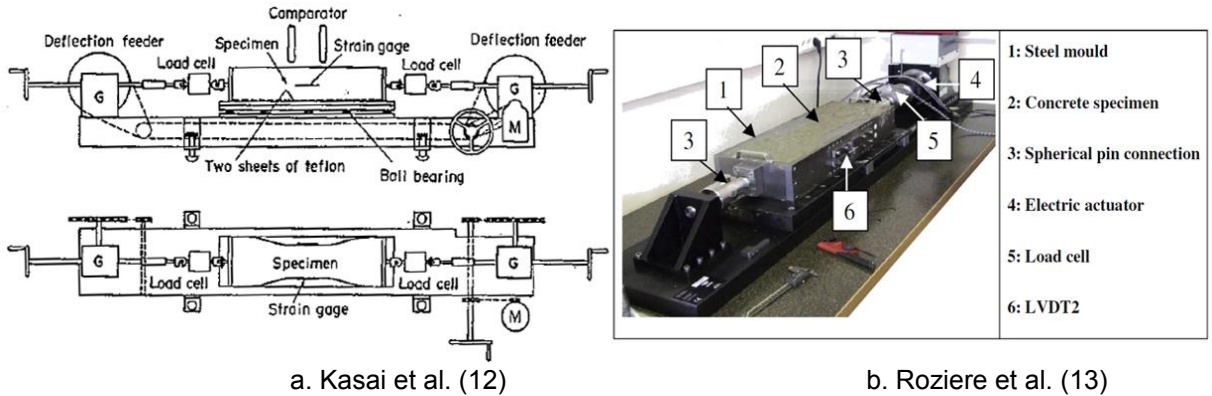
In this paper, current knowledge of tensile properties of concrete during the first several hours after casting, together with techniques for their measurement, are first reviewed. On that basis, an improved testing system that effectively overcomes major drawbacks in current test setups is described. Finally,

initial test results derived from the obtained full stress-strain curves of very young concrete are presented. These include tensile strength, Young’s modulus, tensile strain capacity, and fracture mechanics parameters.

**2. Review of Tensile Properties of Early-age Concrete and Tests for their Measurement**

Despite their significance in assessing associated early-age cracking risk in concrete structures, tensile properties of concrete during the first several hours after casting have been investigated by *only few* researchers (9-11) – due mainly to the considerable practical problems to be overcome when testing early-age concrete. Specifically:

- Due to its low tensile strength, minimisation of friction between test specimens and supporting surface during testing becomes highly critical. Various measures have been attempted (9, 10), including several layers of special materials such as Teflon (12) or PTFE (13). The best available measure is possibly the air-bearing box which “floats” the test specimen on a thin layer of air, thus effectively eliminating all friction – The system was initially proposed by Hannant’s group (10) and subsequently further improved by Dao et al. (11).
- Due to its fragility, disturbance to test specimens must be minimised throughout the moulding, handling and testing processes.
- The fragility of concrete has important implications on reliable deformation measurement – Methods for deformation measurement in previous research can be categorised into three groups:
  - i. Strain gauges are attached to the mould (14, 15), giving total deformation of the whole specimen – Deformation over the region of interest has to be estimated from the measured total deformation, typically by finite element modelling. This “estimation” procedure inevitably has introduced additional uncertainties that has not been appropriately taken into account, raising doubts over the reliability of obtained results.
  - ii. Strain gauges are attached to the posts cast into concrete (16, 17) – The likely movement of the posts in young concrete and the resulting disturbance may have significantly compromised the measurement accuracy; but again, the effect of this disturbance could not be quantified.
  - iii. Digital image correlation (13, 18): DIC is a form of data extraction through image analysis, and has been one of the most effective ways for macroscopic displacement tracking, mechanical and structural testing both in 2D and 3D areas. Although DIC has been widely employed in testing of mature-age concrete (19-22), its application to concrete during its first day is very limited. In order to apply DIC, concrete surfaces need to be treated with appropriate materials to create a sufficiently contrast pattern for the cameras to recognize, while respecting its continuity and strength. Wet-, soft- and dark coloured surfaces of the specimen at early age make the pattern application a real challenge. Nguyen and Dao (18) appeared to be the first to report the successful use of DIC for tensile testing of very early-age concrete. Another such DIC application was recently published by Roziere et al. (13).



**Figure 1. Typical direct tensile testing systems.**

Also, due to the weak nature of very early-age concrete, vertical test specimens as in (23, 24) cannot be used - Specimens have to be tested in horizontal position (12, 13, 15, 16) (Figure 1). Test specimens typically have a dog-bone shape with two enlarged end regions, a reduced middle region to

promote failure therein, and curved transition zones to minimise stress concentrations that could initiate undesirable cracking outside the middle region (Figures 1 and 4). Prismatic specimens have also been used (23-26) but generally for concrete of more than 12 hours only when sufficient strength has developed enabling adequate gripping of specimen ends. Furthermore, prismatic specimens applied in those systems with glued grips at two ends (24) or a centrally embedded bar (23, 25, 26) might raise questions on the effectiveness of the glue on young concrete, as well as on stress concentration at the embedded bar.

During testing, specimens are subject to either load-controlled or displacement-controlled loading. To capture complete stress-strain behaviour, displacement-controlled loading has to be applied. The chosen displacement rate should be slow enough but not too slow to enable full stress-strain curves to be captured while minimising the test time for each specimen. Displacement rate representative of actual early cracking conditions has also been used (13), although it seems too high to produce a full stress-strain curve.

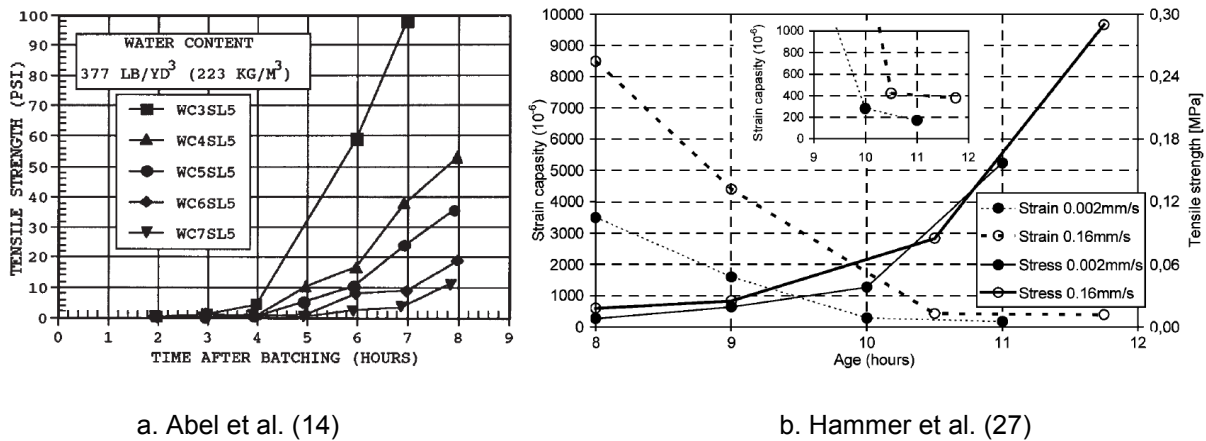


Figure 2. Typical development of early-age tensile strength.

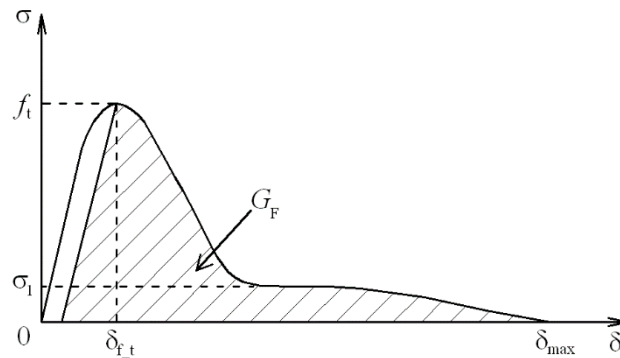


Figure 3. Typical stress-displacement curve (11).

Using the above-mentioned test systems, initial relevant data have been collected – However, useful data are still very limited, with full stress-strain curves reported by only few groups (10, 11), enabling somewhat improved knowledge of tensile properties of very early-age concrete:

- The stress-displacement relationship for early-age concrete generally follows the typical response of a quasi-brittle material in tension (10, 11) (**Figure 3**). However, as highlighted earlier, the accuracy and reliability of measured displacements in previous studies may have been compromised due to limitations inherent in their test setups.
- There was a dormant period during the first several hours after casting in which the tensile strength and Young's modulus of concrete increase very slowly, followed by a period of significantly more rapid development (11, 14, 27) (**Figure 2**).
- Tensile strain capacity tends to decrease rapidly at first, then slightly increases to a stable level after several days of age (12-15, 27).

- However, reported development rates are different between studies due to variations in testing (and associated reliability) as well as types of concrete tested.
- Fracture characteristics are also reported by Dao et al. (11) based on very limited test results.

An ongoing research program at The University of Queensland aims at providing a more comprehensive reliable knowledge of very early-age concrete through addressing the above-mentioned limitations of current test systems. Key details of that research are presented in subsequent sections.

### 3. Experimental Program with Improved Testing System

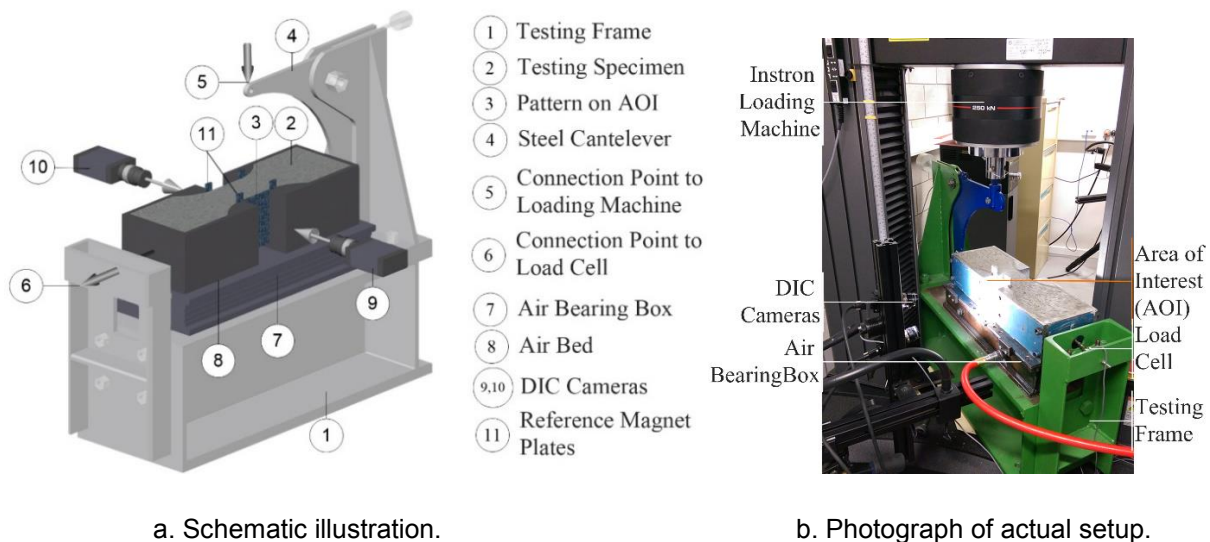
#### 3.1. Direct Tensile Testing System

The improved direct tensile testing system used in this study is shown in **Figure 4**. The test apparatus comprises an air-bearing box ③ and a lever arm ④ attached to a small steel frame①. The lever arm was pin-connected to the frame and was self-balanced in the test position, enabling the direction but not the magnitude of the force applied through the Instron load cell ⑤ to be altered. The specimen ② is placed on top of the air-bearing box ③ with one end pin-connected to the test load cell ⑥ and the other to the lever arm④.

During test, the test apparatus is placed on the horizontal platform of a displacement-controlled Instron testing frame (**Figure 4**). Notable features of this unique test apparatus include:

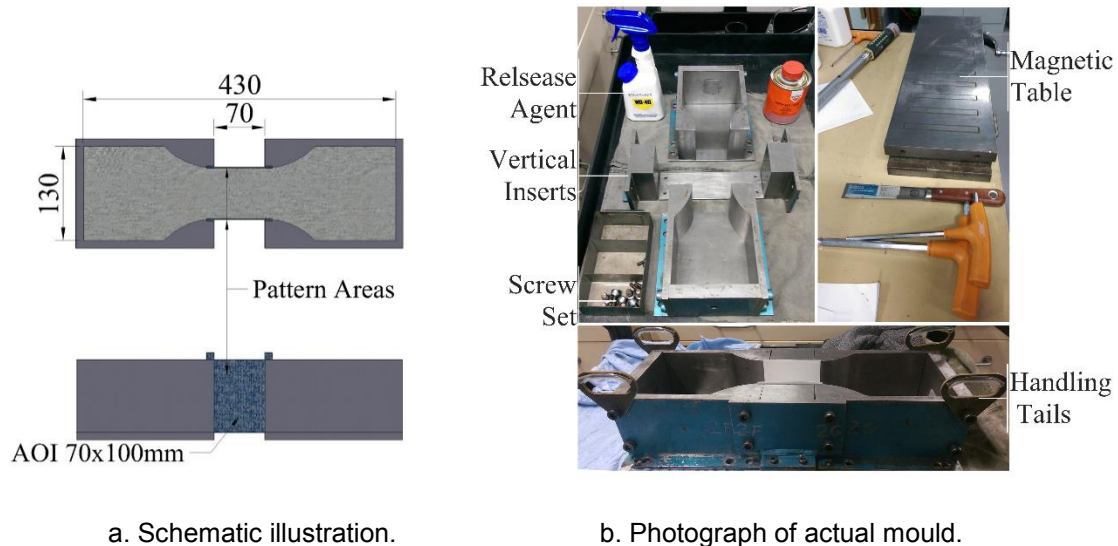
- Air-bearing box: The upper plate of the air-bearing box has 32 holes, 1 mm diameter each symmetrically distributed under the two halves of the mould. The levelness of the upper surface of the air-bearing box after placement in the test position is ensured by using an electronic leveller with an accuracy of 0.1 degrees. During testing, the air bearing box provides a uniform air cushion to float the test specimen that effectively eliminates friction between the specimen and the supporting base
- Digital Image Correlation (DIC): The novel application of DIC enables the desired deformation over the whole areas of interest (AOIs) to be reliably captured in a non-contact way. The successful use of DIC in testing of concrete several hours after casting has thus effectively addressed major shortcomings of previous set-ups.

High resolution professional cameras (⑨,⑩ in **Figure 4**) are employed at both sides of the exposed neck (i.e. AOIs) to capture required displacement fields. All cameras are synchronized to work together with the loading process by a “sync” software developed at UQ Structures Laboratory. Four reference magnet plates [11] attached to the steel mould at the upper corners of AOIs provide a direct mean to verify displacement analysis from DIC system. More details about the verification will be provided in the subsequent section.



**Figure 4. Direct tensile test setup.**

The steel mould is made of 11 different parts connected to each other by a set of screws. Two mould sides are firmly connected by two vertical inserts (Figure 5b), forming a rigid formwork and nurturing the specimen inside. A magnetic table is employed to assist the mould assembling, ensuring a planar bottom surface. The reduced middle region of test specimen (i.e. AOI or Area of Interest) has 100x70mm<sup>2</sup> in cross-section and 70mm in length.



**Figure 5. Testing mould.**

### 3.2. Testing Procedure

Mixing is carried out in the laboratory using a 0.07 m<sup>3</sup> rotary drum mixer. Concrete placing temperature is assumed equal to laboratory temperature (20°C), provided that all the mix ingredients are stored in the laboratory conditions for at least 7 days before being collected. Age zero is determined at the time water is added.

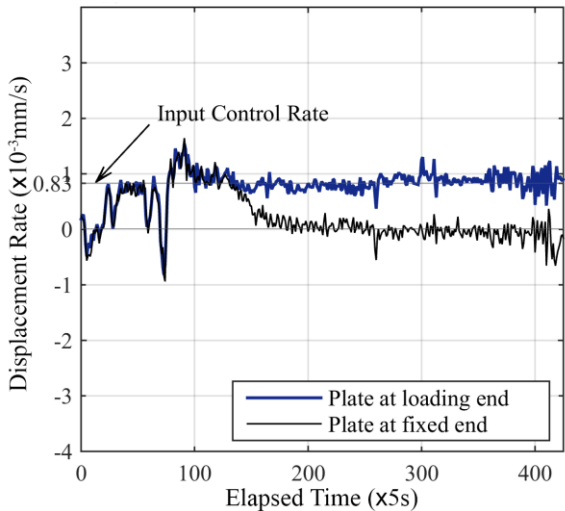
Upon preparation, test specimens are immediately covered by damp clothes to minimise any moisture loss until actual testing in an air-conditioned room with negligible wind, stable temperature (18-20°C) and humidity (60%).

Typical test procedures are as outlined below:

- When ready, test specimen is carefully placed on the air-bearing box and connected to the testing frame. An air pressure of 140kPa is supplied to facilitate the process and float the specimen on a thin layer of air to eliminate friction between test specimen and supporting surface.
- The air is then turned off for further manipulation. Two centre vertical inserts are unscrewed and removed, exposing the concrete neck for pattern application.
- In order to create surface pattern with appropriate contrast, white paint is first applied, followed by a reasonable waiting time for the paint to dry out *before* the application of black paint. Provided that both white and black paint do not form a continuous layer on AOIs, the paint does not affect recorded tensile properties of concrete.
- Two camera systems are then installed with the camera axes perpendicular to concrete captured surfaces (AOIs). Distance from the camera lens to concrete surface is 20-25 cm. Pixel resolution of the cameras is 2448x2048, and intensity resolution is 8 bit.
- The loading process starts with camera capturing. Displacement rate chosen is 0.03-0.05mm/min (compared to a constant rate of 0.05mm/min in (15), 0.3-1.2mm/min in (12) and 0.75mm/min in (16)). Readings from the load cell and Instron machine are recorded along with image capturing until cracking. Post calibration of DIC cameras is to be conducted after removing the specimen, using calibration boards with appropriate size and shape. After the calibration is successfully finished, captured images can be imported and analysis starts.

The reliability of the improved test setup and procedures has been verified using several methods. One such verification is the displacement rate as measured by DIC compared with the applied

displacement rate: The four reference magnet plates with surface patterns similar to concrete AOIs are attached onto the two steel mould halves, two on each half (**Figure 4**). It is evident from **Figure 6** that the reference plates move relative to each other at a rate identical to the applied displacement rate, giving confidence on the reliability of DIC readings.



**Figure 6. Reference plates moving at applied displacement rate, giving credibility to DIC reliability.**

**4. Initial Results**

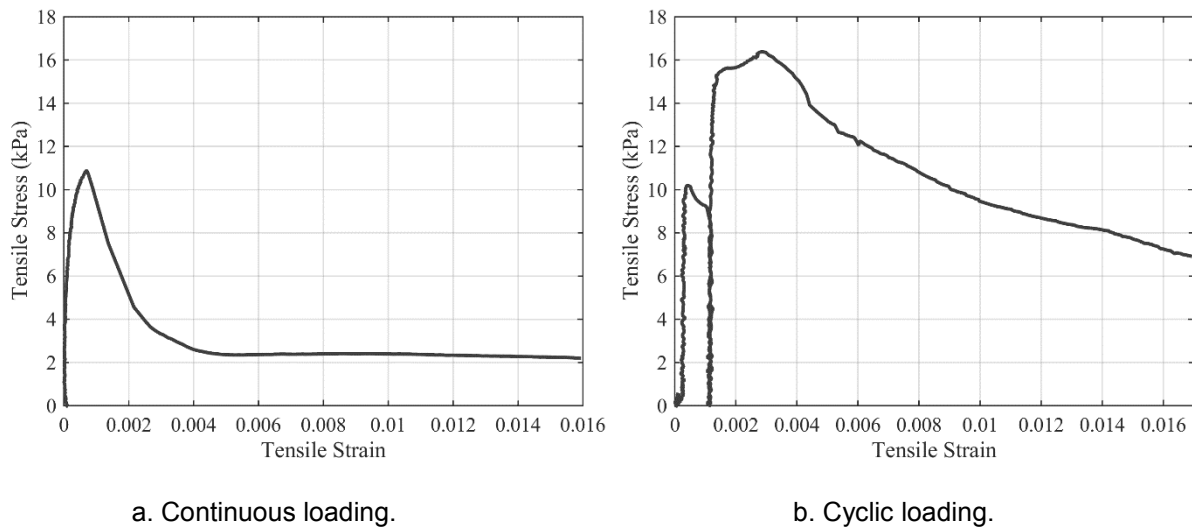
One test series has been conducted using the improved test system detailed above. Mix design used is as shown in Table 1.

**Table 1 – Concrete Mix Design**

Ingredients	GP Cement (kg)	10mm Aggregate (kg)	5mm Aggregate (kg)	Coarse Sand (kg)	Fine Sand (kg)	Water (L)	Slump (mm)
Quantity/m <sup>3</sup>	380	520	435	490	295	240	80

In this study, besides a test series in which displacement-controlled loading is increased continuously until failure (**Figure 7a**), another series in which *cyclic loading* is applied to investigate tensile properties during unloading (**Figure 7b**) – This tensile behaviour during unloading has not been studied in previous research.





**Figure 7. Typical stress-strain curves.**

As illustrated in **Figure 7**, in both cases of loading a complete tensile stress-strain relationship is successfully established. Stress values are obtained from load cell's data file, assuming uniform stress distribution across the section. Strain values are averaged from both DIC systems. From each side, a full field of displacement/strain also allows further comparison/judgement at different positions. In cyclic loading, the first cycle starts at the beginning to approximately 30-40% of the estimated tensile strength, then comes the unloading process. When tensile stress reduces to zero, the second cycle initiates and continuously increase to failure.

#### **4.1. Tensile strength $f_t$**

As illustrated in **Figure 8a**, concrete tensile strength is very low during the first 3 hours but accelerates quickly to several times larger in the next few hours. An obvious development trend is also observed, although slightly deviating from previous study for the same mix design (15) – This deviation is possibly due mainly to the different curing applied: While moisture loss from test specimens are minimized by effective covering in this study, such covering of specimens was not provided in (15).

Tensile strength and its development described are consistent with the hydration process: The dormant period with minimal hydration lasts for approximately 2-4 hours for normal concrete as used in this study. Following this dormant period, initial set commences (28, 29) and significant ongoing hydration results in rapid increase in tensile strength.

#### **4.2. Tensile strain capacity $\epsilon_{max}$**

Tensile strain capacity in early age concrete were reported to firstly decrease sharply over time, from thousands of micro-strain to possibly as low as tens of micro-strain (12, 30, 31), then gradually increases to a relatively stable value.

The tensile strain capacity derived from data obtained in this study, as in **Figure 8b**, appears to agree well with that from previous study for similar mix design (15).

#### **4.3. Young's modulus $E$**

In this study, due to the nature of early-age concrete, the range of stress in the ascending curve for linear fitting proposed is between 5%-20% of the ultimate stress instead of the widely instructed range 5%-40% in current standards (32). A narrower stress range ensures the linear elastic characteristics of concrete to be illustrated more effectively and reduces scattering in calculated results. Young's modulus increases quickly over time, from only about  $10^4$  kPa at 3hr age to  $(2.5-3.0) \times 10^4$  kPa at 8hr age (**Figure 8c**). The developing rate is much lower compared to that in (15) (**Figure 8d**), possibly due to (i) the lower tensile strength and (ii) more importantly, the more reliable measured strains in this study. Detailed analysis of displacement field recorded by DIC in this study indicates that the

correlation assumed in (15) between deformation over the region of interest and measured total deformation of the whole specimen may be inaccurate in many cases.

In **Figure 8h**, Young's moduli obtained from different loading stages in a cyclic series show some characteristics, including: (i) fast growing of modulus from (3-4) hour to 7 hour age and (ii) significant variation between the first and the second loading stages. For specimen at 3h15m age, Young's modulus in the second loading is approximately 30% higher, illustrating the sensitivity of very young concrete to early loading due to its visco-elastic nature.

#### **4.4. Fracture properties**

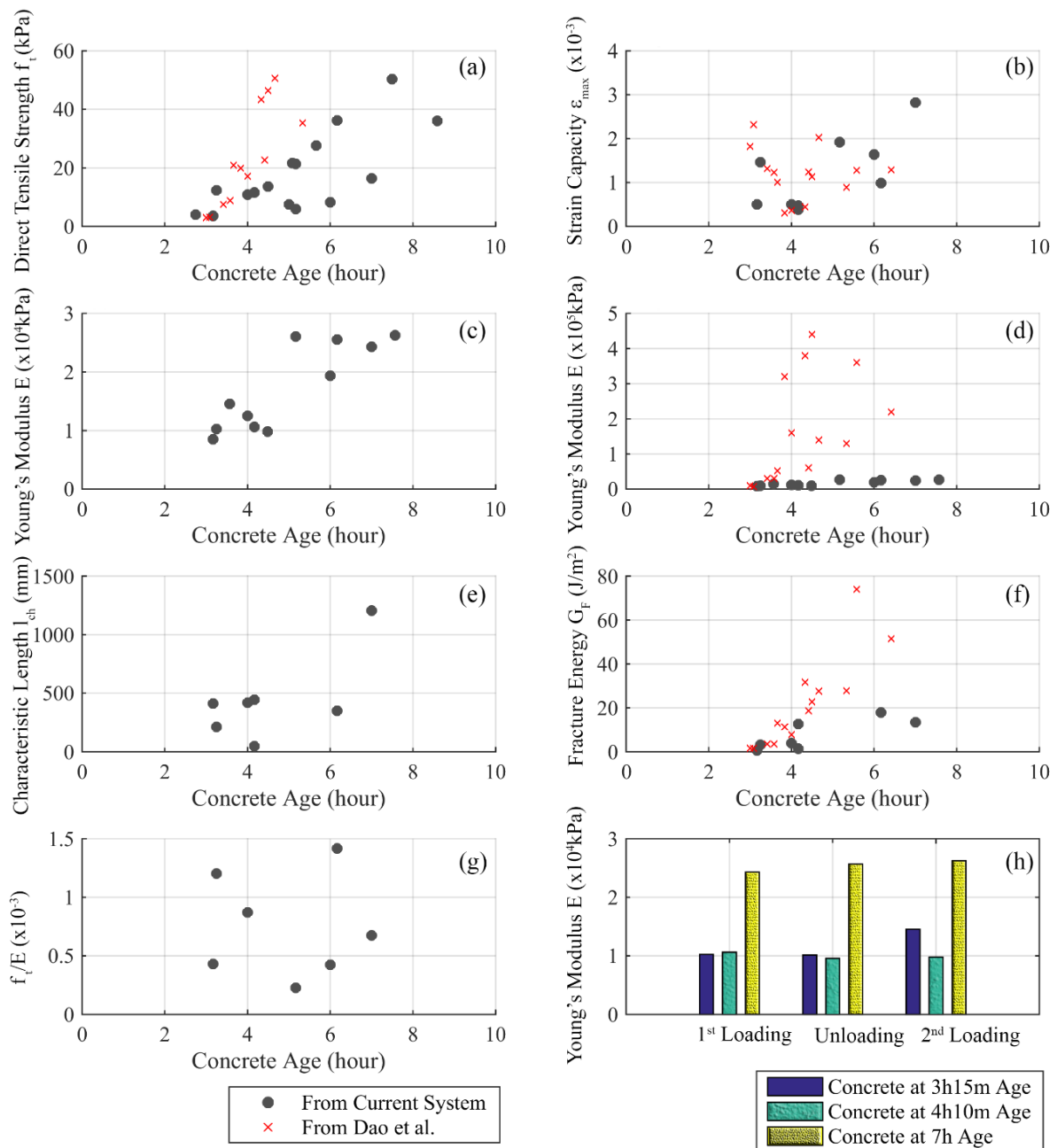
From obtained test data, stress-crack opening relationship can be extracted, from which fracture properties can be derived. Important fracture properties include  $G_F$  (**Figure 3**) and  $l_{ch}$ , which is given as:

$$l_{ch} = \frac{G_F E}{f_t^2} \quad (1)$$

**Figure 8f** provides fracture energy development over time. The increasing trend is generally observed, however the developing rate of fracture mechanics in this study is significantly lower compared to that in (15), similar to the case of Young's modulus. Again, this difference is possibly due mainly to the use of DIC for displacement measurement in this study: The displacement recorded by DIC is much smaller than that estimated in (15) from displacement measured by LVDTs attached on the steel mould. This clearly highlights the need to have an accurate and reliable system for displacement measurement – Further improvement is being underway at The University of Queensland to develop such system.

In **Figure 8e**, there seems to be an increasing trend of characteristic length  $l_{ch}$  over the first several hours. However further data are needed before development trends can be identified with confidence.





**Figure 8. Initial test results: (a) Tensile strength, (b) Tensile strain capacity, (c) to (d) Young's modulus from this study and from (15), (e) Characteristic length, (f) Fracture energy, (g) Tensile strength to Young's modulus ratio and (h) Young's modulus in cyclic loading series.**

## 5. Summary and Conclusions

This paper first provides a critical review of current knowledge of tensile properties of concrete during the first several hours after casting and of techniques for their measurement. The current dearth of useful data on tensile properties of very early-age concrete, despite their significance in assessing associated cracking risk, has been highlighted. This is argued as a result of the considerable practical problems to be overcome when testing very early-age concrete due to its weak nature.

On that basis, the paper outlines key features of an improved testing system that effectively addresses major drawbacks in current test setups. Notable features of this system include (i) an air-bearing box to float test specimen, thus effectively eliminating friction and (ii) the novel use of DIC for reliable, non-contact capturing of the required displacement fields. Finally, initial test results derived from the obtained full stress-strain curves of very young concrete are presented:

- The obtained stress-displacement/strain curves and development trend for different tensile properties are similar to those in previous research.
- However, displacements as directly measured by DIC in this study appear much smaller than those estimated from LVDTs readings in previous research. This has resulted in significantly smaller Young's modulus and fracture energy. The substantial variation also highlights the need for an accurate and reliable displacement measuring system. Further improvement is being underway at The University of Queensland to develop such system.

Importantly, the above-described improved system for direct tensile testing of very early-age concrete can now be used to obtain full stress-strain curves for various concrete mixtures typically used in practice. This will form a solid basis for more reliable assessment of cracking risk in concrete structures at early age, and thus more effective control of such cracking risk.

## References

1. Springenschmid, R., *"Thermal cracking in concrete at early ages"*, 1994, London: E & FN Spon.
2. Springenschmid, R., *"Prevention of thermal cracking in concrete at early ages"*, T.F. Routledge, Editor, 1998.
3. Wiss, J., Elstner Associates, Inc., *"On-call structural concrete bridge deck cracking investigation services, in WJE No. 2009.2643"*, 2011, Wiss, Janney, Elstner Associates, Inc.: Emeryville, California 94608.
4. Ba, H., A. Su, et al., *"Cracking tendency of restrained concrete at early ages"*, Journal of Wuhan University of Technology-Materials Science Edition, 04/2008, 23: p. 263 - 267.
5. Dux, P.F. and V.T.N. Dao, *"Early-age Cracking"*, 2012: Concrete Institute of Australia.
6. Byard, B.E., A.K. Schindler, et al., *"Cracking tendency of bridge deck concrete"*, Transportation Research Record, 2010(2164): p. 122-131.
7. British Standard, *"Eurocode 2: Design of concrete structures, in Part 1-1: General rules and rules for buildings"*, 2004, British Standard: UK. 230 p.
8. JSCE Concrete Committee, *"English version of standard specification for Concrete Structures - 2007, in Design"*, 2007, Japan Society of Civil Engineers: Japan. 503 p.
9. Kasai, Y., K. Yokoyama, et al., *"Tensile properties of early-age concrete, in Mechanical Behaviour of Materials - Proceedings of the International Conference on Mechanical Behaviour of Materials"*, 1972, The Society of Materials Science: Kyoto, Japan, p. 288-299.
10. Hannant, D.J., J. Branch, et al., *"Equipment for tensile testing of fresh concrete"*, Magazine of Concrete Research, 1999, 51(4): p. 263-267.
11. Dao, V.T.N., P.F. Dux, et al., *"Tensile properties of early-age concrete"*, ACI Materials Journal, 2009, 106(6): p. 1-10.
12. Kasai, Y., K. Yokoyama, et al., *"Tensile properties of early-age concrete"*, 1974: p. 433-441.
13. Roziere, E., R. Cortas, et al., *"Tensile behaviour of early age concrete: New methods of investigation"*, Cement and Concrete Composites, 2015, 55: p. 153-161.
14. Abel, J. and K. Hover, *"Effect of water/cement ratio on the early age tensile strength of concrete"*, Transportation Research Record: Journal of the Transportation Research Board, 1998, 1610(-1): p. 33-38.
15. Dao, V.T.N., P.F. Dux, et al., *"Tensile properties of early-age concrete"*, ACI Materials Journal, 2009, 106(6): p. 483-492.
16. Hannant, D.J., J. Branch, et al. *"Equipment for tensile testing of fresh concrete"*, Magazine of Concrete Research, 1999, 51, 263-267.
17. Branch, J., D.J. Hannant, et al. *"Factors affecting the plastic shrinkage cracking of high-strength concrete"*, Magazine of Concrete Research, 2002, 54, 347-354.
18. Nguyen, D. and V. Dao, *"A novel method for tensile testing of very early-age concrete, in The 23rd Australasian Conference on the Mechanics of Structures and Materials (ACMSM23)"*, S.T. Smith, Editor, 2014: Byron Bay, Australia. p. 47-52.
19. Sutton, M., *"Digital Image Correlation for Shape and Deformation Measurements, in Springer Handbook of Experimental Solid Mechanics"*, W.N. Sharpe, Jr. Editor, 2008, Springer US, p. 565-600.
20. Destrebecq, J.F., E. Toussaint, et al., *"Analysis of cracks and deformations in a full scale reinforced concrete beam using a digital image correlation technique"*, Experimental Mechanics, 2011, 51(6): p. 879-890.
21. Küntz, M., M. Jolin, et al., *"Digital image correlation analysis of crack behavior in a reinforced concrete beam during a load test"*, Canadian Journal of Civil Engineering, 2006, 33(11): p. 1418-1425.

22. Skarżyński, Ł., J. Kozicki, et al., "Application of DIC technique to concrete—study on objectivity of measured surface displacements", *Experimental Mechanics*, 2013, 53(9): p. 1545-1559.
23. Swaddiwudhipong, S., H.-R. Lu, et al., "Direct tension test and tensile strain capacity of concrete at early age", *Cement and Concrete Research*, 2003, 33(12): p. 2077-2084.
24. Jin, X. and Z. Li, "Investigation on mechanical properties of young concrete", *Materials and Structures*, 2000, 33(10): p. 627-633.
25. Yoshitake, I., W. Zhang, et al., "Uniaxial tensile strength and tensile Young's modulus of fly-ash concrete at early age", *Construction and Building Materials*, 2013, 40(0): p. 514-521.
26. Mimura, Y., I. Yoshitake, et al., "Uniaxial tension test of slender reinforced early age concrete members", *Materials*, 2011, 4(8): p. 1345-1359.
27. Hammer, T.A., K.T. Fosså, et al., "Cracking tendency of HSC: Tensile strength and self generated stress in the period of setting and early hardening", *Materials and Structures*, 2007, 40(3): p. 319-324.
28. Neville, A.M., "Properties of concrete", 1986, London: Longman Scientific & Technical.
29. Department of Transportation Federal Highway Administration (USA), "Integrated Materials and Construction Practices for Concrete Pavement: A State-of-the-Practice Manual", 2007, FHWA: USA.
30. Comite Euro-International du Beton, "Durable Concrete Structures", 1992, Telford: Great Britain.
31. Brameshuber, W. and H.K. Hilsdorf, "Development of Strength and Deformability of Very Young Concrete, in *Fracture of Concrete and Rock*", S. Shah and S. Swartz. Editors, 1989, Springer New York, p. 409-421.
32. Standards Australia, "Methods of testing concrete - AS1012.17, in *Method 17: Determination of the static chord modulus of elasticity and Poisson's ratio of concrete specimens*", 1997: Australia.
33. Tang, T., D.G. Zollinger, et al., "Fracture toughness of concrete at early ages", *Materials Journal*, 1993, 90(5): p. 463-471.

# Experimental study of creep and shrinkage in early-age concrete

Inamullah Khan<sup>1</sup>, Angus Murray<sup>2</sup>, Arnaud Castel<sup>3</sup> and Raymond Ian Gilbert<sup>4</sup>

<sup>1</sup> Research Associate, <sup>2</sup> PhD Student, <sup>3</sup> Associate Professor, <sup>4</sup> Emeritus Professor  
Centre for Infrastructure Engineering and Safety, School of Civil and Environmental Engineering,  
UNSW Australia, Sydney, NSW, Australia

**Abstract:** Early-age contraction of concrete may cause excessive cracking in restrained concrete structures within the first few days after casting. The magnitude and rate of development of early-age deformation of Australian concrete is often not known reliably and restraint to shrinkage is often poorly modelled in structural design. In order to accurately quantify the early-age deformational characteristics of concrete, including shrinkage and tensile creep, a comprehensive experimental program is being conducted at the Centre for Infrastructure Engineering and Safety at UNSW. Dog bone-shaped specimens were tested in portable creep rigs specially designed to test the specimens in direct tension. The specimens were loaded at the ages of 1, 2, 3, 5 and 7 days in order to measure the tensile creep coefficients at different loading ages. Shrinkage was also measured on accompanying specimens. The tests were performed under constant sustained tension. Autogenous shrinkage was measured on dog bone specimens. Compressive creep was also investigated for the same concrete mix. Comparisons of the creep coefficient versus time curves for tensile and compressive creep at different loading ages are presented in this paper. Tensile creep was found to be significantly larger than compressive creep for the same loading level.

**Keywords:** Compressive creep, cracking, early-age concrete, laboratory tests, shrinkage, tensile creep.

## 1. Introduction

Early age concrete is a continuously changing material due to the fact that it undergoes chemical and physical changes as soon as it interacts with the environment. It is also a highly variable material, with early-age deformational characteristics varying significantly from specimen to specimen. At early ages, concrete is prone to volumetric changes due to thermal and moisture related shrinkage. When there is restraint and concrete is prevented from shrinking freely, tensile stresses develop in the restrained concrete and, because of its low tensile strength, particularly at early ages, these stresses often exceed the tensile strength of concrete and cause cracking in the young concrete. Early age cracking of concrete is, and has always been, a concern for engineers.

All concrete structures are restrained to some extent, whether externally by the supports or by adjacent parts of the structure or internally by the embedded reinforcement. In a restrained concrete member, as the concrete shrinks, the tensile stress that develops in the concrete is relaxed by tensile creep. Early-age cracking in restrained concrete is therefore dependent on the tensile creep of concrete at early ages, as well as the magnitude of shrinkage, the development of the tensile strength of concrete with time and the degree of restraint. To predict early-age cracking, it is important to accurately quantify the early-age tensile creep and shrinkage of concrete.

Despite its importance for the assessment of cracking, the tensile creep characteristics of concrete are rarely measured and even more rarely considered in structural design. Traditional focus has been on measuring and predicting the creep of concrete in compression and assuming that the creep behaviour in tension is similar to that in compression. In the literature, there is limited information on the tensile creep of concrete loaded in direct tension at early ages. Accurate measurements of tensile creep are difficult to obtain. Because of the necessarily low stress levels, the tensile strains to be measured in a tensile creep test are small. When the concrete is also shrinking, the specimen in direct tension may actually be shortening and the measured strains will be compressive. Even in specimens where drying is prevented, autogenous shrinkage will be taking place in the first few days and weeks after casting rendering the measurement of tensile creep problematic. The large variability of shrinkage and creep from specimen to specimen in concrete at early ages further complicates the issue. Because of these difficulties, some researchers (1-4) have used uniaxially restrained shrinkage test to indirectly measure the tensile creep characteristics of concrete. Relatively few experimental programs (5-7) have been conducted where tensile creep was measured in direct tension tests. In this paper, an experimental program to measure early-age tensile creep using uniaxial direct tensile loading tests is described. In order to examine the effect of the age at loading on tensile creep, tests are conducted on specimens loaded at different ages under similar environmental conditions and with the same stress-strength level. Early-age compressive creep on specimens loaded at the same ages

as the tensile specimens has also been measured and the results are compared with early age tensile creep measurements.

## 2. Experimental program

A series of tensile creep tests has been undertaken as part of a more comprehensive experimental program carried out at the Centre for Infrastructure Engineering and Safety (CIES) at UNSW Australia. The aim is to calibrate and quantify the early age deformational characteristics of Australian concrete. In this paper, the effect of loading age on early age tensile creep is investigated and comparisons are made between tensile creep and compressive creep. All tests are to be performed on one type concrete – a 32 MPa normal class concrete (GP cement and w/c = 0.55). Further testing is currently underway to determine the effects of varying the type of cement, the type and grade of aggregate and the water cement ratio. As the main objective of the research program is to better characterise and evaluate the potential cracking of on-site concrete at early-ages in restrained shrinkage conditions, creep and shrinkage tests were conducted under ambient conditions. The relative humidity varied between 55-70% and the temperature varied from 15°C to 22°C (day and night temperature). Comparisons are made between results for tests performed simultaneously.

### 2.1 Concrete mix

In the first stage, a normal concrete mix was selected and a sufficient number of cylinders and prisms were cast and tested to determine evolution of compressive strength, tensile strength and elastic modulus at the age of 0.75, 1, 2, 3, 7 and 28 days. For each material test, three specimens were tested in order to assess the statistical variation and this practice was repeated for each batch. Table 1 shows the mix design selected for this experimental program.

**Table 1. Mixture proportions of concrete (kg/m<sup>3</sup>)**

Components	GP Cement	Sand	Gravel (10mm Basalt)	Water
Mass	380	545	1265	210

After selecting the desired concrete mix, cylinders and prisms were subjected to compressive, indirect tensile or Brazilian and flexure tests according to Australian Standards to study the strength evolution in concrete. The evolution of concrete mechanical properties is presented in Table 2. Specimens were cured in laboratory ambient conditions after demoulding because all the creep tests were also performed inside the laboratory under similar environmental conditions. For each concrete batch, compressive strength, elastic modulus, indirect tensile strength and modulus of rupture were measured. The statistical variation of mechanical characteristics of concrete for all the batches was less than 10%.

**Table 2. Mechanical characteristics of concrete**

Age (days)	Compressive strength (MPa)	Modulus of rupture (MPa)	Indirect tensile strength (MPa)	Elastic modulus (GPa)
0.75	13.18	2.57	1.20	18.35
1	15.28	3.11	1.40	20.35
2	21.55	3.785	2.10	22.05
3	24.64	4.03	2.54	22.7
7	32	4.56	2.94	27.78
28	37	4.84	3.47	28.58

## 2.2 Creep tests

### 2.2.1 Tensile creep

In order to measure tensile creep, a creep rig specifically designed for this project was used to test dog bone specimens loaded in direct tension. The sustained stress is applied to each creep specimen by a simple lever arm arrangement using dead weights. The dimensions of the dog bone specimens were 200 x 300 x 35 mm and are shown in Figure 1.

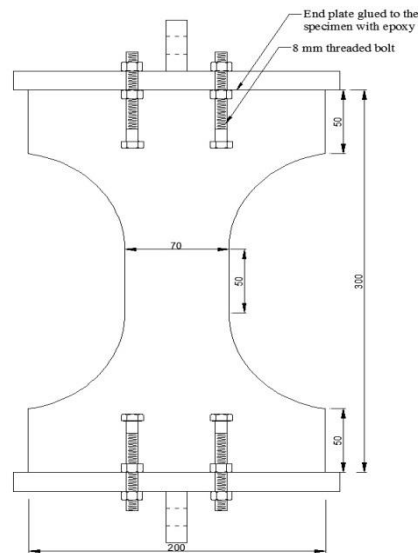


Figure 1. Dog bone specimen

The dog bone specimens are fixed into the creep rig by means of two steel plates glued to each end of the specimen with high strength epoxy. Two threaded bolts are also cast in the specimen and are further connected to the steel plates at each end as shown. The purpose of gluing steel plate to the specimen is to ensure an even stress distribution from the applied tensile load. Strains are measured using strain gauges attached to each 35 mm thick face of the dog bone specimen at the centre position at mid-height where the width of the specimen is 70 mm. The strains are recorded at regular intervals with a data acquisition system.

Creep rigs were installed in the laboratory and tests were performed under ambient conditions. A total of 12 creep rigs were constructed on two platforms with each platform able to test six specimens simultaneously, as shown in the Figure 2. As early-age creep was of interest, the tensile creep tests were performed over a two to three week period. All specimens were loaded to the same stress level, namely 50% of the tensile strength of the concrete measured at an age of 2 days. To examine the effect of age at first loading, specimens were loaded at an age of either 1, 2, 3, 5 or 7 days.

The load was transferred to the specimens by lever arms with the help of high strength steel chains in order to induce a purely uniaxial force and to avoid any bending of the specimen. With the lever arm ratio of 5 to 1, a steel block of 50 kg mass imparted a maximum uniform stress of 1 MPa across the 70 mm by 35 mm section at the mid-height of the specimen, representing 50% of the tensile strength of concrete at the age of 2 days. S-type load cells were used to check the applied load in each individual test rig.

### 2.2.2 Compressive creep

Compressive creep was measured in standard creep rigs in accordance with Australian Standard AS 1012.16 AS 1012.16-1996 (R2014) : "Methods of testing concrete - Determination of creep of concrete cylinders in compression. Concrete cylinders of 100 mm diameter and 200 mm height were loaded in the creep rig. A total of three specimens were stacked in the creep rig for simultaneous loading. Longitudinal strains were measured using a 100 mm Demec gauge. On each specimen, a total of three Demec targets were attached at the mid-height of each cylinder and evenly spaced around the circumference at 120 degrees. Two cylinders were kept in the same environmental conditions to serve as companion specimens to measure the free shrinkage strain.



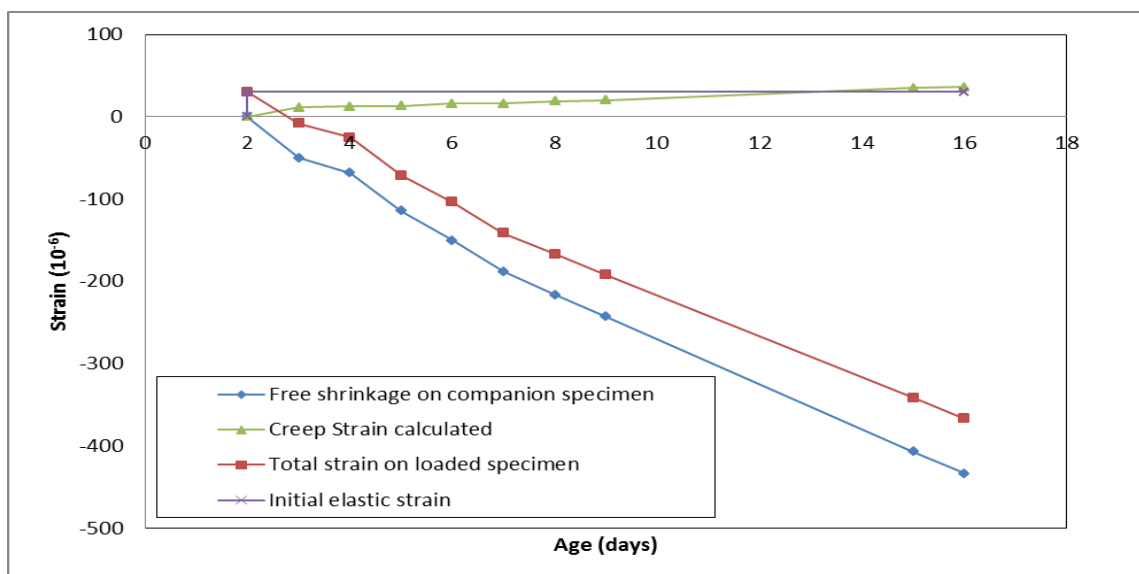
**Figure 2. Tensile creep rigs**

All specimens were covered with wet burlap and polyethylene during a 24-hour period after casting. They were then removed from their moulds and left in laboratory ambient conditions. The compressive creep tests were run over a period of 18 to 20 days.

Compressive creep was also measured on unsealed cylindrical specimens loaded at either 1, 2, 3, 5 or 7 days and a comparison was made between tensile creep and compressive creep for the same concrete mix, loaded at similar stress level and at the same age.

### 3. Experimental results and discussion

Tensile creep was calculated by subtracting the initial elastic strain and the shrinkage strain (measured on an identical companion specimen) from the total strain recorded on each loaded specimen. Creep coefficients were calculated by dividing the creep strain by the initial elastic strain. Due to the fact that the initial stress applied to the concrete specimens (50% of the tensile strength) is low, the initial elastic strain was small. As the shrinkage strain was predominant, the total strains recorded on the loaded specimens changed from positive to negative in less than a day. Figure 3 shows a comparison between the development of total strain recorded on the specimens loaded at an age of 2 days and the shrinkage strain recorded on the companion specimens. Also shown are the initial elastic strain and the calculated tensile creep strain. The curves are the average of the responses all three specimens loaded at age 2 days.



**Figure 3. Development of strains in the specimens**

### 3.1 Effect of loading age on tensile creep

Figure 4 shows the tensile creep coefficients measured at different loading ages. As expected, the specimens loaded at day 1 had the highest creep coefficient, reaching a value of 1.9 after 21 days of loading. For a loading period of 15 days, the creep coefficient of specimens loaded at the age of 1 day was 1.85 (i.e. at age 16 days), while for the specimens loaded at the age of 7 days the creep coefficient after 15 days under load (i.e. at age 22 days) was 0.51. Clearly, the age at first loading has a very significant effect on early-age tensile creep, particularly for concrete loaded in the first one or two days. This is the case for many concrete structures, where tensile stresses begin to develop due to restrained shrinkage soon after the concrete sets.

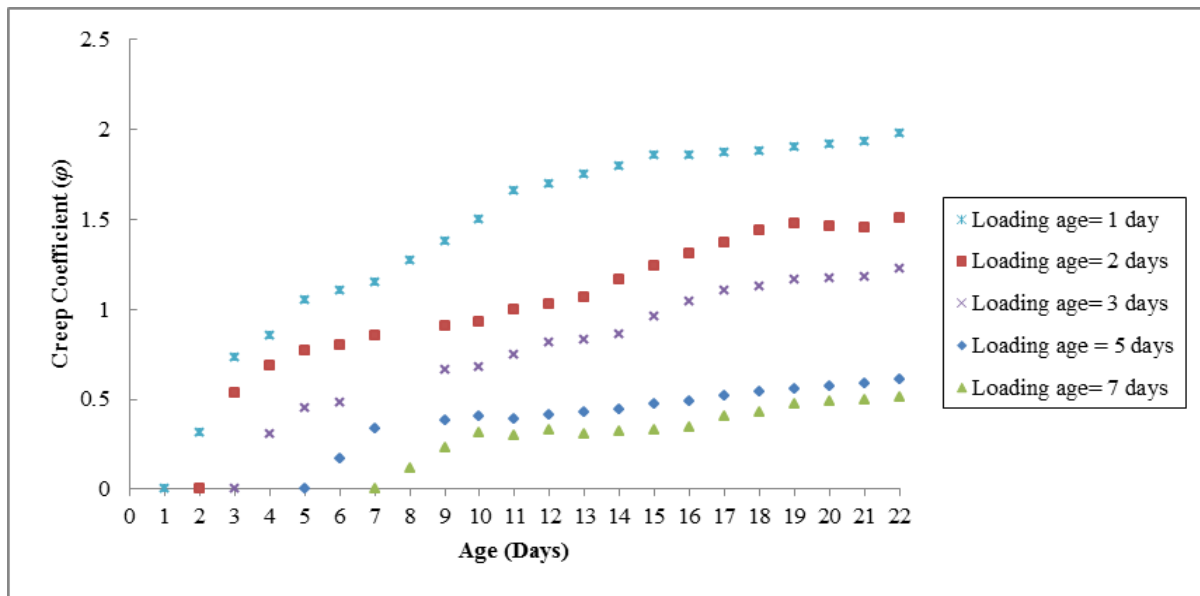


Figure 4. Creep coefficients at different loading ages

The specific creep  $C$  is defined as creep strain  $\varepsilon_{cc}$  per unit stress. For a specimen subjected to a constant stress  $\sigma_0$ :

$$C = \frac{\varepsilon_{cc}}{\sigma_0} \quad (1)$$

Figure 5 shows the specific tensile creep versus time after loading. A relatively high creep response is observed when concrete is loaded at either 24 hrs or 48 hrs after casting and a significantly stiffer response is observed when the concrete is a few days older when loaded. These observations are in accordance with earlier findings of Østegaard et al. (2).

### 3.2 Comparison of compressive creep and tensile creep

Figure 6 shows a typical comparison between the compressive creep coefficients and tensile creep coefficients for similar test conditions and the same age at first loading.

Early age tensile creep is more prominent than early age compressive creep for same the concrete mix under similar loading conditions. These results are contradictory to earlier findings by Briffault et al. (7) and Rossi et al. (5). Briffault et al. found similar basic creep behaviour for normal concrete under compression and tension when specimens were loaded at the age of 5 days. Rossi et al. found that basic compressive creep was significantly greater than basic tensile creep while compressive creep and tensile creep under drying conditions were equivalent when specimens were loaded at 64 days.



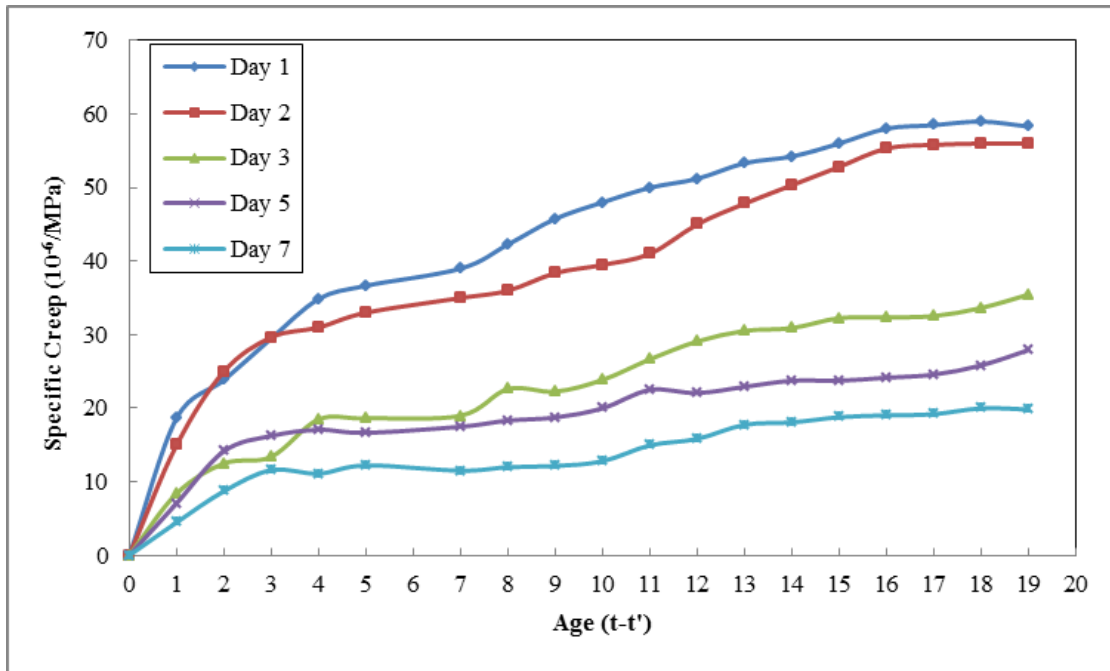


Figure 5. Specific Creep at different loading ages

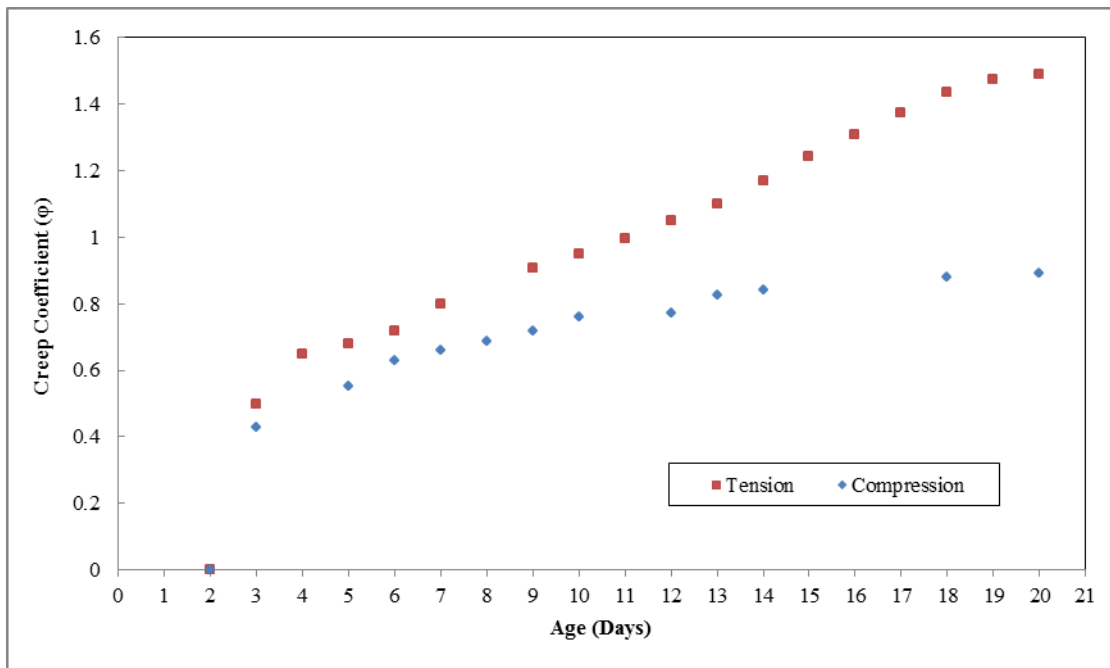


Figure 6. Compressive and tensile creep coefficient

### 3.3 Autogenous and total shrinkage

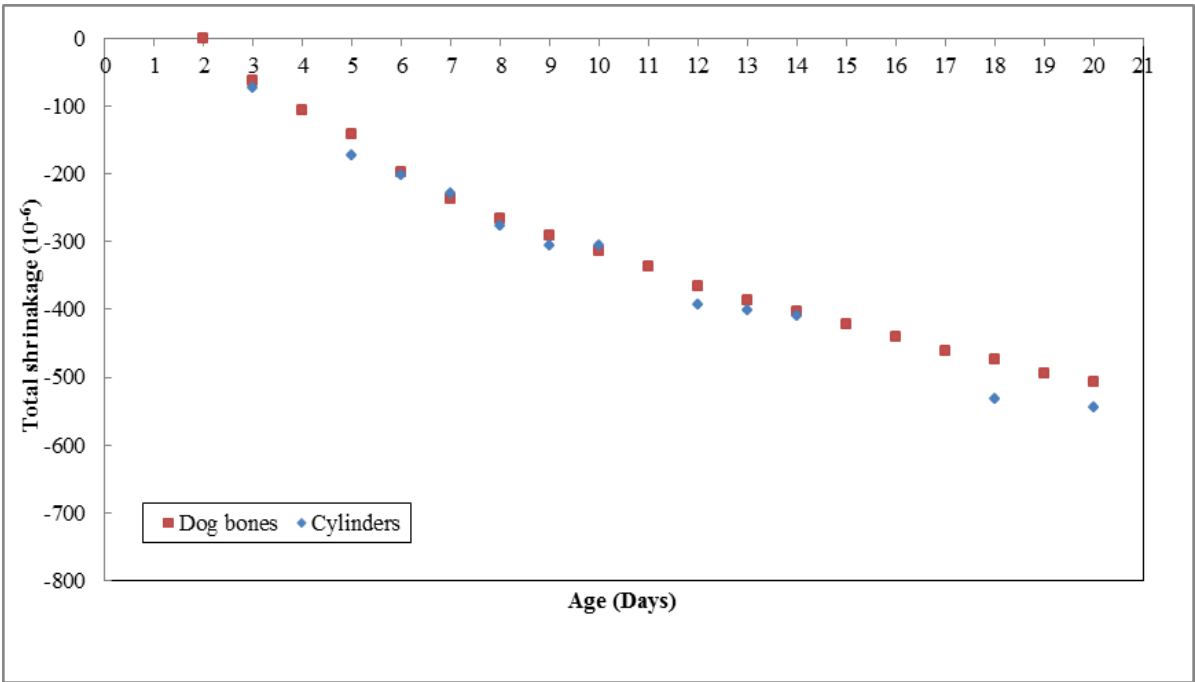
In order to draw comparisons between the total shrinkage strains measured on both types of specimens, i.e. the dog bones and cylinders, the hypothetical thicknesses  $t_h$  as defined in AS3600-2009 (10) have been calculated for both specimens as follows:

$$t_h = \frac{2A}{u} \quad (2)$$

where  $A$  is the cross-sectional area of the specimen and  $u$  is the perimeter of the specimen exposed to the atmosphere. Excellent agreement between the total shrinkage strains measured on the dog

bones and those measured on the cylinders is obtained if the cylinder strains are modified using Eq. (3). This comparison is shown in Figure 7.

$$(\epsilon_{cs})_{\text{dogbone}} = \frac{(t_h)_{\text{cylinder}}}{(t_h)_{\text{dogbone}}} * (\epsilon_{cs})_{\text{cylinder}} \tag{3}$$



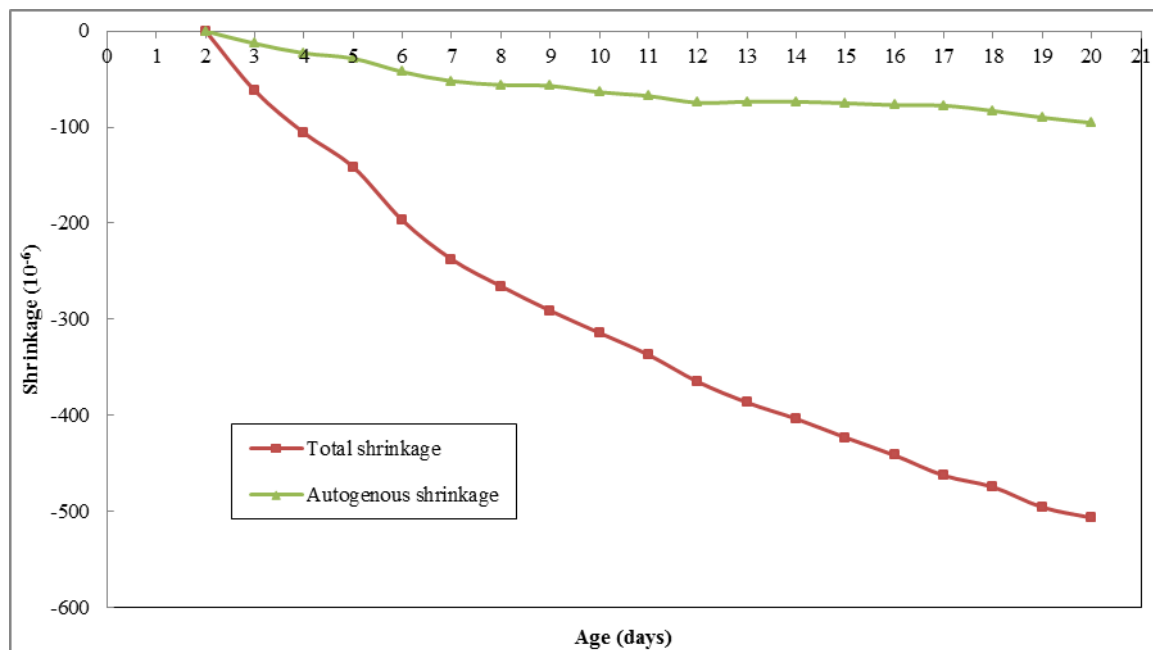
**Figure 7. Total shrinkage strains in dog bones and cylindrical specimens**

Autogenous shrinkage was measured on the dog bone specimens only. Autogenous shrinkage is a volume change resulting from chemical reactions in the concrete and is not associated with drying. Autogenous shrinkage is measured on specimens where there is no moisture transfer to the surrounding environment. The autogenous shrinkage specimens were wrapped in self-adhesive aluminium foil soon after demoulding, as shown in Figure 8.



**Figure 8 Specimen wrapped in self-adhesive foil to eliminate drying.**

Figure 9 shows the total shrinkage and autogenous shrinkage strain versus time curves measured on the dog bone specimens. After 20 days of exposure to laboratory ambient conditions, the contribution of the autogenous shrinkage to the total shrinkage was 19% for a concrete mix of w/c ratio 0.55. This is consistent with Tazawa & Miyazawa (9) who found that for w/c ratios of 0.40, 0.23 and 0.17, the autogenous shrinkage was 40%, 80% and 100% of the total shrinkage.



**Figure 9. Total shrinkage and autogenous shrinkage**

#### 4. Conclusions

An experiment program has been carried out to quantify early age tensile creep of OPC concrete with a water-cement ratio of 0.55 and to examine the effects of age at first loading. It was found that early age tensile creep is strongly affected by the loading age, with tensile creep decreasing as the age at first loading increases. Early-age tensile creep was found to be significantly greater than early age compressive creep.

These experiments are part of a major research program to quantify the early age properties of concrete. These results, together with the results of future experiments, will be used to accurately model the early-age cracking of concrete.

#### Acknowledgement

This research was supported by the Australian Research Council's Discovery Project funding scheme (project number DP130102966).

#### 5. References

1. Kovler K. "Testing system for determining the mechanical behavior of early age concrete under restrained and free uniaxial shrinkage." *Materials and Structures*, 1994, 27, No. 170, 324–330.
2. Lennart Østergaarda, David A. Langeb, Salah A. Altoubatb, Henrik Stanga "Tensile basic creep of early-age concrete under constant load." *Cement and Concrete Research* 31 (2001) 1895 – 1899
3. T. Aly and J. G. Sanjayan, "Shrinkage cracking properties of slag concretes with one-day curing", *Magazine of Concrete Research*, 2008, 60, No. 1, 41–48.

4. Ya Wei and Will Hansen. "Tensile Creep Behavior of Concrete Subject to Constant Restraint at Very Early Ages." *Journal of Materials in Civil Engineering*, 2013, 25(9): 1277-1284.
5. Pierre Rossi, Jean-Louis Tailhan, Fabrice Le Maou (2013). "Comparison of concrete creep in tension and in compression: Influence of concrete age at loading and drying conditions." *Cement and Concrete Research* 51: 78-84.
6. G. M. Ji, T. Kanstad ,Ø. Bjøntegaard , E. J. Sellevold, "Tensile and compressive creep deformations of hardening concrete containing mineral additives", *Materials and Structures* (2013) 46:1167–1182
7. Matthieu Briffaut, Farid Benboudjemab, Jean-Michel Torrentic, Georges Nahas. "Concrete early age basic creep: Experiments and test of rheological modelling approaches." *Construction and Building Materials*, 2012, 36: 373-380.
8. AS 1012.16-1996 (R2014) : "Methods of testing concrete - Determination of creep of concrete cylinders in compression", Standards Australia, 2014.
9. Tazawa, E. and Miyazawa, S., "Experimental Study on Mechanisms of Autogenous Shrinkage of Concrete," *Cement and Concrete Research*, 1995b Vol. 25, No. 8, 1633 - 1638.
10. AS3600-2009, "Australian Standard for Concrete Structures", Standards Australia, 2009.

# Self-Compacting Concrete

# The Combined Influence of Paste Volume and Volumetric Water-to-Powder Ratio on Robustness of Fresh Self-Compacting Concrete

Farid Van Der Vurst<sup>1</sup>, Steffen Grünewald<sup>2</sup>, Dimitri Feys<sup>3</sup> and Geert De Schutter<sup>4</sup>

<sup>1</sup>Ph.D. student, Ghent University

<sup>2</sup>Postdoctoral researcher, Ghent University and Delft University of Technology

<sup>3</sup>Assistant Professor Materials Engineering, Missouri University of Science and Technology

<sup>4</sup>Full Professor Concrete Technology, Ghent University

**Abstract:** In order to avoid durability problems caused by an inadequate consolidation of concrete, self-compacting concrete (SCC) has been developed. The mix design of SCC aims at balancing a minimum flowability allowing air bubbles to escape and a maximum flowability in order to avoid segregation. Because of the higher demands on mix design and additional requirements related to casting, SCC mixtures are in general more sensitive to small variations in its mix composition compared to conventional vibrated concrete. Besides improving the robustness of SCC with admixtures like Viscosity-Modifying Agents (VMAs), it is also important to find out why certain mixtures are more robust than others. This paper investigates the influence of the paste volume and the water-to-powder ratio (volumetric) on the robustness of fresh SCC mixtures. Nine SCC mixtures with a paste volume of 350, 375, and 400 l/m<sup>3</sup> and a volumetric water-to-powder ratio of 0.75, 0.90, and 1.05 were subjected to a variation of  $\pm 8$  l/m<sup>3</sup> water. The robustness of the produced mixtures was quantified measuring the slump flow, V-funnel time, L-box ratio, and sieve stability.

**Keywords:** Robustness, Self-Compacting Concrete, Rheology, Paste Volume, Water-to-Powder ratio

## 1. Introduction

### 1.1. Self-compacting concrete

After investigating many durability problems of post-war Japanese concrete structures, Okamura and his team found that a majority of problems originated in a poor consolidation of concrete during the casting process. As a solution to avoid similar problems, a new type of concrete was developed for which external vibration was no longer needed to assure a good compactation: self-compacting concrete (SCC) [1, 2]. In order to combine sufficient fluidity – allowing air-bubbles to escape and complete formwork filling – and sufficient stability to avoid segregation, the high fluidity concrete contains higher powder content compared to conventional vibrated concrete, superplasticizer(s), and sometimes a viscosity-modifying admixture (VMA). However, because the target range for sufficient fluidity, sufficient segregation resistance, and to avoid an excessive stickiness is much smaller than the optimum range of conventional vibrated concrete, self-compacting mixtures are generally more sensitive to small variations in the mix proportions, materials properties, and casting circumstances.

To counter this larger sensitivity to small variations, also referred to as reduced robustness, a more severe quality control and better trained workers are needed. The use of SCC is nowadays still limited to cases where all conditions are well-controlled and situations in which an external compaction would cause great difficulties. To facilitate the use of SCC in general and especially for applications with specific requirements for fresh concrete, it is necessary to investigate the origin of the robustness of concrete.

### 1.2. The origin of the robustness

Although many parameters such as material characteristics [3-11], temperature [12-14], and shear history [15-18] affect the fresh behaviour of self-compacting concrete, most robustness studies focus on the influence of small changes in the material proportions [11, 19-42]. Of all changes in material proportions, inaccuracies in the water amount are responsible for the largest variations of the fresh behaviour of SCC [43, 44]. Therefore, many studies on the robustness of fresh SCC focus on the influence of small variations of the water content ( $\pm 5$  to 10 l/m<sup>3</sup>). According to these publications, the sensitivity to small variations of the water content decreases as:

- A surplus of fine aggregates is included in the aggregates grading curve, preventing the coarse aggregates from becoming dominant [19-21, 45].
- The powder content increases [20, 21, 23].
- Part of the cement is substituted by silica fume or fly ash [22, 24].
- A VMA is added to the mixture [20, 28-39, 46].
- Certain types of superplasticizers are used [25-27].
- Opposing conclusions are drawn about the influence of the water-to-cement and water-to-powder ratio [19, 38]

The mechanisms and combination of influences of the powder content, the water-to-powder ratio, mineral additions and admixtures on the robustness are still unknown. Some authors indicate the importance of the paste volume, the paste density, and the paste viscosity [20, 21, 23], while others focus on the excess water in the concrete mix design [38] or make a link between the thixotropy and robustness [47, 48]. This paper attempts to determine the causes behind the influence of paste volume and volumetric water-to-powder ratio on the robustness of SCC.

## 2. Experimental work

### 2.1. Materials and mixing sequence

All mixtures are made with the same raw materials: Rhine sand 0/5, river gravel 2/8 and 8/16 (with a density of respectively 2630 kg/m<sup>3</sup>, 2670 kg/m<sup>3</sup>, and 2660 kg/m<sup>3</sup>), Portland cement CEM I 52.5 N (with a density of 3126 kg/m<sup>3</sup> and a Blaine fineness of 370 m<sup>2</sup>/kg), limestone filler (with a density of 2685 kg/m<sup>3</sup> and a specific surface area of 424 m<sup>2</sup>/kg, based on the particle size distribution), and a PCE superplasticiser with a solid content of 35%. The grading curve of the aggregates is illustrated in

Figure 1 and the chemical composition of the cement as determined by an XRF analysis is given in Table 1. After premixing the cement, filler, and dry aggregates for one minute in a planetary pan mixer, water was added to the mixer and mixing continued for another minute. Finally, the superplasticizer was added and the concrete was mixed for two more minutes.

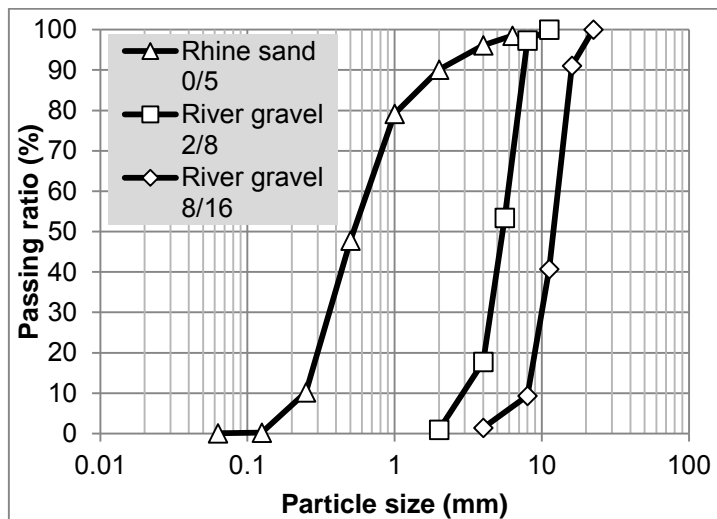


Figure 1. Grading curve of the aggregates

Table 1. Chemical composition of the cement

	Cement [%]
CaO	62.30
SiO <sub>2</sub>	18.77
Al <sub>2</sub> O <sub>3</sub>	6.00
Fe <sub>2</sub> O <sub>3</sub>	4.06
MgO	1.07
K <sub>2</sub> O	0.58
Na <sub>2</sub> O	0.51
CO <sub>2</sub>	0.60
SO <sub>3</sub>	3.35
Cl <sup>2-</sup>	0.067
L.O.I.	1.82
Insoluble rest	0.41

### 2.2. Mixture compositions

The robustness of nine SCC mixtures was determined by measuring the slump flow, V-funnel time, L-box ratio, sieve stability, air content and density of the mixtures subjected to a variation of  $\pm 8$  l/m<sup>3</sup> water. The mixtures, given in Table 2, have different paste volumes (350, 375, and 400 l/m<sup>3</sup>) and volumetric water-to-powder ratios (0.75, 0.90, and 1.05), keeping the water-to-cement ratio constant. These paste volumes and volumetric water-to-powder ratio's correspond with the 20%, 50%, and 80% fractals of a database summarizing the properties of SCC mixes used in more than 175 papers [49,

50]. The superplasticizer dosage was always determined such that the Sieve Stability Index (S.S.I., tested according to EN 12350-11) of the reference mixture is between 8 and 12%.

**Table 2: Mix proportions of reference SCC mixes**

Paste volume / water-to-powder ratio (by volume) [l/m <sup>3</sup> ] / [-]	Sand 0/5 [kg/m <sup>3</sup> ]	Gravel 2/8 [kg/m <sup>3</sup> ]	Gravel 8/16 [kg/m <sup>3</sup> ]	Cement I 52 N [kg/m <sup>3</sup> ]	Limestone filler [kg/m <sup>3</sup> ]	Water [kg/m <sup>3</sup> ]	SP dosage [l/m <sup>3</sup> ]
400 / 0.75	800	279	459	312	346	171	3.31
400 / 0.90	800	279	459	344	269	189	2.50
400 / 1.05	800	279	459	373	204	205	1.95
375 / 0.75	835	291	478	292	324	161	3.95
375 / 0.90	835	291	478	323	252	178	2.80
375 / 1.05	835	291	478	349	191	192	2.00
350 / 0.75	869	303	498	273	302	150	5.31
350 / 0.90	869	303	498	301	236	166	3.63
350 / 1.05	869	303	498	326	178	179	2.38

### 3. Experimental results

Table 3 and Table 4 summarize the fresh properties of the nine reference mixtures. In Table 4, for each workability test, the values for the reference mixtures are listed together with the change of the test response per liter water of the parameter (eg.  $\Delta SF / 16 \text{ l/m}^3$ ) and the ratio of the interval divided by the mean value (eg.  $\Delta SF / SF_{ref}$ ). All workability tests except the L-box ratio gave a good picture of the impact of fluctuations of the water content on the fresh behaviour of the mixtures.

**Table 3: Fresh state properties of nine reference SCC mixes**

Paste volume / water-to-powder ratio [l/m <sup>3</sup> ] / [-]	Slump flow [mm]	V-funnel time [s]	L-box ratio [-]	S.S.I. [%]	Density [kg/m <sup>3</sup> ]	Air content [%]
400 / 0.75	673	13.7	0.82	9.4	2475	2.5
400 / 0.90	680	6.3	0.85	12.2	2369	1.6
400 / 1.05	688	3.5	0.83	12.0	2369	1.2
375 / 0.75	705	17.6	0.96	11.2	2394	1.9
375 / 0.90	680	8.0	0.91	10.1	2375	1.8
375 / 1.05	680	4.0	0.86	12.3	2372	1.4
350 / 0.75	865	15.9	1.00	10.5	2406	0.9
350 / 0.90	750	10.5	0.98	9.4	2375	1.5
350 / 1.05	675	5.3	0.80	8.0	2369	1.5

**Table 4: The robustness of nine SCC mixes**

	400 / 0.75	400 / 0.90	400 / 1.05	375 / 0.75	375 / 0.90	375 / 1.05	350 / 0.75	350 / 0.90	350 / 1.05
<b>Slump flow [mm]</b>	<b>673</b>	<b>680</b>	<b>688</b>	<b>705</b>	<b>680</b>	<b>680</b>	<b>865</b>	<b>750</b>	<b>675</b>
$\Delta SF$	260	163	210	155	138	133	90	130	148
$\Delta SF / 16 \text{ l/m}^3$	16.3	10.2	13.1	9.7	8.6	8.3	5.6	8.1	9.2
$\Delta SF / SF_{ref}$	0.39	0.24	0.31	0.22	0.20	0.19	0.10	0.17	0.22
<b>V-funnel time [s]</b>	<b>13.7</b>	<b>6.3</b>	<b>3.5</b>	<b>17.6</b>	<b>8.0</b>	<b>4.0</b>	<b>15.9</b>	<b>10.5</b>	<b>5.3</b>
$\Delta VF$	11.4	3.8	3.8	18.4	5.4	2.2	21.8	5.4	2.8
$\Delta VF / 16 \text{ l/m}^3$	0.71	0.24	0.24	1.15	0.34	0.14	1.36	0.34	0.18
$\Delta VF / VF_{ref}$	0.83	0.60	1.07	1.04	0.68	0.56	1.37	0.51	0.53
<b>L-box ratio [-]</b>	<b>0.82</b>	<b>0.85</b>	<b>0.83</b>	<b>0.96</b>	<b>0.91</b>	<b>0.86</b>	<b>1.00</b>	<b>0.98</b>	<b>0.8</b>
$\Delta LB$	0.78	0.19	0.35	0.06	0.27	0.15	0.02	0.02	0.19
$\Delta LB / 16 \text{ l/m}^3$	0.049	0.012	0.022	0.004	0.017	0.009	0.001	0.002	0.012
$\Delta LB / LB_{ref}$	0.95	0.22	0.41	0.06	0.29	0.17	0.02	0.02	0.23
<b>S.S.I. [%]</b>	<b>9.4</b>	<b>12.2</b>	<b>12.0</b>	<b>11.2</b>	<b>10.1</b>	<b>12.3</b>	<b>10.5</b>	<b>9.4</b>	<b>8.0</b>
$\Delta SSI$	16.7	8.1	12.9	13.8	8.0	8.4	9.1	4.5	5.0
$\Delta SSI / 16 \text{ l/m}^3$	1.04	0.51	0.80	0.86	0.50	0.52	0.57	0.28	0.31



### 3.1. Variations of the slump flow

Because the superplasticizer dosage was always adjusted in order to have a S.S.I. of  $10\% \pm 2\%$ , the slump flow of the nine mixtures is not related to their paste volume or water-to-powder ratio (Table 3). However, as shown in Table 4 and Figure 2, the sensitivity of the slump flow to changes in the water content depends on the paste volume: the robustness of the flow decreases as the paste volume increases. Table 4 shows that the water-to-powder ratio of the mixtures has no clear influence on the robustness of the slump flow.

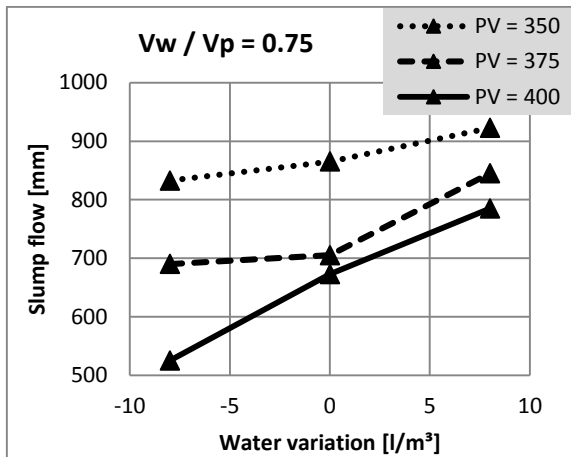


Figure 2a: Influence of the paste volume on the slump flow

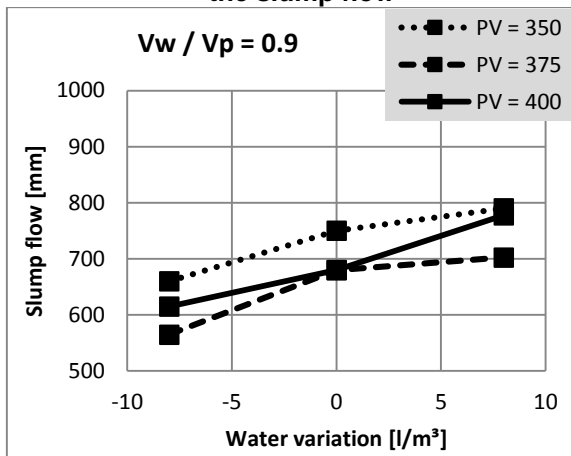


Figure 2b: Influence of the paste volume on the slump flow

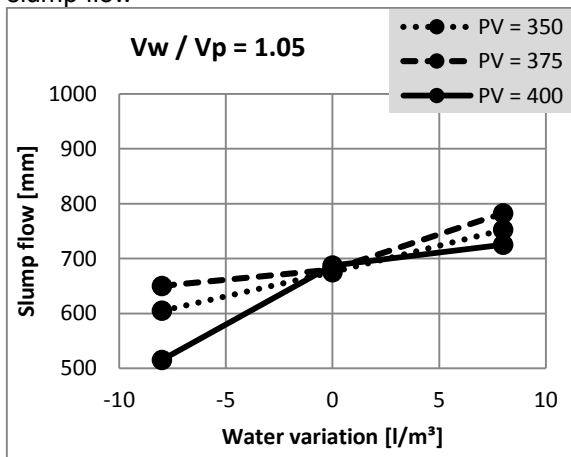


Figure 2c: Influence of the paste volume on

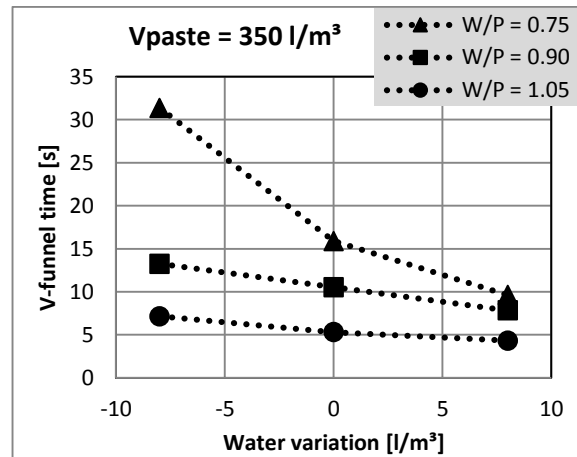


Figure 3a: Influence of the volumetric water-to-powder ratio on the V-funnel time

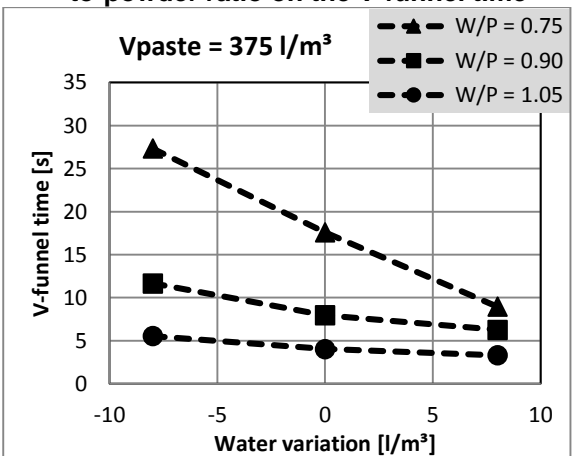


Figure 3b: Influence of the volumetric water-to-powder ratio on the V-funnel time

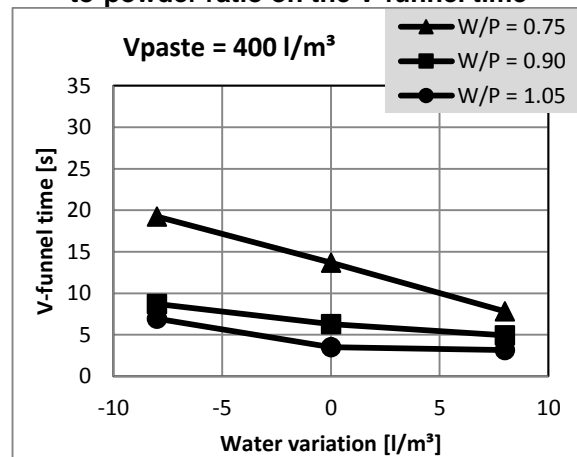


Figure 3c: Influence of the volumetric water-

**3.2. Variations of the V-funnel time**

When the paste volume increases, the V-funnel time of the mixtures decreases slightly (about 3 sec difference between 350 and 400 l/m<sup>3</sup> for the same water-to-powder ratio); the sensitivity of the V-funnel time to variations in the water content also seems to be independent of the paste volume of the mixture. Mixtures with a higher water-to-powder ratio have a significant lower V-funnel time than mixtures with a lower water-to-powder ratio (see Tables 3 and 4). Especially, mixtures with a water-to-powder ratio of 0.75 are very sensitive to a decrease in the water content, making them very sticky and not easy to process. The robustness determined by changes in the V-funnel time therefore increases when the water-to-powder ratio increases (Figure 3).

**3.3. Variations of the L-box ratio**

Table 4 reveals no clear influence of the test responses on the L-box ratio results. The results are also difficult to interpret because of the poor flowability of the mixtures with 8 l/m<sup>3</sup> less water, a paste volume of 400 l/m<sup>3</sup> and volumetric water-to-powder ratios of 0.75 and 1.00, which have a slump flow of respectively 525 and 515 mm.

**3.4. Variations of the sieve stability**

As shown in Table 4 and Figure 4, an increase in the paste volume increases the sensitivity of the S.S.I. to variations in the water content. The paste volume has a larger effect than changes in the water-to-powder ratio.

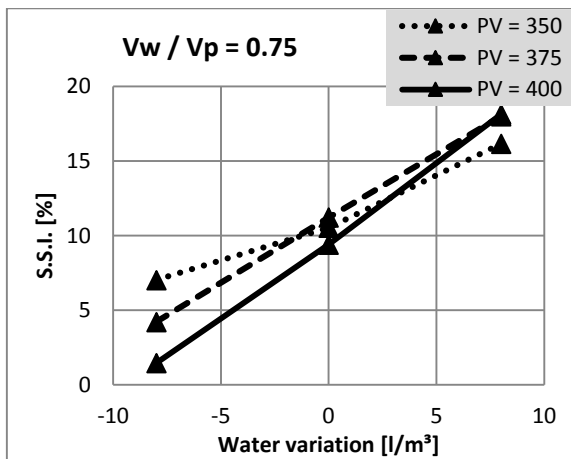


Figure 4a: Influence of the paste volume on the sieve stability

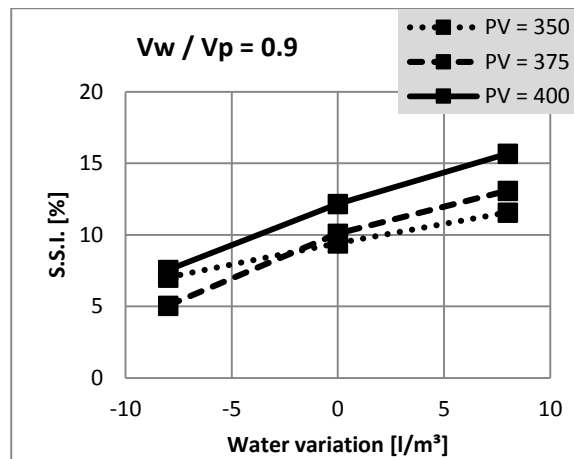


Figure 4b: Influence of the paste volume on the sieve stability

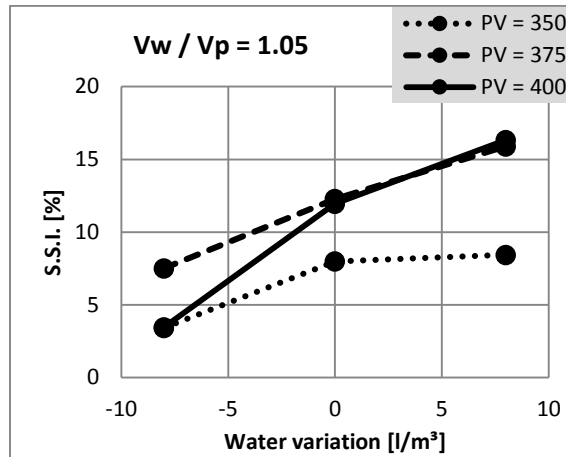


Figure 4c: Influence of the paste volume on the sieve stability

#### 4. Discussion of influence parameters

Mixtures were designed to show a specific level of sieve stability, regardless of the fluidity of the mixture. As static segregation must be avoided in all cases, the S.S.I. was chosen as “reference mix design parameter”. The conclusions of this study may therefore deviate from other results in literature.

##### 4.1. Workability tests for the robustness

Variations induced by changes in the water content affect the filling ability, the passing ability, and the segregation resistance and may result in a rejected mixture. Because a lack of robustness of an SCC mixture is most often not caused by the three key characteristics of SCC at the same time, it is not evident to grasp the variations of the slump flow, V-funnel time, L-box ratio, and sieve stability index into one global ‘robustness value’. A better approach is to judge robustness of each mixture based on its most critical parameter: a poor flowability or a too viscous and sticky mixture when the mixture contains 8 l/m<sup>3</sup> less water; or a severe segregation of the coarse aggregates or extreme bleeding occurring when 8 l/m<sup>3</sup> water in excess is added to the mixture.

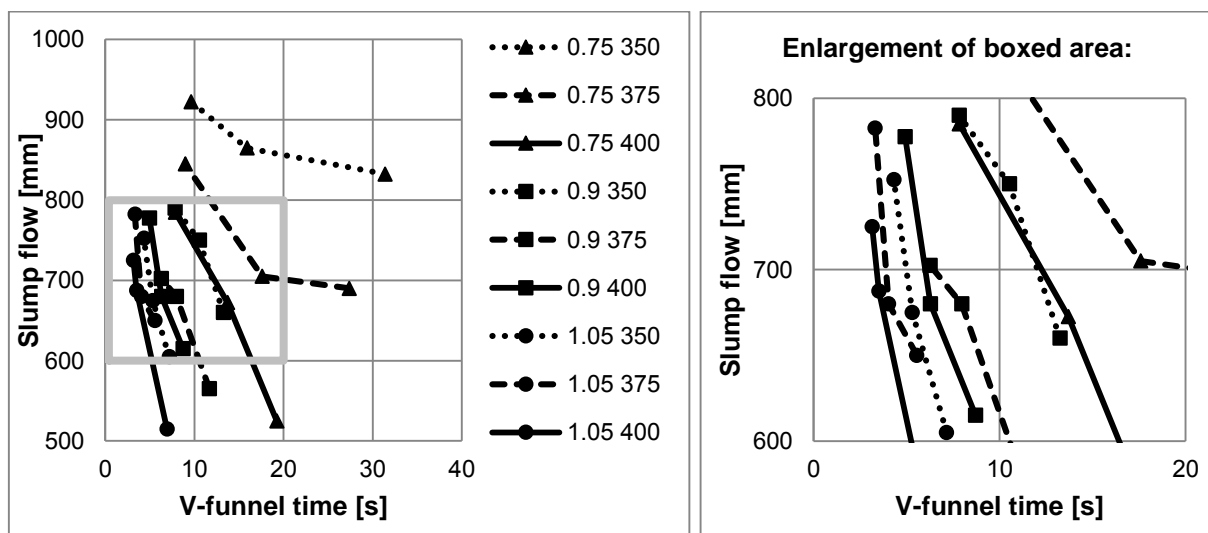


Figure 5: The robustness of all mixtures illustrated in a workability box

##### 4.2. Influence of the paste volume

When the paste volume increases, the robustness to variations in the water content of the slump flow and S.S.I. decreases while the sensitivity of the V-funnel time is constant (Table 4 and Figure 3 to 5). As shown in Figure 5, the SCC mixtures with a higher paste volume (full lines) have a lower slump

flow to achieve similar stability and are thus more sensitive to a poor flowability when the water dosage is decreased by 8 l/m<sup>3</sup> or have a more than proportional increase in S.S.I. when 8 l/m<sup>3</sup> water is added to the mixture.

#### **4.3. Influence of the volumetric water-to-powder ratio**

The robustness determined by changes in the V-funnel time increases when the water-to-powder ratio increases (Table 4, Figure 3, and Figure 5, lines with circles). Because the superplasticizer dosage added to the mixtures decreases with a higher water-to-powder ratio to achieve similar stability, the resulting effect on the sensitivity of the slump flow and S.S.I. is rather limited. Mixtures with a higher water-to-powder ratio have a lower plastic viscosity, making them more dependent on the yield stress to assure a stable mix design. Therefore, the robustness of these mixtures should be assured by increasing the aggregates volume and thus reducing the paste volume. When the water-to-powder ratio of a mixture is rather low, the plastic viscosity might become too high when reducing water by 8 l/m<sup>3</sup> and the robustness should be guaranteed by a larger paste volume. The paste volume, however, should also not be too high, since this increases the sensitivity of the slump flow of the mixture.

### **5. Recommendations**

Every application of SCC imposes specific demands towards the mix design of the concrete [24]. In order to combine specific workability demands with a sufficient robustness, the following is recommended regarding the paste volume and water-to-powder volume combination while assuming the stability of the mixture, summarized in Table 5.

**Table 5: The recommended paste volume and water-to-powder ratio depended on the application**

<b>Application</b>	<b>Recommended paste volume</b>	<b>Recommended volumetric water-to-powder ratio</b>
Large horizontal elements (floors and plates)	Low	High
Long horizontal elements (reinforced beams)	Low	Intermediate
Long vertical elements (walls)	Intermediate	Low
Slender vertical elements (columns)	High	Low

#### **5.1. Large horizontal elements (floors and plates)**

To facilitate the casting of large horizontal elements, SCC mixtures with high volumetric water-to-powder ratios should be used. Because the stability of such a mixture is provided by its high yield stress, the robustness can be improved by decreasing the paste volume of the mixture.

#### **5.2. Long horizontal elements (reinforced beams)**

A slow, but far flowing SCC mixture with a low paste volume and low water-to-paste ratio should be applied. In such a mixture, the stability is achieved by the high plastic viscosity. With a sufficiently high but not too high volumetric water-to-powder ratio, the needed robustness concerning changes in the water content is achieved.

#### **5.3. Long vertical elements (walls)**

In order to flow slowly and without segregation in between the reinforcement of long vertical elements, mixtures should have a low yield stress and a high plastic viscosity for its segregation resistance. The high plastic viscosity can be achieved with a low volumetric water-to-powder ratio. A maximum robustness is achieved by a higher paste volume, which should not be too high preventing the yield stress from becoming dominant and thus increasing the sensitivity to an too low flowability.

#### 5.4. Slender vertical elements (columns)

In columns and slender walls, the mixture should have a high plastic viscosity and without specific demands towards the yield stress. Because the stability to segregation can be provided by a combination of an intermediate plastic viscosity and yield stress, the mixture needs a low volumetric water-to-powder ratio to obtain the required plastic viscosity and a relatively high paste volume.

### 6. Conclusions

An experimental program including nine SCC mix compositions with different paste volumes and volumetric water-to-powder ratio's demonstrates that the robustness of SCC should be tested with several workability parameters in order to determine the most critical parameter of the mixture for a specific application. Because the L-box ratio does not always provide clear trends, the analysis in this experimental program is based on the slump flow, V-funnel, and sieve stability measurements. For all mixtures, the superplasticizer dosage was adjusted to achieve a specific stability level (S.S.I. =  $10 \pm 2\%$ ).

The robustness of the slump flow increases when the paste volume decreases, because mixtures with a lower paste volume depend mainly on their larger aggregate volume in order to obtain sufficient segregation resistance. The paste volume only has a minor influence on the V-funnel time and its sensitivity. A lower volumetric water-to-powder ratio increases the V-funnel time and increases the risk for the mixture of becoming too viscous when a small decrease of the water content occurs. The limited influence of the water-to-powder ratio on variations of the slump flow is probably caused by the lower superplasticizer dosage of the mixtures with a higher water-to-powder ratio.

### 7. Acknowledgements

The authors would like to thank the Science Foundation Flanders (FWO) for their financial support, and Tom Stulemeijer and Nathan Lampens for their assistance during the experimental work.

### 8. References

- [1] De Schutter G, Bartos PJM, Domone P, Gibbs J. Self-compacting concrete. Dunbeath, Scotland, UK: Whittles Publishing 2008.
- [2] Ozawa K, Maekawa K, Kunishima M, Okamura H. Development of high performance concrete based on the durability design of concrete structures. In: Okamura H, Shima H, eds. *Second East-Asia and Pacific Conference on Structural Engineering and Construction*. Chiang-Mai, Thailand 1989.
- [3] Nunes S, Milheiro-Oliveira P, Sousa Coutinho J, Figueiras J. Rheological characterization of SCC mortars and pastes with changes induced by cement delivery. *Cement & Concrete Composites*. 2011;33(1):103-15.
- [4] Kubens S. Interaction of cement and admixtures and its effect on rheological properties. Göttingen: Bauhaus-Universität Weimar 2010: Doctoral thesis.
- [5] Kubens S, Peng H, Oesterheld S, Wallevik OH. Some effects of silica fume on variations in rheology of mortar due to production date of cement. *Annual Transactions of the Nordic Rheology Society*. 2008;16:4.
- [6] Wallevik OH, Kubens S, Müller F. Influence of cement-admixture interaction on the stability of production properties of SCC. In: De Schutter G, Boel V, eds. *5th International RILEM Symposium on Self-Compacting Concrete*. Ghent, Belgium: RILEM Publications SARL 2007:211-6.
- [7] Nunes S, Oliveira PM, Coutinho JS, Figueiras J. Rheological characterization of SCC mortars and pastes with changes induced by cement delivery. *Cement & Concrete Composites*. 2011;33(1).
- [8] Juvas K, Käppi A, Salo K, Nordenswan E. The effects of cement variations on concrete workability. *Nordic Concrete Research*. 2001;26:39-46.
- [9] Westerholm M, Lagerblad B, Silfwerbrand J, Forssberg E. Influence of fine aggregate characteristics on the rheological properties of mortars. *Cement & Concrete Composites*. 2008;30(4):274-82.
- [10] Kristensen LF. Influence of different Danish glacial deposited sands on SCC properties. In: Wang K, Shah SP, eds. *Fifth North American Conference on the Design and Use of Self-Consolidating Concrete*. Chicago, IL, USA 2013.
- [11] Yurugi M, Sakai G. A Proven QA System for Flowable Concrete. *Concrete International*. 1998;20(10):44-8.

- [12] Yamada K, Yanagisawa T, Hanehara S. Influence of temperature on the dispersibility of polycarboxylate type superplasticizer for highly fluid concrete. In: Skarendahl A, Petersson Ö, eds. *First International RILEM Symposium on Self-Compacting Concrete*. Stockholm, Sweden: RILEM Publications 1999:437-48.
- [13] Jolicoeur C, Simard M-A. Chemical admixture-cement interactions: phenomenology and physico-chemical concepts. *Cement and Concrete Composites*. 1998;20(2):87-101.
- [14] Schmidt W. Design concepts for the robustness improvement of self-compacting concrete - Effects of admixtures and mixture components on the rheology and early hydration at varying temperatures. Eindhoven, The Netherlands: Eindhoven University of Technology 2014:Doctoral thesis.
- [15] Van Der Vurst F, Ghafari E, Feys D, De Schutter G. Influence of addition sequence of materials on rheological properties of self-compacting concrete. *The 23rd Nordic Concrete Research Symposium*. Reykjavik, Iceland: Norsk betongforening 2014:399-402.
- [16] Ng IYT, Ng PL, Fung WWS, Kwan AKH. Optimizing mixing sequence and mixing time for SCC. In: Shi C, Yu Z, Khayat KH, Yan P, eds. *Second International Symposium on Design, Performance and Use of Self-Consolidating Concrete*. Beijing, China: RILEM 2009:105-13.
- [17] Mazanec O, Schiessl P. Mixing Time Optimisation for UHPC. In: Fehling E, Schmidt M, Stürwald S, eds. *Second International Symposium on Ultra High Performance Concrete*. Kassel, Germany: Kassel University Press 2008:401-8.
- [18] Schiessl P, Mazanec O, Lowke D. SCC and UHPC - Effect of mixing technology on fresh concrete properties. In: Grosse CU, ed. *Advances in Construction Materials*. Heidelberg, Germany: Springer 2007:513-22.
- [19] Kwan AKH, Ng IYT. Optimum superplasticiser dosage and aggregate proportions for SCC. *Magazine of Concrete Research*. 2009;61(4):281-92.
- [20] Bonen D, Deshpande Y, Olek J, Shen L, Struble L, Lange DA, et al. Robustness of self-consolidating concrete. In: De Schutter G, Boel V, eds. *5th International RILEM Symposium on Self-Compacting Concrete*. Ghent, Belgium: RILEM Publications SARL 2007:33-42.
- [21] Jonasson J-E, Nilsson M, Utsi S, Simonsson P, Emborg M. Designing robust SCC for industrial construction with cast in place concrete. In: Shah SP, ed. *Second North American Conference on the Design and Use of Self-Consolidating Concrete; Fourth International RILEM Symposium on Self-Compacting Concrete*. Chicago, IL, USA: Hanley Wood, LLC 2005:1251-7.
- [22] Kwan AKH, Ng IYT. Improving performance and robustness of SCC by adding supplementary cementitious materials. *Construction and Building Materials*. 2010;24(11):2260-6.
- [23] Nunes S, Oliveira PM, Coutinho JS, Figueiras J. Evaluation of SCC Mixture Robustness. In: De Schutter G, Boel V, eds. *5th International RILEM Symposium on Self-Compacting Concrete*. Ghent, Belgium: RILEM Publications SARL 2007:131-6.
- [24] BIBM - CEMBUREAU - EFCA - EFNARC - ERMCO. The European Guidelines for Self-Compacting Concrete - Specification, Production and Use. 2005.
- [25] Haldenwang R, Fester VG. The influence of different superplasticisers on the flowability and reproducibility of a SCC mix. In: Wallevik O, Khrapko M, eds. *9th International Symposium on High Performance Concrete*. Rotorua, New Zealand: New Zealand Concrete Society 2011.
- [26] Bosiljkov VB, Gasperic N, Zevnik L. New type of superplasticizer for SCC mixtures with increased robustness. In: Roussel N, Bessaies H, eds. *7th International RILEM Symposium on Self-Compacting Concrete*. Paris, France 2013.
- [27] Naji S, Hwang S-D, Khayat KH. Robustness of self-consolidating concrete incorporating different viscosity-enhancing admixtures. *ACI Materials Journal*. 2011;108(4):432-8.
- [28] Billberg P, Westerholm M. Robustness of fresh VMA-modified SCC to varying aggregate moisture. *NCR Journal*. 2008;38(7):103-19.
- [29] Grünwald S, Walraven JC. Robust flowable concrete with viscosity agents. In: Mechtcherine V, Schroefl C, eds. *International RILEM Conference on Application of superabsorbent polymers and other new admixtures in concrete construction*. Dresden, Germany: RILEM Publications 2014:385-94.
- [30] Sakata N, Yanai S, Yoshizaki M, Phyfferoen A, Monty H. Evaluation of S-657 Biopolymer as a new viscosity-modifying admixture for self-compacting concrete. In: Ozawa K, Ouchi M, eds. *Second International Symposium on Self-Compacting Concrete*. Tokyo, Japan 2001:229-36.
- [31] Phyfferoen A, Monty H, Skags B, Sakata N, Yanai S, Yoshizaki M. Evaluation of the biopolymer, diutan gum, for use in self-compacting concrete. In: Shah SP, Daczko JA, Lingscheit JN, eds. *First North American Conference on the Design and Use of Self-Consolidating Concrete*. Evanston, IL, USA 2002:147-52.
- [32] Grünwald S, Walraven JC. The effect of viscosity agents on the characteristics of self-compacting concrete. In: Shah SP, ed. *Second North American Conference on the Design and Use of*

*Self-consolidating Concrete / 4th International RILEM Symposium on Self-Compacting Concrete*. Addison, IL, USA: Hanley Wood 2005:9-15.

- [33] Domone PL. Self-compacting concrete: An analysis of 11 years of case studies. *Cement & Concrete Composites*. 2006;28(2):197-208.
- [34] Berke NS, Cornman CR, Jeknavorian AA, Knight GF, Wallevik O. The effective use of superplasticizers and viscosity-modifying agents in self-consolidating concrete. In: Shah SP, Daczko JA, Lingscheit JN, eds. *First North American Conference on the Design and Use of Self-Consolidating Concrete*. Evanston, IL, USA: North Western University 2002:173-8.
- [35] Sakata N, Yanai S, Yokozeki K, Maruyama K. Study on new viscosity agent for combination use type of self-compacting concrete. *Journal of Advanced Concrete Technology*. 2003;1(1):37-41.
- [36] Garcia L, Valcuende M, Balasch S, Fernández-Lebrez J. Study of robustness of self-compacting concretes made with low fines content. *Journal of Materials in Civil Engineering*. 2013;25(4):497-503.
- [37] Gettu R, Shareef SN, Ernest KJD. Evaluation of the robustness of SCC. *The Indian Concrete Journal*. 2009;83(6):13-9.
- [38] Billberg PH. Influence of powder type and VMA combination on certain key fresh properties of SCC. In: Wallevik O, Khrapko M, eds. *9th International Symposium on High Performance Concrete*. Rotorua, New Zealand: New Zealand Concrete Society 2011.
- [39] Höveling H. Robustheit von selbstverdichtendem Beton (SVB) - Robustness of self-compacting concrete (SCC), in German. *Faculty of Civil Engineering and Geodesy*. Hannover, Germany: University of Hannover 2006:Doctoral thesis.
- [40] Leemann A, Winnefeld F. The effect of viscosity modifying agents on mortar and concrete. *Cement & Concrete Composites*. 2007;29(5):341-9.
- [41] Van Der Vurst F, De Schutter G. Improving the robustness of fresh self-compacting concrete using small quantities of fine additions. In: Shi C, Ou Z, Khayat KH, eds. *Third International Symposium on Design, Performance and Use of Self-Consolidating Concrete*. Xiamen, China: RILEM 2014.
- [42] Georgiadis AS, Sideris KK, Anagnostopoulos NS. Properties of SCC produced with limestone filler or viscosity modifying admixture. *Journal of Materials in Civil Engineering*. 2010;22(4):352-60.
- [43] Rigueira JW, García-Taengua E, Serna-Ros P. Robustness of SCC dosages and its implications on large-scale production. In: De Schutter G, Boel V, eds. *5th International RILEM Symposium on Self-Compacting Concrete*. Ghent, Belgium: RILEM Publications SARL 2007:95-101.
- [44] Rigueira JW, García-Taengua E, Serna-Ros P. Self-consolidating concrete robustness in continuous production regarding fresh and hardened state properties. *ACI Materials Journal*. 2009;106(3):301-7.
- [45] Lohaus L, Ramge P. Robustness of UHPC - A new approach for mixture proportioning. In: Fehling E, Schmidt M, Stürwald S, eds. *2nd International Symposium on Ultra High Performance Concrete*. Kassel, Germany: Kassel University Press 2008:113-20.
- [46] Phan TH. Thixotropic behaviour of self-compacting pastes (in french). *XXIVèmes Rencontres Universitaires de Génie Civil 2006* 2006.
- [47] Bonen D, Deshpande Y, Olek J, Shen L, Struble L, Lange DA, et al. Robustness of SCC. In: Lange DA, ed. *Self-consolidating concrete*. Urbana, IL, U.S.A.: The Center for Advanced Cement Based Materials (ACBM) 2007.
- [48] Bouras R, Chaouche M, Kaci S. Influence of viscosity-modifying admixtures on the thixotropic behaviour of cement pastes. *Applied Rheology*. 2008;18(4):45604-1 - -8.
- [49] Desnerck P, Van Itterbeeck P, Boel V, Craeye B, De Schutter G. Survey on the mechanical properties of SCC: 20 years of research. In: Tam CT, Ong KCG, Teng S, Zhang MH, eds. *36th Conference on Our World in Concrete & Structures : 'Recent Advances in the Technology of Fresh Concrete'*. Singapore, Singapore: Ghent University, Department of Structural engineering 2011:231-9.
- [50] Craeye B, Van Itterbeeck P, Desnerck P, Boel V, De Schutter G. Modulus of elasticity and tensile strength of self-compacting concrete: Survey of experimental data and structural design codes. *Cement and Concrete Composites*. 2014;in press.

# Instantaneous and Time-Dependent Behaviour of Reinforced Self-Compacting Concrete Slabs

Farhad Aslani<sup>1</sup>, Shami Nejadi<sup>2</sup> and Bijan Samali<sup>3</sup>

<sup>1</sup>Centre for Infrastructure Engineering and Safety, School of Civil and Environmental Engineering, University of New South Wales, Australia

<sup>2</sup>Centre for Built Infrastructure Research, School of Civil and Environmental Engineering, University of Technology Sydney, Australia

<sup>3</sup>Institute for Infrastructure Engineering, University of Western Sydney, Australia

**Abstract:** One of the developments in concrete technology is Self-Compacting Concrete (SCC). SCC refers to highly flowable, non-segregating concrete that can be spread into place, fill the formwork, and encapsulate the reinforcement without the aid of any mechanical consolidation. In this study, cracking in reinforced SCC and Fibre Reinforced Self-Compacting Concrete (FRSCC) slabs with particular emphasis on the development of flexural cracking have been investigated both experimentally and analytically. Two series tests were conducted on the one-way reinforced SCC and FRSCC slabs to study the development of short-term and long-term flexural cracking under monotonically increasing loads and caused by the combined effects of constant sustained service loads and shrinkage, respectively. Deflections, crack patterns, crack widths, steel strains and concrete surface strains at the steel level were recorded 'in the instantaneous cracking and post-cracking range for short-term tests' and 'both immediately after loading and up to 240 days under sustained loads for long-term tests'. Analytical models were developed to simulate SCC and FRSCC instantaneous and time-dependent flexural cracking. Also, available tension chord models for CC and FRC were modified and used in the proposed model to study the SCC and FRSCC tension zone of a flexural member and the effect of creep and shrinkage with time. Moreover, the crack width and spacing calculation procedures of the available codes of practice were assessed and some deficiencies in the existing approaches exposed. Finally, a comprehensive parametric study for the instantaneous and time-dependent behaviour of the slabs by FEM analyses has been conducted.

**Keywords:** self-compacting concrete, fibre reinforced self-compacting concrete, flexural cracking, crack control, time-dependent.

## 1. Introduction

Developments in concrete technology provide engineers, designers, suppliers and contractors with new methods of approaching engineering problems. Many of these developments are engineered solutions to technical and commercial problems, by either improving the current practices or overcoming limitations in the existing technology. One of the developments is Self-Compacting Concrete (SCC). SCC refers to 'highly flowable, non-segregating concrete that can be spread into place, fill the formwork, and encapsulate the reinforcement without the aid of any mechanical consolidation' as defined by the American Concrete Institute (1). SCC is regarded as one of the most promising developments in concrete technology due to significant advantages over Conventional Concrete (CC). Many different factors can influence a decision to adopt SCC over CC ranging from structural performance to associated costs. These decisions should be well informed and based on a sound understanding of such factors. Recently, SCC has gained wider use in many countries for different applications and structural configurations. SCC can also provide a better working environment by eliminating the vibration noise. Such concrete requires a high slump that can be achieved by superplasticizer addition to a concrete mix and special attention to the mix proportions. SCC often contains a large quantity of powder materials that are required to maintain sufficient yield value and viscosity of the fresh mix, thus reducing bleeding, segregation, and settlement. As the use of a large quantity of cement increases costs and results in higher temperatures, the use of mineral admixtures such as fly ash, blast furnace slag, or limestone filler could increase the slump of the concrete mix without increasing its cost (2).

In addition, Fibre Reinforced Self-Compacting Concrete (FRSCC) is a relatively new composite material which congregates the benefits of the SCC technology with the profits derived from the fibre addition to a brittle cementitious matrix. Fibres improve many of the properties of SCC elements including tensile strength, ductility, toughness, energy absorption capacity, fracture toughness and cracking. FRSCC can mitigate two opposing weaknesses: poor workability in Fibre Reinforced Concrete (FRC) and cracking resistance in plain concrete (3).



Generally, strength and serviceability are the two main criteria to be satisfied in the design of reinforced concrete structures. Strength is the ability of the structure to carry the design ultimate loads without collapsing. The strength of a structure may usually be determined with reasonable accuracy because reinforced concrete structures are commonly designed to provide ductile failure, i.e., yielding of the reinforcement before failure of the concrete. Serviceability refers to the behaviour of structures at working loads, with particular reference to cracking and deflection. Both cracking and deflection are primarily dependent on the properties and behaviour of the concrete but are more difficult to predict because of the non-linear, inelastic and time-dependent nature of the concrete. If structural designers do not adequately account for this non-linear behaviour, serviceability problems may result. Therefore, crack control is an important aspect of the design of reinforced concrete structures at the serviceability limit state (4). Because concrete is low in tensile strength, cracks are inevitable in reinforced concrete structures. Therefore, studying the cracking behaviour and controlling the width of cracks in reinforced concrete members are absolutely necessary.

For a structure that is made by SCC and FRSCC (e.g. bridges and tall buildings) to remain serviceable, crack widths must be small enough to be acceptable from an aesthetic point of view, small enough to avoid waterproofing problems and to prevent the ingress of water that may lead to corrosion of the reinforcement. Despite its importance, building code provisions for crack control mostly have been developed from laboratory observations of the instantaneous behaviour of reinforced SCC and FRSCC members under load and fail to account adequately for the time-dependent development of cracking. In this study cracking caused by external loads in reinforced SCC and FRSCC elements is examined experimentally and numerically (5).

## **2. Research Significance**

Limited researches have been undertaken to understand cracking and crack control for SCC and FRSCC members. Also, the time-dependent mechanisms and interactions are still not completely understood. In addition, a reliable and universally accepted design procedure has not been developed. There exists a need for both theoretical and experimental research of the critical factors which affect time-dependent cracking of SCC and FRSCC. The major objectives of this study were:

- (a) To gain a better understanding of the mechanisms associated with SCC and FRSCC flexural cracking of slab, and the influence of those factors that affect the spacing and width of flexural cracks under short-term and long-term loading.
- (b) To obtain benchmark, laboratory-controlled data to assist in the development of rational design-oriented procedures for the control of cracking and the calculation of crack widths on the short-term and long-term response of one-way slabs made by SCC and FRSCC.
- (c) To develop analytical models those accurately predict hardened mechanical properties of SCC and FRSCC.
- (d) To develop analytical models for flexural cracking that describe in appropriate detail the observed cracking behaviour of the SCC and FRSCC flexural one way slabs tested.
- (e) To effectively model CC, SCC, and FRSCC slabs under short-term and long-term loading. The Finite Element Method (FEM) was used to model the slabs with the aid of a computer program to process the finite element model. The models will be critiqued on their ability to properly replicate real cracking and deflection behaviour in practice models. There are multiple methods for determining the deflection of slabs as well as calculating crack spacing and crack width with regard to short term loading and under sustained load.

## **3. Experimental Study**

In this study, (a) short-term flexural load tests on eight reinforced SCC and FRSCC specimens slabs were conducted to study the development of flexural cracking under increasing short-term loads from first cracking through to flexural failure and (b) long-term flexural load tests on eight reinforced SCC and FRSCC specimens slabs were monitored for up to 240 days to measure the development of cracking and deformations under service loads. For this purpose, four SCC mixes – two plain SCC (N-SCC-a, b), two steel fibre (D-SCC-a, b), two polypropylene fibre (S-SCC-a, b), and two hybrid fibre (DS-SCC-a, b) FRSCC slab specimens – are considered in the test program. In this study, all testing and measurement requirements are based on the Nejadi (4) research study and we aimed to compare SCC and FRSCC slab series experimental results with CC (4) slab series experimental results. Deflections at mid-span,

crack patterns, crack widths, steel strains and concrete surface strains at the steel level were recorded 'in the instantaneous cracking and post-cracking range for short-term tests' and 'both immediately after loading and up to 240 days under sustained loads for long-term tests'. Detailed material properties, mix proportions, and fresh and hardened properties can be found in Aslani (5).

### 3.1 Mechanical properties, shrinkage and creep tests

Specimens for testing the hardened properties are prepared by direct pouring of concrete into moulds without compaction. The compressive and tensile strengths, modulus of elasticity and modulus of rupture specimens are tested at 3, 7, 14, 28, 56, and 91 days. Also, shrinkage and creep are monitored up to 240 days.

### 3.2 Short-term SCC and FRSCC slabs tests

Eight singly reinforced SCC and FRSCC slab specimens were cast and moist cured for 28 days. The slab specimens were each nominally 3500 mm long by 400 mm wide (see Figure 1). In all slabs the nominal distance from the soffit to the centroid of the main reinforcement was 25 mm and distance among bars is 103 mm. Slabs series were each reinforced with 4N12. All the specimens were tested to failure to investigate the distribution and extent of primary and secondary cracking under short-term loading using two equal point loads applied at the third points on the span, at ages greater than 28 days. Crack widths were monitored on the side face of the specimens from initial cracking up to a load sufficient to cause the tensile steel to yield. The schematic diagram of the test set-up is shown in Figure 2. Two identical specimen "a" and "b" were constructed for each SCC mix.

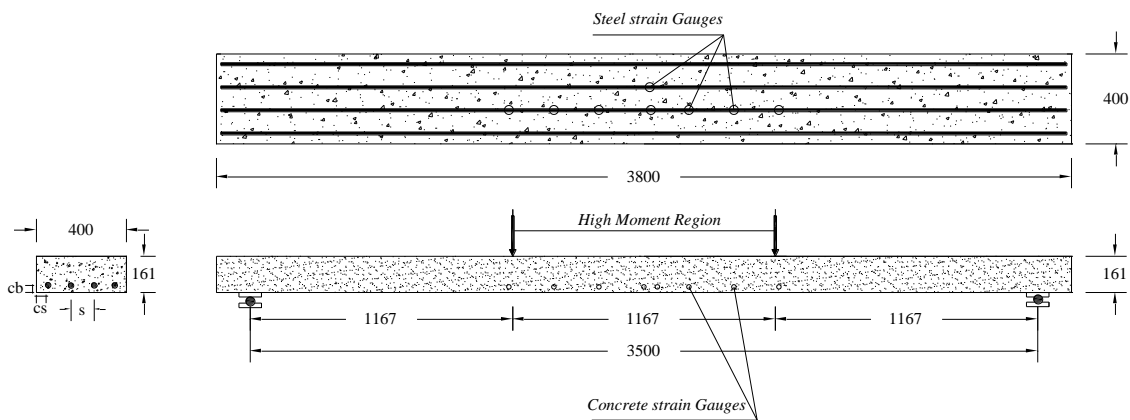


Figure 1. Dimensions and reinforcement details for slab specimens.



Figure 2. Short-term flexural test arrangement for all specimens.

### 3.3 Long-term SCC and FRSCC slabs tests

A total of eight SCC and FRSCC slabs with the same cross-section and details were monitored for up to 240 days to measure the time-dependent development of cracking and deformations under service loads. Details of the cross-sections and reinforcement layouts for slab specimens are shown in Figure 1. A general view of the test specimens is shown in Figure 3. All slab specimens were subjected to different gravity loads, consisting of self-weight plus superimposed sustained loads via carefully constructed and arranged concrete blocks supported off the top (of the specimens). To provide the sustained loading, rectangular concrete blocks of predetermined size and weights were cast and weighed prior to the commencement of the test. The blocks were suitably arranged on the top surface of each specimen to achieve the desired sustained load level. Two sustained load levels were considered, namely 50% and 30% of the ultimate design load, and designated load conditions “a” and “b”, respectively. The slab specimens were subjected to uniformly distributed sustained loads, UDL + self-weight. All measurements were taken within the high moment region, i.e. the middle third of the span for beams and for slabs where  $M \geq 90\% M_{max}$  (5).



Figure 3. General view of flexural long-term tests under load.

## 4. Experimental Results

The compressive and tensile strengths, modulus of elasticity and modulus of rupture results are presented in Table 1. The measured shrinkage strain and creep coefficients for SCC loaded at age 14 days is presented in Tables 2 and 3. Also, the results from short-term and long-term flexural tests are presented in Tables 4 and 5.

Table 1. Mechanical properties results of SCC and FRSCC.

Age (days)	Compressive strength (MPa)				Tensile strength (MPa)			
	N-SCC	D-SCC	S-SCC	DS-SCC	N-SCC	D-SCC	S-SCC	DS-SCC
3	12.45	18.50	13.65	14.30	1.65	2.32	1.16	1.76
7	21.80	25.30	22.50	26.30	2.26	3.38	1.93	2.51
14	29.05	34.30	32.45	38.10	2.80	3.87	3.05	3.54
28	33.30	38.00	38.10	45.00	3.60	4.54	3.56	4.09
56	40.60	50.50	42.90	50.75	4.17	5.35	4.02	4.33
91	46.40	51.15	47.65	52.00	4.57	5.44	4.41	4.80
	MOE (GPa)				MOR (MPa)			
Age (days)	N-SCC	D-SCC	S-SCC	DS-SCC	N-SCC	D-SCC	S-SCC	DS-SCC
3	25.23	24.45	25.36	26.78	2.50	3.35	3.13	2.47
7	27.84	26.57	27.87	30.13	3.35	4.10	4.26	3.81
14	32.24	29.14	29.68	31.26	4.66	5.40	4.60	4.80
28	35.39	35.76	35.76	36.10	5.00	6.37	5.00	5.40
56	35.58	36.44	36.32	37.03	5.87	6.72	6.50	6.52
91	37.79	37.58	37.47	38.12	7.13	7.23	6.76	7.21

**Table 2. The measured shrinkage for SCC and FRSCC.**

Age (days)	15	17	20	21	28	35	42	70	98	126	154	182	210	240
Shrinkage strain (microstrain)														
N-SCC	12	52	121	150	242	329	403	567	693	756	793	827	848	870
D-SCC	42	105	166	204	339	419	479	631	713	757	803	816	830	844
S-SCC	22	81	119	150	251	348	404	565	650	709	749	780	811	823
DS-SCC	36	95	172	210	310	394	436	596	688	758	830	849	869	882
N-CC*	15	41	97	109	227	315	341	526	598	724	748	769	778	785

\* N-CC: normal conventional concrete (4)

**Table 3. The measured creep coefficient for SCC and FRSCC.**

Age (days)	15	17	20	21	28	35	42	70	98	126	154	182	210	240
Creep coefficient, $\phi_{cc}$														
N-SCC	0.36	0.7	0.96	1.01	1.15	1.28	1.36	1.55	1.7	1.76	1.82	1.85	1.91	1.96
D-SCC	0.39	0.52	0.67	0.73	1.02	1.12	1.2	1.43	1.6	1.67	1.72	1.76	1.82	1.86
S-SCC	0.36	0.59	0.75	0.78	0.96	1.12	1.19	1.41	1.5	1.58	1.64	1.72	1.77	1.82
DS-SCC	0.2	0.35	0.55	0.6	0.74	0.85	0.95	1.1	1.21	1.27	1.32	1.38	1.41	1.45
N-CC	0.1	0.17	0.35	0.36	0.55	0.75	0.83	1.07	1.15	1.25	1.33	1.37	1.42	1.49

**Table 4. Summary of the short-term flexural tests results.**

Specimen	Testing age (days)	$(W_{max})^*_{final}$ (mm)	$(W_{ave})^*_{final}$ (mm)	$(S_{ave})^*_{final}$ (mm)	Failure Load (kN)	Deflection at failure load (mm)	$W_{max}/W_{ave}$
N-SCC-a	62	0.20	0.154	95	49.0	180	1.29
N-SCC-b	63	0.25	0.195	94	48.5	163	1.17
D-SCC-a	65	0.18	0.138	106	53.0	205	1.10
D-SCC-b	66	0.23	0.172	96	52.0	177	1.33
S-SCC-a	67	0.18	0.132	102	50.0	185	1.36
S-SCC-b	69	0.23	0.189	100	48.0	167	1.21
DS-SCC-a	71	0.15	0.120	95	56.0	220	1.24
DS-SCC-b	72	0.20	0.156	98	54.0	182	1.15
N-CC-a	62	0.18	0.130	90	50.0	136	1.38
N-CC-b	63	0.23	0.180	117	47.0	156	1.28

\*  $W_{max}$  is the maximum crack width,  $W_{ave}$  is the average crack width, and  $s_{avg}$  is the average crack spacing

**Table 5. Summary of the long-term flexural tests results.**

Specimen	Instantaneous				Time-dependent				$(S_{ave})_{final} / (S_{ave})_{inst.}$	$\delta_{inst.}$ (mm)	$\delta_{final}$ (mm)
	$W_{min}^*$ (mm)	$W_{ave}^*$ (mm)	$W_{max}^*$ (mm)	$S_{ave}^*$ (mm)	$W_{min}$ (mm)	$W_{ave}$ (mm)	$W_{max}$ (mm)	$S_{ave}$ (mm)			
N-SCC-a	0.03	0.07	0.11	99	0.06	0.15	0.24	97	0.98	12.11	24.76
N-SCC-b	0.03	0.05	0.08	100	0.03	0.11	0.18	95	0.95	5.89	18.08
D-SCC-a	0.04	0.07	0.11	96	0.06	0.13	0.22	95	0.99	7.65	17.76
D-SCC-b	0.02	0.05	0.07	99	0.02	0.09	0.14	95	0.96	7.59	16.78
S-SCC-a	0.03	0.07	0.12	96	0.07	0.15	0.22	94	0.98	6.41	22.27
S-SCC-b	0.02	0.04	0.07	93	0.05	0.10	0.15	91	0.98	2.91	20.25
DS-SCC-a	0.03	0.06	0.10	102	0.04	0.14	0.20	98	0.96	8.98	21.31
DS-SCC-b	0.02	0.04	0.06	94	0.04	0.09	0.14	90	0.96	5.14	15.83
N-CC-a	0.05	0.09	0.10	153	0.10	0.15	0.22	102	0.67	11.80	32.10
N-CC-b	0.03	0.04	0.08	141	0.08	0.14	0.20	136	0.96	5.04	21.92

\*  $W_{max}$ ,  $W_{min}$ ,  $W_{ave}$  are the maximum, minimum, average crack widths,  $s_{avg}$  is the average crack spacing,  $\delta$  is the deflection

## 5. Numerical analysis

### 5.1 Short-term and long-term bond shear stresses

The force in the bar is transmitted to the surrounding concrete by bond shear stress  $\tau_b$ . Due to this transfer, the force in a reinforcing bar changes along its length. The transfer of forces across the interface by bond between concrete and steel is of fundamental importance to many aspects of reinforced concrete behaviour. Under service conditions  $\sigma_s < f_{sy}$  and according to Marti et al. (6),  $\tau_b = 2 f_{ct}$ . To investigate the influence of the assumed short-term bond shear stress on the predicted crack width, four different values for bond shear stress ( $\tau_b = f_{ct}$ ,  $\tau_b = 1.5 f_{ct}$ ,  $\tau_b = 2 f_{ct}$  and  $\tau_b = 3 f_{ct}$ ) have been considered. Moreover, following the CEB proposal which accounts for the breakdown of tension stiffening under long-term, each value was reduced by a factor of one half ( $\tau_b(t) = 0.5 f_{ct}$ ,  $\tau_b(t) = f_{ct}$  and  $\tau_b(t) = 1.5 f_{ct}$ ) for time-dependent behaviour. For each assumed bond shear stress, the crack widths were calculated and compared with the measured crack widths for each load increment. Instantaneous and time-dependent crack width calculations for concrete reinforced with bars are different from concrete reinforced with bars and fibres. Detailed calculation procedures have been presented in Aslani (5). The proposed bond shear stress models for short-term behaviour which have been applied in the crack width and spacing calculations can be presented as follows:

$$\text{N-SCC: } \tau_b = \begin{cases} 1.50 f_{ct} & \sigma_{s,max} < 180 \text{ MPa} \\ 1.50 f_{ct} & f_{sy} > \sigma_{s,max} \geq 180 \text{ MPa} \end{cases} \quad (1)$$

$$\text{D-SCC: } \tau_b = \begin{cases} 1.25 f_{ct} & \sigma_{s,max} < 180 \text{ MPa} \\ 1.30 f_{ct} & f_{sy} > \sigma_{s,max} \geq 180 \text{ MPa} \end{cases} \quad (2)$$

$$\text{S-SCC: } \tau_b = \begin{cases} 1.50 f_{ct} & \sigma_{s,max} < 180 \text{ MPa} \\ 1.70 f_{ct} & f_{sy} > \sigma_{s,max} \geq 180 \text{ MPa} \end{cases} \quad (3)$$

$$\text{DS-SCC: } \tau_b = \begin{cases} 1.50 f_{ct} & \sigma_{s,max} < 180 \text{ MPa} \\ 1.60 f_{ct} & f_{sy} > \sigma_{s,max} \geq 180 \text{ MPa} \end{cases} \quad (4)$$

The proposed bond shear stress model for long-term behaviour which has been applied in the crack width and spacing calculations can be presented as follows:

$$\tau_b = 1.5 f_{ct} \quad (5)$$

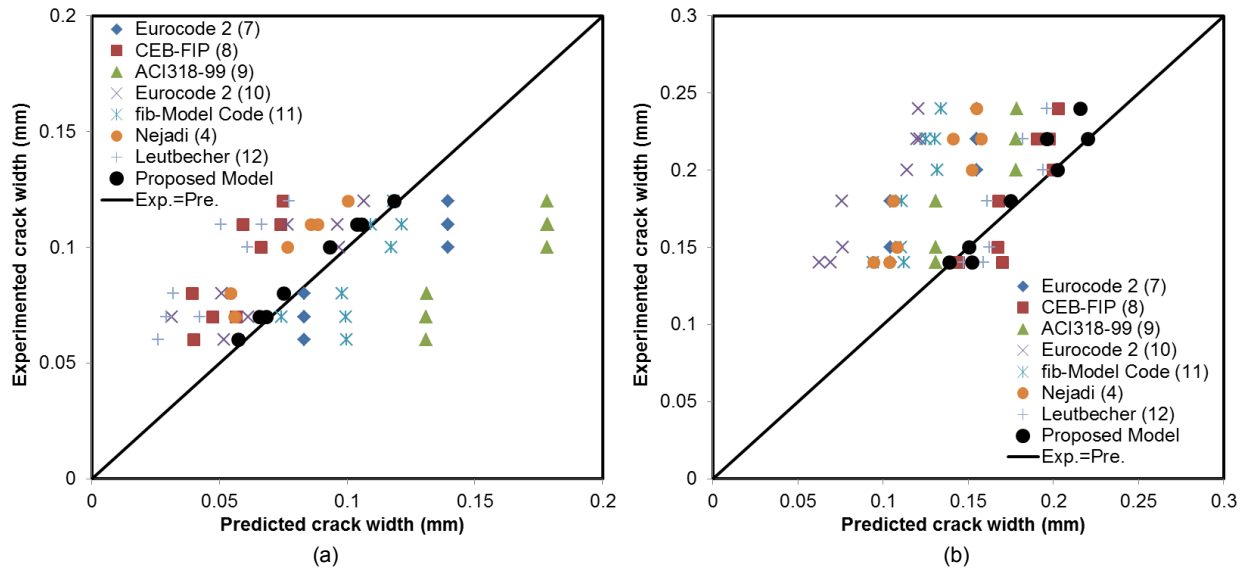
### 5.2 Instantaneous and time-dependent flexural cracking models

To control the crack width at the flexural member tension surface, designers can use the guidelines prescribed in various design codes. These guidelines are based on certain analytical solutions to crack width for CC that were developed by various researchers. There is no study about analytical models for instantaneous and time-dependent flexural cracking of reinforced SCC and FRSCC one-way slabs. The crack width and crack spacing calculation procedures outlined in five international codes, namely Eurocode 2 (7), CEB-FIP (8), ACI318-99 (9), Eurocode 2 (10), and fib-Model Code (11), are presented and crack widths and crack spacing are accordingly calculated. Then, the results are compared with the proposed analytical models and the measured experimental values, and discussed in detail separately. The proposed crack width and crack spacing models in this study for prediction of instantaneous and time-dependent crack widths for SCC and FRSCC are based on the Leutbecher (12) models. The Leutbecher (12) models include crack widths for initial crack and stabilized cracking phases. These models are proposed for Conventional Reinforced Concrete (CRC) and CRC with fibres. The flexural cracking modelling of fibre reinforced concrete is very complicated but the proposed models by Leutbecher (12) are very convenient and effective. The proposed models of Leutbecher (12) are more suitable when they are combined with the proposed effective tensile area of concrete by Nejadi (4) and the calculated results are more in agreement with the measured experimental results. Proposed SCC and FRSCC flexural cracking models are presented through Table 6. In these equations, the proposed these bond shear stress models, equations (1-5), should be used. Detailed calculation procedures and notations have been presented in Aslani (5). In order to make a comparison between the models, crack width and crack spacing were also

calculated in accordance with Eurocode 2 (7), CEB-FIP (8), ACI318-99 (9), Eurocode 2 (10), fib-Model Code (11), Nejadi (4), Leutbecher (12), and proposed model in this study. Comparison between the experimental results, proposed analytical model and international codes are presented in Figure 4.

**Table 6. Proposed SCC and FRSCC flexural cracking models.**

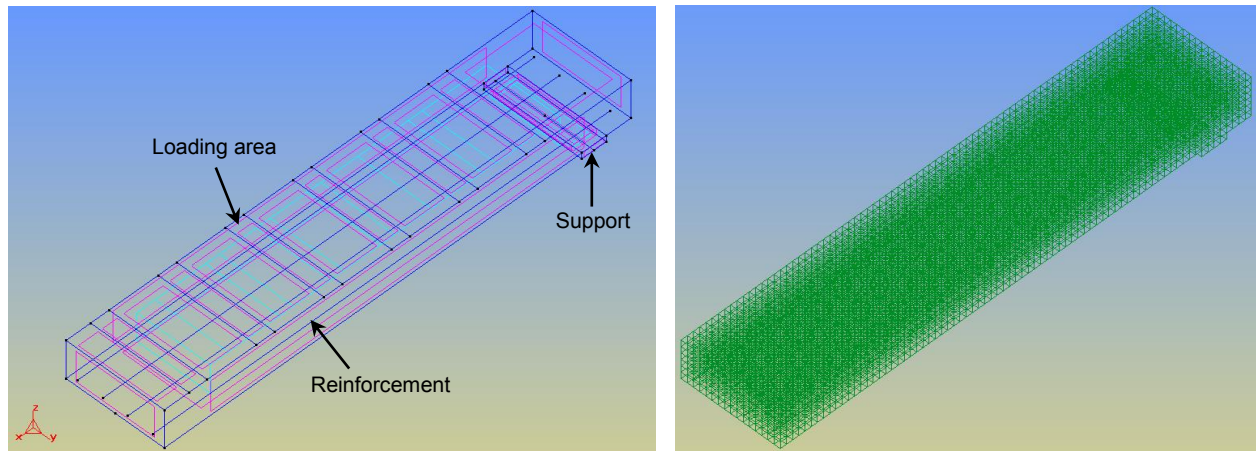
Proposed models	Equations
instantaneous crack width initial crack phase - SCC	$w = \frac{0.25 f_{ct}^2 d_b}{E_s \tau_b \rho_s^2} \left( 1 + \frac{E_s}{E_c} \rho_s \right)$
time-dependent crack width initial crack phase - SCC	$w = \frac{0.25 \left( \frac{\sigma_s}{1 + \frac{E_s}{E_c} \rho_s} - \varepsilon_{s,shr} E_s \right)^2}{E_s \tau_b} d_b \left[ 1 + \frac{E_s}{E_c} \rho_s \right]$
instantaneous crack width stabilized cracking phase - SCC	$w = \frac{s_r}{E_s} \left[ \sigma_s - \frac{s_r \tau_b}{d_b} \left( 1 + \frac{E_s}{E_c} \rho_s \right) \right]$
time-dependent crack width stabilized cracking phase - SCC	$w = \frac{s_r}{E_s} \left[ \sigma_s - \left( \frac{s_r \tau_b}{d_b} + \varepsilon_{s,shr} E_s \right) \left( 1 + \frac{E_s}{E_c} \rho_s \right) \right]$
instantaneous crack width initial crack phase - SCC	$w_s = \frac{0.25 \left[ \sigma_s - \frac{\sigma_{cf,cr}^i \frac{E_s}{E_c}}{\gamma} \right] d_b}{E_s \tau_b} (\sigma_s)$
instantaneous crack width initial crack phase - FRSCC	$w_s = \frac{0.25 \left[ \sigma_s - \frac{\sigma_{cf,cr}^i \frac{E_s}{E_c}}{\gamma} \right] d_b}{E_s \tau_b} (\sigma_s)$
time-dependent crack width initial crack phase - FRSCC	$w_s = \frac{0.25 \left[ \sigma_s - \varepsilon_{s,shr} E_s \left( 1 + \frac{E_s}{E_c} \rho_s / \gamma \right) - \frac{\sigma_{cf,cr}^i \frac{E_s}{E_c}}{\gamma} \right] d_b}{E_s \tau_b} (\sigma_s - \varepsilon_{shr}^* E_s)$
instantaneous crack width stabilized cracking phase - FRSCC	$w_s = s_r \left[ \frac{\sigma_s}{E_s} - \left( \frac{s_r \tau_b}{d_b E_s} \left( 1 + \frac{E_s}{E_c} \rho_s / \gamma \right) + \frac{\sigma_{cf}}{\gamma E_c} \right) \right]$
time-dependent crack width stabilized cracking phase - FRSCC	$w_s = s_r \left[ \frac{\sigma_s}{E_s} - \left( \frac{s_r \tau_{sm}}{d_b E_s} \left( 1 + \frac{E_s}{E_c} \rho_s / \gamma \right) + \frac{\sigma_{cf}}{\gamma E_c} - \varepsilon_{f,shr}^* \frac{E_f}{E_c} \eta \rho_f \right) - \varepsilon_{shr}^* \right]$
instantaneous and time-dependent crack spacing	$(s_r)_{max} = \frac{f_{ct} d_b}{2 \tau_b \rho_{ef}}; (s_r)_{min} = \frac{1}{2} (s_r)_{max}; (s_r)_{ave} = \frac{(s_r)_{max} + (s_r)_{min}}{2}$



**Figure 4. Comparison between crack widths experimental results, proposed analytical model and codes for (a) instantaneous and (b) time-dependent behaviour.**

### 5.3 Finite element modelling

This section deals with the finite element analysis of the flexural time-dependent behaviour of SCC and FRSCC slabs. A new finite element model procedure is developed using the commercial FEM program ATENA based on the proposed material properties, bond-slip, and creep and shrinkage constitutive models (proposed models can be found in Aslani and Nejadi (3, 13-14) and Aslani (5)) for SCC and FRSCC. In the FEM parametric study, mentioned proposed models for SCC and FRSCC are used together with the default ATENA models, to simulate and analysis of instantaneous and time-dependent cracking behaviours SCC and FRSCC one-way slabs. General and mesh views of slabs modelled in ATENA are presented in Figure 5.



**Figure 5. General and mesh views of slabs modelled in ATENA.**

The parametric study methods are as follows:

1. Using the default models of ATENA program (i.e. CC3DNonLinCementitious2 for material, CCModelB3Improved for creep and shrinkage, and bond-slip).
2. Applying default ATENA's CCModelB3Improved creep and shrinkage model then using the CC3DNonLinCementitious2User by utilizing the proposed models presented in Aslani and Nejadi (3), and default ATENA's bond-slip model.



3. Using default ATENA's CCMoelB3Improved creep and shrinkage model then using the CC3DNonLinCementitious2User and bond-slip model by utilizing the proposed models presented in Aslani and Nejadi (13, 3).

4. Using proposed creep and shrinkage models by utilizing the proposed models in presented in chapter 4 and using the CC3DNonLinCementitious2User and bond-slip model by utilizing the proposed models presented in Aslani and Nejadi (3, 13-14).

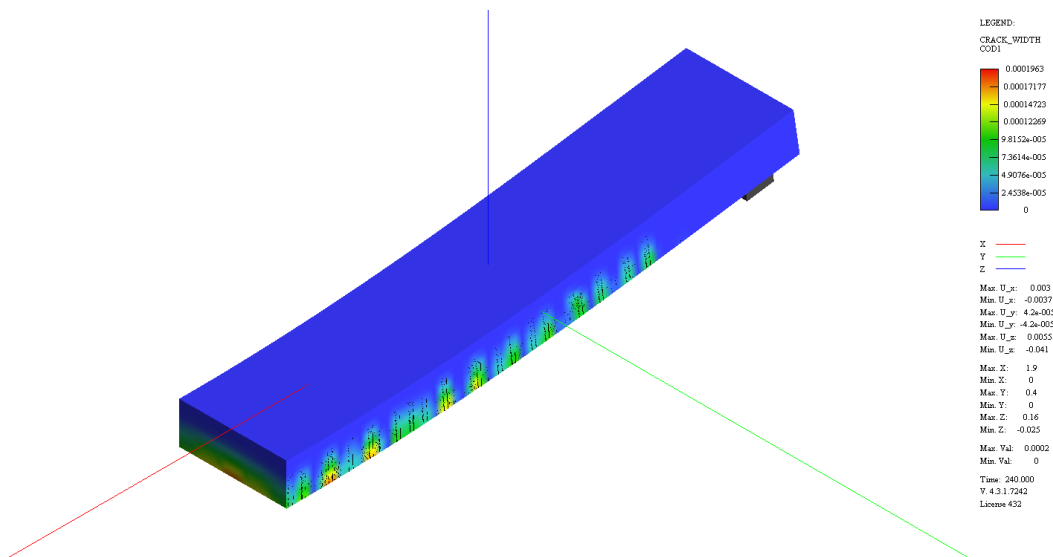
The results from parametric study have been presented in Tables 7 and 8. The results show that by using each proposed model (e.g. material properties, bond-slip, and creep and shrinkage), accuracy of the crack widths and deflections prediction increased. Also, when the analysis is combined with the proposed models the accuracy of the crack width and deflection prediction is in the best agreement with the experimental results. Typical FEM analysis result is shown in Figure 6.

**Table 7. Comparison between crack widths experimental results and FEM results.**

FEM Parametric study method	Time-dependent crack widths (mm)									
	N-SCC-a	N-SCC-b	D-SCC-a	D-SCC-b	S-SCC-a	S-SCC-b	DS-SCC-a	DS-SCC-b	N-CC-a	N-CC-b
Experimental Results	0.24	0.18	0.22	0.14	0.22	0.15	0.20	0.14	0.22	0.20
1	0.32	0.25	0.32	0.20	0.31	0.21	0.29	0.19	0.32	0.27
2	0.28	0.22	0.28	0.18	0.27	0.18	0.24	0.16	0.28	0.23
3	0.27	0.21	0.27	0.17	0.26	0.17	0.22	0.15	0.27	0.22
4	0.25	0.19	0.24	0.16	0.23	0.16	0.21	0.14	0.25	0.21

**Table 8. Comparison between deflections experimental results and FEM results.**

FEM Parametric study method	Deflections (mm)									
	N-SCC-a	N-SCC-b	D-SCC-a	D-SCC-b	S-SCC-a	S-SCC-b	DS-SCC-a	DS-SCC-b	N-CC-a	N-CC-b
Experimental Results	24.7	18.1	17.7	16.7	22.2	20.2	21.3	15.8	28.7	21.2
1	39.8	16.7	38.6	15.4	38.8	16.6	37.4	15.4	40.3	16.8
2	30.8	17.6	30.0	16.2	30.0	18.0	29.1	15.3	35.1	17.8
3	33.6	17.5	32.7	16.2	32.8	17.7	31.9	15.9	33.0	18.1
4	25.1	18.1	18.2	17.0	22.8	20.1	22.1	16.4	29.0	20.5



**Figure 6. Typical FEM time-dependent crack width result for N-SCC-a slab.**



## 6. Conclusions

In this study, cracking in reinforced SCC and FRSCC slabs with particular emphasis on the development of flexural cracking due to the combined effects of constant sustained service loads and shrinkage have been investigated both experimentally and analytically. The results have been compared with the CC slabs flexural cracking behaviour available in the literature. Also, this study provides a rational method for designers to control flexural cracking in reinforced SCC and FRSCC slabs and thereby improve the serviceability of concrete structures.

The crack widths calculated in accordance with proposed models and FEM at steel stress levels up to 250 MPa shows that predicts crack widths which are in good agreement with the measured experimental results at all steel stress levels. Also, long term deflections were accurately modelled with a maximum error of about 5% and the models showed appropriate flexural cracking behaviour.

## 7. Acknowledgement

This work was supported by Centre for Built Infrastructure Research, School of Civil and Environmental Engineering, University of Technology Sydney, Australia. The authors would like to express their appreciation to BORAL, BOSFA, and Concrete companies.

## 8. References

1. American Concrete Institute, "Self-consolidating concrete (ACI 237R-07)", ACI Committee 237, 2007, Michigan.
2. Aslani, F., Nejadi, S., "Mechanical properties of conventional and self-compacting concrete: an analytical study", *Construction and Building Materials*, 36, 2012, pp 330-347.
3. Aslani, F., Nejadi, S., "Self-compacting concrete incorporating steel and polypropylene fibers: compressive and tensile strengths, moduli of elasticity and rupture, compressive stress-strain curve, and energy dissipated under compression", *Composites Part B: Engineering*, 53, 2013, pp 121-133.
4. Nejadi, S., "Time-dependent cracking and crack control in reinforced concrete structures", PhD Thesis, 2005, The University of New South Wales.
5. Aslani, F., "Experimental and numerical study of time-dependent behaviour of reinforced self-compacting concrete slabs", PhD Thesis, 2014, University of Technology, Sydney.
6. Marti, P., Alvarez, M. et al., "Tension chord model for structural concrete", *Structural Engineering International*, 4, 1998, pp 287-298.
7. Eurocode 2, "Design of concrete structures – Part 1: General rules and rules for buildings", 1991, European Committee for Standardization, Brussels.
8. CEB-FIP, "High-strength concrete state of the art report", Thomas Telford, 1990, London.
9. American Concrete Institute, "Building code requirements for structural concrete (ACI 318-99)", ACI Committee 318, 1999, Michigan.
10. Eurocode 2, "Design of concrete structures – Part 1: General rules and rules for buildings", 2004, European Committee for Standardization, Brussels.
11. fib Model Code, "First complete draft Volume 1, fib Bulletin 55", 2010, Switzerland.
12. Leutbecher, T., "Rissbildung und Zugtragverhalten von mit Stabstahl und Fasern bewehrtem Ultrahochfesten Beton (UHPC)", Doktors der Ingebiurwissenschaften genehmigte Dissertation, 2007, der Universitat Kassel.
13. Aslani, F., Nejadi, S., "Bond behavior of reinforcement in conventional and self-compacting concrete", *Advances in Structural Engineering*, 15(12), 2012, 2033–2051.
14. Aslani, F., Nejadi, S., "Creep and shrinkage of self-compacting concrete with and without fibers", *Journal of Advanced Concrete Technology*, 11(10), 2013, pp 251-265.

# Foam concrete-aerogel composite for thermal insulation in lightweight sandwich facade elements

Nelson Silva<sup>1</sup>, Urs Mueller<sup>2</sup>, Katarina Malaga<sup>3</sup>, Per Hallingberg<sup>4</sup>, Christer Cederqvist<sup>5</sup>

<sup>1</sup>Researcher, CBI Swedish Cement and Concrete Research Institute

<sup>2</sup>Senior Researcher, CBI Swedish Cement and Concrete Research Institute

<sup>3</sup>CEO, CBI Swedish Cement and Concrete Research Institute

<sup>4</sup>Export Sales Manager, Aercrete Technology AB

<sup>5</sup>Technical Director, Aercrete Technology AB

**Abstract:** This paper describes the initial steps towards the development of a foam concrete-aerogel composite for thermal insulation in lightweight sandwich facade elements. Fire safety is an important issue pertaining insulation materials. Therefore, the need for low-density inorganic, non-flammable materials is rapidly increasing. Foam concrete is a lightweight material with good thermal characteristics; densities as low as 400 kg/m<sup>3</sup> and thermal conductivities as low as 100 mW/m·K can easily be achieved. The main advantage when compared to typical inorganic insulations (e.g. autoclaved aerated concrete or mineral wool) is that foam concrete has a much lower embodied energy, in particular due to the simplicity of the manufacturing process. However, in order to be competitive as an effective insulation material, the thermal conductivity needs to be drastically reduced which can be achieved by reducing the density and by incorporating silica aerogels (both measures affecting the compressive strength).

**Keywords:** Foam concrete, aerogel, insulation, facade, fire safety.

## 1. Introduction

The redirection of the construction sector towards Sustainable Construction is the core of the EU 2020 strategy, mainly through increased energy savings in buildings. The major goal is that by 2050, new buildings shall become energy neutral and have zero CO<sub>2</sub> emissions.

The building stock in Europe is around 160 million buildings, 70% of which built after 1945, thus with major potential for retrofitting applications. Residential buildings represent about 80% of the total building stock, where multifamily houses and high rise buildings account for 47% of the total number of building stock in EU25.

In a building, it is assumed that about 20% of the total embodied energy is associated with materials and transportation whereas the remaining 80% is consumed at the user stage. Thus, it is important to consider the user stage when considering the total energy use. This means that the buildings shall have low embodied energy, low weight of construction materials and enhance thermal properties. Breakthroughs will be in the area of the application of nanomaterials for the development of multifunctional products and components in order to address energy efficiency, fire resistance and living comfort aspects with processes that are more robust and cost-effective.

The most important part of a building from an insulation perspective is the building envelope. One way to decrease the energy consumption in buildings and thus increase the energetic efficiency of the building envelopes is by improving the thermal insulation. Better insulation materials in terms of performance, durability and embodied energy are therefore required. This concerns both new buildings as well as refurbishment applications.

### 1.1 Project concept

Facade elements made of concrete have a long tradition in the built environment. Typical pre-fabricated concrete sandwich elements are very heavy and thick; they consist of an outer panel (80-100 mm thick) made reinforced concrete, an insulation layer (100-200 mm thick) in EPS or mineral wool and an inner load-bearing panel (100-150 mm thick) made of reinforced concrete.

There is a huge and growing demand for new solutions concerning the energetic retrofitting of buildings made of this type of prefabricated sandwich elements. Such solutions should not only be energy efficient, but also fire safe as well as promoting a healthier indoor environment.

The SESBE project (*Smart Elements for Sustainable Building Envelopes*) aims to develop new lightweight façade elements that are energy efficient, non-combustible and have multifunctional properties. The new sandwich elements totally based on inorganic cementitious materials, use carbon fibre reinforced reactive powder concrete as structural material and aerogel modified foam concrete for the insulation layer. In addition, the project proposes cost-effective use of nanomaterials and nanotechnology as a tool to custom design functional and performance properties such as easy-to-clean/self-cleaning surfaces, increased heat reflectivity by a heat reflective layer and moisture control in the insulation using nano-clays.

## **1.2 Foam concrete: a fire-safe insulation material**

Foam concrete, also known as cellular lightweight concrete (CLC), can be defined as a cementitious material with a minimum of 20% by volume of mechanically entrained air in the fresh cement paste or mortar [1]. It differs from autoclaved aerated concrete (AAC) in which the spherical voids are chemically generated by the reaction between aluminium powder and the alkali hydroxides in the cement.

The basic components of foam concrete are cement, sand, water and foam (water, air and a surfactant). Typically, the air content varies between 40 to 80% of the total volume with void sizes ranging from 0.1 to 1.5 mm in diameter, although coalescence can produce larger voids, especially at lower densities [2]. Although the composition of the cementitious matrix and air void content influences the properties of the material, there is a good correlation between the dry density and compressive strength, typically varying between 400 and 1600 kg/m<sup>3</sup> and from 1 to 10 MPa, respectively. Due to the low density and highly porous structure, foam concrete presents good functional properties such as fire resistance, thermal conductivity and acoustic performance; for example, at a density of 400 kg/m<sup>3</sup>, the  $\lambda$ -value is approximately 100 mW/(m·K).

Due to its pumpability and self-compacting behaviour, foam concrete is majorly used as filling material for sealing sewage pipes, wells, mines, storage tanks and tunnels. Other applications include: soil stabilisation; bridge abutments; floor and roof screeding; road sub-bases; insulation of foundations in industrial and domestic housing; sandwich fill for precast units and concrete blocks [2].

So far, in building applications, the use of foam concrete is limited to social housing projects where a large number of units need to be produced in a short time and where densities of around 600 kg/m<sup>3</sup> constitute an affordable and sustainable alternative when both structural and insulation characteristics are required. To our knowledge however, the use of foam concrete as a high performance insulation material has not been proven.

The reason for using foam concrete in the SESBE project is to increase the fire-safety of the sandwich elements by developing a non-flammable inorganic insulation material. Standard insulation materials present several disadvantages: organic materials such as polystyrene (EPS/XPS) and polyurethane (PUR) are highly flammable and release toxic fumes during fire; inorganic materials such as mineral wool, although non-flammable, have a large embodied energy due to the high temperatures during the production process; state-of-the-art vacuum insulation panels (VIP) are expensive and require cautious handling and installation in order not to be perforated leading to the potential loss of their insulation properties.

As mentioned previously, the  $\lambda$ -value of foam concrete with a density of 400 kg/m<sup>3</sup> is around 100 mW/(m·K). In fact for such low density cementitious foams nearly all data available in the literature reports to the thermal performance of chemically generated foam concrete. Proshin et al. [3] reported thermal conductivities in the range of 60 to 160 mW/(m·K) for foam concretes, partially filled with polystyrene beads, with densities between 200 and 650 kg/m<sup>3</sup>. Akthar and Evans [4] reported values of 110 and 135 mW/(m·K) for cement foams with densities of 193 and 220 kg/m<sup>3</sup>, respectively. Finally, Zheng and Chung [5] reported thermal conductivity of 46 mW/(m·K) for a density of 152 kg/m<sup>3</sup>.

Silica aerogels are nano-porous heterogeneous solid materials, with pore diameters in the range of 1 to 100 nm. Aerogels consist of approximately 90 to 95% air in volume and therefore have low densities (80 to 150 kg/m<sup>3</sup>) and very low thermal conductivities (12 to 25 mW/(m·K)). Due to its nano-porous structure, they possess a very high specific surface area (up to 800 m<sup>2</sup>/g). Typically, aerogels are produced via a super-critical drying process meaning that they are often quite expensive. However, in the SESBE project, aerogels produced via the ambient pressure drying method [6] will be used contributing to the competitiveness of the final insulation product.

The incorporation of aerogels into the foam concrete is expected to significantly decrease the thermal conductivity. In a study by Serina et al. [7], the  $\lambda$ -value of a UHPC formulation decreased from 2300 to 310 mW/(m·K) when 80% in volume of aerogel was used (the density of the UHPC-aerogel composite was around 800 kg/m<sup>3</sup>). In another study by Hub [8] a cement paste containing 75% in volume of aerogel showed a  $\lambda$ -value of 61 mW/(m·K) (the density of the composite was around 370 kg/m<sup>3</sup>).

The main goal of the SESBE project is to develop a foam concrete-aerogel composite insulation material with a thermal conductivity around 30-35 mW/(m·K) at a density of about 150 kg/m<sup>3</sup>.

## 2. Material development

At present, the material development consisted on the selection of the type of cement most appropriate for the production of very low density foam concrete, design of the basic mix (w/c ratio, superplasticizer) and incorporation into the foam. The main goal was to characterize the state-of-the-art foam concrete (to be used as a reference) as well as the new formulation, with regards to the following fresh and hardened properties: density ratio, i.e. fresh density/design density (as an indicator of the homogeneity of the final mix); stability (tendency to collapse); compressive strength and thermal conductivity.

There are two main types of foaming agents used for the production of foam concrete; protein-based and synthetic. Protein-based foam is in general more stable than synthetic foam; however, protein-based foaming agents have a foul smell and dark brown colour, leaving a sticky residue after drying. The resulting foam has a pale yellow colour; the odour is present in the foam and can linger in the foam concrete for a long time after production, subject to drying conditions and ventilation. Because proteins are organic substances, foam concrete made with protein-based foam has a greater tendency to facilitate mould growth and other microorganisms and for that reason should be avoided in residential and commercial buildings. Synthetic foams on the other hand are odourless, bright white and dissolve easily in water without leaving any residue. For this reason, in this project, only synthetic foam was used.

In the first stage of design of the basic mix, a multi-binder system based on CEM I 52.5 R and incorporating high volume of mineral additions was tested. Table 1 lists the materials and mix proportions for the foam concrete developed. Most of the foam concrete mixes collapsed within the first 2 to 4 hours after casting and only 2 out of 16 could be tested for compressive strength. In most cases, the plastic density was below the design density. A number of possible reasons for the behaviour of the mixes tested are pointed:

- Due to the high viscosity of the cementitious matrix, homogenization of the foam concrete becomes difficult resulting in segregation. Depending on the level of segregation of the mixture, this leads in the first place to lower densities than design and eventually collapse as the cell structure is not able to support itself (not enough binder);
- The fact that some of the mixes didn't harden means that there is an unbalance between the amount of cement and the volume of mineral additions in the mixture. When water is added to the cement, the main products from the reaction are calcium hydroxide (CH) and calcium-silicate-hydrates (CSH-gel). Additionally, other alkali-hydroxides are formed; these are important to activate the pozzolanic reaction and contribute to the strength gain (setting and hardening) of the concrete;
- Silica fume, metakaolin and quartz filler have a higher specific surface than cement requiring more water. This water can be taken from the foam leading to segregation and eventually collapse;
- The high volume of mineral additions (mainly fly ash and metakaolin) and quartz filler negatively influences the stability of the foam concrete since it increases the setting time, thus increasing the tendency to collapse.

**Table 1. Mix proportions for foam concrete based on multi-binder system (in kg per m<sup>3</sup> of foam concrete).**

Material	CEM	SF	FA	MK	QF	Sand	Acc	SP	w/c	Foam (l)	Design Density
(kg/m <sup>3</sup> )	44-148	14-37	22-59	22-35	28-71	129-318	2.8-5.6	0.4-7.1	0.3-0.5	690-910	250-700

SF, silica fume; FA, fly ash; MK, metakaolin; QF, quartz filler; Acc, accelerator; SP, superplasticizer

Given the unsucceeded first stage, a second approach was based on a single-binder system. For that, 4 different cements were selected and tested. Table 2 lists the materials and mix proportions for the foam concrete developed. For each cement, at least 3 different series, i.e. 3 different densities within the range shown in Table 2, were produced. The results clearly indicated that some of the cements were not suitable for the formulation of low density foam concrete. Except for CEM I 52.5 R SR3-LA, all other cements led to collapse of the foam concrete, presumably due to the following reasons:

- Despite the fast setting time, CEM I 52.5 R is not suitable for the production of foam concrete mainly due to its high alkalinity which interacts with surfactant leading to the collapse of the foam;
- CEM I 52.5 R SR3-LA is also a rapid hardening cement but with a much finer particle size distribution and lower  $d_{50}$  (4-5  $\mu\text{m}$  as opposed to 15-16  $\mu\text{m}$ ) when compared to CEM I 52.5 R. This fast setting associated with the low alkalis content enables the production of low density foam concrete;
- CEM II/A-LL 42.5 R and CEM II/A-V 52.5 N are not suitable for the production of very low density foam concrete. Both cements include around 16% mineral additions (limestone and fly ash, respectively), with prolonged setting time which might lead to collapse of the foam.

**Table 2. Mix proportions for foam concrete based on single-binder system (in kg per  $\text{m}^3$  of foam concrete).**

Material	CEM I 52.5 R	CEM I 52.5 R SR3-LA	CEM II/A-LL 42.5 R	CEM II/A-V 52.5 N	SP	w/c	Foam (l)	Design Density
( $\text{kg}/\text{m}^3$ )	278-299	155-300	153-296	152-175	0.4-1.5	0.3-0.4	800-890	250-450

### 3. Material properties

Based on the results from the second stage of development of the mix design, CEM I 52.5 R SR3-LA was selected for further studies of material properties. The w/c ratio was set to 0.35; the superplasticizer to 0.5% by mass of cement and, for lower densities, the use of accelerator was set to 5% by mass of cement. The objective was to evaluate the dependency of the compressive strength and thermal conductivity with density. Table 3 shows the mix proportions for foam concrete of different densities.

**Table 3. Mix proportions for foam concrete of various densities (in kg per  $\text{m}^3$  of foam concrete).**

Material	Design Density ( $\text{kg}/\text{m}^3$ )					
	800	600	500	400	300	200
CEM I 52.5 R SR3-LA	572	413	338	266	186	109
Superplasticizer	2.8	1.9	1.6	1.3	0.9	0.5
Accelerator	x	x	x	x	x	5.4
Water	200	145	118	93	65	34
Foam (l)	615	722	773	821	875	926

#### 3.1 Compressive strength

The compressive strength was measured on foam concrete cubes 150 x 150 x 150 mm at the age of 28 days, according to EN 826 [9]. As expected, the results in Figure 1 indicate a clear dependency of the compressive strength with the density of foam concrete. Although foam concrete is intended to be used as insulation material and therefore serves no structural purpose, it is still important to quantify the compressive strength because during manufacturing, transportation, assembly and usage, the material will be subject to some mechanical loads. The apparent linear relation between compressive strength and density is, in the present case, the result of a common base mix for all the densities tested.

Yet some scatter can be observed, as a result of the manufacturing process, e.g. differences in the mixing time between foam concrete of different densities. Similarly low values were obtained by Tonyan and Gibson [10] who reported compressive strengths of 0.04 and 0.12 MPa for foam concrete with densities of 160 and 224 kg/m<sup>3</sup>, respectively, while higher values were reported by others: Zheng and Chung [5] reported values of 0.5–0.9 MPa for densities between 130 and 190 kg/m<sup>3</sup>; Van Deijk [1] reported a value of 0.6 MPa for a density of 240 kg/m<sup>3</sup> and in ACI 523.1R [11], 0.48 MPa were obtained for a density of 240 kg/m<sup>3</sup>.

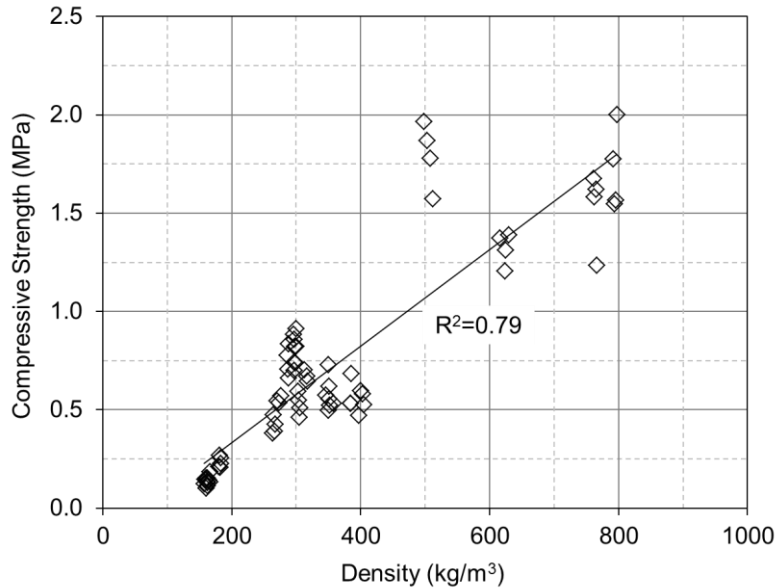


Figure 1. Compressive strength of foam concrete as a function of the density.

### 3.2 Thermal conductivity

Thermal conductivity measurements were performed in foam concrete plates 400 x 400 x 50 mm, according to EN 12667 [12]. The results in Figure 2 show that there is a fairly good linear correlation between  $\lambda$ -value and density. Note that, without the aerogel, the thermal conductivity of the foam concrete with a density of 130 kg/m<sup>3</sup> is 46 mW/(m·K). These results are in line with those reported in the literature (see section 1.2). Naturally, there is some variability of the results which is associated to the mixing process and the air-void size and distribution. Depending on the density, there is a dominant pore size, which increases as the density decreases (see Figure 3) due to the higher quantity of foam used. In addition, other factors such as coalescence voids (mainly at low densities) and degree of hydration (note the presence of large unhydrated cement grains in Figure 3 middle) will have an impact on the thermal properties of the foam concrete.

As a first trial, 50% in volume of aerogel was also incorporated into a cement paste. The thermal conductivity of the aerogel particles is approximately 20 mW/(m·K). The result in Figure 2 show a reduction of more than 60% in the  $\lambda$ -value when compared to the reference and that this value lies clearly below the  $\lambda$ -value versus density trend line.

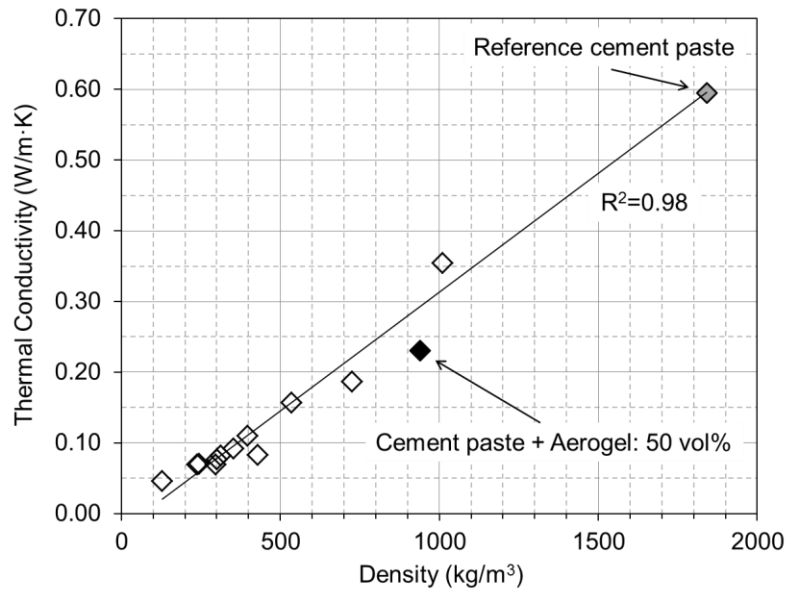


Figure 2. Thermal conductivity of foam concrete as a function of the density.



Figure 3. Pore sizes in foam concrete of various densities.

#### 4. Conclusions

The present paper reports the preliminary results towards the development of a foam concrete-aerogel composite material to be used as thermal insulation in lightweight sandwich façade elements.

A multi-binder system based on minimization of cement clinker and replacement by high volumes of supplementary cementitious materials was tested without success. It was found that such systems are not suitable for very low density foam concrete due to increased specific surface area which increases the water demand and delayed setting.

A formulation for very low density foam concrete was developed, based on single-binder system, using a commercial cement of the type CEM I 52.5 R SR3-LA. For a design density between 200 and 300 kg/m<sup>3</sup>, the cement content ranges from 110 to 190 kg/m<sup>3</sup>.

At a density of 130 kg/m<sup>3</sup>, the compressive strength is around 0.2 MPa and the thermal conductivity around 46 mW/(m·K). Preliminary experiments with aerogel incorporated into ordinary cement paste showed a reduction of the  $\lambda$ -value by more than 60%, for a degree of replacement of 50% by volume.

## 5. Future work

The work so far demonstrated that it is possible to produce very lightweight foam concrete with acceptable mechanical performance and good thermal characteristics. The incorporation of aerogels is expected to further enhance the thermal conductivity of the foam concrete, representing a competitive and safer alternative insulation material. However, the incorporation of aerogels is not expected without challenges.

Firstly, the mixing method must be optimized to ensure that the aerogel becomes part of the skeleton structure of the foam concrete rather than being entrapped in the air voids. Then, it is important that the aerogel maintains its physical and chemical integrity and is not destroyed (partially or totally) during mixing (shear action).

Secondly, the amount of aerogel needs to be optimized towards maximum performance at minimum level of incorporation, i.e. in a cost-effective way. This implies that modifications to the basic mix (in terms of w/c ratio, superplasticizer) might be necessary.

Thirdly, to achieve such low densities, the basic mix is composed only by cement (and aerogel). This means that the foam concrete is prone to chemical shrinkage and eventually cracking, as it is restrained by the inner and outer reactive powder concrete layers as well as mechanical connectors. In order to reduce the stiffness of the material, PVA fibers will be incorporated, the amount of which needs to be optimized with regards to the mechanical performance but without compromising the thermal performance.

Finally, acoustic performance and fire resistance tests will be carried to assess the suitability for use; aerogels are nanoporous materials which may significantly influence the sound transmission/absorption properties.

## 6. Acknowledgement

This research study was made possible with the support of the European Union's Seventh Framework Programme for research, technological development and demonstration under grant agreement no. 608950 (SESBE, [www.sesbe.eu](http://www.sesbe.eu)).

## 7. References

1. Van Deijk, S., "Foam concrete", *Concrete*, 1991, 49-53.
2. Brady, K.C., Watts G.R.A. and Jones, M.R., "Specification for foamed concrete", Project Report PR/IS/40/01, 2001, TRL Limited.
3. Proshin, A., Beregovoi, V.A., Beregovoi, A.M. and Eremkin, I.A., "Unautoclaved foam concrete and its constructions adapted to the regional conditions", in: *Use of foamed concrete in construction*, R.K. Dhir, M.D. Newlands MD and A. McCarthy, editors, 2005, London, Thomas Telford, pp. 113-120.
4. Akthar, F.K. and Evans, J.R.G., "High porosity (>90%) cementitious foams", *Cement and Concrete Research*, 2010, 40:352-358.
5. Zheng, Q. and Chung, D.D.L., "Microporous calcium silicate thermal insulator", *Materials Science and Technology*, 1990, Vol. 6, pp. 666-669.
6. Li, T. and Wang, T., "Preparation of silica aerogel from rice hull ash by drying at atmospheric pressure", *Materials Chemistry and Physics*, 2008, Vol. 112, pp. 398-401.
7. Serina, Ng, Sandberg, L.I.C. and Jelle, B.P., "Insulating and strength properties of an aerogel-incorporated mortar based on UHPC formulations", *Key Engineering Materials*, 2015, Vols. 629-630, pp. 43-48.
8. Hub, A., "Integriertes Konzept zur nachhaltigen Errichtung von Gebäuden in massiver Elementbauweise", 2012, PhD Thesis, University of Stuttgart (in German).
9. EN 826: "Thermal insulating products for building applications – Determination of compression behaviour", 2013, European Committee for Standardization.



10. Tonyan, T.D. and Gibson, L.J., "Structure and mechanics of cement foams", *Journal of Materials Science*, 1992, Vol. 27, pp. 6371-6378.
11. ACI 523.1R: "Guide for cast-in-place low density concrete", 1992, American Concrete Institute.
12. EN 12667: "Thermal performance of building materials and products. Determination of thermal resistance by means of guarded hot plate and heat flow meter methods. Products of high and medium thermal resistance", 2001, European Committee for Standardization.

Fib C6

# Prefabricating in Unusual Environments

Marco Menegotto<sup>1</sup> and Luciano Marcaccioli<sup>2</sup>

<sup>1</sup>Professor of Civil Engineering, Sapienza University of Rome, Italy

<sup>2</sup>General Manager, Construction Division, Piccini Group, Perugia, Italy

**Abstract:** Three building projects were realized in environments that, given the local economic and natural conditions, were theoretically not fit for industrialized construction. Prefabrication, although not common in any of the respective contexts, turned out to be the key solution and, perhaps, the only way in which the projects could have been carried out, given the requirements in terms of quality, cost and timeframe. Completing the projects with traditional construction methods would have been, if not impossible, much more lengthy and costly, with lower quality results.

**Keywords:** Prefabrication, Environment, Climatic conditions, Concrete structures, Prestressing, Cellular concrete (non-autoclaved).

## 1. Introduction

The feasibility of structural prefabrication is commonly believed to be limited to industrialized areas, where it can offer its typical advantages in meeting construction needs. However, applications can be valuable and convenient also in areas that are far from any industrial environment, in particular when large projects are to be developed and insufficient traditional construction facilities are available nearby. In such conditions, prefabrication can prove more appropriate in meeting projects' requirements and in making the best use of the local technical and logistic means as well as of the local human and natural resources.

This paper aims at showing how the above can be put in practice by presenting three case studies in which the authors were involved from the conceptual stage and throughout the planning, design, production and construction, and where optimum solutions were developed for both the building features and the construction processes.

In all these cases, the final option was precast concrete; structural systems and production procedures customized for the individual cases were conceptualized, and "unconventional" prefabrication plants reflecting the needs of each specific environment were installed. All projects were completed successfully.

Since then, the buildings in object have been in use, showing how the solutions adopted in the different cases proved to be successful, not only with respect to their structural features.

## 2. Self-construction housing

### 2.1 Needs to meet

A housing project in the Costa Rican highlands, Central America, planned for low-cost self-construction by private individuals, was launched by the Government of Costa Rica in the early 1980s. At the time, the country was not industrialized and had practically no experience in prefabrication.

The project framework required that the local applicants owned a piece of land and that the government would contribute to construction expenses by providing "coupons" to people with lower incomes. The government's contribution was approximately US\$ 4,000 per low-income family and was directed at supporting procurement of required materials.

Requirements were rather specific and directly related to the social and natural environments in which the projects were to be developed. While realizing a low-cost self-construction system for individual family houses was considered to be the main goal, security was also a requirement, including protection from the intrusion of small animals. With temperatures ranging always within 22-27 °C, climate conditions posed no problems for thermal insulation, but protection against the very intense daily rainfall was needed.

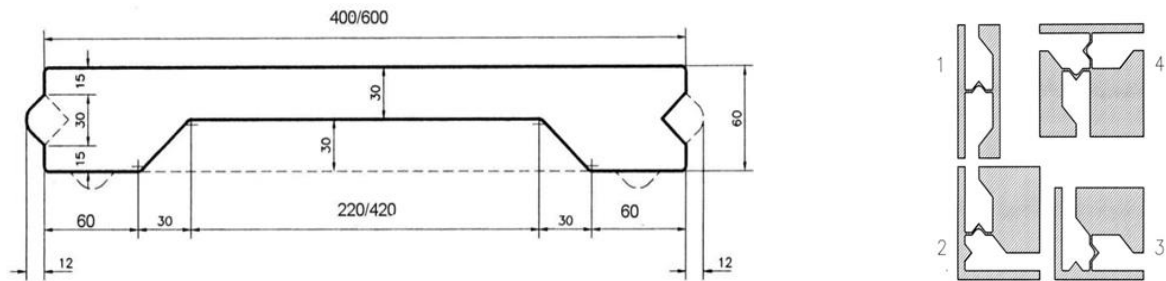
The devised design was based on very light load-bearing precast concrete wall panels, which constituted the core part of the solution through realizing inner and outer partitions with the required structural performance and protection functions.

## 2.2 The construction system

The construction system was composed of precast pre-stressed concrete panels with a very thin ribbed cross-section (30-60mm). The structure was made of those panels, clamped in a channel to the foundation, also made of U shaped small precast concrete units, and linked together on top by a wooden rod. Moreover, wooden truss-beams supported a light roof as well as forming a horizontal diaphragm. The light weight structural elements allowed their movement, handling and erection by a small number of unskilled persons, without the need for machinery or lifting equipment. A complete single-family house could then be easily built by the end-users with some external assistance in the shortest possible period.

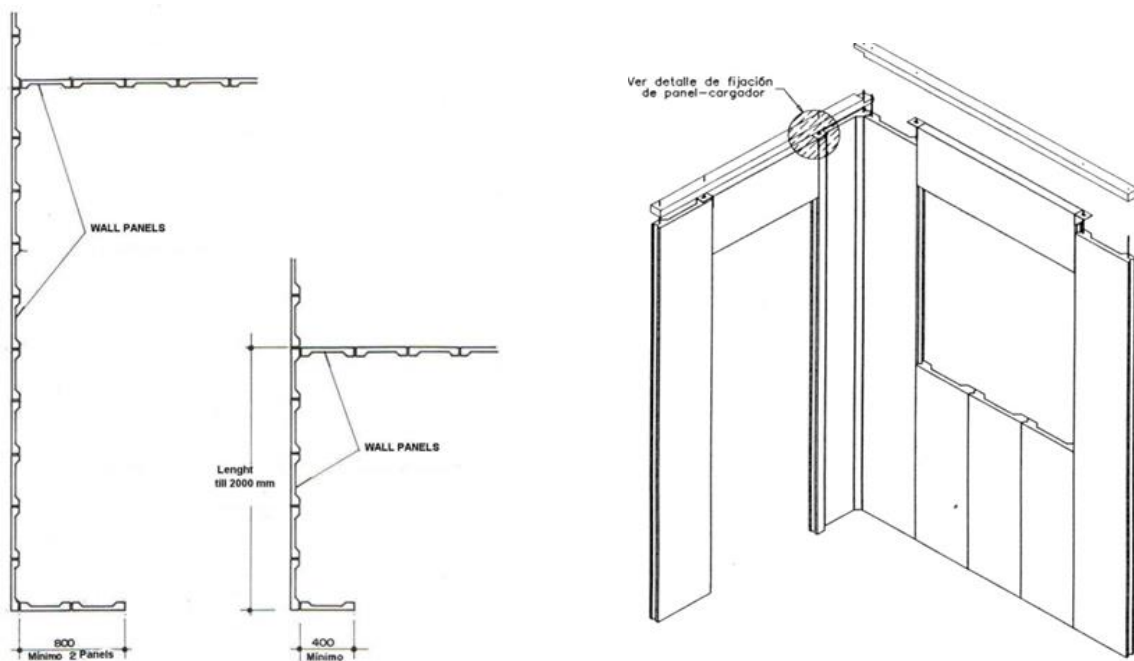
The main features of this system are: safety, dimensioned against wind and seismic actions (in fact, resistance to both vertical and lateral actions is distributed along the whole base, yet continuous, contrary to most systems); security (concrete walls); flexibility of layout and ease of adding rooms for enlarging the house; economy (self-construction); last but not least, pleasant look.

The system consists of a series of precast prestressed concrete elements, the dimensions of which are shown in fig. 1. The production system was a purpose made long line pre-tensioning bed. The industrial components are panels and clamping rails, embedded into a cast-in-situ raft foundation, quite simple and easy to build, thanks to the lightweight construction. The other building elements were the roof, normally made of timber trusses with metal sheathing (according to local customs and abilities) and complementary finishes (doors, windows, floor finishes, false ceiling, piping), all items that could be handled and installed by the end-users themselves, with the help of craftsmen, possibly available within their community.



**Figure 1. Plan cross section of a typical wall panel (mm) and edge dry connections schemes**

Typical elements have a standard height of 2.6 m, with part heights used to create openings (fig. 2).

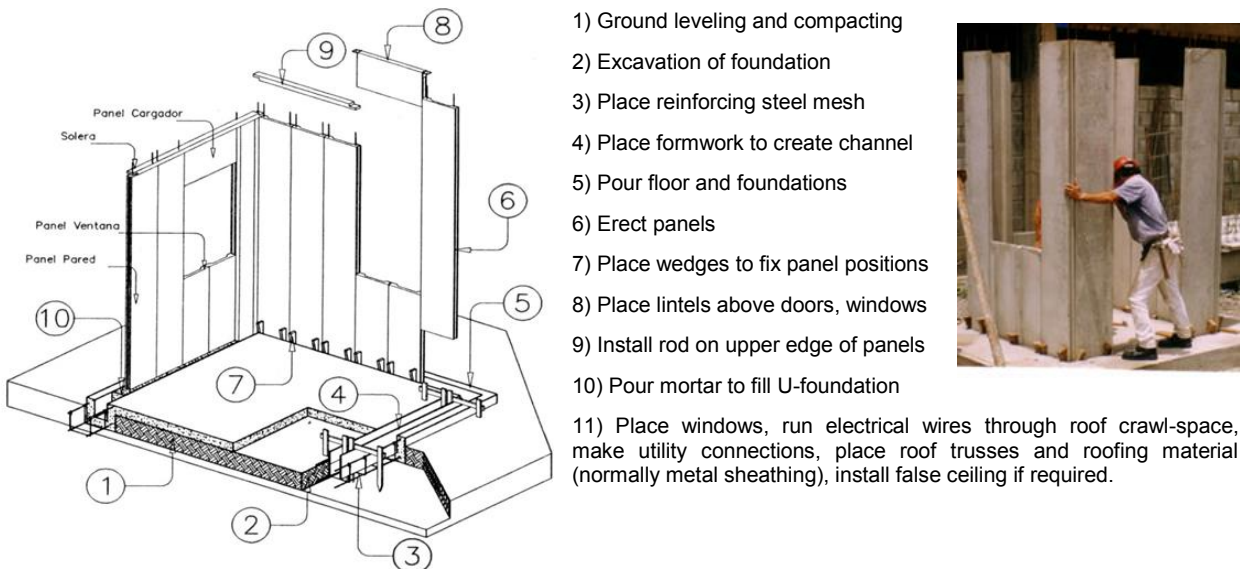


**Figure 2. Plan and isometric view of assembled walls**

Concrete is added with propylene fibers, allowing very thin sections with high level of resistance to cracking and failure, pre-stressed with 2x4mm + 2x3mm indented wires and reinforced with steel bars. It is designed to develop sufficient early strength to release the wires at 12 hours after casting under summer conditions, without use of heat. During winter, 2-4 hours of heat is used, to ensure a daily production cycle.

Panels are divided into five types, with sub types, allowing for a very large number of choices for internal distribution of areas as well as window positions.

The joints between the panels are dry type; expanded bitumen polyurethane band can be placed between the joints, to prevent any seepage. The connections to the foundation, by filling the channel with mortar, are structural, as well as those with the top rod and realize fixed end restraints (fig. 3).



**Figure 3. Assembly sequence of a house**

The precast panels offer smooth finishes on both sides, ready for painting, which allows to give the finished house a pleasant aesthetic appearance, as shown in figure 4.



**Figure 4. A typical house built according to the system: a) structure completed; b) finished**

More than 1,200 houses were built using this very effective system for low-cost housing, under the umbrella of the mentioned government grant program.

### 3. In the desert

#### 3.1 Boundary conditions

Gas fields located in the middle of the Sahara desert in Algeria, where exploitation was mobilizing in the early 1990s, needed dwelling, social and service buildings for large worker settlements. Surroundings were lacking access roads or basic facilities; materials and supplies including natural coarse aggregates for concrete, were only available at locations over one thousand kilometers from the sites.

The main requirements included resistance to wind and seismic actions, thermal insulation, construction speed. The work was not limited to personal dwelling but also included social buildings and workshops.

The ideal structural solution would involve loadbearing walls, for providing stiffening elements and acting as cladding, partitions at the same time. Ultimately, a design solution was devised to use precast concrete loadbearing panels and solid slabs.

At first stage, two villages (one of them appearing in fig. 5) were built, with forty dwelling buildings, six social buildings (for meetings, healthcare, religious functions, shopping, restaurants, ...) and ten workshops were built using lightweight cellular (foamed) non autoclaved concrete for walls and slabs. On the other hand, for a limited number of additional elements in areas requiring ample and unobstructed free space, standard precast concrete frames with columns, beams and roof elements were used. Throughout, the panels performed an important structural function, either providing both bearing and lateral resistance, in one or two-story buildings, or being only large cladding wall panels for lateral stiffening of the R/C frames. Moreover, foamed concrete was used for the foundations, sensibly reducing their cost.



Figure 5. Workers' settlement near gas fields in the Sahara desert

Given the lack of coarse aggregate, concrete was made with local sand (sieved and washed), cement, superplasticizer and foam, with the great advantage of achieving a low density product. This generated two decisive features: low self-weight of the elements, making the application possible for slabs as well, and very good thermal properties (mass and conductivity combined), making additional insulating material unnecessary. It is worth noting that temperatures in the area reach up to 55 °C.



Figure 6. a) The prefabrication plant; b) oversized units



As the performance proved to provide optimum results, a prefabrication plant was first built (in steelwork) on the site (fig. 6a), followed by a quick start in precast element production. It should be noted that the transport of the precast elements was possible without problems on the existing desert tracks, including the transport of oversized elements (fig. 6b).

### 3.2 Structural system

The use of foamed concrete as a structural material was not in the scope of structural standards and codes at the time. Therefore, ad hoc rules were agreed with the authorities and the client. In fact, the system was to be used for one- and seldom for two-story buildings with short floor spans, making the solid panels subject to low-level stresses in service. Specific tests were made to assess properties like strength, elastic modulus, behavior under long term loading and bond with rebars.

Foundations of dwellings were 0.30 m deep rafts with a similar concrete, of a density of  $1800 \text{ kg/m}^3$ , cast in-situ.

Precast elements were made of cellular concrete of  $1600 \text{ kg/m}^3$  with a compressive strength (cubic) of  $15 \text{ N/mm}^2$ . External walls were precast panels 3.2 m high and 250mm thick, providing a coefficient of thermal conductivity of  $K = 1.4 \text{ kcal / m}^2 \text{ h } ^\circ\text{C}$ ; internal partitions are 160mm thick. Upper floor or roof are made of 200mm deep solid slabs of the same concrete, simply supported on four sides by internal and external wall panels, with spans less than 4m; roofs were in some cases sloped as well as the top of their bearing panels (Fig. 7)

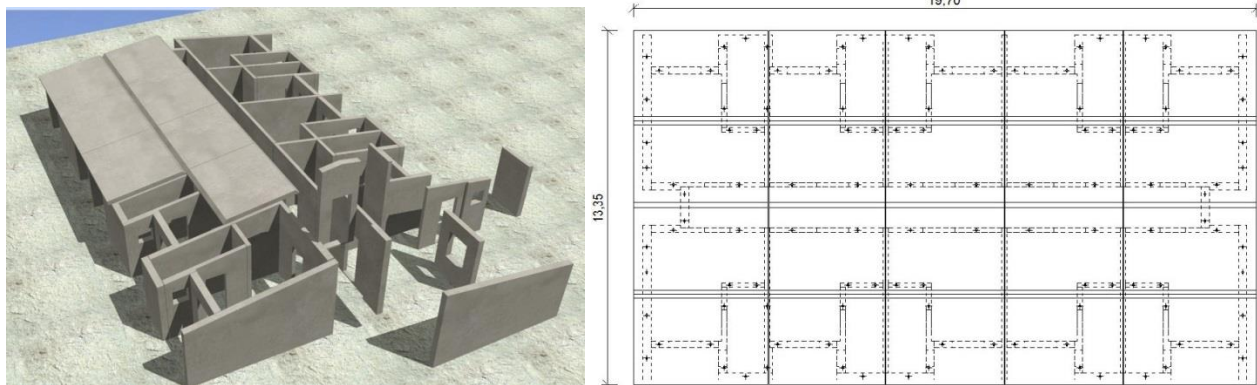
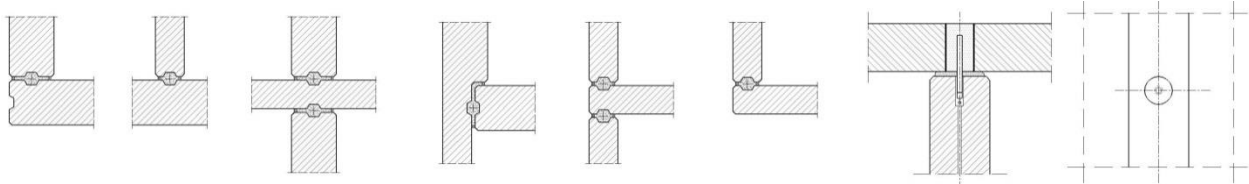


Figure 7. Scheme of a typical house and plan of the roof with the points of connection to walls



Figure 8. Finished houses, and a foundation raft for an additional one

Connections were specially devised for maximum simplification, taking advantage of the low level of stressing. Vertical joints between panels were continuous recesses of 25 x 80 mm on both sides, without keys for vertical shear, filled with mortar and relying on adhesion only. In fact, they are not required to perform a structural function, i.e., walls do not need to be connected to form **T** or **I** cross-sections. Joints were finished and closed with sealants. Supports of wall and slab panels rested on a thin layer of mortar and they interacted as a whole in a boxed system behavior that was ensured by vertical pin rods protruding from the wall panels into holes of the slabs, wide enough to account for all tolerances and again filled with mortar. Verifications against wind and seismic actions showed that the walls did not need to be anchored to the foundation, in the absence of tensile resultant forces. Joints between slab units, welded in two points and filled with mortar, ensured the compatibility of deflections. For two-story buildings, the rods continued throughout the slab and into the upper wall panel.



**Figure 9. Typical panel-to-panel connections (1-6: horizontal cross-sections) and panel-to-roof connections (7: vertical cross section; 8: plan view)**

In this way, a typical “non-emulative” system was built up, with elements connected to each other by means of linear hinges.

Panels were also molded with decorative reliefs depicting local architecture and then painted, as shown in the figures below.



**Figure 10. Examples of houses built with cellular concrete precast wall panels**

The system proved to be effective from all standpoints: construction speed, economy, quality and overall efficiency. Further settlements were then constructed.



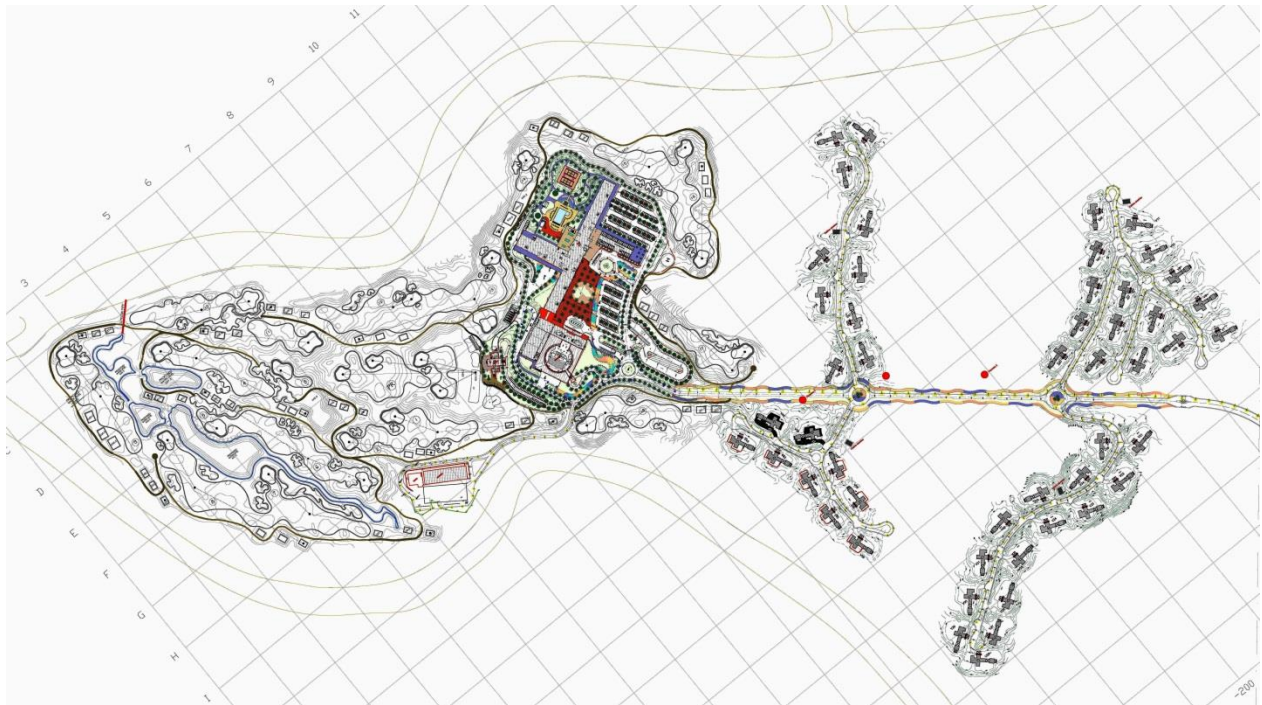
## 4. In the equatorial rain forest

### 4.1 The environment

The project was a large conference center and hotel compound, located within the African rainforest in Equatorial Guinea, about 200 km from any town or even road, at the moment.

It was the first ever construction to take place in an region where the completely new metropolitan area of Oyala was planned to be built.

The site, a river peninsula, was previously fully covered by a dense rainforest jungle, making the work on the final layout only possible after site clearing (fig. 11).



**Figure 11. General plan of the compound with hotel, conference center, park and villas**

Temperatures in the area are not extreme but rainfall is, with 3,100 mm per year, which may be critical for the works planning and invites to reduce outdoor operations.

To cater for the Project's size, installing a prefabrication plant in the vicinity, in spite of the difficult and adverse surrounding conditions, was identified as a sound and ideal investment.

Firstly, the presence of source of natural aggregates needed to be identified and, fortunately enough, optimum quality and abundant granite was found in a nearby location. A quarry was established as well a high capacity crushing plant, producing fine and coarse aggregates.

As for the project in the Sahara desert described above, short range transportation was rather easy and oversize was not a problem for the units' transport to the working site, whereas long range transport was problematic.

The compound comprises a five-star-luxury hotel with 450 rooms, suites, restaurants, roof gardens, shops, fitness center and SPA, business center, underground car parks and all related services, as well as a congress hall, a medical clinic, and outdoor resort amenities like a 18 holes golf course, swimming pools and tennis courts, with a built up area of 150,000 m<sup>2</sup>, within an area totaling 250 hectares.

Fifty high-standard two-story individual "villas", 700 m<sup>2</sup> each, are also part of the compound.

## 4.2 The buildings



Figure 12. The five-star luxury hotel and conference center – front view



Figure 13. Plan of the hotel and conference center

Regarding the structures, the production of high quality precast concrete, with a compressive strength of  $50 \text{ N/mm}^2$ , was made possible by the mentioned conditions and the design was performed together with the study of the elements required.

For the hotel, the foundations were a grid of surface beams, cast in place, as well as the columns of the underground garage and the first level. The upper part is divided in blocks, up to 8-story high, made of precast frames and cast-in-place stairs-elevators shafts. The latter provided most of the resistance to lateral forces of the whole construction. All floors were constructed using precast pre-stressed hollow-core slabs.

All connections were of a wet type, with overlapped or welded reinforcement, in order to achieve a continuous “emulative” concrete structure, i.e., matching the behavior of fully cast-in-situ structures. The façade was also made of precast concrete elements. Only the hall’s roof and its inner flyovers were in steelwork.

Structures of the villas (fig. 15) were also made of precast load bearing wall panels.





**Figure 14. Hotel's structural 3D model and a construction phase**



**Figure 15. One group of the villas, built with precast concrete panels,**

Most interesting is the construction of the prefabrication plant itself. Contrary to the previous case, this was built with precast concrete elements. In fact, it is an example of self-prefabrication, within the jungle (fig. 16). After installing a crushing plant for the aggregate, a concrete mixing plant and the prestressing beds, pocket foundations, columns, pre-stressed beams and pre-stressed joists were produced for mounting the plant's 10,000 m<sup>2</sup> hall itself.



**Figure 16. The plant during its own "self-prefabrication"**

What was called “self-prefabrication” of the plant was chosen for two main reasons: (i) the high local cost of steelwork compared with concrete produced on site and (ii) the possibility of training local unskilled personnel with the prefabrication techniques.



**Figure 17. The 10,000 m<sup>2</sup> prefabrication plant in full operation**

Thereafter, the plant became operational for the construction of the compound (fig. 17). Later on, it has been used for other projects nearby.

## **5. Conclusions**

Structural prefabrication has been thought often as a means for selling closed systems. In fact, little of this remains at that stage. Through research and application, concrete prefabrication, has significantly advanced over the decades and has succeeded in overcoming many challenges, being adopted in the rarest and most difficult environments, too.

In this respect, the cases presented above show how it has been possible to build concrete structures with special requirements in unusual environments, that could have hardly been met using traditional means. The case studies illustrated in the paper are examples of the ability to adapt to local resources, which is a way of transforming imagination and theoretical research into actual and practical realizations. This without forgetting the typical advantages of prefabrication, such as the quality of the final product and the speed of construction.

In the examples shown above, prefabrication made the projects feasible, where traditional construction techniques would have encountered overwhelming obstacles, making such undertakings extremely difficult and perhaps even unachievable.

Paradoxically, in a non-industrialized context, prefabrication can be by far the best if not the only solution for uncommon construction. The authors keenly await further opportunities for getting involved in other unusual environments in which, by facing different conditions and challenges, they could once again test and confirm this statement.

# Paddington Rail Station

George Jones

Member of *fib* Commission 6

Director, Commercial Design Concepts Ltd (CDC Ltd)

**Abstract:** The Paddington Rail Station is at the London end of the First Great Western Line from Bristol. The station is presently undergoing major renewal and expansion as part of the Crossrail project. It is one of the largest and most significant infrastructure projects being undertaken in Europe.

Part of the Station extension involves the installation of precast concrete ceiling panels then the use of “top down” construction from ground to track level, enabling work at ground level to be carried out as excavation proceeds.

The Station has significant geometrical complexity and the use of BIM modelling was essential to achieve the satisfactory coordination of services within the concrete envelope. The complex, but regular, ceiling profile favoured the use of precast concrete to achieve the required consistency of finish and profile, and to maximise the benefits of repetition.

**Keywords:** Railways, Precast Concrete, Top Down, BIM

## Project Background

A new station is being constructed and integrated with the existing Paddington Station as part of the Crossrail project across London. The mainline Paddington Station was at the eastern end of the First Great Western Line, undertaken by Isambard Kingdom Brunel and opened in 1854. The existing station is a central London railway terminus and London Underground station complex served by four underground lines. It is also the London gateway for international passengers arriving from Heathrow.

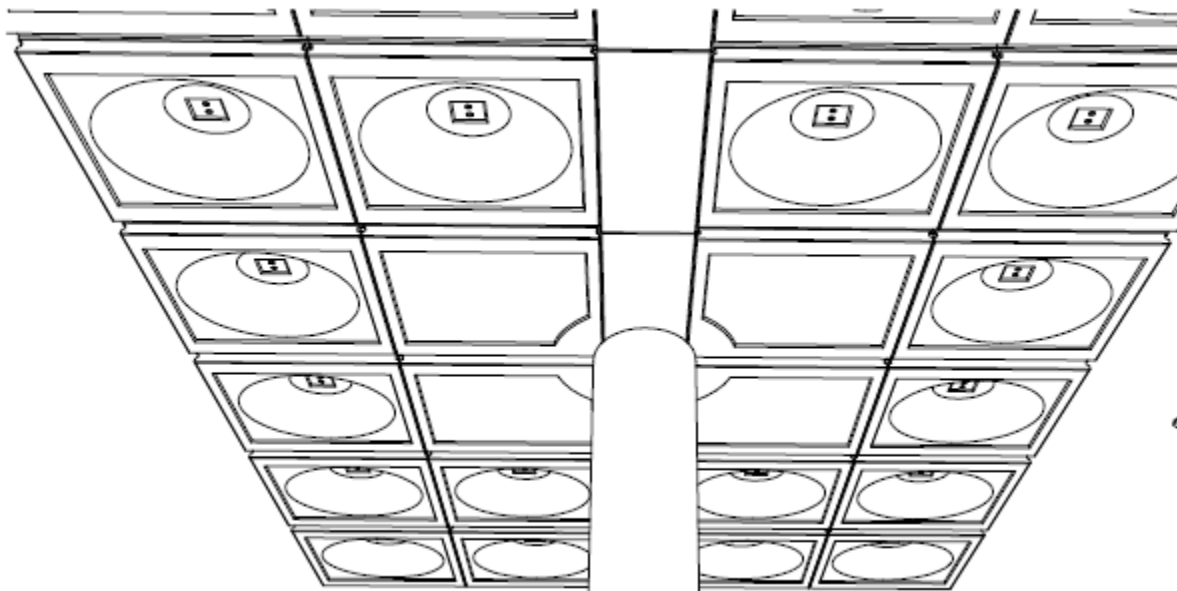


**Figure 1: Architect's section through new station**

## Selection of Precast Concrete for Ceilings

The ceilings to the main platforms and concourse areas are formed as curved coffers with lighting at the top of the curve of each coffer. The coffers are of consistent profile and are set out in regular patterns. Fair and consistent finish for the ceilings is a contract requirement. This could only be achieved economically using precast concrete.

In order to limit the amount of mouldage and to achieve consistency the coffers were cast individually through repeated use of the same moulds, and installed in the required patterns. Each coffer had a plan area of 2.5m square and depth of 160mm. A total of 1132 precast ceiling elements were supplied as part of the contract, of these 286 were coffered units. The original cast in place scheme required 180 coffer moulds to meet both programme and quality targets. The precast solution used only four glass fibre coffer moulds.



**Figure 2: View of part of ceiling from platform**

The trackside platform is over 250m long and the coffered ceiling fully covers the platform area. Cast in place concrete is provided over the tracks themselves.

The precast concrete coffers act as permanent formwork to a structural slab of varying depth between 1500 and 1800mm. The coffers are designed to withstand the construction loading from cast in place concrete and also the possibility of blast loading during service.

In order to accept precast concrete as a solution for the ceilings Crossrail required a full size mock-up of a typical bay to be constructed at the Contractor's precast production facility. The mock-up had to take account of construction conditions and incorporate all the service conduits required. The Contractor was using "top down" construction (See later section also). Therefore, to reflect the site conditions each precast slab spanned between temporary supports onto white neoprene bearing strips to provide an even bearing surface and minimise marking from the bearing medium. A slab of 1800mm depth was cast onto the precast concrete permanent formwork.

The mock-up result was considered satisfactory by Crossrail and precast concrete coffers were accepted as the solution for achieving the specified ceiling finish and profile.

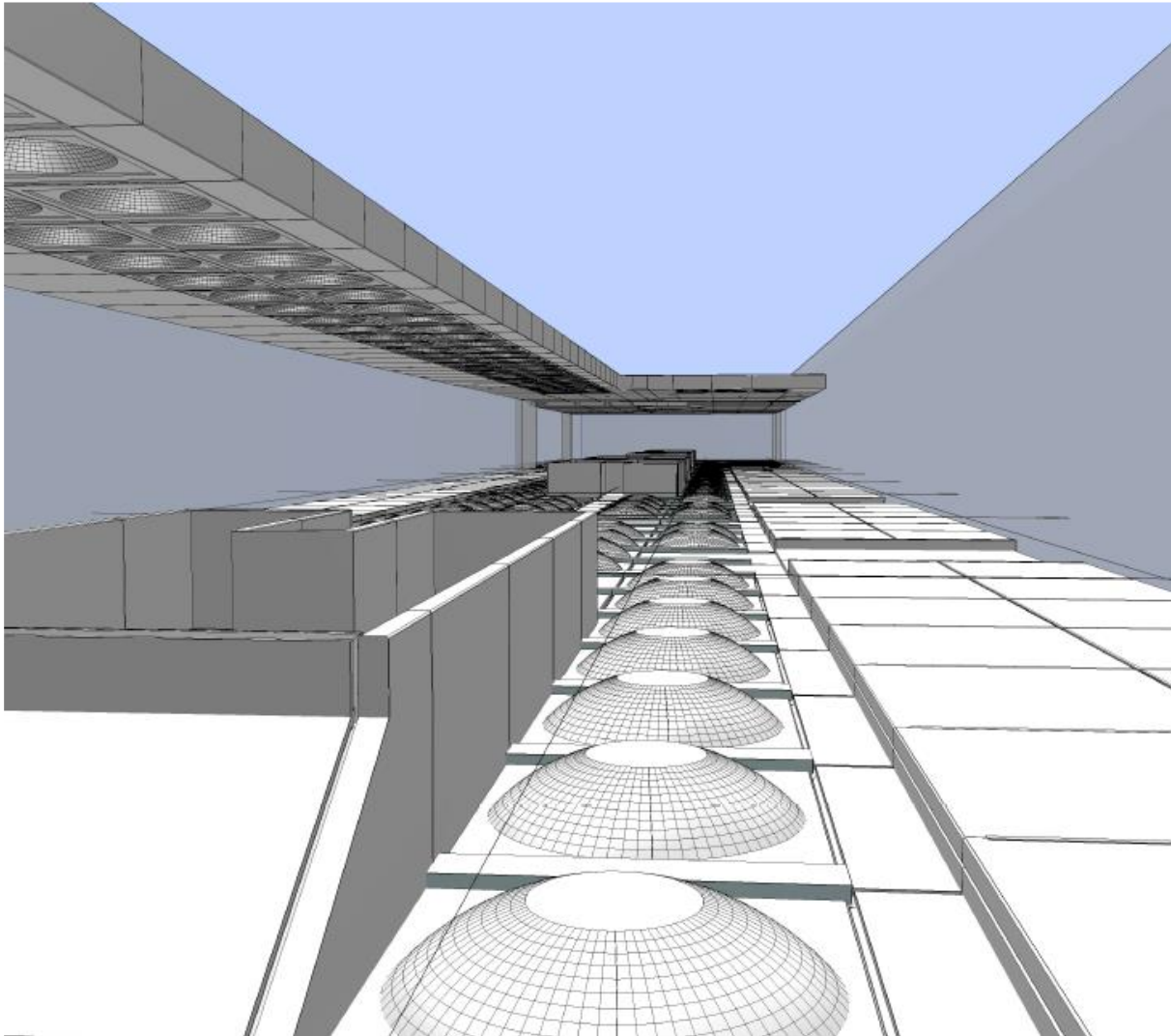


## Use of BIM Modelling for Precast Coffers

Close coordination between the precast concrete arrangement and the architectural layout was required to achieve the building form required by Crossrail.

It was decided at an early stage that the precast arrangement would need to be developed first, in line with general architectural and service parameters, and the finer detail relating to services and finishing was then integrated into the precast arrangement. The Architect's early 3D model was used as a basis for the precast arrangement. A 3D model of the precast arrangement was then developed in close collaboration with the Architect and the Services Engineer, with the precast team taking the lead role at this stage. Services requirements were added to the precast model by the Design team to achieve a fully integrated solution.

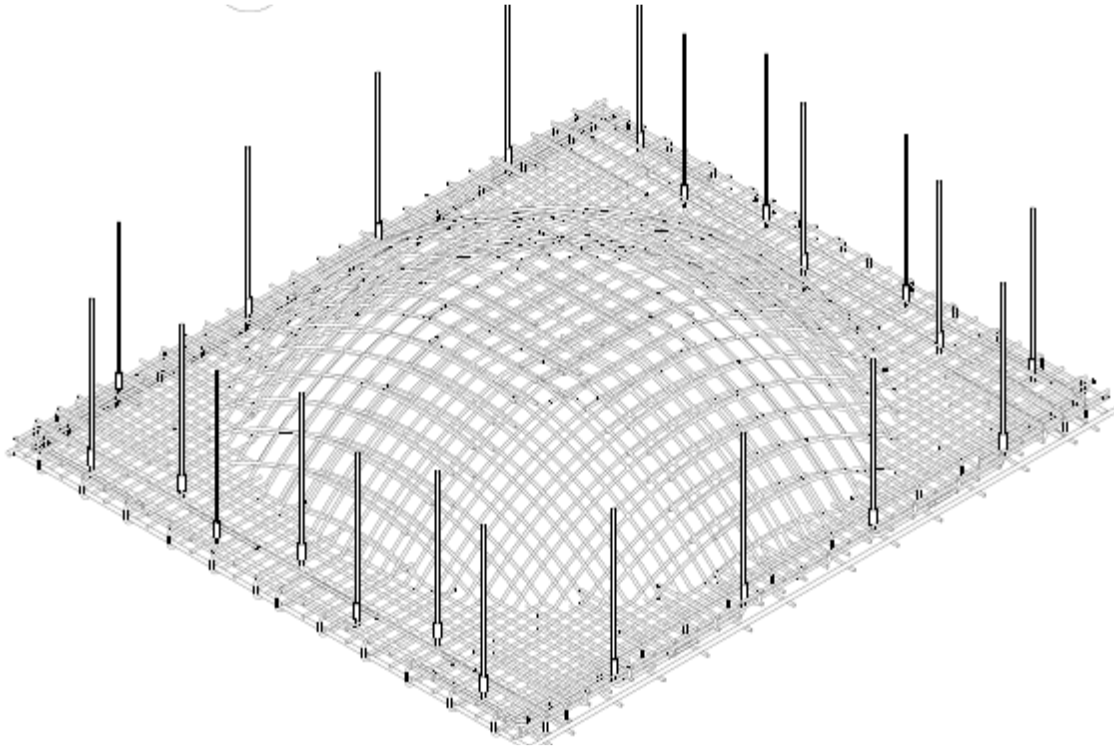
Figure 3 below is an extract from the model and shows a top view of the precast concrete elements only, forming the ceiling above the station platforms, with all other building elements removed. Precast concrete vertical elements were also used to form the finished wall face alongside the main station escalators to achieve uniformity of finish. An intermediate level of coffered slabs above the Concourse is also shown in Figure 3.



**Figure 3: Precast model extract at platform ceiling/concourse level**  
(Top of coffered slabs shown at Concourse Level before receiving insitu structural slab concrete)

The formwork requirements were challenging, and a model of the individual coffer was prepared and issued to the mould supplier. A master glass fibre mould was then produced by the supplier from his own 3D software, and thereafter three further identical moulds delivered to achieve profile consistency through the project.

Reinforcement detailing also became part of the BIM process with 3D versions of the coffer bar arrangement produced for fabrication by the precast producer. Structural design of the coffers was carried out using finite element software.



**Figure 4: 3D Model of Coffers Reinforcement**

Factory production rates exceeded site delivery requirements and project programme and budgetary targets were satisfied. Quality control and supervision had to be of the highest order to meet both aesthetic and technical requirements.

## **Top Down Construction**

Many projects in London now use “Top Down” as part of the construction process to avoid open excavations and allow other construction activities to run in parallel, which would be impossible using traditional methods.

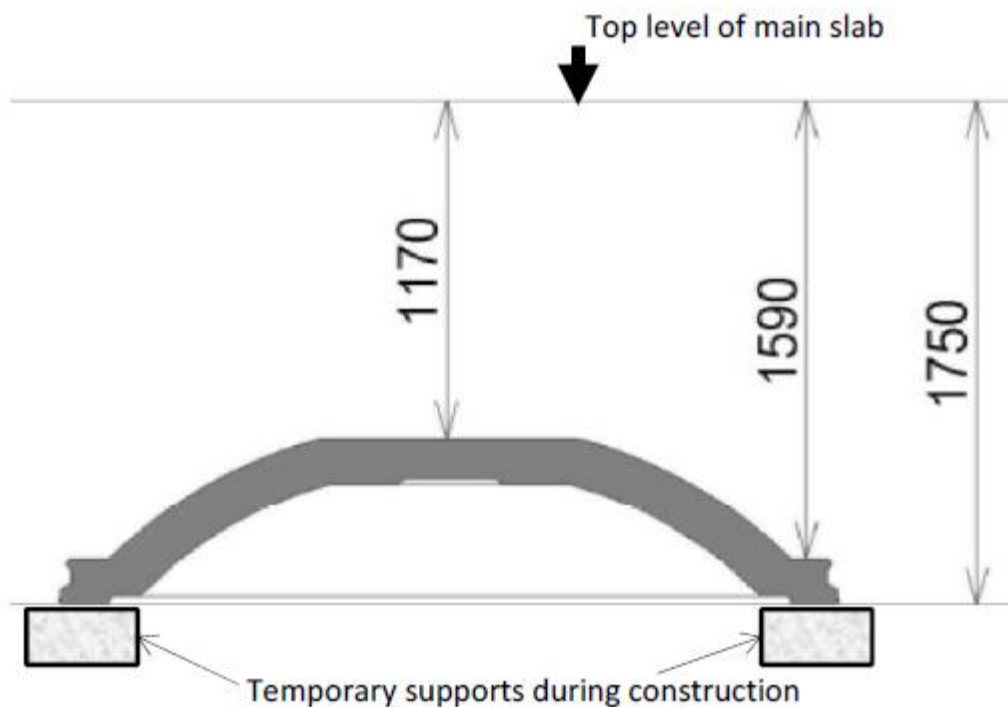
“Top Down”, as its name suggests, involves firstly constructing at ground level and above, with work below ground following either later or in parallel.

To enable use of this method a temporary supporting system for the superstructure has to first be installed. In this case steel piles were driven to act as temporary columns (See exposed temporary steel piles penetrating the concrete ceilings in Figure 8 below). At permanent column locations the steel piles will be encased in insitu concrete forming an elliptical visual section. At other locations the temporary columns are removed once the permanent concrete columns are constructed and the slab penetrations closed with custom made precast concrete cover slabs matching the general ceiling finish.



The top surface level structure was then constructed onto the ground surface. Once the ground structural slab had reached a satisfactory strength the strata below was excavated to expose the ceiling. This approach involves greater risk with regard to achieving the required surface finish as an extra digging operation is introduced. Also, the surface is not exposed to view until many weeks after installation. Use of precast concrete minimises these risks as each element surface can be inspected before delivery and corrective action taken at an early stage before it becomes critical.

The main precast concrete ceiling is above platform level. Excavation was completed from Ground to Concourse Level and temporary concrete strip footings then poured to support the precast ceiling panels as shown in Figure 5. The panels were landed onto neoprene strips (See mock-up reference earlier), joints sealed, and then the main structural slab reinforcement cage fixed on top of the precast ceiling as shown in Figure 6 below. The structural slab was then poured.



**Figure 5: Section through a Precast Concrete Coffered at Concourse Slab Construction Phase**

Once the Concourse structural slab had acquired its design strength excavation beneath Concourse resumed. The temporary footings were removed as part of the excavation operation. The precast concrete ceiling was now mechanically anchored to the structural slab via vertical tie bars that had been coupled to the reinforcement in the precast ceiling elements; see projecting vertical anchor bars in Figure 4.

Distribution of the precast elements at underground levels had been achieved through use of a crane gantry system. Elements were delivered to a designated distribution point at ground level alongside a "mole hole". "Mole holes" were located along the station as points for vertical delivery and removal of materials from the underground site. After delivery below ground by tower crane the elements then had to be distributed horizontally to their individual locations using the crane gantries. A gantry can be seen in the background in Figure 6.

Following completion of the Concourse structural slab an intermediate ceiling above was installed using traditional methods supported from the completed structural slab below.



**Figure 6: Structural slab reinforcement being fixed on precast concrete ceiling panels**

An excellent result was achieved with the ceiling finish. The temporary supporting system along the panel edges had resulted in minimal panel deformations and surface blemishing.



**Figure 7: Exposed Coffers Slabs**





**Figure 8: Exposed platform ceiling**  
(Note temporary steel piles penetrating the concrete ceiling)

## **Conclusions**

A challenge arose to provide a high quality fair faced concrete ceiling at the new underground station at Paddington, London. There were a number of other constraints that included a pattern of coffered elements forming the ceiling, the integration of complex services and finishes, the production of a cost effective and risk reduced formwork system, and the accommodation of “top down” construction in the process.

Precast concrete was chosen to provide a high and consistent standard of finish, certainty of profile and minimal, highly repetitive, cost effective formwork. BIM modelling achieved the technical end result required through close collaboration with the Design Team. Finally, a highly professional team foresaw potential problems at an early stage, solved them and achieved a commendable result.

## **Acknowledgements**

The following staff at Byrne Brothers (Formwork Ltd), the concrete contractor at Paddington Station:

Alexander MacCorquodale-Precast Manager

Colin McFadden-Senior Project Engineer (Construction)

Craig Nicolson-Senior Project Engineer (Design)

BIM consultant: Josef Buday-Buday and Partners Ltd

# PCI Design Awards Program

Jason Krohn, Precast/Prestressed Concrete Institute

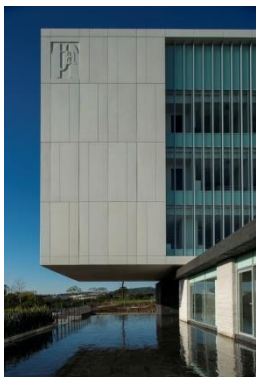
Daniel Roman, Southern Illinois University

Karla Vazquez, Southern Illinois University



For over 50 years, the PCI Design Awards program recognizes design excellence and construction quality using precast concrete. The program has helped the design and construction community innovate and advance by showcasing ideas that push the envelope, overcome challenges, and improve upon existing concepts. The program demonstrates how designers are continuing to utilize high performance precast/prestressed concrete to achieve sustainable, more cost-effective, aesthetically-pleasing, and quickly-constructed projects. All winning projects are showcased at the PCI Convention and National Bridge Conference, as well as included in summary articles published in the PCI Journal, Ascent and Aspire magazines. Together these publications reach more than 60,000 industry stakeholders. There are entries from across the country and even international entries. In 2014 a couple international entries won and received honorable mentioned. The following winners are selected from the 2014 competition results.

The winner for the category of “The Best Government or Public Building” was Salas Regionales del Golfo, located in Veracruz, Mexico. The architect was Tribunal Federal de Justicia and the precaster was Pretecsa. The building is the legal system headquarters for the state government. The façade was made up of 373 architectural



**White architectural precast panels**

precast panels. The architect opted for the white and beige marble aggregates and light acid etched finished. It took approximate 60 days

to erect all 373 precast panels (5873.5 m<sup>2</sup>). Along with the precast panels, the structure also has large curtain walls that look over the exceptional surrounding views. The precast manufacturing started late May of 2012 and installation was completed in July 2012. By using precast concrete, the project was able to maintain a clean working environment and not allow pollution to spread to local areas. The quickness of the erection of the precast allowed for a quick closure, which aided against the bad weather that the site is prone to receiving.

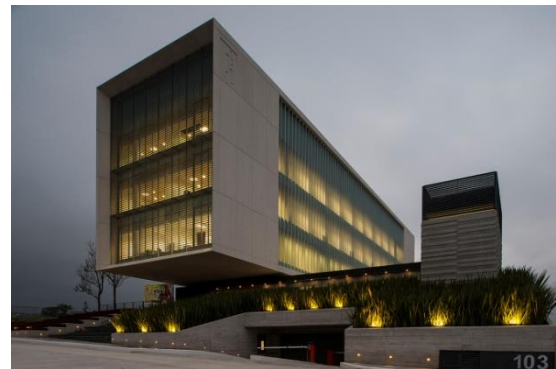
Another successful project that took place in Mexico, this time in Mexico City, was the Kinder Monte Sinai, which won “The Best K-12 School”, the architect was LBR&A and the precaster was Pretecsa. A



**Precast panel wall installation**

grade school with many of the basic amenities but with a modern touch, it houses a library, main courtyard, and 18 classrooms that are elevated 11m from the parking lot. Out of the 18 classrooms, 12 are whitewashed

precast concrete panels with drippers, perfect round window cuts at various



**Main entrance of Regionales del Golfo,**



**The Kinder Monte Sinai with window cut outs on its façade**

elevations. To allow for this stacking effect, the architect needed a material that was light. Glass-reinforced precast concrete panels reduced the weight to about one-third in comparison to the competing material. The cubes required 285 very slim precast panels, which contained white marble aggregates and were hand polished. It took approximately two months to erect the precast.

From schools to malls, internationally precast is being utilized and is being pushed to new grounds, as in the following project. Fiber optics were taken into consideration when designing this precast structure. La Maison Simons is a mall located in Montreal, Quebec, Canada. Designed by LEMAYMICHAUD Architecture Design and the precast provided by BPD L Beton Prefabrique. Requiring a material that allowed the flexibility to install fiber optics into the walls, designers quickly looked into precast concrete. The fiber optics light up the structure throughout the day. A total of 140 white double wythe insulated panels were used. The molds were created with recesses in various locations. They had to be designed to accommodate rain and other inconveniences. The fiber optics were woven into the panels to activate the eye catching effect. A challenge that was encountered was that each mold had around 600 recesses. With different variations of the panels along with the recesses, different molds had to be made to accommodate for the design. The project had to be efficient and appealing to the client.



LED illumination of La Maison

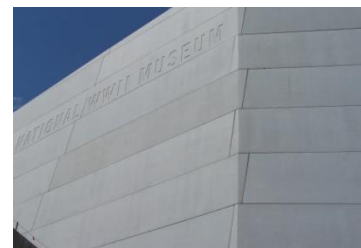
An honorable Mention under the Multi-Family Housing was awarded to the Hotel Staff Accommodation in Dubai, UAE. The structure houses 320 residential units for employees for a local corporation. The whole structure was precast, from load-bearing walls to hollow-core slabs, and cladding. The cladding is insulated sandwich wall panels, with no thermal bridges. The 21,368 m<sup>2</sup> structure is located in a developing zone of the city. Precast is even more cost effective when designing in a modular manner. The designer took advantage of that and was able to reuse a lot of the same structure and aesthetics throughout the design. To make the living complex more visually pleasing, greenery was added along with a pool and a green terrace. The precast erection took place from March 2013 to August 2013.



Top: Main entrance to Boeing Center  
Bottom Right: Boeing Center corner condition

particular project, which in fact is able to withstand hurricane forces. At approximate 30.5 m tall, it is the tallest building in the museum campus. They needed to enclose the building quickly to continue working on what the interior

The winner of the Government or Public Building was the U.S. Freedom Pavilion/The Boeing Center at the World War II Memorial. This project is part of an addition to an ongoing expansion to the museum in New Orleans, Louisiana, USA. The designer, Voorsanger Mathes LLC, used interlocking precast concrete elements which allowed an interesting corner condition. Gate Precast Co, provided the precast for this



was going to house, actual aircraft that would hang from the interior structure. The erection time was from September 2012 to October 2012. The precast panels were designed without any 90 degree angles. Horizontal joints align but are tapered, and the vertical joints are offset. The flexibility of precast made for these aesthetically pleasing details to be created. In total 253 gray, light sandblast finish panels were used in the project. The typical height of the panels is 2.4 m, about 23 panels were over 12m long. One panel was over 15m long.

The Sanford Heart Hospital in Sioux Falls, South Dakota, USA, was the winner under the category of Healthcare/Medical Structure. Designed by AECOM and precast provided by Gage Brothers, the owner of Sanford Heart Hospital primarily wanted the building to be constructed of masonry. Due to its tight location and possible disturbance that a full crew of masonry workers would have to the area, the designers had to look for an alternative. Precast was the solution for such conflict. The use of thin-brick-clad precast concrete panels allowed for a close resemblance to the buildings in the area. By using precast, the owner was able to save over \$1 million US dollars and the building was completed about 3 to 4 months quicker. A couple months were taken in the manufacturing of the precast, but it only took a little over 20 days to erect all of the precast. There was about 936 pieces that covered about 11982 m<sup>2</sup>



Finish perspective of thin brick cladding of Sanford Heart Hospital's clock tower



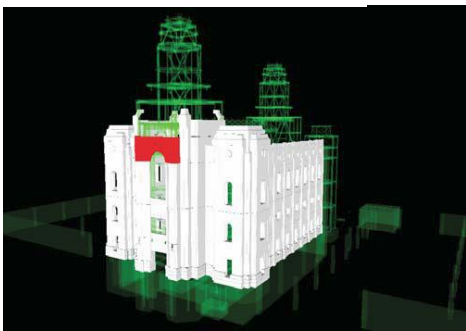
Z parking structure, close to being done

Car parks have been constructed out of precast concrete for a very long time. Some architects are taking the design aspect and are having fun with the limitless possibilities that precast concrete can offer. The Z in Detroit, Michigan, USA, won the Parking Structure category. It is a multipurpose 10 level structure that holds 1282 cars with retail and restaurant space in the lower level. The exterior façade uses repetitive formwork to create a frame pattern. The pattern was designed to reduce the scale of the 10 level building. The precast was manufactured from January 2013 to November 2013 and the erection of the precast was from April 2013 to November 2013. Since a lot of the manufacturing is being done indoors, the winter exposure that workers had to endure was really low. In total there was about 2,385 pieces from columns, double tees, to architectural finish panels.





North East view of Brigham Temple

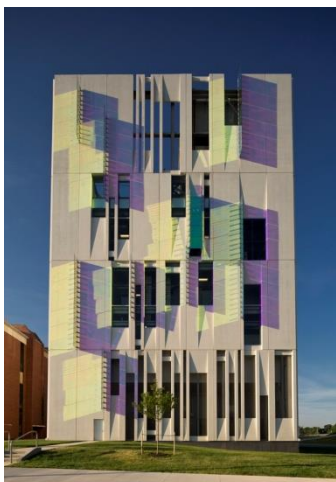


3D model utilized for construction planning and coordination.

The Religious Structure award was awarded to the Brigham Temple. The Architects from FFKR Architects were asked to design a temple with a stone façade. After calculating the cost and time frame it would take, they knew they had to go with precast concrete. With precast, they were able to obtain the look and quick construction all at a much lower price. The structure is clad entirely in sparkling white dolomite aggregate-based precast concrete panels. A total of 337 precast pieces were used: seven large panels were used to make the base; 100 panels were used for different ornamentation along the building site; and 230 panels were used on the main temple. The temple's spires are 45.7 m tall, that makes the temple visible from other local landmarks. "The architectural versatility and plasticity of concrete to accommodate several integral design features and create a complex façade of dramatic depth and bold character was

taken as an advantage" as one judge commented. The amount of detail that was integrated into the project would have been really hard to replicate with other materials or methods. There are about 40 different cornice details that were able to be reproduced to use again. A challenge, that was encounter during construction, were the steeples. Comprised of architectural precast "wedges", the tower was supported with interior steel framing and pre-assembled at the precast plant. When it was delivered they were lifted and attached to the structural. A 3D Bim modeling program was used to make sure all the design work

Ohio State University Chiller Plant located in Columbus, Ohio, USA, won the award for Best Custom Solution. The architecture firm Champlin Architecture worked with High Concrete group, the precasters, on this 10 story 5011 m<sup>2</sup> plant. Precast Concrete was utilized for its ability to be reproduced in



Shadows casted due to glass fins

such number of forms. There were 11 different forms that were used to produce about 200 different panels that went into constructing this building. These panels were arrange in such manner that allowed for fenestrations to view them inside but still able to keep the interior temperature consistent and the energy use regulated. The façade is more than just a concrete box, it also has a high polish finish and "fins" of diachronic glass. These "fins" cast different colors on to the concrete, and it varies on the time of day, season, and



Erection of custom sized precast panels

location of whoever is looking upon it. 3D modeling was used at different times during the project. In one occasion in which it was helpful was during the design of the connection between the steel and precast cladding. Over 100 of the connections were pre-connected to the steel frame as it was fabricated, which saved a lot of time during erection. The erection took from December 2011 to January 2012. According to the architect, “By using such a small number of panel types, a significant reduction in precast cost was realized because the manufacturer was able to utilize these forms multiple times, in lieu of constructing new forms.” The design team also wanted to design the largest size panels in order to accelerate the installation process. Transportation criteria dictated the final panel sizes. The size of the panels are 3.75 m x 9.1 m, with the top panels being 10.6 m tall to enclose the cooling towers. The precaster’s involvement during the design was key to the success of the precast work on this project.

Not all projects are meant to last forever; the G8WAY Pavilion in Washington, DC, USA, is a temporary structure that is a great example of how to utilize ultra-high performance concrete (UHPC). With Gate Precast providing the precast and Architect Davis Brody Bond as the designer, this pavilion with sloping canopy and rooftop terrace won the Best Custom Solution Award. A total of 181 light weight precast ultra-high performance panels that measure 45mm thick were used to construct the pavilion. As the result of increasing the size of the precast panels to match the structural steel, the architect was able to minimize the number of extra reinforced steel members. It took roughly 19 days to make 181 UHPC panels and the erection was completed in one month. The roof structure is about 122 m long by 7.6 m high by 18.2 m wide and an impressive 44.45 mm thick. The strength, durability, and aesthetics that UHPC offered helped in multiple functional benefits and creative design possibilities. The panels and the supplemental hollow structural section attached to the back of the panels were incorporated into the structure, which created an appealing, yet structurally safe pavilion. The architect was able to eliminate the need for additional steel framing to support the architectural roof panels by using lightweight UHPC. No waterproofing system was required below the panels because of the UHPC roof system. This saved more money for the owner.



Elevation view of G8Way Pavilion



UHPC being installed on G8Way Pavilion

Various number of bridges were entered into the competition. The PCI Design Awards program divides the bridges into many different categories; a few categories are Best Bridge with Span over 46m, Best Non Highway Bridge, Best Rehabilitated Bridge, and Best Transportation Special Solution. The winner for Best Bridge with Main Span over 46m was the Foothills Parkway Bridge No. 2, located in Wears Valley, Tennessee, USA. The engineer was Corven Engineering, Inc while the precaster was Ross Prestressed Concrete Inc. The bridge is 241 m long.

Since the site is on an uneven mountain terrain, a temporary work trestle was used. It granted access along the entire bridge alignment and could be reconfigured as work shifted from foundation and precast concrete segmental piers to superstructure segment erection. The winner of the Best Non Highway Bridge was the North Milliken Avenue Underpass value Engineering Redesign, in Ontario, Canada. The precaster, Oldcastle Precast, worked closely with the Engineer, T.Y. Lin International, to be



Segments of precast being placed



Rehabilitation of New York Avenue bridge  
Permanent concrete girder system

able to create this bridge. The underpass measures at 52 m long by 16 m wide. The use of precast saved about \$900,000 US dollars over the original plan of using steel. I-5 Bridge over the Skagit River in Burlington/Mount Vernon, Washington, USA, won the award for best Rehabilitated Bridge. The rehabilitation came after a crash caused a 49 m long part of the bridge to collapse. Precast concrete was chosen for its time and cost effectiveness. This precast option would minimize the need to close the interstate. The Rehabilitation of New York Avenue Bridge in Washington, DC, USA, won the Best Transportation Special

Solution. The project engineer was T.Y. Lin international, and the Precaster was The Fort Miller Co. Inc. This particular bridge spans and connects Maryland and Washington DC. Being a major transportation outlet, it is used by over 87,000 cars a day. The design used precast, post-tensioned concrete deck panels that cantilever 4 m over the exterior girders. Rehabilitation and repair of the existing substructure to sustain the multi-beam superstructure systems was accomplished by constructing post-tensioned pier caps that rest on the retrofitted pier columns. The deck replacement was achieved through the innovative erection of longitudinally and transversely post-tensioned precast concrete deck panels.



Foothills Parkway Bridge Completed



West elevation of Terracotta finished panels

Some Buildings are awarded multiple awards such as the following entry, the University Of Missouri Henry W. Bloch Executive Hall Of Entrepreneurship and Innovation. It was awarded the Harry H. Edwards Industry Advancement Award and Best Higher Education Building. The precaster on the project was Enterprise Precast Concrete, Inc. and the Architects were BNINM Architects and Moore Ruble Yudell Architects & Planners. This project took a material which has been used in architecture for many years. With



the help of the precaster and the innovations of precast, they were able to take terra-cotta to a whole new level.



Erection of terracotta panels

Terra-cotta was used in the large 3.65m wide, fully insulated precast panels. It was quickly realized that by choosing set wall conditions, other factors were going to work out perfectly, such as the wall system supplying a great rain barrier without the intricate fabrication of a rain screen system. In reward to its great thermal performance, it was awarded LEED Gold Registered. A lot of research and tests were conducted. Everything was explored from the coefficient of thermal expansion to the amount of precast bowing that the tiles could withstand before cracking, the optimal thickness of the tile, reaction of the panel during freeze-thaw cycles, and much more. The terra-cotta company is given a lot of credit for being hands on when it came to testing and answering any questions the architects or precasters had. “Once the building became thermally stable, it allowed us to bridge the budgetary objective together in one solution,” noted the senior project architect. The structure was comprised of 159 pieces (total of 5,852 m<sup>2</sup>). The panels were 3.65m wide and about 280 mm thick.

The University of Kentucky Albert B. Chandler Hospital Pavilion A won the Sustainable Design Award. Located in Lexington, Kentucky, USA the hospital was designed by GBBN Architects and the precast was provided by Gate Precast Co. The precast concrete panels consisted of 75 mm front wythe of concrete with another 16 mm layer of thin brick, a 50 mm center of polyisocyanurate insulation with ship-lapped edges, and interior 100 mm structural wythe. The nominal panels are 2.03 m tall and 11 m long. The main concern when completing the project was enclosing the interior as quickly as possible so that the complex interior could be worked on as soon

as possible. This requirement went hand in hand with having the building all continuously insulated without any cold spots. No thermal bridge was allowed at the connection points, because it was crucial to meet energy requirements. The insulated panels came into perspective in a great manner later on when it was realized that it had other benefits such as; inherent mold and mildew resistance, excellent indoor air quality due to the lack of off-gassing or other chemical interactions, noise dampening from exterior sources due to its high mass and elimination of air penetration, fire resistance due to



Finished perspective of The University of Kentucky Albert B. Chandler Hospital Pavilion



Pre-insulated thin brick precast panels

concrete inorganic composition, and reduced trades on site during construction. A total of 1,758 panels were erected.

The Rich street Bridge in Columbus, Ohio, USA won the All-Precast Concrete Solution & Bridge with Main Span from 23-45 m. The Project engineer, Burgess and Niple, Inc and precaster, Prestress Services Industries, LLC were in charge of constructing this bridge. The modern ribbed bridge spans 717 m, it is constructed of semi-lightweight precast, post-tensioned concrete arch ribs. The primary design called for cast-in-place arches, but it was realized that it would take more time and more money to accomplish. Using precast instead allowed the project to be completed approximately 7 months earlier and reduced the cost by about 10 million US dollars. The modern arch structure uses precast beam, arch rib, and arch apex segments stitched together with a combination of pre-stressing and field post-tensioning to create a fully continuous frame, eliminating intermediate expansion joints and spandrel columns. The bridge has five spans and three lanes, utilities integrated in the bridge railing and sidewalks for use during festivals and community events. The bridge also has an open design that provides more transparent views and reduces flooding impacts.



Aerial view of the Rich Street Bridge



Precast rib arches



Close up view of the rib arches with post-tensioning ducts

# Sustainability of Structures with Precast Elements

D. Fernández-Ordóñez<sup>1</sup>, B. González-Rodrigo<sup>1</sup>, J. Ramírez<sup>1</sup>, R. Valdivielso<sup>1</sup>

<sup>1</sup> Universidad Politécnica de Madrid (Technical University of Madrid), Madrid, Spain

**Abstract:** Prefabrication has evolved in depth and breadth from its beginnings, bringing many of the advantages of industrialisation to construction, while solving some of the problems that arose in the early years. Today prefabrication, compared to traditional construction methods, and concrete as a material, feature a number of beneficial characteristics.

As prefabrication makes optimal use of materials, its potential for savings is much greater than in cast-in-situ construction. Structural performance and durability are also enhanced through design, modern manufacturing equipment and carefully planned working procedures.

This paper deals with the very interesting subject of Sustainability of building structures and taking a close look at precast concrete structures. It reviews the specific aspects of industrialized construction in enclosed factories. These factories make possible that production conditions are controlled for the quality point of view of the precast elements. Also the conditions that make possible a better quality control than the normal on site work make possible that sustainability conditions are better met. Sustainability conditions take into account from the simple control of emissions, the working conditions of the workers to the possibility of recycling and reuse.

**Keywords:** prefabrication, thermal mass, sustainability, concrete technologies, environmental production.

## 1. Introduction

The production of precast concrete elements normally takes place under controlled climatic conditions in enclosed factories. This makes control of waste, emissions, noise levels, etc. easy compared to the same process at a traditional building site. Working environment is also easily controlled.

Moreover the use of new technologies like self-compacting concrete (SCC) can significantly reduce the noise and vibration in the production process. The use of high performance concrete (HPC) enables design and production of more reliable and more durable structures with optimized shape. The potential for savings in structural material consumption and consequently natural resources is evident.

The environmental burden of prefabrication is mainly the impact caused by the raw materials of concrete (especially production of cement and steel) which is similar as other concrete construction structures but in a reduced way because of the reduced use of materials in comparison with in situ construction. The environmental burden caused by raw materials is approximately three times larger than that caused by the production process of the elements, as indicated by the examples of environmental product declarations.

The thermal inertia of heavy materials is well known for both in warm and cold climates. Most people have experienced the comfort of coming into a comparatively cool stone building on a hot day in a warm climate. In precast structures several constructive systems have been developed using this characteristic.

## 2. Precast structures

### 2.1 Service Life

In the First International Conference on Sustainable Construction in 1994, sustainable construction was defined as the creation and the responsible maintenance of a healthy constructed environment, based on ecological principles and with an efficient use of resources. (Hendriks, 2000)

This definition resumes most of the essential functional characteristics, as the use of energy, internal ambience conditions and flexibility. A very important aspect for sustainability, and for the life cycle assessment for the construction of a building, consists of taking into account a design life for different structures and systems that are in the building following the principles life cycle analysis, and this means as follows:

- Primary System= External facades and structural design > 80 years
- Secondary System = main interior load bearing partitions > 30 years
- Tertiary System = interior non load bearing partitions > 10 years

Therefore, both durability and recycling possibilities are two very important aspects of life cycle design as can be observed in Figure 1.

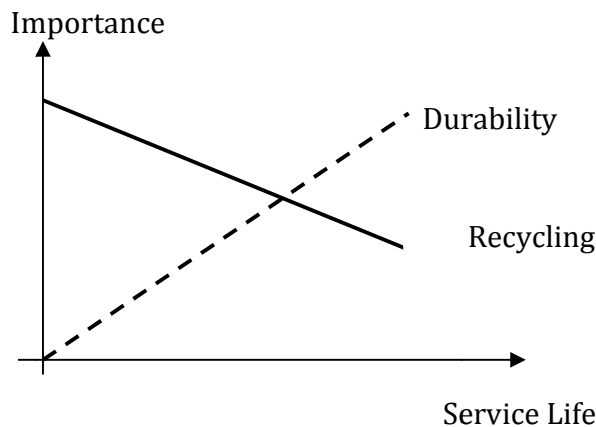


Figure 1. Principles for optimization in service life (Óberg, 2000)

## 2.2 Structural Systems

Some examples there have been compared the structures of buildings with several heights for buildings of both homes and office. The functional unit is one square meter of ground used by the building for the life of the building, including both horizontal and vertical structural components and supplementary materials, i.e., the total environmental load of the building. Lifetime expectation was taken as 50 years. Several schemes for handling the demolition debris were investigated. Differences can be seen in Figure 2

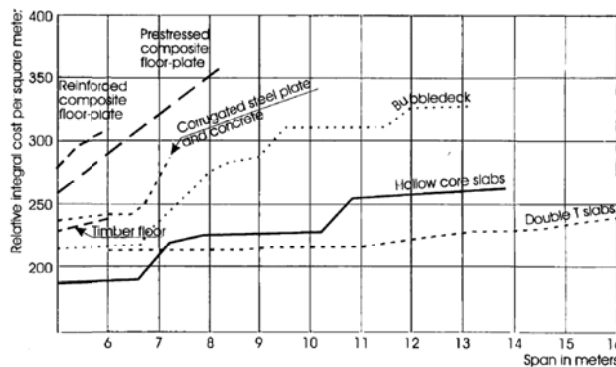


Figure 2. Relative Costs of different kind of decks for housing. (CIMbéton, 2002)

The example is basically a revision of the environmental contributions of each kind of structure to a given number of ambient hazards, like the greenhouse effect or acidification. The example has been developed in the Netherlands, and can be adjusted according to local conditions. The different effect categories are weighted according to local political environmental goals and regulations.

In the production of the structure of the load bearing components, it is generated from 75 to 95% of the environmental burden. Total Cost is set as the sum of the environmental burden and economic integral cost. Loads are calculated in two environments that must be articulated in monetary terms.

This is done by calculating or estimating the costs necessary to restore the environmental impact caused by the use of raw materials, energy, water, etc. These effects could be further normalized according to the ISO 14041 normative. In any comparison, it is of great importance that the functional unit always includes the same parameters, in this case regardless of soil type. The functional unit may include a selection of parameters such as structural performance, safety, comfort, etc.

### **3. Durability and flexibility**

The production of precast elements, under climatic controlled conditions, allows a precise control of the outcome, such as tolerances and concrete quality. Usually, there are higher design concrete strengths in precast concrete structures than in ordinary in situ structures. These two facts, high strength and controlled curing of concrete, have the potential to produce very dense and durable concrete.

The most common damage in concrete structures is reinforcement corrosion. In the production of precast concrete cover this damage is easy to secure and therefore, durable components are created. Furthermore, concrete used in precast elements has usually high resistance and therefore, it is a dense material that inhibits or delays deterioration.

These improved properties of high-quality concrete allow it to be used with minor requirements for a useful life span or with improved lifetime while maintaining the same cover. The utmost symbol of durability is to be able to use for longer time old structures. In sheltered from the weather concrete, for instance in all building structures., expectancy life is a hundred years.

If the structure is made so that the building can be changed without major demolition process, no doubt the building itself may have a long life, it will only need to adapt its inner architectural layout for new uses. Lately the practice of reusing concrete structures with old concrete removed for new buildings has become more and more frequent, as well as detaching existing structures and reassemble them again. Several examples are well known in the Netherlands, Sweden and Norway.

Precast structures are flexible in many respects. First, when using prestressing, design spans are usually long, so it is easy to adapt the building to future needs of change or forthcoming use demands. After then, life design for the structure and external walls is at least 50 to 100 years, while for the inner partitions is just about 10 years. After those 10 years the experience is that the building has to be redesigned for a change in use.

Connections are an essential part of the design and the construction of precast concrete buildings. With regard to durability, it is necessary to consider the risk of corrosion of reinforcing steel and cracking and spalling of concrete with due attention to the actual environment. Steel exposed to aggressive environment should be provided with a permanent protection. This can be achieved by applying a layer of



epoxy, rust proof paint or bitumen, or by casting-in with concrete or mortar. In many cases the connections cannot be inspected or maintained after the building has been completed. In such a case the connection, without maintenance, should have life expectancy that exceeds that of the structure.

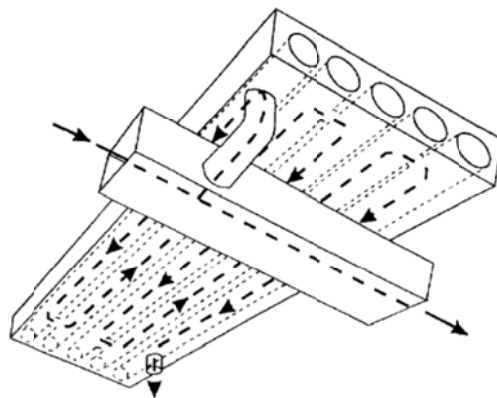
In the secondary buildings that have structures built with precast elements, such as mezzanine floors in industrial buildings, structures can be installed or removed at request. When buildings are designed as demountable, in can be advised to use bolted connections that are demountable and provide immediate fixity. Several systems that are fully demountable are in use for precast buildings. However, to overcome constructional deviations, tolerances in three-dimensional space must be accommodated.

#### 4. Thermal Mass

Thermal inertia of precast concrete deck elements can be used to reduce the energy used for cooling and heating the whole structure. Heating capacity of reinforced concrete is about  $2.20\text{-}2.50\text{MJ/m}^3\text{K}$ . With an average volume of  $30\text{ m}^3$  concrete per apartment, this energy of about  $70\text{ MJ}$ , is stored in the concrete structure for each degree as the temperature rises. This energy can be released and can contribute to heating when the temperature decreases. An example of this system of using thermal mass is the Elizabeth Fry Building, University of East Anglia 1998.

To get an idea of how much energy it is about, it can be compared with the total energy required to heat an apartment in a modern building on a Nordic country. On an annual basis the energy needed it is up to  $150\text{ kWh/m}^2$ , which is  $45\text{GJ}$  in an apartment of  $80\text{ m}^2$ . Therefore daily energy consumption in the cold season will be at least  $250\text{ MJ}$ . (Obergh, 2000).

It is well known that in a life cycle perspective, energy consumption while using the building is essential. Hence, any measure that would reduce energy consumption when the building is in use will have a significant effect on the environmental record of the construction. It is this aspect that makes visible the energy savings potential of all systems that use the thermal mass of concrete that are important from the environmental point of view, in addition to the economic benefit for the owner of the building.



**Figure 3. Example of the use of thermal mass in precast decks**

Another important benefit is that the concrete mass also provides excellent properties for acoustic insulation and is ideal as exterior walls for the houses overlooking the roads with heavy traffic, as well as isolation between different areas of a building, and as noise barriers along railways and roads.

Several systems have been developed in precast structures by using this characteristic. There is a representative system of these solutions in which the air is distributed in the voids of the hollow core slab elements.

This system minimizes the installed power and generates energy savings in both heating in cold weather. It also allows cooling in the warmer months. This system can achieve an energy heating saving of about 35% and a reduction in cooling power consumption of 40%. (Environmental Aspects of Concrete, 1998)

To maximize benefits of concrete precast structures, surfaces on roofs should be exposed. Eliminating false ceiling systems allows great savings in the overall height of the building that can provide 5% to 7% of construction cost savings. The concrete slabs behave as a normal steel duct. There are reports done by independent agencies confirming this. Thus the ducts can be used and maintained just the same as normal steel ducts.

Comfortable indoor temperature improves productivity of people working in the building. Another possibility is to use false open ceilings elements to allow air exchange between the upper part and lower part. Figure 4 offers an example about the use of thermal mass in reinforced or prestressed precast concrete floors at night time conditions on summer.

On summer nights, fresh air is blown through the roof with hollow core slabs using mechanical ventilation fans. This air cools the concrete slab and acts as a cold store space for the next day. Thus, intensive energy air conditioning demand can be reduced to a great extent or even eliminated. Another advantage is that cooling elements can operate with cheap electricity rates at night, while the traditional electric cooling is required during peak hours during the day.



**Figure 4. Example of the use of thermal mass in decks during summer: a) night and b) day**

In summer daytime conditions, with warm days, cold from the previous night stored in the hollow core slab roof improves comfort in two ways:

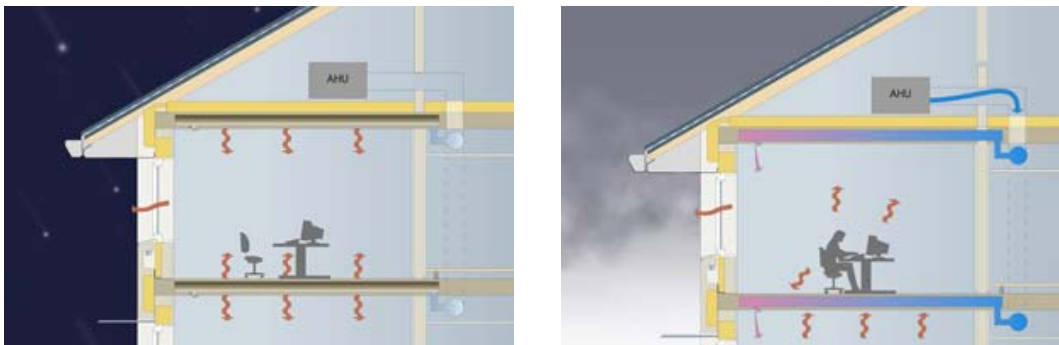
- It absorbs the heat produced by people and machinery.
- Cool air goes through the roof slab and cools before entering the room

The use of thermal mass instead of other cooling methods saves energy and allows more freedom for the occupants because if necessary, they can open the windows.

On the other hand, in winter night time situations as seen in Figure 5, the building is closed at night to keep heat gains, produced by people and machinery during the day. Anyhow in very cold climates additional heating may be required.

Therefore ventilation heating will start two hours before the working hours to ensure that the room temperature is suitable at the beginning of the working day. If the building cools at night below the preset limits, air conditioning equipment will initiate air recirculation, and a slight warming will start. There is no fresh air ventilation when the building is empty. There will be no fresh air ventilation in an empty dwelling.

With regard to winter conditions, even though in daylight conditions, the heat generated by the occupants and machinery will be radiated to the hollow core slabs and it will be also recuperated from the exhaust air, which goes again through the slab across the rooms. This design using these systems reduces ventilation needs for heating and cooling ducts or ventilation, and hence reduces cost and improves space utilization. It also uses very efficiently the available thermal mass.



**Figure 5. Example of use of thermal mass in decks during Winter: a) night and b) day**

There is no additional capital cost as the use of thermal mass doesn't add any extra material or equipment. In fact, since the installed AC-equipment is small-sized, generally about half of a conventional installation, the installation cost is lower than in a conventional system.

- 20-50% Lower Energy Consumption and thus lower CO<sub>2</sub> Emissions.
- 70-90% savings in power demand during peaks
- The building height is also reduced as no false ceilings are needed (lower construction costs)
- The system is silent and there are no draughts. The hollow cores act as efficient silencers which make the system completely silent. Since the supply air is warmed or cooled when passing through the slabs before entering the room, the temperature of the supply air is very similar to the room temperature.

There are benefits in Hot Climates as experiences from several buildings in the Middle East show a 50% reduction in installed cooling capacity required for the thermal mass systems compared to conventional air-conditioning systems. This results in reduced capital costs for air-conditioning by 15-30% due to much smaller dimensions on chillers, fans, etc. Also, the total energy costs will be 30-50% lower compared to an identical building due to lower energy consumption (the ambient air is cooler at night, which increases the efficiency of the chiller & night cooling can be used during parts of the year). The reduced installed power means lower electrical connection and distribution charges.

There are also benefits in Cold and Temperate Climates as in milder climates, such as Sweden and UK, the slabs are primarily cooled during night with the outdoor air. Small chillers, if any, are needed. Heating will also be reduced since the heat accumulated in the slabs during daytime can be used to warm the building during cold nights. The energy savings will therefore be very high, up to 50 %.

### 3. Conclusions

This paper emphasizes the importance of sustainability in precast concrete buildings taking into account the full life of the structure, even with the consideration of reuse and recycling. Taking into account these aspects, the contribution of thermal mass specific uses in precast concrete are considered.

- (1) The use of industrialization or prefab in construction provides the advantage of applying industrial methods for construction.
- (2) The use of available resources in industry provides materials optimization and means of implementation for structures. It can be either because they minimize work at site, or because structures can be performed with less materials and higher quality.
- (3) The greatest impact that involves industrialized elements transfer at site is compensated by the advantages of industrial means within controlled premises.
- (4) Thus environmental impact of industrial structures implementation is less than with traditional means directly on site.

### 4. Acknowledgement

The authors would like to express their sincere gratitude to the Civil Engineers School at the Technical University of Madrid (UPM).

### 5. References

1. Alexander, Sven (1995) Can Lightweight Aggregate be used with Advantage in Precasting? Symposium proceedings, Structural Lightweight Aggregate Concrete. Sandefjord.
2. Alexander, Sven (1997) Precast concrete manufacture seen from an ecological point of view. Symposium proceedings, Prefabrication - facing the new century. Helsinki.
3. Alexander, Sven (1997) Taking advantage of the environmental challenges facing the precasting industry. FTP symposium proceedings, The concrete way to development. Johannesburg.
4. Asunmaa, Otto-Ville Anttoni (1999) Optimizing Environmental Effects of Prefabricated Concrete Building Frames. Helsinki University of Technology
5. CIMbéton ( 2002) Bétons & environnement. Analyses de cycle de vie de bétons. Paris.
6. Elizabeth Fry Building, University of East Anglia (1998) The Feedback for designers and clients. New Practice Final Report 106. The Department of the Environment, Transport and the Region's Energy Efficiency, London.
7. Fib (2003) Environmental issues in Prefabrication. Bulletin 21 FIB
8. Fib (2004) Environmental Design. Bulletin 28. FIB
9. Fib (2008) Environmental Design of Concrete Structures. Bulletin 47. FIB
10. Fluitman, A; deLange, V.P.A. (1996) Comparison of the environmental effects of three concrete story floors. CREM Report no. 95.107Amsterdam.
11. Hendriks, Ch. F.(2000) Durable and sustainable construction materials, Aeneas,.
12. Jacobs, F.; Hunkeler, F. (1999) Design of self compacting concrete for durable concrete structures. RILEM symposium proceedings, Self-compacting concrete. Stockholm.
13. Óberg, M. (2000) The optimal concrete building. Lund Technical University. Division of Building Materials. Lund.
14. Paus, Kjeld (1996) Platsbygge - prefabbygge inom Sticklingshyden- idingi. Byggforskningsrådet, Stockholm.
15. Punkki, Jouni (2001) Sustainable Prefabrication. FIB Symposium proceedings, Concrete and Environment. Berlin.
16. Steen, B; Ryding, S-O. (1991) EPS, The Enviro-Accounting Method, An application of environmental principles for evaluation and valuation of environmental impact in product design. The Swedish Environmental Research Institute, (IYL), Gothenburg,
17. Straatman, Remco (2000) Environmental Related Issues in Precast Demountable Construction. Delft University of Technology, Faculty of Civil Engineering,
18. Swiss Society of Engineers and Architects (1998) Environmental Aspects of Concrete. Information on environmental compatibility, Zurich.

19. Tellus Institute The (1992) The Tellus packaging study. Assessing the impacts of production and disposal of packaging and public policy measures to alter its mix. Boston
20. NEW PRACTICE FINAL REPORT 106. The Elizabeth Fry Building, University of East Anglia – feedback for designers and clients.
21. Thermal Mass. A Concrete Solution For The Changing Climate. The Concrete Centre. Ref. TCC/05/05 ISBN 1-904818-13-7 First published 2005
22. Concrete for energy efficient buildings The benefits of thermal mass. Published by the European Concrete Platform ASBL Editor, Belgium
23. Energy Storage In Concrete Slabs Reduce Energy Consumption And Peak Cooling Loads At No Increase In Capital Costs. A. Engström, L-O. Andersson. Termodeck International Ltd
24. Elizabeth Fry Building. Building Services Journal April 1998

# Major Project Case Studies

# Christchurch Art Gallery Foundation Strengthening and Building Re-Level

James O'Grady<sup>1</sup>, William Lindsay<sup>2</sup> and Russell Deller<sup>3</sup>

<sup>1</sup>Sales Manager, Mainmark Ground Engineering,

<sup>2</sup>General Manager, Mainmark Civil & Mining

<sup>3</sup>General Manager, Mainmark Ground Engineering NZ

**Abstract:** The four-storey Christchurch Art Gallery was badly shaken by the 2010 and 2011 earthquakes. The 6500 square meter basement slab sank unevenly and was out of level by up to 182 mm. A global tender was called for the remediation of the foundation ground and re-leveling of the building. Mainmark Ground Engineering (trading as Uretek Ground Engineering at that time) was the successful tenderer. The re-level contract held many challenges; an occupied building housing priceless artworks needed to be raised and leveled from the basement which was located below the water table. Mainmark Ground Engineering installed a reaction platform with jet grout columns. Over 1800 tonnes of cement were used in the jet grout column formation. A computer controlled cement grout leveling system was then used to level the building by lifting off the reaction platform. The movement of the basement slab and structure was monitored in real time using wireless Trimble S8 Robotic Stations and prisms. The consultants and building owner were able to monitor the movement in real-time, with the basement contours being updated every 45 minutes during the lifting process. The foundation ground of the structure was strengthened and the building restored to its original level across the 6500 square meter slab. A value-added consequence of the re-leveling work is the reaction platform and leveling grout has strengthened the ground beneath the gallery, providing the existing building with improved behaviour under seismic loads.

**Keywords:** Christchurch, Earthquake, Art Gallery, Foundation remediation, Subsidence.

## 1. Christchurch

Christchurch is located on the Canterbury plains on the east coast of New Zealand's south island, and is well known for its historic timber houses and stone churches. The Avon River winds through the centre of the city.

In 2010 and 2011 a series of earthquakes struck Christchurch, New Zealand's second largest city. In the four years from 4 September 2010, 4,558 earthquakes of magnitude 3 or higher were recorded in the Canterbury region. The earthquakes destroyed almost one third of the buildings within the CBD. There were four major earthquake events; 4 September 2010, 22 February 2011, 13 June 2011 and 23 December 2011.

The initial earthquake event occurred on 4 September 2010 and was centred 40 kilometres west of Christchurch at a depth of 11 kilometres. The peak ground acceleration at the epicentre was 1.25g, however at Christchurch the acceleration had reduced to 0.37g (2). The 7.1 earthquake was the largest in New Zealand since 1931. Severe building damage occurred in Christchurch; however there was no loss of life.

The 22 February 2011 earthquake event occurred 10 kilometres south east of the Christchurch CBD and was much shallower, only 5 kilometres deep. Peak ground accelerations of up to 2.20g were measured in Christchurch suburbs. Severe building damage occurred and 185 lives were lost. Liquefaction was extensive, particularly in the eastern suburbs, with approximately 400,000 tonnes of silt being forced to the surface, burying streets and properties and damaging essential services such as water, sewerage and electricity.

The third earthquake event occurred 10 kilometres south east of Christchurch on 13 June 2011 and the fourth occurred 20 kilometres east of Christchurch on 23 December 2011. The peak ground acceleration was 0.68g and 0.44g respectively.

**Table 1. 25 Largest Earthquakes for Christchurch (1)**

Magnitude	Depth	Date	Time
7.1	11km	4/09/10	04:35
5.6	10km	4/09/10	04:56
5.4	5km	4/09/10	16:55
5.3	9km	4/09/10	11:12
5.4	6km	6/09/10	23:40
5.3	15km	7/09/10	03:24
6.3	5km	22/02/11	12:51
5.9	7km	22/02/11	14:50
5.8	6km	22/02/11	13:04
5.3	9km	16/04/11	17:49
5.2	12km	10/05/11	03:04
5.5	9km	6/06/11	09:09
5.5	10km	6/06/11	09:09
6.4	7km	13/06/11	14:20
5.9	9km	13/06/11	13:01
5.4	9km	21/06/11	22:34
5.3	12km	22/07/11	05:39
5.5	8km	9/10/11	20:34
6.2	7km	23/12/11	15:18
5.8	10km	23/12/11	13:58
5.5	7km	23/12/11	14:06
5.2	8km	23/12/11	14:00
5.6	8km	2/01/12	05:45
5.3	9km	2/01/12	05:45
5.3	8km	7/01/12	01:21

## 2. Christchurch Art Gallery Building

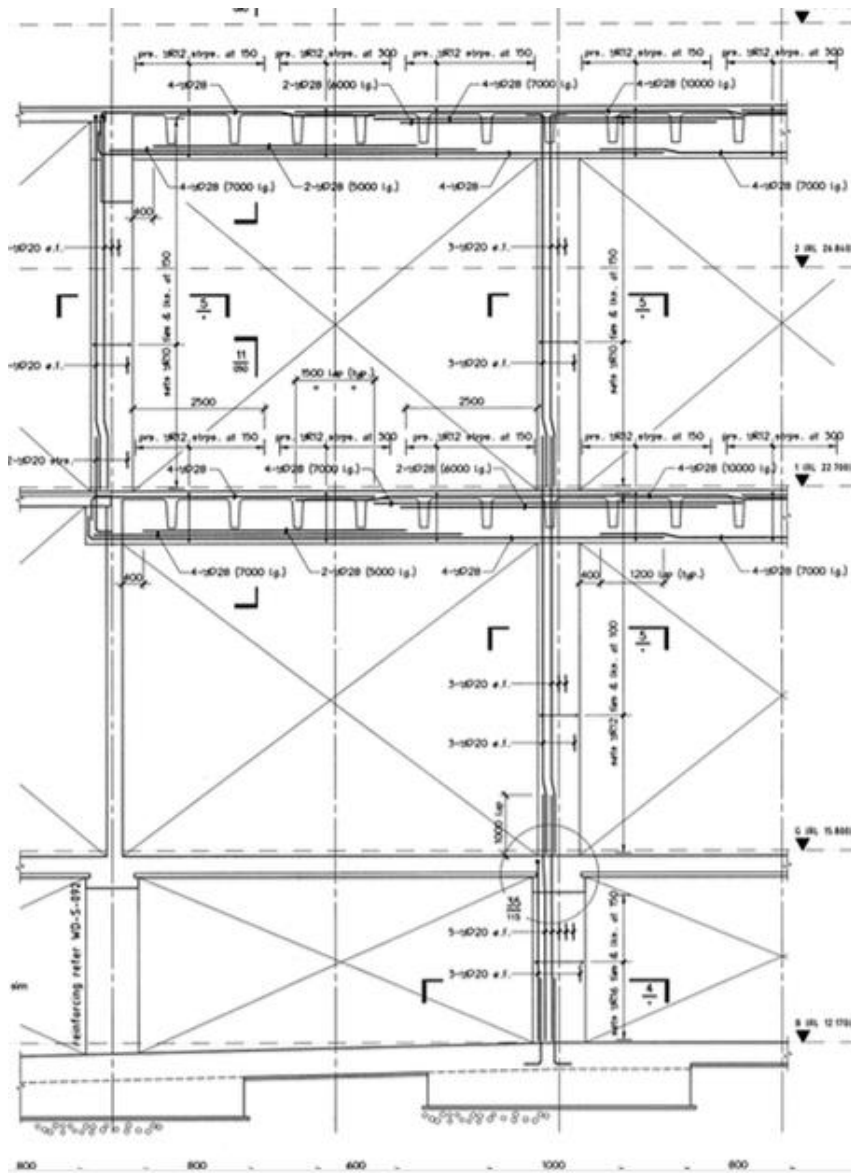
The Christchurch Art Gallery is located in the heart of Christchurch, approximately 100 metres from the Avon River. The public art gallery houses one of New Zealand's finest art collections and hosts major international exhibitions. The Christchurch City Council owns the gallery.

The art gallery building, with its distinctive curved glass façade, was opened in May 2003.

The four-storey building weighs 30,000 tonnes and has a 6500 square metre basement slab. Due to the earthquake risk, the gallery was designed as a raft slab to evenly distribute earthquake forces through the structure.

**Figure 1. Structural Section Through Art Gallery**





No	Date	Description	By
1	26.07.04	For Tender	
2	28.10.04	For Construction	

**CHRISTCHURCH**  
CITY COUNCIL - YOUR PEOPLE - YOUR CITY

**CARSON**  
Leading People Driving Projects

- SOFTA WISSELL (LANDSCAPE ARCHITECTS)
- NO 042 042 CHRISTCHURCH
- PO BOX 988 NEWTON FAY 022 861 700
- BUCHAN GROUP (ARCHITECTS)
- NO 042 042 CHRISTCHURCH
- PO BOX 101 NEWTON FAY 022 861 700
- CARSON GROUP LTD (PROJECT MANAGERS)
- NO 042 042 CHRISTCHURCH
- PO BOX 101 NEWTON FAY 022 861 700
- CONNELL WARDER (MECHANICAL, HYDRAULIC ENGINEERS)
- NO 042 042 CHRISTCHURCH
- PO BOX 101 NEWTON FAY 022 861 700
- GLASSON POTTS GROUP LTD (RESOURCE CONSULTANTS)
- NO 042 042 CHRISTCHURCH
- PO BOX 101 NEWTON FAY 022 861 700
- HOLMES FIRE & SAFETY (FIRE ENGINEERS)
- NO 042 042 CHRISTCHURCH
- PO BOX 101 NEWTON FAY 022 861 700
- MARSHALL DAY & ASSOCIATES (ACOUSTICS)
- NO 042 042 CHRISTCHURCH
- PO BOX 101 NEWTON FAY 022 861 700
- PEDERSEN READ LTD (ELECTRICAL ENGINEERS)
- NO 042 042 CHRISTCHURCH
- PO BOX 101 NEWTON FAY 022 861 700
- SEARLENSONS (QUANTITY SURVEYORS)
- NO 042 042 CHRISTCHURCH
- PO BOX 101 NEWTON FAY 022 861 700
- TRAFFIC DESIGN GROUP (TRAFFIC ENGINEERS)
- NO 042 042 CHRISTCHURCH
- PO BOX 101 NEWTON FAY 022 861 700

**HolmesCruslingGroup**

61 Courtenay  
Terrace  
PO Box 791  
Christchurch  
New Zealand

Telephone  
366 3366  
Facsimile  
379 2169

**CHRISTCHURCH ART GALLERY**  
FOR  
**CHRISTCHURCH CITY COUNCIL**

frame elevation grid C & D

Figure 2. Basement Plan



The Art Gallery is a reinforced concrete structure. As the basement slab is approximately 1 metre below the level of the water table, it was designed as a water retaining structure. The basement slab is typically 400 mm thick with N20 bars at 350 centres each way top and bottom. The column pads are typically local thickenings beneath the basement slab. Included in the basement slab is the 150 mm thick car park entry ramp to the East of the site,

Although the basement slab had subsided and the building was over 180 mm out of level as a result of the 2010 and 2011 earthquakes, the structure of the gallery survived the earthquakes remarkably well, sustaining only secondary damage. After the earthquakes, the gallery was used as the Emergency Operating Centre for the recovery effort.

**3. Contractual Requirements**

Jenny Harper, Director of Christchurch Art Gallery, stated “It is essential for the gallery to have ‘a gold-plated engineering certificate’ so international and local galleries will be confident enough to lend works and bring exhibits to the city”.

The re-level of the Art Gallery was an international tender; to restore the building to its original level and, as a value add, to provide additional earthquake stabilization work. The requirements to submitting a conforming tender included:

- All level correction works to be carried out from within the basement level of the building.
- No impact to the external landscape, including car park toppings, footpaths and roads.
- Guarantee a maximum 25 mm settlement under static load.
- The back up power and computer servers servicing the adjacent Civic Building (Christchurch City Council Main Administrative Centre) were located in the Gallery basement and were not to be interrupted.
- An 11,000 KVA Zone Sub Transformer Station servicing Christchurch’s CBD and surrounding residential population was located in the lowest level of the basement, power supply was not to be interrupted
- The Art Gallery Structure was anchored in place with 73 No. 12m long post tensioned grouted tendons, required to resist hydraulic uplift as a result of a seasonally high water table due to glacier melt and the proximity of the Avon River

- The site had a history of hydrocarbon and high levels of organic volatile contamination
- There was to be no vibration and dust particles were to be minimised.
- All existing art was to remain on site.
- The Art Gallery was to remain occupied by management and tenants.

Following a long design process, Mainmark Ground Engineering was the successful tenderer to perform the lifting and level correction works at the Art Gallery.

### **3.1 Site Challenges**

The site conditions provided several challenges.

As gallery staff and tenants were to occupy the building during the works, all services had to be maintained for the duration of the works. Electricity, water, sewerage and data services could not be interrupted during work hours. The zone substation and council computer back up servers located on the site had to stay in operation at all times.

The gallery building services, surrounds and environment had to be protected during the works. The basement extends under the large forecourt in front of the gallery. However the forecourt was not designed for vehicle loads and could not be used as a staging area for the works.

Access to the basement was via a vehicle ramp with only 2.1 metre head height. Only compact machinery could be mobilised and used in the basement. The head height of the access ramp meant trucks could not deliver into or pick up from the basement. The head height within the basement itself was as low as 2.25 metres.

The basement slab is approximately one and a half metres below the water table.

The ground water flow through the site was to the Avon River, about 100 metres from the site. Real time monitoring of the pH was required, both of the ground water and of water in the Avon. If water sampling revealed pH outside the range 5.5 to 8.5, work had to stop immediately.

There was a requirement that minimal reinforcement be disturbed by the works, consequentially all slab and wall reinforcement was required to be located using ground penetrating radar. Before any reinforcement was cut, approval had to be obtained from Aurecon, the engineers for the Art Gallery. Every penetration through the slab had to be approved, annotated and documented prior to drilling or coring.

There were seventy-three ground anchors, approximately twelve meters in length, tied into the basement raft slab. These anchors were required to resist upward floatation forces due to variable ground water levels. It was not known if the earthquakes and subsequent settlement had compromised the integrity of the anchors. Each of these anchors had to be located and the concrete about the anchor heads excavated. The tension in the anchors had to be controlled, requiring the anchor heads to be backed off at the same rate as the level correction of the adjacent slab. Upon completion of the project the anchors were required to be tested, re-tensioned and locked off,

The artwork stored in the gallery had to be protected from construction dust. A custom dust extraction and filtration system was designed and constructed to ensure there was no risk of cement dust entering the Art Gallery ventilation system.

## **4. Mainmark's Solution**

The objectives of the Mainmark solution were:

- To raise the gallery building back to its pre-earthquake design levels.
- To release the tension stresses caused by the differential settlement of the foundation.
- To complete all work from the building basement.
- To ensure zero business disruption to the gallery staff and tenants.
- To maintain the structural integrity of the superstructure throughout the level correction exercise.

To achieve this Uretek proposed a combination of 124 JetGrout columns with 350 JOG integrated computer levelling locations monitored by 6 Trimble robotic stations in real time.

The Mainmark solution was modelled by KGA Geotechnical Investigations Christchurch and Geotecnia Lisbon. The modelling determined that in addition to providing a platform to level the structure, the proposal also improved the building's ability to withstand future earthquakes and improved the performance of the footing system to meet the new New Zealand building code earthquake requirements. "The relevel solution of the Christchurch Art Gallery provides a non-liquefiable crust of at least 6.5 m below foundation, which is considered to minimize the manifestation of liquefaction damage at foundation level."(3)

The solution presented for this landmark project was the first of its kind in the world, utilizing these combined technologies.

#### **4.1 Jet Grout Columns**

In order to guarantee lift of the structure, a reaction platform had to be constructed beneath the structure. This reaction platform was constructed with 124 Jet Grout soil mix columns of 3 and 4 metre diameter.

The 3 and 4 metre diameter Jet Grout columns were placed through 200 mm diameter cores through the slab onto a gravel layer approximately 6.5 metres below the basement slab. The cement paste was injected into the soil through rotating horizontal jets. The force of the jets cut through the soil and enveloped the gravels, mixing with the soil to form soil-cement columns. The gravel lenses encountered across the site consisted of cobbles up to 300 mm in diameter. Excess soil cement slurry was extracted from the core and pumped to a basement holding tank, before being pumped from the basement to an external tank before being removed from site. The JetGrout columns extended from the gravel layer at 6.5 m below the top of slab to 2 metres below top of slab.

Over 1,800 tonnes of cement were used to install the 124 JetGrout columns. The JetGrout columns were installed on a triangular grid at 7,500 mm centres. The columns about the perimeter of the structure were 4 metres diameter and the internal columns were 3 metres diameter.

The 124 Jet Grout columns were installed within 52 working days.

#### **4.2 JOG Integrated Computer Levelling**

Once the Jet Grout columns were installed, cement grout was injected into the soil beneath the slab, levelling the building and providing a load transfer layer between the Jet Grout columns and raft slab, using JOG integrated computer grouting technology.

The JOG process provided a hydraulic lift of the building, gradually and gently lifting the building back to level. The building was lifted to its original position by injecting a variable mobility laminar cement grout beneath the building basement slab at 350 locations contemporaneously. All 350 injectors were connected via eight kilometres of delivery hoses back to injection pumps located within a temporary batch plant constructed within the basement car park.

The purpose-made batching plant was constructed to guarantee grout quality. The five colloidal mixers and ten high-pressure grout pumps were linked back to the computer controllers.

The injection array was designed considering the building loads, degree and distribution of lift required, and mitigation against any new stresses being imposed on the structure during the lifting process. Injection ports were installed through 40 mm diameter cored holes in the raft slab.

The lifting process was computer controlled. The basement was divided into 10 zones, with up to sixty-four injectors in a zone. A network of five computers controlled the rapid succession in which the injections took place, the amount of modified cement grout that was injected at each location, the delay between injections and the delivery time of each injection. During each sequence, only a very small volume of cement grout was injected at each location.

Over 16,500 25kg bags of cement were used in the lifting of the art gallery slab. A total of 1.5 million litres of grout was injected during the levelling operation. The levelling of the building was completed in 44 working days.

**Figure 3. Initial Slab Contours**

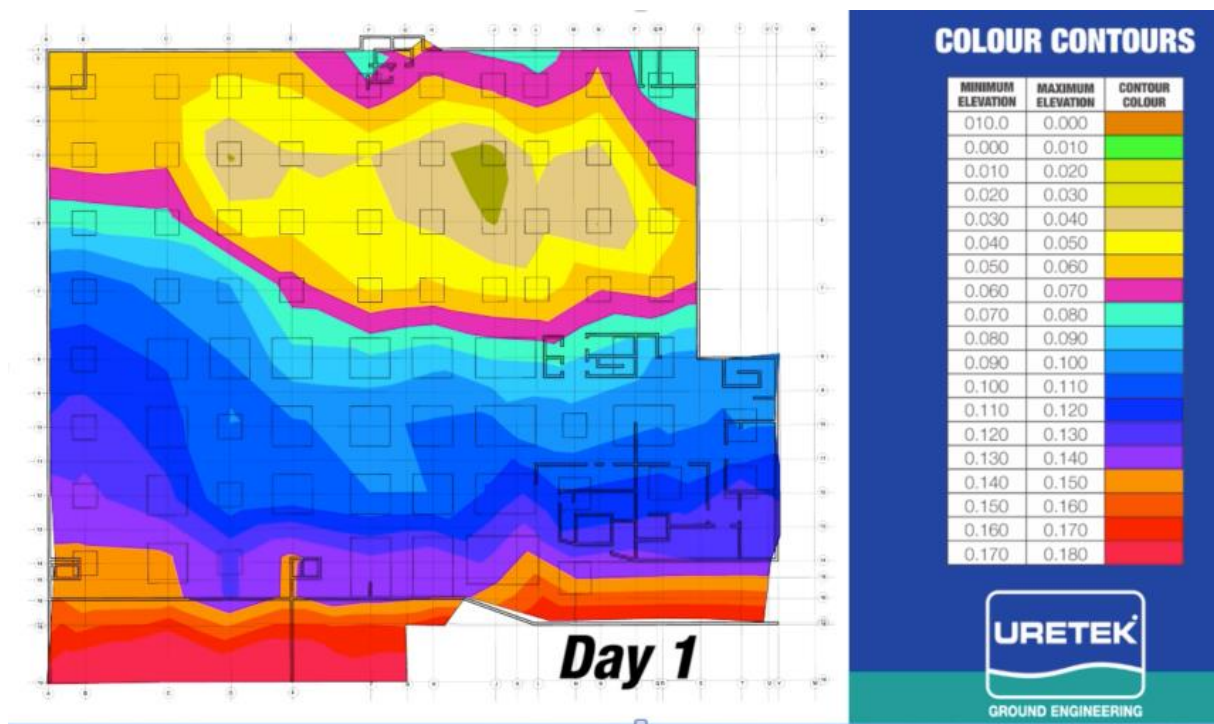
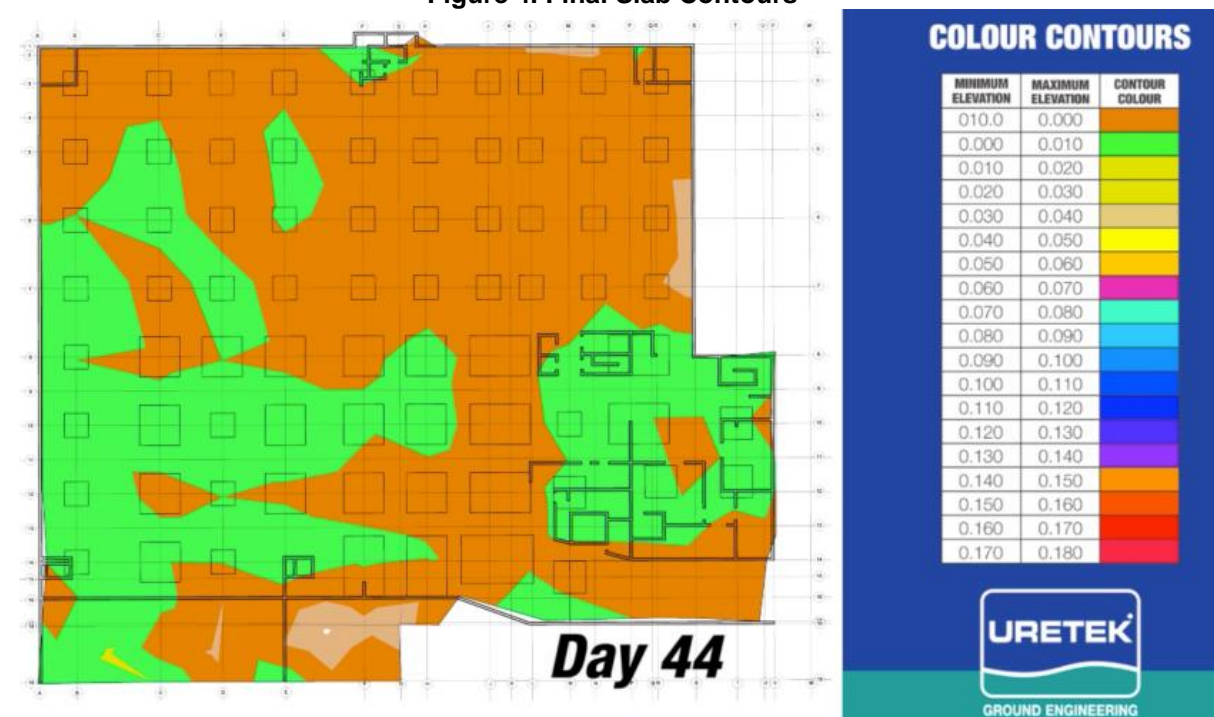


Figure 4. Final Slab Contours



#### 4.3 Trimble Total Station Monitoring

Prior to commencement of the correction works, a 3D laser scan of the basement, building interior, external façade and surrounding properties was undertaken to determine the exact location of the structure. This scan, with over one billion points, provided a virtual building model that could be entered at any time to determine the condition and location of the building prior to the work commencement. The building model was used to confirm the degree of settlement and to examine existing and potential new stresses on the structure.

A network of 5 Trimble S8 robotic stations placed in the basement and 1 Trimble S8 external to the building was used to monitor the building 24 hours a day during the lifting process. The Trimble S8 stations continuously monitored the movement and rotation of over 400 locations throughout the



basement and building exterior. Over 300 prisms were mounted in the basement. Every column, the centre of each beam and the upper surface of the basement slab were monitored.

The external station was required to transfer true levels from outside the building back to the stations located in the basement. As the entire building was being lifted, there was no internal zero point that could be used as a reference during the works.

The data from the S8 stations was fed back to the control room computers by wireless MOXA communication equipment. The real time monitoring of the movement of the building provided feedback to the JOG injection sequence, allowing the technicians to slow down or speed up the lift of discrete parts of the structure. This ensured the building was lifted smoothly and prevented additional stresses being applied to the building during the process.

The complex output of the Trimble S8 stations was used to provide contour maps of the basement slab every 45 minutes. These contour maps were loaded onto a web site where the Art Gallery, Council, Aurecon and Trimble could monitor the progression of the building lift during the work.

The basement slab was levelled to within +/- 10 mm.

## **5. Conclusions**

From possession of the site in August 2013 to completion in January 2014, the project took a total of five months. The project was completed on time and on budget. The 6500 square meter floor plate was levelled to within +/- 10 mm.

Mainmark's solution was a surgical approach, installing the lifting columns and lifting the structure through penetrations of 200 mm diameter and smaller. The structural integrity of the building was not compromised. All work was completed from within the basement level of the building.

The work was completed with zero business interruption to the art gallery, and all artwork and art gallery personnel remained on site. All building services were maintained throughout the process.

## **6. Acknowledgement**

Uretek acknowledge the support and assistance of the Christchurch Art Gallery Te Puna o Waiwhetu, The Christchurch City Council, Aurecon, KGA Geotechnical Investigations, Geotecnia Lisbon, Kevin O'Connor and Associates, Geosystems New Zealand and Trimble in the delivery of the re-leveling of the Christchurch Art Gallery.

## **7. References**

1. Nicholls, P., [Christchurchquakemap.co.nz/recent](http://Christchurchquakemap.co.nz/recent), The University of Canterbury, Christchurch, New Zealand, February 2015
2. Geonet, [info.geonet.org.nz](http://info.geonet.org.nz)
3. Nogueira, A., et al, "Jet Grout Columns Operating as a Reaction Platform for Christchurch Art Gallery Relevel Uplift and Soil Liquefaction Mitigation", XVII Congresso Brasileiro de Mecanica dos Solos e Engenharia Geotecnica, September 2014, Brasil

# Design of Berthing Dolphins on Curtis Island LNG Jetties

Jesper Jensen<sup>1</sup>, Peter Kastrup<sup>2</sup> and Matt Hodder<sup>3</sup>

<sup>1</sup>Engineer, Arup

<sup>2</sup>Queensland Maritime Leader and Senior Engineer, Arup

<sup>3</sup>Senior Engineer, Arup

**Abstract:** The demand for energy in South East Asia and the Pacific region has seen vast growth in gas exploration across the continent of Australia. With the approval of a number of liquefied natural gas (LNG) export facilities across the Australian seaboard, Arup Australasia has put its multi-disciplinary capabilities to full use in the delivery of a number of LNG Jetties in Gladstone, Queensland in a design and construct collaboration with contractor John Holland Group (JHG). One of the most vital elements of an LNG Jetty, both from a design and construction point of view, is the berthing dolphins. While the structural form may vary considerably across various project sites, this structure is consistent in functionality which is to resist the lateral forces associated with berthing and mooring of vessels. With the world's energy demands growing and sea going vessels increasing in size and volume for coal and LNG transportation, berthing dolphins are growing both in size and complexity in design. This paper presents the design and construction of berthing dolphin structures accommodating berthing and mooring of vessels of up to 220,000 m<sup>3</sup> in capacity, which is the result of close collaboration between JHG and Arup.

**Keywords:** LNG Jetty Design, Constructability, Pile Group Analysis, BIM, Maritime Construction

## 1. Introduction and Project Background

In 2010, the Queensland Government approved the Queensland Curtis LNG (QCLNG), Gladstone LNG (GLNG), and Australia Pacific LNG. The project partners across the three projects are (at the time of writing):

- QCLNG – QGC(BG), China National Offshore Oil Corporation (CNOOC)
- GLNG – Santos, PETRONAS, Total, KOGAS
- Australia Pacific LNG – Origin, ConocoPhillips, Sinopec

Bechtel was awarded as the engineering, procurement, and construction contractor of the three jetties. JHG was awarded the marine subcontracts, including procurement, fabrication, construction and commissioning of the structural, mechanical and electrical components of the product loading facility. JHG appointed Arup in a Design and Construct (D&C) collaboration for the permanent works design of the three LNG jetty facilities. Arup was also the engineer of record during construction, certifying that the works met the design intent.

With three different project stakeholders, the projects are considered as three separate projects. As such, each project required an individual assessment of the project-specific design requirements, geotechnical profile, and environmental conditions. The three LNG plants are located on the south-western shoreline of Curtis Island and are only accessible by water. The three project sites are illustrated in Figure 1.

Early collaboration with the client to understand the ancillary functional requirements of the dolphins such as furniture, early Arup input during fender selection and involvement with the contractor to understand the constructability needs, was key to a successful scheme development.



**Figure 1. Top left: Overview of the Curtis Island LNG plants (from the bottom; Australia Pacific LNG, QCLNG and GLNG). Top right: GLNG. Bottom left: Australia Pacific LNG. Bottom right: QCLNG. ©Bechtel**

Concerns over positional tolerance of the driven piles from a floating barge meant that a reinforced concrete pile cap was adopted as the contractor's preferred solution. This was seen as the most efficient method to accommodate the large bending moments resulting from a significant cantilevering length between the fender unit load application level and design mudline level of up to 25m, including allowance for scour and over-dredge. Arup designed a complex reinforced concrete pile cap to accommodate the 4 no. driven tubular steel piles. Bored rock sockets were specified where the geotechnical axial tension capacity, provided by the driven steel tube shaft friction, was inadequate to resist the design axial pile tension.

The high variability of ground conditions in Gladstone Harbour and concerns over geotechnical risk governed the contractor's early decision to adopt a vertical pile solution. This was chosen over raking piles for the ease of installation and flexibility while the bored in-situ concrete rock sockets could be practically extended where required to counteract the ground condition variability and manage geotechnical uncertainty.

## **2. Key Design Inputs**

Before the dolphin design could be developed, a number of key design inputs were required. Of particular importance was the berthing and mooring analysis to determine an envelope of forces and angles for the range of operational vessels for input into the analysis. A metocean study was needed to determine the operational and ultimate limit state wind, wave and current conditions specific to Gladstone harbour and the subsequent loads for input into the analysis. The different design lives for each project had a significant impact on the metocean design criteria.

A geotechnical/geological assessment of the local ground conditions was also undertaken. The assessment included carrying out detailed geotechnical studies and development of site-specific ground models to inform pile types and installation methodologies, in addition to determination of geotechnical parameters for input into the structural and geotechnical analyses.



## **2.1 Berthing Analysis and Fender Selection**

Assessment of normal and abnormal berthing was carried out in accordance with PIANC Guidelines for the Design of Fender Systems (Guidelines for the Design of Fender Systems, PIANC, MarCom WG33, 2002) including factors for manufacturing tolerance, angle, temperature performance and velocity correction. Due to the non-linear energy performance behaviour, normal berthing proved to govern the loading from the fenders chosen on these projects.

The fender cone was inverted to minimise the height of the concrete dolphin cap and subsequent concrete volume. The fender type and size was also confirmed to be acceptable for the required fender thrust, determined as part of the mooring analysis.

## **2.2 Mooring Analysis and Mooring Hook Selection**

The objective of the mooring analysis was to confirm that the berth layout provides a safe and efficient mooring system. In the mooring analysis, the vessels at berth were subjected to a range of survivability and operational conditions. A large number of combinations of wind, wave and current input was varied in direction and intensity, hence an advanced software package was used. This included the metocean criteria specified by the Oil Companies International Marine Forum (OCIMF) (Oil Companies International Marine Forum (OCIMF), Mooring equipment guidelines (MEG3), 2008) applied to each design vessel moored port and starboard.

The movement outputs of the analysis were checked against project specific criteria as well as criteria from OCIMF (Oil Companies International Marine Forum (OCIMF), Mooring equipment guidelines (MEG3), 2008) the Society of International Gas Tanker and Terminal Operators Ltd (SIGTTO) and the World Association for Waterborne Transport Infrastructure (PIANC).

During the analysis, prismatic and spherical tank vessels were found to have noticeably different mooring characteristics. Spherical carriers tend to have large windage areas combined with offset manifolds. This resulted in notable yaw movements for some spherical vessels when the design metocean forces were applied.

Passing ship analysis was performed and demonstrated that while a passing ship does have an effect on the vessel at berth, the project specific effects were minimal and negligible when considered probabilistically.

The key dolphin design outputs from the mooring analysis were confirmation of line loads, hook size and load angle envelope.

## **2.3 Metocean Conditions and Loading (Water Levels, Wave and Current Loading)**

Each of the projects specified different design life requirements and hence different requirements for metocean condition design return periods. Joint probability was considered where possible, which provided optimized design basis for water level, wave height & period as well as current – which in turn optimised loading and structural design.

Wave and current loads on the piles were determined using Morison's equations. Stokes 5th order wave theory was used to determine the water particle velocities and accelerations. Fenton's Fourier approximations and stream theory were also used. Marine growth was prescribed as a design criterion, which also varied across the projects. Typically, an increased marine growth thickness requirement between Highest Astronomical Tide (HAT) and Mean Sea Level (MSL) meant that the typical wave load profile had a load spike in the HAT to MSL range.

Each project had different design wave crest and pile cap levels. This meant that wave loading on the dolphin pilecap had to be considered in some cases, but not others.

## **2.4 Geotechnical Assessment**

In order to inform foundation analysis and dolphin design, Arup undertook a detailed geological and geotechnical assessment to evaluate the site ground conditions.

During the initial site evaluation, the prevailing ground conditions on site were found to consist of alluvial soils overlying metasedimentary and deformed rocks; typically comprising mudstones, sandstones, siltstones and chert (scattered sporadically). It was identified that following deposition of the underlying geological formations as horizontal sedimentary layers during the Late Devonian to Early Carboniferous period, the region was subjected to intense metamorphism and deformation during the Late Carboniferous period. This is when fault bound tectonic blocks were thrust up against each other which resulted in the tilting of the underlying formations.

Critical to the selection of pile type and installation methodology was the identification of highly variable ground conditions and the underlying steeply dipping (typically between 60 and 80 degrees to horizontal) rocks beds. Tilting of the rock beds resulted in significant vertical and horizontal variations in stratigraphy and the variable strength and weathering resistance of the rock materials encountered at the site.

## **3. Pile Group and Structural Analysis**

One of the key stages during the detailed design process was the development of the analysis models to determine both the load effects on the structure and on the ground. Generally, the Arup in-house geotechnical analysis program, 'Oasys ALP' was used for lateral geotechnical analysis, however the dolphins were analysed using a pile group software. Soil-structure interaction analysis of the pile group was undertaken to design a number of key elements in the dolphin structures and also to check the ultimate limit state geotechnical lateral stability of the pile group. Seamless interface between the structural and geotechnical disciplines was crucial in the delivery of an efficient design approach. The geotechnical analysis of the dolphin structures was undertaken using numerical analysis incorporating non-linear lateral 'p-y' pile-soil interaction springs and group interaction factors to model pile group behaviour under applied loads. The pile cap was considered as a rigid body and the piles were modelled with a non-linear relationship between pile bending moment and curvature. The soil was specified in a series of horizontal layers of variable thickness. Input soil parameters were converted to non-linear springs and applied at the pile interface to represent the ground behaviour. Both upper bound and lower bound cases were analysed using models with corresponding pile toe levels derived from the pile driveability analyses, and with ground material strength representative of each dolphin characteristic ground profile.

Three types of pile group analysis were performed to satisfy the design requirements:

- SLS design action effect analysis performed to determine deflections and material stresses at serviceability limit state.
- ULS design action effect analysis performed to determine ultimate limit state pile design actions for structural and geotechnical design
- ULS geotechnical lateral stability analysis performed to check ultimate limit state geotechnical lateral stability of the pile group

In the ultimate geotechnical lateral stability analyses, both 'short' and 'long' pile failure mechanisms were checked. Ultimate geotechnical lateral stability was satisfied by ensuring that the lateral ground pressure (modified for lateral group effects) was not mobilised, and the number of plastic hinges required for the structure to form a mechanism had not formed. Non-linear pile bending moment-curvature relationships were adopted in the analyses, which allowed the redistribution of load throughout the system as the ultimate bending moment capacity of the piles is reached and plastic hinges are formed.

Structural modelling of the dolphin structures was undertaken using the Arup in-house structural analysis program, 'Oasys GSA'. In order to model the lateral pile-soil interaction within Oasys GSA, equivalent linear springs were derived from the non-linear p-y curves derived from the geotechnical analyses. The equivalent linear spring stiffnesses were derived considering loading magnitude and pile deflection in response to lateral loading, and for both upper bound and lower bound cases. For critical load cases, the

equivalent linear spring stiffnesses were iterated until similar pile deflections and structural actions were calculated using Oasys GSA and the geotechnical analysis software.

As part of the structural analysis and design of the dolphin structures, analyses were carried out to determine the deformations of the structure and the impacts on the design load effects, requiring the use of the rigorous method of analysis to AS5100.5 Cl. 7.4 (Australian Standard, AS5100-2004, Bridge Design). Staged Analysis was carried out to replicate the construction sequence and accurately account for locked-in stresses. The Arup in-house structural section analysis program, 'Oasys AdSec' was used for the reinforced concrete design.

#### **4. Pile Cap Analysis & Design**

The Arup in-house software Oasys GSA was used to create the structural analysis model. The ability to easily import and export data was crucial and the ease with which design actions can be managed was a factor in reducing the time required for analysis.

In determining the design actions for the pile cap the non-flexural pile cap was idealised by a truss consisting of compression struts and tension ties connected at nodes to form a load-resisting system. Early conceptual assessments indicated that vertical ties were required between the piles. Further refinements determined the spacing of the vertical ties to optimise the utilisation of the compressive struts.

Non-linear analysis was required to reach equilibrium between the applied external loads, the axial forces in the 3D strut and tie grid, and the pile reactions. This allowed determining the reinforcement requirements to limit serviceability limit states steel stresses and ensure adequate strength at ultimate limit state. Local confinement reinforcement was carefully detailed in the rupture zones near the piles.

Thermal modelling following the guidelines of CIRIA C660 (CIRIA C660, Early-age Thermal Crack Control in Concrete, 2007) was required to assess the deleterious effects due to the heat of hydration. This effect was controlled by designing surface reinforcement to control cracking associated with the anticipated differential temperature. The input to the thermal modelling is further discussed in section 7.

#### **5. Pile to Pile Cap Connection and Pile Design**

A challenge associated with using vertical piles is the relatively high design actions at the connection between the pile cap and piles, when the structure is subject to lateral loadings. The local effects at this load transfer zone require careful attention and detailing.

The design actions were of a magnitude exceeding the maximum capacity of the reinforced pile plug, which is used to transfer design loads between the pile cap and piles. Increasing the diameter of the steel pile liner was not desirable due to limitations on the lift capacity of the barge crane and would also increase the total steel tonnage. As such, Arup developed a solution with further embedment of the steel pile liner into the pile cap to provide the necessary strength to resist the combinations of design loads as well as meeting operational and serviceability requirements. Development of this solution was key to determining the reinforcement arrangement within the pile cap itself and the temporary works solution.

Relying on composite action of the steel liner and reinforced concrete pile plug introduce a requirement for weld beads to resist the associated interface shear stresses. Significant extents of the pile would have required weld beads to overcome the high ground variability, for which this option was considered not to be feasible. Instead, superimposed behaviour was investigated in collaboration with the Arup Advanced Technology and Research team. Studying the compatibility conditions of the two bodies led to a formulation of the load sharing under serviceability limit state and ultimate limit state conditions. Rigorous analysis was required to assess whether the steel pile liner had adequate strength, and in order to account for the buckling behavior. The anticipated long term corrosion varies dependent on the exposure classification, yielding a varying cross-section along the member. 6 mm corrosion was required for the splash zone. Marine grade coating and sacrificial anodes were adopted for corrosion protection for the steel liner, however the design criteria requirement for corrosion allowance was still applicable. Below For piles in compression, the modified member slenderness was therefore used when determining the nominal member capacity to AS4100 Cl. 6.3.4 (Australian Standard, AS4100-1998, Steel Structures) by use of a modal buckling analysis associated with each individual load case.

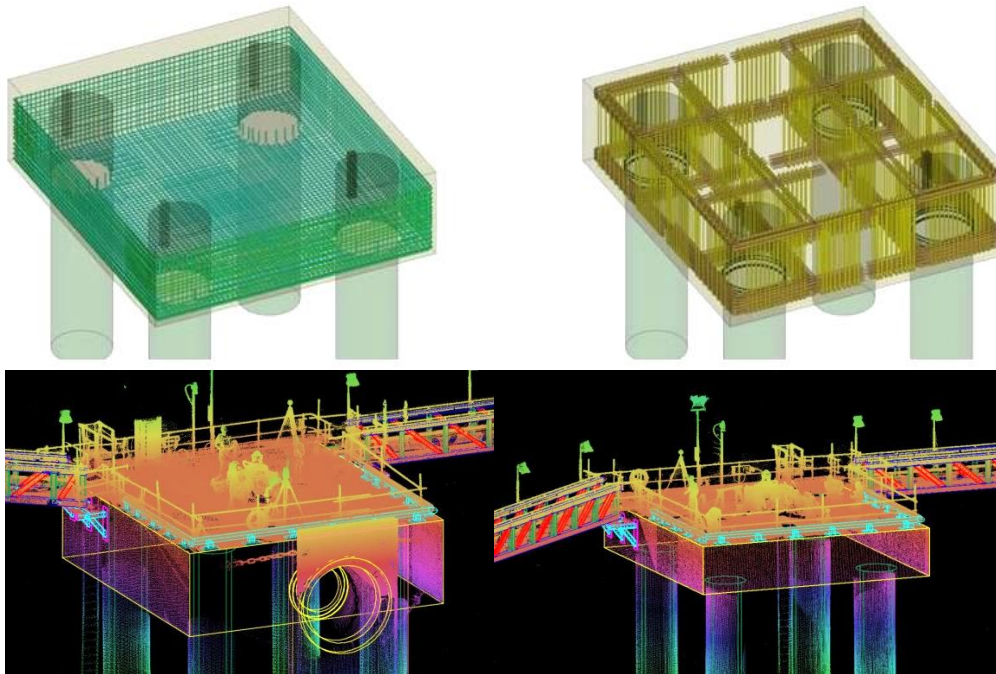
## 6. Reinforcement Clash Detection

As the projects were delivered in a high labour cost environment, pre-fabricated solutions were developed by Arup in collaboration with JHG. Adopting this type of modular construction had a positive impact on the critical path of the construction programme.

In addition to the coordination of temporary works and the reinforcement, it was also a priority to develop a solution maintaining a safe working environment. Particularly the positioning of vertical tension ties was optimised to allow for personnel access within the pile cap. In zones such as the pile to pile cap connection and where the fender unit cast-in bolts were located, a significant challenge was present in avoiding congestion and allowing safe placement of reinforcement.

The solution to overcome this challenge was the development of a fully coordinated and integrated 3D building information model (BIM) of the pile cap reinforcement, including cast-in items for the fender unit, mooring hook, walkway supports, ladder supports, cable ladder supports, rope rail guards, handrails and several types of electrical equipment. The immediate benefit was the visualization of the heavily reinforced structure aiding to undertake reinforcement clash detection and aiding drawing production. Beyond this, sharing the BIM model with JHG ensured a fully integrated design and construct relationship. This proved to be an extremely useful tool allowing JHG to further develop the temporary works solution by carrying out clash detection with the temporary works supports and cast-in items for the formwork, prior to procurement and construction. It furthermore allowed accurate construction sequence planning that, by use of visual effects, enhanced the understanding of the construction process and fixing sequence.

Additional benefits from the 3D design philosophy were identified during construction in being able to promptly react to changes, which ultimately yielded program savings. Furthermore, the as-built condition was incorporated in the BIM model at the final project stage using 3D laser scanning technology. An example of the BIM model and 3D laser point survey is shown in **Figure 2**.



**Figure 2 Top: Design BIM Model. Bottom: 3D Laser Point As-Built Survey. ©Arup**

An opportunity exists to create a 6D BIM model by including links to product data and details, maintenance/operation manuals, specifications, warranty data, maintenance requirements and

manufacturer information and contacts. This would further assist the project stakeholders and facilities managers in the operation and maintenance of the jetty throughout the life cycle.

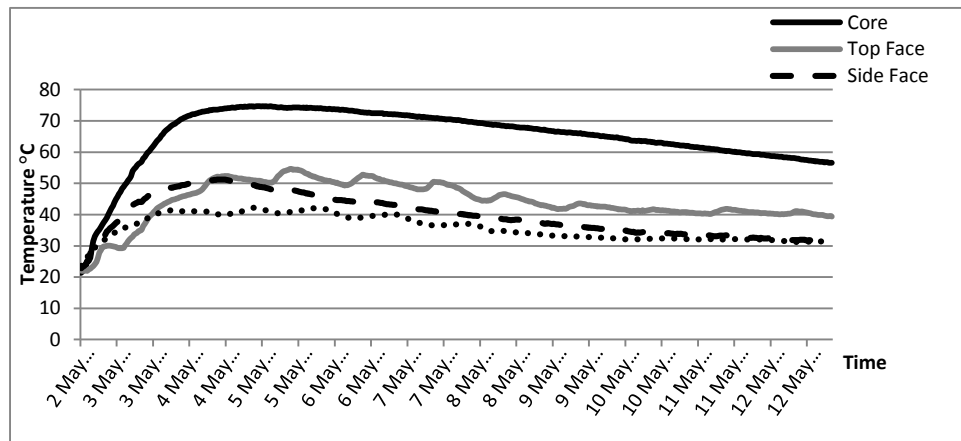
## **7. Concrete Supply and Impacts on Design**

Arup undertook detailed assessments of the proposed concrete mix, placement methods, construction sequence and pour dates to ensure the concrete temperature was within the specified limits. This was coordinated closely with JHG to ensure full compatibility between aspects related to construction processes and the Arup design. Thermocouples were used to measure and record the concrete core and face temperature during the initial curing process.

Different methods and techniques were used for winter and summer concrete cooling and transport in order to satisfy placement requirements.

On one of the three project sites, the construction of berthing dolphins was started prior to completing construction of the access trestle and loading platform. As such, concreting of sockets, pile plugs, and pile caps was done by use of a barge mounted boom pump. On average 40 no. concrete agitators were delivered to the site on barges to complete an in-situ berthing dolphin pile cap pour. Each barge delivery would hold 7 no. agitators. A transportation time of minimum 90 minutes from the point of batching to the point of discharge led to an increase in placement temperature. Therefore, concreting had to be done during winter, to avoid excessive peak temperatures. The temperature development for a berthing dolphin pile cap poured in May 2014 is shown in Figure 3.

Another method adopted was to use a line pump to complete the in-situ pile cap pours where direct access to the dolphins was possible via the access trestle, loading platform and access walkways. This reduced the transportation time to 20 minutes. Where this placement method was applied, the construction programme required concreting during the summer months. Although the transportation time was reduced, the minimum achievable placement temperature was at a level such that, in combination with the expected adiabatic temperature rise, the peak temperature would reach an unacceptable level. The solution was to inject liquid nitrogen (LN) into the ready-mix truck immediately before the point of discharge. A fully automated and controlled setup was implemented in a secured area only accessible to trained operators. A test determined the efficiency of the LN injection as 7 minutes of injection to cool the mix by 10 °C. A target placement temperature was defined which controlled the active injection time for each delivery. By implementing the LN injection no peak temperatures exceeded the allowable limit.



**Figure 3 Top: Injection of liquid nitrogen to reduce concrete placement temperature during summer. ©Bechtel/Arup. Bottom: Temperature development for a berthing dolphin pile cap pour. ©Arup**

Arup defined the requirements related to the performance of the concrete during the early stages of the detailed design programme, which made allowance for preparation of the concrete mix and verifying performance by a test pour before commencing construction activities.

## 8. Conclusion

Achieving an efficient design that meets the environmental, metocean and vessel design criteria, while satisfying the challenging ground variability and construction constraints, was a testament to the positive collaborative relationship between the design team and contractor. Early engagement and an aligned understanding of the constraints helped in paving the way to designing efficient structures. In addition fluid communication between structural, geotechnical, maritime, and electrical design teams was paramount in achieving the design which produced holistically positive outcomes. The implementation of BIM modelling was useful during both design and construction stages to both Arup and JHG, yielding improved visualisation and construction planning.

First gas was shipped from Curtis Island on 5 January 2015 from QCLNG. GLNG and Australia Pacific LNG are expected to commence shipping later in 2015.





**Figure 4 Methane Rita Andrea LNG Vessel at the QCLNG Berth (first vessel to ship gas from Curtis Island). ©QGC.**

## **9. Acknowledgements**

This paper is published with the permission of John Holland Group, Bechtel, QCLNG, GLNG, and Australia Pacific LNG. The authors acknowledge the encouragement of these parties in supporting this paper. Many people have contributed to these projects and the preparation of this article. The authors thank everyone involved and for the opportunity to deliver such challenging projects.

## **10. References**

1. Guidelines for the Design of Fender Systems, PIANC, MarCom WG33, 2002
2. Oil Companies International Marine Forum (OCIMF), Mooring equipment guidelines (MEG3), 2008
3. Australian Standard, AS5100-2004, Bridge Design
4. CIRIA C660, Early-age Thermal Crack Control in Concrete, 2007
5. Australian Standard, AS4100-1998, Steel Structures

# Lady Cilento Children's Hospital

Ken Gallie<sup>1</sup> and Darryl Feodoroff<sup>2</sup>

<sup>1</sup>Structural Team Leader and Principal, Cardno

<sup>2</sup>Principal, Cardno

**Abstract:** The Lady Cilento is a new tertiary children's hospital, a state of the art health facility and an iconic building. Works commenced in 2007 and construction completed in 2014 at an overall project cost \$1.5 billion.

The Architects for the project were Conrad Gargett Lyons. Town planning, civil, structural and traffic engineering was undertaken by Cardno and services were by AECOM. Lend Lease were the Managing Contractor.

The building has four basement parking levels, eight main hospital levels, four ward levels and three upper levels for services. In order to achieve openness, light and connectivity within the large footprint, there are two central atriums with large radiating open spaces. The footprint and atrium size vary for each of the main hospital levels and have landscaped roof areas.

The varying footprint, voids and column grid created challenges which required an efficient structural system suitable for construction, operation, installation of complex building services and be adaptive in the long term. A band beam and slab system with post tensioned beams was adopted to minimise depths and control deflections. The slabs were designed with conventional reinforcement to maintain flexibility for the installation of services.

The ward level floors have a different column grid and were fully post tensioned to minimise weight at the transfer level.

The concrete specified for the project included shrinkage control mix in the slabs, strengths up to 80 MPa in columns and specialised concrete mixes for thick walls. Metal decking was used as permanent formwork for slabs.

**Keywords:** Concrete composite column, post-tensioned, reinforced

## 1. General Project Description

The Lady Cilento Children's Hospital is a tertiary healthcare facility serving paediatric clients in Queensland. It replaces the Royal Children's Hospital and the Mater Children's Hospital and is located on a brown field site in South Brisbane, adjacent to the Mater Hospital Campus.

The Lady Cilento Children's Hospital is the major component of a new health precinct which includes a separate energy building, a medical research building, and a multi-storey short term parent's accommodation facility. The energy and research buildings are linked to the main hospital building with tunnels for both services and pedestrians.

The new precinct was occupied by a variety of buildings and open spaces, including a multi-level car park and a telephone exchange. To allow for construction of the new hospital building, a new multi-level carpark had to be constructed on an adjacent site. Once the new carpark had been completed, it allowed the original carpark to be demolished.

The telephone exchange occupied a corner of the site which was key to the overall redevelopment of the precinct. Initial studies included relocating the exchange within the Lady Cilento Children's Hospital, however ultimately the exchange was decommissioned and the building demolished. The hospital construction had to be staged around the exchange building to allow sufficient time for all of the existing telephone services to be relocated.

The project brief was to provide a state of the art building that brought together all paediatric services in one location, providing a positive experience for patients and families, conducive to achieving healthy outcomes.





Photograph 1. The Lady Cilento Children's Hospital

The architectural design incorporates a 'trunk and branch' concept with two internal atria forming the *trunks*. Each trunk has large radiating public spaces or *branches* at different levels throughout the building which extend from the atria to the face of the building. The branches seek to open up the internal parts of the building and provide views of some of Brisbane's landmarks. The branches also cantilever through the façade of the building creating a distinctive feature of the building.

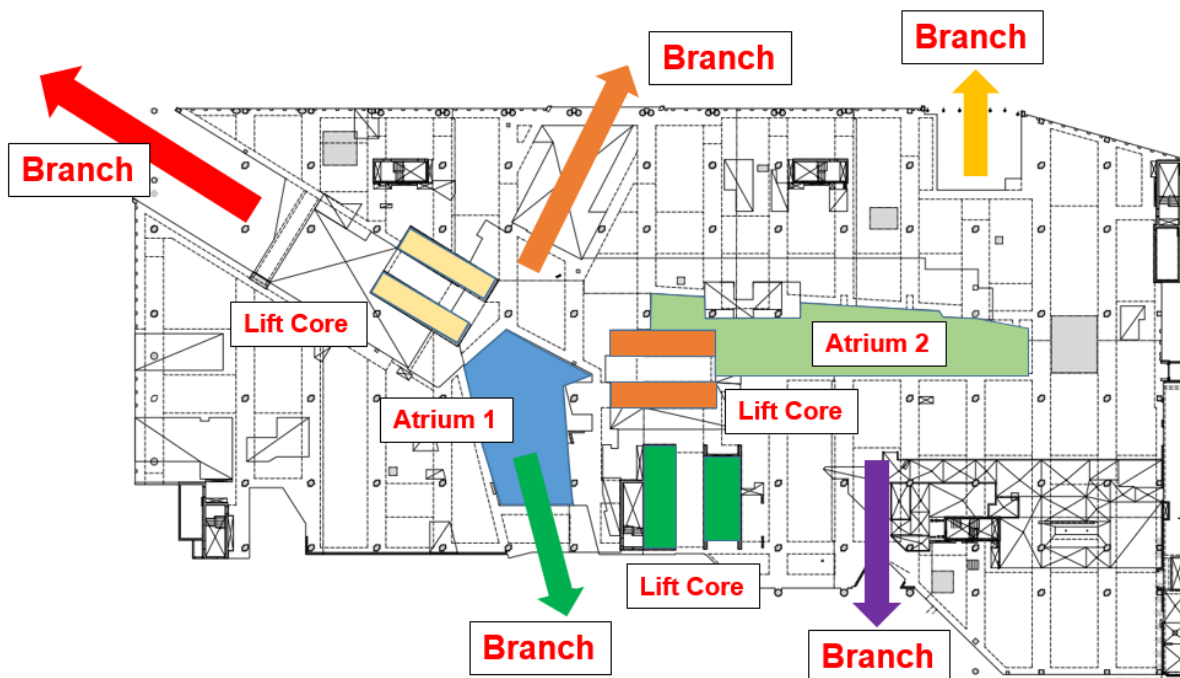


Figure 1. Trunk and Branch Concept

The Lady Cilento Children's Hospital has over 110,000 square metres of floor space, spread across eight main floors (Levels 1 to 8) which cater for clinical, administrative and other facilities. Each of the levels has a varying footprint with the atria and branches altering in size and orientation. The building form steps back progressively creating a series of landscaped rooftop spaces, which provide areas for patients and staff, as well as providing rest areas for families.

There are four ward floors which start at Level 9 and have a completely different footprint to the main floors of the building. Above the ward floors is an open rooftop area incorporating plant rooms and an elevated helipad. The helipad is supported by steel trusses which cantilever up to 13 m off concrete columns.

Externally the development included reconfiguring the adjacent road intersection and street improvements to improve traffic flows, plus the creation of landscaped open spaces which link to the nearby South Bank Parklands. An open children's play area and pet visiting area are located external to the hospital at Level 2.

Vehicle access is provided to the off-street drop off zones at the Stanley Street and Raymond Terrace entry points. Due to the complexity of the underground services and the heavy local traffic, tunnel boring was adopted as the only viable alternative to upgrading and relocating many of the services in the precinct including electricity, water, gas and telecommunications services.

Early construction works commenced on the site in 2008 and the hospital opened in late 2014.

## **2. Primary Structural Concrete Elements**

### **2.1 Foundations and Basement Floors**

The geotechnical site investigation revealed that the site was underlain by rocks of the Bunya Phyllite which is a weakly metamorphosed fine grained rock. Seven boreholes were drilled to depths of up to 18 metres during the geotechnical investigation. There were three weathered rock profiles encountered in the boreholes including phyllite, metasandstone and metagreywacke. The depths to the weathered rock increased in the north eastern corner of the site. Generally improving with depth, the rock strength varied from very weak to strong.

There are four basement levels of car-parking which allows for up to 650 vehicles. The excavation of the basements were completed in stages. Bored piers were installed and then anchors installed as the basement was excavated. Although 600 mm diameter piers were used in some areas, generally 750 mm diameter piers at approximately 2.5 m centres were adopted. In addition to the lateral earth pressures, the piers were also designed to support the loads from the building where required. To resist the retention loads, the bored piers were temporarily anchored into rock using 15.2 mm diameter stressed strands. 150 mm thick spray-crete walls were constructed between the piers prior to the next stage of excavation commencing.

Due to the proximity of the project to the South Brisbane Bus Tunnel (under Stanley Street), an extensive geotechnical study was required to satisfy the Department of Main Roads and Transport that the existing tunnel would not be adversely affected by the excavation of the basement including the construction of ground retention system and the building generally. Real time monitoring was carried out during construction to ensure that there were no movements within the tunnel structure.

High level pad footings were used to support the building internally and were sized on the basis of an allowable bearing pressure of 1500 kPa. To reduce the amount of rock over-break, a rock saw was used to cut the rock to suit the size of the footings.

While the lowest levels of the basement floors were slab on ground construction, upper suspended levels consisted of reinforced band beams and one way slabs. To allow for creep and shrinkage of the floor slabs, special details were required for the connection of the band beams and suspended slabs to the retention piers. The gaps between the slabs and the piers were later grouted allowing the temporary rock anchors to be de-stressed.

## **2.2 Typical Floors Levels 1 to 8**

The slabs at these levels have a large footprint and are interrupted by two atriums of varying size and three lift cores. The footprint varies floor to floor, with the western and eastern ends stepping back progressively to create a series of useable roof areas. The column grids vary to optimise floor planning and as a result, beams and slabs are required to have medium to large spans.

Hospitals are highly serviced and the floor structure needs to be able to maximise the ceiling space. To cater for changes in service delivery and technological advancement, hospitals also need to be able to adapt to changes over time. The floor structure needs to;

- Provide for the functional and technical aspects of the design brief
- Be serviceable, with appropriate vibration performance for the various functions, particularly in the operating theatre suites and diagnostic imaging areas
- Be economical, durable and provide adequate fire resistance
- Cater for a high level of services cores, risers and voids of varying sizes
- Allow flexibility for future re-planning, including provision for setbacks for wet areas and services installation
- Have provision for heavy loading and suit the installation of a wide variety of clinical and imaging equipment, data processing and mechanical plant
- Have medium to large spans to provide the most flexibility in planning
- Minimise depths to provide the maximum clear ceiling space for services runs
- Cater for column transfers
- Provide radiation shielding in radiography areas

A number of floor systems were investigated to satisfy these issues, including flat slab, flat plate and banded slab. Precast systems were discounted as they constrained flexibility needed to suit potential planning changes. A banded slab system was adopted as the preferred system. The slabs are generally conventionally reinforced with strategic use of post-tensioning to allow for future flexibility and installation of services.

Post tensioning was introduced in band beams to minimise depths and control deflections on the larger spans and to cater for transfer loads. Post tensioning was also introduced in some internal slab areas to suit heavy loadings and in some floors to suit construction programming and to minimise back propping. External slab areas were post tensioned to aid in waterproofing.

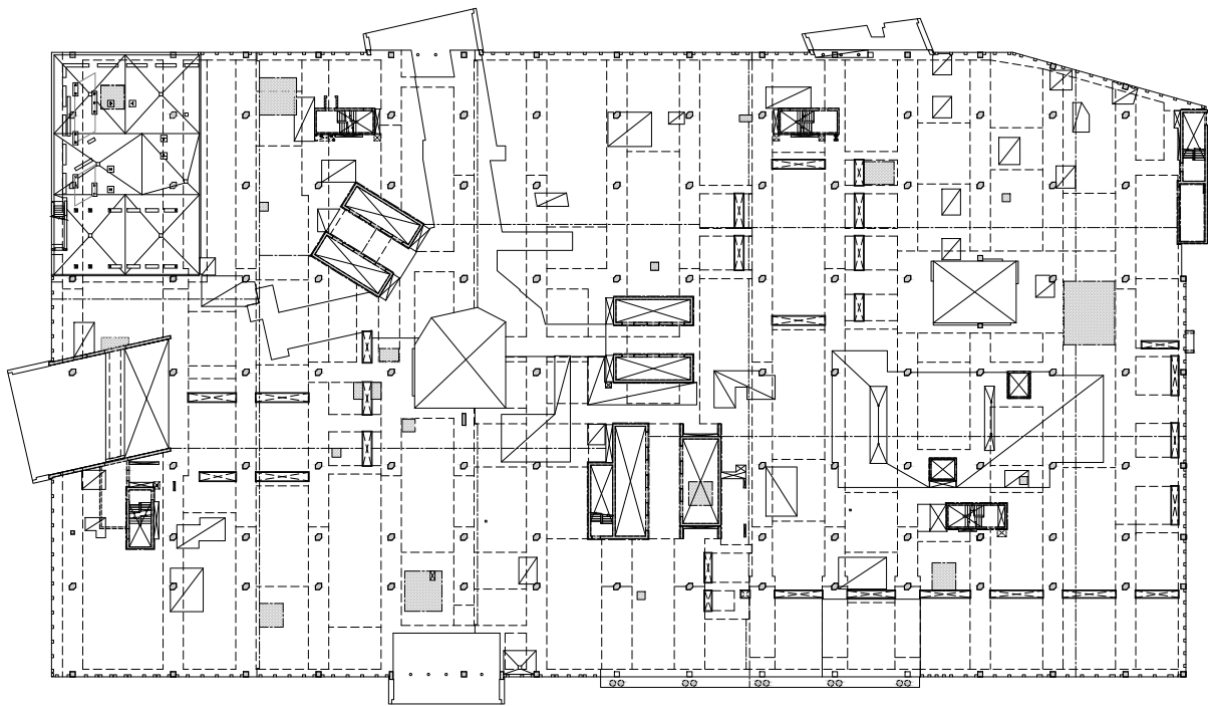
Flexibility for the provision of future wet areas was provided by topping the slabs at some levels. It was considered uneconomic to top all of the floors within the building. A study of possible future planning changes was carried out and particular floors were identified as requiring a topping. To reduce the impact on the construction program and to avoid issues with delamination, a topping integral with the slab was adopted rather than a separately applied topping or screed.

Conventional formwork was used for the beams, areas of varying slab shapes (in plan) and other particular zones. Metal decking was typically used as permanent formwork for the slab soffits between the beams.

During construction there were up to five tower cranes, six concrete placing satellite booms and three material and personnel hoists rising within the building. The large number of temporary voids necessary to suit these had a significant effect on the design and construction of the slabs. These were all ultimately closed in as the plant was removed.

The external roof slab areas created by the building setbacks have a variety of uses, from patient and staff areas to recreational and quiet spaces for families. These areas have surface falls to drainage outlets and have various surface finishes including turf and pavers.

Movement joints were provided in the slab to allow for the initial shrinkage of the concrete due to the large floor plates and the effects of the three internal lift cores. To avoid impacts on the construction program, a lockable dowelled joint system was used. These joints were left as long as possible before the dowels were locked and the joint gaps that had opened since casting the slab were grouted.



**Figure 2. Level 5 Slab Key Plan**

In this heavily serviced building there are a large number of slab penetrations for services. While as many as possible of these services had pipework or sleeves built in when the slab was poured, there were still a large number installed after the floor had been cast.

Late changes also occurred due to planning changes and some of the detailed services design lagging behind the construction program. To manage this and avoid inadvertent drilling and cutting causing structural issues, a permit system was introduced. The permit system required sign off by all parties and all services installers were required to follow this procedure.

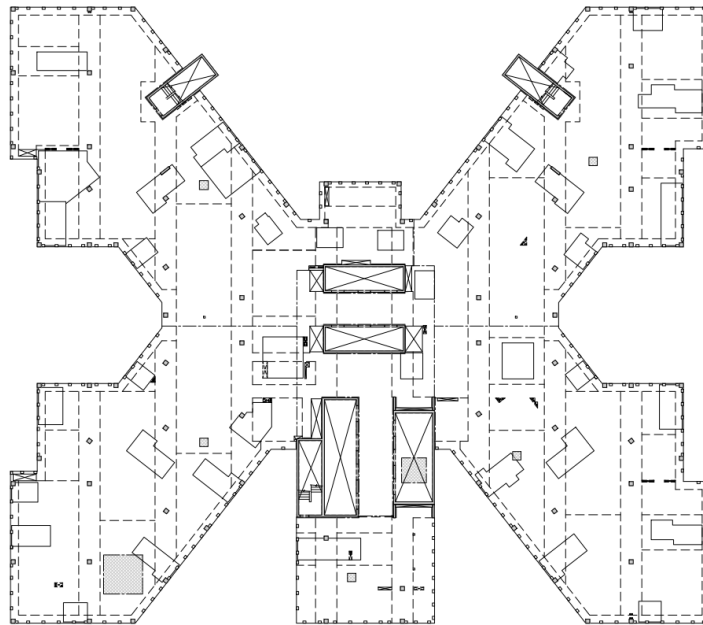
### **2.3 Levels 9 to 12 - Ward Floors**

The ward areas are located in the upper four levels of the building. To suit the ward planning and overall form of the building, these floors have a completely different footprint to the building below.

The column layout is significantly different on the ward levels requiring a transfer floor at Level 9. The band beams are significantly deeper on Level 9 than the lower floors and are more heavily reinforced with an increased level of post tensioning.

A fully post tensioned banded slab system was used for the ward levels to reduce weight, minimise the transfer loads and to keep floor to floor heights to a minimum.

Generally 50 mm deep set downs were provided for wet areas in the ward levels. Level 12 was designed as a shell floor and incorporated extended set down areas to suit any planning changes that may occur in the future fitout.



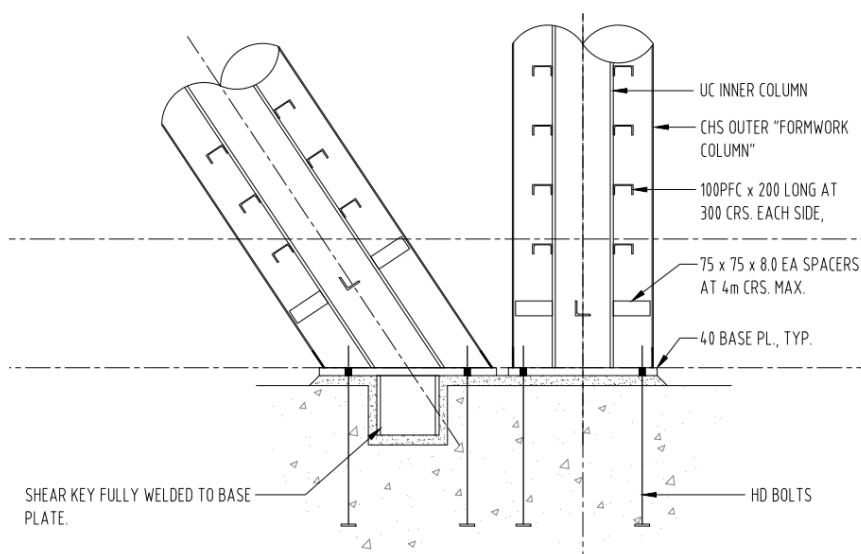
**Figure 3. Level 11 Slab Key Plan**

## **2.4 Composite Structural Steel & Concrete Columns**

Early design studies for the building investigated a cantilevered building perimeter, however the depth of the supporting beams was found to be a constraint to providing sufficient clear ceiling space for services. An alternative solution of raking columns was adopted for the perimeter of the building. The geometry of the columns vary to suit the building form and are coordinated with vehicle access to the Raymond Terrace and Stanley Street patient drop off zones. The columns form a striking feature of the building.

The raking columns comprise an outer steel circular hollow section (CHS) with an inner universal column (UC) section encased in concrete. The inner core relies on composite action between the UC section and the concrete. As the CHS is sacrificial in the case of fire, it was assumed to not contribute to the overall structural capacity of the column.

The columns found on bored pier foundations and as the columns on the Stanley Street frontage rake outwards significantly, the foundations to these have tie beams back to the main structure to cater for the lateral forces that arise.



**Figure 4. Typical details of raking columns**

Some of the earliest construction using composite concrete columns was in Brisbane, Melbourne, Perth and Adelaide in the late 1980's and early 90's. There was no Australian Standard covering the design of composite columns in buildings when the raking columns were being designed for the Lady Cilento Children's Hospital. Our research indicated that composite columns in Australia have been designed using Eurocode 4: Design of Composite Steel and Concrete Structures - Part 1-1. This design code was adopted which satisfied the performance requirements of the BCA (rather than the deemed to comply requirements).

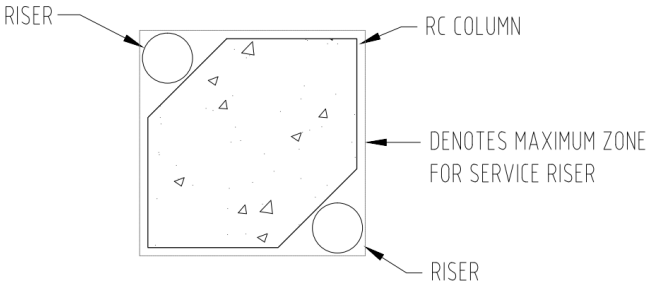
Due to the three dimensional geometry, the columns had to be temporarily propped with falsework to position them and maintain their stability, until they were cast in with the floor slabs. Differential deflections of the columns was also factored into the design.

**2.5 Vertical Elements**

The building has three main multiple lift cores and a number of stair cores. The columns range in shape and size up through the building. Walls and columns were designed as cast in-situ reinforced concrete. The column grid is fairly regular in the long direction of the building, but varies at end spans and across the short direction of the building to optimise planning. There are column transfers at various locations to suit planning and the atriums. Column and wall sizes have been minimised by the use of high strength concretes, particularly in the basement parking areas to optimise parking arrangements.

The lift cores terminate at different levels to suit the planning requirements and were constructed using a jump form system. The lift cores provide lateral stability to the structure for wind and seismic loading. Due to the complex shape of the building, a wind model study was carried out to provide more complete information than could be derived from Code provisions. Three dimensional computer modelling, including dynamic loads from seismic actions, was employed to analyse the building frame and optimise the structural wall sizes and layout.

An innovation, promoted by the Project Architect, was to shape the main building columns to suit the installation of services.



**Figure 5. Typical Concrete Column Shape**

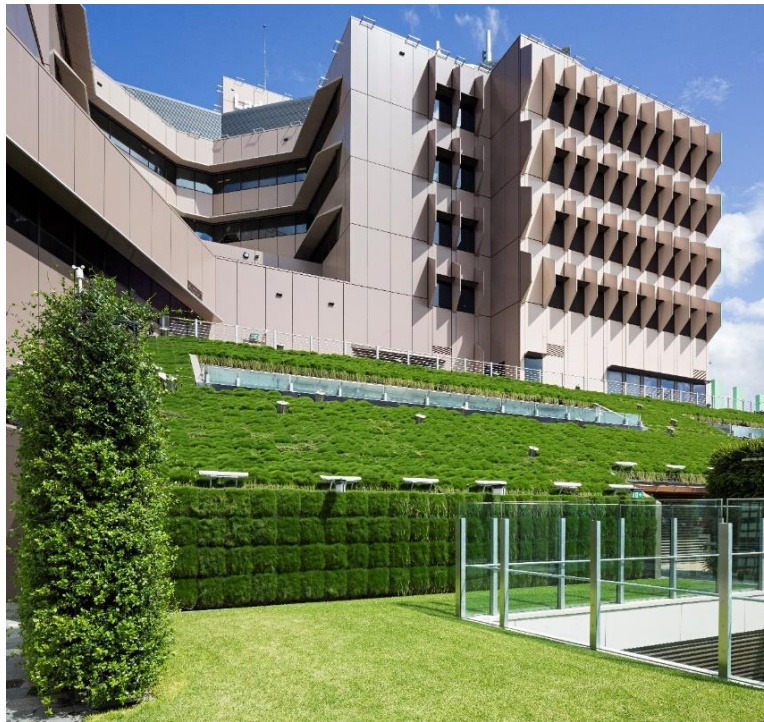
Apart from the lift and stair cores, there are reinforced concrete walls for rainwater and potable water storage tanks and transfer walls. Some walls were also provided for shielding in radiography zones. Loadbearing walls were kept to a minimum to provide flexibility for future reutilisation. Loadbearing blockwork was generally avoided.

**2.6 Sloping Green Wall**

The sloping green wall is a significant landscaping feature of the building. Located on the western side of the building, the sloping green wall traverses two floors, starting at Level 6 and continuing to Level 8. The slope of the green wall is approximately 30 degrees which presented some challenges during construction. The main feature of the sloping green wall is the landscaping element which consisted of planting contained in *baskets*. The baskets were designed to hold the soil and planting in place on the slope.

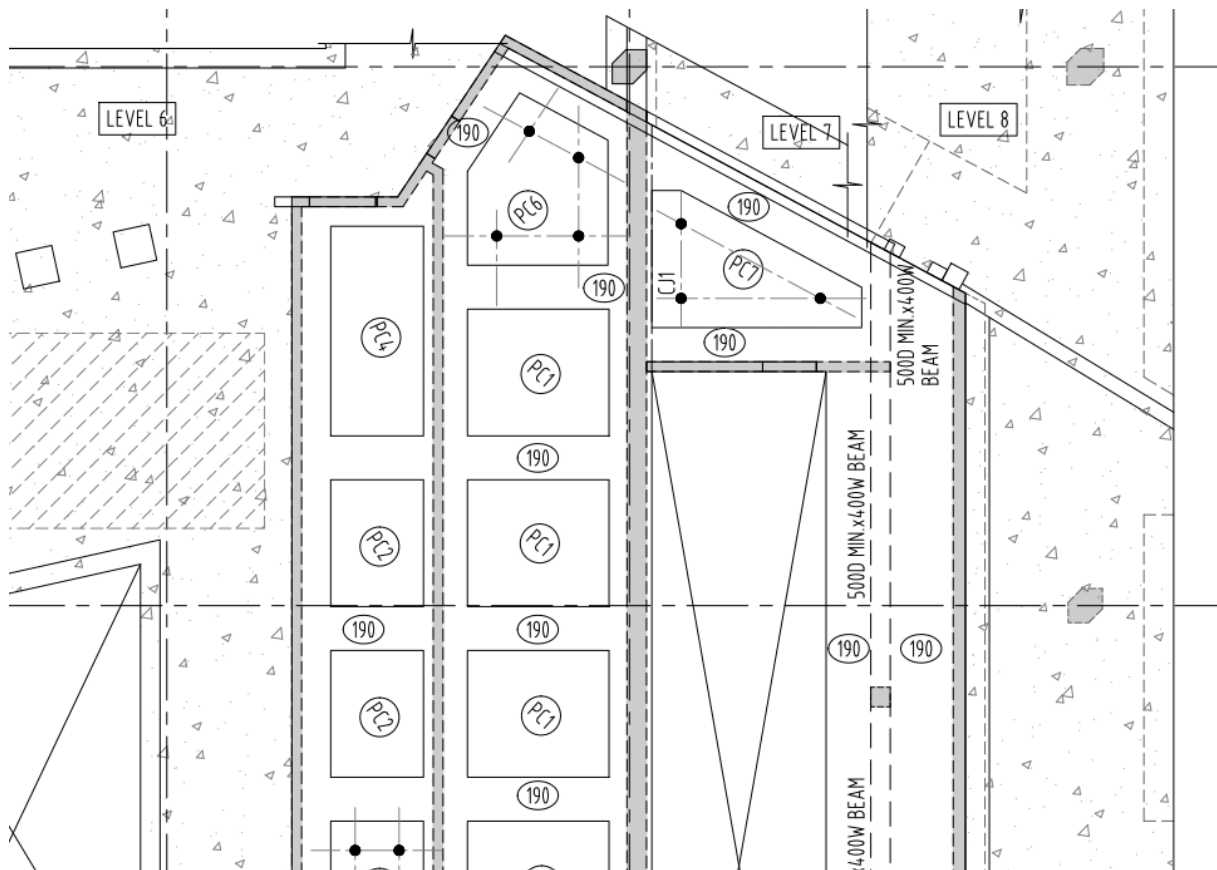
During the early phases of design development, a number of options were considered including in-situ concrete, precast concrete, structural steel and composite/fiberglass. Fire, durability and waterproofing considerations eventually ruled out structural steel and the composite/fiberglass options. A moving stage would have been required to finish the concrete had a full insitu option been adopted.





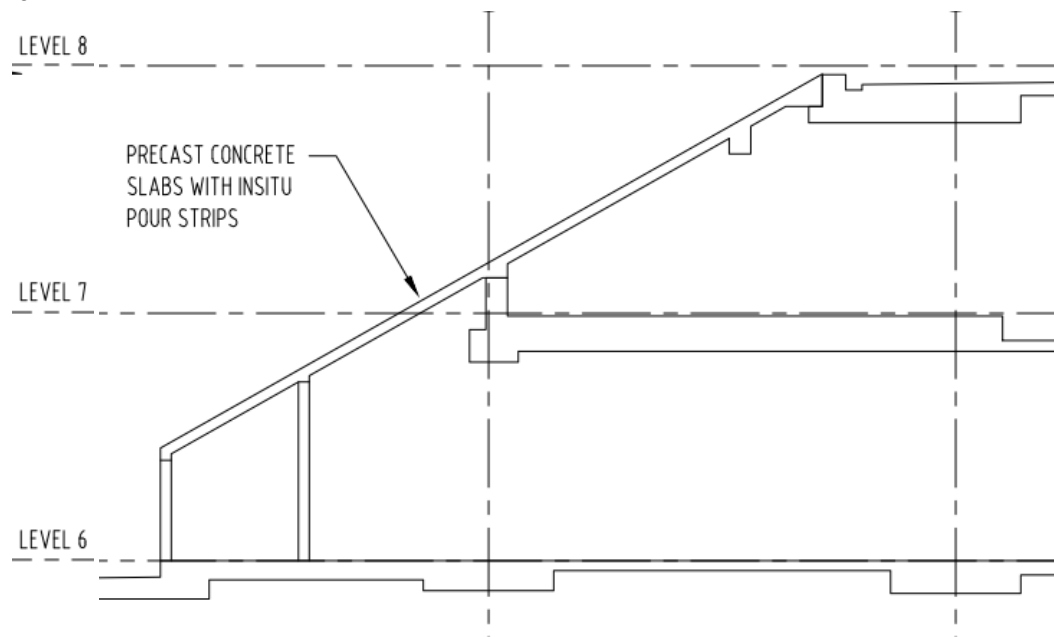
**Photograph 2. Sloping green wall**

A combination of 3.5 tonne, 190 mm thick precast concrete slabs with in-situ concrete pour strips was adopted in conjunction with the Managing Contractor and the formwork sub-contractor. The precast slabs were laid on falsework and the infill strips were then constructed. The precast slabs allowed a safe zone for the steel fixers and the concreters to work from. The number of identical precast slabs was maximised to allow the panels to be stack cast adjacent to the green wall.



**Figure 6. Part Plan showing precast concrete slabs to sloping green wall**

Once the concrete operations had been completed and backpropping removed, a waterproof membrane was applied and the baskets were installed. Stainless steel straps were used to prevent the baskets from sliding down the sloping surface. Safety lines were installed at the top to allow abseilers to maintain the green wall.



**Figure 7. Typical cross sections of sloping green wall**

## **2.7 Use of Precast Concrete**

To minimise falsework, the lift motor room floors and roof slabs to the water tanks were constructed using precast panels with a cast in situ topping. The topped panels were designed to suit the elevator plant loads and to suit forming and pouring the roof slab over. Craneage requirements dictated the size of the precast slabs in some instances. The precast slabs were typically 180 mm thick and weighed up to 6 tonnes. The number, size and location of penetrations in the lift motor room precast slabs were a primary issue for the design. Steel beams were used to provide temporary support of the panels during construction.

## **3. Concrete Materials**

As expected for a project of this complexity, a wide range of concrete mixes were used. There was over 60,000 cubic metres of concrete placed, at an average of over 120 cubic metres per day during the building structure construction.

Mixes were developed to suit the various building components and the extensive surrounding paved areas. Concrete mixes supplied to the project included:

- 40 to 80 MPa strength in columns and walls. High strength concrete was used in the basement parking zones to minimise the column size and optimise parking arrangements
- Generally special class 32 MPa in slabs, with shrinkage control and high early strength to suit post tensioning
- 65 MPa concrete in thick water tank walls with temperature controls to reduce thermal effects
- Topping mixes
- 32 MPa special aggregate mixes for exposed aggregate paving
- A number of special mixes were also supplied for particular situations or where there were constraints on delivery and placing

Aggregate sizes and slumps varied to suit the particular situations, pumping and placing.

The site was very constrained on all sides, with insufficient area to establish a concrete delivery and pumping site close to the building. To overcome this problem, the Managing Contractor established a remote concrete delivery site on an adjacent street and the concrete was pumped to the site through



underground pipelines. Delivery to the satellite boom pumps on the site was controlled through a manifold system in the basement. Up to six boom pumps across the site were established to suit concrete placing.

#### **4.0 Structural Steel**

##### **4.1 Branches**

The branches offer a unique statement to the façade of the building form. The branches cantilever over the streetscape and are typically over two floors. The branches form a balcony that allow users of the hospital to view the city skyline. The side walls of the branches were designed as structural steel trusses enabling the structure to cantilever from the concrete columns at the building interface.

Concrete columns were specifically shaped to allow the structural steel from the branch to connect into the building fabric and also to provide an interface for the curtain wall. The branch walls, ceilings and roofs were clad with alpolic. Branch floors were constructed using in-situ concrete over steel formwork supported on structural steel framing.

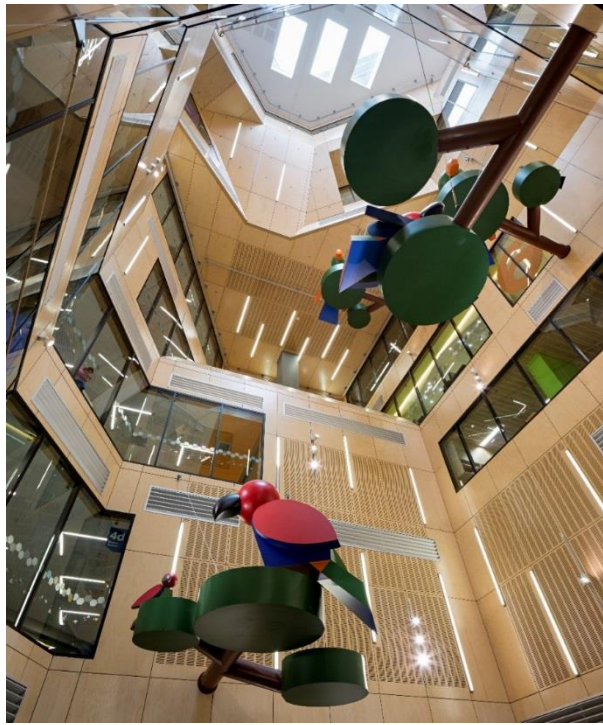
The layout of the structural steel floor framing were set out so that the steel formwork did not require propping during construction.



**Photograph 3. Northern Branches**

##### **4.2 Atriums**

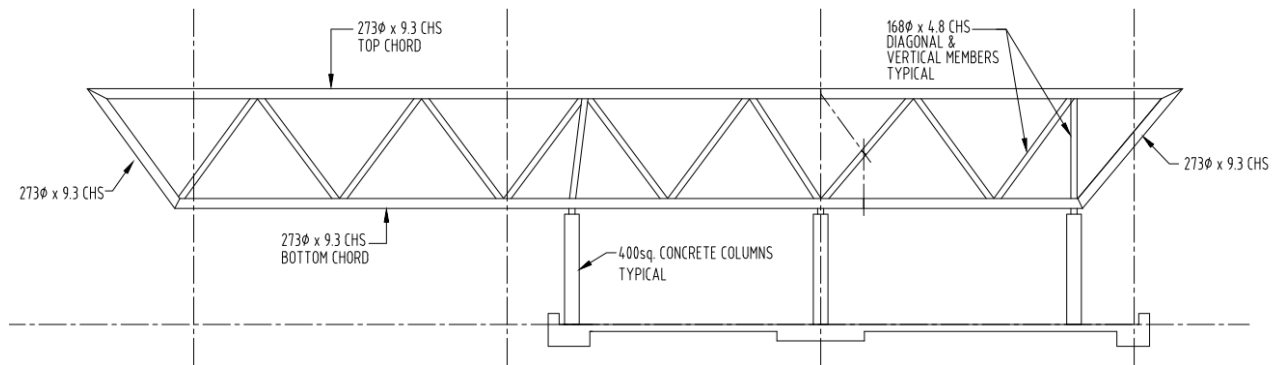
Two atriums were part of the living tree concept for the project. The first of these commenced at Level 2 and continued to Level 10. The walls of the atrium were multi-faceted with a significant number of inclined faces. The walls were framed using structural steel and light steel stud framing. Complexity of the architectural form, fire-rating, maintenance and cleaning were key issues during the design and documentation.



**Photograph 4. Atrium 1**

### **4.3 Helideck**

Located at Level 14, the Lady Cilento's emergency helipad measures approximately 27m x 23m. There are two components of the helipad being the primary support structure and the helipad deck. The primary support structure consisted on four structural steel trusses that were supported on concrete columns. Two of the trusses were required to cantilever up to 13 metres and were designed to support emergency services helicopters weighing up to 8.0 tonnes. The 3.0 metre deep trusses were fabricated using 273 x 9.3 CHS top and bottom chords with 168 x 4.8 CHS diagonal members.



**Figure 8. Typical cross section through Helideck structure**

## **5. Design Codes and Loads**

The various building uses were considered in determining the types of loads onto the structural elements. There are special load areas within the building to cater for uses such as medical imaging, records, plant and landscaping. Planning for the heavy equipment included defined load routes through the building for the installation and replacement of the same. Provision was also made for access points into the building, through the façade and via a hatch through the Level 2 slab. Provision for specific vibration sensitive functions was also made to suit operational requirements.

The structural design parameters were set by the Project Brief, the Building Code of Australia, Australian Standards and Regulations. International codes were adopted when there was no appropriate Australian Standard.

## 5.1 *Dead and Live Loads*

A Building Code of Australia Importance Level 4 was adopted for the building structure. Floor and general loadings were adopted in accordance with AS1170 Part 1. Loads in excess of AS1170.1 have been used in some areas to permit future flexibility. Special load cases apply in various parts of the building for plant, imaging equipment and landscaping. Generally, loads were as follows;

- Superimposed dead loads from partitions, etc, (excluding slab toppings) 1 kPa
- Live load generally 3 kPa; public areas 4 kPa; plant areas 5 kPa;
- Special loads as required for medical imaging and other equipment

## 5.2 *Wind Loads*

A wind tunnel study was commissioned to examine the wind pressures on the complex façade including branch structures. The wind study also provided advice on the effect that the operable louvres that occur at the branch ends would have on the internal walls and ceilings. The operable louvres automatically closed once the wind speed exceeds 10m/s.

The external walls (excluding the main façade), internal atrium walls and general internal walls were designed in accordance with the requirements of the design guidelines and the Building Code of Australia.

### 5.2.1 *Basic Wind Pressure*

The wind loads were assessed in accordance with the Building Code of Australia and AS 1170 Part 2. The wind speed was assumed to vary with the height of the building. For practical reasons the wind pressures were calculated in groups of three storeys above Level 1. The ultimate design wind pressure (at Level 13) was 3.20kPa.

Region	B
Importance Level (BCA)	4
Topographic Multiplier	Mt = 1.0
Shielding Multiplier	Ms = 1.0
Terrain Category	2.5

### 5.2.2 *Pressurised Internal walls*

Typically the pressurised internal walls bound the open spaces created in the centre of the building between Levels 1 and 4. These spaces have natural ventilation from the louvres in a number of the Branches that allow natural light to permeate through the building. Above Level 4, the atrium splits off into two smaller isolated atriums that extend to roof level.

## 5.3 *Earthquake Loads*

The building was designed to withstand a 1 in 1500 year seismic event (Seismic Design Category III) which required a dynamic assessment to be undertaken. As noted earlier, lateral loads were resisted by the lift and stair cores.

## 6. *Conclusion*

The Lady Cilento is a new tertiary children's hospital, a state of the art health facility and an iconic building, designed to serve Queensland. At an overall cost of \$1.5 billion, works commenced in 2008 and construction completed in 2014.

The building has four basement parking levels, eight main hospital levels, four ward levels and three upper services levels. In order to achieve openness, light and connectivity within the large footprint of the main floors, there are two central atriums with radiating branches which connect through to the façade.

The footprint and atrium size vary for each of the main hospital levels and have landscaped roof areas. The western façade includes a raking wall which supports specialised landscaping.

Reinforced and post-tensioned slabs and band beams were generally adopted for the floor structures as these were considered to be the most efficient and adaptable system.

## **7. Acknowledgements**

The authors would like to acknowledge the Managing Contractor, Lend Lease, for their assistance in providing some of the background information for this paper. The authors would also like to acknowledge the invaluable contribution from the Project Architects, Conrad Gargett Lyons for their assistance with the images and other details.

## **8. References**

1. The design of Circular Concrete Filled Steel Tubes - M.D.O'Shea & R.Q.Bridge Centre for Advanced Structural Engineering, The University of Sydney.
2. Eurocode 4: Design of composite steel and concrete structures - Part 1-1, General rules and rules for buildings.
3. European Convention for Constructional Steelwork (ECCS) - Technical Committee 11 - Composite Structures - Publication No 72 - 1993, Composite Beams and Columns to Eurocode 4.
4. Soil Surveys Geotechnical Investigation Report for the Proposed Queensland Children's Hospital, August 2008.
5. Windtech Consultants Report for the Façade Cladding and Internal Pressure Study for the Proposed Development known as the Queensland Children's Hospital, Brisbane, October 2010.

# Documentation of Bridge Deck Construction Using Industrially Produced Internally Cured, High Performance Concrete

Timothy J. Barrett<sup>1</sup> Albert E. Miller<sup>2</sup> and W. Jason Weiss<sup>3</sup>

<sup>1</sup>PhD Candidate, Purdue University

<sup>2</sup>Graduate Research Assistant, Purdue University

<sup>3</sup>Jack and Kay Hockema Professor of Civil Engineering, Purdue University

**Abstract:** In 2013, the Indiana Department of Transportation (INDOT) commissioned the construction of four bridge decks using an internally cured concrete designed to achieve an increase in durability through reductions in ionic transport and reductions in the potential for cracking. In an effort to improve the durability, a blended cementitious system was used containing ordinary portland cement, fly ash or slag, and silica fume was specified for use at moderate water-to-cementitious materials ratios, of less than 0.43. Since higher performance concretes show an increased susceptibility for shrinkage cracking, the process of internal curing using a pre-wetted fine lightweight aggregate was used to reduce the potential for cracking. This paper presents a case study on the construction of these internally cured, high performance concrete bridge decks with a focus on its impact of implementation on practice. Basic testing results such as strength and stiffness will be presented with a focus on the lack of necessity for revisions to code equations or design practices due to the presence of internal curing. In addition, a new quality control technique for the rapid determination of lightweight aggregate moisture states will be reviewed while recommendations for the daily field implementation of internally cured concrete will also be presented. This research is intended to provide a succinct overview of the successful field implementation of internally cured concrete, which offers the potential to produce concrete that may have a lower susceptibility to cracking, leading to realized improvements in the service life of high performance concretes.

**Keywords:** Internal curing, high performance concrete, construction documentation, service life, shrinkage.

## 1. Introduction

The Indiana Department of Transportation (INDOT) constructed four bridge decks utilizing internally cured high performance concrete (IC HPC) during the summer of 2013. These decks are being considered as one method to reduce cracking and to improve the durability of the bridges [1]. While the laboratory results of internally cured concrete have shown great promise, few studies have documented field performance [2]. The objective of this research is to provide documentation of the construction of four IC HPC bridge decks that were constructed in Indiana during 2013 and to quantify the properties and performance of these decks from samples procured at each site. The data obtained from each of these mixtures will be compared with equivalent high performance concretes (HPC) that contained no internal curing for each respective mixture and contrasted with a typical bridge deck concrete that is used in Indiana (so-called Class C concrete) [3]. The purpose of this documentation is to provide data that can be used to quantify the performance of industrially produced internally cured concrete with the goal of developing recommended procedures to implement new technology and developing future strategies to determine if and where internal curing should be used. The documentation provided by this project will focus on three main areas:

1. Documentation of construction/measurement of the constituent materials, variability, and fresh concrete properties.
2. Documentation of the properties of the concrete used in these bridges
3. Documentation of the shrinkage cracking resistance with a comparison of IC HPC and reference (non-internally cured) concrete.

## 2. Specification Overview

As a part of this work, a new specification was developed and implemented which incorporated both prescriptive and performance based measures which were intended to produce a concrete of high durability, low permeability, and low cracking potential [4]. This section will review the specified measures intended to provide higher performance and internal curing using prewetted fine lightweight aggregates (LWA).

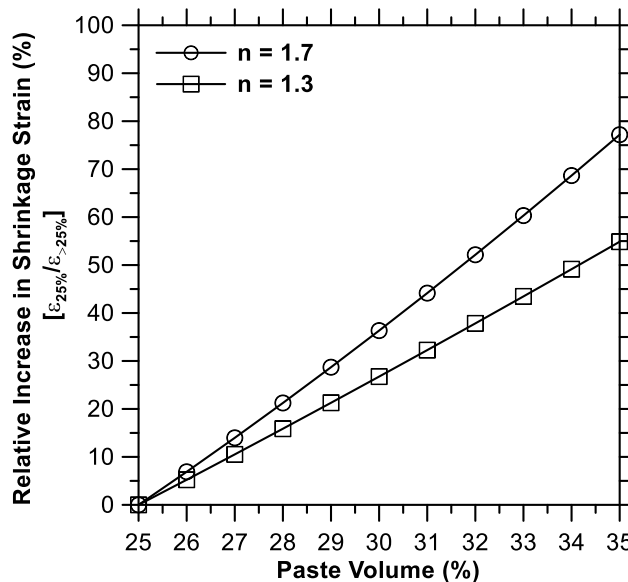
## 2.1 Higher Performance Specifications

The higher performance inherent to the IC HPC comes from three key specification measures. The first is through the use of two supplementary cementitious materials in combination with the portland cement which will result in a refinement of the pore network, consumption of calcium hydroxide, and a microstructure that is more dense overall [5]. The specification requires a minimum of 231 kg/m<sup>3</sup>, a content of 20 to 25% of Class F or C fly ash (by mass), and a content of 3 to 7% of silica fume (by mass). It is permitted to substitute ground granulated blast furnace slag (ggbfs) in an amount of 15 to 20% (by mass) in lieu of fly ash. An additional benefit of the use of supplementary cementitious materials is the net reduction in cement consumption for the production of concrete bridge decks. IC-HPC conforming to this specification may result in a net reduction in cement usage of 23 to 32% (18 to 27% using ggbfs).

The second aspect of the specification that improves the performance of the mixture is a limitation of total paste volume to 25% with a tolerance of  $\pm 1.0\%$  on batched quantities. This limitation was intended to limit the shrinkage potential of high performance mixtures, based on research presented in the FHWA/IN/JTRP-2008/29-2 report where it is recommended that a paste volume of less than 24% be targeted [6]. This report reflects previous recommendations from Schmitt and Darwin which studied 33 monolithically cast bridge decks constructed prior to 1994, where it was documented that measured cracking increased with increasing paste volumes [7]. The survey indicated that the volume of paste should not exceed 27%, based on a sample of 9 bridge decks at moderate w/c of 0.42 or 0.44. This data was then reproduced in 1999 [8], 2004 [9], and again in 2005 [10] with the culmination of these results being used as the basis of mixture proportioning for a low-cracking, high-performance concrete with a maximum paste content of 24% and performance being measured in relation to crack density alone [11].

This body of work recognizes the importance of paste volume, as shrinkage in cementitious systems is derived primarily through chemical reactions, osmotic or disjoining pressures, and/or the development of capillary stresses occurring within the paste [12]. The connection of shrinkage to paste volume has been observed experimentally for many years, with numerous models having been proposed to estimate contributions of paste shrinkage to the overall shrinkage observed in concretes. Picket proposed a simple relationship in 1956 which relates the total shrinkage in concrete to the shrinkage of the matrix and the volume of paste, as shown in Equation 1 (with the volume of paste being represented by  $(1 - V_{\text{aggregate}})$ , where  $V_{\text{aggregate}}$  is the volumetric fraction of the concrete which is aggregate) [13]. Figure 1 shows this relationship, normalized by the total estimated shrinkage of a concrete with a paste volume of 25%, with values of  $(n)$  which reasonably estimate the range of typical concretes. From this, the relative increase in shrinkage of concretes with higher paste contents can be seen to be approximately linear, with a 5.5 to 7.7% (for  $(n)$  equal to 1.3 and 1.5, respectively) increase in shrinkage for a 1% increase in paste. With this in mind, a few points of emphasis should now be made. The first is that excessively low paste volumes for industrially produced concretes may result in technical challenges with placement and achieving proper consolidation. Secondly, as the volume of paste is reduced, the potential for the interfacial transition zone to percolate, resulting in increased permeabilities [14]. Finally, it should be highlighted that internal curing is intended to mitigate significant early age shrinkage, making this limitation less necessary for the intent of shrinkage reduction (revisions to the specification in 2014 have relaxed the limit on total paste volume to 26% and may be able to be further relaxed without significant changes in the shrinkage behaviour of the IC HPC mixtures).

$$\varepsilon_{\text{concrete}} = \varepsilon_{\text{matrix}}(1 - V_{\text{aggregate}})^n \quad (1)$$



**Figure 1. Estimated relative increase in shrinkage strain of a concrete, normalized to a paste content of 25%. Relationship is based on Pickett's Law [13].**

A secondary effect of the limitation on paste volume is the inherent maximum cementitious materials content of the concrete mixture. In current specifications for Class C bridge deck concretes, this limitation does not exist. During the production of this concrete, producers target minimum strength values which can be easily achieved through the addition of cement to the mixture. A recent study concluded that Class C bridge deck concretes frequently have cement contents in excess of 386 kg/m<sup>3</sup> which may lead to increased susceptibility to the formation of transverse cracking in bridge decks [15].

The final specification measure which promotes higher performance is the limitation on water-to-cementitious materials ratio (w/cm) of 0.36 to 0.43, with a stated allowable tolerance of  $\pm 0.025$ . This limitation on w/cm leads to the production of concrete that, when a high degree of hydration is reached, will have minimized the capillary porosity [16]. The minimization of capillary porosity will result in concrete that has a lower permeability and diffusivity [5]. A secondary consequence of specifying the low paste volume and w/cm is the inherent necessity for producers to perform accurate aggregate moisture tests and account for excess water in the mixture at all times during the production of IC HPC.

## 2.2 Internal Curing Specifications

The internal curing in the IC HPC is specified to be achieved using a pre-wetted fine lightweight aggregate. The amount of LWA used for internal curing is intended to supply 7 kg of water per 100 kg of cementitious materials [17]. This quantity was multiplied by 1.025 by INDOT to account for an additional margin of safety in the specification (i.e., supply a total of 7.17 kg of water per 100 kg of cement). The approved mixture design was used to ensure a fixed volume of LWA is supplied (not less than 20% of the total volume of fine aggregate volume) based upon laboratory measured values for the LWA absorption and specific gravity at 24 hours. According to the specification, at the time of production the LWA absorption and specific gravity is to be measured. The target batch weight of LWA is then specified to be determined by multiplying the weight of dry LWA necessary to supply 7.17 kg of water per 100 kg of cement (as determined by the 24 hour laboratory moisture properties of the LWA) multiplied by the total moisture of the LWA measured on the day of production.

In preparation for the production of IC HPC, the producer is required to wet the lightweight aggregate with a suitable sprinkler system for a minimum of 48 hours or until the absorption of the LWA is consistently maintained above the design absorption value. The stockpile of LWA is to be drained for 12 to 15 hours immediately prior to its use in IC HPC construction. Manipulation of the stockpile should be done as necessary to achieve a uniform moisture state while wetting and draining. To determine the LWA moisture state on the day of production, the specification cited the provisions in Appendix B of ACI 211.2 which utilizes a centrifuge spinning at 500 rpm for 20 minutes in order to achieve a pre-wetted surface dry condition for absorption testing [18]. Since the inception of this research, this technique has been improved upon by Miller et al. to utilize a centrifuge spinning at 2000 rpm for 3 minutes to achieve a pre-wetted surface dry condition of the LWA [19] and has been subsequently standardized by the state of Indiana in Indiana Testing Method 222 [20]. A variability study has also been conducted [21] showing that the centrifuge method reduces the coefficient of variation in measured moisture contents of LWA

by an order of magnitude compared to the so-called “paper towel” test, recommended in ASTM C 1761 [22].

In order to ensure that the IC HPC mixtures achieve the stated goals of improved durability and reduced permeability, certain performance measures based on standardized tests were specified. At the point of placement, the concrete mixture is to have a measured slump between 63 to 140 mm, a target air content of 6.5%, and the measured relative yield shall not be excessively high or low. The specified compressive strength at 28 days shall be a minimum of 34 MPa. Finally, the IC HPC shall achieve a target resistance to chloride ion permeability of no greater than 1500 coulombs as measured by the rapid chloride penetration test (ASTM C 1202/ AASHTO T277) at 56 days of age [23]. It should be noted that the specification for Class C concrete does not include any limitations on measures of resistance to chloride penetration, only specifying a maximum w/cm of 0.443 and a minimum 28 day compressive strength of 30 MPa. The performance criteria have been summarized in Table 1.

**Table 1. Internally cured, high performance structural concrete specification parameters [4].**

<b>IC HPC Specification Criteria</b>	
Batching Tolerance	± 1%
Slump Range	63 - 140 mm
Target Air Content	6.5%
w/cm	0.36 - 0.43
f <sub>c</sub> , 28 d	> 34 Mpa
RCP Test, 56 d	< 1500 C
Internal Curing Water	7.17 kg/kg cem

### 3. Project Information and Mixture Designs

The IC HPC bridge decks that were cast were made by four separate producers, located in four different regions of Indiana and being supervised by four different INDOT district engineering units. The bridges had varying span lengths (maximum span lengths ranged from 8.5 m to 26 m) and varying structural configurations (single span composite with steel girders, three span continuous composite with steel girders, and two span continuous composite with prestressed concrete beams with an integrally cast pier).

The specimens obtained in this study were produced on the same day that each bridge deck was cast using the same mixture proportions, batching and mixing system, and aggregate moisture adjustments as was used for the bridge deck. Upon completion of the deck pour, two separate concrete trucks were ordered at each producer’s facility, containing 2.3 m<sup>3</sup> (three cubic yards) of concrete each. The first truck contained the IC HPC as batched that morning while the second truck contained the equivalent HPC, where the LWA in the mixture was replaced with normal weight fine aggregate.

The cementitious materials used in the study include Type I ordinary portland cement, Class C fly ash or ground granulated blast furnace slag (GGBFS), and densified silica fume. The aggregate consisted of a normal weight natural fine aggregate and a normal weight limestone conforming to INDOT gradation 9 [24]. To achieve internal curing, an expanded shale lightweight fine aggregate was used to replace a portion of the normal fine aggregate. The moisture state of the LWA was determined using the centrifuge method [25] where, at the time of batching, the measured absorption ranged from 18.7 to 20.2% for all mixtures. The measured surface moisture contents of the LWA for all mixtures ranged between 6.6 to 9.9%.

The as-batched mixture proportions of the concretes used in this study can be seen in Table 2. The naming convention of each mixture is denoted by the concrete mixture type (IC HPC or HPC) and a numeral indicating the base mixture for each bridge deck in no particular order. Concrete mixtures IC HPC 1 and HPC 1 were made using the same mixture proportions with the only difference being the replacement of fine aggregate with LWA for the purposes of internal curing. Air entraining admixture, high range water reducing admixture (HRWRA), mid-range water reducing admixture (MRWRA), and retardant admixtures were added at the discretion of each producer in order to meet specifications for air content and slump. Inspection of Table 2 shows that variation in the w/cm exists throughout these mixtures. Based on field observation it is advised that special attention be paid to all sources of excess water during production (e.g., surface moisture of aggregates, wash water in the truck, and batching



error). In general, the target fresh properties were obtained with the exception of those marked. Table 3 shows the price of the IC HPC and HPC mixtures in this study, indicating that the additional cost for internal curing may be minimal. As a part of one of the contracts involved in this study, two identical bridge decks were replaced with one bridge deck consisting of the mixture referred to herein as IC HPC 1 while the other bridge deck was constructed with a traditional Class C concrete. The constructed cost difference of these bridge decks is \$35/yd<sup>3</sup> (~\$27/m<sup>3</sup>), representing a premium of 0.13% of the cost of one bridge deck replacement to implement the internally cured, high performance concrete.

**Table 2. As-batched mixture proportions [26].**

	IC HPC 1	HPC 1	IC HPC 2	HPC 2	IC HPC 3	HPC 3	IC HPC 4	HPC 4
W/CM	0.405	0.428	0.396	0.403	0.447	0.422	0.465	0.398
Cement	234	236	263	263	256	256	260	272
Fly Ash	74	74	-	-	67	67	-	-
GGBFS	-	-	59	58	-	-	71	74
Silica Fume [kg/m <sup>3</sup> ]	15	15	15	15	10	10	15	15
Coarse Aggregate	1083	1088	1069	1069	1027	1023	1084	1067
Fine Aggregate	442	725	463	792	486	794	505	821
Lightweight Aggregate	195	-	205	-	249	-	301	-
Air Entrainer	73	104	36	36	54	58	70	67
HRWRA [mL/kg]	917	810	333	335	580	617	913	867
MRWRA	-	-	-	-	120	116	220	212
Retarder	122	231	183	183	-	-	-	-
Measured Air Content [%]	6.5	7.1	5.1	5.2	1.8*	5.9	8.1	7.1
Slump [mm]	90	150	200	180	50	50	230	230
Paste Content [%]	24	25	24.4	24.6	26.0*	25.2*	24.5	25.3*

\*Denotes measures which were beyond the limits set for in the specification.

**Table 3. Price (\$/yd<sup>3</sup>) for each mixture in this study. (1 yd<sup>3</sup> = 0.765 m<sup>3</sup>)**

	Volume [yd <sup>3</sup> ]	Material Only [\$/yd <sup>3</sup> ]	Constructed [\$/yd <sup>3</sup> ]	Deck Concrete Cost [% of Total Contract]
IC HPC 1	154	126	680	10.2
HPC 1	-	126	-	-
IC HPC 2	280.4	203	900	27.5
HPC 2	-	104	-	-
IC HPC 3	75.6	116	750	11.7
HPC 3	-	116	-	-
IC HPC 4	239	165	500	11.2
HPC 4	-	159	-	-
Class C*	154	110	645	9.6

\*Twin interstate overpass bridges were constructed as a part of one contract, where IC HPC 1 was used for the northbound bridge deck and Class C concrete used in the southbound bridge deck.

#### 4. Laboratory Measured Properties

A series of tests were performed to characterize the overall behavior and performance of the IC HPC and HPC materials. Table 4 lists the results of mechanical behavior as measured through ASTM C 39 [27], ASTM C469 [28], and ASTM C496 [29], and the result of the rapid chloride permeability (RCP) test (ASTM C1202 [23]), allowing for the assessment of the performance in relation to the limits set forth in the specification. In addition to this information, the linear unrestrained autogenous shrinkage strain at 7 days is provided (as measured by ASTM C1698 [30], with a modified geometry of 72 mm diameter and 305 mm length for concrete) as well as the total shrinkage due to drying for 91 days in a 50% relative humidity (RH) environment, a modified version of ASTM C157 [31] performed on 72 mm by 72 mm by 286 mm prisms with the drying beginning after 24 hours of curing in molds (i.e., no additional water

curing was provided). The results of these tests are reported as strain in the concrete, where negative strain values indicate shrinkage. Finally, the diffusion based service life of these mixtures (where cracking was not considered) was estimated using an extended Nernst-Planck equation coupled with non-linear moisture diffusion [32]. The full results of the testing performed on these mixtures are available in a report by Barrett et al. [26]. In an effort to put the performance of the IC HPC class of concrete into perspective, data from previous research by Di Bella et al. performed on an industrially produced Class C concrete has also been provided [2]. Inspection of the results from laboratory testing of each of these mixtures indicates four main conclusions:

1. All of the IC HPC mixtures met (even well exceeded) the limitations set in the specification.
2. Internal curing in the IC HPC mixtures significantly reduced the autogenous shrinkage after 7 days of curing.
3. Improvements in the performance of IC HPC mixtures compared to the traditional Class C concrete are substantial, even when compared to the lowest performing IC HPC mixture.
4. The IC HPC mixtures tested in this study provide a bridge deck material that achieves an estimated service life of nearly 60 years or more, and when accounting for propagation time for corrosion, a service life of 75 years is achievable (AASHTO design life for bridges is 75 years [33]).

**Table 4. Selected material properties and performance of IC HPC, HPC, and Class C concretes.**

	$f'_c$ (28 d) [MPa]	$E_c$ (28 d) <sup>1</sup> [GPa]	$f'_t$ (28 d) <sup>1</sup> [MPa]	RCP Test [C]	$\epsilon_{Auto}$ (7 d) <sup>2</sup> [ $\mu\text{m}/\text{m}$ ]	$\epsilon_{Tot}$ (91 d) <sup>3</sup> [ $\mu\text{m}/\text{m}$ ]	Est. Service Life <sup>4</sup> [Years]
<b>Class C</b> <sup>5</sup>	30	26	3	3175	-70	-516	18
<b>IC HPC Class</b> <sup>6</sup>	> 34	> 28	> 3.3	< 1500	N/A	N/A	N/A
<b>IC HPC 1</b>	57	37	4.1	420	55	-470	92
<b>HPC 1</b>	62	35	4.7	435	90	-510	85
<b>IC HPC 2</b>	42	31	3.6	1105	-5	-570	62
<b>HPC 2</b>	37	33	3.0	1410	-40	-600	37
<b>IC HPC 3</b>	57	38	4.5	945	-30	-340	59
<b>HPC 3</b>	51	36	4.4	1420	-90	-510	32
<b>IC HPC 4</b>	50	39	3.9	550	-20	-340	73
<b>HPC 4</b>	58	44	4.3	560	-75	-400	100

<sup>1</sup> $E_c$  and  $f'_t$  are inferred for IC HPC Class based on AASHTO C5.4.2.4-1 and 5.8.2.2 (this will be discussed in the next section) [33]. These values were measured directly for all other mixtures in this study.

<sup>2</sup>Autogenous shrinkage strain as measured by a modified version of ASTM C 1698 for concrete [30].

<sup>3</sup>Total shrinkage strain of prisms undergoing drying at 50% RH after 1 day of sealed curing [31].

<sup>4</sup>Estimated service life based on extended Nernst-Planck equation simulated using Stadium® software [34].

<sup>5</sup>Class C concrete strength and RCP values reported by Di Bella et al. [2]; service life estimation reported by Weiss et al. [35].

<sup>6</sup>IC HPC Class concrete performance requirements according to special provisions established by the INDOT [4].

## 5. Discussion of Field Observations

This section will summarize the major observations from the construction process of the four IC HPC bridge decks. While avoidable issues during construction were witnessed, two points should be emphasized. First, four bridge decks utilizing internal curing are now in service and the concrete materials produced for each of bridge decks in this study achieve higher performance in laboratory testing (strength, shrinkage, and chloride resistance) than traditional INDOT Class C bridge deck materials. Second, a mixed specification of prescriptive and performance based parameters was successfully used to produce these bridge decks, resulting in higher performance concretes. In addition to these observations, comments on the impact of IC HPC mixtures on current design specifications and the potential for cracking of these mixtures will be discussed.

## 5.1 Summary of Lessons Learned from the Trial Batch, Production, and Construction

The key areas of emphasis to the successful implementation of internally cured, high performance concretes in field have been listed.

- Prewetted lightweight aggregate can be successfully used in the production of internally cured concrete if the moisture condition of the aggregates are understood, controlled, and accounted for in production. This study implemented a new testing technique that utilizes a centrifuge to rapidly condition the lightweight aggregate to a surface-dry condition and reduces variability in testing over previous testing methods [19]–[21].
- Variability in moisture states within a stockpile of prewetted lightweight aggregate should be controlled through appropriate means (working the stockpile, proper soaking and draining) or measured and accounted for throughout concrete production.
- Batching issues were observed which would be present regardless of the concrete mixture proportions, whether the concrete mixtures are internally cured or not, or regardless of the constituent materials used during production. Special attention, training, and education for batch plant operators to fully understand how to properly make moisture adjustments and change scale jog rates (i.e., the rate at which the gates on the aggregate bins open and close to drop aggregate on the scale) when producing mixtures containing lightweight aggregates may serve to avoid potential issues.
- Pumping issues were observed which would be present regardless of the concrete mixture proportions, whether the concrete mixtures are internally cured or not, or regardless of the constituent materials used in concrete production and are avoidable with additional training and education.
- Segregation issues was potentially observed on one deck that was independent of whether the concrete mixtures are internally cured or not and are avoidable with additional training and education.
- Trial batches should be used to identify and solve potential issues for production prior to date of construction, as exemplified by the third bridge deck in this study.
- Previous research has shown that the pressure based air meter and the volumetric air meter yield the same result for internally cured concrete mixtures, indicating that the use of the pressure based meter is permissible for IC HPC materials [36].

## 5.2 Impact on Design Specifications

The codified equations for predicting the modulus of elasticity ( $E_c$ ) and the splitting tensile strength ( $f_{ct}$ ) using the square root of the measured compressive strength show good agreement with experimental data within the tolerance of the estimation ( $\pm 20\%$ ). The equations have been provided here [33]:

$$E_c = 1,820\sqrt{f'_c(ksi)} \quad \text{AASHTO C5.4.2.4-1}$$

$$f_{ct} = \frac{1}{4.7}\sqrt{f'_c(ksi)} \quad \text{AASHTO 5.8.2.2}$$

## 5.3 Impact on Shrinkage and Cracking

As briefly discussed previously, the unrestrained shrinkage of the IC HPC and HPC mixtures were characterized using modified versions of ASTM C1698-09 and ASTM C157-08. In addition to these tests, the restrained shrinkage behaviour was characterized using the dual ring test [37], [38]. This test utilizes two concentric rings made of invar to provide restraint to expansion and shrinkage under sealed conditions (i.e., autogenous shrinkage only). After 7 days, the temperature of the test is reduced at a standard rate in an attempt to induce thermal cracking and assess how close the concrete sample was to cracking. The results of this testing are summarized here:

- The IC HPC mixtures exhibited a reduction in measured linear autogenous shrinkage strain of 70 to 90%, with the maximum measured strain of any IC HPC sample at 7 days being  $30 \mu\epsilon$ .
- The IC HPC mixtures exhibited a reduction in measured residual tensile stress due to autogenous shrinkage of 80% with the maximum measured stress of any IC HPC sample at 7 days being 0.5 MPa (72 psi), or approximately 10% of the available tensile strength.

- The IC HPC mixtures exhibited a reduction in measured peak induced thermal stress of 25 to 55% and is likely associated with a reduction in the coefficient of thermal expansion of the internally cured mixtures.
- The IC HPC mixtures exhibited a reduction up to 50% in the rate of induced stress due to temperature reduction and is likely associated to the more compliant nature of the internally cured mixtures.

Collectively, these results indicate that the presence of internal curing reduces the residual tensile stress due to autogenous shrinkage to negligible quantities while also providing a more robust response to thermal loading at early ages.

## 6. Summary and Conclusions

Internal curing is a practice-ready, engineered solution that may lead to the production of higher performance concretes which have a reduced potential for cracking. To aid practitioners in the implementation of internal curing in practice, spreadsheets which automate calculations necessary for quality control for lightweight aggregates, mixture proportioning, and moisture adjustments are available [26]. The authors emphasize that the implementation of such technologies alone does not guarantee higher performance however, as the production of such concrete requires a degree of technical competence in design, production, and construction of concrete materials. As is the case with the production of any concrete, internally cured or not, performance will be directly tied to the careful accounting of water, be it on the surface of aggregates, in the mixing drum after washing, or elsewhere. Special attention should be paid to the proper operation of batching systems, while placement techniques should be reviewed to minimize unwanted effects, and proper finishing and curing techniques must always be practiced. The results of laboratory testing carried out on field produced samples indicates that the concretes met the performance limitations set in the standard specification. The IC HPC concretes cast in the state of Indiana in 2013 achieve an estimated service life improvement of 3 to 4.5 times that of the conventional bridge deck concrete specified and the results from restrained shrinkage testing indicate that the IC HPC mixtures reduce the residual tensile stress due to autogenous shrinkage to negligible quantities. Collectively, these results indicate that IC HPC materials may provide longer service life with a lower potential for cracking, but only after performing the basics of concrete production properly will the full benefits of internal curing be actualized.

## 7. Acknowledgement

The research performed in this study was conducted in the Charles Pankow Materials Laboratory at Purdue University. The authors would like to express their deepest gratitude and acknowledge those who have made the laboratory and its operation possible. This work was supported in part by the Joint Transportation Research Program administered by the Indiana Department of Transportation and Purdue University under SPR 3752.

## 8. References

- [1] J. L. Schlitter, R. Henkensiefken, J. Castro, K. Raoufi, and W. J. Weiss, "Development of Internally Cured Concrete for Increased Service Life," *FHWA/IN/JTRP-2010/10*. Joint Transportation Research Program, Indiana Department of Transportation, and Purdue University, West Lafayette, IN, 2010.
- [2] C. Di Bella, J. L. Schlitter, N. Carboouneau, and W. J. Weiss, "Documenting the Construction of a Plain Concrete Bridge Deck and an Internally Cured Bridge Deck." Indiana LTAP Center, West Lafayette, IN, 2012.
- [3] Indiana Department of Transportation, "Section 700 - Structures," *2014 Standard Specifications*. Indianapolis, IN, 2014.
- [4] Indiana Department of Transportation, "Section 502 - Special Provisions for Internally Cured, High Performance, Structural Concrete for Bridge Decks," *2013 Standard Specifications*. Indianapolis, IN, 2013.
- [5] S. Mindess, J. F. Young, and D. Darwin, *Concrete*, 2nd ed. Prentice Hall, 2003.
- [6] M. Radlinski and J. Olek, "High-Performance Concrete Bridge Decks: A Fast-Track Implementation Study, Volume 2: Materials," *FHWA/IN/JTRP-2008/29-2*, vol. 2. Joint Transportation Research Program, Indiana Department of Transportation, and Purdue University, West Lafayette, IN, 2010.

- [7] T. R. Schmitt and D. Darwin, "Cracking in Concrete Bridge Decks," *No. KU-94-1*. The Kansas Department of Transportation and University of Kansas Center for Research, Inc., 1995.
- [8] T. R. Schmitt and D. Darwin, "Effect of Material Properties on Cracking in Bridge Decks," *Journal of Bridge Engineering*, vol. 4, pp. 8–13, 1999.
- [9] D. Darwin, J. Browning, and W. D. Lindquist, "Control of Cracking in Bridge Decks: Observations from the Field," *Cement, Concrete, and Aggregates*, vol. 26, no. 2, pp. 1–7, 2004.
- [10] W. D. Lindquist, J. P. Browning, and D. Darwin, "Final Report Cracking and Chloride Contents in Reinforced Concrete Bridge Decks a Cooperative Transportation Research Program Between : Kansas Department of Transportation," no. November, 2005.
- [11] J. A. Browning, D. Darwin, D. Reynolds, and B. Pendergrass, "Lightweight aggregate as internal curing agent to limit concrete shrinkage," *ACI Materials Journal*, vol. 108, no. 108, pp. 638–644, 2011.
- [12] Z. Bazant and F. Wittmann, *Creep and shrinkage in concrete structures*. Chichester: Wiley, 1982.
- [13] G. Pickett, "Effect of aggregate on shrinkage of concrete and a hypothesis concerning shrinkage," *ACI Journal Proceedings*, vol. 52, no. 1, 1956.
- [14] D. N. Winslow, M. D. Cohen, D. P. Bentz, K. A. Snyder, and E. J. Garboczi, "Percolation and pore structure in mortars and concrete," *Cement and concrete ...*, vol. 24, 1994.
- [15] R. J. Frosch, S. Gutierrez, and J. S. Hoffman, "Control and Repair of Bridge Deck Cracking," *FHWA/IN/JTRP-2010/04*. Joint Transportation Research Program, Indiana Department of Transportation, and Purdue University, West Lafayette, IN, 2010.
- [16] T. C. Powers and T. L. Brownyard, "Studies of the Physical Properties of Hardened Portland Cement Paste. Part 6. Relation of Physical Characteristics of the Paste to Compressive Strength," *Journal of the American Concrete Institute*, vol. 18, no. 845, pp. 845–857, 1947.
- [17] D. P. Bentz and K. A. Snyder, "Protected paste volume in concrete: Extension to internal curing using saturated lightweight fine aggregate," *Cement and Concrete Research*, vol. 29, pp. 1863–1867, 1999.
- [18] ACI Committee 211, "ACI 211 . 2-98 , Standard Practice for Selecting Proportions for Structural Lightweight Concrete," 1998.
- [19] a. Miller, R. Spragg, F. Antico, W. Ashraf, T. Barrett, a. Behnood, Y. Bu, Y. Chiu, B. Desta, Y. Farnam, H. Jeong, W. Jones, C. Lucero, D. Luo, F. Macobatti, C. Nickel, P. Panchmatia, K. Pin, S. Qiang, C. Qiao, H. Shagerdi, Q. Tian, R. Tokpotayeva, C. Vilani, a. Wiese, S. Woodard, and W. J. Weiss, "Determining the Moisture Content of Pre-Wetted Lightweight Aggregate: Assessing the Variability of the Paper Towel and Centrifuge Methods," *4th International Conference on the Durability of Concrete Structures*, no. July, pp. 1–5, 2014.
- [20] Indiana Department of Transportation, "ITM 222-14T, Specific Gravity Factor and Absorption of Lightweight Fine Aggregate." Indianapolis, IN, 2014.
- [21] A. E. Miller, R. P. Spragg, F. Antico, W. Ashraf, T. Barrett, A. Behnood, Y. Bu, Y. Chiu, B. Desta, Y. Farnam, H. Jeong, W. Jones, C. Lucero, D. Luo, F. Macobatti, C. Nickel, P. Panchmatia, K. Pin, S. Qiang, C. Qiao, H. Shagerdi, Q. Tian, R. Tokpotayeva, C. Vilani, A. Wiese, S. Woodard, and W. J. Weiss, "Determining the Moisture Content of Pre-Wetted Lightweight Aggregate: Assessing the Variability of the Paper Towel and Centrifuge Methods," in *4th International Conference on the Durability of Concrete Structures*, 2014, pp. 1–5.
- [22] ASTM C1761/C1761M-12, "Standard Specification for Lightweight Aggregate for Internal Curing of Concrete," *ASTM International, West Conshohocken, PA, USA*, 2012.
- [23] AASHTO T277-07, "Standard Test Method for Electrical Indication of Concrete's Ability to Resist Chloride Ion Penetration," 2007.
- [24] Indiana Department of Transportation, "Section 904.03, Table (e)," *2014 Standard Specifications*. Indianapolis, IN, 2014.
- [25] A. E. Miller, T. J. Barrett, A. R. Zander, and W. J. Weiss, "Using a Centrifuge to Determine Moisture Properties of Lightweight Fine Aggregate for Use in Internal Curing," *Advances in Civil Engineering Materials*, 2014. .
- [26] T. J. Barrett, A. E. Miller, and W. J. Weiss, "Documentation of the INDOT Experience and Construction of the Bridge Decks Containing Internal Curing in 2013," *SPR 3752*. Joint

Transportation Research Program, Indiana Department of Transportation, and Purdue University, West Lafayette, IN, p. (Submitted), 2015.

- [27] ASTM C39/C39M-10, "Standard Test Method for Compressive Strength of Cylindrical Concrete Specimens," *ASTM International, West Conshohocken, PA, USA*, 2010.
- [28] ASTM C469-02, "Standard Test Method for Static Modulus of Elasticity and Poisson's Ratio of Concrete," *ASTM International, West Conshohocken, PA*, 2002.
- [29] ASTM C496/C496M-04, "Standard Test Method for Splitting Tensile Strength of Cylindrical Concrete Specimens," *ASTM International, West Conshohocken, PA, USA*, 2004.
- [30] ASTM C1698-09, "Standard Test Method for Autogenous Strain of Cement Paste and Mortar," *ASTM International, West Conshohocken, PA, USA*, 2009.
- [31] ASTM C157/C157M-08, "Standard Test Method for Length Change of Hardened Hydraulic-Cement Mortar and Concrete," *ASTM International, West Conshohocken, PA, USA*, 2008.
- [32] T. J. Barrett, A. E. Miller, A. R. Zander, and W. J. Weiss, "Service Life Estimation of Commercially Produced Internally Cured, High Performance Concrete," in *International RILEM Conference on Application of Superabsorbent Polymers and other New Admixtures in Concrete Construction*, 2014.
- [33] AASHTO LRFD, *Bridge Design Specifications*, 6th ed. Washington, DC: American Association of State Highway and Transportation Officials, 2012.
- [34] SIMCO Technologies Inc., "Stadium V2.99 Technical Guide." Quebec City, Quebec, Canada, 2010.
- [35] J. Weiss, Y. Bu, C. Di Bella, and C. Villani, "Estimated performance of as-built internally cured concrete bridge decks and thoughts on performance related specifications," in *RILEM International Workshop on Performance-Based Specification and Control of Concrete Durability*, 2014.
- [36] W. A. Jones, M. W. House, and W. J. Weiss, "Internal Curing of High Performance Concrete Using Lightweight Aggregates and Other Techniques," *CDOT-2013-3*. Colorado Department of Transportation, Denver, CO, 2014.
- [37] J. L. Schlitter, A. H. Senter, D. P. Bentz, T. E. Nantung, and W. J. Weiss, "A Dual Concentric Ring Test for Evaluating Residual Stress Development due to Restrained Volume Change," *Journal of ASTM International*, vol. 7, no. 9. American Society for Testing and Materials, Sch. of Civil Eng., Purdue Univ., West Lafayette, IN, United States, 01-Oct-2010.
- [38] J. L. Schlitter, D. P. Bentz, and W. J. Weiss, "Quantifying stress development and remaining stress capacity in restrained, internally cured mortars," *ACI Materials Journal*, vol. 110, no. 110, 2013.

# Poster Presentations

# Physical Properties of Extrusion Panel Using Ground Granulated Blast-Furnace Slag and Electric Arc Furnace Slag

Ha Seog Kim<sup>1</sup> and Sea Hyun Lee<sup>1</sup> and Dae Hyun Back<sup>1</sup>

<sup>1</sup>Korea Institute of Construction Technology/Advanced Building Research Division

**Abstract:** Carbon dioxide generated from construction materials and construction material industry among the fields of construction is approximately 67 million tons. It is about 30% of the carbon dioxide generated in the fields of construction. In order to reduce carbon dioxide in the fields of construction, it is necessary to control the use of fossil fuel consumed and decrease carbon emission by reducing the secondary and tertiary curing generating carbon dioxide in construction material industry. Therefore, this study produced an extrusion panel by using cement as the base materials and substituting binding materials up to 40% to analyze strength characteristics.

According to the results of strength characteristics by the replacement binder (Low energy curing Admixture) showed an apparent active strength improvement. In particular, specimens substituting binder as 45% indicated the greatest strength improvement. When binding materials was used with substitution, it showed strength characteristics similar or higher than specimens made from tertiary autoclave curing as secondary steam curing.

**Keywords:** Carbon dioxide, Steam curing, Ground granulated blast-furnace slag, Electric arc furnace slag

## 1. Introduction

The dramatic industrial development in recent years has led to the improvement of living standards for mankind. However, fossil fuel has been the primary energy source, accounting for 80 to 85% of all energy sources used to support such industrial activities, and this has led to the massive generation of greenhouse gases (GHGs), contributing to global warming.

Korea rose in the global rankings according to the national CO<sub>2</sub> emissions from 9th to 8th place in 2008, with the CO<sub>2</sub> emissions measured to be 528.7 million tons as of 2009. Of the GHGs emitted, 42.3% are generated in the construction fields. Accordingly, the Korean government has set a target to reduce the GHG emissions to 30% of BAU by 2020 including the GHG emissions in the construction fields. Of the construction fields, which are the source of 42.3% of the CO<sub>2</sub> emissions in Korea, the construction material industry generates 670,000 tons of CO<sub>2</sub>, which accounts for 30% of the total CO<sub>2</sub> emissions generated in the construction fields.

In recognition of the fact that the construction materials generating the largest volumes of CO<sub>2</sub> are cement and structural steel, efforts have been made to reduce the CO<sub>2</sub> generated from these materials, but they have been largely unsuccessful due to the limitations of the reduction technology and materials in use. Thus, there needs to be more diverse measures proposed with the aim to reduce the CO<sub>2</sub> emissions in the construction material industry.

Generally, in the construction material industry, curing at room temperature as well as secondary and tertiary curing processes are performed following product formation for the purpose of acquiring target performance, realizing the desired strength in the early stages, improving productivity and promoting workability. It is the combustion of fossil fuel during these curing processes that causes the generation of CO<sub>2</sub> in large volumes, and countermeasures are urgently needed.

On the other hand, cement extrusion panel is one of the main dry walls used in the industry that is a lightweight yet strong material with many other advantages such as excellent dimension stability, constructability and moisture tolerance. However, the areas of its use are relatively limited due to its high production costs compared to gypsum boards and lightweight concrete panels resulting from the use of large amounts of cement compared to silica, the use of high-cost raw materials such as fiber and viscosity agents as well as the secondary steam curing and tertiary autoclave curing processes following its formation.

Accordingly, this study was conducted with the aim to reduce the use of fossil fuels and carbon emissions by lowering the need for the secondary and tertiary curing processes in the construction material industry as part of the efforts to reduce CO<sub>2</sub> emissions in the construction fields according to the domestic GHG reduction policy.

The possibility of eliminating the tertiary autoclave curing process was confirmed by using steam curing high-strength admixture based on the blast furnace and electric arc furnace slags according to the findings of the preceding research. The cement binder used in the extrusion panel was replaced with the admixture according to the level as a means to review the applicability to secondary concrete products.



## 2. Experimental Plan and Method

### 2.1 Experimental plan

In this study, an extrusion panel was fabricated by substituting cement, which is the conventional binder, with low-energy curing admixture (LA) in order to determine its applicability of LA in the production of extrusion panels.

Table 1 shows the experimental plan in which the experimental factor was set as the LA substitution rate, while Table 2 shows the composition of the low-energy curing high-strength admixture used in the experiment and Table 3 shows the mixing ratio used in the experiment.

**Table 1. Experimental plan of extruding mixture**

Factors	Levels	Test items
Replacement ratio(%)	20%	- Compressive strength - Flexural strength - Density - Moisture content ratio - Absorption ratio
	30%	
	40%	

**Table 2. Composition of Admixture(LA)**

Sum	P	K	S	C	G	K <sub>2</sub> SiF <sub>6</sub>
100%	50%	17%	15%	5%	7.9%	0.1%

P = Ground Granulated Blast-Furnace Slag K = Kaolin, S = CSA, C = Electric Arc Furnace Slag  
G = Glauberite, K<sub>2</sub>SiF<sub>6</sub> = Fluosilicate salt

**Table 3. Experimental mix**

Mix ID	W/P (%)	Powder(%)					Fiber(%)			M.C (%)
		C	L.A	S.P	S.S	C.P	P.P	W	Pulp	
Base	27	42.8	0	22.5	21.2	4.54	2.42	5.05	0.76	0.69
L20		34.2	8.6	22.5	21.2	4.54	2.42	5.05	0.76	
L30		30	12.8	22.5	21.2	4.54	2.42	5.05	0.76	
L40		25.7	17.1	22.5	21.2	4.54	2.42	5.05	0.76	

L.A = Low energy curing Admixture, S.P = Silica Powder, S.S = Silica Sand, C.P = Crush Sand, W = Wollasonite  
P.P = Polypropylene fiber, M.C = Methyl cellulose

### 2.2 Experimental method

The extrusion specimen was fabricated as a 300×1,000×35 mm panel using the extruder model SY-05S of Japanese manufacturer I. The specimen was then cut at a length of 12 mm to test the flexural and compressive strengths of the extruded specimen according to KS L ISO 679.

### 2.3 Curing method

As for the curing of the specimen formed by extrusion, room-temperature curing and atmospheric steam curing processes were performed. In the case of the base specimen, in which only cement was used, autoclave curing was performed. Room-temperature curing was performed in a constant temperature and humidity chamber at 20±1°C and RH 60±5%. On the other hand, atmospheric steam curing was performed

at 80°C and RH 100%, during which the conditions were raised for 4 hours and maintained for 5 hours prior to the natural cooling process. For the atmospheric steam cured specimens, autoclave curing was performed under the conditions of 180°C, 10 atm, RH 100%, during which the conditions were raised for 4 hours and maintained for 5 hours prior to the natural cooling process.

## 2.4 Used material

The materials used include Type 1 ordinary Portland cement sold by domestic company A, as well as Type 3 BF slag produced as a byproduct of the pig iron process by company U with a Blaine fineness of 7,400 cm<sup>2</sup>/g and CSA produced by domestic company H with 36.5% Al<sub>2</sub>O<sub>3</sub> content and a Blaine fineness of 4,500 cm<sup>2</sup>/g.

Calcined kaolin refers to kaolinite calcined in the metakaolin manufacturing process, and the calcined kaolin produced by domestic company B with a Blaine fineness of 4,200 cm<sup>2</sup>/g was used as it is low in cost even though it has low reactivity compared to metakaolin.

The CAC used was atomized EAF slag that was ground to have a Blaine fineness of 5,000 cm<sup>2</sup>/g. It had similar chemical composition as ultra-rapid hardened CA, and characterized by high heat of hydration and quick-setting property. Also, glauberite and fluosilicate salt was used in order to contribute to the pozzolanic reaction of slag and calcined kaolin. These two materials promote the pozzolanic reaction involving the calcium hydroxide produced from the cement hydration reaction after the transition into soluble silica caused by hydrolysis in the cement matrix, and this is known to improve durability through the inhibition of crack formation and an increase in hydration heat, neutralization, and enhancement of freezing-thawing resistance. The characteristics of each of these materials are summarized in Table 4 to 8.

Also, the viscosity agent used to adjust the viscosity and improve the lubrication characteristics during the extrusion process was a product manufactured by domestic company S with viscosity of 40,000 cps and density of 1.26 g/cm<sup>3</sup>. In addition, inorganic Wollastonite, organic pulp and artificial fiber polypropylene (PP) were used as fiber materials to enhance the tensile strength.

**Table 4. Physical and chemical properties of OPC**

Density (g/cm <sup>3</sup> )	Blain (cm <sup>2</sup> /g)	Setting time						LSF
		Start(min)		Finish(min)				
3.15	3,240	290		380				
Chemical component (%)								LSF
LOI	SiO <sub>2</sub>	Al <sub>2</sub> O <sub>3</sub>	Fe <sub>2</sub> O <sub>3</sub>	CaO	MgO	SO <sub>3</sub>	K <sub>2</sub> O	
0.35	21.88	5.02	3.66	64.18	2.01	1.83	0.92	

**Table 5. Properties of blast furnace slag**

Blain (cm <sup>2</sup> /g)	Chemical component (%)								Total
	SiO <sub>2</sub>	Al <sub>2</sub> O <sub>3</sub>	Fe <sub>2</sub> O <sub>3</sub>	CaO	MgO	Na <sub>2</sub> O	SO <sub>3</sub>	K <sub>2</sub> O	
7,400	33.4	15.8	0.6	41.8	5.3	0.3	1.5	0.3	99.0

**Table 6. Properties of CSA**

Blain (cm <sup>2</sup> /g)	Chemical component (%)								lg-loss
	SiO <sub>2</sub>	Al <sub>2</sub> O <sub>3</sub>	Fe <sub>2</sub> O <sub>3</sub>	CaO	MgO	SO <sub>3</sub>	Na <sub>2</sub> O	K <sub>2</sub> O	
4,500	4.14	36.5	0.4	38.17	3.00	6.14	0.11	11.02	0.52

**Table 7. Properties of HK**

Blain (cm <sup>2</sup> /g)	Chemical component (%)							
	SiO <sub>2</sub>	Al <sub>2</sub> O <sub>3</sub>	Fe <sub>2</sub> O <sub>3</sub>	CaO	MgO	SO <sub>3</sub>	Na <sub>2</sub> O	K <sub>2</sub> O
4,200	52.1	41.0	4.32	0.07	0.19	-	0.31	0.58

**Table 8 Physical and chemical properties of CAC**

Blain (cm <sup>2</sup> /g)	Chemical component (%)							
	SiO <sub>2</sub>	Al <sub>2</sub> O <sub>3</sub>	Fe <sub>2</sub> O <sub>3</sub>	CaO	MgO	SO <sub>3</sub>	Na <sub>2</sub> O	K <sub>2</sub> O
4,200	7.0	21.0	0.5	50.0	4.43	3.03	0	0

### 3. Results and Discussion

Table 4 shows the results of the experiment, indicating that substitution of more than 30% of the cement with LA resulted in a strength level that was equivalent to or higher than that of autoclave cured products.

**Table 4. Test results**

	L20	L30	L40
Moisture content ratio	1.05	0.32	0.28
Absorption ratio	18.05	17.47	15.26
Density	1.63	1.7	1.59
Compressive strength	36.8	38.96	38.96
Flexural strength	13.31	14.98	17.44

#### 3.1 Moisture content

All three types were equivalent to the reference moisture content as shown in Fig. 1. Of particular note, L30 and L40 had moisture content, ranging from 0.32 to 0.28. High moisture content in extrusion panels is known to cause reduced strength as a result of twisting and cracks caused by drying shrinkage. Thus, low moisture content is considered advantageous in terms of physical performance and durability.

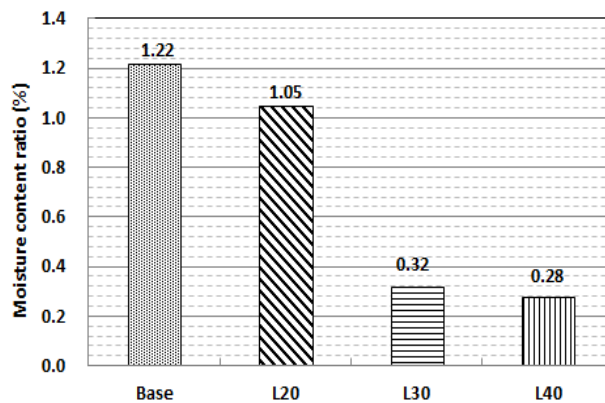


Figure 1. A variation of moisture content ratio according to curing process and LA replacement ratio.

### 3.2 Absorption ratio

The absorption rates of all three types of specimen that varied according to the LA substitution ratio were equivalent to the reference absorption rate as shown in Fig. 2. Of particular note, L40 had the lowest absorption rate at 15.26. In the case of extrusion panels used in the exterior, because they are exposed to open air, high absorption rate can cause issues related to stability and aesthetics due to increased weight, cracks and discoloration resulting from water absorption in the rainy season. Thus, exterior panels are required to have low absorption rate to prevent such problems.

### 3.3 Moisture content

Fig. 3 shows the varying density characteristics according to the LA substitution ratio. L40, in particular, had the lowest density at 1.59. The lowered density is deemed to be due to the fact that the density of the substituting material, LA, is lower than that of cement. Conventional cement-based extrusion panels have high density, which causes difficulties in construction due to the increased unit weight. Accordingly, it is deemed that substituting cement with LA, with lower density, will facilitate construction.

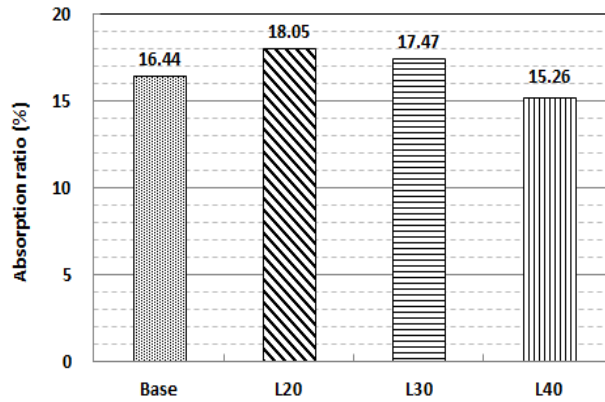


Figure 2. A variation absorption ratio according to curing process and LA substitution ratio.

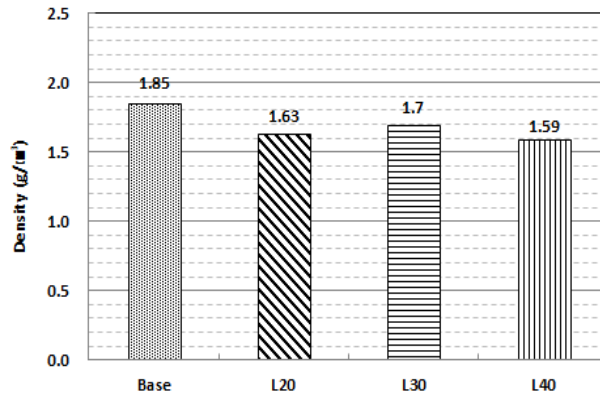


Figure 3. A variation of density according to curing process and LA substitution ratio.

### 3.4 Strength

Fig. 4 shows the compressive strengths of the specimens according to the LA substitution ratio. All three types were shown to be lower than the reference level. L20 had the lowest compressive strength at 36.8 N/mm<sup>2</sup>, whereas L30 and L40 had compressive strength of 38.96 N/mm<sup>2</sup>, which was near the reference strength of 39.2 N/mm<sup>2</sup>. Generally, BF slags are known to be a potentially hydraulic material, which does not contribute to early hydration and reacts to stimulants such as alkali. Thus, compared to the general room-temperature curing process, steam curing promotes hydration of cement in the matrix, leading to the generation of large amounts of calcium hydroxides, which then activate BF slags and contribute to the promotion of strength. Similar results were observed in this experiment. In addition, CSA is thought to have

contributed to the promotion of matrix strength as a result of the active production of ettringite due to the rapid hydration of  $C_3A$  in the early ages and the increase in the  $SO_3^-$  content.

As shown in Fig. 5, the flexural strength was observed to rise with increased LA substitution ratio, similar to compressive strength, and the specimens, except for L20, satisfied the standard level. The flexural strength of the base was shown to be 15.2 N/  $mm^2$  after the autoclave curing process. Although the flexural strength of L30 was observed to slightly lower than that of the base at 14.98 N/  $mm^2$ , it still satisfied the standard level for extrusion panels, which is 14.0 N/  $mm^2$ . Also, L40 had flexural strength of 17.44 N/  $mm^2$ , which was higher than that of the base containing cement as the binder that had been autoclave cured. This result is thought to be due to the fact that low LA substitution rate leads to poor hydrate production and insufficient heat of hydration for the strengthening of the internal area of the matrix.

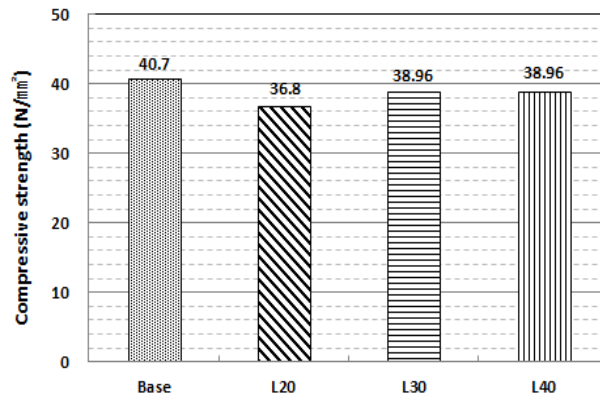


Figure 4. A variation of compressive strength according to curing process and LA substitution ratio.

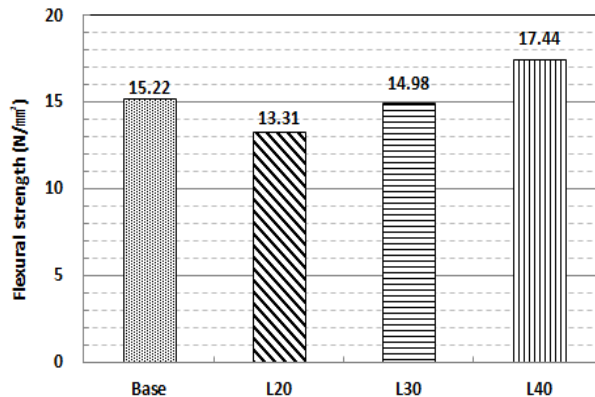


Figure 5. A variation of flexural strength according to curing process and LA substitution ratio.

#### 4. Conclusion

The following conclusions were reached based on the results of the experiment in which cement was substituted with BF slag-based LA as a means to reduce the number of curing processes during the production of extrusion panels, which are secondary concrete products:

- a. Based on the results of measuring the moisture content according to the LA substitution ratio, it is deemed that lower substitution ratio is more advantageous as it results in lower moisture content and improves the physical performance and durability of the extrusion panel.
- b. Based on the results of measuring the absorption rate according to the LA substitution ratio, higher LA substitution ratio resulted in lower absorption rate, which enhances the stability and aesthetics of extrusion panels that are used in the exterior.

- c. Higher LA substitution ratio was shown to lower the density of the extrusion panel and this is deemed to be more advantageous compared to cement-based extrusion panels, which cause difficulty in construction due to high weight.
- d. As for the strength characteristics, specimens containing LA that were steam cured had equivalent or higher strengths compared to the autoclave cured specimen.
- e. Based on the experimental and empirical research results above, it is deemed that substitution with LA will make it possible to eliminate the autoclave curing process and reduce the duration of the steam curing process; however, further research is necessary to determine the long-term durability, resistance in connection with exposure to the external environment, and optimum mixing ratio for the extrusion panel manufacture.

### **Acknowledgement**

This research was supported by a grant(Code 11-Technology Innovation-F04) from Construction Technology Innovation Program(CTIP) funded by Ministry of Land, Transportation and Maritime Affairs(MLTM) of Korean government.

### **5. References**

1. Sipilä, J. Teir, S. and Zevenhoven, R., 2008, Carbon dioxide sequestration by mineral carbonation; Literature review update 2005-2007, Report VT2008-1, Åboakademi university.
2. Yang D.O., Park H.G., and Ko S.S., A Study of the Physical Characteristics of Blast Furnace Slag Concrete, Architectural Institute of Korea: A Collection of Papers Presented at the Academic Conference, 28(1), 2008
3. Lee J.R., Lim S.J. Song I.M. Yun J.H., and Jung S.J., An Experimental Study of the Basic Properties of Concrete in which Durability-enhancing Admixture Was Added to Blast Furnace Slag Powder, Korea Institute of Building Construction: A Collection of Papers Presented at the Spring Academic Conference, 7(1), 2007
4. Jung Y.B., Yang G.H., Hwang H.J., and Jung H.S., Dynamic Performance Assessment of Concrete Containing Red Clay and Blast Furnace Slag Powder, Journal of the Architectural Institute of Korea, 22(5), 2006
5. Ryu D.W., Kim W.J., Yang W.H., Yoo J.H., and Ko J.W., An Experimental Study of the Salt Damage and Freezing-Thawing Resistance of Concrete with High Blast Furnace Slag Powder Content, Journal of the Korea Institute of Building Construction, 12(3), 2012
6. Choi S.M., Kim J.H., Shin S.C., Oh S.Y., and Kim J.M., A Study of the Chemical Characteristics of Electric Arc Furnace Slag, a Byproduct of Various Steel Manufacturing Processes, Korea Institute of Building Construction: A Collection of Papers Presented at the Spring Academic Conference, 24(1), 2012, pp.195~196
7. Choi H.G., Jung E.H., Kwak E.G., Kang C., Seo J.P., and Kim J.M., Korea Institute of Building Construction: A Collection of Papers Presented at the Spring Academic Conference, 6(1), 2006
8. Choi D.J., Development and Performance Assessment of Fireproof Extrusion Panels for Housing Border Walls, doctorate dissertation, Kongju National University, 2013
9. H. F. W. Taylor, The Chemistry of Cements, Third printing, Academic Press INC, 1979, pp.173

10. Powers, T. C., Some Physical Aspects of the Hydration of Portland Cement, J. Res. Dev. Labs. Portland cement Ass, 3(1), 1965, pp.47~56
11. Odler, I. and Gebauer, J., Cement Hydration in Heat Treatment, Zement-Kalk-Gips, 55(6), 1966, pp.276~281, German
12. P. Paulini, Reaction Mechanism of Concrete Admixture, Cement and Concrete Research, 20(1), 1990, pp.910~918
13. Lee, Myung-Kue, et al., Strength of Recycled Concrete with Furnace Slag Cement under Steam Curing Condition, Journal of the Korea Concrete Institute, 17(4), 2005, pp.613~620
14. Sho, K. H et al., Utilization of Separator Bag Filter Dust for High Early Strength Cement Production, Construction and Building Materials, 2011, pp.2318~2322

# Finite Element Modeling of Shape Memory Alloy Confined Reinforced Concrete Column

Khaled Abdelrahman<sup>1</sup> and Raafat El-Hacha<sup>2</sup>

<sup>1</sup>PhD Candidate, Department of Civil Engineering, University of Calgary

<sup>2</sup>Associate Professor, Department of Civil Engineering, University of Calgary

**Abstract:** Strengthening and repair of critical structural elements such as concrete columns is an ongoing research state that seeks for innovative and practical ideas. Recently, the use of smart materials such as Shape Memory Alloys (SMA) has been introduced to civil engineering applications for repair and strengthening of concrete columns. The thermo-mechanical properties of the SMA allows for practical and reliable active confinement mechanism, compared to the passive confinement mechanism applied by the conventionally used materials such as Fibre Reinforced Polymers wraps and concrete/steel jackets. In addition, SMA materials provide significant ductility making them potentially attractive for seismic applications. Despite the many structural benefits of using SMA as confinement material, the current literature include very limited numerical attempts to predict the behaviour of SMA confined concrete columns. Thus, the main objective of this study is to develop a numerical finite element (FE) model capable of predicting the stress-strain characteristics of SMA confined concrete subjected to uni-axial compression loading. The validity of the developed FE model was verified by comparing the results with the experimental data conducted on SMA confined concrete. The results clearly show the capability of the FE model to capture accurately the stress-strain characteristics of SMA confined concrete.

**Keywords:** Confinement, Concrete, Finite Element, Shape Memory Alloy (SMA)

## 1. Introduction

Catastrophic failure due to seismic events has been mainly attributed to the collapse of critical structural elements such as columns. Attaining reliable, safe and efficient designs of our current infrastructure can be achieved through numerous strengthening techniques of the deficient concrete columns. Traditional strengthening techniques include confining the concrete columns with concrete or steel jackets. However, these methods were considered inefficient as the strengthening materials suffered from the same deterioration effects as the parent material. The evolvement of non-corrosive and light-weight composite materials such as Fibre Reinforced Polymers (FRP) became attractive to researchers worldwide. FRP wraps/jackets have been experimentally proven to increase the strength and ductility of concrete columns. However, the FRP wraps/jackets confine the concrete column through a passive confinement mechanism, which means that the concrete requires to undergo significant damage prior to the activation of the FRP. Research studies have shown that engaging the confinement material prior to achieving any damage to the concrete through active confinement mechanism is deemed to provide superior performance in terms of the strength and ductility of the concrete. Several attempts have been made using traditional strengthening materials to actively confine concrete columns [1-3]. However, these proposed techniques to provide active confinement were considered costly, impractical, and required extensive labor time. Recently, the use of smart materials such as Shape Memory Alloys (SMA) has been introduced to civil engineering applications for repair and strengthening of concrete columns [4, 5]. The thermo-mechanical properties of the SMA allows for practical and reliable active confinement mechanism that overcomes all the drawbacks associated with the current active confinement techniques.

The SMA's are a class of alloy that exhibit shape memory recovery (up to 8%) inherited through its unique thermo-mechanical properties. The most commonly used type of SMA for confinement applications include Nickel ( $Ni$ ) and Titanium ( $Ti$ ) as its composition elements. The SMA's have two distinctive phases, a high temperature phase called austenite ( $A$ ) and a low temperature phase called martensite ( $M$ ). The austenite phase is considered as the parent phase and the martensite phase is considered as the product phase. The transformation from one phase to the other can occur by either applying an external stress or by changing the temperature. The SMA's are characterized by four distinctive temperatures; austenite start temperature ( $A_s$ ), austenite finish temperature ( $A_f$ ), martensite start temperature ( $M_s$ ) and martensite finish temperature ( $M_f$ ). The confinement technique using SMA rely on the recovery stress generated as the SMA material transforms to its original (un-deformed) state. The confinement methodology simply involves wrapping a pre-strained SMA wire along the perimeter of the concrete column. Then, heating the alloy above a predefined transformation temperature would trigger the shape memory characteristics of



the SMA wire. Constraining the ends of the SMA wire to the concrete column and since the concrete column is basically incompressible, a reactive force is created by the pre-strained SMA wire as they attempt to regain their original (un-deformed) state producing an active confinement pressure. This confinement technique has been tested experimentally and the results showed that the actively SMA confined concrete specimens exhibited superior performance in terms of the strength and ductility when compared to unconfined concrete specimens [6-14]. The SMA's currently emerging as a new strengthening material for civil engineering applications have a relatively high material cost constricting the diversity of experimental research to be conducted. Thus, adopting a computerized numerical method using finite element approach would allow to further investigate the confinement characteristics of the SMA confined concrete efficiently. Thus, the main objective of the study presented in this paper is to develop a numerical finite element model using a non-linear finite element program capable of predicting the stress-strain characteristics of SMA confined concrete subjected to uni-axial compression loading.

## 2. Finite Element Modeling

### 2.1 General

Several parameters are subject to investigation in order to achieve a successful numerical model capable of simulating the complete behaviour of SMA confined concrete under axial compressive loading. Therefore, a realistic definition of the constitutive relationship of the materials involved is necessary, in this case, namely the concrete and the SMA wire, and the interfacial bond between them. In addition, this section also includes the geometric modeling and the list of elements used to model the SMA confined concrete.

### 2.2 Constitutive behaviour and material model

The non-linearity of the concrete can be modeled using the Concrete Damage Plasticity (CDP) predefined in the *ABAQUS* software. The CDP requires the definition of the concrete stress-strain relationship in compression and tension, as well as certain parameters to define the plastic flow and the yield surface criteria. In order to input the most appropriate concrete model for this numerical problem, the stress-strain characteristics of the SMA confined concrete was first investigated. Figure 1 displays the experimental results of SMA confined concrete cylinder subject to uni-axial compression loading tested by the authors as a part of a preliminary investigation to assess the stress-strain characteristics of SMA confined concrete. The results show that SMA confined concrete possess distinctive features from solely active or solely passive confinement behaviour. Prior to loading, the SMA actively confines the concrete through a confinement pressure equivalent to the residual recovery stress generated by the SMA wire. During loading, as the concrete gains significant dilations, the SMA wire passively engages to confine the concrete until failure of the SMA wire is achieved.

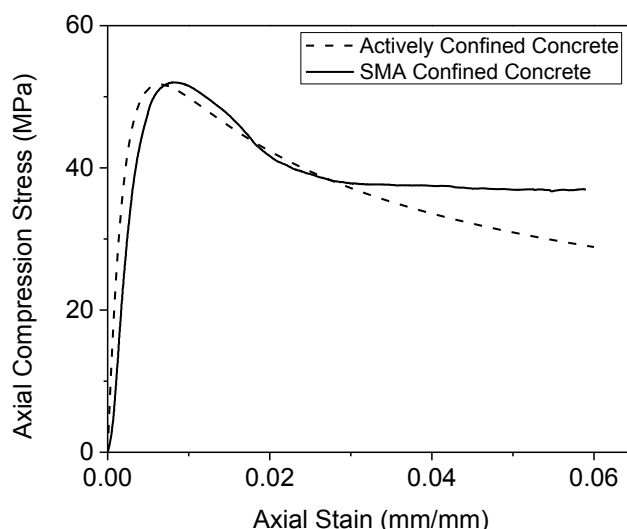


Figure 1. Stress-strain behaviour for SMA confined and actively confined concrete

In order to compute the active confinement pressure generated by the SMA wire onto the concrete column, the equation proposed by Mander et al. [8] was adopted. The equation quantifies the amount of lateral confinement pressure ( $f_l$ ) produced by the transverse reinforcement on a circular concrete section and is defined by:

$$f_l = \frac{2f_h A_{sp}}{s d_s} \quad (1)$$

where,  $f_h$  is the tensile stress of the transverse reinforcement,  $A_{sp}$  is the area of the transverse reinforcement,  $s$  is the center-to-center spacing for circular hoop or the pitch spacing for spiral hoop, and  $d_s$  is the cross-sectional diameter of the concrete specimen.

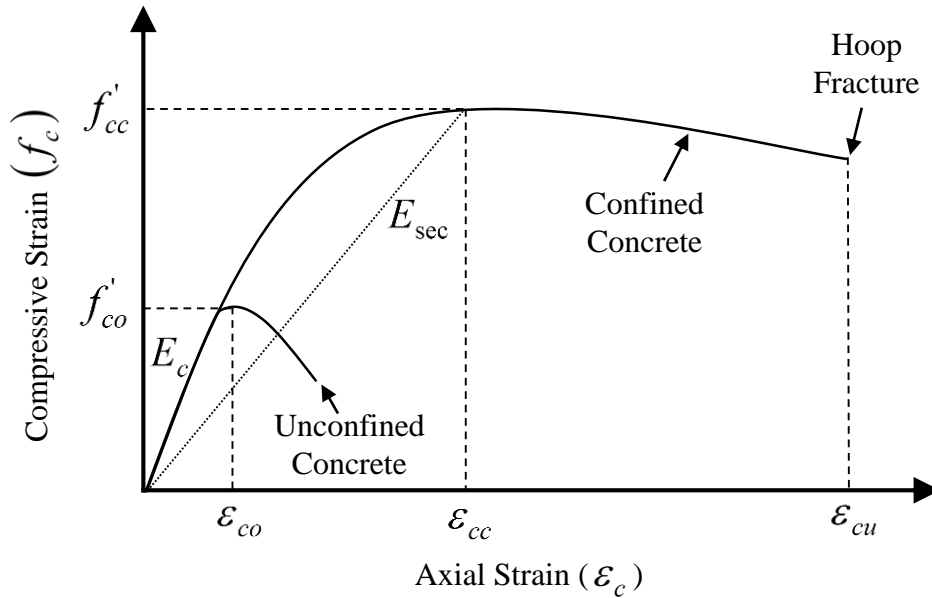


Figure 2. Stress-strain behaviour for confined and unconfined concrete (Mander et al.,[8]).

Mander et al. [8] also proposed a unified stress-strain approach for confined concrete transversely reinforced by circular ties or spirals (Figure 2). Although the model was developed based on transverse steel reinforcement, once the steel yields and reaches a state of constant stress, this represents an active confinement state. This concept can be further extended to represent the active confinement state induced by the constant recovery stress generated by the SMA wire. The proposed equation to determine the longitudinal compressive concrete stress ( $f_c$ ) is defined by:

$$f_c = \frac{f'_{cc} x r}{r - 1 + x^r} \quad (2)$$

where,  $f'_{cc}$  is the confined concrete compressive strength defined by:

$$f'_{cc} = f'_{co} \left( -1.254 + 2.254 \sqrt{1 + \frac{7.94 f'_l}{f'_{co}}} - 2 \frac{f'_l}{f'_{co}} \right) \quad (3)$$

where,  $f'_{co}$  is the unconfined concrete strength, and

$$x = \frac{\epsilon_c}{\epsilon_{cc}} \quad (4)$$

where,  $\epsilon_c$  is the longitudinal compressive concrete strain.

$$\varepsilon_{cc} = \varepsilon_{co} \left[ 1 + 5 \left( \frac{f'_{cc}}{f'_{co}} - 1 \right) \right] \quad (5)$$

where,  $\varepsilon_{co}$  is the unconfined concrete strain, and

$$r = \frac{E_c}{E_c - E_{sec}} \quad (6)$$

where,  $E_c$  is the modulus of elasticity of the concrete in MPa

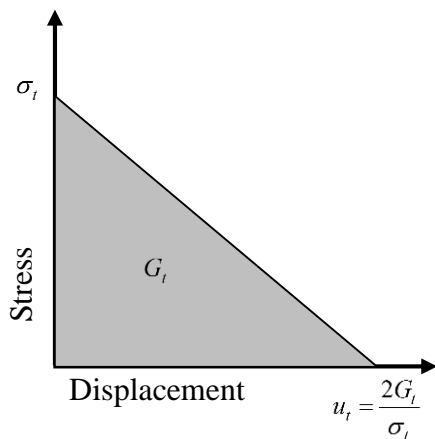
$$E_c = 5000 \sqrt{f'_{co}} \quad (7)$$

and  $E_{sec}$  is secant modulus of elasticity of the concrete in MPa

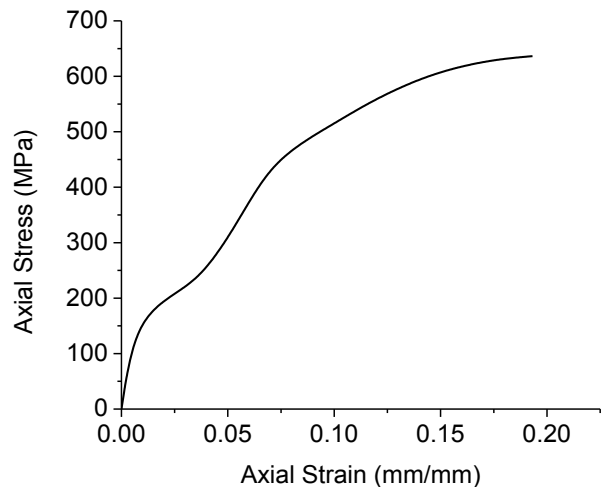
$$E_{sec} = \frac{f'_{cc}}{\varepsilon_{cc}} \quad (8)$$

The above set of equations was used to develop a stress-strain relation of concrete specimen actively confined by a constant confinement pressure equivalent to the initial active confining pressure from the SMA spirals. As shown in Figure 1, the initial stress-strain response of the SMA confined concrete follows the paths of the purely active confined concrete with an initial active confining pressure from the SMA spirals. As the concrete dilates and reaches its peak strength, the SMA spirals engages passively and deviates away from the path of the purely active confinement case. Thus, it reasonable to assume that the behaviour of the SMA confined concrete follows the behaviour of an equivalent purely active confinement case until the peak load. The post peak behaviour critically relies on the passive confinement mechanism that cannot be captured using Mander et al. [8] model. Thus, the initial active confinement pressure is accounted for in the input compression model and the finite element model captures the post peak behaviour considering the passive confinement mechanism of the SMA spirals.

The parameters defined for the CDP include the dilation angle ( $\psi$ ), which controls the amount of plastic volumetric strain. Based on experimental research, a dilation angle of  $30^\circ$  was selected [9]. Secondly, the ratio of the initial equilibrium yield stress to the initial uniaxial compressive yield stress is defined with a default value of 1.16 [15]. Thirdly, the flow potential eccentricity ( $\epsilon$ ) is defined with a default value of 0.1 [15]. This ensures that the dilation angle remains almost constant over a wide range of confinement pressures. Lastly, the ratio of the second stress invariant on the tensile meridian, to that on the compressive meridian ( $K_c$ ) is defined with a default value of 0.667 [15].



**Figure 3. Tensile stress-displacement relationship of concrete**



**Figure 4. Axial tensile stress-strain behaviour of SMA wire**

The tensile constitutive model of the concrete defined for the CDP was expressed as the relationship between the tensile stress and the cracking displacement (Figure 3). The cracking displacement ( $u_t$ ) at which complete loss of strength occurs is defined through Equation 9. The fracture energy ( $G_f$ ) varies with the compressive strength of the concrete. In order to accurately capture the behaviour of the SMA spirals, the property was based on the SMA wire tensile coupon test results after the stress recovery to account only for the passive confinement generated by the SMA wire during loading. The result of the SMA tensile coupon test is plotted in Figure 4.

$$u_t = \frac{2G_f}{\sigma_t} \quad (9)$$

where,  $\sigma_t$  is the cracking stress of the concrete.

### 2.3 Geometric modeling

The concrete cylinder was modeled with full geometry in three dimensions (3D) as there was no computational expense involved. The boundary conditions of the specimens were simulated by restraining the rotational and displacement degrees of freedom for the nodes located at the bottom end of the cylinder (Figure 5). A displacement control mode was applied to the opposite end of the cylinder until failure was achieved by rupture of the SMA wire to simulate the failure mode achieved experimentally. Based on experimental evidence found by visually investigating the contact behaviour between the concrete and the SMA wire at various intervals during the experimental testing, no form of slippage behaviour was recognizable. Thus, it can be concluded that, a good bond was usually maintained between the concrete surface and the SMA wire. Accordingly, the interaction between the concrete and the SMA wire was modeled using a surface tie. This constraint ties the two surfaces together for the duration of the simulation. The concrete was modeled using an eight node linear brick element C3D8 and the SMA wire was modeled using as two node linear 3-D truss element T3D2 (Figure 6). These elements were selected from the standard element library in *ABAQUS*.

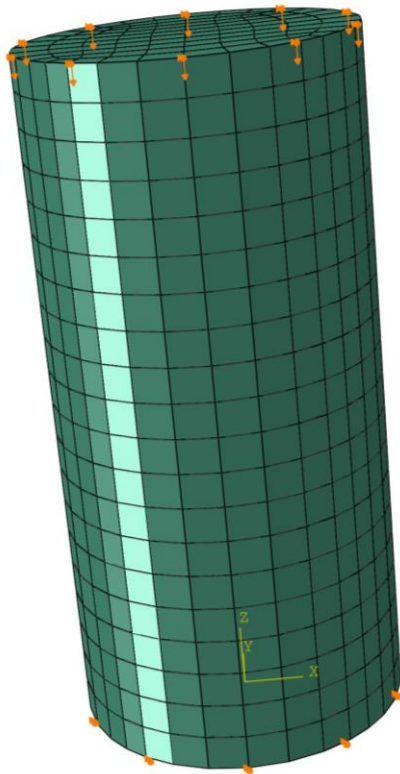


Figure 5. Boundary conditions of the FE model

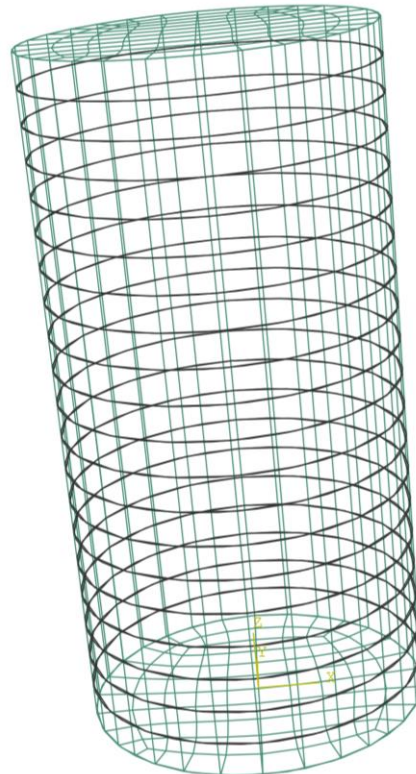


Figure 6. Mesh detailing of the FE model

### 3. Verification of the Finite Element Model

To validate the finite element model, the experimental data conducted by the authors on SMA confined concrete was utilized. The concrete cylinder used in this study measured 100 mm in diameter and 200 mm in height. The type of SMA wire used was NiTi with a smooth cross-sectional diameter of 1.9 mm. According to the manufacturer [16], the mechanical characteristics of the SMA wire, which include the ultimate tensile strength, elastic modulus and strain at failure of the SMA wires were 818 MPa ( $\pm 50$  MPa), 462 MPa ( $\pm 5$  MPa), and 41 % ( $\pm 5\%$ ), respectively. Based on the recovery stress test performed on the SMA wire, the maximum recovery stress and the residual stress attained by the SMA wire was 581 MPa and 485 MPa, respectively. The SMA wires were wrapped circumferentially around the perimeter of the column at a pitch spacing of 10 mm. At the ends of the cylinder, the SMA wires were coiled with two additional turns that were fixed and tightened to the concrete cylinder using U-clamp connectors. As the SMA wires were shipped in predefined lengths, the intermediate splices of the SMA wires were connected with U-clamps to ensure continuity of the wires across the height of the cylinder. The SMA confined specimen was subjected to uni-axial compression loading at a loading rate of 10 kN/sec to failure.

The comparison between the experimental data and the FE prediction model is shown in Figure 7. The results clearly show the FE model can capture accurately the axial stress-axial strain and the axial stress-hoop strain relationships of the SMA confined concrete, taking into account the softening branch of the concrete behaviour. The model also captured accurately the peak strength achieved by the SMA confined concrete specimen with a percentage difference of less than 1 % between the experimental and the predicted peak strength. To further investigate the behaviour of the SMA confined concrete specimen, the stress and strain nephograms of the SMA wire and the stress nephogram of the concrete cylinder are shown in Figure 8. It can be clearly seen that the maximum lateral stress and strain experienced by the SMA wire and the concrete cylinder were found at the mid-height of the cylinder. Due to the relatively low aspect ratio of the test cylinder, the platen effects that were accounted for by imposing representative boundary condition, significantly affects the deformation shape of the cylinder forming a bell shaped curve (Figure 8). This effect amplifies the lateral strain measurements of the SMA wire and the concrete cylinder at the mid-height of the specimen eventually leading to rupture of the SMA wire and concrete spalling at this mid-height zone.

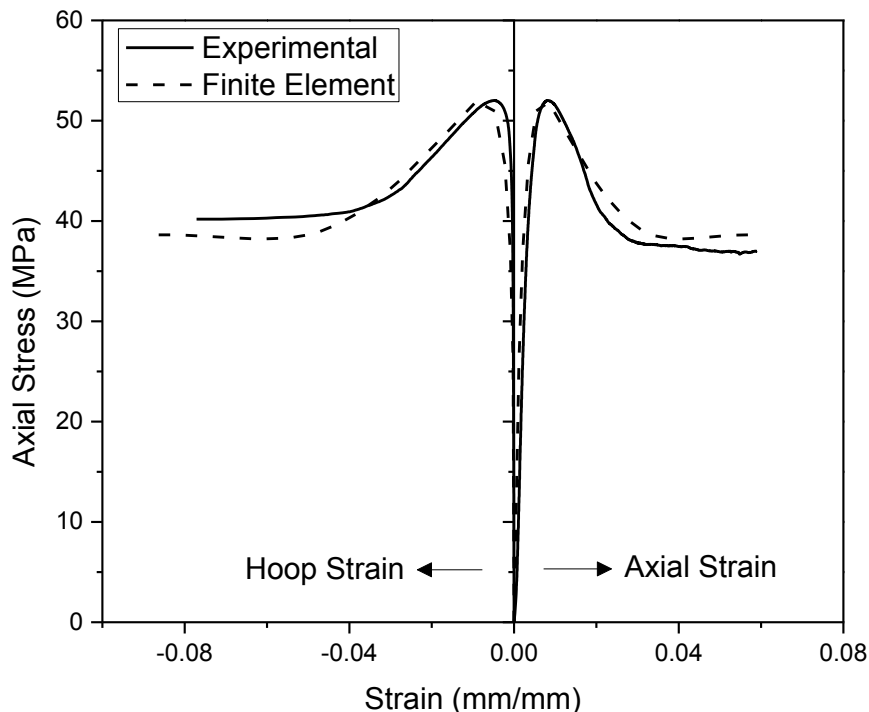
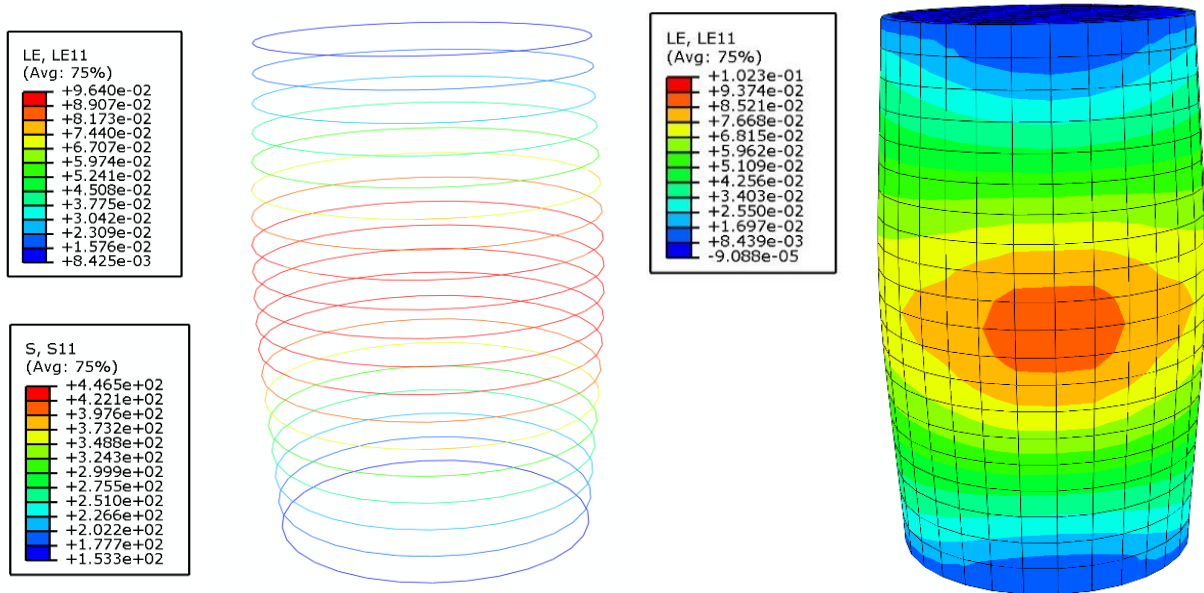


Figure 7. Comparison between FE predicted results and the experimental data



**Figure 8. Lateral stress and strain nephograms of the SMA wire and the strain nephogram of the concrete cylinder.**

#### 4. Conclusions

This paper presented a 3-D FE model to predict the stress-strain characteristics of actively SMA confined concrete. The model is capable of simulating the overall stress-strain response, as well as accurately predicts the peak strength and the post peak softening behaviours of the confined concrete. In addition, the numerical results from the FE model showed good agreement with the experimental data. The FE model is currently being extended to simulate the behaviour of large-scale reinforced concrete columns confined with SMA wires. Once developed, the FE model can be used as a valuable tool to investigate several parameters such as varying the concrete strength, the pitch spacing of the SMA wire, slenderness effects, size effects, and the eccentricity loading. These results produced by the FE model can be used in the development of simple design models to be implemented in the design codes.

#### 5. Acknowledgement

The authors would like to express their gratitude for the financial support provided by the University of Calgary.

#### 6. References

1. Mortazavi, A., Pilakoutas, K. et al., "RC column strengthening by lateral pre-tensioning of FRP", Construction and Building Materials, 17, 2004, pp 491-497.
2. Yan, Z., Pantelides, C.P. et al., "Seismic retrofit of bridge columns using fibre reinforced polymer composite sheels and shape modifications", The 14<sup>th</sup> World Conference on Earthquake Engineering, October 12-17, 2008, Beijing, China.
3. Reisi, M., Mostofinejad, D. et al., "M-P curves for strengthened concrete columns with active confinement", The 14<sup>th</sup> World Conference on Earthquake Engineering, October 12-17, 2008, Beijing, China.
4. Alam, M.S, Youssef, M.A. et al., "Utilizing shape memory alloys to enhance the performance and safety of civil infrastructure: A review", Canadian Journal of Civil Engineering, 34, 2007, pp 1075-1086.
5. Janke, L., Czaderski, M. et al., "Applications of shape memory alloys in civil engineering structures – overview, limits and new ideas", Materials and Structures, 38, 2005, pp 578-592.

6. Krstulovic-Opara, N., Thiedeman, P.D., "Active confinement of concrete members with self-stressing composites", ACI Materials Journal, 93(3), 2000, pp 297-308.
7. Choi, E., Nam, T-H. et al., "The behavior of concrete cylinders confined by shape memory wires", Smart Materials and Structures, 17, 2008, 10pp.
8. Destrebecq, J-F., Balandraud, X., "Interaction between concrete cylinders and shape memory wires in the achievement of active confinement", Materials with Complex Behaviour, Advanced Structural Materials, 6, Springer-Verlag Berlin Heidelberg, 2010, pp 19-34.
9. Mirzaee, Z., Motavalli, M. et al., "Experimental investigation of compressive concrete elements confined with shape memory Ni-Ti wires", Fracture Mechanics of Concrete and Concrete Structures – Assessment, Durability, Monitoring and Retrofitting of Concrete Structures, Korea Concrete Institute, Seoul, ISBN 978-89-5708-181-5, 2010, pp 1173-1178.
10. Shin, M., Andrawes, B., "Experimental investigation of actively confined concrete using shape memory alloys", Engineering Structures, 32, 2010, pp 656-664.
11. Zuboski, G.R., "Stress-strain behaviour for actively confined concrete using shape memory alloy wires", Master of Science Thesis, The Ohio State University, USA, 2013, 213pp.
12. Tran, H., Balandraud, X., "Improvement of the mechanical performances of concrete cylinders confined actively or passively by means of SMA wires", Elsevier Urban & Partner Sp. z 0.0., <http://dx.doi.org/10.1016/j.acme.2014.04.009>, 2014, 8pp.
13. Mander, J.B., Priestley, M.J.N. et al., "Theoretical stress-strain model for confined concrete", Journal of Structural Engineering, 114(8), 1988, pp 1804-1826.
14. Jankowaik, T., Lodygowski, T., "Identification of parameters of concrete damage plasticity constitutive model", Foundations of Civil and Environmental Engineering, No. 6, Publishing house of Poznan Univeristy of Technology, Poznan, 2005.
15. ABAQUS 6.9, ABAQUS user's manual, ABAQUS Inc. Rising Sun Mills, 166 Valley Street, Providence, RI 02909-2499, USA, 2009.
16. Memry SEAS Group Company, <http://www.memry.com/products-services/material/wire>, retrieved on 15 January 2015.

# Modelling the Reactivity of Nano-silica in Cement Paste

Madhuwanthi Rupasinghe, Rackel San Nicolas and Priyan Mendis

Department of Infrastructure Engineering, The University of Melbourne.

**Abstract:** Integration of nano materials into concrete with the aim of improving its performance is a key research area at present. While various attempts has been made to find out the significance of nano-silica on concrete, there is a lack of in-depth understanding over the effects of its substitution on hydration of cement and its role in the microstructural evolution of the binder. In this study the effects of commercial colloidal nano-silica in substitution of cementitious pastes, in fractions from 0 to 12w% are analysed using Calorimetry, Thermal Gravimetric Analysis (TGA) and Backscattered electron (BSE) imaging. A model to predict the hydration characteristics of the nano modified cement paste is developed. Through both modelling and experimentation, results reveal that nano-silica in substitution of cement improves the hydration and increases the compressive strength. The optimum composition of replacement level was found at 8w% by of cement.

**Keywords:** Cement paste, nano-silica, CH content, hydration, pozzolanic activity

## 1. Introduction

With the increasing research focus on nano-materials and nano-technology within the past couple of decades, the effects of nano-particles on construction materials has been of great research interest. Concrete is the most widely used man made material in the world. Most of the current research on nano-engineering concrete has been focused on including nano-materials into concrete with the aim of increasing its performance. These include increasing strength characteristics, reduction of porosity and increasing durability. Nano-materials that have been included in concrete include Carbon Nano-Tubes[1], nano-silica [2-6], nano-TiO<sub>2</sub> [7] nano-Fe<sub>2</sub>O<sub>3</sub>, nano-Al<sub>2</sub>O<sub>3</sub> [8, 9] and nano-clay [10]. Nano-materials facilitates cement hydration through providing more nucleation sites for the cement particles to hydrate and acts as a filler material within the paste [6]. This paper focuses the effects of nano-SiO<sub>2</sub> on cement paste and it mainly concentrates on the pozzolanic reactivity of the nano-material.

Nano-silica is available in both powder form and colloidal dispersion. Research has been carried out on including both these forms in concrete [6, 11-13] . The colloidal form, when compared with the powder form, has the advantage of better dispersion within the cement paste, thus reducing the probability of forming agglomerates [12]. In contrast to many of the nano-materials previously studied, nano-silica not only provides nucleation sites for cement hydration, but also participates in the hydration process by reacting with the Calcium Hydroxide (CH) produced during cement hydration, which is known as the pozzolanic reaction [3, 6]. Ordinary cement hydration produces Calcium Silica Hydrate (CSH) and CH [14, 15]. CSH is the main strength carrying material in the cement paste, and CH is considered to have a detrimental effect on strength characteristics of concrete [14]. Nano-silica reacts with the CH and produces more CSH into the paste, thereby increasing the overall strength characteristics of the cement paste [6].

However, despite these previous studies, there is still a lack of in-depth understanding of the mechanism of incorporation of nano-silica on the hydration of a cement binder, and its role in microstructural evolution and gel chemistry. This is crucial in understanding the long-term mechanical and durability performance of concrete. Therefore, this study reports the microstructural changes taking place in nano-silica/cement binders up to the age of 28 days, as a function of the time of curing and the nano-silica content in the range 0-12%, using thermogravimetry and Backscattered Electron Imaging(BSE).



## 2. Materials and methods

### 2.1 Materials

The cement used in this study was a General purpose cement as per AS 3972-2010 (Australian Standard for General purpose and blended cements). An amorphous colloidal nano-silica suspension, Cembinder 8, was used which was produced by Akzo Nobel, Germany[16]. Table 1 and Table 2 below provide the chemical composition of cement specifications of nano- silica, respectively.

**Table 1: Chemical composition of cement**

Compound	Chemical composition (%)
Silica (SiO <sub>2</sub> )	20.38
Alumina (Al <sub>2</sub> O <sub>3</sub> )	7.89
Iron oxide (Fe <sub>2</sub> O <sub>3</sub> )	0.75
Calcium oxide (CaO)	65.02
Magnesium oxide (MgO)	0.98
Sulphur trioxide (SO <sub>3</sub> )	2.21

**Table 2: Specifications of nano-silica**

Property	
Density (g/cm <sup>3</sup> , 20°C)	1.4
pH	9.5
Viscosity (mPas)	<15
Solid content (% w/w)	50

### 2.2 Introduction to Thermal Gravimetric Analysis (TGA)

Thermal Gravimetric Analysis (TGA) is a widely used method for the quantification of the pozzolanic reaction extent. In this method, the sample is gradually heated from room temperature to a defined maximum temperature, and the weight of the sample and the temperature is monitored and recorded. As the temperature is increased, the mass of the sample reduces at particular temperature ranges due to decomposition of its chemical components. Through obtaining the reduction of the mass at the corresponding temperature range and following the necessary calculation steps, the amount of the chemical component that was decomposed at that temperature range can be quantified. This method was used to quantify the amount of CH in the samples, and is described further in the section below.

### 2.3 Sample preparation and testing

For the preparation of the cement paste samples, constant water to binder ratio of 0.3 was used for all cement pastes. The water content of the nano-silica suspension was taken into consideration, and the externally added water content was altered to maintain a constant w/b ratio. Table 3 provides the description of the samples. Isothermal calorimetry was carried out just after mixing the samples, and rest of the paste was poured into moulds to harden.

Isothermal calorimetric was carried out using a TAM Air isothermal calorimeter. The base temperature was  $25 \pm 0.02^\circ\text{C}$ . Fresh paste was mixed externally, weighed into an ampoule, and immediately placed in the calorimeter, and the heat flow was recorded for the first 40 hours.

For TG analysis, the cement paste samples were de-moulded after 1 day, and were cured at a constant temperature of  $20^\circ\text{C}$ . Crushed samples were obtained from the hardened cement pastes at different ages 1, 3, 7 and 28 days. The proceeding of the hydration reaction was stopped using acetone, and the samples were tested for TGA in a Perkin Elmer Diamond instrument. In the TGA procedure, the following steps were adhered [17].

- I. Hold the sample at  $30^\circ\text{C}$  for 20 minutes
- II. Heat from  $30^\circ\text{C}$  to  $1000^\circ\text{C}$  at  $10.00^\circ\text{C}/\text{min}$
- III. Hold at  $1000^\circ\text{C}$  for 5 minutes
- IV. Cool back to  $30^\circ\text{C}$  at a rate of  $40^\circ\text{C}/\text{min}$

The microstructural analyses of the cement pastes at 28 days were carried out under FEI Quanta Scanning Electron Microscope (ESEM). The backscattered electron (BSE) imaging mode of the SEM was used to obtain the micrographs.

**Table 3: Sample descriptions**

Sample ID	% Nano-silica (by weight)	Cement (g)	Cembinder (g)	Water(g)	w/b
CO	0	100	0	40	0.3
NS4	4	96	8	36	0.3
NS8	8	92	16	32	0.3
NS12	12	88	24	28	0.3

## 2.4 Calculation of the CH content

The pozzolanic reactivity of nano-silica is calculated based on the CH content of the cement paste samples at different ages. Details of the evaluation of CH content based on TG data can be found in [18]. The CH content of the hydrated paste samples is calculated as at time  $t$ ,  $CH(t)$

$$CH(t) = \frac{74.09}{18.01} \cdot \frac{m_{420}(t) - m_{540}(t)}{m_s} \quad (1)$$

where  $m_{420}(t)$  and  $m_{540}(t)$  are the mass of the sample recorded at 420°C and 540°C during the TGA test, and  $m_s$  is the anhydrous mass of the sample. (74.09/18.01) is the molar mass ratio between CH and H<sub>2</sub>O.

To get an idea on the pozzolanic reaction compared to the performance of the plain cement paste at time  $t$ , the CH contents are normalized as follows.

$$CH_{norm}(t) = \frac{CH(t)}{CH_{ref}(t) \cdot f_c} \quad (2)$$

$CH_{norm}(t)$  and  $CH_{ref}(t)$  are the normalized CH content of the paste and the CH content of the reference paste at time  $t$ , respectively.  $f_c$  is the fraction of cement present in the sample.

## 3. Results and Discussion

Figure 1 shows the results of isothermal calorimetric analysis. It can be seen that nano-silica accelerates the initial hydration process by 3-4 hours. As the percentage of nano-silica increases in the paste, the quicker the peak occurs. It can also be noted that peak heat flow is also increased as nano-silica content increases within the paste. The curves for NS8 and NS12 are almost the same, indicating that after 8% replacement, significant changes on heat of hydration are not achieved. This gives an indication 8% replacement level is a threshold limit for the acceleration of the initial reactivity of the cement paste. Beyond 8% replacement, there is limited possibility of nano-silica accelerating the hydration reaction.

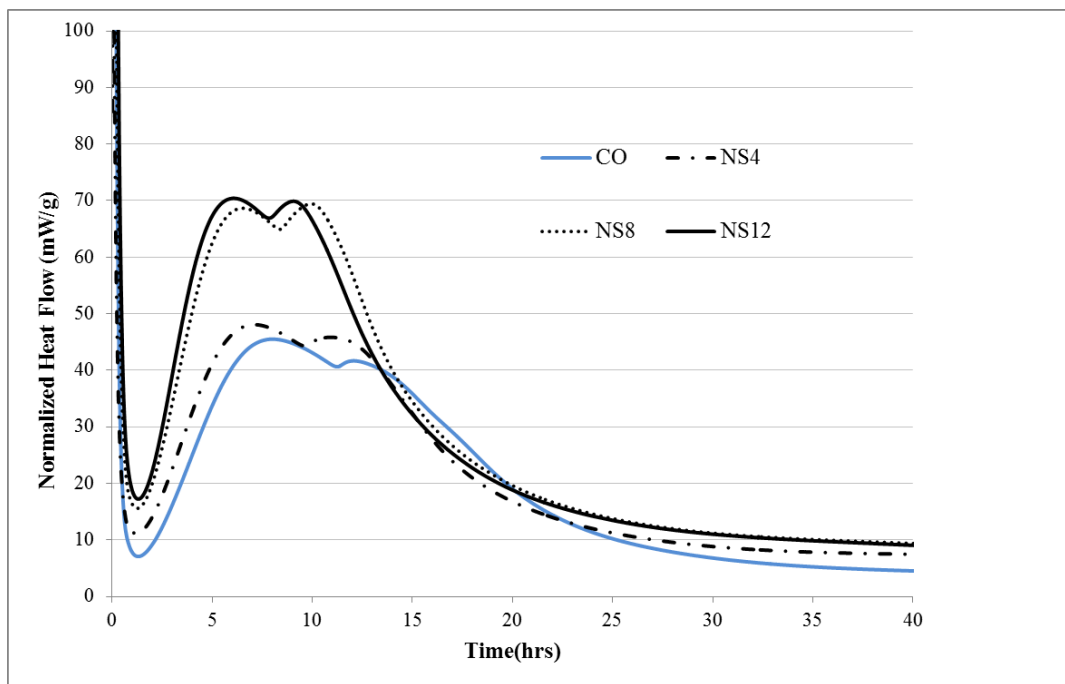


Figure 1. The heat release curves of the samples

Figure 2 illustrates a curve obtained from TGA, along with a plot of the first derivative of the TG curve (DTG). Three main peaks can be seen on the DTG curve, and among them, the peaks occurring around 420°C-540°C and 600°C-800°C are the peaks corresponding to the decomposition of CH and CaCO<sub>3</sub>, respectively [18].

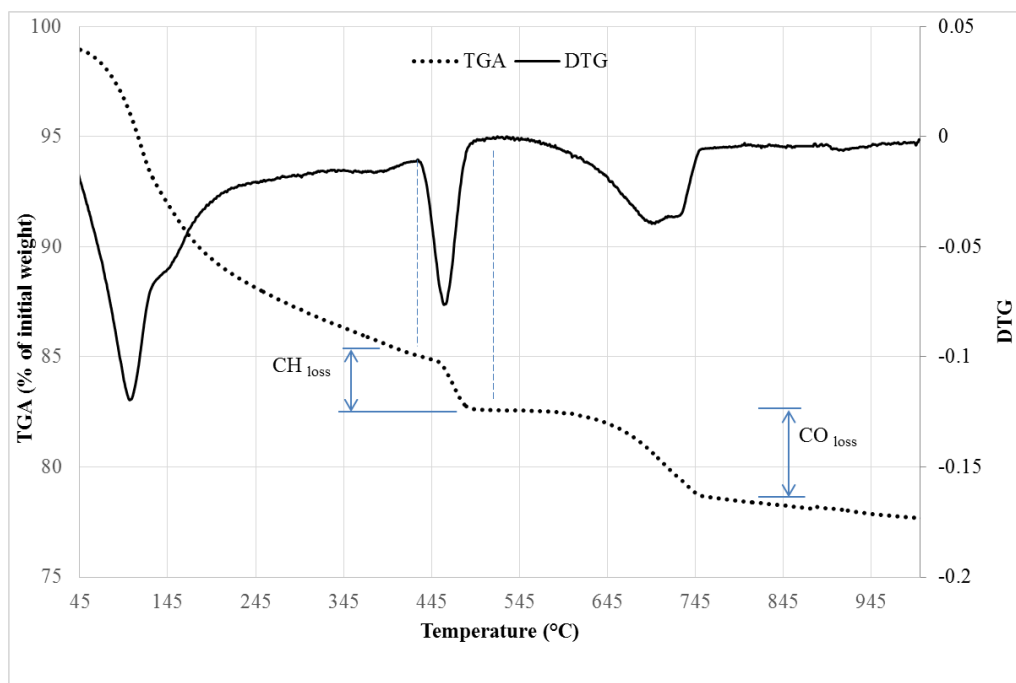


Figure 2. The TG curve and the DTG curve for one sample

The normalised CH contents obtained through analysing the TG curves of different samples at 1 day, 3 day, 7 day and 28 day are shown in Figure 3. The normalised CH content reflects the CH content of the

paste with respect to a plain cement paste having the same amount of cement content. Therefore, a lower normalised CH content implies less CH content and more hydrated phase present in the mix. The normalised CH content of the mix decreases as the nano-silica content is increased, up to 7 days. But at 28 days, the performance of NS12 seems to be less than that of NS8, as NS8 exhibits the lowest normalised CH content among the pastes tested. Less CH contents implies that more CSH is produced in the mix, and a denser paste structure is achieved. Pozzolanic activity can result in higher amounts of strength carrying CSH into the paste, which ultimately makes the nano-modified paste to have higher compressive strength [4, 6]. These results suggest that 8% replacement level is the optimum cement replacement level with nano-silica with regards to the pozzolanic reactivity.

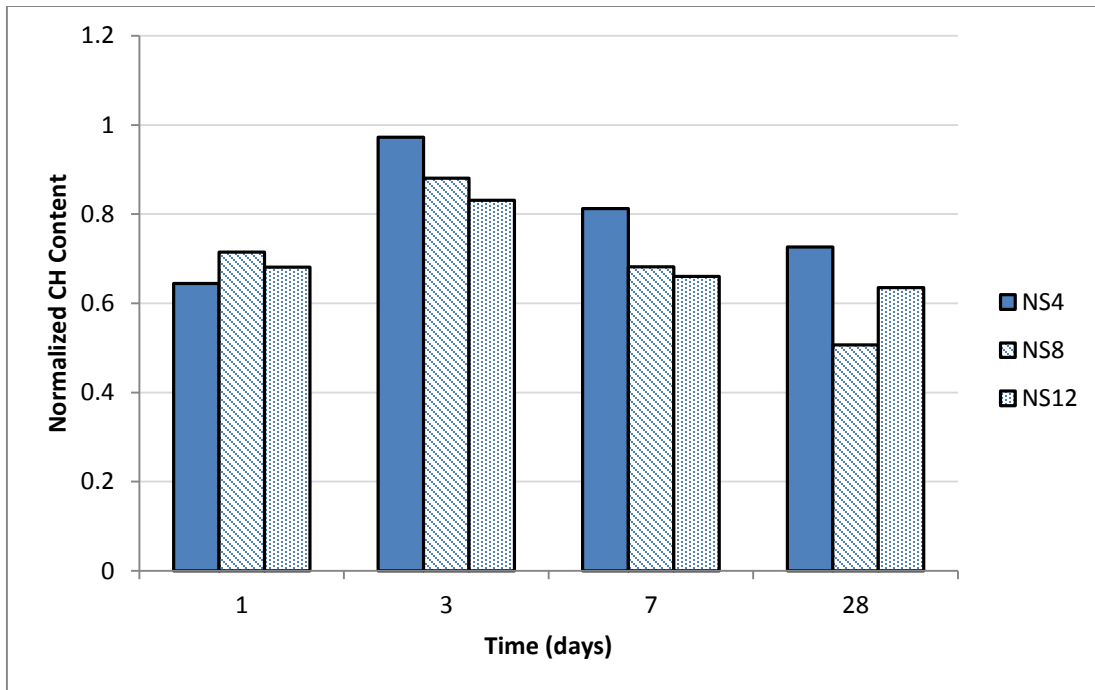


Figure 3. The normalized CH content of the paste samples over time

Figure 4 below shows a BSE images for the samples obtained at 28 days. Depending on the mean atomic number of a particular phase, the brightness of the phase on the BSE image differs. For a typical cement paste, unhydrated cement particles appears as the brightest. It is then followed by CH, C-S-H, and the epoxy filled pores [19]. Through comparing the microstructures in figure 4, it can be seen the amount of capillary pores (i.e. the darkest area) is less for NS8 than for the other samples. NS12 seems to have the least amount of unhydrated cement.

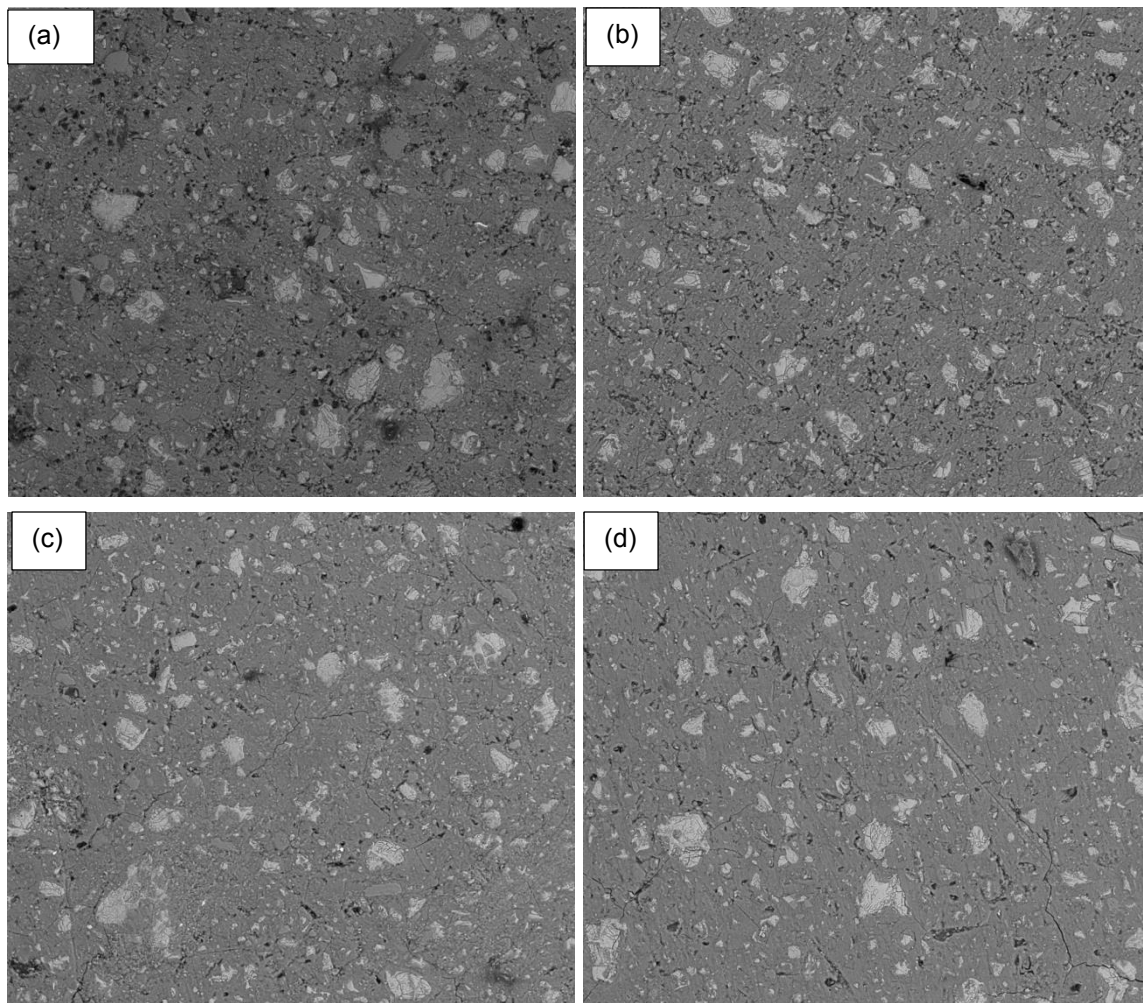


Figure 4. BSE images for the (a) Control sample (b) NS4 (c) NS8 (d) NS12 at 28 days

The microstructural images obtained in this study were quantified based on the grey scale using an image processing software ( MeVisLab). Figure 5 shows the results of the image quantification analysis. It can be observed that the quantity of unhydrated cement decreases with the increase of nano-silica content. This is because increasing nano-silica content also implies a decrease in the cement content of the mix, as nano-silica is included as a cement replacement material. The more important phenomenon is the variation of the quantity of capillary pores. It can be seen that NS 8 has the lowest capillary pore content out of the mixes tested. Lower capillary pore content implies a higher amount of hydrated phase in the paste, and a dense paste structure. Thus, through hydration quantifications of TGA and image quantification of BSE microstructural images, it is clearly observed that 8% cement replacement with nano-silica is the optimum replacement with regards to a dense microstructure with minimum amounts of CH content.

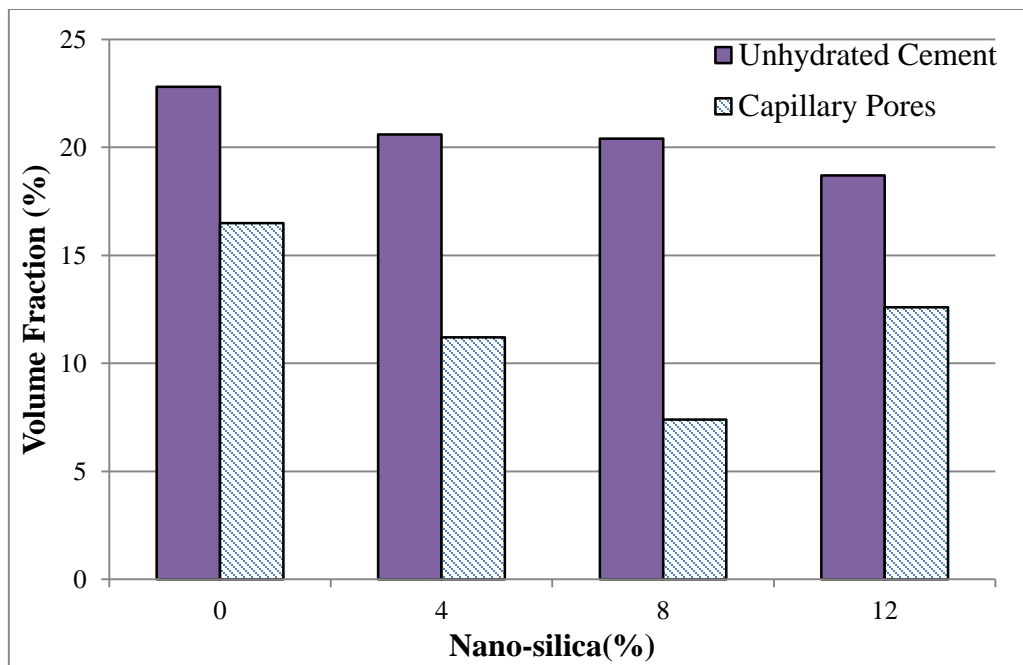


Figure 5. The unhydrated cement content and the capillary pore content of the cement pastes through BSE image quantification

#### 4. Conclusions

Following the hydration reactions and investigating the microstructure of the nano-silica substituted matrices brings a new understanding of the microstructural evolution and sustainability of this system. From the results, it can be concluded that nano-silica actively reacts with the CH from the hydration of the cement paste through the pozzolanic reaction. It can also be concluded that 8% cement replacement with nano-silica is the optimum replacement level. The above characterisation of samples over the time of curing has enhanced our understanding of the behaviour of binders with nano-silica when replacing cement. Such a micro-scale understanding is essential for predicting the macro-scale mechanical and durability performance of nano-silica/cement based construction materials.

#### 5. Acknowledgement

The authors would like to acknowledge the commitment and support provided by Laura Jukes for the experimental component of this research.

#### 6. References

- [1] Konsta-Gdoutos, M.S., Metaxa, Z. S. et al., "Highly dispersed carbon nanotube reinforced cement based materials," *Cement and Concrete Research*, 40, 2010, pp. 1052-1059.
- [2] Belkowitz J.S., Armentrout, D., "An Investigation of Nano-silica in the Cement Hydration Process," *Concrete Sustainability Conference*, 2010.
- [3] Li, H., Xiao, H. et al., "Microstructure of cement mortar with nano-particles," *Composites Part B: Engineering*, 35, 2004, pp. 185-189.
- [4] Qing Y., Zenan Z. et al., "Influence of nano-SiO<sub>2</sub> addition on properties of hardened cement paste as compared with silica fume," *Construction and Building Materials*, 21, 2007, pp. 539-545.
- [5] Senff, L., Hotza, D. et al., "Mortars with nano-SiO<sub>2</sub> and micro-SiO<sub>2</sub> investigated by experimental design," *Construction and Building Materials*, 24, 2010 pp. 1432-1437.

- [6] Sobolev, K., Flores, I. et al., "Engineering of SiO<sub>2</sub> Nanoparticles for Optimal Performance in Nano Cement-Based Materials," 3rd International Symposium on Nanotechnology in Construction, Prague, Czech Republic, 2009, pp. 139-148.
- [7] Nochaiya, T., Chaipanich, A., "The effect of nano-TiO<sub>2</sub> addition on Portland cement properties," IEEE 3rd International Nanoelectronics Conference (INEC 2010), 3-8 Jan., Piscataway, NJ, USA, 2010, pp. 1479-80.
- [8] Nazari, A., Riahi, S. et al., "Influence of Al<sub>2</sub>O<sub>3</sub> nanoparticles on the compressive strength and workability of blended concrete," Journal of American Science, 6, 2010, pp. 6-9.
- [9] Nazari, A., Riahi, S. et al., "The effects of incorporation Fe<sub>2</sub>O<sub>3</sub> nanoparticles on tensile and flexural strength of concrete," Journal of American Science, 6, 2010, pp. 90-93.
- [10] Tregger, N., Pakula, M. et al., "Influence of micro- and nanoclays on fresh state of concrete," Transportation Research Record, 2010, pp. 68-74.
- [11] Jo, B., Kim, C. et al., "Characteristics of cement mortar with nano-SiO<sub>2</sub> particles," Construction and Building Materials, 21, 2007, pp. 1351-1355.
- [12] Said, A. M., Zeidan, M. S. et al., "Properties of concrete incorporating nano-silica," Construction and Building Materials, 36, 2012, pp. 838-844.
- [13] Shih, J., Chang, T. et al., "Effect of nanosilica on characterization of Portland cement composite," Materials Science and Engineering A, 424, 2006, pp. 266-274.
- [14] Mehta, P. K., Monteiro, P. J. M. Concrete Microstructure, Properties, and Materials, Third Edition ed. McGraw-Hill Companies, 1986.
- [15] Neville, A. M., Properties of Concrete, Fourth Edition ed.: Pearson Education(Singapore) Pte. Ltd., Indian Branch, Delhi, India, 1995.
- [16] Akzo Nobel. (2014, 26/07/2014). *AkzoNobel*. Available: <https://www.akzonobel.com/>
- [17] Neithalath, N., Persun, J. et al., "Hydration in high-performance cementitious systems containing vitreous calcium aluminosilicate or silica fume," Cement and Concrete Research, 39, 2009, pp. 473-481.
- [18] Marsh B. K., Day, R. L., "Pozzolan and cementitious reactions of fly ash in blended cement pastes," Cement and Concrete Research, 18, 1988, pp. 301-310.
- [19] Scrivener, K. L., "Backscattered electron imaging of cementitious microstructures: understanding and quantification," Cement and Concrete Composites, 26, 2004, pp. 935-945.

# A Study on the Estimation of ASR Expansion Based on CPT

Kazuo Yamada<sup>1</sup>, Shoichi Ogawa<sup>2</sup>, Yuichiro Kawabata<sup>3</sup>, Yasutaka Sagawa<sup>4</sup>, Masahiro Osako<sup>5</sup> and Takamasa Ochiai<sup>6</sup>

<sup>1</sup>Senior Researcher of Research Center for Material Cycles and Waste Management, National Institute for Environmental Studies.

<sup>2</sup>General Manager of Sales & Development Department, Taiheiyo Consultant Co., Ltd.

<sup>3</sup>Senior Researcher of Structural Engineering Division, Port and Airport Research Institute and Visiting Researcher of Materials and Structures Department, IFSTTAR, Université Paris-Est

<sup>4</sup>A Associate Professor of Faculty of Engineering, Kyushu University

<sup>5</sup>Director of Research Center for Material Cycles and Waste Management, National Institute for Environmental Studies.

<sup>6</sup>Chief Project Manager of Nuclear Safety Research Division, Mitsubishi Research Institute, Inc.

**Abstract:** Concrete prism tests (CPT) were performed on samples having various alkali content and at various temperature. Assuming the shape of the expansion curve, three parameters describing expansion were obtained by data fitting. Then the dependence of these parameters on alkali amount and temperature were calculated. By using the basic information, expansion behavior measured in field exposure test was reproduced. There are some necessities to modify some parameters, so that appropriate ASR estimation in arbitrary condition becomes possible. The effect of SCMs can be taken into account with the decrease in alkali amount due to their substitution to cement.

**Keywords:** CPT, ASR, expansion estimation, fitting, field exposure.

## 1. Introduction

Durability design of concrete is the center of recent concrete technology. Modeling concrete degradation is based on material characters, environmental conditions, and so on. However, regarding to alkali-silica-reaction (ASR) expansion, although various mitigation procedures have been proposed, quantitative estimation of expansion and damage is still hardly established and there are difficulties in preparing countermeasures and maintenance only based on environmental conditions and grade of structures. In this study, based on expansion curves from concrete prism test (CPT) performed under different temperature conditions and with different alkali amounts, expansion in real condition is estimated and the results are compared with exposed concrete blocks. Then, some factors affecting the estimation of ASR expansion are discussed.

## 2. Importance of modeling

The final goal of this study is not the only expansion estimation by ASR but integrated evaluation system of the soundness of some existing concrete structures. Especially, for nuclear power plants (NPP), advanced aging management technical evaluation is required for prolonging its service life. In Japan, the evaluation procedure of alkali reactivity of aggregate has some limitations because the tests being used are classical chemical method and mortar bar test in general and CPT wrapped by a set paper. Of course, chemical method and mortar bar test cannot detect compositional and size pessimum effects and late expansive aggregate. In Figure 5, the relationship between various factors affecting ASR and aging effects on the performance of concrete members is shown. Reactivity of aggregate is the only one part of even for concrete members not the integrated system. Based on the nature of aggregate, various factors such as alkali amounts, mix proportion including pessimum effects, environments including temperature and humidity, and details of member including thickness and confinements affect ASR of members in concrete structure.

ASR does not affect equally the performance of various members in NPP because each member has each requirement in the integrated system. The goal of ASR management is the safety evaluation of facilities in future based on present state. The fundamental concept is summarized in Figure 4. From usual visual inspection and monitoring, when features of damages are detected, petrographic analysis and accelerated expansion test for cores will be carried out. Then, future performance and safety will be evaluated. In this paper, a method of modeling of ASR expansion estimation is proposed.



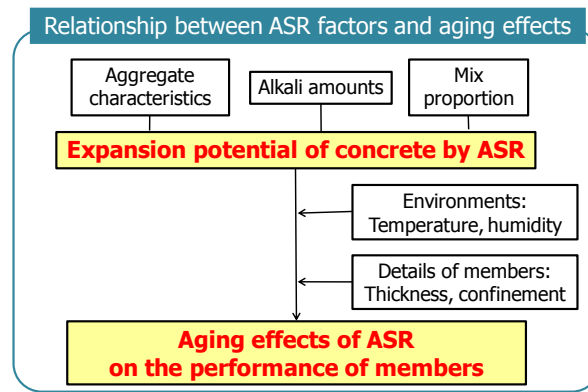


Figure 1. Relationship between various factors affecting ASR and aging effects on the performance of concrete members.

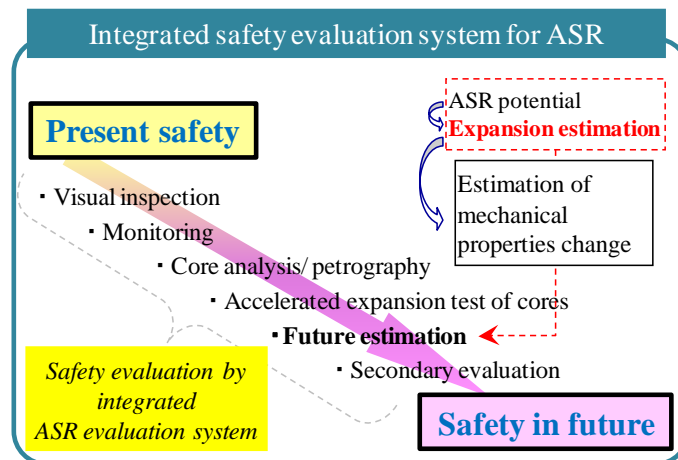


Figure 2. Meaning of modeling of ASR expansion in integrated safety evaluation system for ASR.

### 3. Experiments

#### 3.1 Materials

Two kinds of coarse aggregate, Agg-A and Agg-D were used. Agg-A is a rapid expansive type of andesite containing a large amount of cristobalite and opal and showing compositional pessimum effect. Agg-D is a late expansive type of sandstone origin hornfels containing cryptocrystalline quartz. According to the chemical methods JIS A1145, Agg-A is not innocuous and Agg-D is innocuous. According to the mortar bar test JIS A 1146, Agg-A is not innocuous and Agg-D is innocuous. According to accelerated mortar bar test ASTM C1260, Agg-A is potentially harmful and Agg-D is obscure. As non-reactive aggregate, pure limestone was used because its reactivity was judged as innocuous by a reference.

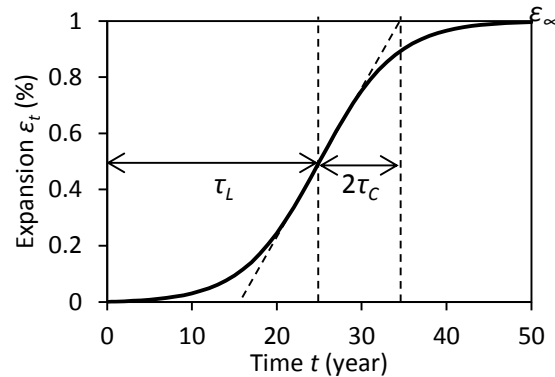
Cement used was normal Portland cement of 52.5 class having density of 3.16 g/cm<sup>3</sup> and Blaine specific surface area of 3110 cm<sup>2</sup>/g. Fly ash used was classified type II according to JIS A6201 having density of 2.30 g/cm<sup>3</sup> and Blaine specific surface area of 4190 cm<sup>2</sup>/g. Blast furnace slag used was composed of 95.6 % of glass having density of 2.89 g/cm<sup>3</sup> and Blaine specific surface area of 4400 cm<sup>2</sup>/g.

#### 3.2 Concrete Prism Test

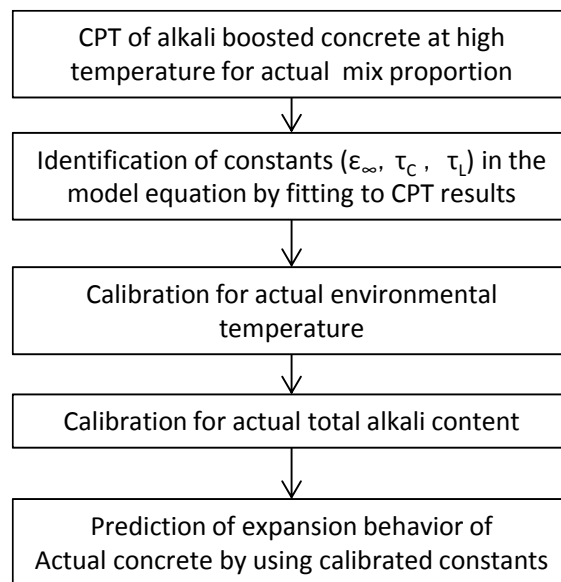
According to RILEM AAR-4, CPT was carried out by keeping demolded concrete prisms of 7.5x7.5x25 cm in stainless steel containers and in humid condition at 60°C. However, for Agg-D, only prism size was modified to 10x10x40 cm and wrapped with wet paper.

In order to examine the effect of alkali amounts (Na<sub>2</sub>O<sub>eq</sub>), from Na<sub>2</sub>O<sub>eq</sub> = 5.5 kg/m<sup>3</sup>, which is the standard of RILEM AAR-4, alkali amounts were reduced to several levels. Fly ash was also added in some mixtures.

Regarding mixture proportion, for the sake of being representative of Japanese usual concrete, following conditions were selected: water to binder ratio  $W/B = 0.55$ , unit water content  $W = 160 \text{ kg/m}^3$ . Reactive aggregates were used as coarse aggregate. In order to check the behavior of pessimum effect of Agg-A, the ratio of coarse aggregate was set as Agg-A : limestone = 3 : 7. Agg-D is used as 100% of coarse aggregate. Fine aggregate was non reactive limestone. As legend, abbreviations such as "A30FA25" stand for Agg-A of 30% and fly ash of 25% replacement, which means aggregate type/ reactive aggregate ratio (%) / fly ash (when used only) / fly ash replacement, are used.



**Figure 3. Modeling of ASR expansion [2].**



**Figure 4. Estimation flow of ASR expansion.**

### 3.3 Estimation Method of ASR Expansion

Estimation of ASR expansion of concrete based on CPT was carried out according to previous study [1]. In this estimation, ASR expansion is assumed to be described by expansion curve shown in Figure 3 [2] and by Eq. (1). By the chart flow shown in Figure 4, each parameter included by Eq. (1) was obtained, and those are calibrated by temperature and alkali amounts, then, the expansion at target temperature and alkali amount was estimated.

$$\varepsilon_t = \varepsilon_\infty \frac{1 - \exp(-t/\tau_C)}{1 + \exp\{-(t - \tau_L)/\tau_C\}} \quad (1)$$

Here,  $\varepsilon_t$ : expansion (%) at the age of  $t$ ,  $\varepsilon_\infty$ : maximum expansion (%),  $\tau_C$ ,  $\tau_L$ : time constants related to required time to the initiation of expansion (years) and expansion rate (years), respectively [2].

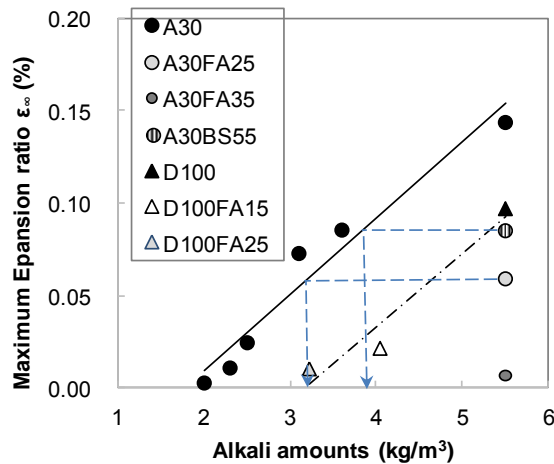


Figure 5. Correlation between alkali amounts and maximum expansion rate  $\epsilon_{\infty}$  by CPT

## 4. Results and Discussions

### 4.1 Correlation between Alkali Amounts and Maximum Expansion Ratio $\epsilon_{\infty}$

By plotting  $\epsilon_{\infty}$  obtained from CPT as a function of the different initial alkali amounts, the correlation is shown in Figure 5. Alkalis from fly ash were counted. Regarding to Agg-D, because CPT was carried out only at 5.5 kg/m<sup>3</sup> of alkali amount, assuming fly ash addition reduces alkali amount apparently, some points were plotted as follows. Alkali content in fly ash was considered. According to previous study [3], even when fly ash or blast furnace slag are used in some quantity, regardless of the kind and amounts of supplemental cementitious materials, there is a proportional correlation between ASR expansion and OH<sup>-</sup> concentration and the OH<sup>-</sup> concentration is determined by alkali concentration in solution phase. Based on this study, from the alkali amount of A30FA25 (5.5 kg/m<sup>3</sup>), by using regression line (solid line in Figure 3) between alkali amounts and for Agg-A, alkali amount can be assumed to decrease to 3.23 kg/m<sup>3</sup> by the replacement of 25% fly ash. Similarly for D100FA25, assuming for Agg-D a parallel regression line to Agg-A (chain line in Figure 3), the apparent alkali amount was assumed to decrease to 3.23 kg/m<sup>3</sup> from the original 5.5 kg/m<sup>3</sup>. For D100FA15, the decrease of alkali in case of substitution of fly ash is assumed to be proportional to the replacement ratio by fly ash, the apparent total alkali of D100FA15 was calculated as 4.04 kg/m<sup>3</sup>. From Figure 5, the alkali threshold of A30 not to expand ( $R_{lim}$ ) can be determined as 1.79 kg/m<sup>3</sup>.  $R_{lim}$  of D100 is 3.07 kg/m<sup>3</sup>. Based on these results, Agg-A of rapid expansive type is thought to be possibly reactive even under the condition of alkali limit of 3.0 kg/m<sup>3</sup>. Although Agg-D of late expansive type is judged as innocuous by the chemical method and the mortar bar test, there is a possibility of expansion, when alkali amounts exceed 3.0 kg/m<sup>3</sup>. Besides, the reactivity of Agg-D can be detected by RILEM AAR-4 since the expansion at 20 weeks exceeded the threshold 0.04% and the acceleration at 60 °C can detect the reactivity of late expansion aggregate.

### 4.2 Comparison between Expansion Estimation in Real Environment and Field Exposure.

Considering the concrete block (40x40x60cm) exposure tests results, carried out using the same origin but a different lot of Agg-A [4], the expansion behaviours are estimated based on the results of CPT with an adaptation to the temperature and alkali amount conditions of field exposure tests. The results are shown in Figure 6. Although there have been studied about the effect of temperature [2] and alkali amount on ASR expansion, behaviours will be different for different aggregate and the dependencies are required to be evaluated. In previous study [1], because of the lack of data,  $R_{lim}$  is assumed as 1.2 kg/m<sup>3</sup> for highly reactive aggregate. However, in this study,  $R_{lim}$  was evaluated and the value was used. As for temperature condition, annual average temperature 17 °C was used for all age of estimation. The estimation was too much during first one year and then the calculation became under estimate more and more for longer ages. However, alkali dependence of expansion, i.e. less expansion in less alkali amounts, was reproduced as a trend. Especially, in the small alkali amount condition, the expansion behaviour was successfully reproduced by the method proposed in this study.

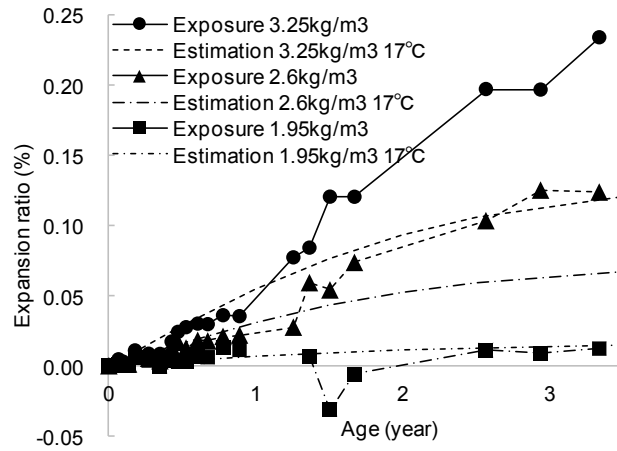


Figure 6. Expansion behaviors of field exposure concrete blocks having different alkali amounts and expansion estimation results based on CPT

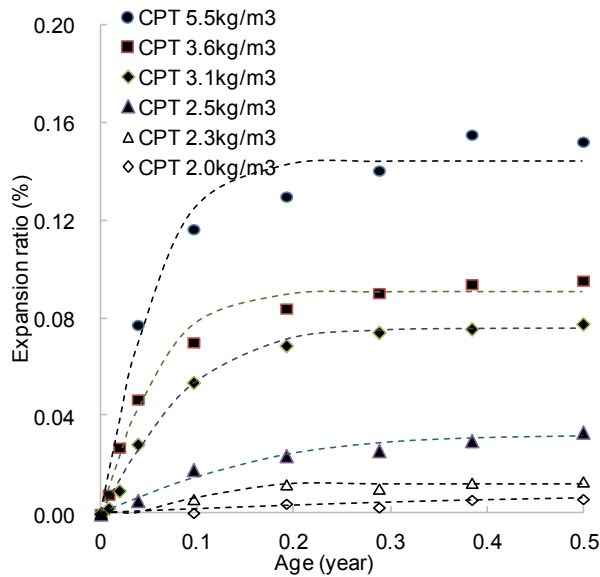


Figure 7. Expansion behaviors of CPT for Agg-A with various alkali amounts and fitting results.

### 4.3 Discussion on the Differences between Field Exposure and Estimation.

#### 4.3.1 Problems in fitting

Temperature effect on ASR expansion for existing structure is described in LCPC guideline [6]. Because this study is aimed to estimate the field expansion of newly built concrete structure based on CPT, both effects by temperature and alkali amounts have to be considered and special attention has to be paid for alkali leaching. In this study, unfortunately, there are limitations to consider the effects of alkali leaching and the effects are ignored.

The results of CPT for Agg-A having various alkali amounts and fitting results are shown in Figure 7. For the expansion estimation of field exposure condition, fitting parameters obtained from the data of 5.5 kg/m<sup>3</sup> of alkali amounts has been chosen in order to shorten test period. In Figure 7, there are some scattering of data but there are clear tendency of discrepancy between data obtained and regression curves in the alkali amounts of 3.6 or 5.5kg/m<sup>3</sup>. In the earlier ages 0.2 or 0.3, the regression overestimated but in longer ages 0.4 or 0.5 years, the regression underestimated. For the prism containing 5.5 kg/m<sup>3</sup> of alkali, the expansion continues to increase for all period of experiments although

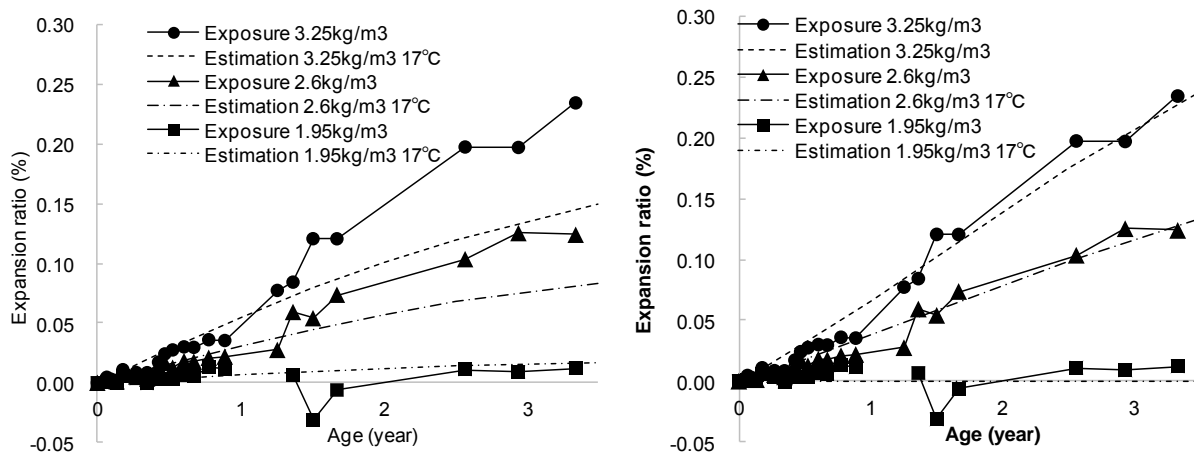
the estimated fitting result reached saturation  $\varepsilon_t$  in the age of 0.2 years (10 weeks). Therefore, the  $\varepsilon_t$  used in estimation was underestimated compared to field exposure and then the estimation underestimated. This result suggests the inappropriateness of fitting CPT data to a model indicated in Figure 3.

#### 4.3.2 Effects of temperature on each parameter

In Figure 6, because an appropriate fitting result was obtained in the smallest alkali amount condition, the results of A30 with 3.1 kg/m<sup>3</sup> of alkali were compared to the alkali amount 3.25 kg/m<sup>3</sup> of field exposure. Each parameter was obtained and estimation results are shown in Figure 8 left. However, only slight improvements were observed. Even in limited alkali amounts, in high temperature condition, it is indicated that the expansion of CPT became limited.

There may be some possible reasons for this behaviour such as 1) at high temperature such as 60 °C, the expansion mechanism became different such as generated ASR gel became fluid and dispersed in paste without significant expansion, 2) as pointed out by previous studies [5], at high temperature, alkalis tend to leached out from concrete prisms, and 3) activation parameter  $U_\infty$  [1] calibrating temperature dependence was too small. The calibration of each parameter against temperature and alkali amounts are based on some limited number of experiments and expected to contain significant error. And also, temperature and humidity change surely affect the ASR expansion in field that are not considered in this study.

Therefore, selecting two parameter  $\varepsilon_\infty$  and  $\tau_L$  having significant effects, these two parameters were adjusted to the expansion curve of field exposure and the results are shown in Figure 8 right. The expansion behaviors of field exposure test were successfully reproduced by this equation. In this estimation, the calibration of  $\tau_C$  was carried out according to reference [1], and so, if appropriate  $\varepsilon_\infty$  and  $\tau_L$  can be obtained from CPT, the accuracy of the estimation of ASR expansion will be improved. For this purpose, there is necessity to accumulate CPT results for various temperature and alkali amounts.



**Figure 8. Expansion behaviors of field exposure concrete blocks having different alkali amounts and the expansion estimation results based on CPT A30 with 3.1 kg/m<sup>3</sup> of alkali amounts (right) and parameters used were calibrated for best fitting (left).**

## 5. Conclusions

By the discussion of the effect of parameters on the estimation of ASR expansion, although the data for various temperature and alkali amounts are not enough and there remain problems in accuracy, it is possible to estimate ASR expansion quantitatively based on appropriate expansion parameters. Another unique point of this study is the consideration of the adding effect of SCMs by exchanging its addition to the reduction of alkali amounts. Expansion estimation in field based on CPT with various mixtures is expected useful for the durability design of structure. In future, appropriate procedure of CPT will be also applied for concrete core accelerated expansion test required for reasonable maintenance.

## Acknowledgement

This study has been carried out as a part of NRA project for advanced aging management technical evaluation of concrete structures in NPP.

## References

1. Kawabata, K., Yamada, K., Ogawa, S., Sagawa, Y., "Simplified Prediction of ASR Expansion of Concrete Based on Accelerated Concrete Prism Test", Cement Science and Concrete Technology, 67, 2013, pp 449-455 (in Japanese).
2. Larive, C., "Apports Combinés de l'Experimentation et de la Modelisation à la Comprehension de l'Alcali Reaction et de ses Effects Mecaniques", Laboratoire Central des Ponts et Chaussées, 1998 (in French).
3. Kawabata, Y., Yamada, K., Matsushita, H., "Relation of Phase Composition of Cement Hydrates with Supplementary Cementitious Materials to the Suppressing Effect on ASR Expansion", Journal of JSCE, Ser. E2, 69, 2013, pp 402-420 (in Japanese).
4. Sagawa, Y, Yamada, K., Karasuda, S., Eriguchi, R., "Expansion Behavior of Concrete using Aggregate Showing Pessimism Effect in Accelerated and Exposure Tests", Concrete Research and Technology, 25, 2014, pp 135-145 (in Japanese)
5. Lindgård, J, Thomas, M.D.A., Sellevold, E.J., Pedersen, B., Andic-Cakir, O., Justnes, H., Ronning, T.F., "Alkali-silica reaction (ASR)-performance testing: Influence of specimen pre-treatment, exposure conditions and prism size on alkali leaching and prism expansion", Cement and Concrete Research, 53, 2013, pp. 68-90
6. Laboratoire Central des Ponts et Chaussees: Aide a la gestion des ouvrages atteints de reactions de gonflement interne, 2003 (in French)

# Enhancing Mechanical and Durability Properties of Recycled Aggregate Concrete

George Dimitriou<sup>1</sup> and Michael F. Petrou<sup>2</sup>

<sup>1</sup>Research fellow, University of Cyprus

<sup>2</sup>Professor, Department of Civil and Environmental Engineering, University of Cyprus

**Abstract:** The main difference between Recycled Concrete Aggregate (RCA) and Natural Aggregate (NA) is the amount of cement paste attached on the former. This investigation examines the effect of RCA to concrete and a method to improve the properties of recycled aggregates and the properties of the Recycled Aggregate Concrete (RAC). Three types of coarse RCA and two types of mineral admixtures were used. Mineral admixtures (industrial by-products), namely Fly Ash (FA) and Silica Fume (SF) were used as partial replacements of cement to improve the durability properties of concrete. The coarse aggregates were evaluated according to their resistance to fragmentation, soundness, absorption and density. The RAC mixtures were evaluated according to their compressive strength, flexural and splitting tensile strength, modulus of elasticity, chloride permeability, sorptivity and porosity. The results revealed that an adequate quality concrete can be produced from RCA and it can be used for construction activity. The RAC quality can be even further improved using a simple treatment method and the durability properties can be improved by the incorporation of mineral admixtures. Finally, cost analysis showed that RAC mixtures can be less expensive than NA mixtures even with the additional cost of the treatment.

**KEYWORDS:** Recycled concrete aggregates, attached cement paste, treatment method, mineral admixtures, recycled aggregate concrete, mechanical and durability properties

## 1. Introduction

According to the World Commission on Environment and Development (WCED), "sustainable development is a development that meets the needs of the present without compromising the ability of future generations to meet their own needs" (1). When considering the total amount of natural resources in a large scale, in Europe for example, the exploitation of resources might not be as significant as in a smaller scale, in Cyprus for instance, where the increased exploitation may reduce the resources to a crucial level, due to country's small size, compromising the needs of the following generations.

There is a significant research activity regarding the mechanical performance of RAC which in most cases shows that the strength of RAC is adequate for use as structural concrete. On the contrary, the replacement level of natural with recycled aggregates and the durability properties of RAC are still researched, since a wide variability in the results is reported. In fact, the durability properties are still under examination and so the RCA are used only for secondary level construction activities, as road base and landfilling materials.

The difference between recycled and natural aggregates stems from the fact that during the recycling process of the old concrete, a certain amount of mortar from the original cement remains attached on the aggregate particles. Hence RCA consists of two materials: natural aggregate and attached cement paste. The drawbacks come from the cracks and fissures, which are formed during processing and mainly from the existence of an old interfacial transition zone (ITZ) and a layer of adhesive mortar on the aggregates. In order to enhance the properties of RCA, it is fundamental to elaborate a treatment method that is capable to remove the adhering mortar at such level that diminishes the negative effects.

The microstructure of RAC is much more complicated than that of conventional concrete since it includes two kinds of ITZ, one between the RCA and the new cement paste and a second one between the RCA and the old cement attached. The old cement paste possesses many micro-cracks and fissures and has high porosity (2), thus it becomes the weakest link in RAC, since its strength is the upper limit of the strength of concrete. As the paste-aggregate bond strength increases, the concrete strength also increases (3,4). RAC are weaker than NA and the failure happens through the aggregates themselves (including the old ITZ) instead of the new ITZ (5,6). Like the high strength concrete, the recycled aggregate concrete fails through the aggregate in addition to failure of the old ITZ (2,7). The presence of the attached cement paste is significant since recycled aggregates consist of 65-70% by volume of natural coarse aggregate and 30-35% by volume of old cement paste (4).

In general, RCA are of lower quality than NA. RCA have higher absorption value and lower density. The water absorption of RCA ranges from 3 to 15% (4,7). The presence of the mortar hinders the density value of the recycled aggregates (2200 to 2400 kg/m<sup>3</sup>) (4). Furthermore, the resistance to fragmentation is lower and their texture is more porous, rough and irregular due to crushing of the old concrete.

The lower quality aggregates have an immediate effect on the quality of the hardened concrete. The increase in the replacement ratio of RCA decreases the compressive strength of RAC. Generally, the compressive strength can be 10-25% lower than conventional for 100% replacement. Etxeberria et al. reported losses of 20-25% for 100% replacement, maintaining the same effective w/c ratio (0.50) and the same cement content (5). However, the use of 20%-30% RCA produces no significant changes with respect to the control mixture with 0% RCA (2,5,8).

There is a drop of 10-35% of the splitting tensile strength using 100% RCA (2). Tabsh and Abdelfatah found a 10-35% drop in tensile strength (9). During the determination of splitting tensile strength many researchers concluded that the failure initiated not only from the interfaces between the recycled aggregates but also from the recycled aggregates themselves (2).

Regarding the modulus of elasticity, Rao et al. found a reduction of 34.8% using 100% RCA compared to the control concrete (10). Xiao et al. noticed a reduction up to 45% for modulus of elasticity with 100% replacement of RCA (2).

The durability properties of RAC deteriorate at a further extend than mechanical properties, with the increase in RCA content. Thomas et al. noted that the open porosity of RAC increases with w/c ratio and the degree of replacement and concluded that a 20% replacement of NA with RCA decreases the density value around 5% than in the case of control concrete (8). Kou and Poon found 9.5% lower resistance to chloride permeability for the 100% RCA mixture (11). Rao et al. reported 7.37% water absorption for concrete with 100% RA and 6.54% for concrete with 50% RCA (10).

The use of fly ash and silica fume (or microsilica), creates some minor negative effects on the mechanical properties of the concrete but it improves substantially the durability properties of RAC. The use of fly ash presents reduced permeability and better workability. Silica fume due to its small size and its large surface area is changing the microstructure of concrete and improves it, creating a denser matrix. Although fly ash and silica fume have some drawbacks, such as reduced early strength and increased water demand respectively, the synergistic effect using both mineral admixtures as cement replacements is important and more beneficial than using each other alone.

The objective of this research is to determine whether a mix design incorporating RCA as replacement of NA and mineral admixtures as partial replacement of cement is able to achieve an adequate performance for structural applications. Furthermore, RCA are subjected to a treatment method to reduce the amount of the attached cement paste and improve their properties.

Apart from the mechanical and durability properties, the environmental and economic aspects of the RAC are of equal importance and a comparison of NA with RCA is presented. The potential environmental and economic benefits could ameliorate RAC image to the public and boost its usage.

## **2. Experimental program**

### **2.1 *Materials and testing methods***

In order to be able to quantify the cement paste attached, the aggregates were subjected to a thermal treatment method as described, in detail, in Sanchez de Juan and Gutierrez (12). It contains several cycles of high temperatures (500 °C) and soaking in water. The thermal method was selected as it can be used for all types of aggregates (including limestone), is more consistent and it is easier to perform. It was also proved to be the most effective and it had lower variability compared to other methods (13).

Both mechanical and durability properties were determined according to international standards. The coarse aggregates were evaluated according to their resistance to fragmentation (EN 1097-2:2010), weathering properties (EN 1367-2:2009), absorption and density (EN 1097-6:2000). The RAC mixtures were evaluated according to their compressive strength (EN12390-3:2009), flexural (EN 12390-5:2009) and splitting tensile strength (EN 12390-6:2009), modulus of elasticity (ASTM C 469 –



02), chloride permeability (ASTM C 1202-97), sorptivity (capillary absorption) and porosity (open porosity).

## 2.2 Concrete Constituents

Four types of coarse aggregates were used in this research, namely three RCAs and one NA. The RCAs tested are:

- RCA-L (laboratory), aggregates from crushed good quality laboratory concrete which represent the best case scenario of RCA.
- RCA-F (field), aggregates from crushed field concrete, provided by a local supplier.
- RCA-T (treated), aggregates from crushed field concrete (same as RCA-F) that were subjected to a treatment method to remove the attached cement paste.

A simple low-cost treatment method was used on field recycled aggregates in order to improve their mechanical properties. RCA-F aggregates were placed into an 8 m<sup>3</sup> modified concrete mixer. The mixer was rotated at a speed of 10 rpm for 5 hours. A total of around 3000 rotations were performed. During this process water was added removing smaller particles, dust and the weaker adhering mortar. At the end of the rotation period, the aggregates were sieved through a modified sieve in order to discard aggregates with sizes lower than 4 mm. The final product was named RCA-T and presented substantially better properties, as it is described in the following sections.

Coarse natural aggregates were used, with nominal sizes 4/10 mm and 8/20 mm. Only natural fine aggregates were used in all mixtures. The water used was drinkable tap water from the laboratory. All mixtures contained Superplasticizer (Sika Viscocrete 4000). Three binders were used: Ordinary Portland Cement (OPC), CEM I 42.5 R, as the main binder, Microsilica and fly ash as partial replacements of cement. Binders' properties are presented in Table 1.

**Table 1: Constituents of Binders**

Property	Fly Ash	Silica Fume	Portland Cement
SiO <sub>2</sub> content, %	40	85 to 97	21
Al <sub>2</sub> O <sub>3</sub> content, %	17	-	5
Fe <sub>2</sub> O <sub>3</sub> content, %	6	-	3
CaO content, %	24	<1	62
Surface area, m <sup>2</sup> /kg	420	15000 to 30000	370
Specific gravity	2.38	2.22	3.15

## 2.3 Concrete mixtures

A total of 12 mixtures were cast. The mix design is presented in Table 2. The same mix design was adopted for all mixtures. The effective w/c ratio was kept constant at 0.48. All aggregates and cement replacements were made by weight and the design method used in this study was the Direct Weight Replacement (DWR) method, which has been used extensively throughout the literature, mainly because its simplicity. Two series of mixtures were cast. In the first series, of 8 mixtures, there is a replacement of NA with different types of RCA while in the second series, of 4 mixtures, there is additionally a replacement of cement with mineral admixtures. The second series' specimens were also tested at 56 days due to the presence of mineral admixtures. For the mixtures without mineral admixtures the 28-day period of curing was considered adequate. The replacement ratios of the mixtures are presented in Table 3. The code names of each one consist of "R" for RCA, "L" (laboratory), "F" (Field), "T" (Treated), depending to the type of RCAs. "100" or "50" represent the replacement ratio of aggregates. "F25" represent the utilization of fly ash and the replacement ratio of cement with fly ash. Finally, "S5" represent the use of silica fume and its replacement ratio. Cubes of 100mm were used to determine the compressive strength, the sorptivity and the porosity. Cylinders  $\Phi$ 100 x 200 mm were used to determine the rapid chloride permeability, while the  $\Phi$ 150 x 300 mm cylinders were used to determine the tensile splitting strength and the modulus of elasticity. Prisms 100 x 100 x 500 mm were used to determine the flexural tensile strength.

**Table 2: Mix proportions**

Constituents	Quantity (kg/m <sup>3</sup> )
Cement	400.0
Water	192.5
Coarse Aggregates 8/20 mm	655.4
Coarse Aggregates 4/10 mm	263.8
Sand 1 (natural sand) 0/4 mm	559.5
Sand 2 (extra fine limestone)	108.4
Superplasticizer	6.4

**Table 3: Replacement Ratios**

Mixtures	Replacement ratio of coarse aggregates	Type of aggregate	Fly Ash	Silica fume
Control	0%	Natural	-	-
RL100	100%	RCA-L	-	-
RF100sa	100%	RCA-F	-	-
RF100ps	100%	RCA-F	-	-
RF100	100%	RCA-F	-	-
RT100	100%	RCA-T	-	-
RF50	50%	RCA-F	-	-
RT50	50%	RCA-T	-	-
RF100F25	100%	RCA-F	25%	0%
RF100F25S5	100%	RCA-F	25%	5%
RT100F25	100%	RCA-T	25%	0%
RT100F25S5	100%	RCA-T	25%	5%

## 2.4 Casting and curing

Concrete mixtures were prepared using a mixer available in the Laboratory of Civil and Environmental Engineering, University of Cyprus. Aggregates were in air-dried condition (except for "RF100ps" mixture) and the proper water corrections were made, according to aggregates' moisture and absorption values. Slump tests were performed with a slump target of  $200 \pm 30$ mm, aiming to create a relatively fluid and workable concrete. The desired slump was achieved by adjusting the amount of superplasticizer added in the concrete mix. The vibration was applied quite carefully to avoid segregation. The samples were removed from the moulds after 24 hours and were placed in water tanks at a constant temperature of 21 C°.

## 3. Results and discussion

The results of the tests are discussed in the following section with an emphasis on the mechanical and durability properties of hardened concrete but also on the effect of the treatment method on aggregates.

### 3.1 Properties of aggregates

The mechanical and physical properties of the four types of aggregates used for this research are presented in Table 4.

**Table 4: Mechanical and Physical Properties of Aggregates**

Properties	NA	RCA-T	RCA-F	RCA-L
LA (%)	29	15	32	29
Apparent Particle Density (Mg/m <sup>3</sup> )	2.69	2.74	2.72	2.60
Particle Density (Mg/m <sup>3</sup> )	2.52	2.49	2.28	2.21
Particle Density in SSD (Mg/m <sup>3</sup> )	2.58	2.58	2.44	2.37
Moisture Content (%)	0.5-0.6	2.6-2.8	2.7-2.9	2.1-2.2
W.A. 24 (%)	2.5	3.7	7.2	7.0
Soundness (%)	30	14	41	-
Mortar content (%)	0	9	24	23

NA in Cyprus present higher absorption values, reaching up to 4.5% (14) and thus the 2.5% is considered lower. The RCA-T aggregates had much lower absorption values, compared to RCA-F and RCA-L (around 50%). From the tests performed on aggregates it is clear that:

- The density and absorption values are related to the amount of the cement paste attached.
- The treatment method, which resembled a prolonged Los Angeles test, removed not only a major amount of cement paste but also some weaker or fractured aggregates keeping only the stronger and sounder ones producing the RCA-T aggregates that had very good resistance to fragmentation.
- The treatment method decreased the total amount of the attached cement paste by 62% and produced sounder and rounder aggregates.
- RCA-T aggregates proved to be of a better quality than the other types of RCA and in some tests they performed even better than NA.

### 3.2 Workability

The shape and texture of the aggregates and the attached cement paste has an impact on the workability. The mixture "RF100sa" was cast in order to examine the effect of the shape and texture of aggregates on the workability, thus the amount of superplasticizer used was kept the same as "Control". This resulted in a low slump value of 50mm. Table 5 presents the slump and superplasticizer values of each mixture.

**Table 5: Slump and Amount of Superplasticizer**

Mixtures	Slump (mm)	Superplasticizer (Kg/m <sup>3</sup> )	Superplasticizer/cement ratio (%)
Control	198	3.50	0.87
RL100	220	3.00	0.75
RF100sa	50	3.50	0.87
RF100ps	190	2.50	0.62
RF100	170	4.60	1.15
RT100	185	2.50	0.62
RF50	194	3.25	0.81
RT50	195	2.00	0.50
RF100F25	170	5.90	1.48
RF100F25S5	190	6.25	1.56
RT100F25	196	2.58	0.65
RT100F25S5	195	2.90	0.73

The slump test results showed that:

- The mixtures containing RCA-T aggregates needed less superplasticizer in order to reach the target slump value. Due to the rounder shape, RCA-T aggregates had better workability compared to RCA-F aggregates but even to the natural aggregates.
- The replacement of cement with mineral admixtures increased greatly the amount of the superplasticizer that was needed. Especially the microsilica-mixtures demanded the biggest amount. This occurred due to the higher surface area of microsilica particles that increased the water requirement.
- Presoaking the aggregates affected the workability since having the same w/c ratio, "RF100ps" mixture needed 0.62% (of the amount of cement) superplasticizer while "RF100" needed 1.15%.

### **3.3 Mechanical properties**

Table 6, presents the results of the mechanical properties of all concrete mixtures tested.

#### **3.3.1 Compressive Strength**

The compressive strength test results indicate that the use of RCA affected negatively the strength of the concrete. The results for the 100% substitution of NA coarse aggregates with RCA showed losses of 16.8%, 34.1% and 13.8% for "RL100", "RF100" and "RT100" respectively. For a replacement ratio of 50% the losses were 25.7% and 11% for "RF50" and "RT50", respectively. The use of SSD aggregates had only a minor impact on the 28-day strength. It should be noted that despite the decrease, the RAC mixtures manage to reach high compressive strength values. The difference between the RCA-T and RCA-F aggregate mixes is substantial; there is a 23.6% and 16.5% difference in compressive strength for incorporation ratios of 100% and 50% respectively.

In the second series, the difference between mixtures, consisted of the two different field aggregates (RCA-T, RCA-F), is also clearly noticed. Regarding the use of mineral admixtures, although the 28-day compressive strength was low, the 56-day strength presented only a slight decrease compared to the mixtures without mineral admixtures. The lower early strength can be attributed to the slow pozzolanic reaction of fly ash. For the optimal scenario of 100% NA replacement and 25% and 5% replacement of cement with fly ash and microsilica, respectively, "RT100F25S5", the 56-day strength reached a compressive strength of 60.3 MPa. The use of fly ash and microsilica produced only minor losses compared to the mixtures without mineral admixtures. Comparing the use of fly ash with the use of both fly ash and microsilica, it can be noticed that the use of microsilica did not provide higher early strength, as it was expected due to its rapid pozzolanic reaction. Regarding the 56-day compressive strength, microsilica did not have neither positive nor negative effects.

Taking into account all the compressive strength test results:

- All RAC mixtures provided good compressive strength values that decreased as the replacement ratio of NA with RCA increased.
- Differences between RAC containing RCA-T and RAC containing RCA-F aggregates were particularly significant for both series of mixtures and underlined the effect of a simple treatment method.
- The 28-day compressive strength of concrete mixtures decreased with the increase in recycled aggregate content. This was due to the presence of the old ITZ that worsens the mechanical and physical properties of the recycled aggregates.
- Comparing the "RN100ps" with "RN100", it can be concluded that the effect of presoaking the aggregates was insignificant.
- The use of fly ash and microsilica as partial replacement of cement produced a low early strength but their 56-day strength was almost the same as the 28-day strength of mixtures without mineral admixtures.
- Despite the use of recycled aggregates, that according to literature should present high variability, the standard deviation was relatively low for all the tests (ranging between 1-6% of the mean values). Though, standard deviation of compressive strength increased with the increase of recycled aggregates in concrete. The Control mixture presented the lowest deviation.

**Table 6: Summary of Results**

Mixtures	Compressive strength (MPa)			Flexural strength (MPa)	Indirect tensile (MPa)	Modulus of elasticity (GPa)	Porosity (%)		Sorptivity (mm <sup>2</sup> /min)		Rapid Chloride Permeability (Coulombs)	
	7 days	28 days	56 days				28 days	56 days	28 days	56 days	28 days	56 days
Control	58.5	72.1	-	8.6	4.22	27.28	17.44	-	0.092	-	3473	-
RL100	45.8	60.0	-	6.9	4.06	24.03	22.28	-	0.122	-	4870	-
RF100sa	38.6	47.5	-	5.4	2.81	18.25	22.17	-	0.120	-	4861	-
RF100ps	39.5	50.6	-	6.0	3.04	21.33	20.98	-	0.109	-	5822	-
RF100	39.1	47.1	-	6.6	3.14	20.09	21.28	-	0.116	-	5248	-
RT100	40.8	62.2	-	7.2	3.09	29.64	18.19	-	0.101	-	3444	-
RF50	43.6	53.6	-	7.4	3.10	25.37	19.60	-	0.098	-	4154	-
RT50	50.6	64.2	-	7.2	2.88	25.85	18.05	-	0.091	-	3867	-
RF100F25	29.1	35.6	46.4	6.3	2.03	20.00	22.47	22.35	0.120	0.116	5303	3095
RF100F25S5	26.0	38.2	45.8	6.3	2.22	19.89	22.41	22.76	0.087	0.095	3466	1652
RT100F25	36.0	50.8	58.2	6.2	2.98	25.84	18.95	18.73	0.095	0.083	4553	1887
RT100F25S5	34.2	50.9	60.3	6.9	2.30	22.97	19.05	18.19	0.071	0.070	2989	1200

### 3.3.2 Flexural strength

It can be seen that flexural strength decreased with the increase of recycled aggregate content. The results for the 100% substitution of NA with RCA showed losses of 19.6%, 23.7% and 16.7% for “RL100”, “RF100” and “RT100” respectively. Like the compressive strength test, the “RT100” presented the lowest loss in strength compared to the control mixture. This is an indication of the difference in the mechanical and physical properties of the aggregates. Regarding the SSD aggregates, there was a slight decrease in flexural strength. Etxeberria et al. noted that the recycled aggregates should not be saturated, as that would probably result in the failure of an effective transition zone between the saturated recycled aggregates and the cement paste (5). Regarding the use of mineral admixtures, there was only a slight effect in flexural strength with the incorporation of FA and SF.

### 3.3.3 Splitting tensile strength

There is a drop of 5%-25% of the splitting tensile strength using 100% RCA. The “RF100” presented higher tensile splitting strength than “RT100”. This shows, as expected, that the shape and texture of aggregates affect the strength of the concrete. Matias et al. concluded that the rough and angular contact area allows a better adherence to the new cement paste than NA (15). As a result, “RF100” had higher splitting tensile than “RT100” with the rounder aggregates. The same pattern exists also for the 50% replacement level (“RF50”, “RT50”). The splitting tensile strength test provided a good opportunity to examine the failure mechanism that exists in concrete as the cylinder sample was broken in half at the end of the test. The failure of conventional concrete derives from the interfacial transition zone that is the weakest link. Regarding the RAC, the failure occurs through the aggregates themselves. The control mixture had a matrix failure. The failure surface did not pass through the aggregates but around them, since failure occurred along the ITZ. On the other hand, in most of the cases of the recycled concrete the failure occurred through the aggregates themselves. The RCA-T aggregates though presented a different pattern. There was a combination of the two cases described. The partial replacement of cement with mineral admixtures decreased the splitting tensile strength.

### 3.3.4 Modulus of elasticity

The modulus of elasticity of the recycled aggregate concretes was reduced when the recycled aggregates percentage increased. There was a difference between the RCA-T and RCA-F aggregates. It can be noted that the partial replacement of cement with mineral admixtures had a minor negative effect for RCA-F aggregate concrete but decreased at greater level the RCA-T aggregate concrete.

### 3.4 Durability Properties

The durability tests results are presented in Table 6. The density of the “Control” was typical for normal concrete. The mixtures with RCA had lower density due to the lower density of the attached cement paste. “RT100” however had almost the same density as “Control” indicating the good quality aggregates. The use of mineral admixtures did not have any serious impact on density. Porosity followed the same pattern as density, “RT100” achieved close enough values to “Control” while the use of mineral admixtures had only a minor effect.

Using RCA, the reduction in permeability and the increase of sorptivity, were expected since the recycled aggregates contained a certain amount of mortar and had undergone a crushing process, which was likely to leave cracks in the weaker mortar or weaker aggregates. These cracks would in turn create paths for the fluids to pass through. The increase of the sorptivity coefficient of RAC can also be attributed to the higher absorption capacity of the recycled aggregates compared with natural. The difference though between RCA-T aggregates and RCA-F or RCA-L was evident. Especially the “RT100” mix presented around the same properties as the control mixture while “RL100” and “RF100” presented lower quality.

For the second series of mixtures the RCP and sorptivity values were greatly improved since the use silica fume restructure the matrix leaving fewer paths for the liquid to pass through. Silica fume with high value of fineness filled both the interfaces and the bulk paste and the capillary pores were reduced, hence, the sorptivity and permeability of concrete decreased. The use of fly ash and microsilica refined the distribution of pore size and pore shape of concrete. In concrete mixtures with FA, the average particle size of the mineral admixture was higher compared to microsilica and the pores in bulk paste and the interfaces were not filled adequately. Due to the higher fineness, the use of microsilica seems to react better and produces better values for both RCA-T and RCA-F aggregates. Finally, there was good correlation among durability properties, especially the sorptivity-porosity correlation ( $R^2=0.92$ ) and sorptivity-Rapid Chloride Permeability ( $R^2=0.72$ ).

## 4. Economic aspect

Regarding the cost analysis conducted for this research, some valuable conclusions emerged. The cost of mineral admixtures found to be extremely high, in Cyprus, to be used in a large scale. The cost is much lower in countries with production sources of industrial by-products. The import of these materials raises the cost and makes it much higher than the cost of cement. Table 7 presents the costs of the materials used and the final cost of the mixtures. RCA-F aggregates were the cheapest. The treatment method (for RCA-T) raised the cost of the aggregates but was still lower than the cost of NA. The 50% substitution level of NA with RCA-T (RT50 mixture) was the most cost-effective of all mixtures, in terms of €/MPa. RT50 mixture produced a cheaper concrete that had around the same quality as “Control”. Finally, a useful conclusion is that although RCA-F aggregates were cheaper than RCA-T, the mixtures produced from RCA-F were more expensive since they required greater amount of superplasticizer in order to reach the same level of workability.

**Table 7: Cost of mixtures (€)**

	Unit cost (€/tn)	Control	RT100	RF100	RF50	RT50	RF100 F25	RF100 F25S5	RT100 F25	RT100 F25S5
Cement	84.0	33.6	33.6	33.6	33.6	33.6	25.2	23.5	25.2	23.5
Fly Ash	200.0	-	-	-	-	-	20.0	20.0	20.0	20.0
Microsilica	250.0	-	-	-	-	-	-	5.0	-	5.0
NA	9.3	6.2	-	-	3.0	3.0	-	-	-	-
RCA-F	3.5	-	-	2.3	1.1	-	2.3	2.3	-	-
RCA-T	6.5	-	4.3	-	-	2.1	-	-	4.3	4.3
Sand	10.8	7.2	7.2	7.2	7.2	7.2	7.2	7.2	7.2	7.2
Superplasticizer (€/lt)	3.3	11.6	8.3	15.2	10.7	6.6	19.5	20.6	8.5	9.6
Water	0.9	0.2	0.2	0.2	0.2	0.2	0.2	0.2	0.2	0.2
Sum		58.5	53.4	58.3	55.7	52.6	74.2	78.7	65.3	69.6
€/Mpa		0.8	0.9	1.2	1.0	0.8	1.6	1.7	1.1	1.2

## 5. Conclusions

Useful conclusions were derived from this research aiming to dispel fears regarding the utilization of RCA into concrete. The key conclusion of this research is that the RAC can provide adequate quality in order to be used in major construction activities. A simple treatment method, in the recycling process of RCA, is capable to reduce the attached cement paste at such level that diminishes the negative effects and to create a better quality RAC which is competitive to normal concrete. The main findings of the research are:

- Properties of aggregates
  - RCA-F aggregates consisted of 24% attached cement paste. A simple treatment method though can reduce the cement paste to 9%, producing aggregates with fewer amount of cement paste, rounder and more sound (RCA-T aggregates).
  - RCA had higher water absorption values, lower density and higher LA and soundness values. Treated recycled aggregates (RCA-T) showed great improvement in all of the tests that were performed, reaching or even surpassing the properties of natural aggregates.
- Replacement ratio of NA with RCA
  - Increasing the replacement ratio resulted in lower quality of concrete compared to normal concrete. Both mechanical and durability properties are negatively affected by the increase of the replacement ratio.
- Type of aggregates
  - RCA-F aggregates provided good quality concrete, taking into account the low quality of aggregates. RCA-T aggregates provided good quality concrete, competitive to control concrete.
  - Presoaking aggregates did not have any clear positive effect on mechanical properties of concrete and instead, a slight decrease in some of the durability properties was noticed.
- The combined effect of mineral admixtures (fly ash and silica fume) proved to be quite significant and improved substantially the durability properties. Especially the use of silica fume had a crucial impact on sorptivity and chloride permeability values. The mechanical properties were relatively the same, though a low early compressive strength was presented due to the delayed pozzolanic activity of fly ash.
- RAC were cheaper than NA resulting to a slightly cheaper concrete. A 50% replacement of NA with RCA-T produces a less expensive mixture with almost the same quality as "Control". In Cyprus, mineral admixtures are much more expensive than cement and their utilization resulted to a higher total cost.

## 6. Acknowledgement

The authors are grateful to Skyrra Vassas Ltd for providing the recycled concrete aggregates and to Vasiliko Cements Public Company Ltd for providing the OPC.

## 7. References

1. **Brundtland Commission.** *Report of the World Commission on Environment and Development.* s.l. : United Nations, 1987.
2. **Xiao, Jianzhuang, Wengui, Li, et al.** An overview of study on recycled aggregate concrete in China (1996-2011). *Construction and Building Materials.* 2012, 31, pp. 364-383.
3. **Mindness, Sidney, Young, Francis, et al.** *Concrete.* s.l. : Prentice Hall, 2003.
4. **Poon, C.S., Shui, Z.H. and Lam, L.** Effect of microstructure on compressive strength of concrete prepared with recycled aggregates. *Construction and Building Materials.* 2004, 18, pp. 461-468.
5. **Etxeberria, M., Vasquez E., et al.** Influence of amount of recycled coarse aggregates and production process on properties of recycled aggregate concrete. *Cement and Concrete Research.* 2007, 37, pp. 735-742.
6. **Corinaldesi, Valeria and Moriconi, Giacomo.** Influence of mineral additions on the performance of 100% recycled aggregate concrete. *Construction and Building Materials.* 2009, 23, pp. 2869-2876.
7. **Rao, Akash, Jha, Kumar N., et al.** Use of aggregates from recycled construction and demolition waste in concrete. *Resources Conservation & Recycling.* 2006.

8. **Thomas, C., Setien, J., et al.**, Durability of recycled aggregate concrete. *Construction and Building Materials*. 2013, 40, pp. 1054-1065.
9. **Tabsh, Sami W. and Abdelfatah, Akmal S.** Influence of recycled concrete aggregates on strength properties of concrete. *Construction and Building Materials*. 2009, Vol. 23, pp. 1163-1167.
10. **Rao, Chakradhara, Bhattacharya, S. K., et al.** Influence of field recycled coarse aggregate on properties of concrete. *Materials and Structures*. 2010.
11. **Kou, Shi-Cong and Poon, Chi-Sun.** Long-term mechanical and durability properties of recycled aggregate concrete prepared with the incorporation of fly ash. *Cement & Concrete Composites*. 2013, 37, pp. 12-19.
12. **Sanchez de Juan, Marta and Gutierrez, Pilar Alaejos.** Study on the influence of attached mortar content on the properties of recycled concrete aggregate. *Construction and Building Materials*. 2009, 23, pp. 872-877.
13. **Butler, L., West, J.S. et al.** The effect of recycled concrete aggregate properties on the bond strength between RCA concrete and steel reinforcement. *Cement and Concrete Research*. 2011, Vol. 41.
14. **Kanellopoulos, Antonios, Nicolaidis, Demetrios, et al.** Mechanical and durability properties of concretes containing recycled lime powder and recycled aggregates. *Construction and Building Materials*. 2014, Vol. 53.
15. **Matias, D., De Brito, J., et al.** Mechanical properties of concrete produced with recycled coarse aggregates - Influence of the use of superplasticizers. *Construction and Building Materials*. 2013, 44, pp. 101-109.



# Effects of Silane Impregnation on Drying Shrinkage of Cement-based Compounds

Pedram H. Mojarad<sup>1</sup> and Gary Boon<sup>2</sup>

<sup>1</sup> Product Manager, Sika Australia

<sup>2</sup> Technology Manager, Sika Australia

**Abstract:** Drying shrinkage can result in shrinkage cracking and durability issues. There are different types of shrinkage reducing/compensating admixtures or methods in concrete industry, which affect the drying shrinkage mechanism in different ways.

On the other hand, there are types of hydrophobic impregnation products in the market, e.g. silanes, siloxanes or their combinations which when applied on concrete surfaces, provide water repellency and bring about reduction of moisture ingress or any deleterious agents dissolved in water, and of course, enhance the durability of cement-based elements. The other aspect of silane impregnation on cement-based compounds is the reduction in capillary water absorption.

Current research project is studying the effect of silane impregnation, applied at early age, on the drying shrinkage of cement-based mortar specimens. Experimental tests have been carried out on sets of OPC mortars, of which some are treated with different silane combinations. Two types of silane products have been used, i.e. liquid and cream, and the specimens were stored in controlled drying environment.

Results illustrate that the application of silane impregnation reduced the amount of drying shrinkage of mortars. Further investigations has shown the shrinkage reduction mechanism was through the reduction of moisture loss through reduction of surface tension of pore water.

**Keywords:** Silanes, hydrophobic, capillary water, drying shrinkage, mortar.

## 1. Introduction

Drying shrinkage is the major contributor to total shrinkage of normal strength concrete [1]. Once mortar and concrete are exposed to dry environment, they begin to lose water and consequently shrink [2]. The loss of free water from large cavities present in paste microstructure may not result in tangible shrinkage; however, the loss of adsorbed water and water held in small capillary pores result in a reduction in disjoining pressure, which is considered to be the principal cause of drying shrinkage [3, 4].

Formation of cracks in cement-based materials can be due to tensile stresses originating from applied loads or different forms of shrinkage when the specimen is restrained. Once the cement-based material cracks, chemicals can enter and diffuse through the cementing matrix. Therefore, controlling shrinkage can bring about cracking control.

Shrinkage Reducing Admixtures (SRA) are one of the methods that are widely used in the concrete industry. The mechanism through which SRAs reduce the drying shrinkage is reduction of surface tension of capillary pores [5]. SRAs are used as admixtures into the concrete during mix.

Silane based products are now being increasingly used in construction jobs. The main reason of using hydrophobic impregnations on concrete and masonry surfaces is that they may bring about water repellency on the surface, which can result in immense reduction of water adsorption. This characteristic is claimed to be achieved by reducing the surface tension of concrete or masonry surface. There are reported literatures showing the influence of silanes (hydrophobic impregnation) on corrosion rate control of reinforced concrete [6, 7].

As defined by EN 1504-2 [8], hydrophobic impregnation is a treatment of concrete to produce a water-repellent surface. The pores and capillaries are internally coated and there is no film on the surface of the concrete. Hydrophobic impregnation products are mainly categorized based on their ability to penetrate into concrete, i.e. <10 mm or >10mm [8].

Different research studies have investigated the influence of silanes on concrete samples. Tittarelli and Moriconi [7] showed that silane can block the corrosion process in uncracked concrete specimens, whereas in cracked concrete specimens, corrosion of steel reinforcements was unexpectedly more severe in hydrophobic specimens rather than in non-treated ones. Using silane as water repellent agent was

found to improve the durability of recycled aggregate concrete [9]. In addition, positive effects of incorporating organosilanes in cementitious system, in regards to workability and strength were reported in research publications [10, 11]. However, limited information on how silanes influence concrete properties have been reported.

This article endeavors to examine the idea that whether reduction of surface tension of concrete surface using silane treatment on surface, can affect the drying shrinkage of concrete samples. This is done through drying shrinkage measurement of samples treated with surface applied commercially available silane products, and comparing them with control specimens.

## 2. Experiments

Two classes of silane molecules based products have been used in this research. Liquid silane contains 99% of active content and also cream-based technology with greater than 80% active content are the silanes used in this project.

Australian Standards were used in the experiments. Standard prismatic test specimens for drying shrinkage were utilized, based on test specifications in AS 2350-13 [12]. For the first 22–24 hours after mixing and casting, all specimens were stored in a moist environment where the relative humidity was more than 95% [13]. After demoulding, all shrinkage specimens were maintained inside a humidity-controlled (23 C and 50% relative humidity) cabinet, for the entire testing period [12].

### 2.1. Raw materials, hydrophobic impregnation treatment

A ready mixed cementitious grout/mortar, readily available in the market was used as cementitious samples in this research project. The cementitious mortar was a general purpose mortar with a drying shrinkage reported greater than of high performance ones. The reason for choosing this mortar was to use the most similar mix to the standard one defined in AS2350.11, in order to compare shrinkage more easily. Mortar was mixed based on manufacturer’s instruction.

Mixing, casting and all tests were carried out at  $22 \pm 1$  C and  $60 \pm 5$  %RH. In order to obtain comparable results for the evaluation of silane treatments, 12 sets (including control sets) were prepared under the same environmental ambient. **Table 1** tabulates the silane treatment regime on concrete samples. Preparation of mortar mixes was carried out in accordance with AS 2350.12 [14].

**Table 1. Specimen labelling, based on treatment regime**

Treatment regime	Silane treatment 2 h after demoulding and after initial measurements	Silane treatment 24 h after demoulding and after initial measurements	Silane treatment 72 h after demoulding and after initial measurements	No silane treatment
Liquid silane @ 150 g/m <sup>2</sup>	LSA-2h	LSA-24 h	LSA-72 h	Control 1
Liquid silane @ 300 g/m <sup>2</sup>	LSB-2h	LSB-24 h	LSB-72 h	Control 2
Cream silane @ 200 g/m <sup>2</sup>	CS-2h	CS-24 h	CS-72 h	Control 3

As shown in **Table 1**, two types of silanes have been used, i.e. liquid silane and cream silane, with active content of 99% and >80 %, respectively.

Liquid silane has been applied in two different consumption rate (based on manufacturer's recommendation), i.e. 150 and 300 g/m<sup>2</sup>. The cream type silane was only applied at a consumption rate, i.e. 200 g/m<sup>2</sup>. Both liquid and cream silanes have been applied by brush onto concrete surfaces, following the treatment regime. As tabulated above, for each set of testing: 1- silane has been applied, only 2h after demoulding, 2- 24 h after demoulding and in the third sets, 3- 72h after demoulding. All Control specimens were left without any silane treatments.

In order to have consistency over all mixes, LSA (set of samples treated with liquid silane at 150 g/m<sup>2</sup>) and LSB (another set with liquid silane at 300 g/m<sup>2</sup>) samples were all mixed in one batch. CS (cream silane treated at 200 g/m<sup>2</sup>) specimens were mixed in a separate batch.

## 2.2. Shrinkage measurement and physical properties

Immediately after demoulding, all specimens were measured for initial length to the nearest 0.001 mm, using a length comparator and stored in a humidity controlled cabinet at a temperature of 23 ±1C and a relative humidity of not less than 50%. Subsequent measurements were after 2, 3, 7, 28 and 56 days of casting. The drying shrinkage was calculated by  $\Delta L/L$ , where  $\Delta L$  is the difference between the initial length measurement taken immediately after demoulding, and the length reading at the particular age, and L is the original length of the sample at initial stage and defined in AS2350.13.

Mass changes of specimens were also monitored in this research, in order to figure out any possible shrinkage reduction mechanism.

## 3. Test results

Results of subsequent shrinkage measurements have been reported in Figures 1-3.

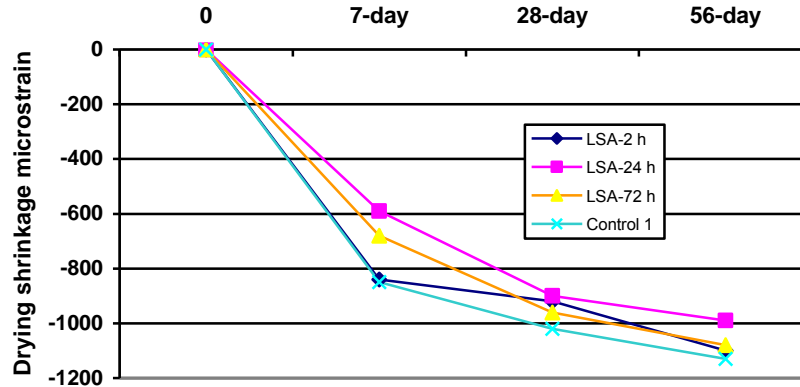


Figure 1. Shrinkage measurement of liquid silane treatment @ 150 g/m<sup>2</sup>

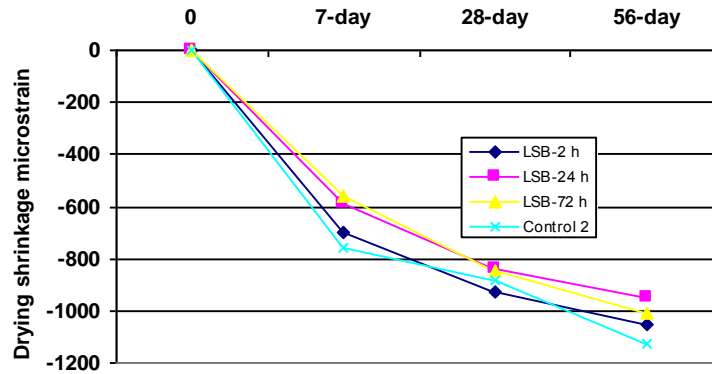


Figure 2. Shrinkage measurement of liquid silane treatment @ 300 g/m<sup>2</sup>

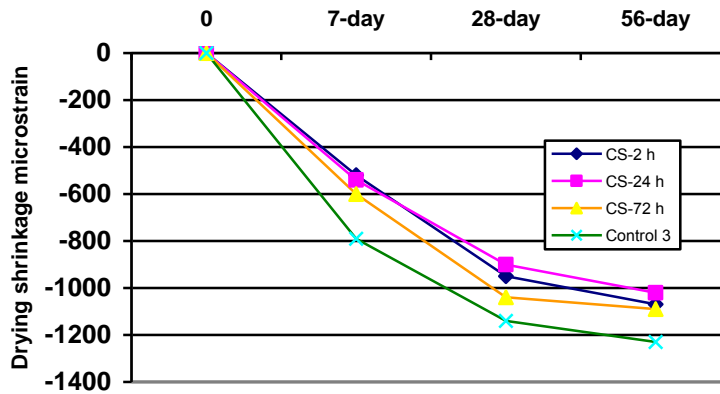


Figure 3. Shrinkage measurement of cream silane treatment @ 200 g/m<sup>2</sup>

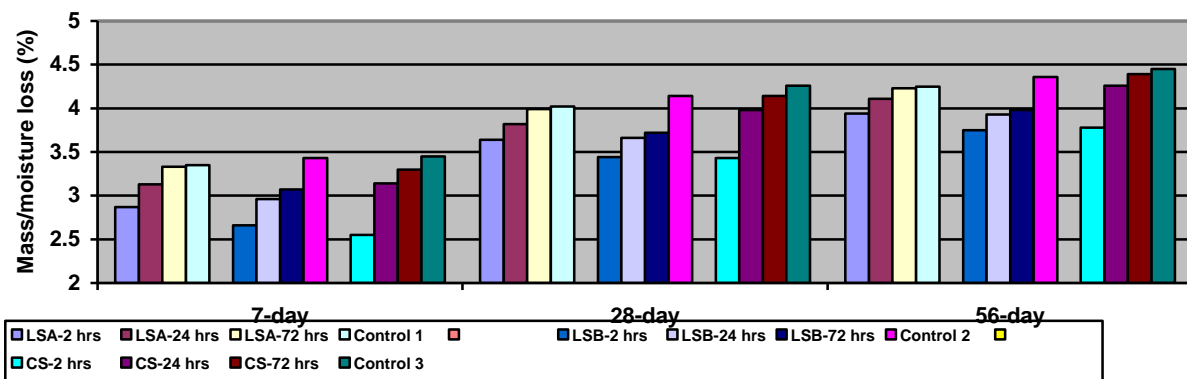


Figure 4. Mass change (%) of sample with and without silane treatment

#### 4. Discussion and conclusions

Figures 1-3 display reduction of shrinkage at 28 and 56 days in samples treated with silanes. Silane treatment on existing concrete and cementitious specimens has clearly demonstrated trend of reduction in drying shrinkage of mortar specimens. However, different results were obtained as a function of different consumption rate and type of silanes. In addition, a direct relationship between shrinkage reduction and specimen moisture loss indicating, the lower the moisture loss, the less the drying shrinkage, was observed for each mix.

In terms of drying shrinkage, those samples which were treated with silane 24 h after demoulding show lower shrinkage than those which were treated 2h and 72 h after. The effect of treating 2h after demoulding and 72h after demoulding were very similar.

In these samples and under these conditions, 24hr treatment seems to be the optimum in regards to shrinkage reduction. This might be due to appearance of cracks which may result in deeper penetration of silane into concrete specimens.

The mechanism proposed for shrinkage reduction using silane treatment can possibly be the interruption of moisture transfer from the capillary structures in the mortar due to the presence of hydrophobic molecules near the concrete surface, which results in decrease in water transfer from inner layers and pores of matrix to the surface and consequently decreasing moisture loss of sample. Figure 4 supports this mechanism, since the changes in mass of mixes with silane treatment were less than of that in control samples.

Hydrophobic impregnation is now widely used as concrete protection system on new and existing concrete structures. These findings support extra advantages of using these systems on concrete, specifically at early stages (onset of cracking in concrete). Therefore, when applied properly and with the correct consumption rate, not only do hydrophobic impregnation protect the concrete surface against the ingress of water soluble aggressive ions, but also may bring about shrinkage reduction mechanisms which will mean less cracking of concrete.

A new shrinkage reduction method was introduced and assessed in this project. The highest reduction belonged to 300 g/m<sup>2</sup> of liquid silane, then 200 g/m<sup>2</sup> of cream silane and finally to 150 g/m<sup>2</sup> of liquid silane, all treated after 2 h of demoulding. Thus, this can be concluded that the consumption rate also does have a direct effect on shrinkage reduction of concrete specimens as well as the time of application.

#### 5. References

1. Lamond, J.F. and J.H. Pielert, *Significance of tests and properties of concrete and concrete-making materials*. Vol. 169. 2006: ASTM International.
2. Kovler, K. and S. Zhutovsky, *Overview and future trends of shrinkage research*. Materials and Structures, 2006. **39**(9): p. 827-847.
3. Mehta, P.K., P.J. Monteiro, and M.-H. Education, *Concrete: microstructure, properties, and materials*. Vol. 3. 2006: McGraw-Hill New York.
4. Bentur, A. and S. Mindess, *Fibre reinforced cementitious composites*. 2006: CRC Press.
5. Hamedanimojarrad, P., *Development of High Performance Shrinkage Resistant Concrete, Using Novel Shrinkage Compensating Admixtures*, 2012, University of Technology, Sydney.
6. Holmes, N., R. O'Brien, and P. Basheer, *Engineering performance of a new siloxane-based corrosion inhibitor*. Materials and Structures, 2014. **47**(9): p. 1531-1543.
7. Tittarelli, F. and G. Moriconi, *The effect of silane-based hydrophobic admixture on corrosion of reinforcing steel in concrete*. Cement and Concrete Research, 2008. **38**(11): p. 1354-1357.

8. Standard, B., *Products and systems for the protection and repair of concrete structures — Definitions, requirements, quality control and evaluation of conformity — Part 2: Surface protection systems for concrete BS EN 1504-2*, 2004.
9. Zhu, Y.-G., et al., *Influence of silane-based water repellent on the durability properties of recycled aggregate concrete*. *Cement and Concrete Composites*, 2013. **35**(1): p. 32-38.
10. Itul, A., *Interactions entre organo-silanes et ciment*, 2012, Citeseer.
11. Felekoğlu, B., *A method for improving the early strength of pumice concrete blocks by using alkyl alkoxy silane (AAS)*. *Construction and Building Materials*, 2012. **28**(1): p. 305-310.
12. Australia, S., *Methods of testing portland, blended and masonry cements Method 13: Determination of drying shrinkage of cement mortars; AS 2350.13*, 2006.
13. Neville, A.M., *Properties of concrete*. 1981.
14. Australia, S., *Methods of testing portland, blended and masonry cements Method 12: Preparation of a standard mortar and moulding of specimens, AS 2350.12*, 2006.

# Fresh Property and Matrix Distribution for Amorphous Steel Fiber Reinforced Concrete

Byoungil Kim<sup>1</sup> and Sea Hyun Lee<sup>1</sup>

<sup>1</sup>Korea Institute of Civil Engineering & Building Technology/Building & Urban Research Institute

**Abstract:** The research was conducted to analyze workability and fiber distributions of amorphous steel fiber reinforced concrete by changing fiber length and fiber addition ratio. The inverted slump cone and vebe tests as well as slump test was performed to understand the fluidity of amorphous steel fibers which have quite different appearance compared to conventional steel fibers. Test results showed that thin plate type of amorphous steel fibers required different test approach to figure out workability since the reduction of workability from slump test was different that from inverted slump cone and vebe tests. In conclusion, fluidity of amorphous steel fibers reinforced concrete was significantly degraded as fiber length and addition ratio increase. Also, fibers spacing in cement matrix was apparently reduced as the increase of fiber length and addition ratios without fiber balling.

**Keywords:** Amorphous steel fiber, Fiber addition ratio, Workability, Fiber distribution, Compressive strength

## 1. Introduction

As the buildings in Korea become taller and larger, the types of admixture added to concrete are also becoming diverse. As the demand for high performance construction material rapidly increased, heavy investment and study on development of high performance cement and concrete composite material by adding the fiber type material are ongoing. Generally, PP, steel, PVA or nylon fibers are added to cement and concrete to distribute the stress generated inside the structure by the pullout mechanism to the homogeneously dispersed fibers in order to reinforce the initial crack control and ductility after bending failure. The crack control mechanism depends on the diameter, thickness, length, tensile strength, mixing ratio, etc. of the fiber. Higher mixing ratio of fibers homogeneously dispersed in the cement matrix particularly is known to not only reinforce the strength but also greatly increase the crack control and energy absorption capability after the flexural behaviors. The leading super-high performance cement-concrete composite materials with fiber content include UHPC (ultra-high performance concrete) and ECC (engineered cementitious composite).

UHPC is the fiber reinforced cement composite with the compression strength of 150 MPa or more and design basis splitting tensile strength of 5 MPa or more. UHPC is the pozzolan type admixture consisting of Portland cement, silica fume or blast-furnace slag fine particles; filling material having aggregates with diameter of 0.5mm or less and SiO<sub>2</sub> content of 90% or more; and other admixture. It has the water-binding material ratio of 0.24 or less and tensile strength of 2,000MPa or more and is mixed with reinforced fibers with diameter of 0.2~0.25mm and length of 10~20mm for 2% or more of total volume<sup>6)</sup>. ECC is the cementitious composite having the pseudo strain hardening and multiple crack properties to show increasing stress as the strain rate increases without degradation of strength even after the cracks are generated under the bending moment or direct stress. Added with organic fiber such as the micron polyethylene (PE) fiber and vinyl (PVA) fiber or the steel fiber, it has 4~8% deformation capacity. The materials included the cement, admixture, fine aggregates, and additives (high performance water reducing agent and viscosity agent).

Unlike the conventional steel fiber requiring the complex and long manufacturing process, the amorphous steel fiber used in this study is rapidly cooled in the plate shape to omit the process after melting and thus the energy consumption is reduced and CO<sub>2</sub> is reduced because there is not carbon removal process. As such, it can be used as the eco-friendly construction material. The amorphous Fe used in the experiment had the tensile strength of 1400~1700 MPa and flexible straight type. Compared to conventional hook type steel fiber, it is easier to process and more durable because of corrosion resistance. The fiber was reinforced to the concrete to experimentally study the fiber dispersion by deducing the workability evaluation method and optimum mixing as well as observing the micro structure according to the change of fiber length and mixing ratio.

## 2. Experimental Plan

### 2.1 Experimental Materials

This study used the class 1 conventional Portland cement and the standard sand with specific gravity of 1.54 and fineness

modulus of 2.8 as the fine aggregates. For the coarse aggregates, the grinded aggregates with maximum size of 19mm and specific gravity of 2.72 were used. The steel fiber used in the experiment is the amorphous steel fiber manufactured by a foreign manufacturer and had the lengths of 10mm, 20mm and 30mm, width of 1.3mm and thickness of 35 $\mu$ m. The amorphous steel fiber is a thin plate type manufactured by rapidly cooling the molten steel so that the nuclei of the generated crystals are not grown to freeze the liquid structure. The specific gravity is 7.2 which is slightly lower than the specific gravity of conventional steel fiber of 7.8, and the apparent volume is much large.

## 2.2 Mixing Design

Fig. 1 shows the research flow to deduce the optimum mixing design to ensure the flowability and dispersibility with the length and mixing ratio as the variables. To ensure the appropriate flowability and homogeneous dispersion of fibers by mixing the amorphous steel fiber, documents related to concrete mixing design here and abroad were surveyed to select the materials (fibers, aggregates and mixing materials) for optimum mixing of amorphous steel fiber. The concrete mixing such as the high performance fiber reinforced concrete (HPFRC), ECC and UHPC, which adds 2% or more fibers to maximize the dynamic property of fibers in the cement matrix and reinforce the tensile strength, flexural strength and flexural toughness in order to reduce the crack and prevent its spread, were considered.

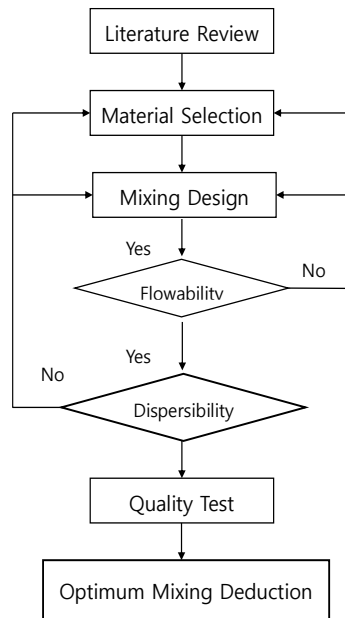


Figure 1. Research flow for optimized mix design

In the reference mixing experiment before the actual mixing, the mixing design factors required for optimum mixing of amorphous steel fiber was studied with the preliminary experiment of W/C ratio, fine aggregate ratio, maximum aggregate size, water reducing agent, viscosity agent and air-entraining agent, and then the flowability and dispersibility experiments were conducted. Lastly, the inverted slump and Vebe tests specific to the high mix amorphous steel fiber were conducted to deduce the optimum mixing for the fiber length and mixing rate to complete the mixing design for quality test of fiber reinforced concrete.

Table 1 shows the mixing design of amorphous steel fiber with length of 10 mm and 20 mm and mixing ratio of 0.2%, 0.4% and 0.6%. The water-cement ratio of 0.45 was selected to maintain the conventional concrete strength. For each fiber length, 0.2%~0.6% fibers to total volume were added. Generally, fiber lumping in the fiber reinforced concrete can be mainly divided into three types. First, lumping of fibers occur due to the difference of the aspect ratio (ratio of length and diameter) of fiber and particles such as the cement and sand when a large volume of fibers is added. Second, it is because of greatly different specific gravities of fiber and concrete materials. The typical fiber gravity of 7.8 is different from that of cement (3.15) or sand (2.5), and thus they are separated from each other during mixing, and the materials of similar specific gravity tend to lump together. Last, lumping of fiber occurs during the compaction work to fill the concrete in the concrete form after mixing. The widely used rod vibrator uses an internal vibrator to fill the concrete in the every corner of the concrete form. After the vibrator is used for a long period, the fibers tend to be compacted in a direction due to the vibration and the effect of adding the fibers decreases. When the compaction is excessive, the steel fibers with high specific gravity settle below and the organic fibers with low specific gravity rise above, and that causes the reinforcing effect of fibers greatly.

In the conventional fiber mixing, if the small amount of fibers is added, it is considered as the additive and the volume change is disregarded in mixing design. If a large amount of fibers is added, it is considered as the mixing material and the volume of aggregate is lowered by the apparent volume of fibers to ensure the fiber dispersibility. To minimize the effect, this study added



the high performance water reducing agent and cellulose viscosity agent to minimize the decrease of flowability due to addition of large amount of fibers. The apparent volume of relatively larger amorphous steel fiber is substituted by the volume of aggregates and deducted. Then the fine aggregates in the same amount as the deducted volume is added to maintain the specific level of granular materials and flowability appropriate to the work.

**Table 1. Mix design**

Symbols	G <sub>max</sub> (mm)	Slump (mm)	Air Content (%)	W/B	S/a (%)	Unit weight (kg/m <sup>3</sup> )						
						W	C	S	G	F (%)	SP (C*%)	VMA (C*%)
OPC	19	230	4.5	0.45	55	175	390	568	822	-	0.4	-
AF-10-0.2	19	240	5.5	0.45	56	175	390	576	803	0.2	0.6	-
AF-10-0.4	19	200	6.0	0.45	57	175	390	585	783	0.4	0.8	0.03
AF-10-0.6	19	180	6.3	0.45	58	175	390	593	763	0.6	1.5	0.03
AF-20-0.2	19	210	4.0	0.45	56	175	390	576	803	0.2	0.6	-
AF-20-0.4	19	200	6.5	0.45	57	175	390	585	783	0.4	1.0	0.03
AF-20-0.6	19	130	4.5	0.45	58	175	390	593	763	0.6	2.0	0.03

The forced twin shaft mixer was used to mix the concrete. The fine aggregates and coarse aggregates were poured first and dry mixed for one minute. Then the cement was added and mixed for one minute. The minimum amount of high performance water reducing agent and viscosity agent diluted in water was added to complete mixing. After the mixing, the slump, air content, inverted slump and Vebe time were measured to study the unhardened concrete property. Moreover, to study the dynamic property of hardened fiber reinforced concrete, the unhardened concrete was poured into the compression strength test piece specimen, and the test sample was initially cured indoor with  $23 \pm 2^\circ\text{C}$  temperature and  $50 \pm 2\%$  relative humidity for 24 hours. The concrete was removed from the specimen and cured in a wet curing room with 100% relative humidity for 28 days. Then the compression strength and flexural strength tests were conducted.

### 3. Experiment Method

#### 3.1 Properties of fresh concrete

When the fibers are added to the concrete, the flowability generally deteriorates because of increased stiffening during the mixing. The workability can be improved when the water reducing agent is added or mixing design is changed. However, to accurately measure the workability of fiber reinforced concrete, an approach different from the slump test used for the conventional concrete is needed. That is because the loss of slump and loss of workability when the fibers are added do not exactly match. This experiment observed the effect of change of flowability of each fiber and its correlation with slump test through the slump test, which is the typical workability measurement method, and inverted slump cone test and Vebe test which are the plasticity characteristics test methods.

The inverted slump time was developed for simple field test to measure the workability of fiber reinforced concrete at low cost. Although the fiber reinforced concrete can show the improved workability, each fiber has the role of increasing thixotropy (a phenomenon of decreasing viscosity when the liquid is subject to shear stress such as agitation and increasing velocity when the shear stress is stopped). The study that showed the slight decreased slump in the mix of PP reinforced fiber and increased workability in the compacting factor test highlights that more accurate workability evaluation is needed<sup>2)</sup>. Moreover, many steel fiber and synthetic fiber manufacturers report that the general slump test is not suitable to evaluate the workability of fiber reinforced concrete and recommend the flowability evaluation by inverted slump test using the vibration to accurately evaluate the workability of fiber reinforced concrete. The test apparatus such as the vibrator, slump cone, bucket and stopwatch can be easily obtained in the field. To maintain the unification of the slump cone and bucket during the vibration, the slump cone is fixed with a wooden frame and the bucket is inserted at the top. In this study, the slump cone was fixed upside down with a wooden frame and placed at the top of the bucket so that there was around 10cm gap between the bucket bottom and inverted slump cone. The inverted slump cone was filled with the concrete in three steps, and the stopwatch was pressed as soon as the bottom plate began vibrating and the time until the inverted slump cone was completely removed of concrete was measured to evaluate the flowability and consistency of the fiber reinforced concrete. As the workability and flowability of the concrete significantly decreased due to the fiber, the bottom hole of the slump cone was instantly plugged, and the fiber reinforced concrete did not naturally flow.

The Vebe consistometer (BS 1881-104) is a tool to measure the remolding ability of the very dry concrete. It measures the energy required for the concrete collapsed by vibration to be remolded. A metal cylindrical vessel is placed on a vibrating table to induce the sinusoidal vibration, and the slump cone is placed at the center of the cylinder. Like the standard slump test, the slump cone is filled with concrete in three steps and then a plastic disk is placed at the top. The time until the concrete is completely collapsed by falling disk is measured. The purpose of Vebe test is to measure the consistency of the very dry concrete. For this

experiment, a slump cone was placed on top of a vibrating table and filled with concrete in three steps. Then the slump cone was removed, and the plastic plate on top was placed in contact with the concrete surface. Then the timer is pressed as soon as the vibration begins, and the time till the slump is completely collapsed is measured.

### 3.1 Compressive Strength Test

To evaluate the impact of fiber reinforcement in the cement matrix according to the amorphous steel fiber amount (0.2%, 0.4% or 0.6% ) and length (10 mm or 20 mm) change, the compression strength of 28-day wet cured cylindrical test piece specimen with 10 mm diameter and 200 mm height was measured using UTM with 2,000 kN capacity.

### 3.2 Secondary electron microscope

For dispersibility of fiber according to the change of length and mixing ratio of amorphous steel fiber, the microstructure of the fiber was observed using a scanning electron microscope (SEM) to compare the dispersion of fibers in the cement matrix, bonding of fiber on the interface, and directional nature of fibers. The magnification of SEM was set to 60~80 times and the spaces between the fibers were measured to evaluate the dispersibility of the fibers at each length (10 or 20 mm) and mixing ratio (0.2, 0.4 or 0.6%).

## 4. Experiment Result

### 4.1 Slump

Table 1 shows the change of workability according to the change of amorphous steel fiber length and mixing ratio. When the fiber length was 10 mm, there was not much change of workability in comparison with OPC when the mixing ratio increased from 0.2% to 0.4%. In the case of 20 mm fiber length, the slump had the relatively smaller value than 10 mm, and the slump value reached 130 mm at 0.6% mixing ratio. In conclusion, the viscosity and flowability decreased as the fiber length and mixing ratio increased. The decrease of workability was the largest at 0.6% mixing ratio.

### 4.2 Inverted slump cone time

Fig. 1 shows the result of inverted slump test at different fiber mixing ratios and lengths. In the case of OPC mixing, the inverted slump time was 5 seconds. The very short inverted slump time is attributed to relatively large flowability. At 10 mm fiber length and 0.2% mixing rate, the inverted slump time increased by around 60% from OPC although the slump value was higher than OPC. In the case of 0.4% mixing ratio, the change of slump value was around 30 mm, or around 13% decrease, but the inverted slump time changed by 320%. As such, the workability decreased much larger than the slump. In the case of 0.6% mixing ratio, the decrease of workability due to the increased inverted slump time greatly increased. For the change of workability at the fiber length of 20 mm at mixing ratio of 0.2%, the inverted slump time increased by 23 seconds for the slump value decrease, indicating much greater decrease than the workability decrease by OPC slump decrease. In the case of 0.4% mixing ratio, the workability decrease was slightly larger than 0.2% mixing ratio, but the concrete flowability greatly decreased by sharp increase of inverted slump time in the case of 0.6% mixing ratio.

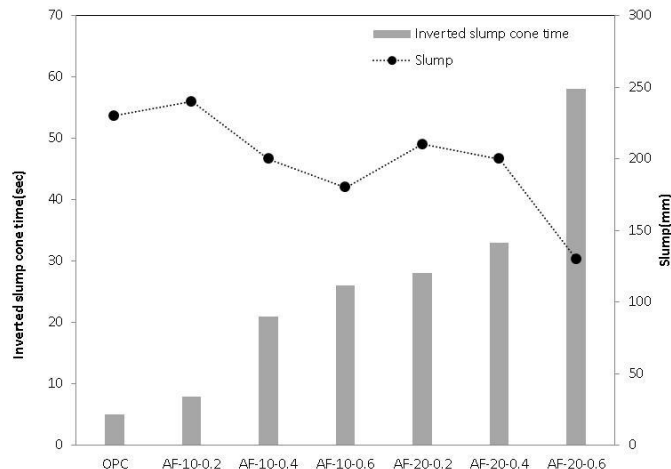


Figure 1. Inverted slump cone time vs. slump

### 4.3 Vebe time

Fig. 2 shows the Vebe time at different fiber mixing ratios and lengths. In the case of OPC mixing, the Vebe time was 1.3 seconds. The very short time was attributed to relatively larger flowability. For the workability change at the fiber length of 10 mm, there was little change of Vebe time at 0.2% mixing ratio, then the Vebe time increase twice at 0.4% mixing ratio. At the 0.6% mixing ratio, the Vebe time greatly increased. For the workability change at the fiber length of 20 mm, the rate of flowability decrease by increased Vebe time was around 10 larger than change of workability when the slump decreased by 20 mm compared to OPC slump of 230 mm at the 0.2% fiber mixing ratio. In the case of 0.4% fiber mixing ratio, the result was similar to the 0.2% mixing ratio, and the workability slightly increase. In the case of fiber mixing ratio of 0.6%, the Vebe time by decreased slump greatly increased, and the change of workability was even greater.

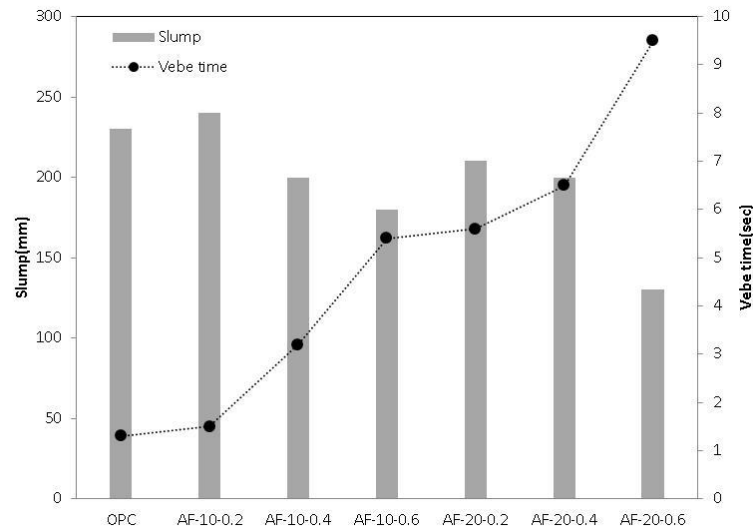


Figure 2. Vebe time vs. slump

### 4.4 Compressive strength

Table 2 summarizes the result of compressive strength test with the amorphous steel fiber reinforced cement. Generally, the fiber is mostly used to defer the crack by reinforcing the flexural strength and flexural toughness rather than increasing the compressive strength. The analysis of compressive strength test conducted in this study shows much clear increase of compressive strength than less than 10% change in conventional test. In the case of 10 mm fiber length, the compressive strength increased by around 30% by reinforcing with the fiber regardless of mixing ratio. In the case of 20 mm fiber length, the increase was more than 30%. In conclusion, the increase of compressive strength by fiber reinforcement was clear, and the best result was at the fiber lengths of 20 mm.

Table 2. Test results of compressive strength


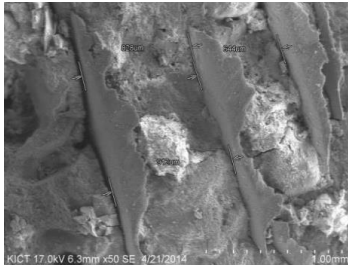
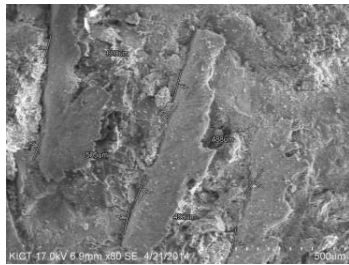
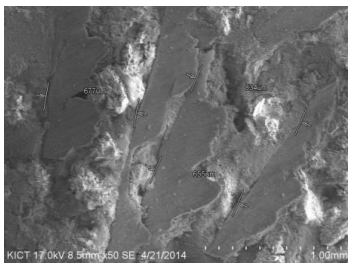
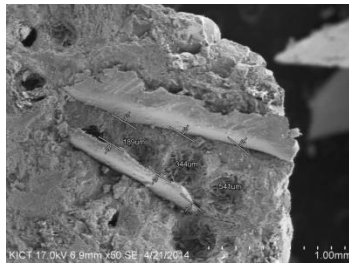
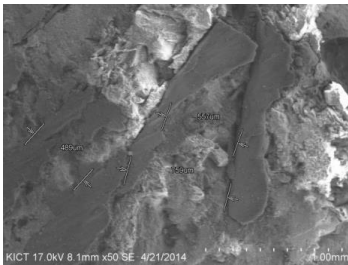
Symbols	Compressive Strength(Mpa)			
	1	2	3	Ave
OPC	34.14	34.05	33.31	33.84
AF-10-0.2	41.05	43.01	42.18	42.08
AF-10-0.4	43.5	41.47	42.26	42.41
AF-10-0.6	42.6	40.78	43.33	42.24
AF-20-0.2	42.12	42.12	42.97	42.4
AF-20-0.4	48.63	45.86	46.89	47.13
AF-20-0.6	43.5	42.95	44.44	43.63

### 4.4 Secondary electron microscope

Table 3 summarizes the SEM observation of micro structure and dispersibility of amorphous steel fibers. In the case of 10 mm fiber length, the spaces between fibers were 816~895  $\mu\text{m}$ (0.2%), 488~628  $\mu\text{m}$ (0.4%), and 189~541  $\mu\text{m}$ (0.6%) indicating that the space between fibers decreased as fiber mixing ratio increased. The fibers were uniformly dispersed with no lumping because of overall stable bonding with cement matrix.

In the case of 20 mm fiber length, the spaces between fibers were 644~912  $\mu\text{m}$ (0.2%), 655~834  $\mu\text{m}$ (0.4%) and 489~759  $\mu\text{m}$ (0.6%) indicating that the space between fibers decreased as fiber mixing ratio increased. Like the case of 10 mm fiber length, the fibers were uniformly dispersed with no lumping because of overall stable bonding with cement matrix. In conclusion, the space between fibers tended to decrease as the fiber length increased and mixing ratio increased. There was not much ununiform dispersion of fibers by fiber lumping regardless of length and mixing ratio.

**Table 3. Microstructure of amorphous steel fibers in concrete matrix**

Fiber content rate	10mm	20mm
0.2%		
0.4%		
0.6%		

## 5. Conclusion

This study compared the result of effective experimental evaluation of flowability and workability of concrete reinforced with amorphous steel fiber, which has benefit of CO<sub>2</sub> reduction and cost saving from simplified manufacturing process, with the fiber length and mixing ratio as the variables. It also conducted the basic research experiment to check if it can be used as the future construction material based on the dynamic characteristics.

- The flowability and workability evaluations through the slump test showed very different result from the Vebe test and inverted slump test.
- Although the Vebe test and inverted slump test showed similar change workability of amorphous steel fiber reinforced concrete to change of fiber length and mixing ratio, the inverted slump test showed clearer change of viscosity to change of mixing ratio.
- Adding the amorphous steel fiber increased the compressive strength by 20~30% in all mixing ratios. The increase of compressive strength was clearer in fiber length of 20 mm.
- Observation of micro structure of fibers using SEM indicated that the space between fibers decreased as the fiber length increased and fiber mixing ratio increased. Generally, the dispersibility of the fibers were excellent, and the bonding structure with cement matrix was stable also.

- e. It is considered that it is more effective to test the flowability and quality with inverted slump test than the conventional slump test to evaluate flowability change from addition of amorphous steel fiber.

### **Acknowledgement**

This research was supported by a grant(20150116-001-01-Seed) from Ministry of Science, ICT and Future Planning

### **6. References**

1. Yang, K.H. : Slump and Mechanical Properties of Hybrid Steel-PVA Fiber Reinforced Concrete, Journal of the Korea Concrete Institute, Vol. 22, No. 5, pp. 651 ~ 658 (2010)
2. ACI Committee 544 : Fiber Reinforced Concrete, ACI Special Publication SP-81, American Concrete Institute (1984)
3. Shah, S. P., Ludirdja, D., Daniel, J. I., and Mobasher, B. : Toughness-Durability of Glass Fiber Reinforced Concrete System, ACI Materials Journal, Vol. 85, No. 5, pp. 352 ~ 360 (1988)
4. Johnston, C. D. : Steel Fibre Reinforced Mortar and concrete-A Review of Mechanical Properties, Fiber Reinforced Concrete, SP-44, ACI, pp. 127 ~ 142 (1974)
5. Cha, S. W., Kim, K. H., Kim, S. W., Park, J. J., and Bae, S. G. : Models for hydration Heat Development and Mechanical Properties of Ultra High Performance Concrete, Journal of the Korea Concrete Institute, Vol. 22, No. 3, pp. 389 ~ 397 (2010)
6. Kang, S. T., and Ryu, G. S. : The Effect of Steel-Fiber Contents on the Compressive Stress-Strain Relation of Ultra High Performance Cementitious Composites (UHPC), Journal of the Korea Concrete Institute, Vol. 23, No. 1, pp. 67 ~ 75 (2011)
7. Jang, Y. I., Park, S. B., and Lee, B. J. : An Experimental Study on the Mechanical Properties of Ultra-High Strength Steel Fiber Reinforced Mortar Using Composite Slag Fine Aggregate, Journal of Korea Society of Waste Management, Vol. 27, No. 3, pp. 204 ~ 211 (2010)
8. Kim, Y. Y., Kim, J. S., Kim, H. S., Ha, G. J., and Kim, J. K. : Mechanical Properties of an ECC(Engineered Cementitious Composite) Designed Based on Micromechanical Principle, Journal of the Korea Concrete Institute, Vol. 17, No. 5, pp. 709 ~ 716 (2005)
9. Kim, Y. Y. : Mechanical and Repair Performance of Sprayed Ductile Fiber Reinforced Cementitious Composite(ECC), Journal of the Korea Concrete Institute, Vol. 15, No. 3, pp. 462 ~ 469 (2003)
10. Mindess, S., Young, J. F., and Darwin, D. : Concrete, Prentice Hall, pp. 599 ~ 617 (2003)
11. ASTM C 995 : Standard Test Methods for Time of Flow of Fiber-Reinforced Concrete through Inverted Slump Cone, Annual Book of ASTM Standards, (2004)
12. BS 1881-104 : Testing concrete. Method for determination of vebe time, British Standards Institution, (2004)
13. Kim, B. : Transport Coefficients and Effect of Corrosion Resistance for SFRC, Journal of the Korea Concrete Institute, Vol. 22, No. 6, pp. 867 ~ 873 (2010)

# Application of FRP Composite to Self-anchored Cable-stayed Bridge for Emergency Disaster Relief

Fang-Yao Yeh<sup>1</sup>, Kuo-Chun Chang<sup>2</sup>, Yu-Chi Sung<sup>3</sup>, Hsiao-Hui Hung<sup>1</sup>

<sup>1</sup>Research Fellow, National Center for Research on Earthquake Engineering (NCREE)

<sup>2</sup>Professor of Civil Engineering, National Taiwan University (NTU)

<sup>3</sup>Professor of Civil Engineering, National Taipei University of Technology (NTUT)

**Abstract:** Owing to recent extreme climates, typhoons, floods, and earthquakes have become large natural disaster threats in Taiwan over the years. Such natural disasters have caused damage to some bridges, consequently isolating residential communities located on mountains, and hampering the ability to delivery emergency relief supplies to those communities. In order to provide quick emergency relief, the simple construction of a temporary bridge becomes critical for the transportation of food and medical supplies into the emergency disaster areas. While composite materials for footbridges and vehicular traffic applications have been widely used overseas, they are not suitable for disaster relief applications. The objective of this paper is to present a novel bridge structure for a portable, reusable, and lightweight bridge. This paper focuses on the design concept and experimental verification of a temporary composite bridge for disaster relief. Ultimately, it advocates composite bridges for disaster relief applications.

**Keywords:** composite emergency bridge, cable-stayed composite bridge, lightweight, portable, reusable bridge.

## 1. Introduction

Owing to resented extreme climates, typhoons, floods, and earthquakes have become the large natural disaster threats in Taiwan over the years. For instance, 88 floods were caused by Typhoon Morakot in 2009, causing damage to more than 200 bridges and washing away more than 100 bridges (Fig. 1a). Chi-Chi Earthquake in 1999 also caused damage to more than 150 bridges (Fig. 1b), resulting in isolated mountain communities to which emergency relief supplies could not be easily delivered.

Advanced composite materials have found expanded use in the aerospace, marine, and automobile industries during the past few years due to favorable engineering properties such as high specific strength and stiffness, lower density, high fatigue endurance, and high damping. The advantages of fiber reinforced polymer (FRP) composites make them attractive for use in replacement decks or in new bridge systems, such as (1) bridge decks, including FRP rebar reinforced concrete deck systems, FRP grid and grating reinforced concrete deck systems, deck systems made completely from FRP composites, and hybrid FRP plate reinforced concrete deck systems; (2) FRP composite bridge girders and beams, including glass fiber reinforced polymer (GFRP) composite girders, carbon fiber reinforced polymer (CFRP) composite girders, and hybrid girders; and (3) slab-on-girder bridge systems [1].



(a) Morakot Typhoon



(b) Chi-Chi Earthquake.

**Figure 1. Damage of a bridge and disaster rescue.**

FRP bridge technology has progressed rapidly from laboratory prototypes to actual demonstration projects in this field. It is noteworthy that the world's first pedestrian bridge constructed entirely of FRP composites dates back to 1972, and is a single span (span length of 24 m and a width of 1.8 m) bridge in Tel Aviv, Israel, with a total weight of 2.5 tons of GFRP [2]. The world's first vehicle bridge, Miyun Traffic Bridge, constructed entirely of FRP dates back to 1982, and is a single span (span length of 20.7 m), two-lane (width of 9.2 m) bridge in Beijing, China with GFRP girders made from a hand lay-up process [3]. The bridge was constructed by approximately 20 workers within two weeks assisted only

by a light gin pole and capstan winches. Furthermore, the world's first cable-stayed bridge, the 133 m Aberfeldy Foot-Bridge located in Scotland, is built entirely from composites (GFRP for the super-structure and aramid fiber for the cables) [1].

A movable temporary bridge that is foldable, stretchable, and made with aluminum was designed by using stress base optimization methods [4]. The prototype bridge with a length of 1 m after folding and a maximum length of 5.2 m after extending could bear the weight of three adults. The operating procedure is very simple; only one person is required to complete the assembly of the whole bridge within two minutes. Meanwhile, a new type of scrolling lightweight arched bridge is being researched in the US [5]. The prototype model has a length of 3 m and a width of 0.25 m. The bridge consists of a motor and a cable reel to control the entire retracting, stretching, and recovery. The advantage of a temporary bridge is that only one reel motor is required for the complete assembly of the bridge. A deployable lightweight bridge for transport facility and reduced assembling and erection time used of GFRP pipe and steel adapter for combination of truss bridges, and placed in pre-strength steel cable into GFRP tube to increase the stiffness of the bridge [6]. The current experimental test body is 13 m long, and its advantages over the assembly process without the use of any of the co-bolt assembly steps can be reduced, assembly parts and greatly reduced assembly time.

Nowadays, FRP composites are used mostly in deck systems, footbridges, and vehicle bridges. This paper focuses on the advantages of FRP composites in applications for typhoon, flood, and earthquake disaster rescue in Taiwan. The objective of this paper is to present a novel bridge structure for a portable, reusable, and lightweight bridge. It also focuses on the design concept and experimental verification of a temporary composite bridge for disaster relief and promotes composite bridges for disaster relief applications.

## **2. Concept of a temporary bridge for emergency disaster relief**

### **2.1 Conceptual design of temporary bridge**

In order to design a lightweight bridge that is portable, reusable, and suitable for transportation, the following design requirements are considered: (1) for disaster relief and transportation of goods, the design goals for the temporary bridge are set to a span length of 20 m, a width of 3 m, a live load of 5 tons (for transportation of rescue goods by a truck weighing 3.5 tons), and a deflection-to-span ratio of  $L/400$  (the design goal may be modified by the actual requirement of a disaster region); (2) for satisfying the lightweight requirement, the advantages of composite materials are used for the temporary bridge; and (3) for the short to medium span bridge, a beam-type or truss-type bridge is considered; meanwhile, for the medium to long span bridge, a cable-stayed bridge or suspension bridge is considered.

### **2.2 The major challenges of composite bridges**

The report "FRP bridge – technologies and prospects" [7] showed that the drawbacks of a FRP composite bridge includes (1) the low modulus of materials (compared to steel) and low stiffness of the FRP components which leads to large deflection of the structure, (2) requirement for the joints and connections to be simplified, and (3) the high price of composite materials requiring cost-effective problems to be addressed.

Based on the above literature reviews, the major challenges to be addressed for the design of a FRP temporary composite bridge are as follows: (1) the stiffness of the composite structure system should be improved to meet the deflection-to-span ratio requirement; (2) the effective and simplified joints and connections of the composite structure should be studied; (3) for a lightweight structure that has sufficient strength, acceptable stiffness, and is affordable at a reasonable price, the cost-effectiveness of the composite materials should then determined their use; and (4) a novel bridge structure for the lightweight bridge possessing portable, reusable, and suitable capabilities for manual transportation needs to be innovatively created.

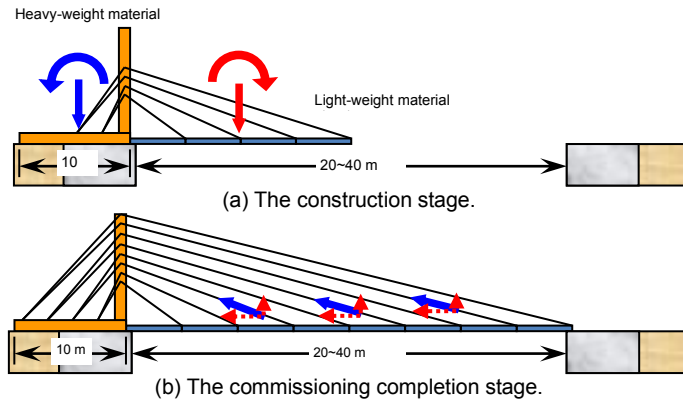
### **2.3 Concept and construction sequences**

The development of a suitable bridge type with the function of quickly to restoring traffic and providing emergency disaster relief is important. This bridge should be constructed within a short time and limited by few manpower and simple tools and should also be portable and reusable.

This study develops a temporary bridge system by using a self-weight balance approach and a cantilever incremental launching method. An asymmetric self-anchored cable-stayed bridge is proposed. The structural segments constructed by heavyweight materials (e.g., steel and concrete) are used as counter-weights at the rescue end and the cross-river segments are constructed by lightweight materials (e.g., composite materials) in order to increase the span to easily reach the isolated island end without any supports or foundations (Fig. 2).

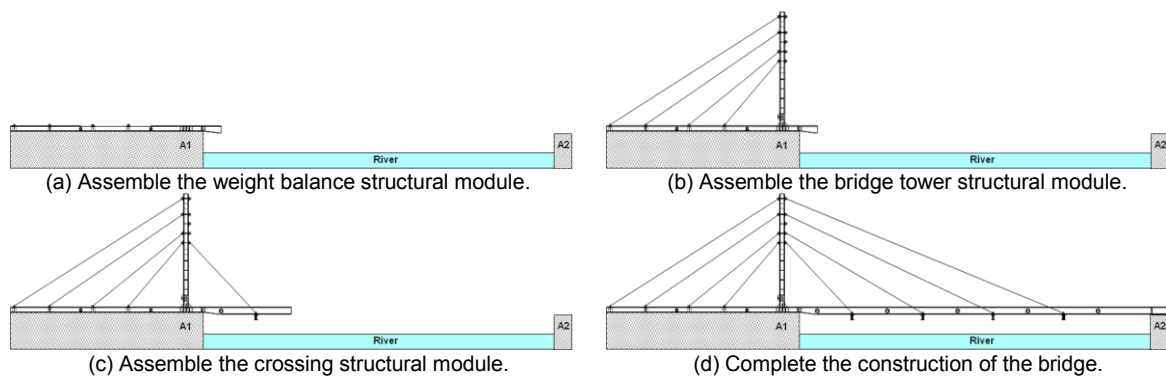


The advantages of this composite bridge include the following: (1) during the construction stage, the asymmetric self-anchored cable-stayed bridge is easily constructed from the rescue end to the isolated island end by using the self-weight balance of heavyweight structural segments and lightweight cross-river segments. The wires of the cable-stayed bridge are helpfully for the construction of cross-river segments by using the cantilever incremental launching method (Fig. 2a); further, (2) during the commissioning completion stage, these wires are effective in reducing the deformation of the bridge caused by live loads from traffic (Fig. 2b).



**Figure 2. Innovation and concept of a composite bridge for emergency disaster relief.**

The lightweight temporary composite bridge system includes a weight balance structural module, a bridge tower structural module, a crossing structural module, and connection cables. The weight balance structural module and the bridge tower structural module are constructed of steel, concrete, and any other heavyweight materials as structural segments. The crossing structural module is constructed of composites and any other lightweight materials. The construction sequences is as follows: (1) assemble the structural segments to complete the weight balance structural module (Fig. 3a); (2) assemble the structural segments to complete the bridge tower structural module, fix the bottom part to the weight balance structural module, and couple the top part to the weight balance structural module via at least one connection cable (Fig. 3b); and (3) assemble the crossing segments between the rescue end and the isolated island end gap (Fig. 3c) to complete the crossing structural module and couple it to the top part of the bridge tower structural module via at least one connection cable (Fig. 3d).



**Figure 3. Construction sequences of composite bridge for emergency disaster relief.**

### 3. Material properties and connection of composite girders

#### 3.1 Material properties of the GFRP girder

The pultruded H-shaped GFRP girders were produced by a local manufacturer in Taiwan. The 410 mm × 20 mm × 200 mm × 18 mm H-shaped composite girders, with a length of 8.0 m, are cut into two parts with lengths of 6.5 m and 1.5 m. The 6.5 m long girder provides moment capacity and bolted connection test for the composite girder as illustrated in the next section. Part of the 1.5 m long girder is cut as specimens for the material property test and as multiple fasteners for the bolted connections test. The experimental results of the material property test for the GFRP girder shows the linear relation of the stress-strain curves for the tensile specimens of the GFRP girder. The elastic moduli



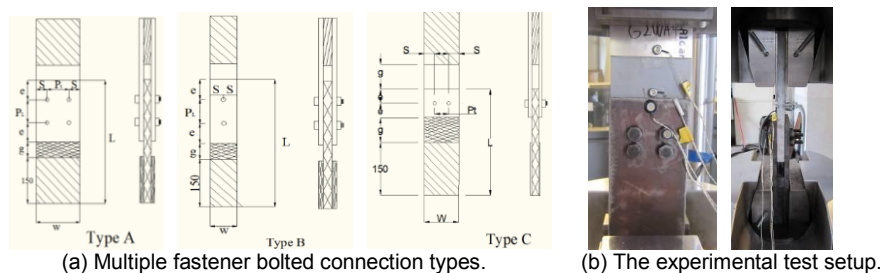
can be obtained from the linear regression of the stress-strain curve, which are 12.73 GPa in the web and 28.30 GPa in the flange of the GFRP girder. Table 1 shows the theoretical and experimental results of the material property test for the GFRP girders. The elastic modulus of the theoretical and experimental results on the web of the composite girder is very similar; however the value shows some difference in the flange of the GFRP girder.

**Table 1. Material properties of the GFRP girder.**

Material type	Position	Elastic modulus E (GPa)	
		Theoretical	Experimental
GFRP	Flange	23.24	28.30
	Web	12.82	12.73

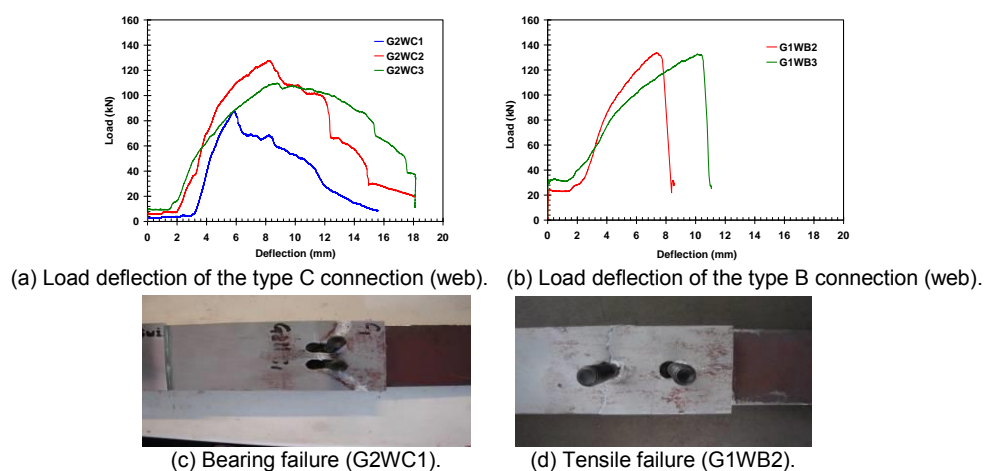
### 3.2 Bolted connection of the GFRP plate

Many researchers have focused on the joints and connections of FRP composite frames [8, 9, 10]. Mechanical connections may be used alone or in combination with other methods of joining composites, either to themselves or to other materials. The literature shows that it is very difficult to achieve a joint resistance in exceed of the FRP materials being jointed with mechanical fastening. This article attempts to employ bolted connections with composite and steel fasteners as the joints of composite frames with H-shaped GFRP girders having cross section of 410 mm × 20 mm × 200 mm × 18 mm and conduct tests for the three types of multiple fastener connections as shown in Fig. 4a. The test setup of bolted connection specimens of composite plates cut from GFRP girders are shown in Fig. 4b.



**Figure 4. Bolted connection test of the GFRP plate.**

The test results are shown in Fig. 5 and Table 2. Fig. 5 shows the typical load deflection curves and failure modes of a bolted connection GFRP plate. There are two types of failure modes that occurred during this test, namely (1) bearing failure mode: the behaviours are ductile and some contact failures are shown in Fig. 5a and 5c; and (2) tensile failure mode: the behaviours are brittle and some cracking failures along the plate are shown in Fig. 5b and 5d. Table 2 shows the test results of multiple fastener bolted connections of composite plates. It is evident that the longitudinal pitch and transverse pitch should be greater than or equal to four times the bolt diameter (4d) for the web and flange of the GFRP girder.



**Figure 5. Load deflection curves and failure modes of the bolted connection GFRP plate.**

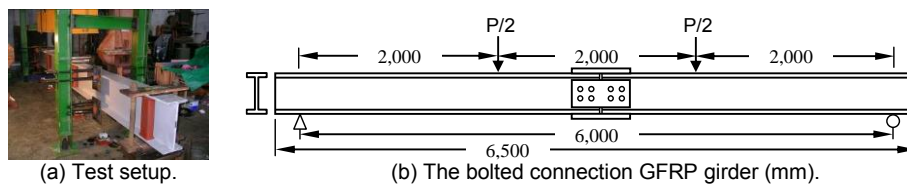
**Table 2. Test results of the multiple fastener bolted connection of the composite plate.**

Specimen	Type	Location	Width (mm)	PL (mm)	PT (mm)	Predicted Force (kN)	Test Force (kN)	Force/Per bolt (kN)	Failure Mode*
G1WA1	A	Web	100	40(4d)	40(4d)	178.6	222.4	55.6	TF
G1WA2	A	Web	80	40(4d)	20(2d)	178.6	121.2	30.3	TF
G1WA5	A	Web	100	60(6d)	40(4d)	178.6	236.1	59.1	TF
G1FB1	B	Flange	60	20(2d)	-	72.3	66.2	33.1	BF
G1FB2	B	Flange	60	40(4d)	-	72.3	72.3	36.1	BF
G2WC1	C	Web	80	-	20(2d)	87.8	87.8	43.9	BF
G2WC2	C	Web	100	-	40(4d)	87.8	127.4	63.7	BF
G2WC3	C	Web	120	-	60(6d)	87.8	109.8	54.9	BF
G1WB2	B	Web	60	40(4d)	-	132.7	133.8	66.9	TF
G1WB3	B	Web	60	60(6d)	-	132.7	132.7	66.3	TF

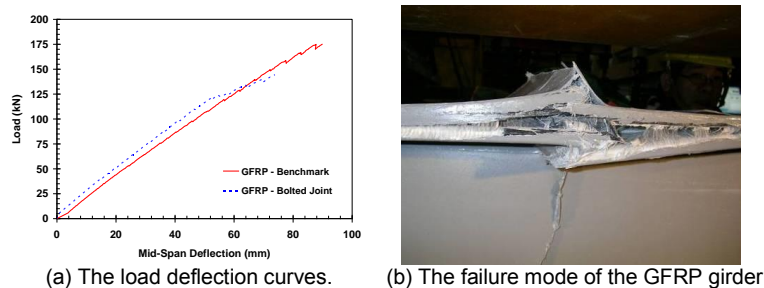
\*Note: TF = tensile failure, BF = bearing failure

### 3.3 Bolted connection of the GFRP girder

This article attempts to use bolted connections with composite and steel fasteners as joints of composite frames of a 410 mm × 20 mm × 200 mm × 18 mm H-shaped GFRP girder. Testing for the moment capacity of the composite girder is shown in Fig. 6. The test setups of a four point bending test of a bolted connection of the GFRP girders are shown in Fig. 6a. The test results are shown in Fig. 7 and they indicate that the typical load deflection curves of composite girders and effective modulus can be derived from the slope of the curves; the effective modulus is 20.03 GPa for the girder (Fig. 7a). The failure mode of the GFRP girder is local buckling on its top flange (Fig. 7b). The theoretical and experimental results of effective modulus are compared in Table 3.



**Figure 6. Four point bending test of the benchmark and bolted connection GFRP girder.**



**Figure 7. Load deflection curves and the failure mode of the GFRP girders.**

**Table 3. Effective modulus of the GFRP girder.**

Material type	Position	Effective modulus $E_{eff}$ (GPa)	
		Theoretical	Experimental
GFRP	Flange	23.24	21.16
	Web	12.82	20.03

## 4. Design and laboratory testing of a composite bridge

### 4.1 Detail design of a composite bridge

The composite bridge is composed of structural steel and GFRP composite materials. In this paper, steel structural design follows the Taiwan local code of steel building construction [11] and composite structure using the design code proposed by the U.S. Department of Agriculture (USDA) Forest Service [12] and the American Association of State Highway and Transportation Officials (AASHTO) [13]. The following equations are used for the design of the steel components in the temporary composite bridge system:

$$\frac{f_a}{0.6F_a} + \frac{f_{bx}}{F_{bx}} + \frac{f_{by}}{F_{by}} \leq 1.0 \quad (1)$$

$$\frac{f_a}{F_a} + \frac{C_{mx}f_{bx}}{\left(1 - \frac{f_a}{F'_e}\right)F_{bx}} + \frac{C_{my}f_{by}}{\left(1 - \frac{f_a}{F'_e}\right)F_{by}} \leq 1.0 \quad (2)$$

$$\frac{f_v}{F_v} \leq 1.0 \quad (3)$$

In these equations, the expressions  $f_a$  and  $f_b$  represent the actual axial and bending stress, respectively;  $F_a$  and  $F_b$  denote the allowable axial and bending stress, respectively;  $C_m$  corresponds to a modification factor;  $F'_e$  represents Euler's critical buckling stress;  $f_v$  denotes the actual shear stress; and  $F_v$  represents the allowable shear stress.

Parallel FRP girder bridge systems are studied to meet the design requirements of a span of 10 m, a width of 3 m, a live load of 5 tons (for transportation of rescue goods via a truck weighing 3.5 tons), and a deflection-to-span ratio of  $L/400$ , which is suggested by AASHTO [13]. The 410 mm × 20 mm × 200 mm × 18 mm H-shaped composite girders are used in the bridge system. The material properties of GFRP are as follows: Young's modulus = 20.03 GPa; density = 1.72 g/cm<sup>3</sup>; and allowable stress = 207 MPa. The detailed design results are shown in Fig. 8. Fig. 8a shows the detailed design drawing and Fig. 8b shows the details of the bolted connection by using bolts and steel connection plates. The numerical results for the number of parallel girders and deflection-to-span ratios are shown in Table 4. The results indicate that a five parallel GFRP girder bridge system could meet the requirement of a deflection-to-span ratio of  $L/400$  under a live of 5 tons.

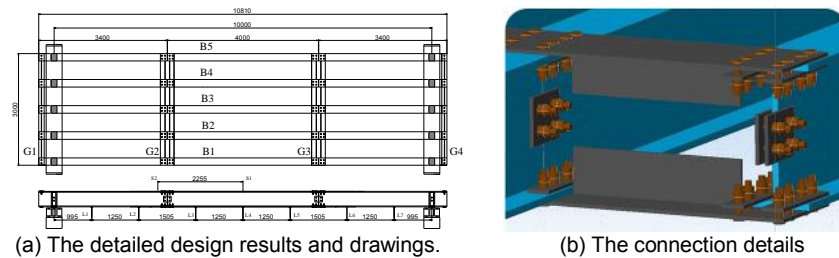


Figure 8. Design results of the GFRP composite bridge.

Table 4. Numerical results of the GFRP composite bridge.

Material	$E_{eff}$ (GPa)	No. of girders	Deflection (cm)	$L/400$ (cm)	No. of bolts
GFRP	20.03	5	2.508	2.500	240

#### 4.2 Flexural test of the GFRP composite bridge

The experimental setup of the GFRP composite bridge is shown in Fig. 9a and the loading position in order to simulate a small truck weighing 3.5 tons is shown in Fig. 9b. The test program includes a flexural test, a fatigue test, and a strength test. The results of the flexural test are shown in Fig. 10. Fig. 10a shows the linear relation of the load deflection curve. The deformed shapes are shown in Fig. 10b. The maximum displacements are 26.58 mm ( $P = 50$  kN) and 52.94 mm ( $P = 100$  kN), which occurred at the middle span of the B4 girder. The maximum longitudinal strains are  $5.681 \times 10^{-4}$  ( $P = 50$  kN) and  $1.162 \times 10^{-3}$  ( $P = 100$  kN), which occurred at the bottom flange of the B2 girder (Fig. 10c). The flexural test results indicate that the deflection-to-span ratio is approximately  $L/376$ , which is very close to the design requirement of  $L/400$ , under a live load of 5 tons.

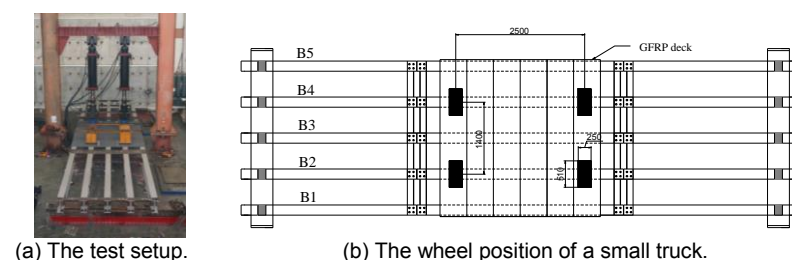
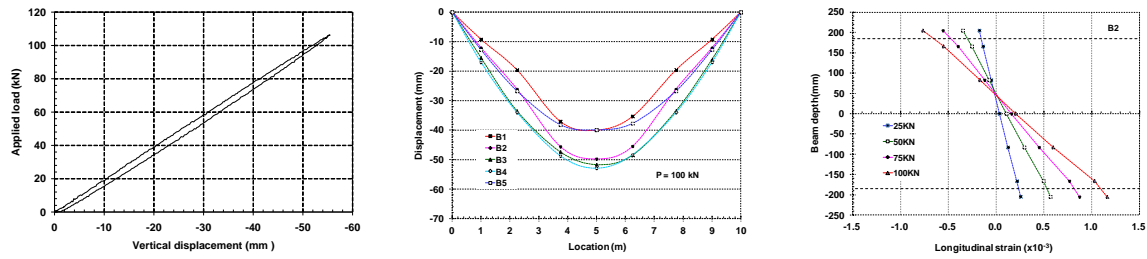


Figure 9. The experimental setup of the GFRP composite bridge.

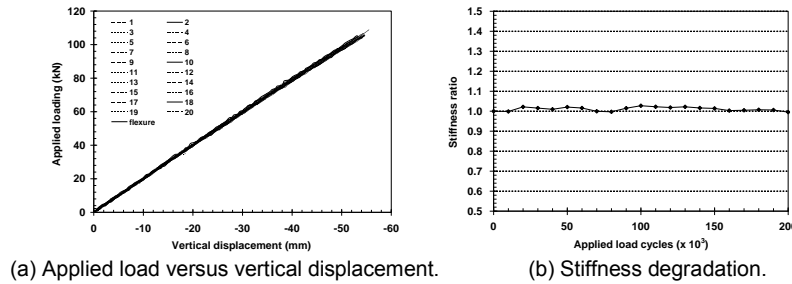


(a) Applied load versus vertical displacement. (b) Deformed shape (100 kN). (c) Longitudinal strain along the depth of B2 girder.

**Figure 10. Flexural test results of the GFRP composite bridge.**

### 4.3 Fatigue test of the GFRP composite bridge

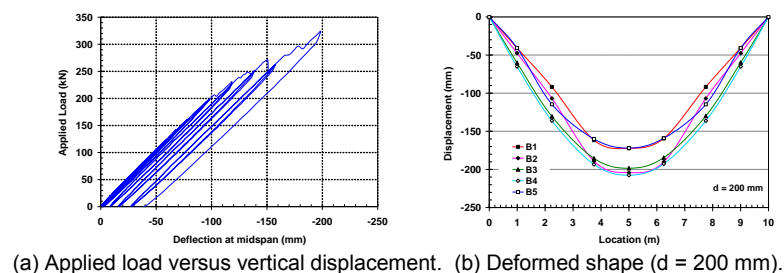
The test setup for the fatigue test of the GFRP composite bridge is identical to that of the previous section and is shown in Fig. 9. The frequency of fatigue loading is 1 Hz and a total of  $2 \times 10^5$  cycles of loading with amplitude for a target design loading of 50 kN are applied to the specimen. Additionally, the specimen is subjected to a static flexural loading after every  $1 \times 10^4$  cycles to examine the stiffness degradation. The test results are shown in Fig. 11. Fig. 11a shows the linear relation of the load deflection curve after every  $1 \times 10^4$  cycles. The stiffness degradation curve is shown in Fig. 11b. The stiffness ratio is defined as the ratio of the stiffness measured after every  $1 \times 10^4$  cycles of loading to the stiffness measured in the first flexural test. The test results show that there is no stiffness degradation over  $2 \times 10^5$  cycles of loading with amplitude for a target design loading of 50 kN.



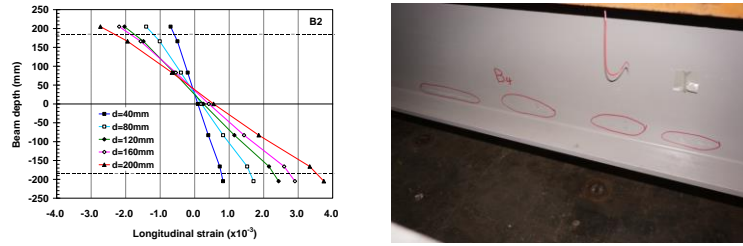
**Figure 11. Fatigue test results of the GFRP composite bridge.**

### 4.4 Strength test of the GFRP composite bridge

The test setup for the strength test of the GFRP composite bridge is identical to that of previous section and is shown in Fig. 9. The specimen is tested in flexure to failure to examine its residual strength and failure mode. The test protocol includes the displacements, which ranged from 1 cm to 8 cm. Three cycles were applied for each displacement level; two cycles were applied when the displacement amplitude ranged from 10 cm to 16 cm, while only one cycle were applied when the amplitude was 20 cm. The test results are shown in Fig. 12. Fig. 12a shows the load deflection curve at the middle span of the B3 girder; when the displacement is less than 10 cm, the loading and unloading curves are very much linear and elastic, and when the displacement is equal to 20 cm, the maximum load is around 324 kN. The deformed shapes are shown in Fig. 12b. The maximum displacements of 207.56 mm, 204.21 mm, and 198.49 mm occurred at the middle span of the B4, B2, and B3 girder, respectively. The maximum longitudinal strains of  $3.743 \times 10^{-3}$  occurred at the bottom flange of the B2 girder (Fig. 12c). The failure of the specimen was due to the slippage at the connection, but not the GFRP girder itself (Fig. 12d). The strength test results indicate that the design of the proposed composite bridge is deflection-driven, instead of being strength-driven. It also shows that the proposed design has strength higher than is required for a safety factor of more than 4.



(a) Applied load versus vertical displacement. (b) Deformed shape (d = 200 mm).



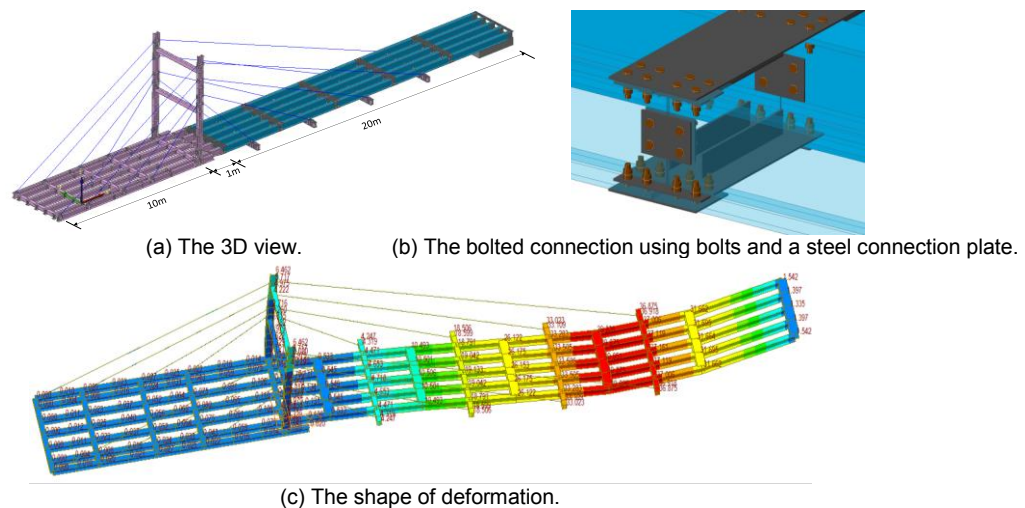
(c) Longitudinal strain along the depth of the B2 girder. (d) Failure mode of the girder.

**Figure 12. Strength test results of the GFRP composite bridge.**

## 5. Experimental verification of the composite bridge for emergency disaster relief

### 5.1 Scenario and design thinking

In order to confirm the construction and usability of the lightweight temporary bridge for disaster relief, a potential scenario for testing is required, and is as follows: a bridge with a span of 20 m was damaged in a disaster area, and thus, a temporary bridge for the transportation and delivery of relief supplies is needed. The concept of weight balance and the incremental launching method proposed in Section 2.3 are considered in the novel emergency bridge design. The design codes and material properties are identical to Section 4.1. We have designed a steel-composite cable-stayed bridge with a span of 20 m, a width of 3 m, and a live load of 5 tons (for transportation of rescue goods via a truck weighing 3.5 tons) and a deflection-to-span ratio of  $L/400$  for the assembled and river-crossing test. Fig. 13 shows the design results of the asymmetric self-anchored cable-stayed bridge. Seven parallel steel girders and H-shape pillars using A572 grade 50 steel with a 294 mm × 200 mm × 8 mm × 12 mm cross section on the A1 side abutment are used as the weight balance structural module, five parallel FRP girders using GFRP with a 410 mm × 200 mm × 18 mm × 20 mm cross section are used as crossing structural module, and double-H-shape steel cross beams are used to aid the crossing of the river (Fig. 13a). We used a steel frame on the A1 side abutment as a counterweight and a cable-stayed type bridge to quickly assemble the lightweight GFRP temporary bridge via the incremental launching method to cross the river and therefore achieve the goal of providing disaster relief. By using the same capacity for connection design (details of the connection are shown in Fig. 13b), the numerical result shows that connection between the steel girder and the GFRP girder is not the critical connection; instead, the critical connection is located at connection G4 between GFRP segment C and GFRP segment D (Fig. 13c).



**Figure 13. Design results of the 20 m span temporary composite bridge.**

### 5.2 Construction sequences and river-crossing tests

The construction sequence is shown in Fig. 14 and is as follows: (1) step 1: assembly of seven parallel steel girders with 294 mm × 200 mm × 8 mm × 12 mm cross sections and a total length of 12 m (3@4m), and a bolted connection at the web of the girder with box cross beams (200 mm × 200 mm × 6 mm) (Fig. 14a and 14b); (2) step 2: assembly of H-shape pillars with 18 connection devices for the steel cable, with 294 mm × 200 mm × 8 mm × 12 mm cross sections and a total height of 6.5 m (Fig.



14c), and a bolted connection with the top flange of the outer girders of the seven parallel steel girders at the third segment (Fig. 14d); (3) step 3: assembly of the first segment of the five parallel GFRP girders (Fig. 14e) and then connection to the third segment of the weight balance structural module (Fig. 14f); (4) step 4: assembly of the second segment of the five parallel GFRP girders by using the same sequence as the previous step (Fig. 14g) and then connection to the first segment of the crossing structural module (Fig. 14h); and (5) step 5: assembly of the third to final segment of the five parallel GFRP girders by using the same procedure as the previous step (Fig. 14i) and completion of the construction sequence to cross the river (Fig. 14j). The test results show that the 20 m span temporary composite bridge for emergency disaster relief was constructed by 30 workers within 6 hours via manpower, simple tools, and a small truck with a crane – ultimately meeting the requirements for emergency disaster relief.

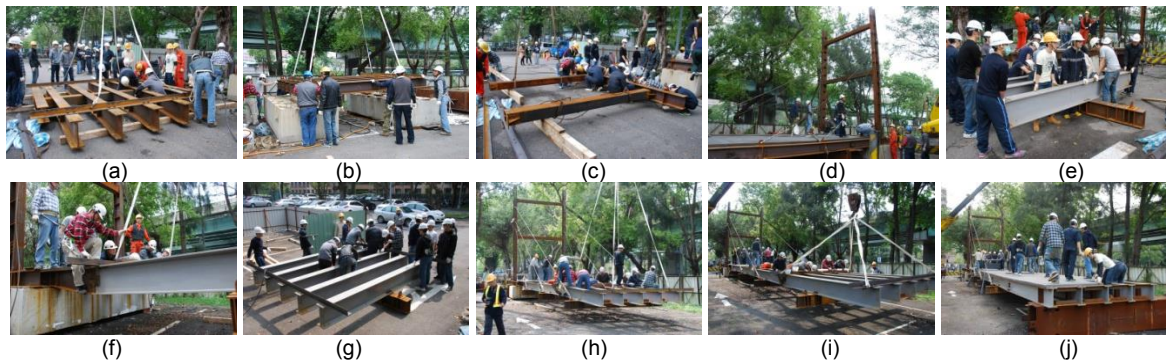


Figure 14. Construction sequence of the 20 m span temporary composite bridge.

### 5.3 In situ full scale flexural and dynamic tests

The experimental setup of a temporary composite bridge with a span of 20 m is shown in Fig. 15a and the different loading positions of a small truck weighing 3.5 tons (total weight 5 tons) is shown in Fig. 15b. The test program includes a flexural test, an off-axis flexural test, and a dynamic test. The results of the flexural and dynamic tests are shown in Fig. 16. The deformed shapes are shown in Fig. 16a. The maximum displacements are 53.41 mm (flexural test) and 56.23 mm (off-axis flexural test) and occurred at connection G4. The maximum longitudinal strains are  $5.05 \times 10^{-4}$  (flexural test) and  $-5.53 \times 10^{-4}$  (off-axis flexural test) and occurred on B3 at the left hand side of connection G4 (Fig. 16b). The deflection versus time at connection G4 is shown in Fig. 16c. The flexural and dynamic test results indicate that the deflection-to-span ratio is around  $L/356$ , which is very close to the design requirement of  $L/400$ , for a live load of 5 tons.

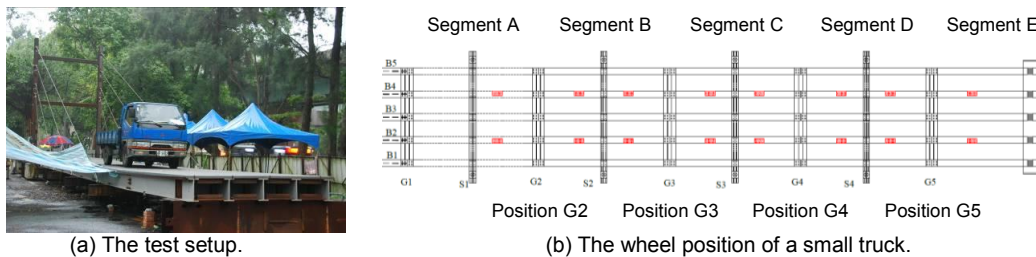


Figure 15. The experimental setup of the 20 m span temporary composite bridge.

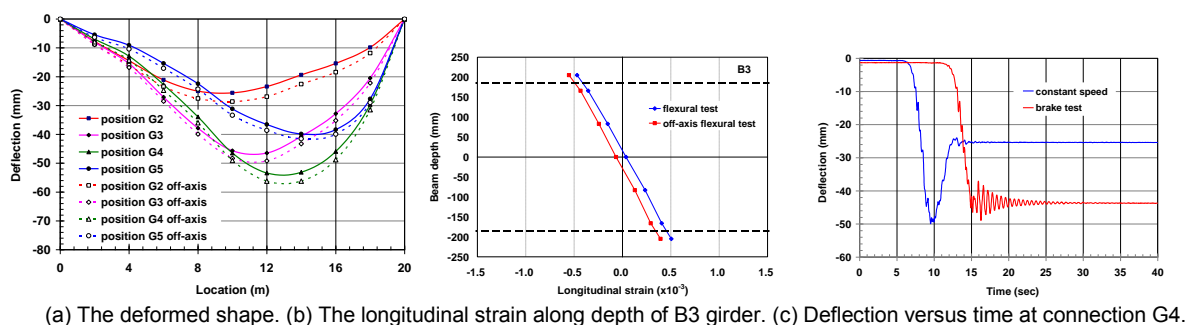


Figure 16. Flexural and dynamic test results of the 20 m span temporary composite bridge.

## 6. Concluding remarks

This paper developed a lightweight, portable, and reusable temporary composite bridge for emergency disaster relief. This bridge is an asymmetric self-anchored cable-stayed bridge designed using steel-FRP composite materials to improve the stiffness of the composite frame, reduce the deflection of the bridge, and allow easy travel across a river without any supports or foundations. All of these achievements ultimately reach the goal of disaster relief through the use of the concept of weight balance and the incremental launching method. The current research results are summarized as follows: (1) for bolted connections of the GFRP girder, the longitudinal pitch and transverse pitch should be greater than or equal to four times the bolt diameter ( $4d$ ) for the web and the flange of the girder; (2) for the flexural test of the GFRP bridge with a span of 10 m, the deflection-to-span ratio is around  $L/376$ , which is very close to the design requirement of  $L/400$ , under a live load of 5 tons; (3) for the fatigue test of the GFRP bridge with a span of 10 m, there is no stiffness degradation over  $2 \times 10^5$  cycles of loading with amplitude of target design loading 50 kN; (4) for the strength test the GFRP bridge with a span of 10 m, the design of the proposed composite bridge is deflection-driven, instead of being strength-driven, and the strength is higher than is required for a safety factor more than 4; (5) for the in situ test of a 20 m temporary composite bridge for emergency disaster relief, the novel bridge was constructed by 30 workers within 6 hours through the use of manpower, simple tools, and a small truck with a crane to meet the requirements of emergency disaster relief. The flexural and dynamic test results indicate that the deflection-to-span ratio is around  $L/356$ , which is very close to the design requirement of  $L/400$ , for a live load of 5 tons.

## 7. Acknowledgement

This work was supported by the National Science Council of Taiwan R.O.C., under the grant number NSC 100-2119-M-492-008 and NSC 101-2119-M-492-001. The facilities and technical supports from the National Center for Research on Earthquake Engineering (NCREE) are also gratefully acknowledged.

## 8. References

1. Cheng, L., Karbhari V.M., "New bridge systems using FRP composites and concrete: a state-of-the-art review", readers write, *Progress in Structural Engineering Materials*, 8(4), 2006, pp 143-154.
2. Hollaway, L.C., "The evolution of and the way forward for advanced polymer composite in the civil Infrastructure", *Proceedings of the International Conference on FRP Composites in Civil Engineering*, Hong Kong, Elsevier Science Ltd., 2001, pp 27-40.
3. Seible, F., Sun, Z. et al., "Glass fiber composite bridges in China", ACTT-93/01, University of California, San Diego, 1993.
4. Ario, I., "Development of a prototype deployable bridge based on origami skill", *Automation in Construction*, 32, 2013, pp 104-111.
5. Lederman, G., "A novel deployable tied arch bridge", *Engineering Structures*, 70, 2014; pp 1-10.
6. Teixeira, A.M.A.J., "Structural evaluation of a GFRP truss girder for a deployable bridge", *Composite Structures*, 110, 2014, pp 29-38.
7. JSCE, "FRP Bridge—Technologies and Prospects", Japan Society of Civil Engineers, December, 2004. (In Japanese)
8. Sedlacek, G., Trumpf, H., "Mobile light-weight fixed bridges out of pultruded fiber-reinforced polymer profiles", *Science and Engineering of Composite Materials*, 10(6), 2002, pp 383-395.
9. Erki, M.A., Shyu, C.R. et al., "Multiple bolted connections in pultruded FRP composites", *Proceedings, Annual Conference—Canadian Society for Civil Engineering*, 2005, GC-218-1-7.
10. Nguyen, D.H., Hiroshi, M., "Behavior of bolted/bonded joints in pultruded hybrid CFRP/GFRP composites", *Journal of Structural Engineering*, 56A, 2010, pp 23-31.
11. CPAMI, "Specification for structural steel buildings: allowable stress design", Construction and Planning Agency, Ministry of Interior, R.O.C. , 2010. (In Chinese)
12. USDA Forest Service, "A guide to fiber-reinforced polymer trail bridges", United States Department of Agriculture, second edition, 2011.
13. AASHTO, "Guide specifications for design of FRP pedestrian bridges", American Association of State Highway and Transportation Officials, first edition, 2008.

# Quick Uplift Rehabilitation for Differential Sunken Concrete Structure of Slab Ballastless Track

Xinguo Zheng<sup>1</sup>, Weichang Xu<sup>2</sup>, Fei Cheng<sup>3</sup>, Zhiyuan Zhang<sup>4</sup>, Youneng Wang<sup>5</sup> and Jing Liu<sup>6</sup>

<sup>1</sup>Program Manager, Railway Engineering Research Institute of China Academy of Railway Science

<sup>2</sup>Senior engineer, Shanghai Railway Bureau

<sup>3</sup>Senior engineer, Shanghai- Hangzhou Railway Passenger Dedicated Line Co., Ltd.

<sup>4</sup>Senior engineer, Shanghai Railway Bureau

<sup>5</sup>Project Engineer, Shanghai Railway Bureau

<sup>6</sup>Program Manager, Railway Engineering Research Institute of China Academy of Railway Science

**Abstract:** The concrete slab ballastless track is an advanced track structure with high stability and integrity. However, when the foundation of ballastless track appears large differential sunken deformation, compared with ballast track which can be restored by increasing the ballast under the sleepers simply, the smoothness of concrete slab ballastless track can only be restored by adjusting the thickness of the base plates of fastener system accordingly. But if continuous sunken deformation exceeds specified adjustable range of fastener system, the smoothness of concrete slab ballastless track cannot be restored timely and completely, and then the speed of passing trains has to be limited to ensure the safety. To solve this problem without disturbing the regular operation of the railway lines, we systematically studied a complete set of new quick uplift rehabilitation technology through a series of indoor reduced scale tests and field full scale simulations with real concrete slabs and combined with practical application. Results indicated this technology can restore the smoothness of sunken concrete slab ballastless track quickly and accurately. These will provide valuable references for the rehabilitation of sunken concrete slab ballastless structure.

**Keywords:** grouting, uplift, concrete structure, ballastless track, rehabilitation.

## 1. Introduction

Nowadays, the slab ballastless track with excellent performance, such as low maintenance requirement, a long service life and reduced structure height, etc., is regarded as an advanced track structure [1-2]. In China, it has been widely used in many high-speed railways such as the Shanghai-Hangzhou intercity railway, Beijing-Wuhan high-speed railway and Hangzhou-Changsha high-speed railway and so on. There are currently more than 10,000 kilometres of the slab ballastless track railway, both in operation and in construction. The slab ballastless track commonly includes the rail, fastener, concrete track slab, cement emulsified asphalt mortar layer, and concrete bottom slab [3]. However, when the foundation of ballastless track appears large differential sunken deformation, compared with the ballast track which can be restored by increasing the ballast under the sleepers simply, the track height of the ballastless track can only be restored by adjusting the thickness of the base plates within the range allowed by the fasteners. This has greatly limited the regularity adjustment and restorability of the concrete slab ballastless track. The uncontrollable post-construction foundation settlement of few sections of the high speed railway roadbed is caused by various complex geological conditions. And if continuous sunken deformation exceeds specified adjustable range of fasteners, the smoothness of the slab ballastless track cannot be restored timely and completely, and then the speed of passing trains has to be limited to ensure the safety. This is a big challenge for the high-speed railway operation. These limits seriously affect the operation of high speed railways in some differential sunken concrete structure sections of ballastless track line.

To solve this problem without disturbing the regular operation of the railway lines, we systematically studied a complete set of new quick uplift rehabilitation technology through a series of indoor reduced scale tests and field full scale simulations with real concrete slabs and combined with practical application. We have created a new set of technology and engineering practice to uplift the concrete structure of ballastless track successfully, with no negative effect on existing railway operation. The track smoothness can be restored quickly and accurately. This new technology has been applied successfully to the settlement rehabilitation for the ballastless track line of Daxi Yongji North Station.

This article introduces this new grouting uplifting technology for concrete structure of ballastless track from its uplifting theory, grouting materials, construction process and practical application, in the hope of providing valuable reference for rehabilitation of the differential sunken ballastless track concrete structure of high-speed railway all over the world.



## 2. Uplifting theory

The grouting materials is injected in the ground at discrete locations under the concrete bottom slab to correct differential settlement and to apply compactive forces to the foundation layer. The two components of the foam, which mix as they are injected through a grouting pipe. The expansion pressure it exerts is used to lift the ballastless track structure, remediating a differential settlement problem without excavation. During the overall grouting uplifting of ballastless track concrete structure, the grouting materials is filled into the surface layer of graded broken stone foundation bed through the special grouting equipment, under a certain grouting pressure. The uplifting is realized by the expansibility of the grouting materials and the hydraulic transmission effect resulting from the liquid grouting materials and grouting pressure. The uplifting can be divided into two stages, namely the filling & compacting stage and the uplifting & filling stage.

In the filling & compacting stage, the grouting materials will fill and compact the gaps such as the ones between the supporting layer and graded broken stone layer or those inside the graded broken stone layer. And the track structure will not be uplifted at this stage.

In the uplifting & filling stage, the filled grouting materials and the grouting pressure from grouting equipment will cause hydraulic transmission effect. Meanwhile, the volume expansion from the grouting material solidification will cause expansive upliftiing forces. With the effects of these two factors, the concrete structure can be uplifted continuously and stably, and the gaps between concrete structure and graded broken stone layer due to uplifting can also be filled completely and densely.

## 3. Grouting Material

The grouting material applied is a kind of two component chemical grouting materials [4-5]. After mixing, the material will gel and react to form hardeded concretion within a short time (see Figure 1). This Gel is able to form different volumes and expand as needed. Compared with other grouting materials, the grouting materials have the following features:



Figure 1. Hardened concretion of the grouting materials.

### (1) High adaptability for the construction environment

The grouting material is non-water reactive. The grouting material will cure in both air and water if the ambient temperature is above 5°C.

### (2) High ability of permeation, diffusion and filling

With a certain grouting process, the diffusion diameter can reach up to more than 5 meters and it has a certain volume expansion too (the free expansion ratio can reach up to 20:1 ). The filling ability is outstanding, meanwhile, it can compact the substructure of the filling range to form the sandwich structure (see Figure 2).



**Figure 2. Sandwich structure of grouting material foam layer and graded broken stone layer.**

(3) Filling range controllable

After the mixture of grouting materials, the liquid state will transform into plastic state and then the solid state within a short time. Thus, the filling range is easy to adjust by controlling the reaction speed of two component grouting materials, with no need to set special curtains to prevent the slurry from overflow.

(4) Low density and weight

The structure density formed by this grouting material is around  $100 \text{ kg/m}^3 \sim 300 \text{ kg/m}^3$ , far less than the water density. So compared with cement grouting materials, it does not increase the additional structural load significantly.

(5) Fast in setting and hardening, fast in strength development

The grouting material can reach up to more than 90% of the design strength just within 15 minutes, which can completely meet the strength requirements for railway line operation. As a result, the traffic can be resumed in time after the uplifting of concrete structure.

(6) High volume stability

It almost has no volume shrinkage after the hardened structure formed and will have the feature of a perfect elastomer before 80% of the failure load.

(7) High durability

The hardened grouting materials possess a high durability property with high water proof, frost resistance and chemical erosion resistance.

#### **4. Practical application**

Located at Yuncheng, Shanxi Province, Daxi Yongji North Station, its railway line was designed to be 4 lines of track (see Figure 3). Due to the differential settlement of the roadbed, the concrete structures of slab ballastless track sunken obviously. Therefore, four tracks had serious problems with the smoothness within a range of 80 meters. The maximum settlement of some sections even exceeded 50 millimeters. The railway speed in this sunken section of this line had to be limit to 160 km/h.

In March, 2014, the settlement ballastless track of Yongji North Station was rehabilitated by this overall grouting uplifting technology (see Figure 4). During rehabilitation, when the grouting equipment operated smoothly and the materials reached a stable performance, the grouting uplifting rehabilitation was carried out according to the specified grouting procedure. The electronic level was adopted to monitor the rail elevation change and the total station was adopted to monitor the center line misalignment of concrete structure. When the uplifting height reached the expected height, stop grouting and the high-strength non-shrinking cement material was used to block up the injection holes. It only took 20 days to fulfill this repair work of this sunken section. The concrete structure had no cracking due to uplifting construction.

After rehabilitation, the smoothness of four tracks was improved significantly (see Figure 5 for the track elevation comparison before and after the grouting uplifting rehabilitation). The maximum uplifting height of the concrete structure was up to 52 millimeters (No cracking). The railway speed in this

section had recovered to the design speed of 250 km/h and the dynamic response of the ballastless track in this section showed normally.



Figure 3. North Station of Daxi High-Speed Railway.



Figure 4. Grouting quick uplifting rehabilitation construction of Yongji North Station on site.

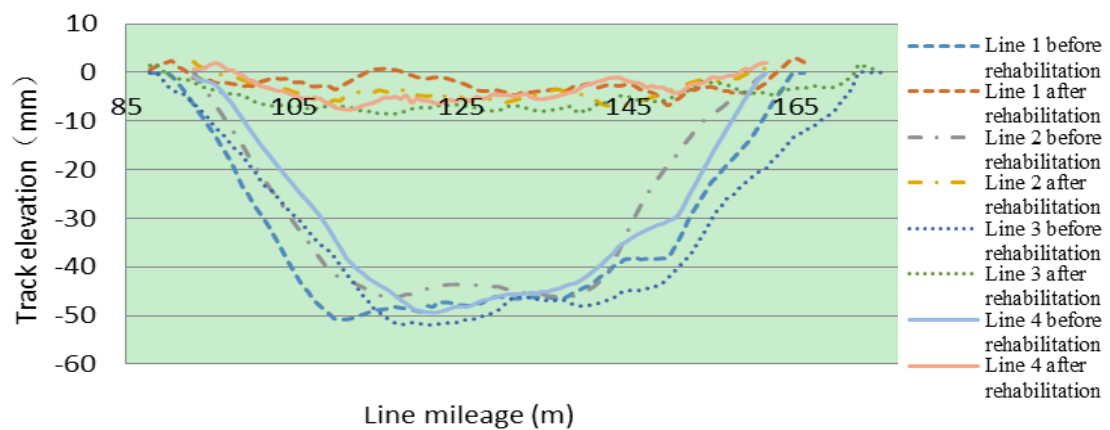


Figure 5. Comparison of the elevation of four tracks before and after uplifting rehabilitation.

## 5. Conclusion

The overall grouting uplifting rehabilitation technology for ballastless track has the advantages of rapid restoration, good effect, simple construction, no disturbing railway line operation and little destruction to the existing concrete structure. It is also a rapid, simple and practical method to rehabilitate the ballastless track of the settlement section in a manner that can neither affect the track structure stress adversely nor affect the traffic safety, which is promising in the settlement rehabilitation of the ballastless track in operation. The properties of this two component grouting materials and the resulting solid foam are very versatile and with stringent quality control, this uplift rehabilitation technology can be more effectively and successfully applied to many other construction projects.

## 6. Acknowledgement

This research was supported by China Railway Corporation Science and Technology Research and Development Program under Grant No. 2013G008-D, National Basic Research Program of China (973 Program) under Grant No. 2010CB736102 and China Academy of Railway Science Foundation under Grant No. 2010YJ75 and No. 2014YJ017 and Shanghai Railway Bureau Foundation under Grant No.HHKZ2013-01.

The authors are grateful to Prof. Yongjiang Xie, Zhenting Li and Youneng Wang for their useful comments and suggestions. The authors are also grateful to Shuming Li, Dejun Yang, Zhicai Weng and Zhi Zeng for their support with material preparation and field experiments. The authors are also grateful to Prof. Wang (SiChuan University) and Prof. Zhang (Wuhan University of Technology) for helping with English writing.

## 7. References

1. Zheng X. G., Liu J. et al., "Preparation of Cement Emulsified Asphalt Mortar for CRTS II Slab Ballastless Track", Railway Engineering, (8), 2009, pp 121-124 (in Chinese).
2. Jin, S. H., Chen, X. F. et al., "Key technologies of CA mortar for slab track", China Railway Science, 27(2), 2006, pp 20–24 (in Chinese).
3. Zeng, Z., Zheng, X. G. et al., "Construction technology of cement-emulsified asphalt mortar used in CRTS II ballastless slab track", Railway Engineering, (9), 2009, pp 97–100 (in Chinese).
4. O. Buzzi, S. Fityus, Y. Sasaki et al., "Structure and properties of expanding polyurethane foam in the context of foundation remediation in expansive soil", Mechanics of Materials, 40, 2008, pp 1012-1021.
5. Seo D, Youn J.R., "Numerical analysis on reaction injection molding of polyurethane foam by using a finite volume method", Polymer, 46, 2005, pp 6482–6493.
6. Byung-Sik Chun, Dong-Seong Ryu., "A Study on Applications of Polyurethane Injection Material for Ground Improvement", Journal of Civil Engineering, 4(2), 2000, pp 113-118.
7. Aksoy CO., "Chemical injection application at tunnel service shaft to prevent ground settlement induced by groundwater drainage: a case study", International Journal of Rock Mechanics and Mining Sciences, 45, 2008, pp 376–383.
8. Ahmet Varol, Suleyman Dalgic., "Grouting applications in the Istanbul metro Turkey", Tunnelling and Underground Space Technology, 21, 2006, pp 602–612.

# Investigation of Strain and Energy Ductility in SFRP-Wrapped Concrete Cylinders

Nisreen Salameh<sup>1</sup>, Raafat El-Hacha<sup>2</sup>, and Khaled Abdelrahman<sup>3</sup>

<sup>1</sup>MSc student, University of Calgary

<sup>2</sup>Associate Professor, University of Calgary

<sup>3</sup>PhD Candidate, University of Calgary

**Abstract:** Ductility plays a significant role in evaluating the suitability and the degree of reliability of Fiber Reinforced Polymer (FRP) material used in retrofitting applications especially in earthquake prone zones. Ductility enhancement for concrete columns wrapped by Carbon FRP (CFRP), Glass FRP (GFRP) and Aramid FRP (AFRP) sheets has been extensively investigated and many literatures can be found on the subject, however literature on strengthening applications of concrete columns using Steel FRP (SFRP) is rather limited and few has examined the effect of the concrete compressive strength and the number of SFRP layers on ductility. To that end, an experimental program has been conducted on plain concrete cylinders (150 mm x 300 mm), which consists of eighteen SFRP-wrapped cylinders, and six unwrapped control cylinders for comparison purposes. The parameters investigated are the concrete compressive strength and the thickness of the SFRP jacket. The two main ductility indices investigated in the current study are; the energy ductility index, which represents the ratio of the total energy absorption at failure of the SFRP-confined concrete over the total energy absorption of the unconfined concrete, and the strain ductility index, which represents the ratio of the SFRP-confined concrete ultimate strain to the axial strain corresponding to the unconfined peak concrete strength. Results showed significant enhancement in ductility of the SFRP-wrapped cylinders as compared to the unconfined cylinders. It is further observed that strain ductility index and energy ductility index were higher for higher concrete strength and thicker SFRP jacket.

**Keywords:** Fibre Reinforced Polymer, ductility, energy, ductility index, lateral stiffness, lateral confinement ratio.

## 1. Introduction and background

The concept of ductility in structural engineering commonly refers to the ability of a structural element to undergo large inelastic deformation, and hence implies the ability to dissipate inelastic energy, without excessive loss in the structural element load carrying capacity [1]. It is required by code and design guidelines, specifically in seismic prone areas, to design and detail structural concrete members to achieve certain degree of ductility. In concrete compression members, ductile behavior is assured by provision of sufficient transverse reinforcement, which can be internal in the form of stirrups or spiral reinforcement [2] or external in the form of externally bonded fiber reinforced polymer (FRP) jacket [3-16].

Mashrik and El-Hacha [3, 4] performed extensive experimental testing on small-scale plain concrete cylinders wrapped by SFRP jacket, where the effects of various concrete strengths, SFRP jacket thicknesses and section shapes (circular and square) were investigated. Their findings indicate substantial overall performance enhancement in terms of axial strength and ductility. Although their study included the effect of the concrete strength and jacket thickness on ductility, the study was limited to the energy ductility enhancement while the strain ductility enhancement was not investigated. Abdelrahman and El-Hacha [5] investigated the effect of slenderness ratio (defined by the ratio of the height to the diameter to the cylinder) on the ductility of SFRP-wrapped concrete cylinders. The slenderness ratios investigated were 2, 4 and 6. They reported a reduction in the wrapped cylinders ductility as the slenderness ratio increased. Abdelrahman and El-Hacha [6] further compared the ductility performance of large-scale reinforced concrete columns wrapped by SFRP sheets exposed to room temperature and environmental freeze-thaw cycles. The findings from this investigation showed no change in ductility performance of the SFRP confined concrete after freeze-thaw exposure, when compared to the unconditioned columns. It is clear that literature regarding the SFRP-wrapped cylinders ductility is limited and the subject has not been adequately addressed. In this paper, the ductility aspect of SFRP confined concrete is quantified and the effect of several parameters on ductility enhancement is investigated.

Ductility has been traditionally measured in terms of various indices, a common ductility index is known as the strain ductility index,  $\mu_{cc}$ , and is defined as the ratio of the FRP-confined concrete ultimate strain to the

axial strain corresponding to the unconfined concrete strength at peak, as shown in Figure 1 (a). Strain ductility index is calculated as per the following equation:

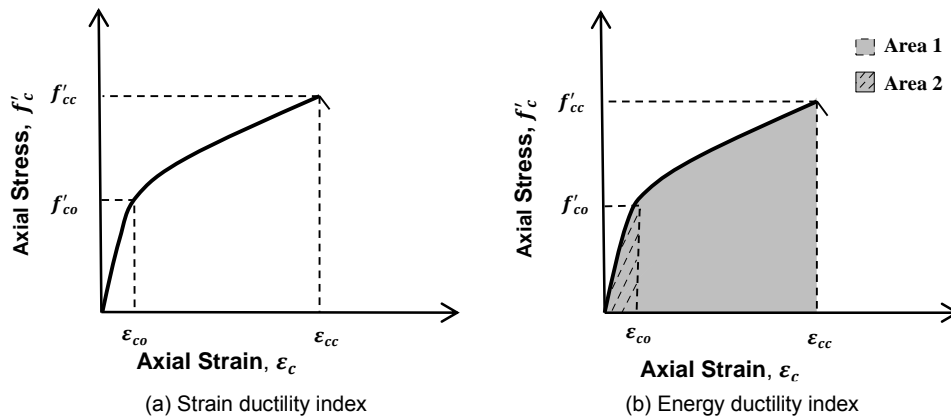
$$\mu_{cc} = \frac{\varepsilon_{cc}}{\varepsilon_{co}}$$

where,  $\varepsilon_{cc}$  is the axial strain corresponding to the rupture of the FRP jacket and  $\varepsilon_{co}$  is the axial strain corresponding to the unconfined concrete strength at peak.

The ductility of FRP confined concrete can be also expressed through an energy ductility index,  $\omega_{cc}$ . The energy ductility index is defined as the ratio of the total area under the stress-strain curve up to the failure of FRP jacket  $f'_{cc}$  (*Area 1*) over the area of the unconfined state up to  $f'_{co}$  (*Area 2*) as shown in Figure 1 (b). Energy ductility index is calculated as per the following equation:

$$\omega_{cc} = \frac{\text{Area 1}}{\text{Area 2}}$$

Figure 1 shows the definition of the different parameters of the ductility indices for a bilinear stress-strain response of the SFRP confined concrete.



**Figure 1. Ductility indices parameters.**

## 2. Experimental Program

### 2.1 Test matrix

A total of twenty-four small-scale unreinforced concrete cylinders measuring 150 mm in diameter and 300 mm in height were fabricated and tested under monotonic uniaxial compression load. The test matrix, as summarized in Table 1 includes eighteen SFRP-wrapped cylinders and six control unwrapped cylinders. The main experimental parameters investigated in this study include the thickness of the SFRP jacket (1, 2 and 3 layers), and the unconfined concrete strength (37.3 MPa and 42.4 MPa). For each combination of testing parameters, three identical specimens were fabricated and tested for repeatability purposes.

The SFRP sheets were applied over the full height of the cylinder in a wet layup process, however, due to the non-flexible nature of SFRP sheets and the tendency of the sheets to open out and detach from the concrete substrate, a day prior to SFRP fabric installation; one edge of the SFRP sheet were attached to the concrete substrate over 20mm of epoxy strip. In addition, the newly SFRP-wrapped cylinders were further wrapped by a flexible plastic sheet and clamped to ensure a complete contact between the concrete surface and the SFRP sheets. The cylinders were left for one day to cure at room temperature before clamps and plastic wrap were removed. In order to avoid premature failure at the overlap zone, sufficient overlap length of 100 mm was provided in all cases.



**Table 1. Test matrix and cylinders details**

Confinement Designation	Number of cylinders tested	Cylinder geometry			Concrete strength $f'_{co}$ (MPa)	FRP Strengthening Scheme			
		X-section	Diameter D (mm)	Height H (mm)		Type	No. of layers	Thickness (mm)	
C37.3-UW	3	Circular	150	300	37.3	-			
C37.3-SFRP1	3					SFRP	1	1.2	
C37.3-SFRP2	3						2	2.4	
C37.3-SFRP3	3						3	3.6	
C42.4-UW	3					42.4	-		
C42.4-SFRP1	3						SFRP	1	1.2
C42.4-SFRP2	3				2			2.4	
C42.4-SFRP3	3				3			3.6	

The designation system adopted in this paper for tested cylinders takes the following general form: C(F)-FBR(N)-SP#(M) where C refers to cylinder; F refers to concrete 28-day compressive strength; FBR refers to fiber type; N refers to number of layers; SP refers to specimen number representation; and M refers to specimen number ( $1 \leq M \leq 3$ ). It should be noted that when N=0, that is, when the cylinder is unwrapped, the notation FBR(N) will be simply replaced by UW notation (unwrapped). It should also be noted that when it is referred to the group of FRP configuration rather than a particular cylinder, the notation SP(M) will be discarded.

## 2.2 Material properties

### 2.2.1. Concrete

Two different concrete mixtures were used in this experimental program; one mixture was prepared at the laboratory of the University of Calgary, the second mixture was provided by a concrete supplier. The average compressive strength of the unconfined concrete was 37.3 MPa ( $\pm 0.7$  MPa) and 42.4 MPa ( $\pm 1.4$  MPa) for the two mixtures, respectively.

### 2.2.2. SFRP jacket

Commercially available steel/epoxy SFRP strengthening system was used to provide the external confinement. The SFRP sheet used in this research was of type 3×2-20-12 made from unidirectional brass coated ultra-high strength twisted steel wires [17]. The 3×2 indicates the number of filament wires per cord. Each individual SFRP cord consists of three straight wires wrapped by two wires at a high twist angle. The third digit indicates density, 20 wires per inch. The final digit indicates the width of the sheet in inch. The mechanical properties of the SFRP sheet reported by the manufacturer are summarized in Table 2. To verify the manufacturer's properties, direct tension tests were also performed according to ASTM [18] on three SFRP coupons and the reported material properties along with their respective standard deviations for the ultimate tensile strength, modulus of elasticity, and strain at failure were 878 MPa ( $\pm 50$  MPa), 68800 MPa ( $\pm 1400$  MPa) and 1.38 % ( $\pm 0.077\%$ ), respectively.

**Table 2. FRP system mechanical properties [17]**

Properties	SFRP 3x2-20-12
Sheet thickness (mm)	1.23
Net cross-sectional area of	0.38mm <sup>2</sup> /mm
Ultimate tensile stress (MPa)	986
Effective modulus (GPa)	66.1
Tensile elongation (%)	1.5

The mechanical properties of the Sikadure® 330 epoxy adhesive reported by the manufacturer for the tensile strength, elastic modulus and elongation at failure are 30MPa, 3.8GPa and 1.5%, respectively [19].

### 3. Test Results

Typical stress-strain curves for tested cylinders from each confinement configuration are shown in Figure 2 (a) and Figure 2 (b) for C37.3 and C42.4 concrete, respectively. Stress-strain curves for corresponding unconfined concrete are also shown for comparison. The substantial increase in the ultimate axial strain due to the SFRP confinement when compared to the unconfined cylinders is apparent in all cases.

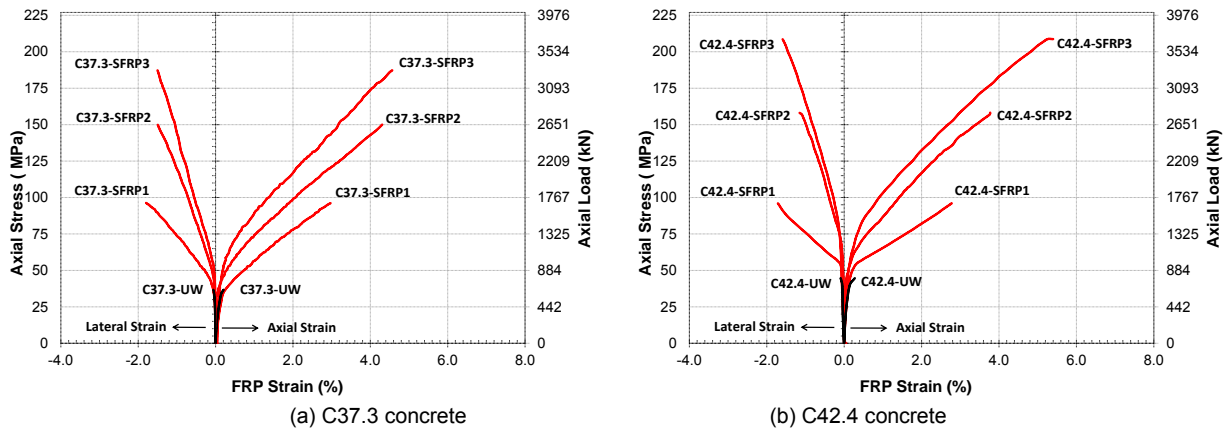


Figure 2. Typical stress-strain curves for SFRP-confined cylinders

The strain ductility indices and energy ductility indices for the SFRP-wrapped cylinders are summarized in Table 3. The axial stress data used for calculating the ductility indices were obtained by dividing the load results over the cylinder cross sectional area, the axial strain data used for calculating the ductility indices were obtained from the measurement of conventional 120 Ω foil strain gauge installed at the mid height of the cylinder directly opposite to the SFRP overlap end edge.

Table 3. Ductility indices for SFRP-wrapped cylinders

Cylinder Designation	Strain ductility index		Energy ductility index	
	$\mu_{cc}$	average	$\omega_{cc}$	average
C37.3-SFRP1-SP#1	18	16	35	33
C37.3-SFRP1-SP#2	15		31	
C37.3-SFRP1-SP#3	16		33	
C37.3-SFRP2-SP#1	24	22	69	67
C37.3-SFRP2-SP#2	21		63	
C37.3-SFRP2-SP#3	22		68	
C37.3-SFRP3-SP#1	23	28	89	108
C37.3-SFRP3-SP#2	32		132	
C37.3-SFRP3-SP#3	28		103	
C42.4-SFRP1-SP#1	15	15	39	41
C42.4-SFRP1-SP#2	16		41	
C42.4-SFRP1-SP#3	16		42	
C42.4-SFRP2-SP#1	18	19	77	78
C42.4-SFRP2-SP#2	21		88	
C42.4-SFRP2-SP#3	17		68	
C42.4-SFRP3-SP#1	26	27	129	139
C42.4-SFRP3-SP#2	24		121	
C42.4-SFRP3-SP#3	31		167	



## 4. Discussion

### 4.1 Effect of SFRP jacket thickness

The thickness of SFRP jacket, i.e. the number of SFRP layers, plays a significant role in improving the concrete behavior in terms of ductility as indicated by the ductility indices summarized in Table 3 and shown in Figure 3 (a) and Figure 3 (b). This is expected as increasing the thickness of the SFRP jacket directly increases the jacket lateral stiffness and hence increases the effectiveness of SFRP jacket in restraining concrete core lateral expansion. The test results showed that, for cylinders with concrete strength of 37.3 MPa, the strain ductility index was increased by 36% and 70% when the SFRP jacket thickness doubled and tripled, respectively, while, for cylinders with concrete strength of 42.4 MPa, the strain ductility index was increased by 23% and 75% when the SFRP jacket thickness doubled and tripled, respectively.

For cylinders within similar concrete compressive groups, the energy ductility index improved significantly due to the increase of the SFRP jacket thickness. Comparison of the test data shows that SFRP-wrapped cylinders of unconfined concrete strength of 37.3 MPa wrapped with one, two and three layers of SFRP sheets exhibited higher ductility indices by 33, 67 and 108, respectively, when compared to their corresponding unconfined concrete cylinders. This also means that the energy ductility index was increased by 103% and 229% when SFRP jacket thickness has been doubled and tripled, respectively. Similarly, the ductility indices of SFRP wrapped concrete cylinders of unconfined concrete strength of 42.4 MPa and wrapped with one, two and three layers of SFRP sheet was higher by 41, 78 and 139, respectively, when compared to their corresponding control specimens. This also implies that the energy ductility index was increased by 91% and 242% when SFRP jacket thickness has been doubled and tripled, respectively.

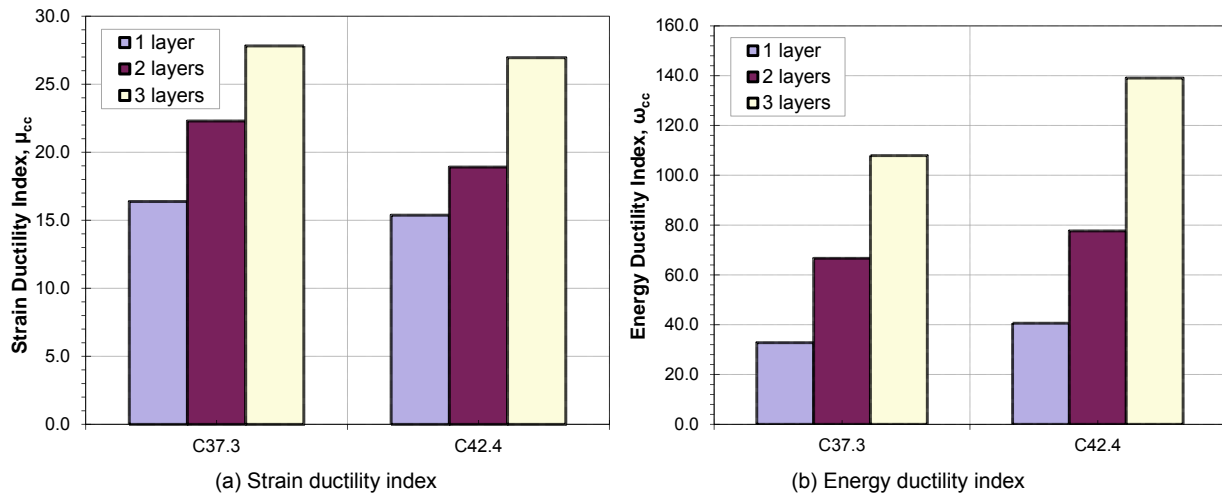


Figure 3. Effect of jacket thickness on ductility indices

### 4.2 Effect of concrete compressive strength

The effect of the unconfined compressive strength on ductility indices is graphically presented in Figure 4. It can be clearly seen that for the same SFRP confinement configuration, an increase in the unconfined concrete compressive strength,  $f'_{co}$ , results in a reduction in the strain ductility index. It is well-known that increasing  $f'_{co}$  reduces the FRP lateral confinement ratio. The FRP lateral confinement ratio,  $\frac{f_{lu}}{f'_{co}}$ , is defined in the following equation:

$$\frac{f_{lu}}{f'_{co}} = \frac{2E_{FRP}\epsilon_{FRP}t_{FRP}}{Df'_{co}}$$

where  $E_{FRP}$  is the FRP modulus of elasticity,  $\epsilon_{FRP}$  is the FRP rupture strain,  $t_{FRP}$  is the thickness of FRP jacket,  $D$  is the concrete cylinder diameter and  $f'_{co}$  is the unconfined concrete compressive strength.

To develop a solid understanding on how the FRP lateral confinement ratio affect the strain ductility properties, the strain at ultimate from the constitutive model proposed by Ottosen for concrete under triaxial state of stress should be revisited [12,13].

$$\varepsilon_{cc} = \frac{\varepsilon_{FRP}}{v_{secu}} + \frac{\varepsilon_{co}(1 - v_{secu} - 2v_{secu}^2)}{v_{secu}} \frac{f_{lu}}{f'_{co}} \left[ 1 + 4 \left( \frac{k_l - 1}{\sqrt{3}} \right) \frac{f_{lu}}{f'_{co}} \right]$$

where  $E_{secu}$  is the concrete ultimate secant modulus of elasticity,  $v_{secu}$  is the concrete ultimate secant Poisson's ratio and  $k_l$  is the confinement effectiveness coefficient.

Hence, it would be expected that based on the above equations and given that the same FRP type is used, SFRP, i.e, the rupture strain is the same, cylinders with lower concrete compressive strength feature higher  $\frac{f_{lu}}{f'_{co}}$  and attain higher ultimate axial strains and hence, higher strain ductility indices. This closely match the test results as strain ductility reduces by 6%, 15% and 3% for one, two, and three layers of SFRP jacket, respectively, when concrete compressive strength increases from 37.3 MPa to 42.4 MPa.

On the other hand, the energy ductility index increases as  $f'_{co}$  increases as shown in Figure 4 (b). The increase of the concrete compressive strength from 37.3 MPa to 42.4 MPa results in energy ductility index increase by 24%, 17% and 6%, for concrete cylinders wrapped with one, two and three layers of SFRP sheets, respectively. As oppose to the strain ductility index, which depends only on the ultimate axial strain, which in turn is a function of FRP rupture strain and FRP lateral confinement ratio, energy ductility index is, by definition, a function of the whole stress-strain response. As concrete compressive strength increases, the ultimate axial strain, for the same type of FRP, slightly decreases, as discussed previously, however, the ultimate axial stress increases as concrete compressive strength increases as indicated by the majority of the proposed FRP-confinement models and are generally expressed by the following expression:

$$f'_{cc} = f'_{co} + k_l f_{lu}$$

where  $f'_{cc}$  is the confined concrete compressive strength, and  $f_{lu}$  is the ultimate lateral confinement pressure exerted by the FRP sheets on the concrete core and is represented mathematically by the following equation:

$$f_{lu} = \frac{2E_{FRP}t_{FRP}\varepsilon_{FRP}}{D}$$

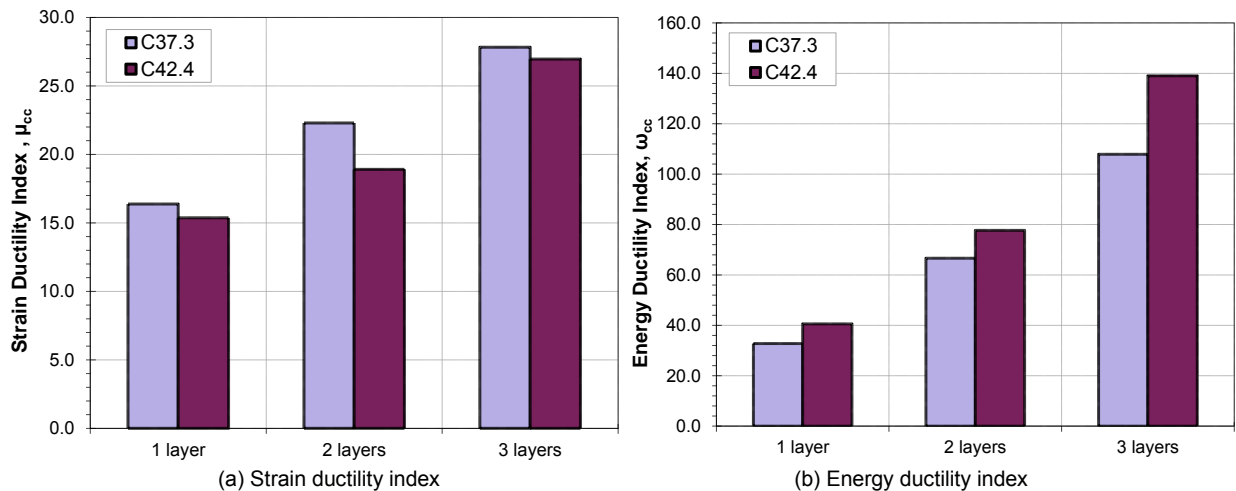


Figure 4. Effect of unconfined compressive strength on ductility indices

## 5. Conclusions

This paper presents the experimental results of externally bonded SFRP-wrapped concrete cylinders subjected to monotonic axial loading. Investigation of ductility enhancement due to the effect of the thickness of FRP jacket and concrete compressive strength has been conducted as two ductility indices, namely strain ductility index and energy ductility index have been quantified. The following conclusions can be drawn,

1. Wrapping concrete cylinders with SFRP jacket significantly enhances the ductility performance of confined concrete.
2. Strain ductility index for SFRP-wrapped cylinders increases as the thickness of FRP jacket increases and decreases as the concrete unconfined compressive strength increases.
3. Energy ductility index for SFRP-wrapped cylinders increases as the thickness of FRP jacket increases and concrete unconfined compressive strength increases.

In conclusion, strain ductility index and energy ductility index are both good indicators of ductility, however, strain ductility index measures the deformation capacity of structural member while energy ductility index gives a more realistic indication of the energy absorption capacity of the structural member and hence deemed more suitable to be used in seismic design application.

## 6. Acknowledgement

The authors would like to thank Hardwire for providing the SFRP sheets, Sika Canada for providing the epoxy adhesives, and Lafarge Canada for providing the ready-mix concrete.

## 7. References

1. Wang, H., and Belarbi, A., "Flexural behavior of fiber-reinforced-concrete beams reinforced with FRP rebars", Proceedings of the 7th International Symposium on Fibre-Reinforced Polymer Reinforcement for Concrete Structures, (FRPRCS-7), ACI Special Publications SP-230, Kansas City, USA, November 6–9, 2005, paper SP-230—51, Vol.2, pp. 895-914.
2. Park, P., Priestley, M.J.N., Gill, W.D., and Potangaroa, R.T. "Ductility and Strength of Reinforced Concrete Columns With Spirals or Hoop Under Seismic Loading", Proceedings of the 7<sup>th</sup> World Conference on Earthquake Engineering, Vol. 7, 1980, Istanbul, Turkey.
3. El-Hacha, R, and Mashrik, M.A., 2012. "Effect of SFRP confinement on circular and square columns". *Engineering Structures*, 2012, 36: 379-393.
4. Mashrik, M.A., El-Hacha, R, and Tran, K., "Performance Evaluation of SFRP-Confined Circular Concrete Columns". Proceedings of the 5<sup>th</sup> International Conference on FRP Composites in Civil Engineering (CICE 2010), September 27-29, 2010, Beijing, China, 4p.
5. El-Hacha, R., and Abdelrahman, K., "Slenderness effect of circular concrete specimens confined with SFRP sheets", *Composites Part B Engineering*, 44(1), 2012, pp.152-166.
6. Abdelrahman, K., "Effectiveness of steel-fibre reinforced polymer for confining circular concrete columns". MSc Thesis, 2011, Department of Civil Engineering, University of Calgary, Calgary, Canada.
7. Mirmiran, A., and Shahawy, M., "Behavior of Concrete Columns Confined by Fiber Composites", *Journal of Structural Engineering*, ASCE, Vol. 123, No. 5, 1997, pp. 583-590.
8. Nanni, A, and Bradford, NM., "FRP jacketed concrete under uniaxial compression". *Construction and Building Materials*, 9(2), 1995, pp 115-124.
9. Shahawy, M., Mirmiran, A., and Beitelman, T., "Tests and Modeling of Carbon-Wrapped Concrete Columns", *Journal of Composites: Part B*, Vol. 31, No. 6-7, 2000, pp. 471-480.
10. Xiao, Y., and Wu, H., "Compressive Behavior of Concrete Confined by Carbon Fiber Composites Jackets", *Journal of Materials in Civil Engineering*, ASCE, Vol. 12, No. 2, 2000, pp. 139-149.

11. Yousef, M., Feng, M., and Mosallam, A., "Stress-Strain Model for Concrete Confined by FRP Composites", *Journal of Composites: Part B*, Vol. 38, No. 5-6, 2007, pp. 614-628.
12. Ottosen NS. Constitutive model for short-time loading of concrete. *J. Eng Mech Div, ASCE* 1979; 105(1), pp. 127-141.
13. Lam, L., and Teng, J.G., "Design-Oriented Stress-Strain Model for FRP-Confined Concrete", *Construction and Buildings Materials*, Vol. 17, No. 6-7, 2003, pp. 471-489.
14. Lam L., and Teng, J.G., "Ultimate Condition of Fiber Reinforced Polymer-Confined Concrete", *Journal of Composites for Construction, ASCE*, Vol. 8, No. 6, 2004, pp. 539-548.
15. Toutanji, H., "Stress-strain characteristics of concrete columns externally confined with advanced fiber composite sheets", *ACI Materials Journal*, 96(3), 1999, pp. 397-404.
16. Toutanji, H, and Deng, Y., "Strength and durability performance of concrete axially loaded members confined with AFRP composite sheets", *Composites Part B: Engineering*, 33(4), 1999, pp 255-261.
17. Hardwire LLC, "Hardwire Composite Armor System" <http://www.hardwirellc.com>
18. ASTM INTERNATIONAL, "Standard test method for tensile properties of polymer matrix composite materials, ASTM D3039/D3039M-00, Vol. 15, No. 3, American Society of Testing Material West Conshohocken, PA, USA
19. Sikadure®-330, "Product Data sheet: 2-Part Epoxy Impregnation Resin". Edition 13/6/2006. <http://www.sikacanada.com>

# The possibility of using inhibitors in new repair materials

Vit Cerny<sup>1</sup>, Rostislav Drochytka<sup>2</sup>, Jiri Bydzovsky<sup>3</sup> and Pavel Dohnalek<sup>4</sup>

<sup>1</sup>Junior researcher, Brno University of Technology, AdMaS Centre

<sup>2</sup>Professor of Civil Engineering, Brno University of Technology, AdMaS Centre

<sup>3</sup>Senior researcher, Brno University of Technology, AdMaS Centre

<sup>4</sup>Executive head, Head of Research, BETOSAN s.r.o.

**Abstract:** Reinforced concrete is the world's most widely used construction material. Exposure of structures to the aggressive mediums from environment in various latent form leads to degradation of concrete and thus significant reduction of lifetime. The corrosion of steel reinforcement is a very serious issue. One of the ways to prevent the corrosion of steel is the use of secondary protection of reinforced concrete structures using advanced technology of migrating corrosion inhibitors. Very often it is a transparent coating emulsion which contains active substances migrating through the concrete matrix to the reinforcement that protects creating a protective film on the surface and passivate the surrounding concrete. There are a number of products from reputable manufacturers that use this technology on the Czech market. This paper is focused on testing a number of selected materials whose effectiveness is evaluated by Ohm's methods of measurement of electrical resistance, which is non-destructive method with high ability to detect state of steel reinforcement.

This research work verifies possibility of application of alternative raw materials in developed renovation coating material. 10% addition of slag was selected as the optimal one. In the consequent step, the corrosion inhibitor was applied with the aim of protecting placed reinforcement against the effect of corrosive environment. As a part of the experimental work, the effectiveness of developed inhibitor with the mark 16 considerably reducing extent of corrosion was verified.

**Keywords:** inhibitors, repair materials, concrete, corrosion.

## 1. Introduction

Corrosion of steel reinforcement is one of the main problems that civil engineering has to face. Concrete is porous material and its matrix can be penetrated by aggressive chlorides, nitrogen oxides and other corrosive substances, which increase the risk of corrosion of steel reinforcement. Aggressive substances also reduce the value of pH of concrete below 10 (pH of rust is 9.6) and the thin layer of stable corrosion products (oxides) on the surface, which was stable before, becomes porous and dissolve. This effect causes penetration of humidity, oxygen and even various ions onto non-corroded steel. This is the cause of increased corrosion of the steel element in concrete. Because it is well known that corrosion products have higher volume (2.5 times larger) than original material, cracks form in concrete and finally the covering concrete layer falls off. (1)

Secondary protection of reinforcement by means of inhibitors of corrosion is a modern and effective way of protection, which can prolong life-time of concrete structures. The basic advantage of the proposed solution is multi-functional utilization of repair material not only for repair of the construction (leveling out) but also its protection by means of integrated corrosion inhibitor, which acts on the original reinforcement built in the structure.



**Figure 1. Corrosion of reinforcement in reinforced concrete structure.**



**Figure 2. Detail of a corroded bar; surrounding concrete is damaged by expansion of corrosion products.**

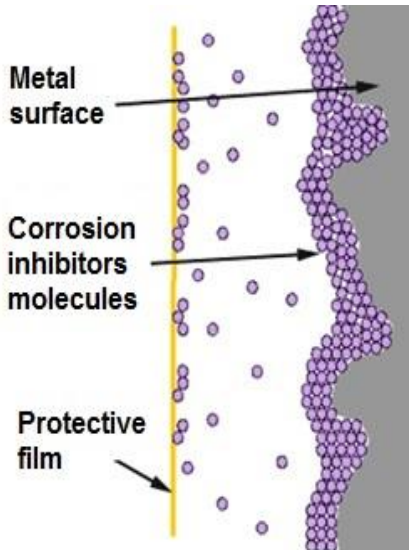
Corrosion inhibitors are generally all substances preventing corrosion or slowing it down. From the point of their principle, inhibitors are divided into anodic, cathodic and “combined”.

Anodic inhibitors slow down or eliminate reaction on the anode usually by means of reacting with corrosion products and create a protective layer on the surface of the product (steel).

Cathodic inhibitors prevent reaction on the cathode. Reaction products of cathodic inhibitors usually do not stick to the surface of metal as strongly as the anodic ones, and therefore are less effective.

Combined inhibitors influence reaction speed on both cathode and anode, which is advantageous for steel reinforced concrete.

From the point of view of prevailing interaction with metal, the inhibitors are divided into (i) inhibitors creating adsorption layer, (ii) oxidizing inhibitors, (iii) inhibitors creating passivated layer and (iv) “traps”, inhibitors bonding undesired ions from around the corroding steel. (2)



**Figure 3. Principle of action of corrosion inhibitors.**

The aim of this part of the paper is detailed research of the effectiveness of developed corrosion inhibitor interacting with polymer-cement compound and underlying concrete. As the result unique compound was

developed. This product is capable of protecting steel reinforcement in repaired concrete element thanks to the addition of corrosion inhibitor.

## 2. Test methods

Test methods are generally based on proving effectiveness of the new type of the compound as regards protecting steel reinforcement placed in repaired concrete. Test specimens were designed and manufactured from a mortar of lower quality to simulate slightly degraded concrete of initial structure including placing of steel reinforcement. Then, the test specimens were treated with the compound with the corrosion inhibitor and without it. Consequently, the test specimens were subjected to accelerated action of aggressive environment. Development of corrosion was observed on both types of the test specimens (with the corrosion inhibitor and without it) with appropriate test methods in the course of 18 months. The chapters below present individual test methods.

### 2.1 Design and preparation of test specimens

A series of test samples for verification of functionality and corrosion-inhibition properties of the compound were made from mortar, with composition given below, in the forms of dimensions 40 x 40 x 160mm with inserted reinforcement bars. After hardening of mortar and removal of formwork, the corrosion inhibiting compound was applied onto the surface.

Composition of mortar – 1m<sup>3</sup>:

- 400 kg of cement CEM II/B – S 32.5
- 1400 kg of sand, size fraction 2 – 4 mm
- 225 l of water

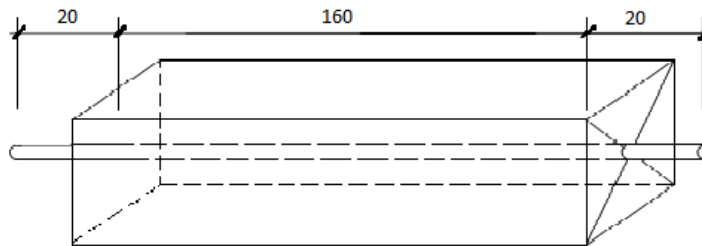


Figure 4. Diagram of the test specimens

It was necessary to adjust the formwork so that the reinforcement bar could be placed straight in the axis of the beam with overlap ca 20 mm. For this reason, the faces of the forms were designed and made from plywood with dimensions corresponding with the standard steel formwork.



Figure 5. Adjusted form for manufacture of test specimens with holes for placing and fixing steel reinforcement



## **2.2 Apparatus for automatic cycling of test specimen in aggressive environment**

The basis of the apparatus is a set of two tanks, one above another, made from specially treated plastic resistant to aggressive chemicals. Heat resistance of this material is increased to more than 100°C, which ensures its stability during thermal load when the test specimens are dried out. The top tank is divided into three levels by means of stainless perforated racks for easy placing of test specimens in the shape of a beam with dimensions 40 x 40 x 160 mm with 200 mm steel reinforcement built in the test specimen. In the bottom part of the tank there is an outlet valve with time switch for letting out the aggressive liquid, which is 3% solution of sodium chloride (NaCl) or 5.12% solution of sodium sulphate (Na<sub>2</sub>S<sub>4</sub>) in our case.

Cycles go in 12 hour intervals, where influence of a corrosive liquid is regularly changed with drying. The bottom tank is a reservoir of the aggressive liquid, which is stored there for the drying period and then again pumped into the top tank.



**Figure 6. Apparatus for accelerated process of degradation of test specimens**

## **2.3 Ohm method of measuring electric resistance**

Measuring changes of electric resistance of a metal sample is a method, which can be used for non-destructive testing of condition of a steel reinforcement built in a concrete matrix. This method uses changes of the cross-section of the metal which decreases as a consequence of corrosive process and dependence of electric resistance value on this change is known.

This measurement requires a very accurate desk multimeter with the range at least 100 Ω - 100 GΩ, coil ammeter for regulation of the current for measuring circuit, connection leads for connecting the whole circuit and an electric source producing sufficient current.





**Figure 7. Set for measuring with Ohm method**

### **2.5 Detection of corrosion inhibitors by means of dansyl chloride**

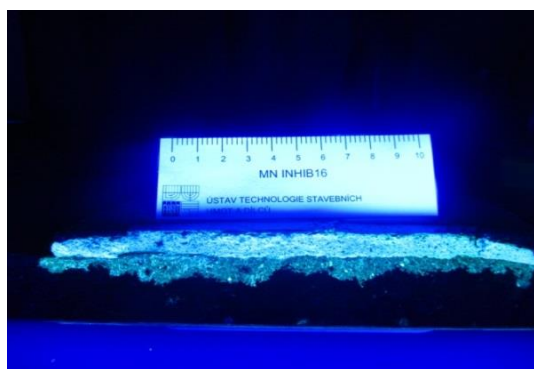
As a part of the solution, a new method for determination of presence of corrosion inhibitors was developed and is based on amino-alcohols and amino-groups. This is very important for practice. It is necessary to detect the presence of the inhibitor directly on the structure.

The method is based on the reaction of amino-groups with the chemical agent dansyl chloride in alkaline environment. The results of the chemical reaction are fluorescent products, which can be observed with naked eye when illuminated by ultraviolet light with appropriate wave-length.

Using this method in situ on building structures is not applicable, because dansyl chloride is basically a salt, which has negative influence on construction materials in general. This method is more suitable for laboratory purposes and for cases, when the silicate based test specimens are not tested by means of dansyl chloride for longer time. (3)



**Figure 8. Fracture surface of mortar applied on the underlying concrete body**



**Figure 9. Observation of corrosion inhibitors by means of an indicating agent – a picture under UV lamp – view of the fracture area**

### **3. Design of the material composition of the compound.**

The focus of the research is development of a unique compound in cooperation with manufacturer of renovation materials. The compound is developed for both horizontal and vertical area application with thickness of the layer up to 3 mm while the aesthetic qualities of the surface are accentuated. The main purpose of the compound is planary unification of the surface of concrete structure, where the surface layers were not destructed as a consequence of corrosion of built in steel reinforcement. In this sense, it is a preventive action with the aim of considerable, difficult and time-consuming renovation.

Below mentioned proportion of components was selected for the basic part of the mixture, because it has been verified by the manufacturer as an optimal compound for further development and implementation of secondary raw materials and corrosion inhibitors. The mixture is divided into two basic types of mixes, which will be consequently manufactured separately as a dry (packed) and liquid components.

**Table 1. Basic material composition of the compound**

Material	Proportion (%)
<b>Dry component</b>	
Cement	27.4
Additive	0.14
Fine sand	39.7
Lime filler	22.1
Fibers	0.04
Filler	10.6
<b>Liquid component</b> (mixing proportion 6.25 : 1)	
Defoaming agent	0.7
Plasticizer	3.6
Water dispersion	64.3
Water	31.4

#### 4. Raw materials

##### 4.1 Secondary raw materials

First of all, secondary raw materials with considerable ecological and economic advantage were selected. Based on literature search, blast furnace slag and fly ash were selected as the most appropriate

**Table 2. Chemical composition of slag**

SiO <sub>2</sub> [%]	Al <sub>2</sub> O <sub>3</sub> [%]	MnO [%]	MgO [%]	CaO [%]	S total [%]
37.9	5.8	0.6	11.9	40.0	0.7

**Table 3. Chemical composition of fly ash**

SiO <sub>2</sub> [%]	Al <sub>2</sub> O <sub>3</sub> [%]	Fe <sub>2</sub> O <sub>3</sub> [%]	FeO [%]	MnO [%]	MgO [%]	CaO [%]	K <sub>2</sub> O [%]
50.16	27.5	13.8	3.96	0.06	1.46	2.51	1.35

**Table 4. Sieve analysis of secondary raw materials**

Mesh size [mm]	Rest on the sieve [%]	
	Slag	Fly ash
2.000	0.00	0.00
1.000	0.00	0.00
0.500	0.00	0.24
0.25	0.00	6.17
0.125	1.58	19.62
0.063	7.25	56.77
<0.045	22.00	65.23

## 4.2 *Inhibitor*

### 4.2.1 *Characteristics*

This type of corrosion inhibitor was developed in the project in cooperation with Technical University in Brno and cooperating manufacturer of renovation materials. It is a completely new type of addition inhibitor of corrosion made from inland raw materials, the properties of which should be comparable with existing products of competitors available on home market. This inhibitor of corrosion presents an added value of newly developed renovation materials built in their material composition. Its task is to penetrate into the underlying concrete, passivate it and thus protect the steel reinforcement.

### 4.2.2 *Typical properties*

**Table 5. Parameters of the inhibitor**

Appearance	White powder
Bulk weight	1.06 g/cm <sup>3</sup>
Dosing	3.0 – 4.0 % by weight of cement.

### 4.2.3 *Application*

Powder inhibitor is dosed in the amount of 3-4% by weight of cement. If it is not mixed in the dry mix, it has to be properly mixed in the dry component by mixing for at least 3 minutes (depending on the amount of material). Addition into the material already mixed with water is not recommended because of its powder form, which can influence workability and mixing can be uneven.

### 4.2.4 *Field of application*

- All structures made from steel reinforced concrete, precast concrete, pre-stressed concrete, post-tensioned concrete and concrete used in naval architecture
- Bridges, highways and roads from steel reinforced concrete exposed to corrosive environment (carbonation, de-icing salts and weather influences)
- All structures made from steel reinforced concrete at sea-shore areas
- Addition into the mortar straight at the manufacturer's to increase anti-corrosion effect

### 4.2.5 *Advantages*

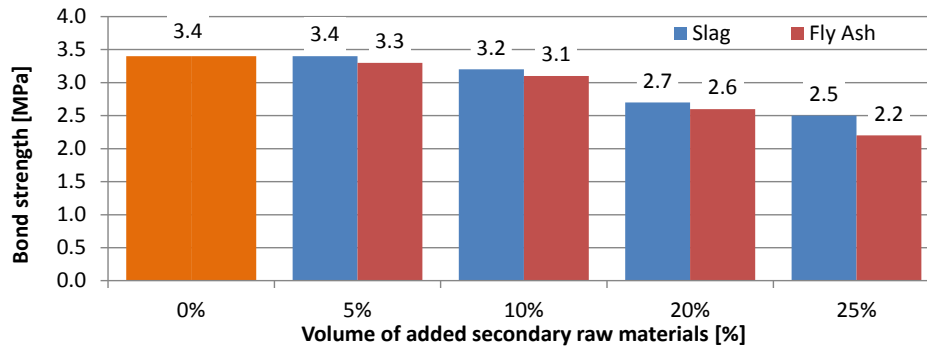
- Considerable prolonging of life of steel reinforced concrete structures
- Composition in dry mortar mix
- Non toxic or harmless
- The product has no influence on the basic characteristics of concrete mix
- Soluble in water, inflammable, easy to manipulate
- Protects reinforcement at both anodic and cathode areas
- Migrates through concrete, where it seeks and consequently protects built in reinforcement

## 5. *Results of experimental testing*

### 5.1 *Optimization of addition of secondary raw material*

For the reason of initial experimental verification of optimal addition of secondary raw material in the compound, addition of blast furnace slag and fly ash with dosage 5%, 10%, 20% and 30% by weight of cement were tested. These were in parallel compared with reference test specimen (0% addition of secondary raw materials). Test specimens were placed in water for 7 days and then in climatic chamber at the temperature of 21°C and relative humidity 65% until the age of 28 days.

Evaluation of suitability of secondary raw materials for the renovation compound was focused mainly on the influence of the dosage of addition on bond strength, which was determined with Pull Off test stated in EN 1542:1999.



**Figure 10. Determination of bond strength by means of a pull off test in accordance with EN 1542:1999**

The test results imply that slag is more appropriate raw material. Experimental determination of bond strength by pull off test in accordance with EN 1542:1999 shows gradual decrease of bond strength as the proportion of alternative component is increased. Minimal requirement of the standard EN 1504-3:2005 for bond strength of mortars on base material is 2.0 MPa for class R4. Based on practical experience from renovation works, the level 3.0 MPa is recommended. This determines the optimal addition of 10% of slag.

## 5.2 Verification of selected type of inhibitor

The principle of protection is based in releasing corrosion inhibitors from the renovation compound after its application on the concrete structure. Newly developed compound was considered and developed as a bi-component polymer-cement mortar mix for renovation of concrete structures, onto which any type of a secondary protection can be coated depending on the exposition of the structure. The second aim is to prolong the life of the treated structure using the corrosion inhibiting technology. All these aspects were taken into account when individual components and their proportions were designed.

**Table 6. Material composition of the compound (SH INHB)**

Material	Proportion (%)
<b>Dry component</b>	
Cement	26.4
Slag	2.6
Additive	0.14
Fine sand	39.7
Lime filler	22.1
Fibers	0.04
Filler	10.6
Addition of corrosion inhibitor (4 % by the amount of cement)	1.06
<b>Liquid component</b> (mixing proportion 6.25 : 1)	
Defoaming agent	0.7
Plasticizer	3.6
Water dispersion	64.3
Water	31.4

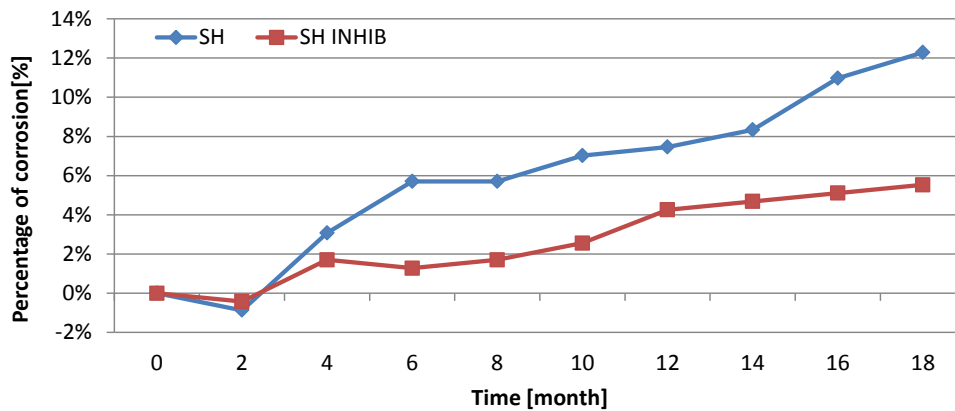
Individual mix-designs were used to manufacture test specimens; after 28 days of maturing basic physical-mechanical properties stated in the table below were determined. Mixture from Table 1 is used as a reference (SH).

**Table 7. Results of basic tests of the compound**

Compound	Volume weight of fresh mix [kg/m <sup>3</sup> ]	Volume weight of hardened mix [kg/m <sup>3</sup> ]	tensile bending strength: [MPa]	Compressive strength [MPa]	Bond strength to base material [MPa]
SH	1800	1796	10.3	29.6	3.4
SH IHIB	1892	1890	13.0	33.2	3.8

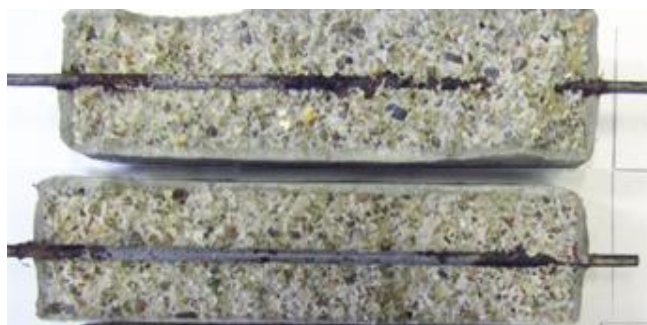
The results show that developed renovation compound (SH INHIB) has higher volume weight, but also higher tensile bending strength, compressive strength and bond strength.

From the point of view of suitability of selected inhibitor, it is necessary to focus on the primary function - protection of reinforcement. Renovation compound was applied on the samples of base concrete (defined in chapter 2), thickness of the layer was 3 mm. Then, the samples were placed in a humid environment for 28 days. Then they were repeatedly exposed to aggressive environment of 3% sodium chloride (NaCl) solution for 18 months. The samples were once a month tested by Ohm method. The table below states percentage of total corrosion of the compound exposed to aggressive environment cycles.



**Figure 11. Percentage of corrosion of the reinforcement**

The values of percentage of corrosion of the reinforcement determined by Ohm method shows that after 18 months exposure the samples treated with inhibiting compound show half rate corrosion than the untreated SH sample. Very low extent of corrosion is apparent on the sample, which was treated with renovation compound with the Inhibitor 16. This was verified also by means of a destructive test and visual assessment, when individual specimens were broken longwise. Figure 5 shows very low corrosion of the specimen with the inhibitor, where corrosion can be observed only at peripheral areas. These are the areas, where aggressive medium penetrates the porous structure at the border line steel-concrete.



**Figure 12. Visual assessment of compounds exposed to chloride environment (SH top, SH INHIB bottom)**

## **6. Conclusion**

There were two options for research verified in this work. First was a possibility of application of alternative raw materials in developed renovative coating material and secondly the possibility of increasing its corrosion protection. As additive of secondary material was 10% of slag selected as an optimum. It ensured bond strength at least by 3 MPa. The consequent step was application of the corrosion inhibitor with the aim of protecting reinforcement against the effect of corrosive environment in the form of 3% solution NaCl. Effectiveness of addition of developed corrosion inhibitor together with the compound was verified; the compound showed unambiguously lower extent of corrosion of reinforcement compared with renovation compound without the inhibitor. The results were verified by measurement of electrical methods and visual assessment after destruction of the test specimens. Further research will verify possibilities of using secondary raw materials and corrosion inhibitors in other types of renovation materials.

## **7. Acknowledgement**

This paper has been worked out under the project No. LO1408 "AdMaS UP - Advanced Materials, Structures and Technologies", supported by Ministry of Education, Youth and Sports under the „National Sustainability Programme I" and under the project FR-TI4/369 "New repair materials for reinforced concrete structures with high fire resistance" supported from funds of the state budget through the Ministry of Industry and Trade.

## **8. References**

1. Drochytka, R., "Durability of Building Materials", Technical University in Brno, 2007.
2. Inhibitors of corrosion of metals, [online], [cit. 22. 10. 2014], Available at: [http://old.vscht.cz/met/stranky/vyuka/labcv/labor/koroze\\_inhibitory/index.htm](http://old.vscht.cz/met/stranky/vyuka/labcv/labor/koroze_inhibitory/index.htm).
3. Fiedlerová, M., Taranza, L. et al. M. "Determination of presence of corrosion inhibitors in hardened mortars" Conference on testing and quality in building industry. 2014. Technical University in Brno. 2014. pp. 63 - 70. ISBN 978-80-214-5032-5.
4. Drochytka, R.; Dohnálek J. et al. "Technical Conditions for Repair Work of Concrete Structures TP SSBK III", Brno 2012, ISBN 978-80-260-2210-7.
5. EN 1542: 1999 Products and systems for the protection and repair of concrete structures - Test methods - Measurement of bond strength by pull-off.
6. EN 1504-3: 2005 Products and systems for the protection and repair of concrete structures. Definitions, requirements, quality control and evaluation of conformity. Structural and non-structural repair.

# Numerical Investigation of the Flexural Performance of RC Beam Strengthened with Iron-Based Shape Memory Alloys Bar

Hothifa Rojob<sup>1</sup> and Raafat El-Hacha<sup>2</sup>

<sup>1</sup>PhD Candidate, Department of Civil Engineering, University of Calgary

<sup>2</sup>Associate Professor, Department of Civil Engineering, University of Calgary

**Abstract:** The use of shape memory alloys (SMA) in structural engineering applications was limited to small-scale projects and not adapted in practical application due to the high cost of constitutive materials and production schemes. Recently, the iron-based SMA (Fe-SAM) is being developed. The inexpensive constitutive materials of the Fe-SMA and the availability of mass production facilities of steel products makes this material more suitable for large structural engineering applications than the most common shape memory alloys (i.e. NiTi). SMA is mainly characterized by the Shape Memory Effect (SME) phenomenon. The SME represents the ability of the SMA to recover its original shape after being deformed beyond the elastic limits through heating. This paper reports on the finite element modeling of 150×305×2000 mm RC beam strengthened in flexure with NSM Fe-SMA bar. The pre-strained Fe-SMA bar is anchored inside a groove in the tension side of the RC beam and then heated up to 350 °C where the transformation from martensite to austenite phase occurs causing a prestressing force developed in the Fe-SMA bar that counteracts the applied loads. Two beams were modeled; a control unstrengthened beam, and a beam strengthened by NSM Fe-SMA bar. The 3D FE model is validated against experimental test results.

**Keywords:** Near-Surface Mounted, Iron-Based Shape Memory Alloy, Strengthening, Prestressing, Finite Element Modeling.

## 1. Introduction

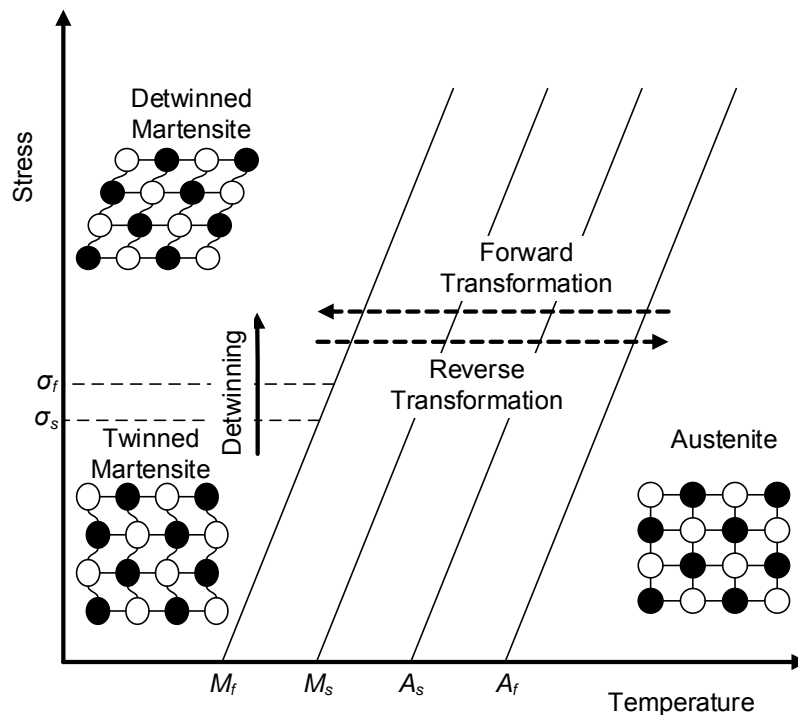
Structural retrofitting become important as structures worldwide are facing deterioration and increasing load demand. Fiber Reinforced Polymers (FRPs) are widely used to strengthen/retrofit existing structures. In the case of Reinforced Concrete (RC) flexural member, FRPs are applied in the form of sheets, strips, bars, and plates. Several techniques are used to attach the non-prestressed FRPs to the concrete, the Near Surface Mounted technique (NSM), Externally Bonded technique (EB), and Mechanically Fastened technique (MF) [1–3]. One common characteristics of the above listed techniques is the passivity of the strengthening system. In other words, the FRP material will not be activated unless a further deflection occurs to the beam. Therefore, the FRP will only contribute in enhancing the ultimate load capacity. In order to enhance the flexural capacity of the RC beam at service load, few researchers proposed to prestress the FRP. It was proven that the prestressing FRP system has contributed in enhancing the flexural performance of the RC beams in service and ultimate load states [4]. However, the application of the prestressing force to the FRP is challenging. El-Hacha and Gaafar [5] developed anchorage system to prestress the NSM FRP against the RC beam using hydraulic jack. Hadiseraji and El-Hacha [6] proposed the use of Nitinol (NiTi) Shape Memory Alloy (SMA) bar as a prestressing tool to apply prestressing force to the EB FRP sheets and NSM FRP strips. SMAs are known by the ability to recover part of the induced deformation upon heating. This phenomenon is called the Shape Memory Effect (SME) [7, 8]. The current research project proposes a new strengthening technique where SMA bars are utilized as strengthening reinforcements instead of FRPs. The NSM technique is adopted by embedding the pre-deformed SMA bar in a groove cut on the tension side of the beam. Because both ends of the bar are restrained through a steel anchorage plates, the application of heat results in a prestressing force in the bar without the need for jacking tools.

This paper reports on the results of Finite Element Modeling (FEM) of RC beam strengthened in flexure with NSM Iron-Based SMA (Fe-SMA). The results of the FEM is compared to the experimental results. The properties of the SMAs is firstly discussed followed by a brief description of the experimental test results. After that, the FE model is described. Finally, the comparison between the FEM results and the experimental results is presented.

## 2. Shape Memory Alloys

The Shape Memory Alloys (SMA) are metallic alloys and considered as type of smart materials. They are mainly known by the ability to recover part of the deformation upon heating. This unique behavior is attributed to the temperature and stress dependent phase transformation. SMAs exist in two different crystallographic phases, the low symmetry phase called the Martensite phase exist at low temperatures, and the high symmetry phase called Austenite phase at high temperature. The martensite transformation is the key feature of SMAs which occurs by shear lattice distortion rather than atom diffusion. The martensite transformation (austenite to martensite, also called forward transformation) starts at temperature value  $M_s$  (martensite start). The transformation continues until temperature  $M_f$  (martensite finish) where all the material become in martensite form. When the material is heated in absence of stress it will start to transform to austenite at a temperature marked as  $A_s$  (austenite start) in a process called reverse transformation. The material will totally transform to austenite at  $A_f$  (austenite finish) as shown in **Figure 1**. During the cooling process below  $M_f$ , no macroscopic shape change will occur because of the twinning process, where multiple variants coexist, and the phase is called twinned martensite. The martensite variants can be forced to orient (detwin) in a single variant through mechanical loading. The detwinning starts at a stress level  $\sigma_s$  (detwinning start) and finishes at stress level  $\sigma_f$  (detwinning finish) causing macroscopic inelastic strain. Upon heating above  $A_f$  the detwinned martensite phase transforms to the parent austenite phase causing recovery of the inelastic strain. This process is called the Shape Memory Effect (SME) as presented in **Figure 2** [7, 8]. If the ends of the SMA bar are restrained, no recovery strain will occur, alternatively, a recovery stress will develop. The recovery stress results from the SME process can be utilized to introduce stresses to structures.

The most common type of SMA is the Nitinol (NiTi), which is mainly composed of Nickle and Titanium. Nitinol stands for Nickel Titanium Naval Ordnance Laboratory [9]. The application of this material is mainly limited to small-scale applications because of the expensive constitutive materials. On the other hand, the Iron-based shape memory alloys (Fe-SMA) are considered to be the future best candidate for structural engineering applications due to the cheap constitutive materials and production scheme [10–14]. Czaderski et al. [11] used Fe-SMA strips to apply prestressing force to small concrete bars. Soroushian et al. [15] were the first to use Fe-SMA for external tensioning to repair bridge girder in shear.



**Figure 1. Phase diagram of typical SMA, after Lagouda [8]**



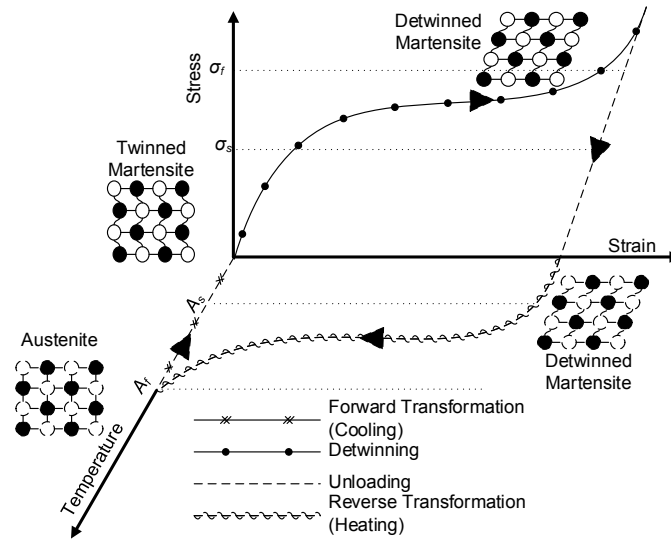


Figure 2. Shape Memory Effect process, after Lagouda [8]

### 3. Description of the experimental program

The experimental program includes the testing of two beams, the control beam (C-B) was tested by Hadiseraji and El-Hacha [6], and the other beam strengthened with NSM Fe-SMA bar (SMA-B) was tested as part of the ongoing research project. **Figure 3** shows the details of the RC beams strengthened with NSM Fe-SMA bar. The bar was initially strained to 6% and then anchored inside a groove cut on the tension side of the beam. The bar was then heated to 350 °C. The heating process caused the activation of the reverse transformation process. Because both ends of the bar were restrained through steel anchors mounted on the beam, a tensile stress developed in the bar causing a prestressing force at the bottom of the RC beam. The groove was then filled with epoxy adhesive. The strengthened beam was tested in four-point bending setup as shown in **Figure 3**.

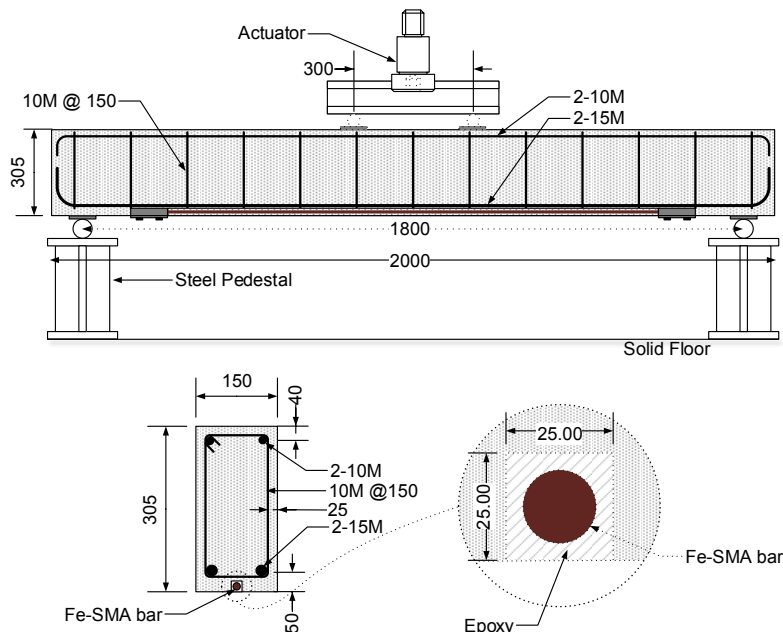
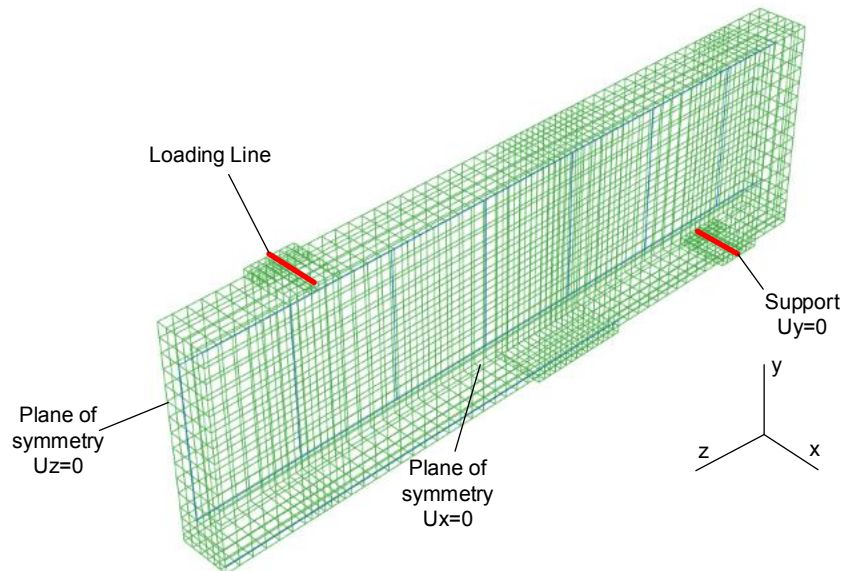


Figure 3. Details of SMA-B.

The beam was instrumented with four Linear Strain Conversion (LSC) at the mid-span of the beams to monitor the concrete strains (two LCSs were placed on each side of the beam in which one of each is mounted at the level of the longitudinal bottom and top steel; and two LCSs were mounted on the top compression surface of the beam). Two strain gauges (SG) were installed on the tension steel and one was installed on the compression steel, at mid-span of the steel bars. Two laser transducers were used to measure the vertical deflection at the mid-span of the beam.

#### 4. Description of the finite element model

A 3D Finite Element Model (FEM) was developed using the commercial software ABAQUS. Quarter of the beam was modeled by making use of two planes of symmetry, one plane divides the beam in half longitudinally, and one plane divides the beam in half transversely. The symmetry was imposed by boundary conditions as shown in **Figure 4**. The concrete, support, and loading plate were modeled with 8-Node reduced integration continuum element which has three degrees of freedom, translation in x, y, and z directions. Steel reinforcements and Fe-SMA bar were modeled using 2-Node truss elements with three translational degrees of freedom at each node (i.e. x, y, z). The interaction behavior of the reinforcements and the concrete was modeled using the embedded region option, where the response of the host elements (i.e. concrete) used to constrain the translational degrees of freedom of the embedded nodes. The beam was loaded in time-independent displacement controlled mode. The support was imposed by applying boundary conditions. The prestressing force was applied to the Fe-SMA as initial tensile stress value that corresponds to the actual stress value developed in the Fe-SMA bar after heating. The size of mesh was optimized to reduce the computational efforts at the same time making sure that the results are mesh-independent.



**Figure 4. Boundary conditions.**

#### 4.1 Material properties

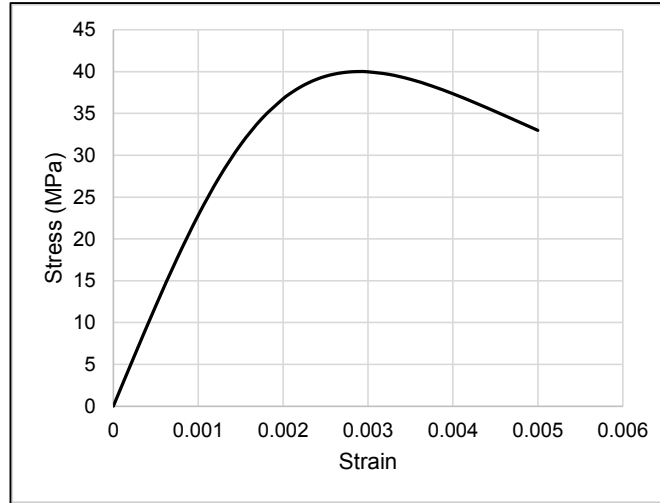
##### 4.1.1 Concrete

The concrete behaviour was modelled using damaged plasticity model [16]. The compression stress strain behavior was obtained using Carreira and Chu model [17] as presented in Equations 1 to 3.  $f_c$  is the concrete stress,  $\epsilon_c$  is the concrete strain, and  $E_{it}$  is the initial tangent modulus. The concrete compressive strength was about 40 MPa. **Figure 5** shows the stress strain curve of concrete under compression obtained using Equation 1.

$$f_c = f_c' \left( \frac{Bx}{B-1+x^B} \right) \quad (1)$$

$$B = \left( \frac{1}{1 - \frac{f'_c}{\varepsilon_o E_{it}}} \right); \text{ and } x = \frac{\varepsilon_c}{\varepsilon_o}; \varepsilon_o = 0.0029 \quad (2)$$

$$E_{it} = 3320\sqrt{f'_c} + 6900 \quad (3)$$



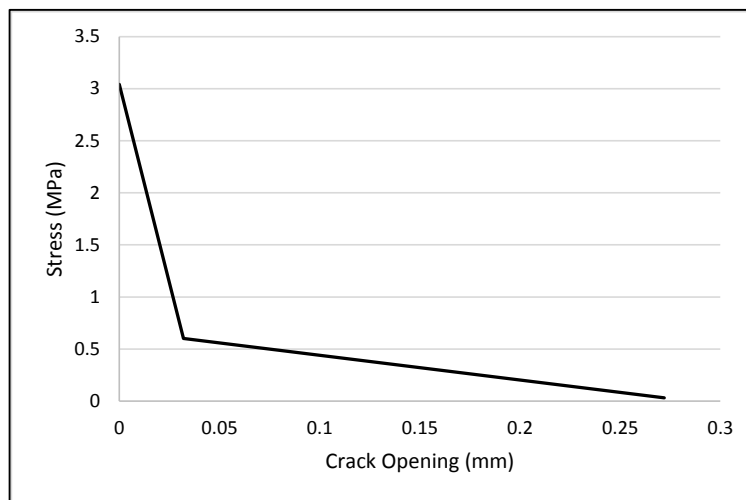
**Figure 5. Stress-strain of concrete under compression.**

The behaviour of concrete in tension was modelled using tensile stress-crack opening curve as recommended by Coronado and Lopez [18]. This curve is defined based on the tensile strength ( $f_t$ ) and the fracture energy of concrete ( $G_F$ ). Both  $f_t$  and  $G_F$  were obtained using the CEB-FIP model [19] as presented in Equation 4 and Equation 5, respectively. **Figure 6** shows the tensile stress-crack opening relationship.

$$f_t = 1.4 \left( \frac{f'_c - 10}{8} \right)^{2/3} = 3.04 \text{ MPa} \quad (4)$$

$$G_F = (0.0469d_a^2 - 0.5d_a + 26) \left( \frac{f'_c}{10} \right)^{0.7} = 0.0917 \text{ N/mm} \quad (5)$$

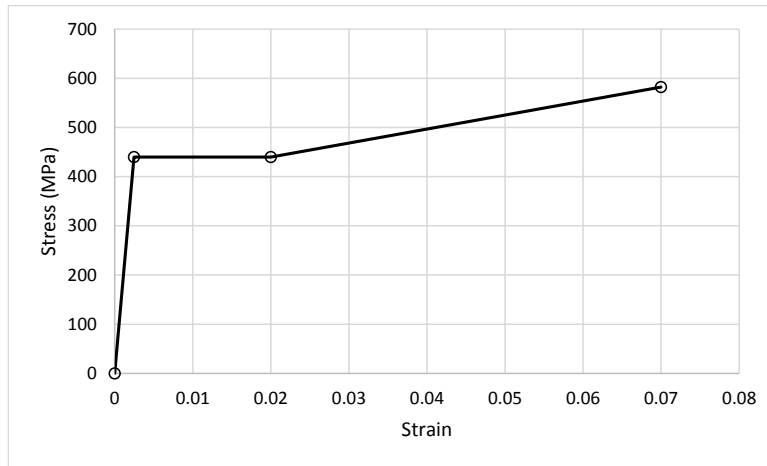
where  $d_a$  is the maximum aggregate size, it was taken as 20 mm.



**Figure 6. Tensile stress-crack opening relationship of concrete.**

#### 4.1.2 Steel

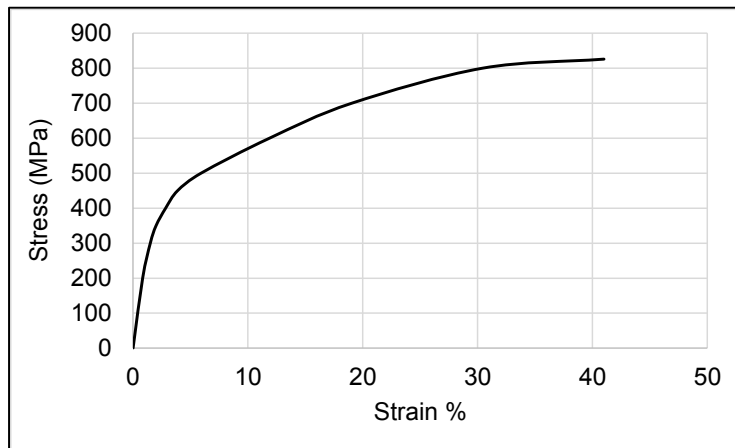
A tri-linear stress-strain curve of steel was simplified from the actual test results reported by Oudah [20] as shown in **Figure 7**. All the steel reinforcements have the same mechanical properties. The yield stress is 440 MPa and the modulus of elasticity is 180 GP.



**Figure 7. Simplified stress-strain curve of steel.**

#### 4.1.3 Fe-SMA bar

The diameter of the Fe-SMA bar was 14.3 mm. The bar was 1.1 m long centered in the groove on the tension side of the RC beam. The stress-strain curve of the bar as given by the manufacturer [12] is shown in **Figure 8**.



**Figure 8. Stress-strain curve of Fe-SMA, after Awaji [12].**

### 5. Model Validation

The model is validated against experimental results of a control beam (C-B) tested by Hadiseraji and El-Hacha [6], and a beam strengthened with NSM Fe-SMA bar (SMA-B) tested as part of this ongoing research project. **Figure 9** and **Figure 10** shows the numerical and experimental load deflection curves of C-B and SMA-B, respectively. The load deflection curves obtained numerically shows a good agreement with the experimental results. This indicates the validity of the FE model to simulate the behavior of the modeled beam. The FE model of SMA-B shows slightly higher stiffness and yielding loads, this might be attributed to the loss of prestressing force in the Fe-SMA bar occurred during the experiment due to

anchorage setting. The failure mode of all the numerical models of the beams occurred by crushing of concrete after the yielding of steel bars and Fe-SMA bar respectively, which is in agreement with the experimental results. **Table 1** shows a comparison between the results of the FE models and the experimental results.

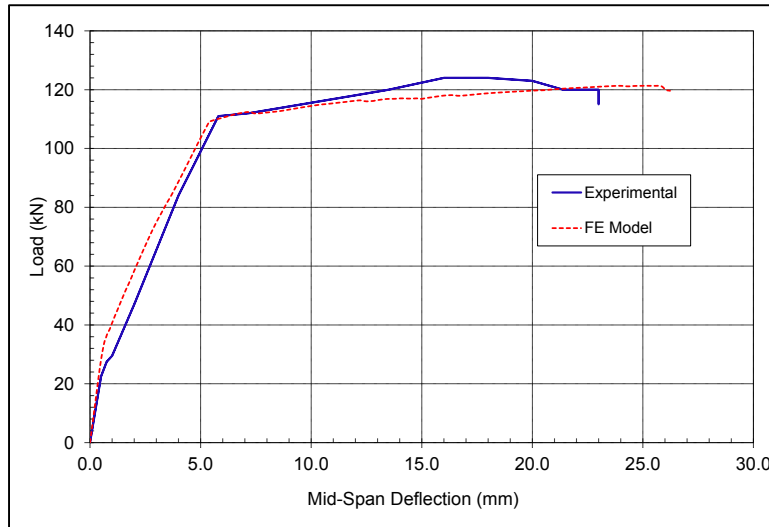


Figure 9. FE model results against the experimental results for B-C.

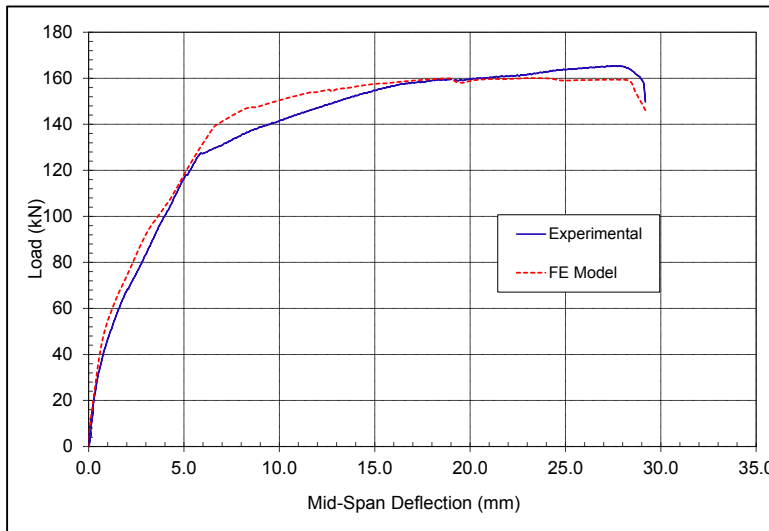


Figure 10. FE model results against the experimental results for SMA-B.

Table 1. Comparison between the numerical and experimental results

Beam →	C-B			SMA-B		
Variable ↓	Exp. Results	FE Results	%Δ	Exp. Results	FE Results	%Δ
Cracking Load: $P_{cr}$ (kN)	19	30	58	40	40	0
Yielding Load: $P_y$ (kN)	104	109	5	127.4	139	9
Ultimate Load: $P_u$ (kN)	124	121.3	2	165.4	160.1	3

## 6. Conclusions

The FE model was validated against the experimental results. The FE model was able to simulate the control beam, and the beam strengthened with Fe-SMA bar. The model can be further used to study the behavior of RC beams strengthened with NSM Fe-SMA bars at different level of prestressing forces, and different Fe-SMA materials. A future work will include the use of comprehensive constitutive model of the Fe-SMA material that will allow the simulation of the behavior of the Fe-SMA bar during heating, including the martensite transformation process and thermal expansion. The model will spot more light on the behavior of the strengthened RC beam during the heating process of Fe-SMA bar.

## 7. Acknowledgement

The authors would like to acknowledge the University of Calgary and the Natural Sciences and Engineering Research Council of Canada (NSERC) for their financial support towards this research project.

## 8. References

- [1] A. J. Lamanna, L. C. Bank, and D. W. Scott, "Flexural strengthening of reinforced concrete beams using fasteners and fiber-reinforced polymer strips," *ACI Struct. J.*, vol. 98, pp. 368–376, 2001.
- [2] H. A. Baky, U. A. Ebead, and K. W. Neale, "Flexural and Interfacial Behavior of FRP-Strengthened Reinforced Concrete Beams," *Journal of Composites for Construction*, vol. 11, pp. 629–639, 2007.
- [3] R. El-Hacha and S. H. Rizkalla, "Near-surface-mounted fiber-reinforced polymer reinforcements for flexural strengthening of concrete structures," *ACI Struct. J.*, vol. 101, pp. 717–726, 2004.
- [4] M. Gaafar and R. El-Hacha, "Strengthening reinforced concrete beams with prestressed near surface mounted FRP strips,". Proceedings, Fourth International Conference on FRP Composites in Civil Engineering, Zurich, Switzerland, pp. 22–24 2008.
- [5] R. El-Hacha and M. Gaafar, "Flexural strengthening of reinforced concrete beams using prestressed, near-surface-mounted CFRP bars," *PCI J.*, vol. 56, no. 4, pp. 134–151, 2011.
- [6] M. Hadiseraji and R. El-Hacha, "Flexural strengthening of reinforced concrete beams with prestressed externally bonded CFRP sheets," in *5th International Conference on Concrete Repair-Concrete Solutions 2014*, pp. 273–277, 2014.
- [7] C. Cismasiu, *Shape Memory Alloys*. Rijeka, Croatia: Sciyo, 2010.
- [8] D. C. Lagoudas, *Shape Memory Alloys, Modeling and Engineering Applications*. New York, USA: Springer Science, 2008.
- [9] G. Kauffman and I. Mayo, "The Story of Nitinol: The Serendipitous Discovery of the Memory Metal and Its Applications," *Chem. Educ.*, vol. 2, no. 2, pp. 1–21, 1997.
- [10] F. C. Nascimento-Borges, "Iron Based Shape Memory Alloys: Mechanical and Structural Properties, Shape Memory Alloys - Processing, Characterization and Applications," *Shape Mem. Alloy. – Process. Charact. Appl.*, pp. 116–128, 2013.
- [11] C. Czaderski, M. Shahverdi, R. Brönnimann, C. Leinenbach, and M. Motavalli, "Feasibility of iron-based shape memory alloy strips for prestressed strengthening of concrete structures," *Constr. Build. Mater.*, vol. 56, pp. 94–105, 2014.
- [12] Awaji Materia, "Shape Memory Alloys," *Characteristics and applications of Fe-Mn-Si-based shape memory alloys*, 2014. [Online]. Available: [http://www.awaji-m.jp/english/r\\_and\\_d/about.html#alloy](http://www.awaji-m.jp/english/r_and_d/about.html#alloy). [Accessed: 01-Dec-2014].
- [13] K. Li, Z. Dong, Y. Liu, and L. Zhang, "A newly developed Fe-based shape memory alloy suitable for smart civil engineering," *Smart Mater. Struct.*, vol. 22, pp. 1–7, 2013.
- [14] Z. Dong, U. E. Klotz, C. Leinenbach, A. Bergamini, C. Czaderski, and M. Motavalli, "A novel Fe-Mn-Si shape memory alloy with improved shape recovery properties by VC precipitation," *Adv. Eng. Mater.*, vol. 11, no. 1, pp. 40–44, 2009.

- [15] P. Soroushian, K. Ostowari, A. Nossoni, and H. Chowdhury, "Repair and strengthening of concrete structures through application of corrective posttensioning forces with shape memory alloys," *Transp. Res. Rec.*, no. 1770, pp. 20–26.
- [16] SIMULIA, "Abaqus theory manual, Concrete damaged plasticity" 2014. [Online]. Available: [www.oulu.fi/tietohallinto/unix/abaqus\\_docs/v6.13/](http://www.oulu.fi/tietohallinto/unix/abaqus_docs/v6.13/). [Accessed: 06-Feb-2015].
- [17] D. J. Carreira and K.-H. Chu, "Stress-Strain Relationship for Plain Concrete in Compression," *ACI J. Proc.*, vol. 82, pp. 797–804, 1985.
- [18] C. A. Coronado and M. M. Lopez, "Sensitivity analysis of reinforced concrete beams strengthened with FRP laminates," *Cem. Concr. Compos.*, vol. 28, no. 1, pp. 102–114, Jan. 2006.
- [19] CEB-FIP, *CEB-FIP Model Code 90*. London: Thomas Telford Ltd., 1993.
- [20] F. Oudah, "Fatigue Performance of RC Beams Strengthened using Prestressed NSM CFRP," MSc. Thesis, University of Calgary, 2011.

# Development of Double-Slotted Beam-Column Connection for the Seismic Design of Structures

Fadi Oudah<sup>1</sup> and Raafat El-Hacha<sup>2</sup>

<sup>1</sup>Post-Doctoral Engineering Specialist, Amec Foster Wheeler (formerly PhD Candidate at University of Calgary)

<sup>2</sup>Associate Professor, Department of Civil Engineering, University of Calgary

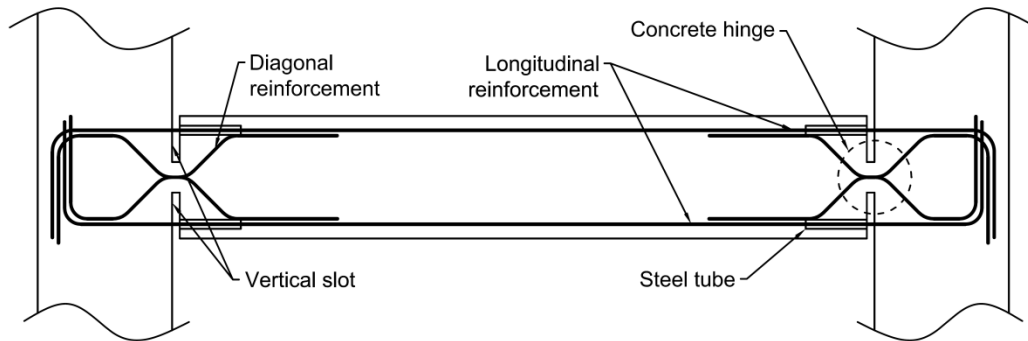
**Abstract:** The Double-Slotted Beam (DSB) system is a new beam-column connection proposed and verified in this research. The DSB system is made of a strong column and a weak beam slotted from both the top and the bottom sides. Both top and bottom reinforcements act as energy dissipation devices in which the energy imposed on the system are dissipated via their hysteretic responses. The DSB system maintains a non-tearing action to the slab attached to the beam member. In this paper, the key design aspects of the newly developed system are discussed followed by experimental evaluation of large-scale beam-column connections. The test results are analyzed with respect to the hysteretic response and energy dissipation. Test results indicate the superior performance of the developed system in terms of achieving a stable and fat hysteretic response with no signs of pinching shear. However, it experienced lower equivalent viscous damping as compared with conventional connections, which open the doors for further enhancements of the system.

**Keywords:** Beam, Concrete, Connection, Slotted.

## 1. Introduction

The continuous development in seismic design of concrete structures is driven by the need to achieve resilient, yet, practical designs of beam-column connections as they represent the most critical components in the lateral loading resisting system. The degradation of the load lateral load carrying capacity and the tearing action of the attached slabs are among the main challenges encountered in the design of conventional concrete beam-column connections (1,2). As such, research in connection design should aim at mitigating the consequences associated with these design difficulties.

An innovative connection design is proposed and validated in this research. The design philosophy of the new system is based on attaining higher drift capacity, achieving a more stable hysteretic response, and attaining a non-tearing action to the attached slab. The system is called 'Double Slotted Beam (DSB)' as it includes two vertical slots made into the beam member at the face of the column (Figure 1).



**Figure 1. Schematic drawing of the DSB connection.**

The DSB system is made of a strong column and a weak beam. A large amount of longitudinal reinforcement is placed in-between the slots in order for it to remain elastic during the plastic rotation of the beam. The top and the bottom reinforcements yield under positive and negative bending, and thus, they act as energy dissipation devices. The energy imposed on the system is dissipated via the hysteresis response of both reinforcements. The advantages of the DSB system are as follows:

1. Non-tearing action. The top slot is anticipated to open and close during the seismic loading. However, if a construction joint is made in the slab at the location of the top slot, a non-tearing action of the slab can be achieved.



2. High drift capacity. The neutral axis at the vertical slot is approximately equal to half of the beam depth. This will lead to higher drift capacity since the strain level in the tension reinforcement decreases with increasing depth of the neutral axis.
3. Plastic hinge relocation. Moving the vertical slot away from the face of the column is anticipated to relocate the plastic hinge effectively.
4. Minimal repair cost. The plastic rotation is concentrated at the slot. Therefore, minimal concrete cracking is anticipated when the connections is subjected to lateral loading.

The design of the connection is discussed briefly following by examining its response via experimental testing. The behavior of the connection is also compared with conventional connection designed to achieve approximately the same ultimate strength.

## 2. Design of Connections

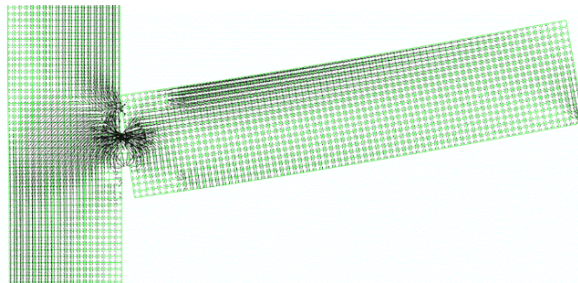
### 2.1 Flexural design

The beam is designed to have similar positive and negative moment capacities. Therefore, the dimensions of the upper and the lower slots along with the amount of the bottom and top reinforcement are set to be equal. A portion of the concrete hinge will be subjected to compression forces, and thus, the stresses induced in the bottom and the top reinforcement will not be the same. The magnitude of the compression forces in the concrete hinge depends on its dimensioning and the width of the cracks developed when the connection is subjected to lateral loading. Each of the top and the bottom reinforcement consisted of 2-15M steel reinforcement (Grade 440).

### 2.2 Shear design

Finite Element (FE) simulation is used to examine the flow of forces within the connection in order to help in designing the amount of stirrups in the beam and the joint. The simplified 2D model intends to provide a general representation of the deformation mechanism and not to provide accurate results in term of load and deflection. Only longitudinal steel (in the beams and columns) and concrete sections were considered in the model. The steel was modeled as a linear elastic material with a modulus of elasticity of 200 GPa. The concrete was also modeled as linear elastic material with a modulus of elasticity equal to 28.5 GPa (3). The concrete section and the steel reinforcement were modeled using 4-node plane strain and beam elements, respectively, in ABAQUS. The tip of the beam was subjected to upward 10 mm deflection upward to induce a positive moment. The column was subjected to 405 kN (determined based on the analysis of the structure included). The column was also hinged at the top and the bottom sides. The size of the mesh was chosen such that to provide adequate level of accuracy. The bottom and top reinforcement in the DSB connections were debonded from the surrounding concrete using the Tube-to-Tube elements for a distance of 200 mm.

The visualization of the minimum principal strains (compressive strains) in the DSB system under positive bending are shown in Figure 2. The behavior under negative bending is similar to that under positive bending due to its symmetric nature, and thus, only positive bending is considered herein. High levels of compressive strains are induced in the concrete hinge. Diagonal compression struts are formed transferring the forces from the edge of the unbonded reinforcement in the beam section to the concrete hinge. Also, two diagonal compression struts are formed in the joint.



**Figure 2. Visualization of the compressive strains in the DSB connection.**

Based on the discussion presented above, the beam is divided into two regions in terms of the detailing of the stirrup reinforcement. In this research, the recommendation on the length of regions are adopted from the Paulay and Priestley (1). Even though the recommendations by Paulay and Priestley (1) are concluded based on the behavior of beams with diagonal reinforcement as a mean for relocating the plastic hinges, their recommendations are applicable to be used in the DSB system based on the observations made about the FE analysis. Region I extends for  $1.5b_d$ , where  $b_d$  is the beam depth. Region I extends from the edge of Region II to the tip of the beam. Region I is a non-critical region in which the conventional design procedure of shear reinforcement is adopted whereas special detailing is required in Regions II. The special detailing of the stirrups adopted in this study was based on the anti-buckling requirements for the design of RC members in CSA-A23.3-04 (3). It is noted that the area of the stirrups right at the face of the vertical slot was doubled in order to accommodate the high shear demand at this region. Diagonal reinforcements are also used to enhance the shear transfer mechanism near the slots as shown in Figure 3. The diagonal reinforcement passes through the concrete hinge extends from the concrete hinge to the top and the bottom concrete fibers. The concrete compression strut that extends between the concrete hinge and the corner of the joint may induce premature failure since the beam in this region acts like a deep beam. Thus, it was determined to include distributed longitudinal reinforcement (4-10M) in this region in order to better resist the shear force and to control the cracking pattern.

### 2.3 Joint design

Based on the observations made with regard to the behavior of the connections in Figure 2, the applied forces onto the joint along with the deformation inside the joint is presented schematically in Figure 3 ( $C$ ,  $T$ , and  $V$  refer to compression, tension, and shear, respectively, subscripts  $c$ ,  $s$ ,  $co$ , and  $b$ , refer to concrete, steel, column, and beam, respectively). Placing the vertical slots at the face of the column in the DSB system leads to the formation of two diagonal compression struts; one transferring a portion of the compression forces from the compression reinforcement to the upper opposite corner of the joint,  $S_1$ , while the other transfers the compression forces in the concrete hinge to the upper opposite corner of the joint,  $S_2$ . The forces in the joint are transferred via two mechanisms; compression strut and truss mechanisms (1). In the former, forces are transferred via the concrete while they are transferred via the transverse steel reinforcement in the latter. For design purposes, only the joint shear value needs to be determined in the joint in order to be able to calculate the amount of the required transverse steel.

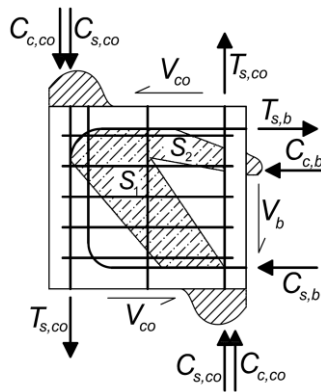


Figure 3. Joint shear mechanism in the DSB connection.

### 2.4 Slot width

The width of the slot is designed such that to prevent the closure of the slot under high drift ratios. The width of the slot is calculated using the expression proposed by Oudah (4) (Equation 1) for the design of slotted-beam connections. The width of the slot is found to be 25 mm.

$$S_w = \lambda_{sf} \cdot \theta_d \cdot l_o \quad (1)$$

where  $S_w$  is the width of the slot,  $\lambda_{sf}$  safety factor,  $\theta_d$  design rotation, and  $l_o$  is the distance from the neutral axis to the centroid of the bottom reinforcement.

### 3. Experimental Program

Two specimens were tested under quasi-static loading; one DSB connection and one conventional connection. The specimen details are shown in Figure 4 while the test setup is shown in Figure 5. Four types of instrumentations were used to monitor the behavior of the connections during testing; Linear Strain Conversion (LSC) devices, Laser displacement sensors, Strain Gauges (SG), and the Digital Image Correlation Technique (DICT). The LSC devices were mounted on the beams, columns, and joints in order to measure the concrete deformations while the laser displacement sensors were positioned on the laboratory floor in order to measure the displacement of the beam members under positive and negative bending. The DICT was used to measure the deformation within the joint.

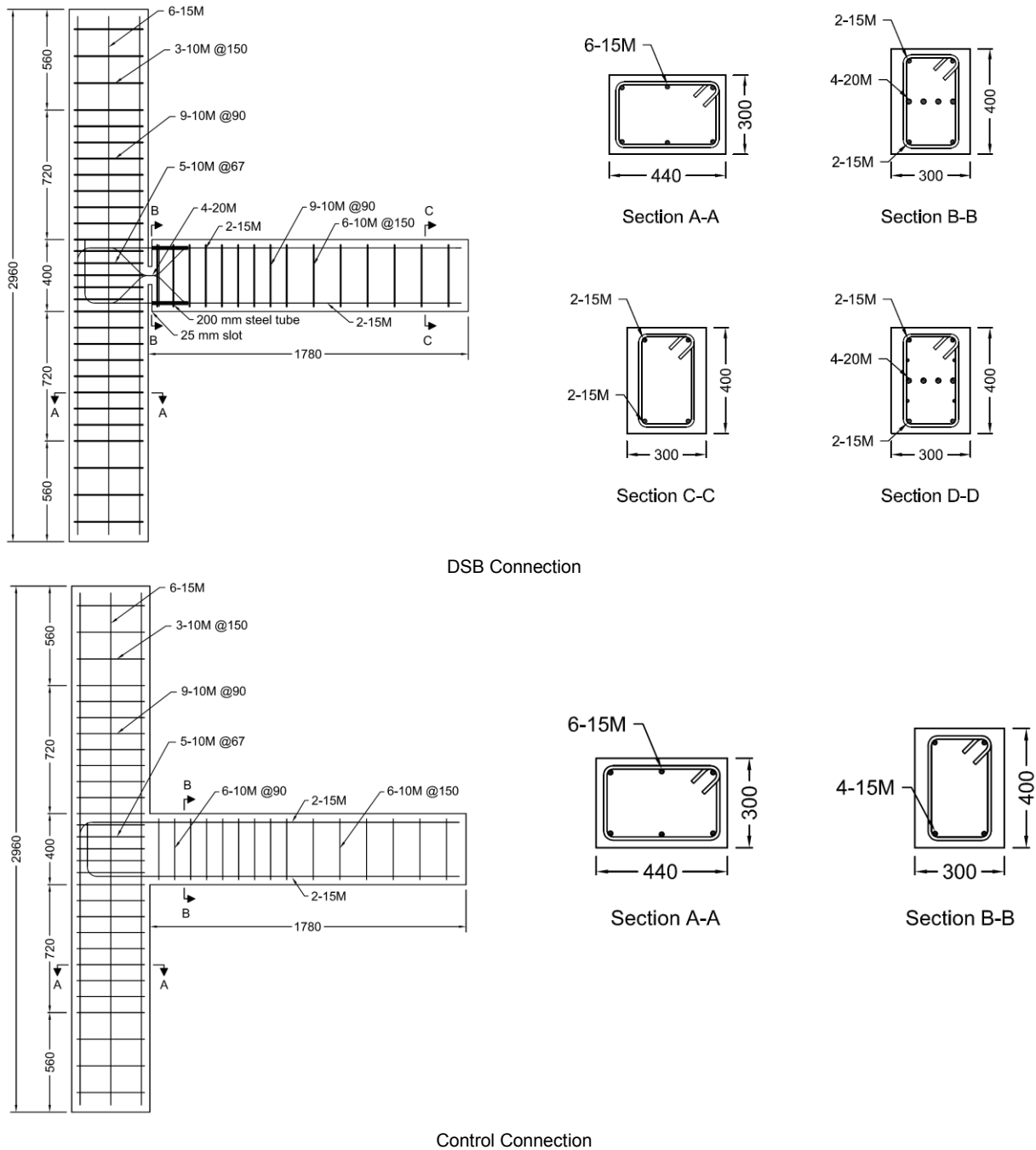
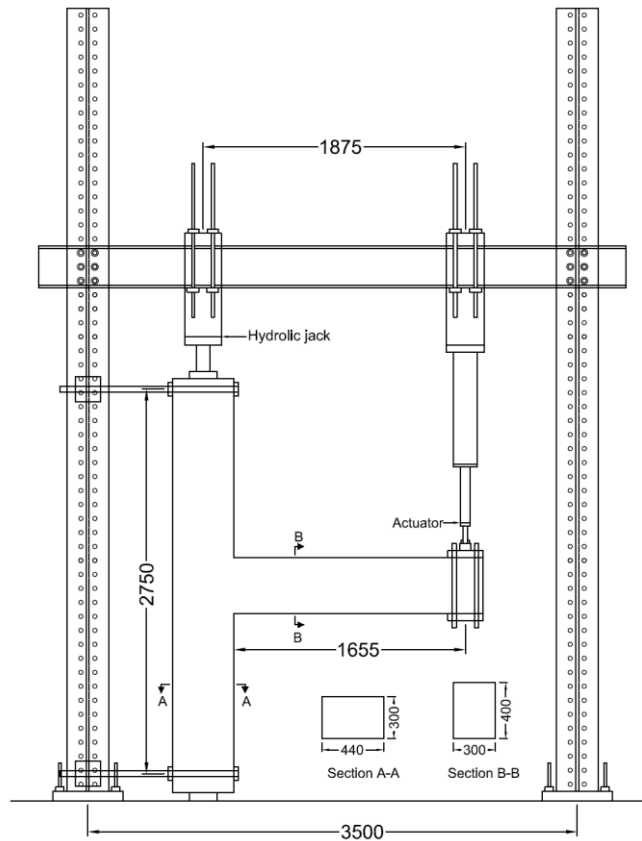


Figure 4. Specimen details.



**Figure 5. Test setup.**

The average 28 days concrete compressive strength is  $40.9 \pm 4.2$  MPa in accordance with ASTM C39/C39M (5). The steel properties of the three rebar diameters; 10 M, 15 M, and 20 M were determined in accordance to ASTM A370 (6). The modulus of elasticity is 187.1 GPa, 180.5 GPa, 194.8 GPa, the yield stress is 484.8 MPa, 484.0 MPa, 435.6 MPa, the yield strain is 0.0026, 0.0027, 0.0022, and the ultimate stress is 730.4 MPa, 729.5 MPa, and 588.2 MPa for the 10 M, 15 M, and 20 M bars, respectively.

## 4. Analysis Results

### 4.1 Hysteretic response

The hysteretic responses are shown in Figure 6. The Control connection failed by crushing of the concrete followed by the fracture of the steel reinforcement in the beam at the face of the column (plastic hinge location) while the DSB connection failed by fracture of the steel reinforcing bar at the slot due to low-cyclic fatigue. The Control connection experienced the typical hysteretic response of conventional beam column connections. The load carrying capacity increased with increasing drift until the maximum capacity is reached. After that, a gradual decrease in the capacity is noticed due to the widening of the cracks and the development of sliding shear plane at beam plastic hinge (located at the face of the column). These actions lead to the so called 'pinching shear'. The increase in the width of the cracks with increasing drift demand makes it difficult for the cracks to close, and hence, to provide a compression force upon the reversal in the bending moment. The delay in the closure of the cracks leads to a reduced stiffness upon the reversal of loading. This behavior is referred to the pinching shear effect and results in the reduction of the amount of energy dissipated during the cyclic loading (7). In the DSB connection, the top and bottom reinforcements provide the main source of resistance for positive and negative bending while a relatively low compression force is transferred in the concrete hinge. Therefore, the effect of the increase in the crack width on lowering the stiffness of the connections is not observed in the DSB connection. Instead, a fat and stable hysteretic response is achieved with no signs of pinching shear.

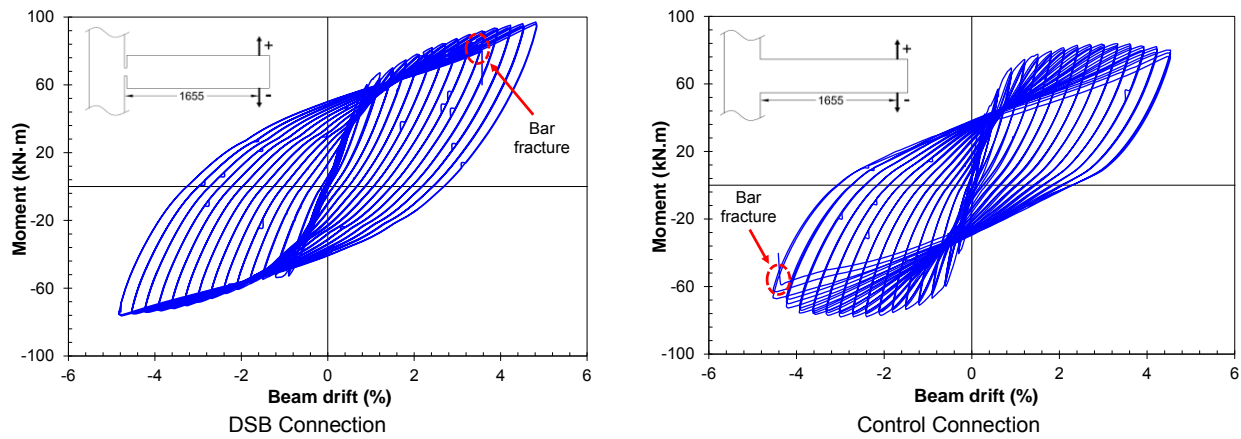


Figure 6. Hysteretic responses.

#### 4.2 Energy and Damping

The energy dissipation is evaluated using two approaches; cumulative energy,  $E_{cum}$ , and equivalent viscous damping,  $\xi_{eq}$ . The  $E_{cum}$  is simply the cumulative hysteretic energy calculated as the summation of the areas enclosed by the hysteretic loops:

$$E_{cum} = \sum_{i=1}^N E_i \quad (2)$$

where  $E_i$  is the energy per cycle  $i$ .

The  $\xi_{eq}$  is also used to evaluate the energy dissipation capacity of the connections and to assess the potential damage. It is a property of the system and depends on the mass and the stiffness (8). The  $\xi_{eq}$  represents the simplest form of damping since the governing differential equation of motion is linear and it can be evaluated using simple experimental test. The  $\xi_{eq}$  ratio is calculated as function of  $E_{cum}$ , and elastic energy,  $E_{el}$ , as follows:

$$\xi_{eq} = \frac{1}{4\pi} \frac{E_{cum}}{E_{el}} \quad (3)$$

The cumulative energy dissipation and the equivalent viscous damping are compared in Figure 7 (a). Even though the post-yielding stiffness of the DSB connection experienced insignificant degradation (Figure 6), the cumulative energy trends of both connections is similar. This is explained by the lower pre-yielding stiffness of the DSB connection as compared with the Control connection. The neutral axis is located approximately at the mid-section in the DSB connection, which contributes in experiencing lower stiffness as compared with conventional connections. The equivalent viscous damping of the DSB connection is lower than that of the Control connection as shown in Figure 7 (a) (0.86 times that of Control connection at drift of 2.5% - drift corresponding to the collapse limit (9)). The lower damping of DSB connection as compared with the Control connection is due to the higher elastic energy in the former as compared with the latter, which is calculated as the product of the load and displacement at each drift amplitude.

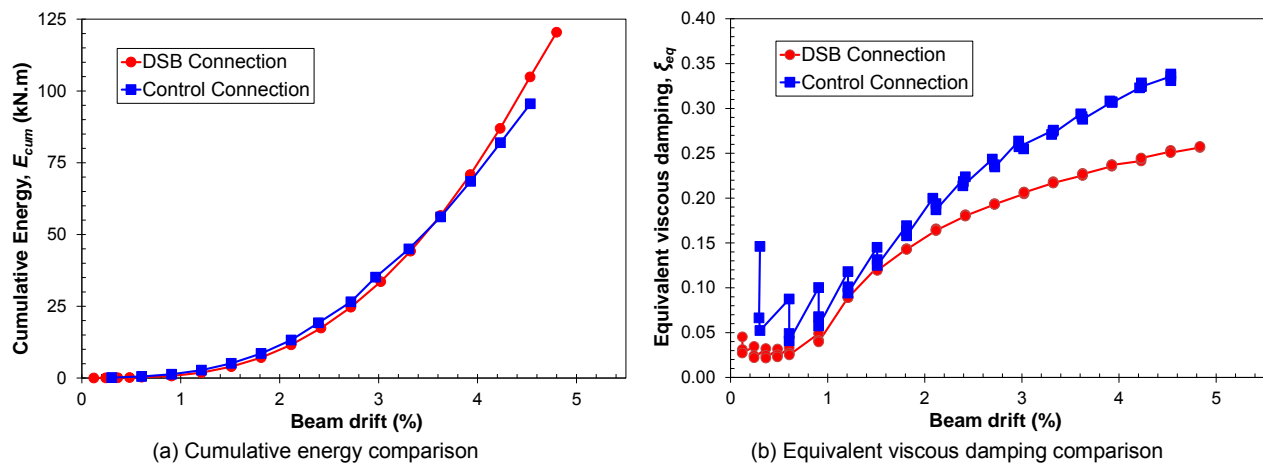


Figure 7. Energy evaluation of the DSB connection.

## 5. Conclusions

A new concrete connection was developed in this study (Double Slotted Beam (DSB)). The flexural, shear, and joint design of the connection were discussed followed by examining its performance experimentally. Large-scale DSB connection was tested and compared with conventional connection. Analysis results indicated the superior performance of the DSB connection in terms of achieving fat, stable, and pinching-shear free response as compared with the conventional one. Cumulative energy comparison indicated that the cumulative energy of the newly developed system follows a similar trend to that of the conventional connection. However, lower equivalent viscous damping was attained by the DSB connection. Thus, further research is needed to enhance the damping property of the DSB system before being introduced into the construction industry.

## 6. Acknowledgement

The authors would like to acknowledge the University of Calgary and the Natural Sciences and Engineering Research Council of Canada for their financial support towards this research project.

## 7. References

1. Paulay, T. and Priestley, M., "Seismic design of reinforced concrete and masonry buildings", John Wiley & Sons, 1992, New York.
2. Ohkubo, M., Matsuoka, T., et al., "Shear transfer mechanism of reinforced concrete beams with a slot at the beam-end", Proc. of Japan Concrete Institute, 1999, 21(3), 523-528.
3. CSA A23-04. "Concrete materials and methods of concrete construction / Methods of test and standard practices for concrete" CSA International, 2014, Toronto.
4. Oudah, F., "Development of innovative design of self-centering concrete beam-column connections using shape memory alloys" Ph.D. thesis, Civil Engineering Dept., University of Calgary, 2014, Calgary, Canada.
5. ASTM C39/C39M, "Standard test method for compressive strength of cylindrical concrete specimens", Vol. 04.02, American Society for Testing Material, 2010, West Conshohocken, PA, USA.
6. ASTM A370, "Standard test methods and definitions for mechanical testing of steel produces", Vol. 04.02, American Society for Testing Material, 2010, West Conshohocken, PA, USA.
7. Derecho A., Kianoush M., "Seismic design of reinforced concrete structures", In: Naeim F (ed) The seismic design handbook, 2<sup>nd</sup> edn. Kluwer Academic, 2001, Boston, MA, USA, pp 463-562.
8. Chopra, A., "Dynamics of structures: theory and applications to earthquake engineering", Third Edition, Person Prentice Hall, Upper Saddle River, 2007, N.J., USA.
9. Elnashai A., Di Sarno L., "Fundamentals of earthquake engineering", John Wiley & Sons, 2008, New York.

# Development of a Finite Element Analysis Design Tool for Future Study of a Novel Hybrid Steel-Free Multi-Girder Bridge Deck System

Donna Chen<sup>1</sup> and Raafat El-Hacha<sup>2</sup>

<sup>1</sup>Junior Structural Engineer in Training, ISL Engineering and Land Services (formerly PhD Candidate at University of Calgary)

<sup>2</sup>Associate Professor, Department of Civil Engineering, University of Calgary

**Abstract:** The research summarized in this paper focuses on the development of a validated finite element model as a design tool for future studies and analysis on a novel hybrid steel-free multi-girder bridge deck system. Good correlation between finite element analysis and experimental test results was found in regards to global behaviour, particularly for predictions of peak load condition and failure sequence in the progressive failure mechanism. The developed finite element model was found applicable for use in future design optimization studies as well as investigations for structural response under additional types of wheel load configurations.

**Keywords:** hybrid, bridge, steel-free, finite element, FRP, UHPC.

## 1. Introduction

In the field of structural bridge engineering, significant progress has been made in recent years towards the design of sustainable infrastructure, as a means of addressing the current infrastructure deficit in Canada. The infrastructure deficit, valued at \$12.7 billion dollars for costs directly associated with transportation infrastructure [1], is mainly due to continued deferral of regular maintenance procedures and extended usage of existing structures past their original design life; this is a critical issue with a significant and direct impact on the future of Canadian society. One branch of research focuses on the development of new infrastructure construction methods that limit the vulnerability of the structure to environmental effects, thus reducing maintenance costs throughout the duration of the design lifespan. By ensuring more resilient and cost-effective replacement structures, steps can be taken to resolve the infrastructure deficit.

The use of high performance materials to replace the conventional materials currently used in construction is a feasible approach. Many high performance materials are resistant to the effects of corrosion, which is a primary cause for structural deterioration in current infrastructure due to the presence of structural steel components. In particular, Fibre Reinforced Polymers (FRPs) and Ultra-High Performance Concrete (UHPC) have been successfully adopted in a wide variety of structural applications [2-21]. Nevertheless, the majority of these structural applications include the usage of high performance materials in conjunction with conventional structural materials, such as reinforced concrete, structural steel and prestressed concrete, as composite structures so that the influence of corrosion is minimized but not completely eliminated. Recently, the authors have developed a new design concept for a hybrid bridge deck system that incorporates only high performance materials, without any structural steel components [22]. Extensive large-scale experimental testing of the hybrid bridge deck system specimen under seven different wheel load configurations has confirmed good structural performance that exceed current Canadian code standards for ultimate and serviceability limit states [22].

To evaluate further the feasibility of the proposed hybrid design for practical implementation, however, additional studies are required. The first would be to investigate the performance of the bridge system under a wider set of loading configurations not yet explored during experimental testing, such as multiple lane loadings and the inclusion of more than two truck axles. An additional aspect to consider would be potential design optimizations that can be made to maximize the full structural capacity of the bridge system while minimizing costs. In order to conduct a comprehensive examination, the use of traditional large-scale experimental testing is highly cost-prohibitive and impractical. An alternative to experimental testing, however, is the use of finite element analysis as a tool to implement the crucial studies. Finite element modelling has been used by many researchers as a mean to conduct detailed investigations in the performance of many structural systems, ranging from examinations of small-scale local behaviours [23-26] to global representations of large-scale structural systems [27]. To ascertain the accuracy of developed model and the parameters used to idealize the various components, validation of the finite

element model must first be conducted with direct comparisons with experimental test results. If reasonable accuracy between the experimental data and predicted finite element analysis behaviour is achieved, then the developed finite element model is deemed suitable for use as a design tool for future studies.

The desired outcome of this research program is the development of a finite element model that can reasonably predict the performance of the hybrid steel-free multi-girder bridge deck system without the need for additional experimental testing. As a design tool, the critical parameters that need to be obtained from the finite element model would include the global prediction of peak load and failure modes. To a lesser degree, determination of the local performance in individual structural components using the finite element model, to aid in future design optimizations and modifications in dimensions, would be a valuable asset.

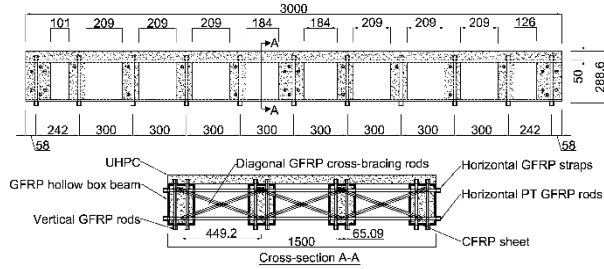
## **2. Description of hybrid steel-free multi-girder bridge deck system design**

The central objective for the design of the hybrid steel-free multi-girder bridge deck system was the successful incorporation of distinct high performance structural elements with linear-elastic material properties into a cohesive bridge system that is capable of exhibiting global pseudo-ductile behaviour. The desired characteristic for successful integration of pseudo-ductile behaviour would be the clear display of a progressive failure mechanism prior to ultimate failure of the hybrid bridge deck system. Thus, with this focus, high performance materials were carefully selected based upon their material properties, particularly in regards to the ultimate strain capacity. Fibre Reinforced Polymers (FRPs) were chosen, with pultruded Glass FRP (GFRP) hollow box beams serving as the core girders of the system as well as the stay-in-place formwork along with Carbon FRP (CFRP) sheets bonded to the bottom face of each GFRP hollow box beam for additional strength and stiffness to the girder system. The pultruded GFRP hollow box beams [28] had an outer depth and width of 228.6 mm and 152.4 mm, respectively, with an all-around wall thickness of 11.11 mm. The bonded CFRP sheets [29, 30] had a thickness of 1.0 mm. Four of the composite FRP girders were spaced side-by-side, with a single 50 mm thick slab of cast-in-place Ultra-High Performance Concrete (UHPC) overtop. The UHPC used is a proprietary concrete product [31] that does not include the use of internal steel reinforcement bars.

To ensure sufficient bond between the UHPC slab and composite FRP girder below, a two-part system was used. The two-part system consisted of an epoxy bonded coarse silica sand aggregate layer bonded directly to the top surface of the composite FRP girder prior to casting of the UHPC slab [24, 32] along with a series of full-depth vertical GFRP threaded rods spaced at regular intervals along the longitudinal span of each composite girders. A combination of horizontal GFRP straps, post-tensioned GFRP rods and diagonal cross-bracing bars were used for composite action and constraint through the transverse cross-section. To reinforce the GFRP hollow box beam at the locations where the composite action GFRP threaded rods traversed the girder system, internal UHPC stiffener blocks were cast within the interior of the hollow box beam. The horizontal and vertical GFRP threaded rods were installed as unbonded structural elements, with PEX tubing serving as ducts to prevent contact between the rods and the UHPC stiffener blocks. All of the GFRP rods (vertical, horizontal and diagonal) were fabricated using a two-step pultrusion process, first of the inner longitudinal load bearing rod, followed by the fabrication of the outer transverse threading [33]. 5/8" 11 UNC threaded rods were chosen for use in the hybrid bridge deck system design, which had a nominal diameter of 15.875 mm. The matching GFRP nuts had an outer diameter of 31.75 mm along with a thickness of 22.225 mm.

During previous stages of the research program, studies were conducted to evaluate the performance of individual hybrid FRP-UHPC girders [4, 5, 9], including optimization studies to ensure the desired pseudo-ductile behaviour was exhibited [11]. Based on the findings obtained from the previous studies, a quarter-scale specimen of the proposed hybrid steel-free multi-girder bridge deck system was constructed for testing. The resulting design dimensions for the quarter-scale hybrid bridge deck system, with associated photographs of the completed specimen, are shown in Figure 1.





**Figure 1. Dimensions and photograph of quarter-scale hybrid steel-free multi-girder bridge deck system.**

**3. Summary of experimental test program and results**

In-depth description and examination of the experimental test results have been presented in another publication [22] and will not be repeated in this publication. A summary of the experimental program and the key experimental findings, necessary for comparison and validation with the finite element analysis (FEA) results, will be presented in this section.

Testing of the hybrid bridge deck system was performed using both service and ultimate condition loading. A simultaneously applied four-wheel load formation was used, based upon the positions of axle 2 and 3 of the CL-625 design truck from the Canadian Highway Bridge Design Code [34]. As mentioned previously in this paper, a quarter-scale specimen of the hybrid bridge deck system was constructed for experimental testing; this was due to constraints in the actuator capacity and space available in the structural lab. Thus, all dimensions and associated parameters were scaled down using scale factors determined through dimensional analysis. Seven different concentric and eccentric load configurations (Load Configurations C1 – C3 and E1 – E4) were examined under service load conditions, with the final ultimate load condition conducted using Load Configurations C1. Diagrams showing the transverse placement of the wheel loads are provided in Table 1. The spacing of the wheel loads in the longitudinal direction was 300 mm about the center of the longitudinal span for all load configurations except for Load Configuration C2, where a longitudinal spacing of 600 mm was used.

**Table 1. Wheel load configurations tested under service and ultimate load condition testing [22]**

Concentric Configurations			Eccentric Configurations		
C1	E1a	E2a			
C2	E1b	E2b			
C3	E3	E4			

Service load condition tests were performed using step-wise quasi-static loading up to a maximum load level of 50 kN. Linear-elastic behaviour was observed within the load range tested for all load configurations with no signs of stress relaxation or creep caused by repeated loading. The final ultimate load condition test was initiated with a similar set of step-wise loading regime up to a maximum total load of 200 kN, after which a loading rate of 0.75 mm/min was applied up until ultimate failure of the specimen. Progressive failure was achieved during experimental testing, with signs of longitudinal tensile cracking in the UHPC slab, buckling in the GFRP cross-bracing bars, tension shear block failure in the GFRP web and tensile fracture in the CFRP sheet and GFRP bottom flange after reaching peak load condition.

## 4. Finite element model

### 4.1 Model development

A three-dimensional (3D) finite element model (FEM) was developed using ABAQUS, a commercial software package. Preliminary validation of FEM results with experimental results was performed and summarized in another publication [35]. A detailed tabulated list of the chosen mesh size and element type used to characterize each structural component is provided in Table 2. The material properties for the structural components used in the FEM, obtained through in-house experimental testing, are provided in Tables 3 to 6.

**Table 2. Basic FE analysis parameters used for the 3D FEM of the hybrid bridge deck system**

Structural component	Element type		Average mesh size (mm)		
	Description	Name	Longitudinal	Transverse	Through depth
GFRP hollow box beam	Continuum shell	SC8R	25	15	5
CFRP sheet	Continuum shell	SC8R	10	10	1
UHPC slab	Solid linear brick	C3D8	25	25	25
UHPC stiffener block	Solid linear brick	C3D8	25	25	25
GFRP rod	Linear beam	C3D8	5	N/A	N/A
GFRP bolt	Linear triangular prism	C3D6	5	9	N/A
Steel plate	Solid linear brick	C3D8	50	50	50
Steel rollers	Linear triangular prism	C3D6	50	6	50

**Table 3. Material property parameters for GFRP hollow box beam [9, 28]**

Material elasticity	$E_1$ (MPa)	21000 (flanges), 16000 (webs)	
	$E_2$ (MPa)	5520	
	$G_{12}$ (MPa)	2930	
	$G_{13}$ (MPa)	2930	
	$G_{23}$ (MPa)	2930	
	$\nu$	0.33	
Hashin damage	$\sigma_1$ (MPa)	207 (tension), 207 (compression)	
	$\sigma_2$ (MPa)	48.3 (tension), 103 (compression)	
	$\tau_{12}$	31	
	$\tau_{23}$	31	

**Table 4. Material property parameters for UHPC [31]**

Material elasticity	$E$ (MPa)	50000				
	$\nu$	0.2				
Compression hardening	Compressive stress (MPa)	96.5	110.3	137.9	165.5	189.6
	Plastic strain (-)	0.0000000	0.0000284	0.0000720	0.0001410	0.0004140
Tension stiffening	Maximum tensile stress (MPa)	15.9		15.9		0
	Plastic strain (+)	0.000000		0.00836		0.00900
Damage plasticity parameters	Dilation angle	15°				
	Eccentricity	0.1				
	$f_{bo}/f_{co}$	1.16				
	$K$	2/3				

**Table 5. Material property parameters for CFRP sheet, GFRP rods and steel plates**

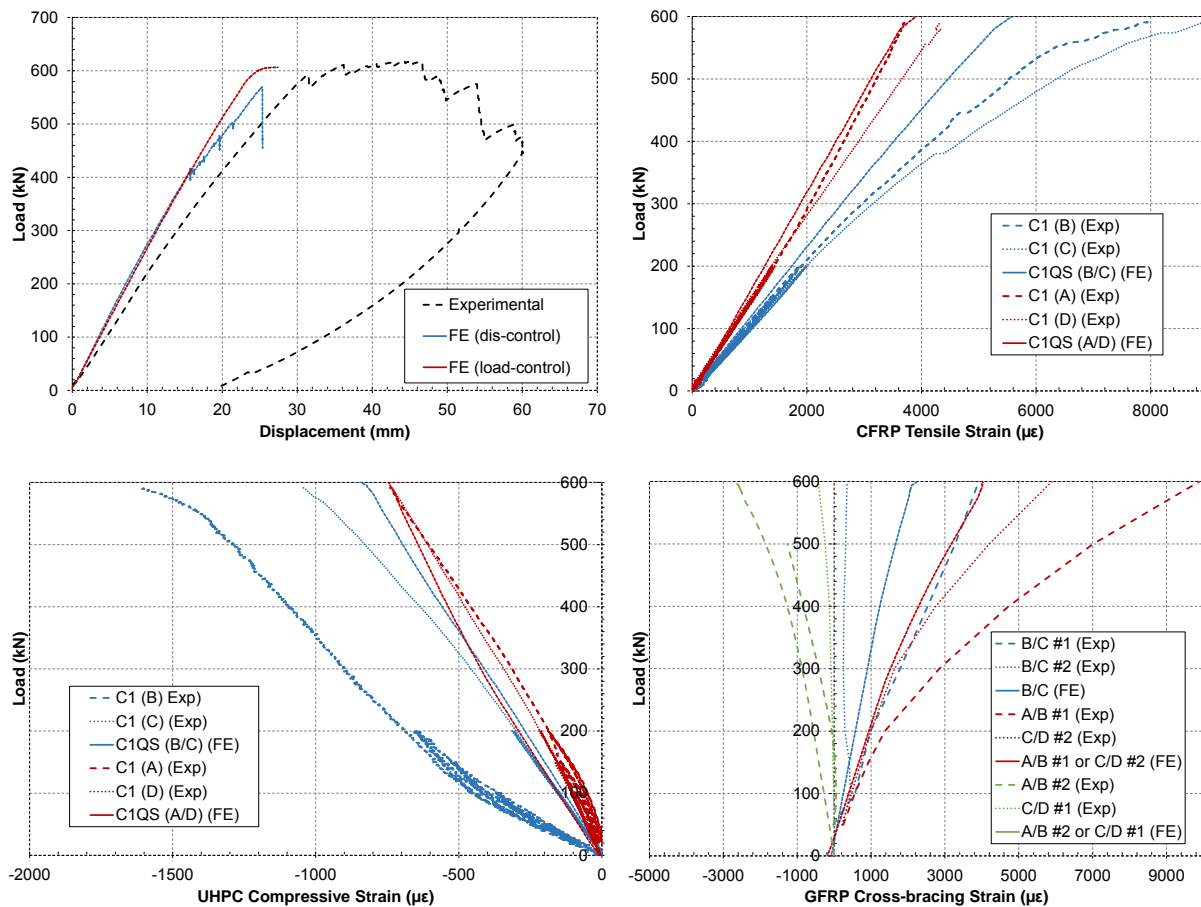
Parameters	CFRP [29, 30]	GFRP rods [33]	Steel plates
$E$ (MPa)	95800	21000	200000
$\nu$	0.3	0.29	0.2

**Table 6. Material property parameters for GFRP-UHPC bond interface [24]**

Bond interface elasticity	$K_{nn}$ (MPa/m)	200
	$K_{ss}$ (MPa/m)	600
	$K_{tt}$ (MPa/m)	600
Quadratic stress traction-separation parameters	$\sigma_n$ (MPa)	2
	$\sigma_s$ (MPa)	6
	$\sigma_t$ (MPa)	6
Linear energy damage evolution power law	$G_1$ (kJ/m)	0.3
	$G_2$ (kJ/m)	0.9
	$G_3$ (kJ/m)	0.9

#### 4.2 Comparison of results: Experimental vs. finite element analysis results

The full spectrum of experimentally tested concentric and eccentric load configurations were implemented and analysed using finite element analysis. Comparison between experimental and FEA behaviour for Load Configuration C1 under ultimate load condition is presented in Figure 2. The labels “A, B, C, and D” refer to transverse positions directly in line with the longitudinal girders whereas labels “A/B, B/C, and C/D” refer to positions directly in line with the middle of the inter-girder space.



**Figure 2. Comparison of experimental and FEA results for Load Configuration C1 tested at ULS.**

The comparison shown in Figure 2 clearly demonstrate a reasonable degree of accuracy between the experimental and finite element analysis results. It is worth noting that FEA conducted under load-controlled conditions provided load-deflection behaviour past the peak load condition that was more consistent with experimental results than FEA results using displacement-controlled load steps. In general, the data obtained through finite element analysis indicated a stiffer global response than observed experimentally. There was good prediction of the peak load, regardless of higher global stiffness of the modelled bridge deck system. Looking at the local responses in the key structural elements (as presented in Figure 2), equally good correlation was observed for load-strain behaviour in the CFRP sheet and UHPC slab. In the case of strain behaviour in the GFRP cross-bracing bars, particularly in the case of bars acting in compression, there were several discrepancies between the experimental and finite element analysis results. This indicates the possible need for further refinements in the modelling of the transverse composite action system.

Whereas the FEA was conducted past peak condition for all of the seven configurations examined, the set of ultimate load condition experimental data was only available for Load Configuration C1. For comparison with the FEA results, linear extrapolations of the experimental data obtained during the service load condition tests for the other six load configurations were used. Since near linear-elastic behaviour was exhibited by the hybrid bridge deck system during experimental testing, the extrapolation of service load condition data was deemed as a safe approximation. To fulfill the length limits of this publication, the full comparison between experimental and finite element analysis results are not presented here for the remaining service load conditions tests. Overall, the predicted behaviour displayed the same key characteristics observed from the ultimate load condition test comparison, with generally higher global stiffness, good correlation of strain behaviour in the CFRP sheet and UHPC slab, as well as moderate correlation in the structural elements making up the transverse composite action system.

## 6. Discussion and analysis

Judging from the extensive comparison of strain behaviour in the various structural elements obtained from experimental testing and FEA, it can be concluded that the developed FEM can be used to adequately predict the global behaviour of the hybrid bridge deck system. Good prediction of local strain behaviours in the CFRP sheet and UHPC slab can also be attained; however, adjustments must be made to the formulation of GFRP cross-bracing bars in order to achieve proper modelled load distribution within the transverse composite action system. Using the modelled global response of the hybrid bridge deck system, detailed assessment of the accuracy of FEA results as compared with experimental behaviour will be discussed in this section.

### 6.1 Live load distribution factor

Firstly, the shear live load distribution factor (LLDF) was examined. As detected previously, there were observed discrepancies in load-strain responses of the GFRP cross-bracing bars obtained from the finite element analysis. This influence on the modelled transverse composite action system may affect the calculated load distribution between adjacent longitudinal girders. A comparison of the shear LLDF is provided in Table 7, showing the fraction of load carried for each girder as well as the percent error in the finite element analysis results as compared with experimental data.

**Table 7. Comparison of shear live load distribution factor between experimental and FEA results**

Load configuration	Experimental				Finite element				Percent error (%)			
	A	B	C	D	A	B	C	D	A	B	C	D
C1	0.20	0.28	0.31	0.21	0.19	0.29	0.29	0.19	-6	3	-4	-13
E1	0.12	0.24	0.31	0.33	0.07	0.25	0.35	0.36	-40	2	14	8
E2	0.05	0.17	0.32	0.46	0.00	0.15	0.30	0.59	-92	-11	-5	27
E3	0.36	0.29	0.22	0.13	0.42	0.25	0.21	0.13	17	-15	-6	-4
E4	0.27	0.29	0.24	0.20	0.29	0.29	0.26	0.15	8	-3	7	-24
C2	0.20	0.32	0.30	0.19	0.17	0.32	0.32	0.17	-16	0	6	-12
C3	0.25	0.27	0.24	0.24	0.25	0.25	0.25	0.25	1	-9	2	7

The shear LLDF obtained through FEA was generally consistent with the experimental results for the seven load configurations tested. For the inner girders, a maximum percent difference of 15% was found. In terms of the outer girders, an initial assessment of the comparative results for the LLDF of the outer girders showed a percent difference of 92%, obtained for Girder A under Load Configuration E2, the most highly eccentric load configuration. Nevertheless, when analyzed in more detail, the low experimental value of LLDF attributed to Girder A (equal to 5% of the total applied load) as compared with a negligible distribution found during FEA (found equal to 0%) resulted in the appearance of an elevated percent difference. If this value was excluded, the maximum percent difference for the LLDF of outer girder would be 40%, found for Girder A when subjected to Load Configuration E1 wheel load placement. Thus, the distribution of forces throughout the hybrid bridge deck system were more accurately predicted by the developed FEM for concentric loading configurations rather than eccentric loading configurations. Overall, there was higher concentration of load within the immediate area of the applied wheel loads from the data obtained from the FEM as compared with experimental results. This is further indication that the modelled system was less effective at distributing load transverse throughout the hybrid bridge deck system than the as-built transverse composite action system.

## 6.2 Peak load condition

Another major objective in the development of the FEM was the ability to predict peak load conditions for additional loading configurations not tested during the experimental program. To assess the accuracy of the FEM, validation was first performed with regards to the peak load of the hybrid bridge deck system under Load Configuration C1, which was tested up to ultimate failure, as well as the linearly extrapolated peak load values from the other experimental tests conducted using service loading conditions. Extrapolation of the service load condition test results to the peak load condition was performed using the percent utilization of ultimate strain capacity in various structural elements during service load conditions tests. Using the experimental set of peak condition strain data under Load Configuration C1 as the defined maximum limit, the strain in the individual structural components under service loading conditions were extrapolated to the maximum limit with a proportionally derived peak load. The governing failure mode at the extrapolated ultimate load condition, and thus the peak load associated with failure of the governing structural element, was determined. A summary of the maximum percent utilization of the governing structural elements during the service loading condition tests is provided in Table 8.

**Table 8. Percent utilization of ultimate strain capacity in key structural elements for all load configurations**

Load Configuration	UHPC		GFRP	CFRP	GFRP rod			
	Compression	Tension			Cross-bracing	PT Rod	Strap	Vertical Rod
C1	3%	10%	5%	4%	4%	18%		
E1	3%	16%	6%	5%	4%	17%		
E2	4%	9%	8%	8%	2%	16%		
E3	3%	5%	7%	6%	2%	16%		
E4	3%	9%	5%	5%	2%	17%		
C2	2%	14%	3%	2%	3%	18%		
C3	6%	12%	5%	4%	1%	16%		
C1 (ULS)	34%	111%	86%	82%	50%	51%	19%	6%

These values represent the maximum percent utilization observed; however, for the transverse tensile strain in the UHPC slab, a large number of strain gages malfunctioned during experimental testing. This prevented a thorough and reliable analysis of peak condition extrapolation to be performed using the tensile strain data set. Instead, the longitudinal compressive strain in the UHPC slab was chosen as a representative parameter for the UHPC failure mode. A final tabulation of the extrapolated experimental peak load associated with each failure mode alongside a direct comparison with peak load calculated through FEA is presented in Table 9.

**Table 9. Summary of extrapolated peak load for service load configurations**

Loading configuration	Extrapolated minimum peak load (kN)						Governing peak load (kN)
	Vertical displacement	UHPC		CFRP tensile strain	Cross-bracing bar		
		Compressive strain	Tensile strain		Compressive strain	Tensile strain	
C1	578	438	552	689	725	539	438
E1	450	348	347	493	279	293	279
E2	341	282	635	380	106	254	106
E3	435	402	1053	486	114	643	114
E4	567	421	621	552	1022	587	421
C2	623	428	384	671	788	610	384
C3	637	270	464	631	182	502	182

The comparison of peak load between experimental results and FEA predictions, shown in Table 9, shows that failure in the UHPC slab was the governing mode of failure for all of the load configurations tested, excluding Load Configuration C2, where the extrapolated data from the mid-span vertical displacement was the limiting parameter. The percent difference between the extrapolated experimental results and the FEA predictions for peak load ranged between 0 – 12% for the governing failure mode in the UHPC whereas a higher variation of 39% was found for Load Configuration C2. It should be kept in mind that the predicted compressive failure in the UHPC slab would be a secondary mechanism following the initial tensile cracking at the top surface of UHPC slab, as a sequence in the progressive failure mechanism observed during experimental testing.

## 8. Conclusions

The outcome from the research presented in this paper is the successful development of a three-dimensional FEM capable of predicting representative global behaviour of the novel hybrid steel-free multi-girder bridge deck system. The FEM provides, with reasonable accuracy, predictions for the peak load condition and failure mode of the hybrid bridge deck system under various load configurations, confirmed through validation with experimental test results. With the globally validated FEM, design optimizations as well as additional examinations into the performance of the hybrid bridge deck system under other load configurations not yet tested in the experimental program can be evaluated. Experimental testing and analytical result both confirm that the initiation of failure commences within the inter-girder region of the UHPC slab, making the transverse tensile strength of the UHPC slab within the two outer inter-girder regions the most critical parameter of the design. Design optimization can be performed to increase the peak load of the hybrid bridge deck system by decreasing the transverse girder spacing, thereby reducing the tensile demand on the UHPC slab. This would also promote higher utilization of material capacity in the other load resisting structural elements.

Overall, the work summarized in this paper combined with the extensive experimental testing conducted previously within this research program confirms the feasible application of the developed hybrid steel-free multi-girder bridge deck system. The analysis performed demonstrates the versatility of the hybrid bridge deck system to carry a wide variety of wheel load configurations. With the aid of the developed finite element model, a reliable means of predicting the expected failure mechanism and load resistance of the hybrid bridge deck system for any load combination is readily available, without the need for extensive experimental testing.

## 9. Acknowledgements

We would like to thank the following companies for their generous donation of materials used in this research project: Lafarge Canada, Pultrall Inc., and Sika Canada Inc. Additionally, we would like to acknowledge the National Sciences and Research Council (NSERC) of Canada and the University of Calgary for their financial support.

## 10. References

1. Mirza, S. Danger ahead: The coming collapse of Canada's municipal infrastructure. Ottawa, ON: Federation of Canadian Municipalities, 2007.
2. Alnahhal W, Aref A, and Alampalli S. Composite behaviour of hybrid FRP-concrete bridge decks on steel girders. *Composite Structures* 2008; 84(1): 29-43.
3. Braimah A, Green MF, and Soudhki KA. Polypropylene FRC bridge deck slabs transversely prestressed with CFRP tendons. *Journal of Composites for Construction* 1998; 2(4): 149-157.
4. Chen D. (2011). Behaviour of hybrid FRP-UHPC bridge deck system under static and fatigue loading. Calgary, Alberta: University of Calgary, 2011. 356p.
5. Chen D and El-Hacha R. Behaviour of hybrid FRP-UHPC beams in flexure under fatigue loading. *Composite Structures* 2011; 94(1): 253-266.
6. Cheng L, and Karbhari VM. Fatigue behavior of a steel-free FRP-concrete modular bridge deck system. *Journal of Bridge Engineering* 2006; 11(4): 474-488.
7. De Lorenzis L, and Teng JG. Near-surface mounted FRP reinforcement: An emerging technique for strengthening structures. *Composites: Part B* 2007; 38(2): 119-143.
8. Deskovic N, Triantafillou TC, and Meier U. Innovative design of FRP combined with concrete: short-term behavior. *Journal of Structural Engineering* 1995; 121(7): 1069-1078.
9. El-Hacha R, and Chen D. Behaviour of hybrid FRP-UHPC beams subjected to static flexural loading. *Composites Part B: Engineering* 2012; 43(2): 582-593.
10. El-Hacha R, and Rizkalla SH. Near-surface-mounted fiber-reinforced polymer reinforcements for flexural strengthening of concrete structures. *ACI Structural Journal* 2004; 101(5): 717-726.
11. Elmahdy A. (2010). Experimental and analytical study of new hybrid beams constructed from high performance materials. Calgary, Alberta: University of Calgary, 2010. 242p.
12. El-Salakawy E, Benmokrane B, El-Ragaby A, and Nadeau D. Field investigation on the first bridge deck slab reinforced with glass FRP bars constructed in Canada. *Journal of Composites for Construction* 2005; 9(6): 470-479.
13. Grace NF, Jensen EA, and Noamesi DK. Flexural performance of carbon-fiber-reinforced polymer prestressed concrete side-by-side box beam bridge. *Journal for Composites for Construction* 2011; 15(5): 663-671.
14. Hejll A, Täljsten B, and Motavalli M. Large scale hybrid FRP composite girders for use in bridge structures - theory, test and field application. *Composites: Part B* 2005; 36(8), 573-585.
15. Keller T, and Gürtler H. Design of hybrid bridge girders with adhesively bonded and compositely acting FRP deck. *Composite Structures* 2006; 74(2): 202-212.
16. Keller T, Schaumann E, and Vallée T. Flexural behavior of a hybrid FRP and lightweight concrete sandwich bridge deck. *Composites: Part A* 2007; 38(3): 879-889.
17. Kitane Y, Aref AJ, and Lee GC. Static and fatigue testing of hybrid fiber-reinforced polymer-concrete bridge superstructure. *Journal of Composites for Construction* 2004; 8(2): 182-190.
18. Moon DY, Zi G, Lee DH, Kim BM, and Hwang YK. Fatigue behavior of the foam-filled GFRP bridge deck. *Composite: Part B* 2009; 40(2): 141-148.
19. Park K-T, Kim S-H, Lee Y-H, and Hwang Y-K. Pilot test on a developed GFRP bridge deck. *Composite Structures* 2005; 70(1): 48-59.
20. Saleem MA, Mirmiran A, Xia J, and Mackie K. Ultra-high-performance concrete bridge deck reinforced with high-strength steel. *ACI Structural Journal* 2011; 10(5): 601-609.
21. Zhu J, and Lopez MM. (2014). Performance of a lightweight GFRP composite bridge deck in positive and negative bending regions. *Composite Structures* 2014; 113: 108-117.
22. Chen, D., and El-Hacha, R. Novel steel-free high performance multi-girder bridge deck system - performance of large-scale test specimen. *Journal of Composite for Construction*. (Under review).

23. Camanho PP, and Dávila CG. Mixed-mode decohesion finite elements for the simulation of delamination in composite materials. NASA/TM-2002-211737. Hampton, Virginia, USA: NASA, 2002.
24. Chen D. and El-Hacha R. Cohesive fracture study of a bonded coarse silica sand aggregate bond interface subjected to mixed-mode bending conditions. *Polymers* 2014; 6(1): 12-38.
25. De Moura MFSF, Campilho RDSG, and Gonçalves JPM. Pure mode II fracture characterization of composite bonded joints. *International Journal of Adhesive and Adhesion* 2009; 46(6): 1589-1595.
26. Da Silva LFM, Esteves VHC, and Chaves FJP. Fracture toughness of a structural adhesive under mixed mode loadings. *Materials Science and Engineering Technology* 2011; 42(5): 460-470.
27. Federal Highway Administration (FHWA). Finite element analysis of ultra-high performance concrete: modeling structural performance of an AASHTO type II girder and a 2nd generation Pi-Girder (FHWA-HRT-11-020). McLean VA: FHWA, 2010.
28. Strongwell. EXTRENE® fiberglass structural shapes and plate. Bristol, VA, 2009.
29. Fyfe. Tyfo® SCH-41 Composite using Tyfo® S-T Epoxy. San Diego, USA, 2009.
30. Fyfe. Tyfo® S Saturant Epoxy. San Diego, USA, 2009.
31. Lafarge. Fiche de caractéristiques techniques: Ductal® -FM Gris. Lafarge, Paris, France, 2007.
32. Chen D and El-Hacha R. Bond strength between cast-in-place ultra-high performance concrete and glass fibre reinforced polymer plates using epoxy bonded coarse silica sand. *Journal of ASTM International* 2012; 9(3): 17p.
33. Strongwell. FIBREBOLT® fiberglass studs and nuts. Bristol, VA, 2014.
34. Canadian Standard Association (CSA). Canadian Highway Bridge Design Code (CSA S6-06). Mississauga, Ontario, 2006.
35. Chen D. and El-Hacha R. The use of appropriate finite element modelling techniques for the idealization of a novel hybrid multi-girder bridge deck system. Istanbul Bridge Conference, Istanbul, Turkey. August 11-13, 2014.



# Investigation of Strength and Thermal Intake of Concrete Curing Through Means of Heated Water and Insulation Applied to the Exterior Surface

Jamie Warr<sup>1</sup>

<sup>1</sup>Civil Engineering Student, University of Tasmania

**Abstract:** Producing in-situ and pre-cast components at a fast rate drove research into curing methods to accelerate strength gain which remains a highly researched topic. Options to accelerate curing for in-situ operations are limited, even for pre-cast work some methods are impractical.

This paper investigates the effectiveness of accelerated curing using an insulation plus hot water (55 °C) combination that's suitable both in-situ and for pre-cast work. This reduces costs and optimises sustainability by reusing and reducing consumables.

In this research four identical concrete 'wingwalls' (slabs) are cured simultaneously each using a different part of the combination curing method, the combination itself and a control. Core temperatures were recorded and test cylinders were cured under equivalent conditions to determine compressive strengths.

In a 21 hour interval the combination produced a 120% increase in degree-hours and 83% strength increase relative to the control, the insulation produced 43% less degree-hours and 17% less strength than the combination, slightly more than the hot water method. A finite element model was produced under simplified conditions that imitated the shape of the experimental temperature-time curves.

This straightforward, effective, portable and chemically free method to cure concrete results in a significant strength gain over the short term.

**Keywords:** in-situ curing, insulation, hot water, accelerated curing, sustainability.

## 1. Introduction

Concrete has maintained a vital role in a broad range of infrastructure and civil based projects because of its compressive strength, workability, availability and cost compared to alternatives.

This significance has spurred a great deal of research into many aspects of the concreting process. For instance, attempting to configure the concretes durability, tensile or compressive strength. The quality of curing for concrete is a determining process for many of these aspects - by definition it is the application or moderation of moisture and heat to achieve the desired strength in concrete. This is why it has been the focus of concrete research for a considerable amount of time.

One of the main issues facing concrete usage is curing efficiency. Builders, engineers and many other users constantly strive for the most economical curing solution available. This obviously, but crucially, enables cheap and fast growth with financial ease on the scale of the project.

This research investigates how a reusable and portable curing system affects the heat intake and compressive strength of concrete over a period of days. A system comprising of hot water at 55 degrees Celsius irrigated on the concrete surface using soaker hoses and a 'bubble wrap' insulation overlay, is used.

The effectiveness of heat intake and compressive strength of the system is found using the Nurse-Saul maturity method by contrasting the maturity (in degree-hours) accumulated and compressive strengths of a control, to each component of the curing regime and the combination of hot water and insulation. With the aid of a computer, a model and transient thermal analysis of the systems components was created and compared with the experimental results in an attempt to obtain an approximate analytical solution.

## 2. Slab/'Wingwall' Testing

### 2.1. Procedure

Supplied concrete conformed to bridgework specifications outlined by The Department of State Growth (DSG) of Tasmania [1].

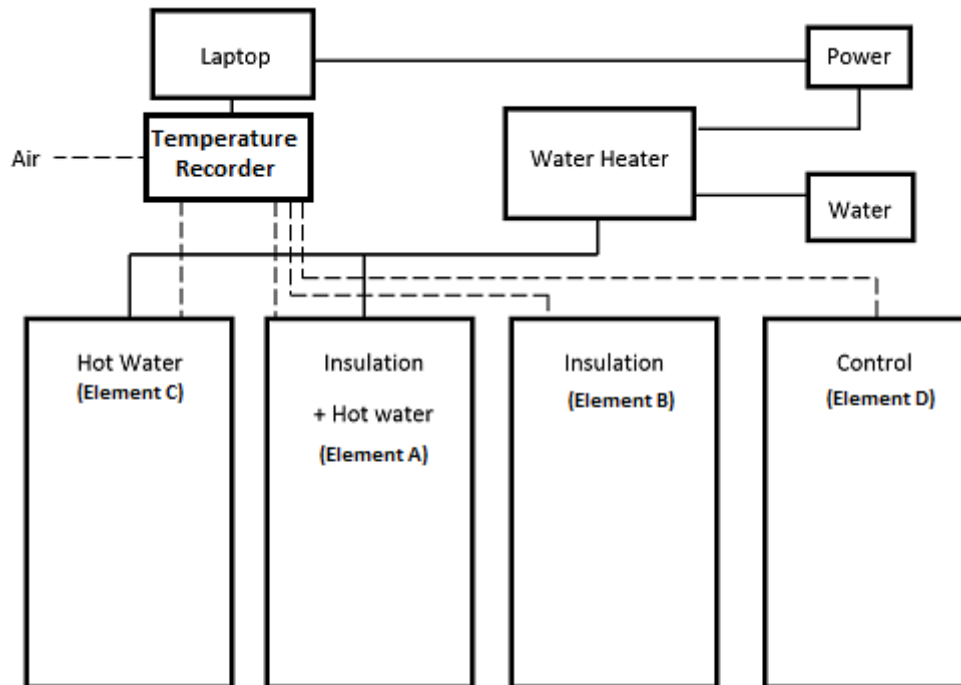
Concrete was poured into four parallel steel moulds. These moulds were rectangular of uniform thickness with dimensions of approximately 2500 x 1300 x 175 mm with a rectangular section removed from one corner (approximately 610 x 750 mm).

Each concrete element was cured under cover and outside in Latrobe (Tasmania), with one of four curing regimes:

- A control which had no curing regime (element D).
- Hot water at 55 °C using sufficient soaker hoses to uniformly saturate the surface (element C). A flow rate of  $5.7 \times 10^{-2}$  L/s was used.
- A single layer of insulation 4.5 mm thick with a thermal resistance (R value) of  $0.11 \text{ m}^2 \text{ CW}$  (element B).
- A layer of insulation with hot water irrigated between it and the concrete slab (element A).

Temperatures were measured with a thermo-resistor sensor and analogue controller system at a 30 second sample rate with an accuracy of  $\pm 1$  °C. The sensor were inserted at the approximate center of mass of the concrete element after two and a half hours from the concrete pour. Partial solidification was necessary to hold the soaker hoses. Data was then recorded for approximately 21 hours starting at 3:00 pm on the 23<sup>rd</sup> of May 2014 to 12:00 am on the 24<sup>th</sup> of May.

The curing system used can be seen in *figure 1*. An in-situ system that was previously used can be found in Appendix A (*figure A.1*).



**Figure 1. Curing system schematic.**

## **2.2. Results**

Below, *figure 2* shows the results of the temperature measurements of each concrete slab. Concrete was poured at approximately 12:40 pm.

The temperature sensor for element C proved faulty around 3.5 to 5.0 hours after commencement. Interpolation with a power law was required with existing valid data to produce the best fit curve.

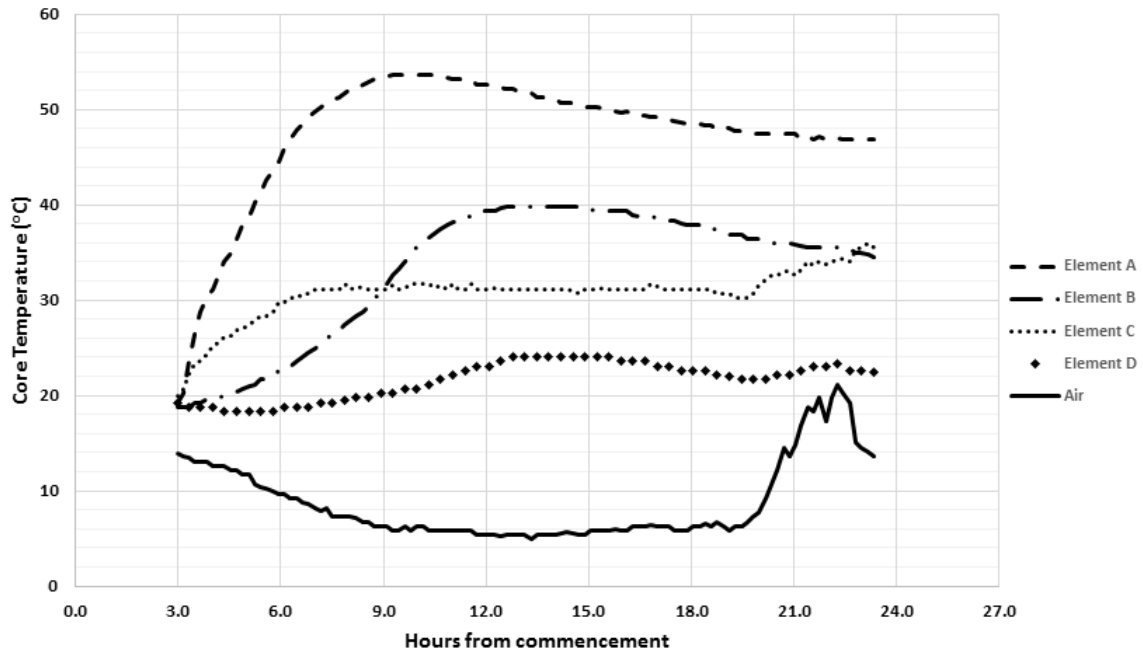


Figure 2. Temperature-time curves of slab core temperatures.

### 3. Equivalent Cylinder Testing

For this research the commonly used Nurse-Saul maturity function was applied to achieve equivalent curing conditions, it appears as:

$$M(t) = \frac{1}{3600} \sum (T_a - T_o) \Delta t \quad (1)$$

Where:

$T_a$  = average temperature during period of time  $\Delta t$  (degrees Celsius).

$\Delta t$  = time interval (seconds).

$T_o$  = temperature datum at which point no strength gain occurs, typically -10 to 0 (degrees Celsius).

$M(t)$  = maturity or temperature time factor at time  $t$  (°C-hours)

For constant time intervals and the temperature datum at zero, *equation 1* above may be simplified to:

$$M(t) = \frac{\Delta t}{3600} \sum (T_a) \quad (2)$$

This maturity method is measure of the extent of hydration based on the transient energy input in the form of heat. The underlying theory is a large amount of heat in small time will progress the hydration process to the same extent as a small amount of heat in a large amount time.

Research suggests this maturity method provides a reasonable approximation for equivalent work under seven days [2]. As the hydration of the concrete isn't a linear function of temperature and the concretes life, errors tend to progress to unreasonable approximations past this time. It was also found large temperature differentials contribute to higher inaccuracies. Another maturity method that better accommodates the changes, such as the Arrhenius maturity function, should be used instead [3].

It's also suggested that the method be used for relative strength gains and not absolute strength to provide higher accuracy [2], as was used for this research

To find the error in the maturity of the concrete slabs we can modify *equation 2* by substituting the measured temperature ( $T_a$ ) with the error bound of the temperature recording system ( $\pm 1$  °C). This leads to *equation*

3 below. With  $\Delta t$  as the 30 second recording time interval, we sum over each of the 2,392 measurements made.

$$Err(t) = \frac{30}{3600} \sum_{n=1}^{2392} 1 = 19.9 \text{ } ^\circ\text{C} - \text{hours} \quad (3)$$

From the data collected in section 2.1, using equations 2 and 3, table 1 below is created.

**Table 1. Concrete maturity and error bounds.**

Element	Maturity ( $^{\circ}\text{C} - \text{hours}$ )	Difference from control (%)	Percentage of Error (%)
Element A	949.4	120	2.1
Element B	665.4	54.2	3.0
Element C	613.8	42.2	3.2
Element D	431.6	0	4.6

### 3.1. Procedure

A total of 33 Australian Standard 200 x 100 mm cylinders were cast to determine equivalent compressive strengths at 21 hours (duration of slab/element test), 7 days and 28 days for each of the elements. Element B at 28 days provided insufficient test cylinders. Three cylinders were used to determine the compressive strength at each time period, using an Avery 1000 kN universal test machine.

For concrete batch creation, casting and water bathing methods, Australian Standards 1012.1, 1012.8, 1012.8.1, 1012.9.2 were followed where applicable and appropriate. Some aggregates from the original batch were not identical for the cylinder tests, however proportions and sizes were maintained. General Purpose cement was used. Reinforcement was not considered for testing with the equivalent concrete cylinders.

The water bath held six cylinders at a time. It allowed for the moderation of the concretes maturity using a fish-tank water heater to maintain a constant temperature. After the maturity was accumulated as per table 1 above, the cylinders were allowed to sit in a humidifier maintained at a constant 21  $^{\circ}\text{C}$  for the duration of the time period required to test them.

### 3.2. Results

Table 2 below shows the compressive strengths found from the two closest results if in agreement.

**Table 2. Compressive strength results from equivalent tests.**

Element	21 Hour Equivalent Test (MPa)	7 Day Test (MPa)	28 Day Test (MPa)
Element A	17.8	29.2	33.2
Element B	15.6	26.5	-
Element C	12.9	27.4	29.5
Element D	9.7	19.2	26.7

## 4. Transient Thermal Analysis

A finite element analysis package (FEA) was used to model and solve a transient thermal analysis of each curing regime. Finite element analysis programs rely on the discretisation of an object (a model) to perform numerical analysis on a nominal segment or a vertex of the segment that is typically magnitudes smaller than the model itself. These segments are generally quadrilateral or triangular.

The numerical analysis in this case involves solving the heat equation (equation 4 below) at each vertex (coordinates of x, y and z), to determine the temperature distribution with time.

$$\frac{\partial T}{\partial t} = \frac{k}{c_p \rho} \left( \frac{\partial^2 T}{\partial x^2} + \frac{\partial^2 T}{\partial y^2} + \frac{\partial^2 T}{\partial z^2} + Q_{internal} \right) \quad (4)$$

Where k is the thermal conductivity of the object,  $c_p$  the specific heat,  $\rho$  the density of the medium, instantaneous time t and the instantaneous temperature T. As the concrete generates heat the variable Q provides addition for the heat generated per unit volume.

The model included the steel casting bed, convective affects from the air and hot water, internal heat generation, and effects of the insulation. Each face of the element received a different heat transfer coefficient due to the variation of wind velocity over the element, this was simplified into two cases, the back and underside of the element, and the front (wind facing) and top of the element.

The overall approach to finding a solution centred on 'guess and check'. Given the complexity of the transient thermal analysis being replicated and the limited equipment available, it was impossible to repeat the systems entirety from prior knowledge for a theoretical approach.

For every variable change the internal heat generated by the concrete was calibrated with the control element such that the output core temperature solution was significantly close to the measured values (see figure 3 (a)).

The general process was as follows:

1. Determine the internal heat generated using the control (element D) as a calibration.
2. Determine the thermal conductivity and specific heat of concrete using the insulation experimental data (element B) as the calibration. The insulation had the most accurate parameters and so using the data would allow the use of another system to calibrate without the addition of unknown variables.
3. Repeat step 1 and 2 as necessary.
4. Using the resulting thermal conductivity and specific heat of concrete found in the previous steps, determine the hot water film coefficient using the experimental data (element C).
5. Using values from the above steps produce the output for the combination curing effect (element A).

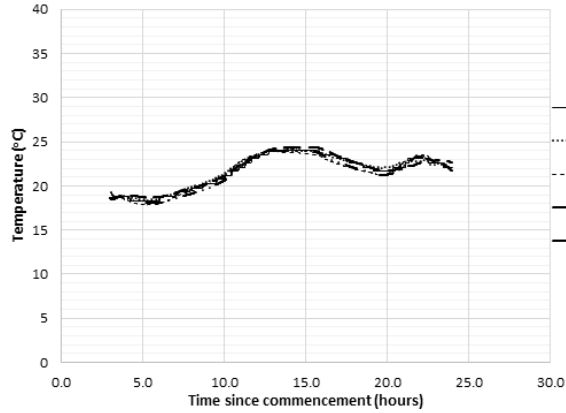
Table 3 below contains properties and boundaries researched and derived for the model.

**Table 3. Values and ranges used for thermal analysis.**

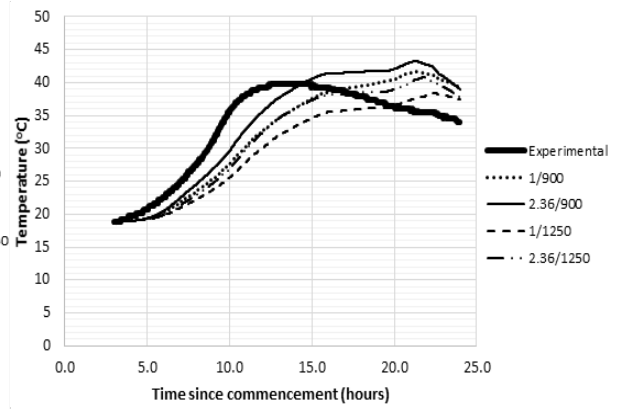
Parameter	Range	Derived from
Concrete thermal conductivity	1.00-2.36 W/m°C	[5] [6] [7]
Concrete specific heat	900-1250 J/kg°C	[5] [7]
Concrete density	2488 kg/m <sup>3</sup>	Given (batch supplier)
Insulation thermal conductivity	0.041 W/m°C	Calculated from given thermal resistance and thickness
Insulation specific heat	1155 J/kg°C	Calculated [2] [3]
Insulation density	96.2 kg/m <sup>3</sup>	Calculated (given properties)
Steal thermal conductivity	60.5 W/m°C	Given (FEA program)
Steal specific heat	434 J/kg°C	Given (FEA program)
Steal density	7850 kg/m <sup>3</sup>	Given (FEA program)
Hot water film coefficient	10-1600 W/m <sup>2</sup> °C	Empirical formulas [4]
Front/top film coefficient	29 W/m <sup>2</sup> °C	Empirical formula based on local wind speed [8]
Back/underside film coefficient	20 W/m <sup>2</sup> °C	Empirical formula based on local wind speed [8]

The starting values for the thermal conductivity and specific heat of concrete were found through general rules of mixture. Where the total value is the sum of the weighted values of each component. Further research into the properties of each component yielded a total thermal conductivity of 1.2 W/m°C and a specific heat of 1,100 J/kg°C.

#### 4.1. Results



(a) FEA analysis temperature output of control and experimental.



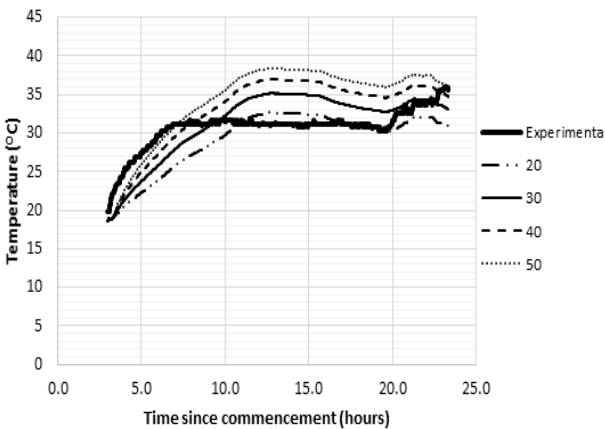
(b) FEA analysis temperature output of insulation and experimental.

**Figure 3. Transient thermal analysis outputs of the control/element D (a) and the insulation regime/element B (b). Plot names are in the form of thermal conductivity/specific heat for concrete of the value that was used in  $W/m^{\circ}C$  and  $J/kg^{\circ}C$  respectively.**

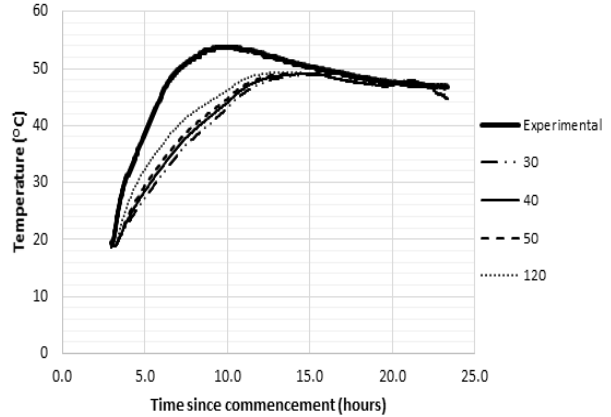
A table of  $R^2$  values to determine closeness of fit (*table 4* below) resulted in a thermal conductivity of 2.36  $W/m^{\circ}C$  and a specific heat of 900  $J/kg^{\circ}C$  for the concrete being the optimal solution. These values were used for the analysis of elements A and C.

**Table 4. Closeness of fit values from the curves generated for figure 3 (b).**

Curve (thermal conductivity/specific heat)	$R^2$ Value
1/900	0.719
2.36/900	0.798
1/1250	0.690
2.36/1250	0.738



(a) FEA analysis temperature output of hot water and experimental



(b) FEA analysis temperature output of combination and experimental.

**Figure 4. Transient thermal analysis outputs of the hot water regime/element C (a) and the combination regime/element A (b). Plot names are the hot water convection film coefficient ( $W/m^2^{\circ}C$ ) that was tested.**

## 5. Discussion

### 5.1. Equivalent Cylinder Testing

*Figure 2* and *Table 1* shows a significant difference in temperature between elements A (insulation and hot water combination) and D (control) leading to an 83% increase in compressive strength within the first 21 hours and 24% after 28 days. Elements B (insulation) and C (hot water) produced a closer maturity yielding a 61% and 33% in increase compressive strength respectively, relative to element D. The seven day tests show elements B and C converge to approximately the same compressive strength. This convergence is expected given only limited amounts of products to hydrate and a decreasing concentration.

Overall we found no immediate correlation between relative strength gain and relative thermal intake of the concrete mass, other than the fact a significant increase in thermal intake will obviously lead to an increase in compressive strength at 21 hours, as expected (see *Table B.1* and *Table 1*).

The strength gain over a period of 28 days for the hot water (55°C) test disagrees with the conclusions drawn from the research conducted by Feyne et al. (2003). They cured and tested concrete compressive strength under a variety of ambient temperatures and type III cement mixtures, with a relative humidity of 50% to 60%. They found almost all mixtures produced inferior strength at 28 days compared to a standard control. For some mixtures this lower strength gain occurred for 24 hour tests.

This research used type I (GP) cement, typically more coarse than type III, however the key difference is humidity. This research essentially used 100% humidity to cure concrete for both experimental components, allowing the hydration to occur continually and at an accelerated rate from the heat input.

We also found element C surpasses element B in compressive strength at seven days (3.4% difference in strength) which highlights the existence of random variance in test cylinders. This can be reduced by testing a greater sample size.

Reinforcement in the elements used for testing was assumed to have negligible effects for both relative strength measurements of the test cylinders and the heat differential between the concrete mass and atmosphere. As the reinforcement has a high thermal conductivity and low specific heat this would have the effect of a faster internal heat transfer. However it would not affect the concrete's hydration process or act as noticeable insulate.

We expect some difference in compressive strength and thermal intake between the cast slabs and test cylinders due to variations in aggregate properties between batches (as mentioned in *section 3.1*). This variation would undermine direct comparison of compressive strength results and thermal intake between slab and cylinder testing. However this study was specifically limited to the relative strength gain of test cylinders, with no comparison between the two tests. The overall thermal properties of the concrete between tests would vary slightly because of this, however similar aggregates were used and proportions were closely maintained to limit the variation.

Error bounds from the equipment tended to be small with *Table 1* above showing a possible maximum error of 4.6% of the total maturity accumulated.

In *Figure 2* near 20-23 hours after commencement, we see that hot water exposed to the atmosphere and concrete slab is noticeably affected by air temperature. A sharp rise in local temperature results in the core temperature of element C to greatly increase. Element D responds with a more latent and shallow increase in core temperature, with element A plateauing. This validates Grove's (1989) suggestion that ambient temperatures could have a negative impact on temperature gains of blanket (insulated) curing. The hot water test (element C) is amplified by this local increase in heat, with the insulation (element B) having no noticeable response.

### 5.2. Transient Thermal Analysis

The finite element model generated for each combination of test proved to have a very weak correlation between the experimental data recorded. This was due to the complexity of the experiment with several unknown properties left to be determined.

The hot water film coefficient for instance, that provided optimal results, tended to be relatively low – between 20 to 60 W/m<sup>2</sup>°C (see *figure 4 (a)*). For the combination regime *figure 4 (b)* shows minimal variance in core temperature when a relatively low film coefficient is used. A relatively high thermal conductivity and low specific heat of concrete produce the best results. This was expected as a sharp increase in temperature followed by a decrease was required (see *figure 3 (b)*). The high thermal conductivity in this case enables a faster internal heat transfer, where a lower specific heat promotes a responsive change.

The lack of reinforcement modelled in the analysis may cause the thermal conductivity to be higher than the true value, however the holistic approach to modelling the thermal properties of the concrete could have included this.

The major inconsistencies derive from a dynamic air convection (wind speed and temperature) throughout the 21 hour curing period that acted with varying magnitudes on each surface of the pre-cast elements.

There were however some general patterns found in the generated data. Some sections of the experimental and computer generated curve for element A appear to have superposition like qualities of the separate curves generated for elements B and C. Suggesting both curing methods have a noticeable effect in combination.

## 6. Conclusions

We began by introducing a new curing regime using insulation and hot water applied to the exterior surface of concrete. With the aim to research the extent of accelerated strength gain and the heat it imparts to the concrete this combination method provides.

Experimenting with a portable system we have demonstrated a significant increase in heat of the concrete for independent curing tests of insulation, hot water and the combination. This translated into a significant increase in compressive strength from a 21 hour equivalent test to a period of 28 days for all tests compared to a control.

The following conclusions can be drawn:

- Hot water and insulation in combination maintain a noticeably higher compressive strength than each component separately and a control, over a 28 day period.
- For this concrete mixture and scenario, the insulation maintains a slightly higher average internal temperature than irrigating the surface of the concrete with hot water.
- Local air temperature can have a significant effect on the internal temperature of the hot water curing method.
- Both insulation and hot water tests converge in compressive strength quickly, reaching a similar strength near seven days.
- The effects of insulation and hot water on the thermal intake and strength of concrete will vary significantly depending on the constituents of concrete.
- Convection of air and hot water were sensitive to the model, and dynamic over 21 hours.
- Tests of hot water (55 °C) and insulation provided some superposition effects on the temperature and the magnitude of degree-hours accumulated for the combination curing method.

## 7. Acknowledgements

The author would like to thank BridgePro Engineering for their major input of resources to the project and fostering the original idea



## 8. References

1. *Bridgeworks specification: B10- supply of concrete* (2006). Department of State Growth. Retrieved from [http://www.transport.tas.gov.au/data/assets/pdf\\_file/0019/11971/b10\\_conc\\_supply\\_806.pdf](http://www.transport.tas.gov.au/data/assets/pdf_file/0019/11971/b10_conc_supply_806.pdf)
2. Schindler, A. K., Barnes, R. W., & Wade, S. A. (2008). *Evaluation of the maturity method to estimate concrete strength in field applications* (No. ALDOT Project 930-590). Highway Research Center, Auburn University.
3. Wilde, W. J. (2013). *Development of a Concrete Maturity Test Protocol* (No. MN/RC 2013-10).
4. Gaur, U., & Wunderlich, B. (1981). *Heat capacity and other thermodynamic properties of linear macromolecules. II. Polyethylene*. Journal of Physical and Chemical Reference Data, 10(1), pp. 119-152.
5. Gaur, U., & Wunderlich, B. (1981). *Heat capacity and other thermodynamic properties of linear macromolecules. IV. Polypropylene*. Journal of Physical and Chemical Reference Data, 10(4), pp. 1051-1064.
6. Lienhard, J. I., & Lienhard, J. V. (2011). *A heat transfer textbook (4th ed.)*. Cambridge, MA: Phlogiston Press.
7. Howlader, M. K., Rashid, M. H., Mallick, D., & Haque, T. (2012). *Effects of aggregate types on thermal properties of concrete*. ARPN Journal of Engineering and Applied Sciences, 7 (7), pp. 900 - 907.
8. ISO, I. (2008). 10456: *Building materials and products—Hygrothermal properties—Tabulated design values and procedures for determining declared and design thermal values*. International Organization for Standardization, Geneva.
9. Guo, D. S., Chen, E. Y., Low, G. L., & Yang, J. L. (2001, August). *Experimental Modeling of Temperature Rise of Mass Concrete by FDM Method*. The 26th International Conference on Our World in Concrete & Structures, pp. 27-28.
10. Kumaran, M. K., Sanders, C., Tariku, F., Blocken, B., Carmeliet, J., Hens, H., Paepe, M. & Janssens, A. (2008). *Boundary conditions and whole building HAM analysis*.
11. Kröger, D. G. (2002). *Convection heat transfer between a horizontal surface and the natural environment*. R and D Journal, 18(3), pp. 49-54
12. Freyne, S. F., Russell, B. W., & Bush Jr, T. D. (2003). *Heat curing of high-performance concrete containing type III cement*. ACI Materials Journal, 100(6).
13. Grove, J. D. (1989). *Blanket curing to promote early strength concrete*. Office of Materials, Highway Division, Iowa Department of Transportation.

## Appendix A

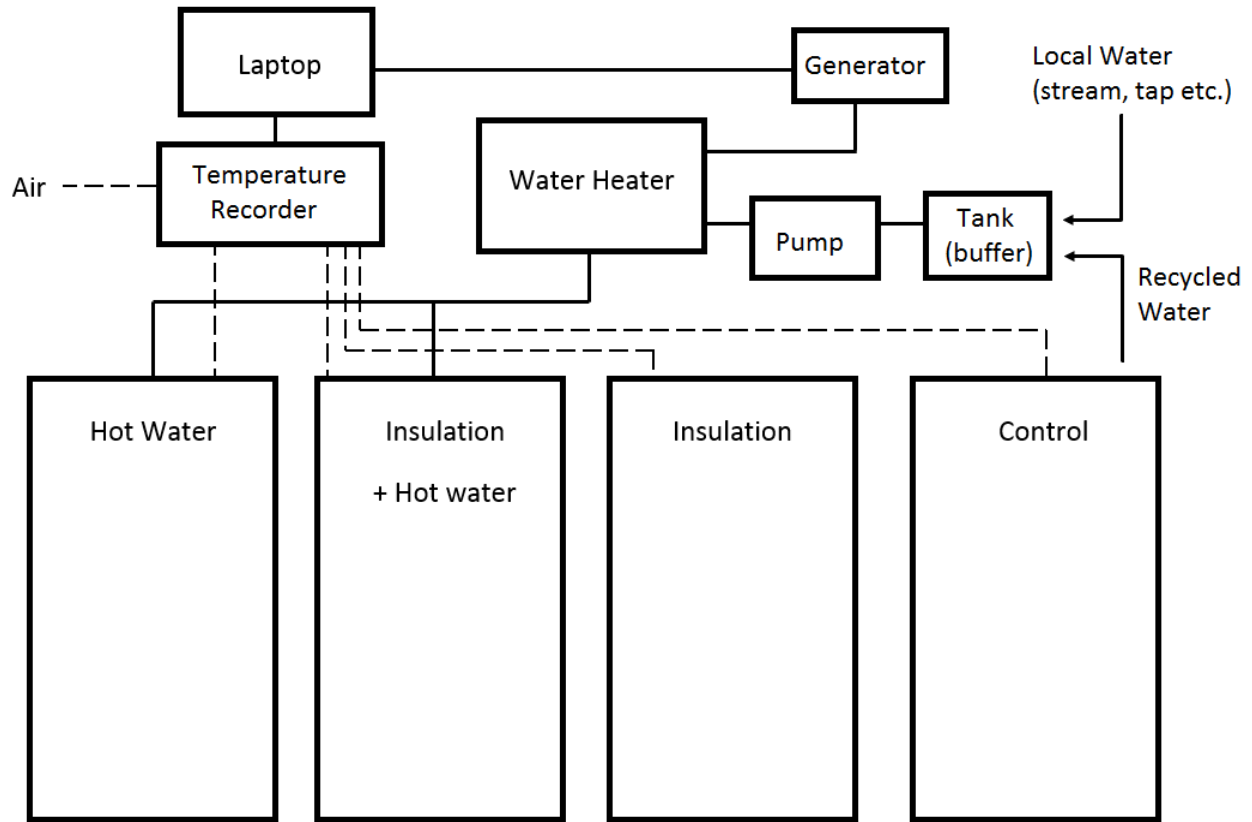


Figure A.1 – Curing system schematic for in-situ operations

## Appendix B

Table B.1. Relative compressive strength results to control (element D).

Element	21 Hour Equivalent Test (%)	7 Day Test (%)	28 Day Test (%)
Element A	83.5	52.1	24.3
Element B	60.8	38.0	-
Element C	33.0	42.7	10.5
Element D	0	0	0

# Comparative Performance of Recycled Plastic and Polypropylene Commercial Fibres with Plain Concrete

Badr S. Al-Tulaian<sup>1</sup>, Mohammad J. Al-Shannag<sup>2</sup>, Abdulrahman M. Al-Hozaimy<sup>3</sup>

<sup>1</sup>Patent Specialist of Civil Engineering, Saudi Patent Office

<sup>2&3</sup>Professor of Civil Engineering, King Saud University

**Abstract:** Manufacturing of fibres from industrial or postconsumer plastic waste is an attractive approach with such benefits as concrete performance enhancement, and reduced needs for land filling. The main objective of this study is to investigate the effect of Plastic fibres obtained locally from recycled waste on plastic shrinkage cracking of concrete. The results indicate that recycled plastic RP fibre of 50 mm length is capable of controlling plastic shrinkage cracking of concrete to some extent, but are not as effective as polypropylene PP fibres when added at the same volume fraction. Furthermore, test results indicated that there was the increase in flexural strength of RP fibres and PP fibres concrete were 12.34% and 40.30%, respectively in comparison to plain concrete. RP fibres caused a significant increase in compressive strengths up to 13.02% compared to concrete without fibre reinforcement.

**Keywords:** Concrete, Plastic, Shrinkage Cracking, Compressive Strength, Flexural Strength, Toughness, RF Recycled Fibres, Polypropylene PP Fibres.

## 1. Introduction

Plastic shrinkage cracking of concrete is still a major problem in concrete members with large surface areas, such as slabs on grade, bridge decks and concrete pavements. Plastic shrinkage occurs in all fresh cement-based materials within the first few hours after they have been placed, Toledo et al. [1], especially during hot, windy and dry weather which can cause a fast rate of surface water evaporation. When the rate of evaporation exceeds the rate of bleed water rising to the surface, the concrete mixture will begin to shrink, Wang et al. [2]. If the shrinkage is restrained, tensile stress develops and can cause cracks.

The fibres provide bridging forces across cracks and thus prevent the cracks from growing. In addition, the large pores that are introduced at the fibre-matrix interfaces are believed to provide bleeding channels which supply water to replenish the water lost from the surface. As a results, the capillary stress between the solid particles, and hence the free plastic shrinkage potential, is reduced [3].

Saudi Arabian Basic Industries Company (SABIC) has been a leading force in the development of the Kingdom of Saudi Arabia plastic industries. There are around 450 thermoplastic processing units in KSA with an overall market demand of 400 ktpa (kilo ton per annual) polyethylene, 200 ktpa polyvinyl chloride (PVC), 100 ktpa polystyrene (PS), 70 ktpa polyethylene terephthalate (PET) and 30 ktpa polyester (PES) fibres, Alhozaimy et al. [4]. Polyethylene terephthalate (PET) is a plastic material commonly used in beverage containers and other products.

Study, Parviz et al. [5], demonstrated the effect of discrete reinforcement systems of recycled plastic fibres on enhancing the resistance of concrete to restrained shrinkage cracking and decrease the maximum crack width. They investigated that improvements in restrained shrinkage crack control and impact resistance was particularly significant and comparable to those of virgin fibres. Discrete reinforcement systems also delay the initiation of cracking. Alhozaimy and Alshannag [4] test results indicated a significant improvement in crack-arresting mechanism of the concretes reinforced with recycled plastic of low density polyethylene fibres (LDPE) compared to plain concrete. They observed that increasing the recycled fibre volume up to 3% caused no plastic shrinkage cracking of concrete slabs.

The use of recycled fibres from industrial or postconsumer waste could offer effective reinforcement for concrete and additional advantages of waste reduction and resources conservation. Limited researches have been conducted on the use of recycled fibres in concrete to control shrinkage cracking. This research provides a more comprehensive testing program to explore the various parameters influencing the performance of recycled plastic RP fibres as crack arrestors in concrete and compare their performance with that of commercial polypropylene PP fibres particularly under hot-dry environment.

## 2. Experimental Program

Ordinary Portland cement (Type I) was used. Coarse aggregates were crushed limestone obtained from quarries around Riyadh and were a blend of 3/4" (20 mm) and 3/8" (10 mm) sizes. The fine aggregate was a blend of crushed sand and red sand obtained from the crushed limestone. The specific gravity and absorption capacity of the coarse and fine aggregates were determined in accordance with (ASTM C 127) and (ASTM C 128), [6, 7]. The specific gravity of coarse aggregate of 3/4" (20 mm) and 3/8" (10 mm) sizes were 2.66 and 2.69, respectively and their absorption capacities were 1.13% and 1.48%, respectively. The specific gravities of the crushed sand and red sand were 2.64 and 2.66, respectively and their absorption capacities were 1.62% and 0.38%, respectively. The material properties of coarse and fine aggregates are given in Table 1.

The recycled Plastic RP fibres were obtained from small workshops operating in Jeddah. Process of recycling plastic includes; first, placing the plastic waste in a machine to be cut into small pieces. Second, these small pieces of plastic will be melted at a temperature depending on the plastic type. Third, the melted plastic will pass through perforated plate and extracted as a plastic wire with the width of 2.0 mm size. Finally, the plastic wires were cut into small pieces to be in the form of fibres. For the present study, recycled PET fibres of 2.0 mm width will be cut into 50 mm long pieces and used as reinforcing fibres for concrete at volume fraction 1.0%. commercial polypropylene PP fibres of 30 mm length at volume fraction 0.50% (Figures 1, 2) shows images of the manufactured recycled PET fibres and PP fibres, respectively. The basic properties of fibres are presented in Table 2.

**Table 1. Coarse and fine aggregate material properties**

Type	Specific gravity	Fineness modulus	Water absorption (mass %)	Unit weight (kg/m <sup>3</sup> )	Moisture content (%)
3/4"	2.66	7.05	1.13	1533	0.32
3/8"	2.69	5.83	1.48	1305	0.59
Crushed Sand	2.64	4.6	1.62	1580	0.55
Red Sand	2.66	1.02	0.38	1668	0.12

**Table 2. Properties recycled PET and Virgin PP fibres**

Fibre type	Strand shape	Specific gravity	Tensile strength (MPa)	Length (mm)	Width (mm)
RPF - (PET)	Flat	1.38	310	50	2.0
Virgin - (PP)	Circular	0.90	450	30	1.0



Fig. 1 : Picture of 50 mm long RP fibres used in the study.



Fig. 2 : Picture of Virgin PP fibres used in the study.

Plastic shrinkage cracking test plan, flexural strength and compressive strength tests were conducted for the various types of fibres. Two different series of RP fibres for concrete mixtures were used for casting ordinary concrete designated as R.P.C.3, R.P.C.4 and PP fibres as P.P.C.5, P.P.C.6 and plain mixture as N.F.C.1, N.F.C.2 without fibres were cast in the concrete laboratory as shown in Table 3. The mold of slab used in the test was a 1000 x 1000 x 100 mm, standard 100 mm of concrete cubes for compressive strength tests according to (BS 1881 Part 116), [8], 600 x 150 x 150 mm prisms for the flexural tests according to (ASTM C 78) and (JSCE-SF4), [9, 10] were used. For all mixtures, measurements of outdoor temperature during the time of casting ranged between 41°C to 45°C, relative humidity (RH) between 18% to 20 % and maximum wind speed 3.00 to 4.50 m/s. It was monitored for 24 h, during which time visible cracks appeared.

**Table 3. List of specimens and the number of specimens used for each combination.**

Design Mix.	Fibre volume fraction (%)	No. slabs Plastic shrinkage	No. specimens flexural strength	No. specimens compressive strength
N.F.C.1	----	2	2	6
N.F.C.2	----	2	2	6
R.P.C.3	1.00	2	2	6
R.P.C.4	1.00	2	2	6
P.P.C.5	0.50	2	2	6
P.P.C.6	0.50	2	2	6

The concrete mixes were prepared outdoor under hot-dry environment conditions to observe the plastic shrinkage cracking on the slabs. Proportions of mixtures ingredients used in this study were designed as given in Table 4. All mixtures were prepared in a rotary planetary mixer with capacity of 180 liters. The coarse and fine aggregate and absorption water were measured and placed into the mixer and mixed for 1.0 minute. After that the cement, the rest of the free water were added and mixed for three minutes followed by 2.0 minutes break and then another 3.0 minutes mixing was performed. Next, the fibres were added into the mixer and then mixed for three minutes.

**Table 4. Properties recycled PET and Virgin PP fibres**

Design Mix.	Fibre length (mm)	Fibre volume fraction (%)	Cement: Coarse Agg.: Fine Agg.: Water
N.F.C.1	----	----	1.00 : 2.40 : 2.66: 0.55
N.F.C.2	----	----	
R.P.C.3	50	1.00	1.00 : 2.40 : 2.66: 0.55
R.P.C.4	50	1.00	
P.P.C.5	30	0.50	1.00 : 2.40 : 2.66: 0.55
P.P.C.6	30	0.50	

The mix proportions of plain, RP fibres and PP fibres reinforced concrete used in this study are as follows:

Free w/c ratio = 0.55

In case of fibrous concrete the weight of RP and PP fibres for different volume fractions was calculated by Equation 1 as follows:

$$W_f = G_s \times \left(\frac{V_f}{100}\right) \times 1000 \quad (1)$$

Where,

$W_f$  : Weight of RP/ PP fibres ( $\text{kg/m}^3$ ).

$V_f$  = Volume fraction of fibres (%).

$G_s$  = Specific Gravity of RP/ PP fibres.

Using the above expression the weight of RP and PP fibres per  $1.00 \text{ m}^3$  of concrete is given in the Table 5.

**Table 5. Quantity of RP and PP fibres in fibrous concretes.**

Fibre type	Volume fraction $V_f$ (%)	Specific Gravity, $G_s$	Weight of Fibre ( $\text{kg/m}^3$ )
RP fibres	1.00	1.38	20.7
PP fibres	0.50	0.92	4.6

## 2.1 Tests on Fresh Concrete

### 2.1.1 Temperature and Slump Tests

Temperature of the materials of the mixtures fresh concrete was measured using the digital thermometer shown in Table 6. This temperature was determined in accordance with (ASTM C1064), [11] standard.

The digital thermometer was also used for measuring the temperature of the concrete. The slump test was used to measure workability of all the concrete mixes and was conducted in accordance with (ASTM C143), [12] as shown in Table 7. The slump of plain and fibrous concrete was determined at the concrete laboratory.

**Table 6. Temperature test for fresh concrete.**

Design Mix.	N.F.C.1	N.F.C.2	R.P.C.3	R.P.C.4	P.P.C.5	P.P.C.6
Cement Temp. °C	40.1	40.1	31.0	31.0	24.3	24.3
Coarse Agg. Temp. °C	40.3	40.3	30.1	30.1	34.6	34.6
Coarse Agg. Temp. °C	37.5	37.5	30.5	30.5	37.1	37.1
Crushed Sand Temp. °C	40.3	40.3	31.1	31.1	36.5	36.5
Red Sand Temp. °C	40.0	40.0	31.3	31.3	36.8	36.8
Water Temp. °C	23.0	23.0	22.5	22.5	22.0	22.0
Casting Temp. °C	32.1	32.1	28.6	28.6	29.1	29.1
Ambient Temp. °C	44.0	44.0	42.0	42.0	41.0	41.0

**Table 7. Slump test for fresh concrete.**

Design Mix.	Fibre volume fraction (%)	Fibre Length (mm)	Slump of Slab 1 (mm)	Slump of Slab 2 (mm)	Average Slump (mm)
N.F.C.1	Plain	0.00	75	85	80
N.F.C.2	Plain	0.00			
R.P.C.3	50	1.00	70	83	77
R.P.C.4	50	1.00			
P.P.C.5	30	0.50	75	90	82
P.P.C.6	30	0.50			

### 2.1.2 Wind Speed and Rate of Evaporation Tests

The anemometer device used for measuring the wind speed was placed on the surface of the mixture. This wind speed was determined in accordance with (ASTM D 5527), [13] standard. Plastic shrinkage cracking generally occurs in fresh concrete when the evaporation rate is high. High evaporation rates are caused by high temperatures, high wind speeds and low relative humidity.

The percentage of water evaporated was calculated as the ratio of water evaporated to the total water added to the mix. The rate of water evaporation was evaluated by recording the change in weight using a digital balance of 0.01-g sensitivity. The rate of evaporation investigate was measured by using Equation 2. The evaporation rate were recorded and presented in Table 8. A graphical method to estimate evaporation rate is described in (ACI 305R), [14]. The concrete temperature recorded was 29°C to 32°C and the average wind speed, ambient temperature and humidity were in the range of 3.00 m/s to 4.50 m/s, 41°C to 45°C and 18% to 20%, respectively. The evaporation rate for concrete slabs approaches 1.20 kg/m<sup>2</sup>/h, the chance of plastic shrinkage cracking occurring is high (ACI 305R).

**Table 8. The rate of evaporation recorded.**

Time	Weight of water (kg)	Loss water weight $L_w$ (kg)	Rate of Evaporation $R_{evp}$ (kg/m <sup>2</sup> /h)	Average of evaporation rate (kg/m <sup>2</sup> /h)
12:25	2.880	----	----	1.12
1:25	2.825	0.055	0.83	
2:25	2.730	0.095	1.43	
3:25	2.672	0.078	1.18	
4:25	2.612	0.070	1.06	
5:25	2.550	0.072	1.10	

$$R_{evp} = \frac{W_L}{A_{cont}} \quad (2)$$

Where,

$R_{evp}$  : Rate of Evaporation (kg/m<sup>2</sup>/h).

$W_L$  : Loss of water weight (kg).

$A_{cont}$  : Area of container (0.3 m , 0.22 m) .

## 2.2 Tests on Hardened Concrete

### 2.2.1 Compressive and Flexural Strength Tests

The compressive strength test was performed on a 100 mm cube specimen tested for concrete at right angles to the position of cast according to British Standard (BS 1881: part 116), [8]. Compressive strength test consisted of applying a continuous compressive axial load at a rate of 0.5 MPa/s until failure occurs.

Flexural strength was measured using prism specimens 600 x 150 x 150 mm under third point loading in accordance with (ASTM C 78), [9]. The toughness was calculated in accordance with (JSCE-SF4), [10] Japanese Standard . The specimens tested were turned on their sides with respect to their position as molded.

The specimens were loaded at a rate of 0.50 mm/minute using displacement control. The prisms were loaded in an Amsler press using a displacement rate of 0.50 mm/minute. The loads and mid span deflections were measured using 10 KN load cell and 25 mm LVDT respectively. The load-deflection data was recorded by using a data logger. The reading from the data logger was transferred to a computer to plot the load-deflection curve during testing.

The flexural strength ( $f_s$ ) was determined in accordance with (ASTM C 78), as an average value of three specimens, the flexural strength or modulus of rupture was calculated using simple beam bending Equation 3, using the first peak load value in the load-deflection curve, according to the following equation:

$$f_s = \frac{PL}{bh^2} \quad (3)$$

Where:

$f_s$  = The flexural strength in MPa.

$P$  = The peak load in N. (first peak for load-deflection curve with multiple peaks).

$L$  = The supported span in mm (450 mm).

$b$  and  $h$  = The width and the depth of specimen ( $b = h = 150$  mm for the tested prism).

Toughness ( $T$ ) is defined as the total energy absorbed prior to complete separation of the specimen. It was calculated as the area under the load-deflection curve up to a deflection of 1/150 times the span, which is equivalent to 3.0 mm for the prism specimen tested (span= 450 mm) as shown in Figure 3. Numerical approach (trapezoidal method) was used, to determine the area under the curve, by dividing the area under the curve into trapezoids. The toughness is calculated by summing up all the trapezoid areas up to 3.0 mm deflection. The toughness which is equal to the area under load-deflection curve up to 3.0 mm according to (JSCE-SF4) , [10] Japanese Standard.

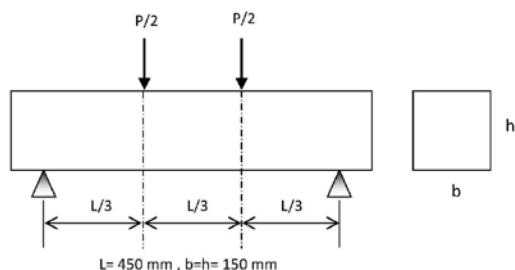


Fig. 3 : Flexural characteristics testing setup.

## 2.2.2 Plastic Shrinkage Cracking Measurement

After casting the plastic shrinkage slabs described in results, the following day, the cracks on the hardened concrete surface were mapped to obtain pattern, length of cracking, crack width and total area of cracking. For mapping 10 mm grid was drawn on the surface of the slabs and the cracks on the slab were mapped on graph sheet. The width of each crack was measured at regular intervals along its length using a microscope as shown in Figure 4. The length of each crack was determined by placing a string along the crack and then measuring the length of string. The summation of product of average width and length of crack for all the cracks in a slab was calculated to obtain total crack area per square meter.



Fig. 4 : The microscope used for measuring crack width.

## 3. Results And Discussions

### 3.1 Plastic Shrinkage Cracking

All the plastic shrinkage slabs were placed outdoor in hot-dry environment condition during the month of September in Riyadh. The average wind speed, ambient temperature and humidity were in the range of 3.00 m/s to 4.50 m/s, 41°C to 45°C and 18% to 20% respectively. The evaporation rate for concrete slabs approaches 1.20 kg/m<sup>2</sup>/h, the chance of plastic shrinkage cracking occurring is high (ACI 305R), [14].

Plastic shrinkage cracks were mapped for all the slabs. These mapping patterns are presented in Figure 5. From these mappings, it is clearly seen that RP fibre with 1.00% and PP fibre with 0.50% concrete content exhibited less cracking.

The influence of adding different fibre types on crack measurements of plastic shrinkage in terms of the average crack width, maximum crack width, average crack length, total crack area and crack numbers is illustrated in Table 9. Average crack width was 0.27 mm/m, the maximum crack width was 0.40 mm for plain control specimens. Average crack length was 903 mm/m; total crack area was 254 mm<sup>2</sup>/m<sup>2</sup> and crack numbers were 2 cracks for plain control slabs.

A comparison of average crack width, crack length and total crack areas obtained for plain, RP fibre and PP fibre concrete is shown in Figures 6A thru 6C. The average crack width and total crack area decreased for both types of RP fibre and PP fibre. The significant reduction in plastic shrinkage cracks was obtained at a volume fraction of 1.00% RP fibre and 0.50% PP fibre concrete, there was no plastic shrinkage cracks in one of the slabs and cracks in the other was negligible. Plastic shrinkage cracking was shown to be connected with initial crack time. This result is clearly reflected in the data of initial crack time for three mixtures given in Table 10.

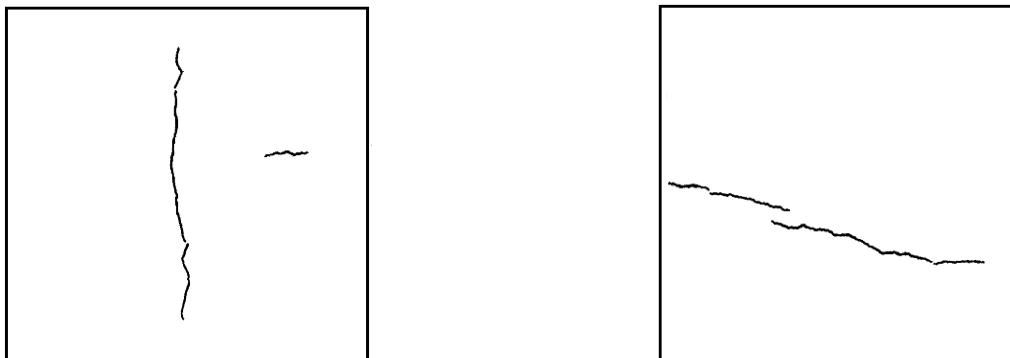


Fig. 5 : Plastic shrinkage cracking at 0.00% .

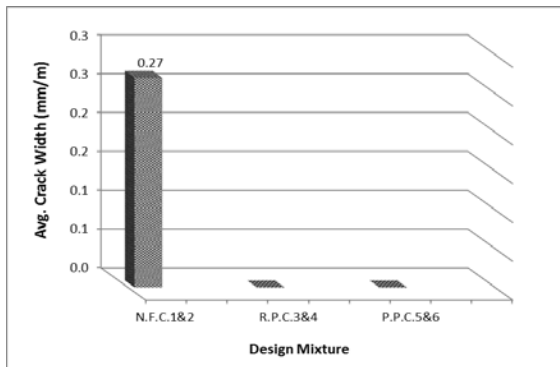


**Table 9. Plastic shrinkage of plain and RF fibres concrete slabs**

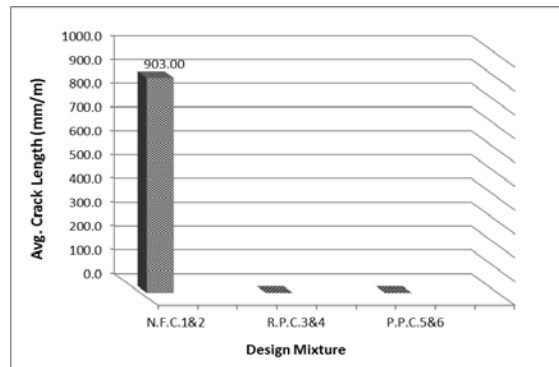
Design Mix.	Crack Measure	Slab No.1	Slab No.2	Average
N.F.C. 1&2 VF = 0%	Avg. Crack Width (mm/m)	0.21	0.32	0.27
	Max. Crack Width (mm/m)	0.30	0.50	0.40
	Total Crack Length (mm/m)	841	965	903
	Total Crack Area (mm <sup>2</sup> /m <sup>2</sup> )	186	321	254
	Crack Numbers	2	2	2
R.P.C. 3&4 VF =1.0%	Avg. Crack Width (mm/m)	No Cracks	No Cracks	No Cracks
	Max. Crack Width (mm/m)			
	Total Crack Length (mm/m)			
	Total Crack Area (mm <sup>2</sup> /m <sup>2</sup> )			
	Crack Numbers			
P.P.C. 5&6 VF = 0.5%	Avg. Crack Width (mm/m)	No Cracks	No Cracks	No Cracks
	Max. Crack Width (mm/m)			
	Total Crack Length (mm/m)			
	Total Crack Area (mm <sup>2</sup> /m <sup>2</sup> )			
	Crack Numbers			

**Table 10. Summary of the initial cracking for concrete specimens**

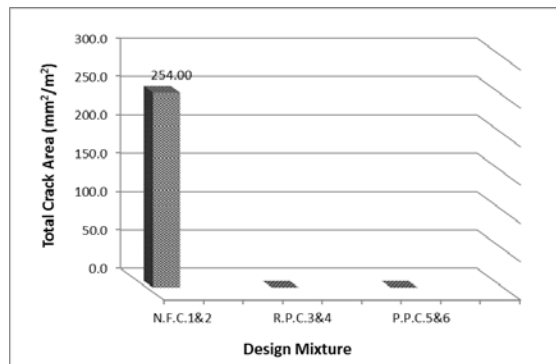
Specimen	Design Mix.	Slabs in outdoor of lab			
		Casting time	Initial crack time	Crack time (hr.)	Average Crack time (hr.)
Plain	N.F.C.1	11:50	2:00	2:10	2.00
	N.F.C.2	1:10	3:00	1:50	
Specimen with RPF	R.P.C.3	3:10	----	----	----
	R.P.C.4	3:35	----	----	
Specimen with PPF	P.P.C.5	3:00	----	----	----
	P.P.C.6	3:25	----	----	



**Fig. 6A : Average crack width of all concrete specimens.**



**Fig. 6B : Average crack length of all concrete specimens.**



**Fig. 6C : Total crack area of all concrete specimens.**

### 3.2 Compressive and Flexural Strength of Concrete

The results for the plain, RP fibres and PP fibres concrete ( i.e. average of three cubes) compressive strength test are summarized in Table 11. The comparison of compressive strength at 7, 14 and 28 days for control, RP fibres and PP fibres contents of volume fraction 1.00% and 0.50% respectively. The results indicate an increase in compressive strength of RP fibre and PP fibre concrete compared to plain concrete.

The increase in compressive strength for concrete content of RP fibre and PP fibre at 7 days was 3.00% and 26.44% respectively, whereas the increase at 14 days was 10.70% and 24.14% respectively and at 28 days was 13.02% and 15.60% respectively, compared to control. The plain concrete specimens failed in a brittle manner and shattered into pieces. In contrast, all the RP fibres and PP fibres samples after reaching the peak load could still remain as integral piece, with fibres holding the mortar matrices tightly together.

**Table 11. Compressive strength of all concrete specimens**

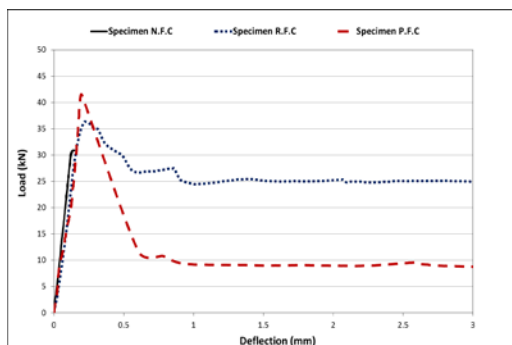
Specimen	Design Mix.	Fibre Volume Fraction (%)	Compressive strength (MPa)		
			7-Days Average	14-Day Average	28-Day Average
Plain	N.F.C.1	0.00	25.15	29.00	34.95
	N.F.C.2	0.00			
Specimen with RPF	R.P.C.3	1.00	25.90	32.10	39.50
	R.P.C.4	1.00			
Specimen with PPF	P.P.C.5	0.50	31.80	36.00	40.40
	P.P.C.6	0.50			

The results for the plain, RP fibres and PP fibres concrete ( i.e. average of two prism) flexural strength test and toughness are summarized in Table 12. Load-deflection behavior under flexure for different fibres types of RP and PP concretes are presented in Figures 7A thru 7D. The curves presented in each of these figures represent plain and containing RP and PP fibres of concrete.

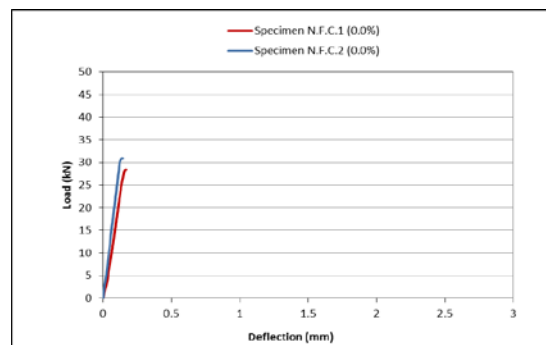
The results indicate an increase in flexural strength and toughness of RP fibre concrete compared to plain concrete. In each of these figures one curve represent the RP fibres and PP fibres concrete is plotted with the control. The plain concrete specimens broke into two pieces once the peak load was reached, with very little energy absorption. The fibres of concrete specimens, on the other hand, exhibited a virtual ductile behavior with RP fibres and PP fibres bridging the cracks.

**Table 12 Flexural strength and toughness of all concrete specimens**

Specimen	Design Mix.	Flexural Strength (MPa)	Average Flexural Strength (MPa)	Toughness (N.mm)	Average Toughness (N.mm)
Plain	N.F.C.1	3.81	3.97	17.95	15.11
	N.F.C.2	4.12		12.25	
Specimen with RPF	R.P.C.3	4.85	4.46	77.22	72.34
	R.P.C.4	4.05		67.63	
Specimen with PPF	P.P.C.5	5.52	5.57	38.24	38.25
	P.P.C.6	5.60		38.26	



**Fig. 7A: Comparison of flexural strength for plain**



**Fig. 7B: Flexural strength of plain concrete specimen.**

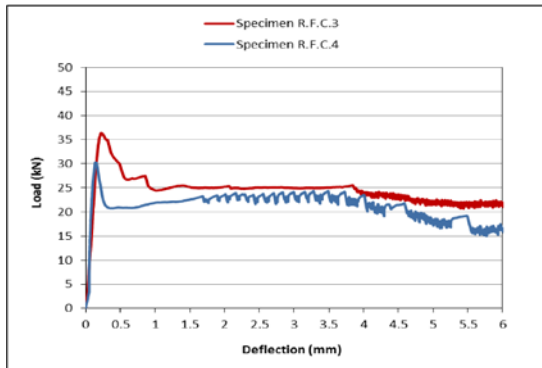


Fig. 7C: Flexural strength at 1.00% RP fibre, length 50 mm.

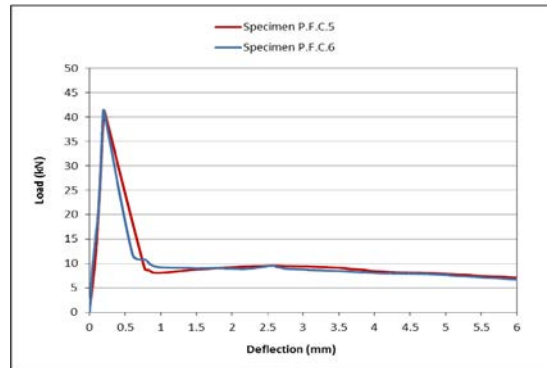


Fig. 7D : Flexural strength at 0.50% PP fibre, length 30 mm.

A comparison of flexural strength and toughness obtained for plain, RP fibres and PP fibres is shown in Figures 8A and 8B. The increase in flexure strength for RP fibres, at 1.00% volume fraction was 12.34%, whereas the increase in flexure strength for P.P fibres, at 0.50% volume fraction was 40.30% compared to control of concrete. The increase in toughness for R.P fibres, at 1.00% volume fraction was 379.00%, whereas the increase in toughness for P.P fibres, at 0.50% volume fraction was 153.00% compared to control of concrete.

The load-deflection curves of RP fibres and PP fibres specimens mainly consisted of three regions. First region is the region up to the point of maximum load called the pre crack (linear elastic behavior) region. Second region is between post crack and load stable regions, and third region is the load stable region. The second and third regions are the post crack regions. In contrast, load-deflection curves of the plain concrete specimens consisted of only first region up to the point of maximum load.

The flexural strengths of all the mixes obtained from the load–deflection relationships. The increase in flexural strength of RP fibres and PP fibres concrete were in range from 12.34% to 40.30% in comparison to plain concrete. Therefore, it may be concluded that the addition of RP and PP fibres to concrete affect the flexural strength significantly. The peak load in the in the third region was higher for mixes with higher volume fraction of RP fibres. The increase in the peak load for 0.50 % content PP fibre was 40.30% higher when compared with plain concrete of 0.0% RP fibre.

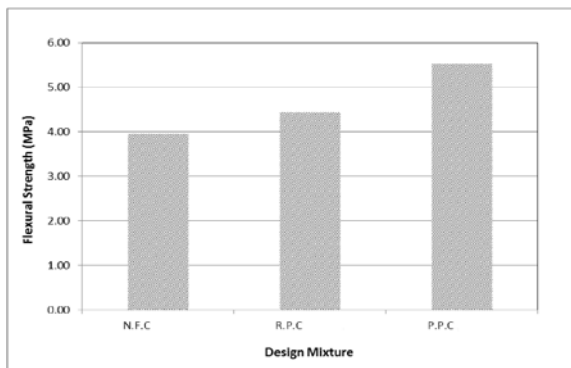


Fig. 8A : Comparison of flexural strength for all specimens.

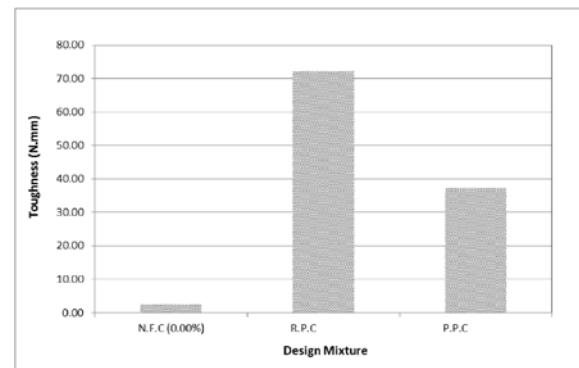


Fig. 8B : Comparison of toughness for all specimens.

Toughness of fibrous concrete was calculated following (JSCE-SF4) guidelines, as the area under the load-deflection curve up to a specified deflection. In this study the limit on the final deflection was fixed at 3.0 mm. Because of the fibres bridging cracks in matrix, the toughness of fibre reinforced concrete was significantly higher than that of plain concrete. The RP and PP fibre also seems to affect toughness. Increasing the volume fraction of RP fibres to 1.00% caused a substantial increase in toughness compared to PP fibres at 0.50% volume fraction.

#### 4. Conclusion

This study investigated the performance of recycled plastic RP fibres as concrete reinforcement with commercially available polypropylene PP fibres. Also, To show the effect of recycled plastic RP/PP fibres

on the flexural strength, toughness and compressive strength of concrete. Based on the results of this investigation following conclusions are made:

- No plastic shrinkage cracks were observed in concrete slabs at 1.00% and 0.50% volume fraction of (recycled plastic) RP and (commercial Polypropylene) PP fibres, respectively.
- RP fibre showed a substantial increase in toughness and a slight decrease in flexural strength of plain concrete at a fibre volume fraction of 1.00% compared to PP fibres at fibre volume fraction of 0.50%.
- RP fibres caused a significant increase in compressive strengths, at the fibre volume fraction used up to 13.02% compared to concrete without fibre reinforcement.
- Based on this study, it is concluded that recycled plastic Polyethylene Terephthalate (PET) of 50 mm length may be used as a reinforcing fibres at 1.00 % volume fraction to control plastic shrinkage cracking and increase flexural toughness of concrete .

## 5. Acknowledgment

The authors acknowledge the support provided by the Department of Civil Engineering and the General Directorate for Research Grants, King Abdul-Aziz city for Science and Technology.

## 6. References

1. Toledo Filho, R. D. and Sanjuan, M. A. (1999). " Effect of low modulus sisal and polypropylene fibre on the free and restrained shrinkage of mortars at early age", *Cement and Concrete Research*. 29(10): 1597-1604.
2. Wang K., Shah S. P., Pariya P. (2001). " Plastic shrinkage cracking in concrete materials influence of fly ash and fibres". *ACI Materials Journal*, 96(6): 458–64.
3. Qi, C. (2003). " Quantitative assessment of plastic shrinkage cracking and its impact on the corrosion of steel reinforcement". Ph.D. Thesis, Department of Civil Engineering, Purdue University, West Lafayette, Indiana, USA.
4. Alhozaimy A. M. and Alshannag M. J. (2009). " Performance of concrete reinforced with recycled plastic fibres". *Magazine of Concrete Research*. 61, No. 4, May, pp. 293-298.
5. Parviz S. , Jesus P. and Siavosh R. (2003). " Assessment of Reinforcing Effects of Recycled Plastic and Paper in Concrete". *ACI Materials Journal*, V. 100, No. 3.
6. ASTM C 127 - 12. (2012), " Standard Test Method for Density, Relative Density (Specific Gravity), and Absorption of Coarse Aggregate", American Society for Testing and Materials, USA, 6 pp.
7. ASTM C 128 - 12. (2012), " Standard Test Method for Density, Relative Density (Specific Gravity), and Absorption of Fine Aggregate", American Society for Testing and Materials, USA, 6 pp.
8. BS 1881 - 116. (2003), " Method for determination of compressive strength of concrete cubes ", British Standard, BS, 11 pp.
9. ASTM C 78 / C 78M - 10. (2010), " Standard Test Method for Flexural Strength of Concrete (Using Simple Beam with Third - Point Loading) ", American Society for Testing and Materials, USA, 4 pp.
10. JSCE - SF4, "Standard for Flexural Strength and Flexural Toughness, Method of Tests for Steel Fibres Reinforced Concrete", Concrete Library of JSCE, Japan Concrete Institute (JCI), 1984, pp. 58-66.
11. ASTM C 1064 / C 1064M - 12. (2013), " Standard Test Method for Temperature of Freshly Mixed Hydraulic-Cement Concrete ", American Society for Testing and Materials, USA, 3 pp.
12. ASTM C 143 / C 143M - 12. (2012), " Standard Test Method for Slump of Hydraulic-Cement Concrete ", American Society for Testing and Materials, USA, 7 pp.
13. ASTM D 5527 – 12. (2011), " Standard Practices for Measuring Surface Wind and Temperature by Acoustic Means", American Society for Testing and Materials, USA, 4 pp.
14. ACI Committee 305, Hot - weather Concreting, ACI 305R - 99, American Concrete Institute, Farmington Hills, Michigan, 1999, 17 pages. ASTM C 150.

The proceedings contain 171 papers across 14 themes. All the papers included in the proceedings have been selected on the basis of at least two peer reviews which were provided by independent reviewers (referees) who were experts in the subject field of the paper.

The theme of the conference is Research into Practice. The Concrete Institute of Australia is an industry led association whose primary charter is to promote good practice in concrete construction. The theme is in line with this charter and is relevant in the current climate where the Australian industry is being asked for greater participation in R&D while the researchers are being asked to show greater impact and practical outcomes of their research. The proceedings contain papers from 20 different countries. Nearly half of them are from Industry and half from Researchers.



Published by Concrete Institute of Australia, 2015